

Encyclopedia of Sustainability Science  
and Technology Series

*Editor-in-Chief: Robert A. Meyers*

SPRINGER  
REFERENCE

Timothy E. Lipman  
Adam Z. Weber *Editors*

# Fuel Cells and Hydrogen Production

A Volume in the Encyclopedia of  
Sustainability Science and Technology,  
Second Edition

 Springer

---

# Encyclopedia of Sustainability Science and Technology Series

**Editor-in-Chief**  
Robert A. Meyers



The Encyclopedia of Sustainability Science and Technology series (ESST) addresses the grand challenge for science and engineering today. It provides unprecedented, peer-reviewed coverage in more than 600 separate articles comprising 20 topical volumes, incorporating many updates from the first edition as well as new articles. ESST establishes a foundation for the many sustainability and policy evaluations being performed in institutions worldwide.

An indispensable resource for scientists and engineers in developing new technologies and for applying existing technologies to sustainability, the Encyclopedia of Sustainability Science and Technology series is presented at the university and professional level needed for scientists, engineers, and their students to support real progress in sustainability science and technology.

Although the emphasis is on science and technology rather than policy, the Encyclopedia of Sustainability Science and Technology series is also a comprehensive and authoritative resource for policy makers who want to understand the scope of research and development and how these bottom-up innovations map on to the sustainability challenge.

More information about this series at <https://link.springer.com/bookseries/15436>

---

Timothy E. Lipman • Adam Z. Weber  
Editors

# Fuel Cells and Hydrogen Production

A Volume in the Encyclopedia of  
Sustainability Science and  
Technology, Second Edition

With 580 Figures and 128 Tables

 Springer

*Editors*

Timothy E. Lipman  
TSRC, University of California  
Berkeley TSRC  
Berkeley, CA, USA

Adam Z. Weber  
Lawrence Berkeley Nat. Lab.  
Berkeley, CA, USA

ISBN 978-1-4939-7788-8                      ISBN 978-1-4939-7789-5 (eBook)

ISBN 978-1-4939-7790-1 (print and electronic bundle)

<https://doi.org/10.1007/978-1-4939-7789-5>

Library of Congress Control Number: 2018948011

© Springer Science+Business Media, LLC, part of Springer Nature 2019

This work is subject to copyright. All rights are reserved by the Publisher, whether the whole or part of the material is concerned, specifically the rights of translation, reprinting, reuse of illustrations, recitation, broadcasting, reproduction on microfilms or in any other physical way, and transmission or information storage and retrieval, electronic adaptation, computer software, or by similar or dissimilar methodology now known or hereafter developed.

The use of general descriptive names, registered names, trademarks, service marks, etc. in this publication does not imply, even in the absence of a specific statement, that such names are exempt from the relevant protective laws and regulations and therefore free for general use.

The publisher, the authors and the editors are safe to assume that the advice and information in this book are believed to be true and accurate at the date of publication. Neither the publisher nor the authors or the editors give a warranty, express or implied, with respect to the material contained herein or for any errors or omissions that may have been made. The publisher remains neutral with regard to jurisdictional claims in published maps and institutional affiliations.

This Springer imprint is published by the registered company Springer Science+Business Media, LLC part of Springer Nature.

The registered company address is: 233 Spring Street, New York, NY 10013, U.S.A.

---

## Series Preface

Our nearly 1000-member team recognizes that all elements of sustainability science and technology continue to advance as does our understanding of the needs for energy, water, clean air, food, mobility, and health, and the relation of every single aspect of this vast and interconnected body of knowledge to climate change. Our Encyclopedia content is at a level for university students, professors, engineers, and other practicing professionals. It is gratifying for our team to note that our online First Edition has been heavily utilized as evidenced by over 500,000 downloads which of course is in addition to scientists' utilization of the Encyclopedia and individual "spin-off" volumes in print.

Now we are pleased to have a Living Reference on-line which assures the sustainability community that we are providing the latest peer-reviewed content covering the science and technology of the sustainability of the earth. We are also publishing the content as a Series of individual topical books for ease use by those with an interest in particular subjects, and with expert oversight in each field to ensure that the second edition presents the state-of-the-science today. Our team covers the physical, chemical and biological processes that underlie the earth system including pollution and remediation and climate change, and we comprehensively cover every energy and environment technology as well as all types of food production, water, transportation and the sustainable built environment.

Our team of 15 board members includes two Nobel Prize winners (Kroto and Fischlin), two former Directors of the National Science Foundation (NSF) (Colwell and Killeen), the former President of the Royal Society (Lord May), and the Chief Scientist of the Rocky Mountain Institute (Amory Lovins). And our more than 40 eminent section editors and now book editors, assure quality of our selected authors and their review presentations.

The extent of our coverage clearly sets our project apart from other publications which now exist, both in extent and depth. In fact, current compendia of the science and technology of several of these topics do not presently exist and yet the content is crucial to any evaluation and planning for the sustainability of the earth. It is important to note that the emphasis of our project is on science and technology and not on policy and positions. Rather, policy makers will use our presentations to evaluate sustainability options.

Vital scientific issues include: human and animal ecological support systems, energy supply and effects, the planet's climate system, systems of agriculture, industry, forestry, and fisheries and the ocean, fresh water and human communities, waste disposal, transportation and the built environment

in general and the various systems on which they depend, and the balance of all of these with sustainability. In this context, sustainability is a characteristic of a process or state that can be maintained at a certain level indefinitely even as global population increases toward nine billion by 2050. The population growth, and the hope for increase in wealth, implies something like a 50% increase in food demand by as early as 2030. At the same time, the proportion of the population that lives in an urban environment will go up from about 47% to 60%. Global economic activity is expected to grow 500%, and global energy and materials use is expected to increase by 300% over this period. That means there are going to be some real problems for energy, agriculture, and water, and it is increasingly clear that conflicting demands among biofuels, food crops, and environmental protection will be difficult to reconcile. The “green revolution” was heavily dependent on fertilizers which are manufactured using increasingly expensive and diminishing reserves of fossil fuels. In addition, about 70% of available freshwater is used for agriculture. Clearly, many natural resources will either become depleted or scarce relative to population.

Larkspur, CA, USA  
June 2018

Robert A. Meyers, Ph.D.  
Editor-in-Chief

---

## Volume Preface

Hydrogen is an abundant element that is found in many forms on Earth. In its molecular form of H<sub>2</sub> (two protons and two electrons), it is not readily found but rather needs to be extracted or “reformed” from hydrocarbon fuels, both fossil and biological, or extracted from water using a “water splitting” process called electrolysis. Hydrogen is a widely produced and used industrial commodity for fertilizer production, oil refining, food production, and metallurgy, used at a level of tens of millions of tons per year around the world. Hydrogen is also now being used as an energy carrier for stationary power and transportation markets using various fuel cell technologies. There are many means of hydrogen production, from established ones such as steam methane reforming, where half of the produced hydrogen comes from natural gas or biogas and half comes from steam used in the reaction to grid-powered electrolysis that uses electricity to split water molecules in hydrogen and oxygen. Various other hydrogen production methods are becoming commercially viable, including gasification or pyrolysis processes of various types of feedstocks (e.g., biogas, biosolids, fossil fuel production residues, etc.), biological production through fermentation processes, and from industrial byproducts such as in chlor-alkali production. Further from commercialization but under active study are more recently developed electrochemical, photo-electrochemical, and thermochemical processes, with potential to produce renewable hydrogen to meet growing demand for hydrogen use at larger scale in the future.

Fuel cells are devices that electrochemically convert the chemical free energy of gaseous or liquid reactants into electrical energy. Due to this electrochemical rather than thermal process, fuel cells are not limited by Carnot efficiency, thereby allow for higher efficiencies. Furthermore, the solid-state nature of these devices and components enables the design of high-rate architectures, which are critical for power-dense applications such as transportation. In addition, as they are open flow systems, unlike batteries, they scale well for longer- and larger-scale operation. For these reasons fuel cells are being explored and commercialized for large-scale energy conversion and electricity generation, automotive and truck applications, materials handling equipment, and auxiliary power units, to name a few. Fuel cells are classified nominally based on their electrolyte, which is highly correlated to operating temperature. At the high end of the temperature scale are solid-oxide fuel cells (SOFCs) that can operate on various gaseous and liquid fuels and operate around 700 °C and above with ceramic materials and oxygen anion conducting species. At decreasing temperatures are the molten carbonate

(carbonate anions), and then the proton conducting cells including phosphoric acid (and related high-temperature membrane) cells, and finally the polymer-electrolyte fuel cells that require operation at 100 °C or lower due to membrane hydration. Because of this temperature requirement, these cells typically operate on hydrogen although may work with denser carriers including methanol. Overall, fuel cells offer intriguing possibilities and will play key roles in the future green energy landscape, although some performance and durability hurdles remain from both engineering and materials standpoints.

Berkeley, CA, USA  
June 2018

Timothy E. Lipman  
Adam Z. Weber

---

# Contents

## Volume 1

<b>Fuel Cells and Hydrogen Production: Introduction</b> .....	1
Adam Z. Weber and Timothy E. Lipman	
<b>Part I Fuel Cells</b> .....	9
<b>Fuel Cell Comparison to Alternate Technologies</b> .....	11
Julia Kunze-Liebhäuser, Odysseas Paschos, Sethu Sundar Pethaiah and Ulrich Stimming	
<b>Fuel Cell Systems: Total Cost of Ownership</b> .....	27
Max Wei, Ahmad Mayyas, Timothy E. Lipman, Hanna Breunig, Roberto Scataglini, Shuk Han Chan, Joshua Chien, David Gosselin and Nadir Saggiorato	
<b>Fuel Cell Types and Their Electrochemistry</b> .....	83
Günther G. Scherer	
<b>Polymer Electrolyte (PE) Fuel Cell Systems</b> .....	99
John F. Elter	
<b>Polymer Electrolyte Membrane (PEM) Fuel Cells: Automotive Applications</b> .....	135
Shyam S. Kocha	
<b>PEM Fuel Cells: Materials and Design Development Challenges</b> .....	173
Stephen J. Paddison and Hubert A. Gasteiger	
<b>PEM Fuel Cell Materials: Costs, Performance, and Durability</b> ...	195
A. de Frank Bruijn and Gaby J. M. Janssen	
<b>PEM Fuel Cells: Modeling</b> .....	235
M. Secanell, A. Jarauta, A. Kosakian, M. Sabharwal and J. Zhou	
<b>PEM Fuel Cells and Platinum-Based Electrocatalysts</b> .....	295
Junliang Zhang	



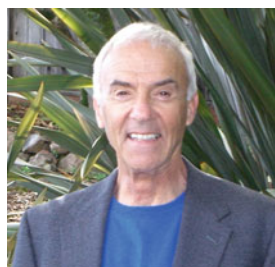
<b>Proton-Exchange Membrane Fuel Cells with Low-Pt Content</b> . . .	323
Anusorn Kongkanand, Wenbin Gu and Mark F. Mathias	
<b>Polymer Electrolyte Membrane Fuel Cells (PEM-FC) and Non-noble Metal Catalysts for Oxygen Reduction</b> . . . . .	343
Ulrike I. Kramm, Peter Bogdanoff and Sebastian Fiechter	
<b>Membrane Electrolytes, from Perfluorosulfonic Acid (PFSA) to Hydrocarbon Ionomers</b> . . . . .	387
Kenji Miyatake	
<b>Ionomer Thin Films in PEM Fuel Cells</b> . . . . .	417
Ahmet Kusoglu	
<b>Alkaline Membrane Fuel Cells</b> . . . . .	439
Robert C. T. Slade, Jamie P. Kizewski, Simon D. Poynton, Rong Zeng, and John R. Varcoe	
<b>Proton Exchange Membrane Fuel Cells: High-Temperature, Low-Humidity Operation</b> . . . . .	455
Steven J. Hamrock and Andrew M. Herring	
<b>Polybenzimidazole Fuel Cell Technology: Theory, Performance, and Applications</b> . . . . .	477
Andrew T. Pingitore, Max Molle, Thomas J. Schmidt and Brian C. Benicewicz	
<b>Phosphoric Acid Fuel Cells for Stationary Applications</b> . . . . .	515
Sridhar V. Kanuri and Sathya Motupally	
<b>Molten Carbonate Fuel Cells</b> . . . . .	531
Choong-Gon Lee	
<b>Solid Oxide Fuel Cells</b> . . . . .	569
A. Atkinson, S. J. Skinner and J. A. Kilner	
<b>Volume 2</b>	
<b>Fuel Cells (SOFC): Alternative Approaches (Electrolytes, Electrodes, Fuels)</b> . . . . .	591
K. Sasaki, Y. Nojiri, Y. Shiratori and S. Taniguchi	
<b>Direct Hydrocarbon Solid Oxide Fuel Cells</b> . . . . .	633
Michael Van Den Bossche and Steven McIntosh	
<b>Solid Oxide Fuel Cell Materials: Durability, Reliability, and Cost</b> . . . . .	665
Harumi Yokokawa and Teruhisa Horita	
<b>Solid Oxide Fuel Cells: Marketing Issues</b> . . . . .	701
John Bøgild Hansen and Niels Christiansen	
<b>Solid Oxide Fuel Cells: Sustainability Aspects</b> . . . . .	733
K. U. Birnbaum, Robert Steinberger-Wilckens and P. Zapp	

---

<b>Part II Hydrogen Production Science and Technology</b> .....	781
<b>Hydrogen Production Science and Technology</b> .....	783
Timothy E. Lipman	
<b>Hydrogen Production Through Electrolysis</b> .....	799
Abudukeremu Kadier, Mohd Sahaid Kalil, Washington Logroño, Azah Mohamed and Hassimi Abu Hasan	
<b>Electrochemical Hydrogen Production</b> .....	819
Marc T. M. Koper	
<b>Hydrogen Production from Biological Sources</b> .....	833
Ao Xia, Xun Zhu, and Qiang Liao	
<b>Biohydrogen Production</b> .....	865
Suphi Ş. Öncel and Ayşe Köse	
<b>Biohydrogen Production from Agricultural Residues</b> .....	905
Emmanuel Koukios and Ioannis (John) A. Panagiotopoulos	
<b>Genetic Optimization for Increasing Hydrogen Production in Microalgae</b> .....	919
Cecilia Faraloni and Giuseppe Torzillo	
<b>Advances on Inorganic Membrane Reactors for Production of Hydrogen</b> .....	935
Adolfo Iulianelli and Angelo Basile	
<b>Hydrogen Production Through Pyrolysis</b> .....	947
Ali Bakhtyari, Mohammad Amin Makarem and Mohammad Reza Rahimpour	
<b>Hydrogen Production from Algal Pathways</b> .....	975
Muhammad Aziz and Ilman Nuran Zaini	
<b>Hydrogen Production from Photoelectrochemical Water Splitting</b> .....	1003
Paula Dias and Adélio Mendes	
<b>Hydrogen via Direct Solar Production</b> .....	1055
Shamindri M. Arachchige and Karen J. Brewer	
<b>Photo-Catalytic Hydrogen Production</b> .....	1099
Jiefang Zhu	
<b>Hydrogen Production from High-Temperature Fuel Cells</b> .....	1123
Jacob Brouwer and Pere Margalef	
<b>Nuclear-Assisted Hydrogen Production</b> .....	1151
Rami S. El-Emam and Ibrahim Dincer	
<b>Index</b> .....	1163

---

## About the Editor-in-Chief



### **Dr. Robert A. Meyers**

President: RAMTECH Limited

Manager, Chemical Process Technology, TRW Inc.

Post doctoral Fellow: California Institute of Technology

Ph.D. Chemistry, University of California at Los Angeles

B.A., Chemistry, California State University, San Diego

---

### **Biography**

Dr. Meyers has worked with more than 20 Nobel laureates during his career and is the originator and serves as Editor in Chief of both the Springer Nature *Encyclopedia of Sustainability Science and Technology* and the related and supportive Springer Nature *Encyclopedia of Complexity and Systems Science*.

---

### **Education**

Postdoctoral Fellow:

California Institute of Technology

Ph.D. in Organic Chemistry, University of California at Los Angeles

B.A., Chemistry with minor in Mathematics, California State University, San Diego

Dr. Meyers holds more than 20 patents and is the author or Editor in Chief of 12 technical books including the *Handbook of Chemical Production Processes*, *Handbook of Synfuels Technology*, and *Handbook of Petroleum*

*Refining Processes* now in 4th Edition, and the *Handbook of Petrochemical Production Processes*, now in its second edition, (McGraw-Hill) and *The Handbook of Energy Technology and Economics*, published by John Wiley & Sons; *Coal Structure*, published by Academic Press; and *Coal Desulfurization* as well as the *Coal Handbook* published by Marcel Dekker. He served as chairman of the Advisory Board for *A Guide to Nuclear Power Technology*, published by John Wiley & Sons, which won the Association of American Publishers Award as the best book in technology and engineering.

---

## About the Volume Editors



**Timothy E. Lipman, Ph.D.** is an energy and environmental technology, economics, and policy researcher with the University of California – Berkeley. He is currently serving as Co-Director of the Transportation Sustainability Research Center (TSRC), based at the Institute of Transportation Studies. He is also a Research Affiliate with the Lawrence Berkeley National Laboratory. Dr. Lipman’s research focuses on electric vehicles, fuel cell technology, combined heat and power systems, renewable energy, and electricity and hydrogen production and distribution infrastructure. He completed a Ph.D. degree in Environmental Policy Analysis with the Graduate Group in Ecology at UC Davis (1999) and also holds an M.S. degree from UC Davis in Transportation Technology and Policy (1998) and a B.A. degree from Stanford University (1990). He is Chair of the Alternative Transportation Fuels and Technologies Committee of the Transportation Research Board of the National Academies of Science and Engineering, a member of the Hydrogen and Fuel Cell Technical Advisory Committee (HTAC) for the US Department of Energy, and on the editorial boards of *Transportation Research-D* and the *International Journal of Sustainable Engineering*.



**Adam Z. Weber** holds B.S. and M.S. degrees from Tufts University, the latter under the guidance of Professor Maria Flytzani-Stephanopoulos. Next, he earned his Ph.D. at University of California, Berkeley, in Chemical Engineering under the guidance of John Newman. His dissertation work focused on the fundamental investigation and mathematical modeling of water management in polymer-electrolyte fuel cells.

Dr. Weber continued his study of water and thermal management in polymer-electrolyte fuel cells at Lawrence Berkeley National Laboratory, where he is now a staff scientist and program manager for Hydrogen and Fuel Cell Technologies. His current research involves understanding and optimizing fuel-cell performance and lifetime including component and ionomer structure/function studies using advanced modeling and diagnostics, understanding flow batteries for grid-scale energy storage, and analysis of solar-fuel generators where he is a Thrust coordinator at the Joint Center for Artificial Photosynthesis (JCAP).

Dr. Weber has coauthored over 110 peer-reviewed articles and 10 book chapters on fuel cells, flow batteries, and related electrochemical devices; developed many widely used models for fuel cells and their components; and has been invited to present his work at various international and national meetings. He is the recipient of a number of awards including a Fulbright scholarship to Australia, the 2008 Oronzio and Niccolò De Nora Foundation Prize on Applied Electrochemistry of the International Society of Electrochemistry, the 2012 Supramaniam Srinivasan Young Investigator Award of the Energy Technology Division of the Electrochemical Society, a 2012 Presidential Early Career Award for Scientists and Engineers (PECASE), the 2014 Charles W. Tobias Young Investigator Award of the Electrochemical Society, a Kavli Fellow in 2014, and the 2016 Sir William Grove Award from the International Association for Hydrogen Energy. He is a Fellow of The Electrochemical Society.

---

## Contributors

**Shamindri M. Arachchige** Department of Chemistry, Virginia Polytechnic Institute and State University, Blacksburg, VA, USA

**A. Atkinson** Department of Materials, Imperial College London, London, UK

**Muhammad Aziz** Institute of Innovative Research, Tokyo Institute of Technology, Tokyo, Japan

**Ali Bakhtyari** Department of Chemical Engineering, Shiraz University, Shiraz, Iran

**Angelo Basile** Institute on Membrane Technology of the Italian National Research Council (CNR-ITN), University of Calabria, Rende, CS, Italy

**Brian C. Benicewicz** Department of Chemistry and Biochemistry, University of South Carolina, University of South Carolina NanoCenter, Columbia, SC, USA

**K. U. Birnbaum** Institute of Energy Research, Forschungszentrum Jülich, Jülich, Germany

**Peter Bogdanoff** Helmholtz-Zentrum Berlin für Materialien und Energie GmbH (HZB), Institut für Solare Brennstoffe und Energiespeichermaterialien, Berlin, Germany

**Hanna Breunig** Sustainable Energy Systems Group, Energy Analysis and Environmental Impacts Department, Environmental Energy Technologies Division, Lawrence Berkeley National Laboratory, Berkeley, CA, USA

**Karen J. Brewer** Department of Chemistry, Virginia Polytechnic Institute and State University, Blacksburg, VA, USA  
National Fuel Cell Research Center, University of California, Irvine, CA, USA

**Shuk Han Chan** Department of Mechanical Engineering, University of California, Berkeley, CA, USA

**Joshua Chien** Department of Mechanical Engineering, University of California, Berkeley, CA, USA

**Niels Christiansen** Topsoe Fuel Cell A/S, Lyngby, Denmark

**A. de Frank Bruijn** Energy Research Centre of the Netherlands, Groningen, The Netherlands

**Paula Dias** LEPABE – Faculdade de Engenharia, Universidade do Porto, Porto, Portugal

**Ibrahim Dincer** Faculty of Engineering and Applied Science, University of Ontario Institute of Technology, Oshawa, ON, Canada

**Rami S. El-Emam** Faculty of Engineering, Mansoura University, Mansoura, Egypt

Faculty of Engineering and Applied Science, University of Ontario Institute of Technology, Oshawa, ON, Canada

**John F. Elter** Sustainable-Systems, LLC, Latham, NY, USA

Nanoscale Engineering, College of Nanoscale Science and Engineering SUNY Albany, Albany, NY, USA

**Cecilia Faraloni** Istituto per lo Studio degli Ecosistemi, Sede di Firenze, Firenze, Italy

**Sebastian Fiechter** Helmholtz-Zentrum Berlin für Materialien und Energie GmbH (HZB), Institut für Solare Brennstoffe und Energiespeichermaterialien, Berlin, Germany

**Hubert A. Gasteiger** Department of Chemistry, Technische Universität München, Munich, Germany

**David Gosselin** Department of Mechanical Engineering, University of California, Berkeley, CA, USA

**Wenbin Gu** Fuel Cell Business, General Motors Global Propulsion Systems, Pontiac, MI, USA

**Steven J. Hamrock** 3M Fuel Cell Components Program, 3M Company, St Paul, MN, USA

**John Bøgild Hansen** Haldor Topsøe A/S, Lyngby, Denmark

**Hassimi Abu Hasan** Department of Chemical and Process Engineering, Faculty of Engineering and Built Environment, National University of Malaysia (UKM), Bangi, Selangor, Malaysia

**Andrew M. Herring** Department of Chemical and Biological Engineering, Colorado School of Mines, Golden, CO, USA

**Teruhisa Horita** National Institute of Advanced Industrial Science and Technology (AIST), Tsukuba, Ibaraki, Japan

**Adolfo Iulianelli** Institute on Membrane Technology of the Italian National Research Council (CNR-ITN), University of Calabria, Rende, CS, Italy



- Gaby J. M. Janssen** Energy and Sustainability Research Institute Groningen, University of Groningen, Groningen, The Netherlands  
Energy Research Centre of the Netherlands, Petten, The Netherlands
- A. Jarauta** Energy Systems Design Laboratory, Department of Mechanical Engineering, University of Alberta, Edmonton, AB, Canada
- Abudukeremu Kadier** Department of Chemical and Process Engineering, Faculty of Engineering and Built Environment, National University of Malaysia (UKM), Bangi, Selangor, Malaysia
- Mohd Sahaid Kalil** Department of Chemical and Process Engineering, Faculty of Engineering and Built Environment, National University of Malaysia (UKM), Bangi, Selangor, Malaysia
- Sridhar V. Kanuri** Doosan Fuel Cell America, South Windsor, CT, USA
- J. A. Kilner** Department of Materials, Imperial College London, London, UK
- Jamie P. Kizewski** Department of Chemistry, University of Surrey, Guildford, UK
- Shyam S. Kocha** Hydrogen Technologies and Systems Center, National Renewable Energy Laboratory, Golden, CO, USA
- Anusorn Kongkanand** Fuel Cell Business, General Motors Global Propulsion Systems, Pontiac, MI, USA
- Marc T. M. Koper** Leiden Institute of Chemistry, Leiden University, Leiden, The Netherlands
- A. Kosakian** Energy Systems Design Laboratory, Department of Mechanical Engineering, University of Alberta, Edmonton, AB, Canada
- Ayşe Köse** Department of Bioengineering, Ege University, Izmir, Turkey
- Emmanuel Koukios** Department of Synthesis and Development of Industrial Processes, School of Chemical Engineering, National Technical University of Athens, Athens, Greece
- Ulrike I. Kramm** Brandenburg University of Technology Applied Physics and Sensors, Cottbus, Germany
- Julia Kunze-Liebhäuser** Institute of Physical Chemistry, University of Innsbruck, Innsbruck, Austria
- Ahmet Kusoglu** Energy Conversion Group, Energy Technologies Area, Lawrence Berkeley National Laboratory, Berkeley, CA, USA
- Choong-Gon Lee** Department of Chemical and Biological Engineering, Hanbat National University, Daejeon, South Korea
- Qiang Liao** Key Laboratory of Low-grade Energy Utilization Technologies and Systems (Ministry of Education), Chongqing University, Chongqing, China  
Institute of Engineering Thermophysics, Chongqing University, Chongqing, China

**Timothy E. Lipman** Transportation Sustainability Research Center,  
University of California Berkeley, Berkeley, CA, USA

**Washington Logroño** Department of Biotechnology, University of Szeged,  
Szeged, Hungary

Centro de Investigación de Energías Alternativas y Ambiente, Escuela  
Superior Politécnica de Chimborazo, Chimborazo, Ecuador

**Mohammad Amin Makarem** Department of Chemical Engineering, Shiraz  
University, Shiraz, Iran

**Pere Margalef** National Fuel Cell Research Center, University of California,  
Irvine, CA, USA

**Mark F. Mathias** Fuel Cell Business, General Motors Global Propulsion  
Systems, Pontiac, MI, USA

**Ahmad Mayyas** Department of Civil Engineering, Transportation  
Sustainability Research Center, University of California, Berkeley, CA, USA

**Steven Mcintosh** Department of Chemical Engineering, University of  
Virginia, Charlottesville, VA, USA

Department of Chemical Engineering, Lehigh University, Bethlehem, PA, USA

**Adélio Mendes** LEPABE – Faculdade de Engenharia, Universidade do  
Porto, Porto, Portugal

**Kenji Miyatake** Clean Energy Research Center, University of Yamanashi,  
Kofu, Yamanashi, Japan

**Azah Mohamed** Department of Electrical, Electronic and System  
Engineering, Faculty of Engineering and Built Environment, National  
University of Malaysia (UKM), Bangi, Selangor, Malaysia

**Max Molleo** Department of Chemistry and Biochemistry, University of  
South Carolina, University of South Carolina NanoCenter, Columbia, SC,  
USA

**Sathya Motupally** Doosan Fuel Cell America, South Windsor, CT, USA

**Y. Nojiri** International Research Center for Hydrogen Energy, Kyushu  
University, Fukuoka, Japan

**Suphi Ş. Öncel** Department of Bioengineering, Ege University, Izmir,  
Turkey

**Stephen J. Paddison** Department of Chemical and Biomolecular  
Engineering, University of Tennessee, Knoxville, TN, USA

**Ioannis (John) A. Panagiotopoulos** Elin Biofuels SA, Athens, Greece

**Odysseas Paschos** BMW AG, Munich, Germany

**Sethu Sundar Pethaiah** Gashubin Engineering Private Limited, Singapore,  
Singapore

**Andrew T. Pingitore** Department of Chemistry and Biochemistry,  
University of South Carolina, University of South Carolina  
NanoCenter, Columbia, SC, USA

**Simon D. Poynton** Department of Chemistry, University of Surrey,  
Guildford, UK

**Mohammad Reza Rahimpour** Department of Chemical Engineering,  
Shiraz University, Shiraz, Iran

**M. Sabharwal** Energy Systems Design Laboratory, Department of  
Mechanical Engineering, University of Alberta, Edmonton, AB, Canada

**Nadir Saggiorato** Sustainable Energy Systems Group, Energy Analysis and  
Environmental Impacts Department, Environmental Energy Technologies  
Division, Lawrence Berkeley National Laboratory, Berkeley, CA, USA

**K. Sasaki** International Research Center for Hydrogen Energy, Kyushu  
University, Fukuoka, Japan

International Institute for Carbon-Neutral Energy Research (WPI), Kyushu  
University, Fukuoka, Japan

Faculty of Engineering, Kyushu University, Fukuoka, Japan

**Roberto Scataglini** Sustainable Energy Systems Group, Energy Analysis  
and Environmental Impacts Department, Environmental Energy Technologies  
Division, Lawrence Berkeley National Laboratory, Berkeley, CA, USA

**Günther G. Scherer** Electrochemistry Laboratory, Paul Scherrer Institute,  
Villigen, Switzerland

**Thomas J. Schmidt** General Energy Research, Laboratory of  
Electrochemistry, Paul Scherrer Institute, Villigen, Switzerland

**M. Secanell** Energy Systems Design Laboratory, Department of Mechanical  
Engineering, University of Alberta, Edmonton, AB, Canada

**Y. Shiratori** International Research Center for Hydrogen Energy, Kyushu  
University, Fukuoka, Japan

Faculty of Engineering, Kyushu University, Fukuoka, Japan

**S. J. Skinner** Department of Materials, Imperial College London, London,  
UK

**Robert C. T. Slade** Department of Chemistry, University of Surrey,  
Guildford, UK

**Robert Steinberger-Wilckens** School of Chemical Engineering, University  
of Birmingham, Birmingham, UK

**Ulrich Stimming** Newcastle University, Chemistry – School of Natural and  
Environmental Sciences, Newcastle upon Tyne, UK

**S. Taniguchi** International Research Center for Hydrogen Energy, Kyushu  
University, Fukuoka, Japan

**Giuseppe Torzillo** Istituto per lo Studio degli Ecosistemi, Sede di Firenze, Firenze, Italy

**Michael Van Den Bossche** Department of Chemical Engineering, University of Virginia, Charlottesville, VA, USA

**John R. Varcoe** Department of Chemistry, University of Surrey, Guildford, UK

**Adam Z. Weber** Lawrence Berkeley National Laboratory, Berkeley, CA, USA

**Max Wei** Sustainable Energy Systems Group, Energy Analysis and Environmental Impacts Department, Environmental Energy Technologies Division, Lawrence Berkeley National Laboratory, Berkeley, CA, USA

**Ao Xia** Key Laboratory of Low-grade Energy Utilization Technologies and Systems (Ministry of Education), Chongqing University, Chongqing, China  
Institute of Engineering Thermophysics, Chongqing University, Chongqing, China

**Harumi Yokokawa** Advanced Research Laboratories, Tokyo City University, Tokyo, Japan

National Institute of Advanced Industrial Science and Technology (AIST), Tsukuba, Ibaraki, Japan

**Ilman Nuran Zaini** Institute of Innovative Research, Tokyo Institute of Technology, Tokyo, Japan

**P. Zapp** Institute of Energy Research, Forschungszentrum Jülich, Jülich, Germany

**Rong Zeng** Department of Chemistry, University of Surrey, Guildford, UK

**Junliang Zhang** Fuel Cell Business, General Motors Global Propulsion Systems, Pontiac, MI, USA

**J. Zhou** Energy Systems Design Laboratory, Department of Mechanical Engineering, University of Alberta, Edmonton, AB, Canada

**Jiefang Zhu** Department of Materials Chemistry, Ångström Laboratory, Uppsala University, Uppsala, Sweden

**Xun Zhu** Key Laboratory of Low-grade Energy Utilization Technologies and Systems (Ministry of Education), Chongqing University, Chongqing, China  
Institute of Engineering Thermophysics, Chongqing University, Chongqing, China



## Fuel Cells and Hydrogen Production: Introduction

Adam Z. Weber<sup>1</sup> and Timothy E. Lipman<sup>2</sup>

<sup>1</sup>Lawrence Berkeley National Laboratory, Berkeley, CA, USA

<sup>2</sup>Transportation Sustainability Research Center, University of California Berkeley, Berkeley, CA, USA

### Article Outline

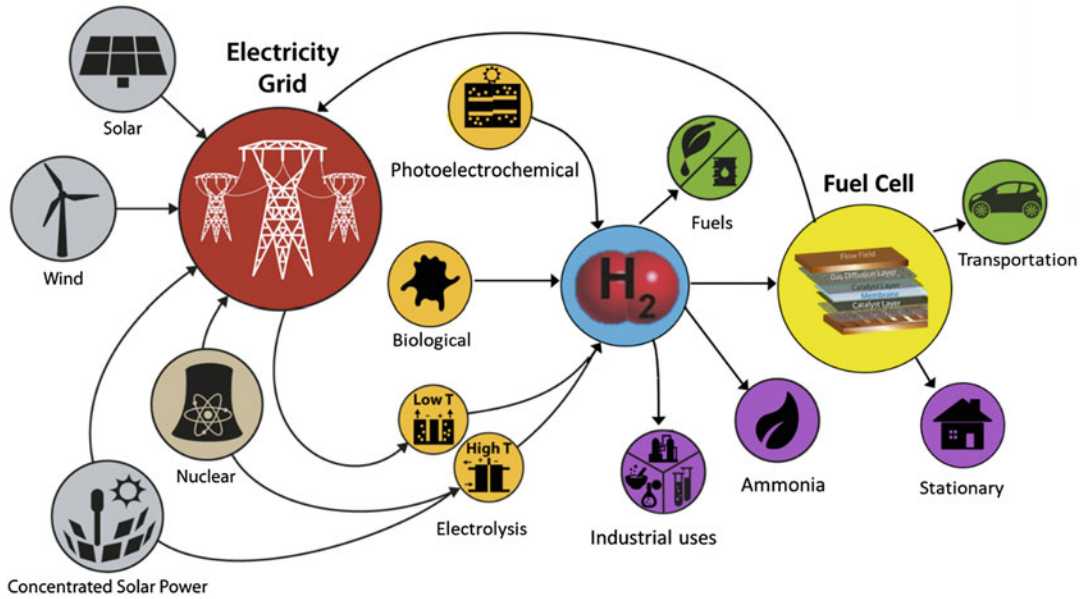
Hydrogen Production Section  
Fuel Cell Section  
Bibliography

Hydrogen is a widely produced and used commodity, now being used as an energy carrier for stationary power and transportation markets. Tens of millions of tons of hydrogen are produced each year globally, mostly for large-scale industrial uses. As awareness grows for the need to reduce greenhouse gases and enable new energy paradigms, hydrogen is being seen as playing a critical role as shown in Fig. 1 [1]. Hydrogen provides chemical storage of electrical energy and can be efficiently converted to electricity on demand for distributed applications, thus enabling the global electrification trends. The H2@SCALE initiative in the United States, the commercialization of hydrogen technologies in Japan, and the focus on power-to-gas and hydrogen utilization in Europe all point toward a renaissance for hydrogen generation and utilization based on its ability to improve efficiency and reduce emissions across many sectors.

Major uses of commercial hydrogen are for oil refining, where hydrogen is used for “upgrading” of crude oil as part of the refining process to improve the hydrogen-to-carbon ratio of the fuel, food production (“hydrogenation”), treating metals and semiconductor manufacturing, and

producing ammonia for fertilizer and other industrial uses. There are many means of hydrogen production, from established ones such as steam methane reforming, where half of the produced hydrogen comes from natural gas or biogas and half comes from steam used in the reaction, and grid-powered electrolysis that uses electricity to split water molecules in hydrogen and oxygen. Various other hydrogen production methods are becoming commercially viable and still others are emerging or being tested in laboratories. Emerging options include various pathways using biogas or other bio-feedstocks such as wood waste using gasification or pyrolysis processes, along with newly developed electrochemical, photo-electrochemical, and thermochemical processes. These include using microbial electrolysis cells as well as tailored molecules and integrated assemblies that can facilitate the splitting of water molecules into hydrogen and oxygen with lower energy requirements than conventional electrolysis. Other concepts include hydrogen production from bio-algae systems, thermo-chemical water splitting processes, and through high-temperature nuclear-power system combined processes. Concomitant with hydrogen production is its efficient utilization via fuel cells, as well as additional concepts such as power-to-gas (where hydrogen is produced from excess renewable electricity and injected into natural gas pipelines) and methanization processes to produce bio-methane.

Fuel cells are devices that electrochemically convert the chemical “free energy” of gaseous or liquid reactants into electrical energy. The basic concepts of fuel cell chemistry have been known for nearly 200 years where they were conceptually identified first in the late 1830s. Christian Friedrich Schönbein recognized and described the appearance of “inverse electrolysis” [2], shortly before Sir William Grove, the inventor of the platinum/zinc battery, constructed his first “gas voltaic battery” that is recognized as



**Fuel Cells and Hydrogen Production: Introduction, Fig. 1** Schematic illustration of hydrogen production and utilization. (Figure adapted from H2@SCALE vision courtesy of Bryan Pivovar) [1]

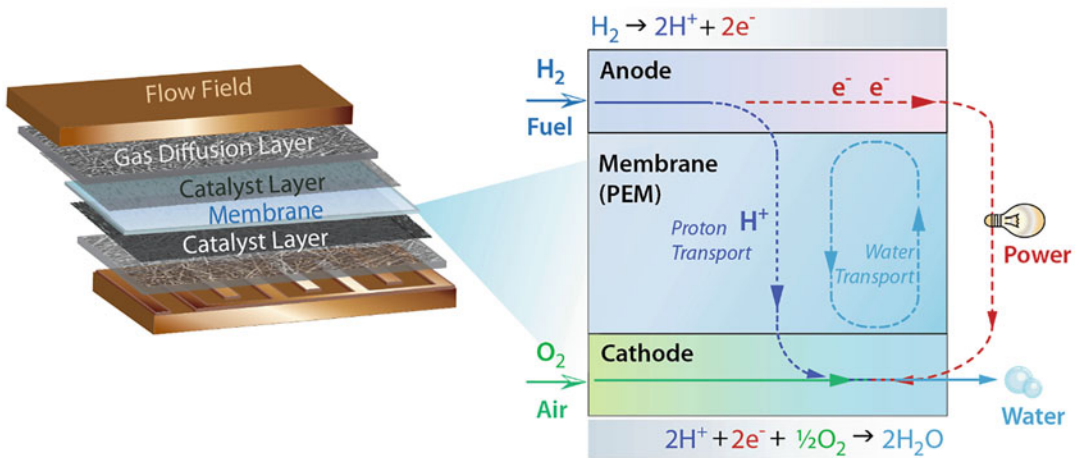
the first example of an early fuel cell device [3]. Grove had previously used platinum electrodes and a dilute sulfuric acid as a proton-conducting electrolyte. It is interesting to note that modern low-temperature polymer-electrolyte fuel cells still make use of related materials (carbon-supported platinum and perfluoro-sulfonic-acid (PFSA)-ionomer membranes).

The basic concept for high-temperature fuel cells dates back to the 1930s, about 100 years after the existence of the lower temperature concepts. In an attempt to prove the concept of “Brennstoff-Ketten mit Festleitern” (fuel chains with solid conductors), Emil Baur and Hans Preis tested different solid electrolytes [4], and they came to the conclusion that the “Nernst-Masse” is “unübertroffen” (unrivaled). At that time “Nernst-Masse” had the composition 85%  $\text{ZrO}_2$  and 15%  $\text{Y}_2\text{O}_3$ , and this is still close to what is used in current SOFCs (solid oxide fuel cell) as electrolyte material. Moreover, even in these initial experiments they tested “masses” containing Ceria ( $\text{CeO}_2$ ), and this is still discussed as a base for alternative SOFC electrolyte materials.

As in a battery or electrolysis cell, the reactants/products are prevented from chemically reacting by separating them with an electrolyte, which is in contact with electro-catalytically active porous electrode structures (Fig. 2). Apart from effectively separating the anode and cathode gases and/or liquids (i.e., fuel and air), the electrolyte mediates the electrochemical reactions taking place at the electrodes by conducting a specific ion at very high rates during operation. In the simplest case of a fuel cell, operating with hydrogen (fuel) and oxygen (air) as reacting gases, a proton or hydroxide or oxide ionic current is driven through the electrolyte and converted to electronic current at the electrodes, which can then be used to perform work (see Fig. 2). Running a similar device in the opposite direction (i.e., electrolysis) can be used to generate hydrogen. When run in both electrolysis and fuel-cell mode, a unitized energy-storage-system can be realized.

During the operation of polymer-electrolyte fuel cells, many interrelated and complex phenomena occur. These processes include mass and heat transfer, electrochemical reactions, and ionic

### Polymer-Electrolyte Membrane (PEM) Fuel Cell



**Fuel Cells and Hydrogen Production: Introduction, Fig. 2** Schematic illustration of electrochemical energy-conversion fuel-cell architecture. (Schematic designed and provided by Ahmet Kusoglu)

and electronic transport. Most of these processes occur in the through-plane direction as shown in Fig. 2. This sandwich comprises multiple layers including diffusion media that can be composite structures containing a macroporous gas-diffusion layer and microporous layer, catalyst layers, flow fields or bipolar plates, and a membrane. During operation fuel is fed into the anode flow field, moves through the diffusion medium, and reacts electrochemically at the anode catalyst layer to form hydrogen ions and electrons. The oxidant, usually oxygen in air, is fed into the cathode flow field, moves through the diffusion medium, and is electrochemically reduced at the cathode catalyst layer by combination with the generated protons and electrons. The water, either liquid or vapor, produced by the reduction of oxygen at the cathode exits the cell through either the cathode or anode flow field.

The electrons generated at the anode pass through an external circuit and may be used to perform work before they are consumed at the cathode. An electrolysis cell is essentially the same but where electrons are supplied and the reverse reactions occur within the catalyst layers. Because of the applied voltage for this process, materials are often different in terms of catalysts and backing layers in the oxygen electrode.

A fuel cell converts the intrinsic chemical energy of a fuel into electrical and heat energies, whereas an electrolyzer takes electrical energy and converts that into chemical energy. Thus, both are energy-conversion and not storage devices (i.e., a fuel cell by itself is not a battery). From the first law of thermodynamics,

$$\Delta H = Q - W_s \tag{1}$$

one sees that the net release of energy is in the form of heat ( $Q$ ) or work ( $W_s$ ). The work performed by the system is simply the power as expressed by the cell current multiplied by its operation voltage:

$$P = IV \tag{2}$$

The net energy due to the electrochemical reaction is the difference between the heat of formation of the products and reactants,  $\Delta H$ , which can be converted to an electrochemical potential, resulting in the enthalpy potential,

$$U_H = \frac{\Delta H}{z_i F} \tag{3}$$

where  $z_i$  is the charge number of species  $i$  and  $F$  is Faraday's law. Using the above power equation, the expression for the heat released becomes

$$Q = i(U_H - V) \quad (4)$$

Thus, if the cell potential equals the enthalpy potential, there is no net heat loss, which is why the enthalpy potential is often termed the thermo-neutral potential. However, the enthalpy energy is not fully accessible as it is composed of both reversible or entropic ( $Q_{\text{rev}} = T\Delta S$ ) as well as irreversible components. The maximum energy that is convertible to electrical energy is related to the free energy of the fuel,

$$\Delta G = \Delta H - T\Delta S \quad (5)$$

The potential corresponding to the Gibbs free energy is defined as the equilibrium potential,

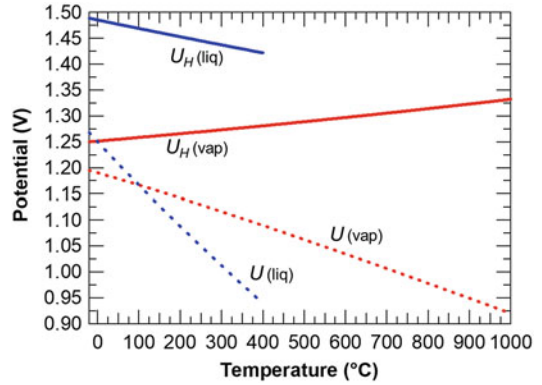
$$U^\theta = \frac{\Delta G}{z_i F} \quad (6)$$

Usually, the fuel cell is operated at a temperature greater than the standard temperature of 25 °C, which can be accounted for by integrating the state properties. For hydrogen and oxygen reacting to become water, the enthalpy and equilibrium potentials are shown in Fig. 3 as calculated from handbooks [5]. Depending on whether the product water is vapor or liquid, one arrives at different potentials due to the latent heat and free energy difference between liquid and vapor water as the reaction product. Thus, as the cell temperature increases, the amount of usable work from the fuel decreases (assuming the generated heat is expelled to the atmosphere), while the amount of heat generated increases for a given operating potential. Figure 3 clearly shows how significant the latent heat of water can be (~200 mV).

To account for local concentration changes, one can use a Nernst equation for the reaction

$$U = U^\theta - \frac{RT}{2F} \ln \left( \frac{p_{\text{H}_2} \sqrt{p_{\text{O}_2}}}{p_{\text{H}_2\text{O}}} \right) \quad (7)$$

where  $R$  is the ideal-gas constant,  $T$  is the temperature, and  $p_i$  is the partial pressure of species  $i$ .



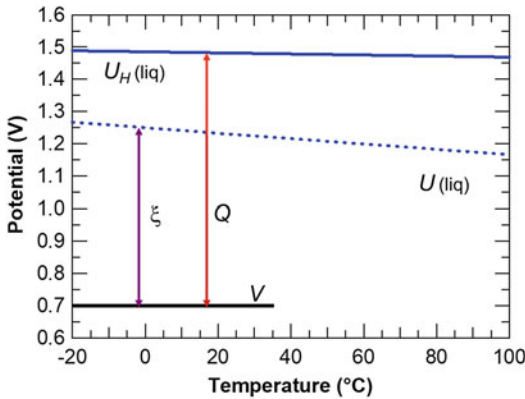
**Fuel Cells and Hydrogen Production: Introduction, Fig. 3** Thermodynamic based potentials for  $\text{H}_2 + \frac{1}{2}\text{O}_2 \rightarrow \text{H}_2\text{O}$

Looking at fuel cells in such a principal way as above may lead one to the conclusion that they are perfect energy-conversion systems superior to any heat engine, for which the efficiency is strictly limited due to the Carnot cycle. However, the issue is more complex in practical systems, and it is still an open question what role fuel cells will play in future energy supply systems. The reason is that when current flows, the available energy or potential of the cell decreases for fuel cells due to losses in the cell. Such losses are termed overpotentials and are derived from resistances to electron and ion migration, surface concentrations that differ from the bulk due to mass-transfer limitations, and intrinsic losses in the kinetic reaction steps. Thus, the net heat lost from the cell is

$$\begin{aligned} Q_{\text{loss}} &= Q_{\text{rev}} + Q_{\text{irrev}} \\ &= i(U_H - U^\theta) + i(U^\theta - V) \quad (8) \end{aligned}$$

which is summarized in Fig. 4 for a polymer-electrolyte fuel cell. Thus, if the cell operates at a potential between the equilibrium and enthalpy potentials, the process is endothermic; whereas if the operating potential is above the enthalpy potential or below the equilibrium potential, the process is exothermic. So for fuel cells, the operation is almost always exothermic, whereas electrolyzers





**Fuel Cells and Hydrogen Production: Introduction, Fig. 4** Efficiency and heat generation of a fuel cell

(devices that convert water to hydrogen and oxygen with application of electrical current) are typically operating much closer to thermo-neutral.

Also as shown in Fig. 4, for fuel cells, the efficiency of the cell,  $\eta_{\text{eff}}$ , is typically defined relative to the maximum free energy available for electrical work,

$$\eta_{\text{eff}} = 1 - \frac{V}{U} \quad (9)$$

One must also be cognizant of whether the efficiency is defined in terms of the equilibrium or enthalpy values, and what the reference state is for the calculation (i.e., vapor or liquid water). This is especially important when comparing different fuel cells as well as with fuel cells to other systems. For example, solid-oxide fuel cells operate at temperatures (600–900 °C) where the heat generated can be recovered to electrical energy, thereby making efficiency greater than 100% possible using the definition above. Thus, it is more advisable to use the heating-value or enthalpy or enthalpy potential of the fuel as the metric for efficiency since this also allows for a better comparison among technologies (e.g., combustion engines to fuel cells). This is also often used as the efficiency value when looking at electrolysis.

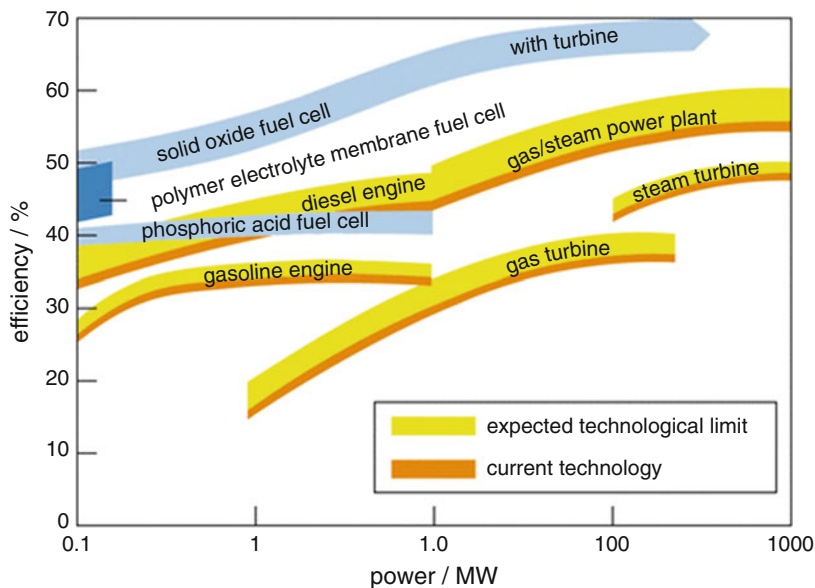
Notwithstanding the above efficiency considerations, we note that the thermodynamic efficiency limits of all relevant fuel cell reactions are

actually below unity (in the range 80–100%) and that irreversibilities (losses) occur in practically all parts of the cells as mentioned above. Nonetheless, electric efficiencies of more than 50% (hydrogen to electricity in fuel cells) and greater than 70% (electricity to hydrogen in electrolyzers) have been demonstrated commercially. Considering the fact that heat engines (e.g., steam turbines) reach such high efficiencies only for very large units operating at high temperatures, the high fuel efficiency of both large and small fuel-cell systems appears to be a unique feature (see Fig. 5) and enables distributed devices and networks.

The potential expanded use of hydrogen involves many technical and infrastructure-related challenges. For example, dispensing hydrogen to wider consumer and fleet-use markets, such as for private and fleet vehicles and for stationary power uses, includes issues related to hydrogen's low energy density (by volume) and other unusual characteristics (i.e., small molecule size, relative ease of ignition in air, metals embrittlement behavior, need for high gas purity when used in certain applications such as in polymer fuel cells, etc.). Hydrogen storage and advanced fuel dispensing and safety systems are active areas of research. Also important are ongoing efforts to study the full economics and lifecycle emissions implications of various hydrogen production and use pathways through total cost of ownership (TCO) and life-cycle impact assessment (LCIA) methods. Various analyses have shown that the capital costs and TCO of both high and low temperature fuel cells systems can be greatly reduced as a function of higher production volume, and with significant overall environmental and social cost benefits when used in different applications.

Over the past 20 years, there has been great progress in fuel-cell system cost reduction, increases in power density, and extended system durability. These improvements have brought commercial fuel cells into specialized applications (e.g., materials handling, military, and remote power applications) as well as initial entry into potentially much larger transportation

**Fuel Cells and Hydrogen Production: Introduction,**  
**Fig. 5** Efficiency versus power for different fuel cell types compared to other energy conversion technologies



(including cars, vans, buses, trucks, and rail systems) and stationary power markets. However, widespread use of the different types of fuel cell systems still requires further fundamental research and engineering efforts. This volume provides detailed insight into the current status of the diverse hydrogen-production and fuel cell technologies and identifies future directions based on critical analyses of the state of the art.

## Hydrogen Production Section

While hydrogen is the most abundant element on earth, it is not readily found in its basic molecular form and has to be produced through one of a variety of processes. This is however also a benefit as it can be produced in many different ways and using a variety of feedstocks. Major efforts are now exploring the options for expanded use of hydrogen for industrial, power generation, and transportation systems (e.g., H2@Scale by US DOE as shown Fig. 1) as well as additional recent work on hydrogen produced using renewable resources (e.g., the US DOE HydroGen – Advanced Water Splitting Materials Consortium).

As discussed above, a range of potential hydrogen production methods and pathways include reformation, gasification, electrolysis, and other

advanced processes. The most common pathway today is steam reforming of natural gas, but it is mainly produced as an industrial input; that is, hydrogen is not being used extensively as an energy carrier. Electrolysis of water to produce hydrogen is well proven at small and larger scales but remains an active area of continued research for improved efficiency and capital cost reduction (chapters ▶ [“Electrochemical Hydrogen Production”](#) and ▶ [“Hydrogen Production Through Electrolysis”](#)). There is a need to leverage the understandings gained and knowledge developed in fuel cells for further development of next-generation electrolyzer systems.

Production of hydrogen from biomass and algae sources using a variety of gasification and pyrolysis technologies is also a very active area of research, using local feedstocks and appropriate processes (chapters ▶ [“Hydrogen Production from Biological Sources”](#), ▶ [“Biohydrogen Production from Agricultural Residues”](#), ▶ [“Hydrogen Production Through Pyrolysis”](#), ▶ [“Hydrogen Production from Algal Pathways”](#), and ▶ [“Genetic Optimization for Increasing Hydrogen Production in Microalgae”](#)).

Moving forward, some countries are even considering the use of excess nuclear energy (electricity and heat) for producing hydrogen (chapter ▶ [“Nuclear-Assisted Hydrogen Production”](#)),

and others want to rely completely on renewables such as wind and solar (chapters ▶ [“Hydrogen via Direct Solar Production”](#) and ▶ [“Photo-catalytic Hydrogen Production”](#)). Making large quantities of hydrogen with sunlight, directly or indirectly, is still some years away, but this is possible at a range of scales from kilowatts to many megawatts with only solar energy and water as inputs.

Some of the latest hydrogen-generation technologies utilize electrons and electrochemical devices including more advanced concepts where they are combined with thermochemical processes (chapter ▶ [“Hydrogen Production from High-Temperature Fuel Cells”](#)). In addition to traditional electrolyzers, there has been a recent focus on utilizing solar light in an electrochemical cell (chapter ▶ [“Hydrogen Production from Photoelectrochemical Water Splitting”](#)), where efficiencies of solar to hydrogen of around 20% are now demonstrated, although longevity and associated durability concerns remain. Additional concepts include improved hydrogen production through improved chemical reactor systems that can be applied to different feedstocks and settings (chapter ▶ [“Advances on Inorganic Membrane Reactors for Production of Hydrogen”](#)).

## Fuel Cell Section

In an overall sense, fuel cells can be classified by their type of electrolyte (chapter ▶ [“Fuel Cell Types and Their Electrochemistry”](#)). The electrolyte type is highly correlated with the operating temperature regime of the fuel cell as the ions used must be mobile in order to conduct the ionic current. Lower temperature fuel cell systems tend to use relatively pure hydrogen as the reactant fuel, but for higher temperature solid-oxide and molten carbonate fuel cells, other fuels including hydrocarbon fuels can be reacted more directly (chapter ▶ [“Direct Hydrocarbon Solid Oxide Fuel Cells”](#)). Durability and reliability issues are critical for higher temperature fuel cells (chapter ▶ [“Solid Oxide Fuel Cell Materials: Durability, Reliability, and Cost”](#)) as are the main components and architectures (chapters ▶ [“Fuel](#)

[Cells \(SOFC\): Alternative Approaches \(Electrolytes, Electrodes, Fuels\)”](#) and ▶ [“Solid Oxide Fuel Cells”](#)). At the higher temperature range, molten-carbonate fuel cells also are commercially available after decades of development (chapter ▶ [“Molten Carbonate Fuel Cells”](#)), and at lower temperatures, polymer electrolyte membrane (PEM), phosphoric acid (chapter ▶ [“Polybenzimidazole Fuel Cell Technology: Theory, Performance, and Applications”](#)), and polybenzimidazole (used as a matrix for phosphoric acid) (chapter ▶ [“Polybenzimidazole Fuel Cell Technology: Theory, Performance, and Applications”](#)) types are also well established.

The most researched and deployed fuel-cell technology to date is the PEM technology that uses a sulfonic acid membrane and noble-metal catalyst material coated on the electrodes and operates traditionally at about 80 C, below the boiling point of water. While tremendous progress has been made over the past few decades, there are still several critical materials issues related to cost and durability requirements, especially for automotive applications, that must be overcome (chapter ▶ [“PEM Fuel Cells: Materials and Design Development Challenges”](#)). The electro-catalyst layers are a key cost and performance component, where there is a current need for higher performance and more durable materials (chapter ▶ [“PEM Fuel Cells and Platinum-Based Electro-catalysts”](#)). Experiments have shown that one can reduce the amount of noble catalyst, but that at least thus far this is not without drawbacks in terms of performance (chapter ▶ [“Proton-Exchange Membrane Fuel Cells with Low-Pt Content”](#)). Alternatively, non-noble metal catalysts are increasingly being researched (chapter ▶ [“Polymer Electrolyte Membrane Fuel Cells \(PEM-FC\) and Non-noble Metal Catalysts for Oxygen Reduction”](#)) to reduce overall cell cost.

A key material for realizing gains in low temperature systems is the PEM itself (chapter ▶ [“Membrane Electrolytes, from Perfluoro-sulfonic Acid \(PFSA\) to Hydrocarbon Ionomers”](#)) and its interplay with environmental conditions (chapter ▶ [“Proton Exchange Membrane Fuel Cells: High-Temperature, Low-Humidity Operation”](#)). A better ability of fuel cells systems to

adapt to local environmental conditions may help to reduce the system cost, especially by reducing the size of the cooling system, the amount of noble-metal catalyst, and the purity requirements for the fuel used (relatively pure hydrogen). Efforts are also constantly underway to find cost reductions by using non-noble metal catalysts, potentially through use of more effective anion or hydroxide exchange membranes (chapter ► [“Alkaline Membrane Fuel Cells”](#)). Beyond the polymer electrolyte as a membrane separator, there is an increasing focus on its existence as thin films in the catalyst layers and potential swelling of the layers over time that can inhibit performance (chapter ► [“Ionomer Thin Films in PEM Fuel Cells”](#)).

As noted, fuel cells are complex devices and to understand the various interplays and complexities researchers are routinely turning to mathematical modeling (chapter ► [“PEM Fuel Cells: Modeling”](#)). Fuel cells act as energy-conversion modules in various systems and applications (chapter ► [“Polymer Electrolyte \(PE\) Fuel Cell Systems”](#)), especially automotive for polymer-electrolyte fuel cells (chapter ► [“Polymer Electrolyte Membrane \(PEM\) Fuel Cells: Automotive Applications”](#)) and stationary for solid-oxide fuel cells. Of course, when discussing the system aspects one must be aware of the cost and design issues (chapters ► [“PEM Fuel Cell Materials: Costs, Performance, and Durability”](#) and ► [“Solid Oxide Fuel Cells: Marketing Issues”](#)), including LCA (chapters ► [“Fuel Cell Systems: Total Cost of Ownership”](#) and ► [“Solid Oxide Fuel Cells: Sustainability Aspects”](#)) and comparisons to alternative technologies (chapter ► [“Fuel Cell Comparison to Alternate Technologies”](#)).

We conclude this introduction by noting that various types of power systems based on

heat engines and electrochemical energy devices (mainly batteries but now including fuel cells as well) have existed side by side since the late 1800s. Over the intervening years the abundance of fossil fuels has driven the development of combustion engines and turbines and slowed the development of more efficient and cleaner energy conversion devices. As the “oil age” continues but is expected to wane over time, the transition may include an increase in the importance of an array of now commercially available systems for a cleaner and more efficient future energy system. These include solar photovoltaic, wind power, geothermal, and biomass-based renewable energy systems, as well as transitional solutions based on natural gas and nuclear power, amid which hydrogen and fuel cells have an important role to play.

## Bibliography

1. Pivovar B (2017) H2@Scale, National Renewable Energy Laboratory, U.S. Department of Energy Fuel Cell Technologies Office
2. Schönbein CF (1839) X. On the voltaic polarization of certain solid and fluid substances. *Philos Mag Ser 3* 14(85):43–45. <https://doi.org/10.1080/14786443908649658>
3. Grove WREMAMRI (1839) XLII. On a small voltaic battery of great energy; some observations on voltaic combinations and forms of arrangement; and on the inactivity of a copper positive electrode in nitro-sulphuric acid. *Philos Mag Ser 3* 15(96):287–293. <https://doi.org/10.1080/14786443908649881>
4. Baur E, Preis H (1937) Über Brennstoff-Ketten Mit Festleitern, *Ztschr. Elektrochem* 43(9):727–732
5. Perry RH, Green DW (1997) Perry’s chemical engineers’ handbook. McGraw-Hill, New York

---

**Part I**

**Fuel Cells**



## Fuel Cell Comparison to Alternate Technologies

Julia Kunze-Liebhäuser<sup>1</sup>, Odysseas Paschos<sup>2</sup>, Sethu Sundar Pethaiah<sup>3</sup> and Ulrich Stimming<sup>4</sup>

<sup>1</sup>Institute of Physical Chemistry, University of Innsbruck, Innsbruck, Austria

<sup>2</sup>BMW AG, Munich, Germany

<sup>3</sup>Gashubin Engineering Private Limited, Singapore, Singapore

<sup>4</sup>Newcastle University, Chemistry – School of Natural and Environmental Sciences, Newcastle upon Tyne, UK

### Article Outline

Glossary

Definition of the Subject and Its Importance

Introduction

Classical Heat Engines

Electrochemical Systems

Electromobility: An Example for Combining Key Energy Technologies

Future Directions

Bibliography

### Glossary

**Battery** A battery or voltaic cell consists of one or more electrochemical cells which store and convert chemical energy into electric energy.

**Electrochemical capacitor** An electrochemical capacitor (supercapacitor, ultracapacitor, or double-layer capacitor) is an electrochemical device that can store and convert energy by charging/discharging the electrochemical double-layer of two electrodes with large surface areas and thus large double layer capacitances.

**Electromobility** Electromobility is a mobility concept in which electric vehicles instead of vehicles powered by internal combustion engines are used.

**Fuel cell** A fuel cell is an electrochemical cell that can convert the chemical energy stored in a given fuel into electrical energy.

**Ragone plot** A Ragone plot compares the performances of different energy storing devices by plotting power densities or specific power [W/kg] versus energy densities or specific energy [Wh/kg].

### Definition of the Subject and Its Importance

The actual energy demand and consumption issues make it necessary to critically discuss and compare different energy conversion and storage systems. At present, only one third of the primary energy is converted into end energy, for example, electrical energy. Losses are associated with a high consumption of fossil fuels and large CO<sub>2</sub> emissions. They can be avoided by considering important electrochemical processes for energy conversion, using batteries, fuel cells, supercapacitors and electrochemical photovoltaics and by incorporating energy storage, employing rechargeable batteries, supercapacitors, generation of hydrogen via electrolysis, and generation of methanol.

Fuel cells can offer clean power generation and have the potential to convert fuels directly into electrical energy with high efficiencies. Today, however, they cannot compete with heat engines because of much higher costs, inferior power performance, and insufficient durability and lifetime. As yet, no single electrochemical power source can match the characteristics of the internal combustion engine. A competitive system in comparison to heat engines can be envisioned when available electrochemical power systems are combined. In such hybrid electrochemical power systems, batteries and/or supercapacitors would provide high power and the fuel cells would deliver electricity with high efficiency. The consequence would be to considerably reduce costs of the electrochemical systems.

Moreover, when we compare different systems, we face the genuine problem of geometry and thus the costs related to the space needed for the processes involved. The latter explains the so far success of thermodynamic-based systems (e.g., heat engines) compared to alternative energy technologies (e.g., fuel cells). This is also evident when the power output of a coal power plant which lies in the GW range is compared to the power that a fuel cell can deliver which lies in the MW range. A possible strategy would be to develop highly efficient fuel cell systems that can push their power to larger outputs. Current research is aiming at increasing the power output of a fuel cell without compromising its efficiency; however, the advantages of conventional systems cannot be ignored.

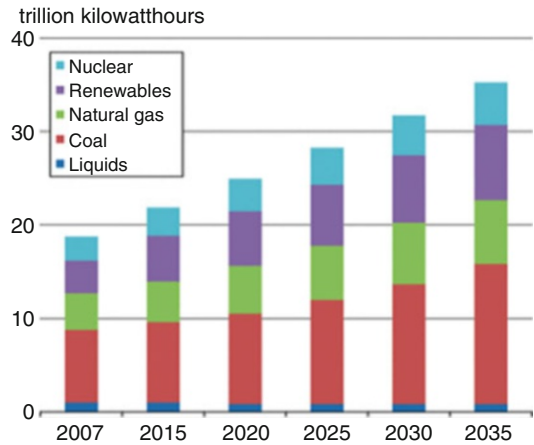
## Introduction

Our present situation concerning major (fossil) energy carriers and energy consumption is characterized by limited reserves and resources as well as emission problems, considering crude oil, natural gas, coal, and uranium as primary energy sources. At the same time, the worldwide demand for electrical energy has increased from 8.3 million GWh in 1980 to 18.9 million GWh in 2006 and is estimated to further increase up to 30.7 million GWh in 2030 ([1] (Fig. 1).

The problem of the energy management is of a rather complex nature. Increasing contributions of renewable energies such as wind power, solar power, and wave power tend to complicate the grid management. Therefore, generation of electrical energy is only part of the challenge. The management and storage of electrical energy will become essential in order to maintain the present grid quality [2].

Energy conversion processes today are under special consideration because of two issues associated with them:

1. The limited availability of primary energy carriers
2. The emission of pollutants with local and global negative effects on the environment



**Fuel Cell Comparison to Alternate Technologies, Fig. 1** Worldwide demand for electrical energy (From Ref. [1])

On average, energy conversion processes aiming at generating electrical power reveal efficiencies not much higher than 30%. This indicates that losses in the form of heat or chemical substances amount to more than two thirds of the primary energy. Conventional processes, for example, those in a heat engine-based power plant, are volume processes such as combustion, which results in mechanical and then in electric energy. By contrast, other technologies such as photovoltaics, batteries, fuel cells, or supercapacitors are based on interfacial transfer of energy and/or charge. In contrast to the performance of heat engines which is limited by the Carnot efficiency, interfacial reactions are usually of much higher thermodynamic efficiency.

## Classical Heat Engines

Thermodynamic considerations lead to the first heat engines that were used to generate mechanical or electrical energy. Since the eighteenth century, conventional reciprocating steam engines have served as mechanical power sources, with notable improvements being made by James Watt. The first commercial central electrical generating stations in New York and London, in 1882, used steam engines [3]. These first-generation heat engines are still serving as power plants today.



Further developments lead to the introduction of combined cycle power plants. Here, usually a combination of several cycles, operating at different temperatures yields considerably higher system efficiency. Heat engines are only able to use a portion of the energy, usually 35–41%. The remaining heat is generally wasted.

In a combined cycle power plant (CCPP), or combined cycle gas turbine (CCGT) plant, a gas turbine generator produces electricity and the waste heat is used to make steam for generating additional electricity via a steam turbine; this last step enhances the efficiency for electricity generation to about 60%, because the temperature difference between the input and output heat levels is higher leading to an increase in the Carnot efficiency. Most modern power plants in Europe and in North America are of this type.

If the waste heat of a conventional thermal power station is utilized for district heating, it is called cogeneration. This heat gives an additional efficiency of about 40–50% which leads to an increase of the overall efficiency to ~90%. The fuels used in these engines comprise black and brown coal and nuclear power.

In contrast to the stationary systems described above, mobile engines are needed in many energy production applications. The best known mobile engines are the four-stroke (Otto), the diesel, and the Stirling engine.

Heat engines have limited efficiencies which are determined by the Carnot cycle. Practical issues reduce the efficiency of steam engines, due to limits of convective heat transfer and viscous flow (friction). There are also mechanical considerations, for example, limitations imposed by the materials such as nonideal properties of the working gas, thermal conductivity, tensile strength, creep, rupture strength, and melting point.

## Electrochemical Systems

### Energy Conversion and Storage

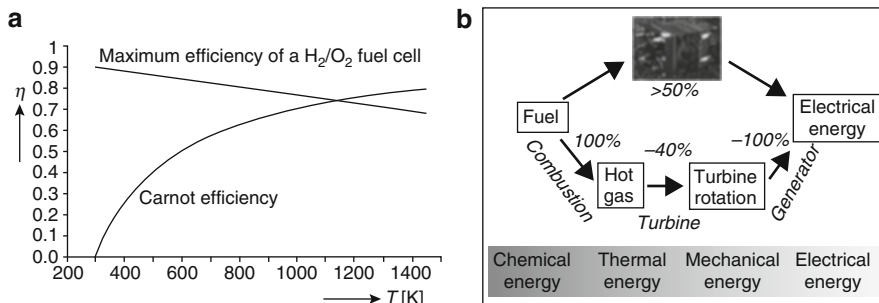
Alternatively to conventional Carnot-based heat engines, electrochemical systems have the potential to be employed to generate and store energy.

Important electrochemical processes for energy conversion are considered in batteries, supercapacitors, electrochemical solar cells, and fuel cells, and energy storage is incorporated by employing rechargeable batteries, supercapacitors, generation of hydrogen via electrolysis, and generation of methanol from electrochemically generated hydrogen and  $\text{CO}_2/\text{CO}$  – containing synthetic gas.

Electrochemical energy conversion systems are not subject to the Carnot cycle limitations and may operate with much higher efficiencies than combustion engines and related devices. Heat engine cycle processes are volume processes, whereas all electrochemical systems that are used for energy conversion and storage are based on reactions that take place at an interface. This makes them dependent on the surface morphology and its physical and chemical properties.

A fuel cell is an electrochemical conversion device. It produces electricity from fuel on the anode side and an oxidant on the cathode side, which react in the presence of an electrolyte. Fuel cells can operate continuously as long as the necessary flows of reactants and reaction products are maintained [4]. They are thus thermodynamically open systems. Many combinations of fuel and oxidant are possible. A hydrogen cell uses hydrogen as fuel and oxygen, usually from air, as oxidant. Other fuels include hydrocarbons and alcohols. Other oxidants include chlorine and chlorine dioxide. The principle of fuel cells is already known for 165 years. In 1838, Christian Friedrich Schönbein discovered that an electrical voltage is measured between two platinum wires in an electrolyte solution surrounded by hydrogen and oxygen. He published these results under the title “On the Voltaic Polarization of Certain Fluid and Solid Substances.” Sir William Robert Grove investigated the new effect intensely and was the first to develop useful fuel cells. He connected several elements in series and called these systems “gas batteries.” The further development of this concept to a really efficient electrical source proved to be so difficult that it took 100 years until it improved essentially. After the design of the first electrical dynamo by Werner von Siemens in 1867, electrical generators were energy sources that efficiently delivered electricity in almost





**Fuel Cell Comparison to Alternate Technologies, Fig. 2** (a) Ideal thermodynamic efficiency of polymer electrolyte membrane fuel cells (PEMFCs) compared to

that obtained in the Carnot process. (b) Comparison of processes in a cogenerated heat engine with fuel cell performance (From Ref. [2])

unlimited amounts. This was the reason why fuel cells were practically replaced completely. Fuel cells have the potential for high conversion efficiencies of chemical energy into electrical energy; at the moment the attainable efficiency is up to 65%, depending on fuel and conditions. Fuel cells can substitute other technologies or be operated in synergy, for example, with combustion engines in cogeneration of electricity and of heat and cold, in residential or mobile applications.

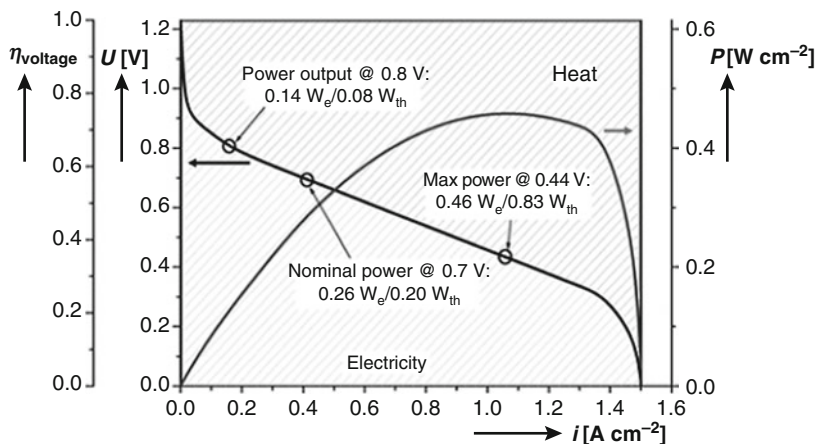
Figure 2 shows a comparison of the thermodynamic efficiencies of a hydrogen/oxygen fuel cell and of a Carnot cycle. In the future, fuel cells might be able to convert the used fuels into electrical energy with efficiencies of >70%. The difference between the theoretical and practical energy storage capabilities is related to several factors, including (1) inert parts of the system such as conductive diluents, current collectors, containers, etc., that are necessary for its operation, (2) internal resistances within the electrodes and electrolyte and between other cell components, resulting in internal losses, and (3) limited utilization of the active masses, as, for example, parts of the fuel in a fuel cell leave the cell without reaction or as, for example, passivation of electrodes makes them partially electrochemically inactive. Fuel cells offer a very clean power generation. They are quiet in operation and can be located close to the application. They produce much less greenhouse emissions and can be more efficient in conversion of the energy in a fuel into power than gasoline engines or utility thermal power plants. Fuel cells are best utilized

as a steady energy source and not as a power source to supply dynamic demands. For applications that require varying power demands, such as automotive propulsion, the use of the fuel cell in a hybrid configuration with a battery or an electrochemical capacitor is envisioned. The fuel cell provides steady power delivery while the battery or the electrochemical capacitor handles the surge for regenerative braking and acceleration as well as initial start-up. There is a *certain number of fuel cells under development*. Usually fuel cells are classified by the electrolyte that they are using. The electrolyte is a major component of the fuel cell since it determines the operating temperature, fuel, oxidant, poisons, catalysts, electrode design, and system design. According to the type of electrolyte that is used, fuel cells can be classified into six major categories.

The polymer electrolyte membrane fuel cell (PEMFC) uses a solid-type electrolyte that typically cannot withstand high temperatures, and the relatively low operating temperature results in slow reaction rates. The operating temperature of a PEMFC is typically between 50 °C and 100 °C. The slow reaction rate is overcome by using highly active catalysts such as platinum. The fuel utilized is pure hydrogen and the electrical power that it produces is typically less than 250 kW. The fuel and oxidant must be free of carbon monoxide, which is a poison because it gets strongly adsorbed by the catalyst reducing the active surface area. To overcome this issues present research is focused onto high-temperature proton exchange membrane [HTPEM] fuel cell

### Fuel Cell Comparison to Alternate Technologies,

**Fig. 3** Conversion of chemical energy in fuel cells (voltage efficiency  $\eta_{\text{voltage}}$  vs. current density  $i$ ). Black line: cell voltage  $U$ ; gray line: power density  $P$



technology. HTPEM has better CO tolerances in hydrogen feeds, so reformed hydrogen gas can be used instead of purified hydrogen. Moreover heat and water management also simplified and reaction kinetics are faster at higher temperatures. Hence, HTPEM is a suitable technology for transport applications [5].

The direct methanol fuel cell (DMFC) is similar to the PEMFC but methanol is used as a fuel instead of hydrogen. It can be used for portable applications such as laptops, cell phones, and MEMS devices. Maximum power of DMFCs is typically less than 10 kW.

Figure 3 shows a typical polarization curve of a low-temperature PEMFC. The curve is similar for all the other types of fuel cells as same trends are observed. At high operation voltages, the power output of a fuel cell is controlled mainly by the electrocatalytic properties of the catalyst. In this region ( $>0.8$  V), the current density is controlled by the charge transfer and the dissipated heat is minimized. Challenges in fuel cell catalyst research are to obtain high electric power density, high electric conversion efficiency, and low material costs. At high electric power density, mass transport is the dominant factor affecting the fuel cell operation. This region can be expanded by careful engineering design of the fuel cell system. A general research trend is to obtain as high current densities as possible at high operation voltages.

For high electric conversion efficiency, one should aim at the use of less cogenerated heat

which would also allow for a simplification of the design and the need of less fuel (hydrogen) for the same electrical energy. To guarantee low material costs, less noble metal should be incorporated, because high catalyst utilization is needed, and highly efficient catalysts are needed for anode and cathode side. The goal in fuel cell research must therefore be a deeper understanding of the parameters controlling electrocatalytic activity which would enable us to propose rational structures for catalysts in fuel cells in the future.

Alkaline fuel cells (AFCs) were used to provide electrical power for many manned spacecrafts. The electrolyte is KOH and the catalysts include silver, nickel, and different metal oxides. AFC catalysts are relatively inexpensive compared to catalysts used for other types of fuel cells. The fuel and oxidant used in an AFC must be completely free of  $\text{CO}_2$  since even a small amount reacts strongly with the electrolyte, producing forms of carbonates that poison the ionic conductivity of the electrolyte. Therefore, pure hydrogen and oxygen must be used, limiting the use of the AFC to special applications, like spacecrafts and submarines, where cost of the fuel and oxidant is not a major issue.

The phosphoric acid fuel cell (PAFC) was the first fuel cell to be commercialized and shares some technologies with the PEMFC, such as the porous electrodes and the platinum catalysts. The liquid phosphoric acid allows high operating temperatures, around  $200^\circ\text{C}$ . Fuels must be free of carbon monoxide, as with the PEMFCs. With

rated power over 50 kW, PAFC systems are used for stationary applications.

Molten carbonate fuel cells (MCFCs) operate at temperatures around 650 °C. The electrolyte is a mixture of molten carbonate salts, such as lithium and potassium carbonate. At the operating temperature, the carbonates melt and become conductive to carbonate ions. Due to the high temperature, high reaction rates can be achieved with low-cost catalysts such as nickel. Rated power for MCFC systems is typically greater than 1 MW.

The last fuel cell system is the solid oxide fuel cell (SOFC). Typical operating temperature for the SOFC is between 600 °C and 1000 °C. It has the same advantages of the MCFC (high reaction rates, inexpensive catalysts, and natural gas can be used as a fuel). The electrolyte is in solid form, the most common kind being yttria (Y<sub>2</sub>O<sub>3</sub>) stabilized with zirconia (ZrO<sub>2</sub>), which is a ceramic and therefore makes the fabrication process complex and difficult. The power output can be greater than 200 kW, making the SOFC ideal for large stationary applications, such as power stations.

High-temperature fuel cells such as *molten carbonate fuel cells (MCFC)* or *solid oxide fuel cells (SOFC)* deliver off heat at high temperature level ( $T > 600$  °C). This can be used in high-temperature fuel cell cogeneration for district heating (heat extraction), for absorption refrigerators and heat pumps. As the energy demand in residential applications is complementary for heating and for cooling over the year, such a combination would be very useful.

A *battery* or voltaic cell consists of one or more electrochemical galvanic cells which store and convert chemical energy into electric energy. Since the invention of the first voltaic pile in 1800, the battery has become a common power source for many household and industrial applications. The name “battery” was coined by Benjamin Franklin for an arrangement of multiple Leyden jars, an early type of capacitor. There are different types of batteries which comprise nonrechargeable batteries (primary batteries) in which chemical energy is stored internally, the discharging reaction, that takes place at the electrode/electrolyte interface, is irreversible, and rechargeable batteries or

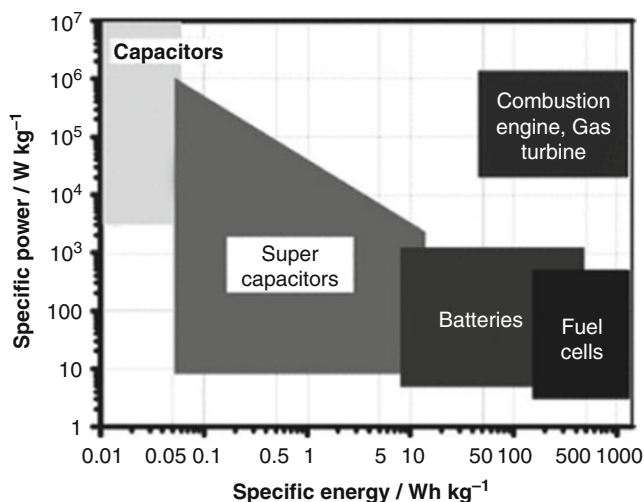
accumulators (secondary batteries) having a reversible discharging reaction [6].

In the nineteenth century, no difference was made between *batteries and fuel cells*. Today the *definitions* have been refined: batteries convert and store electrical energy and hence represent a thermodynamically closed system; energy storage and conversion occur in the same compartment. Fuel cells are open systems where the anode and cathode are just charge-transfer media and the active masses undergoing the redox reactions are delivered from outside the cell, either from the environment, for example, oxygen from air, or from a tank, for example, fuels such as hydrogen and hydrocarbons. Energy storage (in the tank) and energy conversion (in the fuel cell) are thus locally separated.

Electrochemical capacitors (EC), also called supercapacitors, store energy using either ion adsorption or fast surface redox reactions. In the first case, they are called electrochemical double layer capacitors (EDLC), in the second case they are called pseudocapacitors. They can complement or replace batteries in electrical energy storage and harvesting applications, when high power delivery or uptake is needed. Several types of ECs can be distinguished, depending on the charge storage mechanism as well as the active materials used. EDLCs, the most common devices at present, use carbon-based active materials with high surface areas. Pseudocapacitors or redox supercapacitors use fast and reversible surface or near-surface reactions for charge storage. Transition metal oxides as well as electrically conducting polymers are examples of pseudocapacitive active materials. Electrochemical capacitors currently fill the gap between batteries and conventional solid state and electrolytic capacitors. They store 100–1000 times more charge than the latter due to a much larger surface area (1000–2000 m<sup>2</sup> g<sup>-1</sup>) available for charge storage in EDLC. They have a lower energy density than batteries, and this limits the optimal discharge time to less than a minute, whereas many applications clearly need more [7]. Since the early days of EC development in the late 1950s, there has not been a good strategy for increasing the energy density; only incremental performance improvements were achieved

### Fuel Cell Comparison to Alternate Technologies,

**Fig. 4** Simplified Ragone plot of the energy storage domains for the various electrochemical energy conversion systems compared to an internal combustion engine and turbines and conventional capacitors (From Ref. [9])



from the 1960s to 1990s. The increase in performance that has been demonstrated in the past few years is due to the discovery of new electrode materials and improved understanding of ion behavior in small pores, as well as the design of new hybrid systems combining faradic and capacitive electrodes [8].

To compare the power and energy capabilities of fuel cells, batteries, and supercapacitors, a representation known as the *Ragone plot* has been developed. The terms *specific energy* [Wh/kg] and *energy density* [Wh/L] are used to compare the energy contents of a system, whereas the rate capability is expressed as *specific power* [W/kg] and *power density* [W/L]. A simplified Ragone plot (Fig. 4) discloses that fuel cells can be considered to be high-energy systems, whereas supercapacitors are considered to be high-power systems. Batteries have intermediate power and energy characteristics. There is some overlap in energy and power of supercapacitors or fuel cells with batteries. Batteries with thin-film electrodes exhibit power characteristics similar to those of super capacitors.

Not all systems can be described using these definitions, since there are also combined systems such as metal-air batteries [10–12] which contain a battery electrode (metal anode) and a fuel cell electrode (air cathode), or redox flow batteries [13, 14] which are a form of rechargeable battery in which electrolyte containing one or more

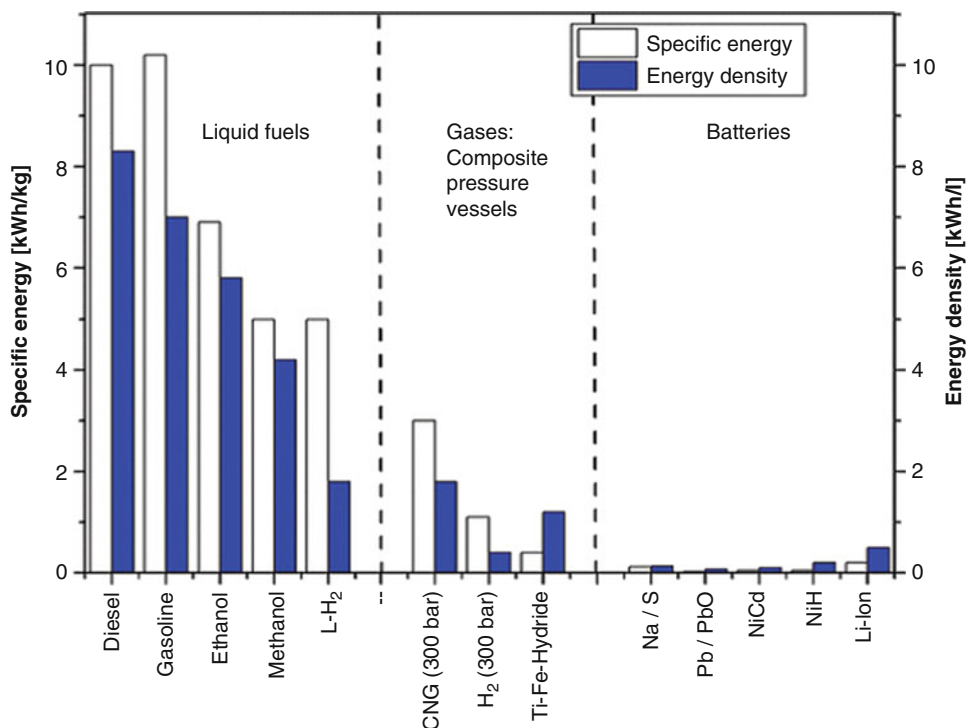
dissolved electroactive species flows through an electrochemical cell. Additional electrolyte is stored externally, generally in tanks, and is usually pumped through the cell of the reactor. Redox flow batteries (RFBs) are classified by the solvated ions they employ for their low- and high-potential half-cell [15, 16]. The first system that can be called RFB was the Fe/Cr system developed by the NASA in the 1970s. The ferrous/ferric redox couple with a standard potential of  $U_0 = 0.77$  V versus NHE is employed for the high potential side, while chromic/chromous ions ( $U_0 = -0.41$  V vs. NHE) form the low potential half-cell. The system suffers from a relatively low open-circuit potential as well as crossover of solvated ions through the membrane. This leads to chemical contamination and self-discharge. By mitigating the significance of the crossover problem, the all-vanadium RFB was a real step forward and is the most successful system today [17]. It makes use of the many oxidation states of vanadium ions and uses V(II)/V(III) ions in the low-potential half-cell and V(IV)/V(V) ions in the high potential half-cell. Therefore, crossover causes only a loss in efficiency, but no chemical contamination and the initial concentrations can be restored during charge. Contemporary problems are the relatively low energy density (25–35 Wh/l) and the low power density. The low obtainable current densities are an immediate result of the sluggish electron transfer kinetics of

the  $\text{VO}^{2+}/\text{VO}_2^+$ -reaction [15, 18]. Energy density is limited by the solubility of the  $\text{VO}_2^+$ -ions and therefore additives such as HCl are mixed into the electrolyte to enhance solubility [19], or the vanadium on the high potential side is replaced by bromine. The latter approach was reported to yield a significantly improved energy density of 35–70 Wh/l [20]. Since toxic bromine-vapor can potentially be released complexing agents need to be added to the electrolyte. Despite their shortcomings in terms of energy – and power density RFBs show some intrinsic advantages. Energy content and obtainable power scale independently, larger electrolyte storage tanks increase the capacity of the battery while a bigger power-converter (larger electrode-electrolyte interface) boosts current density and hence power. RFBs are said to be relatively inexpensive and efficient storage systems. A recent study analyzing the cost sensitivity of an all-vanadium RFB found that the electrolyte is the most expensive single component (37% capital cost) for a 12 MWh system. Depending on the power capacity the capital cost per kWh varies between 370 US\$ (1000 kW) and 750 US\$ (3000 kW) [21]. For comparison, automotive Li-Ion cells are estimated to cost about 400 US\$/kWh while the full battery pack is priced at roughly 800 US\$/kWh. This is large overhead is due to the need for electronic and thermal management [22]. Flow batteries can be rapidly recharged by replacing the electrolyte while simultaneously recovering the spent material. Due to the overlapping properties of batteries and fuel cells, it is nowadays considered to find a definition that recombines the two systems again, to no longer differentiate between batteries and fuel cells like in former times. In order to bridge the gap between batteries and electrochemical capacitors, a capacitive or pseudocapacitive electrode can be combined with a battery electrode. Batteries exhibit usually high energy densities, while capacitors can deliver high power at the cost of low energy storage. Research efforts have been focused to increase the gravimetric energy of electrochemical capacitor electrodes by using materials with enhanced gravimetric capacitances (gravimetric charge storage per volt) [23]. The latter can be achieved by using carbon

subnanometer pores for ion adsorption or by incorporating the pseudocapacitance of nanostructured transition metal oxides. A recent report by S.W. Lee et al. [24] demonstrated that by using a novel class of electrodes for lithium storage high gravimetric energy ( $200 \text{ Wh kg}_{\text{electrode}}^{-1}$ ) was delivered at a high power of  $100 \text{ kW kg}_{\text{electrode}}^{-1}$ . Those electrodes were based on functionalized multiwalled carbon nanotubes (MWNTs) that included stable pseudocapacitive functional groups and were assembled using a layer-by-layer technique. Therefore, it was shown that it is possible to benefit from both the capacitor and the battery properties.

A critical parameter of fuel selection is its energy density. The latter should be as high as possible. Additionally, the choice of fuel is also affected by the ease of transportation and storage which in general should be as easy and uncomplicated as possible. The choice of the fuels determines which problems, including environmental problems, will arise.

Figure 5 shows the theoretical specific energies [(kWh)/kg] and energy densities [(kWh)/l] of various rechargeable battery systems in comparison to fuels, such as gasoline, natural gas, and hydrogen. The inferiority of batteries is evident. These values are an indication for the maximum energy content of certain systems. The practical values are significantly lower than the theoretical ones. A rechargeable battery has a practical energy content which is 25% of its theoretical value while a primary battery normally yields more than 50% of its theoretical value. The theoretical efficiencies of fuel cells for the conversion of fuels into electrical energy are higher than 70%. A number of factors influence the observed differences between theoretical and practical energy storage capabilities. The systems contain inert parts such as conductive diluents, current collectors and containers, and internal resistances which results in internal losses and limited utilization of the active masses. Parts of the fuel can, for example, leave the fuel cell without having reacted or partial passivation of the electrodes can make parts of the surface area inactive. For practical use, however, as batteries and fuel cells are not subject to the Carnot cycle limitations, they may operate with much higher



**Fuel Cell Comparison to Alternate Technologies, Fig. 5** Theoretical specific energies [k Wh/kg] and energy densities [k Wh/l] of various rechargeable battery systems

compared to fuels, such as gasoline, natural gas, hydrogen, and alcohols

efficiencies than combustion engines and related devices. The efficiencies of PEMFCs, batteries, and supercapacitors are summarized for comparison in Table 1.

*Electrochemical photovoltaics* are a specific type of photovoltaic systems to convert solar energy, that is, solar radiation into electrical energy. Today, there is a variety of solar cells already on the market. Difference must be made between electrochemical photovoltaic cells and conventional silicon (Si)-based photovoltaic cells; in electrochemical photovoltaic cells two interfaces exist at which charge transport switches from electronic to ionic and back. In photo-electrochemistry a photoactive semiconducting working electrode is used together with a metallic counter electrode. Both are immersed in an electrolyte containing a suitable redox couple. Upon radiation of the semiconductor-electrolyte interface with light having a higher energy than the bandgap of the semiconductor, electron-hole pairs are formed and separated. Photogenerated

majority carriers accumulate at the backside of the semiconductor, minority carriers travel to the semiconductor-electrolyte interface. The majority carriers are collected with a charge-collecting substrate and transported to the counter electrode where they electrochemically react with the redox couple in the electrolyte. In the 1970s, wet-type electrochemical photovoltaic cells were discovered [25–27]. Michael Grätzel demonstrated that dye molecules can be adsorbed onto nanocrystalline TiO<sub>2</sub> working electrodes and thus extended the concept to dye-sensitized solar cells (DSSCs) [28–31].

It is noteworthy that electrochemical photovoltaic cells without dyes have working (semiconductor) and counter electrodes that are both immersed in the redox electrolyte. After the formation of electron/hole pairs, specific reactions occur at the semiconductor electrode and at the metal counter electrode. Charge balance is maintained via oxidation and reduction processes, and electrodes are often instable in aqueous



**Fuel Cell Comparison to Alternate Technologies, Table 1** Practical efficiencies of fuel cells, batteries, and supercapacitors

System	Process	Efficiency (%)
PEMFCs	Electrolysis-H <sub>2</sub> storage – FC operation	40
Batteries	Charging – discharging	80
Supercapacitors	Charging – discharging	95

media. Photoelectrochemical photovoltaic cells could only replace Si-based photovoltaics if a stable semiconductor material with a bandgap of  $\sim 1.4$  eV is found [32–35]. In dye-sensitized solar cells, a dye-sensitized porous nanocrystalline TiO<sub>2</sub> photoanode with a 1000-fold surface area compared to flat electrodes has been used. Furthermore, the charge transport of the photo-generated electrons passing through all the particles and grain boundaries is highly efficient [36]. The conversion efficiency of DSSCs has improved to 11.5% [37] since it was first reported with an efficiency of 7.1% [35]. Their efficiencies are now comparable with amorphous silicon solar cells [38] but at a much lower cost.

### Electromobility: An Example for Combining Key Energy Technologies

Concerns about global warming and the depletion of petroleum resources demand a shift in automotive transportation from petroleum-based internal combustion engines to electrically driven vehicles (EVs). In the concept of electromobility, all the abovementioned technologies should be united and combined in order to synergistically provide power to an EV.

Hybrid electric vehicles are a first step, where an internal combustion engine is assisted by a battery-driven electric motor, enabling increased fuel efficiencies when using high-power and low-energy (ca. 1 kWh) batteries. Further reduction or even elimination of petroleum-based fuels can be achieved by successively increasing the onboard stored electrical energy, thus enabling plug-in

hybrid electric vehicles, short-range electric vehicles and, ultimately, long-range electric vehicles. Such a development would be the perfect solution to realize electric traction in general.

Together with batteries and supercapacitors, fuel cells are a key component that must be investigated in order to build electric vehicles suitable for continuous use, especially in public transport. Fuel cells have the potential to offer clean power generation, are quiet in operation, and can be located close to the application. They produce much less greenhouse emissions and can be more efficient in conversion of the energy in a fuel into power than gasoline engines or utility thermal power plants. Fuel cells are best utilized as a steady energy source and not as a power source to supply dynamic demands. For applications that require varying power demands, such as automotive propulsion, the use of the fuel cell in a hybrid configuration with a battery or an electrochemical capacitor is required. The fuel cell provides steady power demand while the battery or the electrochemical capacitor handles the surge for regenerative braking and acceleration as well as initial start-up. This makes fuel cells an essential component for hybrid vehicles with adequate ranges as they are required for public transport and goods traffic.

Fuel cells, batteries, and supercapacitors have a similar configuration, that is, two electrodes separated by an electrolyte. The latter are designed for high power and long life service. Currently nonetheless, the status of batteries, supercaps, and fuel cells does not allow for a satisfactory use in electric vehicles due to tremendous weight and safety issues, too high costs, and too short ranges. Thus, fundamental research is necessary to develop novel battery, supercapacitors, and fuel cell concepts for a new generation of electric vehicles.

Nowadays, also concepts are developed in which photovoltaic cells integrated on the roof or in the windows of EVs can be used to recharge the batteries. It is known from literature that EVs suffer from too short ranges and too high weight [9, 39]. Fig. 6 shows typical driving ranges of battery-powered cars compared to ranges of cars powered by modern combustion engines. As it

can be seen, for EVs powered with any secondary battery system (i.e., lead acid, nickel metal hydride, sodium sulfur, and lithium ion), the driving ranges that they possess are inferior compared to those of conventional combustion engines. Therefore, it is illustrated clearly why rather fuel cells and not batteries should be considered for replacement of combustion engines.

Fuel cells and batteries can be used to build full electric vehicles and thus provide pure electrification solutions for different mass and usage segments of automotive application. Battery powered EVs based on lithium ion technology will be limited to small-vehicle low-mileage-per-day applications which is due to the low specific energy and long charging times. The required 300 mile range has been reached with hydrogen fuel cell vehicles and the latter have also been proven to be able to operate in all climates. Nevertheless, the costs of the Pt-based catalysts needed in a fuel cell are too high, the hydrogen infrastructure is not present, and cost-effective renewable sources of primary energy are not yet efficiently used. Drastic decreases in the amount of Pt used are required which is put into practice via a number of strategies currently under development [39].

A very promising approach to energy conversion in electric vehicles is the use of metal-air batteries, for example, Li-air systems. As was discussed in the earlier section, the metal-air battery combines fuel cells with batteries. In the latter example, substitution of the conventional lithium intercalation cathode with an air cathode is projected to increase the cathode specific capacity by a factor of  $\sim 3.5$ . Additionally, the concept of Li-air systems has another major advantage; it can drastically decrease the weight of the battery pack. Specifically, for the case of short-range EVs ( $\sim 25$  kWh), the total battery would weigh only  $\sim 40$  kg. For the case of a full-range EV, the projected Li-air battery-pack weight is only 120 kg. This is significantly smaller compared to the minimum weight of 330 kg for a best case Li-ion battery pack. Therefore, the Li-air battery technology would be a very promising and enabling technology for full-range EVs. Li-air batteries give promise of extending the range, but scientists and engineers will have to face

many challenges in order to prove the research in this area effective.

The electrical energy required on board to travel a certain range before refueling is provided by the energy storage/generation system and is determined by the total gross energy consumed minus the energy recovered from regenerative braking ( $Wh_{net}/mile$ ). All loads on board can be major drains of energy since they are powered by the electrical storage/generation system which affects the driving range. Loads that severely affect the driving ranges are heating and cooling devices in the car. The vehicle mass ( $m$ ) including the mass of the powertrain system and of the passengers, the frontal area ( $A$ ), the drag coefficient ( $C_d$ ), and the drive cycle are elements that influence the  $Wh_{net}/mile$  requirement to the electric motor the most. Furthermore, the rolling resistance and the ancillary loads mentioned above have strong influence.

An equation has been developed to correlate the different parameters [40]:

$$\text{Energy required} = a_1 \times m + a_2 \times C_d \times A + a_3$$

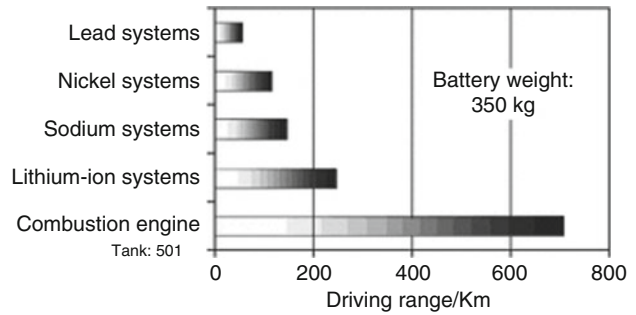
$a_1$ ,  $a_2$ , and  $a_3$  are obtained from modeling results. The model is primarily based on the greenhouse gases, regulated emissions, and energy use in transportation (GREET) software developed by the Argonne National Lab [40]. In Table 2 [39], estimates are listed that start from a small subcompact car ( $C_d \times A = 0.6 \text{ m}^2$ ) with a total vehicle mass of 1200 kg for which the energy required to drive the Environmental Protection Agency (EPA) city or highway cycle is 138 or 156  $Wh_{net}/mile$ , respectively. The energy required for a van ( $C_d \times A = 1.56 \text{ m}^2$ ) weighing 2500 kg is 283 or 361  $Wh/mile$  for city or highway cycle, respectively. The energy requirement for driving in the city is lower because the vehicle has less resistance to overcome at lower speed, electricity generation is more efficient at lower loads, and the use of regenerative braking preserves these advantages for the city cycle [39].

The above given examples show that the range problem is the most severe problem of batteries used to power electric vehicles. Fuel cells have the



### Fuel Cell Comparison to Alternate Technologies,

**Fig. 6** Comparison of the driving ranges for a vehicle powered by various battery systems or a gasoline-powered combustion engine (From Ref. [9])



potential to overcome this issue. On one hand, rather cheap materials are used in Li ion batteries, while on the other hand they require a very large surface area of very finely controlled thin layers, interfaces, and separators. Li ion batteries are already mass produced for use in portable electronic devices and thus, many of the opportunities for cost reduction through scale have already been taken. Nowadays, the development and implementation of improved materials must be the way to further reduce costs.

In fuel cells, however, more expensive materials are employed even though their amount can be tremendously reduced. The total geometric surface area of the cells shows a 30-fold decrease due to higher current densities obtained with more conductive fuel cell electrolytes. Fuel cells can be built in a bipolar construction with cells stacked in series with the negative current collector of one cell serving as the positive current collector of the adjacent cell. Fuel cells require a hydrogen tank and an air compressor which makes their balance of plant more complex.

Strong investment is necessary to develop EVs based on the concept of electromobility. The advantages of all available energy conversion and storage technologies need to be utilized in order to achieve efficient full vehicle electrification. It is very likely that both battery and fuel cell technologies will be developed for automotive application, since batteries are well suited for the use in small short-range vehicles and fuel cells are able to deliver electric power for long-range vehicles. Super capacitors can aid with their high power density output whenever it is needed, for example, for regenerative braking and acceleration. Photovoltaics integrated in the EV can

convert the solar energy and charge the batteries. The main point is that until now no single technology shows the potential to monopolize the implementation into an electrical vehicle. For fuel cells specifically, research needs to focus into identifying novel catalyst materials that can reduce the amount of expensive catalysts currently used (e.g., Pt). Additionally, it faces lot of challenges in the areas of hydrogen production, storage, infrastructure development, transportation, and cost. Hence, fuel cell technologies based on alternative fuels other than hydrogen need to be developed. For all suited energy technologies applicable in EVs, the key challenge is their smart combination in order to build long-range vehicles which produce less greenhouse gas emissions than cars powered by combustion engines.

### Future Directions

In summary, even though the world is becoming aware of an upcoming energy crisis, according to all statistical data currently available, most of the worldwide energy demand is still delivered via fossil fuels, while renewables unfortunately still account only for a small part. It is a fact that use of fossil fuels results in greenhouse gas emissions to the atmosphere. For this reason, the industrialized states, under the Kyoto protocol, have committed themselves to reduce their greenhouse gas emissions by a total of 5% in the period of 2008–2012 compared to 1990.

Most of the CO<sub>2</sub> emitted is a result of the inefficient conversion and distribution systems that we use. The current system efficiencies for energy

**Fuel Cell Comparison to Alternate Technologies, Table 2** Electrical energy required as a function of the vehicle type and mass (analysis assumes 70% recovery of braking energy through regenerative braking)

	Vehicle type Mass (kg) <sup>a</sup>	$C_d \times A$ (m <sup>2</sup> )	City (Wh <sub>net</sub> /mile)	Highway (Wh <sub>net</sub> /mile)
Subcompact	1200 (2)	0.60	138	156
Compact car	1400 (4)	0.64	154	171
Midsize car	1550 (4)	0.67	166	183
Full-size car	1700 (5)	0.71	178	194
Minivan	2200 (7)	0.93	224	250
Van	2500 (8)	1.56	283	361

Taken from Ref. [39]

<sup>a</sup>The mass includes 65 kg passengers weight shown in parentheses

conversion and distribution allow approximately only 30% of the primary energy to be delivered as usable energy. If we manage to increase the system efficiency, CO<sub>2</sub> emissions will be reduced drastically. Therefore, there is the urgent need to develop efficient energy conversion and distribution systems that emit either no or very little CO<sub>2</sub>. A technology that has the potential to help in the reduction of CO<sub>2</sub> emissions is fuel cells.

Fuel cells have the potential to efficiently convert chemical energy to electricity. Even though as discussed the concept of fuel cells is not new and research efforts worldwide have been devoted to advance the technology, there are still many ways that need to be covered before bringing them into the market. Some of the key issues related to fuel cells that need to be tackled before even discussing about a broad commercialization of the technology are:

1. Low efficiency at high power densities
2. Use of hydrogen which is only a secondary energy carrier
3. Large amount of noble metal required for widespread applications
4. Cost and availability of Pt which is commonly used as catalyst
5. Durability and lifetime of the system

The first issue is the low efficiencies at high power densities of current fuel cell systems. For example in PEMFCs, typical power densities delivered are  $\sim 1 \text{ W cm}^{-2}$  at 0.7 V operating voltage. That accounts for a voltage efficiency of  $\sim 56\%$  while the overall system efficiency is

even lower. The power output at the high voltage regime is controlled by electrocatalytic properties and suffers from losses attributed mainly to the slow kinetics of the oxygen reduction reaction. In order to achieve a high-power, high-efficiency system, it is necessary to identify and develop highly active catalyst materials that could push the power output to  $\sim 1 \text{ W cm}^{-2}$  at 0.85–0.9 V.

The second issue relates to hydrogen which is the employed fuel for low-temperature fuel cells. The advantage of using hydrogen is that water is the only product. Nonetheless, we need to take into consideration that hydrogen is only a secondary energy carrier which is not freely available and is currently produced by “nonclean” methods, for example, reforming of natural gas. Hydrogen can be produced by regenerative sources but those suffer from low efficiencies. It would be beneficial to fabricate systems that can directly convert alternative fuels such as bioderived alcohols which have higher energy densities and can be produced efficiently. Direct methanol fuel cells are a starting point but at their current status not a satisfying solution. Bioethanol is a very attractive candidate. It can be produced by cellulosic biomass, has high energy density, is nontoxic, and its liquid form allows using the current fuel infrastructure. Research should also aim at identifying highly active catalysts toward ethanol oxidation and electrolytes with low ethanol permeability that will result in designing an efficient system that will directly convert ethanol to electricity.

The last three issues refer to the current material systems used in fuel cells. Pt supported on carbon (Pt/C) is commonly used in PEMFCs as

catalyst and in order to achieve desirable power densities high amounts of noble metal are required. Even though Pt possesses high catalytic activity, it is also associated with limited resources and high price. Efforts to reduce the metal loading and alloy Pt with other inexpensive and more abundant elements, that is, metals, rare earths have shown improvements; however, there is no system found that would lead PEMFCs to a broader commercialization. Carbon is commonly used as support material in several fuel cell systems since it is inexpensive with high electronic conductivity and high availability. Carbon though is the main reason of the low lifetime since it undergoes corrosion. Efforts to nanostructure carbon, that is, nanotubes, nanofibers, have shown only unsubstantial improvements. Pt and C are materials that have been extensively investigated for many years but have not brought fuel cells to the market. Therefore research should focus to identify novel catalyst/support systems that would replace Pt and C.

Two possible future scenarios for stationary electricity production and road traffic can be envisioned. For the first scenario small units (<1 MW) based on SOFC with natural gas, biogas, or ethanol could be implemented. In niche markets, electricity storage could be achieved with electrolysis to produce hydrogen that could subsequently be stored and then used in a fuel cell system. For larger units (>10 MW), SOFCs could be used with natural gas, biogas, carbon from biomass. For the latter, a negative CO<sub>2</sub> effect is possible (electricity will decrease CO<sub>2</sub> concentration in the atmosphere). For the second scenario of road traffic, two options are possible.

City travel could be handled with battery-operated motor bikes and small cars, possibly in combination with a small (1–5 kW) fuel cell. Long-range travel could be achieved with larger vehicles using mid-temperature (200–300 °C) bioethanol fuel cells hybridized with batteries. In both systems, supercapacitors could be employed to handle the high power needs. For both scenarios, all other energy conversion technologies (e.g., solar, wind) can be used in order to convert and subsequently store energy (i.e., battery recharging).

In conclusion, higher targets need to be set for the future and achieved before fuel cells can be a commercially viable technology. There have been numerous efforts to improve fuel cells but all solutions proposed so far are only small steps that address partially only one of the above-mentioned issues. High-risk, high-profit solutions are required that will drastically improve the current fuel cell status and will lead them to their broad commercialization. In fuel cell development, we need to match the available energy source with the application. Hydrogen does not seem to be an option. A direct conversion of an available fuel in a fuel cell would be more desirable. For example, alcohol oxidation at all temperatures and (hydro-) carbons could be used at high temperatures. In all situations, fuel cell research has to acknowledge the fuel problem. Therefore, if one believes that we are close to the end of research for fuel cells and other energy technologies then the reality is different ... we are only at the beginning.

## Bibliography

1. DOE/EIA-0484 (2010) National energy information center, EI-30, U.S. Energy Information Administration, Forrestal Building, Washington, DC 20585
2. Kunze-Liebhäuser J, Stimming U (2009) Electrochemical versus heat engine energy technology: a tribute to Wilhelm Ostwald's visionary statements. *Angew Chem Int Ed* 48:9230–9237
3. Black WZ, Hartley JG (1985) *Thermodynamics*. Harper & Row, New York, pp 339–429
4. Sundar Pethaiah S, Paruthimal Kalaignan G, Sasikumar G, Ulaganathan M, Swaminathan V (2013) Development of nano-catalyzed membrane for PEM fuel cell applications. *J Solid State Electrochem*. <https://doi.org/10.1007/s10008-013-2211-3>
5. Sundar Pethaiah S, Subiantoro A, Stimming U (2013) The application of intermediate temperature fuel cell for auxiliary power unit of the air conditioning system in an electric vehicle. In: 223rd ECS meeting, Toronto
6. Armand M, Tarascon J-M (2008) Building better batteries. *Nature* 45:652–657
7. Kotz R, Carlen M (2000) Principles and applications of electrochemical capacitors. *Electrochim Acta* 45:2483–2498
8. Simon P, Gogotsi Y (2008) Materials for electrochemical capacitors. *Nat Mater* 7:845–854
9. Winter M, Brodd RJ (2004) What are batteries, fuel cells, and supercapacitors? *Chem Rev* 104:4245–4269

- Jacoby M (2010) Rechargeable metal-air batteries. *Chem Eng News* 88:29–31
- Cairns EJ, Albertus P (2010) Batteries for electric and hybrid-electric vehicles. *Annu Rev Chem Biomol Eng* 1:299–320
- Girishkumar G, McCloskey B, Luntz AC, Swanson S, Wilcke W (2010) Lithium-air battery: promise and challenges. *J Phys Chem Lett* 1:2193–2203
- Zhang HM, Zhang Y, Liu ZH, Wang XL (2009) Redox flow battery technology. *Prog Chem* 21:2333–2340
- De Leon CP, Frias-Ferrer A, Gonzalez-Garcia J, Szanto DA, Walsh FC (2006) Redox flow cells for energy conversion. *J Power Sources* 160:716–732
- Weber AZ, Mench MM, Meyers JP et al (2011) Redox flow batteries: a review. *J Appl Electrochem* 41: 1137–1164
- Ponce de Leon C, Friasferrer A, Gonzalezgarcia J et al (2006) Redox flow cells for energy conversion. *J Power Sources* 160:716–732
- Skyllas-Kazacos M, Grossmith F (1987) Efficient vanadium redox flow cell. *J Electrochem Soc* 134: 2950–2954
- Friedl J, Bauer C, Rinaldi A, Stimming U (2013) Electron transfer kinetics of the VO<sub>2</sub><sup>+</sup>/VO<sub>2</sub><sup>+</sup> reaction on multi-walled carbon nanotubes. *Carbon* 63:228–239
- Li L, Kim S, Wang W et al (2010) A stable vanadium redox-flow battery with high energy density for large-scale energy storage. *Adv Energy Mater* 1: 394–400
- Skyllas-Kazacos M, Chakrabarti MH, Hajimolana SA et al (2011) Progress in flow battery research and development. *J Electrochem Soc* 158:R55–R79
- Zhang M, Moore M, Watson JS et al (2012) Capital cost sensitivity analysis of an all-vanadium redox-flow battery. *J Electrochem Soc* 159:A1183–A1188
- Cluzel VC, Dougles C (2012) Final Report for the Committee on Climate Change. Cost and performance of EV batteries. Cambridge
- Chmiola J, Yushin G, Gogotsi Y, Portet C, Simon P, Taberna PL (2006) Anomalous increase in carbon capacitance at pore sizes less than 1 nanometer. *Science* 313:1760–1763
- Lee SW, Yabuuchi N, Gallant BM, Chen S, Kim B-S, Hammond PT, Shao-Horn Y (2010) High-power lithium batteries from functionalized carbon-nanotube electrodes. *Nat Nanotechnol* 5:531–537
- Gerischer H, Tributsch H (1968) Electrochemical studies on the spectral sensitization of ZnO single crystals *Ber unsenges. Phys Chem* 72:437–445
- Hauffe K, Danzmann HJ, Pusch H, Range J, Volz H (1970) New experiments on the sensitization of zinc oxide by means of the electrochemical cell technique. *J Electrochem Soc* 117:993–999
- Myamlin VA, Pleskov YV (1967) *Electrochemistry of semiconductors*. Plenum, New York
- Gratzel M (2003) Applied physics: solar cells to dye for. *Nature* 421:586–587
- Gratzel M (2004) Conversion of sunlight to electric power by nanocrystalline dye-sensitized solar cells. *J Photochem Photobiol A* 164:3–14
- Hagfeldt A, Gratzel M (1995) Light-induced redox reactions in nanocrystalline systems. *Chem Rev* 95: 49–68
- Hagfeldt A, Gratzel M (2000) Molecular photovoltaics. *Acc Chem Res* 33:269–277
- Ellis AB, Kaiser SW, Wrighton MS (1976) Visible light to electrical energy conversion. Stable cadmium sulfide and cadmium selenide photoelectrodes in aqueous electrolytes. *J Am Chem Soc* 98:1635–1637
- Ellis AB, Bolts JM, Wrighton MS (1977) Characterization of n-type semiconducting indium phosphide photoelectrodes. *J Electrochem Soc* 124:1603–1607
- Hodes G, Manassen J, Cahen D (1976) Photoelectrochemical energy conversion and storage using polycrystalline chalcogenide electrodes. *Nature* 261:403–404
- Miller B, Heller A (1976) Semiconductor liquid junction solar cells based on anodic sulfide films. *Nature* 262:680–681
- Wurfel U, Peters M, Hinsch A (2008) Detailed experimental and theoretical investigation of the electron transport in a dye solar cell by means of a three-electrode configuration. *J Phys Chem C* 112: 1711–1720
- Chen C, Wang M, Li J, Pootrakulchote N, Alibabaei L, Ngoc-le C, Decoppet J-D, Tsai J-H, Grätzel C, C-G W, Zakeeruddin SM, Grätzel M (2009) Highly efficient light-harvesting ruthenium sensitizer for thin-film dye-sensitized solar cells. *ACS Nano* 3:3103
- Gratzel M (2007) Photovoltaic and photoelectrochemical conversion of solar energy. *Philos Trans R Soc A* 365:993–1005
- Wagner FT, Lakshmanan B, Mathias MF (2010) Electrochemistry and the future of the automobile. *J Phys Chem Lett* 1:2204–2219
- Wang MQ (2007) Greenhouse gases, regulated emissions, and energy use in transportation (GREET). The Argonne National Laboratory, Argonne. [www.transportation.anl.gov/modeling\\_simulation/GREET/index.html](http://www.transportation.anl.gov/modeling_simulation/GREET/index.html)



## Fuel Cell Systems: Total Cost of Ownership

Max Wei<sup>1</sup>, Ahmad Mayyas<sup>2</sup>, Timothy E. Lipman<sup>3</sup>, Hanna Breunig<sup>1</sup>, Roberto Scataglini<sup>1</sup>, Shuk Han Chan<sup>4</sup>, Joshua Chien<sup>4</sup>, David Gosselin<sup>4</sup> and Nadir Saggiorato<sup>1</sup>

<sup>1</sup>Sustainable Energy Systems Group, Energy Analysis and Environmental Impacts Department, Environmental Energy Technologies Division, Lawrence Berkeley National Laboratory, Berkeley, CA, USA

<sup>2</sup>Department of Civil Engineering, Transportation Sustainability Research Center, University of California, Berkeley, CA, USA

<sup>3</sup>Transportation Sustainability Research Center, University of California Berkeley, Berkeley, CA, USA

<sup>4</sup>Department of Mechanical Engineering, University of California, Berkeley, CA, USA

### Article Outline

Glossary

Definition of the Subject

Introduction

Modeling Approach

Fuel Cell System Designs and Functional Specifications

Total Cost of Ownership Modeling Results Summary

Future Directions

Bibliography

### Glossary

**Fuel cell** an electrochemical technology that can produce electricity or heat from a cell or a repeating unit that converts chemical energy from a fuel into electricity.

**PEM fuel cell** a type of fuel cell which operates at low temperature (50–100 °C) and has a

polymer electrolyte membrane between the cell anode and cathode.

**SOFC fuel cell** a type of fuel cell (solid oxide fuel cell) that operates at higher temperatures (500–1000 °C) and which has a solid oxide or ceramic electrolyte.

**MEA (membrane electrode assembly) and EEA (electrode electrolyte assembly)** the electrochemical unit cell for PEM and SOFC, respectively, with anode/electrolyte/cathode layer composition specific to each technology.

**Fuel cell stack** a collection of unit fuel cells connected in series form a fuel cell stack.

**Fuel cell system** a fuel cell stack and associated balance of plant components that together make up an entire system.

**Balance of plant** the balance of system components that are needed to form a complete fuel cell system such as electronic components, pumps and compressors, meters and sensors, heat exchange equipment, enclosures, etc. but not including the fuel cell stack itself.

**CHP (combined heat and power)** a form of distributed generation (e.g., internal combustion engine or fuel cell system) that produces both electricity and heating energy at a local site, e.g., at a building or industrial site.

**Criteria air pollutants** six common air pollutants found all over the USA (ground level ozone, carbon monoxide, sulfur dioxide, particulate matter, lead, and nitrogen dioxide). These pollutants can be harmful to human health and the environment and cause property damage. Fuel combustion can be one source of criteria air pollutants.

**Externalities** in this context externalities refer to criteria pollutants and CO<sub>2</sub> that are produced by a power generation source and whose net health and environmental effects may not be reflected in the cost of that generation source.

**Life-cycle cost (LCC) model** an LCC model for a fuel cell system includes capital and installation costs, fuel and operations, stack replacements, and end-of-life costs.

**Life-cycle impact assessment (LCIA) model** an LCIA model provides an estimation

of monetized health and greenhouse gas (GHG) costs from avoided emissions of CO<sub>2</sub> and criteria pollutants during fuel cell system operation, in addition to conventional life-cycle costs.

**Total cost of ownership** the total costs of owning and operating an energy system such as fuel cell CHP system including capital and installation costs, fuel costs, operating and maintenance costs, and ancillary financial costs and benefits such as carbon credits, avoided heating or cooling equipment, valuation of externalities, and any end-of-life equipment or material recovery costs.

**FCS** Fuel cell system.

## Definition of the Subject

Fuel cells are an electrochemical technology that are reaching the market in transportation and are a growing market in stationary power systems for backup power, primary power, combined heat and power, and materials handling equipment.

The first part of this entry describes the manufacturing cost reductions from PEM and SOFC technologies that are estimated from higher-volume fuel cell manufacturing from economies of scale and improvements in overall yield.

Fuel cells combined heat and power systems have the capability to displace grid electricity and on-site fuel combustion. In general CHP systems can be used in industrial and commercial building applications. This work focuses on FC CHP in commercial building applications.

Depending on the building application and location, the FCS can result in lower CO<sub>2</sub> and criteria emissions, and this can lead to better societal outcomes in human health and the environment.

This second part of this entry describes the treatment of total cost of ownership for fuel cell systems illustrating the valuation of these externality benefits in different cities in the USA and how they can reduce the TCO of these systems.

This entry highlights the importance of including externalities in overall societal cost calculations in cleaner forms of energy supply systems and should be included in policy discussions for fuel cell systems that comprehend overall both public and private costs and benefits.

## Introduction

As the world moves toward a more carbon-constrained economy, a better understanding of the costs and benefits of “cleaner” technology options such as fuel cells is critically needed as industry and governments make research, development, and deployment funding decisions and as organizations and individuals make long-term investment decisions. In addition to automotive applications, fuel cell systems are also being considered for a range of stationary and specialty transport applications due to their ability to provide reliable power with clean direct emissions. Existing and emerging applications include primary and backup power, combined heat and power [1], auxiliary power applications in shipping and trucking, and material handling applications such as forklifts and pallet trucks.

As an electrochemical energy-conversion process, fuel cells have intrinsically higher efficiency and much lower criteria pollutant emissions than coal or gas combustion-based plants. Current fuel cell applications range between automotive, residential, and commercial applications. Unlike automotive applications, stationary applications of the fuel cells are also less constrained to the weight and size limitations of vehicles. Fuel cells can serve as a reliable source of baseload power in comparison to variable wind or solar photovoltaic supply sources. If fuel cells become more widely deployed, they could improve public health outcomes due to the reduction air pollutants such as SO<sub>x</sub> and fine particulate matter from traditional coal-based power plants. Fuel cell systems can also be used as distributed generation systems with supplying power close to load, where they avoid transmission line construction or line losses. Natural gas supplied fuel cell systems result in lower overall CO<sub>2</sub> emissions than the average US grid emissions.

Fuel cells offer a promising role in addressing energy security and carbon emissions due to their efficient energy conversion processes and clean emission profiles in comparison with fossil fuel combustion-based systems [2, 3]. In particular, CHP fuel cell systems are potentially attractive applications from both an economic and



environment standpoint due to their ability to produce both power and useful heat on-site, thus augmenting any additional heat needed to meet heating demands [4]. Low-temperature polymer electrolyte membrane (PEM) fuel cells and solid oxide fuel cells (SOFC) are the primary fuel cell technologies considered here. Solid oxide fuel cells (SOFC) are ceramic-based electrolyte fuel cells that operate between 600 °C and 1000 °C. They are of particular interest in the CHP applications due to their high fuel-to-power conversion efficiency and the high quality waste heat produced [5].

Despite the numerous advantages over conventional and alternative power generation sources, fuel cells are not yet manufactured in high volumes. One main adoption barrier is the high capital costs of fuel cells [6]. Over the last decade, the Department of Energy (DOE) has supported several cost analysis studies for fuel cell systems for both automotive [7–9] and nonautomotive systems [10–13]. Most all of these studies primarily focus on the manufacturing costs associated with fuel cell system production.

This entry expands the scope and modeling capability from existing direct manufacturing cost modeling in order to quantify more fully the broader economic benefits of fuel cell CHP systems by taking into account life-cycle assessment, air pollutant impacts, and policy incentives. TCO modeling becomes important in a carbon-constrained economy and in a context where health and environmental impacts are increasingly valued.

From the perspective of the CHP system operator and owner, direct or private costs are associated with equipment costs, operations and maintenance and fuel costs, end-of-life recycling, and potential reduced costs for building operation. The key point here is that private (or direct costs) alone are not the full picture and that including both private costs and public or societal costs (e.g., health and environmental externalities and carbon credits) using a total cost of ownership framework provides a more complete assessment of overall costs and benefits. This entry in turn can be valuable input for a more comprehensive formulation of environmentally friendly technology deployment programs and policies (e.g.,

standards, incentives, education and training programs, etc.).

This entry addresses some key barriers to greater deployment of stationary fuel cell systems (FCS): high capital and installation costs with a failure to address reductions in externalized costs and the fact that potential policy and incentive programs may not value fuel cell (FC) total benefits. The model considers fuel cell systems ranging from 10 to 250 kW<sub>e</sub> of net electrical power for PEM and SOFC combined heat and power (CHP) systems and various annual production rates (100 to 50,000 systems per year) to estimate the direct manufacturing costs for key fuel cell stack components. Sensitivity analysis is then performed to gain insight into the impacts of manufacturing parameters on fuel cell stack costs.

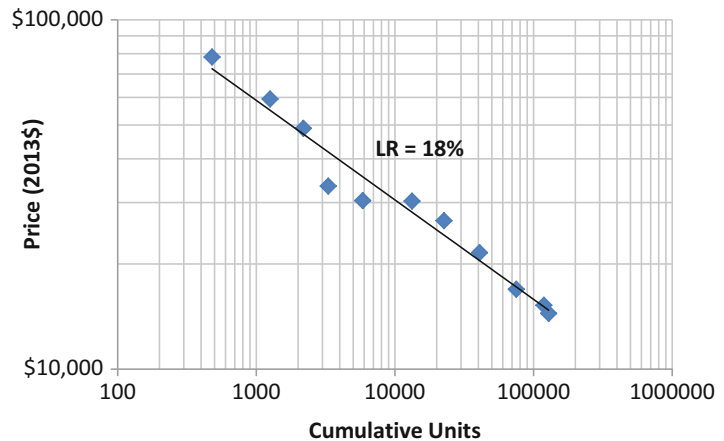
### Fuel Cell Markets

Globally, fuel cell shipments have grown at 15% by MW and 37% by unit per year from 2009 to 2014, led by the stationary sector which shipped over 80% of the units in 2014 [14]. About two-thirds of MW shipped in 2014 was in Asia, led by Japan, with about 30% of total MW shipped to North America. Solid oxide fuel cell (SOFC) MW shipments have increased from 1.1 MW in 2009 to 32.3 MW in 2014 with molten-carbonate fuel cells (MCFC) growing from 18 to 70 MW. Currently, the transportation market is a very small fraction of the overall fuel cell market, but that may shift if fuel cell vehicles continue to be introduced and are more widely adopted. Toyota introduced a fuel cell passenger vehicle in November 2014 and Honda in March 2016.

Conceptually, fuel cell markets can be thought of as global markets. For example, fuel cell stack produced for vehicles should be available for the vehicles in a global market. Still, there are fuel cell systems which are geared toward specific more local markets. For example, Japan has shipped more than 100,000 micro-CHP units domestically since 2005 with an impressive overall learning rate of 18% from 2005 to 2015 (Fig. 1, where the learning rate is the empirical cost reduction in system price for every doubling of overall production volume) [15].

### Fuel Cell Systems: Total Cost of Ownership,

**Fig. 1** Observed cost reduction for Japan micro-CHP system cost from 2005 to 2015 with a learning rate of 18% [15]



## Modeling Approach

Modeling the “total cost of ownership” (TCO) of fuel cell systems involves considering capital costs, fuel costs, operating costs, maintenance costs, “end-of-life” valuation of recoverable components and/or materials, valuation of externalities, and comparisons with a baseline or other comparison scenarios. When externalities are included in TCO analysis, both “private” and “total social” costs can be considered to examine the extent to which they diverge and there are unpriced impacts of project implementation. These divergences can create market imperfections that lead to suboptimal social outcomes but in ways that are potentially correctible with appropriate public policies (e.g., applying prices to air and water discharges that create pollution).

In this section the total cost of ownership modeling framework as shown in Fig. 2 is briefly described. More details on each component of the TCO model are presented in subsequent sections of this entry. The TCO model accepts assumptions about the application/size of the fuel cell system, annual manufacturing volume and year, the location of operation, prices, policies, fuel inputs, etc. The TCO model itself consists of three key components:

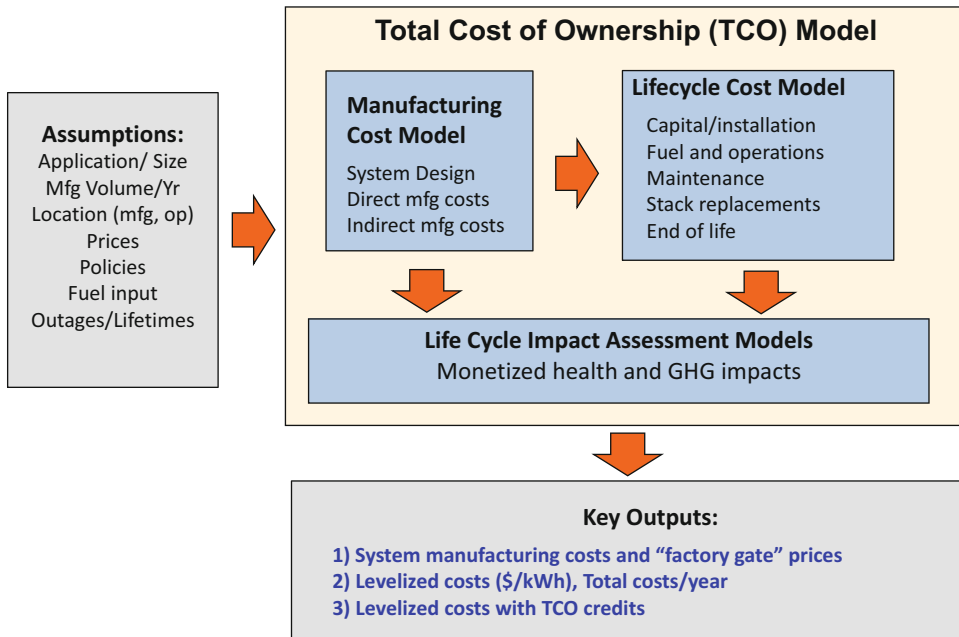
1. A direct manufacturing cost model for direct and indirect manufacturing costs (e.g., administrative costs)
2. A life-cycle cost (LCC) model which includes capital and installation costs, fuel and operations, stack replacements, and end-of-life costs
3. A life-cycle impact assessment (LCIA) model that provides an estimation of monetized health and greenhouse gas (GHG) costs from avoided emissions of CO<sub>2</sub> and criteria pollutants

Key outputs of the model include system manufacturing costs, levelized costs of power and total direct costs per year for operation, and TCO costs including broader social costs. Note however that the intent and scope of this entry is not an optimization of the fuel cell design or CHP sizing for a given commercial application but rather an illustration of the valuation of externalities.

### Direct Cost Modeling Approach for Stack

This section describes the direct manufacturing cost model, which provides bottom-up costing of fuel cell stack components. Some key aspects of this modeling are shown in Fig. 3. The first step is to define the fuel cell configuration and functional specifications. Next, literature reviews and industry inputs are used to obtain functional and operational stack and system parameters referred to here as functional specifications. The system configuration and functional specifications define the system type, system size, key subsystems and system components, FC stack features, and stack and system performance specifications. These





**Fuel Cell Systems: Total Cost of Ownership, Fig. 2** Total cost of ownership modeling framework

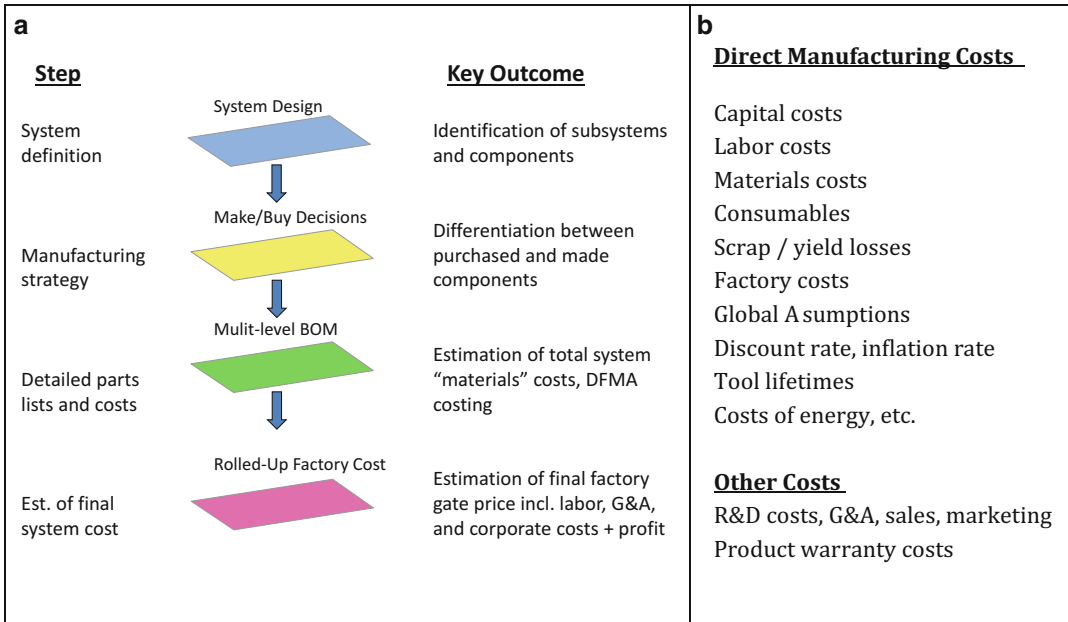
form the basis for direct manufacturing cost modeling which includes capital costs, labor costs, materials costs and consumables, scrap/yield losses, and factory building costs subject to global assumptions such as discount rate, inflation rate, and tool lifetimes. Note that process modeling or optimization of the stack design from a detailed thermodynamic and thermo-chemical point of view is not the focus of this entry. Rather, a “medium fidelity” design, based on feedback from industry advisors, is used to be representative of actual fuel cell systems.

The bottom-up or design for manufacturing and assembly (DFMA is a registered trademark of Boothroyd Dewhurst, Inc. and is the combination of the design of manufacturing processes and design of assembly processes for ease of manufacturing and assembly and cost reduction. It also refers to bottom-up cost modeling, and it is that usage that is used here.) analysis includes the following items shown in Fig. 3b for direct manufacturing costs, global cost assumptions, and other non-product costs. For each manufactured component, first a patent and literature search was done and industry advisor input elicited, followed by selection of a base

manufacturing process flow based on these inputs, an assessment of current industry tooling and direction, and engineering judgment as to which process flows can support high-volume manufacturing in the future.

Balance of plant or nonfuel cell stack components such as compressors, tubing, and power electronics is largely assumed to be purchased components, and stack components are largely manufactured in-house, with carbon fiber paper and Nafion® membrane, the key exceptions for reasons as described below. Vertical integration is assumed for stack manufacturing, i.e., a fuel cell manufacturer is assumed to manufacture all stack components as described below. This assumption is geared toward the case of high-volume production. At lower production volume, some purchase of finished or partially finished stack components may be cost beneficial because at very low volumes, the investment costs for vertical integration are prohibitive and equipment utilization is inefficient.

Overall manufacturing costs are then quoted as the sum of all module or component costs normalized to the overall production



**Fuel Cell Systems: Total Cost of Ownership, Fig. 3** (a) Generalized roll-up steps for total system cost; (b) scope of direct manufacturing costs for components produced in-house (Wei et al. [2])

volume in kWe. Direct manufacturing costs are quoted in cost per kWe of production and are often quoted in cost per meter squared of material for roll-to-roll goods such as GDL and catalyst-coated membrane. Global costing assumptions include discount rate, inflation rate, tool lifetimes, and costs of energy (e.g., electricity and fuel). Direct manufacturing costs are quoted as the sum of fuel cell stack component manufacturing and balance of plant components. A further corporate markup will include nonmanufacturing costs such as general and administrative, sales and marketing, research and development costs, and profit margin to determine the final "factory gate" price to the customer. The installed price to the customer will also need to take into account installation costs and any other fees (e.g., permits, inspections, insurance, service contracts, etc.). Delivery/installation costs for CHP systems are expected to be highly site and project specific. The focus of this entry is on direct manufacturing costs and does not provide a detailed analysis for corporate markups or installation costs.

### Manufacturing Cost Analysis: Shared Parameters

Shared parameters for the cost analysis are summarized in this section, with manufacturing cost shared parameters summarized in Table 1. References are shown in the table and are a mixture of general industry numbers (e.g., annual operating days, inflation rate, tool lifetime) together with fuel cell-specific industry assumptions (discount rate, web width, hourly wage).

An annualized cost of tool approach is adopted from Haberl [16]. The annualized cost equation and components are as follows:

$$C_y = C_c + C_r + C_{oc} + C_p + C_{br} + C_i + C_m - C_s - C_{int} - C_{dep} \quad (1)$$

where

$C_y$  is the total annualized cost

$C_c$  is the capital/system cost (with interest)

$C_r$  is the replacements or disposal cost

$C_{oc}$  is the operating costs (e.g., electricity) excluding labor

$C_p$  is the property tax cost

$C_{br}$  is the building or floor space cost

**Fuel Cell Systems: Total Cost of Ownership, Table 1** General manufacturing cost parameters [3]

Parameter	Symbol	Value	Units	Comments
Operating hours	$t_{hs}$	Varies	Hours	8 h base shift; (2–3 shifts per day)
Annual operating days	$t_{dy}$	240	Days	52 weeks*5 days/week, 10 vacation days, 10 holidays
Avg. inflation rate	$j$	0.023		US average for past 10 years <sup>a</sup>
Avg. mortgage rate	$j_m$	0.051		Trading economics <sup>b</sup>
Discount rate	$j_d$	0.10		
Energy inflation rate	$j_e$	0.056		US average for last 3 years <sup>a</sup>
Income tax	$i_i$	0		No net income
Property tax	$i_p$	0.01035		US average <sup>c</sup>
EOL salvage value	$k_{eol}$	0.02		Assume 2% of end-of-life value
Tool lifetime	$T_t$	15	Years	Typical value in practice
Energy tax credits	$ITC$	0	Dollars	
Energy cost	$c_e$	0.10	\$ kWh <sup>-1</sup>	Typical US value
Floor space cost	$c_{fs}$	1291	\$ m <sup>-2</sup>	US average for factory <sup>d</sup>
Building depreciation	$j_{br}$	0.031		US Department of Commerce <sup>e</sup>
Building recovery	$T_{br}$	31	Years	US Department of Commerce <sup>e</sup>
Hourly labor cost	$c_{labor}$	30	\$ hr <sup>-1</sup>	Hourly wage per worker

<sup>a</sup>Forecast-Chart, <http://www.forecast-chart.com/forecast-inflation-rate.html>, 2015

<sup>b</sup>Trading Economics, <http://www.tradingeconomics.com/united-states/mortgage-rate>, 2015

<sup>c</sup>Tax-rates.org, <http://www.tax-rates.org/taxtables/property-tax-by-state>, 2015

<sup>d</sup>RSMeans, <http://learn.rsmeans.com/rsmeans/models/factory2/>, 2017

<sup>e</sup>US Department of Commerce, Bureau of Economic Analysis, <https://www.bea.gov/>, 2015

$C_i$  is the tool insurance cost

$C_m$  is the maintenance cost

$C_s$  is the end-of-life salvage value

$C_{int}$  is the deduction from income tax

$C_{dep}$  is the deduction due to tool depreciation

In the current version of the model  $C_r$ , the replacements or disposal cost and  $C_i$ , the tool insurance cost, are assumed to be zero. No net income for fuel cell manufacturers is assumed, as is currently the case for PEM manufacturers and thus income tax credits such as interest tax credits do not factor into the calculations below.

Factory area is incorporated by incrementally adding factory area to each specific process module. In general, factory cost contributions are found to be very small factors, especially as production volumes exceed 1000 systems per year.

The cost analysis utilizes largely existing manufacturing equipment technologies and existing materials with key exceptions to be noted (e.g., injection molding composite material for bipolar plates). It does not assume new high-speed manufacturing processes nor major fuel cell technology advances such as much lower cost catalysts or membranes, although the

manufacturing readiness of these technologies applied to fuel cell-specific modules was not evaluated. This entry is thus a “potential cost reduction” study for future costs with existing manufacturing technologies and mostly existing materials, and DOE cost targets for 2020 are used as a benchmark comparison for the cost estimates here. This entry assumes that higher overall volumes will drive significant improvements in yield, but it is not a market adoption or market penetration study and therefore timelines will vary according to the assumptions made for market adoption. Stationary fuel cell systems may also benefit from growth in the transportation sector and higher volumes achieved for fuel cell components in that sector over the next few years may reduce the cost of components for stationary applications (e.g., GDL, membranes, metal plates, etc.).

**PEM Balance of Plant Cost Analysis Approach**

The general approach for balance of plant costing is a cost of component costing analysis based on the system designs shown below and using information from existing fuel cell systems, industry advisors, and various FCS specification sheets for data

sources. Balance of plant components as mentioned above is assumed to be primarily purchased components.

Methods of determining the representative components found in systems models range from inspection of existing stationary fuel cell systems, information gathered through surveys of industry members, discussions and price quotes with component vendors, and utilization of components used for common but similar functions in other applications.

### Life-Cycle Cost Modeling

Life-cycle cost modeling or use-phase modeling is defined as the costs associated with the ownership and operational phase of the fuel cell system when it is functioning in the field as a CHP system. For most stationary power applications, the use-phase is the most demanding phase among LCIA phases in terms of energy and cost and has the greatest GHG impact among all phases [2]. Figure 4 shows the sequence of steps in developing the use-phase model. The current use-phase model is developed for a CHP system operating on reformat fuel produced from natural gas input fuel, with the reforming process assumed to be on-site. GHG emission analysis is based on the emissions associated with the reforming process and does not include fuel extraction and transportation.

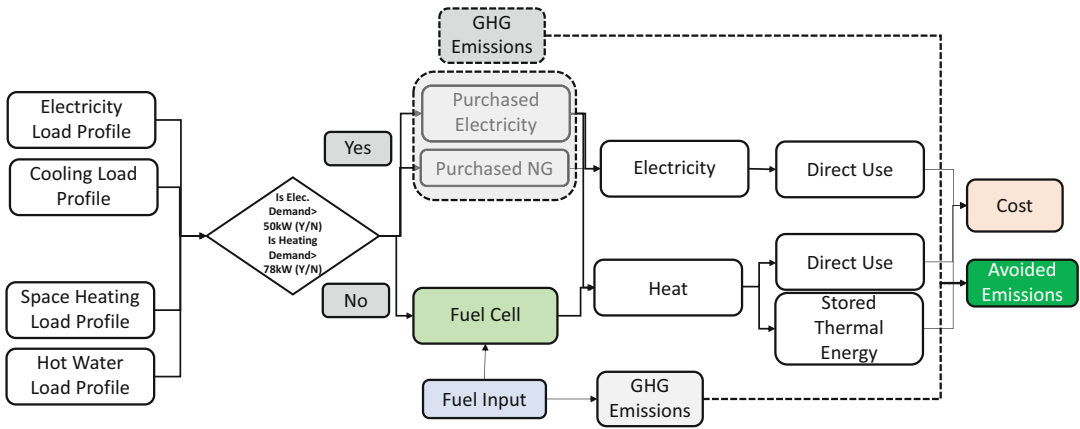
Figure 4 shows the life-cycle cost (or use-phase) modeling elements for the example of a 50 kW PEM FC combined heat and power (CHP) system. This model has four inputs: electricity demand excluding cooling loads, electricity demand for space cooling using traditional electrically driven vapor compression air conditioners, hot water heating demand, and space heating demand as a function of time, as recorded in daily load curves for 3 different days per month (weekday, weekend, and peak day). These load shapes are collected from an NREL modeling simulation [17]. The operating mode of this system will follow the total electricity load (sum of “non-cooling electricity load” and “electricity for cooling load”), so that the fuel cell system will cover all of the electrical demand at any time when total electricity demand is less than or equal to 50 kWe; however, if the total demand

exceeds fuel cell capacity (i.e., total electricity loads >50 kWe), then the system will cover the 50 kWe maximum level and the remaining will be purchased directly from the grid. Similar logic is used for heating demand. The costs of operation of the fuel cell and the purchased grid electricity and fuel for supplementary on-site heating can then be calculated in addition to the greenhouse gas (GHG) emissions associated with the fuel cell operation and those from the electricity grid and on-site combustion of any fuels.

In general, building types with relative high fraction of heat loads relative to overall on-site energy consumption are favorable to CHP systems. In this entry small hotels in five cities are used as building examples. Building load shapes are drawn from five cities representing different climate zones in the USA (New York, Chicago, Minneapolis, Houston, and Phoenix). Utility tariffs are drawn from the OpenEI database ([http://en.openei.org/wiki/Utility\\_Rate\\_Database](http://en.openei.org/wiki/Utility_Rate_Database)) of national utility rates and include electricity rates in \$/kWh, demand charges (\$/kWe (max) per month), and other fixed charges. Natural gas fuel prices are based on the average state commercial price of gas from 2011 to 2014 for each location, since prices are variable and a point estimate for prices may be misleading.

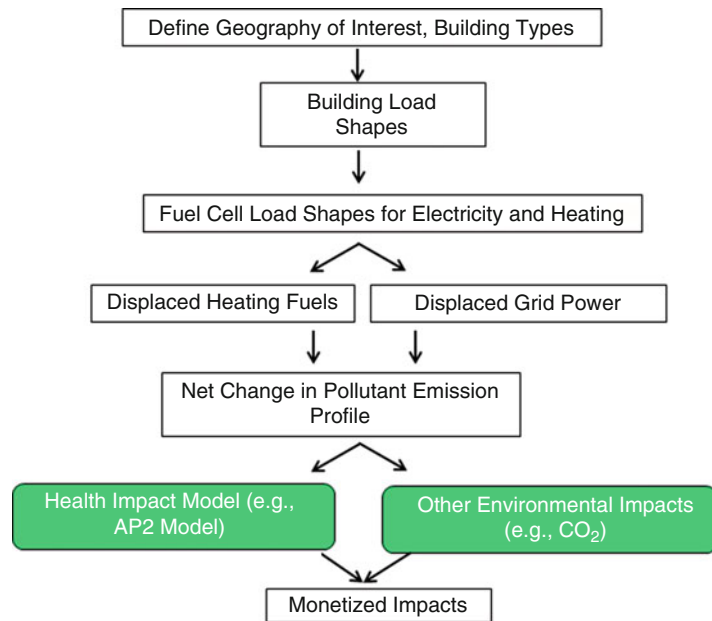
### Life-Cycle Impact Assessment Modeling

Figure 5 shows the elements of the life-cycle impact assessment (LCIA) model to quantify the environmental and human health impacts and/or benefits attributable to the use of fuel cell systems in commercial buildings. The model provides spatial resolution at the state level for electricity generation impacts and at the county level for on-site fuel consumption. The motivation for the development and application of this model is the need to assess the cost of health and environmental externalities associated with fuel cells. The use of fuel cells can impose impacts that arise from the manufacturing of the cells, the extraction of raw materials for manufacturing, fuel cell operation, and the production of energy for manufacturing, transportation, and servicing of the cell [18]. The



**Fuel Cell Systems: Total Cost of Ownership, Fig. 4** Fuel cell system life-cycle cost modeling for a combined heat and power fuel cell system [2]

**Fuel Cell Systems: Total Cost of Ownership, Fig. 5** Life-cycle impact assessment for environmental and health externalities [2]



impact assessment characterizes the use-phase of the fuel cell system. The use of on-site fuel cells will also offset the production of electricity in the region where the cells supply power. Fuel cell-based CHP can also offset on-site criteria pollutant emissions due to the combustion of heating fuel. This offset or net change in emissions can have health benefits that will depend on the sources of electricity in a region and the impacts associated with that electricity production.

Commercial building surveys [19] are used to estimate the mix of heating fuel types by region that is displaced by the FCS. Externalities to be valued include morbidity, mortality, impaired visibility, recreational disruptions, material damages, agricultural and timber damages, and global warming.

In this approach, a fuel cell system in a given building displaces some fraction of building electricity demand that otherwise would be purchased from the grid and some fraction of heating

demand fuel, as described in the LCC modeling section above. From this, the displaced heating fuels and displaced grid power are computed, and together with the criteria emission factors of the grid, heating fuels and the FCS, the net change in pollutant emissions is derived. Valuation of health and environmental externalities for grid-based electricity and on-site fuel consumption are calculated according to the input parameters in Table 2. Total damages or externality damages for each criteria pollutant from grid electricity, on-site heating fuel from conventional heating, and the fuel cell system are then given by

$$\begin{aligned} & \text{Health and environmental externality valuation} \\ & \text{for pollutant } i \left( \frac{\$}{MWh} \right) \text{ from grid electricity} \\ & = MEF_i^* MBA_i = \frac{\text{Ton of pollutant } i^*}{MWh(el)} \frac{\$}{\text{Ton of pollutant } i} \end{aligned} \quad (2)$$

$$\begin{aligned} & \text{Health and environmental externality} \\ & \text{valuation for pollutant } i \left( \frac{\$}{MWh} \right) \\ & \text{from heating fuel} = MEF_i^* MBA_i \\ & = \frac{\text{Ton of pollutant } i^*}{MWh(\text{thermal})} \frac{\$}{\text{Ton of pollutant } i} \end{aligned} \quad (3)$$

$$\begin{aligned} & \text{Health and environmental externality valuation} \\ & \text{for pollutant } i \left( \frac{\$}{MWh} \right) \text{ from fuel cell system} \\ & = MEF_i^* MBA_i \\ & = \frac{\text{Ton of pollutant } i^*}{MWh(el)} \frac{\$}{\text{Ton of pollutant } i} \end{aligned} \quad (4)$$

where MEF is the marginal emission factor, MBA is the marginal benefit of abatement, MWh is the quantity of electricity production or thermal energy from heating fuel in units of MWh, and the assumed emission factors and spatial regime and temporal regimes are defined as in Table 2. The externality valuations above can be interpreted as the savings to society per every unit of energy avoided from each respective source (the grid, heating fuel, or the fuel cell system). Note that electricity emissions are assumed to be stack-height level, i.e., above ground level for air-mixing purposes, and that the spatial regimes varies across the four factors. Electricity MEFs are taken from eGRID subregional factors (eGRID 2015), electricity and fuel MBAs are given by the AP2 model [20], and fuel MEFs are given by the EIA and

**Fuel Cell Systems: Total Cost of Ownership, Table 2** LCIA impact assessment calculations assumptions. LCIA modeling for health/environmental valuation includes both displaced electricity and displaced on-site fuel

Type	Item	Units	Assumed source of emissions	Spatial regime	Temporal regime	Reference
Electricity from grid	MEF	Tons/MWh	Stack-height level	eGRID subregions	Annual	[21]
	MBA	\$/ton	Stack-height level	State level	Annual	[20]
Fuel for conventional heating	MEF	Tons/MWh	Ground level	Site level	Annual	[22, 23], various
	MBA	\$/ton	Ground level	County level	Annual	[20]
Electricity from fuel cell system	MEF	Tons/MWh	Ground level	Site level	Annual	Various, FCS technology-dependent
	MBA	\$/ton	Ground level	County level	Annual	[20]

*MEF* marginal emission factor, *MBA* marginal benefit of abatement

various sources for fuel combustion equipment. The net externalities valuation (or savings) of

the FCS can then be estimated using the net change in criteria pollutants as below:

---


$$\begin{aligned}
 & \text{Net health and environmental externality savings for pollutant } i \text{ from } FCS \\
 & = \Delta GWh (\text{grid electricity}) * \text{Valuation of grid electricity} \\
 & + \Delta GWh (\text{heating fuel thermal energy}) * \text{Valuation of heating fuel} \\
 & - \text{Valuation from } FCS
 \end{aligned} \tag{5}$$


---

where  $\Delta GWh$  (grid electricity) electricity and  $\Delta GWh$  (heating fuel thermal energy) are the savings in grid electricity and heating fuel, respectively.

This approach provides a greater degree of spatial resolution compared to taking national averages for MBA values, and a comparison of this treatment versus the use of national averages will be addressed in future work.

#### Electricity and Fuel Emission Factors

In this entry, stationary fuel cells provide electricity and heat to commercial buildings in different cities in the USA. Electricity from fuel cells displaces energy and emissions from local electricity grids, comprised of conventional and renewable generators. Over long periods of time (on the order of decades), a large reduction in demand for grid electricity may lead to the retirement of conventional generators. Only short-term displacement is considered and measured using regional marginal emission factors. Marginal emission factors (MEFs) express the avoided carbon dioxide (CO<sub>2</sub>-eq), sulfur dioxide (SO<sub>2</sub>), and nitrogen oxides (NO<sub>x</sub>), emissions from displaced marginal generators. It is difficult to know exactly which generators are operating at the margin, but the set of generators that will be deployed to meet electricity demand during high-demand periods (commonly called peaker plants) can be estimated using dispatch models and historical regressions. Subregional non-baseload emission factors from eGRID (2015) [21] are used for CO<sub>2</sub> (Fig. 6) and criteria emission factors. A second set of estimates based on historical regressions is provided for comparison [24]. Note that there is more than a factor of two between regional CO<sub>2</sub> non-baseload emission rates indicating the high range of

emission factors that exist on the US grid depending on region.

The approach here is to use MEFs for greenhouse gases (GHG) (CO<sub>2</sub>, CH<sub>4</sub>, and N<sub>2</sub>O), NO<sub>x</sub>, and SO<sub>x</sub>. MEFs for direct particulate matter emissions (PM<sub>10</sub> and PM<sub>2.5</sub>) are not included since a dominant portion of PM from electricity generation comes from reactions of SO<sub>x</sub> and NO<sub>x</sub> in the atmosphere. Subregional MEFs for grid-based electricity are shown in Table 3. MEFs for on-site combusted fuels are also shown [22, 23]. Commercial building surveys [19] were utilized to estimate the mix of heating fuel types by region that is displaced by the FCS.

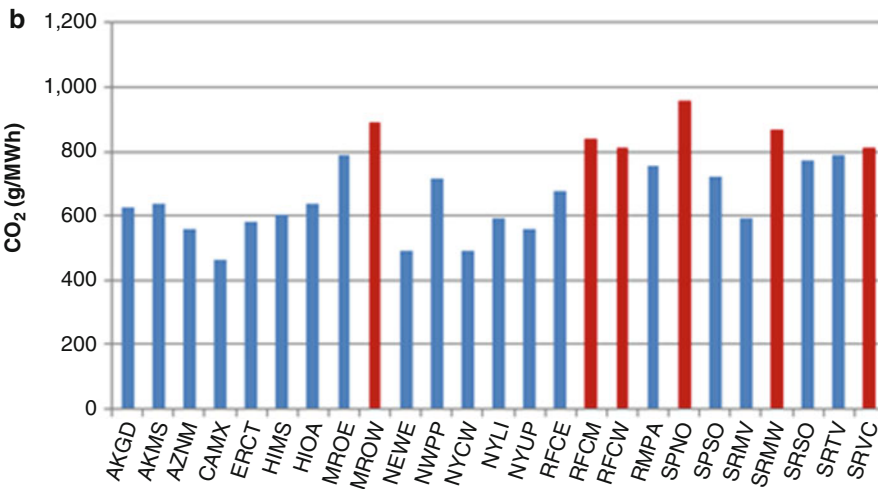
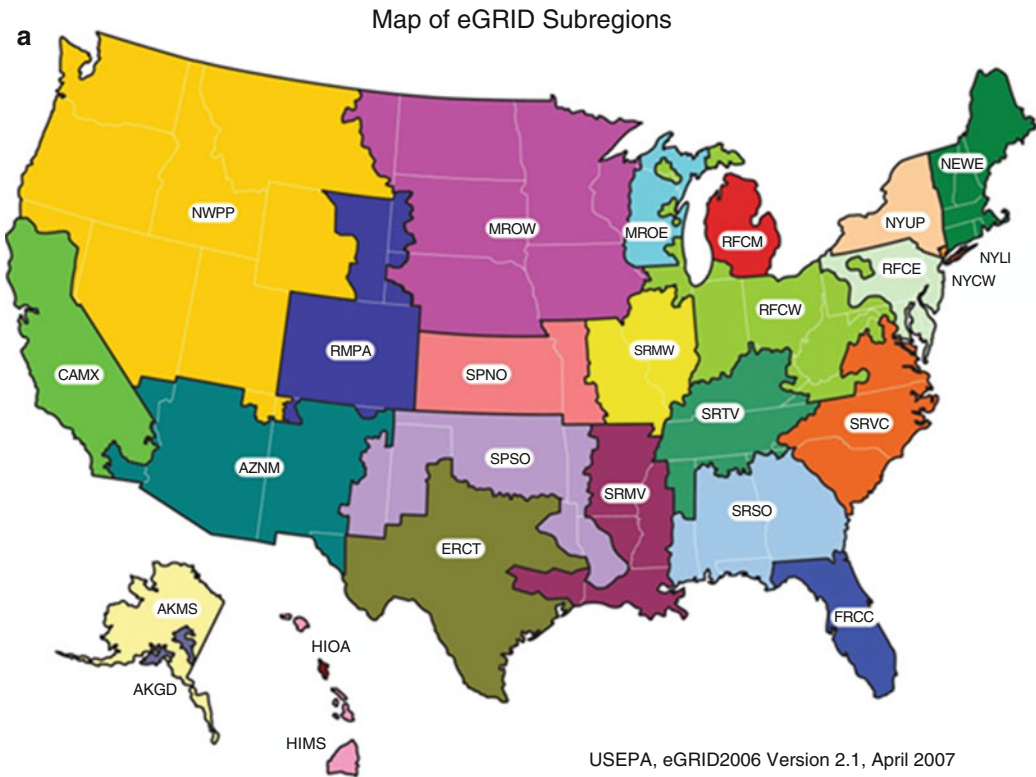
#### AP2 Damage Factors

The benefit of reducing emissions through FCS adoption can be monetized using conversion factors that express marginal benefit of abatement. These factors estimate the damage that a unit of emitted pollutant will cause if released in a specific location, thus explaining their alternative name “damage factors”.

In this entry, a set of damage factors are described and applied in the Air Pollution Emission Experiments and Policy (APEEP) analysis model and its revised version (AP2). Alternatively other studies could be used for damage factors as discussed in a recent dissertation [54].

AP2 monetizes human health and environmental damages associated with SO<sub>2</sub>, volatile organic compounds (VOC), NO<sub>x</sub>, ammonia (NH<sub>3</sub>), fine particulate PM<sub>2.5</sub>, and coarse particulate PM<sub>10</sub> emissions from power plants (The subscript on PM indicates the greatest particle diameter in micrometers that is captured in the particle measurement.) [22] and ground level sources. The idea in APEEP and AP2 is to introduce an





**Fuel Cell Systems: Total Cost of Ownership, Fig. 6** eGRID subregions and non-baseload emission rates by subregion [21]

additional metric ton of pollutant from a specific source and determine the change in national damages. This process is repeated for each pollutant type at about 10,000 sources, generating a set of

marginal damages that are more reliable than an approach based on national averages. Atmospheric chemistry models and air transport models were used to estimate downwind primary and



**Fuel Cell Systems: Total Cost of Ownership, Table 3** Regional marginal emission factors for electricity and emission factors for heating fuels. All emission

factors are from eGRID [21] except for CO<sub>2</sub> emissions from Siler Evans [24] (note that kWh are used as heating fuel units here for natural gas, fuel oil, and propane)

	tCO <sub>2</sub> /kWh	tCO <sub>2</sub> /kWh [24]	tCH <sub>4</sub> /kWh	tN <sub>2</sub> O/kWh	tNO <sub>x</sub> /kWh	tSO <sub>x</sub> /kWh
Electricity (Chicago)	8.13E-04	7.31E-04			7.5E-07	2.6E-06
Electricity (Houston)	5.81E-04	5.27E-04			3.3E-07	9.23E-07
Electricity (Minneapolis)	8.92E-04	8.34E-04			1.15E-06	2.23E-06
Electricity (New York City)	4.91E-04	4.89E-04			2.87E-07	1.23E-08
Electricity (Phoenix)	5.61E-04	4.86E-04			4.69E-07	1.48E-07
Electricity (San Diego)	4.62E-04	4.86E-04			1.6E-07	1.27E-07
Natural gas	1.81E-04		1.71E-08	3.41E-10	1.51E-07	9.21E-10
Fuel oil	2.50E-04		1.02E-08	2.05E-09	3.44E-07	1.73E-06
Propane	2.10E-04		6.82E-12	3.41E-10		

secondary pollution doses. For example, SO<sub>2</sub> forms PM<sub>2.5</sub> (sulfate), and NO is converted to NO<sub>2</sub>, which reacts with VOC to form ozone (O<sub>3</sub>) and PM<sub>2.5</sub> (nitrate). Once the emissions and the resulting pollutants are calculated, human exposures are estimated from a database of county-level receptor populations (humans, materials, crops, timber, etc.). Damage factors were calculated for “ground level”: (less than 250 m off the ground), “medium high” (<500 m), and “tall-smoke stack” sources (>500 m). Concentration-response models are used to convert exposure to physical responses such as morbidity, mortality, visibility impairment, reduced recreation, lower agricultural and timber yields, and material degradation. Finally, economic models convert these physical responses to dollar values. In this entry, the value of a statistical life is assumed to be \$6 million and a social discount rate of 3% is assumed [20]. The implication of these values is that morbidity and mortality are valued more when they occur in younger people than in older people. The total damage from a pollutant emission from a given source is estimated by multiplying the pollutant damage factor with the mass of emitted pollutant. Given the multiple sources of uncertainty in this type of modeling, there is generally a wide range of estimates of health and environmental damages. The scope of this entry does not include a detailed uncertainty analysis of externality damages nor a comparison of outputs of AP2 and other models (see, e.g., [25]).

Marginal benefit of abatement or damage factors are shown in Tables 4 and 5 for ground level and stack-height level emissions, respectively, for the regions of the USA studied.

#### Emissions from Fuel Cells

Direct emission factors reported in recent literature on fuel cells allowed us to determine reasonable EF for CO<sub>2</sub>, CH<sub>4</sub>, N<sub>2</sub>O, CO, NO<sub>x</sub>, SO<sub>x</sub>, PM<sub>10</sub>, and VOC (Table 6). PEM values are based on Colella [26], and SOFC values are from NETL [27] and [1].

Fuel cell emissions are modeled as ground level emissions and were converted to damages using AP2 county ground level damage factors. CO<sub>2</sub>, CH<sub>4</sub>, and N<sub>2</sub>O are converted to CO<sub>2</sub>eq using 100-year GWP factors of 1, 21, and 310, respectively ([http://www.ipcc.ch/publications\\_and\\_data/ar4/wg1/en/ch2s2-10-2.html](http://www.ipcc.ch/publications_and_data/ar4/wg1/en/ch2s2-10-2.html), accessed September 25, 2009).

The total masses of emissions emitted from the fuel cell over a year are calculated by multiplying each EF by the power (P) provided by the fuel cell in our scenarios. Emissions from the fuel cell are modeled as ground level emissions and are converted to damages using AP2 county-specific ground level conversion factors shown in Table 4.

Greenhouse gas emissions were converted to CO<sub>2</sub>eq using a 100-year global warming potential and monetized by assuming a social cost of carbon (SCC), of \$44/tCO<sub>2</sub>eq. Values for the social cost of carbon have been compiled by the

Interagency Working Group on Social Cost of Carbon [28], for use in regulatory analysis. As a base value for additional examination, an intermediate value of \$37/tCO<sub>2</sub> (\$2007) is used and adjusted for inflation to get ~\$44/tCO<sub>2</sub> as an approximate value of the current social cost of carbon.

**Emission Factor Projections with Proposed Clean Power Plan**

The analysis described above provides a snapshot in time of the health and environmental impacts of a fuel cell CHP system for a given year, e.g., for eGRID emission factors for 2012, the most recent year available from the EPA. Of course, the electricity grid is not a static entity in terms of its generation portfolio and emission factors. The proposed EPA Clean Power Plan (The CPP is still being

reviewed in US Court of Appeals but is assumed to be enacted for the purposes of this study. It is unclear at the time of this writing if the CPP will be rolled back in scope or replaced with new legislation. As of April 28, 2017, “the US Court of Appeals for the District of Columbia Circuit this morning granted the White House’s request for pause in litigation on the Clean Power Plan, holding the case in abeyance for 60 days.” (<http://www.utilitydive.com/news/dc-circuit-halts-clean-power-plan-case-in-win-for-trump/441554/>, accessed May 29, 2017.) (CPP) to 2030 if enacted would result in a cleaner grid electricity than that of 2012 [29] and would reduce the health and environmental benefits from fuel cell CHP. The CPP improve emissions from existing coal plants and shift from coal to natural gas and build more renewable sources of electricity. The key objective here is to try to estimate the impact that

**Fuel Cell Systems: Total Cost of Ownership, Table 4** Marginal benefit of abatement for ground level emissions in dollars per metric ton for the six counties in this study (in 2014 dollars). Statistical life value of \$6 million is assumed [20]

City	County	State	Ammonia	Nitrogen oxides	Sulfur dioxide	Volatile Organic compounds	Particulate matter	Particulate matter
			\$/ton NH <sub>3</sub>	\$/ton NO <sub>x</sub>	\$/ton SO <sub>2</sub>	\$/ton VOC	\$/ton PM <sub>2.5</sub>	\$/ton PM <sub>10</sub>
Chicago	Cook	IL	10,497	90,199	169,705	44,959	471,416	18,335
Houston	Harris	TX	11,526	5695	27,349	5151	53,952	5679
Minneapolis	Hennepin	MN	3808	70,544	122,325	30,186	316,990	13,771
New York	New York	NY	102,744	33,935	166,045	71,370	765,320	30,403
Phoenix	Maricopa	AZ	4254	23,003	39,007	10,256	109,293	3005
San Diego	San Diego	CA	16,948	62,821	330,921	32,929	350,036	13,313

**Fuel Cell Systems: Total Cost of Ownership, Table 5** Marginal benefit of abatement for stack-height level emissions in dollars per ton (in 2014 dollars) for the

six states in this study (point sources with height >250 m and <500 m and statistical life value of \$6 million) [20]

State	Ammonia	Nitrogen oxides	Sulfur dioxide	Volatile organic compounds	Particulate matter	Particulate matter
	\$/ton NH <sub>3</sub>	\$/ton NO <sub>x</sub>	\$/ton SO <sub>2</sub>	\$/ton VOC	\$/ton PM <sub>2.5</sub>	\$/ton PM <sub>10</sub>
Arizona	2642	4989	11,142	1250	13,208	469
California	12,462	4005	24,704	3490	37,052	1689
Illinois	5977	9052	27,370	3531	36,767	1213
Minnesota	3090	8252	23,669	2256	23,516	853
New York	42,470	3155	23,705	5792	61,371	2024
Texas	1976	6120	10,448	1621	17,020	594

these changes to the electricity grid would have on the externality benefits of fuel cell CHP.

Table 7 shows estimated CPP impacts to grid electricity carbon intensity and criteria emission intensity. Demands from the AEO2015 base case for 2025 are extrapolated to 2030 and assume a nominal 7% demand reduction from energy efficiency to 2030 demands from the Clean Power Plan in all regions per [30]. CO<sub>2</sub> reductions are taken from mass-based reduction targets in the Clean Power Plan. Note that the regulations for CO<sub>2</sub>, SO<sub>2</sub>, and NO<sub>x</sub> emissions are not the same. The Clean Power Plan regulates CO<sub>2</sub>, and this impacts SO<sub>2</sub> and

NO<sub>x</sub>; but SO<sub>2</sub> and NO<sub>x</sub> have existing regulations with a base emission reduction in tons of 70% and 25%, respectively, in 2025 from 2012 (Mercury and Air Toxics Standards or MATS). Here, it is assumed that the same percentage reduction in MEF from the CPP as the estimated percent reduction in AEF from CPP. For regions where gas is already on the margin, this may be an overestimate, but for regions for which coal is currently on the margin, this may be an underestimate in the percentage reduction.

**Fuel Cell Systems: Total Cost of Ownership, Table 6** Fuel cell emission factors in metric tons per kWh for a PEM FC CHP system with reformat and natural gas fuel input

Pollutant	Emissions in tons/kWhe PEM	Emissions in tons/kWhe SOFC
CO <sub>2</sub>	5.43E-04	3.4E-04
NO <sub>x</sub>	7.5-09	Negligible
SO <sub>x</sub>	Negligible	Negligible
PM <sub>10</sub>	Negligible	Negligible
VOC	Negligible	Negligible
CH <sub>4</sub>	5.6E-07	5.6E-07
CO	1.9E-08	Negligible
N <sub>2</sub> O	6.5E-08	6.5E-08

**Levelized Cost of Electricity with Total Cost of Ownership Credits**

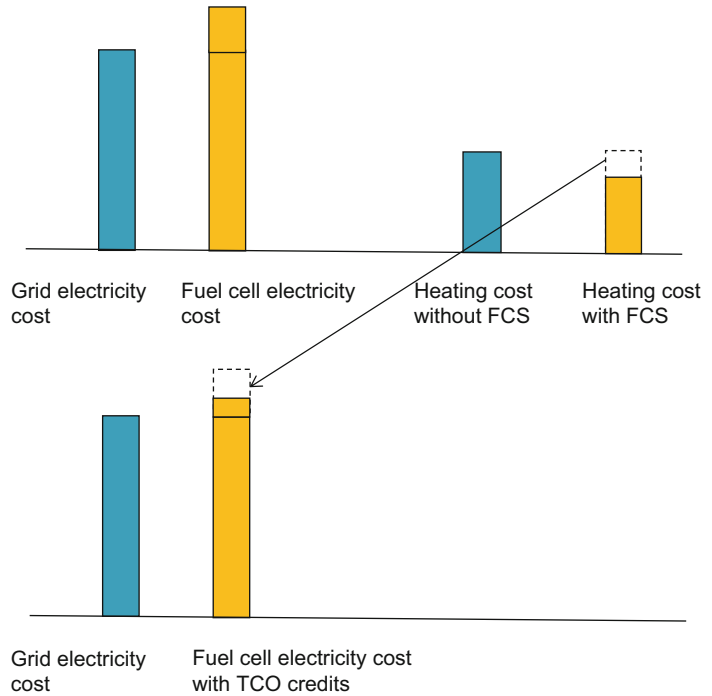
Figure 7 illustrates the conceptual approach used to compare the case of fuel cell CHP total cost of ownership with a reference case of no FCS, grid-based electricity, and conventional heating equipment. A fuel cell CHP system will typically increase the cost of electricity but provide some savings by offsetting heating energy requirements. The cost of fuel cell electricity in this case is taken to be the “levelized cost of electricity” (LCOE) or the levelized cost in \$/kWh for the fuel cell system taking into account capital costs, operations and maintenance (O&M), fuel, and capital replacement costs (inverter, stack replacement, etc.) only. In

**Fuel Cell Systems: Total Cost of Ownership, Table 7** Estimated Clean Power Plan impacts for six representative regions

City	eGRID subregion	kg/MWh			kg/MWh			% Reduction 2030 from 2012		
		eGRID for 2012			2030 Projection with Clean Power Plan			CO2	SO2	NOx
		CO2 AEF eGRID	SO2 AEF eGRID	NOx AEF eGRID	CO2 AEF	SO2 AEF	NOx AEF			
Minneapolis	MROW	646	1.33	0.73	489	0.25	0.45	24%	81%	38%
NYC	NYCW	316	0.03	0.15	322	0	0.05	-2%	97%	64%
Chicago	RFCW	626	1.54	0.55	510	0.4	0.34	19%	74%	37%
Houston	ERCT	518	0.87	0.28	440	0.09	0.11	15%	90%	61%
Phoenix	AZNM	523	0.2	0.59	459	0.07	0.3	12%	64%	50%
San Diego	CAMX	295	0.09	0.15	259	0.03	0.08	12%	62%	46%
Average								<b>13%</b>	<b>78%</b>	<b>49%</b>

**Fuel Cell Systems: Total Cost of Ownership,**

**Fig. 7** Cost of energy service for fuel cell CHP and conventional electricity and heating systems. A fuel cell CHP system will typically increase the levelized cost of electricity (upper left two bars). But if waste heat is utilized, the cost of heating is reduced (upper right two bars). In this treatment, all nonelectricity credits (heating fuel savings, carbon credits, societal health, and environmental benefits) are applied to an LCOE with TCO credits or a “total cost of electricity”



this entry, in addition to crediting the heating fuel savings to the  $LCOE_{FC}$ , carbon credits from net system savings of  $CO_{2eq}$  and net avoided environmental and health-based externalities are credited to the fuel cell system cost of electricity. The resultant quantity is the “cost of electricity with total cost of ownership credits or savings.” This allows comparison of fuel cell cost of electricity with TCO credits to the reference grid electricity cost (\$/kWh).

More specifically, this comparison is described by the equations below. For a representative commercial building (e.g., hotel, hospital, college dormitory), the “no fuel cell system” case has an overall cost of electricity as follows:

$$\text{Cost of electricity } \left( \frac{\$}{kWh} \right) = \frac{\text{Annual energy cost} + \text{Annual demand charges} + \text{Other Charges}}{\text{Total electricity consumption } (kWh)} \tag{6}$$

where the energy cost is the cost of electricity (as charged per kWh consumption) and demand

charges are charges incurred based on the peak load in kW per month and any other fixed annual charges incurred by the rate plan (e.g., for meters, public goods fees, etc.). The building electricity bill will be determined by the particular tariff structure local to the building’s geographical location. Any on-site fuel costs for building heating such as on-site boilers, water heaters, or furnaces are tracked separately.

In comparison, the fuel cell CHP system has the following costs:

$$\begin{aligned} \text{Cost of electricity } \left( \frac{\$}{kWh} \right) &= f * \text{Cost of } FC \text{ electricity} \\ &+ (1 - f) * \text{Cost of electricity from grid} \end{aligned} \tag{7}$$

where the cost of electricity consists of the levelized cost of electricity provided by the fuel cell system ( $LCOE_{FC}$ ) times the fraction  $f$  of electricity consumption provided by the fuel

cell and any cost of electricity that is purchased from the grid if the fuel cell-provided electricity is not sufficient to meet all the electricity demands from the building:

$$\begin{aligned} & \text{Cost of } FC \text{ Electricity } \left( \frac{\$}{kWh} \right) \\ & = LCOE_{FC} = \frac{\text{Installed Cost} * CRF + \text{Annual Maintenance} + \text{Annual Fuel Costs}}{\text{Total electricity provided by FCS } [kWh]} \end{aligned} \quad (8)$$

$$\begin{aligned} & \text{Cost of electricity from grid } \left( \frac{\$}{kWh} \right) \\ & = \frac{\text{Annual energy cost} + \text{Annual demand charges} + \text{Other Charges}}{(\text{Total electricity consumption} - \text{Electricity provided by FCS}) [kWh]} \end{aligned} \quad (9)$$

and

$$\begin{aligned} & LCOE \text{ with } TCO \text{ Credits} \\ & = f * LCOE_{FC} \text{ with } TCO \text{ Credits} \\ & \quad + (1 - f) * \text{Cost of electricity from grid} \end{aligned} \quad (11)$$

$CRF$  = Capital Recovery Factor

$$= \left[ \frac{i(1+i)^n}{(1+i)^n - 1} \right] \quad (10) \quad \text{where}$$

The levelized cost of electricity with TCO credits is then defined as follows:

$$\begin{aligned} & LCOE_{FC} \text{ with } TCO \text{ Credits} \\ & = LCOE_{FC} - TCO \text{ Credits} \end{aligned} \quad (12)$$

$$\begin{aligned} & TCO \text{ Credits } \left( \frac{\$}{kWh} \right) \\ & = \frac{(\text{Fuel Savings} + \text{Savings from } CO_2 + \text{Savings from Health and Environment})_{\text{Annual}}}{\text{Electricity provided by FCS } (kWh)} \end{aligned} \quad (13)$$

The method for calculating the savings from health and environmental externalities was discussed above. This approach allocates any fuel savings, savings from CO<sub>2</sub> reductions, and savings from health and environmental externalities to the LCOE of the fuel cell, and the total LCOE with TCO credits is defined as in Eqs. 11 and 12.

In the discussion below, capital costs are drawn from the modeled costs below assuming low-volume production of 100 units per year for 10 kWe and 50 kWe FCS or 1 MWe and 5

annual production, respectively. The LCOE of FC power in this definition includes all of the fuel purchased for FCS operation, but none of the fuel purchased for conventional heating that augments the FCS waste heat utilization.

Other studies have looked at health and environmental benefits of solar and wind [31] where renewable electricity displaces grid electricity. This entry considers CHP which displaces both grid electricity and on-site fuel combustion for heating.

## Fuel Cell System Designs and Functional Specifications

### PEM Functional Requirements and System Designs

PEM FC system designs and functional specifications have been developed for a range of systems sizes including (1) CHP systems with reformat fuel from 10 to 250 kW<sub>e</sub>. These choices are based upon a search of relevant fuel cell literature and patents, industry system spec sheets, as well as industry advisor input.

The choice of these system designs and functional specifications defines the operational parameters for each respective fuel cell system and defines the system components or balance of plant (BOP) that will be the basis for cost estimates. Functional requirements for the stack further define the stack geometries and stack sizing (number of cells per stack) for the DFMA direct manufacturing cost analysis below. The functional specifications also refer to the rated power of the system. Operating at partial load would result in slightly higher efficiency across most of the turndown ratio of the system.

System designs are meant to be “medium fidelity” designs that are representative of actual fuel cell systems to provide the basis for the costing estimates that are the main focus of this entry. As such, this treatment is not scoped with process modeling or optimization of the system design in terms of detailed pressure management, flow rates, or detailed thermal balances. However, the designs are a reasonable starting points for costing based on feedback from industry advisors and for showing key system components, subsystems, and interconnections that are important for understanding system “topography” for analysis and costing purposes.

The systems represented in this entry reflect the authors’ best assessment of existing or planned systems but do not necessarily capture all system components with exact fidelity to existing physical systems, and hence there does not necessarily exist a physical system that is exactly the same as that described here.

### PEM System and Component Lifetimes

System and component lifetime assumptions are shown in Table 8 for CHP applications, respectively. These specifications are shared across the system power range for each application. In the application of TCO to a CHP system, overall system life is assumed to be approximately 15 years currently and anticipated to increase to 20 years in the future (2015–2020 time frame). Stack life is 20,000 h in the near term and projected to double to 40,000 h per industry and DOE targets. Subsystem component lifetimes vary from 5 to 10 years, with somewhat longer lifetimes expected in the future compared with the present.

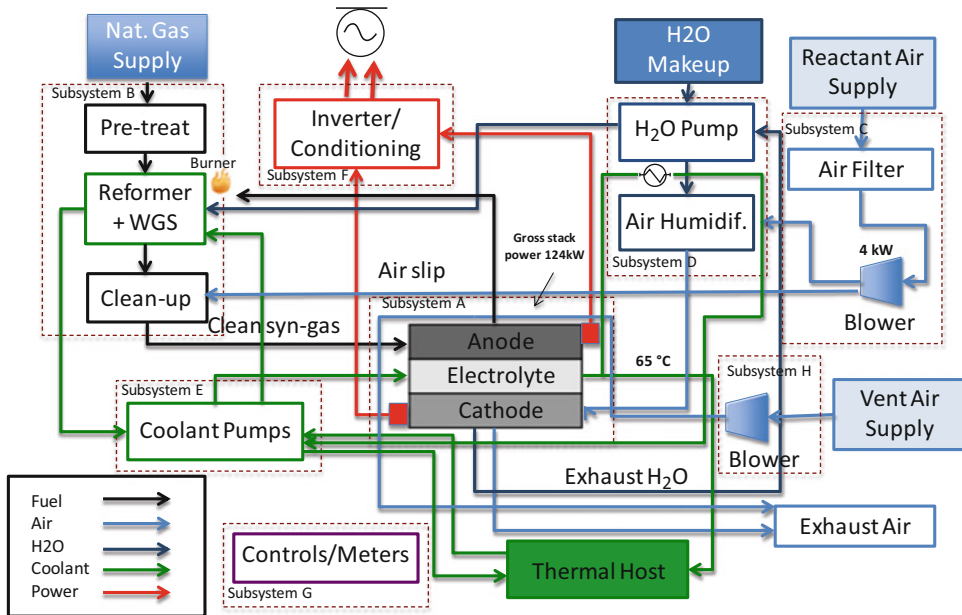
The system turndown ratio is defined as the ratio of the system peak power to its lowest practical operating point (e.g., running at 33 kW<sub>e</sub> on a 100 kW<sub>e</sub> system is a turndown ratio of 3:1). The stack cooling strategy for all CHP systems is assumed to be liquid water circulation, consistent with CHP system duty cycles and stack lifetime requirements.

### PEM CHP System Designs

A representative system design for an PEM fuel cell CHP systems operating on reformat fuel is shown in Fig. 8. Delineation into subsystems is

**Fuel Cell Systems: Total Cost of Ownership, Table 8** CHP application common specifications [2]

CHP application – PEM	Near-term	Future (2015–2020)	Units
System life	15	20	Years
Stack life	20,000	40,000	Hours
Reformer life (if app.)	5	10	Years
Compressor/blower life	7.5	10	Years
Water management subsystem life	7.5	10	Years
Battery/startup system life	7.5	10	Years
Turndown ratio	3:1	3:1	Ratio
Expected availability	96	98	Percent
Stack cooling strategy	Liquid	Liquid	Cooling



**Fuel Cell Systems: Total Cost of Ownership, Fig. 8** System design for 100 kW PEM CHP system using reformat fuel [2]

provided for modularity of design and also to facilitate the tracking and classification of balance of plant components and costing. The CHP systems are subdivided further into subsystems as follows: (1) fuel cell stack, (2) fuel supply system, (3) air supply, (4) water makeup loop, (5) coolant system, (6) power conditioning, (7) controls and meters, and (8) ventilation air supply.

To improve fuel utilization, the CHP system with reformat fuel has a fuel burner to utilize anode tail gas fuel and also includes an air slip input (approximately 2% concentration) for greater CO tolerance. Note that in some cases where there is not a steady demand for waste heat, there may need to be additional parasitic fans and radiators to dissipate the waste heat.

**PEM CHP Functional Specifications**

Functional specifications for the 10 kW and 100 CHP systems with reformat fuel are shown in Table 9. These functional specifications were developed based on a variety of industry sources, publically available product specifications, and literature review and include calculated

parameters for stack and system efficiencies for an “internally consistent” set of reference values. A detailed description of the functional specification focused on the 10 kW and 100 system sizes follows below.

The determination of gross system power reflects about 28% overall parasitic power at 10 kW and about 24% at 100 kW, including losses through the inverter. DC to AC inverter efficiency is assumed to be 93% and constant across the system power ranges. Additional parasitic losses are from compressors, blowers, and other parasitic loads and are assumed to be direct DC power losses from the fuel cell stack output power.

The waste heat grade from the coolant system is taken to be 65 °C for all system sizes although a range of other temperatures are possible, mostly over the range of 50–70 °C. The heat exchanger configuration can also depend on the demand temperatures for the heating streams, and the exact cooling and heating loops will be location and system specific. In the use-phase cost model described later in the report, hot water is generated as the main waste heat application with



**Fuel Cell Systems: Total Cost of Ownership, Table 9** Functional specifications for CHP fuel cell system operating on reformat fuel [2]

Parameter	CHP system with reformat fuel, 10 kWe	CHP system with reformat fuel, 100 kWe	Unit
Gross system power	12.8	124	kWe
Net system power	10	100	kWe
Electrical output	480 V AC	480 V AC	Volts AC or DC
DC/AC inverter efficiency	93	93	%
Waste heat grade	65	65	Temp. °C
Reformer efficiency	75	75	%
Fuel utilization, overall	90–95	90–95	%
Net electrical efficiency	32	33	% LHV
Thermal efficiency	49	50	% LHV
Total efficiency	81	83	Elect. + thermal (%)
Stack power	12.8	9.5	kWe
Total plate area	360	360	cm <sup>2</sup>
CCM coated area	259	259	cm <sup>2</sup>
Single-cell active area	220	220	cm <sup>2</sup>
Gross cell inactive area	39	39	%
Cell amps	111	111	A
Current density	0.5	0.51	A/cm <sup>2</sup>
Reference voltage	0.7	0.7	V
Power density	0.35	0.35	W/cm <sup>2</sup>
Single-cell power	77.8	77.9	W

(continued)

**Fuel Cell Systems: Total Cost of Ownership, Table 9** (continued)

Parameter	CHP system with reformat fuel, 10 kWe	CHP system with reformat fuel, 100 kWe	Unit
Cells per stack	164	122	Cells
Stacks per system	1	13	Stacks
Parasitic loss	2	16	kWe

enhancement to space heating as an additional possibility. In the reformat fuel case, additional waste heat streams from the anode and cathode exhaust can be routed to the fuel processor reactor burner.

Overall fuel utilization is assumed to be up to 95% for reformat fuel systems with a “single pass” fuel utilization of 80%. This assumes that there is a fuel afterburner in the reformat case.

At the reference cell voltage of 0.7 volts, the net electrical efficiency is 32–33% (LHV) for the reformat systems. These overall electrical efficiency levels are similar to those reported in the literature (e.g., see [32]). Fuel reformer efficiency is estimated to be 75%.

The total overall efficiency of 81–83% is viewed as a benchmark value for the case where a large reservoir of heat demand exists and represents the maximal total efficiency of the system. Actual waste heat utilization and total efficiency will be highly dependent on the site and heating demands. For example, a smaller overall heat efficiency can result if waste heat utilization is confined to building water heating and the building has a relatively low demand for hot water.

There is a well-documented tradeoff of peak power and efficiency. The functional specifications are defined for operation at full-rated power. Moving away from the peak power point to lower current density, the cell voltage increases and thus the stack efficiency improves. Partial load operation has higher efficiency but less power output. For the PEM technology considered here, the system is assumed to be load following, or capable of



ramping its power level up and down to follow electrical demand (to the turndown limit described in Table 8). This system flexibility is an advantage for PEM over higher temperature fuel cell systems and will be included in the use-phase modeling described later in the report.

**PEM Cell Stack Sizing**

Total fuel cell plate area is taken to be 363 cm<sup>2</sup> based on inferences and interpretation of publically available industry spec sheets (All functional specifications (e.g., gross and net system power, cell sizes, stack current density, etc.) are based on inferences and interpretations of publically available data, patents, and literature by members of the research team from LBNL and UC-Berkeley and should not be interpreted as actual product data from any other fuel cell stacks or component vendors.). Catalyst-coated membrane area is about 72% of this area due to plate border regions and manifold openings. Single-cell active area has an additional 15% area loss. As described further in the DFMA costing section below, this is due to the overlap and alignment area loss associated with the frame sealing process. The tradeoff here is a longer anticipated frame lifetime (20,000 h) and higher reliability from this frame sealing process for continuous power applications versus the lower area loss with an alternative edge sealing process.

**SOFC System and Component Lifetimes**

System and component lifetime assumptions for SOFC CHP systems are shown in Table 10. These specifications are shared across the system power

range for each application. Overall system life is assumed to be approximately 15 years currently and anticipated to increase to 20 years in the future (2015–2020 time frame). Stack life is assumed to be 20,000 h in the near term and projected to double to 40,000 h per industry and DOE targets. Subsystem component lifetimes are assumed to vary from 5 to 10 years, with longer lifetimes around 20 years expected in the future. Direct air and off-gas cooling strategy is utilized for stack cooling for cost savings and BOP design specifications.

**System Design and Functional Specifications for SOFC CHP Systems**

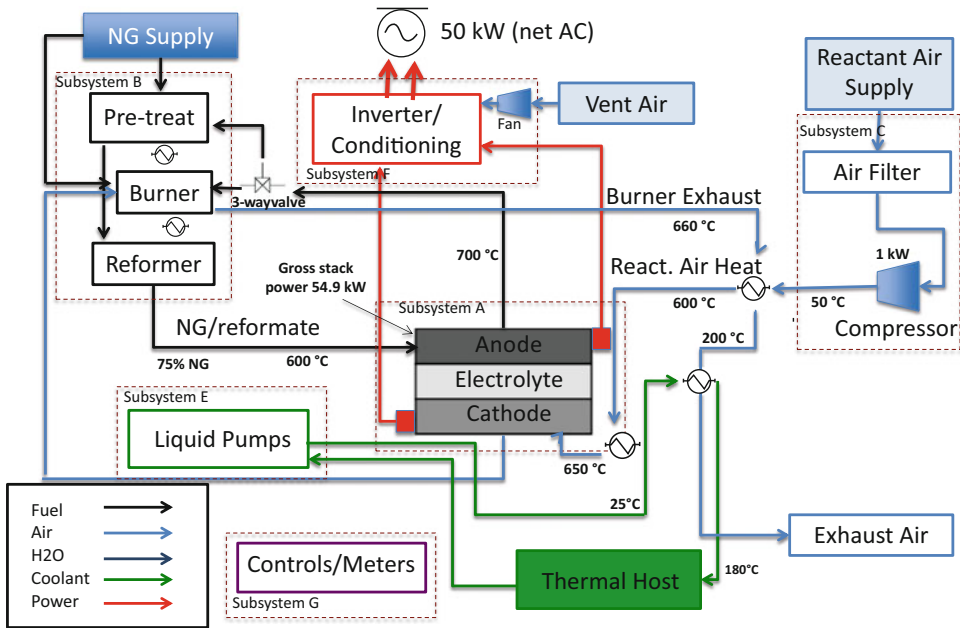
System designs for both a SOFC CHP operating on reformat fuel will be discussed in this section. System design rationale and operations will be discussed in greater detail.

Figure 9 shows the system design for a SOFC CHP system operating on reformat fuel. Delineation into subsystems is provided for modularity of design and also to facilitate the tracking and classification of balance of plant components and costing. Similar to the PEM case above, the CHP systems are subdivided further into subsystems as follows: (1) fuel cell stack, (2) fuel supply system, (3) water recirculation, (4) power conditioning, (5) coolant subsystem, and (6) controls and meters.

Functional specifications for the 10 and 50 kWe CHP systems with reformat fuel are shown in Table 11. These functional specifications were developed based on a variety of

**Fuel Cell Systems: Total Cost of Ownership, Table 10** Specifications and assumptions for SOFC CHP system [3]

CHP application – SOFC	Near-term	Future	
System life	15	20	Years
Stack life	20,000	40,000	Hours
Reformer life (if app.)	5	10	Years
Compressor/blower life	7.5	10	Years
Water management subsystem life	7.5	10	Years
Battery/start-up system life	7.5	10	Years
Turndown % (>50 kW)	0	25	Percent
Turndown % (<50 kW)	25	50	Percent
Expected availability	96	98	Percent
Stack cooling strategy	Air + off-gas	Air + off-gas	Cooling



**Fuel Cell Systems: Total Cost of Ownership, Fig. 9** SOFC CHP system design schematic for 50 kW CHP system [3]

industry sources and literature and include calculated parameters for stack and system efficiencies for an “internally consistent” set of reference values. A detailed description of the functional specification focused on the 10 and 50 kW system sizes follows below. The determination of gross system power reflects about 10% overall parasitic power at 10 kW and about 9.7% at 100 kW, including losses through the inverter. DC to AC inverter efficiency is assumed to be 95% and constant across the system power ranges. Additional parasitic losses are from compressors, blowers, and other parasitic loads and are assumed to be direct DC power losses from the fuel cell stack output power.

The waste heat grade from the coolant system is taken to be 220 °C for all system sizes although a range of other temperatures are possible, mostly over the range of 50–70 °C. The heat exchanger configuration can also depend on the demand temperatures for the heating streams, and the exact cooling and heating loops will be location and system specific. In the use-phase cost model described later in the report, hot water and space heating are generated as the

main waste heat application with enhancement to absorption chilling as an additional possibility. Additional waste heat streams from the anode and cathode exhaust can be routed to the fuel processor reactor burner.

At the reference cell voltage of 0.8 volts, the net electrical efficiency is 59% (lower heating value, or LHV) for the reformat systems. These overall electrical efficiency levels are similar to those reported in the literature [11]. The total overall CHP system efficiency of 84% is viewed as a benchmark value for the case where a large reservoir of heat demand exists and represents the maximal total efficiency of the system. Actual waste heat utilization and total efficiency will be highly dependent on the site and heating demands. For example, a smaller overall heat efficiency can result if waste heat utilization is confined to building water heating and the building has a relatively low demand for hot water.

Total fuel cell plate area is taken to be 540 cm<sup>2</sup>. Active catalyzed area is about 61% of this area due to plate border regions and manifold openings, and single-cell active area has an additional 10% area loss due to the frame sealing process.

**Fuel Cell Systems: Total Cost of Ownership, Table 11** Functional specifications for CHP system operating on reformat fuel [3]

Parameter	10 kWe CHP system reformat fuel	50 kWe CHP system with reformat fuel	Units
Gross system power	11.0	54.9	kW DC
Net system power	10	50	kW AC
Electrical output	220 V AC	480 V AC	Volts AC or DC
DC/AC inverter efficiency	95	95	%
Waste heat grade	220	220	Temp. °C
Fuel utilization % (overall)	N/A	N/A	%
Net electrical efficiency	59	59	% LHV
Thermal efficiency	24	24	% LHV
Total efficiency	84	84	Elect. + thermal (%)
Stack power	11.0	54.9	kW
Total plate area	540	540	cm <sup>2</sup>
Actively catalyzed area	329	329	cm <sup>2</sup>
Single-cell active area	299	299	cm <sup>2</sup>
Gross cell inactive area	45	45	%
Cell amps	105	105	A
Current density	0.35	0.35	A/cm <sup>2</sup>
Reference voltage	0.8	0.8	V
Power density	0.28	0.28	W/cm <sup>2</sup>
Single-cell power	84	84	W
Cells per stack	130	130	Cells
Stacks per system	1	5	Stacks
Parasitic loss	0.5	2.5	kW AC

The 10 kWe system consists of 130 cells in a single stack, while the 50 kW system has 5 stacks of 130 cells each.

### Total Cost of Ownership Modeling Results

#### PEM Fuel Cell System Manufacturing Costs

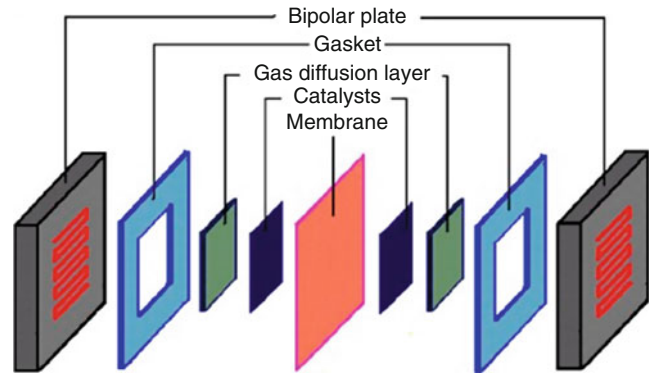
A PEM unit cell consisting of bipolar plate/gasket/GDL/CCM/GDL/gasket is shown in Fig. 10 where the gasket represents the cell frame/seal. Many sequential cells assembled together form a fuel cell stack. Typically the stack is assembled with some compression mechanism such as tie rods or compression bands with conductive endplates on both sides of the stack.

For this entry, bottom-up cost analysis is done for each of the critical stack cost components, namely, the catalyst-coated membrane (CCM), gas diffusion layer (GDL), MEA frame/seal, bipolar plate (BPP), and stack assembly. Details of process costing can be found in Wei et al. [2]. To illustrate the bottom-up analysis, a more detailed discussion for two key process modules is provided: the catalyst-coated membrane and bipolar plates. The cost critical bill of materials is shown in Table 12.

Component process yield is assumed between 60% and 99.5%, line availability between 85% and 95%, and daily setup time between 60 and 5 min. All are scaled with production volume and range from current values to achievable future values. These assumptions have been obtained through consultation with industry sources including Ballard Power Systems and assessment of the current published literature. Yield, availability, and setup time differs from module to module due to differences of the manufacturing processes, difficulties handling the different materials, and embedded value of the product further down the manufacturing line. The process yield assumption represents an intermediate value between the very high-yield assumptions in [7] and the low-yield assumptions of 60% to 70% in ACI Technologies [33] and explicitly assumes that the yield is dependent on the production volume. Implicit in this assumption is

### Fuel Cell Systems: Total Cost of Ownership,

**Fig. 10** Schematic of PEM fuel cell unit



**Fuel Cell Systems: Total Cost of Ownership, Table 12** Key bill of materials for stack manufacturing

Material	Component	Cost	Reference
Teflon perfluoroalkoxy (PFA) film	CCM	\$9.78 m <sup>-2</sup>	Professional plastics
Platinum	CCM	\$1402 troy ounce <sup>-1</sup>	Richest group, Shanghai, China
Carbon fiber	GDL	\$9.50–9.72 m <sup>-2</sup>	Sinha [8]
Polytetrafluorethylene (PTFE)	GDL	\$22.17 kg <sup>-1</sup>	Sinha [8]
Polypropylene	Carbon BPP	\$1.597 kg <sup>-1</sup>	2011 Market price
Graphite	Carbon BPP	\$6.761 kg <sup>-1</sup>	2011 Market price
Carbon black	Carbon BPP	\$6.35 kg <sup>-1</sup>	2013 Market price
Carbon epoxy	Carbon BPP	\$97.38 L <sup>-1</sup>	Eccobond 60 L
SS316L	Metal BPP	\$4 kg <sup>-1</sup>	James et al. [7]
Chromium nitride (CrN)	Metal BPP	\$50 kg <sup>-1</sup>	
Polyethylene naphthalate (PEN)	Frame/seal	\$5 kg <sup>-1</sup>	CES 2012 <sup>a</sup>
Fluorinated ethylene propylene (FEP)	Frame/seal	\$10 kg <sup>-1</sup>	CES 2012 <sup>a</sup>

<sup>a</sup>CES 2012: *Cambridge Engineering Selector* computer software. Vers. 2012. Cambridge, UK: Granta Design Ltd., 1999

that “learning-by-doing” leads to higher yield at higher production volumes. Note that the process yield assumed here is the total yield for an individual stack component, not the overall stack yield nor the step by step yield breakdown. Table 13 shows this breakdown. Furthermore, multiple production lines are considered for tooling optimization of low- and high-volume production.

#### Catalyst-Coated Membrane

For this entry, a decal transfer coating process is adopted as a base flow with coating lines for cathode and anode catalyst followed by a

lamination step to combine the two layers to form a catalyst-coated membrane (CCM), all using automated roll-to-roll or web line processing. The flow is similar in concept and materials to US Patent 20090169950 [34].

Slot die coating was chosen as a representative process for catalyst ink deposition since it is a mature technology with a high degree of process control capability in high-volume manufacturing. This approach has been demonstrated for other thin film products and is expected to be able to scale up to larger volumes for the catalyst coating operation. Other deposition techniques could be used such as spray coating, gravure, roll coating,



etc., but were not explored. Ultra-low catalyst loading, e.g., nanostructured thin films, is not required for longer lifetime stationary applications where a higher loading can be amortized over a longer amount of time. On the down side, wet deposition manufacturing issues include the management of volatile and/or explosive solvents for safety and environmental control, wet mixing control of viscosity, particle uniformity, and management of plumbing lines and concentration gradients.

For the slot die coating, catalyst ink is mixed in a tank and extruded through the slot die coater. Following deposition, the coated membrane or backing layer passes through an IR drying oven to bake off the ink solvents. Anode-side and cathode-side catalyst deposition is done on separate lines due to swelling issues during drying and product quality and process control difficulties with concurrent or serial deposition. Anode and cathode layers are pressed together in a heated nip roller to form the final CCM product.

The overall deposition area is enclosed in a clean room environment at Class 1000 to control for contaminants and particles. An inspection is done after each deposition and thermal treatment pass. Fume hoods to thermal oxidizers are employed to control volatile organic compound (VOC), CO, and volatile hazardous air pollutant (HAP) emissions. Overall, both tooling lines (high volume and low volume) and equipment configuration have been validated by both industry advisors and vendor inputs.

The CCM membrane is a Nafion membrane from DuPont with 25.4  $\mu\text{m}$  thickness and is assumed to be a purchased part. The decision to purchase the membrane was based on industry input, the cost and complexity to bring up a membrane manufacturing line, and the fact that Nafion is readily available and is expected to scale in price with higher demand from increasing PEM fuel cell production. Cathode and anode Pt loading are assumed to be 0.4 and 0.1  $\text{mg cm}^{-2}$ , respectively. This loading is similar to that assumed in [33] and Pt loading and price is also a key variable for the sensitivity analysis later in this entry.

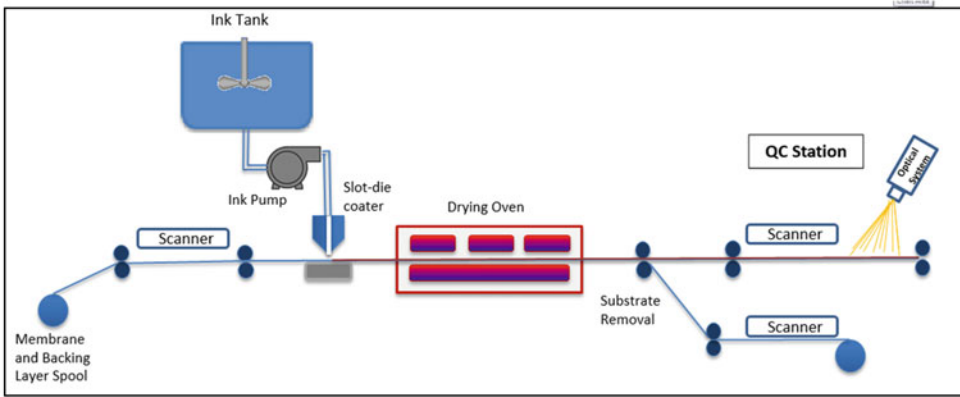
The CCM is made from depositing a catalyst layer (cathode) over a Nafion membrane and depositing an anode layer over Teflon paper then attaching these two layers via a lamination process. Teflon PFA paper is used as a substrate in the decal transfer method for the deposited anode and is then attached to the coated membrane (which was previously coated on one side) to form the final CCM (Fig. 11).

### Bipolar Plates

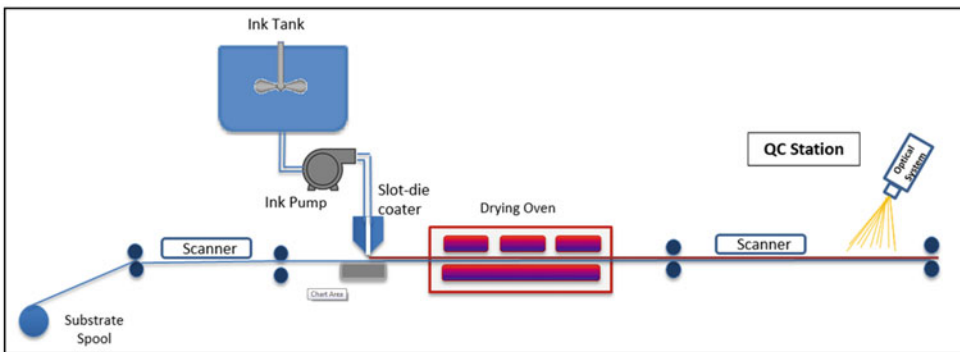
Bipolar plates are conductive plates in the fuel cell stack which separate MEAs and act as an anode for one MEA cell and a cathode for the next cell. Bipolar plates are usually made from metal, carbon, or conductive composite polymer (usually incorporating carbon). Bipolar plates have a number of functions within the fuel cell stack including separating gases between cells, providing a conductive medium between the anode and cathode, providing a flow field channel for the reaction gases, acting as a solid structure for the stack, and transferring heat out of the cell.

Typically, fuel cell plate vendors/developers have used compression molding where resin or polymer materials are blended with conductive filler material or embossing GRAFOIL<sup>®</sup> flexible graphite where graphitic carbon is impregnated with resin. Often, thermal treatment is done after molding to completely cure the material and/or to reduce volatile organic compound (VOC) content. Recently metal plates have also been considered, particularly in the automotive applications; however, a less established plate lifetime (about 5000–6000 h) suggests that using more standard graphite composite-based plates is a more durable option.

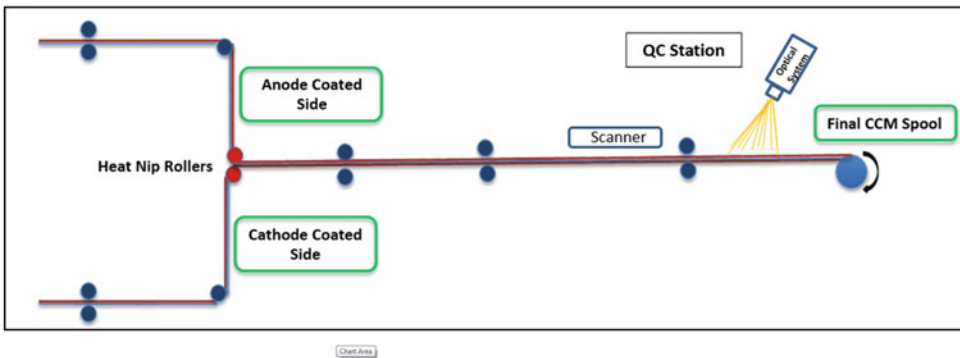
Injection molding is better suited to high-volume manufacturing than compression molding as it offers lower cycle times and established process technology with good dimensional control. However, material issues can make injection molding challenging for fuel cell applications. For example, conductive filler is needed for better conductivity, which adds to material costs and makes the technique more difficult due to higher viscosity and poorly controlled melt properties.



(a) Cathode-side



(b) Anode-side



(c) Final CCM

**Fuel Cell Systems: Total Cost of Ownership, Fig. 11** Schematic diagram for roll-to-roll coating line: (a) cathode line, (b) anode line, and (c) final product

As plates get larger in area, tolerances and control of plate planarity and flatness become larger concerns and need to be evaluated for injection molding. Additionally, plate brittleness can lead to cracking, and therefore plates may need added thickness, which results in undesirable

volume and weight. Nonetheless, recent work from the Center for Fuel Cell Technology (ZBT) at the University of Duisburg-Essen (see, e.g., [35, 36]) has achieved injection molded plates with good electrical and physical performance with a slight increase in plate thickness (2 mm).



As noted in Yeetsorn [37], research and development is needed for better composite materials with maximal electrical conductivity. One cited pathway is the development of more advanced materials with the proper conductive network structure. Here, an analysis of injection molded plates is presented for cost comparison with metal plates. Injection molding was modeled instead of compression molding since this entry is targeted for higher volume and injection molding is expected to yield lower costs.

This implicitly assumes that continued development will occur in composite materials with conductive fillers, potentially including nano-structured materials that will allow injection molding to be viably employed. Stationary applications allow for slightly thicker plates since volume and weight are not as stringent concerns as that for the automotive application. Slightly thicker plates may also achieve better quality in terms of dimensional tolerances, plate stability, and yield.

#### Injection Molded Carbon Plates

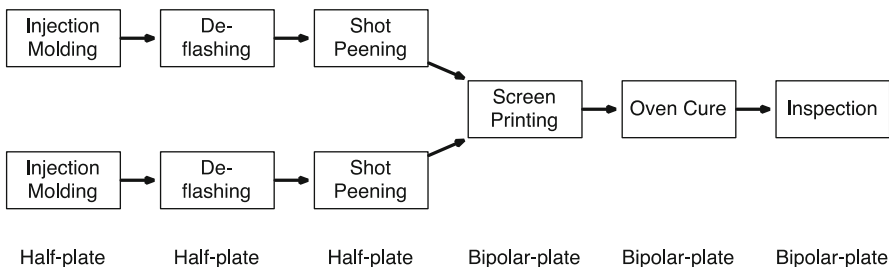
The process flow is shown in Fig. 12. It is assumed that the input material (composite) is already mixed and pelletized. Injection molding machine size, electrical power, and cycle time are determined by a model created by Laboratory of Manufacturing and Sustainability at University of California, Berkeley [38], that results in cycle times estimated to be 30.6 s per half plate (half of a bipolar plate) in a lower-volume configuration and 16.1 s with a higher batch size and two injection cavities. Injection molding is followed by a deflashing (removal of unwanted excess material) and shot peening step. The shot peening

step treats the surface to reduce gas permeability and become a slightly compressive layer. This step is in lieu of a separate resin-curing step typically used to treat the surface. A screen printer is used to coat epoxy on the half plates to form bipolar plates. This is followed by an oven curing step and then a final inspection. Potential plate cleaning steps could also be envisioned and would add to the cost but were not included in this entry due to the uncertainty in cleaning requirements.

Plate materials are assumed to be a combination of polypropylene binder with a mixture of graphite and carbon black conductive filler. Equipment costs are fairly evenly distributed between process modules with the injection molding machine the largest capital cost.

Manufacturing cost is typically high at low production volumes, and therefore individual components would be purchased rather than manufactured in-house. However, it is assumed that all components are manufactured in-house (with exception to the components specifically mentioned in the method section). For this reason, the cost reduction is larger when transitioning from low to high volumes than if there were more purchased components at low-volume production.

Individual component cost breakdowns in  $\$ \text{ kW}^{-1}$  for 100 kW CHP reformate fuel cells are shown in Fig. 13 for the CCM and bipolar plates. The CCM cost is dominated by direct material cost at all production volumes due to the high cost of the platinum catalyst. Other modules such as the GDL and assembly also have very high material cost at high production volumes. This is due to high processing manufacturing



**Fuel Cell Systems: Total Cost of Ownership, Fig. 12** Process flow of bipolar plate manufacturing



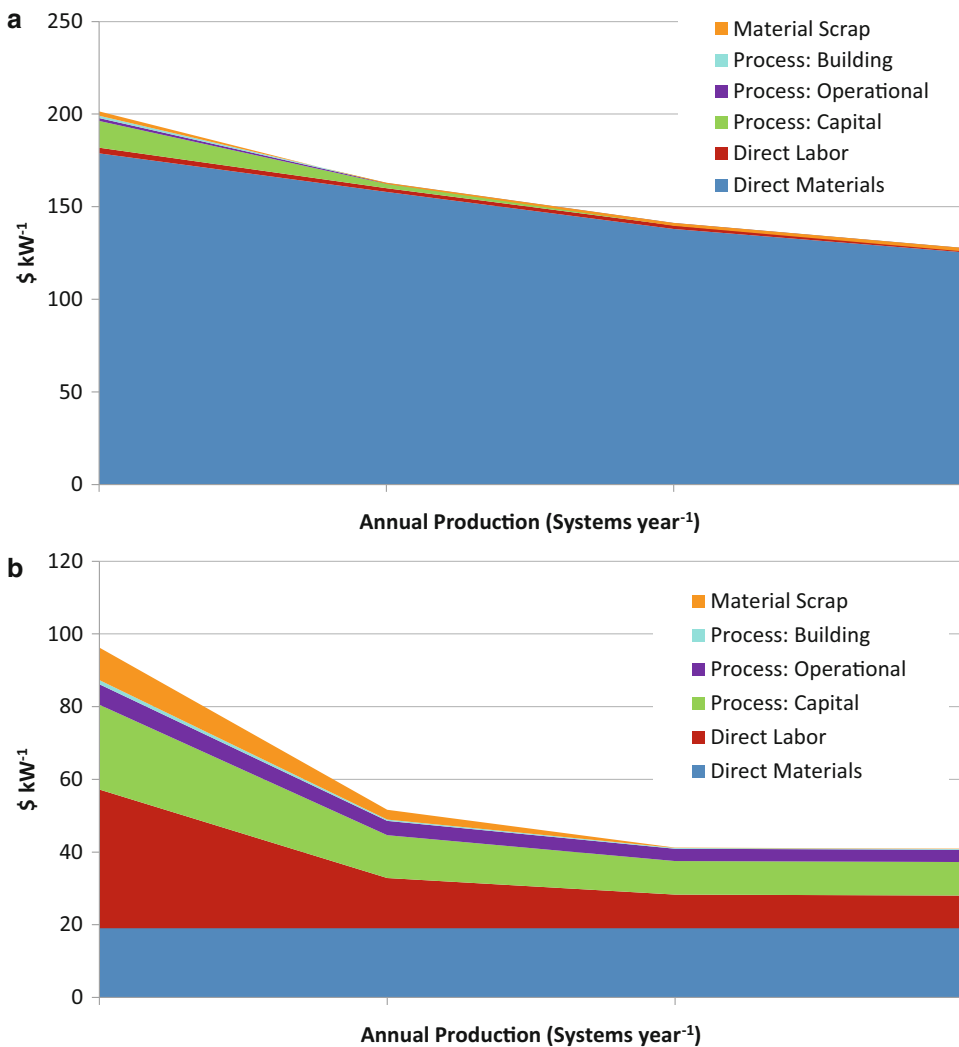
with high line utilization. Also, scrap cost is high for the frame/seal due to high material losses when cutting out the cell sized slot.

**PEM Stack Direct Manufacturing Costs**

Direct stack manufacturing cost vs. annual production volume is shown in Table 14 for CHP systems with reformat fuel and backup power systems, respectively. This provides an indication of future potential PEM fuel cell stack costs with continued process automation, economies of scale, and learning by doing. When production

volume is increased, the stack cost decreases considerably.

Two breakdowns of cost components are shown in Figs. 14 and 15 for a 50 kW system. Figure 14 shows that the CCM is largest cost driver of the stack in part due to the high catalyst cost across process volumes followed by the bipolar plates and the GDL. Figure 15 shows that direct materials and capital costs are the largest cost components at low volume and direct materials dominate costs at higher volumes.

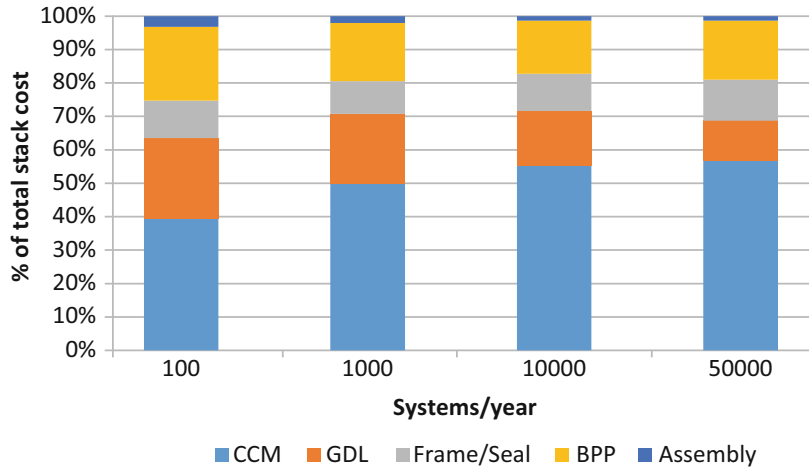


**Fuel Cell Systems: Total Cost of Ownership, Fig. 13** Component cost breakdown of 100 kW CHP(\$ kW<sup>-1</sup>) for (a) catalyst-coated membrane and (b) bipolar plate

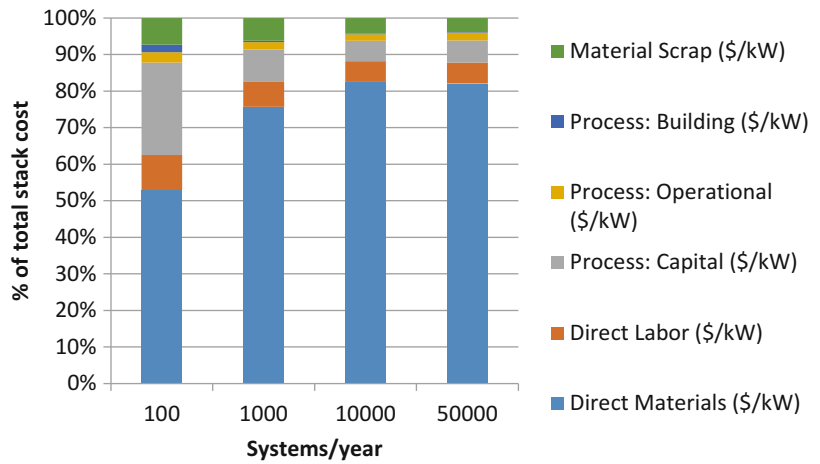
**Fuel Cell Systems: Total Cost of Ownership, Table 14** Stack cost estimate in (\$/kWe) as a function of annual manufacturing volume

System size (kWe)	100 systems/yr	1000 systems/yr	10,000 systems/yr	50,000 systems/yr
10	1340	497	333	284
50	596	352	272	239
100	466	313	249	219
250	377	279	231	203

**Fuel Cell Systems: Total Cost of Ownership, Fig. 14** Disaggregation of stack cost by relative percentage of stack components cost to overall stack cost for 50 kWe systems



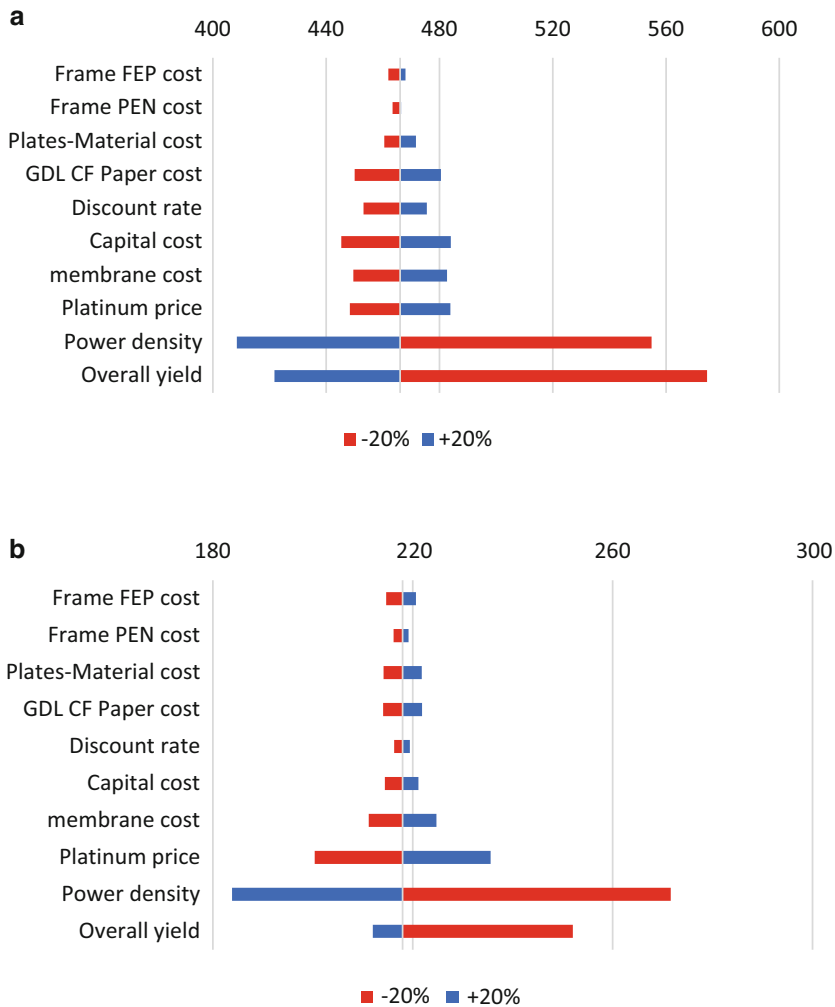
**Fuel Cell Systems: Total Cost of Ownership, Fig. 15** Disaggregation of stack cost by relative percentage of cost components to overall stack cost for 50 kWe systems



**PEM Stack Cost Sensitivity Analysis**

A sensitivity analysis at the stack level is presented in this section for 100 kW systems at different production volumes (as shown in Fig. 16). The impact to the stack cost in \$ kW<sup>-1</sup> is calculated for a ±20% change in the sensitivity parameter being varied.

As it can be seen from these plots, module process yield and power density are the most sensitive cost assumptions. Pt price and Nafion membrane price are among other important factors. This is not surprising for expensive materials and since from the above discussion, material costs dominate at high production volumes. The



**Fuel Cell Systems: Total Cost of Ownership, Fig. 16** Sensitivity analysis for 100 kW stack manufacturing parameters at different production volumes: (a)

100 systems per year<sup>-1</sup> and (b) 50,000 systems per year<sup>-1</sup> (Note: upper bound for yield is 100% and lower bound varies between low and high production volumes)

discount rate and capital cost are not large factors at high volume since material costs dominate the overall cost. Note that yield becomes less sensitive at high volume for two reasons: (1) overall yield is assumed to be very high at high volume ( $\geq 95\%$ ), and (2) material costs dominate at high volume and a significant portion of material costs are recovered from rejected material.

1. Fuel subsystem
2. Air subsystem
3. Coolant subsystem and humidification subsystems
4. Power subsystem
5. Control and meter subsystem
6. Miscellaneous subsystem

**PEM Fuel Cell CHP Balance of Plant and System Costs**

To facilitate the analysis, the BOP is divided into six subsystems or subareas listed below:

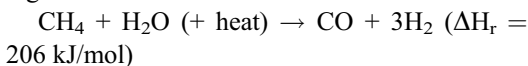
For each subsystem, a detailed list of components and component sizing is generated based on the system design. Subsystem components are estimated using bottom-up system design, component sizing, and vendor discussions. Cost

estimates are based on the cost estimates from publically available sources such as online price quotes or direct quotes from material or component vendors. More details can be found in Wei et al. [2].

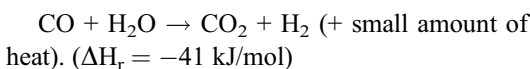
The BOP includes items such as valves, compressors, pumps, wiring, piping, meters, controls, etc. that are associated with the complete operation of the fuel cell system. Six major areas make up the BOP and are shown in Fig. 8. With reference to this figure, the plant is fed by natural gas where it is reformed, shifted, and purified in the reformer to a CO-free hydrogen-rich reformat fuel before entering the stack. The hydrogen-rich fuel enters the anode, and the compressed air enters the cathode side to generate DC electricity in the PEM stack. The generated power is converted to AC power through an inverter for load usage. A coolant loop circulates around the stack for cooling purpose. Thermal power is recovered from the stack and fuel burner for CHP applications. A blower generates vent atmospheric air to cool the stack. Each of the subsystems are listed and described in greater detail in the section below.

#### Fuel Processing Subsystem

The fuel processing subsystem is comprised of components associated with the operation of the fuel reforming process. The purpose of the fuel processor is to convert a hydrocarbon fuel (e.g., natural gas) into a hydrogen-rich gas via steam-methane reforming. In steam-methane reforming, natural gas reacts with steam in the presence of heat to produce hydrogen, carbon monoxide, and a small amount of carbon dioxide via the following chemical reaction:



Subsequently, steam and carbon monoxide are reacted using a catalyst to produce carbon dioxide and additional hydrogen. The reaction is exothermic and is called the water-gas shift reaction:



After that, carbon dioxide and other impurities are then removed from the reformed gas stream.

The cleaned fuel is fed into the fuel cell anode via a piping system that is controlled with manifolds and valves. Additional components include gas sensors for hydrogen level detection throughout the system.

#### Air Subsystem

The air subsystem consists of components associated with oxidant delivery to the fuel cell stack. Air supply from the atmosphere undergoes cleanup with an air filter and is pressurized with a blower. The air is humidified before entering the cathode. In addition, a fan unit takes in vent air for the purpose of stack cooling. Additional components such as piping, manifolds, and valves are employed for air delivery into the fuel cell stack. Gas sensors are also used to monitor oxidant levels throughout the system.

#### Coolant and Humidification Subsystem

The coolant subsystem consists of components associated with water management in the FCS, including cooling of the fuel cell stack. Water coolant from the coolant tank is cooled with a heat exchanger and recirculated through the stack via a pump unit.

#### Thermal Management Subsystem

For CHP operation, the exhaust heat from the burner unit and the fuel cell stack can be utilized to provide both water and space heating (thermal host) through the use of a liquid-liquid and gas-liquid heat exchangers. In order to obtain the costs of the heat exchanger used in the CHP FCS to recover the waste heat, the maximum heat from the fuel cell was calculated using the thermal and electrical efficiencies from the functional specs described above. Using the value, the required heat exchange area was evaluated using the log mean temperature difference method [39], where the required temperatures were obtained from this entry's design specifications. Using the computed areas, the costs of the heat exchangers were computed for both brazed plate and bolted heat exchangers with cost functions available from online database [40].

**Power Subsystem**

The power subsystem includes equipment for power inversion (from direct or “DC” current to “alternating” or AC current) and power regulation. In order for fuel cells to deliver power at the required voltage, a DC-DC converter is used to regulate fluctuating DC fuel cell voltage input to a specified voltage output, particularly for direct DC backup power applications. For most stationary FC applications, the fuel cell will be connected to the electricity grid where AC power is required for residential or utility power. An inverter is necessary for converting the DC power provided by a fuel cell to AC power, and an additional DC-DC converter may or may not be needed depending on the system design and the characteristics of the inverter. A transistor and a transformer were included in the subsystem to account for voltage fluctuations in the cell for the purposes of voltage and current conversions (step-up/step-down) to help meet the fluctuating electrical demands from the facility. Additional components for the working operation of the power subsystem include relays, switches, fuses, resistors, and cables.

**Control and Meter Subsystem**

The control and meter subsystem contains system control-related components for system operation and equipment monitoring. During a fuel cell system’s operation, variables such as flow rates, power output, temperature, and cooling need to be controlled. Sensors, meters, and pressure gauges are used for system monitoring of these variables. A variable frequency drive (VFD) is used to control the system’s actuation units, which include regulation of valves, pumps, switches, etc. A central processing unit (CPU) acts as the primary controller of the system, keeping the fuel cell system operating at the specified condition by monitoring the interaction between the monitoring sensors and actuating parts.

**Miscellaneous Subsystem**

The miscellaneous subsystem comprises external items outside of the stack that provides support, structure, and protection for the FCS. Items included in this subsystem are system enclosure,

fire safety panels, fasteners, tubing, and system assembly labor.

Table 15 shows component and subsystem costs of 10 and 100 kW CHP 100 at 1000 units per year, and Table 16 has a summary of BOP costs for PEM CHP.

The total direct system costs (stack plus BOP) are shown in Fig. 17. Total costs are seen to drop by about 20% for every factor of 10 increase in volume for a given system size, while increasing

**Fuel Cell Systems: Total Cost of Ownership, Table 15** Component and subsystem cost of 10 and 100 kW CHP reformate system at 1000 units per year annual volume

CHP system with reformate fuel component breakdown (for 1000 systems/year)	\$/kW	
System size	10 kW	100 kW
<b>Fuel processing subsystem</b>		
Integrated concentric-shell reformer for reforming natural gas	602	231
<b>Air subsystem</b>		
Air tank, humidification pump, air pump compressor, radiator, manifolds, air piping	246	59
<b>Coolant subsystem</b>		
Coolant tank, pump, coolant piping, external cooling motor	105	59
<b>Thermal management subsystem</b>		
Liquid-liquid heat exchanger, gas-liquid heat exchanger, condenser	182	76
<b>Power system</b>		
Power inverter, braking transistors, transformer, power supply, relays, switches, fuses, bleed resistor, Ethernet switch, power cables, voltage transducer	421	249
<b>Control/meter subsystem</b>		
Variable frequency drive, thermostats, central processing unit, flow sensors, pressure transducer, temperature sensors, hydrogen sensors, sensor heads, virtual private network	231	66
<b>Miscellaneous subsystem</b>		
Tubing, wiring, enclosure, fasteners, fire detection panel, safety leak detection system, ISO containers, labor	390	154
<b>Total in \$/kW</b>	<b>2177</b>	<b>894</b>

Fuel processor subsystem costs were adopted from earlier work by Strategic Analysis Inc. [16]

the system size from 10 to 100 kW results in about 50% lower cost. Note that customer purchase price would be higher than these direct costs, depending on the corporate markup for general and administrative costs, sales and marketing, research and development, installation costs, and any other fees and costs (insurance, warranties). A 50% corporate markup and a nominal 33% additional cost for installation are assumed, and any additional fees and costs, for a customer cost which is approximately double those shown in Fig. 17. For example, the externality modeling below utilizes a 50 kWe system, and a customer cost of \$4000/kWe is estimated at an annual production of 100 units per year.

**PEM Fuel Cell CHP System Life-Cycle Cost and LCIA Model Example**

This section describes the TCO model output for PEM CHP systems in the example commercial building case of a small hotel. More examples of LCIA by building type are provided in [2, 3]. Here, an illustrative example under two

assumptions is provided: a static electricity grid and an evolving electricity grid that is getting progressively cleaner in both carbon and criteria emissions.

Figure 18 shows the externality benefits for six cities for a 50 kW CHP system in a small hotel. These values are found using the methodology shown in Fig. 5 using two different sets of marginal emission factors: those from Siler Evans et al. [24] for large area NERC regions and eGRID subregions [21] and AP2 damage factors in Tables 4 and 5. The average value of externality benefits is fairly well matched in Phoenix, Minneapolis, and Chicago, but is less well matched for New York City and Houston. The average across all six cities is reasonably well matched however. The largest benefits are in the two Midwestern cities, Minneapolis and Chicago, and are dominated by health and environmental savings, driven by the larger electricity grid emission factor in those two locations.

Example output of the LCC and LCIA model for a 50 kW small hotel in five representative cities

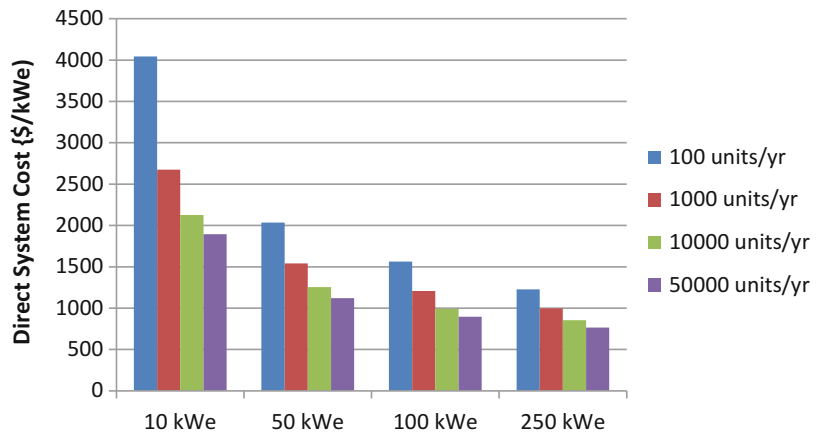
**Fuel Cell Systems: Total Cost of Ownership,**

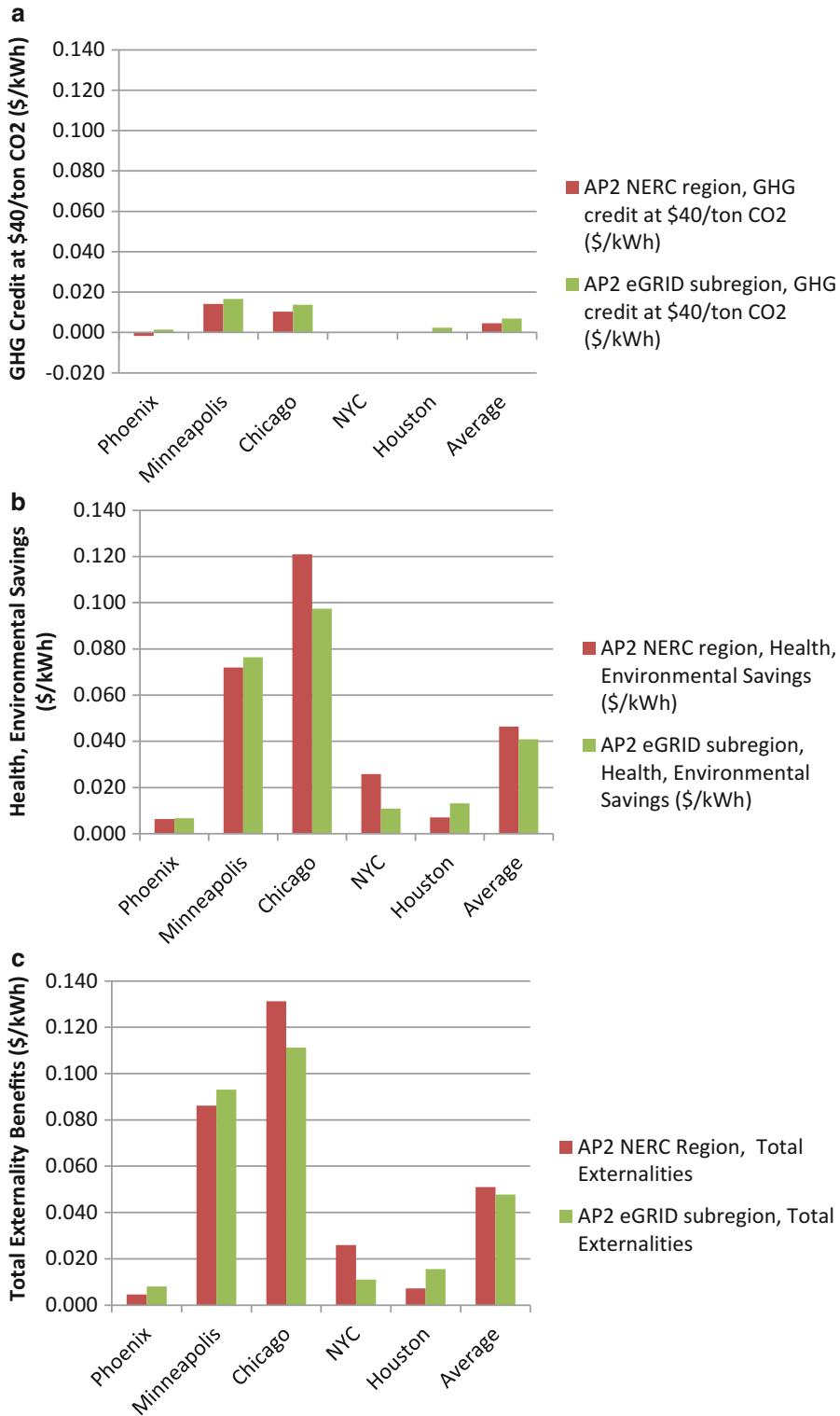
**Table 16** Summary of BOP cost in \$/kW for CHP systems with reformat fuel [2]

System size	Units per year			
	100	1000	10,000	50,000
10 kW	2703	2177	1792	1612
50 kW	1439	1188	982	881
100 kW	1097	894	744	676
250 kW	852	719	622	562

**Fuel Cell Systems: Total Cost of Ownership,**

**Fig. 17** Direct costs for PEM CHP systems as a function of system size and manufacturing volume





**Fuel Cell Systems: Total Cost of Ownership, Fig. 18** Total externality benefits for a 50 kWe PEM CHP system in a small hotel using AP2 health and

environmental impact model and either NERC region marginal emission factors (Siler Evans et al.) [24] or eGRID subregion emission factors (EPA ) [21]

is shown in Table 14. From Fig. 17, a customer cost of \$4000/kWe is assumed or about double the direct system cost at an annual manufacturing volume of 100 systems per year.

The cost of electricity in 2015 is shown in Fig. 19 for the case of a 50 kW PEM fuel cell system in a small hotel at an installed cost of \$4000/kWe. The first bar is the reference cost of electricity for the reference case of no fuel cell system in a 50 kW small hotel; the second bar is the LCOE from the fuel cell system. The third and fourth bars are the reduction in FC LCOE with heating fuel savings and then with health and environmental savings. The final bar is the LCOE with TCO savings for the fuel cell system case with electricity from the fuel cell system and with any purchased electricity from the grid. There is a net reduction in electricity cost in Minneapolis and Chicago which is driven by the health and environmental externality savings (Table 17).

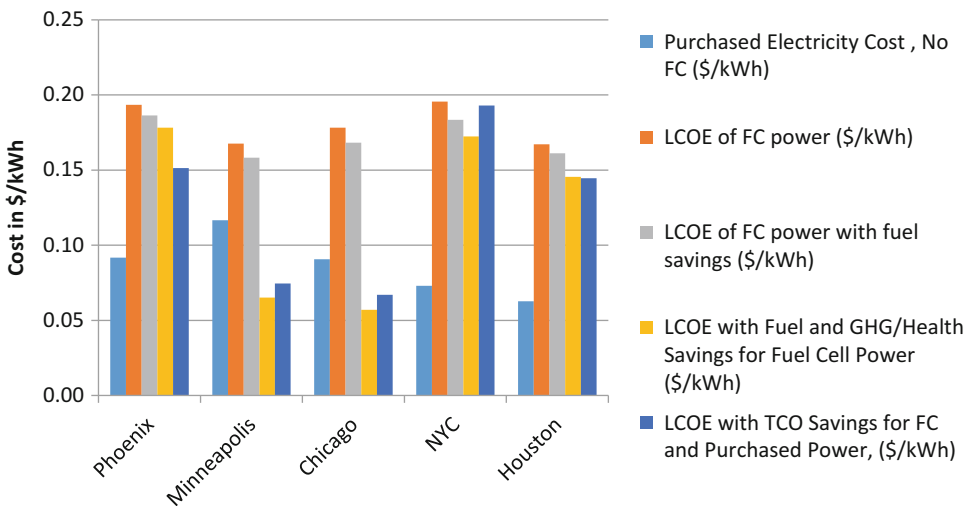
The estimated cost of electricity in 2030 with the estimated future grid emission reductions as described in section “Life-Cycle Impact Assessment Modeling” is shown in Fig. 20 with the same sequence of costs as in Fig. 19. In all cases the LCOE with TCO savings for FC and purchased power is greater than the cost of electricity in the reference case without a fuel cell system.

Cash Flow with Static and Lower Emissions from Electricity Grid

Another view of this is the consideration of cash flow. In this depiction, the capital costs are taken in the first year, and from this initial outlay, the annual difference in operating and fuel costs for a fuel cell system vs. the reference case of no FCS is added. Without externalities and assuming a static case of fixed fuel cell and grid emission factors, the private cash flow is negative for all years since the fuel cell system has higher annual cost for each year of operation.

Figure 21 shows a “societal cash flow” with both private costs and social costs including externalities. This depicts the overall costs to the private owner and to society. Note that this is a notional cash flow since the benefits that accrue to society are not captured by a private entity. In this case, because there is a roughly \$29,000 TCO savings per year (Note that the LCOE with TCO savings above includes the annualized capital costs of the fuel cell system but that the cash flow cash flow treats all equipment cost as an initial cash outlay.), the net cash flow is very favorable after 15 years.

The cash flow for the case of a changing electricity grid with lower emissions due to the Clean Power Plan and other regulations is shown in Fig. 21c. In this case the TCO savings from a

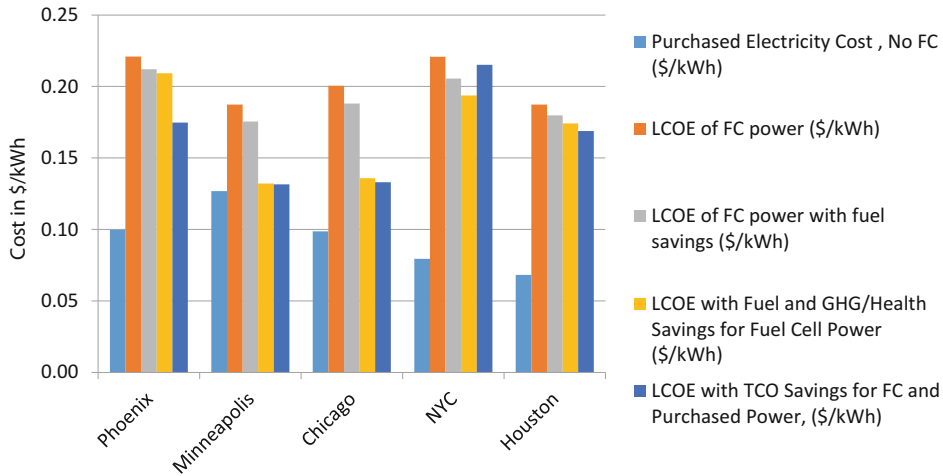


**Fuel Cell Systems: Total Cost of Ownership, Fig. 19** 2015 costs of electricity for a 50 kW PEM CHP system in a small hotel. The fuel cell system’s LCOE with TCO savings is favorable in Minneapolis and Chicago



**Fuel Cell Systems: Total Cost of Ownership, Table 17** LCC and LCIA output results for a 50 kWe PEM CHP system in a small hotel in five cities, assuming \$4000/kWe installed cost

Output	Phoenix, AZ		Minneapolis, MN		Chicago, IL		NYC, NY		Houston, TX	
	No FCS	Fuel cell	No FCS	Fuel Cell	No FCS	Fuel cell	No FCS	Fuel cell	No FCS	Fuel cell
Total electricity demand (kWh/yr)	576,668	576,668	419,590	419,590	424,147	424,147	369,661	369,661	497,656	497,656
Total space heating demand (kWh/yr)	23,307		174,743		135,869		135,869		0	
Total water heating demand (kWh/yr)	76,954		127,112		118,971		116,075		83,071	
Annual generated power by FC (kWh)		382,253		345,368		345,791		314,930		362,313
Annual generated heat by FC (kWh)		565,468		501,840		502,765		454,903		532,839
FC fraction of electricity demand		66%		82%		82%		85%		73%
Capital cost (\$/yr)		19,268		19,268		19,268		19,268		19,268
O&M cost (\$/yr)		11,468		10,361		10,374		9448		10,869
Scheduled maintenance (\$/yr)		1000		1000		1000		1000		1000
Fuel cost for fuel cell (\$/yr)		42,227		27,285		30,998		31,885		29,421
Fuel cost for conv. heating (\$/yr)	3574	831	7780	4504	7450	3972	8351	4504	2185	0
Purchased electricity Energy cost (\$/yr)	47,305	15,360	45,374	6679	32,104	4889	8798	6926	15,427	9524
Demand charge (\$/yr)	5445	3635	3422	1937	6021	3460	16,959	8882	15,490	9422
Fixed charge, electricity (\$/yr)	150	150	131	131	348	348	1241	1241	295	295
Total electricity cost (\$/yr)	52,899	93,108	48,927	66,662	38,473	70,337	26,998	78,650	31,213	79,800
Total cost of electricity (\$/kWh)	0.092	0.161	0.117	0.159	0.091	0.166	0.073	0.213	0.063	0.160
Purchased electricity cost (\$/kWh)	0.092	0.098	0.117	0.118	0.091	0.111	0.07303	0.311	0.063	0.142
LCOE of FC power (\$/kWh)		0.193		0.168		0.178		0.196		0.167
LCOE of FC power with fuel savings (\$/kWh)		0.186		0.158		0.168		0.183		0.161
LCOE with TCO savings for fuel cell power (\$/kWh)		0.178		0.065		0.057		0.172		0.146
LCOE with TCO savings for FC and purchased power, (\$/kWh)		0.151		0.074		0.067		0.193		0.145



**Fuel Cell Systems: Total Cost of Ownership, Fig. 20** 2030 costs of electricity for a 50 kW PEM CHP system in a small hotel with assumed reductions in

electricity grid emissions from the Clean Power Plan. The fuel cell system's LCOE with TCO savings is not favorable in any of the five cities

fuel cell (assuming static emission factors from the FCS) are seen to drop from about \$30,000 per year to about \$5000 per year. In this case the cash flow curve bends downward over time, and the societal cash flow is still net cash positive after 15 years, but the net cash flow in 2030 is reduced by about 80% from the static grid case above.

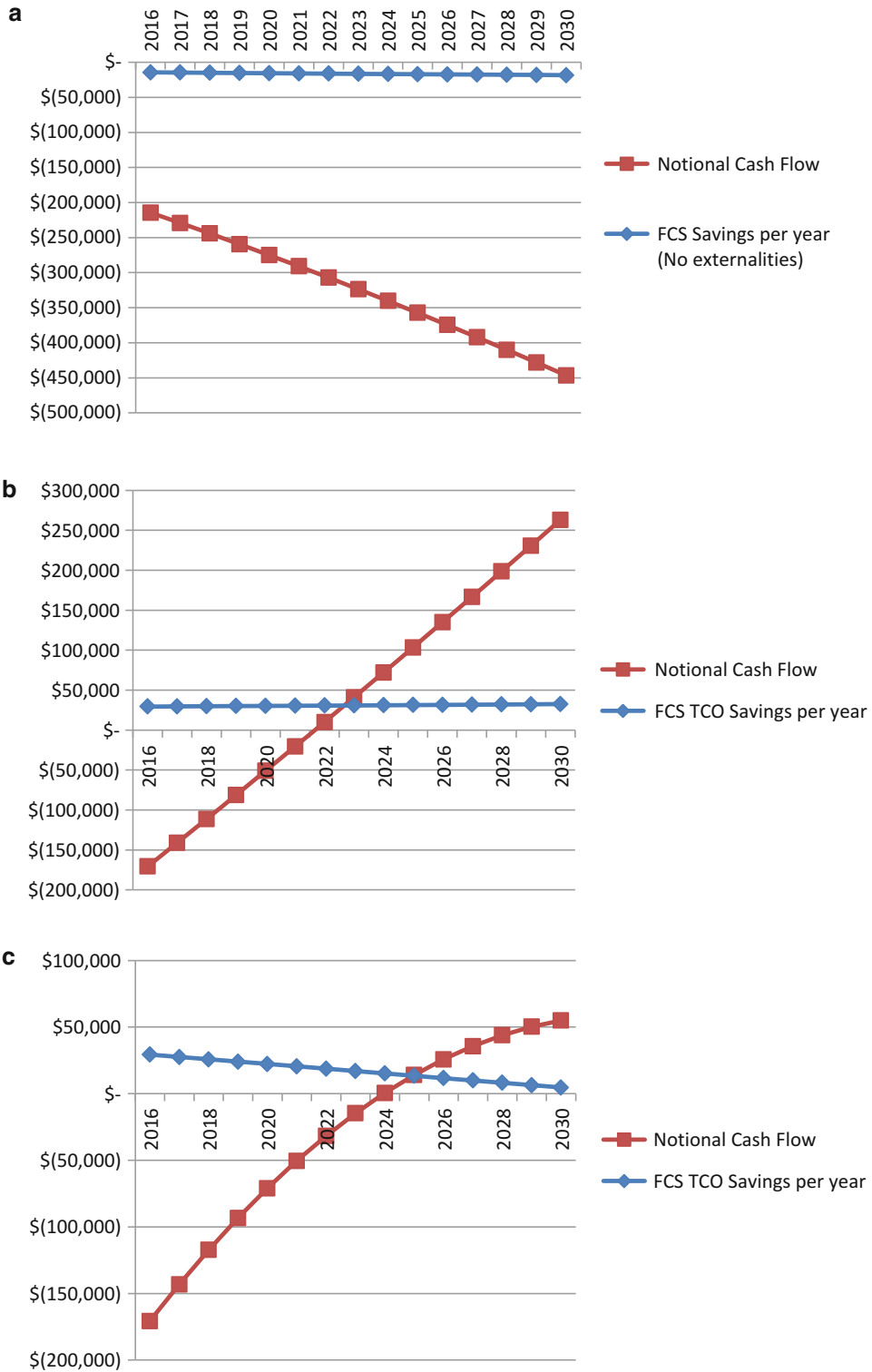
### SOFC Fuel Cell System Manufacturing Costs

A typical SOFC stack is made up of two electrodes (anode and cathode), an electrolyte, seals, interconnect plates, and a frame (Fig. 22). The electrodes and electrolyte form the electrolyte-electrode assembly (EEA) and forms the core component of the fuel cell stack where the electrochemical reactions take place. An anode supporting layer and cathode supporting layer is often added to the EEA, which are designed to support the cathode and anode layers as shown in Fig. 23. This entry is primarily based on FCE/VersaPower's anode-supported cell architecture and reported process steps and stack materials. In an anode-supported cell, the anode layer provides the structural support for the electrically active components.

For an SOFC stack, the electrolyte is typically made up of a ceramic material such as yttria-

stabilized zirconia (YSZ) due to its good ionic conductivity and robust mechanical properties under high-temperature operation. The anode is made up of a porous cermet material composed of nickel mixed with YSZ to allow the fuel to be diffused to the reaction sites close to the electrolyte layer, for the oxygen ions to oxidize the fuel and for the delivered electrons to be conducted to the next cell or to the external load. The composition and manufacturing process for the EEA is summarized in Table 18. The seals prevent the mixing of fuel and oxidant within the stack, leaking of fuel and oxidant from the stack, as well as to provide mechanical bonding for the components [41]. Barium-calcium-aluminosilicate (BCAS), an alkaline earth aluminosilicate glass, is most commonly used for SOFC seals due to its high electrical resistivity, high thermal expansion, and rapid crystallization kinetics [42] and was modeled in this study.

The interconnections provide both electrical contacts and gas channels between individual cells. For SOFC systems, interconnects are usually made from metal material since they need to withstand temperatures up to 1000 °C and usually have a lower manufacturing cost than ceramic-based interconnects. The EEA, seals, and interconnects together form the "stack repeating unit"



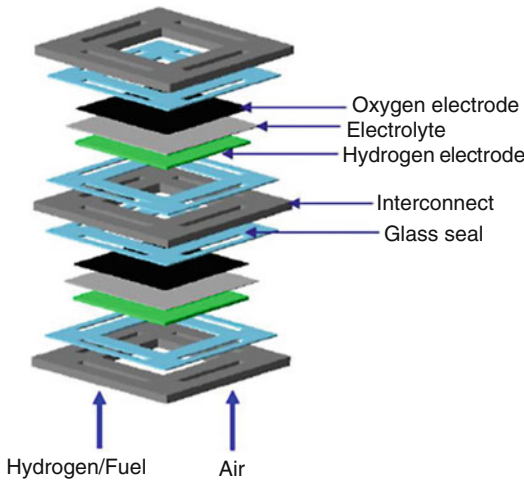
**Fuel Cell Systems: Total Cost of Ownership, Fig. 21** Cash flows for a 50 kW PEM CHP system at \$r000/kWe installed cost for a small hotel in Chicago. (a)

Private cash flow and (b) societal cash flow with private and social costs with a static grid and (c) social cost with a cleaner grid under the Clean Power Plan

(SRU) of the cell. These repeating units are connected together to provide a wide range of power output, forming a “stack.” Finally, a support structure, such as endplates with tie rods, holds the fuel cell stack together to provide structural support. In this study, a base design with SS441 interconnect and frame is assumed where

the interconnect has a thickness of 630 630 μm and a mass of 247 grams [43].

Total fuel cell plate area is taken to be 540 cm<sup>2</sup>. Active catalyzed area is about 61% of this area due to plate border regions and manifold openings. Single-cell active area has an additional 10% area loss due to the frame sealing process. The 10 kWe system consists of 130 cells in a single stack, while the 50 kW system has 5 stacks of 130 cells each. Only bottom-up costing details are presented in this section for the EEA assembly as an example and since this makes up the largest cost component of the SOFC stack. More details can be found in Scatagliini et al. [3].



**Fuel Cell Systems: Total Cost of Ownership, Fig. 22** Typical SOFC stack configuration [18]

**SOFC Stack Manufacturing Process Flow**

Three different process parameters have been taken into account in the cost model: (i) “availability,” or the percentage of time that equipment is available to run during the total possible planned production uptime; (ii) “performance,” a measure of how well the equipment runs within its time of operation; and (iii) “process yield or quality,” a measure of the number of parts that meet specification compared to how many were produced.

A major challenge for fuel cell manufacturing cost modeling is that these parameters are not available since data collected by fuel cell manufacturers are not accessible, and each fuel cell manufacturer uses different toolsets, different manufacturing techniques, and produces no more than 100 MW per year. As in other costing studies [44–46], the model assumes that losses decrease with increasing manufacturing volumes and level of automation due to (i) improvement of in-line inspection with greater inspection sensitivity and more accurate response to defects and

Cathode Functional Layer (50 μm)
Cathode/Electrolyte Interlayer (10 μm)
Electrolyte Layer (10 μm)
Anode/Electrolyte Interlayer (10 μm)
Anode Functional Layer (700 μm)

**Fuel Cell Systems: Total Cost of Ownership, Fig. 23** EEA schematic

**Fuel Cell Systems: Total Cost of Ownership, Table 18** EEA composition and manufacturing process

Component	Materials	Thickness/μm	Process
Anode	Ni/YSZ	700	Tape casting
Anode electrolyte interlayer	50% YSZ 50% NiO	10	Screen printing
Electrolyte	YSZ (yttria-stabilized zirconia)	10	Screen printing
Electrolyte/cathode interlayer	50% YSZ 50% LSM	10	Screen printing
Cathode	LSM (lanthanum strontium manganite)	50	Screen printing

in-line signals, (ii) development of models that relate in-line metrics and measurements to output responses and performance [33], and (iii) utilization of greater feedback systems in manufacturing processing for real-time adjustment of process parameters.

Since vendors and industry advisors do not provide exact information about these parameters, the approach is to assume a range for each parameter as described below and then estimate intermediate values through exponential interpolation depending on annual production volume (Table 19). The advantage of introducing these parameters in the model is because, using sensitivity analysis, it is possible to estimate the impact of these parameters on manufacturing costs.

Line availability is assumed to be 80% and process yield to be 85% at low volumes (<100,000 EEA cells year<sup>-1</sup>, 10 MWe). At the highest volumes (>10,000,000 EEA cells year<sup>-1</sup>, 500 MWe year<sup>-1</sup>), line availability and process yield are assumed equal to 95%. For volumes between 100,000 and 10,000,000 EEA cells year<sup>-1</sup>, the process parameters are found through exponential interpolation. Line performance is considered equal to 89% for manual configuration and 95% for semiautomatic and automatic configurations. As a comparison, Fuel Cell Energy Inc. has reported a fabrication yield of 95% at a production volume of 500 kWe per year<sup>-1</sup> [43].

**SOFC Stack Material Cost**

Material costs are obtained from multiple vendors from Japan, the USA, and China. These countries are the primary suppliers for SOFC materials worldwide. Material prices are priced based on delivery to the geographical center of the USA. Material quality and prices from Chinese suppliers are also evaluated versus US distributors to determine their competitiveness.

Material prices for the EEA used in this study are shown in Table 20. For the EEA, material cost of each layer was calculated using the weight of the slurry constituents multiplied by the corresponding material cost (\$ kg<sup>-1</sup>). For the anode-supported cell design, the anode materials contribute to about 75–82% of the EEA material

cost due to the thickness of the anode layer. Table 21 shows the material prices for the binders, plasticizers, pore formers, and solvents at different order quantities. As shown in the tables, material costs are highly dependent on annual production volume, especially for ceramic materials used in the fabrication of the EEA cells.

At high volumes, material cost is one of the dominant cost drivers in a SOFC stack. In most cases, material prices from Chinese suppliers are competitive with US-based suppliers, while prices from Japanese suppliers were the highest among all vendors.

**Electrode-Electrolyte Assembly (EEA) Functional Cell**

Based on a literature search and discussions with industry experts, the steps required for the fabrication of the EEA functional cell are:

1. Preparing the anode slurry using a two-step ball milling process
2. Sieving and de-airing of the anode slurry
3. Tape casting and infrared drying of the anode tape

**Fuel Cell Systems: Total Cost of Ownership, Table 19** EEA manufacturing line process parameters for all annual production volumes

Power	Systems/year	Process yield (%)	Availability (%)	Line performance (%)
10	100	88%	80%	89%
	1000	91%	81%	95%
	10,000	92%	88%	95%
	50,000	93%	93%	95%
50	100	90%	80%	89%
	1000	92%	86%	95%
	10,000	93%	93%	95%
	50,000	94%	95%	95%
100	100	91%	81%	95%
	1000	92%	88%	95%
	10,000	94%	95%	95%
	50,000	95%	95%	95%
250	100	91%	84%	95%
	1000	93%	910%	95%
	10,000	94%	95%	95%
	50,000	95%	95%	95%

**Fuel Cell Systems: Total Cost of Ownership, Table 20** Anode-supported cell material prices

Vendor/country	Material	Order quantity/kg	Price/\$ kg <sup>-1</sup>	Comments
Daiichi JITSUGYO (Japan)	Nickel oxide	1000	68.5	CIF USA by sea
		5000	42.5	CIF USA by sea
		10,000	37	CIF USA by sea
		20,000	34	CIF USA by sea
Daiichi JITSUGYO (Japan)	8YSZ (8 mol%YSZ)	100	78	CIF USA by sea
		1000	68	CIF USA by sea
		5000	63	CIF USA by sea
Daiichi (Japan)	8YSZ (8 mol%YSZ)	10	97	CIF USA by sea
		100	95	CIF USA by air
		1000	83	CIF USA by sea
Inframat Advanced Materials (USA)	8YSZ (8 mol%YSZ)	1	139.2	By rail or truck
		5	115.8	By rail or truck
		10	94.5	By rail or truck
		50	71.6	By rail or truck
		100	49.7	By rail or truck
		1000	35.2	By rail or truck
		10,000	29.8	By rail or truck
Inframat Advanced Materials (USA)	LSM powder	100	170	By rail or truck
		1000	95	By rail or truck
		10,000	70	By rail or truck
Qingdao Terio Corporation (China)	LSM powder	10	250	CIF USA by air
		100	150	CIF USA by air
		200	125	CIF USA by air
		500	105	CIF USA by air
		1000	80	CIF USA by air
		2000	75	CIF USA by air
5000	60	CIF USA by air		

*CIF* price including cost, insurance, and freight

- Rolling in a take-up roll of the green tape
- Cutting and blanking into sheets of the green tape
- Screen printing and infrared drying of subsequent layers (anode-electrolyte interlayer, electrolyte, cathode-electrolyte interlayer, and cathode layer) above the anode sheet
- First quality check (infrared imaging and ultrasonic spectroscopy)
- Bonding together the mini-stack of five layers by placing it in a furnace at elevated temperature (~1300–1400 °C) for 24 h [47, 48]
- Laser cutting of the EEA cell to the proper dimensions;
- Final quality check (infrared imaging, ultrasonic spectroscopy, and vacuum leak test)

In this entry, slurries are prepared by a two-step ball milling process. In the first step, solid powders are ball milled for 12 h in solvent. In the second step, binder and plasticizer are added and then ball milled for another 12 h [49]. Quantities of slurry to mill per day are estimated based on number of cells casted per day and slurry weight of each layer. Slurry drying time is estimated using the average evaporation rate value of aqueous slurry described by Mistler et al. [50] as suggested in a Battelle report [51]. Assuming that the ratio of the freshly deposited layer thickness to the dried tape thickness is two [52] and multiplying this freshly deposited layer thickness by its corresponding liquid density, it was possible to obtain the quantity of liquid removed per unit area. The corresponding slurry drying time

**Fuel Cell Systems: Total Cost of Ownership, Table 21** Binders, plasticizers, pore formers, and solvent prices

Vendor/country	Material	Order quantity/kg	Price/\$ kg <sup>-1</sup>	Comments
Jiangsu Xiangcanghongrun Trade Co., Ltd. (China)	N-butyl acetate 99,5%	100	4.34	CIF USA by sea
		1000	1.516	CIF USA by sea
		10,000	1.29	CIF USA by sea
ChemPoint Inc. (USA)	Methocel A4M	1–45,400	18.5–29.6	CIF price
Dowd & Guild, Inc. (CA)	Butvar B-76	63.5	23.37	By rail or truck
		200	21.42	By rail or truck
		500	19.47	By rail or truck
		1000	18.36	By rail or truck
		2000	17.14	By rail or truck
		5000	16.07	By rail or truck
Univar (USA)	Santicizer 160	Confidential information from vendor		
Cancarb Limited (USA)	Thermax <sup>®</sup> N990 thermal carbon black	Confidential information from vendor		
Jinan Shijitongda Chemical Co., Ltd. (China)	2-Butoxyethanol	1000	3.07	CIF USA
		10,000	3.07	CIF USA
		100,000	2.53	CIF USA
		1000,000	2.32	CIF USA
		10,000,000	2.29	CIF USA

*CIF* price including cost, insurance, and freight

is estimated dividing the quantity of liquid removed per unit area by an average evaporation rate of the solvent equal to  $2.22 \times 10^{-5}$  g cm<sup>-2</sup> s<sup>-1</sup> at room temperature for an air flow rate of 75 l min<sup>-1</sup> [51]. Estimated slurry drying times are 24.7 min for the anode slurry, 0.48 min for the electrolyte slurry, 2.2 min for the cathode slurry, and 0.44 min for interlayer slurries. In reality, evaporation rates may be expected to be faster than the ones considered in this study since water evaporates more slowly than most organic solvents as n-butyl acetate or 2-butoxyethanol [53].

Equipment size, cycle times, and level of automation vary with annual production rates. Tape casting machines are sized depending on production volume, slurry drying time, and casting speed. Tape casting speed varies with annual production volume

and machine size from 0.25 to 1 m min<sup>-1</sup>. Subsequent process modules included in the production line are sized based on the estimated production capacity and cycle time of the tape casting machine.

#### SOFC Stack Direct Manufacturing Costs

Table 22 shows the cost model results for all system sizes and production rates. Considering the base design, stack cost per unit of electrical power (\$ kWe<sup>-1</sup>) decreases both with increasing system size and increasing annual production rate. When comparing the two key cost drivers, cost seems to be somewhat more sensitive to system size than to production rate, and the impact of system size diminishes at higher production volumes.

**Fuel Cell Systems: Total Cost of Ownership, Table 22** SOFC stack costs [3]

System size (kW)	100 systems/yr	1000 systems/yr	10,000 systems/yr	50,000 systems/yr
10	1039	342	197	178
50	478	215	176	170
100	339	194	171	168
250	249	181	167	166

Figure 24 shows stack manufacturing costs broken out by component for 10 kWe systems. The largest contributor to the stack manufacturing cost is the EEA, which constitutes about 50% of total cost in all cases analyzed. Interconnect and cell-to-frame seal each constitute 11–15% of the stack cost and decrease with production volume. Stack assembly and conditioning process remains constant at about 9% of the stack cost. The relative contribution of frame manufacturing cost to overall stack cost increases with production volume since at low volumes, it is assumed that interconnect manufacturing lines are used and there is no capital cost and building cost associated with the frames.

At low volumes, process capital and labor costs are the categories that most affect the stack cost, whereas at high volume, material cost dominates followed by process capital cost. Figure 25 demonstrates that with increasing production, volume process/operational costs increase and labor cost decreases at greater level of automation. Capital and building costs decrease due to the higher equipment utilization, and scrap cost decreases since the cost model assumes lower defective rate at higher production volumes.

### SOFC Balance of Plant and System Costs

The balance of plant analysis approach is similar to that for PEM FCS described above (Table 23). Since the SOFC is a higher-temperature process than PEM, the overall balance of plant is simpler in terms of requiring fewer components and has overall lower cost. For example, the SOFC unit in Fig. 9 has a smaller reformer unit, no post-reformer cleanup, and no air humidification system. Again the BOP is subdivided into six subsystems:

1. Fuel subsystem
2. Air subsystem

3. Heat management subsystem
4. Power subsystem
5. Control and meter subsystem
6. Miscellaneous subsystem

Overall the BOP cost for SOFC systems is estimated to be about 35% lower per kWe than PEM at annual production rates of greater than about 10 MW.

For the CHP reformat system, the power subsystem represents the largest subsystem cost for the 100 kWe system, representing approximately 40% of the total BOP, following by the control and meter subsystem. In particular, the power inverter is a dominant cost driver, representing approximately 80% of the cost in the power subsystem (Table 15).

Direct system costs for CHP are shown in Fig. 26. For a 50 kWe system at 100 units per year, a customer cost of \$3000/kWe for an installed system is assumed, or about double the direct system cost assuming similar corporate markup and installation costs as for the PEM case above.

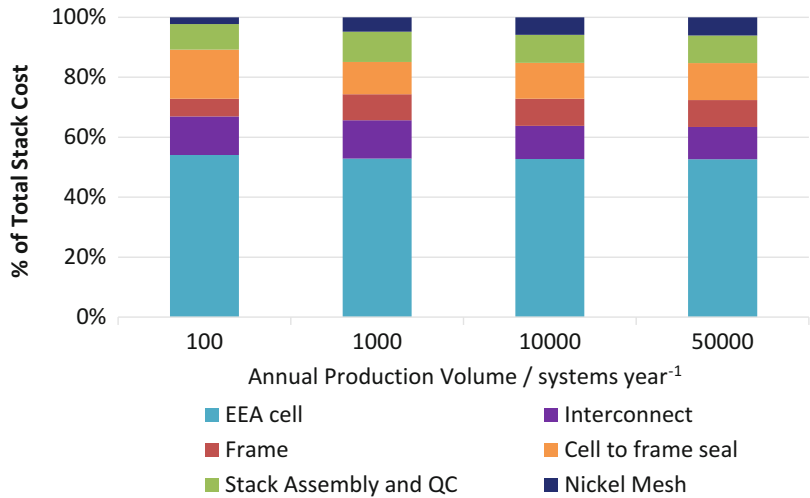
### SOFC vs. PEM Fuel Cell CHP Balance of Plant and System Costs

A summary of fuel cell stack, balance of plant, and direct system costs for SOFC and PEM fuel cell CHP systems is shown in Table 24. Focusing on the 50 kWe system size, the stack cost is estimated to be lower for SOFC by about 20–30% across manufacturing values, the BOP is between 30% and 40% lower, and the overall direct cost is about 25–35% lower. For both PEM and SOFC, the BOP is the dominant component of cost at about 70–80% of direct system cost with the BOP share of cost increasing as annual volume increase.



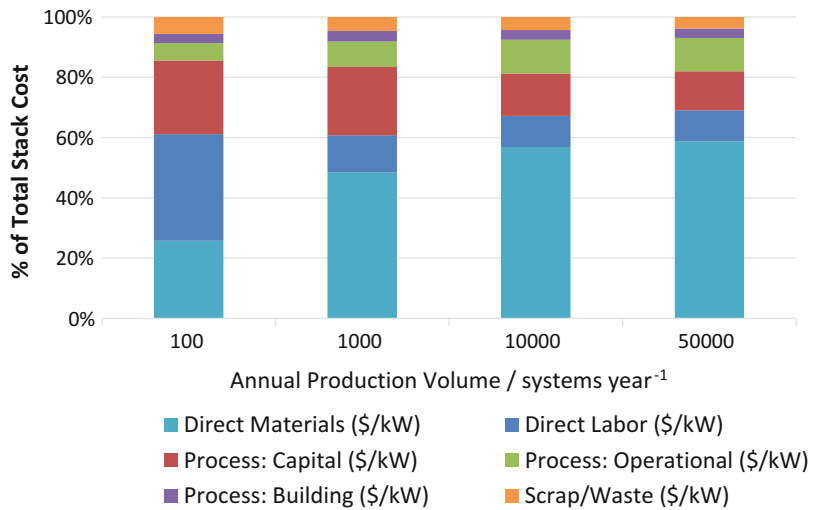
**Fuel Cell Systems: Total Cost of Ownership, Fig. 24**

Disaggregation of stack cost by relative percentage of stack components cost to overall stack cost for 50 kWe systems [3]



**Fuel Cell Systems: Total Cost of Ownership, Fig. 25**

Disaggregation of stack cost by relative percentage of cost components to overall stack cost for 50 kWe systems [3]



**Fuel Cell Systems: Total Cost of Ownership, Table 23** Summary of BOP costs in \$/kWe for SOFC CHP [3]

System size	100 units/year	1000 units/year	10,000 units/year	50,000 units/year
250 kWe	\$ 693	\$ 488	\$ 419	\$ 365
100 kWe	\$ 807	\$ 564	\$ 479	\$ 422
50 kWe	\$ 1002	\$ 721	\$ 611	\$ 537
10 kWe	\$ 1638	\$ 1217	\$ 1027	\$ 925

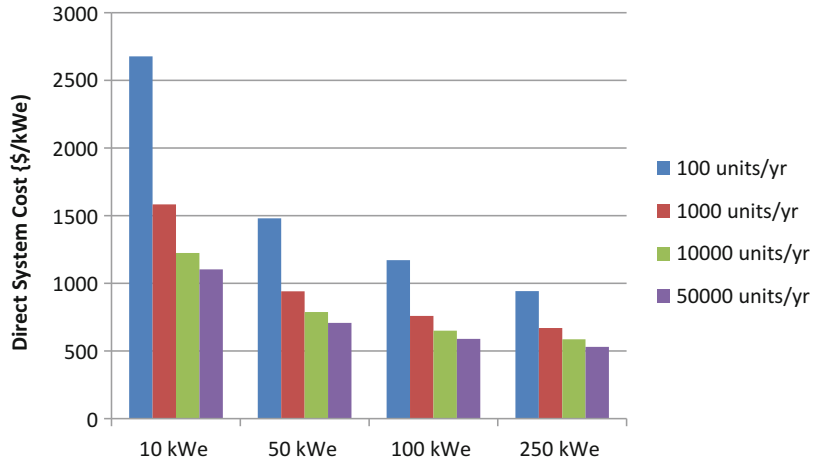
**SOFC CHP System Life-Cycle Cost and LCIA Model Example**

Example output of the LCC/LCIA model for a 50 kW small hotel in five representative cities is shown in Table 25. The cost of electricity in 2015 is shown in Fig. 27 for the case of a 50 kW SOFC fuel cell system in a small hotel at an installed cost of

\$3000/kWe. As in the PEM FC technology case above, the first bar is the reference cost of electricity for the reference case of no fuel cell system in a 50 kW small hotel and the second bar is the LCOE from the fuel cell system. The third and fourth bars are the reduction in FC LCOE with heating fuel savings and then with health and environmental

### Fuel Cell Systems: Total Cost of Ownership,

**Fig. 26** Direct costs for SOFC CHP systems as a function of system size and manufacturing volume [3]



savings, respectively. The final bar is the LCOE with TCO savings for the fuel cell system case with electricity from the fuel cell system and with any purchased electricity from the grid. There is a net reduction in electricity cost in Minneapolis and Chicago which is driven by the health and environmental externality savings.

The estimated cost of electricity in 2030 is shown in Fig. 28 with the same sequence of costs as above assuming a cleaner electricity grid under the Clean Power Plan. In this case, the LCOE with TCO savings for FC and purchased power is still lower than the cost of electricity in the reference case without a fuel cell system in Minneapolis and Chicago.

Figure 29a, b shows the private cash flow and societal cash flow in the case of a static electricity grid. As with the PEM system, the private cash flow is negative, but TCO savings in the latter case generates positive cash flow after about 2 years. Even with the Clean Power Plan and a lower polluting electricity grid, the societal cash flow is strongly net positive in 2030 (Fig. 29c).

## Summary

### Discussion

All fuel cell stack components (CCM, GDL, framed MEA, plates and stack assembly for PEM and EEA, plate, frame, and stack assembly for SOFC) are assumed to be manufactured in-house with high throughput processes and

high yield ( $\geq 95\%$ ) assumed for all modules at high manufacturing volumes. Direct cost results for the stack will be highly dependent on the yield assumptions for each process module. Here, nearly fully automated roll-to-roll processing is modeled for the critical catalyst-coated membrane and for the GDL.

The assumed yield rates are a key uncertain variable in estimating fuel cell stack manufacturing costs. While it was not in the scope of this entry to do a detailed yield feasibility analysis, well-established methodologies exist for improving yield using similar process modules in other industries, and learning by doing and improvements in yield inspection, detection, and process control are implicitly assumed. This entry assumes that high yield is achieved at high manufacturing volumes. This stems from several implicit assumptions.

Learning by doing over the cumulative volume of fuel cell component production and greater process optimization will drive yield improvement both within a given vendor and from vendor to vendor through industry interactions (conferences, IP, cross vendor personnel transfers, etc.):

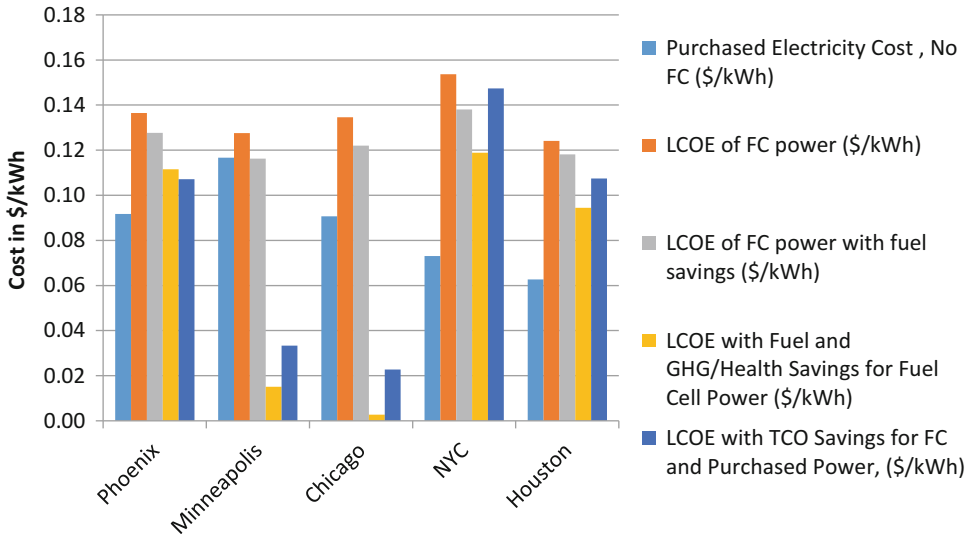
- In-line inspection improvement with greater inspection sensitivity and more accurate response to defects and in-line signals.
- Greater development and utilization of “transfer functions” (Manhattan Projection [33]), e.g., development of models that relate in-line

**Fuel Cell Systems: Total Cost of Ownership, Table 24** Direct costs for PEM and SOFC CHP fuel cell systems as a function of system size and annual manufacturing volume

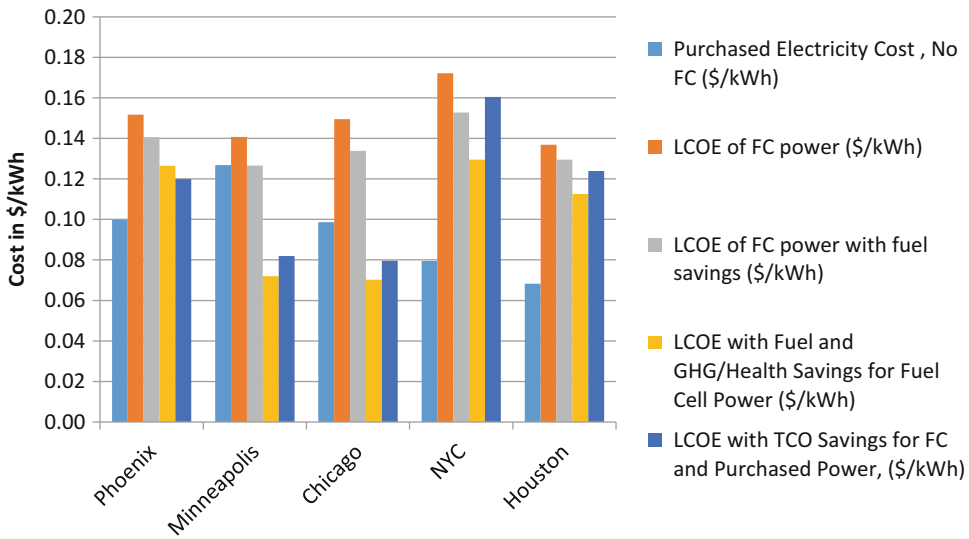
System size {kW}	Fuel cell stack (PEM)				Fuel cell stack (SOFC)				SOFC cost reduction (stack)			
	100 units/year-1	1000 units/year-1	10,000 units/year-1	50,000 units/year-1	100 units/year-1	1000 units/year-1	10,000 units/year-1	50,000 units/year-1	100 units/year-1	1000 units/year-1	10,000 units/year-1	50,000 units/year-1
10 kWe	340	497	333	284	1039	342	197	178	22%	31%	41%	37%
50 kWe	596	352	272	239	478	215	176	170	<b>20%</b>	<b>39%</b>	<b>35%</b>	<b>29%</b>
100 kWe	466	313	249	219	339	194	171	168	27%	38%	31%	23%
250 kWe	377	279	231	203	249	181	167	166	34%	35%	28%	18%
	Balance of plant (PEM)				Balance of plant (SOFC)				SOFC cost reduction (BOP)			
System size {kW}	100 units/year-1	1000 units/year-1	10,000 units/year-1	50,000 units/year-1	100 units/year-1	1000 units/year-1	10,000 units/year-1	50,000 units/year-1	100 units/year-1	1000 units/year-1	10,000 units/year-1	50,000 units/year-1
10 kWe	2703	2177	1792	1612	1638	1217	1027	925	39%	44%	43%	43%
50 kWe	1439	1188	982	881	1002	721	611	537	<b>30%</b>	<b>39%</b>	<b>38%</b>	<b>39%</b>
100 kWe	1097	894	744	676	807	564	479	422	26%	37%	36%	38%
250 kWe	852	719	622	562	693	488	419	365	19%	32%	33%	35%
	System direct cost (PEM)				System direct cost (SOFC)				SOFC cost reduction (SYSTEM)			
System size {kW}	100 units/year-1	1000 units/year-1	10,000 units/year-1	50,000 units/year-1	100 units/year-1	1000 units/year-1	10,000 units/year-1	50,000 units/year-1	100 units/year-1	1000 units/year-1	10,000 units/year-1	50,000 units/year-1
10 kWe	4043	2674	2125	1896	2677	1559	1224	1103	34%	42%	42%	42%
50 kWe	<b>2035</b>	1540	1254	1120	<b>1480</b>	936	787	707	<b>27%</b>	<b>39%</b>	<b>37%</b>	<b>37%</b>
100 kWe	1563	1207	993	895	1146	758	650	590	27%	37%	35%	34%
250 kWe	1229	998	853	765	942	669	586	531	23%	33%	31%	31%
	BOP share of total cost (PEM)				BOP share of total cost (SOFC)							
System size {kW}	100 units/year-1	1000 units/year-1	10,000 units/year-1	50,000 units/year-1	100 units/year-1	1000 units/year-1	10,000 units/year-1	50,000 units/year-1				
10 kWe	67%	81%	84%	85%	61%	78%	84%	84%				
50 kWe	<b>71%</b>	<b>77%</b>	<b>78%</b>	<b>79%</b>	<b>68%</b>	<b>77%</b>	<b>78%</b>	<b>76%</b>				
100 kWe	70%	74%	75%	76%	70%	74%	74%	72%				
250 kWe	69%	72%	73%	73%	74%	73%	72%	69%				

**Fuel Cell Systems: Total Cost of Ownership, Table 25** LCC and LCIA output results for a 50 kWe SOFC CHP system in a small hotel in five cities, assuming \$3000/kWe installed system cost

Output	Phoenix, AZ		Minneapolis, MN		Chicago, IL		NYC, NY		Houston, TX	
	No FCS	Fuel cell	No FCS	Fuel cell	No FCS	Fuel cell	No FCS	Fuel cell	No FCS	Fuel cell
Total electricity demand (kWh/yr)	576,668	576,668	419,590	419,590	424,147	424,147	369,661	369,661	497,656	497,656
Total space heating demand (kWh/yr)	23,307		174,743		135,869		135,869		0	
Total water heating demand (kWh/yr)	76,954		127,112		118,971		116,075		83,071	
Annual generated power by FC (kWh)		382,253		345,368		345,791		314,930		362,313
Annual generated heat by FC (kWh)		90,829		145,416		142,764		142,049		78,340
FC fraction of electricity demand		66%		82%		82%		85%		73%
Capital cost (\$/yr)		14,451		14,451		14,451		14,451		14,451
O&M cost (\$/yr)		11,468		10,361		10,374		9448		10,869
Scheduled maintenance (\$/yr)		1000		1000		1000		1000		1000
Fuel cost for fuel cell (\$/yr)		25,252		18,254		20,705		23,481		18,629
Fuel cost for conv. heating (\$/yr)	3574	201	7780	3875	7450	3102	8351	3447	2185	39
Purchased electricity energy cost (\$/yr)	47,305	15,360	45,374	6679	32,104	4889	8798	6926	15,427	9524
Demand charge (\$/yr)	5445	3635	3422	1937	6021	3460	16,959	8882	15,490	9422
Fixed charge, electricity (\$/yr)	150	150	131	131	348	348	1241	1241	295	295
Total electricity cost (\$/yr)	52,899	71,316	48,927	52,813	38,473	55,227	26,998	65,428	31,213	64,191
Total cost of electricity (\$/kWh)	0.092	0.124	0.117	0.126	0.091	0.130	0.073	0.177	0.063	0.129
Purchased electricity cost (\$/kWh)	0.092	0.098	0.117	0.118	0.091	0.111	0.07303	0.311	0.063	0.142
LCOE of FC power (\$/kWh)		0.136		0.128		0.135		0.154		0.124
LCOE of FC power with fuel savings (\$/kWh)		0.128		0.116		0.122		0.138		0.118
LCOE with TCO savings for fuel cell power (\$/kWh)		0.111		0.015		0.003		0.119		0.094
LCOE with TCO savings for FC and purchased power (\$/kWh)		0.107		0.033		0.023		0.147		0.107



**Fuel Cell Systems: Total Cost of Ownership, Fig. 27** 2015 costs of electricity for a 50 kW SOFC CHP system in a small hotel. The fuel cell system’s LCOE with TCO savings is favorable in Minneapolis and Chicago



**Fuel Cell Systems: Total Cost of Ownership, Fig. 28** 2030 costs of electricity for a 50 kW SOFC CHP system in a small hotel with assumed reductions in

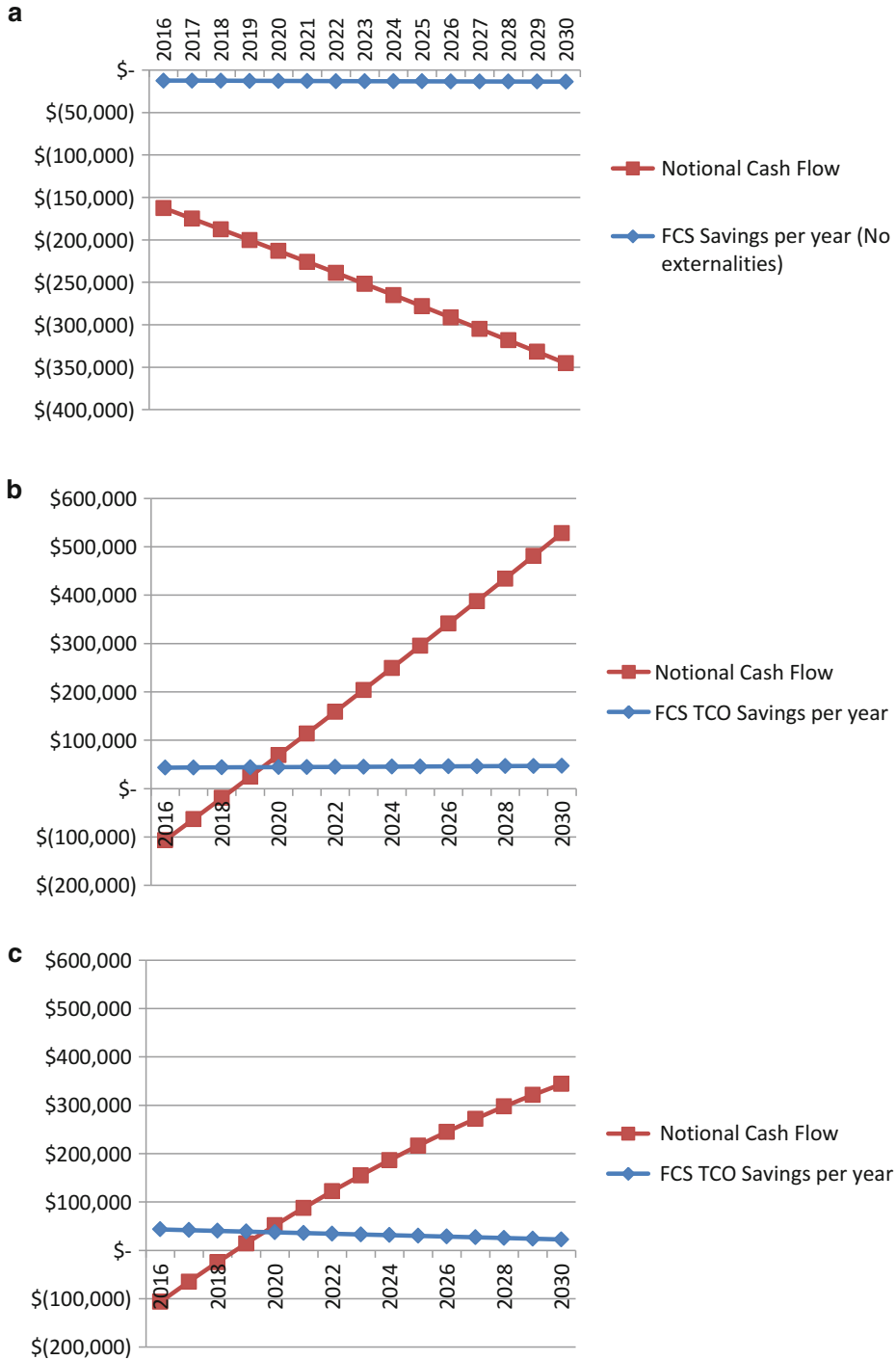
electricity grid emissions from the Clean Power Plan. The fuel cell system’s LCOE with TCO savings is still favorable in Minneapolis and Chicago

metrics and measurements to output responses and performance, and resultant improvement in in-line response sensitivity and process control.

- Utilization of greater feedback systems in manufacturing processing such as feed-forward sampling, for real-time adjustment of

process parameters (e.g., slot die coating thickness and process parameter control).

- Systematic, integrated analysis to anticipate and prepare for yield excursions, e.g., FMEA (failure modes and effect analysis).
- Consideration of yield limiting mechanisms or FMEA-type analysis as a function of



**Fuel Cell Systems: Total Cost of Ownership, Fig. 29** Cash flows for a 50 kW SOFC CHP system at \$3000/kWe installed cost for a small hotel in Chicago. (a)

Private cash flow and (b) societal cash flow with private and social costs with a static grid and (c) social cost with a cleaner grid under the Clean Power Plan

process tooling assumptions is out of scope here and would be very challenging in this type of analysis entry without access to manufacturing data.

At low volumes, PEM stack cost is sharply reduced when moving from a production volume of 100 to 1000 systems per year since tool utilization increases rapidly and capital costs drop sharply. At high volumes, the stack cost is seen to fall at a rate between 20% and 30% per decade increase in volume. This is driven by improved yield and lower direct material costs (e.g., membrane and carbon fiber paper).

Direct material costs dominate PEM stack costs at high volume. For fuel cell stacks in CHP systems with reformat fuel at high production volumes, CCM manufacturing is about 55% of manufacturing cost, with plates at about 20%, and frame and seal about 15%. In terms of cost dominating factor, it was found that yield, power density, and Pt price are the most contributing factors to the overall stack cost.

For SOFC stacks, the EEA makes up about 50% of the stack cost at all annual production volumes, followed by the cell-sealing process at 10–18%, and interconnects at 10–15% of the stack manufacturing cost. The process yield and power density are the most sensitive parameters for the stack cost at both low and high annual production volumes. At low production volumes (5MWe per year), line performance and labor rate are the next most sensitive parameters, while at high production volume (2500 MWe per year), material costs and tool availability also become important cost sensitivities.

Under the assumptions of this entry, SOFC stack and system cost are significantly lower than PEM FCS. A representative 50 kWe system SOFC stack costs us 20–30% lower than PEM, BOP costs are 30–40% lower, and overall direct manufacturing cost is 25–35% than PEM. The SOFC stack does not require a precious metal catalyst, and the SOFC balance of plant has a lower number of components because of higher-temperature operation, and these factors lead to overall lower manufacturing cost.

This entry did not consider detailed DFMA-type cost analysis for balance of plant components. The case of BOP components built in-house was not considered (i.e., “make” versus “buy”) because many BOP components are commodity parts (e.g., pumps, compressors, tanks, motors, cabinets, variable frequency drives, tubing, piping, inverters, valves, heat exchangers, switches, flow sensors) for especially the larger CHP systems. Hence, this assumes that it would be less expensive to purchase these commodity components rather than manufacturing them in-house. Fuel cell manufacturers are unlikely to embark upon a program of producing BOP commodity parts in-house, with some exceptions still being investigated. Thus, the BOP is largely assumed to be comprised of purchased components that are either assembled or integrated by a fuel cell system manufacturer. The downside of this approach is that a fuel cell system provider may be forced to make nonoptimal design choices based on the availability of component part sizes. In some cases, customized design of non-commodity parts is required, as in the case of a manifold block for lower-power systems, but in these cases, the part is assumed to be designed by the fuel cell system provider and purchased from a contract manufacturer. However, many of these components could be readily produced in larger volume in the future, e.g., machined aluminum blocks, and perhaps as more integrated subassemblies. BOP integration and cost reductions realized therein seem more critical at lower system sizes where BOP costs are expected to comprise a larger fraction of overall system costs. In such cases, a FC manufacturer might work closely with a contract manufacturer or part vendor to prototype and develop such subassemblies. This type of part integration and subassembly design was not explicitly considered in this entry, but may represent further cost-reduction opportunities. Similarly, a rigorous examination of in-house manufacturing vs. external purchase was not done for every part and may also yield cost saving opportunities for some balance of plant components or assemblies. Since BOP is estimated to be a large fraction of overall costs,

**Fuel Cell Systems: Total Cost of Ownership, Table 26** US Department of Energy equipment cost targets for 2020 and estimated costs in this entry

System	Units/yr	2020 DOE target with markup (\$/kW)	PEM direct cost (\$/kW)	PEM cost with 50% markup (\$/kW)	SOFC direct cost (\$/kW)	SOFC cost with 50% markup (\$/kW)
		DOE targets	This work			
10 kW CHP system	50,000	\$1700	\$1896	<b>\$2844</b>	\$1103	<b>\$1655</b>
100 kW CHP system	1000	\$1000	\$1207	<b>\$1810</b>	\$758	<b>\$1137</b>

this general area of part integration and consolidation and design optimization is a critical area for future work.

#### Comparison to DOE 2020 Targets

The output of this entry can also be compared with DOE targets for 2020 (Table 26). For 10 kWe CHP systems at 50,000 units per year, the DOE target is \$1700/kWe, and for 100 kWe and 1000 units per year, the equipment cost target is \$1000/kWe. This entry estimates that PEM equipment cost (direct cost with an assumed 50% equipment markup is about 70–80% higher than the DOE targets, while the SOFC system is meeting the 10 kWe target and within 15% of the 100 kWe target.

#### Conclusions

Direct costs are estimated for PEM and SOFC FC CHP systems from 10 to 250 kWe sizes and for annual manufacturing volumes of 100 systems per year to 50,000 systems per year. Key assumptions include vertically integrated manufacturing and high speed, relatively high-yield stack deposition processes for the membrane electrode or electrode/electrolyte assembly, and cost reductions in material costs with higher-volume purchases from material suppliers. Implicit in these assumptions is the assumption of continuous “learning by doing” as manufacturing volumes increase to improve process yields and accumulation of knowledge regarding best manufacturing processes and defect mode characterization and understanding.

Bottom-up DFMA costing analysis for fuel cell stack components in this entry shows that, for

stationary applications, PEM fuel cell stacks alone can approach a direct manufacturing cost of \$200 per kWe of net electrical power at high production volumes (e.g., 250 kW CHP systems at 50,000 systems per year). Overall system costs including corporate markups and installation costs are estimated to reach \$2200/kWe (\$1600/kWe) for 50 kW (250 kW) CHP systems at 50,000 systems per year.

SOFC fuel cell stacks can approach a direct manufacturing cost of \$165 per kWe of net electrical power at high production volumes (e.g., 250 kWe CHP systems at 50,000 systems per year). Overall SOFC system costs including corporate markups and installation costs are estimated to reach \$1400/kWe and \$1100/kWe for 50 kW (250 kW) CHP systems at 50,000 systems per year.

For both PEM and SOFC, balance of plant costs including the fuel processor makes up about 70–80% of total direct costs for 50 kWe CHP systems across the range of production volumes and is thus a key opportunity for further cost reduction. In general, the BOP has a lower rate of decrease in cost as a function of volume as the fuel cell stack in part because many components are already manufactured in reasonable volume and do not benefit in the same way from increased economies of scale as the fuel cell stack. This result is also influenced by the different methodologies applied to stack vs. BOP costing: a DFMA analysis was applied to the stack, whereas BOP costs were estimated based on largely purchased components and vendor price quotes.

The cost of electricity with and without total cost of ownership TCO credits for a fuel cell CHP



system has been demonstrated for buildings in five US cities. This approach incorporates the impacts of offset heating demand by the FCS, carbon credits, and environmental and health externalities into a total levelized cost of electricity (\$/kWh). This “LCOE with total cost of ownership credits” can then be compared with the baseline cost of grid electricity. This entry combines a fuel cell system use-phase model with a life-cycle integrated assessment model of environmental and health externalities. Total cost of electricity is dependent on the carbon intensity of the electricity grid and heating fuel that a FC system is displacing and thus highly geography dependent.

For example, in commercial building types considered here (small hotels), overall TCO costs of fuel cell CHP systems at current low production volume (e.g., 50 kWe systems at 100 systems per year) relative to grid power exceed prevailing power rates in Phoenix, New York City, and Houston, but can be competitive in regions of the country with higher carbon intensity grid electricity. Including total cost of ownership credits can bring the levelized cost of electricity below the cost of electricity purchased from the grid in Minneapolis and Chicago for both PEM and SOFC CHP systems. Health and environmental externalities can provide large savings if electricity or heating with a high environmental impact is being displaced. These externality benefits from fuel cell CHP systems are expected to diminish as the electricity grid becomes cleaner, assuming that FCS systems continue to be fueled by natural gas. In the modeled scenario here, simulating the impact of the proposed Clean Power Plan, the levelized cost of electricity with TCO credits becomes higher than the cost of grid electricity in 2030 for Minneapolis and Chicago in the PEM case, but remains lower than the cost of grid electricity in 2030 for these two locations in the SOFC case.

Overall, this type of total cost of ownership analysis quantification is important to identify key opportunities for direct cost reduction, to fully value the costs and benefits of fuel cell

systems in stationary applications, and to provide a more comprehensive context for future potential policies.

## Future Directions

Key uncertainties in this type of modeling are the exact “state-of-the-art” design details for PEM and SOFC stacks, the actual process yields of stack process modules, and the details of stack composition and materials. Reverse engineering of a commercial fuel cell through stack performance characterization and cross sectional analysis of an actual fuel cell stack would provide valuable information but is beyond the scope of this entry. Additional future work includes further detailed study of lower power (1–5 kWe) fuel cell stack design and manufacturing and expanding the scope of the analysis to include more detailed study of balance of plant costs (e.g., balance of plant designs, supply chains, and comparisons to analogous industries).

As noted above, for both PEM and SOFC, balance of plant costs including the fuel processor make up about 70–80% of total direct costs for 50 kWe CHP systems across the range of production volumes and are thus a key opportunity for further cost reduction.

Further work in TCO analysis and modeling should explore providing a greater degree of temporal resolution for the marginal emission factors for the electricity system and higher temporal and spatial resolution of marginal benefit of abatement factors from the electricity grid. As in this entry, future modeling should try to incorporate the dynamic nature of the electricity grid portfolio and projected fuel prices as well as incorporate future projected equipment prices or learning rates in estimating future FCS CHP benefits.

From a policy standpoint, the illustration here of TCO costs that have appreciable credits in certain regions of the country is an important result that suggests that regionally specific policies and incentives may be appropriate. A key policy question is how to monetize these externalities, for example, where to provide incentives along the supply chain and how best to design policies for various stakeholders.

## Bibliography

### Primary Literature

- Darrow K, Tidball R, Wang J, Hampson A (2015) Catalog of CHP technologies. U.S. EPA (Environmental Protection Agency) Combined heat and power partnership. [https://www.epa.gov/sites/production/files/2015-07/documents/catalog\\_of\\_chp\\_technologies.pdf](https://www.epa.gov/sites/production/files/2015-07/documents/catalog_of_chp_technologies.pdf)
- Wei M, Lipman T, Mayyas A, Chien J, Chan SH, Gosselin D, Breunig H, Stadler M, McKone T, Beattie P, Chong P, Colella WG, James BD (2014) A total cost of ownership model for low temperature PEM fuel cells in combined heat and power and backup power, LBNL-6772E. Lawrence Berkeley National Laboratory, Berkeley
- Scataglini R, Mayyas A, Wei M, Chan SH, Lipman T, Gosselin D, D'Alessio A, Breunig H, Colella WG, James BD (2015) A total cost of ownership model for solid oxide fuel cells in combined heat and power and power-only applications. Lawrence Berkeley Laboratory Report LBNL-1005725
- Colella WG (2003) Modelling results for the thermal management sub-system of a combined heat and power (CHP) fuel cell system (FCS). *J Power Sources* 118:129–149
- Ormerod RM (2003) Solid oxide fuel cells. *Chem Soc Rev* 32:17–28
- DOE (2014) – Multi-year research, development and demonstration plan. [http://energy.gov/sites/prod/files/2014/12/f19/cto\\_myrrdd\\_fuel\\_cells.pdf](http://energy.gov/sites/prod/files/2014/12/f19/cto_myrrdd_fuel_cells.pdf)
- James BD, Kalinoski JA, Baum KN (2010) Mass production cost estimation for direct H<sub>2</sub> PEM fuel cell systems for automotive applications, 2010 Update. Directed Technologies, Arlington
- Sinha J (2010) Direct hydrogen PEMFC manufacturing cost estimation for automotive applications, 2010 DOE annual merit review, Washington, DC, 9 June 2010. Project ID # FC019
- Marcinkoski J, James BD, Kalinoski JA, Podolski W, Benjamin T, Kopasz J (2011) Manufacturing process assumptions used in fuel cell system cost analyses. *J Power Sources* 196(12):5282–5292. ISSN 0378-7753, <https://doi.org/10.1016/j.jpowsour.2011.02.035>
- Mahadevan, K, Contini V, Goshe M, Price J, Eubanks F, Griesemer F (2010) Economic analysis of stationary PEM fuel cell systems. In: 2010 annual merit review proceedings, Department of energy, hydrogen and fuel cells program, Washington, DC
- James BD, Spisak AB, Colella WG (2012) Manufacturing cost analysis of stationary fuel cell systems. Strategic Analysis, Inc, Arlington
- Krullam K, Iyengar A, Kearns D, Newby D (2013) Assessment of the distributed generation market potential for solid oxide fuel cells, DOE/NETL-342/093013
- Staffell I, Green R (2013) The cost of domestic fuel cell micro-CHP systems. *Intl J Hydrogen Energy* 38:1088–1102
- E4tech (2014) The fuel cell industry review 2014. Available at 727 <http://www.e4tech.com/fuelcellindustryreview/>. Accessed on 10 Dec 2015
- Wei M, Smith SJ, Sohn MD (2017) Experience curve development and cost reduction disaggregation for fuel cell markets in Japan and the US. *Appl Energy* 191(1):346–357. ISSN 0306-2619, <https://doi.org/10.1016/j.apenergy.2017.01.056>
- Haberl JS (1993) Economic calculations for ASHRAE handbook. Texas A&M University. [Report Number:] EST-TR-93-04-07, Energy Systems Laboratory, College Station, Texas
- Deru M, Field K, Studer D, Benne K, Griffith B, Torcellini P, Liu B, Halverson M, Winiarski D, Rosenberg M, Yazdaniyan M, Huang J, Crawley D (2011) U.S. Department of energy commercial reference building models of the national building stock. Report NREL/TP-5500-46861, Golden CO, pp 1–118
- Rooijen JV A life cycle assessment of the PureCell™ stationary fuel cell system: providing a guide for environmental improvement. A report of the Center for Sustainable Systems, Report No. CSS06–09. 30 June 2006 Salt River Project. <http://www.srpnet.com/about/facts.aspx#ownership>. Accessed Aug 2013
- CBCECS Database website. <http://www.eia.gov/consumption/commercial/index.cfm>
- Muller NZ (2014) Toward the measurement of net economic welfare: air pollution damage in the U.S. national accounts–2002, 2005, 2008. In: Jorgenson DW, Landefeld JS, Schreyer P (eds) *Measuring economic sustainability and progress volume*. University of Chicago Press, pp 429–459
- EPA (2015) eGRID 2012 summary tables, 5 Oct 2015
- U.S. Energy Information Agency (EIA) (2011) Voluntary reporting of greenhouse gases program. Emission factors and global warming potentials. [http://www.eia.gov/survey/form/eia\\_1605/emission\\_factors.html](http://www.eia.gov/survey/form/eia_1605/emission_factors.html). Accessed Aug 2013, Revised 28 Apr 2011
- U.S. Energy Information Agency (EIA). Total district heat consumption and expenditures. Table C25. Table 1.3–1 and 1.3–4. <http://www.eia.gov/>. Accessed Sep 2013
- Siler-Evans K, Lima Azevedo I, Morgan MG (2012) Marginal emissions factors for the U.S. electricity system. *Environ Sci Technol* 46:4742–4748
- Barbose G, Wiser R, Heeter J, Mai T, Bird L, Bolinger M, Carpenter A, Heath G, Keyser D, Macknick J, Mills A, Millstein D (2016) A retrospective analysis of benefits and impacts of U.S. renewable portfolio standards. *Energy Policy* 96:645–660. ISSN 0301-4215, <https://doi.org/10.1016/j.enpol.2016.06.035>
- Colella WG, Pilli SP (2012) Energy system and thermo-economic analysis of combined heat and power fuel cell systems. In: *Proceedings of the ASME 6th international conference on energy sustainability*, San Diego, 23–25 July 2012. ESFuelCell2012–91481

27. National Energy Technology Laboratory (NETL) (2009) Natural gas-fueled distributed generation solid oxide fuel cell systems. Report Number: R102 04 2009/1
28. White House (2013) Technical support document: technical update of the social cost of carbon for regulatory impact analysis – under executive order 12866 – interagency working group on social cost of carbon, United States Government, May 2013
29. EPA (2015) Regulatory impact analysis for the Clean Power Plan final rule, 23 Oct 2016
30. EPA (2015) Clean Power Plan fact sheet. <http://bio.tech.lsu.edu/blog/fs-cpp-ee.pdf>. Accessed 20 June 2017
31. Siler-Evans K, Azevedo IL, Morgan MG, Apt J (2013) Regional variations in the health, environmental, and climate benefits of wind and solar generation. *Proc Natl Acad Sci* 110:11768–11773
32. Nishizaki K, Hirai K (2009) Commercialization of residential PEM fuel cell CHP “ENE FARM”, White paper by Tokyo Gas Co. and Osaka Gas Co.
33. ACI Technologies, Inc. (2011) Manufacturing fuel cell Manhattan project, Report under U.S. government contract no. N00014–08-D-0758
34. Prugh DN, Tannenbaum HP (2009) U.S. Patent, US 20090169950
35. Heinzl A et al (2004) Injection moulded low cost bipolar plates for PEM fuel cells. *J Power Sources* 131(1):35–40
36. Yeetsom R, Fowler M, Tzoganakis C, Yuhua W, Taylor M (2008) Polypropylene composites for polymer electrolyte membrane fuel cell bipolar plates. *Macromol Symp* 264:34–43
37. Yeetsom R, Fowler M, Tzoganakis C (2011) A review of thermoplastic composites for bipolar plate materials in PEM fuel cells, Chapter 16. In: Cuppoletti J (ed) *Nanocomposites with unique properties and applications in medicine and industry*. InTech, Rijeka
38. Chien JM (2013) Ph.D. dissertation, University of California, Berkeley
39. Incropera FP, DeWitt DP, Bergman TL, Lavine AS (2007) *Fundamentals of heat and mass transfer*. <https://doi.org/10.1016/j.applthermaleng.2011.03.022>
40. Rafferty KD (1998) Heat exchangers, pp 261–277. <http://www.oit.edu/docs/default-source/geoheat-center-documents/publications/heat-exchangers/tp54.pdf?sfvrsn=2>
41. Stevenson J (2003) Paper presented at the SOFC seal meeting, SECA core technology program. Sandia National Laboratory, Albuquerque
42. Jung GB (2013) Can be found under <http://www.enedu.org.tw/files/DownloadFile/20131010130452.pdf>
43. Ghezal Ayagh H (2014) Paper presented at the 15th annual SECA workshop, National energy technology laboratory, Pittsburgh
44. Borglum B (2008) Development of solid oxide fuel cells at Versa Power Systems. In: Williams M, Krist K, Garland N (eds) *ECS transactions, fuel cell seminar 2008*. The electrochemical society, Pennington, pp 9–13
45. Carlson EJ, Yang Y, Fulton C (2004) Tiax report for national energy technology laboratory
46. H.K. Woodward (2003) M.S. Thesis, Worcester Polytechnic Institute, Worcester
47. Schafbauer W, Menzler NH, Buchkremer HP (2014) Tape casting of anode supports for solid oxide fuel cells at Forschungszentrum Jülich. *Intl J App Ceramic Tech* 11:125–135
48. Thorel A (2010) Tape casting ceramics for high temperature fuel cell applications. In: Wunderlich W (ed) *Ceramic materials*. InTech, Rijeka, pp 49–67
49. Liu Q L et al (2011) IOP Conf. Ser.: Mater. Sci. Eng. 18 132006. <https://doi.org/10.1088/1757-899X/18/13/132006>
50. Mistler RE, Runk RB, Shanefield DJ (1978) Tape casting of ceramics. In: Onoda GY, Hench LL (eds) *Ceramic processing before firing*. Wiley, New York, pp 411–448
51. Battelle Memorial Institute (2014) Report for U.S. Department of energy under Contract No. DE-EE0005250
52. Burggraaf AJ, Cot L (1996) *Fundamentals of inorganic membrane science and technology*. Elsevier, Amsterdam
53. Weimar MR, Gotthold DW, Chick LA, Whyatt GA (2013) Cost study for manufacturing of solid oxide fuel cell power systems, PNNL-22732. Pacific Northwest National Laboratory, Richland
54. Breunig HM (2015) Parameter variation and scenario analysis in impact assessments of emerging energy technologies. University of California, Berkeley

## Reviews and Other References

- Bar-On I, Kirchain R, Roth R (2002) Technical cost analysis for PEM fuel cells. *J Power Sources* 109:71–75
- Mehta V, Cooper JS (2003) Review and analysis of PEM fuel cell design and manufacturing. *J Power Sources* 114:32–53
- Sopian K, Wan Daud WR (2006) Challenges and future developments in proton exchange membrane fuel cells. *Renew Energy* 31:719–727
- Tietz F, Buchkremer HP, Stöver D (2002) Components manufacturing for solid oxide fuel cells. *Solid State Ionics* 152–153:373–381
- Verrey J, Wakeman MD, Michaud V, Månson J-AE (2006) Manufacturing cost comparison of thermoplastic and thermoset RTM for an automotive floor pan. *Compos A: Appl Sci Manuf* 37:9–22
- Wannek C, Glösen A, Stolten D (2010) Materials, manufacturing technology and costs of fuel cell membranes. *Desalination* 250:1038–1041



## Fuel Cell Types and Their Electrochemistry

Günther G. Scherer  
Electrochemistry Laboratory, Paul Scherrer  
Institute, Villigen, Switzerland

### Article Outline

Glossary  
Definition of the Subject  
Introduction  
What Is a Fuel Cell?  
The Role of the Electrolyte  
Classification of Fuel Cell Types  
The Role of Electrocatalysis and the Electrode /  
Electrolyte Interface  
Fuel Cell Families  
Future Directions  
Bibliography

### Glossary

**AFC** Alkaline fuel cell  
**EC** Electrocatalysis  
**FC** Fuel cell  
**GDE** Gas diffusion electrode  
**GDL** Gas diffusion layer  
**HOR** Hydrogen oxidation reaction  
**HT-PEFC** High temperature polymer electrolyte  
fuel cell  
**MCFC** Molten carbonate fuel cell  
**ORR** Oxygen reduction reaction  
**PAFC** Phosphoric acid fuel cell  
**PEFC** Polymer electrolyte fuel cell  
**SOFC** Solid oxide fuel cell

### Definition of the Subject

Fuel cells are efficient energy converters, based on electrochemical principles. They convert the

chemical energy (heating value) of a fuel directly into electricity, circumventing the various steps of thermal conversion and electricity generation. Fuel cells can be designed and constructed on the basis of a multitude of material combinations for electrolyte and electrodes, opening the choice of different fuels. The electrocatalytic reactions of fuel and oxygen are major challenges to obtain high conversion efficiency. The electrochemical basics of different fuel cell types considered today for technical applications are described in this contribution.

### Introduction

Fuel cell technologies have seen a revival in recent years, due to several reasons. Global warming and local air pollution caused by various energy utilization processes have created a multitude of environmental concerns, promoting the development of novel technologies with high conversion efficiencies and low emissions, possibly zero emission, with respect to green house gases and other pollutants [1, 2]. Peak oil is another reason for the renewed interest in fuel cell technologies, in particular for automotive applications [3, 4]. Although this fact is discussed in a highly controversial manner, limitation in crude oil supply is obvious in the long-term perspective. This particular aspect of fossil fuel resources is strongly interlinked to the future perspective of the “oil price” and, hence, its economic competitiveness to other fuels, e.g., fuels from renewable sources. In this context, the installation of new supply infrastructures for alternative fuels, e.g., H<sub>2</sub>, is an important additional economical and political factor. Dedicated analysis has clearly shown that energy conversion in fuel cells has to be based on fuels, in particular hydrogen, derived from renewable sources [5]. Further, the geographical distribution of oil reserves causes concerns about the supply security in industrial centers around the world.

Overall, there exist several reasons to ask for novel efficient conversion technologies for

mobility (electromobility) and combined heat and power systems (CHP) with independence on fossil fuels, in particular crude oil. Another area of interest in fuel cell technology is portable electric and electronic applications, where the argument of potentially higher energy density as compared to today's available battery technologies, hence, longer time of operation, is of prime interest [6].

Electricity generation via fuel cells is an idea, based on fundamental research carried out by Christian Friedrich Schönbein at the University of Basel in the early nineteenth century. Schönbein's basic investigations of the respective reaction of  $H_2$  gas (oxidation) and  $O_2$  gas (reduction) dissolved in the electrolyte at an electrode/electrolyte interface, representing the fundamental fuel cell reactions, led William Robert Grove to the design and construction of the first operating fuel cell. He utilized  $H_2$  as fuel and  $O_2$  as oxidant at platinum metal electrodes in two separated closed compartments, filled with the respective reactant (hydrogen electrode, oxygen electrode), and joined by sulfuric acid as common electrolyte [7].

As will be shown in this chapter, the basic electrochemistry of a fuel cell, an electrochemical gas battery, is determined by the choice of the electrolyte and the two different electrodes immersed therein. In the course of time since this fundamental work of Schönbein and Grove, many combinations of electrolytes and electrode materials have been tested and fuel cell types derived upon there. This development has also been driven in the past by the choice of available fuel and possible application in view, in particular by space and military applications.

This introductory chapter will give an overview on the basic electrochemistry of some fuel cell types, developed today for dedicated technological applications. The respective electrochemistry will depend on the materials composition of the fuel cell, in particular, on the nature of the electrolyte and the temperature of operation. This further determines the choice of fuel, due to the strong influence of temperature on the mechanism of the respective electrocatalytic processes.

Engineering issues of fuel cell stack and systems design will be dealt with in the following

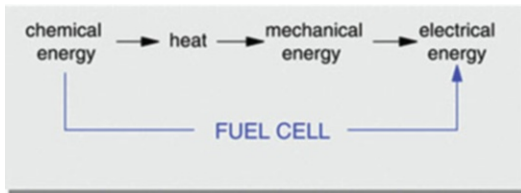
chapters. Hence, issues of, e.g., coflow or counterflow within one cell, stoichiometry and utilization of fuel and oxidant, temperature and current distribution in a fuel cell of technical scale, and, certainly, issues of stacking cells into a bipolar arrangement will not be discussed here.

## What Is a Fuel Cell?

A fuel cell is an electrochemical device, converting the chemical energy (Gibbs free energy) stored in a gaseous or liquid fuel, e.g., hydrogen, methane, methanol, ethanol, others, directly into *work of electrical energy (direct current electricity)* at constant temperature (Fig. 1). This type of energy conversion process is different from the classical thermomechanical energy conversion process and is not limited by the Carnot principle (see below).

In short, in a fuel cell, the fuel is oxidized at an electrochemical interface (electrode called anode), accepting electrons and donating these electrons at a second electrochemical interface (electrode called cathode, separated from the anode) to an oxidant, e.g., oxygen, which is reduced by accepting these electrons. Both electrochemical interfaces have to belong to a common electrochemical cell and are joined in the cell by a common medium, an ion-conducting electrolyte. Both electrodes have to be connected electronically by an external circuit, containing the electrical device to be operated, in which the electrons, due to the potential difference created by the two electrode reactions, travel from the anode to the cathode delivering electrical work (Fig. 2). Fuel and oxidant are supplied in gas channels of the cell housing (bipolar plate in stacked cells) on the backside of the porous electrodes (not displayed in Fig. 2) Both gases have to be transported through the porous gas diffusion layers (GDLs) with pores typically in the micrometer range (blue and red bodies in Fig. 2) to the electroactive catalyst layers (ECLs, black dots in Fig. 2) at the interface to the electrolyte. Colloquially, GDL and ECL together are called gas diffusion electrode (GDE).

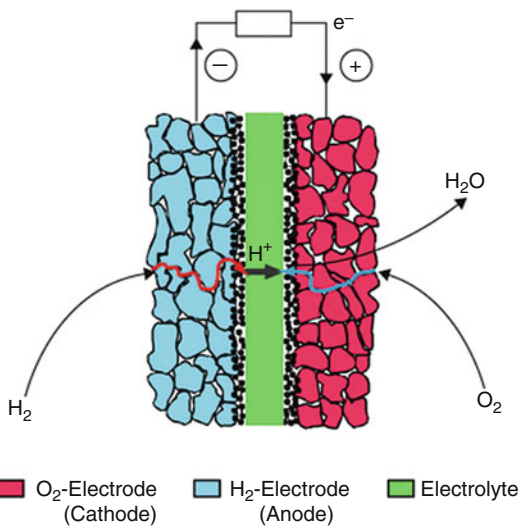
The fuel cell and its electrochemically active components, i.e., electrodes, electrolyte, etc., as well as its (electrochemically inert) structure



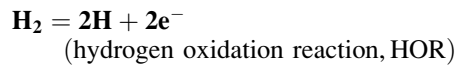
**Fuel Cell Types and Their Electrochemistry, Fig. 1** Scheme of direct energy conversion in an electrochemical cell as compared to “conventional” thermal conversion

At the same time, it is a prerequisite that these materials are as conductive as possible because they are responsible for the collection and transmission of the electric current generated at the two interfaces. Hence, ohmic voltage losses in these materials should be as low as possible.

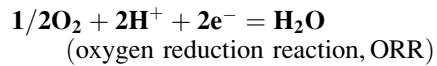
The electrochemistry of the two electrode reactions is exemplified for the simplest and predominant case by the “cold” electrochemical combustion of H<sub>2</sub> with O<sub>2</sub> (pure O<sub>2</sub> or from ambient air) to H<sub>2</sub>O (Fig. 2). The overall reaction is split into two partial reactions, occurring at the two different electrodes of the cell:



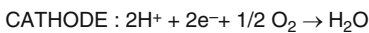
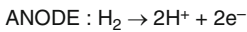
**Anodic reaction :**



**Cathodic reaction :**



**Overall reaction :**



**Fuel Cell Types and Their Electrochemistry, Fig. 2** Simplified fuel cell scheme with an acidic aqueous electrolyte, e.g., the polymer electrolyte fuel cell (PEFC). Fuel: H<sub>2</sub>, oxidant: O<sub>2</sub>. Only porous gas diffusion electrodes and electrolyte are shown, cell housing is not shown [8]

The reaction product(s) of the individual electrode reactions are constituents of the (aqueous) electrolyte (H<sup>+</sup> in the example of an acidic electrolyte, as displayed in the scheme of Fig. 2), which avoids polarization losses in the electrolyte.

Each of the two electrode reactions creates a characteristic potential difference across the interface solid electrode/electrolyte, which is different for the two reactions according to the different reactants. The overall cell voltage between the two electrodes, which are joined by the same electrolyte, allows the electrons generated at the anode (HOR) and consumed at the cathode (ORR) to create work in the external circuit. Hence, chemical energy released by the individual electrode reactions at the locally separated electrodes is directly transferred into electrical energy. This pathway is different from the combustion step in the “classical” thermomechanical power generation, where the oxidation of fuel and reduction of oxidant occur in the same volume element, thereby generating heat only.

materials, i.e., current collectors, cell housing, etc., should be as invariant as possible, i.e., they should not be consumed and, ideally, not age (corrode) over the time of operation. Hence, as an electrochemical reactor, they provide the electrochemically active interfaces (or interphases, see below) and the necessary pathways for mass transport for educts and products to and from these active interfaces through porous media (active electrode layers, gas diffusion layers, internally corrugated cell housing (flow fields) in bipolar plates) with open porosity at different scales.



Generally, the available cell voltage of electrochemical cells depends on the thermodynamics of the two electrode reactions in the prevailing electrolyte, hence the difference in the electrode potentials, and is confined, according to the series of electrochemical potentials, to a few volts [9]. According to the individual electrode potentials of the  $H_2/H^+$  reaction (by IUPAC standard zero volt in the series of electrochemical potentials, acidic electrolyte, standard conditions of 1 atm and 25 °C or 298 K) and the  $O_2/H_2O$  reaction (1.23 V, respectively), a cell with  $H_2$  and  $O_2$  as reactants should yield an ideal cell voltage of 1.23 V at these standard conditions. In practice, a lower value in the range of 1 V is observed, due to different implications (side reactions, depolarization of electrodes due to cross-over of gases through the electrolyte, etc.).

The free energy  $\Delta G$  (Gibbs energy at constant pressure) of the fuel cell reaction is related to the cell voltage under open circuit conditions (open circuit voltage, OCV)  $E^0$  and standard conditions according to

$$E^0 = -\Delta G/nF$$

$n$  being the number of electrons transferred in the respective reaction (equal to 2 for the reaction  $H_2 + \frac{1}{2}O_2 = H_2O$ ) and  $F$  the Faraday constant equal to 96,487 C/mol (electric charge per mol of electrons).

Further,  $\Delta G$  can be expressed as the difference of the free enthalpy  $\Delta H$  of the reaction (thermal cell voltage  $E_H^0$  equivalent to 1.48 V for the  $H_2/O_2$  reaction under standard state conditions) and the term  $T\Delta S$ , ( $T$  absolute temperature) expressing entropy losses (or gains)  $\Delta S$  in the reaction:

$$\Delta G = \Delta H - T\Delta S$$

Hence, the voltage (thermal) efficiency of a reaction under equilibrium conditions can be written as:

$$\epsilon_{th} = \frac{\Delta G}{\Delta H} = 1 - \frac{T\Delta S}{\Delta H}$$

The voltage (thermal) efficiency for the electrochemical conversion of the three different

fuels  $H_2$ ,  $CH_4$ , and  $CO$  reacting with air (oxygen) in dependence of reaction temperature is displayed in Fig. 3. In comparison, also the maximal efficiency  $\eta = (T_1 - T_2)/T_1$  for a Carnot process at the respective higher temperature  $T_1$  and the lower temperature  $T_2$  equal to 0 °C is included. The different temperature dependence of the three conversion reactions is due to the respective entropy changes, e.g.,  $\Delta S = 0$  for the reaction  $CH_4 + 2O_2 = CO_2 + 2H_2O$  and  $\Delta S \neq 0$  for the reactions  $2H_2 + O_2 = 2H_2O$  and  $2CO + O_2 = 2CO_2$ .

Based on thermodynamic arguments only, electrochemical energy conversion offers higher efficiencies within a certain temperature window, depending on the respective reaction.

Introducing Nernst's law for the equilibrium case, the situation when no current (and hence power) is delivered by the cell, the equilibrium cell voltage under nonstandard conditions for a  $H_2/O_2$  cell in dependence of the respective reactant/product concentration (partial pressures) can be expressed as:

$$\begin{aligned} E^{eq} &= -\frac{\Delta G}{n_1 F} = E^{eq,c} - E^{eq,a} \\ &= E^0 + \frac{RT}{2F} \ln \left( \frac{[H_2][O_2]^{1/2}}{[H_2O]} \right) \end{aligned}$$

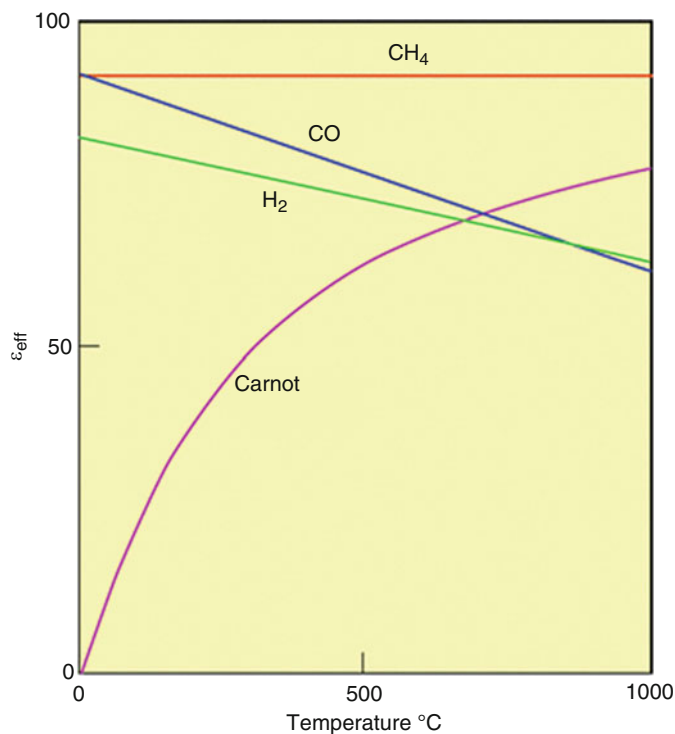
$E^{eq}$  = equilibrium cell potential,  $E^{eq,c}$  = equilibrium potential cathode,  $E^{eq,a}$  = equilibrium potential anode,  $R$  gas constant,  $T$  absolute temperature,  $E^0$  = equilibrium potential under standard state.

$E^{eq}$  is also called "theoretical" open circuit cell voltage, OCV, in dependence of temperature and reactant, respectively product concentrations. Practical OCVs may be observed to be lower, due to losses (mixed potentials due to side reactions or gas crossover, see practical OCV of  $H_2/O_2$  fuel cell) already occurring at zero current flow.

Under current flow, the kinetics of the electrode reactions comes into effect. The Butler-Volmer equation describes the dependency of the current passing through the electrode interface (current density per unit geometric area) on a small voltage excursion (called overvoltage  $\eta$ ) from the respective equilibrium potential  $E^{eq}$ .

### Fuel Cell Types and Their Electrochemistry,

**Fig. 3** Voltage (thermal) efficiency  $\varepsilon_{th}$  for the electrochemical reaction of  $H_2$ ,  $CO$ , and  $CH_4$  as fuel with oxygen from air under equilibrium versus temperature ( $^{\circ}C$ ). In comparison, Carnot efficiency of a thermal process as function of the respective higher temperature in  $^{\circ}C$  and with  $0^{\circ}C$  as lower temperature is displayed



$$i = i_0 [\exp(\alpha n F \eta / RT) - \exp((1 - \alpha) n F \eta / RT)]$$

$i$  = current density at overvoltage  $\eta$ ,  $\eta$  = overvoltage (excursion from the equilibrium potential),  $i_0$  = exchange current density (at  $\eta = 0$ ),  $\alpha$  = symmetry factor, representing the fraction of overvoltage assisting the reaction,  $n$  = number of electrons exchanged,  $F$  = Faraday constant,  $R$  = gas constant,  $T$  = absolute temperature.

The exponential dependency points out that small potential excursions cause a larger change in current, while at larger potential excursions, the current follows a linear behavior. This can be described by the Tafel law, which usually is applied when current densities of technical interest, e.g., several 100 mA per  $cm^2$  geometric surface area in a fuel cell, are passing through the cell.

$$\eta = (RT / \alpha n F) \ln i / i_0$$

For the HOR, exhibiting an exchange current density in the range of  $i_0 = 10^{-3}$  A/ $cm^2$  with platinum as electrode material [9], only a small overvoltage arises even by drawing a current

density of technical interest, e.g., 1 A/ $cm^2$ , due to the fact that the  $H_2$  molecule is easily split into two adsorbed H atoms (Tafel reaction), followed by the transfer of one electron per H atom (Volmer reaction) to the electrode generating two hydrated  $H^+$ . Alternatively, one electron is transferred to an adsorbed  $H_2$  molecule, followed by a split into a hydrated  $H^+$  and an adsorbed H atom. In a consecutive step, the second H atom is oxidized (Heyrovsky reaction).

In contrast, the exchange current density of the ORR at a platinum electrode is in the range of  $i_0 = 10^{-8}$  A/ $cm^2$ . Assuming *direct* reduction of the oxygen molecule, the ORR requires four electrons in total, including the four  $H^+$  generated in the HOR at the counterelectrode (see above). As a consequence, ORR generates a major overvoltage and, hence a major contribution to the overall loss.

In addition to the overvoltage losses due to electrode kinetics, one has to take into account the voltage loss in the ion-conducting electrolyte, due to the finite electrolyte conductivity, and (minimized) losses due to the electric resistance



of electrode and cell materials, including contact resistances.

This relationship between cell voltage and current density is schematically displayed in Fig. 4. The various voltage losses are deducted from the equilibrium cell voltage (zero current), yielding the available cell voltage  $E^*$  at the respective current density  $i^*$ . The difference between  $E_H^0$  and  $E^*$  is expressed as (waste) heat. In terms of voltage efficiency, this (heat) loss should be as low as possible; hence,  $E^*$  should be as high as possible. On the other side, the current density to be drawn has to be as high as possible to utilize power output values (specific power W/kg or power density W/L) of technical interest.

Further, Fig. 4 points to another advantage of (electrochemical) fuel cell technology: Designing a fuel cell to the maximum or rated power for a certain application (power = cell voltage  $E$  times current  $i$ ), one easily realizes that the voltage efficiency  $\epsilon_{\text{eff}}$  increases at lower power (lower current but higher voltage). This fact is particularly important for applications where maximum power (full load) is only required at certain parts of the duty cycle, while in other parts, only part load is necessary. This case is, e.g., exhibited in automotive applications of fuel cell technology.

Generally, the available cell voltage of electrochemical cells depends on the thermodynamics of the two electrode reactions in the prevailing electrolyte, hence the difference in the electrode potentials, and is confined, according to the

Electrochemical Series of Standard Potentials, to a few volts. Cells with an aqueous electrolyte exhibit a limitation given by the stability window of water, namely 1.23 V at standard conditions. As stated above, the  $\text{H}_2/\text{O}_2$  fuel cell allows practical open circuit voltages of around 1.0 V. At cell voltages above 1.23 V, typically around 1.5 V, decomposition of water into  $\text{H}_2$  and  $\text{O}_2$  occurs.

Hence, to accumulate the necessary voltage for technical applications, e.g., 200–400 V, for an electrical power train in a car, cells must be connected in series. Dedicated bipolar arrangements of cells have been designed and put into operation for serial connection, taking into consideration also the necessary parallel mass flow of fuel and oxidant from a manifold into each individual cell and the respective removal of the product. Such an arrangement of cells is called a fuel cell stack, combining the electrical serial connection of individual cells with a parallel connection for mass flow.

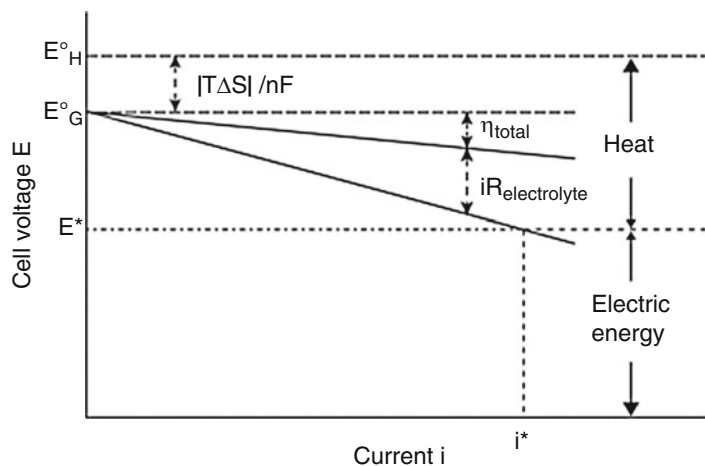
In contrast to batteries, fuel cells are open systems, which convert the chemical energy available in a fuel stored outside the fuel cell, the electrochemical converter. As a consequence, fuel cells need a fuel tank, also a tank for the oxidant, if the oxidant is pure oxygen and not ambient air, and auxiliaries (for temperature, pressure, etc., control) to be operated (Fig. 5).

Mass flow into (reactants) and out of the cell (products) must be allowed and controlled, as well as cooling to remove the waste heat. At a voltage

### Fuel Cell Types and Their Electrochemistry,

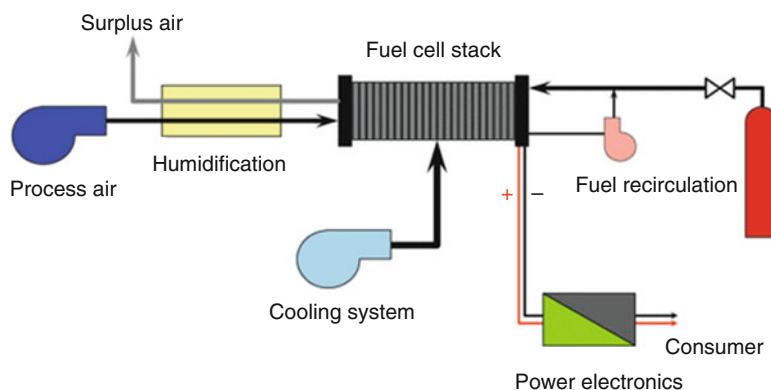
#### Fig. 4 Cell voltage

$E$  versus current  $i$  of a fuel cell, with  $E_H^0$  = thermal cell voltage,  $E_G^0$  = ideal cell voltage based on  $\Delta G$ ,  $\eta$  = sum of overvoltage at anode and cathode,  $R_{\text{Electrolyte}}$  = electrolyte resistance



### Fuel Cell Types and Their Electrochemistry,

**Fig. 5** Simplified scheme of a fuel cell system (Adapted from L. Gubler, Paul Scherrer Institut)



efficiency of 50%, a cell producing 1 kW electric power also generates 1 kW of heat, which has to be removed efficiently not to cause thermal runaway and, hence, degradation of the cell and its components. In summary, this is called a fuel cell system. Engineering issues of mass and heat transfer, current distribution across the active area of a cell, and voltage distribution along the stack, etc., are governing the design of a fuel cell system.

Fuel cells can be operated continuously, as long as they are supplied with fuel and oxidant. Hence, they are not limited by electrical charge-discharge cycles, as batteries are. This fact can be of utmost importance for certain applications, e.g., with respect to refueling time in mobile applications. For mobile or portable applications, the availability of a fuel infrastructure adds another aspect of consideration.

In terms of achievable specific energy (W/kg) and volumetric energy density (W/L), air-fed fuel cells have the advantage that one reaction partner, namely, oxygen, is derived from air, and consequently does not add to the weight and volume of the device. However, ambient air must be processed (cleaned, humidified, etc.), which has to be taken into account. This advantage is also expressed in the concept of metal air batteries, e.g., the Zn/Air or Al/Air battery, which on the anode (metal) consists as half a battery (closed mass flow) and on the cathode as half a fuel cell (open mass flow).

Next to the multitude of material combinations allowing various fuel cell types to be designed and built, the variety of mobile (transport), stationary, and portable applications provokes a multitude of

different cell, stack, and systems designs, guided by the implications of the different fuel cell technologies (see below).

### The Role of the Electrolyte

Generally speaking, the ion conduction in the electrolyte contributes to the losses (ohmic losses, see Fig. 3) in the cell voltage. Hence, one of the major tasks in fuel cell development is the reduction of these losses in the ionic circuit part, because the work available in the external electronic circuit should be as high as possible.

The role of the “electrolyte” in a fuel cell is a multiple one:

1. Transport the charge in ionic form from one interface to the other within the cell. To minimize losses in the ionic circuit, the ion conduction should be carried by an ion, which is produced at one electrode and consumed at the other to avoid losses caused by concentration gradients [10]. This majority ion should carry as much charge as possible through the electrolyte, hence its transport number (Hittorf number) should be as high as possible, ideally one. For high power applications with an aqueous electrolyte, the concentration of this respective anion or cation must be high and exclusively responsible for conduction. Typically, a specific ionic conductivity in the range of 100 mS/cm is required, which at a current density of 1 A/cm<sup>2</sup> and an electrolyte gap of 100 μm would yield an ohmic voltage loss

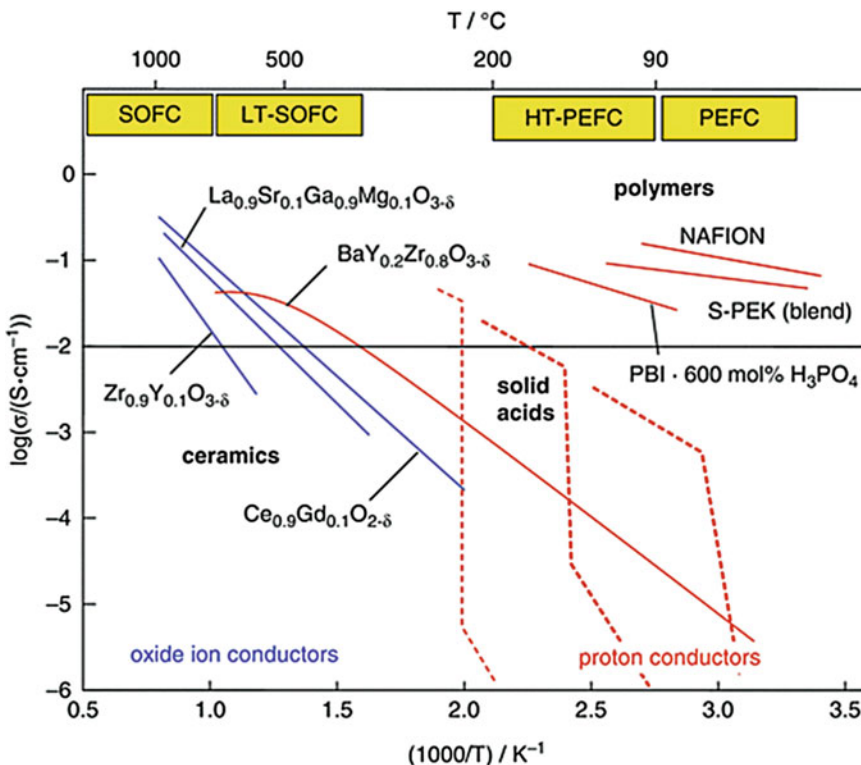
in the range of 100 mV. As seen in Fig. 6, the conductivities of various electrolytes are strongly temperature dependent and cover a wide temperature range, depending on the ion-conducting species in its respective environment (material). Again, electrolytes are of interest, which offer the opportunity that the ionic species is participating in the fuel cell reaction.

2. Act as separator to (1) avoid crossover and, as a consequence, “hot” combustion of the fuel and the oxidant at the respective counterelectrode, and (2) to avoid touching of the electrodes by short circuiting the electronic pathway. Thereby, the electrolyte/separator gap should be as narrow as possible to lower the ohmic contribution to the overall voltage loss. In the case of a liquid electrolyte, it can be absorbed into an inert matrix, providing porosity high enough for an ionic conduction path with low tortuosity for the ion and at the same time a

high enough bubble pressure to suppress gas crossover. An ideal concept is the one of a solid electrolyte, which fulfills the dual electrolyte and separator function at the same time, providing a transfer number of one for the current-carrying ionic species, as in the case of solid polymer electrolytes (ion exchange membranes), thereby excluding a contribution of electronic conduction.

One has to emphasize that the electrolyte has to sustain the potential window of the respective fuel cell reaction, given by the Gibbs free energy, at least over the device lifetime, specified for a certain application.

In aqueous acidic electrolytes, the ionic conduction is provided by an  $H^+$  ion, respectively,  $H(H_2O)_n^+$ . As mentioned above,  $H^+$  is created by the anodic oxidation of  $H_2$  as a fuel, and the conducting species is transported to the cathode, where it is consumed in the direct (ideally four



**Fuel Cell Types and Their Electrochemistry, Fig. 6** Specific conductivity versus temperature of different electrolytes interesting for fuel cell applications (Adapted from K.D. Kreuer)

electrons) cathodic reduction of molecular oxygen. Hereby, water as the reaction product appears at the cathode side of the cell.

In alkaline solution, the ionic conduction is provided by  $\text{OH}^-$  ions, created by the ORR at the cathode. Principally,  $\text{OH}^-$  ions are carriers for the  $\text{O}^{2-}$  ions, produced as intermediate by the cathodic reduction reaction of molecular  $\text{O}_2$  and the follow-up reaction with a water molecule. After conduction,  $\text{OH}^-$  reacts with the  $\text{H}^+$  created at the anode and yields water as a product at the anode side.

Solid polymer electrolytes on the basis of a polymer cation exchange membrane in  $\text{H}^+$  form or an anion exchange polymer membrane in  $\text{OH}^-$  form can be considered as quasi-aqueous electrolytes, whereby the water is absorbed in the phase separated ionic nanomorphology of the respective material. This nanomorphology forms ionic pathways through the polymeric membrane connecting the two fuel cell electrodes.

In cells operated at temperatures below  $100\text{ }^\circ\text{C}$ , liquid water will be the reaction product. For operation temperatures above the boiling point of water, a cell with an aqueous or quasi-aqueous electrolyte can be operated, however, at the expense of pressurizing it to avoid loss of the water and, as a consequence, concentration and conductivity changes in the electrolyte.

An alternative electrolyte for operating temperatures above  $100\text{ }^\circ\text{C}$ , which also gained technical relevance, is orthophosphoric acid,  $\text{H}_3\text{PO}_4$ . "Water-free" orthophosphoric acid is a self-ionizing amphoteric system, which yields  $\text{H}_4\text{PO}_4^+$  and  $\text{H}_2\text{PO}_4^-$ . Protons can be passed along pyrophosphate chains at elevated temperatures of around  $200\text{ }^\circ\text{C}$ , at which product water appears as vapor and can be rejected easily.

Molten salts can also be utilized as electrolytes. Again, the ion responsible for conductivity should be created in one electrode reaction and consumed in the other. However, due to the (1) corrosive nature, (2) the limited thermal stability, and/or (3) the high melting point of many melts, only a few molten salts have been considered. Up to now, the only fuel cell technology based on a molten salt electrolyte has been using a eutectic mixture of alkali metal carbonates,  $\text{Li}_2\text{CO}_3$  and  $\text{K}_2\text{CO}_3$ , at temperatures of around  $650\text{ }^\circ\text{C}$ ,

absorbed in a matrix of  $\text{LiAlO}_2$ . In this molten carbonate fuel cell (MCFC) the ion conducting the current is  $\text{O}^{2-}$  in the form of  $\text{CO}_3^{2-}$ . At the anode,  $\text{CO}_2$  is supplied and reacts with  $\text{O}_2$  and  $4\text{e}^-$  to form  $\text{CO}_3^{2-}$ , which carries the current to the anode, where it is released in the hydrogen oxidation reaction. As a consequence, MCFC, in addition to the mass flow of fuel and oxidant, needs mass flow management of  $\text{CO}_2$ .

At even higher temperatures in the range of  $800\text{--}900\text{ }^\circ\text{C}$ , ionic conduction can also be observed in solid oxides. Certain doped metal oxides become  $\text{O}^{2-}$  conductors; hence, they can be utilized as electrolytes in the solid oxide fuel cell (SOFC). The most common oxide used is yttria-stabilized cubic zirconia ( $\text{ZrO}_2$ ), called YSZ, with a doping level of 8%  $\text{Y}_2\text{O}_3$ . This material is a ceramic; the thermal expansion coefficient of its thin layers has to be matched with the other fuel cell components.

As indicated by the terminology of fuel cells, e.g., PEFC, AFC, SOFC, others (see below), the electrolyte is the decisive cell component, which determines operation temperature, the choice the electrodes (electrocatalytic materials), and finally the specifics of the electrochemistry of the reactants. This, on the other hand, has consequences for the layout of the fuel cell design (balance of plant) and possible applications of the respective fuel cell technology, according to the required duty cycle of the application.

## Classification of Fuel Cell Types

Today's fuel cell types under development can be classified in two different ways: either by the temperature range of operation or by the nature of the electrolyte.

The latter classification distinguishes between acidic and alkaline fuel cells. Acidic fuel cells with  $\text{H}^+$  conduction require other electrode materials than alkaline with  $\text{OH}^-$  conduction. Alkaline fuel cells, at least with an aqueous electrolyte, require a  $\text{CO}_2$ -free fuel, and hence cannot be operated on reformat fuel obtained originally from a C-containing fuel.

The above-described situation displays the fact that there is a temperature gap in the

availability of electrolytes between ca. 200 °C and 650 °C. Today, major research efforts are carried out to extend the range of aqueous  $H^+$  and  $OH^-$  conduction to temperatures beyond 100 °C, for technological reasons (heat rejection in cars, CO tolerance of platinum-based catalysts). On the other hand, oxide materials are developed with improved  $O_2^-$  conductivity at temperatures lower than the operation temperatures of standard SOFCs. Also ceramic proton conductors [11] and proton-conducting salts like  $CsHSO_4$  [12] are considered as electrolytes for this temperature regime.

### The Role of Electrocatalysis and the Electrode /Electrolyte Interface

Next to the voltage losses due to ionic conduction, voltage losses due to the activation overvoltages of the respective electrode reactions arise, as described by the Butler-Volmer, respectively, the Tafel equation. As stated above, at a certain value of the current density, the overvoltage for the HOR is much smaller than for the ORR, due to the simpler electron transfer kinetics. Overvoltage for an electrochemical reaction shows also a strong temperature dependency, as does activation energy, and decreases with increasing temperature.

For fuel cells with an acidic electrolyte, platinum is the electrocatalyst of choice at temperatures up to 200 °C (e.g., PAFC), due to the stability requirements. High dispersion of the catalyst is required, taking into account its nature as a precious metal, to provide a high surface area to volume ratio. Platinum nanoparticles in the diameter range of a few nanometers, typically 2–5 nm, supported on carbon particles are utilized. Different carbons with different surface areas (up to 800  $m^2/g$ ) are used. The amount of platinum in the catalyst powder is specified as wt% per g of carbon and further as mg loading per  $cm^2$  of geometric electrode area.

Platinum is prone to CO adsorption at temperatures of around 100 °C and below. For this reason, care has to be taken with respect to the purity of hydrogen, in particular for hydrogen liberated from a C-containing fuel by a reforming process (steam reforming, partial oxidation, autothermal reforming).

Alkaline electrolytes allow cheaper, non-precious metal catalysts like nickel and its alloys.

High temperature fuel cells, e.g., MCFC or SOFC, require other catalyst materials, which are described in the respective section below.

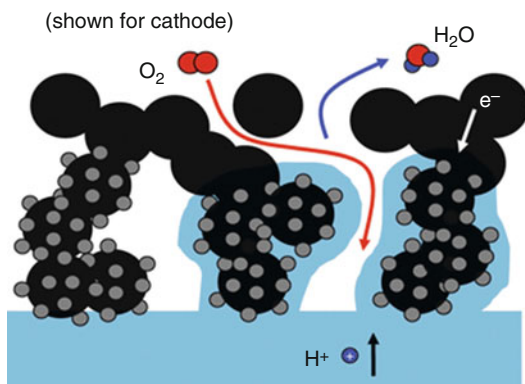
There is a common problem to all material selections for the different fuel cell types, namely, to generate an optimal electrolyte/electrode interface. One has to realize that gaseous molecular reactants are converted into ionic species, solvated/hydrated in their electrolyte medium, by exchanging electrons with the electrode material. This reaction occurs at the so-called triple phase boundary (triple point), where electron conducting, ion conducting, and gas phase (eventually dissolved in the electrolyte) join to each other. To allow a high surface area for current generation, the electrolyte/electrode interface is extended into a three-dimensional *interphase* with a certain thickness. For a polymer electrolyte fuel cell, this *interphase* is drafted in Fig. 7 for the cathode (oxygen) side.

Depending on the respective materials for the different fuel cell types, this three-dimensional *interphase* has to be established by very different preparation/manufacturing procedures. In particular, solid electrolyte materials must be processable to be included into the electrode layer.

### Fuel Cell Families

The various fuel cell types considered today having some technical relevance are displayed schematically in Fig. 8. They are arranged according to the nature of electrolyte, acidic or alkaline, and to their temperature of operation.

The polymer electrolyte fuel cell, PEFC, and the phosphoric acid fuel cell, PAFC, are acidic fuel cells; the PEFC operates in the temperature range below and around 100 °C (PEFC), respectively, and the PAFC at around 200 °C. Hydrogen is the preferred fuel for both types. A PEFC can also be fed by liquid or gaseous methanol, called direct methanol fuel cell, DMFC. Other fuels based on alcohols, e.g., the direct ethanol fuel cell, DEFC, are subject to research. Fuel cell types utilizing an acidic aqueous electrolyte will not be considered here.



**Fuel Cell Types and Their Electrochemistry, Fig. 7** Electrode layer (interphase) with three phase boundary (schematic) of a polymer electrolyte fuel cell (cathode side). Blue: polymer electrolyte, black: carbon particles, gray: platinum nanoparticles (Adapted from L. Gubler, Paul Scherrer Institut)

Most concepts for an alkaline fuel cell in the past have been described with an aqueous alkaline electrolyte. Recently, also anion exchange membranes, alkaline solid polymer electrolytes, have been considered [13].

The molten carbonate fuel cell, MCFC, and the solid oxide fuel cell, SOFC, are high temperature fuel cells, due to their temperatures of operation of around 650 °C, respectively, 800–900 °C. Both can be considered as alkaline fuel cells (chapter ► “[Molten Carbonate Fuel Cells](#)”).

The local appearance of the reaction product is determined by the current-carrying ion. While for acidic fuel cells the reaction product shows up at the cathode (oxidant side), it is the anode (fuel side) for alkaline fuel cells. In case of C-containing fuels, e.g., methanol, a second reaction product containing the oxidized carbon appears at the fuel side. The appearance and hence the removal of the product/s causes consequences for the mass flow engineering of the stack and fuel cell system.

The following ordering of fuel cell types does not reflect the historical development of the various fuel cell technologies.

### Polymer Electrolyte Fuel Cell Types

The idea of using a thin ion-conducting polymer membrane, *solid polymer electrolyte*, as electrolyte

and separator can lead to different concepts of cells. Firstly, when ionic charges, anions or cations, are chemically bound to the polymer (ionomer) network, the respective countercharge can move freely within the polymer volume, provided a certain volumetric charge density within the polymer exists, which on uptake of, e.g., water leads to phase separation into a hydrophobic polymer (backbone) and a hydrophilic, charge-containing phase [14]. As a consequence, the polymer morphology allows the continuous transport of this ion from one electrode interphase to the other. This concept is normally called polymer electrolyte fuel cell (PEFC).

Depending on the fuel, H<sub>2</sub>, MeOH (gas or liquid), or others, the solid polymer electrolyte properties have to be tailored, in particular for their properties toward separation of fuel and oxidant.

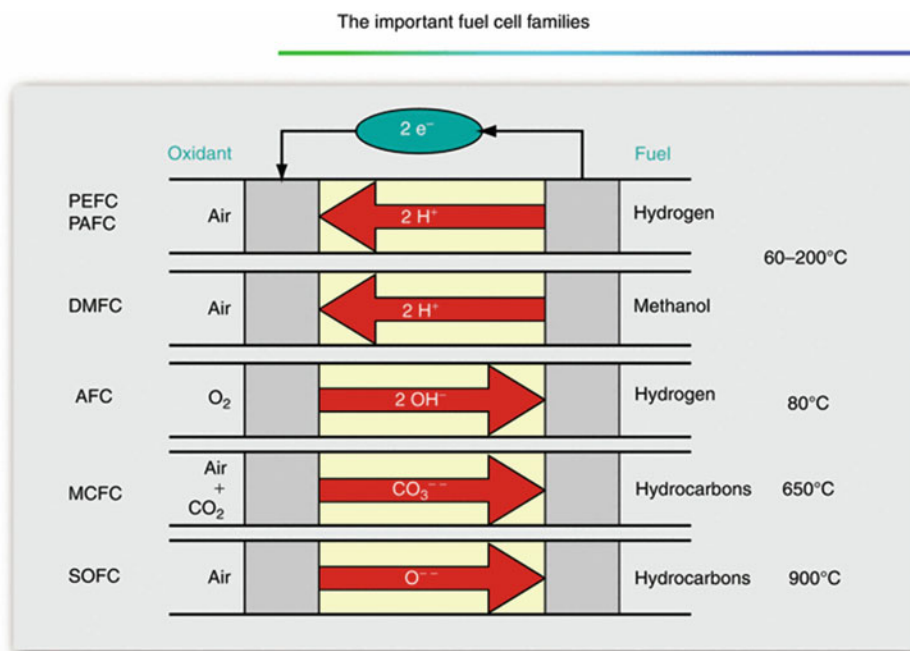
Further, non-ionomeric polymers can absorb an electrolyte, e.g., phosphoric acid H<sub>3</sub>PO<sub>4</sub>, which then renders ion conducting. This concept is realized in the so-called HT-PEFC, high temperature PEFC (ca. 100–200 °C), where a polybenzimidazole film imbibed with phosphoric acid becomes proton conducting due to the mechanism described above for non-aqueous phosphoric acid (see this book, chapter ► “[Polybenzimidazole Fuel Cell Technology: Theory, Performance, and Applications](#)”).

### H<sub>2</sub>-Fed PEFC

This type of H<sub>2</sub>-fed fuel cell, due to its high achievable specific and volumetric power density (in the range of 1 kW/kg and 1 kW/L and above), its cold start behavior, and its fast load following properties, has found interest in the automotive industry and is under development by all major automotive companies.

A thin ion-conducting polymer sheet, typically in the range of 25 μm, is utilized as a solid electrolyte, i.e., electrolyte and separator, in the PEFC (Fig. 1). For thermal stability reasons, only cation exchange membranes in the H<sup>+</sup> form have been considered up to today for technical applications (see also ► “[Alkaline Membrane Fuel Cells](#)”). In comparison to cells with liquid electrolyte, this PEFC concept offers the advantage that the “electrolyte” is chemically bound within the polymer matrix and only



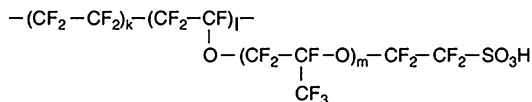


**Fuel Cell Types and Their Electrochemistry, Fig. 8** The important fuel cell families of today

water as reactant, in addition to the gases, appears in the peripheral system components. Membranes are perfluorinated or partially fluorinated polymers, with side chains ending in pendant acid groups, e.g., the sulfonic acid group  $-\text{SO}_3\text{H}$  (Fig. 9).

Under operation, the membrane has to contain some water, e.g., 15 water molecules per sulfonic acid group, to provide the necessary specific conductivity. This fact causes consequences for some of the system auxiliaries, as the gases, hydrogen and air, have to be humidified before flowing into the cell to sustain the hydration level in the membrane.

The acidic electrolyte requires a precious metal catalyst; hence platinum supported on carbon particles serves as electrocatalyst, with typical Pt loadings of ca.  $0.1 \text{ mg/cm}^2$  at the anode side and ca.  $0.4 \text{ mg/cm}^2$  at the cathode side. Platinum nanoparticles, typically a few (3–5) nanometers in diameter, are deposited on various carbon substrates (e.g., 20–40%Pt/C) by wet chemical processes and then further processed in combination with solubilized ionomer material and binder(s) (PTFE) to yield an ink, which then is applied either to the electrolyte membrane surface (CCM, catalyst-coated membrane) or to the GDL to form the GDE.



**Fuel Cell Types and Their Electrochemistry, Fig. 9** Generalized structure formula of Nafion<sup>®</sup> type membranes (DuPont) with  $m = 1$ ,  $l = 1$ ,  $k = 5-7$

Extensive characterization of these electrocatalysts for the fuel cell reactions has shown that the electrocatalytic activity of these nanoparticles is by a factor 10 lower than the activity of a polycrystalline platinum surface for the respective reactions, HOR or ORR [15]. This difference is not fully understood yet.

An interesting proprietary approach has been followed recently by the 3 M Company, creating a continuous electrode area covered by nanoscale Pt whiskers. Reactivity of these electrocatalytic layers is in the range of polycrystalline platinum surfaces [16].

Today, pure hydrogen is considered as the ideal fuel. Due to its CO content, hydrogen derived from C-containing fuels (by steam reforming (SR), partial oxidation (POX), or autothermal

reforming (ATR) followed by preferential oxidation (PROX)) would need specific measures in terms of electrocatalysis, e.g., PtRu as bifunctional electrocatalyst, to allow oxidation of CO. As an alternative, purification methods of the anode gas stream prior to entering the cell down to only a few parts per million CO (depending on operation temperature) are necessary.

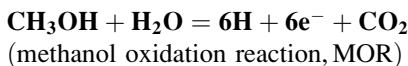
The electrocatalytic layers are contacted by gas diffusion layers, allowing the gases to be passed to the interphase and the product(s), H<sub>2</sub>O with H<sub>2</sub> and O<sub>2</sub> as reactants, which consist of carbon cloth or paper (Fig. 2). This arrangement of membrane, electrocatalytic layers, and gas diffusion layers is colloquially called membrane electrode assembly (MEA).

Most of the applications of this fuel cell type are developed for air operation, taking advantage of utilizing one reactant from the ambient environment. However, there exist also some applications in which pure oxygen is employed as oxidant. Due to the higher partial pressure of oxygen and the absence of electrochemically inert nitrogen as the majority component in the cathodic gas stream, humidification issues of the cell can be strongly simplified [17, 18].

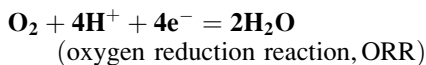
#### Methanol-Fed Fuel Cell (PEFC Type)

The same concept of combination of an acidic solid polymer electrolyte and acid stable precious metal electrocatalysts can also be applied to a methanol-fed fuel cell (direct methanol fuel cell, DMFC). Methanol can be fed in liquid or vapor form, mixed with water. The methanol molecule CH<sub>3</sub>OH is electrochemically converted at the anode:

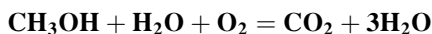
**Anodic reaction :**



**Cathodic reaction :**



**Overall reaction :**



As seen above, during MOR, one molecule of water is consumed, which is necessary to oxidize

carbon in the CH<sub>3</sub>OH molecule to CO<sub>2</sub>, while potentially six protons are liberated. The ORR can be formulated the same way as in a hydrogen-fed cell.

The equilibrium potential for the anode reaction is 0.02 V; hence, a theoretical cell voltage close to the H<sub>2</sub>/O<sub>2</sub> fuel cell should be observed. In practice, the OCV is lower, for several reasons: Due to the similarity of methanol and water as solvents (e.g., solubility parameter), methanol also penetrates into the water-swollen polymer membrane and passes to the cathode (methanol crossover), causing a mixed potential at a lower value than the oxygen potential. Further, the anode reaction requires a binary or ternary bifunctional catalyst, containing next to platinum one metal component (or two) providing the splitting reaction of the water molecule involved to liberate oxygen for the carbon oxidation at lower potentials as compared to platinum. Examples would be Ru, Sn, Mo, others, or even combinations of two of these together with platinum as the hydrogen-liberating catalyst. Intermediate oxidation species of the methanol molecule, e.g., -COH, may adsorb and poison the platinum catalyst surface, thereby impeding the full oxidation reaction.

These kinetic losses at the anode lead to a high anode overvoltage and, therefore, the cell voltage in the DMFC is lower at a respective value of current density as compared to a H<sub>2</sub>-fed cell, as is the achievable power density.

Direct methanol fuel cell concepts with liquid electrolyte have also been considered in the past. One advantage of circulating liquid electrolytes is the option to cool the cell without additional cooling fluid.

#### High Temperature PEFC

As mentioned above, H<sub>3</sub>PO<sub>4</sub> can be absorbed in polybenzimidazole films to yield water-free proton-conducting membranes. The concept is strongly related to the phosphoric acid fuel cell, PAFC. These cells can be operated above 100 °C, typically in the temperature range of 160–180 °C, without humidification, allowing to simplify the balance of plant. Further, due to the higher operation temperature as compared to H<sub>2</sub>-fed cells, CO tolerance is drastically increased. Disadvantages are the loss of H<sub>3</sub>PO<sub>4</sub> during start-stop cycles, i.e.,



excursions to temperatures below 100 °C, where liquid product water causes leaching of the ionic component. In addition, achievable power densities are typically lower than with H<sub>2</sub>-fed cells, due to the fact that phosphate cations strongly adsorb on platinum even at these temperatures, impeding the ORR (chapter ▶ “[Phosphoric Acid Fuel Cells for Stationary Applications](#)”). For more detailed information please see chapter ▶ “[Polybenzimidazole Fuel Cell Technology: Theory, Performance, and Applications](#)”.

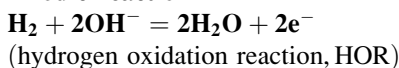
### Phosphoric Acid Fuel Cell

Looking back at the development of fuel cell technologies, the PAFC technology has been the earliest one to be commercialized (chapter ▶ “[Phosphoric Acid Fuel Cells for Stationary Applications](#)”). Several 200 kW<sub>e</sub> power units for co-generation have been delivered to customers over the past 20 years, mainly by the US company UTC Power [19]. Water-free phosphoric acid is absorbed in an inorganic diaphragm and contacted on both sides by platinum-containing gas diffusion electrodes. Advantages and disadvantages are very similar to the ones of the HT-PEFC.

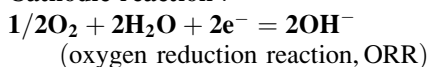
### Alkaline Fuel Cell

Alkaline electrolytes played an important role in the beginning of fuel cell development, due to its less stringent requirements for electrocatalysts. An aqueous solution of NaOH or KOH at higher concentration is absorbed in a matrix, formerly asbestos, today a composite material of an oxide and a polymer binder. The electrochemistry of the respective HOR and ORR can be written the following way:

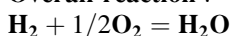
**Anodic reaction :**



**Cathodic reaction :**



**Overall reaction :**



As described above, an alkaline cell generally has to be operated on H<sub>2</sub> and O<sub>2</sub>, due to the CO<sub>2</sub>

problem. As advantage, a non-precious metal, such as Raney nickel, can serve as electrode material. ORR in alkaline solution shows a lower overpotential loss than in acidic solution; hence, higher specific power densities (mW/cm<sup>2</sup>) can be generated in cells.

Recently, some progress in the preparation of anion exchange membranes was reported, leading to the application of the PEFC concept to alkaline fuel cells. However, performance in terms of power output and stability/lifetime is far below the acidic technology [13].

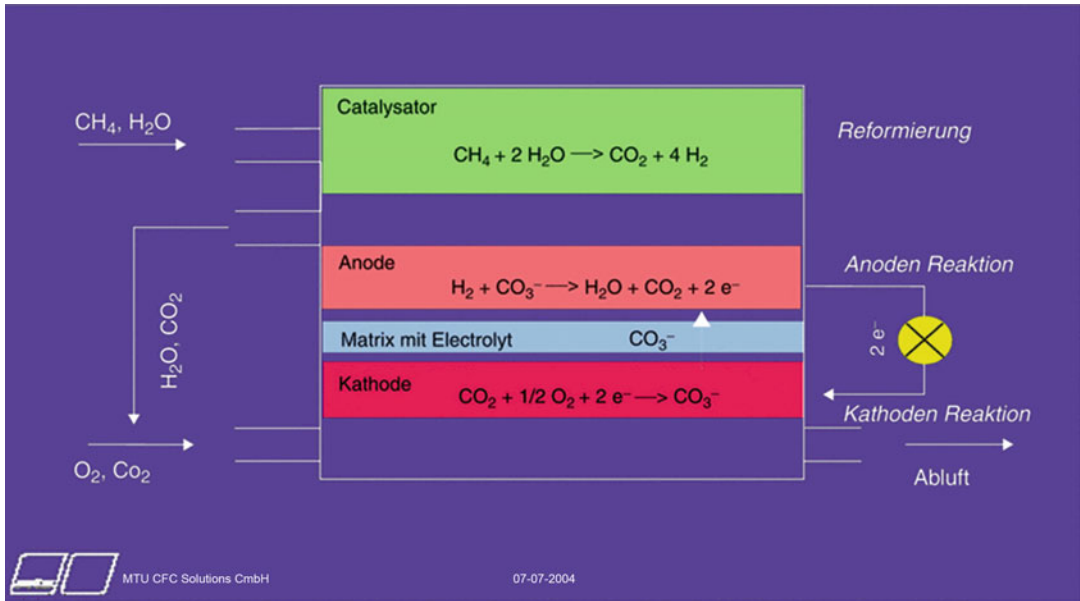
### Molten Carbonate Fuel Cell

As a high temperature fuel cell, which operates in the temperature range around 650 °C, the MCFC can use the waste heat of the fuel cell reactions for internal reforming of C-containing fuels (Fig. 10). No further processing of the reformed fuel is necessary. Reformed hydrogen is oxidized at the anode, consisting of a porous nickel electrode, under consumption of the CO<sub>3</sub><sup>2-</sup> cation, which carries the current through the electrolyte, to H<sub>2</sub>O and CO<sub>2</sub>. The anode reaction product CO<sub>2</sub> has to be recycled to the cathode compartment, where it is consumed during the ORR at a porous Ni-Oxide cathode to CO<sub>3</sub><sup>2-</sup> and taken up by the electrolyte melt again, therefore balancing the CO<sub>3</sub><sup>2-</sup> concentration in the Li<sub>2</sub>CO<sub>3</sub>/K<sub>2</sub>CO<sub>3</sub> eutectic electrolyte, which is absorbed in a LiAlO<sub>2</sub> matrix.

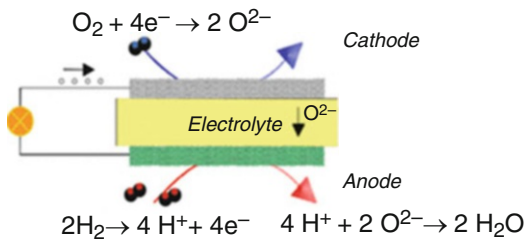
MCFC systems in the power range of 250 kW have been delivered for on-site testing, using a variety of fuels, like biogas, reformed natural gas, and others [20].

### Solid Oxide Fuel Cell

The electrolyte in a solid oxide fuel cell is a thin ceramic body, which is an O<sub>2</sub>-conducting oxide material. O<sup>2-</sup> conduction is established by doping a stoichiometric material like ZrO<sub>2</sub> by Y<sub>2</sub>O<sub>3</sub>, thereby generating O<sup>2-</sup> vacancies in the lattice. Around 8% of Y<sub>2</sub>O<sub>3</sub> are required to stabilize the cubic form of ZrO<sub>2</sub> at temperature of operation. A reasonable specific conductivity for this 8YSZ material is obtained in the range of and above 800 °C (Fig. 11).



**Fuel Cell Types and Their Electrochemistry, Fig. 10** Scheme of the molten carbonate fuel cell, MCFC (Adapted from MTU CFC Solutions)



**Fuel Cell Types and Their Electrochemistry, Fig. 11** Scheme of the planar solid oxide fuel cell, SOFC, and its electrochemistry (Adapted from L. Gauckler, ETH Zürich)

Electrode materials consist of a Ni/8YSZ cermet (mixture of ceramic and metal) as anode and  $La_xSr_yMnO_3$  (perovskite) as cathode.

Ohmic losses in the electrolyte can be lowered by designing cells with thin electrolyte layers, typically 10  $\mu m$  thick, supported on one of the electrode structures, instead of utilizing a thicker, free-standing electrolyte layer.

For many years, also a tubular concept had been developed by Siemens Westinghouse, addressing the challenges in matching the thermal expansion coefficients of the different materials, namely for the electrolyte and the electrodes.

However, the further development of this concept had been abandoned. SOFC technology development mainly addresses stationary co-generation of power and heat, at a power scale of 100 kW<sub>e</sub> and more (e.g., Topsoe Fuel Cell, Denmark), as well as small scale (1 kW<sub>e</sub>) co-generation for private homes (e.g., Hexis Switzerland).

Interestingly, low power application micro-SOFCs are developed as battery alternatives, utilizing materials which allow operation temperatures in the range of 550 °C (One-Bat-Project, ETZ Zürich [21]).

### Future Directions

After two decades of intensive fuel cell research and development, some of the described technologies have come close to the market. This is particularly the case for the PEFC technology developed worldwide by automotive industry. Preliminary market introduction is planned, according to various sources, by the year 2015. However, still issues of cost and reliability remain and provide ample space for further research. Unfortunately, other technologies, e.g., the SOFC and MCFC technology, have

recently seen some setbacks, due to the fact that some longstanding prominent advocates of fuel cell development have decided not to continue their effort (e.g., SOFC by Siemens, MCFC by Tognum (formerly MCFC solutions), others).

## Bibliography

1. International Energy Agency (2011) Clean energy progress report, updated June 2011. International Energy Agency, Paris
2. OECD (2004) Hydrogen and fuel cells, review of National R&D Programs. International Energy Agency/OECD, Paris. ISBN 9789264108837
3. Shell International BV (2011) Shell energy scenarios to 2050, an era of volatile transitions. Shell International BV, The Hague. [http://www-static.shell.com/static/aboutshell/downloads/aboutshell/signals\\_signposts.pdf](http://www-static.shell.com/static/aboutshell/downloads/aboutshell/signals_signposts.pdf)
4. <http://www.peakoil.net/>
5. [http://www.roads2hy.com/pub\\_download.asp?PageIndex=1](http://www.roads2hy.com/pub_download.asp?PageIndex=1)
6. e.g., <http://www.sfc.com/en/>
7. Bossel U (2000) The birth of the fuel cell. European Fuel Cell Forum, Oberrohrdorf. ISBN 3-905592-06-1
8. Scherer GG (1990) *Ber Bunsenges Phys Chem* 94: 1008
9. Hamman CH, Hamnett A, Vielstich W (1998) *Electrochemistry*. Wiley, Weinheim
10. Appleby AJ (1994) *J Power Sources* 49:15
11. Uchida H, Tanaka S, Iwahara H (1985) *J Appl Electrochem* 15:93
12. Haile SM (2003) *Acta Mater* 51:5981
13. Merle G, Wessling M, Nijmeijer K (2011) *J Membr Sci* 377:1
14. Kreuer K-D (2007) Proton conduction in fuel cells. In: Limbach HH, Schowen RL, Hynes JT, Klinman JP (eds) *Hydrogen-transfer reactions*, vol 1. Wiley, New York, pp 709–736
15. Gasteiger HA, Kocha SS, Sompali B, Wagner FT (2005) *Appl Catal B Environ* 56:9
16. [http://www1.eere.energy.gov/hydrogenandfuelcells/pdfs/merit03/72\\_3m\\_mark\\_debe.pdf](http://www1.eere.energy.gov/hydrogenandfuelcells/pdfs/merit03/72_3m_mark_debe.pdf)
17. <http://info.industry.siemens.com/data/presse/docs/m1-isfb07033403e.pdf>
18. Büchi FN, Paganelli G, Dietrich P, Laurent D, Tsukada A, Varenne P, Delfino A, Kötzt R, Freunberger SA, Magne P-A, Walser D, Olsommer D (2007) *Fuel Cells* 07:329
19. <http://www.utcpower.com/products/purecell400>
20. <http://www.fuelcellenergy.com/>
21. <http://www.nonmet.mat.ethz.ch/research/onebat>



---

## Polymer Electrolyte (PE) Fuel Cell Systems

John F. Elter

Sustainable-Systems, LLC, Latham, NY, USA  
Nanoscale Engineering, College of Nanoscale Science and Engineering SUNY Albany, Albany, NY, USA

### Article Outline

Glossary

Definition of Subject

Introduction

The PEM Fuel Cell Industry

Fuel Cell Basics

Critical Parameters/Critical Specifications

Recent Advancements

Fuel Cell System Design

Technical Readiness

System Cost and Reliability

Fuel Cell Systems and Sustainability

Future Directions

Bibliography

### Glossary

**Fuel Cells (FC)** Electrochemical cells that convert chemical energy from a fuel into electrical energy through the controlled transfer of electrical charge driven by the difference in electrochemical potential between two electrodes separated by an electrolyte.

**Electrocatalyst** A material that enhances the rate of an electrochemical reaction, such as the hydrogen oxidation reaction (HOR) or the oxygen reduction reaction (ORR), without itself being consumed in the reaction. In most PEM

fuel cells, the electrocatalysts are nanosized materials made from the precious group metals (PGM), usually platinum, palladium, and ruthenium or alloys of these materials with nickel, cobalt, and manganese.

**Polymer Electrolyte Membrane (PEM)** Cation- or anion-conducting polymer membrane that separates the two electrodes in a fuel cell. In most PEM fuel cells, the polymer is a cation (proton) conductor and in this case PEM can stand for proton exchange membrane.

**Triple-Phase Boundary (TPB)** The place on the catalyst surface within the fuel cell electrodes where protons, electrons, and gaseous reactants meet in order to oxidize hydrogen or reduce oxygen.

**Gas Diffusion Layer (GDL)** A component of the fuel cell used to evenly distribute reactants and electrons across the electrode surface and facilitate the removal of water.

**Membrane Electrode Assembly (MEA)** A manufactured unit consisting of the electrodes, membrane and gas diffusion electrode. Sometimes the MEA can include the gasket used to seal the fuel cell. The MEA, when placed between two electrically conducting plates with channels to provide the fuel and oxygen, constitute a single cell.

**Stack** A collection of individual fuel cells, separated by electrically conducting “bipolar” plates, connected in series. Stacks can range in size from a few watts as in portable fuel cells to hundreds of kilowatts as in stationary fuel cells for combined heat and power or grid assets.

**Fuel Cell System (FCS)** The combination of a fuel cell stack and the subsystems that is required to support its operation for the intended application.

### Definition of Subject

This entry discusses the subject of fuel cells: how they work and how they are designed and

---

John F. Elter is retired from College of Nanoscale Science and Engineering

© Springer Science+Business Media, LLC, part of Springer Nature 2019  
T. E. Lipman, A. Z. Weber (eds.), *Fuel Cells and Hydrogen Production*,  
[https://doi.org/10.1007/978-1-4939-7789-5\\_149](https://doi.org/10.1007/978-1-4939-7789-5_149)

Originally published in  
R. A. Meyers (ed.), *Encyclopedia of Sustainability Science and Technology*, © Springer Science+Business Media LLC 2017  
[https://doi.org/10.1007/978-1-4939-2493-6\\_149-3](https://doi.org/10.1007/978-1-4939-2493-6_149-3)

integrated into a collection of subsystems for application in a variety of applications. Particular focus is placed upon systems utilizing polymer electrolyte membranes and how the properties of the membrane dictate the system design considerations.

Fuel cells themselves were invented over 170 years ago, with the first fuel cell demonstrated by Sir William Robert Grove in 1839. The first commercial use of a PEM fuel cell in a system occurred when General Electric developed the technology with NASA and McDonnell Aircraft for use in the Gemini space program. Since then, fuel cells have been integrated into systems intended for a wide variety of applications, from fuel cells of just a few watts for portable application up to hundreds of kilowatts for some applications in transportation.

## Introduction

The vision of fuel cells running on renewable hydrogen as an energy carrier derived from water, and producing electricity with only water as a by-product, has long captured the imagination of those concerned with the environment. Since the early days of the use of fuel cells in the Gemini space program, various explorations of the potential use of fuel cells have been conducted by individuals, small firms, and large corporations. In each case, the potential of fuel cells has been validated. The long-term benefits of high efficiency and fuel flexibility are clear, especially in today's context, wherein energy security and the need to reduce dependence on foreign oil and the need for sustainable economic development and the reduction of greenhouse gas emissions have been brought into sharp focus by war, weather, and wildlife.

Great progress has been and continued to be made in the development of fuel cells since their first commercial application roughly 50 years ago. This is particularly true of the fuel cells developed for automotive applications, which represents a very demanding application in terms of durability and cost. Progress in the automotive application has had a spillover effect to other applications,

particularly for those being developed for motive power and stationary combined heat and power. This entry will attempt to lay out the status of the technology today, with a focus on the progress made in the past 5 years and where it needs to go in the future. First, a brief overview will be given of the fuel cell industry, followed by a review of some of the basic principles underlying the theory of operation. The notion of critical design parameters and specifications will be discussed as a prelude to a review of some recent advancements and to the system design process as it relates to important considerations for fuel cell systems. Finally, there will be a discussion on future directions.

## The PEM Fuel Cell Industry

In reality, it is fair to say that PEM fuel cells are slowly emerging from their current status as a nascent industry. The long-term benefits of high efficiency and potential fuel flexibility are clear, but cost and durability issues have caused a slow adoption time line. In addition, the nagging issue of the infrastructure needed to provide hydrogen as a fuel has not gone away. Hydrogen availability is still a relevant issue for many of the applications that would have fuel cells as the privileged technology. Other obstacles to profitable commercialization include the excellent low cost, operational flexibility, and lifespan of the incumbent technologies which fuel cells are trying to displace. In response to these important issues, most fuel cell manufacturers, in need of revenues, are focusing on large niche markets for which the technological requirements are best suited to current fuel cell capabilities. These markets, such as backup power, forklift trucks, bus fleets, and small and large combined heat and power, offer the opportunity for fuel cell companies to manufacture sufficient quantities to gain sufficient learning and revenues to attract investors seeking the potential benefits of game-changing technologies. Even in some of these cases, however, government subsidies are needed to help the industry cope with the slow market penetration associated with product immaturity and the risk-adverse nature of the

industries being targeted. Limited revenues from these markets lead to high stock volatility, making valuations difficult, limiting private investment, and further exasperating the situation.

Over the past 5 years, the PEM fuel cell industry has demonstrated a steady year-over-year increase in placements, but at a rate which is not offering the benefit of a strong learning curve and the accompanying economies of scale. On the one hand, there are large automotive players (Honda, Toyota, GM, Hyundai) who continue to make sizeable investments and steady progress in terms of cost and durability. The fuel cell-powered vehicles are now early production models that are being sold and tested in quantities that are compatible with the limited hydrogen dispensing infrastructure. These are providing important feedback on customer acceptance and validation of the fuel cell vehicle performance and reliability. On the other are those established (but still not profitable) smaller fuel cell companies focusing on niche markets (backup, forklift, other mobility applications) that are gaining commercial traction based on recognized value propositions. An example of the latter is Plug Power, which had established strong commercial agreements with both Amazon and Wal-Mart [1]. Feeding fuel cell components to these companies are corporations such as 3M, DuPont, W.L. Gore, and Asahi Glass providing the membrane electrode assemblies, as well as a host of large automotive suppliers providing “balance of plant” components such as blowers, compressors, heat exchangers, and electronics which are a critical part of the maturing supply chain necessary for industry success.

The past 5 years have also witnessed a restructuring of the field in which smaller companies are being consolidated into others as a means of acquiring fuel cell IP, know-how, and additional markets. Examples include Plug Power acquiring ReliOn and its telecom backup power business, Ballard acquiring IdaTech’s backup power assets and UTC’s PEM intellectual property for bus applications, and Hyster-Yale’s purchase of Nuvera for application in its forklift business, which is one of the fuel cell applications which is closest to profitability. In addition, China

is a slumbering dragon which has begun to awaken to the possibilities of fuel cells for both motive and stationary applications, with agreements signed with Ballard, Plug Power, and others as it begins to address its need to build up expertise and its supply chain ecosystems [2].

One reason for the fragmentation of the fuel cell industry is the wide range of potential applications to which fuel cells can be applied. As mentioned, these include transportation applications, material handling, telecommunications backup, consumer electronics, as well as both residential and larger-scale cogeneration. Each of these markets has a well-defined set of operational characteristics and requirements, as defined by the customer. Another and related reason for the fragmentation of the industry is the lack of a dominant design paradigm. Each company has a preferred method of approaching the design of a fuel cell and the system into which it is embedded. Since no single approach has emerged as dominant, there is a lack of standards, *de facto* or otherwise, around which the industry can capture the benefits of economies of scale and of accumulated knowledge.

On the other hand, it might be argued that there *is* a *de facto* dominant design, and it is that standard which, up to now unwittingly adhered to, is limiting the true out-of-the-box thinking needed for step changes in performance at lower cost and improved reliability. In most cases, as we will see, the commercialization issues around each application are driven to a large extent by this underlying “standard” technology and its modes of failure in meeting customer requirements. In this entry, specific attention will be given to these failure modes and how they drive system complexity. In addition, some attention will be paid to the system design and how it can be simplified to enable lower costs.

Finally, as will be discussed here, there has been steady progress over the past 5 years in lowering costs and improving reliability, due in part to sustained government support of fuel cells and the persistence of the key players in the industry. The US DOE in particular has shown a steady willingness to support the technological development of fuel cells, particularly for the

most demanding application, transportation. Indeed, there is hardly a technical nuance that has not received the DOE's support. In many ways the industry is now in the position of developing engineering solutions at the material, component, and system level for minimizing the known deficiencies and failure modes intrinsic to the technology. These will be discussed below.

Still, there is "a lot of room at the bottom" for scientific and engineering innovation. Indeed, the application of nanotechnology as a means of enabling the fuel cell industry to become a sustainable ecosystem should not be underestimated. In fact, most progress within the past 5 years has been in engineering improvements at the nano-scale, thus enabling improvements in cost, performance, and durability. There is ample reason for considerable optimism around PEM fuel cell systems for the sustainable energy applications they support.

## Fuel Cell Basics

Fuel cells are electrochemical devices that transform chemical energy into electrical energy, much the same way a battery converts chemical potential energy into electrical kinetic energy, except that the chemicals consumed in a fuel cell in the reaction are supplied from external sources. The fuel cell enables the generation of electricity while producing pure water by controlling the combining of hydrogen and oxygen:



Ideally, this reaction would take place at a potential of 1.229 V at standard conditions (25 °C and 1 atm) if it were not for losses due to irreversible internal processes. In fact, the reversible potential  $E_r$  of this reaction can be expressed in terms of the change in the Gibbs free energy,  $\Delta G$ :

$$\Delta G = -n F E_r \quad (2)$$

Here  $n$  is the number of electrons involved, and  $F$  is Faraday's constant, which has the value of

96,485 coulombs of charge per mole of electrons. The derivation of Eq. (2) is a straightforward application of thermodynamics, recognizing that in this case, the work done is the product of the amount of charge transferred and the potential. For the case of standard conditions, we know from thermodynamics that  $\Delta G = 237$  kJ/mole when the water is produced as a liquid (corresponding to the higher heating value, HHV) and  $n = 2$  for the  $\text{H}_2/\text{O}_2$  fuel cell reaction. Of course, not all of the energy in the reaction is turned into electricity, and because of this, some portion of hydrogen's HHV is converted into heat. The enthalpy change in the reaction is given by the familiar thermodynamic relationship

$$\Delta H = \Delta G + T\Delta S \quad (3)$$

From thermodynamic tables we find at standard conditions that  $\Delta H = 286$  kJ/mole. It follows that roughly 49 kJ/mole are converted into heat, and the theoretical efficiency  $\eta_{th}$  of a fuel cell operating at standard conditions is

$$\eta_{th} = \Delta G/\Delta H = 237/286 = 83\% \quad (4)$$

In addition, there are various losses which are due to irreversible processes in the cell itself. These losses, which are intrinsic to the cell and are material dependent, reduce the fuel cell efficiencies to around 40–60%, depending on the type of fuel cell and its application. There are numerous references that discuss the theory behind fuel cells in detail [3, 4] as well as the other entries in this encyclopedia. Here only a very cursory overview is given, as the focus of this entry is on the fuel cell *system*.

In a typical fuel cell, there are two electrodes, an anode from which electrons are removed during the oxidation of hydrogen and a cathode to which electrons flow during the reduction of oxygen, an ion-conducting electrolyte which ionically connects the anode and cathode, and an external circuit through which the electrons flow from the anode to the cathode while doing electrical work. In early fuel cells, the electrolyte was generally a liquid such as a solution of KOH, which provided for the flow of  $\text{OH}^-$  anions. In this case, the fuel



cell was termed an “alkaline” fuel cell because of the nature of the electrolyte. In the same way, the electrolyte can be phosphoric acid, in this case providing for the flow of  $H^+$  cations, or protons. Such a fuel cell is called a “phosphoric acid” fuel cell, again in recognition of the electrolyte. In this entry, we will discuss polymer electrolyte fuel cell systems. In this case, the electrolyte is a polymer in the form of a *membrane*, hence the term “polymer electrolyte membrane” or PEM fuel cell. Polymer electrolyte fuel cells, or PEFCs, are electrochemical devices whose characteristics are determined largely by the properties of the polymer electrolyte. One of the main purposes of this entry is to illustrate the extent to which the PEMFC’s performance is in fact *dominated* by the properties of the polymer electrolyte. It is worth noting that in some cases, the acronym PEM is interpreted to mean proton exchange membrane, since in most cases in which the acronym PEM is used, the ion that is transported across the membrane and “exchanged” at the electrodes is the proton. However, here we will interpret the acronym to mean polymer electrolyte membrane to emphasize the point that it is the polymer electrolyte that to a large extent dictates the characteristics of the system.

In a fuel cell, the two reactants, in this case hydrogen and oxygen, are each directed macroscopically by flow channels molded into electrically and thermally conductive plates. The hydrogen on the anode side and the oxygen at the cathode side are each brought into contact with an electrode by the gas diffusion layer or “GDL” which ensures uniform flow across the cell. As discussed, a polymer membrane is provided that serves as the electrolyte, providing good ionic conductivity while maintaining the separation of these reactant gases and preventing the flow of electrons. The membrane needs to make intimate contact with the electrodes to ensure efficient charge transfer across the embedded electrode/electrolyte interface. The electrodes are generally porous to allow the diffusion of the reactant gases while providing a support for the catalysts needed to facilitate the electrochemical reactions. The electrodes also need to provide conductive pathways for the ions and electrons.

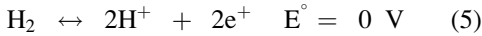
Clearly, the polymer electrolyte membrane, electrodes, and GDL have a complex set of interacting functional requirements. These will be discussed in detail, especially from the point of view of their impact on system design.

In most cases, the polymer electrolyte is basically acidic, in which case the catalysts are usually based upon platinum and its alloys. At the anode electrode, hydrogen gas molecules adsorb onto the supported catalyst material which is used to help strip the hydrogen of its electron, oxidizing it to become a hydrogen cation or proton. This proton is transported through the polymer electrolyte membrane to the cathode electrode. Here, oxygen molecules are fed into cathode electrode, usually by supplying air. Like the active layer at the anode, appropriate nanosized catalyst particles are supported on electrically conducting porous materials. In the current dominant design paradigm, this support is usually a high surface area carbon. Once on the catalyst surface, the oxygen’s covalent bonds are broken, forming oxygen anions. The oxygen anions then combine with protons arriving through the membrane and electrons that have been driven through an external circuit by the difference in the anode and cathode potentials. The *critical point* on the catalyst surface at which protons, electrons, and reactant gases must come together is generally called the *triple-phase boundary* (TPB). All of the necessary components, the gas diffusion media, the porous electrodes, and the polymer electrolyte membrane, and if desired, even the conformable gasket required to provide sealing around the perimeter of the plate, are manufactured as a “membrane electrode assembly” or “MEA” by various suppliers like 3M, Gore, Johnson Matthey, and others. Since a typical PEMFC operates at a voltage of less than 1 V, multiple cells are electrically connected in series to form a “stack” of cells that can be sized for a particular application. In this case, each thermally and electrically conducting plate is shared between the anode of one cell and the cathode of another and is thus termed “bipolar.” The integrated stack design must accommodate a means for managing the products of the fuel cell reaction: electricity, water, and heat. In smaller systems, the stack can be air-cooled, but

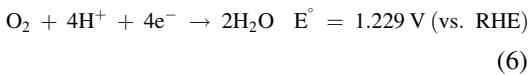


in larger systems, the plates must incorporate channels that allow for the flow of a liquid coolant.

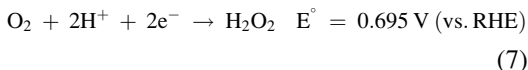
The electrochemical equation governing the hydrogen oxidation reaction (HOR) at the anode of a single cell is



This is a thermodynamically reversible reaction and, with platinum as the catalyst, is a standard reference known as the “reversible hydrogen electrode” (RHE), for which the potential is universally chosen as zero volts. The oxygen reduction reaction (ORR) at the cathode, on the other hand, is thermodynamically irreversible and is generally expressed in terms of the dominant four-electron reaction:



In fact, the ORR is an extremely complicated reaction that depends on the electronic structure and number of the active sites on the catalyst surface, which in turn are influenced by many factors including the size and shape of the catalyst particle, the presence of any contaminant species competing for reaction sites, the presence of oxides which may be formed during potential cycling, the effect of the catalyst support, etc. In addition to the four-electron reaction, there is the possibility for the two-electron peroxide pathway [5]:



In low-temperature PEMFCs, those that operate in the range of 65–80 °C, the peroxide pathway is problematic because if the peroxide is not quickly decomposed into water, it can form radicals that chemically attack the membrane, causing premature failure.

The ORR is a major source of efficiency loss in a PEMFC, but it is not the only source of the so-called overpotential. In general there are also resistive and mass-transport losses. The resistive losses are associated with the finite conductivities of the electrolyte and the electrodes and the contact resistance losses at the plate and GDL

interfaces, whereas mass-transport losses are associated with the lack of adequate fuel or air reaching the reaction sites within the electrode. For low-temperature PEMFC systems that operate below the boiling point of water, mass-transport losses are primarily due to the buildup of liquid water in the electrode or GDL (referred to as “flooding”) that increase the tortuous pathways. Reducing all of these sources of potential losses is important for achieving the highest possible efficiency.

It is perhaps convenient at this point to briefly mention the types of PEM fuel cell that are under development. Low-temperature PEM fuel cells (LTPEMFCs) operate in the range of 65–80 °C. These systems are limited in temperature by the requirement for the membrane to be maintained in a hydrated state in order to have sufficient proton conductivity. Typical of these systems are the perfluorinated sulfonic acid (PFSA) membranes made by DuPont, the standard being Nafion<sup>®</sup>. 3M, Gore, Solvay, Asahi, and others make membranes with similar properties and characteristics. Intermediate-temperature PEMFCs that are capable of operating above the boiling point of water in the region of 120 °C are under development primarily for automotive applications. These are still in the development phase [6] and when available will have a significant impact on PEMFC performance for applications other than just automotive. Still higher-temperature PEMFCs (HTPEMFCs) are based upon phosphoric acid-doped materials such as polybenzimidazole (PBI). These proton-conducting polymer electrolyte membranes allow fuel cells to operate at temperatures in the range of 160–200 °C, thus providing for a high degree of tolerance to certain fuel cell contaminants such as CO, while at the same time offering a source of high-quality heat [7]. PBI-based systems are discussed in detail elsewhere in this encyclopedia and will be mentioned briefly below in terms of their potential to simplify system design.

For a basic understanding of PEM fuel cells, it is important to appreciate how the properties of the polymer electrolyte dictate the requirements on the fuel cell, stack, and system design. A recent comprehensive review of the properties of PFSA

ionomers has been given by Kusoglu and Weber [8]. Here we will discuss just one but critically important example: water management. One of the more well-known and basic properties of the PFSA type of polymer electrolytes is that their protonic conductivity is a strong function of the level of hydration. Sulfonated fluoropolymer membranes are based on a polytetrafluoroethylene (PTFE) backbone that is sulfonated by adding a side chain ending in a sulfonic acid group ( $-\text{SO}_3\text{H}$ ) to the PTFE backbone. The resulting macromolecule contains both hydrophobic regions associated with the backbone and hydrophilic regions associated with the sulfonic acid group. Thus, a hydrated PFSA membrane forms a two-phase system consisting of a water-ion phase that is distributed throughout a partially crystallized perfluorinated matrix phase. As the membrane adsorbs water, the first water molecules cause the sulfonated group to dissociate, forming hydronium ( $\text{H}_3\text{O}^+$ ) ions. The water that hydrates the membrane then forms counterions that are localized on the sulfonated end groups, which act as nucleation sites. As more water is added, the counterion clusters coalesce to form even larger clusters, until a continuous phase is formed with properties that approach those of bulk water. The level of hydration is measured in terms of a parameter  $\lambda$ , which is equal to the number of absorbed waters per sulfonated group. For  $\lambda = 0$ , there is no water, and this anhydrous form of the membrane is uncommon, since complete removal of water requires temperatures near the decomposition temperature of the polymer. Molecular dynamic simulations indicate that the primary hydration shell around the sulfonated group grows to a level of about  $\lambda$  equal to five waters [9]. As more water is added, for  $\lambda > 6$ , the added water is screened by the more strongly bound water of the primary hydration shell, and it can be considered a free phase. Saturation occurs in Nafion<sup>®</sup> at  $\lambda = 14$ . One of the consequences of this strong coupling is that proton transport within the membrane is accompanied by the transport of water. This effect is known as “electroosmotic drag,” and it complicates the required management of the fuel cell by-products: water and heat.

The mechanism and degree of protonic conductivity change as the level of hydration

increases. Kreuer [10] has provided an in-depth review of the physics underlying the basic mechanisms of transport in proton conductors. Transport of the proton can occur by two mechanisms: structural diffusion and vehicle diffusion. The structural diffusion mechanism is associated with the proton “hopping” along water molecules (Grotthuss shuttling). Vehicular diffusion is the classical Einstein diffusive motion. The former is viewed as a discrete mechanism, the latter a continuous mechanism. In the nanosized confined hydrophilic spaces within the membrane, both mechanisms are operative, with the diffusion constant of the discrete mechanism being larger and increasing faster than that of the continuous mechanism at higher levels of hydration. At intermediate and low degrees of hydration, the proton mobility is essentially vehicular in nature. What is important here is that the underlying mechanism of transport in proton-conducting membranes changes as a function of the level of hydration, and it is fundamental to the overall behavior of the fuel cell and therefore the design of the fuel cell system.

Given this fundamental and strong dependence of protonic conductivity with water content, it is necessary to ensure that the polymer electrolyte is safeguarded against localized drying. Indeed, a situation in which the membrane is in a “drying” mode of operation may lead to a catastrophic “death spiral” failure mode, since lower conductivity leads to higher resistances, increased localized temperatures and therefore an ever increasing rate of drying, ultimately resulting in membrane failure. In addition, other failure modes, including attack by hydroxyl radicals, are also accelerated at higher temperature and drier membrane conditions, further exasperating the situation.

Hence, it is necessary to maintain the localized level of membrane hydration through “water management,” the *active* management of the moisture content of the membrane. One method is to design the system so that the relative humidity (RH) of the reactant streams coming into the stack is nearly saturated, an approach used by Plug Power and other fuel cell manufacturers. Another approach is to provide for water injection, an approach used by Intelligent Energy. Or one can

employ porous plates to distribute the product water generated during operation, a technique previously used by United Technologies. More recently, there is also a move toward thinner membranes to enhance the back transport of water. Each of these techniques requires careful stack and system design. The design approach taken likewise needs to avoid the situation where too much water can cause localized “flooding” within the cell, which in turn results in fuel starvation and subsequent permanent performance degradation. In most cases the requirement to manage the polymer electrolyte membrane water content adds considerable system complexity and cost, as well as sources of unreliability.

### Critical Parameters/Critical Specifications

It is clear that in a typical operating fuel cell, the current-voltage characteristics are dependent on the local operating temperature, pressure, flow rate, and composition of the reactant gas streams within the cell. These local conditions within the cell are *critical parameters* that need to be supplied by the careful design of the overall system. The system-level *critical parameters* around which the fuel cell system must be designed in order to achieve and maintain the desired local conditions ultimately determine the desired electrical state of the fuel cell system. Achieving the local critical parameters for adequate cell performance must take into account the design of the overall system and vice versa. It is also obvious that the performance of the fuel cell is also dependent on how well the individual *functional requirements* are met with the *specifications* on the component parts.

From a systems design perspective, it is perhaps worthwhile to describe how these terms are related. To motivate this discussion, it is important to note that a system is “technically ready” when all the required critical parameters can be simultaneously achieved through the intended interactions of the buildup of parts whose specifications can be met with ordinary manufacturing methods. It is assumed that the critical parameters are chosen

to meet the system specifications, while at the same time avoiding all known failure modes. The extent of the range in the critical parameters under which the system can operate over time, without failure, is called the “operating latitude.”

As a simple example, assume that one can write the equations of physics in the linear form

$$F_i = K_{ij}X_j \quad (8)$$

The terms  $F_i$  and  $X_j$  are termed the *critical parameters*, and the  $K_{ij}$  are termed the *critical specifications* that are required to meet the *functional requirements* of the particular component under consideration. The term “critical” is of course an indication that the specification in question is one of the significant few specifications that will be tracked all the way from the voice of the customer down to the factory floor. In a complete PEM fuel cell system, there can be hundreds of specifications that will need to be tracked during the development of the system. Of these, perhaps a few dozen will remain critical even after the product has launched and is in production.

As an example, consider the conduction of protons across the membrane and for the moment neglect the electroosmotic drag of water with the proton. In this case, Eq. (8) takes the simple form of Ohm’s law:

$$d\varphi/dz = -[1/\kappa] i \quad (9)$$

Here  $d\varphi/dz$  is the potential gradient across the membrane,  $i$  is the flux of protons, and  $\kappa$  is the protonic conductivity. The system-level critical parameters (pressure, temperature, flow rate, and composition) establish the conditions for determining the local critical parameters ( $d\varphi/dz$ ,  $i$ ), and these are in turn determined by the functional requirement that the polymer electrolyte has a protonic conductivity,  $\kappa$ . Typical values lie in the range of  $10^{-1}$ – $10^{-2}$  S/cm. Notice that critical parameters are generally *not* dimensions, but are rather forces, fields, affinities, and fluxes. They are the conditions that are required for operation. Specifications, on the other hand, are the items that an engineer can call out on a drawing: dimensions, conductivities (both electrical and thermal),

moduli of elasticity, and so forth. Instead of specifying the protonic conductivity  $\kappa$ , which is fixed by the material chemistry, the design engineer will specify perhaps the membrane equivalent weight and its thickness, thereby affecting not only the resistive losses but also the diffusion rate of gaseous and ionic species across the membrane.

As discussed above, the protonic conductivity is known to be a strong function of the moisture content, which again will be influenced by the system-level critical parameters of flow rate, temperature, pressure, and composition. Hence, in reality, a *constitutive equation* of the dependence of conductivity on moisture content is needed to support larger PEM fuel cell models which are essential to account for and keep track of all the complex interactions between the critical parameters and the specifications for the components of the MEA and other critical components. An early constitutive equation defining these interactions was described by Springer et al. [11] These interactions place stringent demands upon the design of the cell, stack, and ultimately the system. Researchers and engineers have developed sophisticated models in an attempt to describe the current-voltage response of single fuel cells to the significant critical parameters through the specifications of the material properties of the cell components. These models, which are remarkably successful in describing the overall performance of a single cell, are macro-homogeneous in the sense that they use local average properties, such as electrode porosity, conductivity, etc. to describe the materials. Constitutive equations of the conductivity dependence on moisture have been developed to support the fuel cell models [12]. There are also excellent reviews of the models that have been developed to elucidate the various aspects of fuel cell behavior under a variety of conditions, for example, those by Weber and Newman [13] and Wang [14]. A comprehensive review of the mass-transport phenomenon in PEM fuel cells, with a particular focus on multiphase flow, especially on understanding interactions at embedded interfaces within the electrodes, has been conducted by Weber et al. [15]. In addition, there are specialized models that deal with the root cause of specific failures, such as platinum

dissolution [16] and carbon corrosion [17] due to high potentials generated during startup and shutdown [18]. All of these have added considerable insights into how the PEM system runs and how failures are to be avoided. Finally, there are models of the fuel cell system itself. The models predict full system behavior over the range of system-level critical parameters and are useful in developing the algorithms needed in implementing model predictive control strategies.

Extensive cell-/stack-/system-level testing is also needed to assess the system's overall performance. In this case, computational fluid dynamics (CFD) is generally used to guide the cell-/stack-level testing, aiding in the fuel cell system development process. Some of these models have been made commercially available. In particular, models for PEMFCs can be obtained from CD-adapco [19], Fluent [20], Comsol [21], and others. In fact, knowledge of the cell and stack failure modes, and their dependence on the process critical parameters and critical specifications, is fundamental to designing and developing commercially viable fuel cell systems. A more detailed discussion of failure modes will be addressed in what follows. First, however, it is important to understand the current state of the art relative to the component at the heart of the PEM fuel cell, the MEA.

## Recent Advancements

The operation of the fuel cell involves complex interactions at numerous embedded surfaces within the cell, including the triple-phase boundary. These embedded surfaces can mask the ability to probe the detailed nature of these interactions. Today, processes at the nanoscale are a fertile ground for research, enabled by the tremendous advances made in computational nanoscience through the convergence of "nano" and "info" technology. These advancements in computation have allowed theoreticians to explore electrochemical and electromechanical processes at the micro-, meso-, and nanoscales, with meaningful numbers of atoms, thereby improving our theoretical understanding of the basic processes involved.

Furthermore, the rapidly expanding field of nanoscience and nanoengineering is being applied in a variety of fields, to include the synthesis and characterization of nanoscale materials and structures that have direct bearing on energy generation, conversion, and storage.

### Electrocatalysts

Relatively recent advancements have been made in the understanding of heterogeneous ORR catalysis using the combination of molecular- and atomic-level simulation tools, nanoscale fabrication methods, and nanoscale characterization techniques. For example, the early experimental work of Markovic [22], combined with the important theoretical work of Nørskov [23], Mavrakakis [24], Neurock [25], and others, has now given us a deeper understanding not only of the thermodynamics involved in the ORR, and the likely cause of the overpotential associated ORR, but also how variations in the electronic structure determine trends in the catalytic activity of the ORR across the periodic table. This work, coupled with the insights provided by the seminal work of Adzic [26], Stamenkovic [27], and others in the synthesis and performance characterization of Pt alloys and core-shell architectures, has significantly advanced the understanding of the state of the art of catalysts for use in both the HOR and ORR.

The exact mechanisms underlying the ORR are still debatable. However, Nørskov [28] and his group have used density functional theory (DFT) to significantly advance our understanding of the thermodynamics of the various possible reaction pathways and their dependence on surface properties. In combination with detailed DFT calculations, Nørskov and his team were able to provide a detailed description of the free-energy landscape of the electrochemical ORR over Pt as a function of applied bias. In doing so, they found that adsorbed oxygen and hydroxyl species are very stable intermediates at potentials close to equilibrium, and the calculated rate constant for the activated proton/electron transfer to these adsorbed intermediates accounts for the observed kinetics. On this basis, they were able to account for the trends in the ORR rate for a large number of different transition metals. In particular, they

were able to construct “volcano” plots of maximum catalytic activity as a function of the oxygen and hydroxyl adsorption energies, describing known trends and the observed effects of alloying. It is clear that a significant amount of progress has been made in the past several years in our basic understanding of the electrocatalytic processes at the nanoscale. An excellent summary of this and other work has been given in the recent book on fuel cell catalysis by Koper [29].

Of course, the high price of platinum has naturally provided the impetus for reducing the platinum loading by improving the kinetics of the ORR reaction. Considerable experimental effort has gone into the research and development of electrodes that incorporate the advantages of new nanomaterials intended to significantly reduce precious metal catalyst loadings, while maintaining high-power densities. Chief among these are electrodes that incorporate platinum alloys with transition metals of various types as a means of increasing catalytic activity, thereby allowing a reduction in platinum loading. Currently, Pt<sub>3</sub>Co alloys supported on carbon are achieving roughly a 2× improvement over the state-of-the-art Pt/C electrodes. Intermetallic architectures of Pt and other materials have been fabricated by a variety of techniques. Some of these, which yield so-called “core-shell” [30] structures which involve monolayers of Pt particles on Pd cores supported on carbon, are reported to have achieved very significant (≈20) increases in mass activities. The catalysts must not only have high catalytic activities but also good stability, and in this regard, the core-shell architectures offer a challenge in that Pt dissolution is known to occur during voltage cycling.

To deal with this latter problem, researchers are examining the effect nanoparticle structure on not only activity but also stability. In this regard, Adzic [31] and his coworkers have developed a promising new class of Pt-based catalysts having both high activity and high durability for the ORR. In particular, they have achieved this by depositing a Pt shell on an Au core doped with titanium oxide. They experimentally validated that the distinct microstructure of the Ti-Au core-Pt shell on a carbon support (Ti-Au@Pt/C).



The nanoparticles had Au cores, Pt as the shell, with protective titanium oxide located on the low coordination edges and vertex sites of the nanoparticles. Electrochemical measurements using a rotating disk electrode indicate that the mass activity ( $A/mg_{Pt}$ ) of the Ti-Au@Pt/C catalyst exhibits a 13-fold enhancement over that of commercially available Pt/C, whereas the specific activity ( $A/cm^2_{Pt}$ ) showed a fivefold improvement. More impressively, the catalyst exhibited excellent durability after 10,000 cycles of voltage cycling between 0.6 and 1.0 V.

Likewise improvements have been made with the development of catalysts with a “Pt-skin”-type surface structures formed upon annealing Pt-alloy nanoparticles. Stamenkovic, Markovic, and coworkers [32] have explored the activity and stability associated with this class of catalyst structure and have found increased activity and durability through the tailoring of nanomaterials in terms of size, composition, morphology, and architecture, with the objective of balancing the gains in stability with those in activity. They describe a strategy for achieving both high activity and stability as involving the de-alloying of  $Pt_3M$  nanoparticles, followed by annealing which creates a Pt-skin-like surface of several monolayers over a stable alloy-rich core, thereby achieving the desired reduction in PGM loading. Starting with  $PtM_3$  particles, Han et al. [33] have systematically studied the effects of particle size, acid de-alloying, and post-acid treatment annealing on nanoporosity and passivation of the alloy nanoparticles and have achieved unprecedented levels of performance, exceeding the DOE 2017 performance targets in fuel cell tests using MEAs.

Underlying these demonstrated improvements in the activity and stability of Pt-alloy catalysts are important insights gained of the fundamental mechanisms at play at the atomic level. In particular, Stamenkovic, Markovic, and coworkers [34] have performed measurements of dissolution rates of surface atoms and have been able to correlate them to the kinetic rates of electrochemical reactions in real time, allowing for almost “atom-by-atom” structure-activity-stability relationships for Pt single crystals in both acidic and alkaline

environments. They found that the degree of stability is strongly dependent upon the level of coordination of surface atoms, the nature of covalent and non-covalent interactions, the thermodynamic driving force for Pt ion speciation in solution, and the nature of the electrochemical reaction. All of these findings provide the opportunity to further understand and improve upon the activity and stability dependency on nanoparticle electrocatalysts.

### Porous Electrodes

As discussed above, steady progress has been made experimentally in reducing the platinum loadings, particularly in the hydrogen/air fuel cells used in automotive applications. Gasteiger et al. [35] have discussed the strategies to achieve the nearly fivefold reduction in loading needed in order to achieve automotive cost targets. These strategies, which involve increasing the power density at high voltages (while reducing the Pt loading through an increase in the Pt activity and durability) and reducing mass-transport losses in the cell, should also be relevant to backup, motive, and stationary PEMFC applications. The current pathway involves optimizing the Pt-alloy nanoparticle size, composition, and morphology and process optimization, as discussed above.

Most porous electrodes are fabricated from a mixture of ionomer (for proton conduction) and nanoparticles of Pt-alloy catalyst supported on high surface area carbon (for electron conduction) that are all mixed together with a dispersion medium to form an ink-like random material. This ink is then either sprayed, doctored, or jetted onto either a microporous layer on the gas diffusion media or applied directly to the polymer electrolyte. In either case, the density and nature of the local environment at triple-phase boundaries are to a large extent left determined by the random nature of the ink, the interactions among its components, and the application process.

Recent focus has, therefore, shifted to understanding the performance loss of electrodes with low loadings at high current densities. In this case, the flux of reactants at the triple-phase boundary is necessarily high, thereby exposing limitations in mass transport at the nanoscale, including

unexplained resistances that scale with Pt specific area current density. Weber [36] has discussed the nature of these unexplained transport resistances in detail and has proposed that most are caused by the ionomer thin film surrounding the catalyst sites, where confinement and substrate interactions dominate and result in mass-transport limitations. Gostick and Weber [37] have approached this problem by developing a model of the ion conduction in polymer electrolytes as a random resistor network. In the model he accounts for swelling as a function of humidity, as well as spatially varying conductivity within the nano-domains of Nafion<sup>®</sup>. Finally, he included the known confinement effect wherein a substantial drop in conductivity is apparent in films less than 50 nm. Although the model was stated as being overly simplistic, it agrees with experimental data which provide insights into some of the basic mechanisms that limit ion transport in the thin ionomer films within the porous electrode. An important and related finding with regard to the thin ionomer films is their response to annealing. Paul and coworkers [38] have studied the thickness dependence of thin films of Nafion on surface wettability and proton transport. They reported that thermal annealing induces switching of surface wettability of thin films (<55 nm) from hydrophilic to super-hydrophobic and a reduction in proton conductivity. These types of behavior obviously are important factors to consider in the fabrication of porous electrodes.

Recently, Orfanidi et al. [39] have explored the effect of ionomer distribution on oxygen mass transport and proton resistivity of the cathode catalyst layer in H<sub>2</sub>/air fuel cells by functionalizing the carbon support. The functionalization of the commercially available Vulcan XC72 carbon with (–NH<sub>x</sub>) groups was intended to get a more uniform ionomer distribution through interaction with the ionomer's sulfonic acid groups. Detailed experiments using MEAs prepared with differing amounts of ionomer to carbon ratio and ultralow loadings, followed by careful characterization accounting for voltage loss based upon proton resistivity and oxygen transport resistance measurements, provided insights into the major voltage loss contributions. By lowering the ionomer to carbon mass ratio,

thereby reducing the effective ionomer film thickness, oxygen transport resistances were lowered, improving performance. Reducing the ratio further resulted in increased proton resistivity, indicating that low loadings require a balance between good ionomer distribution with a low ionomer/carbon ratio and adequate proton conductivity. These results are consistent with the recent Kongkanand and Mathias [40] review of the challenges of achieving high-power performance at low loadings in PEM fuel cells, in which they conclude that through a concerted effort in the design of materials and electrodes, engineers will be able to resolve the issue of “unexplained losses” at low loadings and achieve a significant improvement in cost and performance. A more detailed discussion can be found in the entry on PFSA thin films within this encyclopedia.

### Nanostructured Electrodes

There is a different class of electrodes based upon highly ordered nanoscale structures that enable both increased performance and better utilization of the precious metals. These so-called thin-film nanostructured electrodes are highly structured by design and enable significant improvement in both performance and durability. To date, the most significant of these structures have been those under development by Debe [41] at 3M, wherein the structure consists of a dense forest of crystalline organic whiskers with areal densities on the order of 3 to about 10 billion whiskers per cm<sup>2</sup>, highly oriented with their long axis normal to the substrate. The whiskers are nanoscale in size (roughly 50 nm by 30 nm by 300–1000 nm) and provide an interesting support for the Pt catalyst. An image of these whiskers, coated with a platinum catalyst, is shown in Fig. 1 below.

High-resolution TEM studies of the sputter that deposited thin catalyst film on the whiskers indicate that the catalyst films grow as polycrystalline layers that expose highly oriented crystallites. The resulting catalyst “whiskerettes” growing on and at an angle of roughly 70° to the surface of crystalline whiskers represent a very interesting hierarchical nanostructure that is providing significant improvements in performance. As proposed by Debe [42], the source of the activity gain of such



**Polymer Electrolyte (PE) Fuel Cell Systems,**  
**Fig. 1** 3M's Pt-coated NSTF electrode

a system might have its contribution rooted in the nature of the metal/support interactions.

How well do these nanostructured thin-film (NSTF) electrodes meet the expected performance targets? Current DOE maturity targets for light-duty vehicle applications specify performance in terms of platinum group metal loading of  $<0.125 \text{ mg/cm}^2_{\text{MEA}}$ , a durability target of at least 5000 h (at temperatures  $<80^\circ\text{C}$ ), a mass activity of at least  $.44\text{A/mg}_{\text{Pt}}$  @  $.9\text{V}_{\text{IRfree}}$ , and a specific activity of  $720 \mu\text{A/cm}^2_{\text{Pt}}$  @  $.9\text{V}_{\text{IRfree}}$ . At a recent DOE Annual Merit Review, 3M reported that they had achieved  $0.19 \text{ mg}_{\text{Pt}}/\text{cm}^2_{\text{MEA}}$  loadings on  $400 \text{ cm}^2$  cells in short stacks, 5000 h of durability (20  $\mu\text{m}$ , 850 EW with no stabilizers),  $0.24 \text{ A/mg}_{\text{Pt}}$  with PtCoMn alloy ( $0.40\text{A/mg}_{\text{Pt}}$  with a new  $\text{Pt}_3\text{Ni}_7$  alloy that needs further development), and specific activity of  $2100 \mu\text{A/cm}^2_{\text{Pt}}$ . This is a substantial improvement in performance over the conventional Pt/C paradigm that has dominated fuel cell MEA designs in the past. There are, however, water management issues with the thin electrode structure, as the reduced thickness of the electrode results in flooding more easily under cold, humid conditions. 3M has addressed this by proposing the use of a unique set of operating conditions and GDL properties on the anode side with an additional cathode interfacial layer in order to reduce the impedance of water transport from the cathode to the anode as a way to improve the “operating robustness” with respect to cathode flooding [43]. In addition to this issue, the NSTF

system is more susceptible to the cumulative effects of contaminants on the long-term stability at operating potentials. In particular, even though the NSTF electrodes show a 20–50X reduction in fluoride emission rates (due to their high specific activity for the ORR), they are more susceptible to poisoning by the products of membrane degradation (due to their low electrochemically active surface area ECSA) [44]; 3M is addressing this by pursuing more stable membranes.

It is important to note that in the pursuit of other types of highly ordered nanostructures, researchers are also taking aim on the issue of the catalyst support from the perspective of its stability. As will be discussed below, the usual carbon materials are used to support the catalyst nanoparticles corrode under certain operating conditions associated with startup and shutdown of the fuel cell, or conditions of localized fuel starvation, and so it is desirable to have a support which is more stable under these dynamic situations. Accordingly, researchers are developing nanostructures in which the typical carbon material is replaced with materials with greater stability. Included in this set of support materials are the use of carbon nanotubes [45] and ceramic materials such as  $\text{TiO}_2$  [46]. It is anticipated that advanced nanostructured electrodes will try to emulate the excellent results and the lessons being learned in the case of the NSTF work underway at 3M, while avoiding problems of water management and contamination.

### Low- and Intermediate-Temperature Proton-Conducting Polymer Electrolyte Membranes

There is also significant research underway addressing the development of alternative classes of polymer electrolytes for fuel cells. For example, sulfonated aromatic polymers, sulfonated polyimides, proton-conducting membranes carrying phosphonic acid groups, and polyphosphazene polymer electrolytes are all being examined as lower cost, more durable alternatives to PFSA-based membranes. There are excellent reviews of the progress being made in the development of these acid-based polymer electrolytes [47].

As noted, PFSA-based polymer electrolyte membranes used in current PEMFCs require



thermal and water management systems to control temperature and keep the membrane humidified. These extra components increase the weight and volume of the fuel cell system and add complexity. The cost and complexity of the thermal and water management systems could be minimized if the fuel cell operated at higher temperatures (up to 120 °C) and at lower relative humidity (RH). In this context it is important to stress the DOE requirement for heat rejection, which reflects itself in the metric of a  $Q/\Delta T$  that has recently been adopted. Currently, this metric is 1.45 kW/°C. The US Department of Energy has therefore initiated a major effort to develop new membranes that can operate at temperatures up to 120 °C without the need for humidification. While it is desired that the fuel cell membrane operates without external humidification, it is recognized that the water generated by the fuel cell itself can be utilized to provide some humidification of the membranes. It is expected that under proper operation, recycling product water from the cathode to the inlet air can provide roughly 25% RH inside a stack operating at 120 °C with inlet feeds at a water vapor partial pressure of <1.5 kPa. This reduces the burden for performance with very low water content, but operation at this low RH still remains a major challenge.

A variety of strategies have been pursued. It is known from extensive molecular level modeling of Nafion<sup>®</sup> that membrane microstructure has a substantial effect on conductivity. With block copolymers, McGrath [48] observed that as the block length increases, the performance under partially hydrated conditions increases, suggesting the presence of hydrophilic domains at higher block lengths through which protons can be transported along the sulfonic acid groups and water molecules. Utilizing block copolymers consisting of hydrophilic oligomers and hydrophobic perfluorinated oligomers, McGrath and his coworkers have prepared a block copolymer that exhibited higher proton conductivity than Nafion<sup>®</sup> 112 at 80 °C at all RH values (30–95%).

FuelCell Energy has attempted a rather sophisticated approach utilizing a four-component composite consisting of a copolymer, a support polymer, a water retention additive, and a protonic

conductivity enhancer. The copolymer, which is intended to provide the basic building block for the membrane, is an advanced perfluoro-sulfonic acid with significantly higher conductivity than state-of-the-art polymers. The support polymer is intended to give a stable cluster structure and to enhance mechanical properties. The functionalized additives are designed to retain water at low RH conditions and to enhance the composite membrane's proton conductivity by providing an alternate proton conduction path for the efficient transport of proton at high temperature as well as at subfreezing conditions. Progress to date has led to a membrane with conductivity about a factor of 2 better than Nafion<sup>®</sup> 112 at 120 °C [49].

3M has recently initiated a study of the use of perfluoroimide acid (PFIA) ionomers in membranes reinforced with electrospun nanofibers made of fluoropolymers [50]. These experimental membranes are exhibiting excellent properties against the DOE targets. However, these are relatively new results, and testing has revealed an unexpected performance loss during open-circuit voltage (OCV). The mechanism of this oxidative decomposition of the PFIA is not yet fully understood.

All of these approaches still rely on water for conduction. Systems utilizing phosphonic acids, heteropolyacids, protic ionic liquids, and heterocyclic bases do not rely on water for conduction. One of the major issues for these systems, however, is that the acid or base aiding proton transport is generally water soluble. The acid or base must be immobilized for use in transportation applications where condensation of liquid water under some of the operating conditions is inevitable. However, enough mobility must be retained by the active group to be able to participate in proton conduction.

In addition to these more advanced studies, progress has been made in developing improvements to the current PFSA polymer electrolyte membranes currently employed in PEMFCs, particularly with regard to degradation caused by mechanical failure due to operationally induced cyclic stresses and from peroxide generated either electrochemically or chemically as the result of

oxygen crossover to the anode. With regard to the former, mechanical reinforcement is often used to improve durability as well as to enable thinner membranes. With regard to peroxide, it is generally accepted that the membrane degradation is the result of the subsequent formation of hydroxyl radicals that attack the side chains of the polymer [51–53]. Here again, dry conditions greatly accelerate the rate of degradation.

What is not generally agreed upon is the location and origin of the hydrogen peroxide formation. Two theories are dominant. One is that the peroxide is formed mainly at the anode due to the diffusion of oxygen across the membrane, at which point the peroxide can form either chemically or electrochemically by the reaction of oxygen with hydrogen. This hypothesis is supported by the fact that the peroxide yield is greatly enhanced in the anode potential region ( $<0.2$  V) of the ORR, as evidenced by rotating ring disk electrode experiments [54]. The other is that the peroxide is formed at the cathode. Experimental results from several sources support this hypothesis. Liu et al. [55], Mittal et al. [56], and Miyake et al. [57] have commonly reported that the membrane degradation rate is higher for an MEA catalyzed only at the cathode side than for one catalyzed only at the anode side. This fact seems inconsistent with the hypothesis that peroxide is formed at the anode. Yu et al. [58], in an effort to identify the origin of the radicals which decompose the membrane, performed a series of experiments after which they concluded, based upon energy dispersive X-ray analysis and IR spectroscopy, that the degradation begins on the cathode and progresses inward. They also found that the formation of radicals within the membrane or near the anode was very low or absent. They postulated the formation of undesirable free radicals involving the catalyst, similar to the hypothesis of Liu and Mittal mentioned above.

Any model of the degradation process would need to propose that formation of hydrogen peroxide forms by distinct mechanisms in the cathode and anode. The commonly accepted mechanism is that the peroxide then forms radicals through Fenton reactions involving metal-ion impurities. The radicals then participate in the decomposition of reactive

end groups in the membrane, to form, among other species, hydrogen fluoride, which can be detected in the product water. Higher fluoride release rates correlate with higher rates of membrane degradation. The degradation occurs through the “unzipping” of the polymer backbone and the cleavage of the polymer side chains. The two conditions which accelerate this degradation mechanism are dry conditions and high temperatures, thinning the membrane until “pinholes” form, allowing gas crossover and cell failure. Therefore, as emphasized earlier, PFSA-like polymer electrolyte materials must be kept under good temperature control and maintained hydrated.

The susceptibility to peroxide radical attack has been attributed to a trace amount of polymer end groups with residual hydrogen containing terminal bonds [59]. It is at these sites that decomposition is initiated. DuPont has reported that the number of hydrogen containing end groups can be reduced by treating Nafion<sup>®</sup> with fluorine gas. 3M has been improving their PEMs by modifying the end groups in the membrane. 3M is investigating modified polymer structures to try to control membrane morphology and has developed a new ionomer with a shorter side chain than standard perfluorosulfonic acid (PFSA) membrane ionomers without the pendant  $\text{CF}_3$  group. They have reported that this structure provides a higher degree of crystallinity and allows for lower equivalent weight membranes with improved mechanical properties and durability under hot, dry conditions. Solvay Solexis also has a short side chain PFSA membrane, Aquivion<sup>™</sup>, that resists peroxide radical attack. In addition, companies are not only modifying the chemical structure but are also incorporating proprietary stabilizers to mitigate the effect of peroxide and the attack by its radicals.

In addition, companies are not only modifying the chemical structure but are also incorporating proprietary stabilizers to mitigate the effect of peroxide attack. Trogadas et al. [60] have investigated the efficacy of cerium oxide as a regenerative free radical scavenger. On the basis of measuring the fluoride emission rate (FER), they determined that membranes prepared with nano-sized ceria particles from 0.5 to 3 wt. % lowered the FER by over one order of magnitude.

Likewise, Coms et al. examined the use of cerium and manganese ions and found that the FER was reduced by factors of approximately 1000 and 100 with  $\text{Ce}^{3+}$  and  $\text{Mn}^{2+}$ , respectively. As a result, companies are not only modifying the chemical structure of the PFSA but are also incorporating proprietary stabilizers to mitigate the effect of peroxide and the attack by its radicals. Recent research is even looking at additives such as microcapsules of Nafion solution that rupture to create self-healing composite membranes [61].

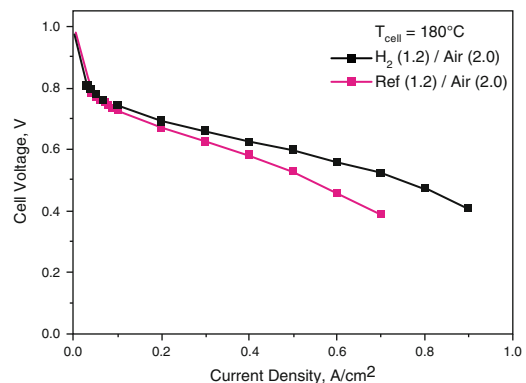
### High-Temperature Polymer Electrolyte Membranes

Early work on the properties of proton-conducting acid polymer blends was carried out by Lassegues et al. [62, 63]. The first detailed study of the effect of doping a high-temperature polymer membrane such as polybenzimidazole with a phosphoric acid in order to achieve proton conductivity in a range suitable for use as a fuel cell was conducted at Case Western Reserve [64]. Polymer electrolyte membranes which do not rely on water as the basis of their proton conductivity offer the potential advantage of simplifying the fuel cell system, if these systems can be operated without complex external humidification schemes. Furthermore, because these systems run at high temperature, they can tolerate higher levels of CO in the reformat, thus further simplifying the system in terms of reforming and control. In addition, the higher operating temperature simplifies thermal management issues and provides a source of high-quality heat for combined heat and power applications.

Advent has recently acquired the rights to PBI-based membranes from BASF, which has restructured its fuel cell business to focus on catalysts and absorbents for fuel cell systems in its catalyst division. Consequently, Advent [65] is developing both PBI-based proton-conducting membranes for high-temperature stationary CHP fuel cell applications, as well as its own high-temperature polymer electrolyte membranes for use in HTPEM fuel cells. These latter are based on aromatic polyether polymers and copolymers containing polar pyridine moieties in the main

chain which have been developed by Advent Technologies, with the idea of creating acid-base interactions in order to obtain high proton conductivity. The developed polymer products are called Advent TPS<sup>®</sup>. Such materials combine the excellent film-forming properties with high mechanical, thermal, and oxidative stability and the ability to be doped with phosphoric acid. Highly conducting polymer electrolyte membranes were produced after treatment with phosphoric acid amounts that could be controlled by varying the pyridine-based monomer content. The polar pyridine groups strongly retain the phosphoric acid molecules, due to their protonation, thus inhibiting leaching out of the phosphoric acid. The performance based on Advent TPS<sup>®</sup> MEA operating at 180 °C with pure hydrogen or reformat with different CO contents and air feed gases is shown in Fig. 2. Here again, because of the high operating temperature, this system tolerates up to 2 volume percent CO poisoning without a significant decrease of performance. The performance shown in Fig. 2 is much improved over that reported earlier by Advent, and this is due to the fact that the TPS<sup>®</sup>-based MEA is now based upon the electrode technology developed at BASF. (DeCastro E, Private communication, 2017).

As is well known, and as discussed by Neyerlin and others, there is an increase in polarization losses with phosphoric acid-based fuel cells, in



**Polymer Electrolyte (PE) Fuel Cell Systems, Fig. 2** Polarization curves of advent TPS<sup>®</sup> (type ABM) at 180° with H<sub>2</sub> or reformat gas (71% H<sub>2</sub>, 2.1% CO, and 26.9% CO<sub>2</sub>) and air, under ambient pressure ( $\lambda_{\text{H}_2} = 1.2$ ,  $\lambda_{\text{air}} = 2$ )

comparison to low-temperature PFSA-based fuel cells, and this effect is due to the presence of phosphoric acid and/or its anions that adsorb onto the surface of the catalyst [66]. Because of this, high-temperature stacks based upon phosphoric acid-based polymer electrolyte membranes are somewhat larger in order to get the same power output. The overall question is whether the benefit in system simplification overcomes the need for these larger stacks, so that there is an overall net system benefit. Reducing the effect of the adsorbed anion species would, of course, have significant benefit at the stack and system levels. One of the approaches suggested by Strmcnik and coresearchers for dealing with this effect is to utilize nanoparticles which are rationally designed to prevent anion adsorption by patterning of platinum surfaces with cyanide absorbates that can block sites for adsorption of spectator electrolyte anions [67].

A more detailed discussion of PBI-based membranes can be found in the entry on PBI in this encyclopedia.

### Alkaline Polymer Electrolyte Membranes

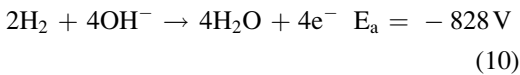
There are also efforts underway to develop alkaline-based polymer electrolytes, which enable the replacement of precious metal catalysts for the ORR by catalysts based on inexpensive transition metals, such as Co, Fe, and Ni. This requires pursuing the development of alkaline technology by transitioning from the proton-conducting polymer electrolyte membrane and ionomer to an OH<sup>-</sup> ion-conducting membrane and ionomer. It is also argued that the alkaline ion-conducting polymer electrolyte membrane provides a much more benign chemical environment which lowers the risk of instability caused by the corrosion processes prevalent in the highly acidic environment of the PEM fuel cell.

Alkaline-based polymer electrolyte membranes are relative newcomers on the scene. It has been widely believed that the quaternary ammonium hydroxide functional group (RN<sub>4</sub><sup>+</sup>, OH<sup>-</sup>), which is the one used in most anion exchange membranes, is “self-destructive,” because the OH<sup>-</sup> ion is likely to attack the RN<sub>4</sub><sup>+</sup>

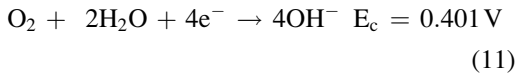
cation. In addition, the specific conductivity of an OH<sup>-</sup>-conducting ionomer was suspected of being at least a factor 3–4 lower than that of the H<sup>+</sup> conducting ionomer, thereby setting a limit on power output. It was also suggested that, as the AEMs developed to date have been based on hydrocarbon, rather than fluorocarbon backbones, the preparation of effective and stable membrane/electrode assemblies would present a significantly tougher challenge vs. the case of PFSA ionomers. Historically, there has always been a concern having to do with the effect of CO<sub>2</sub> from the air feed on the OH<sup>-</sup> conducting ionomer. Since conversion of the OH<sup>-</sup> ion in the alkaline ionomer to bicarbonate (and/or carbonate) ion upon exposure to air, cell performance suffers from the effects on both lower ionomer conductivity and, particularly, the kinetics of electrode processes. Hence, one of the particularly interesting system applications of this technology is for operation on pure oxygen, as would be the case, for example, with a unitized AEM-based electrolyzer/fuel cell operating off of a renewable energy source [68]. (This problem is less severe in KOH systems since it does not form insoluble bicarbonate.)

Tokuyama, a Japanese company specializing for a long time in membrane technology for electro dialysis and desalination, has undertaken development of AEMs in OH<sup>-</sup> form, targeting fuel cell applications. The commercially available membranes, A201 and A901, are currently the standard against which other AEM designs are compared, much like Nafion is the gold standard for acidic membranes [69]. The ionic conductivity of the Tokuyama AEM, while quite satisfactory for many applications, is nonetheless inferior to that of Nafion. Measurements of the water uptake, ionic conductivity, and swelling properties of the A201 membrane have been measured and indicate that, even more so than Nafion<sup>®</sup>, ionic conductivity is a strong function of the hydration state of the membrane [70]. Hence, water management and water transport issues are also a predominant concern in the design of fuel cell systems based on alkaline membranes, especially since water is needed as a reactant at the cathode in order to reduce oxygen to create the OH<sup>-</sup> needed for the anode reaction [71]:

Anode:



Cathode:



Efforts are underway to improve upon the performance of the Tokuyama membranes in terms of its conductivity, water transport properties, and durability. Ren [72] and coworkers have reported improved performance using an approach which mimics the structure of Nafion in the sense that it has poorly ordered bi-continuous hydrophobic and hydrophilic phases. They achieved this by using a styrenic diblock copolymer with a quaternary ammonium-functionalized hydrophilic block with a cross-linkable hydrophobic block. They attributed the improved performance to the reduced tortuosity of the conductive paths, while the hydrophobic network maintains the mechanical integrity, preventing excessive water uptake. Additionally, Pivovar [73] and coworkers are pursuing the use of perfluoropolymer chemistry because of its chemical robustness, enhanced water transport, and conductivity properties compared to hydrocarbon polymers. They are pursuing different strategies to tether different cations to the perfluorosulfonyl fluoride precursor.

There is one final aspect of AEM-based fuel cells that deserves mention. Whereas in acid-based PEM systems the ORR is the predominate source of activation losses, with the hydrogen oxidation reaction being extremely facile, the same cannot be said of alkaline-based systems. For in spite of the fact that non-PGM catalysts can be used for the ORR in alkaline systems, the HOR and HER reactions prove to be problematic at the low Pt loadings normally used for the HOR and HER in acidic systems. Indeed, Durst et al. [74] have reported on the effect of pH effect on the HOR and HER for Pt, Ir, and Pd carbon-supported catalysts, with the data illustrating a 100-fold decrease in activity on all these surfaces when going from low to high pH, pointing to the need for increased understanding of the effect of the materials on binding energies.

Additional information on alkaline membrane fuel cells can be found in the entry on this subject in this encyclopedia.

## Fuel Cell System Design

The *process* of designing of a fuel cell system follows the general design process for any commercial product in which a phase-gated, product development process (PDP) guides activities from initial concept to launch. The PDP is one of the most interesting and well-studied business processes, and usually ends up being tailored to each company's appetite for speed and time to market, balanced by its desire to mitigate risk. Product development is very much a social science, one that integrates business, technology, engineering, and human behavior [75]. Many attempts have been made to study its characteristics and improve the manner by which products are brought to market [76]. Even today it remains a subject of research in most business schools. Before these steps are undertaken, however, usually a *product strategy* is developed which aligns to both the business strategy and the business model of the organization. This product strategy generally takes the form of a *platform strategy*, which shows the relationship between multiple products expected to be developed and launched over a 5–10-year time horizon [77].

## System Requirements and Architecture

The design of the fuel cell system really begins with the "voice of the customer" (VOC). For fuel cell systems, there can be many potential customers: the end user, the OEM, or an intermediate service provider. In any case, the voice of the customer is meant that quality expectation is taken directly from the customer, properly evaluated and deployed within the product development process. One such technique for doing this is the well-known quality function deployment (QFD) process which, if properly used, enables the VOC to be deployed all the way to the factory floor. Without knowing and agreeing on the key customer requirements upfront, the fuel cell system design process cannot be successfully completed.

Developed Country End User CTQs		Customer weight	System Reliability	FC Control & Load Control	Service Provide program	System Serviceability	System Availability	System Design	System kW rating	Cost - Capital and Installation	System Packaging	Cost - O&M	Certification	System Efficiency	Customer Service	Cost - Fuel	System installation
			System Reliability	FC Control & Load Control	Service Provide program	System Serviceability	System Availability	System Design	System kW rating	Cost - Capital and Installation	System Packaging	Cost - O&M	Certification	System Efficiency	Customer Service	Cost - Fuel	System installation
Simple to Operate	5	9	9	9	3	9	3		3	3					3		
Safety	5	9	9	9	9	3	9	3	3	9	3	9	1	1	1		3
Monthly Bill <= current Utility bill	5	9	9	1	3	1	9	9	3	9				9	1	9	1
Supply 100% of electricity needs	5	9	9	9	3	9	3	9	1						3		
Responsive Service	4	3	3	9	9	3	3			3	3				3		
Butter availability than current alternative energy source	3	9	9	9	9	9	9		3	3	1	1		3			3
Ascetics: Appearance & Physical Size	3	3	3		9		3	9	9	9		9	3				3
Environmentally friendly	2	1					3	1				1	9				
Totals		230	228	203	170	159	134	134	116	108	90	77	77	61	45	38	
rank		1	2	3	4	5	6	7	8	9	10	11	12	13	14	15	

**Polymer Electrolyte (PE) Fuel Cell Systems, Fig. 3** Example of a limited set of attributes for a residential fuel cell system

A very much abbreviated and simple example of one of the first steps in the process of developing fuel cell system specifications is shown in Fig. 3. This example is for a residential stationary fuel cell application, but similar requirements are relevant in most other fuel cell applications. Here is shown the high-level VOC, gathered by some technique such as the use of customer interviews or focus groups and the system attributes that will influence their achievement, arranged in order of importance. As shown, some of the key system attributes that are critical to quality (CTQs) and that influence the customer’s demand for clean, quiet, safe, and affordable energy are related to meantime between failure, major component life, load-following capability, turndown ratio, operating and maintenance cost, efficiency, startup time, audible noise, and agency compliance.

Of course, there are a host of other attributes which need to be specified and met, including the expected ranges in ambient temperature and operating altitude, expected number starts and stops, and the quality of air and water needed for operation. All of these external requirements drive the selection of a technology set which, when optimized, needs to provide for acceptable operating

latitude over the life of the system. The US Department of Energy’s Office of Energy Efficiency and Renewable Energy (EERE) has performed a great service in developing a consensus view of some of the more critical CTQs needed for PEM fuel cell systems for a variety of applications, including those for transportation as well as stationary fuel cell systems with combined heat and power. Convening OEM manufacturers, value chain suppliers, and researchers, the EERE set technical targets for 1–25 kW<sub>e</sub> residential and light commercial combined heat and power (CHP) and distributed generation (DG) fuel cell systems operating on natural gas delivered at typical residential distribution line pressures. The most recent set are shown below in Table 1.

Along with this set of targets, the EERE developed a companion low-temperature PEM reference architecture against which it could track progress against the targets. The most recent status for 2015 is given in the table, from which it is seen that the performance in cost and reliability is still off target. It is worth noting that there is considerable “expert” opinion on whether these targets can be met with either low-temperature or high-temperature PEM systems, as the combination



**Polymer Electrolyte (PE) Fuel Cell Systems, Table 1** DOE technical targets for fuel cell systems for stationary (CHP) applications (2015)

Characteristic	Units	2015 status	2020 targets
Electrical efficiency at rated power	%(LHV)	34–40	>45
CHP energy efficiency	%(LHV)	80–90	90
Equipment cost, 5-kW <sub>ave</sub> system	\$/kW	2300–2800	1500
Transient response (10–90% rated power)	min	5	2
Startup time from 20 °C	min	10	20
Degradation with cycling	%/1000 h	<2%	0.30%
Operating lifetime	h	12–20 K	60 K
System availability	%	97	99

of cost, efficiency, and durability targets is quite demanding. In the face of this uncertainty, Japan's Ene-Farm program supported the installation of around 200,000 small micro-CHP PEM units in the <1 kW size, mostly from Toshiba and Panasonic. It is anticipated that government subsidies will continue until 2019, during which time cost reduction efforts through system design simplification and standardization of components will continue [78].

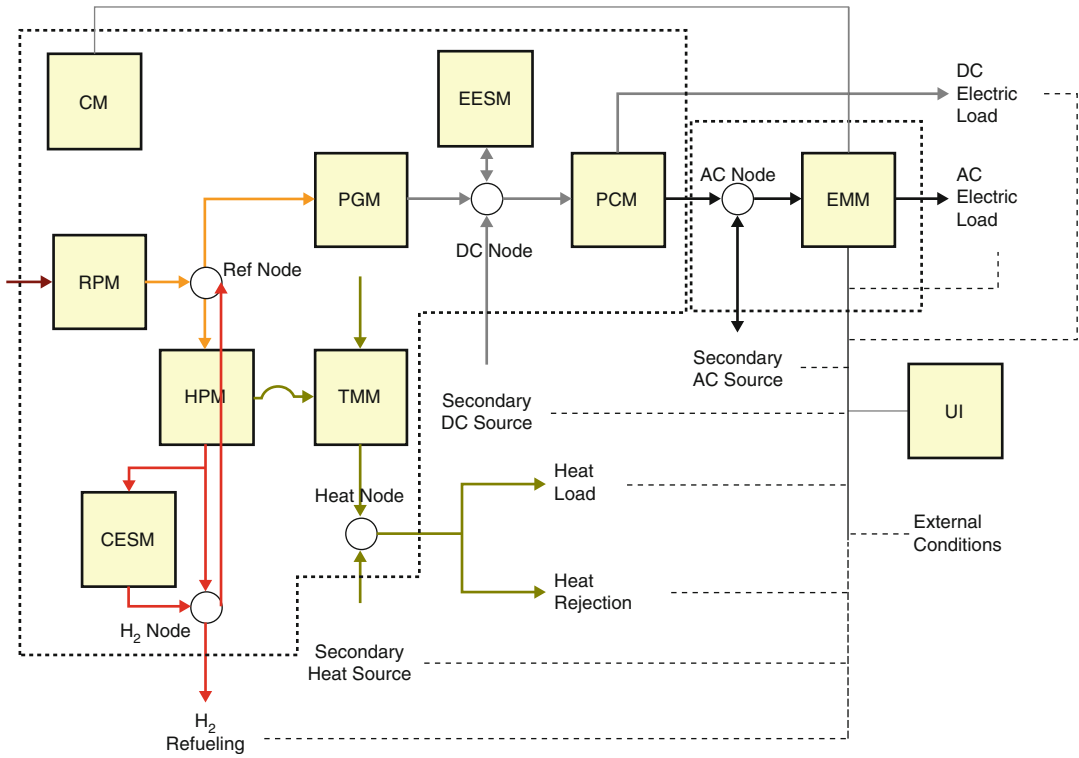
It is clear that one of the key requirements for a successful platform strategy is a well thought out platform *architecture*. The platform architecture enables that product strategy to be executed. As an example, consider the high-level architecture shown in Fig. 4 below. Here one sees the functional breakdown of the system into the major components, which in turn defines requirements for each module in the system.

This figure shows several major subsystems typical of a PEM stationary system. Included are the reactant processing module (RPM), which determines the pressure, temperature, flow rate, and composition of the reactant streams which are delivered to the power generation module or

PGM. Included in the RPM are the desulfurization, reformer and shift reactors, and the required number of heat exchangers which are needed to manage the reforming process. More will be said of this below. The PGM will include the stack and its manifold, and any other subsystems needed to ensure the stack can function properly, such as the subsystems that provide for cathode recirculation and water management. Also shown in this figure is a hydrogen pump module (HPM) that can be used to purify and compress hydrogen for storage in the chemical energy storage module (CESM) for refueling a hydrogen fuel cell car and a thermal management module (TMM) that provides the methods of capturing and directing the flow of heat to either a heat load (such as the RPM) or heat sink. Electrical energy generated by the fuel cell can either be stored in the electrical energy storage module, EESM, or passed through to the power conditioning module (PCM) where it is converted to high-quality power for alternating current loads. A control module (CM) ensures that the required electrical state of the system is achieved over time, as defined by the energy management module (EMM). The CM provides the proper control of the pressure, temperature, flow rate, and composition of the fuel and air streams going into and out of the system. The result of all of this is made visible to "customer" through an appropriate user interface module (UI).

This is a high-level architecture. If the detailed lower-level subsystem requirements that support this "meta-system" are well thought out, it is possible to develop *multiple products* off of the same set of hardware and software components, thereby minimizing the product acquisition spending (PAS). For example, there at least four products that can be derived from this architecture, including a home refueling system, a residential CHP system (eliminating CESM and HPM), a hydrogen fuel cell system for backup applications (further eliminating the RPM system), and a stand-alone hydrogen generator (retaining only the RPM, TMM). Of course, in each case, the controls and user interface have to be modified for the intended application. Furthermore, system-level specifications need to be compatible over the ambient temperature range, etc.





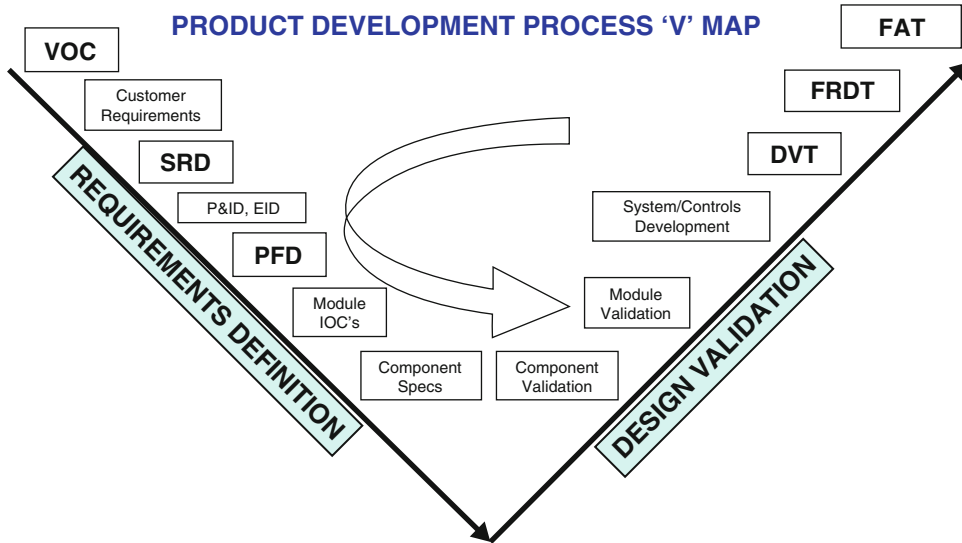
**Polymer Electrolyte (PE) Fuel Cell Systems, Fig. 4** A high-level fuel cell system architecture

Where the intended range of applications does not allow for platform architecture at the meta-system level, the platform products then need to be defined at the system level. In fact, the concept of platform-based architecture can be pursued at the component as well as the system level. Ballard<sup>®</sup>, for example, has defined its platforms at the stack level. It is currently advertising five stack platforms. Each stack platform has a different voltage range, reactant pressure (air and fuel), and cell aspect ratio, optimized for the intended application, whether it be for backup (telecommunications), motive power (forklift trucks), transportation (buses), or residential cogeneration.

While the overall architecture defines the interrelationships among form, fit, and function, *systems engineering* supports the development and achievement of the product specifications. The systems engineering required to enable a product platform strategy is generally quite extensive, requiring many iterations using simulations to

guide the final design at the system, subsystem, and component levels. In general, the requirements for a fuel cell system are quite extensive and complex, and these need to be defined, allocated, and enforced all through the development process.

The key steps in the product development process are shown below in Fig. 5. Most activities are focused on two types: the systems engineering associated with requirements definition, ending with components specifications, and on the actual design and verification process, ending with a successful in-house design verification test (DVT), a field readiness demonstration test (FRDT), and a factory acceptance test (FAT) to validate launch readiness. A key step in the overall process is the development of the systems requirement document (SRD), which enables the development of the process and instrumentation diagram (P&ID), and its companion, the process flow diagram (PFD). The PFD, which is the output of the process engineering analysis using



**Polymer Electrolyte (PE) Fuel Cell Systems, Fig. 5** Product development process map

computational tools such as ASPEN<sup>®</sup>, captures the concepts in flow sheet format and summarizes the heat and material balances characterizing the system design. In short, the PFD, which is the link between concept and reality, defines the critical parameters at each step in the process.

Early on in the process, it is useful to organize the systems engineering effort in pursuit of a collection of interlocking *functionally important topics* which are system-level attributes that need to be allocated to subsystems within the system. One example would be the allocation of efficiency targets between the various major modules. Another high-level example of such an allocation would be the “flow down” of the requirements for cost and reliability. Here the percentage of total allowed cost and failure rate is allocated among the major modules, based upon an initial test of reasonableness followed by refinement during the development process as further information becomes available. Clearly, the initial allocation of the functionally important topics is important, because it drives engineering behavior and subsequent design modifications and, eventually, time to market. The system may have other high-level requirements, such as size, weight, noise, and appearance, and these early requirements are met through systems engineering efforts. Management of the allocation process is achieved through

the use of artifacts such as *input/output/constraint* charts (IOCs) that keep track of both functional (signal) and dysfunctional (noise) attributes of each subsystem, subject to the constraints imposed by the overall system. They track the interactions between subsystems in terms of the critical parameters, and are used to define and guide the robust design optimization process, eventually becoming the “contract” between the subsystem teams and the system engineers. Again, a combination of careful testing and simulation is required to ensure convergence to the subsystem- and system-level allocations.

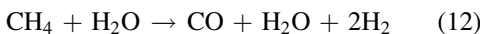
### An Example: Reforming Considerations

In many cases, hydrogen at required purity is not normally available, in which case it must be obtained by the reforming process of stripping hydrogen off a hydrocarbon fuel such as methane, propane, ethanol, and liquid petroleum gases (LPG) or kerosene. Generally, there exist sulfur species that are naturally occurring in the fuel (COS, H<sub>2</sub>S) or are added as odorants (mercaptans, tetrahydrothiophene, THT). Since sulfur poisons the catalysts in the system, the first step in the reforming process generally involves the removal of harmful sulfur-containing species. The level to which sulfur needs to be removed depends upon the operating temperature, but in general, it is safe to assume that

for PEM systems, the level needs to be less than about 50 parts per billion (ppb) [79]. To achieve this level of sulfur impurity, there are several available technologies. At ambient temperatures, these include physical adsorption beds using activated carbon and zeolites and chemisorption beds incorporating nickel-, copper-, and iron-based sorbents. At higher temperatures, one alternative is to use hydrodesulfurization with Co-, Mo-, and Ni-based catalysts. Another option is thermal swing absorption. Ideally, it is desirable to have a single technology in order to have a fuel flexible system that enables the fuel cell system to be sited in a variety of geographical locations. Seasonal and regional variations in sulfur content, as well as catalyst material cost and toxicity, make this a difficult engineering problem. Each of these technologies is well known, and each has its strengths and weaknesses. All add considerable capital cost and complexity to the system, not to mention annual maintenance cost which can also be a significant expense. Consequently, there is a need for continued research into the discovery and development of effective, low-cost desulfurization for fuel cell applications requiring them.

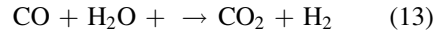
Assuming that the fuel has been adequately desulfurized, there are essentially three alternative processes for extracting hydrogen: steam reforming (SR), catalytic partial oxidation (CPO), and autothermal reforming (ATR). SR is an endothermic process. Heat must be supplied to the reactor, and this is normally accomplished by combusting an additional amount of fuel in a separate, but thermally integrated, reactor. Usually this reactor burns the unused hydrogen which flows through the anode chamber of the fuel cell stack. This component is referred to as the “anode tail-gas oxidizer” or ATO. The ATO is generally considered an integral part of the reactant processing module.

The steam reformation reaction is reversible, and the product gas is a mixture of hydrogen, carbon monoxide, carbon dioxide, and water vapor. In the case of methane, the steam reforming step is



The amount of CO in reformat is a system-level critical parameter, as CO interferes with the

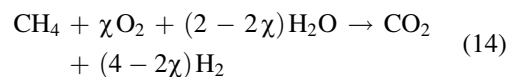
hydrogen oxidation reaction by blocking reaction sites on the platinum catalyst surface. To remove the high levels of CO, this reformat stream is then fed to a “shift” reactor which reduces the CO concentration and makes additional hydrogen:



Following the “shift” reaction, the reformat is generally passed through a preferential oxidation (PROX) step to further reduce the CO content to an acceptable level so as not to poison the anode catalyst. For low-temperature PEM systems, this level is typically less than 10 ppm. To increase the tolerance to the residual CO, ruthenium is added to the anode catalyst layer, but even this is not sufficient to deal with the amount of CO in the reactant stream. In the case of low-temperature PEM systems, there is generally a small amount of “air bleed” fed into the reactant stream to oxidize any residual levels of CO that adsorb onto the catalyst. It is desirable to keep the air bleed to a minimum to reduce the formation of peroxide. Pulsed air bleed techniques have been studied to achieve this purpose [80]. Depending on the reformer design, there may be a high-temperature as well as a low-temperature shift, as well as a single- or two-stage PROX.

Unlike steam reforming, CPO is an exothermic process. It is essentially a combustion but with less than stoichiometric amount of oxygen. As in SR, the reformat gas must go through a shift reaction to produce more hydrogen, though a CPO produces less hydrogen than SR, and unlike SR the product gas contains relatively large amounts of nitrogen from the air used in the process.

Because CPO is an exothermic process, and SR is an endothermic process, these two can be combined in the “autothermal” reforming (ATR) process. The overall reaction of an autothermal process for methane, with the shift reaction included, is



In this equation,  $\chi$  is the number of moles of oxygen per moles of fuel. Its value determines if the reaction (14) is exothermic, endothermic, or

thermoneutral. In practice, the value is chosen to avoid the risk of carbon formation in the reactors, and the amount of steam added is usually in excess of that theoretically required. All of these process steps use specially designed catalysts to facilitate the reaction steps. Catalyst designs are in many cases proprietary, although in most cases references to catalyst materials used in similar reactions can be found in the literature.

For many applications requiring the need to reform a logistical fuel, the reactant processing module represents a significant percentage of the total system cost. This is because the reactant processing module must provide reformat with the proper level of humidity over the entire load range, the required level of CO within the constraints of a single-stage partial oxidation (PROX) step, have rapid startup and load-following capability with near-zero emissions for NO<sub>x</sub>, and this all without resulting in coke formation. To meet the efficiency requirements of the overall system, the reactant processing module must also be thermally integrated into the rest of the fuel cell system. This is a very demanding set of requirements, and the cost of the reactant processing module typically ends up being about one-third of the total system cost.

It is well known that most Japanese residential  $\mu$ CHP fuel cell systems use steam reformers, principally due to their high efficiency. Adachi et al. [81] have recently published the results of their effort to design an autothermal reforming fuel processor for a 1 kW  $\mu$ CHP residential system. They designed and bench tested an ATR system capable of achieving 80% efficiency (on a higher heating value basis) and a reformat containing 48% hydrogen (dry basis) and less than 5 ppm CO. They have studied the ATR principally to address the issues around startup time and the daily start/stop requirements.

A simplified schematic of an ATR-based reformer system is shown below in Fig. 6. Shown in this figure are the desulfurization subsystems, the ATR reactor, a low-temperature shift (LTS) reactor, PROX, ATO, low-pressure steam generators to meet the reformat dew point requirements, and the appropriate heat exchanges.

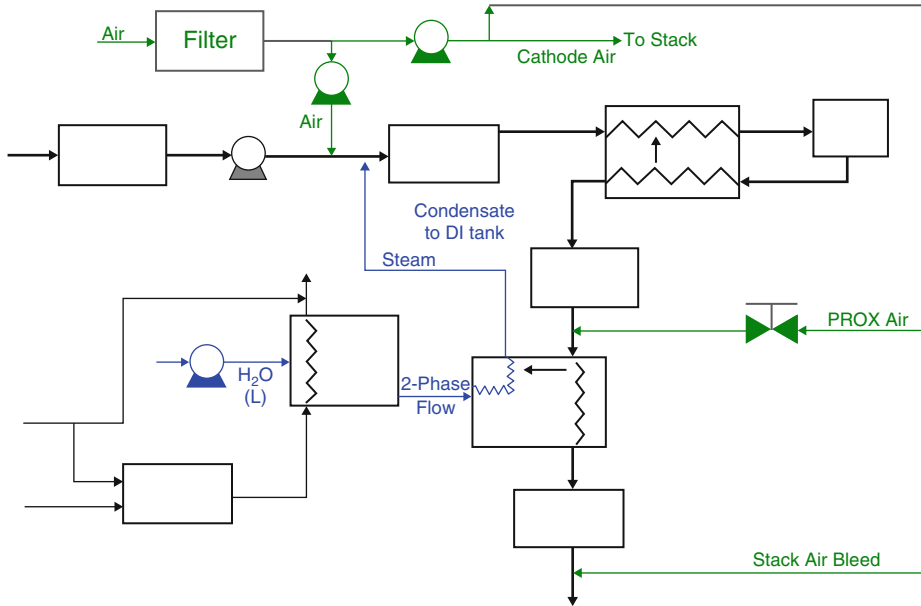
In practice, there are several critical operating requirements placed on the reformer system. First,

the reformat must contain a negligible amount of carbon monoxide (and oxygen) to avoid poisoning the anode catalyst. Likewise, the fractional conversion of fuel in the reformat needs to be specified in order to minimize unburned hydrocarbon emissions. From a system control perspective, it is also desirable to deliver a *predictable* amount of hydrogen for a given fuel input. Finally, because of the dependence of the PEM on the level of hydration, the reformat dew point must also be controlled to a specified value. Given these specifications, Feitelberg and Rohr [82] have shown that two variables, the steam to carbon and oxygen to carbon ratios, define a unique “operating line” for the fuel processor. The operating line defines the required relationship between steam to carbon and oxygen to carbon ratio for a reformer that meets fuel conversion and reformat dew point specifications. An example of the operating line [83] for several dew points is shown in Fig. 7. Operation above this line means that the dew point is greater than that specified, implying that energy has been wasted vaporizing more water than is needed. Operation below the operating line means that the reformat dew point is lower than specified, implying that one should expect reduced MEA life or premature failure. When the PEM system is operating on the line, and the heat generated in the ATO just balances the heat consumed in the reformer, the reforming process has achieved the maximum theoretical efficiency.

In this regard, Feitelberg and Rohr’s analysis has shown that the maximum theoretical efficiency of a SR-based system is only about one percentage point higher than the maximum theoretical efficiency of a typical ATR-based fuel processor. Hence, the ATR technology seems to be a good compromise in performance and efficiency.

## Technical Readiness

A key milestone in the development of a fuel cell (or any other) system is the achievement of technical readiness; that point in the development cycle when commitments to volume manufacturing can be made with confidence. For this



**Polymer Electrolyte (PE) Fuel Cell Systems, Fig. 6** Simplified schematic of an ATR-based reformer subsystem

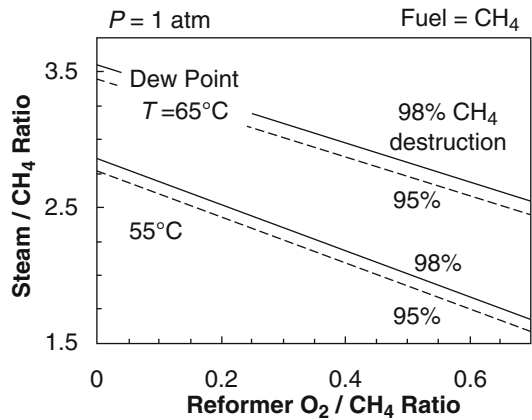
purpose, it is meaningful to define this state of knowledge as:

Technical readiness is achieved when all critical failure modes are known, and when the critical parameters that are required to avoid those failure modes over the required operating range can be achieved through the intended interaction of specified parts which can be manufactured with acceptable process latitude.

In discussing PEM fuel cell systems for stationary, transportation, and portable applications, it is worthwhile to do so in terms of defining those conditions needed to not only meet the intended application but also to avoid the critical failure modes.

**Freezing**

One of the customer-driven requirements associated with fuel cells intended for stationary and transportation applications is the ability to not only survive subfreezing temperatures but to gracefully startup from subfreezing conditions and operate over a large number of expected freeze/thaw cycles. Inasmuch as water is the product of the fuel cell reaction, it is normally carried into the stack with humidified reactants and is fundamental to the transport of protons in the



**Polymer Electrolyte (PE) Fuel Cell Systems, Fig. 7** Reformer operating line analysis [83]

membrane. Most of the work on defining the operating conditions needed for surviving freezing conditions has focused on the behavior of the water within the principle stack components: manifold, plates, flow fields, and MEA. There are three types of water in PFSA-type polymer electrolyte membranes. Water that has strong interactions with the ionic groups in the polymer can withstand temperatures well below the normal freezing point of water without freezing. Water

that finds itself within the nanoscale channels of the polymer electrolyte has a freezing temperature that is dependent on the size and nature of the channel, which in turn is dependent on the degree of hydration of the polymer. This water will therefore have a range of temperatures over which it will freeze, with some of the water having its freezing temperature depressed by the presence of the hydrated ions. Finally, there is “free” water that behaves like bulk water. The result is that there is a distribution of freezing points within the PEM, with no specific “freezing point.” The PEM proton conductivity, for example, varies continuously over a wide range of temperatures, depending on the level of hydration. The proton conductivity below freezing can be an order of magnitude lower than that for normal operation [84], indicating that a large fraction of the water in the membrane is frozen. However, even in this state, the polymer electrolyte membrane is capable of carrying current, increasing with increased thawing. Also, the tightly bound water, while not freezing, has a very low conductivity, since it is not that mobile, as though it were frozen; the resulting membrane resistance is therefore key in generating heat during freeze startup.

Next to the membrane itself, the most critical components in the fuel cell stack relative to startup from freezing and cool down to subfreezing temperatures are the catalyst layer and the GDL. As previously discussed, the GDL is one of the few critical components in the system which can be designed to affect proper water management, including frozen water that exists during storage or operation from subfreezing conditions. However, only a few studies have been published on the effect of freeze/thaw cycles on the properties of the GDL and its subsequent effect on the durability of a PEM fuel cell during cold startup [85, 86]. In fact, due to the wide range of operating conditions and the difference in fuel cell design approaches, reported impacts of freeze/thaw cycles on MEA performance vary considerably.

One of the most descriptive accounts of the factors influencing the cold-start behavior of low-temperature PEM fuel cells has been given by Mao and Wang [87]. They develop a lumped

analysis model of the cold startup of a PEM fuel from subfreezing conditions. The model accounts for the rate of water production, removal, and conversion during startup. The condition for a successful startup is to have the fuel cell raise its temperature beyond the freezing point before being shut down by the formation of ice in the catalyst layer. By accounting for the heat and mass balances within the catalyst layer, the authors were able to investigate the conditions under which ice forms in the catalyst layer, thus restricting the flow of oxygen to the reactions sites. In effect, the authors indicate how to calculate the critical parameter requirements for a successful startup from subfreezing conditions. Initial membrane moisture content, heating rate, and thermal masses need to be chosen so that the temperature within the catalyst layer can reach the melting point before ice can fill up the pores within the catalyst layer and the GDL. Clearly, these critical parameters will depend upon the critical specifications of the components within the MEA, as well as the thermal properties of the bipolar plates.

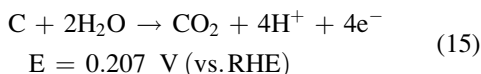
There are a variety of system-level strategies for dealing with freezing, including purging of the stack at shutdown to remove liquid water, heating the stack prior to or during warm-up with auxiliary energy sources, and preventing freezing conditions from occurring (standby idling, etc.). Each of these strategies, however, results in a decrease in overall system efficiency.

### Start/Stop

Every fuel cell system needs to be started up and shut down in a way that meets the requirements of the customer and at the same time ensures long-term operation of the system. Frequent starting and stopping can place the system in a severe electrochemical environment. In particular, when the anode side of the fuel cell is filled with air, as would be the case in standby situation, and the system is started up with the flow of a hydrogen-rich stream through the anode, a hydrogen/air boundary forms on the anode side of the cell [88]. This boundary moves from the anode inlet to outlet and in doing so sets up a high voltage ( $\approx 1.4$  V) situation across the cell. This potential



sets up a reverse current which greatly accelerates the oxidation of carbon, which theoretically can proceed as



In fact, this potential-driven “corrosion” of carbon can be quite severe, causing substantial loss of the electrochemically active surface area as the electrode degrades with the loss of the catalyst support. Enhanced fuel cell degradation can occur under the additional stress conditions associated with cold start and hot stopping [89].

In order to deal with the problem of carbon corrosion due to start/stop, it is necessary to understand the critical parameters associated with the start/stop process, as well as the critical specifications that need to be placed upon the materials. What is required to do this is to have a validated model of carbon corrosion and its dependence on the critical parameters: temperature, pressure, flow rate, and composition. Such a model has been developed, to the first order, by Meyers and Darling [90] in which the potentials driving the reaction are linked to the spatial concentrations of oxygen and hydrogen in the flow channels.

Carbon corrosion can also occur due to fuel starvation on the anode, which sometimes happens when flooding is imminent. Again, this situation sets up localized high potentials and reverse currents. Carbon as a catalyst support is problematic, and for this reason control systems need to provide algorithms to deal with the situation when a particular cell in the stack is behaving in an abnormal fashion (so-called “stack health” algorithms).

### Load Following

In most applications involving fuel cells, the load is dynamic, and it is a requirement that the fuel cell system be able to respond to these load transients nearly instantaneously. This requires careful system design. This requirement translates into the need for having rapid delivery of fuel to the catalyst sites within each cell in the stack. Two transient types of operating modes were described above, startup from subfreezing and start/stop.

Here focus will be on load changes during operation and on applications involving both hydrogen and reformat fuel. In the former, emphasis will be placed on the effects of rapid cycling on durability, whereas in the latter, emphasis will be placed upon achievement of the required critical parameters over the expected range in operating parameters.

Hydrogen-air fuel cells, which are used in transportation, backup power, and material handling applications, respond almost instantaneously, provided that they are fed adequate amounts of fuel. Control schemes for hydrogen-based fuel cell systems for automotive applications are discussed by Pukrushpan et al. [91] in which the primary focus of the discussion is on control of the supply of air and hydrogen. In most cases, the fuel cell system will be “hybrid” with a battery in the overall system architecture. For example, in telecom backup fuel cell systems, a small battery pack (or supercapacitor) is included to ensure the continuous delivery of power within the first millisecond after the grid drops out. In light-duty vehicles, batteries are included as a means of load leveling and energy harvesting during braking. In forklift applications, batteries offer the opportunity to alleviate the load-following requirements on the stack, thereby extending its operating life. In fact, Plug Power sets a stringent set of charging and discharging capacity requirements on the battery to maximize the performance of the system and at the same time life of the stack (Du B, Private communication, 2017). This is another example of adopting a systems engineering approach to systems design. Obviously, it is important from a systems control perspective that one of the key aspects of achieving adequate load-following capability is to develop a comprehensive stack control scheme that incorporates the relevant system-level components, critical parameters, and their linkage to the critical specifications. In most cases, this control scheme must also address both stack health and efficiency.

For reformat-based systems, the control problem becomes particularly difficult because of the strong interactions between subsystems. This is perhaps best seen when considering the function



of the ATO. The ATO is designed to oxidize the unreacted anode gas into water for the reformer, as well as to achieve zero emissions from the fuel cell system. On the other hand, the ATO also serves as the heat source for steam generation. Both the stack and the ATO require an air/oxygen source. To minimize cost, improve efficiency, and increase the operating latitude over which the system can be water independent, it is desirable to use a single air blower to provide air to both the stack and the ATO. However, this shared actuator couples the controls for stack, ATO, steam generation, and reforming, thereby increasing the complexity of the interaction among the control loops.

Another complexity arises due to the lack of in situ measurement of some of the critical parameters, requiring the inference of the value of the critical parameter from the operation of the system itself. This is particularly true when, by design, the relative humidity of the input reactant streams is near or at saturation. In this situation, RH sensors become unreliable, and the RH level needs to be inferred from the system control parameters. In order to accommodate the strong interactions between the subsystems, a considerable amount of modeling and simulating of system performance is required. This can be accomplished by linking process models in ASPEN Dynamics<sup>®</sup> with controls models in Matlab<sup>®</sup>. In this way, nonlinear dependencies in the process can be linearized in a piecewise fashion and exported to Matlab, an environment in which the order of the model can be systematically reduced together with weighting factors to get time-dependent models that can provide unified descriptions of the fuel cell in both steady state and dynamic environments. An example of the result of such an exercise is shown below in Fig. 8, comparing the performance of the ATO during load transients versus the model predictions. In this particular experiment, the system was run in steady state, and the load-following requirements were simulated by suddenly manipulating the cathode air blower in pseudorandom manner. It is seen that the dynamic model is a remarkably good predictor of the ATO performance [92].

### CO Poisoning

One of the challenges facing the fuel cell system is the mismatch in the time constants of the various components in the system. The reformer has the longest time constant, followed by that of the air handling system and stack, and finally the battery. This mismatch can result in large fluctuations in the quality of fuel provided to the stack and can be the source of unwanted excursions in the amount of CO reaching the stack. With validated advanced simulation tools, it is possible to develop robust control strategies that ensure that the overall system can meet the load-following requirements during large and rapid transients. Shown below in Fig. 9 is the transient response of the Plug Power ATR-based fuel processor to large and sudden step changes in electrical load demand. Here it is seen that the control software is able to keep the CO concentration within performance specifications (<10 ppm). In this case, batteries are used to make up the load demand, while the reformer ramps up, illustrating the mismatch in time constants between the stack and reformer subsystems [93].

It is evident that advanced controls, once validated with system verification tests, can be used to maximize the system operational latitude. As shown below in Fig. 10, these controls are used to optimize the operating window for the CO concentration in the reformat stream fed to the stack. Here it is seen that there is a large operational window, in terms of PROX outlet temperature and CO concentration over which the system can operate within its specification.

It is perhaps important at this point to once again discuss the potential advantages of higher-temperature operation. It is well known that fuel cell systems that operate at higher temperatures can tolerate much higher levels of CO. Indeed, tests have shown that stacks at temperatures in the range of 160–200 °C can tolerate CO concentrations on the order of  $10^3$ – $10^4$  ppm. In this case, it is possible to eliminate the PROX and its associated costs and sources of unreliability, while simplifying the controls requirement.

There are, of course, many other potential failure modes that need to be addressed. Only a few are mentioned here. Perhaps the most difficult are

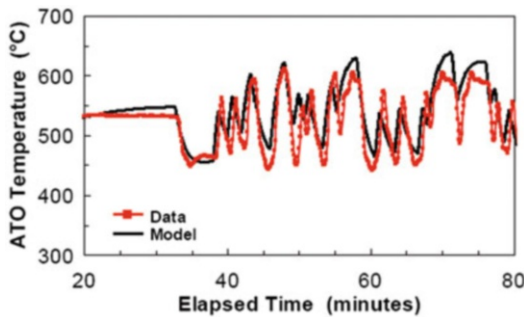
those associated with maintenance of the polymer electrolyte’s required properties over hours of operation and over a wide range of conditions. Temperature, humidity, and potential cycling place severe stress on the polymer electrolyte and its matching electrodes, and minimizing these through great attention to engineering detail is fundamental to the achievement of technical readiness.

### System Cost and Reliability

Two key parameters that are obstacles to widespread fuel cell adoption are system cost and reliability. Both are interrelated through the system design, driven mainly by the complexity of

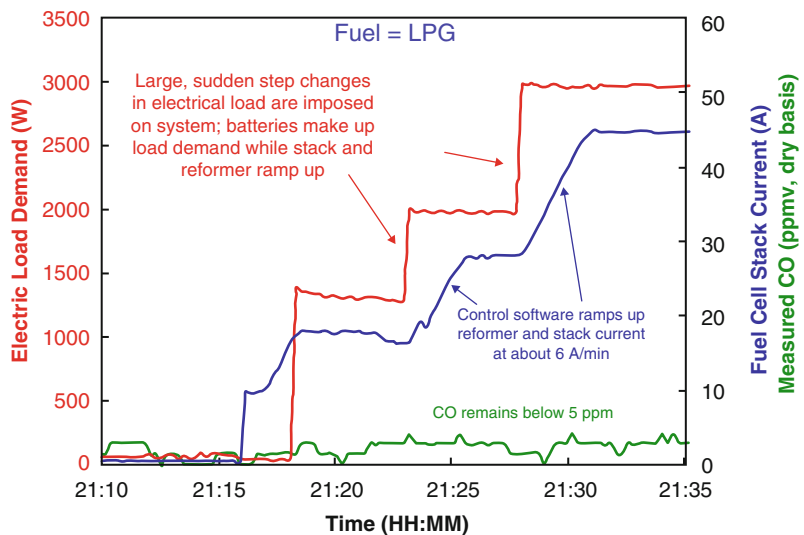
the interactions between the stack and the rest of the system, which in turn is determined by the nature of the polymer electrolyte. However, system complexity is also determined by the customer-driven system specifications. System specifications can vary widely, depending upon the application, and for this reason it is nearly impossible to make specific claims about costs of fuel cell systems without reference to the detailed requirements driving the design.

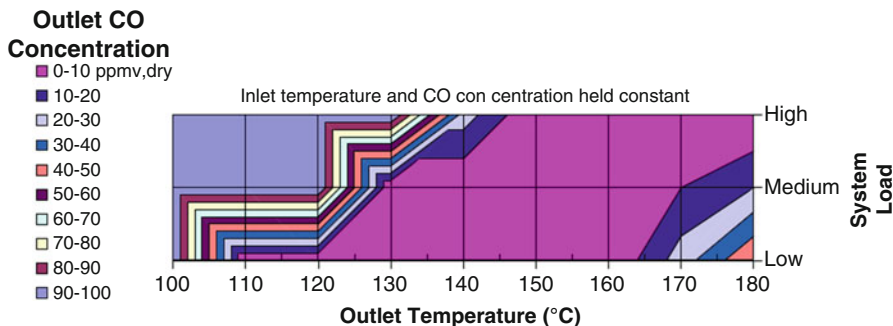
The cost and reliability of PEM fuel cell systems for light vehicles are tracked quite closely as automotive manufacturers are making significant investments in developing fuel cell cars for field entry in the next 5–10 years. The US Department of Energy (DOE) has, in conjunction with industry leaders, developed cost and reliability performance target and track progress against those targets in its annual review process. In addition, the DOE has defined a baseline fuel cell system with which to model performance improvements due to advances in technology and to coordinate those findings with the assumptions in the cost projections. The latest 2017 DOE cost estimates suggest that in high-volume production, total system costs of around \$45/kW<sub>net</sub> can be achieved, with an outlook of \$42/kW<sub>net</sub> in 2020, nearly equal to the DOE 2020 target of \$40/kW<sub>net</sub> at production volumes of 500,000 units/year [94]. This improvement in cost reduction was



**Polymer Electrolyte (PE) Fuel Cell Systems, Fig. 8** Model vs. data comparison for transient operation of ATO [92]

**Polymer Electrolyte (PE) Fuel Cell Systems, Fig. 9** Fuel cell performance during load transients [93]





**Polymer Electrolyte (PE) Fuel Cell Systems, Fig. 10** Prox Co operating latitude in terms of temperature and load [93]

accounted for a combination of advances made in stack power density at low loadings, based upon the data from General Motors on the use of de-alloyed PtCo catalyst on high surface carbon, as well as cost reductions in the processing of coated stainless steel bipolar plates and reduction in hydrogen sensors.

The situation for stationary fuel cells is not as clear. The current DOE performance targets for integrated stationary fuel systems of \$1500/kW<sub>e</sub>, and 60,000 h of durability and 45% electrical efficiency at rated power are difficult targets to meet with a reformat-based system. The system requirements for stationary systems can vary widely, depending upon application. In general, however, the key to cost reduction is through system simplification. One way to accomplish this is through good engineering design, including value analysis/value engineering (VA/VE). VA/VE enables one to reduce the number of parts. Another way is to avoid expensive secondary fastening operations by having parts and modules self-align to each other, eliminating adjustments, using gravity wisely, and designing for “poka-yoke.” (A **poka-yoke** is any mechanism in a lean manufacturing process that helps an equipment operator avoid (yokeru) mistakes (poka).) A third is to specifically employ the design for manufacturing and analysis (DFMA) techniques of Boothroyd-Dewhurst. Readers are also directed to the entry on stationary cost assessments in this encyclopedia.

Currently, stationary fuel cells include the cost burden of the reformer, which makes the achievement of \$1500/kW<sub>e</sub> difficult. As a percentage of

the total system cost, the reactant processing module can be as much as 30% of the total system unit manufacturing and service cost. Whereas the stack can scale downward gracefully as a function of size (kW<sub>e</sub> output), the reformer cannot, making low-cost small residential stationary systems even more challenging. For this reason, it is appropriate to examine *alternative system architectures* that decouple the reformer and provide the required hydrogen from a shared-use centralized reformer. Such architectures are currently under consideration for use in Japan. Lastly, it seems appropriate that at this stage, fuel cell systems should be developed for large niche markets that are appropriate for the current state technical readiness of the technology. Forklift applications are a prime example of matching requirements versus capability. Large stationary fuel cells that are designed for constant base loads with high combined heat and power utilization requirements are another example.

Of course, another way to reduce cost and improve reliability is through clever systems engineering using advances in technology. This is in fact the approach recently taken by Toyota engineers in their pursuit of cost reductions in the Toyota Fuel Cell System (TFCS) known as “Mirai.” In particular, the Toyota engineers pursued an approach of reducing system cost by improving stack performance in terms of power density and by enabling membrane humidification under operating conditions without the cost and complexity of an external humidification system, and in order to achieve these objectives, Toyota engineers took a broad systems perspective. First,

they reduced the number of required cells in the stack by employing a newly adopted boost converter that adjusts the voltage difference between the motor and the inverter. To achieve a system without an external humidifier, Toyota engineers decided to pursue this by ensuring adequate migration of water generated at the cathode to the anode. Three interrelated modifications were made. The first was to reduce the thickness of the membrane by two-thirds, thereby increasing the diffusion of water generated in the downstream air system and improving proton conductivity. The second was to humidify the system using the moisture at the anode, thereby humidifying the cathode inlet by flowing the hydrogen fuel and the air in counter directions. By adjusting the anode operating conditions by increasing the hydrogen circulation in the anode in accordance with the driving conditions, and by reducing the anode inlet pressure, the system was made to enhance the movement of product water to the anode surface [95]. In addition to the steps taken above to eliminate the external humidifier, the Toyota engineers also improved the water management through an innovative cell flow field structure and membrane electrode assembly that enabled a compact and high-performance stack. In particular, an innovative three-dimensional fine-mesh flow field was developed to prevent water accumulation at the cathode by directing the airflow toward the MEA/GDL assembly, promoting oxygen diffusion, and drawing water generated within the MEA/GDL to the back surface of the 3D fine-mesh flow field. An optimized flow field was also developed for the anode to facilitate anode operation, with the material changed to titanium to reduce the weight and cost of the plate-coating process. In terms of the MEA, in addition to reducing the membrane thickness, the amount of platinum was reduced as well, using a de-alloyed PtCo with an improved acid treatment process, coupled with a change in the carbon support to a solid type, reducing the oxygen diffusion resistance. Along with the optimization of the ionomer thickness, the net effect of all of these synergistic modifications was to increase the current density by a factor of 2.4 and to achieve a power density of

3.1 kW/L, reportedly the highest in the industry [96].

The Mirai story described above is important because it demonstrates that a broad-based systemic approach to improving fuel cell cost and performance is within the reach of engineers engaged in the design and development of fuel cell systems. It is an example of combining a combination of clever systems engineering with careful experimentation and design innovation based upon a deep knowledge of fuel cells that has been accumulating over the past 10 years. It also demonstrates the singular importance of increasing power density in order to decrease cell count through dedicated efforts in materials and design engineering.

## Fuel Cell Systems and Sustainability

The connection between fuel cell systems and sustainability is, of course, hydrogen. The lightest and most abundant element on planet Earth is destined to play a central role in the energy landscape of the future. Renewable energy sources can be used to produce hydrogen, which can then be stored as a means of addressing the natural intermittency of the renewable source. In the future, by splitting water with renewable sources of energy such as wind and solar energy and using the stored hydrogen so produced to produce electricity, one can also return the product water to its source, achieving a sustainable energy paradigm for nearly every nation on Earth. This is truly the energy “end game.” Indeed, the fact that as an energy carrier hydrogen can play a key role in the storage of energy produced from renewable resources has received renewed interest among a variety of stakeholders.

Since the fuel cell system will play a key role in the pursuit of sustainable energy, whether in electrifying the automobile for transportation, providing energy for buildings, or converting stored hydrogen generated from renewable sources into electricity, the design of the fuel cell itself should consider its impact on the environment. This encyclopedia addresses the subject of life cycle analysis elsewhere. Here it seems appropriate to

note that Cooper et al. [97] have developed a method to assist in the rapid preparation of life cycle assessments of energy generation technologies and in particular polymer electrolyte fuel cell systems. The method allows one to compare different fuel cell system design approaches, using publically available and peer-reviewed life cycle assessment data, against an environmental impact weighting scheme that reflects various environmental sensitivities. Providing a fuel cell system “designed for the environment,” with the goal that no part ever ends up in a landfill, seems to be a fitting way to approach the objective of truly sustainable energy systems.

## Future Directions

Progress in the development of fuel cell systems for transportation, stationary, and motive power applications will continue as long as the incentives around renewable and clean energy continue to receive public support. This support, in turn, needs to be based upon public awareness of the true cost of the incumbent technologies: environmental and social, as well as financial. The rate of progress made in the past 10 years has been accelerating due to the support of governments tending to the longer range needs of their citizens. With a view of the need for a clean energy future clearly in sight, alternative means of energy generation, conversion, and storage will play an increasing role in shaping the future for our children’s children, a time not too far away.

To meet this challenge, fuel cell research and development will need to continue to pursue a range of subjects from basic understanding of the key factors governing charge transfer at the nanoscale to enabling the simplification of fuel cell systems by developing advanced materials that can relax the constraints currently imposed by the polymer electrolyte membrane. Hence, continued examination of the property and structure relationships in electrocatalysis will be needed to point the way to improved catalyst materials. Research on improved and more stable nanostructured electrodes incorporating advanced and lower cost materials will be needed to reduce

cost while improving durability. The development of new polymer electrolyte membrane materials and structures that enable broader operating latitudes at higher operating temperature and lower relative humidity will be needed to further reduce cost by enabling less complex system designs and improved control. In parallel with this, of course, innovative engineering approaches toward reducing cost while simultaneously increasing reliability will be needed to close the gap between today’s cost-performance curves and those required to enable penetration of commercial markets. In other words, a systemic, broadly based, and steady attack on the issues of unit manufacturing cost, durability, and reliability at the system level is necessary to advance the state of the art around PEM fuel cell systems.

## Bibliography

### Primary References

1. Nassauer S (2017) Wal-Mart, Amazon rivalry spreads to forklifts. *Wall Street Journal*, July 21, 2017. <https://www.wsj.com/articles/wal-mart-amazon-rivalry-spreads-to-forklifts-1500634801>
2. Fuel Cell Industry Review (2016). [www.FuelCellIndustryReview.com](http://www.FuelCellIndustryReview.com)
3. Barbir F (2005) PEM fuel cells. Elsevier, Amsterdam/Boston
4. Srinivasan S (2006) Fuel cells: from fundamentals to applications. Springer, New York
5. Vielstich W, Lamm A, Gasteiger HA (eds) (2003) Handbook of fuel cells. Wiley, Chichester
6. Garland N, Kopasz JP (2007) The United States Department of Energy’s high temperature, low humidity membrane program. *J Power Sources* 172:94–99
7. Mader J, Xia L, Schmidt TJ, Benicewicz BC (2008) Polybenzimidazole/acid complexes as high temperature membranes. In: Fuel cells: advances in polymer science, vol 216. Springer, Berlin/Heidelberg, pp 63–124
8. Kusoglu A, Weber AZ (2017) New insights into perfluorinated sulfonic-acid ionomers. *Chem Rev* 117(3):987–1104
9. Vishnyakov A, Niemark AV (2000) Molecular study of Nafion membrane solvation in water and methanol. *J Phys Chem B* 104:4471–4478
10. Kreuer DK, Paddison S, Spohr E, Schuster M (2004) Transport in proton conductors for fuel cell applications: simulations, elementary reactions, and phenomenology. *Chem Rev* 104:4637
11. Springer TE, Zawodzinski TA, Gottesfeld S (1991) Polymer electrolyte fuel cell model. *J Electrochem Soc* 138:2334–2341



12. Fimrite J, Carnes B, Struchtrup H, Djilali N (2009) Coupled proton and water transport in polymer electrolyte membranes. In: Paddison SJ, Promislow KS (eds) *Device and materials modeling in PEM fuel cells*, Series: topics in applied physics, vol 113. Springer, New York
13. Weber AZ, Newman J (2004) Modeling transport in polymer-electrolyte fuel cells. *Chem Rev* 104: 4679–4726
14. Wang CY (2004) Fundamental models for fuel cell engineering. *Chem Rev* 104:4727
15. Weber AZ, Borup RL, Darling RM, Das PK, Dursch TJ, Gu W, Harvey D, Kusoglu A, Lister S, Mench MM, Mukundan R, Owejan JP, Pharoah JG, Secanell M, Zenyuk IV (2014) A critical review of modeling transport phenomenon in polymer-electrolyte fuel cells. *J Electrochem Soc* 161(12):F1254–F1299
16. Darling RM, Meyers JP (2003) Kinetic model of platinum dissolution in PEMFCs. *J Electrochem Soc* 150: A1523–A1527
17. Meyers JP, Darling RM (2006) Model of carbon corrosion in PEM fuel cells. *J Electrochem Soc* 155: A1432–A1442
18. Reiser CA, Bregoli L, Patterson TW, Yi JS, Yanag JD, Perry MI, Jarvi TD (2005) A reverse current decay mechanism for fuel cells. *Electrochem Solid-State Lett* 8(6):A273
19. [www.cd-adapco.com](http://www.cd-adapco.com)
20. [www.fluent.com](http://www.fluent.com)
21. [www.comsol.com](http://www.comsol.com)
22. Markovic N, Gasteiger H, Ross PN (1997) Kinetics of oxygen reduction on Pt (hkl) electrodes: implications of the crystalline size effect with supported Pt electrocatalysts. *J Electrochem Soc* 144:1591–1159
23. Nørskov JK, Rossmeisl J, Logadottir A, Lindqvist L, Kitchin JR, Bligaard T, Jónsson H (2004) Origin of the overpotential for oxygen reduction at a fuel cell cathode. *J Phys Chem B* 108:17886–17892
24. Mavrikakis M, Hammer B, Nørskov JK (1998) Effect of strain on the reactivity of metal surfaces. *Phys Rev Lett* 81:2819–2822
25. Taylor CD, Wasileski SA, Filhol JS, Neurock M (2006) First principles modeling of the electrochemical interface: consideration and calculation of a tunable surface potential from atomic and electronic structure. *Phys Rev B* 73:65402
26. Adachi H, Ahmed S, Lee SHD, Papadias D, Ahluwalia RK, Bendert JC, Adzic RR et al (2007) Platinum monolayer fuel cell electrocatalysis. *Top Catal* 46:249
27. Stamenkovic V, Mun BS, Mayrhofer KJJ, Ross PN, Markovic NM, Rossmeisl J, Greeley J, Nørskov JK (2006) Changing the activity of electrocatalyst for oxygen reduction by tuning the surface electronic structure. *Angew Chem Int Ed* 45:2897
28. Nørskov JK, Rossmeisl J, Logadottir A, Lindqvist L, Kitchin JR, Bligaard T, Jónsson H (2004) Origin of the overpotential for oxygen reduction at a fuel cell cathode. *J Phys Chem B* 108:17886–17892
29. Koper MTM (ed) (2009) *Fuel cell catalysis*. Wiley, Hoboken
30. Zhang J, Lima FHB, Shao MH, Sasaki K, Wang JX, Hanson J, Adzic RR (2005) Platinum monolayer on non-noble metal-noble metal core-shell nanoparticle electrocatalysts for O<sub>2</sub> reduction. *J Phys Chem B* 109(48):22701–22704
31. Hu J, Wu L, Kuttiyiel KA, Goodman KR, Zhang C, Zhu Y, Vukmirovic MB, White MG, Sasaki K, Adzic RR (2016) Increasing stability and activity of core-shell catalysts by preferential segregation of oxide on edges and vertices: oxygen reduction on Ti-Au@Pt/C. *J Am Chem Soc* 138:9294–9300
32. Kang Y, Yang P, Markovic NM, Stamenkovic VR (2016) Shaping electrocatalysis through tailored materials. *Nano Today* 11:587–600
33. Han B, Carlton CE, Konkanand A, Kukreja RS, Theobald BR, Gan L, O'Malley R, Strasser P, Wagner FT, Shao-Horn Y (2015) Record activity and stability of dealloyed bimetallic catalysts for proton exchange membrane fuel cells. *Energy Environ Sci* 8:258
34. Lopes PP, Strmcnik D, Tripkovic D, Connell JG, Stamenkovic V, Markovic NM (2016) Relationship between atomic level surface structure and stability/activity of platinum surface atoms in aqueous environments. *ACS Catal* 6:2536–2544
35. Gasteiger HA, Kocha SS, Sompali B, Wagner FT (2005) Activity benchmarks for Pt, Pt-alloy and non-Pt oxygen reduction catalysts for PEMFCs. *Appl Catal B Environ* 56:9–35
36. Weber AZ, Kusoglu A (2014) Unexplained transport resistances for low loaded fuel-cell catalyst layers. *J Mater Chem A* 2:17207–17211
37. Gostick JT, Weber AZ (2015) Resistor network modeling of ionic conduction in polymer electrolytes. *Electrochim Acta* 179:137–145
38. Paul DK, Shim HK, Giorgi JB, Karan K (2016) Thickness dependence of thermally induced changes in surface and bulk properties of Nafion<sup>®</sup> nanofilms. *J Polym Sci B Polym Phys* 54:1267–1277
39. Orfanidi A, Madkikar P, El-Sayed HA, Harzer GS, Kratky T, Gasteiger HA (2017) The key to high performance low Pt loaded electrodes. *J Electrochem Soc* 164(4):F418–F426
40. Kongkanand A, Mathias MF (2016) The priority and challenge of high-power performance of low-platinum proton exchange membrane fuel cells. *J Phys Chem Lett* 7:1127–1137
41. Debe MK (2003) Novel catalysts, catalysts support and catalysts coated membrane methods. In: Vielstich W, Lamm A, Gasteiger HA (eds) *Handbook of fuel cells-fundamentals, technology and applications*, vol 3. Wiley, New York. Chapter 45
42. Gancs L, Kobayashi T, Debe MK, Atanasoski R, Wieckowski A. (2008) Crystallographic characteristics of nanostructured thin-film fuel cell electrocatalysts: a HRTEM study. *Chem Mater* 20(7):2444–2454
43. Debe, M. K. (2010) Advanced cathode catalysts and supports for PEM fuel cells. DOE Hydrogen Program Merit Review and Peer Evaluation, Washington, DC
44. Ahluwalia RK, Pang J-K, Wang X, Cullen DA, Steinbach AJ (2017) Long-term stability of

- nanostructured thin film electrodes at operating potentials. *J Electrochem Soc* 164(4):F306–F320
45. Tang JM, Jensen K, Waje M, Li W, Larsen P, Pauley K, Chen Z, Ramesh P, Itkis M, Yan Y, Haddon R (2007) High performance hydrogen fuel cells with ultralow Pt loading carbon nanotube thin film catalysts. *J Phys Chem C* 111(48):17901–17904
  46. Antonlini E, Gonzalez ER (2009) Ceramic materials as supports for low temperature fuel cell catalysts. *Solid State Ionics* 180:746–763
  47. Scherer GG (ed) (2008) Fuel cells II, *Advances in polymer science*, vol 216, Springer, Berlin/Heidelberg
  48. Abhishek R, Yu X, Dunn S, McGrath JE (2009) Influence of microstructure and chemical composition on proton exchange membrane properties of sulfonated-fluorinated hydrophilic-hydrophobic multiblock copolymers. *J Membr Sci* 327(1+2):118–124
  49. Lipp L (2010) High temperature membrane with humidification independent cluster structure. DOE Hydrogen Program Merit Review and Peer Evaluation, Washington, DC
  50. Yandrasits M (2017) New fuel cell membranes with improved durability and performance, project FC109. DOE Fuel Cell Annual Merit Review and Peer Evaluation, Washington, DC
  51. Inaba M (2009) Chemical degradation of perfluorinated sulfonic acid membranes. In: Buechi FN, Inaba M, Schmidt TJ (eds) *Polymer electrolyte fuel cell durability*. Springer Science + Business Media, LLC, New York
  52. Danilczuk M, Coms FD, Schlick S (2008) Fragmentation of fluorinated model compounds exposed to oxygen radicals: spin trapping ESR experiments and implications for the behaviour of proton exchange membranes used in fuel cells. *Fuel Cells (Weinheim, Germany)* 8(6):436–452
  53. Ghassemzadeh L, Marrony M, Barrera R, Kreuer KD, Maier J, Mueller K (2009) Chemical degradation of proton conducting perfluorosulfonic acid ionomer membranes studied by solid-state nuclear magnetic resonance spectroscopy. *J Power Sources* 186(2):334–338
  54. Antoine O, Durand R (2000) RRDE study of oxygen reduction on Pt nanoparticles inside Nafion<sup>®</sup>: H<sub>2</sub>O<sub>2</sub> production in PEMFC cathode conditions. *J Appl Electrochem* 30:839–844
  55. Liu H, Gasteiger HA, Laconti A, Zhang J (2006) Factors impacting chemical degradation of perfluorinated sulfonic acid ionomers operating conditions and catalyst impact on membrane degradation. *Electrochem Soc Trans* 1(8):283–293
  56. Mittal V, Kunz R, Fenton JM (2006) Factors accelerating membrane degradation rate and the underlying degradation mechanism in PEMFC operating conditions and catalyst impact on membrane degradation. *Electrochem Soc Trans* 1(8):275–282
  57. Miyake N, Wakizoe M, Honda E, Ohta T (2006) High durability of Asahi Kasei Aciplex membrane operating conditions and catalyst impact on membrane degradation. *Electrochem Soc Trans* 1(8):249–261
  58. Yu J, Matsuura T, Yoshikawa Y, Islam MN, Hori M (2005) In situ analysis of performance degradation of a PEMFC under nonsaturated humidification. *Electrochemical Solid-State Lett* 8(3):A156–A158
  59. Curtin DE, Lousenberg RD, Henry TJ, Tangeman PC, Tisack ME (2004) Advanced materials for improved PEM performance and life. *J Power Sources* 131: 41–48
  60. Trogadas P, Parronda J, Ramani V (2008) Degradation mitigation in polymer electrolyte membranes using cerium oxide as a regenerative free radical scavenger. *Electrochem Solid-State Lett* 11(7):B113–B116
  61. Wang L, Advani SG, Prasad AK (2017) Self-healing composite membrane for proton electrolyte membrane fuel cell applications. *J Electrochem Soc* 163(10): F1267–F1271
  62. Lassegues JC, Schoolmann D, Trinquet O (1992) Proton conducting acid polymer blends. In: Balkanski T, Takahashi T, Tuller HL (eds) *Solid state ionics*. Elsevier, Amsterdam, pp 443–448
  63. Lassègues JC (1992) Mixed inorganic-organic systems: the acid/polymer blends. In: Colombari P (ed) *Proton conductors: solids, membranes and gel – materials and devices*. Cambridge University Press, Cambridge/New York, pp 311–328
  64. Savinell R, Yeager E, Tryk D, Landau U, Wainright J, Weng D, Lux K, Litt M, Rogers C (1994) A polymer electrolyte for operation at temperatures up to 200°C. *J Electrochem Soc* 141(4):L46–L48
  65. Schmidt TJ (2009) High-temperature polymer electrolyte fuel cells: durability insights. In: Buchi FN, Inaba M, Schmidt TJ (eds) *Polymer electrolyte fuel cell durability*, Springer, New York
  66. Neyerlin KC, Singh A, Chu D (2008) Kinetic characterization of a Pt-Ni/C catalyst with a phosphoric acid doped PBI membrane in a proton exchange membrane fuel cell. *J Power Sources* 176:112–117
  67. Strmcnik D, Escudero-Escribano M, Kodama K, Stamenkovic VR, Cuesta A, Markovic NM (2010) Enhanced electrocatalysis of the oxygen reduction reaction based upon patterning of platinum surfaces with cyanide. *Nat Chem* 2
  68. Xu H, Pivovar B, *Advanced Catalysts and MEAs for reversible alkaline membrane fuel cells*, project FC129, DOE 2016 AMR <https://www.hydrogen.energy.gov/pdfs/review16>
  69. Yanagi H, Fukuta K (2008) Anion exchange membrane and ionomer for alkaline membrane fuel cells. *ECS Trans* 16:257–262
  70. Duan Q, Ge S, Wang C-Y (2013) Water uptake, ionic conductivity, and swelling properties of anion-exchange membrane. *J Power Sources* 243:773–778
  71. Kaspar RB, Letterio MP, Wittkopf JA, Gong K, Gu S, Yan Y (2015) Manipulating water in high-performance hydroxide exchange membrane fuel cells through asymmetric humidification and wetproofing. *J Electrochem Soc* 162(6):F483–F488
  72. Ren X, Price SC, Jackson AC, Pomerantz N, Beyer FL (2014) Highly conductive anion exchange membrane



- for high power density fuel cell performance. *J ACS Appl Mater Interfaces* 6:13330–13333
73. Pivovar B (2016) Advanced ionomers and MEAs for alkaline membrane fuel cells, DOE hydrogen and fuel cell annual merit review, project FC147
  74. Durst J, Siebel A, Simon C, Hasche F, Herranz J, Gasteiger HA (2014) New insights into the electrochemical hydrogen oxidation and evolution reaction mechanism. *Energy Environ Sci* 7:2255–2260
  75. McGrath MF, Anthony MT, Shapiro AR (1992) Product development. Butterworth-Heinemann, Boston
  76. Patterson ML, Fenoglio JA (1999) Leading product innovation. Wiley, New York
  77. McGrath M (2001) Product strategy. McGraw-Hill, New York
  78. [www.FuelCellIndustryReview2016](http://www.FuelCellIndustryReview2016)
  79. Du B, Pollard R, Elter JF, Ramani M (2009) Performance and durability of a polymer electrolyte fuel cell operating with reformat: effects of CO, CO<sub>2</sub>, and other trace impurities. In: Büchi F, Inaba M, Schmidt TJ (eds) *Polymer electrolyte fuel cell durability*. Springer, New York, pp 341–366
  80. Du B, Pollard R, Elter JF CO-air bleed interaction and performance degradation study in proton exchange membrane fuel cells. *Electrochem Soc Trans* 3(1):705–713
  81. Adachi H, Ahmed S, Lee SHD, Papadias D, Ahluwaia RK, Bendert JC, Kanner SA, Yamazaki Y (2009) A natural gas fuel processor for a residential fuel cell system. *J Power Sources* 168:244–255
  82. Feitelberg AS, Rohr DF Jr (2005) Operating line analysis of fuel processors for PEM fuel cell systems. *Int J Hydrog Energy* 30:1251–1257
  83. Feitelberg A (2003) On the efficiency of PEM fuel cell systems and fuel processors, presentation at fuel cell seminar
  84. Mukundan R, Kim YS, Garzon FH, Pivovar B (2006) Freeze/Thaw Effects in PEM Fuel Cells. *ECS Trans* 1(8):403–413
  85. Guo QH, Qi ZH (2006) Effect of freeze-thaw cycles on the properties and performance of membrane-electrode assemblies. *J Power Sources* 160:1269–1274
  86. Lee C, Merida W (2007) Gas diffusion layer durability under steady state and freezing conditions. *J Power Sources* 164:141–153
  87. Mao L, Wang C-Y (2007) Analysis of cold start in polymer electrolyte fuel cells *J Electrochem Soc* 154: B139–B146
  88. Tang H, Qi Z, Ramani M, Elter JF (2006) PEM fuel cell cathode carbon corrosion due to the formation of air/fuel boundary at the anode. *J Power Sources* 158:1306–1312
  89. Du B, Pollard R, Ramani M, Graney P, Elter JF (2007) Impact of cold start and hot stop on the performance and durability of a proton exchange membrane (PEM) fuel cell. *ECS Trans*:271–228
  90. Meyers JP, Darling RM (2006) Model of carbon corrosion in PEM fuel cells. *J Electrochem Soc* 153(8): A1432–A1442
  91. Pukrushpan JT, Stefanopolou AG, Peng H (2005) *Control of fuel cell power systems*. Springer, London
  92. Feitelberg AS, Elter JF. Development, design and performance of plug power's next generation stationary PEM fuel cell system prototype. Presented at 2005 fuel cell seminar, Palm Springs, 14–18 Nov
  93. Elter JF. The design and control of fuel cell systems. Presented at the H<sub>2</sub> fuel cells millennium convergence, Bucharest, 21, 22 Sept 2007
  94. James B, Huga-Kouadio JM, Houchins C (2017) Fuel cell systems analysis, project FC163, DOE annual merit review, Washington, DC. [www.annualmeritreview.energy.gov/](http://www.annualmeritreview.energy.gov/)
  95. Hasegawa T, Imanishi H, Nada M, Ikogi Y (2016) Development of the fuel cell system in the mirai FCV, SAE technical paper 2016-01-1185. doi:<https://doi.org/10.4271/2016-01-1185>
  96. Konno N, Mizuno S, Nakaji H, Ishikawa Y (2015) Development of compact and high performance fuel cell stack. *SAE Int J Altern Power* 4(1). <https://doi.org/10.4271/2015-01-1175>
  97. Cooper J, Lee S-J, Elter J, Boussu J, Boman S (2009) Life cycle design metrics for energy generation technologies: method, data and case study. *J Power Sources* 186:138–157



## Polymer Electrolyte Membrane (PEM) Fuel Cells: Automotive Applications

Shyam S. Kocha  
Hydrogen Technologies and Systems Center,  
National Renewable Energy Laboratory, Golden,  
CO, USA

### Article Outline

Glossary  
Definition of Subject: Automotive PEM Fuel Cells  
Introduction  
Brief History of Automotive Fuel Cells  
Automotive PEMFCS  
Future Directions  
Bibliography

### Glossary

**Automotive PEMFC** Proton exchange membrane fuel cell stacks used to power automotive vehicles typically using hydrogen as a fuel and ambient air as the oxidant

**Electrocatalyst** The material used on the anode and cathode electrodes of fuel cells to catalyze the fuel oxidation and oxygen reduction reactions to produce electrical power and by-products of heat and water. Amount of electrocatalyst used in the anode or cathode of fuel cells is reported in units of  $\text{mg}/\text{cm}^2$

**Fuel cell durability** A measure of the degradation of components of a fuel cell as well as the output power of the entire stack over time. Also defined in terms of the maximum life of the stack before failure or degradation rate of the fuel cell performance in  $\mu\text{V}/\text{h}$

**Fuel cell performance** The voltage produced by a fuel cell stack at a defined current density. A performance or polarization curve refers to a

plot of the cell potential ( $V$ ) versus current density ( $I$ ) under specified conditions of pressure, temperature, humidity, and reactant stoichiometry

**Membrane/PEM** The proton conductive polymer electrolyte used to separate the anode and cathode compartments of fuel cells. The membrane replaces the liquid electrolytes used in some fuel cells.

### Definition of Subject: Automotive PEM Fuel Cells

Since the discovery of fuel cells in the nineteenth century, they have been designed for operation with liquid alkaline, acid, and solid oxide ion conducting electrolytes in different temperature ranges to produce electrical power for stationary, portable, and automotive applications. The liquid acid that provides ionic conduction has been replaced by fairly thin proton conducting membranes such as polystyrenes and perfluorosulfonic acids (PFSAs) like Nafion and more recently with hydrocarbon-based polymers. These fuel cells incorporating a proton-conducting membrane rather than liquid electrolyte to separate the anode and cathode (forming a three-layer sandwich or catalyst coated membrane) are referred to as PEMFCs. PEMFCs are preferred for use in automobiles for a multitude of reasons including their high volumetric and gravimetric power density.

PEMFCs for automobiles have electrodes that are typically constituted of Pt-based catalysts separated by proton-conducting perfluorosulfonic acid (PFSA) or hydrocarbon membranes. The membranes ( $\sim 25 \mu\text{m}$  thick) have proton conductivities of about  $100 \text{ mS}/\text{cm}$  and areal resistances of  $50 \text{ m}\Omega\text{-cm}^2$ . The anode Pt loadings that catalyze the hydrogen oxidation reaction (HOR) are of the order of  $0.05 \text{ mg}/\text{cm}^2$ , while the cathode Pt loadings that catalyze the oxygen reduction reaction (ORR) fall in the range  $0.20\text{--}0.40 \text{ mg}/\text{cm}^2$ . Automotive PEMFCs are

operated in the temperature range from ambient to  $\sim 90$  °C at ambient to  $\sim 300$  kPa and at 30–100% RH. Compressed hydrogen fuel tanks (350–700 kPa) and ambient air pressurized using a compressor are employed as the fuel and oxidant sources. Depending on the size of the vehicle, automotive fuel cell stacks produce 80–140 kW of peak power. Most fuel cell automotives are hybrids and employ a 10–20 kW NiMH or Li ion battery to improve efficiency and to store and provide supplemental power. Automotive PEMFCs are subject to variable operating conditions of high potentials, load cycling, start-up and shutdown cycles, humidity cycles, freeze-thaw cycles, and contamination from ambient air. The main obstacles toward commercialization of PEMFC stacks for automotives are the combination of cost, performance, and durability that are not mutually exclusive. Today's PEMFC-powered automobiles demonstrate driving ranges and lifetimes approaching ( $\sim 70\%$ ) that of ICE vehicles. Major automotive companies have stated that PEMFCs for automotives are slated to arrive at cost levels approaching that necessary for commercialization beginning in 2015.

Currently, ICE-powered vehicles emit  $\sim 1.5$  billion tons  $\text{CO}_2$  equivalent per year at a US urban air pollution cost to society of \$30 billion/year. The consumption of fossil fuels by the human species ( $\sim 6.5$  billion) has resulted in challenges of energy sustainability, environmental pollution, and global warming that need to be addressed urgently. Currently, several technologies that lower the greenhouse gas emissions partially such as gasoline-powered hybrid electric vehicles (HEVs) and gasoline plug-in hybrids (PHEVs), biofuel PHEVs, and batteries (BEVs) are being developed in parallel with fuel cells.

PEMFCs can operate on hydrogen fuel and atmospheric air to produce electrical energy, while exhausting only heat and water. Hydrogen is not available on earth as gas; it is found as a compound bound to oxygen as in water or bound to carbon, and in living things as biomass. Hydrogen is a carrier of energy and needs to be generated and stored efficiently; an infrastructure for hydrogen needs to be developed along with more efficient storage of hydrogen carried on board the

vehicle. Currently about 9 million metric tons of hydrogen per year are generated in the USA that could power 30 million automobiles. Hydrogen can be produced from fossil fuels such as natural gas, and also, renewable sources, such as hydroelectric, wind, geothermal, solar photovoltaics, direct photoelectrochemical, and concentrated solar power ocean (tidal, wave, current, and thermal). The application of  $\text{H}_2$ |Air PEMFCs in automotives is one of the most important components in a renewable hydrogen economy that has the potential to reduce greenhouse gas emissions (to 80% below 1990 GHG levels), lower pollution, and arrest global warming.

## Introduction

Fuel cells have been known to science for more than 150 years. In 1800, British scientists William Nicholson and Anthony Carlisle first demonstrated and explained the phenomena of using electricity to decompose water into hydrogen and oxygen. William Robert Grove (1811–1896), a Welsh scientist who was working on electrolysis of water to hydrogen and oxygen, tested the hypothesis that the reverse might be possible. He placed two platinum strips immersed in dilute sulfuric acid in two separate chambers, one of which was filled with hydrogen and the other with oxygen. A current was found to flow between the two platinum strips and water produced in the chamber confirming the hypothesis [1]. Although Grove was the first to build a working fuel cell, the discovery of the principle and fundamentals of the fuel cell is attributed to Christian Friedrich Schoenbein (1799–1868) [2]. Grove later improved on his original experiments by using a series of four cells to increase the total voltage; he named the device a “gas battery” – now known as a fuel cell stack.

Significant contributions were made in later years on fuel cells powered by various fuels such as that by Mond and Langer [3], Haber, W. V. Jacques [4], Bauer [5], Taitelbaum, Schmid [6], Tobler [7], and others. In addition to the experimental and practical fuel cell devices, a number of

scientists contributed to the science and mechanism of the detailed functioning of fuel cells. Two noteworthy theories were debated to explain the functioning of the fuel cell. One was the “contact” theory originally proposed by Alessandro Volta (1745–1827) to explain his battery and the other was a “chemical” theory that held chemical reactions responsible for the generated power. Both theories had part of the solution which is that reactions that occurred where reactant gases, Pt catalyst, and electrolyte converged. This understanding was advanced by the contributions of Friedrich Wilhelm Ostwald (1853–1932). Other systematic nonempirical contributions were made by Nernst [8], Tafel [9], and Erdey-Gruz and Volmer. A history of the development of fuel cell electrodes between 1839 and 1960 can be found in the reviews of Liebhasvsky and Cairns [10], Vielstich [11], Baur [5], Tobler [7], Maget [12], and Liebhasvsky and Grubb [13].

In 1932, Francis Thomas Bacon replaced the platinum electrodes with cheaper porous nickel metal and the sulfuric acid with potassium hydroxide to demonstrate the first alkaline fuel cell (AFC). Alkaline fuel cells were demonstrated to produce power for practical applications such as welding machines, tractors, powerlifts, etc., in the 1950s. Improved AFCs (2.3 kW) were engineered by Pratt & Whitney/International Fuel Cells (IFC) and were used by NASA in manned US Apollo space missions (1968–1972) and Skylabs for about 54 missions. High power density AFCs using precious metal-based catalysts, static electrolyte (KOH), and operating on hydrogen and oxygen have been used to power (three 12 kW stacks, 92 °C, 400 kPa) space shuttles since 1981 [14]. Other companies that have worked on AFCs include Union Carbide Corp., Siemens AG, and the European Space Agency [15].

Cation exchange resins polymerized as sulfonic acids became available in 1945 for use as deionizers. Around 1959, General Electric (Thomas Grubb and Leonard Niedrach) considered the use of these materials (sulfonated polystyrene) to form solid polymer electrodes (SPEs) as membranes for fuel cells; these materials were predicted to eliminate the system complexity

involved in using liquid electrolytes and lead to the first PEMFCs [10, 16, 17]. The commercial availability of Teflon<sup>®</sup> (discovered in 1938 by Roy Plunkett of Dupont<sup>®</sup>) enhanced the performance of SPEs due to its hydrophobic nature and consequent lowered flooding of electrode pores. Using SPEs, PEM modules were fabricated and used in the Gemini space modules operating under hydrogen and oxygen. The Biosatellite 2 (1967) followed the Gemini program (seven flights, 1962–1966) in which Nafion membrane was used for the first time. GE continued working on PEMFCs and in the 1970s developed PEM water electrolysis technology for undersea life support that was used in US Navy oxygen-generating plants. Some of the technology from GE was acquired by UTC affiliates Hamilton-Standard and IFC in 1984. The British Royal Navy also adopted this technology in the 1980s for their submarine fleet. Siemens A.G. commenced a fuel cell research program on AFCs and in 1984 implemented a 100 kW fuel cell in a German navy submarine; they also have PEMFCs installed in submarines operating with rated power of 34–120 kW with technology that allows a high power density and good thermal management. The efforts described above in all these related areas established the basis and provided the foundation and grounds for pursuing fuel cells for automotive applications.

In 2009, ICE vehicles consumed about 3.5 billion barrels/year gasoline and emitted 1.5 billion tons CO<sub>2</sub> equivalent per year of the greenhouse gases [18]. Figure 1a illustrates the CO<sub>2</sub> emissions over the next century for five different scenarios and Fig. 1b illustrates the well-wheels greenhouse emissions projected for 2010 [19]. In the USA, 28% of the total energy used powers the transportation sector. The fuels commonly used for transportation are gasoline (62%), diesel (22%), jet fuel (9%), and natural gas (2%). The by-products (that have an impact on the environment and human health) of petroleum products include CO<sub>2</sub>, CO, SO<sub>2</sub>, NO<sub>x</sub>, volatile organic compounds (VOCs), fine particulate matter (fine PM), lead, benzene, formaldehyde, acetaldehyde, 1,3 butadiene, etc. Automotives produce a large proportion of the pollution and greenhouse gases on earth;

with global warming becoming an accepted reality, governments and automakers are finally making an effort to lower greenhouse gas emissions. Although a number of intermediate low-emission technologies are being unraveled, PEMFCs are considered to be the best long-term solution since they can operate on hydrogen and atmospheric air to produce electrical energy, while exhausting heat and water with zero emissions.

Although onboard reforming of methanol, gasoline, etc., was seriously considered and attempted, fitting a miniature chemical plant in the limited space of a fuel cell vehicle was found to be untenable. Hydrogen was unanimously selected as the choice of onboard fuel for automotive vehicles in the early twenty-first century with an understanding of its strengths and weaknesses. Hydrogen is not available on earth as gas; it is found as a compound bound to oxygen as in water or bound to carbon, and in living things as biomass. Hydrogen has the highest energy content of any fuel by weight (hydrogen: 143 MJ/kg, gasoline: 43 MJ/kg) and the lowest by volume. Hydrogen can be produced from fossil fuels such as natural gas, and renewable sources, such as hydroelectric, wind, geothermal, solar photovoltaics, direct photo-electrochemical, and concentrated solar power ocean (tidal, wave, current, and thermal). Hydrogen is also classified based on criteria such as primary energy sources (hydro, nuclear, wind, solar, natural gas, etc.); methods of production (reforming, electrolysis, etc.); and renewable/nonrenewable. Currently, about 9 million metric tons of hydrogen per year is generated (~95% steam methane reforming (SMR) and the rest electrolysis); in the USA, this could, in principle, power ~30 million automobiles.

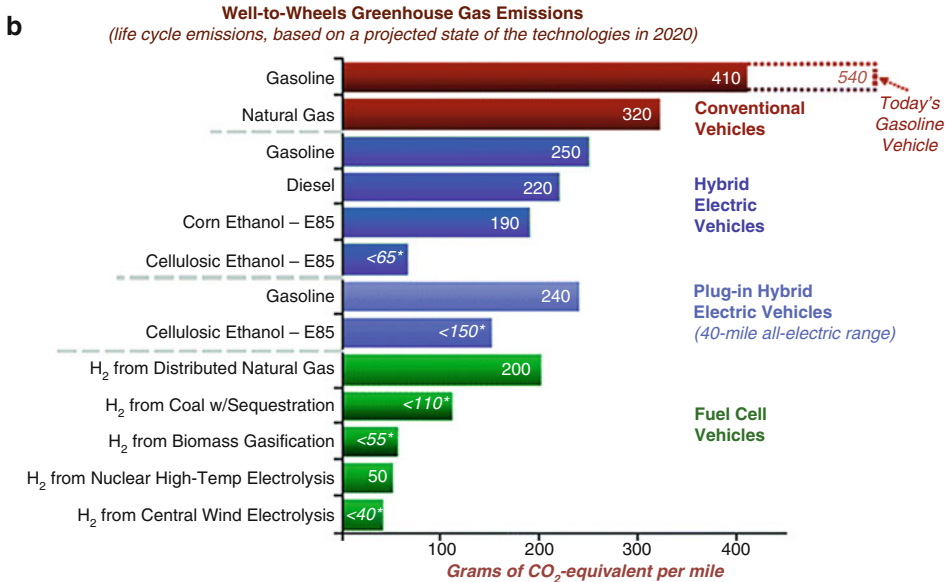
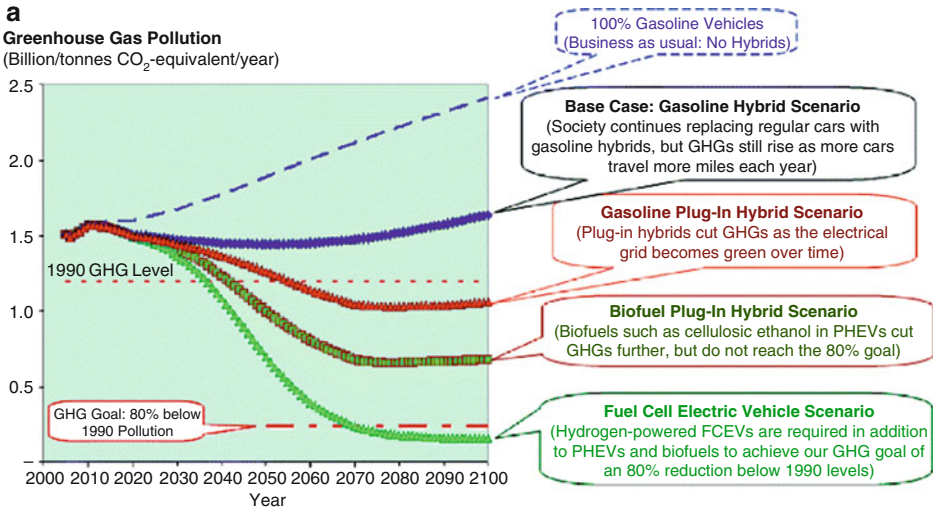
Historically, there have been concerns about the safety of hydrogen, but in actuality, it is as safe and even safer than other flammable fuels such as gasoline and natural gas. A primary safety advantage of hydrogen is that it has very high diffusivity so that it dilutes rapidly to a nonflammable concentration in a reasonably ventilated space. Additionally, due to the absence of carbon and presence of water vapor in the combustion products of hydrogen, hydrogen fires release less

radiant energy thus lowering incidents of secondary fires. The flammability limits, explosion limits, ignition energy, flame temperature, and stoichiometric mixture most easily ignited in air are all well documented for hydrogen. Codes and standards have been established for the safe use of hydrogen. Fuel cell vehicles are subjected to the same safety tests and crash/impact tests as gasoline-powered vehicles and have little trouble passing them.

As the world transitions to a hydrogen economy, a hydrogen infrastructure including a combination of distributed and centralized production is likely to evolve. Hydrogen pipeline networks already exist in some regions, often to provide hydrogen to the refining and food processing industry; transport by trucks is also prevalent. In the USA, at this time, there are 60 hydrogen fueling stations (~350 worldwide), 1,200 miles of hydrogen pipelines, and ~9 million tons of hydrogen produced every year. Hydrogen storage is often categorized as physical (or molecular) and chemical (or dissociative) storage. Onboard physical storage methods include compressed gas, liquid hydrogen, and cryo-adsorbed hydrogen; chemical storage includes metal hydrides and liquid organic carriers. Typically, compressed hydrogen (35–70 MPa) in one or two tanks (~4–8 kg hydrogen depending on the target range) is stored onboard fuel cell vehicles today. Most fuel cell vehicles today closely meet the driving range of their IC engine counterparts.

The application of H<sub>2</sub>|Air PEMFCs in automobiles is one of the most important components in a renewable hydrogen economy that has the enormous potential to reduce greenhouse gas emissions (to 80% below 1990 GHG levels) and arrest global warming. Based on the Intergovernmental Panel for Climate Change (IPCC) study (Fig. 2) by 2050 well-wheels emissions of CO<sub>2</sub> must be reduced by 70% ~ 90% versus 2000 levels [20]. Of all the possible pathways such as gas-electric hybrids, EVs, and fuel cells, only H<sub>2</sub>|Air PEMFCs have the ability to reduce emissions to zero. Thus in attempts to reduce greenhouse gas emissions, lower dependence on imported oil, and limit urban air and water pollution, FCVs are expected to play a very central role.





\*Net emissions from these pathways will be lower if these figures are adjusted to include:

- \* The displacement of emissions from grid power-generation that will occur when surplus electricity is co-produced with cellulosic ethanol
- \* The displacement of emissions from grid power-generation that may occur if electricity is co-produced with hydrogen in the biomass and coal pathways, and is surplus wind power is generated in the wind-to-hydrogen pathway
- \* Carbon dioxide sequestration in the biomass-to-hydrogen process

**Polymer Electrolyte Membrane (PEM) Fuel Cells: Automotive Applications, Fig. 1** (a) CO<sub>2</sub> emissions over the next century for five scenarios where gasoline vehicles, gasoline-hybrid, gasoline plug-in hybrids,

biofuel plug-in hybrids, and fuel cell electric vehicles are used as the power source [18]; (b) well-wheels green house gas emissions based on state of technology in 2020 [19]

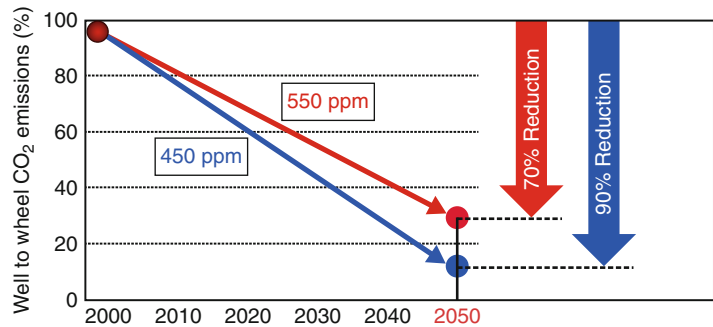
### Brief History of Automotive Fuel Cells

Ballard should be recognized for reigniting the interest in PEMFCs in the late 1980s and 1990s and for the development of improved stacks used

today by several companies in their fuel cell vehicles [21]. All the major automotive companies initiated fuel cell research and development programs as well as small-scale demonstration programs between 1998 and 2010; this was

### Polymer Electrolyte Membrane (PEM) Fuel Cells: Automotive Applications,

**Fig. 2** Reduction in well-wheels CO<sub>2</sub> emissions recommended for 2050 by the Intergovernmental Panel for Climate Change (IPCC) study [20]



augmented by materials and component development by companies in the area of membranes, catalysts, diffusion media, bipolar plates, etc. In 2003, the US government announced a \$1.2 billion FreedomCAR and Hydrogen Fuel Initiative (HFI) to develop hydrogen-powered fuel cells. Together, by 2008, the two initiatives invested about \$1 billion to develop hydrogen-powered fuel cells, hydrogen infrastructure, and advanced automotive technologies. Fuel cells suffered a setback due to the 2009 US government policy that projected a longer 10–20-year forecast for automotive fuel cell commercialization. Nevertheless, most of the US, European, and Japanese automakers continue to support the development of PEMFCs for automobiles internally as well as in public statements and most of the government funding was later restored. Also, in 2009, the European Union (EU) announced €140 million (\$195 million) in available investments for research in energy technology. The funding (European Commission matched by contributions from the private sector) is part of a €1 billion (\$1.4 billion) that the EU plans to invest in fuel cell research and development by 2014. In Japan, the Ministry of Economy, Trade and Industry (METI)'s New Energy and Industrial Technology Development Organization (NEDO) has overseen a lot of the funding for fuel cell and hydrogen research, development, and demonstration. The Japan Hydrogen & Fuel Cell Demonstration Project (JHFC) conducts research and activities for the practical use of fuel cell vehicles and hydrogen stations. The JHFC consists of the Fuel Cell Vehicle-Demonstration Study and the Hydrogen Infrastructures-Demonstration Study; the studies are subsidized by the METI. Many countries now

have hydrogen corridors or hydrogen highways with a number of hydrogen fueling stations already implemented. In this section, for simplicity, the contributions made by a number of stack developers and automotive companies to advance fuel cell technology for automobiles based on publicly available sources will be outlined.

#### Allis-Chalmers

In 1959, a team led by Harry Ihrig developed and demonstrated a 15 kW fuel cell tractor for Allis-Chalmers that was exhibited at state fairs across the USA. The FC stack system used KOH electrolyte and compressed hydrogen and oxygen as the reactants operating at 65 °C. The original fuel cell tractor is on display at the Smithsonian. In 1965, Allis-Chalmers further developed hydrogen-powered FC golf carts. Allis-Chalmers is also experimenting with fuel cell stacks to generate power for spot welders and forklift trucks.

#### General Motors

In 1968, GM's Electrovan was the automotive industry's first attempt at an automobile powered by a H<sub>2</sub>O<sub>2</sub> 125 kW fuel cell. It took a team of 250 people 2 years to demonstrate the potential feasibility of fuel cell technology. The Electrovan weighed more than twice as much as a normal van and could travel at speeds up to ~70 mph for 30 s. In the early 1980s, Los Alamos National Lab (LANL) initiated a PEMFC program and GM was part of the overview board. In 1996, the program moved from LANL to Rochester, NY, and later to Honeoye Fall, NY, where a large fuel cell R&D center still operates. In 1997, GAPC was formed globally at Honeoye Falls, NY; Mainz Kastel, Germany; Warren, MI; and



Torrance, CA. In 1998, the GM/DOE program was successful in demonstrating a 50 kW methanol fuel processor PEM system, and in late 1998, GM methanol Zafira was displayed at Geneva Auto Show. In 2000, focus shifted to hydrogen fuel, and in 2001, HydroGen 3, Zafira was launched. Figure 3 illustrates the history of the various GM FC vehicles from 1968 to 2001 and their latest FCV model. The advancements in volumetric and gravimetric power density of PEMFC stacks designed at General Motors between 1997 and 2004 are depicted in Fig. 4 [22]. Figure 5 is a photograph of their fifth generation stack [23]. GM's Chevrolet Equinox FCV passed 1 million miles with customers using the vehicles in everyday real-world conditions [24, 25]. GM and Honda have been working on fuel cells together since 2013 and the Honda-General Motors' partnership and cooperation on hydrogen fuel cells is approaching a new phase, as both parties intend to build a joint fuel cell plant for FCVs.

### UTC Power/UTC Fuel Cells

For the last 40 years, various groups under the umbrella of United Technologies (IFC, UTC Fuel Cells, UTC Power) have been uninterruptedly involved in the research and development of fuel cell stacks such as the commercial PAFC stack-power plant and the AFC PEMFC stacks/power-plant used in the orbiter/space shuttle [26]. Over the last decade, UTC Power collaborated with several automotive companies to integrate their PEMFC stacks into various automotive platforms. Some of the interesting aspects of the UTC-PEMFC stack are that they operate close to ambient pressure and have unique water transport plates or separators; the plates are porous and have internal channels allowing for circulating water or coolant that performs the function of cooling the stack as well as passive water management. The reactants in the anode and cathode flow fields are, in principle, always humidified and improve the performance and durability of the membrane.

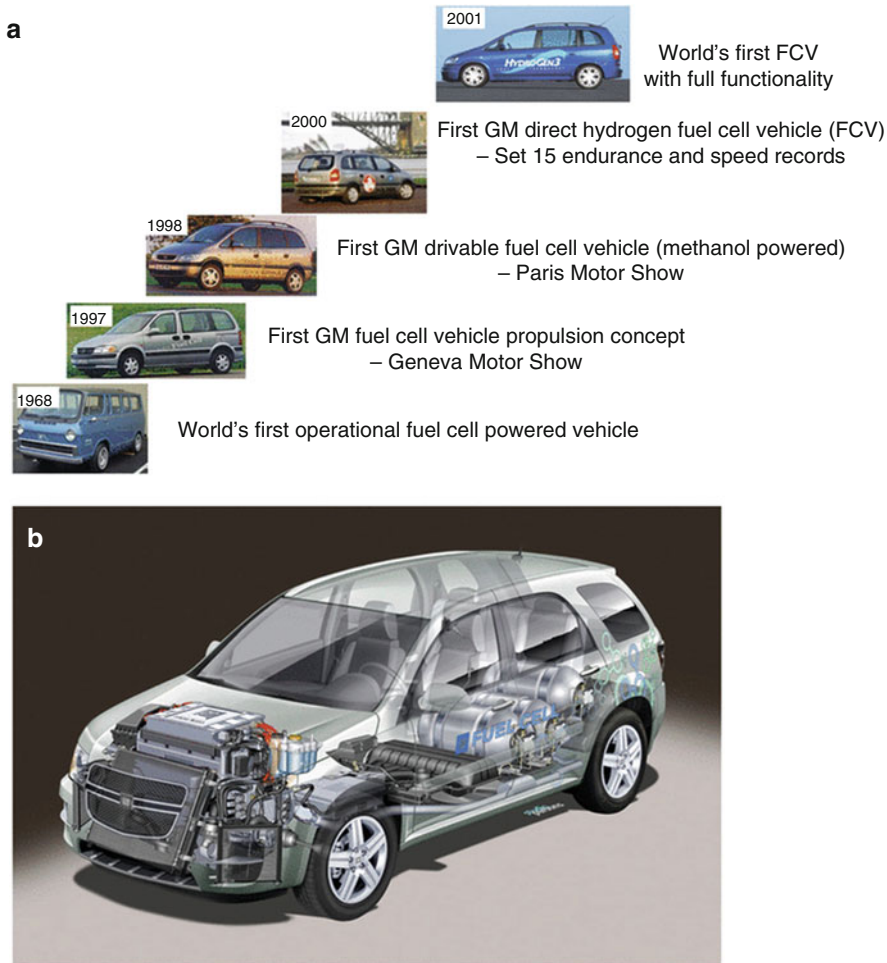
Some of the automotive companies they have worked with include: Hyundai-Kia Motor Company, Chevron Technology Ventures, Nissan, BMW, and a few others. UTC Power has also

developed PEMFC 5 kW auxiliary power units APUs for BMW installed in BMW 7 series vehicles. The PEMFC stack APU provides energy for the vehicle's on-board electrical requirements. The third generation of the APU has been reported to perform for >3,000 h. UTC Power together with Hyundai-Kia Motor Company developed an automotive FCV that was capable of starting and functioning under sub-zero conditions; they were tested in the winter of 2008 in Michigan under the US DOE Hydrogen Fleet and Infrastructure Program. UTC Power also supplied PEMFC stacks for initial generations of Nissan X-TRAIL FCVs.

### Ballard/AFCC

Ballard Power Systems was originally founded in 1979 as Ballard Research Inc. by Dr. Geoffrey Ballard to conduct research on high-energy lithium batteries. In the late 1980s and 1990s, Ballard championed PEMFCs for automotive and other uses and reinvigorated the field. In 1995, Ballard Systems tested PEM cells in buses in Vancouver and Chicago and later in experimental vehicles made by DaimlerChrysler. In late 2007, Ballard pulled out of the hydrogen vehicle sector of its business to focus on fuel cells for forklifts and stationary electrical generation. Established in 2008, the Automotive Fuel Cell Cooperation (AFCC) is a Burnaby, B.C.-based joint-venture private company owned by Daimler AG, Ford Motor Company, and Ballard Power Systems Inc. to develop fuel cell stacks for automotive applications. Today, Daimler and Ford have more than 150 fuel cell vehicles on the road. The fuel cell vehicles of Ford and Daimler are combined together in this subsection since they both generally utilize stacks based on AFCC technology.

DaimlerChrysler unveiled a series of FCVs using Ballard stacks such as the NECAR 1 (50 kW, Compressed H<sub>2</sub>, 1994), NECAR 2 (50 kW, Compressed H<sub>2</sub>, 1996), NECAR 3 (50 kW, liquid methanol, 1997), NECAR 4 (70 kW, liquid H<sub>2</sub>, 1999), and F-Cell (A-class) FCV hybrid delivering 85 kW (Ballard Mark 900) using compressed H<sub>2</sub> in 2002. Most recently, Mercedes announced a series-production of B-class F-Cell powered by an electric motor that generates 136 hp. and 214 lb-ft of



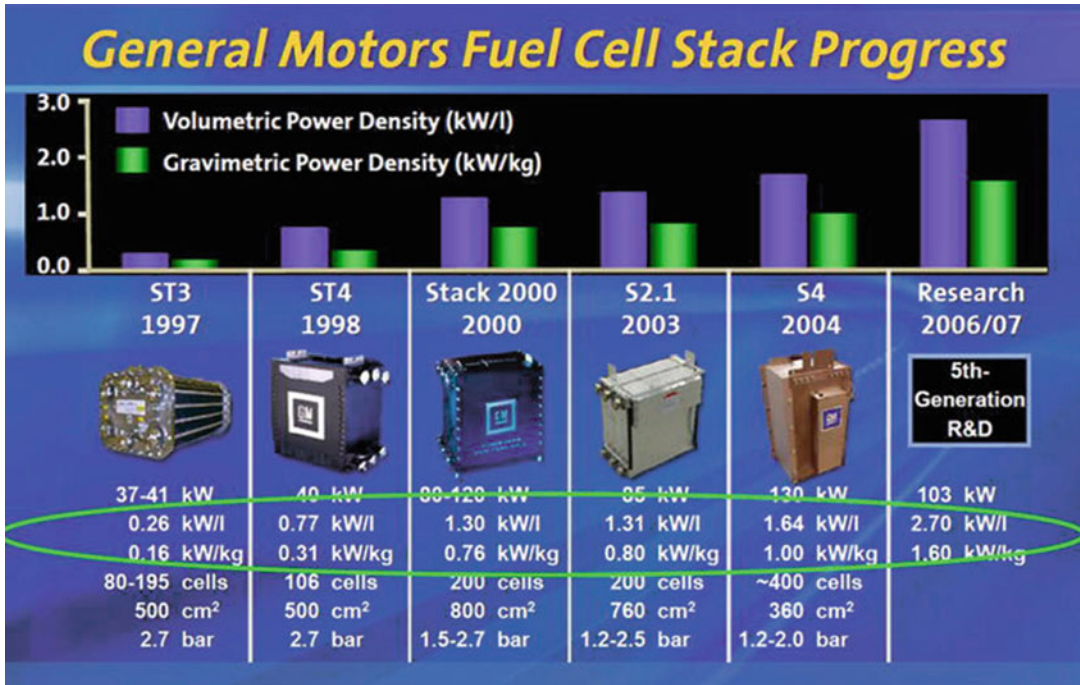
**Polymer Electrolyte Membrane (PEM) Fuel Cells: Automotive Applications, Fig. 3** (a) Timeline of fuel cell vehicle development at General Motors until 2001; (b) 2008 Chevy Equinox fuel cell vehicle [24, 25]

torque, providing a range of 240 miles, and a refueling time of 3 min [27]. Ford Motor Company has also released a series of vehicles using Ballard stacks such as the P200HFC (1999), Focus FCV (2000), and Advanced Focus FCV (2002).

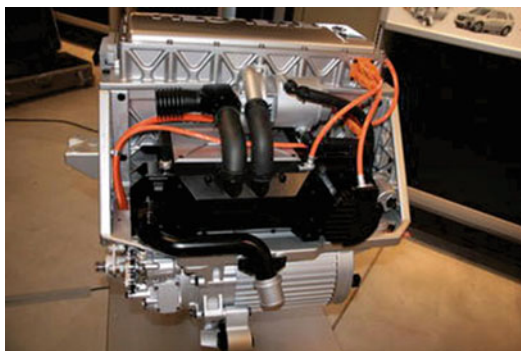
### Toyota

Toyota has been developing fuel cells since about 1996 with vehicles such as the RAV 4 FCEV-hybrid (metal hydride, 1996), RAV 4 FCEV (methanol, 1997), FCHV-3 (metal hydride, 2001), FCHV-4 (compressed  $H_2$ , 2001), and FCHV-5 (reformed gasoline, 2001). Their efforts have resulted in the development of the latest Toyota Fuel-Cell Hybrid Vehicle (FCHV), some

of which are being tested daily at the University of California in Davis and Irvine. Since 2001, a fleet of 25 FCHVs has accumulated more than 100,000 miles. In 2002, Toyota began limited marketing of the hydrogen-powered TOYOTA FCHV (fuel cell hybrid vehicle) in the USA and Japan [28]. Toyota FCHVs have also been successfully tested under subzero conditions. In real-world driving tests carried out in 2008 in collaboration with the US DOE, Savannah River National Laboratory, and National Renewable Energy Laboratory (NREL), the FCHV-adv averaged the equivalent of  $\sim 68$  mpg achieving a range of  $\sim 430$  miles on a single fill of compressed (70 MPa) hydrogen gas. Figure 6 depicts images



**Polymer Electrolyte Membrane (PEM) Fuel Cells: Automotive Applications, Fig. 4** Advancements in the development of the fuel cell stacks designed at General Motors from 1997 to 2004 is depicted [22]



**Polymer Electrolyte Membrane (PEM) Fuel Cells: Automotive Applications, Fig. 5** Photograph of fifth generation of General Motors PEMFC stack and system [23]

of Toyota’s FCHV and an under the hood look at their PEMFC stack [29]. At this time (2017), Toyota has released a commercial FCEV the Toyota Mirai that can be purchased (~USD57,500) in Japan and California. The Toyota Mirai is now available for purchase for \$57,500 with a 312 miles per fill, and 5 mins to refill. The fuel tank consists of a carbon fiber wrapped, polymer lined tank built to

absorb five times the crash energy of steel. About 5 kg of hydrogen is stored at 70 MPa. The fuel consumption is rated at 67 mpg combined. The vehicle has a cold start capability of -30 °C. The vehicle is warranted for 8 years/100,000 miles on key components.

The key specifications are as follows:

Name	Toyota fuel cell stack
Fuel cell stack type	Solid polymer electrolyte fuel cell
Humidification system	Internal circulation system (humidifier-less)
Power output	153 HP (114 kW) MAX
Output density by volume	3.1 kW/L
Output density by weight	2.0 kW/kg
Cell number of cells in one stack	370 (single-line stacking)
Thickness	1.34 mm
Weight	102 g
Flow channel	3D fine-mesh flow field (cathode)
Emission rating	Zero emissions vehicle (ZEV)

**Polymer Electrolyte Membrane (PEM) Fuel Cells: Automotive Applications,**

**Fig. 6** Images of Toyota's FCHV-adv installed with their PEMFC stack [29]



Motor type	AC synchronous electric generator
Power output	151 HP (113 kW) MAX
Peak torque	247 lb-ft (335 Nm)
Storage method	Carbon fiber reinforced tanks
Number of tanks	2

### Nissan

Nissan's foray into the development of FCV technology started in 1996 in collaboration with various stack development partners such as Ballard and UTC Fuel Cells. In 1999, testing of a methanol-reforming fuel cell was initiated and in 2000 Nissan participated in the California Fuel-Cell Partnership (CaFP). Since 2004, Nissan has developed and used an in-house PEMFC stack in their FCVs. Their 2005 FCV employs 70 MPa hydrogen fuel tanks that allow the X-Trail FCV to have a driving range of about 300 miles. Figure 7 depicts the timeline for FCV development at Nissan along with metrics of driving range and acceleration time [30]. The range of their current generation vehicle is ~500 km (310 miles) and is comparable to a similar ICE powered vehicle. In 2007, they have developed a new generation of stacks that have significantly lower catalyst loadings, improved durability, high-rated power of 130 kW, and a volumetric power density approaching 2 kW/L. Specifications of Nissan's 2005 model FCV are detailed in Fig. 8.

### Honda

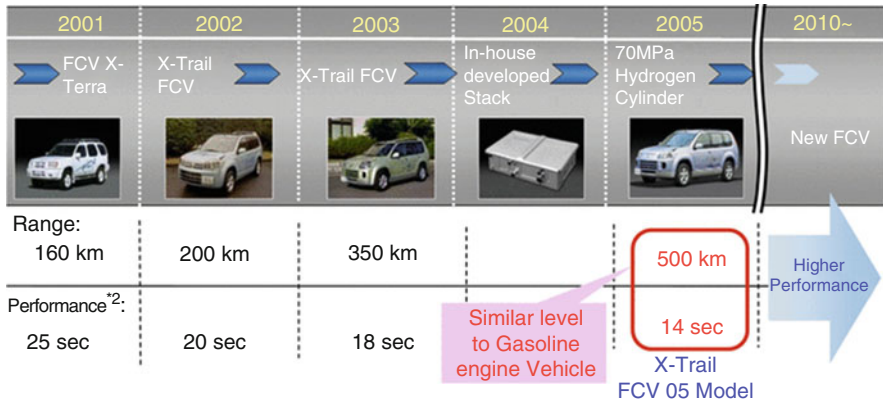
A brief timeline for the development of FCVs by Honda is summarized below. Honda initially employed various 60–85 kW Ballard stacks in

their initial FCVs such as the FCX-V1 (metal hydride, 1999), FCX-V2 (methanol, 1999), FCX-V3 (compressed H<sub>2</sub>, 2000), FCX-V4 with ultra-capacitors (compressed H<sub>2</sub>, 2001), and the FCX (compressed H<sub>2</sub>, 2002) vehicle that was leased in Los Angeles.

The US City of Los Angeles became the first FCX customer, leasing the first of five Honda FCX models for fleet use. In 2003, a next-generation fuel cell stack capable of power generation at temperatures as low as  $-20\text{ }^{\circ}\text{C}$  was announced. In 2005, Honda introduced the second-generation FCX and the first to be powered by a Honda FC stack. FCX Clarity FCEV, a dedicated platform hydrogen fuel cell vehicle, debuted at the LA Auto Show; the new stack was 20% smaller and 30% lighter than its previous generation. Since 2008, FCX Clarity FCEV has been made available as a leased vehicle for consumer use [31].

Some of the interesting aspects of the Honda fuel cell stack are the so-called V-Flow stack configuration that claims easy drainage of water, higher cell stability, aromatic electrolytic membrane, improved thermal management, and improved packaging. Honda has also reported the use of specialized coatings with impregnated electrical contacts on their bipolar plates that reduced the contact resistance while being corrosion resistant. Figure 9a depicts the conventional stack assembly and Fig. 9b and c illustrate their improved efficient stack packaging design. Honda has recently a commercially leasable FCEV, the 2018 Clarity (174 hp) that has a 366 mile EPA-range rating and can be refueled in 3–5 mins.





**Polymer Electrolyte Membrane (PEM) Fuel Cells: Automotive Applications, Fig. 7** Timeline for FCV development at Nissan along with metrics of driving range and 0–100 kmph acceleration time [30]

The 2017 Honda Clarity is also available for commercial sale and has the following key specs:

<i>Engineering</i>	Clarity fuel cell
Proton electrolyte fuel cell (PEFC)	•
Operating range	−22 °F–221 °F
Power output	103 kW
Size	33 L
Weight	114 lbs
Lithium-ion battery	•
Output	346 volts
AC permanent-magnet synchronous electric motor	•
Horsepower (SAE net)	174 @ 4501–9028 rpm
Torque (SAE net)	221 lb-ft @ 0–3500 rpm
<i>EPA mileage ratings<sup>2</sup>/fuel</i>	Clarity fuel cell
5w?>Miles-per-gallon equivalent (MPGe), (city/highway/combined)	69 / 67 / 68
Driving range rating	366
Fuel tank capacity	5.46 kg
Fuel tank pressure	70 MPa / 10,000 psi
Required fuel	Compressed gaseous hydrogen

### Automotive PEMFCS

In this section, the operational modes that fuel cell stacks are subjected to; the 2015 performance, cost, and durability targets that fuel cell technology must achieve; and recent advancements made

by automotive companies toward achieving the targets for commercialization are discussed.

### Operational Modes of Automotive PEMFCS

Unlike residential and stationary fuel cells, automotive PEMFCs undergo the entire slew of aggressive variable loads and environmental conditions that are typically experienced by conventional ICEs. The modes of operation of an automotive PEMFC can be simplified to the following [32]: (1) Idling/low load, (2) acceleration-deceleration/load cycling, (3) start-up shutdown, (4) cold temperatures/freeze-thaw cycles, and (5) contamination/impurities from the environments and cell degradation products. The impact of these modes of operation on the PEMFC stack is briefly discussed below. Unless otherwise specified, the discussion assumes a Pt nanoparticle-based electrocatalyst on a high-surface-area carbon black support, a perfluorosulfonic acid membrane, hydrogen flow on the anode, air flow on the cathode with the reactants partially humidified at the inlet. Testing is performed on a variety of platforms such as liquid electrolyte-half-cells (~0.198 cm<sup>2</sup>), subscale fuel cells (25–50 cm<sup>2</sup>), and full-size single cells or short stacks having active areas as high as 400 cm<sup>2</sup>. The basic diagnostics techniques and characterization of fuel cell components can be found detailed in the literature [33–35].

#### Idling/Low Load

When a vehicle in operation is at rest, for example, at a stop light, the current drawn by the fuel cell

stack is low; essentially power is drawn by the auxiliary equipment in the vehicle. At such low current densities, the cathode potential is high and may approach the open circuit voltage (OCV). Although the thermodynamic reversible potential at 80 °C is about 1.18 V, leakage currents (few mA/cm<sup>2</sup>) especially due to hydrogen crossover across the (~20–50 μm thick) membrane and electronic shorting lower the OCV to about 0.95 V. This high cathode potential leads to several degradation phenomena in the cells. The

Pt-based catalyst dissolves at these potentials and diffuses toward the anode through the membrane and within 48 h forms a band inside the membrane as shown in Fig. 10 [36]. This Pt band formed in the membrane induces chemical degradation of the membrane itself due to formation of OH, hydrogen peroxide, and peroxy radicals resulting in membrane thinning. The chemical degradation is accelerated under low RH conditions and higher temperatures. Degradation of the membrane leads to an increase in hydrogen crossover and can result

Classification		X-TRAIL FCV
Vehicle	Overall length / width / height (mm)	4485/1770/1745
	Curb Weight (kg)	1790(1860)
	Seating capacity	5
	Top speed (km/h)	150
	Cruising range (km)	Over 370 (over 500)
Motor	Type	<b>Co-axial motor integrated with reduction gear</b>
	Max. power (kw)	<b>90</b>
Fuel Cell Stack	Fuel cell	Polymer electrolyte type
	Max. power (kw)	<b>90</b>
	Supplier	In-house
Battery	Type	<b>Compact Lithium-ion Battery</b>
Fueling System	Fuel type	Compressed hydrogen gas
	Max. pressure (MPa)	35 (70)

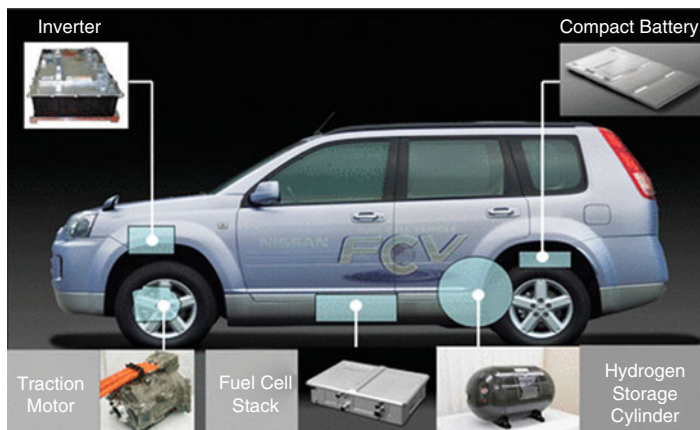
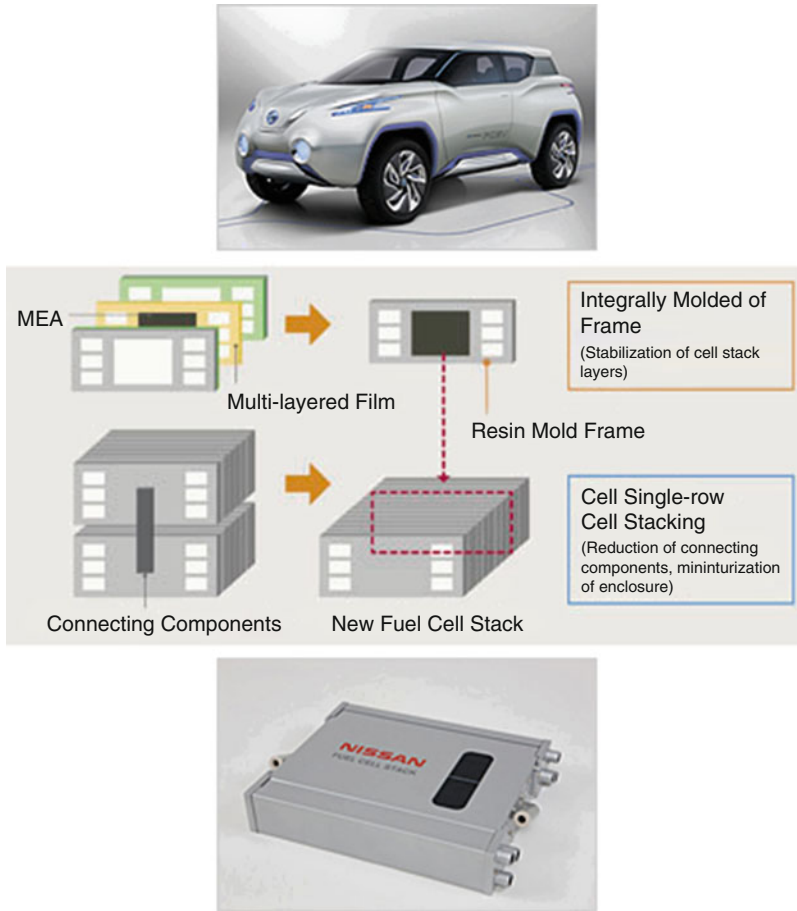


Fig. 8 (continued)



**Polymer Electrolyte Membrane (PEM) Fuel Cells: Automotive Applications, Fig. 8** Detailed specifications of Nissan 2005 X-Trail FCV along with a layout of

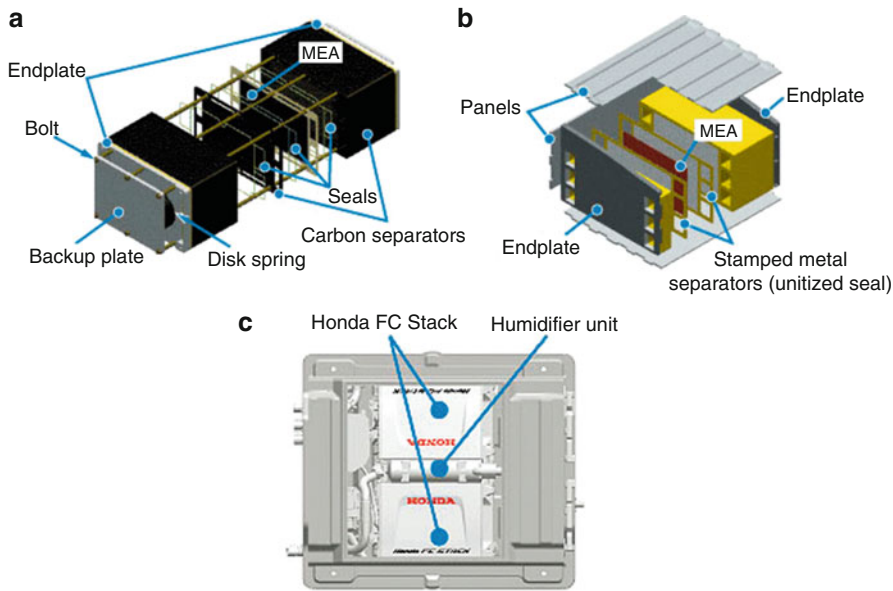
components of the fuel cell stack system. Next generation Nissan Terra SUV concept along with improvements to stack technology is also shown [30]

in thinning, pinholes, and eventually catastrophic failure. Figure 11 shows the fluoride and sulfate elution from the exhaust water of a fuel cell during and after OCV testing [37]. About 6% of the fluorine in the membrane is released during 48 h of OCV hold. If the carbon support (on which the catalyst is dispersed) has a high surface area and therefore susceptible to corrosion, it may first become hydrophilic and over time corrode and oxidize leading to some Pt nanoparticle agglomeration which also leads to cell performance loss. If the fuel cell is a hybrid with a 10–20 kW NiMH or Li-ion battery, it may be possible to minimize the deleterious effects of high cathode potentials by using appropriate system controls and algorithms to lower the high potentials.

**Acceleration/Deceleration**

PEMFC stacks in vehicles are subject to variable power demands that depend on environmental conditions such as the grade of the road as well as the driving behavior of the vehicle operator. As the load changes, the current drawn from the fuel cell and hence the cell voltage changes resulting in the cell being subject to load cycles or potential cycles. Thus, the fuel cell is subject to all kinds of potential cycles with the widest potential range being about 0.60–0.95 V [32, 35, 38–41]. The upper potential corresponds roughly to OCV/idling and the lowest potential corresponds to the potential at peak power (about 0.6 V and a few amperes per square centimeter). The upper limit of the voltage is determined by





**Polymer Electrolyte Membrane (PEM) Fuel Cells: Automotive Applications, Fig. 9** (a) Illustrates conventional stack package design of previous configurations

and (b, c) illustrate Honda's new efficient stack package design [31]

the choice of the membrane (thickness/permeability) and in part by the design of the vehicle system controls. Although peak power is drawn from the stack for only  $\sim 5\%$  of the time, it is necessary for the stack to have an electrical efficiency of  $\sim 55\%$  (to be competitive with ICEs); also, the size of the stack is partly determined based on the peak power point.

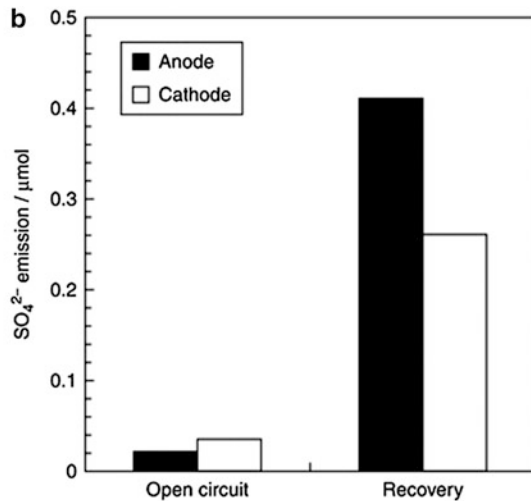
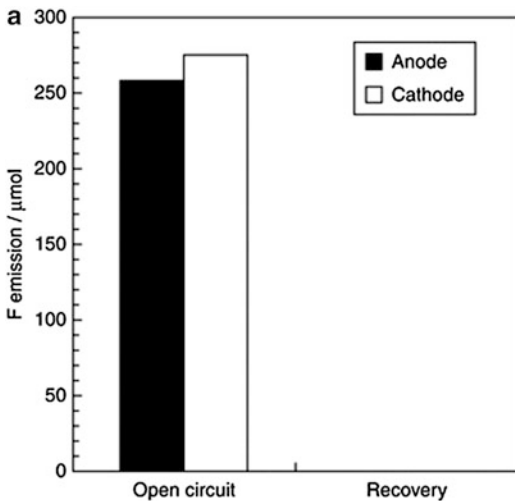
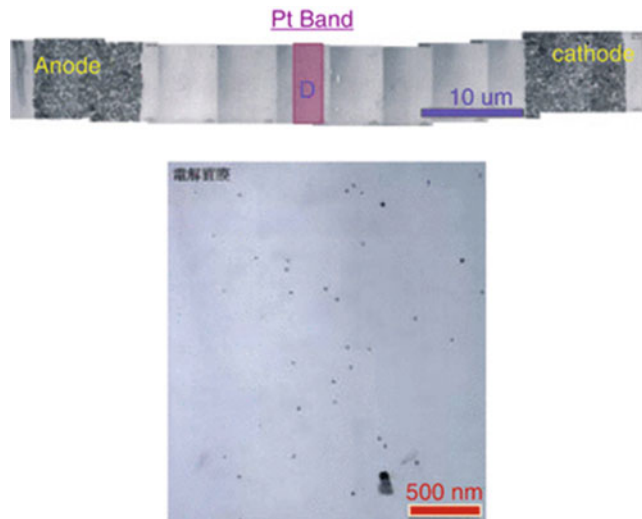
A number of automotive drive cycles (FUDS cycle, US06, NEDC, and Japanese 10–15 mode drive cycles, etc.) are available to represent the statistical usage of a vehicle and are used to determine the mileage of ICE vehicles. Figure 12 is an example of the Japanese 10–15 drive cycle and Fig. 13 an example of the US06 drive cycle. These drive cycles can be systematically converted into voltage-time profiles and applied to estimate the degradation rates of stacks under simulated driving conditions. A generic individual cycle profile is shown in Fig. 14 that represents a superset of all possible profiles [32]. The five elements of the profile that can be varied are: (1) duration at low potential, (2) duration of the ramp-up from low to high potential (or ramp-up rate), (3) duration at high potential, (4) duration of the ramp-down

from high to low potential (or ramp-down rate), and (5) duration at low potential. The high and low potentials can have infinitely different values between the upper and lower limit in the range 0.6–0.95 V.

It has been determined through a large number of studies that the widest potential cycles of 0.60–0.95 V cause the most degradation of the cathode catalyst layer. Automotives typically undergo 300,000 such cycles over their 5,000 h/10 years lifetime. At potentials above 0.95 V, the Pt surface is highly covered with oxide species while below 0.6 V it is almost free of oxide species as is observable from a typical cyclic voltammogram of platinum in acids or in a PEMFC. Thus, the process of cycling in the range 0.60–0.95 V results in the growth (oxidation) and stripping (reduction) of oxide species on the surface and prevents the formation of a stable passivating film. (A more conservative potential regime of 0.70–0.90 corresponding to the  $i_{RFree}$  potential that the catalyst layer experiences is sometimes selected.) Figure 15 depicts both the enhanced activity of PtCo/C electrocatalysts over Pt/C [42] and the surface area

**Polymer Electrolyte Membrane (PEM) Fuel Cells: Automotive Applications,**

**Fig. 10** Formation of a Pt band (with magnified view of the band) in the membrane when held under OCV conditions over a period of 100 h [36]



**Polymer Electrolyte Membrane (PEM) Fuel Cells: Automotive Applications, Fig. 11** Fluoride emission during OCV hold test (6% of fluorine in the membrane is

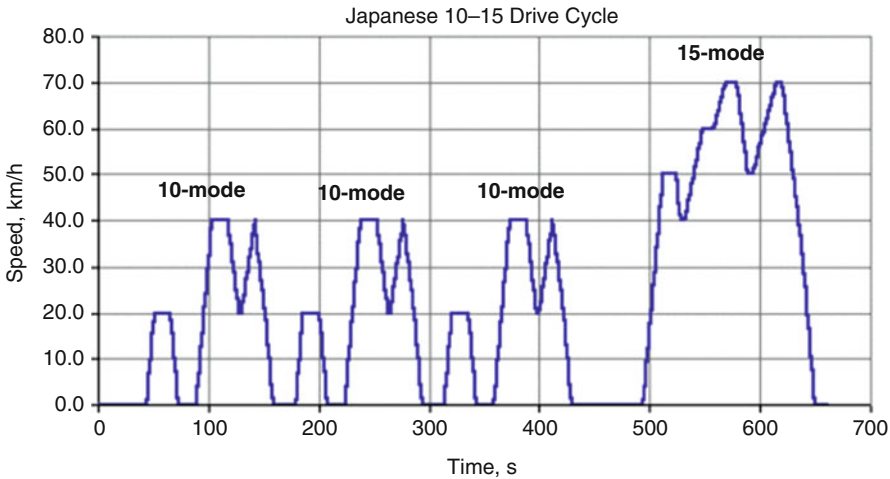
released over a 48 h hold) and sulfate emissions during recovery operation [37]

loss during cycling [39]. Based on recent research, it appears that exposure of bare (oxide-free) Pt to high potentials during the anodic portion of a scan in a cycle has a high impact on the Pt dissolution and degradation of the cathode catalyst layer. Again, practical methods that involve limiting the number of large cycles with the help of a battery in a hybridized system mitigate the losses partially. Pt-based alloys, heat-treated Pt, and other modifications to

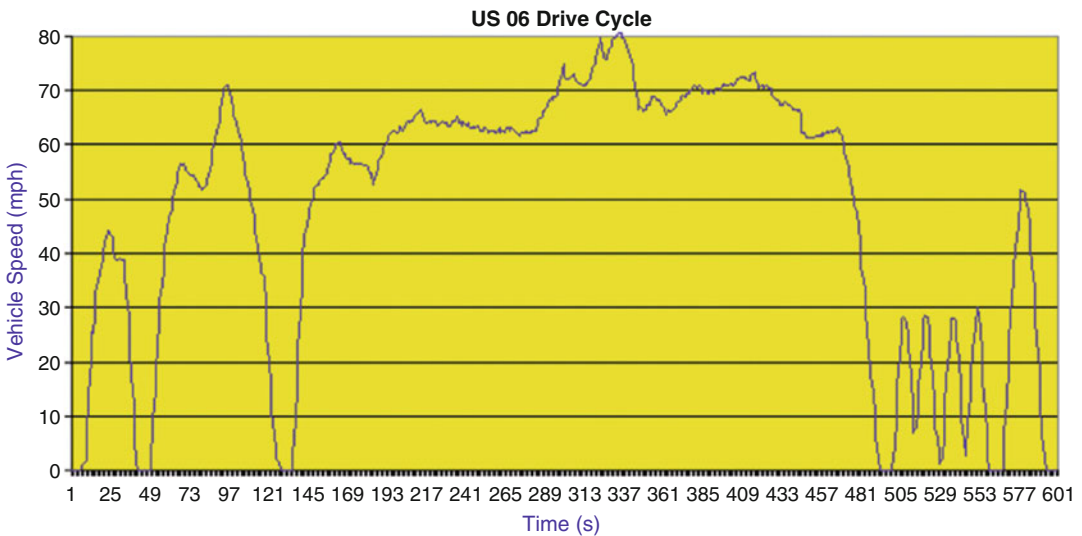
the catalyst layer also provide partial material solutions that restrict the losses.

**Start-Up/Shutdown**

Automotive PEMFC stacks are shut down and started a number of times depending on the needs of the driver; the number of such occurrences is about ~30,000 over the stack life. When an automotive PEMFC stack is allowed to rest for a period of time, both the anode and



**Polymer Electrolyte Membrane (PEM) Fuel Cells: Automotive Applications, Fig. 12** Japanese 10–15 drive cycle for automobiles



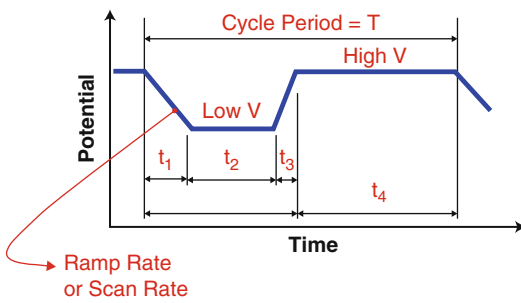
**Polymer Electrolyte Membrane (PEM) Fuel Cells: Automotive Applications, Fig. 13** US 06 drive cycle for automobiles

cathode chambers get filled with ambient air from the atmosphere. When such a stack filled with air is restarted and hydrogen turned on to flow on the anode side, it pushes out the air leading to the formation of a “H<sub>2</sub>-air front.” It was discovered around 2001 that frequent starting and shutting down of fuel cells resulted in a peculiar phenomenon where the cathode becomes subject to potential transients as high as 1.5 V [43–45]. At these high potentials, the

carbon support of the cathode catalyst layer undergoes precipitous corrosion to carbon dioxide. Loss of the carbon leads to agglomeration of the Pt nanoparticles resulting in a loss in catalyst surface area, severe mass-transport issues, and a precipitous loss in cell performance. No losses are observed if the start-up takes place within a short time of shutdown as long as there is residual hydrogen in the anode of the fuel cell; thus the time interval between

start-up and shutdown is an important parameter governing overall degradation rate [46].

Figure 16 below is a schematic of the start-up/shutdown phenomenon and the reactions that occur in the anode and cathode catalyst layers. Interestingly, no damage occurs on the anode-side catalyst layer. Figure 17 depicts the degraded cross section of an MEA (cathode facing up) after ~50 start-up/shutdown cycles. Over the last decade, several mitigation techniques that involve controlling the procedure at start-up and shutdown have been reported and losses have been minimized, albeit at the expense of system

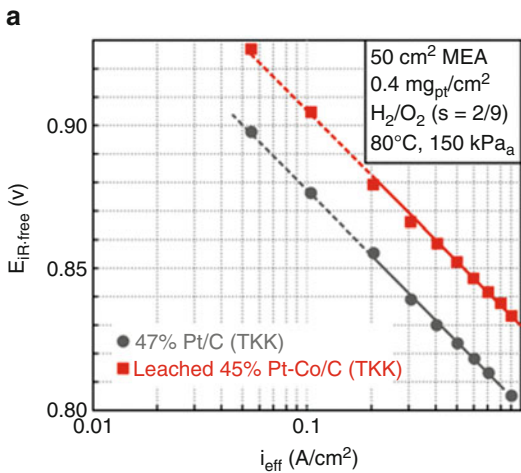


**Polymer Electrolyte Membrane (PEM) Fuel Cells: Automotive Applications, Fig. 14** Schematic representation of an arbitrary cycle extracted from a complex drive cycle illustrating the various parameters that can be varied in the cycle profile

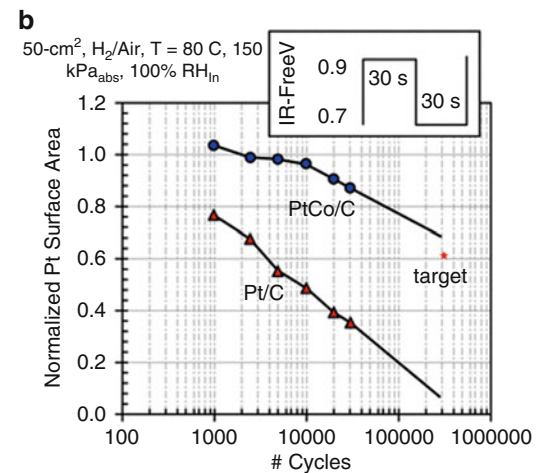
complexity. Some of the mitigating solutions include: (1) shorting the stack to minimize the potential spike, (2) purging the anode using high flows of gases to minimize the H<sub>2</sub>-air front time (to less than 0.5 s), (3) drying the stack after shutdown, (4) lowering the Pt loading on the anode side to lower the ORR with a consequent suppression of the COR on the cathode, and (5) lengthening the time for which residual hydrogen remains in the anode, etc. The search for more durable corrosion-resistant supports to replace carbon is underway so that the fuel cell system can be simplified. Oxides, nitrides, carbides, of tungsten, titanium, etc., are promising candidates but they often suffer from poor electronic conductivity, lower surface area compared to carbon blacks, and it can be difficult to disperse Pt nanoparticles on them [47].

**Cold Temperatures**

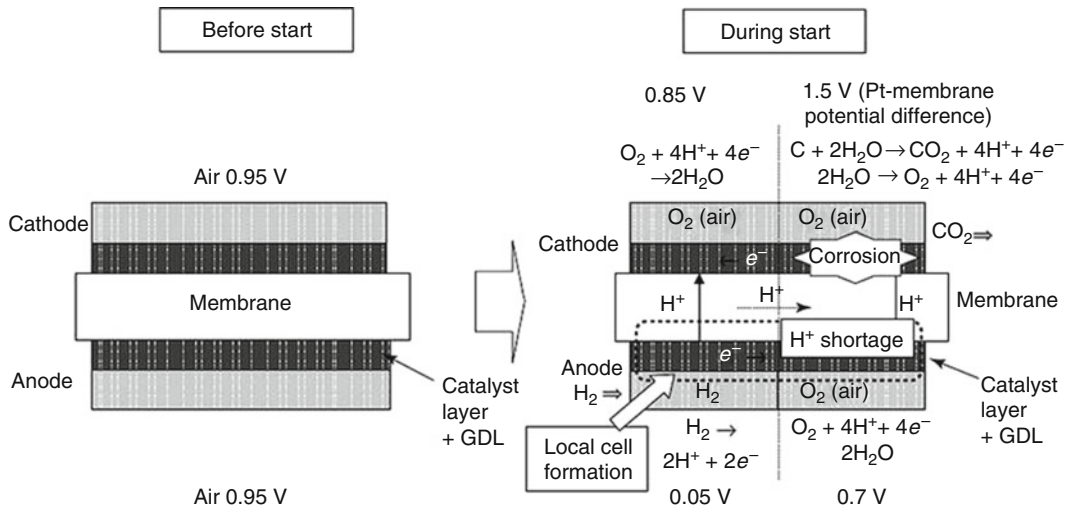
Automotive PEMFCs must be capable of enduring cold weather conditions such as freezing temperatures as low as -40 °C. Even conventional ICE vehicles need help from engine block warmers, etc., in order to be able to start-up from subzero conditions. Under subzero conditions, an operating fuel cell will generate sufficient heat to prevent water from freezing and will likely show



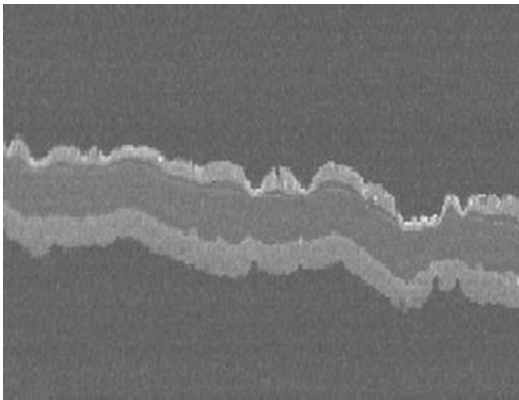
**Polymer Electrolyte Membrane (PEM) Fuel Cells: Automotive Applications, Fig. 15** (a) Enhanced activity (×3) under H<sub>2</sub>/O<sub>2</sub> for pre-leached PtCo/C electrocatalysts compared to Pt/C as tested in subscale fuel cells



[42]; (b) electrochemical area loss for Pt/C versus PtCo/C catalysts over 10,000 cycles in subscale fuel cells illustrates lower degradation for the PtCo/C [39]



**Polymer Electrolyte Membrane (PEM) Fuel Cells: Automotive Applications, Fig. 16** Schematic of start-up/shutdown phenomenon before and during passage of the  $H_2$ -Air front through the anode chamber [43–46]



**Polymer Electrolyte Membrane (PEM) Fuel Cells: Automotive Applications, Fig. 17** SEM cross section of an MEA with the cathode (top) layer showing severe corrosion and degradation after about 50 uncontrolled start-up/shutdown cycles. A light band is also observed near the cathode-membrane interface due to the cycling of potential that takes place between 1 and 1.5 V

little or no loss in performance. The problem arises when a PEMFC has been idle for a long period of time under subzero conditions and is required to start-up.

PEMFCs have the added challenge of liquid water in the system that can freeze, block channels and gas flow paths, and form icicles that may penetrate through the polymer membrane and cause damage. Blockage of channels can lead to

fuel starvation, carbon corrosion, and degradation of the anode/cathode catalyst layer. The use of insulation, heaters, and antifreeze coolants are helpful for short periods of time, but the residual water within the fuel cell will eventually freeze forming ice. The catalyst layer and the diffusion media are especially susceptible to repeated freeze-thaw cycles due to their porous nature and the inherent presence of water (loosely bound and free water) that can expand and contract leading to a disruption of the porous structure that is so important for mass transport. Significant disconnection of the catalyst particles from the ionomer and carbon support could result in degradation in performance due to the loss in protonic and electronic interfacial contact.

Elimination or minimization of the water in the cells by purging with gases or vacuum drying prior to shutting down the stack is a general approach that has been found to be effective. In short, “keeping the stack warm” and “removal of water” are essentially the two main strategies to counter the cold start issue. The principal targets that automotive PEMFC stacks are required to meet are the ability to start unassisted from  $-40^\circ\text{C}$  and a cold start-up time to 50% of rated power in 30 s (from  $-20^\circ\text{C}$ ) with a start-up energy consumption of  $<5$  MJ [48]. Most automotive manufacturers have claimed to have

achieved the targets although research to understand the phenomenon in detail continues.

#### Contamination/Impurities

PEMFCs are very clean systems and act as filters for impurities introduced from ambient air, fuel used, and even degradation products from the cell materials. Both the membrane and the catalyst are susceptible to contamination and poisoning. Electrode degradation of PEMFCs can occur as a result of various impurities found in the fuel feed, air stream, as well as corrosion by-products from fuel cell components such as the bipolar plate, catalysts, or membrane.

Hydrogen for PEMFCs can come from various sources including reformed fossil fuels. Therefore, depending on the reforming technique and degree of posttreatment, small amounts of contaminants such as CO, CO<sub>2</sub>, NH<sub>3</sub>, and H<sub>2</sub>S are expected to be present in the fuel stream [49]. Trade-offs in the level of impurities are unavoidable since ultrahigh purification would lead to elevated costs of hydrogen. The US FreedomCAR technology team has arrived at preliminary fuel mixture specifications that include: >99.9% H<sub>2</sub>, 10 ppb H<sub>2</sub>S, 0.1 ppm CO, 5 ppm CO<sub>2</sub>, and 1 ppm NH<sub>3</sub>. Hydrocarbons such as methane, benzene, and toluene are other common impurity by-products from reforming processes.

Atmospheric air contains 78% nitrogen and 20% oxygen with the remainder being a number of trace gases and particulates depending on the local air quality. Pollutants found in the atmosphere include nitrogen oxides (NO and NO<sub>x</sub>), hydrocarbons, carbon monoxide (CO), ozone, sulfur dioxide (SO<sub>2</sub>), fine primary and secondary particulate matter, and chloride salts from the ocean and deicers. Chloride anions adsorb on Pt, occupy reaction sites, and significantly lower the ORR activity; fortuitously, the loss is recoverable simply by flushing out the anions with generated water. The degradation of performance due to 2.5 and 5 ppm SO<sub>2</sub> in the air stream was reported to be about 50% and 80%, respectively, by Mohtadi et al. [50]. The degradation is due to chemisorption of sulfur species on the Pt catalyst, and oxidation by the application of high potentials (CV) reversed the degradation but operation

under normal potentials did not [51]. The poisoning mechanism by NO<sub>2</sub> was reported to be dependent on the time of exposure rather than bulk concentration and could apparently be reversed by operation under clean air for 24 h. Figure 18 depicts the loss in performance of a subscale fuel cell as a result of contamination of the catalyst in the presence of SO<sub>2</sub>, H<sub>2</sub>S, NO, NO<sub>2</sub>, and NH<sub>3</sub> [51]. The PEM is also easily contaminated by cationic impurities that may enter the stack through water, dissolved catalyst cations [52], as well as corrosion products from the bipolar plate. The loss in cell performance is fairly severe due to the lowering of the conductivity of the membrane.

#### The Status and Targets for Automotive PEMFC Commercialization

The overall status and targets for automotive PEMFC systems as well as hydrogen production, delivery, and storage are outlined in Table 1. All of the targets need to be attained for successful commercialization of fuel cell vehicles.

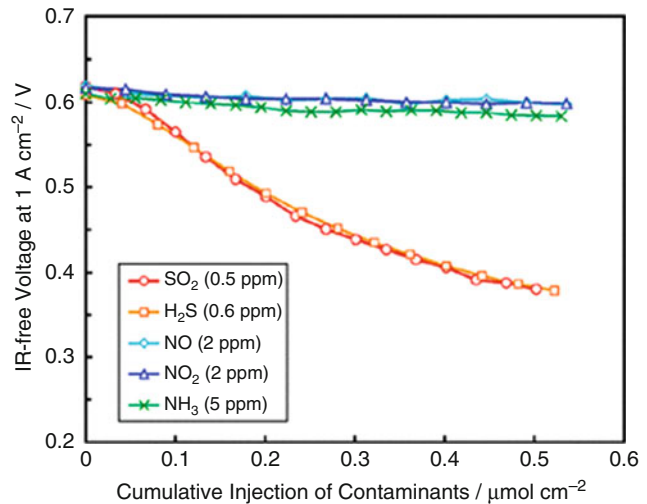
The performance, durability, and cost of PEMFC system and stacks for automobiles are approaching levels such that major automotive manufacturers have projected that commercialization will commence around 2015. The US DOE has had cost analysis conducted by independent organizations and estimates assuming 500,000 units/year indicate that system cost has been lowered from \$275/kW in 2002 to \$73/kW in 2008 [53, 54]. The target for PEMFC system cost in 2015 is \$30/kW. The durability of stacks under automotive conditions is currently around 2,500–3,000 h with the target in 2015 being 5,000 h.

In order to achieve commercialization in 2015, the targets of performance, durability, and cost of the fuel cell components (catalyst, membrane, diffusion media, bipolar plates, etc.) and the system (thermal, fuel, air, and water management, and balance of plant) have to be met simultaneously. For example, high durability can easily be achieved by utilizing high loadings of Pt catalyst, corrosion-resistant bipolar plates with expensive coatings, etc., but this would violate the cost targets. It is required to maintain the performance of PEMFC stacks of today while at the same time lower the precious metal catalyst loadings by a



**Polymer Electrolyte Membrane (PEM) Fuel Cells: Automotive Applications,**

**Fig. 18** The impact of several air contaminants on a fuel cell operated at  $1 \text{ A/cm}^2$  [51]



**Polymer Electrolyte Membrane (PEM) Fuel Cells: Automotive Applications, Table 1** Overall status and targets for PEMFC systems, hydrogen storage, production, and delivery [48]

	Status	Target
Fuel cell system cost	\$61/kW	\$30/kW
Fuel cell system durability	2,000–3,000 h	5,000 h
Hydrogen production	\$3–\$12/gge	\$2–\$3/gge
Hydrogen delivery	\$2.30–\$3.30/gge	\$1/gge
Hydrogen storage gravimetric	3.0–6.5 wt.%	7.5 wt.%
Hydrogen storage volumetric	15–50 g/L	70 g/L
Hydrogen storage cost	\$15–\$23/kWh	\$2/kWh

factor of 4–10 and increase the stack durability by a factor of  $\sim 2$ .

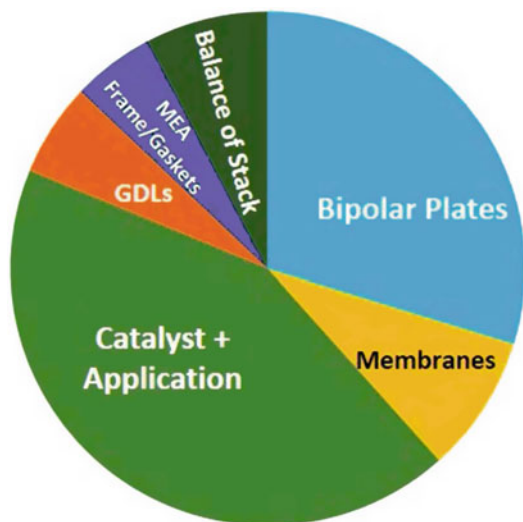
#### Basis for Targets

The targets of performance and durability of PEMFC stacks are loosely based on that of IC engines used in automobiles today. Durability targets are being addressed by organizations such as the US DOE's Office of Energy Efficiency and Renewable Energy's Hydrogen Fuel Cells and Infrastructure (HFCIT) program in close association with national laboratories, universities,

and industry [48], the New Energy and Industrial Technology Development Organization (NEDO) in Japan [55], and the European Hydrogen and Fuel Cell Technology Platform (HFP) and Implementation Panel (IP) in Europe. The Fuel Cell Commercialization Conference of Japan (FCCJ) has also published a booklet defining performance, durability, and cost targets in collaboration with Nissan, Toyota, and Honda and a summary has been reported elsewhere [56]. Overall, the general 2015 target for fuel cell stack durability (in cars) is roughly defined to be 5,000 h (150,000 driven miles) at the end of which  $\sim 10\%$  performance degradation is allowable. This includes  $\sim 30,000$  cycles of start-up/shutdown,  $\sim 300,000$  cycles of wide span load, and hours of idling. So far  $\sim 3,000$  h of stack life with low degradation rates has been demonstrated and steady progress is being made toward the final goal. An additional durability enhancement by a factor of  $< 2\times$  is needed for attaining the commercialization targets of 2015.

The cost breakdown of PEMFC systems is as illustrated in Fig. 19: The most expensive component (22% of system cost) is the precious metal ( $\sim \$40/\text{g}_{\text{Pt}}$ ) catalyst used on the anode and cathode of each cell. Figure 20 shows the estimated reduction in cost of PEMFC stack system that has been achieved between 2002 and 2009. Figure 21 charts the breakdown of cost by subsystem and component for automotive PEMFC stacks.





**Polymer Electrolyte Membrane (PEM) Fuel Cells: Automotive Applications, Fig. 19** Cost structure for automotive PEMFC stack system [53, 54]

**Electrocatalyst Targets** The amount of Pt currently being used in ultra low emission IC engine automobiles (Pt, Pd, Rh, etc.) used in automotive catalytic converters can be as high as 6–10 g. This provides a justification for limiting the amount of Pt in a stack to  $\sim 10$  g (in a typical 100 kW stack) or  $\sim 0.1$  g<sub>Pt</sub>/kW. Recycling of Pt used in fuel cells has been evaluated extensively by Tiax and the conclusion is that more than 90% of the Pt in fuel cell stacks is recyclable. Table 2 outlines the latest targets for automotive PEMFC electrocatalyst activity and costs.

**Membrane Targets** Today's membranes show excellent protonic conductivity ( $\sim 100$  mS/cm) at 100% RH and temperatures below 80 °C. PFSA membranes have been improved over the last few years to also achieve durability values that are approaching the target values of 5,000 h. These improvements involve modification of PFSA membranes by varying the casting conditions, thermal pretreatments, forming composites, employing reinforcements, using different lengths of pendant side chains, fluorinating the end groups, etc. In particular, micro-reinforced membranes (such as those from W. L. Gore [57]) allow for the use of thinner membranes that result in the

use of less ionomer, improve the back diffusion of water, lower the protonic resistance, and generally result in higher power density fuel cells.

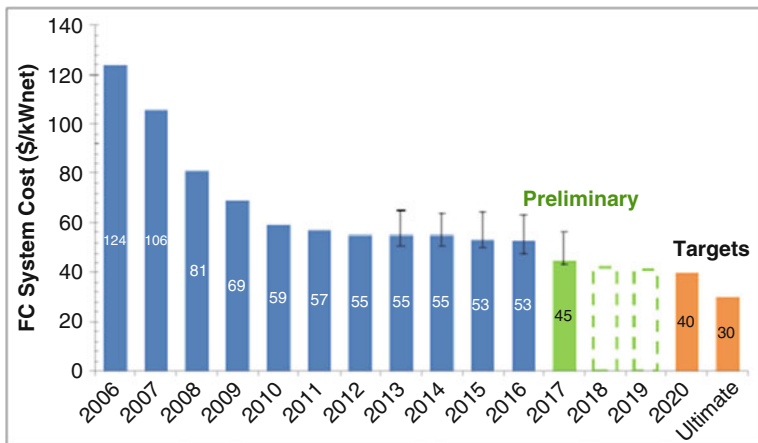
For automotive operation, it would be helpful to have a membrane material that could function with high proton conductivity at a low RH and higher temperatures. It would allow for simplified humidification systems and improved heat rejection (smaller radiator) and improved cell performance (mass transport) is expected due to the absence of liquid water. Membranes that exhibit sufficient conductivity at high temperature by retaining water necessitate the use of higher stack pressures (and higher parasitic compressor-related losses) especially as the temperature exceeds the boiling point of water at ambient pressure.

A cheaper hydrocarbon membrane is also desirable. Hydrocarbon membranes prepared from aromatic block copolymers constituted of alternating rigid sulfonic acid segments with hydrophobic polymeric units that are flexible have been reported. The unique morphology of the membrane provides comparable chemical stability as PFSA commercial membranes with high durability and a wide operating temperature range. Such membranes are already being used by automakers such as Honda. Other hydrocarbon-based membranes that are being actively researched include the use of di-sulfonated poly (arylene ether) sequenced block and random copolymers [58].

The key requirements for survivability and durability of membranes used in PEMFCs are mechanical durability (RH cycling, subzero start-up, shorting) and chemical durability (OCV holds). Survivability refers to the ability of the membrane to withstand operating conditions without the formation of pinholes that would lead to catastrophic hydrogen crossover and stack failure. Under subzero conditions, membranes can fail if the stack is not designed to eliminate most of the water in the flow fields to prevent formation of ice that can penetrate and damage the membrane on start-up. Durability refers to the slow thinning of the membrane over thousands of hours resulting in increased hydrogen crossover, membrane thinning, and

**Fuel Cell Cost Status**

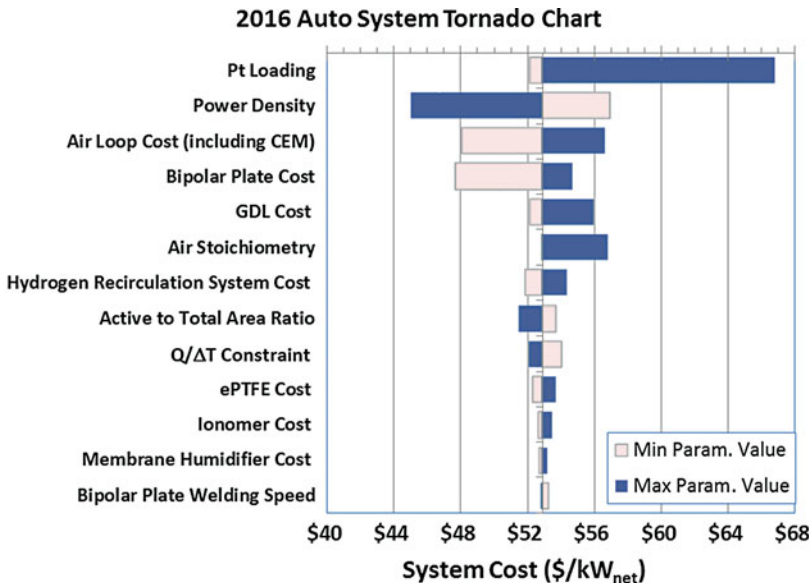
- **\$53/kW\*** for 500,000 units/year
- **\$59/kW\*** for 100,000 units/year
- **\$230/kW†** for currently commercialized technology at 1,000 units/year



**Polymer Electrolyte Membrane (PEM) Fuel Cells: Automotive Applications, Fig. 20** Reduction in cost of PEMFC stack system since 2002 and projected values and target for 2010 and 2015 [53]

**Polymer Electrolyte Membrane (PEM) Fuel Cells: Automotive Applications,**

**Fig. 21** Sensitivity of cost by subsystem and component for automotive PEMFC stacks [53]



consequent loss of cell performance. The membrane (restrained in a cell) is mechanically stressed (fatigue) when the fuel cell RH cycles between dry and wet conditions; thermal cycles also play a role. In the laboratory, tests have shown that nonreinforced PFSA membranes fail in a few hundred hours or ~6,000 cycles while reinforced membranes last as long as 1,000 h or 60,000 cycles. Shorting is a mechanical degradation leading to electronic leakage currents through the membrane that may occur

due to overcompression or penetrating irregularities from the catalyst layer or fibers of the diffusion medium. Shorting failures can be partially mitigated by using lower compression pressures (typically ~1,200 kPa), applying a coating of carbon black-based microporous layer (MPL) on the diffusion medium, etc. Chemical degradation of membranes is accelerated under OCV conditions where the potential is high and no water generated, as well as under generally low RH operation.

**Polymer Electrolyte Membrane (PEM) Fuel Cells: Automotive Applications, Table 2** Targets for automotive PEMFC electrocatalyst activity and costs. Mass Activity @ 0.90 V, H<sub>2</sub>/O<sub>2</sub>, 80 °C, P<sub>H<sub>2</sub></sub>, P<sub>O<sub>2</sub></sub> = 100 kPa (based on multiple sources)

Characteristic	Units	2015 Status	2020 Targets
Platinum group metal total content (both electrodes) <sup>a</sup>	g/kW (rated, <sup>b</sup> gross) @ 150 kPa	0.16 <sup>c,d</sup>	0.125
Platinum group metal (pgm) total loading (both electrodes) <sup>a</sup>	mg PGM/cm <sup>2</sup> electrode area	0.13 <sup>c</sup>	0.125
Mass activity <sup>c</sup>	A/mg PGM @ 900 mV <sub>IR-free</sub>	>0.5 <sup>f</sup>	0.44
Loss in initial catalytic activity <sup>c</sup>	% mass activity loss	66 <sup>c</sup>	<40
Loss in performance at 0.8 A/cm <sup>2,c</sup>	mV	13 <sup>c</sup>	<30
Electrocatalyst support stability <sup>g</sup>	% mass activity loss	41 <sup>h</sup>	<40
Loss in performance at 1.5 A/cm <sup>2,g</sup>	mV	65 <sup>h</sup>	<30
PGM-free catalyst activity	A/cm <sup>2</sup> @ 0.9 V <sub>IR-free</sub>	0.016 <sup>i</sup>	>0.044 <sup>j</sup>

<sup>a</sup>PGM content and loading targets may have to be lower to achieve system cost targets

<sup>b</sup>Rated power operating point depends on MEA temperature and is defined as the voltage at which  $V = 77.6 / (22.1 + T [^{\circ}\text{C}])$ , based on target of  $Q/\Delta T_i = 1.45 \text{ kW}/^{\circ}\text{C}$  and definition of  $Q/\Delta T_i$  from Table 3.4.4, with an approximation of MEA temperature as equal to stack coolant outlet temperature

<sup>c</sup>Steinbach et al. (3 M), "High-Performance, Durable, Low-Cost Membrane Electrode Assemblies for Transportation Applications," 2014 Annual Merit Review, [http://www.hydrogen.energy.gov/pdfs/review14/fc104\\_steinbach\\_2014\\_o.pdf](http://www.hydrogen.energy.gov/pdfs/review14/fc104_steinbach_2014_o.pdf)

<sup>d</sup>Based on MEA gross power at 150 kPa abs. Measured at 0.692 V and 90 °C, satisfying  $Q/\Delta T < 1.45 \text{ kW}/^{\circ}\text{C}$ . At 250 kPa abs status is 0.12 g/kW

<sup>e</sup>Measured using protocol in Table P.1

<sup>f</sup>Kongkanand et al. (General Motors). "High-Activity Dealloyed Catalysts," 2014 Annual Merit Review, [http://www.hydrogen.energy.gov/pdfs/review14/fc087\\_kongkanand\\_2014\\_o.pdf](http://www.hydrogen.energy.gov/pdfs/review14/fc087_kongkanand_2014_o.pdf)

<sup>g</sup>Measured using protocol in Table P.2

<sup>h</sup>B Popov et al. "Development of Ultra-low Doped-Pt Cathode Catalysts for PEM Fuel Cells," 2015 Annual Merit Review, [http://www.hydrogen.energy.gov/pdfs/review15/fc088\\_popov\\_2015\\_o.pdf](http://www.hydrogen.energy.gov/pdfs/review15/fc088_popov_2015_o.pdf)

<sup>i</sup>P. Zelenay (LANL). "Non-Precious Metal Fuel Cell Cathodes: Catalyst Development and Electrode Structure Design," 2016 Annual Merit Review, [https://www.hydrogen.energy.gov/pdfs/review16/fc107\\_zelenay\\_2016\\_o.pdf](https://www.hydrogen.energy.gov/pdfs/review16/fc107_zelenay_2016_o.pdf)

<sup>j</sup>Target is equivalent to PGM catalyst mass activity target of 0.44 A/mg<sub>PGM</sub> at 0.1 mg<sub>PGM</sub>/cm<sup>2</sup>

Chemical degradation of the membrane is measured in terms of the fluoride release rate (FRR in  $\text{g F}^{-}/\text{cm}^2\text{h}$ ) in the collected water; the FRR exhibits Arrhenius dependence with temperature in the range 50–120 °C. The FRR is of the order of  $1.0 \times 10^{-5}$  for typical membranes tested under OCV conditions and has been lowered with newer membranes to  $1.0 \times 10^{-7}$ . It should be noted that the mechanism of membrane degradation is not fully understood and is an area of intensive research. The two commonly invoked mechanisms are based on the assumption that hydrogen peroxide formed in the catalyst layer or at the Pt band in the membrane forms a hydroxyl radical which decomposes the membrane/ionomer by unzipping the less stable end groups or by scission of the main polymer chain. In actuality, mechanical and

chemical degradation occur simultaneously in fuel cells accelerating the failure of the membrane.

The targets for membrane performance and durability based on figures reported by Nissan, USDOE, and the FCCJ are very similar. In order to be able to design a system that can reject heat at peak power, the fuel cell stack needs to operate for short spurts of time at temperatures as high as 90–95 °C. At this time, most fuel cell stacks operate at about 80 °C due to the restrictions of system complexity, parasitic (compressor) losses, and humidification requirements. The membrane is targeted to operate at temperatures above 100 °C (preferably 120 °C) at RH <30% while exhibiting a membrane conductivity of >100 mS/cm. The durability targets are similar to that for the complete fuel cell and includes <10%

performance loss over 5,000 h/10 years of operation under automotive conditions that include start-up/shutdown, load cycling, freeze ( $-40\text{ }^{\circ}\text{C}$ ), and idling. The target cost of the membrane is  $\$10\text{--}20/\text{m}^2$  for production levels of 10 million  $\text{m}^2/\text{year}$ . More detailed membrane performance targets base on USDOE and other sources are detailed in Table 3.

**Bipolar Plate Targets** Graphite bipolar plates have been used for a long time and are still being used in some fuel cell stacks. Graphite has a very high electronic conductivity, low interfacial contact resistance (ICR), and high corrosion resistance.

Disadvantages of graphite bipolar plates are the high cost of material and machining, increased stack volume, high gas permeability, etc., although high volume manufacturability is somewhat better with polymer-carbon fiber and composite bipolar plates. Graphite-polymer composite plates have also been researched to improve the manufacturability of graphite plates while maintaining conductivity and stability with temperature. Bare metal plates do not have the disadvantages mentioned above but suffer from high ICR and poor corrosion resistance that can lead to metal dissolution and possible poisoning of the

**Polymer Electrolyte Membrane (PEM) Fuel Cells: Automotive Applications, Table 3** Targets for selected properties of automotive PEMFC membranes [48]

Characteristic	Units	2015 Status	2020 Targets
Maximum oxygen crossover <sup>a</sup>	$\text{mA}/\text{cm}^2$	2.4 <sup>b</sup>	2
Maximum hydrogen crossover <sup>a</sup>	$\text{mA}/\text{cm}^2$	1.1 <sup>c</sup>	2
Area specific proton resistance at:			
Maximum operating temperature and water partial pressures from 40–80 kPa	$\text{ohm cm}^2$	0.072 (120 $^{\circ}\text{C}$ , 40 kPa) <sup>c</sup>	0.02
80 $^{\circ}\text{C}$ and water partial pressures from 25–45 kPa	$\text{ohm cm}^2$	0.027 (25 kPa) <sup>c</sup>	0.02
30 $^{\circ}\text{C}$ and water partial pressures up to 4 kPa	$\text{ohm cm}^2$	0.027 (4 kPa) <sup>c</sup>	0.03
–20 $^{\circ}\text{C}$	$\text{ohm cm}^2$	0.1 <sup>b</sup>	0.2
Maximum operating temperature	$^{\circ}\text{C}$	120 <sup>c</sup>	120
Minimum electrical resistance	$\text{ohm cm}^2$	$>5,600^c$	1000
Cost <sup>d</sup>	$\$/\text{m}^2$	17 <sup>e</sup>	20
Durability <sup>f</sup>			
Mechanical	Cycles until $>15\text{ mA}/\text{cm}^2\text{ H}_2$ crossover <sup>g</sup>	23,000 <sup>c</sup>	20,000
Chemical	Hours until $>15\text{ mA}/\text{cm}^2$ crossover or $>20\%$ loss in OCV	742 <sup>c</sup>	$>500$
Combined chemical/mechanical	Cycles until $>15\text{ mA}/\text{cm}^2$ crossover or $>20\%$ loss in OCV	–	20,000

<sup>a</sup>Tested in MEA on  $\text{O}_2$  or  $\text{H}_2$ , 80  $^{\circ}\text{C}$ , fully humidified gases, 1 atm total pressure. For  $\text{H}_2$  test methods, see M. Inaba et al. *Electrochimica Acta*, 51, 5746, 2006. For  $\text{O}_2$  test methods, see Zhang et al. *Journal of the Electrochemical Society*, 160, F661–F622, 2013

<sup>b</sup>14  $\mu\text{m}$  PFIA membrane with nanofiber support. M. Yandrasits (3 M), private communication, February 1, 2016

<sup>c</sup>Reinforced and chemically stabilized PFIA membrane. M. Yandrasits et al. (3 M), U.S. Department of Energy Hydrogen and Fuel Cells Program 2015 Annual Progress Report, [https://www.hydrogen.energy.gov/pdfs/progress15/v\\_b\\_1\\_yandrasits\\_2015.pdf](https://www.hydrogen.energy.gov/pdfs/progress15/v_b_1_yandrasits_2015.pdf)

<sup>d</sup>Costs projected to high-volume production (500,000 80 kW systems per year)

<sup>e</sup>Cost when producing membrane for 500,000 systems per year. DOE Hydrogen and Fuel Cells Program Record 15,015, “Fuel Cell System Cost – 2015.” [http://www.hydrogen.energy.gov/program\\_records.html](http://www.hydrogen.energy.gov/program_records.html)

<sup>f</sup>Measured according to protocols in Table P.3, Table P.4, and Table P.5

<sup>g</sup>For air or  $\text{N}_2$  testing, an equivalent crossover metric of 0.1  $\text{sccm}/\text{cm}^2$  at a 50 kPa pressure differential, 80  $^{\circ}\text{C}$ , and 100% RH may be used as an alternative

PEMFC stack components. The dissolved metal ions can contaminate/lower the conductivity of the membrane by taking up ion exchange sites or adsorb on the catalyst and lower its activity. The stacks are generally tolerant to about 5–10 ppm of metal ion contamination. At the compression forces of relevance to PEMFCs, the USDOE bipolar plate areal resistivity target for ICR is  $10 \text{ m}\Omega\text{-cm}^2$ .

Stainless steels, as well as Al-, Ni-, and Ti-based alloys, have been studied extensively as possible candidates for bipolar plates. One of the most well-studied materials for bipolar plates is SS 316/316 L (16–18% Cr, 10–14% Ni, 2% Mo, rest Fe); other candidates are 310, 904 L, 446, and 2205. Bare stainless steel plates form a passive 2–4 nm chromium oxide surface layer under PEMFC conditions that leads to unacceptably high ICRs. A similar trend is observed for the other alloys and therefore surface modification or surface coatings on selected substrate material has to be considered as a pathway to meet the technical targets of low ICR and high corrosion resistance.

Coatings may be metal based, such as gold, TiN, CrN, metal carbides, or carbon based, such as diamond-like carbon, graphite, graphite platelets, carbon-resin composites, conductive tin oxides. Coatings have to be compatible with the substrate bare metal and have good adhesion and peel resistance.

An additional requirement that has to be satisfied is a high level of surface hydrophilicity. Non-wettable plate surfaces result in unstable reactant flows that have to be countered with higher pressure drops and gas stoichiometries and hence higher parasitic power drains. This requirement has led to the development of hybrid coatings that can provide the low ICR and high wettability. At this time, the bipolar plates account for 75% of the total stack weight and x% of the stack cost. Table 4 summarizes some of the targets for bipolar plates for automotive fuel cells.

## Future Directions

Direct hydrogen-fuel-cell-powered vehicles have reached a level of development where the major automotive companies have publicly announced

that initial initiation of commercialization has begun. The targets of performance, durability, and cost agreed upon by various organizations, including the US DOE, appear to be achievable with recent improvements in stack and cell designs as shown in Figures 22, 23, and 24. Well-delineated pathways and strategies have been established to address the barriers of cost and durability of PEMFC stacks and achieve the automotive targets. The principal directions for reduction of cost and enhancement of durability of key fuel cell components, i.e., electrocatalysts, membranes, and bipolar plates are briefly summarized in this section.

Pt-based electrocatalysts will continue to be used in both the anode and cathode of automotive PEMFCs for the next decade. The current status of catalysts in automotive PEMFCs is a Pt-based carbon black-supported catalyst (20–50 wt.% Pt/C, 2–4 nm,  $60\text{--}90 \text{ m}^2/\text{g}$ ) with a loading of  $0.20\text{--}0.35 \text{ mg}_{\text{Pt}}/\text{cm}^2$  on the cathode and about  $0.05 \text{ mg}/\text{cm}^2$  on the anode. About 30 g of Pt are required for a 100-kW-rated stack. The rated power usually corresponds to a voltage of 0.60 V at  $1\text{--}2 \text{ A}/\text{cm}^2$ . The durability of fuel cell stacks under automotive conditions fall in the range of 3,500 h or 75% of the target life.

Progress has already been made over the years in enhancing the activity of the Pt nanoparticles dispersed on carbon support catalysts by alloying Pt with base metals such as Co, Ni, Fe, Rh, Cu, and Ti. The activity enhancements are a factor of 2–4, although the performance decreases over time. The Pt-alloys/C also fortuitously exhibit improved durability in part due to their larger particle size and heat treatment. This is a conventional pathway that has already been explored and proven over the last few decades in PTFE-bonded electrodes used in PAFCs. A correlation to the improved activity from alloying is that the oxygen binding weakens as the d-band center shifts [59–61]; a volcano plot of various metals can be obtained with Pt sitting at the top [62]. Also, an increased number of neighboring metal atoms, 3d metal neighbors, as well as compressive strain have all been reported to weaken the oxygen binding to Pt. A positive shift in the onset of oxide observed in cyclic voltammograms indicating oxophilic nature of the surface has also been

**Polymer Electrolyte Membrane (PEM) Fuel Cells: Automotive Applications, Table 4** Technical targets for automotive PEMFC bipolar plates [48]

Characteristic	Units	2015 Status	2020 Targets
Cost <sup>a</sup>	\$/kW <sub>net</sub>	7 <sup>b</sup>	3
Plate weight	kg/kW <sub>net</sub>	<0.4 <sup>c</sup>	0.4
Plate H <sub>2</sub> permeation coefficient <sup>d</sup>	Std cm <sup>3</sup> /(sec cm <sup>2</sup> Pa) @ 80 °C, 3 atm 100% RH	0 <sup>e</sup>	<1.3 × 10 <sup>-14</sup> . <sup>f</sup>
Corrosion, anode <sup>g</sup>	μA/cm <sup>2</sup>	No active peak <sup>h</sup>	<1 and no active peak
Corrosion, cathode <sup>i</sup>	μA/cm <sup>2</sup>	<0.1 <sup>c</sup>	<1
Electrical conductivity	S/cm	>100 <sup>j</sup>	>100
Areal specific resistance <sup>k</sup>	ohm cm <sup>2</sup>	0.006 <sup>h</sup>	<0.01
Flexural strength <sup>l</sup>	MPa	>34 (carbon plate) <sup>m</sup>	>25
Forming elongation <sup>n</sup>	%	20–40 <sup>o</sup>	40

<sup>a</sup>Costs projected to high volume production (500,000 80 kW systems per year), assuming MEA meets performance target of 1,000 mW/cm<sup>2</sup>

<sup>b</sup>Cost when producing sufficient plates for 500,000 systems per year. DOE Hydrogen and Fuel Cells Program Record 15,015, “Fuel Cell System Cost – 2015.” [http://www.hydrogen.energy.gov/program\\_records.html](http://www.hydrogen.energy.gov/program_records.html)

<sup>c</sup>C.H. Wang (Treadstone), “Low-cost PEM Fuel Cell Metal Bipolar Plates.” 2012 Annual Progress Report, [http://www.hydrogen.energy.gov/pdfs/progress12/v\\_h\\_1\\_wang\\_2012.pdf](http://www.hydrogen.energy.gov/pdfs/progress12/v_h_1_wang_2012.pdf)

<sup>d</sup>Per the standard gas transport test (ASTM D1434)

<sup>e</sup>C.H. Wang (Treadstone), private communication, October 2014

<sup>f</sup>Blunk, et al. J. Power Sources 159 (2006) 533–542

<sup>g</sup>pH 3 0.1 ppm HF, 80 °C, peak active current <1 × 10<sup>-6</sup> A/cm<sup>2</sup> (potentiodynamic test at 0.1 mV/s, –0.4 V to +0.6 V (Ag/AgCl)), de-aerated with Ar purge

<sup>h</sup>Kumar, M. Ricketts, and S. Hirano, “Ex-situ evaluation of nanometer range gold coating on stainless steel substrate for automotive polymer electrolyte membrane fuel cell bipolar plate,” Journal of Power Sources 195 (2010): 1401–1407, September 2009

<sup>i</sup>pH 3 0.1 ppm HF, 80 °C, passive current <5 × 10<sup>-8</sup> A/cm<sup>2</sup> (potentiodynamic test at +0.6 V (Ag/AgCl) for >24 h, aerated solution)

<sup>j</sup>O. Adrianowycz (GrafTech). “Next Generation Bipolar Plates for Automotive PEM Fuel Cells,” 2009 Annual Progress Report. [http://www.hydrogen.energy.gov/pdfs/progress09/v\\_2\\_adrianowycz.pdf](http://www.hydrogen.energy.gov/pdfs/progress09/v_2_adrianowycz.pdf)

<sup>k</sup>Includes interfacial contact resistance (on as received and after potentiostatic test) measured both sides per Wang, et al. J. Power Sources 115 (2003) 243–251 at 200 psi (138 N/cm<sup>2</sup>)

<sup>l</sup>ASTM-D 790–10 Standard Test Method for Flexural Properties of Unreinforced and Reinforced Plastics and Electrical Insulating Materials

<sup>m</sup>D. Haack et al. (Porvair), “Carbon-Carbon Bipolar Plates.” 2007 Annual Progress Report, [http://www.hydrogen.energy.gov/pdfs/progress07/v\\_b\\_3\\_haack.pdf](http://www.hydrogen.energy.gov/pdfs/progress07/v_b_3_haack.pdf)

<sup>n</sup>Per ASTM E8M-01 Standard Test Methods for Tension Testing of Metallic Materials, or demonstrate ability to stamp generic channel design with width depth, and radius

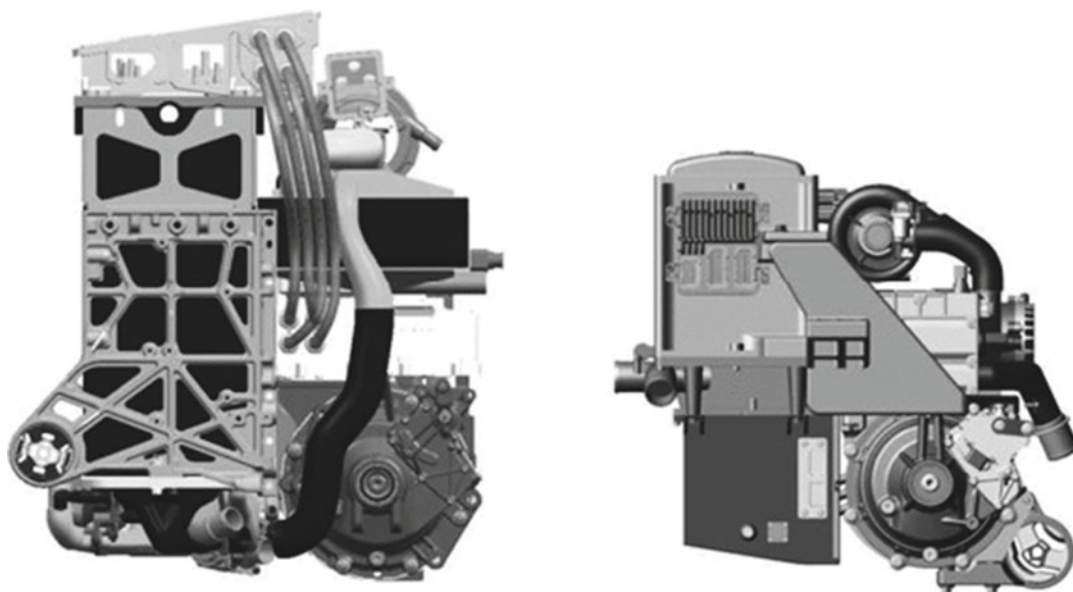
<sup>o</sup>M. Brady et al. (Oak Ridge National Laboratory), “Nitrided Metallic Bipolar Plates.” 2010 Annual Progress Report, [http://www.hydrogen.energy.gov/pdfs/progress10/v\\_1\\_1\\_brady.pdf](http://www.hydrogen.energy.gov/pdfs/progress10/v_1_1_brady.pdf)

directly correlated to enhanced ORR activity. Larger Pt particles, heat-treated Pt particles, and alloys of Pt exhibit oxophobic tendencies and concomitant improved activities. More recently, the understanding of the impact of d-band center on the metal-oxygen bond strength has been refined [63]; the entire valence band structure (density of states vs. binding energy) affects the bond strength and simplification of the band to a single “d-band center” is not valid. To summarize,

the same binary and ternary alloys used previously in acid fuel cells are being implemented in PEMFCs using modified electrode structures.

A well-known weakness of the Pt-alloy approach is the leaching out of the base metal from the surface immediately and from the bulk over time. It has been shown by Stamenkovic et al. [64] that almost all the surface base metal is leached off once in contact with electrolyte; a Pt skeleton structure is formed (or Pt-skin for





GEN1 FCS (GMT101X)		GEN2 FCS (GMT/E)
104	Stack Size (L)	64
80	Platinum (g)	30
405	System Size (L)	191
250	System Mass (kg)	130
62	Peak Power @ 150,000 miles (kW)	78
187	System Part Numbers	120
1903	System Part Count	1100

**Polymer Electrolyte Membrane (PEM) Fuel Cells: Automotive Applications, Fig. 22** Demonstration of improvement in the automotive polymer electrolyte fuel cell stack and system

annealed catalysts) that has higher coordinated Pt atoms and a sublayer enriched in the base metal contributes to the higher activity. Nevertheless, as long as the catalyst activity and fuel cell performance is maintained within the target limits over the life of the stack, it remains an acceptable approach. Fundamental studies on single crystal Pt and Pt-alloys through a “materials by design” approach that involves the simultaneous application of a number of surface spectroscopies to a surface undergoing electrochemistry are being pursued by Markovic et al. [65]. Alloys with controlled crystal orientation such as the PtNi (111) have been demonstrated by Stamenkovic et al. [66] to show extremely high specific activities; it remains a fundamentally important yet difficult approach to implement in practical catalysts.

Perturbations in the approach to the use of alloy catalysts are the use of voltammetrically dealloyed catalysts such as dealloyed Pt<sub>25</sub>Cu<sub>75</sub> and Pt<sub>20</sub>Cu<sub>20</sub>Co<sub>60</sub> nanoparticles [67]. Pt-rich surfaces and alloy-rich cores of such materials have been shown to exhibit significantly improved activity for oxygen reduction in acidic media due to a reduced Pt-Pt atomic distance (lattice strain) and also possess superior durability to commercial Pt/C.

Two other pathways being explored to further drastically reduce the Pt loading are: (1) raising the catalyst mass activity (mA/mg) by using a core of base metal coated with monolayers of Pt and (2) applying the concept of high specific activity-extended thin films to a practical catalyst electrode system. The catalysts in the first pathway are often referred to as core-shell catalysts [68, 69].



**Polymer Electrolyte Membrane (PEM) Fuel Cells: Automotive Applications,**

**Fig. 23** Improvement in automotive fuel-cell system



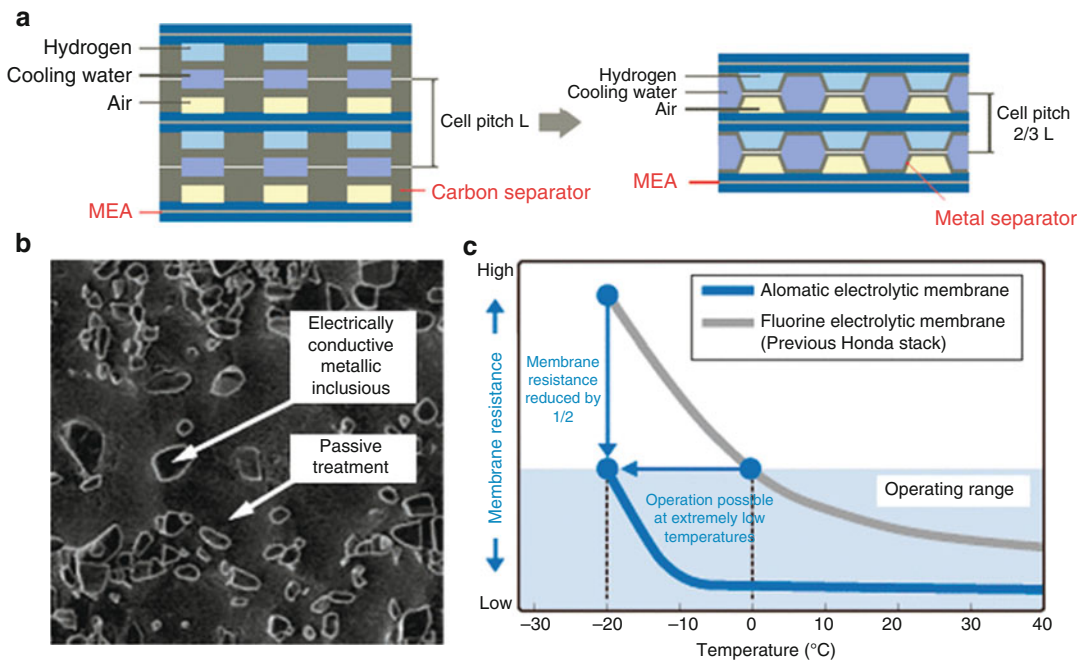
Specifications

Max. Power	90 kW
Volume	90 L
Weight	116 kg



Specifications

Max. Power	130 kW
Volume	68 L
Weight	86 kg



**Polymer Electrolyte Membrane (PEM) Fuel Cells: Automotive Applications, Fig. 24** Improvement in automotive fuel-cell stack and system from Honda showing the advancements in cell bipolar plates and membranes

A deposition technique that involves the replacement of a first UPD metal adlayer with a 2D deposit of a nobler metal monolayer to cover the surface uniformly forms the basis of the technique [70]. In addition to the use of expensive Pt only at the surface where reaction takes place, the use of different subsurface materials enhance the specific activity of the surface Pt layer; a Pt-metal mixed surface monolayer may also be used. About 4–10× enhancement in mass activity has been shown using these catalysts. The use of small

quantities of gold clusters [71] on the surface has also shown to enhance the durability of the catalysts under potential cycling. Latest work in the area includes the generation of hollow Pt spheres (4–8 nm hollow spheres having 1–2 nm Pt shells) prepared from Ni templates exhibiting 5× enhancement of activity over solid nanoparticles (measured in rotating disk electrode liquid electrolyte half cells) [72]. Scale-up and evaluation in fuel cells of several of these technologies is currently underway.

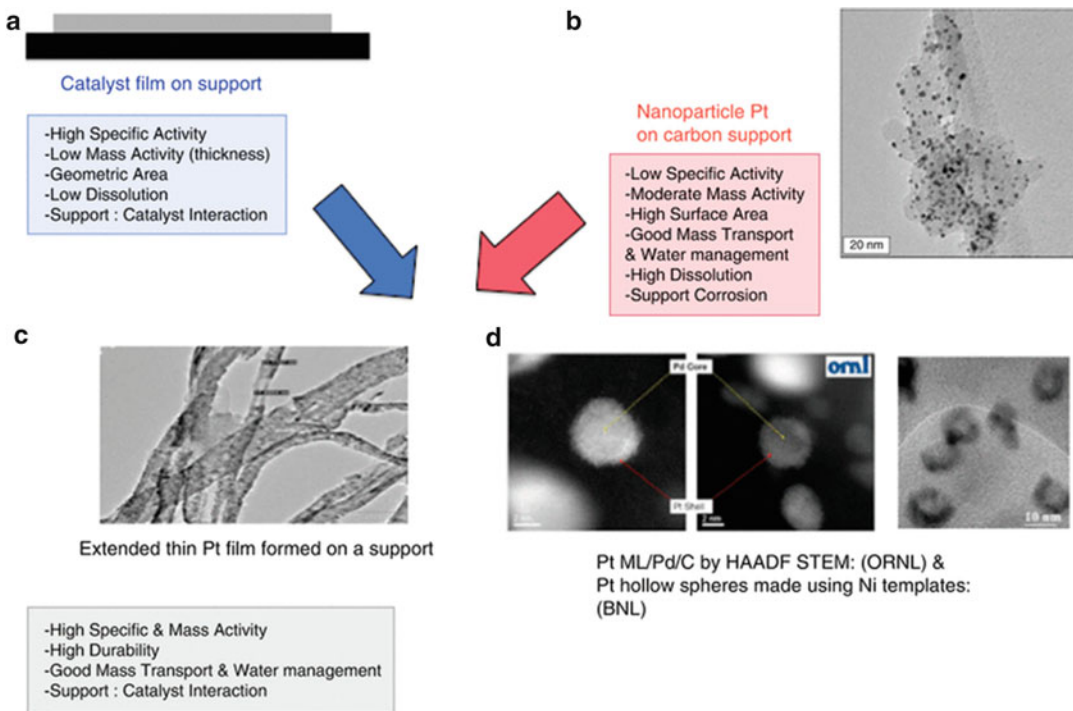
For decades, discussion on the enhanced specific activity of larger nanoparticles has raged. Larger nanoparticles of Pt have been found to have both a higher activity as well as a higher durability by several groups [38, 73, 74]. In addition, bulk polycrystalline Pt has been shown to have  $\sim 10\times$  higher specific activity than Pt nanoparticle in half-cells using ultra pure nonadsorbing liquid electrolytes such as perchloric acid. Over the last decade, the high specific activity of continuous thin films has finally been demonstrated in practical MEAs of fuel cells especially by 3 M with their NSTF catalysts [75, 76]. Two challenges remain in the widespread use of these catalysts in practical fuel cells: the mass specific surface area ( $\text{m}^2/\text{g}$ ) which is ten times lower for these films at this time and significant mass transport resistances due to flooding under humidified conditions due to the thinness of the cathode catalyst layer. Essentially, the catalyst films ( $\sim 30$  nm thick) are not thin enough to provide high mass activity and the electrode structure formed with these catalysts is not thick enough to disperse water easily. Both issues are being addressed by programs funded by the US DOE, and in laboratories elsewhere; the next 5 years will determine the degree of success of this approach [77]. - Figure 25 outlines the main precious metal pathways for future fuel cell electrocatalysts. One of the unexpected problems associated with the use of lower Pt loadings (with Pt-alloys/C) on the cathode is that a higher drop in high current density near peak power is observed compared to higher loaded catalysts. Although not fully resolved, it has been partially attributed to a local resistance at the catalyst ionomer interface as is being currently addressed by major automotive companies and research institutions.

Fundamental research related the formation of surface oxides on Pt [78–80] as well as Pt dissolution [81], although studied in the past, has come to the forefront again. This is due to the current understanding that the dissolution/surface area loss of Pt/C in automotive fuel cells is intensified by the cycling of load and hence potential [35, 40, 82] along with the trend toward core-shell and nanofilms of catalysts. Operational methods to limit the losses through this understanding of mechanisms as

well as material solutions are being actively pursued [32].

An intermediate approach to limit the use of Pt and instead use Pd-based metal alloys has shown reasonable success in activity improvement. Although fairly precious, Pd is currently four times less expensive than Pt. Pd alloyed with Mo, Ta, W, Re, and Cu have all been evaluated. A Pd-Cu (1:1) catalyst composed of 20 nm nanoparticles prepared by co-impregnation showed activity within range of Pt and is being further pursued [63, 83].

Nonprecious metal catalysts (non-Pt group metals/non-PGM) research is still in its infancy and lags in activity and durability by a factor of  $\sim 10$  compared to conventional Pt/C electrocatalysts; they have shown significant progress in terms of improved activity in recently reported work, and research in this field continues as a long-term approach to completely eliminate platinum usage in fuel cells. The target for non-PGM catalyst activity is expressed per unit volume ( $>130 \text{ A}/\text{cm}^3$  @800 mV) since it is the volume/electrode thickness that determines its usability. An example is the C|Fe|N catalyst system that can be synthesized by heat treatment of Fe- $\text{N}_4$  macrocycles as well as individual precursors of the three elements [84, 85]. Lefevre et al. [86] synthesized the catalyst system by utilizing ball-milling to fill microporous carbon with iron ions and pore fillers to obtain higher ORR activity. Carbon supported as well as sputtered transition metal (Cr, Co, Fe)/chalcogens (Se, S) have also been studied with limited success [87]. In research funded by the USDOE, heat-treated, carbon-supported polypyrrole and PANI in the presence of salts of Fe and Co are being investigated in half-cell rotating disk electrodes as well as subscale fuel cells. In comparison to carbon, pyrolyzed carbon, PANI/C, PANI-Co/C, PANI-Fe/C, PANI- $\text{Fe}_3\text{Co}/\text{C}$  exhibited the highest ORR activity of  $27 \text{ A}/\text{cm}^3$  at 800 mV under  $\text{H}_2\text{O}_2$ ; the peroxide yield for PANI- $\text{Fe}_3\text{Co}/\text{C}$  was found to be the lowest at 0.5% [88]. A cyanamide-Fe-C ( $3.5 \text{ mg}/\text{cm}^2$ ) catalyst has shown catalyst activity in fuel cells of  $165 \text{ A}/\text{cm}^3$  @ 800 mV in most recent work [89]. Much work remains to be carried out in the fundamental understanding and characterization of non-PGM catalysts



**Polymer Electrolyte Membrane (PEM) Fuel Cells: Automotive Applications, Fig. 25** Pathways for future electrocatalyst development for automotive PEMFCs. (a) Thick films or bulk single crystal and polycrystalline catalysts that are ideal for fundamental studies on surface structure and mechanisms; these materials need to be modified into (c) and (d) to be applicable to fuel cells. (b) Typical commercial nanoparticles (2–4 nm) on a high-

surface-area carbon support used in fuel cells at this time; (c) Thin continuous films of catalyst on a support such as carbon nanotubes that may provide a physical porous structure for mass transport in a fuel cell; (d) Core-shell catalysts where only the shell consists of precious metals and are supported on a typical high-surface-area support [72, 77, 89]

in terms of identification and quantification of the reaction sites and estimating the turnover frequencies and mechanisms for the ORR.

The high-surface-area carbon supports used today enable the use of small nanoparticles of Pt that are well-dispersed; the price paid in using a high-surface-area carbon black is that it tends to be susceptible to corrosion [90–93]. Carbon is thermodynamically susceptible to corrosion in the entire fuel cell operating regime but the kinetics are fortunately very slow. Near and above the open circuit potential of 0.95 V and especially above 1.1 V, the corrosion currents increase. Potentials in the range 1–1.5 V are seen only during uncontrolled start-up and shutdown of fuel cells [43, 94, 95]. Using mitigation techniques based on operating conditions, the highest potential seen is close to the OCV and the losses

correspondingly lower. Nevertheless, some carbon corrosion is observed over the life of the fuel cell and material solutions are being actively sought. The material solutions will enable system simplification and lower costs. Alternative non-carbon supports such as titanium, tungsten oxides, nitrides, and borides are being studied that can provide a higher corrosion resistance at high potentials and also help anchor the Pt nanoparticles and limit degradation due to particle agglomeration. The main issues with alternative materials is that the corrosion resistance often comes with the cost of lower conductivity, lower surface area, different electrode structure, and the need for new methods to deposit catalysts on them.

Intensive research is being carried out to improve both the membrane performance (conductivity/areal resistance) and durability. The protonic conductivity

is typically improved by the use of low EW ionomers; these ionomers swell with water to a greater extent increasing fatigue stresses. Thinner membranes are also being developed to reduce the areal resistance, but often need to be reinforced to provide mechanical strength and suffer from higher reactant permeability and susceptibility to shorting. Thus, a trade-off between performance and durability is often unavoidable.

Development of new membrane materials that have the capability of sustaining proton conduction under low RH conditions and at temperatures as high as 120 °C has been a struggle. Such a membrane would allow facile water management and also reduce thermal management issues in the stack. Of the two desired properties, a membrane that operates at low RH with sufficient conductivity is more critical since catalyst (both platinum and carbon) degradation is also suppressed under these conditions.

The approach to synthesizing new membrane material candidates involves obtaining the required properties of conductivity, chemical and mechanical durability by: tailoring or modifying water retention, domain interconnectivity, lowering the equivalent weight, use of additives such as metal composites and quenchers, stabilizing bonds and end group terminations, use of short side-chains, using reinforcements and cross-linking, raising the glass transition temperature, the use of amphoteric protogenic groups such as imidazole and phosphonic acid, etc. [96, 97]. Inorganics such as titania, silica, and zirconium phosphate have been incorporated into membranes in attempts to maintain conductivity at low RH through tightly bound water in these compounds. The use of amphoteric protogenic groups such as imidazole [98] and phosphonic acid that allow for proton transport in the absence of water has also been pursued [99]. PBI-PA-based membranes at temperatures above 200 °C have been investigated by several groups [100] and commercialized by PEMEAS<sup>®</sup>. These materials suffer from the leaching of phosphoric acid, complex start-up and shutdown, as well as loss of Pt activity due to phosphate anion adsorption. Modifications to this approach include the use

of sulfonimides, perfluorinated acids, and metal oxides as additives to reduce the anion adsorption and increase the oxygen solubility. Heteropoly acids such as phosphotungstic acid, silicotungstic acid, and sulfonated zeolites have been used with partial success [101]. 10–20 wt.% heteropoly acids (not immobilized) were combined with 3 M PFSA ionomers to cast membranes and prepare MEAs; they showed a reduction in the FRR in fuel cell tests under hot dry conditions [100]. Additives in general may not be stable and may leach out over long periods of time and may also change the mechanical properties of the membrane. High-temperature, water-free/water-insoluble, proton-conducting membranes (protic salt polymer membranes) where a salt repeat unit conducts protons with an adjacent unit without the transport of water are also being researched by Gervasio et al. [102]. The membranes are prepared from solvent-free liquid salts known as protic ionic liquids or pILs that are tailored by selecting an acid and base.

Recently, the use of highly electron-poor poly(phenylene) backbones has resulted in ionomers containing sulfone ( $-\text{SO}_2-$ ) units connecting the sulfonic acid ( $-\text{SO}_3\text{H}$ ) functionalized phenyl rings that exhibit high proton conductivity and stability [103]. Some preparation routes have resulted in highly sulfonated material with an exchange capacity of  $\text{IEC} = 4.5 \text{ meq/g}$  or an EW of 220 g/eq along with low water transport coefficients. These materials though are water soluble and brittle in the dry state but may still be usable as a component in a PEM. The task of synthesizing and developing such membranes is a difficult task, but even partial success such as obtaining a membrane that can operate at similar temperatures as today but at lower RH will help advance PEMFC stack technology considerably. Hydrophobic-hydrophilic multiblock copolymers ( $\text{BPSH}_x\text{-BPS}_y$ ; where  $x = \text{MW of sulfonated poly(arylene ether)}$  and  $y = \text{MW of poly(arylene ether)}$ ) with varying block lengths and controlled morphology that develop order and produce a co-continuous hydrophilic phase for good conductivity at low humidity have also been the subject of research as potential candidates for a new PEM [58].

Incremental engineering modification of membranes is also being carried out with some success. Composite membranes that consist of conductive and nonconductive porous polymer reinforcements have been incorporated for some time into membranes to provide mechanical strength for extremely low thicknesses; they suffer from some loss of conductivity. One approach is to form a composite/polymer blend and decouple the proton conduction from other membrane requirements. Arkema has demonstrated an inexpensive hydrocarbon-based polyelectrolyte blended with polyvinylidene difluoride (PVDF or Kynar) that exhibits similar performance to commercial PFSA membranes [104]. Another approach involves the use of electrospun ionomer fibers embedded in a polymer [105]. 3 M has reported the fabrication of 825 EW nonreinforced membranes with new additives that meet the targets of 20,000 RH cycles and 500 h OCV test in fuel cells [106]. Giner Electrochemical Systems [107] has reported on the development of dimensionally stable membranes (DSM) with laser-drilled supports composed of polysulfone or polyimide (Kapton) or that lowers the swelling of high acid content PFSA ionomers. Asahi Glass Co., [108, 109] has reported a new polymer composite membrane (based on PFSA) in PEMFCs operating at 120 °C, 50% RH for ~4,000 h; the MEA tested in fuel cells had a degradation rate of 75  $\mu\text{V/h}$  and a FRR of less than 1% of the baseline control. Chemical modification of PFSA membranes is being carried out to minimize the non-fluorinated end groups susceptible to degradation. Additives such as  $\text{Ce}^{3+}$  and  $\text{Mn}^{2+}$  ions added in trace quantities into the membrane and ionomer have also been demonstrated to improve the chemical stability.

Although the focus of this entry is on PEMs that are being used in automotive fuel cells today, brief mention must be made of work carried out on alkaline anion exchange membranes (AAEMs). Such membranes have the potential to exhibit sufficient activity when used with nonprecious metal catalysts, may work with fuels such as methanol and ethylene glycol, and provide some of the features that commercial PFSA membranes provide for PEMFCs. A cross-linked, water-insoluble,

$\text{OH}^-$ -conducting, alkaline polymer free of metal ions and consisting of counter ions bound to the quaternary-ammonium containing polymer backbone has been reported with reasonable preliminary results (133–153  $\mu\text{m}$  thick, 0.0092 S/cm @ 30 °C, 100%RH) [110].  $\text{H}_2$ /Air alkaline membrane fuel cells that showed encouraging preliminary results with Pt and transition metal catalyst cathodes in  $\text{CO}_2$  free air have also been reported recently by Acta S.p.A [111].

Graphite-based bipolar plates have been used in PEMFC stacks, they suffer from drawbacks such as higher manufacturing costs, greater thicknesses, higher gas permeability that is necessary for high power density automotive fuel cell stacks. Metal bipolar plates (stainless steel, Ni, Ti, Al-based alloys) on the other hand possess high thermal conductivity, high mechanical and flexural strength, and facile high volume production but tend to corrode and require corrosion-resistant and conductive coatings that increase their cost [112]. New coatings are under development along with thinner stamped plates with most of the details being proprietary at this time. An example is thermal nitriding of thin (0.1 mm foils, Fe-20Cr-4 V and type 2205) stainless steel plates to generate surface layers of  $\text{Cr}_2\text{N}$ , CrN, TiN,  $\text{V}_2\text{N}$ , etc., that lowers the interfacial contact resistance and raises the corrosion resistance simultaneously [113]. The additional requirement of hydrophilicity to facilitate water management in the flow fields has led to the development of hybrid coatings that is capable of providing a low ICR and high wettability. Superhydrophilicity has been shown by layer-by-layer deposition of silica nanoparticles onto bipolar plates, which meets the other requirements [114]. Electrostatic layer-by-layer techniques have been employed to generate 100 nm coating structures that are constituted from 5 to 10 nm graphite platelets and 19 nm silica nanospheres. A low ICR of 4  $\text{m}\Omega\text{-cm}^2$  and a high degree of hydrophilicity are simultaneously achieved by this method.

Figure 23 in the previous section showed the improvement in Nissans latest generation stack achieved by using metal separators instead of carbon. Figure 24 illustrates schematically novel surface treatments on stainless steel bipolar plates



along with electrically conductive inclusions that help maintain high conductivity and corrosion resistance at the same time. Intensive applied research is being carried out to obtain thin, corrosion-resistant conductive bipolar plates modified with coatings that are inexpensive and conducive to high-speed/high-volume manufacturing.

A combination of synergistic improvements in the catalyst, support, gas diffusion layers, membrane, and essentially the entire porous electrode structure in conjunction with bipolar plates/flow fields is expected to improve the mass-transport of reactant gases, protons, and water management. Thus, an increase in the peak current density ( $A/cm^2$ ) and peak power density ( $W/cm^2$ ) will result; this in turn will lower the stack volume, the amount of catalyst, and membrane material used and raise the kW/L, kW/kg, and lower the \$/kW stack metrics. It should be noted that the rated or peak power for automotive stacks is based in part on maintaining an electrical efficiency of  $>50\%$ ; this dictates that the cell voltage has to be maintained above  $\sim 0.60$  V. At this time, volumetric power densities of practical stacks in fuel cell vehicles have been reported to be as high as  $\sim 2$  kW/L [46] and are likely to increase over the next few years contributing to lower stack costs (\$/kW).

Trends in short- and longer-term directions for key fuel cell components including electrocatalysts/supports, membranes, and bipolar plates have been elaborated in this section; improvement of the performance and durability of these components will directly impact the entire automotive fuel cell system requirements, complexity, and cost. Durable catalysts with enhanced ORR activity, durable membranes that perform at very low humidity, and durable bipolar plates that have low contact resistance will not only increase the power density and cost of the fuel cell stack but also simplify and lower/eliminate system component costs of the air compressor, humidification systems, recycle pumps, radiator, start-up/shutdown and freeze-start-related components, etc. A combination of advances in all the fuel cell components discussed above, system simplification, governmental policies that are sensitive to sustainable clean energy, and development of a hydrogen infrastructure will

enable achieving the projected technical and cost targets needed for automotive fuel cell commercialization.

## Bibliography

### Primary Literature

1. Grove WR (1842) On gaseous voltaic battery. *Philos Mag* 3:417
2. Schonbein CF (1839) On the voltaic polarization of certain solid and fluid substances. *Philos Mag* 14:43
3. Mond L, Langer C (1889) A New Form of Gas Battery. *Proc Roy Soc* 46:296
4. Jacques WW (1897) Electricity direct from coal. *Harpers Mag* 94:144–150
5. Baur E, Tobler J (1933) Brennstoffketten. *Z Elektrochem* 39:169–180
6. Schmidt TJ, Paulus UA, Gasteiger HA, Behm RJ (2001) Peroxide rde, anion adsorption effect. *J Electroanal Chem* 508:41–47
7. Tobler J (1933) Studien Über Knallgas-Ketten. *Z Elektrochem* 39:148
8. Nernst W (1904) Theorie der Reaktionsgeschwindigkeit in heterogenen Systemen. *Z Phys Chem* 47:52
9. Tafel J, Emmert B (1905) Ueber die ursache der spontanen depression des kathodenpotentials bei der elektrolyse verduennter schwefelsaeure. *Z Phys Chem* 50:349–373
10. Liebhavsky HA, Cairns EJ (1968) Fuel cells and batteries. Wiley, New York
11. Vielstich W (1965) Fuel cells. Wiley-Interscience, London
12. Maget HJR (1967) In: Berger C (ed) Handbook of fuel cell technology. Prentice-Hall, Englewood Cliffs, pp 425–491
13. Liebhavsky HA, Grubb WT Jr (1961) The fuel cell in space. *ARS J* 31:1183–1190
14. AFC A (2003) Alkaline fuel cells. In: Vielstich W, Lamm A, Gasteiger H (eds) Handbook of fuel cells-fundamentals, technology and applications. Wiley, New York
15. Kordesch KV (1978) 25 years of fuel cell development (1951–1976). *J Electrochem Soc* 125:77 C–91 C
16. Grubb WTJ (1959) US Patent 2,913,511
17. Niedrach LW, Alford HR (1965) A new high-performance fuel cell employing conducting-porous-teflon electrodes and liquid electrolyte. *J Electrochem Soc* 112:117
18. Thomas CES (2007) Greenhouse gas results. [http://www.cleancaroptions.com/html/greenhouse\\_gas\\_results.html](http://www.cleancaroptions.com/html/greenhouse_gas_results.html)
19. DOE US (2010) Well-to-wheels greenhouse gas emissions. [http://www.hydrogen.energy.gov/pdfs/9002\\_well-to-wheels\\_greenhouse\\_gas\\_emissions\\_petrolium\\_use.pdf](http://www.hydrogen.energy.gov/pdfs/9002_well-to-wheels_greenhouse_gas_emissions_petrolium_use.pdf)
20. IPCC (2007) The IPCC assessment reports. <http://www.ipcc.ch/>

21. Koppel T (1999) Powering the future: the ballard fuel cell and the race to change the world. Wiley, New York
22. Taub A (2009) The opportunity in electric transportation. [http://www.ncsc.ncsu.edu/cleantransportation/docs/Events/2009\\_5-27\\_Taub\\_GM-EV.pdf](http://www.ncsc.ncsu.edu/cleantransportation/docs/Events/2009_5-27_Taub_GM-EV.pdf)
23. GreenCarCongress: GM highlights engineering advances with second generation fuel cell system and fifth generation stack; poised for production around 2015. <http://www.greencarcongress.com/2009/09/gm-2gen-20090928.html>
24. ChevyEquinox (2010) Chevy equinox fuel cell. <http://www.gm.com/vehicles/innovation/fuel-cells/>
25. AutoBlogGreen (2010) 2008 chevy equinox fuel cell. <http://green.autoblog.com/photos/2008-chevrolet-equinox-fuel-cell/#380179>
26. UTCPower (2010) UTC power: transportation\automotive. [http://www.utcpower.com/fs/com/bin/fs\\_com\\_Page/0,11491,0151,00.html](http://www.utcpower.com/fs/com/bin/fs_com_Page/0,11491,0151,00.html)
27. F-cell M-BB-c (2010) 2010 mercedes-benz b-class f-cell. [http://www.caranddriver.com/news/car/09q3/2010\\_mercedes-benz\\_b-class\\_f-cell-car\\_news](http://www.caranddriver.com/news/car/09q3/2010_mercedes-benz_b-class_f-cell-car_news)
28. FCHV-adv T (2010) Fuel cell technology. <http://www2.toyota.co.jp/en/tech/environment/fchv/>
29. Pressroom T (2010) Toyota fuel cell vehicle demonstration program expands. <http://pressroom.toyota.com/pr/tms/toyota/toyota-fuel-cell-vehicle-demonstration-151146.aspx>
30. NissanHistory (2010) The history of Nissan's fuel-cell vehicle development. [http://www.nissan-global.com/EN/ENVIRONMENT/CAR/FUEL\\_BATTERY/DEVELOPMENT/FCV/index.html](http://www.nissan-global.com/EN/ENVIRONMENT/CAR/FUEL_BATTERY/DEVELOPMENT/FCV/index.html)
31. Honda (2010) Honda: fuel cell electric vehicle. <http://world.honda.com/FuelCell/>
32. Uchimura M, Sugawara S, Suzuki Y, Zhang J, Kocha SS (2008) Electrocatalyst durability under simulated automotive drive cycles. ECS Trans 16:225–234
33. Kocha SS (2003) Principles of mea preparation. In: Vielstich W, Lamm A, Gasteiger H (eds) Handbook of fuel cells-fundamentals, technology and applications. Wiley, New York, pp 538–565
34. Kocha SS, Yang DJ, Yi JS (2006) Characterization of gas crossover and its implications in PEM fuel cells. AIChE J 52:1916–1925
35. Uchimura M, Kocha S (2007) The impact of cycle profile on PEMFC durability. ECS Trans 11:1215–1226
36. Ohma A, Suga S, Yamamoto S, Shinohara K (2007) Membrane degradation behavior during OCV hold test. J Electrochem Soc 154:B757–B760
37. Sugawara S, Maruyama T, Nagahara Y, Kocha SS, Shinohara K, Tsujita K, Mitsuhashi S, Ota K-i (2009) Performance decay of proton-exchange membrane fuel cells under open circuit conditions induced by membrane decomposition. J Power Sources 187:324–331
38. Gasteiger HA, Kocha SS, Sompalli B, Wagner FT (2005) Activity benchmarks and requirements for pt, pt-alloy, and non-pt oxygen reduction catalysts for PEMFCs. Appl Catal B Environ 56:9–35
39. Mathias MF, Makharia R, Gasteiger HA, Conley JJ, Fuller TJ, Gittleman CJ, Kocha SS, Miller DP, Mittelsteadt CK, Tao X, Yan SG, PT Y (2005) Two fuel cell cars in every garage? Electrochem Soc Interface 14:24–35
40. Uchimura M, Kocha SS (2007) The impact of oxides on activity and durability of PEMFCs. AIChE J. Abstract No. 295b
41. Uchimura M, Kocha SS (2008) The influence of Pt-oxide coverage on the ORR reaction order in PEMFCs. ECS meeting, Honolulu, 12–17 Oct 2008
42. Kocha SS, Gasteiger HA (2004) The use of Pt-alloy catalyst for cathodes of PEMFCs to enhance performance and achieve automotive cost targets. Fuel Cell Seminar, San Antonio
43. Reiser CA, Bregoli L, Patterson TW, Yi JS, Yang JD, Perry ML, Jarvi TD (2005) A reverse-current decay mechanism for fuel cells. Electrochem Solid-State Lett 8:A273–A276
44. Reiser CA, Yang D, Sawyer RD (2005) Procedure for shutting down a fuel cell system using air purge. US Patent 6,858,336, 22 Feb 2005
45. Reiser CA, Yang DJ, Sawyer RD (2005) Procedure for starting up a fuel cell system using a fuel purge. US Patent 7,410,712, 12 Aug 2008
46. Shimoi R, Aoyama T, Iiyama A (2009) Development of fuel cell stack durability based on actual vehicle test data: current status and future work. SAE International 2009-01-1014
47. Merzougui B, Halalay IC, Carpenter MK, Swathirajan S (2006) Conductive matrices for fuel cell electrodes. General motors, US Patent Application 20060251954
48. DOE US (2007) Fuel cell targets. <http://www1.eere.energy.gov/hydrogenandfuelcells/mypp>
49. Borup RL, Meyers JP, Pivovar B, Kim YS, Mukundan R, Garland N, Myers DJ, Wilson M, Garzon F, Wood DL, Zelenay P, More K, Stroh K, Zawodzinski TA, Boncella J, McGrath J, Inaba M, Miyatake K, Hori M, Ota K-i, Ogumi Z, Miyata S, Nishikata A, Siroma Z, Uchimoto Y, Yasuda K, Kimijima K-i, Iwashita N (2007) Scientific aspects of polymer electrolyte fuel cell durability and degradation. Chem Rev 107:3904–3951
50. Mohtadi R, Lee WK, Zee JWV (2004) SO<sub>2</sub> contamination. J Power Sources 138:216–225
51. Nagahara Y, Sugawara S, Shinohara K (2008) The impact of air contaminants on PEMFC performance and durability. J Power Sources 182:422–488
52. Kocha SS, Gasteiger HA (2004) In: Henry B (ed) Platinum alloy catalysts for PEMFCs. Gonzalez Convention Center, San Antonio. <http://www.fuelcellseminar.com/past-conferences/2004.aspx>
53. Satyapal S (2009) Hydrogen program overview. [http://www.hydrogen.energy.gov/pdfs/review09/program\\_overview\\_2009\\_amr.pdf](http://www.hydrogen.energy.gov/pdfs/review09/program_overview_2009_amr.pdf)
54. Satyapal S (2009) Fuel cell project kickoff. [http://www1.eere.energy.gov/hydrogenandfuelcells/pdfs/satyapal\\_doe\\_kickoff.pdf](http://www1.eere.energy.gov/hydrogenandfuelcells/pdfs/satyapal_doe_kickoff.pdf)



55. NEDO (2007) Nedo homepage. <http://www.nedo.go.jp/nenryo/gijutsu/index.html>:
56. Iiyama A, Shinohara K, Igushi S, Daimaru A (2009) Membrane and catalyst performance targets for automotive fuel cells. In: Vielstich W, Gasteiger HA, Yokokawa H (eds) Handbook of fuel cells-advances in electrocatalysis, materials, diagnostics and durability. Wiley, Chichester
57. Cleghorn S, Griffith M, Liu W, Pires J, Kolde J (2007) Gore's development path to a commercial automotive membrane electrode assembly. <http://www.fuelcellseminar.com/past-conferences/2007.aspx>
58. McGrath J (2007) Advanced materials for proton exchange membranes. DOE Hydrogen Program Merit Review Presentation. [http://www.hydrogen.energy.gov/pdfs/review07/fc\\_23\\_mcgrath.pdf](http://www.hydrogen.energy.gov/pdfs/review07/fc_23_mcgrath.pdf)
59. Luczak FJ (1976) Determination of d-band occupancy in pure metals and supported catalysts by measurement of the  $L_{2,3}$  x-ray absorption threshold. *J Catal* 43:376–379
60. Mukerjee S, Srinivasan S, Soriaga MP, McBreen J (1995) Role of structural and electronic properties of Pt and Pt alloys on electrocatalysis of oxygen reduction. *J Electrochem Soc* 142:1409–1422
61. Nagy Z, You H (2002) Applications of surface x-ray scattering to electrochemistry problems. *Electrochim Acta* 47:3037–3055
62. Jalan V, Taylor EJ (1983) Importance of interatomic spacing in catalytic reduction of oxygen in phosphoric acid. *J Electrochem Soc* 130:2299–2302
63. Myers D (2009) [http://www.hydrogen.energy.gov/pdfs/review09/fc\\_20\\_myers.pdf](http://www.hydrogen.energy.gov/pdfs/review09/fc_20_myers.pdf)
64. Stamenkovic VR, Fowler B, Mun BS, Wang G, Ross PN, Lucas CA, Markovic NM (2007) Improved oxygen reduction activity on Pt<sub>3</sub>Ni(111) via increased surface site availability. *Science* 315:494–497
65. Markovic NM, Ross PN (2000) Electrocatalysts by design: from the tailored surface to a commercial catalyst. *Electrochim Acta* 45:4101–4115
66. Stamenkovic VR, Mun BS, Arenz M, Mayrhofer KJJ, Lucas CA, Wang G, Ross PN, Markovic NM (2007) Trends in electrocatalysis on extended and nanoscale Pt-bimetallic alloy surfaces. *Nat Mater* 6:241–247
67. Neyerlin KC, Srivastava R, Yu C, Strasser P (2009) Electrochemical activity and stability of dealloyed Pt-cu and Pt-cu-co electrocatalysts for the oxygen reduction reaction. *J Power Sources* 186:261–267
68. Zhang J, Lima FHB, Shao MH, Sasaki K, Wang JX, Hanson J, Adzic RR (2005) Pt monolayer on noble metal-noble metal core core-shell nanoparticle electrocatalysts for O<sub>2</sub> reduction. *J Phys Chem B* 109:22701–22704
69. Zhang J, Mo Y, Vukmirovic MB, Klie R, Sasaki K, Adzic RR (2004) Pt-Pd core-shell. *J Phys Chem B* 108:10955
70. Brankovic SR, Wang JX, Adzic RR (2001) Metal monolayer deposition by replacement of metal adlayers on electrode surfaces. *Surf Sci* 474: L173–L179
71. Zhang J, Sasaki R, Sutter E, Adzic RR (2007) Stabilization of platinum oxygen reduction electrocatalysts using gold clusters. *Science* 315:220–222
72. Adzic RR (2010) Contiguous platinum monolayer oxygen reduction electrocatalysts on high-stability-low-cost supports. [http://www.hydrogen.energy.gov/pdfs/review10/fc009\\_adzic\\_2010\\_o\\_web.pdf](http://www.hydrogen.energy.gov/pdfs/review10/fc009_adzic_2010_o_web.pdf)
73. Bregoli LJ (1978) The influence of platinum crystallite size on the electrochemical reduction of oxygen in phosphoric acid. *Electrochim Acta* 23:489–492
74. Makharia R, Kocha SS, PT Y, Sweikart MA, Gu W, Wagner FT, Gasteiger HA (2006) Durable PEMFC electrode materials: requirements and benchmarking methodologies. *ECS Trans* 1:3–18
75. Debe M (2005) Advanced meas for enhanced operating conditions, amenable to high volume manufacture. DOE hydrogen program review. [http://www.hydrogen.energy.gov/pdfs/review05/fc3\\_debe.pdf](http://www.hydrogen.energy.gov/pdfs/review05/fc3_debe.pdf)
76. Debe M (2008) Advanced cathode catalysts and supports for pem fuel cells. [http://www.hydrogen.energy.gov/pdfs/review08/fc\\_1\\_debe.pdf](http://www.hydrogen.energy.gov/pdfs/review08/fc_1_debe.pdf)
77. Pivovar B (2010) Extended, continuous pt nanostructures in thick, dispersed electrodes. [http://www.hydrogen.energy.gov/pdfs/review10/fc007\\_pivovar\\_2010\\_o\\_web.pdf](http://www.hydrogen.energy.gov/pdfs/review10/fc007_pivovar_2010_o_web.pdf)
78. Conway BE (1995) Electrochemical oxide film formation at noble metals as a surface-chemical process. *Prog Surf Sci* 49:331–452
79. Conway BE, Barnett B, Angerstein-Kozlowska H (1990) A surface-electrochemical basis for the direct logarithmic growth law for initial stages of extension of anodic oxide films formed at noble metals. *J Chem Phys* 93:8361–8373
80. Conway BE, Jerkiewicz G (1992) Surface orientation dependence of oxide film growth at platinum single crystals. *J Electroanal Chem* 339:123–146
81. Bindra P, Clouser SJ, Yeager E (1979) Pt dissolution in concentrated phosphoric acid. *J Electrochem Soc* 126:1631
82. Wang X, Kumar R, Myers DJ (2006) Effect of voltage on platinum dissolution relevance to polymer electrolyte fuel cells. *Electrochem Solid-State Lett* 9:A225–A227
83. Wang X, Kariuki N, Vaughey JT, Goodpastor J, Kumar R, Myers DJ (2008) Bi-metallic Pd-cu oxygen reduction electrocatalysts. *J Electrochem Soc* 155:B602–B609
84. Jaouen F, Charretre F, Dodolet JP (2006) C-n4. *J Electrochem Soc* 153:A689
85. Medard C, Lefevre M, Dodolet JP, Jaouen F, Lindbergh G (2006) C-n4. *Electrochim Acta* 51:3202
86. Lefevre M, Proietti E, Jaouen F, Dodolet J-P (2009) Iron-based catalysts with improved oxygen reduction activity in polymer electrolyte fuel cells. *Science* 324:71
87. Campbell S (2005) Development of transition metal/chalcogen based cathode catalysts for PEM fuel cells.

- [http://www.hydrogen.energy.gov/pdfs/review05/fc13\\_campbell.pdf](http://www.hydrogen.energy.gov/pdfs/review05/fc13_campbell.pdf)
88. Zelenay P (2009) Advanced cathode catalysts. [http://www.hydrogen.energy.gov/pdfs/review09/fc\\_21\\_zelenay.pdf](http://www.hydrogen.energy.gov/pdfs/review09/fc_21_zelenay.pdf)
  89. Zelenay P (2010) Advanced cathode catalysts. [http://www.hydrogen.energy.gov/pdfs/review10/fc005\\_zelenay\\_2010\\_o\\_web.pdf](http://www.hydrogen.energy.gov/pdfs/review10/fc005_zelenay_2010_o_web.pdf)
  90. Bett JA, Kinoshita K, Stonehart P (1974) Crystallite growth of Pt dispersed on graphitized carbon black. *J Catal* 35:307–316
  91. Bett JA, Kinoshita K, Stonehart P (1976) Crystallite growth of Pt dispersed on graphitized carbon black ii effect of liquid environment. *J Catal* 41:124–133
  92. Cai M, Ruthkosky MS, Merzougui B, Swathirajan S, Balogh MP, Oh SH (2006) Investigation of thermal and electrochemical degradation of fuel cell catalysts. *J Power Sources* 160:977–986
  93. Kinoshita K (1988) Carbon electrochemical and physicochemical properties. Wiley, New York
  94. Yu PT, Gu W, Makharia R, Wagner F, Gasteiger H (2006) The impact of carbon stability on PEM fuel cell start-up and shutdown voltage degradation. ECS 210th Meeting, Abstract 0598.pdf. <http://www.electrochem.org/meetings/scheduler/abstracts/210/0598.pdf>
  95. Yu PT, Kocha SS, Paine L, Gu W, Wagner FT (2004) The effects of air purge on the degradation of PEMFCS during startup an shutdown procedures. Proceedings of AIChE 2004 Annual Meeting, New Orleans, 25–29 Apr 2004
  96. Kreuer KD, Paddison SJ, Spohr E, Schuster M (2004) PEM review. *Chem Rev* 104:4637–4678
  97. Kreuer KD, Schuster M, Obliers B, Diat O, Traub U, Fuchs A, Klock U, Paddison SJ, Maier J (2008) Short-side-chain proton conducting perfluoro-sulfonic acid ionomers: why they perform better in PEM fuel cells. *J Power Sources* 178:499–509
  98. Schuster MFH, Meyer WH, Schuster M, Kreuer KD (2004) Toward a new type of anhydrous organic proton conductor based on immobilized imidazole. *Chem Mater* 16:329–337
  99. Steininger H, Schuster M, Kreuer KD, Kaltbeitzel A, Bingol B, Meyer WH, Schauff S, Brunklaus G, Maier J, Spiess HW (2007) Intermediate temperature proton conductors for PEM fuel cells based on phosphonic acid as protogenic group: a progress report. *Phys Chem Chem Phys* 9:1764–1773
  100. Larson JM, Hamrock SJ, Haugen GM, Pham P, Lamanna WM, Moss AB (2007) Membranes based on basic polymers and perfluorinated acids for hotter and drier fuel cell operating conditions. *J Power Sources* 172:108–114
  101. Meng FQ, Aieta NV, Dec SF, Horan JL, Williamson D, Frey MH, Pham P, Turner JA, Yandrasits MA, Hamrock SJ, Herring AM (2007) Structural and transport effects of doping perfluorosulfonic acid polymers with the heteropoly acids, h3pw12o40 or h4siw12o40. *Electrochim Acta* 53:1372–1378
  102. Gervasio D (2010) Protic salt polymer membranes. [http://www.hydrogen.energy.gov/pdfs/review09/fc\\_06\\_gervasio.pdf](http://www.hydrogen.energy.gov/pdfs/review09/fc_06_gervasio.pdf)
  103. de Araujo CC, Kreuer KD, Schuster M, Portale G, Mendil-Jakani H, Gebel G, Maier J (2009) Poly (p-phenylene sulfone)s with high ion exchange capacity: ionomers with unique microstructural and transport features. *Phys Chem Chem Phys* 11:3305–3312
  104. Yi J (2007) Development of low-cost, durable membrane and MEA for stationary and mobile fuel cell applications. [http://www.hydrogen.energy.gov/pdfs/review07/fc\\_9\\_yi.pdf](http://www.hydrogen.energy.gov/pdfs/review07/fc_9_yi.pdf)
  105. Pintauro P (2010) Nanocapillary network proton conducting membranes for high temperature hydrogen/air fuel cells. [http://www.hydrogen.energy.gov/pdfs/review10/fc038\\_pintauro\\_2010\\_o\\_web.pdf](http://www.hydrogen.energy.gov/pdfs/review10/fc038_pintauro_2010_o_web.pdf)
  106. Hamrock SJ (2010) Membranes and meas for dry, hot operating conditions. [http://www.hydrogen.energy.gov/pdfs/review10/fc034\\_hamrock\\_2010\\_o\\_web.pdf](http://www.hydrogen.energy.gov/pdfs/review10/fc034_hamrock_2010_o_web.pdf)
  107. Mittelsteadt CK (2010) Dimensionally stable membranes. [http://www.hydrogen.energy.gov/pdfs/review10/fc036\\_mittelsteadt\\_2010\\_o\\_web.pdf](http://www.hydrogen.energy.gov/pdfs/review10/fc036_mittelsteadt_2010_o_web.pdf)
  108. Endoh E (2008) Progress of highly durable mea for PEMFC under high temperature and low humidity conditions. *ECS Trans* 12:41–50
  109. Endoh E, Terazono S, Widjaja H, Takimoto Y (2004) OCV degradation. *Electrochem Solid-State Lett* 7: A209–AA211
  110. Varcoe JR, Slade RCT, Yee E (2006) An alkaline polymer electrochemical interface: a breakthrough in application of alkaline anion-exchange membranes in fuel cells. *Chem Commun* 6:1428–1429
  111. Piana M, Boccia M, Filipi A, Flammia E, Miller HA, Orsini M, Salusti F, Santiccioli S, Ciardelli F, Pucci A (2010) H<sub>2</sub>/air alkaline membrane fuel cell performance and durability, using novel ionomer and non-Pt group metal cathode catalyst. *J Power Sources* 195:5875–5881
  112. Wang H, Turner JA (2010) Reviewing metallic PEMFC bipolar plates. *Fuel Cells* 10:510–519
  113. Brady MP, Wang H, Turner JA, Meyer HM, More KL, Tortorelli PF, McCarthy BD (2010) Pre-oxidized and nitrated stainless steel alloy foil for proton exchange membrane fuel cell bipolar plates: part 1. Corrosion, interfacial contact resistance, and surface structure. *J Power Sources* 195:5610–5618
  114. Dadheech G, Elhamid MHA, Blunk R (2009) Nano-structured and self-assembled superhydrophilic bipolar plate coatings for fuel cell water management. *Nanotech Conference & Expo 2009*, vol 3, Technical Proceedings, Austin, TX, pp 18–183

## Books and Reviews

- Alsabet M, Grden M, Jerkiewicz G (2006) Comprehensive study of the growth of thin oxide layers on pt electrodes under well-defined temperature, potential, and time conditions. *J Electroanal Chem* 589:120–127

- Bard AJ, Faulkner LR (1980) *Electrochemical methods*. Wiley, New York
- Bockris JO'M, Reddy AKN (1973) *Modern electrochemistry: an introduction to an interdisciplinary area*, vol 1. Springer, New York
- Borup RL, Meyers JP, Pivovar B, Kim YS, Mukundan R, Garland N, Myers DJ, Wilson M, Garzon F, Wood DL, Zelenay P, More K, Stroh K, Zawodzinski TA, Boncella J, McGrath J, Inaba M, Miyatake K, Hori M, Ota K-i, Ogumi Z, Miyata S, Nishikata A, Siroma Z, Uchimoto Y, Yasuda K, Kimijima K-i, Iwashita N (2007) Scientific aspects of polymer electrolyte fuel cell durability and degradation. *Chem Rev* 107:3904–3951
- Conway BE (1952) *Electrochemical data*. Greenwood Press, Westport
- Conway BE (1964) *Theory of principles of electrode processes*. Ronald Press, New York
- Conway BE (1995) Electrochemical oxide film formation at noble metals as a surface-chemical process. *Prog Surf Sci* 49:331–452
- Conway BE, Jerkiewicz G (1992) Surface orientation dependence of oxide film growth at platinum single crystals. *J Electroanal Chem* 339:123–146
- Gileadi E (1993) *Electrode kinetics*. VCH, New York
- Kinoshita K (1988) *Carbon electrochemical and physico-chemical properties*. Wiley, New York
- Kinoshita K (1992) *Electrochemical oxygen technology*. Wiley, New York
- Kocha SS (2003) Principles of MEA preparation. In: Vielstich W, Lamm A, Gasteiger H (eds) *Handbook of fuel cells-fundamentals, technology and applications*. Wiley, New York, pp 538–565
- Kocha SS, Yang DJ, Yi JS (2006) Characterization of gas crossover and its implications in PEM fuel cells. *AICHE J* 52:1916–1925
- Koppel T (1999) *Powering the future: the Ballard fuel cell and the race to change the world*. Wiley, New York
- Kreuer KD, Paddison SJ, Spohr E, Schuster M (2004) Pem review. *Chem Rev* 104:4637–4678
- Liebavsky HA, Cairns EJ (1968) *Fuel cells and batteries*. Wiley, New York
- Markovic NM, Ross PN (2000) Electrocatalysts by design: from the tailored surface to a commercial catalyst. *Electrochim Acta* 45:4101–4115
- Mathias MF, Makharia R, Gasteiger HA, Conley JJ, Fuller TJ, Gittleman CJ, Kocha SS, Miller DP, Mittelsteadt CK, Tao X, Yan SG, Yu PT (2005) Two fuel cell cars in every garage? *Electrochem Soc Interface* 14:24–35
- Mench MM (2008) *Fuel cell engines*. Wiley, Hoboken
- Pourbaix M (1966) *Atlas of electrochemical equilibrium in aqueous solutions*, 1st edn. Pergamon Press, New York
- Prentice G (1991) *Electrochemical engineering principles*. Prentice Hall, Englewood
- Savadogo O (1998) Emerging membranes for the electrochemical systems: (i) solid polymer electrolyte membranes for fuel cell systems. *J New Mater Electrochem Syst*:47–66
- Vetter KJ (1963) A general thermodynamic theory of the potential of passive electrodes and its influence on passive corrosion. *J Electrochem Soc* 110:597–605
- Wilson MS, Gottesfeld S (1992) High performance catalyzed membranes of ultra-low Pt loadings for polymer electrolyte fuel cells. *J Electrochem Soc* 139:L28–L30
- Zawodzinski TA, Derouin CR, Radzinski S, Sherman RJ, Smith VT, Springer TE, Gottesfeld S (1993) Water uptake by and transport through nafion 117 membranes. *J Electrochem Soc* 140:1041–1047



## PEM Fuel Cells: Materials and Design Development Challenges

Stephen J. Paddison<sup>1</sup> and Hubert A. Gasteiger<sup>2</sup>

<sup>1</sup>Department of Chemical and Biomolecular Engineering, University of Tennessee, Knoxville, TN, USA

<sup>2</sup>Department of Chemistry, Technische Universität München, Munich, Germany

### Article Outline

Glossary

Definition of the Subject and Its Importance

Introduction

Processes in an MEA and Voltage–Loss Terms

Ion and Water Transport in Ionomers

Degradation of Pt-Based Catalysts

Carbon-Support Corrosion

Membrane Development Needs and Approaches

Temperature Targets

Proton Conductivity

Reactant Gas Permeability

Morphology

Choice of the Protogenic Group

Future Directions

Bibliography

### Glossary

**Hydrogen oxidation reaction (HOR)** The electrochemical oxidation of molecular hydrogen occurring at the anode of a fuel cell.

**Membrane electrode assembly (MEA)** The assembly consisting of the electrolyte membrane sandwiched between the anode and cathode.

**Oxygen reduction reaction (ORR)** The electrochemical reduction of molecular oxygen through a four electron transfer at the cathode of a fuel cell.

**Perfluorosulfonic acid (PFSA)** The  $\text{CF}_2\text{SO}_3\text{H}$  group is the protogenic group on ionomers and membranes utilized in catalyst layer and electrolyte in a fuel cell.

**Proton exchange membrane (PEM)** A solid polymer thin film that is proton conducting and functions as the central component of a fuel cell.

### Definition of the Subject and Its Importance

Substantial resources have been devoted over the past decade to the development of proton exchange membrane (PEM) fuel cells that use hydrogen fuel and oxygen from the air to produce electricity for applications including automotive propulsion. Remaining challenges include the design of inexpensive and stable robust catalysts for the electrochemical reaction at the cathode (i.e., the reduction of oxygen) of the fuel cell and the synthesis of robust (i.e., chemical and mechanical stable) electrolyte membranes exhibiting high proton conductivity under hot and dry conditions.

### Introduction

The development of commercially viable proton exchange membrane (PEM) fuel cell systems powered by hydrogen or hydrogen-rich reformat faces a significant number of materials and MEA (membrane electrode assembly) design-related performance and durability challenges, which need to be addressed via:

1. Improvement of current platinum-based catalysts for the oxygen reduction reaction (ORR) and the hydrogen oxidation reaction (HOR) or substitution by platinum-group metal (PGM) free catalysts in order to meet the platinum cost and design constraints for commercial applications [1].

2. Development of more durable ORR and HOR catalysts, which are resistant to the voltage-cycles occurring during the transient operation of fuel cell vehicles (owing to the variable power demand during typical vehicle drive cycles) [2, 3].
3. Substitution of currently used perfluoro-sulfonic acid (PFSA) ionomers and ionomer membranes (e.g., Nafion<sup>®</sup>) by novel materials with substantially improved proton conductivity at low relative humidity (RH), which would eliminate the need for fully humidified reactants and thereby significantly simplify fuel cell system design [2, 4, 5].
4. Modification/development of ionomers and ionomeric membranes to obtain enhanced chemical durability under low-RH conditions [6, 7] as well as increased mechanical stability during RH-cycles, both of which are frequently occurring conditions under automotive fuel cell operation [2, 8].
5. Replacement of current high-surface area carbon supports (e.g., Ketjen blacks) with more corrosion-resistant materials (e.g., fully graphitized carbon supports or noncarbon-based supports) in order to minimize the damage caused by local hydrogen starvation [9, 10] and during fuel cell start/stop processes [11, 12], so that more complex system-design based mitigation strategies can be avoided [13].
6. Design of HOR catalysts which have no activity for the ORR [14] and their integration into anode electrodes, which is an alternative approach to mitigating degradation caused by start/stop.
7. Mitigation of possible cell-voltage reversal caused by temporary hydrogen under-supply during fast transients, which can be achieved by incorporation of efficient oxygen evolution catalysts into the anode electrode [15] or by corrosion-resistant anode catalyst supports (e.g., whisker electrodes developed by 3 M [16]).
8. Optimization of electrode and MEA performance with new electrode materials (catalysts, catalyst supports, and ionomers [2]), particularly for high-current density operation with low platinum loadings.
9. Design of high-performing gas-diffusion media (DM) and microporous layer (MPL) coatings which are resistant to contamination [17] and aging caused by fuel cell system transients (i.e., extensive voltage-cycling, start/stop [18]).
10. Development of ab initio catalyst models, particularly for the ORR catalysis [19] as well as rigorous MEA performance models [20, 21] and in situ diagnostic methods [22–24] in order to provide effective analytical methods required for the screening and implementation of improved electrode materials and MEA designs.

Despite this impressively long list of technical hurdles, the development of fuel cell vehicles has advanced significantly in the past 10 years, and hydrogen fuel cell vehicle fleet tests are now demonstrating drive-cycle efficiencies of 52–58% (lower heating value), real-world vehicle operating life ranging from 700 to 1900 h, and refueling times on the order of 5 min [25], with the capability of starting from temperatures as low as  $-20\text{ }^{\circ}\text{C}$  [26]. Nevertheless, in order to meet the automotive cost targets (<50 US\$ per kW system power), the platinum supply constraints (<10 g platinum per vehicle), and the required durability targets (6000 operating hours), the above listed challenges remain and the cutting-edge research on these topics is being presented in the subsequent entries of this book.

In the following, we will provide only a very brief overview of some of the basic materials and MEA design concepts and the interested reader is referred to the very detailed articles in the remainder of this encyclopedia or to the cited literature.

### Processes in an MEA and Voltage-Loss Terms

In order to define the limiting factors in fuel cell performance, it is helpful to review the various reactions and transport processes occurring in a PEM fuel cell, which are illustrated in Fig. 1. The HOR and ORR reactions catalyzed by the anode and cathode catalysts, respectively, require facile proton transport through the ionomeric membrane and also throughout the porous electrodes which are typically composed of carbon-supported

catalysts and proton-conducting ionomer (exceptions are nanostructured electrodes, for example, those developed by 3 M [16]). At the same time, hydrogen and oxygen supplied via flow-field channels in the bipolar plates (BP, see Fig. 1) need to be supplied via gas-phase diffusion through the porous gas-diffusion layers [27] and throughout the electrodes. At the design point for automotive operating conditions, that is, at an average humidity of the exiting gas-streams of <100% [20], reactant diffusion can be described by a simple effective diffusion coefficient [28]. However, under conditions where the relative humidity of the exiting gas-streams exceeds 100% (e.g., at fuel cell temperatures below 50 °C), the quantitative description of gas transport is more complex due to the presence of liquid water inside the porous layers [29].

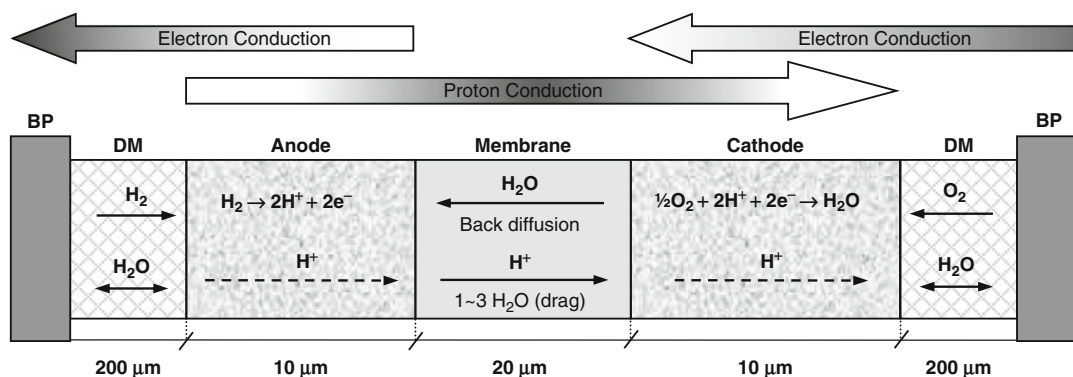
The local relative humidity also determines the proton conductivity of the ionomeric membrane [30] and of the electrodes [31], leading to major voltage losses below 50% RH. An additional voltage loss, particularly at high-current densities and low relative humidity, arises from the dry-out of the anode-side of the membrane, which is due to the electro-osmotic drag of water caused by protons flowing from the anode to the cathode (vide infra). Owing to the drastically increasing proton conduction resistance at low RH [30], the associated voltage loss can be substantial, unless membranes are very thin in order

to allow for fast water back-transport from the cathode to the anode; for this reason, membranes in state-of-the-art PEMFCs are typically not thicker than 15–20 μm.

In addition to the voltage losses caused by the overpotentials of the HOR,  $\eta_{HOR}$ , and the ORR,  $\eta_{ORR}$ , as well as by the proton- and gas-transport resistances, substantial voltage losses can arise from purely electronic resistances from the bipolar plate all the way throughout the electrode,  $R_{electronic}$ . However, the bulk resistances of carbon-black based electrodes, carbon-fiber based diffusion media, and stainless steel or carbon-composite based bipolar plates are generally negligible compared to the electronic contact resistances between electrodes/DMs and DMs/BPs [20], so that the measured electronic resistances are mostly due to contact resistances. The largest contribution here comes from the strongly compression-dependent contact resistance between the bipolar plate and carbon-fiber based diffusion media [27].

The above described voltage losses can be summarized by a conceptually simple equation, describing the fuel cell voltage,  $E_{cell}$ , as a function of current density,  $i$ :

$$E_{cell} = E_{rev.} - i \times (R_{electronic} + R_{membrane}) - \eta_{HOR} - \eta_{ORR} - i \times R_{H^+,eff.} - \eta_{tx,gas(dry)} - \eta_{tx,gas(wet)} \quad (1)$$



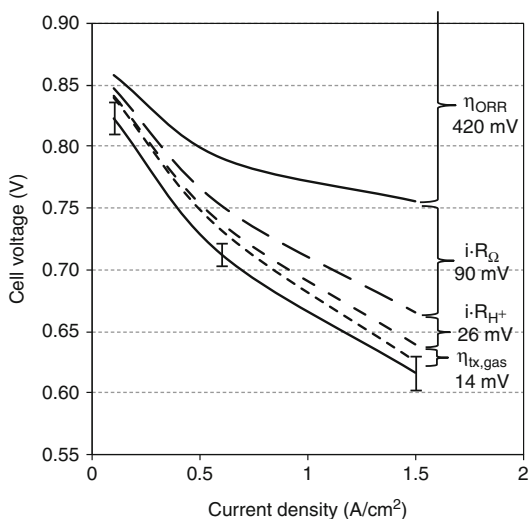
**PEM Fuel Cells: Materials and Design Development Challenges, Fig. 1** Schematic of a PEMFC repeating unit showing the electrode reactions,  $H_2$  and  $O_2$  gas transport, water transport, as well as proton and electron charge

transfer. Typical values of component thickness are shown (not drawn to scale). (Reproduced from W. Gu et al. [20] by permission from Wiley)



where  $E_{rev}$  is the reversible thermodynamic potential depending on temperature and gas partial pressure. The proton conduction resistances of the membrane,  $R_{membrane}$ , and the electrodes,  $R_{H^+,eff}$ , are strongly dependent on the local relative humidity and, in contrast to  $R_{electronic}$ , do also depend on current density and on the local temperature which again is mostly determined by thermal conductivity resistances between the electrode/DM and the DM/bipolar plate interfaces [20, 31, 32]. For fuel cells fed with pure hydrogen and air, the gas-diffusion overpotential,  $\eta_{tx,gas(dry)}$ , is primarily due to the diffusion of oxygen in air through the diffusion medium and the cathode electrode in the absence of liquid water, that is, at operating conditions where the RH of the exiting reactants is  $<100\%$ ; the additional gas-diffusion overpotential losses caused by the presence of liquid water in the diffusion media and the electrodes are here described as  $\eta_{tx,gas(wet)}$  and become significant at wet operating conditions (i.e., at  $>100\%$  RH of the exiting reactants).

The various voltage losses under typical automotive operating conditions are shown in Fig. 2. At the highest current density of  $1.5 \text{ A cm}^{-2}$ , the voltage loss caused by the slow ORR kinetics amounts to approximately 70% of the overall voltage loss, while the voltage loss for the HOR is negligibly small under these conditions ( $\ll 5 \text{ mV}$  [33]). At the maximum power density of  $0.93 \text{ W cm}^{-2}$  ( $0.62 \text{ V}$  at  $1.5 \text{ A cm}^{-2}$ ) and the total platinum loading of  $0.5 \text{ g}_{Pt} \text{ cm}^{-2}$  shown in Fig. 2, the platinum specific power density is  $0.54 \text{ g}_{Pt} \text{ kW}^{-1}$ , implying that  $54 \text{ g}_{Pt}$  would be required for a typical  $100 \text{ kW}$  automotive fuel cell. Even though the fast HOR kinetics allow for a lowering of the anode catalyst loading to  $0.05 \text{ mg}_{Pt} \text{ cm}^{-2}$  without notable performance loss [33], the thus obtained platinum specific power density of  $0.38 \text{ g}_{Pt} \text{ kW}^{-1}$  is still too high for commercially viable fuel cells. Therefore, major foci in current fuel cell R&D is the development of either more active platinum-based ORR catalysts or of PGM-free ORR catalysts [1, 34, 35] as well as the development of suitable electrode structures for these novel catalysts. The other voltage loss terms shown in Fig. 2 are



**PEM Fuel Cells: Materials and Design Development Challenges, Fig. 2** Voltage loss terms in state-of-the-art  $\text{H}_2/\text{air}$  PEMFCs operated under representative automotive conditions. *MEAs*:  $0.2/0.3 \text{ mg}_{Pt} \text{ cm}^{-2}$  (anode/cathode) coated on an  $18 \mu\text{m}$  thick composite membrane and sandwiched between  $\approx 200 \mu\text{m}$  thick DMs (SGL 25 BC). *Operating conditions*:  $\text{H}_2$  and air stoichiometric flows of 2 and 1.8–5.5, respectively, stack pressure of 110–176  $\text{kPa}_{abs}$ , gas inlet humidities of 30–60% RH, and stack temperature of 70–80 °C. For details see [20]. (Reproduced from W. Gu et al. [20] by permission from Wiley)

significantly smaller and dominated by the ohmic resistances,  $R_{\Omega}$ , which represent  $R_{membrane}$  and  $R_{electronic}$  (s. Eq. 1), whereby 60 of the 90 mV losses at  $1.5 \text{ A cm}^{-2}$  are mostly due to the electronic contact resistance between the DMs and the bipolar plates.

From a systems point of view, it would also be desirable to develop ionomers and ionomeric membranes with increased conductivity at low RH, since this would enable the design of fuel cell systems operating with either dry gas-feeds and/or at higher fuel cell temperature [5]. The latter would reduce the vehicle radiator requirements, which are quite demanding for fuel cell vehicles due to the large heat load which has to be dissipated via the radiator [4], contrary to internal combustion engine-based vehicles where a large fraction of the produced heat is discharged via the latent heat of the engine exhaust gases. A brief discussion on the membrane development toward this goal is given below.



## Ion and Water Transport in Ionomers

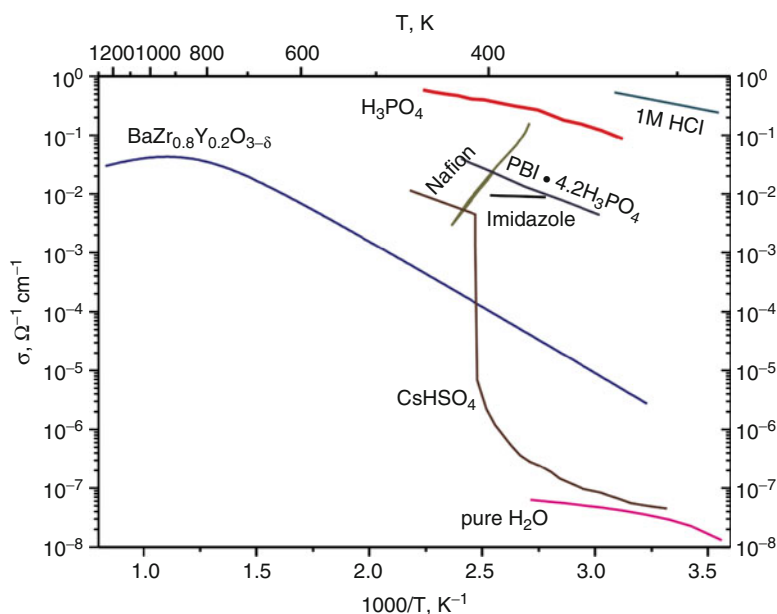
The central component of a PEM fuel cell is a thin film polymer that is an ionomer or ion-containing polymer that critically functions as the separator of gases and electrodes but also as a proton conductor completing the internal circuit. Typically, a proton conductivity of  $0.1 \text{ S cm}^{-1}$  is required for efficient function of the fuel cell. PEMs for automotive applications require that the ionomer function both at high temperature ( $>90 \text{ }^\circ\text{C}$ ) to dissipate waste heat and low pressures ( $<170 \text{ kPa}_{\text{abs}}$ ) to minimize pumping parasitics [2]. This necessitates operation at low relative humidities but currently utilized PFSA-based PEMs require water to facilitate the dissociation and long range transport of protons [36]. Although there are a large number of materials and systems that conduct protons (as shown in Fig. 3), those exhibiting sufficient proton conductivity in the target temperature range (for fuel cell operation) are almost nonexistent. It is also interesting to note that while the majority of the materials substances display an increase in conductivity with increasing temperature, the benchmark PFSA ionomer Nafion<sup>®</sup> exhibits just the opposite if the water vapor pressure remains constant (note: this means that the relative humidity decreases with

increasing temperature). This is, of course, due to the dehydration of the membrane as the temperature approaches and then exceeds the boiling point of water (at a water pressure of 1 atm.). All PFSA ionomers show a sharp decrease in proton conductivity as the water content falls (see the entry on ► “Proton Exchange Membrane Fuel Cells: High-Temperature, Low-Humidity Operation” by Hamrock and Herring). Several different approaches have been used to improve the proton conductivity of PEMs including changes in the backbone and/or side chain chemistry and are described in detail in the entry ► “Membrane Electrolytes, from Perfluorosulfonic Acid (PFSA) to Hydrocarbon Ionomers” by Miyatake.

Several approaches have been devised to reduce the resistance of the membrane at low RH, including increasing the density of the acidic groups and making the membrane thinner. There is, of course, a limit to the extent to which the acid content may be increased, and the membrane thickness decreased. Membranes with a very high ion exchange capacity suffer mechanical robustness as the low degree of crystallinity and high amounts of water result in materials that dissolve and/ or fall apart. Very thin membranes are also prone to mechanical failure and are no longer impermeable to gases which results in both

### PEM Fuel Cells: Materials and Design Development Challenges,

**Fig. 3** Measured proton conductivity for various materials as a function of temperature. In the temperature regime of interest (80–120 °C) for PEM fuel cells, the only presently available conductors are the hydrated ionomers (Nafion<sup>®</sup>, etc.) and display a significant decrease in conductivity as the temperature is increased (due to a decrease in water content)



loss of performance and membrane degradation due to the crossover of the reactant gases. Further details of these issues are provided in the entry on ► “Proton Exchange Membrane Fuel Cells: High-Temperature, Low-Humidity Operation”.

## Degradation of Pt-Based Catalysts

A significant part of the performance degradation of fuel cells with current platinum-based catalysts derives from the dissolution and sintering of platinum. This is due to the relatively high solubility of platinum in the strongly acidic electrolyte [37], whereby the dissolution rate is enhanced by voltage-cycling of the cathode electrode during the dynamic load-following required by the fuel cell in automotive drive cycles [2, 37]. The enhanced Pt dissolution rate is caused by the transition between mostly metallic platinum at high-current density (viz., at high

cathode overpotential) and an oxidized platinum surface at low current density or open circuit potential (viz., at low cathode overpotential) [38, 39]. As illustrated in Fig. 4, dissolved platinum species either redeposit on other platinum particles via an Ostwald ripening process or diffuse in the electrolyte phase toward the membrane, where they precipitate inside the ionomer phase by reaction with hydrogen which is permeating through the membrane from the anode side. Within the ionomer phase, precipitated platinum crystallites form a clearly defined platinum band (see Fig. 4b), the location of which can be predicted by the partial pressure of hydrogen and oxygen in the anode and cathode feed-gases, respectively [40].

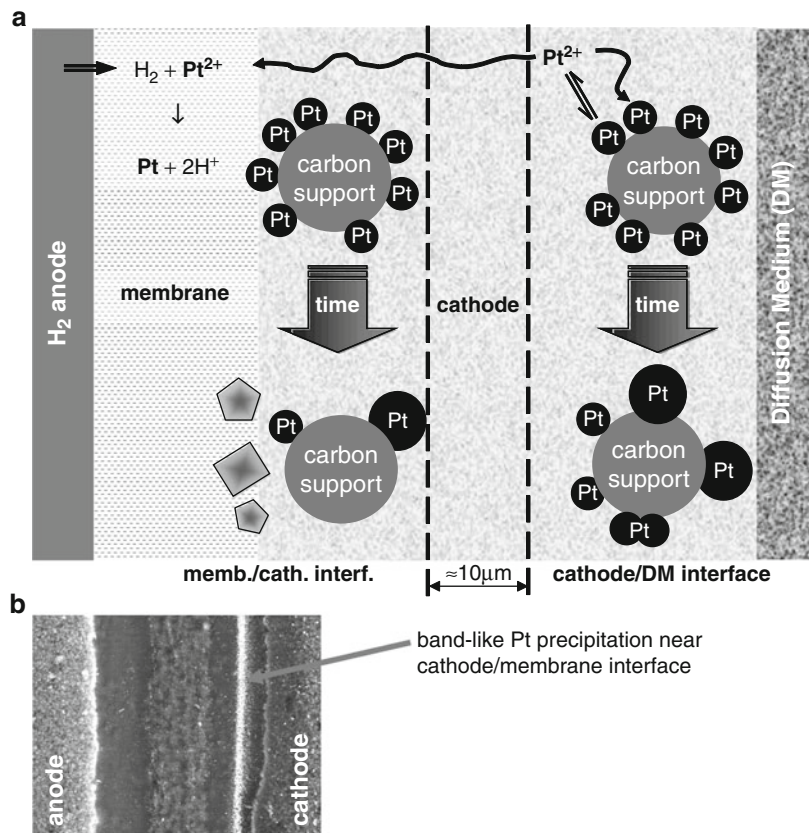
Since several hundred thousand large voltage-cycles would be encountered during the lifetime of an automotive fuel cell [2], the associated significant loss of active platinum surface area must be mitigated either by more dissolution-resistant

### PEM Fuel Cells: Materials and Design

#### Development

#### Challenges, Fig. 4 (a)

Schematic representing platinum surface area loss on (i) the nanometer scale, where platinum particles grow on the carbon support via Ostwald ripening and (ii) the micrometer scale, where dissolved platinum species diffuse toward the membrane, become reduced by hydrogen permeating from the anode through the membrane, and precipitate as platinum particles in the membrane. (b) SEM cross section of a short-stack MEA operating at open circuit voltage for 2000 h, where the bright band in the image indicates platinum deposited in the membrane near the membrane/cathode interface. (Reproduced from P. J. Ferreira et al. [37] by permission from The Electrochemical Society)



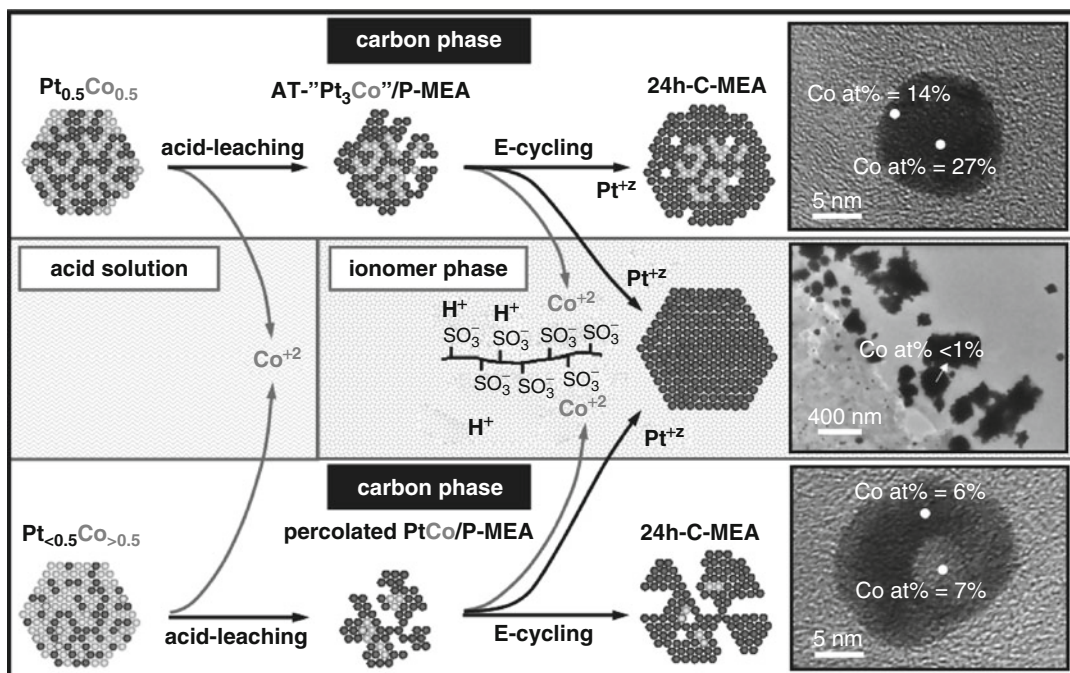
cathode catalysts or by hybridizing a fuel cell system with a large propulsion battery (tens of kW battery power), by which the number of large voltage-cycles can be substantially reduced. In many instances, it was observed that platinum-alloy catalysts displayed an increased resistance to platinum dissolution [2, 3, 41], but much of the effect is due to the larger particle size of platinum-alloys which favorably affects the platinum dissolution rate via the Gibbs-Thomson effect [42]. Indeed, more recent data demonstrated that voltage-cycling of platinum-alloy cathode catalysts leads to core/shell structures, with platinum-shells forming around a platinum-alloy core, so that the initially higher specific activity of platinum-alloys slowly approaches that of pure platinum in the

course of extensive voltage-cycling [43]. This phenomenon is illustrated in Fig. 5.

In summary, while fuel cell/battery hybrid systems reduce the degradation from platinum surface area loss from voltage-cycling to an acceptable level, novel cathode catalysts with increased stability toward voltage-cycling would bring significant benefits and are therefore a very active field of research.

### Carbon-Support Corrosion

The excellent gas-transport properties of fuel cell electrodes are due to their high porosity, with void volume fractions of  $\approx 60\%$  for the typical



**PEM Fuel Cells: Materials and Design Development Challenges, Fig. 5** Schematic of the evolution in morphology and composition of a Pt<sub>0.5</sub>Co<sub>0.5</sub> cathode catalyst caused by acid leaching and voltage-cycling. The *upper panel* represents particles attached to the carbon-support ("carbon phase"), with *skeleton* Pt<sub>x</sub>Co particles obtained after acid leaching, and transforming via Ostwald ripening into *core/shell* particles. The *center panel* represents both the liquid acid phase during pre-leaching and the "ionomer phase" both in the membrane and the electrodes, with large single-crystalline Pt (agglomerates) forming in the

membrane and Co<sup>2+</sup> ion-exchanging into the ionomer phase. The *lower panel* is a proposed mechanism for the formation of *percolated* Pt<sub>x</sub>Co alloy particles deriving from precursors with higher than average Co content ("Pt < 0.5Co > 0.5") and resulting in Pt-rich *spongy particles*. TEM bright-field images and spot-resolved EDS compositions (analysis area of 2.5 nm in diameter) of the various types of aged nanoparticles in the 24 h-C-MEA are shown on the right-hand-side. (Reproduced from S. Chen et al. [43] by permission from The Electrochemical Society)

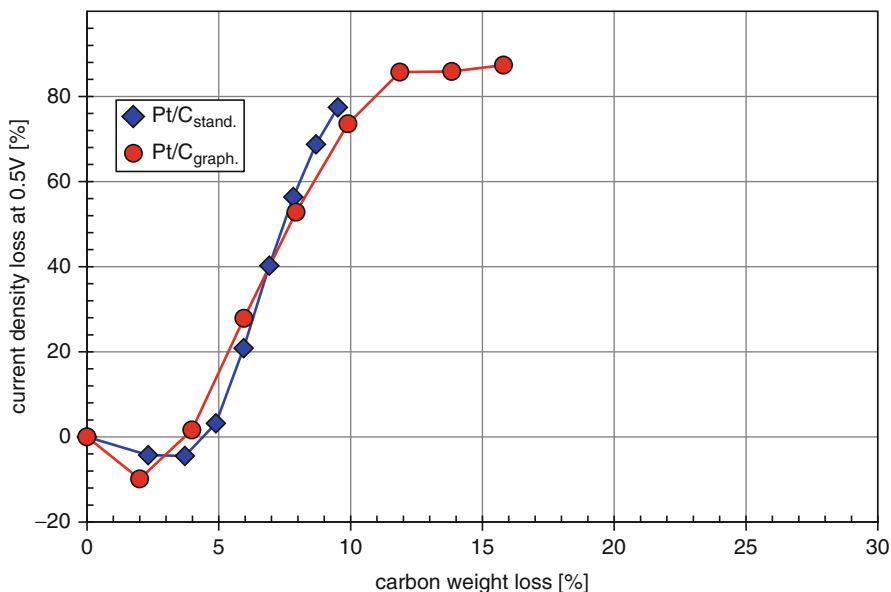
ionomer/ carbon weight ratios of 1/1 (volume fractions of ionomer and carbon being  $\approx 20\%$  each) [20]. This high void volume fraction is due to the use of highly structured carbon blacks (e.g., Vulcan XC72 or Ketjen black), which have an intrinsically low packing density which is maintained up to compressions of  $\approx 100$  MPa (in comparison, MEAs in fuel cell stacks are compressed at  $\approx 1$  MPa). However, at sufficiently high potentials, viz., above  $\approx 1$  V versus the reversible hydrogen electrode (RHE) potential, the electrochemical oxidation of carbon by water ( $C + 2H_2O \rightarrow CO_2 + 4H^+ + 4e^-$ ) is substantial, and after the oxidation of approximately 5–10 wt.% of the carbon support, the carbon structure collapses [44], resulting in a rapid decrease of the fuel cell performance, as is shown in Fig. 6.

Under normal fuel cell operating conditions, the highest oxidative potentials in the cathode range between  $\approx 0.6$  V (vs. RHE) at high-current density and  $\approx 0.95$  V (vs. RHE) at open circuit (the anode potential remains always near 0 V vs. RHE), so that carbon-support corrosion is negligible. However, under start/stop conditions or in the case of localized hydrogen starvation, the

cathode potential significantly exceeds 1 V versus RHE and the associated rapid carbon-support corrosion leads to a loss of electrode void volume which experimentally is observed as a so-called cathode thinning. This is illustrated by the SEM cross section shown in Fig. 7 for a cathode electrode, where 8 wt.% of the carbon support had been oxidized by applying a cathodic potential (the extent of carbon support-corrosion was measured by on-line monitoring of the  $CO_2$  formation rate).

As shown in Fig. 7, the extent of cathode thinning can be monitored by cross section measurements via SEM or optical microscopy [23]. It is accompanied by a loss of electrode void volume as is illustrated in Fig. 8, showing high-resolution SEM cross sections of a nondegraded cathode electrode (left-hand-side) and of a degraded cathode (right-hand-side).

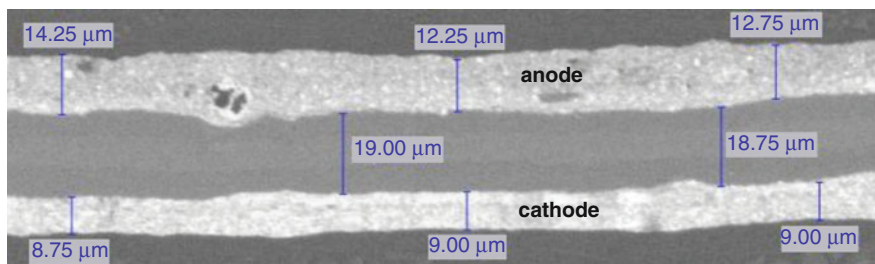
The fundamental start/stop mechanism was first reported by Reiser et al. [11], and occurs when one part of the anode flow-field is partially filled with hydrogen and another part is filled with air, a situation which occurs during the start-up of a fuel cell (hydrogen displacing air in the anode



**PEM Fuel Cells: Materials and Design Development Challenges, Fig. 6** Fuel cell performance loss as a function of the extent of carbon-support corrosion. Conditions:

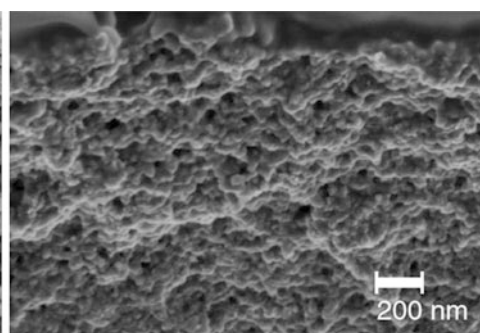
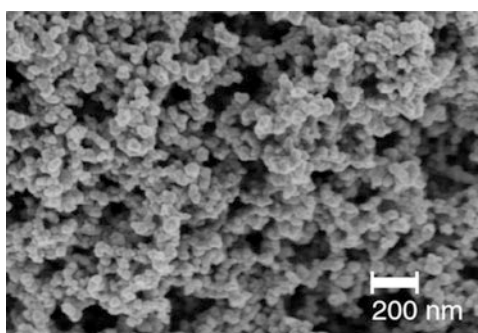
$H_2/air$  ( $s = 2/2$ ) performance at  $80^\circ C$ , 100%RH, 150 kPa<sub>abs</sub> (Reproduced from H.A. Gasteiger et al. [3] by permission from Springer)





**PEM Fuel Cells: Materials and Design Development Challenges, Fig. 7** Scanning electron microscopy (SEM) cross section of an MEA of which 8% wt. of the cathode carbon-support had been corroded (see also

Fig. 6). The initial cathode electrode thickness was identical to the anode electrode thickness shown in the picture. (Reproduced from H.A. Gasteiger et al. [3] by permission from Springer)



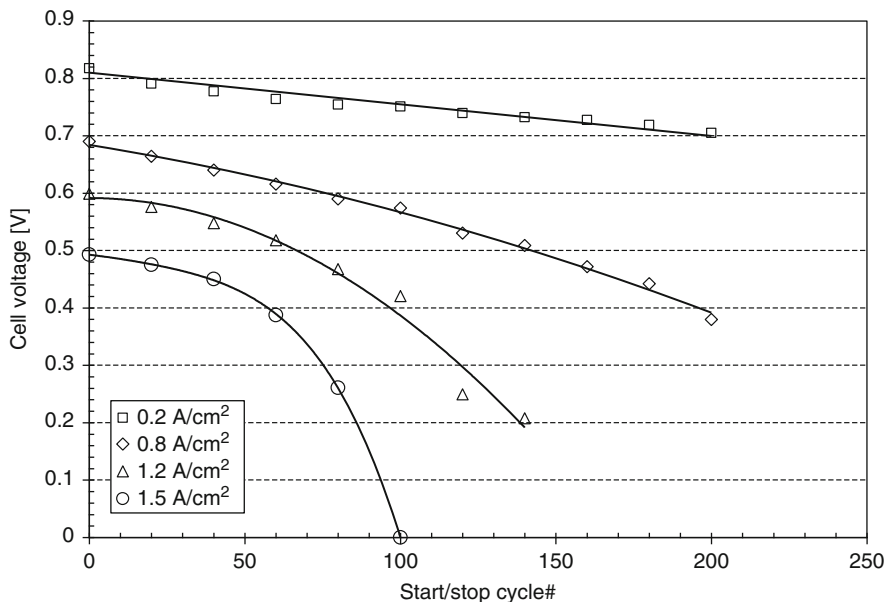
**PEM Fuel Cells: Materials and Design Development Challenges, Fig. 8** SEM micrographs of freeze fractured sections of the cathode electrodes of MEAs. *Left*: non-degraded MEA; *right*: MEA aged by localized hydrogen

starvation. SEM analysis was done without mounting of the MEAs in epoxy. (Reproduced from R.N. Carter et al. [23] by permission from John Wiley & Sons)

flow-field) or during shutdown (air diffusing into a hydrogen filled anode flow-field after the hydrogen supply is shut off). Detailed explanations of the processes which lead to very high voltages on the cathode electrode ( $\gg 1$  V vs. RHE) have been given elsewhere [11, 34] and the interested reader is referred to these references. The voltage degradation rates produced by start/stop can be simulated conveniently by sending  $H_2$ /air fronts through the anode flow-field of a fuel cell (single cell or stack), whereby the voltage degradation rates are proportional to the residence time of the  $H_2$ /air front and increase with increasing current density [12], as would be expected for gas-transport induced voltage losses. Such an experiment is shown in Fig. 9, whereby the  $H_2$ /air-front residence time of 1.3 s is roughly 10 times longer than that which can be achieved during the start-up of a fuel cell stack (residence times much

shorter than 0.1 s are typically not achievable due to engineering constraints). Under these conditions, the cell voltage at  $1.5 \text{ A cm}^{-2}$  decreases to 0 V within only 100 cycles! Under normal start-up conditions, the residence time would be roughly 10 times shorter, so that a maximum of 1000 start-up cycles could be performed, which is far short from the automotive target of  $\approx 40,000$  starts during the life time of a vehicle.

Therefore, mitigation strategies had to be devised and implemented. Currently, most mitigation strategies are based on system design (short residence times, stack storage under hydrogen, cell shorting, etc. [13]), but on the long-term, additional materials-based mitigation strategies are required. These include implementation of graphitized carbon-supports [12, 44, 45] or of more corrosion-resistant alternative support materials, lowering of the anode catalyst loading which



**PEM Fuel Cells: Materials and Design Development Challenges, Fig. 9** Cell-voltage decays for different current densities as a function of start/stop cycles for an MEA with a platinum catalyst supported on a conventional

carbon-support. Conditions: H<sub>2</sub>/air (66% inlet RH) at 150 kPa<sub>abs</sub> and 80 °C, aged at a H<sub>2</sub>/air-front residence time of 1.3 s. (Reproduced from P. T. Yu et al. [12] by permission from The Electrochemical Society)

reduces the ORR activity of the anode electrode or development of anode catalysts with low ORR activity [14], or the incorporation of highly active oxygen evolution catalysts in the cathode electrode. Again, the reader is referred to the literature for a detailed discussion [12, 44, 45].

A mechanism very closely related to the start/stop degradation is the so-called localized hydrogen starvation. It was first discussed by Patterson and Darling [9], and occurs when large sections of the anode flow-field are not being supplied with hydrogen due to blockage of the flow-field channel or of the diffusion medium by liquid water. In that case, oxygen permeating through the membrane from the anode to the cathode side creates an analogous situation to that produced by a H<sub>2</sub>/air front, viz., the simultaneous presence of hydrogen and oxygen in the anode. Consequently, cathode thinning is observed also in the case of localized hydrogen starvation [10, 23], albeit at a slower rate. While the systems mitigation strategies are different from those used in the case of start/stop, the materials mitigation strategies are identical, with one additional materials mitigation

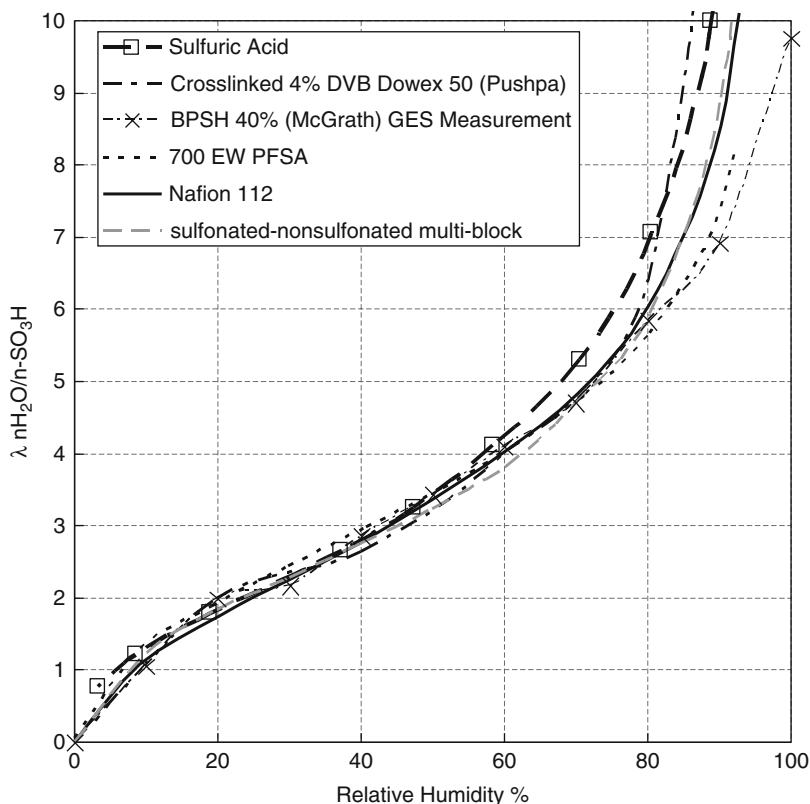
approach: since the maximum carbon corrosion rate is limited by the oxygen permeation rate through the membrane, ionomeric membranes with reduced oxygen permeability (typical for most hydrocarbon-based ionomers) would lower the damage by localized H<sub>2</sub> starvation [10].

## Membrane Development Needs and Approaches

As indicated earlier, water is needed in the membrane to dissociate protons (i.e., making the material proton conducting) from the acid functionality or protogenic groups and then secondly to establish a continuous pathway for long range proton transport. The water content of a PEM decreases with decreasing water activity. It has been observed [30] that the water uptake in sulfonic acid (–SO<sub>3</sub>H)-based PEMs is essentially identical when plotted as function of the water content when the latter is expressed in terms of,  $\lambda$ , the number of water molecules per acid group (i.e.,  $\lambda = \text{H}_2\text{O}/\text{SO}_3\text{H}$ ) as seen in Fig. 10. It is also clear

### PEM Fuel Cells: Materials and Design Development Challenges,

**Fig. 10** Water uptake isotherms of various ionomers and sulfuric acid at 80 °C. Dowex 50 is an ion-exchange resin made of 4% cross-linked polystyrene divinyl benzene; BPSH 40 is a 2-mil 40% randomly sulfonated biphenol sulfone; 700 EW PFSA is a 1-mil membrane with a structure similar to Nafion®; Nafion 112® is a 2-mil extruded membrane; and, PAEK triblock is a 1-mil triblock polyaryl ether ketone with a sulfonated middle block. (Reproduced from C.K. Mittelsteadt and H. Liu [30], by permission from John Wiley & Sons)



from this data that the isotherms of the various PEM are essentially identical to that of sulfuric acid at relatively low levels of hydration (i.e.,  $\lambda < 6$ ), suggesting that it is the enthalpy of hydration of the  $-\text{SO}_3\text{H}$  group which is driving water uptake in the low-RH region.

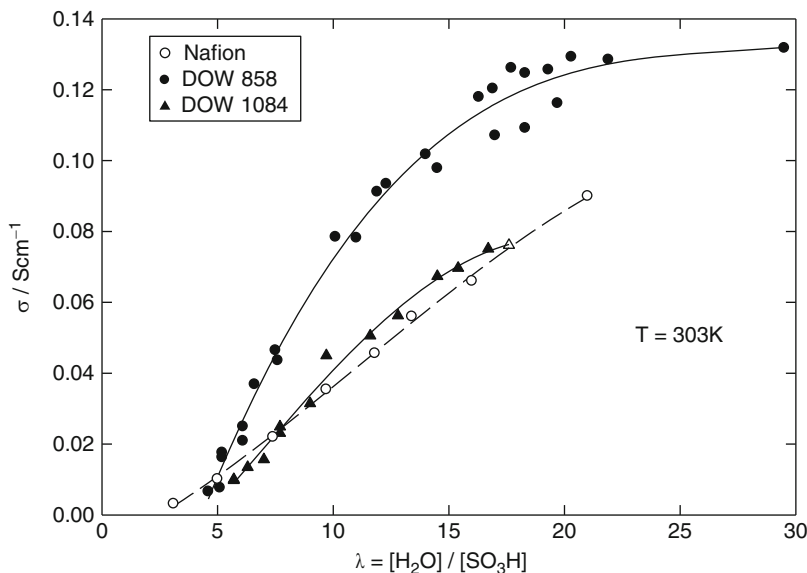
This experimental isotherm has been shown to fit either the Brunauer-Emmett-Teller model [46] or a simple empirical polynomial fit at a given temperature [47]. Finally, above  $\lambda \approx 6$  (i.e.,  $>80\%$  RH) the isotherms diverge, indicating that properties including polymer structure and morphology, charge density, cross-linking, etc., impact the absorption of water at high water content.

### Temperature Targets

For automotive application, it has been determined that a reasonable target for high

temperature membrane operation is between 110 °C and 120 °C for  $\text{H}_2$  fueled fuel cell vehicles [5]. Heat rejection at this temperature with conventional packaging becomes feasible and the purity requirement for onboard  $\text{H}_2$  is reduced as the tolerance for CO improves to approximately 50 ppmv CO without air bleed at low anode catalyst loading ( $0.1\text{--}0.2 \text{ mg}_{\text{noble-metal}} \text{ cm}^{-2}$ ) [48]. Operation of stationary systems at 140–160 °C with hydrocarbon-based  $\text{H}_2$  reformate would result in an increase in CO tolerance to about 0.1–0.5% allowing for a simpler or possibly no preferential oxidation (PROX) reactor. Although there is a small improvements in the oxygen reduction reaction kinetics if the system were operated at 160 °C, this would be offset with a loss of about 70 mV in equilibrium voltage [49]. Furthermore, the strong specific adsorption of phosphate ions on platinum catalysts leads to a reduced ORR activity in the presence of phosphoric acid electrolyte if compared to sulfonic acid-





**PEM Fuel Cells: Materials and Design Development Challenges, Fig. 11** Room temperature proton conductivity of the short side chain (SSC) PFSA ionomer at two different (i.e., Dow 858 and Dow 1084  $g_{\text{ionomer}}$  per  $\text{mol}_{\text{H}^+}$ ) equivalent weights (EW) and Nafion as a function of water

content expressed as  $\lambda = [\text{H}_2\text{O}]/[-\text{SO}_3\text{H}]$ . The data clearly shows the significant effect the equivalent weight has on proton conductivity with the Dow 858 exhibiting conductivity twice that of the higher EW PFSA. (Reproduced from K. D. Kreuer et al. [52] by Elsevier Science)

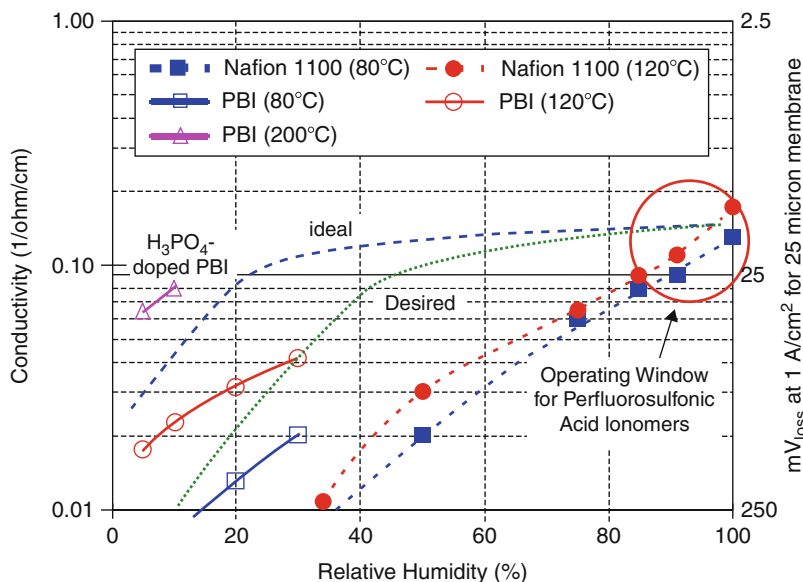
based ionomers (see Table 4 and Fig. 20 in [50]). At temperatures  $>160$  °C, the stability of the carbon-support material is compromised [51].

## Proton Conductivity

Figure 11 displays the results of a seemingly rather subtle change in the length of the side chain in PFSA membranes: the Dow ionomers have a shorter perfluoroether side chain ( $-\text{OCF}_2\text{CF}_2\text{SO}_3\text{H}$ ) than Nafion ( $-\text{OCF}_2\text{CF}(\text{CF}_3)\text{OCF}_2\text{CF}_2\text{SO}_3\text{H}$ ). This plot clearly indicates that the density of the sulfonic acid groups as realized through alteration of the equivalent weight (EW, the grams of polymer per mole of acid) may bring about a fairly large change in the proton conductivity across the majority of the hydration isotherm. The proton conductivity of both ionomers, however, drops precipitously at water contents below 5  $\text{H}_2\text{O}/\text{SO}_3\text{H}$ .

The dependence of proton conductivity on RH for 1100 EW Nafion at 80 °C and 120 °C is shown in Fig. 12 and indicates that although the conductivity falls from about 0.10 to 0.01  $\text{S cm}^{-1}$  as the

relative humidity is decreased from 100% to  $\approx 30\%$  it is essentially independent of temperature [5]. This is in stark contrast to polybenzimidazole (PBI) and phosphoric acid-doped PBI (also plotted in Fig. 12) which although exhibiting the typical fall in proton conductivity as the hydration level is decreased, show significantly higher conductivity at elevated temperatures [54]. Although the PBI systems appear to offer the promise of high temperature fuel cell operation, they suffer from other issues including adsorption on the surfaces of platinum-based catalysts and the leaching of phosphoric acid from the electrolyte. Although a significant body of research has focused on determining the hydrated morphology of PFSA membranes, the connections between the structure and morphology with the transport properties are not fully understood. The microstructure of the PFSA polymer not only affects the proton conductivity but also other properties including methanol permeability (i.e., for direct methanol fuel cells), water diffusion, and electro-osmotic drag.



**PEM Fuel Cells: Materials and Design Development Challenges, Fig. 12** Relationship between proton conductivity and adjoining gas stream humidity at various temperatures for Nafion (1100 EW) [5] and phosphoric acid-doped polybenzimidazole (PBI) [54]. The data clearly demonstrate that the increase in temperature from 80 °C to 120 °C has little effect on the conductivity of Nafion but a

significant effect on the PBI systems. A curve is also shown for a material exhibiting the desired conductivity as a function of the relative humidity that would be ideal for system simplification. (The figure is reproduced from Gasteiger and Mathias [5] with permission from The Electrochemical Society)

## Reactant Gas Permeability

Other important properties of the ionomer include the permeability to both  $H_2$  and  $O_2$  gas. The PEM must not be too permeable to the reactive gases, as excessive gas crossover through the membrane would result in fuel efficiency losses. However, the ionomer in the electrodes must possess sufficient permeability to allow transport of the reactant without imposing any significant concentration gradients and/or mass transfer losses.

The rate of the permeation of gases in PFSA membranes is proportional to the product of the permeability coefficient and the partial pressure (i.e., the driving force) and inversely proportional to the membrane thickness. The permeation leads to a fuel cell crossover efficiency loss due to two components: hydrogen consumption at the anode from  $O_2$  crossover and hydrogen loss to the cathode and subsequent reaction with oxygen. A relatively straightforward analysis [5] based on fuel cell operation with instantaneously

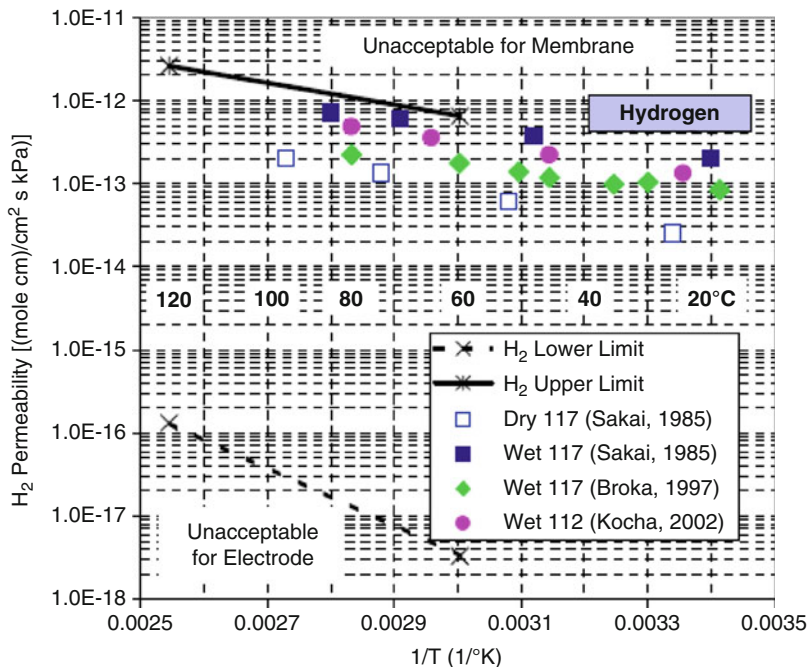
varying loads of  $0.05 \text{ A cm}^{-2}$  at 60 °C and  $2 \text{ A cm}^{-2}$  at 120 °C has estimated both upper and lower limits for the permeability of  $H_2$  and  $O_2$  which are shown as a function of temperature in Figs. 13 and 14, respectively. The permeability window for both reactant gases is approximately 3–4 orders of magnitude. Hence, the permeability coefficient,  $k$ , for  $H_2$  transport must fall within the range:  $1 \times 10^{-17} < k_{H_2} < 1 \times 10^{-12} \text{ mol cm cm}^{-2} \text{ s}^{-1} \text{ kPa}^{-1}$ , and for  $O_2$  transport within the range:  $1 \times 10^{-16} < k_{H_2} < 3 \times 10^{-12} \text{ mol cm cm}^{-2} \text{ s}^{-1} \text{ kPa}^{-1}$ , where the lower limits are dictated by the ionomer in the electrodes and the upper limits by the ionomer in the membrane.

## Morphology

As indicated earlier, all presently available PEMs must be humidified in order to exhibit sufficient proton conductivity to function effectively as the

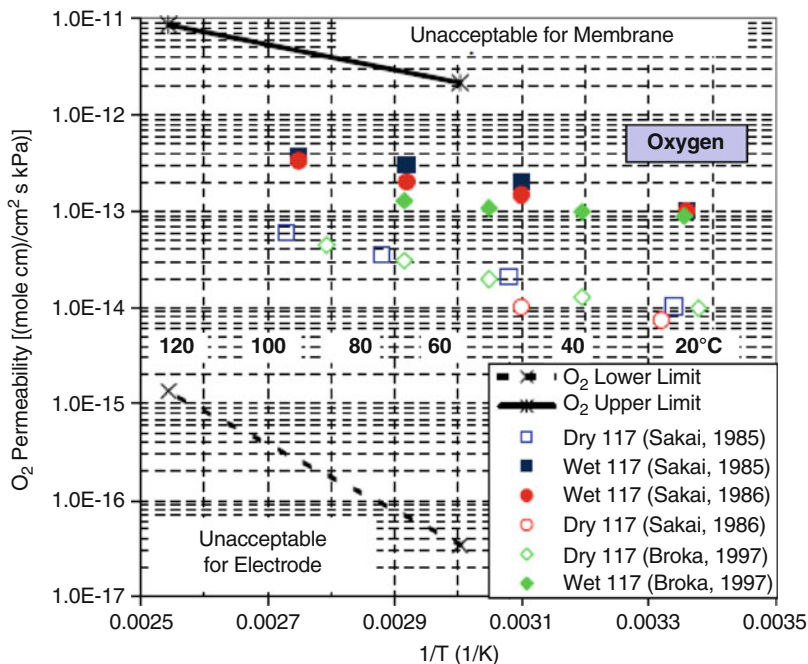
**PEM Fuel Cells: Materials and Design Development Challenges,**

**Fig. 13** Hydrogen gas permeability as a function of both temperature and relative humidity. Upper limit (*solid line*) defined by crossover losses (assuming no contribution from O<sub>2</sub> crossover), lower limit (*dotted line*) defined by the transport requirements of the ionomer in the electrode. Data for both dry and wet Nafion 1100 EW membranes taken from Refs. [55–57]. (Reproduced from H.A. Gasteiger and M.F. Mathias [5] with permission from The Electrochemical Society)



**PEM Fuel Cells: Materials and Design Development Challenges,**

**Fig. 14** Oxygen gas permeability as a function of both temperature and relative humidity. Upper limit (*solid line*) defined by crossover losses (assuming no contribution from H<sub>2</sub> crossover), lower limit (*dotted line*) defined by the transport requirements of the ionomer in the electrode. Data for both dry and wet Nafion 1100 EW membranes taken from Refs. [55–57]. (Reproduced from H.A. Gasteiger and M.F. Mathias [5] with permission from The Electrochemical Society)



electrolyte in a fuel cell. When humidified, the PEMs swell with the absorbed water resulting in a hydrated morphology where the aqueous phase is confined within the polymer to domains that are typically only a few nanometers in dimensions

[56–62]. This morphology and the interactions driving their formation are key to the understanding of the morphological stability of the ionomer and transport properties [63, 64]. Both are of paramount importance for the application of

such materials in PEM fuel cells: morphological stability under operating conditions is not only important for keeping the integrity of the ionomer membrane but also for a stable microstructure of the active electrode layers usually containing a high volume fraction of ionomer. Proton transport is actually a very complex phenomenon [36, 63, 65] comprising different species (protonic charge carriers, water, and gases dissolved therein) and different transport modes (diffusional, hydrodynamic), but the key process here remains the proton conductivity.

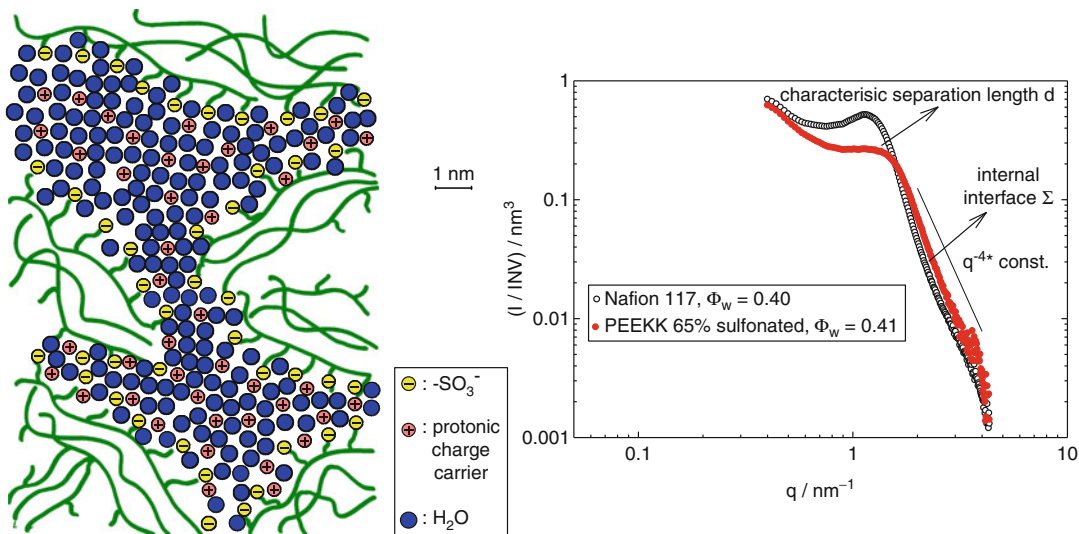
The microstructure is usually the consequence of a constrained hydrophobic/hydrophilic separation, and this can be controlled by adjusting the concentration of protogenic groups (ion-exchange capacity IEC). A high IEC corresponds to a high charge carrier concentration and generally leads to a high uptake of water, both being favorable for high proton conductivity. However, the high IEC leads to severe swelling which goes along with a loss of morphological instability and eventually leads to a complete dissolution of the ionomer. Therefore, the optimum IEC is essentially a tradeoff between these two properties.

Interestingly, this is different for different types of ionomers which is because of the differences in the backbone/backbone interactions and hydrated morphology. Such morphological details are usually obtained from small angle X-ray (SAXS) diffraction experiments (see Fig. 15). A recent interpretation of the SAXS spectra of fully swollen Nafion has attracted considerable attention [62]. The authors claim the existence of parallel cylindrical micelles bearing the water and the dissociated protons. Such a morphology could easily explain the relatively high conductivity of PFSA membranes at low water contents corresponding to a low IEC and low degree of hydration (low RH): cylindrical structures provide high connectivity within the water structure even for low water volume fractions and a high local proton mobility because of their relatively large width compared to water structures of higher dimensionality (a cylinder width of 2.4 nm is suggested which is large compared to about 1 nm suggested by other models). But it should be noted that other groups have raised serious

doubts about this model [67, 68]. It has recently been proposed that the morphology resembles two dimensional water structures, and that it is essentially the tortuosity of locally flat water structures which determines percolation and therefore proton conductivity in such materials.

In any case, there is a clear difference in the morphology of PFSA and hydrocarbon membranes which was first pointed out in a comparative SAXS study [60]. While proton conductivity at high levels of hydration is mainly dependent on the IEC only, the decrease in proton conductivity with decreasing water content is more severe in hydrocarbon membranes. The reason for this characteristic difference is suggested to be the more pronounced hydrophobic/hydrophilic separation of PFSA ionomers which leads to a better connectivity within the aqueous domain and locally to more bulklike properties of the water of hydration. But there are also characteristic disadvantages of PFSA membranes: (1) because of the bulk-like properties of the hydration water, the transport of water has a large hydrodynamic component which shows up as large electro-osmotic water drag and high water/gas permeation coefficients and (2) the viscoelastic properties are severely decaying with temperature. At this stage, it should be noted that so-called short side chain ionomers show a slightly weaker hydrophobic/hydrophilic separation which actually reduces the conductivity for a given IEC. But the significantly higher morphological stability especially at higher temperature (higher  $T_g$ ) allows for significantly higher IECs without significantly compromising the elastic properties (storage modulus). PFSA membranes with shorter side chains (e.g., Dow, 3 M, Aquivion) seem to be a real improvement over the traditional long side chain PFSA membrane Nafion [52].

Despite the disadvantageous conductivity behavior at low levels of hydration, the other alternatives are hydrocarbon membranes. They usually do not show softening in the temperature range of fuel cell operation and the higher dispersion of the hydration water (smaller width of the water domain) leads to significantly lower hydrodynamic water transport. The lower conductivity can actually be increased by introducing another



**PEM Fuel Cells: Materials and Design Development Challenges, Fig. 15** *Left:* A schematic representation of the fully hydrated morphology of a PFSA ionomer (e.g., Nafion) under the assumptions of a cubic lattice model which fitted data from small angle X-ray scattering (SAXS) experiments. *Right:* SAXS spectra of hydrated

Nafion and a hydrated sulfonated polyetherketone. The characteristic hydrophobic/hydrophilic separation lengths are obtained from the position of the ionomer peaks while the internal hydrophobic/hydrophilic interfaces are obtained from the intensities in the Porod regime. (First reported in Ref. [66])

heterogeneity with respect to the degree of sulfonation (IEC) on the 10–100 nm scale. This can lead to a significant increase of proton conductivity provided that bi-continuous morphologies are formed. The reason is the highly nonlinear increase of proton conductivity with increasing IEC. An interesting approach toward such morphologies is the formation of multiblock copolymers consisting of an alternating sequence of highly sulfonated hydrocarbon segments and unsulfonated segments [69]. When cast from solutions, such polymers undergo a constrained microphase separation. The hydrophilic sulfonated phase then still provides a sufficiently high conductivity while the nonsulfonated phase can give the material morphological stability and reduces swelling to an acceptable level (see also the entry in this encyclopedia: ► “[Membrane Electrolytes, from Perfluorosulfonic Acid \(PFSA\) to Hydrocarbon Ionomers](#)” by Miyatake).

Optimizing and controlling the microstructure of such materials is one of the major materials design issues. Here, the main challenges are to maximize the local concentration of sulfonic acid functions within the hydrophilic phase and

to obtain morphological stability with relatively small volume fractions of unsulfonated phase. A recent study on the model system of aqueous methylsulfonic acid ( $\text{CH}_3\text{SO}_3\text{H}(\text{aq})$ ) clearly demonstrates that there is still a huge potential for increasing proton conductivity at low relative humidity [70].

### Choice of the Protogenic Group

The source of the protons in current state-of-the-art PEM fuel cells is the highly acidic sulfonic acid functional group. As pointed out above, hydration is required to dissociate the protons of these groups and to mobilize the protonic charge carriers through solvation (hydration). Since the hydration requirement is one of the issues limiting the operation temperature of sulfonic acid-based electrolytes, there has been an extensive search for other protogenic groups which may enable high proton conductivity at lower water activities [71, 72]. One of the most interesting approaches is to use functional groups which are amphoteric in the sense that they may act both as a proton donor and



as a proton acceptor. Conceptually, they can combine the role of the proton source and the proton solvent in one functional group: high self-dissociation may lead to a sufficiently high charge carrier concentration and structural diffusion (i.e., proton hopping or shuttling) within a dynamically disordered hydrogen bond network and thereby provide high charge carrier mobility. The concept has been proven for imidazole [73] and phosphonic functionalized model compounds [74]. A comparative study, however, of sulfonic acid, phosphonic acid, and imidazole as protogenic groups suggests that only phosphonic acid has some potential to substitute for the sulfonic acid functional group [75, 76]. Experimentally determined proton conductivities of functionalized heptanes examined in this study [75] and corresponding computed proton transfer barriers are shown in Fig. 16. This study actually investigated not only transport but also stability issues and the participation of these groups in the electrochemical reactions. Apart from the fact that the imidazole functionalized oligomer showed the lowest proton conductivity, reaction with oxygen was observed and the platinum catalyst was blocked at high potentials where oxygen reduction takes place. The phosphonic acid-based system showed a clear signature of proton conductivity in the “water free” state, but some water activity was essential to prevent condensation reactions which immediately suppress proton conductivity. It appears that the condensation issue is more severe for systems with immobilized phosphonic acid groups compared to pure liquid phosphonic and phosphoric acid, and it remains a challenge to immobilize phosphonic acid functional groups without increasing the susceptibility for condensation [77].

## Future Directions

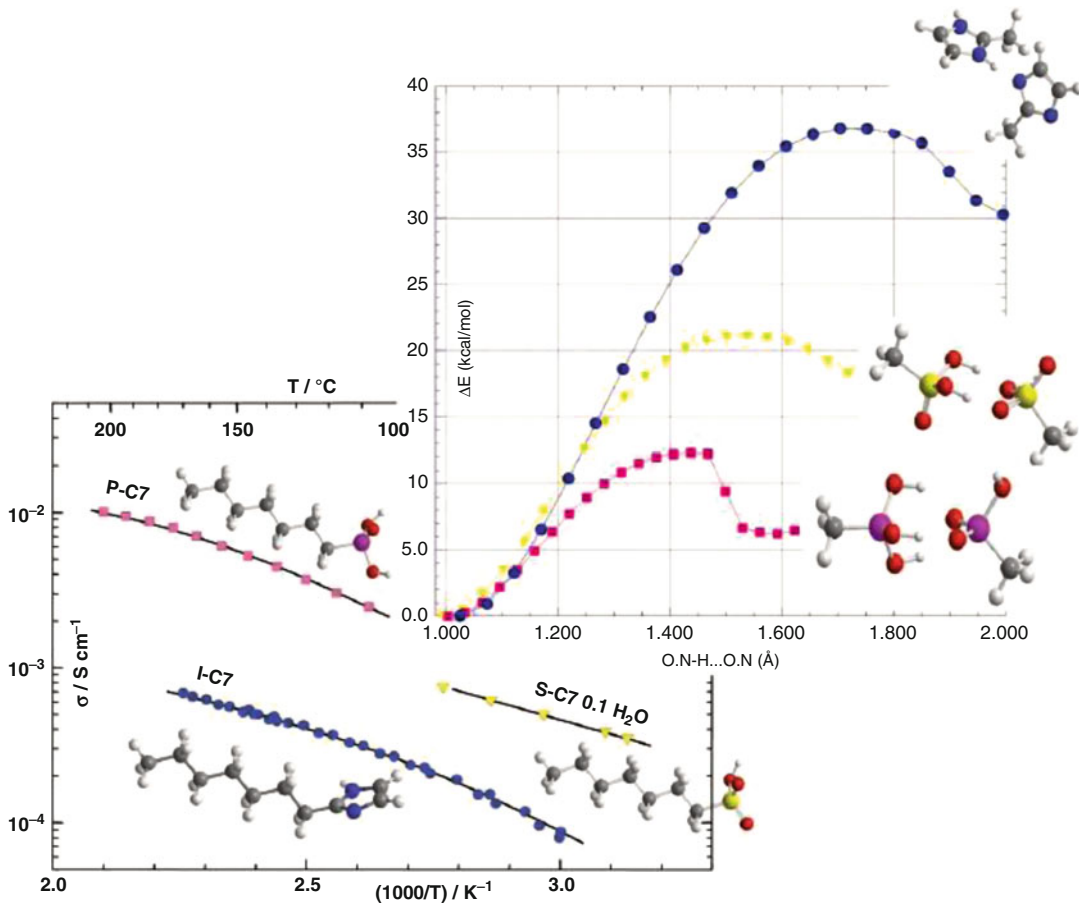
Despite the significant and substantial progress in PEM fuel cell technology achieved during the past couple of decades, the large-scale market introduction of this technology into applications such as vehicular power will require overcoming the high costs associated with the components of the

fuel cell stack (i.e., the anode and cathode catalysts, the ionomeric membrane, bipolar plates, etc.). The platinum or platinum-alloy based electrodes in current state-of-the-art fuel cells will constitute a significant fraction of the overall cost of a PEMFC stack if produced at large number. The precious metal catalysts are the only component in the fuel cell stack that will not benefit from an economies of scale, and hence the research and development of nonprecious metal catalysts is an important challenge that must be overcome.

Although it would be best if the platinum catalysts were replaced at both electrodes, the reduction of oxygen (at the cathode) requires much more Pt and hence the development of nonnoble metal catalysts with sufficient and durable ORR activity is a major focus of current and ongoing research [78–80]. Significant effort and progress has recently been achieved toward the development of catalysts with nitrogen coordinated with either iron or cobalt in a carbon matrix or support (i.e., Fe/N/C or Co/N/C). These systems are showing great promise with turnover frequencies comparable to that of current Pt/C catalysts. A major challenge (and still largely unexplored) is the stability and durability of these catalysts in the hostile electrochemical environment of an operating fuel cell [81].

Although substantial progress has been made on the development of advanced high performance PEMs, there are currently no ionomers that exhibit sufficiently high proton conductivity and durability under hot (i.e.,  $>100\text{ }^{\circ}\text{C}$ ) and “dry” ( $<30\%$  RH) conditions. However, there are several potentially promising routes that may ultimately lead to electrolytes exhibiting both high chemical and thermal stability and not requiring humidification. Increasing the density of sulfonic acid groups (i.e., by lowering the IEC) in PFSA ionomers through shortening the side chain and/or having tethering more than one protogenic group per side chain warrants further research. The development of the highly sulfonated polysulfones also seems to offer some promise as these materials demonstrate that with interpenetrating aqueous domains of very small diameters the proton conductivity is still very high. This class of





**PEM Fuel Cells: Materials and Design Development Challenges, Fig. 16** A compound figure consisting of both experimental [75] and theoretical results [76]. *Lower Left:* Measured proton conductivities under dry conditions versus temperature of three monofunctionalized heptanes: 1-heptylphosphonic acid (P-C7), magenta squares; 1-heptylsulfonic acid (S-C7), yellow triangles; and 2-heptylimidazole (I-C7), blue circles. *Upper Right:*

Computed energetic barriers for neat (i.e., acid to acid) proton transfer for methylphosphonic acid, magenta squares; methylsulfonic acid, yellow triangles; and methylimidazole, blue circles. The combined results suggest that proton conductivity is at least partially a function of the barrier for proton transfer: the experimental proton conductivities are inversely related to the computed proton transfer barrier

materials, however, must be made with lower water solubility in water and with resistance to breakage through elongation.

## Bibliography

- Gasteiger HA, Marković NM (2009) Just a dream – or future reality? Advances in catalyst development offer hope for commercially viable hydrogen fuel cells. *Science* 324:48–49
- Mathias MF, Makharia R, Gasteiger HA, Conley JJ, Fuller T, Gittleman C, Kocha SS, Miller D, Mittelsteadt C, Xie T, Yan SG, Yu PT (2005) Two fuel cell cars in every garage? *Electrochem Soc Interface* 14(2):24–35, Pennington
- Gasteiger HA, Gu W, Litteer B, Makharia R, Brady B, Budinski M, Thompson E, Wagner FT, Yan SG, Yu PT (2007) Catalyst degradation mechanisms in PEM and direct methanol fuel cells. In: Kakac S, Pramuanjaroenkij A, Vasiliev L (eds) Proceedings of the conference of the NATO-advanced-study-institute on mini-micro fuel cells – fundamentals and applications, Cesme Izmir, 22 July–03 Aug. Springer, Dordrecht, pp 225–233
- Masten DA, Bosco AD (2003) System design for vehicle applications – GM/Opel. In: Vielstich W, Lamm A, Gasteiger HA (eds) Handbook of fuel

- cells – fundamentals, technology and applications, vol 4. Wiley, Chichester, pp 714–724
- Gasteiger HA, Mathias MF (2005) Fundamental research and development challenges in polymer electrolyte fuel cell technology. In: Murthy M, Fuller TF, Van Zee JW (eds) Proceedings of the symposium on proton conducting membrane fuel cells III, 202nd ECS Meeting, held in Salt Lake City, Utah in the year 2002, vol PV 2002–31. The Electrochemical Society, Pennington, pp 1–24
  - Endoh E (2009) Highly durable PFSA membranes. In: Vielstich W, Gasteiger HA, Yokokawa H (eds) Handbook of fuel cells – advances in electrocatalysis, materials, diagnostics, and durability, vol 5. Wiley, Chichester, pp 361–374
  - Liu H, Coms FD, Zhang J, Gasteiger HA, LaConti AB (2009) Chemical degradation: correlations between electrolyzer and fuel cell findings. In: Büchi FN, Inaba M, Schmidt TJ (eds) Polymer electrolyte fuel cell durability. Springer, New York, pp 71–118
  - Lai YH, Dillard DA (2009) Mechanical durability characterization and modeling of ionomeric membranes. In: Vielstich W, Gasteiger HA, Yokokawa H (eds) Handbook of fuel cells – advances in electrocatalysis, materials, diagnostics, and durability, vol 5. Wiley, Chichester, pp 403–419
  - Patterson TW, Darling RM (2006) Damage to the cathode catalyst of a PEM fuel cell caused by localized fuel starvation. *Electrochem Solid-State Lett* 9:A183–A185
  - Gu W, Yu PT, Carter RN, Makharia R, Gasteiger HA (2010) Modeling of membrane-electrode assembly degradation in proton-exchange-membrane fuel cells – local H<sub>2</sub> starvation and start-stop induced carbon-support corrosion. In: Pasaogullari U, Wang C-Y (eds) Modeling and diagnostics of polymer electrolyte fuel cells, Modern aspects of electrochemistry, vol 49. Springer, New York, pp 45–85
  - Reiser CA, Bregoli L, Patterson TW, Yi JS, Yang JDL, Perry ML, Jarvi TD (2005) A reverse current decay mechanism for fuel cells. *Electrochem Solid-State Lett* 8:A273–A276
  - Yu P, Gu W, Makharia R, Wagner FT, Gasteiger HA (2006) The impact of carbon stability on PEM fuel cell startup and shutdown voltage degradation. *ECS Trans* 3:797–809
  - Perry ML, Patterson TW, Reiser C (2006) System strategies to mitigate carbon corrosion in fuel cells. *ECS Trans* 3:783–795
  - Genorio B, Subbaraman R, Strmcnik D, Tripkovic D, Stamenkovic VR, Markovic NM (2011) Tailoring the selectivity and stability of chemically modified platinum nanocatalysts to design highly durable anodes for PEM fuel cells. *Angew Chem Int Ed* 50:1–6
  - Ralph TR, Hudson S, Wilkinson DP (2006) Electrocatalyst stability in PEMFCs and the role of fuel starvation and cell reversal tolerant anodes. *ECS Trans* 1:67–84
  - Debe MK, Schmoeckel AK, Vernstrom GD, Atanasoski R (2006) High voltage stability of nanostructured thin film catalysts for PEM fuel cells. *J Power Sources* 161:1002–1011
  - Carter RN, Greszler TA, Baker DR (2009) Technique for measuring gas transport resistance in application-scale aged fuel cell gas diffusion media. *ECS Trans* 25:225–231
  - Perry ML, Patterson T, Madden T (2010) GDL degradation in PEFC. *ECS Trans* 33:1081–1087
  - Stephens IEL, Bondarenko AS, Perez-Alonso FJ, Calle-Vallejo F, Bech L, Johansson TP, Jepsen AK, Frydendal R, Knudsen BP, Rossmeisl J, Chorkendorff I (2011) Tuning the activity of Pt (111) for oxygen electroreduction by subsurface alloying. *J Am Chem Soc* 133:5485–5491
  - Gu W, Baker DR, Liu Y, Gasteiger HA (2009) Proton exchange membrane fuel cell (PEMFC) down-the-channel performance model. In: Vielstich W, Gasteiger HA, Yokokawa H (eds) Handbook of fuel cells – advances in electrocatalysis, materials, diagnostics, and durability, vol 5. Wiley, Chichester, pp 631–657
  - Pasaogullari U (2009) Heat and water transport models for polymer electrolyte fuel cells. In: Vielstich W, Gasteiger HA, Yokokawa H (eds) Handbook of fuel cells – advances in electrocatalysis, materials, diagnostics, and durability, vol 5. Wiley, Chichester, pp 616–630
  - Freunberger SA, Reum M, Büchi FN (2009) Design approaches for determining local current and membrane resistance in polymer electrolyte fuel cells (PEFCs). In: Vielstich W, Gasteiger HA, Yokokawa H (eds) Handbook of fuel cells – advances in electrocatalysis, materials, diagnostics, and durability, vol 5. Wiley, Chichester, pp 603–615
  - Carter RN, Gu W, Brady B, Yu PT, Subramanian K, Gasteiger HA (2009) Membrane electrode assembly (MEA) degradation mechanism studies by current distribution measurements. In: Vielstich W, Gasteiger HA, Yokokawa H (eds) Handbook of fuel cells – advances in electrocatalysis, materials, diagnostics, and durability, vol 5. Wiley, Chichester, pp 829–843
  - Trabold TA, Owejan JP, Gagliardo JJ, Jacobson DL, Hussey DS, Arif M (2009) Use of neutron imaging for proton exchange membrane fuel cell (PEMFC) performance analysis and design. In: Vielstich W, Gasteiger HA, Yokokawa H (eds) Handbook of fuel cells – advances in electrocatalysis, materials, diagnostics, and durability, vol 5. Wiley, Chichester, pp 658–672
  - Wipke K, Sprick S, Kurtz J, Garbak J (2009) Field experience with fuel cell vehicles. In: Vielstich W, Gasteiger HA, Yokokawa H (eds) Handbook of fuel cells – advances in electrocatalysis, materials, diagnostics, and durability, vol 6. Wiley, Chichester, pp 893–904
  - Thompson EL, Gu W, Gasteiger HA (2009) Performance during start-up of proton exchange membrane (PEM) fuel cells at subfreezing conditions. In: Vielstich W, Gasteiger HA, Yokokawa H (eds) Handbook of fuel cells – advances in electrocatalysis,

- materials, diagnostics, and durability, vol 5. Wiley, Chichester, pp 699–717
27. Mathias M, Roth J, Fleming J, Lehnert W (2003) Diffusion media materials and characterization. In: Vielstich W, Lamm A, Gasteiger HA (eds) Handbook of fuel cells – fundamentals, technology and applications, vol 3. Wiley, Chichester, pp 517–537
  28. Baker DR, Caulk DA, Neyerlin KC, Murphy MW (2009) Measurement of oxygen transport resistance in PEM fuel cells by limiting current methods. *J Electrochem Soc* 156:B991–B1003
  29. Caulk DA, Baker DR (2011) Modeling two-phase water transport in hydrophobic diffusion media for PEM fuel cells. *J Electrochem Soc* 158:B384–B393
  30. Mittelstaedt CK, Liu H (2009) Conductivity, permeability, and ohmic shorting of ionomeric membranes. In: Vielstich W, Gasteiger HA, Yokokawa H (eds) Handbook of fuel cells – advances in electrocatalysis, materials, diagnostics, and durability, vol 5. Wiley, Chichester, pp 345–359
  31. Liu Y, Ji C, Gu W, Jorne J, Gasteiger HA (2011) Effects of catalyst carbon support on proton conduction and cathode performance in PEM fuel cells. *J Electrochem Soc* 158:B614–B621
  32. Neyerlin KC, Gu W, Jorne J, Clark A, Gasteiger HA (2007) Cathode catalyst utilization for the ORR in a PEMFC – analytical model and experimental validation. *J Electrochem Soc* 154:B279–B287
  33. Neyerlin KC, Gu W, Jorne J, Gasteiger HA (2007) Study of the exchange current density for the hydrogen oxidation and evolution reactions. *J Electrochem Soc* 154:B631–B635
  34. Gasteiger HA, Baker DR, Carter RN, Gu W, Liu Y, Wagner FT, Yu PT (2010) Electrocatalysis and catalyst degradation challenges in proton exchange membrane fuel cells. In: Stolten D (ed) Hydrogen and fuel cells. fundamentals, technologies, and applications. Wiley-VCH, Weinheim, pp 3–16
  35. Jaouen F, Proietti E, Lefèvre M, Chenitz R, Dodelet J-P, Wu G, Chung HT, Johnston CM, Zelenay P (2011) Recent advances in non-precious metal catalysis for oxygen reduction reaction in polymer electrolyte fuel cells. *Energy Environ Sci* 4:114–130
  36. Paddison SJ (2003) Proton conduction mechanisms at low degrees of hydration in sulfonic acid-based polymer electrolyte membranes. *Annu Rev Mater Res* 33:289–319
  37. Ferreira PJ, la O' GJ, Shao-Horn Y, Morgan D, Makharia R, Kocha SS, Gasteiger HA (2005) Instability of Pt/C electrocatalysts in proton exchange membrane fuel cells: a mechanistic investigation. *J Electrochem Soc* 152:A2256–A2271
  38. Kinoshita K, Lundquist JT, Stonehart P (1973) Potential cycling effects on platinum electrocatalyst surfaces. *J Electroanal Chem* 48:157–166
  39. Kawahara S, Mitsushima S, Ota K-I, Kamiya N (2006) Deterioration of Pt catalyst under potential cycling. *ECS Trans* 3(1):625–631
  40. Zhang J, Litteer BA, Gu W, Liu H, Gasteiger HA (2007) Effect of hydrogen and oxygen partial pressure on Pt precipitation within the membrane of PEMFCs. *J Electrochem Soc* 154:B1006–B1011
  41. Wagner FT, Yan SG, Yu PT (2009) Catalyst and catalyst-support durability. In: Vielstich W, Gasteiger HA, Yokokawa H (eds) Handbook of fuel cells – advances in electrocatalysis, materials, diagnostics, and durability, vol 5. Wiley, Chichester, pp 250–263
  42. Shao-Horn Y, Sheng WC, Chen S, Ferreira PJ, Holby EF, Morgan D (2007) Instability of supported platinum nanoparticles in low-temperature fuel cells. *Top Catal* 46:285–305
  43. Chen S, Gasteiger HA, Hayakawa K, Tada T, Shao-Horn Y (2010) Platinum-Alloy catalyst degradation in proton exchange membrane fuel cells: nanometer-scale compositional and morphological changes. *J Electrochem Soc* 157:A82–A97
  44. Yu PT, Gu W, Zhang J, Makharia R, Wagner FT, Gasteiger HA (2009) Carbon-support requirements for highly durable fuel cell operation. In: Büchi FN, Inaba M, Schmidt TJ (eds) Polymer electrolyte fuel cell durability. Springer, New York, pp 29–53
  45. Gallagher KG, Darling RM, Fuller TF (2009) Carbon-support corrosion mechanisms and models. In: Vielstich W, Gasteiger HA, Yokokawa H (eds) Handbook of fuel cells – advances in electrocatalysis, materials, diagnostics, and durability, vol 5. Wiley, Chichester, pp 819–828
  46. Thampan T, Malhorta S, Tang H, Datta R (2000) Modeling of conductive transport in proton-exchange membranes for fuel cells. *J Electrochem Soc* 147:3242–3250
  47. Springer TE, Zawodzinski T, Gottesfeld S (1991) Polymer electrolyte fuel cell model. *J Electrochem Soc* 138:2334–2342
  48. Springer T, Zawodzinski T, Gottesfeld S (1997) In: McBreen J, Mukerjee S, Srinivasan S (eds) Electrode materials and processes for energy conversion and storage, Proceedings series, vol PV 97–13. The Electrochemical Society, Pennington, pp 15–24
  49. Bernardi DM, Verbrugge MW (1992) A mathematical model of the solid-polymer-electrolyte fuel-cell. *J Electrochem Soc* 139:2477–2491
  50. Gasteiger HA, Garche J (2008) Fuel cells. In: Ertl G, Knözinger H, Schuüth F, Weitkamp J (eds) Handbook of heterogeneous catalysis, 2nd edn. Wiley-VCH, Weinheim, pp 3081–3121
  51. Breault RD (2003) PAFC stack materials and stack design. In: Vielstich W, Lamm A, Gasteiger HA (eds) Handbook of fuel cells: fundamentals, technology, and applications, vol 3. Wiley, Chichester
  52. Kreuzer KD, Schuster M, Obliers B, Diat O, Traub U, Fuchs A, Klock U, Paddison SJ, Maier J (2008) Short-side-chain proton conducting perfluorosulfonic acid ionomers: why they perform better in PEM fuel cells. *J Power Sources* 178:499–509
  53. Alberti G, Casciola M, Massinelli L, Bauer B (2001) Polymeric proton conducting membranes for medium

- temperature fuel cells (110–160°C). *J Membr Sci* 185:73–81
54. Wainwright JS, Litt MH, Savinell RF (2003) High-temperature membranes. In: Vielstich W, Lamm A, Gasteiger HA (eds) *Handbook of fuel cells – fundamentals, technology and applications*, vol 3. Wiley, Chichester, pp 436–446
  55. Sakai T, Takenaka H, Wakabayashi N, Kawami Y, Torikai E (1985) Gas permeation properties of solid polymer electrolyte (SPE) membranes. *J Electrochem Soc* 132:1328–1332
  56. Broka K, Ekdunge P (1997) Oxygen and hydrogen permeation properties and water uptake of Nafion (R) 117 membrane and recast film for PEM fuel cell. *J Appl Electrochem* 27:281–289
  57. Kocha SS (2003) Principles of MEA preparation. In: Vielstich W, Lamm A, Gasteiger HA (eds) *Handbook of fuel cells – fundamentals, technology and applications*, vol 3. Wiley, Chichester, p 538
  58. Hsu WY, Gierke TD (1982) Elastic theory for ionic clustering in perfluorinated ionomers. *Macromolecules* 15:101–105
  59. Gebel G (2000) Structural evolution of water swollen perfluorosulfonated ionomers from dry membrane to solution. *Polymer* 41:5829–5838
  60. Kreuer KD (2001) On the development of proton conducting polymer membranes for hydrogen and methanol fuel cells. *J Membr Sci* 185:29–39
  61. Rubatat L, Gebel G, Diat O (2004) Fibrillar structure of Nafion: matching fourier and real space studies of corresponding films and solutions. *Macromolecules* 37:7772–7783
  62. Schmidt-Rohr K, Chen Q (2008) Parallel cylindrical water nanochannels in Nafion fuel-cell membranes. *Nat Mater* 7:75–83
  63. Kreuer KD, Paddison SJ, Spohr E, Schuster M (2004) Transport in proton conductors for fuel-cell applications: simulations, elementary reactions, and phenomenology. *Chem Rev* 104:4637–4678
  64. Elliott JA, Paddison SJ (2007) Modelling of morphology and proton transport in PFSA membranes. *Phys Chem Chem Phys* 9:2602–2618
  65. Kreuer KD (2000) On the complexity of proton conduction phenomena. *Solid State Ionics* 136:149–160
  66. Ise M (2000) *Polymer Elektrolyt Membranen: Untersuchungen zur Mikrostruktur und zu den Transporteigenschaften für Protonen und Wasser*. PhD thesis, University of Stuttgart
  67. Kreuer KD (2011) *Advances in materials for proton exchange membrane fuel cells systems 2011*. Asilomar, Pacific Grove, 20–23 Feb 2011
  68. Gebel G (2011) *Advances in materials for proton exchange membrane fuel cells systems 2011*. Asilomar, Pacific Grove, 20–23 Feb 2011
  69. Hickner MA, Ghassemi H, Kim YS, Einsla BR, McGrath JE (2004) Alternative polymer systems for proton exchange membranes (PEMs). *Chem Rev* 104:4587–4612
  70. Telfah A, Majer G, Kreuer KD, Schuster M, Maier J (2010) Formation and mobility of protonic charge carriers in methyl sulfonic acid–water mixtures: a model for sulfonic acid based ionomers at low degree of hydration. *Solid State Ionics* 181:461–465
  71. Desmarteau DD (1995) Novel perfluorinated ionomers and ionenes. *J Fluor Chem* 72:203–208
  72. Schaberg MS, Abulu JE, Haugen GM, Emery MA, O’Conner SJ, Xiong PN, Hamrock SJ (2010) New multi acid side-chain ionomers for proton exchange membrane fuel cells. *ECS Trans* 33(1):609–627
  73. Herz HG, Kreuer KD, Maier J, Scharfenberger G, Schuster MFH, Meyer WH (2003) New fully polymeric proton solvents with high proton mobility. *Electrochim Acta* 48:2165–2171
  74. Steininger H, Schuster M, Kreuer KD, Maier J (2006) Intermediate temperature proton conductors based on phosphonic acid functionalized oligosiloxanes. *Solid State Ionics* 177:2457–2462
  75. Schuster M, Rager T, Noda A, Kreuer KD, Maier J (2005) About the choice of the protogenic group in PEM separator materials for intermediate temperature, low humidity operation: a critical comparison of sulfonic acid, phosphonic acid and imidazole functionalized model compounds. *Fuel Cells* 5:355–365
  76. Paddison SJ, Kreuer KD, Maier J (2006) About the choice of the protogenic group in polymer electrolyte membranes: ab initio modelling of sulfonic acid, phosphonic acid, and imidazole functionalized alkanes. *Phys Chem Chem Phys* 8:4530–4542
  77. Steininger H, Schuster M, Kreuer KD, Kaltbeitzel A, Bingöl B, Meyer WH, Schauff S, Brunklaus G, Maier J, Spiess HW (2007) Intermediate temperature proton conductors for PEM fuel cells based on phosphonic acid as protogenic group: a progress report. *Phys Chem Chem Phys* 9:1764–1773
  78. Bashyam R, Zelenay P (2006) A class of non-precious metal composite catalysts for fuel cells. *Nature* 443:63–66
  79. Lefèvre M, Proietti E, Jaouen F, Dodelet JP (2009) Iron-based catalysts with improved oxygen reduction activity in polymer electrolyte fuel cells. *Science* 324:71–74
  80. Wu G, More KL, Johnston CM, Zelenay P (2011) High-performance electrocatalysts for oxygen reduction derived from polyaniline, iron, and cobalt. *Science* 332:443–447
  81. Proietti E, Jaouen F, Lefèvre M, Larouche N, Tian J, Herranz J, Dodelet JP (2011) Iron-based cathode catalyst with enhanced power density in polymer electrolyte membrane fuel cells. *Nat Commun*:2. <https://doi.org/10.1038/ncomms1427>



## PEM Fuel Cell Materials: Costs, Performance, and Durability

A. de Frank Bruijn<sup>1</sup> and Gaby J. M. Janssen<sup>2,3</sup>

<sup>1</sup>Energy Research Centre of the Netherlands, Groningen, The Netherlands

<sup>2</sup>Energy and Sustainability Research Institute Groningen, University of Groningen, Groningen, The Netherlands

<sup>3</sup>Energy Research Centre of the Netherlands, Petten, The Netherlands

### Article Outline

Glossary

Definition of the Subject and Its Importance

Introduction

PEMFC Component Costs and Performance:

Targets, Status and Developments

Operating Conditions Leading to Performance

Loss and Shortening the PEMFC Lifetime

Materials Degradation and the Relation to

Performance Loss and Shortening the PEMFC

Lifetime

Future Directions

Bibliography

### Glossary

**Bipolar plate** Forms the connection between MEAs in a fuel cell stack. The bipolar plate includes the gas flow channels and may also include cooling channels. Bipolar plates are also called flow plates.

**Degradation** The gradual loss of performance. Irreversible degradation is due to change of materials properties. Reversible degradation can be caused by non-optimal operating conditions. Quantitatively, the degradation can be expressed as a voltage decay rate.

**Durability** The capability of the fuel cell to operate in the operating window with limited loss of performance.

**Lifetime** The number of hours that a fuel cell can be operated in the operating window with a pre-defined performance loss relative to the initial performance.

**MEA** Membrane electrode assembly is the result of joining two electrodes and the electrolytic membrane together. Usually, the gas diffusion media are considered to be part of the MEA.

**Operating window** The range of conditions in which the PEMFC can be stably operated. Within this operating window, performance can still depend on the conditions, but irreversible performance loss is limited. The operating window includes the modes of operation, such as start/stop events and load cycling.

**PEMFC** Proton exchange membrane fuel cell. The operating temperature is around 80 °C. Cold start, below 0 °C, is possible. For transport applications, the PEMFC is the fuel cell of choice.

**Robustness** The capability of the fuel cell to operate outside the operating window without a significant irreversible loss of performance.

### Definition of the Subject and Its Importance

The Proton Exchange Membrane Fuel Cell, PEMFC or PEFC, is in development for transport applications as well as for power generators ranging from a few Watts to tens of kilo Watts. Despite the fact that fuel cells have many advantages, such as a high conversion efficiency at partial load, clean exhaust gases, modular design and low noise production, their marketability will depend heavily on whether these fuel cells can compete with the incumbent technologies on performance, cost, and reliability in a specific application. For transport, the benchmark at present is the

internal combustion engine, which has been mass-produced since 1908, and is characterized by high performance, high reliability, and relatively low cost.

### Performance

The internal combustion engine can be cold started within seconds and can be operated worldwide under all climate conditions. It has become quite standard to have 100 kW of engine power under the hood, enabling highway and uphill driving without any concession. A fuel cell vehicle will have to meet the same standards with regard to a fast cold start, availability of power without compromising the available space for the user under all foreseeable conditions. The power density of the complete fuel cell system must be  $650 \text{ W L}^{-1}$  and  $650 \text{ W kg}^{-1}$ , which translates to  $2000 \text{ W L}^{-1}$  and  $2000 \text{ W kg}^{-1}$  for the fuel cell stack [1].

### Lifetime and Reliability

Service intervals for passenger vehicles have dropped to once per 30,000 km or once per 2 years, and vehicles last 10–15 years without major revisions, running more than 250,000 km. Consumers are not used anymore to car breakdowns, especially not within the first 5 years of first ownership. Fuel cell vehicles will have to meet the expectations of today, rather than develop along the line of the internal combustion engine, that is, provide reliability comparable to that of the internal combustion engine of decades ago.

This means that at the time of mass-market introduction, their expected lifetime needs to be 5,000 h, with an end of life performance, which is at least 90% of the performance at the beginning of life. No external conditions, except for severe crashes, might lead to severe deterioration of the fuel cell performance. In practice, this means that the fuel cell system needs to operate between  $-40 \text{ }^\circ\text{C}$  and  $+50 \text{ }^\circ\text{C}$  ambient temperature, under all relative humidities.

### Costs

For the PEMFC to become a viable option for transport, the cost of buying and operating a fuel

cell system, which comprises all parts at present not part of a conventional vehicle, must be comparable to that of an internal combustion engine. A higher investment cost of a fuel cell system can be offset by a lower fuel cost, determined by the cost of hydrogen and the fuel economy of the fuel cell vehicle. Although consumers are increasingly eager to take fuel costs or reduced  $\text{CO}_2$  emissions into account when making their buying decision, there will be limits to the additional price they will want to pay. A cost-neutral switch from the internal combustion engine to a fuel cell system leads to an allowable cost of US\$30/kW for a complete PEMFC system and US\$15/kW for a PEMFC stack, which will be operated on hydrogen [1]. These costs are a reflection of the costs of the components and the assembly of the PEMFC stack and system, with the implicit assumption that it will last for the whole lifetime of the vehicle.

### The Role of Materials

The materials used in the PEMFC play a key role in the fuel cell systems performance, cost, and reliability. This article aims to present a comprehensive treatment of the performance, cost, and durability issues, especially but not exclusively, in light of their application in transport, as this provides so far the most challenging combination of these issues.

## Introduction

As of 2010, fuel cells have matured considerably: Hundreds of fuel cell-driven passenger vehicles have been demonstrated, with an impressive improvement of systems performance. Major car companies such as Honda, Toyota, Daimler, General Motors, Ford, and Hyundai have recently produced a new generation of passenger vehicles that can meet consumer expectations with respect to driving speed, acceleration, and driving range. Furthermore, they can be operated under severe conditions, such as extreme ambient temperature or demanding driving conditions. This accomplishment is based on a combination of advances on both fuel cell components as well as on



systems level. On the one hand, the properties of materials determine the real power density of the fuel cell and the volumetric power density of the fuel cell stack. On the other hand, the systems layout, balance of plant and control strategy determine which conditions the fuel cell materials actually experience.

A schematic presentation of cell and stack components is given in Fig. 1.

The electrolyte of the PEMFC consists of a proton exchange membrane. Besides conducting ions from one electrode to the other, the electrolyte serves as gas separator and electronic insulator. At either side of the membrane, a catalytically active electrode is intimately attached to the membrane, to form a so-called membrane electrode assembly, the MEA. At the anode, hydrogen is oxidized to protons. At the cathode, oxygen is reduced to water. The theoretical voltage at open circuit of a hydrogen-oxygen fuel cell is 1.23 V at 298 K. Under load conditions, the cell voltage is between 0.5 and 1 V, producing a current density up to  $1.5 \text{ A cm}^{-2}$ , depending on conditions.

The type of materials being used in PEM fuel cells has stayed the same since the early 1990s [2].

For the electrolyte, perfluorosulfonic acid/tetrafluoroethylene copolymer membranes (usually referred to as PFSA membranes) have been used for decades. Chemically, this polymer can be considered as a Teflon or polytetrafluoroethylene (PTFE) backbone, with Teflon-like side chains bearing a  $\text{SO}_3\text{H}$  (sulfonic acid) group. Dissociation of this sulfonic acid group leads to mobile protons. Produced as thin, flexible sheets that become conductive when containing water, these membranes enable high volume manufacturing of complete cells by coating the electrodes on these sheets. Originally developed for chlor-alkali electrolyzers, the membranes provide a combination of properties that is unsurpassed: high proton conductivity and a high chemical stability. For optimal conductivity, the water content of the membrane needs to be such that the  $\text{H}_2\text{O}/\text{SO}_3\text{H}$  ratio  $\lambda$  is larger than 14 [3], which for state-of-the-art materials is only achieved at 100% RH. The latest developments on perfluorosulfonic acid/tetrafluoroethylene copolymer membranes that have been applied in fuel cells have been on

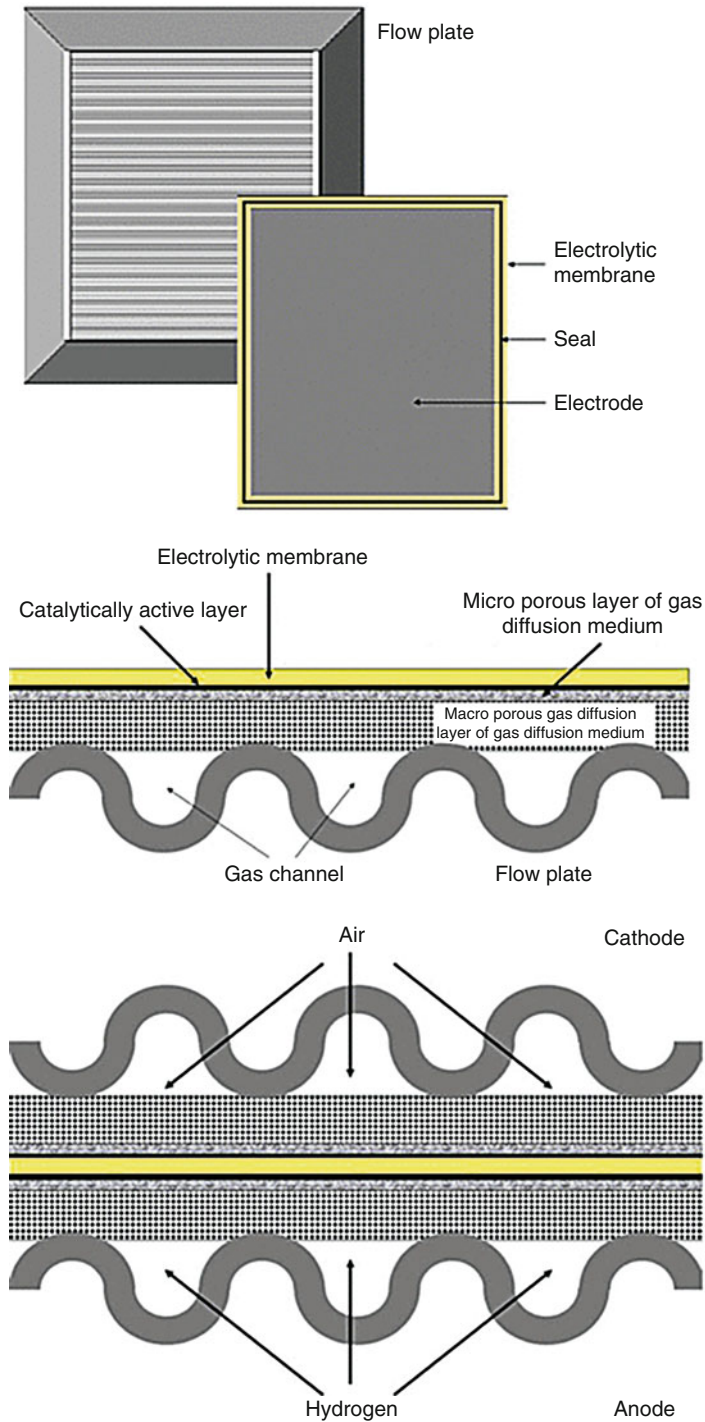
even further improvement of their chemical stability and the development of ever thinner membranes down from 175 to 25  $\mu\text{m}$ , among others by using reinforcements for maintaining strength.

For the electrodes, platinum on carbon catalysts have long been used in both anode and cathode for hydrogen/air fuel cells. Commercial electrodes contain around  $0.2\text{--}0.4 \text{ mg cm}^{-2}$  platinum, generating a power density of  $0.5\text{--}0.7 \text{ W cm}^{-2}$  [2]. Using a total loading of  $0.6 \text{ mg cm}^{-2}$  and a power output of  $0.5 \text{ W cm}^{-2}$ , the platinum usage amounts to  $1.2 \text{ g kWe}^{-1}$ . It has, however, been demonstrated that fuel cells with  $0.4 \text{ g}_{\text{Pt}} \text{ kWe}^{-1}$  are achievable when using clean hydrogen and air [4]. The long-term stability of such cells is, however, not known yet, and the use of reformat prescribes higher loadings of Pt-Ru at the anode,  $0.2 \text{ mg}_{\text{PtRu}} \text{ cm}^{-2}$  at minimum. The ultimate goal is to lower the platinum usage to less than  $0.2 \text{ g}_{\text{Pt}} \text{ kWe}^{-1}$ .

The use of noble metals is an important factor in the cost of the fuel cell. Whereas the cost of many components drops when the scale of manufacturing increases, this is not the case for the noble metal catalysts. The concern of a real shortage of platinum in case of large-scale use of fuel cells in vehicles has been proven not to be substantiated [5], but this is based on a significant reduction of its use to 15 g/vehicle, corresponding to the  $0.2 \text{ g}_{\text{Pt}} \text{ kWe}^{-1}$  mentioned before. The key issue is to minimize the amount of platinum per kW fuel cell power, while maintaining the power density of the present state-of-the-art. It makes no sense to substitute platinum by another metal when this leads to a reduction of the power density.

The catalysts used as a base for electrode manufacturing consist of high loadings of noble metal on carbon, of 40 wt% or even higher. These high loadings are used to render a thin electrode with high enough amount of active sites, typically 10  $\mu\text{m}$  thick. The platinum particle sizes are even at these high noble metal loadings in the range of 2–3 nm [6].

Even in electrodes with a high catalytic activity, the performance is heavily dependent on the electrode structure, as oxygen transport becomes crucial at practical current densities. Water



**PEM Fuel Cell Materials: Costs, Performance, and Durability, Fig. 1** Cell and stack components. Top: top view of separator plate and MEA with seal; middle:

cross-section view of one site of MEA on flow field; bottom: cross-section view of complete cell package

removal plays a key role in this, as the diffusion constant of oxygen in water is a factor of 5,700 lower than that in air at 60 °C. Gas Diffusion Media (GDM) play a decisive role in the water management of the fuel cells. Gas diffusion media, which consist of a macro porous gas diffusion layer (GDL) of 200–400  $\mu\text{m}$  covered by a micro porous layer (MPL) of 30–50  $\mu\text{m}$ , facilitate the transport of gas and electrons between the catalytically active layer and the flow plate. While the macroporous gas diffusion layer needs a certain thickness to distribute the gas in horizontal direction, the microporous layer facilitates the removal of liquid product water, preventing the so-called flooding of the electrode. Effective prevention of such flooding can extend the voltage current curve by around 0.5–1  $\text{A cm}^{-2}$ .

The component that has the highest impact on the weight and volume of the fuel cell stack is the flow plate or bipolar plate. Whereas the flow plates used to be made from high-density graphite, nowadays the material of choice is a moldable graphite/polymer composite material. Although the latter has a somewhat lower conductivity than pure graphite, it enables the use of plates with lower thickness due to its higher mechanical strength and its higher flexibility. This directly leads to reduction of stack weight and volume. A major advantage of polymer/graphite plates is the fact that they can be manufactured by means of injection molding [7]. An alternative to graphite and polymer/graphite material plates is the metal plate. The main advantage of metal plates is the fact that very thin metal sheets can be used, and mass manufacturing techniques are available for forming flow patterns in these sheets [2].

### Operating Window and Performance

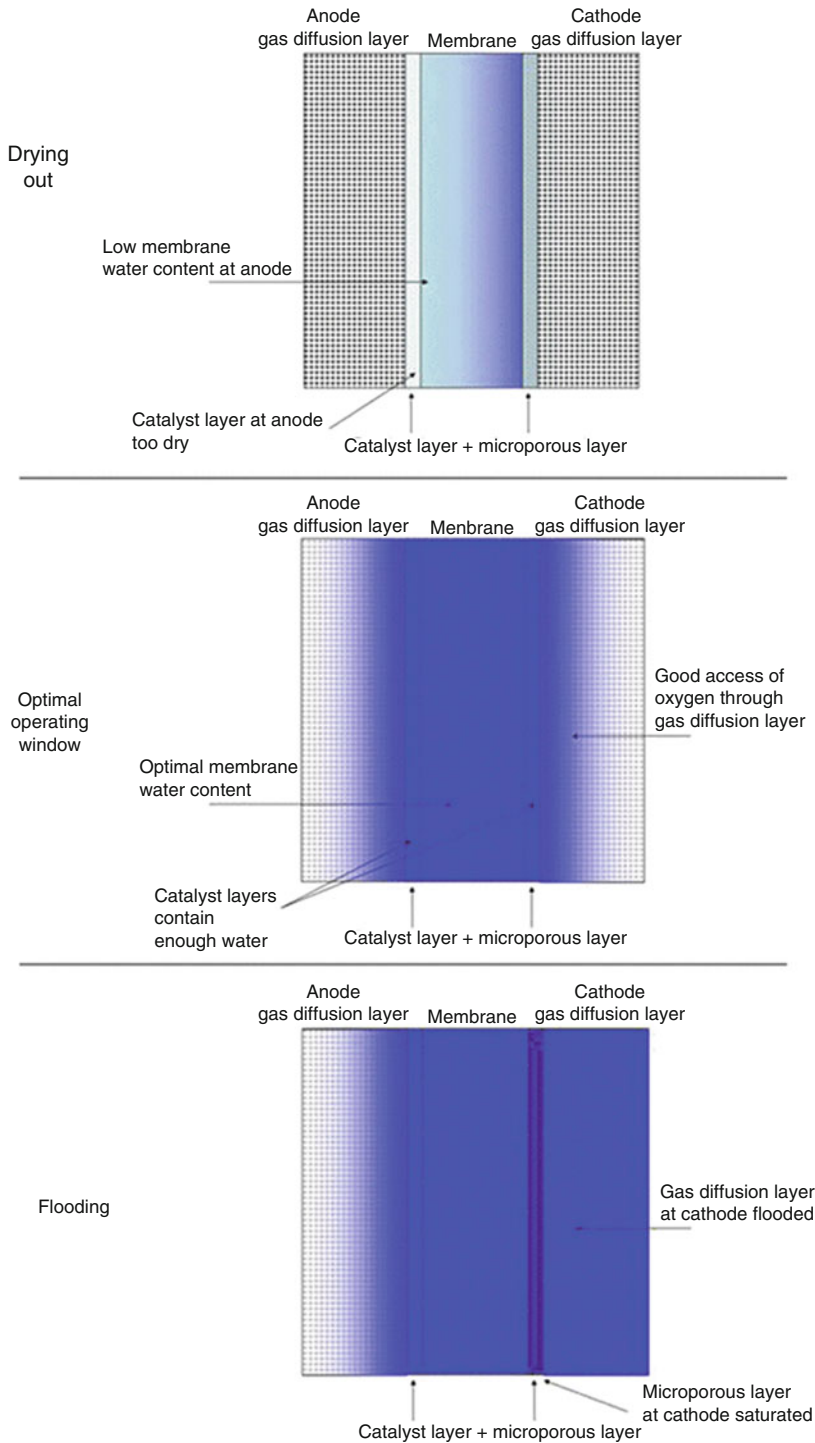
As the area power density of a fuel cell is determining for the overall cost of the system, it is essential to optimize the operating window of the fuel cell stack. Of all conditions, the relative humidity has the largest influence on power density. This relative humidity is governed by the water content of the feed gases and their stoichiometry, the amount of product water, which is directly proportional to the current density, and the cell temperature.

The minimum requirement for water is set by the dependence of the proton conductivity of the PFSA membrane on its water content. In case this minimum requirement is not met, drying out of the membrane and the ionomer phase of the electrode leads to rapid decline of the power density. A maximum is clearly set by the transport of oxygen through the electrode, as liquid water is an effective barrier for the transport of gas to the reaction interface. In the catalytic layer of the cathode, these two factors determine an optimum: sufficient liquid water in the ionomer for proton conduction while simultaneously allowing gas phase transport of oxygen [8]. Figure 2 schematically draws the optimum situation as well as the situation of drying out and flooding.

The water accumulation at the cathode catalyst layer not only originates from product water but also from the electroosmotic drag, that is, protons migrating from anode to cathode also carry water with them. This electroosmotic drag is roughly proportional to the current density. Removal of this accumulated water can take place in two directions. First, water will be transported through the cathode gas diffusion medium to the air gas channel either as vapor or in the liquid form. Second, there will be back-transport of water through the membrane and the anode gas diffusion layer to the fuel gas channel. The respective rates at which these processes take place depend on the driving force for the water transport in either direction and the water permeability of the components [9].

The driving force is the difference in the chemical potential of water (determined by vapor pressure or hydraulic pressure) in the catalyst layer and the gas channel. The first depends strongly on the current density, the second on the relative humidity of the gas channel, factors that can to some extent be controlled and matched.

The water permeability of the components is at least as important. Thin membranes allow for fast water transport to the anode, reducing flooding at the cathode. In thin membranes, the back-transport of water can often overcompensate the water transport that is associated with the electroosmotic drag, thus preventing drying out at the anode.



**PEM Fuel Cell Materials: Costs, Performance, and Durability, Fig. 2** Water content of electrode parts and membrane in optimal operating window, as well as under too dry and too wet conditions

The state-of-the-art gas diffusion media are hydrophobized to such an extent that they allow transport of liquid water, an important mechanism at near-saturated conditions, as well as of water vapor and reactant gases. An important role is played by the micro porous layer (MPL). Because of the presence of small hydrophobic pores, a substantial liquid water capillary pressure can be built up, enabling a good gradient in the chemical potential of water to drier sections [10]. The optimization of gas diffusion media and the application of the MPL have led to significant improvement of the fuel cell performance at saturated conditions, showing their critical role.

The occurrence of flooding leads to an almost immediate drop in power output, which cannot be restored instantaneously. Proper design of the flow field, the cell characteristics, and knowledge of the operating window in which flooding as well as membrane drying can be avoided with the hardware used should lead to system control design avoiding these conditions. Sensors that measure the relative humidity continuously do exist [11] but seem to be too bulky and costly to be applied in a fuel cell system. In fact, the accurate measurement of the water content of gases is very complicated. Most systems therefore rely on the proper functioning of the humidifier, the cell temperature sensor, gas flow sensors, and the preservation of the water management properties of the gas diffusion media. If in the course of the cell lifetime, the water removal capability of the gas diffusion media declines, one could compensate for this by increasing the reactant stoichiometries at high current densities.

A more drastic prevention from flooding would be to work at drier conditions. In such a case, the conditions in the gas channel are such that the driving force for water removal is enhanced. In addition to the strategy of developing membranes and catalysts that do not require a high humidity, the water permeability of the gas diffusion media should be reduced. Whereas mere reduction of gas permeability may also deteriorate the access of especially oxygen, improved water management may come from optimized MPLs. The capability to work at drier conditions would also allow increase of the upper limit of the window of operating temperature.

In the following sections, the fuel cell components are discussed in detail: options and needs for further cost reduction, for operation at more desired conditions, and durability issues.

## **PEMFC Component Costs and Performance: Targets, Status and Developments**

### **Cost and Performance Breakdown**

Directly or indirectly, all R&D efforts on PEMFC materials and components can be brought down to cost reduction. The progress on cost reduction over the last decade has been impressive. Based on high volume numbers, 500,000 systems per year, the cost of a PEMFC system using the materials available in 2009 would be \$61/kW coming from \$275 in 2002 [12]. These costs are a reflection of the costs of the components and the assembly of the PEMFC stack and system, with the implicit assumption that it holds for the rest of the lifetime of the vehicle. The durability requirement of 5,000 h for a passenger vehicle is treated separately.

For commercial applications, operation and maintenance costs are considered as important as the initial investment costs. Durability becomes in that case a matter of maintenance costs, both from the point of replacing individual components, as well as taking into account the time needed to replace these components. An individual seal in a fuel cell stack might cost only 1 dollar, but when the complete stack has to be disassembled to replace that individual seal, it is obviously worthwhile to apply more robust seals that minimize the need for replacement. Similarly, accepting higher fuel costs, caused by a lower cell voltage needed to generate the same fuel cell power after a certain voltage decay has accumulated over time, may be preferred to replacing MEAs or even a complete stack.

The most consistent monitoring of the progress on cost reduction is probably done by the US Department of Energy (DoE). Cost targets are set for 2010 and 2015, where the 2015 target is meant to meet commercial requirements, and the 2010 target is meant as intermediate milestone.

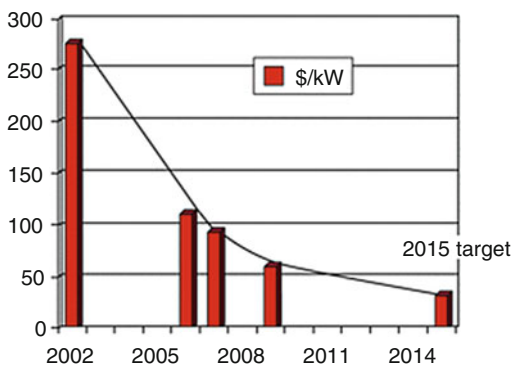


An annual production volume of 500,000 vehicles per year is used to take into account the beneficial effect of mass manufacturing, which does not imply that a learning factor is incorporated in the cost figures. The cost per kW follows from the cost of components used per  $\text{m}^2$  cell area and the power density of such a cell under the specified conditions. The use of expensive components can thus lead to low costs per kW provided the power density of such a cell is high enough.

Figure 3 gives the progressive cost reduction of a PEMFC stack for the years for which enough details are present to make a deeper assessment of the cost breakdown.

It must be noted that the DoE analysis has some tentative aspects. New materials are taken into account in the cost figures without the guarantee that these will actually survive the operating conditions over the full lifetime of the fuel cell. On a cell level, these materials might have survived relevant accelerated tests, but that does not mean that in combination with stack and system hardware, and used under real-life conditions, these materials will qualify. It is at present the only publicly known assessment of fuel cell costs that is regularly updated, and that takes into account all fuel cell stack and system components on an equal basis.

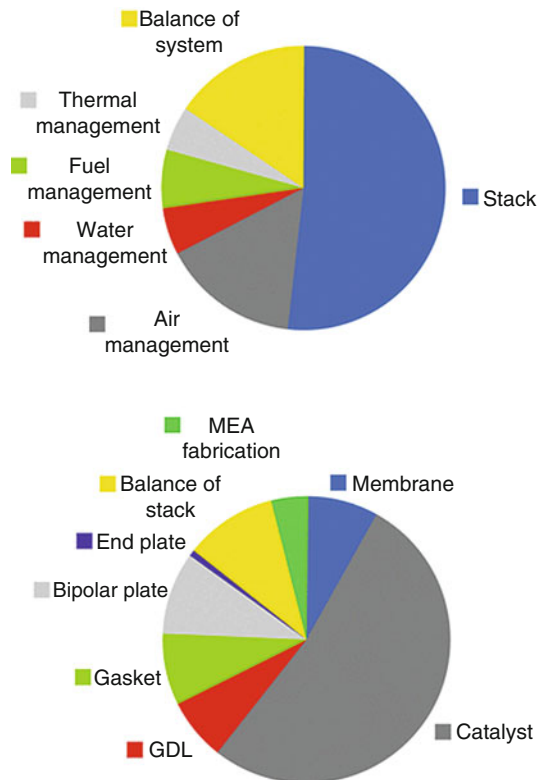
According to the most updated report [13], the cost of an 80 kW PEMFC system, when produced in a quantity of 500,000 systems per year, would amount to \$60–\$80/ $\text{kW}_{\text{net}}$ . The contribution of



**PEM Fuel Cell Materials: Costs, Performance, and Durability, Fig. 3** Cost progress for PEMFC stack, \$ per kW for an 80 kW stack, when manufactured at 500,000 pieces per year (Data from [12])

the stack and systems components is illustrated in Fig. 4.

From Fig. 4, it becomes clear that the stack is the most expensive single component of the fuel cell system, and that on stack level, the catalyst is the most expensive single component. It is important to notice that all costs are expressed per kW system output. It can therefore be important to improve a component that has a big impact on fuel cell performance without being expensive itself. When a better performing membrane or gas diffusion layer leads to a doubling of the power density while the catalysts cost per square meter stays the same, its cost will halve per kW due to this membrane or GDL improvement. Vice versa: It is not helpful to decrease the loading of



**PEM Fuel Cell Materials: Costs, Performance, and Durability, Fig. 4** Contribution of components to total stack costs, taking the cost estimate from Tiax [13]. Top figure: cost breakdown of an 80 kW system; bottom figure: cost breakdown of an 86 kW PEMFC stack. Note that an additional 6 kW is necessary to power balance of system components



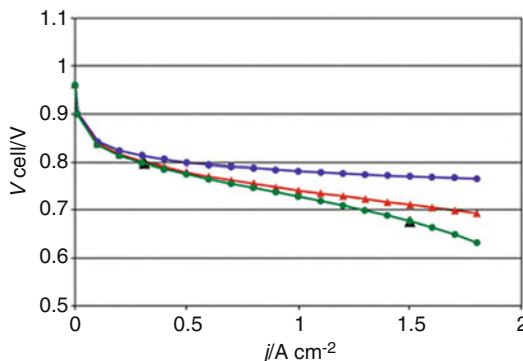
platinum per square meter, when this leads to a lower power density: All components' costs per kW will increase, possibly offsetting the cost gain of the lower platinum cost.

In PEMFC, the cost targets strongly determine the performance targets, which includes MEA performance as well as the allowable operating window. As a result, targets are more demanding for automotive than for stationary applications.

For automotive conditions, the DoE has set for 2015 a target rated cell power density of  $1 \text{ W cm}^{-2}$ , that is,  $1.5 \text{ A cm}^{-2}$  at  $0.68 \text{ V}$  corresponding to 55% LHV electrical efficiency. The requested efficiency at 25% power is 65%, which implies  $0.8 \text{ V}$  at  $0.25 \text{ W cm}^{-2}$  or  $0.31 \text{ A cm}^{-2}$ . Furthermore, the cost requirements demand that the total precious metal loading should not exceed  $0.15 \text{ g kW}^{-1}$ , which results in  $0.2 \text{ mg cm}^{-2}$  [1]. In automotive conditions, the peak power will be achieved at the higher end of the temperature window, in extreme situations near  $120 \text{ }^\circ\text{C}$ , which will mean that the relative humidity will be low, in the order of 25% maximum.

In stationary systems (including APU), the power density may be lower, with  $0.6\text{--}0.7 \text{ W cm}^{-2}$  at  $0.7 \text{ V}$  a typical target but with higher precious metal loadings in the order of  $0.5 \text{ mg cm}^{-2}$ . For reformate fed systems, there is the additional requirement of CO tolerance up to 50 ppm. The temperature and relative humidity can be kept closer to what are called the ideal PEMFC conditions, although increase of temperature up to  $120 \text{ }^\circ\text{C}$ , without increasing the dew point of the gases, would contribute to efficiency of the utilization of heat in  $\mu\text{CHP}$  systems. As automotive performance targets seem to encompass stationary targets with the exception of reformate tolerance, in the following, the emphasis will be on automotive targets.

Figure 5 shows a deconvolution of the total cell voltage compared to the voltage corresponding to the Lower Heating Value. Three different types of losses are usually identified, ohmic loss, activation loss and transport losses. The curves shown correspond to the target situation, that is, the overall ohmic resistance is  $0.04 \text{ } \Omega \text{ cm}^2$ , the total performance matches the efficiency requirements at rated power and 25% rated power, and the activation



**PEM Fuel Cell Materials: Costs, Performance, and Durability, Fig. 5** Deconvolution of the total cell voltage according to DoE targets. The blue line includes activation losses only, the red line includes ohmic losses as well, and the green line gives the overall performance in agreement with the DoE targets (▲)

losses are limited to what may be expected if the catalysts satisfy the targets of the DoE, that is, a mass activity for the oxygen reduction reaction (ORR) of  $0.44 \text{ A mg}^{-1}$  ( $900 \text{ mV}$ ,  $\text{H}_2/\text{O}_2$ ,  $80 \text{ }^\circ\text{C}$ , 100% RH, 150 kPa), and  $0.15 \text{ mg}_{\text{Pt}} \text{ cm}^{-2}$  cathode loading [1]. At  $0.05 \text{ mg}_{\text{Pt}} \text{ cm}^{-2}$  anode loading, anode losses are assumed to be negligible. The difference between the targeted curve and the curve representing activation and ohmic losses reflects the maximum acceptable transport losses.

The most significant contributions to the ohmic losses are due to the membrane, the bipolar/cooling plates and the electrodes (GDM + catalyst layer), including contact resistance between components. In a  $\text{H}_2/\text{air}$ -fed fuel cell, the activation losses are mainly at the cathode. The catalyst layer, the microporous layer (MPL), and the macroporous gas diffusion layer (GDL) of the gas diffusion medium (GDM) as well as the gas channel design (i.e., the bipolar plate) all contribute to transport losses of reactants.

The PEM fuel cell contains a number of components of which the performance varies with operating conditions. This relation can be either instantaneous or become apparent after longer exposure to such conditions. The components that are most sensitive for operating conditions are the proton exchange membrane and the electrodes for hydrogen oxidation and oxygen reduction.

The PEMFC based on perfluorinated sulfonic acid membranes can be operated from sub-freezing conditions to around 80 °C, the upper limit depending on the operating pressure and relative humidity of the inlet gases. Although the PEMFC can be started subzero, systems will generally be controlled in such a way that the cell temperature is allowed to increase to the desired set-point between 60 °C and 80 °C, where power output is at its maximum while improving water management. At low pressures and low relative humidity, this set-point will be close to 60 °C, while at high pressures and high relative humidity, the set-point will be close to 80 °C.

It has been amply demonstrated that the membrane performance is at its maximum when fully wetted by water. The proton conductivity is in this case at its maximum. Under stationary conditions, using fully humidified gases and moderate temperatures not exceeding 70 °C, the stability of the membrane was proven sufficient to sustain stable performance for 26,000 [14] – 36,000 [15].

For the fuel cell electrodes, the picture is more complex, partially because of the various electrode components and functions merged together. For proton conductivity, an ionomer similar to that used for the proton-conducting membrane is dispersed throughout the electrode. As for the membrane, it needs to be wet to provide sufficient proton conductivity. At the same time, an upper limit for wetting exists for the catalyst layer to

prevent flooding. For the electrocatalyst, the electrode potential is the dominant factor determining activity and stability, provided that hydrogen and oxygen are sufficiently available at the reaction interface. For hydrogen oxidation, the activation losses are moderate, so that in practice the anode is between 10 and 50 mV versus RHE. For oxygen reduction, however, the activation losses are substantial; the cathode potential is, depending on the current density, between 500 and 800 mV versus RHE. There has always been a trade-off between efficiency and power output, which can be translated into a trade-off between fuel efficiency and fuel cell investment cost. The relation between cell current density and cell voltage, efficiency, and power density is illustrated in Fig. 6.

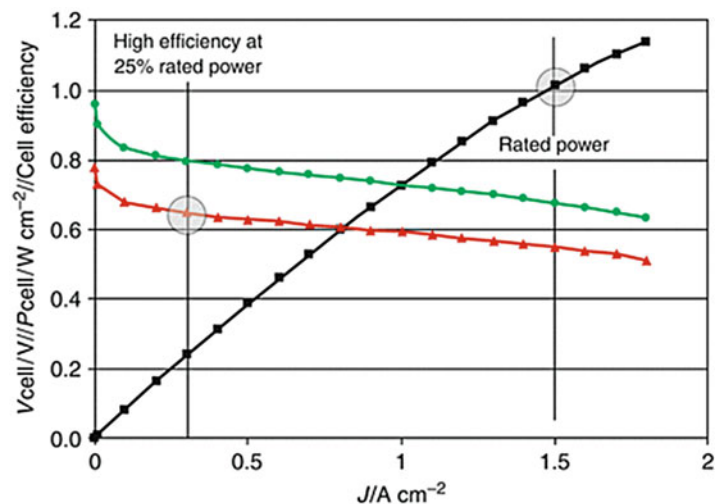
The fuel cell electrical efficiency is directly proportional to the fuel cell voltage  $\Delta E_{\text{cell}}$ :

$$\text{Eff}_{\text{FC,LHV}} = \frac{\Delta E_{\text{Cell}}}{1.23 \text{ V}}, \text{ or } \text{Eff}_{\text{FC,HHV}} = \frac{\Delta E_{\text{Cell}}}{1.48 \text{ V}}$$

for the lower heating efficiency (LHV) and the higher heating efficiency (HHV), respectively, at room temperature. In Fig. 6, the green line represents the relation between cell voltage and current density, which is the same as in Fig. 5; the red line represents the LHV cell efficiency versus current density, according to the equation above, while the black line represents the cell power density versus current density. For the fuel cell and

### PEM Fuel Cell Materials: Costs, Performance, and Durability, Fig. 6

Cell voltage (green), power density (black), and efficiency (red) versus cell current density. The points of rated power and 25% rated power are indicated. Follow vertical lines to find the corresponding cell characteristics at these points



conditions of Fig. 6, the point of rated power density, in this case  $1 \text{ W cm}^{-2}$ , lies at 0.68 V, at which the cell LHV efficiency amounts to 55%. At a cell LHV efficiency of 65%, the power density equals  $0.25 \text{ W cm}^{-2}$  at a cell voltage of 0.8 V. In practice, a system containing a cell with characteristics shown in Fig. 6 will be operated near the high efficiency point for most of its time, while at occasional times, when the rated power is needed, the cell is operated at lower cell voltage. Opposed to internal combustion engines, the operation at low power demands, for example, when idling, leads to higher efficiencies of the fuel cell. At systems level, this is partly offset by the energy consumption of balance of system components.

When developing new materials and components for reducing costs, their durability should be the starting point instead of the sanity check afterward. The durability standard is set by the components used in today's technology, and should only become better. Cheaper alternatives that would lead to lower durability are not welcome, as they would lead to the previously mentioned early replacement of complete stacks or disassembling of the stack to replace individual components.

Moreover, cheaper cell materials leading to lower power density will lead in most cases to higher stack costs at the end. Except for the catalyst, no single component constitutes more than 10% of overall stack costs. Using the overall cost numbers of the Tiax analysis [13], total cost per cell will be \$4,80 including bipolar plates. The power of such a single cell is 196 W, that is, costs are \$24.50 per kW. The membrane, generally regarded as an expensive component, will cost \$0.43 per single cell. Suppose a cheap alternative membrane, costing only \$0.10 per cell, would lead to a performance of 180 W per cell. In this case, a very substantial cost reduction of more than 75% for a particular component leads to a power output loss of less than 10%. Per kW, the cell with the low cost membrane is more expensive, \$24.8 per kW than the cell with the expensive membrane. This simple example shows that improvement of the cell power density rather than mere component cost reduction should be driving materials R&D.

The complexity of the fuel cell system is for a considerable part caused by the large influence of the relative humidity in the cell on the performance of the MEA. The heat removal capacity of a fuel cell system operating at 70–80 °C is limited, since it is directly proportional to the temperature difference between the cooling liquid temperature and the ambient temperature. Moreover, nearly all the heat produced in the fuel cell stack has to be rejected over the coolant/radiator/ambient air heat exchanger, while in the internal combustion engine, much heat is rejected through the tailpipe. Under certain conditions, that is, when delivering full power at a limited speed at high ambient temperature, this can easily lead to stack temperatures up to 120 °C. Volkswagen has a test drive in Death Valley to test their cars on their capability to deal with this [16]. Although the occurrence of such events can be minimized by increasing, for example, the radiator size of the system, from a point of view of system robustness, it is preferred that the stack can operate at such conditions.

However, maintaining a constant high relative humidity at temperatures rising above 70–80 °C is not feasible due to the large amount of water that would need to be circulated as well as the negative effect it would have on the oxygen partial pressure. Therefore, a large R&D effort is currently spent on developing MEAs that do not show a drop in power output at, increasing temperatures with concomitant reduction in relative humidity. Although such widening of tolerable relative humidity range could lead to some reduction in cost for thermal management and water management, see Fig. 4, the prime advantage is on increasing robustness of the system.

In the following sections, the individual cell and stack components are discussed in view of their performance and cost.

## Costs and Performance Developments of Components

### Membranes

The targeted values for the membrane resistance are  $0.02 \text{ } \Omega \text{ cm}^2$  [1]. The accepted commercial standard for membranes (Nafion, Flemion,

Aciplex,) consists of a PTFE backbone with a perfluorovinylether side chain that ends with a sulfonic acid group. Variations in this side chain distinguish the different trade names. The commercial standard membranes have equivalent weights (EW) in the order of  $1,100 \text{ g eq}^{-1}$  (weight per mol sulfonic acid groups). At ideal conditions (i.e.,  $80 \text{ }^\circ\text{C}$ , liquid water present), a conductivity of  $0.1 \text{ S cm}^{-1}$  is a standard value for commercial PFSA membranes. The resistance target therefore corresponds to a maximum thickness of  $20 \text{ }\mu\text{m}$ . Whereas this was a few years ago still at conflict with requirements on gas tightness and durability, the implementation of reinforced membranes has made this feasible as was shown by Gore, Dupont, and 3 M [17–19]. Such a reinforcement is made of PTFE or a ultrahigh molecular weight polyethylene. The latter materials, however, are less suitable for operation near  $120 \text{ }^\circ\text{C}$ . These high EW PFSA membranes of  $25\text{--}30\text{-}\mu\text{m}$  thick, either reinforced (DTI) or not (TIAX), form the basis of the membrane cost in the DoE analysis. These costs amount to  $\$2.4$ (TiAx) or  $\$3.3$  (DTI) per kW [13].

The conductivity of high EW membranes, however, drops dramatically with relative humidity to less than  $5 \text{ mS cm}^{-1}$  at 25% RH, that is, by more than an order of magnitude [20]. Although conductivity values increase slightly with temperature, this implies that at  $120 \text{ }^\circ\text{C}$ , 25% RH these membranes do not meet the target. This fact has motivated considerable research into membranes that can operate at drier conditions, with already quite promising results.

Several routes have been and are to time still being explored, which include (1) low EW PFSA membranes, (2) hybrid inorganic/organic membranes where inorganic additives should take care of water retention and/or proton conductivity, and (3) membranes that enable intrinsically dry proton conduction, such as systems based on imidazole or phosphonic acid rather than water as a proton carrier or relying on phosphoric acid as the proton-conducting medium.

Low EW membranes have higher proton conductivity values at a given humidity. The equilibrium number of water molecules per acid group ( $\lambda$ ) at a certain humidity value is not dependent on

the EW, which results in an increased water uptake per volume or weight unit. In addition, the mobility of the protons tends to increase with decreasing EW, supposedly due to morphological changes associated with the higher water fraction [21]. The combination of higher concentration of protons and enhanced mobility results in conductivity values that at the same  $\lambda$  are higher for low EW polymers. At low EW, however, the degree of crystallinity of the membrane is reduced, which results in water-soluble membranes. Approaches to reduce the water solubility have included modification of the polymer, cross linking, and blending.

A modification of the polymer that has been adopted by various groups is to have shorter side chains as compared to Nafion. Short side chains increase the crystallinity of the PFSA, thus reducing the solubility. Solvay Solexis has developed Aquivion, a membrane based on Hyflon, which is a copolymer of Teflon and sulfonyl fluoride vinyl ether with low EW (790–870) and good crystallinity, with proton conductivity values in the order of  $30 \text{ mS cm}^{-1}$  at  $120 \text{ }^\circ\text{C}$ , 30% RH [22]. A similar approach is followed by 3 M, who have shown 580 EW membranes approaching  $100 \text{ mS cm}^{-1}$  at  $120 \text{ }^\circ\text{C}$  and RH 50% [23]. Gore recently reported values  $>50 \text{ mS cm}^{-1}$  at 30% RH and  $>100 \text{ mS cm}^{-1}$  50% RH with a new, undisclosed ionomers [24]. DuPont recently presented results on MEAs with new ionomer that showed a much reduced dependence on the RH as compared to Nafion-based membranes [17].

Cross-linking can be achieved through the backbone, but also through the acidic groups. Dongyue Shenzhou New Materials uses sulfonimide links to this end [25]. Values of  $200 \text{ mS cm}^{-1}$  at  $80 \text{ }^\circ\text{C}$  and 95% RH to  $12 \text{ mS cm}^{-1}$  at  $120 \text{ }^\circ\text{C}$  and 25% RH have been reported with this material. Also 3 M is considering introducing (aromatic) imide groups to the sulfonic end group either to attach cross-linkable groups or more acid groups per side chain [23]. So far, approaches involving blending of soluble and insoluble material do not seem to have been successful in stopping the dissolution of the soluble material. Reinforcements may also reduce the solubility of low EW materials.

The durability aspects, however, have not been fully established. These will be discussed in section “[Materials Degradation and the Relation to Performance Loss and Shortening the PEMFC Lifetime.](#)”

Also the addition of inorganic materials to enhance water retention and/or proton conductivity has had some success, for example, by adding zirconium phosphate. Such additions have also been successful in increasing the mechanical strength of materials [26, 27].

Hydrocarbon membranes, such as sulfonated PEEK or sulfon imides, usually show lower conductivity values and increased swelling, or water solubility. The proton conductive paths in these materials are not as effective as in PFSA membranes. Not unrelated, however, is the observation of much reduced gas cross-over rates in such membranes [25, 28]. While this may be unfavorable for the application of such materials as proton-conducting phase in the electrode, it has a positive impact on the durability of the membrane as will be discussed in section “[Materials Degradation and the Relation to Performance Loss and Shortening the PEMFC Lifetime.](#)” This has recently given a new incentive to research in this area [29]. Sulfonated PEEK membranes are commercialized by Fumatech GmbH in Germany [30]. Low equivalent weight membranes (EW 675–850) with a conductivity ranging from  $0.04 \text{ S cm}^{-1}$  at  $40 \text{ }^\circ\text{C}$  to more than  $0.08 \text{ S cm}^{-1}$  at  $80 \text{ }^\circ\text{C}$  are offered.

The success of widening the operating temperature for water-based proton conduction system has so far not been matched in the field of intrinsically dry proton conductors. Although interesting developments were reported in the field of polymers having tethered imidazole groups [31–34], these and other approaches based on phosphonated polymers, either in their pure form or as acid-base copolymers or blends, show conductivity values, which are at least an order of magnitude too low [34–36].

The proton conduction based on the phosphoric acid is the basis of HT-PEMFC Celanese technology [37], mostly referred to as phosphoric acid-doped PBI (polybenzimidazole) This membrane enables operation at temperatures as high as

$180 \text{ }^\circ\text{C}$ , without the need for external humidification. Heat dissipation at this temperature is much easier than at the  $70\text{--}80 \text{ }^\circ\text{C}$  operating temperature of fuel cell systems using standard PFSA membranes. The CO tolerance at  $180 \text{ }^\circ\text{C}$  is such that even 1% CO leads to a minor loss of power density compared to that using the same membrane on pure hydrogen. The downside of this membrane is its low conductivity below  $100 \text{ }^\circ\text{C}$ , making a cold start impossible, as well as the lower power density at its optimal temperature.

At  $23 \text{ }^\circ\text{C}$ , the power density of a phosphoric acid-doped PBI-based MEA is quoted to amount to  $8 \text{ mW cm}^{-2}$  [38], while the best performing MEA at  $160 \text{ }^\circ\text{C}$  shows a power density of  $0.28 \text{ W cm}^{-2}$  at  $0.7 \text{ V}$  [39], less than half of the PFSA-based MEAs used for the DoE cost analysis. The only car manufacturer pursuing the use of phosphoric acid-doped PBI membranes has been Volkswagen. For stationary applications, it has been primarily PlugPower that has developed fuel cell systems based on phosphoric acid-doped PBI membranes.

Unassisted start-up at freezing conditions, another automotive requirement, does not seem to be compatible with systems not based on water. First, as already mentioned, their proton conductivity is too low at such temperatures. Secondly, they cannot play the role of water storage medium during start-up. By pre-drying PFSA membranes, the water content can be reduced so much that only non-freezable water remains. This results in a remaining conductivity in the order of  $10 \text{ mS cm}^{-1}$  that is sufficient for a start-up procedure. The low initial performance induces heat generation. In a previously dried system, product water can then be stored, keeping the gas channels in the active layers free from ice [40, 41]. This start-up procedure is not feasible for membranes unable to adsorb liquid water, such as PA-doped systems where water adsorption would lead to washing out of the acid.

In a cost comparison by Gebert et al. [42], it is concluded that sulfonated Polyether ether ketone (S-PEEK) and phosphoric acid-doped polybenzimidazole ( $\text{H}_3\text{PO}_4$ -PBI) could be a factor of five cheaper than Nafion. As discussed earlier, this cost advantage is only helpful when not offset by lower MEA power density.



### Electrodes and Gas Diffusion Media

As noted in the expert review of the two parallel cost estimates for the DoE program [13], the cost reduction realized in the past 3 years is almost entirely caused by the reduction in platinum loading to  $0.25 \text{ mg cm}^{-2}$  at an areal power density of  $0.715 \text{ mW cm}^{-2}$ . It takes into account a prescribed platinum cost of \$1100 per troy ounce (= 31.1 g), to avoid a high volatility of fuel cell cost caused primarily by the volatility of the platinum price. At the same time, the high impact of the platinum price on the fuel cell cost is a serious problem: As the loading target is distilled from the platinum price and the allowable cost per kW, a successful reduction of the platinum loading can easily be offset by an increase in the platinum price. A further reduction of the platinum loading could alleviate this dependence.

The catalytic layer used for the DoE cost review [13] is based on a ternary PtCoMn alloy, either supported by carbon or by organic whiskers, as developed by 3 M, with a platinum loading of  $0.25 \text{ mg cm}^{-2}$  cell area. The cost of the support and the ionomer is insignificant compared to the precious metal cost of the catalytic layer. Most R&D is devoted to decreasing the use of precious metal, primarily platinum, while at the same time preserving power density and durability.

The PtCoMn alloy as developed by 3 M that was adopted for the cost review is so far the only catalyst for which the activity data set by the DoE have been met in MEA tests under relevant conditions, but long-term field data are absent for stacks or systems based on the PtCoMn alloy. The most applied cathode catalyst to date is Pt supported on carbon, while at the anode, either Pt or Pt alloyed with Ru and or Mo is used. At present, these catalysts do not meet yet the target activity.

Further electrode performance improvements, and thus reductions in use of platinum per kW, can either come from a further reduction of ohmic losses, activation losses, or from transport losses.

*Ohmic losses:* The ohmic losses associated with the electrodes are related to electron transport through the gas diffusion media and the catalyst layers. The proton transport in the catalyst layer is

associated with transport losses, as its contribution is not ohmic but depends on current density [43]. In state-of-the-art components, carbon is the electron conductor.

The in-plane as well as the through-plane resistance of the GDM contributes to the ohmic resistance due to their function of evening out the current distribution. As most current GDM's are based upon non-isotropic materials such as paper or woven materials, these differ often by an order of magnitude. The through plane resistance of the material depends strongly upon the compression, a factor that has to be taken into account for application in a fuel cell. In general, the overall ohmic loss through the GDM is quite small, in the order of  $2 \text{ mV}$  at  $1 \text{ A cm}^{-2}$  [44].

The presence of a so-called microporous layer at the interface with the catalyst layer has a positive effect on the contact resistance. For carbon black-based catalyst layers, it is usually assumed that electron transport losses are negligible. This may not be the case when less well-conducting oxide or carbide supports are considered.

*Activation losses:* In an  $\text{H}_2/\text{air}$ -fed fuel cell, the activation losses are mainly at the cathode. The hydrogen oxidation rate is very fast on the standard Pt catalyst, indeed such that it is hard to measure it accurately. Estimates of the exchange current density are in the order of  $0.24\text{--}0.60 \text{ A cm}^{-2}_{\text{Pt}}$  [45]. There is substantial evidence that the anode Pt loading can be as low as  $0.05 \text{ mg cm}^{-2}$  with losses in the order of mV only [4]. Durability issues as well as the presence of CO may require a higher loading; this will be further discussed in the next chapters.

The research is therefore focused at the cathode. The state-of-the-art catalyst Pt/C shows only a low specific activity in the order of  $0.2 \text{ mA cm}^{-2}$  Pt at  $900 \text{ mV}$  (IR-free, at 1 bar  $80^\circ\text{C}$ ) This is compensated by the large Electrochemically Active Surface Area values (ECSA) obtained with these catalysts, which can be in the order of  $60\text{--}90 \text{ m}^2 \text{ g}^{-1}$ . The corresponding mass activities, which are the product of the ECSA and the specific activity, are between  $0.12$  and  $0.18 \text{ A mg}^{-1}$ , about a factor 3 lower than the target, resulting in a required Pt loading in the order of  $0.4\text{--}0.6 \text{ mg cm}^{-2}$  Pt [46].



A further increase of the ECSA does not seem useful; this would imply particles smaller than 2 nm, which are not very active. Specific activity decreases with particle size or specific surface area due to more low coordinated Pt atoms and longer Pt-Pt bond distances, which have a pronounced effect on the electronic structure. Ensuing strong OH adsorption blocks the sites for oxygen adsorption. Whereas 0.2 mA cm<sup>-2</sup> seems a sort of maximum for Pt nanoparticles, the maximum specific activity for pure Pt with well-defined crystal faces is much higher, in the order of 2.2 and 1.9 mA cm<sup>-2</sup> for Pt (110) and (111), respectively, measured in HClO<sub>4</sub>, an electrolyte that due to its non-adsorbing anions mimics PFSA best [47]. For Pt black and Pt polycrystalline disk, higher values for the specific activity are also found [46]. 3 M showed with their so-called Pt Nano-Structured Thin Films (NSTF) a specific activity of up to 1.7 mA cm<sup>-2</sup> Pt at 900 mV (IR-free, at 1 bar 80 °C) with ECSA values in the order of 10–15 m<sup>2</sup> g<sup>-1</sup> [48, 49]. The NSTF is a continuous layer of polycrystalline Pt deposited on non-conductive, inorganic whiskers [50], with a surface mostly showing Pt (111) facets [51].

Several ways to improve the mass activity are currently explored. In the concept of nanoparticles on carbon black, alloying Pt with other metals is intensively studied. It is well known that the specific activity of Pt can be improved by alloying. The effect is ascribed mostly to changes in the electronic structure, which bring the system nearer to the optimum where both O-O bond dissociation and OH formation take place [52, 53]. Very high specific activity values were recently reported for certain Pt<sub>3</sub>M alloys (M = Ni, Co, Fe), where the activity of Pt<sub>3</sub>Ni (111) was shown to be ten times that of Pt (111), that is, 19 mA cm<sub>Pt</sub><sup>-2</sup> [53, 54]. These findings have motivated studies into supported Pt binary and ternary nano-sized catalysts as well as extended Pt alloy catalysts.

Nano-sized binary alloys of Pt with Cr, Co, Mn, Ti, Co have been widely studied indicating a three to four fold increase in specific activity, but also identifying serious stability problems [6, 46, 55, 56]. More recently, ternary systems including

PtIrCo, PtIrCr, and PtMnCo are considered with the aim to improve durability. Mass activity values of some PtIrM catalysts come close or exceed the 0.44 A mg<sup>-1</sup> target value [57]. Increased activity can also be achieved by Pt skin nanoparticles. Here the core of a particle is made of cheap transition metal with a skin of Pt. By carefully selecting the base material, the skin Pt atoms may be more active than the Pt on the outside of a pure Pt nanoparticle [58]. High mass activities have been reported for particles consisting of a Pt or PtIr monolayer on Pd<sub>3</sub>Co cores (order 0.7 A mg<sup>-1</sup>Pt) [59].

A relatively new class of catalysts are pre-leached alloys, e.g., Cu-Pt. It was found that after leaching of Cu from the outer layers of Pt<sub>0.25</sub>Cu<sub>0.75</sub>, the remaining Pt<sub>1-x</sub>Cu<sub>x</sub> showed a Pt-rich surface with high activity, again most likely due to favorable Pt-Pt distances and related electronic effects [60, 61]. Also Pt-free precious metal alloys, such as Pd with a transition metal, are currently being investigated [62].

Changing the support material may also have an effect on the mass activity. In many cases, it was found that on low surface area carbon supports, which are expected to be more stable, the Pt cannot be so well dispersed resulting in lower specific surface area and mass activity. However, it may be envisaged that either through inducing a certain particle morphology or by an electronic interaction, the specific activity may increase in such a way that this outweighs the loss of surface area. Examples of this have recently been reported for Pt on nitrogen-modified carbon [63]. Other such effects have been reported for WC and VC supports. Other alternative supports include conducting oxides, which can also have an enhanced electronic effect [63, 64].

Non-supported catalysts seem a way not only to avoid durability issues related to the support (such as carbon corrosion), but also introduce extended surfaces and therefore the possibility of higher activity. The NSTF is an example, but also improved Pt black, Pt nano-wires or tubes, Pt-coated carbon nanotubes, or mesoporous Pt structures. Although such structures have been made, they have, with the exception of Pt black and NSTF, not yet been extensively tested in fuel

cells. The high mass activity of NSTF Pt was already mentioned. By using extended alloys, that is, NSTF of PtCoMn, the DoE target has been exceeded for PtCoMn ( $>0.44 \text{ A mg}^{-1}$ ) [49].

The last class to mention are non-metal catalysts. The use of catalysts not using metallic catalysts at all has intrigued many researchers for long time. Inspiration has come from nature, where hemoglobin structures in mammals bind oxygen, while porphyrin structures do so in plants. The most promising class of non-metal catalysts are the composite catalysts derived from heteroatomic organic precursors (e.g., polyaniline, polypyrrole, cyanamide, etc.), transition metals (Co or Fe), and carbon [65, 66]. The mechanism has not been completely clarified, but it is becoming increasingly clear that four M-N bonds are required. An essential step in the preparation is heat treatment at 600–1100 °C and subsequent activation steps. A target here is a volume activity of  $130 \text{ A cm}^{-3}$  at 0.80 V-IR-free. This target is not so much derived from cost considerations but from the requirements on the dimension of the electrode [46]. Still, here stability problems are reported as well as intrinsic mass transport losses [66, 67].

The effect of the humidity on activity has not been well explored due to a lack of suitable systems. It has been reported that activity drops when  $\text{RH} < 50\%$ , due to reduced proton activity [68]. Key to a high mass activity is the utilization of the catalyst, which is determined by accessibility for reactants. Under well-humidified conditions, supports with small pores show good utilization due to the presence of liquid water, which transport protons. This becomes critical at low humidity although smaller pores dry out less easily than larger.

*Transport losses:* The catalyst layer, the MPL, the GDL and the gas channel design (i.e., the bipolar plate) all contribute to transport losses of reactants. In the catalyst layers, both proton transport as well as transport of reactants takes place. At the anode side, transport losses are usually negligible. Hydrogen transport is fast, and the reaction seems to take place close to the membrane interface. At the cathode, the problems can be considerable due to the lower partial pressure

of oxygen in air and the water accumulation. This implies the reaction does not just take place at the interface, and therefore, proton transport also plays an important role. Transport losses increase with current density. The oxygen gain, which usually gives a fair indication of mass transport losses, can be as high as 150 mV at  $1.5 \text{ A cm}^{-2}$  [69].

The proton resistance of the catalyst layer can be reduced by adding more ionomer phase or low EW ionomer to the system, but this is outweighed by reduced oxygen transport. As gas phase diffusion is several orders of magnitude faster than diffusion through liquid water, it is essential to create a system that does not completely fill with liquid water, that is, contains fairly hydrophobic materials and not too small pore sizes. The state-of-the-art carbon blacks do not seem to meet this criterion. CNT or other more graphitic structures seem better suited. Also alternative supports should be selected with their potential for improved mass transport. Oxides may be less suitable in that respect but this certainly requires further investigations. At low RH, the requirements may be different, to some extent the structure needs to retain water for proton conductivity, as well as for proton activity. It has been observed that dry ionomers of the PFSA type are not very well permeable for gases. Reduced catalytic activity and more specifically increased transport losses are the reason why present state-of-the-art MEAs still have a poor performance at low RH and high T, in spite of acceptable ohmic resistance of the membrane. This requires improved ionomer to be used also in the electrode [70].

In general, thin catalyst layers will have the lower proton resistance. However, they may also fill up more easily with water as is, for example, the case with the very thin NSTF electrodes by 3 M, which only seem to function well at non-saturated conditions. Also for start-up under freezing conditions, a thicker electrode, or at least a higher pore volume, seems to be an advantage as complete filling with ice is even more detrimental.

A certain amount of mass transport problems must be ascribed to the GDL and MPL. The presence of an MPL usually prevents the GDL from becoming saturated with water; in most state-of-

the-art GDL's, the diffusion through the microporous layer is not limiting, although this may change upon aging. The MPL, although relatively dense, improves the transport by optimizing the water management [10]. When the fuel cell is to be operated at relatively dry conditions, water retention is more important than water removal. Also in this case, the GDM plays a critical role [71].

The cost of Gas Diffusion Media (MPL + GDL) [13] is quoted to be around \$10–\$15 per  $\text{m}^2$ , and is likely to be primarily determined by processing costs. Both carbon/graphite paper as woven structures are being used as substrate, which is made hydrophobic by, for example, a PTFE coating. The microporous layer mostly consists of carbon powder mixed with a PTFE emulsion, which is cured by a heat treatment. Clear directions for cost reduction have not been found. As the gas diffusion media play a critical role in the performance of the PEMFC, especially determining the maximum power output makes it worthwhile to focus on the GDM performance, rather than on the cost per  $\text{m}^2$ .

### Bipolar Plates

For bipolar plates, a total (bulk and contact) resistance value of  $10 \text{ m}\Omega \text{ cm}^2$  is usually specified [72]. This would result in  $0.02 \Omega \text{ cm}^2$  (two plates, coolant between), which at  $1.5 \text{ A cm}^{-2}$  would result in 30 mV voltage loss. Bipolar plates are made of carbon, carbon/polymer composite, or metal. Both the resistance and weight/volume aspects demand thin bipolar plates. This has to be combined with low  $\text{H}_2$  permeability ( $<2 \times 10^{-6} \text{ cm}^3 \text{ cm}^{-2} \text{ s}^{-1}$ ) and good mechanical integrity.

From a materials durability point of view, carbon/polymer composite materials are to be preferred. However, metal-based bipolar plates enable the use of very thin plates, thus leading to an increase in volumetric power density. Major car manufacturers such as Honda and Toyota are using metal-based bipolar plates in the fuel cell stacks that are used in their latest generation fuel cell vehicles. Power density of  $1.9 \text{ kW L}^{-1}$  by both Honda [73] and Nissan [74] is ascribed to the use of metal-based bipolar plates.

From the total costs for metal bipolar plates as stated in the DoE cost review report, the costs of

the metal plates amount to  $\$20 \text{ m}^{-2}$  active cell area, which will be at maximum 10% lower per  $\text{m}^2$  metal area. For the metal-based bipolar plates, the materials costs are significantly higher than the processing costs. As metal, coated 316 L stainless steel is selected.

The use of metal-based bipolar plates brings two concerns [2]. At the anode, corrosion leads to the release of metal ions that can exchange with protons in the ionomer in the electrode as well as in the membrane, resulting in increased resistance of the electrode and membrane. At the cathode, the major concern is an increase in contact resistance, caused by the buildup of an oxide layer that has lower bulk conductivity than the metal itself. The stack compression force has an important effect on the contact resistance; the lower the compression force, the higher the contact resistance [75].

Various approaches are therefore being followed. A material, such as a stainless steel with high corrosion resistance, and with a low tendency to form a high resistance oxide layer, could be applied as plate material. Stainless steels need the right amount of chromium, nickel, and nitrogen to form a thin corrosion resistant layer on the surface that does not have a too negative effect on the contact resistance. Examples of stainless steels that have been qualified are 904 L, and to a lesser extent 316 L and 310S [76].

Recently, incorporation of nitrogen into the surface of especially nickel-based alloys by thermal nitration was shown feasible. In this way, the contact resistances are reduced and the corrosion resistance of the materials is increased, thus meeting the targets set by the DoE [77]. Nitration of cheaper Fe-based stainless steels is being considered.

Another approach is to select steels that qualify when coated with a coating [2], that either prevents direct contact with the electrolyte and is not oxidized at the cathode. In this respect, ceramic metal nitride coatings are considered (Cr, Ti, TiAl nitride) [78]. If the coating is perfectly dense and stable, any base material could be applied. Alternative base metals being considered are aluminum or titanium [79].

The coating may be applied before or after the flow pattern is stamped in the plate, depending on

whether it is possible to avoid damaging the coating layer during the forming process. Some stack manufacturers advocate the use of thin gold coating, which results in a well-conducting coating but needs to exceed a thickness of several nanometers to be sufficiently dense and hence may not meet the cost targets [13]. Conductive polymers have also been suggested as coatings, although their stability under the fuel cell conditions is a concern [80].

Graphite/polymer composite materials made of a graphite, and carbon combined with a polymeric resin, are less susceptible to corrosion, and have low contact resistance but higher bulk resistance than metals. Also the gas permeability is higher than in metals. This results in thicker plates, which may still be acceptable for stationary applications. Target values for the bulk conductivity are in the order of  $>10 \text{ S cm}^{-1}$  [79].

Expanded graphite foil, as alternative to metal plates, would cost  $\$18 \text{ m}^{-2}$  [13, 81]. With respect to plate thickness and processibility [82], expanded graphite foil is similar to metal plates, enabling a stack power density of  $2.1 \text{ kW L}^{-1}$  [81].

Note that the flow field design of the bipolar plate is a critical factor for reactant supply and water management of stack and individual cells. As will be discussed later, a suboptimal flow field and manifold design can lead to an uneven distribution of reactants, and by this to fuel and air starvation.

### Seals and Edge Protection

The seals or gaskets provide protection to leakage of gases and coolants outside their compartments. They also control the stack height and compensate for tolerances in material thickness. These materials consist of several components, the amount and type of which determines the final properties. Usually a base rubber is selected, to which additional fillers for mechanical strength and a plasticizer for flexibility are added. The seals have to be thermally stable as well as stable against hydrogen, oxygen, acid media, and coolants, and be compatible with other stack parts such as the bipolar plate.

Base rubbers may be based on silicone, fluoropolymers, or hydrocarbons. Although silicone rubbers such as silicone S and G have been applied in stacks, it has become clear that they are not sufficiently stable [83–85]. Materials like ethylene-propylene-diene-monomer (EPDM), butyl rubber (IRR), or fluororubbers (FKM such as Viton<sup>®</sup>) seem better suited. Further research is carried out to optimize properties like hardness, tensile strength, and stress relaxation. Also the morphology is being considered, with apparently a preference for profiled over flat gaskets.

Seals can be provided as separate stack components, but preferentially they are integrated in the MEA or the bipolar plate. This of course puts demands to the processibility of the base materials and the manufacturing process, which may involve curing to achieve cross-linking of the polymeric materials.

Misalignments of the anode and cathode, compression forces from the GDM, fibers stretching out from the GDM may all put electrochemical, chemical, and mechanical stress on the membrane, which the thin, state-of-the-art membranes cannot withstand. Therefore, some manufacturers advise the inclusion of edge-protection on the membrane, that is, a layer of gas-tight and non-conducting material covering the membrane not covered by catalyst and GDL, and protruding slightly onto the area between the GDL (or catalyst layer) and membrane at the edges of the GDL. Suggested materials include polyimide [86]. These materials are there to reduce degradation of the membrane, but add to the complexity of the MEA and introduce yet other materials. Another option would be to let the edges of the electrodes coincide with the MEA, but this puts larger demands on the seals as well introduces the risk of shortening [13].

From the DoE cost review [13], it can be concluded that sealing of the cells comprises a higher cost than the electrolytic membrane. Depending on the design, one needs one frame per MEA, or even three frames per MEA. The lack of literature on seals development is at least remarkable. Although sealing is a quite generic topic that plays a role in many devices where leakage of gases or liquids has to be prevented, the sealing

in fuel cells is extra demanding, both due to the aggressive environment as well as due to the sensitivity of the PEMFC for contaminants.

## Operating Conditions Leading to Performance Loss and Shortening the PEMFC Lifetime

### Definitions and Targets

Besides cost reduction, durability is a key topic in the PEMFC R&D. The projected operational lifetime of a passenger vehicle is 5,000 h. While until recent years, PEM fuel cells R&D was especially focused on increasing the power density and decreasing the cost; attention during the last years has been shifted to durability issues. It has been recognized that during operation, the PEMFC cannot always be kept in its ideal window of operation, which has been found out to be steady operation at a constant voltage between 0.5 and 0.7 V, under fully humidified conditions and mild temperatures (70 °C) using clean hydrogen and air [87]. Under these conditions, operating times far exceeding the required 5,000 h have been demonstrated with voltage decay rates of 1–2  $\mu\text{V h}^{-1}$ , which would limit the total voltage loss during a life of 5,000 h to 10 mV, which translates into a loss of efficiency of only 1%.

The numerous lifetime and durability studies on PEMFC in situ as well as on individual components ex situ have identified the main sources for performance decay and the related materials issues. A gradual decay of performance is mainly ascribed to effects in the cathode, notably loss of catalyst activity and increase of mass transport losses. The loss of activity was shown to result from dissolution and coarsening of the catalyst nanoparticles. The increased mass transport losses were ascribed to a decrease of the hydrophobicity of both catalyst layer and gas diffusion layer. Other factors contributing to the gradual decay are similar processes occurring in the anode and degradation of the bipolar plates and the seals of the MEA. The cause of sudden failure of the PEMFC was identified as the membrane losing its integrity, as a result of chemical as well as mechanical stresses. These principal degradation

mechanisms were found to be strongly dependent on conditions, where deviations from ideal conditions (70 °C, 100% RH, constant load) usually exacerbate the effects. These deviations also include the presence of contaminants, either as degradation products from the system itself (bipolar plates, seals, catalyst ions, membrane fragments) as well as contaminants in the fuel, (CO, H<sub>2</sub>S, CH<sub>4</sub>, NH<sub>3</sub>) and in the air (SO<sub>x</sub>, NO<sub>x</sub>, NH<sub>3</sub>).

The targets currently accepted for automotive application are 5,000 h operation under drive cycle conditions or 40,000 h for stationary conditions with less than 10% performance decay. Such requirements imply that the decrease of mass activity should be limited and that the membranes will have to be able to perform without failure during the envisaged lifetime. The increase of mass transport losses should be minimal, putting demands on the stability of the support.

In this section, operating conditions and modes that contribute to voltage decay or limit performance will be discussed. In section “[Materials Degradation and the Relation to Performance Loss and Shortening the PEMFC Lifetime](#),” the durability issues related to the different components of the fuel cell, that is, catalyst, the gas diffusion layers, membranes, bipolar plates, and seals will be presented in more detail.

### Real-Life Conditions that Have an Impact on Fuel Cell Performance

PEM fuel cells are in development to be ultimately deployed in the real world. The real world can vary considerably, from indoor use in buildings or warehouses to outdoor use under arctic conditions. Load variations can vary from continuous idle with occasional periods at maximum power for backup power systems, to highly dynamic operation in transport applications or working at continuous power for Combined Heat and Power systems. The level of control over all relevant parameters can be limited in a fuel cell system, and malfunctioning of control hardware can lead to conditions that fall outside the intended operating window. When compared to testing an MEA in a fuel cell laboratory in test hardware that excludes all influences but those



deliberately applied by the operator, a large number of imperfections can be listed:

- The cell voltage is not constant during operation; extremes can be caused by systems malfunctioning
- The temperature and humidity control in the cell are limited, and are not constant; extremes can be caused by systems malfunctioning
- The feed of anode and cathode feeds can be fully interrupted due to systems malfunctioning, or become sub-stoichiometric in individual cells
- The inlet air will contain contaminants
- The hydrogen will contain contaminants, and for many applications other than road transport, only be a part of the anode feed
- Wear of cell and systems components may generate contaminants that can diffuse to other cell components susceptible to these contaminants
- The system might be placed in climate conditions, which are much harsher than anticipated in the design phase

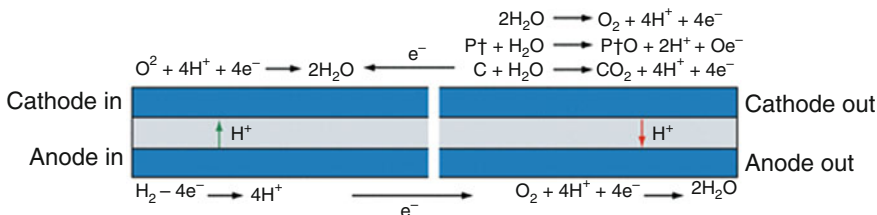
### Cell Voltage Variations and Excursions

Especially in fuel cell vehicles, the load demand to the drive train is characterized by a very dynamic pattern. When viewed over the entire lifetime of the vehicle, it is most of the time shut off, in case of a passenger vehicle typically 95% of the time. During operation, the load demand to the drive train contains significant periods of idling, load cycles, and start-up/shut off periods. It has become apparent that especially those events

leading to relatively high voltages, that is, low power demands, lead to durability problems.

In two recent papers by Nissan and Toyota [74, 88], degradation in fuel cells used in actual vehicles has been linked to the type of drive pattern and occurrence of non-steady state periods. In the paper by Nissan [74], it is shown that the correlation between performance loss on the one side and total vehicle operation hours and vehicle mileage on the other side is rather weak. It is especially the occurrence of start/stop cycles, idling and load cycling that contribute to the performance loss of the fuel cell stacks. Based on a model, verified with actual vehicle data, an estimate is made that 44% of performance loss can be attributed to start/stop cycles, 28% to idling, and 28% to load cycling. Vehicles used in Japan and the USA show different ratios, where start/stop cycles were occurring more frequently in Japan than in the USA, and the relative contribution of idling and load cycling is highly dependent on individual vehicle use.

During standstill, oxygen leaks in the anode compartment. In all cases where a hydrogen/air front arises, two horizontal fuel cell processes can take place as illustrated in Fig. 7. At open circuit, the electrons can only be exchanged horizontally in the same compartment, while protons will take the shortest distance in vertical direction through the membrane. In the bottom side, representing the anode, hydrogen is oxidized by oxygen. As the upper side, representing the cathode, lacks hydrogen, other oxidizable components can be oxidized, where the local potential is defined by the pull on electrons and protons by the oxygen reduction at both left and bottom of this cell



**PEM Fuel Cell Materials: Costs, Performance, and Durability, Fig. 7** Electrochemical reactions take place when both hydrogen and air are present in the anode

compartment (Figure previously published by the authors in Fuel Cells [87])



section. This can lead to local potential values exceeding 1.5 V versus NHE. This mechanism has been previously described by Reiser [89]. The length of standstill appears to be an important factor as well: the longer the standstill period, the higher the oxygen concentration in the anode compartment becomes, and the more severe degradation becomes [74].

In the paper by Toyota [88], a marked difference is shown between performance loss and the type of simulated driving conditions. Whereas 20% performance loss is obtained after less than 100,000 km under low speed or congested conditions, it takes 350,000 km to reach this 20% performance loss under medium- to high-speed conditions. Analysis of the Japanese 10–15 drive cycle shows that 58% of the time the vehicle speed is zero or declining, that is, the fuel cell stack is operated at reduced power. Avoidance of high potentials leads to a sixfold decrease in the rate of performance loss: While operation between 0.65 V and OCV leads to 20% performance loss in less than 1,000 h, a lowering of 50 mV of the maximum potential (OCV being equal to 1.0 V) leads roughly to a doubling of this time to reach 20% performance loss. However, it is clearly shown in the Toyota paper that this lowering of the upper voltage is at the expense of system efficiency, that is, better materials need to be developed to enable the high cell voltage excursions at periods of low power demand.

### Interruption of Anode and Cathode Feeds

Individual cells as well as complete stacks can be deprived of the fuel and air they need. In case of suboptimal stack design, the gas distribution over the individual cells becomes uneven, especially at high utilization. This can lead to individual cells running on sub-stoichiometric feeds, generally called fuel starvation when occurring at the anode, and air starvation when occurring on the cathode. When only individual cells are starved, these cells, placed in a series of hundreds of cells, are forced to generate the current that all other cells generate. When starved of fuel, other components present in the anode compartment are oxidized, starting those with the lowest Nernst potential and activation barrier. Carbon corrosion

and platinum dissolution are two processes widely reported to take place under such conditions [90–92]. As water is relatively easy to oxidize as well, one of the mitigation strategies to protect the carbon and platinum is to include catalysts, such as iridium, that oxidize water at a lower potential than pure platinum. Knights et al. [90] have elegantly shown how the current generation requirement leads to a progressively increasing anode potential upon depleting the anode compartment of oxidizable species, up to the point that the anode potential surpasses that of the cathode, leading to cell reversal.

Air starvation is less well documented, and is believed to be less detrimental than fuel starvation. As the lack of oxygen needs to be replaced by other components to be reduced, this will generally lead to the reduction of protons to form hydrogen, which on itself leads to a negative cell voltage, as the proton reduction potential lies below the hydrogen oxidation potential [90].

One should be aware of the fact that fuel and air starvation lead to current-driven processes, with the resulting potential being an indication of the reaction taking over the normal fuel cell reaction. It is not an external potential imposed on the electrode that leads to an oxidation or reduction process.

### Shortage of Water: Temperature Overshoots and Concomitant Reduction of Relative Humidity

Cell temperature can differ from the design temperature structurally because of improper stack design, as well as occasionally due to malfunctioning of temperature probes or failing cooling systems. Over the cell area, there is always a limited temperature variation due to a finite heat transfer from cell to cooling medium. In air-cooled stacks, the temperature variations are generally bigger than when using liquid cooling media. Continuous higher temperatures of a few degrees than the design temperature will lead to a higher voltage decay rate, as many degradation mechanisms show a positive relation between degradation rate and temperature [87].

More severe in the context of PEMFC is the strong dependence of the relative humidity on the

temperature. The delicacy of the water balance in the PEMFC has been described in section “[Introduction](#).” The water vapor pressure required for 100% relative humidity increases strongly with temperature. Extreme temperature excursions caused by malfunctioning of thermo couples or the cooling circuit, most probably, leads to drying of the MEA, which is difficult to restore in the fuel cell stack.

### Impact of Air Contaminants

In most fuel cell applications foreseen, a continuous flow of atmospheric air will be taken in while the system is in operation. This exposes the cathode, in the absence of air filters, directly to the substances present in the air, their concentrations possibly diminished as a result of air humidification.

For transport, air contaminants such as CO, volatile organic components, nitrogen oxides, and sulfur dioxide are likely to be encountered, their concentration varying with the local air quality. Especially in the first period of introduction, where the fraction of zero emission vehicles is close to zero, while heavily polluting diesel engines are abundant, the fuel cell vehicle is likely to inhale dirty air. The mean value of typical contaminant concentrations in European cities are:  $42 \mu\text{g m}^{-3}$  for  $\text{NO}_2$  and  $12 \mu\text{g m}^{-3}$   $\text{SO}_2$  [93],  $1 \mu\text{g m}^{-3}$  is approximately 1 ppb. However, especially in Asia, much higher levels are common. In Shanghai, China,  $\text{SO}_2$  concentrations exceeding  $150 \mu\text{g m}^{-3}$  and  $\text{NO}_2$  concentrations exceeding  $170 \mu\text{g m}^{-3}$  have been measured [94]. In the end report of the HyFleet Cute project [95], a fuel cell buses demonstration project in eight European cities as well as Perth, Australia and Beijing, China, it is specifically mentioned that air contaminants in Beijing caused performance problems of the fuel cell stacks. In volcanic regions in Japan,  $\text{SO}_2$  concentrations as high as 20 ppm and  $\text{H}_2\text{S}$  concentrations as high as 4.5 ppm have been measured [96]. A drive cycle pattern developed by the Japanese FCCJ even includes a period for driving by a hot spring [97]. Some contaminants are very specific for certain applications of fuel cells, such as sulfur-

containing combat gases as mustard gas for military use or salt-containing aerosols near the sea.

For rural areas, exposure to  $\text{NH}_3$  is likely to occur near intensive livestock farming. Ammonia concentration of 10 ppm is not uncommon, and was shown to lead to rapid drop in performance of around 10% in 2–4 h [98], of which 5% proved to be irreversible.

The influence of those contaminants on the MEA level has been assessed in a number of studies [96, 99] as well as reviewed in [100]. A linear dependence of the voltage drop on the  $\text{NO}_x$  concentration was observed at a current density of  $0.175 \text{ A cm}^{-2}$ , the above quoted  $42 \mu\text{g m}^{-3}$  would lead to a voltage drop of around 15 mV, while  $\text{NO}_2$  concentrations exceeding  $170 \mu\text{g m}^{-3}$  would lead to a voltage drop of 60 mV [99].

Narusawa et al. assessed the allowable concentrations of air contaminants on platinum cathodes [96]. While CO did not lead to any measurable poisoning at the cathode, presumably because the oxygen present oxidizes CO at a high rate,  $\text{NO}_2$  and  $\text{SO}_2$  do lead to a loss in performance, albeit reversible. The allowable concentration of the air contaminants, defined as the concentration of a contaminant leading to a performance loss equal to 2 ppm of CO in the anode feed when using a Pt-Ru anode, is 257 ppm for CO, 2.6 ppm for  $\text{NO}_2$ , and 1.8 ppm for  $\text{SO}_2$ .

With respect to this reversibility, the data shown in [96] are not conclusive, as no graph demonstrates full recovery after exposure to  $\text{NO}_2$  or  $\text{SO}_2$  is stopped. In [98], exposure of a Pt cathode to 0.5 ppm  $\text{SO}_2$  during consecutive periods of 2–4 h, leads during the first periods to a 5% decline in performance per period, without any intermediate recovery. Lower performance levels following next  $\text{SO}_2$  periods were recoverable, but never to more than 90% of the original performance.

The simplest mitigation for air contaminants is the use of an air filter [101]. Activated carbon is widely applied as air filter for many applications requiring contaminant free air, as it has a quite generic adsorption capacity for both organic and inorganic contaminants. Although the application of an air filter comes at the cost of a pressure drop, which leads to extra compressor power, it

is a relatively easy precaution that's worth considering. As the exposure to contaminants is unpredictable in the type and concentration of the contaminants, the breakthrough of the filter is unpredictable; frequent replacement of the air filter is probably the most practical and safe approach.

Mitigation of the influence of air contaminants by adapting the composition of the cathode catalyst is so far not applied.

### Impact of Hydrogen Contaminants

Technically, the hydrogen can be made as pure as necessary. For laboratory purposes, hydrogen quality is quoted as the percentage of hydrogen present in the gas. Hydrogen 6.0 stands for a gas containing 99.9999% of hydrogen, that is, the maximum of all other contaminants totals 0.0001%. For fuel cells, this quality standard is not helpful, as the standard does not discriminate between inert components and those with a detrimental effect on fuel cell performance.

Components that poison the fuel cell anode or membrane might have an adverse effect at even lower concentrations than 0.0001% (=1 ppmv, parts per million by volume). Inert components can be tolerated toward a certain level, as their only effect is that of diluting the hydrogen. Although recycling hydrogen at the anode would lead to building up of such inert contaminants [102], it shouldn't lead to such strict purity requirements, as nitrogen cross-over from the cathode through the membrane takes place anyway. For the purpose of defining fuel cell grade hydrogen specifications, international actions are being pursued to identify the tolerable contaminants for PEM fuel cells [103]. Sixty components are suggested to have a potential harmful impact on fuel cell performance.

Much knowledge on the effect of poisons has been generated in connection to reformer-based PEMFC systems. Both for transport as well as for stationary applications, the presence of CO, CO<sub>2</sub>, NH<sub>3</sub> has to be taken into account besides N<sub>2</sub> and H<sub>2</sub>O [100]. For reformer-based systems that are operated dynamically, that is, including many cold starts and load variations, CO concentrations exceed the 10 ppm level frequently [104]. The

effect of CO is studied most extensively. For unalloyed platinum electrodes, CO concentrations as low as 10 ppm lead to a performance loss of 100 mV [105] at 70 °C. When reformer-based systems are fueled with logistic fuels, such as diesel and kerosene, other contaminants than CO and CO<sub>2</sub> are present in the reformat. Especially aromatics and unsaturated hydrocarbons can poison the fuel cell anode fast and irreversibly, even in concentrations so low that they are hardly detectable with state-of-the-art analytics.

Narusawa et al. assessed the allowable concentrations of hydrogen contaminants on platinum and platinum-ruthenium anodes [96]. Using the effect of 2 ppm CO on Pt-Ru anodes as benchmark, the allowable concentration of hydrogen contaminants is on Pt-Ru 0.33 ppm for HCHO (formaldehyde), 6.8 ppm for HCOOH (formic acid), 15 ppm for C<sub>6</sub>H<sub>6</sub> (benzene), 3.3 ppb for H<sub>2</sub>S (hydrogen sulfide), and 11 ppb for SO<sub>2</sub> (sulfur dioxide). On Pt anodes, these allowable concentrations are 0.05 ppm for CO, 0.56 ppm for HCHO, 17 ppm for HCOOH, 24 ppm for C<sub>6</sub>H<sub>6</sub>, 8.4 ppb for H<sub>2</sub>S and 10 ppb for SO<sub>2</sub>. Methane did not generate any effect at concentrations as high as 1,000 ppm.

The persistent issue of fuel cell poisoning in combination with fuel processor complexity has driven the vehicle manufacturers to pure hydrogen as the preferred fuel. For stationary and some off-road transport applications, the use of gaseous and liquid carbon-based fuels is still preferred so that tolerance toward higher concentrations of species as CO is still pursued. The development of high temperature PEMFCs, such as phosphoric acid-doped PBI, that can be operated at 150–200 °C, show a remarkable high tolerance toward CO. Concentrations as high as 3% CO can be tolerated at 200 °C; at 125 °C concentrations of 1,000 ppm, CO leads to only a minor voltage drop [106].

### Wear of Cell and Systems Components

Due to the sensitivity of the MEA components to fouling, wear of stack and systems components can have a negative influence on MEA performance. Best described is probably the effect of corrosion products when metal-based bipolar

plates are used in stacks [2]. In addition, metal ions can be formed in other parts of the fuel cell system, upon contact with demineralized water used for cooling or humidification. The metal ions can exchange with protons on the electrolytic membrane, as well exchange the ionomer in the electrodes. As the conductivity of metal ions is much less than that of protons, this exchange effectively leads to a higher cell resistance.

Metal deposition on the electrocatalysts active sites can take place as well. Although elements such as chromium are used to enhance the activity of cathode catalysts, it must be in the alloyed form for such enhancement, while in the case of corrosion of metal plates, it will form an adlayer on the catalytic surface, blocking platinum atoms becoming inactive for oxygen or hydrogen dissociation.

Components leaching from seals are a potential cause for loss of MEA performance as well, although no such examples have been found. In long-term tests, seals have been noted to deteriorate completely, probably leading to the release of components as softeners and polymer fragments [87]. The direct influence of such components has not widely been reported.

### Freezing

Both transport systems, as well as outdoor installed stationary systems are exposed to climate conditions depending on their location. The vehicle DoE demonstration fleet, that is monitored by NREL, has been shown to be operated at ambient temperatures between  $-10\text{ }^{\circ}\text{C}$  and  $+50\text{ }^{\circ}\text{C}$  [107].

In most developed countries, freezing conditions occur during winter. The effect of freeze/thaw cycles has been studied to some extent. An immediate effect of freezing can occur during start-up. At  $-10\text{ }^{\circ}\text{C}$ , the conductivity of Nafion, around  $0.025\text{ S cm}^{-1}$  [108], is enough to start the cell. As the water saturation pressure at this temperature is extremely low, liquid water will be formed and ice formation can easily occur, blocking the gas diffusion media pores, preventing start-up. It is among others for this reason that car manufactures have switched to metal bipolar plates, leading to a lower thermal mass

of the fuel cell stack, and thus to a quick rise in temperature during start-up [109].

Without precautions, freeze/thaw cycles have a negative effect on cell performance, especially when liquid water in the MEA is still present under freezing conditions. Especially interfacial stresses can lead to delamination, while increasing ohmic resistances in membrane and electrode have been reported. The Daimler/EVO city buses demonstrated in the CUTE project were therefore always parked indoors overnight. In the latest systems, freezing of liquid water is avoided by water removal procedures when cooling down. Most passenger vehicles and buses of the major OEMs do not need indoor parking anymore.

Stationary PEMFC systems are even operated under arctic conditions, with a guaranteed lifetime of 4000 h by Dantherm Power [110].

## Materials Degradation and the Relation to Performance Loss and Shortening the PEMFC Lifetime

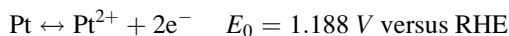
### Catalyst Issues

#### Pt Coarsening/Dissolution

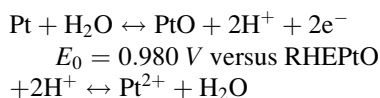
Pt catalysts in PEMFCs gradually lose their activity, mostly as a result of loss of ECSA. With present materials, the loss of ECSA can be in the order of 60% over 10,000 h of constant load operation, and is found to be accelerated by load variations [87]. It has been well established that the loss of ESCA is due to growth of Pt particles as well as to loss of Pt into the ionomer phase of the MEA [111–113]. In a review by Shao-Horn et al. [114], four mechanisms are distinguished: (1) an electrochemically induced Ostwald ripening (2) electrochemical dissolution and deposition in the ionomer phase (3) migration of crystallites on the carbon support followed by coalescence, and (4) detachment from the carbon support.

The Ostwald ripening and electrochemical dissolution are strongly related. Although Pt is one of the most stable elements in the Periodic Table, thermodynamics predict electrochemical Pt dissolution in acid media at the potentials as

encountered at the cathode [115], either directly according to the reaction:



or indirectly through oxide formation



Electrochemical studies on Pt thin films, Pt wires, and Pt nanoparticles on carbon have shown that at potentials  $<0.85$  V, the dissolution process has a Nernstian potential dependence and that the equilibrium electrochemical potential of the Pt dissolution decreases with particle size [116]. Accordingly, higher equilibrium  $\text{Pt}^{2+}$  concentrations were measured for Pt/C than predicted for bulk Pt [111] at  $80^\circ\text{C}$ . According to mechanism 1,  $\text{Pt}^{2+}$  dissolved into the ionomer phase can redeposit on other (larger) particles in the cathode, due to the higher equilibrium potential of dissolution on these particles [117]. These particles need to be on the carbon support in order to allow for the exchange of electrons. The difference in dissolution potential is considered to be related to the surface tension. The above mechanism of dissolution and redeposition is an example of Ostwald ripening, that is, minimization of the surface energy is the driving force. The  $\text{Pt}^{2+}$  ions may also be reduced in the ionomer phase of electrode or in the membrane by  $\text{H}_2$  crossing over from the anode side (mechanism 2).

At potentials above  $0.85$  V versus RHE, it has been observed that Pt dissolution does not show the strong Nernstian potential dependence, and even has a maximum around  $1.15$  V [111, 118, 119]. This is ascribed to formation of the oxide layer, which impedes further Pt dissolution. However, upon lowering the potential, these oxides are reduced accompanied by Pt dissolution. It is thought that oxide formation is related to the observation that potential cycling enhances the Pt dissolution. Kawahara et al. have studied the dissolution of Pt during cycling ex situ [120, 121]. It is known from literature of the early 1990s that fast cycling leads to oxides that are

difficult to reduce, often called  $\beta$ -oxides [122, 123], and that the reduction of these  $\beta$ -oxides is accompanied by dissolution of platinum [124]. At potentials higher than  $1.2$  V, the formation of an oxygen skin was observed, with Pt atoms replacing oxygen atoms at even higher potentials leading to disintegration of the Pt surface [125].

Mechanism 3 and 4 are not electrochemical processes. For mechanism 3, Brownian motion is the assumed driving force, causing surface diffusion of particles with random collisions leading to coalescence [126]. Usually the fact that sintering does not occur significantly in catalysts in the gas phase at temperatures below  $500^\circ\text{C}$  is considered to be an indication that coalescence is not the prevailing mechanism [111, 127, 128]. Still, although both mechanisms 1 and 3 lead to an increase of the average particle size with an asymptotic particle size distribution (PSD), the coalescence mechanism has a log-normal distribution (tail at large sizes) and the Ostwald ripening has a tail at the smaller particle sizes but with a maximal particle size cut-off [129]. In many studies, a log-normal distribution of Pt particle sizes was found in virgin and used electrodes [111, 112, 127, 129, 130]. However, it must be noted that such analysis requires a good sampling also of small particles and results can be affected by the fact that several mechanisms are active at the same time [111, 127].

Accelerating factors are increasing temperature, potential cycling with the upper voltage limit being critical, and high relative humidity [130–132]. The effect of temperature on electrochemical dissolution is very strong, ex situ studies have shown an increase of orders of magnitude between  $65^\circ\text{C}$  and  $80^\circ\text{C}$  [118, 133]. It should be noted that reduction of the Pt loading, as required for cost reduction result, makes the system more sensitive for degradation to the extent that increased degradation rates were observed [132].

Non-nano-sized Pt is not immune for oxide formation or dissolution, but the equilibrium potential of oxide formation is higher compared to nano sized particles. Pt black and NSTF electrodes have either much larger Pt particles or even a continuous phase Pt. This results in lower specific surface area but more stable activity as was



convincingly demonstrated by the life-time studies carried out on NSTF electrodes by 3 M [49].

### Stability of Alloys

Both at the anode and cathode, binary Pt-M alloys are proposed, either to enable operation on CO containing fuel or to increase the activity for the oxygen reduction reaction. The M-metal is usually a transition metal, that is, Co, Ni, Fe, Mn, Ir. These metals themselves are thermodynamically less stable than Pt. As regards the stability of the alloy, several factors play a role: the degree of alloying, the particle size, and the degree of ordering in the alloy.

When a Pt-M particle contains unalloyed M, this will easily dissolve at potentials of 0.6–0.9 V versus NHE. This has led to the use of pre-leached catalysts, some of which show improved stability even compared to pure Pt in this potential range [46]. However, recent work, which includes also cycling to potentials as low as 0 V versus NHE showed a strong decrease of activity. During this cycling, oxides that are formed at high potential and that have a passivating effect are reduced by cycling to low potential, followed by dissolution of the metal. On the other hand, the Pt seems to become less soluble [132].

The loss of the alloyed non-noble metal does not always lead to a decrease of activity. As already mentioned, in some cases, an increase of activity was found, ascribed to as surface roughening or electronic effects [61]. On the other hand, in other cases, the activity decreases because the beneficial effect on the electronic structure of Pt is lost. In any case, metal ions leaching from the catalyst will have a negative effect on the membrane and ionomer phase in the electrode.

Accelerating factors are similar to the factors accelerating the Pt coarsening and dissolution, that is, elevated temperature, potential cycling and high humidity, but for cathode catalysts, cycling to low potentials (i.e., 0 V vs. NHE) seems to be an additional stressing factor [132].

Mitigating effects are also the same as the same as for Pt degradation. Large alloy particles are in general more stable than small particles [55], and at drier conditions, dissolution seems to be slower.

### Contaminants for Catalysts

Chemical species present in the fuel cell can further deactivate the catalyst, either through surface poisoning or by (electro)chemical reactions, which drastically modify the catalyst. Such chemical species are then called contaminants, they can have their source outside as well as inside the system.

*At the anode:* CO adsorbs strongly on Pt at the fuel cell operating temperatures. Even at 10 ppm, the cell voltage loss is in the order of 100 mV. The effects are reversible and mitigated by increased temperature. Some Pt alloys mitigate the CO poisoning, either because the adsorption is less strong or because they facilitate the CO oxidation at low potentials. Among these alloys, well-dispersed Pt-Ru supported on carbon is widely accepted as the standard catalyst for reformat feeds. Tolerance is improved to 100 ppm, with a loss <20 mV at 500 mA cm<sup>-2</sup> at 80 °C, using 0.5 mg cm<sup>-2</sup> Pt-Ru at the anode. These loadings seem high, but reformat application is only considered for stationary applications where such loadings may be acceptable. There is some debate on the mechanism of CO tolerance of Pt-Ru. For well-alloyed material, the interaction with CO is less strong, and on both alloyed and non-alloyed material, OH adsorption followed by CO oxidation can take place at low potential. Both mechanisms are probably involved, which one dominates will depend on the composition and preparation of the catalyst. The hydrogen oxidation on Pt-Ru is still sufficiently fast, even when just a part of the surface area is available.

Other catalysts, such as PtMo, mainly favor the CO oxidation. This is effective only if sufficient CO is oxidized at low potential, which is not always the case. Bilayer electrodes have been proposed to separate the CO oxidation from the H<sub>2</sub> oxidation. In this concept, CO oxidation takes place in a layer adjacent to the GDL, catalyzed, for example, by PtMo, and hydrogen oxidation in Pt-Ru layer adjacent to the membrane. This improved the CO tolerance significantly compared to the tolerance obtained with monolayer system of either catalyst [134, 135].

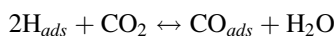
Dissolution of Ru or Mo from Pt alloys in anodes and migration to the cathode have been



reported, and seem enhanced at high anode potentials, such as occurring during fuel starvation and severe poisoning [136]. PtWO<sub>x</sub> is expected to be much more stable, but the activity relies on the capacity to form bronzes, for which H<sub>2</sub> needs to dissociate on Pt. As the Pt becomes poisoned, these materials lose their activity [137].

Mixing small amounts (2–4%) of air into the fuel, the so-called air bleeds, can also be effective. The CO is then chemically oxidized. Air bleeds can have detrimental effect on durability, both on the catalyst as the chemical oxidation induces heat effects, as well as on the membrane as detrimental radicals such as OH• can be formed.

Reduction of the CO content in reformat feeds below 10 ppm is usually not advantageous, since the resulting feed still contains high fractions (10–25%) of CO<sub>2</sub>. On Pt in the potential range where adsorbed H is present, CO<sub>2</sub> reacts along the so-called reverse Water Gas Shift reaction:



The reaction product is adsorbed CO, poisoning the catalyst. Again this effect is mitigated on Pt-Ru due to the strong adsorption [138–140].

The tolerance for H<sub>2</sub>S is usually <0.1 ppm. H<sub>2</sub>S will decompose on the anode surface and poison the Pt, an effect, which can be irreversible at high potential or with high S concentration when Pt-S is formed (thermodynamically at very low potential already). H<sub>2</sub>S can migrate to the cathode and form Pt-S there as well. The only way to remove Pt-S is to oxidize it at very high potential (1.2 V vs. NHE). Pt-based catalysts promoting S oxidation at low temperature are not yet known [100].

A remarkable finding in the previously cited study by Narusawa [96] is that while alloying of platinum with ruthenium mitigates the poisoning of CO, it aggravates the poisoning of many other contaminants, such as HCHO (formaldehyde), HCOOH (formic acid), H<sub>2</sub>S (hydrogen sulfide), and C<sub>6</sub>H<sub>6</sub> (benzene). For all contaminants studied, the addition of an alloying metal does not make irreversible adsorption reversible, that is, the decrease of the potential at which oxygen and hydroxyl adsorption start is not high enough to

shift the onset of the oxidation of adsorption to a useful potential range.

*At the cathode:* Contaminants with a strong interaction with the cathode catalyst might accumulate over time and lead to performance loss after reaching a certain threshold.

When a fuel cell is operated during 5,000 h at an air stoichiometry of 2, the accumulated number of contaminant molecules present in a concentration of 1 ppmv outnumbers the amount of platinum surface atoms by a factor of 300. Molecules that adsorb irreversibly on platinum will easily poison the platinum surface to such an extent that fuel cell performance is bound to approach zero in the course of 5,000 h. While the surface coverage of the contaminant slowly builds up, the available sites for oxygen reduction decrease. As two adjacent platinum sites are needed for oxygen desorption, the oxygen reduction activity at constant potential is proportional to  $(1-\theta_c)^2$ , in which  $\theta_c$  stands for the degree of coverage by the contaminant.

Except for ammonia, all air contaminants are believed to lead to poisoning of the catalytic sites. Ammonia is thought to lead to a loss of ionic conductivity in the ionomer in the cathode layer, as a result of an acid-base reaction between the basic ammonia and the acidic sulfonic acid group of the ionomer.

SO<sub>2</sub> in air can chemically adsorb on the catalyst, but also reduction of SO<sub>2</sub> on Pt leads also to Pt-S formation, with Pt-SO as intermediate product. Surface adsorption of NO on Pt has also been reported. The effect of NO<sub>2</sub>, on the other hand, is not related to surface adsorption, rather NH<sub>4</sub><sup>+</sup> is formed by electrochemical reduction, which poisons the membrane conducting phase see below) [100, 141].

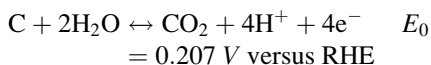
*Internal sources:* Some metal ions may deposit on the catalyst, that is, such as Ru on Pt cathode [136], which will deactivate them. Also Cl<sup>-</sup>, which may be present as a result of the catalyst manufacturing is a strong poisoning for Pt catalysts [142].

### Carbon Corrosion

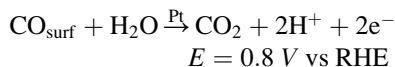
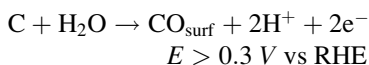
Both electrochemical oxidation and thermal degradation of carbon in humid air at temperatures

<125 °C have been reported, and it seems established that these corrosion mechanisms are accelerated by the presence of Pt. Carbon corrosion will first modify the surface of the support, which will become less hydrophobic. It has also been reported that carbon corrosion may enhance the mobility of Pt on the surface, accelerating the Pt sintering discussed above. Further carbon corrosion will degrade the electron-conducting network, rendering Pt particles inactive.

Thermodynamically carbon is less stable in acid media than, for example, Pt, but due to the slow reaction kinetics, carbon can still be used in fuel cell [143]. Carbon (graphite) can be electrochemically oxidized to CO<sub>2</sub> at quite low potentials:



Electrochemical ex situ studies [131, 144, 145] in the temperature range 25–80 °C have shown that at a potential higher than 0.3 V versus RHE, CO<sub>surf</sub> starts to form irreversibly on the carbon particle surface. One specific species is the quinone group that is electrochemically active with a redox peak at 0.55 V versus RHE that can be identified in cyclic voltammetry. The presence of Pt catalyzes the subsequent oxidation to CO<sub>2</sub>. The carbon corrosion mechanism consists of the following steps:



In the absence of Pt, CO<sub>2</sub> emission was observed only at potentials above 1.1 V versus RHE. Carbon corrosion is often quantified in potential hold tests, where the catalyst is held at potentials >1.2 V [145, 146].

The thermal degradation of carbon and platinum-loaded carbon in air is not expected to take place below 100 °C [147], although at higher temperatures, it was shown to be accelerated by the presence of Pt nanoparticles. However,

the humidification of air substantially enhances the thermal corrosion rate of carbon, by providing an additional pathway for chemical carbon oxidation through a direct reaction with water [148, 149].

In most carbon corrosion studies, it is observed that the corrosion rate (in g h<sup>-1</sup>) increases with the specific surface area (m<sup>2</sup> g<sup>-1</sup>). High surface area carbons have more edge features and are therefore sensitive to oxidation centers [144]. An effective method to reduce the carbon corrosion is therefore to decrease the number of dangling bonds, that is, use a more graphitic carbon. Heat-treated carbon was shown to be more stable as were materials that by nature have a more graphitic surface such as carbon nanotubes, as well as some type of carbon nanofibers. Good stability has been shown in fuel cell accelerated stress tests but a drawback is the lower surface area of these materials, which results in larger metal particles or lower metal loading [150, 151].

Accelerating conditions for carbon corrosion include high potentials as during air/hydrogen fronts and fuel starvation. The role of humidity is still under some dispute. On the one hand, the carbon corrosion reactions require the presence of water; on the other hand, oxidation of water may proceed at higher rate than carbon corrosion. The recent research into water oxidation catalysts to mitigate carbon corrosion is based on this. However, it must be noted that the inclusion of such (metal-alloyed) catalysts has concomitant durability issues.

### Gas Diffusion and Microporous Layers

The GDL and MPL experience conditions much similar to the catalyst layer, only there is no ionomer to provide protons, and there is no Pt catalyst to enhance reactions. The water phase is acidic due to the presence of degradation products from other components (CO<sub>2</sub>, SO<sub>3</sub><sup>-</sup>, F<sup>-</sup>), resulting in a pH of about 4 [152]. The presence of fluorinated binders in MPL and GDL protects the carbon to some extent, but surface oxidation or even oxidation to CO or CO<sub>2</sub> can occur in the environment of liquid water, with O<sub>2</sub> present in the gas phase and dissolved in water. Schulze et al.

present evidence for decomposition of PTFE on the basis of XPS data, but a mechanism has not been proposed [133].

The result of these degradation mechanisms is that the GDL and the MPL both lose their hydrophobic character [133, 153, 154], and that the pore structure of the materials changes. The relation between microstructure and surface properties and mass transport properties has been the subject of several recent experimental studies [155, 156], which indicate that indeed mass transport can be seriously affected by the hydrophobicity of the GDL and MPL as well as by the pore size. This will contribute to the gradual decay of the performance, though it is hard to distinguish the effects of changes in the GDL/MPL to those of changes in the catalyst layer.

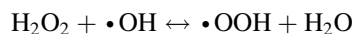
The decreased hydrophobicity can result in widening the window in which flooding can occur. Flooding itself is not regarded as a main cause for degradation. Although in some overviews it is stated that flooding might lead to accelerated carbon corrosion and platinum dissolution, one should realize that the occurrence of both flooding and a high cathode potential is unlikely. The potentials needed to lead to significant platinum dissolution and carbon corrosion are 0.9 V and higher [87, 157], hardly a potential that occurs at the cathode during high power output.

An important function of the GDL is to even out the compression forces in the stack. These compression forces are also a source for degradation. Lee and Mérida concluded from *ex situ* experiments that the compressive strain increased with the applied pressure but even more strongly with temperature, and the GDL strain was influenced by the PTFE stability [158]. Properties such as in-plane electrical resistivity, surface contact angle, bending stiffness, and porosity were not affected. However, it was found that convective airflow through the GDL under strain can lead to loss of material. The GDL degradation can also contribute to sudden failure as GDL fibers can puncture the membrane, either when as a result of degradation they do not distribute the compression forces well any more or when they are even broken themselves.

## Membranes

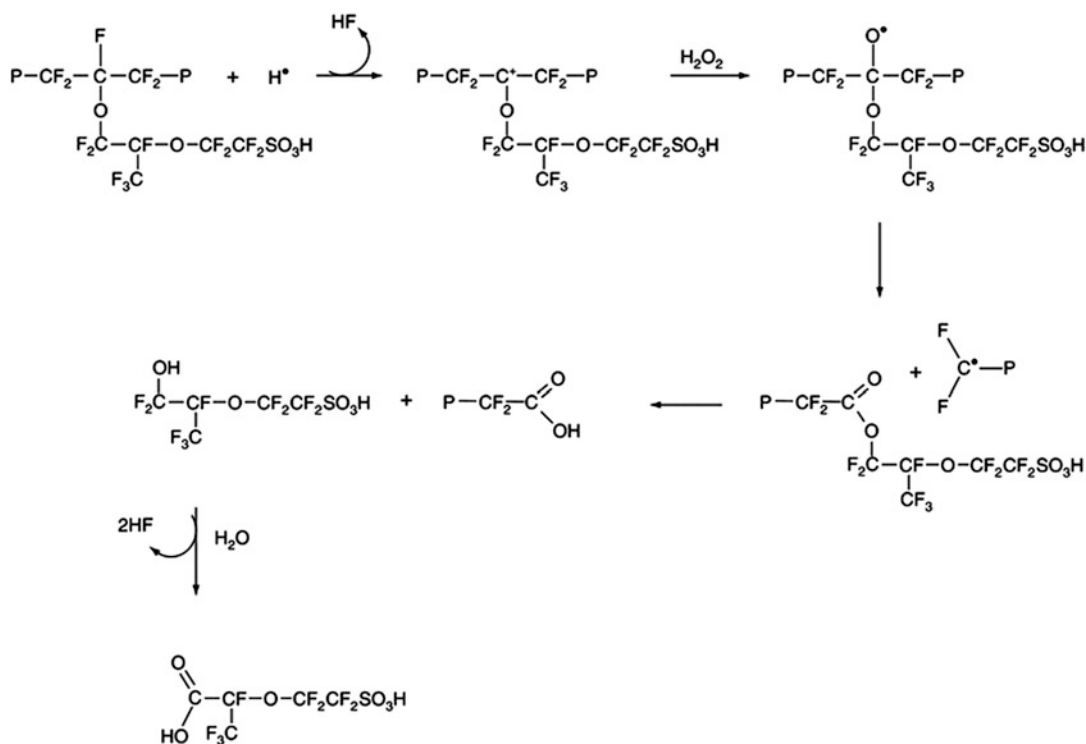
### Chemical Stability

Chemical instability of membranes has always been associated with the formation of peroxide in the PEMFC. Peroxide and related radicals can attack aliphatic groups, resulting in chemical degradation. Therefore, perfluorinated or highly aromatic polymers have been considered only, with perfluorinated materials now being the commercially available option. The removal of end-groups like carboxyl or H has resulted in a much enhanced stability. An important recent development has been the identification of the hydroxyl ( $\cdot\text{OH}$ ) radical as the detrimental species rather than peroxide [159]. For this radical to form from  $\text{H}_2\text{O}_2$ , the presence of oxidizable metal ions such as  $\text{Fe}^{2+}$  is required; hence, it was thought that contaminating ions were required to induce radical formation. Recently, however, it was reported [160, 161] that they can be formed under fuel cell operation in a direct reaction of  $\text{H}_2$  and  $\text{O}_2$ . It is now assumed that  $\text{H}_2\text{O}_2$ ,  $\cdot\text{OH}$ , and  $\cdot\text{OOH}$  are formed due to gas cross-over reaction of  $\text{H}_2$  and  $\text{O}_2$  either chemically at electrodes and in the membrane or electrochemically at the anode, and that their concentrations are related through the equilibrium:

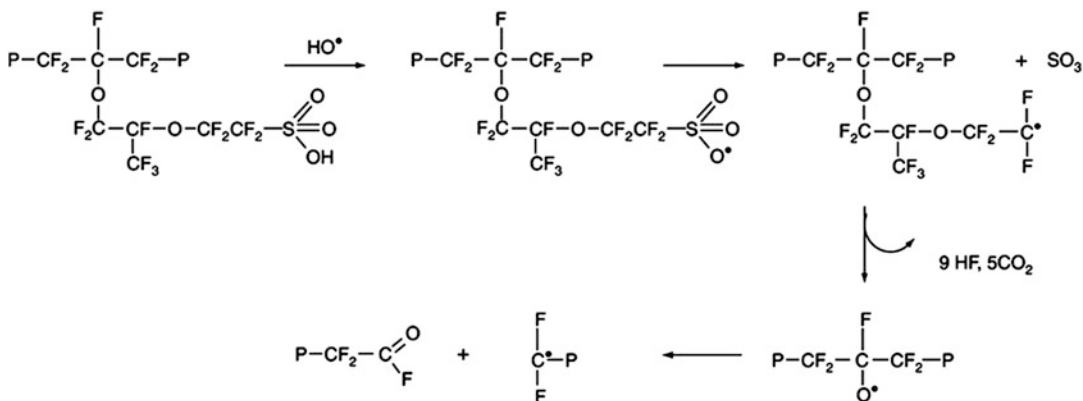


The presence of these radicals would lead to the classical unzipping mechanisms induced by an attack on C-H and COOH groups, present in small quantities in the polymer after manufacturing. This mechanism would result in continuous HF release, no chain scission, and “ideal PFSA,” not containing such reactive end-groups, would not be vulnerable [162].

Still, also improved PFSA materials suffer from chemical degradation as was established by increasing HF release, which indicates a chain scission process [159]. Further analysis showed that the  $\cdot\text{OH}$  radical can react with  $\text{H}_2$  to form  $\text{H}\cdot$ , which can react with the tertiary fluorine atom, thus initiating a main chain scission process, as shown in Fig. 8.



**PEM Fuel Cell Materials: Costs, Performance, and Durability, Fig. 8** Scheme showing the degradation of “ideal” PFSA induced by the attack of a  $H^\bullet$  radical on a tertiary fluorine atom (After reference [159])



**PEM Fuel Cell Materials: Costs, Performance, and Durability, Fig. 9** Scheme showing the degradation of PFSA in dry conditions initiated by an  $\bullet OH$  radical (After reference [159])

A second mechanism involving  $\bullet OH$  is exacerbated by dry conditions, when the deprotonation of the sulfon groups is incomplete. The proton on the sulfon group reacts with the  $\bullet OH$  radical, leaving a sulfonyl radical, which has a weak

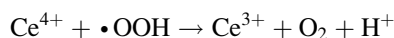
bond to the carbon atom. This initiates another scission mechanism. This is illustrated in Fig. 9.

Recognition of these two mechanisms has led to the conclusion that  $\bullet OH$  is the “killer species” [159]. A possible mitigation strategy is the

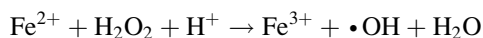
addition of radical scavengers, such as  $Ce^{3+}$  or  $Mn^{3+}$ , which react with  $\bullet OH$



and which are recovered through reaction with  $H_2O_2$ ,  $\bullet OOH$ ,  $H_2O$ ,  $H_2$



Unlike  $Fe^{2+}$  ions, the mitigating ions should *not* reduce  $H^+/H_2O_2$  as this would result in  $\bullet OH$  formation, as is the basis of Fenton's test [87].



This requirement involves careful matching of reduction potentials and reaction rates but has led to much increased stability [163–165].

The relation between the chemical degradation of the membrane and cross-over of the reactant gases has also shed new light on the stability of (aromatic) hydrocarbon-based membranes such as sulfonated PEEK. Although such materials perform dramatically bad in the Fenton's test, which shows that they are vulnerable for attack by  $\bullet OOH$  and  $\bullet OH$ , stable performance has been obtained for such membranes [28, 166]. This may be associated with the gas cross-over rates that are lower in hydrocarbon membranes than in PFSA membranes by a factor 5–40 [28, 167], thus reducing the rate of radical

formation. However, depending on the degree of aromaticity of some non-fluorinated compounds such as PEEK are susceptible to the loss of the sulfonic acid group by hydrolysis at wet conditions [166], while others like polysulfones are much more stable [168].

Chemical degradation of PFSA membranes seems to be accelerated by elevated temperature, OCV conditions, low relative humidity, and elevated gas pressures. The main mitigation is the addition of radical scavengers and removal of non-perfluorinated groups. Note, that the amount of metal scavenger ions added to the membrane is limited and does not affect much the conductivity.

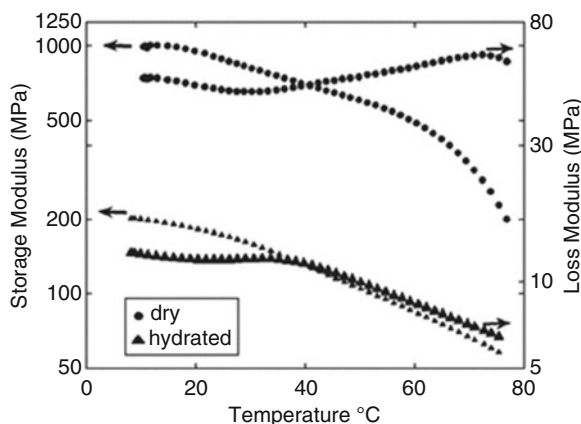
### Mechanical Degradation

Sulfonated membranes take up liquid water, which enables them to conduct protons, but which also results in swelling of the membrane. Hence, stresses occurring during temperature and humidity cycling [169, 170] can lead to mechanical failure of the membrane. Mechanical failure can also result from nonuniform contact pressure [171], high differential initial gas pressure over the membrane, and punctures as well as fatigue from stresses occurring.

Fig. 10 shows the effect of both temperature and hydration on the storage and loss modulus of Nafion NRE212, as measured by dynamic mechanical analysis [172]. While temperature has already a marked effect on the elasticity of Nafion, as expressed by the drop of the storage modulus, hydration leads to a decrease in the

### PEM Fuel Cell Materials: Costs, Performance, and Durability,

**Fig. 10** Storage modulus and loss factor as a function of temperature for dry and hydrated as-received Nafion NRE212 (Reprinted from [172]; with permission from Elsevier)



storage modulus over the whole temperature range.

Therefore, most commercial membranes are now reinforced, for example, by a porous polyethylene or PTFE [170, 173] material that enhances the dimensional stability and reduces the shrinkage stress in the membrane during drying. Reinforced membranes show a lower decrease of the OCV [169] and longer lifetime at elevated temperature and low humidity [173].

A successful way to achieve good proton conduction at low humidity has been through low EW PFSA. A durability problem is that these low EW materials suffer loss of crystallinity and therefore are also easily water soluble, resulting in a lack of mechanical integrity, which shows, for example, during humidity cycling. Several solutions have been suggested such as cross linking, either of the backbone or of the sulfonic groups, blending and changing the protogenic group as was discussed in section “[PEMFC Component Costs and Performance: Targets, Status and Developments.](#)”

#### Freezing Conditions

Freezing conditions result in a reduction of the conductivity of the PFSA membranes but do not seem to induce irreversible changes [174]. In a PFSA membrane, 90% of the water can freeze, but some water is non-freezable. The temperature at which freezing is observed varied with the water content. McDonalds et al. studied N112 membranes that underwent up to 385 F/T cycles between  $-40\text{ }^{\circ}\text{C}$  and  $+80\text{ }^{\circ}\text{C}$ . These materials were in a relatively dry state (only humidified by ambient conditions). These studies did not indicate any serious physical or chemical damage. The toughness of membranes seemed to decrease somewhat, as well as the permeability of the membrane for oxygen. It was suggested that a rearrangement of the sulfonic acid groups in the ionomer might have occurred.

#### Contamination by Ionic Species

Metal ions that originate from other parts of the system (electrode, bipolar plates, coolant, BOP) or from the fuel or air can be absorbed into the membrane.  $\text{NH}_3$  present in the fuel or in air will

migrate into the membrane to form  $\text{NH}_4^+$ . Another source of  $\text{NH}_4^+$  is  $\text{NO}_2$ , that can be present in air and can be electrochemically reduced at the cathode [141]. The sulfonate sites have a stronger affinity to cations except  $\text{Li}^+$ , than for protons, leading to exchange of the protons by the metal ion when present. The direct effect is a reduction of the proton conductivity that is proportional to the decrease in proton concentration [171, 175]. An indirect effect is the lower hydrophilicity of metal ions in comparison to protons, which can result in partial drying out of membrane, thus also reducing the proton conductivity.

#### Bipolar Plates

Bipolar plates are made from graphite, graphite/polymer composite, or metal. A loss of mechanical integrity of the bipolar plate would result in mixing of the fuel or oxidant with the coolant, or even of mixing fuel with air, leading to severe degradation of performance or failure. Moreover, the electronic current is passed from one cell to the other by the polar plate, which means that any change in intrinsic resistance or contact resistance will affect the ohmic losses. The conditions experienced by the bipolar plates are similar to the ones experienced by the GDLs, with the addition of exposure to the coolant.

For graphite and graphite composite plates, corrosion and release of contaminants are under normal operation not an issue. At normal operating conditions, the cathode potential is not high enough for oxide formation on the surface, and the contact resistance remains constant during fuel cell operation [75, 176]. Especially under start/stop or fuel starvation conditions, electrodes can be exposed to higher potentials but the pH is about 4 [152], that is, much higher than the catalyst layer. However, chemical degradation is possible by oxidation of carbon in a reaction with  $\text{H}_2\text{O}_2$ , which may be formed due to  $\text{O}_2$  gas crossing over to the anode during a stop period [177]. The polymer of the composite plate may be subject to similar degradation effects, which may in the end lead to embrittlement, leaching from the coolant or gas cross-over. A serious durability issue with graphite/composite plates is the



prolonged exposure to temperatures in the order of 120 °C, which may result in creep and deformation of some resins, or the brittleness of thermosetting resins.

The use of metal bipolar plates brings about serious durability issues, as was already discussed in section “**Bipolar Plates**” Most metals form a passive layer on the surface at the potential in which the cathode operates, which affects the contact resistance. As discussed, this requires either a dense, stable, and conductive coating or a surface modification that enhances contact resistances as well as improves stability. At the anode, the conditions are usually not such that oxide layers are formed, but during starvation, poisoning or start/stop oxidation is accelerated resulting in metal ions being directly released into the fuel cell. Similarly, low potentials occurring at the cathode may result in reduction of the passivating layer, thus releasing metal ions. Such ions will further contaminate membrane and catalysts.

### **Seals Degradation [87]**

Fuel cell stacks contain seals on the MEA side as well as on the coolant side of the bipolar plate. Not only are they meant to prevent leakage of the gases and the coolants outside their containments, seals function as electrical insulation, stack height control, and variability control as well [178]. The degradation phenomena connected to seals do not only refer to the loss of the functionality of the seals themselves, but also to the leakage of seal components that could poison the MEA.

Degradation phenomena on seals are in general poorly understood, and only a very few number of papers have been published on seal degradation [84, 85, 178, 179]. Papers from Frisch [178] and Du [179] report on the selection of seals that meet fuel cell requirements. PlugPower used an ex situ method to test the seals resistance against a specific coolant as well as against acids that mimic the fuel cell environment [179]. Weight change and the release of contaminants are used as indicators for the compatibility of the seals. Without giving hints to specific materials, the differences between various materials appeared to be huge.

Dow Corning [178] considered silicone elastomers as seals. The stability against coolant is not

seen as a problem by Dow Corning for these silicone elastomers, while there is concern about the stability in the MEA compartment. Exposure of sealing materials to a mixture of various acids in a 1 M concentration at undefined temperature is used as ex situ aging test. General purpose silicone elastomers show cracks after 336 h in such a test, while special fuel cell grade silicone elastomers survive such a test for over a year without showing cracks.

In a study by Tan [85], the stability of various sealing materials has been tested in simulated environment at 60 °C and 80 °C. This simulated environment consisted of solutions containing HF and H<sub>2</sub>SO<sub>4</sub>, in two different concentrations. It was concluded that Silicone S and Silicone G are heavily degraded in the concentrated solutions as well as the diluted concentrations, although most of the data are collected in the concentrated solutions. Degradation reveals itself by weight loss, complete disintegration, as well as by leaching of Mg and Ca. The latter stem from magnesium oxide and calcium carbonate, which are used as fillers for obtaining the desired tensile strength, hardness, and resistance to compression. When these components are leached out, mechanical properties will be lost, and one might expect a negative influence on fuel cell performance as well, as these components can replace protons in the membrane as well as affect the properties of gas diffusion media and electrodes. An increase in temperature, as well as exposure to stress accelerates the degradation. The degradation mechanism is thought to involve de-crosslinking as well as backbone scission. Materials that much better survive the exposure to the solutions are ethylene-propylene-diene-monomer (EPDM) and fluoroelastomers.

Only in a couple of long-term experiments was seal degradation observed, and this might have been the consequence of an inappropriate materials selection. Silicone seals in direct contact with a perfluorosulfonic acid membrane suffer from degradation, at the anode as well as at the cathode [84]. The degradation is probably caused by acidic decomposition of the sealing material, leading to coloration of the membrane and detectable amounts of silicon on the electrodes. No fuel cell

performance loss or increase in gas leakage along the seal has been observed. The same observation has been made by St. Pierre et al. after an 11,000 h test with a Ballard Mark 513 stack [180]. The seals were visibly oxidized, albeit more in the humidification section than in the active section. In the 26,000 h testing by Gore, complete degradation of the glass-reinforced silicone seal has been observed [14]. It forced them to increase the compression force to keep the cell gas tight. This might have had an impact on effective porosity of the gas diffusion media. The silicon of the seal could be detected throughout the MEA, especially on the gas diffusion media.

## Future Directions

Fuel cell vehicles are being demonstrated worldwide, and have reached a maturity that allows daily driving in demonstration schemes while offering a performance that meets consumer expectations. The latest generation fuel cell vehicles combine the user characteristics of modern passenger cars, such as a maximum speed of around 160 km h<sup>-1</sup>, a driving range of 400 km or more, with a low energy use. Refueling can be done in a couple of minutes. The progress in materials development from the past years has brought the cost, performance, and durability targets set for market introduction of road transport applications in sight. The *caveat* with respect to costs as presented in this contribution is that they are based on an annual production volume of 500,000 vehicles. The fuel cell systems in the first generation of commercially produced vehicles will certainly be more expensive than those projected for the 500,000 vehicles volume.

As cost reduction and durability improvement will not automatically go hand in hand, it is important to define priorities. For the acceptance of a new technology, robustness and performance are crucial, more than costs. With many alternative drive trains and energy carriers foreseen to be introduced in the coming decade, failures on robustness and performance will not be tolerated by consumers. If market stimulation packages by governments to stimulate the sales of clean

vehicles are put in place, the last part of the cost reduction can be postponed to next generation vehicles, when the technology already has been adopted. In any case, the options for further cost reduction should be present.

For cost reduction, the major contribution has to come from alternative electrodes, in which the mass activity of platinum is driven to its maximum, and transport limitations are driven to their minimum. A better control on catalyst layer and gas diffusion medium structures will be crucial in this respect, both on design and on maintaining the beginning-of-life properties. In this respect, the focus should be directed more than in the past on materials that are intrinsically stable under the harsh fuel cell conditions. Theoretically, the targets are achievable with presently known materials.

For robustness, it seems of key importance to use proton-conducting materials that can be used at higher temperatures and lower relative humidities than presently used materials. Application of such materials in the membrane as well as in the electrodes can lead to a considerably simpler and more robust fuel cell system. The combination of new components with other new or already existing components that need to be integrated in a new MEA is part of the development work that should not be underestimated. Given the benefits that fuel cells offer for clean and efficient transport, it will be worth the effort.

## Bibliography

### Primary Literature

1. US Department of Energy (2007) Multi-year research, development and demonstration plan, hydrogen, fuel cells & infrastructure technologies program. DOE/GO-102007-2430
2. de Bruijn FA, Makkus RC, Mallant RKAM, Janssen GJM (2007) Materials for state-of-the-art PEM fuel cells, and their suitability for operation above 100°C. In: Zhao T, Kreuer KD, Nguyen T (eds) *Advances in fuel cells*. Elsevier, Amsterdam
3. Zawodzinski TA Jr, Derouin C, Radzinski S, Sherman RJ, Smith VT, Springer TE, Gottesfeld S (1993) Water uptake by and transport through Nafion<sup>®</sup> 117 membranes. *J Electrochem Soc* 140:1041–1047
4. Gasteiger HA, Panels JE, Yan SG (2004) Dependence of PEM fuel cell performance on catalyst loading. *J Power Sources* 127:162–171

5. TIAX LLC (2003) Platinum availability and economics for PEMFC commercialization, DOE report number: DE-FC04-01AL67601
6. Ralph TR, Hogarth MP (2002) Catalysis for low temperature fuel cell Part I. The cathode challenges. *Platin Met Rev* 46:3–14
7. Heinzel A, Mahlendorf F, Niemzig O, Kreuz C (2004) Injection moulded low cost bipolar plates for PEM fuel cells. *J Power Sources* 131:35–40
8. Stumper J, Stone C (2008) Recent advances in fuel cell technology at Ballard. *J Power Sources* 176:468–476
9. Janssen GJM (2001) A phenomenological model of water transport in a proton-exchange-membrane fuel cell. *J Electrochem Soc* 148:A1313–A1323
10. Weber AZ, Newman J (2005) Effects of microporous layers in polymer electrolyte fuel cells. *J Electrochem Soc* 152:A677–A688
11. Hurvitz N (2008) An in-situ, real-time gas humidity sensor for fuel cells, fuel cells durability and performance. The Knowledge Press, Brookline, pp 231–244
12. Satayapal S (2009) Overview of hydrogen and fuel cell activities, 27-10-2009. Fuel Cells & Hydrogen Joint Undertaking Stakeholders General Assembly, Brussels
13. Ernst WD, Stone C, Wheeler D (2009) Fuel cell system cost for transportation-2008 Cost Estimate, NREL/BK-6A1-45457
14. Cleghorn SJC, Mayfield DK, Moore DA, Moore JC, Rusch G, Sherman TW, Sisofo NT, Beuscher U (2006) A polymer electrolyte fuel cell life test: 3 years of continuous operation. *J Power Sources* 158:446–454
15. Yamazaki O, Oomori Y, Shintaku H, Tabata T (2005) Evaluation study of PEFC single cell at Osaka gas, 2005 fuel cell seminar abstracts. Courtesy Associates, Washington, DC
16. Huth H (2008) Volkswagen's high temperature polymer electrolyte fuel cell. In: 4th annual international conference fuel cells durability and performance, Cambridge, 9-12-2008
17. Perti D (2009) DuPont next generation membrane and membrane electrode assembly development. In: FC Expo 2009, Tokyo
18. Johnson WB, Bazkowski C, Berta T, Crum M, Greene L, Kunitz B, Mao H, Priester S, Rudolph J, Ryan K, Seligura C (2011) MEA degradation issues opportunities and challenges using thin, reinforced polymer electrolyte membranes. In: 2nd international workshop on degradation issues on fuel cells, Thessaloniki, 21–23 Sept 2011
19. Hicks MT (2006) MEA and stack durability for PEM fuel cells. DOE hydrogen program FY 2006 annual progress report, Washington, DC pp 722–726
20. Sone Y, Ekdunge P, Simonsson D (1996) Proton conductivity of Nafion 117 as measured by a four-electrode AC impedance method. *J Electrochem Soc* 143:1254–1259
21. Maalouf M, Pyle B, Sun CN, Wu D, Paddison SJ, Schaberg M, Emery M, Lochhaas KH, Hamrock SJ, Ghassemi H, Zawodzinski TA (2009) Proton exchange membranes for high temperature fuel cells: equivalent weight and end group effects on conductivity. *ECS Trans* 25:1473–1481
22. Aquivion PFSA membrane performance data. [http://www.solvaysites.com/sites/solvayplastics/EN/specialty\\_polymers/Specialties/Pages/Aquivion\\_PFSA.aspx](http://www.solvaysites.com/sites/solvayplastics/EN/specialty_polymers/Specialties/Pages/Aquivion_PFSA.aspx)
23. Hamrock S (2009) Membranes and MEAs for dry, hot operating conditions. DOE hydrogen programme FY 2009 annual progress report, Washington, DC pp 1042–1047
24. Cleghorn S, Griffith M, Liu W, Pires J, Kolde J (2007) Gore's development path to a commercial automotive membrane electrode assembly. 2007 fuel cell seminar. Courtesy Associates, Washington, DC
25. Zhang YM, Li L, Tang J, Bauer B, Zhang W, Gao HR, Taillades-Jacquin M, Jones DJ, Roziere J, Lebedeva N, Mallant R (2009) Development of covalently cross-linked and composite perfluorosulfonic acid membranes. *ECS Trans* 25:1469–1472
26. Jones DJ, Roziere J (2003) Inorganic/organic composite membranes. In: Vielstich W, Gasteiger HA, Lamm A (eds) Handbook of fuel cells-fundamentals, technology and applications, vol 3. Wiley, Chichester, pp 447–455
27. Kerres J (2005) Blended and cross-linked Ionomer membranes for application in membrane fuel cells. *Fuel Cells* 5:230–240
28. Aoki M, Asano N, Miyatake K, Uchida H, Watanabe M (2006) Durability of sulfonated polyimide membrane evaluated by long-term polymer electrolyte fuel cell operation. *J Electrochem Soc* 153:A1154–A1158
29. de Araujo CC, Kreuer KD, Schuster M, Portale G, Mendil-Jakani H, Gebel G, Maier J (2009) Poly(p-phenylene sulfone)s with high ion exchange capacity: ionomers with unique microstructural and transport features. *Phys Chem Chem Phys* 11: 3305–3312
30. FumaPem – High performance membranes for fuel cells. Products section of company website [www.fumatech.com](http://www.fumatech.com)
31. Herz HG, Kreuer KD, Maier J, Scharfenberger G, Schuster MFH, Meyer WH (2003) New fully polymeric proton solvents with high proton mobility. *Electrochim Acta* 48:2165–2171
32. Scharfenberger G, Meyer WH, Wegner G, Schuster M, Kreuer KD, Maier J (2006) Anhydrous polymeric proton conductors based on imidazole functionalized polysiloxane. *Fuel Cells* 6:237–250
33. Schuster MFH, Meyer WH, Schuster M, Kreuer KD (2004) Toward a new type of anhydrous organic proton conductor based on immobilized imidazole. *Chem Mater* 16:329–337
34. Bozkurt A, Karadedeli B (2007) Copolymers of 4(5)-vinylimidazole and ethyleneglycol methacrylate phosphate: synthesis and proton conductivity properties. *React Funct Polym* 67:348–354
35. Steininger H, Schuster M, Kreuer KD, Maier J (2006) Intermediate temperature proton conductors based on

- phosphonic acid functionalized oligosiloxanes. *Solid State Ionics* 177:2457–2462
36. Bozkurt A, Meyer WH, Gutmann J, Wegner G (2003) Proton conducting copolymers on the basis of vinylphosphonic acid and 4-vinylimidazole. *Solid State Ionics* 164:169–176
  37. Seel DC, Benicewicz BC, Xiao L, Schmidt TJ (2009) High-temperature polybenzimidazole-based membranes. In: Vielstich W, Yokokawa H, Gasteiger HA (eds) *Handbook of fuel cells-fundamentals, technology and applications*, vol 5. Wiley, Chichester, pp 300–312
  38. PBI/H<sub>3</sub>PO<sub>4</sub> fuel cell starts up at room temperature. *Fuel Cells Bulletin* November 2008, p 10
  39. Li Q, Jensen JO, Savinell RF, Bjerrum NJ (2009) High temperature proton exchange membranes based on polybenzimidazoles for fuel cells. *Prog Polym Sci* 34:449–477
  40. Ahluwalia RK, Wang X (2006) Rapid self-start of polymer electrolyte fuel cell stacks from subfreezing temperatures. *J Power Sources* 162:502–512
  41. Oszcipok M, Hakenjos A, Riemann D, Hebling C (2007) Start up and freezing processes in PEM fuel cells. *Fuel Cells* 7:135–141
  42. Gebert M, Hoehlein B, Stolten D (2004) Benchmark cost analysis of main PEFC ionomer membrane solutions. *J Fuel Cell Sci Technol* 1:56
  43. Springer TE, Wilson MS, Gottesfeld S (1993) Modeling and experimental diagnostics in polymer electrolyte fuel cells. *J Electrochem Soc* 140:3513–3526
  44. Mathias MF, Roth J, Fleming J, Lehnert W (2003) Diffusion media materials and characterisation. In: Vielstich W, Gasteiger HA, Lamm A (eds) *Handbook of fuel cells – fundamentals, technology and applications*, vol 3. Wiley, Chichester, pp 515–537
  45. Neyerlin KC, Gu W, Jorne J, Gasteiger HA (2007) Study of the exchange current density for the hydrogen oxidation and evolution reactions. *J Electrochem Soc* 154:B631–B635
  46. Gasteiger HA, Kocha SS, Sompalli B, Wagner FT (2005) Activity benchmarks and requirements for Pt, Pt-alloy, and non-Pt oxygen reduction catalysts for PEMFCs. *Appl Catal B* 56:9–35
  47. Markovic NM, Ross PN (2002) Surface science studies of model fuel cell electrocatalysts. *Surf Sci Rep* 45:117–229
  48. Bonakdarpour A, Stevens K, Vernstrom GD, Atanasoski R, Schmoedel AK, Debe MK, Dahn JR (2007) Oxygen reduction activity of Pt and Pt-Mn-Co electrocatalysts sputtered on nano-structured thin film support. *Electrochim Acta* 53:688–694
  49. Debe MK, Schmoedel AK, Vernstrom GD, Atanasoski R (2006) High voltage stability of nano-structured thin film catalysts for PEM fuel cells. *J Power Sources* 161:1002–1011
  50. Debe MK (2003) Novel catalysts, catalyst support and catalyst coated membrane methods. In: Vielstich W, Gasteiger HA, Lamm A (eds) *Handbook of fuel cells-fundamentals, technology and applications*, vol 3. Wiley, Chichester, pp 576–590
  51. Gancs L, Kobayashi T, Debe MK, Atanasoski R, Wieckowski A (2008) Crystallographic characteristics of nanostructured thin-film fuel cell electrocatalysts: a HRTEM study. *Chem Mater* 20:2444–2454
  52. Zhang JL, Vukmirovic MB, Xu Y, Mavrikakis M, Adzic RR (2005) Controlling the catalytic activity of platinum-monolayer electrocatalysts for oxygen reduction with different substrates. *Angew Chem Int Ed* 44:2132–2135
  53. Stamenkovic VR, Mun BS, Mayrhofer KJJ, Ross PN, Markovic NM, Rossmeisl J, Greeley J, Norskov JK (2006) Changing the activity of electrocatalysts for oxygen reduction by tuning the surface electronic structure. *Angew Chem Int Ed* 45:2897–2901
  54. Stamenkovic VR, Fowler B, Mun BS, Wang G, Ross PN, Lucas CA, Markovic NM (2007) Improved oxygen reduction activity on Pt<sub>3</sub>Ni(111) via increased surface site availability. *Science* 315:493–497
  55. Antolini E, Salgado JRC, Gonzalez ER (2006) The stability of Pt-M (M=first row transition metal) alloy catalysts and its effect on the activity in low temperature fuel cells. *J Power Sources* 160:957–968
  56. Mukerjee S, Srinivasan S (1993) Enhanced electrocatalysis of oxygen reduction on platinum alloys in proton exchange membrane fuel cells. *J Electroanal Chem* 357:201–224
  57. Murthi VS (2009) Highly dispersed alloy catalyst for durability. DOE hydrogen programme FY 2009 annual progress report, US DOE in Washington, DC, pp 1075–1080
  58. Adzic RR, Zhang J, Sasaki K, Vukmirovic MB, Shao M, Wang JX, Nilekar AU, Mavrikakis M, Valerio JA, Uribe F (2007) Platinum monolayer fuel cell electrocatalysts. *Top Catal* 46:249–262
  59. Ball SC, Burton SL, Fisher J, ÓMalley R, Tessier BC, Theobald B, Thompsett D, Zhou WP, Su D, Zhu Y, Adzic R (2009) Structure and activity of novel Pt core-shell catalysts for the oxygen reduction reaction. *ECS Trans* 25:1023–1036
  60. Neyerlin KC, Srivastava R, Yu C, Strasser P (2009) Electrochemical activity and stability of dealloyed Pt-Cu and Pt-Cu-Co electrocatalysts for the oxygen reduction reaction (ORR). *J Power Sources* 186: 261–267
  61. Strasser P (2009) Dealloyed Pt bimetallic electrocatalysts for oxygen reduction. In: Vielstich W, Yokokawa H, Gasteiger HA (eds) *Handbook of fuel cells-fundamentals, technology and applications*, vol 5. Wiley, Chichester, pp 30–47
  62. Wang X, Kariuki N, Niyogi S, Smith MC, Myers DJ, Hofmann T, Zhang Y, Bar M, Heske C (2008) Bimetallic palladium-base metal nanoparticle oxygen reduction electrocatalysts. *ECS Trans* 16:109–119
  63. Zhou Y, Holme T, Berry J, Ohno TR, Ginley D, ÓHayre R (2009) Dopant-induced electronic structure modification of HOPG surfaces: implications for

- high activity fuel cell catalysts. *J Phys Chem C* 114: 506–515
64. Shao Y, Liu J, Wang Y, Lin Y (2009) Novel catalyst support materials for PEM fuel cells: current status and future prospects. *J Mater Chem* 19:46–59
65. Bashyam R, Zelenay P (2006) A class of non-precious metal composite catalysts for fuel cells. *Nature* 443:63–66
66. Lefevre M, Proietti E, Jaouen F, Dodelet JP (2009) Iron-based catalysts with improved oxygen reduction activity in polymer electrolyte fuel cells. *Science* 324:71–74. Washington, DC
67. Wu G, Artyushkova K, Ferrandon M, Kropf AJ, Myers D, Zelenay P (2009) Performance durability of polyaniline-derived non-precious cathode catalysts. *ECS Trans* 25:1299–1311
68. Neyerlin KC, Gasteiger HA, Mittelstaedt CK, Jorne J, Gu W (2005) Effect of relative humidity on oxygen reduction kinetics in a PEMFC. *J Electrochem Soc* 152:A1073–A1080
69. Kocha SS (2003) Principles of MEA preparation. In: Vielstich W, Gasteiger HA, Lamm A (eds) *Handbook of fuel cells-fundamentals, technology and applications*, vol 3. Wiley, Chichester, pp 538–565
70. Xie Z, Zhao X, Gazzarri J, Wang Q, Navessin T, Holdcroft S (2009) Identification of dominant transport mechanisms in PEMFC cathode catalyst layers operated under low RH. *ECS Trans* 25:1187–1192
71. Quick C, Ritzinger D, Lehnert W, Hartnig C (2009) Characterization of water transport in gas diffusion media. *J Power Sources* 190:110–120
72. Hermann A, Chaudhuri T, Spagnol P (2005) Bipolar plates for PEM fuel cells: a review. *Int J Hydrog Energy* 30:1297–1302
73. Morikawa H, Kikushi H, Saito N (2009) Development and advances of a V-flow FC stack for FCX clarity. *SAE Int J Engines* 2:955–959
74. Shimoi R, Aoyama T, Iiyama A (2009) Development of fuel cell stack durability based on actual vehicle test data: current status and future work. *SAE Int J Engines* 2:960–970
75. Makkus RC, Janssen AHH, de Bruijn FA, Mallant RKAM (2000) Use of stainless steel for cost competitive bipolar plates in the SPFC. *J Power Sources* 86:274–282
76. Suria OV, Bruno M, Bois P, Maggiore P, Cazzolato C (2009) Fuel size and weight reduction due to innovative metallic bipolar plates: Technical process details and improvements, *SAE Technical Papers Series*, pp 2009-01-1009
77. Brady MP, Yang B, Wang H, Turner JA, More KL, Wilson M, Garzon F (2006) The formation of protective nitride surfaces for PEM fuel cell metallic bipolar plates. *JOM* 58:50–57
78. Cho EA, Jeon US, Hong SA, Oh IH, Kang SG (2005) Performance of a 1-kW-class PEMFC stack using TiN-coated 316 stainless steel bipolar plates. *J Power Sources* 142:177–183
79. Mepsted GO, Moore JM (2003) Performance and durability of bipolar plate materials. In: Vielstich W, Gasteiger HA, Lamm A (eds) *Handbook of fuel cells-fundamentals, technology and applications*, vol 3. Wiley, Chichester, pp 286–293
80. Joseph S, McClure JC, Sebastian PJ, Moreira J, Valenzuela E (2008) Polyaniline and polypyrrole coatings on aluminum for PEM fuel cell bipolar plates. *J Power Sources* 177:161–166
81. Ahluwalia R, Wang X, Lasher S, Sinha J, Yang Y, Sriramulu S (2007) Performance of automotive fuel cell systems with nanostructured thin film catalysts, 2007 fuel cell seminar, 15-10-2007. Courtesy Associates, Washington, DC
82. Dobrovol'skii YA, Ukshe AE, Levchenko AE, Arkhangel'skii IV, Ionov SG, Avdeev VV, Aldoshin SM (2007) Materials for bipolar plates for proton-conducting membrane fuel cells. *Russ J Gen Chem* 77:752–765
83. Cleghorn SJC, Mayfield DK, Moore DA, Moore JC, Rusch G, Sherman TW, Sisofo N, Beuscher U (2006) A polymer electrolyte fuel cell life test: 3 years of continuous operation. *J Power Sources* 158:4–455
84. Schulze M, Knöri T, Schneider A, Gülzow E (2004) Degradation of sealings for PEFC test cells during fuel cell operation. *J Power Sources* 127:222–229
85. Tan J, Chao YJ, Van Zee JW, Lee WK (2007) Degradation of elastomeric gasket materials in PEM fuel cells. *Mater Sci Eng A* 445-446:669–675
86. Ralph TR, Barnwell DE, Bouwman PJ, Hodgkinson AJ, Petch MI, Pollington M (2008) Reinforced membrane durability in proton exchange membrane fuel cell stacks for automotive applications. *J Electrochem Soc* 155:B411–B422
87. de Bruijn FA, Dam VAT, Janssen GJM (2008) Review: durability and degradation issues of PEM fuel cell components. *Fuel Cells* 8:3–22
88. Noto H, Kondo M, Otake Y, Kato M (2009) Development of fuel cell hybrid vehicle by Toyota, *SAE technical paper series*, pp 2009-01-1002
89. Reiser CA, Bregoli L, Patterson TW, Yi JS, Yang JD, Perry ML, Jarvi TD (2005) A reverse-current decay mechanism for fuel cells. *Electrochem Solid-State Lett* 8:A273–A276
90. Knights SD, Colbow KM, St-Pierre J, Wilkinson DP (2004) Aging mechanisms and lifetime of PEFC and DMFC. *J Power Sources* 127:127–134
91. Ferreira-Aparicio P, Chaparro AM, Gallardo B, Folgado M, Daza L (2009) Anode degradation effects in PEMFC stacks by localized fuel starvation, 2009 fuel cell seminar. Courtesy Associates, Washington, DC
92. Schmittinger W, Vahidi A (2008) A review of the main parameters influencing long-term performance and durability of PEM fuel cells. *J Power Sources* 180:1–14
93. Baldasano JM, Valera E, Jimenez P (2003) Air quality data from large cities. *Sci Total Environ* 307:141–165

94. Huang W, Tan J, Kan H, Zhao N, Song W, Song G, Chen G, Jiang L, Jiang C, Chen R, Chen B (2009) Visibility, air quality and daily mortality in Shanghai, China. *Sci Total Environ* 407:3295–3300
95. A Report on the achievements and learnings from the HyFleet: CUTE project 2006–2009
96. Narusawa K, Myong K, Murooka K, Kamiya Y (2007) A study regarding effects of proton exchange membrane fuel cell poisoning due to impurities on fuel cell performance, SAE technical paper series, pp 2007-01-0698
97. Adjemian K, Iiyama A (2008) MEA development for automotive applications, fuel cells durability and performance, 3rd edn. The Knowledge Press, Inc., Brookline, pp 5–16
98. Veldhuis JBJ, de Bruijn FA, Mallant RKAM (1998) Fuel cell seminar abstracts, 16-11-1998. Courtesy Associates, Washington, DC, p 598
99. Knights SD, Jia N, Chuy C, Zhang J (2005) Fuel cell seminar abstracts, 14-11-2005. Courtesy associates, Washington, DC
100. Cheng X, Shi Z, Glass N, Zhang L, Zhang J, Song D, Liu ZS, Wang H, Shen J (2007) A review of PEM hydrogen fuel cell contamination: Impacts, mechanisms, and mitigation. *J Power Sources* 165:739–756
101. Kennedy DM, Cahela DR, Zhu WH, Westrom KC, Nelms RM, Tatarchuk BJ (2007) Fuel cell cathode air filters: methodologies for design and optimization. *J Power Sources* 168:391–399
102. Matsuda Y (2009) Accumulation behavior of impurities in fuel cell hydrogen circulation system, 2009 fuel cell seminar, 16-11-2009. Courtesy associates, Washington, DC
103. Papasavva S (2005) Developing hydrogen (H<sub>2</sub>) specification guidelines for proton exchange membrane (PEM) fuel cell vehicles, SAE technical series papers, pp 2005-01-0011
104. Recupero V, Pino L, Vita A, Cipiti F, Cordaro M, Lagana M (2005) Development of a LPG fuel processor for PEFC systems: Laboratory scale evaluation of autothermal reforming and preferential oxidation subunits. *Int J Hydrog Energy* 30:963–971
105. de Bruijn FA, Rietveld G, van den Brink RW (2007) Hydrogen production and fuel cells as the bridging technologies towards a sustainable energy system. In: Centi G, Santen RA (eds) *Catalysis for renewables*. Wiley-VCH, Weinheim, pp 299–336
106. Li Q, He R, Gao J-A, Jensen JO, Bjerrum NJ (2003) The CO poisoning effect in polymer electrolyte fuel cells operational at temperatures up to 200°C. *J Electrochem Soc* 150:A1599–A1605
107. Wipke K, Sprik S, Kurtz J, Ramsden T (2009) Controlled hydrogen fleet and infrastructure demonstration and validation project, NREL/NREL/TP-560-46679
108. Mallant RKAM, Lebedeva NP, Zhang YM, Li L, Tang JK, Bukhtiyarov VI, Romanenko AV, Voropaev I, Bauer B, Zhang W, Jones DJ, Rozière J, Gao HR (2009) Significant steps towards medium temperature/low RH PEMFC, 2009 fuel cell seminar. Courtesy Associates, Washington, DC
109. Bono T, Kizaki M, Mizuno H, Nonobe Y, Takahashi T, Matsumoto T, Kobayashi N (2010) Development of new Toyota FCHV-adv fuel cell system. *SAE Int J Engines* 2:948–954
110. Power backup solutions for telecom and related networks. Dantherm Power Catalogue 2008
111. Ferreira PJ, la Ó GJ, Shao-Horn Y, Morgan D, Makharia R, Kocha S, Gasteiger HA (2005) Instability of Pt/C electrocatalysts in proton exchange membrane fuel cells. *J Electrochem Soc* 152: A2256–A2271
112. Xie J, Wood DL, More KL, Atanassov P, Borup RL (2005) Microstructural changes of membrane electrode assemblies during PEFC durability testing at high humidity conditions. *J Electrochem Soc* 152: A1011–A1020
113. Guilminot E, Corcella A, Charlot F, Maillard F, Chatenet M (2007) Detection of Pt<sup>[sup z+]</sup> Ions and Pt nanoparticles Inside the membrane of a used PEMFC. *J Electrochem Soc* 154:B96–B105
114. Shao-Horn Y, Sheng WC, Chen S, Ferreira PJ, Holby EF, Morgan D (2007) Instability of supported platinum nanoparticles in low-temperature fuel cells. *Top Catal* 46:285–305
115. Pourbaix M (1974) *Atlas of electrochemical equilibria in aqueous solutions*. National Association of Corrosion Engineers, New York
116. Darling RM, Meyers JP (2003) Kinetic model of platinum dissolution in PEMFCs. *J Electrochem Soc* 150:A1523–A1527
117. Virkar AN, Zhou Y (2007) Mechanism of catalyst degradation in proton exchange membrane fuel cells. *J Electrochem Soc* 154:B540–B547
118. Dam VAT, de Bruijn FA (2007) The stability of PEMFC electrodes. *J Electrochem Soc* 154: B494–B499
119. Wang X, Kumar R, Myers DJ (2006) Effect of voltage on platinum dissolution. *Electrochem Solid-State Lett* 9:A225–A227
120. Kawahara S, Mitsushima S, Ota K, Kamiya N (2006) Deterioration of Pt catalyst under potential cycling. *ECS Trans* 3:625–631
121. Kawahara S, Mitsushima S, Ota K, Kamiya N (2006) Consumption of Pt catalyst under electrolysis and fuel cell operation. *ECS Trans* 1:85–100
122. Burke LD, Buckley DT (1994) Anomalous stability of acid-grown hydrous platinum oxide films in aqueous media. *J Electroanal Chem* 366:239–251
123. Burke LD, ÓDwyer KJ (1992) Multilayer oxide growth on Pt under potential cycling conditions. *Electrochim Acta* 37:43–50
124. Birss VI, Chang M, Segal J (1993) Platinum oxide film formation-reduction: an in-situ mass measurement study. *J Electroanal Chem* 355:181–191
125. Nagy Z, You H (2002) Applications of surface X-ray scattering to electrochemistry problems. *Electrochim Acta* 47:3037–3055



126. Kinoshita K (1992) *Electrochemical oxygen technology*. Wiley, New York
127. Guilminot E, Corcella A, Chatenet M, Maillard F, Charlot F, Berthome G, Iojoiu C, Sanchez JY, Rossinot E, Claude E (2007) Membrane and active layer degradation upon PEMFC steady-state operation. *J Electrochem Soc* 154:B1106–B1114
128. Honji A, Mori T, Tamura K, Hishinuma M (1988) Agglomeration of platinum particles supported on carbon in phosphoric acid. *J Electrochem Soc* 135: 355–359
129. Ascarelli P, Contini V, Giorgi R (2002) Formation process of nanocrystalline materials from x-ray diffraction profile analysis: application to platinum catalysts. *J Appl Phys* 91:4556–4561
130. Borup RL, Davey JR, Garzon FH, Wood DL, Inbody MA (2006) PEM fuel cell electrocatalyst durability measurements. *J Power Sources* 163:76–81
131. Mathias MF, Makharia R, Gasteiger HA, Conley JJ, Fuller TJ, Gittleman CJ, Kocha SS, Miller DP, Mittelsteadt CK, Xie T, Yan SG, Yu PT (2005) Two fuel cell cars in every garage. *Electrochem Soc Interface* 14(Fall):24–35
132. Haas HR, Davis MT (2009) Electrode and catalyst durability requirements in automotive PEM applications: technology status of a recent MEA design and next generation challenges. *ECS Trans* 25: 1623–1631
133. Schulze M, Wagner N, Kaz T, Friedrich KA (2007) Combined electrochemical and surface analysis investigation of degradation processes in polymer electrolyte membrane fuel cells. *Electrochim Acta* 52:2328–2336
134. Janssen GJM, de Heer MP, Papageorgopoulos DC (2004) Bilayer anodes for improved reformate tolerance of PEM fuel cells. *Fuel Cells* 4:169–174
135. Yu H, Hou Z, Yi B, Lin Z (2002) Composite anode for CO tolerance proton exchange membrane fuel cells. *J Power Sources* 105:52–57
136. Piela P, Eickes C, Brosha E, Garzon F, Zelenay P (2004) Ruthenium crossover in direct methanol fuel cell with Pt-Ru black anode. *J Electrochem Soc* 151: A2053–A2059
137. Lebedeva NP, Rosca V, Janssen GJM (2010) CO oxidation and CO<sub>2</sub> reduction on carbon supported PtWO<sub>3</sub> catalyst. *Electrochim Acta* 55:7659–7668
138. de Bruijn FA, Papageorgopoulos DC, Sitters EF, Janssen GJM (2002) The influence of carbon dioxide on PEM fuel cells anodes. *J Power Sources* 110: 117–124
139. Janssen GJM (2004) Modelling study of CO<sub>2</sub> poisoning on PEMFC anodes. *J Power Sources* 136:45–54
140. Ahluwalia RK, Wang X (2008) Effect of CO and CO<sub>2</sub> impurities on performance of direct hydrogen polymer-electrolyte fuel cells. *J Power Sources* 180:122–131
141. Mohtadi R, Lee W, Van Zee JW (2004) Assessing durability of cathodes exposed to common air impurities. *J Power Sources* 138:216–225
142. Paulus UA, Schmidt TJ, Gasteiger HA (2003) Poisons for the O<sub>2</sub> reduction reaction. In: Vielstich W, Gasteiger HA, Lamm A (eds) *Handbook of fuel cells-fundamentals, technology and applications*, vol 2. Wiley, Chichester, pp 555–569
143. Kinoshita K (1988) *Carbon. Electrochemical and physicochemical properties*. Wiley, New York
144. Giordano N, Antonucci PL, Passalacqua E, Pino L, Arico AS, Kinoshita K (1991) Relationship between physicochemical properties and electrooxidation behaviour of carbon materials. *Electrochim Acta* 36:1931–1935
145. Ball SC, Hudson SL, Thompsett D, Theobald B (2007) An investigation into factors affecting the stability of carbons and carbon supported platinum and platinum/cobalt alloy catalysts during 1.2 V potentiostatic holds regimes at a range of temperatures. *J Power Sources* 171:18–15
146. Garland N, Benjamin T, Kopasz J (2007) DOE fuel cell program: durability technical targets and testing protocols. *ECS Trans* 11:923–931
147. Stevens DA, Dahn JR (2005) Thermal degradation of the support in carbon-supported platinum electrocatalysts for PEM fuel cells. *Carbon* 43:179–188
148. Stevens DA, Hicks MT, Haugen GM, Dahn JR (2005) Ex situ and in situ stability studies of PEMFC catalysts. *J Electrochem Soc* 152: A2309–A2315
149. Cai M, Ruthkosky MS, Merzougui B, Swathirajan S, Balogh MP, Oh SE (2006) Investigation of thermal and electrochemical degradation of fuel cell catalysts. *J Power Sources* 160:977–986
150. Shao Y, Yin G, Gao Y, Shi P (2006) Durability study of Pt/C and Pt/CNTs catalysts under simulated PEM fuel cell conditions. *J Electrochem Soc* 153: A1093–A1097
151. Tang Z, Ng HY, Lin J, Wee ATS, Chua DHC (2010) Pt/CNT-based electrodes with high electrochemical activity and stability for proton exchange membrane fuel cells. *J Electrochem Soc* 157:B245–B250
152. Healy J, Hayden C, Xie T, Olson K, Waldo R, Brundage M, Gasteiger H, Abbott J (2005) Aspects of the chemical degradation of PFSA ionomers used in PEM fuel cells. *Fuel Cells* 5:302–308
153. St-Pierre J, Wilkinson DP, Knights SD, Bos M (2000) Relationships between water management, contamination and lifetime degradation in PEFC. *J New Mater Electrochem Syst* 3:99–106
154. Wood D, Davey J, Garzon F, Atanassov P, Borup R (2005) Mass-transport phenomena and long-term performance limitations in H<sub>2</sub>-air PEMFC durability testing, 2005 fuel cell seminar abstracts, 14-11-2005. Courtesy Associates, Washington, DC
155. Jordan LR, Shukla AK, Behrsing T, Avery NR, Muddle BC, Forsyth M (2000) Diffusion layer parameters influencing optimal fuel cell performance. *J Power Sources* 86:250–254
156. Williams MV, Begg E, Bonville L, Kunz HR, Fenton JM (2004) Characterization of gas diffusion

- layers for PEMFC. *J Electrochem Soc* 151: A1173–A1180
157. de Bruijn FA, Dam VAT, Janssen GJM, Makkus RC (2009) Electrode degradation in PEMFCs as studied in model systems and PEMFC testing. *ECS Trans* 25:1835–1847
  158. Lee C, Merida W (2007) Gas diffusion layer durability under steady-state and freezing conditions. *J Power Sources* 164:141–153
  159. Coms FD (2008) The chemistry of fuel cell membrane chemical degradation. *ECS Trans* 16:235–255
  160. Liu H, Gasteiger HA, LaConti AB, Zhang J (2006) Factors impacting chemical degradation of perfluorinated sulfonic acid ionomers. *ECS Trans* 1:283–293
  161. Mittal VO, Kunz HR, Fenton JM (2007) Membrane degradation mechanisms in PEMFCs. *J Electrochem Soc* 154:B652–B656
  162. Curtin DE, Lousenberg RD, Henry TJ, Tangeman PC, Tisack ME (2004) Advanced materials for improved PEMFC performance and life. *J Power Sources* 131:41–48
  163. Coms FD, Liu H, Owejan JE (2008) Mitigation of perfluorosulfonic acid membrane chemical degradation using cerium and manganese ions. *ECS Trans* 16:1735–1747
  164. Endoh E (2008) Development of highly durable PFSA membrane and MEA for PEMFC under high temperature and low humidity conditions. *ECS Trans* 16:1229–1240
  165. Trogadas P, Parrondo J, Ramani V (2008) Degradation mitigation in polymer electrolyte membranes using free radical scavengers. *ECS Trans* 16:1725–1733
  166. Rozière J, Jones DJ (2003) Non-fluorinated polymer materials for proton exchange membrane fuel cells. *Annu Rev Mater Res* 33:503–555
  167. Zhang L, Ma CS, Mukerjee S (2003) Oxygen permeation studies on alternative proton exchange membranes designed for elevated temperature operation. *Electrochim Acta* 48:1845–1859
  168. Schuster M, Kreuer KD, Andersen HT, Maier J (2007) Sulfonated poly(phenylene sulfone) polymers as hydrolytically and thermooxidatively stable proton conducting ionomers. *Macromolecules* 40:598–607
  169. Escobedo G, Raiford K, Nagarajan GS, Schwiebert KE (2006) Strategies for mitigation of PFSA polymer degradation in PEM fuel cells. *ECS Trans* 1:303–311
  170. Stone C, Calis GHM (2006) Improved composite membranes and related performance in commercial PEM fuel cells, 2006 fuel cell seminar abstracts. Courtesy Associates, Washington, DC
  171. LaConti AB, Hamdan M, McDonald RC (2003) Mechanisms of membrane degradation. In: Vielstich W, Lamm A, Gasteiger HA (eds) *Handbook of fuel cells*, vol 3. Wiley, Chichester, pp 647–663
  172. Silberstein MN, Boyce MC (2010) Constitutive modeling of the rate, temperature, and hydration dependent deformation response of Nafion to monotonic and cyclic loading. *J Power Sources* 195: 5692–5706
  173. Liu W, Ruth K, Rusch G (2001) Membrane durability in PEM fuel cells. *J New Mater Electrochem Syst* 4:227–231
  174. McDonald RC, Mittelsteadt CK, Thompson EL (2004) Effects of deep temperature cycling on Nafion® 112 membranes and membrane electrode assemblies. *Fuel Cells* 4:208–213
  175. Okada T (2003) Ionic Contaminants. In: Vielstich W, Lamm A, Gasteiger HA (eds) *Handbook of fuel cells*, vol 3. Wiley, Chichester, pp 627–646
  176. Davies DP, Adcock PL, Turpin M, Rowen SJ (2000) Bipolar plate materials for solid polymer fuel cells. *J Appl Electrochem* 30:101–105
  177. Gallagher KG, Wong DT, Fuller TF (2008) The effect of transient potential exposure on the electrochemical oxidation of carbon black in low-temperature fuel cells. *J Electrochem Soc* 155:B488–B493
  178. Frisch L (2001) PEM fuel cell stack sealing using silicone elastomers. *Seal Technol* 2001:7–9
  179. Du B, Guo R, Pollard R, Rodriguez D, Smith J, Elter J (2006) PEM fuel cells: status and challenges for commercial stationary power applications. *JOM* 58(8):45–49
  180. St-Pierre J, Jia N (2002) Successful demonstration of Ballard PEMFCs for space shuttle applications. *J New Mater Electrochem Syst* 5:263

## Books and Reviews

- Barbir F (2005) *PEM fuel cells, theory and practice*. Elsevier, Amsterdam
- Büchi FN, Inaba M, Schmidt TJ (eds) (2009) *Polymer electrolyte fuel cell durability*. Springer, New York
- Larminie J, Dicks A (2003) *Fuel cell systems explained*, 2nd edn. Wiley, Chichester
- Scherer GG (ed) (2008) *Fuel cells I, advances in polymer science*, vol 215. Springer, New York
- Scherer GG (ed) (2008) *Fuel cells II, advances in polymer science*, vol 216. Springer, New York
- Vielstich W, Lamm A, Gasteiger HA (eds) (2003) *Handbook of fuel cells, fundamental, technology and applications*, 4th edn. Wiley, Chichester
- Vielstich W, Yokokawa H, Gasteiger HA (eds) (2009) *Handbook of fuel cells: advances in electrocatalysis, materials, diagnostics and durability*, vol 5 & 6. Wiley, Chichester
- Zhang J (ed) (2009) *PEM fuel cell electrocatalysts and catalyst layers*. Springer, New York
- Zhao TS, Kreuer KD, Van Nguyen T (eds) (2007) *Advances in fuel cells I*. Elsevier, Amsterdam



## PEM Fuel Cells: Modeling

M. Secanell, A. Jarauta, A. Kosokian,  
M. Sabharwal and J. Zhou  
Energy Systems Design Laboratory, Department  
of Mechanical Engineering, University of  
Alberta, Edmonton, AB, Canada

### Article Outline

Glossary  
Definition of the Subject  
Introduction  
Fuel Cell Components and Operation  
General Models  
Microscale Simulation for Parameter Estimation  
Implementation  
Conclusion  
Future Directions  
Bibliography

### Glossary

**Proton exchange membrane fuel cells (PEMFCs)** are energy conversion devices that transform chemical energy in a fuel directly to electricity by means of two electrochemical reactions divided by a proton conductive membrane.

**Mathematical modeling** is the development of partial differential equations for describing the physical and electrochemical processes that govern a physicochemical system, in this entry, a PEMFC.

**Numerical modeling** is the development of numerical analysis and software tools to solve the partial differential equations that describe a physicochemical system, in this entry, a PEMFC.

**Gas diffusion layers (GDL)** are porous, electrically conductive layers made of carbon fibers, a binder, and usually coated with PTFE that are

placed between a fuel cell gas channel and the catalyst layer.

**Catalyst layers (CLs)** are porous, electronically and ionically conductive composite layers made of ionomer and supported catalysts. They are the heart of the fuel cell as it is in these layers that the electrochemical reactions take place.

**Proton exchange membranes (PEM)** are ion conductive membranes, usually made of a perfluorosulfonic acid (PFSA) polymer, that are used to separate anodic and cathodic reactions in a fuel cell.

**Ohmic transport losses** are cell voltage losses associated with the transport of charge within the fuel cell components.

**Mass transport losses** are cell voltage losses associated with either inappropriate reactant distribution to the reaction site or slow product removal.

**Kinetic losses** are cell voltage losses associated with the irreversible potential required to accelerate the rate of the electrochemical reactions.

**Open-source fuel cell software** is numerical analysis software for fuel cells where the source code is made available with a license in which the copyright holder provides the rights to study, change, and distribute the software to anyone and for any purpose. Open-source software is ideal for collaborative development.

### Definition of the Subject

Proton exchange membrane fuel cell (PEMFC) operation involves multiphase mass, charge, and heat transport, complex electrochemical reactions, and physical processes that occur at multiple spatial and time scales, e.g., from double-layer effects occurring in milliseconds to catalyst degradation which becomes only significant after many hours of operation. PEMFC design is therefore a complex endeavor that requires the optimization of a multitude of objectives, such as minimizing cost

and maximizing specific current density, efficiency, and durability, by modifying a large design data set that includes the geometry, composition, and microstructure of each of the components that form the cell. In order to achieve an optimal design, multidisciplinary computational design and optimization is required. The heart of numerical design and optimization is a numerical model of the system under study, in this case a numerical model of the PEMFC. Mathematical and numerical modeling of PEMFCs is therefore critical in order to understand the physical and chemical processes occurring inside the fuel cell and to design a PEMFC system that can meet current targets for PEMFC commercialization.

The modern era of PEMFC modeling started with the pioneering work of Springer et al. [1] and Bernardi and Verbrugge [2] in the early 1990s, where one-dimensional full-cell models were considered and has continued to present time with the development of complex three-dimensional PEMFC models including multicomponent mass transport, charge and heat transport, two-phase flow, and multistep electrochemical reactions [3–6]. In recent years, advancement in image analysis has led to the development of microscale numerical models [7–18]. In this entry, the reader is first introduced to the physicochemical properties and function of each component in a fuel cell. Then, based on the expected physical processes in each component, general models are developed to describe the physicochemical behavior of the PEMFC components. Common simplifications applied to the most general governing equations are highlighted in order to reach the most common set of governing equations used in numerical modeling software. Then, microscale models are reviewed and discussed. Finally, strategies used to solve the PEMFC governing equations are discussed with emphasis on the use of open-source software as a novel tool for collaborative development on numerical models for PEMFC.

## Introduction

PEMFCs convert the energy in a chemical fuel, such as hydrogen, directly to electricity by means

of two electrochemical reactions separated by a polymer electrolyte membrane. PEMFCs present a viable alternative to the internal combustion engine and lithium-ion batteries in transportation, portable, and backup power applications. The transportation sector, which is currently responsible for nearly 30% of all greenhouse gas (GHG) emission in North America, could be fueled by hydrogen gas produced using electricity from intermittent renewable sources, such as wind and solar. PEMFC vehicles, fueled with hydrogen produce only water vapor as a by-product and could then eliminate nearly all particulate matter and greenhouse gas emissions associated with the sector as well as provide added value to excess electricity from renewable resources during low demand. PEMFC vehicles have already demonstrated all attributes that customers expect, such as quick start-up and refueling, long range, and durability [19]. An increase in market penetration of PEMFC vehicles, however, will depend on further production cost reductions as well as performance and durability improvements [20].

In order to reduce the cost of transportation PEMFC stacks to commercialization targets, i.e., \$ 30/kW (2020 US Department of Energy targets), PEMFC stacks need to be designed to achieve higher power density, and reduce or eliminate the use of expensive catalysts, such as platinum [20]. To increase durability, PEMFCs need to be designed and operated at conditions that minimize membrane damage, catalyst dissolution, and catalyst support corrosion [21]. For example, hydrogen depletion/starvation in the anode during start-up/shutdown leads to carbon corrosion [22], and oxygen starvation due to local water accumulation leads to oxygen peroxide formation which damages the polymer membrane [23]. To design such PEMFC stacks, an excellent understanding of the steady-state and transient mass, charge, and heat transport and electrochemical processes occurring at the nano-, micro-, and macroscale inside each component of the fuel cell is required. PEMFC stack design is therefore a multiscale, multidisciplinary problem which aims at achieving multiple objectives while conforming to very stringent constraints regarding cost, durability, and reliability. Such complex design problem is

best tackled by numerical design and optimization which require accurate mathematical and numerical modeling tools [24, 25].

Mathematical models are a requirement for PEMFC design, but they can also provide insight into the physical and electrochemical phenomena occurring inside PEMFCs, insight that is especially challenging to obtain experimentally due to the submillimeter scales of most fuel cell components and the lack of visual access. Along with physical experiments and visualization, mathematical modeling can be used to estimate transport and electrochemical properties of new PEMFC materials and components by means of least square parameter estimation [26, 27], experimental data fitting with numerical macrohomogeneous models [28], or direct pore-scale simulation using imaging data [18, 29].

The modern era of PEMFC modeling started with the pioneering work of Springer et al. [1] and Bernardi and Verbrugge [2] in the early 1990s, where one-dimensional full-cell models were considered. It shortly became evident that, for the detailed analysis and design of fuel cells, multidimensional models were needed in order to account for channel/landing interactions [30], oxygen depletion along the channel at low stoichiometries [5], and nonuniform temperature and relative humidity profiles [5]. This leads to two-dimensional [31, 32] and three-dimensional [3–5] models. This entry will provide the reader with the necessary set of governing equations to develop their own mathematical models and numerical implementations; therefore, a detailed review of the many numerical modeling articles in the literature is not provided, and instead these will be cited in the context of the physical processes that they included. A number of excellent reviews have been written in the fuel cell modeling area, e.g. [33–40], the reader can refer to these publications for a detailed chronological review of the numerical models in the literature.

This entry will focus on developing a transient, multidimensional, multiscale mathematical model for a fuel cell. The literature also contains multitude of analytical 1D and quasi-2D models for describing the fuel cell behavior, a collection of which can be found, for example, in references

[41, 42]. These models can be used for quick, rough estimation of a certain effect; however, they are limited by dimensionality assumptions and physical simplifications. Geometry of the reactant flow fields, land-channel interactions, gas-liquid water interaction in channels and in porous media, thermal gradients, anisotropic properties, and microstructural characteristics of the components are only a few of the multitude of effects that are ignored in such analytical and semi-analytical models, thereby making it challenging to analyze any results obtained. Models that are able to account for multidimensional reactant, product, reaction, and heat variations, as well as geometrical, compositional, and morphological features, are required for fuel cell design. The aim of this entry is, therefore, to develop such models instead of the aforementioned analytical 1D and quasi-2D models.

Remarkable progress has been achieved in macroscale numerical modeling of fuel cells. These models, however, cannot account for the effect microscopic features in porous composite materials in PEMFCs have on mass transport properties and reactions. Macroscale mathematical models have thus far used semiempirical or percolation theory-based functions to estimate the effective transport properties [43, 44]. Recent experimental and modeling work has shown that these functions can overpredict effective transport parameters by three to ten times [45–48]. Recent work in low loading electrodes has also shown that large local mass transport losses at catalyst/electrolyte interfaces are present and can only be studied by accounting for the layer's microstructural details [49–51]. During operation, liquid water accumulation in the porous media also leads to dynamic pore blockage, further reducing transport and making the use of semiempirical correlation functions challenging. FIB-SEM and nano-CT methods have recently been used to image catalyst layers (CLs) [52, 53] and micro porous layers (MPLs) [54, 55] with resolutions of 5–20 nm and 30–50 nm, respectively. Scanning TEM has been used to visualize platinum particles in the CLs [56] and the electrolyte network [57]. Electrolyte properties in the CL are also being analyzed [58, 59]. Using imaging data

from FIB-SEM and nano-CT, tortuosity [60], mass transport [18, 29, 55], liquid water injection [54], and reactions [14, 17, 18] have very recently been studied by computer simulation. This entry will, therefore, also cover this emerging area of research.

Mathematical modeling of fuel cells is most commonly performed using commercial software, e.g., ANSYS Fluent [3, 4, 61–70], COMSOL Multiphysics [71–78], STAR-CD [79], and MATLAB/SIMULINK [80, 81]. While commercial software is an attractive option because it does not require much implementation effort and usually has better customer support than open-source analogs, it has a few drawbacks compared to the latter, primarily (a) lack of access to source code, which prevents users from understanding how the equations are solved and limits the flexibility of implementing novel solution and domain decomposition strategies; (b) lack of collaborative development tools for sharing numerical implementation and input parameter databases; (c) higher computational requirements due to the universality of commercial software which leads to a complex logical kernel (e.g., Ref. [82] showed a specialized in-house code solved the same problem three to four times faster than the same model implemented in COMSOL Multiphysics); and (d) license fees, which are expensive, especially for nonacademic use and when running multi-core simulations. The necessity of an open-source software in the area of fuel cells that is available for everyone has led to the development of several open-source software projects, OpenFCST [6, 83] and FAST-FC [84] and OpenPNM [85] for pore network modeling. Details on the implementation of the software to solve the mathematical models proposed in the entry will therefore also be discussed.

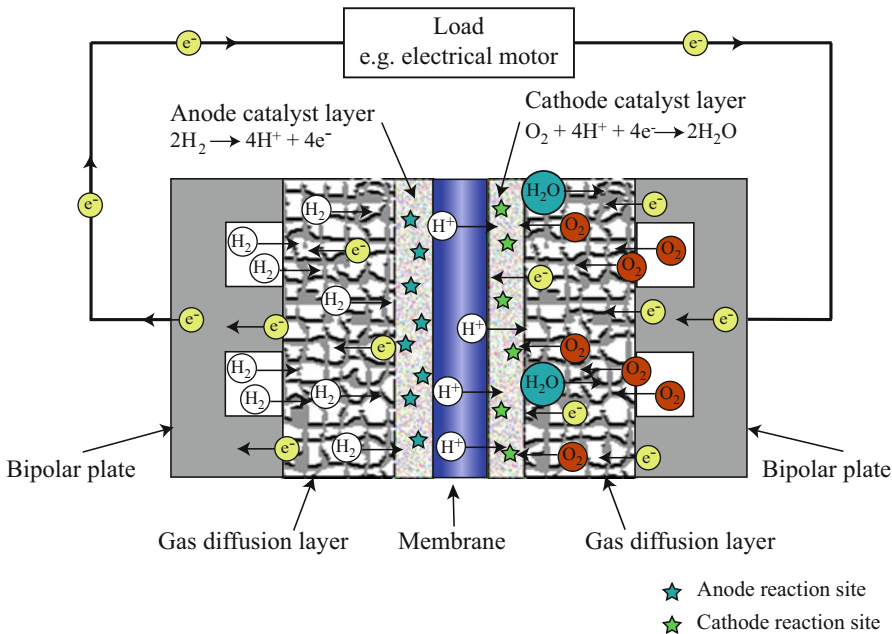
This entry starts with a brief introduction to the functionality and structure of each fuel cell component in section “[Fuel Cell Components and Operation](#).” This insight is then used in order to develop a generalized model for transport and electrochemical reactions in the channels and membrane electrode assembly (MEA) of fuel cells in section “[General Models](#).” As previously discussed, macroscale models depend on a large

number of effective parameters; therefore, section “[Microscale Simulation for Parameter Estimation](#)” introduces the mathematical models currently available to extract average macroscopic parameters from imaging data. Finally, fuel cell mathematical model implementation details are provided in section “[Implementation](#).” The entry does not cover mathematical models involving degradation mechanisms. Even though this area is extremely important, it was excluded in order to limit the scope of the entry. For information in this area, the reader is referred to references [21, 33, 86–88].

## Fuel Cell Components and Operation

A polymer electrolyte fuel cell (PEFC) is an electrochemical energy conversion device that converts the chemical energy in a fuel to electricity by means of two electrochemical reactions that are separated by a gas tight and ion conductive electrolyte. In the case of PEMFCs, which are the subject of this entry, the electrolyte is usually a proton conductive membrane, such as Nafion<sup>®</sup>. To catalyze the electrochemical reactions, both sides of the polymer electrolyte membrane are coated with a 2 – 20  $\mu\text{m}$  porous catalyst layer. The catalyst-coated membrane (CCM) is then sandwiched between two gas transport layers made of a microporous layer and gas diffusion layer (GDL). This assembly, known as the membrane electrode assembly, is finally sandwiched between two conductive plates engraved with microchannels used to deliver the reactant gas mixtures and remove the by-product water. A cross section of a typical PEMFC is shown in Fig. 1. Reactant gases, ions, and electrons are transported through void, electrolyte, and solid phases, respectively, in GDL, MPL, and CL. By-product water in either vapor or liquid forms, and heat are also transported by these layers. Due to their multifunctional nature, these layers are composite materials with a complex microstructure. A detailed description of each layer is provided below, including its composition, functionality, durability, and physical phenomena occurring inside the layer.





**PEM Fuel Cells: Modeling, Fig. 1** A schematic of a PEMFC cross section (Reproduced from [82] with the permission of the author)

## Bipolar Plates

Bipolar plates (BPP) are responsible for:

- Gas reactant supply to the cell
- Electrical connection between the cell and the current collectors
- Transport of the product heat to ambient and to the stack cooling system
- Removal of excess water from the cell

Since bipolar plates need to be electrically conductive, they are made of either carbon-based materials or metals [89–91]. Graphite plates are most commonly used in fuel cell hardware because metal plates suffer corrosion and dissolution under the high humidity and acidity conditions typical of PEMFCs [92–94]. To reduce the risk of degradation, metal plates are usually coated with thin corrosion-resistant films [94], which, however, add to the price of the final product.

Flow field design aims at achieving multiple goals such as improving gas and charge transport to the catalyst site, removing excess liquid water from the channel and MEA, achieving appropriate

compression and sealing, and maintaining a uniform thermal profile. The most popular and simple flow field designs are parallel and serpentine channels, both of which have their advantages and disadvantages. Parallel channels are more prone to water blockage since reactant gases can easily by-pass blocked channels, thereby not allowing the necessary pressure buildup in the channel to remove the liquid water blockage [95]. Serpentine channels, on the other hand, have a long gas flow path leading to substantial pressure drops and gas composition changes along the channel. Interdigitated channels are another common design which incorporates dead-ended inlets and dead-ended outlets that are not connected, forcing the gas through the gas diffusion layer. Although interdigitated channels lead to better liquid water removal from the cell, they exhibit large pressure gradients compared to serpentine and parallel channels and therefore higher parasitic power consumption. For more details on flow field designs, the reader is referred to [96].

Due to reactant, pressure, humidity, and heat variations in the channels, structural land-channel

interactions, and complicated geometries, detailed of bipolar plates analysis can only be performed with three-dimensional models including transport and structural physical processes. Depending on the goal of the simulation, only a cross section of the cell may be considered (red rectangle in Fig. 2). In this case, reactant, heat, and pressure drop along the channel are neglected, and two-dimensional models are used where the channel reactant concentrations are used as boundary conditions. Through-the-channel models, as they are commonly named, are likely appropriate when operating fuel cells with parallel channels and small active area at high gas flow rates, i.e., high stoichiometry, in order to maintain uniform reactant and product concentration in the channel – a testing condition recently referred to as “differential” condition by Kongkanand and Mathias [20] (supplementary material). If reactant depletion along the channel is of primary concern, however, a model considering the green rectangle domain in Fig. 2 could also be developed, known as an along-the-channel model. This model however ignores land to channel effects, which are important in most fuel cells [30], unless porous plates are used [97].

Mathematical models for mass transport in channels are presented in section “[Mass Transport in Channels](#),” including the modeling approaches for liquid water transport in channels in section “[Two-Phase Flow in Channels](#).”

### Gas Diffusion and Microporous Layers

GDLs are responsible for:

- Uniform distribution of the reactant gases to the catalyst layer (see mass transport models in section “[Mass Transport in MEAs](#)”)
- Transport of water and heat generated in catalyst layers to BPPs (sections “[Liquid Water in MEAs](#)” and “[Heat Transport](#)”)
- Electrical connection between the catalyst layer and current collectors (section “[Charge Transport](#)”)
- Improving the mechanical stability of the MEA

GDLs are 100–500  $\mu\text{m}$  thick porous layers made of an electrically conductive material, such

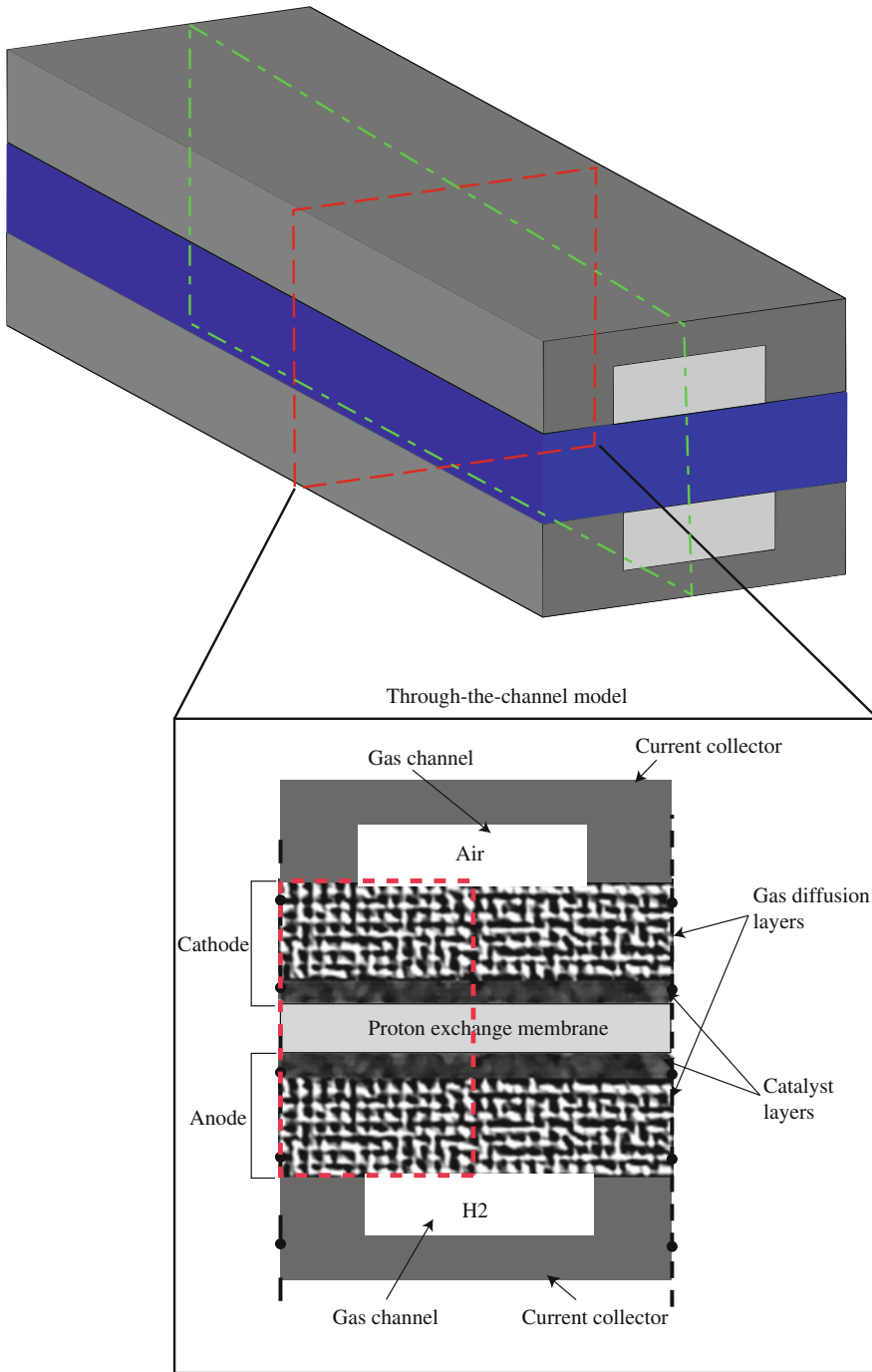
as carbon paper or carbon cloth [98–101]. GDL porosity is between 90% and 70%, depending on manufacturer, type, and compression level [102, 103]. Electron transport in GDLs occurs through the solid network of carbon fibers, while reactant and product gases as well as liquid water are transported through the void, or pore, phase of the GDLs. To aid liquid water removal from the cell and avoid flooding, GDLs are impregnated with polytetrafluoroethylene (PTFE) or other hydrophobic materials [98].

The microporous layer, commonly manufactured by intermixing a hydrophobic polymer, e.g., PTFE, with carbon black, is a porous media between the CL and GDL. The role of the microporous layer is still under debate; however, it has been shown to reduce fuel cell ohmic resistance, increase fuel cell stability, and enhance performance at high current density, especially under fully humidified conditions [104–111]. Based on these studies, the hypothesized MPL functionality includes:

- Increasing the water removal rate [104]
- Providing a better electrical contact [105]
- Alleviating water accumulation by forcing the liquid water from cathode to anode [107]
- Improving the evaporation in the electrodes [110, 111]
- Creating an in-plane diffusion pathway in the partially saturated layers [110]

In the past decade, durability and degradation of fuel cell materials and components has become a major area of research [21, 112–128]. In GDLs, carbon sites may be oxidized and form hydrophilic regions (this is primarily observed on the cathode side) [21]. This leads to increase in water uptake and, as a result, degraded gas transport. Similar carbon degradation, i.e., corrosion and mass loss, is observed in MPLs [21]. Loss of hydrophobicity may also be attributed to disintegration of PTFE binders in GDLs, which is more significant on the anode side [112].

In addition to the layers themselves, GDL/MPL and CL/MPL interfaces have received a great deal of attention in recent years



**PEM Fuel Cells: Modeling, Fig. 2** A schematic of a single-channel PEMFC. Through-the-channel computational domain is shown in the red rectangle. Along-the-

channel computational domain is shown in the green rectangle (Reproduced from [82] with the permission of the author)

[33, 129–136]. Imperfect GDL/MPL and CL/MPL interfacial contact may result in not only additional ohmic resistance due to the loss of contact area [130] but also increased mass transport losses due to water accumulation at the interfacial gaps between the layers [131–134].

### Catalyst Layers

Catalyst layers are responsible for:

- Activation of reaction kinetics (see reaction kinetic models in section “[Electrochemical Reactions](#)”)
- Reactant transport (section “[Mass Transport in MEAs](#)”)
- Charge transport (section “[Charge Transport](#)”)
- Water transport between GDL and PEM (section “[Liquid Water in MEAs](#)”)

In order to achieve the functionality above, these layers are composed of three phases: an electronically conductive solid phase (carbon nanoparticles with attached catalyst particles, often platinum or platinum-based alloys); an ion conductive phase, also known as ionomer phase (usually a perfluorosulfonic acid ionomer (PFSA) dispersion of varying equivalent weight [137–139]); and a void (pore) phase. The solid phase in the catalyst layer includes the catalyst as well as the supporting particles which transfer the electrons. The catalyst serves the purpose of initiating the electrochemical reaction. During the past decade, a wide variety of catalysts have been developed including (a) Pt, (b) Pt-based alloys [140], (c) core-shell [141, 142], (d) non-precious metal catalysts [143–145], and (e) shape-controlled nanocrystals [146, 147]. Among them, Pt/C and Pt-based alloys (e.g., PtCo, PtNi) are used in commercial PEMFC products due to the maturity of these technologies [148, 149]. Reducing the amount of catalyst used in PEMFC is still critical to achieve lighter stack weight and lower PEMFCs cost to meet DOE targets [150, 151]. The catalyst layer thickness is optimized to achieve a high catalyst utilization, resulting in a thickness of 1 – 20  $\mu\text{m}$ . Experimental studies have shown that the optimal

electrolyte loading is between 30% and 40%; however, it varies depending on the catalyst loading and operating conditions [152–156].

The optimal catalyst layer design strikes a balance between the fractions of void space, electrolyte loading, and solid phase. It is more cost-efficient to use a numerical model to perform parametric studies on the catalyst layer compositions. For example, a couple of numerical optimization studies on electrolyte loading have been carried out over the past decades [24, 157–159].

Conceptual models of catalyst layers can be divided into three main categories depending on their complexity: interface models, macro-homogeneous models, and multiscale models. Interface, or zero-thickness, models assume infinitely thin catalyst layers, and reaction kinetics are implemented in the model as a boundary condition between GDL (or MPL) and PEM. It is considered that all properties of the catalyst layer are uniform, and its effects are negligible or are not of primary interest, e.g., when studying water or heat management in a complete cell [5, 160]. This approach cannot provide an adequate description of the cathode overpotential [161, 162] and is clearly not suitable for catalyst layer optimization.

In macro-homogeneous models, the catalyst layer is simulated as a heterogeneous porous structure made of a solid catalyst support (like carbon), a catalyst, and an electrolyte. Electrochemical reactions occur on the surface of the catalytic particles that are sitting on larger supporting particles. All reactants and products need therefore to travel through the catalyst layer to reach or leave those reaction sites. In cathode CLs, electrons are transported through the catalyst and support particles, protons through the ionomer, and oxygen travels through the void space. These transport processes are modeled using a volume-averaged approach with effective transport parameters obtained either by experiments or microscale simulations.

Models that account for both macro- and microstructure features in the catalyst layer are labeled here multiscale models. The key idea of multiscale models is to account not only for reactant and charge transport within the catalyst layer using a volume-averaged approach but also to

include some detail of the local transport processes occurring at the catalyst particle using an idealized model of the local processes. Then, the volume-averaged model and the local models are coupled via the reaction source term. Based on early scanning electron microscopy imaging, a local reaction model idealization was developed to account for observed mass transport losses in the microscale. It was assumed that the carbon particles formed large spherical aggregates of  $0.5 - 2 \mu\text{m}$ , and these carbon aggregates were idealized as a spherical porous catalyst with the pores inside the catalyst filled with ionomer [163–167]. Further refinements to this idealization included covering the agglomerates with ionomer thin films [44, 162, 168–170] and water films [171–173] to further enhance mass transport limitations, as well as replacing the ionomer in the pores by liquid water [174, 175]. Electrochemical reactions in agglomerates were then modeled similarly to those in porous electrodes [176]: oxygen is first transported through the gas pores (macroscale transport); it then dissolves and is transported through the electrolyte/water films around the agglomerate, diffuses through the agglomerate filling, and finally reaches the reaction sites. A detailed comparison of the suggested agglomerate structures and their effects on fuel cell performance can be found in [175].

Recent experimental [53, 177–179] and numerical [53, 180] studies suggest that catalyst support particles arrange into aggregates, but these aggregates are much smaller than those used in previous modeling work, i.e., in the range of 25–200 nm instead of 500–2000 nm [170], and that are only partially covered by an ionomer thin film [57, 181]. Further, given the heterogeneous surfaces in the catalyst layer, it is unlikely a uniform water film will cover these small aggregates. Once agglomerate sizes are reduced to those observed experimentally, bulk ionomer transport values no longer can explain the decrease in performance observed experimentally in conventional and particularly low loading electrodes [18, 27, 49, 182, 183]. Oxygen transport measurements through ionomer thin films supported on platinum [182, 183] and microscale simulation results [18] show negligible local

transport limitations in the gas phase suggesting that transport through the ionomer covering the catalyst particles is the key parameter limiting performance at the local reaction site. If this is the case, a more realistic idealization at the local scale would be the use of a single particle (30–70 nm [177]) or several particles (100–150 nm [178]) covered by an ionomer film with transport properties that are different from those from bulk ionomer, as highlighted by Owejan et al. [49] who stated that ionomer transport properties would have to be an order of magnitude lower to explain the performance degradation observed in low loading electrodes. A simple, yet more realistic, idealization of the catalyst layer is, for example, the ionomer covered catalyst particle (ICCP) model [175, 184] which considers a single catalyst carbon particle with smaller platinum particles evenly residing on its surface, all covered with a thin ionomer film [175]. A similar model by Hao et al. [158] takes into account oxygen transport through a water film that covers the ionomer surface. The ICCP model is provided as an example. This idealization might only be valid from some carbon supports, e.g., low surface area carbon such as Vulcan [179, 185] and it might not be valid for other types of carbon such as high surface area carbons. Local idealizations that are physically meaningful and yet computationally easy to implement and solve are still required. These should be obtained based on catalyst, catalyst support, and catalyst layer microstructure and composition.

The models discussed above are valid at beginning of life (BOL); however, the catalyst layer will undergo degradation during operation. Models are required to understand these processes. Even though such models are not included in this chapter, a basic overview on degradation mechanisms is provided for completeness in the next paragraphs. A number of experimental studies have highlighted two key mechanisms of catalyst layer degradation: (a) loss of the electrochemically active surface area (ECSA) due to platinum particle coarsening [21, 113–115, 117, 186, 187] and (b) carbon corrosion [120, 188–190]. Even though the exact Pt dissolution mechanism remains unclear [187], three pathways leading to

platinum particle coarsening have been identified: (1) Ostwald ripening, where small particles dissolve, diffuse, and redeposit into larger particles; (2) dissolution and re-precipitation into newly formed particles often inside the membrane; and (3) particle coalescence, where two particles in close proximity sinter to form one large particle with lower surface energy [21]. Pt degradation is often approximated with thermodynamic and kinetic models of the reactions of interest, such as platinum dissolution and oxide growth, together with a particle size distribution that evolves over time. Examples of kinetic models to study platinum degradation can be found in references [21, 113, 114, 118, 186, 191–196]. Very few attempts have been made to integrate Pt dissolution models in an MEA model. Franco and Tembeley [192] developed a 0D + 1D model of the whole MEA for modeling aging mechanisms in a PEMFC cathode.

Carbon corrosion kinetic models have also been developed, and, unlike platinum degradation models, they have been integrated into MEA models. Meyers and Darling [119] and Fuller and Gray [197] developed carbon degradation models in 1D and 2D, respectively, in which a Butler-Volmer kinetics model and a cathodic carbon oxidation reaction (in addition to the common PEMFC kinetics) were incorporated (Meyers and Darling [119] used Tafel kinetics for carbon corrosion). Although these models are able to quantify the effect of operating conditions on carbon corrosion, they neglect the instantaneous performance change due to degradation. Franco and Gerard [121] proposed an improved multiscale model (based on the model from [192]) that was capable of predicting the instantaneous performance feedback to carbon aging, e.g., cathode catalyst layer thinning, decrease of platinum surface area in it, and increase in CL-GDL contact resistance. With that model, it was possible to analyze the effect of catalyst layer composition and operating conditions on carbon mass loss during the fuel cell operation. The model by Franco and Gerard has several simplifying assumptions, such as isothermal conditions, single phase, and no coupling between carbon

corrosion and electrode structure; however, it is a starting point for the implementation of carbon corrosion into more sophisticated mathematical models. The kinetic mechanism of carbon corrosion was recently improved by Pandey et al. [120], who suggested several multistep reaction mechanisms at different zones around the platinum particle on the support.

### Polymer Electrolyte Membrane

Polymer electrolyte membranes used in PEMFCs usually belong to the perfluorosulfonic acid (PFSA) family of polymer membranes such as Nafion<sup>®</sup> and Aquivion<sup>®</sup>. Their key functions include:

- Acting as an electrical insulator separating anode and cathode sides of the cell
- Preventing reactant crossover between the two halves of the cell
- Acting as a protonic conductor to provide means for hydrogen protons to reach the cathode

An accurate representation of the membrane in a model is required for a good approximation of ohmic losses and water transport. Ohmic losses are associated with the protonic conductivity of the membrane, which depends on its hydration level. Efficient water management in the fuel cell is required to maintain the membrane and ionomer in the catalyst layers hydrated while removing excessive liquid water.

Most PEM mathematical models consider transport of only two components, protons and water (in liquid or sorbed form), neglecting any reactant crossover that can happen between the electrodes. In PEM fuel cells, crossover effects are usually insignificant; however, they must be taken into account if the model is designed for durability studies.

Proton transport is predominantly modeled with either Nernst-Planck [198–202] or simpler Ohm's law-based [40, 61, 63–71, 73, 76, 78, 203–209] equations, in which the transport parameters, e.g., protonic conductivity, depend on the membrane water content  $\lambda$ , a ratio of the



number of moles of sorbed water to the number of moles of sulfonic groups in the PEM. The simplest models assume that the membrane is always fully hydrated and exhibits its peak protonic conductivity.

An accurate representation of polymer electrolyte membrane requires a model that takes into account water transport, which can be approximated as a diffusion [1] or a hydraulic process [2, 201]. In the former, the membrane is assumed to be a homogeneous and nonporous material, in which water is transported by diffusion and electroosmotic drag. Hydraulic models, on the other hand, suggest that the membrane has two phases, the polymer phase and the pore phase that is filled with liquid water. These models also consider electroosmotic drag, but the other driving force is associated with a pressure gradient. Schlögl's equation is used in such models to compute the liquid water velocity [5]. Applicability of either of the two models might depend on the hydration level of the membrane. Diffusion models appear to be suitable for dry membranes, while hydraulic models might be applicable when the membrane is saturated [210, 211]. An approach that is valid for both cases is thus a better choice for fuel cell modeling. An example of such models can be found in [210, 212]. More recent models are designed in a way that allows them to couple protonic and water transport [213].

Constantly changing temperature and humidity conditions during the typical operation of a fuel cell lead to hygrothermal cycling loading of the membrane and directly affect its durability by significant mechanical stress development and pinhole and crack formation, as shown by viscoplastic, elastoplastic, and viscoelastic-plastic studies [123–125]. Polymer electrolyte membranes can degrade not only mechanically but also chemically through OH and H radical formation and side chain decomposition [126, 127]. Examples of proposed models for membrane degradation are provided in references [126, 127]. A detailed review on membrane properties and degradation mechanisms was recently provided by Kusoglu and Weber [139].

## General Models

### Mass Transport in Channels

Multicomponent gas transport in fuel cell channels is governed by mass, momentum, and energy conservation equations. Most mathematical models, with the exception of the generalized model by Kerkhof et al. [214, 215], formulate this problem using mass, momentum, and energy conservation equations for the gas mixture, and  $N - 1$  combined mass and momentum conservation equations for the  $N$  individual species [176, 216].

The mass conservation equation for the gas mixture is [217, 218]

$$\frac{\partial \rho}{\partial t} + \nabla \cdot (\rho \mathbf{v}) = S, \quad (1)$$

where  $\rho$  is the density of the gas mixture,  $t$  is time,  $\mathbf{v}$  is the mass-averaged velocity of the mixture, and  $S$  is a source term that combines the consumption and/or production of each species in the gas mixture. Due to the consumption of reactants, the density of the mixture will not be constant along the channel, and a compressible form of the mass conservation equation should be used [5, 160, 219]; however, several articles [32, 220–223] assume the density changes are negligible, and then, the incompressible form of the mass conservation is used.

The momentum conservation equation is the result of applying Newton's second law to a fluid particle in motion. For the gas mixture, it is given by

$$\frac{\partial}{\partial t}(\rho \mathbf{v}) + \nabla \cdot (\rho \mathbf{v} \otimes \mathbf{v}) = \nabla \cdot \hat{\boldsymbol{\tau}} + \rho \mathbf{g} + \mathbf{F}, \quad (2)$$

where the operator  $\otimes$  stands for the tensor product,  $\hat{\boldsymbol{\tau}}$  is the Cauchy stress tensor,  $\mathbf{g}$  is gravity vector field, and  $\mathbf{F}$  is a momentum source term, which is equal to zero for one species transport in gas channels. For a Newtonian fluid, the Cauchy stress tensor is given by

$$\hat{\boldsymbol{\tau}} = -(p - \lambda_b \varepsilon_v) \mathbf{I} + 2\mu \mathbf{D}, \quad (3)$$

where  $p$  is the pressure,  $\lambda_b$  is the bulk viscosity,  $\epsilon_v = \nabla \cdot \mathbf{v}$  is the volumetric strain rate,  $\mathbf{I}$  is the identity tensor,  $\mu$  is the dynamic viscosity, and  $\mathbf{D} = \Delta_s \mathbf{v} = \frac{1}{2}(\Delta \mathbf{v} + \Delta^T \mathbf{v})$  is the strain rate tensor. The viscosity of the mixture is given by Chapman-Enskog theory [176, 224, 225]:

$$\mu = \sum_{i=1}^N \frac{x_i \mu_i^0}{\sum_{j=1}^N x_j \xi_{ij}}, \quad (4)$$

where  $x_i$  is the molar fraction of species  $i$ ,  $\mu_i^0$  is the viscosity of a pure substance, and  $\xi$  is the Lennard-Zones interaction parameter [224]. If, in order to simplify the equations, the density of the fluid mixture is assumed constant, the Cauchy stress tensor for an incompressible fluid yields

$$\hat{\boldsymbol{\tau}} = -p\mathbf{I} + \mu(\nabla \mathbf{v} + \nabla^T \mathbf{v}). \quad (5)$$

The first term in Eq. (5) represents the hydrostatic pressure acting on the considered particle, whereas the latter indicates its rate of strain. Combination of Eqs. (1), (2), and (3) results in the Navier-Stokes equations for a compressible fluid.

The energy transport equation for an ideal gas is given by [176]

$$\hat{C}_p \frac{D(\rho T)}{Dt} = \nabla \cdot (k \nabla T) + \frac{Dp}{Dt} + Q, \quad (6)$$

where  $\hat{C}_p$  is the specific heat,  $T$  is the temperature,  $k$  is the thermal conductivity,  $p$  is the pressure, and  $Q$  is a volumetric heat source. However, the vast majority of models that analyze mass transport in fuel cell channels [32, 219–222, 226–234] consider the fluid to be isothermal, and therefore, this equation is not solved.

The transport of individual species is described using a combined mass and momentum conservation for the individual species. This equation can be formulated for each species  $i$  as

$$\frac{\partial \rho_i}{\partial t} + \nabla \cdot \hat{N}_i = S_i, \quad (7)$$

where  $\rho_i$  is the density of species  $i$ ,  $\hat{N}_i = \rho_i \mathbf{v}_i$  is the mass flux of species  $i$ ,  $\mathbf{v}_i$  is the velocity of species  $i$ ,

and  $S_i$  is the source term. Neglecting external body forces, the velocity, for all  $N - 1$  species can be obtained using the Maxwell-Stefan equations, i.e., [216]:

$$\nabla x_i + (x_i - \omega_i) \frac{\nabla p}{p} = - \sum_{i \neq j}^N \frac{x_i x_j}{\mathcal{D}_{ij}} (\mathbf{v}_i - \mathbf{v}_j), \quad (8)$$

where  $\omega_i$  is the mass fraction of species  $i$ , and  $\mathcal{D}_{ij}$  is the binary diffusion coefficient between species  $i$  and  $j$ . Maxwell-Stefan equations account for interactions between species. The model is capable of predicting reverse diffusion, osmotic diffusion, and diffusion barrier effect [216]. The density and velocity for each species can be obtained combining mass and momentum equations for the mixture,  $N - 1$  mass conservation, and Maxwell-Stefan (momentum conservation) equation with the following closure equations:

$$\rho = \sum_{i=1}^N \rho_i, \quad (9)$$

$$\mathbf{v} = \sum_{i=1}^N \omega_i \mathbf{v}_i, \quad (10)$$

$$x_i = \omega_i \frac{\sum_{k=1}^N M_k x_k}{M_i}, \quad (11)$$

where  $M_i$  is the molar mass of species  $i$  and  $\mathbf{v}$  is the mass-average velocity of the mixture. Assuming negligible pressure changes, Eq. (8) can be rearranged in order to obtain an explicit expression for the species mass fluxes such that [216]

$$\hat{N}_i = \sum_{j=1}^N \hat{D}_{ij} \nabla x_j, \quad (12)$$

where tensor  $\hat{D}$  is a function of molecular diffusion coefficients and composition of the mixture. For infinitely dilute species and negligible velocities, the equation above becomes Fick's law of diffusion, and Eq. (7) becomes Fick's second law of diffusion:

$$\frac{\partial \rho_i}{\partial t} = \nabla \cdot (\rho \mathcal{D}_{ij} \nabla \omega_i) + S_i \quad (13)$$

where  $i$  is the solute and  $j$  is the solvent. The binary diffusivity  $\mathcal{D}_{ij}$  can be estimated using Chapman-Enskog theory [176]:

$$\mathcal{D}_{ij} = \frac{188.29 T^{3/2}}{p A_{ij}^2 \Omega_D^*} \sqrt{\frac{1}{M_i} + \frac{1}{M_j}}, \quad (14)$$

where  $T$  is the temperature,  $A_{ij}$  is the collision diameter of a binary mixture,  $\Omega_D^*$  is a correction factor, and  $M_i$  is the molar mass of species  $i$ . The collision diameter  $A_{ij}$  is obtained as the average of the collision diameters  $A_i$  and  $A_j$  of species  $i$  and  $j$ :

$$A_{ij} = \frac{1}{2} (A_i + A_j). \quad (15)$$

The most common method for solving the set of Eqs. (1), (2), and (6) is the finite volume method [235], which has been implemented in many commercial numerical simulation packages, such as ANSYS Fluent [236], and STAR-CCM+ [237], as well as some open-source software, e.g., OpenFOAM [238]. An alternative approach is the finite element method [239], which is available in commercial packages such as COMSOL Multiphysics [240], and in open-source frameworks such as Kratos Multiphysics [241] and deal.II [242].

### Two-Phase Flow in Channels

In order to numerically reproduce two-phase flow in fuel cell channels, the model presented in section “[Mass Transport in Channels](#)” needs to be extended. There are two approaches in literature to study two-phase flow in fuel cell channels: analytical and numerical models. The former approach has been taken by several authors [243–245], but usually these models are an oversimplification of the phenomena and, therefore, are not considered here.

Numerical models use Navier-Stokes and continuity equations to model the mass transport of both gas and liquid phases. The main challenges of two-phase flow models are:

- Identification of the interface between both phases
- Taking into account the changes in the material properties (i.e., density and viscosity)
- Representation of the discontinuity of flow variables, i.e., velocity and pressure
- Modeling surface tension and wetting phenomena

The difference between models basically resides in the chosen kinematic framework. Fixed-grid models use the Eulerian formulation to model both air and water. However, they must include additional techniques to track or reconstruct the interface between the phases. Moving-mesh models use the Lagrangian formulation, allowing to track the air-water interface exactly. In those methods, the numerical domain has to be continuously re-meshed, which can be computationally expensive. An alternative to the previous models is a combination of fixed and moving grids, often referred to as embedded formulations, which have been extensively used in the fluid-structure interaction (FSI) community and have been proven to be a promising method for multi-fluid problems.

Fixed-grid models are the most used methods to solve two-phase problems. The most known fixed-grid method is the volume of fluid (VOF) method, which is a front-capturing technique. It was developed by Hirt and Nichols [246] and, together with Eqs. (1) and (2) for both gas and liquid, includes an additional equation for convecting the interface volume fraction variable  $C_k$ :

$$\frac{\partial}{\partial t} (C_k \rho_k) + \nabla \cdot (C_k \rho_k \mathbf{v}_k) = 0, \quad (16)$$

where  $\rho_k$  and  $\mathbf{v}_k$  are the density and the velocity of the fluid  $k$ , respectively. The volume fraction variable,  $C_k$ , takes the value 0 for the nodes outside the fluid  $k$ , 1 inside the fluid, and between 0 and 1 when the considered element contains the interface between two fluids. In the case of two fluids, therefore, only one equation needs to be solved and  $C_k$  is usually replaced by  $S$ . Piecewise linear interface calculation (PLIC) techniques [247, 248] are the most used nowadays and have been included in

commercial codes [249]. Figure 3 shows a possible distribution of obtained  $C_k$  values in a fixed mesh using the VOF. Cells with a  $C_k$  value between 0 and 1 contain the interface between the two phases, as shown on the right-hand side mesh after interface reconstruction using PLIC technique.

In order to include surface tension effects, an additional force term is added to the right-hand side of Eq. (2). The majority of existing commercial codes, such as ANSYS Fluent [236], COMSOL Multiphysics [240], or STAR-CCM+ [237], use the continuum surface force (CSF) model [250], in which the surface tension is evaluated at the historical time step of the transient problem (i.e., the model is explicit in time). The expression for the surface tension force is

$$\mathbf{f}_{st} = \gamma \rho \hat{\kappa} \frac{\nabla C_k}{0.5(\rho_l + \rho_g)}, \quad (17)$$

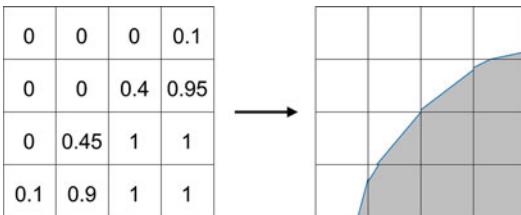
where  $\gamma$  is the surface tension coefficient;  $\rho_l$  and  $\rho_g$  are the densities of liquid and gas phases, respectively; and  $\hat{\kappa}$  is the curvature of the air-water interface defined as the divergence of the unit normal to the interface:

$$\hat{\kappa} = \nabla \cdot \frac{\mathbf{n}}{\|\mathbf{n}\|}, \quad (18)$$

where the normal vector is related to the volume fraction  $C_k$  through

$$\mathbf{n} = \nabla C_k. \quad (19)$$

An alternative to the CSF model is the continuum surface stress (CSS) model, developed by



**PEM Fuel Cells: Modeling, Fig 3** Schematic representation of obtained  $C_k$  values in a fixed mesh using the VOF and interface reconstruction using PLIC technique [247, 248]

Lafaurie et al. [251]. The surface tension term has the following expression:

$$\mathbf{f}_{st} = \nabla \cdot \left( \gamma \left( \|\nabla C_k\| \mathbf{I} - \frac{\nabla C_k \otimes \nabla C_k}{\|\nabla C_k\|} \right) \right), \quad (20)$$

where  $\otimes$  denotes the tensor product. The CSS model has several advantages over the CSF model: it is conservative and it does not require the computation of the curvature  $\hat{\kappa}$ . Moreover, it can be used to solve problems with variable surface tension, whereas CSF model cannot account for this effect.

Earlier studies of droplet dynamics in fuel cell channels include the works by Golpaygan and Ashgriz [226, 252] and Shirani and Masoomi [253]. In these studies, the contact line was fixed and no validation was provided. Other studies analyzed the problem in 3D [227–229, 254–257]; however, validation was again not provided, and the droplets were placed in the channel domain a priori without any particular criteria. The first studies using VOF that included experimental validation in their study were the works of Theodorakakos et al. [258] and Bazylak et al. [231].

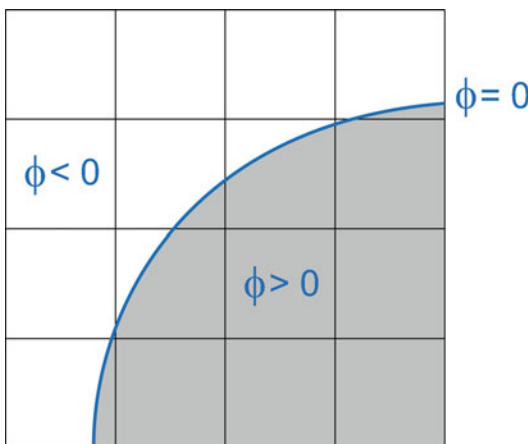
Le and Zhou [259] implemented a model in ANSYS Fluent that integrated a multicomponent, non-isothermal two-phase flow in the channel and GDL with a CL model including electrochemical reactions. The water distribution in the model was qualitatively validated by visual comparison to experimental results; however, no quantitative validation was provided regarding water distribution or cell performance, and the model could not predict water formation in the MEA and posterior emergence into the channels. Instead, they started their simulations with several droplets distributed along the serpentine channels. A review on the application of VOF to the PEMFC field was recently provided in [249].

The level set (LS) method is another fixed-grid technique that was presented by Osher and Sethian in 1988 [260] as a general technique to capture a moving interface. The basic idea of the level set method is to represent the interface by the zero level set of a smooth scalar function  $\phi(x)$  [261, 262]:

$$\phi(x) : \mathbb{R}^n \rightarrow \mathbb{R} \quad \Gamma = \{x : \phi(x) = 0\}. \quad (21)$$

The position of the interface is known implicitly by the nodal values of  $\phi$ : nodes with positive values are inside the fluid, whereas negative values mark nodes outside the fluid domain, as shown in Fig. 4. The position of the interface is then obtained by interpolation of nodal values of function  $\phi$ . The LS method has the advantage of being capable of handling topological changes and complex shapes of the interface. It may, however, give inaccurate results for normal vector and interface curvature, and it also fails at mass conservation. Additional techniques to alleviate these drawbacks have been reported in literature [263, 264–268].

The embedded formulation combines Lagrangian and Eulerian descriptions for the liquid and the gas phases, respectively. The method was proposed in [269] and [270] and was extended later for surface tension-dominated problems in [233] and [234]. The main advantage of this method is that it allows tracking of the interface between air and water, which is critical in surface tension-dominated problems, such as droplet shedding in fuel cell channels. The gas is modeled using the Eulerian formulation, which is the most natural approach, whereas the liquid phase is described using a Lagrangian formulation. The embedded model does not require mesh refinement around the interface to avoid numerical diffusion, contrary

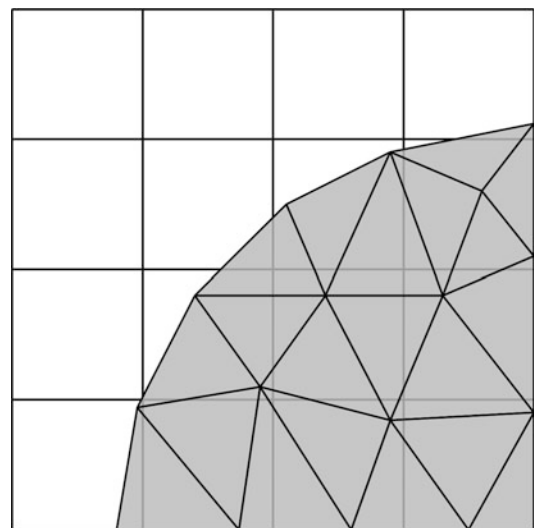


**PEM Fuel Cells: Modeling, Fig. 4** Schematic representation of function  $\phi(x)$  representing the interface in the LS method

to fixed-grid methods. The liquid domain has to be re-meshed in order to update its configuration. Since the water domain usually represents a small fraction of the total domain in fuel cell channels, however, the cost of re-meshing is reduced.

Figure 5 shows a schematic representation of the two meshes used in this method. Since the liquid domain is discretized using a moving mesh embedded into the fixed mesh of the gas domain, a coupling technique must be implemented. The overall solution strategy is:

1. Solve the problem in the moving mesh, i.e., liquid domain, obtaining velocity, and pressure.
2. Identify the position of the interface in the fixed mesh.
3. Project the velocity of the boundary nodes in the moving mesh onto the nodes of the fixed mesh representing the interface.
4. Use this velocity as a Dirichlet boundary condition to solve the problem in the fixed mesh, obtaining velocity and pressure.
5. Use the solution of the fixed mesh to project the whole stress onto the boundary of the moving mesh.
6. Repeat.



**PEM Fuel Cells: Modeling, Fig. 5** Schematic of the moving mesh, representing the liquid domain, overlapped with the fixed mesh, representing the gas domain, in the embedded method

Jarauta et al. [233] showed that the model can accurately describe wetting phenomena on rough surfaces and droplet oscillation in channels. Effects of surface energy and roughness were validated by showing good agreement between experimental and numerical predictions of advancing and receding contact angles of droplets of varying sizes on different substrates and inclined planes. It was also shown that sessile droplets on smooth hydrophobic surfaces, such as PTFE, are more prone to detachment than on rough surfaces, such as GDLs, where droplets experience large deformations before detachment due to the effect of contact line pinning. The model was also able to capture the recirculating pattern observed experimentally in sessile droplets subjected to an airflow [271].

### Mass Transport in MEAs

#### Gas Transport

In porous media, the mass and momentum transport equations of gaseous mixtures in Eqs. (1) and (2) need to be volume averaged [225] and a source term,

$$\mathbf{F} = -\left(\mu \hat{\mathbf{K}}^{-1} \varepsilon_v \mathbf{v} + \hat{\beta} \rho \varepsilon_v^2 |\mathbf{v}| \mathbf{v}\right), \quad (22)$$

representing solid-fluid interactions needs to be added to the momentum equation. In the equation above,  $\varepsilon_v$  is the porosity of the porous media,  $\hat{\mathbf{K}}$  is the permeability tensor,  $\mathbf{v}$  represents the interstitial (intrinsic) mass-averaged velocity vector of the mixture, and  $\hat{\beta}$  is the Forchheimer correction tensor. Equation (1) then results in [225]

$$\begin{aligned} \frac{D(\rho \mathbf{v})}{Dt} - \nabla \cdot \mu (\nabla \mathbf{v} + \nabla^T \mathbf{v}) + \nabla p + \nabla \cdot \left( \frac{2}{3} \lambda_b \varepsilon_v \right) \\ = \rho \mathbf{g} - \left( \mu \hat{\mathbf{K}}^{-1} \varepsilon_v \mathbf{v} + \hat{\beta} \rho \varepsilon_v^2 |\mathbf{v}| \mathbf{v} \right), \end{aligned} \quad (23)$$

where  $\rho$  is the phase (superficial)-averaged density and  $\mathbf{v}$  represents the interstitial (intrinsic) mass-averaged velocity vector of the mixture.

If inertia and viscous effects are assumed to be negligible in the porous media, along with gravity

effects, and assuming steady state, Eq. (23) becomes the Darcy-Forchheimer law of momentum transport in porous media:

$$\nabla p = -\left(\mu \hat{\mathbf{K}}^{-1} \varepsilon_v \mathbf{v} + \hat{\beta} \rho \varepsilon_v^2 |\mathbf{v}| \mathbf{v}\right). \quad (24)$$

If the porosity is higher than 0.6 [272], and if viscous effects cannot be neglected, Brinkman's equation must be used instead:

$$\begin{aligned} \nabla p = -\left(\mu \hat{\mathbf{K}}^{-1} \varepsilon_v \mathbf{v} + \hat{\beta} \rho \varepsilon_v^2 |\mathbf{v}| \mathbf{v}\right) \\ + \hat{\mu} \nabla^2 \varepsilon_v^2 \mathbf{v}, \end{aligned} \quad (25)$$

where  $\hat{\mu}$  is the effective diffusivity [272]. At low velocities, the second term in Eq. (24), can be neglected, giving Darcy's law [5, 32, 164]:

$$\nabla p = -\mu \hat{\mathbf{K}}^{-1} \varepsilon_v \mathbf{v}. \quad (26)$$

For the mass transport of individual species, one option relies on solving the volume-averaged mass and momentum mixture equations and mass and momentum conservation volume-averaged equations for  $N - 1$  of the considered species, i.e., Eqs. (7) and (8). As shown in section "Mass Transport in Channels," mass transport can be modelled using either Fick's law of diffusion or Maxwell-Stefan equations for multicomponent mass transport. An additional momentum conservation model for multicomponent mixtures that accounts for porous media-particle interactions is the dusty gas model (DGM) [224, 225, 273]:

$$\frac{1}{RT} \nabla p_i = \sum_{i=1}^N \frac{x_i N_j - x_j N_i}{D_{ij}^{\text{eff}}} - \frac{N_i}{D_i^K}, \quad (27)$$

where  $R$  is the universal gas constant,  $D_{ij}^{\text{eff}}$  is the effective molecular diffusivity between species  $i$  and  $j$ , and  $D_i^K$  is the Knudsen diffusion coefficient, which is discussed later in this section. Although this model is considered an extension of Maxwell-Stefan equations, Kerkhof [274] pointed out that the model takes viscous forces into account twice and, therefore, is incorrect. In his work, Kerkhof proposed the binary friction



model (BFM) based on Lightfoot's friction model [275]. The governing equation for the binary friction model is given by [224, 225, 274]

$$\frac{1}{RT} \nabla p_i = \sum_{i=1}^N \Phi_{ij} \frac{x_i N_j - x_j N_i}{D_{ij}^{\text{eff}}} - \left( D_i^K + \frac{\hat{K}}{\bar{\kappa}_i} \right)^{-1} N_i, \quad (28)$$

where the coefficient  $\Phi$  is equal to one in the continuum region and zero in Knudsen region [224], and  $\bar{\kappa}$  is the partial viscosity. Pant et al. [224] proposed a modified binary friction model (MBFM) in order to make it valid for mass transport in capillaries.

An alternative model to solving volume-averaged equations for the mixture and  $N - 1$  species is to use the model proposed by Kerkhof and Geboers [214, 215] for all species. In this case, the momentum conservation equation for each species is extended to include a term that accounts for the interaction between species:

$$\frac{D}{Dt} (\rho_i \mathbf{v}_i) = \nabla \cdot \hat{\boldsymbol{\tau}}_{ij} + \rho \mathbf{g} + \mathbf{F} + \mathbf{D}_i, \quad (29)$$

where the term  $\mathbf{D}_i$  is given by

$$\mathbf{D}_i = \sum_{i=1}^N \frac{p_i p_j}{\rho D_{ij}^{\text{eff}}} \hat{\mathbf{I}} (\mathbf{v}_j - \mathbf{v}_i), \quad (30)$$

and where  $\hat{\mathbf{I}}$  is the identity tensor. The term  $\mathbf{D}_i$  accounts for friction effects between species. The option of solving Eqs. (7) and (29) for each species was adopted in Refs. [225, 276]; however, this leads to a computationally intensive model [225]. To date, there is only one study in literature that includes an implementation of the model by Kerkhof and Geboers in porous media [225]. This is still an active area of research [224, 225, 277–280].

The vast majority of models that study mass transport of gaseous species in the porous media consider Navier-Stokes equations for the gas mixture, and then use Fick's law (Eq. 13) or Maxwell-Stefan (Eq. 8) models for the mass transport of

individual species. Quan et al. [256, 257] and Gurau et al. [32] modeled the transport of species in the porous media under a serpentine channel using the Navier-Stokes equations, including a Darcy source term for the momentum transport. A similar approach was taken by Le et al. [259, 281–283], but the transport of individual species was modeled using Fick's equation (7). Other studies have considered the same governing equations [4, 219–222]. Berning et al. [5, 160] also used Navier-Stokes equations for mass transport in the channel; however, they considered Darcy's law in the porous media together with Maxwell-Stefan equations for the transport of individual species.

In order to apply any of the aforementioned models in porous media, permeability and effective diffusion coefficients need to be obtained. Semiempirical correlations are commonly used to estimate these coefficients based on the morphology, porosity, and tortuosity of the material, where the expression constants are obtained by fitting the semiempirical results to experimental values.

A commonly used expression for gas permeability of GDLs is the Carman-Kozeny equation given as [284]

$$\hat{K} = \frac{d_f^2 \varepsilon_v^3}{16 k_{CK} (1 - \varepsilon_v^2)}, \quad (31)$$

where  $d_f$  is the fiber diameter, and  $k_{CK}$  is known as the Carman-Kozeny constant which is considered as a fitting parameter that is obtained experimentally. References [45, 285–294] provide the value of these empirical constants for several GDLs. The permeability of several MPL materials was also estimated in some of the references above, e.g., [292].

The effective diffusion coefficient of dry GDLs and dry CLs can also be estimated using appropriate semiempirical equations that relate effective molecular diffusivity to bulk molecular diffusivity, porosity, and tortuosity of the porous material. One commonly used method to estimate effective diffusion coefficients is using percolation theory, where the effective diffusion

coefficient,  $D_{ij}^{\text{eff}}$ , is computed based on the bulk diffusion coefficient,  $\mathcal{D}_{ij}$ , as [43, 170]

$$D_{ij}^{\text{eff}} = \mathcal{D}_{ij} \left( \frac{\varepsilon_v - \varepsilon_p}{1 - \varepsilon_p} \right)^\mu \Theta(\varepsilon_v - \varepsilon_p), \quad (32)$$

where  $\varepsilon_p$  is the so-called percolation threshold,  $\mu$  is an exponent that depends on the material structure, and  $\Theta(x)$  is the Heaviside step function. When  $\varepsilon_v < \varepsilon_p$ , no transport occurs.

An alternative to the previous approach is the tortuosity model, where the effective diffusion coefficient,  $D_{ij}^{\text{eff}}$ , is computed based on the bulk diffusion coefficient,  $D_{ij}$ , with the random walk method [295]:

$$D_{ij}^{\text{eff}} = \frac{\varepsilon_v}{\tau} D_{ij}, \quad (33)$$

where the tortuosity of the phase  $\tau$  is given by the generalized Archie's law [214, 296]:

$$\tau = \left( \frac{1 - \varepsilon_p}{\varepsilon_v - \varepsilon_p} \right)^\alpha. \quad (34)$$

The resulting equation for the effective diffusion coefficient is

$$D_{ij}^{\text{eff}} = \frac{\varepsilon_v}{\left( \frac{1 - \varepsilon_p}{\varepsilon_v - \varepsilon_p} \right)^\alpha} D_{ij}, \quad (35)$$

where the exponent  $\alpha$  depends on the material structure. These models can be used to describe transport in various structures depending on the parameter used from fibrous structures [284] to randomly distributed cylindrical and spherical particles [297]. For example, setting  $\varepsilon_p = 0$  results in Archie's law,  $\tau = \varepsilon^{-\alpha}$ , and two particular cases of Archie's law are the Bruggemann model for transport in porous media with randomly distributed cylindrical and spherical particles. Respectively, those correspond to  $\alpha = 1$  ( $\tau = \varepsilon^{-1}$ ) and  $\alpha = 0.5$  ( $\tau = \varepsilon^{-0.5}$ ) [297]. The Heaviside step function,  $\Theta(x)$ , may be used in Eq. (35) to limit transport for the case  $\varepsilon_v < \varepsilon_p$ . References [45, 48, 294, 298–301] have fitted some of these expressions to experimental data for different GDL, MPL, and CL materials and

provided estimates for the different empirical constants. Pore-scale numerical modeling can also be used to provide estimates of effective transport properties, e.g., [18, 302].

For porous media where the Knudsen number, i.e., the ratio between the mean free path of the molecules and the pore diameter, is large (approximately larger than 0.1), Knudsen diffusion should be considered in addition to bulk diffusion [30, 51, 303, 304]. In the GDL, the pore sizes are large enough that Knudsen diffusion does not need to be considered; however, it becomes more important in MPL and CLs, where pore sizes are smaller as recently demonstrated experimentally in the case of MPLs by Pant et al. [291] and Carrigy et al. [292]. The Knudsen diffusion coefficient of species  $\alpha$ ,  $D_\alpha^K$  can be estimated as

$$D_\alpha^K = \frac{2r_p}{3} \sqrt{\frac{8RT}{\pi M_\alpha}}, \quad (36)$$

where  $r_p$  is the pore radius. An effective pore radius for MPLs was estimated experimentally in [291, 292].

When the aforementioned equations are applied to model mass transport in fuel cells, source terms  $S_i$  must be included in order to account for mass variations due to the electrochemical reactions. For instance, if mass transport in the MEA is modeled using Fick's law, the governing equations for oxygen and water vapor molar fractions are

$$\varepsilon_v \frac{\partial c_{O_2}}{\partial t} - \nabla \cdot (c D_{O_2}^{\text{eff}} \nabla x_{O_2}) = S_{O_2} \quad (37)$$

$$\varepsilon_v \frac{\partial c_w}{\partial t} - \nabla \cdot (c D_w^{\text{eff}} \nabla x_w) = S_w. \quad (38)$$

Equation (38) needs to be modified if water sorption/desorption effects are taken into account (see section “Liquid Water in MEAs”). Under the assumption of impermeable membrane (no gas crossover), there is no need for additional equations for nitrogen or hydrogen molar fractions since they can be obtained as  $x_{N_2} = 1 - x_{O_2} - x_w$  in the cathode side and  $x_{H_2} = 1 - x_w$  in

the anode side, respectively. Table 1 includes the source terms for hydrogen (if needed), oxygen, and water transport equations (37) and (38), where  $i$  is the volumetric current density and  $F$  is Faraday’s constant. Source terms in Table 1 follow directly from the relation between current density and species flux discussed in section “Charge Transport” and the number of charged species (electrons) per mole of oxygen and water in the electrochemical reaction (73).

**Water Transport in the Polymer Electrolyte**

Water transport in the electrolyte is generally considered either in liquid or sorbed form. In the former approach, based on the works by Bernardi and Verbrugge [2, 201], the membrane is assumed to be a polymer matrix with pores filled with liquid water. The velocity of liquid water in the membrane is computed using the Schlögl equation [2, 5, 201, 305–307]:

$$\mathbf{v} = \frac{\hat{K}_\phi}{\mu} z_f c_f F \nabla \phi_m - \frac{\hat{K}_p}{\mu} \nabla p_l, \quad (39)$$

where  $\hat{K}_\phi$  is the electrokinetic permeability of the membrane,  $\mu$  is the viscosity of the pore fluid,  $z_f$  is the charge number of the sulfonic acid ions attached to the polymer backbone in the membrane,  $c_f$  is their concentration,  $\hat{K}_p$  is the hydraulic permeability of the membrane, and  $p_l$  is the hydraulic pressure. The driving forces considered in this model are associated with the electroosmosis and hydraulic pressure. Velocity (39) is used to describe convective mass transport in the membrane [2, 201]. This approach is generally used for fully humidified membranes, and diffusive transport of water is neglected [5].

A more common approach was proposed by Springer et al. [1], in which the membrane is assumed to be homogeneous and nonporous. In their model, water is transported in the sorbed form and is driven by electroosmosis and back diffusion. The flux of sorbed water due to electroosmosis is proportional to the proton flux in the membrane [1, 82, 304, 308, 309]:

$$N_{\lambda, \text{drag}} = -n_d \frac{\sigma_m^{\text{eff}}}{F} \nabla \phi_m, \quad (40)$$

where  $\sigma_m^{\text{eff}}$  and  $\phi_m$  are the conductivity of the electrolyte and its potential (see section “Charge Transport”) and  $n_d$  is the electroosmosis coefficient (the ratio of the flux of water molecules to the flux of protons in the absence of concentration gradients). In the PEM, the effective value is the bulk value. In the CL, the effective value is obtained using relations such as in Eq. (32) [43, 170]. The electroosmosis coefficient has been studied by various groups over the past decade, e.g., references [1, 310–312] to name but a few. Kusoglu and Weber [139] reviewed previous work and highlighted that most of them report electroosmosis values of 0.9 to 1.4 in vapor-equilibrated membranes ( $\lambda < 14$ ) and 2.5 to 2.9 in liquid water-equilibrated membranes ( $\lambda > 20$ ). Analysis of the results for vapor-equilibrated membranes also shows that, although some authors have reported a constant electroosmosis coefficient of approximately one, e.g., [310, 311], many others have observed a quasi-linear relationship between the number of sorbed water molecules and the electroosmosis coefficient, e.g., [1, 312–314], with a relationship that is similar to that proposed by Springer et al. [1] and given by

$$n_d = \frac{2.5\lambda}{22},$$

where  $\lambda$  is the sorbed water content in the membrane (in moles of sorbed water per number of moles of sulfonate groups  $\text{SO}_3^-$ ). The electroosmosis coefficient also depends on temperature and membrane equivalent weight and type and manufacturing method, e.g., casted or extruded [139].

**PEM Fuel Cells: Modeling, Table 1** Source terms for oxygen and water electrochemical reaction

Parameters	GDL	CCL	ACL	PEM
$S_{H_2}$	0	0	$-\frac{i}{2F}$	0
$S_{O_2}$	0	$-\frac{i}{4F}$	0	0
$S_w$	0	$\frac{i}{2F}$	0	0

The sorbed water flux due to back diffusion is defined as [1, 82, 304, 308, 309]

$$N_{\lambda, \text{diffusion}} = -\frac{\rho_{\text{dry}}}{EW} D_{\lambda}^{\text{eff}} \nabla \lambda, \quad (41)$$

where  $\rho_{\text{dry}}$  is the density of the dry ionomer and  $EW$  is its equivalent weight (in grams of the ionomer per mole of ionic group). The effective diffusion coefficient  $D_{\lambda}^{\text{eff}}$  again will be bulk in the PEM and an effective value in the CL. The bulk diffusion coefficient depends on  $\lambda$  and temperature. The exact functional form of  $D_{\lambda}^{\text{eff}}(\lambda, T)$  depends on the type of the ionomer and is obtained through fitting of experimental data. Examples of such relations for bulk sorbed water diffusivity in Nafion<sup>®</sup> can be found in [31, 315, 316] to name but a few. Zhou et al. recently implemented the latter expressions in a full MEA model in order to study their effect on water transport in Ref. [317]. Kusoglu and Weber [139] provided a detailed review of the water diffusion coefficients reported in the literature.

Under non-isothermal conditions, the sorbed water is also transported due to variations in temperature. This process is called thermo-osmosis [130, 318, 319], and the corresponding flux of the sorbed water is [304, 308, 309]

$$N_{\lambda, \text{thermo-osmosis}} = -\frac{D_T^{\text{eff}}}{M_{H_2O}} \nabla T, \quad (42)$$

where  $D_T^{\text{eff}}$  is the effective thermo-osmosis diffusion coefficient, the values of which vary between the materials [130, 318, 319].

The total sorbed water flux in the electrolyte considering all three modes of transport is given by

$$\begin{aligned} N_{\lambda} &= N_{\lambda, \text{drag}} + N_{\lambda, \text{diffusion}} \\ &\quad + N_{\lambda, \text{thermo-osmosis}} \\ &= -n_d \frac{\sigma_m^{\text{eff}}}{F} \nabla \phi_m - \frac{\rho_{\text{dry}}}{EW} D_{\lambda}^{\text{eff}} \nabla \lambda \\ &\quad - \frac{D_T^{\text{eff}}}{M_{H_2O}} \nabla T, \end{aligned} \quad (43)$$

where in the PEM the bulk values should be used. Thus, the mass conservation equation for sorbed water takes the following form:

$$\begin{aligned} \varepsilon_N \frac{\rho_{\text{dry}}}{EW} \frac{\partial \lambda}{\partial t} - \\ \nabla \cdot \left( n_d \frac{\sigma_m^{\text{eff}}}{F} \nabla \phi_m + \frac{\rho_{\text{dry}}}{EW} D_{\lambda}^{\text{eff}} \nabla \lambda + \frac{D_T^{\text{eff}}}{M_{H_2O}} \nabla T \right) \\ = S_{\lambda}, \end{aligned} \quad (44)$$

where the transient term is present in the form natural for the diffusion type (Eq. (44)) and  $\varepsilon_N$  is the volume fraction of ionomer in the CL and  $\varepsilon_N = 1$  in the PEM. The complexity of the resulting model depends on how many driving forces are considered in Eq. (44). The source term,  $S_{\lambda}$ , is given by [82]

$$S_{\lambda} = \begin{cases} k_t \frac{\rho_{\text{dry}}}{EW} (\lambda_{\text{eq}} - \lambda) & \text{in CLs,} \\ 0 & \text{everywhere else,} \end{cases} \quad (45)$$

where  $k_t$  is a time constant and  $\lambda_{\text{eq}}$  is the equilibrium value of  $\lambda$  in the electrolyte determined by a sorption isotherm [320]. In general,  $\lambda_{\text{eq}}$  depends on the equivalent weight of the ionomer, water vapor mole fraction, and temperature [139]. Experimentally fitted  $\lambda_{\text{eq}}$  can be obtained in the form  $\lambda_{\text{eq}}(a_w, T)$  [321], where the activity of water is defined as

$$a_w = \frac{p_{x_{H_2O}}}{p_{\text{sat}}}.$$

Since water sorption/desorption affects water vapor transport,  $S_{\lambda}$  is also included in Eq. (38) so that it is modified into

$$\varepsilon_v \frac{\partial c_w}{\partial t} - \nabla \cdot (c D_w \nabla x_w) = S_w - S_{\lambda}.$$

For  $k_t < 10^{-2} \text{s}^{-1}$ ,  $S_{\lambda}$  becomes negligible compared to  $S_w$ , and the coupling between water vapor transport and water sorption/desorption is weak [82]. The time required for  $\lambda$  to reach its

equilibrium value is normally of order  $100 - 1,000 \text{ s}^{-1}$  [322]. In steady-state simulations, a value of 10,000 may be used to ensure strong coupling between the equations [82, 308]. Because of the coupling, water vapor will either be sorbed into the ionomer from the pore space or desorbed from the ionomer depending on the relative humidity and temperature conditions.

The effective electrolyte protonic conductivity  $\sigma_m^{\text{eff}}$  used in the sorbed water transport equation (44) and electrolyte potential transport equation (see section “Charge Transport”) is the bulk value and in the CL is an effective value. In general, the bulk conductivity depends on the water content and temperature, as it was discussed in section “Polymer Electrolyte Membrane.” The functional form  $\sigma_m^{\text{eff}}(a_w, T)$  or  $\sigma_m^{\text{eff}}(\lambda, T)$  is obtained experimentally and can be found in [308].

#### Liquid Water in MEAs

Water management is critical to achieving higher current density and improving the durability of fuel cells, especially under cold and wet operating conditions. A large number of models have been proposed in the fuel cell literature during the past decades to study water management [323–331]. Based on these studies, it was identified that the key to appropriate fuel cell water management is to strike a balance between membrane dehydration and water accumulation in the electrode, also known as flooding. When the cell is operating with dry gases, keeping the electrolyte in the PEM and CLs sufficiently hydrated is critical to maintaining good ionic conductivity and reducing ohmic losses. During high relative humidity and high current density operation, removing the excess water generated in the electrodes is critical to avoid water accumulation and achieve high performance.

Liquid water is produced at the cathode CL. At low relative humidity, the generated liquid water evaporates and is transported to the channels in vapor phase. If the electrode gas mixture is saturated with water vapor, liquid water accumulates in the electrode. This leads to a sharp drop in performance which limits the fuel cell maximum current and power densities. When a sufficient

liquid pressure is available to flow through the CL, MPL, and GDL, liquid water removed from the MEA will reach the gas flow channels and negatively affect also the reactant flow as discussed in previous sections.

Natarajan et al. [332] proposed one of the first two-phase cathode models in the literature. Wang et al. [333] also introduced a two-phase model that included a threshold current density to distinguish the single- and two-phase regimes. Weber and Newman proposed the first structure-based two-phase flow model [330]. It included mass and momentum conservation equations for gas and liquid transport in the MEA, and it used a pore size distribution to estimate transport properties. The models above, however, did not account for thermal effects. Thermal effects were accounted for in more recent two-phase models, allowing to study the heat pipe effect as well as phase change-induced flow [209, 304, 323].

Two-phase flow transport in the porous media of fuel cells has usually been studied using a volume-averaged approach at the MEA level [209, 304, 323, 330, 333]. This approach is based on the assumption that there exists a representative elementary volume (REV) in the porous medium where hydrophilic and hydrophobic pore networks are homogeneous. In general, pore-scale models, such as full morphology and pore network models (discussed in the following sections), have been mainly used to study two-phase flow in the GDL, while volume-averaged models incorporating information on the pore size distribution have been used in the MPL and CL. Such choice is appropriate given the length scales in each layer. Conventional CLs and MPLs are  $5 - 15 \mu\text{m}$  and  $40 - 80 \mu\text{m}$  in thickness, respectively. CLs contain pores that are  $5 - 210 \text{ nm}$ , with most pores in the range of  $20 - 80 \text{ nm}$  [18, 29, 334, 335], and MPLs contain pores that are smaller than  $1 \mu\text{m}$  [336]. Given the pore size and layer thickness, there are hundreds of pores across any CL and MPL, and, therefore, an REV is likely to exist. In this case, volume-averaged models are appropriate, and effective properties, such as interfacial area, effective diffusivity, and relative permeability, are likely well

approximated by using statistical theory of heterogeneous media. In the GDL, the layer thickness is 150 – 400  $\mu\text{m}$  and the pore size is between 5 and 60  $\mu\text{m}$ . Due to the size of the pores, an REV for the GDL might be of the same size or even larger than the GDL thickness; thereby, a volume-averaged model should not be used [337]. The use of an REV for the GDL can only be justified on the basis of averaging along the channel to create a two-dimensional model. The use of pore-scale models is more appropriate, however, and the integration of volume-averaged MPL and CL models with a pore-scale model has been recently performed by Zenyuk et al. [338].

The effect of liquid water can be studied by reducing the void fraction available for gas transport in porous layers; however, a mechanism is required in order to estimate the percentage of pores that will be filled with water. In the crudest approximations, the volume fraction is treated as a fitting parameter. Thus, the only effect of liquid water is to decrease the mobility of reactants to diffuse to the electrochemically active site [339, 340]. Most mathematical models in the literature however, assume that capillary pressure is the driving force for pore filling in porous media, an assumption that is justified based on nondimensional analysis that shows that surface tension effects are orders of magnitude larger than gravitational, inertial, and viscous effects. To validate this assumption, Bond [341, 342] (Bo), Weber [342] (We), and capillary [343] (Ca) numbers for GDL and CL are summarized in Table 2; see Ref. [308] for more details. Table 2 clearly shows that surface tension effects are at least three orders of magnitude larger than any of the other effects discussed above.

The transport equations described in section “Gas Transport” are solved for each phase in order to estimate capillary pressure [5, 201, 330]. Assuming the Reynolds number in the porous media for gas and liquid phases is small, i.e., less than one, and using further simplifications, a mass conservation equation, (1), and Darcy’s law for momentum transport, (26), can be obtained for each phase. Two approaches are proposed in literature as the two-phase transport governing equations in the MEA: (a) saturation-based and (b) capillary-based models.

**PEM Fuel Cells: Modeling, Table 2** Estimated dimensionless numbers for an operating PEMFC

Dimensionless characteristic length	Physical meaning	GDL 10 $\mu\text{m}$	CL 0.1 $\mu\text{m}$
Bond	Gravitational force to surface tension	$10^{-3}$	$10^{-7}$
Weber	Inertial force to surface tension	$10^{-10}$	$10^{-12}$
Capillary	Viscous force to surface tension	$10^{-7}$	$10^{-7}$

In saturation-based models, gas pressure changes are assumed negligible, and capillary pressure and saturation are related by an empirical function known as the Leverett J-function. Using these assumptions, Darcy’s law equation for the liquid phase is reformulated as a function of saturation’s, instead of capillary pressure,  $p_c$ , and the former is used as the solution variable. The governing equation can then be expressed as

$$\frac{\partial(\varepsilon_v S \rho_l)}{\partial t} - \nabla \cdot \left( \frac{\rho_l k_{lr}}{\mu_l} \left( \frac{\partial p_c}{\partial s} \right) \nabla s \right) = S_{\text{liquid}}, \quad (46)$$

where  $\varepsilon_v$  is the porosity,  $k_{lr}$  is the effective permeability in liquid phase,  $p_c$  is the capillary pressure, and  $s$  is the saturation variable. Note that in this expression, the interstitial density is used instead of the superficial density in Eq. (1), and the permeability tensor is assumed isotropic. This method is generally used in petroleum engineering applications, particularly for measuring the one-dimensional steady-state transport on packed sand [344]. The saturation approach was first adopted by Natarajan and Nguyen [332] in studying the liquid water transport in the cathode. Since then, a great number of saturation-based models have been proposed in literature to study liquid water transport in the MEA [327, 345–350].

One of the primary concerns of using saturation-based models is that, in most cases, a continuous function is used to approximate the saturation variable even though saturation is likely to be discontinuous at the interface between porous layers, e.g., at MPL-GDL interface, due to the different



wettabilities and pore sizes. Also, the approach is usually limited to fully humidified conditions as the specification of a finite saturation at the GDL/channel boundary implies that some liquid water should already be present in the channel. Even if a value of zero saturation is used, liquid water can flow from the channel to the MEA.

Capillary-based models solve mass and momentum conservation equations for liquid water and gas mixture pressure separately and relate them to saturation by means of the capillary pressure and a set of closure equations using microstructural information [327–331, 351]. The input parameters for the microstructural model are the pore size distribution (PSD) and the wettability of the porous material. Based on this information, a bundle of rejoined capillary model is used to estimate dry and wet transport properties, e.g., liquid and gas permeability and relative permeability. The advantage of this method is that it provides an idealized microscale model that can be used to perform parametric studies in order to find the optimized porous layer design. The use of gas and liquid pressure enforces continuity in the pressure fields, while saturation is allowed to vary at the interface between materials.

The first capillary-based models that proposed the use of a PSD assumed either a hydrophilic or hydrophobic pore network for the whole material [329, 330]. More recently, researchers have introduced a variety of mixed wettability models based on experimental observations proposing that a network of hydrophilic and hydrophobic pores might coexist in fuel cell materials such as GDLs and CLs [352, 353]. Weber et al. [323, 330], Mateo [351], and Mulone et al. [331] have treated hydrophilic (HI) and hydrophobic (HO) pore networks separately either by introducing a continuous wettability distribution [323] or by studying two independent networks [330, 331, 351]. In all previous work, however, due to the difficulty of implementation of

a PSD model in multidimensional computational fluid dynamic solvers, the PSD model was either not integrated in a complete MEA model [329, 331, 351] or was integrated only in a one-dimensional model [323, 330]. Recently, Zhou et al. [304] introduced a multidimensional, two-phase, capillary-based model. The model was shown to be suitable to study fuel cell operation under both dry and wet conditions as well as to predict water distribution in the MEA and water fluxes at the GDL/channel boundaries.

The governing equations for the capillary-based model, which solve for liquid and total gas pressure, respectively, are as follows:

$$\frac{\partial(\rho_g \varepsilon_g)}{\partial t} - \nabla \cdot \left( \frac{\rho_g k_{gr}(p_c)}{\mu_g} \nabla p_g \right) = S_{\text{gas}}, \quad (47)$$

$$\frac{\partial(\rho_l \varepsilon_l)}{\partial t} - \nabla \cdot \left( \frac{\rho_l k_{lr}(p_c)}{\mu_l} \nabla p_l \right) = S_{\text{liquid}}, \quad (48)$$

where  $\rho$  is the interstitial (phase) density,  $\varepsilon_k$  is the volume fraction of phase  $k$ , and subscripts  $g$  and  $l$  refer to gas and liquid phases, respectively. In this entry, the capillary pressure is defined as

$$p_c = p_l - p_g. \quad (49)$$

The corresponding source terms are listed in Table 3. The source term for condensation and evaporation is described by

$$S_{H_2O(\text{evap/cond})} = k_{e/c} a_{lv} \left( \frac{p_v - p_{\text{sat}}(p_c, T)}{p_{\text{sat}}(p_c, T)} \right), \quad (50)$$

where  $k_{e/c}$  is the aerial evaporation or condensation rate constant,  $a_{lv}$  is the liquid-gas interfacial surface area per unit volume, and  $p_v$  is the vapor

**PEM Fuel Cells: Modeling, Table 3** Source terms for two-phase transport

Parameters	GDL, MPL	CCL	ACL	PEM
$S_{\text{gas}}$	$-M_{H_2O} S_{H_2O}(\text{evap/cond})$	$-M_{H_2O} S_{H_2O}(\text{evap/cond}) + \frac{i}{4F} M_{O_2} + S_i M_{H_2O}$	$-M_{H_2O} S_{H_2O}(\text{evap/cond}) + \frac{i}{2F} M_{H_2} + S_i M_{H_2O}$	0
$S_{\text{liquid}}$	$M_{H_2O} S_{H_2O}(\text{evap/cond})$	$M_{H_2O} S_{H_2O}(\text{evap/cond}) - \frac{i}{2F} M_{H_2O}$	$M_{H_2O} S_{H_2O}(\text{evap/cond})$	0

pressure. The effective saturation vapor pressure in a capillary,  $p_{\text{sat}}(p_c, T)$ , is determined by considering the Kelvin effect and the Young-Laplace equation as follows:

$$p_{\text{sat}}(p_c, T) = p_{\text{sat}}(T) \exp\left(\frac{p_c M_G}{RT \rho_g}\right), \quad (51)$$

where  $p_{\text{sat}}$  is the uncorrected saturated vapor pressure of water, and  $M_G$  is the molar mass of water.

The GDL and MPL absolute permeabilities have been reported by various studies [45, 285, 286, 288, 291, 294, 354–356]. It has been shown that the absolute permeability depends on many factors such as level of compression, type of carbon black, percentage of PTFE content, and pore size distribution. The typical GDL permeability falls mostly within the range of  $10^{-12}$ – $10^{-10}$  m<sup>2</sup>. The MPL permeability is usually extrapolated from the measured permeabilities of the GDL and the GDL-MPL assembly, and the estimated value is around  $10^{-13}$  m<sup>2</sup>. The measurement of CL absolute permeability is not yet feasible as the layer is too thin to conduct the experiment.

Measurements of GDL relative permeability have not received much attention during the past decades. Air relative permeabilities were reported by Nguyen et al. [357] and Koido et al. [358]. Relative liquid water permeability was measured by Hussaini et al. [359] and Sole [360]. Alternatively, numerical models, such as pore size distribution [304] and pore network model [361] can be used to estimate the relative permeability with a reasonable agreement with the experimental data.

Determining an appropriate liquid water boundary condition at the GDL/channel interface is important to any two-phase flow model. Zero flux [326, 328, 362] and fixed saturation values are the most commonly used boundary conditions [363]. These boundary conditions either force all water to be vaporized in the MEA or impose the existence of liquid water at the GDL/channel boundary. Their applicability is therefore limited, and a more general boundary condition is needed. Zenyuk et al. [209] recently introduced a step function to switch from a no-flux boundary condition to a Dirichlet condition for liquid pressure.

After reaching a breakthrough pressure, the liquid pressure is considered to be constant. Alternatively, a dynamic boundary condition could be used where once the capillary pressure reaches the given breakthrough pressure, a flux proportional to the liquid pressure is applied [304], i.e.,

$$\begin{aligned} \rho_l \mathbf{v}_l \cdot \mathbf{n} &= -\left(\frac{\rho_l k_{rl}}{\mu_l} \nabla p_l\right) \cdot \mathbf{n} \\ &= k \left(\frac{p_l - p_{l, \text{channel}}}{p_0}\right) g(p_l), \end{aligned} \quad (52)$$

where  $k$  is an unknown proportionality constant that controls the flux of water as a function of the liquid pressure,  $p_{l, \text{channel}}$  is the liquid pressure at the channel-GDL interface, and  $p_0$  is a dimensionless factor. Function  $g(p_l)$  in Eq. (52) is given by

$$g(p_l) = \left[ \frac{\tanh((p_l - p_{l, \text{channel}})/p_0) + 1}{2} \right] \theta(p_l - p_{\text{BT}}), \quad (53)$$

where  $p_{\text{BT}}$  is the liquid breakthrough pressure and  $\theta(p_l - p_{\text{BT}})$  is a step function, i.e., it is set to be zero until  $p_l > p_{\text{BT}}$  is satisfied in the Newton solver loop and not modified further in order to maintain numerical stability. Its validity should be confirmed during post-processing by making sure that the liquid water flux remains positive. In order to prevent liquid water from entering the MEA from the channel, once the step function is set to be one, a tangent function  $\tanh((p_l - p_{l, \text{channel}})/p_0)$  is used, where  $p_{l, \text{channel}}$  is set to be atmospheric pressure considering the droplet volume is large enough so that Laplace pressure is negligible, and  $p_0$  should reflect the channel conditions.

### Charge Transport

In general, transport of charged species in an electrolyte is described by either concentrated solution or dilute solution models. The former are more general but require more information on the interactions between the different species in the solution [33, 198]. Multicomponent diffusion of charged species is generally described by [198]

$$c_i \nabla \hat{\mu}_i = \sum_{j \neq i} K_{ij} (\mathbf{v}_j - \mathbf{v}_i), \quad (54)$$

which is similar to the Maxwell-Stefan equation (8). Here,  $\hat{\mu}_i$  is the electrochemical potential of species,  $i$ ,  $K_{ij}$  are friction coefficients, and  $\mathbf{v}_i$  is the superficial velocity of species  $i$ . The term  $-c_i \hat{\mu}_i$  in Eq. (54) is a volumetric driving force causing the motion of species  $i$ ; the term  $K_{ij}(\mathbf{v}_j - \mathbf{v}_i)$  is the balancing volumetric force of species  $j$  acting on species  $i$  in their relative motion. Coefficients  $K_{ij}$  can be related to the binary interaction coefficients  $D_{ij}$  with [198, 364]

$$K_{ij} = \frac{RTc_i c_j}{cD_{ij}}. \quad (55)$$

Assuming that species  $i$  is minor and the total concentration  $c_{\text{tot}}$  is approximately equal to the solvent concentration  $c_0$ , one can use Eq. (55) and rewrite Eq. (54) as

$$c_i \nabla \hat{\mu}_i = \frac{RT}{D_{i0}} (c_i \mathbf{v}_0 - c_i \mathbf{v}_i). \quad (56)$$

Then, the molar flux of species  $i$  is given by

$$N_i = c_i \mathbf{v}_i = -\frac{D_{i0}}{RT} c_i \nabla \hat{\mu}_i + c_i \mathbf{v}_0. \quad (57)$$

Further, if the solution is diluted, the species-solvent interaction coefficients  $D_{i0}$  can be replaced with the diffusion coefficients  $D_i$ , and the solvent velocity  $\mathbf{v}_0$  can be approximated by the bulk velocity  $\mathbf{v}$ :

$$N_i = -\frac{D_i}{RT} c_i \nabla \hat{\mu}_i + c_i \mathbf{v}. \quad (58)$$

Equation (57) can then be written in the form of the Nernst-Planck equation [198–202]:

$$N_i = -z_i \frac{F}{RT} c_i D_i \nabla \phi - D_i \nabla c_i + c_i \mathbf{v}. \quad (59)$$

Note that, in the case of infinitely dilute solutions, the first term in the right-hand side of Eq. (59) is sometimes written in terms of the

mobility  $u_i$  of species  $i$  instead of its diffusivity using the Nernst-Einstein equation [33, 198, 200]:

$$D_i = RTu_i.$$

Multiplying Eq. (59) by  $z_i F$ , summing over species  $i$ , and using the definition of current density, i.e.,

$$\mathbf{j} = F \sum_i z_i N_i,$$

and conductivity,  $\sigma$ ,

$$\sigma = F^2 \sum_i z_i^2 c_i u_i = F^2 \sum_i z_i^2 c_i \frac{D_i}{RT},$$

the following expression for the current density is obtained:

$$\mathbf{j} = -\sigma \nabla \phi - F \sum_i z_i D_i \nabla c_i. \quad (60)$$

The first term in Eq. (60) is the Ohmic current component of  $\mathbf{j}$ , and the second term is the diffusion current. Since sulfonic acid groups are immovable in the solid electrolytes used in PEMFCs, e.g., Nafion, and assuming the only charged species being transported in the membrane is protons, Eq. (60) simplifies to Ohm's law:

$$\mathbf{j} = -\sigma \nabla \phi. \quad (61)$$

once electroneutrality is assumed, i.e.,

$$\sum_i z_i c_i = 0.$$

Equation (61) is commonly used in the area of fuel cell modeling to relate current density and variation in the potential, although its applicability is limited by the assumptions listed above. In cases where ion transport across the membrane is of interest, i.e., in cases when Pt redeposition is to be studied, Eq. (60) should be used. Finally, if the species of interest is not minor in the solution, then the general model (54) and (55) should be used. In hydrogen PEM fuel cells, there are mainly two types of charged species that are

transported, electrons in the solid phase of GDLs and CLs (and in BPPs) and protons in the PEM and in the ionomer in CLs, and therefore two current densities,  $\mathbf{j}_p$  and  $\mathbf{j}_e$ . They are equal to each other in absolute value and have opposite signs:  $\mathbf{j}_p = -\mathbf{j}_e$ . Each of them is normally assumed to obey Ohm's law (61)

$$\mathbf{j}_p = -\sigma_m^{\text{eff}} \nabla \phi_m,$$

$$\mathbf{j}_e = -\sigma_s^{\text{eff}} \nabla \phi_s,$$

where effective conductivity depends on the structure and composition of the medium and is approximated using the percolation or the random walk method (see section "Mass Transport in MEAs" for details).

The typical effective electrical conductivity values for PEMFC GDLs are in the range of 80 – 200 S/cm in the in-plane direction [285, 365, 366], reaching the higher of the reported values when MPL is dispersed on the side of the diffusion layer [285], and in the range 3 – 70 S/cm in the through-plane direction [285, 365, 366]. In the catalyst layers, effective electrical conductivities are reported to be between 0.1 and 3.0 S/cm for a wide range of solid-phase volume fractions from 0.1 to 0.8 [367, 368].

The bulk proton conductivity in the ionomer phase is a function of temperature and water content [1, 34, 139, 304, 369–371]. The water content, which depends on relative humidity and temperature, can be determined using Eq. (44). Numerical models used to estimate bulk proton conductivity have been proposed by several researchers [1, 210, 372]. One example of the most commonly used model for estimating the bulk proton conductivity is Springer's model [1]:

$$\sigma_m = 0.005139\lambda - 0.00326\exp(1268.0(1.0/303.0 - 1.0/T)). \quad (62)$$

Kusoglu and Weber [139] recently compiled a comprehensive list of the proton conductivity measurements for various PEM types at varying relative humidity and temperature.

The effective proton conductivity in the catalyst layer is of the order  $10^{-4}$ – $10^{-1}$  S/cm [58, 373]. There are a few models proposed in the literature to compute the effective proton conductivity in the catalyst layer such as Bruggeman method, percolation theory, and the correlation proposed by Iden et al. using experiments with a pseudo-catalyst layer on a hydrogen pump [371].

In order to estimate the phase potential, a charge conservation equation is used:

$$\frac{\partial \hat{\rho}}{\partial t} + \nabla \cdot \mathbf{j} = R,$$

where  $\hat{\rho}$  is the free charge density and  $R$  is a source/sink term due to electrochemical reactions and charge redistribution as discussed later in this section. For convenience, models are usually constructed considering the volumetric electronic current density  $i = \nabla \cdot \mathbf{j}_e$ , A/cm<sup>3</sup>. Equations modeling charge transport in PEMFCs are predominantly used in their steady-state form even though other effects may be considered in transient [40, 61, 63–71, 73, 76, 78, 203–209]. This leads to the two equations describing the steady-state transport of charge:

$$-\nabla \cdot (\sigma_m^{\text{eff}} \nabla \phi_m) = R_{H^+}, \quad (63)$$

$$-\nabla \cdot (\sigma_s^{\text{eff}} \nabla \phi_s) = R_{e^-}, \quad (64)$$

where  $R_{H^+}$  and  $R_{e^-}$  are reaction source terms and are defined as

$$R_{H^+} = \begin{cases} -i & \text{in cathode CL,} \\ i & \text{in anode CL,} \\ 0 & \text{everywhere else,} \end{cases} \quad (65)$$

and

$$R_{e^-} = \begin{cases} i & \text{in cathode CL,} \\ -i & \text{in anode CL,} \\ 0 & \text{everywhere else.} \end{cases} \quad (66)$$

The interface between the solid phase and the surrounding electrolyte acts as a capacitor. At a given potential, there exists charge  $q_1$  at the electrode surface and charge  $q_2 = -q_1$  accumulated

as a thin layer in the electrolyte at the interface with the electrode. Such interfacial distribution of charged species and oriented dipoles is called the electrical double layer. A change in the potential causes redistribution of charge at the interface, which gives rise to the transient charging (or capacitive) current.

When no capacitive effects are taken into account, the total volumetric current density,  $i$ , is equal to  $i_f$ , the faradaic current resulting from electrochemical reactions, which can be computed using Eq. (81) or (94) using the kinetic models (described in section “Electrochemical Reactions”). In the presence of a double layer with volumetric capacitance  $C_{dl}$ , F/cm<sup>3</sup>, total current density consists of faradaic and charging current densities [199]:

$$i = i_f + i_c,$$

where

$$i_c = -C_{dl} \frac{\partial \eta}{\partial t}.$$

In this case, the total current is no longer purely faradaic, and the charge conservation equations (63) and (64) include transient terms describing capacitive current due to the rearrangement of charge in the double layers inside CLs in addition to the faradaic current accounted for in the reaction source terms:

$$-C_{dl} \frac{\partial \eta}{\partial t} - \nabla \cdot (\sigma_m^{\text{eff}} \nabla \phi_m) = R_{H^+}, \quad (67)$$

$$C_{dl} \frac{\partial \eta}{\partial t} - \nabla \cdot (\sigma_s^{\text{eff}} \nabla \phi_s) = R_{e^-}, \quad (68)$$

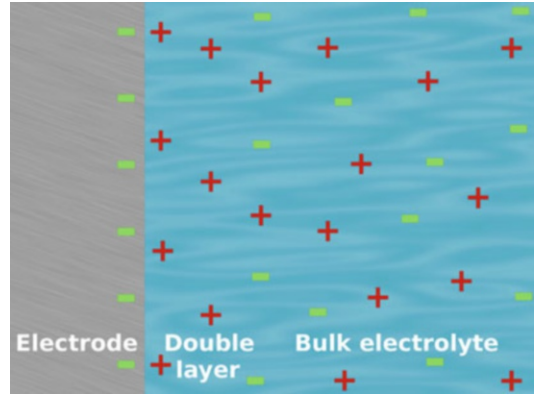
where by

$\eta$  is the local overpotential defined as

$$\eta = \phi_s - \phi_m - E_{th}, \quad (69)$$

and  $E_{th}$  is the theoretical half-cell potential.

In fuel cells, charge transport is always coupled with mass and thermal transport through reaction source terms, and therefore, Eqs. (63) and (64) are never purely steady state when any of the latter two



**PEM Fuel Cells: Modeling, Fig. 6** Illustration of the electrical double layer at the electrode-electrolyte interface

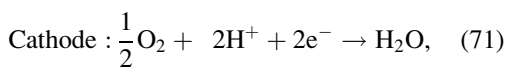
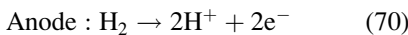
processes are transient. Choice of those equations over their fully transient form (67, 68) is often made with assumption of negligible double-layer effect. Double-layer charging and discharging is normally observed at relatively small time scales that depend on the double-layer capacitance, which is estimated to be between  $8 \cdot 10^{-3}$  and  $10^{-1}$  F/cm<sup>2</sup> [374–380] or between 3 and 9 F/cm<sup>3</sup> [367, 378] (or between 3 and 34 F/cm<sup>3</sup> if recomputed from F/cm<sup>2</sup> using the reported catalyst layer thickness in [374, 376, 377, 379]).

Most of literature disregards double-layer effects, often referring to the work of Wang and Wang [79], who claimed that the time constant of double-layer discharging is of order  $10^{-7}$  s, while the time constant for gas diffusion through GDLs is of order  $10^{-2}$  s and for membrane hydration is of order 10 s. When estimating the charging/discharging time for the double layer, Wang and Wang considered a double-layer capacitance per unit area,  $C_{dl}^a = 2 \cdot 10^{-5}$  F/cm<sup>2</sup>. Peng et al. [62] have simulated a cell with two orders of magnitude larger capacitance (which corresponds to the experimental values listed above) and have shown that such values affect approximately the first 0.15 s of the current density response to a step change in cell voltage, a significantly longer time period than estimated by Wang and Wang. Moreover, since the time constant for the double-layer charging is directly proportional to its capacitance [79], an increase of the double-layer capacitance by just one order of magnitude to order 10 F/cm<sup>3</sup> leads

to charging effects lasting for more than a second [62], “smoothing” the response even further. In contrast, absence of the double layer in the model ( $C_{dl} = 0$ ) may lead to over- and undershoots in the power output of the cell when a change in current or voltage is applied [62, 375]. Peaks in the transient response of the cell are observed experimentally [76, 379]; their size and stabilization time depend not only on the double-layer capacitance but also on the operating conditions [61, 65, 67–69, 73, 76, 79]. Such peaks are commonly attributed to reactant availability after the step change in operating conditions [61, 65, 68, 69, 381] and membrane water content [69]. Further modeling and experimental studies are required to estimate the time scale of the double-layer charging effects at various operating conditions and for various catalyst layer compositions.

### Electrochemical Reactions

Electrochemical reactions taking place in the fuel cell are responsible for generation of electric current by converting the chemical energy of the reactants, i.e., hydrogen and oxygen, to electrical energy. For a hydrogen PEM fuel cell, the half-cell reactions at the anode and cathode are



where the anodic reaction is the hydrogen oxidation reaction (HOR) and the cathodic reaction is the oxygen reduction reaction (ORR). The source terms in mass and charge transport equations in the CL are computed from the HOR and ORR kinetic models. The reaction kinetic models compute the current density (or volumetric current density) as a function of the reactant concentration (partial pressure of gases) and overpotential  $\eta$ .

Butler-Volmer and Tafel kinetics are most commonly used to describe the reaction kinetics for both the HOR [1, 5, 34, 220, 338, 345] and ORR [1, 5, 34, 44, 329, 333, 382]. Using the Butler-Volmer equation, the volumetric current density  $i$  can be written as [184, 345]

$$j = A_v j_0^{\text{ref}} \left\{ \left[ \prod_{i=\text{reactants}} \left( \frac{c_i}{c_j^*} \right)^{\gamma_i} \right] \exp\left(\frac{-\alpha_R F \eta}{RT}\right) - \left[ \prod_{i=\text{products}} \left( \frac{c_i}{c_j^*} \right)^{\gamma_i} \right] \exp\left(\frac{\alpha_P F \eta}{RT}\right) \right\}, \quad (72)$$

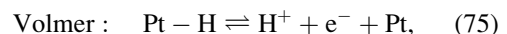
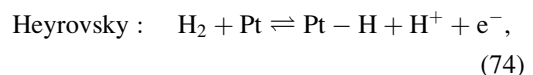
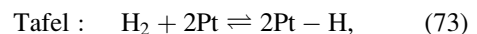
where  $A_v$  is the active area of platinum per unit volume of catalyst layer;  $c_i$  is the concentration of species  $i$  at the electrode surface;  $c_i^*$  is the concentration of species  $i$  at which the exchange current density,  $j_0^{\text{ref}}$ , was measured;  $\alpha_R$  and  $\alpha_P$  are the reaction transfer coefficients; and  $\gamma_i$  is the reaction order with respect to species  $i$ .

For sluggish reactions requiring high negative overpotentials to proceed such as the ORR, the Butler-Volmer equation (72) can be simplified to the Tafel expression:

$$j = A_v j_0^{\text{ref}} \left\{ \left[ \prod_{i=\text{reactants}} \left( \frac{c_i}{c_j^*} \right)^{\gamma_i} \right] \exp\left(\frac{-\alpha_R F \eta}{RT}\right) \right\}.$$

Butler-Volmer and Tafel kinetics are only valid for single electron transfer and multistep reactions with a unique rate determining step. Experimental evidence however suggests that HOR [8, 338, 384] and ORR [385–388] have rate determining step that change with overpotential. Thus, kinetic models which can take into account the multistep reaction mechanisms are required to accurately predict the reaction rates for the HOR and ORR. Complex kinetic models are also required to study Pt dissolution and carbon corrosion.

HOR on Pt catalyst is generally described by the Tafel-Heyrovsky-Volmer mechanism [389–391]:



with two possible pathways, i.e., Tafel-Volmer and Heyrovsky-Volmer, for the oxidation of hydrogen to protons. The Tafel-Volmer pathway involves a dissociative chemisorption of



hydrogen on the Pt surface (Tafel step) followed by the one-electron oxidation reaction of the adsorbed hydrogen atom (Volmer step) which occurs twice. In the Heyrovsky-Volmer mechanism, the first step involves dissociative adsorption of hydrogen along with one-electron oxidation of one of the hydrogen atoms (Heyrovsky step) followed by the one-electron oxidation of the adsorbed hydrogen atom (Volmer step). Studies have shown the relative contributions of the Tafel-Volmer and Heyrovsky-Volmer mechanisms at different overpotentials and limiting mass transport currents [383, 392, 392, 393]. Wang et al. [8] proposed a dual-path kinetic model for the HOR that considered both reaction pathways and was able to accurately model experimental polarization curves for a range of limiting mass transport currents.

For the dual-path model, the reaction rates for each of the elementary steps in Eqs. (73), (74), and (75) are [8]

$$v_T = k_T(1 - \theta_{\text{Pt-H}})^2 c_{\text{H}_2} - k_{-T} \theta_{\text{Pt-H}}^2, \quad (76)$$

$$v_H = k_H(1 - \theta_{\text{Pt-H}}) c_{\text{H}_2} \exp\left(\frac{(1 - \beta_H)FE}{RT}\right) - k_{-H} \theta_{\text{Pt-H}} c_{\text{H}^+} \exp\left(\frac{-\beta_H FE}{RT}\right), \quad (77)$$

$$v_V = k_V \theta_{\text{Pt-H}} \exp\left(\frac{(1 - \beta_V)FE}{RT}\right) - k_{-V} c_{\text{H}^+} (1 - \theta_{\text{Pt-H}}) \exp\left(\frac{-\beta_V FE}{RT}\right), \quad (78)$$

where  $v$  is the rate of the reaction;  $E$  is the half-cell voltage;  $k$  is the equilibrium rate constant (usually computed from experimental data); subscripts T, H, and V denote the Tafel, Heyrovsky, and Volmer reactions; and negative subscripts denote the backward reactions. Wang et al. [8] suggest a value of 0.5 for both  $\beta_H$  and  $\beta_V$ . The coverage  $\theta_{\text{Pt-H}}$  is defined as the fraction of active Pt sites occupied by the intermediate adsorbed species Pt-H. Therefore,  $(1 - \theta_{\text{Pt-H}})$  gives the fraction of active Pt sites available for reaction, as seen in Eqs. (76) and (77). Using

Eqs. (76), (77), and (78), the change in coverage of the intermediate species can be written as

$$\frac{d\theta_{\text{Pt-H}}}{dt} = 2v_T + v_H - v_V. \quad (79)$$

The HOR current density,  $j_{\text{HOR}}$ , can be computed as

$$j_{\text{HOR}} = F(v_H + v_V), \quad (80)$$

which gives the current per unit area of Pt. The volumetric current density,  $i_{\text{HOR}}$ , i.e., current per unit volume of electrode, can be obtained using

$$i_{\text{HOR}} = j_{\text{HOR}} A_v, \quad (81)$$

which is used in the source term in Eqs. (66) and (67) and in Table 3 for the anode.

Equations (76) – (80) summarize the general set of nonlinear system of equations for the dual-path HOR kinetics with six rate constants and two cathodic transfer coefficients. However, for practical implementation into MEA or full-cell models, the kinetic model needs to be simplified so that the overall simulation is feasible and computationally efficient. Further, the rate constants cannot be measured directly from experiments; therefore, they must be fitted to the experimental data by correlating them to the exchange current density, i.e., the current density produced when the reaction is at equilibrium (forward reaction rate is equal to the backward reaction rate). The following assumptions are made to simplify the dual-path kinetic model:

1. Steady-state conditions are assumed for the coverages so that  $\frac{d\theta_{\text{Pt-H}}}{dt} = 0$ .
2. The rate of the Volmer reaction is much higher than the Tafel or Heyrovsky reactions.
3. The coverage of the intermediate species is small so that  $(1 - \theta_{\text{Pt-H}}) \sim 1$ .
4. The concentration of protons ( $c_{\text{H}^+}$ ) is equal to the reference equilibrium proton concentration ( $c_{\text{H}^+}^{\text{eq}}$ ).
5. The cathodic transfer coefficients for Heyrovsky and Volmer reactions are 0.5 ( $\beta_H = \beta_V = 0.5$ ) [8].

Applying these assumptions to Eqs. (76), (77), (78), (79), and (80) and correlating the rate constants to the exchange current density, the coverage of the intermediate species can be written as

$$\frac{\theta_{\text{Pt-H}}}{\theta_{\text{Pt-H}}^0} = e^{\frac{-F\eta}{\gamma_{\text{ads}}RT}} \quad (82)$$

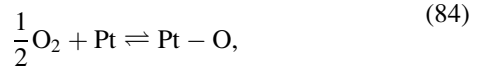
where  $\theta_{\text{Pt-H}}^0$  is the equilibrium coverage of the intermediate species and  $\gamma_{\text{ads}}$  is the potential range constant for adsorption isotherm [8]. The HOR current density can then be computed as [8]

$$j_{\text{HOR}} = j_{0T} \left[ \frac{c_{\text{H}_2}}{c_{\text{H}_2}^{\text{ref}}} - \frac{c_{\text{H}_2}^0}{c_{\text{H}_2}^{\text{ref}}} e^{\frac{-2F\eta}{\gamma_{\text{ads}}RT}} \right] + j_{0H} \left[ \frac{c_{\text{H}_2}}{c_{\text{H}_2}^{\text{ref}}} e^{\frac{F\eta}{2RT}} - \frac{c_{\text{H}_2}^0}{c_{\text{H}_2}^{\text{ref}}} e^{\frac{-F\eta}{\gamma_{\text{ads}}RT}} e^{\frac{-F\eta}{2RT}} \right], \quad (83)$$

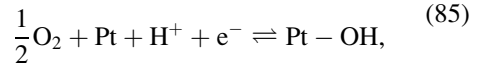
where  $c_{\text{H}_2}^0$  is the equilibrium concentration of hydrogen at the Pt surface,  $c_{\text{H}_2}^{\text{ref}}$  is the saturation concentration of  $\text{H}_2$  under 1 atm pressure, and  $j_{0T}$  and  $j_{0H}$  are the exchange current densities for the Tafel and Heyrovsky reactions, respectively. A detailed derivation of Eqs. (82) and (83) can be found in Ref. [8]. Equation (83) can be implemented in any numerical model, and a similar expression is implemented, for example, in OpenFCST [6, 83].

Several studies have been performed to investigate the ORR mechanism on Pt catalyst [385, 388, 394–397]. Walch et al. [398] summarize the different ORR mechanisms where up to six intermediate adsorbed species, namely,  $\text{O}_{2(\text{ads})}$ ,  $\text{O}_{(\text{ads})}$ ,  $\text{HO}_{2(\text{ads})}$ ,  $\text{H}_2\text{O}_{2(\text{ads})}$ ,  $\text{H}_2\text{O}_{(\text{ads})}$ , and  $\text{OH}_{(\text{ads})}$ , can be present. However, detailed reaction pathways such as those in [398] are generally not used for fuel cell modeling. Only recently, the double trap mechanism proposed by Wang et al. [397], which assumes two intermediate species,  $\text{OH}_{(\text{ads})}$  and  $\text{O}_{(\text{ads})}$ , was used for fuel cell MEA models [51, 304, 317, 338, 399, 400]. The elementary reactions for the double trap mechanism for the ORR on Pt proposed by Wang et al. [397] and later fitted to experimental data by Moore et al. [27] are

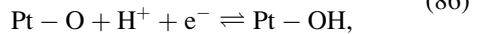
Dissociative adsorption (DA) :



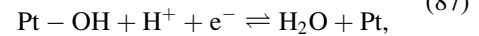
Reductive adsorption (RA) :



Reductive transition (RT) :



Reductive desorption (RD) :



where Pt-O and Pt-OH are adsorbed species on the Pt active sites. The double trap mechanism proposes that ORR can take place via two routes, namely, DA-RT-RD and RA-RD. Markiewicz et al. [388] found that the double trap model was unable to predict their experimental ORR polarization curves for potentials in the range of 0.3–0.7 V. They proposed a modified double trap model with three intermediate species; however, an analytical expression for the current density was not provided, and therefore, the model is not discussed further.

In the double trap model, the reaction rates for the reactions in Eqs. (84), (85), (86), and (87) are

$$v_{\text{DA}} = k_{\text{DA}} \psi c_{\text{O}_2}^{\frac{1}{2}} - k_{-\text{DA}} \theta_{\text{Pt-O}}, \quad (88)$$

$$v_{\text{RA}} = k_{\text{RA}} \psi c_{\text{O}_2}^{\frac{1}{2}} c_{\text{H}^+} \exp\left(\frac{-\beta_{\text{RA}} FE}{RT}\right) - k_{-\text{RA}} \theta_{\text{Pt-OH}} \exp\left(\frac{(1 - \beta_{\text{RA}1}) FE}{RT}\right), \quad (89)$$

$$v_{\text{RT}} = k_{\text{RT}} \theta_{\text{Pt-O}} c_{\text{H}^+} \exp\left(\frac{-\beta_{\text{RT}} FE}{RT}\right) - k_{-\text{RT}} \theta_{\text{Pt-OH}} \exp\left(\frac{(1 - \beta_{\text{RT}1}) FE}{RT}\right), \quad (90)$$

$$v_{RD} = k_{RD}\theta_{Pt-OH}c_{H^+}\exp\left(\frac{-\beta_{RD}FE}{RT}\right) - k_{-RD}\psi\exp\left(\frac{(1-\beta_{RD})FE}{RT}\right), \quad (91)$$

where  $\psi$  is the fraction of active platinum sites available, which is related to the coverage of intermediate species through the following equation:

$$\psi = 1 - \theta_{Pt-O} - \theta_{Pt-OH}. \quad (92)$$

Using the reaction rates from Eqs. (88), (89), (90), and (91), the ORR current density,  $j_{ORR}$ , can be computed using

$$j_{ORR} = -F(v_{RA} + v_{RT} + v_{RD}), \quad (93)$$

where the negative sign is added to follow the convention that reduction current is negative and  $j_{ORR}$  is the ORR current per unit area of platinum. Similar to the HOR, the volumetric current density  $i_{ORR}$  can be obtained as

$$i_{ORR} = j_{ORR}A_v, \quad (94)$$

which is used in the source terms in Eqs. (66) and (67) and in Tables 1 and 3 for the cathode. The following assumptions are made to simplify the expression for  $j_{ORR}$ :

1. Steady-state conditions are assumed for the coverages so that  $\frac{d\theta_{Pt-O}}{dt} = 0$  and  $\frac{d\theta_{Pt-OH}}{dt} = 0$ .

$$\theta_{Pt-OH} = \frac{C g_{DA}(C g_{RA} + g_{-RD} - g_{RT}) - (C g_{RA} + g_{-RD})(C g_{DA} + g_{-DA} + g_{RT})}{(C g_{DA} - g_{-RT})(C g_{RA} + g_{-RD} - g_{RT}) - (C g_{RA} + g_{-RA} + g_{-RT} + g_{RD} + g_{-RD})(C g_{DA} + g_{-DA} + g_{RT})} \quad (98)$$

$$\theta_{Pt-O} = \frac{C g_{DA}(C g_{RA} + g_{-RA} + g_{-RT} + g_{RD} + g_{-RD}) - (C g_{RA} + g_{-RD})(C g_{DA} - g_{-RT})}{(C g_{DA} + g_{-DA} + g_{RT})(C g_{RA} + g_{-RA} + g_{-RT} + g_{RD} + g_{-RD}) - (C g_{RA} + g_{-RD} - g_{RT})(C g_{DA} - g_{-RT})} \quad (99)$$

where  $C$  is the oxygen concentration ratio and is given by

$$C = \left(\frac{c_{O_2}}{c_{O_2}^{ref}}\right)^{1/2}. \quad (100)$$

2. The concentration of protons is constant and equal to the reference equilibrium proton concentration.
3. The equilibrium free energies of the intermediates ( $\theta_{Pt-O}^{eq}$  and  $\theta_{Pt-OH}^{eq}$ ) can be represented using Langmuir isotherms so that

$$\frac{\theta_{Pt-O}^0}{\psi^0} = e^{-\Delta G_{Pt-O}^0}, \quad (95)$$

$$\frac{\theta_{Pt-OH}^0}{\psi^0} = e^{-\Delta G_{Pt-OH}^0}, \quad (96)$$

where  $\Delta G_i^0$  denotes the equilibrium Gibbs free energy for intermediate species,  $i$ ,  $\theta_{Pt-O}^0$  is the equilibrium coverage of the intermediate species,  $O_{ads}$ ,  $\theta_{Pt-OH}^0$  is the equilibrium coverage of the intermediate species  $OH_{ads}$ , and  $\psi^0$  is the equilibrium fraction of free Pt sites.

Applying the assumptions above and relating the rate constants to the free energy of the reactions, the expression for the current density for the ORR is [401]

$$j_{ORR} = j^* \left[ e^{-\frac{\Delta G_{RD}^*}{RT}} \theta_{Pt-OH} - e^{-\frac{\Delta G_{-RD}^*}{RT}} \psi \right], \quad (97)$$

where  $j^*$  is a reference prefactor for the ORR reaction which is set to 1000  $Acm^{-2}$  in [27, 397], and the coverage of the intermediate steps are given as [27, 401]

The  $g_i$  terms in Eqs. (98) and (99) are given by

$$g_i = e^{-\Delta G_i^*/kT} \quad (101)$$

where  $\Delta G_i^*$  are the potential dependent free energies of activation of the  $i$ -th step. These free energies are given by [401]

$$\begin{aligned} \Delta G_{DA}^* &= \Delta G_{DA}^{*0}, \\ \Delta G_{-DA}^* &= \Delta G_{DA}^{*0} - \Delta G_O^0, \\ \Delta G_{RA}^* &= \Delta G_{RA}^{*0} + \beta_{RA}e\eta, \\ \Delta G_{-RA}^* &= \Delta G_{RA}^{*0} - \Delta G_{OH}^0 - \beta_{RA}e\eta, \\ \Delta G_{RT}^* &= \Delta G_{RT}^{*0} + \beta_{RT}e\eta, \\ \Delta G_{-RT}^* &= \Delta G_{RT}^{*0} - \Delta G_{OH}^0 + \Delta G_O^0 - \beta_{RT}e\eta, \\ \Delta G_{RD}^* &= \Delta G_{RD}^{*0} + \beta_{RD}e\eta, \\ \Delta G_{-RD}^* &= \Delta G_{RD}^{*0} + \Delta G_{OH}^0 - \beta_{RD}e\eta, \end{aligned}$$

where  $e$  is the charge of a single electron and  $\eta$  is the applied overpotential, i.e.,  $\eta = E - E_{eq}$ . The free energies of activation at zero overpotential are denoted  $\Delta G_{DA}^{*0}$ ,  $\Delta G_{RA}^{*0}$ ,  $\Delta G_{RT}^{*0}$ , and  $\Delta G_{RD}^{*0}$ , while the free energies of adsorption at zero overpotential are denoted  $\Delta G_O^0$  and  $\Delta G_{OH}^0$ . These six free energies are the unknown kinetic parameters upon which the model is based. These values were obtained by Moore et al. in reference [27]. Detailed derivations for the expressions above can be found in [27, 397, 401]. An implementation of the kinetic model can be found in OpenFCST [6, 83].

### Heat Transport

Thermal effects cannot be neglected in single-cell and stack fuel cell models, especially in cases where phase change is dominant. High temperatures increase reaction rates and species transport while they reduce theoretical cell voltage and membrane conductivity (due to low water content) while increasing hydrogen crossover. If the cell is operated at high current density, localized excessive heat in the catalyst layers may lead to membrane degradation and the appearance of pin holes [402, 403]. Achieving a balance between positive and negative thermal effects, known as heat (or thermal) management, has been an active area of research for many years within the fuel cell

mathematical modeling community and resulted in a large number of fuel cell models aiming at predicting the temperature distribution within the fuel cell which has been measured experimentally to change by several degrees [111].

Nguyen and White proposed a non-isothermal PEMFC model as early as 1993 [31]. Since then, more detailed non-isothermal fuel cell models were developed including three-dimensional studies by Wang et al. [404], Mazumder and Cole [405], and Ju et al. [406, 407]. Unfortunately, some key thermal effects were neglected in those models, such as the heat of the reaction [31], reversible heat of reaction [404, 405], ohmic losses due to electron transport [404, 406, 407], and heat sink due to water evaporation [406, 407]. Other 3D models also lacked a description of ohmic heating [5, 408]. Wang and Wang [409] improved the model by Ju et al. by including two-phase effects. However, a number of simplifying assumptions were still present in their model, e.g., isotropic and homogeneous properties of the fuel cell layers. Geometrical simplifications resulted in several 1D [410–412] and 2D [413–416] models that, due to their lower computational and implementation demands, allowed scientist to introduce more accurate physical representations, including anisotropy of the porous media [414, 415] and two-phase physics [410, 412, 415, 416]. These models however still contained some simplifications. For instance, Rowe and Li [410] and Ramousse et al. [411] did not take into account local thermal effects and assumed either a uniform cell temperature [411] or that the thermophysical properties were given at the average cell temperature [410]. Birgersson et al. [413] and Weber and Newman [412] considered interface models for catalyst layers, thereby neglecting any effects within the catalyst layer. Pasaogullari et al. [414] only studied the GDL and Zamel and Li [416] limited their model to the cathode. Bapat and Thynell [415] only considered heat conduction. Bhaiya et al. [308, 309] recently developed a single-phase, non-isothermal PEMFC model that took into account all thermal effects listed in previous publications, except for water condensation because all water in cathode was assumed to be generated in vapor form. This model was extended later by Zhou et al. [304] into a two-phase, non-isothermal PEMFC model

where the effects of condensation and enthalpy transport of liquid water are included.

Temperature distribution within a cell is governed by the energy conservation equation [32, 160, 303, 417]. A single energy conservation equation is considered in this entry by assuming local thermal equilibrium between phases due to the large interstitial area of the porous materials in a PEMFC [308, 309]. An energy conservation equation could be used for each phase (solid, gas, and liquid); however, this approach is not taken here, and the interested reader is referred to Refs. [418–420] for more information.

During the operation of a fuel cell, the main local sources and sinks of heat can be separated into three major categories depending on their nature: (a) reaction heat, (b) due to changes in the physical state of water, and (c) ohmic heating. Reaction heat (reversible and irreversible) is released in the catalyst layers as the electrochemical reactions proceed. Liquid water is generated in the cathode during ORR and, depending on the local temperature, pressure, and humidity, may evaporate acting as a heat sink, be transported to cooler regions of the cell, and condense there creating a heat source (this is referred to as the heat pipe effect). Water sorption and desorption into and out of the electrolyte also release/absorb heat. Thermal effects may also affect the transport phenomena in PEMFCs, such as in the case of thermo-osmosis, i.e., the transport of sorbed water in the ionomer due to temperature gradients.

Based on the analysis above, treating all gases as ideal, and neglecting viscous heat dissipation and Soret and Dufour effects, the energy conservation equation inside a fuel cell takes the following form:

$$\begin{aligned} \varepsilon_v \frac{\partial(\rho_g \hat{h}_g)}{\partial t} + \nabla \cdot (\varepsilon_v \rho_g \hat{h}_g \mathbf{v}_g) \\ = \nabla \cdot (\kappa^{\text{eff}} \nabla T) - \nabla \cdot \left( \sum \bar{H}_i N_i \right) \\ + \hat{S}_{\text{heat}} - W_{\text{electrical}}, \end{aligned} \quad (102)$$

where  $\hat{h}_g$  is the mass specific enthalpy of the gas,  $\mathbf{v}_g$  is the interstitial velocity of the gas mixture,  $\kappa^{\text{eff}}$  is the effective thermal conductivity,  $\bar{H}_i$  is the molar specific enthalpy of species  $i$ ,  $N_i$  is the molar flux, and  $\hat{S}_{\text{heat}}$  and  $W$  are volumetric rates

of heat production and work done by the system, respectively.

The expression above depends on the mixture velocity and the molar flux of the different species in the porous media; therefore, it has to be expanded for each fuel cell compartment, and its final form depends on the mass transport model used as described in detail in reference [308]. In the cathode compartment of a PEMFC, a steady-state case with negligible convective gas transport, i.e.,  $\mathbf{v}_g \approx 0$ , and Fickian diffusion, the equation above can be expanded and further simplified to achieve the following expression [308]:

$$\begin{aligned} \nabla \cdot (\kappa^{\text{eff}} \nabla T) + D_{O_2, N_2}^{\text{eff}} c \nabla x_{O_2} \\ \cdot (\nabla \bar{H}_{O_2} - \nabla \bar{H}_{N_2}) + D_{H_2O, N_2}^{\text{eff}} c \nabla x_{H_2O} \\ \cdot (\nabla \bar{H}_{H_2O} - \nabla \bar{H}_{N_2}) - N_\lambda \cdot \nabla \bar{H}_\lambda - N_l \\ \cdot \nabla \bar{H}_l + \hat{S}_{\text{heat}} = 0. \end{aligned} \quad (103)$$

For ideal gases, molar enthalpies of gaseous species are function of temperature alone. For sorbed water and liquid water, it is also assumed here that the molar specific enthalpies are only a function of temperature. Thus considering the sorbed water transport due to electroosmotic drag, water diffusion, and thermo-osmotic diffusion, the thermal transport equation inside the cathode catalyst layer can finally be expressed as

$$\begin{aligned} \nabla \cdot (\kappa^{\text{eff}} \nabla T) + D_{O_2, N_2}^{\text{eff}} \left( \frac{\partial \bar{H}_{O_2}}{\partial T} - \frac{\partial \bar{H}_{N_2}}{\partial T} \right) \nabla T \\ \cdot \nabla x_{O_2} \\ + D_{H_2O, N_2}^{\text{eff}} \left( \frac{\partial \bar{H}_{H_2O}}{\partial T} - \frac{\partial \bar{H}_{N_2}}{\partial T} \right) \nabla T \\ \cdot \nabla x_{H_2O} + \frac{n_d \sigma_m^{\text{eff}}}{F} \frac{\partial \bar{H}_\lambda}{\partial T} \nabla T \cdot \nabla \phi_m \\ + \frac{\rho_{dry}}{EW} D_\lambda^{\text{eff}} \frac{\partial \bar{H}_\lambda}{\partial T} \nabla T \cdot \nabla \lambda + \frac{1}{M_{H_2O}} D_T^{\text{eff}} \\ \times \frac{\partial \bar{H}_\lambda}{\partial T} \nabla T \cdot \nabla T + \frac{\rho_l k_{rl}}{\mu_l} \frac{\partial \bar{H}_l}{\partial T} \nabla p_c \cdot \nabla T \\ + \hat{S}_{\text{heat}} = 0, \end{aligned} \quad (104)$$

where in the cathode catalyst layer the term  $\hat{S}_{\text{heat}}$  contains the following:

1. The irreversible heat generation (efficiency losses) due to activation overpotential:

$$\begin{aligned} S_{\text{irrev, ORR}} &= -i\eta \\ &= -i(\phi_s - \phi_m - E_{\text{ORR}}), \end{aligned} \quad (105)$$

where  $\eta$  is the overpotential. Since  $\eta$  is negative for a cathodic reaction, a negative sign is placed in the formula;  $E_{\text{ORR}}$  is the equilibrium potential derived from the Nernst equation [199, 401].

2. Reversible heat generation in the cathode catalyst layer due to ORR is

$$\begin{aligned} S_{\text{rev, ORR}} &= \frac{i}{2F} (-T\Delta\bar{S}_{\text{ORR}}) \\ &= \frac{i}{2F} (-Tf_{\text{ORR}}\Delta\bar{S}_{\text{overall}}), \end{aligned} \quad (106)$$

where  $\bar{S}_{\text{overall}}$  is the overall entropy change per mole of fuel ( $H_2$ ). Since the entropy of the half-cell reaction cannot be explicitly obtained, a factor,  $f_{\text{ORR}}$ , is introduced to account for the fraction of reversible heat produced in the ORR.

3. Heat source term due to phase change:

$$S_{\text{phase, CL}} = M_{H_2O} S_{H_2O(\text{evap/cond})} \hat{L}_{\text{water}}, \quad (107)$$

where  $\hat{L}_{\text{water}}$  is the specific latent heat of vaporization/condensation of water, which is a function of temperature and is reported in [421].

4. The electronic and protonic Ohmic heating (irreversible):

$$\begin{aligned} S_{\text{ohmic, CL}} &= \sigma_m^{\text{eff}} (\nabla\phi_m \cdot \nabla\phi_m) \\ &\quad + \sigma_s^{\text{eff}} (\nabla\phi_s \cdot \nabla\phi_s). \end{aligned} \quad (108)$$

5. Heat source term due to water vapor sorption/desorption in the ionomer:

$$S_{\text{sorption, CL}} = \frac{k_t \rho_{\text{dry}}}{EW} (\lambda_{\text{eq}} - \lambda) \bar{H}_{\text{sorption}}, \quad (109)$$

where  $\bar{H}_{\text{sorption}}$  is heat release due to molar enthalpy change which corresponds to water vapor sorption.

Equation (104) can be implemented in order to estimate the temperature in the cathode CL. For

the GDL and MPL, the same equation can be used excluding the reaction heat terms, i.e., (105) and (106), and water sorption term, i.e., (109). For the anode, a similar expression can be obtained. The interested reader is referred to [308].

## Microscale Simulation for Parameter Estimation

The governing equations of an MEA are described in section “General Models.” Critical to the proposed models are effective transport coefficients such as the effective diffusion coefficient in Eq. (37). Effective medium theories, such as Bruggemann correlation [34, 44, 422] (a particular case of Eq. 35) and percolation theory [304, 329, 423] (shown in Eq. 32), have traditionally been used to estimate the effective transport properties of the porous media by correlating the bulk transport properties to the solid or void volume fraction. However, these approximations do not take into account the intrinsic structure of the porous media and rely upon experimental measurements to estimate the exponents for the expressions in Eqs. (32) and (35). A more accurate alternative to the effective medium theories is the use of microscale simulations to estimate the transport properties, coefficients for condensation and evaporation, and reaction effectiveness.

Advancements in microscopy techniques, such as x-ray computed tomography (X-CT) [29, 53, 55, 103, 424–431], scanning transmission x-ray microscopy (STXM) [432–434], and focused ion beam-scanning electron microscopy (FIB-SEM) [18, 52, 54, 55, 60, 335, 435], have enabled the visualization of the intrinsic structure of the fuel cell porous media. The choice of the technique to be used depends on the application and fuel cell layer to be visualized. Imaging techniques produce large image data sets which often require extensive image analysis to filter external noise and provide meaningful information about the underlying structure. To estimate the transport and electrochemical properties from the image data, a numerical tool must address the following aspects: (a) image analysis of the data to produce



binarized images; (b) conversion of the binarized image data to a computational domain or mesh; (c) modeling of the underlying physics, including simulation of the model, which involves providing parameters and discretization of the equations; and (d) computational requirement.

Image analysis depends on the microscopy technique used to obtain the data. Details for image analysis can be found in the references for the different techniques mentioned above. The goal of image analysis is the segmentation of the structure into different phases (for X-CT and FIB-SEM). This binarized data set can then be used to generate a computational mesh. The mesh can be generated from the images in one of the following ways:

1. Direct conversion of the image voxels into cells (for direct numerical simulation (DNS)) or lattice points (used for Lattice Boltzmann method (LBM)) [9, 12, 18, 366, 436–441] so that the mesh resolution is the voxel size
2. Use of triangulation algorithms to generate meshes from the images [29, 103, 442], typically used for CFD simulations
3. Abstraction of the geometry to simplified networks [361, 428, 437, 440, 443–447], usually employed in pore network models (this method, however, results in the loss of morphological features of the original sample)

Berson et al. [448] reported that the direct conversion of voxels into a mesh, as is the case with the first approach, could lead to an overprediction of the interfacial area depending upon the mesh resolution. However, the use of meshing algorithms to smooth the digitized geometry might not be necessarily accurate, because the smallest recoverable feature or interface depends on the voxel size. Also, it is unlikely that the solid surface in the fuel cell porous media, made up of heterogeneous materials, such as platinum supported on high surface area carbon in CLs, is smooth. Therefore, the first approach of converting image voxels into a computational mesh is acceptable for numerical simulation of the transport and electrochemical performance in the microstructures.

Numerical simulations in PEMFC microstructures have been performed either using the continuum approach (DNS) or (LBM). However, for certain cases like diffusion in the CL, where the pore sizes are in the range of the mean free path of the gas molecules, the continuum approach is an approximation. This has led to the use of higher-order LBM for such cases [15, 424, 449]. However, the large computational cost associated with the LBM (e.g., 6 h on 320 cores for eight million lattice points without consideration of Knudsen effects [15]) makes it unfeasible for performing optimization studies. This, in conjunction with the similar results obtained using continuum and LBM simulations for  $Kn \sim 1$  [14], has led to the continued use of the continuum approach to describe the physics in microstructures. In this section, continuum equations used to compute the effective transport properties for the microstructures are described. Since the effective properties depend only on the steady-state fluxes, transient effects are ignored in the presented models.

Charge transport in the microstructures is simulated using Ohm's law [13, 366, 431, 439, 442, 450, 451]:

$$\nabla \cdot (\boldsymbol{\sigma} \nabla \phi) = 0, \quad (110)$$

where  $\boldsymbol{\sigma}$  is either the bulk electronic or protonic conductivity tensor of the material and  $\phi$  is either the electronic or protonic potential, depending upon the phase under study. Usually, Eq. (110) is simulated in the solid phase of the microstructures, corresponding to the platinum and carbon in the CL and carbon fibers in the GDL. Therefore,  $\phi$  is usually the electronic potential except when the equation is simulated in the ionomer or liquid water phase of the CL where it would be the protonic potential. It is important to note that the source term (usually written on the right side) in Eq. (110) is zero. This is because the effective conductivity is assumed to be a function of the geometry and material of the layer and independent of the electrochemical reactions in the layer. To compute the effective conductivity in the Cartesian directions (X, Y, and Z), Eq. (110) is solved with the boundary conditions:

$$\begin{aligned}
\phi &= \phi^{\text{in}} \text{ on } \Gamma_1, \\
\phi &= \phi^{\text{out}} \text{ on } \Gamma_2, \text{ and} \\
(\boldsymbol{\sigma} \nabla \phi) \cdot \mathbf{n} &= 0 \\
&\text{(no-flux condition) everywhere else,}
\end{aligned} \tag{111}$$

where  $\phi^{\text{in}}$  is the potential at the inlet plane,  $\phi^{\text{out}}$  is the potential at the outlet plane,  $\mathbf{n}$  is the outward normal vector to a surface, and  $\Gamma_1$  and  $\Gamma_2$  are the inlet and outlet cross section planes, respectively, in the direction in which the effective conductivity is to be computed. For example, to compute the effective conductivity in the  $X$ -direction, i.e.,  $\sigma_{XX}^{\text{eff}}$  component of the conductivity tensor,  $\Gamma_1$  and  $\Gamma_2$  would be the  $YZ$  planes at the  $X$ -inlet and  $X$ -outlet. The no-flux boundary condition in Eq. (111) is used to prevent the charge transport across the solid-void interface and assume symmetry on all the outer planes except the inlet and outlet planes. By solving Eq. (110) with boundary conditions given by Eq. (111), the total current,  $I$ , leaving through the outlet plane,  $\Gamma_2$ , can be computed. This can be used to compute the effective conductivity,  $\sigma^{\text{eff}}$ , using

$$\sigma^{\text{eff}} = I \frac{L}{A(\phi^{\text{in}} - \phi^{\text{out}})}, \tag{112}$$

where  $L$  is the distance between the inlet and outlet planes and  $A$  is the cross section area of the outlet plane.

The effective thermal conductivity of the solid phase in the microstructures can be computed using heat conservation based on Fourier's law [450–452]:

$$\nabla \cdot (\boldsymbol{\kappa} \nabla T) = 0, \tag{113}$$

where  $\boldsymbol{\kappa}$  is the bulk thermal conductivity tensor of the solid-phase material in the microstructure. The thermal transport is considered to take place primarily in the solid phase due to difference of three to four orders of magnitude between the thermal conductivity of air and carbon (which is the primary material for most of the fuel cell porous media). Boundary conditions similar to Eq. (111) can be used by replacing  $\phi$  with  $T$  and  $\boldsymbol{\sigma}$  with  $\boldsymbol{\kappa}$ . It is assumed that gas and solid are at a thermal

equilibrium near the solid-void interface; therefore, the no-flux boundary condition can be used at solid-void interface. Further, it is assumed that symmetry conditions apply at the outer planes of the domain except the inlet,  $\Gamma_1$ , and outlet,  $\Gamma_2$ , planes. Similar to the charge transport, Eq. (113) can be solved with the given boundary conditions to compute the total heat flow rate,  $Q$ , through the outlet plane which can be used to compute the effective thermal conductivity,  $\kappa^{\text{eff}}$ , using Eq. (112) with  $I$ ,  $\phi$  and  $\sigma^{\text{eff}}$  replaced by  $Q$ ,  $T$  and  $\kappa^{\text{eff}}$ , respectively.

The thermal and charge transport equations presented here ignore the local contact resistances that might exist between the particles in the microstructure. Kotaka et al. [431] compared the numerically computed effective electronic conductivity, using Eq. (110), with experimentally measured values for GDLs and MPLs and found that the numerical values were 27–32% higher than the experimental values for the GDL and 39 times the experimental value for the MPL. They attributed the huge discrepancy, especially for the MPL sample, to the contact resistance between carbon particles. The effect of contact resistances has also been shown by Espinola et al. [453], where the experimentally measured electrical conductivity for carbon powders was shown to be a function of compression pressure. These results indicate that the contact resistance between particles in porous layers made of carbon powder-based materials, such as MPLs and CLs, is important to accurately estimate the effective electronic conductivity of these materials. Since thermal transport is also assumed to take place via conduction through the solid material, a similar thermal contact resistance should be accounted for in the thermal transport model.

Gas transport in the pores of the microstructures is commonly studied using the steady-state form of Fick's second law of diffusion [13, 18, 448, 451], given in Eq. (37). In this case, the diffusion coefficient for species,  $i$ ,  $D_i$ , is defined as the bulk diffusion coefficient of species  $i$  in the gas for GDLs, where the Knudsen effects are negligible, and using the Bosanquet equation for CLs and MPLs, where pore sizes are in the range of the mean free path of the gas molecules [13, 18, 448, 451]. In the latter case, the diffusion coefficient is given by

$$\frac{1}{D_i} = \frac{1}{\mathcal{D}_{ij}} + \frac{1}{D_i^K}, \quad (114)$$

where  $D_i^K$  is the Knudsen diffusion coefficient for species  $i$ , given by Eq. (36). Since the Knudsen diffusion coefficient depends on the local pore radius, it is specified locally by computing the local pore radius (using sphere fitting [13, 29], average of the wall distance in different directions [13, 439]), or using an effective pore radius for the entire domain [10]. Boundary conditions similar to Eq. (111) can be used by replacing  $\phi$  with  $x_i$  and  $\sigma$  with  $D_i$ . The total flow rate of species  $i$  at the outlet,  $\dot{N}_i$ , can be used to compute the effective diffusivity,  $D_i^{\text{eff}}$ , using Eq. (112) by replacing  $I$ ,  $\phi$  and  $\sigma^{\text{eff}}$  with  $\dot{N}_i$ ,  $x_i$  and  $D_i^{\text{eff}}$ , respectively.

Electrochemical reactions have mainly been studied on the cathode CL microstructure due to the sluggishness of the ORR. These studies have been performed on stochastic [7–15] and FIB-SEM CL reconstructions [16–18]. Chen et al. [15] have used LBM to simulate the electrochemical reactions on a CL reconstruction, but all other studies have used either the finite volume or the finite element methods. Most of the prior studies have used Butler-Volmer or Tafel kinetics to estimate the ORR. As discussed in section “[Electrochemical Reactions](#),” the ORR is a multistep reaction where the rate determining step depends on the overpotential. Therefore, the double trap [397] or the modified double trap model [388], presented in section “[Electrochemical Reactions](#),” would be more appropriate. Sabharwal et al. [18] used the double trap model to study the ORR on a FIB-SEM reconstruction of the CL. However, they assumed constant overpotential in the simulation domain.

The electrochemical reactions in the CL microstructure are studied by simulating Eq. (63) in the ionomer phase, Eq. (64) in the carbon and platinum phase, and the steady-state form of Eq. (37) in the pore phase. These three equations are coupled using the source term which depends on the reaction occurring on the Pt surface and can be computed using the kinetic models in section “[Electrochemical Reactions](#).” For FIB-SEM and nano-CT imaging, only solid and pore phases can be reconstructed; therefore, the solid phase cannot be separated into carbon, platinum, and ionomer

phases. If the domain is small enough so that the overpotential can be assumed constant, then the model proposed by Sabharwal et al. [18] can be used, where only the oxygen diffusion is solved in the pore phase using Eq. (37) (where species  $i$  would now be  $O_2$ ) with boundary conditions:

$$\begin{aligned} x_{O_2} &= x_{O_2}^{\text{in}} \quad \text{at all external walls,} \\ (-D_{O_2} c_{\text{tot}} \nabla x_{O_2}) \cdot \mathbf{n} &= \frac{j}{4F} A_{Pt,s|g} \text{ at } \Gamma_{s|p}. \end{aligned} \quad (115)$$

where  $\Gamma_{s|p}$  indicates the solid-pore interface,  $j$  is the current density per unit area of Pt, and  $A_{Pt,s|g}$  is the ratio of active platinum area in the simulation domain to the solid-pore interface area. The boundary conditions given by Eq. (115) assume that the domain is small enough that the oxygen concentrations at the outer walls of the domain are identical and that the reaction only takes place at the solid-pore interface.

An oxygen transport resistance due to catalyst-ionomer interactions has been proposed as a key factor limiting cathode performance [18, 51, 182, 183, 454, 455]. Zhang et al. [17] and Sabharwal et al. [18] accounted for the mass transport resistance due to the ionomer films in their electrochemical models. The model presented by Sabharwal et al. [18] assumes a fictitious thin film of ionomer to be present at the solid-pore interface as shown in Fig. 7.

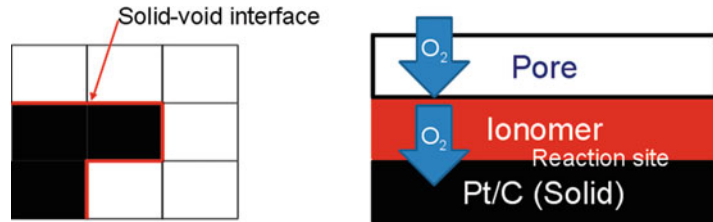
Therefore, for the reaction to take place at the solid-ionomer interface, additional resistances, in the form of an interfacial resistance (considered in the model at the ionomer-gas interface) and diffusion resistance through the ionomer film, are introduced. The mathematical form of these resistances is

$$\begin{aligned} (-D_{O_2} c \nabla x_{O_2}) \cdot \mathbf{n} &= -k_{O_2} (c_{O_2,slf} - c_{O_2slf}^{\text{eq}}), \\ &= \frac{D_{O_2}^{\text{film}}}{\delta_N} (c_{O_2,slf} - c_{O_2}^{\text{react}}), \\ &= \frac{j (c_{O_2}^{\text{react}}, \phi_s, \phi_m)}{4F}, \end{aligned} \quad (116)$$

where  $k_{O_2}$  is the oxygen dissolution rate in the ionomer,  $D_{O_2}^{\text{film}}$  is the oxygen diffusion coefficient

**PEM Fuel Cells:  
Modeling,**

**Fig. 7** Illustration of the solid (black)-pore (white) domain of the CL microstructure with the fictitious ionomer film (red)



in the ionomer film,  $\delta_N$  is the thickness of the ionomer film,  $c_{O_2,slf}$  is the concentration of oxygen in the ionomer phase at the gas-ionomer interface,  $c_{O_2,slf}^{eq}$  is the equilibrium oxygen concentration obtained from Henry's law using the partial pressure of oxygen in the gas phase, and  $c_{O_2}^{react}$  is the oxygen concentration at the ionomer-catalyst interface used for calculating  $j$ . When solved together, Eqs. (37), (115), and (116) can be used to estimate the electrochemical performance in the CL microstructure assuming constant overpotential in the domain. The results of the electrochemical simulations can be used in macroscale simulations to provide a better estimate of the local current density in different regions of the CL based on the macroscale overpotentials and oxygen concentrations. Recently, it has been suggested that the interfacial resistance is likely due to platinum-ionomer interactions instead of oxygen dissolution [454]. In this latter case, the functional form of the equation would remain the same, but the physical meaning of  $k_{O_2}$  would change.

Water management is critical to the operation of a PEMFC. The operation of a fuel cell under wet (high RH) and cold (low temperature) conditions can lead to the production of excess liquid water, which can affect the reactant transport and, in severe cases, cause complete shutdown of the cell due to reactant starvation. It is therefore crucial to understand the effect of liquid water saturation on the gas transport and electrochemical reactions in PEMFC. Microscale models can be used to correlate the morphology of the porous media to the liquid water movement and the corresponding impact on the gas pathways. Liquid water transport in microstructures has been studied using LBM [363, 437, 440, 441, 456–458], PNM [361, 427, 428, 437, 443–447, 459, 460], and full morphology (FM) models [54,

437, 440, 461–463]. PNM is the most commonly used approach to study liquid water intrusion in the fuel cell porous media microstructures. As described earlier, PNMs abstract the geometry into a network of pores and throats which can be generated using microscopy images such as X-CT [363, 428, 464] or random networks [361, 445–447, 459] calibrated with experimental data such as porosity, mercury intrusion porosimetry, or saturation-pressure profiles. PNMs are extremely fast and provide a computationally inexpensive means of obtaining pressure-saturation profiles for porous media and computing the effective transport properties as functions of saturation for the abstract network. FM models study the liquid intrusion in the porous media using a quasi-static capillary-driven water front approach, in which the following equation is used to compute the capillary pressure required to intrude a pore with liquid water:

$$p_c = \frac{2\gamma \cos \theta}{r_p},$$

where  $\gamma$  is the surface tension of water, and  $\theta$  is the contact angle.

The major advantage of FM over PNM is that no geometry abstraction is required and the liquid water transport and corresponding transport properties can be studied on the actual microstructure. However, FM model is computationally more expensive than PNM [440]. LBM can be used to study the intricate liquid water dynamics in the microstructures as opposed to the quasi-static approach used by PNM and FM but is computationally very expensive [440]. The details of the different models are not described in this section and can be found in the references listed above.

Interphase mass transfer between the gas and liquid phase is another mode for the transport of

water in the PEMFC layers. Microscale simulations can be used to compute the evaporation/condensation rates in the different porous media. One such study was performed by Zenyuk et al. [465], who measured the evaporation rates in a GDL microstructure at different saturations. Using X-CT, they reconstructed the partially wetted GDL microstructures to extract the liquid water surface mesh. Diffusive gas transport was simulated using the Maxwell-Stefan equation (8), assuming that the region above the liquid water surface was a macro-homogeneous GDL and partial pressure of water vapor near the liquid water surface was equal to the saturation pressure for water vapor. The results of the simulation were used to compute the evaporation rates by measuring the flux of water through the liquid-gas interface. The approach used by Zenyuk et al. [465] provided good agreements with the experimentally measured evaporation rates. However, better models are needed to accurately take into account the morphology of the microstructures and the local water distributions which might not always be connected and planar. Accurate estimates of the evaporation/condensation rates in different porous media are required for the macroscale models to describe the two-phase flow in PEMFCs and optimize the functionality of different layers.

## Implementation

There are mainly three categories of PEFC models: (a) channel models [231, 258, 333, 466–469], (b) through-the-channel MEA models [161, 209, 304, 309, 327–331, 338, 345–350, 406, 470], and (c) along-the-channel and fuel cell models which account for both gas channels and MEA sandwich [4, 417, 471].

Some channel models consider single-phase flow [466]; however, most of the models studying mass transport in the channel include both air and liquid water in their formulation [231, 258, 333, 467–469]. Early two-phase models, e.g., mixture (or  $M^2$ ) models, solved the transport problem for the gas-liquid mixture using a variable phase composition formulation [333]. The transport of the

gas mixture is solved using mass (1) and momentum (2) conservation equations, and saturation is obtained from the water concentration in the mixture. Other two-phase flow models in channels solve Navier-Stokes equation (2) and continuity equation (1) for both air and liquid water as immiscible phases. Although ANSYS Fluent is the software used for the majority of these studies [231, 467–469], other works use COMSOL Multiphysics [466] or open-source packages such as Gerris flow solver (GFS) [258, 472]. Since ANSYS Fluent and COMSOL are commercial CFD packages, the abovementioned studies do not include discussion on the implementation of the numerical models, and only the reference manual of each software is cited. Some authors, e.g., Wang et al. [467], included a short discussion on the numerical approach, specifying that some terms in the governing equations were implemented using user-specified functions. The only works that mention details on the implementation and solvers used in open-source packages are that from Theodorakakos et al. [258] and Jarauta et al. [233], the latter being implemented in the open-source package Kratos Multiphysics [241].

A typical through-the-channel, single-phase, non-isothermal MEA model includes governing equations for gas, charge, water and heat transport. The transport of gaseous species in the MEA is modeled using Fick's law of diffusion (Eq. 13). Charge transport is commonly modeled using Ohm's law (Eq. 61). Transport of sorbed water in the membrane is modeled using Eq. (44). Heat transfer is modeled using Eq. (104). An example of single-phase non-isothermal MEA model is implemented in open-source software package OpenFCST v0.3 [83].

Two-phase, non-isothermal MEA models that account for the transport of liquid water are implemented using either a one-equation model based on saturation (Eq. (46)) or a two-equation model including Darcy's law for the gas and liquid phases (Eqs. (47) and (48)) together with a set of closure equations. Two-phase model implementations can be found in many modeling packages such as CFdesign [345], STAR-CCM+ [406], ANSYS Fluent [161, 327, 349], COMSOL



Multiphysics [209], and OpenFCST [304, 309, 470]. One of the most complete fuel cell models is the one proposed by Zenyuk et al. [209]. Their governing equations are solved using the general solvers provided by COMSOL Multiphysics 5.0/5.1 [240] and MUMPS. A more recent two-phase model is developed by Zhou et al. [470] which is linearized using Newton-Raphson method, discretized using the Galerkin finite element method, and solved using MUMPS in open FCST.

The models that include both gas flow channel and MEA sandwich are implemented in modeling packages such as ANSYS Fluent [4] and CFX [417, 471]. These models require a high computational power, and the convergence can be very slow. For instance, the model proposed by Nguyen et al. [471] required about 6,000–8,000 iterations to achieve convergence.

The partial differential equations for the abovementioned numerical models are nonlinear. For example, the source terms for mass transport equations for oxygen and water vapor depend on current density, which depends on electronic and solid potentials and reactant availability (Table 1). Therefore, these equations must be linearized using Newton-Raphson and Picard methods.

After a set of linear partial differential equations is obtained, discretization in space is performed. One option relies on using the finite volume method [235] for space discretization. This method is used in many commercial numerical simulation packages such as ANSYS Fluent [236] and STAR-CCM+ [237], and in open-source packages such as FAST-FC [84]. Another well-known method is the finite element method [239], which is available in commercial packages such as COMSOL Multiphysics [240] and in open-source frameworks such as deal.II [473] and OpenFCST [6, 83]. Using both finite volume and finite element methods, the computational domain is discretized into small elements, known as the computational mesh. The resulting mesh must contain sufficient elements in order to obtain a grid-independent solution. The meshes can be classified into structured and unstructured meshes. In a structured mesh, all internal nodes are connected to the same number of neighbor nodes, and the same element pattern is followed

throughout the grid. In an unstructured mesh, the pattern may be irregular, and no requirement on the number of vertices surrounding each node exists. Meshes can be refined based on an error estimator of the approximate solution (e.g., a posteriori error estimator developed by Kelly et al. [474]). Adaptive refinement is applied, for example, in OpenFCST [6, 44]. To further improve the computational efficiency and avoid nonmatching grids, domain decomposition methods (DDMs) are used. DDMs are implemented in commercial (e.g., COMSOL [240], ANSYS Fluent [236]) and open-source (e.g., OpenFOAM [238]) software.

For the reader interested in an open-source implementation of an MEA model, OpenFCST contains several models that can be downloaded and utilized to gain a better understanding of fuel cell modeling [6].

As described in section “[Microscale Simulation for Parameter Estimation](#),” continuum models have been used to describe the physical processes in the microstructures of the fuel cell porous media. The governing equations for these models can be discretized using the finite volume method [11, 13, 14, 439, 451] or finite element method [18, 29, 103]. Additionally, when the electrochemical reactions are considered in a CL microstructure, the resulting system of equations might be nonlinear. These equations are then linearized using Newton-Raphson method [13, 14, 439] or Picard method [18]. The governing equations can then be solved using commercial packages, such as ANSYS Fluent [236], COMSOL [240], and GEODICT<sup>®</sup> [475], or open-source software, such as OpenFCST [6, 83]. Although not described in this entry, lattice Boltzmann method and pore network models have also been used for microstructure simulations. Palabos [476] and OpenPNM [85, 477] are examples of open-source software which employ LBM and PNM, respectively, to study the physics in the fuel cell porous media microstructures.

## Conclusion

Substantial progress has been achieved in the area of fuel cell modeling since the pioneering work of



Springer et al. [1] and Bernardi and Verbrugge [2] in the early 1990s. A deeper understanding of the critical physical phenomena occurring inside the fuel cell coupled with expanding computational resources has allowed researchers to consider higher dimensionality and complex physical and electrochemical processes that were initially neglected due to high computing costs, lack of experimental evidence of their importance, and the difficulty of implementation. To date, several two- and three-dimensional single- and two-phase channel models have been proposed, and novel formulations are still under development, such as the implementation of the generalized Navier-Stokes equations proposed by Kerkhof and Geboers [214] for multicomponent transport or the embedded Lagrangian-Eulerian formulation proposed by Jarauta et al. [233]. MEA and full-cell models have transitioned from one-dimensional, single-phase models with limited access to the source code to open-source implementations of two-phase, non-isothermal MEA models that include multistep reaction kinetics and local mass transport losses [304].

This entry provided an overview of the governing equations used in channel, MEA, and full-cell proton exchange membrane fuel cell modeling. Starting with the function and composition of each component of a PEMFC, the entry provided the most common mathematical models for mass, charge, and energy transport in PEMFCs, as well as the electrochemical reactions of hydrogen oxidation and oxygen reduction. All models are derived following several levels of detail so that the material of this entry can serve as a base for developing novel PEMFC mathematical models with varying levels of complexity depending on the simplifying assumptions. Due to nonlinearity and stiffness, the resulting numerical models are hard to solve and require an adequate solution approach at all levels from discretization (in both space and time) to the selection of appropriate linear, nonlinear, and transient solvers. Therefore, a section on implementation details was also provided outlining the solution methodologies used in the literature and highlighting the importance of open-source numerical software.

The governing equations discussed in this entry for full-cell and MEA modeling depend on many effective transport properties, such as effective diffusivity. Obtaining effective transport properties and accounting for local transport effects in the porous media, such as local transport resistances or evaporation, requires tedious experiments that are usually time consuming. FIB-SEM and CT imaging can now provide three-dimensional reconstructions of GDLs, CLs, and MPLs with high resolution. This entry showed how numerical modeling can be used to interpret the imaging data in order to extract effective transport properties under dry and wet conditions and reaction rates per unit volume.

## Future Directions

The level of detail and overall complexity of PEMFC mathematical models has drastically increased since the 1990s. It is clear, however, that future work is still required in order to remove simplifying assumptions and include additional phenomena. Physical processes such as platinum dissolution and coarsening, carbon corrosion, compression effects, membrane swelling, and mechanical and chemical degradation and local mass transport losses have been shown to be critical to fuel cell performance and durability [21, 33]. These processes take place at different time scales, and therefore, they are seldom integrated into detailed full-cell or MEA models. Numerical models need to be developed with adaptive time stepping algorithms to capture the dynamics of the fuel cell at the various time scales.

Future numerical models should also be able to integrate PEMFC transport and electrochemical processes across various length scales. This requires developing coupling strategies to introduce nanoscale information from molecular dynamics and density functional theory and microscale information from microstructure simulations from FIB-SEM and CT image reconstructions in the macroscale models. Progress has been made recently in this regard by coupling a GDL pore network model (PNM) to a volume-averaged macroscale MEA model [338, 400]. However, for

CLs much more complex couplings might be required, especially to introduce information regarding the electrochemical processes occurring at the pore scale.

In addition to the structure of the porous media, the structure of the interface between the different layers has also been shown to affect the local ohmic resistances [130] and water accumulation [131–134] in the PEFC. Although commonly ignored in the macroscale models, these interfaces can significantly affect the transport processes in the PEFC and, therefore, need to be accounted for in the full-cell models [33]. It is therefore necessary to develop efficient coupling methods to integrate the information about the structure of the porous media and their interfaces into the macroscale models.

In the area of microscale simulations, further development is needed in order to seamlessly integrate modeling into image analysis protocols. Mathematical characterization of the porous media microstructures using multiple statistical functions has seldom been performed in literature. Future studies should aim to characterize the difference in the structure of porous media with different composition and fabrication methods. Correlations also need to be developed between the structure and properties of the porous media. Models to predict ionic transport and wettability of thin ionomer films in the CL and the local mass transport losses identified at the catalyst sites [182, 183, 454, 455] are also required. Recent studies have tried to account for the effects of the ionomer film at micro- [17, 18] and macroscales [51, 158]; however, much work is required to understand the mechanism and mathematical functional form of this so-called interfacial resistance.

Future work will therefore be required in the next decade to further extend, and validate with respect to experimental data, current model implementations. Given the complexity of the current models, such extensions are likely to be only possible within the framework of an open-source collaboration. Non-isothermal MEA models, as well as companion simplified models, that have been validated with respect to experimental data [309] and microscale models are already publicly available in the open-source

fuel cell software OpenFCST at [www.openfcst.org](http://www.openfcst.org). Open-source software should serve as a foundation for further fuel cell model development. It is important that the research community as a collective contributes to the development of open-source software so that the existing knowledge base can be expanded in an efficient manner.

## Nomenclature

$\bar{C}_p$	Molar specific heat, [ $J mol^{-1}K^{-1}$ ]
$\bar{H}$	Enthalpy, [ $J$ ]
$\dot{W}$	Rate of work done by the system, [ $W cm^{-3}$ ]
$\mathbf{g}$	Gravity vector field, [ $cm s^{-2}$ ]
$\hat{C}_p$	Specific heat, [ $J g^{-1}K^{-1}$ ]
$\hat{h}$	Specific enthalpy, [ $J g^{-1}$ ]
$\hat{u}$	Specific internal energy, [ $J g^{-1}$ ]
$\hat{N}$	Mass flux, [ $g cm^{-2} s^{-1}$ ]
$\mathcal{D}$	Maxwell-Stefan diffusion coefficient, [ $cm^2 s^{-1}$ ]
$N$	Molar flux, [ $mol cm^{-2} s^{-1}$ ]
$\mathbf{q}$	Molecular heat flux, [ $W cm^{-2} K^{-1}$ ]
$\mathbf{n}$	Outward normal vector
$\hat{\mathbf{K}}$	Permeability tensor, [ $cm^2$ ]
$\mathbf{v}$	Velocity, [ $cm s^{-1}$ ]
$A_v$	Active area of Pt per unit volume of catalyst layer, [ $cm^2 cm^{-3}$ ]
$a_w$	Water activity
$a_{lv}$	Liquid-gas interfacial surface area per unit volume, [ $cm^2 cm^{-3}$ ]
$c$	Molar concentration, [ $mol cm^{-3}$ ]
$C_k$	Volume fraction of fluid $k$
$D$	Fick's diffusion coefficient, [ $cm^2 s^{-1}$ ]
$D^K$	Knudsen diffusion coefficient, [ $cm^2 s^{-1}$ ]
$D_T$	Thermo-osmotic diffusion coefficient, [ $mol cm^{-1} s^{-1} K^{-1}$ ]
$E$	Half-cell voltage, [ $V$ ]
$EW$	Equivalent weight of the ionomer, [ $g mol^{-1}$ ]
$F$	Faraday's constant, [ $C mol^{-1}$ ]
$h$	Convective heat transfer coefficient, [ $W cm^{-2} K^{-1}$ ]
$H_{g, N}$	Henry's constant, [ $Pa cm^3 mol^{-1}$ ]
$i$	Volumetric current density, [ $A cm^{-3}$ ]
$j$	Current density, [ $A cm^{-2}$ ]
$j_0^{ref}$	Exchange current density, [ $A cm^{-2}$ ]

$k$	Equilibrium rate constant, [ $cm$ $s^{-1} (cm^3 mol^{-1})^{(\alpha-1)}$ ]	$\beta$	Transfer coefficient for cathodic reaction
$k_{elc}$	Evaporation or condensation rate per unit of liquid-gas interfacial surface area, [ $mol cm^{-2} s^{-1}$ ]	$\hat{\boldsymbol{\tau}}$	Cauchy stress tensor, [ $g cm^{-1} s^{-2}$ ]
$K_{i,j}$	Frictional interaction coefficient between species $i$ and $j$ , [ $N s cm^{-4}$ ]	$\Lambda$	Collision diameter, [ $cm$ ]
$k_r$	Effective permeability, [ $cm^2$ ]	$\hat{\kappa}$	Surface curvature, [ $cm^{-1}$ ]
$L$	Characteristic length, [ $cm$ ]	$\eta$	Overpotential, [ $V$ ]
$M$	Molar mass, [ $g mol^{-1}$ ]	$\hat{\boldsymbol{\beta}}$	Forchheimer correction tensor, [ $cm$ ]
$n_d$	Electroosmotic drag coefficient	$\gamma$	Surface tension coefficient, [ $g s^{-2}$ ]
$p$	Pressure, [ $g cm^{-1} s^{-2}$ ]	$\gamma_i$	Order of reaction for reaction $i$
$R$	Universal gas constant, [ $J mol^{-1} K^{-1}$ ]	$\gamma_{ads}$	Potential range constant for adsorption isotherm
$r_p$	Pore radius, [ $cm$ ]	$\hat{\mu}_i$	Electrochemical potential of species $i$ , [ $J mol^{-1}$ ]
$S_{heat}$	Volumetric heat source, [ $W cm^{-3}$ ]	$\hat{\rho}$	Charge density, [ $C cm^{-3}$ ]
$T$	Absolute temperature, [ $K$ ]	$\kappa$	Thermal conductivity coefficient, [ $W cm^{-2} K^{-1}$ ]
$t$	Time, [ $s$ ]	$\lambda$	Sorbed water content in the membrane
$u_{i,k}$	Mobility of species $i$ in phase $k$ , [ $cm^2$ $mol J^{-1} s^{-1}$ ]	$\lambda_b$	Bulk viscosity, [ $g cm^{-1} s^{-1}$ ]
$x$	Molar fraction	$\lambda_{eq}$	Equilibrium sorbed water content in the membrane
$z_i$	Valence (or charge number) of species $i$	$\mu$	Dynamic viscosity, [ $g cm^{-1} s^{-1}$ ]
		$\nu$	Rate of reaction, [ $mol cm^{-2} s^{-1}$ ]
		$\omega$	Mass fraction
		$\phi_k$	Electrostatic potential of phase $k$ , [ $V$ ]
		$\psi$	Fraction of active platinum sites available
		$\rho$	Density, [ $g cm^{-3}$ ]
		$\boldsymbol{\tau}$	Shear stress tensor, [ $g cm^{-1} s^{-2}$ ]
		$\sigma$	Conductivity, [ $S cm^{-1}$ ]
		$\tau$	Tortuosity
		$\theta$	Coverage of intermediate reaction species
		$\varepsilon$	Volume fraction

## Abbreviations

BPP	Bipolar plate
CL	Catalyst layer
CSF	Continuum surface force
CSS	Continuum surface stress
ECSA	Electrochemically active surface area
FEP	Fluorinated ethylene propylene
GDL	Gas diffusion layer
ICCP	Ionomer covered catalyst particle
LS	Level set
MEA	Membrane electrode assembly
MPL	Microporous layer
PEM	Proton exchange membrane
PEMFC	Proton exchange membrane fuel cell
PFSa	Perfluorosulfonic acid
PLIC	Piecewise linear interface calculation
PTFE	Polytetrafluoroethylene
VOF	Volume of fluid

## Greek Letters

$\alpha_i$	Transfer coefficient for reaction $i$
$\bar{\kappa}$	Partial viscosity, [ $g cm^{-1} s^{-1}$ ]
$\bar{v}$	Specific volume, [ $cm^3 g^{-1}$ ]

## Mathematical Operators

$\nabla$	Gradient
$\nabla_s$	Symmetric gradient
$\otimes$	Tensor product
$\Theta(x)$	Heaviside step function

## Subscripts and Superscripts

$DA$	Dissociative adsorption reaction
$g$	Gas mixture
$H$	Heyrovsky reaction
$i, j$	Species indexes
$k$	Phase index
$m$	Electrolyte phase
$p$	Percolation threshold

<i>RA</i>	Reductive adsorption reaction
<i>RD</i>	Reductive desorption reaction
<i>RT</i>	Reductive transition reaction
<i>s</i>	Solid phase
<i>T</i>	Tafel reaction
<i>V</i>	Volmer reaction
<i>v</i>	Void phase

## Bibliography

### Primary Literature

- Springer T, Zawodzinski T, Gottesfeld S (1991) Polymer electrolyte fuel cell model. *J Electrochem Soc* 138(8):2334–2342
- Bernardi DM, Verbrugge MW (1992) Mathematical model of the solid-polymer-electrolyte fuel cell. *J Electrochem Soc* 139(9):2477–2491
- Shimpalee S, Dutta S, Van Zee J (2000) Numerical prediction of local temperature and current density in a PEM fuel cell. *ASME Publ HTD* 366:1–10
- Dutta S, Shimpalee S, Van Zee J (2001) Numerical prediction of mass-exchange between cathode and anode channels in a PEM fuel cell. *Int J Heat Mass Transf* 44(11):2029–2042
- Berning T, Lu D, Djilali N (2002) Three-dimensional computational analysis of transport phenomena in a PEM fuel cell. *J Power Sources* 106(1–2):284–294
- Secanell M, Putz A, Wardlaw P, Zingan V, Bhaiya M, Moore M, Zhou J, Balen C, Domican K (2014) Open-FCST: an open-source mathematical modeling software for polymer electrolyte fuel cells. *ECS Trans* 64(3):655–680
- Wang G, Mukherjee PP, Wang CY (2006) Direct numerical simulation (DNS) modeling of PEFC electrodes Part II. Random microstructure. *Electrochim Acta* 51:3151–3160
- Wang JX, Springer TE, Adzic RR (2006) Dual-pathway kinetic equation for the hydrogen oxidation reaction on Pt electrodes. *J Electrochem Soc* 153(9):A1732–A1740
- Wang G, Mukherjee PP, Wang CY (2007) Optimization of polymer electrolyte fuel cell cathode catalyst layers via direct numerical simulation modeling. *Electrochim Acta* 52(22):6367–6377
- Mukherjee P, Wang CY (2006) Stochastic microstructure reconstruction and direct numerical simulation of the PEFC catalyst layer. *J Electrochem Soc* 153(5):A840–A849
- Mukherjee PP, Wang CY (2007) Direct numerical simulation modeling of bilayer cathode catalyst layers in polymer electrolyte fuel cells. *J Electrochem Soc* 154(11):B1121–B1131
- Siddique N, Liu F (2010) Process based reconstruction and simulation of a three-dimensional fuel cell catalyst layer. *Electrochim Acta* 55(19):5357–5366
- Lange KJ, Sui PC, Djilali N (2010) Pore scale simulation of transport and electrochemical reactions in reconstructed PEMFC catalyst layers. *J Electrochem Soc* 157(10):B1434–B1442
- Lange KJ, Sui PC, Djilali N (2012) Determination of effective transport properties in a PEMFC catalyst layer using different reconstruction algorithms. *J Power Sources* 208:354–365
- Chen L, Wu G, Holby EF, Zelenay P, Tao WQ, Kang Q (2015) Lattice Boltzmann pore-scale investigation of coupled physical-electrochemical processes in C/Pt and non-precious metal cathode catalyst layers in proton exchange membrane fuel cells. *Electrochim Acta* 158:175–186
- Zhang X, Ostadi H, Jiang K, Chen R (2014) Reliability of the spherical agglomerate models for catalyst layer in polymer electrolyte membrane fuel cells. *Electrochim Acta* 133:475–483
- Zhang X, Gao Y, Ostadi H, Jiang K, Chen R (2015) Method to improve catalyst layer model for modeling proton exchange membrane fuel cell. *J Power Sources* 289:114–128
- Sabharwal M, Pant L, Putz A, Susac D, Jankovic J, Secanell M (2016) Analysis of catalyst layer microstructures: from imaging to performance. *Fuel Cells* 16(6):734–753
- Konno N, Mizuno S, Nakaji H, Ishikawa Y (2015) Development of compact and high-performance fuel cell stack. *SAE Int J Altern Powertrains* 4(1):123–129
- Kongkanand A, Mathias M (2016) The priority and challenge of high-power performance of low-platinum proton-exchange membrane fuel cells. *J Phys Chem Lett* 7(7):1127–1137. 42
- Borup R, Meyers J, Pivovar B, Kim Y, Mukundan R, Garland N, Myers D, Wilson M, Garzon F, Wood D, Zelenay P, More K, Stroh K, Zawodzinski T, Boncella J, McGrath J, Inaba M, Miyatake K, Hori M, Ota K, Ogumi Z, Miyata S, Nishikata A, Siroma Z, Uchimoto Y, Yasuda K, Kimijima KI, Iwashita N (2007) Scientific aspects of polymer electrolyte fuel cell durability and degradation. *Chem Rev* 107(10):3904–3951
- Maranzana G, Lamibrac A, Dillet J, Lottin O (2015) Startup (and shutdown) model for polymer electrolyte membrane fuel cells. *J Electrochem Soc* 162(7):F694–F706
- Sethuraman VA, Weidner JW, Motupally S, Protsailo LV (2008) Hydrogen peroxide formation rates in PEMFC anode and cathode. *J Electrochem Soc* 155(1):B50–B57
- Secanell M, Wishart J, Dobson P (2011) Computational design and optimization of fuel cells and fuel cell systems: a review. *J Power Sources* 196(8):3690–3704
- Martins J, Lambe A (2013) Multidisciplinary design optimization: a survey of architectures. *AIAA J* 51(9):2049–2075

26. Carnes B, Djilali N (2005) Systematic parameter estimation for PEM fuel cell models. *J Power Sources* 144(1):83–93
27. Moore M, Putz A, Secanell M (2013) Investigation of the ORR using the double-trap intrinsic kinetic model. *J Electrochem Soc* 160(6):F670–F681
28. Novitski D, Kosakian A, Weissbach T, Secanell M, Holdcroft S (2016) Electrochemical reduction of dissolved oxygen in alkaline, solid polymer electrolyte films. *J Am Chem Soc* 138(47):15465–15472
29. Litster S, Epting WK, A. Wargo E, Kalidindi SR, Kumbur EC (2013) Morphological analyses of polymer electrolyte fuel cell electrodes with nano-scale computed tomography imaging. *Fuel Cells* 13(5):935–945
30. Kulikovskiy A, Divisek J, Kornyshev A (1999) Modeling the cathode compartment of polymer electrolyte fuel cells: dead and active reaction zones. *J Electrochem Soc* 146(11):3981–3991
31. Nguyen T, White R (1993) A water and heat management model for proton-exchange-membrane fuel cells. *J Electrochem Soc* 140(8):2178–2186
32. Gurau V, Liu H, Kakac S (1998) Two-dimensional model for proton exchange membrane fuel cells. *AIChE J* 44(11):2410–2422
33. Weber AZ, Borup RL, Darling RM, Das PK, Dursch TJ, Gu W, Harvey D, Kusoglu A, Litster S, Mench MM, Mukundan R, Owejan JP, Pharoah JG, Secanell M, Zenyuk IV (2014) A critical review of modeling transport phenomena in polymer-electrolyte fuel cells. *J Electrochem Soc* 161(12):F1254–F1299
34. Weber AZ, Newman J (2004) Modeling transport in polymer-electrolyte fuel cells. *Chem Rev* 104(10):4679–4726
35. Wang CY (2004) Fundamental models for fuel cell engineering. *Chem Rev* 104:4727–4766
36. Haraldsson K, Wipke K (2004) Evaluating PEM fuel cell system models. *J Power Sources* 126:88–97
37. Biyikoğlu A (2005) Review of proton exchange membrane fuel cell models. *Int J Hydrog Energy* 30:1181–1212
38. Cheddie D, Munroe N (2005) Review and comparison of approaches to proton exchange membrane fuel cell modeling. *J Power Sources* 147(1–2):72–84
39. Siegel C (2008) Review of computational heat and mass transfer modeling in polymer-electrolyte-membrane (PEM) fuel cells. *Energy* 33(9):1331–1352
40. Song GH, Meng H (2013) Numerical modeling and simulation of PEM fuel cells: progress and perspective. *Acta Mech Sinica* 29(3):318–334
41. Eikerling M, Kulikovskiy A (2014) Polymer electrolyte fuel cells: physical principles of materials and operation. CRC Press, Boca Raton
42. Kulikovskiy AA (2010) Analytical modelling of fuel cells, vol 43. Elsevier, Amsterdam/Boston
43. Eikerling M, Kornyshev A (1998) Modelling the performance of the cathode catalyst layer of polymer electrolyte fuel cells. *J Electroanal Chem* 453(1–2):89–106
44. Secanell M, Karan K, Suleman A, Djilali N (2007) Multi-variable optimization of PEMFC cathodes using an agglomerate model. *Electrochim Acta* 52(22):6318–6337
45. Mangal P, Pant LM, Carrigy N, Dumontier M, Zingan V, Mitra S, Secanell M (2015) Experimental study of mass transport in PEMFCs: through plane permeability and molecular diffusivity in GDLs. *Electrochim Acta* 167:160–171
46. Zamel N, Li X (2013) Effective transport properties for polymer electrolyte membrane fuel cells – with a focus on the gas diffusion layer. *Prog Energy Combust Sci* 39(1):111–146
47. Shen J, Zhou J, Astrath NG, Navessin T, Liu ZSS, Lei C, Rohling JH, Bessarabov D, Knights S, Ye S (2011) Measurement of effective gas diffusion coefficients of catalyst layers of PEM fuel cells with a Loschmidt diffusion cell. *J Power Sources* 196(2):674–678
48. Chan C, Zamel N, Li X, Shen J (2012) Experimental measurement of effective diffusion coefficient of gas diffusion layer/microporous layer in PEM fuel cells. *Electrochim Acta* 65:13–21
49. Owejan JP, Owejan JE, Gu W (2013) Impact of platinum loading and catalyst layer structure on PEMFC performance. *J Electrochem Soc* 160(8):F824–F833
50. Weber A, Kusoglu A (2014) Unexplained transport resistances for low-loaded fuel-cell catalyst layers. *J Mater Chem A* 2(41):17,207–17,211
51. Secanell M, Putz A, Shukla S, Wardlaw P, Bhaiya M, Pant LM, Sabharwal M (2015) Mathematical modeling and experimental analysis of thin, low-loading fuel cell electrodes. *ECS Trans* 69(17):157–187
52. Ziegler C, Thiele S, Zengerle R (2011) Direct three-dimensional reconstruction of a nanoporous catalyst layer for a polymer electrolyte fuel cell. *J Power Sources* 196(4):2094–2097
53. Epting W, Gelb J, Litster S (2012) Resolving the three-dimensional microstructure of polymer electrolyte fuel cell electrodes using nanometer-scale X-ray computed tomography. *Adv Funct Mater* 22(3):555–560
54. Zhang X, Gao Y, Ostadi H, Jiang K, Chen R (2014) Modelling water intrusion and oxygen diffusion in a reconstructed microporous layer of PEM fuel cells. *Int J Hydrog Energy* 39(30):17,222–17,230
55. Wargo E, Kotaka T, Tabuchi Y, Kumbur E (2013) Comparison of focused ion beam versus nano-scale X-ray computed tomography for resolving 3-D microstructures of porous fuel cell materials. *J Power Sources* 241:608–618
56. Thiele S, Fürstnhaupt T, Banham D, Hutzenlaub T, Birss V, Ziegler C, Zengerle R (2013) Multiscale tomography of nanoporous carbon-supported noble metal catalyst layers. *J Power Sources* 228:185–192
57. Lopez-Haro M, Guétaz L, Printemps T, Morin A, Escribano S, Jouneau PH, Bayle-Guillemaud P,

- Chandezon F, Gebel G (2014) Three-dimensional analysis of Nafion layers in fuel cell electrodes. *Nat Commun* 5:5229–5234
59. Liu H, Epting W, Litster S (2015) Gas transport resistance in polymer electrolyte thin films on oxygen reduction reaction catalysts. *Langmuir* 31(36): 9853–9858
  60. Cecen A, Wargo E, Hanna A, Turner D, Kalidindi S, Kumbur E (2012) 3-D microstructure analysis of fuel cell materials: spatial distributions of tortuosity, void size and diffusivity. *J Electrochem Soc* 159(3): B299–B307
  61. Wang XD, JL X, Yan WM, Lee DJ, Su A (2011) Transient response of PEM fuel cells with parallel and interdigitated flow field designs. *Int J Heat Mass Transf* 54(11):2375–2386
  62. Peng J, Shin J, Song T (2008) Transient response of high temperature PEM fuel cell. *J Power Sources* 179(1):220–231
  63. Jo A, Lee S, Kim W, Ko J, Ju H (2015) Large-scale cold-start simulations for automotive fuel cells. *Int J Hydrog Energy* 40(2):1305–1315. 44
  64. Ko J, Ju H (2012) Comparison of numerical simulation results and experimental data during cold-start of polymer electrolyte fuel cells. *Appl Energy* 94: 364–374
  65. Kim H, Jeon S, Cha D, Kim Y (2016) Numerical analysis of a high-temperature proton exchange membrane fuel cell under humidified operation with stepwise reactant supply. *Int J Hydrog Energy* 41(31):13657–13665
  66. Yin Y, Wang J, Yang X, Du Q, Fang J, Jiao K (2014) Modeling of high temperature proton exchange membrane fuel cells with novel sulfonated poly-benzimidazole membranes. *Int J Hydrog Energy* 39(25):13671–13680
  67. Chen X, Jia B, Yin Y, Du Q (2013) Numerical simulation of transient response of inlet relative humidity for high temperature PEM fuel cells with material properties. *Adv Mater Res* 625:226–229. *Trans Tech Publ*
  68. Wu H, Berg P, Li X (2010) Modeling of PEMFC transients with finite-rate phase-transfer processes. *J Electrochem Soc* 157(1):B1–B12
  69. Verma A, Pitchumani R (2015) Analysis and optimization of transient response of polymer electrolyte fuel cells. *J Fuel Cell Sci Technol* 12(1):011005
  70. Gomez A, Raj A, Sasmito A, Shamim T (2014) Effect of operating parameters on the transient performance of a polymer electrolyte membrane fuel cell stack with a dead-end anode. *Appl Energy* 130:692–701
  71. Sousa T, Mamlouk M, Scott K, Rangel C (2012) Three dimensional model of a high temperature PEMFC. Study of the flow field effect on performance. *Fuel Cells* 12(4):566–576
  72. Songprakorp R (2008) Investigation of transient phenomena of proton exchange membrane fuel cells. PhD thesis, University of Victoria
  73. Roy A, Serincan M, Pasaogullari U, Renfro M, Cetegen B (2009), Transient computational analysis of proton exchange membrane fuel cells during load change and non-isothermal start-up. In: ASME 2009 7th international conference on fuel cell science, engineering and technology. American Society of Mechanical Engineers, pp 429–438
  74. Wu H, Li X, Berg P (2007) Numerical analysis of dynamic processes in fully humidified PEM fuel cells. *Int J Hydrog Energy* 32(12):2022–2031
  75. Sousa T, Mamlouk M, Scott K (2010) A dynamic non-isothermal model of a laboratory intermediate temperature fuel cell using PBI doped phosphoric acid membranes. *Int J Hydrog Energy* 35(21): 12065–12080
  76. Qu S, Li X, Ke C, Shao ZG, Yi B (2010) Experimental and modeling study on water dynamic transport of the proton exchange membrane fuel cell under transient air flow and load change. *J Power Sources* 195(19):6629–6636
  77. Bao C, Bessler W (2015) Two-dimensional modeling of a polymer electrolyte membrane fuel cell with long flow channel. Part I. Model development. *J Power Sources* 275:922–934
  78. Balliet R, Newman J (2010) Two-dimensional model for cold start in a polymer-electrolyte-membrane fuel cell. *ECS Trans* 33(1):1545–1559
  79. Wang Y, Wang CY (2005) Transient analysis of polymer electrolyte fuel cells. *Electrochim Acta* 50(6):1307–1315
  80. Wang C, Nehrir M, Shaw S (2005) Dynamic models and model validation for PEM fuel cells using electrical circuits. *IEEE Trans Energy Convers* 20(2): 442–451
  81. Vang J, Andreassen S, Kær S (2012) A transient fuel cell model to simulate HTPEM fuel cell impedance spectra. *J Fuel Cell Sci Technol* 9(2):021005
  82. Secanell M (2007) Computational modeling and optimization of proton exchange membrane fuel cells. PhD thesis, University of Victoria
  83. OpenFCST. <http://www.openfcst.org/>. Accessed on 30 Jun 2017
  84. Fast-FC. <https://www.fastsimulations.com/>. Accessed on 30 Jun 2017 45
  85. OpenPNM. <http://openpnm.org/>. Accessed on 12 Jul 2017
  86. Yu X, Ye S (2007) Recent advances in activity and durability enhancement of Pt/C catalytic cathode in PEMFC. Part II: degradation mechanism and durability enhancement of carbon supported platinum catalyst. *J Power Sources* 172(1):145–154
  87. Wu J, Yuan X, Martin J, Wang H, Zhang J, Shen J, Wu S, Merida W (2008) A review of PEM fuel cell durability: degradation mechanisms and mitigation strategies. *J Power Sources* 184(1):104–119



88. Schmittinger W, Vahidi A (2008) A review of the main parameters influencing long-term performance and durability of PEM fuel cells. *J Power Sources* 180(1):1–14
89. Antunes R, De Oliveira M, Ett G, Ett V (2011) Carbon materials in composite bipolar plates for polymer electrolyte membrane fuel cells: a review of the main challenges to improve electrical performance. *J Power Sources* 196(6):2945–2961
90. Cunningham B, Huang J, Baird D (2007) Review of materials and processing methods used in the production of bipolar plates for fuel cells. *Int Mater Rev* 52(1):1–13
91. Karimi S, Fraser N, Roberts B, Foulkes F (2012) A review of metallic bipolar plates for proton exchange membrane fuel cells: materials and fabrication methods. *Adv Mater Sci Eng* 2012:1–22
92. Tawfik H, Hung Y, Mahajan D (2007) Metal bipolar plates for PEM fuel cell – a review. *J Power Sources* 163(2):755–767
93. Antunes R, Oliveira M, Ett G, Ett V (2010) Corrosion of metal bipolar plates for PEM fuel cells: a review. *Int J Hydrog Energy* 35(8):3632–3647
94. Hermann A, Chaudhuri T, Spagnol P (2005) Bipolar plates for PEM fuel cells: a review. *Int J Hydrog Energy* 30(12):1297–1302
95. Lu Z, Kandlikar S, Rath C, Grimm M, Domigan W, White A, Hardbarger M, Owejan J, Trabold T (2009) Water management studies in PEM fuel cells, part II: ex situ investigation of flow maldistribution, pressure drop and two-phase flow pattern in gas channels. *Int J Hydrog Energy* 34(8):3445–3456
96. Li X, Sabir I (2005) Review of bipolar plates in PEM fuel cells: flow-field designs. *Int J Hydrog Energy* 30:359–371
97. Allen GM, Resnick G (2008) Porous plate for a fuel cell. US Pat Off, US20080160366 A1
98. Mathias MF, Roth J, Fleming J, Lehnert W (2010) Handbook of fuel cells. Wiley, Hoboken
99. Cindrella L, Kannan A, Lin J, Saminathan K, Ho Y, Lin C, Wertz J (2009) Gas diffusion layer for proton exchange membrane fuel cells – a review. *J Power Sources* 194(1):146–160
100. Park J, Oh H, Ha T, Lee Y, Min K (2015) A review of the gas diffusion layer in proton exchange membrane fuel cells: durability and degradation. *Appl Energy* 155:866–880
101. Hartnig C, Jörissen L, Kerres J, Lehnert W, Scholta J (2008) Polymer electrolyte membrane fuel cells. In: *Mater for fuel cells*, 1st edn. CRC Press/Woodhead Publ Ltd, Boca Raton/Boston/New York/Washington DC/Cambridge, pp 101–184
102. Rashapov R, Unno J, Gostick J (2015) Characterization of PEMFC gas diffusion layer porosity. *J Electrochem Soc* 162(6):F603–F612
103. Zenyuk IV, Parkinson DY, Connolly LG, Weber AZ (2016) Gas-diffusion-layer structural properties under compression via X-ray tomography. *J Power Sources* 328:364–376
104. Gostick JT, Ioannidis MA, Fowler MW, Pritzker MD (2009) On the role of the microporous layer in PEMFC operation. *Electrochem Commun* 11(3):576–579
105. Malevich D, Halliop E, Peppley BA, Pharoah JG, Karan K (2009) Investigation of charge-transfer and mass-transport resistances in PEMFCs with microporous layer using electrochemical impedance spectroscopy. *J Electrochem Soc* 156(2):B216–B224. 46
106. Stampino PG, Cristiani C, Dotelli G, Omati L, Zampori L, Pelosato R, Guilizzoni M (2009) Effect of different substrates, inks composition and rheology on coating deposition of microporous layer (MPL) for PEM-FCs. *Catal Today* 147:S30–S35
107. Weber AZ, Newman J (2005) Effects of microporous layers in polymer electrolyte fuel cells. *J Electrochem Soc* 152(4):A677–A688
108. Lin G, Nguyen TV (2005) Effect of thickness and hydrophobic polymer content of the gas diffusion layer on electrode flooding level in a PEMFC. *J Electrochem Soc* 152(10):A1942–A1948
109. Karan K, Atiyeh H, Phoenix A, Halliop E, Pharoah J, Peppley B (2007) An experimental investigation of water transport in PEMFCs the role of microporous layers. *Electrochem Solid-State Lett* 10(2):B34–B38
110. Owejan JP, Owejan JE, Gu W, Trabold TA, Tighe TW, Mathias MF (2010) Water transport mechanisms in PEMFC gas diffusion layers. *J Electrochem Soc* 157(10):B1456–B1464
111. Thomas A, Maranzana G, Didierjean S, Dillet J, Lottin O (2014) Thermal and water transfer in PEMFCs: investigating the role of the microporous layer. *Int J Hydrog Energy* 39(6):2649–2658
112. Schulze M, Wagner N, Kaz T, Friedrich K (2007) Combined electrochemical and surface analysis investigation of degradation processes in polymer electrolyte membrane fuel cells. *Electrochim Acta* 52(6):2328–2336
113. Yang Z, Ball S, Condit D, Gummalla M (2011) Systematic study on the impact of Pt particle size and operating conditions on PEMFC cathode catalyst durability. *J Electrochem Soc* 158(11):B1439–B1445
114. Ahluwalia R, Arisetty S, Wang X, Wang X, Subbaraman R, Ball S, DeCrane S, Myers D (2013) Thermodynamics and kinetics of platinum dissolution from carbon-supported electrocatalysts in aqueous media under potentiostatic and potentiodynamic conditions. *J Electrochem Soc* 160(4):F447–F455
115. Topalov A, Cherevko S, Zeradjani A, Meier J, Katsounaros I, Mayrhofer K (2014) Towards a comprehensive understanding of platinum dissolution in acidic media. *Chem Sci* 5(2):631–638
116. Dubau L, Castanheira L, Maillard F, Chatenet M, Lottin O, Maranzana G, Dillet J, Lamibrac A, Perrin JC, Moukheiber E et al (2014) A review of PEM fuel cell durability: materials degradation, local heterogeneities of aging and possible mitigation strategies. *Wiley Interdiscip Rev Energy Environ* 3(6):540–560

117. Arisetty S, Wang X, Ahluwalia R, Mukundan R, Borup R, Davey J, Langlois D, Gambini F, Polevaya O, Blanchet S (2012) Catalyst durability in PEM fuel cells with low platinum loading. *J Electrochem Soc* 159(5):B455–B462
118. Rinaldo S, Stumper J, Eikerling M (2010) Physical theory of platinum nanoparticle dissolution in polymer electrolyte fuel cells. *J Phys Chem C* 114(13): 5773–5785
119. Meyers J, Darling R (2006) Model of carbon corrosion in PEM fuel cells. *J Electrochem Soc* 153(8): A1432–A1442
120. Pandey A, Yang Z, Gummalla M, Atrazhev V, Kuzminyh N, Sultanov V, Burlatsky S (2013) A carbon corrosion model to evaluate the effect of steady state and transient operation of a polymer electrolyte membrane fuel cell. *J Electrochem Soc* 160(9):F972–F979
121. Franco A, Gerard M (2008) Multiscale model of carbon corrosion in a PEFC: coupling with electrocatalysis and impact on performance degradation. *J Electrochem Soc* 155(4):B367–B384
122. Franco A, Guinard M, Barthe B, Lemaire O (2009) Impact of carbon monoxide on PEFC catalyst carbon support degradation under current-cycled operating conditions. *Electrochim Acta* 54(22):5267–5279
123. Solasi R, Zou Y, Huang X, Reifsnider K, Condit D (2007) On mechanical behavior and in-plane modeling of constrained PEM fuel cell membranes subjected to hydration and temperature cycles. *J Power Sources* 167(2):366–377
124. Khattra N, Karlsson A, Santare M, Walsh P, Busby F (2012) Effect of time-dependent material properties on the mechanical behavior of PFSA membranes subjected to humidity cycling. *J Power Sources* 214(365–376):47
125. Khattra N, Santare M, Karlsson A, Schmiedel T, Busby F (2015) Effect of water transport on swelling and stresses in PFSA membranes. *Fuel Cells* 15(1): 178–188
126. Coulon R, Bessler W, Franco A (2010) Modeling chemical degradation of a polymer electrolyte membrane and its impact on fuel cell performance. *ECS Trans* 25(35):259–273
127. Yu T, Sha Y, Liu WG, Merinov B, Shirvanian P, Goddard W III (2011) Mechanism for degradation of Nafion in PEM fuel cells from quantum mechanics calculations. *J Am Chem Soc* 133(49): 19857–19863
128. Robin C, Gérard M, Quinaud M, d'Arbigny J, Bultel Y (2016) Proton exchange membrane fuel cell model for aging predictions: Simulated equivalent active surface area loss and comparisons with durability tests. *J Power Sources* 326:417–427
129. Park S, Lee JW, Popov BN (2012) A review of gas diffusion layer in PEM fuel cells: materials and designs. *Int J Hydrog Energy* 37(7):5850–5865
130. Kim S, Mench M (2009) Investigation of temperature-driven water transport in polymer electrolyte fuel cell: thermo-osmosis in membranes. *J Membr Sci* 328(1):113–120
131. Kim S, Ahn BK, Mench M (2008) Physical degradation of membrane electrode assemblies undergoing freeze/thaw cycling: diffusion media effects. *J Power Sources* 179(1):140–146
132. Swamy T, Kumbur E, Mench M (2010) Characterization of interfacial structure in PEFCs: water storage and contact resistance model. *J Electrochem Soc* 157(1):B77–B85
133. Kalidindi A, Taspinar R, Litster S, Kumbur E (2013) A two-phase model for studying the role of microporous layer and catalyst layer interface on polymer electrolyte fuel cell performance. *Int J Hydrog Energy* 38(22):9297–9309
134. Hizir F, Ural S, Kumbur E, Mench M (2010) Characterization of interfacial morphology in polymer electrolyte fuel cells: micro-porous layer and catalyst layer surfaces. *J Power Sources* 195(11):3463–3471
135. Zenyuk IV, Taspinar R, Kalidindi AR, Kumbur EC, Litster S (2013) Coupling of deterministic contact mechanics model and two-phase model to study the effect of catalyst layer – microporous layer interface on polymer electrolyte fuel cell performance. *ECS Trans* 58(1):1125–1135
136. Zielke L, Vierrath S, Moroni R, Mondon A, Zengerle R, Thiele S (2016) Three-dimensional morphology of the interface between micro porous layer and catalyst layer in a polymer electrolyte membrane fuel cell. *RSC Adv* 6(84):80700–80705
137. Gebel G, Loppinet B (1996) Colloidal structure of ionomer solutions in polar solvents. *J Mol Struct* 383(1–3):431–442
138. Welch C, Labouriau A, Hjelm R, Orler B, Johnston C, Kim Yu S (2012) Nafion in dilute solvent systems: dispersion or solution? *ACS Macro Lett* 1(12):1403
139. Kusoglu A, Weber AZ (2017) New insights into perfluorinated sulfonic-acid ionomers. *Chem Rev* 117(3):987–1104
140. Huang X, Zhao Z, Cao L, Chen Y, Zhu E, Lin Z, Li M, Yan A, Zettl A, Wang YM et al (2015) High-performance transition metal-doped Pt<sub>3</sub>Ni octahedra for oxygen reduction reaction. *Science* 348(6240): 1230–1234
141. Strasser P, Koh S, Anniyev T, Greeley J, More K, Yu C, Liu Z, Kaya S, Nordlund D, Ogasawara H, Toney M, Nilsson A (2010) Lattice-strain control of the activity in dealloyed core-shell fuel cell catalysts. *Nat Chem* 2(6):454–460
142. Sasaki K, Naohara H, Cai Y, Choi YM, Liu P, Vukmirovic MB, Wang JX, Adzic RR (2010) Core-protected platinum monolayer shell high-stability electrocatalysts for fuel-cell cathodes. *Angew Chem Int Ed* 49(46):8602–8607
143. Wu G, More K, Johnston C, Zelenay P (2011) High-performance electrocatalysts for oxygen reduction derived from polyaniline, iron, and cobalt. *Science* 332(6028):443–447. 48

144. Jaouen F, Proietti E, Lefèvre M, Chenitz R, Dodelet JP, Wu G, Chung HT, Johnston C, Zelenay P (2011) Recent advances in non-precious metal catalysis for oxygen-reduction reaction in polymer electrolyte fuel cells. *Energy Environ Sci* 4(1):114–130
145. Lefèvre M, Proietti E, Jaouen F, Dodelet JP (2009) Iron-based catalysts with improved oxygen reduction activity in polymer electrolyte fuel cells. *Science* 324(5923):71–74
146. Chen C, Kang Y, Huo Z, Zhu Z, Huang W, Xin HL, Snyder JD, Li D, Herron JA, Mavrikakis M et al (2014) Highly crystalline multimetallic nanoframes with three-dimensional electrocatalytic surfaces. *Science* 343(6177):1339–1343
147. Gu J, Zhang YW, Tao FF (2012) Shape control of bimetallic nanocatalysts through well-designed colloidal chemistry approaches. *Chem Soc Rev* 41(24):8050–8065
148. Banham D, Ye S (2017) Current status and future development of catalyst materials and catalyst layers for proton exchange membrane fuel cells: an industrial perspective. *ACS Energy Lett* 2(3):629–638
149. Gasteiger HA, Kocha SS, Sompalli B, Wagner FT (2005) Activity benchmarks and requirements for Pt, Pt-alloy, and non-Pt oxygen reduction catalysts for PEMFCs. *Appl Catal B Environ* 56(1):9–35
150. Wilson A, Marcinkoski J, Papageorgopoulos D (2016). DOE Hydrogen and fuel cells program record #16020
151. Marcinkoski J, Spendelov J, Wilson A, Papageorgopoulos D (2015). DOE hydrogen and fuel cells program record #15015
152. Kim KH, Lee KY, Kim HJ, Cho E, Lee SY, Lim TH, Yoon SP, Hwang IC, Jang JH (2010) The effects of Nafion<sup>®</sup> ionomer content in PEMFC MEAs prepared by a catalyst-coated membrane (CCM) spraying method. *Int J Hydrog Energy* 35(5):2119–2126
153. Jeon S, Lee J, Rios GM, Kim HJ, Lee SY, Cho E, Lim TH, Jang JH (2010) Effect of ionomer content and relative humidity on polymer electrolyte membrane fuel cell (PEMFC) performance of membrane-electrode assemblies (MEAs) prepared by decal transfer method. *Int J Hydrog Energy* 35(18):9678–9686
154. Song J, Cha S, Lee W (2001) Optimal composition of polymer electrolyte fuel cell electrodes determined by the AC impedance method. *J Power Sources* 94(1):78–84
155. Du S, Millington B, Pollet BG (2011) The effect of Nafion ionomer loading coated on gas diffusion electrodes with in-situ grown Pt nanowires and their durability in proton exchange membrane fuel cells. *Int J Hydrog Energy* 36(7):4386–4393
156. Shukla S, Stanier D, Saha M, Stumper J, Secanell M (2016) Analysis of inkjet printed PEFC electrodes with varying platinum loading. *J Electrochem Soc* 163(7):F677–F687
157. Secanell M, Carnes B, Suleman A, Djilali N (2007) Numerical optimization of proton exchange membrane fuel cell cathodes. *Electrochim Acta* 52(7):2668–2682
158. Hao L, Moriyama K, Gu W, Wang CY (2015) Modeling and experimental validation of Pt loading and electrode composition effects in PEM fuel cells. *J Electrochem Soc* 162(8):F854–F867
159. Suzuki A, Sen U, Hattori T, Miura R, Nagumo R, Tsuboi H, Hatakeyama N, Endou A, Takaba H, Williams MC et al (2011) Ionomer content in the catalyst layer of polymer electrolyte membrane fuel cell (PEMFC): effects on diffusion and performance. *Int J Hydrog Energy* 36(3):2221–2229
160. Berning T, Djilali N (2003) Three-dimensional computational analysis of transport phenomena in a PEM fuel cell – a parametric study. *J Power Sources* 124(2):440–452
161. Sivertsen B, Djilali N (2005) CFD based modelling of proton exchange membrane fuel cells. *J Power Sources* 141(1):65–78
162. Sun W, Peppley B, Karan K (2005) An improved two-dimensional agglomerate cathode model to study the influence of catalyst layer structural parameters. *Electrochim Acta* 50(16):3359–3374
163. Broka K, Ekdunge P (1997) Modelling the PEM fuel cell cathode. *J Appl Electrochem* 27(3):281–289. 49
164. Siegel N, Ellis M, Nelson D, Von Spakovsky M (2003) Single domain PEMFC model based on agglomerate catalyst geometry. *J Power Sources* 115(1):81–89
165. Jaouen F, Lindbergh G, Sundholm G (2002) Investigation of mass-transport limitations in the solid polymer fuel cell cathode – I. Mathematical model. *J Electrochem Soc* 149(4):A437–A447
166. Ihonen J, Jaouen F, Lindbergh G, Lundblad A, Sundholm G (2002) Investigation of mass-transport limitations in the solid polymer fuel cell cathode – II. Experimental. *J Electrochem Soc* 149(4):A448–A454
167. Gode P, Jaouen F, Lindbergh G, Lundblad A, Sundholm G (2003) Influence of the composition on the structure and electrochemical characteristics of the PEMFC cathode. *Electrochimica Acta* 48:4175–4187
168. Secanell M, Songprakorp R, Suleman A, Djilali N (2008) Multi-objective optimization of a polymer electrolyte fuel cell membrane electrode assembly. *Energy Environ Sci* 1:378–388
169. Secanell M, Songprakorp R, Djilali N, Suleman A (2010) Optimization of a proton exchange membrane fuel cell membrane electrode assembly. *Struct Multidiscip Optim* 40(1–6):563–583
170. Dobson P, Lei C, Navessin T, Secanell M (2012) Characterization of the PEM fuel cell catalyst layer microstructure by nonlinear least-squares parameter estimation. *J Electrochem Soc* 159(5):B514–B523
171. Shah A, Kim GS, Sui P, Harvey D (2007) Transient non-isothermal model of a polymer electrolyte fuel cell. *J Power Sources* 163(2):793–806

172. Xing L, Liu X, Alaje T, Kumar R, Mamlouk M, Scott K (2014) A two-phase flow and non-isothermal agglomerate model for a proton exchange membrane (PEM) fuel cell. *Energy* 73:618–634
173. Xing L, Mamlouk M, Kumar R, Scott K (2014) Numerical investigation of the optimal Nafion<sup>®</sup> ionomer content in cathode catalyst layer: an agglomerate two-phase flow modelling. *Int J Hydrog Energy* 39(17):9087–9104
174. Wang Q, Eikerling M, Song D, Liu Z (2004) Structure and performance of different types of agglomerates in cathode catalyst layers in PEM fuel cells. *J Electroanal Chem* 573:61–69
175. Wardlaw P (2014) Modelling of PEMFC catalyst layer mass transport and electro-chemical reactions using multi-scale simulations. Master's thesis, University of Alberta
176. Bird RB, Stewart WE, Lightfoot E (2002) Transport phenomena, 2nd edn. Wiley, New York
177. Ma S, Solterbeck CH, Odgaard M, Skou E (2009) Microscopy studies on proton exchange membrane fuel cell electrodes with different ionomer contents. *Appl Phys A Mater Sci Process* 96(3):581–589
178. Xu F, Zhang H, Ilavsky J, Stanciu L, Ho D, Justice MJ, Petrache HI, Xie J (2010) Investigation of a catalyst ink dispersion using both ultra-small-angle X-ray scattering and cryogenic TEM. *Langmuir* 26(24):19,199–19,208
179. Banham D, Feng F, Fürstenthaupt T, Pei K, Ye S, Birss V (2011) Effect of Pt-loaded carbon support nanostructure on oxygen reduction catalysis. *J Power Sources* 196(13):5438–5445
180. Epting W, Litster S (2012) Effects of an agglomerate size distribution on the PEFC agglomerate model. *Int J Hydrog Energy* 37(10):8505–8511
181. More K, Borup R, Reeves K (2006) Identifying contributing degradation phenomena in PEM fuel cell membrane electrode assemblies via electron microscopy. *ECS Trans* 3(1):717–733
182. Kudo K, Suzuki T, Morimoto Y (2010) Analysis of oxygen dissolution rate from gas phase into Nafion surface and development of an agglomerate model. *ECS Trans* 33(1):1495–1502
183. Suzuki T, Kudo K, Morimoto Y (2013) Model for investigation of oxygen transport limitation in a polymer electrolyte fuel cell. *J Power Sources* 222: 379–389
184. Moore M, Wardlaw P, Dobson P, Boisvert J, Putz A, Spiteri R, Secanell M (2014) Understanding the effect of kinetic and mass transport processes in cathode agglomerates. *J Electrochem Soc* 161(8):E3125–E3137
185. Banham D, Feng F, Fürstenthaupt T, Ye S, Birss V (2012) First time investigation of Pt nanocatalysts deposited inside carbon mesopores of controlled length and diameter. *J Mater Chem* 22(15):7164–7171. 50
186. Shao Y, Yin G, Gao Y (2007) Understanding and approaches for the durability issues of Pt-based catalysts for PEM fuel cell. *J Power Sources* 171(2): 558–566
187. Katsounaros I, Cherevko S, Zeradjanin A, Mayrhofer K (2014) Oxygen electrochemistry as a cornerstone for sustainable energy conversion. *Angew Chem Int Ed* 53(1):102–121
188. Roen L, Paik C, Jarvi T (2004) Electrocatalytic corrosion of carbon support in PEMFC cathodes. *Electrochem Solid-State Lett* 7(1):A19–A22
189. Liu Z, Brady B, Carter R, Litteer B, Budinski M, Hyun J, Muller D (2008) Characterization of carbon corrosion-induced structural damage of PEM fuel cell cathode electrodes caused by local fuel starvation. *J Electrochem Soc* 155(10):B979–B984
190. Young A, Stumper J, Gyenge E (2009) Characterizing the structural degradation in a PEMFC cathode catalyst layer: carbon corrosion. *J Electrochem Soc* 156(8):B913–B922
191. Darling RM, Meyers JP (2003) Kinetic model of platinum dissolution in PEMFCs. *J Electrochem Soc* 150(11):A1523–A1527
192. Franco AA, Tembely M (2007) Transient multiscale modeling of aging mechanisms in a PEFC cathode. *J Electrochem Soc* 154(7):B712–B723
193. Rinaldo S, Lee W, Stumper J, Eikerling M (2011) Model- and theory-based evaluation of Pt dissolution for supported Pt nanoparticle distributions under potential cycling. *Electrochem Solid-State Lett* 14(5):B47–B49
194. Holby EF, Morgan D (2012) Application of Pt nanoparticle dissolution and oxidation modeling to understanding degradation in PEM fuel cells. *J Electrochem Soc* 159(5):B578–B591
195. Rinaldo S, Lee W, Stumper J, Eikerling M (2014) Mechanistic principles of platinum oxide formation and reduction. *Electrocatalysis* 5(3):262–272
196. Redmond E, Setzler B, Alamgir F, Fuller T (2014) Elucidating the oxide growth mechanism on platinum at the cathode in PEM fuel cells. *Phys Chem Chem Phys* 16(11):5301–5311
197. Fuller T, Gray G (2006) Carbon corrosion induced by partial hydrogen coverage. *ECS Trans* 1(8): 345–353
198. Newman J, Thomas-Alyea KE (2012) Electrochemical systems. Wiley, New York
199. Bard AJ, Faulkner LR (2001) Electrochemical methods: fundamentals and applications, 2nd edn. Wiley, New York
200. Verbrugge M, Hill R (1990) Ion and solvent transport in ion-exchange membranes I. A macro-homogeneous mathematical model. *J Electrochem Soc* 137(3):886–893
201. Bernardi D, Verbrugge M (1991) Mathematical model of a gas diffusion electrode bonded to a polymer electrolyte. *AIChE J* 37(8):1151–1163
202. Cwirko E, Carbonell R (1992) Interpretation of transport coefficients in Nafion using a parallel pore model. *J Membr Sci* 67(2–3):227–247
203. Zhang Z, Jia L, Wang X, Ba L (2011) Effects of inlet humidification on PEM fuel cell dynamic behaviors. *Int J Energy Res* 35(5):376–388

204. Li HY, Weng WC, Yan WM, Wang XD (2011) Transient characteristics of proton exchange membrane fuel cells with different flow field designs. *J Power Sources* 196(1):235–245
205. Meng H, Ruan B (2011) Numerical studies of cold-start phenomena in PEM fuel cells: a review. *Int J Energy Res* 35(1):2–14
206. Yang X, Yin Y, Jia B, Du Q (2013) Analysis of voltage losses in high temperature proton exchange membrane fuel cells with properties of membrane materials and fluent software. *Adv Mater Res* 625:235–238. *Trans Tech Publ* 51
207. Genevey D, von Spakovsky M, Ellis M, Nelson D, Olsommer B, Topin F, Siegel N (2002), Transient model of heat, mass, and charge transfer as well as electrochemistry in the cathode catalyst layer of a PEMFC. In: ASME 2002 international mechanical engineering congress and exposition. American Society of Mechanical Engineers, pp 393–406
208. Olapade P, Meyers J, Mukundan R, Davey J, Borup R (2011) Modeling the dynamic behavior of proton-exchange membrane fuel cells. *J Electrochem Soc* 158(5):B536–B549
209. Zenyuk IV, Das PK, Weber AZ (2016) Understanding impacts of catalyst-layer thickness on fuel-cell performance via mathematical modeling. *J Electrochem Soc* 163(7):F691–F703
210. Eikerling M, Kharkats YI, Kornyshev AA, Volfkovich YM (1998) Phenomenological theory of electro-osmotic effect and water management in polymer electrolyte proton-conducting membranes. *J Electrochem Soc* 145(8):2684–2699
211. Fimrite J, Struchtrup H, Djilali N (2005) Transport phenomena in polymer electrolyte membranes. Part I: modeling framework. *J Electrochem Soc* 152(9): A1804–A1814
212. Weber AZ, Newman J (2004) Transport in polymer-electrolyte membranes: II. Mathematical model. *J Electrochem Soc* 151(2):A311–A325
213. Fimrite J, Struchtrup H, Djilali N (2005) Transport phenomena in polymer electrolyte membranes. Part II: binary friction membrane model. *J Electrochem Soc* 152(9):A1815–A1823
214. Kerkhof P, Geboers M (2005) Toward a unified theory of isotropic molecular transport phenomena. *AIChE J* 51(1):79–121
215. Kerkhof P, Geboers M (2005) Analysis and extension of the theory of multicomponent fluid diffusion. *Chem Eng Sci* 60(12):3129–3167
216. Taylor R, Krishna R (1993) Multicomponent mass transfer Wiley, New York
217. White F (1991) Viscous fluid flow, 2nd edn. McGraw-Hill, New York
218. Donea J, Huerta A (2003) Finite element methods for flow problems, 1st edn. Wiley, Chichester
219. Meng H, Wang C (2004) Electron transport in PEFCs. *J Electrochem Soc* 151(3):A358–A367
220. Um S, Wang CY, Chen K (2000) Computational fluid dynamics modeling of proton exchange membrane fuel cells. *J Electrochem Soc* 147(12):4485–4493
221. Shimpalee S, Dutta S, Lee W, Zee JV (1999) Effect of humidity on PEM fuel cell performance: part II-Numerical simulation. ASME-PUBLICATIONS-HTD 364:367–374
222. Dutta S, Shimpalee S, Zee JV (2000) Three-dimensional numerical simulation of straight channel PEM fuel cells. *J Appl Electrochem* 30(2):135–146
223. Zamel N, Li X (2008) A parametric study of multi-phase and multi-species transport in the cathode of PEM fuel cells. *Int J Energy Res* 32(8):698–721
224. Pant L, Mitra S, Secanell M (2013) A generalized mathematical model to study gas transport in PEMFC porous media. *Int J Heat Mass Transf* 58(1–2):70–79
225. Balen C (2016) A multi-component mass transport model for polymer electrolyte fuel cells. Msc thesis, University of Alberta
226. Golpaygan A, Ashgriz N (2005) Effects of oxidant fluid properties on the mobility of water droplets in the channels of PEM fuel cell. *Int J Energy Res* 29(12):1027–1040
227. Quan P, Zhou B, Sobiesiak A, Liu Z (2005) Water behavior in serpentine micro-channel for proton exchange membrane fuel cell cathode. *J Power Sources* 152:131–145
228. Jiao K, Zhou B, Quan P (2006) Liquid water transport in parallel serpentine channels with manifolds on cathode side of a PEM fuel cell stack. *J Power Sources* 154(1):124–137. 52
229. Cai Y, Hu J, Ma H, Yi B, Zhang H (2006) Effects of hydrophilic/hydrophobic properties on the water behavior in the micro-channels of a proton exchange membrane fuel cell. *J Power Sources* 161(2): 843–848
230. Choi J, Son G (2008) Numerical study of droplet motion in a microchannel with different contact angles. *J Mech Sci Technol* 22(12):2590–2599
231. Bazylak A, Sinton D, Djilali N (2008) Dynamic water transport and droplet emergence in PEMFC gas diffusion layers. *J Power Sources* 176(1): 240–246
232. Akhtar N, Kerkhof PJAM (2011) Dynamic behavior of liquid water transport in a tapered channel of a proton exchange membrane fuel cell cathode. *Int J Hydrog Energy* 36(4):3076–3086
233. Jarauta A, Ryzhakov PB, Secanell M, Waghmare PR, Pons-Prats J (2016) Numerical study of droplet dynamics in a polymer electrolyte fuel cell gas channel using an embedded Eulerian-Lagrangian approach. *J Power Sources* 323:201–212
234. Ryzhakov PB, Jarauta A, Secanell M, Pons-Prats J (2017) On the application of the PFEM to droplet dynamics modeling in fuel cells. *Comput Part Mech* 4(3):285–295
235. Hyman J, Knapp R, Scovel J (1992) High order finite volume approximations of differential operators on

- nonuniform grids. *Phys D Nonlinear Phenom* 60(1):112–138
236. ANSYS Fluent. <http://www.ansys.com/Products/Fluids/ANSYS-Fluent>. Accessed on 30 Jun 2017
  237. STAR-CCM+. <https://mdx.plm.automation.siemens.com/star-ccm-plus>. Accessed on 30 Jun 2017
  238. OpenFOAM. <http://www.openfoam.com/>. Accessed on 30 Jun 2017
  239. Zienkiewicz O, Taylor R, Taylor R (1977) *The finite element method*, vol 3. McGraw-hill, London
  240. COMSOL Multiphysics. <https://www.comsol.com/>. Accessed on 30 Jun 2017
  241. Dadvand P, Rossi R, Oñate E (2010) An object-oriented environment for developing finite element codes for multi-disciplinary applications. *Arch Comput Methods Eng* 17(3):253–297
  242. Bangerth W, Hartmann R, Kanschat G (2007) Deal. II – a general purpose object oriented finite element library. *ACM Trans Math Softw* 33(4):24/1–24/27
  243. Chen K, Hickner M, Noble D (2005) Simplified models for predicting the onset of liquid water droplet instability at the gas diffusion layer/gas flow channel interface. *Int J Energy Res* 29(12):1113–1132
  244. Kumbur E, Sharp K, Mench M (2006) Liquid droplet behavior and instability in a polymer electrolyte fuel cell flow channel. *J Power Sources* 161:333–345
  245. Jarauta A, Secanell M, Pons-Prats J, Ryzhakov PB, Idelsohn SR, Oñate E (2015) A semi-analytical model for droplet dynamics on the GDL surface of a PEFC electrode. *Int J Hydrog Energy* 40:5375–5383
  246. Hirt C, Nichols B (1981) Volume of fluid (VOF) method for the dynamics of free boundaries. *J Comput Phys* 39:201–225
  247. Youngs DL (1982) Time-dependent multi-material flow with large fluid distortion. *Numer Methods Fluid Dyn* 24:273–285
  248. Gueyffier D, Li J, Nadim A, Scardovelli R, Zaleski S (1999) Volume-of-Fluid interface tracking with smoothed surface stress methods for three dimensional flows. *J Comput Phys* 152:423–456
  249. Ferreira RB, Falcão DS, Oliveira VB, Pinto AMFR (2015) Numerical simulations of two-phase flow in proton exchange membrane fuel cells using the volume of fluid method – a review. *J Power Sources* 277:329–342
  250. Brackbill J, Kothe D, Zemach C (1992) A continuum method for modeling surface tension. *J Comput Phys* 100:335–354
  251. Lafaurie B, Nardone C, Scardovelli R, Zaleski S, Zanetti G (1994) Modelling merging and fragmentation in multiphase flows with SURFER. *J Comput Phys* 113(1):134–147. 53
  252. Golpaygan A, Ashgriz N (2008) Multiphase flow model to study channel flow dynamics of PEM fuel cells: deformation and detachment of water droplets. *Int J Comput Fluid Dyn* 22(1–2):85–95
  253. Shirani E, Masoomi S (2008) Deformation of a droplet in a channel flow. *J Fuel Cell Sci Technol* 5(4):041008
  254. Jiao K, Zhou B, Quan P (2006) Liquid water transport in straight micro-parallel-channels with manifolds for PEM fuel cell cathode. *J Power Sources* 157(1):226–243
  255. Zhan Z, Xiao J, Pan M, Yuan R (2006) Characteristics of droplet and film water motion in the flow channels of polymer electrolyte membrane fuel cells. *J Power Sources* 160(1):1–9
  256. Quan P, Lai M (2007) Numerical study of water management in the air flow channel of a PEM fuel cell cathode. *J Power Sources* 164:222–237
  257. Quan P, Lai M (2010) Numerical simulation of two-phase water behavior in the cathode of an interdigitated proton exchange membrane fuel cell. *J Fuel Cell Sci Technol* 7(1):011017–011030
  258. Theodorakakos A, Ous T, Gavaises M, Nouri J, Nikolopoulos N, Yanagihara H (2006) Dynamics of water droplets detached from porous surfaces of relevance to PEM fuel cells. *J Colloid Interface Sci* 300:673–687
  259. Le A, Zhou B (2008) A general model of proton exchange membrane fuel cell. *J Power Sources* 182(1):197–222
  260. Osher S, Sethian J (1988) Fronts propagating with curvature dependent speed: algorithms based on Hamilton-Jacobi formulations. *J Comput Phys* 79:12–49
  261. Osher SJ, Fedkiw RP (2006) *Level set methods and dynamic implicit surfaces*. Springer, New York
  262. Rossi R, Larese A, Dadvand P, Oñate E (2013) An efficient edge-based level set finite element method for free surface flow problems. *Int J Numer Methods Fluids* 71(6):687–716
  263. Wörner M (2012) Numerical modeling of multiphase flows in microfluidics and micro process engineering: a review of methods and applications. *Microfluid Nanofluid* 12:841–886
  264. Cruchaga M, Celentano D, Tezduyar T (2001) A moving Lagrangian interface technique for flow computations over fixed meshes. *Comput Methods Appl Mech Eng* 191(6):525–543
  265. Barton PT, Obadia B, Drikakis D (2011) A conservative level-set method for compressible solid/fluid problems on fixed grids. *J Comput Phys* 230:7867–7890
  266. Spelt PDM (2005) A level-set approach for simulations of flows with multiple moving contact lines with hysteresis. *J Comput Phys* 207(2):389–404
  267. Zhang YL, Zou QP, Greaves D (2010) Numerical simulation of free-surface flow using the level-set method with global mass correction. *Int J Numer Methods Fluids* 63(6):366–396
  268. Ausas RF, Dari EA, Buscaglia GC (2011) A geometric mass-preserving redistancing scheme for the level set function. *Int J Numer Methods Fluids* 65(8):989–1010
  269. Ryzhakov PB, Jarauta A (2015) An embedded approach for immiscible multi-fluid problems. *Int J Numer Methods Fluids* 81:357–376



270. Marti J, Ryzhakov P, Idelsohn S, Oñate E (2012) Combined Eulerian-PFEM approach for analysis of polymers in fire situations. *Int J Numer Methods Eng* 92:782–801
271. Minor G (2007) Experimental study of water droplet flows in a model PEM fuel cell gas microchannel. Master's thesis, University of Victoria
272. Nield D, Bejan A (2006) *Convection in porous media*, vol 3. Springer, New York
273. Jackson R (1977) *Transport in porous catalysts*, Chemical engineering monographs, vol 4. Elsevier Scientific Pub. Co., Amsterdam/New York
274. Kerkhof P (1996) A modified Maxwell-Stefan model for transport through inert membranes: the binary friction model. *Chem Eng J Biochem Eng J* 64(3): 319–343. 54
275. Lightfoot E (1973) *Transport phenomena and living systems: biomedical aspects of momentum and mass transport*. Wiley, New York
276. Salcedo-Diaz R, Ruiz-Femenia R, Kerkhof P, Peters E (2008) Velocity profiles and circulation in Stefan-diffusion. *Chem Eng Sci* 63(19):4685–4693
277. Datta R, Vilekar SA (2010) The continuum mechanical theory of multicomponent diffusion in fluid mixtures. *Chem Eng Sci* 65(22):5976–5989
278. Vural Y, Ma L, Ingham DB, Pourkashanian M (2010) Comparison of the multicomponent mass transfer models for the prediction of the concentration overpotential for solid oxide fuel cell anodes. *J Power Sources* 195(15):4893–4904
279. Bothe D, Dreyer W (2015) Continuum thermodynamics of chemically reacting fluid mixtures. *Acta Mech* 226(6):1757–1805
280. Akhtar N, Kerkhof P (2012) Predicting liquid water saturation through differently structured cathode gas diffusion media of a proton exchange Membrane Fuel Cell. *J Fuel Cell Sci Technol* 9(2):021010
281. Le A, Zhou B (2009) A generalized numerical model for liquid water in a proton exchange membrane fuel cell with interdigitated design. *J Power Sources* 193(2):665–683
282. Le AD, Zhou B (2009) Fundamental understanding of liquid water effects on the performance of a PEMFC with serpentine-parallel channels. *Electrochim Acta* 54(8):2137–2154
283. Le A, Zhou B (2010) A numerical investigation on multi-phase transport phenomena in a proton exchange membrane fuel cell stack. *J Power Sources* 195(16):5278–5291
284. Tomadakis M, Robertson T (2005) Viscous permeability of random fiber structures: comparison of electrical and diffusional estimates with experimental and analytical results. *J Compos Mater* 39(2): 163–188
285. Williams MV, Begg E, Bonville L, Kunz HR, Fenton J (2004) Characterization of gas diffusion layers for PEMFC. *J Electrochem Soc* 151(8):A1173–A1180
286. Gostick J, Fowler M, Pritzker M, Ioannidis M, Behra L (2006) In-plane and through-plane gas permeability of carbon fiber electrode backing layers. *J Power Sources* 162(1):228–238
287. Feser J, Prasad A, Advani S (2006) Experimental characterization of in-plane permeability of gas diffusion layers. *J Power Sources* 162(2):1226–1231
288. Gurau V, Bluemle MJ, De Castro ES, Tsou YM, Zawodzinski TA Jr, Mann JA Jr (2007) Characterization of transport properties in gas diffusion layers for proton exchange membrane fuel cells: 2. Absolute permeability. *J Power Sources* 165(2):793–802
289. Ismail M, Damjanovic T, Ingham D (2010) Effect of polytetrafluoroethylene-treatment and microporous layer-coating on the in-plane permeability of gas diffusion layers used in proton exchange membrane fuel cells. *J Power Sources* 195:6619–6628
290. Tamayol A, Bahrami M (2011) In-plane gas permeability of proton exchange membrane fuel cell gas diffusion layers. *J Power Sources* 196(7):3559–3564
291. Pant LM, Mitra SK, Secanell M (2012) Absolute permeability and Knudsen diffusivity measurements in PEMFC gas diffusion layers and micro porous layers. *J Power Sources* 206:153–160
292. Carrigy NB, Pant LM, Mitra S, Secanell M (2013) Knudsen diffusivity and permeability of PEMFC microporous coated gas diffusion layers for different polytetrafluoroethylene loadings. *J Electrochem Soc* 160(2):F81–F89
293. Tamayol A, McGregor F, Bahrami M (2012) Single phase through-plane permeability of carbon paper gas diffusion layers. *J Power Sources* 204:94–99
294. Mangal P, Dumontier M, Carrigy N, Secanell M (2014) Measurements of permeability and effective in-plane gas diffusivity of gas diffusion media under compression. *ECS Trans* 64(3):487–499
295. Inoue G, Kawase M (2016) Effect of porous structure of catalyst layer on effective oxygen diffusion coefficient in polymer electrolyte fuel cell. *J Power Sources* 327(1–10):55
296. Tomadakis M, Sotirchos S (1993) Ordinary and transition regime diffusion in random fiber structures. *AIChE J* 39(3):397–412
297. Tjaden B, Cooper S, Brett D, Kramer D, Shearing P (2016) On the origin and application of the Bruggeman correlation for analysing transport phenomena in electrochemical systems. *Curr Opin Chem Eng* 12:44–51
298. Flückiger R, Freunberger SA, Kramer D, Wokaun A, Scherer GG, Büchi FN (2008) Anisotropic, effective diffusivity of porous gas diffusion layer materials for PEFC. *Electrochim Acta* 54(54):551–559
299. LaManna JM, Kandlikar SG (2011) Determination of effective water vapor diffusion coefficient in pemfc gas diffusion layers. *Int J Hydrog Energy* 36(8):5021–5029
300. Hwang G, Weber A (2012) Effective-diffusivity measurement of partially-saturated fuel-cell gas-diffusion layers. *J Electrochem Soc* 159(11):F683–F692
301. Rashapov R, Gostick J (2016) In-plane effective diffusivity in PEMFC gas diffusion layers. *Transp Porous Media* 115(3):411–433

302. Zamel N, Becker J, Wiegmann A (2012) Estimating the thermal conductivity and diffusion coefficient of the microporous layer of polymer electrolyte membrane fuel cells. *J Power Sources* 207:70–80
303. Djilali N, Lu D (2002) Influence of heat transfer on gas and water transport in fuel cells. *Int J Therm Sci* 41(1):29–40
304. Zhou J, Putz A, Secanell M (2017) A mixed wettability pore size distribution based mathematical model for analyzing two-phase flow in porous electrodes I. Mathematical model. *J Electrochem Soc* 164(6):F530–F539
305. Schlögl R (1966) Membrane permeation in systems far from equilibrium. *Ber Bunsenges Phys Chem* 70(4):400–414
306. Singh D, Lu D, Djilali N (1999) A two-dimensional analysis of mass transport in proton exchange membrane fuel cells. *Int J Eng Sci* 37(4):431–452
307. Sundmacher K, Schultz T, Zhou S, Scott K, Ginkel M, Gilles E (2001) Dynamics of the direct methanol fuel cell (DMFC): experiments and model-based analysis. *Chem Eng Sci* 56(2):333–341
308. Bhaiya M (2014) An open-source two-phase non-isothermal mathematical model of a polymer electrolyte membrane fuel cell. Master's thesis, University of Alberta
309. Bhaiya M, Putz A, Secanell M (2014) Analysis of non-isothermal effects on polymer electrolyte fuel cell electrode assemblies. *Electrochim Acta* 147: 294–304
310. Zawodzinski TA, Derouin C, Radzinski S, Sherman RJ, Smith VT, Springer TE, Gottesfeld S (1993) Water uptake by and transport through Nafion<sup>®</sup> 117 membranes. *J Electrochem Soc* 140(4):1041–1047
311. Ye X, Wang CY (2007) Measurement of water transport properties through membrane-electrode assemblies I. membranes. *J Electrochem Soc* 154(7): B676–B682
312. Xu F, Leclerc S, Stemmelen D, Perrin JC, Retournard A, Canet D (2017) Study of electro-osmotic drag coefficients in Nafion membrane in acid, sodium and potassium forms by electrophoresis NMR. *J Membr Sci* 536:116–122
313. Ge S, Yi B, Ming P (2006) Experimental determination of electro-osmotic drag coefficient in Nafion membrane for fuel cells. *J Electrochem Soc* 153(8): A1443–A1450
314. Braff W, Mittelsteadt CK (2008) Electroosmotic drag coefficient of proton exchange membranes as a function of relative humidity. *ECS Trans* 16(2):309–316
315. Motupally S, Becker A, Weidner J (2000) Diffusion of water in Nafion 115 membranes. *J Electrochem Soc* 147(9):3171–3177
316. Fuller TF (1992) Solid-polymer-electrolyte fuel cells, PhD thesis 56
317. Zhou J, Stanier D, Putz A, Secanell M (2017) A mixed wettability pore size distribution based mathematical model for analyzing two-phase flow in porous electrodes II. Model validation and analysis of micro-structural parameters. *J Electrochem Soc* 164(6):F540–F556
318. Tasaka M, Hirai T, Kiyono R, Aki Y (1992) Solvent transport across cation-exchange membranes under a temperature difference and under an osmotic pressure difference. *J Membr Sci* 71(1–2):151–159
319. Villaluenga J, Seoane B, Barragán V, Ruiz-Bauzá C (2006) Thermo-osmosis of mixtures of water and methanol through a Nafion membrane. *J Membr Sci* 274(1):116–122
320. Hinatsu JT, Mizuhata M, Takenaka H (1994) Water uptake of perfluorosulfonic acid membranes from liquid water and water vapor. *J Electrochem Soc* 141(6):1493–1498
321. Liu Y, Murphy M, Baker D, Gu W, Ji C, Jorne J, Gasteiger H (2009) Proton conduction and oxygen reduction kinetics in PEM fuel cell cathodes: effects of ionomer-to-carbon ratio and relative humidity. *J Electrochem Soc* 156(8):B970–B980
322. Berg P, Promislow K, Pierre J, Stumper J, Wetton B (2004) Water management in PEM fuel cells. *J Electrochem Soc* 151(3):A341–A353
323. Weber AZ (2010) Improved modeling and understanding of diffusion-media wettability on polymer-electrolyte-fuel-cell performance. *J Power Sources* 195(16):5292–5304
324. Wang ZH, Wang CY, Chen KS (2001) Two-phase flow and transport in the air cathode of proton exchange membrane fuel cells. *J Power Sources* 94:40–50
325. Meng H, Wang CY (2005) Model of two-phase flow and flooding dynamics in polymer electrolyte fuel cells. *J Electrochem Soc* 152(9):A1733–A1741
326. Siegel N, Ellis M, Nelson D, Von Spakovsky M (2004) A two-dimensional computational model of a PEMFC with liquid water transport. *J Power Sources* 128(2):173–184
327. Nam JH, Kaviany M (2003) Effective diffusivity and water-saturation distribution in single-and two-layer PEMFC diffusion medium. *Int J Heat Mass Transf* 46(24):4595–4611
328. Qin C, Rensink D, Fell S, Hassanizadeh SM (2012) Two-phase flow modeling for the cathode side of a polymer electrolyte fuel cell. *J Power Sources* 197:136–144
329. Eikerling M (2006) Water management in cathode catalyst layers of PEM fuel cells a structure-based model. *J Electrochem Soc* 153(3):E58–E70
330. Weber AZ, Darling RM, Newman J (2004) Modeling two-phase behavior in PEFCs. *J Electrochem Soc* 151(10):A1715–A1727
331. Mulone V, Karan K (2013) Analysis of capillary flow driven model for water transport in PEFC cathode catalyst layer: consideration of mixed wettability and pore size distribution. *Int J Hydrog Energy* 38(1): 558–569
332. Natarajan D, Van Nguyen T (2001) A two-dimensional, two-phase, multicomponent, transient

- model for the cathode of a proton exchange membrane fuel cell using conventional gas distributors. *J Electrochem Soc* 148(12):A1324–A1335
333. Wang Z, Wang C, Chen K (2001) Two-phase flow and transport in the air cathode of proton exchange membrane fuel cells. *J Power Sources* 94(1):40–50
334. Soboleva T, Zhao X, Malek K, Xie Z, Navessin T, Holdcroft S (2010) On the micro-, meso-, and macroporous structures of polymer electrolyte membrane fuel cell catalyst layers. *ACS Appl Mater Interfaces* 2(2):375–384
335. Thiele S, Zengerle R, Ziegler C (2011) Nanomorphology of a polymer electrolyte fuel cell catalyst layer—Imaging, reconstruction and analysis. *Nano Res* 4(9):849–860
336. Gostick J, Ioannidis MA, Pritzker MD, Fowler MW (2010) Impact of liquid water on reactant mass transfer in PEM fuel cell electrodes. *J Electrochem Soc* 157(4):B563–B571
337. Rebai M, Prat M (2009) Scale effect and two-phase flow in a thin hydrophobic porous layer. Application to water transport in gas diffusion layers of proton exchange membrane fuel cells. *J Power Sources* 192(2):534–543. 57
338. Zenyuk IV, Medici E, Allen J, Weber AZ (2015) Coupling continuum and pore-network models for polymer-electrolyte fuel cells. *Int J Hydrog Energy* 40(46):16831–16845
339. Song D, Wang Q, Liu Z, Eikerling M, Xie Z, Navessin T, Holdcroft S (2005) A method for optimizing distributions of Nafion and Pt in cathode catalyst layers of PEM fuel cells. *Electrochim Acta* 50(16):3347–3358
340. Baschuk J, Li X (2000) Modelling of polymer electrolyte membrane fuel cells with variable degrees of water flooding. *J Power Sources* 86(1):181–196
341. Culligan P, Barry D (1996) Scaling immiscible flow in porous media. Technical report, Research Report ED 1207 PC, Centre for Water Research, University of Western Australia, Perth
342. Jiao K, Li X (2011) Water transport in polymer electrolyte membrane fuel cells. *Prog Energy Combust Sci* 37(3):221–291
343. Litster S, Djilali N (2006) Transport phenomena in fuel cells., chapter 5, 1st edn. WIT Press, Ashurst
344. Leverett M, Lewis W (1941) Steady flow of gas-oil-water mixtures through unconsolidated sands. *Trans AIME* 142(01):107–116
345. Siegel N, Ellis M, Nelson D, Von Spakovsky M (2004) A two-dimensional computational model of a PEMFC with liquid water transport. *J Power Sources* 128(2):173–184
346. Natarajan D, Van Nguyen T (2003) Three-dimensional effects of liquid water flooding in the cathode of a PEM fuel cell. *J Power Sources* 115(1):66–80
347. You L, Liu H (2002) A two-phase flow and transport model for the cathode of PEM fuel cells. *Int J Heat Mass Transf* 45(11):2277–2287
348. Hu M, Gu A, Wang M, Zhu X, Yu L (2004) Three dimensional, two phase flow mathematical model for PEM fuel cell: part I. Model development. *Energy Convers Manag* 45(11):1861–1882
349. Meng H (2007) A two-phase non-isothermal mixed-domain PEM fuel cell model and its application to two-dimensional simulations. *J Power Sources* 168(1):218–228
350. Lin G, Van Nguyen T (2006) A two-dimensional two-phase model of a PEM fuel cell. *J Electrochem Soc* 153(2):A372–A382
351. Mateo-Villanueva P (2013) A mixed wettability pore size distribution model for the analysis of water transport in PEMFC materials. Master's thesis, University of Alberta
352. Gostick JT, Ioannidis MA, Fowler MW, Pritzker MD (2009) Wettability and capillary behavior of fibrous gas diffusion media for polymer electrolyte membrane fuel cells. *J Power Sources* 194(1):433–444
353. Zhang FY, Spornjak D, Prasad AK, Advani SG (2007) In situ characterization of the catalyst layer in a polymer electrolyte membrane fuel cell. *J Electrochem Soc* 154(11):B1152–B1157
354. Ihonen J, Mikkola M, Lindbergh G (2004) Flooding of gas diffusion backing in PEFCs: Physical and electro-chemical characterization. *J Electrochem Soc* 151(8):A1152–A1161
355. Prasanna M, Ha H, Cho E, Hong SA, IH O (2004) Influence of cathode gas diffusion media on the performance of the pemfcs. *J Power Sources* 131(1):147–154
356. Dohle H, Jung R, Kimiaie N, Mergel J, Müller M (2003) Interaction between the diffusion layer and the flow field of polymer electrolyte fuel cell experiments and simulation studies. *J Power Sources* 124(2):371–384
357. Nguyen T, Lin G, Ohn H, Hussey D, Jacobson D, Arif M (2006) Measurements of two-phase flow properties of the porous media used in pem fuel cells. *ECS Trans* 3(1):415–423
358. Koido T, Furusawa T, Moriyama K, Takato K (2006) Two-phase transport properties and transport simulation of the gas diffusion layer of a pefc. *ECS Trans* 3(1):425–434
359. Hussaini I, Wang C (2010) Measurement of relative permeability of fuel cell diffusion media. *J Power Sources* 195(12):3830–3840. 58
360. Sole JD (2008) Investigation of water transport parameters and processes in the gas diffusion layer of PEM fuel cells. PhD thesis
361. Gostick JT, Ioannidis MA, Fowler MW, Pritzker MD (2007) Pore network modeling of fibrous gas diffusion layers for polymer electrolyte membrane fuel cells. *J Power Sources* 173(1):277–290
362. He G, Ming P, Zhao Z, Abudula A, Xiao Y (2007) A two-fluid model for two-phase flow in PEMFCs. *J Power Sources* 163(2):864–873
363. Koido T, Furusawa T, Moriyama K (2008) An approach to modeling two-phase transport in the

- gas diffusion layer of a proton exchange membrane fuel cell. *J Power Sources* 175(1):127–136
364. Pintauro P, Bennion D (1984) Mass transport of electrolytes in membranes. I. Development of mathematical transport model. *Ind Eng Chem Fundam* 23(2):230–234
365. Natarajan D, Nguyen TV (2004) Effect of electrode configuration and electronic conductivity on current density distribution measurements in PEM fuel cells. *J Power Sources* 135(1):95–109
366. Becker J, Flückiger R, Reum M, Büchi FN, Marone F, Stampanoni M (2009) Determination of material properties of gas diffusion layers: experiments and simulations using phase contrast tomographic microscopy. *J Electrochem Soc* 156(10):B1175–B1181
367. Suzuki T, Murata H, Hatanaka T, Morimoto Y (2003) Analysis of the catalyst layer of polymer electrolyte fuel cells. *R&D Rev Toyota CRDL* 39(3):33–38
368. Morris DR, Liu SP, Villegas Gonzalez D, Gostick JT (2014) Effect of water sorption on the electronic conductivity of porous polymer electrolyte membrane fuel cell catalyst layers. *ACS Appl Mater Interfaces* 6(21):18609–18618
369. Weber AZ, Newman J (2003) Transport in polymer-electrolyte membranes: I. Physical model. *J Electrochem Soc* 150(7):A1008–A1015
370. Bekkedahl T (2007) In-Plane conductivity testing procedures & results. In: DOE high temperature membrane working group meeting, Arlington
371. Iden H, Ohma A, Shinohara K (2009) Analysis of proton transport in pseudo catalyst layers. *J Electrochem Soc* 156(9):B1078–B1084
372. Fuller TF, Newman J (1993) Water and thermal management in solid-polymer-electrolyte fuel cells. *J Electrochem Soc* 140(5):1218–1225
373. Peron J, Edwards D, Haldane M, Luo X, Zhang Y, Holdcroft S, Shi Z (2011) Fuel cell catalyst layers containing short-side-chain perfluorosulfonic acid ionomers. *J Power Sources* 196(1):179–181
374. Vang J, Zhou F, Andreassen S, Kær S (2015) Estimating important electrode parameters of high temperature PEM fuel cells by fitting a model to polarisation curves and impedance spectra. *ECS Trans* 68(3):13–34
375. Adzakpa K, Agbossou K, Dube Y, Dostie M, Fournier M, Poulin A (2008) PEM fuel cells modeling and analysis through current and voltage transient behaviors. *IEEE Trans Energy Convers* 23(2):581–591
376. Makharia R, Mathias M, Baker D (2005) Measurement of catalyst layer electrolyte resistance in PEFCs using electrochemical impedance spectroscopy. *J Electrochem Soc* 152(5):A970–A977
377. Springer T, Zawodzinski T, Wilson M, Gottesfeld S (1996) Characterization of polymer electrolyte fuel cells using AC impedance spectroscopy. *J Electrochem Soc* 143(2):587–599
378. Baricci A, Zago M, Casalegno A (2014) A quasi 2D model of a high temperature polymer fuel cell for the interpretation of impedance spectra. *Fuel Cells* 14(6):926–937
379. Shamardina O, Kondratenko M, Chertovich A, Kulikovskiy A (2014) A simple transient model for a high temperature PEM fuel cell impedance. *Int J Hydrog Energy* 39(5):2224–2235
380. Tant S, Rosini S, Thivel PX, Druart F, Rakotonrainibe A, Geneston T, Bultel Y (2014) An algorithm for diagnosis of proton exchange membrane fuel cells by electrochemical impedance spectroscopy. *Electrochim Acta* 135(368–379):59
381. Choopanya P, Yang Z (2014) Transient performance investigation of different flow-field designs of automotive polymer electrolyte membrane fuel cell (PEMFC) using computational fluid dynamics (CFD). In: International conference on heat transfer, fluid mechanics and thermodynamics
382. Sun W, Peppley BA, Karan K (2005) Modeling the influence of GDL and flow-field plate parameters on the reaction distribution in the PEMFC cathode catalyst layer. *J Power Sources* 144(1):42–53
383. Chen S, Kucernak A (2004) Electrocatalysis under conditions of high mass transport: investigation of hydrogen oxidation on single submicron Pt particles supported on carbon. *J Phys Chem B* 108(37):13984–13994
384. Gasteiger H, Panels J, Yan S (2004) Dependence of PEM fuel cell performance on catalyst loading. *J Power Sources* 127(1):162–171
385. Damjanovic A, Brusic V (1967) Electrode kinetics of oxygen reduction on oxide-free platinum electrodes. *Electrochim Acta* 12(6):615–628
386. Paucirova M, Drazic D, Damjanovic A (1973) The effect of surface coverage by adsorbed oxygen on the kinetics of oxygen reduction at oxide free platinum. *Electrochim Acta* 18(12):945–951
387. Parthasarathy A, Srinivasan S, Appleby AJ, Martin CR (1992) Temperature dependence of the electrode kinetics of oxygen reduction at the platinum/Nafion<sup>®</sup> interface – a microelectrode investigation. *J Electrochem Soc* 139(9):2530–2537
388. Markiewicz M, Zalitis C, Kucernak A (2015) Performance measurements and modelling of the ORR on fuel cell electrocatalysts—the modified double trap model. *Electrochim Acta* 179:126–136
389. Tafel J (1905) Über die Polarisation bei kathodischer Wasserstoffentwicklung. *Z Phys Chem* 50:641
390. Heyrovský J (1927) A theory of overpotential. *Recueil des Travaux Chimiques des Pays-Bas* 46(8):582–585
391. Volmer M, Erdey-Gruz T (1930). Principles of adsorption and reaction on solid surfaces, Wiley-Interscience, Hoboken
392. de Chialvo MRG, Chialvo AC (2004) Hydrogen diffusion effects on the kinetics of the hydrogen electrode reaction. Part I. Theoretical aspects. *Phys Chem Chem Phys* 6(15):4009–4017
393. Quaino PM, de Chialvo MRG, Chialvo AC (2004) Hydrogen diffusion effects on the kinetics of

- the hydrogen electrode reaction Part II. Evaluation of kinetic parameters. *Phys Chem Chem Phys* 6(18):4450–4455
394. Sepa D, Vojnovic M, Damjanovic A (1981) Reaction intermediates as a controlling factor in the kinetics and mechanism of oxygen reduction at platinum electrodes. *Electrochim Acta* 26(6):781–793
395. Antoine O, Bultel Y, Durand R (2001) Oxygen reduction reaction kinetics and mechanism on platinum nanoparticles inside Nafion<sup>®</sup>. *J Electroanal Chem* 499(1):85–94
396. Eslamibidgoli MJ, Huang J, Kadyk T, Malek A, Eikerling M (2016) How theory and simulation can drive fuel cell electrocatalysis. *Nano Energy* 29: 334–361
397. Wang JX, Zhang J, Adzic RR (2007) Double-trap kinetic equation for the oxygen reduction reaction on Pt (111) in acidic media. *J Phys Chem A* 111(49):12,702–12,710
398. Walch S, Dhanda A, Aryanpour M, Pitsch H (2008) Mechanism of molecular oxygen reduction at the cathode of a PEM fuel cell: non-electrochemical reactions on catalytic Pt particles. *J Phys Chem C* 112(22):8464–8475
399. Moore M, Putz A, Secanell M (2012) Development of a cathode electrode model using the ORR dual-trap intrinsic kinetic model. In: ASME 2012 10th international conference on fuel cell science, engineering and technology collocated with the ASME 2012 6th international conference on energy sustainability. American Society of Mechanical Engineers, pp 367–376
400. Medici E, Zenyuk I, Parkinson D, Weber A, Allen J (2016) Understanding water transport in polymer electrolyte fuel cells using coupled continuum and pore-network models. *Fuel Cells* 16(6):725–733
401. Moore M (2012) Investigation of the double-trap intrinsic kinetic equation for the oxygen reduction reaction and its implementation into a membrane electrode assembly model. Master's thesis, University of Alberta 60
402. Huang BT, Chatillon Y, Bonnet C, Lapicque F, Leclerc S, Hinaje M, Raël S (2012) Experimental investigation of air relative humidity (RH) cycling tests on mea/cell aging in pemfc part II: study of low RH cycling test with air RH at 62%/0%. *Fuel Cells* 12(3):347–355
403. Breaz E, Gao F, Miraoui A, Timovan R (2014) A short review of aging mechanism modeling of proton exchange membrane fuel cell in transportation applications. In: 40th annual conference of the IEEE industrial electronics society, IECON 2014. IEEE, pp 3941–3947
404. Wang L, Husar A, Zhou T, Liu H (2003) A parametric study of PEM fuel cell performances. *Int J Hydrog Energy* 28(11):1263–1272
405. Mazumder S, Cole JV (2003) Rigorous 3-D mathematical modeling of PEM fuel cells II. Model predictions with liquid water transport. *J Electrochem Soc* 150(11):A1510–A1517
406. Ju H, Meng H, Wang CY (2005) A single-phase, non-isothermal model for PEM fuel cells. *Int J Heat Mass Transf* 48(7):1303–1315
407. Ju H, Wang CY, Cleghorn S, Beuscher U (2005) Nonisothermal modeling of polymer electrolyte fuel cells I. Experimental validation. *J Electrochem Soc* 152(8):A1645–A1653
408. Dutta SSS (2000) Numerical prediction of temperature distribution in PEM fuel cells. *Numer Heat Transf Part A Appl* 38(2):111–128
409. Wang Y, Wang CY (2006) A nonisothermal, two-phase model for polymer electrolyte fuel cells. *J Electrochem Soc* 153(6):A1193–A1200
410. Rowe A, Li X (2001) Mathematical modeling of proton exchange membrane fuel cells. *J Power Sources* 102(1):82–96
411. Ramousse J, Deseure J, Lottin O, Didierjean S, Maillat D (2005) Modelling of heat, mass and charge transfer in a PEMFC single cell. *J Power Sources* 145(2):416–427
412. Weber AZ, Newman J (2006) Coupled thermal and water management in polymer electrolyte fuel cells. *J Electrochem Soc* 153(12):A2205–A2214
413. Birgersson E, Noponen M, Vynnycky M (2005) Analysis of a two-phase non-isothermal model for a PEFC. *J Electrochem Soc* 152(5):A1021–A1034
414. Pasaogullari U, Mukherjee P, Wang CY, Chen K (2007) Anisotropic heat and water transport in a PEFC cathode gas diffusion layer. *J Electrochem Soc* 154(8):B823–B834
415. Bapat CJ, Thynell ST (2007) Anisotropic heat conduction effects in proton-exchange membrane fuel cells. *J Heat Transf* 129(9):1109–1118
416. Zamel N, Li X (2010) Non-isothermal multi-phase modeling of PEM fuel cell cathode. *Int J Energy Res* 34(7):568–584
417. Berning T, Djilali N (2003) A 3D, multiphase, multi-component model of the cathode and anode of a PEM fuel cell. *J Electrochem Soc* 150(12):A1589–A1598
418. Hwang J, Chen P (2006) Heat/mass transfer in porous electrodes of fuel cells. *Int J Heat Mass Transf* 49(13):2315–2327
419. Hwang J, Chao C, Wu W (2006) Thermal-fluid transports in a five-layer membrane-electrode assembly of a PEM fuel cell. *J Power Sources* 163(1):450–459
420. Hwang J, Chao C, Chang C, Ho W, Wang D (2007) Modeling of two-phase temperatures in a two-layer porous cathode of polymer electrolyte fuel cells. *Int J Hydrog Energy* 32(3):405–414
421. Popiel C, Wojtkowiak J (1998) Simple formulas for thermophysical properties of liquid water for heat transfer calculations (from 0 °C to 150 °C). *Heat Transf Eng* 19(3):87–101
422. Chung DW, Ebner M, Ely DR, Wood V, Garcia RE (2013) Validity of the Bruggeman relation for porous electrodes. *Model Simul Mater Sci Eng* 21(7): 074009. 61
423. Aharony A, Stauffer D (2003) Introduction to percolation theory. Taylor & Francis, London

424. Ostadi H, Rama P, Liu Y, Chen R, Zhang X, Jiang K (2010) 3D reconstruction of a gas diffusion layer and a microporous layer. *J Membr Sci* 351(1):69–74
425. García-Salaberri PA, Gostick JT, Hwang G, Weber AZ, Vera M (2015) Effective diffusivity in partially-saturated carbon-fiber gas diffusion layers: effect of local saturation and application to macroscopic continuum models. *J Power Sources* 296:440–453
426. García-Salaberri PA, Hwang G, Vera M, Weber AZ, Gostick JT (2015) Effective diffusivity in partially-saturated carbon-fiber gas diffusion layers: effect of through-plane saturation distribution. *Int J Heat Mass Transf* 86:319–333
427. Fazeli M, Hinebaugh J, Bazylak A (2016) Incorporating embedded microporous layers into topologically equivalent pore network models for oxygen diffusivity calculations in polymer electrolyte membrane fuel cell gas diffusion layers. *Electrochim Acta* 216:364–375
428. Hinebaugh J, Fishman Z, Bazylak A (2010) Unstructured pore network modeling with heterogeneous PEMFC GDL porosity distributions. *J Electrochem Soc* 157(11):B1651–B1657
429. Zenyuk IV, Weber AZ (2015) Understanding liquid-water management in PEFCs using X-ray computed tomography and modeling. *ECS Trans* 69(17):1253–1265
430. Zenyuk IV, Parkinson DY, Hwang G, Weber AZ (2015) Probing water distribution in compressed fuel-cell gas-diffusion layers using X-ray computed tomography. *Electrochem Commun* 53:24–28
431. Kotaka T, Tabuchi Y, Mukherjee PP (2015) Microstructural analysis of mass transport phenomena in gas diffusion media for high current density operation in PEM fuel cells. *J Power Sources* 280:231–239
432. Berejnov V, Susac D, Stumper J, Hitchcock AP (2011) Nano to micro scale characterization of water up-take in the catalyst coated membrane measured by soft X-ray scanning transmission X-ray microscopy. *ECS Trans* 41(1):395–402
433. Saha MS, Tam M, Berejnov V, Susac D, McDermid S, Hitchcock AP, Stumper J (2013) Characterization and performance of catalyst layers prepared by inkjet printing technology. *ECS Trans* 58(1):797–806
434. Susac D, Berejnov V, Hitchcock AP, Stumper J (2013) STXM characterization of PEM fuel cell catalyst layers. *ECS Trans* 50(2):405–413
435. Wargo E, Hanna A, Cecen A, Kalidindi S, Kumbur E (2012) Selection of representative volume elements for pore-scale analysis of transport in fuel cell materials. *J Power Sources* 197:168–179
436. Barbosa R, Andaverde J, Escobar B, Cano U (2011) Stochastic reconstruction and a scaling method to determine effective transport coefficients of a proton exchange membrane fuel cell catalyst layer. *J Power Sources* 196(3):1248–1257
437. Sinha PK, Mukherjee PP, Wang CY (2007) Impact of GDL structure and wettability on water management in polymer electrolyte fuel cells. *J Mater Chem* 17(30):3089–3103
438. Becker J, Wieser C, Fell S, Steiner K (2011) A multi-scale approach to material modeling of fuel cell diffusion media. *Int J Heat Mass Transf* 54:1360–1368
439. Lange KJ, Misra C, Sui PC, Djilali N (2011) A numerical study on preconditioning and partitioning schemes for reactive transport in a PEMFC catalyst layer. *Comput Methods Appl Mech Eng* 200(9):905–916
440. Vogel HJ, Tölke J, Schulz V, Krafczyk M, Roth K (2005) Comparison of a lattice-Boltzmann model, a full-morphology model, and a pore network model for determining capillary pressure–saturation relationships. *Vadose Zone J* 4(2):380–388
441. Mukherjee PP, Wang CY, Kang Q (2009) Mesoscopic modeling of two-phase behavior and flooding phenomena in polymer electrolyte fuel cells. *Electrochim Acta* 54(27):6861–6875
442. Pharoah J, Choi HW, Chueh CC, Harvey DB (2011) Effective transport properties accounting for electrochemical reactions of proton-exchange membrane fuel cell catalyst layers. *ECS Trans* 41(1):221–227. 62
443. El Hannach M, Pauchet J, Prat M (2011) Pore network modeling: application to multiphase transport inside the cathode catalyst layer of proton exchange membrane fuel cell. *Electrochim Acta* 56(28):10796–10808
444. El Hannach M, Prat M, Pauchet J (2012) Pore network model of the cathode catalyst layer of proton exchange membrane fuel cells: analysis of water management and electrical performance. *Int J Hydrog Energy* 37(24):18996–19006
445. Wu R, Zhu X, Liao Q, Wang H, Yd D, Li J, Ye D (2010) A pore network study on water distribution in bi-layer gas diffusion media: effects of inlet boundary condition and micro-porous layer properties. *Int J Hydrog Energy* 35(17):9134–9143
446. Wu R, Zhu X, Liao Q, Wang H, Yd D, Li J, Ye D (2010) A pore network study on the role of micro-porous layer in control of liquid water distribution in gas diffusion layer. *Int J Hydrog Energy* 35(14):7588–7593
447. Gostick JT (2013) Random pore network modeling of fibrous PEMFC gas diffusion media using Voronoi and Delaunay tessellations. *J Electrochem Soc* 160(8):F731–F743
448. Berson A, Choi HW, Pharoah JG (2011) Determination of the effective gas diffusivity of a porous composite medium from the three-dimensional reconstruction of its microstructure. *Phys Rev E* 83:026310
449. Kim SH, Pitsch H (2009) Reconstruction and effective transport properties of the catalyst layer in PEM fuel cells. *J Electrochem Soc* 156(6):B673–B681
450. Becker J, Schulz V, Wiegmann A (2008) Numerical determination of two-phase material parameters of a



- gas diffusion layer using tomography images. *J Fuel Cell Sci Technol* 5(2):021006
451. El Hannach M, Singh R, Djilali N, Kjeang E (2015) Micro-porous layer stochastic reconstruction and transport parameter determination. *J Power Sources* 282:58–64
452. El Hannach M, Kjeang E (2014) Stochastic micro-structural modeling of PEFC gas diffusion media. *J Electrochem Soc* 161(9):F951–F960
453. Espinola A, Miguel PM, Salles MR, Pinto AR (1986) Electrical properties of carbons – resistance of powder materials. *Carbon* 24(3):337–341
454. Jinnouchi R, Kudo K, Kitano N, Morimoto Y (2016) Molecular dynamics simulations on  $O_2$  permeation through Nafion ionomer on platinum surface. *Electrochim Acta* 188:767–776
455. Kudo K, Morimoto Y (2013) Analysis of oxygen transport resistance of Nafion thin film on Pt electrode. *ECS Trans* 50(2):1487–1494
456. Hao L, Cheng P (2010) Lattice Boltzmann simulations of water transport in gas diffusion layer of a polymer electrolyte membrane fuel cell. *J Power Sources* 195(12):3870–3881
457. Moriyama K, Inamuro T (2011) Lattice Boltzmann simulations of water transport from the gas diffusion layer to the gas channel in PEFC. *Commun Comput Phys* 9(5):1206–1218
458. Kim KN, Kang JH, Lee SG, Nam JH, Kim CJ (2015) Lattice Boltzmann simulation of liquid water transport in microporous and gas diffusion layers of polymer electrolyte membrane fuel cells. *J Power Sources* 278:703–717
459. Sinha PK, Wang CY (2007) Pore-network modeling of liquid water transport in gas diffusion layer of a polymer electrolyte fuel cell. *Electrochim Acta* 52(28):7936–7945
460. Ji Y, Luo G, Wang CY (2010) Pore-level liquid water transport through composite diffusion media of PEMFC. *J Electrochem Soc* 157(12):B1753–B1761
461. Schulz VP, Wargo EA, Kumbur EC (2015) Pore-morphology-based simulation of drainage in porous media featuring a locally variable contact angle. *Transp Porous Media* 107(1):13–25
462. Schulz VP, Becker J, Wiegmann A, Mukherjee PP, Wang CY (2007) Modeling of two-phase behavior in the gas diffusion medium of PEFCs via full morphology approach. *J Electrochem Soc* 154(4):B419–B426
463. Zamel N, Li X, Becker J, Wiegmann A (2011) Effect of liquid water on transport properties of the gas diffusion layer of polymer electrolyte membrane fuel cells. *Int J Hydrog. Energy* 36(9):5466–5478. 63
464. Fazeli M, Hinebaugh J, Bazylak A (2015) Investigating inlet condition effects on PEMFC GDL liquid water transport through pore network modeling. *J Electrochem Soc* 162(7):F661–F668
465. Zenyuk IV, Lamibrac A, Eller J, Parkinson DY, Marone F, Büchi FN, Weber AZ (2016) Investigating evaporation in gas diffusion layers for fuel cells with X-ray computed tomography. *J Phys Chem C* 120(50):28701–28711
466. Lobato J, Cañizares P, Rodrigo MA, Pinar FJ, Mena E, Úbeda D (2010) Three-dimensional model of a 50 cm<sup>2</sup> high temperature PEM fuel cell. Study of the flow channel geometry influence. *Int J Hydrog Energy* 35(11):5510–5520
467. Wang Y, Basu S, Wang CY (2008) Modeling two-phase flow in PEM fuel cell channels. *J Power Sources* 179(2):603–617
468. Jiao K, Zhou B (2007) Innovative gas diffusion layers and their water removal characteristics in PEM fuel cell cathode. *J Power Sources* 169(2): 296–314
469. Chen L, Cao T, Li Z, He Y, Tao W (2012) Numerical investigation of liquid water distribution in the cathode side of proton exchange membrane fuel cell and its effects on cell performance. *Int J Hydrog Energy* 37(11):9155–9170
470. Zhou J, Shukla S, Putz A, Secanell M (2017) Understanding the role of micro porous layer on fuel cell performance using a non-isothermal two-phase model. *Electrochim Acta* (Under review)
471. Nguyen PT, Berning T, Djilali N (2004) Computational model of a PEM fuel cell with serpentine gas flow channels. *J Power Sources* 130(1):149–157
472. Gerris flow solver. [http://gfs.sourceforge.net/wiki/index.php/Main\\_Page](http://gfs.sourceforge.net/wiki/index.php/Main_Page). Accessed on 12 Jul 2017
473. Arndt D, Bangerth W, Davydov D, Heister T, Heltai L, Kronbichler M, Maier M, Pelteret JP, Turcksin B, Wells D (2017) The deal.II library, version 8.5. *J Numer Math* 25(3):137–145
474. Kelly DW, Gago d SR, JP ZOC, Babuska I (1983) A posteriori error analysis and adaptive processes in the finite element method: Part I – error analysis. *Int J Numer Methods Eng* 19(11):1593–1619
475. Math2Market<sup>®</sup>GmbH (2017). GeoDict<sup>®</sup>
476. Palabos. <http://www.palabos.org/>. Accessed on 25 Jul 2017
477. Gostick J, Aghighi M, Hinebaugh J, Tranter T, Hoeh MA, Day H, Spellacy B, Sharqawy MH, Bazylak A, Burns A et al (2016) Openpnm: a pore network modeling package. *Comput Sci Eng* 18(4): 60–74



## PEM Fuel Cells and Platinum-Based Electrocatalysts

Junliang Zhang  
Fuel Cell Business, General Motors Global  
Propulsion Systems, Pontiac, MI, USA

### Article Outline

Glossary  
Definition of the Subject  
Introduction  
Electrocatalysis of the ORR at Platinum Surfaces  
Pt-Alloy Electrocatalysts  
Pt Monolayer Electrocatalysts  
Pt and Pt-Alloy Nanowire and Nanotube  
Electrocatalysts  
Facet- and Shape-Controlled Pt-Alloy  
Nanocrystal Electrocatalysts  
Future Directions  
Bibliography

### Glossary

**Anode** An electrode where the electrochemical oxidation reaction(s) occurs, generating free electrons that flow through a polarized electrical device and enter the cathode. In a fuel cell, the fuel oxidation reaction happens at the anode.

**Cathode** An electrode where the electrochemical reduction reaction(s) occurs, by consuming the electrons originated from the anode. In a fuel cell, the oxygen reduction reaction happens at the cathode.

**Electrocatalyst** A material that is applied on the surface of an electrode to catalyze half-cell reactions.

**Normal hydrogen electrode (NHE)** Also known as the standard hydrogen electrode (SHE), it is a redox reference electrode which

forms the basis of the thermodynamic scale of oxidation-reduction potentials. The potential of the NHE is defined as zero and based on equilibrium of the following redox half-cell reaction, typically on a Pt surface:  $2\text{H}^+(\text{aq}) + 2\text{e}^- \rightarrow \text{H}_2(\text{g})$  The activities of both the reduced form and the oxidized form are maintained at unity. That implies that the pressure of hydrogen gas is 1 atm and the concentration of hydrogen ions in the solution is 1 M.

**Oxygen reduction reaction (ORR)** An electrode reaction, in which oxygen gas is reduced at the cathode of an electrochemical cell. The product of the reaction can be water molecules, hydroxyl ions ( $\text{OH}^-$ ), or sometimes hydrogen peroxide molecules. It is a very important and much-studied electrochemical reaction because it occurs at the cathode of practically all fuel cells.

**Proton-exchange membrane fuel cells (PEMFC)** Also known as polymer electrolyte membrane fuel cells, these are a type of fuel cells that use proton-conducting-ionomer membrane as the electrolyte to separate anode and cathode. Their distinguishing features include low operating temperature ( $<80^\circ\text{C}$ ), high power density, quick start-up, and quick match to shifting demands for power. They are being developed for transport applications as well as stationary and portable applications.

**Pt mass activity** The kinetic current of the oxygen reduction reaction normalized by the mass of Pt metal contained in the electrocatalyst.

**Pt-specific activity** The kinetic current of the oxygen reduction reaction normalized by the electrochemical surface area of the Pt metal contained in the electrocatalyst.

**Reversible hydrogen electrode (RHE)** This differs from the NHE by the fact that the hydrogen-ion concentration of RHE reaction is the same as that in the actual electrolyte solution used for the working electrode. The potential of RHE is therefore  $(-0.059 \times (\text{pH of the electrolyte}))$  V.

## Definition of the Subject

H<sub>2</sub>/air-powered PEM fuel cells are a future substitute for combustion engines as the green power source for transport application. In PEM fuel cells, because of their low operating temperature and low pH, both anode and cathode reactions are catalyzed by Pt or Pt-based electrocatalysts. Pt is a precious and expensive noble metal, and therefore its loading requirement plays a major role in determining the cost of fuel cells in mass production. The anode hydrogen oxidation reaction on Pt is intrinsically fast and requires very little Pt, while the cathode oxygen reduction reaction (ORR) is a very sluggish reaction that consumes about 90% of the total Pt content in PEM fuel cells. The current Pt loading in the most advanced fuel cell vehicles that use state-of-the-art Pt-based catalysts is about four- to eight-fold higher than the target established for mass-produced fuel cell vehicles. Therefore, lowering the Pt loading at the cathode is the most critical mission for the PEM fuel cell development. To do that, significant depth of knowledge in understanding the ORR on Pt and Pt-based electrocatalysts' surfaces is required; and the search for novel Pt-based electrocatalysts with enhanced ORR activity is seemingly the most productive pathway.

## Introduction

Ever since 1839, when Sir William Robert Grove introduced the first concept of fuel cells [1, 2], researchers have been continuously trying to apply fuel cells for stationary and mobile power sources [3, 4], because of their high energy efficiency and low environmental footprint. Fuel cells can be customarily classified according to the electrolyte employed, with different electrolytes operating at different temperature ranges. The operating temperature then dictates the types of fuels and electrode materials that can be used in a fuel cell. For example, aqueous electrolytes are limited to operating temperatures of about 200 °C or lower because of their high water vapor pressure. At these temperatures the fuel is, in applications requiring high current density and low cost, restricted to hydrogen. To accommodate the slow

kinetics of the electrochemical reactions at such low temperature in acid environments, platinum catalysts are required for both cathode and anode. In high temperature fuel cells, CO or even CH<sub>4</sub> can be used as the fuel, and the catalyst is not necessary to be noble metals, because of the inherently fast electrode reaction kinetics.

Among various types of fuel cells, proton exchange membrane fuel cells (PEMFCs) have attracted the most attention in recent years due to their low operating temperature (about 80 °C), high power density, quick start-up, and quick match to shifting demands for power [3]. Hydrogen/air-powered PEMFCs make them the primary candidate for the power source of light-duty vehicles and buildings. In a recent study by Thomas [5], the author compared fuel cell and battery as the power sources for all-electric vehicles, and found that for any vehicle range greater than 160 km (100 miles), fuel cells are superior than batteries in terms of mass, volume, cost, initial greenhouse gas reductions, refueling time, well-to-wheel energy efficiency (using natural gas and biomass as the source) and life cycle costs. PEMFCs also allow direct use of methanol without a processor, called DMFC. DMFCs are the primary candidates for portable electronic applications; low power densities and high Pt requirements have precluded their use in vehicles to date.

One difficult challenge to make PEMFC vehicles cost-competitive with traditional combustion engine cars is the high platinum catalyst loading and poor catalyst durability of the fuel cells [6, 7]. In the mid- to late-1980s and in the early 1990s, the fuel cell team at Los Alamos National Laboratory (LANL) succeeded in demonstrating high performance H<sub>2</sub>/air fuel cells with a platinum loading less than 0.5 mg Pt/cm<sup>2</sup> per electrode, which was one magnitude lower than its previous level [8–11]. In that effort, Raistrick [8] was the first one to cast ionomer into the electrocatalyst layer by impregnating a Pt/C electrode into the ionomer solution before hot-pressing it onto the membrane, and thus greatly increased the electrocatalyst-electrolyte interfacial contact area. Wilson et al. [9–11] improved that process by mixing the Pt/C powder catalyst with ionomer solution before coating the electrode. Those

research achievements at LANL partly led to the renaissance in PEMFCs in the past 2 decades [4].

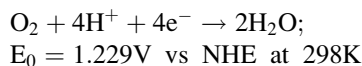
In a PEMFC, if pure hydrogen is used as fuel, the anode reaction is then the hydrogen oxidation reaction (HOR) at the surface of the anode platinum electrocatalyst. The hydrogen oxidation reaction (HOR) and hydrogen evolution reaction (HER) are by far the most thoroughly investigated electrochemical reaction system [12]. Due to the fast electrode kinetics of hydrogen oxidation at platinum surface [12–14], the anode platinum loading can be reduced down to 0.05 mg Pt/cm<sup>2</sup> without significant performance loss [15]. The cathode reaction in a PEM fuel cell is the oxygen reduction reaction (ORR) at platinum surface in an acidic electrolyte. In contrast to HOR at the anode, the cathode ORR is a highly irreversible reaction even at temperatures above 100 °C at the best existing catalyst – the platinum surface [16–19]. Gasteiger et al. [20] found that 0.4 mg Pt/cm<sup>2</sup> was close to the optimal platinum loading for the air electrode using the state-of-the-art Pt/C catalyst and an optimized electrode structure. Further reduction of the cathode platinum loading will result in cell voltage loss at low current densities that follows the ORR kinetic loss. The high platinum loading at the cathode originates from the slow kinetics of (ORR) at platinum surface. To make the fuel cell vehicles commercially viable on the market, the platinum loading on the cathode has to be reduced significantly. As shown in Fig. 1, when Pt loading requirement is translated from the target set for power-specific Pt consumption in g Pt/kW, a fourfold Pt mass activity (activity per unit platinum mass) improvement is required, if combined with a 50% reduction in mass transport-related voltage loss [21]. Recent increases in Pt prices suggest that one should be striving for at least an eightfold improvement.

There are two ways one might think of that could help to reach that goal: further increasing the platinum dispersion (defined as the ratio of surface metal atoms to total number of atoms) by making finer platinum particles, if there is no decrease of Pt-specific activity (activity per unit Pt surface area); or alternatively, increasing the Pt-specific activity. One could also seek a combination of these two approaches.

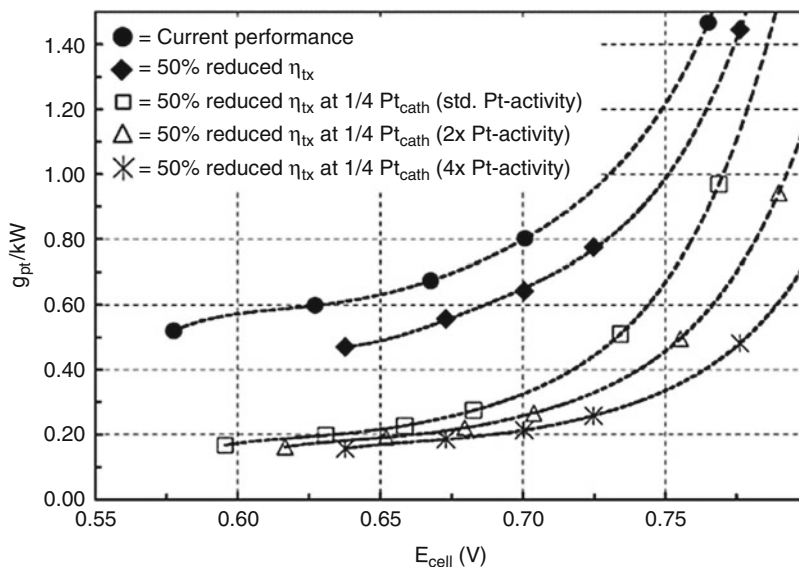
This selected brief review will be focused on the research and development progress on ORR kinetics. The origin of the problem related with the low ORR activity of platinum will be discussed, followed by a review of recent progress in making more active, more durable platinum-based ORR catalysts. These include platinum alloy catalysts, platinum monolayer catalysts, platinum nanowire and nanotube catalysts, and the more recent shape- and facet-controlled platinum-alloy nanocrystal catalysts. The progress in the mechanistic understanding on the correlation between the activity and the electronic and structural properties of surface platinum atoms will be reviewed as well. The future direction of the research on platinum-based catalysts for PEM fuel cell application will be proposed.

## Electrocatalysis of the ORR at Platinum Surfaces

It is widely accepted that the ORR on platinum surfaces is dominantly a multistep and four-electron reduction process with H<sub>2</sub>O being the final product. However, the detailed mechanism of ORR still remains elusive [17]. The overall four electron reduction of O<sub>2</sub> in acid aqueous solutions is



Since the four-electron reduction of oxygen is highly irreversible, the experimental verification of the thermodynamic reversible potential of this reaction is very difficult. The irreversibility of ORR imposes serious voltage loss in fuel cells. In most instances, the current densities practical for kinetic studies are much larger than the exchange current density of ORR; therefore the information obtained from current-potential data are confined only to the rate-determining step (RDS). On the other hand, in the ORR kinetic potential region, the electrode surface structure and properties strongly depend on the applied potential and the time held at that potential, which makes the reaction more complicated. While the relationship between the overall



### PEM Fuel Cells and Platinum-Based Electrocatalysts,

**Fig. 1** Pt-mass-specific power density [ $g_{Pt}/kW$ ] versus cell voltage,  $E_{cell}$  [V], based on a  $50\text{ cm}^2$  single-cell  $H_2$ /air performance.  $\eta_{tx}$  = cell-voltage loss caused by mass transport;  $Pt_{cath}$  = cathode-Pt loading. The cell was tested at  $T_{cell} = 80^\circ\text{C}$ , 100% RH (relative humidity), at a total pressure of  $150\text{ kPa}_{abs}$  and stoichiometric flows of

$s = 2.0/2.0$ . Catalyst-coated membrane (CCM) was based on a ca.  $25\text{ }25\text{ }\mu\text{m}$  low-EW (equivalent weight = 900) membrane, and ca. 50 wt% Pt/carbon ( $0.4/0.4\text{ mg Pt}/\text{cm}^2$  (anode/cathode)). It was assumed that the cell performance could be maintained at a reduced anode loading of  $0.05\text{ mg Pt}/\text{cm}^2$  (Reproduced from [21] with permission)

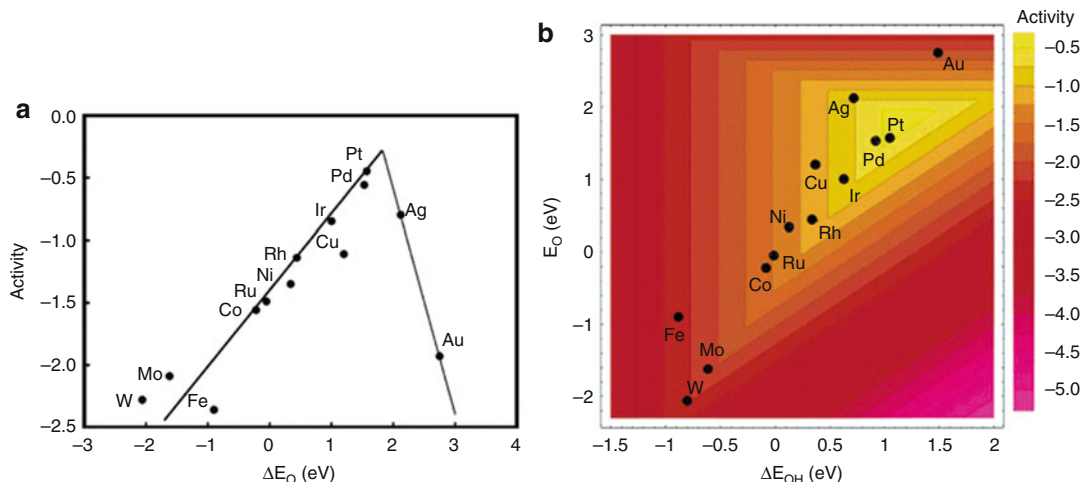
kinetics and the surface electronic properties is not well understood, it is widely accepted that in the multistep reaction, the first electron transfer is the rate-determining step, which is accompanied by or followed by a fast proton transfer [16–18]. Two Tafel slopes are usually observed for ORR on Pt in RDE tests in perchloric acid, from  $-60\text{ mV}/\text{decade}$  at low current density, transitioning to  $-120\text{ mV}/\text{decade}$  at high current density. The lower Tafel slope of the ORR in perchloric acid at low current density has been attributed to the potential dependent Pt oxide/hydroxide coverage at high potentials [22–26].

Recently, by using Density Functional Theory (DFT), Norskov and coworkers [27] calculated the Gibbs free energy of ORR intermediates as a function of cathode potential based on a simple dissociative mechanism, i.e., with the adsorbed oxygen and hydroxide being the only intermediates. They found that oxygen or hydroxide is so strongly bound to the platinum surface at the thermodynamic equilibrium potential that proton and electron transfer become impossible. By

lowering the potential, the stability of adsorbed oxygen decreases and the reaction may proceed. They suggested that these effects are the origin of the overpotential of the ORR on platinum surfaces.

By setting the reference zero potential to be NHE, the proton chemical potential in the electrolyte is related to the electrode potential. The authors made DFT calculations to get the bond energies of  $O^*$  and  $HO^*$  for a number of interesting metals. From this, they can evaluate the reaction free energies of the two basic steps: the hydrogenation of the two adsorbed intermediates  $O^*$  and  $HO^*$ . The larger one of the two reaction free energies was taken as the activation energy barrier of the rate-determining step (RDS) in ORR. By using a microkinetic model they constructed, the rate constant of the RDS, and therefore the ORR activity, can be evaluated based on the activation energy barrier. As shown in Fig. 2a, the model predicts a volcano-shaped relationship between the rate of the ORR and the oxygen adsorption energy, with platinum and



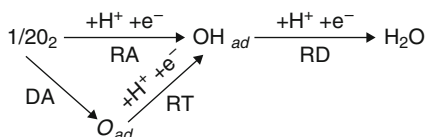


**PEM Fuel Cells and Platinum-Based Electrocatalysts, Fig. 2** (a) Trends in oxygen reduction activity plotted as a function of the O-binding energy. (b) Trends in oxygen

reduction activity plotted as a function of both the O and the OH-binding energy (Reproduced from [27]. With permission)

palladium being among the best metals for electrocatalysis of ORR. Fig. 2b shows that the bonding energy of OH is roughly linearly correlated to that of O, indicating both are nearly equivalent parameters in determining the ORR activity.

More recently, Wang et al. [28] derived an intrinsic kinetic equation for the four-electron ( $4e^-$ ) oxygen reduction reaction (ORR) in acidic media, by using free energies of activation and adsorption as the kinetic parameters, which were obtained through fitting experimental ORR data from a Pt(111) rotating disk electrode (RDE). Their kinetic model consists of four essential elementary reactions: (1) a dissociative adsorption (DA); (2) a reductive adsorption (RA), which yields two reaction intermediates, O and OH; (3) a reductive transition (RT) from O to OH; and (4) a reductive desorption (RD) of OH, as shown below [28] (Reproduced with permission from [28]).



In contrast to a conventional ORR kinetic model, in this work there is no single particular

RDS assumed, as the authors believe that a single RDS assumption may not hold over a wide potential region since the reaction pathway may change with potential, or there may exist two RDSs with similarly high activation barriers. The results indicate that the first electron transfer in the RA reaction ( $\Delta G_{RA}^{*0} = 0.46\text{eV}$ , where  $\Delta G_i^{*0}$  is the activation energy of reaction  $i$  (at equilibrium potential)) is not the rate-determining step (RDS) for the ORR on Pt at high potentials, because dissociative adsorption ( $\Delta G_{DA}^{*0} = 0.26\text{eV}$ ) provides a more active adsorption pathway. However, the reaction intermediates, O and OH, are strongly trapped on the Pt surface, requiring considerable overpotential to overcome the barriers for O to OH transition ( $\Delta G_{RT}^{*0} = 0.50\text{eV}$ ) and OH reduction to water and desorption ( $\Delta G_{RD}^{*0} = 0.45\text{eV}$ ).

Thus, the ORR on Pt is desorption-limited at high potentials, exhibiting a low apparent Tafel slope at those potentials. Wang et al. [29] further used this kinetic model to fit a typical IR-free polarization curve of a PEMFC, by adjusting the parameters to reflect the fuel cell-operating conditions at  $80^\circ\text{C}$ . The results showed that the transition of the Tafel slope occurs at about the same  $0.77\text{V}$  that is the equilibrium potential for the transition between adsorbed O and OH on a Pt surface with low adsorbed O coverage [27].



Neyerlin et al. [30–32] investigated the ORR kinetics on high-surface-area carbon-supported platinum catalyst Pt/C in an operating PEMFC. By assuming the transfer coefficient  $\alpha = 1$  and using a single Tafel slope, i.e.,  $-70$  mV/decade at  $80$  °C, three kinetic parameters could be extracted through fitting the kinetic model to the fuel cell data: the exchange current density or current density at a constant IR-free cell potential, the reaction order with respect to oxygen partial pressure, and the activation energy. One may need to note that the lower limit of the electrode potential after IR and transport correction in this work is about  $0.77$  V, so that this single-Tafel-slope treatment can still be consistent with Wang et al.'s [29] result. Neyerlin et al. [30] were concerned about the accuracy of the kinetic current extracted from low potentials in RDE tests, since at these low potentials the experimental measured current is more than ten times lower than the kinetic current derived from it. The transport correction used in RDE analysis assumes perfect first-order kinetics, which is not strictly true, and errors from this imperfect correction could become large at low potentials. The authors also studied the relative humidity (RH) effects on ORR kinetics in PEMFCs [32]. They found that when RH is above 50–60%, the kinetics are independent of the RH, but they observed significant ORR kinetic losses at lower RH. The reduction of ORR kinetics at low RH was interpreted as most likely due to a lowering of the proton activity (therefore only indirectly related to the lowering of the water activity) via hydration of acidic groups and the sequestering of protons at low RH.

Another factor that plays an important role in determining the minimum loading of Pt catalyst required for PEMFCs is the Pt size effect on ORR, not only through altering the fraction of surface Pt atoms over the number of total Pt atoms, but also through changing the ORR kinetics per surface Pt atom (Pt specific activity). Earlier results by Blurton et al. [33] showed that in 20%  $\text{H}_2\text{SO}_4$  at  $70$  °C, the highly dispersed Pt (with size of about  $1.4$  nm) supported on conductive carbon prepared through ion exchange on resin followed by pyrolysis has a Pt-specific activity 20 times lower than that of crystalline Pt black (with size of about

$10$  nm), though it is not clear to what extent the lower activity could be caused by contamination of Pt and/or a “burying effect” during the catalyst preparation. Blurton et al. [33] correlated the decreased ORR specific activity with the decreased coordination number of surface Pt atoms on smaller Pt particles, causing more severe oxidation of the Pt surface. Peuckert et al. [34] later investigated a series of Pt-on-carbon catalysts with Pt weight percents from 5% to 30% prepared by an impregnation method, with corresponding fractions of metal atoms on the surface from 1.0 (Pt size  $< 1$  nm) to 0.09 (Pt size  $< 12$  nm). The Pt-specific activity toward ORR in  $0.5$  M  $\text{H}_2\text{SO}_4$  at  $298$  K on these catalysts was found to be constant for Pt particle sizes above  $4$  nm but to decrease by a factor of 20 as the particle size decreased from  $3$  to  $1$  nm. Taking into account the larger percentage of buried and these inactive Pt atoms in larger particles, this result suggested that the optimal Pt size for the maximum Pt mass activity is about  $3$  nm. Kinoshita [35] also reviewed and analyzed the particle size effect for ORR on Pt/C catalysts. Based on the literature data of ORR on Pt/C collected in  $\text{H}_3\text{PO}_4$  [36–38] and  $\text{H}_2\text{SO}_4$  [34] solutions, Kinoshita proposed the decrease of Pt-specific activity with decrease of Pt particle size is a consequence of the changing distribution of surface atoms at the (100) and (111) crystal faces. Recent literature data [18] in  $\text{H}_3\text{PO}_4$  reported that when Pt particle size increases from  $2.5$  to  $12$  nm, there is about threefold of increase in Pt-specific activity and confirmed the optimal Pt particle size for maximum mass activity to be around  $3$  nm. Gasteiger et al. [21] investigated Pt/C and Pt black catalysts for ORR in  $\text{HClO}_4$  solution at  $60$  °C, with the Pt particle size ranging from  $2$  nm to over  $10$  nm, and found that the magnitude of activity improvement is comparable to that in literature data [39, 40], although the absolute values are about ten times higher than those reported in Ref. [40], due in part to the use of a less-strongly adsorbing electrolyte.

It is well established that ORR on Pt single crystals is structure-sensitive, depending on the electrolyte. In  $\text{H}_2\text{SO}_4$ , the order of activity of Pt(hkl) increases in the sequence (111)

$\ll(100) \ll(110)$  [19, 41]. The variation in  $\text{H}_2\text{SO}_4$  originates from highly structure-specific adsorption of sulfate/bisulfate anions in this electrolyte, which has a strongly inhibiting effect on the (111) surface. Given that the dominant Pt crystal facets of high-surface-area Pt/C catalysts are  $\{111\}$  and  $\{100\}$ , the Pt size effect on ORR activity in  $\text{H}_2\text{SO}_4$  can be explained by the structure-sensitive adsorption. In perchloric acid, the variation in activity is relatively small between the three low index faces, with activity increasing in the order  $(100) < (111) < (110)$  [42], owing to the structure sensitive inhibiting effect of  $\text{OH}_{\text{ads}}$ , i.e., a stronger inhibiting effect on (100) and smaller effects on (110) and (111) [41]. Norskov and other researchers [43–48], based on their DFT calculations, recently proposed using the concept of averaged d-band center energy to explain the reactivity of metal surface atoms, which was supported by numerous experimental data. According to them, when Pt particle size decreases, the average coordination number of surface Pt atoms decreases, causing the d-band center to move closer to the Fermi level and the reactivity of those atoms to increase. As a result of that, the Pt atoms bind oxygen-hydroxide stronger, and therefore, have a lower ORR activity. A stronger adsorption of OH species on Pt surface when the particle size is reduced to below 5 nm was reported in Ref. [49].

While the Pt particle-size effect on ORR suggests that a further increase of Pt dispersion by decreasing the particle size to much smaller than 3 nm will not improve Pt mass activity, it is worth noting that the Pt-size effect is not universally believed. Recently, Yano et al. [50] studied ORR on a series of carbon-supported Pt-nanoparticle electrocatalysts (Pt/C) with average diameters in the range of roughly 1–5 nm, combined with measurements on  $^{195}\text{Pt}$  electrochemical nuclear magnetic resonance (EC-NMR) spectroscopy. They observed that ORR rate constants and  $\text{H}_2\text{O}_2$  yields evaluated from hydrodynamic voltammograms measurements did not show any particle size dependency. The apparent activation energy of  $37 \text{ kJ mol}^{-1}$ , obtained for the ORR rate constant, was found to be identical to that obtained for bulk platinum electrodes. This was

consistent with the negligible difference in the surface electronic properties of these Pt/C catalysts, revealed from the practically no change of surface peak position of  $^{195}\text{Pt}$  NMR spectra and the spin-lattice relaxation time of surface platinum atoms with the particle size variation.

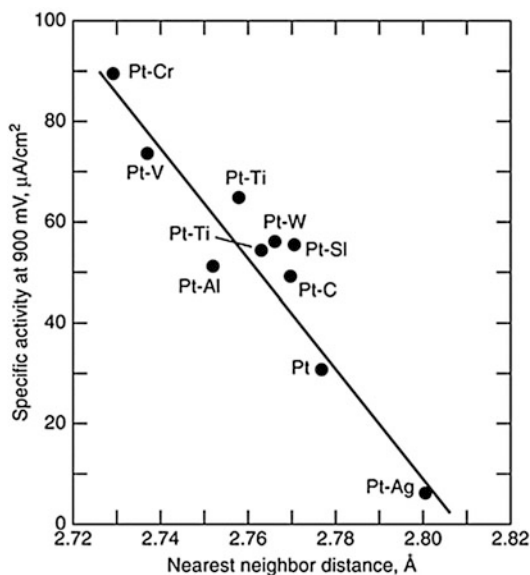
Nevertheless, facilitating the ORR kinetics by augmenting the Pt specific activity is important for the future of fuel cells. A recent perspective in *Science* by Gasteiger and Markovic [51] showed some promising advances in this aspect.

## Pt-Alloy Electrocatalysts

Pt-alloy catalysts, predominantly Pt binary and ternary alloys with 3D transition metals, have been the main focus of catalyst research for PEM fuel cells in the past decades, as they confer enhanced ORR activities over those available from pure Pt catalysts. Great progress has been made in past decades in developing more active and durable Pt alloy catalysts and in understanding the mechanism of their activity enhancements. Two- to threefold specific activity enhancements versus pure Pt were typically reported in literature [21, 40, 52–54], while exceptions existed from earlier results, claiming either no enhancement [55–57], or over an order of magnitude enhancement [58]. As far as which alloy and what alloy compositions confer the highest ORR activity, there seems to be lack of general agreement. This is probably because the measured activity depends highly on the catalyst surface and near-surface atomic composition and structure, on impurities on the surface, and on particle size and shape, all of which could be affected by the preparation method, heat treatment protocol, and testing conditions. For example, to achieve the optimal alloy structure for maximum activity, different Pt alloy particles may require different annealing-temperature protocols to accommodate the distinctions between metal melting points and particle sizes [59, 60]. In a number of earlier papers [61–63] it was shown that Pt-Cr is the most active ORR cathode catalyst in phosphoric acid fuel cells, while some recent results reported that in the PEMFC-oriented settings, the most

active Pt alloy ORR catalyst could be Pt-Co [64], Pt-Fe [58, 65], Pt-Cr [52], Pt-Ni [66], or Pt-Cu [67] at specific atomic ratios of Pt to the alloying elements. Several representative mechanisms have been proposed in the literature to explain the enhanced activities observed on Pt alloy catalysts: (1) a surface roughening effect due to leaching of the alloy base metal [68, 69]; (2) decreased lattice spacing of Pt atoms due to alloying [52, 61, 70]; (3) electronic effects of the neighboring atoms on Pt, such as increased Pt d-band vacancy [52, 58, 65, 71] or depressed d-band center energy upon alloying [42, 64, 67, 72, 73]; and/or (4) decreased Pt oxide/hydroxide formation at high potential [52, 74–76]. The increased Pt surface roughness alone may help increase Pt mass activity but will not increase the Pt-specific activity. Other mechanisms are correlated with each other, for example, the decreased lattice spacing may affect the electronic structure of Pt atoms, which in turn may inhibit the Pt oxide/hydroxide formation. A more detailed discussion follows.

Jalan and Taloy [61] believed that the nearest-neighbor distance between Pt atoms plays an important role in the ORR, based on the reaction model proposed by Yeager et al. [16], i.e., the rate-determining step being the rupture of O-O bond via various dual site mechanisms. They proposed that the distance between nearest-neighbor atoms on the surface of pure Pt is not ideal for dual site adsorption of O<sub>2</sub> or “HO<sub>2</sub>” and that the introduction of foreign atoms that reduce the Pt nearest-neighbor spacing would result in higher ORR activity. By testing a number of carbon-supported Pt-M alloy catalysts fabricated into gas diffusion electrodes, with various nearest-neighbor Pt atom distances determined from X-ray diffraction, a linear relationship was obtained between the activity and the distance, with Pt-Cr exhibiting highest ORR activity and smallest nearest-neighbor distance, as shown in Fig. 3. While the geometric distance between the neighboring Pt atoms is shorter in alloys, the surface electronic structure of Pt alloys is different from that of pure Pt as well, so it is difficult to separate the two factors. Yet other studies [55, 68, 69] claimed no activity enhancement was observed on Pt-Cr alloy



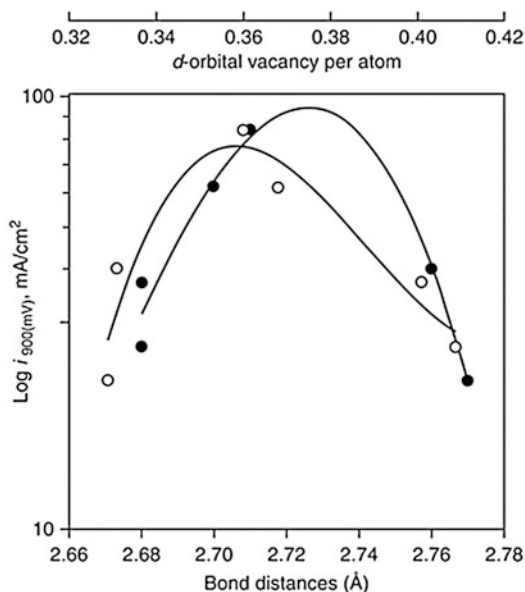
**PEM Fuel Cells and Platinum-Based Electrocatalysts, Fig. 3** Specific activity for the ORR versus electrocatalyst nearest-neighbor distance (Reproduced from [61] with permission)

over pure Pt, except for the increased surface roughness [68, 69], but this has not been supported by more recent literature [52, 70].

Mukerjee and coworkers did a series of studies [52, 74, 77, 78] on Pt binary alloys for ORR applying in situ X-ray absorption spectroscopy (XAS) to electrochemical systems. The spectra consist of two parts, the near-edge part XANES (X-ray absorption near-edge structure), which gives chemical information and EXAFS (extended X-ray absorption fine structure), which gives the structural information around the element of interest. In a related study, Mukerjee et al. [52] investigated five binary Pt alloys (PtCr/C, PtMn/C, PtFe/C, PtCo/C, and PtNi/C) supported on high-surface-area carbon for ORR in a proton exchange membrane fuel cell. The electrode kinetic studies on the Pt alloys showed a two- to threefold increase in ORR activity relative to a reference Pt/C electrocatalyst, with the PtCr/C alloy exhibiting the best performance. Contractions in the Pt-Pt bond distances were observed by both EXAFS and XRD. In addition, they found that in the double-layer potential region (0.54 V versus RHE), the alloys possess

higher Pt d-band vacancies than Pt/C, while in the high potential region (0.84 V versus RHE), Pt/C shows higher d-band vacancy relative to alloys. This was interpreted by the adsorption of OH species at high potential on Pt/C but to a lesser extent on Pt alloys. Correlation of the electronic (Pt d-band vacancies) and geometric (Pt-Pt bond distance) with the electrochemical performance characteristics exhibits a volcano-type behavior with the PtCr/C alloy being at the top of the curve, shown in Fig. 4. They rationalized the enhanced activity on alloys on the basis of electronic and geometric effects, and of inhibition of OH adsorption. Similar observations were also reported from the ORR measurements in phosphoric acid [66], and in alkaline solution [79–81].

Surface segregation of Pt has been experimentally observed in a wide range of Pt-M binary alloys, such as Pt-Fe [82], Pt-Ni [83], Pt-Co [84], Pt-Ru [85], and has also been reported in theoretical calculations [86, 87]. Furthermore, it has been reported that the topmost layer is composed of pure Pt while the second layer is enriched in the transition metal M for Pt-rich Fe, Co, and Ni alloys [72, 76, 88], produced by displacement of Pt and M atoms in the first two layers to minimize the surface free energy during annealing. Stamenkovic et al. [76] studied polycrystalline Pt<sub>3</sub>Ni and Pt<sub>3</sub>Co alloys for electrocatalysis of ORR in acid electrolytes using the rotating ring disk electrode (RRDE) method. Polycrystalline bulk alloys of Pt<sub>3</sub>Ni and Pt<sub>3</sub>Co were prepared in ultra-high vacuum (UHV) having two different surface compositions: one with 75% Pt (by sputtering) and the other with 100% Pt (by annealing). The latter was called a “Pt-skin” structure and is produced by an exchange of Pt and Co in the first two layers. Activities of Pt-alloys for the ORR were compared to those of polycrystalline Pt in 0.5 M H<sub>2</sub>SO<sub>4</sub> and 0.1 M HClO<sub>4</sub> electrolytes. It was found that in H<sub>2</sub>SO<sub>4</sub>, the activity increased in the order Pt<sub>3</sub>Ni > Pt<sub>3</sub>Co > Pt; in HClO<sub>4</sub>, however, the order of activities was “Pt-skin/Pt<sub>3</sub>Co” > Pt<sub>3</sub>Co > Pt<sub>3</sub>Ni > Pt. The catalytic enhancement was greater in 0.1 M HClO<sub>4</sub> than in 0.5 M H<sub>2</sub>SO<sub>4</sub>, with the maximum enhancement observed for the “Pt-skin” on Pt<sub>3</sub>Co in 0.1 M HClO<sub>4</sub> being three to four times



**PEM Fuel Cells and Platinum-Based Electrocatalysts, Fig. 4** Correlation of the ORR performance of Pt and Pt-alloy electrocatalysts in PEMFC with Pt-Pt bond distance (solid circles) and the d-band vacancy of Pt (empty circles) obtained from in situ XAS (Reproduced from [52] with permission)

that for pure Pt. The activity enhancement was attributed to the inhibited Pt-OH<sub>ad</sub> formation on an alloy, even one covered with pure Pt, relative to the surface of a pure-Pt electrode, and the ORR reaction mechanism (pathway) was found to be the same on alloys as on a pure-Pt electrode. In a more recent study, Stamenkovic et al. [64] investigated polycrystalline Pt<sub>3</sub>M (M = Ni, Co, Fe, Ti, V) surfaces for ORR in 0.1 M HClO<sub>4</sub>, for both “Pt-skin” and sputtered alloy surfaces. The activity was correlated to the d-band center energy obtained in UHV via ultraviolet photoemission spectroscopy (UPS). A “volcano behavior” was revealed with the Pt<sub>3</sub>Co has the highest activity for both “Pt-skin” and sputtered surfaces. The “Pt-skin” surface was found to be more active than sputtered surface again for each Pt<sub>3</sub>M. The electrochemical and post-electrochemical UHV (ultra-high vacuum) surface characterizations revealed that Pt-skin surfaces are stable during and after immersion to an electrolyte. In contrast, all sputtered surfaces formed Pt-skeleton

outermost layers due to dissolution of transition metal atoms [89].

By using DFT calculations, Xu et al. [47] studied the adsorption of O and O<sub>2</sub> and the dissociation of O<sub>2</sub> on the (111) faces of ordered Pt<sub>3</sub>Co and Pt<sub>3</sub>Fe alloys and on monolayer Pt skins covering these two alloys. Results were compared with those calculated for two Pt(111) surfaces, one at the equilibrium lattice constant and the other laterally compressed by 2% to match the strain in the Pt alloys. The absolute magnitudes of the binding energies of O and O<sub>2</sub> follow the same order in the two alloy systems: Pt skin < compressed Pt(111) < Pt(111) < Pt<sub>3</sub>Co(111) or Pt<sub>3</sub>Fe(111). The reduced bonding strength of the compressed Pt(111) and Pt skins for oxygen was rationalized as being due to the shifting of the d-band center increasingly away from the Fermi level. They proposed that an alleviation of poisoning by O and enhanced rates for reactions involving O could be some of the reasons why Pt skins are more active for the ORR.

Chen et al. [88, 90] recently studied carbon supported Pt<sub>3</sub>Co nanoparticles for ORR and correlated their activity with the chemical composition and structural information of individual particles. Conventional and aberration-corrected high-angle annular dark-field (HAADF), scanning transmission electron microscopy (STEM), and high resolution transmission electron microscopy (HRTEM) were used to obtain the particle compositional and structural information. For the acid treated Pt<sub>3</sub>Co nanoparticles, they observed the formation of percolated Pt-rich and Pt poor regions within individual nanoparticles, analogous to the skeleton structure observed for sputtered polycrystalline Pt alloy surfaces after acid leaching [89]. The acid treated alloy nanoparticles yielded about two times the specific activity of pure-Pt nanoparticles. After annealing of the acid-treated particles, sandwich-segregation surfaces of ordered Pt<sub>3</sub>Co nanoparticles were directly observed, with the topmost layer being pure Pt atoms. The specific activity of annealed nanoparticles was about four times that of pure Pt nanoparticles. The enhanced Pt-specific activity toward ORR was attributed to the reduced binding energy of oxygenated species, owing to

combined two effects, i.e., the increased compressive strain in Pt atoms, and the ligand effect from underlying Co atoms.

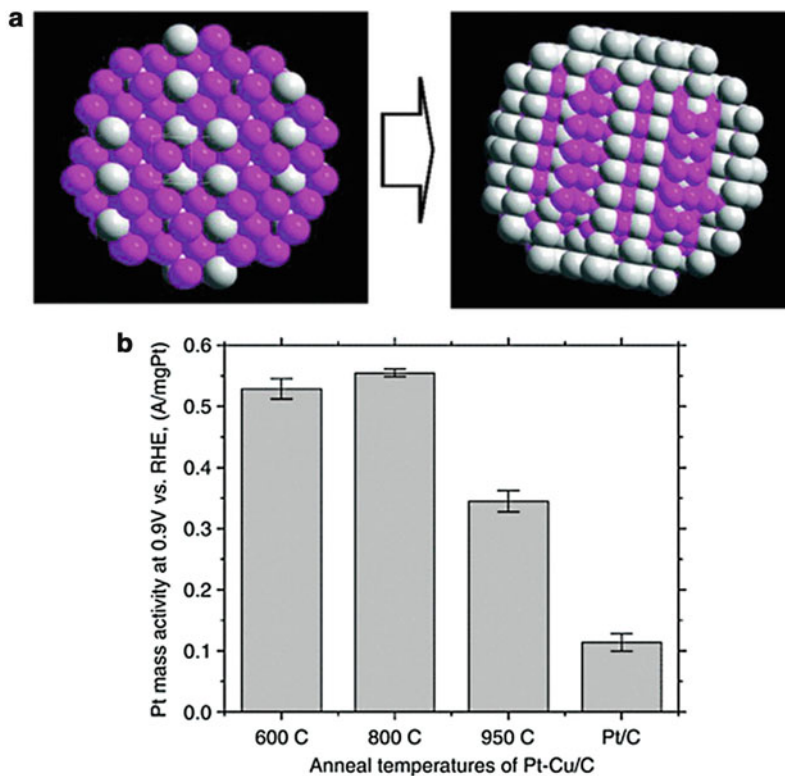
Strasser et al. [59, 67, 91–94] recently applied a freeze-drying technique in the synthesis of Pt alloy nanoparticle catalysts with enhanced ORR activity. The Pt-Cu alloy catalyst after electrochemical dealloying was reported to have both mass and specific activities about four to six times those of a standard commercial Pt/C catalyst, in both RDE and MEA tests. The synthesis involved an impregnation/freeze-drying route followed by annealing. Preparation started with impregnation and sonication of a commercial 30 wt% Pt/C catalyst with an aqueous solution of a copper nitrate, with Pt:Cu atomic ratio of 1:3, followed by freezing in liquid N<sub>2</sub>. The frozen sample was subsequently freeze-dried under a moderate vacuum (0.055 mbar). Reduction and alloying of Pt and Cu on the carbon support was thermally driven under a reductive H<sub>2</sub> atmosphere in a tube furnace. Electrochemical etching (voltammetric dealloying) was employed to remove the surface Cu atoms from Cu-rich Pt-Cu alloy precursors. Bulk and surface structural and compositional characterization suggested that the dealloyed active catalyst phase consists of a core-shell structure in which a multilayer Pt rich shell is surrounding a Pt-poor alloy particle core. This work constitutes significant progress on initial activity, since a fourfold of increase of Pt mass activity is the performance target for commercially viable fuel cell cathode catalyst [21]. Fig. 5a shows a schematic of the dealloying process, and Fig. 5b exhibits the Pt mass activities of Pt-Cu/C synthesized at different temperatures, compared with the Pt/C catalyst.

As to the mechanistic origin of the activity enhancement in dealloyed Pt-Cu catalyst, the authors believe geometric effects play a key role, because the low residual Cu near-surface concentrations make significant electronic interactions between Pt and Cu surface atoms unlikely. Therefore, they suspect that the dealloying creates favorable structural arrangements of Pt atoms at the particle surface, such as more active crystallographic facets or more favorable Pt-Pt interatomic distances for the electroreduction of oxygen, as



### PEM Fuel Cells and Platinum-Based Electrocatalysts,

**Fig. 5** (a) The schematic model of a Pt-Cu alloy particle before and after electrochemical dealloying of the near-surface Cu atoms (*pink balls* = Cu atoms; *gray balls* = Pt atoms); (b) Pt mass activities of Pt-Cu/C catalysts at various annealing temperatures compared to that of Pt/C catalyst (Reproduced from [67] with permission)



predicted by DFT calculations [47]. A fourfold enhancement in Pt mass activity on mono-dispersed Pt<sub>3</sub>Co nanoparticles with particle size of 4.5 nm was also reported recently [95].

Watanabe and coworkers carried out a series of studies on the mechanism for the enhancement of ORR activity on Pt-Fe, Pt-Ni, and Pt-Co alloys [53, 58, 65, 71, 96, 97]. By using X-ray photoelectron spectroscopy combined with an electrochemical cell (EC-XPS) [96, 97], they identified quantitatively oxygen-containing species adsorbed on electrodes of a pure Pt and a Pt skin layer (generated by acid treatment, not annealing, and therefore equivalent to the “skeleton” layers described by Stamenkovic et al. [89]) formed on Pt-Fe and Pt-Co alloys’ surface from N<sub>2</sub>- and O<sub>2</sub>-saturated 0.1 M HF solution. Four types of species were distinguished with binding energies at 529.6, 530.5, 531.1, and 532.6 eV; the first two were assigned to O<sub>ad</sub> and OH<sub>ad</sub>, while the latter two were assigned to the bilayer water molecules, H<sub>2</sub>O<sub>ad,1</sub> and H<sub>2</sub>O<sub>ad,2</sub>. The XPS results showed that the Pt skin layer exhibited a higher

affinity to O<sub>ad</sub> but less to H<sub>2</sub>O compared to pure Pt, particularly in the O<sub>2</sub>-saturated solution. The enhanced ORR activity at the Pt skin/Pt-alloy electrode was ascribed to higher coverage of O<sub>ad</sub> than that at pure Pt. They also found that such an enhancement is induced without changing the activation energy but the corresponding frequency factor value in the pre-exponential term from that of pure Pt. From the measurements in a flow channel with 0.1 M HClO<sub>4</sub>, in the temperature range of 20–50 °C, a two to fourfold of ORR-specific activity enhancement was reported for those Pt alloys [53].

Pt metal dissolution in fuel cells has been reported to play a key role in Pt surface area loss and cell performance loss [98]. While Pt-alloy catalysts with fourfold enhancement in both Pt mass activity and specific activity relative to standard Pt/C catalyst seem achievable, as has been shown above, the long-term durability of the alloy catalysts is still a concern, due to dissolution of the base metal from the alloys [21, 99]. For Pt-Cu alloy catalysts, an additional possible risk is that



the dissolved Cu may migrate from cathode through membrane to anode and deposit on the anode Pt surface, causing a poisoning effect on anode hydrogen oxidation kinetics, as the Cu redox potential is higher than the anode hydrogen redox potential. Fortunately, the durability of the cathode catalyst can be compensated by careful system control, mainly through lowering the cathode upper potential limit and narrowing its operating potential window [100, 101].

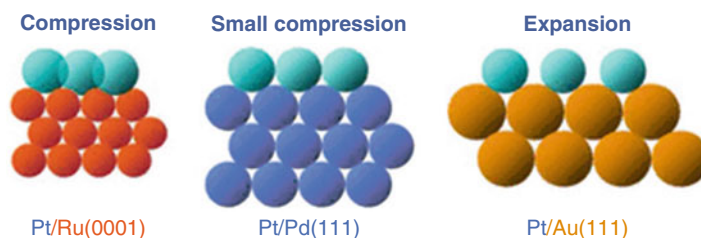
## Pt Monolayer Electrocatalysts

Pioneered by Adzic et al. [102, 103], the idea of a Pt monolayer electrocatalyst has been one of the key concepts in reducing the Pt loading of PEM fuel cells in recent years. Pt submonolayers deposited on Ru nanoparticles had been earlier demonstrated to give superior performance with ultra-low Pt loading compared to commercial Pt/C or Pt-Ru alloy catalysts for the anode CO-tolerant hydrogen oxidation reaction [103–107]. More recently, Adzic and coworkers applied this concept in making novel Pt monolayer catalysts for the cathode ORR, which will be the focus of the review in this section. In general, the new method of synthesizing Pt monolayer catalysts involves underpotential deposition (UPD), a technique well known to produce an ordered atomic monolayer to multilayer metal deposition onto a foreign metal substrate [108–110]. Specifically, the method consists of two steps [111, 112]: first, a monolayer of a sacrificial less-noble metal is deposited on a more noble metal substrate by UPD, such as Cu UPD on Au or Pd; second, the

sacrificial metal is spontaneously and irreversibly oxidized and dissolved by a noble metal cation, such as a Pt cation, which is simultaneously reduced and deposited onto the foreign metal substrate. The whole procedure can be repeated in order to deposit multilayers of Pt (or another noble metal) on the foreign metal.

The advantages of Pt monolayer catalysts include (1) full utilization of the Pt atoms that are all on the surface, and (2) that the Pt activity and stability can be tailored by the selection of the substrate metals. For example [102], when a Pt monolayer is deposited onto different substrate metals, as shown in Fig. 6, due to the lattice mismatch between the metals, it can experience compressive or tensile stress, which is known to affect the Pt activity by adjusting its d-band center energy [43, 47] and consequently its ORR activity.

Pt monolayer deposits on Pd(111) single crystals (Pt/Pd(111)) and on Pd/C nanoparticles (Pt/Pd/C) have been studied for ORR [112], and improved activities compared to Pt(111) and commercial Pt/C, respectively, were reported. The ORR reaction mechanism of the monolayer catalysts was found to be the same as that on pure Pt surface. Pt/Pd(111) was found to have a 20 mV improvement in half-wave potential versus Pt(111), and the Pt/Pd/C had a Pt-mass activity five- to eight-times higher than that of Pt/C catalyst. If the total noble metal amount (Pt + Pd) is counted, the mass activity is about 80% higher than that of Pt/C catalyst [112]. The enhanced ORR activity is attributed to the inhibited OH formation at high potential, as evidenced from XAS measurements. In a real fuel cell test, 0.47 g Pt/kW was demonstrated at 0.602 V [113].



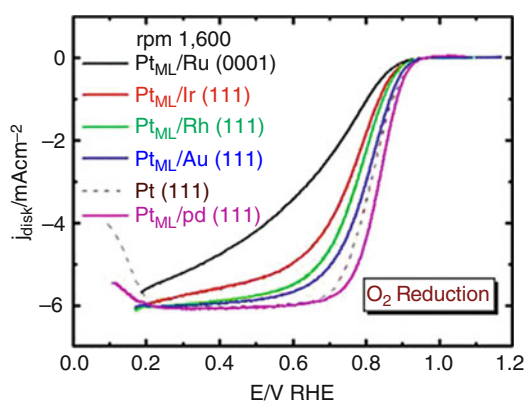
**PEM Fuel Cells and Platinum-Based Electrocatalysts, Fig. 6** Models of pseudomorphic monolayers of Pt on three different substrates inducing compressive strain (Ru

(0001) and Pd(111)) and tensile strain (Au(111)). (Reproduced from [102] with permission)

In order to understand the mechanism for the enhanced activity of a Pt monolayer deposited on Pd metal, the ORR was investigated in  $O_2$ -saturated 0.1 M  $HClO_4$  solution on platinum monolayers supported on Au(111), Ir(111), Pd(111), Rh(111), and Ru(0001) single-crystal RDE surfaces [114]. A comparison of the polarization curves at 1600 rpm is shown as in Fig. 7. The trend of the ORR activities increase in the sequence  $Pt/Ru(0001) < Pt/Ir(111) < Pt/Rh(111) < Pt/Au(111) < Pt(111) < Pt/Pd(111)$ .

The authors further correlated the kinetic activities of the “monolayers” with the Pt d-band center energies (not shown) and Pt-O binding energies, and found a “volcano” relationship, with the Pt/Pd(111) having the optimal d-band center, as well as  $Pt_{ML}$ -O-binding energy, for the maximum ORR activity. The “volcano” behavior was rationalized as being controlled by the two key steps in ORR, the O-O bond dissociation which is followed by the other step, the O-H bond formation. As shown in Fig. 8, the activation energies of the two steps both correlated linearly with the  $Pt_{ML}$ -O-binding energies (and with the d-band center energies, not shown), but in the opposite trend, indicating the  $Pt_{ML}$ -O binding can be neither too strong, nor too weak, for the best ORR activity.

For further fine-tuning of the monolayer Pt/Pd ORR activity, they further introduced mixed metal + Pt monolayer catalysts [115], which contained

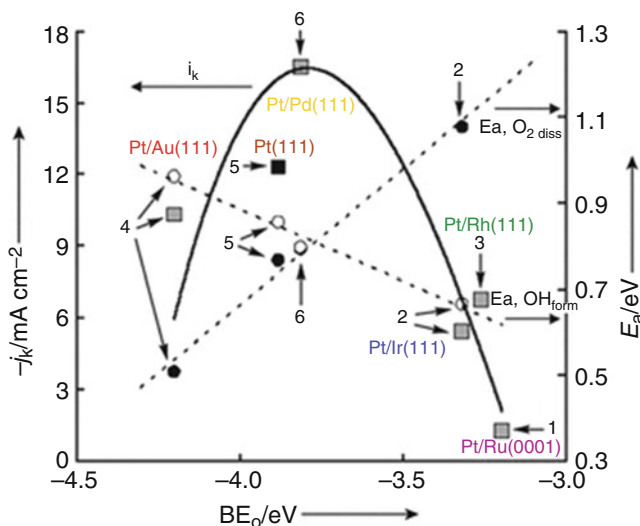


**PEM Fuel Cells and Platinum-Based Electrocatalysts, Fig. 7** Polarization curves for  $O_2$  reduction on platinum monolayers in 0.1 M  $HClO_4$  solution on a RDE. Rotation rate = 1,600 rpm (Reproduced from [114] with permission)

0.2 monolayer of a foreign metal from selection of (Au, Pd, Rh, Ir, Ru, Os, and Re) combined with 0.8 monolayer of Pt co-deposited on Pd(111) or on Pd/C nanoparticles. The foreign metals have either a weaker M-OH bond (for the case of Au-OH), or a stronger M-OH bond (for the rest of the cases) than the Pt-OH bond. DFT calculations [115] showed that, in addition to altering the Pt d-band center energies, the  $OH_{(-M)} - OH_{(-Pt)}$  (or  $O_{(-M)} - OH_{(-Pt)}$ ) repulsion plays an important role in augmenting the ORR activity, as shown below in Fig. 9. Instead of adjusting the composition of the top2most Pt monolayer, replacing the substrate Pd(111) with  $Pd_3Fe(111)$  to generate  $Pt/Pd_3Fe(111)$  was recently reported to also have an enhanced ORR activity [116].

Another type of Pt monolayer catalyst showing improved ORR activities are Pt monolayers deposited on (noble metal)/(non-noble metal) core-shell nanoparticles [117]. The synthesis approach started with impregnation of high surface carbon into a mixed solution of noble metal precursor and non-noble metal precursor, followed by stir-drying in air. Core-shell metal substrates were formed by surface segregation of the noble metal at elevated temperature in a reductive atmosphere. A Pt monolayer was then deposited on the core/shell substrates by galvanic displacement of a Cu monolayer that was UPD-deposited onto the core-shell substrate particles. Three combinations were investigated: Pt/Au/Ni, Pt/Pd/Co, and Pt/Pt/Co. The enhancement of Pt mass activity of the best case (Pt/Au/Ni) was reported as being over an order of magnitude relative to the commercial Pt/C catalyst. The total noble metal mass activities were reported to be 2.5–4 times higher than that of Pt/C, with the Pt/Pt/Co having the highest number. The enhancement of activities was attributed to the geometric effect induced by the fine-tuning of the Pt lattice spacing with the substrate core-shell particles and to the inhibited PtOH formation because of lowering of the d-band center position relative to the Fermi level.

In a related study, Zhang et al. [118] investigated a partial monolayer of Au deposited on Pt(111) and on Pt/C nanoparticles for ORR. The catalysts were synthesized by Au displacement

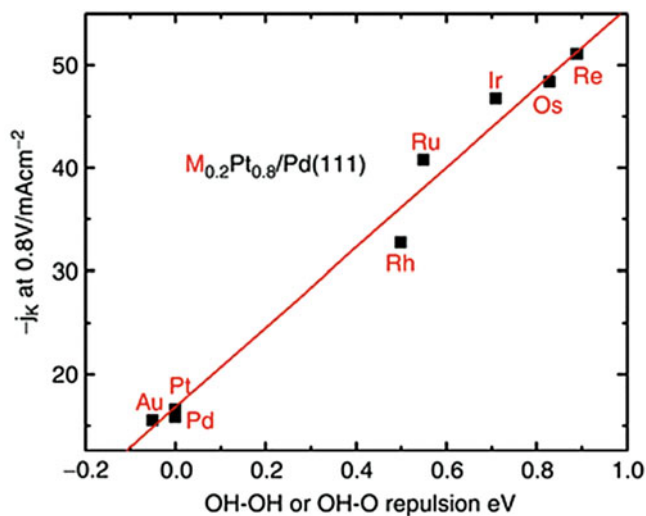


**PEM Fuel Cells and Platinum-Based Electrocatalysts, Fig. 8** Kinetic currents ( $j_k$ ; square symbols) at 0.8 V (versus RHE) calculated from Fig. 7 for ORR and the activation energies for  $O_2$  dissociation (solid circles) and for OH formation (empty circles) on Pt/Ru(0001) (1); Pt/Ir

(111) (2), Pt/Rh(111) (3), Pt/Au(111) (4), Pt(111) (5) and Pt/Pd(111) (6), as functions of the calculated binding energy of atomic oxygen (BEO) (Reproduced from [114] with permission)

**PEM Fuel Cells and Platinum-Based Electrocatalysts,**

**Fig. 9** Kinetic current at 0.80 V as a function of the calculated interaction energy between two OHs, or OH and O. Positive energies indicate more repulsive interaction compared to Pt/Pd(111) (Reproduced from [115] with permission)



of a monolayer Cu that was deposited with UPD onto the Pt(111) or Pt/C substrates. Due to the valence-state difference between  $Au^{3+}$  and  $Cu^{2+}$ , two thirds of a monolayer of Au was deposited onto each of the Pt surfaces. The Au atoms appeared to form clusters on Pt surfaces. While the ORR activities of the Au/Pt(111) and Au/Pt/C catalysts were slightly lower than those of pure Pt

(111) and Pt/C catalysts, respectively; the stability of the Au/Pt/C was superior compared to that of Pt/C catalyst. Potential cycling tests were performed on RDE in 0.1 M  $HClO_4$  solution, with the potential cycling window between 0.6 and 1.1 V, for 30,000 cycles. The catalytic activity of Au/Pt/C, measured as half-wave potentials on the  $O_2$  reduction polarization curves obtained

before and after potential cycling, showed only a 5 mV degradation in over the cycling period. In contrast, the corresponding change for Pt/C amounted to a loss of 39 mV. In situ X-ray absorption near-edge spectroscopy (XANES) with respect to the potential applied on the catalyst surfaces revealed the oxidation of Pt nanoparticles covered by Au at high potentials was decreased in comparison with the oxidation of Pt nanoparticles lacking such coverage.

More recently, Wang et al. [119] investigated the ORR on well-defined Pt/Pd and Pt/PdCo core-shell nanoparticles for the effects of particle size, facet orientation, and Pt shell thickness. The Pt shell was generated and the shell thickness was controlled by a novel method called the Cu-UPD-mediated electrodeposition method, in which repeated Cu-UPD/stripping, potential cycling, and Pt irreversible deposition occurred simultaneously in the same electrolyte, with the Pt deposition under diffusion control, until a desired thickness of Pt was achieved. Atomic level analysis using Z-contrast scanning transmission electron microscopy (STEM) coupled with element-sensitive electron energy loss spectroscopy (EELS) showed that well-controlled core-shell particles were obtained. ORR tests on RDE showed that Pt-monolayer catalysts on 4 nm Pd and 4.6 nm Pd<sub>3</sub>Co cores exhibited 1.0 and 1.6 A/mg Pt mass activities at 0.9 V, respectively, about five- and ninefold enhancements over that of 3 nm Pt nanoparticles. Also, two- and threefold enhancements in specific activity were observed respectively, which were mainly attributed to the nanosize- and lattice-mismatch-induced contraction in (111) facets based on the DFT calculations using a nanoparticle model. Scale-up methods were developed for synthesis of the core-shell particles [120].

In summary, Pt monolayer catalysts show a promising pathway toward solving one of the major problems facing PEM fuel cells by enhancing the Pt-specific activity and the utilization of Pt atoms, and therefore reducing the cost of the cathode catalyst, although more fuel cell tests of durability are needed before the monolayer catalysts can be put in fuel cell vehicles. There is still a need for a reduction in the total noble metals in these catalysts.

## Pt and Pt-Alloy Nanowire and Nanotube Electrocatalysts

As has been discussed in the introduction, low activity and limited durability are the two major issues related to the high-surface-area-carbon-dispersed Pt nanoparticle catalysts (Pt/C) in PEM fuel cells. Shao-Horn et al. [121] have given a comprehensive review on the instability considerations of Pt/C catalysts. Conventional PEM fuel cell catalysts typically consist of Pt nanoparticles in size of 2–3 nm that are supported on high-surface carbon with 20–50 nm primary carbon particles for electrical conductivity and high levels of catalyst activity. As it has been shown above, this kind of catalyst has already approached the maximum Pt mass activity as a pure Pt/C catalyst, as the Pt particle size is close to the optimal value. However, the 2–3 nm Pt nanoparticles are intrinsically not stable enough under PEM fuel cell operating conditions if no system-mitigation methods are applied. As an example, for a fuel cell short stack operating at steady-state open-circuit voltage (OCV, <0.95 V versus RHE), with H<sub>2</sub>/air flows (stoichiometric reactant flows of  $s = 2/2$ ) at 80 °C, fully humidified and 150 kPa<sub>abs</sub> for 2000 h, the Pt surface area decreased from <70 m<sup>2</sup>/g Pt to <15 m<sup>2</sup>/g Pt, corresponding to an almost 80% of Pt surface area loss [98]. If accompanied by a similar percentage loss of activity, this is not acceptable for commercialization of fuel cell vehicles. In addition, corrosion of carbon support makes the situation even more serious [122, 123]. One way to address this issue is to lower the upper voltage limit of the fuel cell through system mitigation [100, 101], or alternatively, to improve the intrinsic Pt stability through catalyst design, such as using Pt or Pt-alloy nanowire/nanotube catalysts. The local curvature of the nanowire/nanotube Pt or its alloy is expected to be small (in at least one direction), and it consequently has a lower surface free energy and higher stability. On the other hand, the Pt-specific activity of the nanowire/nanotube is expected to be higher than its nanoparticle counterpart, as it should bind OH/O less strongly.

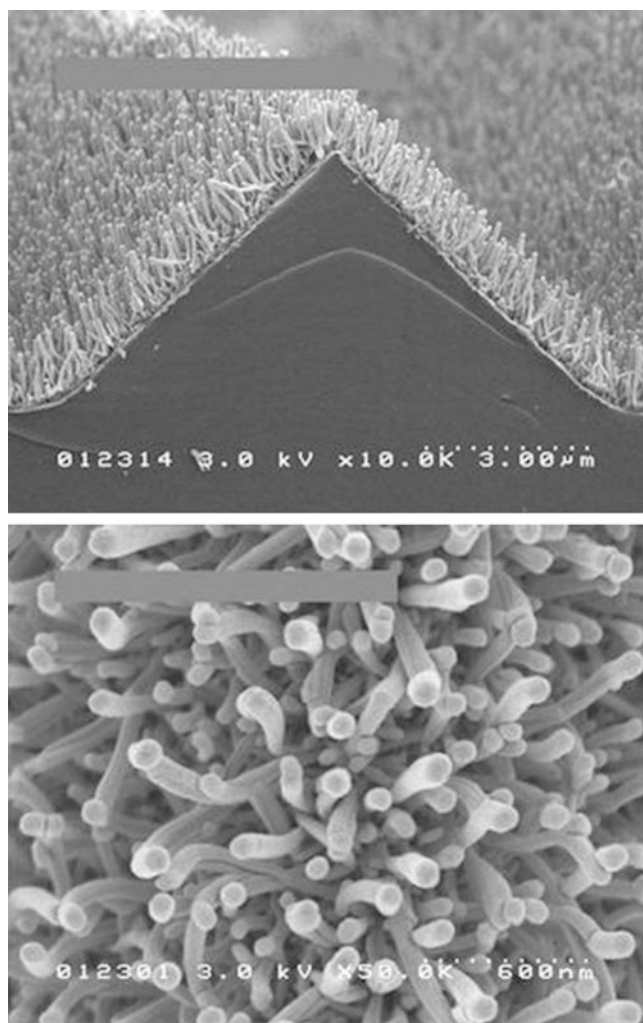
The 3M nanostructured thin film (NSTF) catalyst is such a non-conventional catalyst [124, 125]. The support particle is a crystalline organic pigment material, perylene red (PR), which is vacuum-deposited and converted to an oriented whisker phase by thermal annealing. The result is a uniquely structured thin film composed of highly oriented, densely packed crystalline organic whiskers [126]. A crystalline Pt coating can be vacuum-deposited on the whiskers. Fig. 10 shows SEM images of the NSTF catalyst-coated whiskers prior to incorporation onto the surfaces of a PEM to form a catalyst-coated membrane [127]. The cross section of the whiskers is on the order of 50 nm, and the lengths of the whiskers are

controllable by the thickness of the as-deposited PR film, typically in the range of 0.5–2  $\mu\text{m}$ . For a practical loading of  $<0.2 \text{ mg Pt/cm}^2$ , the typical Pt crystallite size of the coated PR whiskers is 10–11 nm, and the specific surface areas of the NSTF-Pt catalysts are  $<10 \text{ m}^2/\text{g Pt}$  [124].

Bonakdarpour et al. [128] investigated Pt/NSTF and Pt-Co-Mn/NSTF for ORR by using the rotating ring disk electrode (RRDE). The nominal chemical composition of the ternary alloy was calculated to be  $\text{Pt}_{0.68}\text{Co}_{0.3}\text{Mn}_{0.02}$ . The catalyst-coated whiskers were carefully brushed off of the original substrate web and applied onto the glassy carbon disk of the RRDE. The measurements were done in  $\text{O}_2$ -saturated 0.1 M  $\text{HClO}_4$  at room

### PEM Fuel Cells and Platinum-Based Electrocatalysts,

**Fig. 10** Scanning electron micrographs of typical NSTF catalysts as fabricated on a microstructured catalyst transfer substrate, seen (*top*) in cross section with original magnification of  $\times 10,000$ , and (*bottom*) in plain view with original magnification of  $\times 50,000$ . The dotted scale bar is shown in each micrograph (Reproduced from [127] with permission)





temperature. The Pt-specific activity of the Pt/NSTF was found to be close to that of a Pt polycrystalline disk. A twofold gain of Pt specific activity was observed on Pt-Co-Mn/NSTF versus Pt/NSTF. In PEMFC measurements for the same loading of  $0.2 \text{ mg Pt/cm}^2$ , using GM recommended conditions for measuring specific and mass activity at  $80^\circ\text{C}$ , saturated  $\text{H}_2/\text{O}_2$  at  $150 \text{ kPa}_{\text{abs}}$ , at  $900 \text{ mV}$ , the NSTF Pt-Co-Mn catalyst-coated membrane (CCM) generated specific activities of  $2.93 \text{ mA/cm}^2\text{Pt}$ , and mass activities of  $0.18 \text{ A/mg}^1 \text{ Pt}$ . The specific activity is  $<12$  times higher, and mass activity is about two times higher than those of TKK 47 wt% Pt/C.

To investigate the NSTF electrode stability under high voltage cycling, Debe et al. [129] tested a series of NSTF Pt and NSTF Pt-ternary catalysts along with Pt/C (Ketjen Black) and Pt/C (graphitic) types by scanning at  $20 \text{ mV/s}$ , between  $0.6$  and  $1.2 \text{ V}$  under saturated  $\text{H}_2/\text{N}_2$  at  $80^\circ\text{C}$ . The MEA's contained the same 3 M-ionomer PEM having a 1000 equivalent weight (EW), and the same 3 M-coated GDL. The NSTF electrodes had loadings of  $0.1 \text{ mg/cm}^2$ , while the carbon- and graphitic-carbon-supported catalysts had loadings of  $0.4 \text{ mg/cm}^2$ . Fig. 11 compares the normalized surface area as a function of the number of CV cycles for all the samples. It is interesting to note that for the NSTF samples the Pt and ternary

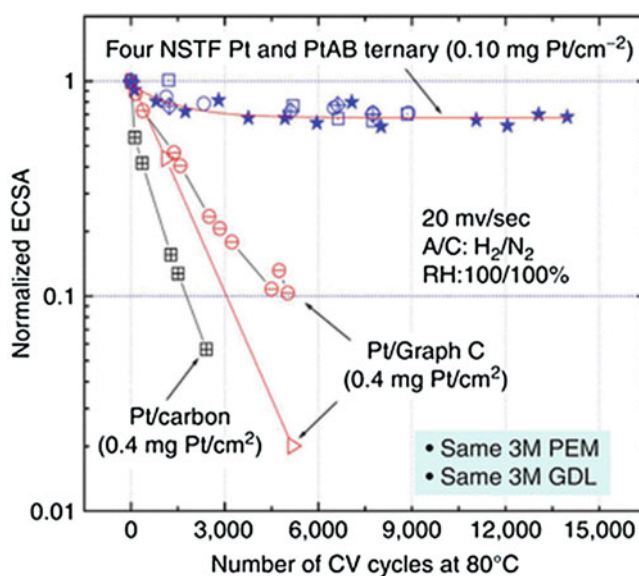
catalysts behave similarly and lose approximately 30% of the surface area out to 14,000 cycles. The Pt/C and Pt/graphitic carbon, on the other hand, lose substantially more surface area in significantly fewer cycles. The superior ability of the NSTF catalyst to withstand thousands of fast voltage scans over the potential range most critical for Pt dissolution and Pt agglomeration demonstrated a significant differentiating feature over carbon-supported catalysts [129].

Recently, Chen et al. [130] developed supportless Pt nanotubes (PtNTs) and Pt-alloy nanotubes (e.g., Pt-Pd alloy nanotubes (PtPdNTs)) as cathode catalysts for PEMFCs. PtNTs were synthesized by a galvanic replacement of silver nanowires (AgNWs) by following a similar method developed by Xia and coworkers [131, 132]. The AgNWs were synthesized using a polyol method [133] and were subsequently heated at reflux temperature with  $\text{Pt}(\text{CH}_3\text{COO})_2$  in an aqueous solution. For the preparation of PtPdNTs, mixed aqueous  $\text{Pt}(\text{CH}_3\text{COO})_2$  and  $\text{Pd}(\text{NO}_3)_2$  solutions were used. The diameter (Fig. 12a, b) and length of AgNWs are about  $40 \text{ nm}$  and  $10 \mu\text{m}$ , respectively. After Pt replacement, the diameter, wall thickness (Fig. 12c, d), and length of the PtNTs are about  $40 \text{ nm}$ ,  $6 \text{ nm}$ , and  $10 \mu\text{m}$ , respectively.

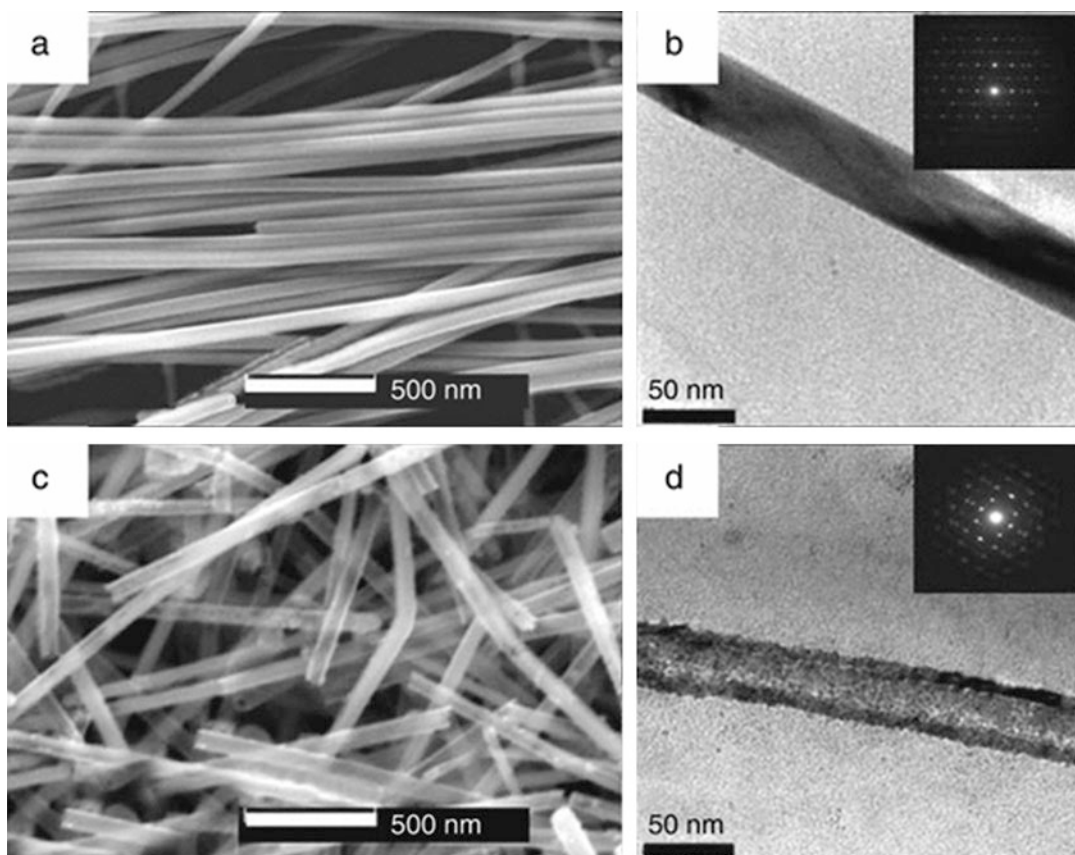
Chen et al. [130] tested the durability of these materials by cycling the electrode between 0 and

#### PEM Fuel Cells and Platinum-Based Electrocatalysts,

**Fig. 11** Normalized surface area versus number of CV cycles from  $0.6$  to  $1.2 \text{ V}$  for four NSTF catalyst samples and three Pt/carbon catalysts at  $80^\circ\text{C}$ . All MEAs used the same 3 M ionomer PEM and GDL (gas diffusion layer) (Reproduced from [129] with permission)







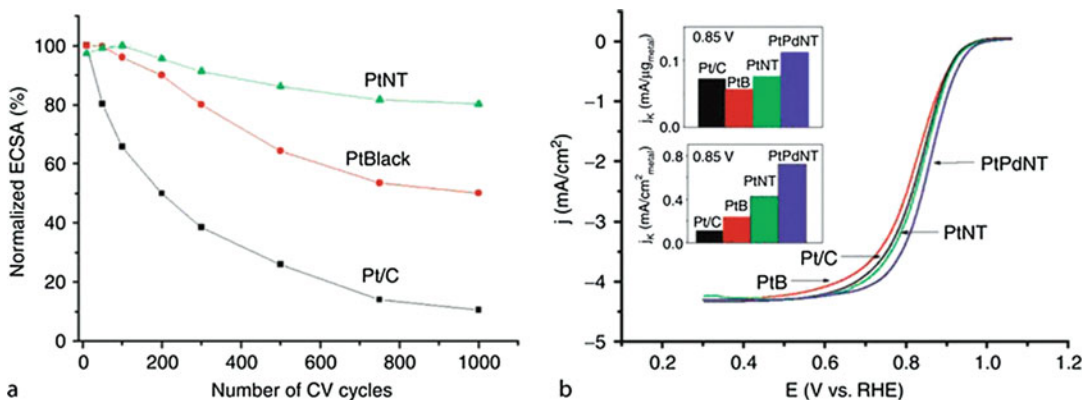
**PEM Fuel Cells and Platinum-Based Electrocatalysts, Fig. 12** (a) SEM image of AgNWs. (b) TEM image and electron diffraction pattern (inset) of AgNWs. (c) SEM

image of PtNTs. (d) TEM image and electron diffraction pattern (inset) of PtNTs (Reproduced from [130] with permission)

1.3 V versus RHE at a scan rate of 50 mV/s in argon-purged 0.5 M  $\text{H}_2\text{SO}_4$  solution at 60 °C. As shown in Fig. 13a, the electrochemical surface area (ECSA) of the PtNTs decreased by about 20% after 1000 cycles, while the Pt-black and Pt/C catalysts lost about 51% and 90% of their platinum ECSA, respectively. Fig. 13b shows the comparison of typical ORR polarization curves of the respective catalysts obtained at room temperature in  $\text{O}_2$ -saturated 0.5 M  $\text{H}_2\text{SO}_4$  using a rotating disk electrode (RDE) at 1600 rpm. At 0.85 V versus RHE, the mass activity of PtNTs was reported slightly higher than that of Pt/C, and 1.4 times higher than that of Pt-black catalysts. The specific activity of the PtNTs was 3.8 times and 1.8 times higher than those of Pt/C and Pt-black catalysts, respectively. For PtPdNTs, the mass activity was

measured 1.4 times and 2.1 times higher than those of Pt/C and Pt-black catalysts, while the specific activity was 5.8 times and 2.7 times higher than those of Pt/C and Pt-black catalysts, respectively.

The examples given above illustrate that it is possible to achieve both activity and durability goals of Pt-based catalysts through special morphology and structural design of the catalyst and electrode. There are many other important advancements not discussed here on nanostructured Pt and Pt-alloy catalysts/electrodes showing improvements in activity and/or durability for ORR, such as single-crystal-Pt nanowires grown on continuous carbon-layer-coated Sn-fiber 3D electrodes [134], Pt-Pd bimetallic nanodendrites [135, 136], faceted Pt nanocrystals [137], nanoporous Pt alloy electrodes [138–140].



**PEM Fuel Cells and Platinum-Based Electrocatalysts.** **Fig. 13** (a) Loss of electrochemical surface area (ECSA) of Pt/C (E-TEK), platinum-black (PtB; E-TEK), and PtNT catalysts with number of potential cycles in Ar-purged 0.5 M H<sub>2</sub>SO<sub>4</sub> solution at 60°C (0–1.3 V versus RHE, sweep rate 50 mV/s). (b) ORR curves (shown as current-

voltage relations) of Pt/C, platinum black (PtB), PtNTs, and PdPtNTs in O<sub>2</sub>-saturated 0.5 M H<sub>2</sub>SO<sub>4</sub> solution at room temperature (1,600 rpm, sweep rate 5 mV/s). Inset: Mass activity (*top*) and specific activity (*bottom*) for the four catalysts at 0.85 V (Reproduced from [130] with permission)

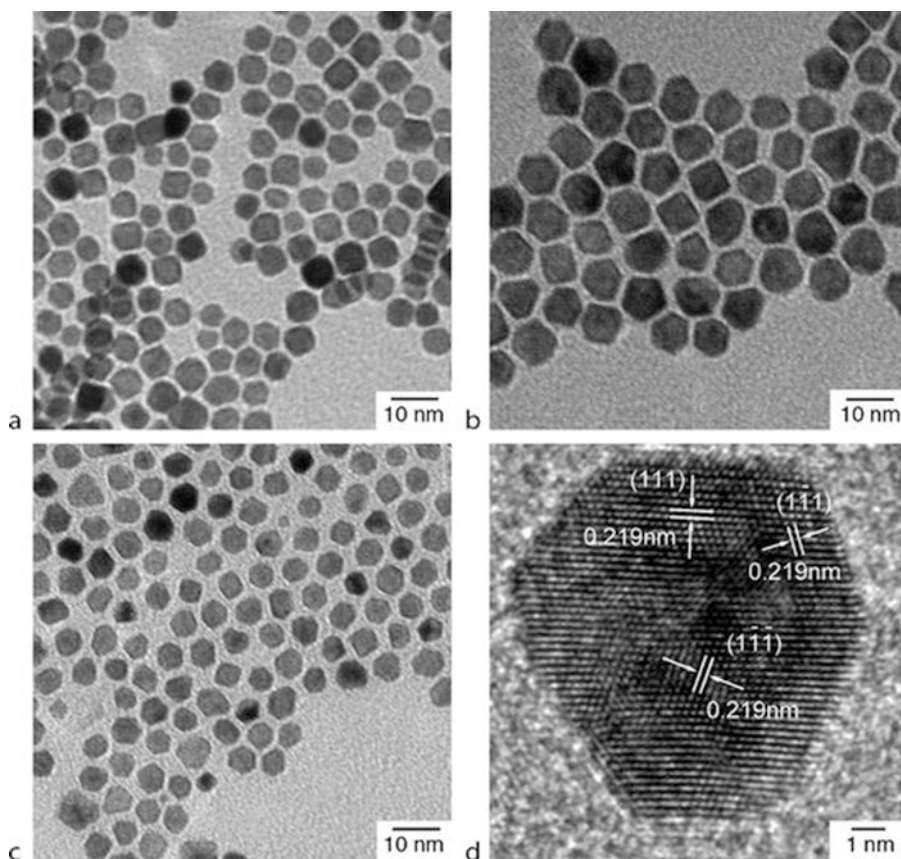
### Facet- and Shape-Controlled Pt-Alloy Nanocrystal Electrocatalysts

Stamenkovic and coworkers [42] demonstrated in HClO<sub>4</sub> that on RDE Pt<sub>3</sub>Ni(111) single-crystal surfaces of <6 mm in diameter, the specific activity for ORR is about an order of magnitude higher than on the Pt(111) surface and is about 90 times higher than on Pt/C catalyst, while the other two low-index surfaces, [Pt<sub>3</sub>Ni(100) and Pt<sub>3</sub>Ni(110)] are much less active than Pt<sub>3</sub>Ni(111). This result is very intriguing in that it suggests that if one can make Pt<sub>3</sub>Ni nanocrystals with all exposed surfaces having {111} orientations, one can hope to gain an enhancement of specific activity by up to two orders of magnitude relative to state-of-the-art Pt/C catalysts. Recently, two interesting papers [141, 142] have shown progress on synthesizing such Pt alloy nanocrystals.

Wu et al. [141] recently reported an approach to the preparation of truncated-octahedral Pt<sub>3</sub>Ni (*t*,*o*-Pt<sub>3</sub>Ni) catalysts that have dominant exposure of {111} facets. The shape-defined Pt-Ni nanoparticles were made from platinum acetylacetonate [Pt(acac)<sub>3</sub>] and nickel acetylacetonate [Ni(acac)<sub>2</sub>] in diphenyl ether (DPE) using a mixture of borane-*tert*-butylamine complex (TBAB) and hexadecanediol as the reducing agents. Long-alkane-chain amines were used as

the main capping agents, and adamantane-carboxylic acid (ACA) or adamantaneacetic acid (AAA) was used to affect the reaction kinetics. The population of truncated octahedral crystals could be adjusted by the types and amounts of the reducing agents and capping agents. Three sets of Pt<sub>3</sub>Ni nanocrystals were generated with various truncated-octahedral crystal populations; see Fig. 14.

While Fig. 14a, b contain 30% and 10% of Pt<sub>3</sub>Ni cubes (with the remaining particles being truncated-octahedrons), respectively, Fig. 14c contains only truncated-octahedrons. The particle size is on the order of 5 to 7 nm. Only two types of facets are exposed of all the nanocrystals, i.e., the {111} and {100}. The fractions of the {111} surface area over the total surface area could be calculated based on the geometries of the shapes and the population statistics. The ORR kinetics of the nanocrystals were studied on RDEs in O<sub>2</sub>-saturated 0.1 M HClO<sub>4</sub>, at room temperature, at 1600 rpm, with a potential scan rate of 10 mV/s. Fig. 15 shows comparison of polarization curves, cyclic-voltammetry curves, mass activities, and specific activities of the Pt<sub>3</sub>Ni nanocrystals to the standard TTK Pt/Vulcan carbon catalyst. As shown in Fig. 15d, almost-linear correlations were obtained for both mass activities and specific activities versus the fraction of the



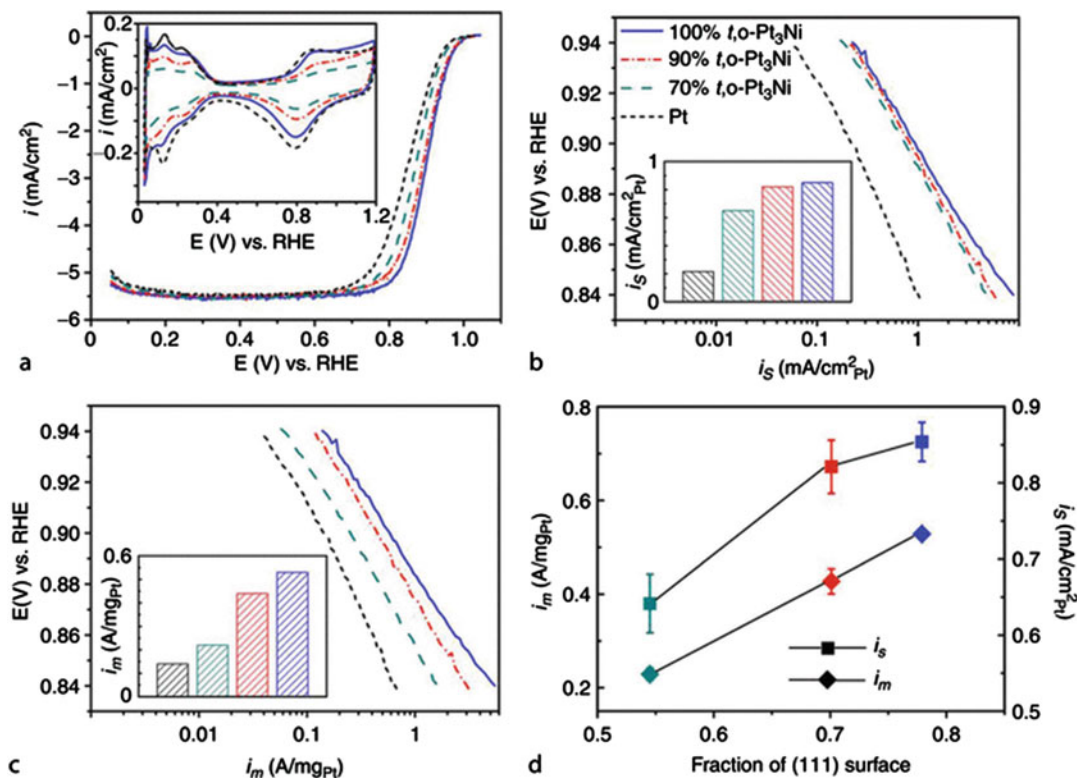
**PEM Fuel Cells and Platinum-Based Electrocatalysts, Fig. 14** TEM images of  $\text{Pt}_3\text{Ni}$  nanocrystals with truncated octahedron population of (a) 70%, (b) 90%, (c) 100%, and

(d) HR-TEM image of a truncated octahedron showing the (111) lattice (Reproduced from [141] with permission)

(111) surface area over the total surface area. A tabulated kinetic activity comparison is shown in Table 1. The mass activity and specific activity comparisons were made at 0.9 V versus RHE. Roughly  $4\times$  mass-activity and specific-activity enhancements were observed on the 100% truncated octahedral  $\text{Pt}_3\text{Ni}$  nanocrystals over the Pt/C catalyst. While the {111} facets of the nanocrystals showed much higher specific activity than the {100} facets, as indicated in Fig. 15d, in agreement with trend found on bulk  $\text{Pt}_3\text{Ni}$  single crystal disks, the absolute values of the specific activities of the nanocrystals are still far below those observed on bulk single-crystal surfaces [42].

Another interesting report is from Zhang et al. [142] on the synthesis and ORR activity of  $\text{Pt}_3\text{Ni}$

nano-octahedra and nanocubes, with the two shapes of nanocrystals having only {111} facets and {100} facets exposed, respectively. The monodispersed  $\text{Pt}_3\text{Ni}$  nano-octahedra and nanocubes were synthesized via a high-temperature organic solution chemistry approach, which involved using mixed oleylamine and oleic acid at elevated temperature as the reducing agent and capping agent, and tungsten hexacarbonyl  $\text{W}(\text{CO})_6$  as the shape controlling agent. Detailed procedures for synthesis of the nanocrystals can be found in Ref. [142]. Fig. 16 shows the SEM and TEM images of those shape and size controlled nano-octahedral (a-e) and nanocube (f-j) crystals. The chemical compositions of the crystals were analyzed by using combined ICP-MS and EDS techniques (from both TEM and SEM),



**PEM Fuel Cells and Platinum-Based Electrocatalysts, Fig. 15** (a) Polarization curves and CV curves (*inset*), (b) area (mA/cm<sup>2</sup>Pt), (c) mass (A/mg Pt) specific ORR activity for the *t,o*-Pt<sub>3</sub>Ni and reference Pt catalysts; and

(d) the correlations between specific activities and fractions of (111) surfaces of these Pt<sub>3</sub>Ni catalysts. The ORR polarization curves were collected at 1,600 rpm (Reproduced from [141] with permission)

**PEM Fuel Cells and Platinum-Based Electrocatalysts, Table 1** ECSA, mass- and area- specific ORR activities of Pt<sub>3</sub>Ni and Pt/catalysts (at 0.9 V versus RHE) (Reproduced from [141] with permission)

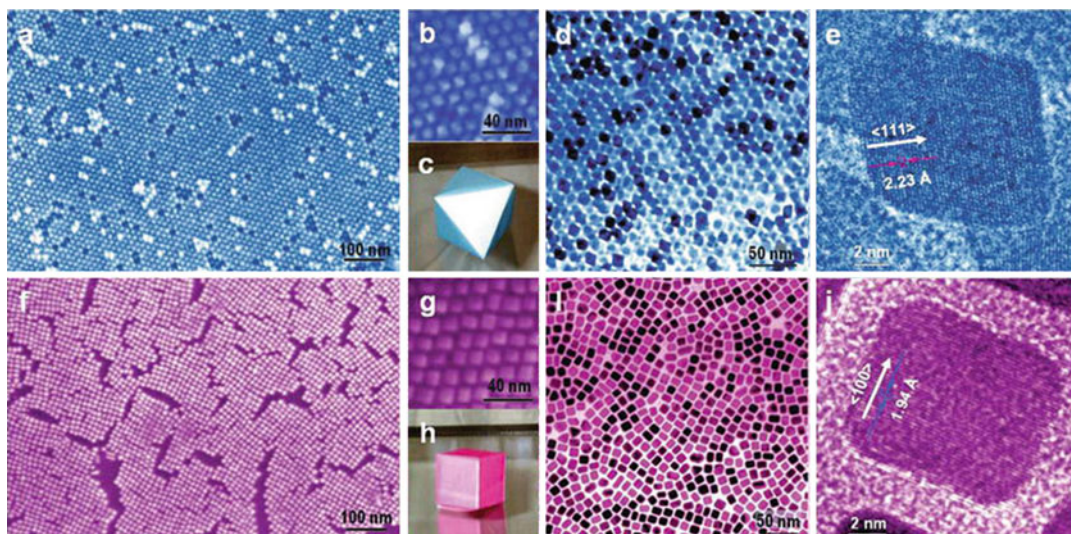
Sample name	Pt loading [ $\mu\text{g}_{\text{Pt}}/\text{cm}_{\text{disk}}^2$ ]	ECSA [ $\text{m}^2/\text{g}_{\text{Pt}}$ ]	Mass activity [ $\text{A}/\text{mg}_{\text{Pt}}$ ]	Specific activity [ $\text{mA}/\text{cm}_{\text{Pt}}^2$ ]
100% <i>t,o</i> -Pt <sub>3</sub> Ni	9.3	62.4	0.53	0.85
90% <i>t,o</i> -Pt <sub>3</sub> Ni	9.3	53.7	0.44	0.82
70% <i>t,o</i> -Pt <sub>3</sub> Ni	9.3	33.8	0.22	0.65
Pt/C (TKK)	11	65	0.14	0.215

and the results suggested that the average molar ratio of Pt over Ni was 3:1.

Zhang et al. [142] further investigated ORR activities of the shape controlled nanocrystals by using RDE measurements. The ORR measurements were conducted in an O<sub>2</sub>-saturated 0.1 M HClO<sub>4</sub> solution at 295 K. A characteristic set of polarization curves at 900 rpm for the ORR on

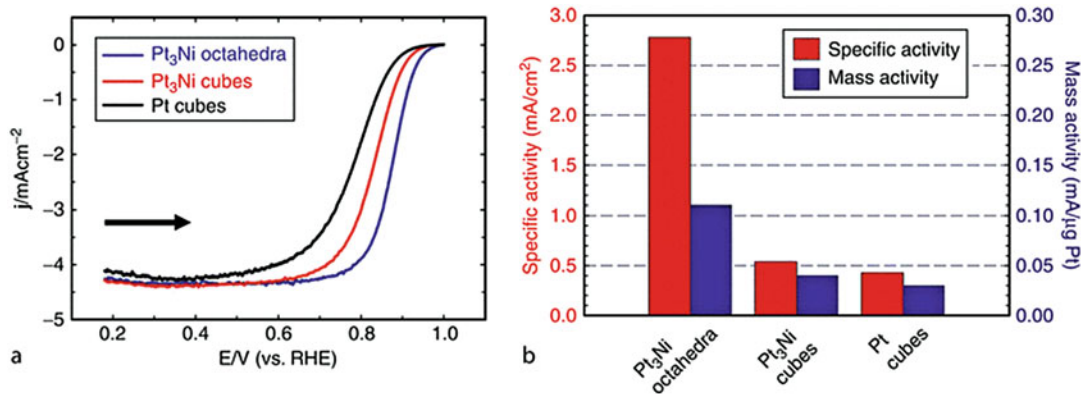
Pt<sub>3</sub>Ni nano-octahedra, Pt<sub>3</sub>Ni nanocubes, and Pt nanocubes are displayed in Fig. 17a. After mass transport correction using Koutecky-Levich equation, and normalizing by the Pt surface area and mass, the kinetic activities (specific activity and mass activity) at 0.9 V were plotted in Fig. 17b. The Pt-specific activity of Pt<sub>3</sub>Ni nano-octahedra were determined to be 5.1 times of that of the





**PEM Fuel Cells and Platinum-Based Electrocatalysts, Fig. 16** (a–e) Images for  $\text{Pt}_3\text{Ni}$  nano-octahedra. (f–j) Images for  $\text{Pt}_3\text{Ni}$  nanocubes. (a, f) Field-emission SEM images. (b, g) High-resolution SEM images. (c) 3D model

of an octahedron. (d, i) TEM images. (e, j) High-resolution TEM images of single nanocrystals. (h) 3D model of a cube (Reproduced from [142] with permission)



**PEM Fuel Cells and Platinum-Based Electrocatalysts, Fig. 17** (a) Polarization curves for ORR on  $\text{Pt}_3\text{Ni}$  nano-octahedra,  $\text{Pt}_3\text{Ni}$  nanocubes, and Pt nanocubes supported on a rotating glassy carbon disk electrode in  $\text{O}_2$ -saturated 0.1 M  $\text{HClO}_4$  solution at 295 K; with scan rate = 20 mV/s; rotation rate = 900 rpm. Catalyst loading in terms of Pt mass:  $\text{Pt}_3\text{Ni}$  octahedra, 3.0  $\mu\text{g}$ ;  $\text{Pt}_3\text{Ni}$  cube, 2.0  $\mu\text{g}$ ; Pt cube,

1.1  $\mu\text{g}$ . Current density was normalized to the glassy carbon geometric surface area (0.196  $\text{cm}^2$ ). The arrow indicates the potential scan direction. (b) Comparison of the ORR activities on the three types of catalysts. Specific activity and mass activity were all measured at 0.9 V versus RHE at 295 K (Reproduced from [142] with permission)

$\text{Pt}_3\text{Ni}$  nanocubes and  $<6.5$  times that of the Pt nanocubes, while the Pt mass activity of the  $\text{Pt}_3\text{Ni}$  nano-octahedra was  $<2.8$  times of that of  $\text{Pt}_3\text{Ni}$  nanocubes and  $<3.6$  times of that of Pt nanocubes. The significant shape dependence of ORR activity agreed with the observation from the extended  $\text{Pt}_3\text{Ni}$  single crystal surfaces,

although the absolute values of specific activities observed on  $\text{Pt}_3\text{Ni}$  nanocubes and nano-octahedra were about four- to sevenfold lower than those reported in Ref. [42], respectively. One apparent puzzle in these reported results is that the Pt surface area or ECSA of the nanocrystals derived from the specific activity and mass activity

(ECSA per unit mass of Pt = mass activity/specific activity) is 5–10 times lower than one would expect from the size of particles revealed by SEM and TEM images. The discrepancy may come from the low utilization of the surface area because of impurities or from overlap of the non-supported nanocrystals. Another set of data for the high surface carbon supported those nanocrystals was reported in the online supporting information of the paper, and this showed a better agreement between measured ECSA and diameter to TEM, suggesting that particle aggregation caused the low area observed for the unsupported catalysts.

In summary, the size- and shape-controlled synthesis of nanocrystal Pt-based electrocatalysts has shown a promising path to high Pt-specific activity, although the absolute number of the activity is still not comparable to that observed on extended Pt alloy single-crystal surface, probably due to the size effect, residual impurities and defects in the nanocrystal surface, and incomplete formation of smooth, segregated Pt layers on the facet surfaces. The Pt mass activity achieved for the best case is already about four times higher than state-of-the-art Pt/C catalyst. If the core of the nanocrystals can be replaced with some corrosion-resistant material but keeping the surface of the Pt alloy shell still in {111} facets, one could expect a significant further reduction of the Pt loading required for the cathode catalyst. In addition, the size of the particles can be larger to gain the benefits of the particle size effect, as the Pt consumption is determined by the thickness of the shell. The durability of such nanocrystals could be expected to be high because of the lack of low-coordination atoms in their surfaces.

## Future Directions

Low platinum loading, high activity, and more durable catalysts still remain as critical challenges for PEFCs for automotive applications. Further fundamental understanding of the correlations between activity, stability, and structural properties at the atomic level are most desired from both theoretical and experimental perspectives. Studies of the connections between the activities of

controlled-facet-orientation nanoparticles and extended single-crystal surfaces would be helpful. Structure- and surface-controlled syntheses of catalysts (Pt monolayer catalysts, nanostructured catalysts and electrodes, size- and facet-controlled Pt alloy nanocrystals, combined with core-shell structure) should provide a practical viable path to achieving fuel cell catalyst loadings required for large-scale commercialization.

## Bibliography

### Primary Literature

1. Andujar JM, Segura F (2009) Fuel cells: history and updating. A walk along two centuries. *Renew Sust Energ Rev* 13(9):2309–2322
2. Grimes PG (2000) Historical pathways for fuel cells – the new electric century. *IEEE Aerosp Electron Syst Mag* 15(12):7–10
3. Appleby AJ (1990) From Sir William Grove to today: fuel cells and the future. *J Power Sources* 29(1–2):3–11
4. Perry ML, Fuller TF (2002) A historical perspective of fuel cell technology in the 20th century. *J Electrochem Soc* 149(7):S59–S67
5. Thomas CE (2009) Fuel cell and battery electric vehicles compared. *Int J Hydrog Energy* 34(15):6005–6020
6. Gottesfeld S (2007) Fuel cell techno-personal milestones 1984–2006. *J Power Sources* 171(1):37–45
7. Mathias MF, Makharia R, Gasteiger HA, Conley JJ, Fuller TJ, Gittleman CJ, Kocha SS, Miller DP, Mittelsteadt CK, Xie T, Yan SG, Yu PT (2005) Two fuel cell cars in every garage? *Electrochem Soc Interface* 14(3):24–35
8. Raistrick ID (1986) In: Zee JWV, White RE, Kinoshita K, Burney HS (eds) Diaphragms, separators, and ion-exchange membranes, the electrochemical society proceedings series. The Electrochemical Society, Pennington, p 172
9. Wilson MS, Gottesfeld S (1992) Thin-film catalyst layers for polymer electrolyte fuel cell electrodes. *J Appl Electrochem* 22(1):1–7
10. Wilson MS, Gottesfeld S (1992) High performance catalyzed membranes of ultra-low Pt loadings for polymer electrolyte fuel cells. *J Electrochem Soc* 139(2):L28–L30
11. Wilson MS, Valerio JA, Gottesfeld S (1995) Low platinum loading electrodes for polymer electrolyte fuel-cells fabricated using thermoplastic ionomers. *Electrochim Acta* 40(3):355–363
12. Conway BE, Tilak BV (2002) Interfacial processes involving electrocatalytic evolution and oxidation of H<sub>2</sub>, and the role of chemisorbed H. *Electrochim Acta* 47(22–23):3571–3594
13. Gasteiger HA, Markovic NM, Ross PN (1995) H<sub>2</sub> and CO electrooxidation on well-characterized Pt, Ru, and



- Pt-Ru.2. rotating disk electrode studies of CO/H<sub>2</sub> mixtures at 62-degrees C. *J Phys Chem* 99(45): 16757–16767
14. Mukerjee S, McBreen J (1996) Hydrogen electrocatalysis by carbon supported Pt and Pt alloys – an in situ x-ray absorption study. *J Electrochem Soc* 143(7):2285–2294
  15. Neyerlin KC, WB G, Jorne J, Gasteiger HA (2007) Study of the exchange current density for the hydrogen oxidation and evolution reactions. *J Electrochem Soc* 154(7):B631–B635
  16. Tarasevich MR, Sadkowsky A, Yeager E (1983) Oxygen electrochemistry. In: Conway BE, Bockris JO, Yeager E, Khan SUM, White RE (eds) *Comprehensive treatise in electrochemistry*. Plenum Press, New York, p 301
  17. Adzic RR (1998) Recent advances in the kinetics of oxygen reduction. In: Lipkowsky J, Ross PN (eds) *Electrocatalysis*. Wiley-VCH, New York, pp 197–241
  18. Kinoshita K (1992) *Electrochemical oxygen technology*. Wiley, New York
  19. Markovic NM, Gasteiger HA, Ross PN (1995) Oxygen reduction on platinum low-index single-crystal surfaces in sulfuric-acid-solution – rotating ring-Pt(Hkl) disk studies. *J Phys Chem* 99(11):3411–3415
  20. Gasteiger HA, Panels JE, Yan SG (2004) Dependence of PEM fuel cell performance on catalyst loading. *J Power Sources* 127(1–2):162–171
  21. Gasteiger HA, Kocha SS, Sompalli B, Wagner FT (2005) Activity benchmarks and requirements for Pt, Pt-alloy, and non-Pt oxygen reduction catalysts for PEMFCs. *Appl Catal B Environ* 56(1–2):9–35
  22. Damjanovic A, Brusica V (1967) Electrode kinetics of oxygen reduction on oxide-free platinum electrodes. *Electrochim Acta* 12(6):615–628
  23. Wang JX, Markovic NM, Adzic RR (2004) Kinetic analysis of oxygen reduction on Pt(111) in acid solutions: intrinsic kinetic parameters and anion adsorption effects. *J Phys Chem B* 108(13):4127–4133
  24. Markovic NM, Gasteiger HA, Grgur BN, Ross PN (1999) Oxygen reduction reaction on Pt(111): effects of bromide. *J Electroanal Chem* 467(1):157–163
  25. Adzic RR (1992) Surface morphology effects in oxygen electrochemistry. In: Scherson D, Tryk D, Xing X (eds) *Proceedings of the workshop on structural effects in electrocatalysis and oxygen electrochemistry*. The Electrochemical Society, Pennington, p 419
  26. Uribe FA, Wilson MS, Springer TE, Gottesfeld S (1992) Oxygen reduction (ORR) at the Pt/recast ionomer interface and some general comments on the ORR at Pt/aqueous electrolyte interfaces. In: Scherson DD, Tryk D, Xing X (eds) *Proceedings of the workshop on structural effects in electrocatalysis and oxygen electrochemistry*. The Electrochemical Society, Pennington, p 494
  27. Norskov JK, Rossmeisl J, Logadottir A, Lindqvist L, Kitchin JR, Bligaard T, Jonsson H (2004) Origin of the overpotential for oxygen reduction at a fuel-cell cathode. *J Phys Chem B* 108(46):17886–17892
  28. Wang JX, Zhang JL, Adzic RR (2007) Double-trap kinetic equation for the oxygen reduction reaction on Pt(111) in acidic media. *J Phys Chem A* 111(49): 12702–12710
  29. Wang JX, Uribe FA, Springer TE, Zhang JL, Adzic RR (2008) Intrinsic kinetic equation for oxygen reduction reaction in acidic media: the double Tafel slope and fuel cell applications. *Faraday Discuss* 140:347–362
  30. Neyerlin KC, WB G, Jorne J, Gasteiger HA (2006) Determination of catalyst unique parameters for the oxygen reduction reaction in a PEMFC. *J Electrochem Soc* 153(10):A1955–A1963
  31. Neyerlin KC, Gu W, Jorne J, Clark A, Gasteiger HA (2007) Cathode catalyst utilization for the ORR in a PEMFC – analytical model and experimental validation. *J Electrochem Soc* 154(2):B279–B287
  32. Neyerlin KC, Gasteiger HA, Mittelsteadt CK, Jorne J, WB G (2005) Effect of relative humidity on oxygen reduction kinetics in a PEMFC. *J Electrochem Soc* 152(6):A1073–A1080
  33. Blurton KF, Greenberg P, Oswin HG, Rutt DR (1972) The electrochemical activity of dispersed platinum. *J Electrochem Soc* 119(5):559–564
  34. Peuckert M, Yoneda T, Betta RAD, Boudart M (1986) Oxygen reduction on small supported platinum particles. *J Electrochem Soc* 133(5):944–947
  35. Kinoshita K (1990) Particle size effects for oxygen reduction on highly dispersed platinum in acid electrolytes. *J Electrochem Soc* 137(3):845–848
  36. Ross PN (1986) Structure-property relations in noble metal electrocatalysis. In: *The Gordon conference on chemistry at interfaces*. Lawrence Berkeley Laboratory, Berkeley/Meriden, p LBL-21733
  37. Ross PN (1980) Oxygen reduction on supported Pt alloys and intermetallic compounds in phosphoric acid. Final report prepared for the electric power research institute. Electric Power Research Institute, Palo Alto, September 1980
  38. Sattler ML, Ross PN (1986) The surface structure of Pt crystallites supported on carbon black. *Ultramicroscopy* 20:21–28
  39. Landsman DA, Luczak FJ (2003) Catalyst studies and coating technologies. In: Vielstich W, Gasteiger H, Lamm A (eds) *Handbook of fuel cells*. Wiley, Chichester, p 811
  40. Thompsett D (2003) Pt alloys as oxygen reduction catalysts. In: Vielstich W, Gasteiger H, Lamm A (eds) *Handbook of fuel cells – fundamentals, technology and applications*. Wiley, Chichester, p 467
  41. Markovic N, Gasteiger H, Ross PN (1997) Kinetics of oxygen reduction on Pt(hkl) electrodes: implications for the crystallite size effect with supported Pt electrocatalysts. *J Electrochem Soc* 144(5):1591–1597
  42. Stamenkovic VR, Fowler B, Mun BS, Wang GF, Ross PN, Lucas CA, Markovic NM (2007) Improved oxygen reduction activity on Pt<sub>3</sub>Ni(111) via increased surface site availability. *Science* 315(5811):493–497
  43. Hammer B, Norskov JK (2000) Theoretical surface science and catalysis – calculations and concepts. In:

- Gates BC, Knozinger H (eds) *Advances in catalysis*, vol 45. Academic, San Diego, pp 71–129
44. Norskov JK, Bligaard T, Logadottir A, Bahn S, Hansen LB, Bollinger M, Bengaard H, Hammer B, Slijivančanin Z, Mavrikakis M, Xu Y, Dahl S, Jacobsen CJH (2002) Universality in heterogeneous catalysis. *J Catal* 209(2):275–278
  45. Lopez N, Janssens TVW, Clausen BS, Xu Y, Mavrikakis M, Bligaard T, Norskov JK (2004) On the origin of the catalytic activity of gold nanoparticles for low-temperature CO oxidation. *J Catal* 223(1):232–235
  46. Xu Y, Mavrikakis M (2003) Adsorption and dissociation of O<sub>2</sub> on gold surfaces: effect of steps and strain. *J Phys Chem B* 107(35):9298–9307
  47. Xu Y, Ruban AV, Mavrikakis M (2004) Adsorption and dissociation of O<sub>2</sub> on Pt-Co and Pt-Fe alloys. *J Am Chem Soc* 126(14):4717–4725
  48. Greeley J, Rossmeisl J, Hellman A, Norskov JK (2007) Theoretical trends in particle size effects for the oxygen reduction reaction. *Z Phys Chemie-Int J Res Phys Chem Chem Phys* 221(9–10):1209–1220
  49. Mukerjee S, McBreen J (1998) Effect of particle size on the electrocatalysis by carbon-supported Pt electrocatalysts: an in situ XAS investigation. *J Electroanal Chem* 448(2):163–171
  50. Yano H, Inukai J, Uchida H, Watanabe M, Babu PK, Kobayashi T, Chung JH, Oldfield E, Wieckowski A (2006) Particle-size effect of nanoscale platinum catalysts in oxygen reduction reaction: an electrochemical and Pt-195 EC-NMR study. *Phys Chem Chem Phys* 8(42):4932–4939
  51. Gasteiger HA, Markovic NM (2009) Just a dream-or future reality? *Science* 324(5923):48–49
  52. Mukerjee S, Srinivasan S, Soriaga MP, McBreen J (1995) Role of structural and electronic-properties of Pt and Pt alloys on electrocatalysis of oxygen reduction – an in-situ Xanes and EXAFS investigation. *J Electrochem Soc* 142(5):1409–1422
  53. Wakabayashi N, Takeichi M, Uchida H, Watanabe M (2005) Temperature dependence of oxygen reduction activity at Pt-Fe, Pt-Co, and Pt-Ni alloy electrodes. *J Phys Chem B* 109(12):5836–5841
  54. Paulus UA, Wokaun A, Scherer GG, Schmidt TJ, Stamenkovic V, Markovic NM, Ross PN (2002) Oxygen reduction on high surface area Pt-based alloy catalysts in comparison to well defined smooth bulk alloy electrodes. *Electrochim Acta* 47(22–23):3787–3798
  55. Glass JT, Cahen JGL, Stoner GE, Taylor EJ (1987) The effect of metallurgical variables on the electrocatalytic properties of PtCr alloys. *J Electrochem Soc* 134(1):58–65
  56. Paffett MT, Daube KA, Gottesfeld S, Campbell CT (1987) Electrochemical and surface science investigations of PtCr alloy electrodes. *J Electroanal Chem* 220(2):269–285
  57. Beard BC, Ross JPN (1990) The structure and activity of Pt-Co alloys as oxygen reduction electrocatalysts. *J Electrochem Soc* 137(11):3368–3374
  58. Toda T, Igarashi H, Uchida H, Watanabe M (1999) Enhancement of the electroreduction of oxygen on Pt alloys with Fe, Ni, and Co. *J Electrochem Soc* 146(10):3750–3756
  59. Koh S, Hahn N, CF Y, Strasser P (2008) Effects of composition and annealing conditions on catalytic activities of dealloyed Pt-Cu nanoparticle electrocatalysts for PEMFC. *J Electrochem Soc* 155(12):B1281–B1288
  60. Schulenburg H, Muller E, Khelashvili G, Roser T, Bonnemann H, Wokaun A, Scherer GG (2009) Heat-treated PtCo<sub>3</sub> nanoparticles as oxygen reduction catalysts. *J Phys Chem C* 113(10):4069–4077
  61. Jalan V, Taylor EJ (1983) Importance of interatomic spacing in catalytic reduction of oxygen in phosphoric acid. *J Electrochem Soc* 130(11):2299–2302
  62. Jalan V, Taylor EJ (1984) Importance of interatomic spacing in the catalytic reduction of oxygen in phosphoric acid. In: McIntyre JDE, Weaver MJ, Yeager EB (eds) *The electrochemical society softbound proceedings series. The Electrochemical Society, Pennington*, p 546
  63. Landsman DA, Luczak FJ (1982) Noble metal-chromium alloy catalysts and electrochemical cell. US Patent 4,316,944, United Technologies Corporation: US
  64. Stamenkovic VR, Mun BS, Arenz M, Mayrhofer KJJ, Lucas CA, Wang GF, Ross PN, Markovic NM (2007) Trends in electrocatalysis on extended and nanoscale Pt-bimetallic alloy surfaces. *Nat Mater* 6(3):241–247
  65. Toda T, Igarashi H, Watanabe M (1999) Enhancement of the electrocatalytic O<sub>2</sub> reduction on Pt-Fe alloys. *J Electroanal Chem* 460(1–2):258–262
  66. M-k M, Cho J, Cho K, Kim H (2000) Particle size and alloying effects of Pt-based alloy catalysts for fuel cell applications. *Electrochim Acta* 45(25–26):4211–4217
  67. Koh S, Strasser P (2007) Electrocatalysis on bimetallic surfaces: modifying catalytic reactivity for oxygen reduction by voltammetric surface dealloying. *J Am Chem Soc* 129(42):12624
  68. Gottesfeld S (1986) The ellipsometric characterization of Pt + Cr alloy surfaces in acid solutions. *J Electroanal Chem* 205(1–2):163–184
  69. Paffett MT, Beery JG, Gottesfeld S (1988) Oxygen reduction at Pt<sub>0.65</sub>Cr<sub>0.35</sub>, Pt<sub>0.2</sub>Cr<sub>0.8</sub> and roughened platinum. *J Electrochem Soc* 135(6):1431–1436
  70. Mukerjee S, Srinivasan S (1993) Enhanced electrocatalysis of oxygen reduction on platinum alloys in proton exchange membrane fuel cells. *J Electroanal Chem* 357(1–2):201–224
  71. Toda T, Igarashi H, Watanabe M (1998) Role of electronic property of Pt and Pt alloys on electrocatalytic reduction of oxygen. *J Electrochem Soc* 145(12):4185–4188
  72. Mun BS, Watanabe M, Rossi M, Stamenkovic V, Markovic NM, Ross PN (2005) A study of electronic structures of Pt<sub>3</sub>M (M = Ti, V, Cr, Fe, Co, Ni) polycrystalline alloys with valence-band photoemission spectroscopy. *J Chem Phys* 123(20):204717

73. Greeley J, Stephens IEL, Bondarenko AS, Johansson TP, Hansen HA, Jaramillo TF, Rossmeisl J, Chorkendorff I, Norskov JK (2009) Alloys of platinum and early transition metals as oxygen reduction electrocatalysts. *Nat Chem* 1(7):552–556
74. Mukerjee S, Srinivasan S, Soriaga MP, McBreen J (1995) Effect of preparation conditions of Pt Alloys on their electronic, structural, and electrocatalytic activities for oxygen reduction-XRD, XAS, and electrochemical studies. *J Phys Chem* 99(13):4577–4589
75. Uribe FA, Zawodzinski TA (2002) A study of polymer electrolyte fuel cell performance at high voltages. Dependence on cathode catalyst layer composition and on voltage conditioning. *Electrochim Acta* 47(22–23):3799–3806
76. Stamenkovic V, Schmidt TJ, Ross PN, Markovic NM (2002) Surface composition effects in electrocatalysis: kinetics of oxygen reduction on well-defined Pt<sub>3</sub>Ni and Pt<sub>3</sub>Co alloy surfaces. *J Phys Chem B* 106(46):11970–11979
77. Murthi VS, Urian RC, Mukerjee S (2004) Oxygen reduction kinetics in low and medium temperature acid environment: correlation of water activation and surface properties in supported Pt and Pt alloy electrocatalysts. *J Phys Chem B* 108(30):11011–11023
78. Teliska M, Murthi VS, Mukerjee S, Ramaker DE (2005) Correlation of water activation, surface properties, and oxygen reduction reactivity of supported Pt-M/C bimetallic electrocatalysts using XAS. *J Electrochem Soc* 152(11):A2159–A2169
79. Lima FHB, Ticianelli EA (2004) Oxygen electrocatalysis on ultra-thin porous coating rotating ring/disk platinum and platinum-cobalt electrodes in alkaline media. *Electrochim Acta* 49(24):4091–4099
80. Lima FHB, Giz MJ, Ticianelli EA (2005) Electrochemical performance of dispersed Pt-M (M = V, Cr and Co) nanoparticles for the oxygen reduction electrocatalysis. *J Braz Chem Soc* 16(3 A):328–336
81. Lima FHB, Salgado JRC, Gonzalez ER, Ticianelli EA (2007) Electrocatalytic properties of PtCoC and PtNiC alloys for the oxygen reduction reaction in alkaline solution. *J Electrochem Soc* 154(4):A369–A375
82. Creemers C, Deurinck P (1997) Platinum segregation to the (111) surface of ordered Pt<sub>80</sub>Fe<sub>20</sub>: LEIS results and model simulations. *Surf Interface Anal* 25(3):177–189
83. Gauthier Y, Joly Y, Baudoing R, Rundgren J (1985) Surface-sandwich segregation on nondilute bimetallic alloys: Pt<sub>50</sub>Ni<sub>50</sub> and Pt<sub>78</sub>Ni<sub>22</sub> probed by low-energy electron diffraction. *Phys Rev B* 31(10):6216–6218
84. Gauthier Y, Baudoing-Savois R, Bugnard JM, Hebenstreit W, Schmid M, Varga P (2000) Segregation and chemical ordering in the surface layers of Pt<sub>25</sub>Co<sub>75</sub>(111): a LEED/STM study. *Surf Sci* 466(1–3):155–166
85. Gasteiger HA, Ross PN Jr, Cairns EJ (1993) LEIS and AES on sputtered and annealed polycrystalline Pt-Ru bulk alloys. *Surf Sci* 293(1–2):67–80
86. Ruban AV, Skriver HL, Norskov JK (1999) Surface segregation energies in transition-metal alloys. *Phys Rev B* 59(24):15990–16000
87. Ma Y, Balbuena PB (2008) Pt surface segregation in bimetallic Pt<sub>3</sub>M alloys: a density functional theory study. *Surf Sci* 602(1):107–113
88. Chen S, Ferreira PJ, Sheng WC, Yabuuchi N, Allard LF, Shao-Horn Y (2008) Enhanced activity for oxygen reduction reaction on “Pt<sub>3</sub>CO” nanoparticles: direct evidence of percolated and sandwich-segregation structures. *J Am Chem Soc* 130(42):13818–13819
89. Stamenkovic VR, Mun BS, Mayrhofer KJJ, Ross PN, Markovic NM (2006) Effect of surface composition on electronic structure, stability, and electrocatalytic properties of Pt-transition metal alloys: Pt-skin versus Pt-skeleton surfaces. *J Am Chem Soc* 128(27):8813–8819
90. Chen S, Sheng WC, Yabuuchi N, Ferreira PJ, Allard LF, Shao-Horn Y (2009) Origin of oxygen reduction reaction activity on “Pt<sub>3</sub>Co” nanoparticles: atomically resolved chemical compositions and structures. *J Phys Chem C* 113(3):1109–1125
91. Koh S, Leisch J, Toney MF, Strasser P (2007) Structure-activity-stability relationships of Pt-Co alloy electrocatalysts in gas-diffusion electrode layers. *J Phys Chem C* 111(9):3744–3752
92. Mani P, Srivastava R, Strasser P (2008) Dealloyed Pt-Cu core-shell nanoparticle electrocatalysts for use in PEM fuel cell cathodes. *J Phys Chem C* 112(7):2770–2778
93. Srivastava R, Mani P, Hahn N, Strasser P (2007) Efficient oxygen reduction fuel cell electrocatalysis on voltammetrically dealloyed Pt-Cu-Co nanoparticles. *Angew Chem Int Ed Engl* 46(47):8988–8991
94. Neyerlin KC, Srivastava R, CF Y, Strasser P (2009) Electrochemical activity and stability of dealloyed Pt-Cu and Pt-Cu-Co electrocatalysts for the oxygen reduction reaction (ORR). *J Power Sources* 186(2):261–267
95. Wang C, Van Der Vliet D, Chang KC, You H, Strmcnik D, Schluter JA, Markovic NM, Stamenkovic VR (2009) Monodisperse Pt<sub>3</sub>Co nanoparticles as a catalyst for the oxygen reduction reaction: size-dependent activity. *J Phys Chem C* 113(45):19365–19368
96. Watanabe M, Wakisaka M, Yano H, Uchida H (2008) Analyses of oxygen reduction reaction at Pt-based electrocatalysts. *ECS Trans* 16:199–206
97. Wakisaka M, Suzuki H, Mitsui S, Uchida H, Watanabe M (2008) Increased oxygen coverage at Pt-Fe alloy cathode for the enhanced oxygen reduction reaction studied by EC-XPS. *J Phys Chem C* 112(7):2750–2755
98. Ferreira PJ, la OGI, Shao-Horn Y, Morgan D, Makharia R, Kocha S, Gasteiger HA (2005) Instability of Pt/C electrocatalysts in proton exchange membrane fuel cells – a mechanistic investigation. *J Electrochem Soc* 152(11):A2256–A2271

99. Colon-Mercado HR, Popov BN (2006) Stability of platinum based alloy cathode catalysts in PEM fuel cells. *J Power Sources* 155(2):253–263
100. Morita T, Kojima K (2008) Development of fuel cell hybrid vehicle in Toyota. *ECS Trans* 16:185–198
101. Uchimura M, Sugawara S, Suzuki Y, Zhang J, Kocha SS (2008) Electrocatalyst durability under simulated automotive drive cycles. *ECS Trans* 16(2):225–234
102. Adzic RR, Zhang J, Sasaki K, Vukmirovic MB, Shao M, Wang JX, Nilekar AU, Mavrikakis M, Valerio JA, Uribe F (2007) Platinum monolayer fuel cell electrocatalysts. *Top Catal* 46(3–4):249–262
103. Brankovic SR, Wang JX, Adzic RR (2001) Pt sub-monolayers on Ru nanoparticles – a novel low Pt loading, high CO tolerance fuel cell electrocatalyst. *Electrochem Solid State Lett* 4(12):A217–A220
104. Sasaki K, Mo Y, Wang JX, Balasubramanian M, Uribe F, McBreen J, Adzic RR (2003) Pt sub-monolayers on metal nanoparticles – novel electrocatalysts for H<sub>2</sub> oxidation and O<sub>2</sub> reduction. *Electrochim Acta* 48(25–26):3841–3849
105. Wang JX, Brankovic SR, Zhu Y, Hanson JC, Adzic RR (2003) Kinetic characterization of PtRu fuel cell anode catalysts made by spontaneous Pt deposition on Ru nanoparticles. *J Electrochem Soc* 150(8):A1108–A1117
106. Brankovic SR, McBreen J, Adzic RR (2001) Spontaneous deposition of Pt on the Ru(0001) surface. *J Electroanal Chem* 503(1–2):99–104
107. Sasaki K, Wang JX, Balasubramanian M, McBreen J, Uribe F, Adzic RR (2004) Ultra-low platinum content fuel cell anode electrocatalyst with a long-term performance stability. *Electrochim Acta* 49(22–23):3873–3877
108. Kolb DM, Przasnyski M, Gerischer H (1974) Underpotential deposition of metals and work function differences. *J Electroanal Chem* 54(1):25–38
109. Herrero E, Buller LJ, Abruna HD (2001) Underpotential deposition at single crystal surfaces of Au, Pt, Ag and other materials. *Chem Rev* 101(7):1897–1930
110. Aramata A (1997) Underpotential deposition on single-crystal metals. In: Bockris JO, White RE, Conway BE (eds) *Modern aspects of electrochemistry*. Plenum, New York
111. Brankovic SR, Wang JX, Adzic RR (2001) Metal monolayer deposition by replacement of metal adlayers on electrode surfaces. *Surf Sci* 474(1–3):L173–L179
112. Zhang J, Mo Y, Vukmirovic MB, Klie R, Sasaki K, Adzic RR (2004) Platinum monolayer electrocatalysts for O<sub>2</sub> reduction: Pt monolayer on Pd(111) and on carbon-supported Pd nanoparticles. *J Phys Chem B* 108(30):10955–10964
113. Zhang J, Vukmirovic MB, Sasaki K, Uribe F, Adzic RR (2005) Platinum monolayer electrocatalysts for oxygen reduction: effect of substrates, and long-term stability. *J Serb Chem Soc* 70(3):513–525
114. Zhang JL, Vukmirovic MB, Xu Y, Mavrikakis M, Adzic RR (2005) Controlling the catalytic activity of platinum-monolayer electrocatalysts for oxygen reduction with different substrates. *Angew Chem Int Ed Engl* 44(14):2132–2135
115. Zhang JL, Vukmirovic MB, Sasaki K, Nilekar AU, Mavrikakis M, Adzic RR (2005) Mixed-metal Pt monolayer electrocatalysts for enhanced oxygen reduction kinetics. *J Am Chem Soc* 127(36):12480–12481
116. Zhou WP, Yang XF, Vukmirovic MB, Koel BE, Jiao J, Peng GW, Mavrikakis M, Adzic RR (2009) Improving electrocatalysts for O<sub>2</sub> reduction by fine-tuning the Pt-support interaction: Pt monolayer on the surfaces of a Pd<sub>3</sub>Fe(111) single-crystal alloy. *J Am Chem Soc* 131(35):12755–12762
117. Zhang J, Lima FHB, Shao MH, Sasaki K, Wang JX, Hanson J, Adzic RR (2005) Platinum monolayer on nonnoble metal-noble metal core-shell nanoparticle electrocatalysts for O<sub>2</sub> reduction. *J Phys Chem B* 109(48):22701–22704
118. Zhang J, Sasaki K, Sutter E, Adzic RR (2007) Stabilization of platinum oxygen-reduction electrocatalysts using gold clusters. *Science* 315(5809):220–222
119. Wang JX, Inada H, LJ W, Zhu YM, Choi YM, Liu P, Zhou WP, Adzic RR (2009) Oxygen reduction on well-defined core-shell nanocatalysts: particle size, facet, and Pt shell thickness effects. *J Am Chem Soc* 131(47):17298–17302
120. Sasaki K, Wang JX, Naohara H, Marinkovic N, More K, Inada H, Adzic RR (2010) Recent advances in platinum monolayer electrocatalysts for oxygen reduction reaction: scale-up synthesis, structure and activity of Pt shells on Pd cores. *Electrochim Acta* 55(8):2645–2652
121. Shao-Horn Y, Sheng WC, Chen S, Ferreira PJ, Holby EF, Morgan D (2007) Instability of supported platinum nanoparticles in low-temperature fuel cells. *Top Catal* 46(3–4):285–305
122. PT Y, Gu W, Makharia R, Wagner FT, Gasteiger HA (2006) The impact of carbon stability on PEM fuel cell startup and shutdown voltage degradation. *ECS Trans* 3:797–809
123. Yu PT, Kocha S, Paine L, Gu W, Wagner FT (2004) The effects of air purge on the degradation of PEM fuel cells during startup and shutdown procedures. In: 2004 AIChE spring national meeting, conference proceedings, New Orleans, pp 521–527
124. Debe MK (2003) Novel catalyst, catalyst support and catalyst coated membrane methods. In: Vielstich W, Gasteiger HA, Lamm A (eds) *Handbook of fuel cells – fundamentals technology and applications*. Wiley, Chichester
125. Gancs L, Kobayashi T, Debe MK, Atanasoski R, Wieckowski A (2008) Crystallographic characteristics of nanostructured thin-film fuel cell electrocatalysts: a HRTEM study. *Chem Mater* 20(7):2444–2454

126. Debe MK, Drube AR (1995) Structural characteristics of a uniquely nanostructured organic thin film. *J Vac Sci Technol B Microelectron Nanometer Struct* 13(3):1236–1241
127. Debe MK, Schmoeckel AK, Vernstrom GD, Atanasoski R (2006) High voltage stability of nanostructured thin film catalysts for PEM fuel cells. *J Power Sources* 161(2):1002–1011
128. Bonakdarpour A, Stevens K, Vernstrom GD, Atanasoski R, Schmoeckel AK, Debe MK, Dahn JR (2007) Oxygen reduction activity of Pt and Pt-Mn-Co electrocatalysts sputtered on nano-structured thin film support. *Electrochim Acta* 53(2):688–694
129. Debe MK, Schmoeckel AK, Hendricks SM, Vernstrom GD, Haugen GM, Atanasoski RT (2005) Durability aspects of nanostructured thin film catalysts for PEM fuel cells. *ECS Trans* 1:51–66
130. Chen ZW, Waje M, Li WZ, Yan YS (2007) Supportless Pt and PtPd nanotubes as electrocatalysts for oxygen-reduction reactions. *Angew Chem Int Edit Engl* 46(22):4060–4063
131. Mayers B, Jiang X, Sunderland D, Cattle B, Xia Y (2003) Hollow nanostructures of platinum with controllable dimensions can be synthesized by templating against selenium nanowires and colloids. *J Am Chem Soc* 125(44):13364–13365
132. Sun Y, Tao Z, Chen J, Herricks T, Xia Y (2004) Ag nanowires coated with Ag/Pd alloy sheaths and their use as substrates for reversible absorption and desorption of hydrogen. *J Am Chem Soc* 126(19):5940–5941
133. Sun Y, Yin Y, Mayers BT, Herricks T, Xia Y (2002) Uniform silver nanowires synthesis by reducing AgNO<sub>3</sub> with ethylene glycol in the presence of seeds and poly(vinyl pyrrolidone). *Chem Mater* 14(11):4736–4745
134. Sun SH, Zhang GX, Geng DS, Chen YG, Banis MN, Li RY, Cai M, Sun XL (2010) Direct growth of single-crystal Pt nanowires on Sn@CNT nanocable: 3D electrodes for highly active electrocatalysts. *Chem Eur J* 16(3):829–835
135. Peng ZM, Yang H (2009) Synthesis and oxygen reduction electrocatalytic property of Pt-on-Pd bimetallic heteronanostructures. *J Am Chem Soc* 131(22):7542
136. Lim B, Jiang M, Camargo PHC, Cho EC, Tao J, Lu X, Zhu Y, Xia Y (2009) Pd-Pt bimetallic nanodendrites with high activity for oxygen reduction. *Science* 324(5932):1302–1305
137. Lim BW, XM L, Jiang MJ, Camargo PHC, Cho EC, Lee EP, Xia YN (2008) Facile synthesis of highly faceted multioctahedral Pt nanocrystals through controlled overgrowth. *Nano Lett* 8(11):4043–4047
138. Erlebacher J, Snyder J (2009) Dealloyed nanoporous metals for PEM fuel cell catalysis. *ECS Trans* 25:603–612
139. Zeis R, Mathur A, Fritz G, Lee J, Erlebacher J (2007) Platinum-plated nanoporous gold: an efficient, low Pt loading electrocatalyst for PEM fuel cells. *J Power Sources* 165(1):65–72
140. Erlebacher J (2009) Materials science of hydrogen/oxygen fuel cell catalysis. In: Ehrenreich H, Spaepen F (eds) *Solid state physics – advances in research and applications*. Academic, New York, pp 77–141
141. Wu J, Zhang J, Peng Z, Yang S, Wagner FT, Yang H (2010) Truncated octahedral Pt<sub>3</sub>Ni oxygen reduction reaction electrocatalysts. *J Am Chem Soc* 132(14):4984–4985
142. Zhang J, Yang H, Fang J, Zou S (2010) Synthesis and oxygen reduction activity of shape-controlled Pt<sub>3</sub>Ni nanopolyhedra. *Nano Lett* 10(2):638–644

### Books and Reviews

- Bard AJ, Faulkner LR (2001) *Electrochemical methods, fundamentals and applications*, 2nd edn. Wiley, New York
- Lipkowski J, Ross P (eds) (1998) *Electrocatalysis (frontiers in electrochemistry)*. Wiley-VCH, Danvers
- Markovic NM, Ross PN Jr (2002) Surface science studies of model fuel cell electrocatalysts. *Surf Sci Rep* 45(4–6):117–229
- Newman J, Thomas-Alyea KE (2004) *Electrochemical system*, 3rd edn. Wiley, Hoboken
- Vielstich W, Gasteiger H, Lamm A (eds) (2003) *Handbook of fuel cells: fundamentals, technology, applications*. Wiley, Chichester
- Vielstich W, Gasteiger H, Lamm A (eds) (2009) *Handbook of fuel cells: advances in electrocatalysis, materials, diagnostics and durability*, vol 5 and 6. Wiley, New York
- Wieckowski A, Savinova ER, Vayenas CG (eds) (2003) *Catalysis and electrocatalysis at nanoparticle surfaces*, 1st edn. Boca Raton, CRC Press
- Zhang J (ed) (2008) *PEM fuel cell electrocatalysts and catalyst layers: fundamentals and applications*, 1st edn. London, Springer



## Proton-Exchange Membrane Fuel Cells with Low-Pt Content

Anusorn Kongkanand, Wenbin Gu and Mark F. Mathias  
Fuel Cell Business, General Motors Global Propulsion Systems, Pontiac, MI, USA

### Article Outline

Glossary  
Definition of the Subject  
Introduction  
PEM Fuel Cell Electrodes  
Performance of Low-Pt Fuel Cell  
Local Transport Resistance  
Ionomer Thin Film and Ionomer-Pt Interface  
Catalyst Roadmap  
Durability of Low-Pt Fuel Cell  
Other Challenges  
Future Directions  
Bibliography

### Glossary

#### Electrochemically active surface area (ECSA)

The surface area of Pt catalyst that is electrochemically active, requiring access to both protons and electrons. It is generally normalized to Pt mass (e.g.,  $\text{m}^2/\text{g}_{\text{Pt}}$ ), and is the primary measure of Pt dispersion.

**Fuel cell catalyst** Materials that catalyze the electrochemical reactions. Pt or Pt alloy nanoparticles (3–5 nm in diameter) deposited on carbon blacks are commonly used with the goal of maximizing the available reaction site surface area per Pt mass.

**Hydrogen PEMFC vehicle** Vehicle that uses proton-exchange membrane fuel cell (PEMFC) as its primary power generator, commonly known as fuel cell electric vehicle (FCEV). It uses pure hydrogen gas fuel

reacting electrochemically with oxygen gas from the atmosphere to generate electricity and emit only water. Generally requires Pt as electrocatalyst on both anode and cathode.

**Ionomer** Ion conducting polymer is used in the membrane and electrodes. In PEMFCs, the conducted ion is a proton, and the environment is strongly acidic with effective  $\text{pH} < 1$ . Perfluorosulfonic acid (PFSA) such as Nafion<sup>®</sup> (DuPont tradename) is the most common.

**Local transport loss** Performance (i.e., voltage) loss due to the transport of oxygen and protons in close (<30 nm) proximity to the Pt reaction site. Characteristically, this loss is inversely proportional to the Pt roughness factor (i.e., low  $\text{m}^2_{\text{Pt}}/\text{m}^2_{\text{MEA}}$ ) and is most prevalent at high-current density.

**Membrane-electrode assembly (MEA)** The MEA is at the heart of the fuel cell where the electrochemical reactions occur. Hydrogen oxidation reaction (HOR) occurs in the anode. Oxygen reduction reaction (ORR) occurs in the cathode. The polymer membrane, sandwiched between the two electrodes, conducts proton across from the anode to cathode and acts as an electrical and reactant separator.

**Oxygen reduction reaction (ORR)**  $\text{O}_2$  is electrochemically reduced to water on the cathode. ORR is responsible for most of the overall voltage (i.e., efficiency) loss in a fuel cell even with heavy use of Pt catalyst. Therefore, research on high-activity ORR catalyst is of high priority. ORR kinetic activity is commonly expressed by either normalizing to its Pt mass (mass activity) or to its available Pt surface area (area-specific activity).

**PGM** Platinum group metals (Pt, Pd, Ir, Ru, Rh, and Os) and other precious metals (Au, Ag, Re) must be minimized or avoided to enable affordable fuel cells.

**Pt roughness factor (r.f.)** The Pt surface area on an electrode for electrochemical reaction per MEA geometric area ( $\text{m}^2_{\text{Pt}}/\text{m}^2_{\text{MEA}}$ ). This is a product of Pt ECSA ( $\text{m}^2/\text{g}_{\text{Pt}}$ ) and the MEA Pt loading ( $\text{g}_{\text{Pt}}/\text{m}^2_{\text{MEA}}$ ).



## Definition of the Subject

Widespread commercialization of fuel cell electric vehicles (FCEV) relies on further reduction of PGM (platinum group metals) usage. Although enhancements in the activity and stability of the catalyst are necessary, those alone are insufficient. In a fuel cell with low PGM content, transport of reactants (oxygen and protons) to a small area of catalyst can cause large performance loss at high power. Because it is this high-power point that determines the required fuel cell area, these losses drive up the size, and thus the cost, of the fuel cell stack. This entry discusses fuel cell cost reduction with special focus on the challenges and opportunity associated with Pt reduction.

## Introduction

PEM fuel cells offer a zero-emission tank-to-wheels solution for sustainable transportation, extending to a well-to-wheels solution when renewable hydrogen is used. Although a few automotive manufacturers, notably Hyundai, Toyota, and Honda, have begun to commercialize fuel cell electric vehicles (FCEV), their high cost limits market penetration. The availability of hydrogen stations is also limited. Yet, major fuel cell developers have defined plausible pathways to reduce the fuel cell vehicle total cost of ownership (vehicle plus fuel cost over life) to approach that of incumbent gasoline-engine vehicles in the long term. Two critical elements of this roadmap include decreasing material cost of the fuel cell system and reducing manufacturing cost through economies of scale.

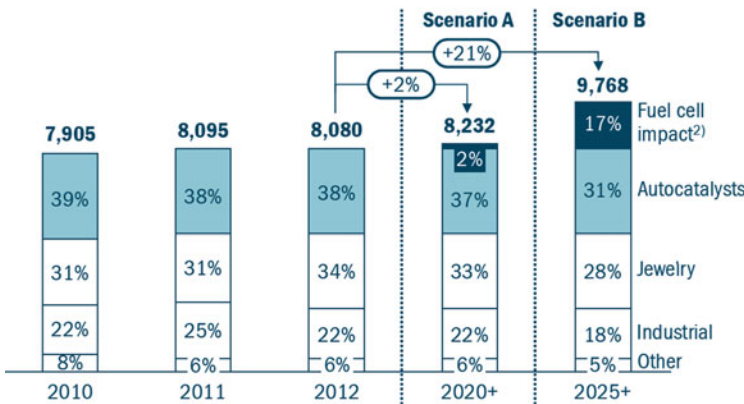
An automotive fuel cell typically requires about 10 m<sup>2</sup> of electrochemically active area which is distributed over 250–400 individual cells in series, each with 400–250 cm<sup>2</sup> of active area. Each cell is a high-current (>500A) and low-voltage (~0.6 V) device, and cells are stacked in series to deliver high DC power required for vehicle propulsion. The trade-off defining the number of cells and active area is dictated by a cost optimization involving the

power electronics that are used to interface the fuel cell stack with the high-voltage electrical system [1], a topic outside of the scope of this entry. Instead, this entry focuses on the issue of reducing overall electrochemically active area needed to produce a given power, an issue that is independent from the trade-off determining the selection of the number of cells.

State-of-the-art FCEVs use about 30 g of Pt [2, 3], the only PGM used in the fuel cell system. At today's (June 2017) Pt price of \$30 per gram, the cost of Pt metal itself is about \$900, a small fraction of a vehicle cost. But it is significantly larger than what is used in the current clean light-duty internal combustion engine (ICE) vehicle catalytic converter (<5 g PGM, comprising Pt, Pd, and Rh) [4, 5]. Pt is rare, and because of its high resistance to corrosion, it is used in many applications. Of the 218 tons of platinum sold in 2014, 45% was used for vehicle emission control devices, 34% for jewelry, and 9% for chemical production and petroleum refining [6]. The remainder was consumed in other industries including electronics, glass manufacturing, and the medical and biomedical industries. Because Pt is such a well-established commodity, increase in demand will put pressure on its availability and price. Analysis in Fig. 1 shows a significant increase in Pt demand once FCEVs with 10 g<sub>Pt</sub> penetrate the mass market (scenario B, assumes five million FCEVs/year, about 5% of global vehicle market), generating upward pressure on Pt price [7]. This supply-demand scenario indicates the need for technologies to reduce Pt usage well below 10 g/vehicle in the long run.

Figure 2 illustrates the relationship between cathode Pt loading and the cost of major fuel cell stack components assuming a 2016 state-of-the-art current-voltage curve [2]. Although the Pt cost is a large portion of the stack cost at 0.3 mg<sub>Pt</sub>/cm<sup>2</sup> (~30 g<sub>Pt</sub>/vehicle), reducing Pt loading below 0.2–0.1 mg<sub>Pt</sub>/cm<sup>2</sup> results in only a marginally lower stack cost, and decreasing to 0.05 mg<sub>Pt</sub>/cm<sup>2</sup> actually results in a stack cost increase. This is due to poor high-power performance of the low-Pt cathode, to be discussed in more detail below, making it necessary to increase stack area and

**Platinum demand<sup>1)</sup> by application ['000 oz]**



**Comments**

**Scenario A:**  
Next-generation technology will reach 0.15 mg/cm<sup>2</sup> platinum load in the MEA – By 2020, a global production volume of 300,000 vehicles is assumed

**Scenario B:**  
FCEVs will improve significantly in costs and required platinum load decreases to <0.10 mg/cm<sup>2</sup> in the MEA. FCEVs become a global success story with a yearly production volume of 5 million units

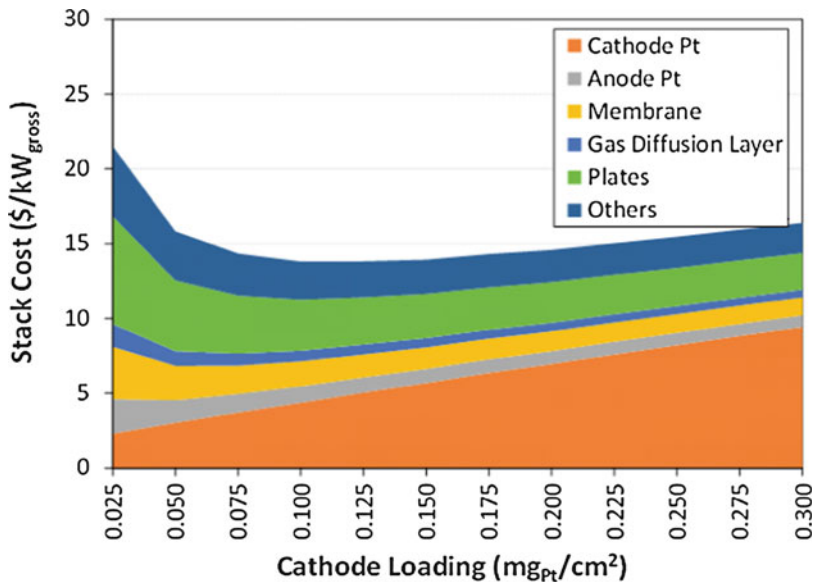
1) Excluding movement in stocks      2) Underlying assumption: 300,000 FCVs with each 16 g platinum in Scenario A, 5 million FCVs each with <10 g platinum/vehicle in Scenario B

Source: Johnson Matthey; Roland Berger

**Proton-Exchange Membrane Fuel Cells with Low-Pt Content, Fig. 1** Impact of fuel cell vehicles on Pt consumption (Reprinted with permission from Ref. [7]. Copyright 2013 Roland Berger LLC)

**Proton-Exchange Membrane Fuel Cells with Low-Pt Content, Fig. 2**

Effect of cathode Pt loading on stack cost. Anode Pt loading is kept constant at 0.025 mg<sub>Pt</sub>/cm<sup>2</sup>. Cost estimated using SA/DOE 2013 cost study, 90 kW<sub>gross</sub> system, 500 k system/year [8] (Reprinted with permission from Ref. [2] Copyright 2016 American Chemical Society)



overcoming the benefit of the Pt areal-loading decrease. Improvement in the high-power performance of the low-loaded cathode will minimize stack cost and decrease the Pt loading at which the minimum cost occurs. This analysis also indicates that further reduction of Pt loading below 0.1 mg<sub>Pt</sub>/cm<sup>2</sup> (~10 g<sub>Pt</sub>/vehicle) must be done

with the objective of lowering the overall fuel cell stack cost. Whereas reduction below 0.1 mg<sub>Pt</sub>/cm<sup>2</sup> with current fuel cell performance may not necessarily be a major vehicle-level cost saver, it would be important to mitigate demand on the global Pt market and thus enable high market penetration of automotive fuel cells.

If 10 g<sub>Pt</sub>/vehicle could suppress FCEV mass-market penetration due to supply-demand factors, what level is needed to eliminate this barrier? Reductions to a level comparable to the catalytic converter (~5 g PGM/vehicle) would largely neutralize the demand increase due to the corresponding decrease in catalytic converter demand. Thus, 5 g PGM/vehicle is a reasonable long-term target [2]. Other important factors could involve broader PGM market shifts. For example, an average wedding ring weighs about 5 g; thus, many married couples own approximately an FCEV equivalent of Pt. Consider this reference point and the fact that the world is consuming 34% of total Pt consumption for jewelry. Thus, a shift in consumer preference to use Pt to enable emission-free future transportation and to use other metals (tungsten, gold, etc.) for jewelry could have a large beneficial impact on Pt availability and cost for FCEV use.

The ultimate goal of fuel cell catalyst development is to entirely eliminate the need for PGM. Significant progress has been made by packing as many active sites as possible into carbon-nitrogen-based non-PGM catalysts [9–11]. However, their stability is currently unacceptably poor [12]. In addition, their useable power density is only about one-tenth of the PGM catalyst system, making vehicle packaging and cost (e.g., of other stack components that scale with surface area) impractical. Finally, if PGM use is successfully reduced to a level comparable to incumbent vehicle technology (~5 g<sub>PGM</sub>/vehicle), the economic benefit of an alternative may not be favorable.

Alkaline membrane fuel cells (AMFC) operate under less corrosive conditions, and low-cost non-PGM cathode catalysts may be used [13, 14]. However, palladium is currently still required on the anode to achieve power density, and thus stack size reduction, approaching that possible with PEMFCs. Furthermore, the instability of AMFC membrane candidates at high temperature (80–100 °C) and the deactivation of its ionic carriers due to CO<sub>2</sub> in air are other major technology hurdles [15–17]. These performance, durability, and cost uncertainties have thus far prevented AMFC technology from mounting a serious challenge to PEMFC for automotive

applications. AMFC technology status and trajectory is described in detail in a separate entry in this volume.

In this entry, we will provide an overview of the challenges and most promising research directions to develop automotive PEM fuel cell technology with sustainable Pt use.

## PEM Fuel Cell Electrodes

The hydrogen oxidation reaction (HOR) on the anode is so fast that less than 1 g of Pt can suffice [18]. And when pure hydrogen is used, fast HOR rate and diffusion minimize the voltage loss on the anode. Therefore, the primary focus has been on improving the sluggish oxygen reduction reaction (ORR) on the cathode. Much progress has been made in improving the activity and stability of the ORR catalysts in the past 15 years. Many advanced catalysts (e.g., shape-/size-controlled alloy [19–24], Pt monolayer catalysts [25–27], etc.) have shown promising activity in rotating disk electrode (RDE) tests, although they have not shown comparable activities in fuel cell membrane-electrode assemblies (MEA). Fortunately, a more gradual improvement using a dealloying approach [28–31] on spherical PtNi and PtCo to control the “Pt skin” and subsurface composition has yielded materials that approach the required activity and stability in a fuel cell for a ~5 g<sub>Pt</sub>/vehicle [2, 31, 32].

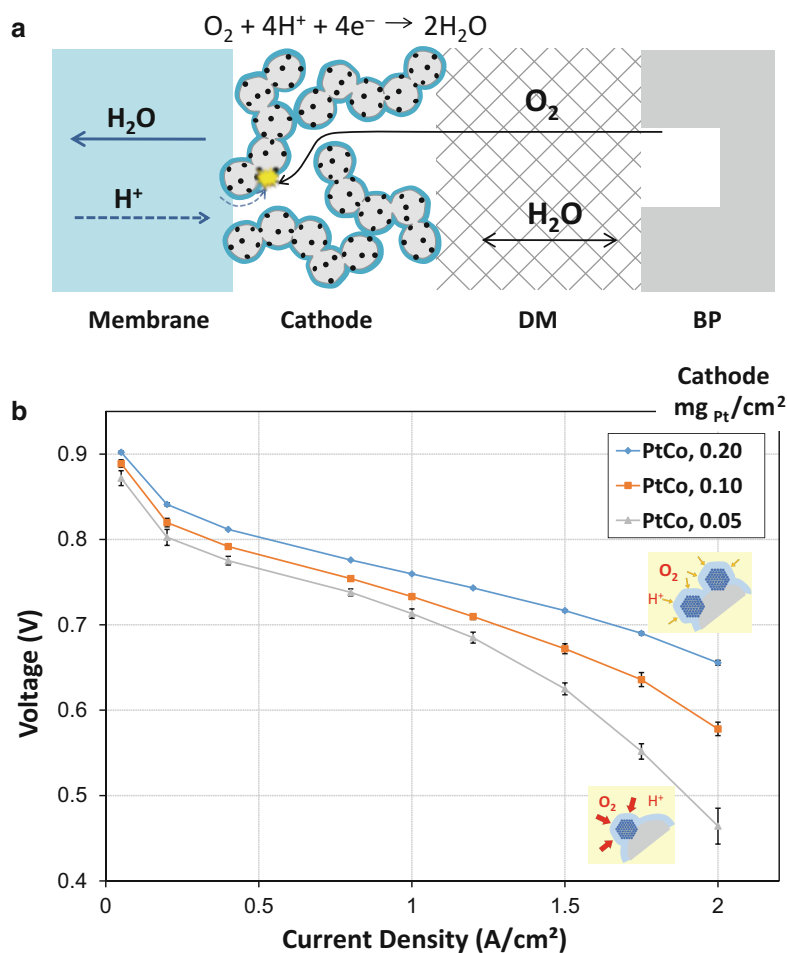
As shown in Fig. 3a, the ORR requires efficient delivery of oxygen, protons, and electrons at the same location. Facile transport of these species, which occur through different phases, to the active site is essential to allow high-power output. The electrodes are generally made of mixtures of proton-conducting polymers (ionomer, blue) and carbon-supported Pt nanoparticle (gray and black circles) catalysts. This design gives a porous layer (~60% porosity) that is good for gas transport and a large active area (roughness factors >30 cm<sup>2</sup><sub>Pt</sub>/cm<sup>2</sup><sub>MEA</sub>) for the reaction [33, 34].

Carbon black is the preferred support to disperse Pt-based nanoparticles, thanks to its high electronic conductivity, high surface area for nanoparticle deposition, relatively high stability,

### Proton-Exchange Membrane Fuel Cells with Low-Pt Content, Fig. 3

(a) Schematic of transport reaction in the fuel cell cathode. (DM = diffusion media; BP = bipolar plate). (b) Fuel cell polarization curves of PtCo/C catalyst at different cathode Pt loadings.

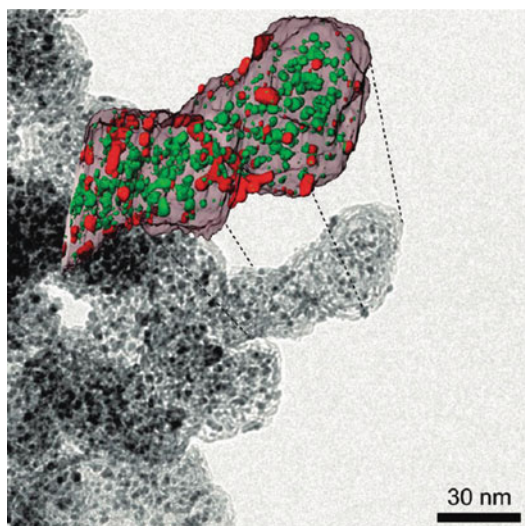
Operating conditions in the order of anode/cathode: H<sub>2</sub>/air, 94 °C, 65/65% RH, 250/250 kPa<sub>abs,outlet</sub>, stoichiometries of 1.5/2. Single cell, 50 cm<sup>2</sup> active area (Reprinted with permission from Ref. [2]. Copyright 2016 American Chemical Society)



and low cost. The morphology and properties of carbon play a critical role in determining the performance and stability of the catalyst [35–39]. Some popular carbons such as KetjenBlack (KB) possess a large number of internal micropores within its carbon particles, making it possible to achieve good Pt particle dispersion and thus high Pt surface area [40, 41]. Figure 4 shows a transmission electron micrograph of a Pt/KB catalyst. Tomography analysis on a section of the catalyst reveals the location of Pt particles in relation to the carbon particle. The red and green coloring represent Pt particles that are located on the surface and within the carbon, respectively.

The presence of the internal Pt adds another set of reactant transport considerations within a fuel cell electrode (Fig. 5). The internal particles have been

shown to be mostly electrochemically active and are believed to have access to proton and O<sub>2</sub> through small openings (1–5 nm) in the carbon micropores [40, 41]. But it is believed that the pores are too small for ionomer to intrude and form a direct proton conduction path to the Pt surface [39, 42–45]. Although it is hypothesized that condensed water can conduct protons in these pores, much remains unclear on the exact mechanism and the magnitude of the proton conductivity [46–48]. Additionally, ionomer can form a layer blocking the transport of O<sub>2</sub> and water at the opening leading to increased voltage loss [49, 50]. These complexities may make it appealing to use carbons that do not possess internal porosity. However, it has been shown that porous carbons could offer better Pt dispersion, Pt alloy quality, ORR activity, and catalyst stability [37–39]. Therefore, the best carbon



**Proton-Exchange Membrane Fuel Cells with Low-Pt Content, Fig. 4** Transmission electron micrograph of Pt nanoparticles deposited on KetjenBlack carbon particles. Color inset shows the tomography of an area of the catalyst and the location of Pt particles. Red surface Pt. Green internal Pt (Reprinted with permission from Ref. [41]. Copyright 2010 American Chemical Society)

support for each user may vary depending on their needs and materials-system trade-off.

### Performance of Low-Pt Fuel Cell

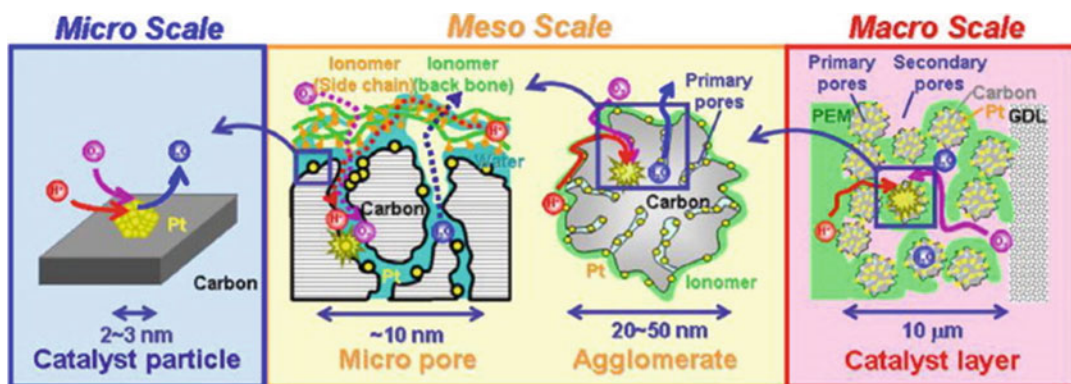
At higher power, transport phenomena (oxygen, proton, and electron) in a fuel cell will contribute to the voltage loss. As Pt loading and the available Pt area for ORR are reduced, higher  $O_2$  and proton fluxes must be delivered to the Pt surface which can lead to noticeable and even severe voltage losses. This is particularly noticeable below  $0.1 \text{ mg}_{Pt}/\text{cm}^2_{MEA}$  (Fig. 3b), corresponding to  $<10 \text{ g}_{Pt}/\text{vehicle}$ . These internal losses in energy within the fuel cell are converted into waste heat which must be removed from the fuel cell using coolant and a radiator. The size of the radiator, and thus the amount of this heat removal, is limited by the frontal area of the vehicle. Depending on system design and requirement, cell voltage at the stack high-power (i.e., rating) point is generally required to be higher than 0.55–0.65 V to allow for waste heat removal from the vehicle

and maintain sufficient hydrogen conversion efficiency ( $>50\%$ ) [1, 51]. Assuming that the fuel cell stack is sized at 0.58 V, one can estimate current densities from Fig. 3b of 1.65 and  $2.0 \text{ A}/\text{cm}^2$  for 0.05 and  $0.1 \text{ mg}_{Pt}/\text{cm}^2_{MEA}$ , respectively. This results in power densities at these points of 0.96 and  $1.16 \text{ W}/\text{cm}^2$ , translating for a  $100 \text{ kW}_{gross}$  stack to requirements of approximately 10.4 and  $8.6 \text{ m}^2$  of fuel cell area, respectively. This case illustrates that although it is in principle desirable to reduce the Pt loading, worse fuel cell performance at the stack rating voltage translates to a 20% increase in overall stack size. Depending on the cost of the fuel cell components that scale with area (e.g., plates, membrane, and diffusion media), this can result in an increase in stack cost even with lower-Pt areal loading, as also shown in Fig. 2 at cathode Pt loadings less than  $0.1 \text{ mg}_{Pt}/\text{cm}^2$ .

A fuel cell performance mathematical model provides a useful tool to help understand the various internal voltage losses. One can build a model using known physics involved in a PEMFC that uses inputs from a number of in situ electrochemical diagnostics and ex situ characterization methods [34, 45]. Figure 6 illustrates the voltage loss terms estimated for various components as a function of current density. While a realistic fuel cell is operated under a wide range of conditions that vary over the fuel cell area, a simplified “differential cell” (i.e., high gas flow and constant temperature condition) is often used, and is modeled here, for diagnostic purposes. By far, ORR kinetic loss is the largest contributor. As current density increases, transport phenomena (oxygen, proton, and electron) contribute to the voltage loss. Ohmic loss (membrane protonic resistance and electronic resistance of other components),  $O_2$  transport loss in the gas diffusion layers, and proton conduction loss in the electrodes are also noticeable. However, these losses do not change with Pt amount and are thus not the focus of this entry. More detail on these losses can be found elsewhere [34, 45].

As Pt loading and its surface area decrease, transport of protons and  $O_2$  to the reaction sites becomes more challenging. Characteristically, this type of loss increases with decreasing Pt





**Proton-Exchange Membrane Fuel Cells with Low-Pt Content, Fig. 5** Illustration showing transport of proton,  $O_2$ , and water at different length scales in the cathode

electrode (Reprinted with permission from Ref. [42]. Copyright 2011 Elsevier)

roughness factor and is called a “local transport loss,” postulated to be at or near the Pt surface [52]. As will be discussed in the next section, a portion of this loss can be attributed to the transport of  $O_2$  through an ionomer thin film covering the Pt particle (yellow area). However, there remains voltage loss at high-current density that has not yet been accounted for by known physics or chemistry (orange area). Both losses grow rapidly as current is further increased or as Pt surface area drops further during long-term fuel cell operation. Therefore, they must be understood and minimized for the long-term Pt loading target to be met.

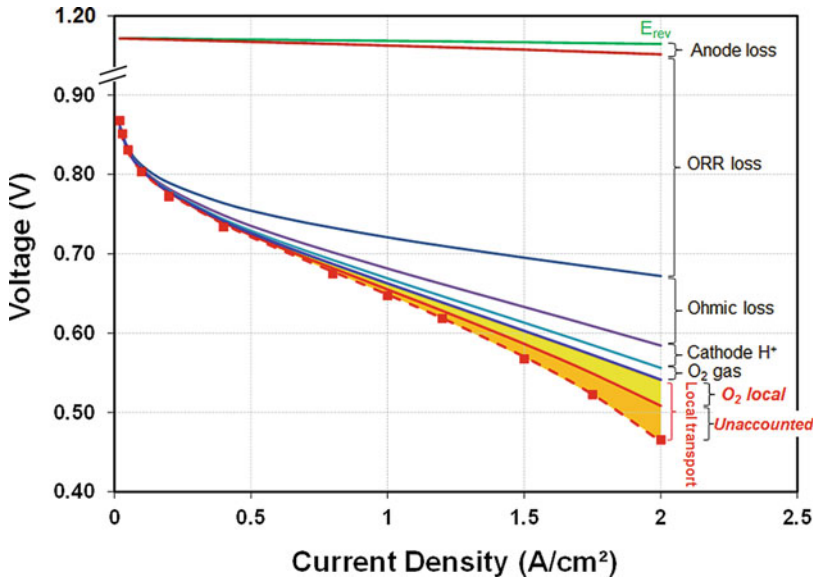
### Local Transport Resistance

As discussed in Fig. 6, the local transport resistance can be divided into two components: (a)  $O_2$  transport associated with ionomer thin film (yellow area) and (b) an unaccounted-for resistance (orange area). The latter component is hypothesized to result from proton and  $O_2$  transport through nanometer-sized pores shown in Fig. 5. Some studies constructed “agglomerate” models, simulating impact of 50–500 nm diameter spherical elements filled with water and/or ionomer, in attempts to simulate the voltage loss [45, 49, 50, 53]. Indeed, there are examples indicating that this unaccounted-for loss (orange area) can be largely eliminated when nonporous

carbons are used [39, 54–56]. However, due to the complex structural heterogeneity of the electrode (ionomer distribution [57, 58], Pt location [40, 41], carbon pore morphology [42, 44, 59], etc.) as well as engineering phenomena (e.g., localized water generation, drying due to local temperature increase), such models have been difficult to unambiguously test and validate. This area remains in need of improved diagnostics and modeling tools to definitively identify the source of this unaccounted-for loss.

The “ $O_2$  local” component in Fig. 6 can be characterized by a resistance called  $R_{O_2}^{Pt}$ , and this can be quantified by operating an MEA under  $O_2$  transport-limiting conditions [52, 60]. In this so-called  $O_2$  limiting-current measurement, both the Fickian (pressure-dependent component representing bulk gas transport,  $R_F$ ) and non-Fickian (pressure-independent component representing Knudsen or through-film transport,  $R_{NF}$ ) components of the  $O_2$  transport resistance can be determined. Fickian transport represents bulk gas transports in gas-diffusion media and large pores in the microporous layer and electrode. Fickian transport resistance does not change with Pt loading. It is the  $R_{NF}$  that strongly correlates with high-current-density (HCD) performance of low-Pt electrodes. Physically,  $R_{NF}$  is made up of three transport resistances – one from the small pores in the microporous layer (MPL), another from the small pores in the cathode catalyst layer (CCL), and the third for a region close to the Pt surface [52]:





**Proton-Exchange Membrane Fuel Cells with Low-Pt Content, Fig. 6** Voltage loss terms in a low-Pt PEMFC operated under differential cell conditions (i.e., high gas flow and constant temperature):  $\text{H}_2/\text{air}$ , 150 kPa<sub>abs</sub>, 80 °C, and 100% RH. The *symbols* represent the experimental data. The *lines* are the thermodynamic equilibrium cell

voltage ( $E_{\text{rev}}$ ) subtracting various voltage losses calculated based on the measured component material and transport properties and electrode kinetics. MEAs: Pt/C anode and Pt/KB cathode (0.025 and 0.056 mg<sub>Pt</sub>/cm<sup>2</sup>, respectively) coated on an 18 μm thick composite membrane

$$R_{\text{NF}} \approx R_{\text{NF}}^{\text{MPL}} + R_{\text{NF}}^{\text{CCL}} + \frac{R_{\text{O}_2}^{\text{Pt}}}{r.f.} \quad (1)$$

Figure 7a summarizes the  $R_{\text{NF}}$  as a function of Pt roughness factor (r.f.) for a variety of cathode catalysts [61]. Electrodes with low r.f. (low Pt loading) show high  $R_{\text{NF}}$  because more  $\text{O}_2$  must be delivered to a smaller Pt surface resulting in a higher apparent electrode  $\text{O}_2$  transport resistance. As shown in Eq. 1, one can determine the  $R_{\text{O}_2}^{\text{Pt}}$  by plotting  $R_{\text{NF}}$  vs  $1/r.f.$  (inset). In this case, the  $R_{\text{O}_2}^{\text{Pt}}$  is determined to be 11.2 s/cm from the slope. In Fig. 7b, we summarize the fuel cell performance at 1.75 A/cm<sup>2</sup> as a function of roughness factor. The fuel cell voltage drops precipitously once the r.f. is below about 50, as the shrinking available surface area drives up the local reactant flux.

In contrast to the dispersed carbon-supported catalysts discussed above, the 3M nanostructured thin-film (NSTF, blue squares) catalyst shows impressive fuel cell performance despite its very low-Pt r.f. [62–64]. The majority of the 3M NSTF surface is free of ionomer and therefore relies on

proton conduction on the Pt surface. However, when a thin (2–4 nm) ionomer film was coated on the NSTF surface, the catalyst exhibited similar behavior to that of the carbon-supported Pt nanoparticle-based (and presumably thin ionomer film coated) catalysts [61, 65, 66].

### Ionomer Thin Film and Ionomer-Pt Interface

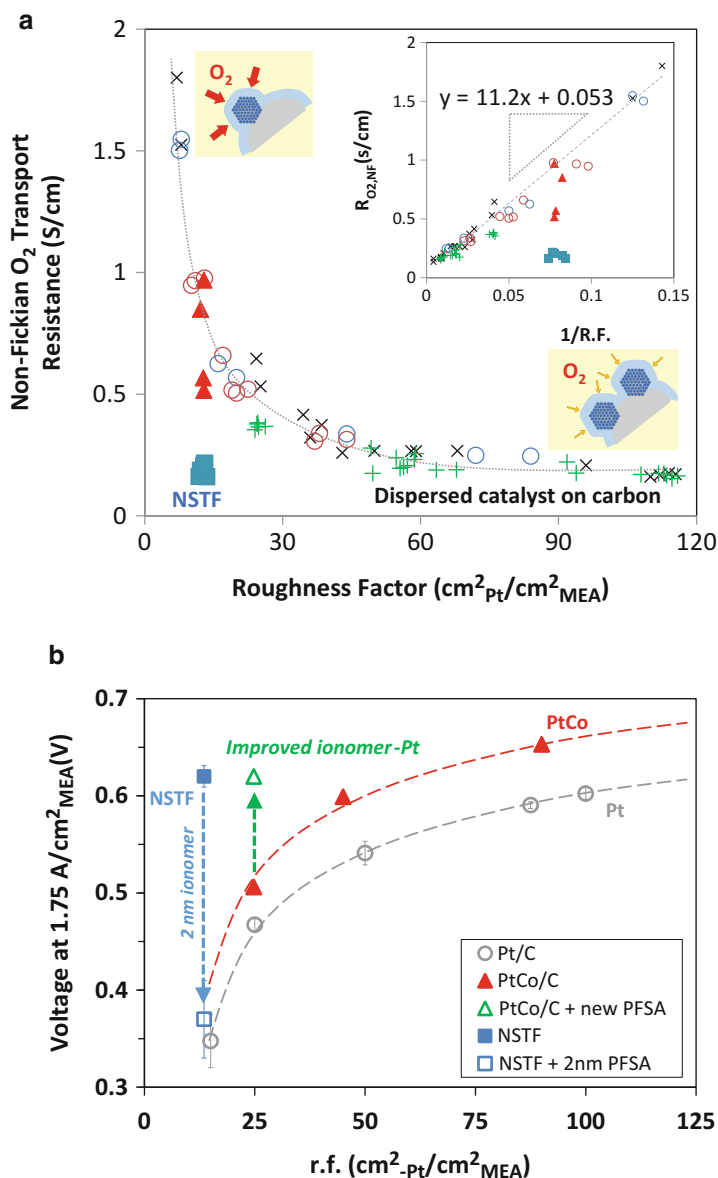
The above results strongly indicate that ionomer thin film (<5 nm) on the Pt surface contributes to the rise of the “local  $\text{O}_2$ ” resistance (yellow shaded area in Fig. 6). In this section, we discuss potential mechanisms by which the ionomer induces this resistance. Known  $\text{O}_2$  permeability of a thick membrane (e.g., a 10–20 μm membrane such as typically used in the fuel cell) cannot explain the large  $\text{O}_2$  transport loss observed in the fuel cell electrodes, as there is a factor of 3–10 increase in the apparent resistivity of a thin film [52]. In bulk perfluorosulfonic acid (PFSA)

### Proton-Exchange Membrane Fuel Cells with Low-Pt Content,

**Fig. 7** (a) Non-Fickian  $O_2$  transport resistance ( $R_{NF}$ ) as a function of total Pt area on an MEA cathode

(roughness factor is defined as the product of Pt loading and ECSA of the catalyst) for different catalysts. Inset is a plot of  $R_{NF}$  vs  $1/r.f.$ . Pt/C ( $\times$ ), PtCo/C ( $\circ$ ), Pt-ML/Pd/C ( $+$ ), NSTF ( $\blacksquare$ ), NSTF with 2–4 nm ionomer coatings ( $\blacktriangle$ ) (Reprinted with permission from Ref. [2]. Copyright 2016

American Chemical Society (b) Voltage at  $1.75 \text{ A/cm}^2$  showing the impact of r.f. and ionomer)



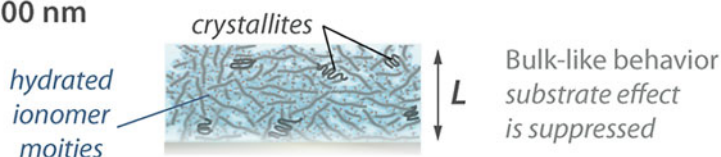
membrane, the ionomer phase segregates into hydrophobic regions and water-containing domains with 2–5 nm diameter channels. This efficiently segregated two-phase morphology is believed to be an important feature responsible for the superior proton conductivity as well as increased water and  $O_2$  transport rates as compared to non-PFSA membranes [67–69]. In a fuel cell electrode where ionomer exists as a 1–5 nm thin film on Pt and carbon, the dimensions

are too small to allow development of the two-phase morphology present in thicker films. The resulting increased importance of interfacial properties and interactions with solid substrates are expected to induce changes in its structure and transport properties (Fig. 8).

When the ionomer film thickness approaches the characteristic domain size of the ionomer, structure and transport properties of the ionomer can change due to the so-called confinement

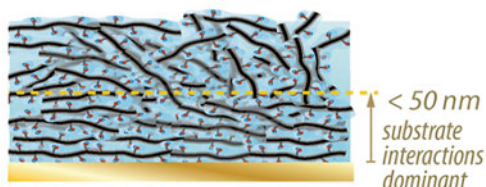
## Thicker (Bulk-like) Film Regime

$L > 200 \text{ nm}$

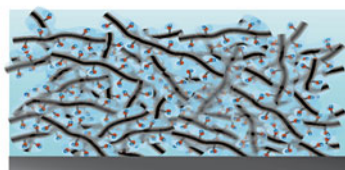
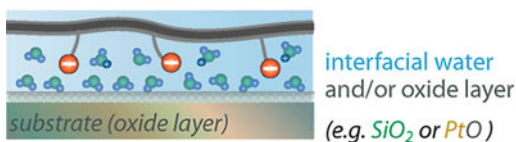
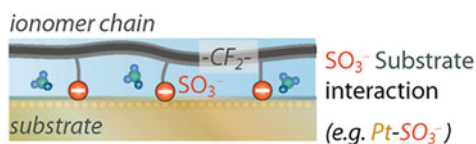


## Thin Film Regime

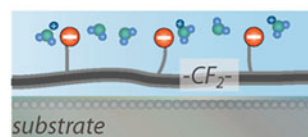
$L < 100 \text{ nm}$  Confinement with strong substrate/film interaction



**Hydrophilic or metallic substrates** - stronger interactions

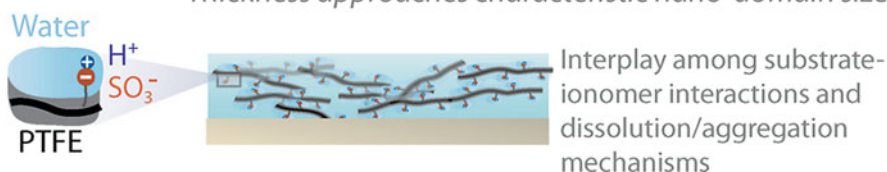


**Hydrophobic Substrates**  
Weaker interactions



## Ultra-Thin Film

$L < 20 \text{ nm}$  Dispersion-like behavior with weak phase-separation  
Thickness approaches characteristic nano-domain size



**Proton-Exchange Membrane Fuel Cells with Low-Pt Content, Fig. 8** Thickness dependence and substrate interaction of ionomer thin film (Reprinted with permission from Ref. [70]. Copyright 2017 American Chemical Society)

effect. Many ex situ techniques such as X-ray scattering, neutron and X-ray reflectivity, TEM, XPS, AFM, and FTIR were employed to study this effect [57, 71–78]. Some effects include a formation of multilamellar nanostructure and

reduced transport properties such as lower water uptake and uptake rate [59, 72, 74–77, 79–82]. These effects are highly dependent on treatment condition, substrate type, and operating environments [76, 83]. These findings corroborate

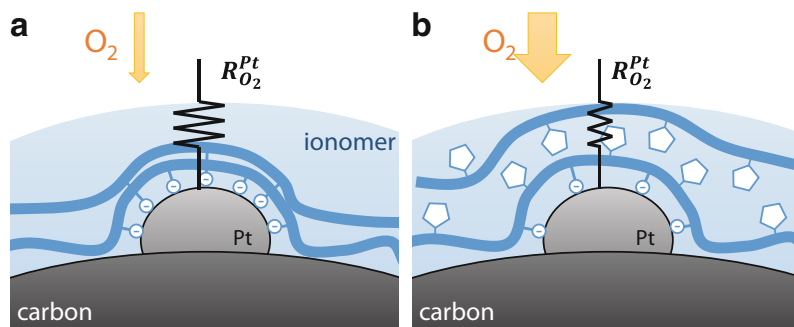
the notion based on domain-size arguments that transport properties of ionomer in a fuel cell electrode are very different from those in bulk membranes. A comprehensive discussion can be found in the PFSA ionomer thin-film entry in this volume and a review by Kusoglu and Weber [70].

Sulfonate groups on the ionomer can adsorb on Pt and reduce ORR activity [84, 85]. The adsorption of the acid group immobilizes the ionomer chain reducing its degrees of freedom [86–88]. Electrodes with higher acid group concentration (lower equivalent weight ionomer) were shown to have higher apparent local  $O_2$  resistance [89]. Some studies showed that different ionomer acid groups and ionic liquid additives can improve ORR activity [24, 90–92]. Furthermore, ex situ  $O_2$  permeability measurement by Litster and coworkers showed that there was no such increase in thin ionomer  $O_2$  resistance when as low as 50 nm thick ionomer films were coated on a polycarbonate substrate and placed in the diffusion path, but not in direct contact with the Pt surface [93]. This result indicates that ionomer interaction with the Pt surface is associated with the increase of the local  $O_2$  resistance.

As an alternative consideration to sulfonate group interaction with Pt, molecular dynamics and DFT simulation by Jinnouchi et al. indicated that it is energetically preferable for the large number of  $CF_2$  groups on the ionomer backbone to fold on the Pt surface [94]. Such a dense layer adjacent to Pt can reduce the  $O_2$  concentration and may be a root cause for the local  $O_2$  resistance.

Published studies using alternative ionomer structures in the electrodes are limited. In general, use of hydrocarbon ionomers results in poor fuel cell performance [95–99]. This is primarily due to their characteristically lower gas permeability which, although favorable when used as a membrane, is detrimental in the electrodes. Among the PFSA ionomers, decrease in the ionomer equivalent weight (increase in the acid group concentration per mass of ionomer) was shown to worsen HCD performance in one study [89]. Ionomers with short side chain or rigid backbone have been shown to mitigate reversible degradation of the electrode [92]. Some acid groups are found to adsorb less strongly to the Pt surface which might translate to higher activity and improved transport properties, although its HCD benefits were not confirmed in actual fuel cell performance [90]. The most significant impact observed is when a small cyclical ring is inserted into the ionomer backbone in order to create a sterically enhanced  $O_2$  permeability through a more open structure (Fig. 9) [100–102]. This results in a substantial improvement in HCD voltage as shown in Fig. 7b (green triangle). These are very encouraging initial results. However, stability and processability concerns still remain.

Altering the process when forming the catalyst layer by changing the solvent system or mixing procedure was shown to improve HCD performance [103–105]. However, it is uncertain whether these enhancements are due to local transport (characteristically scales with Pt



**Proton-Exchange Membrane Fuel Cells with Low-Pt Content, Fig. 9** Schematics of hypothesized ionomer structure at the Pt surface for conventional ionomer (a) and high-oxygen-permeable ionomer (b) (Reprinted with permission from Ref. [2]. Copyright 2016 American Chemical Society)

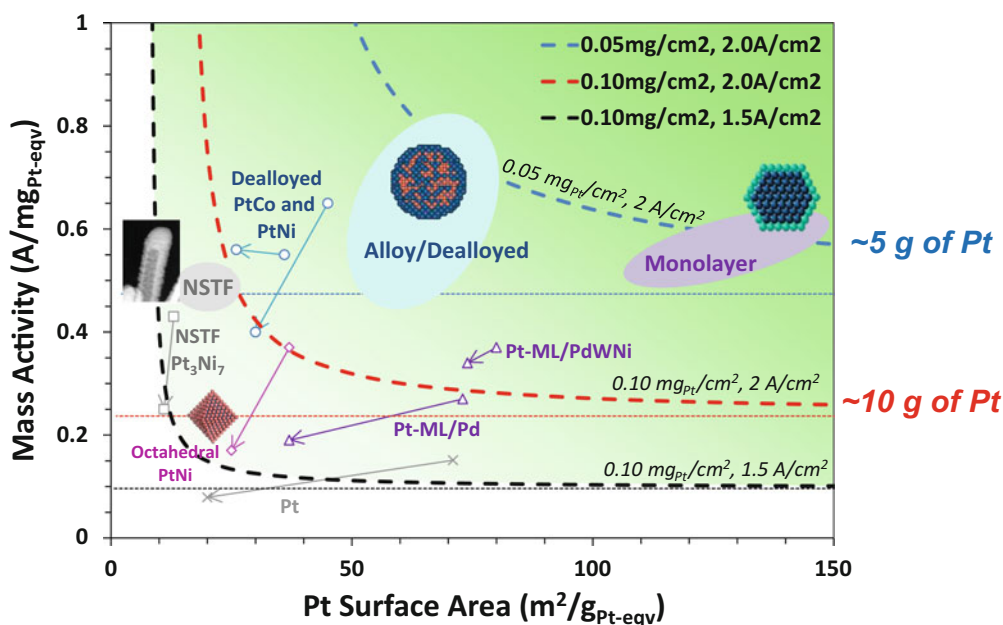
loading) or optimization of ionomer distribution in the electrode.

Recent studies on ionomer thin films have identified many changes in the microstructure and physical properties of the ionomer; however, large gaps still remain in understanding how these changes affect its transport properties (oxygen, proton, and water) within the cathode as well as how the ionomer structure might change with operating conditions in a fuel cell. These topics are critical future research areas that could have significant positive impact on cathode performance and durability.

## Catalyst Roadmap

The mathematical model discussed above can also be used to create catalyst roadmaps that consider the impact of the local transport resistance,

indicating critical ex situ measured parameter requirements needed to achieve performance targets. Figure 10 shows catalyst requirements, ORR mass activity, and Pt surface area (ECSA), needed for acceptable performance ( $>0.58$  V) at 1.5 and 2.0 A/cm<sup>2</sup> for cathode catalyst loadings of 0.05 and 0.1 mg<sub>Pt</sub>/cm<sup>2</sup>. Requirements with (parabolic dashed lines) and without the local resistance (horizontal dotted lines) are shown. Parameters must be higher than the dashed parabolic lines in order to meet the associated requirement, and materials with values in the upper right-hand portion of the plot are most desirable. Some experimental data are also shown on the map – open symbols are representative MEA data before and after durability tests for four well-known catalyst families. The arrows show significant deleterious impact of degradation during operation, representing a large opportunity if catalyst behavior could be stabilized close to beginning-of-life



**Proton-Exchange Membrane Fuel Cells with Low-Pt Content, Fig. 10** ORR mass activity and Pt ECSA targets which enable the cathode to meet vehicle requirements (0.58 V) at the indicated current density and cathode catalyst loadings. Local resistance of 12 s/cm was used in the analysis. *Dashed lines and dotted lines* show the minimum values to meet the requirement with and without local resistance, respectively. Catalysts that are above and to

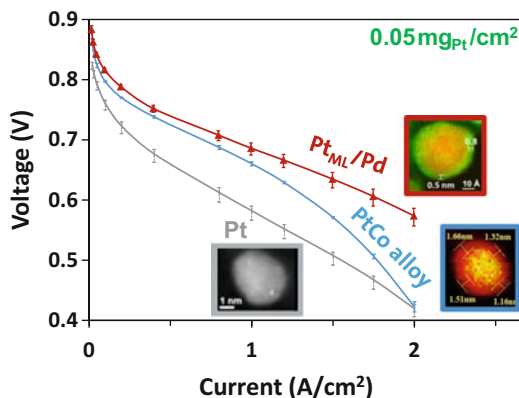
the right of a given boundary are sufficient to meet or exceed the voltage requirement. Data points from MEAs before (*arrow start*) and after (*arrow end*) accelerated durability tests are shown for various catalyst systems [31, 106, 107], and shaded areas indicate estimate of achievable targets (Reprinted with permission from Ref. [2]. Copyright 2016 American Chemical Society)



values. The shaded ovals represent an optimistic expectation of what each approach may achieve in the next 10 years.

Pt alloy catalysts are the most mature. The Toyota Mirai FCEV, introduced to the market in 2014, already uses this type of catalyst although at a higher Pt loading [3, 108]. The high ORR mass activity and moderate Pt surface area suggest that the current catalysts can meet requirement at 10  $\text{g}_{\text{Pt}}/\text{vehicle}$  (red dashed line) but fall short of 5  $\text{g}_{\text{Pt}}/\text{vehicle}$  (blue-dashed line) [31, 32]. Increase in both ORR activity and Pt surface area over operating life is required. Other promising advanced catalysts (e.g., shape-/size-controlled alloy [19–24], Pt monolayer catalysts [25–27], etc.) have shown some encouraging initial results but have generally not yet shown competitive stability in fuel cell MEA testing. Furthermore, they are still made in small quantities at lab scale, and processes amenable to high-volume production remain to be developed.

The Pt monolayer catalyst family pioneered by Brookhaven National Laboratory, shown toward the upper right-hand portion of Fig. 10, is conceptually appealing in that it places essentially all Pt atoms on the particle surface and does not waste Pt atoms in the particle core [25, 26]. This construction gives the highest Pt surface area possible, and representative data are shown in Fig. 11. On a Pt content basis, this catalyst outperforms other types of catalyst, thanks to its high Pt ECSA [27]. However, at the current stage, a relatively large amount of Pd is needed to form Pt monolayer shell, and Pd is subject to leaching out from the core resulting in destabilization of the Pt monolayer [26, 27, 109]. Furthermore, global tightening of automotive emissions standards has raised the price of Pd in recent years to the point that economical advantage of Pd over Pt is minimal. (Both are about \$30/g in June 2017.) Some early work on platinum-monolayer shell on palladium-tungsten-nickel core catalyst (Pt-ML/PdW<sub>Ni</sub>), in which half the Pd core has been replaced by less expensive materials, has shown promising performance and durability (middle of Fig. 10). Further work along these lines, pursuing reduction of Pd use and stabilization of the core materials, appears to be a worthwhile development direction.



**Proton-Exchange Membrane Fuel Cells with Low-Pt Content, Fig. 11**  $\text{H}_2/\text{air}$  polarization curves of different catalysts with Pt loadings of  $0.05 \text{ mg}_{\text{Pt}}/\text{cm}^2$ . Pt<sub>ML</sub>/Pd catalyst contains 15 wt% Pt and 25 wt% Pd (Reprinted with permission from Ref. [27]. Copyright 2016 American Chemical Society)

## Durability of Low-Pt Fuel Cell

Usable performance of the fuel cell must extend over the lifetime of the vehicle (>12 years). Automotive producers generally aim to allow less than 10–20% performance degradation over its life. In the context of Fig. 10, one will need at the end of expected life a catalyst that remains higher than the required ORR activity and Pt ECSA. Characteristics of the degradation of the catalyst and electrode can be observed through decrease in ORR activity and Pt ECSA and loss of transport properties. These losses can be either permanent or reversible. The major degradation mechanisms include Pt and transition metal dissolution, particle migration and coalescence, carbon corrosion, and contaminant adsorption. An extensive review of this topic is available in Ref. [110].

Although one might expect the degradation of a catalyst to be relatively independent of Pt loading, more systematic study is warranted. And even if degradation mechanisms and rates in a low-Pt electrode are the same as in a higher-Pt electrode, the impact on voltage loss will be higher in the low-Pt case. This is because, as discussed in Figs. 7b and 10, the voltage drops precipitously at low r.f. since the resistance (and thus loss) is inversely proportional to this factor. Therefore, research to develop and implement low-Pt



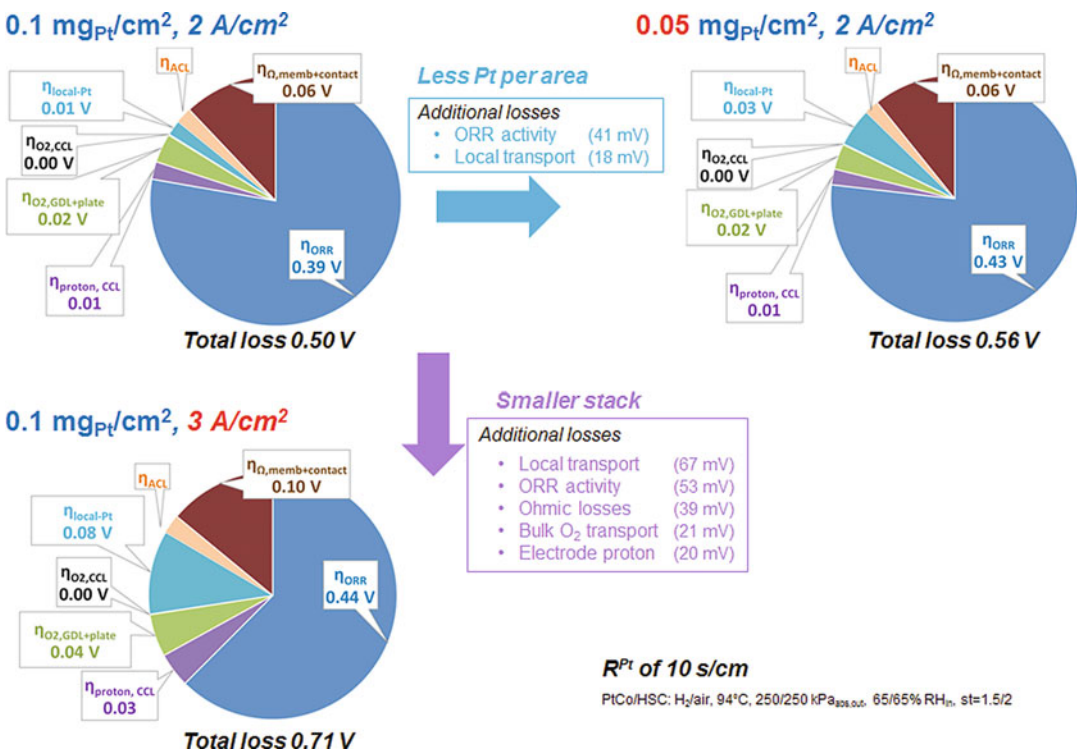
catalysts that start and end life with high ECSA and specific activity is critical to the pursuit of affordable automotive fuel cells.

As the total Pt surface area is reduced in a low-Pt fuel cell, the electrodes become more susceptible to contamination. Some chemical degradation is reversible, and performance can be recovered during normal vehicle operating modes. On the anode, H<sub>2</sub> fuel quality is critical to allow Pt reduction (<0.025 mg<sub>Pt</sub>/cm<sup>2</sup>), where contaminants such as CO and H<sub>2</sub>S must be carefully controlled. On the cathode side, a chemical air filter may be required to remove potential contaminants (SO<sub>x</sub>, H<sub>2</sub>S, NO<sub>x</sub>, volatile organic compounds, etc.) from intake air [111, 112]. In addition to external contaminants, degradation products (sulfate and organic compounds from the membrane [66, 113–115]; cobalt from the catalyst [116, 117]) from within the fuel cell MEA can also decrease fuel cell cathode performance. Development of more stable MEA components and strategies to mitigate degradation are

needed to enable low-Pt fuel cells under real-world application.

## Other Challenges

In this entry, we have focused on the performance of the catalyst and cathode electrode. However, for further improvement other components in the fuel cell must also be developed. Figure 12 breaks down the sources of the voltage loss at high-current density for the near-term target of 0.1 mg<sub>Pt</sub>/cm<sup>2</sup> at 2 A/cm<sup>2</sup> (upper left, about 10 g<sub>Pt</sub>/vehicle) and possible paths toward further improvement. For further Pt and cost reduction, one can reduce the Pt loading or increase the maximum current density. To decrease Pt loading (mg<sub>Pt</sub>/cm<sup>2</sup>) at the same current density (move to right in Fig. 12), improvement in ORR activity and local transport are key enablers. To increase current density at the same Pt loading



**Proton-Exchange Membrane Fuel Cells with Low-Pt Content, Fig. 12** Two pathways to reducing cost further [1]: decreasing Pt loading and [2] increasing current density. Losses are estimated using a fuel cell voltage loss model

(move downward in Fig. 12), improvement in ORR activity and local transport remain of highest priority, but important issues broaden to include ohmic loss reduction, bulk O<sub>2</sub> transport, and cathode proton conduction in the cathode. This downward path can have higher cost reduction impact since smaller stack size will also reduce the amount of bipolar plate, membrane, electrode, and diffusion media material required.

Finally, in order to realize a truly sustainable technology, more precious metals must be recycled. Although growing in recently years, recycling currently only accounts for 30% of the global PGM supply [6]. Pt global recycling rates (60–70%) are better than those of other PGMs thanks to its favorable recycling economics. However, in the automotive sector, the recycling rate only reaches 50–55% [118]. Recycling of PGM is not only technically feasible and environmental friendly but also profitable. Recycling rates can be increased through improved waste collection mechanisms, as well as shifting public perspective from “waste management” to “resource management” [119]. Management of PGM life cycle ultimately needs to expand across many markets and applications including automotive, jewelry, and electronics. For this to occur, strong support will likely be needed from policy makers at state, federal, and international levels.

## Future Directions

Fuel cell electric vehicles with about 30 g of Pt are now on the road [2, 3], and next-generation FCEVs are expected to use about 10–25 g of PGM. These are significant accomplishments and encouraging progress toward commercializing this sustainable transportation technology. However, considering commercial factors as well as promising catalyst technologies early in the pipeline, a long-term PGM target is warranted at a level comparable to that used in automotive catalytic converters (~5 g<sub>PGM</sub>). Progress in Pt-based catalysts in recent years has been due to alloy optimization resulting in notable activity gains, but opportunities remain to achieve better Pt surface area (ECSA) and alloy stability over

operating life. In addition to these structure and kinetics considerations, fundamental understanding of the origin of the local transport resistance is needed in order to optimally engineer the nanostructure near the catalyst active surfaces. Development of ionomer specifically designed for this purpose is a promising research direction, as encouraging early data exists. New issues will be encountered as the use of low-Pt roughness factor increases contamination susceptibility, and fundamental studies to conclusively identify poisoning mechanisms and mitigations approaches will also be needed. Judging from the steady progress made in the past decades, we are optimistic that the concerted efforts of materials developers and electrode designers can resolve these issues, enabling fuel cell vehicles that are affordable for the mass market.

**Acknowledgments** This work was partially supported by the US Department of Energy, Office of Energy Efficiency and Renewable Energy under grant DE-EE0007271.

## Bibliography

### Primary Literature

1. Masten DA, Bosco AD (2010) System design for vehicle applications: GM/Opel. In: Handbook of fuel cells. Wiley, Hoboken
2. Kongkanand A, Mathias MF (2016) The priority and challenge of high-power performance of low-platinum proton-exchange membrane fuel cells. *J Phys Chem Lett* 7(7):1127–1137
3. Gröger O, Gasteiger HA, Suchsland J-P (2015) Review – electromobility: batteries or fuel cells? *J Electrochem Soc* 162(14):A2605–A2622
4. Fornalczyk A, Saternus M (2009) Removal of platinum group metals from the used auto catalytic converter. *Metalurgija* 48(2):133–136
5. Nguyen T., Andress D.; Howden, K.; Toops, T., Das S (n.d.) Platinum Group Metals (PGM) for light-duty vehicles. [https://www.hydrogen.energy.gov/pdfs/16006\\_pgm\\_light\\_duty\\_vehicles.pdf](https://www.hydrogen.energy.gov/pdfs/16006_pgm_light_duty_vehicles.pdf)
6. Loferski PJ (2014) Minerals yearbook; Platinum-Group Metals. <http://minerals.usgs.gov/minerals/pubs/commodity/platinum/myb1-2014-plati.pdf>
7. Bernhart W, Riederle S, Yoon M (n.d.) Fuel cells – a realistic alternative for zero emission? [https://www.rolandberger.com/en/Publications/pub\\_fuel\\_cells\\_a\\_realistic\\_alternative\\_for\\_zero\\_emission.html](https://www.rolandberger.com/en/Publications/pub_fuel_cells_a_realistic_alternative_for_zero_emission.html)
8. James BD, Moton JM, Colella WG (n.d.) Mass production cost estimation of direct H<sub>2</sub> PEM fuel cell systems

- for transportation applications: 2013 update. Strategic Analysis, Inc. [http://energy.gov/sites/prod/files/2014/11/f19/feto\\_sa\\_2013\\_pemfc\\_transportation\\_cost\\_analysis.pdf](http://energy.gov/sites/prod/files/2014/11/f19/feto_sa_2013_pemfc_transportation_cost_analysis.pdf)
- Proietti E, Jaouen F, Lefèvre M, Larouche N, Tian J, Herranz J, Dodelet J-P (2011) Iron-based cathode catalyst with enhanced power density in polymer electrolyte membrane fuel cells. *Nat Commun* 2:416
  - Wu G, More KL, Johnston CM, Zelenay P (2011) High-performance electrocatalysts for oxygen reduction derived from polyaniline, iron, and cobalt. *Science* 332(6028):443–447
  - Jaouen F, Proietti E, Lefèvre M, Chenitz R, Dodelet J-P, Wu G, Chung HT, Johnston CM, Zelenay P (2011) Recent advances in non-precious metal catalysis for oxygen-reduction reaction in polymer electrolyte fuel cells. *Energy Environ Sci* 4(1):114
  - Banham D, Ye S, Pei K, Ozaki J-I, Kishimoto T, Imashiro Y (2015) A review of the stability and durability of non-precious metal catalysts for the oxygen reduction reaction in proton exchange membrane fuel cells. *J Power Sources* 285:334
  - Varcoe JR, Slade RCT (2005) Prospects for alkaline anion-exchange membranes in low temperature fuel cells. *Fuel Cells* 5(2):187–200
  - Merle G, Wessling M, Nijmeijer K (2011) Anion exchange membranes for alkaline fuel cells: a review. *J Membr Sci* 377(1–2):1–35
  - Yanagi H, Fukuta K (2008) Anion exchange membrane and ionomer for alkaline membrane fuel cells (AMFCs). *ECS Trans* 16:257–262
  - Einsla BR, Chempath S, Pratt LR, Boncella JM, Rau J, Macomber C, Pivovar BS (2007) Stability of cations for anion exchange membrane fuel cells. *ECS Trans* 11:1173–1180
  - Pan J, Lu S, Li Y, Huang A, Zhuang L, Lu J (2010) High-performance alkaline polymer electrolyte for fuel cell applications. *Adv Funct Mater* 20(2):312–319
  - Neyerlin KC, Gu W, Jorne J, Gasteiger HA (2007) Study of the exchange current density for the hydrogen oxidation and evolution reactions. *J Electrochem Soc* 154(7):B631
  - Zhang J, Yang H, Fang J, Zou S (2010) Synthesis and oxygen reduction activity of shape-controlled Pt(3)Ni nanopolyhedra. *Nano Lett* 10(2):638–644
  - Wu J, Zhang J, Peng Z, Yang S, Wagner FT, Yang H (2010) Truncated octahedral Pt<sub>3</sub>Ni oxygen reduction reaction electrocatalysts. *J Am Chem Soc* 132(14):4984–4985
  - Carpenter MK, Moylan TE, Kukreja RS, Atwan MH, Tessema MM (2012) Solvothermal synthesis of platinum alloy nanoparticles for oxygen reduction electrocatalysis. *J Am Chem Soc* 134(20):8535–8542
  - Choi SI, Xie S, Shao M, Odell JH, Lu N, Peng H-C, Protsailo L, Guerrero S, Park J, Xia X, Wang J, Kim MJ, Xia Y (2013) Synthesis and characterization of 9 Nm Pt – Ni octahedra with a record high activity of 3.3 A/mg. *Nano Lett* 13:3420–3425
  - Gan L, Cui C, Heggen M, Dionigi F, Rudi S, Strasser P (2014) Element-specific anisotropic growth of shaped platinum alloy nanocrystals. *Science* 346(6216):1502–1506
  - Chen C, Kang Y, Huo Z, Zhu Z, Huang W, Xin HL, Snyder JD, Li D, Herron JA, Mavrikakis M, Chi M, More KL, Li Y, Markovic NM, Somorjai GA, Yang P, Stamenkovic VR (2014) Highly crystalline multimetallic nanoframes with three-dimensional electrocatalytic surfaces. *Science* 343(6177):1339–1343
  - Zhang J, Mo Y, Vukmirovic MB, Klie R, Sasaki K, Adzic RR (2004) Platinum monolayer electrocatalysts for O<sub>2</sub> reduction: Pt monolayer on Pd(111) and on carbon-supported Pd nanoparticles. *J Phys Chem B* 108(30):10955–10964
  - Sasaki K, Naohara H, Cai Y, Choi YM, Liu P, Vukmirovic MB, Wang JX, Adzic RR (2010) Core-protected platinum monolayer shell high-stability electrocatalysts for fuel-cell cathodes. *Angew Chemie Int Ed* 49(46):8602–8607
  - Kongkanand A, Subramanian NP, Yu Y, Liu Z, Igarashi H, Muller DA (2016) Achieving high-power PEM fuel cell performance with an ultralow-Pt-content core-shell catalyst. *ACS Catal* 6(3):1578–1583
  - Oezaslan M, Heggen M, Strasser P (2012) Size-dependent morphology of dealloyed bimetallic catalysts: linking the nano to the macro scale. *J Am Chem Soc* 134(1):514–524
  - Jia Q, Caldwell K, Ziegelbauer JM, Kongkanand A, Wagner FT, Mukerjee S, Ramaker DE (2014) The role of OOH binding site and Pt surface structure on ORR activities. *J Electrochem Soc* 161(14):F1323–F1329
  - Caldwell KM, Ramaker DE, Jia Q, Mukerjee S, Ziegelbauer JM, Kukreja RS, Kongkanand A (2015) Spectroscopic in situ measurements of the relative Pt skin thicknesses and porosities of dealloyed PtMn (Ni, Co) electrocatalysts. *J Phys Chem C* 119(1):757–765
  - Han B, Carlton CE, Kongkanand A, Kukreja RS, Theobald BR, Gan L, O'Malley R, Strasser P, Wagner FT, Shao-Horn Y (2015) Record activity and stability of dealloyed bimetallic catalysts for proton exchange membrane fuel cells. *Energy Environ Sci* 8(1):258–266
  - Kongkanand A (n.d.) DOE final report: high-activity dealloyed catalysts. <http://www.osti.gov/scitech/servlets/purl/1262711>
  - Gasteiger HA, Kocha SS, Sompalli B, Wagner FT (2005) Activity benchmarks and requirements for Pt, Pt-alloy, and non-Pt oxygen reduction catalysts for PEMFCs. *Appl Catal B Environ* 56(1–2):9–35
  - Gu W, Baker DR, Liu Y, Gasteiger HA (2009) Proton exchange membrane fuel cell (PEMFC) down-the-channel performance model. In: Vielstich W, Gasteiger HA, Lamm A, Yokokawa H (eds) *Handbook of fuel cells: fundamentals, technology and applications*. Wiley, Hoboken
  - Antolini E (2009) Carbon supports for low-temperature fuel cell catalysts. *Appl Catal B Environ* 88(1–2):1–24

36. Yu PT, Gu W, Makharia R, Wagner FT, Gasteiger HA (2006) The impact of carbon stability on PEM fuel cell startup and shutdown voltage degradation. *ECS Trans* 3:797–809
37. Tuavev X, Rudi S, Strasser P (2016) The impact of the morphology of the carbon support on the activity and stability of nanoparticle fuel cell catalysts. *Cat Sci Technol* 6(23):8276–8288
38. Park YC, Tokiwa H, Kakinuma K, Watanabe M, Uchida M (2016) Effects of carbon supports on Pt distribution, ionomer coverage and cathode performance for polymer electrolyte fuel cells. *J Power Sources* 315:179–191
39. Kongkanand A, Yarlagadda V, Garrick T, Moylan TE, Gu W (2016) Electrochemical diagnostics and modeling in developing the PEMFC cathode. *ECS Trans* 75(14):25
40. Ito T, Matsuwaki U, Otsuka Y, Hatta M, Hayakawa K, Matsutani K, Tada T, Jinnai H (2011) Three-dimensional spatial distributions of Pt catalyst nanoparticles on carbon substrates in polymer electrolyte fuel cells. *Electrochemistry* 79(5):374–376
41. Jinnai H, Spontak RJ, Nishi T (2010) Transmission electron microtomography and polymer nanostructures. *Macromolecules* 43(4):1675
42. Ohma A, Mashio T, Sato K, Iden H, Ono Y, Sakai K, Akizuki K, Takaichi S, Shinohara K (2011) Analysis of proton exchange membrane fuel cell catalyst layers for reduction of platinum loading at Nissan. *Electrochim Acta* 56(28):10832–10841
43. Iden H, Mashio T, Ohma A (2013) Gas transport inside and outside carbon supports of catalyst layers for PEM fuel cells. *J Electroanal Chem* 708:87–94
44. Shinozaki K, Yamada H, Morimoto Y (2011) Relative humidity dependence of Pt utilization in polymer electrolyte fuel cell electrodes: effects of electrode thickness, ionomer-to-carbon ratio, ionomer equivalent weight, and carbon support. *J Electrochem Soc* 158(5):B467
45. Weber AZ, Borup RL, Darling RM, Das PK, Dursch TJ, Gu W, Harvey D, Kusoglu A, Litster S, Mench MM, Mukundan R, Owejan JP, Pharoah JG, Secanell M, Zenyuk IV (2014) A critical review of modeling transport phenomena in polymer-electrolyte fuel cells. *J Electrochem Soc* 161(12):F1254–F1299
46. Zenyuk IV, Litster S (2012) Spatially resolved modeling of electric double layers and surface chemistry for the hydrogen oxidation reaction in water-filled platinum-carbon electrodes. *J Phys Chem C* 116(18):9862–9875
47. Zenyuk IV, Litster S (2014) Modeling ion conduction and electrochemical reactions in water films on thin-film metal electrodes with application to low temperature fuel cells. *Electrochim Acta* 146:194–206
48. Nouri-Khorasani A, Malek K, Malek A, Mashio T, Wilkinson DP, Eikerling MH (2016) Molecular modeling of the proton density distribution in a water-filled slab-like nanopore bounded by Pt oxide and ionomer. *Catal Today* 262:133–140
49. Nonoyama N, Okazaki S, Weber AZ, Ikogi Y, Yoshida T (2011) Analysis of oxygen-transport diffusion resistance in proton-exchange-membrane fuel cells. *J Electrochem Soc* 158(4):B416
50. Sadeghi E, Eikerling M, Putz A (2013) Hierarchical model of reaction rate distributions and effectiveness factors in catalyst layers of polymer electrolyte fuel cells. *J Electrochem Soc* 160(10):F1159–F1169
51. Ahluwalia RK, Wang X, Steinbach AJ (2016) Performance of advanced automotive fuel cell systems with heat rejection constraint. *J Power Sources* 309:178
52. Greszler TA, Caulk D, Sinha P (2012) The impact of platinum loading on oxygen transport resistance. *J Electrochem Soc* 159(12):F831–F840
53. Epting WK, Litster S (2012) Effects of an agglomerate size distribution on the PEFC agglomerate model. *Int J Hydrog Energy* 37(10):8505–8511
54. Murata S, Imanishi M, Hasegawa S, Namba R (2014) Vertically aligned carbon nanotube electrodes for high current density operating proton exchange membrane fuel cells. *J Power Sources* 253:104–113
55. Kongkanand A (2017) Highly accessible catalysts for durable high-power performance. Annual merit review DOE hydrogen and fuel cells and vehicle technologies programs. Washington, DC. [https://www.hydrogen.energy.gov/pdfs/review17/fc144\\_kongkanand\\_2017\\_o.pdf](https://www.hydrogen.energy.gov/pdfs/review17/fc144_kongkanand_2017_o.pdf)
56. Neyerlin KC, Christ JM, Zack JW, Gu W, Kumaraguru S, Kongkanand A, Kocha SS (2016) New insights from electrochemical diagnostics pertaining to the high current density performance of Pt-based catalysts. *Meet Abstr MA2016-02(38):2492*
57. Lopez-Haro M, Guétaz L, Printemps T, Morin A, Escribano S, Jouneau P-H, Bayle-Guillemaud P, Chandezon F, Gebel G (2014) Three-dimensional analysis of Nafion layers in fuel cell electrodes. *Nat Commun* 5:5229
58. Cullen DA, Koestner R, Kukreja RS, Liu ZY, Minko S, Trotsenko O, Tokarev A, Guetaz L, Meyer HM, Parish CM, More KL (2014) Imaging and microanalysis of thin ionomer layers by scanning transmission electron microscopy. *J Electrochem Soc* 161(10):F1111–F1117
59. Iden H, Sato K, Ohma A, Shinohara K (2011) Relationship among microstructure, ionomer property and proton transport in pseudo catalyst layers. *J Electrochem Soc* 158(8):B987
60. Baker DR, Caulk DA, Neyerlin KC, Murphy MW (2009) Measurement of oxygen transport resistance in PEM fuel cells by limiting current methods. *J Electrochem Soc* 156(9):B991
61. Makharia R (2010) Challenges associated with high current density performance of low Pt-loading cathodes in proton exchange membrane (PEM) fuel cells. In: ASME 8th international fuel cell science, engineering & technology conference, Brooklyn, 2010
62. Debe MK (2012) Effect of electrode surface area distribution on high current density performance of PEM fuel cells. *J Electrochem Soc* 159(1):B54

63. Sinha PK, Gu W, Kongkanand A, Thompson E (2011) Performance of nano structured thin film (NSTF) electrodes under partially-humidified conditions. *J Electrochem Soc* 158(7):B831
64. Debe MK (2012) Electrocatalyst approaches and challenges for automotive fuel cells. *Nature* 486(7401):43–51
65. Kongkanand A, Owejan JE, Moose S, Dioguardi M, Biradar M, Makharia R (2012) Development of dispersed-catalyst/NSTF hybrid electrode. *J Electrochem Soc* F676–F682
66. Kongkanand A, Zhang J, Liu Z, Lai Y-H, Sinha P, Thompson EL, Makharia R (2014) Degradation of PEMFC observed on NSTF electrodes. *J Electrochem Soc* 161(6):F744–F753
67. Gierke TD, Munn GE, Wilson FC (1981) The morphology in Nafion perfluorinated membrane products, as determined by wide- and small- angle X-ray studies. *J Polym Sci Polym Phys Ed* 19(11):1687–1704
68. Schmidt-Rohr K, Chen Q (2008) Parallel cylindrical water nanochannels in Nafion fuel-cell membranes. *Nat Mater* 7(1):75–83
69. Kreuer K-D, Paddison SJ, Spohr E, Schuster M (2004) Transport in proton conductors for fuel-cell applications: simulations, elementary reactions, and phenomenology. *Chem Rev* 104(10):4637–4678
70. Kusoglu A, Weber AZ (2017) New insights into perfluorinated sulfonic-acid ionomers. *Chem Rev* 117(3):987
71. Dura JA, Murthi VS, Hartman M, Satija SK, Majkrzak CF (2009) Multilamellar interface structures in Nafion. *Macromolecules* 42(13):4769
72. Eastman SASA, Kim S, Page KAKA, Rowe BWB, Kang S, Soles CLCL, Yager KGKG (2012) Effect of confinement on structure, water solubility, and water transport in Nafion thin films. *Macromolecules* 45(19):7920–7930
73. Modestino MA, Paul DK, Dishari S, Petrina SA, Allen FI, Hickner MA, Karan K, Segalman RA, Weber AZ (2013) Self-assembly and transport limitations in confined Nafion films. *Macromolecules* 46(3):867
74. Kusoglu A, Kushner D, Paul DKDK, Karan K, Hickner MAMA, Weber AZAZ (2014) Impact of substrate and processing on confinement of Nafion thin films. *Adv Funct Mater* 24(30):4763–4774
75. Bass M, Berman A, Singh A, Konovalov O, Freger V (2011) Surface-induced micelle orientation in Nafion films. *Macromolecules* 44(8):2893–2899
76. Kusoglu A, Dursch TJ, Weber AZ (2016) Nanostructure/swelling relationships of bulk and thin-film PFSA ionomers. *Adv Funct Mater* 26(27):4961
77. Page KA, Kusoglu A, Stafford CM, Kim S, Kline RJ, Weber AZ (2014) Confinement-driven increase in ionomer thin-film modulus. *Nano Lett* 14(5):2299–2304
78. Ohira A, Kuroda S, Mohamed HFM, Tavernier B (2013) Effect of interface on surface morphology and proton conduction of polymer electrolyte thin films. *Phys Chem Chem Phys* 15(27):11494–11500
79. Kongkanand A (2011) Interfacial water transport measurements in Nafion thin films using a quartz-crystal microbalance. *J Phys Chem C* 115(22):11318–11325
80. Siroma Z, Kakitsu R, Fujiwara N, Ioroi T, Yamazaki SI, Yasuda K (2009) Depression of proton conductivity in recast Nafion film measured on flat substrate. *J Power Sources* 189(2):994–998
81. Mohamed HFM, Kuroda S, Kobayashi Y, Oshima N, Suzuki R, Ohira A (2013) Possible Presence of hydrophilic SO<sub>3</sub>H nanoclusters on the surface of dry ultra-thin Nafion® films: a positron annihilation study. *Phys Chem Chem Phys* 15(5):1518–1525
82. Paul DK, Giorgi JB, Karan K (2013) Chemical and ionic conductivity degradation of ultra-thin ionomer film by X-ray beam exposure. *J Electrochem Soc* 160(4):F824
83. Paul DK, Karan K, Docoslis A, Giorgi JB, Pearce J (2013) Characteristics of self-assembled ultrathin Nafion films. *Macromolecules* 46(9):3461
84. Subbaraman R, Strmcnik D, Paulikas AP, Stamenkovic VR, Markovic NM (2010) Oxygen reduction reaction at three-phase interfaces. *Chem Phys Chem* 11(13):2825–2833
85. Kocha SS, Zack JW, Alia SM, Neyerlin KC, Pivovar BS (2012) Influence of ink composition on the electrochemical properties of Pt/C electrocatalysts. *ECS Trans* 50(2):1475–1485
86. Masuda T, Ikeda K, Uosaki K (2013) Potential-dependent adsorption/desorption behavior of perfluoro-sulfonated ionomer on a gold electrode surface studied by cyclic voltammetry, electrochemical quartz microbalance, and electrochemical atomic force microscopy. *Langmuir* 29(7):2420–2426
87. Kunimatsu K, Yoda T, Tryk DA, Uchida H, Watanabe M (2010) In situ ATR-FTIR study of oxygen reduction at the Pt/Nafion interface. *Phys Chem Chem Phys* 12(3):621–629
88. Ayato Y, Kunimatsu K, Osawa M, Okada T (2006) Study of Pt electrode/Nafion ionomer interface in HClO<sub>4</sub> by in situ surface-enhanced FTIR spectroscopy. *J Electrochem Soc* 153(2):A203
89. Ono Y, Ohma A, Shinohara K, Fushinobu K (2013) Influence of equivalent weight of ionomer on local oxygen transport resistance in cathode catalyst layers. *J Electrochem Soc* 160(8):F779–F787
90. Kodama K, Shinohara A, Hasegawa N, Shinozaki K, Jinnouchi R, Suzuki T, Hatanaka T, Morimoto Y (2014) Catalyst poisoning property of sulfonimide acid ionomer on Pt (111) surface. *J Electrochem Soc* 161(5):F649–F652
91. Snyder J, Livi K, Erlebacher J (2013) Oxygen reduction reaction performance of [MTBD][beti]-encapsulated nanoporous NiPt alloy nanoparticles. *Adv Funct Mater* 23(44):5494–5501
92. Jomori S, Komatsubara K, Nonoyama N, Kato M, Yoshida T (2013) An experimental study of the effects of operational history on activity changes in a PEMFC. *J Electrochem Soc* 160(9):F1067–F1073



93. Liu H, Epting WK, Litster S (2015) Gas transport resistance in polymer electrolyte thin films on oxygen reduction reaction catalysts. *Langmuir* 31(36):9853–9858
94. Jinnouchi R, Kudo K, Kitano N, Morimoto Y (2016) Molecular dynamics simulations on O<sub>2</sub> permeation through Nafion ionomer on platinum surface. *Electrochim Acta* 188:767–776
95. Béléké AB, Miyatake K, Uchida H, Watanabe M (2007) Gas diffusion electrodes containing sulfonated polyether ionomers for PEFCs. *Electrochim Acta* 53(4):1972–1978
96. Omata T, Tanaka M, Miyatake K, Uchida M, Uchida H, Watanabe M (2012) Preparation and fuel cell performance of catalyst layers using sulfonated polyimide ionomers. *ACS Appl Mater Interfaces* 4(2):730–737
97. Dru D, Baranton S, Bigarré J, Buvat P, Coutanceau C (2016) Fluorine-free Pt nanocomposites for three-phase interfaces in fuel cell electrodes. *ACS Catal* 6(10):6993–7001
98. Park J-S, Krishnan P, Park S-H, Park G-G, Yang T-H, Lee W-Y, Kim C-SJ (2008) A study on fabrication of sulfonated poly(ether ether ketone)-based membrane-electrode assemblies for polymer electrolyte membrane fuel cells. *J Power Sources* 178(2):642–650
99. Yoon YJ, Kim T-H, Yu DM, Park J-Y, Hong YT (2012) Modification of hydrocarbon structure for polymer electrolyte membrane fuel cell binder application. *Int J Hydrog Energy* 37(18):13452–13461
100. Takami M (2013) Ionomers and ionically conductive compositions for use as one or more electrode of a fuel cell
101. Fuel Cell Development Progress 2013 Report (n.d.). New Energy and Industrial Technology Development Organization (NEDO). <http://www.nedo.go.jp/content/100575921.pdf>
102. Kinoshita S, Tanuma T, Yamada K, Hommura S, Watakabe A, Saito S, Shimohira T (2014) Development of PFSA ionomers for the membrane and the electrodes. *ECS Trans* 64(3):371–375
103. Takahashi S, Mashio T, Horibe N, Akizuki K, Ohma A (2015) Analysis of the microstructure formation process and its influence on the performance of polymer electrolyte fuel-cell catalyst layers. *Chem Electro Chem* 2(10):1560–1567
104. Kim YS, Welch CF, Mack NH, Hjelm RP, Orler EB, Hawley ME, Lee KS, Yim S-D, Johnston CM (2014) Highly durable fuel cell electrodes based on ionomers dispersed in glycerol. *Phys Chem Chem Phys* 16(13):5927–5932
105. Amemiya, K.; Kobayashi, N.; Yoshida, T (2013) Fabrication process and its microscopic structure characteristics for high performance PEFC electrodes. In: Japanese society of automotive engineering. p 20135108
106. Adzic RR (2014) Contiguous platinum monolayer oxygen reduction electrocatalysts on high-stability-low-cost supports. Annual merit review DOE hydrogen and fuel cells and vehicle technologies programs. Washington, DC. [https://www.hydrogen.energy.gov/pdfs/review14/fc009\\_adzic\\_2014\\_o.pdf](https://www.hydrogen.energy.gov/pdfs/review14/fc009_adzic_2014_o.pdf)
107. Steinbach A (2014) High performance, durable, low cost membrane electrode assemblies for transportation applications. Annual merit review DOE hydrogen and fuel cells and vehicle technologies programs. Washington, DC. [https://www.hydrogen.energy.gov/pdfs/review14/fc104\\_steinbach\\_2014\\_o.pdf](https://www.hydrogen.energy.gov/pdfs/review14/fc104_steinbach_2014_o.pdf)
108. Konno N, Mizuno S, Nakaji H, Ishikawa Y (2015) Development of compact and high-performance fuel cell stack. *SAE Int J Altern Powertrains* 4(1):2015-01-1175
109. Sasaki K, Naohara H, Choi Y, Cai Y, Chen W-F, Liu P, Adzic RR (2012) Highly stable Pt monolayer on PdAu nanoparticle electrocatalysts for the oxygen reduction reaction. *Nat Commun* 3:1115
110. Borup R, Meyers J, Pivovar B, Kim YS, Mukundan R, Garland N, Myers D, Wilson M, Garzon F, Wood D, Zelenay P, More K, Stroh K, Zawodzinski T, Boncella J, McGrath JE, Inaba M, Miyatake K, Hori M, Ota K, Ogumi S, Miyata S, Nishikata A, Siroma Z, Uchimoto Y, Yasuda K, Kimijima K-I, Iwashita N (2007) Scientific aspects of polymer electrolyte fuel cell durability and degradation. *Chem Rev* 107(10):3904–3951
111. St-Pierre J, Zhai Y, Angelo MS (2014) Effect of selected airborne contaminants on PEMFC performance. *J Electrochem Soc* 161(3):F280
112. St-Pierre J, Zhai Y, Ge J (2016) Relationships between PEMFC cathode kinetic losses and contaminants' dipole moment and adsorption energy on Pt. *J Electrochem Soc* 163(3):F247
113. Teranishi K, Kawata K, Tsushima S, Hirai S (2006) Degradation mechanism of PEMFC under open circuit operation. *Electrochem Solid-State Lett* 9(10):A475
114. Ohma A, Yamamoto S, Shinohara K (2008) Membrane degradation mechanism during open-circuit voltage hold test. *J Power Sources* 182(1):39
115. Zhang J, Litteer BA, Coms FD, Makharia R (2012) Recoverable performance loss due to membrane chemical degradation in PEM fuel cells. *J Electrochem Soc* 159(7):F287
116. Okada T (1999) Theory for water management in membranes for polymer electrolyte fuel cells. Part 2. The effect of impurity ions at the cathode side on the membrane performances. *J Electroanal Chem* 465(1):18
117. Cai Y, Kongkanand A, Gu W, Moylan TE (2015) Effects of cobalt cation on low Pt-loaded PEM fuel cell performance. *ECS Trans* 69(17):1047
118. Graedel TE, Allwood J, Birat J, Reck BK, Sibley SF, Sonnemann G, Buchert M, Hagelüken C (2011) Recycling rates of metals – a status report. A report of the Working Group on the Global Metal Flows to the International Resource Panel, United Nations Environment Programme, Paris



119. Hagelüken C (2012) Recycling the platinum group metals: a European perspective. *Platin Met Rev* 56(1):29–35

### Books and Reviews

- Gu W, Baker DR, Liu Y, Gasteiger HA (2009) Proton exchange membrane fuel cell (PEMFC) down-the-channel performance model. In: Vielstich W, Gasteiger HA, Lamm A, Yokokawa H (eds) *Handbook of fuel cells: fundamentals, technology and applications*. Wiley, Hoboken
- Kongkanand A, Mathias MF (2016) The priority and challenge of high-power performance of low-platinum proton-exchange membrane fuel cells. *J Phys Chem Lett* 7(7):1127–1137
- Kusoglu A, Weber AZ (2017) New insights into perfluorinated sulfonic-acid ionomers. *Chem Rev* 117(3):987
- Weber AZ, Kusoglu A (2014) Unexplained transport resistances for low-loaded fuel-cell catalyst layers. *J Mater Chem A* 2(c):17207–17211
- Zhang J (2013) PEM fuel cells and platinum-based electrocatalysts. In: Kreuzer K-D (ed) *Fuel cells: selected entries from the encyclopedia of sustainability science and technology*. Springer, New York, pp 305–340



# Polymer Electrolyte Membrane Fuel Cells (PEM-FC) and Non-noble Metal Catalysts for Oxygen Reduction

Ulrike I. Kramm<sup>1</sup>, Peter Bogdanoff<sup>2</sup> and Sebastian Fiechter<sup>2</sup>

<sup>1</sup>Brandenburg University of Technology Applied Physics and Sensors, Cottbus, Germany

<sup>2</sup>Helmholtz-Zentrum Berlin für Materialien und Energie GmbH (HZB), Institut für Solare Brennstoffe und Energiespeichermaterialien, Berlin, Germany

## Article Outline

Glossary

Definition of the Subject

Introduction

Transition Metal Carbides, Nitrides, and Chalcogenides

Non-noble Metal Catalysts with Molecular Centers

NNMC and Their Potential for PEM-FC Application

Future Direction

Bibliography

## Glossary

**Fe-N-C catalyst** Group of catalysts for which it is believed that molecular FeN<sub>4</sub>- or FeN<sub>2+2</sub>-centers are responsible for the reduction of oxygen.

**Macrocycle** Complex, organic molecule; in the context of this report, usually porphyrins, phthalocyanines, tetraazaannulenes, i.e., characterized by a tetrapyrrole core.

**NNMC** Non-noble metal catalysts: Catalysts prepared without any noble metals. As a result, the fabrication costs of such materials should be essentially lower as all basic-components are cheap.

**ORR** Oxygen Reduction Reaction. In this contribution, it stands for the electrochemical reduction of oxygen. The favored pathway is the direct reduction to water whereas the indirect pathway via the formation of peroxides is undesirable for fuel cell application.

**Pyrochelates** Macrocycles which were heat-treated ( $T > 300\text{ }^{\circ}\text{C}$ ). During pyrolysis, the initial molecular structure is transferred into a carbon matrix. As also some fractions of the molecular centers of the precursor are preserved, the resulting product is sometimes assigned as pyrochelate.

**R(R)DE** Rotating (Ring) Disk Electrode. This technique is an electrochemical standard method; in this work, the measurements are performed to determine the catalytic activity towards the oxygen reduction in liquid oxygen-saturated electrolytes. Depending on the rotation rate, the diffusionlimited current changes. Measurements at different rotation rates enable the calculation of the kinetic current by using the Koutecky-Levich equation.

**Site density ( $S_p$ )** Number of active sites per volume of catalyst. For the calculation of site densities of Me-N-C catalysts, often two assumptions have to be made: (1) the density is similar to other carbonbased catalysts ( $0.4\text{ g/cm}^3$ ) and (2) each metal atom is related to an active site. In some cases, authors determine the exact mass density and/or number of active sites, so that the value becomes more accurate. In all other cases, it is usually overestimated as not all metal atoms are associated with active sites.

**Transition metal chalcogenides** A chemical compound which is composed of at least one chalcogen (O, S, Se, Te) anion and one or more transition metal cations.

**Turnover frequency (TOF)** The TOF gives the number of electrons which are transferred from the active site per site and second. Similar to the site density also here often assumptions have to be made.

## Definition of the Subject

More efficient energy conversion systems may help to reduce the use of fossil fuels and the emission of greenhouse gases. Polymer Electrolyte Membrane Fuel Cells are such devices which are of particular interest for automotive applications. Unfortunately, cost issues are still limiting the application of this technology in a highly competitive market. An important part of this is the inherently high cost of platinum which is commonly used as electrocatalyst. But recently, the replacement of platinum by NNMC has come into the focus of reach. The most promising approaches – comprising the use of crystalline phases and catalysts with molecular active centers – are described in this entry; limitations of both classes of materials are discussed.

## Introduction

Although platinum and platinum alloys are the state-of-the-art electrocatalysts for PEM fuel cell applications, the platinum loading required to reduce the effective overpotential of the oxygen reduction reaction at high current densities (1–2 A/cm<sup>2</sup>) to an acceptable level is still quite high for standard electrode structures (0.2–0.5 mg/cm<sup>2</sup>). Therefore, there have been many attempts to improve the dispersion of the nano-scaled platinum particles and to optimize the electronic states of the catalytically active platinum interface with the aim to increase the mass-related activities of the platinum catalysts.

Pt-alloys PtMe (Me = Cr, Mn, Co, Ni, V, Ti) were investigated early on, since they show an increased specific activity with respect to ORR [1, 2]. Enrichments and depletions of alloying metals on the particle interface were found, which influenced the electrochemical activity significantly. Predominant scientific success was achieved in the field of “Pt-monolayer catalysts” [3], the concept of “Pt-skin electrocatalysts” [4], and the concept of “unalloyed Pt bimetallic catalysts” [5].

Some authors report a rise in the mass specific activity of these catalysts by a factor up to 20 in

PEM fuel cells [6]. Considering the complex production methods, it remains a question to what extent this concept will effect a real cost reduction. Furthermore, it has to be proven to which extent these sub-nanometerstructured catalysts remain stable in an operating fuel cell under corrosive conditions. Commercial platinum catalysts already show a significant reduction of the active platinum surface especially under changing loading conditions during the long-term operation of a fuel cell due to dissolution and aggregation of Pt particles, which leads to a decline of the fuel cell efficiency [7, 8].

Further challenges remain unsolved concerning the ability of platinum to catalyze the oxidation of the carbon support and the poisoning of the platinum interface in the presence of traces of toxic gases such as CO or H<sub>2</sub>S, present in the environment, which arrive at the fuel cell via the cathodic air flow. It needs to be mentioned that novel research activities aim to operate the PEM fuel cells at higher temperatures (>100 °C, HT-PEM-FC) in order to obtain enhanced reaction kinetic and, therefore, higher efficiencies. However, due to the elevated temperature, the dissolution of platinum as well as the platinum-catalyzed carbon oxidation both will increase.

In spite of the success in the optimization of platinum catalysts, a major breakthrough in the field of fuel cells is yet to be achieved. Especially, the desire for a significant cost reduction by the replacement of platinum motivates international research activities investigating new catalyst concepts for cathodes. Thereby, the cathodes have to be sufficiently stable under fuel cell conditions; the alternative non-noble metal catalysts (NNMC) need to have a high selectivity for direct reduction of oxygen to water. The US department of energy (DOE) defined 25% of the achievable current density of a commercial platinum catalyst as target value for 2015. For fuel cell application, the catalysts should be producible in such a nano-structured form that suitable gas diffusion structures can be built.

Even if the numerous investigated non-noble material systems cannot yet fulfill all necessary demands, they do highlight new ways and principles in the electroreduction of oxygen, which

could become applicable after a further aim-oriented development of these groups of materials. In the next sections, a selection of NNMC will be presented, which constitute a promising potential due to their catalytic properties.

## Transition Metal Carbides, Nitrides, and Chalcogenides

As reported so far, one of the best platinum-free ORR catalysts of chalcogenide-type structure is a selenium-modified ruthenium catalyst ( $\text{RuSe}_x/\text{C}$ ) [9–20]. State-of-the-art catalysts are composed of carbon-supported nano-scaled ruthenium particles whose surface was modified with selenium [9–14]. The modification leads to 10 times higher ORR activity, protects the ruthenium particles against electrooxidation, and suppresses the  $\text{H}_2\text{O}_2$  formation. As  $\text{RuSe}_x/\text{C}$  is insensitive to methanol, it might be particularly suitable as an alternative cathode material in direct methanol fuel cells (DMFC) where platinum shows potential losses due to the methanol crossover [15–18]. However, ruthenium is still a costly and rare noble metal and seems not to be a feasible alternative to platinum. Therefore, readers who are interested in this type of catalyst are referred to the cited literature.

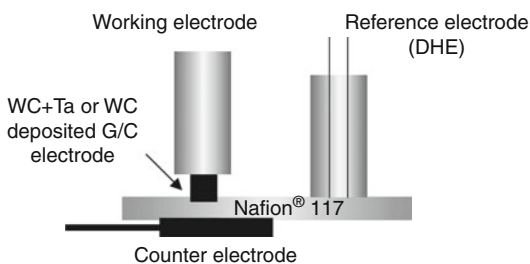
Because of a high electrical conductivity, transition metal carbides and nitrides are promising materials for electrocatalysis. Tungsten carbide has proven to possess platinum-like characteristics in terms of the valence band structure at the Fermi level and the chemisorption of oxygen and hydrogen [21–24]. Therefore, it was intensively investigated for the electrooxidation of hydrogen and methanol [25–28] as well as for the electro-reduction of oxygen. Mazza and Trasatti [29] studied several transition metal carbides (TMe: Ti, Ta, W) in sulfuric acid and selected WC as the most active material for the ORR among the others. However, tungsten carbide revealed poor corrosion stability in acidic electrolytes. More recent investigations on WC by Lee et al. [30] demonstrated that the stability and activity of these catalysts can significantly be increased by the addition of tantalum. They prepared pure WC

and WC + Ta layers onto glassy carbon substrates by RF-sputtering and analyzed the electrochemical behavior in a solid state cell with Nafion<sup>®</sup> 117 as an electrolyte (Fig. 1).

This solid state cell has the advantage that the experimental conditions are close to those in a PEM-FC compared to investigations in an  $\text{H}_2\text{SO}_4$  electrolyte of conventional electrochemical cells. CV measurements under  $\text{N}_2$  atmosphere of WC at 30 °C and 60 °C showed corrosion with an onset potential of about 0.5 V (DHE), attributed to an oxidation of WC to  $\text{WO}_3$  and  $\text{CO}_2$ . In contrast to this observation, the WC + Ta sample only showed very small anodic currents that points to a significant improved electrochemical stability at both 30 °C and 60 °C (Fig. 2). In voltammograms, the ORR onset potential of 0.45 V (DHE) for pure WC was shifted to 0.8 V (DHE) for the WC + Ta catalyst, pointing to an improved performance after.

Possibly motivated by the high chemical and mechanical stability of metal nitrides as wear- and erosion-resistant coatings [32], the ORR activity of metal nitrides (Me = W, Mo) was investigated by Zhong et al. [33, 34]. The authors prepared tungsten and molybdenum nitrides as cathode catalysts by the following procedure: In the first step, a carbon black (XC-72R) impregnated with an ammonium salt of the respective metal was calcinated (500 °C,  $\text{N}_2$ ). Subsequently, nitridation was performed by a temperatureprogrammed reaction under  $\text{NH}_3$  gas flow ( $T_{\text{final}} = 750$  °C and 700 °C for tungsten and molybdenum). X-ray diffraction (XRD) of the final conditioned materials revealed the formation of  $\beta\text{-W}_2\text{N}$  and  $\gamma\text{-Mo}_2\text{N}$  nano-crystals.

From CV measurements in 0.5 M  $\text{H}_2\text{SO}_4$ , the authors concluded a high stability of the  $\beta\text{-W}_2\text{N}/\text{C}$  catalyst under  $\text{N}_2$  atmosphere and determined an onset potential for ORR at about 0.6 V, which is inferior compared to the reference measurement with a commercial Pt/C catalyst (onset potential of 1 V (NHE), 20 wt% Pt/C, Johnson Matthey) (Fig. 3a). In PEM-FC measurements at  $T = 80$  °C, the  $\beta\text{-W}_2\text{N}/\text{C}$  and  $\gamma\text{-Mo}_2/\text{C}$  catalysts reached power densities of 39  $\text{mW}/\text{cm}^2$  ( $\beta\text{-W}_2\text{N}/\text{C}$ , Fig. 3b) and 65  $\text{mW}/\text{cm}^2$ , respectively. Both catalysts revealed a good stability within an



### Polymer Electrolyte Membrane Fuel Cells (PEM-FC) and Non-noble Metal Catalysts for Oxygen Reduction, Fig. 1

Schematic drawing of the solid state cell as used for the electrochemical measurements of WC and WC + Ta layers by Lee et al.; as counter electrode a platinum foil with platinum black was used. (The figure was taken from [30], reproduced with permission of Elsevier modification with tantalum). X-ray-induced photoelectron spectroscopy (XPS) evidenced that the WC + Ta material consisted of WC, a W-Ta alloy, TaC<sub>x</sub>, Ta and carbon (overall composition: W<sub>42</sub>Ta<sub>24</sub>C<sub>34</sub>). Among these components, the W-Ta alloy had the highest chemical stability in acidic solutions but exhibited no noteworthy ORR activity [31]. As a reason for the beneficial effect of tantalum, the authors considered that the W-Ta alloy protects the catalytically active WC-phase against corrosion that enabled the WC to reduce oxygen even at those potentials where electrooxidation was observed for the pure material

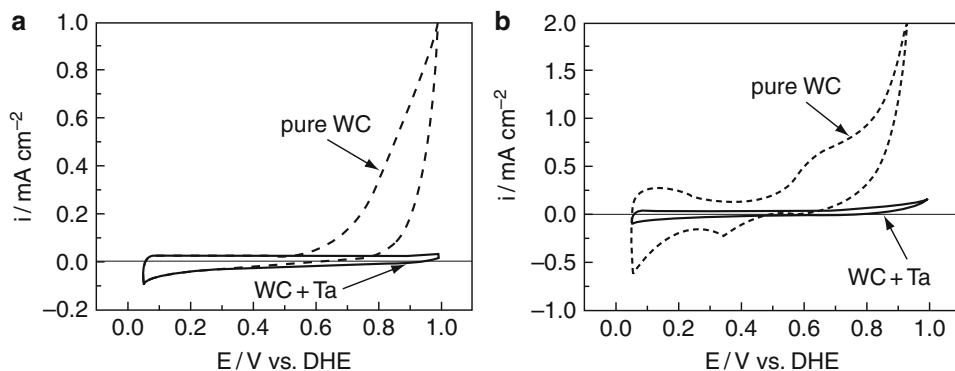
operating time of  $\geq 60$  h in galvanostatic tests (120 mA/cm<sup>2</sup> for  $\beta$ -W<sub>2</sub>N/C and 200 mA/cm<sup>2</sup> for  $\gamma$ -Mo<sub>2</sub>N/C, both at 80 °C).

A slightly higher performance in PEM-FC tests was reported by Atanasoski (3 M company) using a C-N<sub>x</sub>:Fe catalyst which had been prepared by vapor deposition onto a non-woven carbon support [35, 36]. They achieved 70 mW/cm<sup>2</sup> (0.1 A/cm<sup>2</sup> at 0.7 V, 75 °C, H<sub>2</sub>/air) and an open circuit potential of 0.9 V which is very close to that of platinum [35]. However, durability tests at 0.65 V revealed a decline of the catalyst's performance to below 10% of the initial value within 10 h. In order to improve the stability, other conductive materials like carbides, silicides, and nitrides were tested as substrates. A considerable improvement in the stability of the catalyst was found by using titanium carbide TiC. No noteworthy decrease of the fuel cell performance within 1,000 h of operation was observed. This remarkable result points out that the interaction between the support and the catalytic sites could be a very crucial factor for

the optimization of catalysts. Concerning the structure of the catalytically active centers in the C-N<sub>x</sub>:Fe catalyst, Atanasoski et al. [36] concluded from Extended X-ray Absorption Fine Structure (EXAFS) analysis and Ultraviolet Photoelectron Spectroscopy (UPS) that the iron atoms are coordinated to nitrogen very similar to the FeN<sub>x</sub>/C (x = 2, 4) centers which had been detected in pyrolyzed transition metal macrocycles [37–42]. Such pyrolyzed macrocycles and related materials are currently the most active catalysts among all noble metal-free catalysts and will therefore be described in detail in section “Catalysts Prepared by Carbonization of Macrocycles” of this contribution.

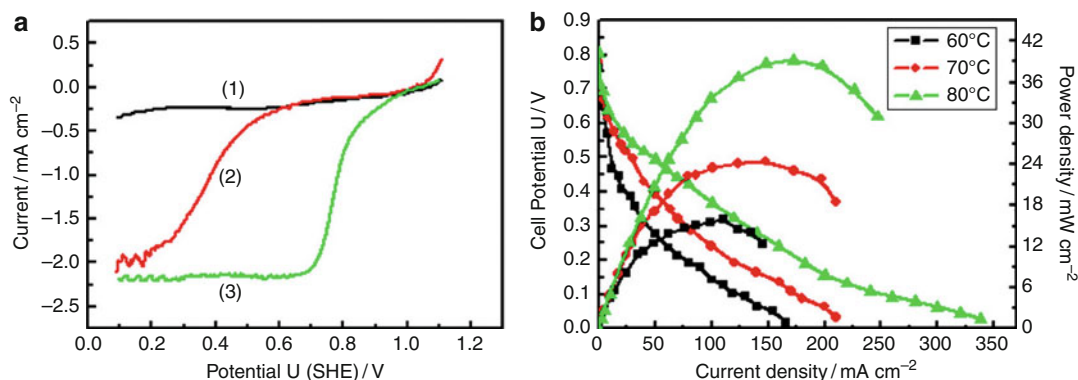
Following the idea of pyrolyzed macrocycles, indeed a heat treatment of the vapor-deposited layers at 650 °C led to a significantly improved ORR activity. The authors correlated this to an increased atomic order and by the introduction of a second coordination shell around the Fe atom. Similar results have been reported for iron carbon nitride layers prepared by magnetron sputtering in a combinatorial approach [43]. However, the activities are still below that of state-of-the-art pyrolyzed macrocycles. Nevertheless, these explorative works might disclose a new way to prepare similar high catalytically active structures like those known from pyrolyzed macrocycles.

Already in the 1970s, numerous transition metal oxides of perovskite- and spinel-type structure showed promising results for oxygen reduction in alkaline electrolyte; however, only moderate activities and stabilities could be achieved in acidic media. Thus, the interest to use this class of materials for the PEM-FC was nearly abandoned. In 2007, Ota's group investigated metal oxides of type Me<sub>x</sub>O<sub>y</sub> for Me = Zr, Ti, Nb, Co, Sn, deposited as thin layers by reactive magnetron sputtering on glassy carbon substrates [44]. Significant activities toward ORR in strong acidic media were found for zirconium oxide ZrO<sub>2-x</sub> with an onset potential of about 0.64 V (NHE) followed by oxides in the sequence Co<sub>3</sub>O<sub>4-x</sub> (0.26 V) > TiO<sub>2-x</sub> ≈ SnO<sub>2-x</sub> (0.24 V) > Nb<sub>2</sub>O<sub>5-x</sub> (0.14 V). From CV measurements (N<sub>2</sub>-saturated 0.1 M H<sub>2</sub>SO<sub>4</sub> at 30 °C), the authors concluded a sufficiently high electrochemical stability for all oxides in the potential



**Polymer Electrolyte Membrane Fuel Cells (PEM-FC) and Non-noble Metal Catalysts for Oxygen Reduction, Fig. 2** Cyclic voltammograms on Nafion electrolyte

under  $N_2$  atmosphere, scan rate  $100 \text{ mV s}^{-1}$ , measurements were performed at  $30 \text{ }^\circ\text{C}$  (a) and  $60 \text{ }^\circ\text{C}$  (b). (The figures were taken from [30], reproduced with permission of Elsevier)



**Polymer Electrolyte Membrane Fuel Cells (PEM-FC) and Non-noble Metal Catalysts for Oxygen Reduction, Fig. 3** Cyclic voltammograms (a) for a  $W_2N/C$  (43 mg  $W_2N$ ) in the  $0.5 \text{ M H}_2\text{SO}_4$  solution saturated with nitrogen (1) and oxygen (2), respectively. For reasons of comparison, the linear scan of a 20% Pt/C catalyst

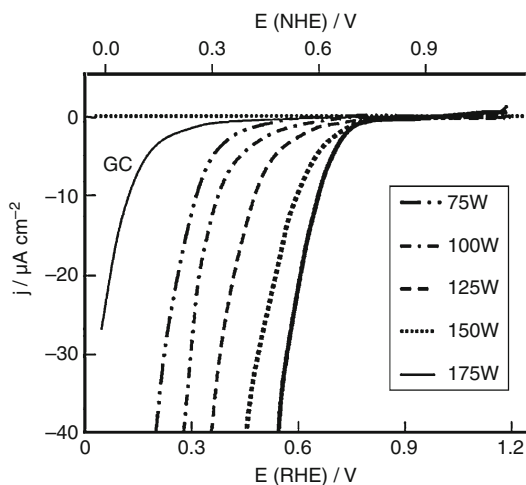
(12 mg Pt) in oxygen-saturated solution is given (3), all measurements were performed with a scan rate of  $5 \text{ mV s}^{-1}$  and at  $T = 25 \text{ }^\circ\text{C}$ . In (b), polarization curves as obtained at different temperatures using a  $W_2N/C$  catalyst (18% W) as cathode material are shown. (Figures were taken from [33], reproduced with permission of Elsevier)

range from 0.65 to 0.85 V (1.15 V for  $ZrO_{2-x}$ ), except for  $Co_3O_{4-x}$ . For  $ZrO_{2-x}$ , it was found that with increasing RF-power, the onset potential of the ORR current is shifted to more positive potentials, reaching 0.88 V (NHE) at 175 W RF-power (Fig. 4) [45]. From XPS analysis, the authors concluded that the increased amount of oxygen defects at the surface of the partially reduced  $ZrO_{2-x}$  ( $x = 0.15$ ) might serve as adsorption sites for oxygen, enhancing the ORR activity. Surface defects are discussed by many researchers to be responsible for the adsorption of oxygen molecules on metal oxide surfaces [46–48]. Additionally, the increasing number of defects could be

responsible for the observed decrease in the ionization potential and the increase in the conductivity of the n-type material with increasing RF-power.

On studying  $TiO_2$  layers, an increasing ORR activity was correlated with an increasing fraction of rutile crystallites characterized by a (110) face habit leading to a decreasing ionization potential of the layers [49]. All these investigations have proven that the catalytic activity of the oxides is dependent on the crystal structure and the degree of crystallinity as well as on the electronic structure at the interface. Unfortunately, no information on the selectivity of the catalysts in the ORR was given. Mentus found on anodically oxidized





**Polymer Electrolyte Membrane Fuel Cells (PEM-FC) and Non-noble Metal Catalysts for Oxygen Reduction, Fig. 4** Potential – current curves of glassy carbon (GC) and  $ZrO_{2-x}$ -layers deposited at different RF-power (as given in the figure caption) in  $O_2$ -saturated 0.1 M  $H_2SO_4$  at 30 °C (scan rate: 5  $mVs^{-1}$ ). (The figure was taken from [45], reproduced with permission of Elsevier)

Ti nanorods that in an acidic electrolyte, oxygen is predominantly reduced via a two-electron transfer pathway while in alkaline electrolytes, a four-electron transfer pathway is preferred [50]. Until now, the observed catalytic activities of these single metal oxides are smaller compared to Pt/C catalysts. Nevertheless, in contrast to Pt/C, these materials show no mixed potentials in the presence of methanol, which could make them attractive for an application in the Direct Methanol Fuel Cell (DMFC).

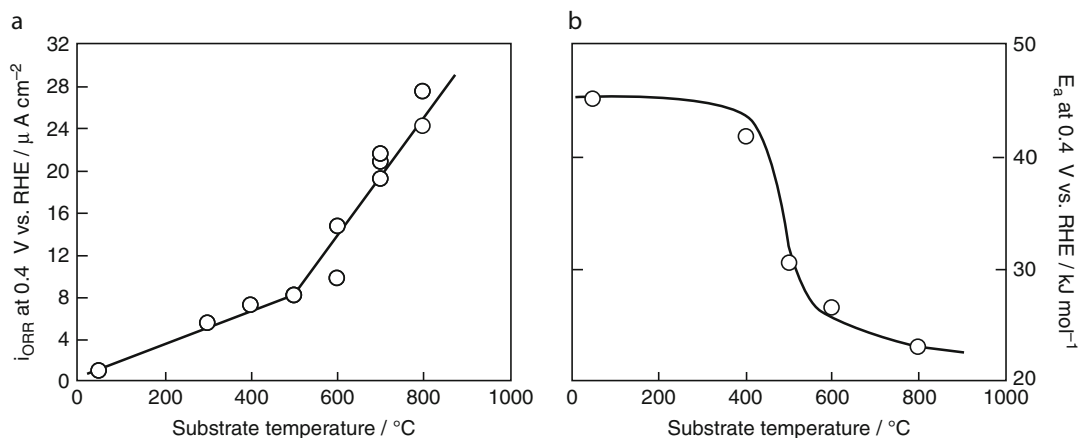
Based on the results with metal oxides and nitrides, research on the catalytic behavior toward ORR of metal oxynitrides has been intensified in the last few years. Nitrides and oxynitrides of subgroup IV and V elements have been intensively investigated as photo-catalysts for water oxidation showing remarkable stabilities and electrochemical activities in acidic electrolytes [51, 52]. Due to their partly high metal d-band concentration at the Fermi level, these materials might also be promising as ORR catalysts.

PEM-FC tests with carbon-supported zirconium oxide  $ZrO_2$  and zirconium oxynitrides  $ZrO_xN_y$  as cathode catalysts have been reported

by Liu et al. [53]. Although the maximum power density of the cell reached only one tenth of a Pt/C reference, the beneficial effect of the nitrogen incorporation into the  $ZrO_2$  lattice on the ORR activity has been clearly demonstrated. Furthermore, a good stability of the nitrogen-modified catalysts can be observed even at operation temperatures of 80 °C. Zirconium oxynitrides have also been investigated in detail by Ota's group [54, 55]. Thin layers were prepared by RF-magnetron sputtering onto heated glassy carbon substrates. As shown in Fig. 5, they observed a strong influence of the substrate temperature on the ORR activity. Up to 500 °C, a moderate increase of activity was observed, whereas at higher substrate temperatures, the enhancement was accelerated much stronger (Fig. 5a). This shift in activity increase was attributed to a decrease of the overall activation energy of the ORR at 500 °C from 42 to about 22  $KJ mol^{-1}$  (Fig. 5b); a change in the adsorption enthalpy of  $O_2$  is assumed to be responsible for the change in the activation energy [54]. In accordance with Yeager's group [56], they proposed that the rate-determining step can be attributed to a dissociative adsorption of oxygen, remaining unchanged at approximately unity over the complete investigated temperature range.

Furthermore, the ionization potential can be decreased by introducing nitrogen into monoclinic  $ZrO_2$ . However, the nitrogen concentration detected in samples annealed at 800 °C was relatively small ( $ZrO_{1.7}N_{0.2}$ ). Similar to Liu's observations [53], CV measurements in 0.5 M  $H_2SO_4$  at 30 °C gave no hint on any electrochemical corrosion of  $ZrO_xN_y$ . For the most active  $ZrO_xN_y$  sample, deposited at a substrate temperature of 800 °C, an onset potential for the ORR of about 0.7–0.8 V was stated. More recently, an onset potential of even 0.9 V had been reported for a ZrOCN catalyst which had been prepared by oxidation of ZrCN (potentials with respect to NHE) [55].

It is interesting to compare zirconium oxynitride ( $ZrO_xN_y$ ) with tantalum oxynitride ( $TaO_xN_y$ ), which was investigated by Ishihara et al. [57]. The authors reported a remarkable chemical and electrochemical stability for  $TaO_xN_y$  in 0.1 M  $H_2SO_4$  at 30 °C, that was attributed to the



**Polymer Electrolyte Membrane Fuel Cells (PEM-FC) and Non-noble Metal Catalysts for Oxygen Reduction, Fig. 5** Relationship between the ORR current density at 0.4 V (RHE) (a) and the activation energy (b), both

with respect to the substrate temperature for sputtered zirconium oxynitride thin films. (The figures were taken from [54] (Figs. 6 and 10); reproduced by permission of ECS – The Electrochemical Society)

fact that in this oxide, tantalum is present in the highest possible oxidation state  $\text{Ta}^{5+}$  [57].

The material was prepared by nitridation of a  $\text{Ta}_2\text{O}_5$  powder in  $\text{NH}_3$  atmosphere. The reaction product consisted of a non-stoichiometric  $\text{TaO}_x\text{N}_y$  (highest activity for  $x = 0.92$  and  $y = 1.05$ ) that reached a similar high onset potential as  $\text{ZrO}_x\text{N}_y$  of about 0.8 V (NHE) in 0.1 M  $\text{H}_2\text{SO}_4$ . From XRD measurements, it was concluded that the films consisted of a mixture of  $\text{Ta}_3\text{N}_5$  and  $\beta\text{-TaON}$ . The authors excluded ORR activity for  $\text{Ta}_2\text{O}_5$  and  $\text{Ta}_3\text{N}_5$  and concluded that the  $\beta\text{-TaON}$  which crystallizes in the same structure (monoclinic) as  $\text{ZrO}_2$  is responsible for the catalytic activity. On the basis of this result, one might assume that the monoclinic  $\text{ZrO}_2$  structure type has a promoting effect toward the ORR. On the other hand, in a more recent work, the authors showed good ORR activity (onset potential  $\approx 0.8$  V [RHE], type of electrolyte not mentioned) for  $\text{Ta}_2\text{O}_5$  which had been grown onto TaCN by a slight oxidation under low oxygen pressure of  $10^{-5}$  Pa at 1,273 K [58]. By using an adopted conversion electron yield x-ray absorption method (CEY-XAS), they concluded that oxygen vacancies are likely to be responsible for the ORR activity as stated by other groups (see above).

In a recent paper, Domen et al. introduced the use of an arc-plasma gun technique in a controlled

$\text{O}_2/\text{N}_2$  atmosphere for the preparation of niobium (oxy) nitride catalysts onto carbon blacks [59]. They showed that this technique leads to finely dispersed particles in the nanometer and sub-nanometer range which show excellent activity for the ORR compared to other non-noble metal catalysts (ORR onset potential at 0.8 V (NHE) in 0.1 M  $\text{H}_2\text{SO}_4$ ). Also here, oxygen vacancies or reduced sites in the  $\text{Nb}_2\text{O}_5$  phase were proposed to be responsible for the ORR activity. Highest ORR onset potentials were observed for a  $\text{N}:\text{Nb}_2\text{O}_5$  catalyst (0.86 V (RHE)) which was sputtered in a reactive gas composition of  $\text{N}_2/\text{O}_2 = 3:1$ . A further increase of the nitrogen concentrations led to the formation of less active oxynitride or nitride phases whereas lower nitrogen ratios produced less active niobium oxide ( $\text{Nb}_2\text{O}_5$ ) phases. As no nitrogen could be detected by XPS in the most active  $\text{N}:\text{Nb}_2\text{O}_5$  material, only small amounts of nitrogen are obviously causing the promoting effect by doping or by forming defects in the crystalline  $\text{N}:\text{Nb}_2\text{O}_5$  phase. The high deposition rate of this technique enables the rapid synthesis of highly dispersed catalysts onto high surface area substrates that is necessary for an application in fuel cells [59].

In a further paper, they reported on another alternative preparation method called polymerized complex method (PC) for niobium oxynitride

supported on carbon (Nb-O-N/CB). The preparation involves the addition of carbon black (CB) during the polymerization process followed by nitridation in ammonia [60]. Such catalysts showed significantly enhanced ORR activity and also a better distribution and homogeneity of the catalyst's nanoparticles compared to a material prepared via conventional impregnation method. They attributed this effect mainly to an improved electrical contact of the catalytic active sites to the carbon substrate [60]. Obviously the use of N<sub>2</sub> instead of O<sub>2</sub> during the required heat treatment step allows the carbonization of organic precursor material which is favorable for contacting the catalyst's particles to the carbon support. Corresponding to this thesis, the authors found improved ORR current densities with increasing heat treatment temperature, probably because of an improved graphitization process.

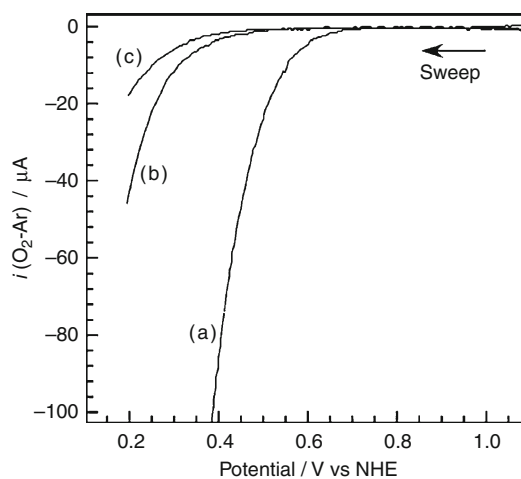
A further doping of the Nb-O-N/CB catalyst with barium led to a considerable increase of the ORR activity by a factor of about 100 at 0.4 V (NHE) compared to the barium-free sample (Fig. 6). RRDE measurements revealed no H<sub>2</sub>O<sub>2</sub> production at potentials positive of 0.25 V (NHE), what points to a direct reduction of O<sub>2</sub> to water (four-electron pathway). Based on XRD, the authors found an increased fraction of niobium oxide Nb<sub>2</sub>O<sub>5</sub> crystallites after adding barium to the precursor. This result was confirmed by XPS where in the Ba-Nb-O-N/CB samples, an increased signal of niobium in the oxidation state Nb<sup>5+</sup> instead of Nb<sup>4+</sup> had been detected. Therefore, the authors supposed local niobium Nb<sup>5+</sup> structures close to barium atoms to be responsible for the promoting effect of the ORR activity [60].

As the examples above show, it should be pointed out that it is difficult to compare the different catalytic materials because not only the intrinsic activity but morphological parameters such as particle size, particle distribution, or electronic coupling to the substrate also play an important role in the observed activities. It has to be expected that most of the materials investigated so far can be remarkably improved in catalytic efficiency by optimizing these parameters.

## Non-noble Metal Catalysts with Molecular Centers

Already in 1964, Jasinski demonstrated that different metal phthalocyanines (Me: Co, Pt, Ni and Cu) can act as oxygen reduction catalysts in alkaline media [61]. During the following years, it was confirmed that several metallomacrocycles can act as ORR catalysts even in acidic environment. Later, it was found that pyrolysis leads to enormous improvements of the ORR activity even if instead of macrocycles, cheaper and less complex precursors are used [62, 63]. This will be discussed in detail in the section "Alternative Center Generation during Heat Treatment."

The current densities and stabilities of macrocycles are insufficient for fuel cell applications; nevertheless, due to their well-defined molecular structure, they are useful as model systems in order to get a better understanding of the factors that might cause the high oxygen reduction ability of the Me-N-C catalysts prepared via pyrolysis.



**Polymer Electrolyte Membrane Fuel Cells (PEM-FC) and Non-noble Metal Catalysts for Oxygen Reduction, Fig. 6** ORR voltammograms for (a) Ba-Nb-O-N/CB composit catalyst; (b) the Ba-free Nb-O-N/CB catalyst, and (c) bare CB. All materials were prepared by two heating steps (N<sub>2</sub> at 773 K, NH<sub>3</sub> at 1123 K). Measurements in oxygen- and argon-saturated 0.1 M H<sub>2</sub>SO<sub>4</sub> were performed with a sweep rate of  $-5 \text{ mV s}^{-1}$ , the vertical axis ( $i_{(\text{O}_2-\text{Ar})}$ ) denotes the difference in current under O<sub>2</sub> and Ar atmospheres. (The figure was taken from [60], reproduced by permission of ECS – The Electrochemical Society)

Therefore, this chapter will first summarize the most important factors that affect ORR activity of non-pyrolyzed macrocycles.

### Non-pyrolyzed Macrocycles

In nature, numerous redox and transport processes are associated with metallomacrocycles. As an example, FeN<sub>4</sub>-centers of hemoglobin are responsible for the transport of oxygen in blood. In this particular case, oxygen binds reversibly to the FeN<sub>4</sub>-unit. Besides the binding, reduction of oxygen to water requires a multielectron transfer and the reaction with protons. Therefore, (1) all intermediate products have to be bonded strongly (but reversibly) enough to the metal center and (2) the final product of water should only have a weak bonding so that the centers are not blocked and can continue to participate in the reduction process.

The reactivity of a macrocycle will depend on the energetic position of its highest occupied molecular orbital (HOMO<sub>Macrocycle</sub>) related to the lowest unoccupied molecular orbital of the oxygen molecule (LUMOO<sub>2</sub>). A narrow gap between both will make it reactive while a larger gap stabilizes the complex [64, 65].

Jahnke et al. investigated various macrocycles, characterized by different ligands such as nitrogen, oxygen, and sulfur (Me-N<sub>4</sub>, Me-S<sub>4</sub>, Me-O<sub>4</sub>, Me-N<sub>2</sub>O<sub>2</sub>, Me-N<sub>2</sub>S<sub>2</sub>), each under the same experimental conditions. For iron and copper, highest kinetic current densities were found if the metal center was fourfold coordinated by nitrogen (FeN<sub>4</sub> and CuN<sub>4</sub> centers); in the case of cobalt, the so-called Pfeiffer complex with a CoN<sub>2</sub>O<sub>2</sub>-center enabled the best results [62]. If oxygen or sulfur were the only ligands, the complexes were not or only poorly active toward oxygen reduction for all investigated metal centers.

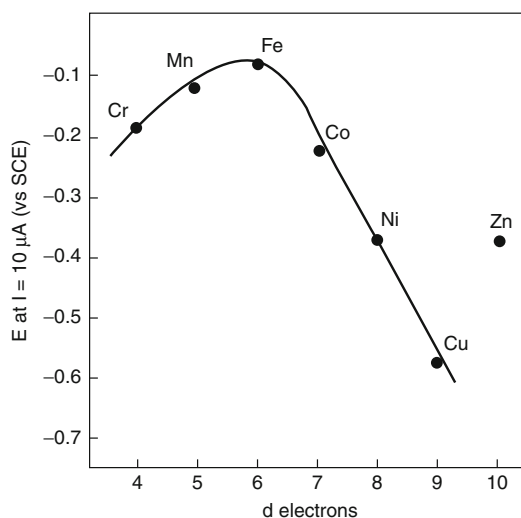
Due to their low electric conductivity, macrocycles were usually impregnated on a conducting substrate, in most cases on a carbon black. Besides electron conductivity, also the active surface area is increased by the impregnation. It was found that quinone and/or carboxyl groups on the carbon surface interact electronically with the metal centers of the macrocycles. This was supposed to enhance the electronic coupling of oxygen toward

the active MeN<sub>4</sub>-site enabling higher ORR activities [66, 67]. Indeed, with Mössbauer spectroscopy, Melendres was able to confirm that due to interaction with the carbon support, Mössbauer parameters of iron phthalocyanine (FePc) were changed confirming the different electronic structures of such interacting FeN<sub>4</sub>-centers in comparison to FeN<sub>4</sub>-sites in pure FePc [68].

An oxygen reduction ability was described for MeN<sub>4</sub>-complexes with Fe<sup>2+</sup>, Fe<sup>3+</sup>, Co<sup>2+</sup>, Ni<sup>2+</sup>, Mn<sup>2+</sup>, Ru<sup>2+</sup>, Cu<sup>2+</sup>, and Zn<sup>2+</sup> as central ion [62, 64, 66, 67, 69–78].

Best results were found for iron, but also for cobalt, manganese, and nickel [62, 67, 79], which was explained by the 3d electron orbital occupation. It was proposed that MeN<sub>4</sub>-centers with 3d<sup>6</sup> configuration should enable the best oxygen reduction ability [65, 77]. The related volcano plot is given in Fig. 7.

The nature and number of macrocycle substituents and axial ligands are both influencing the electron density at the metal center, leading to variations of the oxidation and/or the spin state and the electron donor capacity of the complex



**Polymer Electrolyte Membrane Fuel Cells (PEM-FC) and Non-noble Metal Catalysts for Oxygen Reduction, Fig. 7** Volcano plot depicting the ORR onset potential of different bivalent Me(II)-TSPs for the oxygen reduction in alkaline media as a function of the number of d electrons (TSP denotes tetrasulphonatophenylporphyrin), the figure was taken from [65], reproduced with permission of Elsevier

[64, 80–84]. It was shown by STM that macrocycles with a fully occupied  $3d_z^2$  orbital are nearly ORR inactive. For the binding of oxygen, this orbital should be either empty or only partially filled [78].

Concentrating on complexes with the same metal center, it was shown that the intensity of backbonding to the complex is related to the ORR activity. As a measure for the strength of backbonding, the position of the  $\text{Co}^{3+}/\text{Co}^{2+}$  redox peak was used, i.e., depending on the macrocycle substituents, the redox peak position was shifted in the CV diagrams, the higher the redox potential the higher the kinetic current density was [85, 86].

The electron donor properties of the metal centers are affected by the type of substituents. Donating groups like phenyl or methoxy groups cause an increase of the electron density at the metal center whereas electron-withdrawing groups like sulfinyle have no or even a negative effect [62]. Induced by a higher electron density on the metal center, the oxygen molecule can be more easily activated enabling higher ORR activities [77, 87, 88].

In general, the macromolecular structure enables an extended system of conjugated  $\pi$ -electrons that provides electrons, making multi-electron transfer processes even on monomolecular centers possible. Experimentally, a direct reduction of oxygen to water was confirmed for iron and manganese  $\text{N}_4$ -macrocycles [65, 67, 79, 88–91]. For non-pyrolzsed cobalt complexes with single  $\text{CoN}_4$ -centers, only a two-electron reduction to hydrogen peroxide is possible. However, in 1980, it was shown that the so-called face-to-face dicobalt-porphyrins can catalyze a direct reduction of oxygen to water [92]. It was proposed that the oxygen molecule binds to two  $\text{CoN}_4$ -centers in a trans-configuration, which was suggested as bimolecular center even for pyrolyzed materials [92–97].

The formation of  $\text{H}_2\text{O}_2$  is crucial for the stability of such complexes. Hydrogen peroxide initiates a weakening or even breaking of the bonds between the tetrapyrrole core and the substituents. The resulting smaller electron donor capacity will cause a decrease of ORR activity [41, 85, 98]. On the other hand, metal ions especially in strong

acidic solutions can be removed from the tetrapyrrole core by leaching. It was observed that such demetallation is a further reason for a decreased activity [71, 99–101]. As discussed in the following, both activity and stability can be enhanced by a heat treatment.

### Molecular Centers in Carbonized Materials

In 1976, it was demonstrated that the catalytic activity and stability of carbon-supported macrocycles can be enhanced significantly by a heat treatment [62, 69]. Since the 1980s, it is known that after pyrolysis, some of the metal species formed can be dissolved in acidic solution [41, 42, 63, 71, 79, 98, 102–106]. The remaining  $\text{MeN}_4$ -centers must either reduce oxygen with a higher turnover frequency or other, more active sites (e.g., N-C-sites) have to be formed. Until now, it is still under debate whether the  $\text{MeN}_4$ -centers become more active or whether the released metal acts as catalyst during the heat treatment for the formation of a certain active carbon structure (e.g., N-C-sites). It should also be noted that more than one type of catalytic center might be present in the catalysts. Possibly, both  $\text{MeN}_4$ -centers and metal-free N-C-sites could act as centers for the reduction of oxygen.

In the following, the literature will be discussed separated according to the author's assignment of active site constitution. Hence, one will also find certain metal-containing catalysts, but where the activity was assigned to N-C-sites, already discussed in the following section.

### Carbon-Based Materials with Carbon and/or Nitrogen Sites as Active Centers

It is known that the efficiency of catalysts is not only a function of the kind of active site, but also dependent on the constitution of the carbon support, that will influence the overall electronic properties of the catalyst material [96, 107–109]. For platinum-based catalysts, it was shown that by nitrogen doping of the carbon support, the platinum particles are stronger linked to the support material compared to the not-modified carbon. The resultant smaller particles with a more homogeneous distribution enabled higher

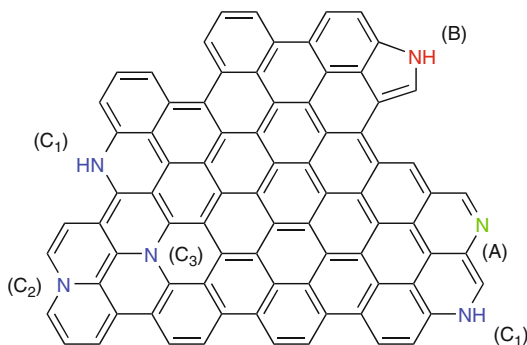


ORR activity and an improved long-term stability [107, 110].

However, beside the function as a catalyst support, it was reported that nitrogen-doped carbon itself can be active as a metal-free catalyst for the ORR. The nitrogen atoms will (1) change the electronic character of the carbon and (2) the obtained defect structure (in comparison to the inert surface of graphene sheets) might enable an easier adsorption of oxygen and a subsequent reduction to water or hydrogen peroxide.

In 2000, Strelko et al. published theoretical calculations of the electronic character of carbon related to the integration of nitrogen, phosphorous, and boron heteroatoms [111]. In the first step, they investigated the electronic changes that depended on different positions of these atoms in the carbon matrix (i.e., pyridinic, pyrrolic, graphitic). As an example, a scheme of a graphene layer with the different type of nitrogen atoms is given in Fig. 8.

While pyridinic nitrogen atoms only contribute one electron to the  $\pi$ -electron system of the carbon, pyrrolic and graphitic nitrogen atoms increase the  $\pi$ -electron density as they contribute



**Polymer Electrolyte Membrane Fuel Cells (PEM-FC) and Non-noble Metal Catalysts for Oxygen Reduction, Fig. 8** Different types of nitrogen atoms incorporated in a graphene plane. Pyridinic nitrogen atoms (A) only contribute with one electron to the  $\pi$ -electron system of the carbon matrix while pyrrolic (B) and graphitic nitrogen atoms (C) contribute by two electrons. Graphitic nitrogen atoms can be bonded in one  $C_6$ -ring ( $C_1$ ), or between two ( $C_2$ ) or three ( $C_3$ )  $C_6$ -rings, respectively. (The figure was adapted from Figs. 3, 4, 5, 6, and 7 of [112], Südwestdeutscher Verlag für Hochschulschriften)

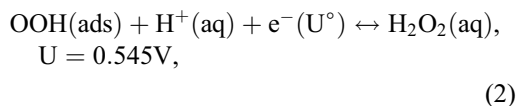
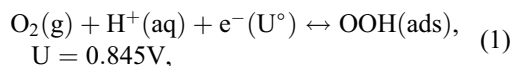
two electrons. Therefore, pyridinic atoms (N, P, B) should be insensitive to an improvement of the electron donor properties of the carbon. For pyrrolic and graphitic nitrogen heteroatoms, a lowering of the graphene bandgap had been calculated, enhancing the electron donor capacity in the order of  $B < N < P$  [111].

It was first stated by Wiesener that electronically modified carbon itself can act as oxygen reduction catalyst [102]. He measured ORR activity after heat treatment of  $MeN_4$ -chelates (without acid leaching). As during long-term measurements, some of the metals were dissolved without significantly affecting the ORR activity, he concluded that the metal could not be a part of active sites but catalyzes the formation of certain active N-C-sites during the heat treatment [98, 102]. Later other authors also assigned the observed ORR activity to the presence of graphitic or pyridinic N-C-sites in carbon-based materials [113–119].

The behavior of graphitic nitrogen atoms integrated in carbon was systematically investigated by Sidik et al. [120]. The catalysts were prepared starting from the soot Ketjen Black EC 300 J, which was treated in HCl and  $HNO_3$  to remove metallic impurities and then heat-treated in  $NH_3$  at  $900^\circ C$ . Induced by nitridation, ORR activity was increased but the high concentration of hydrogen peroxide that was formed (75%  $H_2O_2$  at  $U = 0.3 V$ ) indicated a predominant two-electron transfer process for this material. At higher overpotentials,  $H_2O_2$  production decreased, which was explained by an ORR process leading to water formation via two two-electron transfer processes. Cluster calculations were performed modeling the nitridation of the basal plane sheet of graphite by substitution of carbon by nitrogen atoms. For carbon atoms at different positions in the graphene sheet, the adsorption energies of reaction intermediates related to ORR were calculated as pointed out in Fig. 9.

On the basis of their calculations, the authors concluded that it is most likely that the oxygen reduction should take place on carbon atoms adjacent to in-plane N-atoms (position a in Fig. 9). With respect to the calculated potentials, for a two-step reduction





especially, the second value was in good agreement with their experimental observation of an onset potential of 0.51 V (NHE). Therefore, this work evidences in experiment and theory that carbon doped with graphitic nitrogen indeed is able to reduce oxygen, but only via a two-electron pathway, to hydrogen peroxide at low onset potentials [120].

Table 1 summarizes further attempts to prepare metal-free catalysts for the ORR. Some of these materials were formed by a heat treatment of nitrogen-rich organic precursors (lines 1–2, 6); others are carbon blacks which had been heat-treated in a reactive nitrogen-rich atmosphere at appropriate temperatures (No. 4–5 in Table 1). The highest nitrogen concentration is found for carbon nitride (line 1), in which both graphitic and pyridinic nitrogen atoms have been found. Due to its good electrochemical stability, carbon nitride C<sub>3</sub>N<sub>4</sub> has gained interest for several catalytic applications [109, 121–123]. As this material exhibits the largest concentration of nitrogen known for N-C-based materials, it was also suggested to be of interest for the ORR. Lyth et al. investigated the electrochemical reduction of oxygen on C<sub>3</sub>N<sub>4</sub> which was prepared by the reaction of cyanuric chloride with sodium azide (in benzene) at 220 °C [122]. The achieved catalytic activity was only slightly better compared to pure carbon black. However, after impregnation of C<sub>3</sub>N<sub>4</sub> onto the same carbon black (50/50 C<sub>3</sub>N<sub>4</sub>/CB, CB not further specified), an enhanced ORR activity was observed. The increased kinetic current density might be related to a higher active surface area and/or an improved electronic conductivity (compare Table 1, No. 1). The authors assigned the catalytic activity which was highest after a 1,000 °C pyrolysis to graphitic nitrogen atoms [123]. In contrast to Wiesener [98, 102], they did not observe an improved formation of

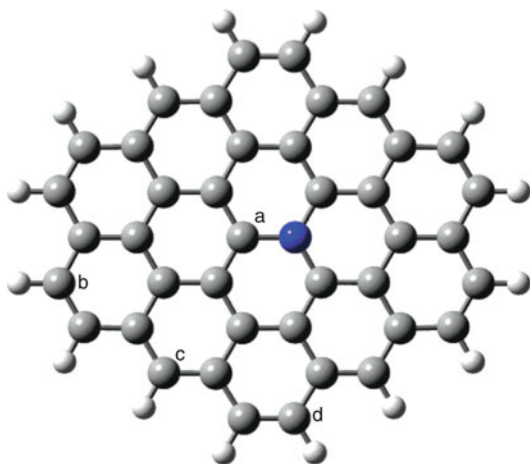
catalytically active graphitic sites by integration of iron during the heat treatment.

Nabae et al. [124] pyrolyzed iron phthalocyanine mixed with phenolic resin (FePc/PhR) in inert gas at different temperatures, each for 5 h, and found best catalytic activity toward ORR at 600 °C. A comparison to metal-free H<sub>2</sub>Pc/PhR reference samples, as shown in Fig. 10 (a: H<sub>2</sub>Pc/PhR, b: FePc/PhR), evidenced significant higher current densities and higher onset potentials for the samples prepared with iron phthalocyanine.

Similar to earlier works [104, 128], the authors observed an increased concentration of nitrogen in the carbon structure for the iron-containing catalysts. They attributed the metal species to be more important in the enrichment of nitrogen rather than in participation in the ORR [124].

Matter et al. [129] and Maldonado and Stevenson [116] attributed the catalytic activity to pyridinic nitrogen atoms at edge-planes of “cub-stacked carbon nanotubes” [129] and carbon nanofibers [116], respectively. The authors proposed that the present metal only enhances the integration of active pyridinic nitrogen atoms.

In order to achieve a high concentration of pyridinic nitrogen atoms – without the presence of any metal source – phenanthroline was pyrolyzed in the presence of ammonium oxalate (Table 1, No. 6) [127]. The oxalate-supported pyrolysis was established for transition metal macrocycles [130–133] (compare section “Catalysts Prepared by Carbonization of Macrocycles”), but works also for metal-free phenanthroline as first shown by Herrmann et al. [134]. If ammonium oxalate is pyrolyzed together with phenanthroline, only a low active carbon-based material was obtained [127]. When the ammonium oxalate was replaced by an ammonium iron oxalate, however, a highly active catalyst was yielded whose onset potential (at 0.1 mA/cm<sup>2</sup>) was shifted to significantly higher values compared to even the best metal-free catalyst of Table 1 (U = 0.8 V compared to 0.5 V). For this iron-containing catalyst, RRDE measurements revealed a predominantly direct reduction of oxygen to water. In this case, however, the much higher activity of the



**Polymer Electrolyte Membrane Fuel Cells (PEM-FC) and Non-noble Metal Catalysts for Oxygen Reduction, Fig. 9** Model cluster used for the calculation of absorption energies on (graphitic) nitrogen-doped carbon. The calculations were performed for carbon atoms at different electronic positions in the N-doped graphene plane as indicated by the letters a, b, c, and d. (The figure was taken from [120], reproduced with permission of the American Chemical Society)

Me-containing catalyst was attributed to the presence of  $\text{FeN}_4$ -centers [127].

This finding is in accord with theoretical calculations by Kurak and Anderson [135]. Using the VASP code, the authors estimated the extent to which oxygen reduction can take place on carbon, doped with pyridinic nitrogen atoms. Similar to the experimental observation, nitrogen atoms bonded near an edge of a graphene plane magnify the reactivity toward bonding radical molecules in the first step. The strong binding, however, would make large overpotentials necessary in order to enable ORR (often 1.8 V, i.e.,  $U_{\text{onset}} = -0.6$  V). Only for one specific configuration which is shown in Fig. 11, an onset potential of 0.695 V was determined, but only with hydrogen peroxide as product.

The related electron transfer mechanism for the reduction to hydrogen peroxide is shown in Fig. 12. The authors concluded that there are no evidences for a direct reduction to water, but that the integration of transition metals might enhance the catalytic interaction to enable the four-electron transfer process [135].

Liu et al. prepared catalysts by a multistep preparation [115]. In the first step on either carbon or silica supports, metal complexes were formed by the reaction of  $\text{Co}(\text{NO}_3)_2$  and  $\text{FeSO}_4$  with ethylenediamine. These precursors were heat-treated twice at 800 °C in inert gas whereas after the first pyrolysis, an acid leaching was performed in order to remove soluble metal species. The authors came to the conclusion that in the surface region accessible for ORR, all metal-containing species should have been removed and could therefore be excluded as components of any active sites. The presence of any  $\text{FeN}_4$ -centers, stable in acidic solution, was excluded, in the first place. XPS confirmed the presence of pyridinic and graphitic nitrogen atoms. The authors proposed both to be catalytically active whereas pyridinic nitrogen atoms should have a higher activity but poorer stability (compare section “Stability”) [115].

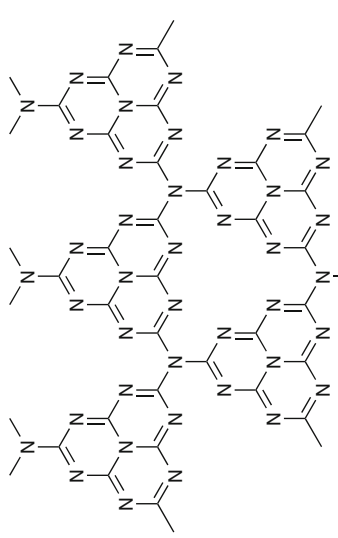
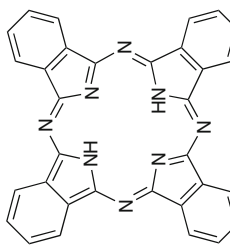
The results presented so far have shown that in most cases, catalysts reached higher ORR activities and selectivity for a direct reduction when a metal source was present during heat treatment. This makes it difficult to finally assign the role of metals in these catalysts. Nevertheless, unquestionable is the crucial role of nitrogen atoms incorporated in the carbon structure. Even in materials, in which a metal-based  $\text{MeN}_4$ -center has undoubtedly been identified as the active site, it has been observed that graphitic nitrogen atoms (i.e., not associated to the metal) can enhance the oxygen reduction of the catalysts [136]. Further investigations are necessary to clarify the mechanism of ORR in these materials.

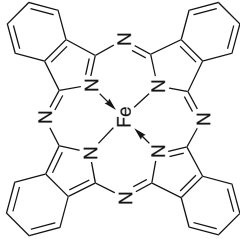
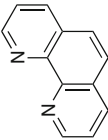
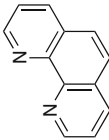
### Me–N–C Catalysts with $\text{MeN}_4$ and/or $\text{MeN}_2 + \text{N}_2$ -Centers

#### Catalysts Prepared by Carbonization of Macrocycles

As already mentioned, one can enhance ORR activity and stability of macrocycle-based catalysts by performing a heat treatment [62]. This result has led to intensive studies of the pyrolysis behavior of different  $\text{N}_4$ -chelates [37–42, 79, 100, 103, 104, 128, 137–153]. For some carbon-supported macrocycles, the effect of heat treatment on ORR activity is shown in Fig. 13.

**Polymer Electrolyte Membrane Fuel Cells (PEM-FC) and Non-noble Metal Catalysts for Oxygen Reduction, Table 1** Comparison of different carbon-based electrocatalysts and their electrochemical characteristics

	Catalyst sample		N content (wt%)	Fe content (wt%)	Onset potential V vs. NHE (@ 0.1 mA/cm <sup>2</sup> )	Lit.
1	C <sub>3</sub> N <sub>4</sub> <sup>a</sup>		60.9	–	0.4	[122, 123]
2	H <sub>2</sub> Pc/PhR <sup>b</sup>		2.0	–	0.53	[124]

3	FePc/PhR <sup>c</sup>		3.75	–	0.77	
4	BP 2000 NH <sub>3</sub> treated <sup>d</sup>	N:CB	1.10	–	0.4	[125]
5	Vulcan + AN <sup>e</sup>	N:CB	4.77	–	no activity	[126]
6	Phen/AmOx <sup>f</sup>		n.d.	0.04	<0.0	[127]
7	Phen/AmFeOx <sup>g</sup>		n.d.	13.9	0.82	

<sup>a</sup>(Cyanuric acid + sodium azide) precipitated at 220 °C in benzene

<sup>b</sup>(H<sub>2</sub>Pc + phenolresin), heat-treated at 700 °C for 5 h

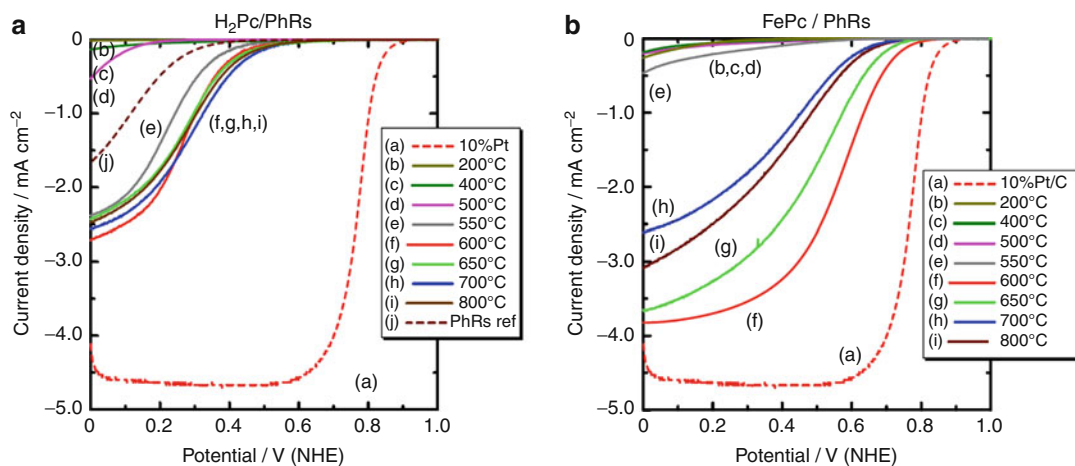
<sup>c</sup>(FePc + phenolresin), heat-treated at 600 °C for 5 h (<sup>a,b</sup>; compare Fig. 3.3)

<sup>d</sup>BP2000 heat-treated in NH<sub>3</sub>/N<sub>2</sub> at 800 °C for 30 min

<sup>e</sup>Vulcan pyrolyzed at 1000 °C in acetonitrile-enriched Ar for 2 h, weight gain: 65%

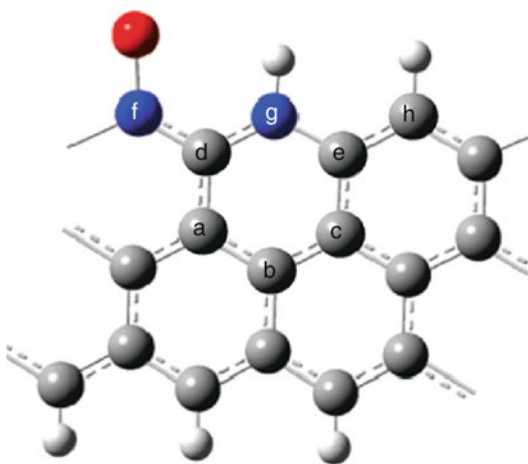
<sup>f</sup>Phenanthroline + ammonium oxalate hydrate precursor

<sup>g</sup>Phenanthroline + ammonium iron oxalate trihydrate, both samples (<sup>f,g</sup>) were heat-treated at 800 °C for 30 min followed by a subsequent acid leaching



**Polymer Electrolyte Membrane Fuel Cells (PEM-FC) and Non-noble Metal Catalysts for Oxygen Reduction, Fig. 10** RDE voltammograms (0.5 M  $\text{H}_2\text{SO}_4$ , 1 mV/s, catalyst loading 0.2 mg/cm<sup>2</sup>) of (a)  $\text{H}_2\text{Pc}/\text{PhR}$  and (b) the  $\text{FePc}/\text{PhR}$  catalysts, respectively. The

$\text{FePc}/\text{PhR}$  precursor contained 3 wt% Fe, pyrolysis was performed for 5 h for all samples. All given catalysts were not acid-leached after the heat treatment. (The figures were taken from [124]; reproduced with permission of Elsevier)



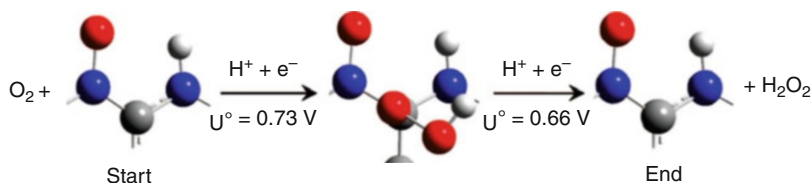
**Polymer Electrolyte Membrane Fuel Cells (PEM-FC) and Non-noble Metal Catalysts for Oxygen Reduction, Fig. 11** Proposed ON...NH edge sites on graphene sheets as catalytic sites for the oxygen reduction. (The figure was taken from [135]; reproduced with permission of the American Chemical Society)

Due to the temperature-induced graphitization, an additional carbon support is not needed a priori (see below). Nevertheless, in order to increase the active surface area and thereby the current density, one can use carbon blacks as a substrate. Depending on (1) the choice of the macrocycle, (2) the pyrolysis conditions, and

(3) the macrocycle loading, the maximal achievable current density will be obtained during pyrolysis in inert gas flow at temperatures between 600 °C and 1000 °C. For such impregnation catalysts, an optimal loading is obtained when a double setting of the available carbon surface is given. In this approximation, the fraction of surface area which is in pores smaller than the macrocycle expansion must not be considered [145, 154]. This explains why the metal content at which highest ORR activity is found varies within the reports.

A comparison of different metal-containing and metal-free macrocycles showed that the metal centers seem to stabilize the tetrapyrrole core [104, 128, 144]. As a result, the second decomposition step is shifted to much higher temperatures compared to the metal-free porphyrin and the overall mass loss is much smaller, as it becomes apparent from Fig. 14. Furthermore, the mass fragments related to the decomposition of the tetrapyrrole core (HCN) are detected at significantly higher temperatures in the coupled mass spectrometer for metal-containing macrocycles compared to the metal-free ones [104, 112, 128, 144].

The disadvantage of the impregnation technique is that above the optimal loading, no further activity increase is possible, even a decline of the



**Polymer Electrolyte Membrane Fuel Cells (PEM-FC) and Non-noble Metal Catalysts for Oxygen Reduction, Fig. 12** Predicted catalytic cycle for the two-electron

reduction on catalytic ON...NH edge sites in pyridinically doped carbon. (The figure was taken from [135]; reproduced with permission of the American Chemical Society)

activity can be observed [130]. This fact hinders the optimization for FC application where higher densities of active sites are required.

For this reason, several alternative production methods were developed which enable higher site densities. In principle, the carbonization can also be reached applying low-temperature plasma. This was first shown by Herrmann et al. in 2005 [155]. The direct comparison to the pyrolyzed equivalent showed that the carbon structure of the final product contained less disordered carbon phases after an Ar-plasma treatment (20 min, 250 W) compared to a pyrolysis at 700 °C (for which one of the highest ORR activity was obtained) [156]. Furthermore, as only a local carbonization is reached, a sintering of the macrocycles can be prevented even without carbon support [155–157].

In order to yield higher site densities, macrocycles can either be impregnated on a template or mixed with it prior to a heat treatment. In such a case, it is always mandatory to remove the template in a subsequent acid leaching. For instance, a sintering of macrocycle molecules is inhibited if fumed silica is used as a template [158–161]. The silica is removed by leaching in HF.

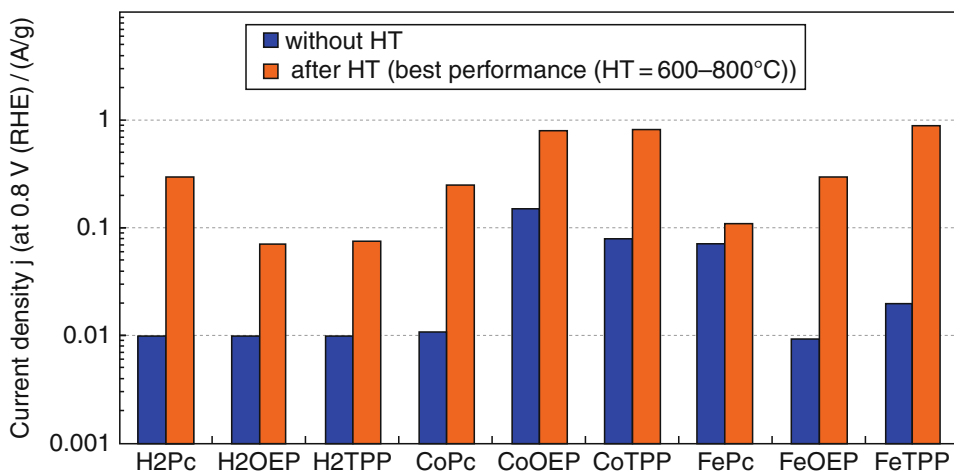
Another template-assisted method that enables high site densities is the so-called oxalate-supported pyrolysis. In this preparation approach, it is utilized that the porphyrine melts shortly before the carbonization takes place [130], whereas in the same temperature range, a decomposition of many metal oxalates occurs [132]. On the one hand, the released CO<sub>2</sub> contributes to a generation of porosity; on the other hand, the metal/metal oxide framework serves as template during the further heat treatment [39, 132, 133, 162, 163]. The advantage of this method is the

achievement of a homogenous distribution of active centers over the whole catalyst material [39, 160, 162]. In a second pyrolysis, further porosities can be generated so that due to the surface increase and an increase of participating MeN<sub>4</sub>-centers, significant enhancements of kinetic current density can be achieved [39, 162]. It was shown that the addition of sulfur enables much higher current densities due to (1) an easier removal of inactive metal species during the acid leaching, (2) higher site densities, and (3) changed carbon morphology [133]. By in-situ investigation of the pyrolysis process by high-temperature X-ray diffraction (HT-XRD) and TG-MS, it was found that without sulfur addition, iron carbide formation occurs at T > 580 °C, causing an additional release of HCN fragments (related to MeN<sub>4</sub> decomposition). By the addition of sulfur, the formation of Fe<sub>3</sub>C is inhibited as FeS is formed instead. Therefore, a larger fraction of MeN<sub>4</sub>-centers remained intact and so higher current densities were gained. Obviously, the carbide formation (or related graphitization) should be excluded during catalyst's preparation [163].

Structural analyses showed that non-leached catalysts are often dominated by decomposition products [37, 38, 41, 42, 104, 116, 164]. In such a case, with TEM, XRD, Mößbauer spectroscopy, and EXAFS analysis, mostly metal particles, carbides, nitrides, and sometimes oxides were detected. In Fig. 15, a Mößbauer spectrum of an as-prepared catalyst (HT 800, 2 h at 800 °C in Ar) and its acid-leached product (HT 800, washed) are shown.

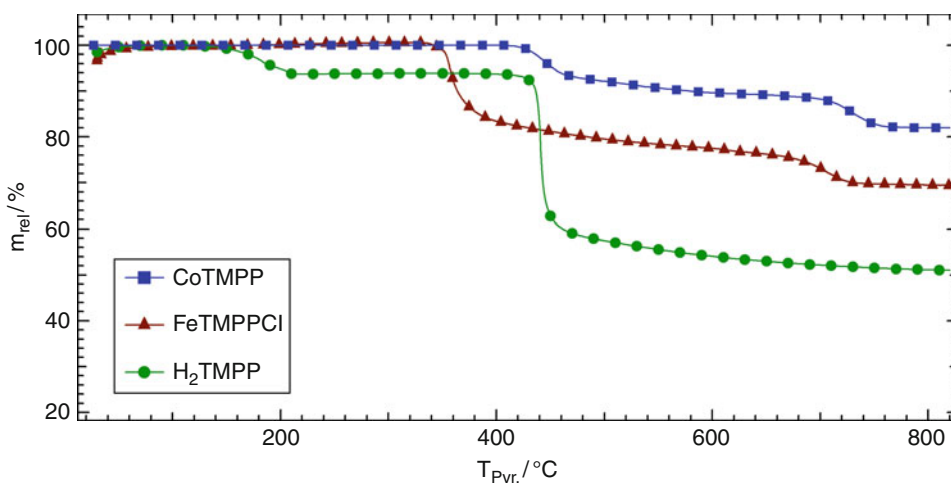
By a sufficient leaching of the catalyst, large amounts of inorganic species can be removed without negatively affecting the kinetic current density [38, 136].





**Polymer Electrolyte Membrane Fuel Cells (PEM-FC) and Non-noble Metal Catalysts for Oxygen Reduction, Fig. 13** Effect of heat treatment on the kinetic current density for oxygen reduction for some Co, Fe, and metal-free macrocycles (Pc: phthalocyanine, OEP: octaethylporphyrin and TPP: tetraphenylporphyrin). All

samples were supported on the same carbon black; for the pyrolyzed samples, the highest kinetic current densities are given, achieved after a heat treatment at temperatures ranging from 600 °C to 800 °C. Current values were taken from [41], Fig. 1

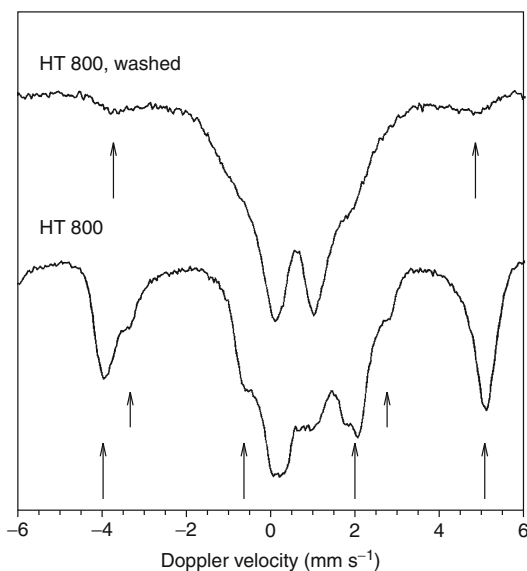


**Polymer Electrolyte Membrane Fuel Cells (PEM-FC) and Non-noble Metal Catalysts for Oxygen Reduction, Fig. 14** Thermogravimetric measurements of different tetramethoxyphenylporphyrins (TMPP). The metal-

free H<sub>2</sub>TMPP reveals a much larger mass loss starting at 450 °C in comparison to both metal porphyrins. (The figure was adapted from Fig. 5–3 of [112], Südwestdeutscher Verlag für Hochschulschriften)

A comparison of both catalysts in Fig. 15 shows that the non-leached catalyst HT 800 is dominated by two sextets (indicated by the two different type of arrays); further Fe-containing species in the material are difficult to assign. Induced by the acid leaching the sextets nearly vanished. Thus, it becomes easier to assign the

remaining species which in this case were related to different FeN<sub>4</sub>-centers [38]. Several authors have shown that even after a treatment at 1,000 °C, about 30% of MeN<sub>4</sub>-centers remain intact [37, 38, 41, 42, 136]. These results show clearly that in order to understand the role of metal in the final catalysts, structural analysis should



**Polymer Electrolyte Membrane Fuel Cells (PEM-FC) and Non-noble Metal Catalysts for Oxygen Reduction, Fig. 15** Mössbauer spectra of a catalyst as prepared from carbon-supported FeTPPCI and pyrolyzed at 800 °C for 2 h (HT 800) and its acid-leached product (HT 800, washed). The velocity scale is given relative to sodium nitroprusside (0.26 mm/s vs.  $\alpha$ -Fe). (The figure was adapted from Fig. 4 of [38]; reproduced with permission of the American Chemical Society)

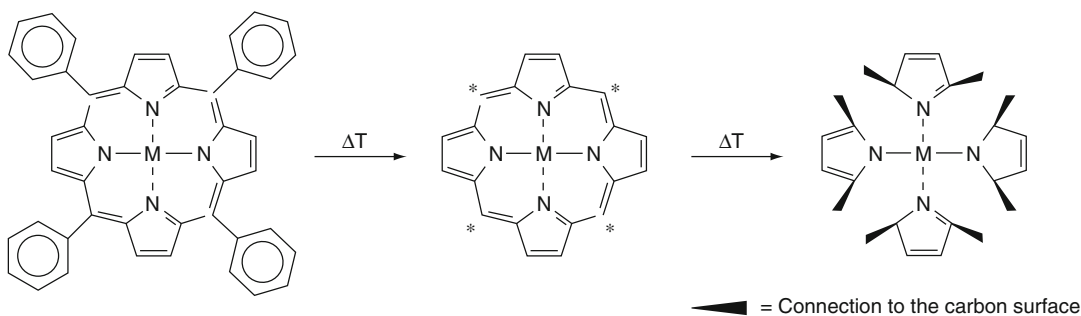
better be performed on the already acid-leached catalysts. As  $\text{MeN}_4$ -centers are still remaining, Van Veen et al. concluded that these sites are also responsible for the catalytic activity in the pyrochelates (similar to non-pyrolyzed macrocycles) [41, 42]. The authors proposed that an enhanced electronic structure is the main reason for an increased turnover frequency (TOF) of the remaining  $\text{MeN}_4$ -centers. In Fig. 16, a model for the processes occurring during heat treatment of porphyrins is shown [38]. According to this observation, even after high-temperature treatments, units of the tetrapyrrole core remain intact but interact with the carbon support.

In 2008, a direct correlation of the ORR activity and the overall concentration of all or at least one specific  $\text{MeN}_4$ -centre was proven for the first time [42]. In this work by Koslowski et al., the catalysts were produced by the oxalate-supported pyrolysis of FeTMPPCI or  $\text{H}_2\text{TMPP}$ . Variations of ORR activity and concentration of different iron

modifications were obtained by different subsequent treatments whereas the heat treatment temperature was always kept constant. It was found that the obtained catalytic activity was proportional to the number of a specific  $\text{FeN}_4$ -center which is a major hint to the participation of this center in the oxygen reduction process. The correlation is shown in Fig. 17a. In a recent work, carbon-supported FeTMPPCI (FeTMPPCI/KB600) pyrolyzed at different temperatures was thoroughly structurally characterized before and after an acid leaching [136]. The results showed clearly that up to 600 °C, the whole nitrogen remained in the system. Due to the carbonization, only a reorganization of the  $\text{FeN}_4$ -centers was observed, while the pyrolysis at 600 °C was sufficient to essentially improve ORR activity [39, 136].

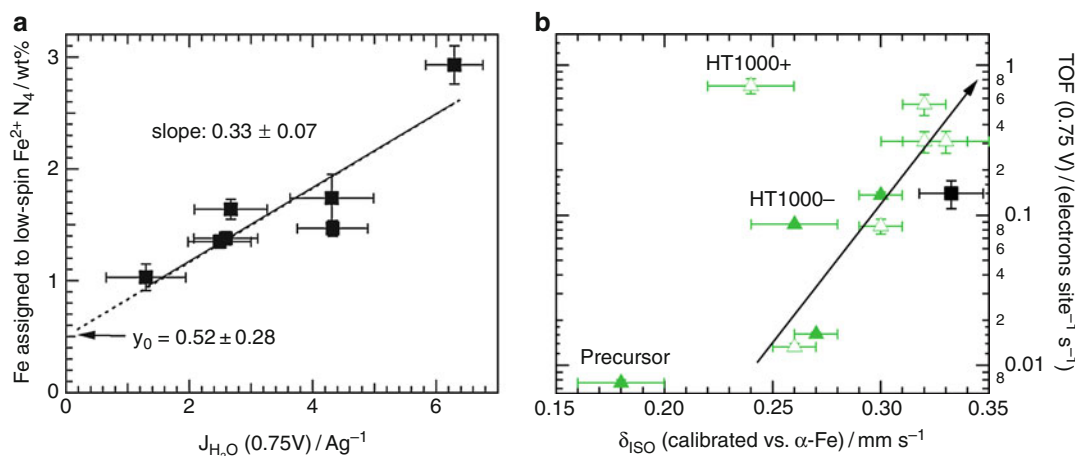
A comparison of XPS and Mössbauer spectroscopic results allows an explanation why significantly higher current densities could be achieved despite a decreasing concentration of active  $\text{FeN}_4$ -centers. Both, the N1 s bonding energy and the isomer shift assigned to the active  $\text{FeN}_4$ -centers changed with the TOF [136]. The results were interpreted by an increasing bond-strength between iron and the surrounding nitrogen atoms which obviously leads to a higher 3d electron density on the metal center. As a result, oxygen might be activated faster so that higher TOFs can be obtained. A similar relation was already found for non-pyrolyzed macrocycles as discussed in section “Non-pyrolyzed Macrocycles” [65]. The relation between TOF and  $\delta_{\text{ISO}}$  assigned to the active sites is shown in Fig. 17b. According to these results, a mesomerically bonded  $\text{FeN}_4$ -center with ferrous iron in the low-spin state is assigned as catalytic active center in FeTMPPCI-based catalysts pyrolyzed in inert gas atmosphere [39, 136]. Apart from these findings, graphitic nitrogen atoms seem to enhance the electron donor capacity, thus enabling higher ORR activities [136].

A related positive effect emerged also after a second pyrolysis of Me-N-C catalysts in ammonia [112, 160, 162, 165–167]. Since a huge increase in the concentration of pyridinic nitrogen atoms was observed, it was suggested that either different, but more active sites were formed or an



**Polymer Electrolyte Membrane Fuel Cells (PEM-FC) and Non-noble Metal Catalysts for Oxygen Reduction, Fig. 16** Visualization of the carbonization process of a porphyrin during the heat treatment. (The figure was taken from [38]; reproduced with permission of the

American Chemical Society). During the first decomposition step of porphyrins (compare Fig. 14), the substituents are released. In the following heating process, the active centers are integrated into or onto the carbon framework



**Polymer Electrolyte Membrane Fuel Cells (PEM-FC) and Non-noble Metal Catalysts for Oxygen Reduction, Fig. 17** Correlation of the concentration of low-spin  $\text{Fe}^{\text{II}}\text{N}_4$ -centers with the ORR current density for different Fe-N-C catalysts (a). Relation between turnover frequency (TOF) and isomer shift  $\delta_{\text{ISO}}$ . (b) The isomer shift  $\delta_{\text{ISO}}$  is related to the electron density at the iron nucleus. In this work, a higher  $\delta_{\text{ISO}}$  is in accord with an increased 3d electron density. The precursor and impregnation catalysts

prepared at 1000 °C (HT1000+: acid-leached, HT1000-: without acid leaching) are indicated. For reasons of comparison, the point ■ related to the catalysts discussed in [39] is added (average values of  $\delta_{\text{ISO}}$  and TOF). (Data were taken from [39, 136], reproduced with permission of the American Chemical Society (for figure a), and permission by ECS – The Electrochemical Society (for figure b), respectively)

enhanced electronic structure of the carbon matrix enabled the higher ORR activity [115, 117, 118, 126, 129, 165, 168–173]. In general, the utilization of  $\text{NH}_3$  allows an alternative generation of catalysts where instead of complex macrocycles, simple and cheap substances can be used. This matter will be discussed in the following.

#### Alternative Center Generation During Heat Treatment

In 1989, Gupta and coauthors showed that highly active catalysts can be prepared from less complex molecules [63]. In their work, they impregnated a carbon black with polyacrylonitril (PAN) and an iron or cobalt acetate. The precursors were heat-

treated at different temperatures and the ORR activity was measured. It was found that one can generalize the preparation of Me-N-C catalysts: Whenever a metal precursor is heat-treated with nitrogen and carbon sources at temperatures of  $\geq 600\text{ }^\circ\text{C}$  (Co) or  $\geq 700\text{ }^\circ\text{C}$  (Fe), an active catalyst can be obtained. A scheme of their preparation route and the achieved ORR activities (as a function of pyrolysis temperature) are given in Fig. 18.

Since then, this approach was adapted by several working groups [43, 97, 113, 115–118, 126, 152, 165, 166, 168, 171, 173–186]. Extensive studies were made by Dodelet's group, who tested a wide gamut of metal, nitrogen, and carbon sources, in order to find highest current densities by this screening technique. It could be demonstrated that metal acetates and ammonia are especially suited as precursors to achieve highly active catalysts [179, 187]. Besides ammonia, other nitrogen precursors such as acetonitrile (AN), metal-free  $\text{N}_4$ -macrocycles, phenanthroline (Phen), polypyrrole (PPy), polyaniline (PAN), and others can equally be used as demonstrated by several groups [113, 126, 127, 134, 165, 174, 176–178, 186, 188, 189].

Varying the metal acetate in the precursor, the obtained ORR activity was studied by He et al. [187]. It was found that the kinetic current density increases in the order  $\text{Ni} (3d^8 4s) \approx \text{Cu} (3d^{10} 4s) < \text{Mn} (3d^5 4s^2) < \text{Cr} (3d^5 4s) \ll \text{Co} (3d^7 4s^2) < \text{Fe} (3d^6 4s^2)$ . If the ORR activity is plotted versus the 3d orbital occupation a volcano plot with a maximum at  $3d^6$  will be obtained (For the ease of comparison, the electron configuration of the metals is given in brackets). It should be pointed out that this order nearly reflects the relation between ORR onset potentials and the number of 3d electrons as shown for non-pyrolyzed porphyrins in Fig. 7.

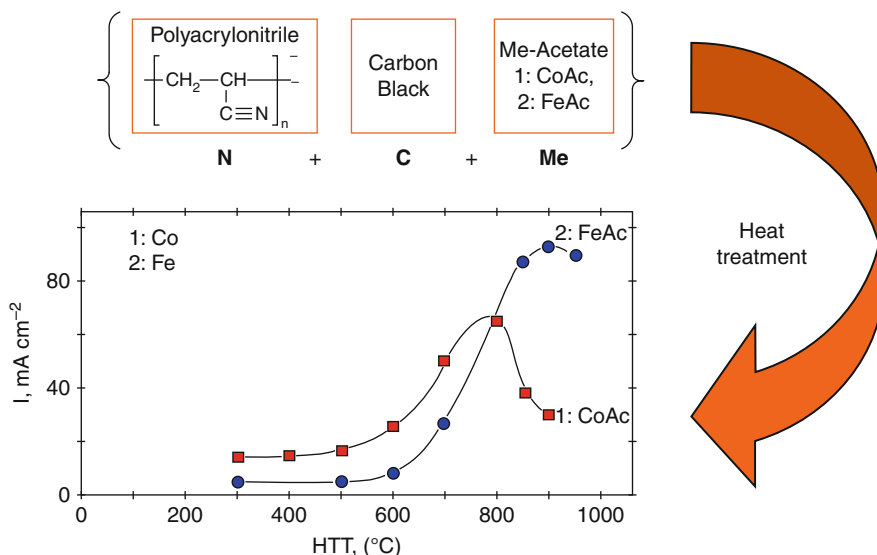
It has been observed that besides the type of metal and its content, the fractions of micropores and pyridinic nitrogen atoms play a crucial role for the active site formation. Both are generated during the ammonia treatment [168, 171, 180, 182, 187]. The authors assumed that  $\text{MeN}_{2+2}$ -centers were built in micropores, a scheme of the center is given in Fig. 19 [168]. Experiments performed with the goal to increase the amount

of active centers by annealing the nonporous carbon black impregnated with iron acetate in the presence of  $\text{NH}_3$  failed. Even catalysts with more than 0.2 wt% Fe turned out to reveal only smaller turnover frequency. Above 2 wt% iron, the activity dropped remarkably [172].

Mössbauer analysis of such catalysts evidenced that besides less active  $\text{FeN}_4$ -centers (similar to those in heat-treated porphyrin-based catalysts), a new type of  $\text{FeN}_4$ -centers was found [190]. This high-spin  $\text{Fe}^{2+}$ -center was not present in any heat-treated  $\text{N}_4$ -macrocycle-based catalyst, making it most probable that it is related to the proposed active site. In conclusion, the  $\text{FeN}_{2+2}$ -centers differ from porphyrin-based ones by the different spin state, the pyridinic coordination of the iron ion and the placement in micropores. The different electronic state might explain why the  $\text{FeN}_{2+2}$ -centers can reach much higher turnover frequencies in their "highly active state" (please note: the electron density on iron is higher for  $\text{Fe}^{2+}$ , HS compared to  $\text{Fe}^{2+}$ , LS); on the other hand, these centers can be deactivated, e.g., in contact with acid, as will be discussed in the section "Stability" [190, 191].

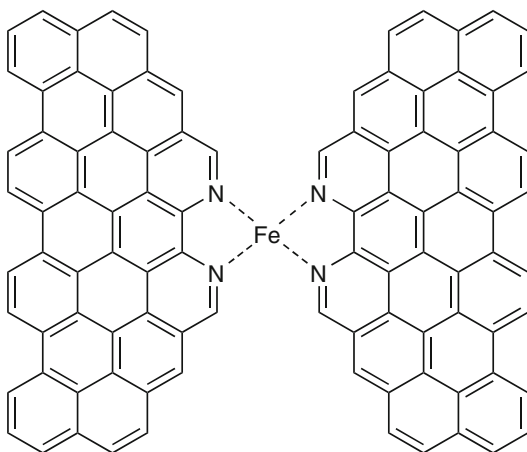
Very high activities are obtained when phenanthroline is used as nitrogen source [134, 165, 178]. In 2009, such catalysts exhibited the highest catalytic activity within the system Fe-N-C. The authors assigned their preparation method as pore-filling method (PFM) because especially this step within the preparation process seems to play a crucial role to achieve a high ORR activity [165]. In order to obtain the precursor, a microporous carbon was impregnated with phenanthroline and iron acetate. In the next step, a low-energy ball milling was performed with the aim to press iron acetate and phenanthroline into the micropores. The precursor was pyrolyzed two times (first  $1050\text{ }^\circ\text{C}$  in Ar, second at  $950\text{ }^\circ\text{C}$  in  $\text{NH}_3$ ) [165]. Highest ORR activities were achieved when the total weight loss from both pyrolysis steps amounted to the weight percentage of phenanthroline, the best having a phenanthroline content of 50 wt% [165, 192].

A homogeneous distribution of active sites was obtained when the phenanthroline is pyrolyzed in the presence of iron oxalate. Such catalysts



**Polymer Electrolyte Membrane Fuel Cells (PEM-FC) and Non-noble Metal Catalysts for Oxygen Reduction, Fig. 18** Scheme of Gupta's precursor selection (*top*) and ORR activity of catalysts as a function of the heat treatment temperature and metal precursor, 1: CoAc, ■

and 2: FeAc, • (*bottom*). ORR activity was measured in 4 M NaOH. The temperature-dependent current curve was taken from [63], Fig. 3; reproduced with permission of Springer Publishing Group



**Polymer Electrolyte Membrane Fuel Cells (PEM-FC) and Non-noble Metal Catalysts for Oxygen Reduction, Fig. 19** FeN<sub>2+2</sub>-center embedded in a micropore, as assumed by Charreteur [168]. (The figure was taken from [112], Fig. 3–9; Südwestdeutscher Verlag für Hochschulschriften)

exhibited an excellent performance in RDE measurements, even without sulfur addition [134]. As indicated by a change of color, already during the mixing of the precursors, a complexation of iron with phenanthroline occurs. These catalysts show

similar structural features in Mößbauer spectroscopy and exhibit similar iron contents as those catalysts prepared by the oxalate-supported pyrolysis of porphyrins.

A further preparation approach uses nitrogenbearing monomers to synthesize catalytic active sites [177, 186, 189], e.g., when pyrrole is impregnated on a carbon black in the presence of a metal source. An oxidation agent induces the polymerization process. Without any heat treatment, only small ORR activity was obtained; however, this catalyst showed a stable performance of more than 500 h in potentiostatic fuel cell tests [177]. Although a heat treatment enhanced the catalyst's activity (similar to the pyrolysis of macrocycles), the stability was moderate. Nevertheless, recent results have shown that by further optimization of the preparation method (including a heat treatment), both, a high activity and a remarkable stability, could be realized [189]. This fact will further be discussed in section "NNMC and Their Potential for PEM-FC Application."

The preparation of catalysts by utilization of monomers with a subsequent polymerization

reaction and heat treatment was also applied by other groups [159, 160, 193, 194]. Dahn's team impregnated silica with pyrrole and iron chloride. The polymerization was induced in a hot acid steam. Directly after complete polymerization, the sample was pyrolyzed in Ar at 900 °C. The silica template was removed afterward by a doubled leaching in 5% and 40% HF, respectively [159, 160].

Relatively high iron contents are found for self-supported iron-polypyrrole catalysts which were prepared by spray pyrolysis. The authors proposed high site densities; however, comparatively low current densities with respect to other Fe-N-C catalysts make it most probable that only a small fraction of the overall iron is bonded in active sites. Nevertheless, the shape of these catalysts is interesting because porous carbon spheres with diameters of 100 up to 1000 nm are formed [194].

In conclusion, it can be summarized that active sites in Me-N-C catalysts can be prepared via several different preparation routes. Optimization of each parameter (e.g., amounts of precursors [metal, nitrogen, and carbon], ratios of precursors, annealing temperature, and post treatment) is necessary in order to achieve highest ORR activity. If a heat treatment is performed, one will always achieve a mixture of different metal modifications, whereas it seems that only a fraction of the modifications formed is connected with ORR activity. This observation supports the importance of a subsequent acid leaching and of highly sensitive analysis techniques that can distinguish between the different phases, especially between FeN<sub>4</sub>-centers of different oxidation and spin states.

## NNMC and Their Potential for PEM-FC Application

With respect to the alternative materials discussed so far, Fe-N-C catalysts seem to be the most promising cathode catalysts for FC application [165, 195]. For that reason, the discussion is focussed on this material system in this chapter. Alternative fuel cell catalysts have to be (1) simple in their preparation, (2) economical in production,

and (3) they should generate an adequately high volumetric current density ( $J_{vol}$  in A/cm<sup>3</sup>). In order to meet the DOE-target value of the volumetric current density, a certain site density ( $S_D$  in sites/cm<sup>3</sup>) and a sufficiently high turnover frequency (TOF in electrons sites<sup>-1</sup> s<sup>-1</sup>) have to be gained to enable commercial application. Besides, a catalyst stability of several 1,000 h is expected, even under high load conditions of the fuel cell.

Today, catalysts that reach high volumetric current densities often exhibit only low stability while different, less active materials perform nearly stable, even over periods of weeks. Therefore, activity and stability will be discussed separately. The section "Future Direction" will give a final outlook regarding the commercial applicability of NNMC.

### Activity

Up-to-date non-noble metal catalysts only partially fulfill the demands in activity for a fuel cell application. To boost activity, the catalyst loading on the cathode can be increased. It was noticed, however, that above a certain layer thickness, mass transport properties hinder a further increase of the current density. For this reason, the specific volumetric activity has to be improved.

The target values for 2010 (the year in which this article was written) and for 2015 are 10% (130 A/cm<sup>3</sup>) and 25% (325 A/cm<sup>3</sup>), respectively, of the volumetric ORR activity of a commercial Pt/C catalyst [160, 166, 195]. Standard conditions are fulfilled if the measurements are performed at 80 °C ( $T_{CELL} = 80$  °C) with oxygen and hydrogen partial pressures of 1 bar ( $p_{O_2} = 1$  bar,  $p_{H_2} = 1$  bar) and a relative humidity of RH = 100.

In Table 2, different catalysts are compared with respect to their volumetric ORR activity, site density, kinetic current density, and turnover frequency. The knowledge of these different parameters enables the identification of the factors that have to be further optimized. The catalysts are sorted according to their achieved volumetric current density calculated from fuel cell measurements (column I, Eq. 3). The so far best Fe-N-C catalyst is listed below the DOE-target value followed by the other materials given in the sequence of decreasing volumetric activity. If the



**Polymer Electrolyte Membrane Fuel Cells (PEM-FC) and Non-noble Metal Catalysts for Oxygen Reduction, Table 2** Comparison of several catalysts concerning their site density  $S_b$  (column C), their kinetic current densities (columns D and E), turnover frequency (columns G and H), and their achieved Volumetric current density (column I). The values in Columns D–I are all given for a potential of 0.8 V. To enable a comparison, for several catalysts values were calculated from the original data as described in the beginning of the chapter

A	B	C	D	E	F	G	H	I	J
		$S_b$	RDE	FC	FC/ RDE	RDE	RDE	FC	
Shortname	Lit.	$\times 10^{20}/$ sites/ $S_{cat}$	J (0.8 V)/A/g	J (0.8 V)/A/g		TOF (0.8 V)/ electrons/(site s)	TOF (0.8 V)/ electrons/(site s)	vol curr. Jv/(A/cm <sup>3</sup> )	Description
1	Target NNMC 2010	DOE						130	
2	Target NNMC 2015	DOE						325	
3	CM-Fe-C	208	–		–	–		127	CM: Cyanamide, Fe-source: FeSO <sub>4</sub> ·7H <sub>2</sub> O, C-source: sucrose, leaching in KOH
4	PFM1: Fe/Phen/BP-HT1050Ar-HT950NH <sub>3</sub>	192	–	429	–	–	12.42	99	optimized PFM-catalyst, Fe-source: iron acetate
5	PFM2: Fe/Phen/BP-HT1050Ar-HT950NH <sub>3</sub>	165	–	246	–	–	7.12	98.3	catalyst after optimization, Fe-source: FeAc
6	PANI-Fe/EDA-Co-C	208	–	90	6.55	–		72	PANI-Fe/EDA-Co-C
7	PFM4: Fe/PTCDA/BP-HT1050NH <sub>3</sub> (“M786”)	160	3	80	26.67	0.23	6.2	32	HT 1050 °C, 5 min NH <sub>3</sub> , Fe-source: FeAc
8	Fe/Fe/S-HT800N <sub>2</sub> -HCl+BM-HT800NH <sub>3</sub>	209	0.71	76.4	107.61	0.01	0.93	30.6	Fe/Fe/S denotes mixture of FeTMPPCI + iron oxalate + sulfur, Leaching in 1 M HCl, 15 min ball milling (BM)
9	Fe/Fe/S-HT800N <sub>2</sub> -HCl-HT800NH <sub>3</sub>	209	4.48	31	6.92	0.08	0.45	12.4	Fe/Fe/S denotes mixture of FeTMPPCI + iron oxalate + sulfur, Leaching in 1 M HCl
10	3 M-NiANI-HT_NH <sub>3</sub> *-HT_NH <sub>3</sub> *	166	–	30	–	–	1.45	12	iron-source: FeCl <sub>3</sub> , NiANI: Nitroanilin, NH <sub>3</sub> *: gas mixture of 25% NH <sub>3</sub> and 75% N <sub>2</sub> , HT at 800–1000 °C, same T for both steps
11	Fe/Fe/S-HT800N <sub>2</sub> -HCl-HT800N <sub>2</sub> /H <sub>2</sub> -HCl-HT800CO <sub>2</sub> (“UK63”)	160	18	20.7	1.15	0.33	0.38	8.3	Leaching in 1 M HCl; N <sub>2</sub> /H <sub>2</sub> : Forming Gas 10% H <sub>2</sub> ; Fe/Fe/S denotes mixture of FeTMPPCI + iron oxalate + sulfur
12	PFM3: Fe/Phen/BP-HT1050Ar	165	–	13.8	–	–	0.4–0.8	5.5	only heat treatment in Ar, Fe-source: FeAc

13	Co/Fe/S-HT800N <sub>2</sub> -HCl-HT800N <sub>2</sub> / H <sub>2</sub> -HCl-HT800CO <sub>2</sub> ("UK65")	160	3.3	10	10.3	1.03	0.19	0.19	4.1	For leaching 1 M HCl; N <sub>2</sub> /H <sub>2</sub> ; Forming gas with 10% H <sub>2</sub> ; Co/Fe/S denotes mixture of CoTMPP + iron oxalate + sulfur
14	(PANI-Fe <sub>3</sub> Co-KB300)-HT900N <sub>2</sub> -H <sub>2</sub> SO <sub>4</sub>	186	2.7	1.3	9.8	7.54	0.03	0.23	3.9	Fe- and Co-sources: hydrated Fe/Co-sulfates, leaching in 0.5 M H <sub>2</sub> SO <sub>4</sub>
15	μPMI: Fe/npCB-HT950NH <sub>3</sub> ("FC280")	160	0.3	4.2	5.8	1.38	0.92	1.27	2.3	μPM: Micropore method; Fe-source: FeAc; npCB: non-porous carbon black
16	GAdFeCu-HT1000Ar-H <sub>2</sub> SO <sub>4</sub> ("GAdFeCu")	160	3.0	0.55	5.7	10.36	0.01	0.12	2.3	G: Glucose, Ad: Adenin, Fe- and Cu-source: hydrated Fe/Cu-gluconate
17	"DAL900c": (DAL900a + Fe)-HT900NH <sub>3</sub>	160	1.5	1.1	5	4.55	0.05	0.21	2	DAL900a + Fe: impregnation of DAL900a with FeAc previous to HT
18	CoTMPP/SiO <sub>2</sub> -HT700N <sub>2</sub> -KOH ("CoTMPP700")	160	6.8	1	3.2	3.20	0.01	0.03	1.3	CoTMPP was impregnated on porous silica previous to HT
19	"DAL900a": (FeCl <sub>3</sub> /SiO <sub>2</sub> + PPy/HCl)-HT900Ar-HF	160	0.5	0.4	2.7	6.75	0.05	0.36	1.1	PPy/HCl: Polymerization of pyrrole by HCl-vapor; HF: leaching in 5% and 40% HF-solution
20	Fe/Fe/S-HT800N <sub>2</sub> -HCl-BM	209	4.3	0.4	2.3	5.75	0.01	0.03	0.9	Fe/Fe/S denotes mixture of FeTMPPCl + iron oxalate + sulfur; BM: 15 min ball milling
21	Hem-HT600Ar-G-HT900CO <sub>2</sub> -H <sub>2</sub> SO <sub>4</sub> ("CHb200900")	160	1.2	0.4	2.3	5.75	0.02	0.12	0.9	Hem: grounded Hemoglobin; G: grounded, CO <sub>2</sub> *: gas mixture of 10% CO <sub>2</sub> and 90% Ar, leaching in 0.5 M H <sub>2</sub> SO <sub>4</sub>
22	Co-PPy-C (Vulcan + PPy/H <sub>2</sub> O <sub>2</sub> ) + Co (NO <sub>3</sub> ) <sub>2</sub> /(NaBH <sub>4</sub> + NaOH)	177	4.1	-	1.8	-	-	0.03	0.72	Vulcan was impregnated with pyrrole, polymerization was done by H <sub>2</sub> O <sub>2</sub> ; product was mixed with Co(NO <sub>3</sub> ) <sub>2</sub> , which was reduced by NaBH <sub>4</sub> + NaOH
23	Fe/Fe/S-HT800N <sub>2</sub> -HCl	209	3.9	0.19	1.7	8.95	<0.01	0.03	0.7	Forleaching 1 M HCl; Fe/Fe/S denotes mixture of FeTMPPCl + iron oxalate + sulfur
24	3 M-NiANI-HT_NH <sub>3</sub> *	166	1.3	-	1	-	-	0.05	0.4	iron-source: FeCl <sub>3</sub> , NiANI: Nitroanilin, NH <sub>3</sub> *: gas mixture of 25% NH <sub>3</sub> and 75% N <sub>2</sub> , HT at 800-1000 °C
25	FeCl <sub>3</sub> /SiO <sub>2</sub> + PPy/HCl-HT900Ar-HF	159	2.2	1.3	1	0.77	0.04	0.03	0.4	PPy/HCl: Polymerization of pyrrole by HCl-vapor; HF: leaching in 5% and 40% HF-solution

(continued)

Polymer Electrolyte Membrane Fuel Cells (PEM-FC) and Non-noble Metal Catalysts for Oxygen Reduction, Table 2 (continued)

A	B	C	D	E	F	G	H	I	J
		$S_D$	RDE	FC	FC/ RDE	RDE	FC	FC	
		$\times 10^{20}/$ sites/ g <sub>cat.</sub>	J (0.8 V)/A/g			TOF (0.8 V)/ electrons/(site s)		vol curr. Jv/(A/cm <sup>2</sup> )	Description
26	Lit. 194	2.9	0.14	0.4	2.86	0.02	<0.01	0.16	Polymerization of pyrrole + K <sub>3</sub> [Fe(CN) <sub>6</sub> ] in H <sub>2</sub> O + H <sub>2</sub> O <sub>2</sub> induced by FeCl <sub>3</sub> ; US spray pyrolysis (800 °C, 2.4 MHz), leaching in 10% HF-solution
27	119	6.5	0.28	0.1	0.36	<0.01	<0.01	<0.01	CB-HCl-HNO <sub>3</sub> : carbon was first leached in conc. HCl then in conc. HNO <sub>3</sub> ; Co/Fe/N: Co (NO <sub>3</sub> ) <sub>2</sub> + FeSO <sub>4</sub> + Ethylenediamide; final leaching in 0.5 M H <sub>2</sub> SO <sub>4</sub>
28	197	0.5	0.02	0.03	1.50	<0.01	<0.01	<0.01	GGL: Mixture of 0.49:0.49:0.02 mol Glucose:Glycin:Fe-lactate; leaching in 0.5 M H <sub>2</sub> SO <sub>4</sub>
29	174	1.2	0.51	-	-	0.03	-	-	Complexation of phantrolinone with hydrated Fe-sulfate

authors did not provide any magnitude of the volumetric current density, the value was calculated under the assumption of a catalyst density of  $\rho = 0.4 \text{ g/cm}^3$  [172, 196].

Volumetric current density  $J_{\text{vol}}$  (in  $\text{A cm}^{-3}$ ):

$$J_{\text{vol}} = \frac{J_{\text{A/g}}}{\rho_{\text{g/cm}^3}}, \quad (3)$$

Presently, none of the Fe-N-C catalysts meet the target value of  $J_{\text{vol}}$ , even if some of the given data were extrapolated to 0.8 V from the Tafel region of the polarization curve. For highly active catalysts even at 0.8 V, some mass transport limitation is visible so that the measured values of the current density are smaller compared to the extrapolated ones.

An increase of the volumetric current density can be obtained either by enhancing the site density  $S_{\text{D}}$  and/or the turnover frequency TOF. Column C in Table 2 lists the site densities of the catalysts as far as the metal content is known. The calculations were made under the assumption that each metal atom is coordinated in an active  $\text{MeN}_4^-$  or  $\text{MeN}_{2+2}$ -center.

Site density  $S_{\text{D}}$  (in sites/ $\text{g}_{\text{cat}}^{-1}$ ):

$$S_{\text{D}} = \frac{[\text{Me}]_{\text{wt}\%}}{100 \cdot M(\text{Me})_{\text{g/mol}}} N_{\text{A}}, \quad (4)$$

In the equation,  $[\text{Me}]_{\text{wt}\%}$  is the concentration of metal species in the catalyst,  $M(\text{Me})_{\text{g/mol}}$  is the molar mass (if several metal species are present, the average related to the contents of different metals is used), and  $N_{\text{a}}$  represents Avogadro's number. Since the density for many of the catalysts is unknown, a weighting related to the volume was neglected.

As described in the section “Non-noble Metal Catalysts with Molecular Centers,” it is still controversially discussed, what structural unit (or units) in Me-N-C catalysts causes the oxygen reduction reaction. Furthermore, it was shown for different catalysts that besides the presumably active  $\text{MeN}_4^-$ -center also inactive metal-containing

modifications exist [39, 40, 117, 129, 131–133, 136, 162, 163, 170, 172, 175, 185, 197, 198]. Consequently, the given site density  $S_{\text{D}}$  can merely be regarded as a rough approximate. Nevertheless, it helps to estimate if the site density is a distinct value which has to be adapted.

From the site density  $S_{\text{D}}$  and the kinetic current density  $J_{\text{K}}$  (at 0.8 V), one can determine the turnover frequency TOF (0.8 V), which is given in Table 2 for both, RDE as well as fuel cell measurements (columns G and H).

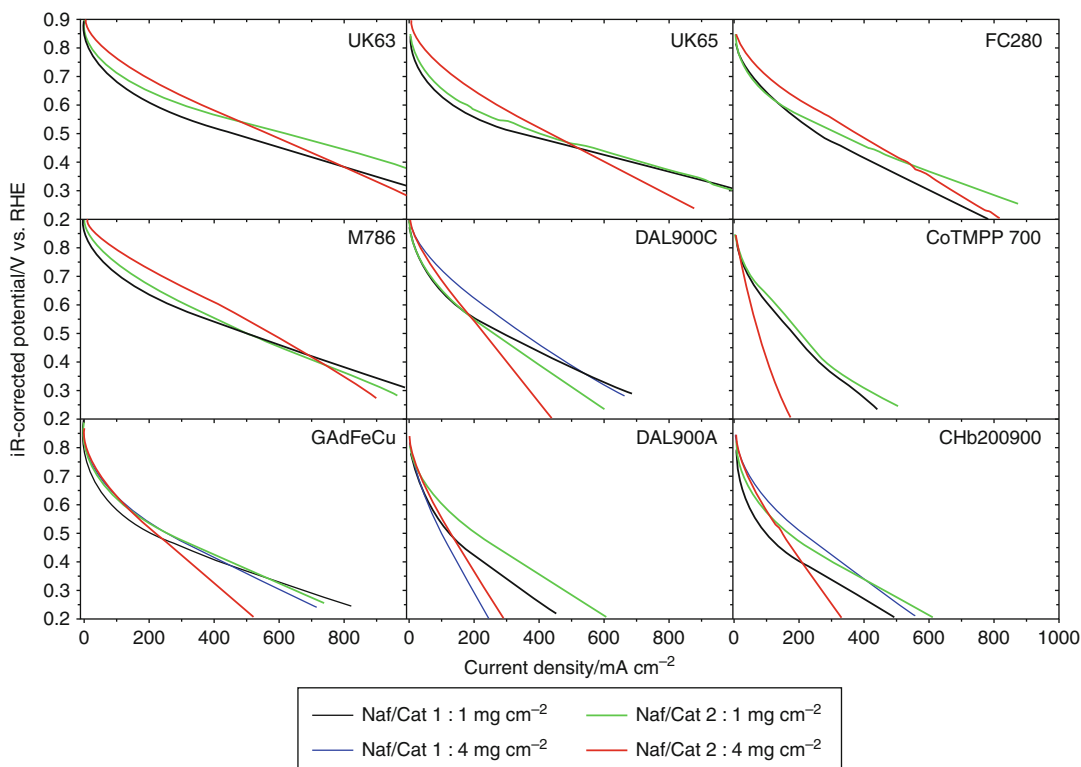
Turnover frequency TOE (in electrons  $\text{site}^{-1} \cdot \text{s}^{-1}$ ):

$$\text{TOF} = \frac{J_{\text{K(A/g)}}}{S_{\text{D(sites/g)}}} \cdot \frac{1}{e}, \quad (5)$$

In this equation,  $e$  stands for the elementary charge of the electron.

Fuel cell measurements excellently reflect the actual performance of a catalyst and its applicability. Besides the kinetic behavior, however, the mass transport properties (proton, electron, and oxygen transport as well as water removal) and the internal resistance affect the performance in fuel cells. Thus, it becomes difficult to estimate the kinetic properties of a catalyst just from FC measurements. Rotating (Ring) Disk Electrode (R(R)DE) measurements more precisely reflect the kinetic properties (ORR activity and selectivity). Therefore, in this work also, R(R) DE measurements were taken into account. A comparison of publications showed that measurement conditions (for PEM-FC and R(R)DE) often vary considerably from one laboratory to another, which hinders a direct comparison of the different materials [7, 114, 115, 160, 165, 166, 168–171, 173, 175, 177, 196–206]. In order to enable a better evaluation, F. Jaouen initiated a cross-laboratory comparison of FC and RDE measurements for various Me-N-C catalysts [160]. In Fig. 20, fuel cell measurements of these catalysts are shown.

It was found that the catalysts from different institutes behaved completely different when changing, e.g., the Nafion content or the catalyst loading in FC and RDE tests, as shown for FC measurements in Fig. 20.



**Polymer Electrolyte Membrane Fuel Cells (PEM-FC) and Non-noble Metal Catalysts for Oxygen Reduction, Fig. 20** Fuel cell tests of NNMC prepared by different preparation methods (for catalyst's preparation routes,

compare Table 2 and [160]). The given FC measurements were made with different Nafion-to-catalyst ratios (Naf/Cat). (The figure was taken from [160]; reproduced with permission of the American Chemical Society)

Regarding the volumetric current density, best Fe-N-C catalysts yield about 25–40% of the DOE target of  $325 \text{ A/cm}^3$  envisaged for 2015 (see lines 3–6, in Table 2) [165, 207, 208]. P. Zelenay's working group published for one of their catalysts a volumetric activity of 40% of the DOE target for 2015 (line 3) [208]. In that preparation route, catalysts were prepared from a mixture of cyanamide, iron sulfate, and sucrose. Further details of the preparation procedure are not yet published. The activity of the so-called PANI-based catalysts of the same group was boosted by optimization of the preparation steps and the addition of ethylenediamine [189, 207, 208]. Comparing the results of lines 6 and 14, it becomes apparent that by the optimization, the volumetric activity was increased by a factor of 18.

The catalysts in lines 4–5 have been produced via the pore-filling method (PFM) [165]. The

preparation is described in the section “[Alternative Center Generation During Heat Treatment.](#)” A catalyst produced in this manner achieved about 50% of the electron transfer rate of commercial platinum. Similar catalysts, but without ball milling, were already described by Bron et al. in 2002 [174, 178, 188]. The comparison clearly shows that the ball milling has a considerable influence on the achievable activity (lines 4, 5, and 29).

Comparing the volumetric current densities in column I related to the catalyst manufacturing method, it becomes apparent that all catalysts in the upper third of Table 2 were produced in a multistep preparation and/or optimization process. Furthermore, in nearly all procedures, one preparation step is performed in ammonia at  $T > 800 \text{ }^\circ\text{C}$ . In 2008, different groups have shown that by performing a second pyrolysis step in ammonia, the kinetic current density can

be enhanced drastically [162, 166, 167], a less pronounced improvement was found when other gases (like  $\text{CO}_2$ ,  $\text{N}_2$ ) were used [112, 162]. If previous to the  $\text{NH}_3$ -treatment a high-energy ball milling is performed, an up to 30-fold increase in current density was achieved as can be learned from columns 8 and 20 in Table 2. The ball milling itself does not affect the kinetics of the catalyst; however, it can lead to enhanced mass transport properties [209]. Induced by the ball milling, the carbon agglomerates formed during this template-assisted preparation were cracked down allowing subsequently the  $\text{NH}_3$  to react more efficiently with the catalyst (compare lines 8 and 9) [209]. Induced by the burn-off, higher site densities are obtained, and a formation of new and/or different catalytic centers might appear [63, 129, 167, 170]. On the other hand, the turnover frequency of the catalysts is improved. To illustrate this behavior, compare lines 4, 5, 12; lines 17, 19; lines 8, 20 and lines 9, 23. Possible reasons for the enhanced kinetics could be (1) the formation of additional, maybe different catalytic centers (i.e.,  $\text{FeN}_4$  vs.  $\text{FeN}_{2+2}$  in micropores, compare section “Molecular Centers in Carbonized Materials,” Figs. 16 and 19), (2) a general change of the reduction mechanism, or (3) an improvement of the carbon matrix with respect to its electron donor properties [112, 136, 167, 191].

As described in section “Alternative Center Generation During Heat Treatment,” some preparation approaches failed by the attempt to increase the site density above a certain critical value [170, 172]. In Table 2, column C, the site densities are listed. It can be deduced that catalysts prepared by the use of a carbon support usually reveal smaller site densities compared to those where exclusively organic precursor molecules were used as carbon sources. In template-assisted preparation processes, an acid leaching (removal of the template) was performed after a first pyrolysis and before the catalyst was further processed [39, 115, 130–133, 159, 160, 162, 177, 186, 189, 197, 201, 209]. The obtained catalysts exhibit site densities of  $3 \cdot 10^{20}$  up to  $7 \cdot 10^{20}$  centers per gram (compare Table 2). In contrast, the utilization of carbon blacks as support often leads to site densities  $< 1.5 \cdot 10^{20}$  centers per gram. In these

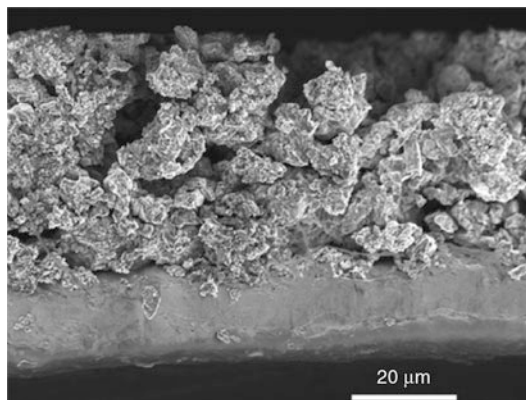
catalysts, the number of active sites should be further increased for FC application.

When high current densities are requested, a lack in the presence of one (or more) of the reactants at the three phase boundary often limits the performance. Another issue concerns the removal of reaction water out of the micro- and mesopore structure which is lowering the kinetics of reactive centers. Thus, in order to optimize the mass transport properties, either the electron or proton conductivity has to be augmented or the pore structure of the catalyst has to be improved to enable better oxygen diffusion to the active centers. Furthermore, the catalyst should be sufficiently hydrophobic in order to guarantee a fast removal of the water to prevent any blocking of active sites. Preferentially, surface groups on the carbon increase the hydrophilicity of the catalyst. Especially disordered carbon can provide higher concentrations of such groups caused by a high number of defects in comparison to well-ordered carbon. Thus, in turn, a high degree of graphitization is beneficial for the water transport properties [207]. As discussed in the next section, graphitic carbon can also enhance the long-term stability.

When switching from RDE to fuel cell measurements, an increase of catalytic activity is expected, simply because of the higher operation temperature. Column F lists the ratio of achieved activities in fuel cell and RDE measurements ( $J_{\text{FC}}/J_{\text{RDE}}$ ) at  $U = 0.8$  V. Looking at catalysts, which were produced without commercial carbon support, difficulties in the fuel cell application (as expressed by a low current ratio FC/RDE in column F) can be recognized with the exception of the catalyst in line 8 of Table 2. This catalyst is similar to the one in line 9 except of a ball milling previous to the ammonia treatment. Therefore, a main reason might be the presence of substantially larger carbon agglomerates, which inhibit a homogeneous preparation of the gas diffusion electrode (GDE) [160, 162, 209], as shown in Fig. 21.

Looking at the template-assisted preparation techniques, the physicochemical properties of the in-situ formed carbon could be of lower quality compared to commercial carbon supports. For fuel cell application, an optimization with respect





**Polymer Electrolyte Membrane Fuel Cells (PEM-FC) and Non-noble Metal Catalysts for Oxygen Reduction, Fig. 21** GDE of a catalyst prepared by the oxalate-supported pyrolysis. (The figure was taken from [162], reproduced by permission of ECS – The Electrochemical Society)

to (1) the electrical conductivity, (2) the agglomerate or particle size, and (3) the transport properties (hydrophilicity) is necessary. However, optimal physicochemical properties of the carbon might not be obtained at the maximum of volumetric current density (determined by SD and TOF). Therefore, approaches to improve catalysts with an in-situ formed carbon should be also done under utilization of FC measurements in order to evaluate the mass transport kinetics. Nevertheless, optimization remains challenging as a good balance between carbon properties and ORR performance must be found. Not-optimized carbon could not only lower the achievable activity, it could also affect the long-term stability as will be discussed in the following section.

### Stability

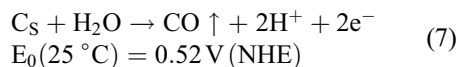
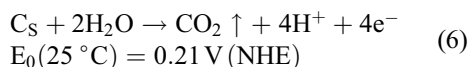
In this part, possible degradation mechanisms and the currently most promising catalysts with respect to longterm stability will be discussed. For the final implementation, the observed stability is crucial. To optimize the material system, however, it has to be rationalized which processes lead to a decrease of ORR activity.

Regarding non-pyrolyzed macrocycles, hydrogen peroxide formed in the reduction cycle can lead to broken bonds between the substituents and the tetrapyrrole core. Changes in the electronic

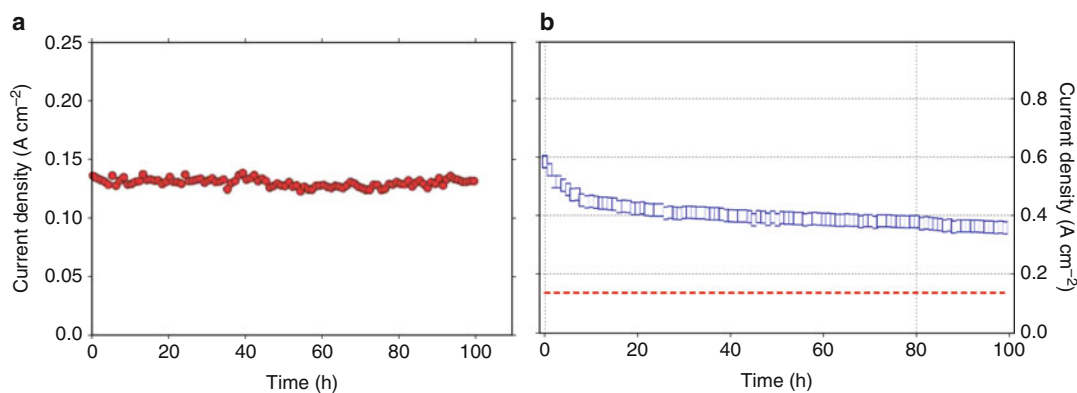
structure connected therewith cause a decrease of the reduction activity. In acidic conditions as given in PEM-FC, demetallation can also cause an activity decline [71, 87, 98, 102, 210, 211]. Furthermore, carbon monoxide is able to bind irreversibly to the metal centers and thereby deactivating them [212]. With respect to Eq. 7, carbon monoxide might be formed by carbon oxidation during FC operation.

Better stabilities were achieved investigating heat-treated catalysts (section “Molecular Centers in Carbonized Materials”). Nevertheless, in most of the cases, even after the heat treatment, considerable decreases of performance were already observed after a few hours of operation time [69, 159, 168, 184, 188, 213–216]. For catalysts prepared by a heat treatment of either iron porphyrin or iron phthalocyanine, it was shown that they are tolerant toward CO [217, 218]. Therefore, we assume that in general, CO-poisoning can be ruled out as degradation mechanism for carbonized materials. Possible degradation mechanisms could be addressed to (1) a corrosion of carbon as known from platinum catalysts, (2) an inactivation by leaching of active sites, or (3) a deactivation of active species (e.g., by blocking of the centers by intermediates or the final products) [71, 98, 99, 102, 190, 191, 210, 211, 219, 220].

The thermodynamic process of carbon oxidation already starts at potentials  $>0.21$  V. For Pt/C catalysts, SEM cross-sectional images illustrated a significant decrease of the carbon layer thickness, causing a detachment of the platinum particles or an increase of the particle size [8, 110, 220]. In Eqs. 6 and 7, the oxidation reactions of carbon to carbon dioxide (Eq. 6) and carbon monoxide (Eq. 7) are given.



Both reactions are initiated by the presence of water. This fact again underlines the importance of an optimized water management. Independent



**Polymer Electrolyte Membrane Fuel Cells (PEM-FC) and Non-noble Metal Catalysts for Oxygen Reduction, Fig. 22** Stability measurements of (a) a Co-PPy-CB and (b) a Fe/CB-PFM catalysts. Both catalysts were measured under nearly the same conditions at 80 °C, backpressures of 2 atm, gases at 100% RH with catalyst

loadings of 6 mg/cm<sup>2</sup> and 5.6 mg/cm<sup>2</sup> for the Co-PPy-CB and Fe/CB-PFM catalysts, respectively. (The figure in (a) was taken from [177]; copyright 2006, reproduced with permission of Nature Publishing Group. The figure in (b) was taken from [165], reprinted with permission from AAAS)

of the nature of the active centers in Me-N-C catalysts, they are presumably integrated into a carbon matrix, either as nitrogen heteroatoms (Fig. 8), MeN<sub>4</sub>-centers (Fig. 16), or as MeN<sub>2+2</sub>-centers in micropores between two adjacent graphene layers (Fig. 19). As discussed above, in N<sub>4</sub>-macrocycles, a decrease of the conjugated  $\pi$ -electron system causes a lowering of the ORR activity [41, 42, 80, 81, 221]. It can be assumed that a carbon burn-off in heat-treated materials can cause a similar effect (see below, discussion related to Fig. 25).

Herranz et al. showed that FeN<sub>2+2</sub>-centers have two different states of catalytic activity depending on whether an NH<sup>+</sup>-group or an NH-anion-group is present in its environment [191]. For the first case, very high turnover frequencies are reported. The anion blocking causes a drastic decrease of the turnover frequency and will appear during RDE or FC tests. Nevertheless, it was found that this deactivation process is reversible and that the centers can be activated by performing a thermal or chemical recover treatment [191]. As such treatments are not applicable during FC operation, however, the effect in general should be inhibited if it is the main reason for activity decay of a specific catalyst.

In 2006, Bashyam and Zelenay published a stable performance of a catalyst entirely produced without heat treatment obtaining stability for a runtime of 100 h. The performance of the catalyst is shown in Fig. 22a. It was prepared by polymerization of pyrrole in the presence of a carbon-supported cobalt salt. Caused by the polymerization, an extended  $\pi$ -electron system was formed leading to good electron conductivity. At that time, the authors suggested that cobalt ions – two-fold coordinated by nitrogen atoms – are responsible for the activity [177].

However, the disadvantage of this material was a low catalytic activity (23 A/g at 0.4 V at a catalyst loading of 6 mg/cm<sup>2</sup>). Recent approaches of the same group showed that besides pyrrole, also other nitrogen heterocycles and metal salts can be used as nitrogen and metal sources, respectively [189, 208]. Similar to non-pyrolyzed macrocycles, the activity can be enhanced by a heat treatment [177, 189]. A comparison of different nitrogen heterocycles used in the preparation showed that the selection of the polymer significantly affects activity and stability – even after a heat treatment. The Fe/PANI/C-catalyst supported on multiwall carbon nanotubes (MWCNT) achieved an activity of 75 A/g (at 0.4 V) and showed no degradation within the

investigated time of 500 h [186, 189]. Therefore, this catalyst is currently the most stable Fe-N-C catalyst, exhibiting even a good catalytic activity (remark: considering catalysts, which have been investigated in fuel cells with respect to their stability). The preparation is similar to that of a pyrrole-based catalyst.

The currently most active catalysts prepared by the Pore-Filling-Method (PFM) from J.-P. Dodelet's group show an average degradation of 0.38%/h for 100 h potentiostatic operation with respect to the initial activity (compare [165, 192]), the related curve is shown in Fig. 22b. The measuring conditions thereby were more or less identical to Bashyam's and Zelenay's experiments. It seems that for the degradation of this PFM-catalyst, one can distinguish an initial fast degradation ( $t < 20$  h) which is superimposed by a weaker and slower one ( $t > 20$  h:  $-0.08\%/h$ ).

In the work of Wu et al., structural changes of a Fe/PANI/KB300 catalyst were investigated before and after a runtime of 500 h [189]. After a long-term test, the percentage of oxygen in the matrix was drastically increased, that the authors attributed to the oxidation of carbon and nitrogen atoms. Particularly striking were a complete loss of sulfur (which was present in the polymerization agent) and a slight decrease of the total nitrogen content (from 6.3% to 5.6%). Changes in the relative composition of the N1 s spectra were significant. A comparison of the spectra before and after 500 h fuel cell test time is shown in Fig. 23. It is evident that the long-term performance causes an energetic shift of the nitrogen species toward higher bonding energies. This was mostly attributable to the oxidation of pyridinic nitrogen atoms. In the investigated timeframe, the catalyst lost 17% of its initial activity. Similar shifts in the XPS N1s-spectra were observed by Liu et al. and by Kramm [112, 115].

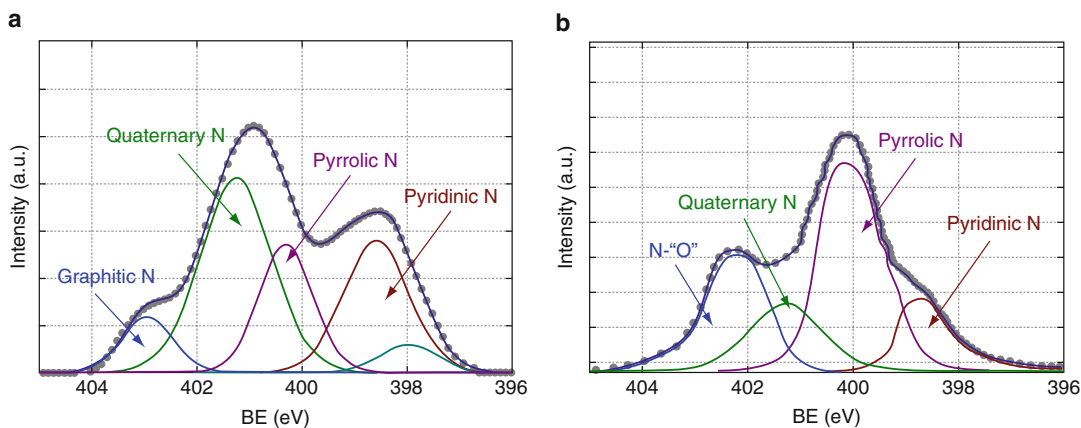
In the case of Liu et al., significantly higher activity losses compared to Wu et al. were observed ( $-0.46\%/h$  vs  $-0.04\%/h$ ), while Kramm did not observe any significant loss (compare Fig. 25). Liu et al. assigned the overall ORR activity to highly active pyridinic and less active graphitic nitrogen atoms (both without iron participation) [115]. They explained their XPS

results with a protonation of pyridinic nitrogen atoms in contact with an acidic electrolyte; this process was proposed to be the main reason for the observed deactivation. On the other hand, graphitic nitrogen atoms were assigned to be less active but more stable in acidic environment [115]. Kramm investigated the structural changes of a Fe-N-C catalyst via XPS, NAA and  $^{57}\text{Fe}$  Mößbauer spectroscopy [112]. The catalyst was produced by the sulfur-assisted oxalate-supported pyrolysis of FeTMPPCI; in a subsequent acid leaching step, excess iron was removed. Before the long-term measurement was performed, the electrode was kept in distilled water for 24 h in order to initiate a complete swelling of the PTFE previous to the stability test shown in Fig. 24.

The preconditioned electrode showed no loss in activity over a period of 4 weeks and no significant change of the composition in Mößbauer spectra or iron content. The changes of the N1 s spectra, however, were similarly pronounced as described by Wu et al. [112, 189]. A comparison of the three references discussed above leads to the conclusion that pyridinic nitrogen atoms might affect the activity of the catalysts up to a certain degree. However, it has been demonstrated that pyridinic nitrogen atoms cannot explain the catalytic activity alone [112].

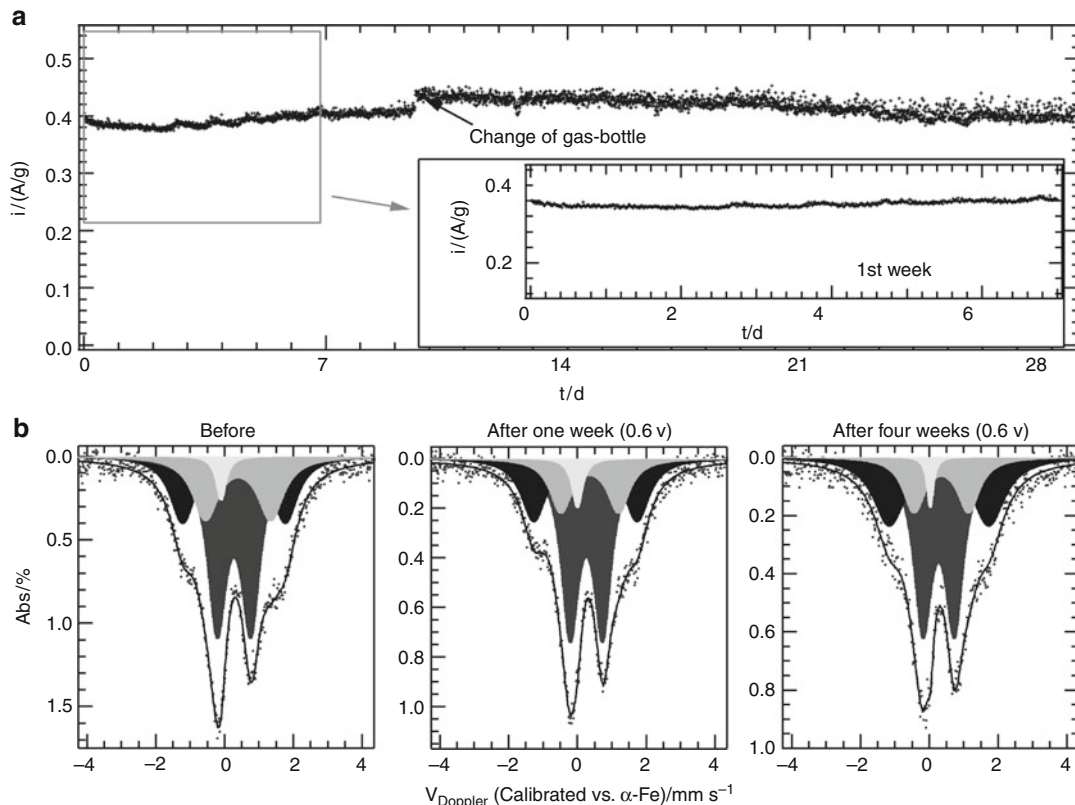
In an early work of Faubert et al. [140], the influence of the pyrolysis temperature on the stability of MeTPP/C was investigated (Me = Fe, Co). Figure 25 shows the changes of the current density (related to the surface area and the metal content) as a function of performance time. It is evident that catalysts prepared from FeTPP achieve higher current densities and better stabilities than CoTPP-based catalysts. Apart from a pronounced loss in activity within the first 5 min, the FeTPP/C catalysts, produced at 800 °C and 900 °C, demonstrated a nearly stable performance. At even higher pyrolysis temperatures, the stability performance was similar to that of the platinum catalyst (2 wt% Pt/C), which was measured as a reference. The authors assigned the enhanced stability to an increased amount of graphitic carbon [140].

Recent results published by the same group [222, 223] and the comparison of various



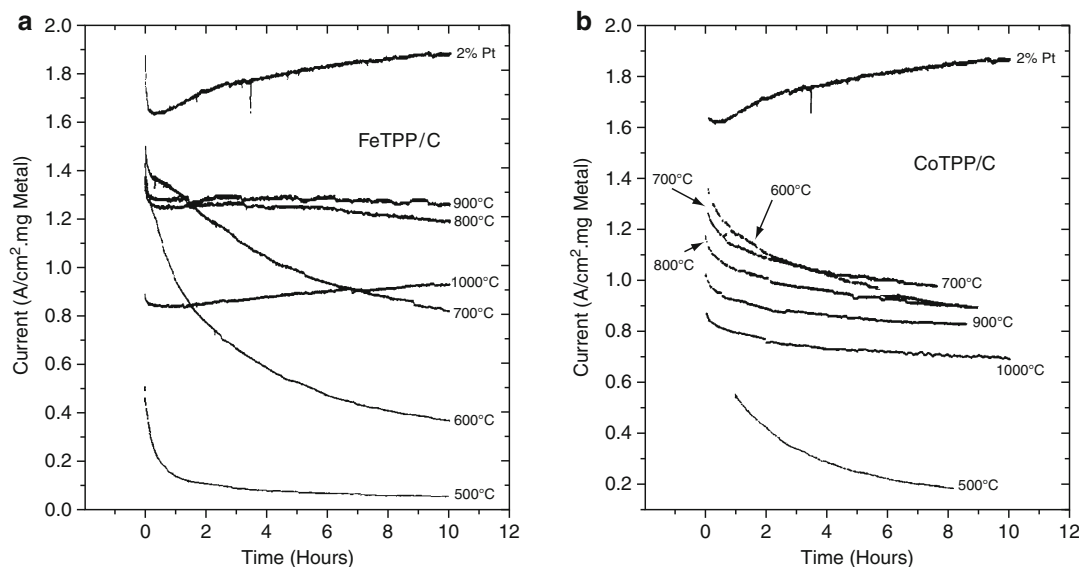
**Polymer Electrolyte Membrane Fuel Cells (PEM-FC) and Non-noble Metal Catalysts for Oxygen Reduction, Fig. 23** N 1s XP spectra of a Fe-PANI-C catalyst

(a) before and (b) after a 500-h long-term stability test. (The figure was taken from [189]; reproduced by permission of ECS – The Electrochemical Society)



**Polymer Electrolyte Membrane Fuel Cells (PEM-FC) and Non-noble Metal Catalysts for Oxygen Reduction, Fig. 24** Potentiostatic ( $U = 0.6\text{ V}$ ) long-term stability test in  $\text{O}_2$ -flushed  $0.5\text{ M H}_2\text{SO}_4$  of a Fe-N-C-catalyst at RT (a). The insert gives a magnification of the first week of measuring time. The catalyst was prepared by the sulfur-

assisted oxalate-supported pyrolysis of  $\text{FeTMPPCl}$  ( $800\text{ }^\circ\text{C}$ ,  $\text{N}_2$ ), with acid leaching. The structural features related to iron were studied by Mößbauer spectroscopy at RT; (b) before, after 1 week and after 4 weeks of measuring time. (The figure is adapted from Figs. 7–7 and 7–8 of [112]; copyright 2009 by Südwestdeutscher Verlag für Hochschulschriften)



**Polymer Electrolyte Membrane Fuel Cells (PEM-FC) and Non-noble Metal Catalysts for Oxygen Reduction, Fig. 25** Stability tests of carbon-supported FeTPP

(a) and CoTPP (b), both pyrolyzed at various temperatures as indicated in the graphs. (The figures were taken from [140], reproduced with permission of Elsevier)

carbon-supported Fe/PANI/C catalysts confirm this observation [189]. One might summarize that in fuel cells, obviously the long-term stability seems to depend on the corrosion resistivity of the carbon matrix for both, Fe-N-C and Pt/C catalysts [8, 224].

In order to avoid any activity loss, the catalysts must be stabilized: For Pt/C catalysts, it was shown that the implementation of metal oxide particles into the carbon matrix can enhance the corrosion resistivity substantially. Furthermore, as far as possible, the catalysts should comprise fractions of graphitic carbon which prevent a fast oxidation.

It is believed that the search for alternative supports for Fe-N-C catalysts will become dominant in the future. Especially, different transition metal oxynitrides ( $\text{TiO}_x\text{N}_y$ ,  $\text{TaO}_x\text{N}_y$ ,  $\text{ZrO}_x\text{N}_y$ ), and Nb- or Sb-doped  $\text{TiO}_2$  or  $\text{SnO}_2$  or PANI appear to be promising in this context [55, 224–227]. It will remain a major challenge to enable the implementation of molecular centers onto the surface of the new support material. It has already been pointed out that PANI possesses a considerable potential with this respect [189]. Since none of the other promising support materials contain carbon, it is questionable how catalytically active Fe-N-C catalysts could be implemented.

With this respect, the work from Atanasoski and coworkers is promising (compare section “Transition Metal Carbides, Nitrides and Chalcogenides”) [35]. By performing a heat treatment of their sputtered  $\text{C-N}_x\text{:Fe}$  films, the activity was drastically enhanced but still much lower compared to macrocycle-based catalysts. However, when titanium carbide was used as support instead of carbon, a high stability was obtained. The fact that by changing the support, an essentially better durability was obtained is an important result as it shows that even for catalysts based on molecular centers, alternative support materials can be utilized and that the interaction between the support and the catalytic centers might be crucial for the optimization of those catalysts for a fuel cell application.

However, it has to be kept in mind that a major challenge of these catalysts is to improve their transport properties which are by far not ideal as can be recognized from Tafelplots deduced from RDE measurements. To investigate the water management in platinum-based fuel cells, the use of neutron scattering has meanwhile proven to be an effective tool [228, 229]. Such investigations could also play a major role for further optimization of Fe-N-C catalysts.

**Polymer Electrolyte Membrane Fuel Cells (PEM-FC) and Non-noble Metal Catalysts for Oxygen Reduction, Table 3** Comparison of different Fe-N-C catalysts with respect to their stability

A	B	C	D	E		G	H
				Start	End		
	Catalyst	Lit.	Comm.	mW/cm <sup>2</sup>	time/h	Performance (%)	
1	(FeTMPPCl/non-ppCB)-HT950Ar, 5.2 wt%Fe	222	FC80, H <sub>2</sub> /O <sub>2</sub> : 1 bar, 2 mg/cm <sup>2</sup>	2.58	6.24	15	9.46
2	(FeTMPPCl/non-ppCB)-HT950Ar-H <sub>2</sub> SO <sub>4</sub> , 5.2 wt%	222	FC80, H <sub>2</sub> /O <sub>2</sub> : 1 bar, 2 mg/cm <sup>2</sup>	5.1	6.6	15	1.96
3	PANI-Fe-MWCNT (HT900, N <sub>2</sub> -H <sub>2</sub> SO <sub>4</sub> )	189	FC80, H <sub>2</sub> /Air: 2 bar, 4 mg/cm <sup>2</sup>	120	120	500	0.00
4	PPy-Co-C	177	FC80, H <sub>2</sub> /Air: 2 bar, 4 mg/cm <sup>2</sup>	56	56	100	0.00
5	PPy-Co-C	177	FC80, H <sub>2</sub> /O <sub>2</sub> : 2 bar, 6 mg/cm <sup>2</sup>	24.5	24.5	50	0.00
6	Fe/Fe/S-HT800N <sub>2</sub> -HCl, 24h_swelling_inH <sub>2</sub> O	112	T = 25 °C, 0.5 M H <sub>2</sub> SO <sub>4</sub> , O <sub>2</sub> , 4 mg/cm <sup>2</sup>	0.96	0.96	672	0.00
7	3 M-NiANI-HT_NH <sub>3</sub>	166	FC80, H <sub>2</sub> /O <sub>2</sub> : 3/4, 3 bar	0.0024	0.0024	0.5	0.00
8	PANI-Fe <sub>3</sub> Co-C (HT900, N <sub>2</sub> -H <sub>2</sub> SO <sub>4</sub> )	189	FC80, H <sub>2</sub> /Air: 2 bar, 4 mg/cm <sup>2</sup>	148	132	600	-0.02
9	PANI-Fe <sub>3</sub> Co-C (HT900, N <sub>2</sub> -H <sub>2</sub> SO <sub>4</sub> )	186	FC80, H <sub>2</sub> /Air: 2 bar, 4 mg/cm <sup>2</sup>	140	130	400	-0.02
10	PANI-Fe-C (HT900, N <sub>2</sub> -H <sub>2</sub> SO <sub>4</sub> )	189	FC80, H <sub>2</sub> /Air: 2 bar, 4 mg/cm <sup>2</sup>	120	100	500	-0.03
11	((CB-HCl-HNO <sub>3</sub> ) + Co/Fe(N) - HT900Ar-H <sub>2</sub> SO <sub>4</sub>	119	FC80, H <sub>2</sub> /O <sub>2</sub> , no backpressure	70	60	450	-0.03
12	PANI-Fe-KB300 (HT900, N <sub>2</sub> -H <sub>2</sub> SO <sub>4</sub> )	189	FC80, H <sub>2</sub> /Air: 2 bar, 4 mg/cm <sup>2</sup>	116	90	500	-0.04
13	PANI-Co-C (HT900, N <sub>2</sub> -H <sub>2</sub> SO <sub>4</sub> )	189	FC80, H <sub>2</sub> /Air: 2 bar, 4 mg/cm <sup>2</sup>	100	90	180	-0.06
14	Fe/Fe/S-HT800N <sub>2</sub> -HCl	112	GDE, T = 25 °C, O <sub>2</sub> , 4 mg/cm <sup>2</sup>	0.96	0.7032	168	-0.16
15	(FeCo)/EDA + SiO <sub>2</sub> -HT1000Ar-NaOH-H <sub>2</sub> SO <sub>4</sub> -HT1000Ar	115	FC75, H <sub>2</sub> /Air: 2 bar, 2 mg/cm <sup>2</sup>	140	110	100	-0.21
16	CHb200900	204	FC80, H <sub>2</sub> /Air:50/250, 10 mg/cm <sup>2</sup>	-	-	200	-0.22
17	CHb350900C	204	FC80, H <sub>2</sub> /Air:50/250, 10 mg/cm <sup>2</sup>	-	-	200	-0.33
18	PFM1: Fe/Phen/BP-HT1050Ar-HT950NH <sub>3</sub>	165	FC80, H <sub>2</sub> /Air: 2 bar, 5.6 mg/cm <sup>2</sup>	240	150	100	-0.38
19	(Fe,Co)/EDA + SiO <sub>2</sub> -HT800Ar-NaOH-H <sub>2</sub> SO <sub>4</sub> -HT800Ar	115	FC75, H <sub>2</sub> /Air: 2 bar, 2 mg/cm <sup>2</sup>	204	120	90	-0.46
20	PPy-Fe-C (HT900, N <sub>2</sub> -H <sub>2</sub> SO <sub>4</sub> )	189	FC80, H <sub>2</sub> /Air: 2 bar, 4 mg/cm <sup>2</sup>	196	100	100	-0.49
21	PFM1: Fe/Phen/BP-HT1050Ar-HT950NH <sub>3</sub>	165	FC80, H <sub>2</sub> /O <sub>2</sub> : 2 bar, 5.6 mg/cm <sup>2</sup>	385	165	100	-0.57
22	(FePhen3 + BP2000)-HT900Ar	178	GDE, T = 25 °C, 0.5 M H <sub>2</sub> SO <sub>4</sub> , Air	13.5	3	40	-1.94
23	(Graphite + BM5)-FeAc-HT950NH <sub>3</sub>	184	FC80, H <sub>2</sub> /O <sub>2</sub> : 4/2 bar, 1.1 mg/cm <sup>2</sup>	135	69	24	-2.04
24	(Graphite + BM0.5)-FeAc-HT950NH <sub>3</sub>	184	FC80, H <sub>2</sub> /O <sub>2</sub> : 4/2 bar, 1.1 mg/cm <sup>2</sup>	102	37.5	24	-2.63
25	(Graphite + BM10)-FeAc-HT950NH <sub>3</sub>	184	FC80, H <sub>2</sub> /O <sub>2</sub> : 4/2 bar, 1.1 mg/cm <sup>2</sup>	43.5	14.4	24	-2.79
26	(FeTMPPCl/non-ppCB)-HT950Ar, 0.4 wt%aFe	222	FC80, H <sub>2</sub> /O <sub>2</sub> : 1 bar, 2 mg/cm <sup>2</sup>	108	13.2	15	-5.85
27	(FeTMPPCl/non-ppCB)-HT950Ar, 0.4 wt% Fe	222	FC80, H <sub>2</sub> /O <sub>2</sub> : 1 bar, 2 mg/cm <sup>2</sup>	6	0.66	15	-5.93



## Future Direction

Comparing the different types of NNMC, the Fe-N-C catalysts are presently the most promising candidates to replace platinum or other noble metal catalysts. These materials exhibit the highest activities and catalyze with high selectivity the direct reduction of oxygen to water. Since 2009, a significant improvement in comparison to previous results was made; here especially the work of Dodelet and coworkers and Zelenay and coworkers should be mentioned [165, 189]. In general, stable fuel cell performance over periods of up to 1,000 h has already been demonstrated (Table 3). Although long-term stability and high catalytic activity appear to be difficult to combine into one material, based on today's knowledge of the structural characteristics that affect activity and/or stability, further improvements of FC performance are expected. One major step to an improved stability may be through alternative support materials.

Apart from this "hot" topic, one should keep in mind that catalysts based on transition metal chalcogenides, nitrides, and carbides also have the potential to be used without carbon support. Considering the tremendous carbon corrosion problems especially at higher temperature ( $>110\text{ }^{\circ}\text{C}$ ), carbon-free electrode structures will be an important aspect of future research.

## Bibliography

1. Markovic NM, Radmilovic V, Ross PN (2003) Catalysis and electrocatalysis at nanoparticle surfaces. Marcel Dekker, New York/Basel
2. Mukerjee S, Srinivasan S (1993) Enhanced electrocatalysis of oxygen reduction on platinum alloys in proton exchange membrane fuel cells. *J Electroanal Chem* 357:201–224
3. Zhang J, Lima FHB, Shao MH, Sasaki K, Wang JX, Hanson J, Adzic RR (2005) Platinum monolayer on non-noble metal-noble metal core-shell nanoparticle electrocatalysts for  $\text{O}_2$  reduction. *J Phys Chem B* 109:22701–22704
4. Stamenkovic VR, Mun BS, Mayrhofer KJJ, Ross PN, Markovic NM (2006) Effect of surface composition on electronic structure, stability and electrocatalytic properties of Pt-transition metal alloys: Pt-skin versus Pt-skeleton surfaces. *J Am Chem Soc* 128:8813–8819
5. Strasser P, Koh S, Anniyev T, Greeley J, More K, Yu C, Liu Z, Kaya S, Nordlund D, Ogasawara H, Toney MF, Nilsson A (2010) Lattice-strain control of the activity in dealloyed core – shell fuel cell catalysts. *Nat Chem* 2:454–460
6. Adzic RR, Zhang J, Sasaki K, Vukmirovic MB, Shao M, Wang JX, Nilekar AU, Mavrikakis M, Valerio JA, Uribe F (2007) Platinum monolayer fuel cell electrocatalysts. *Top Catal* 46:249–262
7. Zhang S, Yuan XZ, Hin JC, Wang H, Friedrich KA, Schulze M (2009) A review of platinum-based catalyst layer degradation in proton exchange membrane fuel cells. *J Power Sources* 194:588–600
8. Mayrhofer KJJ, Meier JC, Ashton SJ, Wiberg GKH, Kraus F, Hanzlik M, Arenz M (2008) Fuel cell catalyst degradation on the nanoscale. *Electrochem Commun* 10:1144–1147
9. Delacote C, Bonakdarpour A, Johnston CM, Zelenay P, Wieckowski A (2008) Aqueous-based synthesis of ruthenium – selenium catalyst for oxygen reduction reaction. *Faraday Discuss* 140:269–281
10. Fiechter S, Dorbandt I, Bogdanoff P, Zehl G, Schulenburg H, Tributsch H, Bron M, Radnik J, Fieber-Erdmann M (2007) Surface modified ruthenium nanoparticles: structural investigation and surface analysis of a novel catalyst for oxygen reduction. *J Phys Chem C* 111:477–487
11. Guinel MJF, Bonakdarpour A, Wang B, Babu PK, Ernst F, Ramaswamy N, Mukerjee S, Wieckowski A (2009) Carbonsupported, selenium-modified ruthenium – molybdenum catalysts for oxygen reduction in acidic media. *ChemSusChem* 2:658–664
12. Haas S, Hoell A, Zehl G, Dorbandt I, Bogdanoff P, Fiechter S (2008) Structural investigation of carbon supported Ru-Se based catalysts using anomalous small angle X-ray scattering. *ECS Trans* 6:127–138
13. Lopotov KN, Kriventsov VV, Nagabhushana KS, Boennemann H, Kochubey DI, Savinova ER (2009) Combined in situ EXAFS and electrochemical investigation of the oxygen reduction reaction on unmodified and Se-modified Ru/C. *Catal Today* 147:260–269
14. Zehl G, Schmithals G, Hoell A, Haas S, Hartnig C, Dorbandt I, Bogdanoff P, Fiechter S (2007) On the structure of carbonsupported selenium-modified ruthenium nanoparticles as electrocatalysts for oxygen reduction in fuel cells. *Angew Chem Int Ed* 46:7311–7314
15. Cremers C, Scholz M, Seliger W, Racz A, Knechtel W, Rittmayr J, Grafwallner F, Peller H, Stimming U (2007) Developments for improved direct methanol fuel cell stacks for portable power. *Fuel Cells* 7:21–31
16. Garsuch A, Michaud X, Böhme K, Wagner G, Dahn JR (2009) Fuel cell performance of templated Ru/Se/C-based catalysts. *J Power Sources* 189:1008–1011

17. Whipple DT, Jayashree RS, Egas D, Alonso-Vante N, Kenis PJA (2009) Ruthenium cluster-like chalcogenide as a methanol tolerant cathode catalyst in air-breathing laminar flow fuel cells. *Electrochim Acta* 54:4384–4388
18. Wippermann K, Richter B, Klafki K, Mergel J, Zehl G, Dorbandt I, Bogdanoff P, Fiechter S, Kaytakoglu S (2007) Carbon supported Ru – Se as methanol tolerant catalysts for DMFC cathodes part II: preparation and characterization of MEAs. *J Appl Electrochem* 37:1399–1411
19. Lee J-W, Popov BN (2007) Ruthenium-based electrocatalysts for oxygen reduction reaction – a review. *J Solid State Electrochem* 11:1355–1364
20. Zhang L, Zhang J, Wilkinson DP, Wang H (2006) Progress in preparation of non-noble electrocatalysts for PEM fuel cell reactions. *J Power Sources* 156:171–182
21. Bennett LH, Cuthill JR, McAlister AJ, Erickson NE, Watson RE (1974) Electronic structure and catalytic behavior of tungsten carbide. *Science* 184:563–565
22. Colton RJ, Huang JJ, Rabalais JW (1975) Electronic structure of tungsten carbide and its catalytic behavior. *Chem Phys Lett* 34:337–339
23. Levy RB, Boudart M (1973) Platinum-like behavior of tungsten carbide in surface catalysis. *Science* 181:547–549
24. Ross PN Jr, Stonehart P (1975) Surface characterization of catalytically active tungsten carbide (WC). *J Catal* 39:298–301
25. Binder H, Köhling A, Kuhn W, Lindner W, Sandstede G (1969) Tungsten carbide electrodes for fuel cells with acid electrolyte. *Nature* 224:1299–1300
26. Bronoel G, Museux E, Leclercq G, Leclercq L, Tassin N (1991) Study of hydrogen oxidation on carbides. *Electrochim Acta* 36:1543–1547
27. Machida K, Enyo M (1990) Preparation of WC<sub>x</sub> thin films by RF sputtering and their electrocatalytic property for anodic methanol oxidation. *J Electrochem Soc* 137:871–876
28. Sokolsky DV, Palanker VS, Baybatyrov EN (1975) Electrochemical hydrogen reactions on tungsten carbide. *Electrochim Acta* 20:71–77
29. Mazza F, Trassatti S (1963) Transition metal oxides as DMFC cathodes without platinum. *J Electrochem Soc* 110:847–849
30. Lee K, Ishihara A, Mitsushima S, Kamiya N, Ota K (2004) Stability and electrocatalytic activity for oxygen reduction in WC + Ta catalyst. *Electrochim Acta* 49:3479–3485
31. Bhattarai J, Akiyama E, Habazaki H, Kawashima A, Asami K, Hashimoto K (1998) The passivation behavior of sputter-deposited W-Ta alloys in 12 M HCl. *Corros Sci* 40:757–179
32. Chou WJ, Yu GP, Huang JH (2003) Corrosion resistance of ZrN films on AISI 304 stainless steel substrate. *Surf Coat Technol* 167:59–67
33. Zhong H, Zhang H, Liang Y, Zhang J, Wang M, Wang X (2007) A novel non-noble electrocatalyst for oxygen reduction in proton exchange membrane fuel cells. *J Power Sources* 164:572–577
34. Zhong H, Zhang H, Liu G, Liang Y, Hu J, Yi B (2006) A novel nonnoble electrocatalyst for PEM fuel cell based on molybdenum nitride. *Electrochem Commun* 8:707–712
35. Atanasoski R (2007) Novel approach to non-precious metal catalysts. DOE hydrogen program FY2007 annual progress report 820–824
36. O'Neill DG, Atanasoski R, Schmoekel AK, Vernstrom GD, O'Brien DP, Jain M, Wood TE (2006) Vacuum deposited non-precious metal catalysts for PEM fuel-cells. *Mater Matters* 1:17–19
37. Blomquist J, Lang H, Larsson R, Widellöv A (1992) Pyrolysis behaviour of metalloporphyrins: part2: a Mössbauer study of pyrolysed Fe<sup>III</sup> tetraphenylporphyrin chloride. *J Chem Soc Faraday Trans* 88:2007–2011
38. Bouwkamp-Wijnoltz AL, Visscher W, van Veen JAR, Boellaard E, van der Kraan AM, Tang SC (2002) On active-site heterogeneity in pyrolysed carbon-supported iron porphyrin catalysts for the electrochemical reduction of oxygen: an in situ Mössbauer study. *J Phys Chem B* 106:12993–13001
39. Koslowski UI, Abs-Wurmbach I, Fiechter S, Bogdanoff P (2008) Nature of the catalytic centres of porphyrin based electrocatalysts for the ORR – a correlation of kinetic current density with the site density of Fe–N<sub>4</sub> centres. *J Phys Chem C* 112: 15356–15366
40. Lefèvre M, Dodelet J-P, Bertrand P (2002) Molecular oxygen reduction in PEM fuel cells: evidence for the simultaneous presence of two active sites in Fe-based catalysts. *J Phys Chem B* 106:8705–8713
41. van Veen JAR, van Baar JF, Kroese KJ (1981) Effect of heat treatment on the performance of carbon-supported transition-metal chelates in the electrochemical reduction of oxygen. *J Chem Soc Faraday Trans* 77:2827–2843
42. van Veen JAR, Colijn HA, van Baar JF (1988) On the effect of a heat treatment on the structure of carbon-supported metalloporphyrins and phthalocyanines. *Electrochim Acta* 33:801–804
43. Bradley Easton E, Bonakdarpour A, Dahn JR (2006) Fe-C-N oxygen reduction catalysts prepared by combinatorial sputter deposition. *Electrochem Sol State Letts* 9:A463–A567
44. Liu Y, Ishihara A, Mitsushima S, Kamiya N, Ota K (2007) Transition metal oxides as DMFC cathodes without platinum. *J Electrochem Soc* 154: B664–B669
45. Liu Y, Ishihara A, Mitsushima S, Ota K (2010) Influence of sputtering power on oxygen reduction reaction activity of zirconium oxides prepared by radio frequency reactive sputtering. *Electrochim Acta* 55:1239–1244
46. Descorme C, Madier Y, Duprez D (2000) Infrared study of oxygen adsorption and activation on cerium–zirconium mixed oxides. *J Catal* 196:167–173

47. Lisebigler AL, Lu G, Yates JT (1995) Photocatalysis on  $\text{TiO}_2$  surfaces: principles, mechanisms, and selected results. *Chem Rev* 95:735–758
48. Witko M, Tokarz-Sobieraj R (2004) Surface oxygen in catalysts based on transition metal oxides: what can we learn from cluster DFT calculations? *Catal Today* 91–92:171–176
49. Kim J-H, Ishihara A, Mitsushima S, Kamiya N, Ota K-I (2007) Catalytic activity of titanium oxide for oxygen reduction reaction as a non-platinum catalyst for PEFC. *Electrochim Acta* 52:2492–2497
50. Mentus SV (2004) Oxygen reduction on anodically formed titanium dioxide. *Electrochim Acta* 50:27–32
51. Kudo A, Miseki YCSR (2009) Heterogeneous photocatalyst materials for water splitting. *Chem Soc Rev* 38:253–278
52. Osterloh FE (2008) Inorganic materials as catalysts for photochemical splitting of water. *Chem Mater* 20:35–54
53. Liu G, Zhang HM, Wang MR, Zhong HX, Chen J (2007) Preparation, characterization of  $\text{ZrO}_x\text{N}_y/\text{C}$  and its application in PEMFC as an electrocatalyst for oxygen reduction. *J Power Sources* 172:503–510
54. Doi S, Ishihara A, Mitsushima S, Kamiya N, Ota K (2007) Zirconium-based compounds for cathode of polymer electrolyte fuel cell. *J Electrochem Soc* 154:B362–B369
55. Ohgi Y, Ishihara A, Matsuzawa K, Mitsushima S, Ota K (2010) Zirconium oxide-based compound as new cathode without platinum group metals for PEFC. *J Electrochem Soc* 57:B885–B891
56. Clouser SJ, Huang JC, Yeager E (1993) Temperature dependence of the Tafel slope for oxygen reduction on platinum in concentrated phosphoric acid. *J Appl Electrochem* 23:597–605
57. Ishihara A, Lee K, Doi S, Mitsushima S, Kamiya N, Hara M, Domen K, Fukuda K, Ota K (2005) Tantalum oxynitride for a novel cathode of PEFC. *Electrochem Solid State Lett* 8:A201–A203
58. Imai H, Matsumoto M, Miyazaki T, Fujieda S, Ishihara A, Tamura M, Ota K (2010) Structural defects working as active oxygen-reduction sites in partially oxidized Ta-carbonitride core-shell particles probed by using surface-sensitive conversion-electron-yield X-ray absorption spectroscopy. *App Phys Lett* 96:191905
59. Ohnishi R, Katayama M, Takanabe K, Kubota J, Domen K (2010) Niobium-based catalysts prepared by reactive radiofrequency magnetron sputtering and arc plasma methods as non-noble metal cathode catalysts for polymer electrolyte fuel cells. *Electrochim Acta* 55:5393–5400
60. Takagaki A, Takahashi Y, Yin F, Takanabe K, Kubota J, Domen K (2009) Highly dispersed niobium catalyst on carbon black by polymerized complex method as PEFC cathode catalyst. *J Electrochem Soc* 156:B811–B815
61. Jasinski R (1964) A new fuel cell cathode catalyst. *Nature (Lond)* 201:1212–1213
62. Jahnke H, Schönborn M, Zimmermann G (1976) Organic dyestuffs as catalysts for fuel cells. *Top Curr Chem* 61:133–182
63. Gupta SL, Tryk D, Bae I, Aldred W, Yeager EB (1989) Heattreated polyacrylonitrile-based catalysts for oxygen electroreduction. *J Appl Electrochem* 19:19–27
64. Fierro C, Anderson AB, Scherson DA (1988) Electron donor/acceptor properties of porphyrines, phthalocyanines, and related ring-chelates: a molecular orbital approach. *J Phys Chem* 92:6902–6907
65. Zagal JH (1992) Metallophthalocyanines as catalysts in electrochemical reactions. *Coord Chem Rev* 119:89–136
66. Kobayashi N, Nishiyama Y (1984) Catalytic electroreduction of molecular oxygen at glassy carbon electrodes with immobilized iron porphyrins containing zero, one, or four amino groups. *J Electroanal Chem* 181:107–117
67. van Veen JAR, Visser C (1979) Oxygen reduction on monomeric transition metal phthalocyanines in acid electrolyte. *Electrochim Acta* 24:921–928
68. Melendres CA (1980) Mössbauer and Raman spectra of carbon-supported iron phthalocyanine. *J Phys Chem* 84:1936–1939
69. Bagotzky VS, Tarasevich MR, Radyushkina KA, Levina OA, Andrusyova SI (1977–1978) Electro-catalysis of the oxygen reduction process on metal chelates in acid electrolyte. *J Power Sources* 2:233–240
70. Beck F (1977) The redox mechanism of chelate-catalysed oxygen-cathode. *J Appl Electrochem* 7:239–245
71. Blomquist J, Helgeson U, Moberg LC, Johansson LY, Larsson R (1982) Simultaneous electrochemical and Mössbauer measurements on polymeric iron phthalocyanine oxygen electrodes. *Electrochim Acta* 27:1453–1460
72. Brezina M, Khalil W, Koryta J, Musilová M (1977) Electroreduction of oxygen and hydrogen peroxide catalyzed by heme and phthalocyanines. *J Electroana Chem* 77:237–244
73. Johansson LY, Mrha J, Larsson R (1973) Elektrokatalyse der  $\text{O}_2$ -Reduktion in saurer Lösung mit Hilfe der polymeren Phthalocyanine. *Electrochim Acta* 18:255–258
74. Kazarinov VE, Tarasevich MR, Radyushkina KA, Andreev VN (1979) Some specific features of the metalloporphyrin/electrolyte interface and the kinetics of oxygen electroreduction. *J Electroanal Chem* 100:225–232
75. Larsson R, Mrha J (1973) Katalytische Sauerstoffelektrode in sauren Lösungen. *Electrochim Acta* 18:391–394
76. Maroie S, Savy M, Verbist JJ (1979) ESCA and EPR studies of monomer, dimer, and polymer iron phthalocyanines: involvements for the electrocatalysis of  $\text{O}_2$  reduction. *Inorg Chem* 18:2560–2567
77. Zagal JH, Páez M, Tanaka AA, dos Santos JR, Linkous CA (1992) Electrocatalytic activity of

- metal phthalocyanines for oxygen reduction. *J Electroanal Chem* 339:13–30
78. Zagal JH, Páez M, Silva JF (2006) Fundamental aspects on the catalytic activity of metallo-macrocyclics for the electrochemical reduction of O<sub>2</sub>. In: Zagal JH, Bedioui F, Dodelet JP (eds) N<sub>4</sub>-macrocyclic metal complexes. Springer, New York, pp 41–82
79. Yeager EB (1984) Electrocatalysts for O<sub>2</sub> reduction. *Electrochim Acta* 29:1527–1537
80. Ohya T, Kobayashi N, Sato M (1987) Bonding character in tetracoordinate (phthalocyanato) iron (II) complexes with electron-withdrawing substituents as studied by Mößbauer spectroscopy. *Inorg Chem* 26:2506–2509
81. Ohya T, Sato M (1997) Mössbauer and visible spectra of iron(III) complexes of para-substituted tetraphenylporphyrins – electronic effects of substituents and axial ligands. *J Inorg Biochem* 67:126, Abstract: 126
82. Schlosser K, Hoyer E, Arnold D (1974) Mößbauer Untersuchungen zur  $\pi$ -Rückbindung in Tris (1,2-diimin) Eisen (II) chelaten. *Spectrochim Acta* 30:1431–1436
83. Taube R (1974) New aspects of the chemistry of transition metal phthalocyanines. *Pure Appl Chem* 38:427–438
84. Walker FA (2003) Pulsed EPR and NMR spectroscopy of paramagnetic iron porphyrinates and related iron macrocycles: how to understand patterns of spin delocalization and recognize macrocycle radicals. *Inorg Chem* 42:4526–4544
85. Steiger B, Anson FC (1995) Evidence for the importance of back-bonding in determining the behavior of ruthenated cyanophenyl cobalt porphyrins as electrocatalysts for the reduction of dioxygen. *Inorg Chem* 34:3355–3357
86. Zagal JH, Gulppi M, Isaacs M, Cárdenas-Jirón G, Aguirre MJ (1998) Linear versus volcano correlations between electrocatalytic activity and redox and electronic properties of metallophthalocyanines. *Electrochim Acta* 44:1349–1357
87. Alt H, Binder H, Lindner W, Sandstede G (1971) Metal chelates as electrocatalysts for oxygen reduction in acid electrolytes. *J Electroanal Chem* 31: A19–A22
88. Vasudevan P, Santosh MN, Tyagi S (1990) Transition metal complexes of porphyrins and phthalocyanines as electrocatalysts for dioxygen reduction. *Transition Metal Chem Lond* 15:81–90
89. Kozawa A, Zilionis VE, Brodd RJ (1970) Oxygen and hydrogen peroxide reduction at a ferric phthalocyanine-catalyzed graphite electrode. *J Electrochem Soc* 117:1470–1474
90. Okunola A, Kowalewska B, Bron M, Kulesza PJ, Schuhmann W (2009) Electrocatalytic reduction of oxygen at electropolymerized films of metalloporphyrins deposited onto multiwalled carbon nanotubes. *Electrochim Acta* 54:1954–1960
91. Okunola AO, Nagaiah TC, Chen X, Eckhard K, Schuhmann W, Bron M (2009) Visualization of local electrocatalytic activity of metalloporphyrins towards oxygen reduction by means of redox competition scanning electrochemical microscopy (RC-SECM). *Electrochim Acta* 54:4971–4978
92. Collman JP, Denisevich P, Konai Y, Marrocco M, Koval C, Anson FC (1980) Electrode catalysis of the four-electron reduction of oxygen to water by dicobalt face-to-face porphyrins. *J Am Chem Soc* 102:6027–6036
93. Biloul A, Coowar F, Contamin O, Scarbeck G, Savy M, van den Ham D, Riga J, Verbist JJ (1993) Oxygen reduction in an acid medium: electrocatalysis by CoNpc(1,2)-bilayer impregnated on a carbon black support: effect of loading and heat treatment. *J Electroanal Chem* 350:189–204
94. Collman JP, Wagenknecht PS, Hutchison JE (1994) Cofaciale Bis(metallo)diporphyrine als potentielle molekulare Katalysatoren für Mehrelektronenreduktionen und – oxidationen kleiner Moleküle. *Angew Chem* 106:1620–1639
95. Liu HY, Weaver MJ, Wang C-B, Chang CK (1983) Dependence of electrocatalysis for oxygen reduction by adsorbed dicobalt cofacial porphyrins upon catalyst structure. *J Electroanal Chem* 145:439–447
96. Biloul A, Contamin O, Scarbeck G, Savy M, Palys B, Riga J, Verbist JJ (1994) Oxygen reduction in acid media: influence of the activity of conpc(1,2)-bilayer deposits in relation to their attachment to the carbon black support and role of surface groups as a function of heat treatment. *J Electroanal Chem* 365:239–246
97. Tributsch H, Koslowski U, Dorbandt I (2008) Experimental and theoretical modeling of Fe-, Co-, Cu-, Mn based electrocatalysts oxygen reduction. *Electrochim Acta* 53:2198–2209
98. Wiesener K, Ohms D, Neumann V, Franke R (1989) N<sub>4</sub> Macrocyclus als electrocatalysts for the cathodic reduction of oxygen. *Mater Chem Phys* 22:457–475
99. Blomquist J, Helgeson U, Moberg LC, Johansson LY, Larsson R (1982) Electrochemical and Mössbauer investigations of polymeric iron phthalocyanine oxygen electrodes. *Electrochim Acta* 27:1445–1451
100. Scherson DA, Fierro C, Tryk D, Gupta SL, Yeager EB, Eldridge J, Hoffman RW (1985) In situ Mössbauer spectroscopy and electrochemical studies of the thermal stability of iron phthalocyanine dispersed in high surface area carbon. *J Electroanal Chem* 184:419–426
101. Scherson DA, Fierro C, Yeager EB, Kordesch ME, Eldridge J, Hoffman RW, Barnes A (1984) In situ Mössbauer spectroscopy on an operating fuel cell. *J Electroanal Chem* 169:287–302
102. Wiesener K (1986) N<sub>4</sub> chelates as electrocatalysts for the cathodic oxygen reduction. *Electrochim Acta* 31:1073–1078
103. Tanaka AA, Fierro C, Scherson DA, Yeager EB (1989) Oxygen reduction on adsorbed iron

- tetrapyridinoporphyrazine. *Mater Chem Phys* 22:431–456
104. Tarasevich MR, Radyushkina KA (1989) Pyropolymers of  $N_4$ -complexes: structure and electrocatalytic properties. *Mater Chem Phys* 22:477–502
  105. Franke R, Ohms D, Wiesener K (1989) Investigation of the influence of thermal treatment on the properties of carbon materials modified by  $N_4$ -chelates for the reduction of oxygen in acidic media. *J Electroanal Chem* 260:63–73
  106. Joyner RW, van Veen JAR, Sachtler WMH (1982) Extended X-ray absorption fine structure (EXAFS) study of cobaltporphyrin catalysts supported on active carbon. *J Chem Soc Faraday Trans* 78:1021–1028
  107. Saha MS, Li R, Sun X, Ye S (2009) 3-D composite electrodes for high performance PEM fuel cells composed of Pt supported on nitrogen-doped carbon nanotubes grown on carbon paper. *Electrochem Commun* 11:438–441
  108. Biniak S, Szymanski G, Siedlewski J, Swiatkowski A (1997) The characterization of activated carbons with oxygen and nitrogen surface groups. *Carbon* 35:1799–1810
  109. Lacerda M, Lejeune M, Jones BJ, Barklie RC, Bouzerar R, Zellama K, Conway NMJ, Godet C (2002) Electronic properties of amorphous carbon nitride  $a-C_{1-x}N_x$ : H films investigated using vibrational and ESR characterisations. *J NonCryst Solids* 299–302:907–911
  110. Chen Y, Wang J, Liu H, Li R, Sun X, Ye S, Knights S (2009) Enhanced stability of Pt electrocatalysts by nitrogen doping in CNTs for PEM fuel cells. *Electrochem Commun* 11:2071–2076
  111. Strelko VV, Kuts VS, Thrower PA (2000) On the mechanism of possible influence of heteroatoms of nitrogen, boron and phosphorus in a carbon matrix on the catalytic activity of carbons in electron transfer reactions. *Carbon* 38:1499–1503
  112. Kramm UI (2009) Strukturelle Untersuchungen alternativer Katalysatoren für die PEM-BZ – Eine Fe-57-Mößbauer-spektroskopische Studie pyrolysierter Eisenporphyrin-Elektrokatalysatoren. Südwestdeutscher Verlag für Hochschulschriften, Saarbrücken
  113. Biddinger EJ, Ozkan US (2007) Methanol tolerance of  $CN_x$  oxygen reduction catalysts. *Top Catal* 46:339–348
  114. Kothandaraman R, Nallathambi V, Artyushkova K, Barton SC (2009) Non-precious oxygen reduction catalysts prepared by high-pressure pyrolysis for low-temperature fuel cells. *Appl Catal B* 92:209–216
  115. Liu G, Li X, Ganesan P, Popov BN (2010) Studies of oxygen reduction reaction active sites and stability of nitrogen-modified carbon composite catalysts for PEM fuel cells. *Electrochim Acta* 55:2853–2858
  116. Maldonado S, Stevenson KJ (2005) Influence of nitrogen doping on oxygen reduction electrocatalysis at carbon nanofiber. *J Phys Chem B* 109:4707–4716
  117. Matter PH, Biddinger EJ, Ozkan US (2007) Non-precious metal oxygen reduction catalysts for PEM fuel cells. *Catalysis* 30:338–366
  118. Matter PH, Wang E, Millet J-M, Ozkan US (2007) Characterization of the iron phase in  $CN_x$ -based oxygen reduction reaction catalysts. *J Phys Chem C* 111:1444–1450
  119. Nallathambi V, Li X, Lee J-W, Popov BN (2008) Development of nitrogen-modified carbon-based catalysts for oxygen reduction in PEM fuel cells. *ECS Trans* 16:405–417
  120. Sidik RA, Anderson AB, Subramanian NP, Kumaraguru SP, Popov BN (2006) O<sub>2</sub> reduction on graphite and nitrogendoped graphite: experimental and theory. *J Phys Chem B* 110:1787–1793
  121. Fischer A, Antonietti M, Thomas A (2007) Growth confined by the nitrogen source: synthesis of pure metal nitride nanoparticles in mesoporous graphitic carbon nitride. *Adv Mater Weinheim* 19:264–267
  122. Lyth SM, Nabae Y, Moriya S, Kuroki S, Kakimoto M-a, Ozaki J-i, Miyata S (2009) Carbon nitride as a nonprecious catalyst for electrochemical oxygen reduction. *J Phys Chem C* 113:20148–20151
  123. Lyth SM, Nabae Y, Islam NM, Kuroki S, Kakimoto M-a, Miyata S (2011) Electrochemical oxygen reduction activity of carbon nitride supported on carbon black. *J Electrochem Soc* 158:B194–B201
  124. Nabae Y, Moriya S, Matsubayashi K, Lyth SM, Malon M, Wu L, Islam NM, Koshigoe Y, Kuroki S, Kakimoto M-a, Ozaki K, Miyata S, Ozaki J-I (2010) The role of Fe species in the pyrolysis of Fe phthalocyanine and phenolic resin for preparation of carbon-based cathode catalysts. *Carbon* 48:2613–2624
  125. Plejewski P, Fiechter S (2011) Investigation of the oxygen reduction ability of different metal-free C/N-based materials, in preparation
  126. Lalande G, Côté R, Guay D, Dodelet J-P, Weng LT, Bertrand P (1997) Is nitrogen important in the formulation of Fe-based catalysts for oxygen reduction in solid polymer fuel cells? *Electrochim Acta* 42:1379–1388
  127. Martinaiou I, Bogdanoff P, Fiechter S, Kramm UI (2011) Synthesis of nitrogen-rich Fe-N-C catalysts for the oxygen reduction in acidic media, in preparation
  128. Scherson DA, Tanaka AA, Gupta GP, Tryk DA, Fierro C, Holze R, Yeager EB, Lattimer RP (1986) Transition metal macrocycles supported on high area carbon: pyrolysis-mass spectroscopy studies. *Electrochim Acta* 31:1247–1258
  129. Matter PH, Zhang L, Ozkan US (2006) The role of nanostructure in nitrogen-containing carbon catalysts for the oxygen reduction reaction. *J Catal* 239:83–96
  130. Bogdanoff P, Herrmann I, Hilgendorff M, Dorbandt I, Fiechter S, Tributsch H (2004) Probing structural effects of pyrolysed CoTMPP-based electrocatalysts for oxygen reduction via new preparation strategies. *J New Mat Elect Syst* 7:85–92

131. Herrmann I, Bogdanoff P, Schmithals G, Fiechter S (2006) Influence of the molecular and mesoscopic structure on the electrocatalytic activity of pyrolysed CoTMPP in the oxygen reduction. *ECS Trans* 3:211–219
132. Herrmann I, Kramm UI, Fiechter S, Bogdanoff P (2009) Oxalate supported pyrolysis of CoTMPP as electrocatalysts for the oxygen reduction reaction. *Electrochim Acta* 54:4275–4287
133. Herrmann I, Kramm UI, Radnik J, Bogdanoff P, Fiechter S (2009) Influence of sulphur on the pyrolysis of CoTMPP as electrocatalyst for the oxygen reduction reaction. *J Electrochem Soc* 156: B1283–B1292
134. Herrmann I, Barkschat C, Fiechter S, Bogdanoff P, Iwata N, Takahashi H (2007) Electrode catalyst for fuel cells, a method of preparing an electrode catalyst for fuel cells, and a polymer electrolyte fuel cell. Patent application number PCT/JP2007/074369
135. Kurak KA, Anderson AB (2009) Nitrogen-treated graphite and oxygen electroreduction on pyridinic edge sites. *J Phys Chem C* 113:6730–6734
136. Kramm UI, Abs-Wurmbach I, Herrmann-Geppert I, Radnik J, Fiechter S, Bogdanoff P (2011) Influence of the electron density of FeN<sub>4</sub>-centers towards the catalytic activity of pyrolysed FeTMPPI-based ORR-electrocatalysts. *J Electrochem Soc* 158:B69–B78
137. Biloul A, Coowar F, Contamin O, Scarbeck G, Savy M, Van den Ham D, Riga J, Verbist JJ (1990) Oxygen reduction in acid media on supported iron naphthalocyanine – effect of isomer configuration and pyrolysis. *J Electroanal Chem* 289:189–201
138. Bouwkamp-Wijnoltz AL, Visscher W, van Veen JAR (1998) The selectivity of oxygen reduction by pyrolysed iron porphyrin supported on carbon. *Electrochim Acta* 43:3141–3152
139. Faubert G, Côté R, Guay D, Dodelet J-P, Dénès G, Bertrand P (1998) Iron catalysts prepared by high-temperature pyrolysis of tetraphenylporphyrins in polymer electrolyte fuel cells. *Electrochim Acta* 43:341–353
140. Faubert G, Lalande G, Côté R, Guay D, Dodelet J-P, Weng LT, Bertrand P, Dénès G (1996) Heat-treated iron and cobalt tetraphenylporphyrins adsorbed on carbon black: physical characterization and catalytic properties of these materials for the reduction of oxygen in polymer electrolyte fuel cells. *Electrochim Acta* 41:1689–1701
141. Gojkovic SL, Gupta S, Savinell RF (1998) Heat-treated iron(III) tetramethoxyphenyl porphyrin chloride supported on high area carbon as an electrocatalyst for oxygen reduction part I: characterization of the electrocatalyst. *J Electrochem Soc* 145:3493–3499
142. Gojkovic SL, Gupta S, Savinell RF (1999) Heat-treated iron(III) tetramethoxyphenyl porphyrin chloride supported on high area carbon as an electrocatalyst for oxygen reduction part II: kinetics of oxygen reduction. *J Electroanal Chem* 462:63–72
143. Gojkovic SL, Gupta S, Savinell RF (1999) Heat-treated iron(III) tetramethoxyphenyl porphyrin chloride supported on high area carbon as an electrocatalyst for oxygen reduction part III: detection of hydrogen-peroxide during oxygen reduction. *Electrochim Acta* 45:889–897
144. Ikeda O, Fukuda H, Tamura H (1986) The effect of heat-treatment on group VIII porphyrins as electrocatalysts in the cathodic reduction of oxygen. *J Chem Soc Faraday Trans* 82:1561–1573
145. Lalande G, Faubert G, Côté R, Guay D, Dodelet J-P, Weng LT, Bertrand P (1996) Catalytic activity and stability of heat-treated iron phthalocyanines for the electroreduction of oxygen in polymer electrolyte fuel cells. *J Power Sources* 61:227–237
146. Savy M, Coowar F, Riga J, Verbist JJ, Bronoël G, Besse S (1990) Investigation of O<sub>2</sub> reduction in alkaline media on macrocyclic chelates impregnated on different supports: influence of the heat treatment on stability and activity. *J Appl Electrochem* 20:260–268
147. Sawaguchi T, Itabashi T, Matsue T, Uchida I (1990) Electrochemical reduction of oxygen by metalloporphyrin ion-complexes with heat-treatment. *J Electroanal Chem* 279:219–230
148. Schulenburg H, Stankov S, Schünemann V, Radnik J, Dorbandt I, Fiechter S, Bogdanoff P, Tributsch H (2003) Catalysts for the oxygen reduction from heat-treated iron(III) tetramethoxyphenylporphyrin chloride: structure and stability of active sites. *J Phys Chem B* 107:9034–9041
149. Sheng T-C, Rebenstorf B, Widelöv A, Larsson R (1992) Pyrolysis of metalloporphyrins part 1: Fourier-transform infrared study of Fe-tetraphenylporphyrin chloride. *J Chem Soc Faraday Trans* 88:477–482
150. Sun G-Q, Wang J-T, Gupta S, Savinell RF (2001) Iron(III) tetramethoxyphenylporphyrin (FeTMPP-Cl) as electrocatalyst for oxygen reduction in direct methanol fuel cells. *J Appl Electrochem* 31:1025–1031
151. Sun G-Q, Wang J-T, Savinell RF (1998) Iron(III) tetramethoxyphenylporphyrin (FeTMPP) as methanol tolerant electrocatalyst for oxygen reduction in direct methanol fuel cells. *J Appl Electrochem* 28:1087–1093
152. Wang H, Côté R, Faubert G, Guay D, Dodelet J-P (1999) Effect of the pre-treatment of carbon black supports on the activity of Fe-based electrocatalysts for the reduction of oxygen. *J Phys Chem B* 103:2042–2049
153. Widelöv A (1993) Pyrolysis of iron and cobalt porphyrins sublimated onto the surface of carbon black as a method to prepare catalysts for O<sub>2</sub> reduction. *Electrochim Acta* 38:2493–2502
154. Lalande G, Côté R, Tamizhmani GD, Dodelet J-P, Dignard-Bailey L, Weng LT, Bertrand P (1995) Physical, chemical and electrochemical characterization of heat-treated tetracarboxylic cobalt phthalocyanine



- adsorbed on carbon black as electrocatalyst for oxygen reduction in polymer electrolyte fuel cells. *Electrochim Acta* 40:2635–2646
155. Herrmann I, Brüser V, Fiechter S, Kersten H, Bogdanoff P (2005) Electrocatalysts for oxygen reduction prepared by plasma treatment of carbon-supported cobalt tetramethoxyphenylporphyrin. *J Electrochem Soc* 152:A2179–A2185
  156. Herrmann I, Kramm UI, Fiechter S, Brüser V, Kersten H, Bogdanoff P (2010) Comparative study of the carbonisation of CoTMPP by low temperature plasma and by heat-treatment. *Plasma Process Polym* 7:515–526
  157. Harnisch F, Savastenko NA, Zhao F, Steffen H, Brütner V, Schröder U (2009) Comparative study on the performance of pyrolyzed and plasma-treated iron(II) phthalocyaninebased catalysts for oxygen reduction in pH neutral electrolyte solutions. *J Power Sources* 193:86–92
  158. Atanassov P (2005) Non-platinum electrocatalysts for fuel cells. *FC Techn, Aiche*
  159. Garsuch A, d'Eon R, Dahn T, Klepel O, Garsuch RR, Dahn JR (2008) Oxygen reduction behaviour of highly porous nonnoble metal catalysts prepared by a template-assisted synthesis. *J Electrochem Soc* 155: B236–B243
  160. Jaouen F, Herranz J, Lefèvre M, Dodelet J-P, Kramm UI, Herrmann I, Bogdanoff P, Maruyama J, Nagaoka T, Garsuch A, Dahn JR, Olson TS, Pylypenko S, Atanassov P, Ustinov EA (2009) A cross-laboratory experimental review of non-noble metal catalysts for oxygen electro-reduction. *Appl Mater Interfaces* 1:1623–1639
  161. Olson TS, Chapman K, Atanassov P (2008) Non-platinum cathode catalyst layer composition for single membrane electrode assembly proton exchange membrane fuel cell. *J Power Sources* 183:557–563
  162. Koslowski UI, Herrmann I, Bogdanoff P, Barkschat C, Fiechter S, Iwata N, Takahashi H, Nishikoro H (2008) Evaluation and analysis of PEM-FC performance using nonplatinum cathode catalysts based on pyrolysed Fe- and Co-porphyrins – influence of a secondary heat-treatment. *ECS Trans* 13:125–141
  163. Kramm UI, Herrmann I, Fiechter S, Zehl G, Zizak I, Abs-Wurbach I, Radnik J, Dorbandt I, Bogdanoff P (2009) On the influence of sulphur on the pyrolysis process of FeTMPP-Cl-based electro-catalysts with respect to oxygen reduction reaction (ORR) in acidic media. *ECS Trans* 25:659–670
  164. Maldonado S, Stevenson KJ (2004) Direct preparation of carbon nanofiber electrodes via pyrolysis of iron(II) phthalocyanine: electrocatalytic aspects for oxygen reduction. *J Phys Chem B* 108:11375–11383
  165. Lefèvre M, Proietti E, Jaouen F, Dodelet J-P (2009) Iron-based catalysts with improved oxygen reduction activity in polymer electrolyte fuel cells. *Science* 324:71–74
  166. Wood TE, Tan Z, Schmoekkel AK, O'Neill D, Atanasoski R (2008) Non-precious metal oxygen reduction catalyst for PEM fuel cells based on nitroaniline precursor. *J Power Sources* 178:510–516
  167. Kramm UI, Herrmann-Geppert I, Bogdanoff P, Abs-Wurbach I, Fiechter S (2011) Effect of an ammonia treatment on the structural composition and ORR activity of Fe-N-C catalysts. *J Phys Chem C*, in preparation
  168. Charreteur F, Jaouen F, Ruggeri S, Dodelet J-P (2008) Fe/N/C non-precious catalysts for PEM fuel cells: influence of the structural parameters of pristine commercial carbon blacks on their activity for oxygen reduction. *Electrochim Acta* 53:2925–2938
  169. Charreteur F, Ruggeri S, Jaouen F, Dodelet J-P (2008) Increasing the activity of Fe/N/C catalysts in PEM fuel cell cathodes using carbon blacks with a high disordered carbon content. *Electrochim Acta* 53:6881–6889
  170. Dodelet J-P (2006) Oxygen reduction in PEM fuel cell conditions: heat-treated non-precious metal-N<sub>4</sub> macrocycles and beyond. In: Zagal JH, Bedioui F, Dodelet JP (eds) N<sub>4</sub>-macrocyclic metal complexes: electrocatalysis, electrophotochemistry & biomimetic electroanalysis. Springer, New York, pp 83–147
  171. Herranz J, Lefèvre M, Larouche N, Stansfield B, Dodelet J-P (2007) Step-by-step synthesis of non-noble metal electrocatalysts for O<sub>2</sub> reduction under proton exchange membrane fuel cell conditions. *J Phys Chem C* 111:19033–19042
  172. Jaouen F, Dodelet J-P (2007) Turn-over frequency of O<sub>2</sub> electro-reduction for Fe/N/C and Co/N/C catalysts in PEFCs. *Electrochim Acta* 52:5975–5984
  173. Matter PH, Wang E, Arias M, Biddinger EJ, Ozkan US (2006) Oxygen reduction reaction catalysts prepared from acetonitrile pyrolysis over alumina-supported metal particles. *J Phys Chem B* 110: 18374–18384
  174. Bron M, Radnik J, Fieber-Erdmann M, Bogdanoff P, Fiechter S (2002) EXAFS, XPS and electrochemical studies on oxygen reduction catalysts obtained by heat treatment of iron phenanthroline complexes supported on high surface area carbon black. *J Electroanal Chem* 535:113–119
  175. Nallathambi V, Lee J-W, Kumaraguru SP, Wu G, Popov BN (2008) Development of high performance carbon composite catalyst for oxygen reduction reaction in PEM proton exchange membrane fuel cells. *J Power Sources* 183:34–42
  176. Wu T-M, Lin S-H (2006) Characterization and electrical properties of polypyrrole/multiwalled carbon nanotube composites synthesized by in situ chemical oxidative polymerization. *J Polym Sci Pol Phys* 44:1413–1418
  177. Bashyam R, Zelenay P (2006) A class of non-precious metal composite catalysts for fuel cells. *Nat Lond* 443:63–66

178. Bron M, Fiechter S, Hilgendorf M, Bogdanoff P (2002) Catalysts for oxygen reduction from heat-treated carbon-supported iron phenantroline complexes. *J Appl Electrochem* 32:211–216
179. Côté R, Lalonde G, Guay D, Dodelet J-P (1998) Influence of nitrogen-containing precursors on the electrocatalytic activity of heat-treated Fe(OH)<sub>2</sub> on carbon black for O<sub>2</sub> reduction. *J Electrochem Soc* 145:2411–2418
180. Jaouen F, Lefèvre M, Dodelet J-P, Cai M (2006) Heat-treated Fe/N/C catalysts for O<sub>2</sub> electroreduction: are active sites hosted in micropores? *J Phys Chem B* 110:5553–5558
181. Jaouen F, Marcotte S, Dodelet J-P, Lindbergh G (2003) Oxygen reduction catalysts for polymer electrolyte fuel cells from the pyrolysis of iron acetate adsorbed on various carbon supports. *J Phys Chem B* 107:1376–1386
182. Lefèvre M, Jaouen F, Dodelet J-P, Li XH, Chen K, Hay A (2006) Fe-based catalyst for oxygen reduction: functionalization of carbon black and importance of the microporosity. *ECS Trans* 3:201–210
183. Maruyama J, K-i S, Kawaguchi M, Abe I (2004) Influence of activated carbon pore structure on oxygen reduction at catalyst layers supported on rotating disk electrodes. *Carbon* 42:3115–3121
184. Proietti E, Ruggeri S, Dodelet J-P (2008) Fe-based electrocatalysts for oxygen reduction in PEMFCs using ballmilled graphite powder as a carbon support. *J Electrochem Soc* 155:B340–B348
185. Wang P, Ma Z, Zhao Z, Jia L (2007) Oxygen reduction on the electrocatalysts based on pyrolysed non-noble metal/poly-o-phenylenediamine/carbon black composites: new insight into the active sites. *J Electroanal Chem* 611:87–95
186. Wu G, Chen Z, Artyushkova K, Garzona FH, Zelenay P (2008) Polyaniline-derived non-precious catalyst for the polymer electrolyte fuel cell cathode. *ECS Trans* 16:159–170
187. He P, Lefèvre M, Faubert G, Dodelet J-P (1999) Oxygen reduction catalysts for polymer electrolyte fuel cells from the pyrolysis of various transition metal acetates adsorbed on 3,4,9,10 perylenetetracarboxylic dianhydride. *J New Mater Electrochem Sys* 2:243–251
188. Bron M, Fiechter S, Bogdanoff P, Tributsch H (2002) Thermogravimetry/mass spectrometry investigations on the formation of oxygen reduction catalysts for PEM fuel cells on the basis of heat-treated iron phenantroline complexes. *Fuel Cells* 2:137–142
189. Wu G, Artyushkova K, Ferrandon M, Kropf AJ, Myers D, Zelenay P (2009) Performance durability of polyaniline-derived nonprecious cathode catalysts. *ECS Trans* 25:1299–1311
190. Kramm UI, Herranz J, Arruda TM, Larouche N, Lefèvre M, Jaouen F, Bogdanoff P, Fiechter S, Abs-Wurmbach I, Stansfield B, Mukerjee S, Dodelet JP (2011) The role of Fe-modifications in the activity of Fe/N/C catalysts for the O<sub>2</sub>-reduction in PEM fuel cells, in preparation
191. Herranz J, Jaouen F, Lefevre M, Kramm UI, Proietti E, Dodelet JP, Bogdanoff P, Fiechter S, Abs-Wurmbach I, Bertrand P, Arruda TM, Mukerjee S (2011) Unveiling N-protonation and anion binding effects on Fe/N/C-catalysts for O<sub>2</sub> reduction in PEM fuel cells. *J Phys Chem C*, submitted (2011-05-10)
192. Lefèvre M, Proietti E, Jaouen F, Dodelet J-P (2009) Iron-based catalysts for oxygen reduction in PEM fuel cells: expanded study using the pore-filling method. *ECS Trans* 25:105–115
193. Lee K, Zhang L, Lui H, Hui R, Shi Z, Zhang J (2009) Oxygen reduction reaction (ORR) catalyzed by carbon-supported cobalt polypyrrole (Co-PPy/C) electrocatalysts. *Electrochim Acta* 54:4704–4711
194. Liu H, Shi Z, Zhang J, Zhang L, Zhang J (2009) Ultrasonic spray pyrolyzed iron-polypyrrole mesoporous spheres for fuel cell oxygen reduction electrocatalysts. *J Mater Chem* 19:468–470
195. Gasteiger HA, Markovic NM (2009) Just a dream – or future reality? *Science* 324:48–49
196. Gasteiger HA, Kocha SS, Sompalli B, Wagner FT (2005) Activity benchmarks and requirements for Pt, Pt-alloys, and non-Pt oxygen reduction catalysts for PEMFCs. *Appl Catal B Environ* 56:9–35
197. Maruyama J, Abe I (2007) Fuel cell cathode catalyst with heme-like structure formed from nitrogen of glycine and iron. *J Electrochem Soc* 154:B297–B304
198. Nallathambi V, Wu G, Subramanian NP, Kumaraguru SP, Lee J-W, Popov BN (2007) Highly active carbon composite electrocatalysts for PEM fuel cells. *ECS Trans* 11:241–247
199. Bezerra CWB, Zhang L, Liu H, Lee K, Marques ALB, Marques EP, Wang H, Zhang J (2007) A review of heat-treatment effects on activity and stability of PEM fuel cell catalysts for oxygen reduction reaction. *J Power Sources* 173:891–908
200. Ekström H, Hanarp P, Gustavsson M, Fridell E, Lundblad A, Lindbergh G (2006) A novel approach for measuring catalytic activity of planar model catalysts in the polymer electrolyte fuel cell environment. *J Electrochem Soc* 153:A724–A730
201. Liu G, Li X, Ganesan P, Popov BN (2009) Development of nonprecious metal oxygen-reduction catalysts for PEM fuel cells based on N-doped ordered porous carbon. *Appl Catal B Environ* 93:156–165
202. Ma Z-F, Xie X-Y, Ma X-X, Zhang D-Y, Ren Q, Heß-Mohr N, Schmidt VM (2006) Electrochemical characteristics and performance of CoTMPP/BP oxygen reduction electrocatalysts for PEM fuel cell. *Electrochem Commun* 8:389–394
203. Maruyama J, Abe I (2006) Carbonized hemoglobin functioning as a cathode catalyst for polymer electrolyte fuel cells. *Chem Mater* 18:1303–1311
204. Maruyama J, Fukui N, Kawaguchi M, Abe I (2008) Application of nitrogen-rich amino acids to active

- site generation in oxygen reduction catalyst. *J Power Sources* 182:489–495
205. Papakonstantinou G, Daletou MK, Kotsifa A, Paloukis F, Katerinopoulou K, Ioannides T, Neophytides SG (2009) Non noble metal electrocatalysts for high temperature PEM fuel cells. *ECS Trans* 25:181–189
206. Yang J, Liu D-J, Kariuki NN, Chen LX (2008) Aligned carbon nanotubes with built-in FeN<sub>4</sub> active sites for electrocatalytic reduction of oxygen. *Chem Commun* 3:329–331
207. Jaouen F, Proietti E, Lefèvre M, Chenitz R, Dodelet J-P, Wu G, Chung HT, Johnston C, Zelenay P (2011) Recent advances in non-precious metal catalysis for oxygen-reduction reaction in polymer electrolyte fuel cells. *Energy Environ Sci* 4:114–130
208. Zelenay P (2010) Advanced cathode catalysts, hydrogen program annual merit review and peer evaluation meeting. Project ID: fc005
209. Kramm UI, Herrmann-Geppert I, Proietti E, Jaouen F, Lefèvre M, Bogdanoff P, Dodelet J-P, Fiechter S (2011) Effect of a highenergy ball milling on the PEM-fuel-cell performance of Fe-N-C catalysts for the oxygen reduction. *J Power Sources*, in preparation
210. Beck F (1973) Voltammetrische Untersuchungen an elektrokatalytisch wirksamen Phthalocyaninen und Tetraazaannulenen in konzentrierter Schwefelsäure. *Ber Bunsen Ges fuer Phys Chem* 77:353–364
211. Meier H, Albrecht W, Tschirwitz U, Zimmerhackl E (1973) Zum Einfluß der Leitfähigkeit von Phthalocyaninen bei der Elektrokatalyse in Brennstoffzellen. *Ber Bunsen Ges fuer Phys Chem* 77:843–849
212. Bae IT, Scherson DA (1998) In situ X-ray absorption of a carbon monoxide-iron porphyrin adduct adsorbed on high area in an aqueous electrolyte. *J Phys Chem B* 102:2519–2522
213. Appleby AJ, Savy M, Caro P (1980) The role of transition element multiple spin crossover in oxygen transport and electroreduction in porphyrin and phthalocyanine structures. *J Electroanal Chem* 111:91–96
214. El Hourch A, Belcadi S, Moisy P, Crouigneau P, Léger JM, Lamy C (1992) Electrocatalytic reduction of oxygen at iron phthalocyanine modified polymer electrodes. *J Electroanal Chem* 339:1–12
215. Lefèvre M, Dodelet J-P (2003) Fe-based catalysts for the reduction of oxygen in polymer electrolyte membrane fuel cell conditions: determination of the amount of peroxide released during electroreduction and its influence on the stability of the catalysts. *Electrochim Acta* 48:2749–2760
216. Ziegelbauer JM, Gatewood D, Gullá AF, Ramaker DE, Mukerjee S (2006) X-ray absorption spectroscopy studies of water activation on Rh<sub>x</sub>S<sub>y</sub> electrocatalyst for oxygen reduction reaction application. *Electrochem Solid State Lett* 9:A430–A434
217. Bae IT, Tryk DA, Scherson DA (1998) Effect of heat treatment on the redox properties of iron porphyrins adsorbed on high area carbon in acid electrolytes: an in situ Fe K-Edge X-ray absorption near-edge structure study. *J Phys Chem B* 102:4114–4117
218. Birry L, Zagal JH, Dodelet J-P (2010) Does CO poison Fe-based catalysts for ORR? *Electrochem Commun* 12:628–631
219. Borup RL, Meyers J, Pivovar B, Kim YS, Mukundan R, Garland N, Myers D, Wilson M, Garzon F, Wood D, Zelenay P, More K, Stroh K, Zawodzinski T, Boncella J, McGrath JE, Inaba M, Miyatake K, Hori M, Ota K, Ogumi Z, Miyata S, Nishikata A, Siroma Z, Uchimoto Y, Yasuda K, K-i K, Iwashita N (2007) Scientific aspects of polymer electrolyte fuel cell durability and degradation. *Chem Rev* 107:3904–3951
220. Young AP, Stumper J, Gyenge E (2009) Characterizing the structural degradation in a PEMFC cathode catalyst layer: carbon corrosion. *J Electrochem Soc* 156:B913–B922
221. Baker R, Wilkinson DP, Zhang J (2008) Electrocatalytic activity and stability of substituted iron phthalocyanines towards oxygen reduction evaluated at different temperatures. *Electrochim Acta* 53:6906–6919
222. Charreteur F, Jaouen F, Dodelet J-P (2009) Iron porphyrin-based cathode catalysts for PEM fuel cells: influence of pyrolysis gas on activity and stability. *Electrochim Acta* 54:6622–6630
223. Meng H, Larouche N, Lefèvre M, Jaouen F, Stansfield B, Dodelet J-P (2010) Iron porphyrin-based cathode catalysts for polymer electrolyte membrane fuel cells: effect of NH<sub>3</sub> and Ar mixtures as pyrolysis gases on catalytic activity and stability. *Electrochim Acta* 55:6450–6461
224. Wesselmark M, Lagegren C, Lindbergh G (2009) Degradation studies of PEMFC cathodes based on different types of carbon. *ECS Trans* 25:1241–1250
225. Ettingshausen F, Weidner A, Zils S, Wolz A, Suffner J, Michel M, Roth C (2009) Alternative support materials for fuel cell catalysts. *ECS Trans* 25:1883–1892
226. Huang S-Y, Ganesan P, Zhang P, Popov BN (2009) Development of novel metal oxide supported Pt catalysts for Polymer electrolyte membrane and unitized regenerative fuel cells applications. *ECS Trans* 25:1893–1902
227. Shoyama M, Tomimura T, Okubo Y, Nambu H, Lin M-L, Hara K, Fukuoka A, Ishihara A, K-I O (2009) Synthesis of Ta-oxide based nano-sized cathode catalyst on highly ordered mesoporous carbon for PEM fuel cells. *ECS Trans* 25:1903–1908
228. Mukundan R, Borup RL (2009) Visualising liquid water in PEM fuel cells using neutron imaging. *Fuel Cells* 9:499–505
229. Manke I, Hartnig C, Grünerbel M, Kaczerowski J, Lehnert W, Kardjilov N, Hilger A, Banhart J, Treimer W, Strobl M (2007) Quasi-in situ neutron tomography on polymer electrolyte membrane fuel cell stacks. *App Phys Lett* 90:184101-(01–03)



## Membrane Electrolytes, from Perfluorosulfonic Acid (PFSA) to Hydrocarbon Ionomers

Kenji Miyatake  
Clean Energy Research Center, University of  
Yamanashi, Kofu, Yamanashi, Japan

### Article Outline

Definition of the Subject and Its Importance  
Introduction  
Perfluorosulfonic Acid Ionomer Membranes  
Hydrocarbon Ionomer Membranes  
Future Directions  
Bibliography

### Glossary

**Hydrophilic/hydrophobic phase separation** Phase-separated morphology of ionomer membranes based on the differences in the hydrophilicity (and hydrophobicity) of the components.

**Ion exchange capacity** Amount of acidic or ion-exchangeable sites per weight or volume unit of ionomer membranes, often abbreviated as IEC. EW (equivalent weight or weight of ionomer membranes per acidic or ion-exchangeable site) is a reciprocal of IEC.

**Ionic channels** Network of acidic groups and water molecules, through which proton and/or hydronium ions can migrate.

**Ionomers** Originally defined as copolymers having one ionic group per polymer repeating unit, where composition of ion-containing copolymer unit is less than 20%, and, nowadays, often used to be synonymous with polymer electrolytes.

**Perfluorosulfonic acid ionomers** Copolymers composed of poly(tetrafluoroethylene) and

poly(trifluoroethylene) with perfluorosulfonic acid ether side chains.

**Proton exchange membranes** Membranes that can exchange protons with other cations or that can transport protons.

### Definition of the Subject and Its Importance

Proton exchange membranes (PEMs) are one of the key materials in low-temperature fuel cells, proton exchange membrane fuel cells (PEMFCs), and direct methanol fuel cells (DMFCs). Especially, recent trend in the research and development of low-temperature fuel cells focuses on PEMFCs for transportation (electric vehicle) applications due to the impact on economy and environment. The most important role of PEMs is to transport protons formed as a product of oxidation reaction of fuels at the anode to the cathode, where oxygen reduction reaction takes place to produce water. In addition to this, there are a number of requirements for PEM materials for the practical fuel cell applications, which include:

1. Proton conductivity (higher than 0.01 S/cm, hopefully 0.1 S/cm).
2. Chemical, physical (mechanical and dimensional), and thermal stability.
3. Impermeability of fuels (hydrogen, methanol) and oxidants (air, oxygen).
4. Water transport capability (high water flux) from the cathode to the anode.

These properties have to be assured under a wide range of temperature and humidity (−30–120 °C, nominal 0–100% relative humidity (RH)) considering the fabrication of membrane electrode assemblies (MEAs).

5. Easy processability and compatibility with the electrodes are also crucial factors.

For wide dissemination of fuel cells:

6. Environmental adaptability (recyclability or disposability).
7. Low cost (final target for electric vehicle applications would be cheaper than US\$ 10/m<sup>2</sup>) needs to be taken into account. While a number of PEMs have been developed, no single membranes fulfill all of these requirements. Currently, the most promising PEMs are perfluorosulfonic acid (PFSA) ionomers. Another candidate second to the PFSA ionomers is non-fluorinated (or in some cases only slightly fluorinated) hydrocarbon ionomers. The aim of this entry is to review the most recent progress on these two classes of ionomer membranes for low-temperature fuel cell applications.

US DOE (Department of Energy) has set technical targets in PEMs for transportation applications (Table 1) [1]. The targets are for gas crossover (permeability), area-specific resistance, operating temperature, cost, and durability. In 2015, car companies will make a decision whether they continue their endeavor to commercialize fuel cell vehicles. The membrane scientists are facing a big challenge in order to help them go further with fuel cells.

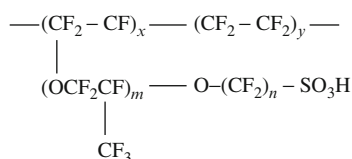
## Introduction

PFSA ionomers are copolymers of poly(tetrafluoroethylene) (PTFE) and poly(trifluoroethylene) with pendant perfluorosulfonic acid groups. There are several industrial companies that supply the PFSA ionomers as resins, membranes, or solution. Such companies include DuPont, 3M, Asahi Kasei, Asahi Chemicals, and Solvay Solexis. A general chemical structure of the PFSA ionomers is shown in Fig. 1. They share the similar chemical structure, and the differences in them lie in the copolymer composition and the length of the pendant side chains and/or the presence of trifluoromethyl groups. Originally, DuPont developed the PFSA in the 1950s. The PFSA membranes have a history as separator membranes in the chlor-alkali electrolysis industry. In this application, the PFSA membranes are used as single ion (Na<sup>+</sup>) conductor. Typical PFSA membranes survive electrolysis operation under strongly basic conditions (>30% NaOH aq.) for more than several years retaining high current efficiency (>95%). Due to the hydrophobicity of fluorinated polymer main chains and strong acidity of the flexible side chains, the PFSA ionomer membranes show distinct hydrophilic/

**Membrane Electrolytes, from Perfluorosulfonic Acid (PFSA) to Hydrocarbon Ionomers, Table 1** US Department of Energy (DOE) targets in PEMs for transportation applications

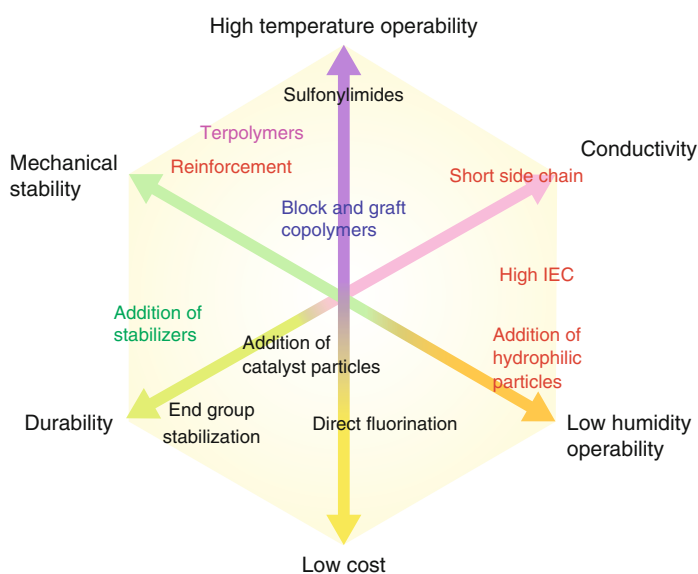
Characteristics	Units	Year	
		2010	2015
O <sub>2</sub> crossover	mA/cm <sup>2</sup>	2	2
H <sub>2</sub> crossover	mA/cm <sup>2</sup>	2	2
Area-specific resistance at			
Maximum operating temperature and water partial pressures from 40 to 80 kPa	ohm cm <sup>2</sup>	0.02	0.02
80 °C water and water vapor partial pressure from 25 to 45 kPa	ohm cm <sup>2</sup>	0.02	0.02
30 °C water and water vapor partial pressure up to 4 kPa	ohm cm <sup>2</sup>	0.03	0.03
−20 °C	ohm cm <sup>2</sup>	0.2	0.2
Maximum operating temperature	°C	120	120
Unassisted start from low temperature	°C	−40	−40
Cost	\$/m <sup>2</sup>	20	20
Durability with cycling			
Mechanical	Cycles with <10 sccm crossover	20,000	20,000
Chemical	mA/cm <sup>2</sup> (H <sub>2</sub> crossover)	200	20

hydrophobic phase separation. The sulfonic acid groups aggregate to form hydrophilic domains, while fluorinated main chains form hydrophobic domains with some crystallinity. Hydrated, hydrophilic domains (5–6 nm in diameter) contain water molecules and become interconnected, which are responsible for high proton transport capability or high proton conductivity. The morphology of PFSA membranes has been analyzed by small-angle X-ray scattering (SAXS), X-ray diffraction (XRD), small-angle neutron scattering (SANS), transmission electron microscopy (TEM), atomic force microscopy (AFM), and differential scanning calorimetry (DSC) techniques and well reviewed in the books and articles. Short side chain and, thus, high ion exchange capacity (IEC) and highly proton-conductive PFSA were developed by Dow, and the membranes were used by Ballard Power Systems to realize high-



**Membrane Electrolytes, from Perfluorosulfonic Acid (PFSA) to Hydrocarbon Ionomers, Fig. 1** General chemical structure of the perfluorosulfonic acid (PFSA) ionomers

**Membrane Electrolytes, from Perfluorosulfonic Acid (PFSA) to Hydrocarbon Ionomers, Fig. 2** Recent research trends in perfluorosulfonic acid (PFSA) membranes

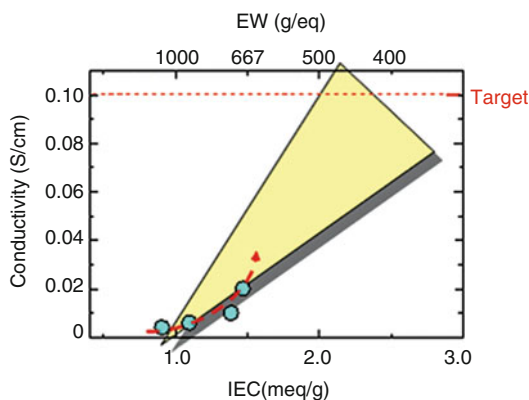


performance PEMFCs in the mid-1980s. Since then, the PFSA have been and will be the most studied PEMs for fuel cells. The recent research trends in PFSA membranes are summarized in Fig. 2. In order to fulfill the abovementioned requirements, a considerable effort has been consumed especially in the last decade. They can be classified into six items: high-temperature operability, low-humidity operability, proton conductivity, mechanical stability, durability, and cost. Details of each approach can be found in the literature, and because of the limited space, only some of the representative examples are described in the next section.

Hydrocarbon ionomers have a rather longer history (ca. 100 years) as cation exchange resins. Original hydrocarbon ionomers were based on the sulfonated polystyrenes or phenol resins. In the earliest stage of the PEMFC research, such ionomer membranes were investigated. General Electric (GE) invented PEMFC with hydrocarbon ionomer membranes in the early 1960s. The operation time of the initial PEMFCs was limited by the membrane durability. PFSA membranes have replaced them in the mid-1960s, and since then they have been the main option. However, the hydrocarbon ionomer materials have been reexamined in more detail in the last decade due to their possible lower production cost, more







**Membrane Electrolytes, from Perfluorosulfonic Acid (PFSA) to Hydrocarbon Ionomers, Fig. 4** Proton conductivity of perfluorosulfonic acid (PFSA) membranes at 110 °C and 20 % RH

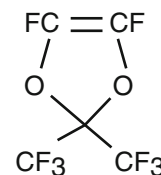
membrane material. However, there is still a gap in the conductivity between the current level and the target. The question is how high IEC would be required to reach 0.1 S/cm. Extrapolating the current line gives a rough value of IEC, 2–3 meq/g. Such high-IEC membranes probably suffer from low mechanical and dimensional stability, which has to be addressed by appropriate molecular modifications such as cross-linking. Reinforcing with compatible resins (e.g., porous substrates or fabrics of PTFEs) may also be a possible option.

In addition to the proton-conducting properties, short side chain provides additional advantages, such as high glass transition temperature and high decomposition temperature. For example, Solvay Solexis' short side chain PFSA, known as Aquivion, show  $\alpha$ -relaxation transition at 160 °C, which is ca. 50 °C higher than that of the conventional long side chain PFSA. This is a consequence of higher crystallinity of the short side chain PFSA [5, 6]. Therefore, higher-IEC membranes can be prepared from the short side chain PFSA with the same crystallinity (e.g., similar thermal and mechanical properties) with the long side chain PFSA or the same IEC membranes with the higher crystallinity.

### Terpolymers

Asahi Glass has investigated the effect of third compounds and found that cyclic vinyl compounds,

**Membrane Electrolytes, from Perfluorosulfonic Acid (PFSA) to Hydrocarbon Ionomers, Fig. 5** Chemical structure of bulky comonomer for the perfluorosulfonic acid (PFSA) terpolymers



for example, 2,2-bis(trifluoromethyl)-4,5-difluoro-1,3-dioxole, function well to improve the thermal and dimensional stability (Fig. 5) [7]. Similar to the short side chain ionomers, the terpolymer PFSA showed higher elastic modulus and ca. 40 °C higher softening temperature than those of the conventional long side chain PFSA. The water absorbability of the terpolymers was nearly half in a wide range of temperature.

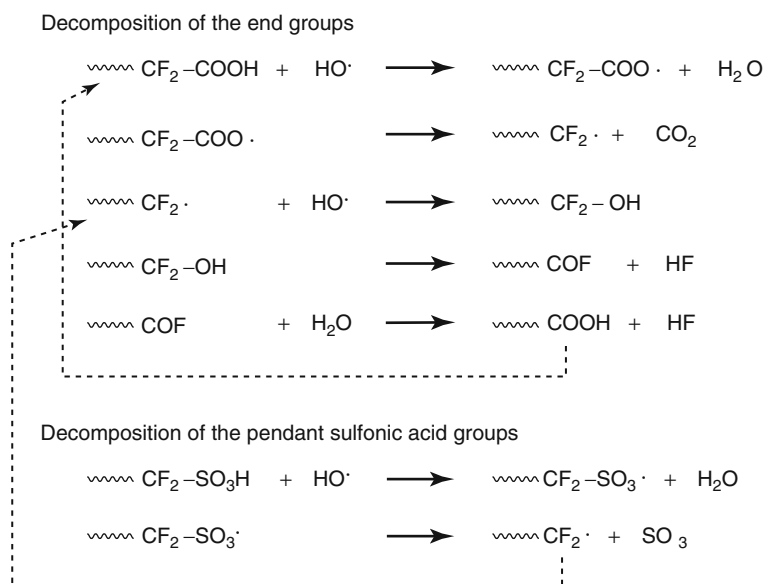
There seems to be a number of other candidates suitable as a third comonomer (e.g., trifluorovinyl monomers containing phosphonic acid, sulfonamide, sulfonimide, and/or cross-linkable moieties) [8–12]; however, high production cost of these rather complex perfluorinated vinyl compounds may be an obstacle to the practical industrial applications.

### Stabilized PFSA

Despite the established durability of PFSA as separator membranes in the chlor-alkali electrolysis, they fail to function as proton exchange membranes for longtime fuel cell operation. Typical PFSA membranes degrade and have pinholes within several hundred hours of operation under high-temperature, low-humidity, and open-circuit voltage (OCV) conditions. It is generally recognized that the degradation of PFSA membranes is caused by hydroxide ( $\text{HO}^-$ ) radical, which is generated by the homolysis or the Fenton's reaction (catalyzed by  $\text{Fe}^{2+}$  ions) of hydrogen peroxide. When oxygen reduction reaction (ORR) occurs via four-electron process, the product is water. Instead, two-electron process provides hydrogen peroxide as the product, which may occasionally form both at the cathode and the anode. At the anode where oxygen permeated through the membrane can react with hydrogen at the lower potential than that of the cathode, the ORR is more likely to proceed via two-electron process. Hydroperoxide ( $\text{HOO}^\cdot$ ) radical would also

**Membrane Electrolytes,  
from Perfluorosulfonic  
Acid (PFSA) to  
Hydrocarbon Ionomers,**

**Fig. 6** Possible degradation mechanisms of perfluorosulfonic acid (PFSA) involving oxidative radical species



form in the operating fuel cells and cause membrane degradation similarly.

The probable degradation mechanisms (Fig. 6) of the PFSA membranes involving the radicals are:

1. Decomposition of the end groups [13–15]

PFSA contains carboxylic acid groups at the end of polymer main chains as a result of the initiator in the polymerization reaction. The terminal carboxylic acid groups can be attacked by the radical species to produce shortened carboxylic acid groups and hydrogen fluoride. The repetition of this reaction causes unzipping degradation of polymer main chains.

2. Decomposition of the pendant sulfonic acid groups [16–18]

In the side chains of PFSA ionomers, the sulfonic acid groups are likely to be attacked by the radicals. Under dry or low-humidity conditions, in particular, most sulfonic acid groups are not dissociated and prone to hydrogen abstraction reaction by the radicals. The reaction gives  $\text{---CF}_2\cdot$  radicals and initiates the unzipping degradation of polymer main chains.

In addition to these mechanisms, there may be another degradation mechanism, in which fluorocarbons ( $\text{---CF}_2\text{---}$ ) are hydrogenated to  $\text{---CH}_2\text{---}$  with hydrogen gas and then attacked by radicals. It is shown by solid-state NMR spectroscopy that

the side chain degradation is severer than the main chain degradation for the stabilized PFSA.

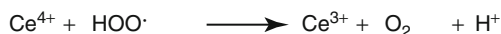
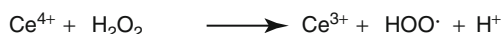
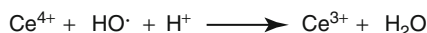
It has been proposed that the terminal carboxylic acid ( $\text{---COOH}$ ) groups can be converted to trifluoromethyl ( $\text{---CF}_3$ ) groups by treating the ionomers with fluorine gas under heated conditions [15]. The degradation could be mitigated significantly with the trifluoromethylated ionomers. However, there remains ca. 10% of the degradation even extrapolating the content of terminal carboxylic acid groups to zero. The remaining degradation is considered to be the side chain degradation.

While some transition metal ions promote radical formation and ionomer degradation, other transition metal ions act as radical quencher and mitigate the ionomer degradation (Fig. 7) [16, 17, 19–21]. Such ions include  $\text{Ce}^{3+}$  and  $\text{Mn}^{2+}$ , having reduction potential at 1.74 and 1.51 V at 25 °C, respectively. These ions can reduce hydroxide radicals or hydrogen peroxide to water, but not reduce hydrogen peroxide to hydroxide radicals. The oxidized ions,  $\text{Ce}^{4+}$  and  $\text{Mn}^{3+}$ , could be reduced to  $\text{Ce}^{3+}$  and  $\text{Mn}^{2+}$  by hydrogen permeating through the ionomer membranes from the anode to the cathode. Typically, a few to 10% of sulfonic acid groups are ion exchanged to such transition metal ions in order to obtain improved durability and acceptable proton conductivity. Some membranes have been claimed to survive OCV test at 120 °C

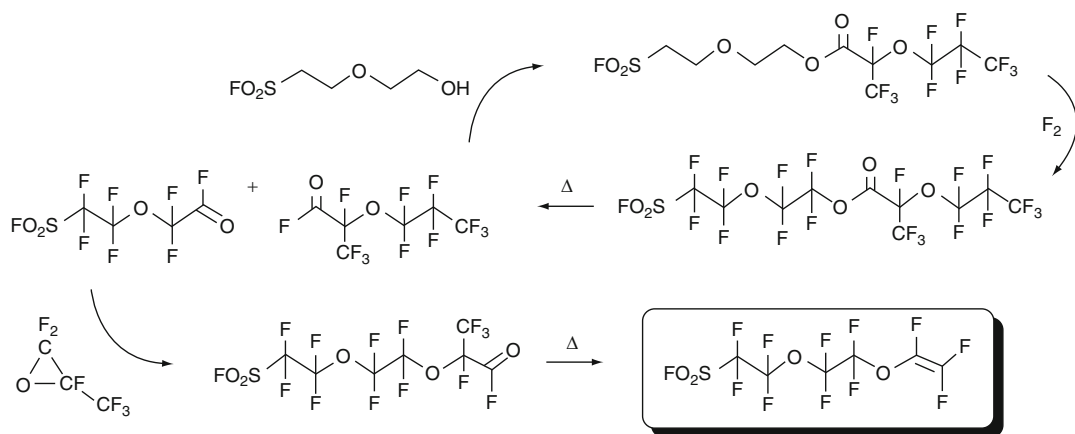
and 18% RH and constant current (0.2 A/cm<sup>2</sup>) operation at 120 °C and 50% RH for several thousand hours. In addition to the role as effective mitigants of chemical degradation, the multivalent transition metal ions function as ionic cross-linkers to render better mechanical properties to the ionomer membranes.

### New Synthetic Routes

Synthetic approaches of sulfonated perfluorovinyl monomers are limited and require many steps. Fluorinated cyclic compounds (sultones and epoxides), which are often used as raw materials, need careful attention in handling. Such synthetic complexity is one of the reasons of their high production cost. A unique methodology to produce sulfonated perfluorovinyl monomers has been developed by Asahi Glass (Fig. 8) [7, 22]. The synthetic process, as they name PERFECT (PERFluorination of an Esterified Compound then Thermal elimination) process, involves perfluorination of partially fluorinated aliphatic



**Membrane Electrolytes, from Perfluorosulfonic Acid (PFSA) to Hydrocarbon Ionomers, Fig. 7** Radical quenching mechanism with cerium ions



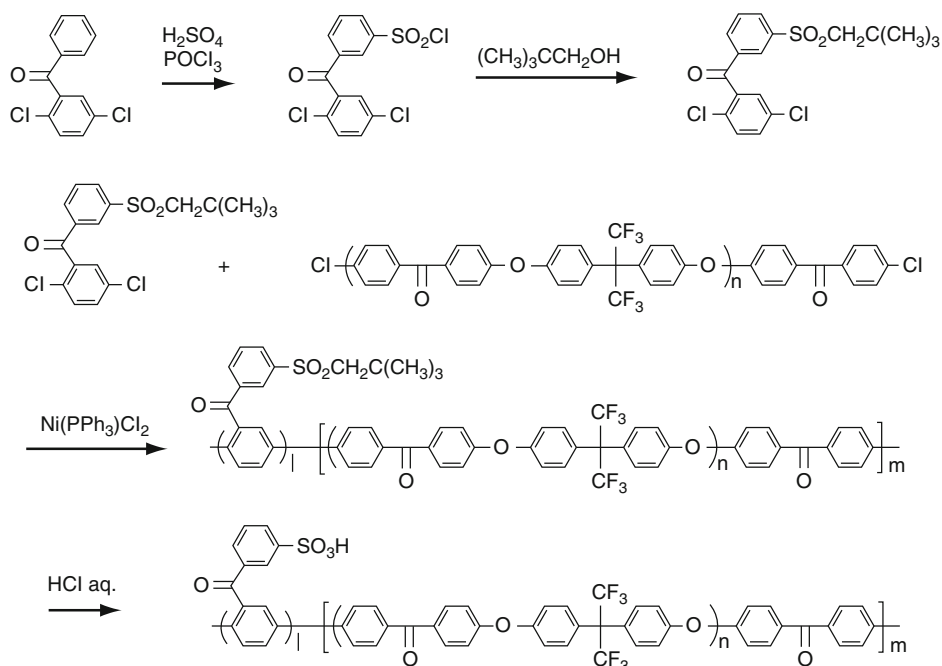
**Membrane Electrolytes, from Perfluorosulfonic Acid (PFSA) to Hydrocarbon Ionomers, Fig. 8** Synthetic route of sulfonated perfluorovinyl monomers via direct fluorination of partially fluorinated compounds

esters containing sulfonyl fluoride groups. The perfluorination reaction with fluorine ( $\text{F}_2$ ) is carried out in solution. The thermal decomposition of the perfluorinated esters gives acetyl fluorides, which can be converted to the corresponding vinyl monomers via conventional reaction pathway. This process may be applicable to a variety of aliphatic esters to provide new vinyl monomers with fewer steps and at lower production cost.

### Hydrocarbon Ionomer Membranes

#### High-IEC Ionomers with Rigid Rod Backbone

Poly(phenylene)s are probably one of the most attractive polymer backbones for hydrocarbon ionomers in terms of chemical stability and long-term durability since their main chains are composed of pure  $\text{C}_{\text{aromatic}}-\text{C}_{\text{aromatic}}$  bonds, which afford rigid rod structure to the polymers. Most other hydrocarbon ionomers suffer from chemical degradation, which often takes place at heterolinkages, especially electron-donating ether and aliphatic groups, under fuel cell operating conditions. The challenge is how to synthesize soluble high molecular weight poly(phenylene) ionomers (high enough to provide self-standing membranes) and how to introduce ionic groups. There are not many synthetic options available for poly(phenylene) derivatives compared to the other aromatic polymers with heteroatom linkages. Therefore, there have been a limited number of reports for poly(phenylene) ionomers. Among



**Membrane Electrolytes, from Perfluorosulfonic Acid (PFSA) to Hydrocarbon Ionomers, Fig. 9** Synthesis of sulfonated poly(p-phenylene) copolymers

them, poly(p-phenylene) ionomers developed by Goto et al. of JSR Corporation, Japan, are one of the most successful examples. They have discovered that poly(p-phenylene)s with 3-sulfobenzoyl groups give appropriate properties as fuel cell membranes [23]. A typical synthetic approach is summarized in Fig. 9. The key monomer, neopentyl 3-(2,5-dichlorobenzoyl)benzenesulfonate, synthesized from 2,5-dichlorobenzophenone, was copolymerized with hydrophobic dichloro compounds via nickel-catalyzed coupling reaction. The neopentyl ester groups in the resulting polymers were removed via hydrolysis to obtain the title ionomers.

The striking feature of the poly(p-phenylene)-based ionomers is that the membranes obtained therefrom show well-developed hydrophilic/hydrophobic microphase separation. Such morphology can be controlled by (1) copolymer composition, (2) chemical structure of the hydrophobic component, (3) sequenced structure and length of hydrophilic and hydrophobic components, and (4) membrane preparation conditions. Another characteristic of the poly(p-phenylene)-based ionomers is that the IEC

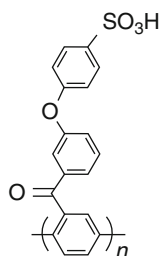
can be higher than 3 meq/g without sacrificing good mechanical and chemical stability of the membranes. In Table 3 are summarized properties of typical JSR membranes. According to the disclosed data, the JSR membranes absorb more water and show higher proton conductivity, better thermal and mechanical stability, comparable hydrolytic stability, and much lower gas permeability compared to those of the conventional perfluorinated ionomer membranes. It has been recently claimed that the introduction of basic groups such as pyridine and imidazole as a third comonomer component could improve the durability of the poly(p-phenylene)-based ionomers. The JSR membranes have been successfully installed on Honda FCX Clarity fuel cell electric vehicles.

Rikukawa et al. of Sophia University have also developed a series of poly(p-phenylene) ionomers [24–26]. The main differences from the JSR membranes are that sulfophenylene groups are connected with ether bonds in the side chain because of the synthetic reason (Fig. 10). (According to JSR, such extra phenoxy groups

**Membrane Electrolytes, from Perfluorosulfonic Acid (PFSA) to Hydrocarbon Ionomers, Table 3** Properties of the sulfonated poly(p-phenylene) copolymer (JSR) membranes

Proton conductivity	70 °C, 80 % RH	0.1 S/cm
	95 °C, 80 % RH	0.16 S/cm
Mechanical strength	Elongation at break at 23 °C, 50 % RH	100 %
	Stress at break at 23 °C, 50 % RH	130 MPa
Gas permeability	H <sub>2</sub> at 80 °C, dry	9 barrer
	O <sub>2</sub> at 40 °C, 90 % RH	6 barrer
Stability	IEC change after 1,000 h in 95 °C water	0 %
	Weight change after 1,000 h in 95 °C water	0 %

**Membrane Electrolytes, from Perfluorosulfonic Acid (PFSA) to Hydrocarbon Ionomers, Fig. 10** Sulfonated poly(p-phenylene) containing phenoxy side chains



do not have positive effect on the properties of the resulting ionomer membranes in terms of the proton conductivity and stability.) Rikukawa's group has applied post-sulfonation method so that the phenyl groups need to be activated with electron-donating ether groups. The advantage is that synthesis of monomers and high molecular weight polymers is easier. Their membranes showed similar properties to the JSR membranes, supporting the validity of the strategy to utilize rigid rod-like main chains.

Sulfonated poly(2,5-benzophenone)s, derivatives of poly(p-phenylene)s with sulfobiphenylene-carbonyl side chains, were synthesized by McGrath and Ghassemi of Virginia Polytechnic Institute and State University [27]. The base (unsulfonated) polymers were thermally stable up to ca. 480 °C in air and nitrogen; however, their film-forming capability was insufficient due to rather low molecular weight. They have also synthesized multiblock copolymers composed of the sulfonated oligo(2,5-benzophenone)s and oligo(arylene ether sulfone)s to achieve higher molecular weight and better film-forming capability (Fig. 11) [28]. The block copolymers showed high glass transition temperature (225 °C) due to

the arylene ether sulfone units. Proton conductivity of the membrane (IEC = 1.20 meq/g) was measured under specific conditions (in water at 30 °C) to be 0.036 S/cm.

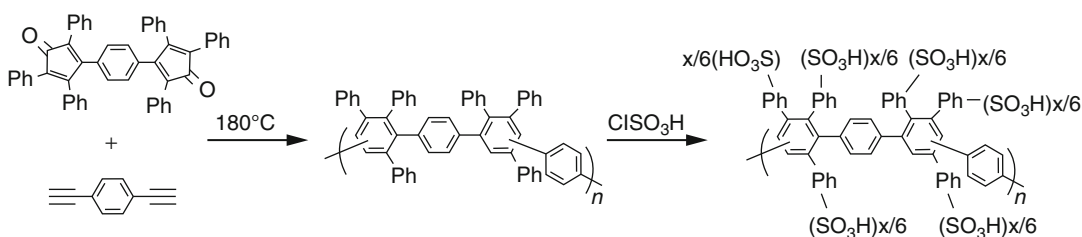
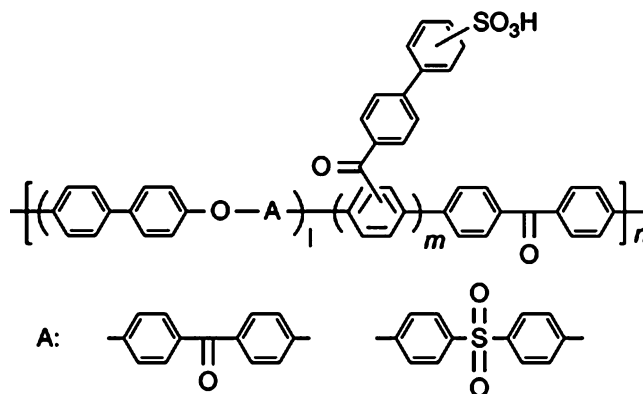
Cornelius et al. have synthesized a series of unique poly(phenylene)-based polyelectrolytes by Diels-Alder polymerization followed by post-sulfonation (Fig. 12) [29–32]. The ionomers are composed of sulfonated, highly phenylated poly(phenylene)s and do not carry any heteroatoms as their constituents except for the sulfonic acid groups. The complete aryl backbone resulted in a tough rigid rod material with no Tg below the decomposition temperature. The stiffness of the ionomer backbone did not negatively affect the membrane properties such as water uptake (21–137%, in water) and proton conductivity (13–123 mS/cm, in water at 30 °C) with IECs ranging from 0.98 to 2.2 meq/g.

More recently, poly(p-phenylene) ionomers with simpler chemical structure have been proposed by the group of Litt of Case Western Reserve University (Fig. 13). They have synthesized poly(p-phenylene)s with sulfonic acid groups directly attached on the main chains via Ullmann coupling reaction. Their membranes seem promising for high-temperature operable fuel cells in terms of the proton conductivity; the proton conductivity of the membranes was 0.1 S/cm at 75 °C and 15% RH, which was approximately three orders of magnitude higher than that of Nafion membrane and meets the requirements of DOE for the year of 2015. However, it is difficult to obtain high molecular weight polymers via the Ullmann coupling reaction, which causes poor mechanical properties of the membranes.

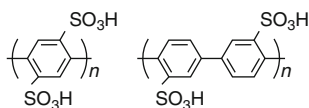


**Membrane Electrolytes, from Perfluorosulfonic Acid (PFSA) to Hydrocarbon Ionomers,**

**Fig. 11** Multiblock copolymer of sulfonated copolymer of poly(p-phenylene) and poly(arylene ether sulfone)



**Membrane Electrolytes, from Perfluorosulfonic Acid (PFSA) to Hydrocarbon Ionomers, Fig. 12** Synthesis of polysulfophenylated poly(phenylene) via Diels-Alder polymerization followed by sulfonation



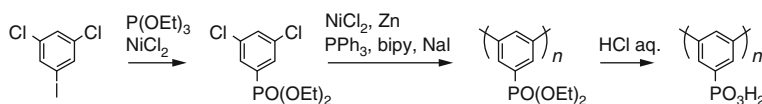
**Membrane Electrolytes, from Perfluorosulfonic Acid (PFSA) to Hydrocarbon Ionomers, Fig. 13** Poly(p-phenylene)s with sulfonic acid groups on the main chains

This issue may be improved by copolymerizing with appropriate hydrophobic comonomers that are more reactive in the Ullmann coupling reaction and also give flexibility to the membranes.

Phosphonic acid containing poly(phenylene)s were investigated by Kreuer's group of Max Planck Institute (Fig. 14) [33, 34]. *m*-Dichlorobenzene containing phosphonic acid ester was polymerized by nickel-catalyzed polycondensation reaction. The ester groups were hydrolyzed with acid to provide poly(*m*-phenylene phosphonic acid). Compared to the sulfonated poly(phenylene) ionomers, phosphonated analogues showed lower proton

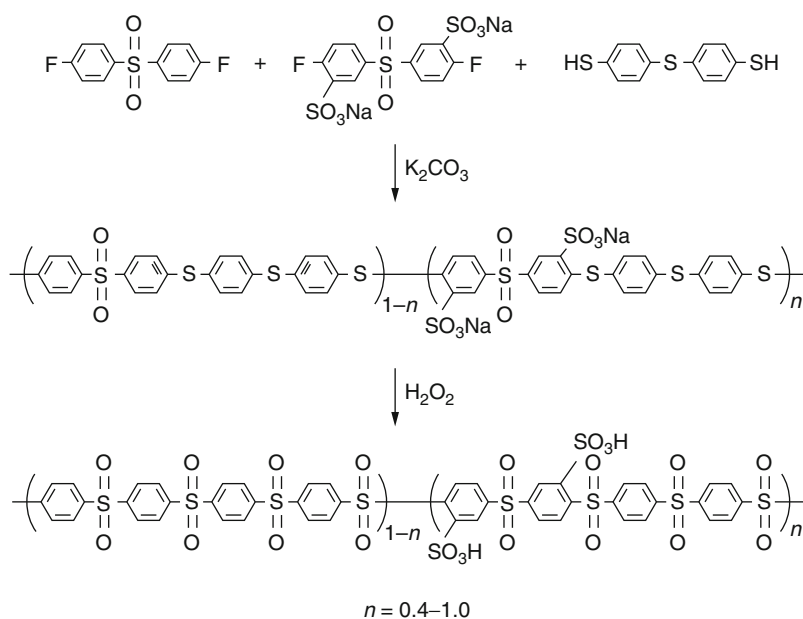
conductivity and better thermal stability due to the lower water affinity. The ionomer membranes are probably not suitable for fuel cells with dry or slightly humidified hydrogen as a fuel but may find applications using liquid fuels such as direct methanol fuel cells. In any case, the ionomers have to be cross-linked or incorporated with hydrophobic moieties in order to prevent excess swelling or dissolving in water.

A new synthetic approach has been developed by the same group to produce poly(phenylene) ionomers containing merely sulfone units connecting the phenylene rings (SPSO<sub>2</sub>) (Fig. 15) [35, 36]. In the ionomers, each phenylene ring contains one sulfonic acid group (100% degree of sulfonation), which corresponds to very high IEC of 4.5 meq/g. The synthesis was carried out in a two-step process, in which bis(sulfophenyl)sulfone was polymerized with sodium sulfide and then the subsequent oxidation reaction of sulfide linkages to sulfone gave the title ionomers. Since phenylene rings in the main



**Membrane Electrolytes, from Perfluorosulfonic Acid (PFSA) to Hydrocarbon Ionomers, Fig. 14** Synthesis of poly(*m*-phenylene phosphonic acid)

**Membrane Electrolytes, from Perfluorosulfonic Acid (PFSA) to Hydrocarbon Ionomers, Fig. 15** Synthesis of sulfonated poly(phenylene sulfone)s (sPSO<sub>2</sub>)



chains are connected solely with strong electron-withdrawing sulfone groups and not with electron-donating groups such as ether and sulfide, the ionomers show high hydrolytic (no practical desulfonation at 180 °C and high water activity) and thermooxidative stability (decomposition in air above 300 °C). The high IEC afforded the ionomer membranes very high proton conductivity in the wide temperature range from 110 °C to 160 °C at a constant water vapor pressure (1 atm), which corresponds to ca. 50% and 15% RH, respectively. The proton diffusion coefficient (calculated from the conductivity data by the use of Nernst-Einstein equation) increased with IEC values (Fig. 16). While the conductivity overcomes that of Nafion by a factor of 5–7, the ionomers are soluble in water and become brittle in the dry state. Approaches such as blends and graft and block copolymers are under investigation. The materials have been registered as

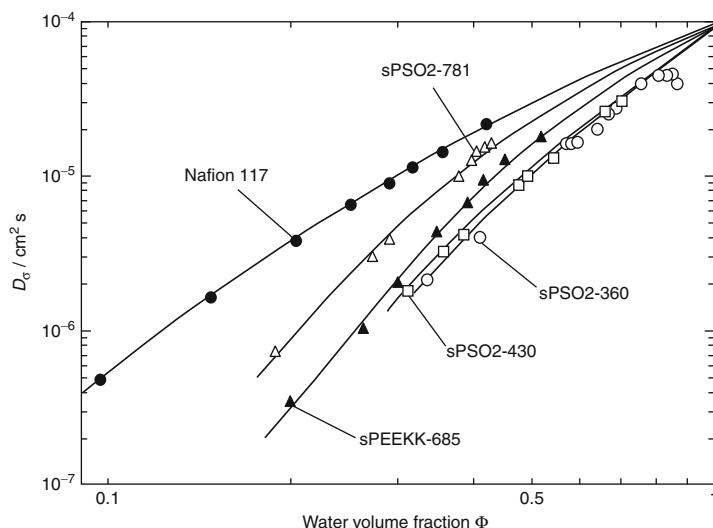
fumapem S (granular resin, solution, or dispersion) and fumion S (membranes) by the FuMA-Tech company for commercialization.

### Block Copolymers

Block copolymers have been utilized in order for the hydrocarbon ionomer membranes to have well-developed and interconnected ionic domains. The strategy seems to work in many ionomers of different molecular structures. The block copolymer membranes show considerably higher proton conductivity than that of the random copolymer membranes with similar values of IEC. For example, Kawakami et al. of Tokyo Metropolitan University have proved that the block copolyimides containing hexafluoropropylene groups in the hydrophobic segment are much more proton conductive than the random equivalents [37–40]. The differences in the conductivity were much more pronounced at low humidity.

### Membrane Electrolytes, from Perfluorosulfonic Acid (PFSA) to Hydrocarbon Ionomers,

**Fig. 16** Proton diffusion coefficient of sPSO<sub>2</sub>, sulfonated poly(ether ether ketone ketone), and Nafion 117 membranes as a function of water volume fraction at 30 °C (Reprinted from Schuster et al. [36] with permission from the American Chemical Society)



The proton conductivity of the block copolyimide membranes depended strongly upon the block chain lengths. The longer the block length was, the higher the conductivity became. They ascribe this effect to ionic channels of which formation depends on the block chain length.

Similar effect was confirmed by the group of Miyatake et al. of University of Yamanashi with other series of sulfonated polyimides of different main chain structures [41]. They have investigated the effect of block copolymer architecture on sulfonated polyimides containing aliphatic segments in the hydrophobic main chains and in the hydrophilic side chains. The block copolymer with longest block segments (the number of repeating unit was 150 for both hydrophilic and hydrophobic blocks) showed the highest proton conductivity of  $2 \times 10^{-2}$  S/cm at 80 °C and 48% RH, which was comparable to that of the conventional perfluorinated ionomer membrane (Fig. 17). Well-connected hydrophilic domains, which looked like a cloudlike belt with several hundred nanometers in width, were observed in the transmission electron microscopic images (Fig. 18).

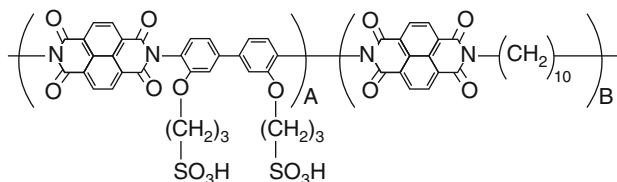
McGrath's group has done an extensive and systematic study on their sulfonated poly(arylene ether sulfone) block copolymers (Fig. 19) [42–51]. The block copolymers are composed of biphenol-based disulfonated arylene ether sulfone (the so-called BPSH) units and the unsulfonated equivalents (BPS). The investigated properties of

the block copolymer membranes include synthetic details with different main chain linkages, spectroscopic analyses of the chemical structure, water uptake, diffusion of water, proton conductivity at a wide range of temperature and humidity, thermal transition and decomposition, morphological analyses (atomic force microscopic (AFM) and transmission electron microscopic (TEM) imaging and small-angle X-ray scattering (SAXS) profile), mechanical strength, and fuel cell performance. A brief summary is:

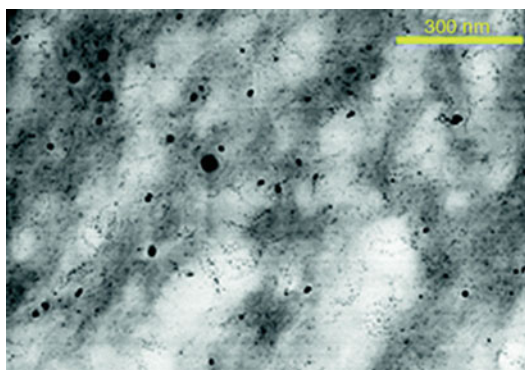
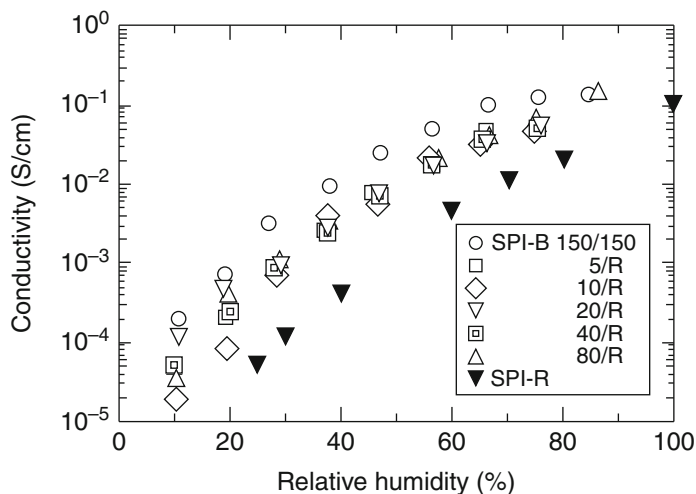
- High molecular weight block copolymers were obtained when reactive perfluorinated linkage (nonafluorobiphenylene or pentafluorophenylene) groups were attached at the both ends on unsulfonated hydrophobic oligomers.
- The linkage groups had some effect on the membrane properties. The fluorinated biphenylene groups seemed to promote nano-phase separation and thus water uptake and proton conductivity at low humidity than the fluorinated phenylene groups.
- The block copolymer membranes performed much better as proton exchange membranes for fuel cells than the random copolymers with similar IEC, especially in terms of proton conductivity at low humidity (on the order of mS/cm at 80 °C and 30% RH, IEC = 1.5 meq/g).
- The block length rather than the IEC was more important to dominate water uptake and proton

**Membrane Electrolytes, from Perfluorosulfonic Acid (PFSA) to Hydrocarbon Ionomers,**

**Fig. 17** Humidity dependence of the proton conductivity of sulfonated block copolyimide membranes at 80 °C



SPI-B (A: random or 5–150, B: random or 150)



**Membrane Electrolytes, from Perfluorosulfonic Acid (PFSA) to Hydrocarbon Ionomers, Fig. 18** Scanning transmission electron microscopic image of SPI-B 150/150

conductivity, where longer block length led to higher water uptake and higher proton conductivity. So were the nanophase separation (or connection of hydrophilic domains) (Fig. 20) and water diffusion coefficient.

- In the hydrated block copolymers, more freezing water (free and loosely bound water to sulfonic acid groups) existed than in the random copolymers due to the developed

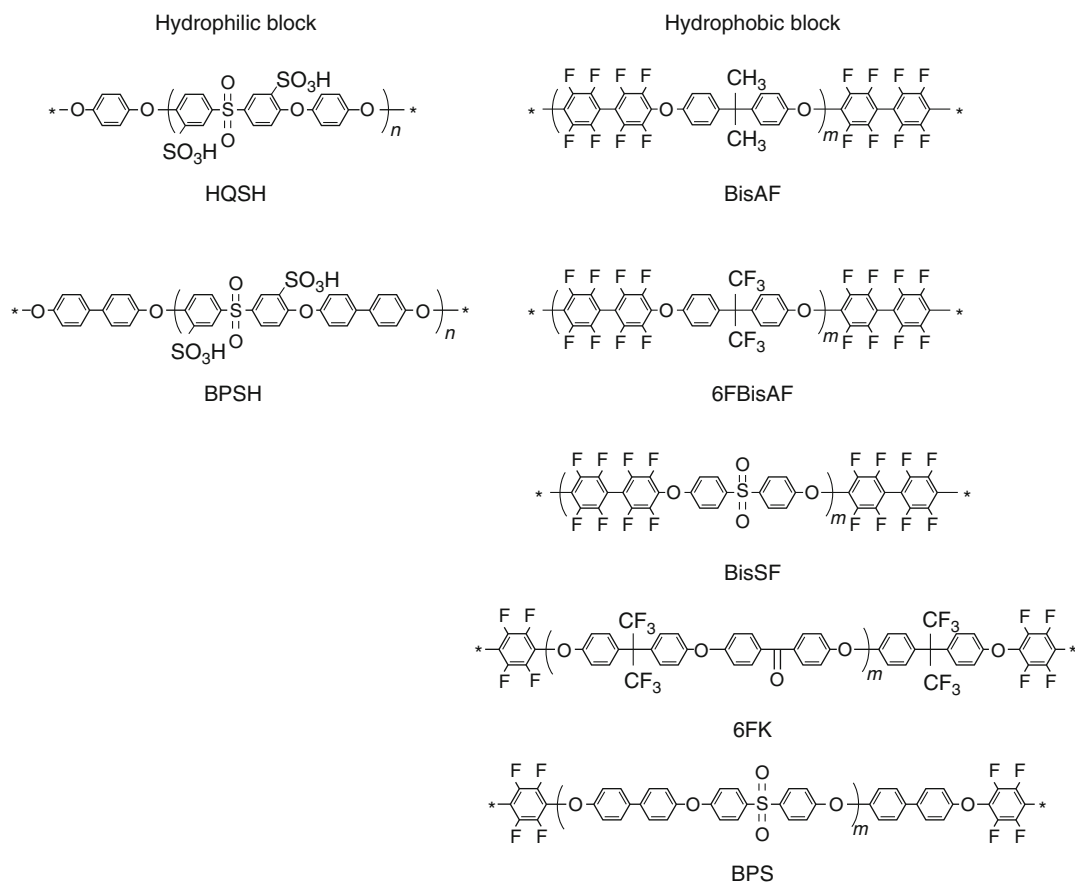
morphology (Table 4). The block length should be longer than 10 kDa in order to have noticeable improvement on the morphological order and proton conductivity.

- In addition to the block length and IEC values, casting conditions (such as the solvent and drying temperature or solvent removal rate) did have significant impact on membrane morphology and properties.
- The block copolymer membrane performed in an H<sub>2</sub>/air fuel cell at 100 °C and 40% RH comparable to Nafion membrane.

These findings are, more or less, applicable to the other hydrocarbon ionomers and useful to tailor the higher order structure and properties of ionomer membranes.

### Polymers with Sulfonic Acid Clusters

In order to overcome the trade-off relationship between water uptake and proton conductivity (high conductivity can be achieved with high-water-absorbing membranes), Hay's group at



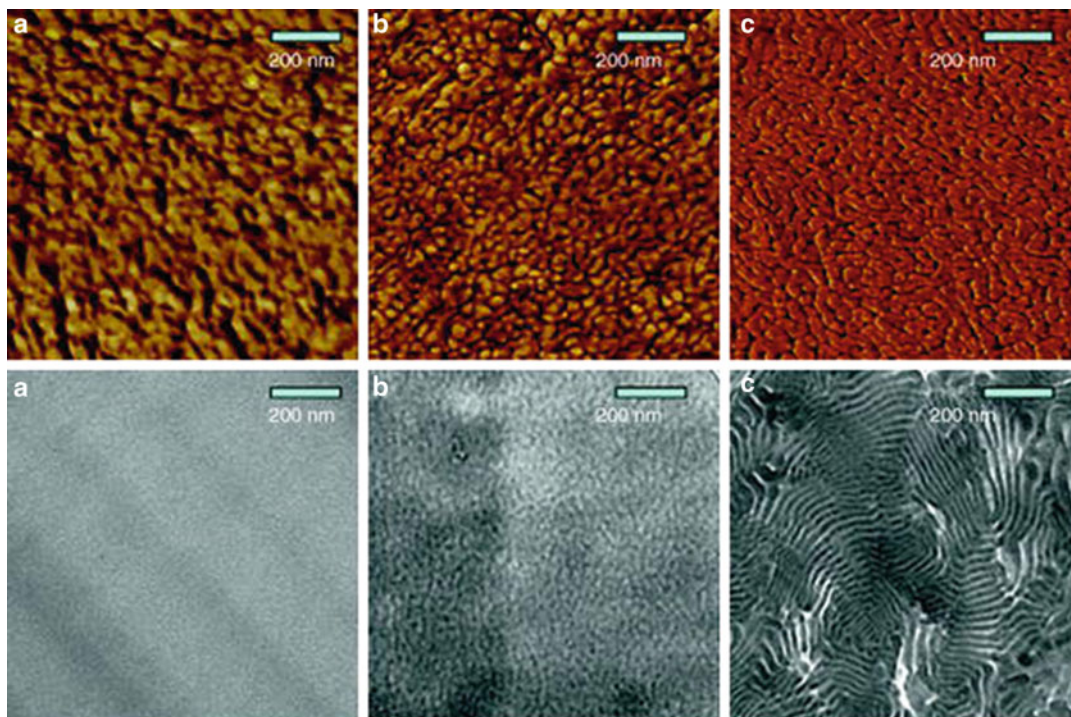
**Membrane Electrolytes, from Perfluorosulfonic Acid (PFSA) to Hydrocarbon Ionomers, Fig. 19** Chemical structure of BPSH block copolymers and their derivatives

McGill University has proposed a unique strategy. They have synthesized poly(arylene ether)s containing nanoclusters of up to 18 sulfonic acid groups either tethered on the end groups or distributed in the main chains (Fig. 21) [52–58]. Membranes therefrom showed significantly phase-separated (worm-like or large hydrophilic domains) and highly connected morphology in the TEM images. The highest proton conductivity at 120 °C was 3.1 mS/cm at 10% RH and 10.5 mS/cm at 30% RH for a membrane with IEC = 1.0 meq/g. The reported conductivity values were extremely high compared to those of the other hydrocarbon ionomer membranes with such low IEC and even higher than those of Nafion under the same conditions, 1.7 mS/cm (at 10% RH) and 4.0 mS/cm (at 30% RH),

respectively. The membrane absorbed ca. double amount of water compared to the Nafion membrane, which is thought to be responsible for the high proton conductivity.

Ueda and his coworkers of Tokyo Institute of Technology confirmed this strategy with their sulfonated poly(arylene ether sulfone)s (Fig. 22) [59–61]. Their polymers contain highly sulfonated moieties (up to ten sulfonic acid groups per repeating unit) randomly distributed in the main chains. Large difference in the polarity between highly sulfonated units and hydrophobic units caused the formation of defined phase-separated structures and well-connected proton pathways. The proton conductivity of the ionomer membrane with IEC = 2.38 meq/g was comparable to that of Nafion 117 at >30% RH, 80 °C.





**Membrane Electrolytes, from Perfluorosulfonic Acid (PFSA) to Hydrocarbon Ionomers, Fig. 20** Atomic force microscopy (AFM) (*top*) and transmission electron microscopy (TEM) (*bottom*) images of BPSH-6FK multi-block copolymer membranes: (a) BPSH5-6FK5, (b)

BPSH10-6FK10, and (c) BPSH10 for AFM or BPSH15 for TEM-6FK15. Numbers represent molecular weight of each block component in kDa (Reprinted from Lee et al. [47] with permission from Wiley Interscience)

**Membrane Electrolytes, from Perfluorosulfonic Acid (PFSA) to Hydrocarbon Ionomers, Table 4** States of water molecules in the BPSH (random), BPSH-BPS (block), and Nafion membranes

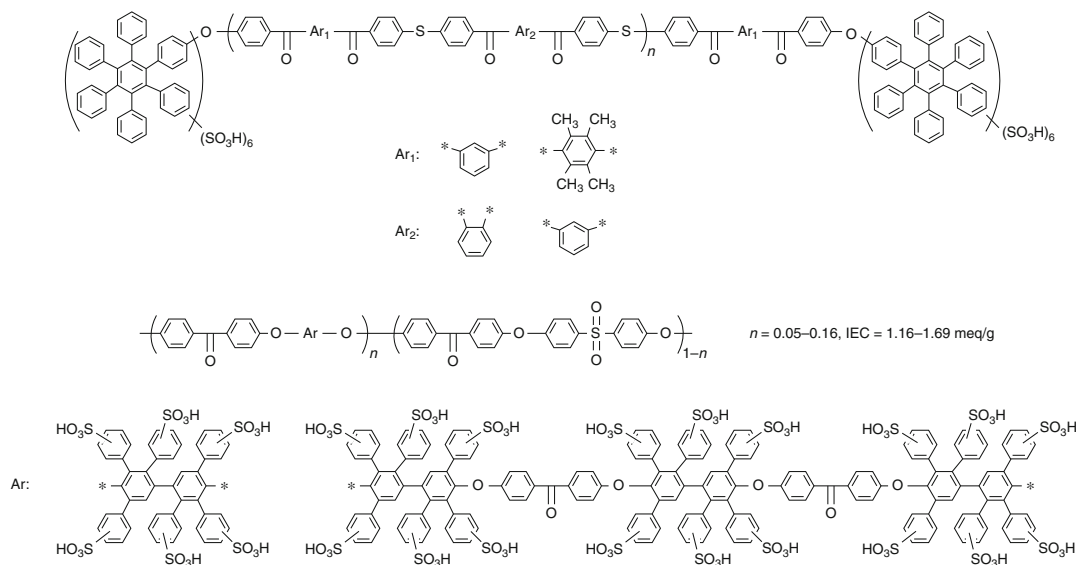
Membrane	IEC (meq/g)	Total water ( $\lambda^a$ )	Tightly bound water ( $\lambda^a$ )	Loosely bound water ( $\lambda^a$ )	Free water ( $\lambda^a$ )
BPSH30	1.34	12	4	8	0
BPSH3-BPS3	1.33	12	7	5	0
BPSH5-BPS5	1.39	13	8	5	0
BPSH10-BPS10	1.28	26	10	8	8
Nafion 112	0.90	17	3	9	5

<sup>a</sup>Number of water molecules absorbed per sulfonic acid group

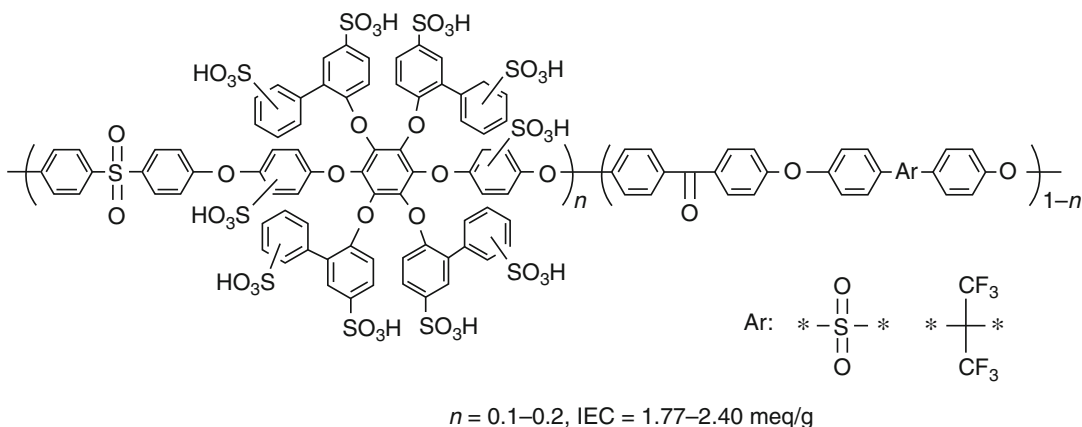
Miyatake et al. have combined two strategies in a single polymer architecture (multiblock copolymers containing sulfonic acid clusters in their hydrophilic blocks) [62]. They have successfully synthesized a series of multiblock poly(arylene ether sulfone ketone)s (SPESKs) containing fully sulfonated fluorenylidene

biphenylene units (Fig. 23) [63, 64]. The well-controlled post-sulfonation reaction of the precursor polymers enabled preferential sulfonation on each aromatic ring of the fluorenylidene biphenylene groups with 100% degree of sulfonation. The ionomer membranes showed unique morphology with well-developed hydrophilic/

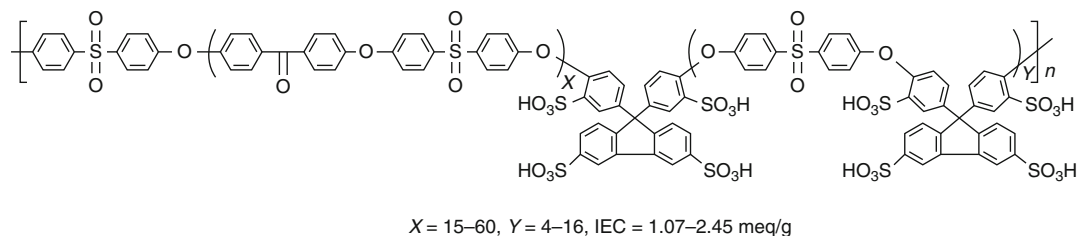




**Membrane Electrolytes, from Perfluorosulfonic Acid (PFSA) to Hydrocarbon Ionomers, Fig. 21** Poly(arylene ether)s containing sulfonic acid clusters

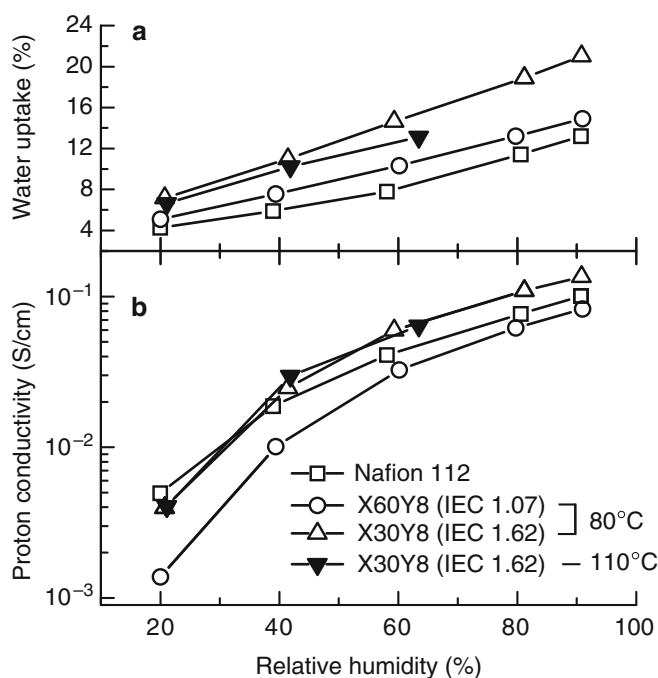


**Membrane Electrolytes, from Perfluorosulfonic Acid (PFSA) to Hydrocarbon Ionomers, Fig. 22** Poly(arylene ether sulfone)s with up to ten sulfonic acid groups per repeating unit



**Membrane Electrolytes, from Perfluorosulfonic Acid (PFSA) to Hydrocarbon Ionomers, Fig. 23** Multiblock poly(arylene ether sulfone ketone)s (SPESKs) containing fully sulfonated fluorenylidene biphenylene units

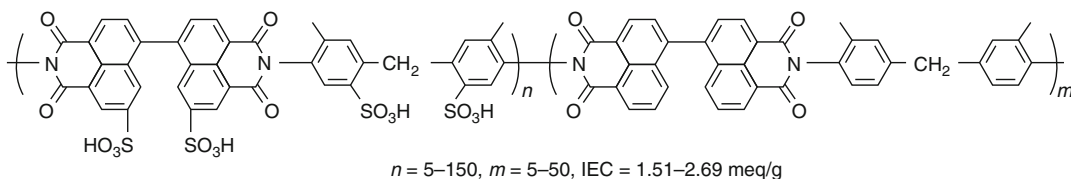
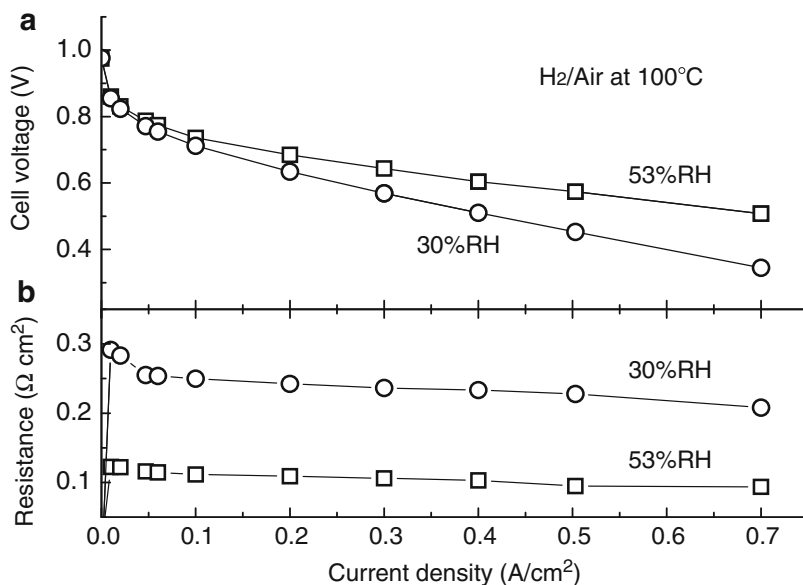
**Membrane Electrolytes, from Perfluorosulfonic Acid (PFSA) to Hydrocarbon Ionomers, Fig. 24** (a) Water uptake and (b) proton conductivity of Nafion 112 and block SPESKs (where IEC is in meq/g) as a function of relative humidity at 80 and 110 °C (Reprinted from Bae et al. [64] with permission from Wiley Interscience)



hydrophobic phase separation, depending on the block length of each segment. It was concluded that longer block length and/or higher IEC resulted in larger and better-connected hydrophilic clusters under dry conditions, while the morphology was less dependent on these factors under fully hydrated conditions. The multiblock copolymer membrane with IEC = 1.62 meq/g showed much higher proton conductivity than that of the random copolymer membrane with similar chemical structure and IEC (Fig. 24). The proton conductivity was similar or even higher compared to that of Nafion over a wide humidity range. The membrane retained high proton conductivity at 110 °C. The high conductivity resulted from the high proton diffusion coefficient. Longer block length seemed effective in increasing proton diffusion coefficient, which coincided with the morphological observations. The multiblock copolymer membranes were stable to hydrolysis in water at 140 °C for 24 h or at 100 °C for 1,000 h. The membranes degraded to some extent under harsh oxidative conditions (in Fenton's reagent), which is the fate of hydrocarbon ionomer compounds. Oxidative degradation is likely to occur at phenylene

carbon atoms *ortho* to the ether bonds by the attack of highly oxidative hydroxyl radicals. The multiblock copolymer membrane showed much lower gas permeability than Nafion, while humidity dependence of the permeability was different between hydrogen and oxygen. Hydrogen permeability showed reverse volcano-type dependence on the humidity, decreased slightly with humidification, and then increased with further humidification. Oxygen permeability simply increased with humidity. Such humidity dependency of oxygen permeability was similar to that of Nafion, however, not observed in the random copolymer membranes. The low gas permeability could mitigate their oxidative instability since hydrogen peroxide as a by-product is potentially less produced when the gas permeation through the membranes is low. A fuel cell was successfully operated with the multiblock copolymer membranes at 30% and 53% RH and 100 °C (Fig. 25). The current density was 250 mA/cm<sup>2</sup> at 30% RH and 410 mA/cm<sup>2</sup> at 53% RH at a cell voltage of 0.6 V. The high proton conductivity of the membrane at low RH and high temperature was well confirmed in practical fuel cell operation.

**Membrane Electrolytes, from Perfluorosulfonic Acid (PFSA) to Hydrocarbon Ionomers, Fig. 25** (a)  $H_2$ /air fuel cell performances including ohmic resistance voltage losses and (b) ohmic resistances of SPESK X30Y8 (IEC = 1.62 meq/g) at 100 °C with humidification at 53 % and 30 % RH for both electrodes (Reprinted from Bae et al. [64] with permission from Wiley Interscience)



**Membrane Electrolytes, from Perfluorosulfonic Acid (PFSA) to Hydrocarbon Ionomers, Fig. 26** Multiblock copolyimides with highly sulfonated hydrophilic block

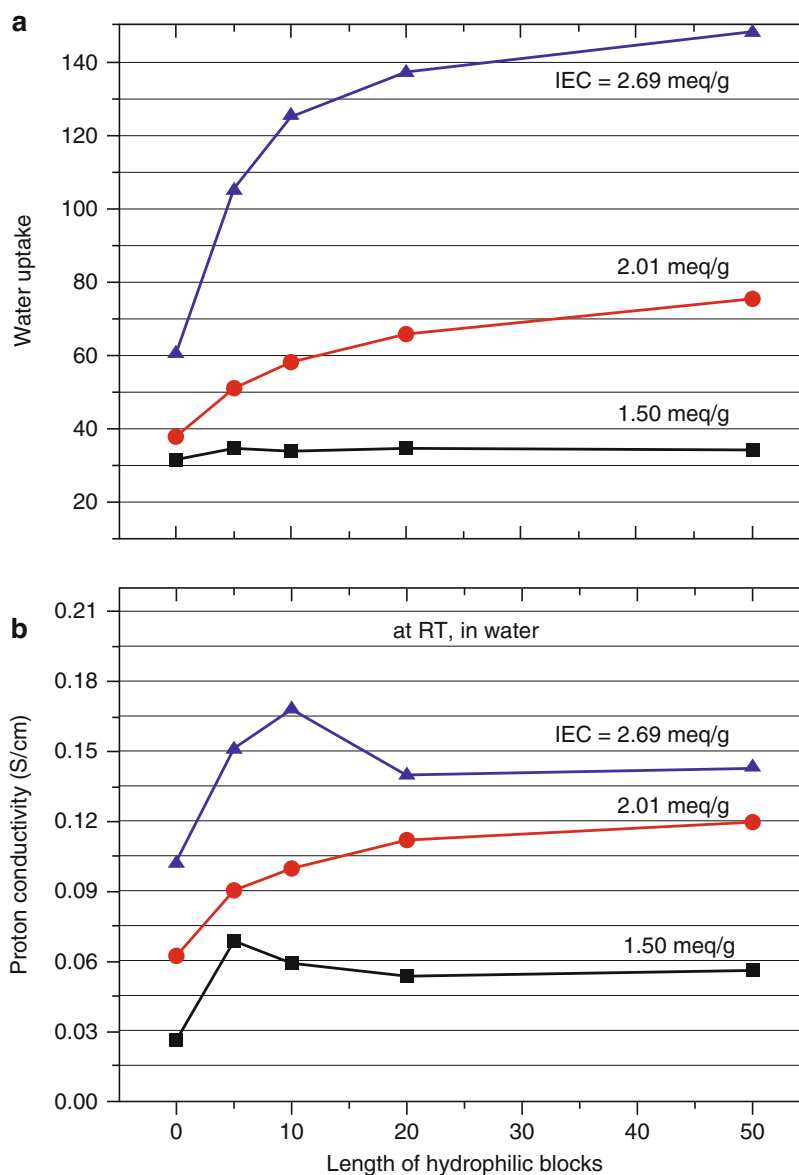
Zhang et al. of Changchun Institute of Applied Chemistry have also confirmed the similar strategy with their unique multiblock copolyimide ionomers, in which hydrophilic blocks were composed of disulfonated dianhydride and disulfonated diamine (each aromatic ring was sulfonated) (Fig. 26) [65]. While they have not done morphological investigations, the high concentration of the sulfonic acid groups in the hydrophilic block was effective in enhancing water absorbability and proton conductivity of the polyimide ionomer membranes (Fig. 27). For example, their high-IEC (2.69 meq/g) block copolymer membranes were much more proton conductive than the random equivalent, and the highest conductivity at 50% RH and 70 °C was  $3.2 \times 10^{-2}$  S/cm for the multiblock copolyimide with the 50 repeating units in the hydrophilic blocks. The multiblock copolyimides showed lower proton concentration as a consequence of the higher

water uptake; however, higher proton mobility compensated the proton concentration. Hydrolysis remains an issue for the polyimides, and the block copolymer architecture did not help improve the hydrolytic stability (the fact is that the block copolymers were more susceptible to hydrolysis due to the higher water uptake).

### Polymers with Pendant Acidic Groups

One of the reason for Nafion to have well-developed phase separation and interconnected ionic channels lies on its chemical structure that contains acid groups at the end of flexible perfluoroalkyl ether side chains. The introduction of pendant sulfonic acid groups has been investigated for the aromatic polymers such as polybenzimidazoles, polyimides, and poly(arylene ether)s, to confirm whether a similar effect can be obtained without perfluorinated chains (Fig. 28). In most cases, flexible side chains

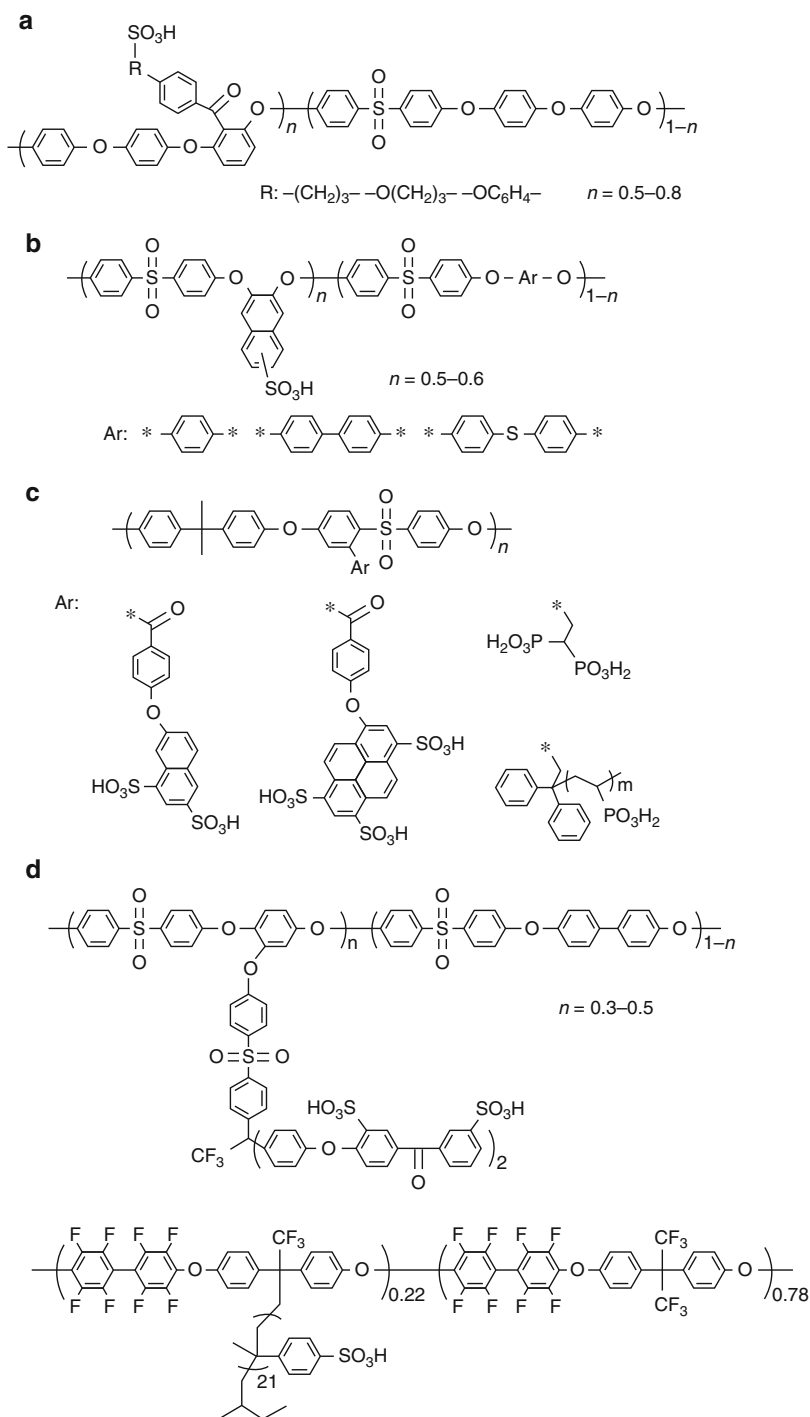
**Membrane Electrolytes, from Perfluorosulfonic Acid (PFSA) to Hydrocarbon Ionomers, Fig. 27** (a) Water uptake and (b) proton conductivity of multiblock copolyimides with different IECs as a function of hydrophilic block length (Reprinted from Li et al. [65] with permission from Elsevier)



between the aromatic main chains and the acid groups improve morphology and proton conductivity but not as striking as that in Nafion. For example, Jiang et al. of Jilin University have developed a series of poly(arylene ether sulfone)s containing long pendant acidic (sulfopropylbenzoyl, sulfopropoxybenzoyl, or sulfophenoxybenzoyl) groups [66–71] (a), in which membrane ionic clusters of ca. 10–20 nm in diameter were confirmed via TEM observation but rather isolated from one another. When

relatively higher sulfonic acid concentration was applied, ionic clusters became larger (ca. 40 nm in diameter) and better interconnected. Poly(arylene ether sulfone)s containing pendant sulfonaphthyl groups (b) were synthesized by Manthiram's group at the University of Texas at Austin [72]. Their membranes outperformed Nafion 115 membrane in DMFC operation, while the effect of pendant naphthyl groups was not well investigated. Jannasch et al. of Lund University proposed poly(arylene ether sulfone)s tethered

**Membrane Electrolytes, from Perfluorosulfonic Acid (PFSA) to Hydrocarbon Ionomers, Fig. 28** Aromatic polymers with pendant acidic groups



with hyper-acidified pendant groups (two or more sulfonic or phosphonic acid groups per pendant unit) (c) [73, 74]. By concentrating acidic groups locally onto the side chains, a distinct phase

separation between hydrophobic polymer main chains and hydrophilic pendant groups was achieved. The water uptake of these kinds of ionomer membranes seemed rather high, and

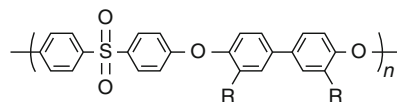
thus cross-linking or incorporation of inorganic additives may be needed to avoid excess swelling.

Recently, more developed ideas on the pendant acidic groups have been proposed by several research groups. Such include graft copolymers or comb-shaped ionomers, in which ionic grafts were substituted onto aromatic main chains. Jannasch et al. have further developed their above ideas by grafting poly(vinylphosphonic acid) (PVPA) onto poly(phenylene ether sulfone)s (c) [75]. Such molecular architecture caused phase separation and dual glass transition temperature due to the inherent miscibility of the stiff and hydrophobic polymer backbones and strongly hydrogen-bonded phosphonic acid side chains. The membrane with 57 wt% of the PVPA content showed 4.6 mS/cm (dry) and 93 mS/cm (100% RH) at 120 °C. Still, the water uptake of the membrane was rather high and should be improved.

Guiver et al. of the National Research Council, Canada, developed comb-shaped poly(arylene ether) electrolytes containing two to four sulfonic acid groups on aromatic side chains (d) [76]. Their membranes showed relatively high proton conductivity and well-developed and continuous ionic domains. However, trade-off relationship between water uptake and proton conductivity of their membranes was not better than that of Nafion. In order to pronounce the hydrophilic/hydrophobic differences, another series of comb-shaped aromatic ionomers with highly fluorinated main chains and flexible poly( $\alpha$ -methyl styrene sulfonic acid) side chains were developed [77]. The membranes seemed to have better properties than their previous version; however, chemical instability of the side chains needed to be improved.

### Hydrocarbon Polymers with Superacid Groups

One of the significant differences between hydrocarbon ionomers and perfluorosulfonic acid polymers is acid groups. The  $pK_a$  value of benzenesulfonic acid ( $\text{PhSO}_3\text{H}$ ) is  $-2.5$  and that of trifluoromethanesulfonic acid ( $\text{CF}_3\text{SO}_3\text{H}$ ) is  $-13$ . The  $pK_a$  value was estimated to be ca.  $-1$  for sulfonated polyether ketone and ca.  $-6$  for



R: H,  $-(\text{CF}_2)_2\text{O}(\text{CF}_2)_2\text{SO}_3\text{H}$  IEC = 0.95–1.58 meq/g

**Membrane Electrolytes, from Perfluorosulfonic Acid (PFSA) to Hydrocarbon Ionomers, Fig. 29** Poly(arylene ether sulfone)s with superacid groups

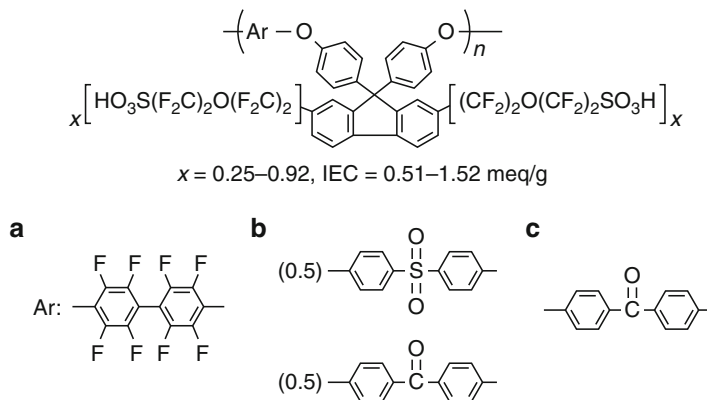
Nafion membranes [78]. Therefore, the effective proton concentration and proton mobility should be lower in the hydrocarbon ionomer membranes. Without appropriate molecular design such as multiblock copolymer and sulfonic acid clusters as mentioned above, hydrocarbon ionomer membranes lack well-developed ionic channels due to less pronounced hydrophilic and hydrophobic phase separation, which causes the lower proton conductivity at low humidity.

Yoshimura and Iwasaki of Sumitomo Chemical Co. have synthesized aromatic ionomers containing pendant perfluorosulfonic acid groups (Fig. 29) [79]. Poly(arylene ether sulfone) was brominated and then perfluorosulfonated via Ullmann coupling reaction in the presence of copper catalyst. The IEC was controllable up to 1.58 meq/g. The obtained ionomer membranes behaved very differently from the typical sulfonated aromatic ionomer membranes. Characteristic hydrophobic/hydrophilic separation (ca. 3–4 nm) was observed in the small-angle X-ray scattering (SAXS) analyses of the hydrated samples. The ionic clusters were slightly smaller than those of Nafion membrane. The superacid groups were effective in improving thermal and mechanical properties of poly(arylene ether sulfone) ionomers as confirmed by dynamic mechanical analyses (DMA) and tensile testings. The superacidified ionomer membranes showed several times higher proton conductivity than that of the typical sulfonated poly(arylene ether sulfone) ionomers with similar IEC at 80 °C, 50–90% RH.

Miyatake et al. have also confirmed the positive effect of superacid groups on the properties of the poly(arylene ether) ionomers [80, 81]. They have synthesized poly(arylene ether)s containing pendant superacid groups on fluorenyl groups (FSPEa-c) (Fig. 30) via similar method as that of

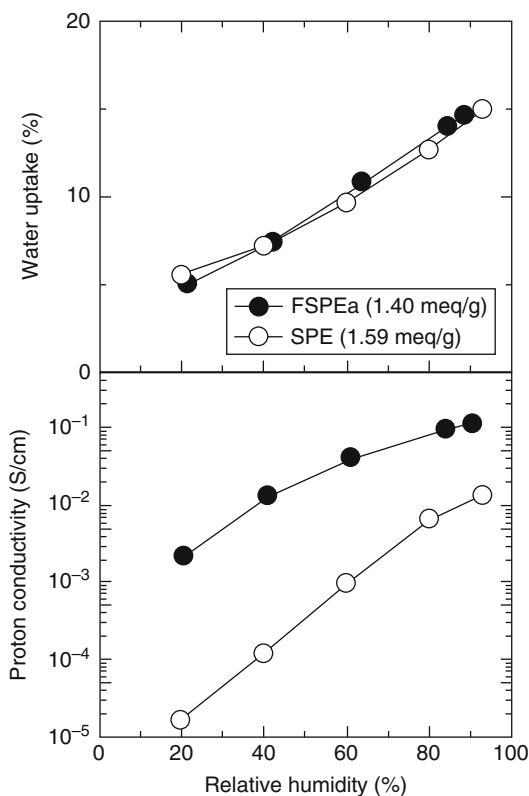


**Membrane Electrolytes, from Perfluorosulfonic Acid (PFSA) to Hydrocarbon Ionomers, Fig. 30** Poly(arylene ether)s containing superacid groups on fluorenyl groups



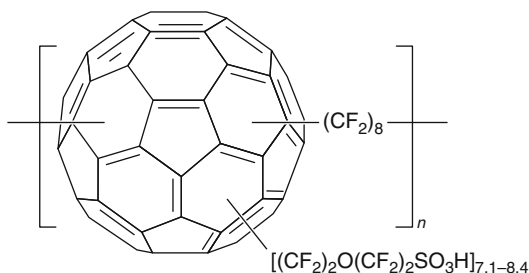
Sumitomo Chemical Co. The superacid-containing ionomer membranes showed similar thermal and gas permeation properties to those of the conventional sulfonated aromatic ionomers. Instead, their morphology was more similar to that of Nafion. Well-developed hydrophilic/hydrophobic phase separation was observed, while the hydrophilic clusters were somewhat smaller than those of Nafion. More significant difference was observed in water uptake and proton conductivity (Fig. 31). For example, proton conductivity of superacid-containing ionomer membrane ( $\text{IEC} = 1.40$  meq/g) was ca. 2 mS/cm at 80 °C and 20% RH, which was considerably higher than that (0.02 mS/cm) of conventional sulfonated poly(arylene ether)s (SPE,  $\text{IEC} = 1.59$  meq/g) under the same conditions. The two membranes showed very similar water uptake behavior at a wide range of humidity. The results imply that the superacid groups utilize water molecules more efficiently for proton conduction than arylsulfonic acid groups. Their study revealed that the main chain structure seemed to affect the properties and could be optimized for further improvement of the properties. The membrane showed good fuel cell performance at 80 °C and 78 or 100% RH; however, the performance became lower under lower-humidity conditions.

Hirakimoto et al. of Sony Co. have developed a unique ionomer containing superacid-substituted fullerene groups in the main chain (Fig. 32) [82]. Fullerene was substituted by averaging 7.1–8.4 superacid groups and was polymerized and cross-linked with 1,8-diiodoperfluorooctane to give the polymer with  $\text{IEC} = 1.88$



**Membrane Electrolytes, from Perfluorosulfonic Acid (PFSA) to Hydrocarbon Ionomers, Fig. 31** Humidity dependence of water uptake and proton conductivity of fluorene-containing poly(arylene ether)s with superacid groups (FSPEa) and conventional sulfonic acid groups (SPE) at 80 °C

meq/g. The ionomer was thermally stable up to 240 °C as confirmed by TG analyses in dry nitrogen and showed high proton conductivity ( $2 \times 10^{-2}$  S/cm) at 25 °C and 50% RH as a pellet.



**Membrane Electrolytes, from Perfluorosulfonic Acid (PFSA) to Hydrocarbon Ionomers, Fig. 32** Superacid-modified polyfullerene

Since the material did not seem to have good film-forming capability by itself, composite membranes with poly(vinylidene difluoride) (PVDF) were investigated. The composite membrane containing 20 wt% of PVDF outperformed Nafion membrane in DMFC operation. The maximum power density of ca. 110 mW/cm<sup>2</sup> was achieved.

### Composite Membranes

It has been proposed that modification of ionomer materials with hygroscopic oxides such silica, titania, tungsten oxide, zirconia, and zirconia phosphate could improve membrane properties. Introduction of nanoparticles of such oxides has been claimed to increase water affinity and reduce evaporation of water at high temperature and/or low humidity. The original research stems from Nafion composites [83–85], and recently, considerable effort has been devoted to apply the methodology to hydrocarbon ionomers. Some of the composite membranes showed better mechanical properties and lower gas or methanol permeability; however, the composite effect on the proton conductivity was not very obvious or even negative in some cases. In addition to the chemical and physical state of the inorganic additives, membrane fabrication procedure also seems a crucial factor since it affects membrane morphology and miscibility of inorganic additives with the matrix. Therefore, detailed and careful analyses are required to discuss the effect of additives. It is beyond the scope of this entry to review the composite membranes. A few of the recent examples are introduced.

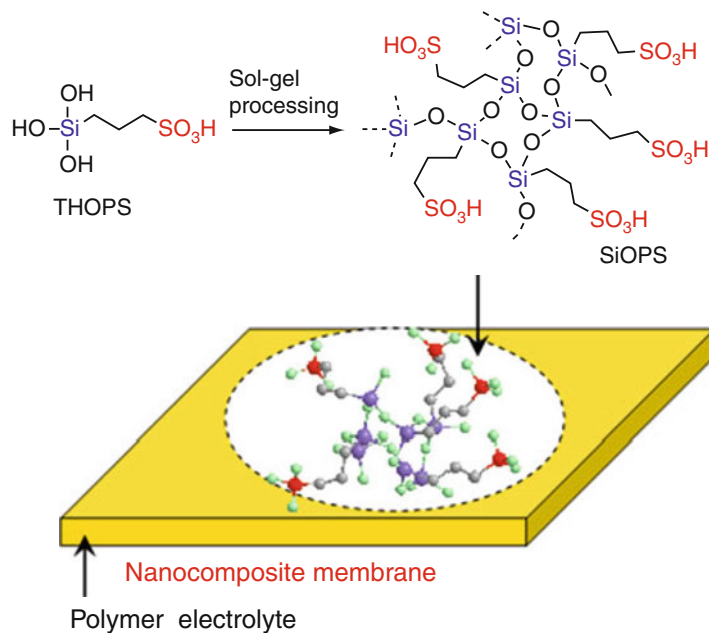
The group of GKSS Research Centre, Germany, extensively researched the effect of a variety of inorganic nanoparticles on the properties of aromatic ionomer membranes [86–93]. Composite membranes were prepared from silicates and sulfonated poly(ether ketone)s or sulfonated poly(ether ether ketone)s. For DMFC applications, the composite membranes showed promising properties with lower methanol and water permeability and comparable (or higher) proton conductivity compared to the parent polymer membranes. The flux of water and methanol decreased with the increase in content of silicates.

In the case of sulfonated poly(phthalazinone ether ketone)s being used as a matrix, composite membranes showed less swelling in water and methanol and better mechanical and thermal stability, but lower proton conductivity [94, 95]. The results suggest that the amount of inorganic additives has to be optimized for each ionomer material and fuel cell operation conditions. Addition of 5 wt% of silica was optimum for poly(phthalazinone ether ketone)s to obtain high OCV and high power density of DMFC with 3M methanol at 70 °C.

It has been proposed that hybrid membranes are more proton conductive at low humidity than the parent polymer membranes. For example, zirconia phosphate (ZrP) was formed in the sulfonated poly(arylene ether sulfone). Nanoparticles of zirconia phosphate were homogeneously distributed in the membranes as crystalline  $\alpha$ -zirconium hydrogen phosphate hydrate [96]. The composite membrane (with ZrP up to 50 wt%) showed  $3.7 \times 10^{-3}$  S/cm of the proton conductivity at 90 °C, 30% RH, which was ca. 5 times higher than that of the parent polymer membrane under the same conditions. It is claimed that the composite effect depends upon interfacial contact between the polymer matrix and additives and inappropriate preparation procedure could result in opposite effects.

In order to take more advantage of the effect of incorporated inorganic additives and to produce highly proton-conductive composite membranes, Miyatake et al. have utilized 3-trihydroxysilyl-1-propanesulfonic acid (THOPS) as a precursor of the inorganic component (Fig. 33) [97]. THOPS

**Membrane Electrolytes, from Perfluorosulfonic Acid (PFSA) to Hydrocarbon Ionomers, Fig. 33** Schematic representation of the proton-conductive nanocomposite membranes composed of ionomer (matrix) and sulfopropylated polysilsesquioxane (SiOPS) (Reprinted from Miyatake et al. [97] with permission from Wiley Interscience)



has a sulfonic acid group covalently bonded to a silicon atom through aliphatic chain. The in situ sol-gel process in the polymer electrolyte matrices gave composite membranes containing sulfopropylated polysilsesquioxane ( $\{\text{SiO}_{3/2}(\text{CH}_2)_3\text{SO}_3\text{H}\}_n$ ; SiOPS). Two different ionomers, sulfonated polyimides and sulfonated poly(arylene ether)s, were used as matrices. In the STEM images of the Ag-stained membrane samples, the ionic domains of approximately 5 nm in diameter were observed which were well connected to each other. The connectivity of the ionic domains was significantly improved compared to that of the parent matrix membrane, while the size of the spherical ionic clusters did not alter. It is thought that the ionic domains result from the aggregation of sulfonic acid groups both from the matrix polymer and SiOPS. Energy Dispersive X-ray (EDX) analyses of the composite samples support highly dispersed SiOPS. These results suggest that well-dispersed nanocomposite membranes were formed. Nanocomposite membranes thus obtained showed much higher proton conductivity (up to 30 times) than that of the original membranes and accordingly less dependence of the conductivity upon the humidity. The ionomer properties such as thermal, hydrolytic, and oxidative stability and gas permeability were rather

unaffected by the SiOPS. The methodology seems to be versatile as confirmed by the two different series of polymer electrolytes, although the miscibility with SiOPS depended on the matrix polymer.

### Future Directions

The success of fuel cell industry depends greatly on the membrane technology. Since the biggest market of fuel cells will lie in the electric vehicles, most of the effort on the development of proton exchange membranes has been and will be devoted to high-temperature and low-humidity (or nominally dry) operable membranes. In the last decade, PFSA has achieved a significant progress and probably meet most of the requirements for the commercialization of fuel cell vehicles. At least, reasonable performance and durability can be obtained under well-controlled operating conditions using relatively large balance of plant (BoP). On a long-term basis, the current situation is not acceptable, and more effort has to be made in developing better (possibly, non-fluorinated) ionomer membranes that fulfill all the abovementioned requirements. This indicates that investment in such research is essential.

There is no doubt that the PFSA membranes take initiative in this field and contribute a great deal in the commercialization and wide diffusion of fuel cells in the early stage. In terms of environmental compatibility (recyclability or disposability) and production cost, the PFSA membranes would better be replaced with non-fluorinated alternative materials within the next decade. Challenge is how to achieve comparable conductivity and durability with the non-fluorinated membranes. Unfortunately, no alternative materials have overcome the trade-off relationship between these two incompatible properties. Aromatic hydrocarbon ionomers are one of the possible candidates and run next to PFSA in the race of membrane development. While a number of effective approaches have been proposed, there still remains a significant gap between them. Alternative membranes can show comparable conductivity to PFSA by absorbing more water; however, such excessive hydrophilicity results in chemical and mechanical instability. All hydrocarbon membranes tend to show severer decrease of proton conductivity with decreasing RH compared to the conductivity of PFSA membranes. A technological breakthrough is certainly required.

Due to the limited space, the other important role of proton-conducting materials as a binder in the gas diffusion electrode has not been mentioned in this entry. In order to maximize potential activity of catalysts (both for the oxygen reduction and hydrogen oxidation catalysts), the ionomer materials are expected to function differently from the membranes. In addition to the basic properties such as proton conductivity and durability, the binder materials are required to permeate reactant gases and discharge product water. Excess swelling under hydrated conditions often disturbs oxygen from diffusing onto the catalyst surface. The membranes are generally flat and rather thick ( $>10\ \mu\text{m}$ ), while the binders cover uneven nanostructured catalysts on carbon black in several nm thickness. The ionomers may behave differently in such thin layers; however, there have been few research works on this topic, particularly for non-fluorinated ionomers. Although some non-fluorinated ionomers are claimed to perform

comparably to Nafion as membranes, they show considerably lower performance as a binder in the gas diffusion electrode in most cases. These issues need to be addressed more carefully and extensively in order to realize high-performance fluorine-free fuel cells.

## Bibliography

### Primary Literature

1. <http://www1.eere.energy.gov/hydrogenandfuelcells/mypp/>
2. Arenz M, Schmidt TJ, Wandelt K, Ross PN, Markovic NM (2003) The oxygen reduction reaction on thin palladium films supported on a Pt(111) electrode. *J Phys Chem B* 107:9813–9819
3. Aieta NV, Stanis RJ, Horan JL, Yandrasits MA, Cookson DJ, Ingham B, Toney MF, Hamrock SJ, Herring AM (2009) Clipped random wave morphologies and the analysis of the SAXS of an ionomer formed by copolymerization of tetrafluoroethylene and  $\text{CF}_2 = \text{CFO}(\text{CF}_2)_4\text{SO}_3\text{H}$ . *Macromolecules* 42:5774–5780
4. Emery M, Frey M, Guerra M, Haugen G, Hintzer K, Lochhaas KH, Pham P, Pierpont D, Schaberg M, Thaler A, Yandrasits M, Hamrock S (2007) The development of new membranes for proton exchange membrane fuel cells. *ECS Trans* 11:3–14
5. Arcella V, Troglia C, Ghielmi A (2005) Hyflon ion membranes for fuel cells. *Ind Eng Chem Res* 44:7646–7651
6. Kreuer KD, Schuster M, Obliers B, Diat O, Traub U, Fuchs A, Klock U, Paddison SJ, Maier J (2008) Short-side-chain proton conducting perfluorosulfonic acid ionomers: why they perform better in PEM fuel cells. *J Power Sources* 178:499–509
7. Yoshitake M, Watakabe A (2008) Perfluorinated ionic polymers for PEFCs (including supported PFSA). *Adv Polym Sci Fuel Cells I* 215:127–155
8. Appleby AJ, Velez OA, LeHelloco JG, Parthasarthy A, Srinivasan S, DesMarteau DD, Gillette MS, Ghosh JK (1993) Polymeric perfluoro bis-sulfonimides as possible fuel cell electrolytes. *J Electrochem Soc* 140:109–111
9. Kotov SV, Pedersen SD, Qiu W, Qiu Z-M, Burton DJ (1997) Preparation of perfluorocarbon polymers containing phosphonic acid groups. *J Fluor Chem* 82:13–19
10. Thomas BH, DesMarteau DD (2005) Self-emulsifying polymerization (SEP) of 3, 6-dioxo-Delta 7-4-trifluoromethyl perfluorooctyl trifluoromethyl sulfonimide with tetrafluoroethylene. *J Fluor Chem* 126:1057–1064
11. Thomas BH, Shafer G, Ma JJ, Tu M-H, DesMarteau DD (2004) Synthesis of 3, 6-dioxo-Delta 7-4-trifluoromethyl perfluorooctyl trifluoromethyl sulfonimide: bis[(perfluoroalkyl)sulfonyl] superacid monomer and polymer. *J Fluor Chem* 125:1231–1240

12. Uematsu N, Hoshi N, Koga T, Ikeda M (2006) Synthesis of novel perfluorosulfonamide monomers and their application. *J Fluor Chem* 127:1087–1095
13. Coms FD (2008) The chemistry of fuel cell membrane chemical degradation. *ECS Trans* 16:235–255
14. Curtin DE, Lousenberg RD, Henry TJ, Tangeman PC, Tisack ME (2004) Advanced materials for improved PEMFC performance and life. *J Power Sources* 131:41–48
15. Schiraldi DA (2006) Perfluorinated polymer electrolyte membrane durability. *Polym Rev* 46:315–327
16. Danilczuk M, Perkowski AJ, Schlick S (2010) Ranking the stability of perfluorinated membranes used in fuel cells to attack by hydroxyl radicals and the effect of Ce(III): a competitive kinetics approach based on spin trapping ESR. *Macromolecules* 43:3352–3358
17. Endoh E (2008) Development of highly durable PFSA membrane and MEA for PEMFC under high temperature and low humidity conditions. *ECS Trans* 16:1229–1240
18. Ghassemzadeh L, Kreuer KD, Maier J, Muller K (2010) Chemical degradation of nation membranes under mimic fuel cell conditions as investigated by solid-state NMR spectroscopy. *J Phys Chem C* 114:14635–14645
19. Coms FD, Liu H, Owejan JE (2008) Mitigation of perfluorosulfonic acid membrane chemical degradation using cerium and manganese ions. *ECS Trans* 16:1735–1747
20. Danilczuk M, Schlick S, Coms FD (2009) Cerium(III) as a stabilizer of perfluorinated membranes used in fuel cells: in situ detection of early events in the ESR resonator. *Macromolecules* 42:8943–8949
21. Trogadas P, Parrondo J, Ramani V (2008) Degradation mitigation in polymer electrolyte membranes using cerium oxide as a regenerative free-radical scavenger. *Electrochem Solid-State Lett* 11:B113–B116
22. Okazoe T, Murotani E, Watanabe K, Itoh M, Shirakawa D, Kawahara K, Kaneko I, Tatematsu S (2004) An entirely new methodology for synthesizing perfluorinated compounds: synthesis of perfluoroalkanesulfonyl fluorides from non-fluorinated compounds. *J Fluor Chem* 125:1695–1701
23. Goto K, Rozhanskii I, Yamakawa Y, Otsuki T, Naito Y (2008) Development of aromatic polymer electrolyte membrane with high conductivity and durability for fuel cell. *Polym J* 41:95–104
24. Bae JM, Honma I, Murata M, Yamamoto T, Rikukawa M, Ogata N (2002) Properties of selected sulfonated polymers as proton-conducting electrolytes for polymer electrolyte fuel cells. *Solid State Ion* 147:189–194
25. Kobayashi T, Rikukawa M, Sanui K, Ogata N (1998) Proton-conducting polymers derived from poly(ether-etherketone) and poly(4-phenoxybenzoyl-1, 4-phenylene). *Solid State Ion* 106:219–225
26. Yanagimachi S, Kaneko K, Takeoka Y, Rikukawa M (2003) Synthesis and evaluation of phosphonated poly(4-phenoxybenzoyl-1, 4-phenylene). *Synth Met* 135:69–70
27. Ghassemi H, McGrath JE (2004) Synthesis and properties of new sulfonated poly(p-phenylene) derivatives for proton exchange membranes. I. *Polymer* 45:5847–5854
28. Ghassemi H, Ndip G, McGrath JE (2004) New multi-block copolymers of sulfonated poly(4'-phenyl-2, 5-benzophenone) and poly(arylene ether sulfone) for proton exchange membranes. II. *Polymer* 45:5855–5862
29. Fujimoto CH, Hickner MA, Cornelius CJ, Loy DA (2005) Ionomeric poly(phenylene) prepared by Diels-Alder polymerization: synthesis and physical properties of a novel polyelectrolyte. *Macromolecules* 38:5010–5016
30. He L, Fujimoto CH, Cornelius CJ, Perahia D (2009) From solutions to membranes: structure studies of sulfonated polyphenylene ionomers. *Macromolecules* 42:7084–7090
31. Hickner MA, Fujimoto CH, Cornelius CJ (2006) Transport in sulfonated poly(phenylene)s: proton conductivity, permeability, and the state of water. *Polymer* 47:4238–4244
32. Stanis RJ, Yaklin MA, Cornelius CJ, Takatera T, Umemoto A, Ambrosini A, Fujimoto CH (2010) Evaluation of hydrogen and methanol fuel cell performance of sulfonated diels alder poly(phenylene) membranes. *J Power Sources* 195:104–110
33. Rager T, Schuster M, Steininger H, Kreuer K-D (2007) Poly(1, 3-phenylene-5-phosphonic acid), a fully aromatic polyelectrolyte with high ion exchange capacity. *Adv Mater* 19:3317–3321
34. Steininger H, Schuster M, Kreuer KD, Kaltbeitzel A, Bingoel B, Meyer WH, Schauff S, Brunklaus G, Maier J, Spiess HW (2007) Intermediate temperature proton conductors for PEM fuel cells based on phosphonic acid as protogenic group: a progress report. *Phys Chem Chem Phys* 9:1764–1773
35. Schuster M, de Araujo CC, Atanasov V, Andersen HT, Kreuer K-D, Maier J (2009) Highly sulfonated poly(phenylene sulfone): preparation and stability issues. *Macromolecules* 42:3129–3137
36. Schuster M, Kreuer K-D, Andersen HT, Maier J (2007) Sulfonated poly(phenylene sulfone) polymers as hydrolytically and thermooxidatively stable proton conducting ionomers. *Macromolecules* 40:598–607
37. Kashimura Y, Aoyama S, Kawakami H (2009) Gas transport properties of asymmetric block copolyimide membranes. *Polym J* 41:961–967
38. Nakano T, Nagaoka S, Kawakami H (2005) Preparation of novel sulfonated block copolyimides for proton conductivity membranes. *Polym Adv Technol* 16:753–757
39. Nakano T, Nagaoka S, Kawakami H (2006) Proton conductivity of sulfonated long-chain-block copolyimide films. *Kobunshi Ronbunshu* 63:200–204
40. Niwa M, Nagaoka S, Kawakami H (2006) Preparation of novel fluorinated block copolyimide membranes for gas separation. *J Appl Polym Sci* 100:2436–2442
41. Asano N, Miyatake K, Watanabe M (2006) Sulfonated block polyimide copolymers as a proton-conductive

- membrane. *J Polym Sci A: Polym Chem* 44:2744–2748
42. Badami AS, Lane O, Lee H-S, Roy A, McGrath JE (2009) Fundamental investigations of the effect of the linkage group on the behavior of hydrophilic-hydrophobic poly(arylene ether sulfone) multiblock copolymers for proton exchange membrane fuel cells. *J Membr Sci* 333:1–11
  43. Badami AS, Roy A, Lee H-S, Li Y, McGrath JE (2009) Morphological investigations of disulfonated poly(arylene ether sulfone)-b-naphthalene dianhydride-based polyimide multiblock copolymers as potential high temperature proton exchange membranes. *J Membr Sci* 328:156–164
  44. Ghassemi H, McGrath JE, Zawodzinski TA (2006) Multiblock sulfonated-fluorinated poly(arylene ether)s for a proton exchange membrane fuel cell. *Polymer* 47:4132–4139
  45. Lee H-S, Lane O, McGrath JE (2010) Development of multiblock copolymers with novel hydroquinone-based hydrophilic blocks for proton exchange membrane (PEM) applications. *J Power Sources* 195:1772–1778
  46. Lee H-S, Roy A, Lane O, Dunn S, McGrath JE (2008) Hydrophilic-hydrophobic multiblock copolymers based on poly(arylene ether sulfone) via low-temperature coupling reactions for proton exchange membrane fuel cells. *Polymer* 49:715–723
  47. Lee HS, Roy A, Lane O, Lee M, McGrath JE (2010) Synthesis and characterization of multiblock copolymers based on hydrophilic disulfonated poly(arylene ether sulfone) and hydrophobic partially fluorinated poly(arylene ether ketone) for fuel cell applications. *J Polym Sci Polym Chem* 48:214–222
  48. Lee M, Park JK, Lee H-S, Lane O, Moore RB, McGrath JE, Baird DG (2009) Effects of block length and solution-casting conditions on the final morphology and properties of disulfonated poly(arylene ether sulfone) multiblock copolymer films for proton exchange membranes. *Polymer* 50:6129–6138
  49. Roy A, Hickner MA, Einsla BR, Harrison WL, McGrath JE (2009) Synthesis and characterization of partially disulfonated hydroquinone-based poly(arylene ether sulfone)s random copolymers for application as proton exchange membranes. *J Polym Sci Polym Chem* 47:384–391
  50. Roy A, Lee H-S, McGrath JE (2008) Hydrophilic-hydrophobic multiblock copolymers based on poly(arylene ether sulfone)s as novel proton exchange membranes – part B. *Polymer* 49:5037–5044
  51. Yu X, Roy A, Dunn S, Yang J, McGrath JE (2006) Synthesis and characterization of sulfonated-fluorinated, hydrophilic-hydrophobic multiblock copolymers for proton exchange membranes. *Macromol Symp* 245(246):439–449
  52. Matsumura S, Hlil AR, Hay AS (2008) Synthesis, properties, and sulfonation of novel dendritic multiblock copoly(ether-sulfone). *J Polym Sci Polym Chem* 46:6365–6375
  53. Matsumura S, Hlil AR, Lepiller C, Gaudet J, Guay D, Hay AS (2008) Ionomers for proton exchange membrane fuel cells with sulfonic acid groups on the end groups: novel linear aromatic poly(sulfide-ketone)s. *Macromolecules* 41:277–280
  54. Matsumura S, Hlil AR, Lepiller C, Gaudet J, Guay D, Shi Z, Holdcroft S, Hay AS (2008) Ionomers for proton exchange membrane fuel cells with sulfonic acid groups on the end groups: novel branched poly(ether-ketone)s. *Macromolecules* 41:281–284
  55. Matsumura S, Hlil AR, Al-Souz MAK, Gaudet J, Guay D, Hay AS (2009) Ionomers for proton exchange membrane fuel cells by sulfonation of novel dendritic multiblock copoly(ether-sulfone)s. *J Polym Sci Polym Chem* 47:5461–5473
  56. Matsumura S, Hlil AR, Du N, Lepiller C, Gaudet J, Guay D, Shi Z, Holdcroft S, Hay AS (2008) Ionomers for proton exchange membrane fuel cells with sulfonic acid groups on the end-groups: novel branched poly(ether-ketone)s with 3, 6-ditrityl-9H-carbazole end-groups. *J Polym Sci Polym Chem* 46:3860–3868
  57. Tian S, Meng Y, Hay AS (2009) Membranes from poly(aryl ether)-based ionomers containing multiblock segments of randomly distributed nanoclusters of 18 sulfonic acid groups. *J Polym Sci Polym Chem* 47:4762–4773
  58. Tian S, Meng Y, Hay AS (2009) Membranes from poly(aryl ether)-based ionomers containing randomly distributed nanoclusters of 6 or 12 sulfonic acid groups. *Macromolecules* 42:1153–1160
  59. Higashihara T, Matsumoto K, Ueda M (2009) Sulfonated aromatic hydrocarbon polymers as proton exchange membranes for fuel cells. *Polymer* 50:5341–5357
  60. Matsumoto K, Higashihara T, Ueda M (2009) Locally and densely sulfonated poly(ether sulfone)s as proton exchange membrane. *Macromolecules* 42:1161–1166
  61. Matsumoto K, Higashihara T, Ueda M (2009) Locally sulfonated poly(ether sulfone)s with highly sulfonated units as proton exchange membrane. *J Polym Sci Polym Chem* 47:3444–3453
  62. Bae B, Miyatake K, Watanabe M (2009) Synthesis and properties of sulfonated block copolymers having fluorenyl groups for fuel-cell applications. *ACS Appl Mater Interfaces* 1:1279–1286
  63. Bae B, Miyatake K, Watanabe M (2010) Sulfonated poly(arylene ether sulfone ketone) multiblock copolymers with highly sulfonated block. *Synth Properties Macromol* 43:2684–2691
  64. Bae B, Yoda T, Miyatake K, Uchida H, Watanabe M (2010) Proton-conductive aromatic ionomers containing highly sulfonated blocks for high-temperature-operable fuel cells. *Angew Chem Int Ed* 49:317–320
  65. Li N, Liu J, Cui Z, Zhang S, Xing W (2009) Novel hydrophilic-hydrophobic multiblock copolyimides as proton exchange membranes: enhancing the proton conductivity. *Polymer* 50:4505–4511
  66. Liu B, Robertson GP, Kim D-S, Guiver MD, Hu W, Jiang Z (2007) Aromatic poly(ether ketone)s with



- pendant sulfonic acid phenyl groups prepared by a mild sulfonation method for proton exchange membranes. *Macromolecules* 40:1934–1944
67. Liu B, Robertson GP, Kim D-S, Sun X, Jiang Z, Guiver MD (2010) Enhanced thermo-oxidative stability of sulfophenylated poly(ether sulfone)s. *Polymer* 51:403–413
  68. Pang J, Zhang H, Li X, Jiang Z (2007) Novel wholly aromatic sulfonated poly(arylene ether) copolymers containing sulfonic acid groups on the pendants for proton exchange membrane materials. *Macromolecules* 40:9435–9442
  69. Pang J, Zhang H, Li X, Liu B, Jiang Z (2008) Poly(arylene ether)s with pendant sulfoalkoxy groups prepared by direct copolymerization method for proton exchange membranes. *J Power Sources* 184:1–8
  70. Pang J, Zhang H, Li X, Ren D, Jiang Z (2007) Low water swelling and high proton conducting sulfonated poly(arylene ether) with pendant sulfoalkyl groups for proton exchange membranes. *Macromol Rapid Commun* 28:2332–2338
  71. Pang J, Zhang H, Li X, Wang L, Liu B, Jiang Z (2008) Synthesis and characterization of sulfonated poly(arylene ether)s with sulfoalkyl pendant groups for proton exchange membranes. *J Membr Sci* 318:271–279
  72. Lee JK, Li W, Manthiram A (2009) Poly(arylene ether sulfone)s containing pendant sulfonic acid groups as membrane materials for direct methanol fuel cells. *J Membr Sci* 330:73–79
  73. Lafitte B, Jannasch P (2007) Proton-conducting aromatic polymers carrying hypersulfonated side chains for fuel cell applications. *Adv Funct Mater* 17:2823–2834
  74. Parvole J, Jannasch P (2008) Poly(arylene ether sulfone)s with phosphonic acid and bis(phosphonic acid) on short alkyl side chains for proton-exchange membranes. *J Mater Chem* 18:5547–5556
  75. Parvole J, Jannasch P (2008) Polysulfones grafted with poly(vinylphosphonic acid) for highly proton conducting fuel cell membranes in the hydrated and nominally dry state. *Macromolecules* 41:3893–3903
  76. Kim DS, Kim YS, Guiver MD, Pivovar BS (2008) High performance nitrile copolymers for polymer electrolyte membrane fuel cells. *J Membr Sci* 321:199–208
  77. Kim DS, Kim YS, Guiver MD, Ding J, Pivovar BS (2008) Highly fluorinated comb-shaped copolymer as proton exchange membranes (PEMs): fuel cell performance. *J Power Sources* 182:100–105
  78. Kreuer KD (2001) On the development of proton conducting polymer membranes for hydrogen and methanol fuel cells. *J Membr Sci* 185:29–39
  79. Yoshimura K, Iwasaki K (2009) Aromatic polymer with pendant perfluoroalkyl sulfonic acid for fuel cell applications. *Macromolecules* 42:9302–9306
  80. Mikami T, Miyatake K, Watanabe M (2010) Poly(arylene ether)s containing superacid groups as proton exchange membranes. *ACS Appl Mater Interfaces* 2:1714–1721
  81. Miyatake K, Shimura T, Mikami T, Watanabe M (2009) Aromatic ionomers with superacid groups. *Chem Commun* 42:6403–6405
  82. Hirakimoto T, Fukushima K, Li Y, Takizawa S, Hinokuma K, Senoo T (2008) Fullerene-based proton-conductive material for the electrolyte membrane and electrode of a direct methanol fuel cell. *ECS Trans* 16:2067–2072
  83. Watanabe M, Uchida H, Emori M (1998) Analyses of self-humidification and suppression of gas crossover in Pt-dispersed polymer electrolyte membranes for fuel cells. *J Electrochem Soc* 145:1137–1141
  84. Watanabe M, Uchida H, Emori M (1998) Polymer electrolyte membranes incorporated with nanometer-size particles of Pt and/or metal-oxides: experimental analysis of the self-humidification and suppression of gas-crossover in fuel cells. *J Phys Chem B* 102:3129–3137
  85. Watanabe M, Uchida H, Seki Y, Emori M, Stonehart P (1996) Self-humidifying polymer electrolyte membranes for fuel cells. *J Electrochem Soc* 143:3847–3852
  86. Dyck A, Fritsch D, Nunes SP (2002) Proton-conductive membranes of sulfonated polyphenylsulfone. *J Appl Polym Sci* 86:2820–2827
  87. Gomes D, Buder I, Nunes SP (2006) Sulfonated silica-based electrolyte nanocomposite membranes. *J Polym Sci Polym Chem* 44:2278–2298
  88. Karthikeyan CS, Nunes SP, Prado LASA, Ponce ML, Silva H, Ruffmann B, Schulte K (2005) Polymer nanocomposite membranes for DMFC application. *J Membr Sci* 254:139–146
  89. Karthikeyan CS, Nunes SP, Schulte K (2005) Ionomer-silicates composite membranes: permeability and conductivity studies. *Eur Polym J* 41:1350–1356
  90. Karthikeyan CS, Nunes SP, Schulte K (2006) Permeability and conductivity studies on ionomer-polysilsesquioxane hybrid materials. *Macromol Chem Phys* 207:336–341
  91. Nunes SP, Ruffmann B, Rikowski E, Vetter S, Richau K (2002) Inorganic modification of proton conductive polymer membranes for direct methanol fuel cells. *J Membr Sci* 203:215–225
  92. Silva VS, Ruffmann B, Silva H, Gallego YA, Mendes A, Madeira LM, Nunes SP (2005) Proton electrolyte membrane properties and direct methanol fuel cell performance. *J Power Sources* 140:34–40
  93. Silva VS, Schirmer J, Reissner R, Ruffmann B, Silva H, Mendes A, Madeira LM, Nunes SP (2005) Proton electrolyte membrane properties and direct methanol fuel cell performance. *J Power Sources* 140:41–49
  94. Su Y-H, Liu Y-L, Sun Y-M, Lai J-Y, Guiver MD, Gao Y (2006) Using silica nanoparticles for modifying sulfonated poly(phthalazinone ether ketone) membrane for direct methanol fuel cell: a significant improvement on cell performance. *J Power Sources* 155:111–117
  95. Su Y-H, Liu Y-L, Sun Y-M, Lai J-Y, Wang D-M, Gao Y, Liu B, Guiver MD (2007) Proton exchange membranes modified with sulfonated silica nanoparticles for direct methanol fuel cells. *J Membr Sci* 296:21–28

96. Anilkumar GM, Nakazawa S, Okubo T, Yamaguchi T (2006) Proton conducting phosphated zirconia-sulfonated polyether sulfone nanohybrid electrolyte for low humidity, wide-temperature PEMFC operation. *Electrochem Commun* 8:133–136
97. Miyatake K, Tombe T, Chikashige Y, Uchida H, Watanabe M (2007) Enhanced proton conduction in polymer electrolyte membranes with acid-functionalized polysilsesquioxane. *Angew Chem Int Ed* 46:6646–6649
- Hickner MA, Ghassemi H, Kim YS, Einsla BR, McGrath JE (2004) Alternative polymer systems for proton exchange membranes (PEMs). *Chem Rev* 104:4587–4612
- Kreuer KD, Paddison SJ, Spohr E, Schuster M (2004) Transport in proton conductors for fuel-cell applications: simulations, elementary reactions, and phenomenology. *Chem Rev* 104:4637–4678
- Rikukawa M, Sanui K (2000) Proton-conducting polymer electrolyte membranes based on hydrocarbon polymers. *Prog Polym Sci* 25:1463–1502
- Scherer GG (2008) *Advances in polymer science: fuel cells I & II*. Springer, Berlin

### Books and Reviews

- Colomban P (1992) *Proton conductors: solids, membrane and gels – materials and devices*. Cambridge University Press, Cambridge
- Tant BR, Mauritz KA, Wilkes GL (1997) *Ionomers – synthesis, structure, properties and applications*. Blackie Academic & Professional, New York



## Ionomer Thin Films in PEM Fuel Cells

Ahmet Kusoglu  
Energy Conversion Group, Energy Technologies  
Area, Lawrence Berkeley National Laboratory,  
Berkeley, CA, USA

### Article Outline

Glossary  
Definition of the Subject  
Introduction: Ionomers in Fuel Cells  
Ionomer Thin Films  
Summary and Remarks  
Future Directions  
Bibliography

### Glossary

**Ionomer membranes** ionomers that are cast, fabricated, and used as a bulk material with a thickness on the order of micrometers. Most PEMs in fuel cells are 10 to 200  $\mu\text{m}$  thick but are expected to be thinner and robust for sustainable cell performance.

**Ionomer thin films** ionomers that are cast on, and interact with, a support material (substrate) thereby forming a thin film with a thickness on the order of nanometers. In fuel cell catalyst layers (CLs), ionomers exist as nanometer-thick electrolyte film responsible for transporting ions and reactants to catalyst sites, where electrochemical reactions occur.

**Ionomer** an ion-containing polymer chemically composed of charged (ionic) groups tethered to an electrically neutral polymer backbone. The fixed ionic groups are neutralized by the mobile counterions of opposite charge, which

act as charge carriers, thereby giving the ionomer its inherent ion-conductive functionality. Ionomers are commonly used as the PEM in fuel cells.

**PFSA (perfluorosulfonic acid)** a fluorocarbon-based sulfonated ionomer, which is a random copolymer of a polytetrafluoroethylene (PTFE) backbone and a randomly tethered polysulfonfyl fluoride vinyl ether side chain terminated by the polar sulfonic acid ionic group,  $\text{SO}_3^-$ , that is associated with a specific counterion, most commonly a proton (e.g.,  $\text{SO}_3^- + \text{H}^+ \rightarrow \text{SO}_3\text{H}$ ). Nafion<sup>®</sup> is a commercially available PFSA developed by DuPont in the 1960s, which has since been adopted as a benchmark PEM in fuel cells.

**Proton exchange membrane (PEM)** a polymeric membrane that separates the electrodes in an electrochemical device, such as a fuel cell, and conducts protons between the electrodes while separating their reactant gases.

### Definition of the Subject

In polymer-electrolyte fuel cells (PEFCs), ionomers play a key role not only as a proton exchange membrane (PEM) but also as nanometer-thick electrolyte “thin films” within porous catalyst layer (CL) structures, where they bind and cover the catalytic particles and provide transport pathways for the ions and reactant species. An ionomer’s properties and functionality are governed by its hydration-dependent nanostructure, which separates into hydrophilic transport pathways and hydrophobic polymer matrix. As the ionomer is confined to nanometer thicknesses in the CLs, its intrinsic nano-morphology and resulting transport properties deviate from bulk membrane behavior. These deviations in properties manifest themselves as additional resistance to transport of active species that are key for driving the desired electrochemical reactions. Thus, some of the performance losses observed in the cell are rooted in the catalyst ionomer and its

local environment and interactions therein. In thin-film form, the ionomer forms dynamic interfaces with the air and substrate, which impose stronger impact on ionomer's structure/functionality. This interplay between the confinement and dynamic interactions controls the catalyst ionomer's properties, which affects the local transport resistances in CLs, and ultimately PEFC performance.

## Introduction: Ionomers in Fuel Cells

Perfluorosulfonic acid (PFSA) ionomers are ion-conducting polymers commonly used as the solid electrolyte/separator in electrochemical energy conversion and storage devices where they provide multiple functionalities such as ion conductivity, gas separation, and solvent transport. Similarly, in polymer electrolyte fuel cells (PEFCs), PFSA ionomers have been widely studied and used as the PEM with a thickness on the order of micrometers (10 to 200  $\mu\text{m}$ ); yet, increasingly important, but less explored, is the role of ionomers as thin films and the interfaces they form within the heterogeneous catalyst layer structures, where electrochemical reactions occur (see Fig. 1). In particular, the latter phenomenon of confinement could have important implications for the mass-transport limitations in catalyst layers and PEFC performance, which are strongly related to the transport resistances occurring within the ionomer thin film and at its interfaces.

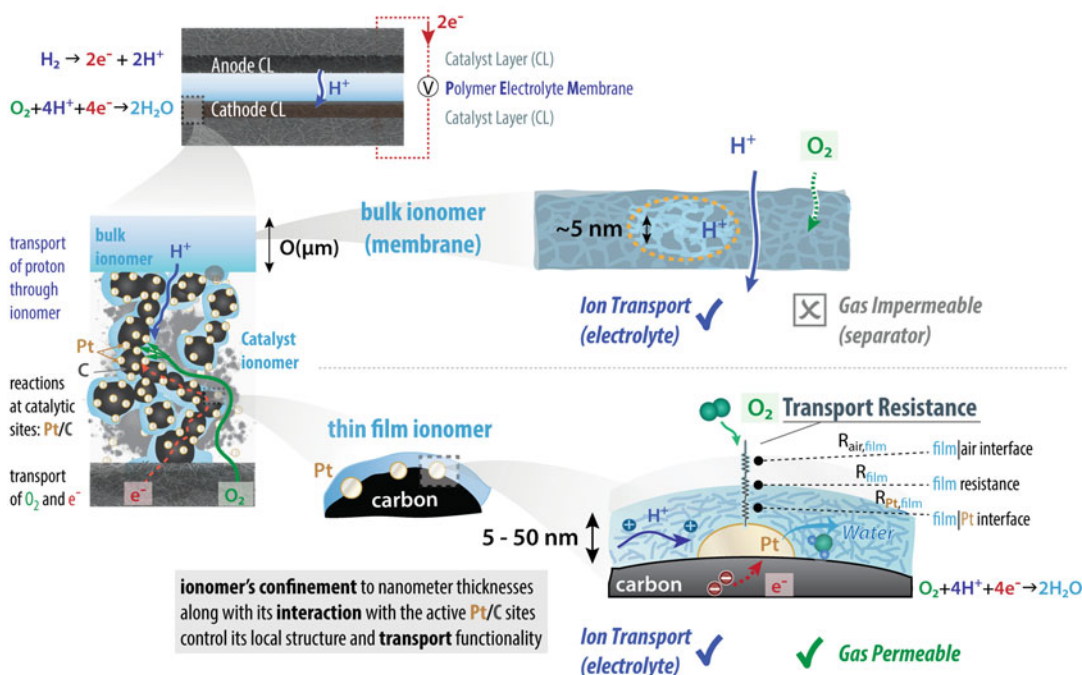
In a catalyst layer (CL), the ionomer functions as nanometer-thick electrolyte film binding the catalyst particles together and facilitating proton transport through the layer and gas and water transport to and from the catalytic sites. A CL is a heterogeneous porous structure to increase electrocatalytically active surface area, where the ionomer thin film provides proton transport pathways to platinum particles, the carbon particles provide electron conduction, and the pores enable gas/liquid transport (see Fig. 1). Thus, while the ionomer's proton transport functionality persists throughout the membrane-electrode assembly, i.e., from PEM to CLs, and is critical to the cell performance, the ionomer's gas transport

functionality differs significantly within the cell. Ionomer as a PEM functions not only as a solid electrolyte but also as a (gas) separator requiring low  $\text{O}_2$  permeability, whereas the ionomer in the cathode CL must allow ingress of  $\text{O}_2$  molecules from pores to the catalytic Pt sites, where they meet electrons (transferred through carbon) and reduce  $\text{O}_2$  to water (Fig. 1). Hence, an ionomer's gas transport functionality exhibits a striking contrast between PEM (gas impermeable) and CL (gas permeable), understanding and optimization of which is critical for cell design and performance [1–15].

The current state of CL diagnostics data suggests that the local resistance arising from the ionomer/Pt interfaces in CL decreases with increasing Pt loading, [1, 2, 6–15] exemplifying how the performance and cost could be intertwined [1, 7] (also see the chapter ▶ “Proton-Exchange Membrane Fuel Cells with Low-Pt Content” by A. Kongkanand). The overall reaction rate in the cathode CL is slow due to the formation of water, the four-electron process of  $\text{O}_2$  reduction, and the use of air as the  $\text{O}_2$  carrier, thereby resulting in dramatic performance losses. Because the oxygen reduction reactions (ORR) take place at the ionomer/Pt interface, ionomer interactions are believed to play a key role in controlling the transport resistance in CLs. The contributions to the  $\text{O}_2$  transport resistance in CLs illustrated in Fig. 1: (i)  $\text{O}_2$  transport at the ionomer/air interface, (ii)  $\text{O}_2$  permeation and diffusion through the ionomer film, and (iii)  $\text{O}_2$  permeation at the ionomer/Pt interface. Despite distinct physicochemical natures of each mechanism, they are all related to the behavior of ionomer moieties and their interaction with the water and gas molecules, as well as the substrate composition. Given the unequivocal goal of reducing the Pt loading (and cost), these transport phenomena create an intriguing performance-cost trade-off, which is considered one of the most critical challenges that must be addressed in PEM fuel cells to make them a competitive technology [1, 2, 7].

Ionomers exist in CLs with a distribution of thicknesses ranging from 7 to 15 nm [2, 4, 16], which could be influenced by several design parameters, such as the ratio of carbon to ionomer (C/I), porosity, Pt loading, as well as CL

### Polymer-Electrolyte Fuel Cells (PEFCs): Role of Ionomers



**Ionomer Thin Films in PEM Fuel Cells, Fig. 1** Role of ionomers in PEM fuel cells as an ion-conducting polymer electrolyte membrane (PEM) and catalyst ionomer in the electrodes

fabrication method. Thus, the ionomer thickness (distribution) is likely to change with the ionomer fraction in the CL, which affects the surface area and mass activity of CL therein [10–12, 17]. Similarly, water uptake behavior of catalyst ionomer changes with C/I ratio [3, 9, 10, 17, 18], type of carbon support [6], Pt loading [18], as well as pretreatment [18]. The nature of Pt surface also impacts the water uptake; catalyst ionomer under reducing environment absorbs less water due to the removal of oxide layer, the presence of which creates an oxide-rich PtO layer that is more polar and hydrophilic [19]. The complex structure of CL, wherein the ionomer film formation and properties are controlled by a multitude of parameters listed in Table 1, has driven the need for developing model systems for ionomers. Thin-film ionomers serve this purpose with an idealized representation of CL ionomers (Table 1). Thin films are prepared by casting a diluted ionomer dispersion onto a uniform, homogenous support substrate followed by thermal treatments and

other post-processing treatments. The most commonly used technique is spin casting, where the ionomer dispersion with a dilute concentration of solid is cast on a substrate spinning at a controlled rate, followed by other methods such as self-assembly or drop casting on a substrate. Due to the distinct nature of these processes, casting methods and conditions influence the structure/property relationship of the ionomer film, as do the substrate and the dispersion solvents, because of their interaction with the ionomer moieties [20]. As the casting and dispersion solvent also affects both the CL structure and PEM [2, 21–23], fundamental investigation of such processing effects in ionomer thin films could be beneficial for developing material solutions for improved cell performance. The key aspects and parameter space of thin films and their diagnostics are shown in Table 1 and Fig. 2, respectively. Even though thin films underestimate the heterogeneity and binary interactions in CL ionomers, they nonetheless provide a mean to isolate and study some of

**Ionomer Thin Films in PEM Fuel Cells, Table 1** Comparison of ionomers in fuel cell catalyst layers and ionomer thin films as model systems

	Catalyst layer ionomer	Ionomer thin film
Use/function	PEM fuel cell electrode	Thin-film model system
Film formation	Through casting and processing of catalyst inks containing ionomer dispersion	Casting from a dispersion onto a support substrate (e.g., spin casting)
Design and structure	Heterogeneous porous structure where ionomer covers particles on nonplanar surfaces	Homogeneous, macroscopically uniform structure on a planar substrate surface
Design and material parameters	Carbon and Pt type and fraction, ionomer content, CL thickness and porosity, coating method and conditions, ionomer chemistry, casting solvent	Substrate, ionomer chemistry, casting solvent (dispersion), casting method and conditions
Thickness	Varies with spatial distribution, C:I ratio, and Pt loading	Constant film thickness controlled during casting
Interactions	Dynamic interactions with catalytic particles including carbon and platinum	Interactions with the substrate
Operational parameters	RH, T, potential and time	RH, T, potential and time
Conditioning	Cell conditioning and break-in protocols affecting ionomer	Thermal and solvent annealing of films after casting

these effects in an effort to identify the governing factors and phenomena. Thus, ionomer thin films allow characterizing an ionomer's morphology, measuring its swelling and transport properties, and probing its interactions with the substrate, under controlled environments. Such investigations, in most cases, require techniques specifically suited for thin films that are distinct from those used to characterize bulk membranes (see Fig. 2).

The challenges common to these techniques include significantly less volume occupied by the thin films and the influence of the substrate composition on the ionomer, which requires a careful examination and analysis of the measured properties. Nevertheless, most surface characterization techniques are applicable to both bulk and thin-film form of the ionomer, and any observed difference between the two could also be used to study the interfacial effects and their domain of influence through the thickness of the ionomer.

### Ionomer Thin Films

A PFSA ionomer is comprised of hydrophilic domains of 3 to 6 nm that are interconnected


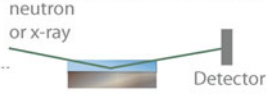
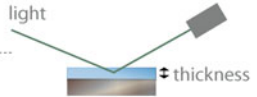
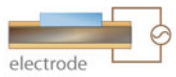

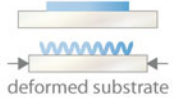
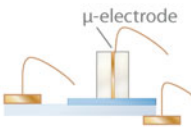
and form a phase-separated network at longer length scales (100s of nm), which ultimately controls its macroscopic properties. When the thickness of ionomer is reduced to 100 nm or below, its constituent chains and moieties are confined to volumes comparable to its characteristic domain size, thereby losing their ability to form a bulk-like morphology. Such nanoconfinement of an ionomer also amplifies the overall impact of the substrate interactions on the thin film, which, in turn, could further restrict the ionomer moieties' mobility and cause additional nanostructural changes, as highlighted in Fig. 3.

Even though confinement effects in polymer thin films have long been of interest [47–52], their application to charge-containing ionomer thin films used in PEM fuel cells has garnered interest only recently [6, 9, 20, 25, 27, 30, 32, 33, 36, 37, 53–57], due primarily to the need for understanding the ionomer behavior in PEFC electrodes [1, 2, 7–9, 13, 14].

Confinement effects are strongly intertwined with the surface morphology and properties of bulk ionomers (i.e., PEM), where the ionomer forms a thin layer of interfacial “skin” that behaves differently from the ionomer in the



### Ionomer Characterization and Diagnostics

<b>Bulk membrane</b>	<b>Thin Film (on a substrate*)</b>	
<i>Thickness: 10 to 200 μm</i>	<i>Thickness: 10 to 500 nm</i>	
<hr style="border-top: 1px dashed #ccc;"/>		
<b>Morphology</b>		
X-ray scattering (XS)	Grazing-incidence XS	
Neutron scattering	Neutron reflectivity	
<b>Swelling</b>		
Dimensional change	Spectroscopic Ellipsometry	
<b>Water Uptake</b>		
Gravimetric (weight)	Quartz-crystal microbalance	
<b>Ion Transport (Conductivity)</b>		
Electrochemical cell or impedance setup (e.g., four-probe in-plane or thickness direction)	Impedance measurement of film on a inter-digitated array (substrate)	
<b>Mechanical Response</b>		
Stress-Strain testing	Buckling on a support	
DMA, TMA	Cantilever beam bending	
<b>Gas Transport permeation</b>		
	microelectrode setup	
<b>Techniques Probing Surface</b>		
AFM, contact angle, FTIR/ATR, XPS		

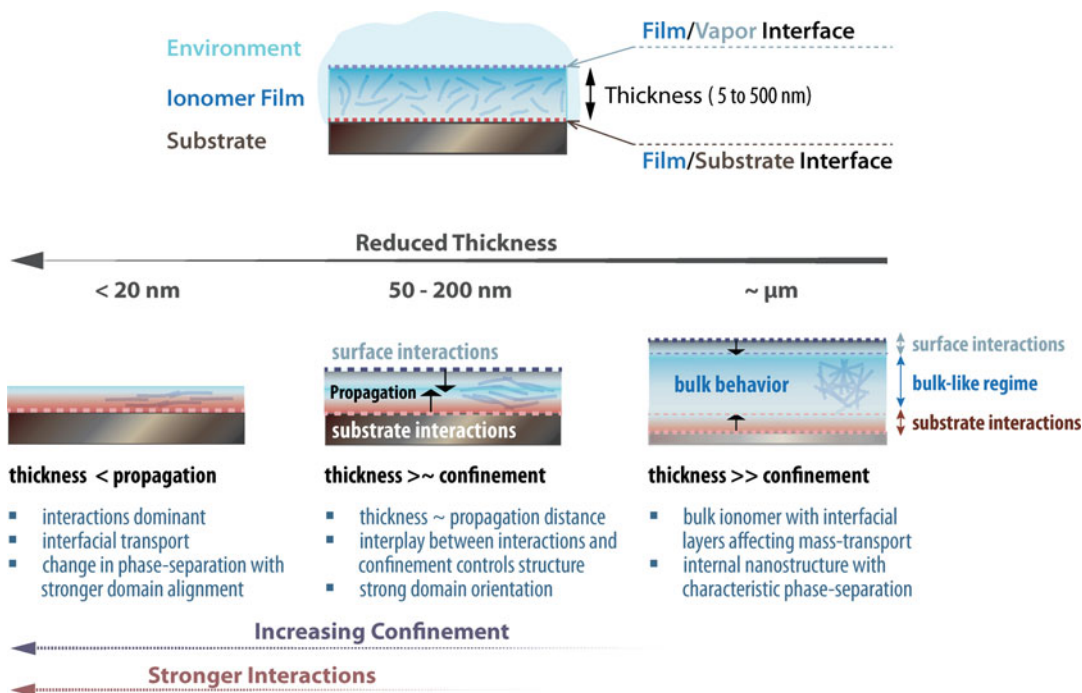
\* ionomer film's property is measured on a support substrate, and affected by the substrate and its interaction with the film

**Ionomer Thin Films in PEM Fuel Cells, Fig. 2** Comparison of characterization and diagnostic techniques commonly used for bulk ionomers and thin-film ionomers, which are conceptualized with simplified schematics for selected techniques. Additional information

on technique can be obtained in the references [20, 24] and [25–29] for morphology [20, 27, 30–33], for swelling and uptake [34–37], for conductivity [26, 38], for mechanical properties [8, 13, 15, 39], for microelectrode [40–46], and for spectroscopy techniques

internal regions (see Fig. 3). This surface layer in bulk ionomer could influence the membrane's transport properties by controlling the mass transport of species through its interface [58–61], although the membrane's overall behavior is still controlled by its internal regions, which constitute the majority of the material's volume (Fig. 3). As the thickness of the ionomer is reduced to sub-micrometer values, however, the interfacial effects are more pronounced. In the thin-film motif, in contrast with the ionomer's open surface

that creates an interfacial layer, its other surface interacts with the solid substrate. Therefore, an ionomer thin film's behavior is influenced by these two key interactions, both of which propagate through the ionomer thin film, but in the opposite directions, and perhaps with different strengths (Fig. 3). Once the film thickness reaches below 100 nm, a strong interplay between the confinement and substrate interactions controls the ionomer's nanostructure and properties. As the film thickness approaches 10s of nanometers,



**Ionomer Thin Films in PEM Fuel Cells, Fig. 3** Impact of thickness on properties of PFSA ionomers from bulk membrane to the confined thin films highlighting the

interplay between the surface/substrate interactions and confinement controlling the morphology of the ionomer

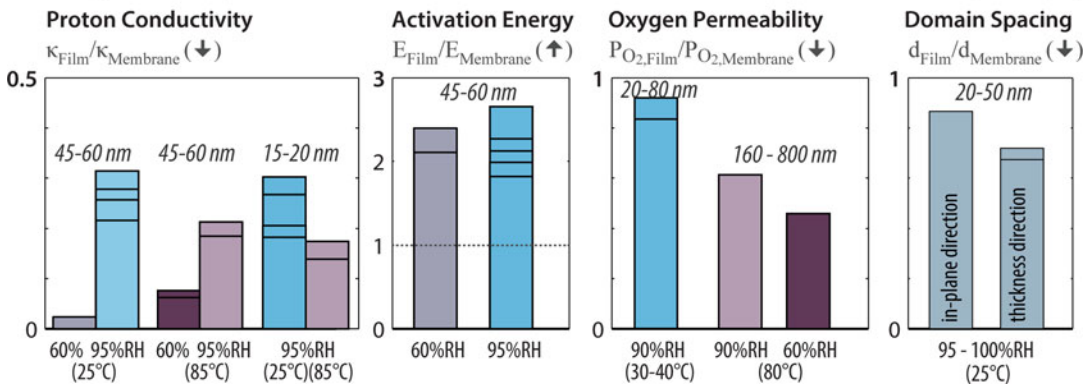
i.e., comparable to CL ionomers, the impact of substrate interactions becomes dominant. Thus, in the thin-film regime, ionomer properties deviate significantly compared to its bulk form (i.e., PEM), and the magnitude of these deviations depends on the substrate and the environment (Fig. 4).

Recent years have witnessed a significant effort dedicated toward understanding PFSA thin films, which exhibit reduced transport properties compared to those of bulk films due to abovementioned confinement effects [1, 20, 27, 32, 33, 36, 37, 53–57, 62–65]. Compared to bulk membrane, Nafion<sup>®</sup> films of ~100 nm or thinner have been shown to exhibit reduced swelling [20, 27, 33, 66, 67], water uptake amounts and rates [20, 24, 27, 32, 33, 36, 54, 56, 57, 64, 65, 68], reduced ionic conductivity and increased activation energy [5, 34, 36, 37, 53, 56, 64, 69, 70], lower rate of water diffusion [27, 54, 65, 68, 71, 72], lower intrinsic permeation [73], lower contact angle [45, 67, 70], higher fraction of hydrophilic surface area [70], higher modulus

[26, 38], and lower oxygen permeability [8, 13, 39]. Figure 4 highlights the relative changes in selected properties of Nafion thin films compared to their values for thicker Nafion. Upon confinement to nanometer thicknesses, transport properties for proton and oxygen in Nafion decrease up to more than 50%, while their activation barrier increases indicating an overall significant increase in the transport resistance. The fact that the magnitude of these changes depends on the measured property and the environmental conditions reflects the complex nature of ionomer film's structure and interactions with the substrate (on which the properties are measured).

These studies demonstrate trends reflecting the confinement effects below 100 nm, and significant shifts in the values along with stronger effect of substrates as the film thickness reduces below 50 nm and approaches 10 nm [20, 24, 27, 31–33, 36, 37, 40, 45, 53–56, 63–67, 70]. Confinement, along with the substrate-/surface-specific interactions, affects the molecular ordering of the backbone chains as evidenced from FTIR [40], NR

Change in the Properties of Nafion Thin Films relative to their value for Nafion bulk Membrane (25-50 μm)



**Ionomer Thin Films in PEM Fuel Cells, Fig. 4** Relative change in properties of a Nafion thin film with respect to its value for thicker Nafion membrane under the same conditions. Values are determined based on the reported values for proton conductivity and activation energy for conductivity (using interdigitated substrates) [34, 35, 37, 64, 67], oxygen permeability (from microelectrode studies)

[8, 13, 39], and hydrophilic-domain spacing (from GISAXS) [24]. Thickness values of films are matched and grouped together, but the substrates could differ among the studies due to the distinct nature of setups and techniques used to probe each property. (Values from different reports are shown as individual bars plotted together for similar thicknesses.)

[25, 28, 65], and GISAXS [20, 24] data, where orientation of the backbone chains and ionic domains resulted in reduced water uptake [27, 33, 57, 62] and transport processes [27, 33, 57, 62]. The increase in ionomer’s transport resistance under confinement can be explained by the changes in swelling and morphology of the thin film, as described in the following sections.

**Swelling and Sorption Behavior**

A key driving force behind an ionomer’s structure/property relationship is hydration. Owing to their hydrophilic nature, the ionic moieties absorb water molecules from the surrounding humid environment. The amount of water in the hydrated ionomer is usually quantified by the local *water content*, λ (= mol H<sub>2</sub>O/mol SO<sub>3</sub><sup>-</sup>) [74], which is described as

$$\lambda \equiv \frac{n(\text{H}_2\text{O})}{n(\text{SO}_3^-)} = \left(\frac{M_w}{M_p}\right) \frac{\bar{M}_p}{\bar{M}_w}, \text{ and} \quad (1)$$

$$\bar{M}_p = EW = \frac{1}{IEC}$$

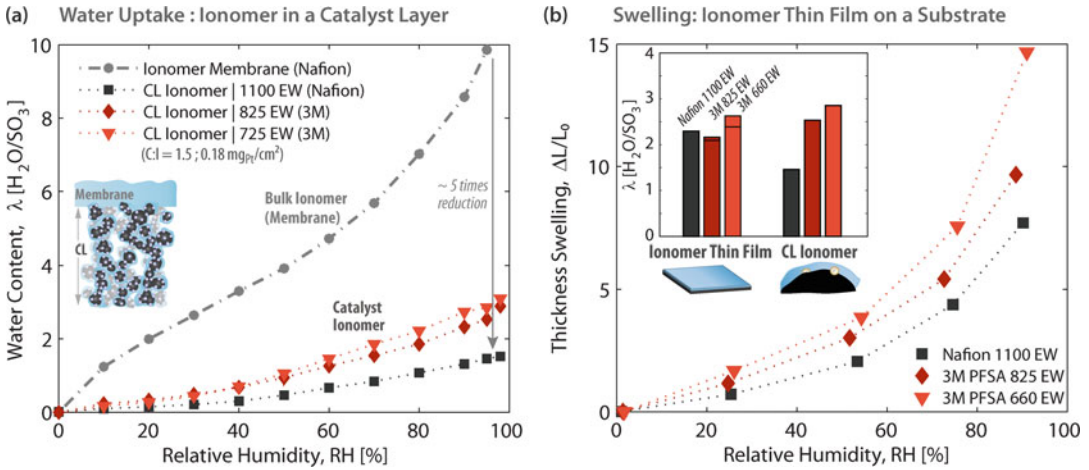
where  $M_{i(=w,p)}$  and  $\bar{M}_{i(=w,p)}$  are the mass and molar mass of phase *i*, respectively, and the subscripts *w* and *p* stand for water and dry polymer, respectively. The degree of sulfonation in PFSA

ionomers is commonly represented by the equivalent weight (EW), which is inversely proportional to the ion exchange capacity (IEC). The ionomer accommodates the absorbed water molecules in its hydrophilic nano-domains, which grow with hydration and separate from the hydrophobic polymer backbone. Thus, hydration drives the ionomer’s phase-separated nanostructure, which results in a volumetric swelling at macroscopic level. The volume change at a given RH with respect to dry state can be related to dimensional change in each direction (*i*),  $L_i/L_{dry}$ , as follows:

$$\frac{V_{dry} + V_w}{V_{dry}} = \left(\frac{\bar{V}_{dry} + \Delta\lambda\bar{V}_w}{\bar{V}_{dry}}\right) = \prod_i \frac{L_i(\lambda)}{L_{dry}} \equiv \left(1 + \frac{L_{iso}(\lambda)}{L_{dry}}\right)^m, \quad (2)$$

where  $\bar{V}$  represents the molar volume. If one assumes isotropic swelling,  $L_i(\lambda) = L_{iso}(\lambda)$ , then a simplified expression could be obtained for swelling as a function of λ. In the expression above, the swelling dimension, *m*, takes the value of 3 for three-dimensional (3-D) swelling.

The water uptake and swelling of PFSA membranes are well established based on measurements at a controlled water vapor activity,  $a_w$  (or relative



**Ionomer Thin Films in PEM Fuel Cells, Fig. 5** Comparison of (a) water uptake behavior of catalyst layer (CL) ionomer (measured without the membrane) and (b) ionomer thin films of 50 nm spin cast on silicon substrate, measured at 25 °C. The ionomers are 1100 EW Nafion and

825 and 725 EW 3 M PFSA. Water uptake profile for bulk Nafion 212<sup>®</sup> membrane was included in (a) for comparison. The inset in (b) shows the water content at 95% RH converted from the uptake and swelling data for CL ionomer and for thin films, respectively

humidity, RH), at a given temperature [75]. Hydration behavior of PFSA thin films is usually characterized using quartz crystal microbalance (QCM) and ellipsometry (Fig. 2). While QCM determines the mass change of a thin film on a quartz crystal substrate based on the change in sample frequency during hydration, ellipsometry measures the thickness swelling,  $\Delta L/L_0$ , of a film by measuring the change in its optical response. PFSA thin films' mass uptake can be characterized by QCM using the Sauerbrey analysis, which determines the mass change in the film during hydration,  $\Delta M$ , from the resonance frequency change,  $\Delta f$ , of the quartz crystal [20, 25, 30, 32, 33, 55, 69]. Such analysis holds for ionomer films of less than 600 nm where they do not exhibit dissipation or viscoelastic losses [33, 55]. Ellipsometry also provides properties such as the refractive index of the ionomer, which must be modeled to determine the film thickness. The wavelength dependence of the refractive index  $n(\lambda_{\text{wave}})$  is analyzed using the Cauchy model [31, 76]:

$$n(\lambda_{\text{wave}}) = A + \frac{B}{\lambda_{\text{wave}}^2} + \frac{C}{\lambda_{\text{wave}}^4} \quad (3)$$

where  $A$ ,  $B$ , and  $C$  are coefficients determined through the data modeling. With the above

expression, a thin film is modeled as a Cauchy layer that describes the dispersion of light in transparent media with minimal light absorption and is used to determine the film's thickness.

Figure 5 summarizes hydration behavior of PFSA ionomers as a membrane (PEM), catalyst ionomer film, and thin film. Compared to a bulk membrane, ionomers in the CLs have much lower water content at a given RH. Moreover, as the ionomer IEC increases, the catalyst ionomer's water uptake capacity increases. A similar effect of IEC on ionomer is observed from the thickness swelling data of PFSA thin films on a silicon substrate. In fact, the calculated water content values are comparable for the ionomer films in CL and on a flat substrate, which demonstrates the potential of ionomer thin films as model systems (Fig. 5b).

Comparison of swelling (ellipsometry) and uptake,  $\lambda$  (QCM), values could provide insight into ionomer's hydration behavior [20]:

$$1 + \underbrace{(\lambda)}_{\text{QCM}} \frac{\bar{V}_w}{\bar{V}_p} - \frac{\bar{V}_{\text{mix}}}{\bar{V}_p} = \underbrace{\left(1 + \frac{\Delta L}{L_{\text{dry}}}\right)^m}_{\text{Ellipsometry}} \quad (4)$$

where the (partial) volume of mixing  $\bar{V}_{\text{mix}}$  accounts for the contribution due to nonideal

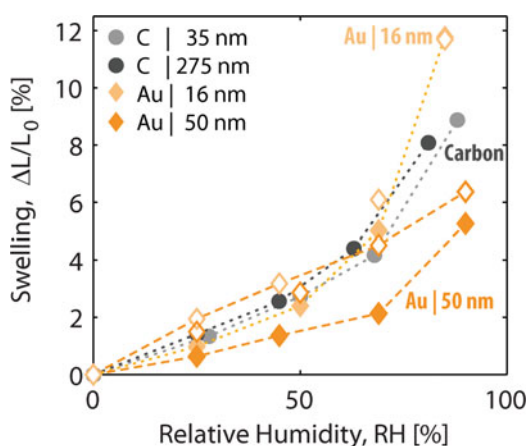
mixing [77]. A fair approximation for thin films is  $m = 1$  as they are confined on the substrate, which allows them to swell only in the thickness direction [27, 32, 33, 36]. Swelling dimension increases toward 2 as the thickness increases over 200 nm, for the fact that in-plane swelling starts as the film's top surface is less restricted by the constraints imposed by the substrate. A value of  $m = 3$  should be reached as the ionomer approaches the "bulk" regime. As for  $\bar{V}_{\text{mix}}$ , it is known for bulk membranes that the partial molar volumes change as a function of hydration due to the mechanisms of solvation, although with relatively minor effects at higher hydration levels [75]. In the case of 1-D swelling assumed ( $m = 1$ ), the contribution from nonideal mixing could be negligible ( $\bar{V}_{\text{mix}} \approx 0$ ) [27]. Physically, the low volume of mixing effect indicates that confinement alters the solvation process in the ionomer, which is also evident from the shape of the hydration isotherms of thin films (Fig. 5b), which lack the primary solvation regime at low RH (i.e., Langmuir regime for bulk PFSA). The thin-film uptake curve exhibits lower  $\lambda$  for a given RH than for a bulk membrane. This is especially apparent at higher RHs, where hydration is expected to be driven by entropic effects and not primary solvation [78–80]. Thus, confinement effects not only reduce the swelling of ionomer thin films but also change the nature of the associated water (i.e., whether it is strongly bound to an ionic group or freely moving). Overall, the qualitative trends between QCM and ellipsometry are consistent, with the latter being more commonly employed as it works on most substrates, albeit with the caveat of using the correct model for the data analysis and difficulties with converting swelling to water content [53].

Even though limitations in swelling could occur due to confinement, the reality is more complex due to the interplays among confinement and substrate composition, casting, and ionomer chemistry. The current state of understanding of hydration behavior of PFSA thin films can be summarized as follows [20, 24, 69]:

- (i) Ionomer's swelling could be correlated to its water (mass) uptake where a 1-D swelling represents a fair approximation, the accuracy

of which, however, decreases with increasing film thickness (from 100s of nm to 1  $\mu\text{m}$ ) [20, 24].

- (ii) As the film thickness decreases to 50 nm, its swelling continuously reduces relative to its value for thick (bulk) membrane. Once the film is confined to below 15 to 20 nm, however, it enters a different regime with much higher swelling and a stronger dependence on the substrate composition. As an example, swelling of Nafion on Au is comparable on C for 35 to 50 nm thickness, but increases significantly for 16 nm-thick film (Fig. 6).
- (iii) Ionomer's swelling increases with increasing IEC (or lower EW) [24], although differences arising from such effects are less pronounced in terms of water content,  $\lambda$ , which, by definition, accounts for the number of  $\text{SO}_3^-$  groups (see Fig. 5b).
- (iv) Swelling of self-assembled thin films is higher than spin-cast films on gold, but the opposite is true on carbon, caused probably by the substrate-specific interactions changing the adsorption of the PFSA moieties from the solution to the substrate during film formation [20].
- (v) Thermal annealing reduces water uptake and swelling of thin films [20, 24, 66, 70] and increases crystallinity [24], similar to its effect



**Ionomer Thin Films in PEM Fuel Cells, Fig. 6** Thickness swelling (ellipsometry) data of Nafion thin-film spin casts on carbon and gold substrates (from Ref. [20]). Open and closed symbols correspond to unannealed and annealed films, respectively



on bulk membranes. The impact of annealing is substrate dependent where it decreases with decreasing film thickness on gold but increases on carbon (see Fig. 6), owing to the stronger sulfur interactions with gold than carbon. Thinner films on substrates like Au and Pt are strongly interacting with the substrate surface, which pins the ionic moieties onto the substrate, thereby restricting the motion and conformation changes of ionomer chains under thermal conditions, which is also supported by the morphological evidence (from GISAXS studies[20]).

Hence, when it comes to the effects of processing and substrate, the latter could dominate the ionomer's hydration, especially when it strongly interacts with an ionomer confined to less than 50 nm. Such interactions also drive the changes in  $T_\alpha$  [70] and modulus [38], which alter the effect of the thermal treatment process. However, such surface alteration is more restricted in ultrathin films (~10 nm), which require more thermal energy for annealing and therefore a higher annealing temperature. This also explains why the influence of annealing on thin film's hydration changes both with film thickness and substrate.

### Morphology

As with their swelling behavior, the phase-separated morphology of PFSA's also changes under confinement and in the presence of substrate and wetting interactions, as evidenced by various techniques including grazing-incidence small-angle X-ray scattering (GISAXS) [20, 24, 27, 53, 57, 62], neutron or X-ray reflectivity (NR or XR) [25, 27–29], TEM [53], spectroscopic techniques (e.g., XPS or FTIR/ATR) [40–46, 81, 82], cryo-TEM tomography [83], fluorescence [33], AFM [53, 56, 67, 69, 70, 84–87], contact angle [45, 64, 67, 70], PM-IRRAS [68], and positron annihilation lifetime (PAL) spectroscopy [45].

GISAXS and NR in particular are powerful tools to investigate the orientation and spatial distribution of the nano-domains, at and below the thin-film interfaces [20, 25, 28, 29, 57, 88, 89]. As opposed to random, isotropic distribution of

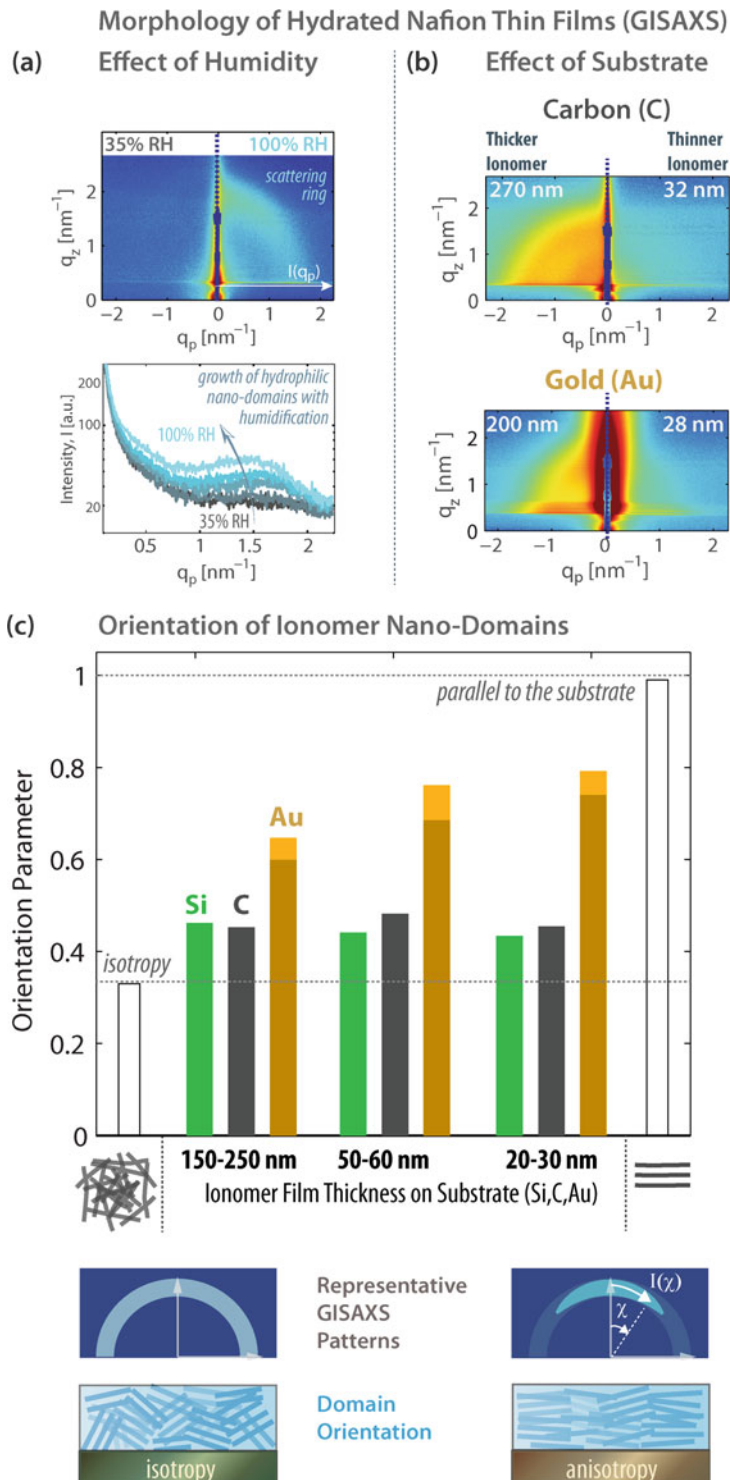
domains in bulk PFSA, in thin films, a hydration-dependent lamellar-like nanostructure forms at the film/substrate interface, with alternating layers of water-rich and polymer-rich domains (Fig. 3) [25, 28]. In addition, on hydrophilic substrates (such as  $\text{SiO}_2$ ), a water-enriched surface with a water layer thickness of 1 to 3 nm is observed due to the excess water at the substrate/film interface [25, 69, 89]. Such ordering at the interface could propagate a significant distance (10s of nm) through subsequent layers in a thin film, inducing a locally ordered morphology with alternating layers of  $\text{SO}_3^-$ -rich hydrophilic domains and fluorocarbon hydrophobic domains (Fig. 3) [24, 25, 55, 69, 88, 89]. A recent FTIR study on a PFSA thin film [40] documented different polarizations in and out of the plane of the film, with stronger z-polarized electric field in thinner films indicative of chain alignment parallel to the surface. Such molecular ordering exhibits a transition around 50 nm and depends on processing such as spin casting. The preferential domain alignment is strongest closer to the interface, depending on the substrate interactions, and diminishes along the successive layers toward the film surface [25, 28, 55, 89] (Figs. 3 and 7). Such changes in film morphology with the substrate, along with the impact of thickness and humidity, were also witnessed in GISAXS studies [20, 24]. Typical GISAXS patterns for Nafion films (of  $90 \pm 10$  nm thickness) on various substrates are compared and analyzed in Fig. 7.

Compared to scattering based on transmission (through membranes), techniques for thin films rely on reflection geometry, where the incident beam applied at a shallow incident angle ( $\alpha_i \ll 1^\circ$ ) enters the film and then reflects from the substrate/film interface [90]. To accomplish this, the incidence angle must be lower than that critical angle,  $\alpha_{\text{cr}}$ , of the film yet lower than that of the substrate,  $\alpha_{\text{cr, film}} < \alpha_i < \alpha_{\text{cr, substrate}}$ . Under such *grazing-incidence* conditions, sufficient beam path could be achieved to collect scattering patterns that probe the local structure of a thin film as well as its interface with the substrate. While the reflection geometry increases the complexity of the scattering, it nonetheless provides a powerful method to characterize polymer thin films [90].



**Ionomer Thin Films in PEM Fuel Cells, Fig. 7**

(a) 2-D GISAXS spectra of 100 nm Nafion thin film on SiO<sub>2</sub> substrate at different humidities and the evolution of the ionomer peak obtained from the intensity profile during humidification. (b) Comparison of GISAXS patterns for vapor-saturated (100% RH) Nafion films of two thicknesses on carbon and gold substrates. (c) Impact of thickness and substrate on the orientation parameter of Nafion film, which was calculated from the distribution of intensity along the azimuthal angle at the ionomer peak position (shown schematically below) (Data are compiled from Kusoglu et al. [20, 24]) (For ease of comparison, only one quadrant of the 2-D images is shown due to their symmetry along the vertical axis,  $q_z$ )



Characteristic features of GISAXS patterns for Nafion thin films shown in Fig. 7 are summarized as follows:

There exists a scattering half-ring that intensifies with humidification indicating hydration-driven phase separation with a correlation length between  $q = 1.5$  and  $2.5 \text{ nm}^{-1}$ , which corresponds to domain spacing of  $d = 2\pi/q \approx 2.5$  to  $4.5 \text{ nm}$  [20, 57]. The degree of phase separation, quantified by the full-width half-max (FWHM) of the ionomer peak, decreases with film thickness and almost disappears for ultrathin films [20, 24, 27, 57]. Nevertheless, this trend is strongly influenced by the IEC (or EW) of the ionomer, increase in which it tends to enhance phase separation at a given thickness due to a higher fraction of ionic moieties [24]. As the film thickness is reduced below  $50 \text{ nm}$ , the ionomer begins to exhibit weaker phase separation, which is evident from the broader ionomer peak in GISAXS [20, 53, 57], more mixing of smaller-size domains in TEM images [53] and AFM [56], as well as the change from hydrophobic to hydrophilic film surface [45, 67, 70].

A rather more important consequence of confinement is the (nano)structural anisotropy. Scattering patterns begin to exhibit slight deviations from isotropy as the film gets thinner since the ionomer chains are topologically confined. A comparison between the intensity profiles taken parallel ( $I_{\text{qp}}$ ) and perpendicular ( $I_{\text{qz}}$ ) to the substrate indicates stronger phase separation in thickness direction, accompanied by smaller domain spacing. Compared to the isotropic d-spacing of a bulk-like ionomer, confinement reduces the ionomer's d-spacing more in the thickness direction ( $d_z < d_p$ ) (Fig. 4). Nevertheless, in the thickness direction, ionomer preserves its phase-separated nanostructure aided by the confinement effects, which induce preferential orientation of domains parallel to the substrate. In such a configuration, domain orientation is influenced also by the strength of the substrate/film interactions.

Figure 7b reveals a sharp contrast in PFSA structure between carbon and metallic substrates. PFSA film's nanostructure exhibits closer to a semicircular (isotropic) ionomer peak on silicon and carbon substrates, whereas it becomes

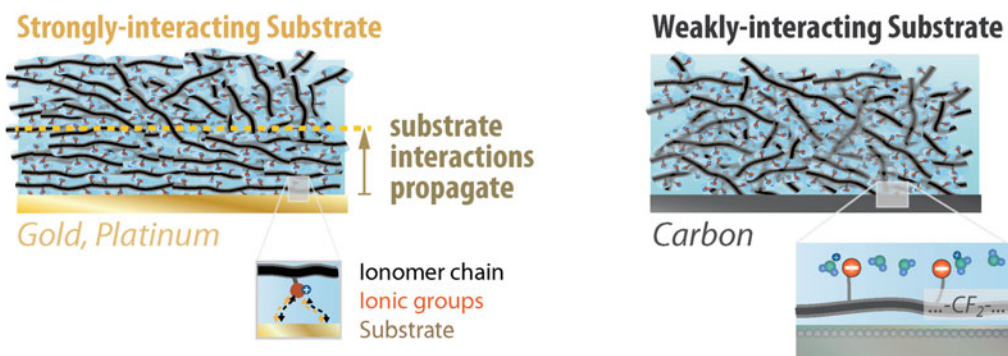
more anisotropic on gold and platinum. Also, the substrate appears to have a stronger impact on domain orientation than on domain spacing. To characterize this nanostructural anisotropy, an *orientation parameter*, O.P., is calculated from the distribution of ionomer peak intensity as a function of azimuthal angle,  $\chi$  (Fig. 7):

$$\begin{aligned} O.P. &= \langle \cos^2 \chi \rangle \\ &= \frac{\int_0^{\pi/2} I(\chi) \sin(\chi) \cos^2 \chi d\chi}{\int_0^{\pi/2} I(\chi) \sin(\chi) d\chi} \end{aligned} \quad (5)$$

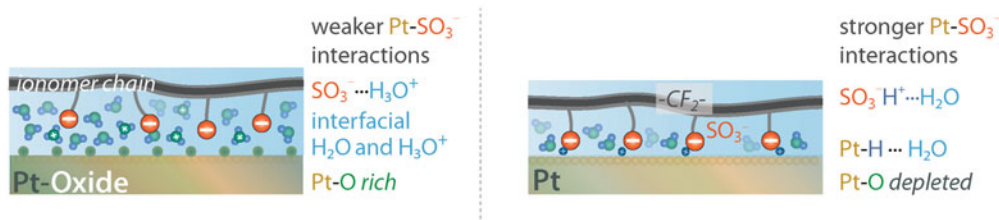
An O.P. of 0 and 1 corresponds to perpendicular and parallel orientations, respectively, while an isotropic distribution of intensity ( $I(\chi) = \text{constant}$ ) yields O.P. = 0.33. As shown in Fig. 7c, the orientation parameter for Nafion thin film depends both on thickness (confinement) and substrate (interactions), with the latter imposing a stronger effect. On silicon and carbon, the O.P. is closer to the isotropic distribution, regardless of thickness. On gold substrates, however, PFSA films exhibit a stronger orientation accompanied by a secondary impact of thickness. As the ionomer is confined on gold to a thickness below  $50 \text{ nm}$ , its O.P. approaches 1, which is the theoretical value for parallel alignment. Hence, the strong interactions of PFSA moieties with metallic substrates lead to substrate-induced ordering, which is enhanced under confinement. Thus, for ultrathin films, the substrate-ionomer interaction is strong enough to propagate the entire film leading to preferential alignment of all the domains therein (Fig. 8a).

An increasing number of studies agree on formation of a partially ordered ionomer domain structure closer to the film/substrate interface [20, 28, 33, 38, 45, 55, 67], albeit with a strong substrate dependence [20, 28, 45, 56, 57]. Such alignment in confined geometries is possible in light of recent evidence on the locally flat, ribbon-like morphology of PFSA (see Ref. [75] for additional reading). It was shown that during humidification of PFSA thin films, hydrophilic d-spacing ( $d(\lambda)/d_{\text{dry}}$ ) increases with thickness swelling ( $L(\lambda)/L_{\text{dry}}$ ) in an affine manner,

### (a) Effect of Confinement and Substrate on Ionomer thin-film Nanostructure



### (b) Effect of PFSA Ionomer - Substrate Interactions on Local Structure



**Ionomer Thin Films in PEM Fuel Cells, Fig. 8 (a)** Impact of substrate interactions on the local orientation of PFSA domains on weakly and strongly interaction

substrates. **(b)** Changes in the nature of Pt/ionomer interface under oxidizing and reducing environment

indicative of locally flat domains [24]. Hence, a bulk PFSA ionomer can also be interpreted as a mesoscale assembly of ionomer structures with local order, like thin films, which could also serve as a model constituent for studying multi-scale transport phenomena.

From these studies, a morphological picture for PFSA thin film emerges where the ionomer domains have stronger packing and preferential orientation nearby the substrate. In the plane of film, however, they maintain their interconnected network with more random orientation. It is instructive to consider that close packing of domains also results in a strong densification of ionomer, thereby giving rise to additional resistance to the transport species perpendicular to the substrate. In such a confined geometry, the polymer chains do not have sufficient energy to orient themselves randomly as they do in a bulk volume, and therefore exhibit preferential alignment,

thereby impacting transport of ions [5, 35–37, 53, 91], water [20, 32, 65, 68, 73], and gases [6, 8, 15, 39]. It should be noted that ionomer chains still have relatively more conformational freedom in the plane, where their mobility is less likely to be restricted compared to that perpendicular to substrate.

In accord with these morphological changes, the surface of a PFSA thin film also changes under confinement, which is probed by methods such as contact angle measurements and electrochemical AFM. The contact angle of a Nafion film exhibits a strong dependence on not only the thickness but also the thermal history. Below a critical thickness,  $L_{cr}$ , the film surface is hydrophilic and becomes more hydrophobic as the thickness increases toward bulk-like values ( $L > L_{cr}$ ) [31, 64, 67]. The contact angle of a Nafion film decreases from  $100^\circ$  to almost  $0^\circ$  around a critical thickness of  $L_{cr} = 50$  to  $60$  nm and then increases

slightly up to 20° for a film of a few nanometer [31, 64, 67]. The hydrophilicity of thin-film surface was also confirmed by PALS, showing an SO<sub>3</sub>-rich surface [45] and NMR [87], which demonstrated that the local hydrogen-bonding structure of a 10 nm film is water rich with a high dissociation of protons and exhibits no further change in <sup>1</sup>H chemical shifts and mobility with temperature [87]. This is in contrast with a 160-nm-thick film, which exhibit a bulk-like behavior with a temperature-dependent proton mobility, and thus does not suffer from the kinetically trapped state with limited mobility that ultrathin films experience [87]. In addition, a Nafion film annealed at C exhibits hydrophobic surface, regardless of the thickness [70]. However, once an annealed film is exposed to liquid water, it becomes hydrophilic again, signifying a surface reorganization that can be switched by means of surface treatments, accompanied by changes in surface roughness [64, 70]. The fact that switching of the surface wettability requires a higher annealing temperature for thin(ner) films indicates the highly restrictive mobility of Nafion as its confinement increases.

### Structure/Property Relationship and Transport

It is clear that a thin film's internal and surface morphology poses significant limitations to transport and overall device performance [7, 27, 33, 56, 57, 62, 65, 91]. Due to similar transport limitations between the Nafion electrolyte films formed in PEFC electrodes [6, 7, 9, 11, 14, 18, 92] and Nafion thin films [20, 27, 32, 33, 36, 57, 91], thin films are used as model systems to investigate and model electrode ionomers [1, 2, 7]. Key for electrode performance is good oxygen permeability with proton conductivity across/through an ionomer thin film on and between carbon/Pt agglomerates. Since both transport properties tend to deteriorate for nm-thick films, understanding the structure/transport properties therein is of great importance. As discussed above, such transport resistance, while being driven by the confinement, is also impacted by the ionomer/Pt interaction, with structural ordering through chemical affinity of SO<sub>3</sub><sup>-</sup> groups onto Pt. With the formation of water-

enriched surfaces near the substrate, which was evidenced by the availability of non-H-bonded water [43] it becomes easier to solvate SO<sub>3</sub> groups with lower energy cost on backbone chain's deformation. In a DPD model of a 10-nm-thick Nafion on carbon, diffusion was found to be anisotropic, higher along the film and lower in thickness direction [93]. Similarly, the conductivity of ionomer films along the ionomer-substrate interface is strongly influenced by the molecular orientation and ordering of the ionomer moieties therein [91]. Thus, the impact of morphological changes on transport is largely dependent on the direction on which the mechanism is probed.

Confinement-driven structural changes and ordering reduce not only the transport properties but also their kinetics. For example, swelling kinetics of thin films have been shown to yield time constants [18, 20, 32, 57, 65] similar to those found for the interfacial transport of bulk membranes, thus revealing the thin-film nature of bulk-membrane interfaces. It must be noted, however, that correlating kinetic effects with confinement is not trivial, especially when probing transport parallel or perpendicular to the substrate. This is because swelling kinetics is strongly intertwined to dynamic of morphological changes, such as formation of interfacial layering [25, 65]. It is worth noting that similar phenomena occur at the open surface of an ionomer, where the humidity-dependent film interface changes the mass transport and its kinetics [59, 61, 94, 95]. An intriguing consequence of this phenomenon is observed when gas transport at the film's interface is probed electrochemically using a Pt electrode, where the electrochemically generated water changes the interface, thereby affecting the measured property and its kinetics [59].

Hence, there exists a strong interplay between the film's morphology and transport phenomena, as dictated by confinement and interactions, whether it is in contact with air or a substrate [8, 14, 20, 34, 53, 55, 67, 68]. When confined to thin films, PFSA exhibits not only lower diffusion [27, 54, 65, 68, 71, 72] but also a few orders of magnitude slower relaxation, indicating more restricted chain dynamics [68]. An important implication of confinement effect for fuel cell

ionomers is the reduced conductivity with decrease in film thickness [5, 34, 36, 37, 53, 64, 70, 91] and substrate dependence [34] (Fig. 4), which can be associated with decreased water uptake [34, 36, 64, 70, 91] and the number of conducting sites (from conductive AFM) [56], as the conductivity- $\lambda$  relationship was shown to extend to the thin-film regime, albeit with differences from that in the bulk regime [69]. Concurrent with the confinement-driven increase in resistance to transport of water and ions, activation energy for conductivity also increases as the film thickness is reduced [34, 35, 37, 64, 67, 91] (Fig. 4). Conductivity of PFSA film decreases also after thermal annealing, the impact of which, however, diminishes for ultrathin (10 nm) films, which exhibit minimal rearrangement in response to heat-treatment processes [35]. A noteworthy observation is that the reduction in conductivity upon heat treatments is more pronounced than that in swelling, which not only reveals the key roles of morphological changes and film interactions on transport resistances [20, 64, 70] but also underscores the enthalpic and entropic contributions to chain dynamics in thin films which are controlled by both kinetic and thermodynamic phenomena.

Similar to conductivity, oxygen permeability also decreases in thin films [6, 8, 13, 15, 39]. Oxygen transport in thin films is measured electrochemically using a microelectrode setup, where one of the dimensions of the Pt electrode is small enough to probe local resistances at the ionomer/Pt interface during oxygen reduction reaction (ORR), thereby mimicking the mechanisms occurring in PEFC cathodes [8, 39, 59, 96–98]. By sweeping potential under various concentrations of  $O_2$ , diffusion-limited current densities are achieved and used to relate for various film thicknesses to the  $O_2$  transport through the film to the interface. With such characterization, one can identify the contributions to the  $O_2$  transport resistance in CLs (shown in Fig. 1) and study the role of ionomer film. However, such analysis is nontrivial due to the nanometer thicknesses probed. Kudo et al. [8, 39] showed that the reduced  $O_2$  permeation in thinner films exhibits a thickness dependence, which is governed by the surface interactions of the film, especially at the Pt/ionomer interface. While an overall interfacial resistance to

gas transport is inferred, separating the oxygen permeation through ionomer's inner regions and at the ionomer/Pt layer is difficult as below 20 nm thicknesses, the entire ionomer film exhibits densification and acts as an "interface."

Furthermore, any preferential alignment is expected to result in local stiffening, which was evidenced by fluorescence showing antiplasticization [33] and correlates to the observed increase in the modulus of thin films [26, 38]. These changes are consistent with the reduced water uptake due to a stronger mechanical force in the mechanical/chemical energy balance that controls swelling equilibrium. One potential strategy for altering this balance and overcoming transport limitations is using PFSA with higher IECs and different side chain chemistries. Lowering the EW of a PFSA ionomer film increases its swelling, which could be favorable for enhancing some of the transport mechanisms, but it could also increase the local order near the Pt substrate (Fig. 8b), thereby affecting the transport of species to that interface. For example, MD simulations showed that increasing the side chain density by lowering the EW enhances the H-bonding and charge-dipole interactions, which impedes water mobility and its self-diffusion [99]. Such an effect is explored in CLs, where low-EW ionomers could increase  $O_2$  transport resistance despite absorbing more water [15]. Thus, changes in ionomer's side chain chemistry and density in the presence of an interacting substrate could significantly alter the transport mechanisms, which result in multiple distinct factors influencing the film's swelling and transport properties and making it challenging to establish their underlying origin.

### Substrate/Film Interactions and Related Phenomena

The nature and composition of the substrate surface, including its oxide layers (e.g.,  $SiO_2$ , PtO), is critical to the understanding of their interactions and response to various stimuli, such as humidity and electrochemical potential [8, 19, 20, 29, 30, 34, 41, 56, 69, 91, 100, 101]. Thus, compared to a hydrophilic Si native-oxide surface, films on hydrophobized Si substrates exhibited less water uptake and strong structural anisotropy with



domains parallel to the substrate [57]. On carbon, the nature of the substrate becomes critical as well [10, 20, 29, 30, 45, 56]. In addition, aging of carbon was shown to cause surface oxidation and rearrangement, accompanied by reduced film thickness and irreversible swelling [29]. Also, when the carbon surface is hydrophobic, the ionomer's interactions occurs via its apolar fluorocarbon chains [10], whereas hydrophilic carbon preferentially interacts with the polar  $\text{SO}_3\text{H}$  groups (Fig. 8a) [102]. Similarly, aggregates of PFSA are randomly adsorbed onto a highly oriented pyrolytic graphite (HOPG) surface, thereby forming an ordered morphology [103]. The favorable interactions between  $\text{SO}_3^-$  groups and a hydrophilic substrate's polar groups [29, 45, 56, 57, 103] become strongest on a Pt substrate [41, 45, 56, 101] (Fig. 8). While the NR studies report higher affinity of  $\text{SO}_3^-$  groups on hydrophilic  $\text{SiO}_2$  compared to metallic substrates [25, 28], GISAXS data show stronger substrate-induced morphological changes on Au and Pt [20], which is likely the cause of stronger domain orientation (Fig. 8c). Nevertheless, due to dynamic and chemically heterogeneous nature of the substrate-ionomer interface, local structure probed therein could also be influenced by the type of excitation, which could explain some of these discrepancies between various techniques. The substrate-specific changes are in accord with simulation results [43, 93, 104–106], confirming the key role of affinity of water to the substrate in an ionomer's molecular rearrangement that affects the morphology [104] and surface hydrophilicity [70, 93, 104, 105].

PFSA( $-\text{SO}_3\text{H}$ )/Pt interactions are well-explored electrochemical cell studies to elucidate the effects of electrochemically formed water and the oxide layer formation on ionomer film behavior [6, 8, 14, 29, 30, 44, 101, 107] with spectroscopic evidence [41–44] and supported by molecular simulations [43, 104, 106] (Fig. 8b). These studies confirmed the high chemical affinity of sulfonate  $\text{SO}_3^-$  groups to the Pt, which was also supported by FTIR [41, 43, 44], XPS [45], PALS [45], and MD studies [10, 43, 99, 104, 108]. PFSA/Pt interactions were shown to be reversible during Pt-oxide formation and reduction such that

adsorption of PFSA moieties onto the Pt surface weakens and disrupts surface oxide formation (e.g., due to applied electrochemical potential) [14, 30, 41, 44, 101, 107]. Thus, in reducing environment as well as at low hydration levels, PFSA's acid groups are embedded on the Pt surface, whereas formation of an oxide layer (PtO) creates a polar, hydrophilic interface between the ionic groups and the Pt particles [41, 44]. Such changes affect the long-range restructuring of the ionomer chains, which was accompanied by the changes in the mobility of  $\text{SO}_3^- \text{H}_3\text{O}^+$  and  $\text{H}_2\text{O}$  [41, 44], ionomer structure [14, 30, 41, 43, 45, 101], and transport resistances [6, 8, 14, 29]. Spectroscopic evidence suggests that with increasing potential,  $\text{SO}_3^-$  preferably adsorbs onto the Pt, which restricts the vibrational mobility of ionic groups (vs- ( $\text{SO}_3^-$ )) and expels the water molecules from the interface [41]. Cyclic voltammetry (CV) studies showed that the  $\text{SO}_3^-$  adsorption/desorption peaks are shifted to lower potentials with ionomer dehydration indicating enhanced adsorption of  $\text{SO}_3^-$  onto Pt under drier conditions, which is attributed to higher local concentration of  $\text{SO}_3^-$  and/or reduced hydration stabilization energy of ionomer [14, 109]. Hence, strong ordering of ionomer chains at the interface aided by the Pt- $\text{SO}_3^-$  interactions restrict the mobility of the pendant chains and reduce the fraction of available (active) ionic groups participating in transport, which could effectively block the gas transport pathways and thereby increase the local  $\text{O}_2$  resistance [7, 8, 11, 14, 15]. This phenomenon is also interpreted as the poisoning effect of the ionomer on the catalyst. The adsorption/desorption of the  $\text{SO}_3^-$  onto/from the Pt could be explained by the balance between an electrode metal spring (Pt- $\text{SO}_3^-$ ) and ionomer spring (backbone- $\text{SO}_3^-$ -cation) [101]. With increasing potential,  $\text{SO}_3^-$  approaches Pt, as the Pt- $\text{SO}_3^-$  interaction dominates the cation/anion interaction within Nafion. For the same reason, for other cations that interact more strongly with  $\text{SO}_3^-$ , a higher activation potential is needed to adsorb the cations onto the electrode surface [101]. Thus, in essence,  $\text{SO}_3^-$  responds to electric potential like single counterions (i.e., forming an electric double layer) [44] and affects the backbone (orientation)



through the flexible side chain [43, 44, 108]. These interactions also change the nature of interfacial water, some molecules of which are relocated to Pt, thereby reducing the hydration of the sulfonate layers (i.e. less  $\text{H}_3\text{O}^+$ ) and hydrogen bonding [43, 107, 108]. Therefore, the potential- and hydration-dependent changes of the Pt surface, including its oxide coverage, influence, chemically, the interaction and mobility of the ionomer's acid groups and, physically, the densification of the ionomer at the interface, which together controls the diffusion pathways. This phenomenon was simulated in a MD study, which showed that closer to the Nafion/substrate interface, the ionomer density increases, but its  $\text{O}_2$  concentration decreases [106].

## Summary and Remarks

In summary, from the current state of understanding of PFSA thin films, the following thickness regimes can be identified (see Fig. 3):

- (i) *Bulk-like regime*: (from  $\mu\text{m}$  down to a few 100 nm) where the majority of ionomer volume behaves like the inner regions of the bulk membrane, albeit still with interfacial effects arising from the presence of a surface layer which may differ from the inner structure.
- (ii) *Thin-film regime*: (between 0 (10) nm to a few 100 nm) where confinement-induced changes begin to influence the structure/transport properties resulting in reduced swelling, slower diffusion, limited transport properties, and anisotropic nanostructure with preferential orientation of ionomer domains parallel to the substrate. Such confinement-driven orientation also enhances the role of substrate/film interactions, which could induce additional changes in morphology including local ordering of the domains at the substrate/film interface, accompanied by higher transport resistances therein.
- (iii) *Ultrathin-film regime*: (less than 20 nm) where the ionomer interactions with the

substrate and open surface cause an intriguing interplay that propagate throughout the film thickness. As the film thickness approaches the characteristic length scale of the ionomer (e.g., domain spacing), the ionomer begins to exhibit reduced phase separation accompanied by increased swelling, resulting in dispersion-like behavior. In the presence of a metallic substrate, strong alignment and densification of ionomer chains at the substrate interface occurs. In such a morphology, the ionomer might begin to lose characteristic features of its mesoscale domain network, with weaker connectivity between its constituent domains and reduced hydrophobic-domain elastic forces, which tend to prevent dissolution of the ionomer [53].

Although the transitions between these regimes are neither well defined nor understood, there still appears to be a *critical thickness* of 50 to 60 nm, around which confinement effects manifest themselves even stronger as discussed above. It must be noted that this critical thickness (or transitions between regimes) could change in the presence of other effects, such as annealing and substrate interactions, and additional deviations might occur for properties that may be dominated by larger-scale morphological reorganization, such as diffusivity, permeability, and mechanical properties. Similarly, for the bulk-like regime (i), QCM and ellipsometry data deviate the most, suggesting that the swelling and water uptake processes are more complicated due to the presence of additional mixing effects, multidimensional swelling, and disruption of locally ordered structure or its diminishing influence over larger thicknesses.

Due to their similarity to the locally hydrated nano-domains of bulk ionomers and their interfacial layers, thin films show promise for modeling ionomer systems and studying their structure/property relationship at multiple length scales. Hence, a bulk PFSA ionomer can also be interpreted as a mesoscale assembly of ionomer structures with local order, like thin films. Thin films possess a higher level of complexity due to

the presence of electrostatic interactions arising from ionic groups responsive to environments, surface and wetting interactions, and confinement. Thus, additional studies are needed to understand how electrochemical potential impact thin-film morphology and properties in these regimes.

Lastly, for a given substrate composition, the impact of EW and chemistry on ionomer's structure/property relationship is stronger in regime (ii), where shorter backbone chain (lower EW) and side chain collectively enhance the structural order and the degree of phase separation in thin films. The effects of EW in PFSA are more pronounced in the thin-film regime (ii), which underlies the important role of ionic interactions on the morphology. Since the ionomer interacts via its pendant chains and  $\text{SO}_3^-$  acid groups, higher IEC could amplify the overall impact of the interactions near the substrate interface thereby enhancing ordering and densification.

## Future Directions

The role of ionomers in state-of-the-art PEFCs has expanded beyond the conventional solid electrolyte separator PEM into catalyst layers, where they maintain their electrolyte functionality as a thin film but also require permeation of reactant gases critical for the electrochemical reactions. In particular, the local resistance to oxygen flux at the CL ionomer/Pt interface leads to significant losses in cell performance, especially at reduced Pt loadings. To overcome the performance limitations without sacrificing cost, one must understand the genesis of the transport resistances in the cell, from membrane to CLs. Thus, ionomer thin films serve as model systems to study, characterize, and understand ionomer behavior in PEFC CLs, where transport resistances imposed by confinement and substrate interactions lead to increased mass-transport limitations. Despite the simplified nature of the thin films on model substrates, they help elucidate properties of CL ionomers and pave the way to mimic their behavior under conditions relevant to cell environment with operando characterization techniques. The

fact that both CL ionomers and ionomer thin films exhibit similar water uptake behavior and trends in terms of restrictions to ion and gas transport suggests that thin films can be used as proxies for the films occurring with the CLs. Nevertheless, there exist significant knowledge gaps in terms of (i) improving model systems with more realistic substrate compositions that enable a better representation of the catalyst ionomer films; (ii) investigation under conditions relevant to PEFC operating environment, including humidity, temperature, time, and potential effects; (iii) characterization of the dynamic nature of the substrate/film interfaces, in particular with ionomer/Pt interactions; and (iv) establishing the structure-property correlations by accounting for ionomer chemistry to model and predict the transport limitations.

In ionomer thin films, the interplay between the interactions and confinement results in preferential orientation and densification of domains, which could pose significant limitations to transport of species occurring through these domains. Most of these transport limitations manifest themselves in terms of reduction in water uptake and diffusion, ion conductivity, and gas permeability, accompanied by higher activation energy barriers. The magnitude of these transport-property reductions changes with many factors, including solvent type, casting and processing conditions (e.g., posttreatment), ionomer chemistry, film thickness, substrate type, composition, and interface, as well as environmental conditions relevant to cell operation (e.g., humidity, temperature, potential), resulting in a wide material parameter space that still remains to be explored fully in order to elucidate the governing phenomena and develop material solutions.

There is a growing body of evidence on changes in PFSA thin films' swelling, water uptake, and morphological features under confinement, which help understand the role of thickness and, to a certain extent, the substrate. Hitherto, most studies on PFSA thin films have focused on silicon substrates, followed by gold. Nevertheless, to better understand the PEFC CL ionomers, there is a need to explore their behavior on carbon- and platinum-mixed substrates and in

thinner regimes. A large fraction of the ionomer films in CLs are below 15 nm thick, yet their structure/function relationship has not been established in model systems, due in part to the challenges associated with probing their morphology and properties at such thicknesses. Furthermore, since thin films exhibit anisotropy in morphology and transport properties, there is a need to explore and model the anisotropy of properties. The thin films highlight the importance of substrate interactions, especially their dynamic nature during operation, such as the formation and reduction of oxide layer on Pt, which expands the required data, needs, and science, most of which are still in early stages. Even though substrate-specific interactions control the ionic moieties' distribution at the interface, a complete picture as to how these interactions control the orientation of ionomer's side and main chain, and their conformation in the morphology propagates through the thickness, has yet to emerge. In particular, there is a need to explore PFSA ionomers beyond Nafion to identify the role of EW and side chain chemistry in controlling thin film's interactions with various substrates and structure/functionality. The fact that permeability of a gas depends on its solubility and diffusion, which respond differently to the environmental and nanostructural changes, makes it difficult to identify the role of chemistry on gas transport near the ionomer/Pt interface.

PFSA ionomers' remarkable transport properties could be associated with its nanoscale environment, where high mobility of bulk-like water aids rapid water and ion transport, and the interconnected mesoscale domain network that governs the macroscopic transport. It is important to understand how this multiscale three-dimensional morphology is disrupted when the ionomer is confined to nanometer thicknesses including anisotropy formation and altered transport properties of various species, which are highly coupled. Moreover, elucidation of the anisotropy in relation to the film's confined domain network requires models and techniques that enable characterization of transport properties beyond scalar values to direction-dependent vectors. Thus, there is a need to build a new knowledge base for PEFC

ionomers, to understand their structure/functionality across the length scales, and in the presence of various dynamic interactions. This is a significant challenge and opportunity to design and implement advanced characterization techniques to probe ionomer-substrate interface and to develop more predictive multiscale models to elucidate transport phenomena.

## Bibliography

### Primary Literature

1. Weber AZ, Kusoglu A (2014) Unexplained transport resistances for low-loaded fuel-cell catalyst layers. *J Mater Chem A* 2(41):17207–17211
2. Holdcroft S (2014) Fuel cell catalyst layers: a polymer science perspective. *Chem Mater* 26(1):381–393
3. Soboleva T, Malek K, Xie Z, Navessin T, Holdcroft S (2011) PEMFC catalyst layers: the role of micropores and mesopores on water sorption and fuel cell activity. *ACS Appl Mater Interfaces* 3(6):1827–1837
4. Lopez-Haro M et al (2014) Three-dimensional analysis of Nafion layers in fuel cell electrodes. *Nat Commun* 5:5229. doi:10.1038/ncomms6229
5. Siroma Z, Ioroi T, Fujiwara N, Yasuda K (2002) Proton conductivity along interface in thin cast film of Nafion (R). *Electrochem Commun* 4(2):143–145
6. Iden H, Ohma A, Shinohara K (2009) Analysis of proton transport in pseudo catalyst layers. *J Electrochem Soc* 156(9):B1078–B1084
7. Kongkanand A, Mathias MF (2016) The priority and challenge of high-power performance of low-platinum proton-exchange membrane fuel cells. *J Phys Chem Lett* 7(7):1127–1137
8. Kudo K, Jinnouchi R, Morimoto Y (2016) Humidity and temperature dependences of oxygen transport resistance of Nafion thin film on platinum electrode. *Electrochim Acta* 209:682–690
9. Iden H, Sato K, Ohma A, Shinohara K (2011) Relationship among microstructure, ionomer property and proton transport in pseudo catalyst layers. *J Electrochem Soc* 158(8):B987–B994
10. Ohma A et al (2011) Analysis of proton exchange membrane fuel cell catalyst layers for reduction of platinum loading at Nissan. *Electrochim Acta* 56(28):10832–10841
11. Mashio T, Iden H, Ohma A, Tokumasu T (2017) Modeling of local gas transport in catalyst layers of PEM fuel cells. *J Electroanal Chem* 790:27–39
12. Shinozaki K, Morimoto Y, Pivovar BS, Kocha SS (2016) Suppression of oxygen reduction reaction activity on Pt-based electrocatalysts from ionomer incorporation. *J Power Sources* 325:745–751
13. Suzuki T, Kudo K, Morimoto Y (2013) Model for investigation of oxygen transport limitation in a

- polymer electrolyte fuel cell. *J Power Sources* 222:379–389
14. Jomori S, Komatsubara K, Nonoyama N, Kato M, Yoshida T (2013) An experimental study of the effects of operational history on activity changes in a PEMFC. *J Electrochem Soc* 160(9):F1067–F1073
  15. Ono Y, Ohma A, Shinohara K, Fushinobu K (2013) Influence of equivalent weight of ionomer on local oxygen transport resistance in cathode catalyst layers. *J Electrochem Soc* 160(8):F779–F787
  16. Morawietz T, Handl M, Oldani C, Friedrich KA, Hiesgen R (2016) Quantitative in situ analysis of ionomer structure in fuel cell catalytic layers. *ACS Appl Mater Interfaces* 8(40):27044–27054
  17. Soboleva T et al (2010) On the micro-, meso- and macroporous structures of polymer electrolyte membrane fuel cell catalyst layers. *ACS Appl Mater Interfaces* 2(2):375–384
  18. Kusoglu A, Kwong A, Clark KT, Gunterman HP, Weber AZ (2012) Water uptake of fuel-cell catalyst layers. *J Electrochem Soc* 159(9):F530–F535
  19. Iden H, Ohma A (2013) An in situ technique for analyzing ionomer coverage in catalyst layers. *J Electroanal Chem* 693:34–41
  20. Kusoglu A et al (2014) Impact of substrate and processing on confinement of Nafion thin films. *Adv Funct Mater* 24(30):4763–4774
  21. Kim TH, Yi JY, Jung CY, Jeong E, Yi SC (2017) Solvent effect on the Nafion agglomerate morphology in the catalyst layer of the proton exchange membrane fuel cells. *Int J Hydrog Energy* 42(1):478–485
  22. Kim YS et al (2015) Origin of toughness in dispersion-cast Nafion membranes. *Macromolecules* 48(7):2161–2172
  23. Welch C et al (2012) Nafion in dilute solvent systems: dispersion or solution? *ACS Macro Lett* 1(12):1403–1407
  24. Kusoglu A, Dursch TJ, Weber AZ (2016) Nanostructure/swelling relationships of bulk and thin-film PFSA ionomers. *Adv Funct Mater* 26(27):4961–4975
  25. Kim S et al (2013) Surface-induced nanostructure and water transport of thin proton-conducting polymer films. *Macromolecules* 46(14):5630–5637
  26. Page KA et al (2015) In situ method for measuring the mechanical properties of Nafion thin films during hydration cycles. *ACS Appl Mater Interfaces* 7(32):17874–17883
  27. Eastman SA et al (2012) Effect of confinement on structure, water solubility, and water transport in Nafion thin films. *Macromolecules* 45(19):7920–7930
  28. Dura JA, Murthi VS, Hartman M, Satija SK, Majkrzak CF (2009) Multilamellar interface structures in Nafion. *Macromolecules* 42(13):4769–4774
  29. Wood DL, Chlistunoff J, Majewski J, Borup RL (2009) Nafion structural phenomena at platinum and carbon interfaces. *J Am Chem Soc* 131(50):18096–18104
  30. Masuda T, Sonsudin F, Singh PR, Naohara H, Uosaki K (2013) Potential-dependent adsorption and desorption of perfluorosulfonated ionomer on a platinum electrode surface probed by electrochemical quartz crystal microbalance and atomic force microscopy. *J Phys Chem C* 117(30):15704–15709
  31. Paul DK, Fraser A, Karan K (2011) Understanding the ionomer structure and the proton conduction mechanism in PEFC catalyst layer: adsorbed Nafion on model substrate. *ECS Trans* 41(1):1393–1406
  32. Kongkanand A (2011) Interfacial water transport measurements in Nafion thin films using a quartz-crystal microbalance. *J Phys Chem C* 115(22):11318–11325
  33. Dishari SK, Hickner MA (2012) Antiplasticization and water uptake of Nafion thin films. *ACS Macro Lett* 1(2):291–295
  34. Ono Y, Nagao Y (2016) Interfacial structure and proton conductivity of Nafion at the Pt-deposited surface. *Langmuir* 32(1):352–358
  35. Paul DK, McCreery R, Karan K (2014) Proton transport property in supported Nafion Nanothin films by electrochemical impedance spectroscopy. *J Electrochem Soc* 161(14):F1395–F1402
  36. Paul DK, Fraser A, Karan K (2011) Towards the understanding of proton conduction mechanism in PEMFC catalyst layer: conductivity of adsorbed Nafion films. *Electrochem Commun* 13(8):774–777
  37. Siroma Z et al (2009) Depression of proton conductivity in recast Nafion (R) film measured on flat substrate. *J Power Sources* 189(2):994–998
  38. Page KA et al (2014) Confinement-driven increase in ionomer thin-film modulus. *Nano Lett* 14(5):2299–2304
  39. Kudo K, Morimoto Y (2013) Analysis of oxygen transport resistance of Nafion thin film on Pt electrode. *ECS Trans* 50(2):1487–1494
  40. Zimudzi TJ, Hickner MA (2016) Signal enhanced FTIR analysis of alignment in NAFION thin films at SiO<sub>2</sub> and Au interfaces. *ACS Macro Lett* 5(1):83–87
  41. Hanawa H, Kunimatsu K, Watanabe M, Uchida H (2012) In situ ATR-FTIR analysis of the structure of Nafion-Pt/C and Nafion-Pt<sub>3</sub>Co/C interfaces in fuel cell. *J Phys Chem C* 116(40):21401–21406
  42. Kunimatsu K, Yoda T, Tryk DA, Uchida H, Watanabe M (2010) In situ ATR-FTIR study of oxygen reduction at the Pt/Nafion interface. *Phys Chem Chem Phys* 12(3):621–629
  43. Kendrick I, Kumari D, Yakoboski A, Dimakis N, Smotkin ES (2010) Elucidating the ionomer-electrified metal interface. *J Am Chem Soc* 132(49):17611–17616
  44. Ayato Y, Kunimatsu K, Osawa M, Okada T (2006) Study of Pt electrode/Nafion ionomer interface in HClO<sub>4</sub> by in situ surface-enhanced FTIR spectroscopy. *J Electrochem Soc* 153(2):A203–A209
  45. Mohamed HF et al (2013) Possible presence of hydrophilic SO<sub>3</sub>H nanoclusters on the surface of dry ultrathin Nafion(R) films: a positron annihilation study. *Phys Chem Chem Phys* 15(5):1518–1525
  46. Paul DK, Giorgi JB, Karan K (2013) Chemical and ionic conductivity degradation of ultra-thin ionomer

- film by X-ray beam exposure. *J Electrochem Soc* 160(4):F464–F469
47. Albert JNL, Epps Iii TH (2010) Self-assembly of block copolymer thin films. *Mater Today* 13(6):24–33
  48. Segalman RA (2005) Patterning with block copolymer thin films. *Mater Sci Eng R* 48(6):191–226
  49. Fasolka MJ, Mayes AM (2001) BLOCK COPOLYMER THIN FILMS: physics and Applications1. *Annu Rev Mater Res* 31(1):323–355
  50. Russell TP, Lambooy P, Kellogg GJ, Mayes AM (1995) Diblock copolymers under confinement. *Physica B* 213(0):22–25
  51. Huang E et al (1998) Using surface active random copolymers to control the domain orientation in diblock copolymer thin films. *Macromolecules* 31(22):7641–7650
  52. Mansky P, Russell TP, Hawker CJ, Pitsikalis M, Mays J (1997) Ordered Diblock copolymer films on random copolymer brushes. *Macromolecules* 30(22):6810–6813
  53. Modestino MA et al (2013) Self-assembly and transport limitations in confined Nafion films. *Macromolecules* 46(3):867–873
  54. Bertonecello P, Ciani I, Li F, Unwin PR (2006) Measurement of apparent diffusion coefficients within ultrathin Nafion Langmuir-Schaefer films: comparison of a novel scanning electrochemical microscopy approach with cyclic voltammetry. *Langmuir* 22(25):10380–10388
  55. Dishari SK, Hickner MA (2013) Confinement and proton transfer in NAFION thin films. *Macromolecules* 46(2):413–421
  56. Ohira A, Kuroda S, Mohamed HFM, Tavernier B (2013) Effect of interface on surface morphology and proton conduction of polymer electrolyte thin films. *Phys Chem Chem Phys* 15(27):11494–11500
  57. Modestino MA, Kusoglu A, Hexemer A, Weber AZ, Segalman RA (2012) Controlling Nafion structure and properties via wetting interactions. *Macromolecules* 45(11):4681–4688
  58. Noguchi H, Taneda K, Minowa H, Naohara H, Uosaki K (2010) Humidity-dependent structure of surface water on Perfluorosulfonated ionomer thin film studied by sum frequency generation spectroscopy. *J Phys Chem C* 114(9):3958–3961
  59. Novitski D, Xie Z, Holdcroft S (2015) Time-dependent mass transport for O<sub>2</sub> reduction at the Pt | Perfluorosulfonic acid ionomer Interface. *ECS Electrochem Lett* 4(1):F9–F12
  60. Tang J, Yuan W, Zhang J, Li H, Zhang Y (2013) Evidence for a crystallite-rich skin on perfluorosulfonate ionomer membranes. *RSC Adv* 3(23):8947–8952
  61. He Q et al (2011) Correlating humidity-dependent ionically conductive surface area with transport phenomena in proton-exchange membranes. *J Phys Chem B* 115(40):11650–11657
  62. Bass M, Berman A, Singh A, Konovalov O, Freger V (2011) Surface-induced micelle orientation in Nafion films. *Macromolecules* 44(8):2893–2899
  63. Koestner R, Roiter Y, Kozhinova I, Minko S (2011) AFM imaging of adsorbed Nafion polymer on mica and Graphite at molecular level. *Langmuir* 27(16):10157–10166
  64. Paul DK, Karan K (2014) Conductivity and wettability changes of ultrathin Nafion films subjected to thermal annealing and liquid water exposure. *J Phys Chem C* 118(4):1828–1835
  65. Ogata Y, Kawaguchi D, Yamada NL, Tanaka K (2013) Multistep thickening of Nafion thin films in water. *ACS Macro Lett* 2(10):856–859
  66. Abuin GC, Cecilia Fuertes M, Corti HR (2013) Substrate effect on the swelling and water sorption of Nafion nanomembranes. *J Membr Sci* 428(0):507–515
  67. Paul DK, Karan K, Docoslis A, Giorgi JB, Pearce J (2013) Characteristics of self-assembled ultrathin Nafion films. *Macromolecules* 46(9):3461–3475
  68. Davis EM, Stafford CM, Page KA (2014) Elucidating water transport mechanisms in Nafion thin films. *ACS Macro Lett* 3(10):1029–1035
  69. Shim HK, Paul DK, Karan K (2015) Resolving the contradiction between anomalously high water uptake and low conductivity of nanothin Nafion films on SiO<sub>2</sub> substrate. *Macromolecules* 48(22):8394–8397
  70. Paul DK, Shim HK, Giorgi JB, Karan K (2016) Thickness dependence of thermally induced changes in surface and bulk properties of Nafion (R) nanofilms. *J Polym Sci Part B Polym Phys* 54(13):1267–1277
  71. Bertonecello P, Wilson NR, Unwin PR (2007) One-step formation of ultra-thin chemically functionalized redox-active Langmuir-Schaefer Nafion films. *Soft Matter* 3(10):1300–1307
  72. Krtil P, Trojanek A, Samec Z (2001) Kinetics of water sorption in Nafion thin films – quartz crystal microbalance study. *J Phys Chem B* 105(33):7979–7983
  73. Nadermann NK, Davis EM, Page KA, Stafford CM, Chan EP (2015) Using indentation to quantify transport properties of nanophase-segregated polymer thin films. *Adv Mater* 27(33):4924–4930.
  74. Springer TE, Zawodzinski TA, Gottesfeld S (1991) Polymer Electrolyte Fuel-Cell Model. *J Electrochem Soc* 138(8):2334–2342
  75. Kusoglu A, Weber AZ (2017) New insights into perfluorinated sulfonic-acid ionomers. *Chem Rev* 117(3):987–1104
  76. Pantelić N, Wansaipura CM, Heineman WR, Seliskar CJ (2005) Dynamic in situ spectroscopic ellipsometry of the reaction of aqueous iron(II) with 2,2'-bipyridine in a thin Nafion film. *J Phys Chem B* 109(29):13971–13979
  77. Bai YJ, Schaberg MS, Hamrock SJ, Tang ZJ, Goenaga G, Papandrew AB and Zawodzinski TA (2017) Density Measurements and Partial Molar Volume Analysis of Different Membranes for Polymer Electrolyte Membrane Fuel Cells. *Electrochim Acta* 242:307–314
  78. Freger V (2009) Hydration of ionomers and Schroeder's paradox in Nafion. *J Phys Chem B* 113(1):24–36

79. Kreuer KD (2013) The role of internal pressure for the hydration and transport properties of ionomers and polyelectrolytes. *Solid State Ionics* 252(0):93–101
80. Kusoglu A, Savagatrup S, Clark KT, Weber AZ (2012) Role of mechanical factors in controlling the structure–function relationship of PFSA ionomers. *Macromolecules* 45(18):7467–7476
81. Kollath VO, Karan K (2016) New molecular scale insights into the alpha-transition of Nafion (R) thin films from variable temperature ATR-FTIR spectroscopy. *Phys Chem Chem Phys* 18(37):26144–26150
82. Singhal N, Datta A (2016) Thickness dependence of acidity and microstructure in Nafion films. *Chemistryselect* 1(10):2277–2283
83. Allen FI et al (2015) Morphology of hydrated as-cast Nafion revealed through Cryo electron tomography. *ACS Macro Lett* 4(1):1–5
84. Umemura K et al (2006) Nanocharacterization and nanofabrication of a Nafion thin film in liquids by atomic force microscopy. *Langmuir* 22(7):3306–3312
85. Hill TA, Carroll DL, Czerw R, Martin CW, Perahia D (2003) Atomic force microscopy studies on the dewetting of perfluorinated ionomer thin films. *J Polym Sci Part B Polym Phys* 41(2):149–158
86. Maeda Y et al (2008) Study of the nanoscopic deformation of an annealed Nafion film by using atomic force microscopy and a patterned substrate. *Ultra-microscopy* 108(6):529–535
87. De Almeida NE, Paul DK, Karan K, Goward GR (2015) <sup>1</sup>H solid-state NMR study of Nanothin Nafion films. *J Phys Chem C* 119(3):1280–1285
88. Kalisvaart WP, Fritzsche H, Merida W (2015) Water uptake and swelling hysteresis in a Nafion thin film measured with neutron reflectometry. *Langmuir* 31(19):5416–5422
89. DeCaluwe SC, Kienzle PA, Bhargava P, Baker AM, Dura JA (2014) Phase segregation of sulfonate groups in Nafion interface lamellae, quantified via neutron reflectometry fitting techniques for multilayered structures. *Soft Matter* 10(31):5763–5776
90. Hexemer A, Müller-Buschbaum P (2015) Advanced grazing-incidence techniques for modern soft-matter materials analysis. *IUCrJ* 2(Pt 1):106–125
91. Nagao Y (2017) Proton-conductivity enhancement in polymer thin films. *Langmuir* 33(44):12547–12558
92. Peron J et al (2011) Fuel cell catalyst layers containing short-side-chain perfluorosulfonic acid ionomers. *J Power Sources* 196(1):179–181
93. Dorenbos G, Pomogaev VA, Takigawa M, Morohoshi K (2010) Prediction of anisotropic transport in Nafion containing catalyst layers. *Electrochem Commun* 12(1):125–128
94. Hwang GS, Parkinson DY, Kusoglu A, MacDowell AA, Weber AZ (2013) Understanding water uptake and transport in Nafion using X-ray microtomography. *ACS Macro Lett* 2(4):288–291
95. Novitski D, Holdcroft S (2015) Determination of O-2 mass transport at the Pt I PFSA ionomer interface under reduced relative humidity. *ACS Appl Mater Interfaces* 7(49):27314–27323
96. Uribe FA, Springer TE, Gottesfeld S (1992) A microelectrode study of oxygen reduction at the platinum/recast-Nafion film interface. *J Electrochem Soc* 139(3):765–773
97. Sambandam S, Parrondo J, Ramani V (2013) Estimation of electrode ionomer oxygen permeability and ionomer-phase oxygen transport resistance in polymer electrolyte fuel cells. *Phys Chem Chem Phys: PCCP* 15(36):14994–15002
98. Zhang L, Ma CS, Mukerjee S (2004) Oxygen reduction and transport characteristics at a platinum and alternative proton conducting membrane interface. *J Electroanal Chem* 568(1–2):273–291
99. Nouri-Khorasani A et al (2016) Molecular modeling of the proton density distribution in a water-filled slab-like nanopore bounded by Pt oxide and ionomer. *Catal Today* 262:133–140
100. Garrick TR, Moylan TE, Yarlagadda V, Kongkanand A (2017) Characterizing electrolyte and platinum interface in PEM fuel cells using CO displacement. *J Electrochem Soc* 164(2):F60–F64
101. Subbaraman R, Strmcnik D, Stamenkovic V, Markovic NM (2010) Three phase interfaces at electrified metal–solid electrolyte systems 1. Study of the Pt(hkl)-Nafion Interface. *J Phys Chem C* 114(18):8414–8422
102. Andersen SM et al (2014) Adsorption behavior of perfluorinated sulfonic acid ionomer on highly graphitized carbon nanofibers and their thermal stabilities. *J Phys Chem C* 118(20):10814–10823
103. Masuda T, Naohara H, Takakusagi S, Singh PR, Uosaki K (2009) Formation and structure of perfluorosulfonated ionomer thin film on a graphite surface. *Chem Lett* 38(9):884–885
104. Damasceno Borges D, Gebel G, Franco AA, Malek K, Mossa S (2015) Morphology of supported polymer electrolyte ultrathin films: a numerical study. *J Phys Chem C* 119(2):1201–1216
105. Mashio T et al (2010) Molecular dynamics study of ionomer and water adsorption at carbon support materials. *J Phys Chem C* 114(32):13739–13745
106. Jinnouchi R, Kudo K, Kitano N, Morimoto Y (2016) Molecular dynamics simulations on O-2 permeation through Nafion ionomer on platinum surface. *Electrochim Acta* 188:767–776
107. Kanamura K, Morikawa H, Umegaki T (2003) Observation of interface between Pt electrode and Nafion membrane. *J Electrochem Soc* 150(2):A193–A198
108. He QP, Suraweera NS, Joy DC, Keffer DJ (2013) Structure of the ionomer film in catalyst layers of proton exchange membrane fuel cells. *J Phys Chem C* 117(48):25305–25316
109. Kodama K et al (2013) Increase in adsorptivity of sulfonate anions on Pt (111) surface with drying of ionomer. *Electrochem Commun* 36:26–28





## Alkaline Membrane Fuel Cells

Robert C. T. Slade, Jamie P. Kizewski,  
Simon D. Poynton, Rong Zeng and  
John R. Varcoe  
Department of Chemistry, University of Surrey,  
Guildford, UK

### Article Outline

Glossary  
Definition  
Introduction  
An Overview of Alkaline Anion-Exchange  
Membranes (AEMs)  
Properties of AEMs  
Synthetic Routes to AEMs  
Development of Alkaline Ionomers  
AMFCs with H<sub>2</sub> as Fuel  
The Application of AEMs in Other Fuel Cell  
Types  
A Brief Overview of the Patent Literature  
Future Directions and Research Challenges  
Bibliography

### Glossary

**AEM** Alkaline (anion) exchange membrane  
**AFC** Alkaline fuel cell  
**AMFC** Alkaline membrane fuel cell (also  
known as AEMFC)  
**DMFC** Direct methanol fuel cell  
**MEA** Membrane electrode assembly  
**OCV** Open circuit voltage  
**PEM** Proton-exchange membrane  
**PEMFC** Proton-exchange membrane fuel cell  
**QA** Quaternary ammonium  
**RG-AEM** Radiation-grafted alkaline (anion)  
exchange membrane

### Definition

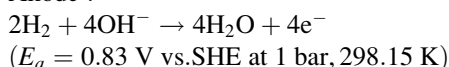
The disruptive approach of applying alkaline anion-exchange membranes (AEMs) in alkaline membrane fuel cells (AMFCs) potentially meets several of the challenges facing other approaches to low temperature fuel cells, including the otherwise high catalyst and fuel costs. Thus, the move to alkaline conditions at the electrodes opens the potential use of a range of low cost non-precious-metal catalysts, as opposed to the otherwise necessary use of platinum-group-metal (PGM) based catalysts. Further, it becomes possible to consider hydrogen fuels containing substantial amounts of impurities, whereas an acidic membrane approach (that in proton exchange membrane fuel cells, PEMFCs) requires high-purity gases and PGM catalysts.

### Introduction

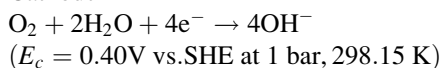
The first entry in the AMFC area was published in 2005 [1], since then activity and interest have continued to increase steeply. Zeng and Varcoe have recently reviewed the developing patent literature [2]. Some researchers have recently termed these systems HEMFCs, hydroxide exchange membrane fuel cells; that terminology is not fully appropriate in view of the complex hydroxide/hydrogen carbonate/carbonate equilibria that are present (even after handling membranes in air), inevitable in the use of air (containing CO<sub>2</sub>(g)) as source of oxidant and also produced in the oxidation of methanol in direct methanol fuel cells (DMFCs). Another acronym applied to these systems, APEMFCs, is also potentially confusing, the first three words of the full form then seemingly being “alkaline proton exchange” (following the very similar PEMFC acronym) but being readable alternatively as alkaline polymer electrolyte membrane fuel cells (possibly AEMFC would be clearer).

Alkaline fuel cells (AFCs, hydrogen-fuelled cells with an alkaline liquid electrolyte such as KOH(aq)) are the best performing of all known conventional hydrogen-oxygen fuel cells operable at temperatures below 200 °C. This is due to the facile kinetics at the cathode and at the anode; cheaper non-noble metal catalysts can be used (such as nickel and silver [3, 4]), reducing cost. McLean et al. gave comprehensive review of alkaline fuel cell technology [5]. The associated fuel cell reactions both for a traditional AFC and also for an AMFC are:

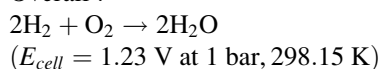
Anode :



Cathode :

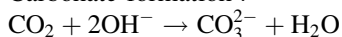


Overall :

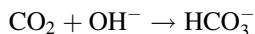


A major issue with traditional AFCs is that of electrolyte and electrode degradation caused by the formation of carbonate/bicarbonate ( $\text{CO}_3^{2-}/\text{HCO}_3^-$ ) on reaction of  $\text{OH}^-$  ions with  $\text{CO}_2$  contamination in the oxidant gas stream [5–7]:

Carbonate formation :



Bicarbonate formation :



The major cause of the degrading performance of AFCs is the consequent precipitation of metal carbonate crystals (most commonly  $\text{Na}_2\text{CO}_3$  or  $\text{K}_2\text{CO}_3$ , depending on the alkaline electrolyte used) in the electrolyte-filled pores of the electrodes, blocking pores and mechanically disrupting and destroying active layers.

The cost of fuel cells still retards commercialization in most markets. AFCs are promising on a cost basis mainly because cheap and relatively abundant non-platinum-group metals (non-PGM) are viable

catalysts, but are hindered by degradation due to formation of precipitates as above. Catalyst electrokinetics (for fuel oxidation and oxygen reduction) are improved in alkaline, as opposed to acidic, conditions (the acid-stability criterion precludes the use of most non-PGM catalysts in PEMFCs). The replacement of the KOH(aq) electrolyte with an alkaline electrolyte membrane (AEM), to give AMFCs, retains the electrocatalytic advantages but introduces  $\text{CO}_2$  tolerance (there being no mobile cations that could give carbonate/bicarbonate precipitates) with the additional advantage of being an all-solid-state fuel cell (as with PEMFCs – i.e., no seeping out of KOH(aq)). Additionally, thin (low electronic resistance) and easily stamped (cheap) metal mono/bipolar plates can be used, with reduced corrosion-derived problems at high pH (the cost of bipolar plates for PEMFCs can be as much as one third of the cost of the stacks themselves). A key and yet to be convincingly met requirement is, however, the development of a dispersible alkaline ionomer (sometimes termed an anionomer) to maximize ionic contact between the catalyst reaction sites and the ion-conductive membranes. As in the case of AFCs, water is produced at anode and consumed at cathode in AMFCs (when fuelled with hydrogen and with four electron reduction of oxygen at the cathode), which is fundamentally different to what occurs in PEMFCs containing acidic electrolytes; this can cause high overpotentials at AMFC anodes, due to suspected flooding [8].

The use of an AEM as a solid electrolyte including no metal cations prevents precipitation of carbonate/bicarbonate salts. (The electrolyte containing the cationic groups is already a solid.) The carbonation process is quick even if the AEM has been exposed to the air for only a short time [9, 10]. The conductivities of the AEMs in  $\text{OH}^-$  form may have been underestimated because most studies to date have not disclosed vigorous  $\text{CO}_2$  exclusion procedures during conductivity measurements. It has been hypothesized that  $\text{OH}^-$  ion conductivities in AEMs can be estimated by measuring the ionic conductivities of  $\text{HCO}_3^-$  from AEMs and multiplying by 3.8 [11]. This carbonation process may not to be a serious problem due to an in situ “self-purging mechanism” because  $\text{OH}^-$  anions are continuously generated at the cathode in AMFCs [12].

AEMs are solid polymer electrolyte membranes that contain positive ionic groups (typically quaternary ammonium (QA) functional groups such as poly-N Me<sub>3</sub><sup>+</sup>) and mobile negatively charged anions. A widely quoted concern with AEMs is membrane stability, especially at elevated temperatures [13, 14]. The general issues are:

1. The diffusion coefficients and mobilities of OH<sup>-</sup> anions are less than that of H<sup>+</sup> in most media, and QA ionic groups are less dissociated than the typical sulfonic acid groups (p*K* *a* for sulfonic acid groups are typically -1 but for QA groups the related p*K* *b* values are around +4); there were concerns that AEMs would not possess adequate intrinsic ionic conductivities for application in fuel cells.
2. The OH<sup>-</sup> anions are effective nucleophiles which potentially cause degradation via (a) a direct nucleophilic displacement and/or (b) a Hofmann elimination reaction when a β-hydrogen is present; methyl (-CH<sub>3</sub>) groups may also be displaced by OH<sup>-</sup> ions forming tertiary amines and methanol [13, 14]. If the AEMs contain good leaving groups (e.g., QA -NMe<sub>3</sub><sup>+</sup> groups) then the chemical stability of the AEMs might have been inadequate for use in fuel cells, particularly at elevated temperatures.
3. Precursor anion-exchange membranes are generally submerged in aqueous NaOH/KOH solutions to exchange them to the OH<sup>-</sup> form AEM; the AEM must have the chemical stability to withstand this process. Despite this, over a decade ago, the stabilities of various benzyltrimethylammonium-based AEMs were found to be stable at up to 75 °C in NaOH(aq) at concentrations up to 6 mol dm<sup>-3</sup> for several days [15].

A major potential application of AMFCs is, however, as power sources for at or near room temperature (as for PEMFCs), which means such degradation can be minimal.

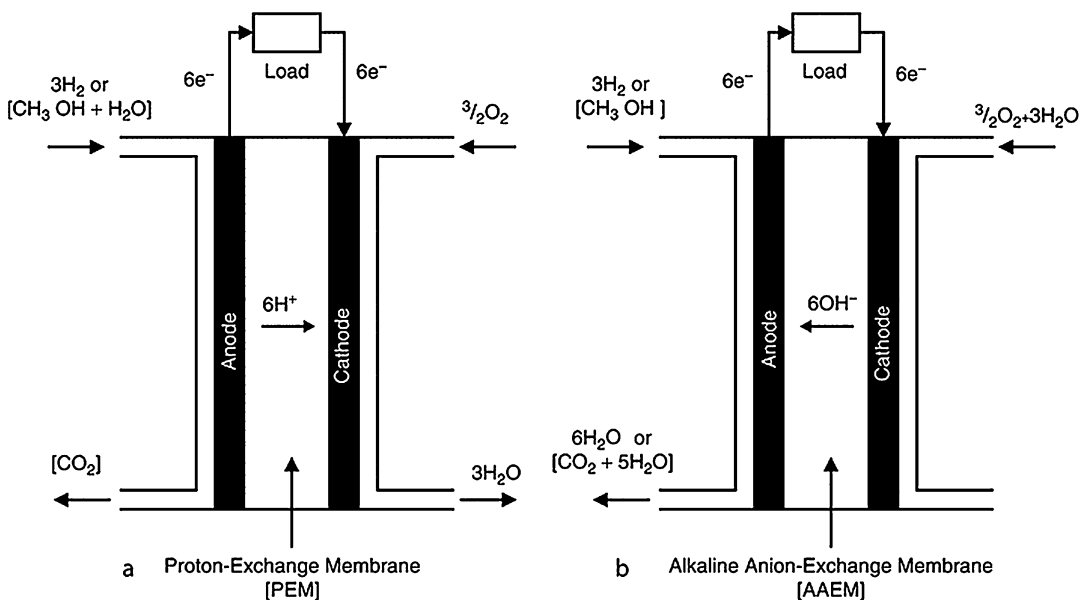
This entry considers the current understanding and application of AEMs in hydrogen-fuelled AMFCs and other fuel cell types employing AEMs. Figure 1 enables comparison between hydrogen- or methanol-fuelled PEMFCs and

AMFCs; the electrode reactions in a hydrogen-fuelled AMFC are discussed above. In contrast to PEMFCs, operation of an AMFC requires the presence of water as a reagent at the cathode (oxygen reduction reaction, ORR – to form OH<sup>-</sup>) and the product water is formed by the hydrogen oxidation reaction (HOR) at the anode (as opposed to being formed at the cathode in PEMFCs). The entry begins with consideration of the main classes of AEMs.

## An Overview of Alkaline Anion-Exchange Membranes (AEMs)

AEMs and alkaline ionomers (anionomers) are key to the successful implementation of AMFCs. Anion-exchange membranes have, for a long time, been used as separation membranes for seawater desalination, the recovery of metal ions from wastewaters, electro dialysis and bio-separation processes, for example [16–26]. These membranes may, however, not be stable or conductive enough to be applied in AMFCs. AEMs used in early AMFC studies were reviewed in 2005 [1] and included polybenzimidazole (PBI) doped with KOH, epichlorohydrin polymer quaternized with 1,4-diazabicyclo [2] octane (DABCO) or quaternized with a 1:1 ratio of DABCO and triethylamine, and commercial membranes such as AHA (Tokuyama Co, Japan), Morgane ADP (Solvey S.A.), Tosflex<sup>®</sup> SF-17 (Tosoh) and 2259-60 (Pall RAI). Most of these fuel cells containing AEMs were, however, being operated in the presence of aqueous alkaline solutions (containing NaOH or KOH).

In the UK (at the University of Surrey), several kinds of QA-containing radiation-grafted AEMs (RG-AEMs) based on poly(vinylidene fluoride) PVDF [27–31], poly(tetrafluoroethylene-co-hexafluoropropylene) FEP [27, 28, 32] and poly(ethylene-co-tetrafluoroethylene) ETFE [32, 33], with good ion-exchange capacities (IEC) and ionic conductivities and with sufficient stabilities to test the proof of concept of using AEMs in fuel cells, have been developed. ETFE base films produce the best AEMs for testing in AMFCs. The radiation-grafted methodology



**Alkaline Membrane Fuel Cells, Fig. 1** A schematic presentation of (a) a proton-exchange membrane (PEMFC) and (b) an alkaline membrane fuel cell

(using gamma rays or electron beams for irradiation) allowed for the production of AEMs of different thicknesses, ion-exchange capacity, physical/mechanical properties, and chemistries that facilitated fundamental investigations. A water-insoluble alkaline ionomer that used *N, N, N', N'*-tetramethylhexane-1,6-diamine as the joint amination and cross-linking agent first enabled studies of the performance of metal-cation-free all-solid-state alkaline fuel cells with stable performance into the medium term at 50 °C [33, 34]. Many other groups have now developed new conductive and chemically and thermally stable AEMs (and candidate alkaline ionomers), as discussed below. AEMs in the hydroxide form typically become brittle if allowed to dry; hydroxide forms are typically prepared just before use, from the chloride form analogue.

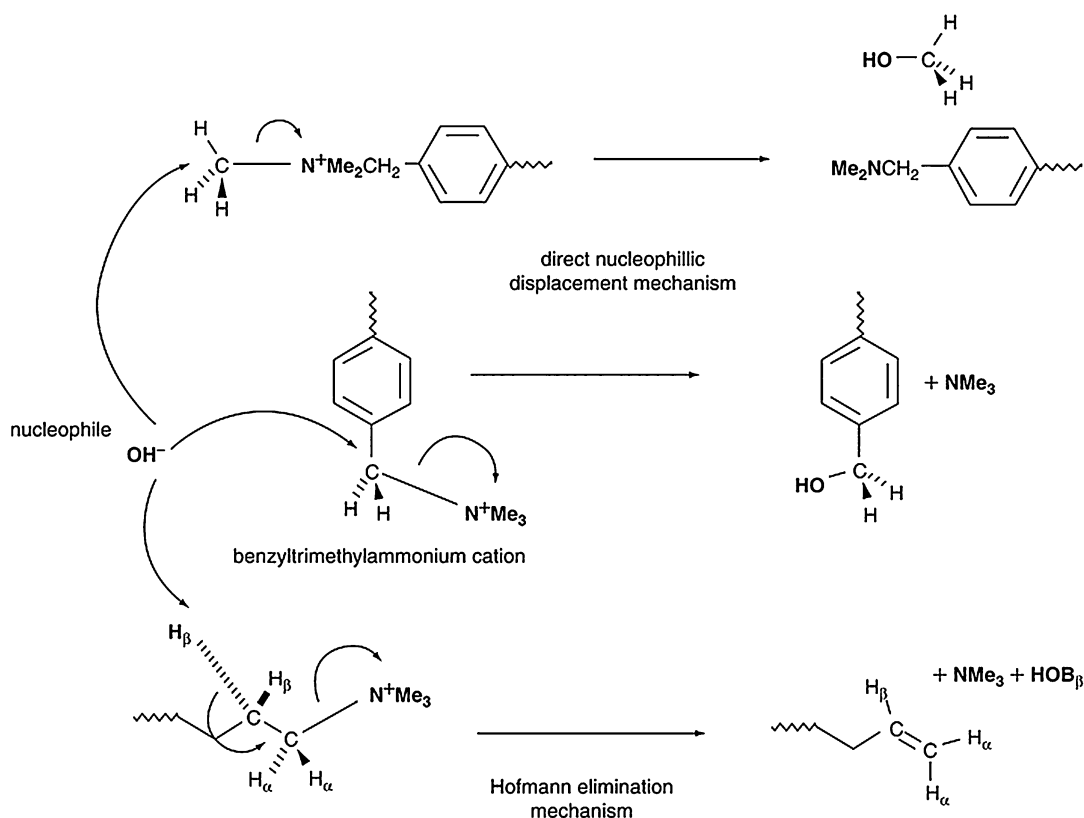
## Properties of AEMs

The most common class of NaOH–/KOH-free AEMs being investigated for use in fuel cells is based on QA chemistry and has reasonable stability in alkaline environments (especially those AEMs

(AMFC), both fuelled either with H<sub>2</sub> gas or directly with methanol (DMFC mode). The stoichiometric ratios of reactants and products are shown in each case

containing benzyltrimethyl ammonium exchange sites). There are three main classes of chemical degradation reaction mechanisms by which nucleophilic OH<sup>−</sup> anions can remove QA groups. The presence of β-hydrogens allows the Hofmann elimination reaction to occur (Scheme 1), often in parallel to the reactions discussed below, yielding alkene (vinyl) groups; this can give rise to QA-AEMs that have low thermal and chemical (to alkali) stabilities. If, as in RG-AEMs, no β-hydrogen atoms are present, direct nucleophilic substitution reactions were traditionally thought to take place yielding alcohol and tertiary amine groups. However, recent density functional theory (DFT) calculations and deuterium exchange experiments at Los Alamos National Laboratory (USA) on model small QA-containing compounds indicate that a mechanism involving an ylide intermediate (trimethyl ammonium methylyde, also known as a 1,2-dipolar ylide compound) may predominate and be more severe when the AEMs are dehydrated [35].

AEMs from Tokuyama Co have good thermochemical stability. The thin (10 μm) Tokuyama “fuel cell grade” AEMs (A010, A201 – formerly A006 and A901) [9, 36–39] and their developmental dispersible alkaline ionomers (A3ver.2



**Alkaline Membrane Fuel Cells, Scheme 1** Alternative mechanisms for degradation of AEMs by displacement of the trimethylammonium groups by hydroxide anions at elevated temperatures

and AS-4) have also been tested at up to  $50^\circ\text{C}$  by several research groups in direct alcohol fuel cells [40–42].

Quaternized pyridinium- or phosphonium-based AEMs were thought to have thermochemical stabilities that are not suitable for use in AEM fuel cells but there are reports of recent work on polysulfone-phosphonium-based AEMs and anionomers (see later).

Surrey's benzyltrimethylammonium-containing S80, S50, and S20 RG-AEMs (the number designating the fully hydrated thicknesses in micrometers) are chemically stable up to  $80^\circ\text{C}$  in aqueous KOH [32–34] (aq,  $1\text{ mol dm}^{-3}$ ) and can exhibit ionic conductivities  $>0.03\text{ S cm}^{-1}$  at room temperature when fully hydrated; the ex situ and in situ ionic conductivity of fully hydrated S80 is  $0.06\text{ S cm}^{-1}$  at  $60^\circ\text{C}$  (cf. Nafion<sup>®</sup> acidic PEMs are typically  $>0.1\text{ S cm}^{-1}$  at these temperatures). AEM conductivities are, however, considerably

reduced at humidities  $\text{RH}/\% < 100$  and drop to values between  $0.01$  and  $0.02\text{ S cm}^{-1}$  after only an hour when exposed to air (especially with very thin membranes) due to the reaction of  $\text{OH}^-$  anions with  $\text{CO}_2$  forming  $\text{CO}_3^{2-}$  and  $\text{HCO}_3^-$  within the membrane. The lower dissociation constant for  $-\text{NMe}_3\text{OH}$  groups (requiring a higher number of water molecules for complete dissociation), compared to  $-\text{SO}_3\text{H}$  groups in PEMs, and a very low number of water molecules directly associated with the ionic groups lead to the poor performance at low RHs (at high humidities much of the water present in AEMs is located in aggregates not directly associated with the ionic groups) [32].

The developing published and patent literature in this area has recently been reviewed by Zeng and Varcoe [2]. Further classes of AEM for fuel cells have included membranes based on quaternized poly(epichlorohydrin), polysulfone, poly(phthalalazinone ether ketone), poly(2,6-

dimethyl-1,4-phenylene oxide), and poly(vinyl alcohol) grafted with (2,3-epoxypropyl) trimethylammonium chloride. Common quaternizing agents include alkyl iodides, trialkylamines,  $N,N,N',N'$ -tetramethylalkyl-1, $n$ -diamines, polyethyleneimine, 1,4-diazabicyclo-[2.2.2]-octane (DABCO), and 1-azabicyclo-[2.2.2]-octane. The final two of these have been used extensively; they contain  $\beta$ -hydrogen but their structures do not permit molecular conformations favored in the Hofmann elimination mechanism. Metal-cation-containing AEMs based on doping polymer films (e.g., polybenzimidazole (PBI), poly(vinyl alcohol) and its composites, and biocompatible chitosan) with NaOH/KOH(aq) are also being investigated, but the presence of mobile cations may introduce problems associated with precipitation of carbonate salts.

Ionic conductivities of AEMs are generally lower than those of comparable PEMs. This is not surprising as the solution mobility of  $\text{OH}^-$  is one third to one half of that of a  $\text{H}^+$  (depending on the environment and if there  $-\mu_o \times 10^4 / \text{cm}^2 \text{V}^{-1} \text{s}^{-1} = 20.64$  for  $\text{OH}^-(\text{aq})$  anions and 36.23 for  $\text{H}^+(\text{aq})$  cations at 298 K) [1, 43]. One strategy for enhanced ionic conductivities is to increase the ion-exchange capacity (IEC) via synthetic methodology, but this often leads to a decrease in the mechanical strength due to excessive water uptakes. Another strategy is to synthesize tailored membranes that will exhibit hydrophilic(ionic)-hydrophobic(nonionic) phase segregation and continuous ionic domains, which is hypothesized to increase ionic conductivities [44, 45].

Recent intensive studies have, however, been reported to lead to AEMs with high ionic conductivities, reportedly comparable to Nafion<sup>®</sup>. These promising AEMs [11, 45–51] are still to be evaluated in AMFCs. Most hydrocarbon AEMs are soluble in various solvents, which is potentially useful for the formulation of alkaline ionomers required for the preparation of high-performance membrane electrode assemblies (MEAs). If the conductive properties reported can be translated into high power outputs, then AMFC performances comparable to those of PEMFCs can be expected in the near future.

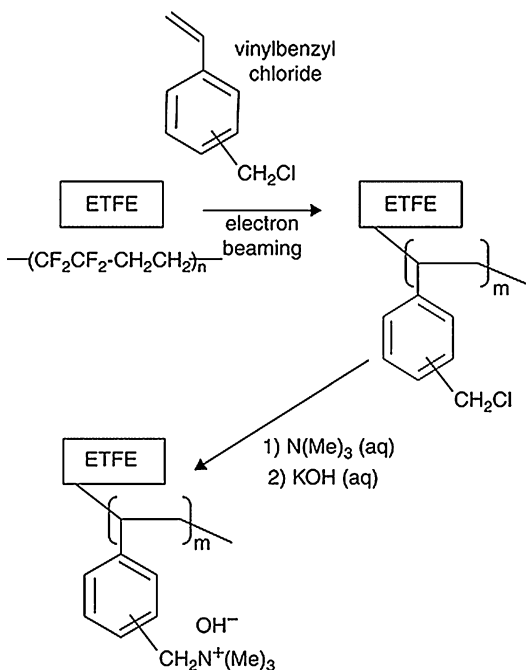
## Synthetic Routes to AEMs

The preparation of applicable AEMs involves a compromise between the properties of the membrane, such as the chemical and thermal stability, ion-exchange capacity (IEC), ion conductivity, mechanical properties, water uptake, and dimensional stability. In general, alkaline anion-exchange polymer electrolytes can be polymerized directly from functionalized monomers, polymerized from monomers with subsequent functionalization or by functionalizing a commercially available polymer. The backbone of the polymer is usually selected for its good chemical and thermal stability and, therefore, typically includes aromatic rings and/or a degree of fluorination: typical polymer classes include polysulfones and polyetherketones, polyimides, poly(phenylene), poly(phthalazinone ether sulfone ketone), polyepichlorohydrin homopolymer, polybenzimidazole (PBI), poly(phenylene oxide), radiation-grafted copolymers, inorganic-organic hybrids, and even perfluorinated membranes such as Nafion. The active functional groups are commonly quaternary ammonium type ( $-\text{NR}_3^+$ ) with a clear preference for trimethylammonium ( $-\text{N}(\text{CH}_3)_3^+$ ) groups ( $\text{pK}_a(\text{H}_2\text{O}) = 9.8$ ).

A suitable AEM will have a high ion-exchange capacity, high ionic conductivity, and thermochemical stability, but will exhibit a low degree of swelling on hydration. There are several general synthetic methodologies for the preparation of AEMs [52, 53]. Fluorine-containing polymers generally show higher thermal stabilities than hydrocarbon polymers. AEMs based on a poly(arylene ether sulfone) containing fluorine atoms show high ionic conductivities (63  $\text{mS cm}^{-1}$  in  $\text{CO}_3^{2-}$  form at 70 °C) [53]; this is a key result as  $\text{CO}_3^{2-}$  anions have dilute solution mobilities that are less than 33% of that of  $\text{OH}^-$  anions. (It is rare to see  $\text{CO}_3^{2-}$  conductivities above 30  $\text{mS cm}^{-1}$ .)

Irradiation of polymer films (and powders, etc.) using X-rays,  $\gamma$ -rays, or electron beams (as at Surrey, see previous section) is a flexible way to introduce various functional groups on the polymer backbones (Scheme 2). A wide range of





**Alkaline Membrane Fuel Cells, Scheme 2** The radiation-grafting of vinylbenzyl chloride onto ETFE and subsequent amination and alkali-exchange, yielding alkaline anion-exchange membranes (RG-AEMs)

chemically and thermal stable polymers, such as ETFE and FEP, can be chosen as the base films for the production of AEMs. Additionally, there is a wide choice of functional monomers available that can be used to introduce ion-exchange groups into the grafted polymeric chains.

A common strategy in the synthesis of AEMs is to introduce halogen alkyl groups onto the backbone or side chains of the polymer via chloroalkylation, fluorination, bromination, or chlorination, followed by amination/quaternization and finally ion exchange. Highly carcinogenic chloromethylethers have traditionally been used as the chloroalkylation agent but safer strategies have been introduced, for example, the chloro methylation agent is generated in situ (e.g., [44, 54–56]). An alternative strategy is the prior introduction of tertiary amine groups into the polymer, followed by quaternization.

The easiest synthetic route is to use inert polymers (as above) doped with concentrated  $KOH(aq)$  (as above): polybenzimidazole (PBI

[57–61], poly(vinyl alcohol) (PVA) [44], composite polymers such as PVA/hydroxyapatite (PVA/HAP) [62], quaternized-PVA/alumina (QPVA/ $Al_2O_3$ ) [63], PVA/titanium oxide (PVA/ $TiO_2$ ) [64, 65], chitosan and cross-linked chitosan [66–68], copolymers of epichlorohydrin and ethylene oxide [69], and cross-linked PVA/sulfosuccinic acid (10 wt.% SSA) [70] have all been doped with  $KOH$  and used as AEMs. Patent US5569559 [71] describes the use of polar polymers (most preferred being polyethylene oxide) doped with alkaline metal hydroxides (such as  $KOH$ ), alkaline earth metal hydroxides or ammonium hydroxides such as tetrabutylammonium hydroxide; PBI doped with  $KOH$  showed the highest ionic conductivity, comparable to Nafion<sup>®</sup> (a standard acidic proton-exchange membrane, PEM). All of these materials could, however, lead to carbonate precipitates.

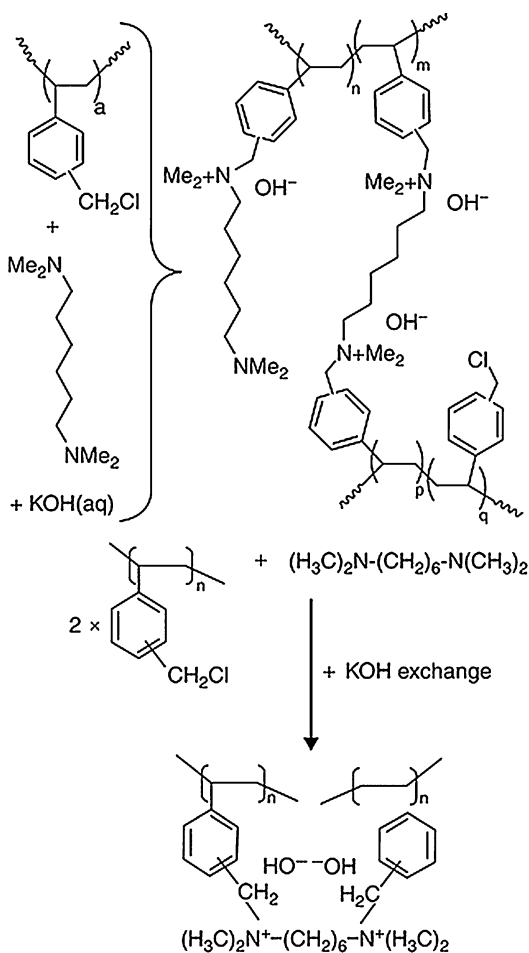
Anion-exchange polymers that contain methacrylate, ester, amide, or other carbonyl ( $C=O$  double bond) functional groups show low stabilities in alkali as these functional groups are highly reactive to nucleophiles such as  $OH^-$ .

## Development of Alkaline Ionomers

Alkaline analogues to the oligomeric perfluoro-sulfonic acid dispersions used to produce optimized ionic contact between the catalyst reaction sites and the PEM in PEMFCs have yet to be convincingly developed and this has resulted in the use of nonideal strategies for the fabrication of alkaline MEAs: the use of Nafion dispersions (acidic, cation exchanging); concepts involving adsorbed potassium hydroxide, and quaternized copolymers made from 4-vinylpyridine monomer at the electrode-AEM interface. Polysulfone-based alkaline ionomers that are compatible with polysulfone AEMs have been developed by various teams. On the commercial front, it has been reported that Fumatech has developed a ionomer concept for use with their commercial Fumasep<sup>®</sup>FAA AEMs, that uses two precursors that react to form a cross-linked polymer when mixed together, and Tokuyama's alkaline

ionomers can be deposited from solution (designated A3 or AS-4) and are chemically compatible with Tokuyama's fuel cell AEMs.

Surrey developed an alkaline ionomer (SION1, Scheme 3) for MEA fabrication, with the objective of developing a system that would allow the testing of different AEMs and electrodes in AMFCs [72]; without this alkaline ionomer, the performances were too low for satisfactory testing. That alkaline ionomer also allowed for the operation of fuel cells in metal-cation-free mode, in contrast to the possible use of doped polymers containing alkali metal hydroxides. An alkaline MEA that was deliberately converted to the  $\text{CO}_3^{2-}$



**Alkaline Membrane Fuel Cells, Scheme 3** The formation of SION1 alkaline ionomer (anionomer) by cross-linkage of poly(vinylbenzyl chloride) with tetramethylhexanediamine (TMHDA)

form operated as well as an  $\text{OH}^-$  form MEA; even more interestingly, the  $\text{CO}_3^{2-}$  content of the carbonated MEA decreased during fuel cell operation with air (containing  $\text{CO}_2$ ) at the cathode. The SION1 ionomer contains  $\beta$ -hydrogen atoms and, therefore, allows the Hofmann elimination degradation mechanism to operate, limiting the thermal stability to below ca.  $60^\circ\text{C}$ . Surrey is currently developing a next-generation  $\beta$ -hydrogen-free alkaline ionomers deposited from aqueous solutions (Patent GB 0814652.4).

Many researchers have reported that alkaline polymers with hydrocarbon backbones can be dissolved in solvents such as DMF, DMAc, and DMSO [47–49, 54, 73, 74], and this allows their use as the ionomer for the preparation of MEAs. Zhuang et al. [73, 75] used a quaternary ammonium polysulfone (QAPS) which can be dissolved in DMF and used as the ionomer; the QAPS polymer (in  $\text{OH}^-$  form:  $\text{IEC} = 1.08 \text{ mmol g}^{-1}$ ) was used to fabricate the membrane, while a QAPS film ( $\text{OH}^-$  form:  $\text{IEC} = 1.18 \text{ meq g}^{-1}$ ) was used as the ionomer.

The development of alkaline ionomers is one of the major challenges for the development of high-performance alkaline membrane containing fuel cells. In state-of-the-art AMFC technology, the role of the ionomer has not been fully investigated or understood; alkaline ionomer solutions/dispersions, comparable to the Nafion dispersions used in PEMFCs, remain highly sought after.

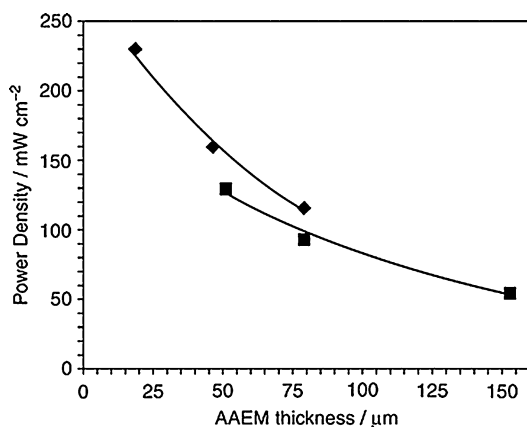
## AMFCs with $\text{H}_2$ as Fuel

Fundamental studies at Surrey revealed the following [31–34]:

*A major source of performance loss is the mass transport of  $\text{H}_2\text{O}$  to the ORR reaction sites.* S80/S50/S20 radiation-grafted RG-AEMs, Solvay's Morgane<sup>®</sup>-ADP, and Tokuyama's A201 were evaluated in  $\text{H}_2/\text{O}_2$  fuel cells at Surrey using both commercial (prefabricated) and in-house produced electrodes containing SION1 ionomer [72]. As discussed earlier, water is required as a stoichiometric reactant for the ORR at the cathode when using AEMs (unlike in PEMFCs).

The primary source of H<sub>2</sub>O to the cathode appears to be the back transport of the H<sub>2</sub>O electro-generated at the anode. Even with the use of fully hydrated gas supplies, evidence for this was that enhanced back transport of H<sub>2</sub>O from the anode, and therefore superior performances, was observed with thinner AEMs: beginning-of-life peak geometric power densities,  $P_{\text{peak}}$ , of 54 → 94 → 130 mW cm<sup>-2</sup> were recorded using 154 → 78 → 51 μm thick AEMs, respectively, under identical test conditions (less than 20 mW cm<sup>-2</sup> was obtained with the 230 μm thick Tokuyama AHA AEM – not developed for use in fuel cells) (Fig. 2). The commercial Pt/C (20% mass – 0.5 mg<sub>Pt</sub> cm<sup>-2</sup> loading)-containing Type A carbon cloth prefabricated cathodes (E-Tek division of BASF) that were used contained PTFE binder (current commercially available fuel cell electrodes are optimized for use with PEMs and not for AEMs) and it was suspected that this restricted the transport of the H<sub>2</sub>O supplied in the humidified oxygen supply to the reaction sites.

Achieving an optimal MEA is still hindered by the available anionomers. Switching to the use of Toray carbon paper commercial electrodes (435 μm thick containing Pt/C (20% mass) catalyst at 0.5 mg<sub>Pt</sub> cm<sup>-2</sup> loading and containing



**Alkaline Membrane Fuel Cells, Fig. 2** Variation in power density for H<sub>2</sub>/O<sub>2</sub> AMFCs as a function of fully hydrated RG-AEM thickness. The cells contained ETFE-derived RG-AEMs. All electrodes were treated with SION1 ionomer and utilized E-TekPt/C (20% mass) catalyst-loaded carbon cloth (squares) or carbon paper (diamonds) supports

PTFE binder – supplied by E-Tek division of BASF) at both the anode and cathode led to an increase in obtainable power densities (Fig. 2).  $P_{\text{peak}} = 230 \text{ mW cm}^{-2}$  and a maximum  $i$  at full discharge of  $1.3 \text{ A cm}^{-2}$  was obtained in a H<sub>2</sub>/O<sub>2</sub> fuel cell at 50 °C with S20 (20 μm). A  $P_{\text{peak}} = 260 \text{ mW cm}^{-2}$  was obtained at 50 °C with Tokuyama A201 using SION1-treated electrodes. Fully satisfactory MEA lamination cannot, however, be achieved with SION1 alkaline ionomer and there are still considerable, variable, contact resistances.

Pt-free electrodes are viable in AMFCs (more evidence is given below). Ag/C (60% mass, 4 mg<sub>Ag</sub> cm<sup>-2</sup>) performed well when used as a cathode catalyst (Ag/C catalyst performed poorly in the cathode of a PEMFC). Open circuit voltages ( $V_{\text{OC}}$ ) were normally in the range 1.0–1.1 V with Solvay ADP and Pt/C electrodes (ca. 100 mV higher than obtained with Nafion-115 PEMFCs); a drop of 100 mV in  $V_{\text{OC}}$  was observed when Pt was replaced with Ag at the cathode.

The activity of the carbon supports needs to be evaluated for each catalyst material to be tested. An important finding was that metal-free Vulcan XC-72R (i.e., carbon black only) cathodes produced significant currents ( $P_{\text{peak}} = 22 \text{ mW cm}^{-2}$  and  $V_{\text{OC}} = 0.88 \text{ V}$  with Solvay ADP at 50 °C). Carbons reduce O<sub>2</sub> primarily through a 2e<sup>-</sup> mechanism at high pH producing hydroperoxide anions (HO<sub>2</sub><sup>-</sup>), which may form highly reactive hydroxyl radical species.

Other groups have been investigating nonradiation-grafted AEMs. A fully non-PGM-catalyst-containing metal-cation-free alkaline membrane fuel cell was first reported by the team at Wuhan University [73], for an AMFC containing a QA-polysulfone AEM and an MEA that did not contain any PGM catalysts; a  $P_{\text{peak}} = 52 \text{ mW cm}^{-2}$  at 60 °C (open circuit voltage, OCV,  $V_{\text{OC}} = 0.94 \text{ V}$ ) was obtained using Ni-based anode catalyst and a Ag cathode catalyst.

Polysulfone-based AEMs (see earlier) have been tested in H<sub>2</sub>/air fuel cells at 60 °C using a polysulfone alkaline ionomer (dew point of the gases was 55 °C). A  $P_{\text{peak}} = 28 \text{ mW cm}^{-2}$  at  $V_{\text{cell}} = 0.47 \text{ V}$  was obtained with Pt/C (40% mass, Johnson Matthey) with loadings of 0.5

$\text{mg}_{\text{Pt}} \text{cm}^{-2}$ .  $P_{\text{peak}} = 30 \text{ mW cm}^{-2}$  at  $V_{\text{cell}} = 0.42 \text{ V}$  was obtained when the cathode contained a Ag/C catalyst (40% mass, E-Tek) at a loading of  $2 \text{ mg}_{\text{Ag}} \text{cm}^{-2}$ . OCVs were 100 mV lower with Ag compared to Pt, which correlates with the results above. A  $P_{\text{peak}} = 365 \text{ mW cm}^{-2}$  at  $0.4 \text{ V}$  ( $V_{\text{OC}} = 1.04 \text{ V}$ ,  $r = 0.152 \Omega \text{ cm}^2$ ) was reported at the 214th Meeting of the Electrochemical Society in 2008 by Wang's team at Penn State University, using Tokuyama's A901 (10  $\mu\text{m}$ ) AEM and AS-4 alkaline ionomer (IEC =  $1.3 \text{ meq g}^{-1}$ ) at  $50 \text{ }^\circ\text{C}$  in a  $\text{H}_2/\text{O}_2$  AMFC with  $0.4 \text{ mg cm}^{-2}$  Pt/C catalysts; these values dropped to  $212 \text{ mW cm}^{-2}$  ( $V_{\text{OC}} = 1.02 \text{ V}$ ,  $r = 0.19 \Omega \text{ cm}^2$ ) when the  $\text{O}_2$  at the cathode was replaced with purified air ( $<1 \text{ ppm CO}_2$ ) and the  $P_{\text{peak}}$  dropped to  $113 \text{ mW cm}^{-2}$  ( $r = 0.22 \Omega \text{ cm}^2$ ). The higher value represents the highest  $\text{H}_2/\text{O}_2$  AMFC performance publicly reported to date.

KOH-doped membranes (see earlier) represent metal-cation-containing AEMs. A  $\text{H}_2/\text{O}_2$  fuel cell has been tested with a KOH-doped PBI membrane ( $t = 40 \mu\text{m}$ ) at  $50 \text{ }^\circ\text{C}$  yielding an  $i = 620 \text{ mA cm}^{-2}$  at  $V_{\text{cell}} = 0.60 \text{ V}$  ( $P = 370 \text{ mW cm}^{-2}$ ) [60]. This performance was similar to that of the same apparatus with a Nafion-117 PEM and also, remarkably, with a PBI AEM doped with both KOH and  $\text{K}_2\text{CO}_3$ . The question of the long-term stability and leaching out of the KOH (if any) remains to be fully addressed for this class of AEM, as does the issue of potential for carbonate/bicarbonate precipitation.

Gu and Yan et al. [76] developed an ionomer, tris(2,4,6-trimethoxyphenyl) polysulfone-methylene quaternary phosphonium hydroxide (TPQPH), which is soluble in low boiling point and water-soluble solvents such as methanol, ethanol, and *n*-propanol. The solubility of this kind of ionomer could be ideal for use in AMFC MEAs;  $196 \text{ mW cm}^{-2}$  was achieved at  $80 \text{ }^\circ\text{C}$  ( $\text{H}_2/\text{O}_2$  gases supplied at 250 kPa back-pressure) using this phosphonium ionomer with a 70  $\mu\text{m}$  thick FAA commercial membrane (Fumatech GmbH) as the AEM. A maximum power of more than  $250 \text{ mW cm}^{-2}$  was obtained in a  $\text{H}_2/\text{O}_2$  fuel cell at  $50 \text{ }^\circ\text{C}$  with a 50  $\mu\text{m}$  AEM and gas back-pressures of 250 kPa. The presence of methoxy ( $-\text{OCH}_3$ ) groups on the aromatic rings that are connected to the phosphonium ion centers seems essential to adequate chemical stability.

## The Application of AEMs in Other Fuel Cell Types

The utility of AEMs as potential electrolytes in fuel cells arises not only from the prospects for the use of non-Pt-group metal (non-PGM) catalysts and cheaper fuel cell components (less corrosive environment) but also from potential for use of alternative fuels.

Alcohols and diols, sodium borohydride ( $\text{NaBH}_4$ ), and hydrazine ( $\text{H}_2\text{NNH}_2$ ) have all been used directly as fuels in AMFCs. Patents [77, 78] introduced more fuels including hydrated hydrazine ( $\text{NH}_2\text{NH}_2 \cdot \text{H}_2\text{O}$ ), hydrazine carbonate ( $(\text{NH}_2\text{NH}_2)_2\text{CO}_2$ ), hydrazine sulfate ( $\text{NH}_2\text{NH}_2 \cdot \text{H}_2\text{SO}_4$ ), monomethyl hydrazine ( $\text{CH}_3\text{NHNH}_2$ ), ammonia ( $\text{NH}_3$ ), heterocycles such as imidazole and 1,3,5-triazine and 3-amino-1,2,4-triazole, and hydroxylamines such as hydroxylamine ( $\text{NH}_2\text{OH}$ ) and hydroxylamine sulfate ( $\text{NH}_2\text{OH} \cdot \text{H}_2\text{SO}_4$ ); the catalysts were co-based for the fuel side (anode) and Ag/C, Pt/C and Ni/C for the oxygen reduction side (cathode). EP2133946 [79] disclosed the use of transition metals as catalysts in AMFCs. There are numerous reports on the use of non-Pt catalyst, such as  $\text{MnO}_2$  [58], Ag/C [74, 75, 79], Au/C [80], FeTPP/BPC (Black Pearl Carbon) [81], CoPPyC [82], FeCo-CNF (Carbon Nanofiber) [83], CoFeN/C-HLH [84] in AMFC cathodes and Cr-decorated Ni/C [73], Fe-Co-Ni/C [85, 86] at anodes.

Zhuang et al. conducted a feasibility analysis of the use of AEMs in DMFCs [87]; this important study concentrated on the thermodynamic disadvantages versus kinetic advantages of such cells by considering the reactions taking place in aqueous solutions and the authors concluded that the thermodynamic voltage losses due to the pH difference across the AEM would be approximately canceled out by the kinetic voltage gains. Ogumi et al. studied direct alcohol fuel cells (methanol and ethylene glycol) with a commercial AEM (Tokoyama AHA, thickness  $\approx 240 \mu\text{m}$ ) [39]. Solutions of ethylene glycol and methanol were made to a concentration of  $1 \text{ mol dm}^{-3}$  dissolved in KOH (aq,  $1 \text{ mol dm}^{-3}$ ), and so the system was not metal-cation-free (common with other AMFCs obtaining reasonable power levels with alcohols as fuels). Cell voltages were around

100 mV higher for ethylene glycol compared to methanol. This fuel cell is *not* quite an alkaline analogue of an acid membrane DMFC, as the authors used alkaline fuel solution. No indication was given concerning completeness of oxidation of the ethylene glycol to  $\text{CO}_2$  and  $\text{H}_2\text{O}$ . Yu and Scott also reported the operation of a direct methanol alkaline fuel cell, with platinized titanium mesh anodes ( $1.5 \text{ mg cm}^{-2}\text{Pt/Ti}$ ) and a commercial alkaline anion-exchange membrane (Morgane ADP membrane from Solvay SA) [88].

It has been proposed that ammonia would make a good energy vector/carrier [6] and an indirect fuel for a hydrogen fuel cell; ammonia is environmentally benign (it is already used as a fertilizer and neutralizes acid rain), already available cheaply, contains 50% more H per  $\text{dm}^3$  than liquid hydrogen, and is a liquid at much lower pressures (8–9 bar); it also has the advantage of a strong smell, allowing the easier location of leaks. Cracking ammonia to form hydrogen free of traces of ammonia for use in traditional PEMFCs requires temperatures of above  $900 \text{ }^\circ\text{C}$ ; PEMFCs cannot tolerate any  $\text{NH}_3$  contamination. An advantage of AFCs is that they will tolerate low levels of  $\text{NH}_3$ , and so cracking can be undertaken at lower temperatures; this has yet to be explored using AMFC approaches.

## A Brief Overview of the Patent Literature

Zeng and Varcoe have recently reviewed in depth the patent literature concerning AEMs [89]. A small number of patents of direct interest to application of AEMs in AMFCs are considered in this section.

In the area of novel AEMs:

- Patents relating to the application of radiation-grafted ion-exchange membranes in fuel cells have been granted to Scherer et al. [89] and to Stone and Steck [90, 91]. These patents mention the functionalization of base polymers with quaternary ammonium groups to yield alkaline polymers. The use of fluorine-substituted styrenic monomers is also claimed to improve membrane chemical stability when utilized in fuel cells (removal of undesired and reactive C-H bonds).

- Fauvarque was granted a patent on aqueous alkaline solid electrolyte based around poly-ether polymer matrices [92].
- Yao et al. were granted related patents on alkaline polymers containing alkyl quaternary ammonium salts, nitrogen containing heterocyclic quaternary ammonium salts, and metal hydroxide salts for potential applications in alkaline batteries and fuel cells [93–95].

In the area of device architecture:

- Jaouen patented a novel cathode structure for a solid polymer fuel cell [96]; that cathode structure consisted of a solid polymer anion-exchange membrane surrounding the catalyst particles (entirely within the cathode structure), which was in contact (surrounded) with a cation-conducting polymer membrane.
- Lu and Zhuang were granted a patent on alkaline-resin-containing fuel cells with direct fuelling with liquid organic fuels [97].
- Related patents from Divisek describe the invention of a methanol fuel cell utilizing an anion-exchange membrane [98, 99].

## Future Directions and Research Challenges

There are a number of research challenges that must be overcome before AEMs can be successfully applied in pre-commercial AMFCs:

1. As a priority and to complement *ex situ* stability measurements, AEMs must be evaluated in  $\text{H}_2/\text{O}_2$ ,  $\text{H}_2/\text{air}$ , and methanol/air fuel cells for several thousand hours to ensure adequate *in situ* membrane stability and assess the effect of and level of  $\text{CO}_2^-/\text{HCO}_3^-$  formation. The effect of adding alkali to the methanol solution must also be thoroughly investigated over long timescales.
2. AEMs must be created with higher conductivities, to ensure good fuel cell performances at high current densities. It should be noted, however, that with application of an alkaline DMFC as a power source for portable devices,



an overriding priority is maximizing the energy density of the fuel and fuel efficiency (cell voltage). These DMFCs will be operated at low-to-medium current densities (higher efficiencies), where electrode overpotentials are the dominant cause of voltage losses.

3. It is essential that a solubilized form of an alkaline anion-exchange polymer be developed to improve the interface between the electrodes and the AEM electrolyte. Success in this effort will decrease MEA resistances. A water-based soluble form which can be rendered water insoluble when cast would be preferred, as there are safety concerns (primarily with industrial scale production) about using organic solvents near finely dispersed (pyrophoric) metal catalysts (unsupported or supported on carbon).
4. If AEMs are to be applied to fuel cells for other applications (such as automotive power etc.), more temperature stable AEMs must be developed. Operation of alkaline-membrane-based fuel cells at elevated temperature would reduce thermodynamic voltage losses due to pH differences across the AEM and would also improve the electrokinetics. Successful, stable over the long term, and being operational at elevated temperatures, all would allow application in fuel cells for the automotive mass market.
5. If AEMs are shown to be stable in fuel cells over thousands of hours, an in-depth investigation into effective and cheaper non-noble metal catalysts (e.g., Ni, Ag etc.) is indicated. There would also be a greater chance of finding methanol-tolerant catalysts for use in the cathodes than in related PEM-based DMFCs.
6. Finally, removal of fluorine from the polymer systems would be of interest to enhance the environmental credentials of the technology (facilitating easier disposal) and reduce costs. The substitution of fully fluorinated FEP with non-fluorinated LDPE is feasible. While oxidative radical degradation is a problem at the cathode and anode (via oxygen diffusion through the membrane) with non-fluorinated PEMs, it has been shown using electron paramagnetic resonance (EPR) studies that such degradation is prevented in highly alkaline (pH > 11.7) conditions pertinent to AEMs [100–102].

## Bibliography

### Primary Literature

1. Varcoe JR, Slade RCT (2005) Prospects for alkaline anion-exchange membranes in low temperature fuel cells. *Fuel Cell* 5:189–200
2. Zeng R, Varcoe JR (2011) Alkaline anion exchange membranes for fuel cells – a patent review. *Recent Pat Chem Eng* 4:93–115
3. Schulze M, Gülzow E (2004) Degradation of nickel anodes in alkaline fuel cells. *J Power Sources* 127:252–263
4. Wagner N, Schulze M, Gülzow E (2004) Long term investigations of silver cathodes for alkaline fuel cells. *J Power Sources* 127:264–272
5. McLean GF, Niet T, Prince-Richard S, Djilali N (2002) An assessment of alkaline fuel cell technology. *Int J Hydrog Energy* 27:507–526
6. Cifrain M, Kordesch KV (2004) Advances, aging mechanism and lifetime in AFCs with circulating electrolytes. *J Power Sources* 127:234–242
7. Gülzow E, Schulze M (2004) Long-term operation of AFC electrodes with CO<sub>2</sub> containing gases. *J Power Sources* 127:243–251
8. Zeng R, Poynton SD, Kizewski JP, Slade RCT, Varcoe JR (2010) A novel reference electrode for application in alkaline polymer electrolyte membrane fuel cells. *Electrochem Commun* 12:823–835
9. Yanagi H, Fukuta K (2008) Anion exchange membrane and ionomer for alkaline membrane fuel cells (AMFCs). *Electrochem Soc Trans* 16:257–262
10. Kizewski JP, Mudri NH, Zeng R, Poynton SD, Slade RCT, Varcoe JR (2010) Alkaline electrolytes and reference electrodes for alkaline polymer electrolyte membrane fuel cells. *Electrochem Soc Trans* 33:27–35
11. Yan JL, Hickner MA (2010) Anion exchange membranes by bromination of benzylmethyl-containing poly(sulfone)s. *Macromolecules* 43:2349–2356
12. Adams LA, Poynton SD, Tamain C, Slade RCT, Varcoe JR (2008) A carbon dioxide tolerant aqueous-electrolyte-free anion-exchange membrane alkaline fuel cell. *Chem Sus Chem* 1:79–81
13. Zagorodni AA, Kotova DL, Selemenev VF (2002) Infrared spectroscopy of ion exchange resins: chemical deterioration of the resins. *React Funct Polym* 53:157–171
14. Neagu V, Bunia I, Plesca I (2000) Ionic polymers – VI. Chemical stability of strong base anion exchangers in aggressive media. *Polym Degrad Stab* 70:463–468
15. Sata T, Tsujimoto M, Yamaguchi T, Matsusaki K (1996) Change of anion exchange membranes in an aqueous sodium hydroxide solution at high temperature. *J Membr Sci* 112:161–170
16. Soda T, Kaisha K (1972) Anion exchange membranes and their production. GB Patent 1401997
17. Hansen RD, Wheaton RM (1966) Separation of acid from polymers by dialysis with anion exchange membrane. US Patent 3244620



18. Imoto R, Kosaka Y, Shimizu A (1966) Process for manufacturing anion-exchange membranes from a graft copolymer of SBR and a vinylpyridine reacted with an epoxy resin. US Patent 3258435
19. Hansen RD, Wheaton RM (1966) Separation of acid by dialysis with anion-exchange membranes. US Patent 3272737
20. Süser A (1973) Preparation of anion exchange membranes from cellulose sheets. US Patent 3714010
21. Scott R, Moulton T, Gough (1990) Anion exchange membranes. Patent EP0382439
22. Altmeier P (1995) Stark basische anionenaustauschermembranen und verfahren zu deren herstellung. Patent WO9506083
23. Altmeier P (1998) Strongly alkaline anion exchange membranes and process for producing the same. US Patent 5746917
24. Ehrikhovich KJ, Viktorovna SN, Aleksandrovich FJ, Semenovich GS, Mikhajlovich AJ, Vladimirovna SI, Alekseevna JN, Fedorovich TS (1997) Method for production of anion-exchange membranes having high penetrability to chloride ion. Patent RU2074204
25. Jurevich TD (2007) Method for modifying anion-exchange membranes MA-40. Patent RU2303835
26. Aminabhavi T, Kulkarni PV, Kariduraganavar MY (2009) Ion exchange membranes, methods and processes for production thereof and uses in specific applications. US Patent 7544278
27. Danks TN, Slade RCT, Varcoe JR (2002) Comparison of PVDF- and FEP-based radiation-grafted alkaline anion-exchange membranes for use in low temperature portable DMFCs. *J Mater Chem* 12:3371–3373
28. Danks TN, Slade RCT, Varcoe JR (2003) Alkaline anion-exchange radiation-grafted membranes for possible electrochemical application in fuel cells. *J Mater Chem* 13:712–721
29. Herman H, Slade RCT, Varcoe JR (2003) The radiation-grafting of vinylbenzyl chloride onto poly(hexafluoropropylene-co-tetrafluoroethylene) films with subsequent conversion to alkaline anion-exchange membranes: optimisation of the experimental conditions and characterization. *J Membr Sci* 218: 147–163
30. Tzanetakis N, Varcoe J, Slade RS, Scott K (2003) Salt splitting with radiation grafted PVDF anion-exchange membrane. *Electrochem Commun* 5:115–119
31. Tzanetakis N, Varcoe JR, Slade RCT, Scott K (2005) Radiation-grafted PVDF anion exchange membrane for salt splitting. *Desalination* 174:257–265
32. Slade RCT, Varcoe JR (2005) Investigations of conductivity in FEP-based radiation-grafted alkaline anion-exchange membranes. *Solid State Ionics* 176: 585–597
33. Varcoe JR, Slade RCT (2006) An electron-beam-grafted ETFE alkaline anion-exchange membrane in metal-cation-free solid-state alkaline fuel cells. *Electrochem Commun* 8:839–843
34. Varcoe JR, Slade RCT, Yee ELH, Poynton SD, Driscoll DJ, Apperley DC (2007) Poly(ethylene-co-tetrafluoroethylene)-derived radiation-grafted anion-exchange membrane with properties specifically tailored for application in metal-cation-free alkaline polymer electrolyte fuel cells. *Chem Mater* 19:2686–2693
35. Chempath S, Einsla BR, Pratt LR, Macomber CS, Boncella JM, Rau JA, Pivovar BS (2008) Mechanism of tetra alkyl ammonium head group degradation in alkaline fuel cell membranes. *J Phys Chem C* 112:3179–3182
36. Piana M, Boccia M, Filpi A, Flammia E, Miller HA, Orsini M, Salusti F, Santiccioloi S, Ciardelli F, Pucci A (2010) H<sub>2</sub>/air alkaline membrane fuel cell performance and durability, using novel ionomer and non-platinum group metal cathode catalyst. *J Power Sources* 195:5875–5881
37. Li YS, Zhao TS, Liang ZX (2009) Performance of alkaline electrolyte-membrane-based direct ethanol fuel cells. *J Power Sources* 187:387–392
38. Kim JH, Kim HK, Hwang KT, Lee JY (2010) Performance of air-breathing direct methanol fuel cell with anion-exchange membrane. *Int J Hydrog Energy* 35:768–773
39. Matsuoka K, Iriyama Y, Abe T, Matsuoka M, Ogumi Z (2005) Alkaline direct alcohol fuel cells using an anion exchange membrane. *J Power Sources* 150: 27–31
40. Li YS, Zhao TS, Liang ZX (2009) Effect of polymer binders in anode catalyst layer on performance of alkaline direct ethanol fuel cells. *J Power Sources* 190:223–229
41. Fujiwara N, Siroma Z, Yamazaki SI, Ioroi T, Senoh H, Yasuda K (2008) Direct ethanol fuel cells using an anion exchange membrane. *J Power Sources* 185:621–626
42. Bunazawa H, Yamazaki Y (2008) Influence of anion ionomer content and silver cathode catalyst on the performance of alkaline membrane electrode assemblies (MEAs) for direct methanol fuel cells (DMFCs). *J Power Sources* 182:48–51
43. Marx D, Chandra A, Tuckerman ME (2010) Aqueous basic solutions: hydroxide solvation, structural diffusion, and comparison to the hydrated proton. *Chem Rev* 110:2174–2216
44. Hibbs MR, Hickner MA, Alam TM, McIntyre SK, Fujimoto CH, Cornelius CJ (2008) Transport properties of hydroxide and proton conducting membranes. *Chem Mater* 20:2566–2573
45. Robertson NJ, Kostalik HA IV, Clark TJ, Mutolo PF, Abruna HD, Coates GW (2010) Tunable high performance cross-linked alkaline anion exchange membranes for fuel cell applications. *J Am Chem Soc* 132:3400–3404
46. Tanaka M, Koike M, Miyatake K, Watanabe M (2010) Anion conductive aromatic ionomers containing fluorenyl groups. *Macromolecules* 43:2657–2659
47. Wang JH, Li SH, Zhang SB (2010) Novel hydroxide-conducting polyelectrolyte composed of a poly(arylene ether sulfone) containing pendant quaternary guanidinium groups for alkaline fuel cell applications. *Macromolecules* 43:3890–3896

48. Guo ML, Fang J, Xu HK, Li W, Lu XH, Lan CH, Li KY (2010) Synthesis and characterization of novel anion exchange membranes based on imidazolium-type ionic liquid for alkaline fuel cells. *J Membr Sci* 362:97–104
49. Wang JH, Zhao Z, Gong FX, Li SH, Zhang SB (2009) Synthesis of soluble poly(arylene ether sulfone) ionomers with pendant quaternary ammonium groups for anion exchange membranes. *Macromolecules* 42:8711–8717
50. Tripathi BP, Kumar M, Shahi VK (2010) Organic-inorganic hybrid alkaline membranes by epoxide ring opening for direct methanol fuel cell applications. *J Membr Sci* 360:90–101
51. Clark TJ, Robertson NJ, Kostalik HA IV, Lobkovsky EB, Mutolo PF, Abruna HD, Coates GW (2009) A ring-opening metathesis polymerization route to alkaline anion exchange membranes: development of hydroxide-conducting thin films from an ammonium-functionalized monomer. *J Am Chem Soc* 131:12888–12889
52. Shevchenko VV, Gumennaya MA (2010) Synthesis and properties of anion-exchange membranes for fuel cells. *Theor Exp Chem* 46:139–152
53. Varcoe JR, Poynton SD, Slade RCT (2009) In: Vielstich W, Gasteiger HA, Yokokawa H (eds) *Handbook of fuel cells – fundamentals, technology and applications, Advances in electrocatalysis, materials, diagnostics and durability*, vol 5. Wiley, Chichester, pp 322–336
54. Zhou J, Unlu M, Vega J, Kohl P (2009) Anionic polysulfoneionomers and membranes containing fluorenyl groups for anionic fuel cells. *J Power Sources* 190:285–292
55. Fang J, Shen PK (2006) Quaternized poly(phthalazinone ether sulfone ketone) membrane for anion exchange membrane fuel cells. *J Membr Sci* 285:317–322
56. Zeng QH, Liu QL, Broadwell I, Zhu AM, Xiong Y, Tu XP (2010) Anion exchange membranes based on quaternized polystyrene-block-poly(ethylene-ran-butylene)-block-polystyrene for direct methanol alkaline fuel cells. *J Membr Sci* 349:237–243
57. Hou HY, Sun GQ, He RH, Wu ZM, Sun BY (2008) Alkali doped polybenzimidazole membrane for high performance alkaline direct ethanol fuel cell. *J Power Sources* 182:95–99
58. Hou HY, Sun GQ, He RH, Sun BY, Jin W, Liu H, Xin Q (2008) Alkali doped polybenzimidazole membrane for alkaline direct methanol fuel cell. *Int J Hydrog Energy* 33:7172–7176
59. Modestov AD, Tarasevich MR, Leykin AY, Filimonov VY (2009) MEA for alkaline direct ethanol fuel cell with alkali doped PBI membrane and non-platinum electrodes. *J Power Sources* 188:502–506
60. Xing B, Savadogo O (2000) Hydrogen oxygen polymer electrolyte membrane fuel cells (PEMFCs) based on alkaline-doped polybenzimidazole (PBI). *Electrochem Commun* 2:697–702
61. Savadogo O (2004) Emerging membranes for electrochemical systems. Part II. High temperature composite membranes for polymer electrolyte fuel cell (PEFC) applications. *J Power Sources* 127:135–161
62. Yang CC, Lin CT, Chiu SJ (2008) Preparation of the PVA/HAP composite polymer membrane for alkaline DMFC application. *Desalination* 233:137–146
63. Yang CC, Chiu SJ, Chien WC, Chiu SS (2010) Quaternized poly(vinyl alcohol)/alumina composite polymer membranes for alkaline direct methanol fuel cells. *J Power Sources* 195:2212–2219
64. Yang CC, Chiu SJ, Lee KT, Chien WC, Lin CT, Huang CA (2008) Study of poly(vinyl alcohol)/titanium oxide composite polymer membranes and their application on alkaline direct alcohol fuel cell. *J Power Sources* 184:44–51
65. Yang CC (2007) Synthesis and characterization of the cross-linked PVA/TiO<sub>2</sub> composite polymer membrane for alkaline DMFC. *J Membr Sci* 288:51–60
66. Wan Y, Peppley B, Creber KAM, Bui VT, Halliop E (2006) Preliminary evaluation of an alkaline chitosan-based membrane fuel cell. *J Power Sources* 162:105–113
67. Wan Y, Creber KAM, Peppley B, Bui VT (2006) Chitosan-based electrolyte composite membranes II. Mechanical properties and ionic conductivity. *J Membr Sci* 284:331–338
68. Wan Y, Creber KAM, Peppley B, Bui VT (2006) Chitosan-based solid electrolyte composite membranes I. Preparation and characterization. *J Membr Sci* 280:666–674
69. Vassal N, Salmon E, Fauvarque JF (2000) Electrochemical properties of an alkaline solid polymer electrolyte based on P(ECH-co-EO). *Electrochim Acta* 45:1527–1532
70. Yang CC, Chiu SJ, Chien WC (2006) Development of alkaline direct methanol fuel cells based on cross-linked PVA polymer membranes. *J Power Sources* 162:21–29
71. Fauvarque JF (1996) Alkaline solid polymer electrolyte, electrode and electrochemical generator containing such as electrolyte. US Patent 5569559
72. Varcoe JR, Slade RCT, Lam How Yee E (2006) An alkaline polymer electrochemical interface: a breakthrough in application of alkaline anion-exchange membranes in fuel cells. *Chem Commun* 13:1428–1429
73. Lu SF, Pan J, Huang AB, Zhuang L, Lu JT (2008) Alkaline polymer electrolyte fuel cells completely free from noble metal catalysts. *Proc Natl Acad Sci* 105:20611–20614
74. Park JS, Park SH, Yim SD, Yoon YG, Lee WY, Kim CS (2008) Performance of solid alkaline fuel cells employing anion-exchange membranes. *J Power Sources* 178:620–626
75. Tang DP, Pan J, Lu SF, Zhuang L, Lu JT (2010) Alkaline polymer electrolyte fuel cells: principle, challenges, and recent progress. *Sci China Chem* 53:357–364
76. Gu S, Cai R, Luo T, Chen ZW, Sun MW, Liu Y, He GH, Yan YS (2009) A soluble and highly

- conductive ionomer for high-performance hydroxide exchange membrane fuel cells. *Angew Chem Int Ed* 48:6499–6502
77. Asazawa K, Yamada K, Tanaka H (2007) Fuel cell. Patent EP1843416
  78. Tanaka H, Yamada K, Asazawa K (2004) Fuel cell. Patent EP1460705
  79. Asazawa K, Yamada K, Tanaka H (2009) Fuel cell. Patent EP2133946
  80. Poynton SD, Kizewski JP, Slade RCT, Varcoe JR (2010) Novel electrolyte membranes and non-Pt catalysts for low temperature fuel cells. *Solid State Ionics* 181:219–222
  81. Ramaswamy N, Mukerjee S (2010) Electrocatalysis of oxygen reduction on non-precious metallic centers at high pH environments. *ECS Trans* 33:1777–1785
  82. Asazawa K, Yamamoto K, Yamada K, Tanaka H, Matsumura D, Tamura K, Nishihata Y, Atanassov P (2010) XAFS analysis of unpyrolyzedCoPPyC oxygen reduction catalyst for anion-exchange membrane fuel cells (AMFC). *Electrochem Soc Trans* 33:1751–1755
  83. Jeong B, Uhm S, Lee J (2010) Iron-cobalt modified electrospun carbon nanofibers as oxygen reduction catalysts in alkaline fuel cells. *Electrochem Soc Trans* 33:1757–1767
  84. Li XG, Popov BN, Kawahara T, Yanagi H (2010) Recent advances in non-precious metal catalysts for oxygen reduction reaction in fuel cells. *Electrochem Soc Trans* 33:1769–1776
  85. Takeguchi T, Takahashi H, Yamanaka T, Nakamura A, Ueda W (2010) Development of direct-ethanol anion-conducting solid alkaline inorganic fuel cell. *Electrochem Soc Trans* 33:1847–1851
  86. Nakamura A, Takahashi H, Takeguchi T, Yamanaka T, Wang Q, Uchimoto Y, Ueda W (2010) Effect of reduction temperature of Fe-Co-Ni/C catalyst on the solid alkaline fuel cell performance. *Electrochem Soc Trans* 33:1817–1821
  87. Wang Y, Li L, Hu L, Zhuang L, Lu J, Xu B (2003) A feasibility analysis for alkaline membrane direct methanol fuel cell: thermodynamic disadvantages versus kinetic advantages. *Electrochem Commun* 5:662–666
  88. Yu EH, Krewer U, Scott K (2010) Principles and materials aspects of direct alkaline alcohol fuel cells. *Energies* 3:1499–1528
  89. Scherer GG, Büchi FN, Gupta G (Paul Scherrer Institut, Switzerland) (1997) US Patent 5656386
  90. Stone C, Steck A (Ballard Power Systems Inc., Canada) (2002) US Patent 6359019
  91. Stone C, Steck A (Ballard Power Systems Inc., Canada) (2000) PCT Patent 01/58576
  92. Fauvarque J-F (CNAM Paris and Electricité de France) (1996) US Patent 5569559
  93. Yao W, Tsai T, Chang Y-M, Chen M (Reveo Inc., USA) (2001) US Patent 6183914
  94. Yao W, Tsai T, Chang Y-M, Chen M (Reveo Inc., USA) (2000) PCT Patent 00/16422
  95. Yao W, Tsai T, Chang Y-M, Chen M (Reveo Inc., USA) (2000) Patent EP1116291
  96. Jaouen F (ABB AB and Volvo, Sweden) (2002) PCT Patent 02/35633
  97. Lu J, Zhuang L (Wuhan University) (2003) Patent CN1402370
  98. Divisek J (Forschungszentrum Jülich, Germany) (2001) PCT Patent 01/61776
  99. Divisek J (Forschungszentrum Jülich, Germany) (2001) Patent EP1256142
  100. Yu J, Yi B, Xing D, Liu F, Shao Z, Fu Y, Zhang H (2003) Degradation mechanism of polystyrene sulfonic acid membrane and application of its composite membranes in fuel cells. *Phys Chem Chem Phys* 5:611–615
  101. Hübner G, Roduner E (1999) EPR investigation of HQ<sup>•</sup> radical initiated degradation reactions of sulfonated aromatics as model compounds for fuel cell proton conducting membranes. *J Mater Chem* 9:409–418
  102. Panchenko A, Dilger H, Möller E, Sixt T, Roduner E (2004) In situ EPR investigation of polymer electrolyte membrane degradation in fuel cell applications. *J Power Sources* 127:325–330



# Proton Exchange Membrane Fuel Cells: High-Temperature, Low-Humidity Operation

Steven J. Hamrock<sup>1</sup> and Andrew M. Herring<sup>2</sup>

<sup>1</sup>3M Fuel Cell Components Program, 3M Company, St Paul, MN, USA

<sup>2</sup>Department of Chemical and Biological Engineering, Colorado School of Mines, Golden, CO, USA

## Article Outline

Glossary

Definition of the Subject

Introduction

Proton-Exchange Membrane Fuel Cells

Electrolyte Membranes

PFSAs

Non-fluorinated or Hydrocarbon PEMs

Mechanical Stabilization of Low EW Membranes

Stabilizing Low EW Membranes Through

Chemical Modification of the Ionomer

Conductivity Enhancing/Stabilizing Inorganic

Additives

Electrodes

Future Directions

Bibliography

## Glossary

**Three-phase boundary** Region in the electrode where protons from the ionomer, electrons from the electrically conducting Pt and/or carbon, and reactant gases meet.

**Electrolyte membrane** A solid polymer ion-conducting membrane used in the center of the fuel cell membrane electrode assembly. Fuel cell electrocatalyst A catalyst that catalyzes either the oxidation of the fuel or the reduction of oxygen in a fuel cell.

**Equivalent weight** A measure of the acid content of an ionomer in the units of grams of polymer per mole of acid. Gas diffusion layer A carbon paper or cloth used as a current collector in fuel cells that can allow the passage of reactant gases and product water to and from the electrodes.

**Hydrogen oxidation reaction (HOR)** Electrochemical oxidation of H<sub>2</sub> at the anode.

**Ionomer** A copolymer of an ion-containing monomer and a nonionic monomer, typically not soluble in water. Membrane electrode assembly (MEA) An ion-conducting membrane sandwiched between two electrodes, an anode at which fuel oxidation occurs, and a cathode at which oxygen reduction occurs.

**Oxygen reduction reaction (ORR)** Electrochemical reduction of O<sub>2</sub> at the cathode. Flooding Liquid water collecting within the electrodes or current collectors, impeding the flow of gases to the catalyst surface.

**Perfluorinated sulfonic acid-containing polymer (PFSA)** A fluorinated sulfonic acid-containing ionomer. The most commonly used polymer in proton-exchange fuel cell membranes today.

## Definition of the Subject

Proton-exchange membrane fuel cells (PEMFCs) together with hydrogen represent an important storage and utilization technology for energy generated from renewable sources such as wind, solar, geothermal, or hydroelectric. This is due in part to their high energy density, low operating temperature, rapid start-up, modular design, flexibility of scale (a few watts to hundreds of kilowatts), and the absence of any point-of-use emissions. One barrier to commercialization and widespread acceptance of this technology is cost, a situation fairly common with the introduction of a new technology. Over the past decade, much work has been done, and very significant progress has been made, in bringing down the manufacturing cost of fuel cell systems [1].

Manufacturing processes have been optimized, volumes manufactured have increased, less expensive materials have been demonstrated, system efficiencies and power outputs have been increased, and the amount of precious metal catalyst required to generate a kilowatt of power has been reduced dramatically. All of these features have contributed to significant cost reductions. In the case of the precious metal catalysts, one of the major costs, a fuel cell stack that can generate enough power for an automobile can now be built using less than 30 g of platinum catalyst (about three to four times as much precious metal as is used in vehicles today), and the auto industry target of 10 g per vehicle appears within reach, and fuel cell vehicles are beginning to appear on our roads [2–4].

There is still work to be done. One area where important improvements are currently being made is in developing materials and constructions that address the need of today's PEMFC systems for high levels of humidification during operation. Materials currently used in PEMFCs require water for optimum performance. The electrolyte membranes require a relatively high level of hydration to provide sufficient conductivity for high performance. The electrodes in use also require water, both to provide ionic conductivity within the electrode and between the electrode and the electrolyte, as well as to maintain high electrocatalytic activity for high efficiency.

This thirst for water within the fuel cell requires strict water management, imposing limitations on the system design and adversely affecting manufacturing cost. Reactant gases entering the cell often must be humidified, adding the expense of humidification equipment and the parasitic power loss from its operation. Toyota has overcome these issues in the Mirai fuel cell car where the humidification equipment is eliminated [5]. This is achieved by the use of reinforced membranes that are 1/3 of the thickness of previous PEMs allowing back diffusion of product water from the cathode to the anode. These thinner membranes, when the inlet gases are introduced in counter flow, allow humidification of the inlet air from the water exhaust from the H<sub>2</sub> fuel side across the membrane. In addition, cell

temperature must be carefully controlled, as overheating can cause the cells to dry out, and so larger capacity cooling systems or radiators are required. This must be balanced with the fact that excess cooling or over humidification can cause water vapor formed in the electrochemical reaction to liquefy and collect within the electrodes or current collectors, impeding the flow of gases to the electrodes, a phenomenon called flooding. These requirements of careful control of humidification and temperature in fuel cells are not consistent with the need for a robust, inexpensive power source. New materials, including new membrane materials and catalysts that are less dependent on water, are needed to address this limitation.

## Introduction

For the last few years, there has been a growing, worldwide public focus on the increasing use of energy. One cannot pick up a newspaper or watch a television news program without being exposed to stories about the growth in the need for energy and the economic and environmental cost of that growth. Concerns about energy cost, energy security, and environmental factors (notably climate change) are driving many toward a shift to cleaner, cheaper, and more sustainable methods of generating and using energy. Much of this discussion has centered on the generation of energy, through the more efficient use of fossil fuels, nuclear energy generation, or renewables such as solar and wind energy. There is also growing recognition that if a movement to more sustainable methods of generating energy is to be made, a change in the way of transporting and storing energy will also be required.

An important area of energy technology that has received attention is the area of energy storage. Advanced batteries, capacitors, pumped hydroelectric, compressed air, flywheels, and other methods of energy storage are being considered [6]. As stated above, many believe that proton-exchange membrane fuel cells (PEMFCs) together with hydrogen represent an important energy storage and utilization technology for a number of application areas to allow the transition

away from fossil fuels. For this reason, significant research and investment in this technology have taken place over the last two decades. PEMFCs are beginning to find use in certain emerging applications, such as backup and primary power supplies for telecommunications, powering material handling fork trucks and providing electricity in remote, off-grid locations. While these represent relatively low volumes of systems in the greater energy market, they are an enabling first step, which is important for the introduction of fuel cells into a marketplace where they must compete with established technologies.

Another application of PEMFCs that has received much media attention and many research dollars over the past few years is transportation. Fuel cell-powered vehicles are now commercially available but still limited to 3000 commercial vehicles sold as of the summer of 2017; they are seen by many as the “end game” for renewable energy-powered vehicles [4]. Hydrogen fuel cells for powering automobiles are attractive for several reasons. Their high energy density can provide driving ranges of 250 miles or more, and compressed hydrogen tanks can be refilled easily in less than 5 min. This allows automakers to provide vehicles with essentially the same functionality as drivers enjoy today. However, the strict limitation on weight and volume in automotive applications, as well as the variation in power requirements during use, mean that these systems must run efficiently and reliably under a wide range of temperatures and humidification levels. The current limitations on temperature and humidification require excessively large cooling systems, or radiators, and humidifiers, which make meeting cost and efficiency targets more difficult.

In addition to the utility of hydrogen for storing energy from renewables such as wind or solar, the conversion of hydrocarbon feedstocks such as renewably derived methane or biomass into hydrogen can be an energy-efficient way of utilizing these resources. Currently, the least expensive route to hydrogen is from the reforming of natural gas, a process that initially produces a mixture of hydrogen gas, water, and carbon dioxide with a high carbon monoxide (CO) content. At the current relatively low temperature of operation of the

PEM fuel cell, 80 °C, CO is a severe poison to the Pt catalyst on the fuel cell anode. It is, therefore, necessary to reduce the CO content of the hydrogen fuel to a few parts per million by use of water gas shift reactors and a final gas cleanup stage that may be a hydrogen-selective membrane, pressure swing adsorption, or a preferential oxidation reactor. Each of these additional unit operations adds expense to the hydrogen production process. If hydrogen from the reforming of biomass is to be cost competitive, then the tolerance for CO on the catalyst must be improved so that less expensive less pure hydrogen can be utilized. One method of doing this is to operate the fuel cell at elevated temperature, e.g., a phosphoric acid fuel cell operating at >180 °C can tolerate a reformed hydrogen fuel containing 2% of CO. The operation of PEM fuel cells at elevated temperatures would, therefore, enable the utilization of biomass-derived hydrogen at a price competitive fuel cost.

For the rate of commercialization of PEMFCs to continue to increase, system costs must continue to decrease. One way to do this is to eliminate the fuel cell temperature and humidification requirements described above, allowing operation over a wide range of temperatures without the need for humidification of the incoming gases. To do this, new materials are needed. These include new ion-conducting materials for membranes and electrodes and new catalysts that can function with less water. This entry will review how these materials function in a PEMFC and some of the approaches to new materials that may overcome the humidification and temperature barriers.

## Proton-Exchange Membrane Fuel Cells

A fuel cell is an electrochemical cell that oxidizes a fuel and reduces oxygen to provide electrical energy. It is similar to an engine in that you provide fuel and air to generate energy, but rather than producing heat to produce mechanical energy, it is similar to a battery in that it is an electrochemical cell that produces electricity. The efficiency of electric motors approaches 99%, so this loss is often neglected. A variety of fuels can be used depending on the type of fuel cell. High-temperature fuel cells, such



as solid oxide fuel cells, can use a wider assortment of fuels because the electrocatalysts are more efficient and less prone to poisoning at these higher temperatures, up to 1000 °C. These fuels include hydrogen, alcohols, and hydrocarbons such as methane. Fuel cells that operate at lower temperatures are typically restricted to using fuels that are more easily oxidized, such as hydrogen or methanol. PEMFCs fall into this class. PEMFCs use a polymeric ion exchange membrane as an electrolyte and operate at lower temperatures, typically up to about 80 °C.

A schematic of the cross section of a single cell, often called a *membrane electrode assembly* (MEA), is shown in Fig. 1. The electrolyte membrane is at the center of two porous, catalyst-containing electrodes. The electrodes are typically formed from carbon-supported platinum particles. These carbon particles are held together by a small amount of an ion-conducting polymer, which act as both a binder and an ion conductor, allowing protons to move through the electrode. Newer types of electrode structures that allow for improved catalyst efficiency and durability are being introduced [7]. This three-layer construction is then positioned between two porous gas diffusion layers that also act as current collectors. Hydrogen is supplied to the negative electrode, or anode, and oxygen, usually in the form of air, is supplied to the positive electrode, or cathode. The product water is formed at the cathode.

A PEMFC system typically comprises a fuel cell stack where MEAs are stacked between electrically conductive bipolar plates that have flow fields embedded in them, allowing the reactive gases to be supplied to the catalyst surface and allowing the reactant water to be carried away. The area of the MEA determines the amount of current that can be passed through a cell, and the number of cells in the stack determines the voltage. Together, these define the power the stack is capable of providing.

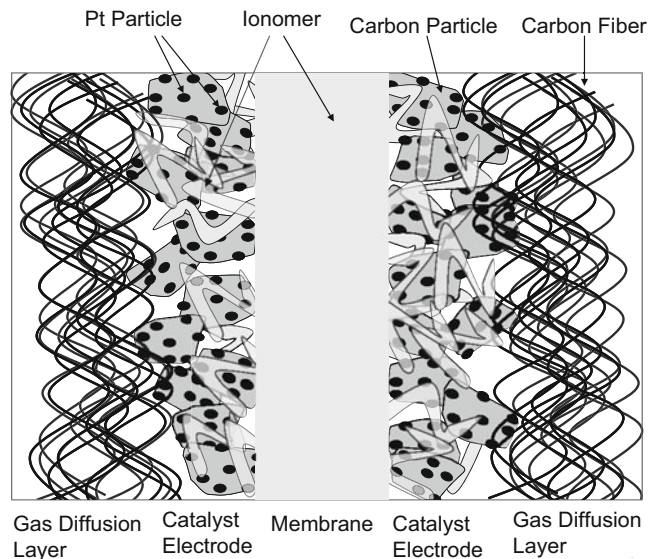
To allow PEM fuel cells to operate under the hotter, drier conditions required for widespread use in applications such as automobiles, new materials are needed. These include new electrolytes with higher proton conductivity and improved durability at low relative humidity (RH) and at higher temperatures. New electrodes that can provide adequate performance with less water are needed.

## Electrolyte Membranes

The electrolyte in a PEMFC, as the name implies, is a proton-exchange membrane, or PEM. It functions by allowing transport of protons from the negative to positive electrode and as a physical barrier to prevent shorting of the electrodes and crossover of the reactant gases. The requirements

### Proton Exchange Membrane Fuel Cells: High-Temperature, Low-Humidity Operation, Fig. 1

A schematic representation of the cross section of an MEA



for an electrolyte membrane in a PEMFC typically include the following:

- High proton conductivity
- Low permeability to reactant gases
- Good mechanical properties both dry and equilibrated with water
- Stability toward leaching of components by liquid water
- Excellent chemical stability (hydrolytic and oxidative)
- Reasonable cost
- The ability to form stable intimate interfaces with the electrodes

A variety of types of materials have been used in electrolyte membranes for PEM fuel cells. Most of these fall into two classes: basic polymers that have been imbibed with an acid and polymers with acidic groups attached.

In the first category, the most commonly used polymers for this are polybenzimidazole (PBI) or analogs imbibed with phosphoric acid [8]. This type of membrane was developed at Case Western Reserve University in the mid-1990s [9]. These membranes are known to have good conductivity at very high temperatures, up to 200 °C, and membranes with high phosphoric acid contents and increased conductivity combined with good mechanical properties have been prepared [10]. MEAs comprising such membranes are commercially available from Advent Technologies and Danish Power Systems.

There are drawbacks to using PBI/Phosphoric acid-based membranes in many fuel cell applications. The highly water-soluble phosphoric acid leads to it being easily leached out of the membrane by liquid water, preventing use in applications where the cell could experience higher humidification or lower temperatures. The phosphoric acid also absorbs to the platinum catalyst surface, inhibiting the electrode kinetics, particularly on the oxygen electrode. To overcome this, high levels of expensive platinum catalysts are required for adequate fuel cell performance. It should be stressed that while PBI/Phosphoric acid-based membranes have drawbacks that prevent their widespread use, they are the only commercially

available membranes that can be used in the temperature range between about 120 °C and 200 °C.

The majority of PEMs used today are from the second class of polymers, those with pendent acidic groups. Specifically, most polymers currently used in PEMs are typically members of a class of polymers called *ionomers*. An ionomer is a copolymer of a strong acid-containing monomer and a nonionic, neutral monomer [11]. When the neutral monomer is relatively nonpolar, ionomers will adapt a phase-separated morphology, where the ionic groups can bind tightly together into ionic aggregates or clusters. These clusters have a significant impact on the physical properties of the ionomer, often behaving as physical cross-links and stiffening the polymer [12]. A few examples of ionomers of this type are commercially available, such as DuPont's Surlyn™, a copolymer of ethylene and a salt of methacrylic acid, which is used in several applications, including the coating on the outside of golf balls.

In order for the protonated form of an ionomer to be suitable for use in a fuel cell, it must be chemically and mechanically stable enough to survive the chemically aggressive, oxidizing environment of a fuel cell. Oxidizing species such as peroxides can be formed during operation, which attack and chemically degrade the membrane [13]. Simultaneously, the membrane is mechanically stressed from the fluxuations in water content resulting from variations in current density and temperature. These combined can cause the membrane to fail, leading to gases crossing over and catastrophic cell failure. For this reason, ionomers used in fuel cells today fall into two categories of polymers that have sufficient chemical stability and mechanical properties. These are perfluorinated sulfonic acid-containing polymers (PFSA's) and aromatic backbone polymers with pendent sulfonic acid groups.

## PFSA's

Perfluorinated sulfonic acid-containing polymers (PFSA's) are the most commonly used membrane materials in fuel cells today. Membranes made from these ionomers provide the benefits of highly acidic pendant acid groups for high proton conductivity, good mechanical properties, excellent

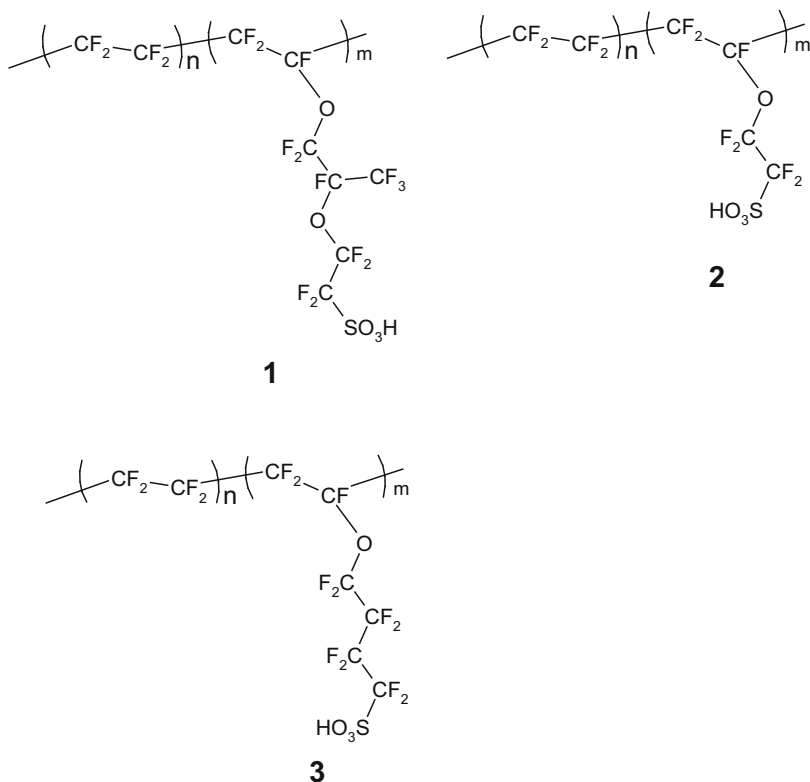
chemical stability, and fairly low cost. The first PFSA used in PEMFCs was DuPont's Nafion™, originally developed in the 1960s for brine electrolysis to produce chlorine [14]. Since then, several other PFSA membranes have been developed and introduced for use in fuel cells [15]. All of these are copolymers of tetrafluoroethylene (TFE) and a sulfonic acid-containing monomer. The chemical structures of some of these polymers are shown in Fig. 2.

When enough acid groups are present in the ionomer, the very hydrophilic sulfonic acid aggregates will absorb water. These hydrated acid groups can provide a continuous, acid-rich, hydrated pathway through the polymer. For PFSA's, in addition to the ionic regions, the TFE segments in the backbone provide another structural feature of the polymer. If the ratio of TFE units to acid-containing monomers is high enough to provide TFE runs of sufficient length (about four or more TFE monomer units), these can crystallize, much like the highly crystalline

polymer, polytetrafluoroethylene. These crystallites in the hydrophobic region of the polymer provide significant mechanical stabilization to the membrane. The amount of acid contained in the membrane is typically expressed as *equivalent weight* (EW), the number of grams of polymer required to provide one mole of acidic protons. For traditional PFSA's such as Nafion™, this value is in the range of 1000–1100. This gives a ratio of TFE to acidic monomers of about 5.5–6.5, enough to provide some stabilizing backbone crystallinity. Such polymers have a good combination of proton conductivity and mechanical properties when fully hydrated. Much work has been done over the years to provide a detailed understanding of the structure of PFSA's, and this is still an active area of research. A comprehensive review on the subject has been written by Mauritz and Moore [16] and recently updated by Kusoglu and Weber [17]. A generalized representation of a hydrated PFSA structure is shown in Fig. 3.

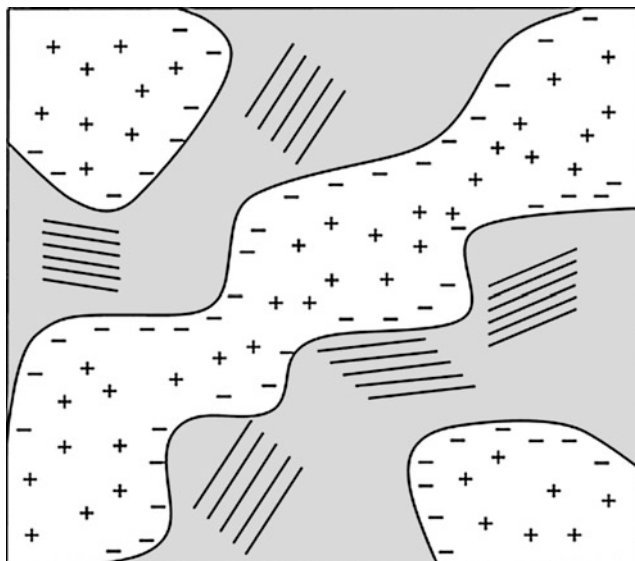
**Proton Exchange  
Membrane Fuel Cells:  
High-Temperature,  
Low-Humidity  
Operation,**

**Fig. 2** Structures of some PFSA's. Polymer 1 is available from DuPont (Nafion™), Asahi Glass (Flemion™), and others; Polymer 2 is the short-side-chain ionomer developed at Dow, currently available from Solvacore; and Polymer 3 is the ionomer available from 3 M Company



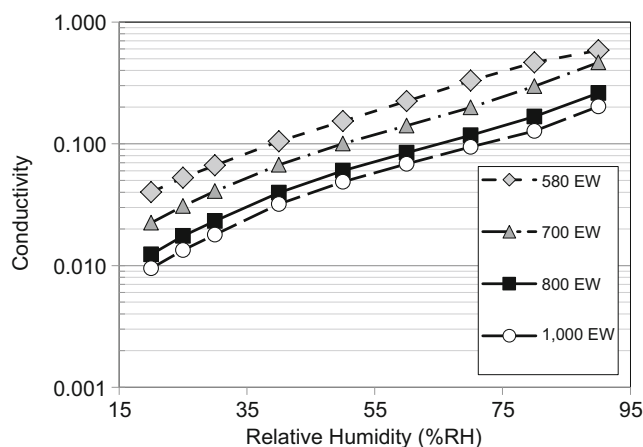
**Proton Exchange Membrane Fuel Cells: High-Temperature, Low-Humidity Operation, Fig. 3**

A general representation of the morphology of a hydrated PFSA. The + represents the hydrated protons, and the - represents the sulfonate groups at the edges of the hydrated region. The parallel lines represent the crystallites formed from the TFE groups of the backbone



**Proton Exchange Membrane Fuel Cells: High-Temperature, Low-Humidity Operation, Fig. 4**

Conductivity vs. relative humidity for several different 3 M Ionomers (Polymer 3) measured by AC impedance spectroscopy at 80 °C

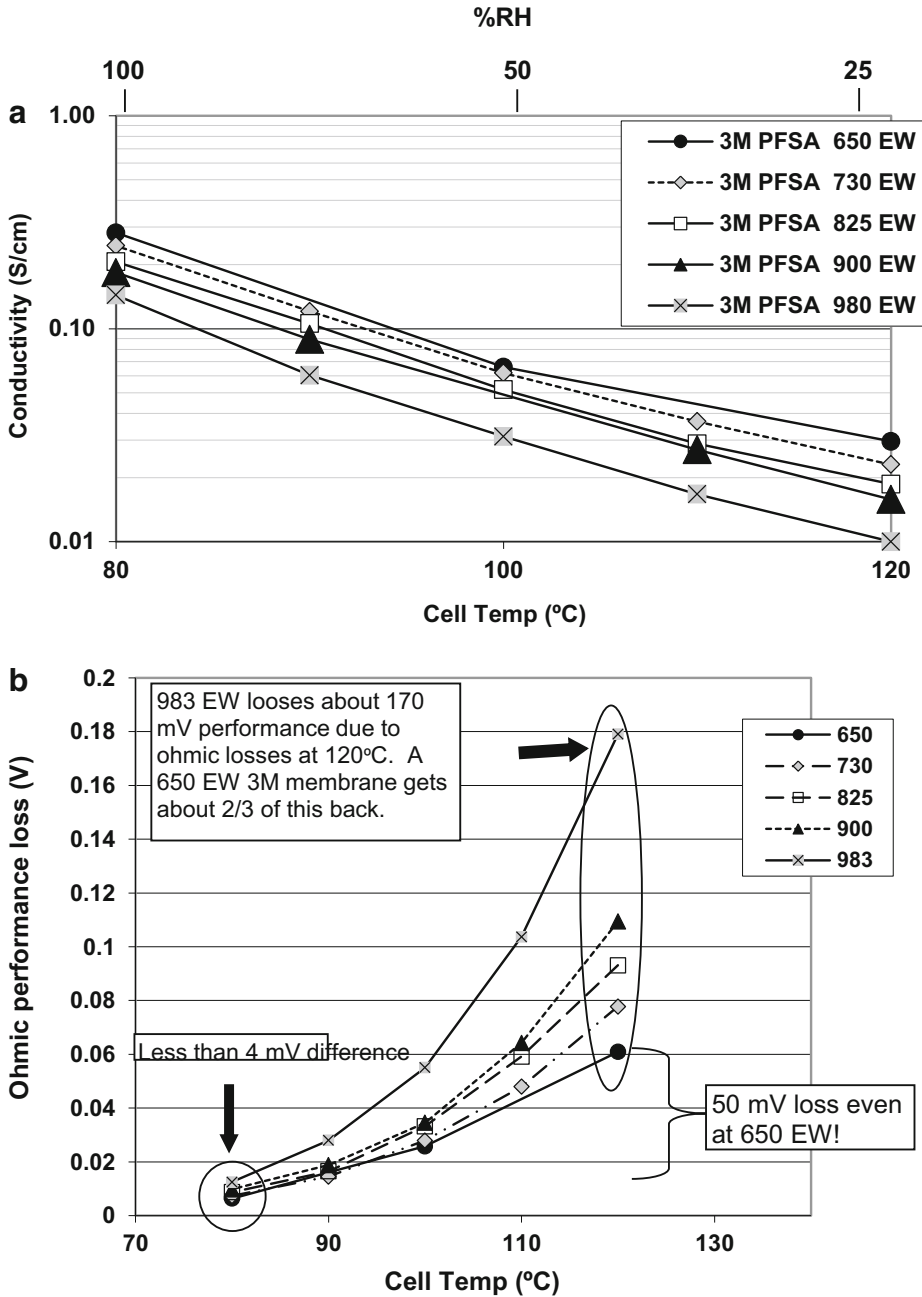


The amount of water present in the hydrated channels of the membrane is a function of the number of sulfonic acid groups present in the membrane and the humidity of the reactant gases [18]. In a typical PFSA membrane, at a given relative humidity, the ratio of water molecules to sulfonic acid groups (referred to as lambda,  $\lambda$ ) is fixed. At low %RH, there are a few tightly bound water molecules. As the %RH is increased, more water is absorbed, and these additional water molecules are less tightly bound and more mobile. It is thought that the less tightly bound, more mobile water molecules that are farther from the sulfonic

acid groups are more able to contribute to proton transport [19]. When the temperature is increased, or humidity levels in the reactant gases are decreased, the membrane will dry out and the conductivity drops. This represents an increase in the resistance of the cell and causes a loss in efficiency and performance.

One method of maintaining high conductivity with less water is to lower the EW, increasing the concentration of sulfonic acid groups in the membrane.

Figure 4 shows the conductivity as a function of relative humidity for several different EW



**Proton Exchange Membrane Fuel Cells: High-Temperature, Low-Humidity Operation, Fig. 5** (a) Conductivity of various EW 3 M ionomer membranes (Polymer 3) as a function of temperature in an atmosphere

with an 80 °C dewpoint. (b) Calculated performance loss due to membrane ohmic losses at 0.6 A/cm<sup>2</sup> for these membranes at 25 micron thickness

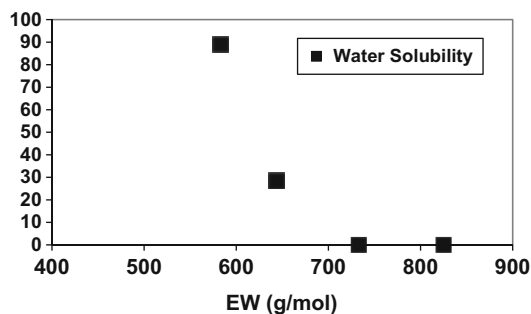
membranes. Lower EW membranes do provide a significant increase although conductivity still drops off at lower relative humidity.

Another way to consider the impact of membrane conductivity on fuel cell performance is shown in Fig. 5. Figure 5a shows the conductivity

of a few different EW membranes as a function of temperature with the atmosphere inside the conductivity cell held at a fixed dew point of 80 °C [20]. When the conductivity cell is at 80 °C, the % RH is 100%. As the temperature of the cell increases, the %RH at a fixed dew point decreases, causing a decrease in the membrane conductivity. This is similar to the situation in some PEMFC applications where the cell temperature may rise, while the humidity level of the incoming gases remains constant. The graph in Fig. 5b uses the same data. Here the conductivity is used to calculate the resistance of a 25  $\mu\text{m}$  membrane, and using Ohms law, that resistance is used to calculate the voltage loss (ohmic loss) one would see in a fuel cell at a 0.6 A/cm<sup>2</sup> current density [20]. This represents the fuel cell performance loss due to the loss of membrane conductivity (certainly not the only performance loss under these conditions!).

At 80 °C, 100% RH, the performance loss is low, about 10 mV. Further, the performance difference between the different EW membranes is also quite low, less than 4 mV. As the temperature increases, the performance losses also increase, and the effect of the different EW ionomers becomes apparent. At 120 °C, the 1000 EW membrane has a large ohmic loss of about 180 mV. This represents a  $\geq 20\%$  loss in the operating voltage of a typical PEMFC at this current density or about  $\geq 15\%$  of the energy contained in the hydrogen fuel being converted to heat. The lower EW membranes do provide a significant improvement, but even at the lowest EW shown here, 650, the ohmic loss is still six times that of the fully humidified cell.

Lowering the EW of the ionomer does seem to provide at least a partial solution to this problem. This suggests the possibility that even lower EW ionomers could allow performance equivalent to the fully hydrated membranes even under these dry conditions. In the case of typical PFSA, this is not a practical approach. This is due in part to the lack of the backbone crystallites mentioned above. At an EW of below about 700, these polymers do not have enough TFE to provide sufficient backbone crystallinity. This renders the membrane effectively water soluble and thus not useful in most PEMFC applications [21]. The



**Proton Exchange Membrane Fuel Cells: High-Temperature, Low-Humidity Operation, Fig. 6** Water solubility of 3 M ionomers (Polymer 3) as a function of EW. The samples were boiled for 3 h

solubility of the 3 M ionomer as a function of EW is shown in Fig. 6.

PFSA ionomers with lower MW side chains should allow additional crystallinity at a given EW. The Polymer 2, shown in Fig. 2, has a side chain that is 100 MW units lower than the 3 M ionomer, so it may allow a more stable membrane at somewhat lower EW. Otherwise PFSA ionomers need to be supported in a matrix such as e-PTFE to act as very thin membranes with low ASRs.

## Non-fluorinated or Hydrocarbon PEMs

A variety of non-fluorinated or partially fluorinated ionomers have been evaluated as alternatives to PFSA for PEM fuel cells. These are typically sulfonated aromatic hydrocarbon polymers. Examples include sulfonated engineering thermoplastics such as polyimides [22], polyetherketones [23], and polysulfones [24] as well as polyphosphazenes [25] or sulfonated polystyrene grafted to fluoroplastics such as polyvinylidene fluoride [26]. Some of the observed or proposed advantages of these membrane materials include lower cost, increased toughness or improved mechanical properties, and lower permeability to oxygen and fuels [27]. Permeation of oxygen through the membrane is thought to lead to formation of hydrogen peroxide on the hydrogen electrode, contributing to chemical degradation of the membrane [28]. One significant



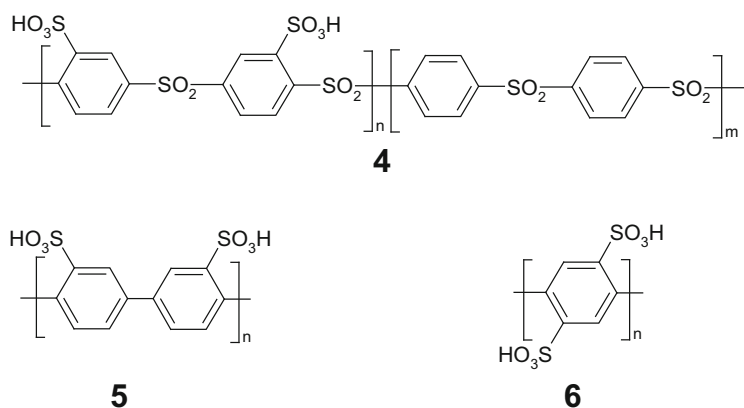
advantage of hydrocarbon-based ionomers that PFSA's do not have is their inherent synthetic versatility, allowing one to more easily design the polymer structure needed for optimum conductivity, physical and mechanical properties, and chemical stability (of course, this assumes one knows what structure one needs).

Many examples of hydrocarbon ionomers have been prepared by exposing aromatic backbone polymers to sulfonating agents, producing ionomers with sulfonic acid moieties attached to the most electron-rich positions on the aromatic rings. By controlling the degree of sulfonation, ionomers can be prepared by this method with suitable swelling characteristics and high proton conductivity at high relative humidity. It should be pointed out that due to the lower density of hydrocarbon-based polymers compared to fluoropolymers, a lower EW is needed in a hydrocarbon ionomer to provide an equivalent volumetric density of acid groups of a PFSA. Differences in the volumetric density of acid groups are more useful when comparing the conductivity of ionomers based on different classes of polymers [29]. Unfortunately, many studies have shown that randomly sulfonated hydrocarbon ionomers often suffer from lower conductivity at low relative humidity compared to PFSA's [23]. This is likely a consequence of a less favorable microstructure for proton transport as well as the lower acidity of the sulfonic acid groups bound to the aromatic ring ( $pK_a = \text{ca. } -2 \text{ to } -4$ ) compared to the sulfonic acid groups of the PFSA ( $pK_a = \text{ca. } -5.5$ ) [23, 30].

Synthetic methods that allow attachment of sulfonic acid groups to more electron-deficient sites on aromatic rings can produce polymers where these groups are not only more acidic but also more stable toward thermal desulfonation [31]. Kreuer and coworkers have prepared such polymers in sulfonated polysulfones with a variety of EWs [32]. The structure is shown as Polymer 4 in Fig. 7. These ionomers have high thermal stability, high conductivity at low levels of hydration, and surprisingly low water solubility. These sulfonated polysulfones are not water soluble at 100 °C at EW values of down to 430. The improved conductivity at low hydration is likely due in part to the low electron density of the aromatic rings of the polysulfone and also possibly due in part to a favorable microstructure for proton transport. To further increase conductivity under very dry conditions, some highly sulfonated hydrocarbon polymers have been shown to have very high proton conductivity, even at low relative humidity. The Kreuer group has also prepared a completely sulphonated polysulfone that is polysulfone with a sulfonic acid group on every aromatic ring (EW = 220). While this ionomer is water soluble, it has conductivity substantially higher than 1100 EW Nafion™, even under dry conditions [34]. Litt and coworkers have prepared highly sulfonated polyphenylenes with one and two sulfonic acid groups per aromatic ring, shown as polymers 5 and 6 in Fig. 7 [33]. The latter has an EW of 118! Both of these ionomers are also water soluble and have very high proton conductivity at low %RH. These ionomers have

**Proton Exchange Membrane Fuel Cells: High-Temperature, Low-Humidity Operation,**

**Fig. 7** Structures of some hydrocarbon ionomers. Polymer 4 is from Ref. [31] and Polymers 5 and 6 are from Ref. [33]



been shown to hold more water at lower %RH than other sulfonic acid-based ionomers. This observation was explained by an increase in the “frozen-in free volume” in these ionomers, that is, that the rod-like morphology of the polymer hindered close packing. Removal of the last few waters of hydration in the voids between these rods would force them closer together into a higher energy state, effectively increasing the heat of vaporization of the bound water molecules.

The studies mentioned above show that through control of the electronic and structural features of hydrocarbon ionomers, increased conductivity can be achieved. However, this is often at the expense of the mechanical stability of the polymer to the point where these materials cannot be used in fuel cells. One potential method of stabilizing these materials is to incorporate them into a stable multiphase or segmented system. A variety of synthetic methods exist that allow generation of different branched or block copolymers, and these have been applied to the synthesis of PEMs [35]. This allows control over the morphology of the phase-separated structures to create interconnected proton-conducting channels that may allow increased proton conductivity. McGrath and coworkers have prepared and evaluated sulfonated multiblock poly arylene ether sulfones with conductivity at low relative humidity equivalent to a Nafion™ membrane [36, 37]. The conductivity has been shown to be a function of the length and the chemistry of both the hydrophilic and the hydrophobic blocks.

### **Mechanical Stabilization of Low EW Membranes**

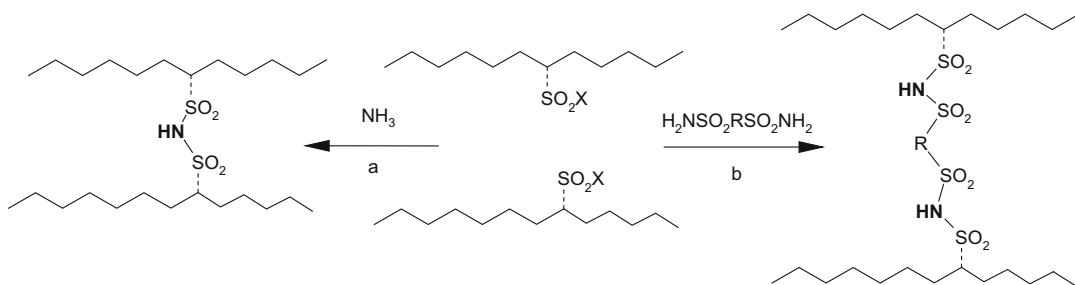
One way of mechanically stabilizing low EW ionomer membranes is to generate a composite membrane using a porous film as an internal reinforcing structure [38, 39]. A PFSA membrane reinforced with a thin expanded polytetrafluoroethylene layer is available from W.L. Gore. Reinforced membranes of this type have been shown to have increased strength and lower in-plane swelling upon hydration, lowering the

potential of damage due to stresses generated during fuel cell operation. This should result in increased fuel cell durability [40]. Composite membranes have also been formed by using the porous phase as the conducting phase and filling the pores with a reinforcing phase. Pintauro and coworkers have made membranes using microfibers of sulfonated polyether sulfone filled with an inert filler to provide a membrane with good mechanical properties and proton conductivity when fully hydrated [41]. This group then used low EW PFSA fibers in this process, which gave a membrane with low swelling and very good conductivity at relatively low %RH (0.10 S/cm conductivity at 80 °C and 50% RH, about two to three times higher than a 1100 EW Nafion™ membrane) [42].

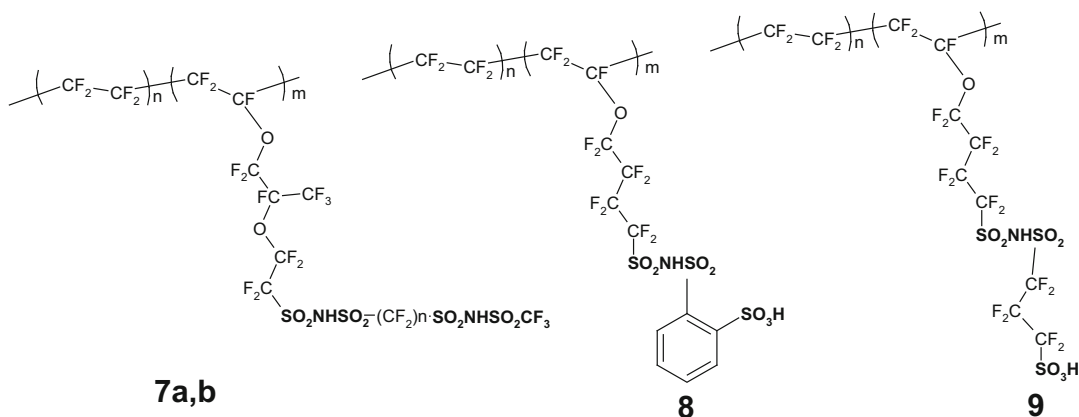
Mechanical stabilizing membranes in this way can allow significant stabilization of low EW ionomers. However, since many applications of PEM fuel cells require not only hotter and/or drier operation conditions but also require that the membrane to be insoluble in liquid water (often hot!) at times during operation, there is a limit to how low this method will allow one to go. In order to allow very low EW ionomers to be feasible, a change in the polymer chemistry will also probably be required.

### **Stabilizing Low EW Membranes Through Chemical Modification of the Ionomer**

One possible method of chemically stabilizing low EW ionomers's toward excessive swelling and dissolution in water is to cross-link the ionomer. Many attempts are being made to cross-link low EW ionomers [43–45]. Generally, there are two “regions” in which ionomers can be cross-linked, in the hydrophilic, conducting region, near the acid groups and in the hydrophobic region, near the backbone. In the case of the former, one method that has been studied is forming a bis-sulfonyl imide from two of the pendent sulfonyl halide groups on the ionomer precursor [46]. Bis-sulfonyl imides are known to have highly acidic protogenic hydrogens and excellent chemical stability [47]. This method has the advantage that the



**Proton Exchange Membrane Fuel Cells: High-Temperature, Low-Humidity Operation, Fig. 8** General method of synthesizing bis-sulfonyl imide containing cross-links from polymers with pendent sulfonyl halide groups



**Proton Exchange Membrane Fuel Cells: High-Temperature, Low-Humidity Operation, Fig. 9** The structure of three multi-acid side-chain ionomers. Polymer 7a,  $n = 4$ , 7b  $n = 2$  are from Ref. [51], Polymers 8 and 9 are from Ref. [53]

cross-links formed have similar acidity to the acid groups consumed. A generalized representation of this method is shown in Fig. 8.

Methods in which the backbone of the polymer can be cross-linked include radiation grafting [48] and through the preparation of a cross-linkable terpolymer by including a reactive third monomer in the polymerization of the ionomer, followed by curing in film form [49–51].

Another approach to providing ionomers with lower EW and suitable mechanical and solubility properties is to have more than one acidic proton per side chain. If the side chain has additional protogenic groups, a low EW ionomer can be prepared having a higher degree of backbone crystallinity and hopefully increased stability toward liquid water. One way to prepare such ionomers is to include a highly acidic bis-sulfonyl

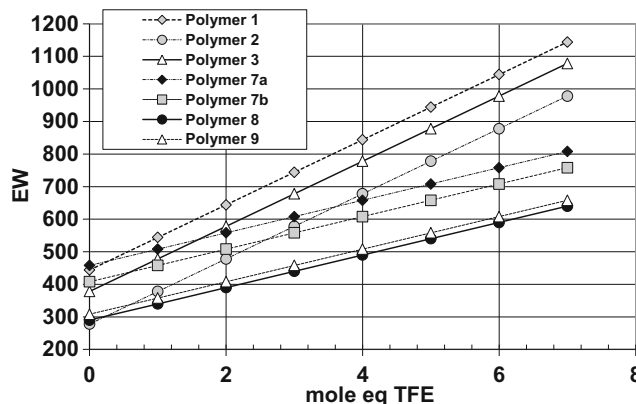
imide acid in the side chain. Such materials were prepared by Desmarteau (Polymers 7a,b) and more recently at 3 M (Polymers 8 and 9) [52–55]. The structures of some of these materials are shown in Fig. 9.

The relationship between the number of TFE units that form the backbone crystallites and EW is shown in Fig. 10. The slope of each line gives the EW of the ionomer/the ratio of TFE units to protons in the polymer, and the intercept is the MW of the acid functional monomer/the number of protons. This shows the utility of having multiple protogenic groups on each side chain in providing polymers having high crystallinity and low EW.

In the case of Polymers 8 and 9, it has been demonstrated that low EW ionomers with higher conductivity, low swelling in boiling water, and good mechanical properties can be prepared [56].

### Proton Exchange Membrane Fuel Cells: High-Temperature, Low-Humidity Operation, Fig. 10

Plot of EW vs. the number of TFE units in the backbone of selected ionomers



### Conductivity Enhancing/Stabilizing Inorganic Additives

Another approach to overcome the inherent deficiencies of ionomers under hot, dry operating conditions has been to investigate the use of inorganic additives to form composite membranes [55]. Three basic functionalities are invoked:

1. Additives that are hygroscopic and designed to retain additional water in the membrane so that no loss of performance is observed when the fuel cell is operated under conditions of reduced RH. If the fuel cell spends significant time under dry operations, these approaches inevitably fail.
2. Additives that have enhanced acidity and can facilitate proton transport and so enhance performance under drier conditions.
3. Additives that are designed to decompose peroxide in situ in the membrane to increase the membrane chemical durability.

A number of additives also have combined functionality.

Probably every common hygroscopic inorganic oxide has at some time been used to prepare a composite membrane for fuel cell use [55]. The perceived benefit of an insoluble inorganic additive is from a surface interaction between the additive particle and the ionomer, and so nano-sized individual particles or mesoporous materials into which the ionomer can penetrate have the larger benefit. Larger particles give no additional

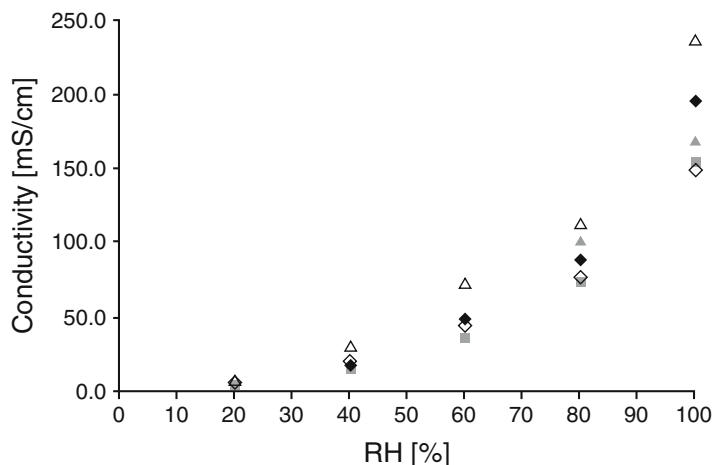
benefit and simply reduce the EW of the ionomer. The inorganic materials are either preformed before being mixed with the ionomer or are formed in situ, typically by a sol-gel process. Of the oxides that can be formed in situ, the most commonly used additive has been silica, but it is unstable to acid, and so its suitability for fuel cell operation is questionable [57]. Titania and zirconia composites would appear to have more promise from a stability viewpoint [58], although they have mostly been found to enhance membrane mechanical properties, as ultimately the water in these additives will also be lost on sustained dry operation. Recently improved performance has been observed under drier operation by combining tin oxide with titania [59]. Clays both natural and synthetic have also been used, but again their benefit to fuel cell under RH cycling is also questionable.

More promising are approaches using either acid-functionalized particles [60] or super acidic inorganic materials that are designed to increase proton mobility. Of these, the two most promising are zirconium phosphonates and the heteropoly acids (HPAs) [61–63]. The effect of these may simply that they are more hygroscopic, or that the phenomena are simply a proton concentration effect, essentially lowering the equivalent weight. However, as they also lower the activation energy for proton transport, it seems that they also act as an effective proton transport promoter, perhaps more effective than the sulfonic acids.

Figure 11 shows proton conductivity data at 100 °C for the 3 M ionomer doped with various

**Proton Exchange Membrane Fuel Cells: High-Temperature, Low-Humidity Operation,**

**Fig. 11** Proton conductivity at 100 °C for the 3 M ionomer (■) and the 3 M ionomer doped with (◇) 1% HPW, (◆) 5% HPW, (△) 1% HSiW, and (▲) 5% HSiW at 20–100% RH (From Ref. [61])



HPAs. Two observations are immediately apparent: (1) that the structure and amount of the additive have a strong influence and (2) that the effect becomes dramatically less as the RH is lowered. Similar results are shown for zirconium phosphonate composites with PFSA ionomer [64].

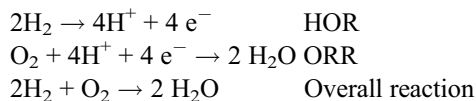
Hydrogen peroxide decomposition catalysts can be added to ionomer membranes in small amounts to slow down the decomposition of the ionomer during fuel cell operation. Additions of cerium and manganese, in both oxide and ionic forms, have been shown to increase the oxidative stability of membranes by orders of magnitude, and fuel cells prepared with such membranes have shown substantial increases in lifetime under aggressive hot and dry operation [65–67]. Unfortunately, these metal ions and oxides can consume ion exchange capacity and negatively impact fuel cell performance.

The ideal additive would enhance proton conductivity and stability. One demonstration of this was in a composite PFSA membrane using Pt nanoparticles supported on titania or silica [68]. The composite membranes when employed in MEAs demonstrated unhumidified fuel cell performance comparable to that of a similar humidified fuel cell. Whether adding Pt to the membrane will help durability or hurt, it is still a matter of some debate [69, 70]. Unfortunately, it is not commercially feasible at this time to add additional Pt to the MEA, and so this approach while novel is not practical. The HPAs are known

peroxide decomposition catalysts, and so these inorganic oxides have been demonstrated to improve performance and decompose peroxide in fuel cells, and if they could be immobilized would present a practical solution to this problem [71].

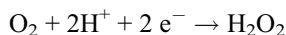
## Electrodes

As stated above, the membrane acts as the proton transporting medium, is an electrical insulator, and separates the reactant gases from direct chemical reaction. On either side of this membrane are placed two electrodes. The anode at which hydrogen is consumed in the hydrogen oxidation reaction (HOR) and the cathode in which oxygen from air is consumed in the oxygen reduction reaction (ORR). The two half-cell reactions and the overall reaction are shown below.



The electrons flow around an external circuit and do work, while the protons pass through the fuel cell membrane. This overall reaction represents the combustion of hydrogen that produces heat, one reason why the membranes function to separate the two reactant gases is critical. Not only would a leak lead to fuel cell inefficiency, but also a hot spot would develop at the site of the leak,

which would result in potential damage to the MEA. Unfortunately, the ORR is not 100% efficient and a  $2e^-$ ,  $2H^+$  reaction results in the formation of hydrogen peroxide as shown below:



This reaction is currently unavoidable and appears to be favored at hot and dry operating conditions of the fuel cell. The peroxide decomposition forms reactive radicals such as hydroxyl,  $\cdot OH$ , and peroxy,  $\cdot OOH$ , that cause oxidative degradation of both the fuel cell membrane and catalyst support [72]. Both electrodes currently use Pt or Pt alloys to catalyze both the HOR and ORR reactions. The catalyst particles are typically supported on a high surface area, heat-treated carbon to both increase the effectiveness of the catalyst and to provide a path for the electrons to pass through to the external circuit via the gas diffusion media (which is typically also made of carbon) and the current collecting bipolar plates. In addition, the catalyst particles are coated in ionomer to facilitate proton transport; however, the electrode structure must also be porous to facilitate reactant gas transport. A schematic of a typical PEM MEA is shown in Fig. 1. A boundary condition exists at the catalyst particle where protons from the ionomer, electrons from the electrically conducting Pt and carbon, and reactant gases meet. This is usually referred to as the *three-phase boundary*. The transport of reactants, electrons, and protons must be carefully balanced in terms of the properties, volume, and distribution of each media in order to optimize operation of the fuel cell.

Typically, a good proton conductor is thought to be one where the proton conductivity is  $\leq 0.1 \text{ S cm}^{-1}$ ; however, from the point of view of fuel cell operation, it is the area-specific resistance (ASR) of the MEA that is more important. If one was to consider the MEA as a series of resistances, an anode resistance would be observed, an interfacial resistance between the membrane and the anode, a membrane resistance, an interfacial resistance between the membrane and the cathode, and a cathode resistance. It is assumed here that the resistance of electrical connection between the anode and the current collectors is negligible compared to those described above;

however, this too can be compromised if there is insufficient pressure between the bipolar plates and the gas diffusion media. All of these resistances must be optimized in order to lower the area-specific resistance of the fuel cell. The effect of the resistances or ohmic losses on the overall performance and efficiency of the fuel cell is illustrated in Fig. 5. While a large amount of current work is concerned with optimizing membrane ionomers for hotter and drier operation, little thought has to date been put into optimizing the electrode ionomer, the ionomer catalyst interface, or the catalytic reactions at the anode or cathode for higher temperature, lower RH operation. If the ionomer in the membrane is not well matched and linked to that in the fuel cell electrodes, a large ASR can result. Of course part of the reason for this, until recently, has been the lack of suitable hot, dry ionomers for practical fuel cell testing.

As stated above, in a conventional, fully humidified fuel cell, part of the reactant gas stream is diluted by water vapor, and the cathode suffers from formation of liquid water blocking the pores, or flooding, as the water is being produced in a water-saturated environment. To overcome this problem, hydrophobic fillers such as Teflon™ may be added to the electrode to facilitate water rejection [73]. These systems have been to a large extent already optimized, and great deal of art pertains to electrode fabrication [74]. One advantage of running a fuel cell hot and dry is that the electrode flooding issue is eliminated. In these fuel cells, there is still water produced on the cathode but possibly not enough to saturate the PFSA polymer in the electrode layer and potentially leaving the anode side of the fuel cell under humidified. However, as it is likely that polymers with low EW will be used for high-temperature operation, back diffusion of water should be increased improving the chance that the anode will not be dried out. With less water in the fuel cell system, freeze issues on start-up in cold climates may also be partially mitigated.

Each of the electrode components is now considered in terms of hot and dry operation, what is known, and what needs to be accomplished to realize these systems.



It is generally thought that as temperature increases so do reaction kinetics. However, the situation in a fuel cell, an electrochemical device, is far more complicated. The reaction mechanism will depend on the surface environment of the catalyst particle and the potential at which the reaction is taking place. The electrode overpotential associated with the ORR represents the largest voltage loss in fully humidified fuel cells, and so it is important that the situation not be exacerbated in running fuel cell under hot and dry conditions. In the kinetically controlled region of the fuel cell operation, the performance can be described by the Tafel equation:

$$E = E_{\text{rev}} + b \log i_0 - b \log i$$

$$b = -2.3 \frac{RT}{\alpha nF}$$

where  $E$ ,  $E_{\text{rev}}$ ,  $b$ ,  $i$ ,  $i_0$ ,  $n$ , and  $\alpha$  are the electrode potential, reversible potential, Tafel slope, current density, exchange current density, the number of electrons transferred in the rate determining step, and the transfer coefficient, respectively [75, 76]. The first observation is that increasing the fuel cell temperature from 60 to 120 °C while maintaining a constant relative humidity (RH) causes the theoretical open circuit voltage (OCV) to decrease from 1.22 to 1.14 V due to the increase in water partial pressure [77], and so again it is desirable to operate the fuel cell at reduced RH. The Tafel slope, a measure of the potential loss of the electrode due to reaction kinetics, is the logarithmic decrease in current density with applied voltage. It is therefore desirable to have as small a Tafel slope as possible. The Tafel slope varies with current density as the surface of the platinum varies with voltage. At high-voltage or low current density, the Pt is oxide coated (Temkin adsorption conditions), and the Tafel slope is 60 mV/decade; at lower voltage, higher current density the Pt is oxide-free (Langmuir adsorption conditions), and the Tafel slope is 120 mV/decade. So above 100 °C, the reaction mechanism may change if the surface coverage is compromised by the lack of water. Experimentally it has been shown for a water-

saturated electrode that the Tafel slope increases with temperature at high voltage but is invariant at low voltage [78].

There are very few studies of the ORR under hot and dry fuel cell operating conditions. Recently, methods have been devised to separate the mass transport effects from the kinetic effects [79, 80], but none of these have been applied to hot and dry fuel cell operation. These studies showed that, under fully humidified conditions up to 70 °C, oxygen reduction had a tenfold higher specific performance for platinum black at 0.90 V compared to Pt on carbon as has been previously reported in the literature [81]. However, this significant benefit of platinum black is shown to rapidly decrease when the potential is shifted to lower, more fuel cell relevant potentials. This is manifested in the Tafel slope, which decreased from ~360 to ~47 mV/decade in the region where the overpotential was <0.35 V. The effect of hot and dry conditions has been studied in a 5 cm<sup>2</sup> MEA where mass transport and kinetics are difficult to separate [78]. At 120 °C, the Tafel slope is found to increase inversely with RH. It is speculated that this is due to the decrease in ionic conductivity in the electrode. RH can also influence water oxidation to form Pt-OH and Pt-O and thereby change the surface condition of the platinum crystals.

It has been shown that the current exchange density increases up to 70 °C, but there is no data for this above 100 °C; again there is a critical need to measure this under real fuel cell conditions. Much work is being undertaken in precious metal alloy catalysts where Pt is combined with one or more other metals and in non-precious metal catalysts [82]. These new catalytic materials are being studied in aqueous acid or in MEAs at 100% RH; very little data exists on how these materials will behave under hot and dry conditions. In fact the development of new catalyst for fuel cells run under hot and dry conditions may require their optimization outside of aqueous or water-saturated systems.

H<sub>2</sub> can be produced from fossil hydrocarbons such as natural gas or renewable biomass via reforming to produce syn gas (H<sub>2</sub> + carbon monoxide, CO), which can be converted to a H<sub>2</sub>-rich

gas via the water gas shift reaction. These processes, while commonplace in chemical engineering practice, do not produce pure  $H_2$ ; the last 1000 ppm or so of CO must be removed by expensive and/or inefficient unit operations such as partial oxidation, pressure swing adsorption, or membrane technology. The great advantage for the fuel cell electrodes in terms of high-temperature operation is on the anode where the effect of adsorbed contaminants that slow the HOR are mitigated. This allows the anode to operate with  $H_2$  contaminated with increasing levels of CO, a by-product of hydrocarbon reforming. At 80 °C, CO levels as low as 10 ppm can cause significant degradations in performance, but at 130 °C, the fuel cell anode can tolerate 1000 ppm of CO allowing the cost of  $H_2$  produced from hydrocarbons to be dramatically reduced.

The optimum particle size for Pt in the catalyst layer is 3–5 nm [83]. Another issue is that the Pt both agglomerates and suffers from dissolution and re-precipitation. Both processes are expected to increase at higher temperature and result in higher particle sizes, lowering the rate of the ORR [84]. As described above, in a typical electrode, the precious metal catalyst is supported on a carbon support that is susceptible to corrosion. It has been shown that the carbon corrodes rapidly if the electrode is held at relatively high potentials and that the reaction is first order with respect to water vapor. Carbon corrosion obviously increases with temperature and Pt loading, Fig. 12 [85]. Doping carbon with N is expected to increase the durability of the carbon.

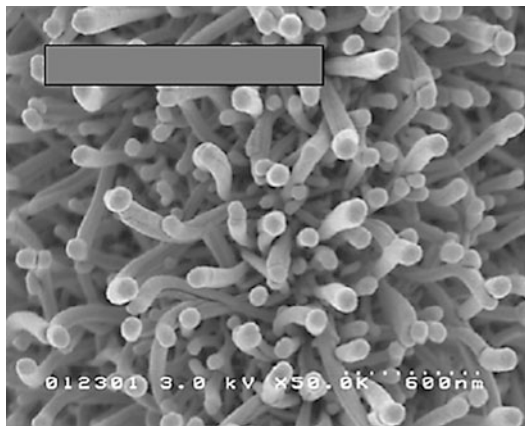
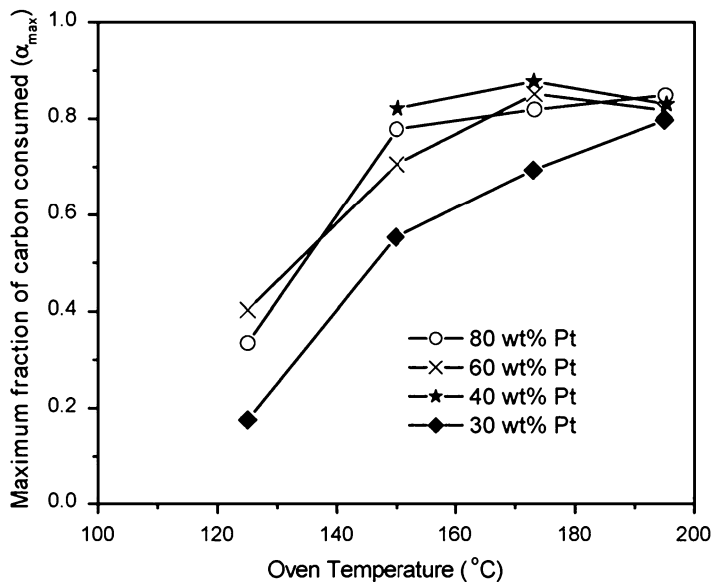
Another solution to both the carbon support and the ionomer contact issue is to use a Pt catalyst that has no support and is embedded in the membrane such as the nano-structured thin film (NSTF) catalyst being developed by 3M [7, 86]. A SEM of the NSTF-Pt catalyst is shown in Fig. 13. In addition to not having a carbon support to corrode, this catalyst system is much less susceptible to Pt dissolution because the small whiskers are coated with a continuous layer of Pt, not Pt nanoparticles, and so behaves more like bulk Pt. MEAs made with these electrodes also produce less  $F^-$  in the effluent water coming from the

fuel cell under hot and dry operating conditions, as shown in Fig. 14. The fluoride content in the effluent water coming from the cell is a common diagnostic for the rate of membrane degradation. Materials known to decompose peroxide have also been added to PEM fuel cell catalyst layer such as  $MnO_2$  [87],  $CeO_2$  [66], and HPA [88], and all have shown a decrease in fluoride emission rates of the fuel cell under hot and dry conditions.

Nafion™ and other PFSA ionomers work very well in conventional PEMFC electrodes because they form a thin layer that allows both gas diffusion and proton transport. For this reason, they are still the ionomer of choice in fuel cell electrodes for hot and dry operation, although under these conditions, the PFSA used usually has a much lower EW to increase proton conductivity at the drier conditions. While the approach of adding a lower EW PFSA ionomer works well for hot and dry operating conditions, the increased swelling and hydrophilicity at lower EW leads to severe flooding if the same fuel cell is operated under high RH. As new ionomers for hot and dry operation are developed, they must be capable of extending their proton connectivity into the electrode without a large interfacial loss due to material incompatibility at the boundary of the electrode and membrane. The consequence of a change in ion-conducting material is that proton transport to and from the catalyst layer may be compromised if conventional ionomers are employed. It is true that at the current time, little work has been done to develop new, stable ionomers suitable for high-temperature applications that will also allow high proton conductivity and high gas permeability in the fuel cell electrodes. One may consider using stable, lower EW version of the new ionomers, functionalizing the carbon support with suitable functional groups or developing new ionomers with higher gas permeability for use as binders in the electrode. It may be necessary to completely redesign fuel cell electrodes for high-temperature, low relative humidity operation using materials that are stable to oxidation, enhance the ORR, proton conductivity, and gas permeability, while maintaining suitable electrical conductivity to maintain the three-phase boundary condition during operation.

**Proton Exchange Membrane Fuel Cells: High-Temperature, Low-Humidity Operation,**

**Fig. 12** Maximum fraction of carbon consumed as a function of temperature for samples with 30–80 wt.% Pt (From Ref. [83])



**Proton Exchange Membrane Fuel Cells: High-Temperature, Low-Humidity Operation,**

**Fig. 13** NSTF catalyst as fabricated and before transfer to a PEM. Plan view at 50,000 X original. The scale bar indicates 600 nm (From Ref. [7])

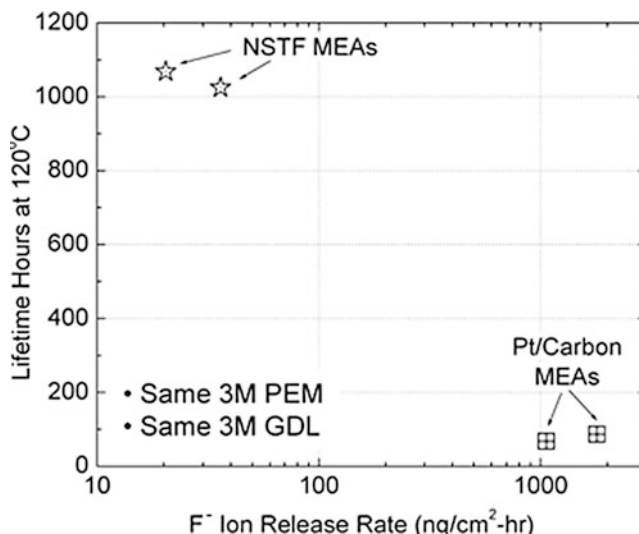
### Future Directions

This entry is by no means comprehensive. It is intended to show important examples of the approaches being taken to address the need for new materials to allow the robust operation of fuel cells under hotter and drier conditions than possible today.

At this point, there are no membranes or ionomers commercially available that will meet both the performance and durability requirements

outlined above, although much progress has been made in the development of polymer membranes, which have improved conductivity and durability under these conditions. More radical approaches to the development of new fuel cell electrolytes including the development of ionomers with a variety of different protogenic groups are being explored [89, 90]. Using imidazole, ionic liquids, and other replacements for water to allow completely dry operation is also being studied [91–93]. The next few years should see significant technical advances and the introduction of improved electrolyte membranes into the marketplace.

Optimization of the electrodes for these fuel cell systems has just started. Work has been done on the optimization of electrode structure for operation under hot, dry conditions but less has been done to study catalysis under these conditions. Part of the reason for this is that as stated above, there are no commercially available polymeric materials available for the development of new electrodes studies. It is hoped that until commercially available materials for this application become available that researchers offer to share their materials. This will, however, be insufficient as the ionomers developed for catalyst layers need different properties than ionomers developed to act as fuel cell membranes. The other major issue is that catalysts for fuel cells run under conditions



**Proton Exchange Membrane Fuel Cells: High-Temperature, Low-Humidity Operation, Fig. 14** Hours of lifetime at 120 °C (before catastrophic failure of the PEM) versus fluoride ion release rates (by IC) for NSTF and Pt/C catalyst -based MEA's having the

same type PEM and GDL. 100 cm<sup>2</sup> cells were operated at 0.4 A/cm<sup>2</sup>, 120 °C, 300kPa, 61%/84% inlet RH. ECSA and cross-over were measured daily at 75 °C. Total lifetimes were ~ 1800 hours for the NSTF MEA's due to diagnostic testing at 75 °C. End-of-life

of water saturation have been developed using liquid phase electrochemical methods. It will be extremely important that new catalyst for fuel cells to be operated under hot, dry conditions be developed by solid-state electrochemistry. New methods must also be developed so that electrodes containing compatible ionomers can be tested.

## Bibliography

### Primary Literature

- Houchins C, Kleen GJ, Spendelow JS, Kopasz J, Peterson D, Garland NL, Ho DL, Marcinkoski J, Martin KE, Tyler R, Papageorgopoulos DC (2012) U.S. DOE progress towards developing low-cost, high performance, durable polymer electrolyte membranes for fuel cell applications, *Membranes*, 2: pp. 855–878
- Nonobe Y (2017) Development of the fuel cell vehicle mirai. *Electron Eng IEEJ Trans Elec* 12:5–9. <https://doi.org/10.1002/tee.22328>
- Hardman S, Chandan A, Shiu E, Steinberger-Wilckens R (2016) Consumer attitudes to fuel cell vehicles post trial in the United Kingdom. *Int J Hydrog Energy* 41(15):6171–6179
- Alaswad A, Baroutaji A, Achour H, Carton J, Makky AA, Olabi AG (2016) Developments in fuel cell technologies in the transport sector. *Int J Hydrog Energy* 41(37):16499–16508
- Yoshida T, Kojima K (2015) Toyota MIRAI fuel cell vehicle and progress toward a future hydrogen society. *Electrochem Soc Interface* 24(2):45–49
- Chen H, Cong NC, Yang W, Tan C, Li Y, Ding Y (2009) Progress in electrical energy storage systems: a critical review. *Prog Nat Sci* 19:291–312
- Debe MK, Schmoeckel AK, Vernstrom GD, Atanasoski R (2006) High voltage stability of nanostructured thin film catalysts for PEM fuel cells. *J Power Sources* 161:1002–1011
- Wainwright JS, Litt MH, Savinell RF (2003) High temperature membranes. In: Vielstien W, Gasteiger HA, Lamm A (eds) *Handbook of fuel cells: fundamentals, technology and applications*, vol 3. Wiley, West Sussex, pp 436–446
- Savinell R, Yeager E, Tryk D, Landau U, Wainwright J, Weng D, Lux K, Litt M, Rogers C (1994) A polymer electrolyte for operation at temperatures up to 200°C. *J Electrochem Soc* 141:L46–L48
- Mader J, Xiao L, Schmidt TJ, Benicewicz BC (2008) Polybenzimidazole/acid complexes as high-temperature membranes. *Adv Polym Sci* 216:63–124
- Pinery M, Eisenberg A (1987) Structure and properties in ionomers, NATO advanced study institute series, vol 198. D. Reidel, Dordrecht
- Bazuin CG, Eisenberg A (1981) Ion-containing polymers: ionomers. *J Chem Educ* 58:938–943
- Laconti AB, Hamdan M, McDonald RC (2003) Mechanisms of membrane degradation. In: Vielstien W, Gasteiger HA, Lamm A (eds) *Handbook of fuel cells: fundamentals, technology and applications*, vol 3. Wiley, West Sussex, pp 647–662

14. Doyle M, Rajendran G (2003) Perfluorinated membranes. In: Vielstien W, Gasteiger HA, Lamm A (eds) Handbook of fuel cells: fundamentals, technology and applications, vol 3. Wiley, West Sussex, pp 351–395
15. Hamrock SJ, Yandrasits MA (2006) Proton exchange membranes for fuel cell applications. *Polym Rev* 46:219–244
16. Maritz KA, Moore RB (2004) The state of understanding of nafion. *Chem Rev* 104:4535–4585
17. Kusoglu A, Weber AZ (2017) New insights into Perfluorinated sulfonic-acid ionomers. *Chem Rev* 117:987–1104
18. Mittelsteadt CK (2010) U.S. department of energy hydrogen program 2010 annual merit review proceedings. [http://www.hydrogen.energy.gov/pdfs/review10/fc036\\_mittelsteadt\\_2010\\_o\\_web.pdf](http://www.hydrogen.energy.gov/pdfs/review10/fc036_mittelsteadt_2010_o_web.pdf)
19. Paddison SJ, Paul R (2002) The nature of proton transport in fully hydrated nafion. *Phys Chem Chem Phys* 4:1158–1163
20. Emery M, Frey M, Guerra M, Haugen G, Hintzer K, Lochhaas KH, Pham P, Pierpont D, Schaberg M, Thaler A, Yandrasits M, Hamrock S (2007) The development of new membranes for proton exchange membrane fuel cells. *ECS Trans* 11:3–14
21. Yandrasits MA, Hamrock SJ (2010) Membranes for PEM fuel cells. In: Herring AM, Zawodzinski TA Jr, Hamrock SJ (eds) Fuel cell chemistry and operation. ACS symposium series. American Chemical Society, Washington, DC, pp 15–29
22. Faure S, Cornet N, Gebel G, Mercier R, Pineri M, Sillion B (1997) Sulfonated polyimides as novel proton exchange membranes for H<sub>2</sub>/O<sub>2</sub> fuel cells. In: Proceedings of the second international symposium on new materials for fuel cell and modern battery systems, Montreal, pp 818–825
23. Kreuer KD (1997, 2001) On the development of proton conducting materials polymer membranes for technological applications. *Solid state Ionics* 97:1–15; Hydrogen and methanol fuel cells. *J Membr Sci* 185:29–39
24. Noshay LM, Robeson J (1976) Sulfonated poly-sulfone. *J Appl Polym Sci* 20:1855–1903
25. Guo Q, Pintauro PN, Tang H, O'Conner S (1999) Sulfonated and cross-linked polyphosphazene-based proton-exchange membranes. *J Membr Sci* 154:175–181
26. Buchi FN, Gupta B, Halim J, Haas O, Scherer GG (1994) A new class of partially fluorinated fuel cell membranes. *Proc Electrochem Soc* 23:220–235
27. Hickner MA, Ghassemi H, Kim YS, Einsla BR, McGrath JE (2004) Alternative polymer systems for proton exchange membranes (PEM's). *Chem Rev* 104:4587–4612
28. Sethuraman VA, Weidner JW, Haug AT, Protsailo LV (2008) Durability of perfluorosulfonic acid and hydrocarbon membranes: effect of humidity and temperature. *J Electrochem Soc* 155:B119–B124
29. Kim YS, Pivovar BS (2009) Comparing proton conductivity of polymer electrolytes by percent conducting volume. *ECS Trans* 25:1425–1431
30. King JF (1991) Acidity. In: Patai S, Rappoport Z (eds) The chemistry of sulphonic acids, esters and their derivatives. Wiley, New York, p 249
31. Iley J (1991) Rearrangements. In: Patai S, Rappoport Z (eds) The chemistry of sulphonic acids, esters and their derivatives. Wiley, New York, p 453
32. Schuster M, Kreuer KD, Andersen HT, Maier J (2007) Sulfonated poly(phenylene sulfone) polymers as hydrolytically and thermo-oxidatively stable proton conducting ionomers. *Macromolecules* 40:598–607
33. Litt M, Granados-Focil S, Kang J (2008) Rigid rod polyelectrolytes with frozen-in free volume: high conductivity at low RH. In: Herring AM, Zawodzinski TA Jr, Hamrock SJ (eds) Fuel cell chemistry and operation. ACS symposium series American Chemical Society, Washington, DC, pp 49–63
34. de Araujo CC, Kreuer KD, Schuster M, Portale G, Mendil-Jakani H, Gebel G, Maier J (2009) Poly(p-phenylene sulfone)s with high ion exchange capacity: ionomers with unique microstructural and transport features. *Phys Chem Chem Phys* 11:3305–3312
35. Higashihara T, Matsumoto K, Ueda M (2009) Sulfonated aromatic hydrocarbon polymers as proton exchange membranes for fuel cells. *Polymer* 50:5341–5357
36. Ghassemi H, McGrath JE, Zawodzinski TA (2006) Multiblock sulfonated-fluorinated poly(arylene ether)s for a proton exchange membrane fuel cell. *Polymer* 47:4132–4139
37. Roy A, Hickner MA, Yu X, Li Y, Glass TE, McGrath JE (2006) Influence of chemical composition and sequence length on the transport properties of proton exchange membranes. *J Polym Sci B Polym Phys* 44:2226–2239
38. Penner RM, Martin CR (1985) Ion transporting composite membranes. *J Electrochem Soc* 132:514–515
39. Cleghorn S, Kolde J, Liu W (2003) Catalyst coated composite membranes. In: Vielstien W, Gasteiger HA, Lamm A (eds) Handbook of fuel cells: fundamentals, technology and applications, vol 3. Wiley, West Sussex, pp 566–575
40. Tang Y, Kusoglu A, Karlsson AM, Santare MH, Cleghorn S, Johnson WB (2008) Mechanical properties of a reinforced composite polymer electrolyte membrane and its simulated performance in PEM fuel cells. *J Power Sources* 175:817–825
41. Choi J, Lee KM, Wycisk R, Pintauro PN, Mather PT (2008) Nanofiber network ion-exchange membranes. *Macromolecules* 41:4569–4572
42. Pintauro P (2009) U.S. department of energy hydrogen program 2009 annual merit review proceedings. [http://www.hydrogen.energy.gov/pdfs/review09/fc\\_09\\_pintauro.pdf](http://www.hydrogen.energy.gov/pdfs/review09/fc_09_pintauro.pdf)
43. Kerres JA (2005) Blended and cross-linked ionomer membranes for application in membrane fuel cells. *Fuel Cells* 5:230–247
44. Yang Y, Holdcroft S (2005) Synthetic strategies for controlling the morphology of proton conducting polymer membranes. *Fuel Cells* 5:171–186



45. Hou H, Di Vona ML, Knauth P (2012) Building bridges: crosslinking of sulfonated aromatic polymers – a review. *J Membr Sci* 423(Supplement C):113–127
46. Mao SS, Hamrock SJ, Ylitalo DA (2000) US Patent 6,090,895 crosslinked ion conductive membranes
47. Koppel IA, Taft RW, Anvia F, Zhu SZ, Hu LQ, Sung KS, DesMarteau DD, Yagupolskii LM, Yagupolski YL, Ignat'ev V, Kondratenko NV, Volkonskii AY, Slasov VM, Notario R, Maria PC (1994) The gas-phase acidities of very strong neutral Bronsted acids. *J Am Chem Soc* 116:3047–3057
48. Gubler L, Gürsel SA, Scherer GG (2005) Radiation grafted membranes for polymer electrolyte fuel cells. *Fuel Cells* 5:317–335
49. Sauguet L, Ameduri B, Boutevin B (2006) Fluorinated, crosslinkable terpolymers based on vinylidene fluoride and bearing sulfonic acid side groups for fuel-cell membranes. *J Polym Sci A Polym Chem* 44:4566–4578
50. Yandrasits MA, Hamrock SJ, Grootaert WM, Guerra MA, Jing N (2006) US Patent 7,074,841 polymer electrolyte membranes crosslinked by nitrile trimerization
51. Yandrasits MA, Hamrock SJ, Hintzer K, Thaler A, Fukushi T, Jing N, Lochhaas KH (2007) US Patent 7,265,162 bromine, chlorine or iodine functional polymer electrolytes crosslinked by e-beam
52. Yandrasits M, Lindell M, Schaberg M, Kurkowski M (2017) Increasing fuel cell efficiency by using ultra-low equivalent weight ionomers. *Electrochem Soc Interface Spring* 26(1):49–53. <https://doi.org/10.1149/2.F05171if>
53. Desmarteau DD (1995) Novel perfluorinated ionomers and ionenes. *J Fluor Chem* 72:203–208
54. Hamrock SJ (2010) U.S. department of energy hydrogen program 2010 annual merit review proceedings. [http://www.hydrogen.energy.gov/pdfs/review10/fc034\\_hamrock\\_2010\\_o\\_web.pdf](http://www.hydrogen.energy.gov/pdfs/review10/fc034_hamrock_2010_o_web.pdf)
55. Herring AM (2006) Inorganic polymer composite membranes for proton exchange membrane fuel cells. *Polym Rev* 46:245–296
56. Schaberg MS, Abulu J, Haugen GM, Emery M, O'Conner SJ, Xiong PN, Hamrock SJ (2010) New multi acid side-chain ionomers for proton exchange membrane fuel cells. *ECS Trans* 33:627–633
57. Iler R (1979) *The chemistry of silica*. Wiley, New York
58. Mauritz KA, Hassan MK (2007) Nanophase separated perfluorinated ionomers as sol-gel polymerization templates for functional inorganic oxide nanoparticles. *Polym Rev* 47:543–565
59. Abbaraju RR, Dasgupta N, Virkar AV (2008) Composite nafion membranes containing nanosize TiO<sub>2</sub>/SnO<sub>2</sub> for proton exchange membrane fuel cells. *J Electrochem Soc* 155:B1307–B1313
60. Kreuer K-D, Paddison SJ, Spohr E, Schuster M (2004) Transport in proton conductors for fuel-cell applications: simulations, elementary reactions, and phenomenology. *Chem Rev* 104:4637–4678
61. Alberti G, Casciola M (2003) Composite membranes for medium-temperature PEM fuel cells. *Annu Rev Mater Res* 33:129–154
62. Malhotra S, Datta R (1997) Membrane-supported non-volatile acidic electrolytes allow higher temperature operation of proton-exchange membrane fuel cells. *J Electrochem Soc* 144:L23–L26
63. Meng F, Aieta NV, Dec SF, Horan JL, Williamson D, Frey MH, Pham P, Turner JA, Yandrasits MA, Hamrock SJ, Herring AM (2007) Structural and transport effects of doping perfluorosulfonic acid polymers with the heteropoly acids, H<sub>3</sub>PW<sub>12</sub>O<sub>40</sub> or H<sub>4</sub>SiW<sub>12</sub>O<sub>40</sub>. *Electrochim Acta* 53:1372–1378
64. Alberti G, Casciola M, Capitani D, Donnadio A, Narducci R, Pica M, Sganappa M (2007) Novel Nafion-zirconium phosphate nanocomposite membranes with enhanced stability of proton conductivity at medium temperature and high relative humidity. *Electrochim Acta* 52:8125–8132
65. Coms FD, Han Liu H, Owejan JE (2008) Mitigation of perfluorosulfonic acid membrane chemical degradation using cerium and manganese ions. *ECS Trans* 16:1735–1747
66. Trogadas P, Parrondo J, Ramani V (2008) Degradation mitigation in polymer electrolyte membranes using cerium oxide as a regenerative free-radical scavenger. *Electrochem Solid State Lett* 11(7):B113–B116
67. Frey MH, Hamrock SJ, Haugen GM, Pham PT (2009) US Patent 7,572,534 fuel cell membrane electrode assembly
68. Watanabe M, Uchida H, Seki Y, Emori M, Stonehart P (1996) Self-humidifying polymer electrolyte membranes for fuel cells. *J Electrochem Soc* 143:3847–3852
69. Endoh E, Hommura S, Terazono S, Widjaja H, Anzai J (2007) Degradation mechanism of the PFSA membrane and influence of deposited Pt in the membrane. *ECS Trans* 11:1083–1091
70. Cipollini NE (2007) Chemical aspects of membrane degradation. *ECS Trans* 11:1071–1082
71. Haugen GM, Meng F, Aieta NV, Horan JL, Kuo M-C, Frey MH, Hamrock SJ, Herring AM (2007) The effect of heteropoly acids on stability of PFSA PEMs under fuel cell operation. *Electrochem Solid State Lett* 10: B51–B55
72. Liu H, Coms FD, Zhang J, Gasteiger HA, LaConti AB (2009) Chemical degradation: correlations between electrolyzer and fuel cell findings. In: Büchi FN, Inaba M, Schmidt TJ (eds) *Chemical degradation: correlations between electrolyzer and fuel cell findings polymer electrolyte fuel cell durability*. Springer, New York, pp 71–117
73. Friedmann R, Van Nguyen T (2010) Optimization of the microstructure of the cathode catalyst layer of a PEMFC for two-phase flow. *J Electrochem Soc* 157: B260–B265
74. Litster S, McLean G (2004) PEM fuel cell electrodes. *J Power Sources* 130:61–76
75. Shao Y, Yin G, Wang Z, Gao Y (2007) Proton exchange membrane fuel cell from low temperature to high temperature: material challenges. *J Power Sources* 167:235



76. Zhang J, Xie Z, Zhang J, Tang Y, Song C, Navessin T, Shi Z, Song D, Wang H, Wilkinson DP, Liu ZS, Holdcroft SJ (2006) High temperature PEM fuel cells. *Power Sources* 160:872
77. Xu H, Song Y, Kunz HR, Fenton JM (2005) Effect of elevated temperature and reduced relative humidity on ORR kinetics for PEM fuel cells. *J Electrochem Soc* 152:A1828–A1836
78. Parthasarathy A, Srinivasan S, Appleby AJ, Martin CR (1992) Temperature dependence of the electrode kinetics of oxygen reduction at the Platinum/Nafion<sup>®</sup> Interface: a microelectrode investigation. *J Electrochem Soc* 139:2530
79. Chen YX, Li MF, Liao LW, Xu J, Ye S (2009) A thermostatic cell with gas diffusion electrode for oxygen reduction reaction under fuel cell relevant conditions. *Electrochem Commun* 11:1434–1436
80. Kucernak AR, Toyoda E (2008) Studying the oxygen reduction and hydrogen oxidation reactions under realistic fuel cell conditions. *Electrochem Commun* 10:1728–1731
81. Gasteiger HA, Kocha SS, Sompalli B, Wagner FT (2005) Activity benchmarks and requirements for Pt, Pt-alloy, and non-Pt oxygen reduction catalysts for PEMFCs. *Appl Catal B* 56:9–35
82. Thompsett D (2003) Pt alloys as oxygen reduction catalysts. In: Vielstien W, Gasteiger HA, Lamm A (eds) *Handbook of fuel cells: fundamentals, technology and applications*, vol 3. Wiley, West Sussex, pp 467–480
83. Tada T (2003) High dispersion catalysts including novel carbon supports. In: Vielstien W, Gasteiger HA, Lamm A (eds) *Handbook of fuel cells: fundamentals, technology and applications*, vol 3. Wiley, West Sussex, pp 481–488
84. Shao Y, Yin G, Gao Y (2007) Understanding and approaches for the durability issues of Pt-based catalysts for PEM fuel cell. *J Power Sources* 171:558
85. Stevens DA, Dahn JR (2005) Thermal degradation of the support in carbon-supported platinum electrocatalysts for PEM fuel cells. *Carbon* 43:179–188
86. Debe MK, Schmoekkel AK, Hendricks SM, Vernstrom GD, Haugen GM, Atanososki RT (2006) Durability aspects of nanostructured thin film catalysts for pem fuel cells. *ECS Trans* 1:51–66
87. Trogadas P, Ramani V (2007) Pt/C/MnO<sub>2</sub> hybrid electrocatalysts for degradation mitigation in polymer electrolyte fuel cells. *J Power Sources* 174(1):159–163
88. Brooker RP, Baker P, Kunz HR, Bonville LJ, Parnas R (2009) Effects of silicotungstic acid addition to the electrodes of polymer electrolyte membrane fuel cells. *J Electrochem Soc* 156:B1317–B1321
89. Paddison SJ, Kreuer KD, Maier J (2006) About the choice of the protogenic group in polymer electrolyte membranes: ab initio modelling of sulfonic acid, phosphonic acid, and imidazole functionalized alkanes. *Phys Chem Chem Phys* 8:4530–4542
90. Horan JL, Genupur A, Ren H, Sikora BJ, Kuo MC, Meng F, Dec SF, Haugen GM, Yandrasits MA, HSJ MA, Frey MH, Herring AH (2009) Copolymerization of divinylsilyl-11-silicotungstic acid with butyl acrylate and hexanediol diacrylate: synthesis of a highly proton-conductive membrane for fuel-cell applications. *ChemSusChem* 2:226–229
91. Doyle M, Choi SK, Proulx G (2000) High-temperature proton conducting membranes based on perfluorinated ionomer membrane-ionic liquid composites. *J Electrochem Soc* 147:34
92. Zhou Z, Li S, Zhang Y, Liu M, Li W (2005) Promotion of proton conduction in polymer electrolyte membranes by 1*H*-1,2,3-triazole. *J Am Chem Soc* 127:10824–10825
93. Jia L, Nguyen D, Halleý JW, Pham P, Lamanna W, Hamrock S (2009) Proton transport in HTFSI-TFSI-EMI mixtures: experiment and theory. *J Electrochem Soc* 156:B136–B151



# Polybenzimidazole Fuel Cell Technology: Theory, Performance, and Applications

Andrew T. Pingitore<sup>1</sup>, Max Molle<sup>1</sup>,  
Thomas J. Schmidt<sup>2</sup> and Brian C. Benicewicz<sup>1</sup>

<sup>1</sup>Department of Chemistry and Biochemistry,  
University of South Carolina, University of South  
Carolina NanoCenter, Columbia, SC, USA

<sup>2</sup>General Energy Research, Laboratory of  
Electrochemistry, Paul Scherrer Institute,  
Villigen, Switzerland

## Article Outline

Glossary

Definition of the Subject

Introduction to Polybenzimidazole Fuel Cell

Sustainability

History and Technical Information of

Polybenzimidazole Membranes

PBI/PA Fuel Cell Systems and Their Applications

Conclusions and Future Directions

Bibliography

## Glossary

**Combined Heat and Power (CHP):** Stationary fuel cell devices that are used to produce both heat and electricity. High temperature PBI fuel cell membranes are well suited for this application.

**Conventional Imbibing:** The original process of impregnating polymer membranes with dopants. The precast, fully dense membranes are placed in baths of dopants and allowed to absorb the dopant which assists in proton conductivity.

**Membrane Electrode Assembly (MEA):** A device that is comprised of a PEM that is sandwiched between two electrodes.

**Polybenzimidazoles (PBIs):** A class of polymers recognized for their excellent thermal

and chemical stability, PBIs have historically been spun into fibers and woven into thermal protective clothing. In the past decade, PBIs have been cast into membranes and incorporated into fuel cells.

**Polymer Electrolyte Membrane (PEM):** Also referred to as Proton Exchange Membranes, PEMs are semi-permeable membranes that conduct and transport protons while preventing the transmission of gases and electrons.

**PPA Process:** A recently developed imbibing process, PBIs are polymerized and cast in a polyphosphoric acid solvent. Under controlled hydrolysis conditions, Polyphosphoric acid, a good solvent for PBI, is converted into phosphoric acid, a poor solvent for PBI. A mechanically stable PBI gel membrane that is highly doped with phosphoric acid is produced by means of a sol-to-gel transition.

**Proton Conductivity:** A measure of how well a material can transfer protons. In fuel cell technology, it is used to gauge the viability of proton exchange membranes.

## Definition of the Subject

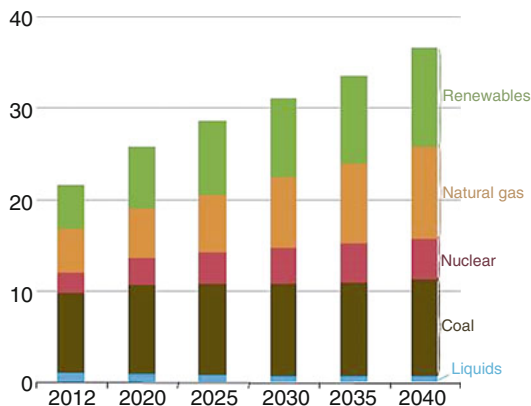
After approximately 15 years of development, polybenzimidazole (PBI) chemistries and the concomitant manufacturing processes have evolved into commercially produced membrane electrode assemblies (MEAs). PBI MEAs can operate reliably without complex water humidification hardware and are able to run at elevated temperatures of 120–180 °C due to the physical and chemical robustness of PBI membranes. These higher temperatures improve the electrode kinetics and conductivity of the MEAs, simplify the water and thermal management of the systems, and significantly increase their tolerance to fuel impurities. Membranes cast by a newly developed polyphosphoric acid (PPA) process possessed excellent mechanical properties, higher phosphoric acid (PA)/PBI ratios, and enhanced proton conductivities as compared to previous methods of membrane preparation. The *p*-PBI and *m*-PBI are

the most common polymers in PBI-based fuel cell systems, although AB-PBI and other derivatives have been investigated. This chapter reports on the chemistries and sustainable usages of PBI-based high temperature proton exchange membrane fuel cells (PEMFCs).

## Introduction to Polybenzimidazole Fuel Cell Sustainability

Alternative energy is often defined as any energy derived from sources other than fossil fuels or nuclear fission. These alternative energy sources, which include solar, wind, hydro, and geothermal energy, are considered renewable because they are naturally replenished and their supply is seemingly limitless. In contrast, the Earth's supply of fossil fuels is constantly being diminished. Fossil fuels, which include crude oil, coal, and natural gas, continue to be the dominating sources of energy in the world (Fig. 1). Fossil fuels provide more than 86% of the total energy consumed globally [1, 2]. In 2009, the electrical power sector was the largest source of carbon dioxide emissions (40% of all energy-related CO<sub>2</sub> emissions) and was followed closely by the transportation sector which was (34% of the total) [3]. It is predicted that the global demand for fossil fuels will continue to increase over the next 10–20 years due to economic growth. One may conclude that the importance of renewable energy will steadily increase as the Earth's supply of fossil fuels continues to be depleted.

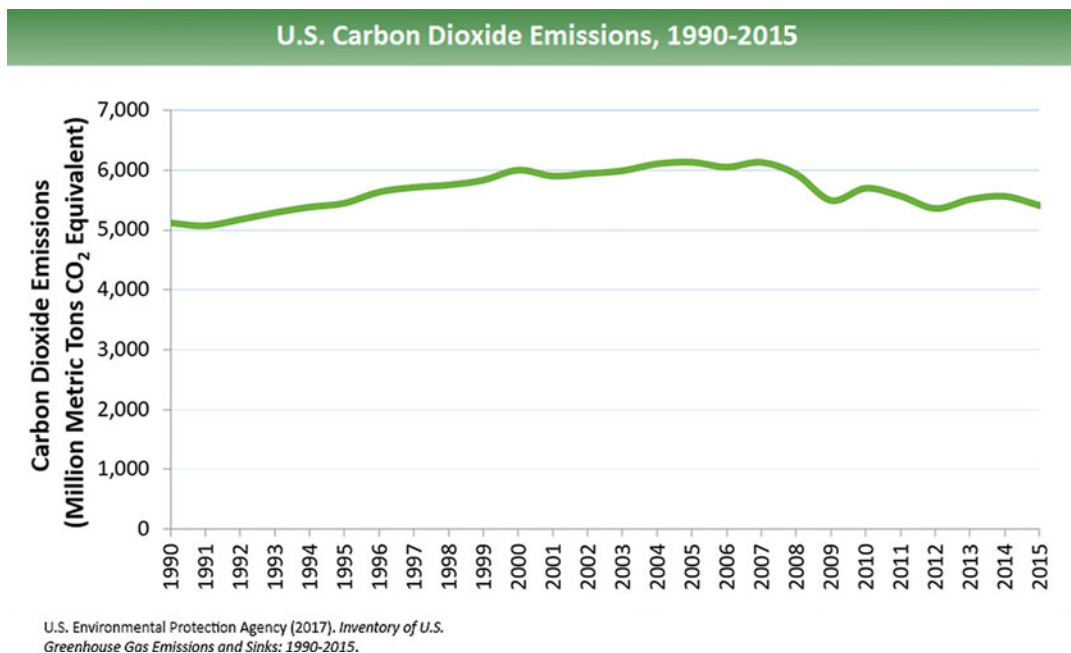
Polymer electrolyte membrane (PEM) fuel cells, also known as proton exchange membrane fuel cells (PEMFCs), are energy conversion devices that could provide the world with clean and efficient energy. Due to their excellent energy production, inexpensive starting materials, and lack of pollutant byproducts, these cells have exponentially gained in popularity over the past decade. Electricity is produced at the heart of the fuel cell by the membrane electrode assembly (MEA), a component that is comprised of a proton exchange membrane sandwiched between two electrodes. Fueled by a hydrogen-based source, a metal catalyst at the anode splits the hydrogen into



**Polybenzimidazole Fuel Cell Technology: Theory, Performance, and Applications, Fig. 1** World net electricity production by source, 2012–2040 (trillion kilowatt hours) [1]

protons and electrons. As the protons are transported through the proton electrolyte membrane to the cathode, the electrons provide electrical work by traveling around the membrane through an external circuit from the anode to the cathode. The protons and electrons react with an oxidant (typically air or pure oxygen) at the cathode to form water, thereby completing the electrochemical cycle. Hydrogen gas is commonly used as a fuel source for the cells, but other fuels such as methane, methanol, and ethanol have been explored.

PEM fuel cells provide multiple advantages over conventional fossil fuel energy production. Because water is the only byproduct of the electrochemical process, these fuel cells are clean and environmentally friendly. If one considers the tremendous amount of carbon dioxide created by energy production on the global scale (Fig. 2), PEM fuel cells offer a method to significantly reduce hazardous gas emissions. Minimal moving parts reduces the amount of maintenance of each cell, and the lack of combustion significantly decreases the amount of harmful pollutants such as sulfur oxides and nitrogen oxides. In addition, PEM fuel cells are much more efficient at producing energy (this is discussed in detail in section “PBI/PA Fuel Cell Systems and Their Applications”), and much like a combustion engine, the cell can run continuously as long as



**Polybenzimidazole Fuel Cell Technology: Theory, Performance, and Applications, Fig. 2** Global production of carbon dioxide annually from 1990 to 2015 [4]

fuel and oxidant are provided. Although fuel cells are an environmentally friendly energy conversion device, one must consider the way hydrogen is gathered. Both hydrogen production and conversion from chemical to electrical energy need to be sustainable to make the overall process sustainable. Hydrogen production, however, will only briefly be discussed in this chapter.

The efficiency of a PEM fuel cell is largely dependent on the materials used and their arrangement in the cell. Fuel cells use an array of different catalysts, electrodes, membranes, and dopants, each of which function under specific operating conditions. Cells that use low-boiling dopants, such as water, operate at approximately 60–80 °C to avoid vaporization of the proton-transfer agent. Large heat exchangers are required to ensure the heat generated by the cell does not vaporize the electrolyte. Consequently, system complexity is increased as extra components and controls are required to ensure that the membrane remains hydrated during operation. Moreover, cell operation at such low

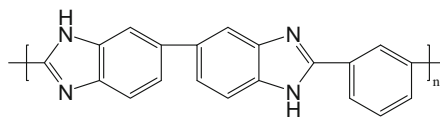
temperatures allows trace amounts of reformat byproducts, especially carbon monoxide, to bind to the catalyst. These highly-competitive, non-reversible reactions “poison” the catalyst, thereby decreasing and possibly terminating the functionality of the fuel cell. Therefore, low temperature fuel cells require an extremely pure fuel source.

In contrast to low-temperature cells, high-temperature PEMs use high-boiling dopants, such as phosphoric acid and sulfuric acid, and function at temperatures of 120–200 °C. Operating at elevated temperatures alleviates the need for excessive heat exchangers and at these temperatures fuel pollutants bind reversibly to the catalyst, which helps to prevent catalyst poisoning. Consequently, high-temperature PEMs can use reformed gases with much higher levels of impurities and lower reformation costs. Furthermore, high temperatures typically improve both the electrode kinetics and operating abilities of the cell. This chapter reports on the chemistries and sustainable usages of PBI-based high temperature PEMFCs.

## History and Technical Information of Polybenzimidazole Membranes

Polybenzimidazoles (PBIs) are a class of polymers recognized for their excellent thermal and chemical stability. PBI is used in multiple applications including matrix resins, high strength adhesives, thermal and electrical insulating foams, and thermally resistant fibers. PBI fibers were originally synthesized in the early 1960s by a cooperative effort of the United States Air Force Materials Laboratory with DuPont and the Celanese Research Company. One of the first PBIs to be widely investigated was poly(2,2'-*m*-phenylene-5,5'-bibenzimidazole), which is commonly referred to as *m*-PBI (Fig. 3). Because *m*-PBI is non-flammable, resistant to chemicals, physically stable at high temperatures, and can be spun into fibers, this polymer has been used in astronaut space suits, firefighter's turnout coats and suits, and high temperature protective gloves.

Polybenzimidazole membranes are excellent candidates for high-temperature fuel cells because of their thermal and chemical stability and proton conducting ability. The stability of PBIs is attributed to its aromatic structure (alternating single and double bonds) and the rigid nature of its bonds [5]. While the membrane structure allows protons to flow from one side to the other, it acts as a barrier to the crossover of gases and electrons. The chemical stability of PBIs allows the membranes to withstand the chemically reactive environments of the anode and cathode. Furthermore, the basic nature of the polymer allows it to be highly doped with phosphoric or sulfuric acid. The dopants interact with the polymer matrix and provide a network through which protons can be transported. These acids are used as electrolytes because of their high conductivity, thermal stability, and enhanced proton-transport capabilities. It is important to note that the proton conductivity of PBI membranes without a dopant is negligible. For liquid phosphoric acid, the proton jump rate is orders of magnitude larger than the diffusion of the phosphoric acid molecule as a whole [6]. Additionally, it has been reported that both protons and phosphate moieties have a substantially decreased diffusion coefficient when



**Polybenzimidazole Fuel Cell Technology: Theory, Performance, and Applications, Fig. 3** Chemical structure of poly(2,2'-*m*-phenylene-5,5'-bibenzimidazole) (*m*-PBI)

blended with basic polymers as opposed to liquid phosphoric acid [7]. Therefore, a heterogeneous, two-phase system in which the PBI membrane is phase-separated and imbibed with phosphoric acid has a higher conductivity than its homogeneous counterpart [8]. More recently, Kreuer et al. demonstrated that the interaction of phosphoric acid and PBI reduces the hydrogen bond network frustration, which in turn reduces phosphoric acid's very high acidity and hygroscopicity; reducing electroosmotic drag as well. They suggest this to be a reason why, in fuel cells, PBI-phosphoric acid membranes perform better than other phosphoric acid containing electrolytes with higher protonic conductivity [9]. As evidence of the growing attention in this area, a book on high temperature PEM fuel cells has recently been released [10].

### Synthesis of Polybenzimidazoles

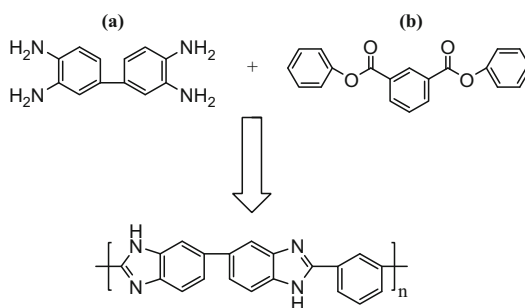
One of the first PBI membranes investigated for fuel cell use was poly(2,2'-*m*-phenylene-5,5'-bibenzimidazole) (*m*-PBI). At the time, there was a vast amount of research previously reported on *m*-PBI and it was renowned for its excellent thermal and mechanical properties [6]. The polymer is synthesized by the reaction of 3,3',4,4'-tetraaminobiphenyl (TAB) with diphenylisophthalate (DPIP) during a melt/solid polymerization (Scheme 1). The resulting polymer is extracted and has an inherent viscosity (IVs) between 0.5 and 0.8 dL g<sup>-1</sup>, which corresponds to a polymer with low to moderate molecular weight. The *m*-PBI is further purified by dissolving it in a solution of N, N-dimethylacetamide and lithium chloride (DMAc/LiCl) under 60–100 psi and 250 °C and then filtering; this step removes any crosslinked

*m*-PBI. The polymer is then cast as a film and dried at 140 °C under vacuum to evaporate the solvent. The *m*-PBI membrane is washed in boiling water to remove any residual DMAc/LiCl solution trapped in the polymer matrix. After the polymer has been dried, an acid bath is used to dope the membrane; the doping level of the membrane can be partially controlled by varying the concentration of acid in the bath. Originally, this conventionally imbibed process created membranes with molar ratios of phosphoric acid/polymer repeat unit (PA/PRU) approximately 6–10 [11]. A “direct acid casting” (DAC) technique was later developed to allow the PBI membrane to retain more PA [12]. Both the conventional imbibing process and DAC were developed following the research performed by Jean-Claude Lasegues, who was one of the first scientists that investigated basic polymeric acid systems (a summary of his work is reviewed in reference [13]). The DAC technique consists of extracting low molecular weight PBI components from PBI powder, and then dissolving the high molecular weight PBI components in trifluoroacetic acid (TFA). Phosphoric acid is added to the TFA/PBI mixture, which is then cast onto glass plates with a casting blade. One may tune the doping level of the polymer by adjusting the amount of phosphoric acid that is added to the TFA/PBI mixture. However, as one increases the PA doping level of a DAC PBI membrane, its mechanical strength decreases to the point where it can no longer be used in a fuel cell. Modern imbibing processes can increase the PA/PBI ratio to 12–16, and these fuel cell membranes are reported to have proton conductivities as high as 0.08 S cm<sup>-1</sup> at 150 °C at various humidities.

A novel synthetic process for producing high molecular weight PBIs, the “PPA Process” was developed at Rensselaer Polytechnic Institute with cooperation from BASF Fuel Cell GmbH. This process has previously been discussed by Xiao et al. [14] The general synthesis of PBI by this method requires the combination of a tetraamine with a dicarboxylic acid in polyphosphoric acid (PPA) in a dry environment. The step-growth polycondensation reaction typically occurs ca. 200 °C for 16–24 h in a nitrogen atmosphere,

producing high molecular weight polymer. This solution is cast directly from PPA as a thin film on a substrate, and upon absorption of water, the PPA hydrolyzes in situ to form phosphoric acid. Note that PPA is a good solvent for PBI while PA is a poor solvent. Under controlled hydrolysis conditions, a mechanically stable PBI gel membrane that is highly doped with phosphoric acid is produced. The multiple physical and chemical transformations that explain the solution-to-gel phase transition are summarized in Fig. 4.

The PA doped *m*-PBI fuel cell membrane maintains thermal and physical stability while operating at high temperature. To illuminate the fundamental differences in polymer film architecture, polymers with similar physical characteristics were prepared by the conventional and PPA Process (Table 1). Even though the ratio of phosphoric acid-to-polymer repeat unit (PA/PRU) achieved by both processes were nearly identical, the PPA Process produces membranes with much higher proton diffusion coefficients and conductivities. One can conclude that the PPA Process creates a membrane with a proton transport architecture superior to that of the conventionally imbibed PBI membrane. The higher proton diffusion coefficients of the membranes produced by the PPA process versus conventionally imbibed membranes were confirmed by NMR [15]. In addition, inherent viscosity data indicates that the PPA Process produces polymers of much higher molecular weight [14]. It was subsequently shown that improved membrane morphology and



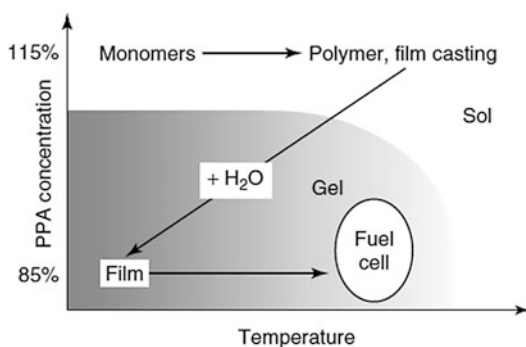
**Polybenzimidazole Fuel Cell Technology: Theory, Performance, and Applications, Scheme 1** Polymerization of 3,3',4,4'-tetraaminobiphenyl (a) and diphenylisophthalate (b) to form *m*-PBI



increased molecular weight allow the polymer to retain much more phosphoric acid than traditionally cast PBI membranes. An increased PA doping level typically improves the conductivity of the membrane and may even increase the performance of the cell.

### Properties and Performance of Synthetically Modified PBI

In this chapter the synthesis of significant PBI membranes (Fig. 5) and their use in fuel cells are described. Synthetically modified PBIs are investigated for enhanced thermo-oxidative stability, solubility, and flexibility; these attributes allow for improved process ability and production of membranes with good chemical and mechanical properties. All PBI membranes are produced by means of step-growth polycondensation reactions and are generally imbibed by either the conventional technique or made by the PPA Process. To synthesize modified polymers, one may either



**Polybenzimidazole Fuel Cell Technology: Theory, Performance, and Applications, Fig. 4** State diagram of the PPA sol-gel process [14]

polymerize modified monomers or use post-polymerization crosslinking or substitution reactions. The following sections briefly detail the syntheses of PBI derivatives and their performances as fuel cell membranes.

### *m*-PBI

One of the first PBI membranes investigated for fuel cell use was *m*-PBI (Fig. 5a). As previously discussed, the film can be processed by using either the conventional imbibing method or the PPA Process. Using the conventional imbibing method, the inherent viscosity of the membrane is usually between 0.50 and 1.00 dL g<sup>-1</sup> at 30 °C, which indicates polymers of moderate molecular weight. In contrast, *m*-PBI membranes synthesized and doped via the PPA Process have inherent viscosities of approximately 1.00–2.35 dL g<sup>-1</sup> at 30 °C, which corresponds to higher molecular weight polymers [11]. Using the PPA process, higher molecular weight polymers have contributed to higher doping levels. Phosphoric acid doping levels for conventionally prepared *m*-PBI ranged from 6 to 10 moles PA/PRU, whereas the doping levels for polymer films prepared via the PPA Process range from 14 to 26 moles PA/PRU [5]. Trends show that the mechanical stability of conventionally prepared membranes decrease as the doping level increases and/or as the molecular weight of the polymer decreases. The doping level, casting technique, temperature, and humidity all influence the conductivity of a *m*-PBI membrane. Under various humidities, conventionally prepared *m*-PBI membranes have been reported having conductivities in the range of 0.04–0.08 S

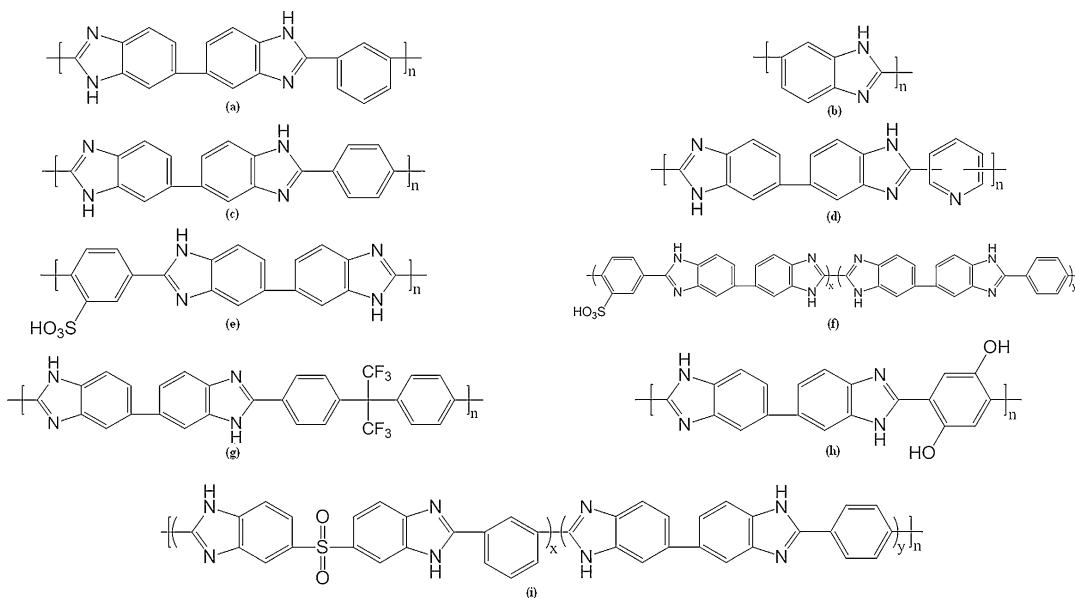
**Polybenzimidazole Fuel Cell Technology: Theory, Performance, and Applications, Table 1** Comparison of conventionally imbibed *m*-PBI vs. *m*-PBI synthesized from the PPA process [16]

IV <sup>a</sup> (dl g <sup>-1</sup> )	Film process	Polymer (wt%)	PA (wt %)	Water (wt%)	PA/PBI (molar ratio)	Proton diffusion coefficient <sup>b</sup> (cm <sup>2</sup> s <sup>-1</sup> )	Conductivity <sup>c</sup> (S cm <sup>-1</sup> )
0.89	Conventionally imbibed	15.6	60.7	23.7	12.2	10 <sup>-7</sup>	0.048
1.49	PPA process	14.4	63.3	22.3	13.8	3 × 10 <sup>-6</sup>	0.13

<sup>a</sup> Inherent viscosity (IV) was measured at a polymer concentration of 0.2 g dl<sup>-1</sup> in concentrated sulfuric acid (96%) at 30 °C, using a Canon Ubbelohde viscometer

<sup>b</sup> Estimation of upper bound for conventionally imbibed *m*-PBI at 180 °C; PPA-prepared *m*-PBI measured at 180 °C

<sup>c</sup> Measured at 160 °C after an initial heating to 160 °C to remove water



**Polybenzimidazole Fuel Cell Technology: Theory, Performance, and Applications, Fig. 5** Various synthetically modified polybenzimidazoles for use in fuel cells. (a) *m*-PBI, (b) AB-PBI, (c) *p*-PBI, (d) py-PBI, (e)

*s*-PBI, (f) *s*-PBI/*p*-PBI segmented block copolymer, (g) 6F-PBI, (h) 2OH-PBI, (i) *m*-SPBI / *p*-PBI segmented block copolymer

$\text{cm}^{-1}$  [17]. Using the PPA Process, the conductivity values of *m*-PBI membranes are typically higher than that of the conventionally imbibed process. One study reported [18] *m*-PBI membranes formed by the PPA process as having a conductivity of  $0.13 \text{ S cm}^{-1}$  at  $160^\circ \text{C}$  under nonhumidified conditions.

Phosphoric acid doped *m*-PBI membranes that have been formed by the conventional imbibing method have been extensively studied for use in fuel cells. Li et al. [19] demonstrated that a membrane with 6.2 PA/PRU doping level obtains a current density of approximately  $0.7 \text{ A cm}^{-2}$  at 0.6 V using hydrogen and oxygen gases; these results were promising because the gases were not humidified. Zhai et al. [20] studied the degradation mechanisms of the PA/*m*-PBI system by continuously operating it at  $0.640 \text{ A cm}^{-2}$  at  $150^\circ \text{C}$  with unhumidified hydrogen and oxygen for 550 h; the fuel cell was operated intermittently the last 50 h with shutoffs every 12 h. The voltage increased from 0.57 to 0.66 V during the beginning 90-h activation period, and the following 450 h period showed a steady decrease to

0.58 V. The performance of the system rapidly decreased in the following 10 h due to agglomeration of the platinum from the catalyst, leaching of the phosphoric acid, and hydrogen crossover. Kongstein et al. [21] employed use of a dual layer electrode to prevent the oxidation of carbon in the polymer membrane, which can occur in acidic environments at high voltages. This electrode would improve the structural integrity of the polymer and help prevent hydrogen crossover from occurring. The PA/*m*-PBI membrane had a maximum of 0.6 V at  $0.6 \text{ A cm}^{-2}$  with a maximum power density of  $0.83 \text{ W cm}^{-2}$  at 0.4 V. These performances were lower than that of other PEM systems, such as Nafion, but were still impressive because they could be run at much higher temperatures.

#### Poly(2,5-polybenzimidazole): AB-PBI

Commonly referred to as AB-PBI, poly(2,5-polybenzimidazole) has a much simpler structure than that of *m*-PBI and other polybenzimidazoles (Fig. 5b). Whereas *m*-PBI is synthesized from

3,3',4,4'-tetraaminobiphenyl and DPIP, AB-PBI is polymerized from a single monomer, 3,4-diaminobenzoic acid (DABA). This monomer is commercially available and is less expensive than the starting materials of *m*-PBI. The polymer membrane can be cast and imbibed with phosphoric acid by the conventional imbibing method in a mixture of methanesulfonic acid (MSA) and phosphorous pentoxide (P<sub>2</sub>O<sub>5</sub>) [22] or DMAc. It can also be cast by direct acid casting using trifluoroacetic acid (TFA) [12, 17] or by the PPA Process [12, 23–25]. AB-PBI membranes prepared by the conventional imbibing method had IV values around 2.0–2.5 dL g<sup>-1</sup> as reported by Asensio et al. [25] and 6–8 dL g<sup>-1</sup> by Litt et al. [17]. Polymers produced from recrystallized DABA by the PPA Process have IV values greater than 10 dL g<sup>-1</sup> [26]; however, membranes of AB-PBI could not be easily formed via the PPA Process because of the polymer's high solubility in acids.

Because AB-PBI has a high concentration of basic sites (amine and imine groups), it has a high solubility and affinity to acids. Due to this affinity, it can be doped with phosphoric acid and sulfonated with sulfuric acid. Sulfonation of AB-PBI (sAB-PBI) is performed by soaking the precast polymer in sulfuric acid followed by treating the mixture with heat. Asensio et al. [25] reported sAB-PBI/PA membranes having an enhanced conductivity over that of AB-PBI/PA and to be both mechanically strong and thermally stable. Using the direct casting method from MSA-P<sub>2</sub>O<sub>5</sub>, Kim et al. [22] produced AB-PBI/PA membranes with conductivities similar that of Asensio, having values ranging from 0.02–0.06 S cm<sup>-1</sup> at 110 °C with no humidification. The conductivity values and physical-chemical properties resemble that of *m*-PBI, making it a good candidate for fuel cell use.

Yu [27] synthesized *p*-PBI-block-AB-PBI membranes to lower the membrane's solubility in acids while maintaining a high acid doping level. Different molar ratios of each polymer block were synthesized, and their conductivities and acid doping levels were investigated. As detailed in Table 2, the proton conductivities of the segmented block copolymers were enhanced

by an order of magnitude over that of native AB-PBI. Stress-strain studies showed that these block copolymers were strong enough to be used in fuel cell tests. Polarization curves (Fig. 6) of these membranes illustrate that copolymers II, III, and IV have excellent fuel cell properties (approximately 0.6 V at 0.2 A cm<sup>-2</sup>); polarization curves for copolymer V and VI could not be measured due to poor thermal stability of the membrane (re-dissolution) at 160 °C.

Poly(2,2'-(1,4-phenylene)5,5'-bibenzimidazole):  
*p*-PBI

Poly(2,2'-(1,4-phenylene)5,5'-bibenzimidazole) (*p*-PBI, Fig. 5c) is one of the highest performing PBI membranes for high-temperature fuel cell use. Due to the rigid nature of *p*-PBI, high molecular weight polymers have typically been difficult to fabricate or process. The first reported high molecular weight *p*-PBI with an IV value of 4.2 dL g<sup>-1</sup> was synthesized in 1974 by the United States Air Force Materials Laboratory [28]. Because it could not be spun into fibers as easily as *m*-PBI, *p*-PBI was not investigated further until after the turn of the century. Using the PPA Process, Xiao et al. [16] and Yu et al. [29] synthesized high molecular weight *p*-PBI with IV values as high as 3.8 dL g<sup>-1</sup>. The PA doping level of the corresponding polymer membranes was >30 mol PA/PRU, allowing the membrane to achieve a conductivity of 0.24 S cm<sup>-1</sup> at 160 °C. Xiao and Yu showed that *p*-PBI membrane achieves a much higher acid doping level and conductivity than that of *m*-PBI, which only achieves a doping level of 13–16 mol PA/PRU with a conductivity of 0.1–0.13 S cm<sup>-1</sup>. Because *p*-PBI had excellent mechanical properties at this high doping level, it was a prime candidate for fuel cell performance tests.

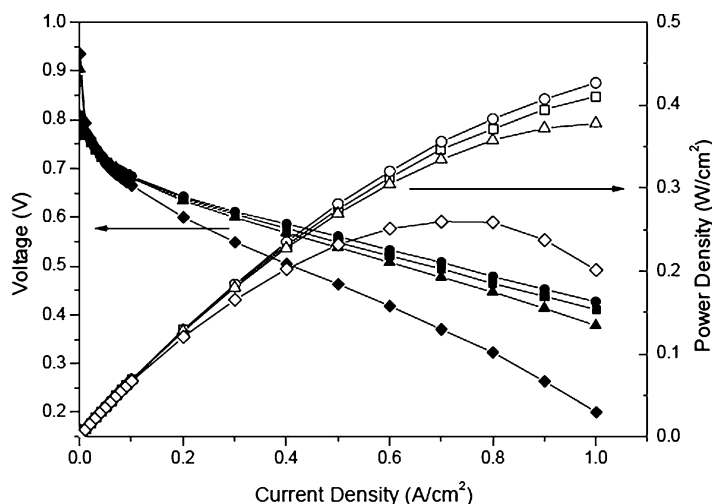
The polarization curves of an MEA using *p*-PBI produced by the PPA Process at various temperatures are shown in Fig. 7. Hydrogen was used as the fuel and air was used as the oxidant. The *p*-PBI outperformed the *m*-PBI at all temperatures, and the performance of the MEA increased as the temperature increased. Using a load of 0.2 A cm<sup>-2</sup>, the cell was able to produce a voltage of 0.606 V at 120 °C; upon raising the temperature

**Polybenzimidazole Fuel Cell Technology: Theory, Performance, and Applications, Table 2** Percent composition, acid doping level, and proton conductivity data for various *p*-PBI-block-AB-PBI membranes [27]

	<i>Para</i> -PBI/AB-PBI (mole ratio, x/y)	Acid doping level (PA/2 benzimidazole)	Proton conductivity (S/cm @ 160 °C)	Membrane composition (%)		
				Polymer	H <sub>3</sub> PO <sub>4</sub>	Water
I	100/0	42.9	0.25	4.13	60.38	35.11
II	75/25	19.1	0.25	8.68	58.09	33.22
III	50/50	24.1	0.27	6.59	54.53	38.88
IV	25/75	21.8	0.23	7.79	63.31	28.90
V	10/90	17.3	0.15	8.84	63.23	27.94
VI	0/100	N/A	N/A			

### Polybenzimidazole Fuel Cell Technology: Theory, Performance, and Applications,

**Fig. 6** Polarization curves (filled symbols) and power density curves (unfilled symbols) of *p*-PBI (Polymer I, ■ □) and *p*-PBI-block-AB-PBI membranes (75/25, Polymer II, ●○, 50/50 Polymer III, ▲△, 25/75, Polymer IV, ◆◇) at 160 °C with H<sub>2</sub> (1.2 stoic)/Air (2.0 stoic) under atmospheric pressure [27]



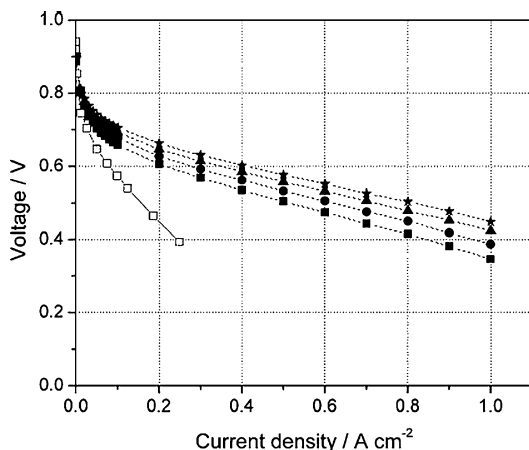
to 180 °C, the voltage increased to 0.663 V. This was especially promising because the gases were unhumidified.

#### Pyridine-PBI

Pyridine polybenzimidazoles (py-PBIs, Fig. 5d) have been investigated for their use in fuel cells because of their high concentration of basic sites (amine and imine groups). Similar to AB-PBI, the high concentration of basic sites allow these polymers to have a high affinity to acids. The pyridine moiety is commonly combined with the traditional PBI structure by including it as part of the backbone structure.

Xiao et al. synthesized an array of py-PBIs that have the pyridine moiety as part of the polymer backbone [14, 30, 31]. These polymers were synthesized by a reaction of 2,4-, 2,5-, 2,6-, or 3,5-pyridine dicarboxylic acid with

3,3',4,4'-tetraaminobiphenyl (TAB) using the PPA Process. Exceedingly pure monomers were required to polymerize the py-PBIs, and IV values of 1.0–2.5 dL g<sup>-1</sup> were obtained. The 2,4- and 2,5-py-PBI membranes formed mechanically strong films, whereas the 2,6-py-PBI membrane was mechanically weak and the 3,5-py-PBI was unable to form films due to high solubility in PPA. All of the py-PBI structures were thermally stable in both nitrogen and air in temperatures up to 420 °C. The 2,5- and 2,6-py-PBI were reported as having conductivities of 0.2 S cm<sup>-1</sup> and 0.1 S cm<sup>-1</sup> at 160–200 °C, respectively. The 2,5-py-PBI was found to have the most mechanically robust structure. It was hypothesized that the enhancement of mechanical properties was due to its *para*-orientation as opposed to the other py-PBIs having a *meta*-orientation. In addition, the doping level of



**Polybenzimidazole Fuel Cell Technology: Theory, Performance, and Applications, Fig. 7** Polarization curves of PPA-processed *p*-PBI MEA using hydrogen/air at 120 °C (squares), 140 °C (circles), 160 °C (triangles), and 180 °C (stars). Open squares represent DMAc cast *m*-PBI MEA at 150 °C [29]

2,5-py-PBI averaged 20 mol of phosphoric acid per polymer repeat unit. Because PPA processed 2,5-py-PBI was an extremely good candidate for fuel cell testing, polarization tests of the MEA were performed (Fig. 8). The platinum loading on the anode and cathode was 1.0 mg cm<sup>-2</sup> with 30% Pt in Vulcan XC-72 carbon black. The active area for the MEA was 10 cm<sup>2</sup>. The membranes used nonhumidified H<sub>2</sub>/O<sub>2</sub> and higher temperatures improved the performances of 2,5-py-PBI MEA.

There have been studies indicating that blends of PBI polymers with pyridine-containing polymers could prove useful in a high-temperature PEM fuel cell. Kallitsis et al. [33] combined commercially supplied *m*-PBI with an aromatic polyether that contained a pyridine moiety in the main chain (PPyPO); these polymer blends were then soaked in 85% wt PA. Dynamic mechanical analysis of a 75/25 PBI/PPyPO block copolymer showed reasonable mechanical strength and flexibility. The conductivity of this copolymer was not reported, but the conductivity of 85/15 PBI/PPyPO block copolymer was 0.013 S cm<sup>-1</sup> at a relatively low PA doping level. Further investigation of these systems is required to prove its utility as a fuel cell membrane.

### Sulfonated PBI

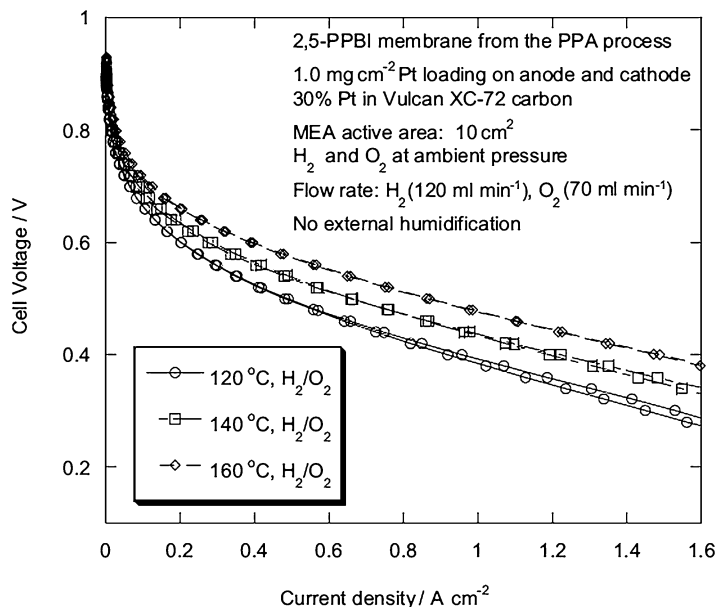
Sulfonated aromatic polymers have been widely investigated [34–44] for fuel cell use due to their enhanced physical and chemical robustness, acid and water retention, and conductivity over that of Nafion and other perfluorosulfonic acid-type polymers. Thus, due to the enhanced properties of PBI, it was logical to investigate the physical and chemical properties of sulfonated PBI (s-PBI) membranes. Sulfonation of PBI typically occurs by either direct sulfonation of the polymer backbone [25, 45, 46], grafting sulfonated moieties onto the backbone [25, 47], or by a polycondensation reaction that bonds aromatic tetra-amines to sulfonated aromatic diacids [48–51]. Compared to other sulfonation methods, polycondensation reactions provide more control over the degree of sulfonation.

Mader investigated the physical and chemical properties of s-PBI with PA as the dopant (Fig. 5e) [50]. The polymer was synthesized by two different synthetic pathways; the first was a direct polycondensation reaction of 2-sulfoterephthalic acid (s-TPA) and TAB using the PPA Process, and the second was a postsulfonation reaction of *p*-PBI using concentrated sulfuric acid. The IV values for the polymer membranes derived from the polycondensation reaction ranged from 1 to 2 dL g<sup>-1</sup>; these polymers had sufficiently high molecular weights to allow strong films to be cast. In addition, these polymer membranes could achieve doping levels between 28 and 53 mol PA/PRU, which resulted in significantly high conductivity values (all above 0.1 S cm<sup>-1</sup> at all temperatures between 100 °C and 200 °C).

Based on the preliminary data, s-PBI polymer membranes were excellent candidates for fuel cell tests. Polarization tests were run using an s-PBI membrane with an IV value of 1.71 dL g<sup>-1</sup>, a PA doping level of 52.33 mol PA/PRU, and a conductivity of 0.248 S cm<sup>-1</sup>; the results are depicted in Fig. 9. The s-PBI membrane exhibited its highest performance at 160 °C, producing 0.6788 V at a current density of 0.2 A cm<sup>-2</sup>. This performance compares well to that of other PBIs produced by the PPA Process, which is typically around 0.6–0.7 V at 0.2 A cm<sup>-2</sup>.

### Polybenzimidazole Fuel Cell Technology: Theory, Performance, and Applications,

**Fig. 8** Polarization curves under hydrogen and oxygen gases at various temperatures of PA-doped 2,5-py-PBI membranes [32]



The s-PBI homopolymer was shown to have both excellent resistance to gas impurities and excellent longevity. A reformat gas composed of 70% hydrogen, 28% carbon dioxide, and 2% carbon monoxide was used as the fuel while air was used as the oxidant. As depicted in Fig. 10, the fuel cell performance increased with increasing temperature; this is explained by the retardation of carbon monoxide poisoning that occurs at high temperatures. The performance loss of s-PBI MEA was measured by holding the MEA at 0.2 A cm<sup>-2</sup> at 160 °C for 1200 h using H<sub>2</sub>/O<sub>2</sub>. After reaching stabilization at the 343rd h, the MEA had a voltage loss of 0.024 mV hr<sup>-1</sup> for the remainder of the test.

Mader also investigated s-PBI/*p*-PBI random copolymers (Fig. 5f) for use in fuel cells [51]. The random copolymer was synthesized by reacting TAB, TPA, and s-TPA in a reaction flask and the membrane was cast via the PPA Process. High molecular weight polymers were achieved with IV values exceeding 1.8 dL g<sup>-1</sup>; this allowed for mechanically strong films to be cast. As the ratio of s-PBI/*p*-PBI decreased, the molecular weight of the polymer proportionally increased. Higher PA loading was seen at lower s-PBI/*p*-PBI ratios, which almost directly corresponded to the

conductivity of the membranes. The 75/25 s-PBI/*p*-PBI membrane had a PA loading value of 20.32 mol PA/PBI and a conductivity of 0.157 S cm<sup>-1</sup>, whereas the 25/75 s-PBI/*p*-PBI membrane had a PA loading value of 40.69 mol PA/PBI and a conductivity of 0.291 S cm<sup>-1</sup>.

Fuel cell performance tests were conducted on the random copolymers. Even though the 25/75 s-PBI/*p*-PBI random copolymer had a higher conductivity than that of *p*-PBI homopolymer, it was found that all of the random copolymers showed lower performance than *p*-PBI. The 50/50 and 75/25 s-PBI/*p*-PBI random copolymers had lower performance than the s-PBI homopolymer at all PA doping levels. However, the 25/75 s-PBI/*p*-PBI random copolymer performed comparably to the s-PBI homopolymer at equivalent PA doping levels.

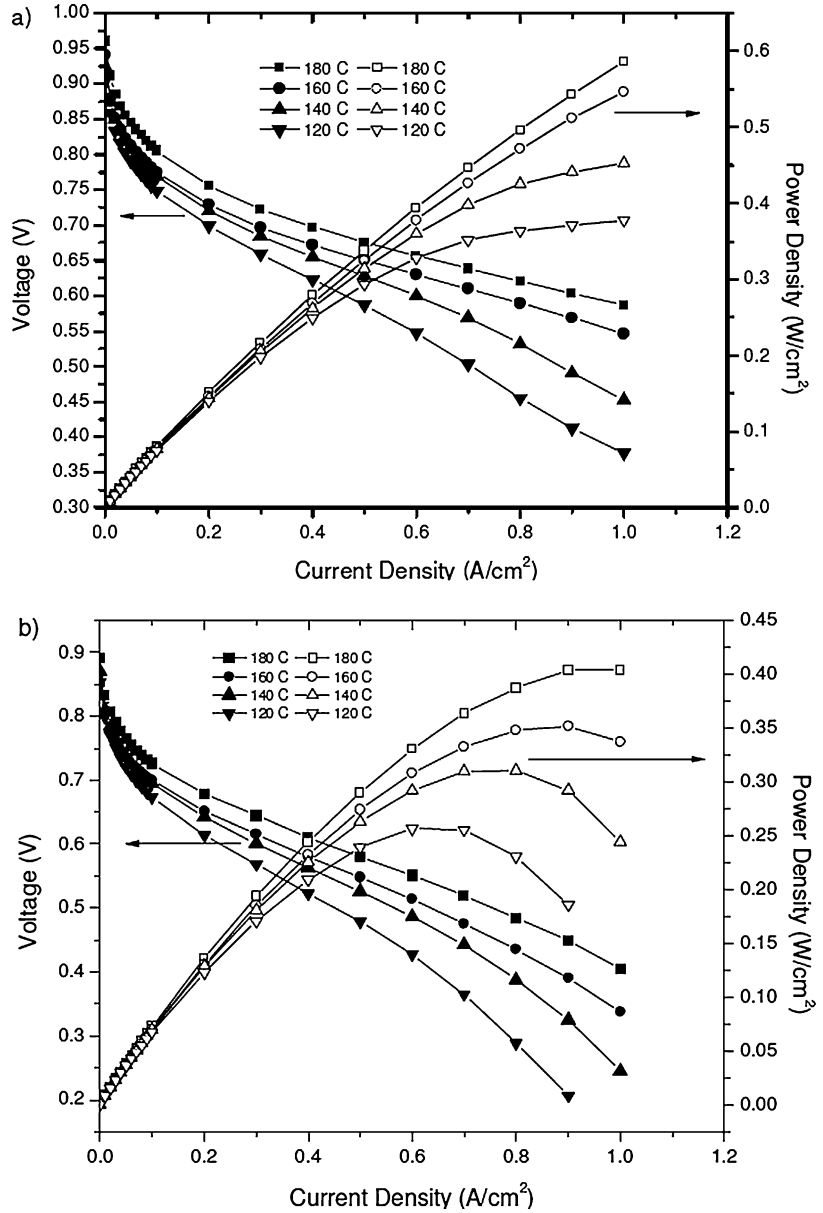
### PBI-Inorganic Composites

For conventionally prepared PBI membranes, as the acid doping levels of PBIs increase, the conductivity and overall performance of the PBI membranes also tend to increase. However, as high acid doping levels are reached for PBI membranes, the mechanical strength of the membrane significantly decreases. Inorganic fillers for PBI



**Polybenzimidazole Fuel Cell Technology: Theory, Performance, and Applications,**

**Fig. 9** Polarization curves (filled symbols) and power density curves (unfilled symbols) of s-PBI using (a) hydrogen and oxygen and (b) hydrogen and air [50]



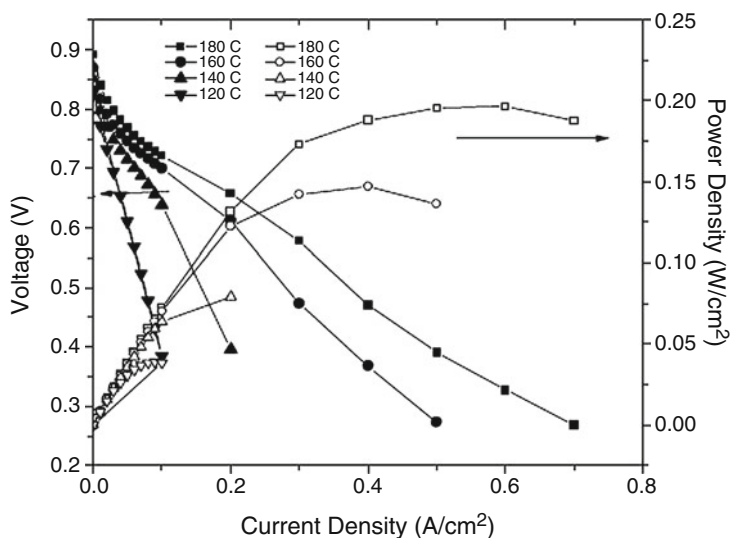
membranes have been investigated to improve membrane film strength, thermal stability, water and acid uptake, and conductivity. These composite membranes have only been examined using *m*-PBI and the conventional casting method.

He et al. investigated the use of zirconium phosphate (ZrP) in a PA/PBI system [52]. The conductivity of *m*-PBI with a doping level of 5.6 PA/PRU increased from 0.068 S cm<sup>-1</sup> to 0.096 S cm<sup>-1</sup> with the addition of 15 wt % ZrP at 200 °C and at 5%

relative humidity. As seen in Fig. 11, the conductivity of the membrane increased as the relative humidity and temperature of its environment increased. Conductivities of other inorganic fillers, such as phosphotungstic acid, silicotungstic acid, and tricarboxylbutylphosphonate, are comparable or lower than that of ZrP. Unfortunately, there have been no fuel cell performance tests published on these systems. Overall, these inorganic fillers improved the conductivity of *m*-PBI membranes.

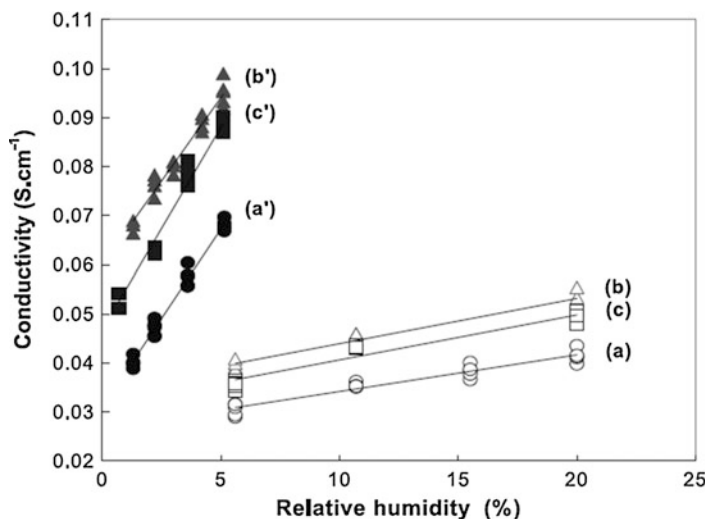
### Polybenzimidazole Fuel Cell Technology: Theory, Performance, and Applications,

**Fig. 10** Polarization curves (filled symbols) and power density curves (unfilled symbols) of s-PBI using reformat and air [50]



### Polybenzimidazole Fuel Cell Technology: Theory, Performance, and Applications,

**Fig. 11** Conductivity study of ZrP/*m*-PBI system for (a) *m*-PBI at 140 °C, (a') *m*-PBI at 200 °C, (b) 15wt% ZrP in *m*-PBI at 140 °C, (b') 15wt% ZrP in *m*-PBI at 200 °C, (c) 20wt% ZrP in *m*-PBI at 140 °C, and (c') 20wt% ZrP in *m*-PBI at 200 °C [52]



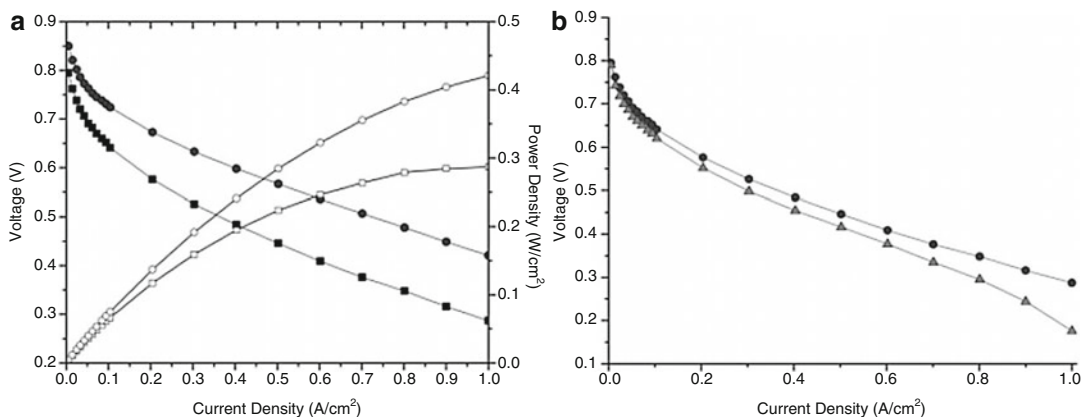
#### Other Modified PBIs

Multitudes of other organically modified PBI membranes exist that include, but are not limited to, fluorinated PBI, ionically and covalently crosslinked PBI, PBI blends, and a wide variety of PBI copolymers. Because there are far too many to describe, this subsection will highlight select PBI membranes that have not been included in the prior subsections.

Qian et al. investigated the use of hexafluoroisopropylidene-containing polybenzimidazole (6F-PBI, Fig. 5g) in fuel cell [53]. The polymer was synthesized via the PPA

Process through the reaction of TAB with 2,2-Bis(4-carboxyphenyl) hexafluoropropane in PPA. High molecular weight polymer with an IV value of  $0.98 \text{ dL g}^{-1}$  was achieved. Although the PA doping level of 6F-PBI was considerably high (30–40 mol PA/PRU), the membrane only achieved a peak conductivity value of  $0.09 \text{ S cm}^{-1}$  at  $180^\circ\text{C}$ . This is lower than that of PPA-processed *p*-PBI that achieved approximately  $0.25 \text{ S cm}^{-1}$  at  $160^\circ\text{C}$ .

The mechanical strength of 6F-PBI at high PA doping levels was strong enough to fabricate a membrane for fuel cell testing. Polarization and



**Polybenzimidazole Fuel Cell Technology: Theory, Performance, and Applications, Fig. 12** Graph (a) Polarization curves (filled symbols) and power density curves (unfilled symbols) of 6F-PBI using H<sub>2</sub>/Air

(squares) and H<sub>2</sub>/O<sub>2</sub> (circles). Graph (b) Polarization curves of 6F-PBI using H<sub>2</sub>/air (circles) and reformat/air (triangles) [53]

power density curves of 6F-PBI using hydrogen and reformat gases as fuel are illustrated in Fig. 12. Using hydrogen as fuel and air as the oxidant, the 6F-PBI MEA achieved a steady-state voltage of 0.58 V at a current density of 0.2 A cm<sup>-2</sup>. When oxygen was used as the oxidant at the same current density, the steady state voltage increased to 0.67 V. Additionally, the MEA showed excellent resistance to carbon monoxide poisoning. When a reformat gas comprised of 40% hydrogen, 40.8% nitrogen, 19% CO<sub>2</sub>, and 0.2% CO was used as fuel and air was used as the oxidant, the CO poisoning effects produced an approximate 3 mV reduction in voltage. This study illustrates that low levels of CO poisoning have little effect on the 6F-PBI MEA operating at this temperature.

Commonly known as 2OH-PBI (Fig. 5h), poly (2,2'-(dihydroxy-1,4-phenylene)5,5'-bibenzimidazole) is another PBI membrane with extremely promising properties. Yu and Benicewicz [54] synthesized 2OH-PBI homopolymer by combining TAB with 2,5-dihydroxyterephthalic acid (2OH-TPA) in PPA and cast it via the PPA Process. Yu also synthesized the 2OH-PBI/*p*-PBI random copolymer by reacting both 2OH-TPA and TPA simultaneously with TAB; the copolymer membrane was also cast using the PPA Process. It was proposed that the 2OH-PBI homopolymer was significantly crosslinked through phosphoric acid ester bridges. Because of this

crosslinking, the polymer was unable to be dissolved and an IV value could not be determined. Upon hydrolysis of the ester bridges by sodium hydroxide, the IV value of the homopolymer was measured as 0.74 dL g<sup>-1</sup>. The acid doping level of 2OH-PBI homopolymer was approximately 25 PA/PRU, and its conductivity at 160 °C was 0.35 S cm<sup>-1</sup>. It is important to note that at all temperatures between room temperature and 180 °C, the conductivity of 2OH-PBI homopolymer was greater than that of *p*-PBI. As the ratio of 2OH-PBI/*p*-PBI decreased in the random copolymer, the doping level and conductivity decreased. It was found that the conductivity of the material was highly dependent on the chemical structure of the PBI membrane and not just the doping level.

Using a Pt anode electrode and a Pt alloy cathode electrode, polarization tests were performed on the homopolymer 2OH-PBI MEA (Fig. 13). The homopolymer produced a voltage of 0.69 V using a load of 0.2 A cm<sup>-2</sup> at 180 °C and H<sub>2</sub>/air; this is greater than the 0.663 V produced by *p*-PBI under the same conditions. The high acid doping level and the membrane chemistry significantly contribute to the excellent performance of the 2OH-PBI membrane. Overall, the fuel cell performance of 2OH-PBI is comparable to that of *p*-PBI.

Segmented PBI block copolymers have also been explored for fuel cell use [55]. Scanlon

synthesized a 52/48 *p*-PBI/*m*-SPBI (Fig. 5i) segmented block copolymer by polymerizing the oligomer of *p*-PBI with that of *m*-SPBI. The oligomers were polymerized in PPA and cast by the PPA Method. Even with an extremely high PA doping level of 91.5 mol PA/PRU, the polymer film had very strong mechanical properties. Under low humidity at 160 °C, the segmented copolymer achieved a conductivity of 0.46 S cm<sup>-1</sup>. Because of the great results, a *p*-PBI/*m*-SPBI MEA was constructed for use in fuel cell performance tests. The polarization curves of the segmented copolymer MEA displayed a voltage of 0.62 V at 0.2 A cm<sup>-2</sup> at 160 °C and 0.65 V at 0.2 A cm<sup>-2</sup> at 200 °C. As implied by the data, these membranes are excellent candidates for high temperature fuel cells.

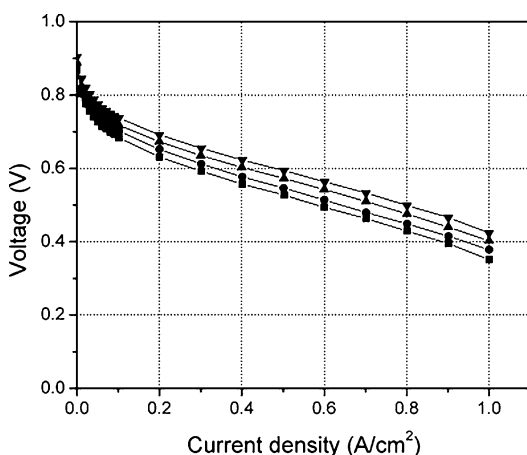
#### Membrane Electrode Assembly Durability

As explained in a previous section, a membrane electrode assembly (MEA) consists of the polymer membrane that is sandwiched between an anode and a cathode electrode, respectively. The electrodes are composed of a conductive carbon network that supports a catalyst on a gas diffusion layer. An additive, such as polytetrafluoroethylene (PTFE), helps bind the Pt/C catalyst to the gas diffusion layer. At the anode, the catalyst facilitates the oxidation of hydrogen into its constituent

electrons and protons. As the protons are passed through the acid-doped membrane to the cathode, the electrons are passed through an external circuit, thereby creating electricity. Finally, the electrons and protons react with oxygen at the cathode electrode to form water as the final reaction product.

Although PBI membranes are highly resistant to degradation, it is possible for the membranes to fail. Common degradation modes for PBI membranes at operating temperatures of 120–200 °C include membrane thinning and pin-hole formation. If there is too much pressure on the membrane, phosphoric acid could be pushed out of the polymer matrix and “thin out” the membrane. An extreme occurrence of membrane thinning results in pin-hole formations. Both of these occurrences result in increased fuel crossover and reduced fuel cell efficiency. Firm gasket materials help to evenly distribute pressure and prevent over-compression of the membrane [56]. Compressive stress of the membrane overtime can also lead to creep, or viscoelastic material flow. Creep and stress relaxation can result in PEM thinning and loss of contact with the electrodes causing degradation in performance.

Chen et al. [57–59] used the compression creep and creep recovery method to study the time-dependent creep behavior of PBI gel membranes. Creep compliance under uniaxial compression offers a direct method to measure viscoelastic deformation under a constant compressive stress. The data was used to directly compare different gel membranes’ creep deformation and can then be rationalized in terms of the polymer solids content and polymer composition. Twenty-three different PBI chemistries and 60 different 24 h creep tests were employed to investigate PBI creep behavior. As intuition would suggest, the membranes creep compliance decreased as the polymer solid content increase, when studying the same membrane composition. However, distinct bands of creep compliances were seen across different membrane compositions, see Fig. 14. For example, let us compare *p*-PBI to *m*-PBI. The *p*-PBI is unable to achieve as high a polymer solids content compared to *m*-PBI but has a lower creep compliance. However, in both compositions creep compliance decreases with increasing



**Polybenzimidazole Fuel Cell Technology: Theory, Performance, and Applications, Fig. 13** Polarization curves of 2OH-PBI using hydrogen as the fuel and air as the oxidant at 120 °C (squares), 140 °C (circles), 160 °C (triangles), and 180 °C (down-triangles) [54]

polymer solids content. This work uncovered the challenge of finding an optimal compromise between factors that increase polymer solubility in PPA and those that increase sol-gel network strength in PA. This becomes somewhat of a trade-off as the characteristics in which make PBI more soluble in PPA (i.e., increased chain flexibility which promote polymer-solvent interactions) typically decrease the gel network strength.

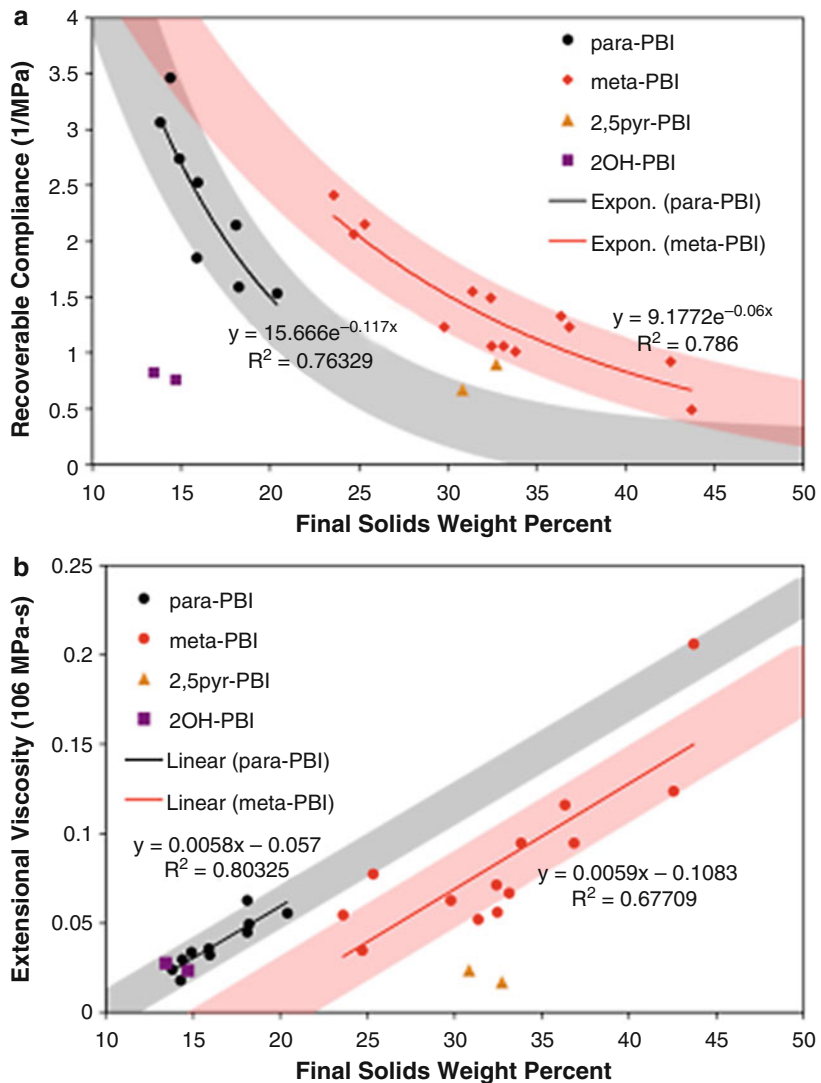
A potential solution to this problem is designing copolymers containing both a more soluble (flexible) polymer with a more rigid type. This

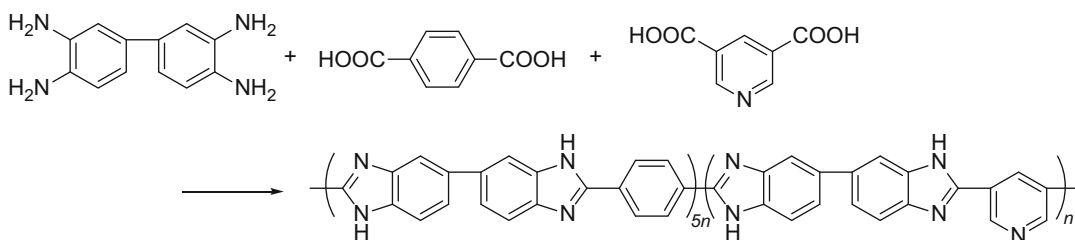
could allow for a higher polymer content while maintaining gel network strength. This was attempted with good results by Benicewicz et al., who looked at multiple different copolymer chemistries. Most notably was the polybenzimidazole 3,5-pyridine-para copolymer made in a 1–5 ratio (83% para and 17% 3,5-pyridine repeat units), Scheme 2.

This copolymer structure allows for the synthesis of a 15% polymer content gel membrane, before preconditioning of the sample, about a 6% increase from the para homopolymer counterpart, with a final post-creep solids content of 31.4%.

**Polybenzimidazole Fuel Cell Technology: Theory, Performance, and Applications,**

**Fig. 14** Steady-state recoverable compliance  $J_s^0$  (a) and extensional viscosity  $\eta_0$  (b) as functions of final solids wt % for para-PBI, meta-PBI, 2,5-pyr-PBI, and 2OH-PBI homopolymers. The solid curves are trend lines fit to the para-PBI and meta-PBI data. The shaded regions are extrapolations of the trend lines, broadened to visually encompass the data points. Each data point is a single compression creep experiment [57]





**Polybenzimidazole Fuel Cell Technology: Theory, Performance, and Applications, Scheme 2** Synthesis of 3,5-pyridine-para copolymer

The increase in polymer solids due to the copolymer structure demonstrates a creep compliance that falls on the extrapolated para-PBI creep compliance curve, boasting a recoverable compliance ( $J_r^0$ ) of  $\sim 0.6 \text{ MPa}^{-1}$ , Fig. 15.

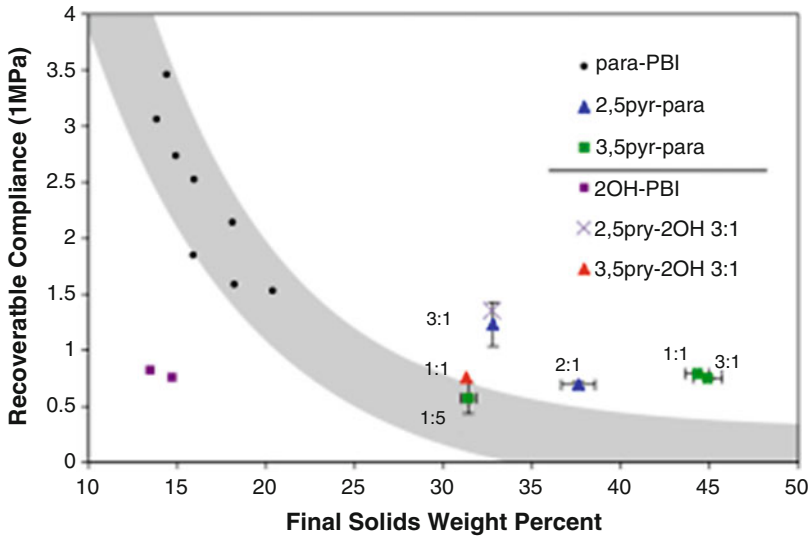
There are other possible avenues to consider when trying to strengthen the polymer network, and those would lie in postmodification techniques. These routes can be employed on both gel and conventionally imbibed PBI membranes. Sondergaard et al. [60] recently published work on enhancing the long-term durability of high temperature PEM fuel cells by thermally cross-linking the PBI membranes. Membranes were fabricated from *m*-PBI by solution casting from *N,N*-dimethylacetamide (DMAc) (a solids content of 10%) on to glass substrates. DMAc was mostly evaporated off by heating the plates to  $60^\circ\text{C}$  for 24 h. The membranes were then thoroughly washed with demineralized water and dried again at  $120^\circ\text{C}$  for an additional 24 h. Following these steps, the membrane underwent a thermal treatment at  $350^\circ\text{C}$  under an argon atmosphere. The now thermally cross-linked membranes were then imbibed with 85% phosphoric acid by soaking in an 85% phosphoric acid bath for 24 h. Long-term fuel cell testing was conducted at  $160^\circ\text{C}$  and a constant current bias of  $0.2 \text{ A/cm}^2$  with hydrogen and air flows on the anode and cathode of stoichiometries of 2 and 4, respectively. Long-term data of these fuel cells suggest that the thermal cross-linking increased stability over the nonthermally treated membrane with respect to the voltage degradation. The thermally cured PBI membrane had an average voltage decay rate relative to peak performance of

$1.4 \mu\text{V h}^{-1}$  in contrast to the  $4.6 \mu\text{V h}^{-1}$  of an equivalent cell without a membrane thermal treatment, over a 13,000 h period. It is important to note that shortly after start-up, the fuel cells without the thermally treated membranes showed better performance than the thermally cross-linked, Fig. 16.

The catalyst-coated electrodes of the MEA must be extremely durable in the presence of harsh physical and chemical environments. The oxidation and reduction processes create immense stress on the electrodes and trigger physical and chemical reactions to occur. A summary of the main MEA and component degradation modes have been previously reported [56, 61]. By means of electrochemical Ostwald ripening, Pt-metal agglomeration causes the loss of electrochemical surface area and decrease of reaction kinetics mainly through a dissolution-recrystallization process [62–64]. Oxidation reactions can also cause corrosion of the gas diffusion layer and carbon components in the electrodes, which would result in acid flooding, an increase in mass transport overpotentials, a decrease of reaction kinetics and also, most severely, the loss of the mechanical integrity of the electrodes. Phosphoric acid can dissolve the Pt-metal catalyst and phosphoric acid anions ( $\text{H}_2\text{PO}_4^-$ ) could adsorb onto the catalyst surface; both of these events would decrease the electrochemical surface area and reaction kinetics. In addition, phosphoric acid evaporation from the catalyst layer would result in similar consequences.

Typical commercial gas diffusion electrodes contain high-surface area carbon supported catalysts, e.g., Pt/Vulcan XC 72. Platinum is

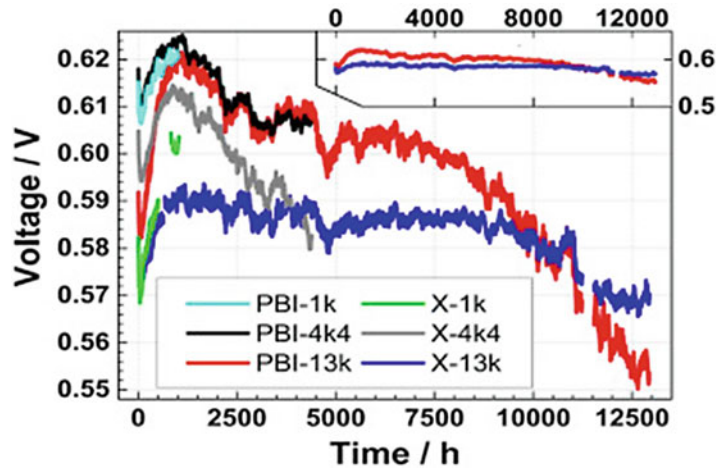




**Polybenzimidazole Fuel Cell Technology: Theory, Performance, and Applications, Fig. 15** Steady-state recoverable compliance as a function of final solids wt % for para-PBI and 2OH-PBI homopolymers and related copolymers. For the para-based copolymers, each data point is an average of 2–4 replicate measurements for

copolymers with the same copolymer ratio (as indicated in the plot). The data points for the homopolymers and the 2OH-based copolymers are single measurements. The shaded region is the extrapolated trend curve for para-PBI homopolymer [57]

**Polybenzimidazole Fuel Cell Technology: Theory, Performance, and Applications, Fig. 16** Steady state lifetime curves for MEAS operated at 160 °C, 200 mA  $\text{cm}^{-2}$ , stoichiometries of 4 and 2 for air and hydrogen respectively. The insert presents an overview of the two MEA samples that were tested the longest [60]



typically used as the catalyst at both the anode and cathode electrodes because it facilitates the reduction and oxidation reactions at high efficiency. However, due to the degradation modes previously mentioned, performance of the catalyst is lost over time. Novel platinum-based catalysts have been developed to increase the stability of the electrode catalysts. Compared to a commercial Pt/C (46.6 wt.% TKK),

Pt<sub>4</sub>ZrO<sub>2</sub>/C catalysts have been shown to decrease the overall performance loss of the MEA [65]. The Pt<sub>4</sub>ZrO<sub>2</sub>/C catalyst showed a higher resistance to Pt-sintering than Pt/C following 3000 cycles of a potential sweep test between 0.6 and 1.2 V versus reversible hydrogen electrode (20 mV s<sup>-1</sup>). The ZrO<sub>2</sub> is thought to act as an anchor to slow the agglomeration of platinum particles.

In order to improve especially the cathode catalyst kinetics and the catalyst stability, alloying of Pt with a base metal such as nickel or cobalt is widely practiced. Origins of these alloys date back to early phosphoric acid fuel cell development [66]. These alloys have been reported to typically improve the cathode kinetics for oxygen reduction by roughly 25–40 mV [66] or a factor of 1.5 to 4 when considering reaction rates. Commercial MEAs using PBI-based membranes also use Pt-base metal alloy catalyst on the cathode [67, 68]. The origin of the kinetic improvements for the Pt-base metal alloys is discussed manifold in the literature [69–77]: (i) modification of the electronic structure of Pt (5-d) orbital vacancies); (ii) change in the physical structure of Pt (Pt-Pt bond distance and coordination number); (iii) adsorption of oxygen-containing species from the electrolyte onto the Pt or alloying element; and/or (iv) redox-type processes involving the first-row transition alloying elements. However, as discussed in detail in the recent work by Stamenkovic et al. [76], the main effect is a shift of the Pt d-band center to lower energy values which induces a surface which adsorbs oxygenated and spectator species to a lower extent and therefore makes more active sites available for the oxygen reduction to proceed.

Other additives to platinum-based electrodes, such as tin-oxide (SnOx) [78], have also been shown to significantly improve the catalytic activity of the oxygen reduction reaction. Using a PPA processed *m*-PBI membrane with a 7 wt.% SnO in Pt/SnO<sub>2</sub>/C catalyst under unhumidified H<sub>2</sub>/O<sub>2</sub> at 180 °C, a voltage of 0.58 V under a load of 0.2 A cm<sup>-2</sup> was produced. Under the same conditions, a *m*-PBI MEA using a Pt/C catalyst produced only 0.4 V at 0.2 A cm<sup>-2</sup>.

PBI has also been investigated as an additive to platinum-based electrodes. It is thought that incorporation of PBI in the catalyst layer would provide a better interface for proton conduction between the electrode and membrane. Qian [79] incorporated 6F-PBI into the electrodes by four different methods: formation of a PBI bilayer inserting a thin 6F-PBI membrane between an E-TEK cathode and *p*-PBI membrane, casting 6F-PBI/PPA directly onto the E-TEK electrodes and

hydrolyzing to form the gel, spraying a 6F-PBI/DMAc solution onto the electrodes, and coating the electrodes with a mixture of 6F-PBI and catalyst (the PBI replaced PTFE). The bilayer method decreased fuel cell performance, and it is proposed that this occurred by creating a large interface resistance between the two PBI layers. Both the casting method and the spraying method improved electrode kinetics, and it is postulated that this occurred due to a lower interface resistance. In addition, a significant decrease in fuel cell performance showed that 6F-PBI could not be used to replace PTFE.

As an outlook to further improvements of catalyst kinetics and durability in low and high temperature polymer electrolyte fuel cells, several possibilities are currently under investigation [80]: (1) extended large scale Pt and Pt-alloy surfaces [76]; (2) extended nanostructured Pt and Pt-alloy films [81]; (3) de-alloyed Pt-alloy nanoparticles [82]; (4) precious metal free catalyst as described by Lefèvre et al. [83], e.g., Fe/N/C catalysts; (5) additives to the electrolyte which modify both adsorption properties of anions and spectator species and also the solubility of oxygen [84]. The latter approach is specific to fuel cells using phosphoric acid as electrolyte.

More recently, catalyst work has been conducted on trying to eliminate the need for expensive platinum. Li et al. [85] have begun work on a platinum-free Fe<sub>3</sub>C based oxygen reduction catalyst. They synthesized hollow microsphere morphologies consisting of a graphite layer encapsulated Fe<sub>3</sub>C nanoparticles by means of high temperature autoclave pyrolysis. The prepared catalysts demonstrated poor performance compared to traditional platinum based oxygen reduction catalysts; high current densities could not be achieved coupled with low initial voltage output and large voltage decay. Nonetheless, creating a working platinum-free catalyst is notable. More work is still needed in this area if platinum-free catalysts are to become a viable option. An often overlooked area of fuel cell construction is of the flow plates themselves. In 2017 Singdeo et al. [86] modified the conventional serpentine flow field by developing a 5 channel, 6 turn configuration. The conventional flow field,

for some time, has been at the forefront of fuel cell research; however, it displays problematic current density gradients across the cell. At the inlet of the serpentine flow plate the current density has been recorded to be 143% above the mean and 50% below the mean at the outlet; when using 1.3 and 1.4 stoichiometries at the anode and cathode, respectively [84]. This corresponds to a uniformity factor of 0.96. However, with the modified serpentine flow pattern the uniformity factor was increased to 0.998, showing the improved current density distribution. Simulated fuel cell performance testing showed that the new gas flow path improved power output by ~22% at 0.57 V. This work demonstrates that the flow field construction can play a pivotal role in fuel cell performance and further research and experimentation should be considered.

## PBI/PA Fuel Cell Systems and Their Applications

*Para*-PBI is one of the most common polymers used in commercial PBI-based fuel cell systems. A mechanically strong and chemically stable polymer, *p*-PBI has proved to be one of the most reliable PBI polymers for MEA use. Load, thermal, and shutdown-startup cycling tests performed on the *p*-PBI MEA indicated that high temperatures (180 and 190 °C) and high load conditions resulted in slightly increased PA loss from the MEA system. However, steady-state fuel cell operation at 80–160 °C studies showed that PA loss would not be a significant factor in fuel cell degradation [61, 87]. Long-term studies showed minimal performance degradation over a two-year span and indicated excellent commercial fuel cell potential [56]. Compared to state-of-the-art phosphoric acid PEMFCs [88], evaporation of phosphoric acid from commercial PBI-based Celtec P1000 MEAs is reduced by a factor of roughly 2–3. This is a key factor of long-term stable operation for PBI-based fuel cells.

For the transition of PBI-based fuel cell science into commercial products, the appropriate manufacturing processes need to be developed. Most companies rely on manual operations [89]

for PBI-based MEA fabrication. Only recently have significant efforts been devoted to developing automated production lines because simple changes in MEA materials and architecture could necessitate the use of different manufacturing equipment. To accommodate the evolution of fuel cell science, a flexible modular manufacturing line has been developed. In 2002, BASF Fuel Cell GmbH (previously PEMEAS) began using the line to accommodate three generations of MEAs. The details of their manufacturing process will be further discussed in section “[Advances in PBI MEA Manufacturing](#).” It is important to mention that BASF Fuel Cell GmbH is no longer in existence; however, they are continuing to supply PBI-based MEAs into the commercial market.

Commercial PBI-based high temperature PEMFCs provide energy to a wide array of electronic devices. Hydrogen fuel cell vehicles, both for the private consumer and public transportation, are growing in popularity as pollution and fossil fuel prices continue to increase. Hydrogen offers 2–3 times the overall efficiency in a fuel cell as gasoline does in a typical combustion engine [90]. High temperature fuel cells are also popular as backup generators and combined heat and power devices for stationary use. These types of systems typically produce 1–10 kW, which is enough energy to power a house or a multifamily dwelling. In addition to providing energy, combined heat and power devices use waste heat to heat water and preheat the fuel cell system components, thereby increasing the overall efficiency of the fuel cell system. Fuel cells also offer applications in mobile electronic devices such as laptops and cell phones. Commonly coupled with a methanol reformer, these fuel cell systems are remarkably portable and can power electronics for many hours of continuous use.

In addition to producing electricity, these PEMs have been used as a purification device for hydrogen gas. Consider the purification device to have the same basic architecture as a fuel cell. A platinum catalyst splits contaminated hydrogen gas into protons and electrons at the anode. Using an external power source, the electrons are driven through an external circuit to the cathode while the protons are allowed to transport across the

membrane from the anode to the cathode. The electrons and protons recombine, thereby creating a higher purity hydrogen gas at the cathode while leaving behind the undesired constituents at the anode. These hydrogen pump devices will be further discussed in section “[H<sub>2</sub> Pump](#).”

### In-Depth Analysis of PPA Processed *p*-PBI MEA

PBI-based high temperature MEAs offer many benefits over more well-known perfluorosulfonic acid PFSA PEMs. Unlike low temperature PFSA MEAs, high temperature PA-doped PBI membranes do not need to be hydrated, and therefore, do not require an external humidification of the gases. Additionally, running at high temperatures generally improves electrode kinetics and proton conductivities while requiring smaller heat exchangers. For PBI fuel cell science to transition into commercially available products, the reliability of PBI fuel cell stacks needs to meet specific requirements. The Department of Energy (DOE) specified durability targets of >5,000 h (>150,000 miles) of automotive fuel cell operation and >40,000 h for stationary applications for 2010. Primarily, the durability of the fuel cell stack dictates the durability of the entire system [91]. In depth durability studies of PBI MEAs have been performed [56, 61, 68, 87, 92–94] to evaluate the viability of commercial PBI fuel cells. In addition to fuel impurity and PA retention tests, load, thermal, and shutdown-startup cycling tests are commonly performed to evaluate the MEAs.

*p*-PBI MEAs have displayed a relatively high resistance to carbon monoxide and sulfur contaminants [87, 92, 95, 96]. While Nafion and other traditional low-temperature PEM fuel cells are often poisoned by small amounts of carbon monoxide (5–50 ppm) in the fuel or oxidant, *p*-PBI and other PBI membranes have been shown to perform with minimal voltage loss in 10<sup>4</sup> ppm of carbon monoxide. Operating the fuel cell at 180 °C with a load of 0.2 A cm<sup>-2</sup> with a reformat gas (70% H<sub>2</sub>, 1.0% CO, and 29% CO<sub>2</sub>), the voltage loss was only 24 mV as compared to pure hydrogen [29]. This decrease in voltage occurred as a result of fuel dilution and carbon monoxide poisoning. As explained in section “[Introduction](#)

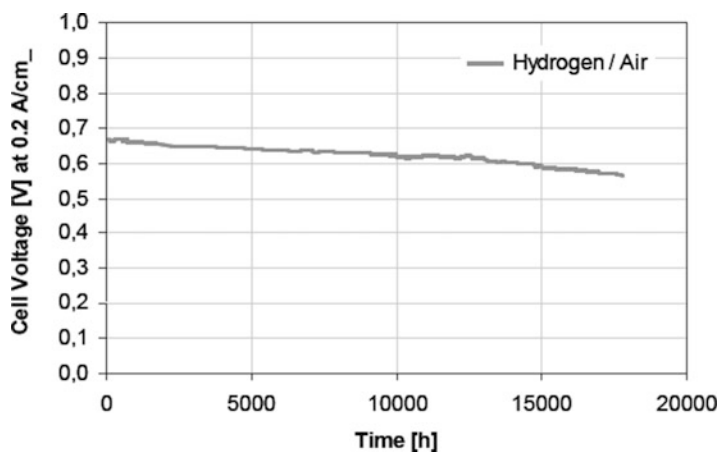
to [Polybenzimidazole Fuel Cell Sustainability](#),” the cell is able to resist poisoning because the high operating temperatures allow for reversible binding of carbon monoxide from the catalyst. Details on the CO adsorption isotherms in the presence of hydrogen under fuel cell operation conditions between 150 °C and 190 °C can be found in literature [96]. Similarly, Garseny et al. [95] reported that a PBI MEA from BASF Fuel Cell GmbH (Celtec-P Series 1000) is 70 times more resistant to sulfur contaminants than Nafion MEAs. Using air contaminated with 1 ppm H<sub>2</sub>S or SO<sub>2</sub> as the oxidant, the performance of Nafion decreased by 82.9% while the performance of the Celtec-P MEA decreased by <2%. Garseny et al. proposed that H<sub>2</sub>S is converted to SO<sub>2</sub>, and that SO<sub>2</sub> adsorbs onto the Pt catalyst surface. At temperatures above 140 °C, this SO<sub>2</sub> is desorbed and flushed out of the system. Schmidt and Baurmeister showed that the H<sub>2</sub>S tolerance of PBI-based Celtec P1000 MEAs is in the range of 10 ppm [92], a value significant larger than typical fuel processing catalyst can tolerate. More than 3000 h operation in reformat with 5 ppm H<sub>2</sub>S and 2% CO was demonstrated. Overall, *p*-PBI-based fuel cells can resist contaminant poisoning far better than traditional low-temperature PEM fuel cells, an effect which can mainly be ascribed to the operation temperature between 150 °C and 190 °C.

Under continuous operation and appropriate stack design and components, the PBI membranes retain phosphoric acid extremely well. Long-term performance tests show that *p*-PBI fuel cells can operate for over two years with minimal performance degradation (Fig. 17). This durability is attributed to the unique nature of PBI membrane formed by the PPA process, which allows it to retain PA under continuous operating conditions. The amount of PA lost from the *p*-PBI MEA per h was approximately 10 ng h<sup>-1</sup> cm<sup>-2</sup>, which is equivalent to a 50 cm<sup>2</sup> cell losing 8.74 mg PA after two years of operation. Such a small loss strongly suggests that the life span of a *p*-PBI PEM fuel cell would not be significantly influenced by PA depletion.

Phosphoric acid loss was also monitored during a selection of dynamic durability tests,

### Polybenzimidazole Fuel Cell Technology: Theory, Performance, and Applications,

**Fig. 17** Long-term durability test of *p*-PBI MEA at 160 °C using hydrogen/air without humidification



including load and thermal cycling tests [87]. A single load cycle test involved measuring the voltage at 160 °C under at three different loads: open circuit voltage (OCV), 0.2 A cm<sup>-2</sup>, and 0.6 A cm<sup>-2</sup>. Air and pure hydrogen were supplied to the MEA as oxidant and fuel, respectively. The voltage of the MEA was measured at OCV for 2 min, followed by 0.2 A cm<sup>-2</sup> for 30 min and then 0.6 A cm<sup>-2</sup> for 30 min. A total of 500 load cycles were performed on a *p*-PBI MEA, and the results indicated that larger loads corresponded to an increased PA loss rate (approximately 20 ng h<sup>-1</sup> cm<sup>-2</sup>). Thermal cycling tests were performed by measuring the voltage of the MEA with a constant applied current density of 0.2 A cm<sup>-2</sup> while either cycling the temperature between 120 °C and 180 °C (for a high temperature cycle) or between 80 °C and 120 °C (for a low temperature cycle). Both the high and low temperature cycles were performed 100 times each. The results showed that higher temperatures were associated with an increased PA loss rate (almost 70 ng h<sup>-1</sup> cm<sup>-2</sup> for the high temperature cycle and 20 ng h<sup>-1</sup> cm<sup>-2</sup> for the low temperature cycle). It was proposed that at the higher load and temperature conditions, more water is generated at the cathode. By means of a steam distillation mechanism, an increased amount of PA is lost from the MEA. As indicated by both cycling tests, phosphoric acid loss becomes a significant factor of cell degradation only under extreme conditions.

Shutdown-startup cycling tests have been extensively studied by Schmidt and Baurmeister

of BASF Fuel Cell GmbH [61, 68]. Two PBI-based PEFC Celtec-P 1000 MEAs were tested under different operation modes; one was run under shutdown-startup cycling parameters (12 h shutdown followed by operation for 12 h at 160 °C under a load of 0.2 A cm<sup>-2</sup>) while the other was continuously operated at 160 °C under a load of 0.2 A cm<sup>-2</sup>. Both MEAs were operated for more than 6000 h, during which the shutdown-startup cycling MEA underwent more than 270 cycles. While the continuously operating MEA had an average voltage degradation rate of roughly 5 μV h<sup>-1</sup>, the cycling MEA averaged a voltage degradation of 11 μV h<sup>-1</sup> or 0.2 mV cycle<sup>-1</sup>. This increase in voltage degradation was attributed to an increased corrosion of the cathode catalyst support, thereby significantly increasing the cathodic mass transport overpotential. The observed corrosion was a result of a reverse-current mechanism that occurs under shutdown-startup cycling conditions [97].

Illustrated by the previously discussed durability tests, *p*-PBI MEAs have been shown to be physically and chemically robust. Highly resistant to fuel contaminants, PBI MEAs are resistant to poisoning effects that would typically expunge a low temperature PFSA fuel cell system. Long term steady-state and dynamic durability tests showed that PA loss typically is not a cause of cell degradation. Additionally, Schmidt and Baurmeister showed that PBI MEAs are susceptible to cell degradation under extreme shutdown-startup conditions. Overall, *p*-PBI MEAs have



exhibited much potential for use in fuel cell systems.

### Advances in PBI MEA Manufacturing

As previously discussed, the manufacturing processes of PBI-based fuel cells need to be improved to make fuel cells a viable commercial product. To put this requirement into perspective, the United States Department of Energy has set a goal of producing 500,000 fuel cell cars each year. If these vehicles are powered using current *p*-PBI membranes, this goal requires the production of seven MEAs per second and approximately 250,000 m<sup>2</sup> of electrode per day. Additionally, the performance of each of these MEAs would need to be tested; this is a process called “burn-in testing.” A typical test stand is 25 ft<sup>2</sup>, costs roughly \$50,000, and can only test one stack of MEAs at a time. If each stack requires a 24 h burn-in test, the test facility size would exceed 34,000 ft<sup>2</sup> and house equipment costing over \$68.5 million. Existing manufacturing processes need to be improved in order to reach this goal.

The Center for Automation Technologies and Systems (CATS) at Rensselaer Polytechnic Institute has developed a flexible manufacturing process for BASF Fuel Cell GmbH to accommodate the evolving science of fuel cells [98–100]. If one changes the fuel cell type, size, materials, MEA architecture, design, or application, the manufacturing line could be significantly affected. Therefore, a modular manufacturing line was developed by CATS in 2002 that could produce a large range of MEA sizes (1–1000 cm<sup>2</sup>), could handle a wide variety of materials (membranes, gaskets, electrodes, etc.), could assemble these materials in different architectures, and could be expanded to integrate additional systems. Each module could be singularly operated or could operate as a subset of the entire process; this modular construction is shown in Fig. 15. Over the past eight years, this manufacturing line has evolved over three generations of MEA devices (Fig. 18).

Members of CATS continue to make great strides in order to reduce costs and improve the overall efficiency of MEA fabrication. Laser

cutting and joining of the PBI membranes both uses less power and delivers tighter tolerances than that of conventional cutting and joining. Ultrasonic technology has also been explored to replace the thermal joining of the three components of an MEA. Preliminary results exhibited a significant reduction in pressing time by approximately 90% in addition to using less energy. Additionally, an automated visual inspection of the MEA has been developed using a high precision motion system, multiple cameras and lighting equipment, and software MAT-LAB 7.0 with Image Processing Toolbox [99]. As fuel cell science continues to evolve, so will the manufacturing processes.

### Combined Heat and Power

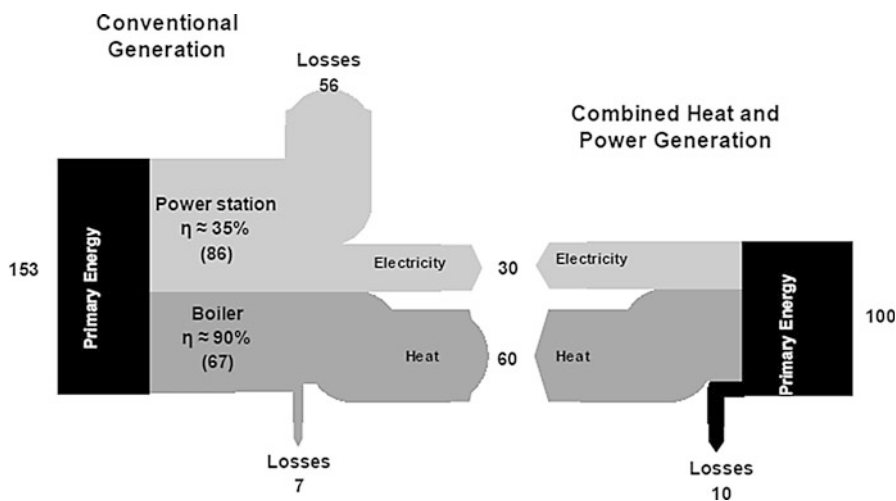
Stationary combined heat and power (CHP) devices are often considered the primary application of high temperature PBI-based fuel cells. These devices are used to provide both electricity and heat (in the form of hot air or water) to small scale residential homes or large scale industrial plants using hydrogen derived from the widely distributed natural gas network. PBI MEAs are ideally situated for combined heat and power devices because they efficiently provide electricity while generating heat as a byproduct. Furthermore, these devices could be used to provide reliable backup power to residential homes, hospitals, servers, etc.

J.-Fr. Hake et al. [101] compared the conventional generation of heat and electricity to that of small scale combined heat and power generation by high temperature fuel cells, and the results of which are shown in Fig. 19. The small scale CHP devices studied were used to provide electricity, space heat, and warm water to both residential and commercial buildings. The conventional generation of electricity is much less efficient than that of small scale CHP devices due to the issues of transportation and storage. In addition to efficiently converting chemical energy into electrical energy, CHP fuel cell systems further act as a sustainable energy conversion device by reducing the total amount of greenhouse gas emissions. Hake et al. considered the penetration of small scale CHP fuel cell technology into the US



**Polybenzimidazole Fuel Cell Technology: Theory, Performance, and Applications, Fig. 18**

A portion of the 2002 pilot line depicting its modular construction [98]

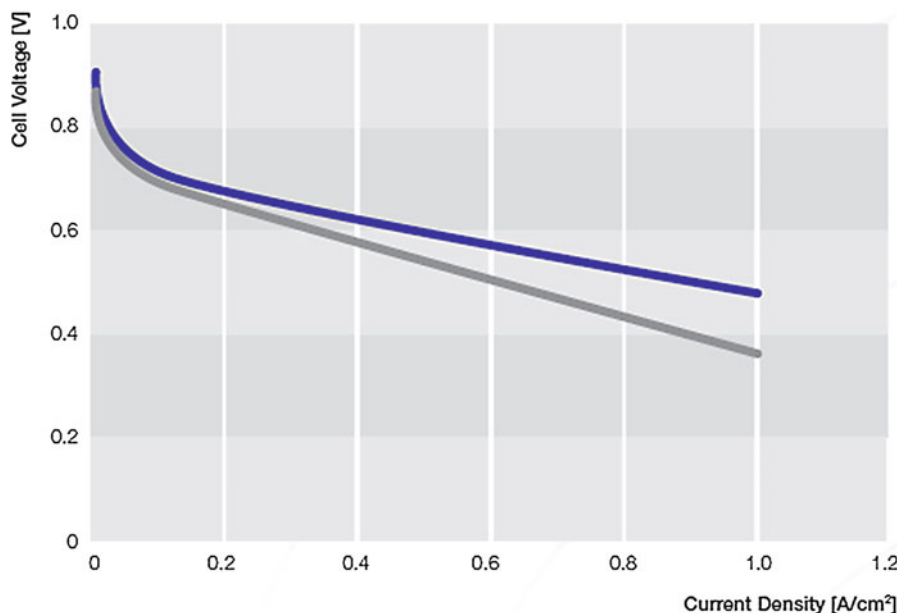


**Polybenzimidazole Fuel Cell Technology: Theory, Performance, and Applications, Fig. 19** Side-by-side comparison of conventional generation of heat and electricity to fuel cell combined heat and electricity generation [101]

residential sector market starting in 2014 until a saturation point as a logarithmic function. To improve the accuracy of the study, Hake considered the trends of the Japanese small scale CHP market [101, 102]. A typical CHP device in Japan costs roughly \$30,000, but analysts expect the price to drop to \$5000 within five years. Analysts also claim that by the year 2050, one in four homes in Japan will run on fuel cells. Also considering current CO<sub>2</sub> emissions, Hake et al. concluded that adoption of this technology in the US

could reduce CO<sub>2</sub> emissions by up to approximately 50 million tons by 2050; this corresponds to a 4% reduction in the residential sector.

As the largest producer of PBI MEAs, BASF Fuel Cell (previously PEMEAS) produces *p*-PBI PEM MEAs for a wide variety of fuel cell applications. The Celtec<sup>®</sup>-P 1000 PEM MEA is typically integrated into either back-up or auxiliary power units and can produce from 0.25 to 10 kW. The MEA is also advertised as maintaining performance for over 20,000 h with only a 6  $\mu\text{V h}^{-1}$



**Polybenzimidazole Fuel Cell Technology: Theory, Performance, and Applications, Fig. 20** Polarization curves of a Celtec<sup>®</sup>-P MEA [103]. The blue line represents

using hydrogen/air as fuel/oxidant. The gray line represents a steam reformat of 70% H<sub>2</sub>, 29% CO<sub>2</sub>, and 1% CO/Air

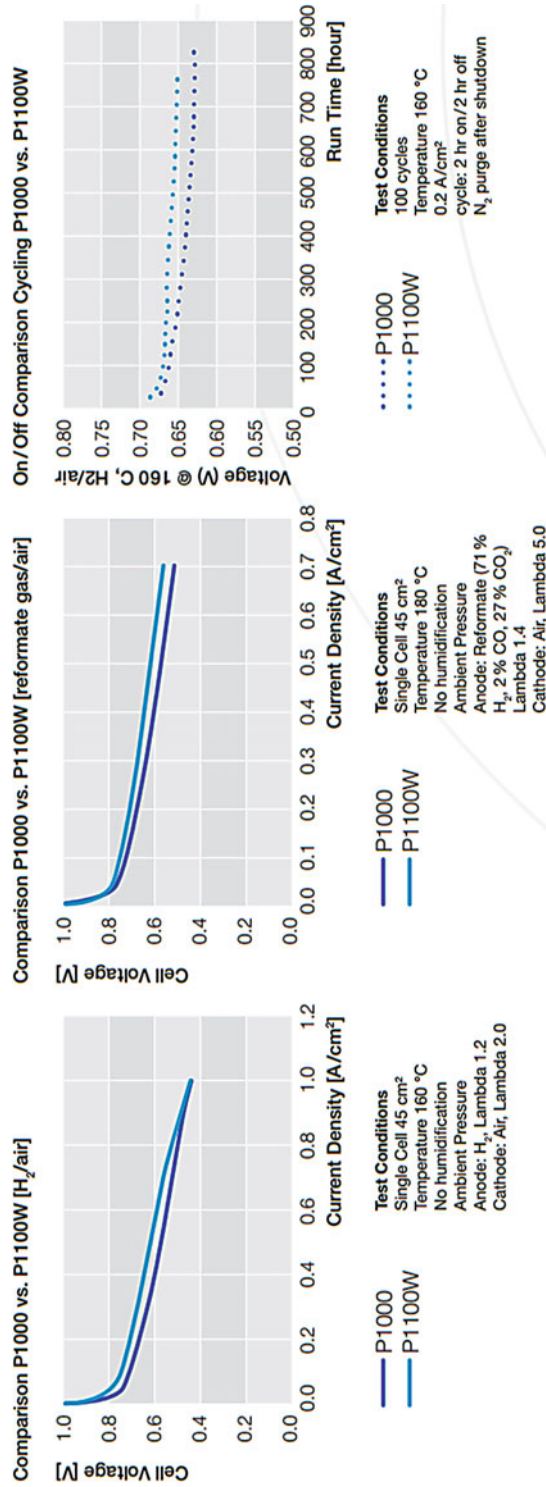
voltage drop at 160 °C [98]. The Celtec<sup>®</sup>-P 2100 PEM MEA is used in stationary CHP systems and is capable of producing 0.74–10 kW. The MEA has a long term stability of over 20,000 h under both steady state and cycling conditions (300 shutdown-startup cycles with 13 μ h<sup>-1</sup> voltage drop). Polarization curves of a Celtec<sup>®</sup>-P MEA at 160 °C using an active area of 45 cm<sup>2</sup> are shown in Fig. 20. PBI-based CHP devices have been commercially test marketed by a variety of companies, including Serenergy, Plug Power, and ClearEdge Power, although large scale adoption has not yet been achieved.

Furthermore, Celtec<sup>®</sup>-P 1100W is an improved version to Celtec<sup>®</sup>-P 1000. It provides more uniformity and a greater degree of manufacturing readiness (Fig. 21) [104].

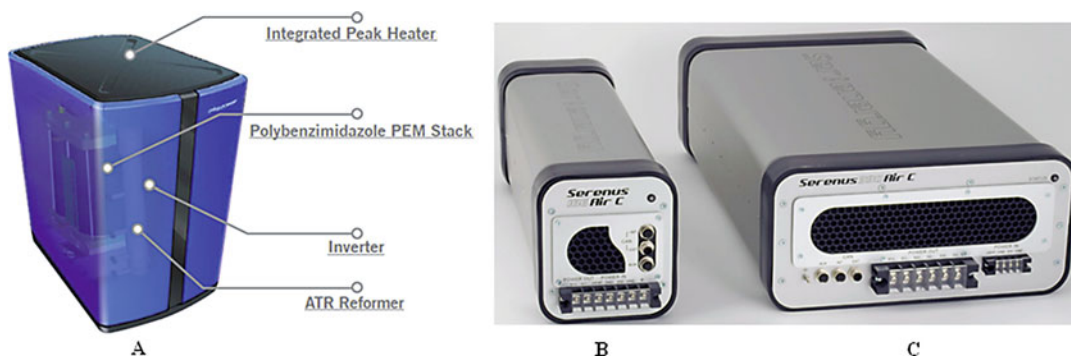
Plug Power of Latham, New York produced a line of PBI-based small scale CHP devices including the GenSys Blue (Fig. 22) [105]. The GenSys Blue was capable of producing 0.5–5 kW of continuous output and capable of reducing home energy costs by 20–40%. An autothermal (ATR) reformer reacts to natural gas (methane) with oxygen and carbon dioxide to produce hydrogen gas

that fuels the PEM stack. An inverter was used to improve the efficiency of the CHP device by specifically supplying enough energy to power the home, thereby minimizing energy losses and reducing CO<sub>2</sub> emissions by 25–35%. Additionally, an integrated peak heater ensures proper heating of the entire home. More recently, Plug Power has focused on integrating low temperature PEMFC's into forklift trucks.

Serenergy, which is based in Hobro, Denmark, also produced a PBI-based fuel cell CHP devices [106]. Serenergy's Serenus 166 Air C v2.5 and 390 Air C v2.5 micro-CHP modules nominally produce 1 and 3.5 kW, respectively. While the 166 model was comprised of one MEA stack of 65 cells, the 390 model uses three MEA stacks each with 89 cells. Both of these systems were able to tolerate fuel impurities up to 5% CO concentrations and 10 ppm H<sub>2</sub>S at 160 °C. Because the excess energy can be used to heat up air or water, Serenergy claims that over 80% of the total heat and power generated can be used and that the system efficiency is as high as 57% (the efficiency data was not available). These systems can also be used as auxiliary energy conversion devices.



Polybenzimidazole Fuel Cell Technology: Theory, Performance, and Applications, Fig. 21 Comparison of Celtec®-P 1100W and Celtec®-P 1000 [104]



**Polybenzimidazole Fuel Cell Technology: Theory, Performance, and Applications, Fig. 22** Plug Power's GenSys Blue (a), Serenergy's Serenus 166 Air C v2.5 (b),

and Serenergy's Serenus 390 Air C v2.5 (c) CHP fuel cell devices [105, 106]

ClearEdge Power produced a line of small scale CHP devices, one of which is the ClearEdge5 [107]. Capable of producing  $5 \text{ kW h}^{-1}$  and up to  $20,000 \text{ BTU h}^{-1}$  while running at  $150^\circ \text{C}$ , the ClearEdge5 couples a methane reformer to a PBI fuel cell stack using MEAs provided by BASF Fuel Cell GmbH. ClearEdge advertised that the CHP device could reduce utility bills by up to 50% and cut  $\text{CO}_2$  emissions by over 33%. Annually, the device was capable of producing 43,000 kWh in electricity and 50,000 kWh (equivalent) in heat. Similar to other CHP devices, the ClearEdge5 offered at-home production of energy, thereby eliminating the losses associated with transferring the energy. However, ClearEdge Power closed operations in 2014.

In 2016 the fuel-cell industry had an estimated total worth of \$3.6 billion and is expected to grow into a \$25.5 billion market by 2024, according to research from Global Markets Insight [108]. With that said, many of the major players listed above are no longer in existence or have very little impact on the industry. For example, BASF-Fuel Cell has reduced its market share considerably and now only supplies Celtec<sup>®</sup>-P 1100W, leaving only Plug Power Inc. and FuelCell Energy Inc. as the major market contributors. However, despite the bullish predictions neither of these two have turned a significant profit. Currently there is uncertainty for the fuel cell technology market, as part of the alternative-energy sector. Hydrogen

and fuel companies do not boast the same government incentives as solar and wind firms, however, if this is levied in the future there might be a possible surge in growth of the technology. With emerging needs of sustainable, clean energy in other countries, like China who has invested \$100 billion into fuel-cell energy to date, there are other possible avenues for the technology to grow. Fuel cells still remain a viable option for clean energy and to reduce dependence on fossil fuels, leaving hope that they might be an integral part of the growing alternative energy sector [108]. With that said, the research and development on fuel cell technologies has laid the foundation for other possible devices that could alleviate the use of fossil fuels. These include both hydrogen pumping, which can be used to purify hydrogen from a mixed gas stream, as well as the hybrid sulfur cycle, which is an enticing thermal-electrochemical process used for the production of pure hydrogen. These will be discussed more in depth in sections "H<sub>2</sub> Pump" and "The HyS Cycle."

### Automotive Transportation

Producing 1.9253 billion metric tons of carbon dioxide, which is roughly 33% of the United States' total carbon dioxide emissions, the transportation sector was the largest contributor to pollution in 2008 [109]. According to another 2009 study by the U.S. Department of Energy [3], all transportation in the US produced

approximately 1850 million metric tons of carbon dioxide emissions. Considering both of these facts, one can conclude that a more sustainable energy source could significantly reduce the carbon footprint of the transportation sector. For the transition of fuel cell science into a viable commercial product to occur, the U.S. Department of Energy has set numerous targets for automotive fuel cell systems. Because a typical internal combustion engine costs roughly \$25–35/kW, a fuel cell system will need to cost roughly \$30/kW to become competitive enough to penetrate the US market. Furthermore, the system must be durable enough to operate for at least 5000 h (or roughly 150,000 miles). Additional issues of system size and management of air, heat, and water will also play a role in automotive fuel cell viability.

Over the past decade, fuel cell technology has been adapted by the major automotive industries as a cleaner, more efficient method of providing energy to vehicles. In addition to the issue of fuel cell automotive viability, issues of hydrogen sources, hydrogen storage, and fueling stations continue to be addressed and solved. The California Fuel Cell Partnership (CaFCP) is a collaboration of auto manufacturers, energy providers, government agencies, and fuel cell technology companies to promote the commercialization of fuel cell vehicles. In 2009, California had only six public hydrogen fueling stations that were used to fuel roughly 200 vehicles [90]. To date, there are 28 fueling stations open for retail business throughout California and 17 more are under construction. The State of California committed funding to design, build, and provide operation and maintenance support for 100 hydrogen stations [110]. The hydrogen used to fuel these stations can be domestically produced as either a low carbon fuel or potentially as a zero-carbon fuel when produced from renewable sources (such as splitting water into oxygen and hydrogen with solar energy). According to California regulations, at least 33% of the hydrogen must come from such renewable sources [111].

SunHydro, one of the world's first hydrogen fueling station chains, has set a goal of providing fueling stations along the entire east coast of the

US. Using solar cell technology, every SunHydro station will harvest solar energy to electrolytically split water into hydrogen and oxygen gases. This process is extremely sustainable and will create much less greenhouse gas emissions. This hydrogen highway will stretch from Scarborough, ME to Miami, FL and consist of eleven stations. Each station will cost an estimated \$2–3 million to construct and will be paid for by private funders. Currently there is one hydrogen refueling station open for retail use in Wallingford, Connecticut with plans for a second station to be opened in Braintree, Massachusetts [112].

Over the past decade, many automotive and fuel cell industries have used PBI technology in the development of fuel cell vehicles. In November of 2008, Volkswagen unveiled the VW Passat Lingyu at a Los Angeles Auto Show [113]. The VW Lingyu uses an AB-PBI based fuel cell stack that utilizes a trade-secret coating that helps prevent PA from leeching out of the membrane. Metha Energy Solutions, in cooperation with Serenergy, revealed a hybrid electric/fuel cell vehicle in December of 2009 [114]. In this system, a methanol reformer is used to provide hydrogen to the PBI-based fuel cell. It was advertised that this vehicle could travel up to 310 miles on one tank of gas and takes only 2 min to refuel. EnerFuel, a subsidiary of Ener1, has also recently produced a hybrid electric/fuel cell vehicle. The EnerFuel EV uses a reformed methanol PBI fuel cell that works in conjunction with a lithium ion battery. The lithium battery is used to start the vehicle and to power the vehicle while driving, while the fuel cell system produces 3–5 kW to continuously recharge the battery. These fuel cell systems would not generate enough power to drive the vehicle but would act as a range extender for the battery system. The target market of the EnerFuel EVs is not for those who drive 200+ miles daily but instead for those with short daily commutes.

In July of 2009, the German Aerospace Center demonstrated that fuel cells have the potential of powering air-transportation vehicles [115, 116]. Designed in cooperation with Lange Aviation, BASF Fuel Cell, DLR Institute for Technical

Thermodynamics, and Serenergy, the Antares DLR-H<sub>2</sub> became the world's first piloted aircraft with a propulsion system powered only by PBI-based fuel cells. Besides creating zero CO<sub>2</sub> emissions during flight, the aircraft also generates much less noise than other comparable motor gliders. Using a fuel cell stack capable of producing up to 25 kW, the Antares DLR-H<sub>2</sub> has a cruising range of 750 km (or 5 h) and can travel at speeds up to 170 km h<sup>-1</sup>. Similar fuel cell systems could be coupled with current commercial and military aircrafts as auxiliary power units (APUs) to improve fuel efficiency.

### Portable

Microelectricalmechanical (MEM) systems utilizing methanol reformers and PBI fuel cells have been developed for portable use. These devices are generally used to generate power in the range of 5–50 W for laptops, communication systems, and global positioning systems. Compared to batteries that offer equivalent amounts of power, these micro-fuel cell systems are lighter, generate less waste, and are overall more cost effective. Similar to other reformed methanol/PBI fuel cell systems, these MEMS are a sustainable technology by reducing the amount of greenhouse gases produced per unit of electricity generated.

UltraCell of Livermore, CA is a well-known producer of PBI MEM fuel cell systems. Funded and field tested by the U.S. Army, the UltraCell XX25 is capable of providing 25 W of continuous maximum power [117]. Depending on the size of the fuel cartridge, the device is capable of delivering 20 W of continuous power from 9 h to 25 days. The fuel cartridge weighs less than a pound and the XX25 MEM system has been shown to power radio gear, mobile computer systems, communication devices, and a variety of other electrical devices. The XX25 provides roughly 70% in weight savings when compared to a typical battery on a 72-h mission (1.24 kg without the cartridge) and is rugged enough to operate in extremely cold or hot environments. In addition, it meets OSHA standards for safe indoor and in-vehicle use. Similar to the

XX25, the newly developed UltraCell XX55 is capable of generating 55 W of continuous power for up to two weeks using the largest fuel cartridge [118]. Only 0.36 kg heavier than the XX25, the XX55 has an optional battery module that can provide a peak power output of 85 W. Similar to the XX25, it is a very rugged device that can be used essentially in any conditions [118].

Larger than the Ultracell devices, Serenergy test marketed the Serenus E-350, which was a reformed methanol/fuel cell hybrid with an approximate mass of 11 kg. At nominal power levels, it was capable of producing approximately 350 W [119]. The device was fueled by a 60–40 methanol-deionized water mixture. It took approximately 45 min to start-up, at which point it consumed fuel at a rate of 0.45 L h<sup>-1</sup>. Serenergy has, since then, stopped producing the smaller device and replaced it with a midsized model; the H<sub>3</sub> 2500 and 5000 (both weighing around 65–75 kg) [120].

### H<sub>2</sub> Pump

Efficient purification of hydrogen is becoming a common interest in both the industrial and energy sectors. In particular, technology which can efficiently purify, pump, and pressurize hydrogen at low to moderate flow rates is needed but is not readily available. Of course, there are existing methods for hydrogen purification which include various combinations of mechanical compression with cryogenic cleanup, palladium membranes, pressure swing absorption, and passive membrane separators to name a few. However, these technologies are challenged by certain limitations: (1) cryogenic cleanup produces high purity hydrogen, but requires costly refrigeration equipment and is suitable for very large-scale specialty applications; (2) palladium membrane purification can be fairly simple in design and construction but requires pressurization to drive the hydrogen separation process and suffers from poor utilization when purifying hydrogen from gases containing low fractions of hydrogen; (3) pressure swing absorption

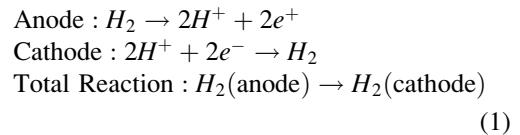


(PSA) is widely used in high volume industrial processes and relies on large, mechanical components that are subject to frequent maintenance and inherent inefficiency. Such devices are not easily scaled to smaller sizes or localized generation/purification needs. Furthermore, it is important to state that all of the above processes require expensive, high maintenance, compressors.

Electrochemical pumping is not a new concept and has in fact been utilized as a diagnostic technique within the electrochemical industry for years. General Electric developed this concept in the early 1970s [121].

The use of polymer electrolyte membranes for electrochemical hydrogen compression has been demonstrated in water electrolysis ( $H_2$  generation) devices at United Technologies Corporation, reaching 3000 psia [122], as well as studied in academic institutions [123]. The electrochemical hydrogen pump, first developed in the 1960s and 1970s, was derived from the original proton exchange membrane fuel cell efforts. The concept is simple, requires little power, and has been shown to pump hydrogen to high pressures. In the original work, the membrane transport medium was a perfluorosulfonic acid (PFSA) material, similar to the material used in many fuel cells today. The process is quite elegant in that like a fuel cell, molecular hydrogen enters the anode compartment, is oxidized to protons and electrons at the catalyst, and then the protons are driven through the membrane while the electrons are driven through the electrically conductive elements of the cell (Fig. 23).

The major difference in this cell as compared to a fuel cell is that the pump is operated in an electrolytic mode, not galvanic, meaning that power is required to “drive” the proton movement. Once the protons emerge from the membrane at the cathode, they recombine to form molecular hydrogen. Thus, hydrogen can be pumped and purified in a single step with a non-mechanical device. The pump concept builds upon the understanding of proton transport membranes. The overall chemicals are described by Eq. 1:



The cell voltage between the anode and cathode can then be described by the Eq. 2. The Nernst potential,  $E_{\text{Nernst}}$ , is given by the Nernst Eq. 3, where  $E^\circ$  is the standard potential of a hydrogen reaction,  $R$  is the gas constant,  $T$  is the temperature in Kelvin,  $F$  is Faraday’s constant, and  $p_{\text{cathode}}$  and  $p_{\text{anode}}$  are the partial pressures of hydrogen at the anode and cathode respectively.

$$E = E_{\text{Nernst}} - E_{\text{polarization}} - E_{\text{ohmic}} \quad (2)$$

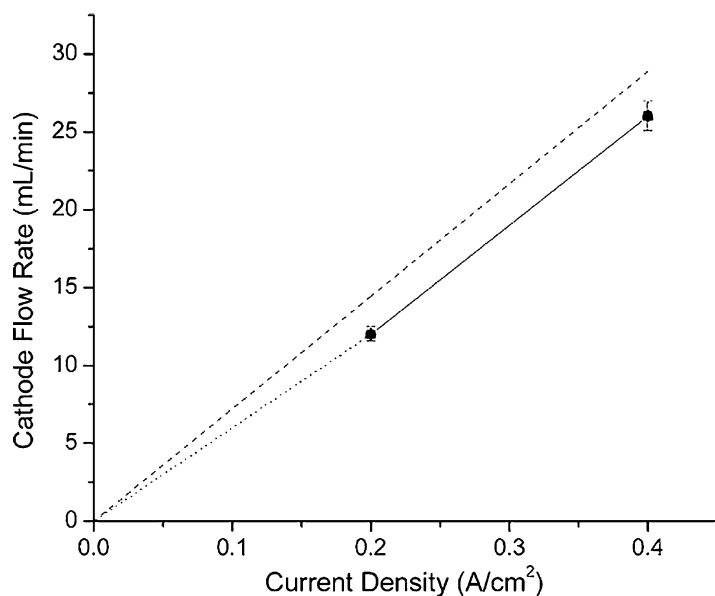
$$E_{\text{Nernst}} = E^\circ - \frac{RT}{2F} \ln \frac{p_{\text{cathode}}}{p_{\text{anode}}} \quad (3)$$

$E_{\text{polarization}}$  is the polarization overpotential which is the sum of the polarization overpotentials at the anode and cathode. This can be described using the Butler-Volmer equation. The polarization overpotential can be approximated at low overpotentials, Eq. 4, where  $R$  is the gas constant,  $T$  is the temperature in Kelvin,  $F$  is Faraday’s constant,  $i$  is the current density, and  $i_0$  is the exchange current density.

$$E_{\text{polarization}} = \frac{RTi}{2Fi_0} \quad (4)$$

Clearly, the proton conducting membrane properties are critical. Desirable properties include: high proton conductivity, mechanical stability, low solubility and permeability of impurity gases, and sufficient operating temperature to support tolerance to impurities ( $CO$  and  $H_2S$ ) found in reformed gases. The application of the PBI membrane to electrochemical hydrogen pumping provides high proton conductivity (0.2–0.4 S/cm), mechanical stability, enhanced gas separation, and up to 180 °C operation. The high operating temperature eliminates water management difficulties typically experienced with the low operating temperatures of PSFA membranes while also providing tolerance to poisonous gas species such as





**Polybenzimidazole Fuel Cell Technology: Theory, Performance, and Applications, Fig. 24** The cathodic flow rates of a hydrogen pump operated at 160 °C and 0% relative humidity and fueled by pure hydrogen (*unfilled squares*), a reformat gas comprised of 35.8% H<sub>2</sub>, 11.9% CO<sub>2</sub>, 1906 ppm CO, and 52.11% N<sub>2</sub> (*filled circles*), and a

reformat gas comprised of 69.17% H<sub>2</sub>, 29.8% CO<sub>2</sub>, and 1.03% CO (*filled triangles*). The values are nearly identical, and thus, the symbols appear superimposed. The dotted line represents the theoretical flow rate at 100% efficiency [124]

composition of the gas feed at the various operating conditions (the data points are superimposed for the different gases). The data demonstrates that the pump was capable of operating at high CO levels (1% in this work) and extracting hydrogen from dilute feed streams (<40% hydrogen). Additionally, the hydrogen pump was capable to producing hydrogen with purities greater than 99%, with the final purity dependent on operating conditions. This device could play a prominent role for both the current industrial hydrogen users, as well as in a future economy that is more heavily reliant on hydrogen as an energy carrier. Commercial development of this device is underway.

### The HyS Cycle

More recently, the hybrid sulfur thermochemical cycle has drawn a great amount of attention due to its potential to provide clean hydrogen on a large scale using considerably less energy than water electrolysis. The hybrid sulfur (HyS) process contains two steps: (1) a high temperature decomposition of sulfuric acid to produce sulfur dioxide,

oxygen, and water and (2) a low temperature electrochemical oxidation of sulfur dioxide in the presence of water to form sulfuric acid and gaseous hydrogen. The entire process recycles sulfur compounds which leave a net reaction splitting water into hydrogen and oxygen. Herein we describe advancements in the low temperature sulfur oxidation step that could be coupled with next generation solar power plants or high temperature nuclear reactors.

Since the HyS process involves the transfer of protons it is not surprising that proton exchange membranes (PEMs) are the most investigated materials. Historically, Nafion has been usually the most widely studied due to its availability. Nafion's performance in the HyS electrolyzer has been thoroughly examined with the prediction of mass transport through the membrane as a function of operating potential and other design variables. Nafion does, however, have many drawbacks including the inability to operate at elevated temperatures (above 100 °C) and since water is needed for its conductivity, there is

decreased performance at high acid concentrations or low water concentrations [125].

Polybenzimidazole (PBI) membranes are high temperature PEMs that are imbibed with acid as its electrolyte. We have shown that PBI membranes are a good alternative to Nafion in fuel cells and offer a solution to the HyS process as an avenue to higher temperature operation, which minimizes voltage losses, as well as the ability to perform under high acid concentration conditions that allow for reduced energy demands necessary for water separation. Weidner et al. show the successful operation of the HyS electrolyzer using sulfuric acid doped PBI membranes and have determined that the area-specific resistance of sulfonated PBI (s-PBI) compares favorably with Nafion, yet is not adversely affected by concentrated sulfuric acid conditions within the electrolyzer. Importantly, the PBI-based cell could be operated at low pressures and without significant water dilution of the sulfuric acid produced. Additionally, a model for high temperature and high-pressure operation of the s-PBI membrane in the electrolyzer has been constructed allowing for further analysis of the system to determine operating conditions for economically viable operation [125, 126].

## Conclusions and Future Directions

After approximately 15 years of development, PBI chemistries and the concomitant manufacturing processes have evolved to produce commercially available MEAs. PBI MEAs can operate reliably without complex water humidification hardware and are able to run at elevated temperatures of 120–180 °C due to the physical and chemical robustness of PBI membranes. These higher temperatures improve the electrode kinetics and conductivity of the MEAs, simplify the water and thermal management of the systems, and significantly increase their tolerance to fuel impurities. Membranes cast by a newly developed PPA Process possessed excellent mechanical properties, higher PA/PBI ratios, and enhanced proton conductivities as compared to previous methods of membrane preparation.

The robustness of *p*-PBI membranes cast by the PPA Process has been tested and characterized by a variety of methods. Under a constant load, *p*-PBI has been shown to perform for well over two years with very little reduction in performance. Using synthetic reformates, *p*-PBI MEAs have demonstrated excellent resistances to impurities such as CO, CO<sub>2</sub>, and SO<sub>2</sub>. *p*-PBI membranes have also been shown to retain PA extremely well, and evidence strongly suggests that this small rate of PA loss would not significantly influence the life span of a MEA. Load, thermal, and shutdown-startup cycling tests of *p*-PBI fuel cells have also indicated comparable or improved results over other commercially available fuel cell systems. *p*-PBI is the most common polymer in PBI-based fuel cell systems, although AB-PBI, *m*-PBI, and other derivatives have been investigated. Recently developed 2OH-PBI, which to date has the highest recorded proton conductivity of all other PBIs, offers much potential for future fuel cell use.

Many fuel cell manufacturers are now considering the benefits of high temperature PBI fuel cells. BASF Fuel Cell, the largest producer of PBI MEAs, has been in operation since March of 2007. BASF offers a wide variety of MEAs for stationary systems (combined heat and power, backup generators, etc.) and portable systems (transportation, microelectricalmechanical systems, etc.). Other companies, such as Plug Power, Serenergy, ClearEdge Power, and UltraCell have incorporated commercially available MEAs into commercial fuel cell systems. Additionally, Danish Power Systems has expanded its offerings and its presence in offering BI-based MEAs with improved durability. Companies such as H<sub>2</sub> Pump LLC developed electrochemical pumping devices that use PBI membranes for the purification of hydrogen gas. Using various reformat gases, the devices have been shown capable of operating at high gas contamination levels and low hydrogen concentrations. Depending on operating conditions, the purity of the extracted hydrogen gas can be greater than 99%. In transportation applications, PBI-based fuel cells show great promise as APUs or range extenders for battery powered electric vehicles.

## Bibliography

1. EIA (2016) International Energy Outlook 2016. U.S. Energy Information Administration
2. EIA (2009) Annual Energy Review 2008. U.S. Energy Information Administration
3. EIA (2011) Emissions of greenhouse gases in the United States 2009. U.S. Energy Information Administration
4. EPA (2017) Overview of greenhouse gases: carbon dioxide emissions. U.S. Environmental Protection Agency. <http://safetynet.dropmark.com/304772/6659915>
5. Wainright J, Wang J, Weng D, Savinell R, Litt M (1995) Acid-doped polybenzimidazoles: a new polymer electrolyte. *J Electrochem Soc* 142(7): L121–L123
6. Dippel T, Kreuer KD, Lassègues JC, Rodriguez D (1993) Proton conductivity in fused phosphoric acid; A  $^1\text{H}/^{31}\text{P}$  PFG-NMR and QNS study. *Solid State Ion* 61(1):41–46. [https://doi.org/10.1016/0167-2738\(93\)90332-W](https://doi.org/10.1016/0167-2738(93)90332-W)
7. Bozkurt A, Ise M, Kreuer KD, Meyer WH, Wegner G (1999) Proton-conducting polymer electrolytes based on phosphoric acid. *Solid State Ion* 125(1):225–233. [https://doi.org/10.1016/S0167-2738\(99\)00179-4](https://doi.org/10.1016/S0167-2738(99)00179-4)
8. Weber J, Kreuer K-D, Maier J, Thomas A (2008) Proton conductivity enhancement by nanostructural control of poly(benzimidazole)-phosphoric acid adducts. *Adv Mater* 20(13):2595–2598. <https://doi.org/10.1002/adma.200703159>
9. Melchior JP, Majer G, Kreuer KD (2017) Why do proton conducting polybenzimidazole phosphoric acid membranes perform well in high-temperature PEM fuel cells? *Phys Chem Chem Phys* 19(1):601–612. <https://doi.org/10.1039/c6cp05331a>
10. Li Q, Aili D, Hjuler HA, Jensen JO (2016) High temperature polymer electrolyte membrane fuel cells. Springer, NY: 545
11. Mader J, Xiao L, Schmidt T, Benicewicz BC (2008) Polybenzimidazole/acid complexes as high-temperature membranes. *Adv Polym Sci* 216(Fuel Cells II):63–124
12. Wainright JS, Savinell RF, Litt MH (2003) High temperature membranes. Handbook of fuel cells, vol 3. Wiley, NY, pp 436–446
13. Colombari P (1992) Proton conductors: solids, membranes, and gels – materials and devices. Cambridge University Press, Cambridge
14. Xiao L, Zhang H, Scanlon E, Ramanathan LS, Choe EW, Rogers D, Apple T, Benicewicz BC (2005) High-temperature polybenzimidazole fuel cell membranes via a sol-gel process. *Chem Mater* 17(21):5328–5333
15. Jayakody JRP, Chung SH, Durantino L, Zhang H, Xiao L, Benicewicz BC, Greenbaum SG (2007) NMR studies of mass transport in high-acid-content fuel cell membranes based on phosphoric acid and polybenzimidazole. *J Electrochem Soc* 154(2): B242–B246. <https://doi.org/10.1149/1.2405726>
16. Seel DC, Benicewicz BC, Xiao L, Schmidt TJ (2009) High-temperature polybenzimidazole-based membranes. Handbook of fuel cells, vol 5. Wiley, NY, pp 300–312
17. Litt M, Ameri R, Wang Y, Savinell RF, Wainright JS (1999) Polybenzimidazole/phosphoric acid solid polymer electrolytes: mechanical and electrical properties. *Mater Res Soc Symp Proc* 548:313–323
18. Zhang H (2004) Novel phosphoric acid doped polybenzimidazole membranes for fuel cells. Ph.D. thesis, Rensselaer Polytechnic Institute, Troy, December
19. Li Q, Hjuler HA, Bjerrum NJ (2001) Phosphoric acid doped polybenzimidazole membranes: physicochemical characterization and fuel cell applications. *J Appl Electrochem* 31(7):773–779
20. Zhai Y, Zhang H, Liu G, Hu J, Yi B (2006) Performance degradation studies on PBI/H<sub>3</sub>PO<sub>4</sub> high temperature PEMFC and one-dimensional numerical analysis. *J Electrochem Acta* 52(2):394–401
21. Kongstein OE, Berning T, Borresen B, Seland F, Tunold R (2007) Polymer electrolyte fuel cells based on phosphoric acid doped polybenzimidazole (PBI) membranes. *Energy* 32(4):418–422
22. Kim H, Cho SY, An SJ, Eun YC, Kim J, Yoon H, Kweon H, YEW KH (2004) Synthesis of poly(2,5-benzimidazole) for use as a fuel-cell membrane. *Macromol Rapid Commun* 25(8):894–897
23. Asensio JA, Gomez-Romero P (2005) Recent developments on proton conducting poly(2,5-benzimidazole) (AB-PBI) membranes for high temperature polymer electrolyte membrane fuel cells. *Fuel Cells* 5(3):336–343
24. Li Q, Jensen JO (2008) Membranes for high temperature PEMFC based on acid-doped polybenzimidazoles. *Membr Technol* 2:61–96
25. Asensio JA, Borros S, Gomez-Romero P (2004) Polymer electrolyte fuel cells based on phosphoric acid-impregnated poly(2,5-benzimidazole). *J Electrochem Soc* 151(2):A304–A310
26. Chen R (2004) Unpublished work. Rensselaer Polytechnic Institute, Troy
27. Yu S (2006) Novel polybenzimidazole derivatives for high temperature PEM fuel cells. Ph.D. thesis, Rensselaer Polytechnic Institute, Troy
28. Delano CB, Doyle RR, Miligan RJ (1974) United States Air Force Materials Laboratory. AFML-TR-74-22
29. Yu S, Zhang H, Xiao L, Choe EW, Benicewicz BC (2009) Synthesis of poly(2,2'-(1,4-phenylene)5,5'-bibenzimidazole) (para-PBI) and phosphoric acid doped membrane for fuel cells. *Fuel Cells* 9(4):318–324
30. Xiao L (2003) Novel polybenzimidazole derivatives for high temperature polymer electrolyte membrane fuel cell application. Ph.D. thesis, Rensselaer Polytechnic Institute, Troy

31. Xiao L, Zhang H, Jana T, Scanlon E, Chen R, Choe EW, Ramanathan LS, Yu S, Benicewicz BC (2005) Synthesis and characterization of pyridine-based polybenzimidazoles for high temperature polymer electrolyte membrane fuel cell applications. *Fuel Cells* 5(2):287–295
32. Xiao L, Zhang H, Jana T, Scanlon E, Chen R, Choe EW, Ramanathan LS, Yu S, Benicewicz BC (2004) Synthesis and characterization of pyridine-based polybenzimidazoles for high temperature polymer electrolyte membrane fuel cell applications. *Fuel Cells* 5(2):287–295
33. Kallitsis JK, Gourdoupi N (2003) Proton conducting membranes based on polymer blends for use in high temperature PEM fuel cells. *J New Mat Electrochem Syst* 6(4):217–222
34. Faure S, Mercier R, Aldebert P, Pineri M, Sillion B (1996) Gas separation polyimide membranes used to prepare ion-exchange membranes for use in manufacture of fuel cells. France Patent 9,605,707
35. Watari T, Fang J, Tanaka K, Kita H, Okamoto KI, Hirano T (2004) Synthesis, water stability and proton conductivity of novel sulfonated polyimides from 4,4'-bis(4-aminophenoxy)biphenyl-3,3'-disulfonic acid. *J Membr Sci* 230(1–2):111–120
36. Luffrano F, Gatto I, Staiti P, Antonucci V, Passalacqua E (2001) Sulfonated polysulfone ionomer membranes for fuel cells. *Solid State Ionics* 145(1–4):47–51
37. Einsla BR, Harrison WL, Tchatchoua C, McGrath JE (2004) Disulfonated polybenzoxazoles for proton exchange membrane fuel cell applications. *Polym Prepr* 44(2):645–646
38. Gil M, Ji X, Li X, Na H, Hampsey JE, Lu Y (2004) Direct synthesis of sulfonated aromatic poly(ether ether ketone) proton exchange membranes for fuel cell applications. *J Membr Sci* 234(1–2):75–81
39. Xing P, Robertson GP, Guiver MD, Mikhailenko SD, Kaliaguine S (2004) Sulfonated poly(aryl ether ketone)s containing the hexafluoroisopropylidene diphenyl moiety prepared by direct copolymerization, as proton exchange membranes for fuel cell application. *Macromolecules* 37(21):7960–7967
40. Gao Y, Robertson GP, Guiver MD, Mikhailenko SD, Kaliaguine S (2004) Synthesis of Copoly(aryl ether ether nitrile)s containing sulfonic acid groups for PEM applications. *Macromolecules* 37(18):6748–6754
41. Xiao GY, Sun GM, Yan DY, Zhu PF, Tao P (2002) Synthesis of sulfonated poly(phthalazinone ether sulfone)s by direct polymerization. *Polym Prepr* 43(19):5335–5339
42. Wang F, Hickner M, Kim YS, Zawodzinski TA, McGrath JE (2002) Direct polymerization of sulfonated poly(arylene ether sulfone) random (statistical) copolymers: candidates for new proton exchange membranes. *J Membr Sci* 197(1–2):231–242
43. Hickner MA, Ghassemi H, Kim YS, Einsla BR, McGrath JE (2004) Alternative polymer systems for proton exchange membranes (PEMs). *Chem Rev* 104(10):4587–4611
44. Kim S, Cameron DA, Lee Y, Reynolds JR, Savage CR (1996) Aromatic and rigid rod polyelectrolytes based on sulfonated poly(benzobisthiazoles). *J Polym Sci Part A* 34(3):481–492
45. Ariza MJ, Jones DJ, Roziere J (2002) Role of post-sulfonation thermal treatment in conducting and thermal properties of sulfuric acid sulfonated poly(benzimidazole) membranes. *Desalination* 147(1–3):189–194
46. Staiti P, Luffrano F, Arico AS, Passalacqua E, Antonucci V (2001) Sulfonated polybenzimidazole membranes – preparation and physico-chemical characterization. *J Membr Sci* 188(1):71–78
47. Bae JM, Honma I, Murata M, Yamamoto T, Rikukawa M, Ogata N (2002) Properties of selected sulfonated polymers as proton-conducting electrolytes for polymer electrolyte fuel cells. *Solid State Ionics* 147(1–2):189–194
48. Asensio JA, Borros S, Gomez-Romero P (2002) Proton-conducting polymers based on benzimidazoles and sulfonated benzimidazoles. *J Polym Sci Part A* 40(21):3703–3710
49. Sakaguchi Y, Kitamura K, Nakao J, Hamamoto S, Tachimori H, Takase S (2001) Preparation and properties of sulfonated or phosphonated polybenzimidazoles and polybenzoxazoles. *J Polym Mater Sci Eng* 84:899–900
50. Mader JA, Benicewicz BC (2010) Sulfonated polybenzimidazoles for high temperature PEM fuel cells. *Macromolecules* 43(16):6706–6715. <https://doi.org/10.1021/ma1009098>
51. Mader JA, Benicewicz BC (2011) Synthesis and properties of random copolymers of functionalised polybenzimidazoles for high temperature fuel cells. *Fuel Cells* 11(2):212–221. <https://doi.org/10.1002/fuce.201000080>
52. He R, Li Q, Xiao GY, Bjerrum NJ (2003) Proton conductivity of phosphoric acid doped polybenzimidazole and its composites with inorganic proton conductors. *J Membr Sci* 226(1–2):169–184
53. Qian G, Benicewicz BC (2009) Synthesis and characterization of high molecular weight hexafluoroisopropylidene-containing polybenzimidazole for high-temperature polymer electrolyte membrane fuel cells. *J Polym Sci, Part A* 47(16):4064–4073
54. Yu S, Benicewicz BC (2009) Synthesis and properties of functionalized polybenzimidazoles for high-temperature PEMFCs. *Macromolecules* 42(22):8640–8648
55. Scanlon E (2005) Polybenzimidazole based segmented block copolymers for high temperature fuel cell applications. Ph.D. thesis, Rensselaer Polytechnic Institute, Troy



56. Schmidt TJ (2006) Durability and degradation in high-temperature polymer electrolyte fuel cells. *ECS Trans* 1(8):19–31
57. Chen XM, Qian GQ, Molle MA, Benicewicz BC, Ploehn HJ (2015) High temperature creep behavior of phosphoric acid-polybenzimidazole gel membranes. *J Polym Sci Pol Phys* 53(21):1527–1538
58. Molle MA, Chen X, Ploehn HJ, Benicewicz BC (2015) High polymer content 2,5-pyridine-polybenzimidazole copolymer membranes with improved compressive properties. *Fuel Cells* 15(1):150–159
59. Molle MA, Chen X, Ploehn HJ, Fishel KJ, Benicewicz BC (2014) High polymer content 3,5-pyridine-polybenzimidazole copolymer membranes with improved compressive properties. *Fuel Cells* 14(1):16–25
60. Sondergaard T, Cleemann LN, Becker H, Aili D, Steenberg T, Hjulder HA, Seerup L, Li QF, Jensen JO (2017) Long-term durability of HT-PEM fuel cells based on thermally cross-linked polybenzimidazole. *J Power Sources* 342:570–578
61. Schmidt TJ (2009) High-temperature polymer electrolyte fuel cells: durability insights. In: Buchi FN, Inaba M, Schmidt TJ (eds) *Polymer electrolyte fuel cell durability*. Springer, New York, pp 199–221
62. Ross PN Jr (1987) Deactivation and poisoning of fuel cell catalysts. In: Petersen EE, Bell AT (eds) *Catalyst deactivation*. Marcel Dekker, New York
63. Ferreira PJ, la O'GJ, Shao-Horn Y, Morgan D, Makharia R, Kocha S, Gasteiger HA (2005) Instability of Pt/C electrocatalysts in proton exchange membrane fuel cells: a mechanistic investigation. *J Electrochem Soc* 152(11):A2256–A2271
64. Tang L, Han B, Persson K, Friesen C, He T, Sieradzki K, Ceder G (2010) Electrochemical stability of nanometer-scale Pt particles in acidic environments. *J Am Chem Soc* 132(2):596–600
65. Liu G, Zhang H, Zhai Y, Zhang Y, Xu D, Z-g S (2007) Pt<sub>4</sub>ZrO<sub>2</sub>/C cathode catalyst for improved durability in high temperature PEMFC based on H<sub>3</sub>PO<sub>4</sub> doped PBI. *Electrochem Commun* 9(1):135–141
66. Landsman DA, Luczak FJ (2003) In: Vielstich W, Lamm A, Gasteiger H (eds) *Handbook of fuel cells – fundamentals, technology and applications*, vol 4. Wiley, Chicester, pp 811–831
67. Neyerlin KC, Singh A, Chu D (2008) Kinetic characterization of a Pt-Ni/C catalyst with a phosphoric acid doped PBI membrane in a proton exchange membrane fuel cell. *J Power Sources* 176(1):112–117
68. Schmidt TJ, Baurmeister J (2008) Properties of high-temperature PEFC Celtec-P 1000 MEAs in start/stop operation mode. *J Power Sources* 176(2):428–434
69. Luczak FJ, Landsman DA (1984) Ordered ternary fuel cell catalysts containing platinum, cobalt and chromium. US Patent 4,447,506
70. Luczak FJ, Landsman DA (1987) Ordered ternary fuel cell catalysts containing platinum and cobalt and method for making the catalyst. US Patent 4,677,092
71. Beard B, Ross PN Jr (1990) The structure and activity of platinum-cobalt alloys as oxygen reduction electrocatalysts. *J Electrochem Soc* 137(11):3368–3374
72. Glass JT, Cahen GL, Stoner GE (1987) The effect of metallurgical variables on the electrocatalytic properties of platinum-chromium alloys. *J Electrochem Soc* 134(1):58–65
73. Mukerjee S, Srinivasan S (1993) Enhanced electrocatalysis of oxygen reduction on platinum alloys in proton exchange membrane fuel cells. *J Electroanal Chem* 357(1–2):201–224
74. Mukerjee S, Srinivasan S, Soriaga MP (1995) Role of structural and electronic properties of Pt and Pt alloys on electrocatalysis of oxygen reduction. An in situ XANES and EXAFS investigation. *J Electrochem Soc* 142(5):1409–1422
75. Paulus UA, Scherer GG, Wokaun A, Schmidt TJ, Stamenkovic V, Radmilovic V, Markovic NM, Ross PN (2001) Oxygen reduction on carbon-supported Pt-Ni and Pt-Co alloy catalysts. *J Phys Chem B* 106(16):4181–4191
76. Stamenkovic V, Fowler B, Mun BS, Wang B, Ross PN, Lucas CA, Markovic NM (2007) Improved oxygen reduction activity on Pt<sub>3</sub>Ni(111) via increased surface site availability. *Science* 315(5811):493–497
77. Stamenkovic V, Schmidt TJ, Ross PN, Markovic NM (2002) Surface composition effects in electrocatalysis: kinetics of oxygen reduction on well-defined Pt<sub>3</sub>Ni and Pt<sub>3</sub>Co alloy surfaces. *J Phys Chem B* 106(46):11970–11979
78. Parrondo J, Mijangos F, Rambabu B (2010) Platinum/tin oxide/carbon cathode catalyst for high temperature PEM fuel cell. *J Power Sources* 195(13):3977–3983
79. Qian G (2008) Fluorine-containing polybenzimidazoles for high temperature polymer electrolyte membrane fuel cell applications. Ph.D. thesis, Rensselaer Polytechnic Institute, Troy
80. Gasteiger H, Markovic NM (2009) Just a dream – or future reality? *Science* 324(5923):48–49
81. Debe MK, Schmoedel AK, Vernstrom GD, Atanoski R (2006) High voltage stability of nanostructured thin film catalysts for PEM fuel cells. *J Power Sources* 161(2):1002–1011
82. Strasser P (2009) Dealloyed Pt bimetallic electrocatalysts for oxygen reduction. In: Vielstich W, Yokokawa H, Gasteiger HA (eds) *Handbook of fuel cells: advances in electrocatalysis, materials, diagnostics, and durability*. Wiley, New York, pp 30–47
83. Lefevre M, Proietti E, Jaouen F, Dodelet J-P (2009) Iron-based catalysts with improved oxygen reduction activity in polymer electrolyte fuel cells. *Science* 324(5923):71–74
84. MCFC and PAFC R&D Workshop Summary Report. US Department of Energy (2010) <http://www1.eere.gov>

- [energy.gov/hydrogenandfuelcells/pdfs/mcfc\\_pafc\\_workshop\\_summary.pdf](http://energy.gov/hydrogenandfuelcells/pdfs/mcfc_pafc_workshop_summary.pdf)
85. Hu Y, Jensen JO, Zhang W, Martin S, Chenitz R, Pan C, Xing W, Bjerrum NJ, Li Q (2015) Fe<sub>3</sub>C-based oxygen reduction catalysts: synthesis, hollow spherical structures and applications in fuel cells. *J Mater Chem A* 3(4):1752–1760. <https://doi.org/10.1039/C4TA03986F>
  86. Singdeo D, Dey T, Gaikwad S, Andreasen SJ, Ghosh PC (2017) A new modified-serpentine flow field for application in high temperature polymer electrolyte fuel cell. *Appl Energy* 195:13–22. <https://doi.org/10.1016/j.apenergy.2017.03.022>
  87. Yu S, Xiao L, Benicewicz BC (2008) Durability studies of PBI-based high temperature PEMFC. *Fuel Cells* 8(3–4):165–174
  88. Okae I, Kato S, Seya A, Kamoshita T (1990) Study of the phosphoric acid management in PAFCs. In: *The chemical society of Japan 67th spring meeting*, p 148
  89. Manufacturing for the Hydrogen Economy: Manufacturing Research and Development of PEM Fuel Cell Systems for Transportation Application (2005) U.S. Department of Energy. [http://www1.eere.energy.gov/hydrogenandfuelcells/pdfs/mfg\\_wkshp\\_fuelcell.pdf](http://www1.eere.energy.gov/hydrogenandfuelcells/pdfs/mfg_wkshp_fuelcell.pdf)
  90. Hydrogen Fuel Cell Vehicle and Station Deployment Plan: A Strategy for Meeting the Challenge Ahead (2009) California Fuel Cell Partnership. <http://www.fuelcellpartnership.org/>
  91. Feitelberg AS, Stathopoulos J, Qi Z, Smith C, Elter JF (2005) Reliability of plug power GenSys fuel cell systems. *J Power Sources* 147(1–2):203–207
  92. Schmidt TJ, Baumeister J (2006) Durability and reliability in high temperature reformed hydrogen PEFCs. *ECS Trans* 3(1):861–869
  93. Mocoteguy P, Ludwig B, Scholta J, Nedellec Y, Jones DJ, Roziere J (2010) Long-term testing in dynamic mode of HT-PEMFC H<sub>3</sub>PO<sub>4</sub>/PBI celtec-P based membrane electrode assemblies for Micro-CHP applications. *Fuel Cells* 10(2):299–311
  94. Mocoteguy P, Ludwig B, Scholta J, Barrera R, Ginocchio S (2009) Long term testing in continuous mode of HT-PEMFC based H<sub>3</sub>PO<sub>4</sub>/PBI celtec-P MEAs for u-CHP applications. *Fuel Cells* 9(4):325–348
  95. Garsany Y, Gould BD, Baturina OA, Swider-Lyons KE (2009) Comparison of the sulfur poisoning of PBI and nafion PEMFC cathodes. *Electrochem Solid-State Lett* 12(9):B138–B140
  96. Schmidt TJ, Baumeister J (2008) Development status of PBI based high-temperature membrane electrode assemblies. *ECS Trans* 16(2):263–270
  97. Reiser CA, Bregoli L, Patterson TW, Yi JS, Yang JD, Perry ML, Jarvi TD (2005) A reverse-current decay mechanism for fuel cells. *Electrochem Sol Let* 8(6):A273–A276
  98. Puffer RH Jr, Hoppes GH (2004) Development of a flexible pilot high temperature MEA manufacturing line. *Fuel Cell Sci Eng Technol*:573–579
  99. Puffer RH Jr, Rock SJ (2009) Recent advances in high temperature proton exchange membrane fuel cell manufacturing. *J Fuel Cell Sci Tech* 6(4):041013/041011–041013/041017
  100. Harris TAL, Walczyk D (2006) Development of a casting technique for membrane material used in high-temperature PEM fuel cells. *J Manuf Process* 8(1):19–31
  101. Reduction of greenhouse gas emissions through fuel cell combined heat and power applications (2008) [www.fuelcells.org/info/residentialsavings.pdf](http://www.fuelcells.org/info/residentialsavings.pdf). Accessed 15–19 June 2008
  102. Schmidt R (2009) Japan working toward fuel-cell reality. *Marketplace*, December 8, p 1
  103. Celtec MEAs: Membrane Electrode Assemblies for High Temperature PEM Fuel Cells (2010) BASF Fuel Cell GmbH. <http://www.basf-fuelcell.com/en/projects/celtec-mea.html>
  104. Celtec® MEAs: Membrane Electrode Assemblies for High Temperature PEM Fuel Cells BASF. [http://www.basf-fuelcell.com/cm/internet/Fuel\\_Cell/en/function/conversions:publish/content/Microsite/Fuel\\_Cell/2474\\_Flyer\\_Celtec\\_P\\_Mea\\_ak3\\_jk.pdf](http://www.basf-fuelcell.com/cm/internet/Fuel_Cell/en/function/conversions:publish/content/Microsite/Fuel_Cell/2474_Flyer_Celtec_P_Mea_ak3_jk.pdf)
  105. High-Temperature Fuel Cell System for Residential Applications (2009) Plug Power. <http://www.plugpower.com/products/residentialgensys/residentialgensys.aspx>
  106. Serenus 166/390 Air C v2.5 (2010) Serenergy. [http://www.serenergy.com/files/assets/documentation/166\\_390%20Air%20C%20v2.5%20data%20sheet\\_v1.1-0210.pdf](http://www.serenergy.com/files/assets/documentation/166_390%20Air%20C%20v2.5%20data%20sheet_v1.1-0210.pdf)
  107. ClearEdge Power, Delivering Smart Energy Today. (2009) <http://www.clearedgepower.com/>. June 2010
  108. Delventhal S (2017) What's ahead for the fuel-cell industry in 2017. *Investopedia*. <http://www.investopedia.com/news/whats-ahead-fuelcell-industry-2017/>
  109. Emissions of Greenhouse Gases Report (2009) U.S. Energy Information Administration. <http://www.eia.doe.gov/oiaf/1605/ggrpt/#ercde>
  110. Why 100 Hydrogen Stations: A California Fuel Cell Partnership White Paper (2017) California Fuel Cell Partnership. <https://cafcp.org/sites/default/files/100-Stations-White-Paper-for-Public.pdf>
  111. A California Road Map: The Commercialization of Hydrogen Fuel Cell Vehicles (2014). <https://cafcp.org/sites/default/files/Roadmap-Progress-Report2014-FINAL.pdf>
  112. SunHydro: Solar Powered Hydrogen Fueling Stations. (2017) SunHydro. <http://www.sunhydro.com/locations/>
  113. Driving VW's fuel-cell prototypes (2008) Telegraph Media Group Limited. <http://www.telegraph.co.uk/motoring/green-motoring/3520714/Driving-VW-s-fuel-cell-prototypes.html>
  114. Innovative Danish technology uses methanol to make fuel cell vehicles competitive (2009, December) <http://www.renewableenergyfocus.com/view/5650/>

- [innovative-danish-technology-uses-methanol-to-make-fuel-cell-vehicles-competitive/](#)
115. DLR Motor Glider Antares Takes Off in Hamburg – Powered by a Fuel Cell (2009) German Aerospace Center. [http://www.dlr.de/en/desktopdefault.aspx/tabid-13/135\\_read-18278/](http://www.dlr.de/en/desktopdefault.aspx/tabid-13/135_read-18278/)
  116. What's Next after the Dreamliner? Think Fuel Cells (2009, September 18) [http://www.designnews.com/article/354516-What\\_s\\_Next\\_after\\_the\\_Dreamliner\\_Think\\_Fuel\\_Cells.php](http://www.designnews.com/article/354516-What_s_Next_after_the_Dreamliner_Think_Fuel_Cells.php)
  117. UltraCell XX25: Mobile Power for Mobile Applications (2008) Ultracell. [http://www.ultracellpower.com/assets/XX25\\_Data\\_Sheet\\_01-22-2009.pdf](http://www.ultracellpower.com/assets/XX25_Data_Sheet_01-22-2009.pdf)
  118. UltraCell XX55: Extreme Mobile Power for Demanding Applications (2008) Ultracell. [http://www.ultracellpower.com/assets/XX55\\_Data\\_Sheet\\_01-27-2009.pdf](http://www.ultracellpower.com/assets/XX55_Data_Sheet_01-27-2009.pdf)
  119. Serenus Methanol fuel cell module – 350W (2010) Serenergy. [http://www.serenergy.com/files/assets/documentation/Serenus%20H3%20E-350\\_datasheet\\_v1.1-0210.pdf](http://www.serenergy.com/files/assets/documentation/Serenus%20H3%20E-350_datasheet_v1.1-0210.pdf)
  120. Methanol Power System: H<sub>3</sub> 2500/3500 SerEnergy. [http://serenergy.com/wp-content/uploads/2016/10/H3-2500-5000-48V\\_datasheet\\_v2.0-0916.pdf](http://serenergy.com/wp-content/uploads/2016/10/H3-2500-5000-48V_datasheet_v2.0-0916.pdf). Accessed 2017
  121. Maget HJR (1970) Process for gas purification. US Patent 3,489,670, January 13.
  122. McElroy JF (1989) SPE regenerative hydrogen/oxygen fuel cells for extraterrestrial surface applications. In: Energy conversion engineering conference, Washington, DC, August. Proceedings of the 24th intersociety. IEEE, pp 1631–1636
  123. Rohland B, Eberle K, Strobel R, Scholta J, Garcke J (1998) Electrochemical hydrogen compressor. *Electrochem Acta* 43(24):3841
  124. Perry KA, Eisman GA, Benicewicz BC (2008) Electrochemical hydrogen pumping using a high-temperature polybenzimidazole (PBI) membrane. *J Power Sources* 177(2):478–484
  125. Weidner JW (2016) Electrolyzer performance for producing hydrogen via a solar-driven hybrid-sulfur process. *J Appl Electrochem* 46(8):829–839. <https://doi.org/10.1007/s10800-016-0962-0>
  126. Garrick TR, Gullette A, Staser JA, Benicewicz B, Weidner JW (2015) Polybenzimidazole membranes for hydrogen production in the hybrid sulfur electrolyzer. *ECS Trans* 66(3):31–40. <https://doi.org/10.1149/06603.0031ecst>



## Phosphoric Acid Fuel Cells for Stationary Applications

Sridhar V. Kanuri and Sathya Motupally  
Doosan Fuel Cell America, South Windsor,  
CT, USA

### Article Outline

Glossary  
Definition of the Subject  
Introduction  
Market Requirements  
Phosphoric Acid Fuel Cells  
Cell Stack Assembly Components  
Cell Stack Assembly Life  
PAFC Applications  
Future Directions  
Bibliography

### Glossary

**ADG** Anaerobic digester gas.  
**BOP** Balance of plant. Involves components other than fuel cell stacks in a power plant.  
**Bubble pressure** Ability of a component filled with acid to withstand a given pressure of gas.  
**Carbonization** This process involves heating resin-impregnated material to  $\sim 1,000^\circ\text{C}$  to carbonize.  
**CH<sub>4</sub>** Methane.  
**CHP** Combined heat and power. Equipment that generates both electrical and thermal energy.  
**Cloud tower** Equipment to deposit catalyst onto GDL.  
**ECA** Electrochemical area, ideally the Pt surface area available for oxygen reduction or Hydrogen oxidation reaction.  
**Efficiency** Energy output/Energy input.  
**ETU** Electrolyte take-up: Quantity of electrolyte (H<sub>3</sub>PO<sub>4</sub>) taken up by a unit weight of carbon.  
**FEP** Fluorinated ethylene propylene.  
**Floc** Mixture of carbon-coated catalyst and PTFE<sup>®</sup>.

**GDL** Gas diffusion layers.

**GDL** Gas diffusion layers or substrates.

**Graphitization** This process involves in heating carbon material to temperatures of  $2,500\text{--}3,000^\circ\text{C}$  to improve thermal conductivity and corrosion resistance.

**H<sub>2</sub>** Hydrogen.

**H<sub>3</sub>PO<sub>4</sub>** Phosphoric acid.

**HT-PEM** High-temperature polymer electrolyte membrane fuel cell.

**Ionic resistance** Resistance for the flow of H<sup>+</sup> through the electrolyte matrix.

**kW** Kilo watts.

**NG** Natural gas.

**O<sub>2</sub>** Oxygen.

**PAFC** Phosphoric acid fuel cell.

**PAN** Polyacrylonitrile.

**Performance decay** Loss of fuel cell performance due to kinetic, ionic, or mass transport losses.

**PTFE<sup>®</sup>** Polytetrafluoroethylene.

**SiC** Silicon Carbide.

### Definition of the Subject

Fuel cells generate power by electrochemically combining fuel such as hydrogen and oxidant such as oxygen in air to produce electrical and thermal energy. Fuel cells generally consist of an anode electrode where fuel is oxidized and cathode electrode where oxygen in air is reduced. The electrolyte which is usually placed between the two electrodes acts as a medium to transport charge carriers (e.g., H<sup>+</sup>, CO<sup>-</sup>). Fuel cells are particularly interesting as energy generating devices because they consume reactants without combustion, thus providing higher efficiencies and avoiding the issue of pollution. A fuel cell reaction typically produces water as a by-product which is usually removed from the cell by reactant exhaust.

There are various types of fuel cells that are under development. The most noticeable ones are polymer electrolyte membrane (PEM) fuel cells, phosphoric acid fuel cells (PAFC), molten

carbonate fuel cells (MCFC), and solid oxide fuel cells (SOFC). PEM fuel cells are mainly being targeted toward transportation needs due to their ability to provide high power densities at reasonable operating temperatures ( $\sim 100$  °C). PAFCs and MCFCs are being developed primarily for stationary applications since their power densities are lower than PEM. SOFCs are currently being developed for both stationary applications and transportation applications but high-temperature material development is needed before they become commercially viable.

## Introduction

Medium-temperature fuel cells can be classified as those operating between 120 °C and 250 °C. Two main categories of fuel cells fall in this category. One is phosphoric acid fuel cell and the other is high-temperature polymer electrolyte membrane fuel cells (HT-PEMFC). While PAFC is the only fuel cell technology that has demonstrated over 70,000 h of field operation it has cost challenges that have to be overcome for commercialization. On the other hand, significant amount of government and private funding is being devoted to the development of HT-PEMFC for automotive and stationary applications [1]. So far HT-PEM has shown little progress in lab-scale evaluation and has a long road to full-scale demonstration.

This temperature range is particularly interesting because it allows the fuel cell to run on reformed fuel and have tolerance to CO which is the main fuel cell poison generated in the reforming reaction. Most importantly, these temperatures allow for combined heat and power (CHP) capability that can be used in most commercial buildings for either space heating, hot water generation, cooling applications, etc. Today, commercial CHP is the best application for fuel cells in the stationary space due to price of electricity, price of gas, the opportunity for customer energy savings, and the impact of such savings on world energy consumption. Fuel cells in CHP applications need to be efficient (80–90% efficiency), cost effective (less than

\$2,000/kW installed), have useable heat (temperatures in the neighborhood of 150–250 °C), and long life times (10 years) to provide the required value proposition to customers. PAFCs fit very well with the above requirements except for cost which is being addressed currently by both industry and government.

## Market Requirements

Stationary fuel cell applications include commercial buildings such as supermarkets, data centers, schools, hotels, and hospitals, and industrial users such as chemical plants and refineries and distribution utilities. The primary driver for acceptance of any energy application is the payback period associated. For reference purposes, the payback period in the energy industry is usually on the 3–5 year time scale. In addition to payback period, strategic factors such as grid congestion and unreliability, rising energy costs, urbanization, global warming, ability to use waste heat, and avoidance of peak load constraints are also factoring more and more into the decision making of customers evaluating fuel cells for stationary applications.

Payback period is usually a function of initial cost of the system and the life cycle costs associated with the system. Initial cost of a PAFC system involves the cost of fuel cell stacks and balance of plant components, cost of integration and assembly of these components and factory acceptance test. Life cycle costs are primarily a function of the efficiency of the system, cost of fuel and maintenance costs. Efficiency in the case of CHP applications involves both electrical and thermal efficiency.

PAFCs have a payback period of 3–5 years (with various government incentives) when the customers use waste heat generated by the fuel cell. These systems have an initial electrical efficiency greater than 40% and an average lifetime electrical efficiency of 38%. Utilization of all of the waste heat generated by the system allows the customer to achieve 90% overall utilization.

## Phosphoric Acid Fuel Cells

PAFCs are the first fuel cells to be commercially available. The major manufacturers of these fuel cells are UTC Power, Toshiba Corporation, HydroGen Corporation, Fuji Electric Corporation and Mitsubishi Electric Corporation. UTC Power introduced for sale a 200 kW PAFC system in 1991, and over 260 units were delivered to various customers worldwide. The design operational lifetime for these units was 40,000 h and most of the fielded units have met or exceeded this requirement. A number of these units are still operational today with fleet leader at Mohegun Sun in Uncasville, Connecticut, USA, accumulating more than 76,000 h [2]. Fuji's phosphoric acid fuel cell power plants, launched in 1998 have also demonstrated 40,000 h of life in field and some units after overhaul have exceeded 77,000 h of operational lifetime [3].

Phosphoric acid fuel cells usually operate on natural gas but they can operate on other fuels such as H<sub>2</sub> exhaust from chemical plants and anaerobic digester gas (ADG) from waste treatment plants. UTC Power's phosphoric acid fuel cell system is usually designed to operate in water balance, i.e., it does not consume water from the site nor produce excess water at the site. These power plants operate at ambient pressures and have the capability to transition between grid connect and grid independent model. This capability allows the customer to draw electricity when required from grid and export excess electricity generated by the fuel cell power plant when the customer loads are lower than the power generated by fuel cell. Basic description of an ambient pressure natural gas operating UTC Power's PAFC system is shown in Fig. 1.

Natural gas is fed to the fuel processor where CH<sub>4</sub> in natural gas is converted to H<sub>2</sub>-rich fuel using steam reforming. H<sub>2</sub>-rich fuel from reformer is fed to the cell stack where it is electrochemically combined with O<sub>2</sub> in air to generate DC power and thermal energy. DC power is sent to power conditioning system where it is converted to AC power. Makeup water is used only during the start-up of power plant to fill the thermal management system or in situations where the power

plant is operated outside its design specifications for extended period of time.

The cell stack assembly is the heart of the power plant which produces both electrical and thermal energy by electrochemically combining H<sub>2</sub> in fuel and O<sub>2</sub> in air. The basic description of a phosphoric acid fuel cell is shown in Fig. 2.

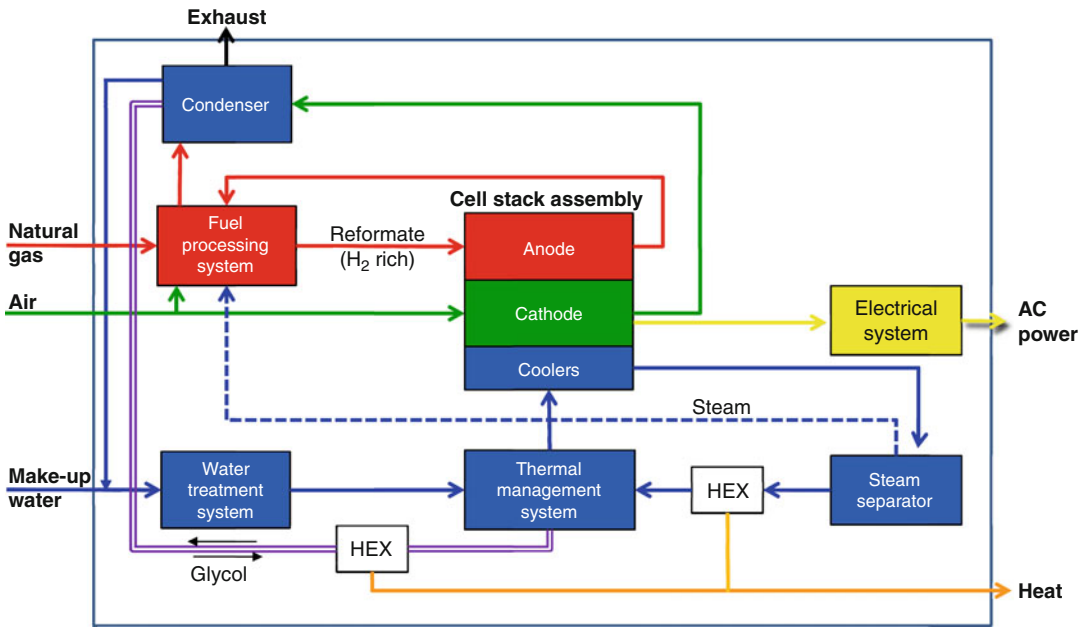
PAFCs operate at temperatures between 150 °C and 225 °C. H<sub>2</sub> from fuel is split into protons and electrons at the anode electrode. The protons travel through the electrolyte (H<sub>3</sub>PO<sub>4</sub>) and reach the cathode catalyst layer where they combine with O<sub>2</sub> in air producing DC power, water, and waste heat. The electrolyte is usually held in a refractory nonconducting matrix like silicon carbide. Water generated in the fuel cell is removed by cathode exhaust. Cathode exhaust is sent to the condenser where generated water is condensed. This condensed water is sent back to the water treatment system where it is purified to minimize the conductivity and sent to the thermal management system. Coolant exhaust from cell stack is sent to steam separator where steam required for fuel processor is separated and the remaining hot coolant water is sent through multiple heat exchangers to supply thermal energy to customers.

## Cell Stack Assembly Components

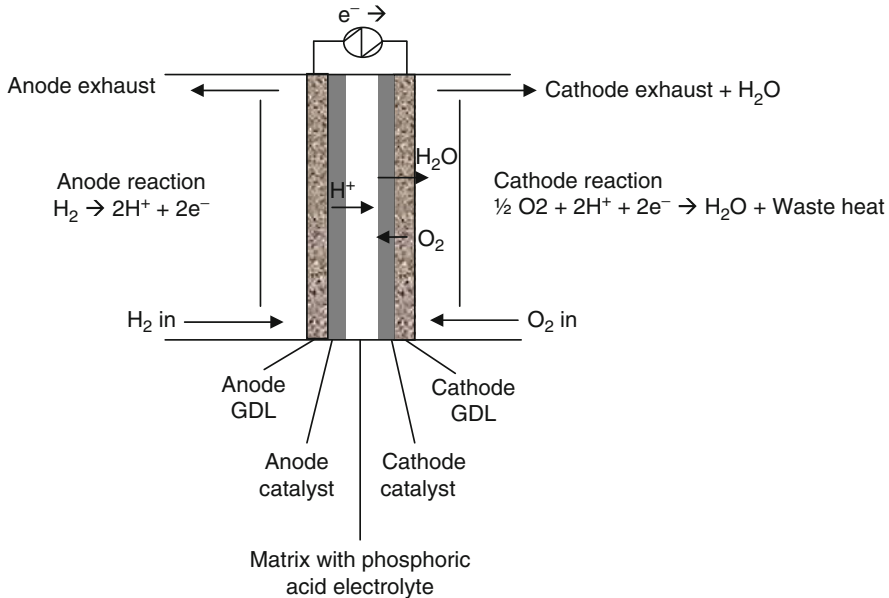
The main components of a PAFC are bipolar plates, gas diffusion layers, catalyst layers, and matrix layer [4]. Typical cell designs include a sandwich of these layers as arranged in Fig. 2 between coolers. Multiple cells per cooler designs are generally employed to improve power density and this unit is called a sub stack. A cell stack assembly consists of multiple sub stacks held between two pressure plates under compression to minimize reactant leakage and contact resistance losses.

*Gas diffusion layers (GDLs):* As the name suggests, GDL allows for gas to diffuse from the bulk flow in channels to the catalyst layer; provides mechanical support to the catalyst layer; allows for water management, i.e., removal of product water to the bulk flow in channels and





**Phosphoric Acid Fuel Cells for Stationary Applications, Fig. 1** Description of an ambient pressure operating PAFC system



**Phosphoric Acid Fuel Cells for Stationary Applications, Fig. 2** Phosphoric acid fuel cell

heat transfer from the catalyst layer to the coolers. GDLs are made by turning polyacrylonitrile (PAN)-based carbon fiber into carbon paper. Carbon paper is then impregnated with a phenolic

resin by a prepreg process, hot laminated to cure the resin in place and to achieve the desired thickness. It is then heat treated at ~1,000 °C to turn the phenolic resin into carbon and then graphitized at

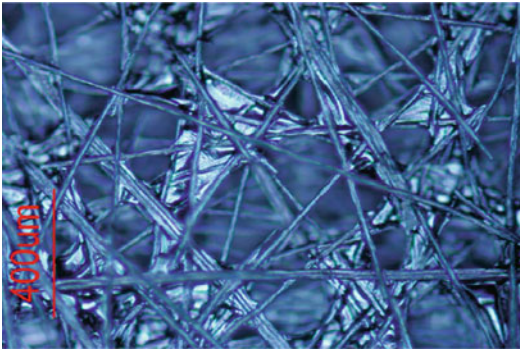
~2,500 °C in an inert atmosphere [5, 6]. Graphitization helps impart better thermal and electrical conductivity to the GDL. A finished substrate is approximately 70% porous with a mean pore size of 25–30 μm. These finished substrates as shown in Fig. 3 are usually hydrophobic and hence they are impregnated with a wettability coating (e.g., Vulcan or Black Pearl Carbon) to facilitate water and acid management.

*Electrolyte matrix:* Matrix in PAFC holds H<sub>3</sub>PO<sub>4</sub> electrolyte and hence facilitates the movement of protons from anode to cathode. The matrix layer should be wettable, sufficiently porous to hold H<sub>3</sub>PO<sub>4</sub> electrolyte, should have minimal reactivity with H<sub>3</sub>PO<sub>4</sub> during operating temperatures, have sufficient electrical isolation to prevent shorting in cells and finally have sufficient bubble pressure (~35 kPa) to minimize reactant crossover. Materials such as wettable PTFE, papers formed using organic polymers and silicon carbide have been evaluated as matrix layers by various fuel cell manufacturers. Wettable PTFE layers failed because they lost their wettable properties over the course of operation leading to expulsion of acid from the matrix layer and hence cell failure due to reactant crossover. Organic polymers such as polyetherketones (PEK) and polybenzimidazoles (PBI) have acceptable beginning-of-life properties but seem to lose desirable properties over the course of time. Silicon carbide matrix layer has been used in UTC Power's PAFC and it has retained its material properties over long life operation. This matrix layer is formed by spraying 5 μm particle size SiC with 5% PTFE as binder onto the catalyst layer and then heating the coated electrode to ~300 °C to evaporate the solvent and form the layer. These layers are typically 25–50 μm to minimize ionic losses, 50% porous, have a bubble pressure of ~70 kPa and an effective ionic resistivity of 6–7 Ω cm [7, 8]. They have worked pretty well in UTC Power's PureCell<sup>®</sup> Model 200 for greater than 70,000 h.

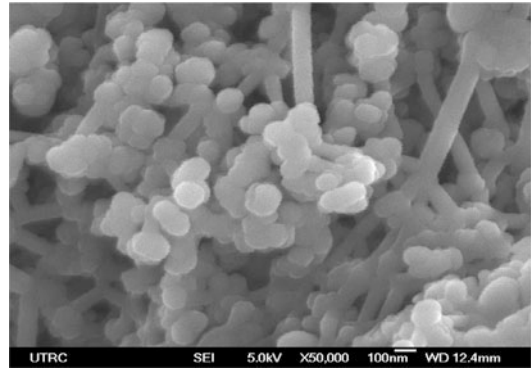
*Cathode catalyst layer:* Cathode catalyst layers in PAFCs are made using a mixture of PTFE and catalyst-coated graphitized carbon. These layers are around 100–125 μm thick and are approximately 70% porous. Catalyst is usually Pt or an

alloy of Pt. Graphitized carbon is used on cathode to ensure minimal carbon corrosion during long life operation. Oxidizing environment on cathode can cause significant corrosion issues during steady state operation and starting/stopping of the power plant. Thus, to minimize carbon corrosion for long life (10–20 years), it is essential to use corrosion-resistant graphitic carbon [9, 10]. PTFE is used in the mixture to produce an optimum balance between hydrophilic and hydrophobic pores in the catalyst layer. Hydrophilic pores take up acid and allow for proton transport while hydrophobic pores allow for reactant air or fuel to reach catalyst sites. It is very critical to achieve this balance to have an optimum electrolyte fill in the catalyst layer while providing enough pathways for gas to reach the catalyst. If the catalyst layers are underfilled or have low electrolyte take-up, it results in the cell having high IR losses; if the catalyst layers are overfilled or have high electrolyte take-up, it results in low cell performance due to flooding or mass transport losses. Hence it is very critical to achieve optimum fill level and remain at that fill level during the course of operation. UTC's catalyst layers have demonstrated the ability to retain this pore structure over the course of field operation. UTC's cathode catalyst layer is manufactured in batch process [11–14]. Graphitized carbon coated with Pt alloy is mixed with PTFE particles to form floc using various wet mixing techniques. This floc is then dewatered and dried to form floc pellets. Floc pellets are then finely ground and deposited onto the GDL using a cloud tower. These electrodes then go through a sintering oven where the PTFE flows over the graphitized carbon to form hydrophilic and hydrophobic pores. SEM image of a typical PAFC electrode where catalyst-coated carbon particles are further coated with PTFE is shown in Fig. 4.

*Anode catalyst layer:* Anode catalyst layers are manufactured using the same process described above but these catalyst layers use carbon instead of graphitized carbon. Since anode electrode is mostly in H<sub>2</sub> environment, there is very little to no corrosion of the anode electrode and hence the use of carbon instead of graphitized carbon [10]. Regular carbon has a higher surface area



**Phosphoric Acid Fuel Cells for Stationary Applications, Fig. 3** Graphitized carbon fibers in PAFC GDL



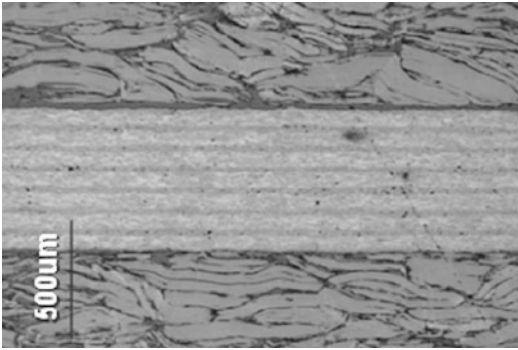
**Phosphoric Acid Fuel Cells for Stationary Applications, Fig. 4** PAFC catalyst particles coated with PTFE

than graphitized carbon thus allowing for better Pt loading characteristics and thus improved  $H_2$  oxidation reaction kinetics. Anode catalyst layers are made slightly more hydrophilic than cathode catalyst layers since  $H_2$  kinetics are fast and thus mass transport losses set in at much higher current densities than operating current densities.

*Bipolar plates:* The main function of bipolar plates is to transport reactants to the catalyst layers, prevent reactant crossover from one cell to another, prevent acid migration from one cell to another, provide good electrical properties to minimize IR loss through the plate and provide good thermal properties to transport heat generated in the cell to the coolers. UTC Power's bipolar plates are usually made of mixture of flaky graphite and FEP. FEP is limited to less than 20% to minimize the impact of IR loss and thermal conductivity loss in the plate. This mixture of FEP and graphite is placed in mold and compacted at high pressures (500–1,000 psi) to make molded performs. The bipolar plates in PAFCs should have very low porosity to reduce electrolyte take-up. Reducing the electrolyte take-up prevents the formation of a continuous electrolyte pathway through the thickness of the plate thereby mitigating electrolyte pumping as discussed in electrolyte management section. In order to achieve this low porosity, two preforms are laminated on either side of a highly nonporous separator plate to form the integral separator plate as shown in Fig. 5. After lamination of molded preforms to the separator plate, channels are either machined or molded in the

plate. Separator plate is manufactured by impregnating carbon paper with a phenolic resin. After resin impregnation, multiple layers of paper are laminated and carbonized in a slow carbonization process at 1,000 °C. The carbonization process has to be slow to prevent the formation of pores in the structure. After carbonization, the plate is graphitized at ~2,500 °C to improve corrosion resistance, thermal and electrical properties. UTC Power's bipolar plates have <5% porosity with very high tortuosity and have performed robustly in the field in mitigating acid transfer through plane in the plate. Channels in these plates are coated with wettable carbon to allow for acid management during fuel cell operation [15]. The perimeter of the plate also needs to be hydrophobic to prevent electrolyte being pumped on the edge of the plate. This hydrophobic break is achieved by placing PTFE flaps around the perimeter [16–23].

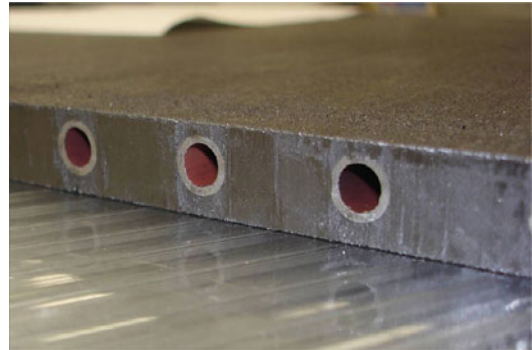
*Edge seals:* UTC Power's cell stack design uses external manifolds to transport reactants in and out of the cell stack. As a result, the edge of the anode GDL in air manifold and similarly cathode GDL in fuel manifold need to be sealed against reactant mixing in these locations. The obvious method of sealing is to fill the perimeter of the GDL with fuel cell-compatible filler material to minimize porosity. UTC Power's design fills the perimeter with a wettable carbon. Some of the previous designs also accomplished edge sealing using silicon carbide. The particle size of this filler material is usually around 5  $\mu m$  and thus



**Phosphoric Acid Fuel Cells for Stationary Applications, Fig. 5** UTC's phosphoric acid fuel cell bipolar plate

when impregnated into the GDL it forms pores that are much smaller than the pores in the GDL. Edge seals are made by forming a viscous ink of these particles and using a screen printing process to apply the ink to the GDL. Subsequent drying of the electrode removes the volatiles used in the ink leaving carbon in the GDL. When these GDLs are filled with acid during the assembly process, the edge seals take up acid due to capillary action and thus form wet seals which prevent gas from leaking into manifolds [24–27].

*Coolers:* Coolers in UTC Power's PAFCs are made of stainless steel tubes embedded in molded material (mixture of FEP and Graphite) as shown in Fig. 6. These coolers use the same manufacturing process as that of the bipolar plates. A serpentine cooler tube is placed between two molded preforms and laminated together at high pressures and temperatures. The ends of the tubes coming out of the molded material are wrapped in PTFE film or coating to prevent attack of stainless steel tubes by phosphoric acid. In UTC Power's PAFC system, water is used as coolant. This coolant enters the cell stack as liquid water and exists as a mixture of steam and liquid water between 150 °C and 180 °C. As a result, the coolant temperature rises as the water is heating up in single phase and once it reaches the saturated pressure, it stays at the same temperature but starts generating steam inside the coolers. The steam from coolant exit is used in the reforming reaction and the remaining hot water is used to supply thermal energy to



**Phosphoric Acid Fuel Cells for Stationary Applications, Fig. 6** UTC Power's PAFC cooler

customers. Due to the two-phase cooling, it is very essential to ensure that the liquid pressure drop is sufficiently greater than the two-phase pressure drop. If not, the variability in performance between cells can cause the system to run into thermal imbalance and as a result some cells would be operating much hotter than other cells, decreasing their life substantially. Increase in liquid pressure drop is obtained by inserting orifices or some other kind of flow restrictors at the coolant inlet to the cell stack. Orifice design has to ensure that there is no potential for clogging of coolant inlet to the cell stack. Thus, in order to mitigate issues associated with clogging, increase in pressure drop is accomplished by using a long tube coiled in front of each cooler [28–31].

*Non-repeat components:* The components described in the previous section are usually referred to as repeat components since every cell has those components with multiple cells present in a cell stack. Non-repeat components are those that are used only once in a cell stack. The main non-repeat components in a cell stack assembly are pressure plates, coolant inlet and outlet manifolds, reactant inlet and outlet manifolds, and manifold seals. Multiple cells placed between coolers are stacked between two stainless steel pressure plates and loaded axially to around 60 psi with the help of tie rods that run the entire length of the cell stack. Reactant manifolds are then assembled onto the cell stack with manifold seals placed between the cell stack and the

manifold. These reactant manifolds are made of stainless steel and coated with PTFE coating to prevent phosphoric acid attack of the manifolds. It is very essential to ensure that there are no pin holes in the PTFE coating for the same reason mentioned above. In phosphoric acid fuel cells, manifold seals made with high fluorine content fluoroelastomers. Fluoroelastomers are very resistant to hot phosphoric acid environment and hence they have lifetimes greater than 10 years. It is very essential that these seals have very low porosity. Seals with high porosity take up acid and due to the potential difference between the top and bottom of the cell stack, acid pumps to the top of the stack thus causing the bottom of the stack to fail due to loss of acid and top of the stack to fail due to flooding by acid. In addition, these seals need to conform to the variations in the layout of cells along the height of the stack. UTC Power uses a seal mechanism where a cured fluoroelastomer is placed adjacent to the manifold and uncured fluoroelastomer placed adjacent to the cell stack. During the heat-up of the cell stack to operating temperature, the uncured manifold seal melts, flows, and cures in place to seal the skyline that is formed due to the variations in the layout of cells.

## Cell Stack Assembly Life

Phosphoric acid fuel cells life is primarily a function of catalyst decay and acid management.

*Catalyst decay:* Catalyst decay occurs due to steady state operation and start-stops. Steady state decay occurs due to agglomeration of Pt particles in the catalyst layer. Pt deposited onto the carbon support in PAFC catalyst has a particle size of approximately 4–5 nm. Due to the high temperature of operation and high operating lifetimes (~80,000–100,000 h), these Pt particles tend to agglomerate and loose surface area. Smaller the particle size, higher the surface area and more sites for O<sub>2</sub> reduction or H<sub>2</sub> oxidation, but these particles are much more unstable and tend to agglomerate quickly. Even though these Pt catalysts tend to have high performance at beginning of life, their performance drops quickly due to Pt

particle agglomeration. UTC Power's PAFCs use a Pt alloy, Pt–Cr–Co on cathode and Pt on anode. The use of alloy on cathode allows for improving the surface area while reducing the agglomeration of catalyst. On anode pure Pt is used with approximately one third loading of that of the cathode. Low loadings are used on anode since H<sub>2</sub> kinetics are fast. These Pt particles are approximately 2–3 nm in size and tend to agglomerate faster than the cathode. As a result, anode catalyst electrochemical area decreases much faster than cathode.

UTC Power has deployed more than 260 Purecell<sup>®</sup> model 200 power plants and their performance decay was as expected in field. This model power plant operated at 200 kW and Fig. 7 shows the operational experience of this model.

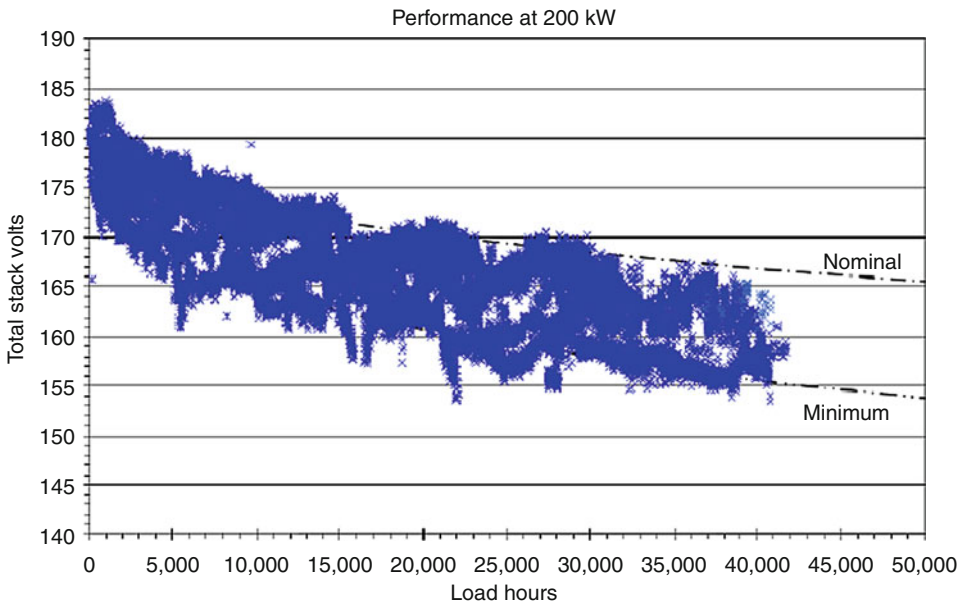
Teardown analysis has been performed on some of these units that have returned from field after their design operational lifetime of 40,000 h. The catalyst in these power plants has degraded as mentioned above. The average ECA of a new catalyst sample is 50 m<sup>2</sup>/g while catalyst that has aged in field for 43,000 h has an average ECA of 6.5 m<sup>2</sup>/g. Field operation increased the particle size from 4–5 nm to 20–25 nm. Figure 8 shows how catalyst ages with operational time.

Based on Model 200 experience, UTC Power has developed model 400 which has a design life of 85,000 h or 10 years. To meet 10 year performance requirements, cell operating conditions have been changed in addition to modification of catalyst properties during manufacture.

In addition to improving the catalyst, system strategies such as using a mixture of H<sub>2</sub>/N<sub>2</sub> as purge gas during shutdown and use of voltage clipping are being deployed to mitigate start/stop losses in model 400. Figure 9 shows performance data of model 400 catalyst vs. design requirements.

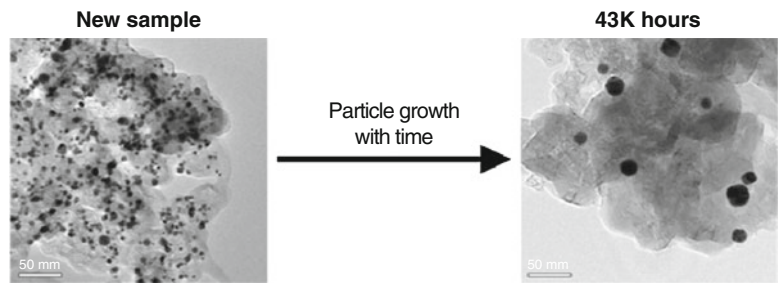
*Electrolyte management:* Phosphoric acid has a finite vapor pressure and a low contact angle with all of the components used in fuel cells except for catalyst layers. As a result, managing evaporation and migration of acid is very critical to maintaining the life of the fuel cell. Evaporation of acid from a cell is controlled by the reactant exhaust temperature. If the reactant exhaust temperature is high, the acid lost in vapor phase





**Phosphoric Acid Fuel Cells for Stationary Applications, Fig. 7** Purecell® model 200 operational performance

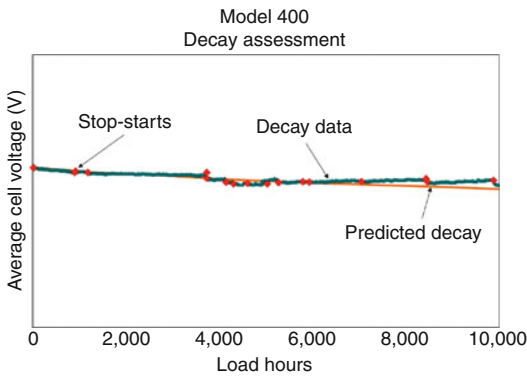
**Phosphoric Acid Fuel Cells for Stationary Applications, Fig. 8** PAFC catalyst on carbon



increases. Acid loss due to temperature is exponential in the region of operation of phosphoric acid fuel cells. In addition, reactant flow has a linear relationship to acid loss. Hence, if the reactant utilization in a cell is low, the loss of acid is high due to higher exit flow. PAFC cell designs need to balance the loss of acid due to exit temperature and flow. UTC’s cell designs operate such that the cell is hot enough to ensure maximum performance with high reactant utilization while the reactant exhaust is cold enough to ensure long life operation [32–34]. This is accomplished by placing coolant inlet to the cell near the reactant exhaust. The cell adjacent to the cooler is the coldest cell and the cell equidistant to coolers on either side is the hottest. Cold cell acid loss is

less than hot cell acid loss, and thus hot cell is the life limiter due to evaporation. Water management is not an issue in phosphoric acid fuel cells. Design features such as incorporating a nonactive condensation zone near the exit location of the reactant stream, having an electrolyte reservoir in the cell, etc., are also used in addition to managing the thermal profile of the cell. UTC Power’s phosphoric acid fuel cells operate at ambient pressures and between temperatures of 150 °C and 225 °C. As a result, water generated in the fuel cell is in vapor phase and leaves with the reactant exhaust. A PAFC cell is generally in water balance. These cells operate between 95% and 105% acid concentration depending on cell operating conditions. If the reactant flow is high, the acid





**Phosphoric Acid Fuel Cells for Stationary Applications, Fig. 9** PureCell® model 400 performance verification

in the cell is more concentrated and more water vapor leaves the cell and vice versa if the flow is low [4].

The movement of acid within the cell is managed using capillary action between various layers. The GDLs have the biggest pore size followed by matrix layer and finally the catalyst layers. During operation, acid is lost due to evaporation from the GDLs as they have the lowest capillary pressure of all the components. Once GDLs reach ~2–3% fill level, the pores in the matrix layer start emptying. Void spots in the matrix layer cause gas crossover between anode and cathode resulting in cell failure.

Acid movement within a cell is a complex phenomenon. During the build of a phosphoric acid fuel cell, acid is deposited onto the porous components [35, 36]. When load is applied to the cell, protons start moving from anode to cathode. Since phosphoric acid is a weak acid, it dissociates and is in the form of  $H^+$  and  $H_2PO_4^-$  in the cell. Thus, in order to maintain charge balance, these phosphate ions start moving from cathode to anode. This flow of acid from cathode to anode is balanced by the liquid pressure difference between anode and cathode. Once acid starts accumulating in the anode, liquid pressure in the anode GDL increases and starts balancing the flow of acid due to charge imbalance. Thus, at steady state, approximately 75% of the acid deposited into the cathode GDL during build moves into the anode GDL. Evaporation over the course of life results in depleting anode and cathode GDL fill

levels, and at end of life, matrix layer starts emptying of acid resulting in reactant crossover.

Acid can also move between cells if appropriate hydrophobic breaks are not inserted between cells [17, 18]. Bipolar plates have very low porosity but they are easily wetted by acid. As a result, the edge of the bipolar plate gets wetted by acid easily and forms a liquid connection between two adjacent cells (referred to as cell 1 and cell 2) across the bipolar plate. In a typical cell one side of the bipolar plate is in reducing environment ( $H_2$  flow channels) and the other side of the plate is in an oxidizing environment (air flow channels). In a simple explanation, electrolyte in cathode GDL of cell 1 is near the cathode potential of the cell 1. The electrolyte potential across this bipolar plate between cell 1 and cell 2 is close to the hydrogen reference potential. As a result, the potential difference across the bipolar plate is equal to that of one cell's voltage. This potential difference can drive a very small shunt current through the acid film that has formed on the edge of the plate thus moving protons from cell 2 to cell 1. Due to movement of protons from cell 2 to cell 1, phosphate ions start moving from cell 1 to cell 2. Over the course of short time intervals, this shunt current can drive enough acid such that cell 1 fails due to dry out and cell 2 fails due to flooding by acid. UTC's cell design includes a hydrophobic break or PTFE flap between cells to mitigate the formation of a continuous film between cells thus mitigating movement of acid due to shunt currents [17, 18].

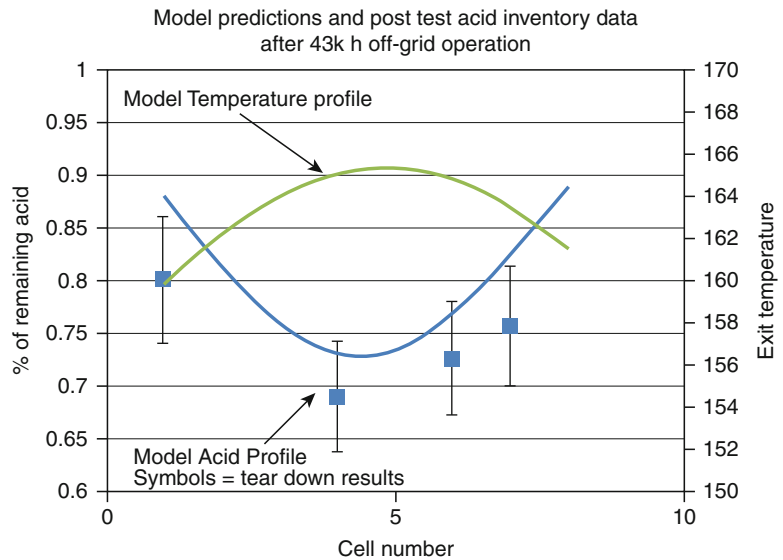
Teardown of UTC's Purecell® Model 200 units from field and measuring the acid content in these cells indicates that the PTFE flap between cells has worked very effectively in mitigating shunt migration of acid between cells. In addition, the loss of acid due to evaporation is very close to model predictions [37] as shown in Fig. 10.

## PAFC Applications

PAFC fuel cells are a natural fit for combined heat and power applications. The use of CHP fuel cell systems in commercial buildings such as supermarkets, office towers, schools, data centers,

### Phosphoric Acid Fuel Cells for Stationary Applications,

**Fig. 10** Acid loss as a function of cell temperature



industrial buildings, etc., improves overall efficiency by displacing low efficiency electricity provided by grid while providing enough thermal energy to displace fuel required for space heating and/or domestic hot water.

UTC's PAFC system has been used in a wide variety of applications and given below is an example of how this application can be used in supermarkets. A typical supermarket's energy needs are met 80% by electricity and remaining by natural gas. For a typical supermarket it has been estimated that a 10% reduction in energy costs is equivalent to increasing net profit margins by 16%. In other words, \$1 in energy savings is equivalent to increasing sales by \$59 [38, 39]. Hence energy-efficient methods of operating stores are a top priority for supermarkets. Supermarket's energy usage is primarily a function of the square footage of the store and its operating hours. Electricity in a supermarket is used mostly for refrigeration while natural gas is used mostly for space heating as shown in Fig. 11.

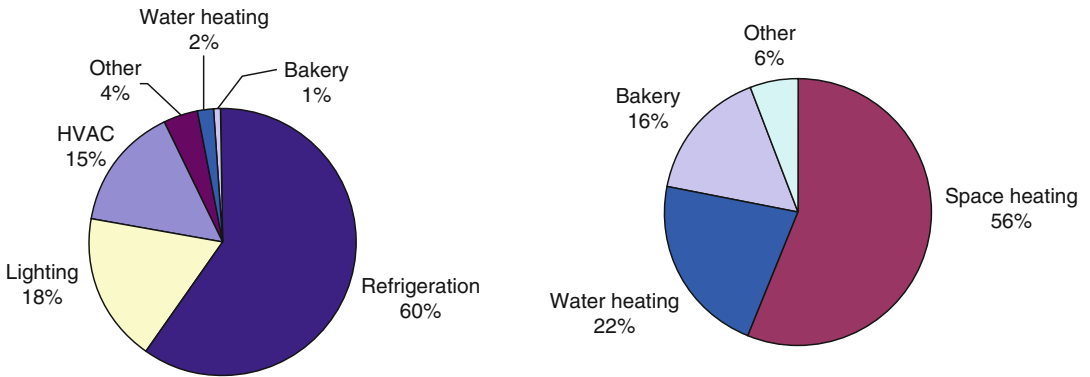
Supermarkets need reliable and low-cost energy to maintain freshness of produce and to improve their margins. Using a fuel cell application with CHP capabilities can improve their efficiencies significantly thereby reducing energy costs. UTC Power's PAFC system is being currently evaluated by various supermarkets to

achieve high efficiency and hence reduced energy costs. Shown in Fig. 12 is a Model 400 application which supplies the store with 324 kW of electricity, 63 kW of high-grade heat which is used for space heating and refrigeration using absorption chilling and 92 kW of low-grade heat for domestic hot water. Absorption chilling is driven by heat energy rather than mechanical energy [39, 40]. The power plant uses 750 kW (LHV) of natural gas to generate above the energy required by the store thus achieving overall efficiency of 65%. As energy costs continue to increase, CHP applications provide the value proposition required by customers to improve their margins.

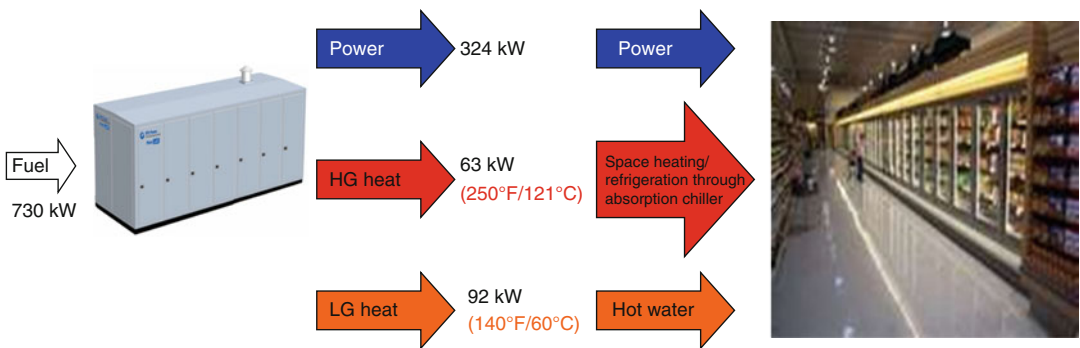
Another example of UTC's Purecell<sup>®</sup> model 200 fuel cell system being used for commercial application is the installation at Mohegun Sun Casino in Uncasville, Connecticut, USA. This facility uses both high-grade and low-grade heat from the fuel cell along with electric power (Fig. 13). Customer needs heating all year long and effective integration allowed for achievement of ~85% efficiency with this unit [39, 40].

### Future Directions

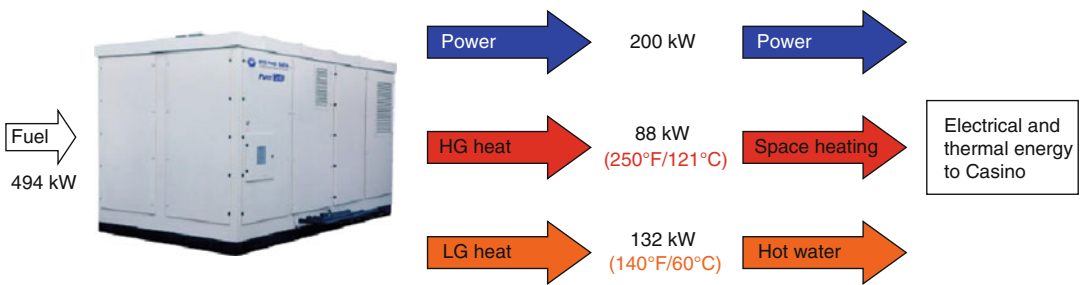
Cost must be reduced aggressively to enable commercialization of combined heat and power



**Phosphoric Acid Fuel Cells for Stationary Applications, Fig. 11** Supermarket energy consumption [38, 39]



**Phosphoric Acid Fuel Cells for Stationary Applications, Fig. 12** Use of a PAFC system for supermarket application



$$\text{Maximum efficiency} = \left( \frac{200+88+132}{494} \right) = 85\%$$

**Phosphoric Acid Fuel Cells for Stationary Applications, Fig. 13** Use of a PAFC system for commercial building application

(CHP) fuel cells. A significant portion of the fuel cell system cost is the cost of cell stack materials and manufacturing processes including labor. Cost of fuel cell components is roughly split half and half between materials and manufacturing

costs. Significant R&D investments to enable continuous efficiency improvements along with operational excellence are essential to drive down manufacturing costs. Development of high-volume manufacturing techniques along

with high-speed quality control process will enable reduction of a significant portion of this cost [41].

Unique processes used in the manufacture of PAFC components result in increased part cost. Current processes for manufacturing GDLs, electrodes, bipolar plates, etc., employ batch processes and require continuous manufacturing processes to reduce cost and also to meet projected high volumes.

GDL manufacturing for high-temperature CHP fuel cells currently involves a lot of batch processes such as turning the fiber into resin-impregnated felt, carbonization, graphitization (for tolerance to high-temperature operation), etc., before electrodes are deposited onto the part. Continuous manufacturing processes for making GDLs can be enabled by use of double belt press, but this requires process development. Double belt press process integrates all of the various steps involved in making GDLs wherein fiber can be fed from one end of the press with finished substrate emerging from the other end of the press. Similarly, bipolar plates used in PAFCs are currently manufactured using unconfined compression molding followed by machining, wet treatment of bipolar plate and incorporation of hydrophobic edges to prevent acid migration from cell to cell. Continuous manufacturing processes such as net-shaped molding can enable integrating these operations into one operation thus enabling high-volume manufacturing and significantly reducing the cost of component. Finally, fuel cell industry needs to move toward manufacturing that can help bring the processes to the part rather than parts moving through the process to reduce factory footprint costs, handling costs, and energy costs, and thus reduce cost of manufacturing. Fuel cell industry currently adopts processes that have been developed in other industries. For example, Gravure coating which is used to coat thin layers at high speeds is being used to coat thick layers of electrolyte matrix at low speeds. The fuel cell industry needs the development of new manufacturing processes for fuel cells that are tailored toward optimum manufacture of a part keeping its fundamental requirements in consideration.

Since every component used in a cell (GDL, catalyst layer, bipolar plate, matrix layer, etc.) is critical for the operation of the cell stack, these components have to be within a very tight specification and meet defined key product characteristics. This requires the implementation of a robust quality control system. For example, substrates in PAFCs have to be checked for porosity, IR, thermal conductivity, thickness, density, compressive strength, flex strength, etc. All of these quality checks impart cost to the substrate. Ability to integrate these measurements into one tool will enable help high-volume manufacturing. Similarly high-speed measurement techniques (e.g., ultrasonic crack detection methods) that can detect defects/cracks in electrode layers and bipolar plates in a few seconds are required for high-volume manufacturing of these components. In addition, improving manufacturing processes to achieve high level of robustness will reduce the number of cell stack rebuilds and/or infant mortalities thus reducing cost. Finally, all of the proposed high-volume manufacturing techniques need to yield product at a very minimal scrap rate to reduce part cost.

Another approach for reducing cost is to improve the efficiency of the power plant. Since cell stack has the lowest efficiency of all the components, improving its efficiency provides maximum benefit but at the same time cell efficiency improvements are not easy to achieve. Improved efficiency can be capitalized by removing cells out of the cell stack to generate the same power at baseline efficiency or it can be used to provide cheaper power to the customer. Phosphate ions poison cathode catalyst, i.e., they occupy valuable sites on Pt catalyst thus reducing the number of sites available for oxygen reduction reaction. This leads to lower cell performance (typically  $<0.25 \text{ W/cm}^2$  of electrode) and hence more number of cells making the stack cost challenging. The only way to eliminate phosphate poisoning is to use a new electrolyte instead of  $\text{H}_3\text{PO}_4$ . New liquid electrolytes which do not have phosphate poisoning effect can lead to significantly improved electrical efficiency. Truls Norby's paper on "Solid state protonic conductors: Principles, properties, progress and

prospects” [42] discusses properties of potential materials that can be used as electrolytes in the temperature ranges discussed. Another way of improving efficiency could be by improving the  $O_2$  solubility/diffusion in  $H_3PO_4$ . Literature shows that additives to  $H_3PO_4$  can improve  $O_2$  solubility in  $H_3PO_4$  and hence improved efficiencies. Additives such as silicon oils, C4 and C6 compounds, Pyrroles, protonated polyamine, etc., evaluated by various researchers have shown performance improvements but further research is needed to determine if these performance improvements are sustainable [43].

Conditioning and qualification of cell stack after it is assembled and final qualification of power plant after integrating cell stacks with balance of plant (BOP) takes significant time increasing product cost. Conditioning of cell stacks involves processes that cure seals and set them in place and enable electrolyte movement into the catalyst layers making them functional. After conditioning, acceptance testing is performed on cell stacks where diagnostics are done to ensure that flow to the cells is appropriate, seals are set in place, catalyst layers are functional, and that the product meets design performance requirements. Ability to assemble hundreds of cells in a power plant in the same manner every time will enable the industry to go to a limited sampling technique rather than testing every power plant thus reducing costs. Developing methods to perform conditioning and acceptance testing on modules of cells rather than on fully assembled cell stack will enable removal of problem parts early in the build and prevent costly teardowns. Further understanding of the electrode manufacturing process at a fundamental level could enable integrating conditioning procedures into manufacturing process thus eliminating post component manufacture conditioning and acceptance testing. R&D aspects that can reduce or eliminate conditioning and acceptance testing of CHP fuel cells should be developed.

Balance of plant (BOP) in fuel cell power plants also adds significant cost to the power plant. The ability to deliver contaminant-free fuel to the cell stacks, ability to provide reactants very quickly as the load changes, etc., add

significant cost to the power plant. The fuel processing system (FPS) is one of the most expensive subsystems in the fuel cell power plant BOP, at 20% of total power plant cost. The catalytic steam reformer (CSR) is the single most expensive component (18%) within the FPS. The CSR is effectively a catalyst-augmented heat exchanger. As such its cost can be significantly reduced by manufacturing designs and techniques to improve heat transfer such as direct application of catalyst to reformer walls (catalyzed walls improve heat transfer by eliminate film losses, thus enabling reduction heat transfer area), improve catalysts to reduce poisons to the stack (such as and sulfur and ammonia which accelerate stack decay and increase stack costs), improve high-volume manufacturing techniques such as spin casting to lower tube costs, and advanced casting techniques to form the reformer burner which is presently made by welding many smaller sheet metal pieces. Automated welding processes are also critical to obtaining repeatable high-quality welds at high volume and low cost. A significant but overlooked BOP cost is piping. Cost reductions can be realized by replacing complex pipe runs requiring threaded or welded assembly with pipe or tube bending. Improved pipe bending capability can reduce manufacturing and assembly time and expense, especially at high volumes.

Heat exchangers are essential in fuel cell power plants to control temperatures for the major components (stack, reformer, shift converter), provide valuable cogeneration energy to customers, and reject waste heat. Brazed plate heat exchangers offer the most cost-effective heat transfer in many applications, but are often limited by poor thermal cycle durability which effects transient capability, especially in CHP power plants where load following and variable customer heat usage cause numerous thermal cycles. Manufacturing development to improve the durability of the brazed plate-type heat exchangers would significantly reduce overall BOP costs by enabling their use in more applications within the CHP fuel cell power plants.

Another critical area of the BOP components is the power conversion system as this system is the customer interface to the fuel cell and contains much of the key product performance

characteristics necessary to achieve the customers' needs. Significant cost reduction could be achieved by developing a modular high-frequency power conversion system. A modular approach would enable use of the same design across the entire product line offered to various customers. Using this same design would allow for improvements in manufacturing volumes as the manufacturing of all current power conversion designs could be consolidated instead of the current mix of various designs in low volume. This would also drive down the cost of the power conversion system by increasing the volume of similar components that would be sourced for the power conversion of the various products offered. Having a modular design would also reduce test time in manufacturing as this would enable improved testing techniques in the supply base (i.e., automated testing) and reduce the mix of power conversion systems encountered at the final assembly.

Development of markets at lower volumes of 50–100 units/year needs to be facilitated so that design-driven cost reduction can be learned out. Demonstration programs where state or federal commercial buildings are converted to using power from fuel cell power plants should be encouraged. Finally, cost reduction as a key aspect of demonstration programs should be emphasized.

**Acknowledgments** The authors would like to acknowledge Tom Jarvi for his valuable input into framing the outline for the entry.

## Bibliography

1. <http://www.fuelcells.org/InternationalH2-FCpolicyfunding.pdf>
2. Kanuri S, Motupally S (2011) Engineering and application of phosphoric acid fuel cell system. ICEPAG, Costa Mesa
3. [www.fujielectric.com](http://www.fujielectric.com)
4. Breault RD (2003) Stack materials and stack design. In: Vielstich W, Lamm A, Gasteiger HA (eds) Handbook of fuel cells: fundamentals, technology and applications, vol 4, Part 4. Wiley, Chichester, pp 797–810. ISBN: 0-471-49926-9
5. Miwa K, Shimizu K, Fukui H (1989) Electrode substrate for fuel cell and process for producing same. US Patent 4,851,304, 25 July 1989
6. Breault R (2006) Electrode substrate for electrochemical cell from Carbon and cross-linkable resin fibers. PCT No: PCT/US2006/041494, 23 Oct 2006
7. Spearin W (1989) Process for forming a fuelcell matrix. European Patent 0,344,089 A1, 29 Nov 1989
8. Breault R (1977) Silicon carbide electrolyte retaining matrix for fuel cells. US Patent 4,017,664, 12 Apr 1977
9. Breault R, Mientek A, Sawyer R (1993) Minimized corrosion fuel cell device and method of making same. US Patent 5,270,132, 14 Dec 1993
10. Breault R, Fredley R, Scheffler G (1998) Corrosion resistant fuel cell assembly. US Patent 5,837,395, 17 Nov 1998
11. Reiser C, Landau M (1980) Method for reducing cell output voltage to permit low power operation. US Patent 4,202,933, 13 May 1980
12. Breault R, Harding R, Kemp F (1977) Method of fabricating a fuel cell electrode. US Patent 4,043,933, 23 Aug 1977
13. Goller G, Salonia J (1981) Dry floc method for making an electrochemical cell electrode. US Patent 4,287,232, 1 Sept 1981
14. Goller G, Salonia J (1982) Dry method for making an electrochemical cell electrode. US Patent 4,313,972, 2 Feb 1982
15. Dufner B (2008) Wettability ink, process and carbon composite articles made therewith. PCT No: PCT/US2007/007045, 25 Sept 2008
16. Breault R, Luoma W, Roche R (2008) Fuel cell separator plate assembly. US Patent 20,080,057,373, PCT No: PCT/US04/44007, 06 Mar 2008
17. Roche R (1993) Extruded fuel cell stack shunt current prevention arrangement. US Patent 5,178,968, 12 Jan 1993
18. Breault R (1983) Method for reducing electrolyte loss from an electrochemical cell. US Patent 4,414,291, 8 Nov 1983
19. Breault R, Martin R, Roche R, Kline R (1996) Cathode reactant flow field for a fuel cell stack. US Patent 5,558,955, 23 Sept 1996
20. Breault R (1980) Fuel cell electrolyte reservoir layer and method for making. US Patent 4,185,145, 22 Jan 1980
21. Breault R, Gorman M (1994) Laminated electrolyte reservoir plate. US Patent 5,366,825, 22 Nov 1994
22. Uemura T, Murakami S (1988) Method for producing a carbon sheet and a fuel cell separator. US Patent 4,737,421, 12 Apr 1988
23. Emanuelson R, Luoma W, Taylor W (1981) Separator plate for electrochemical cells. US Patent 4,301,222, 17 Nov 1981
24. Trocciola J, Schroll C, Elmore D (1975) Wet seal for liquid electrolyte fuel cells. US Patent 3,867,206, 18 Feb 1975
25. Schroll C (1974) Liquid electrolyte fuel cell with gas seal. US Patent 3,855,002, 17 Dec 1974
26. DeCasperis T, Roethlein R, Breault R (1981) Method of forming edge seals for fuel cell components. US Patent 4,269,642, 26 May 1981



27. Singelyn J, Gelting R, Mientek A (1988) Expanded high-temperature stable chemical resistant seal material. US Patent 4,774,154, 27 Sept 1988
28. Grevstad P (1976) Fuel cell cooling system with shunt current protection. US Patent 3,964,929, 22 June 1976
29. Breault R, Sawyer R, DeMarche T (1986) Cooling system for electrochemical fuel cell. US Patent 4,574,112, 4 Mar 1986
30. Breault R, Martin R, Roche R, Scheffler G, O'Brien J (2000) Coolant plate assembly for a fuel cell stack. US Patent 6,050,331, 18 Apr 2000
31. Grasso A, Martin R, Roche R (2000) Composite article. US Patent 6,039,823, 21 Mar 2000
32. Breault R, Fredley R (2007) Fuel cell with electrolyte condensation zone. US Patent Pub. No: US 2007/0224476 A1, 27 Sept 2007
33. Breault R, Rohrbach C (2007) Fuel cell assembly with operating temperatures for extended life. US Patent Pub. No: US 2007/0292725 A1, 20 Dec 2007
34. Breault R, Fredley R (2008) Fuel cell assembly having long life characteristics. US Patent Pub. No: US 2008/0118789 A1, 22 May 2008
35. Congdon J, English J (1986) Method and apparatus for adding electrolyte to a fuel cell stack. US Patent 4,596,749, 24 June 1986
36. Grevstad P (1986) Process for adding electrolyte to a fuel cell stack. US Patent 4,612,262, 16 Sept 1986
37. Ferro J (2009) PAFC history and successes. In: MCFC & PAFC R&D workshop, 2009 Fuel cell seminar, 16 Nov 2009
38. Facility type: Supermarkets and grocery stores. In: Energy star<sup>®</sup> building manual, chap 11. [http://www.energystar.gov/ia/business/EPA\\_BUM\\_CH11\\_Supermarkets.pdf](http://www.energystar.gov/ia/business/EPA_BUM_CH11_Supermarkets.pdf)
39. Supermarkets: An overview of energy use and energy efficiency opportunities, Energy star<sup>®</sup>
40. Jarvi T, Kanuri S (2010) Progress in phosphoric acid fuel cells. FC Expo, Tokyo, 5 Mar 2010
41. Gang X et al (1993) Electrolyte additives for phosphoric acid fuel cells. J Electrochem Soc 140(4):896–902
42. Jarvi T (2009) Fuel cells for combined heat and power applications. University of Pennsylvania, 26 Sept 2009
43. Norby T (1999) Solid-state protonic conductors: principles, properties, progress and prospects. Solid State Ionics 125:1–11
44. [http://www.eere.energy.gov/hydrogenandfuelcells/fuelcells/fc\\_types.html](http://www.eere.energy.gov/hydrogenandfuelcells/fuelcells/fc_types.html)
45. Grevstad P, Gelting R (1976) Fuel cell cooling system using a non-dielectric coolant. US Patent 3,969,145, 13 July 1976
46. Kanuri S (2009) PAFC cost challenges. In: MCFC & PAFC R&D workshop, 2009 Fuel cell seminar, 16 Nov 2009
47. Kanuri S UTC Power response to DOE Request for Information DE-FOA-0000225
48. Goller G, Salonia J, Petraglia V (1979) Dry mix method for making an electrochemical cell electrode. US Patent 4,175,055, 20 Nov 1979



## Molten Carbonate Fuel Cells

Choong-Gon Lee

Department of Chemical and Biological Engineering, Hanbat National University, Daejeon, South Korea

### Article Outline

Glossary

Definition of the Subject

Introduction

Components of MCFC

Performance Analysis

Future Directions

Bibliography

### Glossary

**Activation overpotential** Voltage loss due to slow charge-transfer rate on the electrode surface.

**Anode** A porous electrode where hydrogen is oxidized with carbonate ions ( $\text{CO}_3^{2-}$ ) to steam and carbon dioxide.

**Basicity**  $\text{Log}(K_d)$  of molten carbonates where  $K_d$  is the equilibrium constant of the reaction  $\text{CO}_3^{2-} \rightleftharpoons \text{O}^{2-} + \text{CO}_2$  similarly to the pH of aqueous solutions.

**Cathode** A porous electrode where oxygen is reduced with carbon dioxide to carbonate ions ( $\text{CO}_3^{2-}$ ).

**Effectiveness factor ( $\epsilon$ )** A ratio of overpotential without pore diffusion resistance to that with pore diffusion resistance.

**Electrolyte** Molten carbonates providing ionic paths for the electrode reactions with combinations of  $\text{Li}_2\text{CO}_3$ ,  $\text{Na}_2\text{CO}_3$ , and  $\text{K}_2\text{CO}_3$ .

**Exchange current density ( $i_o$ )** An actual current density of an electrode at net zero current indicating catalytic activity of the electrode.

**Fuel cell** A system of continuous electrochemical energy conversion from chemical energy to electricity mostly by oxidation of hydrogen and reduction of oxygen.

**Internal resistance** Electrical resistance of cell components.

**Mass transfer** Transport of reactants and products to/from the electrode surface.

**Matrix** Ceramic porous material holding molten carbonates by capillary forces.

**Ohmic loss ( $\eta_{\text{IR}}$ )** Voltage loss due to electrical resistance of cell components.

**Open-circuit voltage ( $E_{\text{OCV}}$ )** A cell voltage at net zero current determined by the relation of

$$E_{\text{OCV}} = E^0 + \frac{RT}{2F} \ln \left( \frac{p(\text{H}_2)p(\text{O}_2)^{0.5}p(\text{CO}_2)_{\text{ca}}}{p(\text{H}_2\text{O})p(\text{CO}_2)_{\text{an}}} \right)$$

**Overpotential ( $\eta$ )** Voltage reduction from an open-circuit voltage due to the resistance of electrochemical reactions at an electrode.

**Polarization** A state of deviation from open-circuit voltage due to current flowing in the cell.

**Pore diffusion resistance** Mass-transfer resistance through the pores in the electrodes.

**Reaction kinetics** Charge-transfer rates of electrochemical reactions on electrode surfaces.

**Three-phase boundary** A site of electrode-carbonate electrolyte-gaseous reactants where electrochemical reactions take place.

### Definition of the Subject

Two parts are treated: one is the physical and chemical features of materials of molten carbonate fuel cells (MCFCs) and the other is performance analysis with a 100 cm<sup>2</sup> class single cell. The characteristics of the fuel cell are determined by the electrolyte. The chemical and physical properties of the electrolyte with respect to gas solubility, ionic conductivity, dissolution of cathode material,

corrosion, and electrolyte loss in the real cell are introduced. The reaction characteristics of hydrogen oxidation in molten carbonates and materials for the anode of the MCFC are reviewed. The kinetics of the oxygen reduction reaction in the molten carbonates and state of the art of cathode materials are also described. Based on the reaction kinetics of electrodes, a performance analysis of MCFCs is introduced. The performance analysis has importance with respect to the increase in performance through material development and the extension of cell life by cell development. Conventional as well as relatively new analysis methods are introduced.

## Introduction

A fuel cell, as an emerging power source, generates power directly from the chemical energy of fuel. The fuel cell runs with electrochemical reactions at the electrodes where mostly  $H_2$  oxidation at the anode and  $O_2$  reduction at the cathode occur. The power generation scheme of a fuel cell is very different from that of conventional grid power, where the electricity comes from electromagnetic induction with mechanical rotation. Thus conventional power is produced by several steps of chemical, mechanical, and electrical energy changes. In contrast, a fuel cell converts chemical energy to electrical energy directly, which allows high-energy conversion efficiency and low pollution emission from the fuel cell.

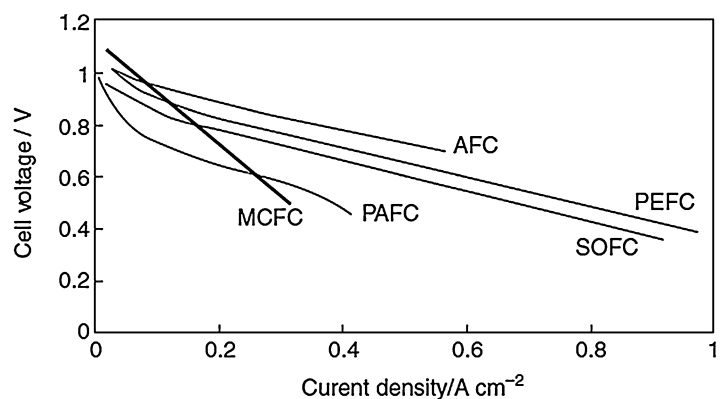
Among the fuel cells, the PEMFC (proton-exchange membrane fuel cell), AFC (alkaline fuel

cell), and PAFC (phosphoric acid fuel cell) are run by  $H^+$  and  $OH^-$  movements in the electrolyte. On the other hand, the MCFC (molten carbonate fuel cell) and SOFC (solid oxide fuel cell) work with carbonate ions ( $CO_3^{2-}$ ) and oxide ions ( $O^{2-}$ ), respectively. The acid ( $H^+$ ) and base ( $OH^-$ ) generally run up to  $200^\circ C$ , whereas carbonate and oxide ions run at over  $600^\circ C$ . Thus the PEMFC, AFC, and PAFC have relatively low operating temperatures compared with the MCFC and SOFC.

The MCFC, running with molten carbonate electrolytes, has an operating temperature of about  $650^\circ C$ . This high temperature facilitates electrochemical reactions at the electrodes, allowing inexpensive metal electrodes such as Ni to be used, while low-temperature fuel cells, that is, PEMFC, AFC, and PAFC, require Pt electrocatalysts. The high operating temperature also gives high efficiency through the bottoming cycle which utilizes exhaust heat. Thus the MCFC has some merits of high efficiency and system economics over the low-temperature fuel cells.

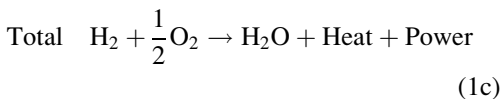
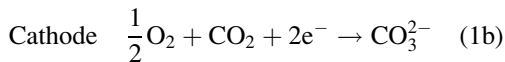
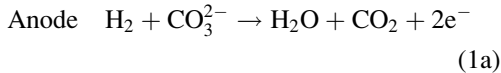
Figure 1 shows current-voltage behaviors of fuel cells. The polarization behavior represents the reaction and performance characteristics of the fuel cells. In principle, the low-temperature fuel cell has a larger absolute Gibbs free energy of  $H_2O$  formation. Thus the PEMFC, AFC, and PAFC have a higher open-circuit voltage ( $E_{OCV}$ ) than the MCFC and SOFC. However, the low-temperature fuel cells also have a sluggish charge-transfer rate in the electrode reaction, which leads to high activation overpotential. In general, the activation

**Molten Carbonate Fuel Cells, Fig. 1** Current-voltage behaviors of various hydrogen fuel cells (From Ref. [1])

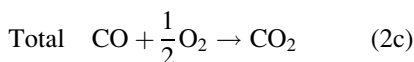
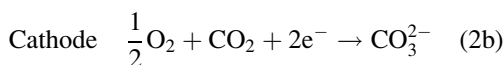
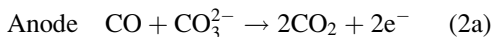


overpotential exponentially decreases voltage due to the applied currents at the early stage of current application (Fig. 1). Moreover, the Pt electrode in a low-temperature fuel cell is oxidized at open-circuit voltage. Therefore, low-temperature fuel cells show an exponential decrease in voltage at around zero current and unclear  $E_{OCV}$  values. On the other hand, the MCFC shows a monotonic decrease in voltage even at the early stage of current application. This indicates that the electrode reactions have very small activation overpotential, probably due to the high-temperature molten carbonate electrolytes. However, the steep current-voltage behavior of the MCFC shows that it has relatively high internal resistance and electrochemical reaction resistance in the cell compared with other fuel cells.

The carbonate ions ( $\text{CO}_3^{2-}$ ) are supplied by the electrolytes: a combination of  $\text{Li}_2\text{CO}_3$ ,  $\text{K}_2\text{CO}_3$ , and  $\text{Na}_2\text{CO}_3$ . Current electrolytes for the MCFC are the eutectics of  $\text{Li}_2\text{CO}_3$ - $\text{K}_2\text{CO}_3$  and  $\text{Li}_2\text{CO}_3$ - $\text{Na}_2\text{CO}_3$ , which have melting temperatures of about 500 °C. Then the electrode reactions with  $\text{H}_2$  and  $\text{O}_2$  in the MCFC are as follows:

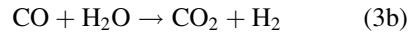
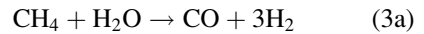


The molten carbonates also allow the use of CO as a fuel. Then the reactions are as follows:



This is a very unique characteristic of a high-temperature fuel cell because CO behaves as a

fuel in the MCFC, while it is a poisonous species for the low-temperature fuel cells. It gives fuel diversity to the MCFC. At present, the  $\text{H}_2$  fuel is supplied by methane steam reforming as follows:



Methane is a main component of natural gas (over 90 vol%), and its infrastructure is relatively well built across the world. Thus natural gas is a main source of  $\text{H}_2$  fuel for fuel cells. However, natural gas is much more expensive than coal, and thus fuel cells are economically inferior to coal power. Coal-based operations have potential to improve the economics of fuel cells. At present, coal gasification is utilized as a clean coal technology, producing  $\text{H}_2$  and CO gases as its main components. Organic materials are also generally decomposed to  $\text{H}_2$  and CO. Thus MCFCs can run with coal and organic wastes, which will enlarge the application of MCFCs.

In the past 40 years, MCFCs have been developed in the world. The primary developer is FCE (FuelCell Energy Co.) in the USA, which has developed an internal reforming type MCFC unit stack of up to 350 kW and provides up to 2.5 MW MCFC systems by combination of the unit stacks. It also reported that a combination of an MCFC and a gas turbine recorded 56% electrical efficiency (based on the lower heating value (LHV) of natural gas) [2]. MTU, a German company, has designed a 250 kW class system, "Hot Module," by adapting FCE's stack. Japan developed MCFC systems of up to 1 MW class during the past 40 years. The 1 MW system was the pressurized external reforming type and IHI (Ishikawajima-Harima Heavy Industry) developed a 300 kW class external reforming type system. Ansaldo Co. of Italy has developed a 500 kW class MCFC system. A 125 kW class external reforming type MCFC system has been developed in Korea. Currently, POSCO Energy Co. in Korea employing FCE technology has commercialized total over 160 MW of MCFC systems in Korea as distributed heat and power sources.

In this work, the characteristics of material for the MCFC such as the electrolyte, electrodes, and matrix are introduced. In addition, the diagnostic tools for MCFC performance are also treated: conventional methods of steady-state polarization, current interruption (C/I), and AC impedance, and novel methods of inert gas step addition (ISA) and reactant gas addition (RA).

## Components of MCFC

### Electrolytes

The MCFC is an electrochemical reaction system where the anode oxidizes  $H_2$  to  $H_2O$  and the cathode reduces  $O_2$  to  $(CO_3^{2-})$  as shown in Eq. 1a and 1b. Thus carbonate materials serve as the electrolyte, which is generally a mixture of various alkali metal carbonates of  $Li_2CO_3$ ,  $Na_2CO_3$ , and  $K_2CO_3$ . Table 1 shows the melting points (m.p.), surface tension ( $\gamma$ ), density ( $\rho$ ), electric conductivity ( $\kappa$ ), and Henry's law constant of  $O_2$  dissolution ( $h_{O_2}$ ) for various eutectic carbonates.

The table also shows the properties of an aqueous solution (1M, KCl). It is found that the eutectics are a kind of electrolyte which have about twice the density, about three times the surface tension, and over ten times the electric conductivity of an aqueous solution. Eutectics also have much lower melting points than at single carbonates:  $Li_2CO_3$  (999 K),  $Na_2CO_3$  (1,131 K), and  $K_2CO_3$  (1,172 K).

In general, the molten carbonates have an equilibrium with oxide ions ( $O^{2-}$ ) and  $CO_2$ :

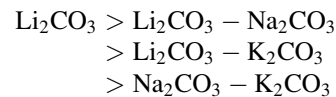


where  $k_d$  is the dissociation constant ( $=[O^{2-}] \cdot p(CO_2)$ ). Molten carbonates also exist in the form of alkali metal cations ( $M^{2+}$ ) and carbonate anions ( $CO_3^{2-}$ ). Thus the activity of oxide ions in the melt determines the characteristics of the melt as the activity of protons ( $H^+$ ) in the aqueous solution (pH) represents the acidity of the solution. By adopting the Lux-Flood acid-base theory, the basicity of the molten carbonate can be defined.

In aqueous solution: acid ( $H_2O$ ) = base ( $OH^-$ ) +  $H^+$   
In carbonate melts: base ( $CO_3^{2-}$ ) = acid ( $CO_2$ ) +  $O^{2-}$

Therefore, we can know that the activity of oxide ions indicates the basicity of the melt and  $CO_2$  in the melt behaves as an acid.

Table 2 shows the dissociation constants ( $k_d$ ) of alkali carbonate melts. The constant rises with Li content and decreases with K and Na contents. Thus the melts become more basic with increasing Li content. The behavior is in agreement with the ionic radius of alkali metals: the smaller ionic radius of alkali metal becomes more basic melts. Then the series of basic melts is as follows:



The oxygen solubility also becomes higher in more acidic carbonate melts. The behavior can be

**Molten Carbonate Fuel Cells, Table 1** Properties of eutectic alkali metal carbonates [3]

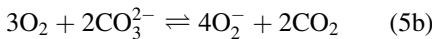
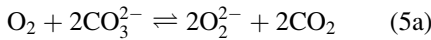
System	Composition (mol%)	m.p. (K)	$\gamma$ (mN/m) at 973 K	$\rho$ (g/cm <sup>3</sup> ) at 973 K	$\kappa$ (S/cm) at 973 K	$h_{O_2}$ (mol/cm <sup>3</sup> atm) at 923 K
$Li_2CO_3:Na_2CO_3$	53:47		239.0	1.937	2.181	$1.83 \times 10^{-7}$
	52:48	774				
$Li_2CO_3:K_2CO_3$	62:38	761	214.1	1.912	1.053	
	50:50	777.5	206.0	1.917		$3.26 \times 10^{-7}$
$Li_2CO_3:Na_2CO_3:K_2CO_3$	43.5:31.5:25	670	219.6	1.984	1.476	$3.91 \times 10^{-7}$
$Na_2CO_3:K_2CO_3$	56:44	983				
1M KCl at 298 K [4]			$\sim 72^a$		0.108	

<sup>a</sup>Value for water

**Molten Carbonate Fuel Cells, Table 2** Dissociation constants ( $k_d$ ) of carbonate melts [5]

Composition	$k_d$		
	823 K	923 K	1,023 K
Li <sub>2</sub> CO <sub>3</sub>	$1.01 \times 10^{-6}$	$2.08 \times 10^{-5}$	$2.37 \times 10^{-4}$
53 mol% Li <sub>2</sub> CO <sub>3</sub> – 47 mol% Na <sub>2</sub> CO <sub>3</sub>	$2.58 \times 10^{-9}$	$1.14 \times 10^{-7}$	$2.41 \times 10^{-6}$
43.5 mol% Li <sub>2</sub> CO <sub>3</sub> – 31.5 mol% Na <sub>2</sub> CO <sub>3</sub> – 25.0 mol% K <sub>2</sub> CO <sub>3</sub>	$2.04 \times 10^{-10}$	$1.23 \times 10^{-8}$	$3.34 \times 10^{-7}$
50 mol% Li <sub>2</sub> CO <sub>3</sub> – 50 mol% K <sub>2</sub> CO <sub>3</sub>	$9.77 \times 10^{-11}$	$6.43 \times 10^{-9}$	$1.86 \times 10^{-7}$
56 mol% Na <sub>2</sub> CO <sub>3</sub> – 44 mol% K <sub>2</sub> CO <sub>3</sub>	$8.53 \times 10^{-14}$	$1.38 \times 10^{-11}$	$8.26 \times 10^{-10}$

interpreted from the ionic radius. The larger ionic radius of alkali metal enhances O<sub>2</sub> solubility. This is due to the increased stability of superoxide ions (O<sub>2</sub><sup>2-</sup>) and peroxide ions (O<sub>2</sub><sup>2-</sup>) in the carbonate melts, which are produced by the following chemical reaction:



The dissociation constants also rise with temperature, indicating that the melts become more basic at a higher temperature.

As another property of molten carbonates, a contact angle is to be introduced. The molten carbonates are transparent liquid and movable. To maintain the molten carbonates in the fuel cell, a porous matrix structure is required. The porous structure holds the carbonate melts by the capillary forces of the pores. The carbonate melts have a very low contact angle with oxide ( $\approx 0^\circ$ ) but very large contact angles with metals [3]. Thus the cathode of the oxide electrode is very well wetted by the carbonates, while the anode electrode, with a metal state under strong reductants of H<sub>2</sub>, is poorly wetted. Based on this concept, a dry agglomerate model for the anode and a well-wetted agglomerate model for the cathode have been suggested [6]. According to the different surface tensions of Li-K and Li-Na carbonate melts as shown in Table 1, the melts have different wetting behaviors. The high surface tension of Li-Na carbonate melts causes poor wetting behavior compared with Li-K melts. This results in a steeper overpotential increase in the Li-Na carbonate electrolyte cell than in the Li-K cell at 600 °C [5, 7].

Gas solubility is also an important parameter for the electrode reaction because the electrode is covered by carbonates and gas reactants must transfer through the carbonate film. So, higher solubility results in less kinetic and mass-transfer resistances during the electrode reaction. In general, CO<sub>2</sub> and H<sub>2</sub> solubilities are approximately  $10^{-5}$  mole cm<sup>-3</sup> atm<sup>-1</sup>, and the O<sub>2</sub> solubility is about one tenth of the H<sub>2</sub> solubility in the carbonate melts. The following dependence of gas solubility on the melt compositions at the same gas condition and temperature was reported [8]:

O<sub>2</sub> solubility: Li-K > Li-Na  $\approx$  Li-Na-K

H<sub>2</sub> solubility: Li-K > Li-Na-K

CO<sub>2</sub> solubility: Li-Na > Li-Na-K > Li-K

### Electrolyte Loss in the Cell

The carbonate electrolytes are contained in the matrices, which are porous ceramic materials placed between the anode and cathode. Since the matrix is comprised of submicron-size pores, most of the pores are filled with carbonate electrolytes. Thus the electrolyte prevents gas leakage between the electrodes. The electrodes are covered by metal separators which provide gas flow paths over the electrodes; the peripheral area of the separators is sealed by matrices and is called the wet seal area. Thus the matrix prevents gas leaks from the inside to the outside of the cell by wet sealing.

Electrolyte loss weakens the gas sealing and shortens cell life. The molten carbonates are very corrosive materials. Since the separator is made of stainless steel, corrosion takes place on the surface of the separator. To reduce the corrosion, the anode side is coated with Ni and the wet seal area with Al.



According to the report on a 2 MW field test at Santa Clara, the causes and amounts of electrolyte losses are as follows: cathode hardware loss, 73%; fixed losses, 17%; vaporization loss, 7%; and unaccounted loss, 3% [9]. The report pointed out that most of the electrolyte loss was due to corrosion at the cathode because the Ni and Al coatings on the anode and wet seal area, respectively, prevented serious corrosion. Mitsubishi Electric Co. reported that about half of the electrolyte loss was due to the corrosion at the cathode current collector and the loss was proportional to the area of the current collector [10].

Among the austenitic stainless steels, 316L and 310 are generally used for the MCFC separator and current collector. The Cr contents of 316L and 310 are about 17% and 25%, respectively, and thus a denser  $\text{LiCrO}_2$  layer occurs on the surface of 310 with more corrosion resistivity. However,  $\text{LiCrO}_2$  has very low conductivity, resulting in a high electrical resistance with 310. Moreover, 310 makes water soluble  $\text{K}_2\text{CrO}_4$  as a corrosion product, and thus electrolyte loss is more severe with 310 than 316L [11].

Li-K and Li-Na carbonate melts had different corrosion behaviors with 316L. These melts showed insignificant corrosion at 650 °C, but severe pit corrosion was observed only in the Li-Na melt under the present  $\text{O}_2$  and  $\text{CO}_2$  condition at around 550 °C [12, 13]. Mitsubishi Electric Co. reported that an inert gas condition in the temperature range could prevent severe corrosion [12]. IHI in Japan also reported that the corrosion is mitigated by pre-oxidation of the surface by steam [13].

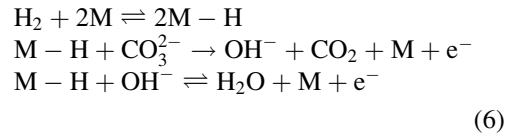
The molten carbonates also react with steam, which produces hydroxides, LiOH, NaOH, and KOH. It was reported that KOH has about twice the vapor pressure of LiOH and the highest vapor pressure among the above hydroxides [14]. However, as reported for the Santa Clara test [9], the electrolyte loss by vaporization was 7% of total loss, which is still low compared with the total loss.

### Anode

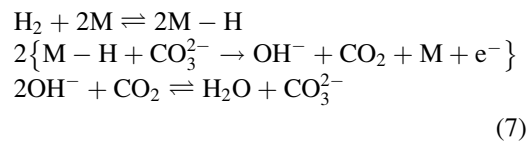
In general,  $\text{H}_2$  oxidation is a quite fast reaction even in the low-temperature fuel cells. The  $\text{H}_2$  oxidation in the high-temperature molten

carbonate is fast enough, as expected. Among the several mechanisms, the following two are mainly discussed:

Ang and Sammells' mechanism [15]



Suski's mechanism [16]



The mechanism of Ang and Sammells was suggested on the basis of experimental results obtained with Ni [15] and Cu [17] electrodes. Other mechanisms were supported by the role of  $\text{OH}^-$  [16], one electron number, and double the rate-determining step [18]. Although the reaction mechanisms are not yet in agreement, the kinetic values are within an acceptable range: Ni has an exchange current density of about  $100 \text{ mA cm}^{-2}$  at 923 K in Li-K melts. Moreover the following reaction orders are in agreement with the experimental results:

$$i_o = i_o^0 p(\text{H}_2)^{0.25} p(\text{CO}_2)^{0.25} p(\text{H}_2\text{O})^{0.25} \quad (8)$$

The positive reaction orders of  $\text{CO}_2$  and  $\text{H}_2\text{O}$  reflect the fact that  $\text{CO}_2$  and  $\text{H}_2\text{O}$  in the anode enhance the reaction kinetics although they are product species.

Owing to the high temperature,  $\text{H}_2$  oxidation is largely insensitive to the chosen anode materials. The exchange current densities of Co [15], Cu [17], Pt [18], Ir [18], Au [18], and Ag [18] were about 45, 69, 85, 27, 26, and 19  $\text{mA cm}^{-2}$ , respectively, at 923 K in Li-K carbonate melts. Considering the possible experimental error, these values indicate that the materials have a similar  $\text{H}_2$  oxidation rate at the anode. In addition, the oxidation potential of Ni in molten carbonate is about  $-0.802 \text{ V}$  under a 1 atm  $\text{O}_2$  condition at 925 K [3]. Thus Ni is metallic at open-circuit voltage and is not oxidized up to a certain potential.

The electrodes in the fuel cell should provide solid-liquid-gas three-phase boundaries to reduce overpotential. Porous-type electrodes are designed, and the carbonate electrolytes are dispersed in the electrode by capillary forces. The anode has a higher contact angle and lower wetting with carbonates than the cathode, which allows a smaller pore size at the anode. As mentioned above, the anode has a very high H<sub>2</sub> oxidation rate. So the active surface area and electrolyte filling in the anode are not critical parameters for its performance. Therefore the anode behaves as an electrolyte reservoir in the MCFC.

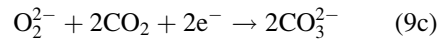
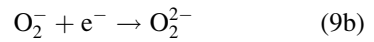
The most plausible life limiting factor is electrolyte depletion in the MCFC. Since the anode serves as electrolyte reservoir, its stable pore structure is very important for the electrolyte management. The Ni-Cr alloy electrodes, however, showed creep behavior which deforms the pore structure due to Ostwald ripening under the suppression in the carbonate melts. Thus the anode thickness is reduced with time, and electrolyte amounts in the anode are also decreased. Consequently, the cell life can be shortened. It was reported that the addition of Al to Ni-Cr resulted in higher creep resistivity than in Ni-Cr [14].

As alternative anodes, Cu-Al alloy and LiFeO<sub>2</sub> were tested, but they had insufficient creep strengths [2].

**Cathode**

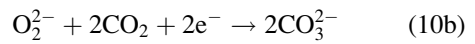
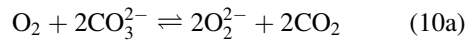
Oxygen reduction is generally much slower than H<sub>2</sub> oxidation. In particular, low-temperature fuel cells have much larger overpotential at the cathode, which is limiting the cell performance. A similar tendency also prevails in MCFCs, and most researches on kinetics have focused on oxygen reduction. In the past 40 years, a lot of works on oxygen reduction in molten carbonates have been done, and several oxygen reduction mechanisms have been suggested. Among them, two mechanisms, superoxide and peroxide paths, have been mainly suggested from half-cell experiments with plain gold electrodes [19, 20]:

Superoxide path [19]



$$i_o = i_o^o p(\text{O}_2)^{0.625} p(\text{CO}_2)^{-0.75} \quad (9d)$$

Peroxide path [20]



$$i_o = i_o^o p(\text{O}_2)^{0.375} p(\text{CO}_2)^{-1.25} \quad (10c)$$

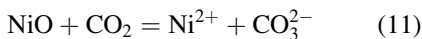
where *i<sub>o</sub>* is the exchange current density, which represents the reaction rate on the electrode surface, and *i<sub>o</sub><sup>o</sup>* is the intrinsic exchange current density. The superoxide path was observed mostly in the acidic carbonate melts of Na-K, whereas the peroxide path was found in the most basic melt of Li<sub>2</sub>CO<sub>3</sub>. In these melts, general agreements were obtained. However, the two mechanisms were separately suggested by the researchers for the widely used Li-K carbonate melts. This ambiguity probably resulted from experimental difficulties with the very hot corrosive carbonate melts. Among the kinetic works on oxygen reduction, the very high exchange current density in oxygen reduction (*i<sub>o</sub>* ≈ 10 mA cm<sup>-2</sup>) was generally accepted. The value is about eight orders higher than that of O<sub>2</sub> reduction in an aqueous solution (*i<sub>o</sub>* ≈ 10<sup>-7</sup> mA cm<sup>-2</sup> [21]). This very high value allows the expectation of very small activation overpotential at the cathode in the MCFC.

The oxygen reduction characteristics were also investigated with 100 cm<sup>2</sup> class single cells by Japanese and Korean groups. In particular, Uchida's group has suggested that oxygen reduction in Li-K melts is a process of mixed diffusion of superoxide and CO<sub>2</sub> in the melts [22]. They analyzed cathodic overpotential with respect to the O<sub>2</sub> and CO<sub>2</sub> gas partial pressures and consistently concluded that the superoxide mechanism prevails under a normal condition of the Li-K carbonate single cells [23, 24].

Under the oxidizing conditions of the cathode, oxides are mostly stable. It was suggested that Au, NiO, and SnO<sub>2</sub> have exchange current densities

( $i_o$ ) of 38.5, 18.3, and 11.2 mA cm<sup>-2</sup>, respectively, indicating that material species are insignificant for the O<sub>2</sub> reduction rate [25]. Since NiO shows comparable catalytic behavior to Au, NiO is the most popular cathode material so far. In general, Ni is oxidized to NiO inside the cell during the pretreatment procedure of MCFC, which is in situ oxidation. During the oxidation, Li ions in the carbonate melts are doped into the NiO. Reportedly about 2% of Li is doped, and the Li-doped NiO has about 33 S cm<sup>-1</sup> electronic conductivity, which is close to metal conductivity [26].

However, NiO at the cathode dissolves into the carbonate electrolyte (Eq. 11), and the Ni ions are reduced to Ni metal in the matrix by H<sub>2</sub> from the anode. Consequently, Ni deposition in the matrix may cause electrical short circuit between the anode and cathode:



It was reported that NiO dissolution is proportional to CO<sub>2</sub> partial pressure and activity [27]. Thus acidic melts have higher NiO solubility. Several methods have been employed to reduce the NiO dissolution: (1) increased basicity of the melts, (2) finding an alternative cathode material, and (3) modification of the NiO electrode. For the first approach, Li-Na melts were considered instead of widely used Li-K melts. It was reported that Li-Na melts have lower solubility [27] and higher electric conductivity than Li-K melts, as shown in Table 1. A Japanese group also reported that a Li-Na carbonate electrolyte cell showed higher performance than a cell with Li-K carbonates in the temperature range 575–675 °C up to 5 atm pressure [7]. The addition of alkali earth metals, MgO, BaO, SrO, and CaO, to the carbonate melts was attempted because alkali earth metal ions behave as a strong base in the melts [28]. They definitely reduced the NiO solubility. However, alkali earth metal ions were segregated in the matrix, and the metal ions were distributed at the anode side. In conclusion, the addition was not effective [29]. As a second approach, oxides such as LiCoO<sub>2</sub> and LiFeO<sub>2</sub> were developed for the cathode material. Although the solubility of LiCoO<sub>2</sub> is about one third of that of NiO [30], the low conductivity and high cost of

LiCoO<sub>2</sub> are obstructions to its use. LiFeO<sub>2</sub> also has low solubility compared with NiO, but very low conductivity is also a barrier [31]. As a third method, modification of NiO with MgO and Fe<sub>2</sub>O<sub>3</sub> was also attempted. The NiO-MgO-LiFeO<sub>2</sub> is a solid solution, and the material has lower NiO solubility due to the stable structure [32]. Industrially, thickening the matrix and reducing the CO<sub>2</sub> partial pressure were attempted, and FCE Co. reported that it could ensure a cell life of 5 years using these methods [2].

## Performance Analysis

The thermodynamic electromotive force of MCFC, called the open-circuit voltage ( $E_{OCV}$ ), is determined by the following equation according to Eq. 1a and 1b:

$$E_{OCV} = E^o + \frac{RT}{2F} \ln \left( \frac{p(\text{H}_2)p(\text{O}_2)^{0.5}p(\text{CO}_2)_{ca}}{p(\text{H}_2\text{O})p(\text{CO}_2)_{an}} \right) \quad (12)$$

where  $E^o$  is the standard potential; the subscripts “an” and “ca” denote the anode and cathode, respectively; and  $p$  is the partial pressure of the gases. Other symbols have their usual meanings.  $E_{OCV}$  is a voltage at zero current, so it represents a theoretically maximum voltage in the cell. When the current flows in the cell, electrical resistance among the cell components and electrochemical resistance at the electrodes reduce the cell voltage. Thus the performance of fuel cells is determined by the voltage loss, which is the difference between the open-circuit voltage ( $E_{OCV}$ ) and the voltage ( $V$ ) at a current load (Eq. 13):

$$V = E_{OCV} - \eta_{IR} - \eta_{an} - \eta_{ca} \quad (13)$$

where  $\eta_{IR}$  is the ohmic loss due to the electrical resistance and  $\eta_{an}$  and  $\eta_{ca}$  are the overpotential at the anode and cathode electrodes, respectively.

The ohmic loss is relatively easy to understand because the electrical resistance of the cell components behaves as a cause of voltage loss.

However, determination of overpotential from the electrochemical reaction resistance at the electrodes has been an interesting research topic. The fuel cell electrodes require a large surface area to increase the reaction rate, and thus porous materials are employed. In addition, the electrode surface is covered by thin electrolyte film to provide the three-phase boundary of gas-liquid-solid where the electrochemical reaction occurs. Thus the electrochemical resistance in MCFC is comprised of charge-transfer resistance on the electrode surface and mass transfer through the liquid film and gas channel as shown in Fig. 2.

At the anode, the following overpotential relations have been suggested based on the electrode kinetics of Eq. 8 by Selman’s group in the USA (Eq. 14a) [33] and CRIEPI (Central Research Institute of Electric Power Industry) in Japan (Eq. 14b) [34]:

$$\eta_{an} = a_1 \cdot p(\text{H}_2)^{-0.42} p(\text{CO}_2)^{-0.17} p(\text{H}_2\text{O})^{-1.0} \cdot i \tag{14a}$$

$$\eta_{an} = a_2 \cdot p(\text{H}_2)^{-0.5} \cdot i \tag{14b}$$

where  $a$  is the constant and  $i$  is the current. Both relations were obtained by the steady-state polarization method. On the other hand, the overpotential relations at the cathode have been

reported by Selman’s group (Eq. 15a) [33] and the CRIEPI group (Eq. 15b) [35]:

$$\eta_{ca} = a_3 \cdot p(\text{O}_2)^{-0.43} p(\text{CO}_2)^{-0.09} \cdot i \tag{15a}$$

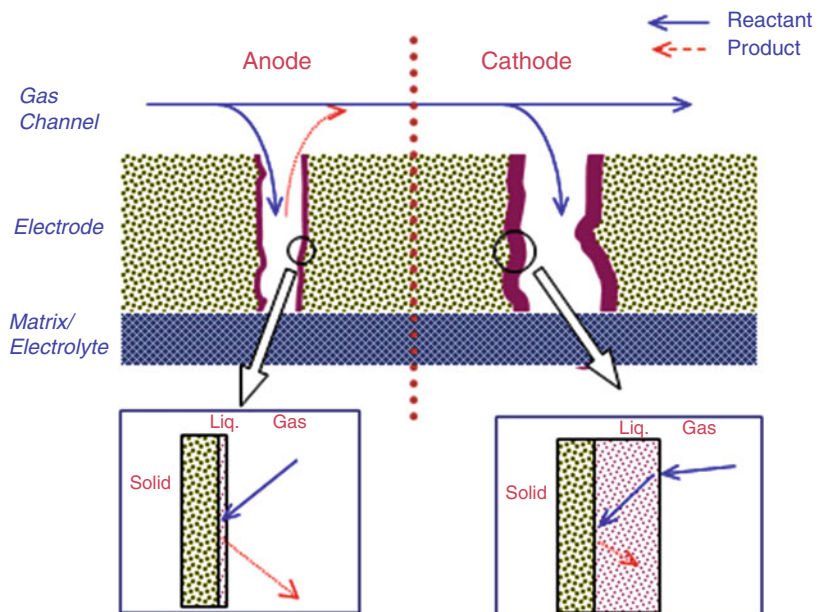
$$\eta_{ca} = \frac{\left( a_4 \cdot p(\text{O}_2)^{-0.75} p(\text{CO}_2)^{0.5} + a_5 \cdot p(\text{CO}_2)^{-1} \right)}{i} \tag{15b}$$

Equation 15a is an empirical relation based on the electrode kinetics of a superoxide path (Eq. 9d). Equation 15b resulted from the assumptions of mass-transfer resistance of superoxide ions and  $\text{CO}_2$  in the carbonate electrolyte film.

Most of the electrode kinetics in molten carbonates has been investigated with half-cell experiments which used smooth surface electrodes. Various experimental techniques could be applied such as the use of rotating disk electrode (RDE) [36], rotating wire electrode [37], ultramicroelectrode [38], potential step [39], AC impedance [39], coulstatic relaxation [39], voltammetry [19], and so on. However, the MCFC uses a porous electrode in the cell. Since it is covered by a thin electrolyte film and has a pore volume of over 50%, the behavior of the porous electrode in the cell would be

**Molten Carbonate Fuel Cells, Fig. 2**

Schematic drawing of reaction characteristics at the anode and cathode of MCFC



significantly different from that of a plain surface electrode in carbonate melts. A limited number of experimental methods could be applied for the investigation of the reaction characteristics of MCFCs. In general, the voltage loss due to ohmic loss and reaction overpotential in the MCFC has been analyzed with steady-state polarization [33], current interruption [40], and AC impedance methods [41]. As relatively new investigation tools, inert gas step addition (ISA) [24] and reactant gas addition (RA) [42] methods are introduced, and the relationship between the methods is treated in this work.

### Reaction Characteristics of MCFC

As shown in Fig. 2, MCFC reactions are comprised of charge-transfer reactions on the electrode surface and mass-transfer processes through the gas and liquid phases in series. Resistances in those processes are reciprocal numbers of reaction rate constant and mass-transfer coefficients which are represented in the overpotential. Thus the overpotential at the anode ( $\eta_{an}$ ) and cathode ( $\eta_{ca}$ ) is the sum of overpotential at each electrode due to the charge-transfer resistance ( $\eta_{ct}$ ) and that due to the liquid-phase mass-transfer resistance ( $\eta_{mt,L}$ ) and that due to the gas-phase mass-transfer resistance ( $\eta_{mt,G}$ ) as follows [24]:

$$\begin{aligned} \eta &= \eta_{ct} + \eta_{mt,L} + \eta_{mt,G} \\ &= \frac{iRT}{n^2F^2ap_0} \left( \frac{h}{k_0} + \frac{h}{k_L} + \frac{RT}{k_G} \right) \end{aligned} \quad (16)$$

where  $i$  is the current,  $a$  is the geometrical area,  $h$  is Henry's law constant,  $p_0$  is the bulk gas pressure,  $k_0$  is the reaction rate constant, and  $k_L$  and  $k_G$  are the mass-transfer coefficients through the liquid electrolyte and gas phase, respectively. Other symbols have their usual meanings.

As mentioned in the chapter of anode electrode, the  $H_2$  oxidation rate is sufficiently fast ( $i_o \approx 100 \text{ mA cm}^{-2}$ ) for the charge-transfer resistance to be neglected. In addition, the electrolyte film on the anode electrode can be assumed to be negligibly thin according to the dry agglomerate model [6], and then the mass-transfer resistance through the electrolyte film can be neglected.

Consequently, the anode is assumed to be only a gas-phase mass-transfer control process. The gas-phase mass-transfer coefficient ( $k_G$ ) was obtained from the mass-transfer coefficient of the boundary layer theory in the case of mass transfer between laminar flow and plain substrates [24]. Then  $k_G$  is expressed as follows:

$$k_G \cong 0.664 \left( \frac{v_f}{L} \right)^{\frac{1}{2}} (D_G)^{\frac{2}{3}} (\nu)^{-\frac{1}{6}} \quad (17)$$

where  $v_f$  is the flow velocity,  $L$  is the electrode length,  $D_G$  is the gas diffusivity, and  $\nu$  is the kinematic viscosity. Other symbols have their usual meanings. Then Eq. 16 can be simplified to Eq. 18 at the anode:

$$\begin{aligned} \eta_{an} &= \eta_{an,ct} + \eta_{an,mt,L} + \eta_{an,mt,G} \\ &\cong \eta_{an,mt,G} = i \frac{R^2T^2}{n^2F^2ap_0} \left( \frac{1}{k_{an,G}} \right) \end{aligned} \quad (18)$$

On the other hand, the linear current-voltage behavior of MCFC (Fig. 1) and the very high reaction rate of the cathode ( $i_o \approx 10 \text{ mA cm}^{-2}$ ) allow the assumption of negligible charge-transfer resistance at the cathode. In fact, the cathode has a relatively thick carbonate electrolyte on the surface as shown in Fig. 2. Thus the following relation has been suggested as the cathodic overpotential [24]:

$$\begin{aligned} \eta_{ca} &= \eta_{ca,ct} + \eta_{ca,mt,L} + \eta_{ca,mt,G} \\ &\cong \eta_{ca,mt,L} + \eta_{ca,mt,G} \\ &= i \frac{RT}{n^2F^2ap_0} \left( \frac{h}{k_{ca,L}} + \frac{RT}{k_{ca,G}} \right) \end{aligned} \quad (19)$$

For the  $k_{ca,G}$ , the same gas-phase mass-transfer relation to Eq. 17 is employed at the cathode because the reactants flow through the gas channel over the electrode and the boundary layer theory is also plausible.

However, the liquid-phase mass-transfer rate,  $k_{ca,L}$ , depends on the gas solubility, diffusivity, and electrolyte film thickness on the cathode. Uchida et al. have suggested that the cathode reaction is mixed diffusion resistance of superoxide ion ( $O_2^-$ ) and  $CO_2$  in the carbonate melts [22], since the superoxide ion is chemically generated



in the carbonate melt according to Eq. 9a. Thus the activity of superoxide ion,  $[O_2^-]$ , is

$$[O_2^-] = \kappa p(O_2)^{0.75} p(CO_2)^{-0.5} \quad (20)$$

where  $\kappa$  is the equilibrium constant of reaction (9a).

When we assume the mixed diffusion of  $O_2^-$  and  $CO_2$  through electrolyte film, the mass-transfer resistance through the liquid electrolyte ( $R_{ca,mt,L}$ ) is to be

$$\begin{aligned} R_{ca,mt,L} &= R_{O_2^-} + R_{CO_2} \\ &= \frac{RT\delta}{3^2 F^2 D_{O_2^-} a \kappa p(O_2)^{0.75} p(CO_2)^{-0.5}} \\ &\quad + \frac{RT\delta h_{CO_2}}{1.5^2 F^2 a D_{CO_2} p(CO_2)} \end{aligned} \quad (21)$$

where  $\delta$  is the electrolyte film thickness. Then the simplified relation of Eq. 22 can be obtained:

$$R_{ca,mt,L} p(CO_2) = A p(O_2)^{-0.75} p(CO_2)^{1.5} + B \quad (22)$$

where  $A$  and  $B$  are constants,  $A = \frac{RT\delta}{3^2 F^2 D_{O_2^-} \kappa^2}$  and  $B = \frac{RT\delta h_{CO_2}}{1.5^2 F^2 D_{CO_2}}$ .

**Steady-State Polarization**

Steady-state polarization (SSP) is a very simple method which measures voltage by applying

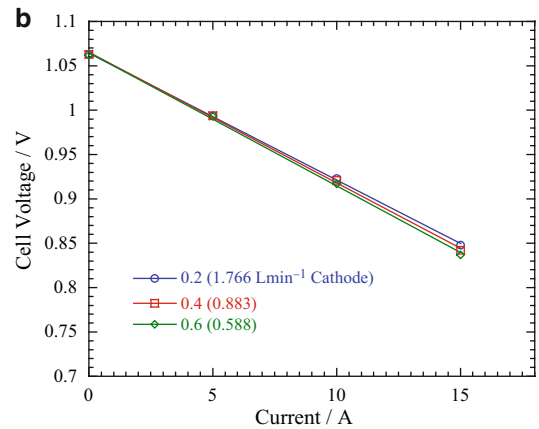
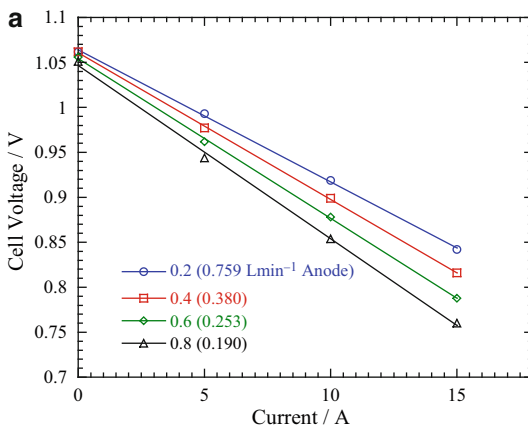
currents with sufficient time intervals. Figure 3 shows some results according to different utilizations. An  $E_{OCV}$  of 1.07 V is observed. It is very close to the theoretical value according to Eq. 12 because the inlet composition of anode gas is  $H_2:CO_2:H_2O = 0.69:0.17:0.14$  atm and that of cathode gas is  $air:CO_2 = 0.7:0.3$  atm.

Since the utilization ( $u$ ) is a ratio of consumed gas amounts to supplied amounts, it indicates a gas flow rate at a fixed current density:

$$u = \frac{\text{consumed gas amounts}}{\text{supplied gas amounts}} \quad (23)$$

The utilizations in the figures are based on currents of 15 A. The linear current-voltage behaviors are observed at the utilizations. This indicates that the MCFC has very low charge-transfer resistance as mentioned in the Introduction. The difference between  $E_{OCV}$  and  $V$  at a current load is the total voltage loss according to Eq. 13. As shown in the figures, SSP cannot distinguish between the voltage losses accounted for by  $\eta_{IR}$ ,  $\eta_{an}$ , and  $\eta_{ca}$ .

Figure 3 also shows that cell voltage is more severely dependent on the anode utilization than on the cathode one. This indicates that anodic overpotential is more affected by the flow rate. It is a specific feature of MCFC that flow rate affects cell voltage.



**Molten Carbonate Fuel Cells, Fig. 3** Steady-state polarization results at various utilizations (15 A current bases) with a 100 cm<sup>2</sup> class MCFC single cell at 650 °C,

1 atm [43]. (a) Anode utilizations at a fixed cathode utilization of 0.4 (b) Cathode utilizations at a fixed anode utilization of 0.4



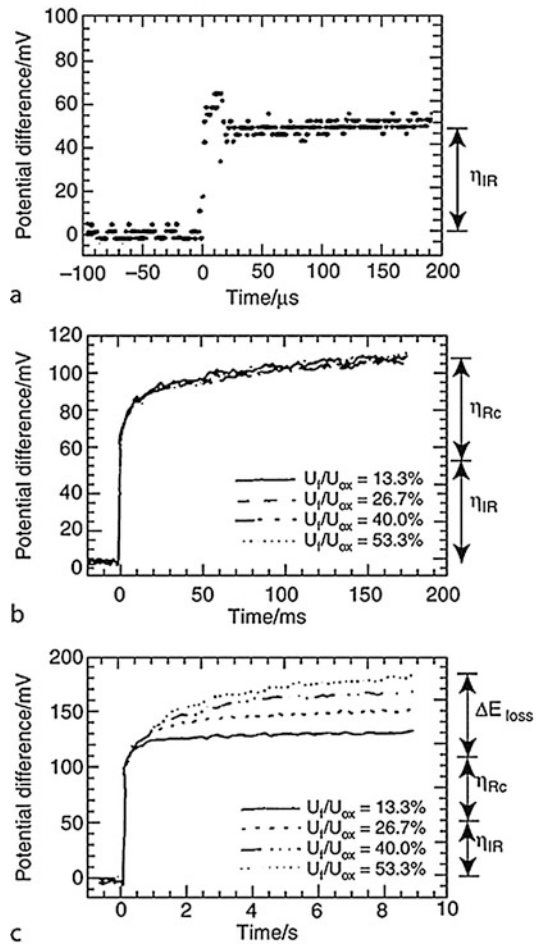
### Current Interruption

Current interruption (C/I) is a voltage relaxation method. The measurement is quite simple: the applied currents are rapidly interrupted, and the following voltage relaxation is recorded. Figure 4 presents some results of C/I measurement. In particular, Fig. 4a shows voltage relaxation during 200  $\mu$ s. At the exact moment of interruption, a voltage jump due to the relaxation of electrical resistance occurs. In the MCFC, most of the electrical resistance is attributed to the ionic resistance in the electrolyte, and thus the voltage jump shows that the ionic resistance is relaxed right after the interruption. Then the flow rate independent time region follows as shown in Fig. 4b. However, voltage relaxation in the time region depends on the oxidant gas composition [40]. This implies that the time region represents the mass-transfer effect through the liquid electrolyte at the cathode. Then the longest time region of 10 s shows that voltage relaxation depends on the anode utilization; higher utilization requires a longer relaxation time. CRIEPI reported that the voltage relaxation for several seconds was ascribed to the relaxation of concentration distribution in the anode electrolyte film [44]. Consequently, the C/I method was found to show ohmic loss and anodic and cathodic overpotential for different time ranges.

### AC Impedance

#### Measurement with 100 cm<sup>2</sup> Class Single Cell

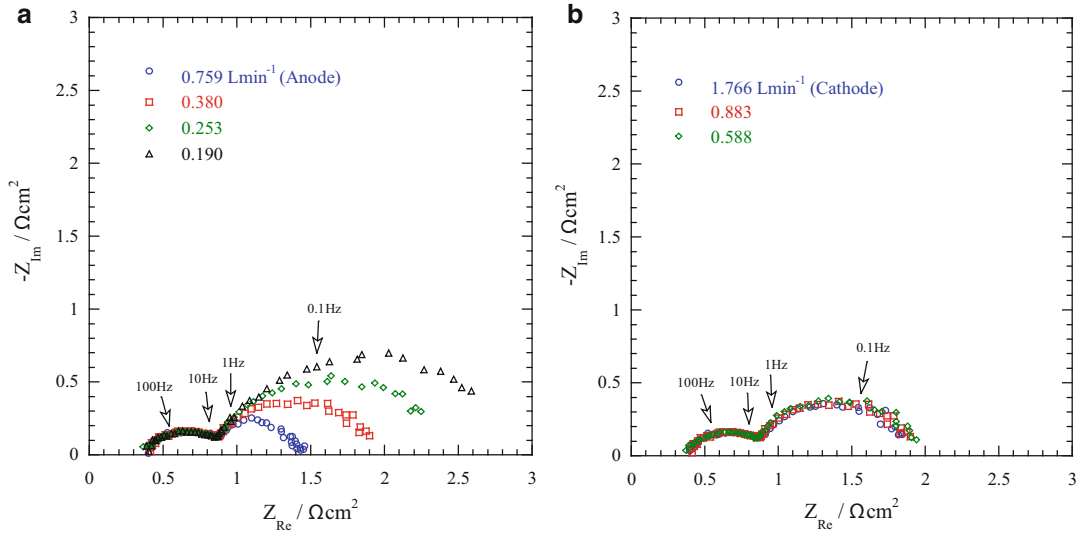
The AC impedance method is a powerful technique for electrode kinetics and mass-transfer investigation. The charge-transfer and mass-transfer resistances are an electrically parallel circuit with an electrochemical double layer which behaves as a capacitor. The parallel circuit of a resistance and a capacitor at a smooth surface electrode has the characteristic behavior of an AC signal: a 90° phase angle between the current and voltage signal at a high-frequency AC signal and 0° at a low-frequency signal. The phase angle is generally represented in the complex plane where the x-axis represents the resistance component and the y-axis the capacitive one. Thus, the impedance of the parallel circuit draws a half circle due to the



**Molten Carbonate Fuel Cells, Fig. 4** Voltage relaxations after current interruption of 10 A current loads at a 100 cm<sup>2</sup> class MCFC single cell (From Ref. [40]). (a) 200  $\mu$ s time range, (b) 200 ms, (c) 10 s

frequency change, and the diameter of the circle represents the resistance value of the circuit.

Interpretation of the AC impedance in the MCFC has not been in agreement, although a lot of theoretical interpretation has been attempted. Difficulties in the interpretation of gas flow effect and porous electrode behaviors are major reasons. Figure 5a, b shows the results of AC impedance with different flow rates at the anode and cathode, respectively. They were measured in an open-circuit state, and thus electrodes were maintained in an equilibrium state. The length of the x-axis



**Molten Carbonate Fuel Cells, Fig. 5** AC impedance results with various gas flow rates with a 100 cm<sup>2</sup> class MCFC single cell at 650 °C, 1 atm, OCV, 5 mV rms signal, 1 kHz to 0.01 Hz [43]. (a) Various anode flow rates at a

fixed cathode flow rate of 0.883 L min<sup>-1</sup>. (b) Various cathode flow rates at a fixed anode flow rate of 0.759 L min<sup>-1</sup>

from 0 to the high-frequency initial point represents the internal resistance of the cell. The high-frequency circle (HFC) on the left has a frequency range of 1 kHz to 5 Hz which does not depend on the anode and cathode flow rate. But it is clear that the low-frequency circle (LFC) depends mostly on the anode gas flow rate. The independence of LFC on the cathode flow rate is in line with the behavior of Fig. 3b that the cathode flow rate does not affect overpotential significantly. On the other hand, it is observed that the cathode gas composition, especially O<sub>2</sub> gas partial pressure, affects the HFC (Fig. 6). The lower O<sub>2</sub> partial pressure leads to the larger HFC, indicating that the HFC is closely related to the cathodic overpotential.

**Simulation of AC Impedance**

The anode and cathode gases flow over the electrodes. Since the Reynolds numbers ( $N_{Re}$ ) are about 15 at the anode and about 300 at the cathode [43], the gas flows at the electrodes are laminar flow. In general, the gas flow over the flat plate generates thin boundary layer due to the

shear stress on the surface. In the laminar flow, the boundary layer thickness ( $\delta_G$ ) is a function of  $N_{Re}$ , electrode length ( $x$ ) and Schmidt number ( $N_{Sc}$ ) as in Eq. 24:

$$\delta_G = \frac{x}{0.664(N_{Re})^{1/2}(N_{Sc})^{1/3}} \quad (24)$$

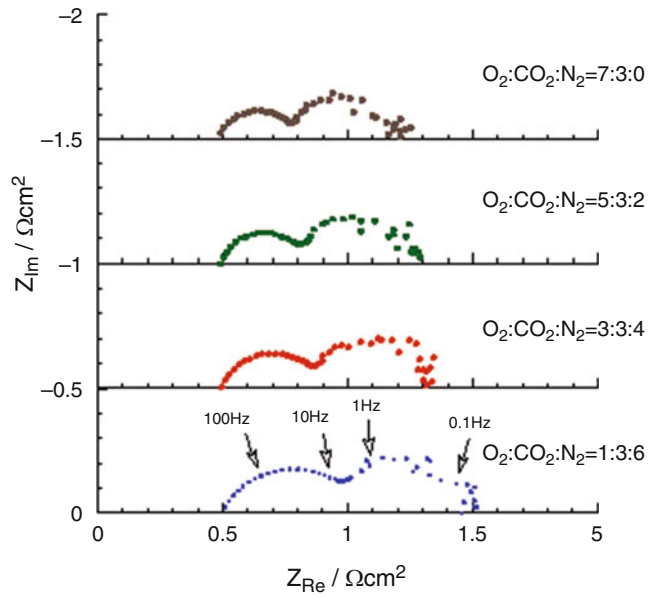
Figure 7 shows the schematic drawing of boundary layer thickness over the electrode and concentration distribution of active species through the pore.

Then, the equivalent circuit of an MCFC can be expressed by Fig. 8. The ionic resistance in the electrolyte is  $R_{\Omega}$ , and the electric double layer capacitance at the anode and cathode are  $C_{d,an}$  and  $C_{d,ca}$ , respectively.  $Z_{f,an}$  and  $Z_{f,ca}$  are the faradaic impedances at the anode and cathode, respectively.

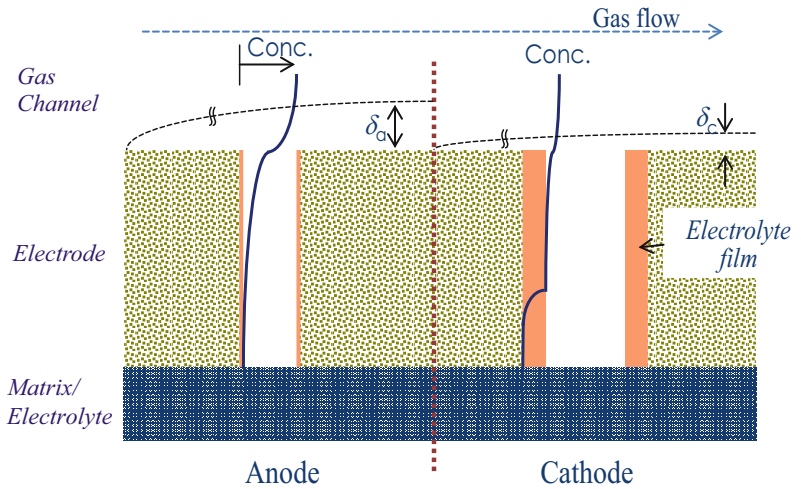
As shown in Eqs. 18 and 19, the anode reaction is mostly gas-phase mass-transfer control process, while the cathode is mixed control process of gas and liquid phases. Thus faradaic impedances at the anode ( $Z_{f,an}$ ) and cathode ( $Z_{f,ca}$ ) can be expressed by mass-transfer impedance:

**Molten Carbonate Fuel Cells, Fig. 6** AC

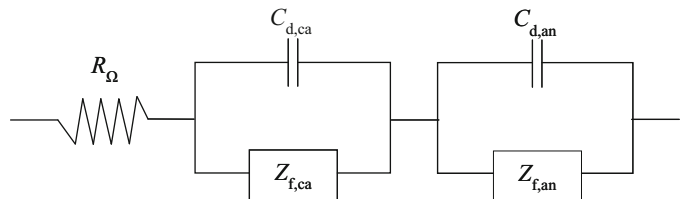
impedance results with different  $O_2:CO_2:N_2$  ratios at a total flow rate of  $0.883 \text{ L min}^{-1}$  and a fixed anode flow rate of  $0.759 \text{ L min}^{-1}$  at  $923 \text{ K}$ ,  $1 \text{ kHz}$  to  $0.01 \text{ Hz}$ , open-circuit state [43]



**Molten Carbonate Fuel Cells, Fig. 7** Schematic drawing of concentration distribution in gas and liquid phases at anode and cathode under a polarization state.  $\delta_a$  and  $\delta_c$  are the gas-phase boundary layer thickness at the anode and cathode, respectively [43]



**Molten Carbonate Fuel Cells, Fig. 8** Equivalent circuit of an MCFC cell [43]



$$Z_{f,an} \approx Z_{an,mt,G} \quad (25a)$$

$$Z_{f,ca} \approx Z_{ca,mt,L} + Z_{ca,mt,G} \quad (25b)$$

Thus, the total impedance ( $Z_{tot}$ ) of Fig. 8 is to be Eq. 26:

$$Z_{tot} = R_{\Omega} + \frac{Z_{f,an}}{1 + j\omega C_{d,an} Z_{f,an}} + \frac{Z_{f,ca}}{1 + j\omega C_{d,ca} Z_{f,ca}} \quad (26)$$

A previous work has reported that mass-transfer impedance through a thin film has following relation [45]:

$$Z_{mt} = \frac{2RT\delta}{n^2 F^2 cD} \cdot \frac{\tanh\sqrt{j\omega/D/\delta^2}}{\sqrt{j\omega/D/\delta^2}} \quad (27)$$

where  $\delta$  is the film thickness,  $D$  is the diffusivity in the fluid,  $c$  is the concentration, and others have their usual meaning. Since the gas-phase mass transfer takes place through the boundary layer in the gas channel and the liquid-phase mass transfer does through the electrolyte film, the relation of Eq. 27 can be employed to the faradaic impedance of Eq. 25a and 25b. Then we have following relation:

$$Z_{f,an} \approx \frac{2RT\delta_G}{n^2 F^2 c_G D_G} \cdot \frac{\tanh\sqrt{j\omega/D_G/\delta_G^2}}{\sqrt{j\omega/D_G/\delta_G^2}} \quad (28a)$$

$$Z_{f,ca} \approx \frac{2RT\delta_L}{n^2 F^2 c_L D_L} \cdot \frac{\tanh\sqrt{j\omega/D_L/\delta_L^2}}{\sqrt{j\omega/D_L/\delta_L^2}} + \frac{2RT\delta_G}{n^2 F^2 c_G D_G} \cdot \frac{\tanh\sqrt{j\omega/D_G/\delta_G^2}}{\sqrt{j\omega/D_G/\delta_G^2}} \quad (28b)$$

where subscripts  $L$  and  $G$  denote liquid and gas phases, respectively. The gas-phase boundary layer thickness,  $\delta_G$ , in Eq. 28a and 28b can be

obtained with a relation of Eq. 24. The concentration in the liquid phase at the cathode,  $c_L$ , can be obtained with the mixed diffusion process of superoxide ion ( $O_2^-$ ) and  $CO_2$  as in Eq. 21, and then we have a relation of  $c_L$ :

$$c_L = \kappa p(O_2)^{0.75} p(CO_2)^{-0.5} + hp(CO_2) \quad (29)$$

With other parameters in Ref. [43], we can simulate AC impedance behavior. Figure 9 shows a simulated Bode plot of the total impedance ( $Z_{tot}$ ), anodic faradaic impedance ( $Z_{f,an}$ ), and cathodic faradaic impedance ( $Z_{f,ca}$ ) with the equivalent circuit in Fig. 8. The imaginary impedance value of the cell generally reflects capacitive elements and diffusion through a layer of finite length in the liquid and gas phases.

The cathodic faradaic impedance ( $Z_{f,ca}$ ) shows two of peak values at around 40 Hz and 0.8 Hz. This can be explained by the diffusion processes through electrolyte film and boundary layer in the gas phase. Since the electrolyte film is assumed to be very thin compared with the boundary layer, the diffusion through the electrolyte film would have much faster response than that of boundary layer. Thus, the value at 40 Hz represents diffusion in the electrolyte film, and the value at 0.8 Hz reflects diffusion through the boundary layer. On the other hand, the anodic faradaic impedance shows only one peak at 0.1 Hz. This is due to the diffusion through the boundary layer in the anode gas channel.

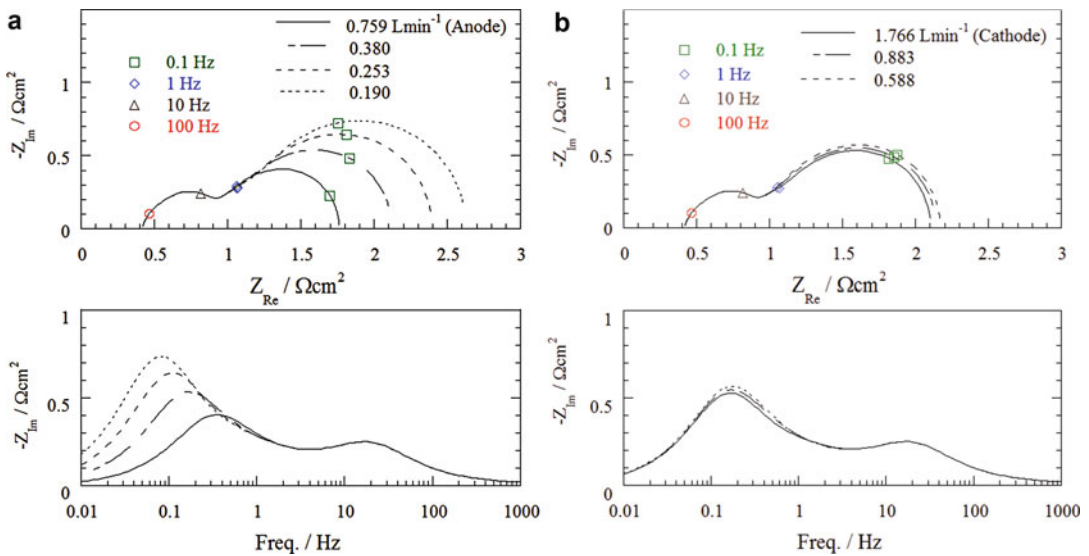
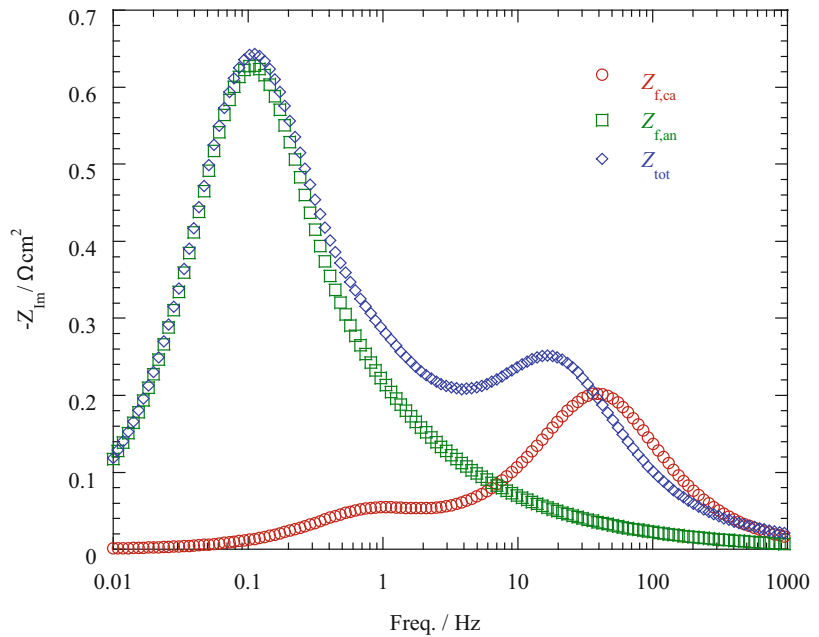
Figure 10 shows the Cole-Cole and Bode plots at different anode (a) and cathode (b) flow rates. The anode gas flow affects the LFC significantly, whereas the cathode gas flow has less influence on the LFC. This is identical behavior to the experimental results in Fig. 5a, b. The effect of concentration in the cathodic electrolyte ( $c_L$ ) on the impedance is shown in Fig. 11. Contrary to the gas flow effect,  $c_L$  affects the HFC in line with the experimental results in Fig. 6.

### Inert Gas Step Addition (ISA)

The above relations of anodic overpotential (Eq. 14a and 14b) and cathodic overpotential (Eq. 15a and 15b) only employ the partial pressure effect of gases. A lot of previous works on the electrode

**Molten Carbonate Fuel**

**Cells, Fig. 9** Imaginary values of  $Z_{f,ca}$ ,  $Z_{f,an}$ , and  $Z_{tot}$  from the simulation result at anode flow rate of  $0.253 \text{ L min}^{-1}$  and cathode flow rate of  $0.883 \text{ L min}^{-1}$  according to the equivalent circuit in Fig. 8 [43]



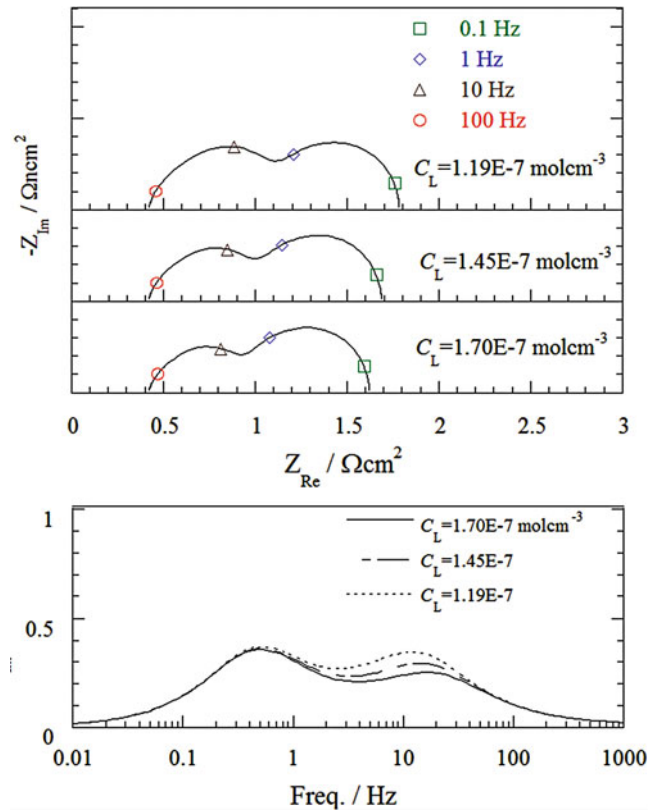
**Molten Carbonate Fuel Cells, Fig. 10** Simulation results with different anode flow rates (a) at a fixed cathode flow rate of  $0.883 \text{ L min}^{-1}$  and cathode flow rates (b) at a

fixed anode flow rate of  $0.759 \text{ L min}^{-1}$  according to the equivalent circuit of Fig. 8 [43]

kinetics have been done with a coin-type single cell which had a geometric electrode area of about  $3 \text{ cm}^2$ . They were carried out with a very low gas utilization that was sufficient to neglect the gas-phase mass-transfer effect. The low utilization, however, was far from the actual condition where

the anode utilization is normally over 70%. In addition, the performance of MCFC depends on the gas flow rate even in the  $100 \text{ cm}^2$  class single cell as shown in Fig. 3. To investigate the flow rate effect in the MCFC, the inert gas step addition (ISA) method has been developed [24]. ISA can vary the

**Molten Carbonate Fuel Cells, Fig. 11** Simulation results with different concentrations in the liquid electrolyte ( $c_L$ ) at cathode and cathode flow rate of  $0.883 \text{ L min}^{-1}$  and anode flow rate of  $0.759 \text{ L min}^{-1}$  [43]



utilization without changing gas compositions, and thus the flow rate effect could be analyzed.

**Measurements**

ISA measurement was mainly carried out with  $100 \text{ cm}^2$  class single cells because it had sufficient anode and cathode gas volumes to show the gas flow effect at the electrodes. In fact, the reactant gases flow through the gas channel over the electrode, and thus an electrode has a certain gas volume between the electrode and cell frame. Figure 12 shows the gas flow path of an electrode. When the gas line volume,  $v_i$ , is bigger than the gas volume of an electrode,  $v_e$ , the added inert gas enlarges the reactant gas flow rate in the electrode during the time range of  $t_{i,a}$  of Fig. 13. The flow rates of reactant gases are enhanced without partial pressure change during  $t_{i,a}$ , which results in a utilization shift. Thus the voltage variation during the time range represents the utilization effect on the overpotential. The added inert gas flows inside the

cell until the step-off of inert gas, which varies the gas partial pressures between  $t_{i,a}$  and  $t_{i,b}$ . Therefore, ISA also provides a partial pressure effect on the overpotential. When the inert gas flow is interrupted, the remaining inert gas in the volume,  $v_i$ , flows in the cell during  $t_{i,b}$ . Thus the reactant flow rate is decreased during the time range. The flow rate of inert gas was controlled with a mass flow controller (MFC). During the flow change, the cell voltage and inert gas flow rate were simultaneously recorded with an oscilloscope.

**Analysis of Overpotential**

As shown in Eq. 18, the anodic overpotential is mainly due to the gas-phase mass-transfer resistance. In addition, the gas-phase mass-transfer rate is a function of gas flow rate as in Eq. 17. Since the gas velocity corresponds to gas flow rate, Eq. 18 can be expressed in terms of utilization ( $u$ ) of Eq. 23. Then Eq. 18 becomes



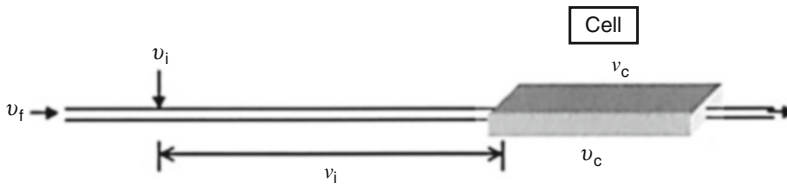
$$\eta_{an} \cong \eta_{an,mt,G} = i \frac{R^2 T^2}{n^2 F^2 a p_0} \left( \frac{1}{k_{an,G}} \right) = q_{an} \cdot u^{0.5} \tag{30}$$

where  $q_{an} = 1.51 \frac{R^2 T^2 (iLs)^{1/2} v^{1/6}}{(n^3 F^3 a^2 p_0)^{1/2} D_G^{2/3}}$  and  $s$  is the cross-sectional area of the gas channel.

Figure 14 shows voltage behaviors with  $0.3 \text{ L min}^{-1} \text{ N}_2$  addition to the anode at various current densities. At the open-circuit state, the voltage increases due to the addition because  $E_{OCV}$  rises with decreasing partial pressure of anode gases according to Eq. 13. However,

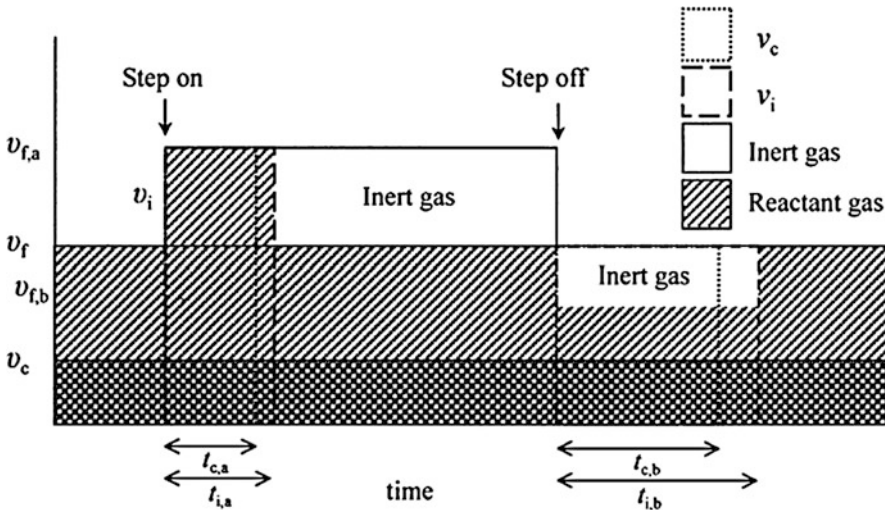
at polarization states, a positive peak, “a,” and a negative voltage peak, “b,” are observed. The peaks are due to the change in the flow rate of reactant gases as shown in Fig. 13. The flow rate increase results in the positive “a” peak, while the flow rate decrease leads to the negative “b” peak. This indicates that the anode reaction is affected by the flow rate of anode reactant gases.

Substituting  $\text{N}_2$  with Ar and He gives identical voltage behaviors [24]. This shows that ISA measurements are available regardless of the inert gas species. However, the voltage between the “a” and “b” peaks was affected by the inert gas species; helium showed the highest voltage among



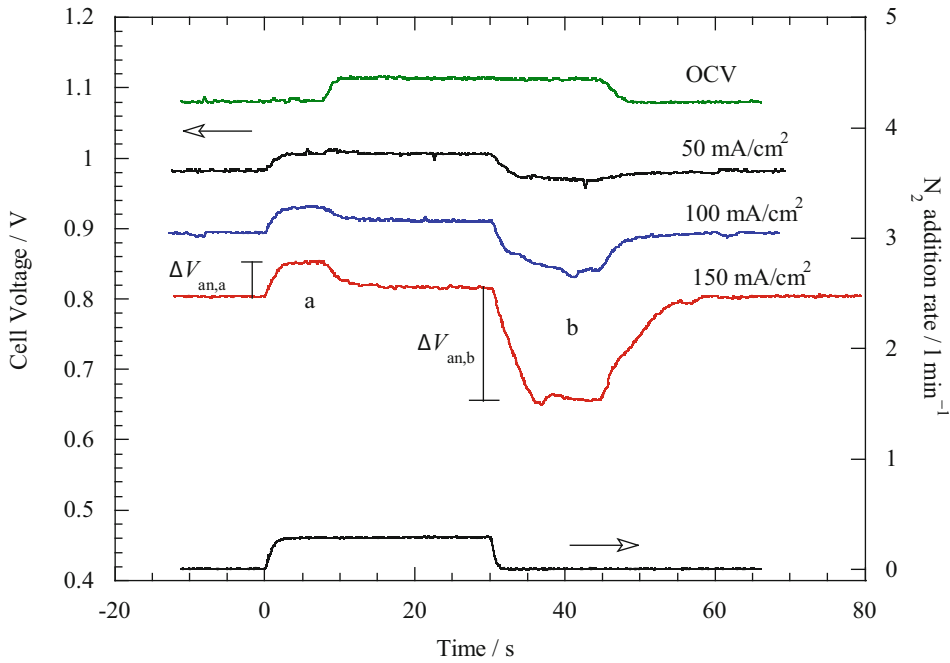
**Molten Carbonate Fuel Cells, Fig. 12** Schematic drawings of gas flow path of an electrode (From Ref. [24]).  $v_f$  is the reactant flow rate,  $v_i$  is the inert gas flow rate,  $v_c$  is the

consumed gas rate by the applied currents,  $v_i$  is the volume between inert gas inlet port and electrode, and  $v_c$  is the volume of gas channel



**Molten Carbonate Fuel Cells, Fig. 13** Schematic drawings of flow rate changes caused by the inert gas addition. The reactant flow rate increases during  $t_{i,a}$  and decreases for  $t_{i,b}$  (From Ref. [24]).  $v_f$  is the reactant flow rate,  $v_i$  is the inert gas flow rate,  $v_c$  is the consumed gas rate due to the applied currents,  $v_{f,a}$  is the flow rate

increase due to the inert gas addition,  $v_{f,b}$  is the flow rate decrease by the interruption of inert gas addition,  $v_i$  is the volume between inert gas inlet port and electrode,  $v_c$  is the volume of gas channel,  $t_c$  is the time to fill  $v_c$ , and  $t_i$  is the time of the gas filled in the volume  $v_i$  to flow over the electrode



**Molten Carbonate Fuel Cells, Fig. 14** Voltage-shift patterns with an addition of 0.3 L min<sup>-1</sup> N<sub>2</sub> to the anode at 650 °C,  $u_f = 0.6(0.253\text{L min}^{-1})$ , and  $u_{ox} = 0.4(0.883\text{L min}^{-1})$  of  $i = 150\text{ mA cm}^{-2}$  (From Ref. [46])

them [24]. During the time range, inert gas flows inside the cell and the gas species may affect the diffusivity of H<sub>2</sub>. Indeed, helium has the highest diffusivity among them, and thus helium provided the lowest mass-transfer resistance in the anode. This strongly implies that the anode reaction is a gas-phase mass-transfer control process.

Since the height of the positive peak,  $\Delta V_{an,a}$ , is an overpotential difference at the flow rate change and the flow rate corresponds to the utilization, the peak height can be expressed in terms of anode utilization ( $u_f$ ):

$$\begin{aligned} \Delta V_{an,a} &= \eta_{an1} - \eta_{an2} = q_{an} u_{f,1}^{0.5} - q_{an} u_{f,2}^{0.5} \\ &= m - q_{an} u_{f,2}^{0.5} \end{aligned} \quad (31)$$

where subscripts 1 and 2 denote before and after the N<sub>2</sub> addition, respectively, and  $m$  is a constant. Thus the peak height has a linear relation with utilization. Figure 15 shows the peak heights with various N<sub>2</sub> addition rates at different anode utilizations and arranges the heights according to the relation of Eq. 31. The linearity of Eq. 31 at the different

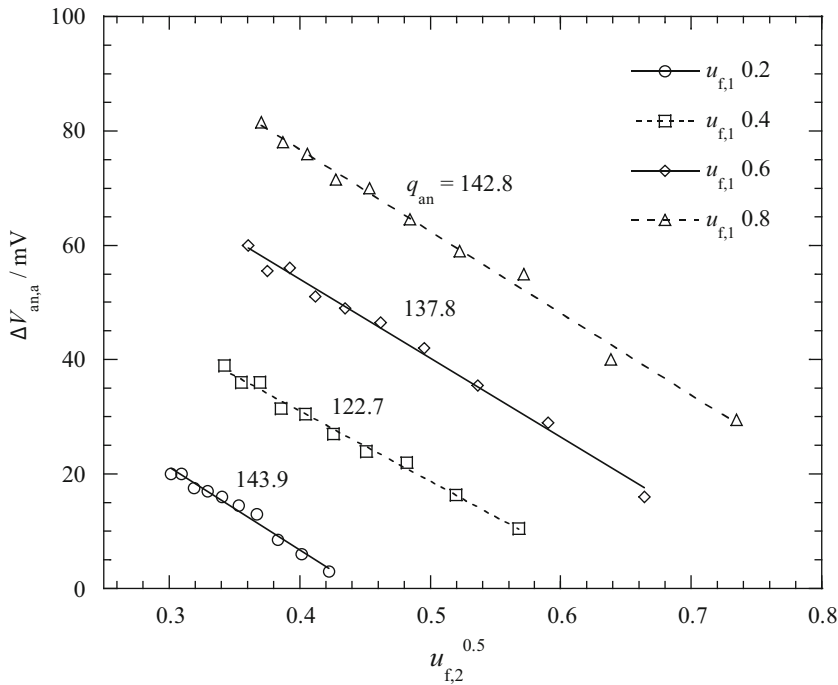
anode gas utilizations verifies the validity of the equation, which shows that the anode reaction is a strong gas-phase mass-transfer control process. The slope of  $q_{an}$  is about 140 mV, and the anodic overpotential can be obtained according to Eq. 30.

On the other hand, the cathode reaction is controlled by the mass-transfer processes through the liquid electrolyte film and boundary layer in the gas channel as in Eq. 19. When the overpotential due to the gas-phase resistance is considered, the following relation can be used:

$$\eta_{ca,mt,G} = i \frac{R^2 T^2}{n^2 F^2 a p_0} \left( \frac{1}{k_{ca,G}} \right) = q_{ca} \cdot u_{ox}^{0.5} \quad (32)$$

$$\text{where } q_{ca} = 1.51 \frac{R^2 T^2 (iLs)^{1/2} v^{1/6}}{(n^3 F^3 a^2 p_0)^{1/2} D_G^{2/3}}$$

The N<sub>2</sub> addition to the cathode brings about two positive and negative voltage peaks in the “B” and “D” time regions as shown in Fig. 16. The origins of the peaks are due to the flow rate and utilization change



**Molten Carbonate Fuel Cells, Fig. 15** Rearrangement of the peak height in Fig. 14 with shifted utilization according to Eq. 31 (From Ref. [24])

similar to the anode as shown in Fig. 14. Applying the relation of Eq. 31 to the cathode, we obtain Eq. 33:

$$\begin{aligned} \Delta V_{ca,a} &= \eta_{ca1} - \eta_{ca2} \\ &= q_{ca} u_{ox,1}^{0.5} - q_{ca} u_{ox,2}^{0.5} \\ &= m - q_{ca} u_{ox,2}^{0.5} \end{aligned} \quad (33)$$

Then the  $q_{ca}$  value of the cathode represents overpotential due to the gas-phase mass-transfer at the cathode.

Figure 17 shows the results of Eq. 33 at the cathode. The value,  $q_{ca}$ , the slope in the figure is very small compared with that at the anode of Fig. 15, although the small positive peak height provides deviations in the  $\Delta V_{ca,a}$ . This means that the cathode has much smaller overpotential due to the gas transport in the cell. In addition,  $q_{ca}$  values are different with cathode utilization; they have larger values at a higher utilization. In general, the cathode showed higher overpotential of over 50% of oxidant utilization [24]. The low diffusivity in

the gas phase and low  $O_2$  solubility in the carbonate melts could be the reason. The  $q_{ca}$  value indicates that the cathodic overpotential also depends on the utilization.

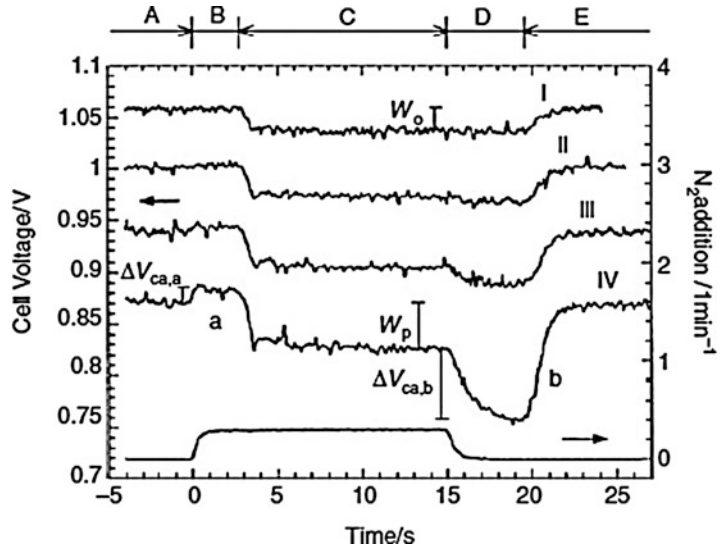
On the other hand, the voltage in the “C” time region of Fig. 16 is a steady-state value of voltage at the  $N_2$  flowing in the cathode. The  $N_2$  in the cell varies the gas partial pressures, and thus the region represents some effects of gas partial pressures on the overpotential. Adding the same amount of  $N_2$  to the various gas partial pressures of  $O_2:CO_2:N_2$  (Table 3) gives overpotential differences ( $\Delta W = W_P - W_O$ ) related to the gas partial pressure. In this case,  $W_P$  is the voltage gap at a polarization state, and  $W_O$  is that at open-circuit state by  $N_2$  addition to the cathode as shown in Fig. 16. Thus  $\Delta W$  has the following relations:

$$\begin{aligned} \Delta W &= \eta_{ca,mt,L,2} - \eta_{ca,mt,L,1} \\ &= (R_{ca,mt,L,2} - R_{ca,mt,L,1}) \cdot i/a \end{aligned} \quad (34)$$

where subscripts 1 and 2 represent before and after  $N_2$  addition, respectively, and  $a$  is the

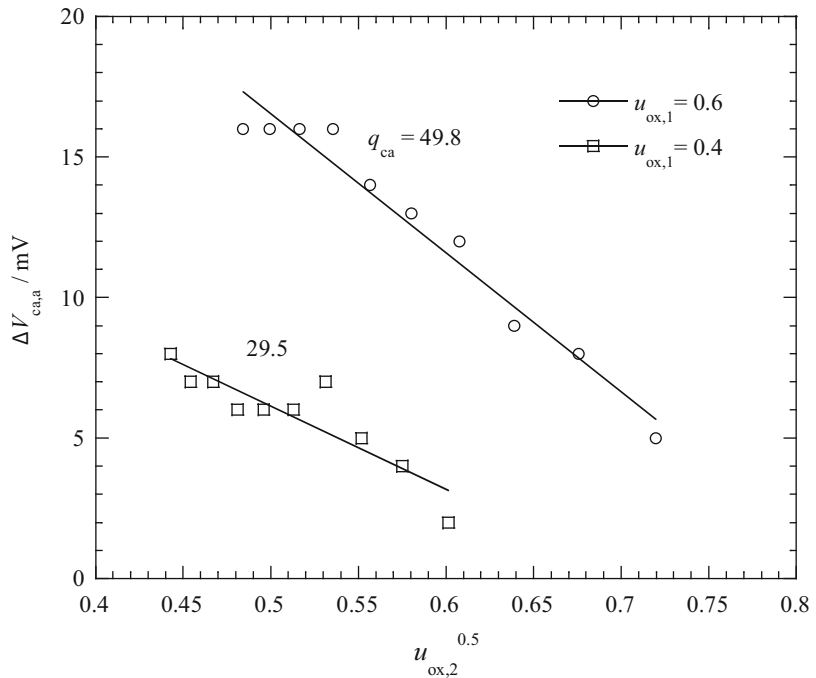
**Molten Carbonate Fuel Cells, Fig. 16**

Cathodic ISA results at different currents with nitrogen addition rate of  $0.3 \text{ L min}^{-1}$  at a cathode flow rate of  $0.589 \text{ L min}^{-1}$  and anode flow rate of  $0.756 \text{ L min}^{-1}$ ,  $923 \text{ K}$ ,  $1 \text{ atm}$ , *I*/0; *II* 50; *III* 100; *IV*  $150 \text{ mA cm}^{-2}$  (From Ref. [24])



**Molten Carbonate Fuel Cells, Fig. 17**

Rearrangement of the peak heights of “a” in Fig. 16 with shifted utilization according to Eq. 33 (From Ref. [24])



geometrical electrode area. Then  $\Delta W$  has a linear relation with gas partial pressure as in Eq. 35:

$$\begin{aligned}
 (\Delta W \cdot a/i)p(\text{CO}_2) &= (R_{ca,mt,L2} - R_{ca,mt,L1})p(\text{CO}_2) \\
 &= A'p(\text{O}_2)^{-0.75}p(\text{CO}_2)^{1.5} + B'
 \end{aligned}
 \tag{35}$$

where  $A' = A(\beta^{-0.25} - 1)$ ,  $B' = B(\beta^{-1} - 1)$ ,

$\beta = p(\text{O}_2)_2/p(\text{O}_2)_1$ ,  $A$  and  $B$  are the constants of Eq. 22, and the subscripts 1 and 2 represent before and after  $N_2$  addition, respectively.

When we assume that the cathode overpotential due to the mass transfer through the carbonate electrolyte is combined diffusion control of superoxide ions and  $\text{CO}_2$ , the overpotential is a function of gas partial pressure as shown in Eqs. 21 and 22.

Equation 35 shows a linear relation between the  $\Delta W$  and gas partial pressures. Figure 18 shows linearity of Eq. 35, indicating that the mass-transfer resistance through the electrolyte film causes cathodic overpotential. From Eq. 35 we can obtain  $A$  and  $B$  values. Then with Eq. 22 we can have  $R_{ca,mt,L}$  and  $\eta_{ca,mt,L}$  at a normal gas partial pressures of  $p(O_2) = 0.15$  atm and  $p(CO_2) = 0.3$  atm. The value of  $\eta_{ca,mt,L}$  under this condition is about 62 mV, which is much larger than  $\eta_{ca,G}(\approx 18\text{mV at } u_{ox} = 0.4)$  from Eq. 32. This means that overpotential at the electrolyte film is much larger than that at the gas phase and the cathodic reaction is mostly the liquid-phase mass-transfer control process.

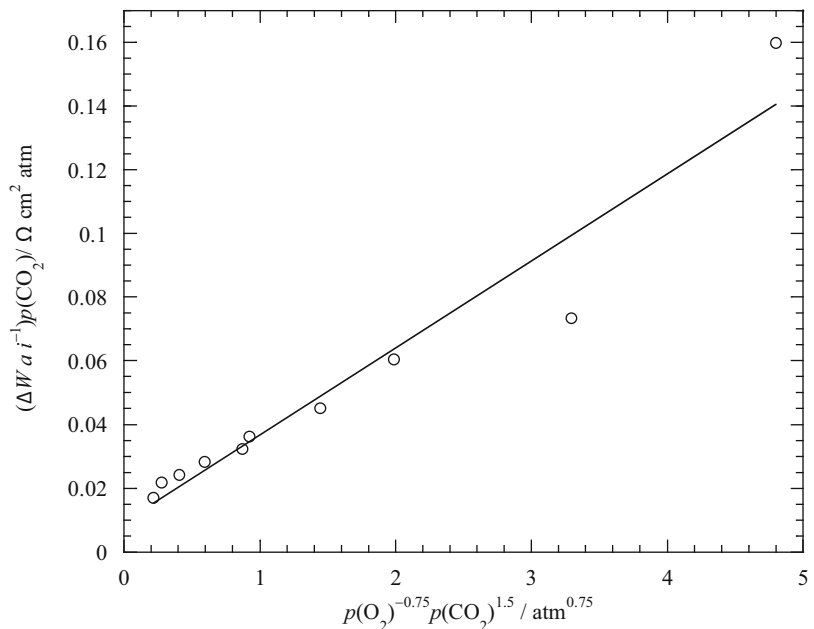
Therefore, total voltage loss can be estimated by the ISA method as shown in Table 4 [24]. The ohmic loss of the cell was 60 mV

**Molten Carbonate Fuel Cells, Table 3** Various compositions of the cathode gases

Gases	Ratio (atm)
O <sub>2</sub> :CO <sub>2</sub> :N <sub>2</sub>	0.9:0.1:0,
	0.7:0.3:0, 0.7:0.1:0.2,
	0.5:0.5:0, 0.5:0.3:0.2, 0.5:0.1:0.4,
	0.3:0.7:0, 0.3:0.5:0.2, 0.3:0.3:0.4,

**Molten Carbonate Fuel Cells,**

**Fig. 18** Relationships of the cathodic overpotentials with partial pressures of oxygen and CO<sub>2</sub> according to Eq. 35 at 923 K, 1 atm (From Ref. [24])



at  $150 \text{ mA cm}^{-2}$ . Considering some of experimental error, the voltage loss estimated by the ISA is very close to that by the experimental value with SSP.

**Temperature Effect on the Overpotential**

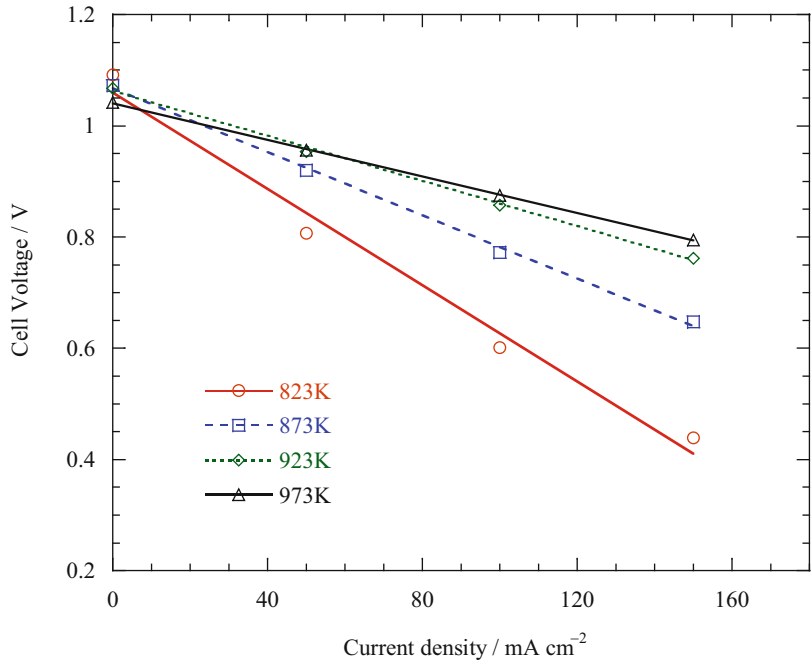
The MCFC runs at very high temperature around 923 K. In general, temperature affects the reaction kinetics and mass-transfer rate. Since the commercial MCFC has about 8,000 cm<sup>2</sup> of electrode area and it generates heat, temperature gradient should be along the flow direction. Investigation of the temperature effect is an important issue for the MCFC research.

Figure 19 shows the steady-state polarization at different temperature with a 100 cm<sup>2</sup> class MCFC single cell. The lowest temperature of 873 K has the highest  $E_{OCV}$  because the standard potential,  $E^o$ , becomes larger at lower temperature. However, the slope of 873 K is the steepest, indicating that internal resistance and reaction resistance at the electrodes are significantly large at the temperature. With increasing temperature, the slope becomes mild because the resistance is decreased. The open-circuit voltage,  $E_{OCV}$ , is also decreased with temperature rising.

**Molten Carbonate Fuel Cells, Table 4** Total voltage loss estimated by ISA and measured by SSP method (Fig. 3)

$u_f$	$\eta_{an,mt,G}/mV$	$u_{ox}$	$\eta_{ca,mt,G}/mV$	$\eta_{ca,mt,L}/mV$	Total voltage loss by ISA at $u_{ox} = 0.4/mV$	Measured total voltage loss by SSP (Fig. 3a)/mV
0.2	61.2	0.4	16.9	66.0	204.1	220.0
0.4	86.5				229.4	246.0
0.6	106.0				248.9	268.0
0.8	122.4				265.3	291.0

**Molten Carbonate Fuel Cells, Fig. 19** Current-voltage behaviors up to  $150\text{ mA cm}^{-2}$  with an anode flow rate of  $0.254\text{ L min}^{-1}$  and a cathode flow rate of  $0.883\text{ L min}^{-1}$  at 1 atm in the temperature range from 823 to 973 K [47]



However, the steady-state polarization in Fig. 19 cannot show the temperature effect of each electrode on the overpotential. Figure 20 shows the AC impedance results at different temperatures. As mentioned at the section “AC Impedance” the HFC represents the cathodic mass-transfer resistance through the electrolyte film, whereas the LFC does the mass-transfer resistance through the boundary layer in the gas channel. Since the anodic boundary layer is much thicker than that of cathode due to the smaller gas flow, the LFC mostly reflects the gas-phase mass-transfer effect at the anode. Then we can suppose from Fig. 20, the internal resistance and cathodic resistance decrease with the temperature rising. This is acceptable that the ionic conductivity in

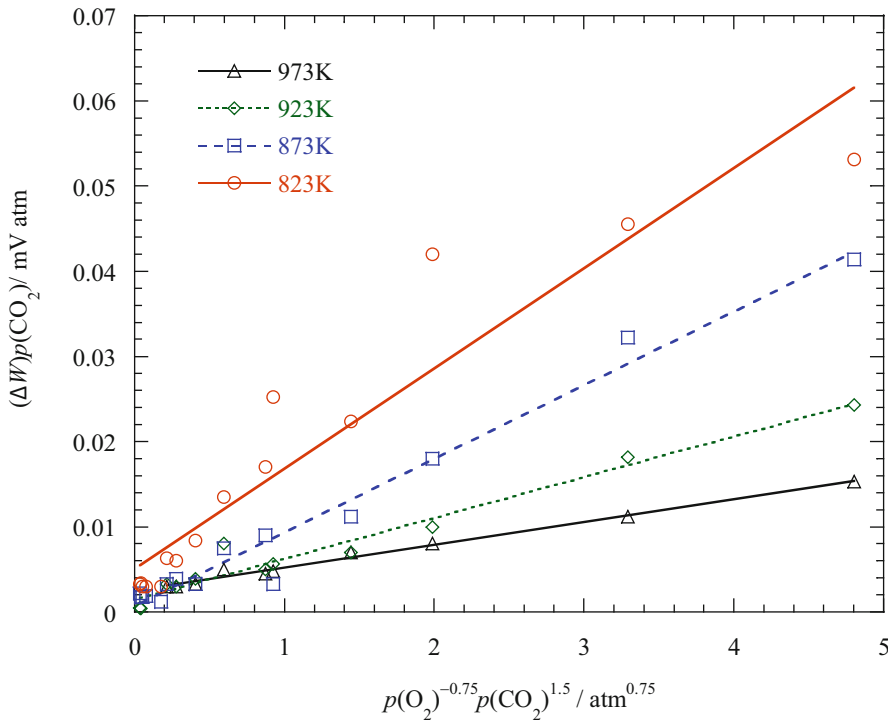
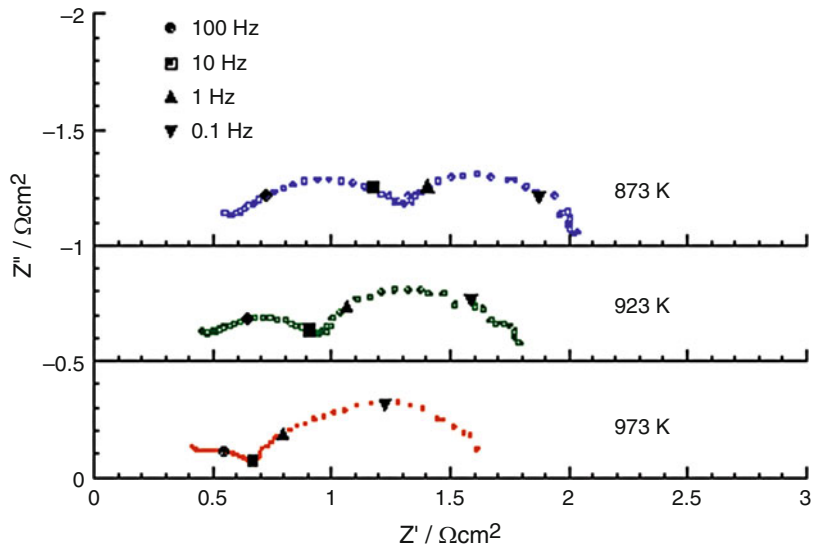
the carbonate electrolyte and the gas solubility and diffusivity rise with temperature. However, the LFC indicating mostly anodic mass-transfer resistance is enlarged with temperature rising. This is a very unique behavior reported recently [48]. In here, the cathodic and anodic overpotential by the temperature rising is investigated serially.

**Cathodic Overpotential** The gas-phase mass-transfer resistance at the cathode is much smaller than the liquid-phase one [24], and  $\eta_{ca, mt, G}$  (a  $u_{ox} = 0.4$ ) 873, 923, 973 K are reported as 30.4, 30.8, and 37.6 mV, respectively, in [47]. Although the values are larger than that in Table 4, it is much less than that of the anode which is about 100 mV



### Molten Carbonate Fuel Cells, Fig. 20

AC impedance results of the anode flow rate of  $0.380 \text{ L min}^{-1}$  and cathode flow rate of  $0.883 \text{ L min}^{-1}$  in open-circuit state at 1 kHz to 0.01 Hz and 5 mV rms in the temperature range from 873 to 973 K [48]



**Molten Carbonate Fuel Cells, Fig. 21** Plot of Eq. 35 obtained  $\Delta W$  at various cathode gas compositions of Table 3 in the temperature range 823–973 K [47]

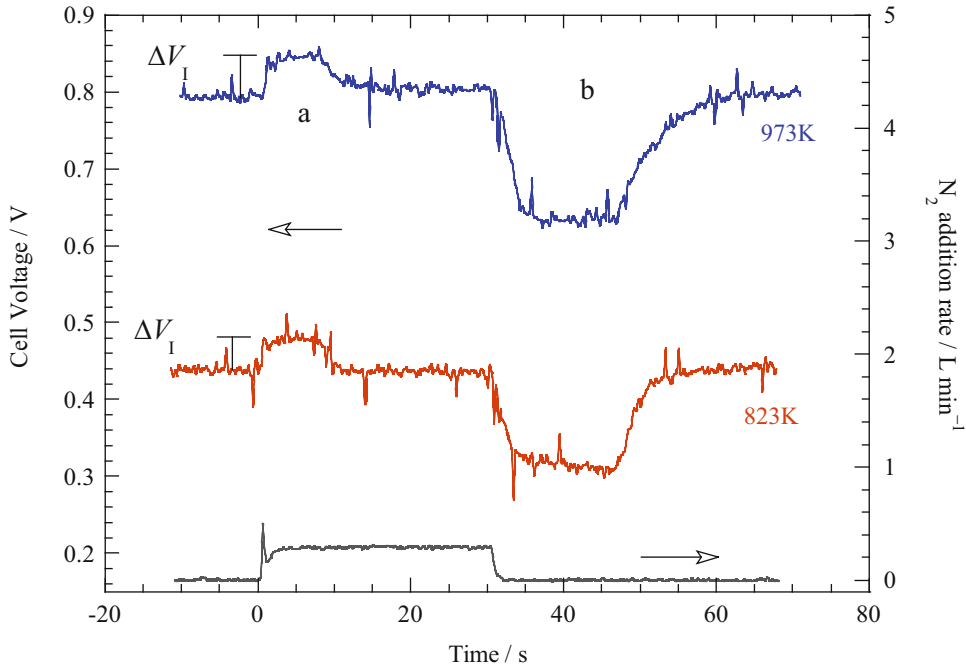
as in the table. In particular,  $\eta_{ca,mt,G}$  does not clearly show temperature effect as in Ref. [47].

On the other hand, the relation of Eq. 35 clearly showed the temperature effect. Figure 21 shows the relation of Eq. 35 at different temperatures.

From the figure, the parameters of  $A'$ ,  $B'$ ,  $A$ , and  $B$  could be obtained (Table 5). Definitely  $\eta_{ca,mt,L}$  is decreased by the temperature rising because the enlarged diffusivity and solubility of reactant species. Thus the impedance behavior of HFC in

**Molten Carbonate Fuel Cells, Table 5** Slopes  $A'$  and intercept  $B'$  from Fig. 21 and calculated  $A$  and  $B$  values and obtained  $\eta_{ca, mt, L}(=i \times R_{ca, mt, L})$  at the various temperatures from Eq. 22 [47]

Temp./K	$A'$	$B'$	$A$	$B$	$\eta_{ca, mt, L}/mV$
823	0.0117720	0.0050783	0.084900	0.0007461	217.0
873	0.0086447	0.0007069	0.062374	0.0010385	145.3
923	0.0047780	0.0015128	0.034474	0.0022220	85.8
973	0.0002670	0.0025539	0.019264	0.0037520	56.4



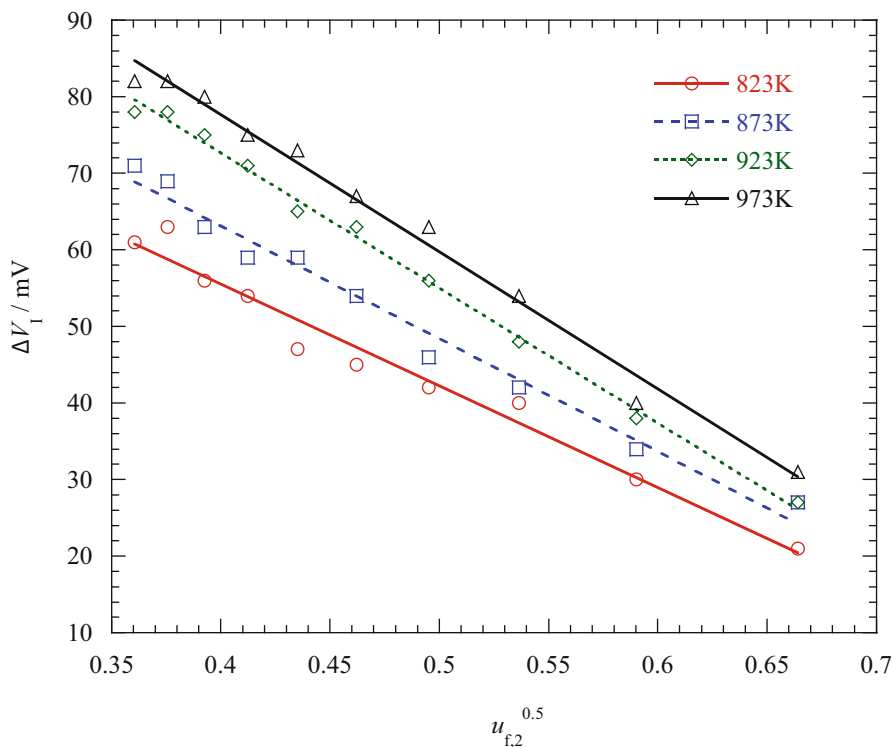
**Molten Carbonate Fuel Cells, Fig. 22** ISA results by the addition of  $0.3 \text{ L min}^{-1}$  of  $\text{N}_2$  to the anode at  $u_f = 0.6(0.254 \text{ L min}^{-1})$ ,  $u_{ox} = 0.4(0.883 \text{ L min}^{-1})$ , current density of  $150 \text{ mA cm}^{-2}$ , and temperatures of 823 and 973 K [48]

Fig. 20 which represents reduced mass-transfer resistance through the electrolyte film at higher temperature is acceptable.

**Anodic Overpotential** Contrary to the HFC-representing cathodic overpotential in Fig. 20, the LFC-reflecting anodic overpotential is enlarged by the temperature rising. Since the anodic overpotential is mostly due to the mass-transfer resistance in the gas phase, it means that the anodic mass-transfer resistance is increased by the temperature rising. Identical behavior that anodic overpotential increase by the temperature rising is obtained with ISA measurement. Figure 22 shows the ISA results at 823 K and

873 K at the anode. Similar to Fig. 14, two of “a” and “b” peaks are observed. When we compare the “a” peaks at 823 K and 973 K, the “a” peak at 973 K is clearly larger than that at 823 K.

Using Eq. 31 the anodic overpotential at 1.0 of utilization,  $q_{an}$ , can be obtained as shown in Fig. 23 which represents clear dependence of  $q_{an}$  on temperature. Larger  $q_{an}$  value at higher temperature is clearly observed (Table 6), which indicates that the anodic overpotential rises with temperature. It is in line with the results of impedance in Fig. 20 where the LFC is enlarged by the temperature rising. But this is an unexpected result because the mass-transfer rate generally has positive relation with the temperature.



**Molten Carbonate Fuel Cells, Fig. 23** Plot of  $\Delta V_f$  shown in Fig. 22 versus  $u_{f,2}^{0.5}$  according to Eq. 31 [48]

**Molten Carbonate Fuel Cells, Table 6**  $q_{an}$  values from Fig. 23

Temperature (K)	$q_{an}$ (mV)
823	132.9
873	149.1
923	176.1
973	179.1

As mentioned in Ref. [48], there are several possibilities in the larger anodic overpotential at higher temperature. One possibility is water-gas-shift reaction in the anode gas. The temperature rising may reduce the  $H_2$  concentration in the gas because the equilibrium constant of Eq. 3b decreases with temperature rising. However, the  $H_2$  flow rate has only  $0.005 \text{ L min}^{-1}$  of difference between 873 and 973 K. They concluded that it is too small to bring about the change in Fig. 20. Second possibility is the change of electrolyte film thickness by the temperature rising. Since the contact angle of carbonate under  $H_2$  environment is

reduced at higher temperature, thicker electrolyte film is expected at higher temperature. If the film thickness may affect the overpotential, the partial pressure should be an important parameter. However, the effect of film thickness at the anode is negligible based on the result that the anodic overpotential depends not on the gas partial pressure but on the gas diffusivity [24]. Thus the effect of film thickness is excluded. The last possibility is the pore diffusion resistance (PDR) which is considered at the catalytic reaction. Since the anode has ca.  $3 \mu\text{m}$  diameter of porous structure where most of reaction takes place and generates product gases, it is very similar to the catalytic reaction. In general, the PDR becomes severe at higher temperature because the increased reaction rate inside pores disturbs gas diffusion through the pore. This can explain the enlarged mass-transfer resistance at the anode by the temperature rising. The PDR effect is expressed by effectiveness factor,  $\varepsilon$  as in Eq. 36:

$$\begin{aligned} \varepsilon &= \frac{1}{\phi} \\ &= \frac{\text{Overpotential without pore diffusion resistance}(\eta_T)}{\text{Overpotential without pore diffusion resistance}(\eta_P)} \end{aligned} \quad (36)$$

where  $\phi$  is the Thiele modulus,  $\phi = L_P \sqrt{\frac{k_0}{D_e r}}$ , and overpotential without PDR ( $\eta_T$ ) is substituted by Eq. 16,  $\eta_T = \frac{iRT}{n^2 F^2 a p_0} \left( \frac{h}{k_0} + \frac{h}{k_L} + \frac{RT}{k_G} \right)$ . Therefore, the overpotential with PDR ( $\eta_P$ ) is expressed by Eq. 37:

$$\eta_P = i \frac{RT}{n^2 F^2 a \cdot p_0} \left( \frac{h}{k_0} + \frac{h}{k_L} + \frac{RT}{k_G} \right) \left( L_P \sqrt{\frac{k_0}{D_e r}} \right) \quad (37)$$

Thus the anodic overpotential relations of Eqs. 18 and 30 are to be Eq. 38:

$$\begin{aligned} \eta_{an} &\cong \eta_{an,mt,G} \\ &= \frac{iR^2 T^2}{n^2 F^2 a p_0} \left( \frac{1}{k_{an,G}} \right) \left( L_P \sqrt{\frac{k_0}{D_e r}} \right) \\ &= \frac{iR^2 T^2}{n^2 F^2 a p_0} \left( \frac{1}{k_{an,G}} \right) \phi = q_{an} u^{0.5} \end{aligned} \quad (38)$$

where  $q_{an} = 1.51 \frac{R^2 T^2 (i \cdot s \cdot L)^{1/2} v^{1/6} \phi}{a \cdot (nF)^{3/2} p_0^{1/2} D_G^{2/3}}$ .

Thus higher temperature has larger  $k_0$  although  $k_{an,G}$  and  $D_e$  are also enlarged. But the temperature dependence of  $k_0$  is much larger than those of  $k_{an,G}$  and  $D_e$ ; thus  $\eta_{an}$  becomes larger at higher temperature. More details of this relation are described in a previous work [48].

### Overpotential Relations

The above results show that the anodic overpotential is mostly attributed to the gas-phase mass-transfer resistance ( $\eta_{an,mt,G}$ ) and additionally to the pore diffusion resistance. Thus larger anodic overpotential is obtained at higher temperature. On the other hand, the cathodic overpotential is a sum of overpotential due to the gas-phase resistance ( $\eta_{ca,mt,G}$ ) and liquid-phase resistance ( $\eta_{ca,mt,L}$ ). In particular,  $\eta_{ca,mt,L}$  is much larger than  $\eta_{ca,mt,G}$ , thus the pore diffusion resistance is not dominant at the cathode. The temperature significantly reduces  $\eta_{ca,mt,L}$  as in Ref. [24]; less cathodic overpotential is

obtained at higher temperature. Thus the following relation can be suggested:

$$\eta_{an} \cong \eta_{an,mt,G} = q_{an} \cdot u_f^{0.5} \quad (39a)$$

$$\begin{aligned} \eta_{ca} &\cong \eta_{ca,mt,G} + \eta_{ca,mt,L} \\ &= q_{ca} \cdot u_{ox}^{0.5} + A'' \\ &\quad \cdot p(\text{O}_2)^{-0.75} p(\text{CO}_2)^{0.5} + B'' \\ &\quad \cdot p(\text{CO}_2)^{-1} \end{aligned} \quad (39b)$$

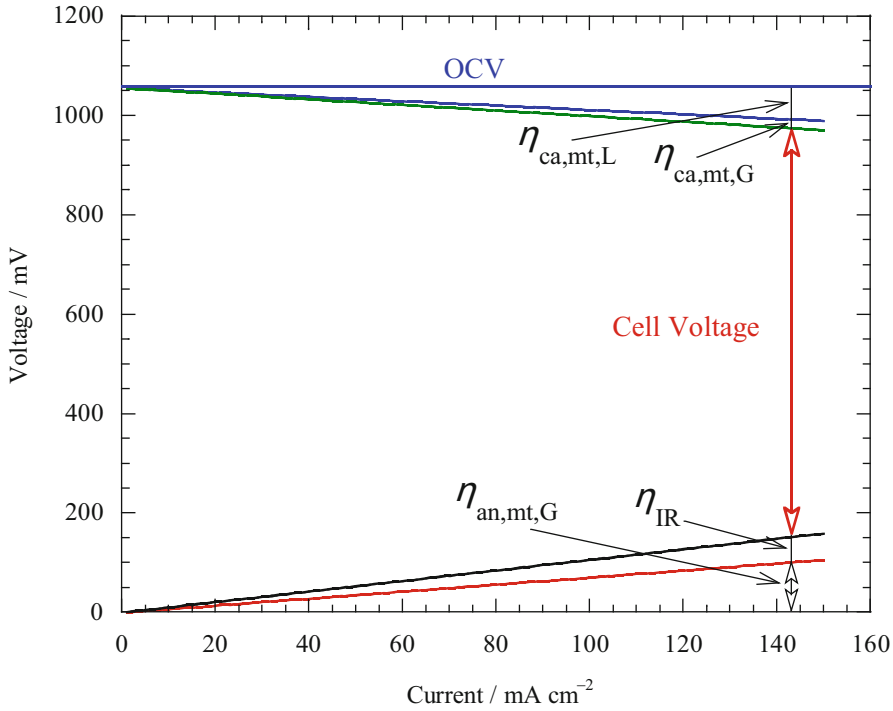
where  $q_{an}$  and  $q_{ca}$  are the constants of Eqs. 38 and 32, respectively,  $A'' = A \cdot i/a$  and  $B'' = B \cdot i/a$ , and  $A$  and  $B$  are the constants of Eq. 22. Figures 24 and 25 show the overpotential behaviors with current density and utilization, respectively.

### Reactant Gas Addition (RA) Method

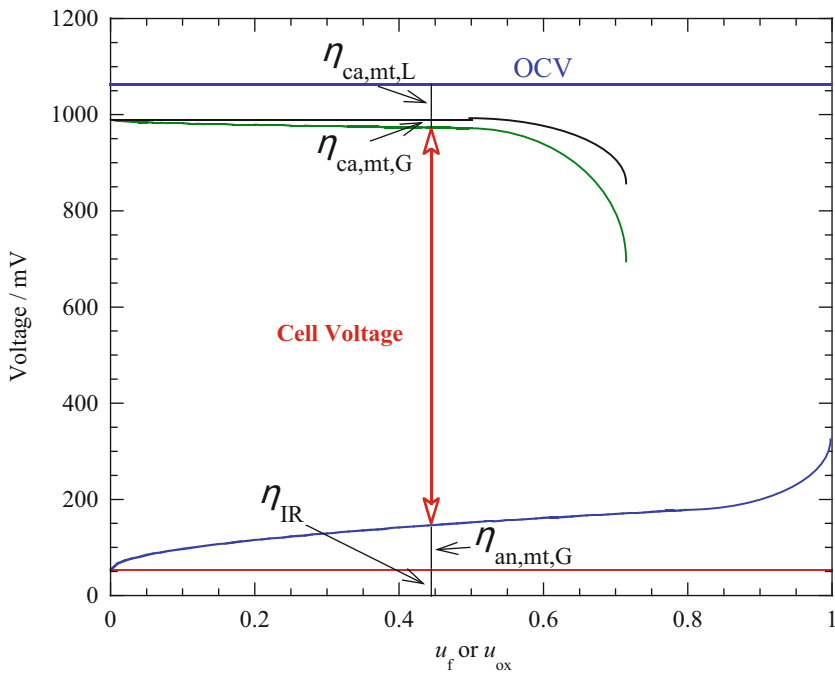
The cathodic overpotential from the ISA method, the sum of  $\eta_{ca,mt,L}$  and  $\eta_{ca,mt,G}$ , is only 80 mV at  $u_{ox} = 0.4$  [24]. This is smaller than the anodic overpotential from the method at  $u_f = 0.4$ , which is about 90 mV according to Eq. 30. This is contradictory to the conventional concept that the cathodic overpotential is larger than the anodic one because of the slow oxygen reduction at the cathode.

Meanwhile, the anode and cathode reactions of Eq. 1a and 1b are multicomponent reaction systems. As mentioned regarding the ISA method, the anode and cathode reactions are mass-transfer control processes. Then the mass-transfer of each species would provide overpotential due to the species. To investigate the overpotential attributed to each species, the reaction gas addition method was attempted. This is very similar to the ISA except that a reactant gas is added to an electrode instead of an inert gas [44]. Figure 26 shows the voltage behaviors due to the addition of a reactant gas. Here, the subscript A denotes a reactant gas species.

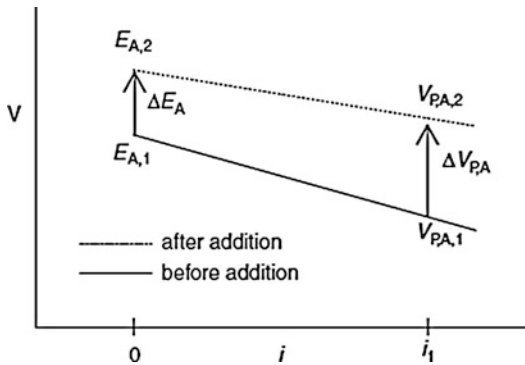
When a certain amount of a reactant gas is added to an electrode at the open-circuit state, the addition changes the partial pressures of the cell and determines  $E_{OCV}$  according to Eq. 12. When the same amounts of reactant gas are added at a polarization state, the voltage is varied by overpotential according to Eq. 13. Thus the gap ( $\Delta V_A$ ) between the voltage shift at the open-circuit



**Molten Carbonate Fuel Cells, Fig. 24** Cell voltage and voltage losses of 100 cm<sup>2</sup> class MCFC as a function of current density with the relations of Eq. 39a and 39b at  $u_f = 0.6$ ,  $u_{ox} = 0.4$ , 1 atm, and 923 K



**Molten Carbonate Fuel Cells, Fig. 25** Cell voltage and voltage losses of 100 cm<sup>2</sup> class MCFC as a function of anodic utilization ( $u_f$ ) and cathodic utilization ( $u_{ox}$ ) with the relations of Eq. 39a and 39b at 1 atm and 923 K



**Molten Carbonate Fuel Cells, Fig. 26** Schematic drawings of voltage-shift behaviors by the addition of a reactant gas at open-circuit ( $\Delta E_A$ ) and polarization states ( $\Delta V_{P,A}$ ) (From Ref. [44])

state ( $\Delta E_A$ ) and at a polarization state ( $\Delta V_{P,A}$ ) is overpotential variation due to the addition:

$$\Delta V_A = \Delta V_{P,A} - \Delta E_A \quad (40)$$

where  $\Delta V_{P,A} = V_{P,2} - V_{P,1}$  and  $\Delta E_A = E_{OCV,2} - E_{OCV,1}$ . When  $\Delta V_A > 0$ , the addition mitigates mass-transfer resistance at the electrode. On the contrary,  $\Delta V_A < 0$  indicates that the addition enlarges the resistance. When  $\Delta V_A = 0$ , the addition does not affect the resistance.

#### Effect of Reactant's Flow Rate

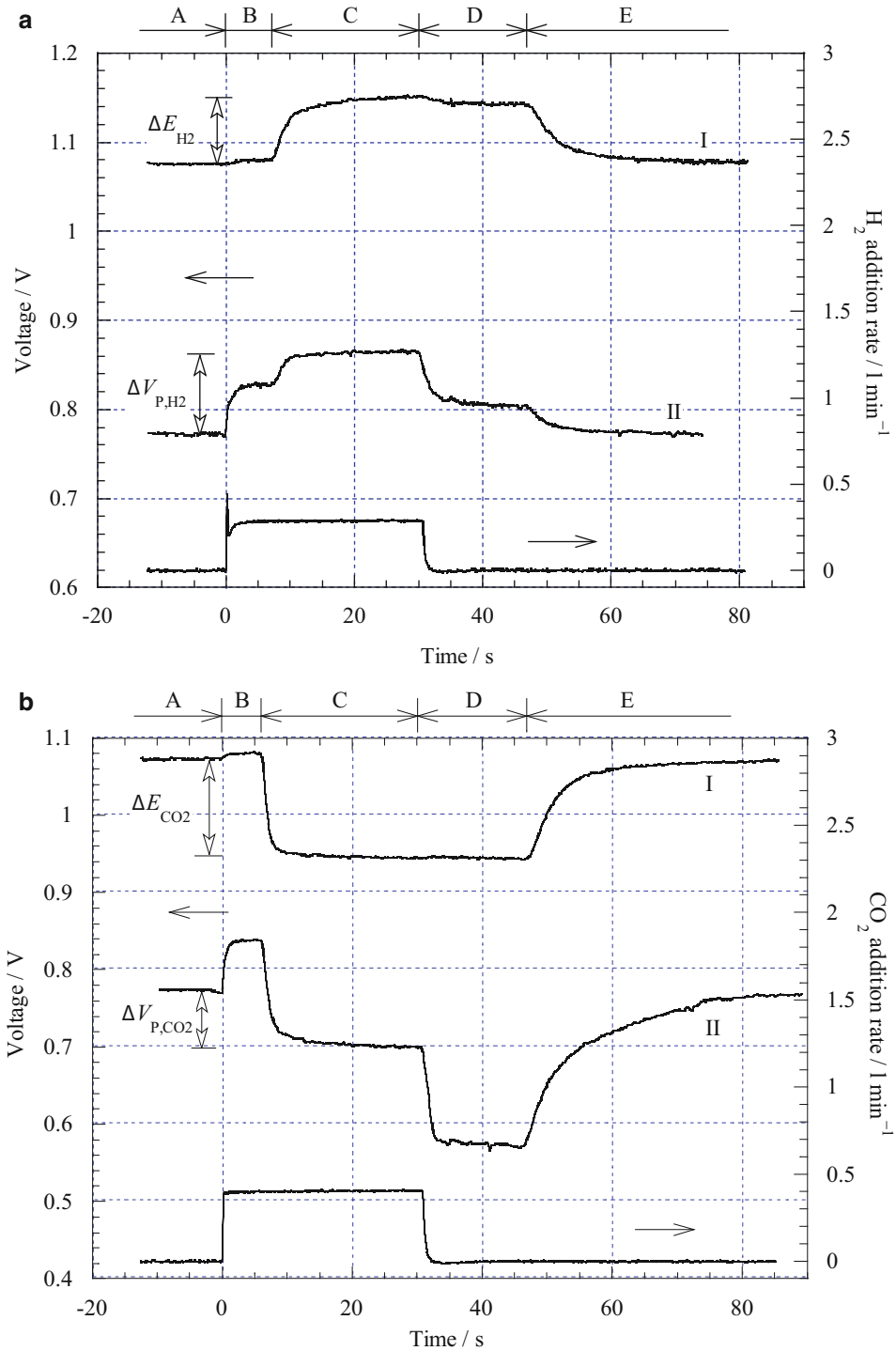
Figure 27a shows RA results with  $H_2$  addition to the anode. At the open-circuit state (curve I) the added  $H_2$  flows inside the cell in the “C” and “D” time regions, which results in a partial pressure and  $E_{OCV}$  increase in these regions. At a polarization state of  $150 \text{ mA cm}^{-2}$  (curve II) two positive voltage steps in the “B” and “C” time regions are observed. The step in the “B” region is due to the increase in flow rate of reactant gases due to the  $H_2$  addition, which is the same as the reason for the positive voltage peak obtained with the ISA method. For the “C” region, the enlarged  $H_2$  flow rate results in the second voltage step, which involves a change in overpotential due to the addition. The voltage shift of curve II ( $\Delta V_{P,H_2}$ ) is larger than that at the open-circuit state ( $\Delta E_{OCV}$ ). In principle, the gas inlet conditions for the two curves are identical. Thus the difference ( $\Delta V_{H_2}$ ) represents variation in overpotential due to the  $H_2$

addition. It results in a positive  $\Delta V_{H_2}$  according to Eq. 40, which shows that  $H_2$  addition reduces the anodic overpotential. It also implies that the anode has overpotential due to the mass-transfer resistance of  $H_2$  species. However, the behavior can provide information on overpotential due to  $H_2$  species through  $\Delta V_{H_2}$ . When the  $H_2$  addition rate was varied from  $0.1$  to  $0.6 \text{ L min}^{-1}$ ,  $\Delta V_{H_2}$  showed consistency in the rates as shown in Fig. 28. This means that the resistance due to the  $H_2$  species is sufficiently reduced by the addition, and then a consistent  $\Delta V_{H_2}$  is obtained. In addition, when anodic utilization,  $u_f$ , is increased,  $\Delta V_{H_2}$  is enlarged [44]. This also implies that anodic overpotential depends on the  $H_2$  flow rate; a lower  $H_2$  flow rate has a larger anodic overpotential.

Figure 27b shows the results of  $CO_2$  addition to the anode. Indeed,  $CO_2$  is a product species of the anode reaction as shown in Eq. 1a. Thus the  $CO_2$  addition reduces  $E_{OCV}$  according to Eq. 12. At open-circuit state, the reduced  $E_{OCV}$  is observed due to the  $CO_2$  addition in the “C” and “D” time regions. At a current density of  $150 \text{ mA cm}^{-2}$ , two voltage peaks are observed; like the voltage peaks obtained using the ISA method, the change in flow rate of anode gas is responsible. The voltage shift due to the addition at the current density ( $\Delta V_{P,CO_2}$ ) is much smaller than that at the open-circuit state ( $\Delta E_{CO_2}$ ). Since those values are negative, the difference ( $\Delta V_{CO_2}$ ) is a positive value. This indicates that  $CO_2$  addition to the anode reduces anodic overpotential. This can be explained by the reaction kinetics of Eq. 8, where the reaction rate has a positive order for the  $CO_2$  species. Therefore raising the  $CO_2$  partial pressure reduces anodic overpotential [44]. Analysis of overpotential with various anode gas compositions shows identical overpotential behavior, whereby increasing  $CO_2$  partial pressure reduces anodic overpotential [49].

Dissimilar to the  $H_2$  addition,  $\Delta V_{CO_2}$  depends on the amount of  $CO_2$  addition (Fig. 29). Furthermore,  $\Delta V_{CO_2}$  values are much larger than  $\Delta V_{H_2}$ , which implies that  $CO_2$  species has higher mass-transfer resistance than  $H_2$  species and anodic overpotential is more dependent on the  $CO_2$  flow rate. The  $CO_2$  addition reduces the resistance, and thus  $\Delta V_{CO_2}$  rises with  $CO_2$  addition amounts as





**Molten Carbonate Fuel Cells, Fig. 27** Results of the RA measurement at the anode with conditions of 923 K, 1 atm at open-circuit state (I) and polarization state of 150 mA cm<sup>-2</sup> (From Ref. [44]). (a) 0.3 L min<sup>-1</sup> H<sub>2</sub> addition, (b) 0.4 L min<sup>-1</sup> CO<sub>2</sub> addition, anode feed rate = 0.253 L min<sup>-1</sup> ( $u_f = 0.6$  at 150 mA cm<sup>-2</sup>), and cathode feed rate = 0.883 L min<sup>-1</sup> ( $u_{ox} = 0.4$  at 150 mA cm<sup>-2</sup>) (From Ref. [44]).

shown in Fig. 29. At certain amounts, from 0.4 to 0.5 L min<sup>-1</sup>,  $\Delta V_{\text{CO}_2}$  has a maximum value. This indicates that the mass-transfer resistance due to the CO<sub>2</sub> species becomes a minimum. Over the amounts the CO<sub>2</sub> species rather signifies the resistance probably due to reducing the mass transfer of H<sub>2</sub> species. Then  $\Delta V_{\text{CO}_2}$  decreases again.  $\Delta V_{\text{CO}_2}$  also depends on the anodic utilization; higher utilization shows larger overpotential. Similarly to the H<sub>2</sub> addition, this indicates that the anode reaction is a mass-transfer control process of CO<sub>2</sub>.

The H<sub>2</sub>O addition also decreased anodic overpotential [44]. The anode gas was humidified with a bubbler which contained water at a certain temperature. Then the partial pressure of H<sub>2</sub>O was controlled by the water temperature in the bubbler. The anodic overpotential decreased monotonously with the increase in H<sub>2</sub>O content [44], although the H<sub>2</sub>O addition reduced  $E_{\text{OCV}}$  according to Eq. 13. In addition,  $\Delta V_{\text{H}_2\text{O}}$  rose with the anodic utilization, which was given larger overpotential by the low H<sub>2</sub>O flow rate. The positive order of H<sub>2</sub>O partial pressure in Eq. 8 is also the reason for the overpotential behavior.

The above results indicate that anode gases of H<sub>2</sub>, CO<sub>2</sub>, and H<sub>2</sub>O provide overpotential due to their mass-transfer limitations. Moreover, the anodic overpotential rises with utilization. These results indicate that the anode reaction is a mass-transfer control process of the species and that the anodic overpotential is a sum of overpotentials due to the mass-transfer resistance of the species. Interestingly  $\Delta V_{\text{CO}_2}$  and  $\Delta V_{\text{H}_2\text{O}}$  are much larger than  $\Delta V_{\text{H}_2}$  under normal operating conditions. The low flow rate of CO<sub>2</sub> and H<sub>2</sub>O under the condition (H<sub>2</sub>:CO<sub>2</sub>:H<sub>2</sub>O = 0.69:0.17:0.14 atm) can be a reason [44].

Figure 30a shows RA results with O<sub>2</sub> addition to the cathode. At open-circuit state the O<sub>2</sub> addition slightly enhances  $E_{\text{OCV}}$ . However, at a current density of 150 mA cm<sup>-2</sup>, a very high voltage shift ( $\Delta V_{P,\text{O}_2}$ ) is observed. The small step at 0 s originates from the increase in the flow of reactant gases due to the addition. As mentioned in the section on ISA, the cathode has very small mass-transfer resistance in the gas phase, and thus the height is rather small. Therefore, we can expect a

large difference ( $\Delta V_{\text{O}_2} = \Delta V_{P,\text{O}_2} - \Delta E_{\text{O}_2}$ ) between voltage shifts at open-circuit state ( $\Delta E_{\text{O}_2}$ ) and at polarization state ( $\Delta V_{P,\text{O}_2}$ ). This shows that the cathode has significant overpotential due to the O<sub>2</sub> species and the cathode reaction is an oxygen mass-transfer limitation process. From the half-cell experiments, it was also suggested that the mass-transfer limitation of O<sub>2</sub> species prevails at the cathode [50].

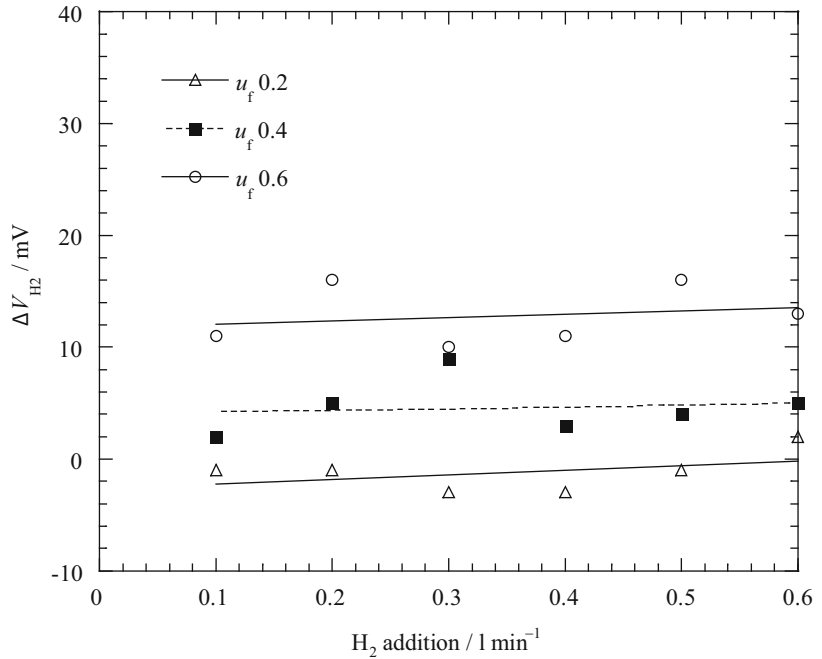
The CO<sub>2</sub> addition to the cathode enhances  $E_{\text{OCV}}$  according to Eq. 12 as shown in Fig. 30b. This is a very similar behavior to the O<sub>2</sub> addition. At a current density of 150 mA cm<sup>-2</sup>, the CO<sub>2</sub> addition gives rise to the two voltage peaks. As mentioned in the section on the ISA method, these are ascribed to the change in cathode flow rate due to the addition; the positive one is due to the increase in flow rate, and the negative one is due to the decrease in flow rate. A dominant feature is that the voltage difference at the current density,  $\Delta V_{P,\text{CO}_2}$ , is almost zero. This means that  $\Delta V_{\text{CO}_2}$  is a negative value and the CO<sub>2</sub> addition to the cathode enlarges cathodic overpotential. Considering that CO<sub>2</sub> has about ten times the gas solubility of O<sub>2</sub> in the molten carbonate and that the mass-transfer resistance of O<sub>2</sub> species is dominant at the cathode, it is plausible that the CO<sub>2</sub> addition reduces O<sub>2</sub> partial pressure and enhances the resistance of O<sub>2</sub> species in the carbonate electrolyte. Consequently, the CO<sub>2</sub> species may not provide cathodic overpotential under normal operating conditions due to its high solubility.

#### Temperature Effect

The temperature effect on the cathodic overpotential has been investigated with ISA method as shown in Fig. 21. The overpotential value of  $\eta_{\text{ca,mt,L}}$  has been decreased by the temperature rising as seen in Table 5. The reduction of  $\eta_{\text{ca,mt,L}}$  by the temperature rising is attributed to the increase of gas solubility and diffusivity. The identical behaviors are observed with RA method. Figure 31 shows the relation of Eq. 40 by the addition of O<sub>2</sub> (a) and CO<sub>2</sub> (b) to the cathode. The positive values of  $\Delta V_{\text{O}_2}$  mean that the cathode has significant mass-transfer resistance due to O<sub>2</sub> species. In addition, less  $\Delta V_{\text{O}_2}$  at higher

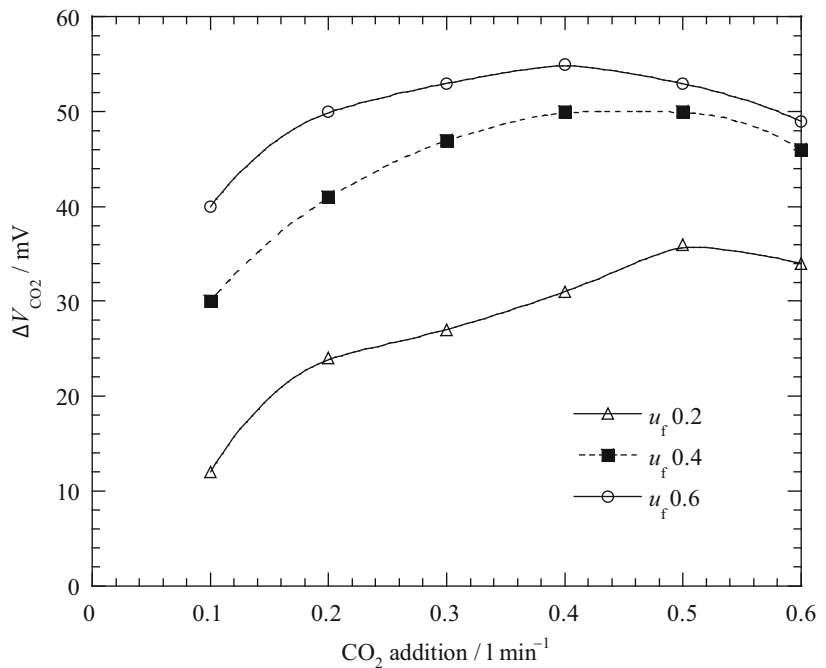
**Molten Carbonate Fuel Cells, Fig. 28**  $\Delta V_{H_2}$

behavior with respect to the  $H_2$  addition amount at the various anode utilizations at 923 K, 1 atm, cathode feed rate = 0.883 L min<sup>-1</sup> (From Ref. [44])



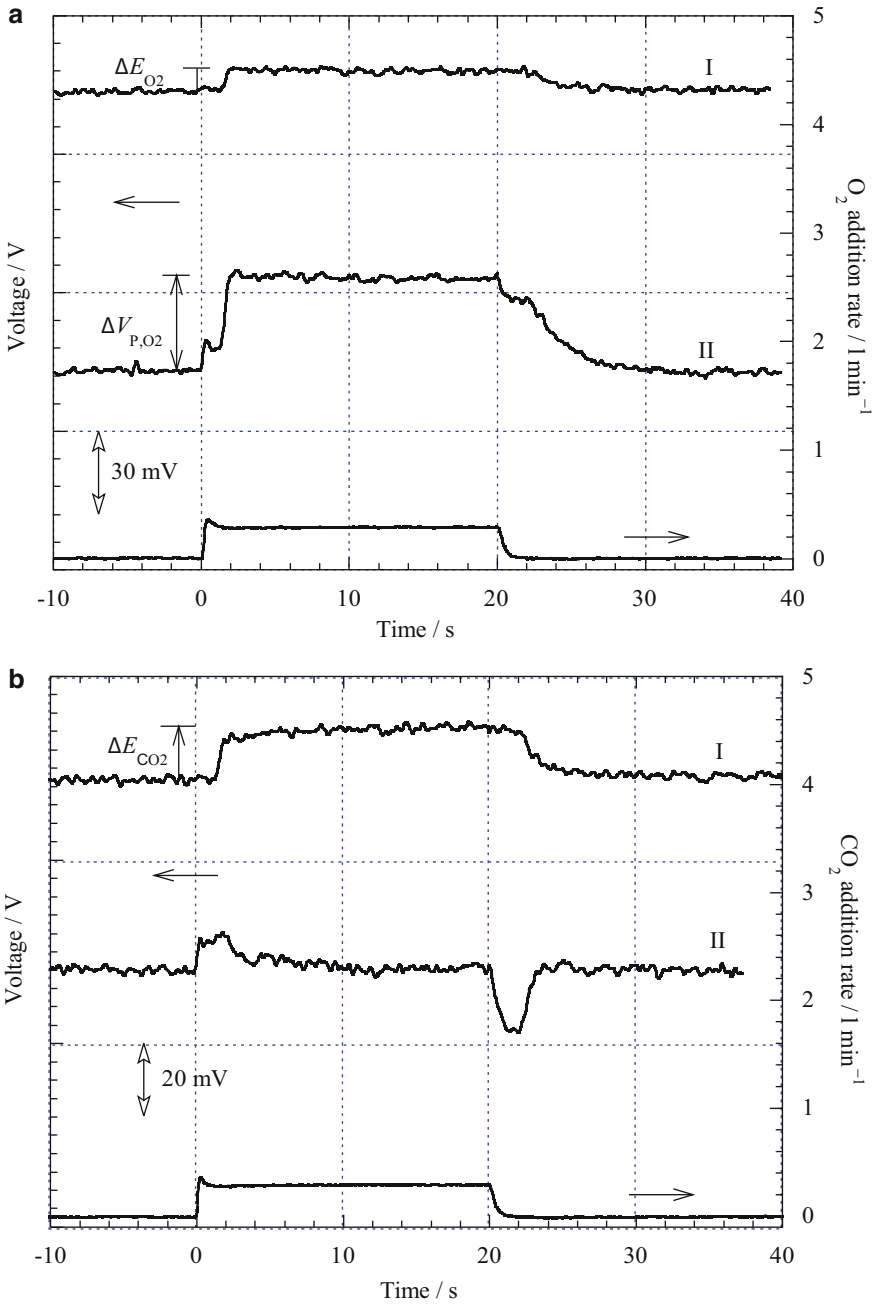
**Molten Carbonate Fuel Cells, Fig. 29**  $\Delta V_{CO_2}$

behavior with respect to the  $CO_2$  addition amount at various utilizations of anode gas at 923 K, 1 atm, cathode feed rate = 0.883 L min<sup>-1</sup> (From Ref. [44])



temperature is observed. At 823 K, about 150 mV of  $\Delta V_{O_2}$  is obtained, whereas only about 30 mV of  $\Delta V_{O_2}$  does at 973 K. The steep decrease of  $\Delta V_{O_2}$  is very similar to the decrease pattern of  $\eta_{ca,mt,L}$  in

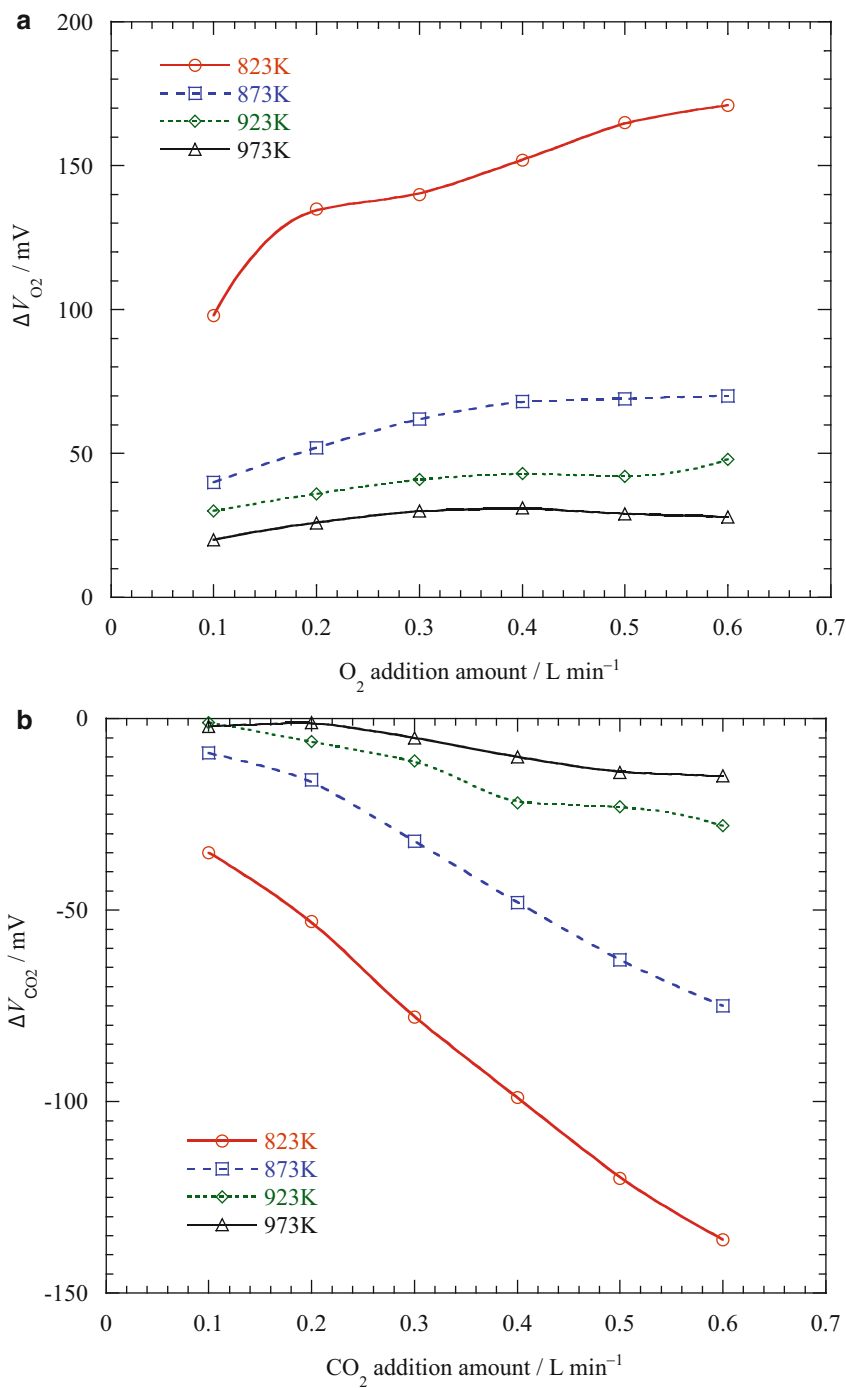
Table 5. This represents that the temperature rising enhances  $O_2$  solubility and diffusivity in the carbonate film and reduces overpotential due to the species. On the contrary,  $\Delta V_{CO_2}$  have negative



**Molten Carbonate Fuel Cells, Fig. 30** Results of RA measurement at the cathode with conditions of 923 K, 1 atm at open-circuit state (I) and 150 mA cm<sup>-2</sup> polarization state (II), anode feed rate = 0.759 L min<sup>-1</sup> ( $u_f = 0.2$  at 150 mA cm<sup>-2</sup>), and cathode feed rate = 0.883 L min<sup>-1</sup> ( $u_{ox} = 0.4$  at 150 mA cm<sup>-2</sup>) (From Ref. [44]). (a) 0.3 L min<sup>-1</sup> O<sub>2</sub> addition, (b) 0.3 L min<sup>-1</sup> CO<sub>2</sub> addition

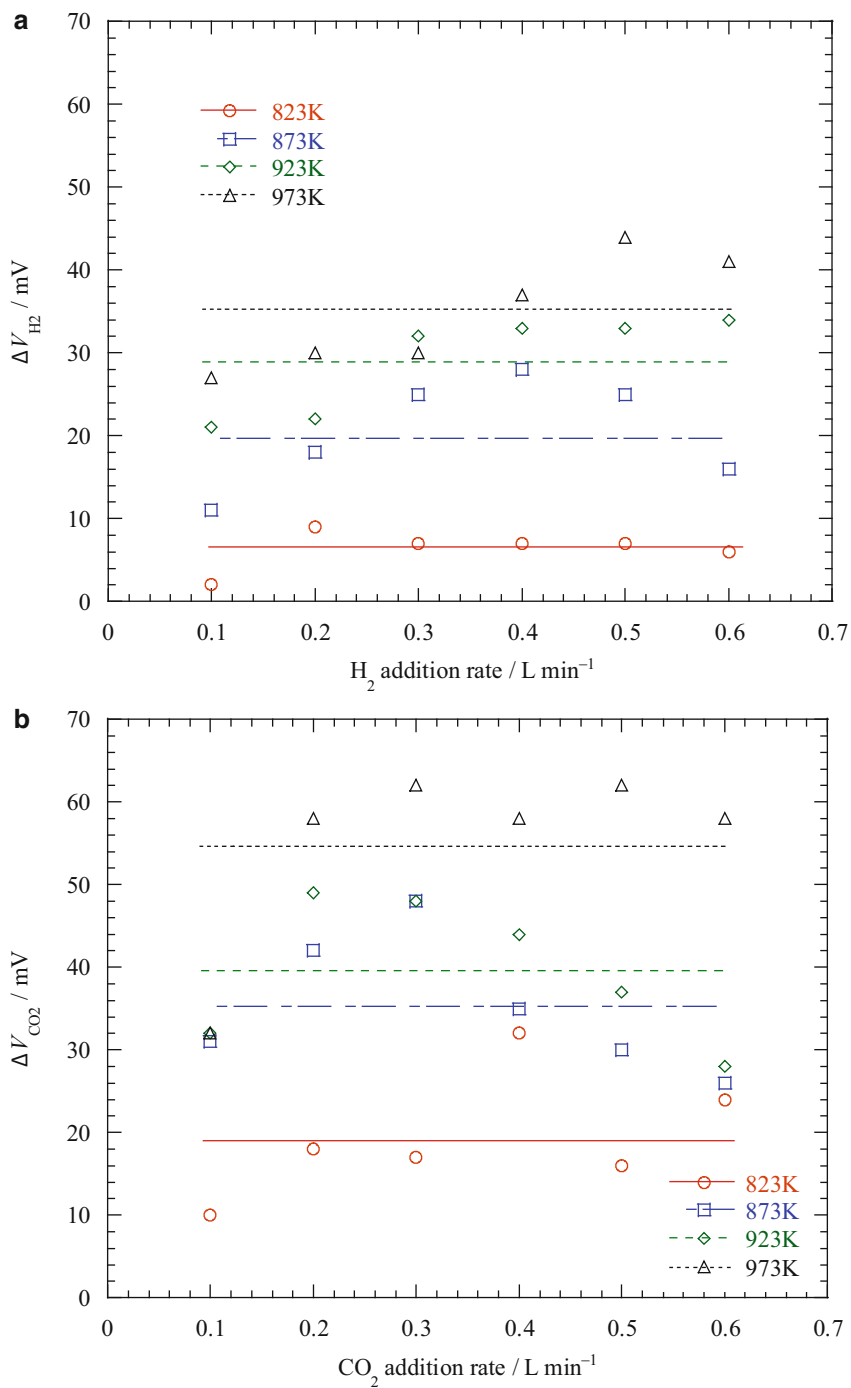
values at all flow rate conditions (Fig. 31b). As shown in Eqs. 9d and 10c, CO<sub>2</sub> species have negative reaction orders in the oxygen reduction

reaction, indicating that raising CO<sub>2</sub> flow rate reduces reaction rate and increases  $\eta_{ca,mt,L}$ . Thus the value of  $\Delta V_{CO_2}$  becomes larger at higher CO<sub>2</sub>



**Molten Carbonate Fuel Cells, Fig. 31**  $\Delta V_{O_2}$  (a) and  $\Delta V_{CO_2}$  (b) obtained at the cathode by the difference of  $\Delta E$  and  $\Delta V_p$  in the temperature range 823–973 K. Anode flow

rate =  $0.381 \text{ L min}^{-1}$  and cathode flow rate =  $0.588 \text{ L min}^{-1}$  and  $0.1\text{--}0.6 \text{ L min}^{-1}$  of  $O_2$  and  $CO_2$  addition rates to the cathode, respectively [47]



**Molten Carbonate Fuel Cells, Fig. 32**  $\Delta V_{H_2}$  (a) and  $\Delta V_{CO_2}$  (b) obtained at the anode due to the difference of  $\Delta E_A$  and  $\Delta V_{p,A}$  in the temperature range of 823–973 K. The

anode flow rate was  $0.254\ L\ min^{-1}$ , and the cathode flow rate was  $0.883\ L\ min^{-1}$ , and the  $H_2$  and  $CO_2$  addition rates were  $0.1$ – $0.6\ L\ min^{-1}$ , respectively [48]



flow rates according to Eq. 21. The largest  $\Delta V_{\text{CO}_2}$  is also observed at 823 K, indicating  $\eta_{\text{ca,mt,L}}$  becomes larger at lower temperature. The reduction of gas solubility and diffusivity at lower temperature would be the main reason as mentioned above.

On the other hand, anodic overpotential becomes larger at higher temperature as shown in Table 6. The similar behavior is observed by the addition of  $\text{H}_2$  to the anode (Fig. 32a). Larger value at high temperature is observed, although there are deviations of  $\Delta V_{\text{H}_2}$  values. Compared with  $\Delta V_{\text{H}_2}$ , the values of  $\Delta V_{\text{CO}_2}$  show more dominant temperature dependence. It represents that the anodic overpotential is due to the severe mass transfer of  $\text{CO}_2$  species than that of  $\text{H}_2$ . This is in line with the results of Figs. 28 and 29. It also supports that anodic overpotential is sum of overpotential due to each species of  $\text{H}_2$ ,  $\text{CO}_2$ , and  $\text{H}_2\text{O}$ .

## Future Directions

MCFCs based on natural gas fuel have been commercialized across the world. In general, natural gas MCFCs are economically inferior to coal power electricity. More economic fuels such as decomposition gas of organic waste and coal gas, and so on, are required for wide-scale use of MCFC. Thus further investigation of the effect of impurities in the fuel gas is necessary to use other fuels. For this more precise performance analysis tools are necessary. The methods in this work can be successfully utilized, but more correct analysis requires sufficient understanding of the reactions in the cells. Then the improvement of analyzing methods of AC impedance, current interruption (C/I), inert gas step addition (ISA), and reactant gas addition (RA) are also necessary. In particular, verification of the relationships is necessary among the measurement tools listed in this work.

Another point to be mentioned for the dissemination of MCFCs is extending their lifetime. Electrolyte management is strongly related to the problem. The molten carbonate electrolyte is depleted mostly by corrosion with metals and weakening of electrolyte holding in the matrices.

Cell design and surface treatment of metal should be considered. It is also necessary to search for appropriate material for the matrix and high performance electrolyte.

Combinations of fuel cells also provide high efficiency. SOFC has been developed as a power system that is comparable to MCFC. SOFC is comprised entirely of solid materials, and thus cracking due to thermal shock is a fundamental problem. The problem confines the SOFC to relatively small power systems so far. In general, SOFC has higher operation temperatures than MCFC. Thus series combination of SOFC and MCFC may enhance power generation efficiency.

## Bibliography

1. Tomczyk P (2006) MCFC versus other fuel cells—characteristics, technologies and prospects. *J Power Sources* 160:858–862
2. Yuh C, Hilmi A, Farooque M, Leo T, Xu G (2009) Direct fuel cell materials experience. *ECS Trans* 17:637–654
3. Selman JR, Maru HC (1981) Physical chemistry and electrochemistry of alkali carbonate melts. In: Mamantov G, Braunstein J (eds) *Advances in molten salt chemistry*. Plenum Press, New York, pp 202–212
4. Lide DR (2008) *Handbook of chemistry and physics*, 88th edn. CRC Press, Boca Raton, pp 6–143. 5–73
5. Hong SG, Selman JR (2004) Wetting characteristics of carbonate melts under MCFC operating conditions. *J Electrochem Soc* 151:A77–A84
6. Yuh CY, Selman JR (1984) Polarization of the molten carbonate fuel cell anode and cathode. *J Electrochem Soc* 131:2062–2069
7. Morita H, Komoda M, Mugikura Y, Izaki Y, Watanabe T, Masuda Y, Matsuyama (2002) Performance analysis of molten carbonate fuel cell using a Li/Na electrolyte. *J Power Sources* 112:509–518
8. Nishina T, Masuda Y, Uchida I (1993) Gas solubility and diffusivity of  $\text{H}_2$ ,  $\text{CO}_2$  and  $\text{O}_2$  in molten alkali carbonates. In: Saboungi ML, Kojima H, Duruz J, Shores D (eds) *Proceedings of the international symposium on molten salt chemistry and technology*. The Electrochemical Society PV93-9, New Jersey, pp 424–435
9. Yuh CY, Farooque M, Maru H (1999) Advances in carbonate fuel cell matrix and electrolyte. In: Uchida I, Hemmes K, Lindbergh G, Shores DA, Selman JR (eds) *Carbonate fuel cell technology*. The Electrochemical Society PV99-20, New Jersey, pp 189–201
10. Fujita Y (2003) Durability. In: *Handbook of fuel cells fundamentals technology and applications*. Wiley, England, pp 969–982

11. Yuh C, Johnsen R, Farooque M, Maru H (1993) Carbonate fuel cell endurance: hardware corrosion and electrolyte management status. In: Shores D, Maru H, Uchida I, Selman JR (eds) Carbonate fuel cell technology. The Electrochemical Society PV93-3, New Jersey, pp 158–170
12. Fujita Y, Nishimura T, Hosokawa JI, Urushibata H, Sasaki A (1996) Degradation of materials in molten carbonate fuel cells with Li/Na electrolyte. In: The 3rd FCDIC fuel cell symposium proceedings. Fuel Cell Development Information Center, Japan, pp 151–155
13. Matsumoto K, Yuasa K, Nakagawa K (1999) Protection against localized corrosion of stainless steel below 843K in molten lithium-sodium carbonate. *Denki Kagaku* 67:253–258
14. Hoffmann J, Yuh CY, Jopek AG (2003) Electrolyte and material challenges. In: Handbook of fuel cells fundamentals technology and applications. Wiley, England, pp 921–941
15. Ang PGP, Sammells AF (1980) Influence of electrolyte composition on electrode kinetics in the molten carbonate fuel cell. *J Electrochem Soc* 127:1287–1293
16. Jewulski J, Suski L (1984) Model of isotropic anode in the molten carbonate fuel cell. *J Appl Electrochem* 14:135–143
17. Lu SH, Selman JR (1984) Electrode kinetics of fuel oxidation at copper in molten carbonates. *J Electrochem Soc* 131:2827–2833
18. Nishina T, Takahashi M, Uchida I (1990) Gas electrode reactions in molten carbonate media IV. Electrode kinetics and mechanism of hydrogen oxidation in (Li+K)CO<sub>3</sub> eutectics. *J Electrochem Soc* 137:1112–1121
19. Appleby AJ, Nicholson SB (1977) Reduction of oxygen in alkali carbonate melts. *J Electroanal Chem* 83:309–328
20. Appleby AJ, Nicholson S (1974) The reduction of oxygen in molten lithium carbonate. *Electroanal Chem Interfacial Electrochem* 53:105–119
21. Kinoshita K (1992) Electrochemical oxygen technology. Electrochemical Society, Wiley, New York, p 37
22. Nishina T, Uchida I, Selman JR (1994) Gas electrode reactions in molten carbonate media V. Electrochemical analysis of the oxygen reduction mechanism at a fully immersed gold electrode. *J Electrochem Soc* 141:1191–1198
23. Yoshikawa M, Mugikura Y, Watanabe T, Ota T, Suzuki A (1999) The behavior of MCFCs using Li/K and Li/Na carbonates as the electrolyte at high pressure. *J Electrochem Soc* 146:2834–2840
24. Lee CG, Kang BS, Seo HK, Lim HC (2003) Effect of gas-phase transport in molten carbonate fuel cell. *J Electroanal Chem* 540:169–188
25. Uchida I, Mugikura Y, Nishina T, Itaya K (1986) Gas electrode reactions in molten carbonate media II. Oxygen reduction kinetics on conductive oxide electrodes in (Li+K)CO<sub>3</sub> eutectic at 650°C. *J Electroanal Chem* 206:241–252
26. Baumgartner C (1984) Electronic conductivity decrease in porous NiO cathodes during operation in molten carbonate fuel cell. *J Electrochem Soc* 131:2607–2610
27. Ota K, Mitsushima S, Kato S, Asano S, Yoshitake H, Kamiya N (1992) Solubilities of nickel oxide in molten carbonate. *J Electrochem Soc* 139:667–671
28. Doyon JD, Gilbert T, Davies G, Paetsch L (1987) NiO solubility in mixed alkali/alkaline earth carbonates. *J Electrochem Soc* 134:3035–3038
29. Kunz HR, Bregoli LJ (1990) Ionic migration in molten carbonate fuel cells. In: Selman JR, Shores DA, Maru HC, Uchida I (eds) Carbonate fuel cell technology. The Electrochemical Society PV90-16, New Jersey, pp 157–168
30. Veldhuis JB, Eckes FC, Plomp L (1992) The dissolution properties of LiCoO<sub>2</sub> in molten 62:38 mol% Li:K carbonates. *J Electrochem Soc* 139:L6–L8
31. Hatoh K, Niikura J, Yasumoto E, Gamo T (1994) The exchange current density of oxide cathodes in molten carbonates. *J Electrochem Soc* 141:1725–1730
32. Motohira N, Senso T, Yamauchi K, Kamiya N, Ota K (1999) Solubility of nickel in molten carbonates—the effect of Mg addition. In: The 6th FCDIC fuel cell symposium proceedings. Fuel Cell Development Information Center, Japan, pp 237–240
33. Yuh CY, Selman JR (1991) The polarization of molten carbonate fuel cell electrodes I. Analysis of steady-state polarization data. *J Electrochem Soc* 138:3642–3648
34. Morita H, Mugikura Y, Izaki Y, Watanabe T, Abe T (1997) Analysis of performance of molten carbonate fuel cell V. Formulation of anode reaction resistance. *Denki Kagaku* 65:740–746
35. Morita H, Mugikura Y, Izaki Y, Watanabe T, Abe T (1998) Model of cathode reaction resistance in molten carbonate fuel cells. *J Electrochem Soc* 145:1511–1517
36. Ramaswami K, Selman JR (1994) Rotating disk studies in molten carbonates III. Diffusion coefficients and bulk concentration in lithium carbonates. *J Electrochem Soc* 141:2338–2343
37. Vogel WM, Smith SW, Bregoli LJ (1983) Studies of the reduction of oxygen on gold in molten Li<sub>2</sub>CO<sub>3</sub>-K<sub>2</sub>CO<sub>3</sub> at 650°C. *J Electrochem Soc* 130:574–578
38. Malinowska B, Cassir M, Devynck J (1994) Design of a gold ultramicroelectrode for voltammetric studies at high temperature in glass-corrosive media (molten carbonate at 650°C). *J Electrochem Soc* 141:2015–2017
39. Uchida I, Nishina T, Mugikura Y, Itaya K (1986) Gas electrode reactions in molten carbonate media I. Exchange current density of oxygen reduction in (Li+K)CO<sub>3</sub> eutectic at 650°C. *J Electroanal Chem* 206:229–239
40. Lee CG, Nakano H, Nishina T, Uchida I, Kuroe S (1998) Characterization of a 100 cm<sup>2</sup> class molten carbonate fuel cell with current interruption. *J Electrochem Soc* 145:2747–2751
41. Yuh CY, Selman JR (1988) Characterization of fuel cell electrode processes by AC impedance. *AICHE J* 34:1949–1958
42. Morita H, Mugikura Y, Izaki Y, Watanabe T (1999) Analysis of performance of molten carbonate fuel cell

- VI. Analysis of Nernst Loss on current interrupt wave. *Electrochemistry* 67:438–444
43. Lee CG (2016) Analysis of impedance in a molten carbonate fuel cell. *J Electroanal Chem* 776:162–169
  44. Lee CG, Lim HC (2005) Experimental investigation of electrode reaction characteristics with reactant gas addition measurement in a molten carbonate fuel cell. *J Electrochem Soc* 152:A219–A228
  45. Becker D, Jüttner K (2003) The impedance of fast charge transfer reactions on boron doped diamond electrodes. *Electrochim Acta* 49:29–39
  46. Lee CG, Kim DH, Lim HC (2007) Electrode reaction characteristics under pressurized conditions in a molten carbonate fuel cell. *J Electrochem Soc* 154: B396–B404
  47. Lee CG (2013) Effect of temperature on the cathodic overpotential in a molten carbonate fuel cell. *J Electroanal Chem* 701:36–42
  48. Lee CG (2017) Influence of temperature on the anode reaction in a molten carbonate fuel cell. *J Electroanal Chem* 785:152–158
  49. Lee CG, Hwang JY, Oh M, Kim DH, Lim HC (2008) Overpotential analysis with various anode gas compositions in a molten carbonate fuel cell. *J Power Sources* 179:467–473
  50. Lee CG, Yamada K, Hisamitsu Y, Ono Y, Uchida I (1999) Kinetics of oxygen reduction in molten carbonates under pressurized Air/CO<sub>2</sub> oxidant gas conditions. *Electrochemistry* 67:608–613



## Solid Oxide Fuel Cells

A. Atkinson, S. J. Skinner and J. A. Kilner  
Department of Materials, Imperial College  
London, London, UK

### Article Outline

Glossary  
Definition of the Subject and Its Importance  
Introduction  
Novel Devices and Configurations  
Microtubular SOFCs  
Mixed Reactant Fuel Cells  
Dual Proton-Oxygen Ion-Conducting Cells  
Novel Materials  
Electrolyte Materials  
Electrode Materials  
Accelerated Materials Discovery  
Development of In Situ Diagnostics  
In Situ Materials Characterization  
Neutron Scattering Studies of Fuel Cell Oxides  
Synchrotron X-Ray Studies  
Raman Spectroscopy  
Summary  
Future Directions  
Bibliography

### Glossary

**Anode** The negative terminal of the SOFC where oxygen ions from the electrolyte react with fuel releasing electrons to the external circuit.

**Cathode** The positive terminal of the SOFC where oxygen molecules from the air are reduced to oxygen ions by absorbing electrons from the external circuit.

**Electrolyte** The central component of the SOFC which conducts electricity by the movement of oxygen ions. This is the solid analogue of the liquid electrolyte used in a battery.

**Fuel cell stack** A fuel cell composed of several individual fuel cell (anode/electrolyte/cathode) units electrically interconnected in order to provide a useful device in terms of power output.

**Heterostructure** A structure consisting of two closely matched materials with properties superior to those of the individual components due primarily to interface effects. Can be further enhanced through creation of multilayer heterostructures where many repeats are generated.

**Planar device** A fuel cell constructed from sequential functional layers of anode, electrolyte, and cathode in a planar geometry.

**Solid oxide fuel cell (SOFC)** An electrochemical device for the conversion of a gaseous fuel into electrical energy using oxide ion-conducting ceramic membranes.

### Definition of the Subject and Its Importance

The Solid Oxide Fuel Cell is an electrochemical device for the conversion of hydrogen or a hydrocarbon fuel directly into electrical power. They are clean, modular, and efficient and retain this efficiency across a wide range of sizes. This fuel flexibility and efficiency makes them very attractive for a number of powergeneration roles, including distributed generation and combined heat and power applications, where they could make a significant impact on carbon-emission reductions and provide a pathway towards an eventual low carbon economy. There are some significant hurdles to be overcome before there is a global uptake of SOFC technology, and it is very likely that the technology will evolve markedly over the next few decades. It is thus important to take a forward look at how the technology may evolve and what kinds of devices, materials, and diagnostics will be needed to assure this continued development.

## Introduction

Although Solid Oxide Fuel Cells (SOFCs) have been investigated since their discovery by Sir William Grove in the nineteenth century, little progress was made until almost a century later when the twin drivers of security of supply and the reduction of carbon emissions provided the necessary financial and political imperatives to accelerate SOFC development. Since that time, there have been a number of generations of devices, from the early tubular cells developed by Westinghouse and Mitsubishi Heavy Industries, through planar electrolyte supported cells, to the current generation of supported thin-film planar devices, which are nearing commercial exploitation, operating at intermediate temperatures (ITSOFCs). Much has been written on the materials and device characteristics in journal articles, conference proceedings, and there are many reference books [1, 2]. The aim of this article is not to replicate these many excellent texts, but to present quite a different view, one which looks towards the future of SOFC technology and what new designs, new materials, and new diagnostic techniques will be required to meet the demands of future SOFC developments.

From the current perspective, the future of SOFC technology looks promising. SOFCs will have many roles to play in the global energy scenario, from large-scale central power generation, distributed generation roles in domestic and district Combined Heat and Power (CHP), to mobile, remote, and standby power. If this outlook is correct, then the SOFC will undergo continued development to achieve improved performance and durability and will become more commercially viable in the very near future, delivering substantial increases in the efficient use of hydrocarbon fuels and a consequent drop in carbon emissions. In considering the future, it is thus important to look at how the technology will develop into new SOFC concepts. These have lagged behind mainstream SOFC development, but could quickly benefit from any significant technological advances made in their development. One thing is clear; these developments are underpinned by the requirements for new

materials and new diagnostic techniques. The materials must meet stringent requirements for electrical and mechanical properties coupled with long-term stability in the appropriate environment. The purpose of this contribution is to describe these possible novel SOFC and SOFC-related concepts, describe their strengths and their drawbacks, and in parallel to explore the advances in materials and materials characterization that will be necessary to ensure application and commercialization in the future.

## Novel Devices and Configurations

SOFCs have largely converged on standard configurations, such as tubular or planar, with the structural support provided by the electrolyte, the anode, the metallic interconnector, or an inert porous support material. Each of these concepts has its own combination of advantages and disadvantages. In this section, some “unconventional” SOFC configurations and devices are discussed, and their performance and potential applications are considered in comparison with the more conventional approaches. This will include microtubular fuel cells, mixed reactant fuel cells, microplanar fuel cells, and dual proton-oxygen ion fuel cells.

### Microtubular SOFCs

Tubular SOFCs are not new and have been developed for large-scale stationary CHP applications with both circular and flat-cross sections. A major advantage of tubular SOFCs is better tolerance of thermal cycling, especially if one end is closed and therefore unconstrained to allow thermal expansion-length changes. A major disadvantage is that the volumetric power density is smaller than for a planar configuration, although this is partially offset with a flat crosssection tube. However, another way of improving the volumetric power density is to make the tubes smaller in diameter. When the diameter is less than approximately 3 mm, these are referred to as microtubular cells and their

development has recently been reviewed by Lawlor et al. [3] and Kendall [4]. The reduction in diameter brings additional advantages in that the small tubes tend to have higher mean strength because the stressed volumes are smaller and lower variability in strength as the processing tends to give a more uniform microstructure. Consequently, microtubular SOFCs tend to have excellent thermal cycling durability.

The most usual configuration is a thin film of electrolyte on an anode support tube and an outer thick-film cathode. However, a major problem with the microtubular concept is with current collection from the electrodes and interconnection into stacks. Since the tubes are so small, large numbers are required for applications requiring appreciable power. For example, a typical tube with diameter 2 mm and length 100 mm operating at  $0.2 \text{ W cm}^{-2}$  only produces 1.25 W. Sammes et al. [5] have described a serpentine interconnection system for anode-supported tubes of conventional SOFC materials that are somewhat larger than the usual microtubular size, being 13 mm diameter and 110 mm long. However, at  $850 \text{ }^\circ\text{C}$ , the maximum power density was only  $0.1 \text{ W cm}^{-2}$  and was limited by the current collection along the cathode.

Suzuki et al. [6, 7] have attempted to overcome this problem with a cubic stack design (Fig. 1) in which microtubular SOFCs are assembled in layers joined by a porous matrix of cathode material. The layers are assembled in stacks in which individual layers are electrically insulated from each other by a glass and the cathodes of one layer are connected to the anodes of the next using silver. Each microtube was 0.8 mm in diameter and 8 mm in length and made from a  $\text{Ni/Ce}_{1-x}\text{Gd}_x\text{O}_{2-\delta}$  (CGO) composite anode material. The electrolyte was CGO and the cathode an  $\text{La}_{1-x}\text{Sr}_x\text{Co}_{1-y}\text{Fe}_y\text{O}_{3-\delta}$  (LSCF)/CGO composite. The stack consisted of 20 cells; 4 layers of 5 cells; and its performance is also shown in Fig. 1. At  $500 \text{ }^\circ\text{C}$ , the power output of a single tube was  $0.32 \text{ W cm}^{-2}$  at 0.7 V, and the total-bundle power at  $490 \text{ }^\circ\text{C}$  and 0.7 V per cell was approximately 1.3 W; corresponding to  $0.25 \text{ W cm}^{-2}$ . These are impressive performance figures at such low operating temperatures.

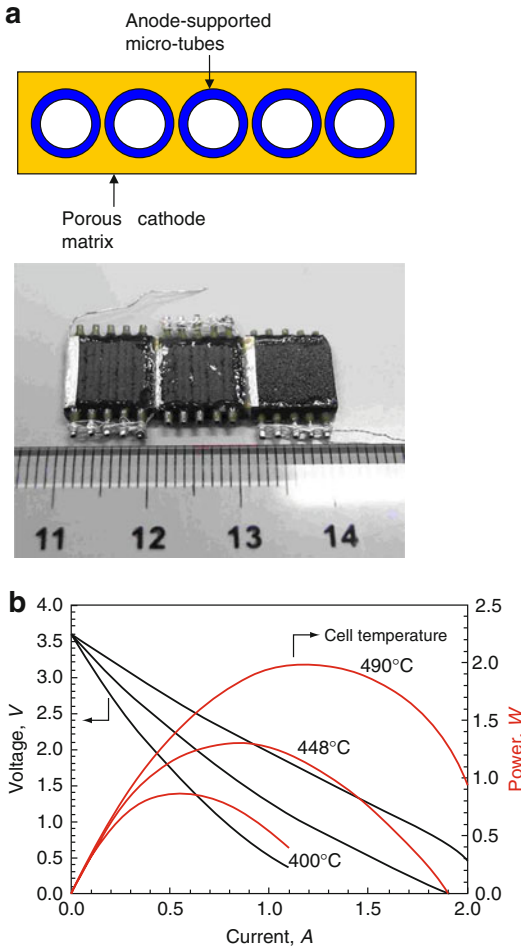
However, the fabrication of these stacks could be difficult to automate and the final structure is monolithic, so that much of the tolerance of the tubular configuration to thermal gradient stresses is compromised.

## Mixed Reactant Fuel Cells

A major problem with almost all SOFC designs is the requirement to seal the structure in order to prevent the fuel and oxidant gases from coming into direct contact and causing direct combustion of the fuel. One possible way around this is to operate the cell at a temperature below which no direct combustion will take place and to allow the fuel and oxidant to mix. The cell then requires very selective electro-catalytic electrodes in order to generate electrochemical power. Ideally, the anode should only catalyze the fuel-electrochemical oxidation and the cathode the electrochemical reduction of the oxidant. Neither electrode should catalyze direct chemical reaction of fuel and oxidant.

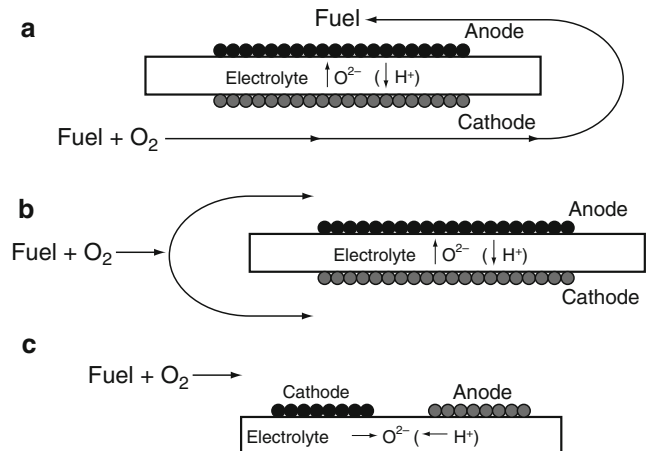
The first attempts at such a configuration were reported by Hibino and Iwahara, [8] and there have been many subsequently. The area has recently been reviewed by Yano et al. [9], and some typical configurations are illustrated in Fig. 2. There are many reports of good power densities when operating on hydrocarbon fuels, which are more resistant to direct oxidation than hydrogen. However, there is always some direct combustion and the cell temperature can be considerably higher than the nominal ambient temperature as a result, which makes the performance difficult to judge. Some direct combustion might even be regarded as an advantage since it can help small SOFCs to be thermally self-sustaining. Riess [10] has discussed the issues involved in mixed-reactant mode and pointed out that to date they can only operate with low fuel utilization and short gas residence times (high-flow rates). He proposes a configuration similar to that being investigated in mixed reactant PEMFCs that is illustrated in Fig. 3. All the components are porous, so that the mixed-reactant gas stream flows through the whole unit. This concept





**Solid Oxide Fuel Cells, Fig. 1** (a) Micro-tubular SOFC stack layer concept and (b) performance of a 20 cell (4 layers) bundle [6, 7]. (Reproduced with permission)

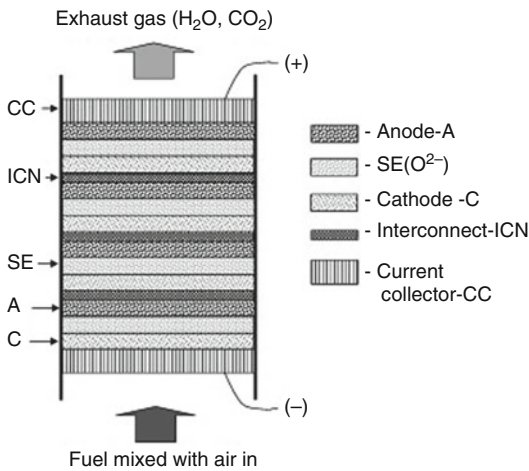
**Solid Oxide Fuel Cells, Fig. 2** Geometries for planar mixed reactant SOFCs [7]



enables high fuel utilization to be achieved in principle, but has not yet been realized in practice since the selectivity of the electrode catalysis is not good enough for the materials investigated thus far.

**Micro-planar SOFCs**

These devices feature the use of micro-fabrication techniques adapted from the micro-electronics industry. These encompass substrate etching, thin-film deposition, lithography, and film-etching steps. This field has recently been reviewed by Evans et al. [11], and all devices exhibit the beautiful structural quality resulting from the micro-fabrication techniques. An example of a micro-planar SOFC fabricated on a silicon substrate is illustrated in Fig. 4 [12]. Figure 4a shows the sequence of fabrication steps used to make the edge-supported SOFC membrane which spans an aperture with dimensions 600 × 600 μm. The yttria stabilized zirconia (YSZ) electrolyte, which is only 70-nm thick, was deposited by atomic-layer deposition and is corrugated in order to increase the active area and accommodate thermal and fabrication strains. An image of the corrugated electrolyte is shown in Fig. 4b. The electrodes are 120-nm thick porous-Pt deposited by sputtering. The performance, of both flat and corrugated cells, on hydrogen is remarkable (Fig. 4c), with a maximum power density of 0.86 W cm<sup>-2</sup> at 450 °C. The shape of the V-I characteristic indicates large



**Solid Oxide Fuel Cells, Fig. 3** Proposed configuration for a flow-through mixed reactant SOFC [10]. (Reproduced with permission)

overpotentials at the electrodes and therefore the possibility of large power density at more useful terminal voltage with improved electrodes.

At this stage of development, the reported results indicate that good performance is likely to be achievable with micro-fabricated SOFCs. However, more problematic are the engineering issues related to thermal management and fuel utilization that are more difficult to deal with as the device becomes smaller. Even if these problems are solved, the power levels and total energies are so small that the impact on sustainable electrical energy generation will be small and the development of these devices will be driven by convenience of operation (e.g., in consumer electronics) rather than energy efficiency.

### Dual Proton-Oxygen Ion-Conducting Cells

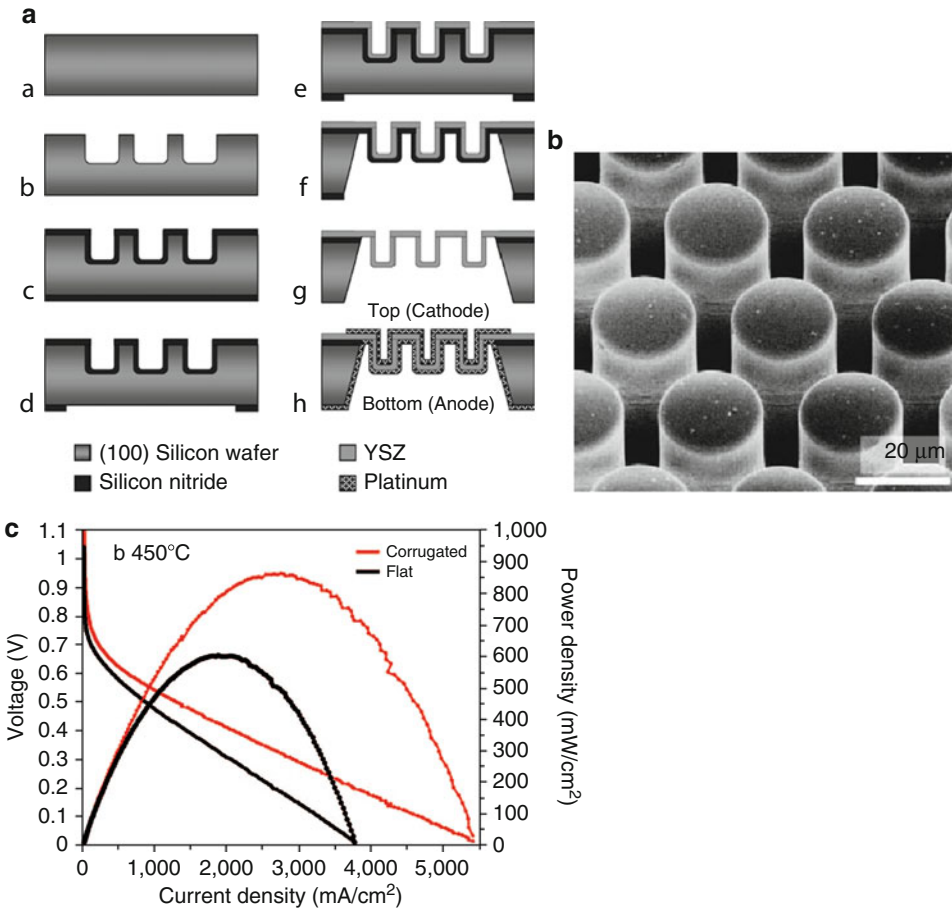
Recently, a new concept (Fig. 5) has been proposed, called the IDEAL-Cell which attempts to combine the advantages of both proton-conducting and oxygen ion-conducting SOFCs [13]. The anode electrode reaction is as in a proton-conducting SOFC, and the cathode reaction as in an oxygen ion-conducting SOFC. In the

central chamber, which contains a porous mixture of the two electrolytes, the protons and oxygen ions combine to give the product water. In this way, the water reaction product does not interfere with either of the electrode reactions. A “proof-of-concept” small cell was fabricated with yttrium-doped barium cerate as the proton-conducting electrolyte and yttrium-doped ceria as the oxygen ion-conducting electrolyte. The test cell achieved an encouraging maximum power output approaching  $0.5 \text{ W cm}^{-2}$  at  $600 \text{ }^\circ\text{C}$  on oxygen and humidified hydrogen. It will be interesting to see whether this concept can actually deliver the anticipated benefits on a larger scale.

### Novel Materials

In the preceding section, new design concepts for the SOFC for application in the near future were discussed. One common feature of most of these new concepts is the lowering of the operating temperature into a new regime ( $400\text{--}600 \text{ }^\circ\text{C}$ ), where high performance materials should make a significant impact. The active components of such solid oxide fuel cells must conform to some very stringent materials requirements. The prime need is to have very high diffusion coefficients for the oxide ion at these low temperatures which will require considerable materials development for both electrolytes and the mixed conductors used as electrodes. In this lower temperature regime, the three active components: anode, cathode, and electrolyte, each contribute towards the overall area specific resistance (ASR) of the cell. Of these three components, the two that have received the most attention are the electrolyte and the cathode, which is known to give rise to the largest ASR below temperatures of  $650 \text{ }^\circ\text{C}$  [2].

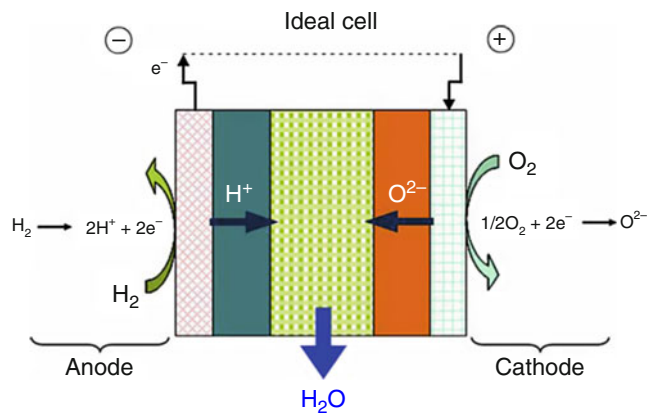
Before moving to the details of these materials, it is instructive to examine the atomistic quantities that govern the transport of oxygen in these oxides. A simple Arrhenius-type expression describes the diffusion coefficient of oxygen,  $D$ , in oxide materials.



**Solid Oxide Fuel Cells, Fig. 4** An example of a micro-planar SOFC produced by micro-fabrication methods. (a) The sequence of fabrication steps, (b) the corrugated

electrolyte membrane before deposition of the electrodes, and (c) the electrochemical performance [12]. (Reproduced with permission)

**Solid Oxide Fuel Cells, Fig. 5** The concept of a dual proton and oxygen ion SOFC [13]. (Reproduced with permission)



$$D = D_0 \exp \left\{ \frac{-E_a}{RT} \right\}$$

where  $D_0$  is the pre-exponential factor which contains terms relating to the concentration of oxygen defects and  $E_a$  is the activation energy for diffusion which can contain terms relating to the formation, association, and migration of the defects on the oxygen sublattice [14]. Both terms are important in achieving high diffusivities. Materials with highly defective oxygen sublattices or high concentrations of interstitials are commonly investigated to give high diffusion coefficients; however, a low activation energy is essential to retaining the high-diffusion coefficient to low temperatures. This means minimizing (or removing) any terms due to the formation or association of defects and ensuring that the mobile oxygen ions can migrate with the minimum of hindrance. These criteria apply to materials that have very high ionic transport numbers for use as electrolyte materials as well as to mixed conducting materials used as electrodes.

An additional criterion for mixed conducting materials used as cathodes is that they should have a high surface exchange rate ( $k$ ) for oxygen. This quantity also follows Arrhenius-type behavior, although the atomistic parameters that govern the exchange process are still somewhat obscure. However, it is well known that materials that have high oxygen-diffusion coefficients usually have high oxygen-exchange coefficients because both are related to the oxygen mobility in the material [15]. It should be remembered that the selection criteria described above are only part of the process of the selection and optimization of new materials for the application in solid oxide fuel cells, and that a significant part of the application of new materials relies upon the development of appropriate ceramic processing to yield a suitable microstructure for the SOFC cathode [16].

In the following paragraphs some of the current materials research that could give rise to suitable materials for applications in SOFCs is described.

## Electrolyte Materials

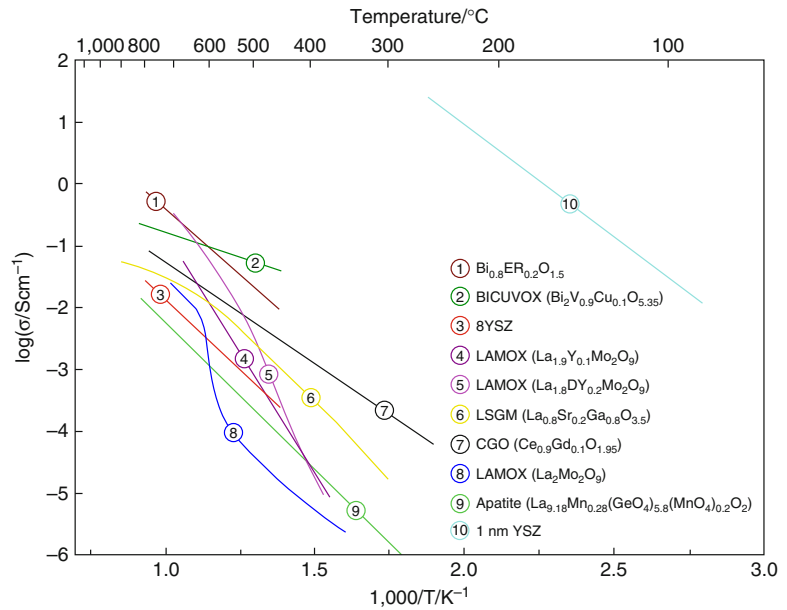
The materials requirements described above for obtaining high oxygen transport can be further developed [17] and have been used for many years in the optimization of new oxygen ion conductors. A good example of this are the materials formed from ceria gadolinia solid solutions that have some of the highest conductivities at low temperatures. Fig. 6 shows an Arrhenius plot of the conductivity of most of the conventional oxide ion conductors used as electrolytes. New ionic conductors are emerging as further compositions are explored, such as the  $\text{La}_2\text{Mo}_2\text{O}_9$  (LAMOX) family and the apatite-structure materials, however they usually offer incremental advantages and do not have either the low-temperature conductivity offered by the cerias or the very high stability offered by the stabilized zirconia materials. At 600 °C, some very high ionic conductivities can be achieved by bismuth-based materials, on the order of  $10^{-1} \text{ S cm}^{-1}$  which is equivalent to that of yttria-stabilized zirconia at 1,000 °C; however, these materials suffer from poor stability in reducing atmospheres and are thus not suitable to act as SOFC electrolytes without some form of protective layer. Other than the bismuth materials, there is a paucity of materials that can display conductivities of this order below temperatures of around 650–700 °C.

## Thin-Film Heterostructures

The continued search for materials that show better ionic transport, especially at low temperatures, has been a quest that has been pursued for many years. In the main, there have been two ways in which this search has been pursued: by the discovery of new materials, i.e., the optimization of the lattice mobility for the oxygen ion, as mentioned above, and more recently, by the investigation of nanomaterials and nanostructures, i.e., by the optimization of the interfacial transport of oxygen. Early work with thin (down to ~15 nm) epitaxial yttria-stabilized zirconia (YSZ) films by Kosacki et al. [27] and Karthikeyan et al. [28] instigated a number of investigations into the effect of interfaces on conductivity. Kosacki

### Solid Oxide Fuel Cells,

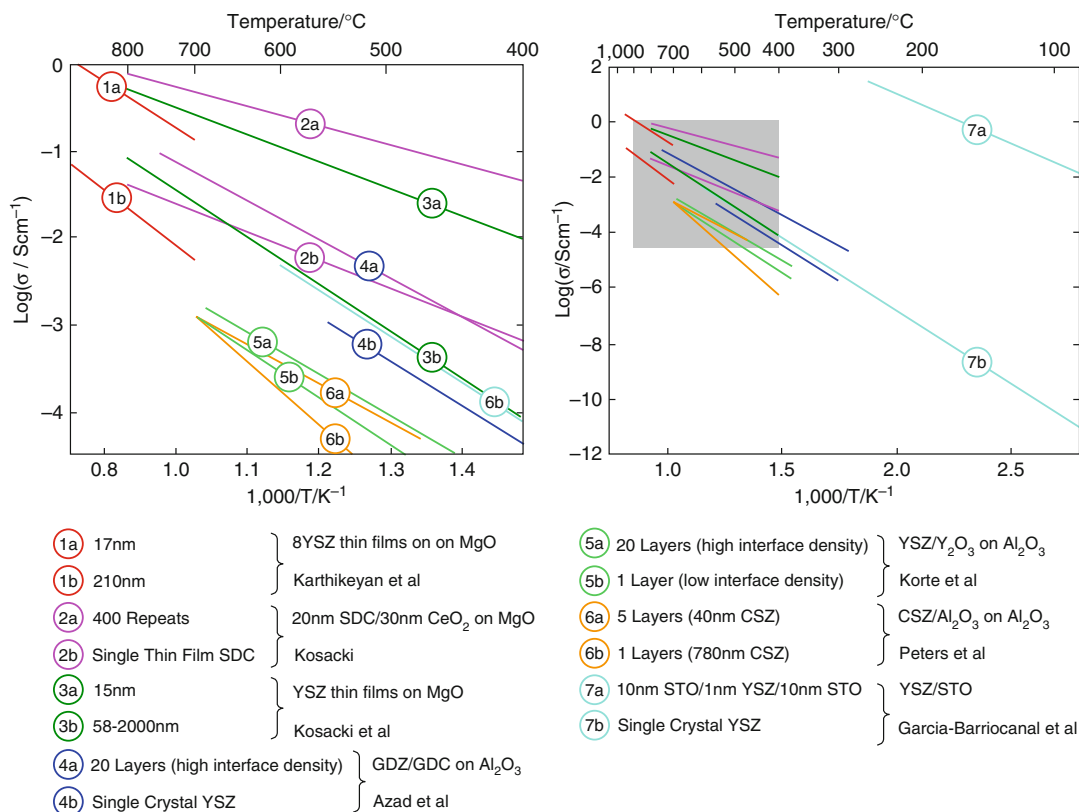
**Fig. 6** Comparison of the lattice conductivity of some well known oxide ion conductors. (Data taken from [18–26])



et al.'s findings implied that the oxygen conductivity of the interfacial layer between the MgO substrate and the YSZ was strongly enhanced, by up to 3 or 4 orders of magnitude, and more significantly, that the activation energy was more than halved from 1.04 to 0.45 eV, important for achieving high values of conductivity at low temperatures. These findings prompted a number of subsequent investigations into the ionic conductivity of heterostructures, produced by pulsed laser deposition, involving thin layers of an oxide ion conductor (mostly YSZ) sandwiched between layers of insulating materials. The temperature dependence of the ionic conductivity for these materials is shown in Fig. 7, which shows that the conductivity can be either enhanced or suppressed over that for single crystal zirconia. By far the most significant result is that obtained by Garcia-Barriocanal et al. [18] (trace 10 in Figs. 6 and 7a in Fig. 7) who investigated very thin layers of YSZ and strontium titanate (STO) in samples made by sputtering. They observe that for epitaxial trilayers of 10 nm STO/1 nm YSZ/10 nm STO the conductivity was highly enhanced (trace 7a in Fig. 7), showing over 8 orders of magnitude of enhancement at 100 °C. This is clearly much larger than any of the enhancements seen by other workers, most of which are grouped around

1–2 orders of enhancement of the conductivity of zirconia, depending upon the temperature. There is still much debate over these findings as, at the date of writing, they have not been repeated and there is controversy over the nature of the carrier, an electronic carrier would be much easier to reconcile with these high conductivities [31–33]. The interfacial strain at the STO/YSZ interface should be on the order of 7% which should not lead to a coherent interface as was observed by electron microscopy. Despite the lack of experimental evidence, there have been some theoretical studies including simulations by Density Functional Theory (DFT) which would tend to support the idea that the observed effects could indeed be ionic [34], although there is some doubt about the magnitude of the conductivity enhancement [35].

The most systematic of the subsequent investigations of heterostructures has been by Korte and coworkers [30, 36, 37], who have investigated a number of different interfaces by fabricating stabilized zirconia-insulator heterostructures using pulsed laser deposition. Recently, Korte et al. [38] have reviewed the current status of their (and other) work on multilayer structures and have classified them according to the degree of coherency of the crystal structure across the



**Solid Oxide Fuel Cells, Fig. 7** Temperature dependence of the conductivity of oxide heterostructures. (Data taken from Karthekeyan et al. [28], Kosacki et al. [27], Azad et al. [29], Korte et al. [30], Garcia-Barriocanal et al. [18])

interfaces. They show that the lattice strain in the zirconia layers is important in determining the magnitude of the change in both conductivity and in activation energy. Tensile strain leads to an enhancement of the conductivity by up to an order of magnitude; however, the largest enhancement seen is in structures formed with calcia-stabilized zirconia (CSZ) and Al<sub>2</sub>O<sub>3</sub> as the insulating layer, which have an incoherent interface and a disordered region and a high density of mismatch dislocations. The enhancement of conductivity seen is around a factor of 60 at 575 °C with a lowering of the activation energy of almost 0.5 eV, a significant decrease, leading to increased low-temperature conductivity.

Korte et al. [38] speculate on the role of any misfit dislocations in the conductivity enhancement. This seems to be a likely explanation, as conductivity enhancement has been seen in YSZ single crystals that have been plastically deformed

at high temperatures. Otsuka and coworkers [39, 40] have shown that the conductivity of material with high dislocation densities does show an enhancement of the conductivity and they estimate that the conductivity could be enhanced by a factor of 10<sup>2</sup>–10<sup>4</sup>. These findings clearly indicate a possible method for the enhancement of low-temperature conductivity in oxygen-ion conductors by the introduction of structures, such as heterointerfaces that give rise to either tensile strain or to large numbers of dislocations.

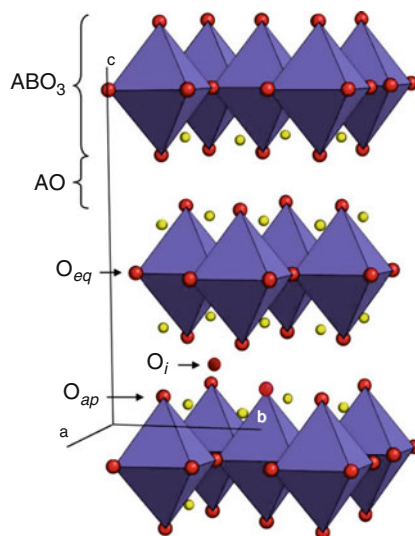
## Electrode Materials

The search for new materials for electrodes has also been a long-term quest similar to the one mentioned above for electrolyte materials. Because of the importance of developing new cathode materials for low-temperature operation,



much recent work has focussed on mixed electronic-ionic conducting materials for this particular application. Like the electrolyte materials, there have been indications that heterogeneous interfaces in mixed conductors can show some enhanced behavior [41], although there has been little published on this subject to date. Much of the conventional bulk materials have been based on highly substituted perovskite materials, such as  $\text{La}_{1-x}\text{Sr}_x\text{CoO}_{3-\delta}$  for which substitution ( $x$ ) can be as high as 0.6. These materials have very high strontium contents and high degrees of non-stoichiometry which give the materials high performance as cathodes, but bring a set of problems. The materials that have the highest levels of oxygen diffusivity, such as the cobalt-based materials mentioned above, also have high values of expansion coefficient ( $>20 \text{ ppm K}^{-1}$ ) [42], making them thermo-mechanically incompatible with the electrolyte materials. In addition, the high strontium contents lead to vulnerability to long-term degradation problems [16] and possibly to chromium poisoning. In order to combat some of these problems, there has been a move towards materials that do not need high degrees of substitution and that could show greater stability while retaining the high electrochemical activity.

Of current interest is the work on layered crystal structures (which are almost a natural analogue of the heterostructures described above) in either polycrystalline or single crystal form. An example of a family of oxides with this layered structure is the  $\text{Ln}_2\text{NiO}_4$  materials such as  $\text{La}_2\text{NiO}_{4+\delta}$  or  $\text{Nd}_2\text{NiO}_{4+\delta}$ . These materials are the first member of the Ruddlesden Popper homologous series with the  $\text{K}_2\text{NiF}_4$  structure, and they are unusual in that they show highly anisotropic conductivity (see for example Fig. 9 next section). The general structure of such  $\text{A}_2\text{BO}_{4+\delta}$  oxides is shown in Fig. 8 and consist of alternating layers of perovskite  $\text{ABO}_3$  and rocksalt  $\text{AO}$  layers. These materials are not substituted, but due to the variable valency of the B, cation tend to oxygen excess in air, i.e.,  $\delta > 0$ , which can reach values of around 0.14. The oxygen interstitials are mobile in the AO layers and can give rise to substantial values of oxygen diffusivity. The expansion coefficients of these materials do not suffer from the very high values

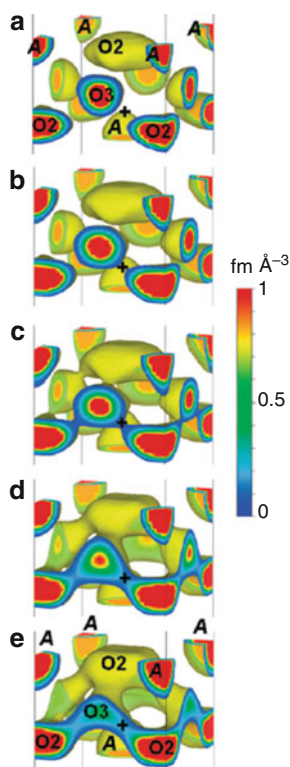


**Solid Oxide Fuel Cells, Fig. 8** Schematic of the crystal structure of  $\text{A}_2\text{BO}_{4+\delta}$

seen for the substituted perovskites, and so these materials are good candidates for next generation cathodes; however, their durability in cathode environments needs to be verified. Their performance, as ITSOFC cathode, has recently been reviewed and their suitability as candidates has been confirmed [43].

## Accelerated Materials Discovery

Accelerated materials discovery is of great interest for the development of the SOFC and a key goal for further development is the lowering of the operational temperature to below  $600 \text{ }^\circ\text{C}$ , the so-called intermediate-temperature regime. In this regime, cheap and readily available materials can be used for the balance of plant. When considering the need for novel materials, it is pertinent to consider the timescales needed for the introduction of new materials into devices to meet emissions reductions targets for 2030 and 2050 and beyond. Historically, the timescales for adoption of new materials/new technologies has been rather long, especially where the drivers (at least initially) are not financial. In order to have significant impact on the reduction of carbon emissions, wide-scale adoption of fuel cells has to



**Solid Oxide Fuel Cells, Fig. 9** Distribution of nuclear density as a function of temperature in  $(\text{Pr}_{0.9}\text{La}_{0.1})(\text{Ni}_{0.74}\text{Cu}_{0.21}\text{Ga}_{0.05})\text{O}_{4+d}$  as determined by MEM fitting of neutron diffraction data at (a) 27 °C, (b) 395 °C, (c) 607 °C, (d) 813 °C, and (e) 1016 °C. (Reproduced with permission from Yashima et al. JACS)

take place over the timescale of the 20–30 years from 2010. Moving back down the development chain, this implies that any new materials must be adopted within the next decade or so, and the real scope of the task becomes apparent. How this can be achieved has been described in a short editorial by Kilner [44].

- Clearly, conventional trial and error methods of materials discovery are not going to meet this aggressive agenda and an accelerated form of materials discovery is needed. The important question is what type of accelerated materials development tools will become available? A new topic of “Materials Informatics” has emerged, which employs the use of large databases of materials properties obtained from conventional, combinatorial, or computational

sources. The databases are then interrogated using techniques, such as data mining, neural networks, etc. This new and developing technique is still in its infancy, and very few databases exist which cover the functional properties of oxide ceramics.

- Much has been made of combinatorial approaches to materials discovery; however, there are many barriers to the introduction of these methods to SOFC materials, not least their suitability to synthesize libraries of complex multicomponent oxides, such as the cathode materials  $\text{La}_{1-x}\text{Sr}_x\text{Co}_{1-y}\text{Fe}_y\text{O}_{3-\delta}$  [45]. In addition to these limitations, there is the requirement for rapid screening methods to allow combinatorial libraries to be measured in an accelerated manner. This is not an easy problem to solve for applications that rely upon measuring complex electro-catalytic activity in very aggressive environments, such as SOFC electrodes.
- Computer simulation offers an alternative way of providing guidelines for materials searching. For example, atomistic simulation of defects and transport in materials is well established; however, it is hardly a rapid process and much of the effort is expended in the rationalization of existing experimental data. A change in scope is needed to exploit the potential of such techniques to predictive materials screening.

It is important that these rather more pragmatic techniques, mentioned above, are developed in parallel with the more conventional intuitive methods to give development engineers rapid access to new materials.

## Development of In Situ Diagnostics

Identifying and developing new materials for all components of a solid oxide fuel-cell system is only the first stage in producing a device. There are several key requirements, such as durability and compatibility, which have to be fully investigated before a material can be incorporated into a

working fuel cell. As detailed earlier, this type of cell operates in a relatively harsh environment with a high temperature of operation and a wide  $pO_2$  range. It is therefore essential to gain a full understanding of the behavior of each of the cell components and the stack itself as a function of all of these parameters in situ. Consequently, there has been an increasing demand for in situ characterization techniques to give real-time insights into device performance. Of course, in situ characterization covers a wide variety of techniques and properties. When discussing in situ characterization, it has to be considered that measurements are obtained as a function of either high temperature, variable  $pO_2$ , or electrical load, or indeed a combination of each of these. Many in situ studies focus on the structural characterization of individual materials, while further studies map the temperature distribution over a single fuel cell. In this section, the current status of in situ characterization of fuel cells and fuel cell materials are considered using a variety of techniques including diffraction and spectroscopy and some of the challenges are detailed that remain in fully understanding all of the processes; mechanical, structural, and electrochemical, that govern fuel-cell performance and durability.

### In Situ Materials Characterization

In considering the development of new materials for fuel cells, many authors have used diffraction techniques to probe the high-temperature stability of individual components and to investigate any potential phase-transformation problems on thermal cycling. Information that can be obtained readily can be classified as either crystallographic (phase evolution/reactivity) or mechanical (stress evolution in ceramics). Initially, users are likely to consider the use of powder x-ray diffraction to investigate all of the individual functional components, given the relative ease of access to the equipment. However, the information obtained from x-ray techniques is limited by a number of factors, including the limited resolution of instruments and the dependence of the x-ray-scattering factors on atomic number, meaning access to

information from elements, such as oxygen, is limited. There are many examples of information being derived successfully from x-ray diffraction studies with perhaps the simplest examples being the study of the reactivity of functional components at operating temperatures. Zhu et al. [46], for instance, have investigated the novel cathode material  $PrBaCo_2O_{5+\delta}$  in contact with  $Ce_{0.8}Sm_{0.2}O_{1.9}$  as a composite, finding no discernible reaction at temperatures up to 1,100 °C, over only a short period of 3 h; while Sayers et al. [47] investigated nickelate cathodes on both  $Ce_{1-x}Gd_xO_{2-d}$  (CGO) and  $La_{1-x}Sr_xGa_{1-y}Mg_yO_{3-d}$  (LSGM) electrolytes, finding differing degrees of reaction depending upon both time and temperature. Significant reactivity was identified by these authors with CGO at temperatures greater than 800 °C. It was however noted that the in situ characterization of these reactions was limited by the data collection time and instrument resolution.

In determining the residual stress of an anode-supported SOFC, Fischer et al. [48] have used x-ray diffraction to map the stress distribution as a function of processing and also have monitored the change in the stress state at room temperature and at 800 °C. However, this study is limited by the operating temperature data having to be recorded after annealing, once the sample has returned to room temperature. Evidently, in situ characterization is of considerable value, but can be limited by the capabilities of the instrumentation/technique, and for SOFCs laboratory, x-ray techniques are certainly restricted.

For either higher resolution or greater phase discrimination, there are two main alternatives to laboratory x-ray techniques: synchrotron powder diffraction or neutron diffraction. Each of these techniques has its own advantages, with neutron-powder diffraction enabling access to light elements while synchrotron-diffraction experiments offer exceptionally high-peak resolution. The use of neutron diffraction at elevated temperature has proven to be invaluable in providing information on cathode materials in particular [49–54], while synchrotron sources have been at the forefront of the development of new techniques, such as 3 dimensional imaging of components.

## Neutron Scattering Studies of Fuel Cell Oxides

Neutron diffraction has long been viewed as an essential tool for the structural characterization of novel materials [55, 56]. It is only relatively recently, however, that neutron diffraction has been used to characterize fuel cell oxides. Recent developments that have attracted researchers to the technique include the production of instruments that can offer small sample sizes and high-temperature stages with variable atmosphere capabilities, extending the in situ capabilities of this technique. Some of the earliest studies of fuel cell oxides were by necessity under ambient conditions and focussed on proton-conducting barium cerates [57–59] in which a structural distortion of  $\text{BaCe}_{1-x}\text{Nd}_x\text{O}_{3-\delta}$  was determined and related to the release of spontaneous strain with increasing Nd content. Since these initial works, several authors have turned to neutron diffraction to gain additional structural information. Slater et al. [60] were among the first to use this technique to characterize an electrolyte material,  $\text{La}_{0.9}\text{Sr}_{0.1}\text{Ga}_{0.8}\text{Mg}_{0.2}\text{O}_{3-\delta}$ . Here the authors identified a significant structural difference between the substituted material and the parent  $\text{LaGaO}_3$ , with the Sr- and Mg-substituted material adopting a more complex monoclinic structure at room temperature and undergoing several phase transitions on heating to 1,000 °C. A tilting of  $\text{GaO}_6$  octahedra was observed and related to the change in activation energy of conduction on heating identified from previous studies.

Use of neutron diffraction to study electrode materials in situ is a relatively recent development, with much of the current interest directed toward the phase evolution in novel cathodes with complex crystallography. Alonso [49] has provided an excellent review of the potential of neutron diffraction for characterizing fuel cell materials and detailed work on the  $\text{La}_2\text{MO}_{4+\delta}$  ( $M = \text{Ni, Cu, Co}$ ) series of cathodes stating that the relationship between M–O distances and electrical properties can be readily determined as a function of temperature. With the  $\text{La}_2\text{MO}_{4+\delta}$  materials, electrical changes occur on introduction

of an A-site substituent, such as Sr, and the relationship between Sr content, apical M–O bond length, and total conductivity is resolved from this high resolution structural data. Further work by Skinner [54] focussed on the location of the oxygen interstitial, a particular strength of neutron scattering, identifying the relationship between oxygen content and phase, varying both temperature and atmosphere. Additionally, the two phase nature of the  $\text{La}_2\text{Ni}_{1-x}\text{Co}_x\text{O}_{4+\delta}$  was clearly determined [61] from in situ studies where previous x-ray techniques had indicated a single phase. Information on the nature of the conduction properties of cathode materials can be inferred from the structural data obtained from these measurements, with Hou et al. [62] arguing that the nature of the Ni redox couple in  $\text{LaNi}_{1-x}\text{Mo}_x\text{O}_3$  cathodes can be determined from the crystallographic data obtained. They also suggest that oxygen deficiency was observed leading to the potentially high oxide ion mobility required for a mixed conductor.

While this information on the crystal chemistry is of importance in determining the potential for new materials, it is the latest advances in data processing and interpretation that enable both structural and chemical information to be extracted from one data set. The advent of the Maximum Entropy Method (MEM) [63] for analysis of neutron-diffraction data has enabled authors to extract chemical-pathway data from the neutron density. Yashima et al. [64, 65] used the MEM technique to visualize the diffusion pathway of the oxide ions in an anisotropic  $\text{Pr}_2\text{NiO}_{4+\delta}$ -based interstitial oxide ion conductor. The data obtained, Fig. 9, at temperatures of up to 812 °C clearly illustrate 2-D diffusional pathways in the *ab* plane of the anisotropic crystal structure. This method has also been used to verify molecular dynamics studies of the isostructural  $\text{La}_2\text{NiO}_{4+\delta}$  material [66], highlighting the benefits of combining both the experimental studies with simulation techniques.

Identification of novel conduction mechanisms is a particular strength of neutron techniques, and these studies have been extended to include the novel electrolyte apatite materials, with local defects identified [67–70]. Further electrolyte

studies have included determining the total conductivity of the potential electrolyte,  $\text{La}_2\text{Mo}_2\text{O}_9$ , in situ through impedance spectroscopy and correlating these time-resolved data with structural transformations revealed through neutron-diffraction measurements [71, 72]. This relies upon the availability of well-designed experimental stages optimized for diffraction beamlines [71]. Engaging with central facilities to design, build, and commission this equipment is therefore essential.

### Synchrotron X-Ray Studies

Synchrotron radiation is incredibly versatile allowing a wide variety of experimental techniques to be developed. Of direct interest to solid oxide fuel-cell science and technology are both diffraction and spectroscopy. Diffraction beamlines offer the potential to access complex structural information that is not revealed by competing diffraction techniques, while the spectroscopic techniques (X-ray Absorption Near Edge Spectroscopy [XANES] and Extended X-ray Absorption Fine Structure [EXAFS]) allow users to access chemical information, such as redox kinetics. The latest developments include 3D tomography of complete cells which give unparalleled information about the microstructure of composite electrodes [73, 74].

**Synchrotron Diffraction** In situ synchrotron x-ray-powder diffraction of fuel cell components has developed significantly over recent years as sample stages, and instrument development has enabled rapid data collection as a function of atmosphere with unprecedented resolution [75]. As the MEM technique can be applied to neutron diffraction data, so it can also be applied to synchrotron diffraction data, with Itoh et al. [76, 77] showing the complementary data obtained from combining both techniques. Through their investigation of  $\text{La}_{1-x}\text{Sr}_x\text{MnO}_{3-\delta}$  (LSM)/ $\text{Ba}_{1-x}\text{Sr}_x\text{Co}_{1-y}\text{Fe}_y\text{O}_3$  (BSCF) composites, they have determined both the ionic and electronic conduction pathways, with the synchrotron data highlighting isotropic Mn–O covalent bonds through which the

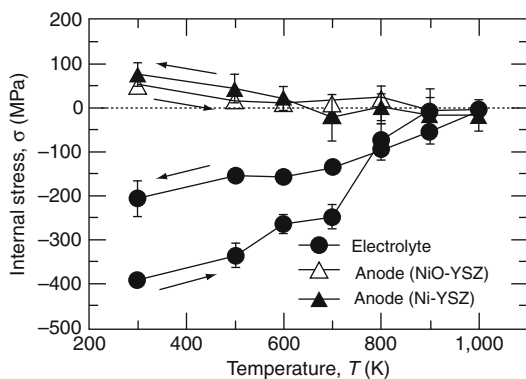
electrons will pass, leading to good electronic conductivity.

As well as obtaining data as a function of temperature and atmosphere, Hagen et al. [78] have demonstrated that depth-resolved data acquisition from NiO/YSZ cermets is possible. Using an advanced data collection mode employing a spiral slit and beamstop, the authors were able to follow the redox process between Ni and NiO. As the distance from the free anode surface increased, a reduction of the reaction rate was observed which is attributed to the difficulty of gas penetration to the electrode/electrolyte interface. As these data were obtained as a function of depth under redox conditions, a logical extension is to include larger operating cells in this environment to fully characterize structural/chemical changes under realistic conditions. These measurements could therefore have a dramatic impact upon cell development.

Residual stress within cells and components is evidently a key concern for developers of SOFCs [79], and analysis of this can readily be achieved using synchrotron x-ray studies. Villanova et al. [80] demonstrated the complementarity of both laboratory and synchrotron x-ray sources through their investigation of all components of the fuel cell. From lab x-ray studies they were able to determine residual stress in an anode-supported SOFC. Macroscopic stresses were determined in each layer through the analysis of lattice deformation. A significant finding of inhomogeneous stress distribution in the electrolyte led these authors to use the synchrotron technique to investigate the local stress from analysis of the stress tensor in the individual electrolyte grains.

A further study [81] examined the development of internal stress as a function of temperature for an anode-supported cell based on a Sc stabilized zirconia (ScSZ) electrolyte with a NiO-3 mol%-YSZ anode, finding that there were significant changes in the internal stress in both NiO and ScSZ that were not fully reversible, Fig. 10. Residual stress in the electrolyte was measured as a function of the reduction cycle and found to be 400 MPa in air, but decreased to 200 MPa on reduction of the NiO, and concluded that this





**Solid Oxide Fuel Cells, Fig. 10** Changes in internal stress of a Scandia stabilized zirconia electrolyte and NiO-YSZ anode as determined by in situ synchrotron measurements. (Reproduced with permissions Sumi et al. [81])

redox cycle would be detrimental to SOFC performance.

While these studies are of importance, there are no studies of stress evolution in a complete functioning cell under electrical load, or indeed in a fuel cell stack, and this is evidently the next development step. The data obtained so far from synchrotron and laboratory x-ray studies highlight the potential of these techniques to advance the current understanding of failure mechanisms in operating SOFCs.

**Spectroscopy – XANES and EXAFS** Spectroscopic techniques complement the diffraction measurements previously discussed as these target the local structure, giving details of the coordination environment surrounding particular chemical species. Thus, through control of the experimental conditions, it is feasible to extract chemical information from in situ measurements of fuel cell materials. There have been a number of initial studies of the room temperature and local structure of SOFC electrolytes, with Yamazaki et al. [82–84] considering the effect of dopants on the defect structure of  $\text{CeO}_{2-\delta}$ -based electrolytes. Further investigation of the Ce  $L_{\text{III}}$  edge spectra of ceria electrolytes was reported by Hormes et al. [85], who have also applied the same techniques to the cathode material  $\text{La}_{1-x}\text{Sr}_x\text{MnO}_{3-\delta}$  (LSM). Each of these studies considered the bulk polycrystalline material, whereas Zhang et al. [86, 87] have used XANES

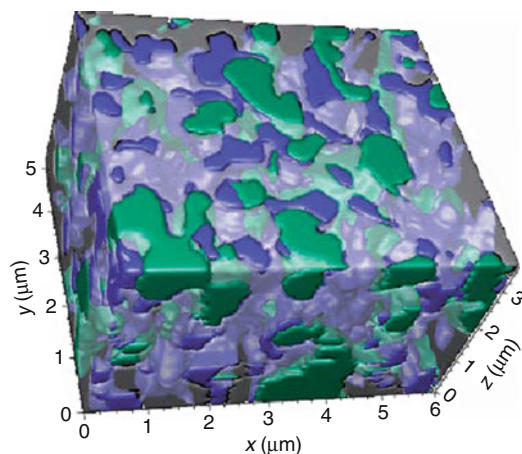
to investigate the growth mechanism and crystallization of  $\text{CeO}_2$  nanoparticles.

In considering LSM samples, significant differences in the local structure of thin film samples when compared with bulk LSM were observed [88], leading to the conclusion that the coordination environment of the Mn species is less distorted in the thin film. With the recent surge in interest in thin-film technologies for fuel cells, this may prove to be a significant finding and highlights the power of x-ray spectroscopy to detect subtle differences that may have a dramatic impact on material performance.

The real strength of x-ray-absorption spectroscopy, however, is in extending these measurements to both time-resolved and temperature-dependent measurements. Species that are commonly found in solid oxide fuel-cell components are easily accessed as the techniques are element specific. As well as accessing element-specific information, the XANES technique is also sensitive to valence state, and hence redox processes and kinetic information can be extracted from in situ data. It is also straightforward to control the atmosphere under which the measurements are undertaken, so kinetics of both anode and cathode materials as functions of temperature, time, and  $p\text{O}_2$  can be obtained. Indeed, this has recently been demonstrated with redox kinetics for fast oxide ion-conducting  $\text{CeNbO}_{4+\delta}$  having been determined from Ce  $L_{\text{III}}$  edge XANES data [89].

**3D Microtomography** Perhaps one of the most exciting developments involving synchrotron radiation has been the advent of three-dimensional tomography [73, 74]. With this technique, it has been shown that detailed information about the internal structure of complex composites can be obtained, enabling researchers to gain vital information on the length of triple phase boundaries (TPB). This also allows the differentiation between active and inactive TPBs and has so far been demonstrated with anode cermets (Ni-YSZ). While not currently available as an in situ measurement, this is an obvious extension and is no doubt a future development for this technique. Currently these measurements are only available at a small number of sites





**Solid Oxide Fuel Cells, Fig. 11** 3D reconstruction of the anode microstructure of a Ni-YSZ anode determined through the use of Focussed Ion Beam Imaging. (Reproduced with permission Wilson et al. Nat Mats)

worldwide, and hence this is a clear limitation. But as interest grows in this technique, it is highly likely that future developments at synchrotron sources will include this capability.

Wilson et al. [74] pioneered this technique using a Focussed Ion Beam slice and view method to allow the electrochemical performance and microstructure of materials to be quantitatively connected. In their pioneering work, a direct measurement of the TPB length was achieved through analysis of the reconstructed 3D anode, Fig. 11. From the analysis, they differentiate between interconnected and unconnected pathways, finding 63% of TPBs are interconnected. A high level of interconnection is required for electrochemical reactions to occur, and quantifying the microstructure in this way enables further optimization to proceed.

Shearing has adapted this process to incorporate a focussed ion beam lift-out technique, and in combination with software development, has shown that detailed phase contrast can be obtained from the Ni-YSZ couple, Fig. 12, leading to greater data quality and reduced uncertainty regarding redeposition of sputtered material. The use of this FIB tomography technique is unfortunately destructive [90], and hence the use of x-ray tomography presents an ideal opportunity to extract similar TPB information

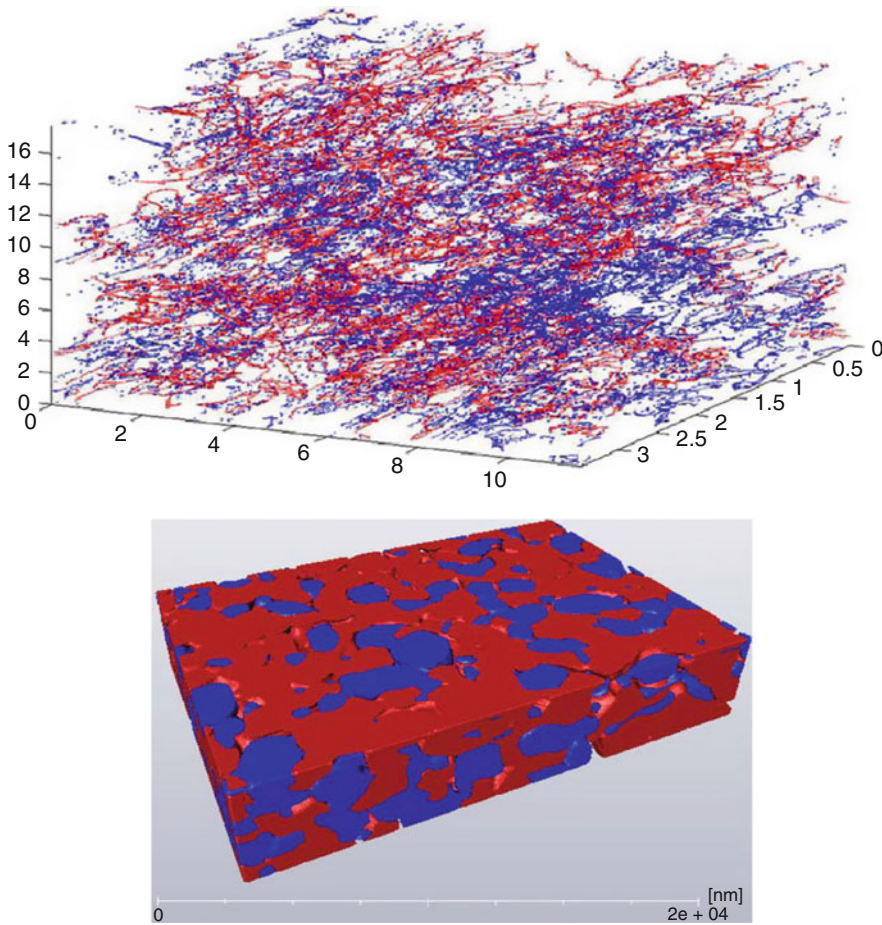
nondestructively [91]. While these data can be collected from standard x-ray systems, the use of a nano-CT system at a synchrotron source will enable higher resolutions to be achieved.

## Raman Spectroscopy

Another promising in situ characterization method to have been proposed recently relies on the use of Raman spectroscopy [90, 92–94] to optically detect changes in the fuel cell under examination. Using Raman spectroscopy is entirely complementary to the previously discussed techniques and delivers data, for instance, on the heat distribution across a cell. Maher et al. [93] have demonstrated the effective use of Raman spectroscopy with a Gd-substituted ceria in which the shift of a characteristic peak at  $460\text{ cm}^{-1}$  can be correlated accurately with temperature and thus provides a method by which temperature distribution with high spatial resolution can be measured. Previously, the use of the Raman technique to determine the chemistry occurring at electrodes in SOFCs was highlighted [90], with particular emphasis on the monitoring of electrochemical processes at the anode. In this work, the disappearance of graphitic carbon was monitored as well as the kinetics of the Ni-NiO redox, and finally it was suggested that phonon modes of YSZ electrolytes could be correlated with lattice parameter changes, leading to a diagnostic for thermal gradients within cells. Subsequent work [95] has highlighted that oxidation processes can be monitored in situ and the effect of using carbon based fuels determined. Deposition of graphitic species (either ordered or disordered) was found to vary depending on carbon source and potential.

## Summary

In situ characterization of solid oxide fuel cells can be achieved through the use of a variety of techniques to produce direct information on the chemistry, structure, and mechanical properties of the material/cell of interest. Rapid developments in test equipment offer ever greater levels of



**Solid Oxide Fuel Cells, Fig. 12** Determination of anode microstructure and the extraction of active TPB length determined through FIB tomography. (Reproduced with permission Shearing et al. Figs. 4 and 5)

detail, with many techniques providing submicron resolution, and below, of the critical processes affecting solid oxide fuel-cell operation. Particularly the non-destructive nature of many of these techniques allows full cycles of operation to potentially be analyzed and the causes of performance degradation to be determined.

### Future Directions

Although the main aim of this article is to look at the future of the SOFC, this has been in the main a look at the near-term future and the possible designs and materials that the SOFC might move

toward. The long-term future of the SOFC is much more difficult to predict because it will depend very heavily upon the diversity of renewable energy sources, what energy vectors are employed, and what fuels evolve to form the future energy mix. Most forecasters agree that the supply of usable hydrocarbons is limited and may already have peaked in the early part of the twenty-first century. The relative roles of newer fuels, such as bio-derived hydrocarbons and hydrogen in this future mix remains unclear; however, because of their high efficiency and fuel flexibility, it is likely that SOFCs will see widespread adoption and continued development in both the short-and long-term future.

## Bibliography

### Primary Literature

- Huang K, Goodenough JB (2009) Solid oxide fuel cell technology principles, performance and operations. Woodhead Energy Series. Woodhead Publishing Ltd, Cambridge, p 344
- Singhal SC, Kendall K (2003) High-temperature solid oxide fuel cells: fundamentals, design and applications. Elsevier Advanced Technology, Oxford, p xvi, 405 p
- Lawlor V, Griesser S, Buchinger G, Olabi AG, Cordiner S, Meissner D (2010) Review of the micro-tubular solid oxide fuel cell: Part I. Stack design issues and research activities (vol 193, p 387, 2009). *J Power Sources* 195(3):936–936
- Kendall K (2010) Progress in microtubular solid oxide fuel cells. *Int J Appl Ceram Technol* 7(1):1–9
- Sammes NM, Du Y, Bove R (2005) Design and fabrication of a 100 W anode supported micro-tubular SOFC stack. *J Power Sources* 145(2):428–434
- Suzuki T, Funahashi Y, Yamaguchi T, Fujishiro Y, Awano M (2008) Cube-type micro SOFC stacks using sub-millimeter tubular SOFCs. *J Power Sources* 183(2):544–550
- Suzuki T, Funahashi Y, Yamaguchi T, Fujishiro Y, Awano M (2009) Performance of the micro-SOFC module using submillimeter tubular cells. *J Electrochem Soc* 156(3):B318–B321
- Hibino T, Iwahara H (1993) Simplification of solid oxide fuelcell system using partial oxidation of methane. *Chem Lett* 1993(7):1131–1134
- Yano M, Tomita A, Sano M, Hibino T (2007) Recent advances in single-chamber solid oxide fuel cells: a review. *Solid State Ionics* 177(39–40):3351–3359
- Riess I (2008) On the single chamber solid oxide fuel cells. *J Power Sources* 175(1):325–337
- Evans A, Bieberle-Hutter A, Rupp JLM, Gauckler LJ (2009) Review on microfabricated micro-solid oxide fuel cell membranes. *J Power Sources* 194(1):119–129
- Su PC, Chao CC, Shim JH, Fasching R, Prinz FB (2008) Solid oxide fuel cell with corrugated thin film electrolyte. *Nano Lett* 8(8):2289–2292
- Thorel AS, Chesnaud A, Viviani M, Barbucci A, Presto S, Piccardo P, Ilhan Z, Vladikova D, Stoyanov Z (2009) IDEAL-cell, a high temperature innovative dual membrane fuel cell. *ECS Trans* 25(2):753–762
- Kilner JA (2000) Fast oxygen transport in acceptor doped oxides. *Solid State Ionics* 129(1):13–23
- Merkle R, Maier J, Bouwmeester HJM (2004) A linear free energy relationship for gas-solid interactions: correlation between surface rate constant and diffusion coefficient of oxygen tracer exchange for electron-rich perovskites. *Angew Chem Int Ed* 43(38):5069–5073
- Tietz F, Mai A, Stover D (2008) From powder properties to fuel cell performance – a holistic approach for SOFC cathode development. *Solid State Ionics* 179(27–32):1509–1515
- Kilner JA (2007) Optimisation of oxygen ion transport in materials for ceramic membrane devices. *Faraday Discuss* 134:9–15
- Garcia-Barriocanal J, Rivera-Calzada A, Varela M, Sefrioui Z, Iborra E, Leon C, Pennycook SJ, Santamaria J (2008) Colossal ionic conductivity at interfaces of epitaxial  $\text{ZrO}_2\text{:Y}_2\text{O}_3\text{/SrTiO}_3$  heterostructures. *Science* 321(5889):676–680
- Georges S, Goutenoire F, Altorfer F, Sheptyakov D, Fauth F, Suard E, Lacorre P (2003) Thermal, structural and transport properties of the fast oxide-ion conductors  $\text{La}_{2-x}\text{R}_x\text{Mo}_2\text{O}_9$  (R=Nd, Gd, Y). *Solid State Ionics* 161(3–4):231–241
- Kendrick E, Knight KS, Slater PR (2009) Ambi-site substitution of Mn in lanthanum germanate apatites. *Mater Res Bull* 44(8):1806–1809
- Lacorre P, Goutenoire F, Bohnke O, Retoux R, Laligant Y (2000) Designing fast oxide-ion conductors based on  $\text{La}_2\text{Mo}_2\text{O}_9$ . *Nature* 404(6780):856–858
- Li Q, Xia T, Liu XD, Ma XF, Meng J, Cao XQ (2007) Fast densification and electrical conductivity of yttria-stabilized zirconia nanoceramics. *Mater Sci Eng B* 138(1):78–83
- Thangadurai V, Weppner W (2005) Studies on electrical properties of  $\text{La}_{0.8}\text{Sr}_{0.2}\text{Ga}_{0.8}\text{Mg}_{0.2}\text{O}_{2.80}$  (LSGM) and LSGM-SrSn $_{1-x}\text{Fe}_x\text{O}_3$  (x=0.8; 0.9) composites and their chemical reactivity. *Electrochim Acta* 50(9):1871–1877
- Tsai D-S, Hsieh M-J, Tseng J-C, Lee H-Y (2005) Ionic conductivities and phase transitions of lanthanide rare-earth substituted  $\text{La}_2\text{Mo}_2\text{O}_9$ . *J Eur Ceram Soc* 25(4):481–487
- Vannier RN, Skinner SJ, Chater RJ, Kilner JA, Mairesse G (2003) Oxygen transfer in BIMEVOX materials. *Solid State Ionics* 160(1–2):85–92
- Verkerk MJ, Keizer K, Burggraaf AJ (1980) High oxygen ion conduction in sintered oxides of the  $\text{Bi}_2\text{O}_3\text{-Er}_2\text{O}_3$  system. *J Appl Electrochem* 10(1):81–90
- Kosacki I, Rouleau CM, Becher PF, Bentley J, Lowndes DH (2005) Nanoscale effects on the ionic conductivity in highly textured YSZ thin films. *Solid State Ionics* 176(13–14):1319–1326
- Karthikeyan A, Chang CL, Ramanathan S (2006) High temperature conductivity studies on nanoscale yttria-doped zirconia thin films and size effects. *Appl Phys Lett* 89(18):183116
- Azad S, Marina OA, Wang CM, Saraf L, Shutthanandan V, McCready DE, El-Azab A, Jaffe JE, Engelhard MH, Peden CHF, Thevuthasan S (2005) Nanoscale effects on ion conductance of layer-by-layer structures of gadolinia-doped ceria and zirconia. *Appl Phys Lett* 86(13):131906
- Korte C, Peters A, Janek J, Hesse D, Zakharov N (2008) Ionic conductivity and activation energy for oxygen ion transport in superlattices – the semicoherent multilayer system YSZ ( $\text{ZrO}_2+9.5 \text{ mol}\% \text{Y}_2\text{O}_3$ )/ $\text{Y}_2\text{O}_3$ . *Phys Chem Chem Phys* 10(31):4623–4635
- Guo X (2009) Comment on “Colossal ionic conductivity at interfaces of epitaxial  $\text{ZrO}_2\text{:Y}_2\text{O}_3\text{/SrTiO}_3$  heterostructures”. *Science* 324(5926):465

32. Cavallaro A, Burriel M, Roqueta J, Apostolidis A, Bernardi A, Tarancón A, Srinivasan R, Cook SN, Fraser HL, Kilner JA, McComb DW, Santiso J (2010) Electronic nature of the enhanced conductivity in YSZ-STO multilayers deposited by PLD. *Solid State Ionics* 181(13–14):592–601
33. Kilner JA (2008) Ionic conductors feel the strain. *Nat Mater* 7(11):838–839
34. Pennycook TJ, Beck MJ, Varga K, Varela M, Pennycook SJ, Pantelides ST (2010) Origin of colossal ionic conductivity in oxide multilayers: interface induced sublattice disorder. *Phys Rev Lett* 104(11):115901
35. Kushima A, Yildiz B (2010) Oxygen ion diffusivity in strained yttria stabilized zirconia: where is the fastest strain? *J Mater Chem* 20(23):4809–4819
36. Schichtel N, Korte C, Hesse D, Janek J (2009) Elastic strain at interfaces and its influence on ionic conductivity in nanoscaled solid electrolyte thin films—theoretical considerations and experimental studies. *Phys Chem Chem Phys* 11(17):3043–3048
37. Peters A, Korte C, Hesse D, Zakharov N, Janek J (2007) Ionic conductivity and activation energy for oxygen ion transport in superlattices – the multilayer system CSZ (ZrO<sub>2</sub>+CaO)/Al<sub>2</sub>O<sub>3</sub>. *Solid State Ionics* 178(1–2):67–76
38. Korte C, Schichtel N, Hesse D, Janek J (2009) Influence of interface structure on mass transport in phase boundaries between different ionic materials experimental studies and formal considerations. *Monatshefte Fur Chemie* 140(9):1069–1080
39. Otsuka K, Matsunaga K, Nakamura A, Ji S, Kuwabara A, Yamamoto T, Ikuhara Y (2004) Effects of dislocations on the oxygen ionic conduction in yttria stabilized zirconia. *Mater Trans* 45(7):2042–2047
40. Otsuka K, Kuwabara A, Nakamura A, Yamamoto T, Matsunaga K, Ikuhara Y (2003) Dislocation-enhanced ionic conductivity of yttria-stabilized zirconia. *Appl Phys Lett* 82(6):877–879
41. Sase M, Yashiro K, Sato K, Mizusaki J, Kawada T, Sakai N, Yamaji K, Horita T, Yokokawa H (2008) Enhancement of oxygen exchange at the hetero interface of (La, Sr)CoO<sub>3</sub>/(La, Sr)<sub>2</sub>CoO<sub>4</sub> in composite ceramics. *Solid State Ionics* 178(35–36):1843–1852
42. Ullmann H, Trofimenko N, Tietz F, Stover D, Ahmad-Khanlou A (2000) Correlation between thermal expansion and oxide ion transport in mixed conducting perovskite-type oxides for SOFC cathodes. *Solid State Ionics* 138(1–2):79–90
43. Tarancon M, Burriel M, Santiso J, Skinner SJ, Kilner JA (2010) Advances in layered oxide cathodes for intermediate temperature solid oxide fuel cells. *J Mater Chem* 20:3799–3813
44. Kilner JA (2009) Accelerated R&D of solid oxide fuel cells with lowering operation temperature vision. *Electrochemistry* 77(2):113–113
45. Rossiny JCH, Julis J, Fearn S, Kilner JA, Zhang Y, Chen LF, Yang SF, Evans JRG (2008) Combinatorial characterisation of mixed conducting perovskites. *Solid State Ionics* 179(21–26):1085–1089
46. Zhu CJ, Liu XM, Yi CS, Pei L, Wang DJ, Yan DT, Yao KG, Lu TQ, Su WH (2010) High-performance PrBaCo<sub>2</sub>O<sub>5</sub>+delta-Ce<sub>0.8</sub>Sm<sub>0.2</sub>O<sub>1.9</sub> composite cathodes for intermediate temperature solid oxide fuel cell. *J Power Sources* 195(11):3504–3507
47. Sayers R, Liu J, Rustomji B, Skinner SJ (2008) Novel K<sub>2</sub>NiF<sub>4</sub>-type materials for solid oxide fuel cells: compatibility with electrolytes in the intermediate temperature range. *Fuel Cells* 8(5):338–343
48. Fischer W, Malzbender J, Blass G, Steinbrech RW (2005) Residual stresses in planar solid oxide fuel cells. *J Power Sources* 150:73–77
49. Alonso JA, Martinez-Lope MJ, Aguadero A, Daza L (2008) Neutron powder diffraction as a characterization tool of solid oxide fuel cell materials. *Prog Solid State Chem* 36(1–2):134–150
50. Aguadero A, Alonso JA, Daza L (2008) Oxygen excess in La<sub>2</sub>CoO<sub>4</sub>+delta: a neutron diffraction study. *Z Naturforsch Sect B J Chem Sci* 63(6):615–622
51. Aguadero A, Alonso JA, Fernandez-Diaz MT, Escudero MJ, Daza L (2007) In situ high temperature neutron powder diffraction study of La<sub>2</sub>Ni<sub>0.6</sub>Cu<sub>0.4</sub>O<sub>4</sub>+delta in air: correlation with the electrical behaviour. *J Power Sources* 169(1):17–24
52. Aguadero A, Perez M, Alonso JA, Daza L (2005) Neutron powder diffraction study of the influence of high oxygen pressure treatments on La<sub>2</sub>NiO<sub>4</sub>+delta and structural analysis of La<sub>2</sub>Ni<sub>1-x</sub>Cu<sub>x</sub>O<sub>4</sub>+delta (0 <= x <= 1). *J Power Sources* 151:52–56
53. Bartolome JF, Bruno G, Deaza AH (2008) Neutron diffraction residual stress analysis of zirconia toughened alumina (ZTA) composites. *J Eur Ceram Soc* 28(9):1809–1814
54. Skinner SJ (2003) Characterisation of La<sub>2</sub>NiO<sub>4</sub>+delta using in situ high temperature neutron powder diffraction. *Solid State Sci* 5(3):419–426
55. Goodenough JB (2004) Electronic and ionic transport properties and other physical aspects of perovskites. *Rep Prog Phys* 67(11):1915–1993
56. Goodenough JB (2003) Oxide-ion electrolytes. *Annu Rev Mater Res* 33:91–128
57. Knight KS, Soar M, Bonanos N (1992) Crystal-structures of gadolinium-doped and yttrium-doped barium cerate. *J Mater Chem* 2(7):709–712
58. Knight KS, Bonanos N (1995) A high-resolution neutron powder diffraction study of neodymium doping in barium cerate. *Solid State Ionics* 77:189–194
59. Jacobson AJ, Tofield BC, Fender BEF (1972) Structures of BaCeO<sub>3</sub>, BaPrO<sub>3</sub> and BaTbO<sub>3</sub> by neutron-diffraction – lattice-parameter relations and ionic radii in O-perovskites. *Acta Crystallogr Sect B Struct Crystallogr Cryst Chem B* 28(Mar 15): 956–961
60. Slater PR, Irvine JTS, Ishihara T, Takita Y (1998) High-temperature powder neutron diffraction study of the oxide ion conductor La<sub>0.9</sub>Sr<sub>0.1</sub>Ga<sub>0.8</sub>Mg<sub>0.2</sub>O<sub>2.85</sub>. *J Solid State Chem* 139(1):135–143

61. Skinner SJ, Amow G (2007) Structural observations on La-2(Ni, CO)O-4 +/--delta phases determined from in situ neutron powder diffraction. *J Solid State Chem* 180(7):1977–1983
62. Hou SE, Alonso JA, Rajasekhara S, Martinez-Lope MJ, Fernandez-Diaz MT, Goodenough JB (2010) Defective Ni perovskites as cathode materials in intermediate-temperature solid-oxide fuel cells: a structure-properties correlation. *Chem Mater* 22(3):1071–1079
63. Sakata M, Mori R, Kumazawa S, Takata M, Toraya H (1990) Electron-density distribution from x-ray-powder data by use of profile fits and the maximum-entropy method. *J Appl Crystallogr* 23:526–534
64. Yashima M, Sirikanda N, Ishihara T (2010) Crystal structure, diffusion path, and oxygen permeability of a Pr<sub>2</sub>NiO<sub>4</sub>-based mixed conductor (Pr<sub>0.9</sub>La<sub>0.1</sub>)(Ni<sub>0.74</sub>Cu<sub>0.21</sub>Ga<sub>0.05</sub>)O<sub>4</sub>+delta. *J Am Chem Soc* 132(7):2385–2392
65. Yashima M, Enoki M, Wakita T, Ali R, Matsushita Y, Izumi F, Ishihara T (2008) Structural disorder and diffusional pathway of oxide ions in a doped Pr<sub>2</sub>NiO<sub>4</sub>-based mixed conductor. *J Am Chem Soc* 130(9):2762
66. Chronos A, Parfitt D, Kilner JA, Grimes RW (2010) Anisotropic oxygen diffusion in tetragonal La<sub>2</sub>NiO<sub>4</sub>+delta: molecular dynamics calculations. *J Mater Chem* 20(2):266–270
67. Guillot S, Beaudet-Savignat S, Lambert S, Vannier RN, Rousse P, Porcher F (2009) Evidence of local defects in the oxygen excess apatite La-9.67(SiO<sub>4</sub>)(6)O-2.5 from high resolution neutron powder diffraction. *J Solid State Chem* 182(12):3358–3364
68. Leon-Reina L, Porras-Vazquez JM, Losilla ER, Aranda MAG (2006) Interstitial oxide positions in oxygen-excess oxy-apatites. *Solid State Ionics* 177(15–16):1307–1315
69. Leon-Reina L, Losilla ER, Martinez-Lara M, Bruque S, Llobet A, Sheptyakov DV, Aranda MAG (2005) Interstitial oxygen in oxygen-stoichiometric apatites. *J Mater Chem* 15(25):2489–2498
70. Leon-Reina L, Losilla ER, Martinez-Lara M, Bruque S, Aranda MAG (2004) Interstitial oxygen conduction in lanthanum oxy-apatite electrolytes. *J Mater Chem* 14(7):1142–1149
71. Engin TE, Powell AV, Haynes R, Chowdhury MAH, Goodway CM, Done R, Kirichek O, Hull S (2008) A high temperature cell for simultaneous electrical resistance and neutron diffraction measurements. *Rev Sci Instrum* 79(9):095104
72. Liu J (2010) Department of Materials. Imperial College London, London
73. Shearing PR, Golbert J, Chater RJ, Brandon NP (2009) 3D reconstruction of SOFC anodes using a focused ion beam lift-out technique. *Chem Eng Sci* 64(17):3928–3933
74. Wilson JR, Kobsiriphat W, Mendoza R, Chen HY, Hiller JM, Miller DJ, Thornton K, Voorhees PW, Adler SB, Barnett SA (2006) Three-dimensional reconstruction of a solid-oxide fuel-cell anode. *Nat Mater* 5(7):541–544
75. Thompson SP, Parker JE, Potter J, Hill TP, Birt A, Cobb TM, Yuan F, Tang CC (2009) Beamline I11 at diamond: a new instrument for high resolution powder diffraction. *Rev Sci Instrum* 80(7):075107
76. Itoh T, Shirasaki S, Fujie Y, Kitamura N, Idemoto Y, Osaka K, Ofuchi H, Hirayama S, Honma T, Hirosawa I (2010) Study of charge density and crystal structure of (La<sub>0.75</sub>Sr<sub>0.25</sub>)MnO<sub>3,00</sub> and (Ba<sub>0.5</sub>Sr<sub>0.5</sub>)(Co<sub>0.8</sub>Fe<sub>0.2</sub>)O<sub>2.33</sub>-delta at 500–900 K by in situ synchrotron x-ray diffraction. *J Alloy Comp* 491(1–2):527–535
77. Itoh T, Shirasaki S, Fujie Y, Kitamura N, Idemoto Y, Osaka K, Hirosawa I, Igawa N (2009) Study of mechanism of mixed conduction due to electrons and oxygen ions in (La<sub>0.75</sub>Sr<sub>0.25</sub>)MnO<sub>3,00</sub> and (Ba<sub>0.5</sub>Sr<sub>0.5</sub>)(Co<sub>0.8</sub>Fe<sub>0.2</sub>)O-2.33 through Rietveld refinement and MEM analysis. *Electrochemistry* 77(2):161–168
78. Hagen A, Poulsen HF, Klemenso T, Martins RV, Honkimaki V, Buslaps T, Feidenshans'l R (2006) A depth-resolved in situ study of the reduction and oxidation of Ni-based anodes in solid oxide fuel cells. *Fuel Cells* 6(5):361–366
79. Atkinson A, Sun B (2007) Residual stress and thermal cycling of planar solid oxide fuel cells. *Mater Sci Technol* 23(10):1135–1143
80. Villanova J, Sicardy O, Fortunier R, Micha JS, Bleuet P (2010) Determination of global and local residual stresses in SOFC by X-ray diffraction. *Nucl Instrum Methods Phys Res Sect B* 268(3–4):282–286
81. Sumi H, Ukai K, Yokoyama M, Mizutani Y, Doi Y, Machiya S, Akiwira Y, Tanaka K (2006) Changes of internal stress in solidoxide fuel cell during red-ox cycle evaluated by in situ measurement with synchrotron radiation. *J Fuel Cell Sci Technol* 3(1):68–74
82. Yamazaki S, Matsui T, Sato T, Arita Y, Nagasaki T (2002) EXAFS study of reduced ceria doped with lanthanide oxides. *Solid State Ionics* 154:113–118
83. Yamazaki S, Matsui T, Ohashi T, Arita Y (2000) Defect structures in doped CeO<sub>2</sub> studied by using XAFS spectrometry. *Solid State Ionics* 136:913–920
84. Ohashi T, Yamazaki S, Tokunaga T, Arita Y, Matsui T, Harami T, Kobayashi K (1998) EXAFS study of Ce<sub>1-x</sub>Gd<sub>x</sub>O<sub>2-x/2</sub>. *Solid State Ionics* 113:559–564
85. Hormes J, Pantelouris M, Balazs GB, Rambabu B (2000) X-ray absorption near edge structure (XANES) measurements of ceria-based solid electrolytes. *Solid State Ionics* 136:945–954
86. Zhang J, Wu ZY, Liu T, Hu TD, Wu ZH, Ju X (2001) XANES study on the valence transitions in cerium oxide nanoparticles. *J Synchrotron Radiat* 8:531–532
87. Zhang J, Wu ZY, Rong LX, Dong BZ (2005) Temperature dependence of the growth of cerium oxide nanoparticles investigated by SAXS and XANES. *Phys Scr T* 115:661–663
88. Gnanasekar KI, Jiang X, Jiang JC, Aghasyan M, Tiltsworth R, Hormes J, Rambabu B (2002) Nanocrystalline bulk and thin films of La<sub>1-x</sub>SrMnO<sub>3</sub>

- ( $0 < x < 0.3$ ). *Solid State Ionics* 148(3–4):575–581
89. Skinner SJ, Packer RJ, Bayliss RD, Illy B, Prestipino C, Ryan MP (in press) Redox chemistry of the novel fast oxide ion conductor  $\text{CeNbO}_4$  determined through an in situ spectroscopic technique. *Solid State Ionics*. <https://doi.org/10.1016/j.ssi.2009.12.008>
90. Pomfret MB, Owrutsky JC, Walker RA (2006) High-temperature Raman spectroscopy of solid oxide fuel cell materials and processes. *J Phys Chem B* 110(35):17305–17308
91. Izzo JR, Joshi AS, Grew KN, Chiu WKS, Tkachuk A, Wang SH, Yun WB (2008) Nondestructive reconstruction and analysis of SOFC anodes using x-ray computed tomography at sub-50 nm resolution. *J Electrochem Soc* 155(5):B504–B508
92. Malzbender J, Steinbrech RW, Singheiser L (2009) A review of advanced techniques for characterising SOFC behaviour. *Fuel Cells* 9(6):785–793
93. Maher RC, Cohen LF (2008) Raman spectroscopy as a probe of temperature and oxidation state for gadolinium-doped ceria used in solid oxide fuel cells. *J Phys Chem A* 112(7):1497–1501
94. Charrier-Cougoulic I, Pagnier T, Lucazeau G (1999) Raman spectroscopy of perovskite-type  $\text{BaCe}_x\text{Zr}_{1-x}\text{O}_3$  ( $0 < x < 1$ ). *J Solid State Chem* 142(1):220–227
95. Pomfret MB, Owrutsky JC, Walker RA (2007) In situ studies of fuel oxidation in solid oxide fuel cells. *Anal Chem* 79(6):2367–2372

### Books and Reviews

- Gellings PJ, Bouwmeester HJM (1997) *The CRC handbook of solid state electrochemistry*. CRC Press, Boca Raton, p 630
- Kisi EH, Howard CJ (2008) *Applications of neutron powder diffraction*. Oxford series on neutron scattering in condensed matter, vol 15. Oxford University Press, Oxford/New York, p xvii, p 486
- Larminie J, Dicks A (2003) *Fuel cell systems explained*, 2nd edn. Wiley, Chichester/West Sussex, p xxii, p 406
- Maier J (2004) *Physical chemistry of ionic materials: ions and electrons in solids*. Wiley, Chichester/Hoboken, p 537
- Rand DAJ, Dell R (2008) *Hydrogen energy: challenges and prospects*. RSC energy series. RSC Pub, Cambridge, p xxxviii, p 300
- Will G (2006) *Powder diffraction: the rietveld method and the two-stage method to determine and refine crystal structures from powder diffraction data*. Springer, Berlin/New York, p ix, p 224





## Fuel Cells (SOFC): Alternative Approaches (Electrolytes, Electrodes, Fuels)

K. Sasaki<sup>1,2,3</sup>, Y. Nojiri<sup>1</sup>, Y. Shiratori<sup>1,3</sup> and S. Taniguchi<sup>1</sup>

<sup>1</sup>International Research Center for Hydrogen Energy, Kyushu University, Fukuoka, Japan

<sup>2</sup>International Institute for Carbon-Neutral Energy Research (WPI), Kyushu University, Fukuoka, Japan

<sup>3</sup>Faculty of Engineering, Kyushu University, Fukuoka, Japan

### Article Outline

Glossary

Definition of the Subject

Introduction

Alternative Electrolyte Materials

Oxygen Ionic Conductors

Protonic Conductors

Alternative Electrode Materials

Anode Materials

Alternative Fuels

Future Directions

Bibliography

### Glossary

**Anode** Electrode for electrochemical oxidation reactions. In solid oxide fuel cells, hydrogen-containing fuels are oxidized by oxygen ions transported through an electrolyte to form water vapor or CO<sub>2</sub> as the reaction products at this electrode. SOFC anodes may also act as fuel reforming catalysts when hydrocarbon-based fuels are supplied to the anodes.

**Cathode** Electrode for electrochemical reduction reactions. In solid oxide fuel cells, oxygen

in ambient air is reduced to oxygen ions at this electrode.

**Electrolyte** Ionic conductor with negligible electronic conductivity, used as a membrane between an oxidation atmosphere and a reduction atmosphere. The essential material to construct electrochemical devices including fuel cells.

**Fuel flexibility** While low-temperature fuel cells (such as polymer electrolyte membrane fuel cells) typically use pure hydrogen gas (or hydrogen gas mixed with CO<sub>2</sub>) as the fuel, high-temperature fuel cells can directly use various kinds of fuels, such as carbon monoxide (CO), which is created by reforming hydrocarbons at the anode to produce hydrogen and carbon monoxide.

**Impurity poisoning** Even though high-temperature fuel cells have good fuel flexibility with various kinds of fuels, some minor constituents (impurities) coming from, for example, low-purity fuels, raw materials, and system components can also react with electrode materials or can be adsorbed on the electrode reaction sites, hindering electrode reactions. Such poisoning phenomena can lead to fuel cell performance degradation with time.

**Mixed ionic electronic conductor** Materials with both high ionic conductivity and high electronic conductivity. Such materials are often attractive for electrodes because of extension of electrochemical reaction sites beyond electrode/electrolyte interface.

**Oxygen ionic conductor** Materials with high oxygen ionic conductivity. Oxides with both high oxygen vacancy (or other charge carrier such as interstitial oxygen atoms) concentration and high oxygen mobility exhibit high ionic conductivities.

**Protonic conductor** Materials with high protonic conductivity. In the presence of oxygen vacancies, water vapor may be dissolved into

oxides forming protons and exhibiting high protonic conductivity.

## Definition of the Subject

While we are realizing commercialization of SOFC systems for residential, industrial, and distributed-power applications, continuous challenges will be needed to develop advanced fuel cells with higher efficiency, higher durability, better flexibility, as well as lower production cost. For realizing next-generation SOFCs, we may apply a broad range of knowledge related to (1) electrolyte and (2) electrode materials for cell development as well as (3) explore alternative fuels. This entry gives an overview on possible alternative approaches for these three important aspects to realize advanced high-performance SOFCs in a future generation.

## Introduction

Fuel cells, environmentally compatible energy systems using hydrogen-containing fuels [1–5], are strongly desired as promising key technologies to realize a sustainable low-carbon society. Compared to internal combustion, electrochemical energy conversion by fuel cells can achieve much higher efficiency. While the direct electrochemical conversion of chemical energy to electricity using fuel cells has received significant attention for several decades, mass marketing of fuel cell systems is often limited by insufficient performance and/or inadequate durability in service.

While the commercialization of fuel cell technologies has just begun in the form of, for example, stationary cogeneration power units for private houses, a broad variety of other application is strongly desired. Even though solid oxide fuel cells (SOFCs) are the most efficient type of fuel cells, partly due to their higher operational temperature compatible with internal reforming of hydrocarbon-based fuels, their application has often been restricted by the limited operational range of electrolyte and electrode materials [1–3]. Although many current research projects

tend to focus on engineering and optimization issues related to cost reduction, durability, and reliability [6–8], in order to take SOFCs closer to full-scale commercialization, breakthroughs in materials and concepts are needed for developing viable fuel cells for broader application. It is therefore essential to consider alternative materials for electrolytes and electrodes and innovative fuel cell concepts including the use of alternative fuels for future-generation fuel cells. For example, alternative electrolyte/electrode materials for lower-temperature SOFCs are needed to improve electrical efficiency in low-power operation, tolerance against thermal cycling, as well as improve longer-term durability. They will help realize alternative fuel cells in real commercial systems. Additionally, morphological control on the nanoscale shows promise in enhancing ionic and electronic transport in nano-ionic systems [9–14], offering an additional degree of freedom in material/device design. A reversing challenge is to harness these effects to the fabrication of practical SOFCs with improved performance.

Alternative device concepts can help realize broader application of SOFCs. SOFCs for automotive applications will enable multi-fuel vehicles capable of being powered by both hydrogen and hydrocarbon fuels. The use of biogas can result in carbon-neutral energy conversion. The use of hydrocarbon fuels and gasified coal gas fuel for SOFCs will achieve more efficient use of such fossil fuels. Portable SOFCs operating with hydrogen, hydrocarbon fuels [15, 16], and solid carbon [17] are attractive as replacements for batteries. Reversible SOFCs can act as both power units and electrolyzers, efficiently converting excess heat and electricity into hydrogen and vice versa [18–20]. If these technologies with SOFCs are realized, a considerable reduction in CO<sub>2</sub> emissions is possible in household, industrial, and transportation sectors.

It is therefore interesting and essential to consider such material/device issues in SOFC R&D to realize future flexible SOFCs with broader application. In this entry, an overview will be given on alternative approaches to SOFCs related to the following three critical material-related issues: electrolytes, electrodes, and fuels.

## Alternative Electrolyte Materials

### Electrolyte Materials: General.

As the ionic conductivity of solid electrolytes is generally much lower than the electronic conductivity of electrode materials, the ionic conductivity of the solid electrolytes may determine the lowest possible operational temperature of SOFCs. Apart from high ionic conductivity, the following properties are required:

1. High ionic transference number around unity
2. Thermochemical stability in both oxidation and reduction atmospheres
3. Near theoretical density for minimum gas leakage
4. High compatibility with other materials in composite device
5. Match of thermal expansion coefficient with other components with minimal defect-induced chemical expansion

In addition, high mechanical strength and reasonable materials cost are required in the case of electrolyte-supported cells.

There are limited numbers of materials satisfying the above-mentioned criteria. Generally,  $Y_2O_3$ -stabilized  $ZrO_2$  (YSZ) is commonly used at high temperatures, that is,  $T > 800$  °C to maintain ionic conductance, while thin-film  $ZrO_2$ -based electrolytes may be applied for operational temperatures around 700 °C. For much lower operational temperatures, alternative electrolyte materials are needed. Ionic conductivity depends strongly on the crystal structure, and oxides with high ionic conductivity have been found among open crystal structures, such as fluorite, pyrochlore, rare-earth, perovskite, and related structures [21, 22].

## Oxygen Ionic Conductors

### Fluorite-Type Materials

#### General

The fluorite structure is relatively open, and it shows exceptional tolerance for high levels of atomic disorder, which may be introduced either

by doping, reduction, or oxidation [23]. Among the binary oxides,  $CeO_2$ ,  $Pr_6O_{11}$ ,  $ThO_2$ ,  $UO_2$ , and  $PuO_2$  possess this structure in the pure state in ambient conditions.  $ZrO_2$  and  $HfO_2$  are stabilized in the fluorite structure by doping with divalent or trivalent oxides (Y, Sc, rare-earth oxides) [23–25]. Beyond stabilization, the addition of such dopants gives rise to the creation of oxygen vacancies responsible for the ionic conduction in these oxides.

Several fluorite-type oxides are known to be excellent oxygen ionic conductors, including  $\delta$ - $Bi_2O_3$ ,  $CeO_2$ ,  $ZrO_2$ ,  $ThO_2$ , and  $HfO_2$ . The  $\delta$ - $Bi_2O_3$  phase possesses an anion-deficient fluorite structure where one-fourth of the normal fluorite anion sites are vacant. This phase exhibits an order to disorder transition above  $\sim 600$  °C (which can be suppressed to some extent through doping) with a consequent increase in conductivity and has the highest oxygen ionic conductivity so far reported for a solid electrolyte [21, 22]. However,  $\delta$ - $Bi_2O_3$  shows poor thermochemical stability, and it is easily reduced at high temperatures.  $ThO_2$  is a radioactive material.  $HfO_2$  has chemical similarity to  $ZrO_2$  but is relatively expensive. Practically available fluorite-type oxides for solid electrolyte are thus limited to  $ZrO_2$  and  $CeO_2$ . Most of the rare-earths, as well as Sc, In, and Y, are trivalent and form sesquioxides of various crystal structures with potential for solid electrolyte membranes. Most of them have the cubic C-type structure ( $Sm_2O_3$ ,  $Dy_2O_3$ ,  $Er_2O_3$ ,  $Sc_2O_3$ ,  $Y_2O_3$ , and  $In_2O_3$ ) which is closely related to the fluorite structure [23], which can be derived from the fluorite structure by removing one-fourth of the oxygen atoms which lie along the four  $\langle 111 \rangle$  directions [23]. SrO-doped  $La_2O_3$  exhibits ionic conductivity close to the  $Y_2O_3$ -doped  $ZrO_2$  electrolyte [21, 22]. However, most of these sesquioxides are mixed ionic and electronic conductors with a substantial electronic conductivity [23, 26–29].

#### $ZrO_2$ -Based Oxide

Pure  $ZrO_2$  exhibits phase changes from monoclinic to tetragonal and cubic, with increasing temperature. Due to its volume change of ca. 5% in the phase transition from monoclinic to tetragonal, pure  $ZrO_2$  cannot be used as a practical solid

**Fuel Cells (SOFC): Alternative Approaches (Electrolytes, Electrodes, Fuels), Table 1** Activation energies and pre-exponential factors of ionic conductivity of ZrO<sub>2</sub> doped with trivalent metal oxides (Y<sub>2</sub>O<sub>3</sub>, Yb<sub>2</sub>O<sub>3</sub>, Er<sub>2</sub>O<sub>3</sub>,

In<sub>2</sub>O<sub>3</sub>, Sc<sub>2</sub>O<sub>3</sub>) [33], based on the relation  $\sigma_{\text{ion}}(\text{S/m}) \times T(\text{K}) = \sigma_0(\text{S/m}) \times \exp(-\Delta E \sigma(\text{eV})/kT)$ , where t and c denote tetragonal and cubic phases

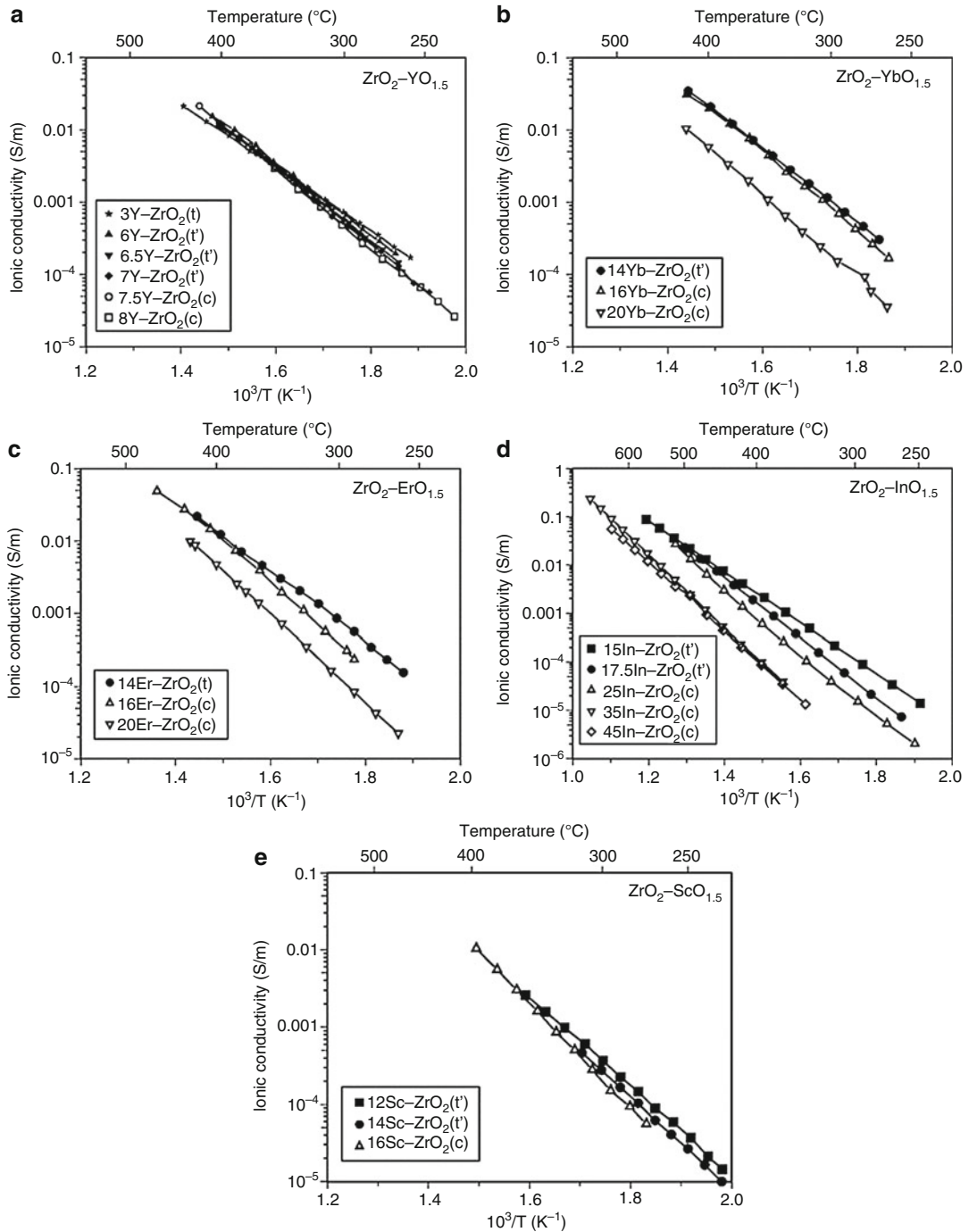
Dopant	mol%(phase)	Intragrain conductivity	
		$\Delta E \sigma(\text{eV})$	$\sigma_0$
YO <sub>1.5</sub>	5.8 (t) <sup>fc</sup>	0.91	$5.11 \times 10^7$
	11.2 (t')	1.04	$5.49 \times 10^8$
	12.0 (t')	1.06	$6.93 \times 10^8$
	12.7 (t')	1.10	$1.34 \times 10^9$
	13.5 (c)	1.09	$1.20 \times 10^9$
	14.3 (c)	1.12	$1.69 \times 10^9$
Yb <sub>1.5</sub>	14(t')	1.07	$1.43 \times 10^9$
	16 (c)	1.13	$3.66 \times 10^9$
	20 (c)	1.19	$3.74 \times 10^9$
ErO <sub>1.5</sub>	14 (t')	1.02	$3.86 \times 10^8$
	16 (c)	1.20	$7.51 \times 10^9$
	20 (c)	1.25	$7.74 \times 10^9$
InO <sub>1.5</sub>	15 (t)	0.80	$6.39 \times 10^6$
	15 (t')	1.10	$2.99 \times 10^8$
	17.5 (t')	1.28	$4.29 \times 10^8$
	25 (c)	1.35	$7.51 \times 10^9$
	25 (c) <sup>fc</sup>	1.22	$5.26 \times 10^9$
	35 (c)	1.56	$3.47 \times 10^{10}$
	35 (c) <sup>fc</sup>	1.14	$1.57 \times 10^8$
	45 (c)	1.48	$8.22 \times 10^9$
	45 (c) <sup>fc</sup>	1.26	$1.83 \times 10^9$
ScO <sub>1.5</sub>	12 (t')	1.20	$6.94 \times 10^9$
	14 (t')	1.24	$1.20 \times 10^{10}$
	16 (c)	1.40	$2.44 \times 10^{11}$

*fc* furnace cooling at a rate of 10 °C/min. *Others*: air quenching

electrolyte material. Group 2 elements of the periodic table or rare-earth elements may be added to stabilize the cubic phase at high temperatures and keep this phase stable also at lower temperatures. As for stabilized ZrO<sub>2</sub> with dopants from the group 2 elements, CaO-stabilized ZrO<sub>2</sub> is widely used mainly for Nernst-type oxygen sensors [30], but it is not used for fuel cells because of its relatively low conductivity [31]. On the other hand, stabilized ZrO<sub>2</sub> using dopants from rare-earth elements such as Y<sub>2</sub>O<sub>3</sub>, Sc<sub>2</sub>O<sub>3</sub>, Yb<sub>2</sub>O<sub>3</sub>, In<sub>2</sub>O<sub>3</sub>, and Er<sub>2</sub>O<sub>3</sub> [21, 22, 32, 33] exhibits higher conductivity suitable for SOFC [34–38]. Ionic conductivity (intragrain conductivity) of ZrO<sub>2</sub> doped with (a) Y<sub>2</sub>O<sub>3</sub>, (b) Yb<sub>2</sub>O<sub>3</sub>, (c) Er<sub>2</sub>O<sub>3</sub>,

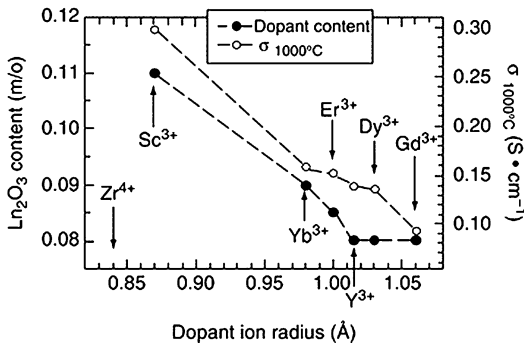
(d) In<sub>2</sub>O<sub>3</sub>, and (e) Sc<sub>2</sub>O<sub>3</sub> measured by impedance spectroscopy is shown in Fig. 1 [33]. In addition, activation energy values for the intragrain ionic conductivity of these doped ZrO<sub>2</sub>,  $\sigma_{\text{ion}}(\text{S/m}) \times T(\text{K}) = \sigma_0(\text{S/m}) \times \exp(-\Delta E \sigma(\text{eV})/kT)$ , are compiled in Table 1.

Yttria-stabilized ZrO<sub>2</sub>, discovered by Nernst [39], is still one of the state-of-the-art SOFC electrolyte materials which was used to demonstrate the first SOFC (and the first solid “electrolyte” fuel cell) in 1937 at ETH-Zürich [40]. Electronic defect concentrations are negligibly low [41]. As can be observed in Fig. 1, the ionic conductivity of fluorite-type oxides stabilized with hypovalent elements exhibits a maximum at a certain dopant



**Fuel Cells (SOFC): Alternative Approaches (Electrolytes, Electrodes, Fuels), Fig. 1** Intragrain conductivity of  $ZrO_2$  doped with (a)  $Y_2O_3$ , (b)  $Yb_2O_3$ , (c)  $Er_2O_3$ , (d)

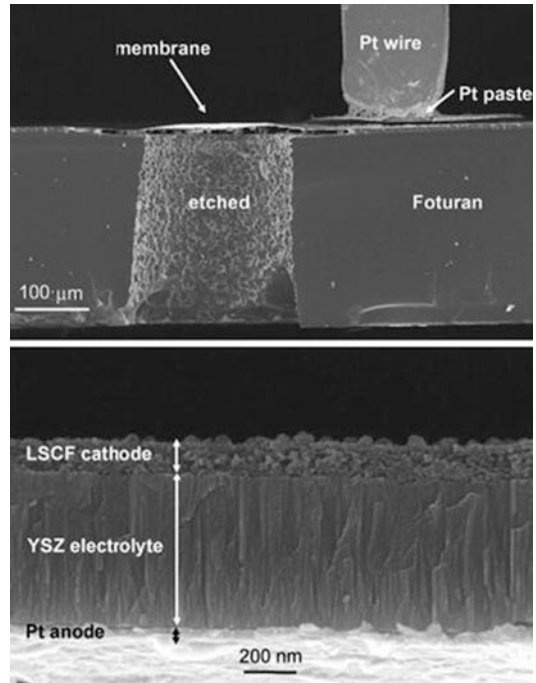
$In_2O_3$ , and (e)  $Sc_2O_3$  measured by impedance spectroscopy, where t and c denote tetragonal and cubic phases [33]



**Fuel Cells (SOFC): Alternative Approaches (Electrolytes, Electrodes, Fuels), Fig. 2** Relation between dopant ionic radius, conductivity, and content of dopant, reported by Arachi et al. [35] (Reproduced by permission of Elsevier)

concentration above which defect interactions occur [42–45]. As shown in Fig. 2, it is known that the peak value of the ionic conductivity becomes higher when the ionic radius of the dopant approaches that of  $Zr^{4+}$  [35], resulting in minimal distortion of the fluorite lattice. Ionic conductivity is the highest in the case of  $Sc^{3+}$ , which is used as a dopant because its ionic radius is almost identical to that of  $Zr^{4+}$  [46]. However,  $Sc_2O_3$  is more expensive than  $Y_2O_3$ , but  $Sc_2O_3$ -stabilized  $ZrO_2$  (ScSZ) has recently become more widely used. In addition, ScSZ with 8 mol%  $Sc_2O_3$  exhibited a high conductivity in the early stages of operation, but the conductivity decreased with operational time due to phase instability [47]. To prevent this decrease in ionic conductivity, ScSZ with 11 mol%  $Sc_2O_3$  was preferably used, but this material had a problem of phase transition in the vicinity of 700 °C [35, 48]. Currently, ScSZ with the addition of  $CeO_2$ , such as  $(ZrO_2)_{0.89}(Sc_2O_3)_{0.1}(CeO_2)_{0.01}$ , is widely used to suppress this phase transition [46, 49].

In addition, tetragonal  $ZrO_2$  and partially stabilized  $ZrO_2$  can also be used as an electrolyte due to their better mechanical properties and their lower activation energy for ionic conductivity. Since the grain size of the tetragonal phase is generally much smaller than that of the cubic phase and grain boundaries impede oxide ion migration, the reduction of grain boundary resistivity is important [50]. Stability of the tetragonal



**Fuel Cells (SOFC): Alternative Approaches (Electrolytes, Electrodes, Fuels), Fig. 3** SEM cross-sectional view of a micro-SOFC prepared on a glass ceramic substrate, as reported by Bieberle-Hütter et al. [51] (Reproduced by permission of Elsevier)

phase for longer time periods should be considered to prevent phase transition from the tetragonal phase to the monoclinic phase when applying this material to SOFC systems.

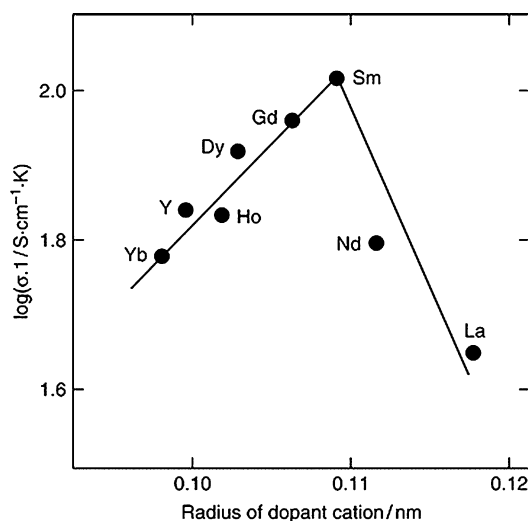
Thin-film technology can also help to realize lower operational temperatures in SOFCs by taking advantage of short transport distance of ions. It is also possible to produce thin-film electrolytes using stabilized  $ZrO_2$ , which enables lower-temperature operation of SOFCs because of its stability in both the oxidation and reduction atmospheres, its sinterability, and its high mechanical strength. Ultrathin YSZ electrolyte layers can be prepared on Si or glass ceramic substrates [15, 16, 51], which can realize, for example, lower-temperature operation of micro-SOFCs for portable applications. Figure 3 shows an SEM cross-sectional view of a micro-SOFC prepared on a glass ceramic substrate with a YSZ electrolyte thickness of less than 1  $\mu m$ , as reported by Bieberle-Hütter et al. [51].



Stabilized  $ZrO_2$  exhibits good chemical compatibility with other materials during SOFC operation below  $1000\text{ }^\circ\text{C}$ . It is possible that stabilized  $ZrO_2$  solid electrolyte reacts with other materials during the cell fabrication processes which often require high temperatures in excess of  $1300\text{ }^\circ\text{C}$ . YSZ does react with  $La_{1-x}Sr_xMnO_{3-\delta}$  (LSM), the state-of-the-art cathode material, to produce  $La_2Zr_2O_7$  or  $SrZrO_3$  at temperatures above  $1100\text{ }^\circ\text{C}$ , with a consequential increase in internal cell resistance [52–54]. In the case of  $LaCoO_3$ - or  $LaFeO_3$ -based oxide cathode materials, reaction with stabilized  $ZrO_2$  becomes worse, so that  $CeO_2$ -based oxides such as  $Gd_2O_3$ -doped  $CeO_2$  are generally used as a buffer layer between the  $ZrO_2$ -based electrolyte and such cathode materials to prevent interfacial reactions from forming [3, 55].

#### $CeO_2$ -Based Oxide

$CeO_2$ -based oxide, partially substituted by a hypovalent rare-earth oxide, exhibits high ionic conductivity in a wider range of compositions in comparison to stabilized  $ZrO_2$ . This is because even pure  $CeO_2$  has the fluorite-type cubic structure rendering stabilization unnecessary. Like  $ZrO_2$ , ionic conductivity of  $CeO_2$  also varies with the substitution of elements. It shows high ionic conductivity when it is partially substituted with alkaline-earth elements such as Ca and Sr [56, 57] and when partially substituted with a rare-earth element, even higher conductivity. As shown in Fig. 4, there is a systematic trend of the conductivity with ionic radius of the substituting element giving the highest conductivity with Sm [58]. Pure  $Sm_2O_3$  has a rare-earth C-type structure, and the similarity of structures between  $Sm_2O_3$  and  $CeO_2$  may lead to high stability. High ionic conductivity can be obtained in a wide range of substitution ratios with  $Sm_2O_3$ .  $Sm_2O_3$ -doped  $CeO_2$ , usually abbreviated as SDC, with 20 mol% partial substitution of  $Sm_2O_3$ , exhibits the highest ionic conductivity. In addition,  $CeO_2$  partially substituted with  $Gd_2O_3$  is also widely used as an electrolyte and, as previously mentioned, interlayer between the stabilized  $ZrO_2$  electrolyte and the cathode, although it shows slightly lower conductivity



**Fuel Cells (SOFC): Alternative Approaches (Electrolytes, Electrodes, Fuels), Fig. 4** Relationship between the dopant ion radius and the ionic conductivity of doped  $CeO_2$  at  $800\text{ }^\circ\text{C}$ , as reported by Eguchi et al. [58] (Reproduced with permission from Elsevier)

than SDC [59]. More recently, double doping with Sm and Nd exhibits one of the highest ionic conductivities reported for ceria [60].

When doped  $CeO_2$  is applied as a solid electrolyte for SOFCs, a change in valence state of  $Ce^{4+}$  to  $Ce^{3+}$  in a reducing atmosphere at the anode results in two main drawbacks. First, it causes n-type electronic conduction in the solid electrolyte which leads to a cell voltage drop. Precisely speaking, when  $CeO_2$  is reduced, both oxygen vacancy and electron are introduced simultaneously. Since the mobility of electrons is much higher than that of oxygen ions, the transference number, that is, the fraction of ionic conductivity from the total, decreases from unity. Second, when lattice oxygen is removed by reduction, the lattice expands, known as chemical expansion. A steep oxygen potential gradient appears in the  $CeO_2$  electrolyte from reducing anode to oxidizing cathode under the operating conditions of SOFCs, and a large mechanical stress in the electrolyte can occur resulting in fracture of the cell [61].

These issues can be overcome partially by using stabilized  $ZrO_2$  as an interlayer between the anode and the electrolyte [62–65]. However,

since there is a thermal expansion mismatch between the  $\text{ZrO}_2$ -based solid electrolyte and the  $\text{CeO}_2$ -based interlayer, this often causes microscopic fracture [64, 65]. GDC with an addition of Pr ( $\text{Ce}_{0.8}\text{Gd}_{0.18}\text{Pr}_{0.02}\text{O}_{2-\delta}$ ) showed enhanced reduction resistance but with the same level of ionic conductivity as SDC [66]. In addition, there have been some attempts to realize lower-temperature operation by fabricating ultrathin membranes of  $\text{CeO}_2$  electrolyte materials which contribute to reduce electrical resistance. Electronic conductivity, caused by reduction, decreases with decreasing temperature, but ionic conductivity also decreases simultaneously. Although making thinner solid electrolytes is accompanied with certain difficulties,  $\text{CeO}_2$ -based electrolytes can be operated at lower temperatures below 600 °C, where the influence of electronic conduction caused by the reduction may not be a fatal problem [67]. For example, Oishi et al. [67, 68] have reported stable operation of metal-supported  $\text{CeO}_2$ -based SOFCs, composed of a porous ferritic stainless steel support, a Ni-Ce<sub>0.8</sub>Y<sub>0.2</sub>O<sub>1.9</sub> anode, a thin Ce<sub>0.9</sub>Gd<sub>0.1</sub>O<sub>1.95</sub> electrolyte, and a La<sub>0.6</sub>Sr<sub>0.4</sub>Co<sub>0.2</sub>Fe<sub>0.8</sub>O<sub>3</sub> cathode, over 1200 h at 600 °C.  $\text{CeO}_2$ -based electrolyte with a thickness of about 10 μm allows operation of SOFCs at rather low temperatures and selection of ferritic steel as a support material, resulting in enhancement of mechanical strength of cells, improvement of redox stability of cell stacks, and minimization of the use of expensive electrode and electrolyte materials [67, 68]. Considering transport in thin-film  $\text{CeO}_2$ -based electrolytes, nano-size effects [12] and mixed conduction [62] should be taken into account to tailor transport phenomena in SOFCs.

**Pyrochlores and Other Fluorite-Type Oxides (Y, Nb, Zr)O<sub>2-δ</sub>**

Pyrochlore-type oxides have the general formula  $\text{A}_2^{3+}\text{B}_2^{4+}\text{O}_7$  in which A is a rare-earth element, such as Gd or Y, and B is Ti or Zr.  $\text{Gd}_2\text{Zr}_2\text{O}_7$  is the typical composition of pyrochlore-type oxides and can be considered as fluorite-type in which ionic defects are regularly arranged. The defect

structure and the mixed conductivity can be controlled by the value of x in, for example,  $\text{Gd}_2(\text{Zr}_x\text{Ti}_{1-x})_2\text{O}_7$ , which is abbreviated as GZT [69]. When the ionic radius of rare-earth elements for the A site is larger than that of Gd, the structure changes from highly defective fluorite to pyrochlore [70, 71].

In the  $\text{Gd}_2\text{Ti}_2\text{O}_7$  series, relatively high ionic conductivity is obtained at the 20 mol% substitution of Gd sites with Ca [72], though its use as an SOFC solid electrolyte is precluded by its electronic conductivity in air, with an ionic transference number lower than that of YSZ [73]. The thermal expansion coefficient of  $\text{Gd}_2\text{Ti}_2\text{O}_7$  ( $10.4\text{--}10.8 \times 10^6 \text{ K}^{-1}$ ) [73, 74] is close to that of LSGM ( $10.4 \times 10^6 \text{ K}^{-1}$ ) [75] and 10ScSZ ( $10.9 \times 10^6 \text{ K}^{-1}$ ) [76].

In addition, the solid solution of  $\text{Y}_4\text{NbO}_{8.5}$  and (Y, Nb, Zr)O<sub>2-δ</sub> also has the fluorite-related structure, and these materials have stimulated research interest due to their oxide ion conduction [77, 78]. Electrical conductivity of  $\text{Y}_4\text{NbO}_{8.5}$  is independent of the oxygen partial pressure, and it is recognized as an ionic conductor [78]. The ionic conductivity is low, enhancement of conductivity by the addition of Zr was reported, and further improvement of ionic conductivity may be expected [77].

## Perovskite-Related Oxides

### General

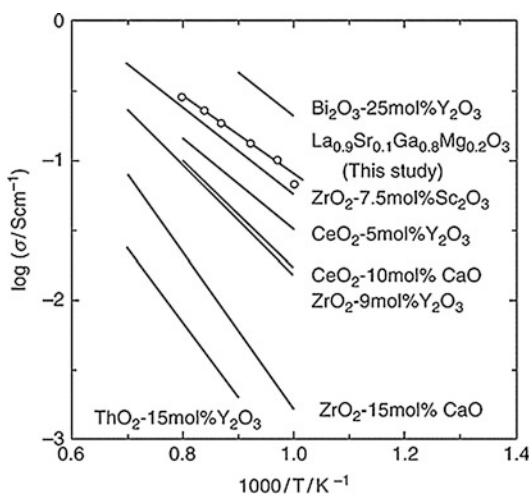
Perovskite-type oxides have the general formula  $\text{ABO}_3$ . The total valence of the A metal and the B metal ions is 6, and various combinations are possible. However, there is a limit to the ionic radius (r) of the constituent metal ions (A and B) and the oxygen ion (O), as the tolerance factor t ( $t = \frac{R_A + R_O}{\sqrt{2}(R_B + R_O)}$ ).

should satisfy  $0.75 \leq t \leq 1$  [79, 80]. Oxides related to  $\text{LaGaO}_3$ ,  $\text{LaAlO}_3$ , and  $\text{Ba}_2\text{In}_2\text{O}_5$  have been well examined as solid electrolyte materials for SOFCs. Takahashi and Iwahara [81] already showed in 1970s that selected perovskite solid solutions exhibited high ionic conductivity around  $5 \times 10^{-3} \text{ S/m}$  at 800 °C [21, 22].

### LaGaO<sub>3</sub>-Based Oxides

Oxygen ionic conductivity in perovskite-type oxide structures has been extensively investigated by Takahashi and Iwahara in their pioneering and detailed studies [81]. High ionic conductivity was observed in the Ti series of perovskite-type oxides. Despite detailed studies, perovskite-type titanate showed poor ionic conductivity compared to that of YSZ. Furthermore, hole conduction was relatively high, so that the ionic transference number was less than unity in oxidizing atmospheres. They also investigated perovskite-type oxides in which trivalent cations were added to both the A site and the B site. LaCoO<sub>3</sub> and LaFeO<sub>3</sub> are known as such kinds of oxides, but these oxides are mixed conductors with predominately high hole conductivity. However, LaAlO<sub>3</sub>, with trivalent metal ions on the B site, showed relatively high ionic conductivity [81].

Building on these results, Ishihara et al. [82] attempted to increase lattice cubic volume by applying Ga to the B site which has a slightly larger ionic radius than Al in the La-based perovskite oxides (Fig. 5). They added various dopants, and the highest oxygen ionic conductivity was

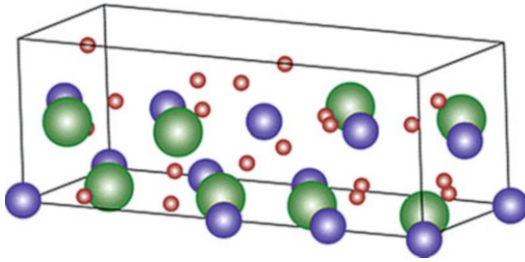


**Fuel Cells (SOFC): Alternative Approaches (Electrolytes, Electrodes, Fuels), Fig. 5** Comparison of the oxygen ionic conductivity of La<sub>0.9</sub>Sr<sub>0.1</sub>Ga<sub>0.8</sub>Mg<sub>0.2</sub>O<sub>3</sub> with conventional oxide ionic conductors with fluorite structures, compiled by Ishihara et al. [82] (Reproduced with permission from American Chemical Society)

obtained in the case where 20 mol% of Sr was added to the A site, which has an approximately equal ionic radius to La [82]. As for the dopant on the B site, the highest ionic conductivity was obtained when 20 mol% of Mg was added to the B site (La<sub>0.8</sub>Sr<sub>0.2</sub>Ga<sub>0.8</sub>Mg<sub>0.2</sub>O<sub>2.6</sub> [83]), since Mg is the only element which satisfies the criteria of both ionic radius and low valence number. La<sub>0.8</sub>Sr<sub>0.2</sub>Ga<sub>0.8</sub>Mg<sub>0.2</sub>O<sub>2.6</sub> (LSGM) shows the same level of ionic conductivity as GDC at temperatures above 650 °C. Electronic conductivity does not become predominant within a wide range of atmospheres from pure oxygen to hydrogen-containing gases [84, 85].

While LSGM exhibits superior properties as an SOFC solid electrolyte, a phase transition from pseudo cubic (monoclinic) to tetragonal was observed at temperatures around 700 °C. In order to give high ionic conductivity to this material even below 650 °C, the B site was partially substituted with Co, which has a similar ionic radius to Mg (La<sub>0.8</sub>Sr<sub>0.2</sub>Ga<sub>0.8</sub>Mg<sub>0.115</sub>Co<sub>0.085</sub>O<sub>3-δ</sub>, denoted as LSGMC) [84]. The crystalline phase at high temperature was then stabilized, and the phase transition did not occur at temperatures around 700 °C, resulting in higher ionic conductivity than that of GDC within a wide temperature range from 500 °C to 1000 °C [85]. It was revealed that oxygen ions tend to be trapped around Mg in LSGM [86], and the addition of Co on the B site is effective for preventing such trapping at lower temperatures.

When an LaGaO<sub>3</sub>-based oxide is applied as a solid electrolyte for SOFCs, reactivity or interdiffusion with electrode materials becomes a critical issue. When LSM was used as the cathode material, interdiffusion of Mn into LSGM was observed [87]. When LSCF was used as the cathode material, interdiffusion of Co and Fe into LSGM was also seen [88–90]. A solid-state reaction also occurs at the interface between the Ni-based anode and the LSGM electrolyte due to the similarity of Ni to Co and Mn in the electrolyte materials [91]. There have been some attempts to prevent such solid-state reactions, for example, by optimizing deposition procedures and by applying a CeO<sub>2</sub> interlayer between the LSC cathode and the LSGM electrolyte.



**Fuel Cells (SOFC): Alternative Approaches (Electrolytes, Electrodes, Fuels), Fig. 6** Crystal structure of  $\text{Ba}_2\text{In}_2\text{O}_5$  (Green: Ba, Blue: In, Red: O)

### $\text{Ba}_2\text{In}_2\text{O}_5$ -Based Oxides

The brownmillerite-type oxide has the general formula  $\text{A}_2\text{B}_2\text{O}_5$ , with the crystal structure presented in Fig. 6. Alkaline-earth metal ions such as Ba occupy the A site, and trivalent typical metal ions such as In occupy the B site [92–99]. At temperatures below 1140 K, it behaves as a mixed conductor which shows both p-type electronic conductivity and oxygen ionic conductivity due to its oxygen excess [92]. When it is heated to 1140–1230 K, ionic conductivity increases, which is associated with the phase transition to the disordered perovskite structure, as shown in Fig. 7 [93]. The ionic transference number also rises drastically to unity.

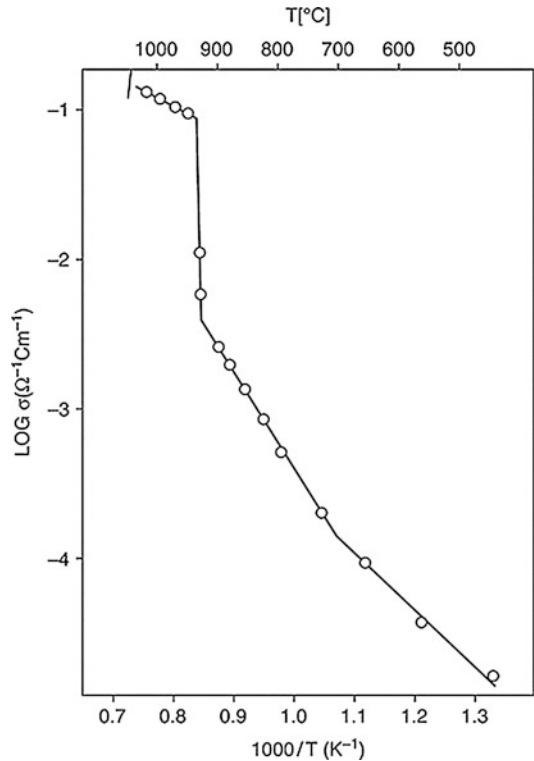
For example, in the case of  $\text{Ba}_2\text{In}_2\text{O}_5$ , the typical brownmillerite-type oxide, the disordered perovskite structure can be stabilized, and ionic conductivity in an intermediate-temperature range can be improved by substituting In with another highly charged cation such as Zr, Hf, and Sn [94, 95]. A similar effect can be obtained by the substitution of Ba, as shown in Fig. 8 [93, 96].

$\text{Ba}_2\text{In}_2\text{O}_5$  is stable in the absence of  $\text{CO}_2$  but decomposes in the presence of  $\text{CO}_2$  in a reducing atmosphere ( $p(\text{O}_2) = 10^{-9}$ – $10^{-13}$  atm), accompanied by the formation of  $\text{BaCO}_3$ . However, in a strongly reducing atmosphere of much lower oxygen partial pressure,  $\text{In}^{3+}$  is reduced to  $\text{In}^+$ , and the brownmillerite structure cannot be maintained anymore [92, 95, 97–99].

### Apatite-Type Oxides

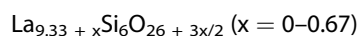
#### General

Apatite is a generic name for minerals with the composition  $\text{A}_{10}(\text{MO}_4)_6\text{X}_2$  [100–102]. Generally,

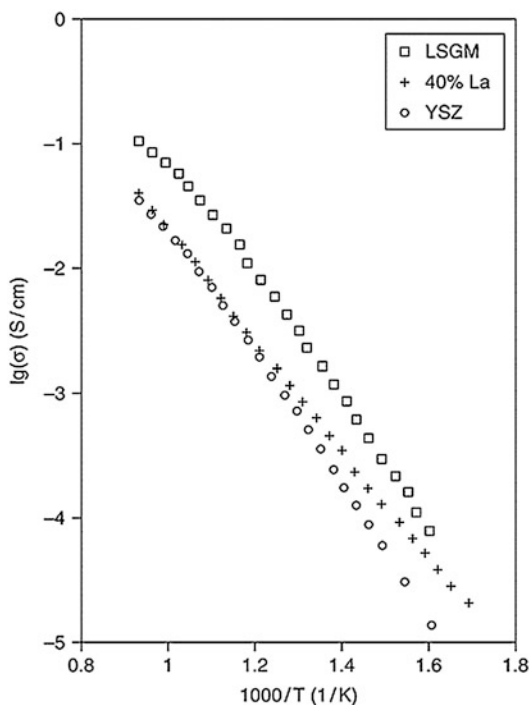


**Fuel Cells (SOFC): Alternative Approaches (Electrolytes, Electrodes, Fuels), Fig. 7** Ionic conductivity of  $\text{Ba}_2\text{In}_2\text{O}_5$ , reported by Goodenough [93] (Reproduced with permission from Elsevier)

the A site can be occupied by alkaline, alkaline-earth, or rare-earth metal ions. The M site can be occupied by elements such as P, Si, and Ge which can have a coordination number of 4. The M site can be partially substituted with transition metal ions. The X site can be occupied by O, OH, F, Cl, and  $\text{CO}_3$ , etc. Moreover, the A-site cations are divided into two kinds: one occupies the 4f site where the coordination number is 7, and the other occupies the 6h site where the coordination number is 9. Hydroxide apatite  $\text{Ca}_{10}(\text{PO}_4)_6(\text{OH})$  is a typical example. It is the principal ingredient of human bone and is practically used for artificial bone [101–103].



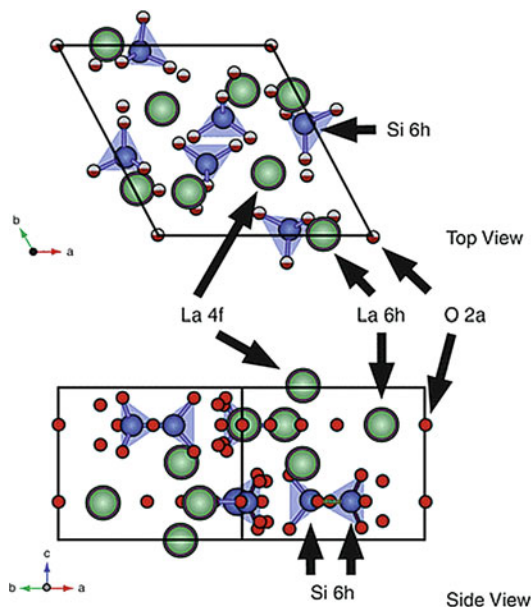
$\text{La}_{9.33}\text{Si}_6\text{O}_{26}$  and  $\text{La}_{10}\text{Si}_6\text{O}_{27}$  have often been studied for their crystallographic interest. It is already known that lattice volume will continuously decrease with the ionic radius of lanthanide ions from La to Lu [102, 104]. In the



**Fuel Cells (SOFC): Alternative Approaches (Electrolytes, Electrodes, Fuels), Fig. 8** Comparison of the oxygen ionic conductivity of  $\text{La}_{0.4}\text{Ba}_{0.6}\text{InO}_{2.7}$  with  $\text{La}_{0.9}\text{Sr}_{0.1}\text{Ga}_{0.8}\text{Mg}_{0.2}\text{O}_{2.85}$  and YSZ, reported by Goodenough [93] (Reproduced with permission from Elsevier)

$\text{Re}_{9.33+x}\text{Si}_6\text{O}_{26}$  system, oxides with  $\text{Re} = \text{La-Dy}$  belong to the hexagonal system apatite structure ( $P6_3/m$ ) and oxides with  $\text{Re} = \text{Y-Yb}$  to the monoclinic system apatite structure ( $I2/a$ ). Specifically,  $\text{La}_{10}\text{Si}_6\text{O}_{27}$  is not regarded as the apatite phase. In the case of silicate and germanate, the oxides with the amount of La from 8 to 9.33 exhibit the apatite phase [105].

The crystal structure of this system is shown in Fig. 9. The La 6h site is fully occupied, while the La 4f site is not fully filled.  $\text{La}_{9.33}\text{Si}_6\text{O}_{26}$  does not have interstitial oxygen ions, but the conductivity improves by partially substituting the La 4f site or by preparing a slightly La-deficient sample ( $\text{La} = 9.0$ ) to introduce oxygen vacancies into the 2a site [105, 106]. For  $x > 0$ , oxygen ions are introduced into the interstitial site, and 1 mol of oxygen is introduced into the unit cell at  $\text{La} = 10$  ( $x = 0.67$ ). When the number of interstitial oxygen ions increases, the conductivity also increases [107]. The ionic conductivity in this

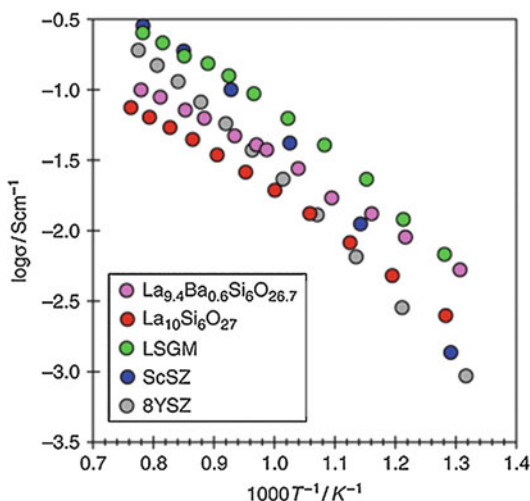


**Fuel Cells (SOFC): Alternative Approaches (Electrolytes, Electrodes, Fuels), Fig. 9** Crystal structure of  $\text{La}_{10}\text{Si}_6\text{O}_{27}$  [110] (Green: La, Blue: Si, Red: O) (Reproduced with permission from Elsevier)

system is strongly anisotropic, as its crystallographic structure is. A single-crystal conductivity measurement of  $\text{Nd}_{9.33}\text{Si}_6\text{O}_{26}$  has revealed that the conductivity along the c-axis is more than 10 times higher than that in the a–b plane [108]. The anisotropy of this conductivity disappears at around 800 °C [109].

As solid electrolytes, the La/Si oxides with  $\text{La} > 9.33$  contain interstitial oxygen ions, which can conduct in the channel (2a site) along the c-axis. The conduction mechanism is quite different from that of other oxide electrolytes in which oxygen vacancies are the mobile charge carriers. For example, in  $\text{La}_{10}\text{Si}_6\text{O}_{27}$ , the activation energy of ionic conductivity via oxygen interstitials is lower than that of YSZ, and the ionic conductivity of this La/Si oxide is higher than that of YSZ at and below 923 K, as described in Fig. 10 [110]. Moreover, it is known that the transference number is unity and that this material remains stable in humidified hydrogen and in  $\text{CO}_2$ -containing atmospheres at and below 1073 K, while p-type conduction can appear at and above 1173 K [111, 112]. The ionic conductivity decreases, and its activation energy increases

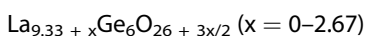




**Fuel Cells (SOFC): Alternative Approaches (Electrolytes, Electrodes, Fuels), Fig. 10** Comparison of the oxygen ionic conductivity of lanthanum silicate with  $\text{La}_{0.9}\text{Sr}_{0.1}\text{Ga}_{0.9}\text{Mg}_{0.1}\text{O}_3$  and oxides with the fluorite structure [110]

with decreasing ionic radius of the rare-earth metal ions in the La site [113, 114]. The substitution sites of dopants should be taken into account in considering ionic conductivities of such materials [106, 107, 110, 115, 116].

These materials are based on inexpensive  $\text{La}_2\text{O}_3$  and  $\text{SiO}_2$  and can be synthesized at relatively low temperatures, but cannot exhibit high conductivity and density without sintering at and above 1873 K [117]. The thermal expansion coefficient of  $\text{La}_{10}\text{Si}_6\text{O}_{27}$  is  $9.7\text{--}10.3 \times 10^{-6} \text{ K}^{-1}$ . This value is very close to that of YSZ ( $10.5 \times 10^{-6} \text{ K}^{-1}$ ) and GDC ( $11.8 \times 10^{-6} \text{ K}^{-1}$ ) [118, 119], indicating that similar oxide electrodes may be used. There are a few reports on fuel cell electrochemical performance using a  $\text{La}_{0.9}\text{Sr}_{0.1}\text{CoO}_{3-\delta}$  cathode with a Ni-SDC cermet anode [110, 116, 119]. The results show 50% better performance than that with Pt electrodes [119]. The interdiffusion of La and Sr in the electrode and in the electrolyte can be technological issues, as observed also in the LSGM electrolyte-based cells.



It has been already reported that La/Ge oxides exhibit a phase transition from triclinic to

hexagonal phase at around 1000 K [120]. This phase transition disappears by substitution of La by Sr [121]. A similar phase transition is observed in  $\text{La}_2\text{GeO}_5$  [122]. The ionic conductivity of  $\text{La}_x\text{Ge}_6\text{O}_{12+1.5x}$  exhibits the highest value in the apatite region, while this result is not the same as in the lanthanum silicates [105, 119, 123]. Due to the volatility of Ge,  $\text{La}_2\text{GeO}_5$  is difficult to synthesize in the stoichiometric ratio of La/Ge [124].

## Protonic Conductors

### General

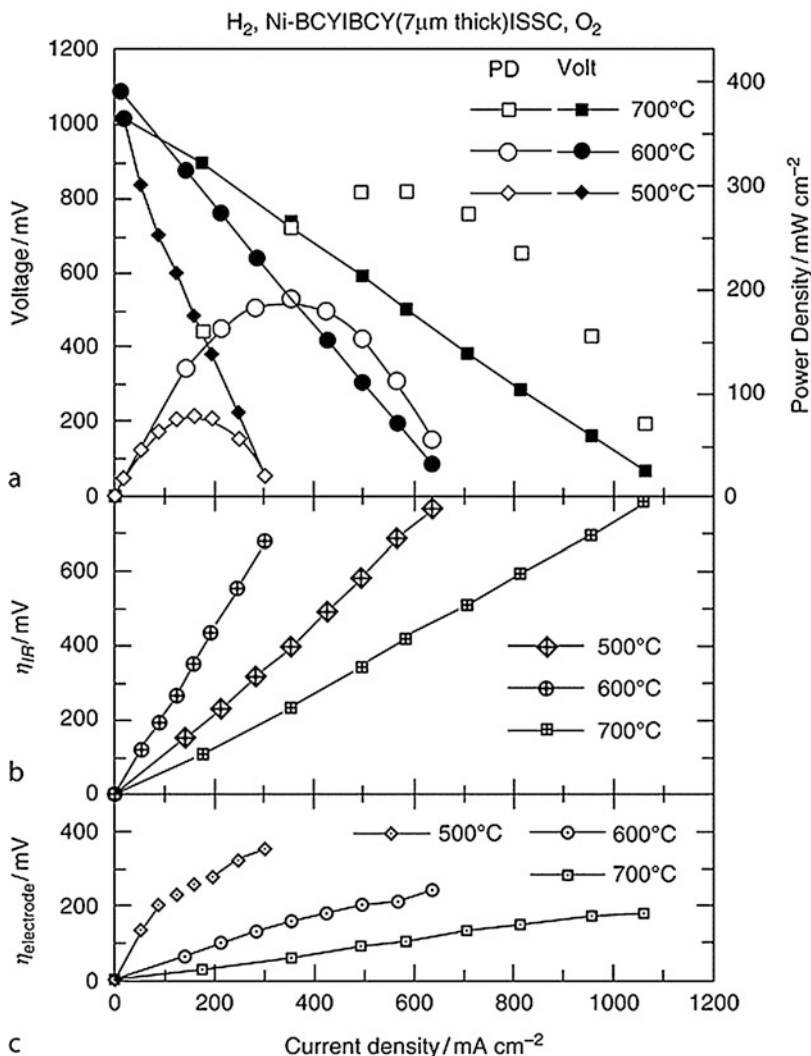
In general, most ionic conductors currently used for solid electrolytes in SOFCs are oxygen ionic conductors. However, the use of proton-conducting oxides allowing for lower-temperature operation is anticipated to have a beneficial effect on durability at long-term operation. There are at least two approaches for this aim from the electrolyte materials selection viewpoint. One approach is to increase the oxygen ionic conductivity of the electrolytes, and another approach is to use a proton-conducting oxide which exhibits smaller temperature dependence (i.e., lower activation energy) of the ionic conductivity.

There are many kinds of proton-conducting oxides widely known in the literature, for example, by Kreuer [125]. In a very early study, C. Wagner had already reported the presence of protons in stabilized  $\text{ZrO}_2$  [126]. Hydrated oxides such as  $\text{WO}_3 \cdot n\text{H}_2\text{O}$ , phosphates such as  $\text{Zr}(\text{HPO}_4)_2$ ,  $\beta$ -alumina,  $\beta''$ -alumina, zeolites, and heteropoly acid are good examples of proton-conducting oxides [9, 125, 127–130]. Acid salts such as  $\text{CsHSO}_4$  are also considered as electrolyte materials for fuel cells operating at lower temperatures [131, 132].

Various perovskite-type oxides [133, 134], as well as  $\text{Ba}_2\text{In}_2\text{O}_5$  [135–137], and  $\text{La}_{10}\text{Ge}_6\text{O}_{27}$  [120, 138, 139] exhibit protonic conductivity. Among these materials, the perovskite-type oxides show outstanding protonic conductivity. To mention a few, SOFCs with  $\text{BaCe}_{0.8}\text{Y}_{0.2}\text{O}_{3-\delta}$  solid electrolytes can be operated at low temperatures above 400 °C [140, 141], and a power



**Fuel Cells (SOFC): Alternative Approaches (Electrolytes, Electrodes, Fuels), Fig. 11** (a)  $I$ - $V$  characteristics (closed symbols) and power density curves (open symbols), (b) ohmic loss and (c) electrode overpotentials (anode + cathode) of a  $H_2$ - $O_2$  proton conductor thin film SOFC operated at 700–500 °C, reported by Matsumoto et al. [141] (Reproduced by permission of Elsevier)



density of 100  $mW/cm^2$  at 500 °C has been achieved (Fig. 11, [141]).

**Perovskite-Type Oxides**

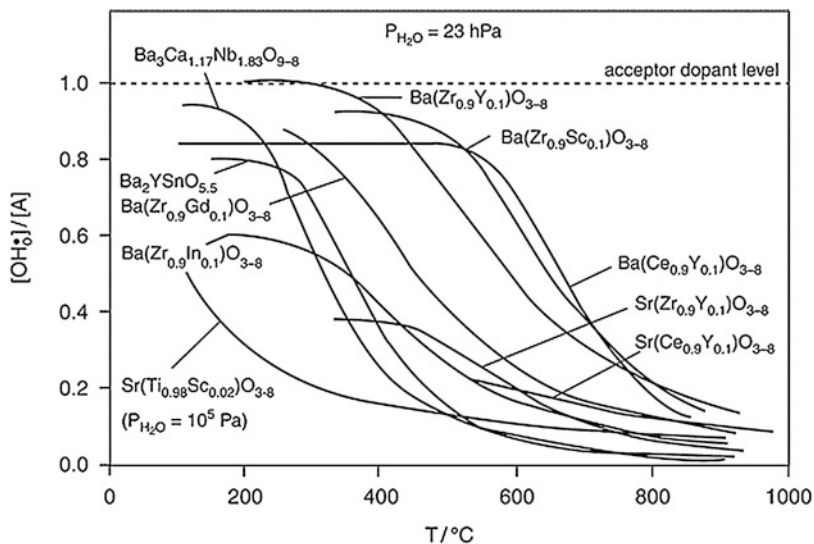
Regarding protonic conduction in perovskite-type oxides ( $ABO_3$ ), Takahashi and Iwahara [81] discovered the interesting phenomenon that protonic conduction appeared in  $SrCeO_3$  at high temperatures, which was associated with the presence of oxygen vacancies [125]. They revealed that  $BaCeO_3$  has high hydrogen solubility by using deuterium absorption measurements [142]. This material exhibited mixed conductivity of oxygen

ions and protons, which was strongly affected by the Ba/Ce ratio [143, 144]. When the Ba/Ce ratio was more than 1.05, such oxides exhibited high protonic conductivity. When the Ba/Ce ratio was less than 1, it behaved as an oxygen ionic conductor, although the conductivity was relatively low [145]. They also investigated the effect of partial substitution in detail [146–153].

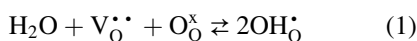
The most important reaction leading to the formation of protonic defects at moderate temperatures is the dissociative absorption of water which requires the presence of oxide ion vacancies  $V_O^{\bullet\bullet}$ . Those defects may be formed intrinsically by varying the ratio of main constituents

### Fuel Cells (SOFC): Alternative Approaches (Electrolytes, Electrodes, Fuels),

**Fig. 12** Normalized hydrogen isobars ( $p_{\text{H}_2\text{O}} = 23 \text{ hPa}$ ) for different perovskites, reported by Kreuer [156]. For  $\text{BaZrO}_3$ -based compositions, data for different hypovalent dopants (Y, Sc, Gd, In) are included (Reproduced by permission of Annual Reviews)



(e.g., in  $\text{Ba}_3\text{Ca}_{1-x}\text{Nb}_{2-x}\text{O}_{9-\delta}$  [154] or  $\text{Ba}_2\text{YSnO}_{5.5}$  [155]), or they may be formed extrinsically to compensate for an acceptor dopant R. In the case of perovskite-type oxides, one generally employs a substitution of up to 25% of the B-site cation by a lower-valence cation (i.e.,  $\text{A}(\text{B}_{1-x}\text{R}_x)\text{O}_{3-\delta}$  in the following denoted  $\text{R}:\text{ABO}_3$ ). In order to form protonic defects, water from the gas phase dissociates into a hydroxide ion filling an oxide ion vacancy and a proton forming a covalent bond with a lattice oxygen. In Kröger-Vink notation, this reaction is written:



by which two hydroxide ions substituting for oxide ions, that is, two positively charged protonic defects ( $\text{OH}_\text{O}^{\bullet}$ ), are formed. The hydroxyl ions form dynamical hydrogen bonds with neighboring lattice oxygen, and proton transfer through these hydrogen bonds combined with the rotational diffusion of this defect allows the protonic charge to migrate [156].

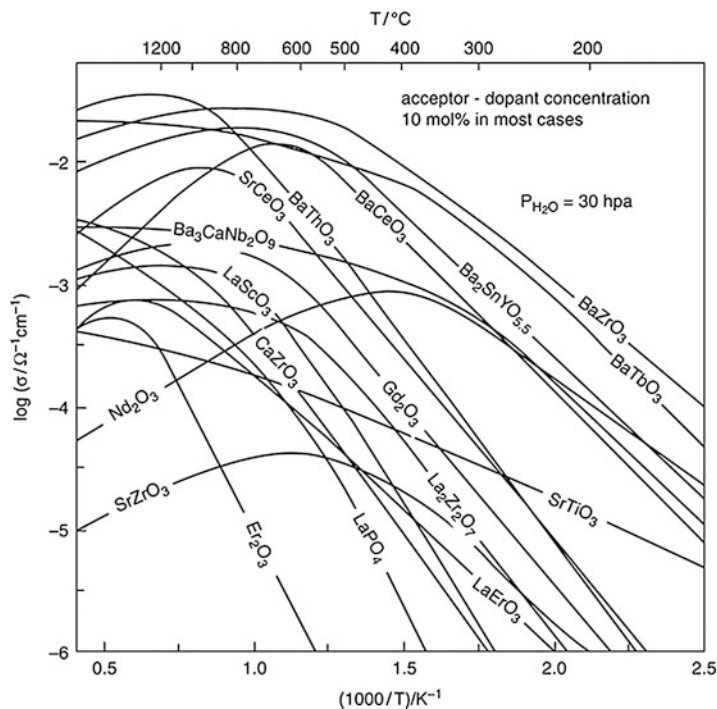
For perovskite-type oxides, the proton solubility decreases, but the stability to  $\text{CO}_2$  increases as the basicity of B-site ions decreases in the order of  $\text{Ce} \rightarrow \text{Zr} \rightarrow \text{Sn} \rightarrow \text{Nb} \rightarrow \text{Ti}$  [156]. The best compromise for high proton conductivity and chemical stability is found for Y-doped  $\text{BaZrO}_3$ , but unfortunately, this material exhibits large

grain boundary resistance, and it still reacts slightly with  $\text{CO}_2$  under certain conditions [157]. Chemical stability against  $\text{CO}_2$  has been demonstrated recently with  $\text{BaCe}_{0.3}\text{Zr}_{0.5}\text{Y}_{0.2}\text{O}_{3-\delta}$  by Fabbri et al. [158].

Proton concentration is proportional to the solubility of water into oxygen vacancies. Such a protonic conductor tends to lose water at high temperatures, which results in a decrease in the carrier density and also a decrease in conductivity. Figure 12 shows the amount of water dissolution measured by the gravimetric analysis for protonic conductors [156]. The perovskite-type proton-conductive oxides have enough carrier density in the temperature range from ca. 300 to 500 °C. On the other hand, mobility changes with temperature according to the Arrhenius equation with activation energy approximately from 0.3 to 0.6 eV. As a result, these protonic conductors exhibit their maximum conductivity at certain temperatures as shown in Fig. 13 [156].

It is extremely important that the ionic transference number is high enough to be used as a solid electrolyte in fuel cells. The  $\text{Ce}^{4+}$  cation has a tendency to be reduced easily, so that electronic conduction caused by the reduction of  $\text{Ce}^{4+}$  ions becomes a problem in the case of the  $\text{CeO}_2$ -containing electrolyte.  $\text{BaCeO}_3$ -based oxides contain Ce ions, exhibiting certain electronic conductivity by reduction [157]. Transport parameters

**Fuel Cells (SOFC):  
Alternative Approaches  
(Electrolytes, Electrodes,  
Fuels), Fig. 13** Ionic  
conductivity of proton-  
conductive perovskite type  
oxides, reported by Kreuer  
[156] (Reproduced by  
permission of Annual  
Reviews)



including activation enthalpies of hole and proton conduction have been reported [157, 159].

It is commonly believed that this is because the band gaps of the perovskite-type protonic conductors are considerably large, ranging from 4.5 to 5 eV or even larger [160]. On the other hand, hole conduction appears in an oxidizing atmosphere. However, the temperature dependence of the hole conductivity is larger than that of the protonic conductivity. Oxygen vacancies are filled with water dissolved in various oxides, as shown in Fig. 12, at temperatures below 500 °C, leading to a high protonic conductivity in an oxidizing atmosphere.

## Alternative Electrode Materials

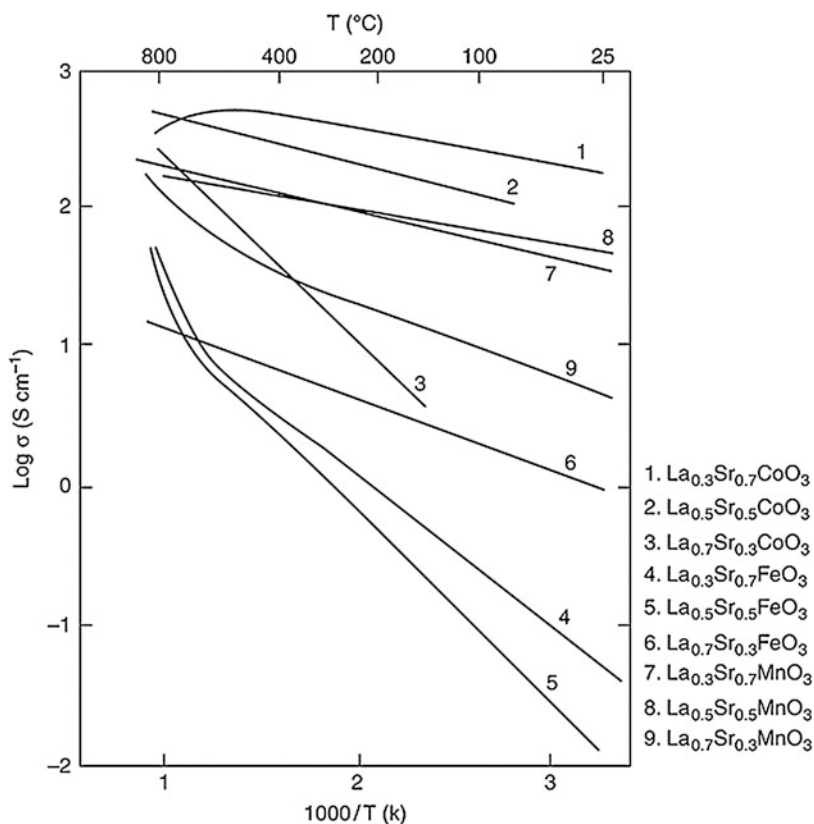
### Cathode Materials

#### Current Cathode Materials

The majority of investigations related to SOFC cathode materials have been concentrated on oxides with the perovskite structure [2–4, 161]. The oxides commonly used are SrO-doped

LaMnO<sub>3</sub> with an A-site deficiency ((La<sub>1-x</sub>Sr<sub>x</sub>)<sub>1-y</sub>MnO<sub>3±δ</sub>; x = 0.1–0.5, 0 ≤ y < 0.1). For example, La<sub>0.86</sub>Sr<sub>0.14</sub>MnO<sub>3</sub> exhibits an electronic conductivity of 1.4 × 10<sup>4</sup> S/m at 1000 °C [162]. The electronic conductivity increases with increasing alkaline-earth cation (Sr<sup>2+</sup>) concentration up to x ≈ 0.5. The increase in Sr content, however, is accompanied with an increase in thermal expansion coefficient [161–168]. The perovskite structure is very tolerant with changes in the ionic radius of the A- and B-site cations, allowing many possibilities to substitute host cations with various dopants. Related perovskite oxides have also been investigated. The A site in this perovskite can be substituted with other rare-earth oxides (e.g., Y<sub>1-x</sub>Ca<sub>x</sub>MnO<sub>3</sub>) [169–172] and with other alkaline-earth oxides (La<sub>1-x</sub>Ca<sub>x</sub>MnO<sub>3</sub>) [173–175]. This structure can also accommodate a high concentration of cation vacancies, particularly on the A site as (La<sub>1-x</sub>Sr<sub>x</sub>)<sub>1-y</sub>MnO<sub>3</sub> [22, 176–179]. By substituting the B site, the electronic conductivity and other properties such as nonstoichiometry, oxygen vacancy concentration, and catalytic activity can be changed considerably

**Fuel Cells (SOFC):  
Alternative Approaches  
(Electrolytes, Electrodes,  
Fuels), Fig. 14** Electronic  
conductivity of SrO-doped  
 $\text{LaBO}_3$  (B = Mn, Co, Fe)  
after Takeda et al. [180]  
(Reproduced by permission  
of ECS – The  
Electrochemical Society)



[163, 180, 181]. The Mn cation has been substituted with Fe, Co, Ni, and Cu, which enhances the electronic conductivity [180, 182]. Transition metal cations can be substituted on the B site like in  $\text{La}_{1-x}\text{Sr}_x\text{Mn}_{1-y}\text{Co}_y\text{O}_3$  or in  $\text{La}_{1-x}\text{Sr}_x\text{Fe}_{1-y}\text{Co}_y\text{O}_3$ , exhibiting excellent ionic conductivity as well as high electronic conductivity [21, 182–190]. The electronic conductivity of several perovskite oxides is shown in Fig. 14 [180]. Those compounds may be favored for their high electronic conductivity, particularly for planar fuel cell configurations, where in-plane electric current flow is essential in the relatively thin cathode layers. In recent SOFC systems under development, Sr-doped  $\text{LaMnO}_3$  is still widely used as the state-of-the-art cathode material for  $\text{ZrO}_2$ -based electrolytes [2–4, 161, 191].

In addition, cathode materials with mixed ionic and electronic conductivities can expand the electrode reaction area, leading to a decrease in cathodic overvoltage [2, 161, 192]. The perovskite oxides exhibit excellent electronic

conductivity, and in specific compounds and conditions, they possess high ionic conductivity. The ionic conductivity of  $\text{La}_{0.6}\text{Sr}_{0.4}\text{MnO}_3$  measured by Steele et al. [193] was  $10^{-5}$  S/m at  $900^{\circ}\text{C}$  in air, which is six orders of magnitude lower than the ionic conductivity of 8 mol%  $\text{Y}_2\text{O}_3$ -doped  $\text{ZrO}_2$  electrolyte. Therefore, the SrO-doped  $\text{LaMnO}_3$ , the state-of-the-art cathode material, is a poor mixed conductor [193]. However, the oxide becomes a mixed conductor in reduced state (at low oxygen partial pressure) [192, 194], as expected from the defect chemistry [22, 163] and electrocatalytic properties [195].

On the other hand, SrO- or CaO-doped  $\text{LaCoO}_3$  and  $\text{LaFeO}_3$  are excellent mixed conductors in ambient atmosphere [22, 180, 186–189, 193], where ionic conduction occurs via the oxygen vacancy mechanism [196]. Teraoka et al. [188] have reported that the  $\text{La}_{1-x}\text{Sr}_x\text{Co}_{1-y}\text{Fe}_y\text{O}_{3-\delta}$  exhibits ionic conductivity ranging from 10 to  $10^3$  S/m, while the ionic conductivity of doped  $\text{ZrO}_2$  electrolyte is

**Fuel Cells (SOFC): Alternative Approaches (Electrolytes, Electrodes, Fuels), Table 2** Thermal expansion coefficients of perovskite oxides for SOFC cathode applications [33, 168, 184, 186]

	Materials	Thermal expansion coefficient ( $\times 10^{-6}/\text{K}$ )	Temp. range ( $^{\circ}\text{C}$ )
ZrO <sub>2</sub>	ZrO <sub>2</sub> -8 mol%Y <sub>2</sub> O <sub>3</sub>	10.5	25-900
LSM	La <sub>0.85</sub> Sr <sub>0.15</sub> MnO <sub>3</sub>	11.7	25-900
	La <sub>0.5</sub> Sr <sub>0.5</sub> MnO <sub>3</sub>	12.6	25-900
	La <sub>0.99</sub> MnO <sub>3</sub>	11.2 <sup>a</sup>	25-1000
	La <sub>0.94</sub> Sr <sub>0.05</sub> MnO <sub>3</sub>	11.7 <sup>a</sup>	25-1000
	La <sub>0.89</sub> Sr <sub>0.10</sub> MnO <sub>3</sub>	12.0 <sup>a</sup>	25-1000
	La <sub>0.79</sub> Sr <sub>0.20</sub> MnO <sub>3</sub>	12.4 <sup>a</sup>	25-1000
	La <sub>0.69</sub> Sr <sub>0.30</sub> MnO <sub>3</sub>	12.8 <sup>a</sup>	25-1000
LSC	La <sub>0.85</sub> Sr <sub>0.15</sub> CoO <sub>3</sub>	18.7	25-900
	La <sub>0.7</sub> Sr <sub>0.3</sub> CoO <sub>3</sub>	18.3	25-900
	La <sub>0.5</sub> Sr <sub>0.5</sub> CoO <sub>3</sub>	22.0	25-900
	La <sub>0.3</sub> Sr <sub>0.7</sub> CoO <sub>3</sub>	15.6	25-900
LSCM	La <sub>0.85</sub> Sr <sub>0.15</sub> Mn <sub>0.8</sub> Co <sub>0.2</sub> O <sub>3</sub>	11.8	25-900
	La <sub>0.85</sub> Sr <sub>0.15</sub> Mn <sub>0.5</sub> Co <sub>0.5</sub> O <sub>3</sub>	14.6	25-900
	La <sub>0.5</sub> Sr <sub>0.5</sub> Mn <sub>0.5</sub> Co <sub>0.5</sub> O <sub>3</sub>	14.9	25-900
	La <sub>0.8</sub> Sr <sub>0.2</sub> Mn <sub>0.8</sub> Co <sub>0.2</sub> O <sub>3</sub>	11.1 <sup>b</sup>	200-800
	La <sub>0.8</sub> Sr <sub>0.2</sub> Mn <sub>0.6</sub> Co <sub>0.4</sub> O <sub>3</sub>	13.7 <sup>b</sup>	200-800
	La <sub>0.8</sub> Sr <sub>0.2</sub> Mn <sub>0.4</sub> Co <sub>0.6</sub> O <sub>3</sub>	16.5 <sup>b</sup>	200-800
	La <sub>0.8</sub> Sr <sub>0.2</sub> Mn <sub>0.2</sub> Co <sub>0.8</sub> O <sub>3</sub>	17.0 <sup>b</sup>	200-800
	La <sub>0.8</sub> Sr <sub>0.2</sub> CoO <sub>3</sub>	17.8 <sup>b</sup>	200-800
LSCF	La <sub>0.8</sub> Sr <sub>0.2</sub> Co <sub>0.8</sub> Fe <sub>0.2</sub> O <sub>3</sub>	18.4	25-900
	La <sub>0.2</sub> Sr <sub>0.8</sub> Co <sub>0.8</sub> Fe <sub>0.2</sub> O <sub>3</sub>	24.0	25-900
	La <sub>0.8</sub> Sr <sub>0.2</sub> CoO <sub>3</sub>	19.7 <sup>c</sup>	100-1000
	La <sub>0.8</sub> Sr <sub>0.2</sub> Co <sub>0.8</sub> Fe <sub>0.2</sub> O <sub>3</sub>	20.7 <sup>c</sup>	100-1000
	La <sub>0.8</sub> Sr <sub>0.2</sub> Co <sub>0.6</sub> Fe <sub>0.4</sub> O <sub>3</sub>	20.0 <sup>c</sup>	100-1000
	La <sub>0.8</sub> Sr <sub>0.2</sub> Co <sub>0.4</sub> Fe <sub>0.6</sub> O <sub>3</sub>	17.7 <sup>c</sup>	100-1000
	La <sub>0.8</sub> Sr <sub>0.2</sub> Co <sub>0.2</sub> Fe <sub>0.8</sub> O <sub>3</sub>	15.1 <sup>c</sup>	100-1000
	La <sub>0.8</sub> Sr <sub>0.2</sub> FeO <sub>3</sub>	12.9 <sup>c</sup>	100-1000

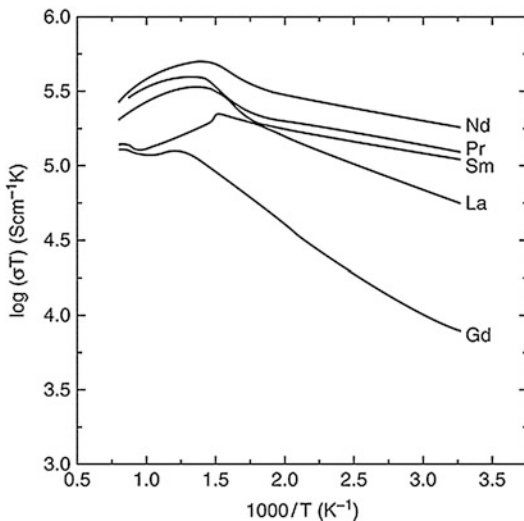
<sup>a</sup>See Ref. [168]<sup>b</sup>See Ref. [184]<sup>c</sup>See Ref. [186]

around 10 S/m. High ionic conductivity in La<sub>0.6</sub>Sr<sub>0.4</sub>CoO<sub>3</sub> has been confirmed by Steele et al. to be 80 S/m at 900 °C [193]. Ionic conductivity also increases by substituting the B-site cations with cations with a larger number of 3d electrons from Fe to Co and Ni [182], consistent with the increase in oxygen vacancy concentration [163]. The thermal expansion mismatch between the cathode and the electrolyte, as compiled in Table 2, leads to insufficient contact and thus the detachment of cathode layers, which limits the SOFC applications of such mixed conducting cathode materials.

### Alternative Cathode Materials

Perovskite oxides using smaller lanthanide elements than La, such as Gd<sub>1-x</sub>Sr<sub>x</sub>CoO<sub>3</sub> [197], Sm<sub>1-x</sub>Sr<sub>x</sub>CoO<sub>3</sub> [198], Pr<sub>1-x</sub>Sr<sub>x</sub>MnO<sub>3</sub>, and Nd<sub>1-x</sub>Sr<sub>x</sub>MnO<sub>3</sub> [199] have been investigated as cathode materials in order to decrease reactivity with the YSZ electrolyte. Compatibility with YSZ electrolyte was further improved for Gd<sub>1-x</sub>Sr<sub>x</sub>Co<sub>1-y</sub>Mn<sub>y</sub>O<sub>3</sub> [200] by substituting Co with Mn on the B site due to lower reactivity and matching of thermal expansion coefficients. Substitution of Co with Fe on the B site also decreases their thermal expansion coefficient.





**Fuel Cells (SOFC): Alternative Approaches (Electrolytes, Electrodes, Fuels), Fig. 15** Temperature dependence of the electrical conductivity for  $\text{Ln}_{0.4}\text{Sr}_{0.6}\text{Co}_{0.8}\text{Fe}_{0.2}\text{O}_{3-\delta}$  ( $\text{Ln} = \text{La}, \text{Pr}, \text{Nd}, \text{Sm}, \text{Gd}$ ), reported by Tu et al. [201] (Reproduced with permission from Elsevier)

Perovskite oxides using Co and Fe for the B site, such as  $\text{Pr}_{1-x}\text{Sr}_x\text{Co}_{1-y}\text{Fe}_y\text{O}_{3-\delta}$ ,  $\text{Nd}_{1-x}\text{Sr}_x\text{Co}_{1-y}\text{Fe}_y\text{O}_{3-\delta}$ , and  $\text{Gd}_{1-x}\text{Sr}_x\text{Co}_{1-y}\text{Fe}_y\text{O}_{3-\delta}$ , exhibit high electrical conductivity above 600 °C as shown in Fig. 15 and exhibit good catalytic activity on GDC electrolytes in the intermediate operational temperature range (600–800 °C) [201, 202], as shown in Fig. 16.

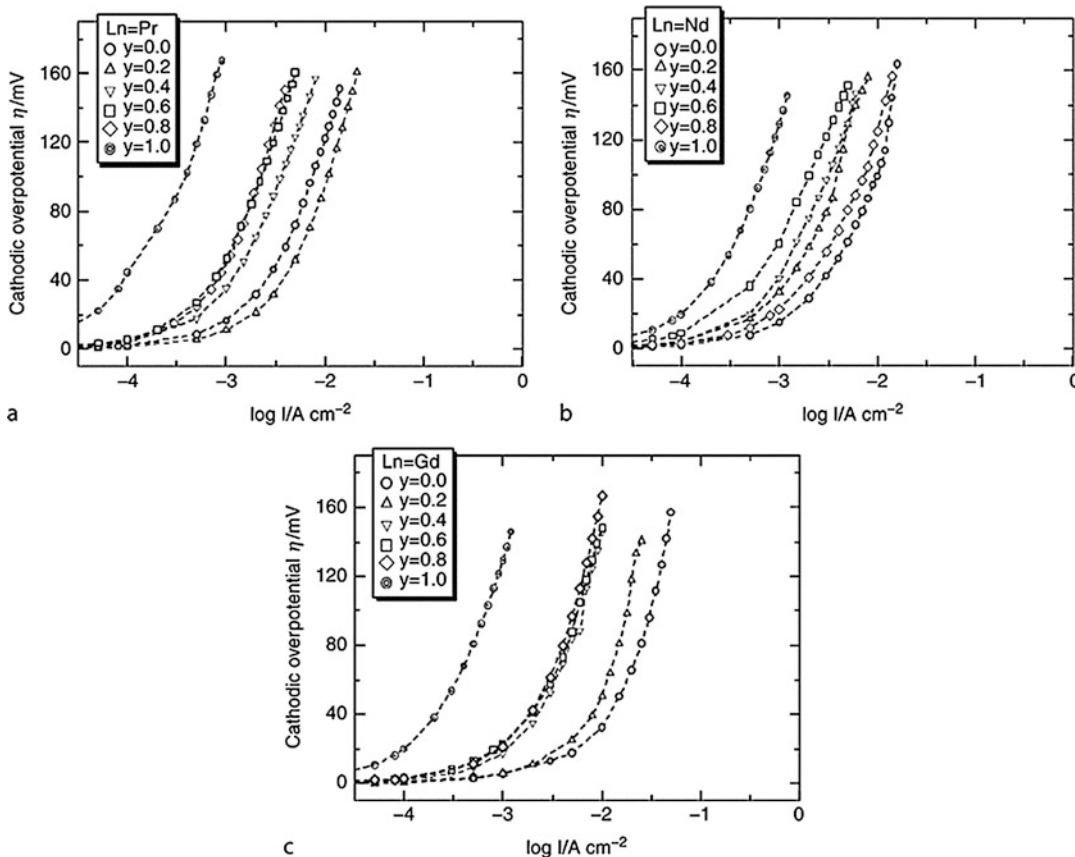
$\text{Sm}_{0.5}\text{Sr}_{0.5}\text{CoO}_3$  has been used as a cathode material for the LSGM electrolyte, and a low cathodic overpotential of less than 50 mV at 0.5  $\text{A}/\text{cm}^2$  was obtained at 873 K [203].  $\text{BaCoO}_3$  was also investigated as a novel cathode material for the LSGM electrolyte.  $\text{Ba}_{0.6}\text{La}_{0.4}\text{CoO}_3$  showed a high surface activity for oxygen dissociation and exhibited the same level of cathodic overpotential as  $\text{Sm}_{0.5}\text{Sr}_{0.5}\text{CoO}_3$  as shown in Fig. 17 [204].

Perovskite oxides containing Ba in the A site were proposed as cathode materials for a lower-temperature operation. Many of them have been investigated in combination with  $\text{CeO}_2$ -based electrolytes. High power density of more than 1  $\text{W}/\text{cm}^2$  was obtained at 600 °C by using  $\text{Ba}_{0.5}\text{Sr}_{0.5}\text{Co}_{0.8}\text{Fe}_{0.2}\text{O}_{3-\delta}$  (BSCF) for the cathode on a thin SDC electrolyte (12–20  $\mu\text{m}$  in thickness)

as shown in Fig. 18 [205]. Enhancement of electrical conductivity by an addition of Sm to BSCF was also reported, which resulted in further improvement of cathode performance at low operational temperatures [206].  $\text{Ba}_{0.5}\text{Sr}_{0.5}\text{Co}_{1-y}\text{Fe}_y\text{O}_{3-\delta}$  possessed low vacancy formation energy with low oxygen migration barrier [207]. However, BSCF cathode could degrade in the presence of  $\text{CO}_2$  in ambient air, owing to the reaction with alkaline-earth elements, resulting in the formation of Ba and Sr carbonates [208, 209].

Regarding durability of SOFC cathodes, Cr poisoning phenomena of cathode materials have been investigated to better understand long-term cell performance. Taniguchi et al. clarified that not only the vapor pressure of Cr species but also the cathodic overvoltage affects the degradation rate for a cell using  $\text{La}_{0.9}\text{Sr}_{0.1}\text{MnO}_3$  [210]. In addition, reaction between the Cr vapor and the cathode material can decrease the vapor pressure and contribute in delaying the beginning of cell performance degradation [211]. Matsuzaki et al. reported that the use of  $\text{La}_{0.6}\text{Sr}_{0.4}\text{Co}_{0.2}\text{Fe}_{0.8}\text{O}_3$  (LSCF) on  $\text{Ce}_{0.8}\text{Sm}_{0.2}\text{O}_{1.9}$  electrolyte drastically reduced the Cr poisoning in comparison with  $\text{La}_{0.85}\text{Sr}_{0.15}\text{MnO}_3$  [212].  $\text{LaNi}_{0.6}\text{Fe}_{0.4}\text{O}_3$  (LNF) was also proposed as a novel cathode material, exhibiting high tolerance to the Cr poisoning. Chiba et al. have first reported that LNF possesses suitable properties for operating at low temperatures [213]. LNF has shown high electronic conductivity of 580  $\text{S}/\text{cm}$  at 800 °C and relatively closer thermal expansion coefficient of  $11.4 \times 10^{-6} \text{K}^{-1}$  (30–1000 °C) to that of YSZ than  $\text{La}_{0.8}\text{Sr}_{0.2}\text{MnO}_3$  (LSM). Furthermore, it is also revealed that LNF has higher tolerance to Cr poisoning than LSM and LSCF [214]. Figure 19 shows the comparison of cathodic overvoltage by Cr poisoning between LSCF and LNF. Concerning the Cr poisoning phenomena, Jiang et al. [215] explained that the deposition of Cr in the LSM cathode is initiated by the nucleation reaction involving the gaseous Cr species and  $\text{Mn}^{2+}$ , which are generated by the cathode polarization and regarded as nucleation agents. SrO is identified as a nucleation agent in the case of LSCF. As a result, they concluded that LNF exhibits high tolerance to





**Fuel Cells (SOFC): Alternative Approaches (Electrolytes, Electrodes, Fuels), Fig. 16** Cathodic polarization curves for  $\text{Ln}_{0.8}\text{Sr}_{0.2}\text{Co}_{1-y}\text{Fe}_y\text{O}_{3-\delta}$  ((a)  $\text{Ln} = \text{Pr}$ , (b)

$\text{Ln} = \text{Nd}$ , (c)  $\text{Ln} = \text{Gd}$ ) cathodes on GDC electrolytes at  $700\text{ }^\circ\text{C}$ , reported by Qiu et al. [202] (Reproduced with permission from Elsevier)

Cr poisoning because it has no nucleation agent under any electrochemical condition [215]. In terms of electrochemical properties at low temperatures, an electrode resistance of approximately  $0.1\ \Omega\ \text{cm}^2$ , corresponding to the cathode polarization, was achieved at  $700\text{ }^\circ\text{C}$  in the case of a LNF-YSZ composite cathode which was made by infiltrating LNF into porous YSZ [216].

Another type of oxide with the general formulation of  $\text{A}_2\text{BO}_4 + \delta$  (e.g.,  $\text{La}_{2-x}\text{Sr}_x\text{NiO}_4 + \delta$  [217],  $\text{Nd}_2\text{NiO}_4 + \delta$  [218, 219],  $\text{Pr}_{1.4}\text{Sr}_{0.6}\text{NiO}_4$  [220], and  $\text{Sm}_{0.5}\text{Sr}_{1.5}\text{CoO}_4 - \delta$  [221]) has also been investigated for intermediate-temperature ( $900\text{--}1000\ \text{K}$ ) operation. Their  $\text{K}_2\text{NiF}_4$ -type structure allows for some slight oxygen overstoichiometry. Oxygen excess, accommodated by oxygen interstitials rather than cation

vacancies, leads to high values of oxygen tracer diffusion coefficient. Current density of  $0.5\ \text{A}\ \text{cm}^{-2}$  at  $0.7\ \text{V}$  was obtained at  $700\text{ }^\circ\text{C}$  with an anode-supported half-cell with a  $\text{Nd}_{1.95}\text{NiO}_4 + \delta$  cathode and a YSZ electrolyte [219].

In order to enhance the catalytic activity of the cathode for oxygen reduction and thus to increase the electrochemical performance, an addition of noble metals has also been investigated [222]. By the addition of silver to a LSCF-CeO<sub>2</sub> composite cathode, an improvement of cathode performance at lower temperatures below  $700\text{ }^\circ\text{C}$  was measured [223, 224]. Consequently, Ag improved the surface exchange step of oxygen from the gas phase into the oxide [223]. Cell performance of more than  $500\ \text{mW}/\text{cm}^2$  at  $0.7\ \text{V}$  at  $700\text{ }^\circ\text{C}$  was obtained using anode-supported cells with LSCF-

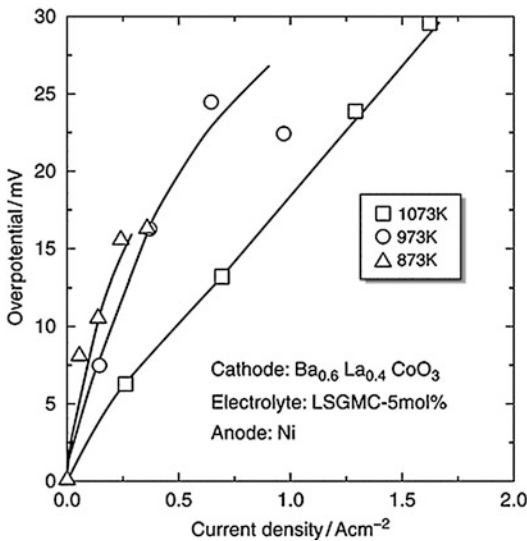
coated Ag cathode and YSZ electrolyte [225]. Generally speaking, Sr-doped LaMnO<sub>3</sub> and related materials are suitable for high-temperature operation of SOFCs, while more electrochemically/catalytically active alternative

cathode materials may be needed especially for lower operational temperatures.

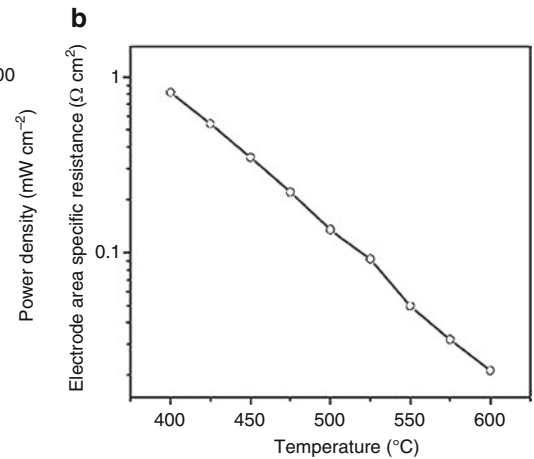
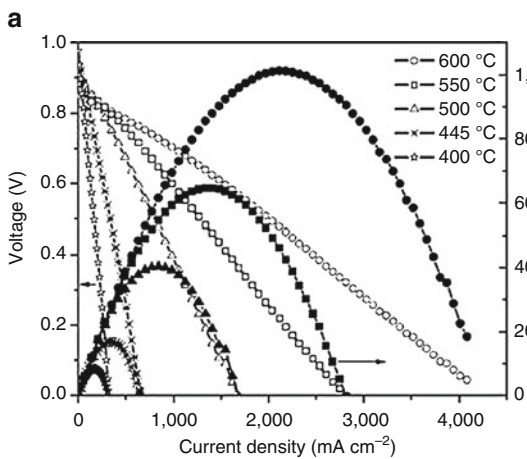
### Anode Materials

#### Current Anode Materials

In state-of-the-art SOFCs, Ni-based cermet anodes are commonly used, which exhibit excellent electrocatalytic activity for anodic electrochemical reactions, fuel oxidation, and internal reforming, as well as sufficient current collection [2–4, 161, 226]. Due to the requirements of operation in reducing environments and high electronic conductivity, pure metallic electrodes are generally used as anodes. Several metals such as Ni, Ru, Pt, and Co have been studied as anode materials [161, 227, 228]. Ni exhibited the lowest anodic overpotentials [161, 227], while Ru could be an excellent anode material [228]. Pure Ni has electronic conductivities of  $1.4 \times 10^5 \text{ Scm}^{-1}$  and  $2.6 \times 10^4 \text{ Scm}^{-1}$  at 298 K and 900 K, respectively, a thermal expansion coefficient of ca.  $14.6 \times 10^6 \text{ K}^{-1}$ , and a melting point of 1455 °C [229]. The transition metals, which show higher activities for the oxidation of hydrogen, tend to change their microstructures at high temperatures under the reducing conditions of the

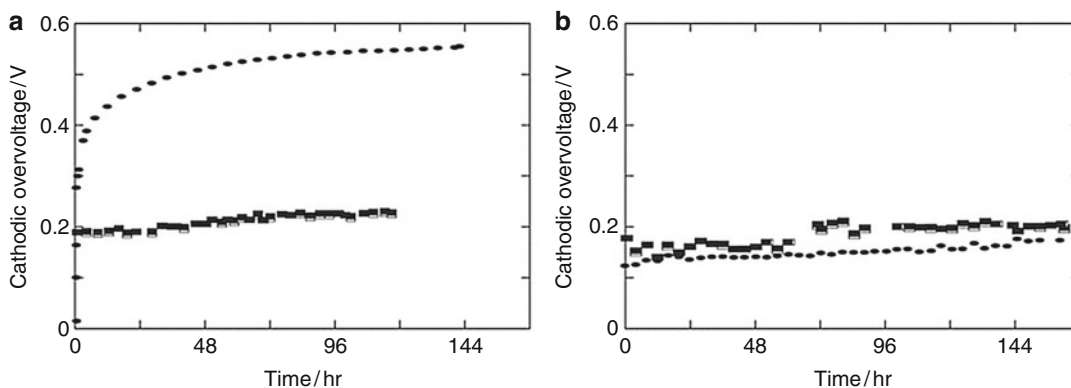


**Fuel Cells (SOFC): Alternative Approaches (Electrolytes, Electrodes, Fuels), Fig. 17** Temperature dependence of cathodic overpotential of the Ba<sub>0.6</sub>La<sub>0.4</sub>CoO<sub>3</sub> cathode on the LSGMC electrolyte as a function of current density, reported by Ishihara et al. [204] (Reproduced with permission from Elsevier)



**Fuel Cells (SOFC): Alternative Approaches (Electrolytes, Electrodes, Fuels), Fig. 18** Performance obtained from a Ba<sub>0.5</sub>Sr<sub>0.5</sub>Co<sub>0.8</sub>Fe<sub>0.2</sub>O<sub>3</sub> – δ (~20 μm) | Sm<sub>0.15</sub>Ce<sub>0.85</sub>O<sub>2</sub> – δ (~20 μm) | Ni + Sm<sub>0.15</sub>Ce<sub>0.85</sub>O<sub>2</sub> – δ (~700 μm) fuel cell. (a) Cell

voltage and power density as a function of current density and (b) area-specific resistances of the electrodes, reported by Shao and Haile [205] (Reproduced with permission from Nature Publishing Group)



**Fuel Cells (SOFC): Alternative Approaches (Electrolytes, Electrodes, Fuels), Fig. 19** Cathodic overvoltage (IR corrected) for cells using (a) LSCF cathode and (b) LNF cathode as a function of time: (•) cell with Inconel

600 at  $0.7 \text{ A cm}^{-2}$  and (•) cell without Inconel 600 at  $0.7 \text{ A cm}^{-2}$ , reported by Komatsu et al. [214] (Reproduced by permission of Elsevier)

anode, that is, coalescence of metal particles leads to anode densification. To stabilize the anode morphology in terms of porosity and thermal expansion coefficients, in general, cermet are used, where the ceramic component provides a rigid network and hinders the porous anode morphology from coalescence. The ceramic component also ensures to make the thermal expansion coefficient similar to that of the electrolyte materials.

Internal reforming of hydrocarbon-based fuels can also occur on the Ni surface in the cermet anode. In an SOFC cermet anode, substantially long triple phase boundaries (TPB) can be achieved, and given that solid networks of two phases (electronic conductors and ionic conductors) are obtained throughout the anode volume. It has been well accepted that the electrochemical reaction occurs around the TPB, where oxygen ion conductor (electrolyte), electron-conducting metal phase (Ni), and gas phase all meet together [2, 161].

### Alternative Anode Materials

#### General

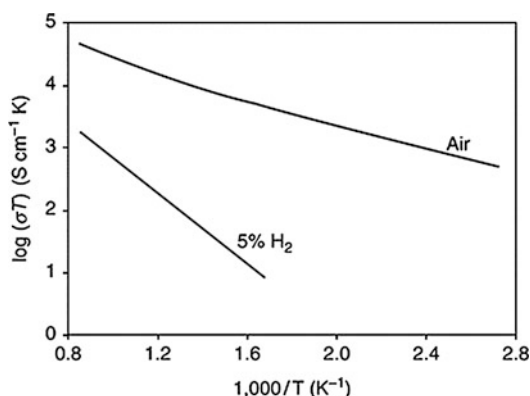
While Ni/YSZ cermet is the most preferred anode material for SOFCs operating with hydrogen-containing fuels, there are several efforts to find alternative materials for the SOFC anode. Many studies on oxide anodes have been made for

perovskite-related oxides.  $\text{LaCrO}_3$  [230–237],  $\text{LaFeO}_3$  [238],  $\text{LaTiO}_3$  [239], and  $\text{SrTiO}_3$  [240–243] systems are considered as possible alternative anode materials.

#### Perovskite-Type Oxide

$\text{LaCrO}_3$ -based oxides are well known as interconnect materials for SOFCs. They have high durability in reducing atmosphere. The oxygen-deficient perovskite  $\text{La}_{0.75}\text{Sr}_{0.25}\text{Cr}_{0.5}\text{Mn}_{0.5}\text{O}_3$ , used as an anode material by Tao et al. [230], is stable in both fuel and air atmospheres and has revealed stable electrode performance, as shown in Fig. 20 [230]. However, this material has a low electronic conductivity in reducing anode atmosphere and is not stable to sulfur impurities in the fuel [231]. Its long-term performance has been proven unsatisfactory [231].  $\text{Sr}_2\text{MgM}_6\text{O}_{6-8}$  exhibited a sulfur tolerance up to 50 ppm  $\text{H}_2\text{S}$  [232]. Experimental results on the  $\text{La}_{0.8}\text{Sr}_{0.2}\text{Cr}_{0.97}\text{V}_{0.03}\text{O}_3$  (LSCV)-YSZ composite anode have demonstrated that the electrochemical performance is comparable to that of Ni/YSZ after 48 h operation [233].

Ruiz-Morales et al. [234] demonstrated symmetrical fuel cells (SFCs) using the same material  $\text{La}_{0.75}\text{Sr}_{0.25}\text{Cr}_{0.5}\text{Mn}_{0.5}\text{O}_{3-\delta}$  (LSCM) on both the anode side and the cathode side. Due to its enhanced electrochemical properties under both reducing and oxidizing conditions, LSCM-based SFCs offered sufficient performances, 0.5 and 0.3



**Fuel Cells (SOFC): Alternative Approaches (Electrolytes, Electrodes, Fuels), Fig. 20** Temperature ( $T$ ) dependence of total conductivity ( $\sigma$ ) of  $\text{La}_{0.75}\text{Sr}_{0.25}\text{Cr}_{0.5}\text{Mn}_{0.5}\text{O}_{3-\delta}$  in air and 5%  $\text{H}_2$ , reported by Tao and Irvine [230] (Reproduced with permission from Nature Publishing Group)

$\text{Wcm}^{-1}$  at 950 °C using  $\text{H}_2$  and  $\text{CH}_4$  as fuels, respectively [234].

Sauvet et al. [235] have studied the electrochemical properties of  $\text{La}_{1-x}\text{Sr}_x\text{Cr}_{1-y}\text{Ru}_y\text{O}_{3-\delta}$  ( $x = 0.2-0.4$ , and  $y = 0.02$  and  $0.05$ ) for hydrogen and methane fuels at 750 and 850 °C. They found the best performances obtained with 30% of Sr doping, and the variation of the ruthenium content, approximately between 0.02 and 0.05, had little influence on the electrochemical results. At 750 °C, the polarization resistance was  $3.7 \Omega \text{ cm}^2$  in hydrogen and  $40 \Omega \text{ cm}^2$  in methane for the YSZ/ $\text{CeO}_2$ /graded  $\text{La}_{0.7}\text{Sr}_{0.3}\text{Cr}_{0.95}\text{Ru}_{0.05}\text{O}_{3-\text{YSZ}}$  structure [235]. Sauvet et al. also studied  $\text{La}_{1-x}\text{Sr}_x\text{Cr}_{1-y}\text{Ni}_y\text{O}_{3-\delta}$  compositions as novel anode materials. They have found that these materials have catalytic activity, but less than that of Ni composites [236, 237].

Lanthanum ferrites have also been investigated as potential anode materials. They are already known for high mixed electronic and ionic conductivity and good oxygen exchange kinetics. However, they have poor stability at lower oxygen partial pressures in the reducing atmosphere. The stability, however, could be improved by mixing with GDC [238].

(La, Sr)TiO<sub>3</sub> has been investigated as alternative SOFC anodes, along with other A-site-deficient lanthanides. Nevertheless, it has poor

conductivity than Ni/YSZ cermet [239]. Doped SrTiO<sub>3</sub> could be an interesting anode material, and the mixed conductivity of La-doped and Fe-doped SrTiO<sub>3</sub> is widely influenced by the chemical composition [240, 244, 245]. SrTiO<sub>3</sub> doped with Y [241] and La [242] exhibits increased electrical conductivity. Unfortunately, the high-temperature electrical conductivity of various perovskite anodes is still lower than that of the conventional Ni/YSZ cermet for the use as SOFC anodes [243].

#### Other Transition Metal Cermets

The Cu-based anode cermet has been extensively studied. For example, Park et al. [246, 247] demonstrated that the anode composed of Cu/ $\text{Sm}_2\text{O}_3\text{-CeO}_2$ /YSZ was active for direct electrochemical oxidation of alkanes and alkenes, such as methane, ethane, butane, butene, hexane, and toluene, at the operating temperature of 700 °C.  $\text{CeO}_2$  plays an important role as a primary catalyst material for oxidizing hydrocarbons, and the main role of Cu is to provide electrical conductivity. Zhou et al. [248] reported good performance of  $\text{CeO}_2\text{-Rh}$  anodes for the direct electrochemical oxidation of waste vegetable oil, which led to stable current density of  $500 \text{ mA cm}^{-2}$  over 100 h under the condition of 0.5 V and 700 °C.

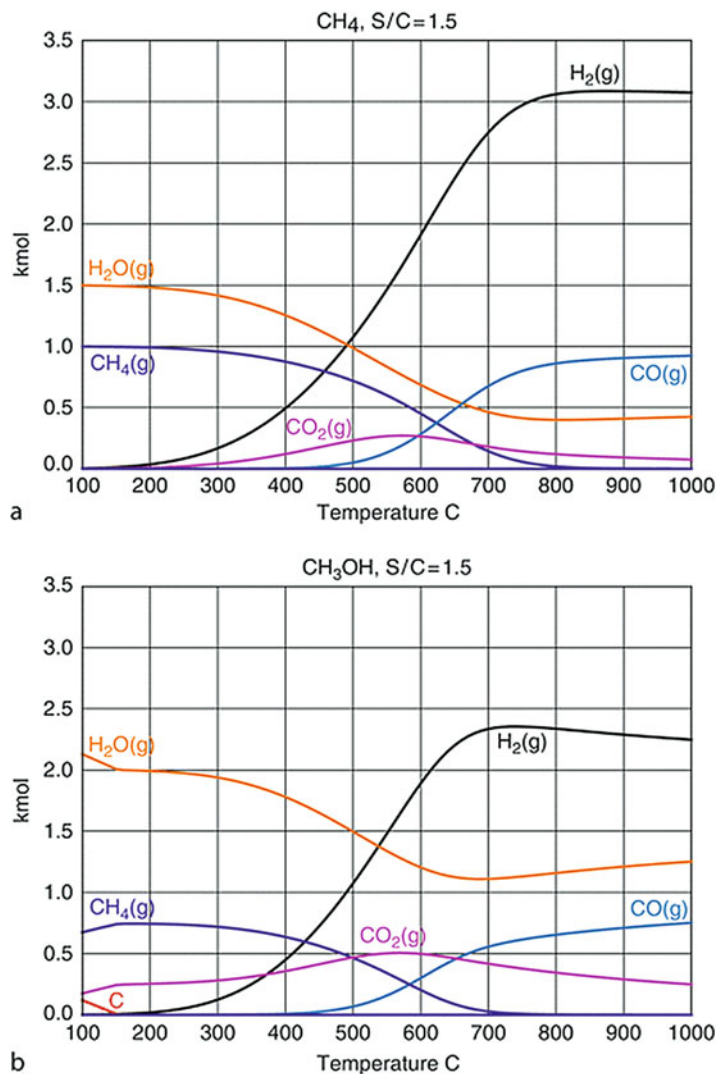
## Alternative Fuels

### Fuel Flexibility

SOFCs are the most flexible fuel cells with respect to the type of fuels [1, 246–255] which can be supplied directly to the anodes. This is partly due to their high operational temperatures suitable for internal reforming within the anodes. Because of their multi-fuel capability, not only hydrogen and carbon monoxide [256] but also various types of fuels such as hydrocarbons, alcohols, and biogas could be used via internal reforming and/or via simple external reforming [246–249, 257–260]. Practical fuels comprise natural gas (consisting mainly of  $\text{CH}_4$  with a small amount of other hydrocarbons such as  $\text{C}_2\text{H}_6$ ), coal gas (consisting mainly of CO and  $\text{H}_2$ ), liquefied petroleum gas (LPG, consisting mainly of  $\text{C}_3\text{H}_8$  with

**Fuel Cells (SOFC):  
Alternative Approaches  
(Electrolytes, Electrodes,  
Fuels),**

**Fig. 21** Equilibrium products from (a) methane- and (b) methanol-based fuels with the steam-to-carbon ratio of 1.5



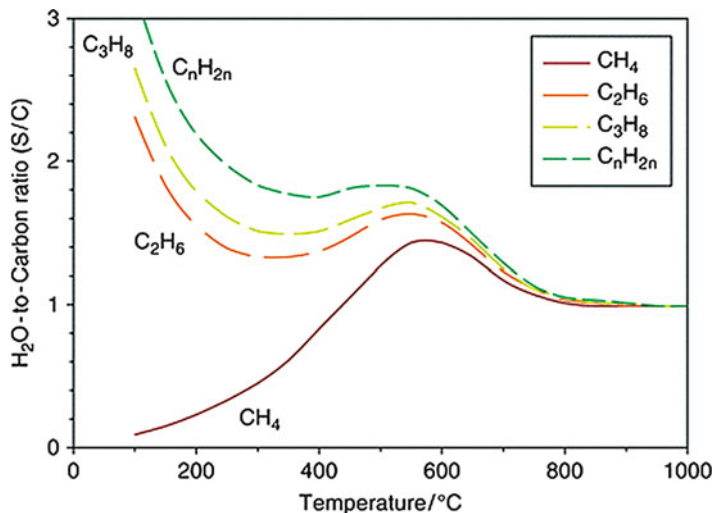
C<sub>4</sub>H<sub>10</sub>), naphtha (consisting mainly of C<sub>5</sub> and C<sub>6</sub> hydrocarbons), gasoline (consisting mainly of hydrocarbons with carbon numbers around 8), kerosene (consisting mainly of hydrocarbons with carbon numbers around 12), diesel fuel (consisting mainly of hydrocarbons with carbon numbers around 14–16), alcohols, dimethyl ether, and biogas (consisting mainly of CH<sub>4</sub>, CO<sub>2</sub>, and H<sub>2</sub>O) [251, 252].

In any case, one of the most important issues to be prevented in SOFC systems is carbon deposition (coke formation) from the fuels. Figure 21 shows the equilibrium products for (a) methane- and (b) methanol-based fuels with the steam-to-

carbon (S/C) ratio of 1.5 at elevated temperatures [251]. Assuming thermochemical equilibrium, carbon deposition is not expected to occur within a wide temperature range. The calculated results for various other fuels mentioned above have been shown elsewhere [251]. The minimum amounts of H<sub>2</sub>O (water vapor) necessary to prevent carbon deposition are shown in Fig. 22 for hydrocarbon fuels. While S/C of 1.5 is enough for CH<sub>4</sub>, higher S/C is needed with increasing carbon number of hydrocarbons, especially at lower temperatures. Such dependencies have also been revealed for O<sub>2</sub> (partial oxidation) and CO<sub>2</sub> (CO<sub>2</sub> reforming) [251] to prevent carbon deposition.



**Fuel Cells (SOFC): Alternative Approaches (Electrolytes, Electrodes, Fuels), Fig. 22** Minimum steam-to-carbon (S/C) ratio needed to prevent carbon deposition in thermodynamic equilibrium for hydrocarbons [251] (Reproduced with permission from ECS – The Electrochemical Society)



It has been found that the major equilibrium constituents in fuel gases are  $H_2(g)$ ,  $H_2O(g)$ ,  $CO(g)$ ,  $CO_2(g)$ ,  $CH_4(g)$ , and  $C(s)$  [251]. Since their equilibrium compositions depend solely on the C–H–O ratio, we can plot, on C–H–O diagrams [252, 253, 255], parameters relevant to optimize operational conditions, including carbon deposition region, gas partial pressures, and electromotive force. Figure 23 shows the positions of various fuel species for fuel cells [252]. Their positions can be shifted by adding  $H_2O$  (steam reforming),  $O_2$  (partial oxidation), and/or  $CO_2$  ( $CO_2$  reforming) as co-reactants. Figure 24 shows the carbon deposition limit lines, the carbon-rich side of which corresponds to the carbon deposition region at each temperature. From Figs. 23 and 24, we see that an addition of co-reactants is necessary to prevent carbon formation at SOFC operational temperatures from most fuels shown in Fig. 23. Once the C–H–O ratio is specified, C–H–O ternary diagrams are useful to derive relevant operational parameters without any additional thermochemical calculations [252].

Apart from such thermochemical processes, also, kinetic phenomena may dominate electrode performance. In the following sections, various practical fuels are experimentally examined, the use of which may enable broader application of SOFCs.

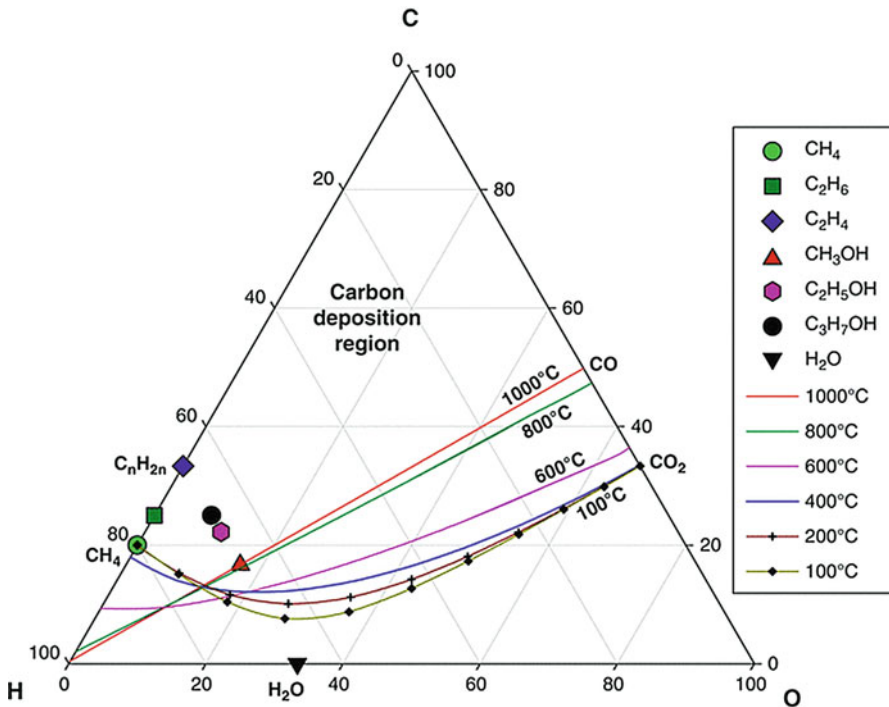
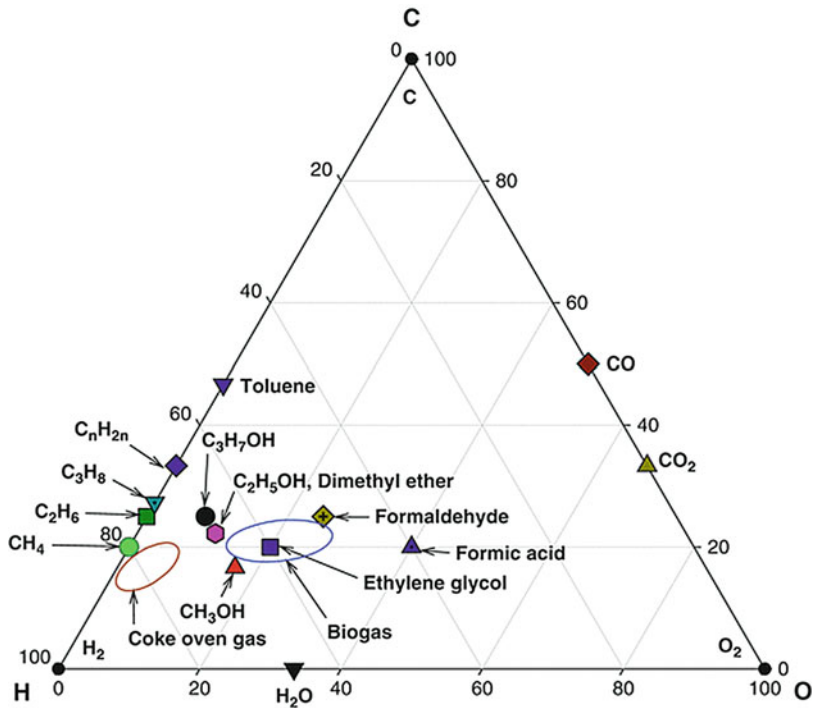
### Practical Fuels

City gas (town gas) is used as the state-of-the-art fuel for the first-generation commercial SOFC systems. City gas, consisting mainly of  $CH_4$  from the natural gas, may be partially pre-reformed before supplying to the SOFC systems. Figure 25 shows the comparison of the current-voltage (I–V) characteristics between a  $H_2$ -based fuel and a typical SOFC fuel (50% pre-reformed  $CH_4$  with  $S/C = 2.5$ ) [261]. The cross section of a typical SOFC used for this electrochemical measurement (see Fig. 25) is shown in Fig. 26. This simulated practical SOFC fuel for distributed cogeneration systems consists of the one-to-one mixture of fully reformed  $CH_4$  with  $S/C = 2.5$  and non-reformed  $CH_4$  with  $S/C = 2.5$ . While too low  $S/C$  may result in carbon deposition, excessive amount of  $H_2O$  causes lower OCV and may cause re-oxidation of Ni at high fuel utilization of the SOFC systems.

As practical SOFC fuels may contain a small amount of sulfur as an impurity,  $H_2S$  poisoning should be considered with respect to various operational conditions [262–266]. As an example, Fig. 27 shows the cell voltage, the anodic polarization, and the ohmic loss on the anode side, measured for 50% pre-reformed  $CH_4$ -based fuel with  $S/C = 2.5$  containing 5 ppm  $H_2S$ . An initial cell voltage drop followed by a



**Fuel Cells (SOFC): Alternative Approaches (Electrolytes, Electrodes, Fuels), Fig. 23** Various hydrocarbons and related species in the C–H–O diagram [252] (Reproduced with permission from ECS – The Electrochemical Society)

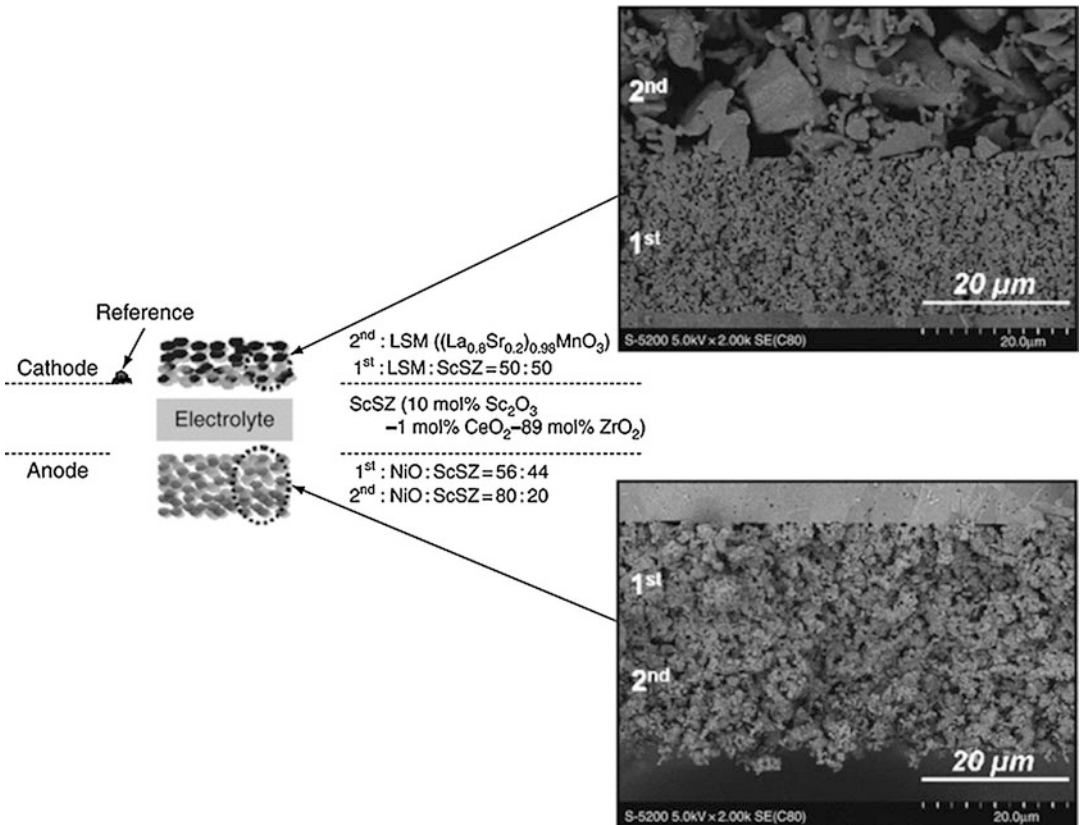
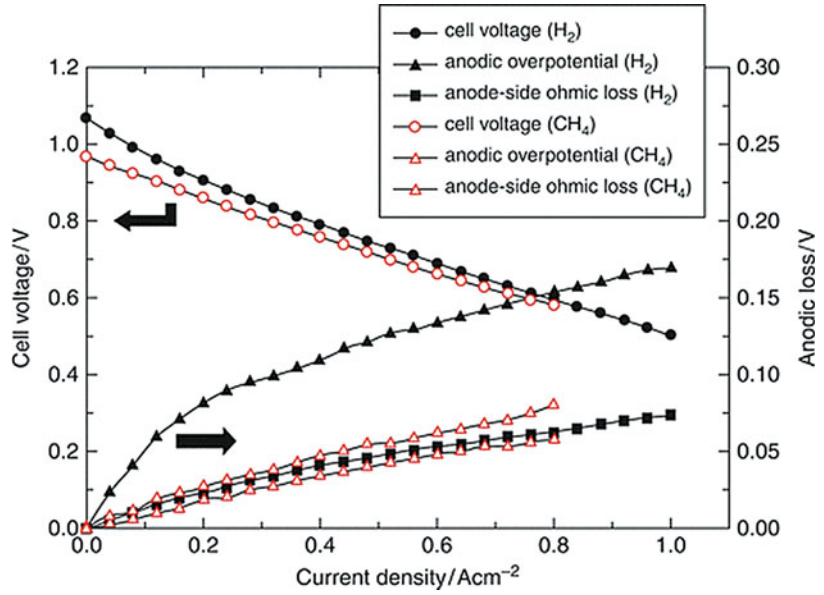


**Fuel Cells (SOFC): Alternative Approaches (Electrolytes, Electrodes, Fuels), Fig. 24** Carbon deposition limit lines at various temperatures in the C–H–O diagram

[252] (Reproduced with permission from ECS – The Electrochemical Society)

**Fuel Cells (SOFC): Alternative Approaches (Electrolytes, Electrodes, Fuels),**

**Fig. 25** Comparison of the cell voltage and anodic losses in using 3% humidified H<sub>2</sub> and 50% pre-reformed CH<sub>4</sub> (S/C = 2.5) as fuels at 800 °C. Anodic loss includes anodic overpotential and anode-side ohmic loss [261] (Reproduced with permission from Dr. Kengo Haga)

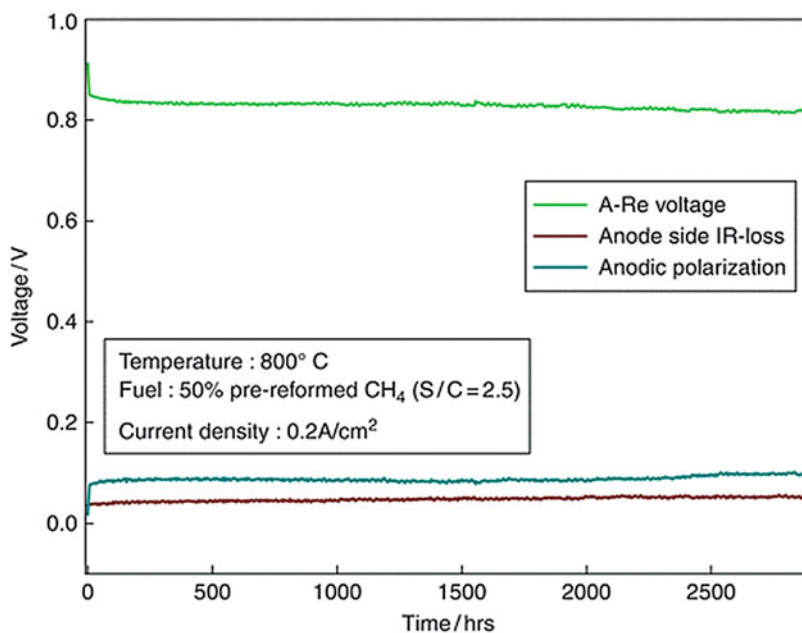


**Fuel Cells (SOFC): Alternative Approaches (Electrolytes, Electrodes, Fuels), Fig. 26** FESEM micrographs of typical cathode and anode. Electrochemical

performance of this cell is shown in Fig. 25. The composition of each electrode layer is also shown [261] (Reproduced with permission from Dr. Kengo Haga)

**Fuel Cells (SOFC):  
Alternative Approaches  
(Electrolytes, Electrodes,  
Fuels), Fig. 27** Cell

voltage, anodic polarization, and anode-side IR loss, measured at 200 mA/cm<sup>2</sup> during H<sub>2</sub>S (5 ppm) poisoning at 800 °C for the 50% pre-reformed CH<sub>4</sub> fuel with S/C = 2.5



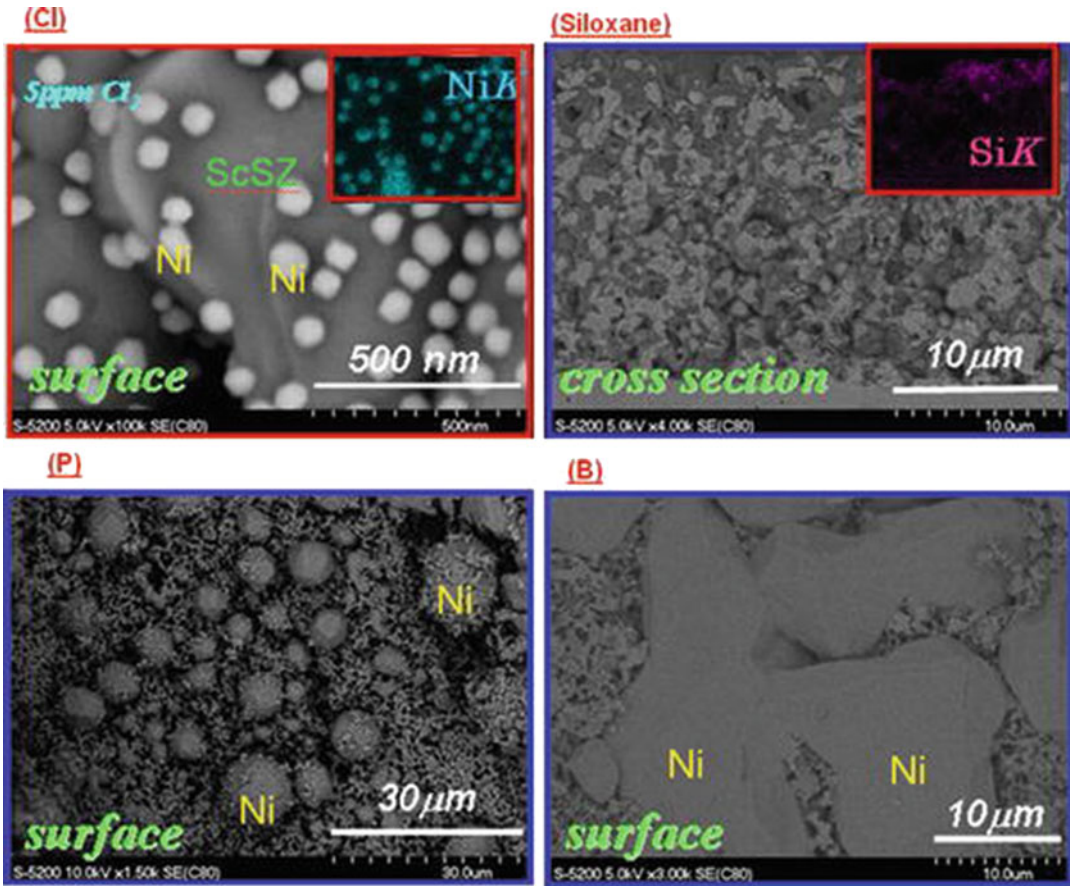
quasi-steady-state cell voltage can be observed associated mainly with an increase in anodic polarization and almost constant IR loss, up to 3000 h [262]. Exactly speaking, cell voltage generally decreased up to ca. 200 h and then remained almost constant but with a slightly higher degradation rate of 0.68%/1000 h with 5 ppm H<sub>2</sub>S, compared to the degradation rate of 0.3%/1000 h without H<sub>2</sub>S impurity [262]. This result clearly shows that SOFC is more tolerant against sulfur poisoning compared to other types of fuel cells, giving more flexibility in practical fuel selection. Even so, it should be noted that carbon deposition phenomena can be affected by the simultaneous presence of sulfur impurities and non-reformed hydrocarbons [262].

Poisoning mechanisms of sulfur, a typical common fuel impurity, have been extensively analyzed for various fuels, including H<sub>2</sub>, H<sub>2</sub>-CO, CH<sub>4</sub>, partially reformed CH<sub>4</sub>, and simulated biogas [263–266]. For relatively low concentrations (ppm level) of sulfur, reversible processes associated with adsorption/desorption of sulfur have been considered as the predominant mechanism [263–265]. At higher sulfur concentration and/or lower operational temperature, an irreversible degradation, associated with the oxidation of

Ni due to a large anodic polarization, has been observed [263, 264]. Sulfur poisoning to internal reforming reactions is also serious, so that much larger cell voltage drop has been observed in the case where CH<sub>4</sub>-rich fuels are supplied [265]. In addition, the C–H–O–Ni–S stability diagram suggests that the formation of Ni<sub>3</sub>S<sub>2</sub> (melting point 787 °C) could be possible for hydrogen-poor fuels. Possible sulfur poisoning mechanisms are summarized elsewhere [262, 265].

Poisoning phenomena have been analyzed for other impurities, including chlorine, siloxane, phosphorus, and boron on the anode side. Figure 28 shows FESEM micrographs of anodes poisoned by these impurities of ppm levels [266]. Chlorine poisoning is associated with the sublimation of NiCl<sub>2</sub> [267], while siloxane poisoning leads to silica deposition [266]. Phosphorus is reactive with Ni to form a eutectic compound [268]. The presence of boron accelerates the grain growth of Ni in the anodes [266].

Various other types of fuels have been examined as possible SOFC fuels. Direct feeding of hydrocarbon fuels has been reported including gaseous fuels such as methane [246, 247, 269], biogas [270], ethane [246, 247], and butane [246, 247], and liquid fuels such as n-decane [271],



**Fuel Cells (SOFC): Alternative Approaches (Electrolytes, Electrodes, Fuels), Fig. 28** Microstructural change of anodes by various impurities: chlorine, siloxane, phosphorus, and boron. Nanocrystalline Ni precipitates after chlorine poisoning, melted Ni particles after phosphorus poisoning, and grown Ni grains after boron poisoning

can be distinguished, while deposited  $\text{SiO}_2$  (dark grains) filling the porous Ni-cermet (bright grain) anode can be seen in the cross section of the anode after the siloxane poisoning [262, 266] (Reproduced with permission from Elsevier)

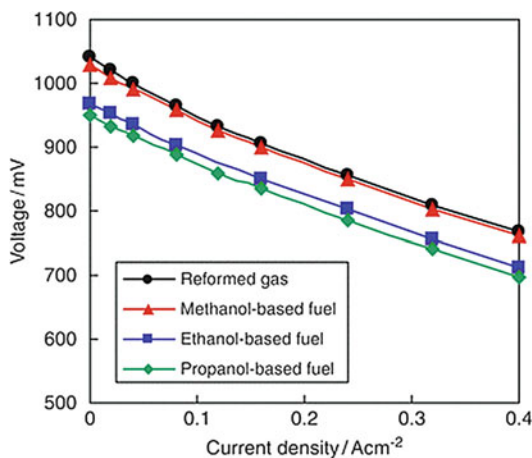
gasoline [271], synthetic diesel [272], crude and jet fuel oils [273], vegetable oil [248], and biodiesel [274]. Generally speaking, the S/C ratio should be optimized to prevent carbon deposition for internal steam reforming, and the oxygen-to-carbon (O/C) ratio should be adjusted for internal partial oxidation. Fuel impurities in such practical fuels should also be taken into account to maintain cell performance and durability.

### Alcohols

The use of alcohols as SOFC fuels is of technological interest, as alcohols (bionoliquids) can be derived from biomass and can be easily reformed.

In addition, direct-alcohol SOFCs could be an alternative to direct-methanol fuel cells, typically using polymer electrolytes at a low temperature [4]. Power generation characteristics for alcohol-based fuels and for the simulated reformed gas (consisting mainly of  $\text{H}_2$ ,  $\text{CO}$ , and  $\text{H}_2\text{O}$ ) are shown in Fig. 29 [257]. All these alcohols were premixed with water, so that the C-H-O ratio was fixed to the same value ( $\text{C:H:O} = 9:38:10$  for all fuels). It has been demonstrated that direct-alcohol SOFCs are feasible, at least, for alcohols with carbon number up to 4 (butanol) [257, 258]. In case that methanol was directly supplied, the I-V characteristics were similar to those for the



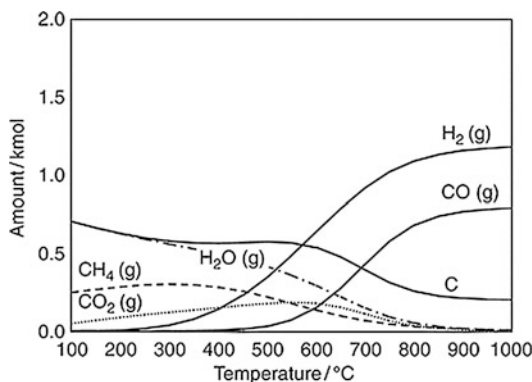


**Fuel Cells (SOFC): Alternative Approaches (Electrolytes, Electrodes, Fuels), Fig. 29** Current-voltage characteristics of SOFCs for alcohol-based fuels at 1000 °C [257] (Reproduced by permission of ECS-The Electrochemical Society)

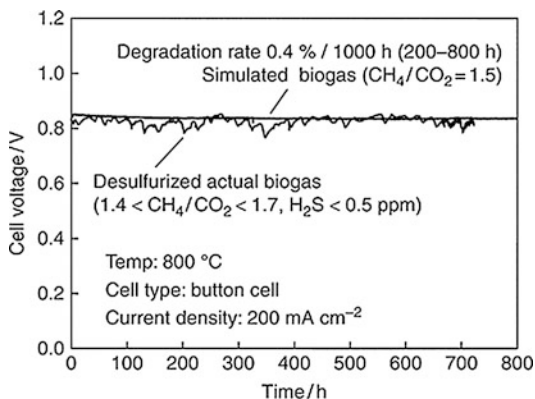
simulated reformed gas. However, with increasing carbon number of alcohols, a decrease in cell voltage was observed. From the gas analysis by gas chromatograph, it has been revealed that the compositions of the simulated reformed gas and the methanol-derived fuel gas were almost the same, well explaining the similar I-V characteristics [257]. However, with increasing carbon number of alcohols, a decrease in  $H_2$  and  $CO$  concentrations associated with a decrease in cell voltage [257] was observed. Therefore, a higher catalytic activity to reform alcohols at fuel electrodes (or pre-reforming) is necessary to optimize the performance of such direct-alcohol SOFCs.

### Biogas

The use of biogas as a fuel for SOFCs is of both technological and environmental interest [3, 4, 251, 260, 270, 275–278]. Biogas can be produced from biomass via various procedures such as fermentation and thermal decomposition. Organic municipal wastes (biowastes) are all metabolized by bacteria under anaerobic conditions producing a mixed gas consisting of ca. 60%  $CH_4$  and 40%  $CO_2$ . Anaerobic fermentation which proceeds in a reducing atmosphere enables us to extract chemical energy of biowastes as  $CH_4$ -rich biogas. Figure 30 shows the equilibrium products from



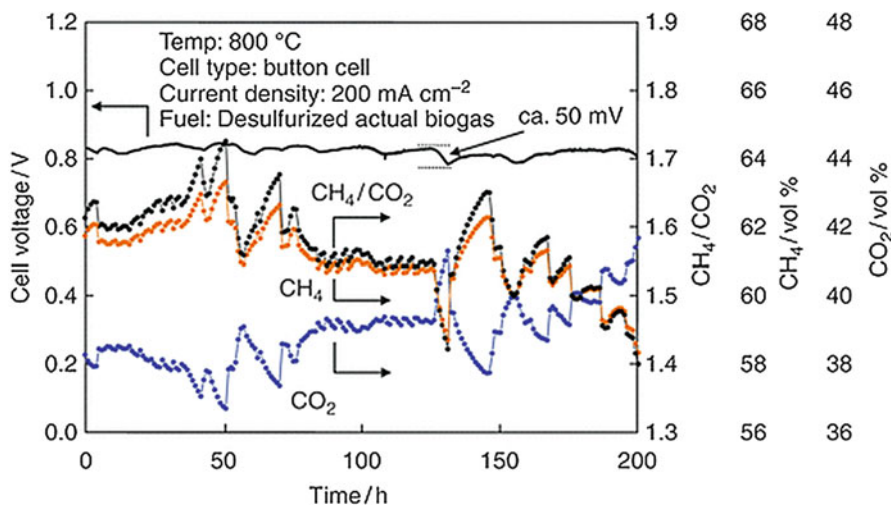
**Fuel Cells (SOFC): Alternative Approaches (Electrolytes, Electrodes, Fuels), Fig. 30** Equilibrium products from biogas ( $CH_4$  60% and  $CO_2$  40%). The calculations are performed by assuming that 1 kmol carbon is supplied



**Fuel Cells (SOFC): Alternative Approaches (Electrolytes, Electrodes, Fuels), Fig. 31** Performance of direct-biogas SOFC: 1 month test of internal reforming SOFC running on simulated and desulfurized actual biogases at 800 °C using anode-supported button cells

biogas initially consisting of  $CH_4$  and  $CO_2$ . High-temperature equilibrium gas from the biogas mainly consists of  $H_2$  and  $CO$ , so that a comparable electrochemical performance with hydrogen-based fuels [275, 277] is expected. This figure also indicates that carbon formation is thermochemically expected, so that an addition of  $H_2O$  (water vapor) and/or  $O_2$  is needed.

As practical examples, Fig. 31 shows the cell voltages of internal reforming SOFC running on biogas measured at  $200 \text{ mA cm}^{-2}$  [278]. Simulated biogas with the  $CH_4/CO_2$  ratio of 1.5 had led



**Fuel Cells (SOFC): Alternative Approaches (Electrolytes, Electrodes, Fuels), Fig. 32** Voltage fluctuation in synchronization with the fluctuation of biogas composition during the long-term test (initial 200 h of Fig. 31 is shown)

to stable cell voltage above 0.8 V for 800 h without pre-reformer and humidifier. The degradation rate of only 0.4%/1000 h has proven that the biogas-fueled SOFC can be operated in the internal reforming mode. As for the actual biogas, a rather high voltage comparable to that obtained by simulated biogas was achieved for 1 month. Monitoring of biogas composition simultaneously with the cell voltage has showed that voltage fluctuation (a maximum of 50 mV level) is related to the fluctuation of the  $\text{CH}_4/\text{CO}_2$  ratio [270] (Fig. 32). Abrupt decrease in  $\text{CH}_4$  concentration (or abrupt increase in  $\text{CO}_2$  concentration) induced temporarily lower cell voltage. The  $\text{CH}_4/\text{CO}_2$  ratio in the actual biogas fluctuated between 1.4 and 1.7, corresponding to a  $\text{CH}_4$  concentration ranging between 58 and 63 vol%. Biogas composition is influenced by many factors, for example, kinds of organic wastes, their physical states, and operational conditions of methane fermentation such as temperature and pH of the waste slurry.

It should be noted that carbon deposition was more noticeable for the desulfurized actual biogas compared to simulated biogas. Judging from the result of the gas analysis, carbon deposition is probably triggered by traces of  $\text{H}_2\text{S}$  in the desulfurized biogas which can cause deactivation of Ni catalyst for the dry reforming of methane [270]. Acceleration of carbon deposition in the

presence of trace  $\text{H}_2\text{S}$  was also reported for SOFCs operated with partially reformed  $\text{CH}_4$ -based fuels [262]. Air addition to biogas is effective in preventing carbon deposition [277]. Solid oxide fuel cells could therefore become a core technology in a carbon-neutral zero-emission renewable energy systems, as biogas can be efficiently converted to electricity and heat, while exhaust  $\text{CO}_2$  gas may be reused in photosynthesis of biomass using solar energy.

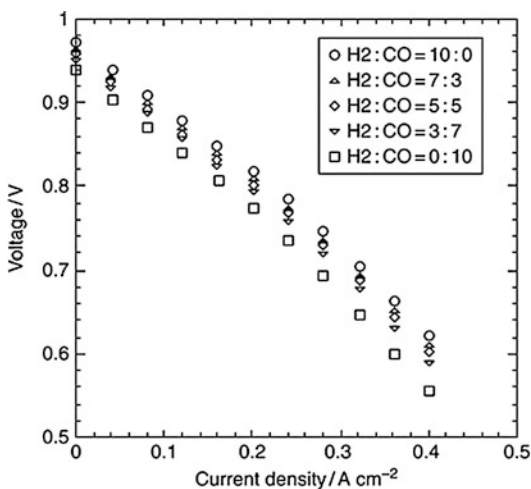
### Coal Gas

As one of the most abundant and inexpensive fossil energy resources [279], coal can be used to produce coal gas, with CO and  $\text{H}_2$  as main constituents. Coal gas could be applied as a fuel for a combined-cycle power plant with coal gasifier, SOFCs, and gas (and steam) turbine(s) [2, 256, 280–284]. The concentration of water vapor and carrier gas in such a gas depends on the gasification procedures for the partial oxidation of coal by air, oxygen, or water [280]. It is therefore of technological relevance to analyze power generation characteristics of SOFCs operated with mixed  $\text{H}_2$  and CO fuel gases, with consideration that coal gas is CO-rich in general.

Figure 33 shows the I-V characteristics of a SOFC at 1000 °C for different  $\text{H}_2$ -to-CO ratios [256]. The open-circuit voltage increased slightly



with decreasing fraction of CO gas, expected from the oxygen partial pressures in thermochemical equilibrium. Figure 33 shows that the I-V characteristics improved, that is, the cell voltage increased for a given current density with decreasing CO concentration of the mixed gas. This change in the I-V characteristics became



**Fuel Cells (SOFC): Alternative Approaches (Electrolytes, Electrodes, Fuels), Fig. 33** Typical I-V characteristics of SOFCs for different H<sub>2</sub>-to-CO ratios at 1000 °C [256] (Reproduced with permission from ECS – The Electrochemical Society)

significant with increasing current density, but this result clearly indicates that the mixture of CO and H<sub>2</sub>, the major constituents of coal gas, can be applied as SOFC fuels, provided that fuel impurity effects can be avoided. It should be noted that raw coal gas contains various kinds of fuel impurities, so that poisoning effects should be carefully examined. Influence of typical fuel impurities in coal gas on electrochemical performance and microstructural stability has been extensively studied and discussed in the literature [262–266, 268, 285–290].

**Future Directions**

The first-generation SOFC systems just commercialized are constructed using the most common materials such as stabilized ZrO<sub>2</sub> electrolytes, La (Sr)MnO<sub>3</sub> cathodes, and Ni cermet, and applying the most conventional fuels such as city gas. However alternative materials and fuels could expand the future applicability of SOFCs. Table 3 briefly summarizes the state-of-the-art and alternative materials for electrolytes, cathodes, and anodes, as well as possible fuels and applications. Advanced materials may offer alternatives too, for example, high-temperature

**Fuel Cells (SOFC): Alternative Approaches (Electrolytes, Electrodes, Fuels), Table 3** State-of-the-art technologies and typical alternatives of SOFC materials, fuels, and applications.

	Electrolyte materials	Cathode materials	Anode materials	Fuels	Possible applications
State-of-the-art technologies	ZrO <sub>2</sub> (Y <sub>2</sub> O <sub>3</sub> ) (YSZ) ZrO <sub>2</sub> (Sc <sub>2</sub> O <sub>3</sub> ) (ScSZ) La(Sr)Ga(Mg)O <sub>3</sub>	La(Sr)MnO <sub>3</sub> , La(Sr)Co(Fe)O <sub>3</sub> , Sm(Sr)CoO <sub>3</sub>	Ni/YSZ Ni/ScSZ Ni/CeO <sub>2</sub> (Gd <sub>2</sub> O <sub>3</sub> )	City gas, LP gas, H <sub>2</sub>	Stational cogenerations, distributed power units, combined power plants (SOFC/turbine)
Typical alternatives	CeO <sub>2</sub> (Gd <sub>2</sub> O <sub>3</sub> ) Gd <sub>2</sub> (Zr <sub>x</sub> Ti <sub>1-x</sub> ) <sub>2</sub> O <sub>7</sub> Ba <sub>2</sub> In <sub>2</sub> O <sub>5</sub> La <sub>9.33</sub> Si <sub>6</sub> O <sub>26</sub> La <sub>9.33</sub> Ge <sub>6</sub> O <sub>26</sub> BaCe(Y)O <sub>3</sub> BaZr(Y)O <sub>3</sub>	Ba(Sr)Co(Fe)O <sub>3</sub> , Gd(Sr)CoO <sub>3</sub> , Sm(Sr)CoO <sub>3</sub> , La <sub>2</sub> (Sr)NiO <sub>4</sub> , Nd <sub>2</sub> NiO <sub>4</sub> , Ag-La(Sr)MnO <sub>3</sub>	La(Sr)Cr(Mn)O <sub>3</sub> , La(Sr)Cr(Ru)O <sub>3</sub> , Sr(La)TiO <sub>3</sub> , CuYSZ(CeO <sub>2</sub> )	Kerosene, gasoline, diesel, alcohol, biogas/biofuel, coal gas, DME	Automotive APU/power units, stational applications with kerosene, coal gas power generation, portable applications, direct-alcohol SOFCs, carbon-neutral power generation using biofuels

polymer electrolyte fuel cells, direct-alcohol fuel cells, and portable fuel cells, as well as fuel cells for power generation, cogeneration, and transportation. Advanced fuel electrode materials may realize flexible SOFCs applicable to wide varieties of fuels. Nanostructural design may considerably improve their electrochemical performance, for example, by tailoring nano-size and stress effects, by reducing grain boundary resistivity, as well as by introducing fast ionic/mixed conducting pathways.

While most of the alternative materials and fuels mentioned in this entry have not yet been tested in fuel cell stacks/systems or even as a single cell, they may have potential for wider varieties of applications in the future. Among others, the following possibilities should be emphasized to consider future directions: (1) High electrical efficiency beyond 50% is attractive to bring about distributed power generation [291], where high ionic conductivity of the electrolyte, low electrode polarization, low contact resistance, and sufficient durability are essential. (2) Low-temperature SOFCs may actualize mobile applications of SOFCs where much higher ionic conductance and electrode activities should be tailored [15, 292–297] and more sophisticated materials design at microscopic levels becomes important [9, 13, 298–300]. (3) As the operational temperature of the low-temperature SOFC approaches that of high-temperature PEFCs, we may also learn much from materials and electrochemical research for PEFCs [301–305], which may lead to an integration of materials research between SOFC and PEFC. (4) Fuel-flexible SOFCs may contribute to energy security by using a wide variety of fuels and carbon-neutral power generation by using regenerable energy resources, for which robustness and poisoning tolerance of electrodes may be critical [255, 260, 262]. SOFC researchers should take responsibilities to fulfill their potentials and possibilities via concept demonstrations of operating materials, devices, and systems.

Readers may read references [9, 21, 23, 24, 26, 28, 29, 79, 100] to understand fundamental materials science related to the topic of this chapter. In order to understand the very early stage of this research field, readers may check references

[39, 40, 126]. Recent development and commercialization of fuel cell technologies including SOFCs have been compiled in Reference [306].

**Acknowledgments** Financial support by the NEDO project “Development of System and Elemental Technology on Solid Oxide Fuel Cells (SOFC)” is gratefully acknowledged. We thank Prof. A. Hayashi and Associate Profs. S. Lyth and Dr. S. Bishop in Kyushu University for carefully reading the manuscript and Ms. A. Zaitzu in Kyushu University for her editorial work.

## Bibliography

1. Steele BCH, Heinzel A (2001) Materials for fuel-cell technologies. *Nature* 414:345–352
2. Minh NQ, Takahashi T (1995) *Science and technology of ceramic fuel cells*. Elsevier, Amsterdam
3. Singhal SC, Kendall K (2003) *High-temperature solid oxide fuel cells: fundamentals, design and application*. Elsevier, Oxford, UK
4. Larminie J, Dicks A (2003) *Fuel cell systems explained*, 2nd edn. Wiley, West Sussex
5. Tagawa H (1998) *Solid oxide fuel cells and global environment*. Agune-Shofudo, Shinjuku. (in Japanese)
6. Steinberger-Wilckens R (2009) European SOFC R&D – status and trends. *ECS Trans* 25(2):3–10
7. Hosoi K, Nakabaru M (2009) Status of national project for SOFC development in Japan. *ECS Trans* 25(2):11–20
8. Surdoyal WA (2009) The status of SOFC programs in USA 2009. *ECS Trans* 25(2):21–27
9. Maier J (2004) *Physical Chemistry of ionic materials: ions and electrons in solids*. Wiley, West Sussex
10. Sata N, Eberman K, Eberl K, Maier J (2000) Mesoscopic fast ion conduction in nanometre-scale planar heterostructures. *Nature* 408:946–949
11. Garcia-Barriocanal J, Rivera-Calzada A, Varela M, Sefrioui Z, Iborra E, Leon C, Pennycook SJ, Santamaria J (2008) Colossal ionic conductivity at interfaces of epitaxial  $ZrO_2:Y_2O_3/SrTiO_3$  heterostructures. *Science* 321(5889):676–680
12. Tuller HL (2000) Ionic conduction in nanocrystalline materials. *Solid State Ionics* 131(1–2):143–157
13. Maier J (2004) Nano-ionics: more than just a fashionable slogan. *J Electroceram* 13(1–3):593–598
14. Araki W, Arai Y (2010) Oxygen diffusion in yttria-stabilized zirconia subjected to uniaxial stress. *Solid State Ionics* 181(8–10):441–446
15. Litzelman SJ, Hertz JL, Jung W, Tuller HL (2008) Opportunities and challenges in materials development for thin film solid oxide fuel cells. *Fuel Cells* 8(5):294–302
16. Evans A, Bieberle-Hütter A, Rupp JLM, Gauckler LJ (2009) Review on microfabricated micro-solid oxide fuel cell membranes. *J Power Sources* 194(1):119–129

17. Ihara M, Hasegawa S (2006) Quickly rechargeable direct carbon solid oxide fuel cell with propane for recharging. *J Electrochem Soc* 153(8): A1544–A1546
18. Hauch A, Jensen SH, Ramousse S, Mogensen M (2006) Performance and durability of solid oxide electrolysis cells. *J Electrochem Soc* 153(9): A1741–A1747
19. Ishihara T, Kanno T (2010) Steam electrolysis using LaGaO<sub>3</sub> based perovskite electrolyte for recovery of unused heat energy. *ISIJ Int* 50:1291–1295
20. Minh NQ (2010) Operating characteristics of solid oxide fuel cell stacks and systems. *ECS Trans* 25(2):241–246
21. Steele BCH (1989) Oxygen ion conductors. In: Takahashi T (ed) High conductivity solid ionic conductors. World Scientific, Singapore, pp 402–446
22. Steele BCH (1992) Oxygen ion conductors and their technological applications. In: Balkanski M, Takahashi T, Tuller HL (eds) Solid state ionics. Elsevier, Amsterdam, pp 17–28
23. Nowick AS (1984) Atom transport in oxides of the fluorite structure. In: Diffusion in crystalline solids. Academic, Orlando, pp 143–188
24. Hayes W, Stoneham AM (1985) Defects and defect processes in nonmetallic solids. Wiley, New York
25. Kilner JA, Steele BCH (1981) Mass transport in anion-deficient fluorite oxides. In: Sørensen OT (ed) Nonstoichiometric oxides. Academic, New York, pp 233–269
26. Kofstad P (1972) Nonstoichiometry, diffusion, and electrical conductivity in binary metal oxides. Wiley, New York
27. Eyring L (1979) The binary rare earth oxides. In: Gschneidner KA Jr, Eyring L (eds) Handbook on the physics and chemistry of rare earths, vol 3. North-Holland, Amsterdam, pp 337–399. Chap 27
28. Tuller HL (1991) Highly conductive ceramics. In: Buchanan RC (ed) Ceramic materials for electronics. Marcel Dekker, New York, pp 379–433
29. Tuller HL (1981) Mixed conduction in nonstoichiometric oxides. In: Sørensen OT, Sørensen OT (eds) Nonstoichiometric oxides. Academic, New York, pp 271–335
30. Shimizu K, Kashiwagi K, Nishiyama H, Kakimoto S, Sugaya S, Yokoi H, Satsuma A (2008) Impedancemetric gas sensor based on Pt and WO<sub>3</sub> co-loaded TiO<sub>2</sub> and ZrO<sub>2</sub> as total NO<sub>x</sub> sensing materials. *Sens Actuators B Chem* 130:707–712
31. Gong J, Li Y, Tang Z, Zhang Z (2000) Enhancement of the ionic conductivity of mixed calcia/yttria stabilized zirconia. *Mater Lett* 46:115–119
32. Gauckler LJ, Sasaki K (1994) Ionic and electronic conductivities of homogeneous and heterogeneous materials in the system ZrO<sub>2</sub>-In<sub>2</sub>O<sub>3</sub>. *Solid State Ionics* 75:203–210
33. Sasaki K (1993) Phase equilibria, electrical conductivity, and electrochemical properties of ZrO<sub>2</sub>-In<sub>2</sub>O<sub>3</sub>. Dissertation, Swiss Federal Institute of Technology, Zürich
34. Stafford RJ, Rothman SJ, Routbort JL (1989) Effect of dopant size on the ionic conductivity of cubic stabilized ZrO<sub>2</sub>. *Solid State Ionics* 37:67–72
35. Arachi Y, Sakai H, Yamamoto O, Takeda Y, Imanishi N (1999) Electrical conductivity of the ZrO<sub>2</sub>-Ln<sub>2</sub>O<sub>3</sub> (Ln = lanthanides) system. *Solid State Ionics* 121:133–139
36. Patterson JW (1971) Conduction domains for solid electrolytes. *J Electrochem Soc* 118:1033–1039
37. Heyne L, Engleson D (1977) The speed of response of solid electrolyte galvanic cells for Gas sensing. *J Electrochem Soc* 124:727–735
38. Tuller HL, Moon PK (1988) Fast ion conductors: future trends. *Mater Sci Eng B1*:171–191
39. Nernst W (1899) Über die elektrolytische Leitung fester Körper bei sehr hohen Temperaturen. *Z Elektrochem* 6(2):41–43
40. Baur E, Preis H (1937) Über Brennstoff-Ketten mit Festleitern. *Z Elektrochem* 44(9):695–698
41. Sasaki K, Maier J (2000) Re-analysis of defect equilibria and transport properties of Y<sub>2</sub>O<sub>3</sub>-stabilized ZrO<sub>2</sub> using EPR and optical relaxation. *Solid State Ionics* 134(3–4):303–321
42. Inaba H, Tagawa H (1996) Ceria-based solid electrolytes. *Solid State Ionics* 83:1–16
43. Sammes NM, Tompsett GA, Näfe H, Aldinger F (1999) Bismuth based oxide electrolytes-structure and ionic conductivity. *J Eur Ceram Soc* 19:1801–1826
44. Mogensen M, Sammes NM, Tompsett GA (2000) Physical, chemical and electrochemical properties of pure and doped ceria. *Solid State Ionics* 129:63–94
45. Yamamoto O, Arachi Y, Sakai H, Takeda Y, Imanishi N, Mizutani Y, Kawai M, Nakamura Y (1998) Zirconia based oxide ion conductors for solid oxide fuel cells. *Ionics* 4:403–408
46. Arachi Y, Asai T, Yamamoto O, Takeda Y, Imanishi N, Kawate K, Tamakoshi C (2001) Electrical conductivity of ZrO<sub>2</sub>-Sc<sub>2</sub>O<sub>3</sub> doped with HfO<sub>2</sub>, CeO<sub>2</sub>, and Ga<sub>2</sub>O<sub>3</sub>. *J Electrochem Soc* 148(5): A520–A523
47. Yamamoto O, Arachi Y, Takeda Y, Imanishi N, Mizutani Y, Kawai M, Nakamura Y (1995) Electrical conductivity of stabilized zirconia with ytterbia and scandia. *Solid State Ionics* 79:137–142
48. Tietz F, Fischer W, Hauber T, Mariotto G (1997) Structural evolution of Sc-containing zirconia electrolytes. *Solid State Ionics* 100:289–295
49. Wang Z, Cheng M, Bi Z, Dong Y, Zhang H, Zhang J, Feng Z, Li C (2005) Structure and impedance of ZrO<sub>2</sub> doped with Sc<sub>2</sub>O<sub>3</sub> and CeO<sub>2</sub>. *Mater Lett* 59:2579–2582
50. Gödickemeier M, Michel B, Orliukas A, Bohac P, Sasaki K, Gauckler LJ, Heinrich H, Schwander P, Kostorz G, Hofmann H, Frei O (1994) Effect of intergranular glass films on the electrical conductivity of 3Y-TZP. *J Mater Res* 9(5):1228–1240
51. Bieberle-Hütter A, Beckel D, Infortuna A, Muecke UP, JLM R, Gauckler LJ, Rey-Mermet S, Murali P, Bieri NR, Hotz N, Stutz MJ, Poulikakos D,

- Heeb P, Müller P, Bernard A, Gmür R, Hocker T (2008) A micro-solid oxide fuel cell system as battery replacement. *J Power Sources* 177:123–130
52. Ji Y, Kilner JA, Carolan MF (2005) Electrical properties and oxygen diffusion in yttria-stabilised zirconia (YSZ)- $\text{La}_{0.8}\text{Sr}_{0.2}\text{MnO}_{3\pm\delta}$ (LSM) composites. *Solid State Ionics* 176:937–943
53. Ralph JM, Rossignol C, Kumar R (2003) Cathode materials for reduced-temperature SOFCs. *J Electrochem Soc* 150(11):A1518–A1522
54. Stochniol G, Syskakis E, Naoumidis A (1995) Chemical compatibility between strontium-doped lanthanum manganite and yttria-stabilized zirconia. *J Am Ceram Soc* 78:929–932
55. Zhao H, Huo I, Sun L, Yu L, Gao S, Zhao J (2004) Preparation, chemical stability and electrochemical properties of LSCF-CBO composite cathodes. *Mater Chem Phys* 88:160–166
56. Yahiro H, Eguchi K, Arai H (1986) Ionic conduction and microstructure of the ceria-strontia system. *Solid State Ionics* 21:37–47
57. Thangadurai V, Kopp P (2007) Chemical synthesis of Ca-doped  $\text{CeO}_2$  – intermediate temperature oxide ion electrolytes. *J Power Sources* 168:178–183
58. Eguchi K, Setoguchi T, Inoue T, Arai H (1992) Electrical properties of ceria-based oxides and their application to solid oxide fuel cells. *Solid State Ionics* 52:165–172
59. Yahiro H, Baba Y, Eguchi Y, Eguchi K, Arai H (1988) High temperature fuel cell with ceria-yttria solid electrolyte. *J Electrochem Soc* 135:2077–2080
60. Shobit Omar S, Wachsmann ED, Nino JC (2008) Higher conductivity  $\text{Sm}^{3+}$  and  $\text{Nd}^{3+}$  co-doped ceria-based electrolyte materials. *Solid State Ionics* 178:1890–1897
61. Bance P, Brandon NP, Girvan B, Holbeche P, O'Dea S, Steele BCH (2004) Spinning-out a fuel cell company from a UK University-2 years of progress at Ceres Power. *J Power Sources* 131:86–90
62. Göedickemeier M, Gauckler LJ (1998) Engineering of solid oxide fuel cells with ceria-based electrolytes. *J Electrochem Soc* 145:414–421
63. Atkinson A (1997) Chemically-induced stresses in gadolinium-doped ceria solid oxide fuel cell electrolytes. *Solid State Ionics* 95:249–258
64. Marques FMB, Navarro LM (1997) Performance of double layer electrolyte cells Part II: GCO/YSZ, a case study. *Solid State Ionics* 100:29–38
65. Tsoda A, Gupta A, Naoumidis A, Skarmoutsos D, Nikolopoulos P (1998) Performance of a double-layer CGO/YSZ electrolyte for solid oxide fuel cells. *Ionics* 4:234–240
66. Kharton VV, Figueiredo FM, Navarro L, Naumovich EN, Kovalevsky AV, Yaremchenko AA, Viskup AP, Carneiro A, Marques FMB, Frade JR (2001) Ceria-based materials for solid oxide fuel cells. *J Mater Sci* 36:1105–1117
67. Oishi N, Atkinson A, Brandon NP, Kilner JA, Steele BCH (2005) Fabrication of an anode-supported gadolinium-doped ceria solid oxide fuel cell and its operation at 550°C. *J Am Ceram Soc* 88(6):1394–1396
68. Oishi N, Yoo Y (2010) Evaluation of metal supported ceria based solid oxide fuel cell fabricated by wet powder spray and sintering. *J Electrochem Soc* 157(1):B125–B129
69. Moon PK, Tuller HL (1990) Evaluation of the  $\text{Gd}_2(\text{Zr}_x\text{Ti}_{1-x})_2\text{O}_7$  pyrochlore system as an oxygen Gas sensor. *Sens Actuators B Chem* 1:199–202
70. Yamamura H, Nishino H, Kakinuma K, Nomura K (2003) Electrical conductivity anomaly around fluorite-pyrochlore phase boundary. *Solid State Ionics* 158:359–365
71. Moon PK, Tuller HL (1988) Ionic-conduction in the  $\text{Gd}_2\text{Ti}_2\text{O}_7$ - $\text{Gd}_2\text{Zr}_2\text{O}_7$  system. *Solid State Ionics* 28–30(1):470–474
72. Kramer SA, Tuller HL (1995) A novel titanate-based oxygen ion conductor:  $\text{Gd}_2\text{Ti}_2\text{O}_7$ . *Solid State Ionics* 82:15–23
73. Kharton VV, Tsipis EV, Yaremchenko AA, Vyshatko NP, Shaula AL, Naumovich EN, Frade JR (2003) Oxygen ionic and electronic transport in  $\text{Gd}_{2-x}\text{Ca}_x\text{Ti}_2\text{O}_{7-\delta}$  pyrochlores. *J Solid State Electrochem* 7:468–476
74. Mori M, Tompsett GM, Sammes NM, Suda E, Takeda Y (2003) Compatibility of  $\text{Gd}_x\text{Ti}_2\text{O}_7$  pyrochlores ( $1.72 \leq x \leq 2.0$ ) as electrolytes in high-temperature solid oxide fuel cells. *Solid State Ionics* 158:79–90
75. Yasuda I, Matsuzaki Y, Yamakawa T, Koyama T (2000) Electrical conductivity and mechanical properties of alumina-dispersed doped lanthanum gallates. *Solid State Ionics* 135:381–388
76. Tietz F (1999) Thermal expansion of SOFC materials. *Ionics* 5:129–139
77. Lee JH, Yoshimura M (1999) Phase stability and electrical conductivity of the  $\text{Zr}_{0.5}\text{Y}_{0.5}\text{O}_{1.75}$ - $\text{Y}_{0.75}\text{Nb}_{0.25}\text{O}_{1.75}$  system. *Solid State Ionics* 124:185–191
78. Lee JH, Yashima M, Yoshimura M (1998) Ionic conductivity of fluorite-structured solid solution  $\text{Y}_{0.8}\text{Nb}_{0.2}\text{O}_{1.7}$ . *Solid State Ionics* 107:47–51
79. West AR (1999) Basic solid state chemistry. Wiley, Chichester
80. Roth RS (1957) Classification of perovskite and other  $\text{ABO}_3$ -type compounds. *J Res Natl Bur Stand* 58:75–88
81. Takahashi T, Iwahara H (1971) Ionic conduction in perovskite-type oxide solid solution and its application to the solid electrolyte fuel cell. *Energy Convers* 11:105–111
82. Ishihara T, Matsuda H, Takita Y (1994) Doped  $\text{LaGaO}_3$  perovskite type oxide as a new oxide ionic conductor. *J Am Chem Soc* 116:3801–3803
83. Ishihara T, Matsuda H, Takita Y (1995) Effects of rare earth cations doped for La site on the oxide ionic conductivity of  $\text{LaGaO}_3$ -based perovskite type oxide. *Solid State Ionics* 79:147–151

84. Ishihara T, Ishikawa S, Yu C, Akbay T, Hosoi K, Nishiguchi H, Takita Y (2003) Oxide ion and electronic conductivity in Co doped  $\text{La}_{0.8}\text{Sr}_{0.2}\text{Ga}_{0.8}\text{Mg}_{0.2}\text{O}_3$  perovskite oxide. *Phys Chem Chem Phys* 5:2257–2263
85. Ishihara T (2001) Current status of intermediate temperature solid oxide fuel cell (in Japanese). *Bull Ceram Soc Jpn* 36:483–485
86. Islam MS, Davis RA (2004) Atomistic study of dopant site-selectivity and defect association in the lanthanum gallate perovskite. *J Mater Chem* 14:86–93
87. Huang K, Feng M, Goodenough JB, Schmerling M (1996) Characterization of Sr-doped  $\text{LaMnO}_3$  and  $\text{LaCoO}_3$  as cathode materials for a doped  $\text{LaGaO}_3$  ceramic fuel cell. *J Electrochem Soc* 143(11):3630–3636
88. Kostogloudis GC, Ftikos C, Ahmad-Khanlou A, Naoumidis A, Stöver D (2000) Chemical compatibility of alternative perovskite oxide SOFC cathodes with doped lanthanum gallate solid electrolyte. *Solid State Ionics* 134:127–138
89. Shaula AL, Kharton VV, Marques FMB (2004) Phase interaction and oxygen transport in  $\text{La}_{0.8}\text{Sr}_{0.2}\text{Fe}_{0.8}\text{Co}_{0.2}\text{O}_{3-(\text{La}_{0.9}\text{Sr}_{0.1})_{0.98}\text{Ga}_{0.8}\text{Mg}_{0.2}\text{O}_3}$  composites. *J Eur Ceram Soc* 24:2631–2639
90. Sakai N, Horita T, Yamaji K, Brito ME, Yokokawa H, Kawakami A, Matsuoka S, Watanabe N, Ueno A (2006) Interface stability among solid oxide fuel cell materials with perovskite structures. *J Electrochem Soc* 153(3):A621–A625
91. Joshi AV, Steppan JJ, Taylor DM, Elangovan S (2004) Solid electrolyte materials, devices, and applications. *J Electroceram* 13:619–625
92. Schober T (1998) Protonic conduction in  $\text{BaIn}_{0.5}\text{Sn}_{0.5}\text{O}_{2.75}$ . *Solid State Ionics* 109:1–11
93. Goodenough JB (1997) Ceramic solid electrolytes. *Solid State Ionics* 94:17–25
94. Goodenough JB, Ruiz-Dias JE, Zhen YS (1990) Oxide-ion conduction in  $\text{Ba}_2\text{In}_2\text{O}_5$  and  $\text{Ba}_3\text{In}_2\text{MO}_8$  (M = Ce, Hf, or Zr). *Solid State Ionics* 44:21–31
95. Manthiram A, Kuo JF, Goodenough JB (1993) Characterization of oxygen-deficient perovskites as oxide-ion electrolytes. *Solid State Ionics* 62:225–234
96. Uchimoto Y, Kinuhata M, Takagi H, Yao T, Inagaki T, Yoshida H (1999) Crystal structure of metal cation-doped  $\text{Ba}_2\text{In}_2\text{O}_5$  and its oxide Ion conductivity. In: *Proceedings of SOFC VI. Electrochemical Society, Pennington*, pp 317–326
97. Schober T, Friedrich J, Krug F (1997) Phase transition in the oxygen and proton conductor  $\text{Ba}_2\text{In}_2\text{O}_5$  in humid atmospheres below 300°C. *Solid State Ionics* 99:9–13
98. Hashimoto T, Inagaki Y, Kishi A, Dokiya M (2000) Absorption and secession of  $\text{H}_2\text{O}$  and  $\text{CO}_2$  on  $\text{Ba}_2\text{In}_2\text{O}_5$  and their effects on crystal structure. *Solid State Ionics* 128:227–231
99. Zhang GB, Smyth DM (1995) Defects and transport of the brownmillerite oxides with high oxygen ion conductivity –  $\text{Ba}_2\text{In}_2\text{O}_5$ . *Solid State Ionics* 82:161–172
100. Kingery WD, Bowen HK, Uhlmann DR (1976) *Introduction to ceramics*, 2nd edn. Wiley, New York
101. Oyane A (2010) Development of apatite-based composites by a biomimetic process for biomedical applications. *J Ceram Soc Jpn* 118(2):77–81
102. Felsche J (1972) Rare earth silicates with the apatite structure. *J Solid State Chem* 5:266–275
103. Park J, Lakes RS (2007) *Biomaterials: an introduction*, 3rd edn. Springer, New York
104. Bonder IA (1982) Rare-earth silicates. *Ceram Int* 8(3):83–89
105. Higuchi Y, Sugawara M, Onishi K, Sakamoto M, Nakayama S (2010) Oxide ionic conductivities of apatite-type lanthanum silicates and germanates and their possibilities as an electrolyte of lower temperature operating SOFC. *Ceram Int* 36:955–959
106. Panteix PJ, Béchade E, Julien I, Abélard P, Bernache-Assollant D (2008) Influence of anionic vacancies on the ionic conductivity of silicated rare earth apatites. *Mater Res Bull* 43:1223–1231
107. Yoshioka H (2006) Oxide ionic conductivity of apatite-type lanthanum silicates. *J Alloys Comp* 408–412:649–652
108. Higuchi M, Masubuchi Y, Nakayama S, Kikkawa S, Kodaira K (2004) Single crystal growth and oxide ion conductivity of apatite-type rare-earth silicates. *Solid State Ionics* 174:73–80
109. Masubuchi Y, Higuchi M, Takeda T, Kikkawa S (2006) Preparation of apatite-type  $\text{La}_{9.33}(\text{SiO}_4)_6\text{O}_2$  oxide ion conductor by alkaloxide-hydrolysis. *J Alloys Comp* 408–412:641–644
110. Nojiri Y, Tanase S, Iwasa M, Yoshioka H, Matsumura Y, Sakai T (2010) Ionic conductivity of apatite-type solid electrolyte material,  $\text{La}_{10-x}\text{Ba}_x\text{Si}_6\text{O}_{27-x/2}$  (X = 0–1), and its fuel cell performance. *J Power Sources* 195:4059–4064
111. Mineshige A, Nakao T, Kobune M, Yazawa T, Yoshioka H (2008) Electrical properties of  $\text{La}_{10}\text{Si}_6\text{O}_{27}$ -based oxides. *Solid State Ionics* 179:1009–1012
112. Nakao T, Mineshige A, Kobune M, Yazawa T, Yoshioka H (2008) Chemical stability of  $\text{La}_{10}\text{Si}_6\text{O}_{27}$  and its application to electrolytes for solid oxide fuel cells. *Solid State Ionics* 179:1567–1569
113. Nakayama S, Kageyama T, Aono H, Sadaoka Y (1995) Ionic conductivity of lanthanoid silicates,  $\text{Ln}_{10}(\text{SiO}_4)_6\text{O}_3$  (Ln = La, Nd, Sm, Gd, Dy, Y, Ho, Er and Yb). *J Mater Chem* 5:1801–1805
114. Nakayama S, Sakamoto M (1998) Electrical properties of new type high oxide ionic conductor  $\text{RE}_{10}\text{Si}_6\text{O}_{27}$  (RE = La, Pr, Nd, Sm, Gd, Dy). *J Euro Ceram Soc* 18:1413–1418
115. Yoshioka H (2007) Enhancement of ionic conductivity of apatite-type lanthanum silicates doped with cations. *J Am Ceram Soc* 90:3099–3105

116. Yoshioka H, Nojiri Y, Tanase S (2008) Ionic conductivity and fuel cell properties of apatite-type lanthanum silicates doped with Mg and containing excess oxide ions. *Solid State Ionics* 179:2165–2169
117. Li B, Liu W, Pan W (2010) Synthesis and electrical properties of apatite-type  $\text{La}_{10}\text{Si}_6\text{O}_{27}$ . *J Power Sources* 195:2196–2201
118. Pivak YV, Kharton VV, Yaremchenko AA, Yakovlev SO, Kovalevsky AV, Frade JR, Marques FMB (2007) Phase relationships and transport in Ti-, Ce- and Zr-substituted lanthanum silicate systems. *J Eur Ceram Soc* 27:2445–2454
119. Nojiri Y, Chen WF, Tanase S, Iwasa M, Matsumura Y, Sakai T, Tanase S (2008) Lanthanum silicate with apatite-type structure as an electrolyte for intermediate temperature SOFCs and the electrode materials. *ITE-IBA Lett* 1(6):498–506
120. León-Reina L, Porras-Vázquez JM, Losilla ER, Aranda MAG (2007) Phase transition and mixed oxide-proton conductivity in germanium oxy-apatites. *J Solid State Chem* 180:1250–1258
121. Arikawa H, Nishiguchi H, Ishihara T, Takita Y (2000) Oxide ion conductivity in Sr-doped  $\text{La}_{10}\text{Ge}_6\text{O}_{27}$  apatite oxide. *Solid State Ionics* 136–137:31–37
122. Ishihara T, Arikawa H, Akbay T, Nishiguchi H, Takita Y (2001) Nonstoichiometric  $\text{La}_{2-x}\text{GeO}_{5-\delta}$  monoclinic oxide as a new fast oxide ion conductor. *J Am Chem Soc* 123:203–209
123. Nakayama S, Higuchi Y, Kondo Y, Sakamoto M (2004) Effects of cation- or oxide ion-defect on conductivities of apatite-type La-Ge-O system ceramics. *Solid State Ionics* 170:219–223
124. Berastegui P, Hull S, García García FJ, Grins J (2002) A structural investigation of  $\text{La}_2(\text{GeO}_4)\text{O}$  and alkaline-earth-doped  $\text{La}_{9.33}(\text{GeO}_4)_6\text{O}_2$ . *J Solid State Chem* 168:294–305
125. Kreuer KD (1996) Proton conductivity: materials and applications. *Chem Mater* 8(3):610–641
126. Wagner C (1968) Die Löslichkeit von Wasserdampf in  $\text{ZrO}_2\text{-Y}_2\text{O}_3$ -Mischkristallen, *Berichte Bunseng. Phys Chem* 72(7):778–781
127. Alberti G, Casciola M (2001) Solid state protonic conductors, present main applications and future prospects. *Solid State Ionics* 145:3–16
128. ZP X, Jin Y, Diniz da Costa JC, GQM L (2008) Zr  $(\text{HPO}_4)_2$  based organic/inorganic nanohybrids as new proton conductors. *Solid State Ionics* 178:1654–1659
129. Ahmad MI, Zaidi SMJ, Ruhman SU, Ahmed S (2006) Synthesis and proton conductivity of heteropolyacids loaded Y-zeolite as solid proton conductors for fuel cell applications. *Miopor Mesopor Mater* 91:296–304
130. Norby T (1999) Solid-state protonic conductors: principles, properties, progress and prospects. *Solid State Ionics* 125:1–11
131. Daiko Y, Nguyen VH, Yazawa T, Muto H, Sakai M, Matsuda A (2010) Phase transition and proton conductivity of  $\text{CsHSO}_4$ -WPA composites prepared by mechanical milling. *Solid State Ionics* 181:183–186
132. Sugahara T, Hayashi A, Tadanaga K, Tatsumisago M (2010) Characterization of proton conducting  $\text{CsHSO}_4\text{-CsH}_2\text{PO}_4$  ionic glasses prepared by the melt-quenching method. *Solid State Ionics* 181:190–192
133. Iwahara H, Esaka T, Uchida H, Maeda N (1981) Proton conduction in sintered oxides and its application to steam electrolysis for hydrogen production. *Solid State Ionics* 3(4):359–363
134. Fukatsu N, Kurita N, Yajima T, Koide K, Ohashi T (1995) Proton conductors of oxide and their application to research into metal-hydrogen systems. *J Alloys Comp* 231:706–712
135. Schwartz M, Link BF, Sammells AF (1993) New brownmillerite solid electrolytes. *J Electrochem Soc* 140:L62–L63
136. Zahang GB, Smyth DM (1995) Protonic conduction in  $\text{Ba}_2\text{In}_2\text{O}_5$ . *Solid State Ionics* 82:153–160
137. Fisher CSJ, Islam MS (1999) Defect, protons and conductivity in brownmillerite-structured  $\text{Ba}_2\text{In}_2\text{O}_5$ . *Solid State Ionics* 118:355–363
138. Orera A, Slater PR (2010) Water incorporation studies in apatite-type rare earth silicates/germinates. *Solid State Ionics* 181:110–114
139. Marrero-López D, Martín-Sedeño MC, Ruiz-Morales JC, Núñez P, Ramos-Barrado JR (2010) Preparation and characterisation of  $\text{La}_{10-x}\text{Ge}_5\text{Al}_{0.5}\text{O}_{26\pm\delta}$  apatites by freeze-drying precursor method. *Mater Res Bull* 45:409–415
140. Ito N, Iijima M, Kimura K, Iguchi S (2005) New intermediate temperature fuel cell with ultra-thin proton conductor electrolyte. *J Power Sources* 152:200–203
141. Matsumoto H, Nomura I, Okada S, Ishihara T (2008) Intermediate-temperature solid oxide fuel cells using perovskite-type oxide based on barium cerate. *Solid State Ionics* 179:1486–1489
142. Ishigaki T, Yamauchi S, Kishio K, Fueki K, Iwahara H (1986) Dissolution of deuterium into proton conductor  $\text{SrCe}_{0.95}\text{Yb}_{0.05}\text{O}_{3-\delta}$ . *Solid State Ionics* 21:239–241
143. Iwahara H, Uchida H, Ono K, Ogaki K (1998) Proton conduction in sintered oxides based on  $\text{BaCeO}_3$ . *J Electrochem Soc* 135:529–533
144. Bonanos N, Ellis B, Mahmood MN (1991) Construction and operation of fuel cells based on the solid electrolyte  $\text{BaCeO}_3$ : Gd. *Solid State Ionics* 44:305–311
145. Ma G, Matsumoto H, Iwahara H (1999) Ionic conduction and nonstoichiometry in non-doped  $\text{Ba}_x\text{CeO}_{3-x}$ . *Solid State Ionics* 122:237–247
146. Taniguchi N, Hatoh K, Niikura J, Gamoto T, Iwahara H (1992) Proton conductive properties of gadolinium-doped barium cerates at high temperatures. *Solid State Ionics* 53–56:998–1003
147. Ma G, Shimura T, Iwahara H (1998) Ionic conduction and nonstoichiometry in  $\text{Ba}_x\text{Ce}_{0.90}\text{Y}_{0.10}\text{O}_{3-x}$ . *Solid State Ionics* 110:103–110
148. Ma G, Shimura T, Iwahara H (1999) Simultaneous doping with  $\text{La}^{3+}$  and  $\text{Y}^{3+}$  for  $\text{Ba}^{2+}$  and  $\text{Ce}^{4+}$  sites



- in BaCeO<sub>3</sub> and the ionic conduction. *Solid State Ionics* 120:51–60
149. Katahira K, Kohchi Y, Shimura T, Iwahara H (2000) Protonic conduction in Zr-substituted BaCeO<sub>3</sub>. *Solid State Ionics* 138:91–98
150. Ranran P, Yan W, Lizhai Y, Zongqiang M (2006) Electrochemical properties of intermediate-temperature SOFCs based on proton conducting Sm-doped BaCeO<sub>3</sub> electrolyte thin film. *Solid State Ionics* 177:389–393
151. XT S, Yan QZ, Ma YH, Zhang WF, Ge CC (2006) Effect of co-dopant addition on the properties of yttrium and neodymium doped barium cerate electrolyte. *Solid State Ionics* 177:1041–1045
152. Gorbova E, Zhuravlev BV, Demin AK, Song SQ, Tsiakaras PE (2006) Charge transfer properties of BaCe<sub>0.88</sub>Nd<sub>0.12</sub>O<sub>3-δ</sub> co-ionic electrolyte. *J Power Sources* 157:720–723
153. Taherparvar H, Kilner JA, Baker RT, Sahibzada M (2003) Effect of humidification at anode and cathode in proton-conducting SOFCs. *Solid State Ionics* 162–163:297–303
154. Du Y, Nowick AS (1995) Structural transitions and proton conduction in nonstoichiometric A<sub>3</sub>B'B<sub>2</sub>'O<sub>9</sub> perovskite-type oxides. *J Am Ceram Soc* 78:3033–3039
155. Murugaraj P, Kreuer KD, He T, Schober T, Maier J (1997) High proton conductivity in barium yttrium stannate Ba<sub>2</sub>YSnO<sub>5.5</sub>. *Solid State Ionics* 98:1–6
156. Kreuer KD (2003) Proton conducting oxides. *Ann Rev Mater Res* 33:333–359
157. He T, Kreuer KD, Baikov YM, Maier J (1997) Impedance spectroscopic study of thermodynamics and kinetics of Gd-doped BaCeO<sub>3</sub> single crystal. *Solid State Ionics* 95:301–308
158. Fabbri E, D'Epifanio A, Di Bartolomeo E, Licoccia S, Traversa E (2008) Tailoring the chemical stability of Ba(Ce<sub>0.8-x</sub>Zr<sub>x</sub>)Y<sub>0.2</sub>O<sub>3-δ</sub> protonic conductors for intermediate temperature solid oxide fuel cells (IT-SOFCs). *Solid State Ionics* 179:558–564
159. Kreuer KD (1999) Aspects of the formation and mobility of protonic charge carriers and the stability of perovskite-type oxides. *Solid State Ionics* 125:285–302
160. He T, Ehrhart P, Meuffels P (1995) Optical band gap and Urbach tail in Y-doped BaCeO<sub>3</sub>. *J Appl Phys* 79:3219–3223
161. Minh NQ (1993) Ceramic fuel cells. *J Am Ceram Soc* 76(3):563–588
162. Mackor A, Koster TPM, Kraaijkamp JG, Gerretsen J, van Eijk JPGM (1991) Influence of La-substitution and -substoichiometry on conductivity, thermal expansion and chemical stability of Ca- or Sr-doped lanthanum manganites as SOFC cathodes. In: Grosz F, Zegers P, Singhal SC, Yamamoto O (eds) *Proceedings of the 2nd international symposium on solid oxide fuel cells*. Commission of European Communities, Luxembourg, pp 463–471
163. Anderson HU (1992) Review of p-type doped perovskite materials for SOFC and other applications. *Solid State Ionics* 52:33–41
164. Kuo JH, Anderson HU, Sparlin DM (1989) Oxidation-reduction behavior of undoped and Sr-doped LaMnO<sub>3</sub>: nonstoichiometry and defect structure. *J Solid State Chem* 83:52–60
165. Kuo JH, Anderson HU, Sparlin DM (1990) Oxidation-reduction behavior of undoped and Sr-doped LaMnO<sub>3</sub>: defect structure, electrical conductivity, and thermoelectric power. *J Solid State Chem* 87:55–63
166. van Roosmalen JAM, Huijsmans JPP, Cordfunke EHP (1991) Sinter behavior and electrical conductivity of (La,Sr)MnO<sub>3</sub> as a function of Sr-content. In: Grosz F, Zegers P, Singhal SC, Yamamoto O (eds) *Proceedings 2nd International symposium on solid oxide fuel cells*. Commission of European Communities, Luxembourg, pp 507–516
167. Hammouche A, Siebert E, Hammou A (1989) Crystallographic, thermal and electrochemical properties of the system La<sub>1-x</sub>Sr<sub>x</sub>MnO<sub>3</sub> for high temperature solid electrolyte fuel cells. *Mater Res Bull* 24:367–380
168. Yamada H, Nagamoto H (1993) Thermal expansion coefficient and electrical conductivity of Mn-based perovskite-type oxides. In: Singhal SC, Iwahara H (eds) *Proceedings of the 3rd International symposium on solid oxide fuel cells*, vol 93–94. The Electrochem Society Inc, Pennington, pp 213–219
169. Nasrallah MM, Anderson HU, Stevenson JW (1991) Defect chemistry and properties of Y<sub>1-x</sub>Ca<sub>x</sub>MnO<sub>3</sub>. In: Grosz F, Zegers P, Singhal SC, Yamamoto O (eds) *Proceedings of the 2nd international symposium on solid oxide fuel cells*. Commission of European Communities, Luxembourg, pp 545–552
170. Stevenson JW, Nasrallah MM, Anderson HU, Parlin DMS (1993) Defect structure of Y<sub>1-y</sub>Ca<sub>y</sub>MnO<sub>3</sub> and La<sub>1-y</sub>Ca<sub>y</sub>MnO<sub>3</sub>. I. Electrical properties. *J Solid State Chem* 102:175–184
171. Stevenson JW, Nasrallah MM, Anderson HU, Sparlin DM (1993) Defect structure of Y<sub>1-y</sub>Ca<sub>y</sub>MnO<sub>3</sub> and La<sub>1-y</sub>Ca<sub>y</sub>MnO<sub>3</sub> II Oxidation-reduction behavior. *J Solid State Chem* 102:185–197
172. Fu B, Huebner W, Trubelja MF, Stubican VS (1993) (Y<sub>1-x</sub>Ca<sub>x</sub>)FeO<sub>3</sub>: a potential cathode material for solid oxide fuel cells. In: Singhal SC, Iwahara H (eds) *Proceedings of the 3rd international symposium on solid oxide fuel cells*, vol 93–94. The Electrochemical Society, Pennington, pp 276–287
173. Yamamoto O, Takeda Y, Imanishi N, Sakaki Y (1993) Electrochemical properties of La<sub>1-x</sub>Ca<sub>x</sub>MnO<sub>3-z</sub> as cathode in SOFC. In: Singhal SC, Iwahara H (eds) *Proceedings of the 3rd international symposium on solid oxide fuel cells*, vol 93–94. The Electrochemical Society, Pennington, pp 205–212

174. Mizusaki J, Tagawa H, Katou M, Hirano K, Sawata A, Tsuneyoshi K (1991) Electrochemical properties of some perovskite-type oxides as oxygen gas electrodes on yttria stabilized zirconia. In: Grosz F, Zegers P, Singhal SC, Yamamoto O (eds) Proceedings of the 2nd international symposium on solid oxide fuel cells. Commission of European Communities, Luxembourg, pp 487–494
175. Mizusaki J, Tagawa H, Tsuneyoshi K, Sawata A (1991) Reaction kinetics and microstructure of the solid oxide fuel cells air electrode  $\text{La}_{0.6}\text{Ca}_{0.4}\text{MnO}_3/\text{YSZ}$ . *J Electrochem Soc* 138(7):1867–1873
176. Dokiya M (1992) A historical review on the SOFC research activity at NCLI, (in Japanese). In: Extended abstracts 1st symposium on solid oxide fuel cells, Japan. Solid Oxide Fuel Cells Society, Tokyo, pp 11–14
177. Yokokawa H, Sakai N, Kawada T, Dokiya M (1991) Chemical thermodynamic compatibility of solid oxide fuel cell materials. In: Grosz F, Zegers P, Singhal SC, Yamamoto O (eds) Proceedings of the 2nd international symposium on solid oxide fuel cells. Commission of European Communities, Luxembourg, pp 663–670
178. Yokokawa H, Sakai N, Kawada T, Dokiya M (1992) Thermodynamic stabilities of perovskite oxides for electrodes and other electrochemical materials. *Solid State Ionics* 52:43–56
179. Otoshi S, Sasaki H, Ohnishi H, Hase M, Ishimaru K, Ippommatsu M, Higuchi T, Miyayama M, Yanagida H (1991) Changes in the phases and electrical conduction properties of  $(\text{La}_{1-x}\text{Sr}_x)_{1-y}\text{MnO}_{3-\delta}$ . *J Electrochem Soc* 138(5):1519–1523
180. Takeda Y, Kanno R, Noda M, Tomida Y, Yamamoto O (1987) Cathodic polarization phenomena of perovskite oxide electrodes with stabilized zirconia. *J Electrochem Soc* 134(11):2656–2661
181. Mizusaki J (1992) Nonstoichiometry, diffusion, and electrical properties of perovskite-type oxide electrode materials. *Solid State Ionics* 52:79–91
182. Teraoka Y, Nobunaga T, Okamoto K, Miura N, Yamazoe N (1991) Influence of constituent metal cations in substituted  $\text{LaCoO}_3$  on mixed conductivity and oxygen permeability. *Solid State Ionics* 48:207–212
183. Ivers-Tiffée E, Schießl M, Oel HJ, Wersing W (1993) Investigations of cobalt-containing perovskites in SOFC single cells with respect to interface reactions and cell performance. In: Singhal SC, Iwahara H (eds) Proceedings of the 3rd international symposium on solid oxide fuel cells, vol 93–94. The Electrochemical Society, Pennington, pp 613–622
184. Iberl A, von Philipsborn H, Schießl M, Ivers-Tiffée E, Wersing W, Zorn G (1991) High-temperature X-ray diffraction measurements of phase transitions and thermal expansion in  $(\text{La,Sr})(\text{Mn,Co})\text{O}_3$ -cathode materials. In: Grosz F, Zegers P, Singhal SC, Yamamoto O (eds) Proceedings of the 2nd international symposium on solid oxide fuel cells. Commission of European Communities, Luxembourg, pp 527–535
185. Mackor A, Spee CIMA, van der Zouwen-Assink EA, Baptista JL, Schoonman J (1990) Mixed conductivity in perovskite SOFC materials  $\text{La}_{1-x}\text{M}_x\text{Mn}_{1-y}\text{Co}_y\text{O}_3$  ( $\text{M} = \text{Ca}$  or  $\text{Sr}$ ). In: Proceedings of the 25th intersociety energy conversion engineering conference, American Institute of Chemical Engineers, vol 3, pp 251–255
186. Tai LW, Nasrallah MM, Anderson HU (1993)  $(\text{La}_{1-x}\text{Sr}_x)(\text{Co}_{1-y}\text{Fe}_y)\text{O}_3$ , A potential cathode for intermediate temperature SOFC applications. In: Singhal SC, Iwahara H (eds) Proceedings of the 3rd international symposium on solid oxide fuel cells, vol 93–94. The Electrochemical Society, Pennington, pp 241–251
187. Chen CC, Nasrallah MM, Anderson HU (1993) Preparation and electrode characteristics of dense  $\text{La}_{0.6}\text{Sr}_{0.4}\text{Co}_{0.2}\text{Fe}_{0.8}\text{O}_3$  thin film by polymeric precursors. In: Singhal SC, Iwahara H (eds) Proceedings of the 3rd international symposium on solid oxide fuel cells, vol 93–94. The Electrochemical Society Inc., Pennington, pp 252–266
188. Teraoka Y, Zhang HM, Okamoto K, Yamazoe N (1988) Mixed ionic-electronic conductivity of  $\text{La}_{1-x}\text{Sr}_x\text{Co}_{1-y}\text{Fe}_y\text{O}_{3-\delta}$ . *Mater Res Bull* 23:51–58
189. Ftikos C, Carter S, Steele BCH (1993) Mixed electronic/ionic conductivity of the solid solutions  $\text{La}_{(1-x)}\text{Sr}_x\text{Co}_{(1-y)}\text{Ni}_y\text{O}_{3-\delta}$  ( $x:0.4, 0.5, 0.6$  and  $y:0.2, 0.4, 0.6$ ). *J Europ Ceram Soc* 12:79–86
190. Inoue T, Seki N, Eguchi K, Arai H (1990) Low-temperature operation of solid electrolyte oxygen sensors using perovskite-type oxide electrodes and cathodic reaction kinetics. *J Electrochem Soc* 137(8):2523–2527
191. Sasaki K, Wurth JP, Gschwend R, Gödickemeier M, Gauckler LJ (1996) Microstructure-property relations of solid oxide fuel cell cathodes and current collectors: cathodic polarization and ohmic resistance. *J Electrochem Soc* 143:530–543
192. Kleitz M (1992) Reaction pathways: a new electrode modelling concept. In: McEvoy A (ed) Fundamental barriers to SOFC performance. Swiss Federal Office of Energy, Bern, pp 4–12
193. Steele BCH, Carter S, Kajda J, Kontoulis I, Kilner JA (1991) Optimisation of fuel cell components using  $^{18}\text{O}/^{16}\text{O}$  exchange and dynamic SIMS techniques. In: Grosz F, Zegers P, Singhal SC, Yamamoto O (eds) Proceedings of the 2nd international symposium on solid oxide fuel cells. Commission of European Communities, Luxembourg, pp 517–525
194. Hammou A (1992) Solid oxide fuel cells. In: Gerischer H, Tobias CW (eds) Advances in electrochemical science and engineering, vol 2. VCH-Verlag, Weinheim, pp 87–139
195. Hammouche A, Siebert E, Hammou A, Kleitz M, Caneiro A (1991) Electrocatalytic properties and nonstoichiometry of the high temperature air

- electrode  $\text{La}_{1-x}\text{Sr}_x\text{MnO}_3$ . *J Electrochem Soc* 138(5):1212–1216
196. Ishigaki T, Yamauchi S, Kishio K, Mizusaki J, Fueki K (1988) Diffusion of oxide ion vacancies in perovskite-type oxides. *J Solid State Chem* 73:179–187
  197. Takeda Y, Ueno H, Imanishi N, Yamamoto O, Sammes N, Phillipps M (1996)  $\text{Gd}_{1-x}\text{Sr}_x\text{CoO}_3$  for the electrode of solid oxide fuel cells. *Solid State Ionics* 86–88:1187–1190
  198. Tu H, Takeda Y, Imanishi N, Yamamoto O (1997)  $\text{Ln}_{1-x}\text{Sr}_x\text{CoO}_3$  (Ln = Sm, Dy) for the electrode of solid oxide fuel cells. *Solid State Ionics* 100:283–288
  199. Sakaki Y, Takeda Y, Kato A, Imanishi N, Yamamoto O, Hattori M, Iio M, Esaki Y (1999)  $\text{Ln}_{1-x}\text{Sr}_x\text{MnO}_3$  (Ln = Pr, Nd, Sm and Gd) as the cathode material for solid oxide fuel cells. *Solid State Ionics* 118:187–194
  200. Phillipps M, Sammes N, Yamamoto O (1999)  $\text{Gd}_{1-x}\text{A}_x\text{Co}_{1-y}\text{Mn}_y\text{O}_3$  (A = Sr, Ca) as a cathode for the SOFC. *Solid State Ionics* 123:131–138
  201. Tu H, Takeda Y, Imanishi N, Yamamoto O (1999)  $\text{Ln}_{0.4}\text{Sr}_{0.6}\text{Co}_{0.8}\text{Fe}_{0.2}\text{O}_{3-\delta}$  (Ln = La, Pr, Nd, Sm, Gd) for the electrode in solid oxide fuel cells. *Solid State Ionics* 117:277–281
  202. Qiu L, Ichikawa T, Hirano A, Imanishi N, Takeda Y (2003)  $\text{Ln}_{1-x}\text{Sr}_x\text{Co}_{1-y}\text{Fe}_y\text{O}_{3-\delta}$  (Ln = Pr, Nd, Gd; x = 0.2, 0.3) for the electrodes of solid oxide fuel cells. *Solid State Ionics* 158:55–65
  203. Ishihara T, Honda M, Shibayama T, Nishiguchi H, Takita Y (1998) Intermediate temperature solid oxide fuel cells using a New  $\text{LaGaO}_3$  based oxide ion conductor. *J Electrochem Soc* 145:3177–3183
  204. Ishihara T, Fukui S, Nishiguchi H, Takita Y (2002) Mixed electronic-oxide ionic conductor of  $\text{BaCoO}_3$  doped with La for cathode of intermediate-temperature-operating solid oxide fuel cell. *Solid State Ionics* 152–153:609–613
  205. Shao ZP, Haile SM (2004) A high-performance cathode for the next generation of solid-oxide fuel cells. *Nature* 431:170–173
  206. Li S, Lu Z, Wei B, Huang X, Miao J, Cao G, Zhu R, Su W (2006) A study of  $(\text{Ba}_{0.5}\text{Sr}_{0.5})_{1-x}\text{Sm}_x\text{Co}_{0.8}\text{Fe}_{0.2}\text{O}_{3-\delta}$  as a cathode material for IT-SOFCs. *J Alloys Comp* 426:408–414
  207. Kotomin EA, Matrikov YA, Kuklja MM, Merkle R, Roytburd A, Maier J (2011) First principles calculations of oxygen vacancy formation and migration in mixed conducting  $\text{Ba}_{0.5}\text{Sr}_{0.5}\text{Co}_{1-y}\text{Fe}_y\text{O}_{3-\delta}$  perovskites. *Solid State Ionics* 188:1–5
  208. Yan A, Cheng M, Dong Y, Yang W, Maragou V, Song S, Tsiakaras P (2006) Investigation of a  $\text{Ba}_{0.5}\text{Sr}_{0.5}\text{Co}_{0.8}\text{Fe}_{0.2}\text{O}_{3-\delta}$  based cathode IT-SOFC I. The effect of  $\text{CO}_2$  on the cell performance. *Appl Catal B Environ* 66:64–71
  209. Yan A, Yang M, Hou Z, Dong Y, Cheng M (2008) Investigation of  $\text{Ba}_{1-x}\text{Sr}_x\text{Co}_{0.8}\text{Fe}_{0.2}\text{O}_{3-\delta}$  as cathodes for low-temperature solid oxide fuel cells both in the absence and presence of  $\text{CO}_2$ . *J Power Sources* 185:76–84
  210. Taniguchi S, Kadowaki M, Kawamura H, Yasuo T, Akiyama Y, Miyake Y, Saitoh T (1995) Degradation phenomena in the cathode of a solid oxide fuel cell with an alloy separator. *J Power Sources* 55:73–79
  211. Taniguchi S, Kadowaki M, Yasuo T, Akiyama Y, Itoh Y, Miyake Y, Nishio K (1996) Suppression of chromium diffusion to an SOFC cathode from an alloy separator by a cathode second layer. *Denki Kagaku* 64(6):568–574
  212. Matsuzaki Y, Yasuda I (2001) Dependence of SOFC cathode degradation by chromium-containing alloy on compositions of electrodes and electrolytes. *J Electrochem Soc* 148(2):A126–A131
  213. Chiba R, Yoshimura F, Sakurai Y (1999) An investigation of  $\text{LaNi}_{1-x}\text{Fe}_x\text{O}_3$  as a cathode material for solid oxide fuel cells. *Solid State Ionics* 124:281–288
  214. Komatsu T, Chiba R, Arai H, Sato K (2008) Chemical compatibility and electrochemical property of intermediate-temperature SOFC cathodes under Cr poisoning condition. *J Power Sources* 176:132–137
  215. Jiang SP, Zhen Y (2008) Mechanism of Cr deposition and its application in the development of Cr-tolerant cathodes of solid oxide fuel cells. *Solid State Ionics* 179:1459–1464
  216. Lee S, Bevilacqua M, Fornasiero P, Vohs JM, Gorte RJ (2009) Solid oxide fuel cell cathodes prepared by infiltration of  $\text{LaNi}_{0.6}\text{Fe}_{0.4}\text{O}_3$  and  $\text{La}_{0.91}\text{Sr}_{0.09}\text{Ni}_{0.6}\text{Fe}_{0.4}\text{O}_3$  in porous yttria-stabilized zirconia. *J Power Sources* 193:747–753
  217. Skinner S, Kilner J (2000) Oxygen diffusion and surface exchange in  $\text{La}_{2-x}\text{Sr}_x\text{NiO}_{4+\delta}$ . *Solid State Ionics* 135:709–712
  218. Mauvy F, Bassat J, Boehm E, Manaud J, Dordor P, Grenier J (2003) Oxygen electrode reaction on  $\text{Nd}_2\text{NiO}_{4+\delta}$  cathode materials: impedance spectroscopy study. *Solid State Ionics* 158:17–28
  219. Lalanne C, Prosperi G, Bassat J, Mauvy F, Fourcade S, Stevens P, Zahid M, Diethelm S, van Herle J, Grenier J (2008) Neodymium-deficient nickelate oxide  $\text{Nd}_{1.95}\text{NiO}_{4+\delta}$  as cathode material for anode-supported intermediate temperature solid oxide fuel cells. *J Power Sources* 185:1218–1224
  220. Nie H, Wen T, Wang S, Wang Y, Guth U, Vashook V (2006) Preparation, thermal expansion, chemical compatibility, electrical conductivity and polarization of  $\text{A}_{2-2\alpha}\text{A}'_{2\alpha}\text{MO}_4$  (A = Pr, Sm; A' = Sr; M = Mn, Ni;  $\alpha = 0.3, 0.6$ ) as a new cathode for SOFC. *Solid State Ionics* 177:1929–1932
  221. Wang Y, Nie H, Wang S, Wen T, Guth U, Vashook V (2006)  $\text{A}_{2-2\alpha}\text{A}'_{2\alpha}\text{BO}_4$ -type oxides as cathode materials for IT-SOFCs (A = Pr, Sm; A' = Sr; B = Fe, Co). *Mater Lett* 60:1174–1178
  222. Haanappel V, Rutenbeck D, Mai A, Uhlenbruck S, Sebold D, Wesemeyer H, Röwekamp B, Tropicz C, Tietz F (2004) The influence of noble-metal-containing cathodes on the electrochemical performance of anode-supported SOFCs. *J Power Sources* 130:119–128

223. Wang S, Kato T, Nagata S, Honda T, Kaneko T, Iwashita N, Dokiya M (2002) Performance of a  $\text{La}_{0.6}\text{Sr}_{0.4}\text{Co}_{0.8}\text{Fe}_{0.2}\text{O}_3\text{-Ce}_{0.8}\text{Gd}_{0.2}\text{O}_{1.9}\text{-Ag}$  cathode for ceria electrolyte SOFCs. *Solid State Ionics* 146:203–210
224. Zhang J, Ji Y, Gao H, He T, Liu J (2005) Composite cathode  $\text{La}_{0.6}\text{Sr}_{0.4}\text{Co}_{0.2}\text{Fe}_{0.8}\text{O}_3\text{-Sm}_{0.1}\text{Ce}_{0.9}\text{O}_{1.95}\text{-Ag}$  for intermediate-temperature solid oxide fuel cells. *J Alloys Compounds* 395:322–325
225. Simner S, Anderson MJ, Coleman JS (2006) Performance of a novel  $\text{La}(\text{Sr})\text{Fe}(\text{Co})\text{O}_3\text{-Ag}$  SOFC cathode. *J Power Sources* 161:115–122
226. Mogensen M, Lindegaard T, Hansen TU, Mogensen G (1994) Physical properties of mixed conductor solid oxide fuel cell anodes of doped  $\text{CeO}_2$ . *J Electrochem Soc* 141(8):2122–2128
227. Setoguchi T, Okamoto K, Eguchi K, Arai H (1992) Effects of anode material and fuel on anodic reaction of solid oxide fuel cells. *J Electrochem Soc* 139:2875–2880
228. Sasaki H, Otoshi S, Suzuki M, Sogi T, Kajimura A, Sugiura N, Ippommatsu M (1994) Fabrication of high power density tubular type solid oxide fuel cells. *Solid State Ionics* 72:253–256
229. Lide DR (2008) CRC handbook of chemistry and physics. CRC Press, Boca Raton
230. Tao SW, Irvine JTS (2003) A redox-stable efficient anode for solid-oxide fuel cells. *Nat Mater* 2:320–323
231. Zha SW, Tsang P, Cheng Z, Liu ML (2005) Electrical properties and sulfur tolerance of  $\text{La}_{0.75}\text{Sr}_{0.25}\text{Cr}_{1-x}\text{Mn}_x\text{O}_3$  under anodic conditions. *J Solid State Chem* 178:1844–1850
232. Huang YH, Dass RI, Denyszyn JC, Goodenough JB (2006) Synthesis and characterization of  $\text{Sr}_2\text{MgMoO}_{6-\delta}$  an anode material for the solid oxide fuel cell. *J Electrochem Soc* 153: A1266–A1272
233. Vernoux P, Guillodo M, Foulrtier J, Hammou A (2000) Alternative anode material for gradual methane reforming in solid oxide fuel cells. *Solid State Ionics* 135:425–431
234. Ruiz-morales JC, Canales-Vázquez J, Peña-Martínez J, López DM, Núñez P (2006) On the simultaneous use of  $\text{La}_{0.75}\text{Sr}_{0.25}\text{Cr}_{0.5}\text{Mn}_{0.5}\text{O}_{3-\delta}$  as both anode and cathode material with improved microstructure in solid oxide fuel cells. *Electrochim Acta* 52:278–284
235. Sauvet AL, Fouletier J (2001) Electrochemical properties of a new type of anode material  $\text{La}_{1-x}\text{Sr}_x\text{Cr}_{1-y}\text{Ru}_y\text{O}_{3-\delta}$  for SOFC under hydrogen and methane at intermediate temperatures. *Electrochim Acta* 47:987–995
236. Sauvet AL, Fouletier J, Gaillard F, Primet M (2002) Surface properties and physicochemical characterizations of a New type of anode material,  $\text{La}_{1-x}\text{Sr}_x\text{Cr}_{1-y}\text{Ru}_y\text{O}_{3-\delta}$ , for a solid oxide fuel cell under methane at intermediate temperature. *J Catal* 209:25–34
237. Sauvet AL, Irvine JTS (2004) Catalytic activity for steam methane reforming and physical characterisation of  $\text{La}_{1-x}\text{Sr}_x\text{Cr}_{1-y}\text{Ni}_y\text{O}_{3-\delta}$ . *Solid State Ionics* 167:1–8
238. Sin A, Kopnin E, Dubitsky Y, Zaopo A, Aricò AS, Gullo LR, Rosa DL, Antonucci V (2005) Stabilisation of composite LSFCE-CGO based anodes for methane oxidation in solid oxide fuel cells. *J Power Sources* 145:68–73
239. Lepe FJ, Fernández-Urbán J, Mestres L, Martínez-Sarrion ML (2005) Synthesis and electrical properties of new rare-earth titanium perovskites for SOFC anode applications. *J Power Sources* 151:74–78
240. Fagg DP, Kharton VV, Kovalevsky AV, Viskup AP, Naumovich EN, Frade JR (2001) The stability and mixed conductivity in La and Fe doped  $\text{SrTiO}_3$  in the search for potential SOFC anode materials. *J Eur Ceram Soc* 21:1831–1835
241. Hui S, Petric A (2002) Evaluation of yttrium-doped  $\text{SrTiO}_3$  as an anode for solid oxide fuel cells. *J Eur Ceram Soc* 22:1673–1681
242. Moos R, Härdtl KH (1997) Defect chemistry of donor-doped and undoped strontium titanate ceramics between 1000° and 1400°C. *J Am Ceram Soc* 80(10):2549–2562
243. Hui SQ, Petric A (2001) Conductivity and stability of  $\text{SrVO}_3$  and mixed perovskites at low oxygen partial pressures. *Solid State Ionics* 143:275–283
244. Bieger T, Waser MJ, Waser R (1992) Optical investigation of oxygen incorporation in  $\text{SrTiO}_3$ . *Solid State Ionics* 53–56:578–582
245. Sasaki K, Claus J, Maier J (1999) Defect chemistry of oxides in partially frozen-in states: case studies for  $\text{ZrO}_2(\text{Y}_2\text{O}_3)$ ,  $\text{SrZrO}_3(\text{Y}_2\text{O}_3)$ , and  $\text{SrTiO}_3$ . *Solid State Ionics* 121:51–60
246. Park S, Gorte RJ, Vohs JM (2000) Applications of heterogeneous catalysis in the direct oxidation of hydrocarbons in a solid-oxide fuel cell. *Appl Catal A Gen* 200:55–61
247. Park S, Vohs JM, Gorte RJ (2000) Direct oxidation of hydrocarbons in a solid-oxide fuel cell. *Nature* 404:265–267
248. Zhou ZF, Kumar R, Thakur ST, Rudnick LR, Schobert H, Lvov SN (2007) Direct oxidation of waste vegetable oil in solid-oxide fuel cells. *J Power Sources* 171:856–860
249. Craciun R, Park S, Gorte RJ, Vohs JM, Wang C, Worrell WL (1999) A novel method for preparing anode cermets for solid oxide fuel cells. *J Electrochem Soc* 146:4019–4022
250. Larminie J, Dicks A (2000) Fuel cell systems explained. Wiley, Chichester
251. Sasaki K, Teraoka Y (2003) Equilibria in fuel cell gases I. equilibrium compositions and reforming conditions. *J Electrochem Soc* 150(7):A878–A884
252. Sasaki K, Teraoka Y (2003) Equilibria in fuel cell gases II. the C–H–O ternary diagrams. *J Electrochem Soc* 150(7):A885–A888

253. Sasaki K, Teraoka Y (2003) Equilibria in fuel cell gases. In: Proceedings of the 8th international symposium on solid oxide fuel cells, vol 2003–2007. Electrochemical Society, Pennington, pp 1225–1239
254. Sasaki K, Kojo H, Hori Y, Kikuchi R, Eguchi K (2002) Direct-alcohol/hydrocarbon SOFCs: comparison of power generation characteristics for various fuels. *Electrochemistry* 70(1):18–22
255. Eguchi K, Kojo H, Takeguchi T, Kikuchi R, Sasaki K (2002) Fuel flexibility in power generation by solid oxide fuel cells. *Solid State Ionics* 152:411–416
256. Sasaki K, Hori Y, Kikuchi R, Eguchi K, Ueno A, Takeuchi H, Aizawa M, Tsujimoto K, Tajiri H, Nishikawa H, Uchida Y (2002) Current-voltage characteristics and impedance analysis of solid oxide fuel cells for mixed H<sub>2</sub> and CO gases. *J Electrochem Soc* 149(3):A227–A233
257. Sasaki K, Watanabe K, Teraoka Y (2004) Direct-alcohol solid oxide fuel cells: current-voltage characteristics and fuel gas compositions. *J Electrochem Soc* 151(7):A965–A970
258. Sasaki K, Watanabe K, Shiosaki K, Susuki K, Teraoka Y (2003) Power generation characteristics of SOFCs for alcohols and hydrocarbons. In: Proceedings of the 8th international symposium on solid oxide fuel cells, vol 2003–2007. Electrochemical Society, Pennington, pp 1295–1304
259. Kishimoto H, Horita T, Yamaji K, Xiong Y, Sakai N, Brito ME, Yokokawa H (2005) Feasibility of n-Dodecane fuel for solid oxide fuel cell with Ni-ScSZ anode. *J Electrochem Soc* 152(3):A532–A538
260. Sasaki K, Watanabe K, Shiosaki K, Susuki K, Teraoka Y (2004) Multi-fuel capability of solid oxide fuel cells. *J Electroceram* 13(1–3):669–675
261. Haga K (2010) Chemical degradation of Ni-based anode materials in solid oxide fuel cells. Dissertation, Kyushu University, Fukuoka
262. Sasaki K, Haga K, Yoshizumi T, Minematsu D, Yuki E, Liu RR, Uryu C, Oshima T, Ogura T, Shiratori Y, Ito K, Koyama M, Yokomoto K (2011) Chemical durability of SOFCs: influence of impurities on long-term performance. *J Power Sources* 196(22):9130–9140
263. Sasaki K, Susuki K, Iyoshi A, Uchimura M, Imamura N, Kusaba H, Teraoka Y, Fuchino H, Tsujimoto K, Uchida Y, Jingo N (2006) H<sub>2</sub>S poisoning of solid oxide fuel cells. *J Electrochem Soc* 153: A2023–A2029
264. Sasaki K, Susuki K, Iyoshi A, Uchimura M, Imamura N, Kusaba H, Teraoka Y, Fuchino H, Tsujimoto K, Uchida Y, Jingo N (2005) Sulfur tolerance of solid oxide fuel cells. In: Proceedings of the 9th international symposium on solid oxide fuel cells, vol 2005–2007. Electrochemical Society, Pennington, pp 1267–1274
265. Sasaki K, Adachi S, Haga K, Uchikawa M, Yamamoto J, Iyoshi A, Chou J-T, Shiratori Y, Itoh K (2007) Fuel impurity tolerance of solid oxide fuel cells. *Solid oxide fuel cells 10 (SOFC-10)*. *ECS Trans* 7(1):1675–1683
266. Haga K, Adachi S, Shiratori Y, Ito K, Sasaki K (2008) Poisoning of SOFC anodes by various fuel impurities. *Solid State Ionics* 179(27–32):1427–1431
267. Haga K, Shiratori Y, Ito K, Sasaki K (2008) Chlorine poisoning of SOFC Ni-cermet anodes. *J Electrochem Soc* 155(12):B1233–B1239
268. Haga K, Shiratori Y, Nojiri Y, Ito K, Sasaki K (2010) Phosphorus poisoning of Ni-cermet anodes in solid oxide fuel cells. *J Electrochem Soc* 157(11): B1693–B1700
269. Park S, Craciun R, Vohs JM, Gorte RJ (1999) Direct oxidation of hydrocarbons in a solid oxide fuel cell: I. Methane oxidation. *J Electrochem Soc* 146:3603–3605
270. Shiratori Y, Oshima T, Sasaki K (2008) Feasibility of direct-biogas SOFC. *Int J Hydrogen Energ* 33:6316–6321
271. Gorte RJ, Kim H, Vohs JM (2002) Novel SOFC anodes for the direct electrochemical oxidation of hydrocarbon. *J Power Sources* 106:10–15
272. Kim H, Park S, Vohs JM, Gorte RJ (2001) Direct oxidation of liquid fuels in a solid oxide fuel cell. *J Electrochem Soc* 148:A693–A695
273. Zhou ZF, Gallo C, Pague MB, Schobert H, Lvov SN (2004) Direct oxidation of jet fuels and Pennsylvania crude oil in a solid oxide fuel cell. *J Power Sources* 133:181–187
274. Shiratori Y, Tran TQ, Takahashi Y, Sasaki K (2011) Application of biofuels to solid oxide fuel cell. *ECS Trans* 35:2641–2651
275. van Herle J, Maréchal F, Leuenberger S, Membrez Y, Bucheli O, Favrat D (2004) Process flow model of solid oxide fuel cell system supplied with sewage biogas. *J Power Sources* 131:127–141
276. Girona K, Laurencin J, Petitjean M, Fouletier J, Lefebvre-Joud F (2009) SOFC running on biogas: identification and experimental validation of “safe” operating conditions. *ECS Trans* 25(2):1041–1050
277. Shiratori Y, Ijichi T, Oshima T, Sasaki K (2010) Internal reforming SOFC running on biogas. *Int J Hydrog Energy* 35:7905–7912
278. Shiratori Y, Ijichi T, Oshima T, Sasaki K (2010) Performance of internal reforming SOFC running on biogas. In: Proceedings of 9th European SOFC Forum, Luzern, pp 4-77–4-87
279. Swaine DJ (1990) Trace elements in coal. Butterworths, London
280. Lobachyov K, Richter HJ (1996) Combined cycle gas turbine power plant with coal gasification and solid oxide fuel cell. *J Energy Resour Technol* 118:285–292
281. Iritani J, Kougami K, Komiyama N, Nagata K, Ikeda K, Tomida K (2001) Pressurized 10kW class module of SOFC. In: Yokokawa H, Singhal SC (eds) Proceedings of the 7th international symposium on solid oxide fuel cells, vol 2001–2016. Pennington, Electrochemical Society, pp 63–71

282. Doctor RD, Molburg JC, Thimmapuram PR (1997) Oxygen-blown gasification combined cycle: carbon dioxide recovery, transport, and disposal. *Energy Convers Manag* 38:S575–S580
283. Timpe RC, Kulas RW, Hauserman WB, Sharma RK, Olson ES, Willson WG (1997) Catalytic gasification of coal for the production of fuel cell feedstock. *Int J Hydrog Energy* 22:487–492
284. Sjunnesson L (1998) Utilities and their investments in fuel cells. *J Power Sources* 71:41–44
285. Cayan FN, Zhi M, Pakalapati SR, Celik I, Wu N, Gemmen RS (2008) Effects of coal syngas impurities on anodes of solid oxide fuel cells. *J Power Sources* 185:595–602
286. Marina OA, Pederson LR, Coyle CA, Thomsen EC, Coffey GW (2005) Ni/YSZ anode interactions with impurities in coal gas. *ECS Trans* 25(2):2125–2130
287. Bao JE, Krishnan GN, Jayaweera P, Perez-Mariano J, Sanjurjo A (2009) Effect of various coal contaminants on the performance of solid oxide fuel cells: part I. accelerated testing. *J Power Sources* 193:607–616
288. Bao JE, Krishnan GN, Jayaweera P, Lau KH, Sanjurjo A (2009) Effect of various coal contaminants on the performance of solid oxide fuel cells: part II. ppm and sub-ppm level testing. *J Power Sources* 193:617–624
289. Bao JE, Krishnan GN, Jayaweera P, Sanjurjo A (2010) Effect of various coal gas contaminants on the performance of solid oxide fuel cells: part III. synergistic effects. *J Power Sources* 195:1316–1324
290. Tremblay JP, Gemmen RS, Bayless DJ (2007) The effect of IGFC warm gas cleanup system conditions on the gas-solid partitioning and form of trace species in coal syngas and their interactions with SOFC anodes. *J Power Sources* 163:986–996
291. Yoshida S, Kabata T, Nishiura M, Koga S, Tomida K, Miyamoto K, Teramoto Y, Mataka N, Tsukuda H, Suemori S, Ando Y, Kobayashi Y (2011) Development of the SOFC-GT combined cycle system with tubular type cell stack. *ECS Trans* 35(1):105–111
292. Ishihara T (2009) *Perovskite oxide for solid oxide fuel cells*. Springer, New York
293. Tsuchiya M, Lai BK, Ramanathan S (2011) Scalable nanostructured membranes for solid oxide fuel cells. *Nat Nanotechnol* 6:282–286
294. Karageorgakis NI, Heel A, Rupp JLM, Aguirre MH, Graule T, Gauckler LJ (2011) Properties of flame sprayed  $\text{Ce}_{0.8}\text{Gd}_{0.2}\text{O}_{1.9-\delta}$  electrolyte thin films. *Adv Funct Mater* 21(3):532–539
295. Bonderer LJ, Chen PW, Kocher P, Gauckler LJ (2010) Free-standing ultrathin ceramic foils. *J Am Ceram Soc* 93(11):3624–3631
296. Ryll T, Galinski H, Schlagenhauf L, Elser P, Rupp JLM, Bieberle-Hutter A, Gauckler LJ (2011) Microscopic and nanoscopic three-phase-boundaries of platinum thin-film electrodes on YSZ electrolyte. *Adv Funct Mater* 21(3):565–572
297. Tuller HL, Litzelman SJ, Jung WC (2009) Microionics: next generation power sources. *Phys Chem Chem Phys* 11:3023–3034
298. Tuller HL, Bishop SR (2011) Point defects in oxides: tailoring materials through defect engineering. *Annu Rev Mater Res* 41:369–398
299. Sasaki K, Maier J (1999) Low temperature defect chemistry of oxides: I. general aspects and numerical calculations. *J Appl Phys* 86(10):5422–5433
300. Sasaki K, Maier J (1999) Low temperature defect chemistry of oxides: II. analytical relations. *J Appl Phys* 86(10):5434–5443
301. Matsumoto K, Fujigaya T, Sasaki K, Nakashima N (2011) Bottom-up design of carbon nanotube-based electrocatalysts and their application in high temperature operating polymer electrolyte fuel cells. *J Mater Chem* 21(4):1187–1190
302. Masao A, Noda Z, Takasaki F, Ito K, Sasaki K (2009) Carbon-free Pt electrocatalysts supported on  $\text{SnO}_2$  for polymer electrolyte fuel cells. *Electrochem Solid-State Lett* 12(9):B119–B122
303. Sasaki K, Takasaki F, Noda Z, Hayashi S, Shiratori Y, Ito K (2010) Alternative electrocatalyst support materials for polymer electrolyte fuel cells. *ECS Trans* 33(1):473–482
304. Hayashi A, Notsu H, Kimijima K, Miyamoto J, Yagi I (2008) Preparation of Pt/mesoporous carbon (MC) electrode catalyst and its reactivity toward oxygen reduction. *Electrochim Acta* 53(21):6117–6125
305. Masuda H, Yamamoto A, Sasaki K, Lee S, Ito K (2011) A visualization study on relationship between water-droplet behavior and cell voltage appeared in straight, parallel and serpentine channel pattern cells. *J Power Sources* 196:5377–5385
306. Sasaki K, Li HW, Hayashi A, Yamabe J, Ogura T, Lyth SM (2016) *Hydrogen Energy Engineering: A Japanese Perspective*. Springer, Tokyo, Japan





## Direct Hydrocarbon Solid Oxide Fuel Cells

Michael Van Den Bossche<sup>1</sup> and  
Steven McIntosh<sup>1,2</sup>

<sup>1</sup>Department of Chemical Engineering,  
University of Virginia, Charlottesville, VA, USA

<sup>2</sup>Department of Chemical Engineering, Lehigh  
University, Bethlehem, PA, USA

### Article Outline

Glossary

Definition of the Subject

Introduction

Background

Copper-Ceria

Lanthanum Chromates

Double Perovskites

Strontium Titanates

Other Materials of Interest

Future Directions

Bibliography

### Glossary

**Electrical conductivity** Also referred to as total conductivity. This total conductivity has three components: electronic n-type (electron charge carriers), electronic p-type (electron hole charge carriers), and ionic conductivity.

**Electrocatalytic reaction** Catalyzed reaction that involves charge transfer.

**Humidified fuel** In this text, humidified fuel refers to fuel that has been passed through room temperature water and hence contains 3 mol% H<sub>2</sub>O.

**OCP** Open Circuit Potential. The potential difference measured between anode and cathode for an SOFC with an open electronic circuit. If the redox reactions occurring at the electrodes are known, the OCP can be predicted using the Nernst equation.

**Overpotential** The decrease in the maximum driving force (OCP), in a working SOFC. This is typically caused by charge transfer processes in the electrodes.

**Oxygen stoichiometry** The oxygen content of a solid oxide material. Most of the materials of interest in this study exhibit variable oxygen stoichiometry as a function of oxygen partial pressure and temperature while maintaining the cation structure.

**Polarization resistance** The electrical resistance of the electrode of an electrochemical device upon polarization.

**SOFC** Solid Oxide Fuel Cell. A fuel cell characterized as having a solid oxide electrolyte that separates the air electrode (cathode) from the fuel electrode (anode).

**TEC** Thermal Expansion Coefficient. Sometimes referred to as the coefficient of thermal expansion (CTE) and refers to the total expansion of the lattice cell as a function of temperature. For oxides with variable oxygen stoichiometry, the TEC consists of the thermal expansion and the chemical expansion. The latter is the expansion due to changes in oxygen stoichiometry. In this text it refers to the total expansion.

### Definition of the Subject

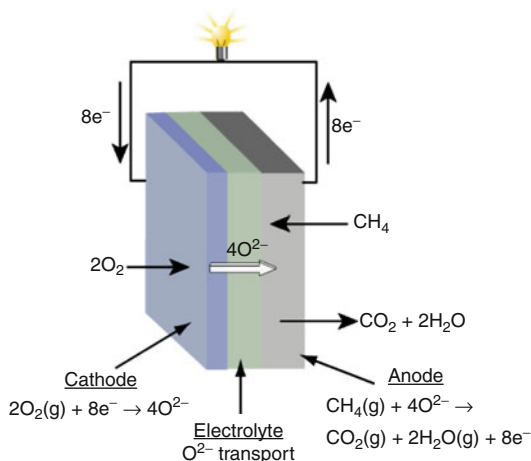
Solid Oxide Fuel Cells (SOFCs) are one of the most promising technologies for future efficient conversion of the chemical energy stored in fuels to electrical energy. One of the primary advantages of SOFCs is the potential to operate with a wide variety of fuels. While H<sub>2</sub> is the fuel of choice for most fuel cells, operation with fossil-derived and bio-derived hydrocarbon fuels would bypass the costly requirement of a new H<sub>2</sub> infrastructure, and accelerate adoption of fuel cell technology. This is feasible as SOFCs transport oxygen anions from the air electrode (cathode) to the fuel electrode (anode). The primary barrier to the realization of fuel flexible SOFCs is the anode material set. Traditional SOFC anodes are

based on Ni composites. While these are very efficient for  $H_2$  and CO fuels, Ni catalyzes graphite formation from dry hydrocarbons, leading to rapid degradation of cell performance and possible mechanical failure. This motivates the development of new anode materials and composites. The principle requirements of an anode are oxygen anion conductivity, electronic conductivity, and electrocatalytic activity toward the desired reaction. This entry reviews the primary issues in direct hydrocarbon anode development and discusses the new materials and composites that have been developed to meet this challenge.

## Introduction

Traditional combustion-based methods of electrical power generation convert the chemical energy of a fuel to electrical energy via an intermediate thermal step. In contrast, electrochemical systems, such as batteries and fuel cells, promise increased efficiency through the direct conversion of chemical to electrical energy. This serves to reduce fuel demand and decrease associated greenhouse gas emissions per unit of electrical energy output. The defining difference between a fuel cell and a battery is that a battery is a closed system with a finite amount of “fuel,” whereas a fuel cell is an open flow system with continuous feed of fuel and oxidant. Where a battery becomes depleted and must be recharged, a fuel cell continues to generate electrical power as long as both fuel and oxidant are supplied to the cell. Therefore, fuel cells are an efficient alternative for continuous power generation from a chemical fuel source.

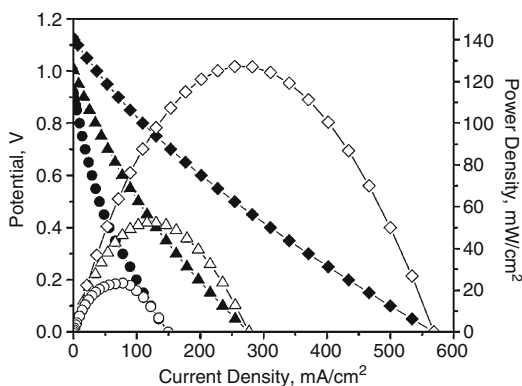
There are many types of fuel cells with the primary differentiators between each type being the ion transported across the electrolyte and the operating temperature range. This entry focuses on solid oxide fuel cells (SOFCs) [1–5]. Like all fuel cells, SOFCs consist of three main components: a cathode (air electrode), an anode (fuel electrode), and an electrolyte (purely ion conducting membrane between the cathode and anode). Figure 1 is a schematic of the SOFC operating principle, showing operation with  $CH_4$  fuel. The distinguishing feature of SOFCs is that



**Direct Hydrocarbon Solid Oxide Fuel Cells,**  
**Fig. 1** Solid Oxide Fuel Cell (SOFC) operating principle

the electrolyte is a dense, oxygen anion conducting but electronically insulating solid oxide. The SOFC operating mechanism is based upon the transport of oxygen anions from an oxygen-rich environment at the cathode (typically air) to an oxygen-lean fuel environment at the anode. The fuel and air chambers are physically and electronically separated by the dense electrolyte and the entire cell is sealed to prevent gas-phase mixing of fuel and air. The anode and cathode are ionically connected via the electrolyte, and electrically connected through an external circuit.

Under operation, electrons from the external circuit are utilized in the electrocatalytic reduction of molecular oxygen to oxygen anions at the cathode. These anions migrate through the electrolyte from the cathode to the anode. Fuel is electrocatalytically oxidized at the anode (consuming the oxygen anions) and the liberated electrons flow back to the cathode via external circuit, providing useful work. The electrochemical driving force for this process is the oxygen chemical potential difference between the cathode and anode compartments. The maximum theoretical thermodynamic driving force, the theoretical open circuit potential (OCP), can be calculated from the Nernst equation. This driving force is consumed as current is drawn from the cell. The current generated for a given potential drop from OCP, or overpotential, is



**Direct Hydrocarbon Solid Oxide Fuel Cells, Fig. 2** Cell potential (*closed symbols*) and power density (*open symbols*) as a function of current density in dry H<sub>2</sub> (diamonds), C<sub>4</sub>H<sub>10</sub> (triangles), and CH<sub>4</sub> (circles) fuels at 700 °C. The cell had an LSM/YSZ cathode, 50 μm thick YSZ electrolyte, and 8/35/57 wt% La<sub>0.75</sub>Sr<sub>0.25</sub>Cr<sub>0.5</sub>Mn<sub>0.5</sub>O<sub>3-d</sub>/Cu/YSZ anode. (Reproduced with permission from [6]. Copyright 2008, The Electrochemical Society)

determined by the magnitude of the resistive processes within the cell electrodes and electrolyte. Assuming a constant cell temperature, electrolyte material, and electrolyte thickness, the cell current is maximized by minimizing losses associated with the reaction and transport in the electrodes. Since power is the product of potential and current, maximizing current at a high potential leads to maximum power output. The typical performance plot for an operating SOFC is a potential-current, or voltage-current (V-I) plot with accompanying power-current curve. An example is shown in Fig. 2 for an SOFC operating with H<sub>2</sub>, CH<sub>4</sub>, and *n*-C<sub>4</sub>H<sub>10</sub> fuels at 700 °C.

The most commonly utilized SOFC electrolyte is 8 mol% yttria-stabilized zirconia (YSZ). YSZ is utilized as it is an almost pure oxygen ion conductor with acceptable conductivity, and is stable in both anode and cathode gas environments. The cathode [7] is a mixture of an electron or mixed oxygen ion and electron conducting oxide and the YSZ electrolyte. Typical cathode materials include La<sub>0.2</sub>Sr<sub>0.8</sub>MnO<sub>3±δ</sub> (LSM) and the La<sub>1-x</sub>Sr<sub>x</sub>Co<sub>1-y</sub>Fe<sub>y</sub>O<sub>3-δ</sub> (LSCF) family. The traditional anode is a combination of Ni metal and YSZ, where Ni provides electronic conductivity and electrocatalytic activity [3].

Due to the high activation energy of ion transport in oxides, current SOFCs require operating temperatures greater than ~700 °C. This high-temperature operation is advantageous in increasing efficiency, enabling the use of relatively inexpensive transition metal and metal oxide catalysts, and removing the issue of CO poisoning that plagues low temperature cells. In addition, the total system efficiency can be increased by utilizing the waste heat to generate more electrical power in a secondary turbine process. However, higher operating temperatures present challenges with regard to balance of plant material costs, startup and shutdown times, and system lifetime.

Full optimization of single cells and cell stacks requires optimization of all components, which is far beyond the scope of a single entry. There are a number of excellent reviews available in the literature that discuss SOFC development [2, 8–10]. The focus of our discussion is the direct utilization of hydrocarbon fuels in SOFC anodes. As such, the discussion here is limited to the anode material challenges and potential solution pathways specific to this goal.

The challenge for researchers is to design electrode materials and composites that provide sufficient ionic and electronic conductivity, and selectively catalyze hydrocarbon fuel oxidation. These materials must operate at high temperatures in highly reducing environments. This entry first provides background regarding the specific challenges and a brief introduction to the relevant materials chemistry. This is followed by more detailed discussions of possible solution pathways, grouped into broad material classes.

## Background

### Anodes for Hydrocarbon Fuels

Irrespective of the power generation route, any method that seeks to maximize electrical energy output via oxidation of a hydrocarbon fuel will emit the carbon content of the fuel as CO<sub>2</sub>. This occurs irrespective of the number of intermediate chemical, electrochemical, or thermal steps. The goals for future power generation are thus to utilize both traditional fossil fuels and future bio-

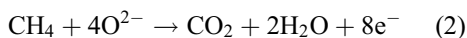
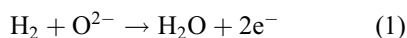
derived hydrocarbons, minimize the amount of fuel used and CO<sub>2</sub> emitted per unit of electrical energy generated, and to generate the CO<sub>2</sub> in a high purity and more easily sequestered form.

Since SOFCs transport the oxidant (oxygen anions) to the fuel, Fig. 1, SOFCs can theoretically operate with any oxidizable fuel that can be supplied to the anode. The simplest and most commonly researched SOFC fuel is H<sub>2</sub> [2]. However, H<sub>2</sub> is not a primary energy source with ~96% of industrial hydrogen generated via energy intensive endothermic steam reforming of hydrocarbons, primarily CH<sub>4</sub>. This is followed by high and low temperature water gas shift reactors to maximize H<sub>2</sub> production, and final product purification. The carbon content of the hydrocarbon is rejected as CO<sub>2</sub> at the point of H<sub>2</sub> generation. The remaining ~4% of industrial H<sub>2</sub> is generated by water electrolysis.

The energy used to produce H<sub>2</sub>, either by reforming or electrolysis, represents a parasitic load on the system that reduces efficiency and increases emissions. Furthermore, while hydrogen has a high mass-based energy density, the volumetric energy density is low and it is currently neither easily stored nor transported at the required scale. Direct utilization of hydrocarbon fuels would remove these barriers to fuel cell adoption and increase system efficiency.

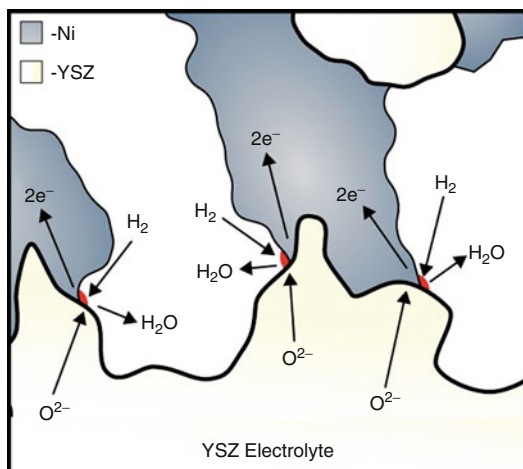
Utilization of CO and H<sub>2</sub> mixtures can be considered a first step along the path to direct utilization of hydrocarbons. As with production of pure H<sub>2</sub>, CO and H<sub>2</sub> mixtures are generated by hydrocarbon steam reforming. However, since the SOFC can utilize CO as a fuel, the water gas shift and H<sub>2</sub> purification steps are unnecessary. Hydrocarbon steam reforming can be performed either in an external reactor or internally on the SOFC anode itself. An external reactor operates as a typical hydrocarbon steam reforming system, while internal reforming requires addition of significant amounts of H<sub>2</sub>O or O<sub>2</sub> to the fuel prior to feeding into the cell anode compartment. While both approaches remove the hydrogen production, storage, and transport demands, the system complexity increases and efficiency decreases compared to the promise of direct hydrocarbon utilization.

The goal for direct hydrocarbon anode design is to realize the complete electrochemical oxidation of the fuel to the total oxidation products H<sub>2</sub>O and CO<sub>2</sub>. This represents the full conversion of the chemical energy potential in the fuel to electrical energy in a single process unit. Where only one oxidation reaction is feasible for H<sub>2</sub>, Eq. 1, hydrocarbons at high temperatures can undergo a large number of oxidation and polymerization reactions. The desired overall reaction is the total oxidation of fuel, shown in Eq. 2 for CH<sub>4</sub>, as this represents complete utilization of the fuel and generates the maximum moles of electrons per mole of fuel consumed.



By considering Eqs. 1 and 2, three clear requirements for SOFC anode materials can be derived. First, oxygen anion conductivity is required to transport the reactant oxygen anions to the reaction site. Second, the anode must selectively facilitate the desired electrocatalytic oxidation of the fuel. Third, facile electrical conductivity is required to transport the product electrons from the reaction site to the current collector wire. These material requirements are in addition to considerations of materials compatibility and stability during cell fabrication and operation, porosity in the electrode for fuel and product gas-phase diffusion, structural integrity, tolerance to impurities in the fuel and anode materials, and redox stability in case of accidental oxidation.

Current anodes for H<sub>2</sub> or humidified CO/H<sub>2</sub> fuelled SOFCs are Ni-YSZ composites. The electrolyte YSZ provides ionic conductivity, while metallic Ni is active for the oxidation of CO and H<sub>2</sub> and is a good electronic conductor. The operation of this anode is shown schematically in Fig. 3. Here operation with H<sub>2</sub> fuel is depicted, with the anode reaction given by Eq. 1. These electrodes are typically fabricated through slurry mixing and tape-casting of NiO and YSZ powders with or without pore former. The two materials are



**Direct Hydrocarbon Solid Oxide Fuel Cells, Fig. 3** Schematic of Ni-YSZ based anode operating with  $H_2$  fuel

then co-fired at high temperature ( $>1,450\text{ }^\circ\text{C}$ ) with the electrolyte. This is possible due to the high melting point of NiO ( $1,960\text{ }^\circ\text{C}$ ) and lack of solid state reaction between NiO and YSZ. One limitation of utilizing two components is that the anode reaction can only take place at the interfaces between the Ni, YSZ, and gas phases as these are the only points at which all of the anode requirements are met – *the triple phase boundary (TPB)* highlighted red in Fig. 3. This disadvantage can be overcome by careful electrode design in terms of porosity and Ni/YSZ particle sizes and interconnectivity, and Ni-YSZ anodes do provide low overpotentials, and thus high cell power output, for  $H_2$  and  $H_2/CO$  fuel mixtures.

The primary barrier to direct hydrocarbon utilization with these traditional anode materials is the activity of Ni toward the formation of graphitic carbon from dry hydrocarbons [11]. These carbon deposits rapidly build up in the anode structure and can generate sufficient stress to fracture the cell. While carbon formation can be suppressed by careful selection of cell operating parameters [12–16], this requires operating an inherently unstable system. For example, Barnett and coworkers demonstrated  $CH_4$  utilization on a Ni-YSZ composite anode by using the oxygen anion flux through the electrolyte to suppress

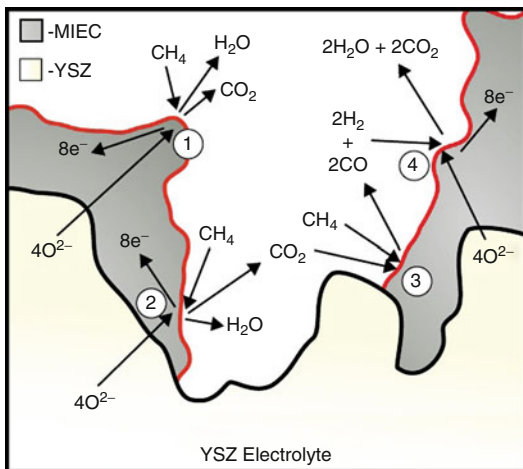
carbon formation [14]. This is impractical for application as the cell must be stable under all potential operating conditions. Thus a considerable effort has been expended to design materials and composites to replace Ni as the electronic and electrocatalytically active component.

### Oxidation of Hydrocarbons in SOFC

Almost all studies regarding direct hydrocarbon SOFCs show comparatively poor performance (lower OCP and higher polarization resistance) with hydrocarbon fuels when compared to  $H_2$  fuel, Fig. 2. Since most of these tests are performed by switching fuel on the same cell, the drop in performance must be linked to the anode. It is possible that the increased polarization resistance may be due to lower diffusivity of the hydrocarbon fuels, but the electrodes are typically highly porous and the current density per unit area is relatively low. In addition, the oxidation of 1 mole of hydrocarbon fuel yields a significantly greater number of electrons than 1 mole of  $H_2$  fuel ( $H_2$ ,  $CH_4$ , and  $C_4H_{10}$  total oxidation yield 2, 8, and 26 moles of electrons, respectively). Furthermore, the cell OCP is an equilibrium, zero current, measurement and is therefore not directly influenced by gas diffusivity. Therefore, it is unlikely that gas diffusivity limits the performance for pure fuels at low conversion. The conclusion must then be that the anode electrocatalytic activity toward hydrocarbon oxidation is the primary factor in reduced SOFC performance.

An ideal anode material would possess sufficient ionic conductivity, electronic conductivity, and electrocatalytic activity. With all of these properties present in a single mixed ionic-electronic conducting (MIEC) phase, the entire anode surface within the active region close to the electrolyte would be active toward fuel oxidation. This is depicted for  $CH_4$  fuel in Fig. 4 with the active surface highlighted in red. The thickness of this active region would be dictated by the relative rates of oxygen ion transport and surface reaction rate [17]. If the surface reaction selectivity were 100% toward total oxidation of hydrocarbon fuel, it may be anticipated that all reactions would follow pathway 1 in Fig. 4. In this case,





**Direct Hydrocarbon Solid Oxide Fuel Cells, Fig. 4** Simplified schematic of an idealized MIEC-YSZ based anode operating with  $\text{CH}_4$

oxygen anions migrate from the electrolyte to the MIEC phase, and are utilized to oxidize  $\text{CH}_4$  to  $\text{CO}_2$  and  $\text{H}_2\text{O}$  in an electrocatalytic surface reaction. The product gases diffuse out of the anode pores with product electrons conducted through the MIEC phase to the surface current collector.

While a number of groups are pushing toward this goal, the idealized MIEC material shown in Fig. 4 has not yet been realized. All of the current materials are lacking in one or more of the critical material requirements. An alternative approach to seeking one multifunctional material is to utilize an increasing number of materials, each one meeting one or more requirements. As with the Ni-YSZ anode for  $\text{H}_2$  and  $\text{CO}$  fuels, the combination of materials meets all of the anode requirements and can provide high performance. However, more solid phases lead to increased complexity of the anode mechanism and increased complexity in device fabrication to ensure sufficient contact between phases.

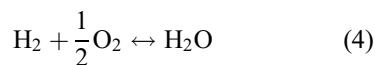
In reality, it is unlikely that the catalyst will be 100% selective and it is also difficult to perceive that the required eight-electron charge transfer reaction will occur at a single point on the catalyst surface. Pathway 1 in Fig. 4 represents an idealized view of the target process. There are numerous alternative reaction pathways, one of which is highlighted by the steps 2–4 in Fig. 4. In this case,

total oxidation of methane occurs as in step 1 above; however, the product  $\text{CO}_2$  can react further in a dry reforming reaction with more  $\text{CH}_4$  to form  $\text{CO}$  and  $\text{H}_2$ , step 3. These products then undergo further electrocatalytic oxidation to  $\text{CO}_2$  and  $\text{H}_2\text{O}$ , step 4. This is, again, a representative oversimplification that serves only to demonstrate the complexity of the system. The number of possible reaction pathways for fuel oxidation is very large as products, intermediates, and reactants interact and compete for active heterogeneous reaction sites, and undergo homogeneous gas-phase reactions at SOFC temperatures. This complexity only increases as the C-number of the hydrocarbon fuel is increased. Fully unraveling all of these possible reactions and their contributions toward determining fuel cell performance is very challenging.

Some insight into the dominant reaction in the anode can be provided by the cell OCP. The theoretical OCP for an electrochemical cell is given by the Nernst equation. For a cell conducting oxygen anions, this is given by:

$$E = -\frac{RT}{2F} \ln \frac{f_{\text{O}_2}^{1/2(a)}}{f_{\text{O}_2}^{1/2(c)}} \quad (3)$$

The fugacity of oxygen at the cathode is usually well determined as the cathode is typically exposed to air. For the anode side of the cell, the fugacity will be set by the reaction equilibria between the fuel and oxidation products. This is well defined for  $\text{H}_2$  fuel as only one reaction can occur:



Substituting this equilibrium expression for the anode fugacity and assuming an ideal gas yields:

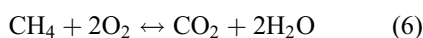
$$E = E^0 - \frac{RT}{2F} \ln \frac{P_{\text{H}_2\text{O}}^{(a)}}{P_{\text{H}_2}^{(a)} P_{\text{O}_2}^{1/2(c)}} \quad (5)$$

where  $E^0$  is the standard potential for the fuel oxidation reaction at the temperature of interest.



The theoretical OCP for humidified H<sub>2</sub> at 700 °C is 1.122 V and an H<sub>2</sub>-fuelled cell should generate this well-defined OCP. Oxygen (or air) leaks through poor cell sealing or residual porosity in the electrolyte should be avoided as they will increase the oxygen fugacity at the anode and decrease the cell OCP. Electronic conductivity within the electrolyte will also reduce the OCP due to the presence of an electrical short circuit within the electrolyte. However, a well-constructed and sealed YSZ-based SOFC will generate the theoretical OCP for hydrogen fuel as YSZ is an almost pure ionic conductor.

The equivalent theoretical anode oxygen fugacity for hydrocarbon fuels is not set by a simple reaction equilibrium due to the complex reaction chemistry of these fuels. There are a large number of elementary steps, potential reaction pathways, and reaction intermediates. The most desirable reaction is the total oxidation of CH<sub>4</sub> to CO<sub>2</sub> and H<sub>2</sub>O, Eq. 2. This provides both the highest OCP value and represents full utilization of the fuel. If the catalyst is 100% selective for this reaction, the anode oxygen chemical potential will be set by this reaction equilibrium:

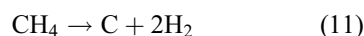
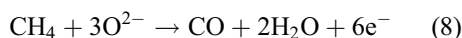


In this case, the cell OCP would be fully defined by substituting this equilibrium expression into Eq. 3 to yield:

$$E = E^0 - \frac{RT}{8F} \ln \frac{P_{\text{H}_2}^{2(a)} P_{\text{CO}_2}^{(a)}}{P_{\text{CH}_4}^{(a)} P_{\text{O}_2}^{2(c)}} \quad (7)$$

However, as discussed with reference to Fig. 4, the complexity is large, even for CH<sub>4</sub>. CH<sub>4</sub> can undergo total oxidation to CO<sub>2</sub> and H<sub>2</sub>O, Eq. 2, or partial oxidation to CO, H<sub>2</sub>, and/or H<sub>2</sub>O, Eq. 8. CH<sub>4</sub> may also undergo surface catalyzed steam or dry reforming with product CO<sub>2</sub> or H<sub>2</sub>O, Eqs. 9 and 10; react to form graphitic carbon and H<sub>2</sub>, Eq. 11; or undergo gas phase cracking and free radical polymerization to deposit tarlike residue. All of these reaction equilibria and chemical species combine to set the anode oxygen fugacity and

OCP. Furthermore, while it is desirable to selectively catalyze the electrochemical total oxidation of CH<sub>4</sub>, this reaction involves the transfer of eight electrons. It is difficult (if not impossible) to ensure that each of these steps will occur electrocatalytically without desorption and further non-electrochemical reaction of partial oxidation products:



The difficulty in defining fugacity, expected variation of anode catalyst reaction selectivity for heterogeneous reactions, and influence of anode gas residence time on the prevalence of homogeneous reactions leads to significant variation in reported cell OCP for hydrocarbon fuels. This also leads to some debate over the definition of “direct” oxidation or utilization. In this entry direct utilization refers to the direct feeding of a hydrocarbon fuel to the anode in the absence of significant diluent, H<sub>2</sub>O, CO<sub>2</sub>, or O<sub>2</sub>, as adopted by McIntosh and Gorte [1].

One barrier to enhancing electrocatalytic activity is the current lack of knowledge regarding the electrocatalytic fuel oxidation mechanism in the anode. There are very few studies in the literature that seek to understand the mechanistic details of this process. In large part this is due to the complexity of the anode system and the relatively extreme anode operating environment. A classical surface science approach is not applicable to the study of SOFC systems. Many of the materials of interest have variable oxygen stoichiometry that controls the ion-electron conductivity and, most likely, catalytic properties of the material. Since oxygen stoichiometry is set by the gas-phase  $p\text{O}_2$ , temperature, and local electrochemical environment, measurements made under vacuum or at low temperature outside of a working electrochemical system are difficult, if not impossible, to relate to the performance and mechanisms of

working SOFC. While one of the most intriguing and challenging aspects of SOFC systems is the unique environment in which the materials are placed, this environment presents considerable challenges to the researcher. For example, while rates of non-electrocatalytic reactions on a powder catalyst sample can be measured, it is not currently possible to accurately probe surface intermediate species under an applied potential. While some groups have attempted to relate externally measured activity to SOFC performance [6, 18–22] and have made steps toward measurements under realistic operating conditions [20], the current lack of in-situ spectroscopic tools is a significant barrier toward rational design of new SOFC electrocatalysts.

### Structures and Defect Chemistry

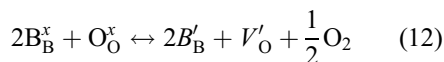
The majority of new materials for SOFCs are perovskite structured oxides of general form  $ABO_{3-\delta}$  [23]. The ideal perovskite structure is a cubic close-packed  $ABO_3$  structure where the B-site cation sits within the octahedral interstices, Fig. 5. This structure is very flexible toward cation composition and tolerates large substitution fractions on either cation site. The Goldschmidt factor, a ratio of A, B, and O ionic radii, is often utilized to predict if a metal oxide will crystallize into the perovskite structure [24]. The A site of the commonly utilized perovskites is typically occupied by La, Ca, Sr, or Ba. The B site is typically a transition metal. Other structures investigated include double perovskites, apatites, and fluorites.

There are a number of excellent reviews and thorough treatments of the defect chemistry of oxides available in the literature, e.g., [25]. The brief overview below serves only to introduce the reader to primary concepts as a basis to the discussion in the rest of this entry. The following discussion is restricted to point defect models as these are predominant for most of the materials discussed.

Oxygen ion transport in these mixed oxides occurs primarily via oxygen anion hopping between oxygen vacancies. Cubic crystal structures are often considered desirable as all of the oxygen sites are geometrically equivalent. Structures with ordered oxygen vacancies may provide

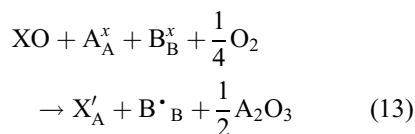
rapid transport through vacancy “channels” but perpendicular transport is frustrated by the ordered structure. In the absence of vacancy trapping or significant structural changes, ionic conductivity increases with increasing density of vacant oxygen sites and increasing mobility. Oxygen vacancies in these oxides are typically denoted as a deviation from the fully occupied lattice, the  $\delta$  in  $3-\delta$ . Oxygen vacancies are formed either by reduction of a cation and/or by aliovalent doping.

Considering the very general system  $A^{3+}B^{3+}O_{3-\delta}^{2-}$ , a fully stoichiometric oxygen sublattice,  $\delta = 0$ , will exist while the combined charge on the A and B-sites is  $6+$ , balancing the negative charge on the three  $O^{2-}$  anions. At elevated temperature and/or reduced gas-phase oxygen partial pressure,  $pO_2$ , the B-site transition metal cation may be reduced with the concomitant formation of oxygen vacancies. In Kröger–Vink notation:



In addition to providing a mechanism for oxygen anion conduction, these oxygen vacancies can act as intrinsic electronic donors, with electronic conductivity occurring via a hopping mechanism between B and  $B'$  sites.

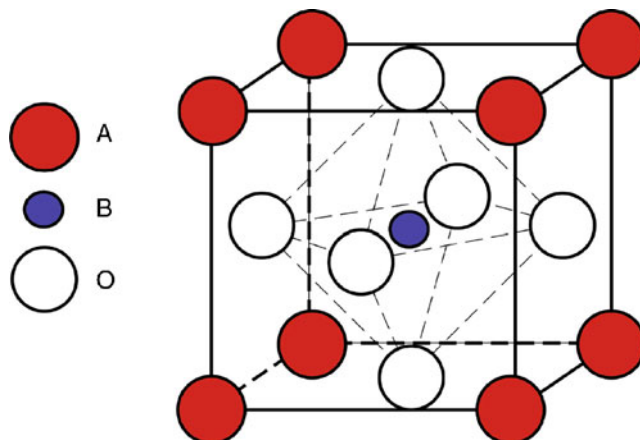
An alternative approach to generate oxygen vacancies is aliovalent substitution of the element on the A or B site. For example, upon substituting  $X^{2+}$  for  $A^{3+}$ , the difference in charge can be compensated by two different mechanisms. The substitution can be compensated for through a change in the oxidation state of B to maintain a fully occupied oxygen sublattice:



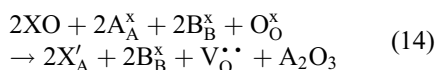
In this case the number of electronic carriers is increased. Alternatively, the B site can maintain a constant charge and the A-site substitution is

### Direct Hydrocarbon Solid Oxide Fuel Cells,

**Fig. 5** Schematic of the cubic perovskite structure



compensated through the formation of oxygen vacancies:



The dominant compensation mechanism, either cation reduction or vacancy formation, is a function of  $pO_2$  and temperature. Thus by selecting materials with differing reducibility in the anode environment, electronic, ionic or mixed ionic, and electronic conductors can be created. An example of oxygen nonstoichiometry data for a candidate anode material is shown in Fig. 6. Note that the oxygen stoichiometry decreases with decreasing  $pO_2$  and increasing temperature within the typical anode  $pO_2$  and temperature range.

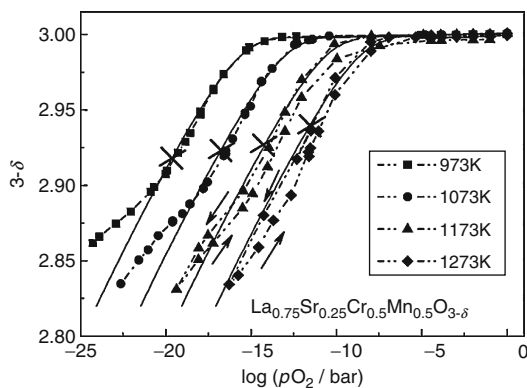
### Electronic Conductivity for Direct Hydrocarbon Anodes

In order to minimize ohmic losses in the anode, the composite structure should have an electronic conductivity greater than 100 S/cm [4]. One option is to replace Ni with a metallic phase that is inert toward catalyzing carbon formation. This is the approach adopted by Gorte, Vohs and coworkers who developed direct hydrocarbon anodes utilizing Cu as the electronic conductor [1]. While this approach is very promising, the list of usable metals is very short as most transition metals either catalyze carbon formation or are prohibitively expensive.

An alternative approach, and one with a wide possible material palette, is to develop stable and highly conductive oxides. The primary challenge is to meet the required target conductivity for both the pure material and a composite. When mixed with an electrolyte, the overall composite electronic conductivity will be considerably lower. Most attempts at this seek to boost the density of p-type carriers in the base lattice by substitution with lower valence cations. Charge compensation upon doping can be either electronic or ionic, and  $n$  or  $p$ -type conductors can be pursued. Details specific to each material are discussed within the relevant sections in this entry.

### Poisoning and Stability

Homogenous gas-phase cracking and subsequent free radical polymerization of hydrocarbon fuels at SOFC operating temperatures leads to the formation of tarlike carbon in the anode compartment [27]. This can lead to blocking of anode active sites but can also lead to improvements in anode electronic conductivity [27, 28]. This is an inherent property of hydrocarbon fuels and, as such, is a hurdle toward long-term operation for any hydrocarbon fuelled SOFC. Methods to control this carbon deposition include utilizing more stable hydrocarbons (typically  $CH_4$ ), reducing cell operating temperature, co-feeding diluent or steam, or develop anodes that aid in removing these deposits by oxidation, steam reforming, and/or dry reforming with product  $H_2O$  and/or  $CO_2$ . It is essential to distinguish between this



**Direct Hydrocarbon Solid Oxide Fuel Cells, Fig. 6** Oxygen non-stoichiometry of  $\text{La}_{0.75}\text{Sr}_{0.25}\text{Cr}_{0.5}\text{Mn}_{0.5}\text{O}_{3-\delta}$  as a function of  $p\text{O}_2$  and temperature. (Reprinted from [26] with permission from Elsevier)

tar-like carbon formation and the catalytic formation of graphitic carbon that occurs on Ni-based anodes. This catalytic graphite formation is a property of Ni metal and must be avoided through the design of new anode materials and composites.

In addition to these undesirable side reactions, impurities in the feed must also be considered. Sulfur can be a significant poison, with its exact concentration and form dependent on the source of hydrocarbon fuel. While sulfur can be removed by preprocessing, at the time of writing (2010), the US Environmental Protection Agency requires a refinery average sulfur content of gasoline fuel of 30 ppm or lower, with a per gallon cap of 80 ppm. Pacific Gas and Electric Company in California allows a total sulfur content of 17 ppm. A number of additional impurities must be considered if coal is to be used as the carbon feedstock, including P, K, Ni, and Cl. While their influence on Ni-based anodes has been considered [29–31], this issue has not been addressed for other anode materials.

### Copper-Ceria

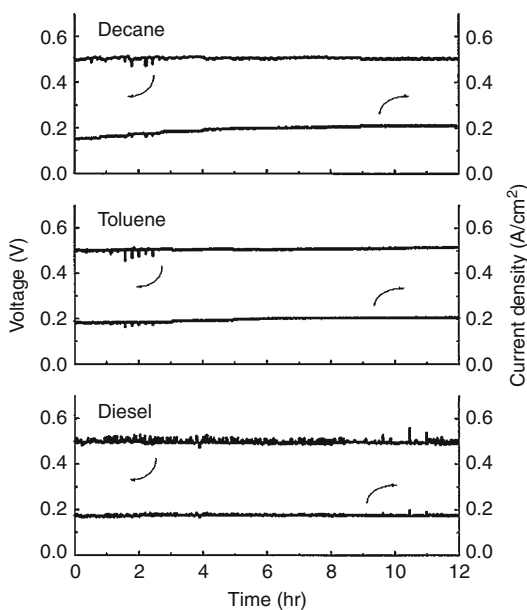
Gorte, Vohs, and coworkers at the University of Pennsylvania pioneered the use of Cu-CeO<sub>2</sub>-YSZ composite anodes for direct hydrocarbon

utilization [1]. Their approach was to separate the anode material requirements between three materials: Cu to provide electronic conductivity without catalyzing graphitic carbon formation, CeO<sub>2</sub> to catalyze the oxidation of hydrocarbon fuel, and YSZ to provide ionic conductivity. These anodes cannot be manufactured utilizing the co-firing approach used for Ni/YSZ due to the relatively low melting point of CuO (1,336 °C). Instead the anodes are fabricated by tape-casting a slurry of YSZ with pore formers [32]. This layer is then co-fired with the electrolyte to form a dense YSZ electrolyte supported on a thicker porous YSZ “skeleton.” Following addition of the cathode, the CeO<sub>2</sub> and Cu phases are added via wet infiltration of metal nitrate salts followed by low temperature calcination (450 °C). This infiltration approach to anode manufacture enables the incorporation of anode materials at lower temperatures. This expands the potential materials palette to materials that would either melt, sinter heavily, decompose, or react with YSZ during high temperature sintering of the YSZ phase. This is a flexible technique that has been demonstrated for both anode and cathode manufacture [33–35]. The largest potential drawback is the time-consuming procedure of adding salt solutions, firing, and repeating until sufficient weight-loading is reached. The associated increases in cell performance must be weighed against increased manufacturing costs.

The ability to utilize hydrocarbon fuels is clearly an advantage to this approach. Cu-CeO<sub>2</sub>-YSZ anodes have been demonstrated to operate with hydrogen fuel and via direct utilization with a range of hydrocarbon fuels from CH<sub>4</sub> to synthetic diesel fuel. Figure 7 shows operation of these cells with a variety of hydrocarbon fuels.

### Conductivity

The YSZ in the Cu-CeO<sub>2</sub>-YSZ composite anode is present as the primary ionic conductor. Since YSZ is a pure electrolyte, the electronic conductivity of the anode must be provided by a second phase. Although reduced CeO<sub>2</sub> has an electronic conductivity of greater than 1 S/cm at 1,000 °C [37], the electronic conductivity in a 15 vol% CeO<sub>2</sub>-YSZ composite was only 0.019 S/cm at



**Direct Hydrocarbon Solid Oxide Fuel Cells, Fig. 7** Cell voltage and current density versus time at 700 °C for a cell with 10/20/70 wt% CeO<sub>2</sub>/Cu/YSZ anode with various hydrocarbon fuels. (Reproduced with permission from [36]. Copyright 2001, The Electrochemical Society)

700 °C in H<sub>2</sub> [38]. While this low electronic conductivity of CeO<sub>2</sub>/YSZ composites is sufficient in a thin anode functional layer [39], a thicker anode structure requires higher electronic conductivity in order to minimize ohmic losses. As such, an additional phase is required. Unlike Ni, Cu does not catalyze the formation of graphitic carbon deposits in the anode, thus enabling the cell to operate with dry hydrocarbon fuel feed.

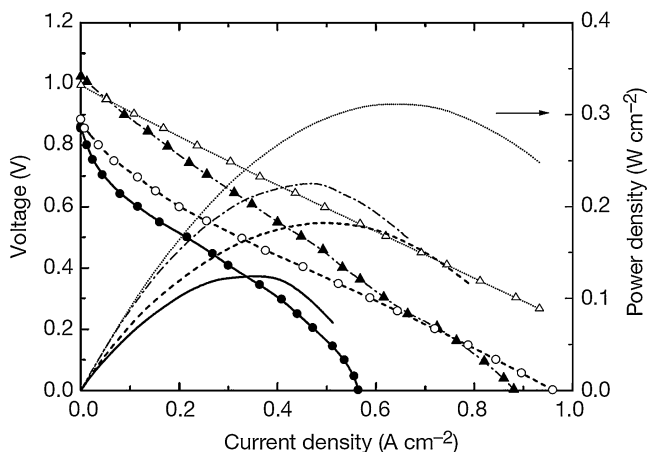
It should also be noted that the electronic conductivity of a porous YSZ-based composite electrode will be significantly lower than that of the pure electronic conducting phases due to the porous and electron blocking YSZ. The loading of the electronic conductor required in the anode composite is dictated by percolation considerations. The electronic conductivity of a 15 vol% Cu-YSZ composite can be as high as 1,190 S/cm [38]. It should be noted that 15 vol% is much lower than the >40 vol% Ni typically utilized in Ni-YSZ anodes. This decrease in required metal loading is due to the difference in fabrication

procedure. The Ni-YSZ powder processing leads to random mixing of the two phases and >40 vol % Ni is required to ensure percolation [3, 40]. In contrast, wet infiltration of Cu salt solution into a preformed porous YSZ structure leads to coating of the pore walls and formation of contiguous conducting pathways at lower volumetric loading. The electronic conductivity of the composite is thus a strong function of Cu loading, and the infiltration must be controlled to form the desired Cu structure [38].

Although Cu does not catalyze graphite formation, most hydrocarbon fuels undergo gas-phase free radical polymerization when fed undiluted into the anode compartment at SOFC operating temperatures. The long-chain and aromatic [22] products of this polymerization lead to tar-like deposits within the Cu-CeO<sub>2</sub>-YSZ anode structure. While excessive deposition of these compounds may lead to blocking of the active sites within the anode, their electronic conductivity has a beneficial influence by reducing ohmic losses within the anode. McIntosh et al. [27] examined the performance of SOFCs with varying Cu loading before and after exposure to dry *n*-C<sub>4</sub>H<sub>10</sub> at 700 °C for 30 min. It was found that the initial ohmic resistance of cells with 10 wt% CeO<sub>2</sub> and either 5, 10 or 20 wt% Cu in H<sub>2</sub> fuel at 700 °C was significantly higher than that calculated for the YSZ electrolyte (i.e., there was a significant ohmic resistance in the electrodes). For the cell with 20 wt% Cu, the ohmic resistance decreased dramatically upon exposure to *n*-C<sub>4</sub>H<sub>10</sub>, reaching the value predicted for the YSZ electrolyte. A cell with 10 wt% CeO<sub>2</sub> and 30 wt% Cu showed no change in ohmic resistance, matching that of the electrolyte before and after exposure to *n*-C<sub>4</sub>H<sub>10</sub>. This shift in ohmic resistance was ascribed to bridging gaps between isolated Cu particles with conducting tar-like carbon deposits. Indeed, further work [21] demonstrated operation of Cu-free cells utilizing only these deposits as the predominant electronic conductor.

### Catalysis

While Cu can be utilized as a catalyst, it does not contribute significantly to the overall catalytic activity of the anode. This was verified by the



**Direct Hydrocarbon Solid Oxide Fuel Cells, Fig. 8** SOFC performance curves for cells with Cu-ceria composite anode. The cell had a 60- $\mu\text{m}$  electrolyte, and data are shown for the following fuels: *filled circles*,

*n*-butane at 700 °C; *open circles*, *n*-butane at 800 °C; *filled triangles*,  $\text{H}_2$  at 700 °C; and *open triangles*,  $\text{H}_2$  at 800 °C. (Reprinted by permission from Macmillan Publishers, Ltd.: Nature [43], copyright 2000)

low performance of Cu-only anodes, particularly in hydrocarbon fuels [22], and the identical performance achieved when Cu is replaced with catalytically inert bulk Au [41]. The role of  $\text{CeO}_2$  as electrocatalyst for fuel oxidation was confirmed by replacing  $\text{CeO}_2$  with other lanthanide oxides and comparing SOFC performance with the activity of the lanthanide toward fuel oxidation [22]. The cell performance tracked well with the  $n\text{-C}_4\text{H}_{10}$  light-off temperature of the lanthanide.

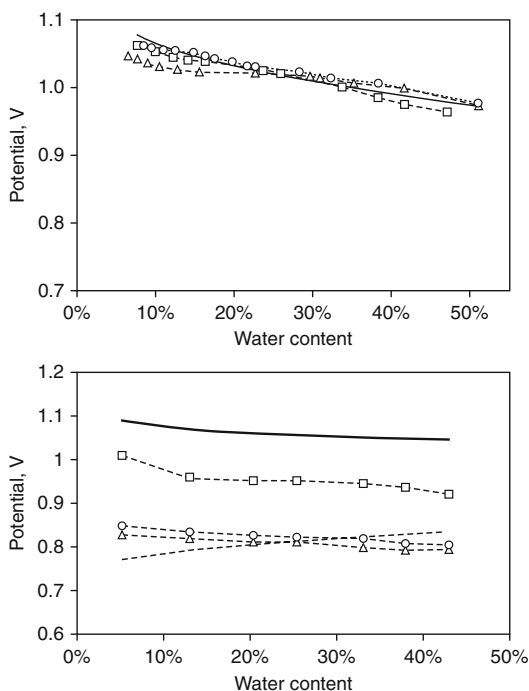
The performance of Cu- $\text{CeO}_2$ -YSZ based cells (in terms of both cell OCP and maximum power density) is consistently lower for hydrocarbon fuels than for  $\text{H}_2$ . For example, Park et al. [42] reported cell OCP values of 1.05 and 0.9 V respectively for  $\text{H}_2$  and  $\text{CH}_4$  fuels at 700 °C, with corresponding maximum power densities of 0.32 and 0.09  $\text{W}/\text{cm}^2$ . A similar decrease is observed when comparing  $\text{H}_2$  and *n*-butane fuel, Fig. 8. Kim et al. reported [36] a cell OCP of 1.1 V with current density at 0.5 V of 0.5  $\text{A}/\text{cm}^2$  at 700 °C in  $\text{H}_2$  fuel; these values decreased to 0.8 V and 0.2  $\text{A}/\text{cm}^2$  in 35 vol% toluene/ $\text{N}_2$  fuel at the same temperature on the same SOFC.

Since the cathode and electrolyte are constant between tests, the electrocatalytic activity of the anode is the primary cause of this decrease. This limitation was partially overcome by utilizing precious metal dopants in the anode [21]. The

addition of 1 wt% Pd added to a C- $\text{CeO}_2$ -YSZ anode resulted in the same OCP, polarization resistance, and hence power density for  $\text{CH}_4$  and  $\text{H}_2$  fuels. The OCP in  $\text{CH}_4$  increased from 1.0 V to 1.25 V and the maximum power density increased from 20 to 280  $\text{mW}/\text{cm}^2$  upon the addition of 1 wt % Pd to nominally identical anodes. This was attributed to the enhanced electrocatalytic activity of Pd- $\text{CeO}_2$  toward  $\text{CH}_4$  oxidation compared to pure  $\text{CeO}_2$ . It should be noted that this cell utilized carbonaceous deposits as the electronic conducting component in the anode due to alloying between Pd and Cu. This result also suggests that care must be taken when utilizing precious metal current collectors to assess the performance of novel anodes. The current collector may inadvertently contribute significant catalytic activity to the anode.

While the influence of the electrocatalyst on cell power output is clear and trends in oxidation activity measured by traditional means track with cell performance, very little is known about the fundamental reaction mechanism occurring in the anode. As discussed above, the thermal stability of hydrocarbons toward homogeneous cracking and free radical polymerization decreases with increasing carbon number. At SOFC operating temperatures, most hydrocarbons will readily undergo these gas-phase reactions in the hot





**Direct Hydrocarbon Solid Oxide Fuel Cells, Fig. 9** OCP as a function of H<sub>2</sub>O content in H<sub>2</sub>-H<sub>2</sub>O (top) feed and CH<sub>4</sub>-CO<sub>2</sub>-H<sub>2</sub>O (bottom) feed with CH<sub>4</sub>: CO<sub>2</sub> ratio of 8. The calculated Nernst potentials for total oxidation of fuel are shown as bold lines (both figures) while the dashed line assumes reforming to form H<sub>2</sub> (bottom). Experimental results are shown for: C-ceria-YSZ (triangles); Cu-ceria-YSZ (circles); and C-Pd-ceria-YSZ (squares) anodes. (Reproduced with permission from [21]. Copyright 2003, The Electrochemical Society)

areas of the fuel feed system and in the anode pores. Examining the OCPs reported for *n*-C<sub>4</sub>H<sub>10</sub> and longerchain hydrocarbons on Cu-CeO<sub>2</sub> anodes finds that the OCPs are all very similar at around 0.8 V [28]. This suggests that the fuel species reaching the anode and the reactions occurring are similar for all these fuels, which makes sense when considering thermal cracking.

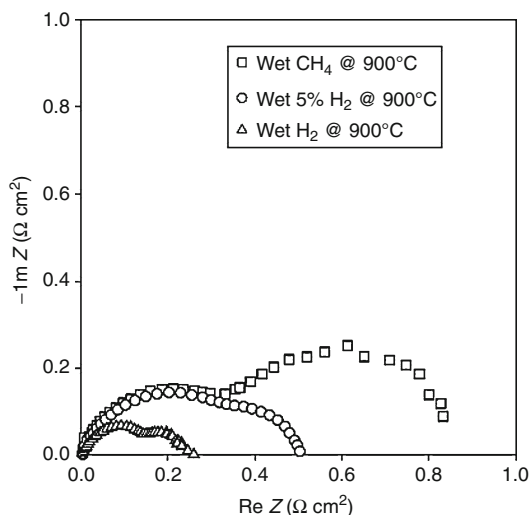
McIntosh et al. [21] studied the trend of OCP with CO<sub>2</sub> and H<sub>2</sub>O content for H<sub>2</sub>, CH<sub>4</sub>, and *n*-C<sub>4</sub>H<sub>10</sub> fuels with CeO<sub>2</sub>-C-YSZ anodes with and without the addition of Pd. For H<sub>2</sub>, the trend of OCP with H<sub>2</sub>O content for both anodes tracked the theoretical trend for total oxidation, as this is the only reaction equilibrium that can be established for H<sub>2</sub> fuel. For CH<sub>4</sub>, Fig. 9, the trend for Pd-free anodes more closely follows the

trend expected if CH<sub>4</sub> first undergoes reforming with the feed CO<sub>2</sub> and H<sub>2</sub>O and it is the product H<sub>2</sub> that reacts at the anode. The trend line was calculated assuming the equilibrium amount of H<sub>2</sub> interacts with the anode. Upon addition of Pd, the measured OCP increased, with the trend line lying between the trend lines calculated for the reforming based mechanism of Pd-free electrodes and for direct CH<sub>4</sub> oxidation. This suggests that Pd-CeO<sub>2</sub> is active toward direct oxidation of CH<sub>4</sub>. While an increase in OCP was measured upon addition of Pd for *n*-C<sub>4</sub>H<sub>10</sub> fuel, the increase was smaller. In addition, it was shown [27, 28] that the tar-like hydrocarbons formed by free radical polymerization are deposited in the anode structure of SOFCs with these longer-chain hydrocarbon fuels. It is likely that these deposits are the primary interaction species at OCP, even with precious metal catalyst dopants, but they may be removed from the active sites in the anode via oxidation with product H<sub>2</sub>O under cell operation [28, 44].

### Poisoning and Stability

The sulfur tolerance of these anodes is primarily dictated by the thermodynamics of ceria sulfide and oxysulfide formation, as the sulfur concentration required for Cu<sub>2</sub>S formation is significantly higher [45]. Kim et al. demonstrated that stable operation could be achieved if the sulfur level in the fuel is reduced to 100 ppmv S as thiophene in 5 mol% *n*-C<sub>10</sub>H<sub>22</sub> – this is below the concentration predicted from thermodynamics for Ce<sub>2</sub>O<sub>2</sub>S formation. This study was followed by work of He et al. who demonstrated stable operation up to 450 ppmv H<sub>2</sub>S in H<sub>2</sub> [46], significantly higher than the tolerance levels reported for Ni-based anodes [47].

As these cells operate at temperatures relatively close to the melting point of Cu (1,085 °C), concerns have been raised regarding the thermal stability of Cu. While Cu will sinter at SOFC operating temperatures, the thermal stability of the Cu phase is shown to be a strong function of the infiltration technique and precursor. These parameters influence the distribution of Cu throughout the anode structure [38]. Alloying



**Direct Hydrocarbon Solid Oxide Fuel Cells, Fig. 10** Electrode impedance of an optimized  $\text{La}_{0.75}\text{Sr}_{0.25}\text{Cr}_{0.50}\text{Mn}_{0.50}\text{O}_{3-\delta}$  anode at 900 °C, in different humidified fuel gas compositions. The electrolyte contribution has been subtracted from the overall impedance. (Reprinted by permission from Macmillan Publishers, Ltd.: Nature Materials [52], copyright 2003)

may be utilized to increase the melting point, although alloy metals and alloy level must be chosen carefully in order to avoid nullifying the benefits of Cu with regard to graphitic carbon formation. Kim et al. [48] demonstrated the use of Cu-rich Ni alloys in preventing graphitic carbon formation and showed 500 h of operation in dry  $\text{CH}_4$  with 80–20 mol% Cu-Ni replacing Cu in the anode. Lee et al. [49] expanded this to include Cu-Co based anodes and proposed that segregation and subsequent surface coverage of the Co by a Cu layer provided stable operation with dry hydrocarbon fuels. With regard to the  $\text{CeO}_2$  phase, doping with Zr has been shown to significantly enhance thermal stability [50].

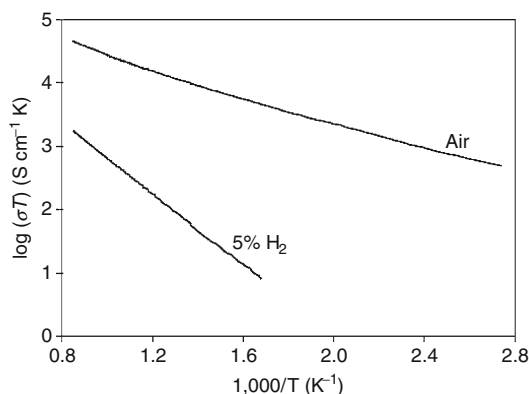
### Lanthanum Chromates

Lanthanum chromate ( $\text{LaCrO}_{3-\delta}$ ) is a reasonable electronic conductor and is stable up to high temperatures (> 1,000 °C) in both oxidizing and reducing ( $p_{\text{O}_2} < 10^{-21}$  atm) environments [51]. Perhaps the most promising

material in the  $\text{LaCrO}_{3-\delta}$  family so far is  $\text{La}_{0.75}\text{Sr}_{0.25}\text{Cr}_{0.50}\text{Mn}_{0.50}\text{O}_{3-\delta}$  (LSCM). Single phase LSCM anodes showed low anode polarization resistances, 0.26 and 0.87  $\Omega\cdot\text{cm}^2$  in humidified  $\text{H}_2$  and  $\text{CH}_4$ , respectively, at 900 °C [52], Fig. 10. High power densities, 0.86 and 0.48  $\text{W}/\text{cm}^2$ , were observed for SOFC with LSCM/Cu composite anodes in 850 °C  $\text{H}_2$  and  $\text{CH}_4$ , respectively [53]. Note that electrolyte thickness, electrode geometry, and cathode material can dictate power density as much as anode material, and that power densities should only be compared between nominally identical cells.

As  $(\text{La,Sr})\text{CrO}_3$  itself is not catalytically active toward hydrocarbon oxidation [54], Cr has been partially substituted with a variety of elements, limited mostly to first-row transition elements (Ti, V, Mn, Fe, Co, and Ni) and Ru, in an effort to enhance catalytic activity [55–58]. These substitutions significantly impact the stability of the perovskites.  $(\text{La,Sr})\text{CrO}_3$  with 5–25 mol% of Ru [59] on the B site or with large amounts (20–50 mol%) of Co [56], Fe [60] or Ni [56, 61] substituting for Cr are unstable, as the dopant cations exsolve from the perovskite lattice under reducing conditions.  $\text{LaCrO}_3$  substituted with Ti is stable in reducing and oxidizing conditions, but has poor catalytic activity for fuel oxidation [56], showing large polarization resistances when used as anodes [62]. This is likely due to the low redox activity of Ti. Finally, the introduction of significant amounts ( $\geq 10$  mol%) of V into the  $(\text{La,Sr})\text{CrO}_3$  lattice requires firing in highly reducing conditions [19]. It is likely that, as with LSV, V-substituted lanthanum chromates will not be stable in air [63].

The best substituent for Cr seems to be Mn, as LSCM shows stable performance in humidified  $\text{CH}_4$  at 900 °C [64], and has some catalytic activity for the total oxidation of hydrocarbons [65]. Although Zha et al. [66] reported that LSCM was stable in pure  $\text{H}_2$  at 950 °C ( $p_{\text{O}_2} < 10^{-20}$  atm), Kawada found significant quantities of the decomposition products  $\text{LaSrMnO}_4$  and  $\text{MnO}$  in LSCM pellets after thermogravimetric measurements at lower temperatures and under less reducing conditions



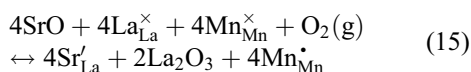
**Direct Hydrocarbon Solid Oxide Fuel Cells, Fig. 11** Temperature ( $T$ ) dependence of total conductivity ( $\sigma$ ) of  $\text{La}_{0.75}\text{Sr}_{0.25}\text{Cr}_{0.5}\text{Mn}_{0.5}\text{O}_{3-\delta}$  in air and 5%  $\text{H}_2$ . (Reprinted by permission from Macmillan Publishers, Ltd.: Nature Materials [52], copyright 2003)

(900 °C,  $p\text{O}_2 = 10^{-20}$  atm) [26]. The same phases were encountered by other researchers after treating LSCM powder in humidified 20%  $\text{H}_2/\text{N}_2$  at 800 °C for 8 h [19]. These differences are expected to be due to variations in treatment times and synthesis procedures. The results indicate that LSCM may not be completely stable in pure fuel at very high temperatures. However, the actual  $p\text{O}_2$  values in a working anode are expected to be higher than the  $p\text{O}_2$  in the surrounding atmosphere due to the transport of oxygen through the SOFC, which could stabilize the anode material.

### Conductivity

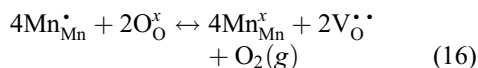
The total conductivity of  $\text{La}_{0.75}\text{Sr}_{0.25}\text{Cr}_{0.50}\text{Mn}_{0.50}\text{O}_{3-\delta}$  was reported to be ~40 S/cm in air, and 1.5 S/cm in 5%  $\text{H}_2$  at 900 °C [64, 67] Fig. 11. While constant at high  $p\text{O}_2$ , total conductivity decreased sharply for  $p\text{O}_2 < 10^{-10}$  atm [67], indicative of  $p$ -type conductivity [64, 68]. Positive values for the Seebeck coefficient under oxidizing conditions confirmed that conductivity in LSCM is  $p$ -type dominant [67, 69]. At low temperatures and in high  $p\text{O}_2$  atm, the net negative charge created by the substitution of  $\text{La}^{3+}$  with  $\text{Sr}^{2+}$  is compensated by an increase in the average oxidation state of Mn,

generating electron holes localized on Mn that are responsible for electronic conductivity [68], Eq. 15.



The activation energy for the conductivity is on the order of 0.1 eV, indicative of conduction through a thermally activated polaron-hopping mechanism.

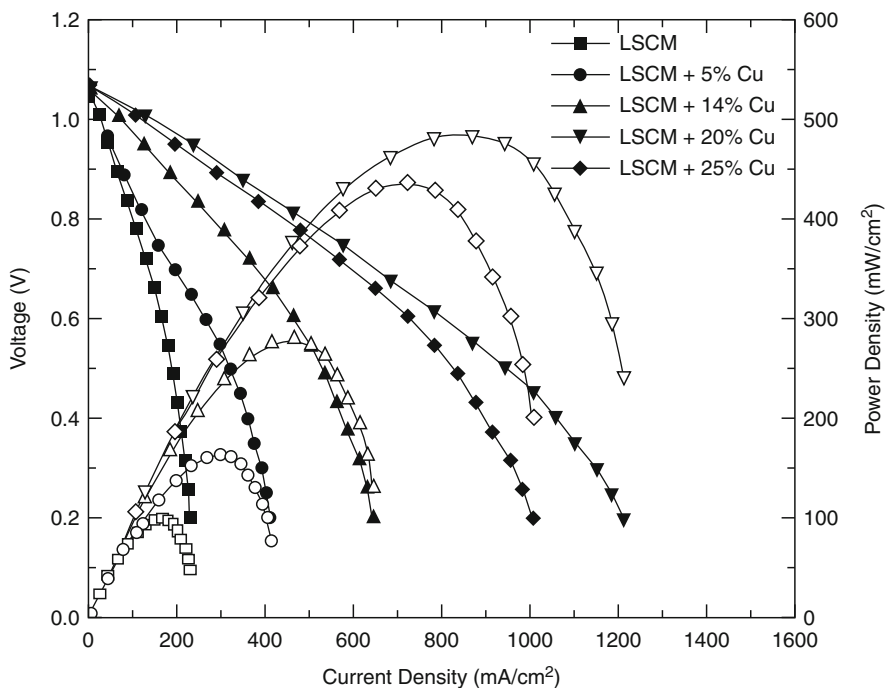
At elevated temperatures and in low  $p\text{O}_2$  atm, Mn is reduced in average oxidation state and the net negative charge is now compensated by the formation of oxygen vacancies, Eq. 16, Fig. 6.



The decrease in electron holes, evident from Eq. 16, results in a decrease in total conductivity in atmospheres with  $p\text{O}_2 < 10^{-10}$  [67, 70]. Due to the generation of oxygen vacancies, this decrease is accompanied by an increase in oxygen ion conductivity, from  $\sim 4 \times 10^{-5}$  S/cm at high  $p\text{O}_2$  to  $\sim 4 \times 10^{-4}$  at  $p\text{O}_2 = 10^{-15}$ , measured at 950 °C. Although the ionic conductivity will be even higher in fuel atmospheres ( $p\text{O}_2 \leq 10^{-21}$  atm), the conductivity under these conditions was found to remain dominated by electron holes [67].

The total conductivity of 1.5 S/cm in 5%  $\text{H}_2$  is further reduced in the SOFC anode and by the use of composite porous GDC/LSCM or YSZ/LSCM anodes, to values of ~0.1 S/cm in humidified  $\text{H}_2$  at 800 °C for a YSZ/LSCM composite [71]. Although this value is much lower than the 100 S/cm suggested by Steele [4], thin YSZ/LSCM anodes with 1 wt% Ni show reasonable performance in  $\text{H}_2$  nonetheless [34].

The substitution of  $\text{La}^{3+}$  with up to 50 mol% of  $\text{Sr}^{2+}$  has been attempted to enhance the electronic conductivity of LSCM [70]. However, the conductivity at low  $p\text{O}_2$  is almost independent of the amount of Sr in the range of 0.20–0.30 mol% Sr [68], and the introduction of more than 0.25 mol% Sr did not significantly enhance electric



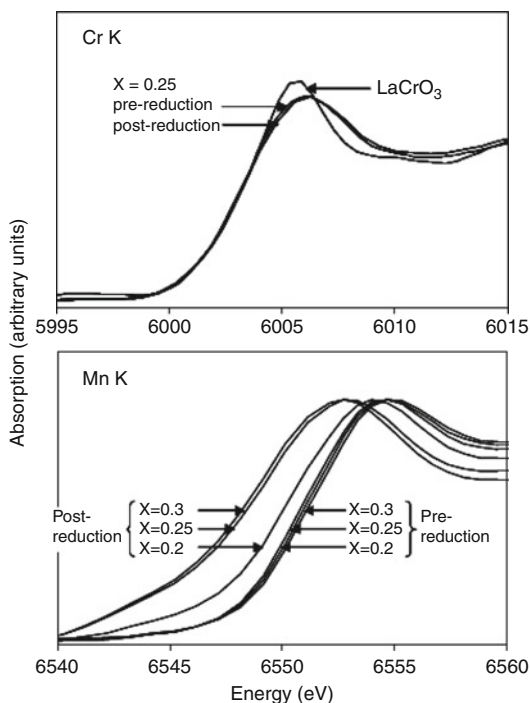
**Direct Hydrocarbon Solid Oxide Fuel Cells, Fig. 12** Voltage and power density for single cells with different LSCM + Cu composite anodes at 850 °C in dry CH<sub>4</sub>. (Reprinted from [53] with permission from Elsevier)

conductivity. Furthermore, the presence of  $\geq 30$  mol% Sr resulted in higher solid state reactivity and decreased the compatibility with the YSZ electrolyte [70]. Increasing the amount of Mn on the B site was reported to enhance the conductivity both in air and reducing atmospheres, but decreased the stability at low  $pO_2$  [66].

Another method is the substitution of  $La^{3+}$  with alkaline earth elements other than Sr. Since the different alkaline earth elements are present in the 2+ oxidation state at the relevant conditions, the number of electron holes is not expected to change significantly for substitution with different alkaline earths. However, changes in lattice parameters and in the distance between the Mn centers, caused by differently sized A-site cations, could affect the electrical conductivity through changes in charge carrier mobility. The electrical conductivity was shown to change when substituting La with Mg and Ba, but this was mostly due to the formation of secondary phases [72]. Apart from Sr, only substitution with Ca

resulted in a phase-pure perovskite, but without an increase in conductivity compared to LSCM [72]. Furthermore, the introduction of Ca is expected to result in the instability of LSCM under reducing conditions [73].

In practice, electronic conductivity has been increased by developing composite anodes of LSCM and an electronic conductor. Cu in particular has been used for the latter [6, 53], since it is an excellent electronic conductor and does not promote hydrocarbon cracking. Therefore, the large amounts of material required to achieve a percolation path can be added without carbon deposition during SOFC operation in hydrocarbon fuels. Although the electronic conductivity was not measured directly, Zhu measured a decrease in anode overpotential and a concomitant increase in SOFC power density with the addition of increasing amounts of Cu to LSCM [53], Fig. 12. The decrease in overpotential was mainly due to a decrease in the ohmic resistance of the SOFC. Since Cu replaced the catalyst LSCM, an optimum in Cu amount was expected.



**Direct Hydrocarbon Solid Oxide Fuel Cells,**  
**Fig. 13** Cr and Mn K XANES spectra for  $\text{La}_{1-x}\text{Sr}_x\text{Cr}_{0.5}\text{Mn}_{0.5}\text{O}_{3-\delta}$ . (Reprinted from [68] with permission from Elsevier)

Indeed, this optimum was observed at 20 wt% Cu, at which point the current density was increased more than fourfold, compared to the pure LSCM anode. With the addition of more Cu, the low-frequency impedance part, ascribed to fuel-related oxidation processes, increased significantly. This may be due to blocking of the active area on the LSCM within the anode.

To our knowledge, a systematic enhancement of the ionic conductivity has not been attempted. Instead, SOFC anodes typically use a composite of LSCM with an electrolyte material, such as YSZ [71] or ceria [74]. Care has to be taken when attributing increases in cell performance to enhanced ionic conductivity, as ceria has some total oxidation activity and could function as a catalyst. Also, at least part of the increase in performance is likely to be structural, since the porous YSZ or GDC scaffold creates a large surface area for the oxidation reaction to take place.

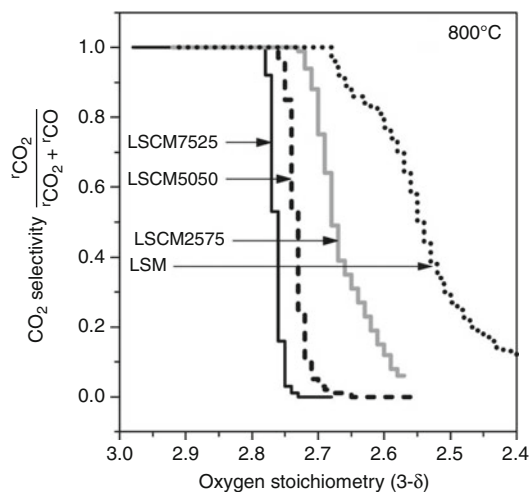
## Catalysis

Although the exact reaction mechanism is unclear, general concepts regarding the fuel oxidation reaction on LSCM have been described in the literature. Yamazoe and Teraoka pointed out that high-temperature oxidation reactions on perovskites typically occur through a reduction-oxidation cycle of the catalysts, otherwise known as a Mars-van Krevelen-type (MvK) mechanism [75], with the B-site elements serving as the redox centers. Studies suggest that this is the case for LSCM.

The active center of LSCM was identified by reducing air-annealed LSCM in fuel atmosphere, and comparing the energy levels of Cr and Mn before and after the reduction using X-ray Adsorption Near Edge Structure (XANES) analysis, Fig. 13. While the Cr K edge energies remained constant, the energy levels were different for Mn before and after reduction, attributed to a difference in oxygen coordination. This indicates that the average oxidation state of Mn decreases during reduction [68], identifying Mn as the active redox center. This is further supported by the poor catalytic activity of  $\text{LaCrO}_{3-d}$  toward hydrocarbons, compared with the higher activity of  $\text{LaMnO}_{3-d}$  [54].

Initial catalytic tests indicated that LSCM catalyzes the oxidation of hydrocarbon fuels, although it also has some activity toward dry reforming [65]. Compared to the conversion of  $\text{CH}_4$  in a blank reactor, LSCM enhanced the reaction rate of  $\text{CH}_4$ , and increased the selectivity toward total oxidation. Even under relatively oxygen-lean conditions ( $\text{CH}_4:\text{O}_2$  gas mixtures of 4:1), LSCM promoted the total oxidation of  $\text{CH}_4$  to  $\text{CO}_2$ , up to 800 °C. At 850 °C, the  $\text{CO}_2/\text{CO}$  selectivity was still 98.6% in favor of  $\text{CO}_2$ . No significant steam reforming activity was measured.

The experiments described above were performed by co-feeding oxygen and  $\text{CH}_4$ , resulting in a  $p\text{O}_2 \sim 10^{-1}$  atm, much higher than the  $p\text{O}_2$  of  $\sim 10^{-20}$  present at a working SOFC anode. Furthermore, the measured reaction rates are not differential rates as they were determined for 100% conversion. In order to determine the oxidation rate and the selectivity for total and partial oxidation of  $\text{CH}_4$  under conditions similar



**Direct Hydrocarbon Solid Oxide Fuel Cells, Fig. 14** Selectivity toward total oxidation of methane at 800 °C. The black solid line is LSCM with 75 mol% Cr and 25 mol% Mn (LSCM7525), dashed line is LSCM5050, gray solid line is LSCM2575 and dotted line is LSM. (Reprinted from [20] with permission from Elsevier)

to those of operating anodes, van den Bossche and McIntosh developed a pulse-type reactor [20]. In this set-up, pulses of  $\text{CH}_4$  (or  $\text{H}_2$ ) are fed to a reactor containing oxidized powder catalyst. No oxygen is co-fed with the fuel; instead, the fuel is oxidized utilizing oxygen from the oxide catalyst surface and bulk. Inert gas is fed between the short pulses of hydrocarbon fuel to allow re-equilibration of the surface oxidation states. This is necessary to prevent the measurement of a bulk oxygen diffusion limited rate. The  $p_{\text{O}_2}$  above the catalyst during a hydrocarbon pulse is that of pure fuel, and the oxygen source is the same as in the anode. Thus the  $\text{CO}_x$  production rates and selectivity are those of the fuel cell. Furthermore, since each pulse titrates a small amount of oxygen from the lattice, multiple pulses and knowledge of the original stoichiometry enable measurement of rates and selectivity as a function of oxygen stoichiometry.

Pulse experiments on  $\text{La}_{0.75}\text{Sr}_{0.25}\text{Cr}_{1-x}\text{Mn}_x\text{O}_{3-\delta}$  ( $x = 0.25-1$ ) indicated that  $\text{CH}_4$  oxidation rates increased with increasing Mn substitution and decreased with decreasing oxygen content. Both observations are in agreement with a modified

MvK mechanism with Mn as the redox center. The oxygen stoichiometry ( $3-\delta$ ) of the perovskite influenced product selectivity. At high lattice oxygen content,  $\delta \approx 0$ , total oxidation was the preferred reaction for all Mn/Cr ratios, with 100% of  $\text{CH}_4$  reacting to  $\text{CO}_2$ , Fig. 14. When less lattice oxygen was present, CO production dominated. The formation of CO was suggested to occur through the partial oxidation of  $\text{CH}_4$ , rather than secondary dry reforming.

Attempts have been made to link this shift in reaction rate and selectivity with oxygen stoichiometry to observed shifts in SOFC anode polarization resistance. At open circuit conditions at 700 °C with  $\text{CH}_4$  fuel, the LSCM oxygen stoichiometry is low as the material is at equilibrium with the fuel gas. This appears to promote cracking as the main reaction, with correspondingly high anode polarization resistance,  $\sim 12.3 \Omega \cdot \text{cm}^2$  [6]. Upon application of current, it is suggested that the oxygen ion flux locally increases the oxygen stoichiometry of the perovskite. The pulse reactor studies suggest that this should shift the reaction mechanism toward total oxidation of the fuel and increase the activity. This is observed as a decrease in anode polarization (to  $1 \Omega \cdot \text{cm}^2$ ) and a shift toward  $\text{CO}_2$  production with increasing SOFC current density.

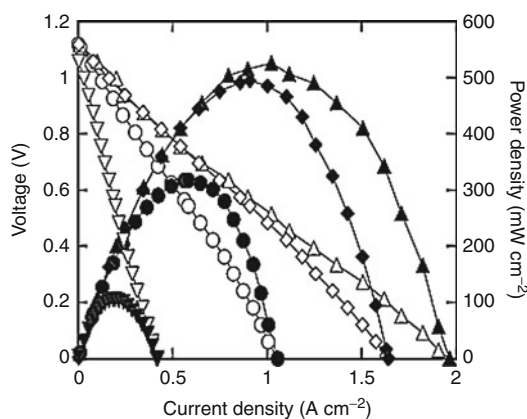
While these results are interesting, SOFC with LSCM anodes show significantly lower power outputs in  $\text{C}_4\text{H}_{10}$  and  $\text{CH}_4$ , when compared with  $\text{H}_2$  fuel [6]. Since the change in fuel only influences anode conditions, the anode activity toward oxidation of hydrocarbons appears to be a performance-limiting process for these anodes. This was further illustrated by electrochemical measurements on SOFCs with dense LSCM films [18]. The OCP values measured for these SOFCs with  $\text{CH}_4$  on the anode were comparable to the values measured in inert gas (He),  $\sim 0.06$  V. It was suggested that the kinetics for  $\text{CH}_4$  oxidation are slow, and that the contact time of the fuel on the relatively smooth surface was too short to set the  $\text{CH}_4$  reaction equilibrium. The addition of small amounts of Pd as a catalyst to the anode resulted in reasonable OCP values,  $\sim 0.87$  V, proving that the catalytic performance of LSCM toward  $\text{CH}_4$  is low and must be improved.



To enhance catalytic activity, the B site of LSCM has been substituted with a third element that is suggested to be more active for hydrocarbon oxidation than Mn. Ni and Fe are attractive choices as their respective lanthanum perovskites show  $\text{CH}_4$  conversion at lower temperatures than  $\text{LaMnO}_3$  [54]. Also, Ni is used as the oxidation catalyst in traditional Ni/YSZ anodes. Although large amounts of Co, Fe, or Ni substitution are unstable [56, 61], small amounts of Ni (10 mol%) were suggested to be kinetically stable in the  $\text{LaCrO}_3$  lattice [73]. Furthermore, the use of relatively small amounts of Co, Fe, or Ni, even if exsolved, is not expected to lead to the mechanical failure that is caused by large amounts of especially Ni, as carbon formation and volume changes upon redox cycling will be limited.

Van den Bossche and McIntosh replaced 10 mol% of Mn with Co, Fe, or Ni and found that  $\text{CH}_4$  oxidation rates were greatly enhanced on LSCMNi and LSCMCo, up to an order of magnitude compared to LSCM. This occurred only after the exsolution of the Co and Ni metals. The degree of carbon formation for LSCMNi and LSCMCo was similar to LSCM [19], suggesting that these compositions can be used as redox-stable, direct oxidation anodes.

Instead of introducing small amounts of catalytic elements into the perovskite, catalysts have also been successfully added to the anode as a separate phase. Again, Ni is the primary focus, as are precious metals such as Pd, Pt, and Rh. By adding a relatively small amount (4 wt%) of Ni to a GDC/LSCM (80% Cr) anode, Liu et al. [74] were able to increase the performance of SOFCs from  $\sim 50$  to  $80 \text{ mW/cm}^2$  in  $750^\circ\text{C}$   $\text{CH}_4$  (the relatively low power output resulted partly from a thick electrolyte). As the small amount of Ni was not expected to significantly increase the electronic conductivity, the increase in power output is mainly due to the enhancement in catalytic activity of the GDC/LSCM-Ni anode. Although the composite anodes with 4% Ni generated a small amount of carbon deposits in  $\text{C}_3\text{H}_8$  fuel under open circuit conditions, no noticeable carbon formation occurred in working SOFCs. This was in contrast to composites with large amounts of Ni, which generated significant amounts of

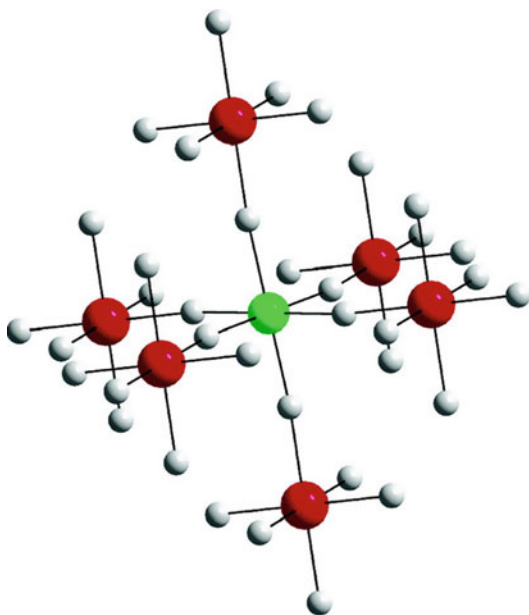


**Direct Hydrocarbon Solid Oxide Fuel Cells, Fig. 15** V-I polarization curves (open symbols) and power densities (filled symbols) in humidified  $\text{H}_2$  at  $700^\circ\text{C}$  for cells having anodes with 45 wt% LSCM in YSZ, using various catalysts: ( $\blacktriangledown$ ) no catalyst, ( $\bullet$ ) with 5 wt% ceria, ( $\blacklozenge$ ) with 0.5 wt% Pd, and ( $\blacktriangle$ ) with 5 wt% ceria and 0.5 wt% Pd. (Reproduced with permission from [34]. Copyright 2009, The Electrochemical Society)

carbon, even under operating conditions. Although the SOFC power output of the GDC/LSCM anode with 4% Ni dropped slightly after a first redox-cycle, performance was stable during the next three cycles. Long-term electrochemical stability studies are required to determine the stability of this composite anode.

Using a similar method, Kin et al. obtained a power output of  $\sim 500 \text{ mW/cm}^2$  in humidified  $\text{H}_2$  at  $700^\circ\text{C}$  utilizing YSZ/LSCM anodes with 0.5–1 wt% of either Pd, Rh or Ni added as a separate phase, Fig. 15. These values are to be compared to the power output of  $\sim 100 \text{ mW/cm}^2$  for YSZ/LSCM without metals added. The addition of 1 wt% Fe to YSZ/LSCM also increased power output to  $400 \text{ mW/cm}^2$  [34]. An enhancement in SOFC performance with the addition of Pd was found by other researchers as well, but not to the extent of a fivefold increase [53]. The smaller impact may be due to other limiting processes, such as low ionic conductivity.

Pd and Rh may be prohibitively expensive for largescale SOFC applications, but Ni or even Fe would be suitable. Long-term fuel cell tests using (sulfur-rich)  $\text{CH}_4$  are required to assess the sulfur tolerance and sintering resistance of Ni in the YSZ/LSCM-Ni anode.



**Direct Hydrocarbon Solid Oxide Fuel Cells, Fig. 16** Mo (green) surrounded by six next-nearest-neighbor Mg (red) in a perfectly B-site ordered material; oxygen ions are white and strontium cations are omitted for clarity. (Reprinted in part with permission from [80]. Copyright 2007 American Chemical Society)

### Stability

The LSCM anode is chemically compatible with the commonly used electrolytes, such as YSZ, up to 1,300 °C [64] and LSGM, up to 1,100 °C [76]. Values for the thermal expansion coefficient (TEC) of LSCM in air varied from 8.9 to 10.8  $\mu\text{K}^{-1}$  at low temperatures ( $< \sim 500$  °C), and from 10.1 to 12.7  $\mu\text{K}^{-1}$  at high temperatures, up to 950 °C [64, 67]. These TEC values match well with those for YSZ (10.8  $\mu\text{K}^{-1}$ ), LSGM (11.1  $\mu\text{K}^{-1}$ ) and GDC (13.5  $\mu\text{K}^{-1}$ ) [8]. The change in TEC in LSCM with temperature is likely due to a change in space group from rhombohedral R-3 C to cubic Pm-3 m, occurring gradually over the range of 500–1,100 °C in air [77]. As the associated change in volume is minimal,  $\sim 1\%$  [64], this is not expected to cause instability during cell heating or cooling. Furthermore, since the Pm-3 m phase is also observed for reduced LSCM, stresses due to redox cycling are expected to be small. Indeed, the difference in volume between the reduced and oxidized unit cells is only 1.7% at room temperature [77], while the

difference in linear expansion between LSCM in air and in reducing atmospheres,  $p\text{O}_2 = 2 \times 10^{-19}$ , is limited to  $\sim 0.2\%$  at 700 °C [67].

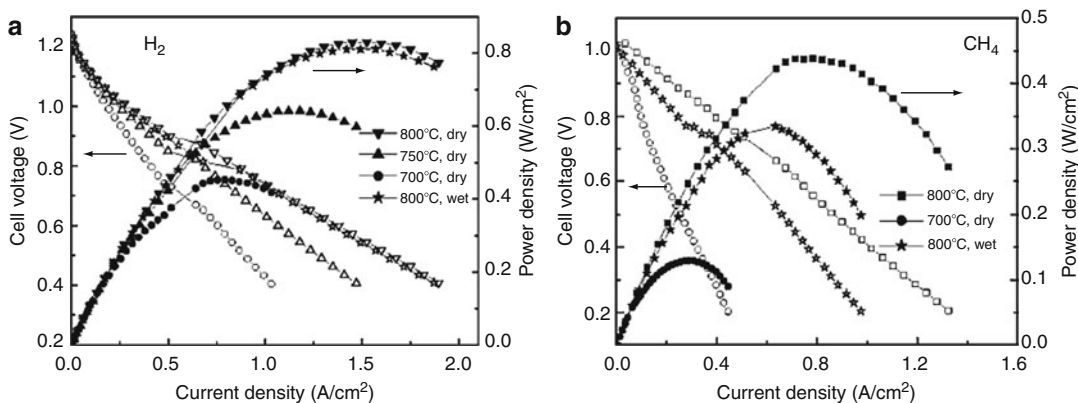
The operation of SOFCs with LSCM anodes in sulfur-rich  $\text{H}_2$  leads to a decrease in cell performance in a short amount of time. Liu reported a decrease in current density of 50% when exposing LSCM to 10%  $\text{H}_2\text{S}/\text{H}_2$  at 950 °C [66]. The decrease occurred over a period of 2 h, after which the performance stabilized. Ten percent  $\text{H}_2\text{S}$  is much higher than the typical ppm levels of sulfur present in natural gas and represents attempts to utilize  $\text{H}_2\text{S}$  as a fuel. However, even in  $\text{H}_2$  with 50 ppmv  $\text{H}_2\text{S}$ , performance was observed to decrease significantly from 0.46  $\text{W}/\text{cm}^2$  to 0.09  $\text{W}/\text{cm}^2$ , again in 2 h, at 850 °C and constant current density of 625  $\text{mA}/\text{cm}^2$  [53]. The large deterioration of LSCM is due to La and Mn reacting with sulfur to form  $\text{La}_2\text{O}_2\text{S}$ , MnS, and  $\alpha\text{-MnOS}$  [66]. Since Mn is the reactive site for fuel oxidation, the formation of these compositions is likely to have an adverse effect on anode performance.

There is no easy solution to decrease the susceptibility of LSCM to sulfur poisoning. Since LSV anodes have been shown to have excellent sulfur resistance [78], operating better in sulfur-rich fuel than in fuel without sulfur, it has been attempted to introduce 10 mol% V on the B site of LSCM. However, no phase-pure material could be obtained [19].

Interestingly, the use of sulfur-rich  $\text{CH}_4$  instead of sulfur-containing  $\text{H}_2$  led to an initial increase in performance on LSCM, compared to  $\text{CH}_4$  without sulfur [56]. After 4–6 h though, the performance in 0.5%  $\text{H}_2\text{S}/\text{CH}_4$  had stabilized to values similar to those in pure  $\text{CH}_4$ . This observation is consistent with the much smaller and slower decrease of power density of SOFC with LSCM anodes in 0.5%  $\text{H}_2\text{S}/\text{CH}_4$ , as compared to  $\text{H}_2\text{S}/\text{H}_2$  mixtures [79].

### Double Perovskites

Double perovskites are described by the general formula  $\text{A}_2\text{B}'\text{B}''\text{O}_{6-\delta}$ , and can be interpreted as a doubling of the regular perovskite  $\text{ABO}_{3-\delta}$ . The



**Direct Hydrocarbon Solid Oxide Fuel Cells, Fig. 17** SMMO/LDC/LSGM/SCF cell voltage and power density as a function of current density in dry and wet: (a)  $\text{H}_2$ ; and (b)  $\text{CH}_4$ . The open symbols represent the

cell voltages while the closed symbols represent the power densities. (Reproduced with permission from [82]. Copyright 2006, The Electrochemical Society)

elements on the  $B'$  site are different from those on the  $B''$  site, and the two sites alternate to form a sublattice with a rock-salt structure. In a perfectly ordered lattice, every  $B'$  ion would be coordinated by six perovskite unit cells with  $B''$  ions and vice versa. This is illustrated in Fig. 16 for  $\text{Sr}_2\text{MgMoO}_{6-\delta}$  (SMMO); the Mo ion (green) is surrounded by 6 Mg ions (red). The ordering is caused by large differences in the radii and charges between the  $B'$  and  $B''$  site ions. For example, in SMMO, the  $B'$  site is occupied by the small  $\text{Mg}^{2+}$  ion, while the  $B''$  site hosts the large and highly charged  $\text{Mo}^{6+}$  ion [80]. Although a regular perovskite can have two different elements on the B site as well, it is this particular B-site structure that classifies these materials as double perovskites.

The most investigated double perovskite anode material is SMMO. It has reasonable electrical conductivity,  $\sim 10$  S/cm in pure  $\text{H}_2$  at  $800^\circ\text{C}$ , good activity for direct  $\text{CH}_4$  oxidation, and operates well in sulfur-containing fuels [81]. The power output of an SOFC with a  $300\text{-}\mu\text{m}$ -thick  $\text{La}_{0.8}\text{Sr}_{0.2}\text{Ga}_{0.8}\text{Mg}_{0.2}\text{O}_{3-\delta}$  electrolyte,  $\text{SrCo}_{0.8}\text{Fe}_{0.2}\text{O}_{3-\delta}$  cathode and SMMO anode reached  $0.84\text{ W/cm}^2$  in dry  $\text{H}_2$  and  $0.44$  and  $0.34\text{ W/cm}^2$  in dry and wet  $\text{CH}_4$ , respectively, at  $800^\circ\text{C}$  [81], Fig. 17. Note that these values were obtained using Pt current collectors, which should be avoided as they contribute toward the catalytic

activity of the anode [83], significantly increasing the performance for hydrocarbon fuels.

### Conductivity

The electrical conductivity of SMMO was found to be  $\sim 1\text{--}4$  S/cm in  $\text{H}_2/\text{Ar}$  and  $10$  S/cm in  $\text{H}_2$ , at  $800^\circ\text{C}$  [82, 84]. The slight differences in the values possibly result from differences in synthesis methods. The conductivity decreases with increasing  $p\text{O}_2$ , indicative of n-type conductivity. The charge carriers are electrons generated by the reduction of  $\text{Mo(VI)}$  to  $\text{Mo(V)}$  to compensate for the charge imbalance created by the formation of oxygen vacancies in the material [84]. No studies have yet been conducted to optimize the electrical conductivity.

### Catalysis

The catalytic activity of SMMO is thought to result from the Mo ion. Whereas the Mg ion keeps a  $2+$  charge, Mo is reduced to some extent from predominantly  $\text{Mo(VI)}$  in air atmospheres, to a mixture of  $\text{Mo(VI)}$  and  $\text{Mo(V)}$  in reducing atmospheres [85]. The presence of a redox center would allow for the oxidation of fuel molecules according to a MvK mechanism, as suggested for the oxidation of  $\text{CH}_4$  on LSCM [20]. Only a small amount of  $\text{Mo(VI)}$  is reduced to  $\text{Mo(V)}$ , resulting in an oxygen non-stoichiometry of  $\sim 0.04\text{--}0.06$  mol O/mol SMMO for samples reduced at  $1,000\text{--}1,200^\circ\text{C}$  in  $5\%$   $\text{H}_2$

[80, 84, 86]. The limited reduction of Mo(VI) could be due to the instability of Mg in a conformation with less than six surrounding oxygen ions. This is confirmed by the decreased B-site order after reduction, indicating that Mg ions relocate to maintain a sixfold oxygen coordination [80].

To increase the electrocatalytic activity of Mo-based double perovskites, Mg has been replaced by a number of transition metals. SOFC anodes have been prepared with  $\text{Sr}_2\text{CoMoO}_6$ ,  $\text{Sr}_2\text{FeMoO}_6$ ,  $\text{Sr}_2\text{MnMoO}_6$  and  $\text{Sr}_2\text{NiMoO}_6$ , but none of those compounds were stable. SMMO with Co, Ni and Zn on the B' site are easily synthesized in air, but are unstable in 5%  $\text{H}_2$  at 800 °C and above, due to exsolution of the metals [87, 88]. Higher initial power outputs were indeed observed for SOFCs made with  $\text{Sr}_2\text{CoMoO}_6$  anodes, compared to similar SOFCs with SMMO anodes, but performance quickly deteriorated, likely due to the decomposition of SCMO.  $\text{Sr}_2\text{FeMoO}_6$  and  $\text{Sr}_2\text{MnMoO}_6$  are stable in reducing atmospheres, but unstable in >400 °C air [88, 89].

More recently, the maximum oxygen non-stoichiometry in SMMO was successfully increased through partial substitution of Mo (VI) by Nb(V), without compromising the stability of the double perovskite [85]. The increase in oxygen non-stoichiometry suggests that more  $\text{Mo}^{6+}/\text{Mo}^{5+}$  redox centers are created, which are expected to increase both oxygen ion conductivity and fuel oxidation rates.

### Stability

As suggested above, a significant challenge in the development of double perovskites is the synthesis of phasepure, redox-stable compositions. The synthesis of SMMO, for example, is successful in air, but requires high temperatures, >1,200 °C, to remove  $\text{SrMoO}_4$  impurities [90]. The firing temperature can be brought down to 900 °C if a 5%  $\text{H}_2$  atm is used, but the use of such a reducing atmosphere could complicate largescale SMMO production.

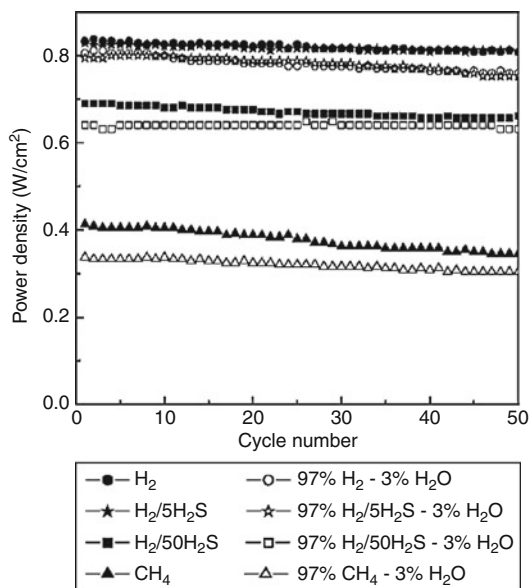
Because of the existence of  $\text{SrMoO}_4$  impurities in air-fired SMMO, it is likely that the same impurities are formed upon treatment of

$\text{H}_2$ -synthesized SMMO in high temperature air. Depending on the thermal and chemical expansion properties of this phase, these impurities could result in a decrease in performance with redox cycling of SMMO. At room temperature in air, SMMO readily forms carbonates, such as  $\text{SrCO}_3$ , resulting in surface degradation and  $\text{SrMoO}_4$  formation [84].

At elevated temperatures in reducing atmospheres, SMMO partly decomposes to  $\text{MgO}$ ,  $\text{SrO}$ , and Mo. The temperature at which decomposition starts is subject to debate. In 5%  $\text{H}_2$ , decomposition temperatures have been reported as low as 900 °C [80] up to 1,000 °C [90] and even 1,200 °C [82]. It has been suggested that the decomposition temperature is influenced by the preparation method, with the high temperatures utilized during air-firing or solid-state synthesis possibly leading to the evaporation of the volatile Mo, decreasing SMMO stability [90]. SMMO synthesized according to an EDTA-complexation route and fired at low temperatures in 5%  $\text{H}_2$  is typically found to be stable up to 1,000 °C in 5%  $\text{H}_2$ , at which point small amounts of the decomposition products appear. SOFC applications however run most efficiently on pure or humidified fuel, atmospheres that are more reducing than 5%  $\text{H}_2$ . The use of pure fuel could therefore lead to decomposition of the SMMO anode at temperatures lower than 900–1,000 °C, which presents a problem for SOFC operating at 700–850 °C.

Another potential issue is the chemical interaction of SMMO with the commonly used electrolytes YSZ and LSGM. When treated in 1,000 °C air for 24 h, SMMO reacts with YSZ to form large amounts of  $\text{SrMoO}_4$  and  $\text{SrZrO}_3$ , and it reacts with LSGM to form  $(\text{La},\text{Sr})\text{Ga}_3\text{O}_7$  [84]. These reaction products have inferior properties compared to the reactants and are therefore to be avoided. In the case of LSGM, this has been done by using a thin ceria-based layer between anode and electrolyte [82]. The thermal expansion of SMMO,  $\sim 11.7\text{--}12.7 \mu\text{K}^{-1}$  [82] is compatible with values for YSZ (10.8), LSGM (11.1) and GDC (13.5).

SOFC with SMMO anodes have shown stable performance in dry  $\text{H}_2$  fuel with 5 ppmv  $\text{H}_2\text{S}$ . The initial power output of fuel cells in 5 ppmv  $\text{H}_2\text{S}/\text{H}_2$  fuel is similar to that in pure  $\text{H}_2$  fuel, Fig. 18, and the cells show a similar decrease in power



**Direct Hydrocarbon Solid Oxide Fuel Cells,**  
**Fig. 18** Maximum power density  $P_{\max}$  at 800 °C versus cycle number in dry and wet  $H_2$ ,  $H_2/H_2S$ , and  $CH_4$ . (Reproduced with permission from [82]. Copyright 2006, The Electrochemical Society)

output, ~3% after 200 h of operation in both fuels at 800 °C [82]. When, under otherwise similar conditions, the concentration of  $H_2S$  is raised to 50 ppmv, the initial power output of the cell was reduced to ~80–85% of its value in  $H_2$  and  $P_{\max}$  decreased by 5% in 200 h.

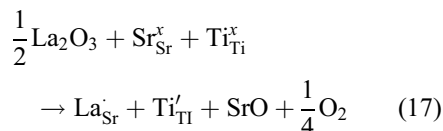
## Strontium Titanates

Pure  $SrTiO_3$  is a simple cubic perovskite that has a good thermal expansion match with YSZ and is stable under reducing conditions. However, undoped  $SrTiO_3$  has insufficient electronic conductivity for an anode material [91]. In contrast, donor-doped (n-type)  $SrTiO_3$  has attracted considerable interest due to its high electronic conductivity under reducing conditions, while maintaining a good thermal expansion match, and resistance to both coking and sulfur poisoning [92, 93]. Unfortunately, the performance of pure STO-based anodes is low, requiring additional catalytic materials to realize acceptable

power densities [94]. As with the other oxides discussed in this entry, the conductivity and stability of this material is dominated by its defect chemistry. There are a number of articles that fully discuss the defect chemistry, for example [91]. This discussion is restricted to the essential points relevant to the use of STO as an SOFC anode.

## Conductivity

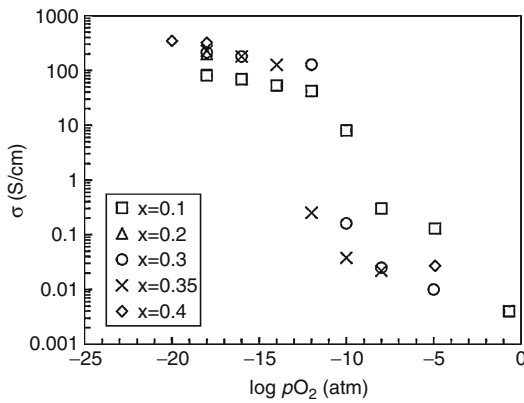
There are two routes to doping of  $SrTiO_3$ : doping of trivalent cations onto the Sr site, and/or doping of pentavalent cations onto the Ti site. The most common trivalent dopants are  $La^{3+}$  and  $Y^{3+}$ .  $La^{3+}$  has high solubility, with only limited distortion of the lattice parameter at high dopant levels (>40%) [95]. Charge compensation upon doping can occur via electronic or ionic compensation, depending on the temperature and  $pO_2$ . At low  $pO_2$ , the compensation mechanism is electronic via reduction of  $Ti^{4+}$  to  $Ti^{3+}$  to form  $Sr_{1-x}La_xTi'_xTi_{1-x}O_3$ :



A similar mechanism occurs for Y-doped STO under reducing conditions [97]. Assuming that dopant carriers dominate, the number of n-carriers is then directly correlated to the dopant level [98]; however, the correlation is not 100% as some electronic defects are associated with the donor atom. The creation of high concentrations of electronic defects leads to high conductivity. For example, Marina et al. reported conductivities for  $La_{0.3}Sr_{0.7}TiO_3$  of over 100 S/cm at low  $pO_2$ , Fig. 19 [96].

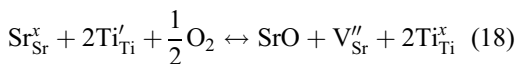
At high  $pO_2$ , the compensation mechanism switches from electronic to cation vacancy compensation (or self compensation), where the donor charge is compensated by the formation of Sr vacancies [98, 99]. This is accompanied by the formation of a secondary Sr-rich phase. The nature of this phase is not fully determined and is suggested to be either an  $Sr_{n+1}Ti_nO_{3n+1}$  phase





**Direct Hydrocarbon Solid Oxide Fuel Cells, Fig. 19** Electrical conductivity as a function of  $pO_2$  for  $La_xSr_{1-x}TiO_3$  sintered at  $1650\text{ }^\circ\text{C}$  in  $H_2$ . Conductivity is measured at  $1,000\text{ }^\circ\text{C}$  from low to high  $pO_2$ . (Reprinted from [96] with permission from Elsevier)

within the matrix [100] or a separate SrO phase [101]. A separate phase is denoted below simply for clarity:

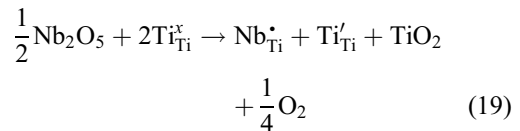


This alternate charge compensation mechanism removes electronic carriers and thus greatly decreases the electronic conductivity of the material [98]. Indeed, the very high conductivities reported for La-doped STO are only created upon sintering at high temperatures under very reducing conditions [92, 93, 96, 102].

Upon exposure to higher  $pO_2$  at SOFC temperatures, the conductivity decreases slowly [96]. This is observed in Fig. 19 as the significant decrease in conductivity for all of the samples as the  $pO_2$  is increased above  $\sim 10^{-14}$  atm. The slow kinetics associated with this may be related to slow cation diffusion [101] and/ or low oxygen mobility in these materials [103]. Slow reoxidation kinetics are beneficial to application in the SOFC anode where accidental and occasional exposure of the anode material to air may be expected. Of course, this assumes that a suitable and cost-effective cell synthesis procedure can be derived to initially form these highly

conductive states. Furthermore, slow reoxidation may indicate slow surface oxygen exchange and low hydrocarbon oxidation activity.

Nb is the most common pentavalent dopant [104–108]. As with the trivalent A-site dopants, the additional charge is compensated by electronic carriers at low  $pO_2$  leading to high electronic conductivity. These carriers are generated by reduction of  $Ti^{4+}$  to  $Ti^{3+}$ :



Nb remains in the pentavalent oxidation state although there is evidence that Nb substitution improves the overlap between Ti atomic orbitals. As with the trivalent doped materials, conductivity decreases upon oxidation due to a shift toward ionic compensation via the formation of Sr vacancies. However, it has been reported that Nb-doped materials can provide adequate conductivity and are very slow to reoxidize [107].

Irvine et al. suggested deliberate introduction of Sr vacancies through the fabrication of A-site deficient materials with the A-site deficiency level set to compensate for the charge introduced through donor doping [103, 109]. While these materials show good electronic conductivity, recent work has suggested that A-site deficiency leads to precipitation of secondary Ti-rich phases [93, 110]. It should be noted that these secondary phases are not always observable by XRD but are observed upon SEM/EDX analysis.

Transition metal acceptor doping of A-site deficient  $Sr_{0.85}Y_{0.1}Ti_{0.95}M_{0.05}O_{3-\delta}$  ( $M = V, Mn, Fe, Co, Ni, Cu, Zn, Mo, Mg, Zr, Al, Ga$ ) leads to a decrease in total conductivity compared to the undoped composition. This is due to the acceptor dopant off-setting the influence of the donor dopant ( $Y^{3+}$  in this case). The ionic conductivity of these materials increases upon acceptor doping but it is still  $\sim 6$  orders of magnitude lower than the electronic conductivity [111].

The ionic conductivity of doped STO is quite low although A-site deficient  $(Y_{0.08}Sr_{0.92})_{1-x}TiO_{3-\delta}$  has been shown to have an ionic conductivity



comparable to YSZ at 700 °C; however, this occurs at the expense of lowering the electronic conductivity [112]. It may not be desirable to introduce significant oxygen ion conductivity as the low mobility of oxygen anions may play a significant role in preventing reoxidation of the material and concomitant loss of electronic carriers [96, 103]. The majority of SOFC anode studies utilize composites of doped STO and YSZ, where STO provide electronic conductivity and YSZ provides ionic conductivity [92].

### Catalysis

Unfortunately, while able to provide sufficient electronic conductivity, the electrocatalytic activity of doped-SrTiO<sub>3</sub> is low [105]. As such, secondary catalysts are required to provide sufficient SOFC performance as cells without additional catalyst provide very low power density. For example, Lee et al. demonstrated a dramatic increasing in performance with H<sub>2</sub> fuel upon addition of 5 wt% CeO<sub>2</sub> and 0.5 wt% Pd. The power density increased from less than 20–780 mW/cm<sup>2</sup> at 800 °C with no change in OCP [35]. Pd doping without CeO<sub>2</sub> has also been shown to enhance activity [94].

Avoiding precious metals, Fu et al. demonstrated a similar enhancement, realizing a two order of magnitude decrease in polarization resistance with an yttria-substituted SrTiO<sub>3</sub>-YSZ composite upon infiltration of 5 vol% Ni [113]. Yang et al. also utilized Ni surface doping but did so in conjunction with Co doping of Sr<sub>0.88</sub>Y<sub>0.08</sub>TiO<sub>3</sub>, finding an enhancement of activity attributed to the reducibility of Co within the lattice [114].

Only limited studies have discussed the activity of these materials toward hydrocarbon utilization. Vincent et al. showed that the performance of cells with La<sub>0.4</sub>Sr<sub>0.6-x</sub>Ba<sub>x</sub>TiO<sub>3</sub> (0 ≤ x ≤ 0.2) based anodes in CH<sub>4</sub> fuel was more than one order of magnitude lower than in H<sub>2</sub> fuel between 800 °C and 950 °C [115]. The performance did increase slightly with an increase in Ba doping level but, perhaps most intriguingly, a more substantial improvement was observed upon the addition of H<sub>2</sub>S to the feed gas. A role for Ba in enhancing oxygen surface exchange rates was confirmed, although with the caveat that it was

measured under oxidizing conditions, when the surface is doped with Sr, Ba, or Ca [116]. Addition of CeO<sub>2</sub> to an Sr<sub>0.88</sub>Y<sub>0.08</sub>O<sub>3</sub>-based anode significantly reduced the anode polarization resistance with both H<sub>2</sub> and CH<sub>4</sub> fuel [117, 118], likely due to enhanced catalytic activity of the composite.

Doping with a more reducible Mn cation to form La<sub>0.4</sub>Sr<sub>0.6</sub>Ti<sub>0.4</sub>Mn<sub>0.6</sub>O<sub>3</sub> leads to a decrease in electronic conductivity although it may slightly increase catalytic activity toward hydrocarbons. The resulting cell shows a low OCP in wet CH<sub>4</sub> of only 0.86 V at 856 °C with a total cell R<sub>p</sub> of ~1.4 Ω·cm<sup>2</sup> compared with an OCP of 1.05 V and total R<sub>p</sub> of ~0.36 Ω·cm<sup>2</sup> in wet Ar/H<sub>2</sub> [119]. The difference in polarization resistance is not as dramatic as shown for Mn-free compositions.

Ruiz-Morales et al. took a unique approach by utilizing multiple dopants to control the oxygen stoichiometry and thus disrupt defect ordering to generate the single-phase perovskite anode material La<sub>4</sub>Sr<sub>8</sub>Ti<sub>11</sub>Mn<sub>0.5</sub>Ga<sub>0.5</sub>O<sub>37.5</sub> [120]. The resulting cell generated 500 mW/cm<sup>2</sup> with H<sub>2</sub> fuel and 350 mW/cm<sup>2</sup> with CH<sub>4</sub> at 950 °C, Fig. 19. The maximum power density and OCP in CH<sub>4</sub> fuel were both significantly higher than with 5% H<sub>2</sub> fuel, Fig. 20, suggesting that homogeneous cracking of CH<sub>4</sub> to form H<sub>2</sub> was not the dominant reaction mechanism and that this material was active toward CH<sub>4</sub> oxidation.

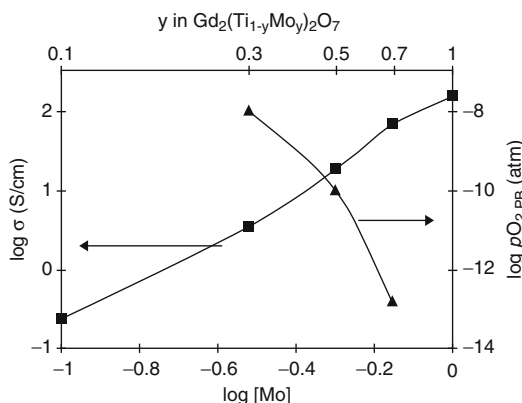
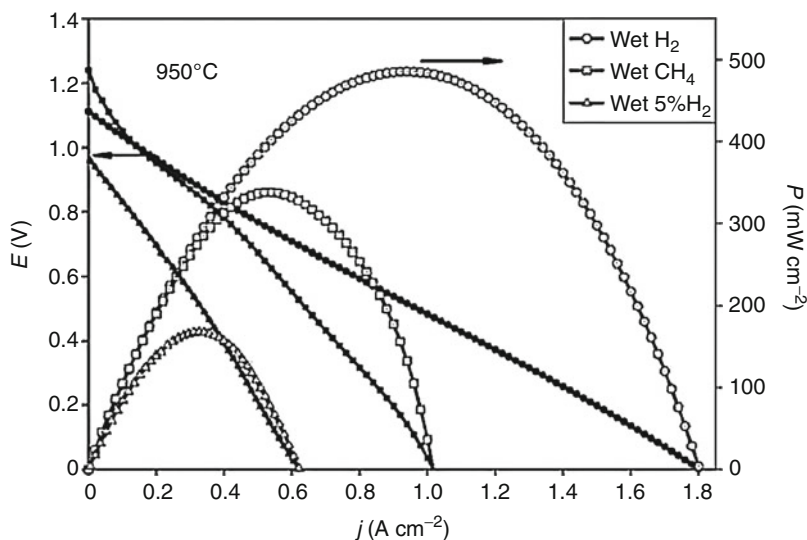
SrTiO<sub>3</sub> based anodes have been shown to be quite tolerant to H<sub>2</sub>S poisoning [121], operating with up to 1% H<sub>2</sub>S [122] and up to 50 ppm H<sub>2</sub>S when surface doped with Pd [94].

### Other Materials of Interest

*Pyrochlore structured oxides* have received some attention for use in SOFC anodes, in particular the series Gd<sub>2</sub>Mo<sub>x</sub>Ti<sub>2-x</sub>O<sub>7</sub>. SOFCs made with 250-micron thick YSZ electrolytes, LSCM cathodes, and Gd<sub>2</sub>Mo<sub>0.6</sub>Ti<sub>1.4</sub>O<sub>7</sub> anodes have shown a stable power output of 340 mW/cm<sup>2</sup> in 950 °C 10% H<sub>2</sub>S/H<sub>2</sub>, and an anode polarization resistance of ~0.23 Ω·cm<sup>2</sup> at OCP [123]. The substitution of Ti in the electrolyte Gd<sub>2</sub>Ti<sub>2</sub>O<sub>7</sub> with large amounts of Mo increases the total conductivity to ~70 and 25 S/cm in 1,000 °C 5% H<sub>2</sub> for 70 and 50 mol%

### Direct Hydrocarbon Solid Oxide Fuel Cells,

**Fig. 20** Fuel cell performance plots at 950 °C of a cell with four-layer optimized  $\text{La}_4\text{Sr}_8\text{Ti}_{11}\text{Mn}_{0.5}\text{Ga}_{0.5}\text{O}_{37.5}$  anode, 330 mm YSZ electrolyte, and  $\text{La}_{0.8}\text{Sr}_{0.2}\text{MnO}_3$  cathode. Fuels humidified with 2.3%  $\text{H}_2\text{O}$ , cathode is in dry  $\text{O}_2$ . (Reprinted by permission from Macmillan Publishers, Ltd.: Nature [120], copyright 2006)



**Direct Hydrocarbon Solid Oxide Fuel Cells,**  
**Fig. 21** Electrical conductivity at  $p\text{O}_2 = 10^{-18}$  bar and the pyrochlore phase boundary at high  $p\text{O}_2$ ,  $p\text{O}_{2,\text{PB}}$ , vs. Mo concentration in  $\text{Gd}_2\text{Ti}_2\text{O}_7$  at 1,000 °C. (Reprinted from [124] with permission from Elsevier)

Mo respectively. The ionic conductivity under these conditions remains high,  $\sim 0.1$  S/cm for 50 mol% Mo [124].

However, the introduction of large amounts of Mo is detrimental to the stability of  $\text{Gd}_2\text{Ti}_2\text{O}_7$ . Compositions with 70 mol% Mo are unstable and exist only in a very narrow  $p\text{O}_2$  range,  $10^{-13}$ – $10^{-15}$  atm at 1,000 °C. This range is extended for lower Mo contents, but even at 30 mol% Mo, compositions are not stable at 1,000 °C in  $p\text{O}_2 > 10^{-8}$  atm [124], Fig. 21.

Sprague reported increased redox stability when co-substituting Ti with Mn instead of just Mo, but this has only been shown for small amounts of Ti substitution,  $< 20$  mol% [125].

More recently, the pyrochlore  $\text{Yb}_{0.96}\text{Ca}_{1.04}\text{TiNbO}_7$  has been suggested as an anode material [126]. Based on  $\text{Yb}_2\text{Ti}_2\text{O}_7$ , the substitution of Yb with Ca increases the ionic conductivity [127], while the introduction of Nb greatly enhances the total conductivity, to 9 S/cm at 800 °C in 5%  $\text{H}_2/\text{N}_2$ . The conductivity is n-type, and is therefore expected to increase further in more reducing atmospheres. In addition,  $\text{Yb}_{0.96}\text{Ca}_{1.04}\text{TiNbO}_7$  is stable up to 1,450 °C in air and 1,350 °C in 5%  $\text{H}_2/\text{N}_2$ . The main drawback of the material appears to be slow oxygen ion exchange, which can be slightly enhanced with further substitution on the B site, for example, with Mn, Cr or Mg/Mo [126].

*Fluorite* anodes, not including ceria, are typically based on YSZ and have been developed to ensure good thermo-mechanical and chemical compatibility with the widely used YSZ electrolyte. A purely ionic conductor, YSZ depends on the substitution of Zr with more reducible elements, such as Ti, to introduce electronic conductivity. The reduction of  $\text{Ti}^{4+}$  to  $\text{Ti}^{3+}$  in  $\text{Y}_{0.18}\text{Zr}_{0.73}\text{Ti}_{0.09}\text{O}_{2-s}$  (YZT) generates electronic charge carriers, but significant amounts of  $\text{Ti}^{3+}$  are only present at high temperatures and low

$pO_2$ . Even at 1,000 °C and  $pO_2 < 10^{-20}$  atm, the total conductivity is low,  $\sim 0.06$  S/cm [128]. An additional drawback of substitution with Ti is the trapping of oxygen vacancies on Ti ions, reducing the ionic conductivity to  $\sim 0.04$  S/cm.

By raising the amount of Ti to 18 at-%, the maximum amount that dissolves in the YSZ lattice, the electrical conductivity of  $Y_{0.15}Zr_{0.67}Ti_{0.18}O_{2-\delta}$  is increased to 0.2 S/cm (at 930 °C and  $pO_2 = 10^{-20}$  atm), while the ionic conductivity is further reduced [129]. Introduction of  $Sc_2O_3$  into YZT (ScYZT) slightly increased the electronic conductivity to 0.14 S/cm at 900 °C [130]. SOFCs with ScYZT anodes were tested in 900 °C 5% humidified  $H_2$  (using Pt as electrode current collectors) and showed an estimated power output of 35 mW/cm<sup>2</sup> and an anode polarization resistance of  $\sim 5.5$   $\Omega \cdot cm^2$  at OCP, using a 2 mm thick YSZ electrolyte and a Pt cathode [131].

Among the *Tungsten Bronzes*, formula  $A_{0.6}BO_3$ , the Nb-based  $Sr_{0.2}Ba_{0.4}Ti_{0.2}Nb_{0.8}O_3$  is the best candidate for SOFC anodes. This composition is redox stable and has reasonable electrical conductivity, 3.4 S/cm at 930 °C in 5%  $H_2/Ar$  [132]. Other compositions are unstable or have lower conductivity [132, 133].  $Sr_{0.2}Ba_{0.4}Ti_{0.2}Nb_{0.8}O_3$  has a much lower TEC than the electrolytes that are commonly used,  $\sim 6.7$   $\mu K^{-1}$ , and reacts with YSZ at 1,200 °C. Also, the power output for symmetrical SOFCs made with this compound are low, with impedance data showing Warburg behavior, suggesting poor oxygen ion exchange and low oxygen ion conductivity [134].

*Vanadates* in the series  $La_{1-x}Sr_xVO_3$  demonstrate sufficient electronic conductivity [63], and reasonable electrocatalytic activity at 1,000 °C [135], coupled with stability toward sulfur poisoning [78]. Aguilar et al. demonstrated operation with 5%  $H_2S$  in both  $H_2$  and  $N_2$  [135]. In the latter case, the LSV-based anode utilized  $H_2S$  as the fuel source. Unfortunately, LSV is only stable at low oxygen partial pressure, for example,  $pO_2 < 10^{-17}$  atm at 800 °C [63]. It transforms to the apatite phase  $Sr_3V_2O_8$  [63] or  $Sr_2V_2O_7$  [78] upon exposure to higher  $pO_2$ . This transformation is irreversible at SOFC operating temperatures [63].

## Future Directions

As discussed in this entry, a number of novel materials and composites have been proposed as potential anodes for direct hydrocarbon solid oxide fuel cells. While many are promising, a commercially viable solution has not yet been found. The discussion in this entry is deliberately framed around the concepts of ionic and electronic conductivity, electrocatalysis, and stability. It is essential for future researchers to address all of these topics when discussing new materials. The schematic in Fig. 4 represents both the complexity of the problem and the simplicity that could potentially be achieved if a material meeting all of these requirements can be found.

One particular challenge for the field as a whole is the measurement of these properties under realistic conditions. Experimental tools to probe the surface or bulk of these materials in situ at the length scales relevant to the anode processes are not currently available. While significant consideration has been given to the bulk transport properties of potential materials, very little is known of the surface chemistry under realistic SOFC conditions. It is also necessary to develop techniques that can measure and quantify the electrocatalytic activity of these materials under operating conditions. While electrochemical impedance techniques can, in principle, provide a wealth of information, the fitting of such data can be ambiguous and it is not a replacement for a direct measurement of a fundamental property. This is a major hurdle that must be overcome if highly active and selective catalytic materials are to be developed for this application.

In combination with this increased knowledge of surface chemistry, a detailed knowledge of the material bulk is essential. It is clear from the discussion in this entry that the target materials set will be a multicomponent oxide with potentially complex cation and anion lattice structures. When material properties depend upon cation configuration, e.g., the double perovskites, or oxygen stoichiometry, these properties must be accurately determined in a working cell.

The barriers to direct hydrocarbon SOFCs will only be overcome through a combination of new material development and more detailed

experimental systems that directly probe fundamental parameters on working SOFC electrodes.

## Bibliography

### Primary Literature

- McIntosh S, Gorte RJ (2004) Direct hydrocarbon solid oxide fuel cells. *Chem Rev* 104:4845–4865
- Minh NQ (2004) Solid oxide fuel cell technology—features and applications. *Solid State Ionics* 174:271
- Minh NQ (1993) Ceramic fuel-cells. *J Am Ceram Soc* 76:563–588
- Steele BCH, Middleton PH, Rudkin RA (1990) Material science aspects of SOFC technology with special reference to anode development. *Solid State Ionics* 40–41:388
- Tao SW, Irvine JTS (2004) Discovery and characterization of novel oxide anodes for solid oxide fuel cells. *Chem Rec* 4:83–95
- Bruce MK, van den Bossche M, McIntosh S (2008) The influence of current density on the electrocatalytic activity of oxidebased direct hydrocarbon SOFC anodes. *J Electrochem Soc* 155:B1202–B1209
- Adler SB (2004) Factors governing oxygen reduction in solid oxide fuel cell cathodes. *Chem Rev* 104:4791
- Jacobson AJ (2009) Materials for solid oxide fuel cells. *Chem Mater* 22:660
- Tsipis EV, Kharton VV (2008) Electrode materials and reaction mechanisms in solid oxide fuel cells: a brief review. *J Solid State Electrochem* 12:1367–1391
- Brett DJL, Atkinson A, Brandon NP, Skinner SJ (2008) Intermediate temperature solid oxide fuel cells. *Chem Soc Rev* 37:1568–1578
- He HP, Hill JM (2007) Carbon deposition on Ni/YSZ composites exposed to humidified methane. *Appl Catal A* 317:284–292
- Gupta GK, Hecht ES, Zhu H, Dean AM, Kee RJ (2006) Gas-phase reactions of methane and natural-gas with air and steam in non-catalytic regions of a solid-oxide fuel cell. *J Power Sources* 156:434–447
- Walters KM, Dean AM, Zhu H, Kee RJ (2003) Homogeneous kinetics and equilibrium predictions of coking propensity in the anode channels of direct oxidation solid-oxide fuel cells using dry natural gas. *J Power Sources* 123:182–189
- Lin YB, Zhan ZL, Liu J, Barnett SA (2005) Direct operation of solid oxide fuel cells with methane fuel. *Solid State Ionics* 176:1827–1835
- Murray EP, Tsai T, Barnett SA (1999) A direct-methane fuel cell with a ceria-based anode. *Nature* 400:649
- Zhan ZL, Barnett SA (2005) An octane-fueled solid oxide fuel cell. *Science* 308:844–847
- Bouwmeester HJM, Kruidhof H, Burggraaf AJ (1994) Importance of the surface exchange kinetics as rate limiting step in oxygen permeation through mixed-conducting oxides. *Solid State Ionics* 72:185
- van den Bossche M, Matthews R, Lichtenberger A, McIntosh S (2010) Insights into the fuel oxidation mechanism of  $\text{La}_{0.75}\text{Sr}_{0.25}\text{Cr}_{0.5}\text{Mn}_{0.5}\text{O}_{3-d}$  SOFC anodes. *J Electrochem Soc* 157:B392–B399
- van den Bossche M, McIntosh S (2010) Pulse reactor studies to assess the potential of  $\text{La}_{0.75}\text{Sr}_{0.25}\text{Cr}_{0.5}\text{Mn}_{0.4}\text{X}_{0.1}\text{O}_{3-d}$  ( $\text{X} = \text{Co}, \text{Fe}, \text{Mn}, \text{Ni}, \text{V}$ ) as direct hydrocarbon solid oxide fuel cell anodes. *Chem Mater* 22:5856–5865
- van den Bossche M, McIntosh S (2008) Rate and selectivity of methane oxidation over  $\text{La}_{0.75}\text{Sr}_{0.25}\text{Cr}_x\text{Mn}_{1-x}\text{O}_{3-d}$  as a function of lattice oxygen stoichiometry under solid oxide fuel cell anode conditions. *J Catal* 255:313–323
- McIntosh S, Vohs JM, Gorte RJ (2003) Effect of precious-metal dopants on SOFC anodes for direct utilization of hydrocarbons. *Electrochem Solid State Lett* 6:A240–A243
- McIntosh S, Vohs JM, Gorte RJ (2002) An examination of lanthanide additives on the performance of Cu-YSZ cermet anodes. *Electrochim Acta* 47:3815–3821
- Bouwmeester HJM, Burggraaf AJ (1997) Dense ceramic membranes for oxygen separation. In: Gellings PJ, Bouwmeester HJM (eds) *CRC handbook of solid state electrochemistry*. CRC Press, Boca Raton
- Goldschmidt VM (1926) *Geochemische verteilungsgesetze der elemente*. Akad Oslo I Mat Nat 2:7
- Knauth P, Tuller HL (2002) Solid-state ionics: roots, status, and future prospects. *J Am Ceram Soc* 85:1654–1680
- Oishi M, Yashiro K, Sato K, Mizusaki J, Kawada T (2008) Oxygen nonstoichiometry and defect structure analysis of B-site mixed perovskite-type oxide  $(\text{La}, \text{Sr})(\text{Cr}, \text{M})\text{O}_{3-d}$  ( $\text{M} = \text{Ti}, \text{Mn}$  and  $\text{Fe}$ ). *J Solid State Chem* 181:3177–3184
- McIntosh S, He HP, Lee SI, Costa-Nunes O, Krishnan VV, Vohs JM, Gorte RJ (2004) An examination of carbonaceous deposits in direct-utilization SOFC anodes. *J Electrochem Soc* 151:A604–A608
- McIntosh S, Vohs JM, Gorte RJ (2003) Role of hydrocarbon deposits in the enhanced performance of direct-oxidation SOFCs. *J Electrochem Soc* 150:A470–A476
- Coyle CA, Marina OA, Thomsen EC, Edwards DJ, Cramer CD, Coffey GW, Pederson LR (2009) Interactions of nickel/zirconia solid oxide fuel cell anodes with coal gas containing arsenic. *J Power Sources* 193:730–738
- Marina OA, Coyle CA, Thomsen EC, Edwards DJ, Coffey GW, Pederson LR (2010) Degradation mechanisms of SOFC anodes in coal gas containing phosphorus. *Solid State Ionics* 181:430–440
- Marina OA, Pederson LR, Thomsen EC, Coyle CA, Yoon KJ (2010) Reversible poisoning of nickel/zirconia solid oxide fuel cell anodes by hydrogen chloride in coal gas. *J Power Sources* 195:7033–7037

32. Gorte RJ, Park S, Vohs JM, Wang C (2000) Anodes for direct oxidation of dry hydrocarbons in a solid-oxide fuel cell. *Adv Mater* 12:1465–1469
33. Vohs JM, Gorte RJ (2009) High-performance SOFC cathodes prepared by infiltration. *Adv Mater* 21(9): 943–956
34. Kim G, Lee S, Shin JY, Corre G, Irvine JTS, Vohs JM, Gorte RJ (2009) Investigation of the structural and catalytic requirements for high-performance SOFC anodes formed by infiltration of LSCM. *Electrochem Solid State Lett* 12:B48–B52
35. Lee S, Kim G, Vohs JM, Gorte RJ (2008) SOFC anodes based on infiltration of  $\text{La}_{0.3}\text{Sr}_{0.7}\text{TiO}_3$ . *J Electrochem Soc* 155:B1179–B1183
36. Kim H, Park S, Vohs JM, Gorte RJ (2001) Direct oxidation of liquid fuels in a solid oxide fuel cell. *J Electrochem Soc* 148:A693–A695
37. Mogensen M, Sammes NM, Tompsett GA (2000) Physical, chemical and electrochemical properties of pure and doped ceria. *Solid State Ionics* 129:63–94
38. Jung S, Lu C, He H, Ahn K, Gorte RJ, Vohs JM (2006) Influence of composition and Cu impregnation method on the performance of Cu/CeO<sub>2</sub>/YSZ SOFC anodes. *J Power Sources* 154:42–50
39. Gross MD, Vohs JM, Gorte RJ (2007) An examination of SOFC anode functional layers based on ceria in YSZ. *J Electrochem Soc* 154:B694–B699
40. Jiang SP, Chan SH (2004) A review of anode materials development in solid oxide fuel cells. *J Mater Sci* 39:4405–4439
41. Lu C, Worrell WL, Vohs JM, Gorte RJ (2003) A comparison of Cu-ceria-SDC and Au-ceria-SDC composites for SOFC anodes. *J Electrochem Soc* 150:A1357–A1359
42. Park S, Gorte RJ, Vohs JM (2001) Tape cast solid-oxide fuel cells for the direct oxidation of hydrocarbons. *J Electrochem Soc* 148:A443–A447
43. Park S, Vohs JM, Gorte RJ (2000) Direct oxidation of hydrocarbons in a solid-oxide fuel cell. *Nature* 404:265
44. Kim T, Liu G, Boaro M, Lee S, Vohs JM, Gorte RJ, Al-Madhi OH, Dabbousi BO (2006) A study of carbon formation and prevention in hydrocarbon-fueled SOFC. *J Power Sources* 155:231–238
45. Kim H, Vohs JM, Gorte RJ (2001) Direct oxidation of sulfurcontaining fuels in a solid oxide fuel cell. *Chem Commun* 22:2334–2335
46. He H, Gorte RJ, Vohs JM (2005) Highly sulfur tolerant Cu-ceria anodes for SOFCs. *Electrochem Solid State Lett* 8:A279–A280
47. Rasmussen JFB, Hagen A (2009) The effect of H<sub>2</sub>S on the performance of Ni–YSZ anodes in solid oxide fuel cells. *J Power Sources* 191:534–541
48. Kim H, Lu C, Worrell WL, Vohs JM, Gorte RJ (2002) Cu–Ni cermet anodes for direct oxidation of methane in solid-oxide fuel cells. *J Electrochem Soc* 149:A247–A250
49. Lee S, Vohs JM, Gorte RJ (2004) A study of SOFC anodes based on Cu–Ni and Cu–Co bimetals in CeO<sub>2</sub>–YSZ. *J Electrochem Soc* 151:A1319–A1323
50. Ahn K, He H, Vohs JM, Gorte RJ (2005) Enhanced thermal stability of SOFC anodes made with CeO<sub>2</sub>–ZrO<sub>2</sub> solutions. *Electrochem Solid State Lett* 8: A414–A417
51. Nakamura T, Petzow G, Gauckler LJ (1979) Stability of the perovskite phase LaBO<sub>3</sub> (B = V, Cr, Mn, Fe, Co, Ni) in reducing atmosphere I. Experimental results. *Mater Res Bull* 14:649
52. Tao SW, Irvine JTS (2003) A redox-stable efficient anode for solid-oxide fuel cells. *Nat Mater* 2:320–323
53. Lu XC, Zhu JH (2007) Cu(pd)-impregnated La<sub>0.75</sub>Sr<sub>0.25</sub>Cr<sub>0.5</sub>Mn<sub>0.5</sub>O<sub>3-d</sub> anodes for direct utilization of methane in SOFC. *Solid State Ionics* 178:1467–1475
54. Doshi R, Alcock CB, Gunasekaran N, Carberry JJ (1993) Carbonmonoxide and methane oxidation properties of oxide solid solution catalysts. *J Catal* 140:557–563
55. Sfeir J, Buffat PA, Mockli P, Xanthopoulos N, Vasquez R, Mathieu HJ, Van Herle J, Thampi KR (2001) Lanthanum chromite based catalysts for oxidation of methane directly on SOFC anodes. *J Catal* 202:229–244
56. Danilovic N, Vincent A, Luo J, Chuang KT, Hui R, Sanger AR (2009) Correlation of fuel cell anode electrocatalytic and ex situ catalytic activity of perovskites La<sub>0.75</sub>Sr<sub>0.25</sub>Cr<sub>0.5</sub>X<sub>0.5</sub>O<sub>3-d</sub> (X = Ti, Mn, Fe, Co). *Chem Mater* 22(3):957–965
57. Prindahl S, Hansen JR, Grahl-Madsen L, Larsen PH (2001) Sr-doped LaCrO<sub>3</sub> anode for solid oxide fuel cells. *J Electrochem Soc* 148:A74–A81
58. Vernoux P, Djurado E, Guillolo M (2001) Catalytic and electrochemical properties of doped lanthanum chromites as new anode materials for solid oxide fuel cells. *J Am Ceram Soc* 84:2289–2295
59. Kobsiriphat W, Madsen BD, Wang Y, Marks LD, Barnett SA (2009) La<sub>0.8</sub>Sr<sub>0.2</sub>Cr<sub>1-x</sub>Ru<sub>x</sub>O<sub>3-d</sub>-Gd<sub>0.1</sub>Ce<sub>0.9</sub>O<sub>1.95</sub> solid oxide fuel cell anodes: Ru precipitation and electrochemical performance. *Solid State Ionics* 180:257
60. Tao SW, Irvine JTS (2004) Catalytic properties of the perovskite oxide La<sub>0.75</sub>Sr<sub>0.25</sub>Cr<sub>0.5</sub>Fe<sub>0.5</sub>O<sub>3-d</sub> in relation to its potential as a solid oxide fuel cell anode material. *Chem Mater* 16:4116–4121
61. Jardiel T, Caldes MT, Moser F, Hamon J, Gauthier G, Joubert O (2010) New SOFC electrode materials: theni-substituted LSCM-based compounds (La<sub>0.75</sub>Sr<sub>0.25</sub>)(Cr<sub>0.5</sub>Mn<sub>0.5-x</sub>Ni<sub>x</sub>)O<sub>3-d</sub> and (La<sub>0.75</sub>Sr<sub>0.25</sub>)(Cr<sub>0.5-x</sub>Ni<sub>x</sub>Mn<sub>0.5</sub>)O<sub>3-d</sub>. *Solid State Ionics* 181:894
62. Pudmich G, Boukamp BA, Gonzalez-Cuenca M, Jungen W, Zipprich W, Tietz F (2000) Chromite/titanate based perovskites for application as anodes in solid oxide fuel cells. *Solid State Ionics* 135:433

63. Hui S, Petric A (2001) Conductivity and stability of  $\text{SrVO}_3$  and mixed perovskites at low oxygen partial pressures. *Solid State Ionics* 143:275–283
64. Tao SW, Irvine JTS (2004) Synthesis and characterization of  $(\text{La}_{0.75}\text{Sr}_{0.25})\text{Cr}_{0.5}\text{Mn}_{0.5}\text{O}_{3-\delta}$ , a redox-stable, efficient perovskite anode for SOFCs. *J Electrochem Soc* 151:A252–A259
65. Tao SW, Irvine JTS, Plint SM (2006) Methane oxidation at redox stable fuel cell electrode  $\text{La}_{0.75}\text{Sr}_{0.25}\text{Cr}_{0.5}\text{Mn}_{0.5}\text{O}_{3-\delta}$ . *J Phys Chem B* 110:21771–21776
66. Zha SW, Tsang P, Cheng Z, Liu ML (2005) Electrical properties and sulfur tolerance of  $\text{La}_{0.75}\text{Sr}_{0.25}\text{Cr}_{1-x}\text{Mn}_x\text{O}_3$  under anodic conditions. *J Solid State Chem* 178:1844–1850
67. Kharton VV, Tsipis EV, Marozau IP, Viskup AP, Frade JR, Irvine JTS (2007) Mixed conductivity and electrochemical behavior of  $(\text{La}_{0.75}\text{Sr}_{0.25})(0.95)\text{Cr}_{0.5}\text{Mn}_{0.5}\text{O}_{3-\delta}$ . *Solid State Ionics* 178:101–113
68. Plint SM, Connor PA, Tao S, Irvine JTS (2006) Electronic transport in the novel SOFC anode material  $\text{La}_{1-x}\text{Sr}_x\text{Cr}_{0.5}\text{Mn}_{0.5}\text{O}_{3+\delta}$ . *Solid State Ionics* 177:2005–2008
69. Wan J, Zhu JH, Goodenough JB (2006)  $\text{La}_{0.75}\text{Sr}_{0.25}\text{Cr}_{0.5}\text{Mn}_{0.5}\text{O}_{3-\delta}$  + Cu composite anode running on  $\text{H}_2$  and  $\text{CH}_4$  fuels. *Solid State Ionics* 177:1211–1217
70. Fonseca FC, Muccillo ENS, Muccillo R, de Florio DZ (2008) Synthesis and electrical characterization of the ceramic anode  $\text{La}_{1-x}\text{Sr}_x\text{Mn}_{0.5}\text{Cr}_{0.5}\text{O}_3$ . *J Electrochem Soc* 155:B483–B487
71. Kim G, Corre G, Irvine JTS, Vohs JM, Gorte RJ (2008) Engineering composite oxide SOFC anodes for efficient oxidation of methane. *Electrochem Solid State Lett* 11:B16–B19
72. Jiang SP, Liu L, Khuong POB, Ping WB, Li H, Pu H (2008) Electrical conductivity and performance of doped  $\text{LaCrO}_3$  perovskite oxides for solid oxide fuel cells. *J Power Sources* 176:82–89
73. Sfeir J (2003)  $\text{LaCrO}_3$ -based anodes: stability considerations. *J Power Sources* 118:276–285
74. Liu J, Madsen BD, Ji ZQ, Barnett SA (2002) A fuel-flexible ceramic-based anode for solid oxide fuel cells. *Electrochem Solid State Lett* 5:A122–A124
75. Yamazoe N, Teraoka Y (1990) Oxidation catalysis of perovskites – relationships to bulk structure and composition (valency, defect, etc.). *Catal Today* 8:175
76. Pena-Martinez J, Marrero-Lopez D, Ruiz-Morales JC, Savaniu C, Nunez P, Irvine JTS (2006) Anodic performance and intermediate temperature fuel cell testing of  $\text{La}_{0.75}\text{Sr}_{0.25}\text{Cr}_{0.5}\text{Mn}_{0.5}\text{O}_{3-\delta}$  at lanthanum gallate electrolytes. *Chem Mater* 18:1001–1006
77. Tao S, Irvine JTS (2006) Phase transition in perovskite oxide  $\text{La}_{0.75}\text{Sr}_{0.25}\text{Cr}_{0.5}\text{Mn}_{0.5}\text{O}_{3-\delta}$  observed by in situ high temperature neutron powder diffraction. *Chem Mater* 18:5453
78. Cheng Z, Zha S, Aguilar L, Liu M (2005) Chemical, electrical, and thermal properties of strontium doped lanthanum vanadate. *Solid State Ionics* 176:1921–1928
79. Chen XJ, Liu QL, Chan SH, Brandon NP, Khor KA (2007) Sulfur tolerance and hydrocarbon stability of  $\text{La}_{0.75}\text{Sr}_{0.25}\text{Cr}_{0.5}\text{Mn}_{0.5}\text{O}_3/\text{Gd}_{0.2}\text{Ce}_{0.8}\text{O}_{1.9}$  composite anode under anodic polarization. *J Electrochem Soc* 154:B1206–B1210
80. Bernuy-Lopez C, Allix M, Bridges CA, Claridge JB, Rosseinsky MJ (2007)  $\text{Sr}_2\text{MgMoO}_{6-\delta}$ : structure, phase stability, and cation site order control of reduction. *Chem Mater* 19:1035–1043
81. Huang YH, Dass RI, Xing ZL, Goodenough JB (2006) Double perovskites as anode materials for solid-oxide fuel cells. *Science* 312:254–257
82. Huang YH, Dass RI, Denyszyn JC, Goodenough JB (2006) Synthesis and characterization of  $\text{Sr}_2\text{MgMoO}_{6-\delta}$  – an anode material for the solid oxide fuel cell. *J Electrochem Soc* 153:A1266–A1272
83. Otsuka K, Wang Y, Sunada E, Yamanaka I (1998) Direct partial oxidation of methane to synthesis gas by cerium oxide. *J Catal* 175:152–160
84. Marrero-López D, Peña-Martínez J, Ruiz-Morales JC, Gabás M, Núñez P, MAG A, Ramos-Barrado JR (2009) Redox behaviour, chemical compatibility and electrochemical performance of  $\text{Sr}_2\text{MgMoO}_6 - [\delta]$  as SOFC anode. *Solid State Ionics* 180:1672
85. Vasala S, Lehtimäki M, Haw SC, Chen JM, Liu RS, Yamauchi H, Karppinen M (2010) Isovalent and aliovalent substitution effects on redox chemistry of  $\text{Sr}_2\text{MgMoO}_{6-\delta}$  SOFC-anode material. *Solid State Ionics* 181:754–759
86. Matsuda Y, Karppinen M, Yamazaki Y, Yamauchi H (2009) Oxygen-vacancy concentration in  $\text{A}_2\text{MgMoO}_{6-\delta}$  doubleperovskite oxides. *J Solid State Chem* 182:1713–1716
87. Huang Y, Liang G, Croft M, Lehtimäki M, Karppinen M, Goodenough JB (2009) Double-perovskite anode materials  $\text{Sr}_2\text{MMoO}_6$  (M = co, ni) for solid oxide fuel cells. *Chem Mater* 21:2319–2326
88. Vasala S, Lehtimäki M, Huang YH, Yamauchi H, Goodenough JB, Karppinen M (2010) Degree of order and redox balance in B-site ordered double-perovskite oxides,  $\text{Sr}_2\text{MMoO}_{6-\delta}$  (M = Mg, mn, fe, co, ni, zn). *J Solid State Chem* 183:1007
89. Marrero-Lopez D, Pena-Martinez J, Ruiz-Morales JC, Martin Sedenio MC, Nunez P (2009) High temperature phase transition in SOFC anodes based on  $\text{Sr}_2\text{MgMoO}_6$ -delta. *J Solid State Chem* 182:1027–1034
90. Marrero-Lopez D, Pena-Martinez J, Ruiz-Morales JC, Perez Coll D, Aranda MAG, Nunez P (2008) Synthesis, phase stability and electrical conductivity of  $\text{Sr}_2\text{MgMoO}_{6-\delta}$  anode. *Mater Res Bull* 43:2441–2450
91. Moos R, Hardtl KH (1997) Defect chemistry of donor-doped and undoped strontium titanate ceramics between 1000° and 1400° C. *J Am Ceram Soc* 80:2549–2562



92. Hui S, Petric A (2002) Evaluation of yttrium-doped SrTiO<sub>3</sub> as an anode for solid oxide fuel cells. *J Eur Ceram Soc* 22:1673–1681
93. Kolodiaznyh T, Petric A (2005) The applicability of sr-deficient n-type SrTiO<sub>3</sub> for SOFC anodes. *J Electroceram* 15:5–11
94. Lu XC, Zhu JH, Yang Z, Xia G, Stevenson JW (2009) Pd-impregnated SYT/LDC composite as sulfur-tolerant anode for solid oxide fuel cells. *J Power Sources* 192:381–384
95. Moos R, Bischoff T, Menesklou W, Hardtl K (1997) Solubility of lanthanum in strontium titanate in oxygen-rich atmospheres. *J Mater Sci* 32:4247–4252
96. Marina OA, Canfield NL, Stevenson JW (2002) Thermal, electrical, and electrocatalytic properties of lanthanum-doped strontium titanate. *Solid State Ionics* 149:21–28
97. Huang X, Zhao H, Shen W, Qiu W, Wu W (2006) Effect of fabrication parameters on the electrical conductivity of YxSr1 – xTiO3 for anode materials. *J Phys Chem Solids* 67:2609–2613
98. Balachandran U, Eror NG (1982) Electrical conductivity in lanthanum-doped strontium titanate. *J Electrochem Soc* 129:1021–1026
99. Flandermeyer BF, Agarwal AK, Anderson HU, Nasrallah MM (1984) Oxidation-reduction behaviour of la-doped SrTiO<sub>3</sub>. *J Mater Sci* 19:2593–2598
100. Battle PD, Bennett JE, Sloan J, Tilley RJD, Vente JF (2000) A-site cation-vacancy ordering in Sr1 – 3x/2LaxTiO3: a study by HRTEM. *J Solid State Chem* 149:360–369
101. Meyer R, Waser R, Helmbold J, Borchardt G (2002) Cationic surface segregation in donor-doped SrTiO<sub>3</sub> under oxidizing conditions. *J Electroceram* 9:101–110
102. Fu QX, Mi SB, Wessel E, Tietz F (2008) Influence of sintering conditions on microstructure and electrical conductivity of yttrium-substituted SrTiO<sub>3</sub>. *J Eur Ceram Soc* 28:811–820
103. Slater PR, Fagg DP, Irvine JTS (1997) Synthesis and electrical characterisation of doped perovskite titanates as potential anode materials for solid oxide fuel cells. *J Mater Chem* 7:2495–2498
104. Blennow P, Hagen A, Hansen KK, Wallenberg LR, Mogensen M (2008) Defect and electrical transport properties of nb-doped SrTiO<sub>3</sub>. *Solid State Ionics* 179:2047–2058
105. Blennow P, Hansen KK, Wallenberg LR, Mogensen M (2009) Electrochemical characterization and redox behavior of nb-doped SrTiO<sub>3</sub>. *Solid State Ionics* 180:63–70
106. Blennow P, Hansen KK, Wallenberg LR, Mogensen M (2007) Synthesis of nb-doped SrTiO<sub>3</sub> by a modified glycine-nitrate process. *J Eur Ceram Soc* 27:3609–3612
107. Hashimoto S, Poulsen FW, Mogensen M (2007) Conductivity of SrTiO<sub>3</sub> based oxides in the reducing atmosphere at high temperature. *J Alloys Compd* 439:232–236
108. Tufte ON, Chapman PW (1967) Electron mobility in semiconducting strontium titanate. *Phys Rev* 155:796
109. Irvine J, Slater P, Wright P (1996) Synthesis and electrical characterisation of the perovskite niobate-titanates, Sr1 – x/2Ti1 – xNbxO3 – d. *Ionics* 2:213–216
110. Blennow P, Hansen KK, Reine Wallenberg L, Mogensen M (2006) Effects of Sr/Ti-ratio in SrTiO<sub>3</sub>-based SOFC anodes investigated by the use of cone-shaped electrodes. *Electrochim Acta* 52:1651–1661
111. Hui S, Petric A (2002) Electrical conductivity of yttrium-doped SrTiO<sub>3</sub>: influence of transition metal additives. *Mater Res Bull* 37:1215–1231
112. Zhao H, Gao F, Li X, Zhang C, Zhao Y (2009) Electrical properties of yttrium doped strontium titanate with A-site deficiency as potential anode materials for solid oxide fuel cells. *Solid State Ionics* 180:193
113. Fu Q, Tietz F, Sebold D, Tao S, Irvine JTS (2007) An efficient ceramic-based anode for solid oxide fuel cells. *J Power Sources* 171:663–669
114. Yang LM, De Jonghe LC, Jacobsen CP, Visco SJ (2007) B-site doping and catalytic activity of sr(Y) TiO<sub>3</sub>. *J Electrochem Soc* 154:B949–B955
115. Vincent A, Luo J, Chuang KT, Sanger AR (2010) Effect of Ba doping on performance of LST as anode in solid oxide fuel cells. *J Power Sources* 195:769
116. Wagner SF, Warnke C, Menesklou W, Argiris C, Damjanovic T, Borchardt G, Ivers-Tiffée E (2006) Enhancement of oxygen surface kinetics of SrTiO<sub>3</sub> by alkaline earth metal oxides. *Solid State Ionics* 177:1607
117. Sun X, Wang S, Wang Z, Qian J, Wen T, Huang F (2009) Evaluation of Sr<sub>0.88</sub>Y<sub>0.08</sub>TiO<sub>3</sub>–CeO<sub>2</sub> as composite anode for solid oxide fuel cells running on CH<sub>4</sub> fuel. *J Power Sources* 187:85–89
118. Sun X, Wang S, Wang Z, Ye X, Wen T, Huang F (2008) Anode performance of LST–xCeO<sub>2</sub> for solid oxide fuel cells. *J Power Sources* 183:114–117
119. Fu QX, Tietz F, Stover D (2006) La<sub>0.4</sub>Sr<sub>0.6</sub>Ti<sub>1–x</sub>Mn<sub>x</sub>O<sub>3–d</sub> perovskites as anode materials for solid oxide fuel cells. *J Electrochem Soc* 153: D74–D83
120. Ruiz-Morales J, Canales-Vázquez J, Savaniu C, Marrero-López D, Zhou W, JTS I (2006) Disruption of extended defects in solid oxide fuel cell anodes for methane oxidation. *Nature* 439:568–571
121. Cheng Z, Zha S, Liu M (2006) Stability of materials as candidates for sulfur-resistant anodes of solid oxide fuel cells. *J Electrochem Soc* 153:A1302–A1309
122. Mukundan R, Brosha EL, Garzon FH (2004) Sulfur tolerant anodes for SOFCs. *Electrochem Solid State Lett* 7:A5–A7
123. Zha SW, Cheng Z, Liu ML (2005) A sulfur-tolerant anode material for SOFCs Gd<sub>2</sub>Ti<sub>1.4</sub>Mo<sub>0.6</sub>O<sub>7</sub>. *Electrochem Solid State Lett* 8:A406–A408

124. Porat O, Heremans C, Tuller HL (1997) Stability and mixed ionic electronic conduction in  $Gd_2(Ti_{1-x}Mo_x)_2O_7$  under anodic conditions. *Solid State Ionics* 94:75
125. Sprague JJ, Tuller HL (1999) Mixed ionic and electronic conduction in Mn/Mo doped gadolinium titanate. *J Eur Ceram Soc* 19:803–806
126. Deng ZQ, Niu HJ, Kuang XJ, Allix M, Claridge JB, Rosseinsky MJ (2008) Highly conducting redox stable pyrochlore oxides. *Chem Mater* 20:6911–6916
127. Kramer S, Spears M, Tuller HL (1994) Conduction in titanate pyrochlores – role of dopants. *Solid State Ionics* 72:59–66
128. Naito H, Arashi H (1992) Electrical-properties of  $ZrO_2$ - $TiO_2$ - $Y_2O_3$  system. *Solid State Ionics* 53:436–441
129. Kaiser A, Feighery A, Fagg D, Irvine J (1998) Electrical characterization of highly titania doped YSZ. *Ionics* 4:215
130. Tao S, Irvine JTS (2002) Optimization of mixed conducting properties of  $Y_2O_3$ - $ZrO_2$ - $TiO_2$  and  $Sc_2O_3$ - $Y_2O_3$ - $ZrO_2$ - $TiO_2$  solid solutions as potential SOFC anode materials. *J Solid State Chem* 165:12–18
131. Tao SW, Irvine JTS (2004) Investigation of the mixed conducting oxide ScYZT as a potential SOFC anode material. *J Electrochem Soc* 151:A497–A503
132. Slater PR, Irvine JTS (1999) Niobium based tetragonal tungsten bronzes as potential anodes for solid oxide fuel cells: synthesis and electrical characterisation. *Solid State Ionics* 120:125–134
133. Slater PR, Irvine JTS (1999) Synthesis and electrical characterisation of the tetragonal tungsten bronze type phases,  $(Ba/Sr/Ca/La)_{0.6}M_xNb_{1-x}O_{3-d}$  ( $M = mg, ni, mn, cr, fe, in, sn$ ): evaluation as potential anode materials for solid oxide fuel cells. *Solid State Ionics* 124:61–72
134. Kaiser A, Bradley JL, Slater PR, Irvine JTS (2000) Tetragonal tungsten bronze type phases  $(Sr_{1-x}Ba_x)_{0.6}Ti_{0.2}Nb_{0.8}O_{3-d}$ : material characterisation and performance as SOFC anodes. *Solid State Ionics* 135:519–524
135. Aguilar L, Zha S, Cheng Z, Winnick J, Liu M (2004) A solid oxide fuel cell operating on hydrogen sulfide (H<sub>2</sub>S) and sulfur-containing fuels. *J Power Sources* 135:17–24

### Books and Reviews

- Atkinson A, Barnett S, Gorte RJ, Irvine JTS, McEvoy AJ, Mogensen M, Singhal SC, Vohs J (2004) Advanced anodes for high temperature fuel cells. *Nat Mater* 3:17–27
- Brandon NP, Skinner S, Steele BCH (2003) Recent advances in materials for fuel cells. *Annu Rev Mater Res* 33:183–213
- Fergus JW (2006) Oxide anode materials for solid oxide fuel cells. *Solid State Ionics* 177:1529
- Fleig J (2003) Solid oxide fuel cell cathodes: polarization mechanisms and modeling of the electrochemical performance. *Annu Rev Mater Res* 33:361–382
- Gellings PJ, Bouwmeester HJM (2000) Solid state aspects of oxidation catalysis. *Catal Today* 58:1–53
- Goodenough JB (2003) Oxide-ion electrolytes. *Annu Rev Mater Res* 33:91–128
- Goodenough JB, Huang Y (2007) Alternative anode materials for solid oxide fuel cells. *J Power Sources* 173:1
- Gong M, Liu X, Trembly J, Johnson C (2007) Sulfur-tolerant anode materials for solid oxide fuel cell application. *J Power Sources* 168:289
- Gorte RJ, Vohs JM (2009) Nanostructured anodes for solid oxide fuel cells. *Curr Opin Colloid Interface Sci* 14:236–244



# Solid Oxide Fuel Cell Materials: Durability, Reliability, and Cost

Harumi Yokokawa<sup>1,2</sup> and Teruhisa Horita<sup>2</sup>

<sup>1</sup>Advanced Research Laboratories, Tokyo City University, Tokyo, Japan

<sup>2</sup>National Institute of Advanced Industrial Science and Technology (AIST), Tsukuba, Ibaraki, Japan

## Article Outline

Glossary

Definition of the Subject

Introduction

Historical Aspects of Reliability, Durability, and Cost Issues

Durability/Reliability of SOFC Systems

Cost Issues

Future Directions

Bibliography

## Glossary

**Acceleration method** Generally speaking, there is no appropriate acceleration method for stack performance degradation as a whole. Therefore, individual factors should be carefully accelerated to know the degradation phenomena. One degradation phenomena should consist of several processes having different activation processes. It is highly required to have an acceleration method which should not create additional sources of different origin and mask the original sources of degradation to be investigated.

**Cr poisoning** Catastrophic degradation of lanthanum manganite-based cathode due to the chromium–oxygen vapors emitted from Cr<sub>2</sub>O<sub>3</sub> oxide scale as a result of reaction with (humidified) air. Cr poisoning for other cathodes such as cobaltite or ferrites are completely

different in mechanism. The SrCrO<sub>4</sub> formation is a key phenomena causing the lowering in cathode performance.

**EVD cells** Sealless tubular cells fabricated by the electrochemical vapor deposition (EVD) technique. The durability is excellent, whereas the fabrication cost is expected to be quite high. This cell can be regarded as the standard cell when the relation among durability, efficiency, and cost is considered.

**First-generation cells** Cells to be operated in the temperature region of 900–1,000° C. Usually oxide interconnects are used together with electrolyte made of YSZ. Since materials compatibility is severe at higher temperatures, stable lanthanum manganite-base cathode is adopted, whereas nickel anodes are used in a similar manner to other types. Electrolyte-self-support or cathode-support types are adopted.

**Metal-support cells** Cells are fabricated on metal substrates. Compared with ceramic substrates, adoptable fabrication conditions are limited to prevent metals from being oxidized severely. Instead, metals as a main structural component provide many benefits such as better stability against thermal shocks and milder temperature distribution inside the stacks, etc.

**Redox stability** When anode-support cells are adopted, the mechanical behavior of anode substrate becomes important. During redox cycles, an anode layer is expanded to destroy the nickel connection or to make cracks on YSZ framework/YSZ electrolyte plate.

**Reliability versus cost reduction** In many cases, achievement of reliability is in trade-off relation to cost reduction. To overcome this, it is required to make breakthroughs in the fabrication technologies

**Second-generation cells** Cells to be operated in the temperature region of around 800° C. Metal interconnects are used together with anode-support cells and sealing materials. The active cathode such as LSCF (lanthanum strontium cobaltite ferrites) is used so that the durability is one of the main issues.

**Stress caused by volume changes** Mechanical stability is dominated by volume changes in components; these are caused by thermal expansion with temperature, chemical volume change due to the valence change within the same lattice at the constant temperature.

**Sulfur poisoning** Degradation of nickel-cermet anodes due to the adsorption of sulfur originated from  $H_2S$  in fuels. An initial drop in performance after introducing  $H_2S$  is maintained without further degradation. After switching back to the normal fuels without sulfur, anode performance is recovered slowly. In cathodes, some degradation is observed due to the contamination as  $SO_2/SO_3$ ; in such a case,  $SrSO_4$  is formed.

**Third-generation cells** Cells to be operated below  $800^\circ C$ . Instead of oxide ceramics, metal is used to support cells. Fabrication technique is most challenging.

## Definition of the Subject

Solid Oxide Fuel Cells (SOFCs) are devices of converting chemical energy (fuels) into electrical energy using an oxide ion conducting materials as electrolyte together with cathode for oxygen incorporation process and anode for oxidation of fuels. For fuel cells to be continuously operated, there arise four flows inside fuel cells: air flow and fuel flow, electrical current, and heat flow. Historically, only a small number of SOFC stack types have been successfully established because it is rather difficult to construct electrochemical cells/stacks with solid materials alone in keeping good electrical contacts among components, good gaseous permeability along the gas channels, or complete gaseous tightness across dense parts such as electrolyte and interconnects [1–3]. This leads to additional requirements concerning the chemical compatibility [4] among the cell components and the mechanical stability [5] of stack as a whole during fabrication and long-term operation including a certain number of thermal cycles. This makes materials selection difficult. Not only the functional properties but also the compatibility with adjacent materials is quite

important. Durability and reliability of SOFC stacks are therefore strongly dependent on such materials compatibility [6]. Stress comes from any volume changes in the cell components; for example, thermal expansion mismatch, chemical volume expansion due to changes in valence state [7], volume change on precipitation of products of reactive diffusion or reaction with gaseous impurities, pore formation, etc. These changes may cause the mechanical instability among the stack components and also affecting the functional parts of cells; that is, the electrical path can be damaged or the gaseous permeability through gas channel to and from the electrochemical reaction sites are influenced. When cracks are formed inside electrolytes or interconnects, fuels and oxidants will meet and burn without generating electricity, causing local heating. The electrochemical performance may also be degraded directly by gaseous impurities attacking the electrochemical reaction sites which are located at the electrode/electrolyte interface region. Changes in microstructure of electrodes also lead to degradation of performance; nickel sintering is a typical example. In these processes, solid-state diffusion makes important contribution [8].

Historically speaking, reliability issues are always associated with an important feature that developments of stack design, fabrication methods, and cell materials are mutually related with each other. Even when the same materials are used in different stack designs, a fabrication method must be different so that materials compatibility appears in different manners. Main issues in the early stage of research and development were interface stability between cathode and electrolyte [9], interconnect chemistry associated with sinterability of lanthanum chromites [10], and chemical volume expansion [7]. Sealless tubular cells fabricated with electrochemical vapor deposition (EVD) [11, 12] were the first ones which have been successfully developed by solving those issues [13, 14]. Durability of the sealless tubular cells was found to be excellent as shown in quite low degradation rates: 0.1%/1,000 h for cell performance and less than 0.1%/1,000 h for system performance at the operation temperature of  $1,000^\circ C$  [10]. Demerits of tubular

cells, however, were analyzed as their low-volume power density and high fabrication cost [15]. These sealless tubular cells are recognized as the first-generation cells. After this success, many attempts have been made to overcome those demerits by testing new materials, new cell designs, and new stack designs. The most typical ones can be called as the second-generation cells which are operated around 750–800° C. Here, metal interconnects were adopted instead of oxide interconnect, active cathodes such as lanthanum strontium cobaltites (LSC) or lanthanum strontium cobaltite ferrites (LSCF) [16] were used instead of stable but less active lanthanum strontium manganites (LSM), and an anode-support-type cell design was adopted. As a result, performance of such second-generation cells has been rapidly improved and in many cases has become much better than that of the first generation. On the other hand, durability was not better because metal interconnects and active cathodes were adopted in spite of their low chemical stability [17]. More recently, the third generation based on the metal support cells [18–20] has attracted much attention, because of its expecting low costs and lower operating temperatures. Based on the idea adopted for this generation, nickel can be regarded as a rather expensive material. Instead, cheaper stainless steel should be utilized as a main cell component. This inevitably leads to a requirement that appropriate fabrication methods should be developed so as to fabricate metal-support cells with a reasonable cost. In other words, chemical stability becomes a big issue even in the fabrication processes.

## Introduction

The most important features associated with fuel cell technologies are energy conversion efficiency, durability (or life time), and cost. These are common characteristic features among various fuel cells such as phosphoric acid fuel cells (PAFC), molten carbonate fuel cells (MCFC), polymer electrolyte fuel cells (PEFC), and solid oxide fuel cells (SOFC). For comparison among fuel cells, applications in which fuel cells are utilized are important aspects of fuel cells:

stationary application in several 100 kW or larger, small stationary applications for residential houses, and automotive or mobile applications.

For the first stationary application, comparison was made in 1980s–mid-1990s among PAFC, MCFC, and SOFC. Efficiency, based on the methane fuel, was regarded as about 40% for PAFC operated at 180° C, 45% for MCFC operated at 650° C and 40% for SOFC operated at 1,000° C when the first attempt by Westinghouse for tubular cells was succeeded [21]. Later, it is clarified that the higher efficiency of MCFC compared with SOFC is due mainly to the operation temperature. Actually, with decreasing operation temperature of SOFCs, the efficiency increases even for SOFCs. The most surprisingly impressive achievement of Westinghouse's SOFCs is their stable performance for a long period of operation time, although their fabrication cost was evaluated to be too high. Alternative efforts of constructing SOFCs in planar design with metal interconnects were, on the other hand, suffered from poor durability in its early stage of development. One of plausible reasons for such technological dead-rock seems to be at a point that the target application was stationary so that they aimed at constructing larger flat cells with sealant materials. In such a larger planar stack, temperature distribution developed within planar cells may cause strong mechanical stresses, leading to failure in sealing or to crack formation.

From the mid-1990s, there arose a new wave in fuel cell applications, that is, the automotive application and closely related applications of small stationary. It began with PEFC. Even so, SOFC has also received the impacts of new applications. This leads to two important efforts on SOFC developments: (1) severer requirements for mechanical stability in automotive applications [22] and (2) smaller stationary application. The former has come from the new application proposed by BMW, Delphi, and Renault to utilize SOFC systems as auxiliary power unit in combustion engine cars. Since BMW and Delphi have cooperated with National Laboratories in their own countries, materials development has been made to improve mechanical instability. Development of simulation technique also helps to improve the stack technologies. The latter case

of the small stationary systems gave rise to a big impact in Japan, Australia, Switzerland, and UK where the SOFC cogeneration systems have attracted strong attention.

Current issues of SOFC technologies, namely, reliability/durability and cost appear in different manners in respective applications which have different historical background.

This entry is organized as follows: In section “[Historical Aspects of Reliability, Durability and Cost Issues](#),” historical aspects are first described to provide essential points of SOFC stack/system development. The technological features of the first-generation cells, namely, sealless tubular cells, will be described in comparison with the second- and the third-generation cells in critical technological issues; these are materials selection of interconnect (oxide or metal), sealing scheme, redox issues of nickel cermets, metal support cells, trade-off relation between reliability and performance, and materials chemistry associated with lowering operation temperature. Section “[Durability/Reliability of SOFC Systems](#)” describes durability/ reliability of SOFC systems. Failures of system operation are first described. Then, failures of stacks and degradation of cell performances are described in detail with focuses on chromium poisoning, nickel sintering, carbon deposition, sulfur poisoning, etc. Results of field tests are also described in relation to reliability. Section “[Cost Issues](#)” describes the cost issue and “Future Directions of SOFC development” are given finally in section “[Future Directions](#).”

## **Historical Aspects of Reliability, Durability, and Cost Issues**

Materials compatibility is important in construction of SOFCs. Particularly, chemical and mechanical stabilities are crucial in simultaneously optimizing materials, materials processing and stack design. First success has been achieved by Westinghouse Power Corp. (later Siemens Westinghouse Power Corp. and now Siemens Power Generation Corp.) in the 1980s by adopting the first-generation cell

materials, the electrochemical deposition technique to fabricate a dense yttria-stabilized zirconia (YSZ) electrolyte film on porous LSM cathode tubes and subsequent Ni anode on the dense YSZ film as described in Fig. 1. This is called sealless tubular cells, because no use of sealing materials is the important key point. The cells exhibit high performance and also long stability; only a small degradation rate of performance (less than 0.1%/1000 h) has been confirmed for more than 70,000 h for the cell level (see Fig. 2) and more than 30,000 h for the system level. Two demerits, however, were pointed out for those cells by Ackermann et al. [15] in Argonne National Laboratory; one is high cost because of the adoption of electrochemical vapor deposition (EVD) technique which utilizes metal chlorides in vacuum vessels, the other one being low-volume power density. Since then, many attempts have been made to overcome these demerits, namely, alternative materials have been investigated, new materials processing methods have been developed, and alternative stack designs have been attempted (Table 1).

In recent years, rapid progress has been made in the development of SOFC cogeneration systems with several kW scale for residential houses [23–26]; its demonstration has been successfully made in real residential circumstances [23]. In such a situation, degradation, durability, and reliability have appeared again as important issues. Now these should be related with cost issues, because it is already well established that the excellent long stability can be achieved with the electrochemical vapor deposition (EVD) technique despite high cost. The most important point is that the low cost has to be obtained at the same time together with high efficiency and long stability.

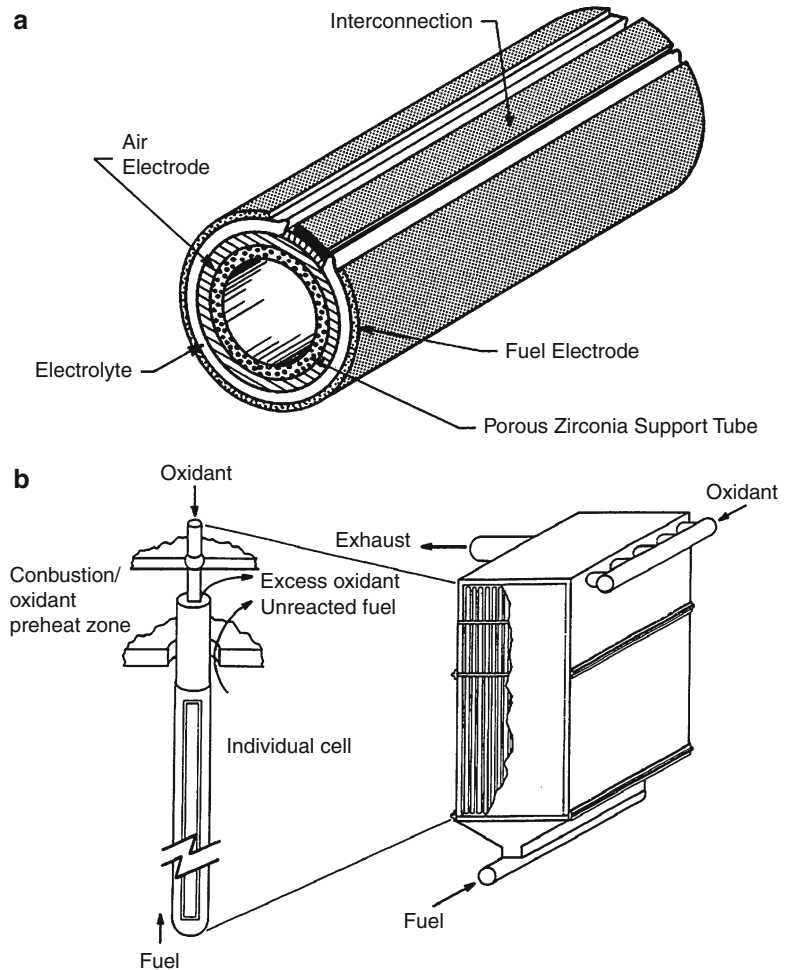
## **First Generation Stack: Sealless Tubular Performance as Standard**

Westinghouse Power Corp. made a breakthrough by adopting sealless tubular cells after examining several other types of SOFC stack design such as planar cells or segment-in-series cells. This implies that the sealless tubular cells have many advantages against other designs. Actually, after the breakthrough, they succeeded in demonstrating



**Solid Oxide Fuel Cell  
Materials: Durability,  
Reliability, and Cost,**

**Fig. 1** Sealless tubular cell: (a) cell configuration and (b) stack configuration  
(From [13, 14])

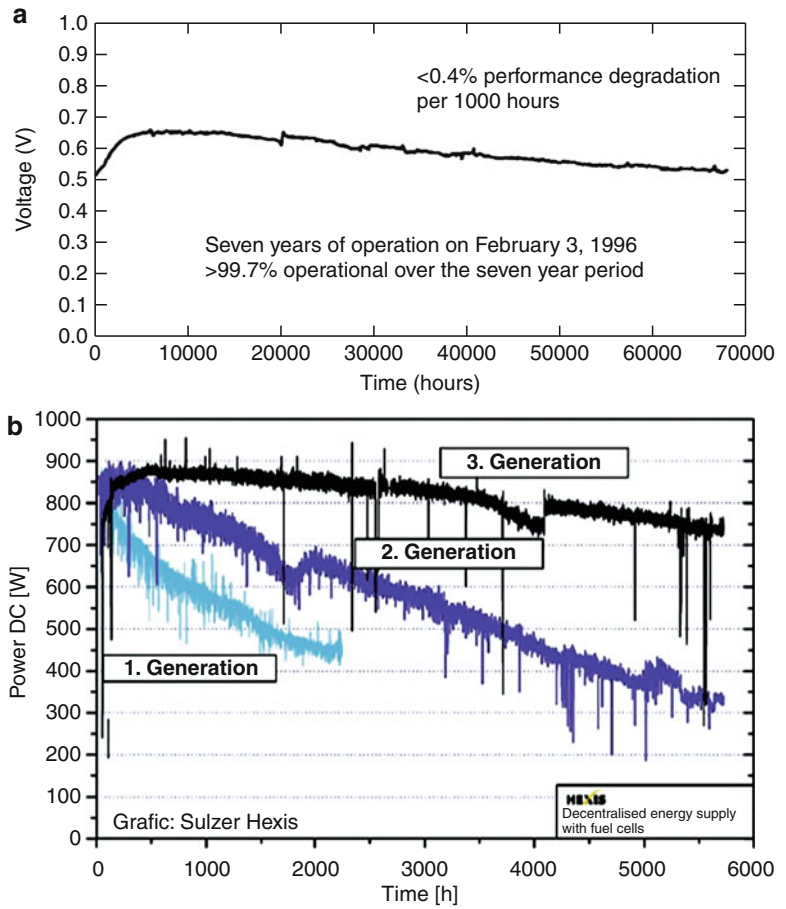


the long-term stability. From the current knowledge of durability of other cells, their success in long-term stability can be ascribed to the following:

1. The electrochemical vapor deposition (EVD) process has been successfully developed as fabricating a dense electrolyte film on porous cathodes and fixing anode nickel particles on the electrolyte plate with YSZ. This provides a nearly ideal micro-structure for electrolyte/electrode interfaces.
2. Sealing materials are not used. Particularly, this cell is free from silica; silica is one of materials to be carefully treated.
3. Other metals than nickel are not used in anode atmosphere or in air. Alloys (Fe-Cr, Ni-Cr)

sometimes caused troubles such as anomalous corrosion. In sealless tubular cells, nickel is used as anode materials and also as cell-to-cell connecting materials. Note that nickel is stable in the fuel atmosphere without forming oxide scale. Furthermore, a small amount of oxygen can be dissolved so that even when oxygen permeates from the air side on nickel in the fuel side, a steady state flow of oxygen can be established across the nickel/LaCrO<sub>3</sub>-based interconnects. Nickel connection can be made because this is the cathode-support cell. Note that when the anode-support tubular cell is adopted in a similar design, cell-to-cell connection has to be made in the air side, leading to a severer materials problem.

**Solid Oxide Fuel Cell Materials: Durability, Reliability, and Cost, Fig. 2** Cell performance degradation of (a) the first generation sealless tubular cells by Westinghouse (Currently Siemens, From [13, 14]) and (b) the second generation planar cells by Sulzer Hexis (Currently Hexis, From [17])



**Solid Oxide Fuel Cell Materials: Durability, Reliability, and Cost, Table 1** Comparison in typical materials and fabrication methods among the first-, second-, and third-generation SOFCs

	First	Second	Third
Cathode	LSM	LSCF	LSCF
Electrolyte	YSZ (50 $\mu\text{m}$ )	YSZ (10 $\mu\text{m}$ ) Ni ScSZ, LSGM GDC	ScSZ, GDC
Anode	Ni/YSZ	Ni/YSZ, Ni/SSZ, Ni/DGC	Ni
Interconnect	LaCrO <sub>3</sub> -based SrTiO <sub>3</sub> -based	Ferritic, Cr-based	Ferritic
Cell to cell connection	Ni	Ferritic	Ferritic
Operation temperature	900–1,000° C	750–800° C	500–650° C
Typical fabrication method	EVD, plasma spray	Wet-sintering	Sintering in reducing atmosphere

4. Alumina tubes are used for providing air at the bottom of the cathode compartment. This is acted as heat exchanger to remove heats out of cells. This provides an excellent situation for thermal management on larger stacks.

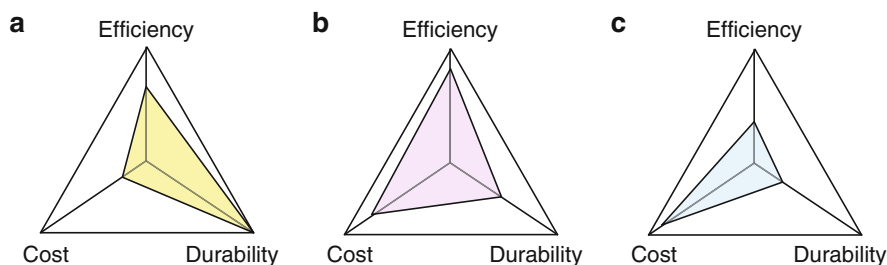
Immediately after the success of sealless tubular cells, one important analysis was made to clarify the technological features by Argonne National Laboratory [15]. Their main conclusions are given as follows:

1. Fabrication cost is too high
2. Power density per unit volume is less

Status of the sealless tubular cells concerning cost, efficiency, and durability can be summarized as shown in Fig. 3a.

After knowing the success of Westinghouse and technological assessments by ANL, many people started to develop various kinds of SOFC stacks to overcome demerits of the sealless tubular cells. Depending on their technological strategies, several different attempts have been made. These can be summarized as follows:

1. Improvement of sealless tubular cells. To improve the volume power density, flatten tube type or delta type designs have been investigated by Siemens (Westinghouse) themselves [27]. To lower the fabrication cost, sintering-wet process has been successfully adopted by TOTO [28], whereas atmospheric plasma spray was adopted by Siemens themselves [27]. These attempts are based on the idea that tubular cells or their modified cells must be superior to other designs.
2. Planar design has been recognized as better in achieving the higher power density in an analogous manner to other fuel cells such as PAFC or MCFC. One approach is to adopt the oxide interconnect, the other being the metal interconnects. Only few developers have adopted the oxide interconnect in planar stacks [29, 30]. One technological reason is that sintering of lanthanum chromite-based ceramics is difficult, particularly in air. Another reason is originated from the cost consideration; when rather thick plates of  $\text{LaCrO}_3$ -based interconnects are used in planar cells, the contribution of La to the total material cost becomes quite large [31]. Adoption of metal interconnects becomes important in stack developments probably because of their technological merits [32, 33]; the use of metal inside SOFC stacks is quite useful for better thermal management, and for controlling the mechanical stress, etc. Even so, demerits can be seen in poisoning of cathodes by Cr originated from oxide scale [34], chemical interactions with sealing materials, and also increasing interface resistivity across the oxide scale. In many cases, utilization of metal interconnect is combined with the adoption of anode support cells.
3. There have been also many efforts in improving stack design such as flatten tubes, micro tubes, or honeycomb type cells. This is mainly from the thermo-mechanical considerations. In order to avoid the thermal shock effectively, utilization of materials having low thermal expansion and high thermal diffusivity are highly required;  $\text{Al}_2\text{O}_3$  and  $\text{Si}_3\text{N}_4$  can be regarded as one of such materials for high-temperature use. Unfortunately, YSZ exhibits high thermal expansion and low thermal conductivity and there is no good way of improving those inappropriate properties. Thus, the most effective way of overcoming thermal shock is to shorten the thermal diffusion length so as to relax changes in temperature on



**Solid Oxide Fuel Cell Materials: Durability, Reliability, and Cost, Fig. 3** Schematic representation of the current status of technology for achieving three targets of fuel cells, namely, efficiency, cost, and durability; (a) the

first generation SOFC based on Electrochemical vapor deposition technique; (b) the second generation SOFC based on anode-support cells with wet-sintering processes; and (c) the third generation based on metal support cells

thermal shocks. For this purpose, micro-tube or honeycomb structures become attractive.

4. Metal support cells are proposed to realize cost reduction from the materials cost and fabrication cost simultaneously. Compared with nickel which is the major component in the anode support cells, the metal support cells aim at using cheaper Fe–Cr alloy as supporting materials [19]. Instead, the fabrication process becomes rather difficult compared with other cell design.

These activities can be summarized as the second or the third generations of SOFCs. These characteristic features are compared with the first generation in fundamental aspects in Fig. 3. Cost and efficiency are expected to be satisfied, whereas durability has not been confirmed yet. Thus, the main issue associated with the second generation becomes the establishment of durability/reliability (Fig. 4).

#### Oxide Interconnect Versus Metal Interconnect

Interconnect materials are quite important in fabricating SOFC stacks. To meet the chemical and mechanical stability requirements under an oxygen potential gradient, only a few materials have remained; some spinel compounds such as  $\text{NiCr}_2\text{O}_4$  or  $\text{CoCr}_2\text{O}_4$  were tested as interconnects in the early stage of development without success because of their poor materials stability. Remaining materials are  $\text{LaCrO}_3$ -based or  $\text{SrTiO}_3$ -based perovskite oxides. The interconnect materials need to meet two requirements: good electrical conductivity (at the same time, essentially no oxide ion conductivity) and the good gaseous tightness. This can be met by fabricating into dense plates/films. Furthermore, an additional requirement is derived from the mechanical point of view, that is, the thermal expansion coefficient should match with that of YSZ, and the chemical volume expansion due to valence change should be small enough [35].

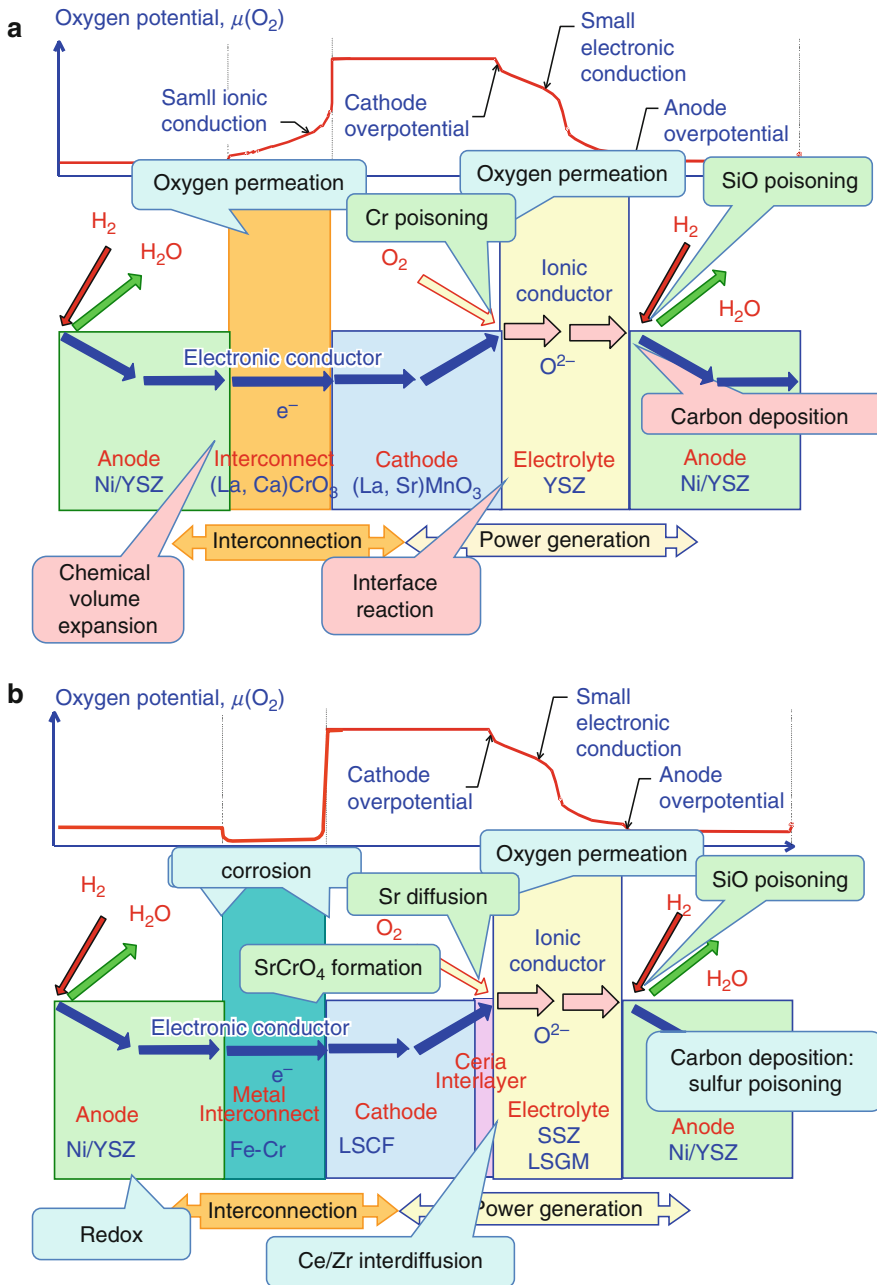
The technical issues associated with oxide interconnect can be summarized as follows:

1. Establishment of inexpensive fabrication process for making dense films of  $\text{LaCrO}_3$ -based

ceramics. This is because the sintering of  $\text{LaCrO}_3$  in air is quite difficult since the chromium component tends to volatilize during sintering and to subsequently deposit at interparticle necks as  $\text{Cr}_2\text{O}_3$ ; This deposited chromia hinders further sintering [10].

2. Thermal expansion coefficient is another issue. The thermal expansion coefficient of non-doped  $\text{LaCrO}_3$  is small compared with YSZ. To match the thermal expansion coefficient, there are two ways: one is the heavy alkaline earth doping up to 30 mol%, the other being addition of alumina to YSZ to reduce the effective thermal expansion coefficient of a mixture of YSZ and  $\text{Al}_2\text{O}_3$  [35]. This makes it possible to adopt the low concentration (about 10%) doping of alkaline earth.
3. The high electrical conductivity is achieved by holes created as a result of doping of alkali earth oxide; however, in reducing atmosphere, hole and  $\text{Cr}^{4+}$  is reduced to  $\text{Cr}^{3+}$  and oxide ion vacancies. This valence change gives rise to the volume expansion, which is called the chemical volume expansion [7]. For the heavily doped system, this chemical volume expansion is too big so that additional B-site doping is necessarily made to reduce the chemical volume expansion.
4. The material cost of lanthanum is high so that the thickness of the oxide interconnects should be thin enough to reduce the amount used in cells [31]. On the other hand, the  $\text{LaCrO}_3$ -based interconnects should be thick enough to prevent the electrochemical oxygen permeation which takes place as the bipolar diffusion of oxide ions and holes inside the interconnect. For such a purpose, Ca-doped  $\text{LaCrO}_3$  is not appropriate because those ceramics are highest in gas permeation among the alkali earth-doped  $\text{LaCrO}_3$  [36, 37].
5. For the  $\text{SrTiO}_3$ -based interconnects, sintering is much easier than  $\text{LaCrO}_3$ -based ceramics, whereas the electrical properties are not good, particularly in the air side [38].

When the metal interconnects are adopted in the second generation stack, there arise other technical issues:



**Solid Oxide Fuel Cell Materials: Durability, Reliability, and Cost, Fig. 4** Schematic representation of the materials and associated degradation issues (a) the first-generation cells and (b) the second-generation cells

1. Metal interconnects typically made of ferritic alloys have slightly higher thermal expansion coefficients than YSZ. A new alloy was produced so as to fit the thermal expansion of YSZ; this is a Cr-based alloy, Cr5Fe1Y<sub>2</sub>O<sub>3</sub>

[39]. Since this alloy is oxide dispersed and therefore quite hard, it is not easy to fabricate it into a desired shape. For this purpose, powder metallurgy process has been developed [40].

2. Most important difference of metal interconnects from oxide interconnects is that such alloys will be oxidized during the cell operation. This inevitably involves kinetic aspects in durability of materials. The most important aspect related with durability is materials behavior under a steep oxygen potential gradient. Electrolyte and interconnect materials should be stable under such a gradient. In addition, alloys have to be stable on both sides of materials, namely, the air side as well as the fuel side, because the oxygen potential inside normal Fe–Cr alloys is maintained to be quite low compared with the fuel atmosphere. One difference from oxide interconnect is that oxygen atoms to be transferred inside oxide interconnects will permeate through the interconnect plate, whereas oxygen atoms reacted with or dissolved into alloys do not permeate but will be accumulated in the surface area to form oxide scale. This increasing amount of oxide scales with operational time becomes an important factor of limiting life time. Note here that in the first-generation sealless tubular cells, only nickel is used in the fuel compartment and such nickel is oxygen permeable when oxygen flux is low enough to maintain the reducing condition.
3. Immediately after starting the utilization of metal interconnects, the chromium poisoning for lanthanum manganite-based cathode was recognized as a severe degradation [34, 41–43]. The  $\text{Cr}_2\text{O}_3$  component of the oxide scales reacts with oxygen molecule in air with/without water vapor to emit the vapors of  $\text{CrO}_3(\text{g})$  or  $\text{CrO}_2(\text{OH})_2(\text{g})$ . Such vapors come to the electrochemically active sites of LSM cathode (namely, three phase boundaries) and deposited as  $\text{Cr}_2\text{O}_3$  or  $\text{MnCr}_2\text{O}_4$ . Although detailed mechanism is different, similar poisoning effects due to Cr vapors were found for other cathodes such as LSCF through the  $\text{SrCrO}_4$  formation.
4. A most effective way of overcoming Cr poisoning is to reduce Cr vapors from oxide scales [44]. As a result, coating technique becomes crucial in the utilization of metal interconnect.

Materials to be coated should meet several requirements concerning the stability under a steep oxygen potential gradient. Such requirements are quite similar to those for the oxide interconnects. Thus, perovskite oxides have been tested as coating materials [45]. As far as the cation diffusivity and the oxygen permeability are concerned, the lanthanum chromite-based materials will be most appropriate. Even so, the fabrication technique to form a dense film on alloys is quite limited. Attempts have been made to try to utilize other perovskite materials such as cobaltites and manganites. Since those perovskites are oxygen permeable, oxide scales should grow under the coating materials. In addition to  $\text{Cr}_2\text{O}_3$ , some spinel phases are formed between the alloys and the coating. Investigations on such complicated oxide layers lead to selection of  $\text{MnCo}_2\text{O}_4$  spinels as coating materials [46].

5. From the viewpoint of cost, utilization of metal interconnects should be considered as the combined technology with coating. Although raw alloy materials are cheaper than lanthanum, the fabrication cost will increase due to the sophisticated coating technique. If coating cannot be avoided, it is essential to reduce the fabrication cost for coating as well as to reduce further the raw materials cost because the development of mother alloys alone cannot lead to low cost enough as interconnects.

From the materials design point of view for those electrical conductive oxides which are stable under an oxygen potential gradient, oxide interconnects and coating materials for alloys are quite similar. From the fabrication method, however, there are several differences. Inexpensive sintering process can be applied for oxide interconnects, whereas high-temperature heat treatment is limited for coating. The low-pressure plasma spray technique was successfully adopted to form dense films; however, from the cost point of view, this is not appropriate. The atmospheric pressure plasma spray is more cost effective, but the quality of fabricated films is not excellent.



## Seals

Seal technology is quite sophisticated among the stacking technologies. As described above, the first success of stacking SOFCs by Westinghouse has been made by adopting the sealless design combined with the electrochemical vapor deposition technique. This clearly indicates that when seals are adopted, there arise many materials problems and without solving those problems, any stacks cannot survive.

The most severe requirements for sealing materials are

1. Appropriate bonding to prevent gaseous leakage. Compared with PEFC which can be easily sealed gas-tightly by just compressing the main cell components, it is impossible for SOFC to achieve the gas-tightness among the ceramic cell components without activation in the atomic level.
2. Sometimes, not quite often, sealing can be achieved by co-sintering two materials to be joined at a relatively high temperature. This can be regarded as a thermally activated process at interfaces.
3. In many cases, glasses or crystallized glasses will be used as sealing materials. This is because glasses are convenient for achieving the gas-tightness due to their deformable nature. Even so, glasses are non-stable materials and tend to undergo the transformation into crystalline phases on reactions with other cell components. This changes the mechanical property or the gas permeability at the bonding places. Such processes are dependent on various factors; temperature, reaction rate, crystallization rate, etc. This implies that their mechanical strength depends on their thermal history. Since there is a large temperature distribution among the places where sealing is needed, deterioration of sealed parts takes place in a different manner from place to place. Note that the durability/reliability of stacks is determined by the weakest place.
4. When no glasses will be used and compression sealing [47] will be adopted, complete gas tightness cannot be necessarily achieved.

Thus effects due to gas leakage will appear in various aspects of stack behavior. Since the SOFC stacks consist of the oxide ion conductive and/or electronic conductive materials, local gas leakage gives rise to those effects which will be spread throughout the stack [48]. In this sense, to make an analysis on gas leakage and to overcome this issue, it will be needed to understand a whole behavior of stacks.

In view of these features, sealing is not the localized materials issue but it is a matter of whole stacks. In this sense, the characteristic features of the adopted stack design and the sequential of fabrication depends on the way of making seals.

## Redox Issues

In a typical case, the stack fabrication will be completed by reducing NiO to Ni metal to form the electrical path in the anode side. On this reduction, the sintered NiO will be reduced by hydrogen to become nickel powders first and then to make an electrical path after some coagulation; during this process, the mechanical constraints introduced at the high temperature heat treatment will be released at the anode side and a new constrained state will start under the oxygen potential gradient [49].

When the sealless structure is adopted and the remaining fuels are combusted inside the stack, there is always some possibility that combusted gases will diffuse backward to the nickel anode area and will reoxidize nickel.

For anode support cells, one needs to have an appropriate method of sealing edges of cells where the porous supporting anode should be appropriately closed. The flatten tubes provide one good way of sealing sides by high-temperature sintering without using seals.

For small power-unit systems such as the SOFC cogeneration systems for the residential applications, usually no purge gas will be used. Thus, there arises a big possibility that the anodes can be reoxidized during the start-up and shut-down cycles.

### Metal Support Cells

The metal support cells can be regarded as the third generation. The major driving forces for making the metal support cells can be summarized as follows;

1. For the mobile/transportation application, it is highly required to start up rapidly, to make stacks mechanically strong enough against mechanical or thermal shocks. For this purpose, ANL adopted the metal-supported cells and they made attempts of fabricating metal parts in essentially the same manner as those for ceramics, that is, they tested to fabricate by sintering metal powders in the reducing atmosphere [18].
2. Another major driving force for metal support cells is cost reduction [19]. For the anode-supported cells, a relatively large amount of nickel will be used because the nickel cermet becomes the major structural supporting component. To achieve a drastic change in raw materials cost, therefore, cheaper alloys should be used as the major component. Note also that from the raw materials point of view, ceramics are more expensive than metals in general.
3. The use of metal as supporting component implies that the operational temperature will be below 800° C which is the typical operational temperature for the second-generation cells. At such a low temperature, brazing will be used instead of glass-based sealing methods. This will make materials chemistry much simpler.

Despite expected low cost, it is expected that the fabrication technology is much more difficult for metal support cells. This is illustrated in Fig. 3c.

### Reliability Versus Performance and Its Relation to Operation Temperature

Utilization of metal interconnects requires lower temperature operation, and this low operation temperature is generally expected to lead to less severe conditions for degradations because of the Arrhenius-type behavior of processes involved in degradations. Accumulated knowledge on

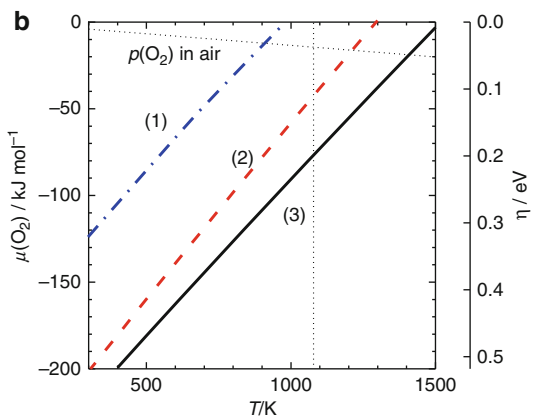
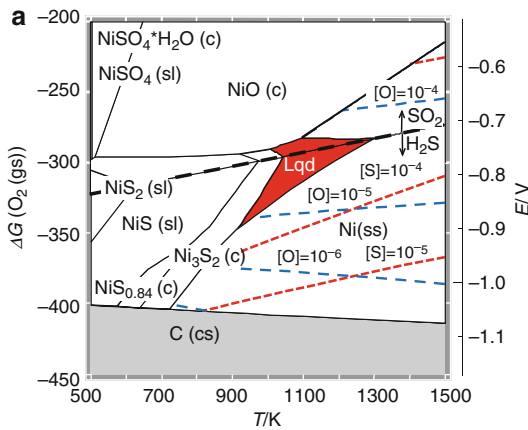
durability, however, exhibits an interesting feature that on contrary to this expectation, some degradations become more severe at lower temperatures. That is because with lowering operation temperature, there arise an increasing number of factors affecting durability as indicated as follows:

1. In order to achieve the same performance as the first generation, the more active electrodes are needed. In particular, cathode performance exhibit rather large temperature dependence [50]. Thus, instead of the stable LSM cathode, it is needed to utilize more active cathodes such as LSCF. The electrode activity of LSCF is high because this material exhibits ionic and electronic mixed conductivity and also shows high surface reaction rate for the oxygen incorporation reaction. These features are originated from the high concentration of oxide ion vacancies in LSCF. This is chemically represented as follows: the SrFeO<sub>3</sub> or SrCoO<sub>3</sub> components in perovskite are reduced to form Fe<sup>3+</sup>/Co<sup>+3</sup> ions together with the oxide ion vacancies. Chemically speaking, the oxide ion vacancy formation is due to the fact that unstable SrFeO<sub>3</sub> is reduced to be SrFeO<sub>3-x</sub> and O<sub>2</sub>(g). In other words, the valence stability of Fe<sup>4+</sup>/Co<sup>+4</sup> is weak compared with that of Mn<sup>4+</sup> in the perovskite lattice.
2. This in turn indicates that LSCF is also reactive to other materials/gases; typical reactions are those with YSZ to form zirconates (SrZrO<sub>4</sub> or La<sub>2</sub>Zr<sub>2</sub>O<sub>7</sub>) and with chromium containing vapors (CrO<sub>3</sub>(g) or CrO<sub>2</sub>(OH)<sub>2</sub>) to form SrCrO<sub>4</sub>. In this reaction, the SrFeO<sub>3-x</sub> component is reductively decomposed into SrO in SrZrO<sub>4</sub>/SrCrO<sub>4</sub> and FeO + O<sub>2</sub>(g). Thus, this chemical reactivity is originated from the same physicochemical properties described above. In this sense, the performance and the durability are in trade-off relation. This is summarized in Table 2 [4, 51].
3. Instead of stable YSZ, use is frequently made of other electrolytes showing higher oxide-ion conductivity; these are ScSZ (Scandia-stabilized zirconia), GDC (gadolinia-doped ceria), and LSGM (lanthanum strontium

**Solid Oxide Fuel Cell Materials: Durability, Reliability, and Cost, Table 2** Comparison of cathodes among lanthanum strontium manganites, ferrites, and cobaltites in

their chemical reactivity, functionality as cathode, and tolerance against Cr poisoning

Items	LSM	LSF	LSC
Valence stability	Mn <sup>4+</sup> Stable	Fe <sup>4+</sup> unstable	Co <sup>4+</sup> Co <sup>3+</sup> unstable
O <sup>2-</sup> conductive	Nearly zero	High	High
Cathode mechanism	Three phase boundaries	Two phase boundaries (surface)	
Reactivity with YSZ	Stable (A-site deficient)	SrZrO <sub>3</sub> formation	La <sub>2</sub> Zr <sub>2</sub> O <sub>7</sub> SrZrO <sub>3</sub> formation
Reactivity with Cr	Cr <sup>3+</sup> substitute	SrCrO <sub>4</sub> /Cr <sup>3+</sup> substitution	SrCrO <sub>4</sub> /Cr <sup>3+</sup> Cr <sup>4+</sup> substitution
Cr poisoning	Significant	Not seen in early stage but causes various deteriorations	



**Solid Oxide Fuel Cell Materials: Durability, Reliability, and Cost, Fig. 5** Ellingham diagrams plotted as  $m(O_2)$  vs.  $T$  (a) Ni-S-O-H system for interaction of nickel and impurities (From [85]); (b) Borderlines for separating SrCrO<sub>4</sub> formation region and LaCrO<sub>3</sub> solid solution

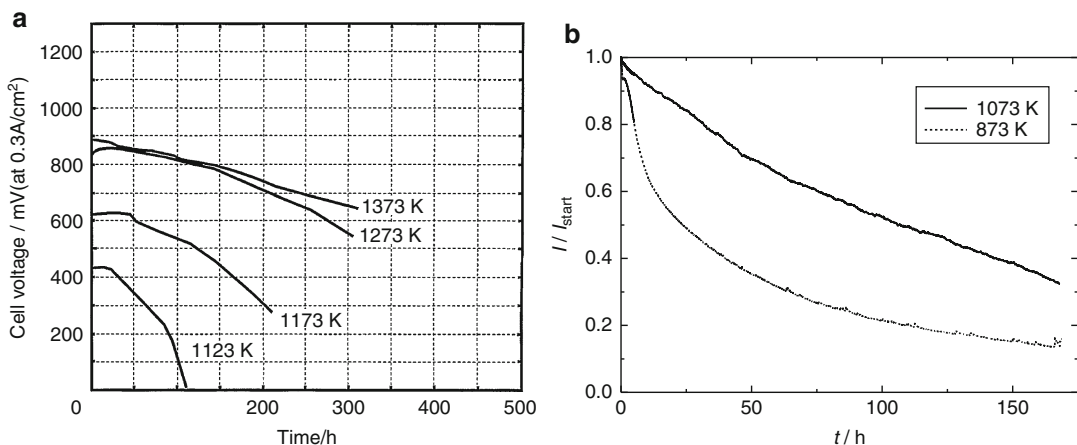
formation region for interaction of perovskite cathodes and chromium containing vapors; (1)  $2SrCrO_4 + 2LaMnO_3 = 2LaCrO_3 + 2SrMnO_3 + O_2(g)$ ; (2)  $1.33SrCrO_4 + 1.33LaFeO_3 = 1.33LaCrO_3 + 1.33SrFeO_{2.5} + O_2(g)$ ; (3)  $2SrCrO_4 = 2SrCrO_3 + O_2(g)$  (From [42])

gallium magnesium oxide). The chemical reactivity of these electrolytes is, however, higher than YSZ. In many cases, ceria is thought to be more stable than zirconia. This is true when comparison is made just between ceria and zirconia. However, when comparison is made among the dopants, this is not the case; dopants in ceria are not well stabilized so that they are more reactive than yttria in YSZ [52].

- Use of metal interconnect gives rise to a new situation that materials are not necessarily used in their most stable states. This means that the durability is determined not only by equilibrium properties but also by kinetic properties. Thus, corrosion becomes one of the main issues at lower temperatures.

- The equilibrium properties tend to shift to a more reactive side with decreasing temperature [52]. In particular, those reactions which involve the condensation of the gaseous component become more favored at lower operation temperatures. A typical example is the adsorption of sulfur from H<sub>2</sub>S gases on nickel. Another important example is the redox reactions which emit or adsorb oxygen gas. At low temperatures, the oxidation becomes thermodynamically favored. Those reactions with gaseous impurities (including water vapor, CO<sub>2</sub>) exhibit the same tendency. With decreasing temperature, the driving force for such reaction increases due to the negative entropy effect. Those features are shown as the oxygen potential vs. temperature plot in Fig. 5.

6. From the Arrhenius behavior of kinetic processes, the reaction rate decreases exponentially at low temperatures. This in turn gives rise to larger driving force for degradation. For example, the overpotential of LSM cathode increases with decreasing temperature as expected. This is understandable from the Arrhenius behavior. This larger overpotential at lower temperatures promotes Cr poisoning because the oxygen potential difference corresponding to the overpotential assists the Cr vapor to reach the electrochemically active sites at the three-phase boundaries (TPBs) and to be electrochemically reduced to form  $\text{Cr}_2\text{O}_3$  (see Fig. 6). In another example using the samarium strontium cobaltite (SSC) cathode, reactions with  $\text{SO}_2$  proceed fast at a high temperature so that only a small amount of  $\text{SO}_2$  can reach the electrochemically active zone. With decreasing temperature, however, this trapping ability is weakened; as a result, a larger amount of  $\text{SO}_2$  can attack the sites, leading to faster degradation compared with high temperature [53, 54]. These examples indicate that one degradation phenomenon consists of several processes which have their own temperature dependence. Thus, the apparent degradation rate becomes fast at lower temperatures.
7. So-called inert metals such as Pt and Ag are not necessarily chemically inert at lower temperatures [55].
8. For active cathodes, an interlayer is inserted between such cathodes and the YSZ electrolyte to prevent chemical reactions, leading to a complicated interconnect/electrode/electrolyte structure. This introduces another technical requirement for fabricating those layers durable enough.
9. Effects of impurities may appear in a more significant manner at low temperatures. One example is sintering of nickel at low temperatures. Compared with the first-generation cells, there are many reports suggesting more significant sintering in the second-generation cells [56]. This is probably due to gaseous impurities which tend to condensate at low temperatures.
10. With decreasing temperature, nature of electro-chemical reactions may change. Particularly, degradation may depend not only on the major electrochemical reactions but also on the secondary reactions. For example, protons in YSZ or GDC do not contribute to the major electrochemical reaction because of its extremely low transport number. However, it is not adequate to neglect completely possible effects of protons in electrolytes or in



**Solid Oxide Fuel Cell Materials: Durability, Reliability, and Cost, Fig. 6** Temperature dependence of cathode degradation (a) Cr poisoning on LSM cathodes (From [34]) (b)  $\text{SO}_2$  poisoning on SSC cathode (From [53])

cathodes. In particular, GDC exhibits two-orders-of-magnitude higher proton solubility than YSZ [57, 58]. This makes it reasonable to assume that protons can contribute to side electrochemical reactions.

When consideration is made on chemical compatibility of cathodes with other components/impurities, it becomes clear that the selection of elements in the major components is critically important. Differences between LSM, LSC, LSF, and LSCF are originated mainly from the thermodynamic activity of SrO component in coexistence with transition metal oxides. Thus, no use of the SrO component in cathodes can be good attempts of avoiding gap between the stability and the performance. Actually, LNF ( $\text{La}(\text{Ni},\text{Fe})\text{O}_3$ ) proposed by NTT [59] seems to indicate some progress in this issue.

## Durability/Reliability of SOFC Systems

### Failures in Flow Systems

The SOFC system is an energy converter from fuels as chemical energy to electricity and heats. There are four flows inside stacks, namely, fuel flow, air flow, electrical flow, and heat flow. In order to maintain the proper function as energy converter, these four flows have to be well maintained and controlled so as to harmonize to generate electricity and remove heats [60].

SOFC systems frequently have to be stopped in their operation due to unexpected failures in controlling systematic flows of fuels, water to be used in reforming, air, or electricity. Typical examples are given as follows:

1. Air flow: When air blower malfunctions, systems will be in trouble. Oxygen starvation takes place in cathodes. Perovskite oxide cathodes will be reduced to provide oxygen if oxygen gas is not sufficiently available. As a result, such cathodes are heavily damaged.
2. Fuel and fuel treatment: Except for hydrogen gas, normal fuels need to be reformed before

utilization. The water reforming needs to add water to hydrocarbons; when water is not supplied in a proper amount, carbon deposition will take place. Deposited carbon can act as catalyst for further carbon deposition, leading to collapse of fuel flow. Similarly, when an amount of air for partial oxidation or autothermal oxidation is not well controlled, essentially the same situation can be reproduced. When fuel supply is stopped accidentally, fuel starvation takes place and nickel anodes will be oxidized by water vapors.

3. Concerning the electrical path, there can be two failure modes: one is shorting, the other being cut-off of path. When shorting will start, the current should pass until generated electrical potential is cancelled out with the ohmic loss in the shorting circuit path; typically, this happens when one of the chemicals (fuel or oxygen) becomes empty. A large current will be concentrated in a limited area, leading to damage in local area. The latter case of cut-off corresponds to the so-called death of the electrochemical cells. This will happen on the electrochemical sites or along the path.
4. Heats are by-products of the electrochemical conversion and therefore have to be removed effectively. Usually this removal of heats is made with the air flow which is supplied in an excess amount to the stoichiometrically required one. When this removal becomes insufficient, the temperature will increase and enhance various kinds of activation processes. The contribution of radiation loss from the stack surface will increase; in other words, temperature distribution inside stacks becomes large.

These failures should be avoided by well-designed and well-trained control systems.

### Field Tests

Field tests of the SOFC systems have been made in several places. In Germany, field test was initiated by the utility companies. Among them, the test on the Sulzer Hexis system has been made in recent years and well documented in the literature [17]. After the field test, Sulzer Hexis made

improvements on the system configurations; these seem to be interesting in knowing what kinds of materials issues were involved. First to be considered is the effect of sulfur. Those SOFC systems in Europe are designed to be utilized with natural gases available from natural gas pipelines. This implies that the sulfur content is rather high and changeable. They chose to operate at a higher temperature instead of applying the desulfurization process. As a result, their cells with Cr-base alloys are operated at around 900° C. Another issue was CaSO<sub>4</sub>. To avoid the contamination by CaSO<sub>4</sub>, they decided not to use the external water.

In Japan, a demonstration program for the SOFC cogeneration systems for residential houses has been initiated for the period 2007–2010. Kyocera reported the statistics of troubles during the demonstration program [61, 62]; this is summarized in Fig. 7. Troubles in systems were well treated to be improved so that a number of troubles decrease year by year.

**Failures/Degradation in SOFC Stacks**

Since there are many kinds of SOFC stacks which are fabricated by different fabrication methods in different sequences, it looks rather hard to describe the failure/degradation modes of stacks

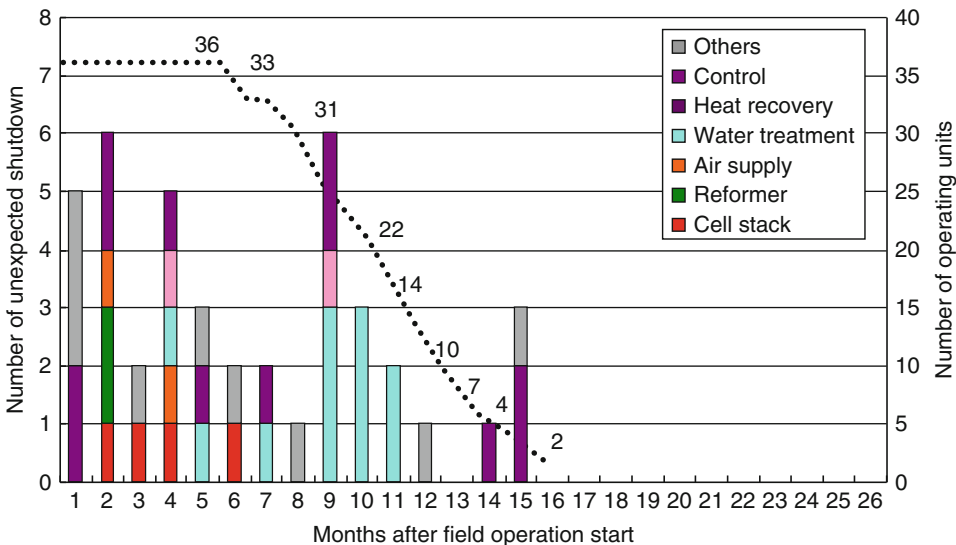
in a proper manner. Even so, it seems possible to extract some common features out of various failure/degradation modes.

**Long-Term Operation** During a long period of operation time, some changes may happen on the following aspects:

1. Deformation due to creep when cells are stacked into a tower consisting of a large number of cells.
2. Change in microstructure and related electrode structure due to diffusion in the vicinity of active sites.
3. Change in mechanical strength due to surface segregation, other aging effects or impurities effects.
4. Those changes in small parts may cause accumulated effects on the durability against thermal shocks or mechanical shocks.

Driving forces for such phenomena are diffusion in solid materials and reactions of solid components with gaseous components. These effects are expected to determine the life time beyond 10,000 h.

These features have been found to be highly correlated with the fabrication method/sequence



**Solid Oxide Fuel Cell Materials: Durability, Reliability, and Cost, Fig. 7** Summary of troubles during the field test for the 2007 fiscal year’s SOFC units. These are

categorized into troubles in Control system, heat recovery system, water treatment system air supply system, reformer, and cell stack itself (From [61])



as well as materials selected. For example, anode support cells have stable anodes but there remain several points to be optimized for a cathode-complex-layer structure.

On contrary, cathode-support cells have the stable performance for cathodes, but anodes may have some changed in microstructure because of nickel sintering [63].

**Failures Originating from Thermal Cycles or Redox Cycles** The SOFC stacks consist all of solid materials. Except for nickel anode and metal interconnects, all other materials are ceramics so that the mechanical instability during thermal cycles and redox cycles can be one of possible failures.

In many cases, failures are associated with stress concentration during thermal cycles or redox cycles. Mechanical stresses are closely related with volume changes of one component leading to mismatch along interfaces.

Volume changes are ascribed to

1. Thermal expansion
2. Chemical volume change due to valence change within the same crystal lattice
3. Redox of the main component such as Ni
4. Precipitation of new phases at interfaces or bonded regions

During operation, temperature distribution can be determined by the current density distribution and related heat release from the surface. This implies that the thermal stress can be properly treated only by the combined analyses on electrochemical performance, gaseous concentration, and thermal conduction. When stacks will be cooled down, temperature distribution can be determined by cooling mechanism so that the thermal stress distribution may change from those under operation.

### Effects Appearing in Stacks

1. Edge effect: Small changes in the shape of repeating elements may be accumulated and appear as an edge effect. In many cases, ceramic cells have their own structure to keep the electrical path and gaseous tightness inside stacks. During a long-term operation or

frequent thermal cycles, deformation can appear as a sum of the accumulated small changes in shape. In this sense, edges tend to have troubles in loss of the electrical loss, gaseous tightness, etc. In addition, temperature gradient tends to be steep in the vicinity of edges. As a result, degradation is apparently worsened in edge parts.

2. Effect of stack weight: When the horizontal cells are vertically stacked to form tower stacks/modules, an effect of gravitational weight may appear at the bottom of the stacks. This is a similar situation to the stacks of MCFC where a large number of horizontal cells are stacked and the effect of creep will appear when the selection of anode materials is not appropriate, for example, copper is recognized as such materials. For the SOFC stacks, no report has been made on creep behavior of the nickel cermet anodes so far. Ferritic steels are recognized as weaker against creep than austenite steels.
3. Gas distribution: Gas manifold system is critically important in the stack technology. When this malfunctions, supplying rate of gases become different from cell to cell, whereas the same electrical current passes through such cells connected in series. As a result, there can be a shortage of fuels in a particular cell, leading to damage of the cell [64].
4. Distribution of current: The SOFC stacks consist of highly electronic conductive electrodes and of highly ionic conductive electrolyte so that the current distribution can be easily reestablished when some parts in flows of fuel or air becomes ineffective or some parts of electrode area are damaged [65]. This electrochemical response to degradation makes it difficult to find out symptom of deteriorated parts while such deterioration continues to take place. In many cases, the degradation of stack performance appears to be linear with operation time.
5. Contamination: The only one appropriate method for investigating on the significance of contamination from other components and on plausible effects on electrode reactivity, electrical resistivity, or gaseous permeability is utilization of secondary ion mass spectrometry (SIMS) [66, 67]. Attempts by AIST

clarified the interesting behavior of elements inside the SOFC stacks [68] as shown in Fig. 8.

(a) Impurities are common in many cases. For example, sodium is quite frequently observed contaminant, whereas potassium is much less than sodium. In addition, aluminum and silicon are also always detected; frequently, but not always, phosphorus is detected. Sulfur is also found to be a frequently observed contaminant.

This is not necessarily derived from fuels. Even in air side, sulfur can be detected. Halogen such as Cl and F can also be detected. Note that Se, As, and Sb are not detected although those elements are major impurities in coal-derived gases.

(b) Impurity levels however depend on stacks/systems. For example, the Na contamination depends largely on raw materials or on the fabrication process.

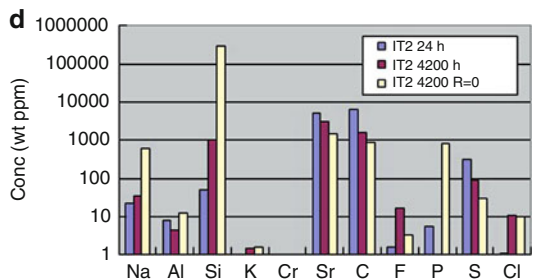
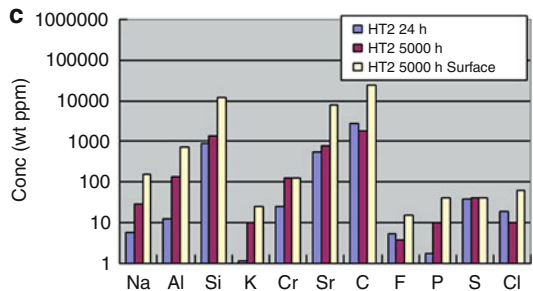
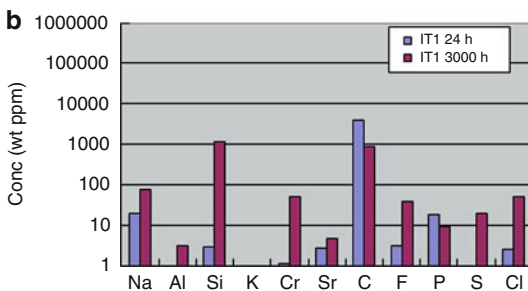
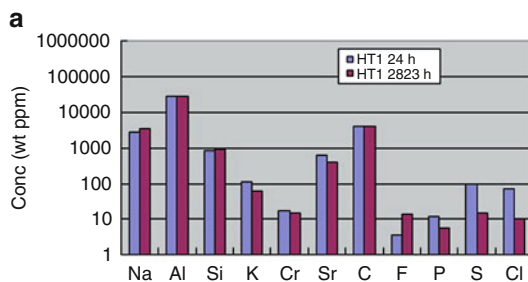
(c) There are several elements which increase in concentration during a long-term operation. Apparently, such elements are

transported as the gaseous species in fuel or air atmospheres. Generally speaking, contamination is much severer in the fuel side compared with the air side. This is due to the presence of water vapors in fuel sides, enhancing the volatilization by forming metal hydroxide vapors or metal suboxide vapors. Actually, the contamination level is higher in many cases in the downstream where water vapors are increased.

(d) Some particular elements are deposited on electrodes. Those elements which are known as poisons for the electrode activity, for example, chromium in cathode and phosphorus in anode, are detected in a more concentrated manner at the three-phase boundaries where the main electrochemical reactions take place.

(e) Sources of contaminants can be suggested as follows: thermal insulating materials, alloys, sealing materials, if any.

6. Behavior during emergency stop: Many durability tests have suffered from emergency stops



**Solid Oxide Fuel Cell Materials: Durability, Reliability, and Cost, Fig. 8** Impurities in anodes for four SOFC stacks with different materials and designs. Impurities were determined with SIMS on the 24 h operation and on the longer (about 5,000 h) operations. (a) High-temperature

segment-in-series cell by MHI, (b) intermediate flattened tubular cell by Kyocera, (c) high temperature sealless tubular cells by TOTO, and (d) intermediate temperature disk-type planar cells by Mitsubishi Materials corp

which are caused, for example, by failures of controlling system for the test facilities. Such accidental stop tends to cause changes in performance or mechanical failure. Severest situation is rapid cooling with the purge gases which will be introduced mandatorily, leading to mechanical failure or heavy damage of cells [69].

### Anomalous Situation

1. Gaseous leakage: Anomalous gaseous leakage can take place as a result of crack formation of electrolyte, interconnect, or seals. In addition, oxygen can be permeable through the oxide electrolyte/ interconnect in a form of bipolar diffusion of oxide ion and electrons. In any case, gaseous leakage gives rise to combustion without generating electricity. This releases heats locally at the place where combustion occurs. This may provide a local hot spot of electrolyte/interconnect. Since gaseous leakage tends to increase with temperature, local heating enhances further gaseous leakage regardless of leakage through pores/cracks or electrochemical oxygen permeation.
2. Shorting: When electrical shorting takes place, current will pass within the shorting circuit until fuel/ air becomes in shortage and as a result, high resistive materials are formed on the electrical path. Current density is determined so as to cancel out electromotive force by the overpotential and ohmic loss inside shortened circuit. Unlike the electro-chemical oxygen permeation, electrons move quite fast. Therefore, combustion rate and heat generation rate are fast. Since the ionic conductivity and the electrode activity are higher at higher temperatures, consumption rate increases until there is shortage of fuel or air.
3. Back diffusion of combusted gases: Some stacks are designed not to have sealing parts. In such a case, combustion of remaining fuels takes place just outside the electricity-generating cell area. In other words, there is a great possibility that the combusted gas will diffuse backward to the electrode area. To

protect particularly nickels against such an oxidative atmosphere, an appropriate distance should be maintained between combusting area and the electrochemical active area.

### Redistribution of Current Flow Among Cells Connected in Parallel or Series

When a cell or a part of a cell is degraded, this should appear as change in cell performances. When the electrical potential decrease takes place in one cell among cells connected in series, it can be detected easily by watching the respective cell performance. On the other hand, when there are many other cells which are connected in parallel with a degraded cell, the current redistribution takes place so as to minimize effects of degraded cells. In such a case, it becomes difficult to detect those degradations from changes in cell performance alone.

### Degradation in Cell Performance

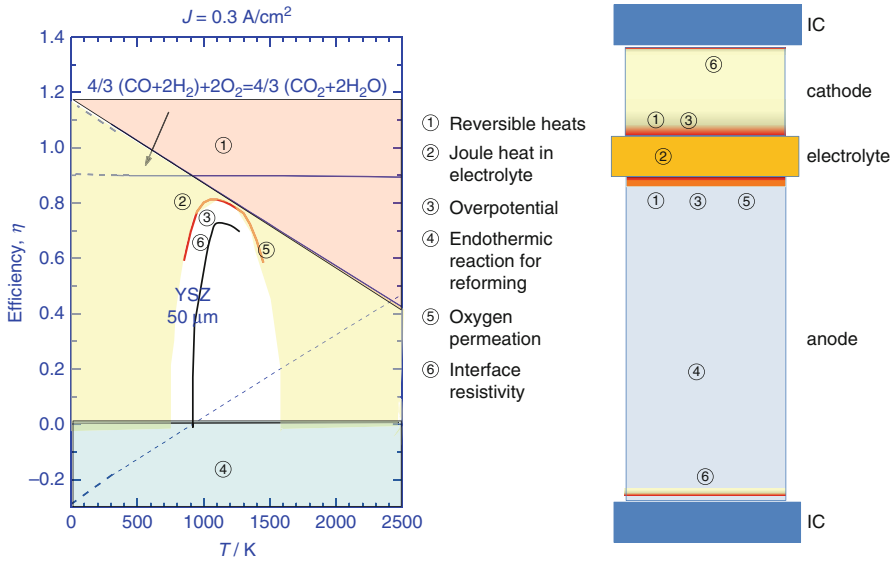
Cell performance is degraded from various reasons. Some degradations are caused from the main components of fuel, others being from contaminants. In many cases, operation temperature plays an important role, whereas the overpotential can become the major factor of controlling degradation. First of all, the places causing potential drops are listed and their relation to other operation conditions is described in section “[Operation Conditions and Their Relations to Degradation of Repeat Elements](#)” and then respective poisoning effects will be described.

### Operation Conditions and Their Relations to Degradation of Repeat Elements

#### 1. Exothermic and Endothermic Effects

Figure 9 summarizes schematically those places where exothermic or endothermic processes take place in repeated elements.

- (a) Most important heat effects are the exothermic process due to the electrochemical reaction at the active reaction sites. This contribution increases with increasing temperature. This is due to the reversible reaction so that this effect cannot be detected in AC impedance spectroscopic measurements under OCV conditions; the



**Solid Oxide Fuel Cell Materials: Durability, Reliability, and Cost, Fig. 9** Analyses on endothermic or exothermic effects in the theoretical efficiency for SOFC and corresponding places inside cells

exothermal and endothermic effects are cancelled out in AC. This effect can appear in the DC polarization measurements; with increasing current density, exothermic heats increase, leading to local heating in the vicinity of the active sites.

- (b) Potential drop due to the electrode overpotential appear also in the electrochemical active sites. This is however irreversible.
- (c) Ohmic loss is also irreversible but appearing along the electrical path with low conductivity.
- (d) Interface resistivity: between cells and interconnects or at cell-to-cell connection potential drop can arise.
- (e) Oxygen permeation, if any, results in local heating due to combustion without generating electricity.
- (f) For internal reforming inside anode layers, local cooling takes place at those places where reforming reactions proceed.

## 2. Effects of current density

In addition to temperature, there are several operational variables which should be examined carefully in their relations to degradation. One of such variables is the current density. In

what follows, plausible effects of increasing current density will be examined in two levels: cell level and stack level.

In cell level:

- (a) With increasing current density, heats are emitted at the electrochemical active sites, therefore, temperature at the active sites increases.
- (b) With increasing current density, the overpotential around the active sites increases. When the overpotential is the driving force, degradation should be given as a function of overpotential as will be shown in Cr poisoning for LSM cathodes.
- (c) When the oxygen potential at the active sites plays an important role in determining the equilibrium for a particular degradation, it can be related to the current density in an indirect way.
- (d) With increasing current density, gaseous flow rates for air and fuel increase if the utilization of air or fuel is kept constant. When poisons for electrode activities are carried with air or fuels, increasing flow rates implies that an amount of transported poisons increases at active sites.

In stacks level:

- (a) Since the conversion efficiency decreases with increasing current density, heats to be removed increase in two aspects: (1) Reversible heats increase linearly with current density and (2) Irreversible heats increase nonlinearly under the same fuel utilization.
- (b) Thermal balance will be achieved (1) when air flow rate increases resulting in lower air utilization or (2) when a larger temperature distribution is allowed to have the larger heat exchange with the same amount of gas flow. For the latter case, the maximum cell temperature should be increased.

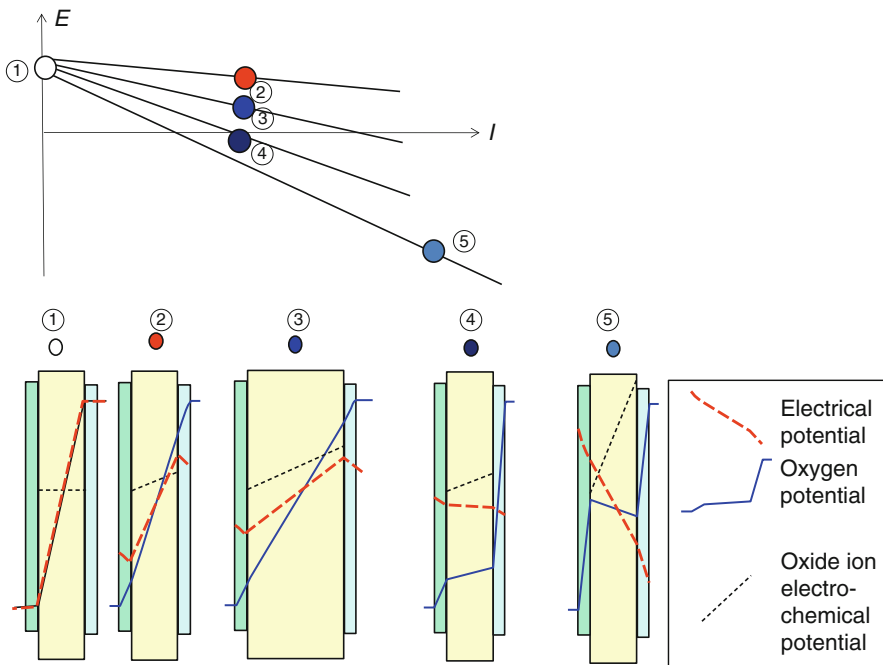
3. Oxygen Potential

Another important variable related with the operation condition is oxygen potential.

When the degradation of electrode performance is considered, the oxygen potential distribution inside electrode layer or at the electrode/electrolyte interfaces becomes important. In particular, the oxygen potential at the electrochemical reaction sites is critical.

Furthermore, oxygen potential distribution may change during operations. Typical examples are schematically shown in Fig. 10. for the oxygen potential ( $\mu(O_2)$ ) distribution in relation to electron electrochemical potential ( $\eta(e^-)$ ) and oxide-ion electrical potential ( $\mu(O^{2-})$ ) and are summarized as follows:

- (a) Normal cases: the electrode overpotential corresponds to a drop of the oxygen potential at the active sites. In cathodes, the overpotential can be interpreted in terms of the oxygen atom diffusion potential on the LSM surface, whereas the oxygen potential drop should appear across the surface of active LSCF cathodes. For nickel anodes, the oxygen potential drop corresponds to the diffusion of hydrogen atoms on nickel. Even when there is a distribution of electrode activity or gaseous concentration inside one cell, the oxygen potential at the active sites is controlled to provide the same electrical potential throughout the cell.



**Solid Oxide Fuel Cell Materials: Durability, Reliability, and Cost, Fig. 10** Typical changes in electrical potential, oxygen potential and oxide ion electrochemical

potential for (1) OCV, (2) normal operation, (3) normal operation with thicker electrolyte, and (4) cathode damaged cell and weakest cell on shorting cells in series

- (b) Fuel/air starvation. Oxygen potential in the starvation side changes drastically from the normal oxygen potential. As a result, some damage may occur on the electrode. In such a case, nickel can be oxidized while LSCF cathodes can be partially decomposed, when the oxygen potential changes beyond the thermodynamic limit.
- (c) Degradation of one electrode of a cell among in-series connected cells. In a series connection, the same current passes through all cells in the series. When one electrode is degraded, the overpotential increases under the same current density. The generating voltage decreases. Even when a damaged cell cannot generate the electricity, the current is mandatorily passed through the cell. In such a case, the oxygen potential at the electrode/electrolyte interface is shifted to an extremely oxidative/reductive side.
- (d) Short circuit with/without outer resistance. When shorting takes place among in-series connected cells, a large amount of current may pass through to cancel out the generated voltage with the resistivity/overpotential of damaged cells. At the beginning, the current is limited by the gas diffusion of air or fuels. Once there appears difference in cell performance including gas diffusion, the generated voltage tends to be cancelled out with the electrode resistivity or gas diffusion resistivity of a particular damaged cell. This suggests that heats are generated locally at the damaged cells. Since the Ohmic loss inside the electrolyte and other places are essentially the same between the damaged and the normal cells, a drastic difference should appear as electrode resistivity. When there are differences in electrode activities among the damaged cells, the current tends to be concentrated in an area with better electrode activity. This will continue to a situation where air or fuel will be in starvation in a major part of cells, leading to lowering in generated voltage.

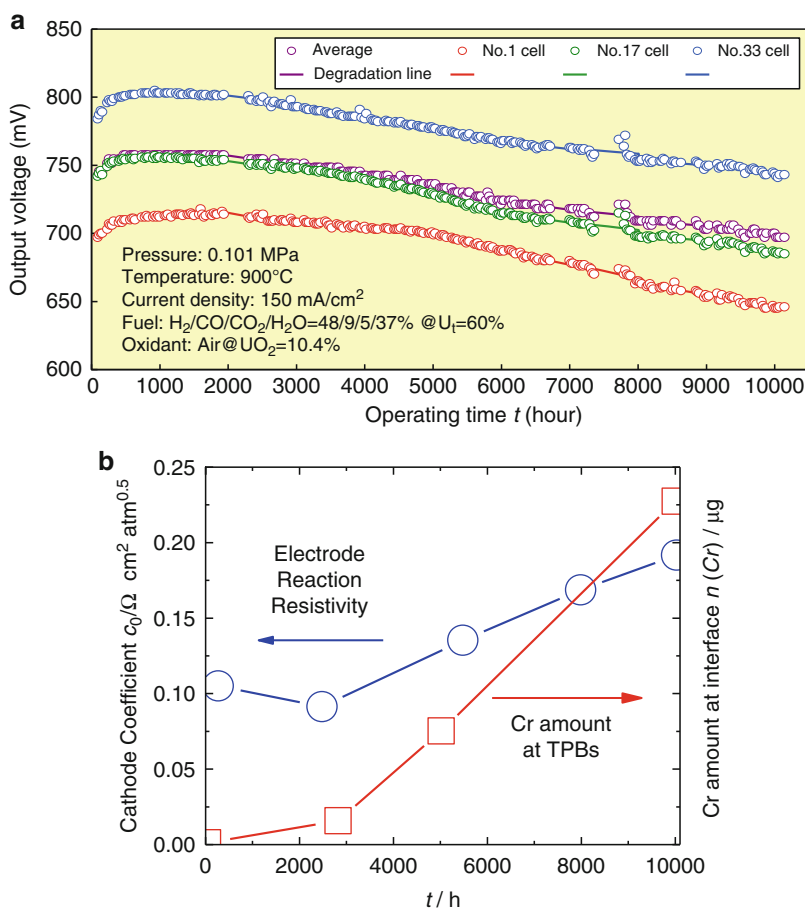
**Chromium Poisoning** Chromium poisoning was first observed during the investigation of utilization of metal interconnect at a rather high temperature like 900° C together with LSM cathodes. Therefore many investigations [34, 70–76] have been made on the chromium poisoning effects of lanthanum strontium manganite cathodes. Among them, the work by Taniguchi et al. [34] is excellent in a sense that from a large number of experimental results obtained by changing cathode materials and testing conditions such as temperature, etc., they eventually found an interesting fact that the half-life time of any manganite cathodes is governed by a simple quantity, namely,  $\log a(O)$ , derived directly from the overpotential of the cathodes with a conversion factor of  $4F/2.303 RT$ . This is well interpreted in terms of the cathode reaction model for the lanthanum strontium manganites [77]; essentially no oxide ion conduction is available in LSM. TPBs become only electrochemically active sites and, as a result, there arises a large oxygen potential gradient in the TPB vicinity which in turn provides a driving force for chromium-containing vapors to attack the electrochemical sites. In an actual segment-in-series cell, the chromium concentration at TPBs was observed by using SIMS technique [68] (see Fig. 11). The observed change in an accumulated amount of chromium was found to have excellent correlation with the cell performance degradation. That is, degradation in a level of several percent in operating potential is caused by the chromium accumulated at TPBs in the order of several hundred parts per million. This strongly suggests that without measuring with SIMS, no proper examination can be made on a long life time of LSM cathodes in an order of several ten thousand hours.

Another interesting finding is obtained by Matsuzaki and Yasuda [69] – they found that the chromium poisoning depends not only on cathode materials but also on electrolyte to be used with cathodes. From four possible combinations made with LSM and LSCF as cathode and YSZ and SDC as electrolyte, they found that the LSCF/SDC combination does not show any degradation under the same conditions. Since then, many efforts have been made on the non-LSM cathode/



### Solid Oxide Fuel Cell Materials: Durability, Reliability, and Cost,

**Fig. 11** (a) The time-dependent degradation of segment-in-series cells by Mitsubishi heavy industry. (b) Correlation of electrode reaction resistivity and the amount of accumulated chromium at the three phase boundaries



ceria interlayer/YSZ systems [78, 79]. In some cases, cell performance is linearly degraded from beginning, whereas the performance is not directly related with the SrCrO<sub>4</sub> formation which is always observed. From analyses on the chemical stability of cathodes and their electrode reaction mechanism based on the mixed conductivity, the generalized degradation mechanism [42, 51] can be derived to cover phenomena occurring at the chemical reactions sites as well as the electrochemically active sites. The important physicochemical feature is the probability of poisoning substances arriving at the sites by penetrating through a trapping zone.

Lanthanum nickel-iron oxide cathodes, La(Ni, Fe) O<sub>3</sub>, have attracted much attention because they show essentially no effects of chromium poisoning [59]. This is mainly because there is

no chance of SrCrO<sub>4</sub> formation. From the thermodynamic point of view, there is a possibility that the La(Ni,Fe)O<sub>3</sub> perovskites react with chromium-containing vapors to form the La(Ni, Fe,Cr) O<sub>3</sub> solid solution [42]. Even so, such perovskites must still be electro-conductive, although some surface kinetic activity will be lowered due to the fact that lanthanum chromite has lower catalytic activity among the transition metal perovskite oxides.

In recent years, an interesting but troublesome fact has been revealed, that is, Pt wire reacts with oxygen in air to form PtO<sub>2</sub>(g) and will be deposited on the three phase boundaries of LSM cathodes [80]. Usually, Pt cathodes are not better than perovskite cathodes so that the electrode activity may be lowered when such Pt will be deposited on cathodes. However, the situation for the

chromium poisoning for the LSM cathode is quite different. When Pt is deposited on TPB of LSM cathodes, the cathode performance can be improved or lowered depending on the state of deposited Pt. This disturbs the effects of chromium on the LSM cathodes. This makes it difficult to examine the chromium poisoning in a laboratory scale.

Other effects such as potassium are reported [81]. The most recent trend to prevent Cr poisoning is to reduce the chromium volatilization from alloys [82]. This is related to the interconnect issues.

**Nickel Sintering** Since the EVD nickel anode is fabricated so as to be firmly fixed to the YSZ electrolyte, the degradation rate of such electrode is small. Compared with the EVD nickel anode, normal Nickel cermet anodes are fabricated by sintering after slurry coating. This implies that the mechanical strength between YSZ and nickel is not necessarily good enough so that pre-annealing process is needed to have a good contact.

For the first-generation cells to be operated at 900–1,000° C, sintering of nickel appears as a result of bulk diffusion based on the normal thermal activation process; note that the melting temperature of nickel is 1,728 K and therefore above two thirds of melting temperature, i.e., 1,152 K = 880° C, sintering can be significant. Actually, experimental observation indicates the change in microstructure in the range of several thousand hours due to sintering.

For the second-generation cells to be operated at 800° C or below, sintering exhibits more complicated features. Sintering depends largely on stacks or cells. This implies that the fabrication as well as operation conditions may affect sintering.

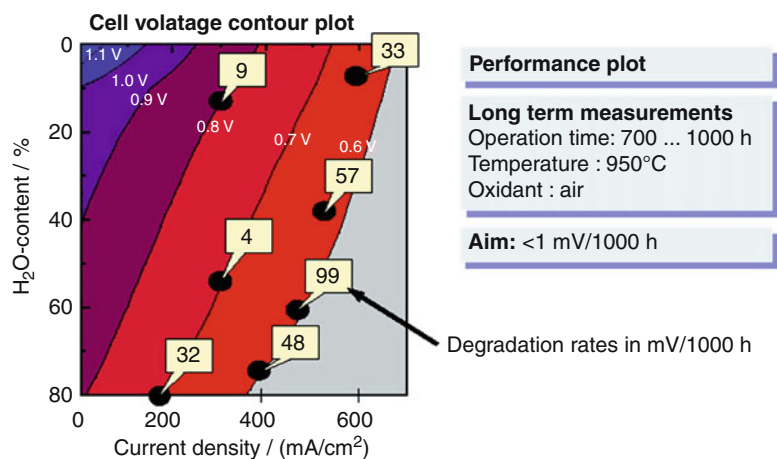
About the operation condition, details of nickel electrode degradation have been investigated by Karlsruhe Institute of technology group [83, 84]; they changed the fuel composition and current density separately with a parameter of operating potential and found that the degradation is severe with increasing water content in fuel and with increasing current density (see Fig. 12). Although there is no examination on relation between such degradation and sintering, this seems to be due to sintering. In a cell test, Topsøe Fuel Cells reported that the degradation of nickel anode is severe in the region where the fuel utilization is high, and correspondingly they observed actual sintering of nickel [56].

An interesting feature associated with sintering is that it can take place on thermal cycles alone between operation temperature and room temperature [63]. It seems plausible due to sulfur contamination on nickel since the nickel–sulfur system exhibits significant lowering of liquidus temperature due to the eutectic formation; thus eutectics appear even below 800° C.

In any case, change in microstructure is a complicated matter, and detailed analyses should be made not only on nickel but also on oxide component or pore [85]. In recent years, the

### Solid Oxide Fuel Cell Materials: Durability, Reliability, and Cost,

**Fig. 12** Systematic investigation on the anode degradation as functions of current density and water content in fuels with a parameter of electrical potential (From [83, 84])



investigation on microstructure with FIB-SEM or XCT has been rapidly progressed [86–88]. It is therefore expected that sintering behavior and related phenomena will be well clarified in its relation to degradation.

**Carbon Deposition** Since hydrocarbons are important fuels for SOFC, carbon deposition should be avoided [89]. When carbon deposition once starts, this destroys the microstructure of Ni-cermet anode and deposited carbon acts as catalyst for further deposition so that a large amount of carbon can block the flow of fuels. Since the decomposition temperature of hydrocarbons decreases with increasing carbon number in hydrocarbons, the possibility of carbon deposition increases with carbon number. On the other hand, water vapors are emitted from the electrochemically active sites and this promotes the steam reforming. Thus, under cell operation, the possibility of carbon deposition decreases in the vicinity of active sites.

**Sulfur Poisoning** Sulfur contaminations inside SOFC stacks depend on the system configuration. For the small stationary applications, desulfurization process is first placed before the reforming process; this is because the reforming catalysis is weak against sulfur contamination. In such a case, essentially no sulfur poisoning can be expected during the normal procedure of SOFC operation.

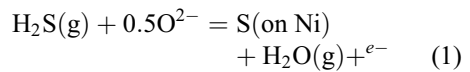
For diesel fuels, on the other hand, the presence of sulfur, and possible sulfur poisoning, is strongly related with the degree of reforming [90].

In recent years, it has been found that sulfur contamination appears even when sulfur-free fuel such as hydrogen is utilized [66]. This strongly suggests that sulfur sources are not only from fuels but also from other components. Most probable source is metal components in stacks and thermal insulating substances containing metal sulfates.

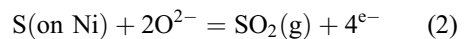
Performance degradation of nickel anode due to sulfur consists typically of two stages [90–100]. The first stage is the prompt response against the introduction of hydrogen sulfur, namely, stepwise decrease of electrical potential. The potential drop is well correlated with the sulfur coverage on Ni [96]. This is usually

recovered when sulfur-containing fuels switch back to noncontaminated fuels; this is quite a slow process. The second stage is a process following the first stepwise change; when concentration is low, there is no further change, whereas some irreversible lowering in electrical potential is observed when concentration is high.

Furthermore, effects of sulfur can appear in a more significant and fatal manner. In an experiment by Julich research center, the cell performance was tested in hydrogen fuel containing 50 ppm H<sub>2</sub>S. After the initial decrease in potential, the performance was maintained at this low level. However, after about 150 h, the cell suddenly died. Posttest examination clarified that NiS spread out in the interface region between YSZ electrolyte and nickel cermets. In addition, NiSO<sub>4</sub> was formed inside the anode layer. These features contradicted with the expected Ni-S interaction predicted from the thermodynamic equilibrium [85]. There must be some mechanism to enhance the effect of sulfur and to accumulate sulfur at the TPB vicinity. One possible explanation is the irreversible nature of the electro-chemical side reactions under the anodically polarized current, that is, the sulfur deposition is described as the following anodic reaction:



On the other hand, the volatilization reaction can be written as follows:



When two reactions take place continuously, adsorption sulfur can be maintained at a certain coverage on Ni. For a long period of operation time, sulfur can be accumulated inside nickel particle as a result of dissolution and diffusion of sulfur.

**Other Impurities** Figure 8 shows the actually observed impurities. Among them, effects of silicon have been extensively investigated [101–106].

Recently, investigation on the impurities derived from coal-base gases has been made

extensively in the SECA project of US Department of Energy (DOE), which promotes the utilization of coals in SOFC [107]. They first made thermodynamic analyses on chemical behavior of impurities in gasification process and hot gas cleaning process, and then categorized impurity elements into several classes [108, 109]; furthermore, they made a series of experiments to examine those elements which are regarded as possible poisoning elements to nickel anodes [110–114]; the following is a brief summary of their results in comparison with other related investigations [115–123].

1. Phosphor and Arsine show the strong affinity with nickel to form intermetallic compounds. In button cell experiments, intermetallic compounds are formed outside of the anode layer, which indicates that the reaction rate is fast and the diffusion of Ni to reaction sites is fast too. For AsH<sub>3</sub> gas, cell performance does not show any changes for a while despite the formation of intermetallic compound and suddenly dies. This is probably because the electrical path was broken due to the nickel deformation. For PH<sub>3</sub>, on the contrary, the cell performance degrades from the starting time. This is probably due to the formation of HPO<sub>2</sub>(g) [116–123] which attacks the electrochemical sites.
2. Sulfur and Selenium exhibit similar behavior when the concentration of H<sub>2</sub>S or H<sub>2</sub>Se is low. Namely, the abrupt initial change occurs first and then constant performance is maintained. Difference can be seen in the recovery behavior from the contaminated fuel to non-contaminated fuel. For H<sub>2</sub>S, a slow recovery process appears, whereas no recovery process appears for H<sub>2</sub>Se. Furthermore, severe damage may be caused for H<sub>2</sub>Se. The common feature is that damage parts are always in the interface region between electrolyte and anodes.

### Generalized Model for Degradation due to Gaseous Impurities

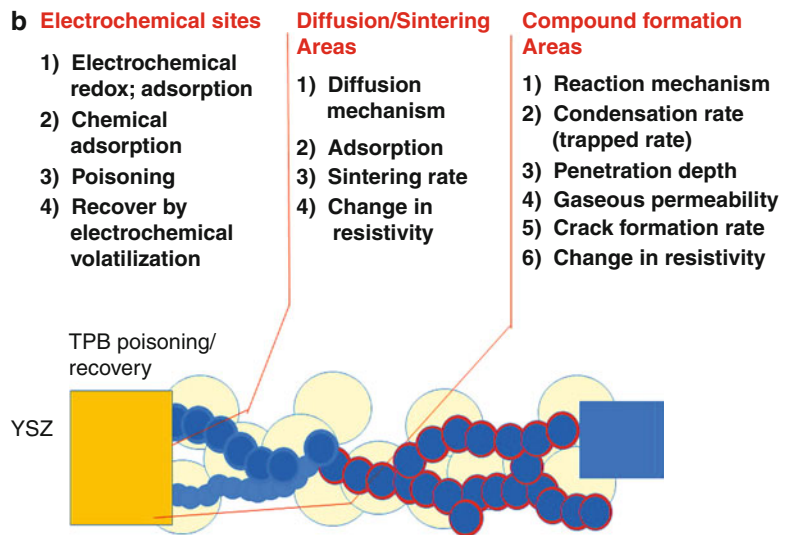
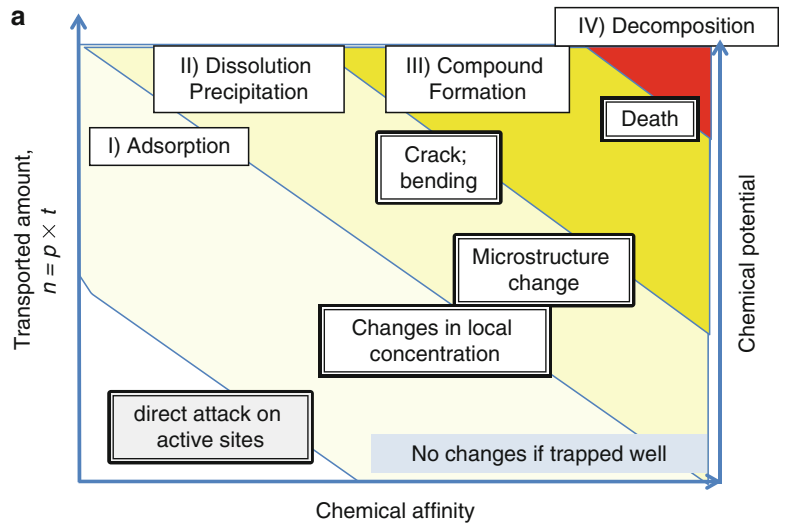
Yokokawa et al. [8] made thermodynamic analyses on the interaction between cathodes/anodes and gaseous impurities. By comparison between the thermodynamic reactivity and the electrode

degradation behaviors, they have extracted generalized models for degradation. It can be summarized as in Fig. 13, where the characteristic features concerning degradations are plotted by using variables for the transported amount of impurities and for the thermodynamic affinity between electrode and gaseous impurities, for example, for perovskite cathodes, the thermodynamic activity of SrO can be adopted, whereas for anodes, the interaction parameters of systems for forming nickel intermetallic alloys can be used. Essential points in the generalized models are:

1. When the electrochemical activity is lowered due to the impurities, the electrochemical reaction sites should be covered by such impurities. In this case, it is no need that the covered atoms have the strong chemical interactions with electrode materials. The deposition or adsorption is enough to disturb the fundamental steps in the electrode reaction mechanisms. On the other hand, when cell performance is changed due to changes in electrical path or gaseous channel, the accumulated amount of deposited or reacted impurities should be large. This difference should be quite significant. For example, in the Cr poisoning, only a thin layer of deposited chromium in the order of several nanometers on reaction sites is enough to lower the cell performance in the order of 10%. On the other hand, since the electrical path or gas channel are made of the particles or pores in the order of several micrometers in size. This implies that a large amount of SrCrO<sub>4</sub> is needed to block the electrical current or the gaseous flow.
2. There can be two different reactions for impurity behaviors, namely, electrochemical side reaction and normal chemical reaction. The most important feature of the degradation is that the degradation reaction takes place under the flow of the electro-chemically active species. This suggests that in the cathodic polarization, the electrochemical reduction (cathodic reaction) is accelerated. For example, chromium-containing vapors, CrO<sub>3</sub>(g) or CrO<sub>2</sub>(OH)<sub>2</sub>(g), can be easily reduced to form Cr<sub>2</sub>O<sub>3</sub> at the electrochemically active sites and

**Solid Oxide Fuel Cell Materials: Durability, Reliability, and Cost, Fig. 13**

Generalized model for electrode-impurity interactions and their relation to degradation: (a) chemical phenomena as functions of transported amount of impurities and chemical affinity between electrode materials and (b) three fundamental regions for electrode-impurity interaction



as a result, the electrochemical activity of active sites decreases due to the coverage of no electrical conductive and no catalytically active substances.

- On the other hand, recovery processes also have two contributions from the chemical and the electro-chemical reactions; the latter is given in Eq. (2), which was derived from considerations on the difference in the recovery process between S and Se.
- When the chemical interaction between the electrode components and the gaseous impurities is strong, there arise many processes inside

the electrode area and respective processes have their own activated process. As a result, their appearance as degradation behavior is quite different from experiment to experiment. Typical example is the effect of Cr vapors on the electrode activity of LSF- or LSC-based active cathodes.

After establishing the general model for degradation due to impurities, it becomes possible to consider all possible effects on a particular case of specified electrode and impurity.

## Cost Issues

### Cost Issues in Relation to Durability/Reliability and Performance

Cost, performance, and durability are important figures of fuel cell systems and for SOFCs, these three aspects are closely related with each other. This can be summarized as follows:

1. Costs consist of materials cost, cell/stack fabrication cost, and system cost. Whenever durability has been improved by changing materials or materials processing, usually it costs more due to additional treatments, etc. Thus, there is a trade-off relation between durability and cost. To overcome this relation, innovative breakthrough is needed to stage up this relation.
2. When cell performance will be improved, this benefit can be used in increasing the conversion efficiency or in increasing operating current density to reduce the mass to realize rated power, leading to cost reduction per rated power.

As described in the introduction, SOFC stack development started with the breakthrough by Westinghouse; the sealless tubular cells can be categorized as stable but expensive stacks. Since then, many efforts have been focused on reducing the fabrication cost in the first-generation cells.

On the other hand, there has been a big wave to construct the second-generation cells to be operated at lower temperatures around 800° C. When the first-generation cells are operated at low temperatures, the Ohmic loss in electrolyte and the overpotential in cathode become quite big. Therefore, in the second-generation cells, use is made of thinner electrolytes and more active cathode materials. Interestingly enough, the performance (conversion efficiency) of second-generation cells becomes much better than that of the first generation. This is mainly because the active cathodes such as LSCF exhibit excellent performance even at low temperatures and also handling of the thinner electrolyte provides some improvement even for fabricating the cathode layer; as a result, performance becomes better. Even so, the active

cathodes such as LSCF are chemically reactive, for example, LSCF reacts with  $\text{CO}_2(\text{g})$ ,  $\text{CrO}_3(\text{g})$  and  $\text{SO}_2(\text{g})$  to form  $\text{SrCO}_3$ ,  $\text{SrCrO}_4$  or  $\text{SrSO}_4$ . This is directly related with the long-term durability.

### Cost in Relation to Applications

Since the first-generation cells were aimed at larger stationary applications, several cost evaluations were made on such applications [31, 124–130]. These considerations are focused on the followings points:

1. Identification of high cost element. The most expensive elements are Y in YSZ, La in cathodes or oxide interconnects; Co in LSCF, Ni in anode can be also categorized as rather expensive materials. To avoid the utilization of such elements, it is required to adopt redesigned stack structure with appropriate fabrication methods.
2. Cheaper materials if acceptable; particularly, impurities will be an issue.
3. Reduction of the number of the components in repetitive units of stacks.
4. Reduction of losses during fabrication.
5. Automation of production.

There are generalized arguments on the relation between cost and performance:

1. Roles of raw materials: as the structural component, the low price materials are thought to be used, whereas for the highly functional materials, there are some arguments: A typical example is the utilization of scandium [131]. Although the raw materials cost for scandium oxides is much higher than that for yttrium oxide, there are many groups who are interested in utilizing ScSZ instead of YSZ. This is based on an idea that despite higher raw materials cost, the higher performance leads to reduction of total cost of stacks to be required to achieve a given rated power.
2. Even when low-cost materials are used, additional procedures are needed to achieve the required reliability and durability. Therefore, cost should be considered in combination of



raw materials cost and fabrication cost. This is particularly true for metal interconnects; metal interconnects are cheap in materials cost compared with La-based oxide but additional procedure of coating increases the fabrication cost.

In 1998, BMW, Delphi, and Renault announced the application of SOFC as APU (Auxiliary Power Units) of automotive. This gave rise to drastic changes in applications of SOFC systems. The US Department of Energy started a new project called SECA (Solid State Energy Converter Alliance). Their cost target is about \$150/kW for stacks and \$700/kW for system in the mass production level. Recently, an interesting analysis [132] has been made on the operation modes of the degraded stacks in its relation to total system cost. There can be two operation modes; one is to keep the same current density, the other being to keep the same electrical potential. This difference gives rise to a large difference in strategies in the replacement of the stack itself and overdesign.

1. Under constant current operation, some degradation leads to lowering the electrical potential and as a result, power output is correspondingly lowered. Since the conversion efficiency is also lowered, heats produced inside stacks increases. To remove excess heats, a larger amount of air has to be flowed. For this purpose, additional energy is required and total efficiency is further decreased. In this sense, operation is continued under a rather severer condition. Further degradation can take place under such a condition. In addition, one needs to keep a large capacity of BOP to ensure the capacity for air flow in an excess amount. In view of these features, this operation mode must only be appropriate for stacks with extremely low degradation rate.
2. Under constant voltage operation, current density decreases largely in contrast and as a result, power output is also correspondingly lowered significantly. However, efficiency is maintained rather constant and therefore there is no need to keep a large capacity of BOP. Since power output per one unit decreases

significantly, additional stack capacity is required to offset for such a loss of capacity. In this operation mode, damage on stacks is not severe so that stacks can be operated for a longer period of time, and this is an important advantage against the constant current operation mode.

## Future Directions

There are a number of degradation issues which are still unclear and need to be addressed in the future:

### Stack Behavior

Stack behaviors are characterized in terms of temperature distribution, current density distribution, flow distribution, etc. Among them, current distribution is very important in determining stack performance, stack temperature distribution, etc., but is hard to be measured in real stacks. In many cases, the information on current distribution is obtained from the simulation technique. In this sense, simulation technique becomes quite important. It is still highly hoped that progress in experimental technique will be made in obtaining the current density distribution in stacks.

From the materials point of view, many stacks consist of ceramics and metals. Ceramics may exhibit oxygen nonstoichiometry and change their volume in a complicated manner as functions of temperature and pressure. On the other hand, metals and alloys can be deformed under stresses/loads. When those two materials are utilized under a long-term operation at constant temperature or under frequent thermal cycles, mechanical interactions between two materials become important.

### Effects of High Conductive Electrolyte

There can be seen one interesting feature in the low temperature SOFC, that is, the cell performance of the anode support cells has been much improved compared with electrolyte self support cells. This is apparently due to the lowering of the ohmic resistance inside electrolyte. Furthermore, the electrode performance is also improved very much. This can be ascribed to better fabrication

procedure. When thin electrolyte is fabricated, very fine structure is designed and fabricated. In a similar manner, cathodes are fabricated carefully so that it is expected that microstructure of cathodes is well established. These features can be summarized as follows: When the conductance is improved and the homogeneous current flow is established inside electrolyte, electrode performance can be maximized by fabricating the electrode layer without faults. This is a matter of the current density distribution inside one cell. This is determined in terms of the homogeneous ionic current, homogeneously distributed electrochemical sites, and homogeneous electronic current. If there is some fault among them, this leads to inhomogeneous current flow and therefore some degradation may take place.

Here, an interesting finding by Watanabe and Uchida [133] should be referred to: that the electrode performance becomes higher with those electrolytes having the higher ionic conductivity. The proper mechanism of this finding has not been given fully but the current density distribution in the vicinity of electrochemically active sites may be different between those electrolytes having different ionic conductivities.

### Advances in Characterization

The electrode performance is determined by many factors. Among them, the microstructure is one of the very important factors. Even so, it has not been easy to make characterization on the microstructure in an appropriate way. For example, in nickel cermet electrode, the connection of nickel is important in addition to the skeleton structure of oxide network. Since nickel is dissolved into acid, it is easy to extract the skeleton structure of zirconia. On the other hand, nickel network is not well determined experimentally. Recent advances in the experimental determination of three-dimensional electrode structures by FIB-SEM or by XCT techniques make it possible to evaluate details of microstructure changes in nickel cermets. For example, the most important physicochemical measure of the electrode is the length of three phase (electrolyte oxide, electronic conductive metal, and gases) boundaries. Recent experimental and related theoretical progress makes it

possible to reconstruct the cermet electrode in computer space and to identify the ionic path, electron path, and electrochemically active sites in combination with appropriate electrode reaction mechanisms. This provides a powerful tool for investigating the mechanism of degradation in terms of fuel cell operation variables such as time, current density, etc. Thus, it is highly recommended to investigate in more details the microstructure and its relation to electrode activity.

### Intermediate Temperature Gaseous Species

Most typical degradation is chromium poisoning. This is caused by the gaseous species such as  $\text{CrO}_3(\text{g})$  or  $\text{Cr}_2\text{O}_2(\text{OH})(\text{g})$ . In order to understand the chromium poisoning, thermodynamic analyses on those gaseous species are essential. Fortunately, those data are available so that detailed analyses were made successfully. For the Ni-P system, the vapors,  $\text{HPO}_x$  ( $X = 1, 2, 3$ ) play an important role according to Bao et al. [116–118]. Without considerations on such gaseous species, no proper transportation mechanism can be obtained. An important point of these analyses is that the partial pressure of such species is extremely small in the range of  $10^{-12}$  to  $10^{-6}$  atm.

Although the accurate determination of the partial pressure of electrochemically important species is highly required, there can be some difficulties:

- (a) Lack of the thermodynamic properties of those gaseous species which can be dominant in the intermediate temperature region. This is particularly true for species which are emitted in the presence of water vapors.
- (b) Some uncertainty in the already available thermo-dynamic data.

Thus, the intermediate temperature gas chemistry should progress for the electrochemical purpose.

### Effects of Minor Species

Minor carriers in electrolyte can also make contributions to degradation, although apparent effects have not been fully clarified. Most

important minor carrier in the fluorite-type oxides is proton. It is well known that the proton concentration in YSZ is in the order of  $10^{-5}$  in mole base. Correspondingly, the transportation number can be evaluated to be in the same order. Normally, it is quite difficult to detect this effect in the electrical performance so that in many electrode reaction models, any role of protons is neglected particularly in cathodes. In the fuel cell operation mode, protons are formed in anode and migrated to cathodes, leading to the emission of water vapors on the cathode side. In view of this nature, it is expected that the formation of hydroxide compounds can be expected as an electrochemical side reaction.  $\text{Sr}(\text{OH})_2(\text{g})$  must be interesting in view of the proposed mechanism of Sr migration in the form of gaseous species. In addition, the  $\text{Cr}_2\text{O}_2(\text{OH})_2(\text{g})$  emission can also be expected from the reaction of deposited  $\text{Cr}_2\text{O}_3$  with transported protons and oxygen atom. This reaction should be considered as the recovering (healing) process of Cr poisoning. Note also that because proton concentrations in doped ceria is two orders of magnitude higher than that in YSZ, the utilization of doped ceria as reaction/diffusion barrier can also provide enhancing effects of such recovering (healing) process. It is hoped to clarify such effects in relation to a long-term stability of cathode materials.

## Bibliography

### Primary Literature

1. Yokokawa H, Sakai N (2003) Part 4. Fuel cell principle, systems and applications, Chapter 13 History of high temperature fuel cell development. In: Vielstich W, Lamm A, Gasteiger HA (eds) Handbook of fuel cells fundamentals technology and application, vol 1. Fundamentals and survey of systems. Wiley, Chichester, pp 219–266
2. Moebius HH (1997) On the history of solid electrolyte fuel cells. *J Solid State Electrochem* 1:2–16
3. Brown JT (1985) High temperature solid-oxide fuel cells (SOFCs). *Energy Int J*:209–229
4. Yokokawa H (2003) Understanding materials compatibility. *Annu Rev Mater Res* 33:581–610
5. Atkinson A, Marquis AJ (2009) Mechanical stability. In: Vielstich W, Yokokawa H, Gasteiger HA (eds) Handbook of fuel cells fundamental technology and applications. Advanced in electrocatalysis, materials, diagnostics and durability: part 2, vol 6. Wiley, Chichester, pp 992–1001
6. Yokokawa H, Tu H, Iwanschitz B, Mai A (2008) Fundamental mechanism limiting solid oxide fuel cell durability. *J Power Sources* 182:400–412
7. Yasuda I, Hishinuma M (1995) Mathematical analysis of stress distribution in acceptor doped lanthanum chromites under an oxygen potential gradient. In: Dokiya M, Yamamoto O, Tagawa H, Singhal SC (eds) Solid oxide fuel cells IV, PV 95-1. The Electrochemical Society, Pennington, pp 924–933
8. Yokokawa H, Yamaji K, Brito ME, Kishimoto H, Horita T (2010) General considerations on degradation of SOFC anodes and cathodes to impurities in gases. *J Power Sources*. <https://doi.org/10.1016/j.powersour.2010.07.093>. (to be published)
9. Yokokawa H, Sakai N, Kawada T, Dokiya M (1991) Thermodynamic analysis of reaction profiles between  $\text{LaMO}_3$  ( $M = \text{Ni, Co, Mn}$ ) and  $\text{ZrO}_2$ . *J Electrochem Soc* 138:2719
10. Yokokawa H, Sakai N, Kawada T, Dokiya M (1991) Chemical thermodynamic considerations in sinterability of  $\text{LaCrO}_3$ -based perovskites. *J Electrochem Soc* 138:1018
11. Pal UB, Singhal SC (1981) Electrochemical vapor deposition of Yttria-stabilized zirconia films. *J Electrochem Soc* 137(9):2937–2941
12. Isenberg AO (1981) Energy conversion via solid oxide electrolyte electrochemical-cells at high-temperatures. *Solid State Ionics* 3(4):431–437
13. Singhal SC (1995) Advance in tubular solid oxide fuel cell technology. In: Dokiya M, Yamamoto O, Tagawa H, Singhal SC (eds) Solid oxide fuel cells IV PV 95-1. The Electrochemical Society, Pennington, pp 195–207
14. Singhal SC (1997) Recent progress in tubular solid oxide fuel cell technology. In: Stimming U, Singhal SC, Tagawa H, Lehnert W (eds) Solid oxide fuel cells V, PV 97-40. The Electrochemical Society, Pennington, pp 37–50
15. Fee DC, Zwick SA, Ackerman JP (1983) Solid oxide fuel cell performance. In: Salzano FJ (ed) Proceedings of the conference on high temperature solid oxide electrolytes anion conductors, vol 1. Brookhaven National Laboratory, Upton, pp 29–38
16. Steele BCH, Hori KM, Uchino S (2000) Kinetic parameters influencing the performance of IT-SOFC composite electrodes. *Solid State Ionics* 135:445–450
17. Frey H, Kessler A, Munch W, Edel M, Nerlich V (2009) Chapter 68 Field experience with molten carbonate fuel cells (MCFCs) and solid oxide fuel cells (SOFCs) with an emphasis on degradation. In: Vielstich W, Yokokawa H, Gasteiger HA (eds) Handbook of fuel cells fundamental technology and applications. Advanced in electrocatalysis, materials, diagnostics and durability: part 2, vol 6. Wiley, Chichester, pp 992–1001

18. Carter JD, Myers D, Kumar R (2006) Recent progress on the development of TuffCell, a metal-supported SOFC/SOEC. In: Presented in the 30th international conference & exposition on advanced ceramics and composites, Cocoa Beach, pp 22–27
19. Tucker MC (2010) Progress in metal supported solid oxide fuel cells: a review. *J Power Sources* 195(15):4570–4582
20. Brandon NP, Blake A, Corcoran D, Cumming D, Duckett A, El-Koury K, Haigh D, Kidd C, Leah R, Lewis G, Matthews C, Maynard N, Oishi N, McColm T, Trezona R, Selcuk A, Schmidt M, Verdugo L (2004) Development of metal supported solid oxide fuel cells for operation at 500–600°C. *J Fuel Cell Sci Technol* 1(1):61–65
21. Hooie DT, Camara EH (1985) Onsite industrial applications for natural gas-fueled fuel cells. *Fuel Cell Semin*:182–185
22. Stolten D, de Haart LGJ, Blum L (2003) Design criteria for SOFC generators. In: Proceedings of the 27th annual Cocoa Beach conference and exposition on advanced ceramics and composites, Cocoa Beach, Florida, USA. American Ceramic Society, Westerville, pp 263–272
23. Suzuki M, Iwata S, Higaki K, Inoue S, Shigehisa T, Miyoshi I, Nakabayashi H, Shimazu K (2009) Development and field test results of residential SOFC CHP system. In: Singhal SC, Yokokawa H (eds) Solid oxide fuel cells XI –part 1. *ECS Trans* 25(2):143–148
24. Mai A, Iwanschitz B, Weissen U, Denzler R, Haberstock D, Nerlich V, Sfeir J, Schler A (2009) Status of Hexas SOFC stack development and the Galileo 1000 N Micro-CHP system. In: Singhal SC, Yokokawa H (eds) Solid oxide fuel cells XI – part 1. *ECS Trans* 25(2):149–158
25. Love J, Amarasinghe S, Selvey D, Zheng X, Christiansen L (2009) Development of SOFC stacks at ceramic fuel cells limited. In: Singhal SC, Yokokawa H (eds) Solid oxide fuel cells XI – part 1. *ECS Trans* 25(2):115–124
26. Hinnells M (2008) Combined heat and power in industry and buildings. *Energy Policy* 36(12):4522–4526
27. Singhal SC (1999) Progress in tubular solid oxide fuel cell technology. In: Singhal SC, Dokiya M (eds) Solid oxide fuel cell VI PV 99-19. The Electrochemical Society, Pennington, pp 39–51
28. Takeuchi H, Nishiyama H, Ueno A, Aikawa S, Aizawa M (1999) Current status of SOFC development by wet process. In: Singhal SC, Dokiya M (eds) Solid oxide fuel cell VI, PV 99-19. The Electrochemical Society, Pennington, pp 879–884
29. Donitz W, Erdle E, Schafer W, Schamm R, Spah R (1991) Status of SOFC development at dornier. In: Grosz F, Zegers P, Singhal SC, Yamamoto O (eds) Proceedings of the 2nd international symposium solid oxide fuel cells. Commission of the European Communities, Brussels/Luxembourg, pp 75–84
30. Nakanishi A, Hattori M, Sakaki Y, Kimura K, Ando Y, Miyamoto H, Oozawa H (2005) Development of MOLB type SOFC. In: Singhal SC, Mizusaki J (eds) Solid oxide fuel cells IX, PV-2005-07. The Electrochemical Society, Pennington, pp 82–88
31. Bagger C, Christiansen N, Hendriksen PV, Jensen EJ, Larsen SS, Mogensen M (1996) Technical problems to be solved before the solid oxide fuel cell commercialized. *Fuel Cell Semin*:44–47
32. Hilpert K, Quadackers J, Singheiser L (2003) Chapter 74 Interconnects. In: Vielstich W, Lamm A, Gasteiger HA (eds) Handbook of fuel cells fundamental technologies and applications. Fuel cell technology and applications, part 2, vol 4. Wiley, Chichester, pp 1037–1054
33. Yang ZG, Stevenson J (2009) Chapter 35 Durability of metallic interconnects and protective coatings. In: Vielstich W, Yokokawa H, Gasteiger HA (eds) Handbook of fuel cells fundamental technology and applications. Advanced in electrocatalysis, materials, diagnostics and durability: part 1, vol 5. Wiley, Chichester, pp 531–542
34. Taniguchi S, Kadwaki M, Kawamura H, Yasuo T, Akiyama Y, Miyake Y, Saitoh T (1995) Degradation phenomena in the cathode of a solid oxide fuel cell with an alloy separator. *Power Sources* 55:73–79
35. Yokokawa H (2001) Recent developments in solid oxide fuel cell materials. *Fuel Cells Fundam Syst* 1(2):1–15
36. Sakai N, Horita T, Yokokawa H, Dokiya M (1996) Oxygen permeation measurement of  $\text{La}_{1-x}\text{Ca}_x\text{CrO}_{3-d}$  by using an electro-chemical method. *Solid State Ionics* 86–88:1273–1278
37. Sakai N, Yamaji K, Horita T, Yokokawa H, Kawada T, Dokiya M, Hiwatashi K, Ueno A, Aizawa M (1999) Determination of oxygen permeation flux through  $\text{La}_{0.75}\text{Ca}_{0.25}\text{CrO}_{3-d}$  by electrochemical method. *J Electrochem Soc* 146(4):1341–1345
38. Nishi T et al (2003) Solid electrolyte fuel cell. *Japan Patent* 3,453,283
39. Köck W, Martinz H-P, Greiner H, Janousek M (1995) Development and processing of metallic Cr based materials for SOFC parts. In: Dokiya M, Yamamoto O, Tagawa H, Singhal SC (eds) Solid oxide fuel cells IV, PV 95-1. The Electrochemical Society, Pennington, pp 841–849
40. Glatz W, Kunschert G, Janousek M, Venskutonis A (2005) P/M processing and properties of high performance interconnect materials and components for SOFC applications. In: Singhal SC, Dokiya M (eds) Solid oxide fuel cell IX, PV 2005-07. The Electrochemical Society, Pennington, pp 1773–1780
41. Yokokawa H, Horita T (2003) Chapter 5. Cathode. In: Singhal SC, Kendall K (eds) High temperature solid oxide fuel cells fundamentals design and application. Elsevier, Oxford, pp 119–147

42. Yokokawa H, Horita T, Sakai N, Yamaji K, Brito ME, Xiong XP, Kishimoto H (2006) Thermodynamic considerations on Cr poisoning in SOFC cathodes. *Solid State Ionics* 177:3193–3198
43. Mentzer NH, Mai A, Stover D (2009) Durability of cathodes including Cr poisoning. In: Vielstich W, Yokokawa H, Gasteiger HA (eds) *Handbook of fuel cells fundamental technology and applications. Advanced in electrocatalysis, materials, diagnostics and durability: part 1, vol 5*. Wiley, Chichester, pp 566–578
44. Hilpert K, Das D, Miller M, Peck DH, Weiss R (1996) Chromium vapor species over solid oxide fuel cell interconnect materials and their potential for degradation processes. *J Electrochem Soc* 143:3642
45. Batawi E, Plas A, Straub W, Honneger K, Diethelm R (1999) New cost-effective ceramic oxide phases used as protective coatings for chromium-based interconnects. In: Singhal SC, Dokiya M (eds) *Solid oxide fuel cells VI, PV 99-19*. The Electrochemical Society, Pennington, pp 767–773
46. Larring Y, Norby T (2000) Spinel and Perovskite functional layers between plannee metallic interconnect (Cr-5 wt% Fe-1wt%  $Y_2O_3$ ) and ceramic ( $La_{0.85}Sr_{0.15}$ ) $_{0.91}MnO_3$  cathode materials for solid oxide fuel cells. *J Electrochem Soc* 147(9):3251–3256
47. Ghosh D, Tang E, Perry M, Prediger D, Pastula M, Boersuma R (2001) Status of SOFC developments at global thermoelectric. In: Yokokawa H, Singhal SC (eds) *Solid oxide fuel cells VII, PV-2001-16*. The Electrochemical Society, Pennington, pp 100–110
48. Wuilleman Z, Autissier N, Nakajo A, Luong M, Van herle J, Favrat D (2008) Modeling and study of the influence of sealing on solid oxide fuel cell. *J Fuel Cell Sci Technol* 5:011016
49. Ivers-Tiffée E, Timmermann H, Leonide A, Mentzer NH, Malzbender J (2009) Methane reforming kinetics, carbon deposition, and redox durability of Ni/8 yttria stabilized zirconia (YSZ) anodes. In: Vielstich W, Yokokawa H, Gasteiger HA (eds) *Handbook of fuel cells fundamental technology and applications. Advanced in electrocatalysis, materials, diagnostics and durability: part 2, vol 6*. Wiley, Chichester, pp 933–956
50. Steinberger-Wilckens R, Blum L, Buchkrember H-P, de Haart LGJ, Pap M, Steinbrech RW, Uhlenbruck S, Tietz F (2009) Overview of solid oxide fuel cell development at Forschungszentrum Juelich. *ECS Trans* 25(2):213–220
51. Yokokawa H, Sakai H, Horita T, Yamaji K, Brito ME, Kishimoto H (2008) Thermodynamic and kinetic considerations on degradations in solid oxide fuel cell cathodes. *J Alloy Compd* 452:41–47
52. Sakai N, Kishimoto H, Yamaji K, Horita T, Brito ME, Yokokawa H (2007) Interface stability of Perovskite cathodes and rare-earth doped ceria interlayer in SOFCs. *J Electrochem Soc* 154(12):B1331–B1337
53. Xiong YP, Yamaji K, Horita T, Yokokawa H, Akikusa J, Eto H, Inagaki T (2009) Sulfur poisoning of SOFC cathodes. *J Electrochem Soc* 156(5): B588–B592
54. Yamaji K, Kishimoto H, Horita T, Yokokawa H, Akikusa J, Kawano M (2010) Effect of temperature on  $SO_2$  poisoning for SSC cathode. In: *Proceedings 77th meeting of electrochemical society of Japan, March 29–31, Toyama, 1G20*, p 209
55. Simner SP, Anderson MD, Pederson LR, Stevenson JW (2005) Performance variability of  $La(Sr)FeO_3$  SOFC cathode with Pt, Ag, and Au current collectors. *J Electrochem Soc* 152:A1851
56. Christiansen N, Hansen JB, Holm-Larsen H, Jørgensen MJ, Larsen P, Hendriksen P, Hagen A, Linderoth S (2008) Solid oxide fuel cell research and development at tops – fuel cell A/S and Risø. In: *Proceedings of the 8th European solid oxide fuel cell forum. The European Fuel Cell Forum, Switzerland, B0201*
57. Yokokawa H, Horita T, Sakai N, Yamaji K, Brito ME, Xiong YP, Kishimoto H (2004) Protons in ceria and their roles in SOFC electrode reactions from thermodynamic and SIMS analyses. *Solid State Ionics* 174:205–221
58. Yokokawa H, Horita T, Sakai N, Yamaji K, Brito ME, Xiong YP, Kishimoto H (2006) Ceria: relation among thermodynamic, electronic hole and proton properties. *Solid State Ionics* 177:1705–1714
59. Komatsu T, Arai H, Chiba R, Nozawa K, Arakawa M, Sato K (2006) Cr poisoning suppression in solid oxide fuel cells using  $LaNi(Fe)O_3$  electrodes. *Electrochem Solid State Lett* 9(1):A9–A12
60. Hartvingsen JJ, Elangovan S, Khandkar AC (2003) Chapter 76 System design. In: Vielstich W, Lamm A, Gasteiger HA (eds) *Handbook of fuel cells fundamentals technology and applications. Fuel cell technology and applications: part 2, vol 4*. Wiley, Chichester, pp 1070–1085
61. Okuda M (2010) Solid oxide fuel cell demonstration program. In: *Proceedings of the report symposium of NEDO projects on fuel cells and hydrogen, Tokyo, July 7–9, NEDO, Kawasaki*, pp 141–148
62. Okuda M (2010) SOFC demonstrative research project. In: *Proceedings of the progress report symposium of solid oxide fuel cell demonstrative research project, March 8, 2010, New Energy Foundation, Tokyo*
63. Yokokawa H (2010) NEDO SOFC project on durability/reliability. In: *Proceedings of the report symposium of NEDO projects on fuel cells and hydrogen, Tokyo, July 7–9, NEDO, Kawasaki*, pp 95–107
64. Yoshida H, Fujita K, Yakabe H, Yamashita S, Sobue T, Seyama T (2006) Subjects to be solved in SOFC system development. In: *15th symposium on solid oxide fuel cells in Japan, extended abstracts. The solid oxide fuel cell society of Japan, Tokyo*, pp 18–21

65. Wuillemin Z, Nakajo A, Muller A, Schuler JA, Diethelm S, Van herle J, Favrat D (2009) Locally-resolved study of degradation in a SOFC repeat element. *ECS Trans* 25(2):457–466
66. Yokokawa H, Sakai N, Horita T, Yamaji K (2009) Impact of impurities on reliability of materials in solid oxide fuel cell (SOFC) stack/modules. In: Vielstich W, Yokokawa H, Gasteiger HA (eds) *Handbook of fuel cells fundamentals technology and application. Advances in electrocatalysis, materials, diagnostics and durability: part 2, vol 6*. Wiley, Chichester, pp 979–991
67. Yamaji K, Sakai N, Kishimoto H, Horita T, Brito ME, Yokokawa H (2009) Application of secondary ion mass spectrometry (SIMS) technique on the durability of solid oxide fuel cell (SOFC). In: Vielstich W, Yokokawa H, Gasteiger HA (eds) *Handbook of fuel cells fundamentals technology and application. Advances in electrocatalysis, materials, diagnostics and durability: part 1, vol 5*. Wiley, Chichester, pp 555–565
68. Yokokawa H, Horita T, Yamaji K, Kishimoto H, Brito ME (2010) Materials chemical point of view for durability issues in solid oxide fuel cells. *J Korean Ceram Soc* 47(1):26–38
69. Wunderlich C (2007) Staxera SOFC stacks in series production. Abstracts for oral presentations for 2007 fuel cell seminar and exposition. October 15–19, 2007, San Antonio, p 322
70. Matsuzaki Y, Yasuda I (2001) Dependence of SOFC cathode degradation by chromium-containing alloy on compositions of electrodes and electrolytes. *J Electrochem Soc* 148:A126
71. Badwal SPS, Deller R, Foger K, Ramprakash Y, Zhang JP (1997) Interaction between chromia forming alloy interconnects and air electrode of solid oxide fuel cells. *Solid State Ionics* 99:297–310
72. Simner SP, Anderson JW, Xia G-G, Yang Z, Pederson LR, Stevenson MD (2005) SOFC performance with Fe-Cr-Mn alloy interconnect. *J Electrochem Soc* 152(4):A740–A745
73. Jiang SP, Zhang JP, Föger K (2000) Deposition of chromium species at Sr-doped LaMnO<sub>3</sub> electrodes in solid oxide fuel cells. *J Electrochem Soc* 147(1):4013–4022; (2000) 147(9): 3195–3205; (2001) 148(7):C447–C455
74. Paulson SC, Birss VI (2004) Chromium poisoning of LSM-YSZ SOFC cathodes I. Detailed study of the distribution of chromium species at a porous, single-phase cathode. *J Electrochem Soc* 151(1): A1961–A1968
75. Konyshva E, Penkalla H, Wessel E, Mertens J, Seeling U, Singheiser L, Hilpert K (2006) Chromium poisoning of Perovskite cathodes by the ODS alloy Cr<sub>5</sub>Fe<sub>1</sub>Y<sub>2</sub>O<sub>3</sub> and the high chromium ferritic steel Croffer 22APU. *J Electrochem Soc* 153(4): A765–A773
76. Konyshva E, Mertens J, Penkalla H, Singheiser L, Hilpert K (2007) Chromium poisoning of the porous composite cathode effect of cathode thickness and current density. *J Electrochem Soc* 154(12): B1252–B1264
77. Tsuneyoshi K, Mori K, Sawata A, Mizusaki J, Tagawa H (1989) Kinetic studies on the reaction at the La<sub>0.6</sub>Ca<sub>0.4</sub>MnO<sub>3</sub>/YSZ interface, as an SOFC air electrode. *Solid State Ionics* 35:263–268
78. Jiang SP, Zhang S, Zhen YD (2006) Deposition of Cr species at (La, Sr) (Co, Fe)O<sub>3</sub> cathodes of solid oxide fuel cells. *J Electrochem Soc* 153(1):A127–A134
79. Kim JY, Sprenkle VL, Canfield NL, Meinhardt KD, Chick LA (2006) Effects of chrome contamination on the performance of La<sub>0.6</sub>Sr<sub>0.4</sub>Co<sub>0.2</sub>Fe<sub>0.8</sub>O<sub>3</sub> cathode used in solid oxide fuel cells. *J Electrochem Soc* 153(5):A880–A886
80. Xiong YP, Yamaji K, Kishimoto H, Brito ME, Horita T, Yokokawa H (2009) Deposition of platinum particles at LSM/ScSZ/air three-phase boundaries using a platinum current collector. *Electrochem Solid State Lett* 12(3):B31–B33
81. Ingram BJ, Cruse TA, Krumpelt M (2007) Potassium-assisted chromium transport in solid oxide fuel cells. *J Electrochem Soc* 154(11):B1200–B1205
82. Stanislawski M, Froitzheim J, Niewolak L, Quadackers WJ, Hilpert K, Markus T, Singheiser L (2007) Reduction of chromium vaporization from SOFC interconnectors by highly effective coatings. *J Power Sources* 164:578–589
83. Muller AC, Weber A, Beie HJ, Krugel A, Gerthsen D, Ivers-Tiffée E (1998) Influence of current density and fuel utilization on the degradation of the anode. In: Stevens P (ed) *Proceedings of the 3rd European solid oxide fuel cell forum. The European Fuel Cell Forum*, pp 353–362
84. Weber A, Sauer B, Muller AC, Herbstritt D, Ivers-Tiffée E (2002) Oxidation of H<sub>2</sub>, CO and methane in SOFCs with Ni/YSZcermet anodes. *Solid State Ionics* 152–153:543–550
85. Kishimoto H, Horita T, Yamaji K, Brito ME, Xiong YP, Yokokawa H (2010) Sulfur poisoning on SOFC Ni anodes: thermodynamic analyses within local equilibrium anode reaction model. *J Electrochem Soc* 157(6):B802–B813
86. Wilson JR, Kobscirphat W, Mendoza R, Chen H-Y, Hiller JM, Miller DJ, Thomson K, Voorhees PW, Adler SB, Barnett SA (2006) Three-dimensional reconstruction of a solid-oxide fuel-cell anode. *Nat Mater* 5:541–544
87. Abbaspour A, Nandakumar K, Luo J, Chuang KT (2006) A novel approach to study the structure versus performance relationship of SOFC electrodes. *J Power Sources* 161:965–970
88. Smith JR, Chen A, Gostovic D, Hickey D, Kundering D, Duncan KL, DeHoff RT, Jones KS, Wachsmann ED (2009) Evaluation of the relation between cathode microstructure and electrochemical behavior for SOFCs. *Solid State Ionics* 180:90–98
89. Timmermann H, Sawady W, Campbell D, Weber A, Reimert R, Ivers-Tiffée E (2008) Coke formation and



- degradation in SOFC operation with a model reformate from liquid hydrocarbons. *J Electrochem Soc* 155(4):B356–B359
90. Mukerjee S, Kerr R, Shaffer S (2009) Solid oxide fuel cell development for transportation and stationary applications: latest update on stack and system performance. In: Abstracts for the oral and poster presentations for 2009 Fuel cell seminar and exposition, November 16–19, 2009, Palm Springs, HRD 24-1
  91. Matsuzaki Y, Yasuda I (2000) The poisoning effect of sulfur-containing impurity gas on a SOFC anode: part I. Dependence on temperature, time, and impurity concentration. *Solid State Ionics* 132:261–269
  92. Sasaki K, Susuki K, Iyoshi A, Uchimura M, Imamura N, Kusaba H, Teraoka Y, Fuchino H, Tsujimoto K, Uchida Y, Jingo N (2006) H<sub>2</sub>S poisoning of solid oxide fuel cells. *J Electrochem Soc* 153(11):A2023–A2029
  93. Lohsoontorn P, Brett DJL, Brandon NP (2008) The effect of fuel composition and temperature on the interaction of H<sub>2</sub>S with nickel-ceria anodes for solid oxide fuel cells. *J Power Sources* 183:232–239
  94. Lohsoontorn P, Brett DJL, Brandon NP (2008) Thermodynamic predictions of the impact of fuel composition on the propensity of sulphur to interact with Ni and ceria-based anodes for solid oxide fuel cells. *J Power Sources* 175:60–67
  95. Dong J, Cheng Z, Zha S, Liu M (2006) Identification of nickel sulfides on Ni-YSZ cermet exposed to H<sub>2</sub> fuel containing H<sub>2</sub>S using Raman spectroscopy. *J Power Sources* 156:461–465
  96. Hansen JB (2008) Correlating sulfur poisoning of SOFC nickel anodes by Temkin isotherm. *Electrochem Solid State Lett* 11(10):B178–B180
  97. Marques AI, Abreu YD, Botte GG (2006) Theoretical investigations of Ni/YSZ in the presence of H<sub>2</sub>S. *Electrochem Solid State Lett* 9(3):A163–A166
  98. Wang J-H, Liu M (2007) Computational study of sulfur-nickel interactions: a new S-Ni phase diagram. *Electrochem Commun* 9:2213–2218
  99. Zha S, Cheng Z, Liu M (2007) Sulfur poisoning and regeneration of Ni-based anodes in solid oxide fuel cells. *J Electrochem Soc* 154(2):B201–B206
  100. Ferrizz RM, Gorte RJ, Vohs JM (2003) Determining the Ce<sub>2</sub>O<sub>2</sub>ScO<sub>x</sub> phase boundary for conditions relevant to adsorption and catalysis. *Appl Catal B* 43:273–280
  101. Chou Y-S, Stevenson JW, Hardy JS, Singh P (2006) Material degradation during isothermal aging and thermal cycling of hybrid mica seal with Ag interlayer under SOFC exposure conditions. *J Electrochem Soc* 153(8):A1591–A1598
  102. Hansen KV, Norrman K, Mogensen M (2004) H<sub>2</sub>-H<sub>2</sub>O-Ni-YSZ electrode performance effect of segregation to the interface. *J Electrochem Soc* 151(9):A1436–A1444
  103. Hauch A, Jensen SH, Bilde-Sørensen JB, Mogensen M (2007) Silica segregation in the Ni/YSZ electrode. *J Electrochem Soc* 154(7):A619–A626
  104. Aravind PV, Ouweltjes JP, Woudstra N, Rietveld G (2008) Impact of biomass-derived contaminants on SOFCs with Ni/Gadolinia-doped ceria anodes. *Electrochem Solid State Lett* 11(2):B24–B28
  105. Yang Z, Meihardt KD, Stevenson JW (2003) Chemical compatibility of barium-calcium-aluminosilicate-based sealing glasses with tge ferritic stainless steel interconnect in SOFCs. *J Electrochem Soc* 150(8):A1095–A1101
  106. Hofmann P, Panopoulos KD, Fryda LE, Schweiger A, Ouweltjes JP, Karl J (2008) Integrating biomass gasification with solid oxide fuel cells: effect of real product gas tars, fluctuations and particulates on Ni-GDC anode. *Int J Hydrog Energy* 33:2834–2844
  107. Marina OA, Pederson LR, Gemmen R, Finklea K, Celik IB (2009) Overview of SOFC anode interactions with coal gas impurities. In: 2009 Fuel cell seminar, Palm Spring, HRD43b-1
  108. Gemmen RS, Trembly J (2006) On the mechanisms and behavior of coal syngas transport and reaction within the anode of a solid oxide fuel cell. *J Power Sources* 161:1084–1095
  109. Trembly JP, Gemmen RS, Bayless DJ (2007) The effect of IGFC warm gas cleanup system conditions on the gas-solid partitioning and form of trace species in coal syngas and their interactions with SOFC anodes. *J Power Sources* 163:986–996
  110. Trembly JP, Gemmen RS, Bayless DJ (2007) The effect of coal syngas containing HCl on the performance of solid oxide fuel cells: investigations into the effect of operational temperature and HCl concentration. *J Power Sources* 169:347–354
  111. Trembly JP, Gemmen RS, Bayless DJ (2007) The effect of coal syngas containing AsH<sub>3</sub> on the performance of SOFCs: investigations into the effect of operational temperature, current density and AsH<sub>3</sub> concentration. *J Power Sources* 171:818–825
  112. Xu B, Zondlo JW, Finklea HO, Demircan O, Gong M, Liu XB (2009) The effect of phosphine in syngas on Ni-YSZ anode-supported solid oxide fuel cells. *J Power Sources* 193:739–746
  113. Trembly JP, Marques AI, Ohrn TR, Bayless DJ (2006) Effects of coal syngas and H<sub>2</sub>S on the performance of solid oxide fuel cells: single-cell tests. *J Power Sources* 158:263–273
  114. Zhi M, Chen X, Finklea H, Celik I, Wu NQ (2008) Electrochemical and microstructural analysis of nickel-yttria-stabilized zirconia electrode operated in phosphorus-containing syngas. *J Power Sources* 183:485–490
  115. Haga K, Adachi S, Shiratori Y, Itoh K, Sasaki K (2008) Poisoning of SOFC anodes by various fuel impurities. *Solid State Ionics* 179:1427–1431
  116. Bao J, Krishnan GN, Jayaweera P, Perez-Mariano J, Sanjurjo A (2009) Effect of various coal contaminants on the performance of solid oxide fuel cells: part I accelerated testing. *J Power Sources* 193:607–616

117. Bao J, Krishnan GN, Jayaweera P, Kau KH, Sanjurjo A (2009) Effect of various coal contaminants on the performance of solid oxide fuel cells: part II. ppm and sub-ppm level testing. *J Power Sources* 193:617–624
118. Bao J, Krishnan GN, Jayaweera P, Sanjurjo A (2010) Effect of various coal gas contaminants on the performance of solid oxide fuel cells: part III Synergistic effects. *J Power Sources* 195(5):1316–1324
119. Burnette DD, Kremer GG, Bayless DJ (2008) The use of hydrogen-depleted coal syngas in solid oxide fuel cells. *J Power Sources* 182:329–333
120. Huang T-J, Chou C-L, Chen W-J, Huang M-C (2009) Coal syngas reactivity over Ni-added LSCF-GDC anode of solid oxide fuel cells. *Electrochem Commun* 11:294–297
121. Marques AI, Ohrm TR, Tremblay JP, Ingram DC, Bayless DJ (2007) Effect of coal syngas and H<sub>2</sub>S on the performance of solid oxide fuel cells part 2 Stack tests. *J Power Sources* 164:659–667
122. Cayan FN, Zhi M, Pakalapati SR, Celik I, Wu NQ, Gemmen R (2008) Effects of coal syngas impurities on anodes of solid oxide fuel cells. *J Power Sources* 185:595–602
123. Casleton KH, Breault RW, Richards GA (2008) System issues and tradeoffs associated with syngas production and combustion. *Combust Sci Technol* 180:1013–1052
124. Itoh H, Mori M, Mori N, Abe T (1993) Development of solid oxide fuel cells – producing cost estimation. Yokosuka Research Laboratory Rep. No. W92028, CRIEPI, Tokyo
125. Itoh H, Mori M, Mori N, Abe T (1994) Production cost estimation of solid oxide fuel cells. *J Power Sources* 49:315–332
126. Romero C, Wright J (1996) The value and manufacturing costs of planar solid oxide fuel cell stacks. Topical Report no. TDA-GRI-96/0210 for Gas Research Institute
127. Krist K, Wright JD, Romero C, Chen TP (1996) Cost projections for planar solid oxide fuel cell systems. In: Fuel cell seminar, Orlando, pp 497–500
128. Krist K, Wright JD, Romero C (1995) Manufacturing costs for planar solid oxide fuel cells. In: Dokiya M, Yamamoto O, Tagawa T, Singhal SC (eds) Solid oxide fuel cells IV, PV 95-1. The Electrochemical Society, Pennington, pp 24–32
129. Ipponmatsu M, Sasaki H, Otoshi S (1996) Evaluation of the cost performance of the SOFC cell in the market. *Int J Hydrog Energy* 21(2):129–135
130. George RA, Bessette N (1998) Reducing the manufacturing cost of tubular SOFC technology. *J Power Sources* 71:131–137
131. Mizutani Y, Tamura M, Kawai M, Nomura K, Nakamura Y, Yamamoto O (1995) Characterization of the Sc<sub>2</sub>O<sub>3</sub>-ZrO<sub>2</sub> system and its application as the electrolyte in planar SOFC. In: Dokiya M, Yamamoto O, Tagawa T, Singhal SC (eds) Solid oxide fuel cells IV, PV 95-1. The Electrochemical Society, Pennington, pp 301–317
132. Thijssen JH, Surdval WA (2009) Stack operating strategies for central station SOFC. In: 2009 Fuel cell seminar and exposition. November 16–19, Palm Springs, HRD32-3
133. Watanabe M, Uchida H, Yoshida M (1997) Effect of ionic conductivity of zirconia electrolytes on the polarization behavior of ceria-based anodes in solid oxide fuel cells. *J Electrochem Soc* 144(5):1739–1743

### Books and Reviews

- Ishihara T (ed) (2009) Perovskite oxide for solid oxide fuel cells. Springer, Dordrecht
- Minh Q, Takahashi T (1995) Science and technology of ceramic fuel cells. Elsevier, Amsterdam
- Singhal SC, Kendall K (eds) (2003) Solid oxide fuel cells. Elsevier, Oxford
- Vielstrich W, Yokokawa H, Gasteiger HA (eds) (2009) Hand book of fuel cells fundamentals technology and application, vols 5 and 6. Advances in electrocatalysis, materials, diagnostics and durability. Wiley, Chichester



## Solid Oxide Fuel Cells: Marketing Issues

John Bøgild Hansen<sup>1</sup> and Niels Christiansen<sup>2</sup>

<sup>1</sup>Haldor Topsøe A/S, Lyngby, Denmark

<sup>2</sup>Topsoe Fuel Cell A/S, Lyngby, Denmark

### Article Outline

Glossary

Definition of the Subject

Introduction

The Global Energy Challenge

Briefly on the SOFC Technology

Markets

Major SOFC Players

Steps in Commercialization

Competitiveness

Summing Up

Future Directions

Conclusions

Bibliography

### Glossary

**APU** Auxiliary power unit – device providing power in addition to main power train.

**DG** Distributed generation. Combined heat and power plant with typical capacities from 50 kW to several MW.

**micro-CHP** Micro-combined heat and power. Capacities up to say 10-kW.

**SOEC** Solid oxide electrolyzer cell.

**SOFC** Solid oxide fuel cell.

### Definition of the Subject

Clean and sufficient energy is an important precondition for the continued growth in global wealth. Solutions must be found to utilize the remaining fossil fuels more efficiently and also to ensure that new environmentally friendly fuels

can secure power production in the post-fossil fuel era. This is the essence of the global energy challenge.

Fuel cells hold the promise of an efficient, low-pollution technology for production of electricity. Because fuel cells rely on electrochemical rather than thermo-mechanical processes in the conversion of fuel into electricity, the fuel cell is not limited by the Carnot efficiency as is the case for conventional generators. High-temperature fuel cells hold the promise of an efficient, low-pollution technology for production of electricity and efficient use of waste heat including low transmission losses. Scalability, decentralization, and load following capabilities are major advantages that can play an effective role in future power grids and power supply.

Solid oxide fuel cells offer the potential of high volumetric power density, cost-efficiency, and fuel flexibility, and significant progress has been made during the last 5 years in bringing SOFC technology closer to commercialization.

This entry will endeavor to answer the question whether SOFC technology is now ready for the market or perhaps put in another way: Is the market ready for SOFC technology and which challenges still need to be addressed?

### Introduction

The entry will describe how SOFC technology can contribute to solving the energy challenges in the future. The current status of the SOFC technology and industry will be briefly discussed and the possible markets described. Three main challenges on the road to competitiveness – lifetime, reliability, and cost – are addressed. Techno-economic studies of the different market segments are used to define the threshold for market entry. The entry ends by looking ahead and concluding that the SOFC technology is ready for the market with respect to the projected cost and lifetimes, but that reliability under real-life conditions still

remains to be demonstrated. The learning investments needed, however, do not appear to be prohibitive considering the benefits which this game-changing technology has to offer.

## The Global Energy Challenge

### Increasing Power Demand

The increasing global demand for energy and power mainly comes from the growth in industrialization, population, and living standards.

Forecasts from International Energy Agency (IEA – all forecasts in the following comes from the publication *World Energy Outlook 2010* [1]) show that the population will grow from 6.7 billion in 2008 to 8.5 billion in 2035. Almost all of the increase will take place in the non-OECD area.

On a global scale, the demand for primary energy is expected to increase by 1.2% per year until 2035. More than one third of the total primary energy consumed is used for power generation (Table 1).

The rapid population growth in the non-OECD area is further followed by a sharp increase in urbanization, which will have a significant impact on the demand for power coming from industrialization and improvements in housing and level of welfare. The demand for electricity generation will therefore increase accordingly and at an even higher rate than the energy demand. Total electricity consumption is expected to increase by 2.5% per year until 2035 (Table 2).

The growth in primary energy demand together with the decreasing accessibility of fossil fuels is expected to result in increasing energy

prices. This makes efficiency in power production an important issue. Technologies with higher efficiency will be in demand.

In 2035, a very large number of people will not have access to power in the quantities known to us in the OECD area today, despite the rapid growth and urbanization within the non-OECD area. Although the total power consumption is expected to double from 2008 to 2035, 38% of the world's power consumption will still be in the OECD area, having only 15% of the world population. While the per capita electricity consumption in the non-OECD countries will be doubled by 2035 to 2600 kWh/year, it will at that time only be around one fourth of the level of the OECD area.

### Significant Structural Investments Needed

In order to meet this high level of consumption, significant investments in energy production and power generation will be needed. The figure below shows the expected growth and the expected investments in power generation capacity (Table 3).

The majority of investments will take place in the non-OECD area. The total growth in capacity, including replacement and expansion, will be about 5700 GW or almost 10 trillion US dollars over the forecasted period. This corresponds to 220-GW new capacity or investments in new plants of 370 billion US dollars per year.

The total investment in new power generation capacity constitutes more than half of the total world energy investments. This means that in future, a high dependency on the power grids remains, and the cost of improving poor grids

**Solid Oxide Fuel Cells: Marketing Issues, Table 1** World primary energy demand

	1980	2008	2020 F	2035 F	Annual growth rate 2008–2035
Energy demand (Mtoe)	7229	12,271	14,556	16,748	1.2%

**Solid Oxide Fuel Cells: Marketing Issues, Table 2** World electricity consumption

TWh	1980	2008	2020F	2035F	Annual growth rate 2008–2035
OECD	4739	8244	10,339	11,566	1.0%
Non-OECD	971	7575	12,841	18,763	3.8%
<b>Total, world</b>	<b>5711</b>	<b>16,819</b>	<b>23,180</b>	<b>30,329</b>	<b>2.5%</b>

**Solid Oxide Fuel Cells: Marketing Issues, Table 3** Projected capacity additions and investment in power infrastructure 2008–2035

	Capacity addition (GW)	Investments, new plants (billion US dollars)
OECD	1985	3992
Non-OECD	3688	5642
<b>Total, world</b>	<b>5673</b>	<b>9634</b>

and in establishing new grids where these do not yet exist will be significant.

Despite the expected high level of investments, the power grid and other power infrastructure will impose a limitation on the capacity and efficiency of the present infrastructure. This will be a driver toward a more decentralized power production with production taking place closer to the end user and with combined production of heat and power.

The transmission losses throughout the grid existing today will also exist in future. On a global average, the energy content of the primary fuel that is actually converted into consumed power will not exceed 35%.

### Renewable-Based Power Production Increase

The increasing scarcity of oil and other fossil fuels makes the exploration efforts more expensive and the transport routes to the consumers longer. This will concentrate the remaining reserves to a limited number of countries. This is a growing concern to the net-importing West-world.

Power generation based on renewables is expected to increase over the forecasted period due to higher fossil fuel prices, growing concerns over pollution and greenhouse gas emissions, and declining technology costs and government support. Renewable electricity generation is expected to grow globally and will in the OECD area constitute 26% of the total power generation in 2035, and in the non-OECD area 22% (Table 4). The rising share of wind and solar power (PV) poses a challenge of integration into the power grid and a challenge of how to match power production with power demand in due

time. Power production from wind and PV fluctuates according to the prevailing conditions with regard to weather, season, and time of the day. Problems due to variability affecting the reliability of a power production system are manageable when the shares of wind and other variable renewable capacity are small, but with a larger share of power from renewables, such problems will increase.

This makes it necessary to balance the growth in renewables in the overall production system with smaller, scalable units capable of equalizing the fluctuations created by solar cells and wind turbines.

### Restrictions on Pollution and Emissions Still Tighter

The extensive use of fossil fuel globally will continue to drive up power-generation-related CO<sub>2</sub> emissions, from 11.9 Gt in 2008 to 14 Gt in 2035 in the base scenario. Nearly all the increase in power-related CO<sub>2</sub> emissions is expected to come from non-OECD countries, where urbanization and higher living standards – together with rising reliance on fossil fuels – are particularly pronounced. The non-OECD area is projected to increase its power-related CO<sub>2</sub> emission by more than 50% by 2035, corresponding to 76% of the total amount.

Continuously, stricter legislation on emissions and pollution is introduced in most countries. This will be supported by incentive schemes given to energy technologies that have inherently lower emissions.

This is already the case in Europe and the USA. The high-growth countries in the Far East and South America have less focus on climate end environment at present. But along with their development, an increasing awareness of the environmental issues is expected to emerge. This will be followed by willingness and ability to pay for advanced, cleaner energy technologies.

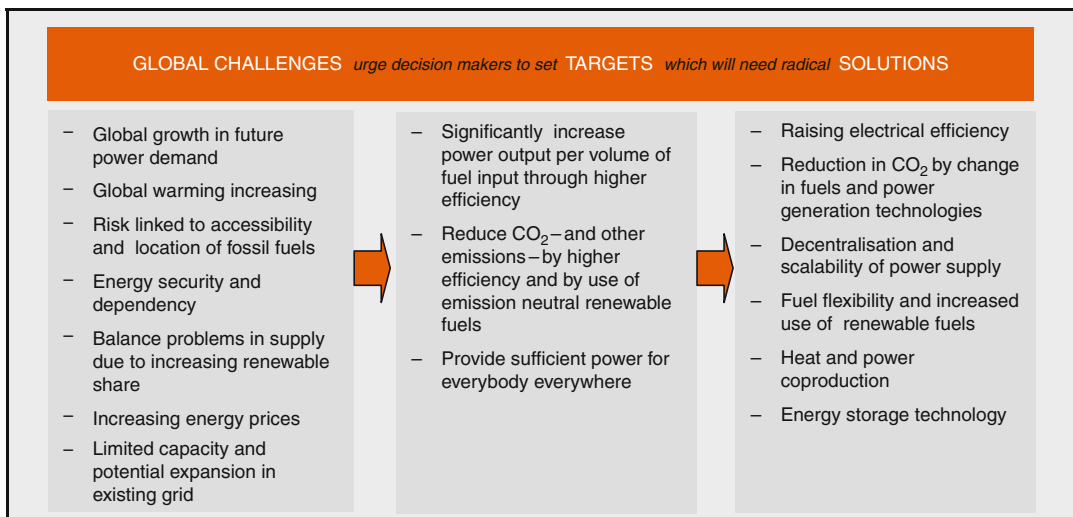
### Global Challenges

All in all, the situation can be summarized in the headlines below. The world urgently needs new technologies that can help solve the challenges of access to clean and sufficient energy (Table 5).

**Solid Oxide Fuel Cells: Marketing Issues, Table 4** Fuel sources of power generation

TWh	1990	2008	2020F	2035F	Annual growth rate 2008–2035
Coal	4427	8273	10,630	11,241	1.1%
Oil	1338	1104	689	480	–3.0%
Gas	1726	4303	5881	7557	2.1%
Nuclear	2013	2731	3712	4883	2.2%
Hydro	2145	3208	4367	5533	2.0%
Biomass	131	267	547	1476	6.5%
Wind	4	219	1229	2851	10.0%
Others	38	79	319	1314	11.0%
<b>Total generation</b>	<b>11,821</b>	<b>20,183</b>	<b>27,373</b>	<b>35,336</b>	<b>2.1%</b>

**Solid Oxide Fuel Cells: Marketing Issues, Table 5** Global challenges in the energy complex



Fuel cells are one of the most promising technologies capable of delivering solutions to the world’s energy challenges.

**Briefly on the SOFC Technology**

A fuel cell system produces electricity from a cleaner and more efficient fuel than conventional technologies. The fuel can be natural gas, diesel, biogas, hydrogen, or similar. Like batteries, a fuel cell generates power by an electrochemical process.

In physical terms, an SOFC fuel cell is a very thin, planar “sheet” of flexible, ceramic material consisting of three functional layers – the anode, the cathode, and the electrolyte (Figs. 1 and 2).

Fuel is supplied and passes over the anode side, and air passes over the cathode. The electrolyte – a thin, gastight, ion-conducting layer – is placed between the anode and the cathode.

An external circuit connects the anode to the cathode and provides the mechanism to power electrical devices (Fig. 3).

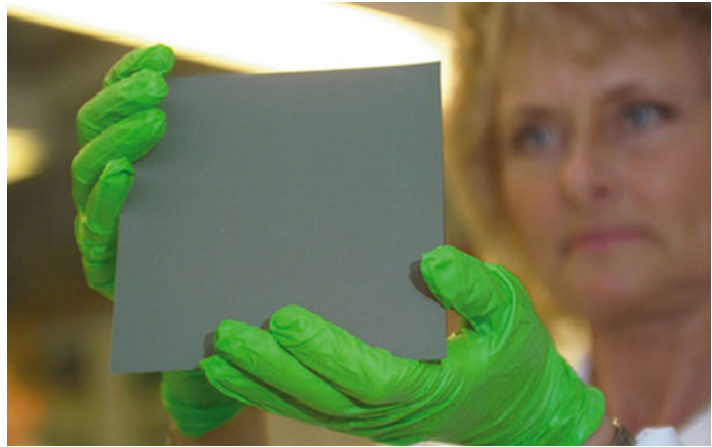
A single fuel cell can create a voltage of approximately 0.7–0.9 V.

The current state-of-the-art SOFC anode-supported cells based on doped zircona ceramic electrolytes, ceramic LSM cathodes, and Ni/YSZ cermet anodes are operated in the temperature range 700–800 °C with a cell area specific resistance (ASR) of about 0.5 Ω/cm<sup>2</sup>.

at 750 °C. Using the more active ceramic lanthanum strontium cobalt ferrite (LSFC)-based



**Solid Oxide Fuel Cells:  
Marketing Issues,  
Fig. 1** Electrolyte/  
electrode assembly

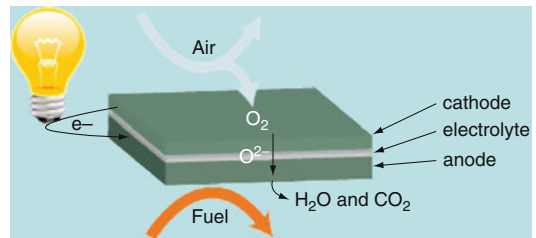


**Solid Oxide Fuel Cells: Marketing Issues,  
Fig. 2** Highly flexible material

cathodes, the ASR is decreased to about  $0.25 \Omega/\text{cm}^2$  at this temperature, which is a more favorable value regarding overall stack power density and cost-effectiveness.

**Fuel Cell Stack, Stack Modules, and  
PowerCore**

Single cells are combined in a stack to generate power in useful quantities.



**Solid Oxide Fuel Cells: Marketing Issues, Fig. 3** The electrochemical process of a fuel cell

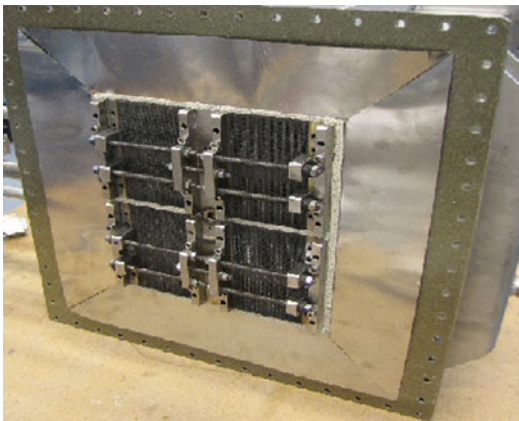
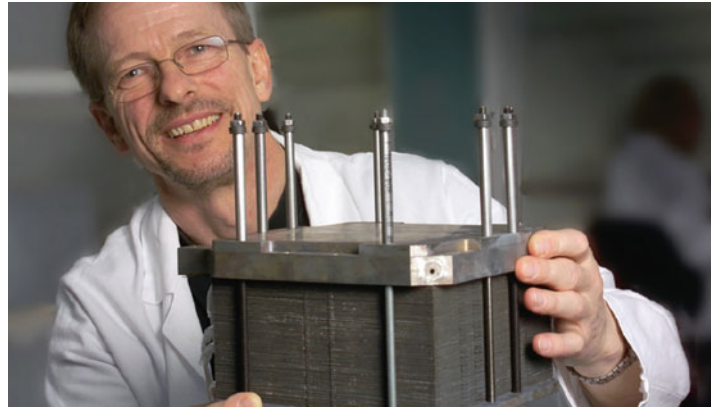
A stack is a multilayer construction of fuel cells separated by metal sheets (the “interconnect plate”) guiding the flow of air and fuel to the individual cells. The number of repeated cell/interconnect plates determines the stack capacity. The stack is the heart of a fuel cell system (Figs. 4 and 5).

With the current technology, a stack can generate up to about 3 kW of power. For larger power levels, stacks are combined into stack modules, which in turn also can be combined, thus providing for power output, in principle, approaching indefinite sizes.

In addition to a stack or stack module, a fuel cell system comprises components for handling of fuel, heat, electric power conditioning, and other components required for the operation.

The fuel cell process on which Topsoe Fuel Cell’s technology is based (SOFC) takes place at temperatures of  $700 - 900 \text{ }^\circ\text{C}$ . The parts of the system operating above  $300 \text{ }^\circ\text{C}$  are integrated into a module called a PowerCore™. The PowerCore is a highly integrated “black box” with defined

**Solid Oxide Fuel Cells: Marketing Issues, Fig. 4** Fuel cell stack



**Solid Oxide Fuel Cells: Marketing Issues, Fig. 5** Stack module

operating responsibility suitable for installation into complete systems (Fig. 6).

### Comparing Fuel Cells to Conventional Technologies

A conventional combustion engine converts the energy stored in the fuel to electricity through a combustion, which in turn drives a generator that produces electricity. In contrast, a fuel cell converts the same initial energy into electricity via a direct electrochemical path. This direct conversion of energy to electrical power means that fuel cells have higher energy efficiency, and at the same time, lower emissions of CO<sub>2</sub>, VOC, and NO<sub>x</sub> than the dominating power generation technologies based on combustion. This makes fuel cell technology economic and very environmentally friendly and accordingly addresses the major challenges of

the energy sector: economy, securing energy supplies, and protection of the environment.

### Different Types of Fuel Cells

Different types of fuel cell technologies exist. They are all based on the same electrochemical principle but differentiated by the materials used for the electrolytes. The six major types are:

- Proton exchange membrane (PEMFC).
- Alkaline (AFC).
- Phosphoric acid (PAFC).
- Molten carbonate (MCFC).
- Direct methanol (DMFC).
- Solid oxide (SOFC).

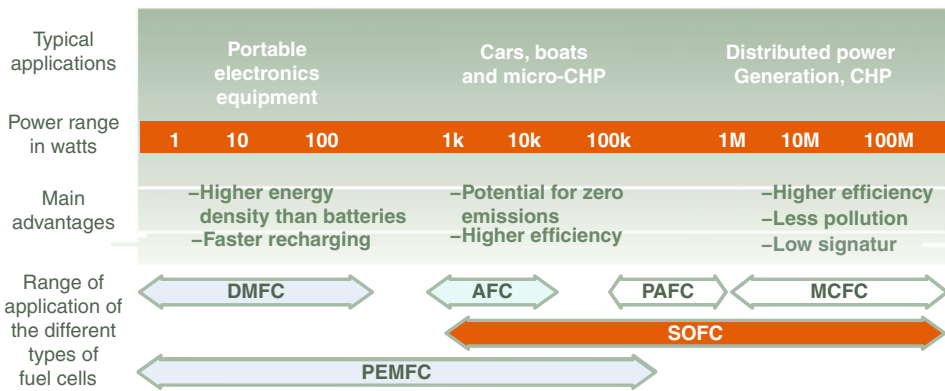
The difference in materials between the fuel cell types results in large differences in performance parameters and operational requirements. This makes the different types specifically suited for different applications.

With some exceptions, higher-temperature systems (MCFC, SOFC, PAFC) tend to be best suited for larger applications, while low-temperature systems (DMFC, PEMFC, AFC) can, in addition to units up to some hundred of kilowatts, be configured to provide as little as a few watts of power or less and hence be applied for portable equipment etc. (Fig. 7).

### Advantages of SOFC Fuel Cells

Analyses made by Haldor Topsøe and Topsoe Fuel Cell have shown that SOFC technology

**Solid Oxide Fuel Cells: Marketing Issues, Fig. 6** PowerCore™



**Solid Oxide Fuel Cells: Marketing Issues, Fig. 7** Primary applications for different fuel cell technologies

possesses the highest potential to become a main contributor to the global power market because of:

*Higher electrical efficiency.* The SOFC technology will be able to provide an electrical efficiency of up to 60%. This efficiency is very high compared to worldwide power plants operating at average electric efficiencies of 30–35% and to existing decentralized, smaller power generation equipment (engines and generators) operating at as low as 5–10% for engines and 15–25% for generators. Application of SOFC units with higher electrical efficiency will result in substantial savings in fuel and money, and for operation on fossil fuels also in a proportional reduction in CO<sub>2</sub> emissions.

*High efficiency for all capacities.* The SOFC technology is scalable and can cover the complete range from 1 kW to 1 MW, or even higher, with almost no loss of efficiency. The technology offers

a very competitive output per weight or volume compared to power plants. Because of this, the SOFC technology addresses a wide range of applications and finds use both in urban and remote areas and both for stationary and mobile purposes.

*Fuel flexibility.* The SOFC technology is (together with MCFC) the only technology among the different fuel cell technologies which is able to effectively generate power directly based on the fossil fuels in use today, and at the same time, the technology has a clear path to renewables and CO<sub>2</sub>-neutral energy systems. This is due to the higher operating temperatures and the superior ability of the SOFC to convert hydrocarbon in the fuel cell stack.

*Lower maintenance cost.* The SOFC system provides a highly effective and direct electrochemical conversion of fuel to power. The only

rotating parts in the system are a fuel pump and a small air blower. Accordingly, maintenance costs are expected to be substantially lower, and operating periods between overhauls are substantially longer than conventional technologies.

*Lower emission and noise levels.* Since no combustion is involved, the acoustic and heat signatures and particle (NO<sub>x</sub> or other particles) emissions will be small. This is crucial for some applications.

*Synergies with coupled technologies.* SOFC systems are very well suited for integration in coupled technologies. Examples include SOFC systems with heat pumps or air-conditioning systems in which SOFC systems can produce power and interchangeable heat or cooling. SOFC can also be coupled with gas turbine to provide extremely high electrical efficiencies up to 70%.

*Solid oxide electrolysis (SOEC).* The SOFC technology deals with conversion of fuel to power. However, the system can be designed to handle the reverse process converting excess production of power to fuel (electrolysis). This is especially interesting in relation to balancing fluctuating power generating sources, like wind turbines or PV systems, but it is also of interest in relation to nuclear power plants, where change from stable base load operation to match supply and demand is not accepted. Commercialization of SOEC is still some years ahead but is an extremely important future feature of the SOFC technology, especially because SOEC is the only

electrolysis technology with the capability to electrolyze CO<sub>2</sub> so that synthesis gas (CO plus H<sub>2</sub>) can be produced. This opens up the possibility of production of renewable transportation fuels from power, water, and CO<sub>2</sub> without having to rely on limited biomass resources and renewable fuels.

**Competing Conventional Power Generation Technologies**

SOFC systems will, in the coming commercial phase, face competition primarily from the conventional power generation technologies such as boilers, Stirling engines, diesel generators, gas engines, batteries, etc., much more than competition from other fuel cell producers. Most of the conventional technologies are advanced, mature technologies (Fig. 8).

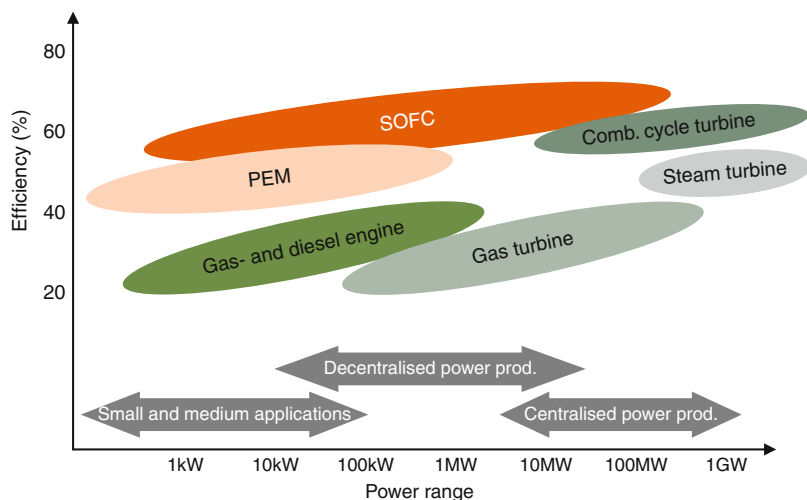
The fuel cell industry in general has to prove that fuel cell systems can provide superior performance (taking all technical, financial, and environmental parameters into account) compared to existing technologies.

The strength of competition from other power generation technologies differs between the different applications and markets.

**Markets**

Solid oxide fuel cells have a higher efficiency than existing power generation technologies,

**Solid Oxide Fuel Cells: Marketing Issues, Fig. 8** SOFC compared with other power production technologies (illustrative figures)



		Small 1–5 kW	Medium 5–50 kW	Large 50–250 kW	Mega large >250 kW
Stationary	Grid	– <i>micro-CHP (residential)</i>	– <i>Apartment buildings</i> – <i>Hotels</i> – <i>Small industry</i>	– <i>Medium industry</i> – <i>Super markets</i> – <i>Hospitals</i>	– Power plants – Airports – Large industry – Electrolysis
	Off-grid	– <i>Telecom base stations</i> – Remote holiday houses	– <i>Military camps</i> – Emergency aid camps – Large screens, light and sound at concerts, circus etc. – Oil and gas industry (power for pipeline pumps and surveillance) – Hotels, ski lifts etc.		– Remote villages and towns – Offshore platforms
Mobile		– <i>Unmanned aerial vehicles</i> – <i>Truck cab power</i> – Recreational vehicles – Yachts – Golf cars	– <i>Military vehicles</i> – Buses – Range extenders (battery charger for electric battery vehicles) – Cooling containers	– Coastal vessels – Airplanes	– Trains – Ocean going vessels
SOEC (electrolysis)					– Storage for renewable energy – Smart grids – Nuclear plants

**Solid Oxide Fuel Cells: Marketing Issues, Fig. 9** Applications for SOFC fuel cells – Topsoe Fuel Cell target applications are highlighted

meaning that attractive and competitive applications of SOFC systems are almost endless – provided the cost and performance targets are met. This includes applications of small and large capacity, stationary and mobile applications, and centralized and decentralized applications, running on fossil fuels as well as on renewables.

Figure 9 groups the potential applications according to power range and mobility. The applications are described in more detail below.

Each market has specific requirements to the technology with regard to, e.g., capacity, cost, and lifetime. Accordingly, there will be a difference as to when the SOFC technology is ready for a given market. Some of the early opportunities, such as smaller units for military applications and secondary power, are characterized by having relatively low capacity requirements and accepting a slightly higher price compared to consumer markets.

Topsoe Fuel Cell uses a classification of the potential target applications in three generic market segments: micro-combined heat and power (micro-CHP), auxiliary power units (APU), and distributed generation (DG). In Fig. 10, the market segments are grouped following this classification.

Topsoe Fuel Cell has chosen initially to target the markets for residential micro-CHP, smaller CHP units (up to 250 kW) within DG, and APU for trucks and military applications first because these applications pose early opportunities for demonstration and at the same time lead to high volume markets later on.

**Micro-combined Heat and Power (micro-CHP)**

micro-CHP units are small stationary systems with an electricity capacity of 1–5 kW intended mainly for private households. The systems are

**Solid Oxide Fuel Cells: Marketing Issues,**  
**Fig. 10** Market segments grouped by Topsoe Fuel Cell segmentation

		Small 1-5 kW	Medium 5-50 kW	Large 50-250 kW	Mega large >250 kW
Stationary	Grid	Micro-CHP	DG		
	Off-grid				
Mobile		APU			
SOEC (electrolysis)		SOEC			

typically based on natural gas using the existing gas pipeline system.

The existing market for domestic power and heating is dominated by gas-based systems, based on an internal combustion engine technology (ICE) or a Stirling engine. In addition, some 8000 PEM fuel cell systems are installed in Japan, and some hundred PEM units have been sold in the USA.

All the existing technologies in the market today provide significantly more heat than power (cf. Fig. 11 below). The electrical power is the more valuable output and should be maximized, but at the same time, legislation dictates that heat must not be wasted. Since heat cannot easily be transported over long distances, it should preferentially be consumed on site. This means that when the need for heating is low, such as during summer, the system must be run at a lower capacity or be turned off, jeopardizing the return on investment. Therefore, a low heat to power ratio will enable the system to run at full capacity during a larger part of the year.

Compared to other technologies, SOFC systems have a superior heat to power ratio as it appears from the figure below.

The attractive markets for micro-CHP products for domestic application are:

- Large markets with access to piped natural gas or other SOFC suited fuel.
- A significant price differential between primary fuel (e.g., natural gas) and power
- Legislation which favors clean technology and distributed generation.

Based on this, the attractive markets are the Northern part of Europe, South Korea, Japan, and the Northeastern USA.

**micro-CHP in Europe** In Europe, there are three main market drivers:

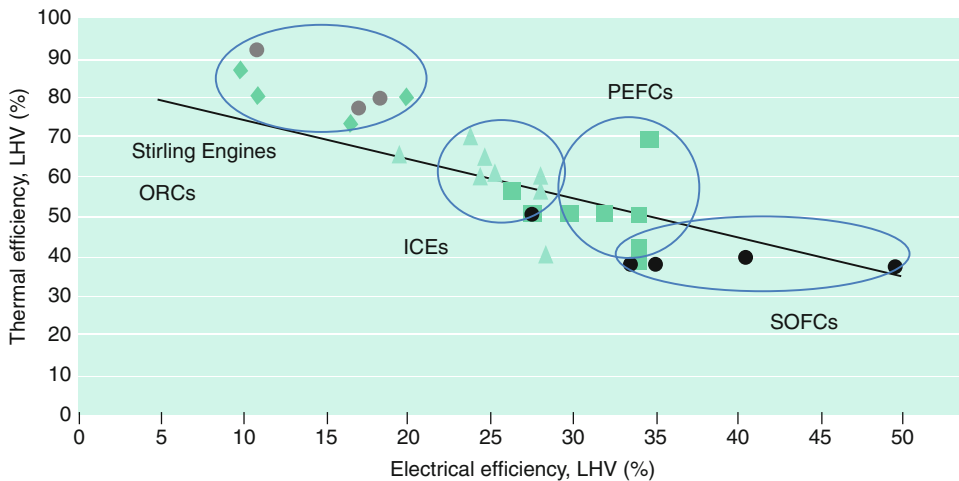
The consumer wants to save money on the combined electricity/gas bill. A more efficient SOFC system with a power generation efficiency which is higher than that of a central power plant will meet this need.

Government subsidies to the households who install fuel cell systems as introduced in a number of countries may further boost the commercialization of the technology.

The energy companies are interested in more decentralized and flexible power generation. SOFC systems installed with consumers will satisfy this demand.

New building regulations demand measures to be taken to reduce the energy consumption when a building is refurbished. In many cases, it is easier to





**Solid Oxide Fuel Cells: Marketing Issues, Fig. 11** SOFC compared with other micro-CHP technologies

replace the domestic heating and power system (with, e.g., an SOFC unit) than to modify an existing system or install additional thermal insulation.

The market potential in Europe is given by the replacement of oil and gas boilers in private homes and by sales to new houses. One of Europe's largest boiler manufacturers, who is also involved in development of micro-CHP systems, estimates this market eventually to be about two million units per year (Western Europe).

**micro-CHP in North America** In North America, there is an increasing focus on energy efficiency and energy conservation. Currently, legislation and programs demanding higher energy efficiency in buildings and production are being implemented. It is estimated that this focus will trickle down to the consumer market. In addition, the demand will be driven by an interest in grid-independent technology because of the relatively unstable electricity grids in many parts of the USA.

In North America, 1.6 million houses are considered eligible for micro-CHP (access to natural gas, attractive ratio between natural gas and electricity price).

**micro-CHP in Japan and South Korea** The demand in Japan and South Korea is driven by both the environmental impact of the technology and its business potential. Japan has made a

massive public investment in fuel cell development, and in South Korea, investment in a fuel cell unit is subsidized. Consultants (Delta EE and Fuel Cell Today) estimate the annual markets to be 1–two million units in Japan and about half a million units in South Korea.

### Auxiliary Power Unit (APU)

Auxiliary power units (APU) range from a few kilowatts to megawatts. They are intended for mobile applications in connection with heavy duty trucks and reefer containers (3–10 kW), leisure applications such as yachts and recreational vehicles (RV), military vehicles, and tanks (10–20 kW). APU systems are used as power generators, either in support of the main engine during peak periods or instead of the main engine when this has been switched off. These systems can also be used in connection with electric cars running on batteries as an integrated, continued charger of the main battery. These systems can be run on diesel, LPG, or methanol.

APUs find their use in many different applications. In the 3–20 kW range, this includes heavy duty trucks, military vehicles, ground generators, and unmanned aerial vehicles (UAV). Each application is described in more detail below.

**APU: Heavy Duty Truck** The primary market for APUs for heavy duty trucks is the USA. Heavy duty trucks commute long distances and often have a sleeper cabin equipped with fridge, consumer electronics, coffee maker, etc., all equipment which requires more power than the battery can supply.



Currently, the power is supplied by an idling main engine or by electrified truck stops. An idling main engine is running at very low efficiency and is polluting, and electrified truck stops do not meet the drivers' demand for flexibility.

An SOFC APU unit will provide a clean and efficient power supply, meeting these demands.

Demand is driven by potential savings in fuel and maintenance costs and by anti-idling legislation, which entails that idling is allowed only for very short time. Based on the current diesel price of 3.1 \$/gal and US Department of Energy standard assumptions on truck driving, Topsoe Fuel Cell calculations show that \$4200 can be saved annually in operational cost by installing an SOFC APU on a truck compared to an idling engine. In addition, all the environmental benefits should be considered.

It is estimated that the potential market in the USA alone is around 200,000 units annually.

**APU: Military Applications** In the military commands, there is an increasing focus on fuel savings, as transport of fuel to the battle field is vulnerable and expensive (between 15 and 40 \$/gal depending on the mode of transport and type of engagement). Any savings in fuel will reduce costs, and low signature energy supply can reduce

casualties. Three applications are of specific interest for SOFC units: as a substitute for diesel generators in military camps, as a silent APU for military vehicles, and as power for unmanned aerial vehicles (UAV):

*Power generator in camps.* Today, diesel generators supply electricity generation in military camps. A lower number of large generators (200 – 750 kW) and some smaller towable generators (5 – 20 kW) are used. The military has an interest in optimizing the energy infrastructure by distributing a larger number of smaller generators in the camp.

*In the field.* Military vehicles have an increasing need for electricity for powering air condition, reconnaissance equipment, and weapon systems. Currently, this electricity need is satisfied by the main engine, by batteries, or by a diesel generator. However, none of the existing solutions are satisfactory.

If a single 10-kW generator is replaced by an SOFC APU, savings in fuel cost will be about \$100 per day or \$40,000 on an annual basis.

Considering the thousands of generators in the field, the potential saving is enormous.

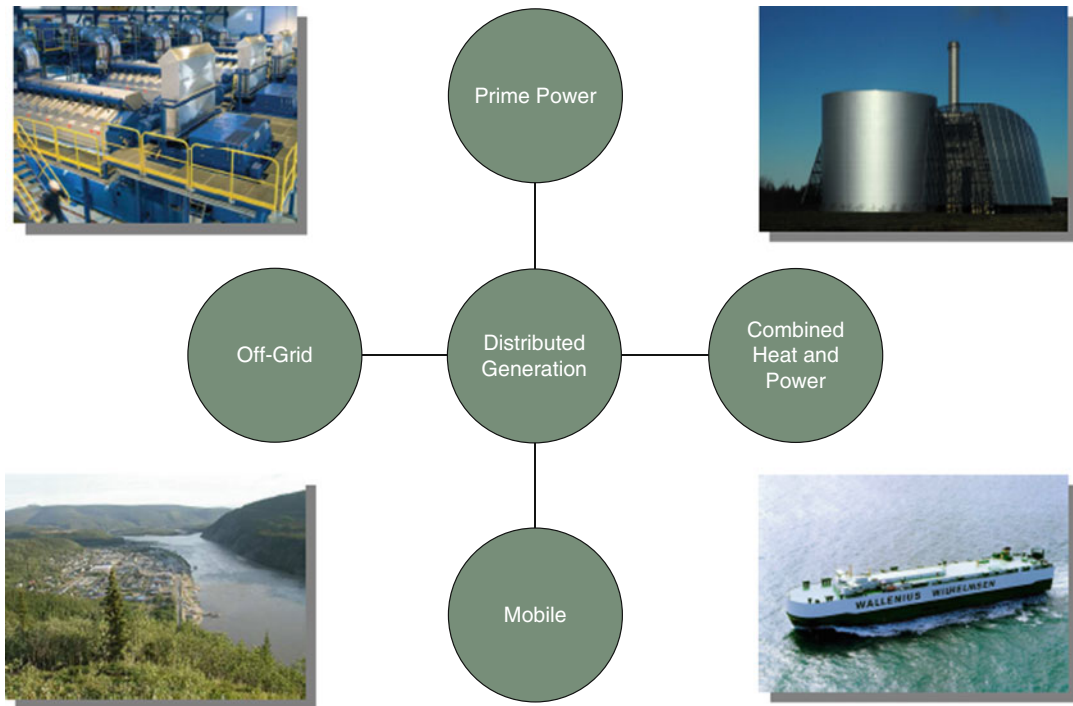
*Reconnaissance from the air.* UAVs come in many different sizes and are today powered by various engines running on jet fuel. Depending of the size of the UAV, it can carry a certain payload including fuel.

There is thus an interest in reducing fuel consumption in order to increase mission length and also in decreasing the signature. Both can be accomplished by a fuel-cell-based generator.

The primary markets for military applications are North America and Europe.

### **Distributed Generation (DG)**

Distributed generation (DG) covers a large range of capacities, from 10-kW for building installations up to the low megawatt range for decentralized power plants. Applications in this size are mostly stationary, but can also be ships and trains and thereby become mobile. These large systems can be used as either primary power generators, as APUs, or as backup support. A wide range of fuels is used for DG. Natural gas from the grid is the most common fossil fuel.



**Solid Oxide Fuel Cells: Marketing Issues, Fig. 12** Sub-segments in the market of distributed generation

Biogas from fermentation, landfill gas, and sewage gas are important renewable fuels. Coal gas is considered for future large-scale power generation. Liquid fuels such as diesel, LPG, or methanol are normally fuels of choice for off-grid applications and for mobile applications. The DG segment can be subdivided into four major sub-segments: prime power, combined heat and power (CHP), off-grid and secondary power, and mobile power (Fig. 12).

**Prime Power** Prime power is defined as megawatt-class power plants, delivering electrical power to the grid. Today, mid-size gas turbines or very large stationary engines are used as prime movers. The demand for SOFC units for prime power is driven by the energy companies' need for load balancing the electricity production because a large and increasing share of the production comes from renewable energy such as wind, solar, and hydro power and from a need to reduce the CO<sub>2</sub> emissions. SOFC units can solve these problems because they are efficient (and consequently has a lower CO<sub>2</sub> footprint), have excellent

load following capabilities, and enable carbon sequestration and storage.

**Combined Heat and Power (CHP)** CHP is an optimal way of utilizing fuel. In a traditional central power station, only about 35–45% of the primary energy is transformed to electrical power, while the remaining is waste heat which is not used. In a CHP plant, the heat is not wasted but used as steam or hot water to provide heat to homes, buildings, or industry. This requires a heat network, and consequently, CHP solutions are primarily implemented as small decentral units situated together with hospitals, hotels, airports, etc., where the heat can be consumed on site.

The CHP market today is dominated by the internal combustion engine technology (ICE), and for high-power systems (above 2 MW) also by gas turbines. These technologies produce more heat than what is typically required by the customer. Since heat is not allowed to be wasted, this limits the time during which a system can operate or limits the overall efficiency. Since the SOFC technology offers a much better power to heat

ratio than competing technologies, the SOFC system can either be operated for a longer time or a higher capacity CHP system can be installed.

**Off-Grid and Secondary Power** Many power consumers are located in areas without electricity grid or in weak grid areas. Examples are telecom base stations and pipeline and border surveillance. In India, many of the telecom base stations are connected to the grid, but the power is very unreliable, and often the power is out for 8–10 h daily. In such areas, an SOFC unit fueled by, e.g., natural gas would provide an attractive alternative since it would offer a reliable power source.

In areas where there is no grid, diesel generators are often used as power sources. The value added by an SOFC unit is higher efficiency (longer time between fueling), less maintenance, and the ability to use nonconventional fuels (in some areas, diesel is often stolen from such sites). Less maintenance and longer time between fueling is of very high value in remote areas because they can often only be reached with off-road vehicles or even helicopters.

**Mobile Applications** The marine industry has an increased focus on the environment because many ports around the world and many coastal regions have started to implement strict emission requirements. One way of fulfilling these requirements is an APU which generates electric power more efficiently and cleaner than the main engine. This unit can be run in ports in order to provide the total load of the ship, but can also be run at sea, reducing the fuel consumption of the main engine.

Once the SOFC technology has been established for marine APUs, the technology can be extended to the main drive of the ship in order to make it even more efficient, more quiet, and less polluting.

Just as in marine transport, the fuel economy and environmental impact of trains can be optimized. Many countries around the world have a desire to switch from diesel engines to electric trains but cannot justify the infrastructure cost of electrifying main train lines, let alone secondary lines. A potential solution to this problem is a battery-powered train that is equipped with a so-called range extender, which is an onboard power plant that constantly recharges the battery,

thereby extending the operating range of the train way beyond the limited capacity of a battery.

In 2009, the world market for power generation equipment (<2 MW) for distributed generation was 28 GW. Geographically, the largest share of this market is in Asia with 12.3 GW annually. Naturally, not all of this potential market is accessible for the fuel cell technology in the short term. Especially interesting in Asia are countries such as South Korea which creates programs for clean energy generation including fuel cells.

In South Korea, the Renewable Portfolio Standard that will come into effect in 2012 demands an increasing share of power generated from renewable sources and fuel cells. It is estimated that the impact of the RPS will be an annual installation of renewable generation capacity including fuel cells of more than 300 MW in 2012 and reaching more than 900 MW toward the end of the decade.

Focusing on Europe, the market for CHP generation equipment has been substantial for more than a decade; from the mid-1990s to 2007, the installed CHP generation capacity has increased from 4.7 GW to 10.6 GW, resulting in average annual sales of about 550 MW. Assuming that the implementation of CHP continues toward the goal set by the European policy (EU directive 2004/8/EC), the annual sales volume over the next decade is expected to be between 600 MW and up to 1 GW toward the end of this decade.

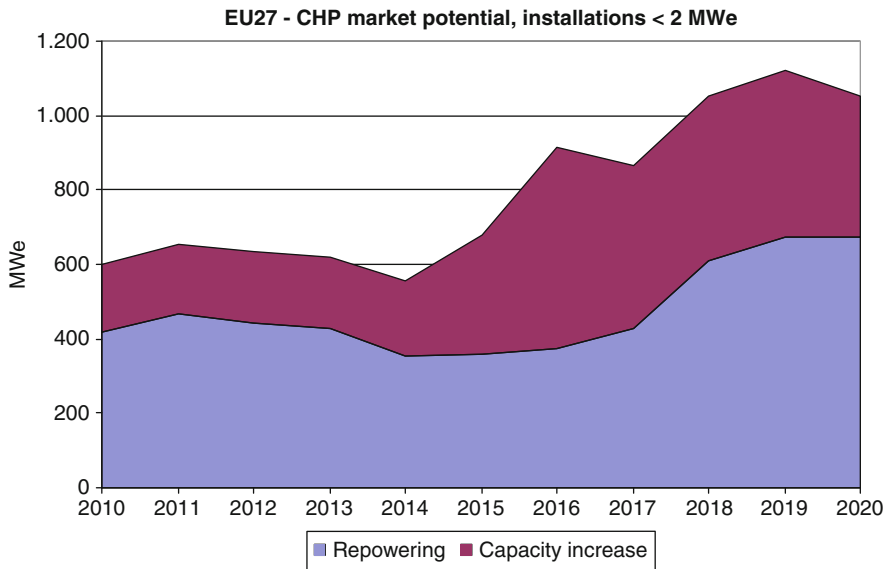
In addition to this figure, there is also a European market for replacement (repowering) of existing CHP installations of about 400 MW annually (Fig. 13).

### Solid Oxide Electrolysis (SOEC)

This reverse SOFC process (SOEC) produces fuel from excess power production. SOEC units will be attractive as energy storage in relation with excess power produced on wind turbines or solar panels. SOEC can be used to help balance supply and demand. This market, as well as the technology serving it, is still some years ahead.

### Market Summary

In all the market segments where commercial SOFC products can be a competitive alternative,



**Solid Oxide Fuel Cells: Marketing Issues, Fig. 13** Potential European market for CHP power generation equipment

**Solid Oxide Fuel Cells: Marketing Issues, Table 6** Primary market drivers and estimated market sizes

	Market drivers	Estimated market size p.a.
micro-CHP	<i>Europe:</i> Economic savings, green image, incentives, lower natural gas price, higher electricity price. <i>North America:</i> Economic savings, reliable electricity supply	Europe: two million units N. America: 1.6 million units Asia: two million units
APU	<i>Europe:</i> Expected anti-idling legislation, savings in diesel consumption (high diesel price). <i>North America:</i> Anti-idling legislation, savings in diesel consumption (high diesel price). <i>Military:</i> Size and weight, low noise, higher efficiency	Truck, USA: 200,000 units
DG	<i>Europe:</i> Economic savings, increasing decentralization of electricity generation, partly driven by the local availability of renewable fuels, increasing requirement for load balancing <i>Asia:</i> Growing demand for electrical power, grid instability, incentives	World: 28 GW Europe: 5.3 GW Asia: 12.3 GW
DG-CHP	<i>Europe:</i> Economic savings, increase in energy efficiency, European and country policies on CHP, feed-in tariffs and incentives	World: 2 GW Europe: 1 GW

the potential market size is overwhelming. All of them are global multibillion-dollar markets.

The size and the market drivers for the market segments are summarized in Table 6.

### Major SOFC Players

A number of important companies are active today within the development of SOFC

technology. Although some of these will ultimately become competitors, they are currently mainly seen as important contributors in a common effort to promote the technology. The main players are listed in the table below (Table 7).

None of the SOFC companies have yet reached a commercial phase. Like Topsoe Fuel Cell, some have started marketing their products and signing up with commercial partners, e.g., CFCL with E.ON and Ceres with Centrica. However,

**Solid Oxide Fuel Cells: Marketing Issues, Table 7** Major SOFC players

Company	Country	Market focus	No. of employees (est)	Ownership	Remarks
Ceramic fuel cell	Australia	micro-CHP	120	Listed	Currently marketing systems. More than fifty systems sold. Partnerships with European utility comp. Close relation to E.ON. Stack manufacturing facility in Germany started 2009. Full in-house system assembly from 2011
Ceres power	UK	micro-CHP	100	Listed	Close partnership with Centrica. Expected launch in 2012
Versa power	USA	DG	40	Owned 42% by Fuel Cell Energy, a leading MCFC company (listed)	Pre-commercial development of 2–10 kW prototype systems. They will be used as building blocks for larger systems which are the focus area. Focus on projects under the public-supported US SECA program
Accumentrics	USA	Sec. power. APU	–	Holding comp. Focusing on UPS for military	Small systems for off-grid use. Focusing on military applications. Developing a 10-kW system together with US military
Hexis	CH	micro-CHP	20	Private	Close relation with EnBW. Focusing on heat-driven products for residential applications
Delphi	USA	APU	–	Part of automotive group	Focus on automotive applications. Group being reconstructed following Chap. 11 after GM collapse
Bloom Energy	USA	DG, CHP	4–500	Venture funds headed by Kleiner Perkins	More than fifty 100-kW systems sold and operating at trophy clients. More than 400 million US dollars invested so far
Kyocera	Japan	micro-CHP	–	Part of larger industrial group	Expected to be close to marketing commercial stacks for micro-CHP
Rolls Royce	USA	DG	80	Part of larger industrial group	Partly relocated to US. Limited commercial activity
Topsoe Fuel Cell	Denmark	micro-CHP, APU, DG	125	Haldor Topsøe A/S	Partnership with Wärtsilä. 5-MW production facilities

everybody in the industry is still on a prototype level without industrial production and sales, thus creating large yearly deficits.

A number of large European and US companies like GE and Siemens Westinghouse with commercial interest in power generation have, during recent years, either withdrawn or dramatically scaled down their participation in SOFC R&D. This means that today, no major player in the industry is directly funded by any of the larger

energy technology companies. These companies will most probably re-enter the market when a commercial breakthrough has occurred. Their strategy has merely changed from home-grown development to acquisition.

Instead, new players originating from Asia (Korea, India, and China) with access to large R&D budgets are entering the industry.

One of the first companies to develop solid oxide fuel cells was Westinghouse in the USA.



They developed a tubular cell design that proved to have advantages such as robustness and easy sealing and manifolding [2]. The tubular cells had a diameter of 2" (25 mm) and a length of 180 cm (150 cm active length) and were building upon a porous ceramic cathode support tube. Each tube was interconnected by nickel felt and bundled to a stack of 1152 tubes for 100-kW<sub>el</sub> overall rating [3]. Tubular cells possess some characteristic advantages compared to other cell designs. The tubular symmetry tolerates larger thermal gradients and offers the possibility to design stacks with very low pressure drop. However, tubular cells have a quite long in-cell current path leading to significant, resistive losses. The internal losses are reduced by operating the cells at high temperatures. Although the tubes are operated at temperatures around 1000°C, long lifetimes of up to 70,000 h could be proven in a ceramic test housing with very low degradation. It is quite likely that avoidance of any impurities and contaminants is a prerequisite for the very low degradation.

In 1998, Siemens acquired Westinghouse SOFC and the tubular SOFC concept. Siemens dropped their leading position with their proprietary planar electrolyte-supported concept and metallic interconnects developed in the early 1990s in Germany. Upscaling of the tubular SOFC concept resulted in two 100-kW<sub>el</sub> prototypes of which one was installed in Arnhem, The Netherlands, in 1999. After successful demonstration of the system, it was refurbished and removed to Torino, Italy, to the Siemens Turbocare plant [4]. Here, it completed a total of 30,000 h of systems operation. Until now, this SOFC concept based on cathode-supported tubular cells is the only one that has surpassed 20,000 h operation on system level. Due to the termination of Siemens' development of the original tubes, the system finally had to be shut down in 2007 [5]. Two Siemens Westinghouse units were built for pressurized operation. Pressurized operation of fuel cells results in an increased cell voltage. A pressure around 4 bar results in approximately 15% higher performance. The Siemens pressurized systems underwent up to 3500 h of testing before being abandoned [6]. Siemens adopted several concepts of improved power density

tubes in which the current path and compactness of the tube bundles was improved. These "high power density" ("HPD") tubes used a "flattened" design with current transporting ribs across the air transport channel. The "Delta 9" was a further improved design based on a flat tubular geometry. Both HPD and Delta were tested in the 5-kW<sub>el</sub> class. Siemens entered the SECA Phase 2 after having completed the SECA Phase 1 with a 5-kW system built in cooperation with Fuel Cell Technologies. Apparently, the manufacturing and volume power density of the different Siemens tubular designs prevented Siemens from suitably reducing the manufacturing costs. The Siemens SOFC operations in Pittsburgh were up for sale in 2008. A number of other SOFC organizations continue to develop SOFC technology based on tubular cells primarily due to their robustness, reliability, and suitability for large pressurized systems.

Global Thermoelectric from Calgary, Canada, acquired the base technology of anode-supported SOFC from Forschungszentrum Ju"lich in 1997 [7].

In 2003, the SOFC operations were bought by the US company FuelCell Energy and transferred into a joint venture with FCE and became Versa Power. Versa successfully accomplished the SECA Phase 1. Today, Versa is the main supplier of large stack units in the SECA Phase 2, working on a 10-kW<sub>el</sub>-plus stack unit [8] which is one of the largest known worldwide with a stack footprint of about 500 cm<sup>2</sup>. Versa is the only SOFC organization that builds and demonstrates stacks with flat planar anode-supported cells with footprint as large as 25 × 25 cm<sup>2</sup> and even 30 × 30 cm<sup>2</sup>. Already, in 2009, they obtained more than 5000 h of continuous testing. The aim is to demonstrate a 250-kW module in 2012 and a 5-MW proof of concept system in 2015. The objective of the DoE/ SECA Phase 2 is to develop the SOFC technology for combination with coal gasification and CO<sub>2</sub> capture.

Bloom Energy, formerly known as Ion America, are active in the development of 100-kW<sub>el</sub>-class SOFC systems [9]. After a long period where little was known of their activities, Bloom disclosed details of their SOFC technology in

April 2010. The 100-kW<sub>el</sub> systems called ES-5000 Energy Server are built of a multitude of stacks of 1–2-kW<sub>el</sub> rating based on planar electrolyte-supported cells with a footprint of about 10 × 10 cm<sup>2</sup> and metallic interconnects. It delivers 480 V AC at an electrical efficiency of about 50% LHV on natural gas. The unit weighs 10 t with the dimensions 224" × 84" × 81". It is well known that for planar cells, a small footprint offers higher stack reliability due to a smaller failure probability for a smaller cell volume. However, small cell footprint leads to increased manifolding cost and use of nonactive stack materials.

In Japan, the main emphasis of SOFC development has been on residential units and distributed generation. Mitsubishi Heavy Industries (MHI) have been working on 150-kW<sub>el</sub> and 200-kW<sub>el</sub> pressurized SOFC system for industrial CHP and larger coal-gas-fueled power plants. These units are based on high-temperature (900 °C) segmented anode-supported tubular cells which have been under development since 1991. By 2009, a 200-kW class system was operated, pressurized for about 3000 h at 52.1% electrical efficiency LHV [10]. The MHI planar MOLB design (Mono Block Layer Build<sup>®</sup>) was developed from about 1995 to 2005. It consists of a “corrugated” electrolyte-supported cell design which integrates functions of interconnect and electrode and operates at a high temperature of around 950 °C. The corrugated cell design has an extended active cell area which promises an increased volume power density compared to more traditional planar stack designs. After the presentation of two units at around 30 kW<sub>el</sub> at the World Exposition in 2005 with few operation hours until failure, activities have reverted back to basic development work.

Ceramic Fuel Cell Ltd. (CFCL) from Australia pursued a 10-kW class design in the 1990s [11]. This was abandoned, and all activities were directed toward small CHP units for residential application. CFCL is now heavily and successfully active in building 1–2 kW<sub>el</sub> units for residential CHP based on planar stack technology in which each repeatable unit consists of four relatively small (7 × 7 cm<sup>2</sup>) anode-supported cells

sealed in a stainless steel window frame. For these small units, they have claimed to have system electrical efficiencies of about 60% due to a strongly integrated system design. Although CFCL possesses a comprehensive experience on development and manufacturing of electrolyte-supported as well as anode-supported cells through many years of engagement in SOFC development, they have decided to outsource their cell manufacturing to leading German ceramic manufacturing companies [12, 13].

Rolls Royce Fuel Cell Systems (UK) is working on medium-sized industrial power generation units up to and above 250 kW, eventually up to several megawatts of electrical power. The basic component is a flattened ceramic tube with a sequence of cells (segmented) printed on it. In contrast to the Siemens concept, fuel flows within the tube and air outside. The design is named as “integrated planar” since it uses characteristics of both tubular (gas supply) and planar (printing on flat surface) designs. The tube units are combined to sub-stacks that are again arranged around a “hub.” This module is pressurized and combined with a turbocharger [14, 15]. In this way, the RRFCS has the possibility to make use of the higher voltage achievable with pressurized operation. RRFCS are targeting the US power generation market with the help of SOFCo, which they acquired in 2007. Recently, considerable funding was awarded by the DoE within the SECA Phase 2 program. At the SECA 2009 workshop, RRFCS announced that their experience with a 125-kW scale up on the way to 250 kW and further MW class units revealed that scale up was much more challenging than anticipated.

A number of smaller European developers adopted the planar SOFC concept. This has now evolved into a high-performance technology, especially with the anode-supported variant. Development groups including cell and stack manufacturers have successfully developed the planar anode-supported technology at a scale above 10 kW<sub>el</sub>. These industrial developers include: Topsoe Fuel Cell (TOFC, Denmark), ProtoTech (Norway), SOFCPower (Italy), Hexis (Switzerland), Staxera (Germany), and Ceres Power (UK).

Ceres Power in UK was founded based on development of low-temperature SOFC carried out at Imperial College in the 1990s. Their cells with ceria electrolyte operate at 500–600 °C and are metal-supported. Both cell and short stack durability have been demonstrated during 2500–3000 h of operation on reformed fuels. The inevitable electronic leakage current in the ceria electrolyte limits the stack efficiency and constricts the operating temperature to 500–600 °C. However, they have, with more than 140 mW/cm<sup>2</sup> at 570 °C, achieved commercially meaningful performance of metal-supported SOFCs. Ceres Power has not provided a public update of recent progress due to commercialization activities. Their primary focus is on the manufacturing of small wall-hanging 1-kW CHP units which are now ready for extended field test [16, 17].

Topsoe Fuel Cell is a subsidiary of the Haldor Topsoe Group. Topsoe Fuel Cell was established as a separate company in 2004, based on more than a decade of fuel cell research activities in Haldor Topsoe. Haldor Topsoe is an internationally recognized company within the catalysis industry with worldwide presence and a turnover exceeding 500 million €. Haldor Topsoe holds a top three position in all of its business areas and has a strong track record for bringing new technology from R&D to global commercial success.

Topsoe Fuel Cell is engaged in development, manufacturing, and marketing of solid oxide fuel cells (SOFC). Until now, 170 million € has been invested in bringing Topsoe Fuel Cell to the leading edge of SOFC technology globally.

Topsoe Fuel Cell is commercializing its technology through a platform strategy where a few basic technology platforms, all coming from the core captive proprietary technology of Topsoe Fuel Cell, can be commercialized and customized to fit into different market segments.

Topsoe Fuel Cell has identified a number of market applications with early commercial opportunities in order to secure a broad market penetration as early as 2013.

Topsoe Fuel Cell has entered into partnerships with a number of important customers, especially for those market applications chosen as early

commercial focus areas. Final product development is a mutual effort of the partnership. Field tests and real-life demonstration projects are scaled up.

TOFC has in 2009 started a pilot-scale facility for production of planar anode-supported cells and stacks. The TOFC stack concept aims at cost-efficiency by using thin-sheet metallic interconnects and minimizing stack component materials. Their stacks have been operated with a stable performance for more than 12,000 h. Currently, TOFC is supplying stacks up to 3 kW and stack modules in the 10-kW size range. Multi-stack arrays are developed for larger systems. For smaller capacities, it is of paramount importance to have a very tight integration, both mechanically and thermally, of all the hot components of the SOFC system. TOFC therefore has a program to develop a so-called PowerCore unit comprising fuel processing, the stack, feed effluent heat exchangers, and catalytic burner(s). A complete 5-kW PowerCore unit based on methanol has been constructed and tested successfully under dynamic load following operating conditions. In similar systems based on diesel fuel, strategies to counteract the impact of sulfur are under investigation. For the micro-CHP applications, 1-kW PowerCore unit has been designed and will be deployed in field tests [18].

Wärtsilä is a Finnish company with a steel and shipbuilding background. Their main interest is the application of SOFC systems as auxiliary power unit (onboard electricity generation) on ships and as multi-sized (100 kW<sub>el</sub> to 100 MW<sub>el</sub>) DG units. With TOFC as a stack supplier, a complete 20-kW demonstration unit based on pre-reforming of natural gas with anode recycle was operated for more than 1000 h with 24 stacks of the 75 cell (12 × 12 cm<sup>2</sup>) type in 2007. Another 24-stack prototype, now based on methanol, was built by Wärtsilä in the project METHAPU, another one for biogas use. The methanol is converted into methane upstream the anode, using a proprietary catalyst. More recently, within the EU project LargeSOFC, Wärtsilä has built a 50-kW<sub>el</sub> system due for operation in 2009/ 2010. This will be the first SOFC system worldwide in this power class operating at ambient pressure and

using planar cells. Follow-up test units of up to 150 kW<sub>el</sub> are expected within the next few years [19–22].

## Steps in Commercialization

Recently, different SOFC companies have been able to show performance records of their fuel cells that prove the commercial viability of the technology.

The proof of competitiveness is taking place in the three phases:

*Validation and proof of concept.* This phase demonstrates that the technology works and that operation can be controlled. This phase has been completed by most of today's SOFC manufacturers.

*Large-scale test and demonstration.* This phase demonstrates that the technology can also work under harsh real-life conditions, and special attention is on robustness and reliability. Most of today's SOFC manufacturers are currently in this phase.

*High-volume field testing and production.* This phase shall go through a very large number of field tests to demonstrate that reproducibility is possible without failures and that competitive manufacturing costs can be achieved. Some SOFC manufacturers are currently preparing for this phase through establishment of manufacturing facilities.

In general, the technology is on its way to prove that it, under real-life conditions, can achieve low production cost, sufficient reliability, and required lifetime to produce an overall performance in line with existing technologies.

## Major Challenges

The major challenges to be focused on are shown below (Fig. 14):

### Lifetime

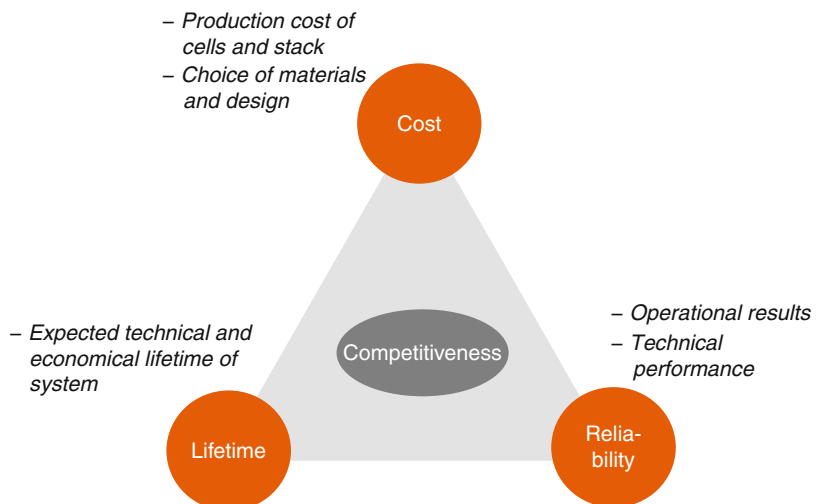
One of the major hurdles on the way to competitiveness for SOFC technology development has been to develop cells and interconnects, which degrades at an acceptable rate to obtain commercially viable lifetimes for the stacks.

In an integrated EU effort to improve the durability of SOFC components, REAL-SOFC, under the Sixth Framework Programme, quite significant progress was made to that effect. The degradation rates were decreased from 2% to 3% voltage drop per 1000 h of operation at 300 mA/cm<sup>2</sup> at the beginning of the project in 2004 to 0.5–0.75%/1000 h at the end of the project in 2009. This reduction in degradation rate was even achieved at a higher current density of 500 mA/cm<sup>2</sup>. More than a 100 thermal cycles from room temperature to 800 °C and 250 full red-ox cycles were also demonstrated [23].

Similar progress has also been demonstrated in the US SECA program: As an example, the

## Solid Oxide Fuel Cells: Marketing Issues,

**Fig. 14** Interrelated challenges in SOFC development



degradation rate has been brought down from 3.6% per 1000 h for the Versa stacks in the 2005–2007 time frame to 1.7% per 1000 h in the 2008–2009 time frame in tests for more than 5000 h [24]. The latest results indicate an aging rate of 0.64%/1000 h for a 32-cell stack operating at 700°C furnace temperature at 390 mA/cm<sup>2</sup> [25].

At Topsoe Fuel Cell, the measured degradation rate has also been dramatically improved as exemplified in Fig. 15 below:

It can thus be concluded that SOFC stacks – under continuous operation – can be expected to have a useful lifetime, defined as a maximum 10–20% loss of performance, in excess of 30,000 h. Strategies to counteract aging – like gradually increasing operating temperature during the lifetime of the stacks and thus keep the internal resistance constant despite degradation – can also be used to maintain system performance [26]. This is a unique opportunity offered by SOFC systems because the stacks can operate in a wide temperature window unlike other fuel cell types.

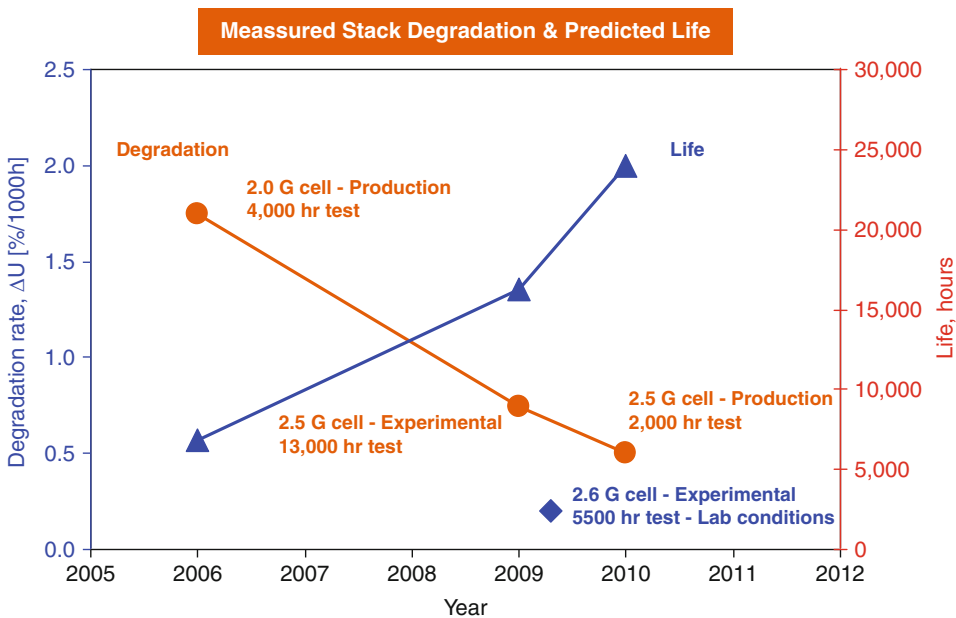
**Reliability**

Many of the demonstrations with ceramic cells in real system operation have until now revealed

problems regarding reliability and degradation in combination with low robustness of system components. Attention to these issues has to be paid in connection with SOFC technology for mobile as well as stationary application. Recent demonstration studies as well as practical experience in the past have proved how upscaling of cells and stacks to larger, more industrially relevant sizes generally leads to lower reliability and some unforeseen challenges. In real system operation failure, abuse or malfunction of auxiliary components can cause harmful conditions for the SOFC stack. Successful verification of long-term operation for more than 10,000 h of current system technologies is still needed and has only been demonstrated so far for the costly tubular designs.

It is important to apply meticulous care in designing *all* the system components in order to avoid operational incidents leading to hard failures [27].

In order to improve durability and cost-efficiency of the cells, the stacks, and the system, much of the development has in the past focused on lower operating temperature, increased power density, and material savings based on reduced cell and stack component thickness.



**Solid Oxide Fuel Cells: Marketing Issues, Fig. 15** Degradation rate for TOFC stacks

Current SOFC technology is relying upon cells made of ceramics with their inherent, somewhat unreliable properties in addition to their intolerance toward thermo-mechanical stresses [28–32]. Therefore, industrialization of SOFC concepts based on the current materials requires implication of large safety factors, which leaves further cost reduction as well as reliability improvements challenging.

The low value of fracture toughness makes ceramic cells sensitive to material defects and unsuspected flaws. The consequence is that the ultimate strength of ceramic cells deviates from their nominal mean value, and significant safety factors (maximum tolerated intrinsic load/applied extrinsic load) have to be used in order to obtain a reasonably safe design. Furthermore, defect sensitivity means that quality control in all manufacturing steps becomes very critical and costly.

One interesting development concept aiming at increased robustness and reduced cost is to replace the critical structural components in cells and stacks with metallic materials [33]. The numbers of R&D activities related to the so-called metal-supported SOFC (also called third-generation SOFC) have increased significantly in recent years. It is expected that many SOFC applications would benefit from increased mechanical ruggedness, red-ox tolerance, and thermal cycling promised by metal-supported cells. Future commercial success depends on a continued development where more emphasis is devoted to an integrated engineering approach and innovative solutions. Introduction of materials such as metals with easily predictive properties makes it possible to design cells, stacks, and system peripheries without over-engineering and without requirements of large safety factors in design. SOFC organizations that have published their development results on metal-supported SOFC are German Aerospace Centre (DLR), Plansee SE, Lawrence Berkeley National Laboratory/Worldwide Energy Inc., JPower, Ikerlan, National Research Council of Canada (NRCIFCI), Ceres Power, and Risø-DTU/Topsoe Fuel Cell A/S. Furthermore, a significant number of R&D institutes worldwide have, during the last 5 years,

initiated development activities on next-generation SOFC technology including metal-supported cells.

### Cost

Although great progress has been made toward solving most of the technical problems associated with the use of SOFC technology, it is generally acknowledged that the cost of the stacks and systems is today about one order of magnitude too high for commercial breakthrough.

**Manufacturing Cost Calculations** There are only a few bottom-up calculations available in the open literature of the manufacturing costs for SOFC stack. The best estimates done by the manufacturers are for obvious reasons not published, but as part of the SECA program, DOE has commissioned three very detailed studies carried out in close contact with major SOFC cell and stack developers. These studies have been used by the DOE to set target and monitor progress of the program [34].

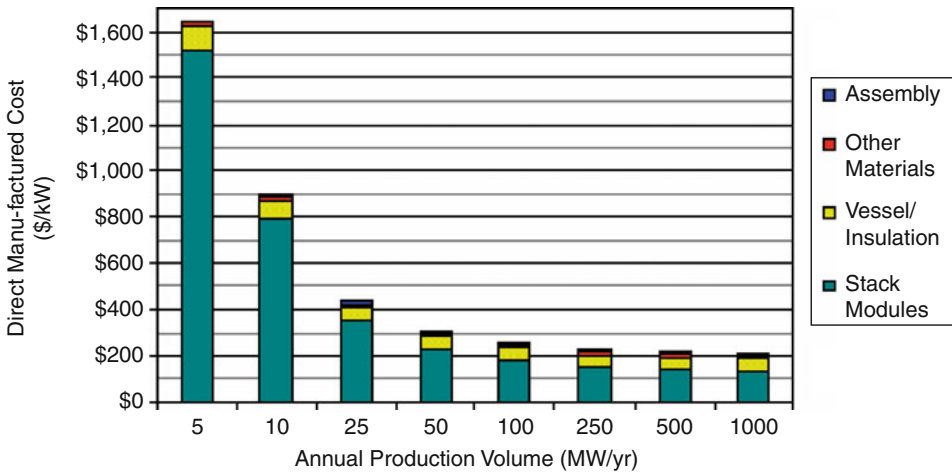
The cost of manufacturing cells and stacks was calculated from the cost of raw materials, manufacturing facility investments, and the operation thereof. The costs were calculated both as function of cell size and manufacturing capacity. It was concluded that the benefits of upscaling the size of the cells from 100 cm<sup>2</sup> to 1000 cm<sup>2</sup> was relatively modest, in the order of 10–20%, mainly due to lower production yields.

The results as function of manufacturing scale for the most competitive option, anode-supported planar cells, are shown in Fig. 16.

It is interesting to note that the cost first of all can reach the DOE goals of 175 \$/kW for the stack but also that the cost can be reduced by a factor 8 by moving from a production capacity of 5–500 MW/year. Even more noteworthy is the reduction by a factor 4 by going to 25 MW/year from 5 MW/year. This indicates that there is a viable stepping stone toward competitive pricing without incurring enormous investment before the major market breakthrough has occurred.

State-of-the-art SOFC cells contain critical rare earth elements. The impact of the dramatic price increases last year, by a factor 4–5 imposed by the mainly Chinese suppliers, has also been





**Solid Oxide Fuel Cells: Marketing Issues, Fig. 16** Manufacturing cost of planar SOFC stacks

**Solid Oxide Fuel Cells: Marketing Issues, Table 8** Cost and availability of rare earth used in SOFC

	REE content of SOFC g/kW	SOFC-driven Net REE demand t/year (2030)	REE production (2009) t/year	Estimated reserves T
<b>Yttria</b>	21	40	9000	540,000
<b>Lanthanum oxide</b>	9.2	95	>12,000	>ten million
<b>Other REE (Ce, Gd, Sm)</b>	<3	<12	20,000	~50 million

calculated for the DOE [35]. The result for the planar, anode-supported cells was an increase in the price of the stack, so that the rare earth component constitutes a cost of 12 \$/kW. In pre-2008 prices, the cost would have been around 1 \$/kW. For the tubular SOFCs, the implications are much more serious, resulting in a dramatic price increase because they contain up to 1.7 kg rare earth elements per kilowatt whereas anode-supported, planar cells only contain 35 g/kW in the stack architecture studied.

The sustainability of using this amount of rare earth elements was also studied, assuming 90% recycling of spent stack material in a scenario where 4-GW new SOFC plants were added per year together with replacement of another 4-GW capacity. The results are shown in Table 8 below:

This demonstrates that the amount of rare earth elements (REE) could be used in a sustainable manner without upsetting the market. It was also

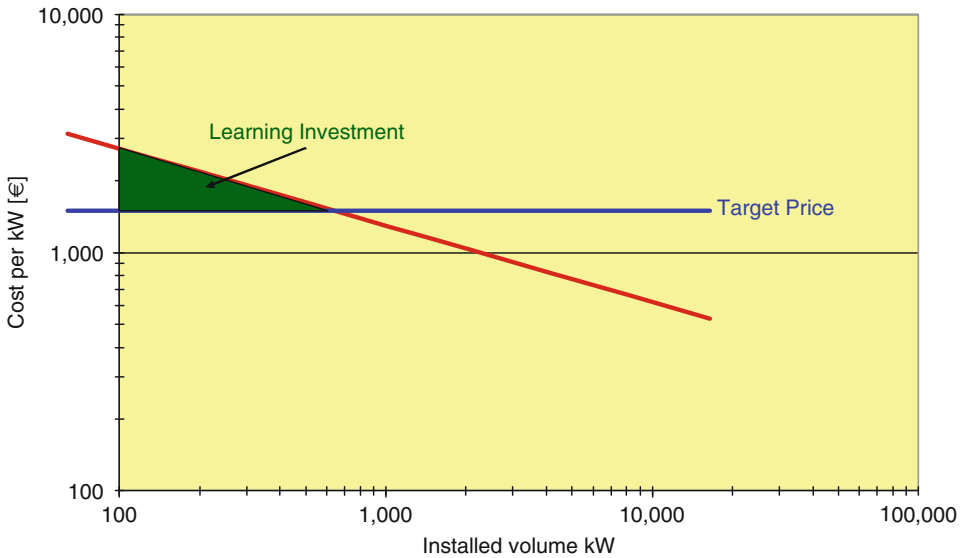
concluded that the price would not rise much further without attracting new mining capacity outside China, thus stabilizing the price level.

**Experience or Learning Curves** Another approach to forecast the future cost is to make use of empirically observed experience curves. Such curves reflect the observation, first made in the aircraft industry and later expanded by the Boston Consulting Group, that the cost of a product drops with the same fraction (the learning rate LR) every time the installed or sold volume has been doubled [36–40].

Mathematically, this can be expressed by the formula:

$$\frac{C_v}{C_0} = \left(\frac{V}{V_0}\right)^\alpha \tag{1}$$

where  $c$  = the unit cost, and  $V$  is the cumulative volume sold or installed;  $\alpha$  is defined by



**Solid Oxide Fuel Cells: Marketing Issues, Fig. 17** Learning or experience curve concept

$$\alpha = \frac{\ln(1 - LR)}{\ln 2} \quad (2)$$

and the subscript 0 refers to the initial state.

If the cost target for the product to reach a competitive level is  $C_{br}$ , then the accumulated volume before market breakthrough occurs,  $V_{br}$ , can be calculated from Eq. 1. The extra cost incurred to reach break-through can be calculated by integrating Eq. 1 from  $V_0$  to  $V_{br}$  and subtract the reference energy cost over the same interval.

The concept is illustrated on Fig. 17.

The learning curve concept clearly breaks down if extrapolated too far because there will always be a floor price set by the raw materials and manufacturing cost and also allowing for a fair profit, so that the producers will enter the market and can recuperate their investment and carry out the necessary R&D to keep abreast of the competition.

The learning investment will obviously have to be paid by somebody, most likely a combination of funding agencies identifying long-term societal benefits, the investors in the industry, and the early adopter customers.

The concept has been used by agencies guiding policy-makers like the IEA or the DOE, and numerous studies have proven their worth.

The learning rate observed varies between 2% and 3% for very mature technologies like gas and steam turbines, whereas emerging technologies with a significant R&D and scale-up potential portion normally have learning rates around 15–25%.

As the accumulated, installed, or produced volumes of SOFC stacks of all varieties are probably below 5-MW and for the most promising, anode-supported planar variety more likely below 1 MW, there is not enough data available to perform analyses yet, but studies have been made on other types of fuel cells like AFC, PAFC, and notably PEMFC where richer data material is available. The studies show learning rates centered around 20–21% with an error around 4% [41–43].

The predictions made by using the experience curve due to its logarithmic nature are obviously very sensitive to the initial assumptions as illustrated in Table 9 where the target cost is assumed to be 1500 €/kW.

The base case in the first row assumes that a cost price of 12,000 €/kW has been attained after production/installation of 1-MW capacity and that the learning rate is 20%. It can then be calculated that 639 MW needs to be installed before the breakthrough cost of 1500 €/kW is reached and the learning investment cost is 439 million €. If

**Solid Oxide Fuel Cells: Marketing Issues, Table 9** Initial cost and volume installed versus learning rate, break even volume and learning investment

Initial cost (€/kw)	V <sub>0</sub> (MW)	Learning (LR, %)	V <sub>br</sub> (MW)	Cost (Mio €)	Beta (%)	Years (to target)
12,000	1	20	639	439	75	10
<b>24,000</b>	1	20	5500	3883	75	14
12,000	<b>5</b>	20	3193	7064	75	13
12,000	1	<b>15</b>	7107	3250	75	15
12,000	1	25	150	141	75	7
12,000	1	20	639	439	<b>100</b>	8
12,000	1	20	639	439	75	13

the installed capacity then increases exponentially by 75% each year, then it would take 10 years to reach the breakthrough target.

In the subsequent rows, the consequences of changing the parameter (in bold) compared to the base case are illustrated. As pointed out by Lund [44] and also Jamasb [45], RTD could bring about a low entry cost and a high learning rate, and it can be seen that such investments in R&D could pay out handsomely.

The learning investment cost may appear very high but is actually quite modest considering the required total investments in new electricity generation capacity discussed in section “The Global Energy Change.” This learning investment is furthermore paid back within a few years provided that the price can be brought below the reference breakthrough price.

## Competitiveness

The break-even point for introduction of SOFC systems is normally defined as the selling price for the system which makes it competitive with respect to incumbent technology. A more precise definition would be that the equivalent annual cost for the owner should provide an acceptable pay-back time for the investment, which will typically be higher than the incumbent technology, but the SOFC will benefit from higher efficiency. Unfortunately, it will normally not be possible to take credit for the lowered environmental impact in the form of lower emissions of CO<sub>2</sub> and the virtual complete avoidance of sulfur, particulates, and NO<sub>x</sub> emissions.

The economic comparison is based on the equivalent annual cost (EAC). The EAC is the cost per year of owning and operating an asset over its entire lifespan. EAC is often used as a decision-making tool in capital budgeting when comparing investment projects. The EAC can be calculated by multiplying the net present value (NPV) of a project by the loan repayment factor LRF. The loan repayment factor (LRF) is calculated by the total time  $n$  (years) of the project and the discount rate ( $i$ ). The net present value (NPV) of a project or investment is defined as the sum of the present values of the annual cash flows  $C_i$  minus the initial investment  $C_0$ .

$$EAC_W = \frac{1}{P_{Net,Average} \cdot t_{Annual}} \cdot \left( C_0 \cdot LRF \cdot \frac{P_{Net,Peak}}{P_{Net,Average}} + \frac{P_{Net,Average} \cdot t_{Annual}}{\eta_{Net}} \cdot C_{Fule} + C_{Maintenance} \right) \quad (3)$$

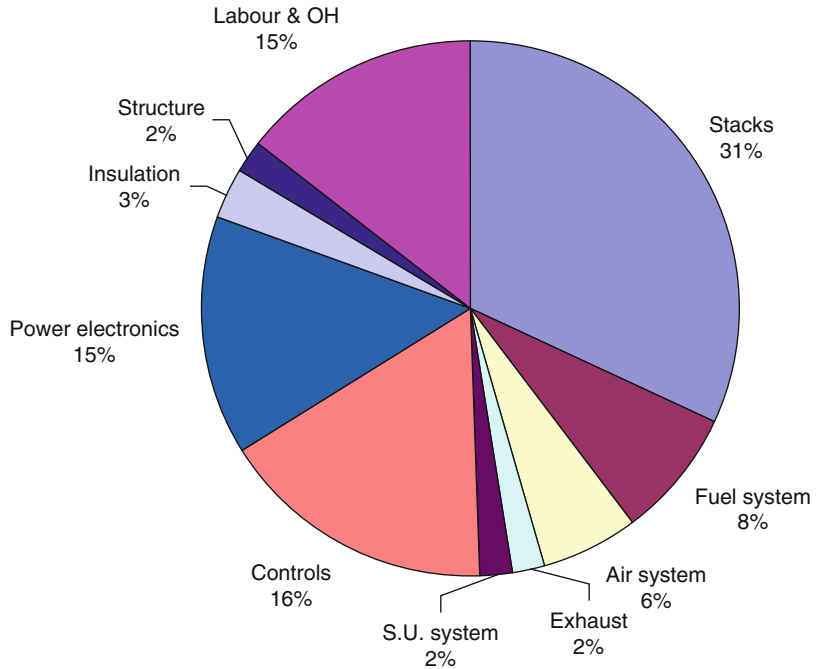
## Distributed Generation

Wärtsilä Corporation and Haldor Topsøe together performed a conceptual study of a 250-kW planar SOFC system for CHP application [46]. They cost estimated the price based on obtained offers or estimated costs for the bottom-up designed components. They found that the major cost components were stacks (31%), power electronics (15%), control system (17%), and labor and overheads (15%) (see Fig. 18 for details).

They also evaluated the competitiveness compared with gas engines, of which Wärtsilä is a major supplier. The lifetime of the stacks was assumed to be 40,000 and 50,000 h in 2015 and 2020, respectively. The cost of the system was

### Solid Oxide Fuel Cells: Marketing Issues,

**Fig. 18** Breakdown of capital cost for 250-kW system



predicted to be between 680 and 1080 €/kW in 2020 when the cost of a gas engine would be 660 €/kW. The efficiency of the SOFC was, however, calculated to be 55% and the net electric and total cogeneration efficiency 90%. For the gas engine, the corresponding numbers were 37% and 81%, respectively, so that the SOFC plant would indeed be the most economical.

It was concluded that the SOFC power unit would become competitive at an investment cost below 1500.

€/kW, e.g., at a stack cost of around 500 €/kW. There should be cost-saving potential by especially simplifying the control system, whereas it was presumed that the cost reduction potential for the power electronics would depend on the general cost development within the technology.

The above analyses emphasize the importance of cost reductions related to the balance of plant components.

### Auxiliary Power Units Based on Diesel

Nehter et al. [47] have analyzed the technology and economics of different fuel processing options for mobile auxiliary power units using ultra-low sulfur diesel as fuel.

At present, trucks generate power when idling by letting the main engine run the generator. The cost of this operation is given in Table 10.

By analyzing the different layouts discussed above and using a payback time of 3 years, the allowable cost of the SOFC APU systems was calculated as function of electrical efficiency. It was found that a system employing an auto-thermal reformer (ATR) with an average efficiency would have an allowable price of 2660 €/kW with the fuel price in Table 10. Operation without desulfurization is feasible even with conventional Ni/ YSZ anodes because the penalty incurred in the form of extra stack area needed is relatively modest with ULSD. Other studies have arrived at similar results [48–52].

### Micro-CHP Units

There are quite a number of techno-economic studies on micro-CHP units based on SOFC for residential use. They exhibit quite different results, mainly due to geographical differences, which give rise to quite different boundary conditions due to climatic conditions, e.g., the need for heat versus electricity and annual variations thereof, operating strategy (electric load versus

**Solid Oxide Fuel Cells: Marketing Issues, Table 10** Cost of truck idling

	Truck idling
Electrical net efficiency	4%
Power average (kWel)	1.3
Power peak (kWel)	3.9
Electrical work (kWh/year) (1830 h/year)	2379
Fuel consumption (gal/year) (37 kWh/gal)	1607
Fuel cost (\$/year) (2.9 \$/gal)	4661
Maintenance cost (\$/h)	0.16
Maintenance cost (\$/year)	292
Variable cost (fuel + maintenance) (\$/year)	4953

**Solid Oxide Fuel Cells: Marketing Issues, Table 11** Advanced power systems with CO<sub>2</sub> capture, compression and storage

	PC baseline	IGCC baseline	IGFC Atm.	IG pressure
Efficiency HHV(%)	28.4	32.6	51.1	57.0
Capital cost \$/kW	3570	3330	2150	2100
Water withdrawal gpm/MW <sub>net</sub>	10.7	18.3	2.5	1.8
Levelized cost-of-electricity ¢/kW-h	15.0	15.1	10.8	10.3

heat load following), sparks spread and installed capacity determined by dwelling size, electrical consumption patterns, state of insulation, need for cooling, etc. [53–63].

In general, it can be said that micro-CHP requirements are quite severe: Low maintenance need is a must, as well as high durability (in some analyses, more than 80,000 h lifetime is required).

**Large Central Power Plants**

The main focus of DOE’s SECA program has been on using SOFC in large coal-fired power plants with CO<sub>2</sub> sequestration. The 2015 goals are:

1. 90% CO<sub>2</sub> capture
2. Less than 10% increase in cost of electricity
3. Efficiency of 60% (without CO<sub>2</sub> capture)

The analyses carried out for DOE have shown that SOFC is the only technology which can lead to these goals [64].

The main results of the analyses are shown in Table 11.

It is interesting to note that the advanced integrated gasification fuel cell plant (IGFC) is in fact producing electricity at a lower cost than the baseline pressurized combustion (PC) plant,

sequesters all the CO<sub>2</sub> instead of only 90%, and uses less than one fifth of the fresh water.

These encouraging results, however, presume that a number of innovative, non-proven technologies can be scaled up – catalytic gasification, dry coal pumps, warm gas clean up, ion transport membranes for oxygen generation, and hydrogen membranes – and finally that the cost of the SOFC power block is lower than 700 \$/kW (stack less than 175 \$/kW). Compared to a plant using pressurized combustion with supercritical steam data without CO<sub>2</sub> capture, it can be calculated that the cost incurred to avoid CO<sub>2</sub> emission is as low as \$18 per ton of CO<sub>2</sub>.

**Summing Up**

It is evident from the discussion above that the criteria for commercialization are or can under the right circumstances be met with respect to lifetime and cost. The required reliability still needs to be proven in long-term demonstration tests under real-life conditions. In fact, it is quite remarkable what has been achieved in the last decade, considering the fact that the total staff engaged in

SOFC development worldwide is probably only a few thousand [65], e.g., less than the R&D Division of many large, industrial companies. One could argue that one of the reasons why a market breakthrough has not occurred before is the somewhat fragmented efforts without the necessary critical mass. International collaboration has on the other hand been quite extensive also among companies, who will eventually become competitors.

There are, however, other challenges than the technical alone. Discussing the challenges of the commercialization process of mainly automotive fuel cells, Hellman et al. [66] have listed the following:

- Immaturity characterized by rapid technological progress still with no dominant design emerging yet, which increases the risk of choosing the wrong technical path.
- Application diversity: This obvious, long-term very beneficial aspect of fuel cell technology does in the short term present the developers with difficulties in business development decisions, and mistakes can be very detrimental especially with respect to timing.
- Replacement technology: Fuel cells basically provide power and heat, two commodities which are already supplied reliably with incumbent technologies. Fuel cell companies thus have to compete/ collaborate with entrenched large OEM's with well-established products, where a lot of investments has been made in R&D, manufacturing equipment, and infrastructure.
- Sub-system of a product: The fuel cell is obviously the heart of the new power/heat plant, but it needs to be carefully integrated into a complete system with many interrelated critical components. It has proven difficult to spur significant interest among balance of plant component suppliers to adapt their equipment in order to obtain the necessary reliability and cost.
- Complexity: Although the SOFC technology requires relatively simple system designs compared to other fuel cell systems, an SOFC system is still rather complex, requiring a broad variety of skills to design and construct.

To this can be added the difficulties in attracting the large amount of capital needed to establish mass manufacturing facilities, which in turn are needed to bring the cost down to a competitive level. The efforts needed to have stakeholders pay for the necessary learning investments should neither be underestimated, and a certain amount of hype and overselling fuel cells in general have not been helpful.

## Future Directions

Despite the remarkable progress made in the last decade, especially with respect to technical performance parameters, it is of course difficult to predict accurately when the commercial breakthrough for SOFC technology will happen because this hinges on several factors beyond the control of the SOFC industry. Among the more important factors can be mentioned:

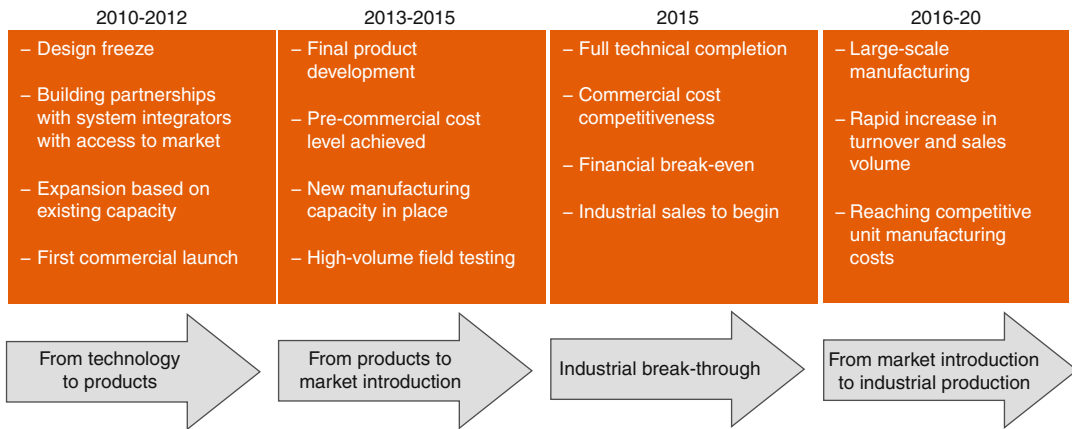
1. The global economic situation in general.
2. The evolution of fuel prices.
3. Legislative initiatives with respect to pollution and greenhouse gases.
4. The funding levels for upscaling and demonstrating the technology.
5. Progress in development and mass production of balance of plant components.
6. The ability of the industry to attract the necessary investment for upscaling manufacturing facilities.

There is, however, a momentum in the industry toward commercialization, and as an example, Topsoe Fuel Cell plans to reduce manufacturing costs by a factor 3 by 2012 and a factor 20 by 2020. The required investments and changes in production methods required to become a high-volume manufacturer have already been defined.

The path toward commercialization of SOFC technology could be envisaged as shown in the Fig 19:

Once the technology has reached commercially competitive levels in performance and cost, the potential market for fuel cells will be a





**Solid Oxide Fuel Cells: Marketing Issues, Fig. 19** SOFC commercialization pathway and timeline

double-digit percentage share of the global power generation market, totaling more than 350 billion US dollars per year.

## Conclusions

The reader should, hopefully, after reading the above, be better equipped to answer the question: Is SOFC ready for the market, or is the market ready for SOFC?

We believe the answer is: Yes, but not quite yet. It will still require some years of development, buildup of manufacturing facilities, and demonstrations before the reservation can be omitted. A significant and concerted effort is still required by the funding authorities, the industry itself, investors, sub-suppliers, and other stakeholders before this promising technology will contribute in a major way to solving the energy challenges ahead. The uncertainties and risks involved are significant but so are the benefits to society at large if the endeavors are successful.

## Bibliography

1. World energy outlook (2010) IEA, Paris
2. Singhal SC (1993) Advances in tubular solid oxide fuel cell technology. In: Dokiya M, Yamamoto Y, Takagawa H, Singhal SC (eds) ECS transactions, PV95-1. Electrochem Soc, Pennington, pp 195-207
3. Kendall K, Minh NQ, Singhal SC (2003) Cell and stack designs. In: Singhal SC, Kendall K (eds) High temperature solid oxide fuel cells - fundamentals, design and applications. Elsevier, Oxford, UK
4. Orsello G, Casanova A, Hoffman J (2008) Latest info about operation of the Siemens SOFC Generators CHP100 and SFC5 in a factory. In: Proceedings of the 8th European fuel cell forum, Lucerne, pp B0204
5. Gariglio M, De Benedictis F, Santarelli M, Calm M, Orsello G (2009) Experimental activity on two tubular solid oxide fuel cell cogeneration plants in a real industrial environment. *Int J Hydrog Energy* 34:4661-4668
6. Hassmann K (2001) SOFC power plants, the Siemens-Westinghouse approach. *Fuel Cells* 1:78-84
7. Borglum B, Fan JJ, Neary E (2003) Following the critical path to commercialization: an update on global thermoelectrics technology and product development. In: Proceedings of the 8th ECS SOFC Symposium, SOFC VIII, Paris. The Electrochemical Society, Pennington, pp 60-69
8. Borglum B, Tang E, Pastula M (2009) The status of SOFC development at versa power systems. *ECS Trans* 25:65-70
9. Seeking Alpha (2009) eBay installing bloom energy fuel cells. <http://seekingalpha.com/article/167936-ebay-installing-bloom-energy-fuel-cells>. Accessed 12 Feb 2011
10. JCN Newswires MHI achieves 3,000 hour operation, unprecedented in Japan for SOFC/MGT combined-cycle power generation systems. 2 Oct 2009
11. Foger K, Love JG (2004) Fifteen years of SOFC development in Australia. *Solid State Ionics* 174:119-126
12. Love J, Amarasinghe S, Selvey D, Zheng X, Christiansen L (2009) Development of SOFC stacks at ceramic fuel cells limited. *ECS Trans* 25:115-124
13. Payne R, Love J, Kah M (2009) Generating electricity at 60% electrical efficiency from 1-2 kWe SOFC products. *ECS Trans* 25:231-239

14. Agnew GD, Collins RD, Jorger M, Pyke SH, Travis RP (2007) The components of a Rolls-Royce 1 MW SOFC system. *ECS Trans* 7:105–111
15. Magistri L, Bozzolo M, Tarnowski O, Agnew G, Massardo AF (2007) Design and off-design analysis of a MW hybrid system based on Rolls-Royce integrated planar solid oxide fuel cells. *J Eng Gas Turbines Power* 129:792–797
16. Bance P, Brandon NP, Girvan B, Holbeche P, O’Dea S, Steele BCH (2004) Spinning-out a fuel cell company from a UK University – 2 years of progress at Ceres power. *J Power Sources* 131:86–90 5-14-2004
17. Brandon NP, Blake A, Corcoran D, Cumming D, Duckett A, El-Koury K, Haigh D, Kidd C, Leah R, Lewis G, Matthews C, Maynard N, Oishi N, McColm T, Trezona R, Selcuk A, Schmidt M, Verdugo L (2004) Development of metal supported solid oxide fuel cells for operation at 500–600°C. *J Fuel Cell Sci Technol* 1:61–65
18. Christiansen N, Hansen JB, Holm-Larsen H, Jørgensen MJ, Wandel M, Hendriksen PV, Hagen A, Ramousse S (2009) Status of development and manufacture of solid oxide fuel cells at Topsoe Fuel Cell A/S and Risø DTU. *ECS Trans* 25:133–142
19. Fontell E (2008) Fuel cell fed with landfill biogas provides power. *Ind Bioprocess* 30:10
20. Fontell E, Jussila M, Hansen JB, Palsson J, Kivisaari T, Nielsen JU (2005) Wärtsilä -Haldor Topsoe SOFC test system. In: *Proceedings of the Electrochemical Society, PV 2005-07*, pp 123–132
21. Fontell E, Phan T, Kivisaari T, Keränen K (2006) Solid oxide fuel cell system and the economical feasibility. *J Fuel Cell Sci Technol* 3:242–253
22. METHAPU. (2012) <http://www.methapu.eu/Oskari2.aspx?cmd=15>. Accessed 10 Jan 2011
23. Steinberger-Wilckens R, Bucheli O, De Haart LGJ, Hagen A, Kiviahho J, Larsen J, Pyke S, Rietveld B, Sfeir J, Tietz F, Zahid M (2009) Real-SOFC – a joint European effort to improve SOFC durability. *ECS Trans* 25:43–56
24. Vora S (2010) SECA program accomplishment and future challenges. In: *11th annual SECA workshop, Pittsburg*
25. Ghezdel-Ayagh H, Borglum B (2010) Coal based SECA program – fuel cell energy. In: *11th annual SECA workshop, Pittsburg*
26. Hansen JB, Palsson J, Nielsen JU, Fontell E, Kivisaari T, Jumppanen P, Hendriksen PV (2003) Design aspects of a 250 kW NG fuelled SOFC system – strategies to counteract stack performance degradation. In: *Abstract fuel cell seminar, vol 3. Miami Beach*, pp 790–793
27. Astrom K, Fontell E, Virtanen S (2007) Reliability analysis and initial requirements for FC systems and stacks. *J Power Sources* 171:46–54
28. Anandakumar G, Kim JH (2010) A thermomechanical fracture modeling and simulation for functionally graded solids using a residual-strain formulation. *Int J Fract* 164:31–55
29. Anandakumar G, Li N, Verma A, Singh P, Kim JH (2010) Thermal stress and probability of failure analyses of functionally graded solid oxide fuel cells. *J Power Sources* 195:6659–6670
30. Nakajo A, Wuillemin Z, Vanherle J, Favrat D (2009) Simulation of thermal stresses in anode-supported solid oxide fuel cell stacks. Part I: probability of failure of the cells. *J Power Sources* 193:203–215
31. Nakajo A, Wuillemin Z, Vanherle J, Favrat D (2009) Simulation of thermal stresses in anode-supported solid oxide fuel cell stacks. Part II: loss of gas-tightness, electrical contact and thermal buckling. *J Power Sources* 193:216–226
32. Zhang Y, Xia C (2010) A durability model for solid oxide fuel cell electrodes in thermal cycle processes. *J Power Sources* 195:6611–6618
33. Tucker MC (2010) Progress in metal-supported solid oxide fuel cells: a review. *J Power Sources* 195:4570–4582
34. Thijssen J (2007) The impact of scale-up and production volume on SOFC manufacturing cost, 4 Feb 2007. <http://www.netl.doe.gov/technologies/coalpower/fuelcells/publications/JT%20Manufacturing%20Study%20Report%20070522.pdf>. Accessed 10 Jan 2011
35. Thijssen J (2010) Market impact of rare element use in solid oxide fuel cells, 18 Oct 2010. <http://www.netl.doe.gov/technologies/coalpower/fuelcells/publications/Rare%20Earth%20Markets%20and%20Solid%20Oxide%20Fuel%20Cells%20101018.pdf>. Accessed 10 Jan 2011
36. Mattsson N, Wene GO (1997) Assessing new energy technologies using an energy system model with endogenized experience curves. *Int J Energy Res* 21:385–393
37. Neij L (1997) Use of experience curves to analyse the prospects for diffusion and adoption of renewable energy technology. *Energy Policy* 25:1099–1107
38. Norberg-Bohm V (2000) Creating incentives for environmentally enhancing technological change: lessons from 30 years of U.S. Energy Technology Policy. *Technol Forecast Soc Change* 65:125–148
39. Rivers N, Jaccard M (2006) Choice of environmental policy in the presence of learning by doing. *Energy Econ* 28:223–242
40. Woerlen C (2004) Experience curves for energy technologies. In: Cleveland CJ (ed) *Encyclopedia of energy*. Elsevier, New York, pp 641–649
41. Schoots K, Kramer GJ, van der Zwaan BCC (2010) Technology learning for fuel cells: an assessment of past and potential cost reductions. *Energy Policy* 38:2887–2897
42. Schwoon M (2008) Learning by doing, learning spillovers and the diffusion of fuel cell vehicles. *Simul Model Pract Theory* 16:1463–1476
43. Staffell I, Green RJ (2009) Estimating future prices for stationary fuel cells with empirically derived experience curves. *Int J Hydrog Energy* 34:5617–5628
44. Lund PD (2010) Importance of integrated strategies and innovations for commercial breakthrough of fuel cells. *Int J Hydrog Energy* 35:2602–2605

45. Jamasb T (2007) Technical change theory and learning curves: patterns of progress in electricity generation technologies. *Energy J* 28:51–71
46. Fontell E, Kivisaari T, Christiansen N, Hansen JB, Pålsson J (2004) Conceptual study of a 250 kW planar SOFC system for CHP application. *J Power Sources* 131:49–56
47. Nehter P, Hansen JB, Larsen PK (2011) *J Power Sources* 196(17):7347–7354
48. Baratto F, Diwekar UM (2005) Life cycle assessment of fuel cell-based APUs. *J Power Sources* 139:188–196
49. Baratto F, Diwekar UM, Manca D (2005) Impacts assessment and trade-offs of fuel cell-based auxiliary power units Part I: system performance and cost modeling. *J Power Sources* 139:205–213
50. Baratto F, Diwekar UM, Manca D (2005) Impacts assessment and tradeoffs of fuel cell based auxiliary power units Part II. Environmental and health impacts, LCA, and multi-objective optimization. *J Power Sources* 139:214–222
51. Hansen JB (2005) Oxygenates as SOFC fuels for APU applications. In: 15th international symposia on alcohol fuels (ISAF XV), San Diego, Sept 2005, 2006
52. Rechberger J, Schauerperl R, Hansen JB, Larsen PK (2009) Development of a methanol SOFC APU demonstration system. *ECS Trans* 25:1085–1092
53. Alanne K, Saari A (2008) Estimating the environmental burdens of residential energy supply systems through material input and emission factors. *Build Environ* 43:1734–1748
54. Alanne K, Saari A, Ugursal VI, Good J (2006) The financial viability of an SOFC cogeneration system in single-family dwellings. *J Power Sources* 158:403–416
55. Alanne K, Salo A, Saari A, Gustafsson SI (2007) Multi-criteria evaluation of residential energy supply systems. *Energy Buildings* 39:1218–1226
56. Bompard E, Napoli R, Wan B, Orsello G (2008) Economics evaluation of a 5 kW SOFC power system for residential use. *Int J Hydrog Energy* 33:3243–3247
57. Braun RJ (2010) Techno-economic optimal design of solid oxide fuel cell systems for micro-combined heat and power applications in the U.S. *J Fuel Cell Sci Technol* 7:0310181–03101815
58. Braun RJ, Klein SA, Reindl DT (2006) Evaluation of system configurations for solid oxide fuel cell-based micro-combined heat and power generators in residential applications. *J Power Sources* 158:1290–1305
59. Hawkes AD, Leach MA (2007) Cost-effective operating strategy for residential micro-combined heat and power. *Energy* 32:711–723
60. Hawkes AD, Aguiar P, Hernandez-Aramburo CA, Leach MA, Brandon NP, Green TC, Adjiman CS (2006) Techno-economic modelling of a solid oxide fuel cell stack for micro combined heat and power. *J Power Sources* 156:321–333
61. Hawkes AD, Aguiar P, Croxford B, Leach MA, Adjiman CS, Brandon NP (2007) Solid oxide fuel cell micro combined heat and power system operating strategy: Options for provision of residential space and water heating. *J Power Sources* 164:260–271
62. Palazzi F, Autissier N, MAM FMA, Favrat D (2007) A methodology for thermo-economic modeling and optimization of solid oxide fuel cell systems. *Appl Thermal Eng* 27:2703–2712
63. Staffell I, Green R, Kendall K (2008) Cost targets for domestic fuel cell CHP. *J Power Sources* 181:339–349
64. Gray D (2010) Current and future technologies for gasification-based power generation. vol 2 – revision 1”, 11 Nov 2010. <http://www.netl.doe.gov/energy-analyses/pubs/Advanced-PowerSystemsPathwayVol2.pdf>. Accessed 10 Jan 2011
65. Steinberger-Wilckens R (2009) European SOFC R&D – Status and trends. *ECS Trans* 25:3–10
66. Hellman HL, van den Hoed R (2007) Characterising fuel cell technology: challenges of the commercialisation process. *Int J Hydrog Energy* 32:305–315



---

## Solid Oxide Fuel Cells: Sustainability Aspects

K. U. Birnbaum<sup>1</sup>, Robert Steinberger-Wilckens<sup>2</sup>  
and P. Zapp<sup>1</sup>

<sup>1</sup>Institute of Energy Research,  
Forschungszentrum Jülich, Jülich, Germany

<sup>2</sup>School of Chemical Engineering, University of  
Birmingham, Birmingham, UK

### Article Outline

Glossary

Definition of the Subject

Introduction

High-Efficiency Energy Converters Based  
on SOFC

CO<sub>2</sub> Emission Reductions from Employing  
SOFCs

Materials Inventory of SOFC Concepts

Environmental Impacts

Future Directions

Bibliography

### Glossary

**BoP** Balance of plant – summary term for all  
components of a fuel cell system, apart from  
the fuel cell stack

**CHP** Combined heat and power

**DG** Distributed generation

**LCA** Life cycle assessment

**LCI** Life cycle inventory

**Life cycle** Period of time and/or use of an object  
(product) spanning the time from the produc-  
tion over use to final disposal (cradle to grave)

**SOFC** Solid oxide fuel cell

**Stack** Fuel cell assembly, including the single  
cells and the interconnecting plates

### Definition of the Subject

The introduction of environmentally relevant issues in the planning, development, and design phase of a product is today an important subject alongside the other relevant technical, economical, social, and legal framework conditions [1]. Fuel cells as a future energy conversion system are expected to have a high potential for environmental benefits. They offer high electrical efficiency, which implies reductions in fossil fuel use and greenhouse gas emissions relative to today's electricity generation, and they can display extremely low local pollutant emission levels.

Especially for new and supposedly environmentally beneficial technology, it is important to prove these benefits and identify any potential pitfalls. Under the headline of “sustainability,” this entry therefore discusses several aspects of the environmental impact of solid oxide fuel cell (SOFC) technology: the improvements delivered by increased (primary) energy efficiency and carbon dioxide emissions on the one hand and the prospective impacts of the materials used in manufacturing the SOFC on the other hand, using an inventory analysis approach.

### Introduction

Solid oxide fuel cells (SOFCs) are one type of high-temperature fuel cells operating in the range of 500–850 °C. The active components consist of ceramics, and the electrolyte is a ceramic layer in most cases made of zirconia or ceria material. Due to the high temperature, the SOFC can use methane directly as a fuel which is then internally converted to hydrogen and carbon monoxide. The electrical efficiency of SOFC systems can reach very high values up to and above 60%, depending on operational parameters, which

---

K. U. Birnbaum has retired.

© Springer Science+Business Media, LLC, part of Springer Nature 2019  
T. E. Lipman, A. Z. Weber (eds.), *Fuel Cells and Hydrogen Production*,  
[https://doi.org/10.1007/978-1-4939-7789-5\\_140](https://doi.org/10.1007/978-1-4939-7789-5_140)

Originally published in  
R. A. Meyers (ed.), *Encyclopedia of Sustainability Science and Technology*, © Springer Science+Business Media LLC 2018  
[https://doi.org/10.1007/978-1-4939-2493-6\\_140-3](https://doi.org/10.1007/978-1-4939-2493-6_140-3)

makes SOFC very interesting for stationary power generation at all scales from one to several hundred kilowatts but also for onboard electricity generation on vehicles.

The first part of this entry looks at the impact of SOFC operation on primary energy efficiency and carbon dioxide emission from electricity generation. These two factors will have a major influence on benefits fuel cell operation will bring to the environmental footprint of the electricity supply system.

The active parts of SOFC (air electrode, electrolyte, and fuel electrode) are made of materials which are not commonly used in conventional power-generating equipment. The second part of this entry presents outlines of an inventory analysis, evaluating the environmental impact of the materials implemented and that of the processing chains involved, using the procedure of life cycle assessment (LCA) [2]. This type of analysis is an important tool in testing the overall advantages of SOFC technology since environmental benefits of operating a technology may be offset by hazards and impacts that emanate from the materials and processes used in manufacturing. Another point of interest is the end-of-use phase of dismantling and recycling.

Fuel cells are an evolving technology and require a very different set of materials for the core system parts (especially the fuel cell stack) than today's power-generating equipment. Consequently, many manufacturing processes are involved which are not yet fully commercialized or well characterized. Moreover, the options for end-of-life material reclamation, recycling, and disposal are less well defined today than for other power equipment.

Much of the analysis presented in this entry is thus of a preliminary nature and is based on laboratory prototypes rather than commercially available products. The data on SOFC referred to here rather reflect differences of concepts and tendencies in development than absolute values. Nevertheless, the information compiled on the materials inventory still can be seen as representative of SOFC technology. Developments continuously take place to introduce novel materials and processes for certain components. Nevertheless,

we still see the "classic" materials today with very little impact of novel solutions. Updates of the analysis presented will be necessary as SOFC technology progresses to the implementation of new materials.

## High-Efficiency Energy Converters Based on SOFC

Worldwide, central electricity generation based on coal, nuclear, and other fossil sources has an average net efficiency of 32% [3]. The remaining 68% of the fuel energy is rejected to the atmosphere as waste heat. Average European or German efficiencies only marginally differ from this figure [4]. Another 5 to 10% of the electricity generated is lost during transport in the supply grids [5, 6]. Central electricity supply based on fossil fuels thus has an overall efficiency of around and below 35% and is one major cause of CO<sub>2</sub> emissions and depletion of fossil fuel resources. This relation can be written as

$$\begin{aligned}\eta_{el} &= E_{el, output} / E_{fuel, input} \\ &= \eta_{conversion} * \eta_{transmission}\end{aligned}\quad (1)$$

Therefore, high-efficiency electricity-producing equipment is of great value in decreasing the environmental impact of electric power production and securing a sustainable use of primary energy resources. In the energy industry, pollution of the atmosphere with CO<sub>2</sub> is measured relative to end energy units, i.e., to the useful energy or energy service, generally in units of kg CO<sub>2</sub> per kWh of delivered energy (thermal or electrical). For carbon-containing fossil fuels, a reduction in primary energy consumption per unit of electricity delivered will obviously immediately translate into a reduction of the carbon footprint of this energy service. This effect will be discussed in the following section.

All fossil primary energy sources (from natural gas all the way to uranium) are limited in availability [7]. Their more efficient use will not automatically lead to a sustainable energy supply system since depletion will simply occur later but not be totally avoided. Nevertheless, increased



energy efficiency buys time to further develop sustainable energy supply technologies, based on renewable energies. As will be shown later, SOFC technology is specifically helpful in such a transition phase since it can use both fossil- and renewables-based fuels.

As indicated in Eq. 1, increases in efficiency can be achieved both by reducing the losses in energy conversion and in the distribution system. While the former calls for improved efficiency in energy conversion, the latter can only partly be met by technology improvements in energy distribution. The concept of “distributed generation” addresses distribution losses of central electricity generation (at least partly) by replacing this by local electricity-generating units that will be considerably closer to the electricity consumers or even are located on-site their premises (with larger building complexes, industrial and commercial facilities, etc.).

Distributed generation has been employed for decades already as a means for companies to produce their own power during periods of peak load or in order to valorize waste gases emanating from a variety of production processes (in chemical industry, steel making, etc.), to supply backup or uninterruptible power, or simply to reduce electricity expenses. The main equipment applied is gas or diesel internal combustion engines and gas turbines. In the region between 1 and 500 kW<sub>el</sub>, these have a limited electrical efficiency ranging from 15% to 35% [8]. The electrical efficiency will in most cases thus be below the average efficiency of central electric power delivery. Therefore, the cost of electricity produced is very sensitive to the spark spread [9], i.e., the price relation between fuel cost and the value of the electricity produced. Especially industrial customers can reduce their electricity bills by exploiting this price difference and produce electricity themselves at competitive cost. Following the sharp increases in the natural gas prices in Europe in the 1990s, though, many DG units were shut down due to a lack of economic competitiveness in regular electricity generation (apart from units operating in peak shaving and backup power generation which have a different business case).

On the other hand, the employment of relatively small generator units (tens of kW<sub>el</sub> to tens of MW<sub>el</sub>) near to the point of use allows for new ways of utilizing the reject heat of the units. Instead of rejecting this to the atmosphere, it can be integrated in heating buildings, in producing hot water, into process heat supply, etc. In this way, the grid losses are minimized and the total efficiency of energy conversion increased. The input of primary energy will now not only result in electricity but also heat supplied. This coupling of energy streams is termed “combined heat and power” (CHP) generation. The overall efficiency of primary energy use will increase by the fraction of thermal energy put to use:

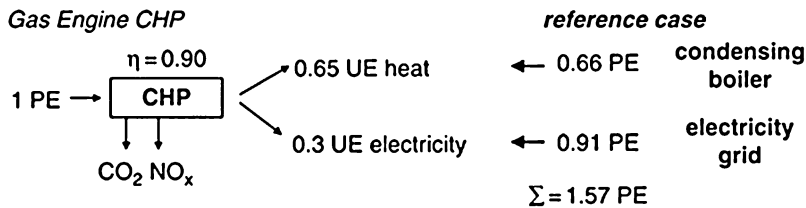
$$\eta_{\text{total}} = \eta_{\text{el}} + \eta_{\text{th}} \quad (2)$$

The European Directive on CHP [10] demands that  $\eta_{\text{tot}}$  be higher than 70% in order for a CHP installation to qualify for the preferred conditions granted for such units in the EU. It has to be noted, of course, that Eq. 2 cannot be based on the maximum theoretical amount of heat that can be extracted but has to take into account what part of the heat generated could actually be put to effective use. Hot weather or hot climate conditions will prevent the utilization of off-heat for heating purposes and limit the operation of the CHP plant to hot water production, unless other applications, for instance, driving cooling units, are further developed. A lack of demand for heat will require the CHP unit to be reduced in power output or even shut down. Ultimately, a heat rejection unit (cooler) can transfer excess heat to the ambient, if electricity demand so requires and the 70% minimum efficiency rule is not violated.

Only large gas turbines of multi-MW<sub>el</sub> size and low rpm diesel engine generators of 1 MW and more can display efficiencies above 40% [11], thus competing with modern coal-fired power plants. Nevertheless, considering the avoidance of grid losses and the dramatically increased total conversion efficiency, a clear case can be made for CHP units with respect to reductions in CO<sub>2</sub> emissions and fossil fuel savings.

Figure 1 shows an energy flow analysis of a gas engine CHP unit. Assuming generalized figures of





**Solid Oxide Fuel Cells: Sustainability Aspects, Fig. 1** Block diagram of a gas engine CHP unit producing heat and electricity. It is compared with a condensing boiler and the German electricity grid as systems of reference with respect to their delivery of useful energy (energy

services). Calibrating to the energy delivery, the total primary energy effort for both scenarios can be compared as 1:1.57, i.e., resulting in a 34% decrease in primary energy effort for the gas engine CHP case

30% electrical and 65% thermal conversion efficiency (relative to the lower heating value, LHV), we obtain an overall primary energy efficiency of 95%. The right side of the graph shows a comparison with a state-of-the-art heating boiler (condensing boiler) and the average electricity supply as a reference. To the right, the primary energy input into the reference system is stated that would lead to the same useful energy delivered to the customer.

The primary energy input is calculated from the useful energy using the efficiencies of 33% and 98% for the electricity delivery and heating boiler, respectively. The summation of primary energy input clearly reveals the superiority of the CHP application and displays a substantial primary energy savings of 34%. As mentioned before, the results of this energy balance of course depends on the amount of heat actually put to use in the system. If excess heat is produced that has to be rejected to the environment, the total efficiency will obviously be lower.

As a result of the typical spark spread observed in Europe in the last decades, CHP units have to be operated as long as possible in order to produce as much electricity as possible. Typically, a minimum of 6000 to 7000 h in operation is required for units to be economically competitive with grid electricity [12]. Switching off units due to lack of heating demand therefore has to be reduced to a minimum.

This means that CHP units are often sized to cover little more than hot water demand in heating systems. The situation only changes when process heat or heat for absorption or adsorption chillers is required as well. Also, the minimum size of units

is more or less limited to around  $5 \text{ kW}_{\text{el}}$  since the efficiency of smaller engines and turbines dramatically drops [8]. Single average family (four persons) buildings in Central Europe will typically require 1 to  $1.5 \text{ kW}_{\text{el}}$  of peak electric power (with an average power demand around  $450 \text{ W}_{\text{el}}$ ) and summer hot water heat demand of 500 to  $750 \text{ W}_{\text{th}}$  [13]. This will limit CHP units to below  $1 \text{ kW}_{\text{el}}$ . Therefore, only very few CHP units suitable for single-family housing (micro-CHP) exist. These mostly use Stirling engines which have an even lower electrical efficiency of anything between 10 and 20%, although their total energy utilization is high. Nevertheless, they suffer from an aggravated problem of heat removal in summer.

SOFC technology, on the other hand, offers interesting options to improve the effectiveness of CHP units. The reasons are multiple: the prospects for high efficiency, low emissions, low noise, scalability, reliability, and, finally, potentially low cost. However, the main attractiveness for CHP applications is the high system efficiency even for small units and at part load operation [14]. Among the most interesting applications are stationary distributed power generation (including CHP), small residential combined heat and power units (micro-CHP), various transport applications (auxiliary power units, APU), and medium-sized portable systems up to  $5 \text{ kW}_{\text{el}}$ .

With a properly designed fuel processing system, SOFC can use many available fuel types. Operating at temperatures above  $600 \text{ }^\circ\text{C}$ , SOFC can reform methane (the main component of natural gas) directly on the fuel electrode or operate on CO-containing gas or even on ammonia.

The fact that thermodynamically some of the heat generated in the electrochemical reaction can be “reinvested” into the chemical fuel conversion explains that SOFCs have the potential to reach a net electrical system efficiency above 60% with natural gas fuel [14]. In a combined cycle system, where the exhaust gas from the high-temperature fuel cell is used to drive a gas turbine, the overall system electrical efficiency may even reach up to 80% [15]. The efficiencies of gas turbines and diesel engines decrease at part load, whereas the efficiency of the fuel cell-based systems will be almost independent of part load up to very high turndown ratios [14].

These high efficiencies are possible due to a marked increase in cell performance during recent years (for instance, [16]), resulting in significantly reduced overpotentials, i.e., increased cell efficiencies. An SOFC CHP unit can reach fossil fuel savings of over 45% (Fig. 2) while delivering the same energy services as the reference system from Fig. 1.

Figure 2 shows a comparison of two systems generating electric power at 50% (upper graph) and 60% (lower graph) efficiency (taking these two values as a lower and upper boundary). Obviously, the increase in primary energy efficiency strongly depends on the efficiency of electricity generation, which is clear since the difference in efficiency between CHP unit and reference system is highest for electricity generation. A high electrical efficiency CHP device will thus bring

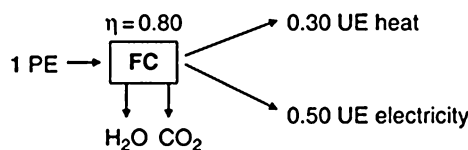
the highest gains in total efficiency. It should be noted that with SOFC CHP units, it is difficult to obtain very high total efficiency values. This is a result of the system flowsheet most of today’s developments use [17], where the cathode airflow is used for cooling as well as for oxygen supply. When cathode and anode off-gas are combined in an afterburner to combust any unconverted fuel, the dilution of the resulting exhaust gas with air is so high that it is virtually impossible to reclaim the sensible heat in the water vapor within the exhaust gas stream. Due to the typically high lambda values of 4 to 8, the dew point temperature of the exhaust gas is far below the 50 °C condensing boilers display. Therefore, Fig. 2 shows the total energy efficiency to remain constant at 80%, independent of electrical efficiency. Total energy efficiency can be increased using larger heat exchangers (which will also imply higher pressure drops and air blower energy requirements). The dew point temperature on the other hand can only be increased by reducing the diluting effect, for instance, by condensing the water out of the anode gas stream before mixing.

Nevertheless, the graphs also show an imminent problem: the more electricity is generated, the less heat is available for further use. This is of course also a result from high conversion efficiencies because due to the second law of thermodynamics, the higher the proportion of electrical energy (useful energy), the lower the losses (entropy), which in the case of CHP are partly

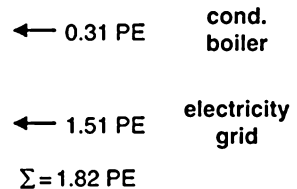
**Solid Oxide Fuel Cells: Sustainability Aspects, Fig. 2**

Modification of Fig. 1 with parameters for a high-efficiency SOFC system. Electrical efficiency is taken as 50% and 60%, while the overall efficiency remains constant (80%). Primary energy use is decreased by 45% and 51%, respectively, for the two energy services

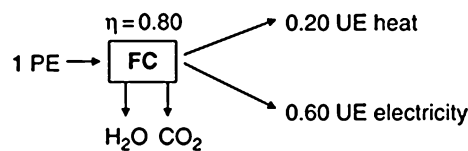
*Natural Gas SOFC Residential System*



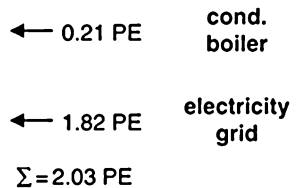
*reference case*



*Natural Gas SOFC Residential System*



*reference case*



turned into useful heat (theoretically, if the fuel cell extracted heat from the environment, the entropy could even be negative and the efficiency higher than 100%; this effect is used in high-temperature electrolysis, SOE). As a result, the units have to be scaled up again in order to produce sufficient heat for a specific application, for instance, summertime hot water demand. High electricity production in a single-family housing, on the other hand, generally means a high fraction of electricity fed to the grid. This is not a problem in itself since low-efficiency generated, centrally produced electricity is displaced by high-efficiency generated electrical energy. Since CHP electricity fed to the grid is supported by guaranteed pricing or regulated tariffs in most parts of Europe [18], though, a high fraction of grid feed-in will make the economics of the unit strongly dependent on the political and regulatory framework. This will often be fragile and may change during the lifetime of the unit, thus causing an operational risk for the owner.

With high-temperature fuel cells, the off-heat offers further possibilities. Polygeneration is the parallel production of electricity, heat, and other products like steam, hydrogen, etc. or heat supplied to air conditioning and cooling equipment. The temperature level of the SOFC exhaust gas is sufficiently high to serve as efficient heat source for both ab- and adsorption chiller regeneration. The exhaust gas from the fuel cell can also be adjusted to a syngas composition with carbon monoxide concentrations that can be used by downstream chemical processes as, for instance, reported in [19].

One final thought should be spent on the heat use in distributed generation. There are applications, for instance, in grid stabilization and peak load production, where the exhaust heat of small electricity-generating units is not used. This can be the case when there are no heat sinks in the vicinity of the DG unit and the electricity-generating costs are competitive even without marketing the off-heat. The aspect of high electrical efficiency will in these cases be the main item of interest, again making an SOFC system or even a hybrid system of SOFC and gas turbine with electricity-generating efficiencies of 60–75%, respectively, specially attractive [20].

## CO<sub>2</sub> Emission Reductions from Employing SOFCs

Working on hydrogen as a fuel, SOFC will obviously achieve a 100% reduction in local CO<sub>2</sub> emissions for a given energy service providing electricity and heat (as, for instance, depicted in Fig. 2). Of course, the environmentally relevant emissions from the hydrogen production process have to be acknowledged for, so that an analysis here cannot be definite as long as the source of hydrogen is arbitrary. Since, on the other hand, the main applications of SOFC are the area of natural gas-based stationary or gas- or diesel-based vehicle systems, the question of hydrogen fuel is – at least for the time being – a marginal one for SOFC.

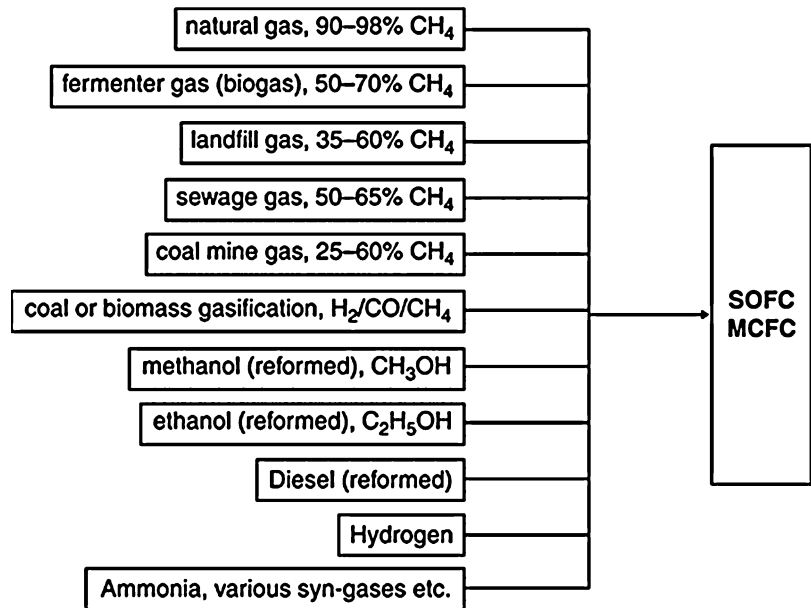
Once large quantities of renewable, fluctuating energy streams have to be stored in order to balance power production and demand in the electricity networks, especially under the framework conditions of a high fraction of renewable energies in the supply system, this situation will change [20, 21]. SOFC and their twin technology, the solid oxide electrolyzers (high-temperature electrolysis) [22], will take over an important role for producing hydrogen and reconvert it to electricity at high efficiencies.

Nevertheless, stationary electricity generation, whether in micro-CHP, CHP, or distributed generation, will heavily rely on carbon-containing fuels for many years to come. This is due to the fact that distributed generation units are generally run on natural gas (more rarely on diesel or fuel oil) [23] and rely on the natural gas distribution infrastructure for fuel supply. Figure 3 shows a selection of fuels suitable for high-temperature fuel cells (in effect, both for molten carbonate fuel cells, MCFC, and SOFC). The conversion of the majority of these fuels will lead to a release of CO<sub>2</sub>. The improvement in electrical efficiency of the conversion as compared to conventional technology will inherently bring considerable reductions in CO<sub>2</sub> emissions, in parallel with the primary energy savings mentioned in the previous section.

The way out of this predicament, though, is of course the use of hydrocarbon fuels, mainly

### Solid Oxide Fuel Cells: Sustainability Aspects,

**Fig. 3** Fuels suitable for high-temperature fuel cells. Most of these are gases and can be converted internally within the fuel cells without preprocessing (apart from eliminating corrosive elements and pollutants). The higher-order hydrocarbons, though, including diesel, generally require reforming (values from [23, 24])



methane, derived from biomass which would then be effectively carbon-free. All carbon released in converting these fuels would be balanced by carbon removed from the atmosphere in the growing of the biomass. Nevertheless, some fossil carbon may be released during the growing, processing, or conversion of the biomass. This would concern tractor fuels, fertilizers, processing energy, etc., none of which, though, would add to the local CO<sub>2</sub> emissions. Even biomass-derived fuels will therefore exhibit a CO<sub>2</sub> footprint, similar to hydro energy and other renewables.

Using wastes as feedstock is regularly considered to be equivalent to biomass since all emissions related to the previous use have been wrapped up into the product footprint. The waste is therefore considered a carbon-free feedstock in further conversion to fuel gases, apart from any contributions originating from the waste treatment itself.

In any case, high-efficiency electricity-producing equipment is key in decreasing the environmental impact of electric power production as it stands today. In the future, this situation will change as more renewable electricity is absorbed into the grids and the network CO<sub>2</sub> footprint is much improved, removing much of the advantages of using SOFC fueled by natural

gas. A transition would then be required to low-carbon or carbon-free fuel gases, such as biogas, gasification syngas, hydrogen from power to gas units, etc.

In energy services, pollution of the atmosphere with CO<sub>2</sub> is measured relative to end energy units, i.e., to the form of energy delivered to the customer (electricity, fuels, etc.), generally in units of kg CO<sub>2</sub> per kWh of energy delivered. The figure not only includes the emissions from the energy conversion itself but also all emissions emanating from the processing steps leading from the primary energy source (oil well, coal mine, gas well, etc.) up to the energy form delivered to the customer.

In order to compare energy conversion processes on-site of the customer, the respective consumption of fuel has to be calculated and the CO<sub>2</sub> emissions evaluated from this. Table 1 compares some processes in building energy supply (heating and electricity). In the CHP processes, the figures for heat and electricity production alone are also stated. They are not practically relevant but show that only the combined use of all energy forms produced leads to the desired increase in system performance. For carbon-containing fossil fuels, a reduction in primary energy demand per unit of electricity produced

**Solid Oxide Fuel Cells: Sustainability Aspects, Table 1** CO<sub>2</sub> emissions per unit of useful energy (kWh electricity or heat) and for combined heat and power generation (From [25] and own calculations)

Process	Fuel	CO <sub>2</sub> emission/kWh useful (end-) energy (LHV)
Condensing boiler	Natural gas	235 g/kWh (heat)
German electricity supply grid (1990)	Various	759 g/kWh (electricity)
German electricity supply grid (2016)	Various	580 g/kWh (electricity)
Gas engine CHP (30% el. eff., 95% total eff.)	Natural gas	362 g/kWh (heat)
		783 g/kWh (electricity)
		247 g/kWh (combined)
SOFC CHP (60% el. eff., 80% total eff.)	Natural gas	1175 g/kWh (heat)
		392 g/kWh (electricity)
		294 g/kWh (combined)

(and delivered) will obviously immediately translate into a reduction of the carbon footprint of the energy service. Comparison of the emission values for gas engine and SOFC CHP shows that values can be misleading, if not properly compared to a reference system. Assuming a high total efficiency of the gas engine (by using latent heat from the exhaust gas water content), the total emission from the energy generated (electric plus thermal) is lower than with the fuel cell. With today's system architecture, the latter will not reach heat removal efficiencies as high as with the gas engine. Nevertheless, looking at the electrical efficiency alone, the SOFC has a clear advantage. A full analysis, though, will have to consider the alternative (or reference) cases as, for instance, shown in Figs. 1 and 2 and compare the emissions with this (see below).

Reduction effects can also be achieved by using primary energy sources with reduced carbon content (for instance, natural gas in place of coal, where the methane in the natural gas contributes three atoms of hydrogen per atom of carbon).

Within Fig. 3, three fossil fuels are mentioned (natural gas, coal, and mineral oil/diesel), all three

of which require some pretreatment, i.e., pre-reforming, gasification, and reforming, respectively. The pretreatment requires heat which again can, at least partly, be recovered from the SOFC exhaust heat. Nevertheless, gas treatment will generally reduce the total efficiency of conversion since these processing steps will incur additional losses.

The gases from renewable sources, on the other hand, have a twofold advantage:

- They only contain ingredients that can be directly fed to an SOFC (apart from pollutants that have to be removed in any case).
- They only contain carbon in the form of methane, carbon monoxide, and carbon dioxide, all of which are either an SOFC fuel or an inert gas (from the perspective of the fuel cell).

Therefore, the use of these gases merely requires gas cleanup but no further processing. The carbon dioxide emissions from electricity generated using biogas (fermenter gas), sewage, coal mine, or landfill gas are extremely low since the carbon chemically bound in the gas molecules was originally extracted from the atmosphere, thus leading to a net zero release. The only remaining carbon dioxide contribution originates from fossil energy that was consumed in growing, harvesting, and transporting the feedstock and in building the plants and devices necessary for producing the gases. In the cases of landfill and coal mine gas, even these contributions may be extremely low since the only effort is to capture and channel the gases which are produced anyhow. Landfills and coal mines as such have been known to be attributed high values of CO<sub>2</sub> equivalent values due to the highly adverse effect methane emissions have to the atmosphere [26]. Once these gases are used for energy production, though, this effect is avoided and the CO<sub>2</sub> footprint is dramatically reduced. Table 2 shows the CO<sub>2</sub> emission factors for various renewable gases from Fig. 3.

In comparing and assessing the carbon reduction potential of SOFC in CHP applications, a balance of emissions has to be drawn in analogy to Fig. 1. Such a balance is shown to the left in

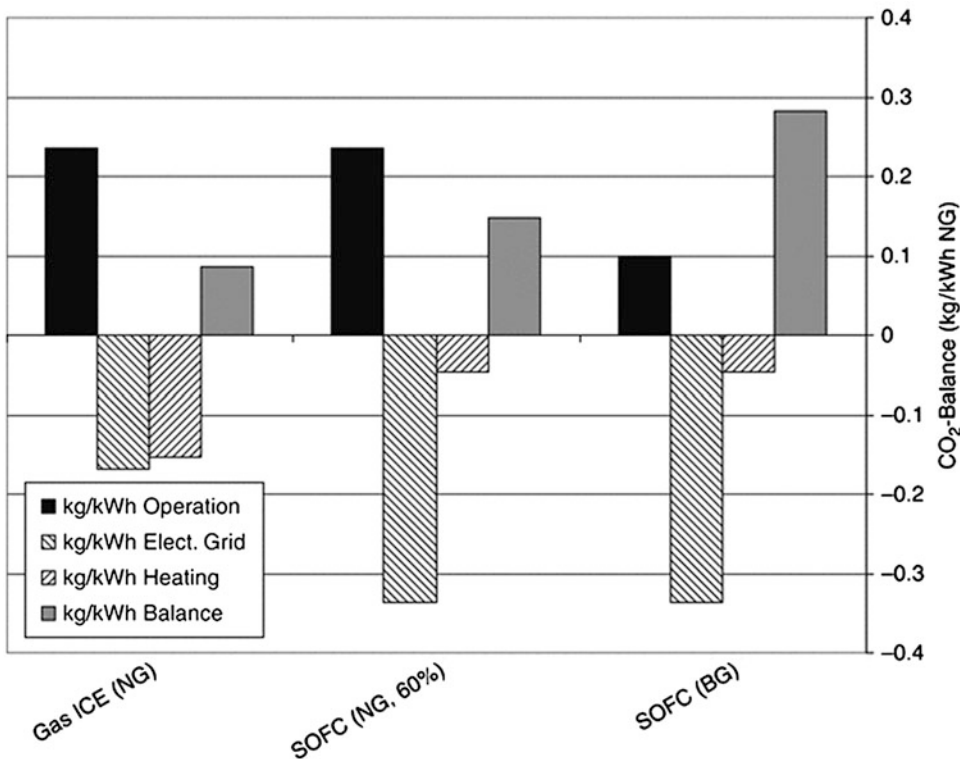
Fig. 4. The black bar above the axis indicates the CO<sub>2</sub> release from 1 kWh of feedstock gas (for instance, natural gas) for an ignition engine CHP unit with a heat and electricity production in the ratio 0.65:0.3 (as indicated in Fig. 1). The

patterned bars below the axis show the carbon dioxide release for the reference case producing the same amount of useful heat and electricity (condensing boiler and grid electricity, emission values as in Table 1 for the German grid 2011). The resulting balance between the two cases is indicated as the gray bar above the x-axis. In the case shown, the CO<sub>2</sub> reduction amounts to 27%. The middle set of bars shows the relationship for an SOFC micro-CHP unit with 60% electrical efficiency (as in Fig. 2).

**Solid Oxide Fuel Cells: Sustainability Aspects, Table 2** CO<sub>2</sub> emission factors for various renewable fuels from Fig. 3 [27, 28]

Fuel	CO <sub>2</sub> emission/kWh (LHV)
Fermenter biogas (energy crops)	~0 g/kWh
Fermenter biogas (manure)	~0 g/kWh
Fermenter biogas (wastes)	~0 g/kWh
Landfill gas	4 g/kWh
Sewage gas	0 g/kWh
Coal mine gas	195 g/kWh

It is clear that the CO<sub>2</sub> emission reduction is considerably higher (–39%) than in the first case due to the increased electrical efficiency, even though the total efficiency is lower. Finally, on the right side, the same (SOFC) case is shown using fermenter biogas. Since the net CO<sub>2</sub> emission of this process is near to zero, the CO<sub>2</sub>



**Solid Oxide Fuel Cells: Sustainability Aspects, Fig. 4** Emission balances for a gas engine CHP system as depicted in Fig. 1 (left) for the SOFC system depicted in Fig. 2 ( $\eta_{el} = 60\%$  case, middle) and the same SOFC system operated on biogas (right). The black bars show the CO<sub>2</sub> emissions from the CHP system. The patterned bars below

the axis represent the CO<sub>2</sub> emission from the reference system (cf. Fig. 1), and the gray bar shows the difference between CHP unit and reference case. If the balance is positive (above the axis), the CHP unit saves the amount of CO<sub>2</sub> shown



emission reduction dramatically increases to minus 74% with the parameters assumed for this example.

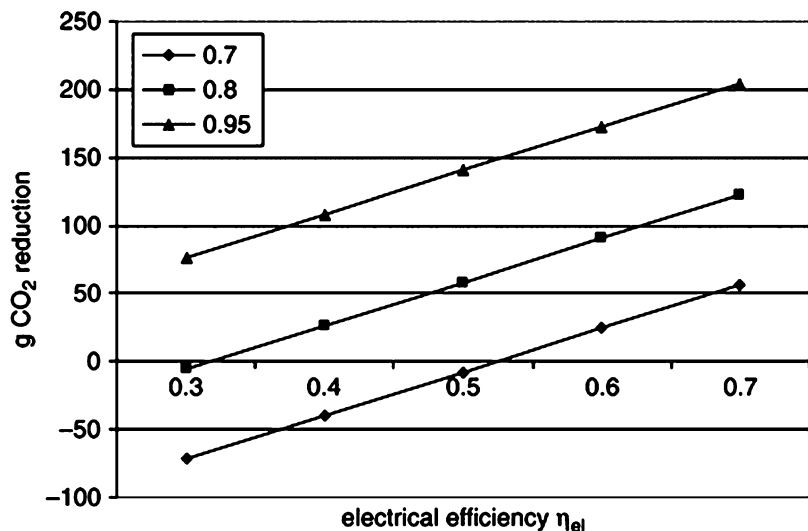
Total CO<sub>2</sub> emission reduction is lower than the primary energy savings since part of the primary energy used in electricity generation is free of CO<sub>2</sub> already today. Therefore, the ratio between the emission factors from Table 1 does not reflect the ratio in efficiencies as displayed in Figs. 1 and 2.

The total energy efficiency of a CHP unit will have a distinct effect on the CO<sub>2</sub> emission reduction. The less energy is lost to the environment; the less CO<sub>2</sub> is effectively emitted per unit of final energy (electricity and heat), especially as the electrical efficiency is increased. On the other hand, the savings in comparison with a reference case will depend on the balance between heat and electricity production (as represented by the respective system efficiencies). This is analyzed in Fig. 5. The y-axis shows the absolute CO<sub>2</sub> reduction in comparison with a German reference system as in Figs. 1 and 2. The three lines correspond to 70%, 80%, and 95% total energy conversion efficiency, as may be attributed to low-, medium-, and high-efficiency CHP units, 70% being the minimum set by the European Regulations [9]. The x-axis shows the electrical efficiency of the CHP unit.

The SOFC CHP installation with the total energy efficiency ( $\eta_{tot}$ ) comparable to up-to-date gas engine units (95%) displays emission savings all across the electrical efficiency ( $\eta_{el}$ ) range. With other words, due to the high  $\eta_{tot}$ , the unit can even save emissions at low  $\eta_{el}$ . On the other hand, the low  $\eta_{tot}$  units will not improve but even deteriorate the CO<sub>2</sub> emission balance at low  $\eta_{el}$ . It is therefore essential to analyze the overall primary energy and emission situation when choosing and installing CHP units. As with many other examples, the simple replacement of conventional technology with technological alternatives will not automatically create a more intelligent solution. It is equally apparent that high  $\eta_{el}$  is a necessary requirement, if major CO<sub>2</sub> emission reductions are targeted and that a high  $\eta_{tot}$  can only partly offset a low  $\eta_{el}$ . Since a condensing boiler displays a conversion efficiency of around 98%, this sets the benchmark for the limiting case of zero electrical efficiency.

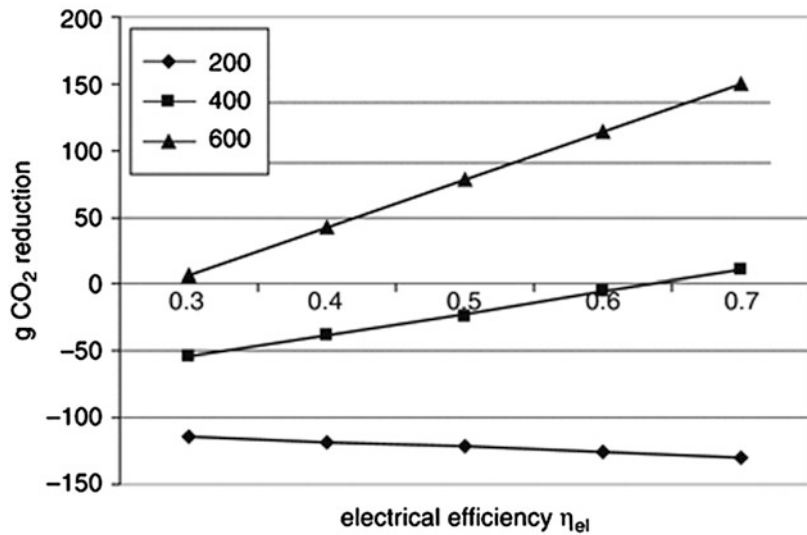
The case of pure electricity generation with an SOFC unit is represented by the data points with equal  $\eta_{el}$  and  $\eta_{tot}$ , for instance, 0.7 and 0.7. At this specific point, the CO<sub>2</sub> reduction is about 35% and not more, due to the considerable loss of 30% of the energy input. A higher electrical efficiency hardly appears feasible, though a combination of an SOFC with a (micro) gas turbine could lead to

**Solid Oxide Fuel Cells: Sustainability Aspects,**  
**Fig. 5** Dependence of total CO<sub>2</sub> savings from a CHP unit running on natural gas on the total energy conversion efficiency  $\eta_{tot}$  (parameter) and the electrical efficiency  $\eta_{el}$  (x-axis). A condensing boiler and the German electricity grid are taken as a reference



### Solid Oxide Fuel Cells: Sustainability Aspects,

**Fig. 6** Dependence of total CO<sub>2</sub> savings from a CHP unit running on natural gas on the electrical efficiency of the unit,  $\eta_{el}$  (x-axis), and the CO<sub>2</sub> footprint of the electricity grid in g CO<sub>2</sub>/kWh<sub>el</sub> (parameter). Again, a condensing boiler and an electricity grid with the respective footprint are taken as a reference. Total energy efficiency ( $\eta_{tot}$ ) of the SOFC CHP unit is set to 80% in this example



$\eta_{el}$  of up to 75% [15]. Total energy efficiency, nevertheless, is doubled.

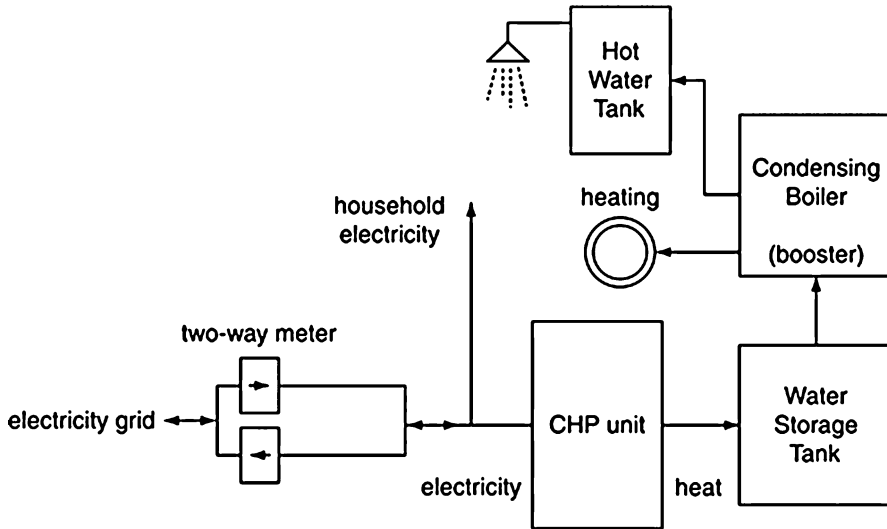
The examples above were calculated for the situation of the German electricity grid and the CO<sub>2</sub> footprint shown in Table 1. It can easily be argued that the CO<sub>2</sub> savings will strongly depend on this footprint, i.e., in a grid with no CO<sub>2</sub> emissions from electricity generation, a CHP installation will not be able to reduce emissions. Figure 6 shows the parameter analysis with 200, 400, and 600 g of CO<sub>2</sub> per kWh of grid electricity delivered to the consumer. The total energy efficiency  $\eta_{tot}$  is set to 80% as a point of reference. As may have been expected, the CHP units cannot deliver emission savings in grid environments with low CO<sub>2</sub> footprint.

If the carbon footprint is lower than that of a condensing boiler, higher electrical efficiencies will even lead to a further deterioration of the emission balance. It is therefore rather obvious that not only the situation at the point of installation but also the total system configuration into which the CHP unit is integrated needs careful analysis.

The analysis up to here has been based on the energy output of a single gas engine or SOFC CHP unit. This is of course a rather limited view, since the requirements of a building or household being supplied with electricity and heat will most probably not be covered by the CHP system alone. Generally, CHP systems are built with the

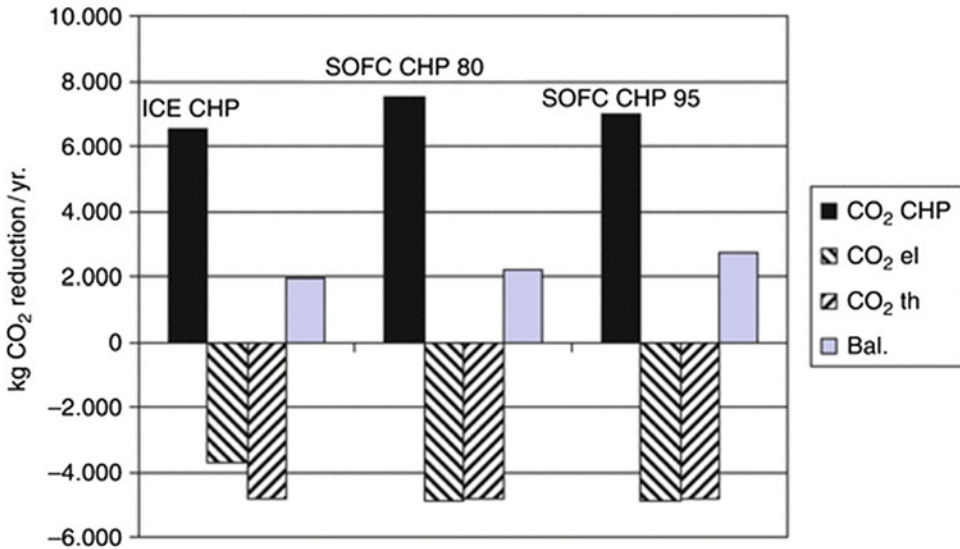
CHP unit as a base load unit supplying the major part of the electricity and some heat, with a (condensing) boiler as the main and backup heat source. Any electricity demand that cannot be covered by the CHP unit – for lack of heat demand, for instance – would be covered by the grid, into which also the excess electricity is fed when heat demand is high and electricity demand not sufficient to use all electrical output.

Due to the higher value of the electricity as compared to heat delivery, CHP units are designed to operate as continuously as possible and mostly at a minimum of 5500–6500 h per year, thus delivering the base load. The layout of such a system is shown in Fig. 7. The total CO<sub>2</sub> balance of such a system will not only depend on the balances for the CHP unit alone, as shown in Figs. 5 and 6, but on the annual displacement of grid electricity and conventional heating. Figure 8 depicts the situation for a household with 20,000 kWh<sub>th</sub> of annual heat demand and a CHP installation of 1 kW<sub>el</sub>. The gas engine CHP unit will deliver 2.17 kW<sub>th</sub>, the two SOFC units (with 80% and 95% total efficiency) 0.33 and 0.58, respectively. A heating boiler is added that will supply the remaining heating and hot water requirements. The gas engine is limited to around 6600 h of annual operation. Above this, the heat demand is lower than the heat produced and the unit is shut down.



**Solid Oxide Fuel Cells: Sustainability Aspects, Fig. 7** Typical layout of a residential CHP system. For typical German households, the heat demand is around 20,000 kWh/year (heating and hot water) and electricity

consumption amounts to 4000 kWh/year [13]. A 1 kW<sub>el</sub> CHP system will therefore require a heating boiler and the electricity grid as backup and as a sink for excess electricity



**Solid Oxide Fuel Cells: Sustainability Aspects, Fig. 8** CO<sub>2</sub> emission balances in analogy to Fig. 4 for a system according to Fig. 7 for three selected CHP units: gas

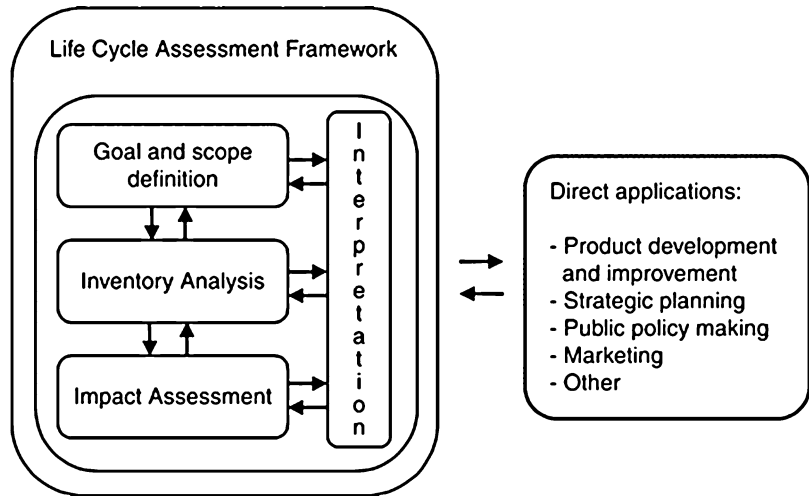
engine (ICE) and SOFC with 80% and 95% total efficiency. Total heating consumption is 20,000 kWh/year and total electricity consumption 4000 kWh/year

Both fuel cell units have a maximum heat production of below and around 500 W. This will just cover the hot water demand of a typical household (12 kWh/day). Therefore, these units

will not be shut down at all, maybe with the exception of holidays.

As a result, the  $\eta_{tot} = 80\%$  SOFC and the gas engine unit are roughly equivalent in CO<sub>2</sub>

**Solid Oxide Fuel Cells: Sustainability Aspects,**  
**Fig. 9** Phases of an LCA according to [2]



reduction. The percentage of reduction, though, is slightly lower because the overall level of CO<sub>2</sub> emission is higher due to the lower  $\eta_{\text{tot}}$ . The  $\eta_{\text{tot}} = 95\%$  SOFC system achieves higher savings in CO<sub>2</sub> emissions. Nevertheless, a comparison with Fig. 4 shows that the differences between the scenarios have been reduced. This is due to the emissions from the heating boiler that amount to roughly half of total emissions in all scenarios and thus form a kind of base emission to which the CHP unit then adds.

The percentage of CO<sub>2</sub> saved is between 22% and 23% (left and middle set of columns) and 28% (right set of columns). These figures are smaller than those displayed in Fig. 4 due to the base level set by the heating system.

## Materials Inventory of SOFC Concepts

### An Introduction to Life Cycle Assessment

An environmental evaluation of the entire life cycle of an SOFC system is necessary to ensure that no environmental effects are neglected, right from the start of the development. A well-developed tool to investigate all stages of a product's life cycle is the life cycle assessment (LCA). It addresses the environmental aspects and potential impacts (e.g., global warming potential, acidification potential, ozone depletion potential, and toxicological potential) throughout the life cycle

of a product or a technique from “cradle to grave” [2]. This not only covers the emissions and energy consumption during operation, as discussed in the previous sections, but also the materials inventory and all environmental effects emanating from the raw materials extraction (for instance, mining, etc.), over the materials processing to the final manufacturing steps. A complete analysis includes the end-of-life provisions, as, for instance, recycling, waste treatment, or waste disposal.

An LCA is divided into four distinct, though interdependent, phases: (1) goal and scope definition, (2) inventory, (3) impact assessment, and (4) interpretation (see Fig. 9).

1. In the first step, the extent of the analysis as well as the specific methods used is described. A precise definition of the product, comparison basis (functional unit), system boundaries, time frame, and geographical coverage, as well as methodological choices such as allocation methods and impact categories of the assessment, are made during this initial phase.
2. In the second step, all environmental inputs and outputs of the investigated system are collected, calculated, and analyzed. For every life cycle stage, inputs (energy and materials) and outputs (emissions to air and water, solid wastes) are gathered and aggregated over the entire life cycle. As one has to deal with a huge

amount of data in this step, databases are usually used. For process technology that is not yet commercially available, the only possibility to collect data is often contact with industrial manufacturers and researchers. When the data situation is unclear, an assumption has to be made, and its influence has to be investigated via a sensitivity analysis in the discussion of the results.

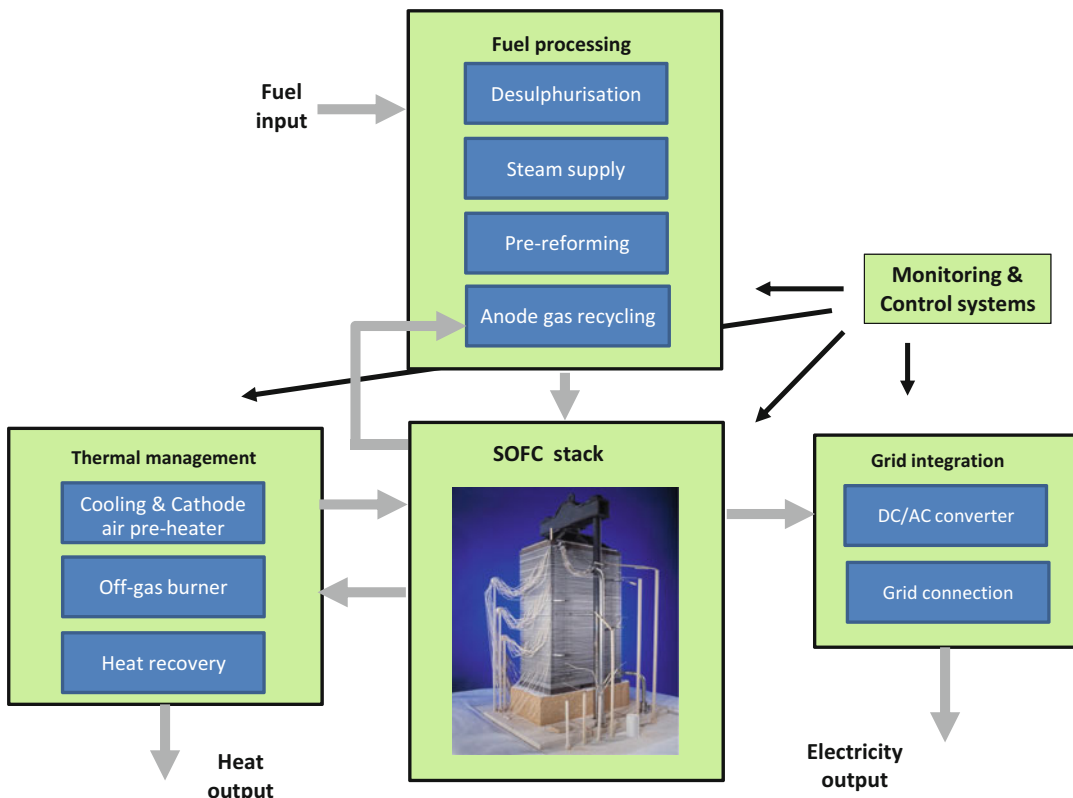
3. In the third step, the inputs and outputs of the system are categorized and allocated to impact categories, such as global warming, acidification, ozone depletion, eutrophication, human toxicity or ecotoxicity, etc. After calculating the environmental effects in the different categories, optional steps are normalization, grouping, and weighting.
4. In the last step, results have to be summarized and discussed as a basis for conclusions and recommendations. Limitations are to be

detected. Sensitivity analysis can be used as an appropriate tool for this purpose. Iteration between life cycle interpretation and the other LCA phases often is performed to refine results, further explore sensitivity of results to assumptions and data variation, or clarify critical problems unveiled in the analysis.

### Demarcation of the Analysis Area

Figure 10 provides an overview of the complexity of an operational fuel cell system which is an ensemble of technical components. Five main sections can be distinguished:

- The fuel cell stack at the center
- The upstream fuel processing unit with desulfurization, pre-reforming (if required), anode gas recycling, and water management



**Solid Oxide Fuel Cells: Sustainability Aspects, Fig. 10** Layout of a fuel cell system with its main components

- The balance of plant (BoP) of which only the off-gas burner, the preheater, and the heat recovery unit are shown
- The monitoring and control system
- The power electronic components such as DC/AC converter and the grid connection unit

Although all components of an operable system should be considered when working out an LCA, the analysis presented here only covers the fuel cell stack and is based on findings of the EU project Real-SOFC [29] in which three different SOFC concepts were analyzed.

These stack concepts include:

- A planar stack with anode-supported ceramic cells (ASC) designed for stationary applications, as, for instance, developed by Forschungszentrum Jülich [30], referred to in the following as “stationary design”
- A planar, lightweight stack with metal-supported cells (MSC) made by plasma spraying, as, for instance, developed by DLR [31], referred to in the following as “lightweight plasma-sprayed design”
- An “integrated planar” stack (IP) as a hybrid between tubular and planar technology, as, for instance, developed by Rolls-Royce Fuel Cell Systems [32], referred to in the following as “IP design”

Currently predominately the ASC design is being commercially exploited. Other designs currently at a pre-commercial or commercial stage include electrolyte-supported cells (ESC), tubular designs, and metal-supported cells with functional layers applied by wet ceramic processes. These are not further described here in order to keep the explanations simple and avoid overlap between key parts of the cell designs. The following will therefore refer to three designs as far separated in details as possible. Insofar the data presented in the following should be considered “indicative” and “typical” rather than describing a specific design in detail. What the data does show, nevertheless, is the principal differences between the concepts and

their weak points that require further consideration in the further development process.

Table 3 shows an overview of typical materials used in different types of SOFC cells. The table shows the different components of the various cell types and the currently mainly employed materials with an indication of possible alternatives less used or with a potential for future use. The following section will be looking into the provenience of some of the materials listed.

### Raw Materials for the Cell Components

The materials for the SOFC, mostly mixtures and not pure elements, have to be extracted/ manufactured from raw materials. Besides iron ore and chromite, which supply the main components for the steel parts, especially rare earths, nickel ore, and alkaline earth minerals are important sources of raw materials. In the LCA of a fuel cell, the upstream mining and processing chains are of equal interest to the processing of the pure materials.

Due to the expected demand in future applications, i.e., batteries for electric mobility, long-term bottlenecks in raw materials availability need to be specifically addressed. This possibly applies to strategically important metals such as rare earth elements or others, as the global distribution of the reserves and resources is very diverse [33].

The following section presents examples of raw materials as a tentative assessment of potential environmental impact and of possible contributions from the upstream processes of materials extraction and purification.

#### Zirconium (Zr)

Zirconium is one of the main constituents of SOFC electrolytes today (in YSZ, yttrium-stabilized zirconia). As indicated in the previous chapter, it is not only the main element in the electrolyte but also an important ingredient in anode substrates and composite cathodes. The YSZ content in a single SOFC cell (depending on design, see above) can be anywhere between 40% and 90% by weight or volume.

**Occurrence** The share of zirconium in the structure of the earth’s crust amounts to roughly 0.02



**Solid Oxide Fuel Cells: Sustainability Aspects, Table 3** Overview of main materials used in different types of SOFC. ASC anode supported cells, ESC

electrolyte supported cells, IP integrated planar, MSC metal supported cells; see text for details of these designs

Cell type	Component	Mainstream material	Alternate materials
ASC, ESC, IP, MSC	electrolyte	yttria stabilised zirconia (YSZ)	Ceria, Scandia stabilised zirconia (ScCeSZ)
ASC, MSC	cathode	perovskites: Lanthanum Strontium Cobalt ferrite (LSCF)	perovskites: Lanthanum Strontium Cobaltite (LSC), Lanthanum Strontium Ferrite (LSF)
ASC, ESC, IP		perovskites: Lanthanum Strontium Manganite (LSM ) composites with YSZ	
ASC, ESC, IP, MSC	anode	Nickel-YSZ composites	Ni-Ceria, Ni-ScCeSZ
ASC, MSC	interconnect	Ferritic stainless steels (chromium content 17 to 22%)	
ESC	interconncet	Iron Chromium Yttrium alloy (CFY), FeCrAlY	Lanthanum Chromite (LaCr)
generic	contacting, anode	nickel mesh	
	contacting, cathode	LSM paste	LSM derivatives, LSCF, LSC
	interconnect protective layers	manganese cobalt (MnCo)	doped MnCo (such as MCFe, MCFeCu, etc.)

weight percentage. It does not occur in pure form in nature. The most important zirconium minerals are alvit (zircon,  $ZrSiO_4$ ) and brasilit and/or baddeleyit (zirconia,  $ZrO_2$ ). Deposits are found on the coasts of Australia, as well as in South Africa, the United States (Florida), Brazil, China, India, Sri Lanka, Madagascar, Scandinavia, Greenland, and GUS states.

**Production** Zirconia is usually produced from zircon,  $ZrSiO_4$ . Zircon sands are first melted with sodium hydroxide and transferred to zirconium (IV) oxide. With addition of coal, the zirconium oxide is transferred to zirconium carbonitride in a plasma arc, which is converted again to zirconium (IV) chloride with chlorine. The chloride is reduced to zirconium with magnesium in a helium atmosphere at 800 °C in the so-called Kroll process:  $ZrCl_4 + 2 Mg \rightarrow Zr + 2 MgCl_2$ .

After the distillation of the magnesium chloride and the separation of excess magnesium, the

retrieved raw zirconium is cleaned in a vapor deposition process.

Australia is the largest producer with a share of nearly 50% of the world production and also has the largest reserves. The second position is held by South Africa, with regard to the annual production as well as to the reserve situation (cf. Table 4).

#### Yttrium (Y)

Yttrium is employed in SOFC cells to stabilize the zirconia lattice in electrolyte materials and increase the oxygen ion conductivity. It is used within a range of 3–10 mol% (3YSZ, 8YSZ, 10YSZ, etc.).

**Occurrence** Yttrium is a rare earth element and occurs in nearly all of the rare earth minerals. Rare earths are defined as a group of 17 elements, comprised of scandium, yttrium, and the lanthanides. The similar radii and oxidation states of the rare earths allow liberal substitution of the rare earths for one another into the crystal lattice sites of

**Solid Oxide Fuel Cells: Sustainability Aspects, Table 4** World production and reserves of zirconium [34]

	Mine production Zircon and baddeleyite		Reserves <sup>6</sup> (thousand metric tons)		Reserve base <sup>6</sup> (thousand metric tons)	
	2005	2006 <sup>c</sup>	ZrO <sub>2</sub> content	HfO <sub>2</sub> content	ZrO <sub>2</sub> content	HfO <sub>2</sub> content
United States	W	W	3400	68	5700	97
Australia	445	480	9100	180	30,000	600
Brazil	35	35	2200	44	4600	91
China	17	20	500	NA	3700	NA
India	20	20	3400	42	3800	46
South Africa	305	310	14,000	280	14,000	290
Ukraine	35	37	4000	NA	6000	NA
Other countries	20	20	900	NA	4100	NA
World total (rounded)	880	920	38,000	610	72,000	1100

minerals. This substitution accounts for their wide dispersion in the earth's crust and the characteristic occurrence as a group of elements within more than 100 minerals. The principal ores of the rare earths are bastnäsite, monazite, and xenotime. Several of the ores occur in unique geologic formations, whereas others are found in similar occurrences worldwide.

Bastnäsite (CeFCO<sub>3</sub>) – a fluorocarbonate of cerium containing 60–70% rare earth oxides (REO), including lanthanum and neodymium – is the world's major source of rare earths. Host rocks include carbonatite, dolomite breccia with syenite intrusives, pegmatite, and amphibole skarn. Since 1985, the bastnäsite production in China has increased rapidly and has dominated the market from the 1990s to the present.

The mineral xenotime (YPO<sub>4</sub>) used to be the principal ore of yttrium and the other heavy rare earth elements. The ion-adsorption lateritic clays from Southern China have now replaced xenotime as the principal source of yttrium and the other heavy rare earth elements in the 1990s. These intensely weathered clays have rare earth ions adsorbed into the clay mineral structure.

Monazite ((Ce,La,Y,Th)PO<sub>4</sub>) is a rare earth phosphate containing 50–78% REO. It is recovered as a component of heavy mineral sands and is a major source of thorium which imparts radioactive properties to the mineral [35, 36].

**Production** World production of rare earths was estimated at just below 127,000 metric tons of

equivalent rare earth oxides in 2016. The graph in Fig. 11 only shows the development of production up to 2006. China was by far the largest producer, with ~80% of the world's total. Smaller amounts of ore came from India and other countries like Australia, Brazil, Malaysia, Thailand, Vietnam, and Russia [37].

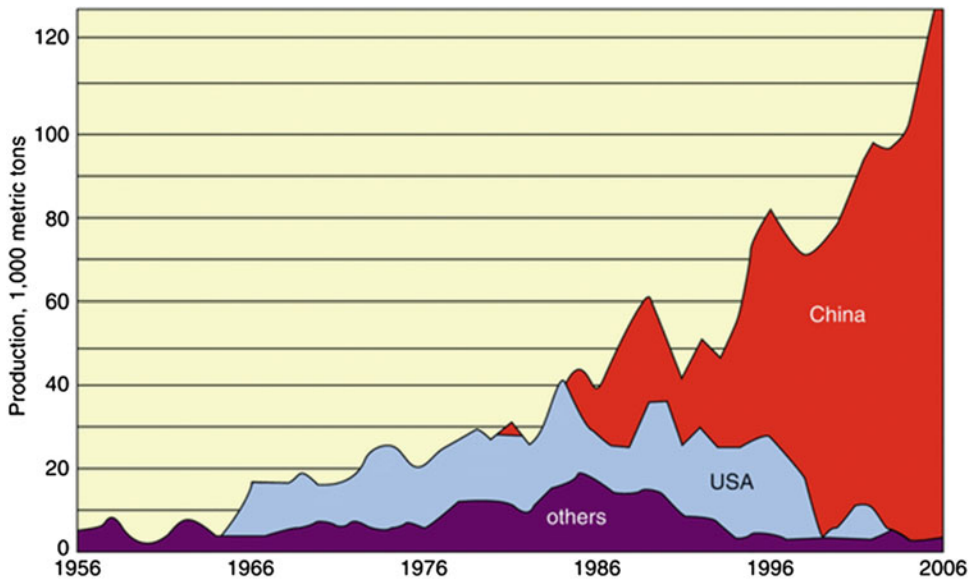
In 2008, the approximate distribution of rare earths by use was as follows: magnets 21%, metal alloy 18%, catalysts 19%, polishing 12%, glass 10%, phosphors 7%, ceramics 6%, and miscellaneous 7% [38].

**Reserves** Large resources of yttrium in monazite and xenotime are available worldwide in ancient and recent placer deposits, carbonatites, uranium ores, and weathered clay deposits (ion-adsorption ore). Additional large subeconomic resources of yttrium occur in apatite-magnetite rocks, deposits of niobium-tantalum minerals, nonplacer monazite-bearing deposits, sedimentary phosphate deposits, and uranium ores. The world's resources of yttrium are probably very large [39].

- Biological rating: No known benefits to life processes [40].
- Biological benefits: Yttrium has no known biological use [40].

Lanthanum, La

Lanthanum is a main constituent of cathode materials but is also used in ceramic interconnects and in electrolytes or contact pastes.



**Solid Oxide Fuel Cells: Sustainability Aspects, Fig. 11** Worldwide rare earth oxide production [36]

**Occurrence** Lanthanum has a share in the earth's crust of 0.0017%. In nature, it always occurs in compounds with other rare earth metals and in minerals like bastnäsit, monazit, cerit, or orthit, with percentages up to 25% and 38%, respectively. Misch metal, used in making lighter flints, contains about 25% of lanthanum.

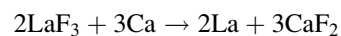
Lanthanum is one of the most reactive of the rare earth metals. It oxidizes rapidly when exposed to air. Cold water attacks lanthanum slowly, and hot water attacks it much more rapidly. The metal reacts directly with elemental carbon, nitrogen, boron, selenium, silicon, phosphorus, sulfur, and halogens [41].

**Production** The most important base minerals are xenotime, monazite, and bastnäsite. The first two are orthophosphate minerals  $\text{LaPO}_4$  and the third is a fluoride carbonate  $\text{LaCO}_3\text{F}$ . Lanthanoids with even atomic numbers are more common. Monazite also contains thorium and yttrium which makes handling difficult since thorium and its decomposition products are radioactive.

For many purposes, it is not particularly necessary to separate the metals, but if separation is required, the process is complex. Initially, the

metals are extracted as salts from the ores by extraction with sulfuric acid ( $\text{H}_2\text{SO}_4$ ), hydrochloric acid (HCl), and sodium hydroxide (NaOH). Modern purification techniques for these lanthanoid salt mixtures are ingenious and involve selective complexation techniques, solvent extractions, and ion exchange chromatography.

Pure lanthanum is available through the reduction of  $\text{LaF}_3$  with calcium metal:



This would work for the other calcium halides as well, but the product  $\text{CaF}_2$  is easier to handle under the reaction conditions (heated to 50 °C above the melting point of the element in an argon atmosphere). Excess calcium is removed from the reaction mixture under vacuum [42].

- Biological rating: No known benefits for life processes in plants and animals.
- Biological benefits: Lanthanum has no known biological use [43].

Lanthanum is mainly obtained from lanthanum-rich monazite and bastnäsite. Other lanthanum-bearing minerals include allanite and

cerite. It is mined in the United States, China, Russia, Australia, and India [43].

### Strontium, Sr

Strontium belongs to group 2 of the periodic table and is one of the alkaline earth metals. Strontium, with atomic number 38, lies between calcium and barium in this group. The discovery of strontium carbonate, which was originally thought to be barium carbonate, is associated with a lead mine located in Strontian, Scotland, hence the name strontium.

**Occurrence** Strontium is present in the earth's crust at an average concentration of 0.04% and is therefore 15th in abundance. Of the naturally occurring strontium compounds, only the minerals strontianite (strontium carbonate,  $\text{SrCO}_3$ ) and celestite (strontium sulfate,  $\text{SrSO}_4$ ) are of economic importance.

Celestite occurs principally as nodules, lenses, beds, and materials filling crevices in sedimentary rocks such as carbonates, gypsums, clays, and evaporites. The economic importance of celestite is considerably greater than that of strontianite.

**Production** Celestite ores are obtained by both open-pit and underground mining. In most cases, only coarsely intergrown rich ores are worked, which can be further enriched by handpicking to give a material containing >90%  $\text{SrSO}_4$ . Demands for increasing purity in chemically produced strontium salts together with the growth of mechanized mining techniques necessitate a continually increasing amount of processing. Finely divided impurities are removed by desliming. By means of density separation, celestite is separated from limestone, quartz, gypsum, and dolomite, which have densities of <3  $\text{g/cm}^3$ , giving end products containing >95%  $\text{SrSO}_4$ . In Spain, a flotation plant for separating finely intergrown celestite ores has been in operation since 1990. The introduction of this technology has markedly increased the number of deposits worldwide that can be profitably worked.

Many important deposits cannot be mined because of unacceptably high levels of barium

and deposit-specific trace elements that cannot be removed by available processing technologies.

**Production of Strontium Carbonate** *Black ash method, reduction with carbon.* To enable the chemical reduction of  $\text{SrSO}_4$ , celestite is mixed with powdered coal and then heated up to about 1100 °C. The chemical reaction follows the equation  $\text{SrSO}_4 + 2\text{C} \rightarrow \text{SrS} + 2\text{CO}_2$  and produces carbon dioxide and strontium sulfide. In the next process step, the strontium sulfide is dissolved in water, before carbon dioxide passes through the solution, forming and precipitating strontium carbonate:  $\text{SrS} + \text{H}_2\text{O} + \text{CO}_2 \rightarrow \text{SrCO}_3 + \text{H}_2\text{S}$ . The by-product sulfur is recovered as elemental sulfur.

*Soda ash process.* Ground celestite ( $\text{SrSO}_4$ ) is converted to strontium carbonate by adding it to hot sodium carbonate solution. Numerous variations of this process have been proposed. Typically, an excess of  $\text{Na}_2\text{CO}_3$  solution is used. The crude product so obtained is not usually acceptable without further treatment. A product sufficiently pure for most applications is obtained by dissolving the crude material in hydrochloric acid, neutralizing with sodium carbonate solution to precipitate iron and aluminum, filtering, and reprecipitating with caustic soda. This process also produces impure sodium sulfate solution as a by-product which must be further treated or disposed. The high consumption of sodium carbonate is a further drawback [44].

**Production of Strontium Metal** Metallic strontium can be produced by aluminothermic reduction of the oxide or by electrolysis in the dry way of a  $\text{SrCl}_2$ -KCl blend. The refining takes place via vacuum distillation.

**Transportation, Storage, and Safety** Due to its reactive nature, strontium must be handled with care. The pure metal and the commercial eutectic alloy (90% Sr, 10% Al) are classified as alkaline earth metals NOS (not otherwise specified), UN no. 1393, for the purposes of transportation. This classification is indicative of materials requiring special approved packaging for transport. These two forms of commercial strontium are packed under an inert atmosphere to prevent formation

of an oxide coating. Strontium is a strong reducing agent and forms explosive hydrogen gas when in contact with water. Strontium is therefore classified as a flammable solid. Hence, strontium is a Class 4.3 material, i.e., one that emits a flammable gas on contact with water. Strontium should therefore be stored in a well-ventilated dry place, avoiding all contact with water. However, commercial alloys of strontium, such as the Sr-Mg-Al master alloy or the family of aluminum-strontium master alloys which contain up to 10% strontium, do not require these special precautions.

**Use** Metallic strontium and master alloys containing strontium have experienced significant expansion in application in modern foundry practice. In aluminum foundries, strontium is used as an additive to Al-Si alloys to enhance their mechanical properties and improve the machining performance. Strontium improves the mechanical properties of Al-Si castings by changing the morphology of the eutectic silicon phase. In an unmodified Al-Si alloy, this eutectic silicon phase precipitates as coarse acicular plates, which causes the casting to exhibit poor mechanical properties. Modification causes the silicon to assume a fine, interconnected fibrous morphology, resulting in higher tensile strength and greatly improved ductility. Impact resistance and machining characteristics are also enhanced through modification.

Strontium improves the properties and processing of wrought aluminum alloys.

In an aluminum alloy sheet which requires high formability, the presence of strontium is reported to reduce the number of intermetallic precipitates. This improves the alloy's formability and reduces the incidence of edge cracking.

In ferrous metallurgy, strontium finds application as a component in certain foundry grades of ferrosilicon, used as inoculants in gray iron casting. The addition of 0.65–1.05% strontium controls the carbon structure in an iron casting and inhibits the chill. The chill, which is in some cases a desired phenomenon, is a rapidly solidified zone in a casting where the formation of mottled iron (cementite and graphite) is favored over a pearlite structure with graphite. By controlling the chill,

the foundry may be able to decrease the minimum section size in a casting keeping it free from the brittle carbides which would most likely form without inoculation. In addition, strontium-bearing inoculants are particularly effective in helping to control internal shrinkage in these castings and thereby enhancing the pressure tightness of the casting [44].

**Economic Aspects and Reserves** Whereas strontianite was the principal starting material used in the production of strontium compounds between 1870 and 1920, it has now been almost completely replaced by celestite for this purpose.

Practically the only use for celestite is the production of other strontium compounds. It is used only to a small extent as a white filler in competition with ground barite (barium sulfate).

World production of celestite in the early 1990s was estimated at ca. 250,000–300,000 t/annum. The most important producing countries are Spain, Turkey, United Kingdom, China, Mexico, Iran, and Morocco.

The world production in 2003 was around 370,000 metric tons of strontium minerals, and the reserves are expected to exceed 1 billion tons.

Large exploited deposits exist in Spain, Mexico, Turkey, China, and Iran. There are much less important deposits in Algeria, Cyprus, Argentina, and Morocco. Mining in the United Kingdom, the traditional producer, ended in 1992.

#### Manganese, Mn

**Occurrence** Manganese is a silver-gray metal, resembling iron. It is hard and very brittle, and its primary uses in a metallic form are as an alloying, desulfurizing, and deoxidizing agent for steel, cast iron, and nonferrous metals. It has a high tendency to oxidize.

Manganese is the twelfth most abundant element in the earth's crust, at 950 ppm (0.095%).

Manganese is contained in many minerals, of which approximately 250 can be regarded as true manganese minerals. The major ores, generally with manganese contents above 35%, are hydrated or anhydrous oxides. The silicates and carbonates occur to a lesser extent.

Economically significant manganese deposits are all of sedimentary origin, having been dissolved from crystalline rocks and deposited as the oxide, hydroxide, or carbonate.

Typically, only ores containing a minimum of 35% Mn are regarded as manganese ores. Ores containing 10–35% Mn are categorized as ferruginous manganese ores, and iron ores with 5–10% Mn are referred to as manganiferous ores.

The three most important areas of application of manganese ores and the specific requirements are as follows:

1. Metallurgical grade ore for the iron and steel industry, which generally contains 38–55% Mn. The phosphorus content should preferably be below 0.1%, and the concentrations of  $\text{Al}_2\text{O}_3$ ,  $\text{SiO}_2$ ,  $\text{CaO}$ ,  $\text{MgO}$ , and S are important. The manganese/iron ratio is critical; a 7.5:1 ratio, e.g., is required for a standard ferromanganese alloy with 78% Mn.
2. Battery grade ore, containing 70–85%  $\text{MnO}_2$  (44–54% Mn). The ore should generally contain less than 0.05% of metals more electro-negative than zinc, such as copper, nickel, cobalt, and arsenic. The suitability of manganese dioxide for use in batteries depends on a number of factors, including the crystal structure, surface area, pore size distribution, particle shape and size, electrical conductivity, surface conditions, chemical composition, and structure defects.
3. Chemical grade ore whose specifications vary considerably depending on the end use. Included in this category are feedstocks for electrolytic manganese and manganese dioxide, manganese chemicals, colorants, and, in the Republic of South Africa, an oxidant in uranium extraction.

**Production** The major producers of manganese ore apply both underground and open-pit mining techniques. In the Republic of South Africa, Samancor extracts ore from the open-cast Mamatwan mine and the underground Wessels mine. At Mamatwan, e.g., the ore body attains a maximum thickness of 45.2 m and is overlain by, on average, 45 m of overburden. The open pit is

approximately 1900 m by 300 m, and the ore is extracted from three benches by drilling, blasting, loading, and hauling to an in-pit crusher. At Wessels, the ore body is located at a depth of ca. 300 m, and a room and pillar mining system is employed. The average stope height is ca. 5 m, and the ore is drilled, blasted, loaded, and hauled to underground primary crushing facilities.

The most important methods for the production of relatively pure manganese metal are the electrolysis of aqueous manganese salts and the electrothermal decomposition of manganese ores [45].

**Reserves** The most important manganese ore deposits are located in the Republic of South Africa, Russia, Australia, Gabon in West Africa, and Brazil. The deposits in India and Mexico are of declining importance, and the majority of the production is consumed domestically.

The largest known land-based manganese deposit is the Kalahari Field, located in the Northern Cape Province of the Republic of South Africa, which contains ca. 78% ( $13,600 \times 10^6$  t) of the world's potential resources. The surface area underlain by this deposit is approximately 320 km<sup>2</sup>. The deposit is sedimentary and interlayered with banded ironstone.

Nickel, Ni

**Occurrence** Nickel is a frequent element and with a share of 0.015% of the earth's crust inhabits the 21st place of the list of frequency of elements. It is more abundant than copper, zinc, or lead. In elemental form, it occurs only in meteorites. On earth, it is a component of so-called nickel ores. An important example is pentlandite which has a close association with other sulfides such as pyrite, chalcopyrite, and pyrrhotite in basic igneous rock intrusions. Garnierite and nickeliferous limonite are other nickel ores of economic significance. The term garnierite is commonly used as a generic name for a series of mixed nickeliferous silicates with a wide range of nickel contents and which can include colloidal mixtures of silica and



nickel hydroxide. Nickeliferous limonite is the term used to describe poorly crystalline nickel-bearing ferric oxides of which the main constituent is goethite ( $\alpha\text{-FeO} \cdot \text{OH}$ ).

**Production** The methods for the extraction and refining of nickel minerals depend on the mineralogical and geological characteristics of the ore. Nickel has mainly been extracted from sulfide and laterite ores.

Nickel sulfide ores are mostly mined underground using drilling, blasting, and other techniques. Milling procedures include liberation, flotation, and magnetic separation. Liberation of the sulfides from the gangue includes grinding of the rock material. Then the sulfides are concentrated by flotation processes. Flotation involves streaming air bubbles through an aqueous slurry of the ore particles in a flotation cell. The particles that are not wetted by the liquid adhere to the air bubbles, rise to the surface of the slurry, and can be removed. The addition of different chemicals to the flotation medium allows the selective flotation of nickel- and copper-rich fractions.

Most of the pyrrhotite (both lump ore and ground ore) can be separated magnetically because of its magnetic properties.

Laterite nickel deposits are mined from open pits using earthmoving equipment.

Both sulfide ore concentrates and laterite ores are subjected to pyro- and hydrometallurgical processes. The pyrometallurgical processing basically involves three operations, i.e., roasting, smelting, and converting.

During roasting, the concentrate is oxidized by hot air. Most of the iron is oxidized, while nickel, copper, and cobalt remain combined with sulfur. Part of the sulfur is removed as gaseous sulfur dioxide.

The roasted product is smelted in a furnace together with a siliceous flux to obtain two immiscible phases, an iron-rich silicate slag and a nickel-rich sulfide matte, which also contains iron, copper, and cobalt.

The matte is treated in a “converter” where more sulfur is driven off and the remaining iron is oxidized and removed as slag.

The matte is allowed to cool and treated in different ways. It may be, for instance, cast into anodes for electrolytic refining or cooled slowly to facilitate crystallization to nickel sulfide, copper sulfide, and a nickel-copper alloy containing the desired metals. These three phases can then be separated by flotation and magnetic separation. The species of nickel likely to be present during roasting, smelting, and converting include the ore, nickel subsulfides, nickel-copper sulfides, nickel oxides, nickel-copper oxides, arsenides, and anhydrous nickel sulfate. The extraction of nickel from laterite ores is similar to the extraction of nickel from sulfide ores with the exception that sulfur (commonly gypsum) has to be added. The molten matte is charged into a converter where the iron is oxidized, and the sulfur combines with nickel to form  $\text{Ni}_3\text{S}_2$ .

Smelting to ferronickel is essentially the same as matte smelting, except that no sulfur is added. It is often applied to laterite ores. The resulting iron-nickel alloy contains 20–50% nickel [46].

Most of the nickel matte obtained from sulfide or laterite ore smelting undergoes further refining techniques, such as electro-, vapo-, or hydrometallurgical refining, but a part of the matte is roasted to marketable nickel oxide sinter.

Hydrometallurgical refining can be applied both to laterite ore and sulfide ore or sulfide ore concentrates. Soluble nickel amines are formed during pressure leaching of the sulfide ore concentrate with strong ammoniacal solution at a moderately elevated temperature. The saturated solution is boiled to drive off ammonia and precipitate copper as sulfide. Sulfur is oxidized. Nickel and cobalt are recovered as pure metal powders by reduction with hydrogen under pressure.

Laterite ores must first be reduced. The reduced ore is leached with an ammonia-ammonium carbonate solution. Nickel dissolves as nickel amine. The saturated solution is heated by steam, ammonia is driven off, and nickel is precipitated as a basic carbonate.

Pure nickel (99.9%) can be produced by electrolytic refining. Generally, an impure metal anode (produced by reducing nickel oxide) and a cathode starting sheet are placed in an acidic

electrolytic solution. When a current flows, nickel and other metals are dissolved from the anode. The electrolyte is then removed, purified, and returned to the cathode compartment, where nickel is deposited on the cathode.

During vapometallurgical refining, impure metal obtained by the reduction of nickel oxide is subjected to the action of carbon monoxide forming volatile nickel carbonyl  $[\text{Ni}(\text{CO})_4]$  (carbonyl or Mond process). This reaction is reversed by heat, and the nickel carbonyl decomposes to pure nickel metal and carbon monoxide. The carbonyl process produces the purest nickel (99.97% or more) [47–51].

**Occupational and Public Health Impacts** Nickel is considered a contact allergen and nickel oxide a carcinogen according to EU classification (Category 1 carcinogen), increasing the risk of lung cancer. Inhalation of NiO in the long term is damaging to the lungs, which is why NiO is viewed as problematic in the working environment.

Nickel hydroxide  $(\text{Ni}(\text{OH})_2)$  apparently does not show these issues and may be the preferred raw material for mass producing SOFC anodes in the future.

## Chromium

**Occurrence** Chromium is practically only found as chromite or chrome iron stone ( $\text{FeCr}_2\text{O}_4$ ), in open-pit mining or in near-surface underground mining. Metallic chromium is obtained by reduction of the ore with aluminum or silicon. Untapped chromite deposits are plentiful and geographically concentrated in Kazakhstan and southern Africa.

**Production** South Africa extracts approximately half of the world's demand of chromite. Other substantial producing countries are Kazakhstan, India, and Turkey.

Approximately 15 million tons of marketable chromite ore were produced in 2000 and converted into approximately 4 million tons of ferrochrome.

**Occupational and Public Health Impacts** Hexavalent chromium ( $\text{Cr}(\text{VI})$ ,  $\text{Cr}^{6+}$ ) is a highly toxic and mutagenic substance when inhaled.  $\text{Cr}(\text{VI})$  is considered a carcinogen upon ingestion and has been linked to stomach tumors. It is also a contact allergen. Therefore automotive industry has been very active over the past two decades in removing any  $\text{Cr}(\text{VI})$  from vehicle components.

The valence of chromium and the composition of chromium compounds potentially released from operating SOFC stacks are little researched and require more attention.

## Stationary SOFC Stack Design

The “stationary” SOFC design used for analysis in the following is based on the F-design stacks as developed by Forschungszentrum Jülich since 2002. This design was established as a laboratory platform for evaluation of SOFC cell developments, protective layers, thermal cycling capabilities, and long-term degradation [30, 52, 53]. Nevertheless, it is also a concept that can be used in stationary fuel cell applications, i.e., for power generation and CHP. For practical, commercial employment, though, some critical parameters, like the amount of steel used for interconnects (see below), will need to be improved to, among other aspects, reduce the manufacturing costs.

The central element of the solid oxide fuel cell stack is the SOFC cell which consists of the fuel electrode (anode), the oxygen electrode (cathode), and the ion-conducting electrolyte. To reach the desired electrical voltage, single cells are stacked (cf. Fig. 11). They are separated by interconnects (plates) and sealed by glass ceramics.

In the case discussed here, the anode substrate is the mechanically supporting component of the fuel cell (ASC concept). The thickness of the anode is set at  $\sim 1000 \mu\text{m}$  due to laboratory manufacturing constraints in warm pressing. More recent anode substrates produced by tape casting have been reduced to  $300\text{--}600 \mu\text{m}$  thickness, still supplying the required mechanical stability. In choosing the anode material, attention must be paid to the fact that the electrochemical reactions are not impaired by the thickness. As the electrolyte has no

mechanical function in this concept, its thickness can be reduced from the typical  $\sim 150\ \mu\text{m}$  seen with electrolyte-supported cells (ESC) to 5 to  $10\ \mu\text{m}$ . Therefore, the contribution of the electrolyte to the overall cell resistance decreases dramatically. This opens up the possibility to reduce the operating temperature to as low as  $650\ ^\circ\text{C}$ , without any efficiency losses by increased activation overpotential. The reduced operating temperature promises several advantages such as lower degradation and longer lifetime, lower thermal losses, and more rapid start-up.

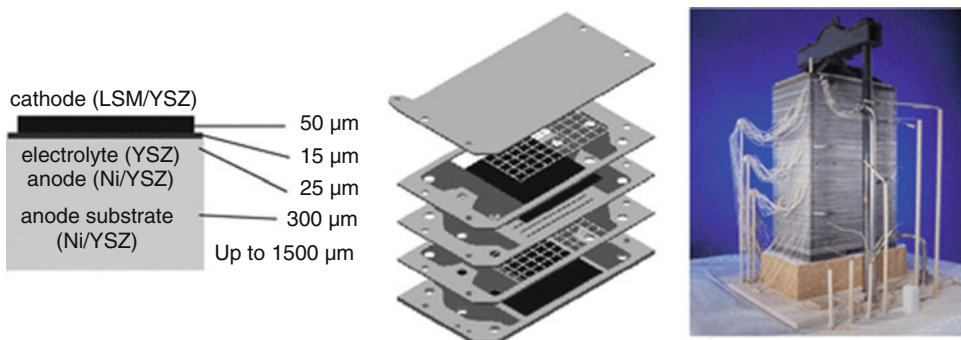
A variety of new materials have been and still are being developed and applied in this SOFC concept. Due to the operating temperature range of  $650\text{--}750\ ^\circ\text{C}$ , heat-resistant steels, ceramics, and glasses are preferentially used. Depending on the function and requirement specifications, the components differ with respect to the choice of materials.

Figure 12 gives an impression of the cell design, the different layers (components), and the materials used in a stack repeating unit (interconnect to interconnect). The respective functions are described on the following pages.

The tasks of the *interconnect* (equivalent to the bipolar plate in low-temperature fuel cells) are the separation of the gas supply streams for the electrodes, guiding the gas flow (providing the flowfield), and the electrical contacting of the cells. An important requirement with contacting is the reduction of the surface resistance between

interconnect and the electrodes of the SOFC. For the guidance of the gaseous fuels, flowfields can be machined into the interconnects. Highly alloyed ferritic steel can be used as material for the interconnect, if the operating temperature of the SOFC is appropriate and not above  $850\ ^\circ\text{C}$ . This condition can be fulfilled with the anode-supported concept. Chromium-nickel alloy steels (such as CroFer22APU or K41) are suitable to fulfill the requirements mentioned. They ensure a permanently good electrical conductivity, and the expansion coefficient differs only slightly from that of YSZ. They fulfill further requirements such as high thermal conductivity, favorable corrosion properties, commercial availability, potentially low production costs, and simple machining [54, 55].

The *cathode* (the air electrode of the fuel cell) supplies the function of reducing the oxygen molecules ( $\text{O}_2$ ) of the air to oxygen ions ( $\text{O}^{2-}$ ) which then migrate through the electrolyte toward the anode. Its porous structure enables the gas transport to the electrolyte surface. It must also supply electrons for the reduction of the oxygen so that good electron conductivity is necessary. Lanthanum strontium manganite (LSM), a complex oxide with a perovskite structure, is one of the standard cathode materials today for operation around  $800\ ^\circ\text{C}$ , with lanthanum strontium cobalt ferrite (LSCF) being the standard for temperatures below  $750\ ^\circ\text{C}$ . The coefficient of thermal expansion again matches well to that of the zirconia-



**Solid Oxide Fuel Cells: Sustainability Aspects, Fig. 12** “Stationary” SOFC concept (based on the F-design of Forschungszentrum Jülich), stacking principle, and example of a 15 kW stack [30, 52, 53]. The F10 stack

shown in the middle has cells of size  $10 \times 10\ \text{cm}^2$  and a footprint of approx.  $12 \times 20\ \text{cm}^2$ . The 15 kW class stack has a footprint of approx.  $22 \times 30\ \text{cm}^2$  and a height of about 40 cm

based electrolyte materials. LSM and LSCF exhibit high electronic conductivity; nevertheless, the ionic conductivity of LSM is nearly zero. Electron-conducting materials like LSM have a disadvantage since the electrochemically active area (“triple-phase boundary” of cathode, electrolyte, and gas space) is limited to the direct vicinity of the electrolyte. To overcome this drawback, the cathode material is mixed with electrolyte material – forming the actual cathode (composite cathode) – and covered with a current-collecting layer of pure cathode material (bilayer cathode) [56]. Some SOFC cells use perovskites where the manganese is replaced by cobalt or iron (LSC or LSF) or a combination of these (LSCF, as mentioned above) [57]. LSCF has the advantage of being a “mixed ionic-electronic conductor” (MIEC) and thus forms TPBs across the whole bulk of material. LSCF cathodes are therefore monolithic and do not need the admixture of YSZ. Further modifications of cathode materials not so prominent in commercial use today include doping with copper or praseodymium or the use of nickelate materials.

To achieve the desired power output, repeating units are layered to form a “stack.” A gastight separation of the anode- and cathode-side gas supply with, at the same time, good electrical contact between the cells is a prerequisite of this design. Two problems occur with this assembly. On the one hand, the cell might be uneven and slightly curved, which can lead to contact problems between cell and interconnect. On the other hand, the process temperature of the fuel cell (600–850 °C) may lead to chromium evaporation from the steel interconnect which can cause an inhibition of the electrochemical process at the cathode side and thereby substantially contributes to the degradation of the cell and to the impairment of the life span of the SOFC [58]. To solve these problems, *contact layers* and chromium evaporation (through the formation of chromium hydroxide) *protective layers* are applied. The requirements for these layers are a good chemical and thermodynamical stability at the operating temperatures of the fuel cell with, at the same time, good electrical conductivity. Furthermore, the layers should not interact chemically with

each other nor the interconnect or the electrodes. For this purpose, special ceramic oxides with perovskite or spinel structure were developed which fulfill these requirements. For the cathode-side contact layer, perovskites based on LSM or LSM itself are often used. Sputtered, plasma-sprayed, galvanically applied, or vapor-deposited perovskite, metal, and metal oxide coatings on the interconnect show good results as chromium evaporation protection [59].

Within the *electrolyte*, the oxygen ions ( $O^{2-}$ ) are transported from the air electrode to the fuel electrode side (anode) to drive the fuel oxidation. Well suitable material is zirconia ( $ZrO_2$ ), which is a poor ionic conductor at ambient conditions, but if heated up to temperatures above 2000 °C, it becomes ionic conducting due to a phase transformation from tetragonal to cubic structure. By adding stabilizing agents like yttria (YSZ), calcium (CSZ), or scandia (ScSZ), the cubic structure is stabilized even at ambient conditions. Because of this stabilization, zirconia already becomes a reasonable ionic conductor at SOFC operating temperatures (600–850 °C) [60]. Other potential electrolyte materials are ceria and lanthanum gallate (LSGM).

The *anode* must be an effective oxidation catalyst so that the oxygen ions, diffused through the electrolyte, react with the fuel hydrogen. Further requirements are, among others, high electronic conductivity and chemical and mechanical stability. Nickel is used both as an electrical conductor for transporting the electrons in the electrode and as the oxidation catalyst. YSZ provides structural support for separating the Ni particles, preventing them from sintering together while matching the thermal expansion coefficient. For fabricating Ni-YSZ anodes, nickel oxide and YSZ are mixed and thermally treated through several steps to form the anode substrate, which has the necessary mechanical stability to be used as the base support structure for the cell. When the SOFC cell is heated up in reducing conditions (for instance, hydrogen atmosphere), the nickel oxide is reduced to metallic nickel, and the resulting ceramic and metal structure, the so-called cermet, is characterized by an excellent electrical conductivity due to its nickel content.

A pore structure is achieved partly through the volume reduction upon nickel oxidation, partly by mixing organic particles into the green substrate which burn out during sintering and permit fuel gas to flow to the anode interface with the electrolyte (TPB). The electrocatalytic effect is based on the metallic nickel, which not only binds hydrogen on its surface but also transports the electrons resulting from the oxidation of the hydrogen. The necessary oxygen ions are supplied by the electrolyte and the ramified YSZ network, whereas the transport of the fuel gas and its corresponding products takes place through the pores. The selective tuning of the pore structure, nickel, and YSZ content leads to an optimized electrochemical conversion [61].

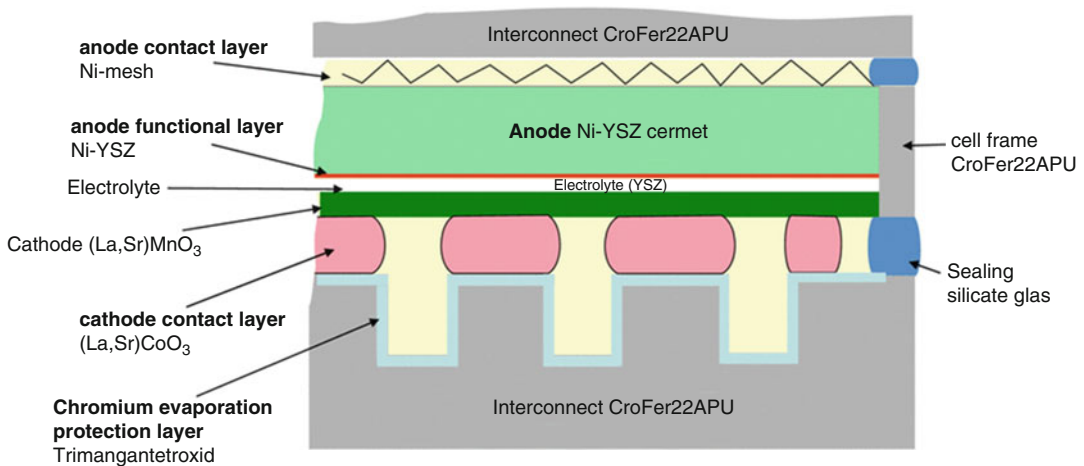
Thermal cyclability and redox stability are crucial requirements for SOFC stacks. Reliable *sealing* of the gas-filled compartments is necessary to ensure a high effectiveness and safe operation of the stacks. The difference in coefficients of thermal expansion (CTE) of the stack components requires long-term separation of the oxidant and fuel gas compartments of planar stacks under dynamic operation conditions. Glass-ceramic sealants have, for instance, been developed on the basis of the ternary system BaO-CaO-SiO<sub>2</sub> with additions of transition metal oxides. Chemical interaction of the sealing glass with the interconnect steel may deteriorate the corrosion

resistance of both chromia-forming and alumina-forming alloys [62]. The inherent brittleness of glass ceramics and the rigid bonding of the stack components limit the compensation of mechanical and thermal stresses and promote growth of defects or cracks at the interconnect/glass-ceramic interface. Due to the stiff stack assembly, the reduction of mechanical or thermal stresses by elastic or plastic deformation or by free expansion and contraction of stack components is limited. Furthermore, a nondestructive dismantling of stacks to replace malfunctioning components is impossible [63].

### Manufacturing of Components and Cells

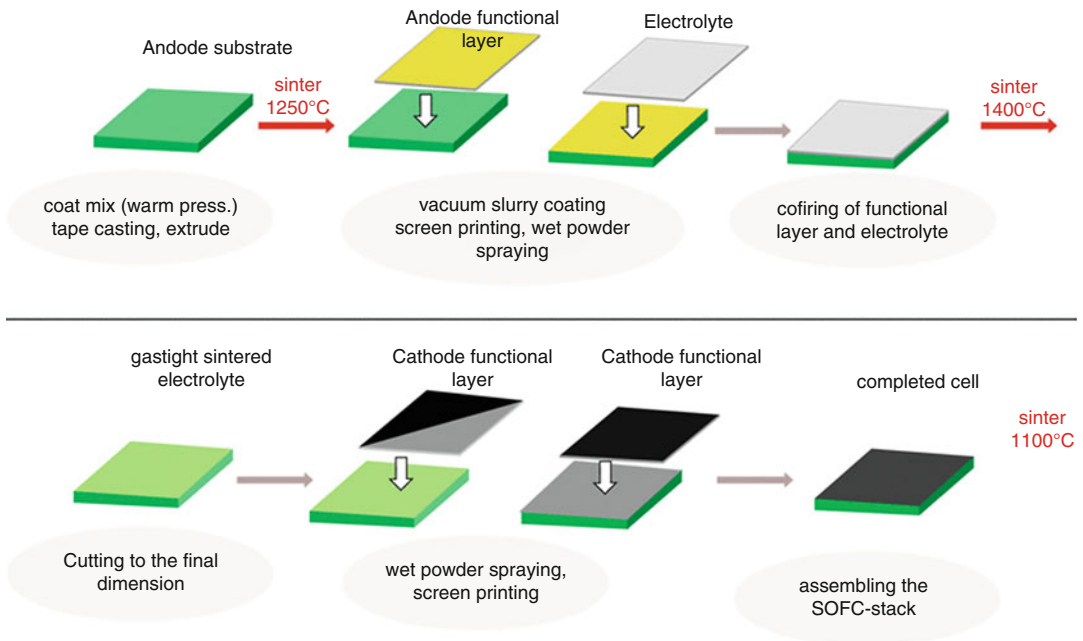
A description of the manufacturing process chain is given for the example of an anode-supported (ASC) SOFC with a substrate produced by warm pressing.

The anode substrate is the mechanical supporting component of the cell (cf. Fig. 13). The substrate consists of nickel oxide (NiO) and yttria-stabilized zirconia (8YSZ) and is fabricated by conditioning of the ceramic powders using the Coat-Mix<sup>®</sup> Process with polymeric resin and subsequent warm pressing; Fig. 14 shows the various processing steps. After burning out the resin, which makes the powder flowable and strengthens the components during pressing, the substrate is fired at temperatures >1000 °C. Thereafter, the



**Solid Oxide Fuel Cells: Sustainability Aspects, Fig. 13** Cross section of a planar SOFC stack single repeating unit [30]





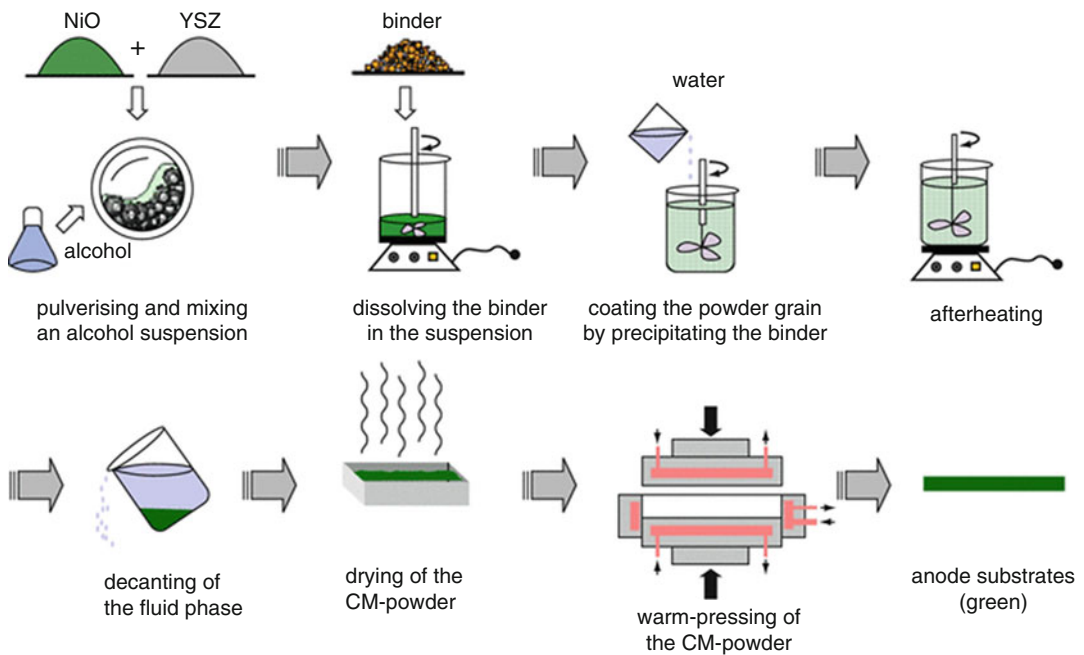
**Solid Oxide Fuel Cells: Sustainability Aspects, Fig. 14** One of several processing chains of Jülich's SOFC (according to the ASC concept; the fabrication

technologies stated for each process step list the potential production technologies) [64]

substrate has sufficient mechanical stability and the necessary porosity for the subsequent coating processes. The substrate does not act as anode since a triple-phase boundary with the electrolyte is necessary for this function. Making the substrate of essentially the same material as the anode, though, reduces problems of CTE matching and chemical compatibility, while it adds considerable reforming capabilities for methane reforming. During the next processing step, the actual anode layer and the electrolyte are deposited by vacuum slip casting. For the coatings, alcoholic suspensions of NiO/8YSZ and pure 8YSZ are deposited in sequence on the substrate, dried, and sintered at a temperature of ca.  $1400^{\circ}\text{C}$  during a co-firing process. After sintering, the electrolyte is gastight, and the "half-cell" can be cut to the required dimensions with a diamond saw or by laser cutting. The cathode layer (e.g., LSM) is then deposited by wet powder spraying or screen printing on the anode-electrolyte unit as a bilayer of differently processed powders. The completed cell is dried and subsequently sintered at about  $1100^{\circ}\text{C}$ .

**Anode** The Coat-Mix<sup>®</sup> Process is a procedure patented by FZ Jülich, in which different non-soluble powders (called fillers) are coated with phenol formaldehyde resin (binder). The manufacturing takes place by mixing NiO, YSZ, and ethanol in a roll container using zirconia balls for milling. The NiO agglomerates, existing in the NiO powder, are destroyed, and both powders are finely ground. Thus, a homogeneous mud-like alcoholic suspension of the raw materials is obtained. After transfer into the coating container, Fig. 15, phenol formaldehyde resin is added to the alcoholic suspension, which dissolves in the existing alcohol after brief heating, so that a slurry in binder-lotion is produced. In the following step, acidified water is added slowly and continuously to this mixture at a defined supply rate. The phenol formaldehyde resin is hardly soluble in water and precipitates again with the addition of the insoluble phase. The powder grains, which are held in suspension by milling, are coated in this phase with the phenol formaldehyde resin and stick together easily to form larger agglomerates (coat mixing). After a subsequent thermal treatment and





**Solid Oxide Fuel Cells: Sustainability Aspects, Fig. 15** Manufacturing the anode substrate by means of the Coat-Mix<sup>®</sup> Process (CM) with subsequent thermal pressing

a washing process, the precipitation settles and the liquid is removed on a suction filter.

The filter cake is transferred to dishes and dried in a vacuum condensation drying furnace at low temperature. The advantage of this manufacturing method is that no further additives are needed in the mixing process. The powder, which is obtained in this way, is well processible after sieving  $<80\ \mu\text{m}$  and is filled into pressing forms. Under low pressure, at temperatures above the melting range of the binder, it is processed to the desired anode substrates [65].

Alternatively to this discontinuous anode production process, tape casting can be used, a standard industrial production technology in electronics, by which the anode substrate can be produced continuously (Fig. 16).

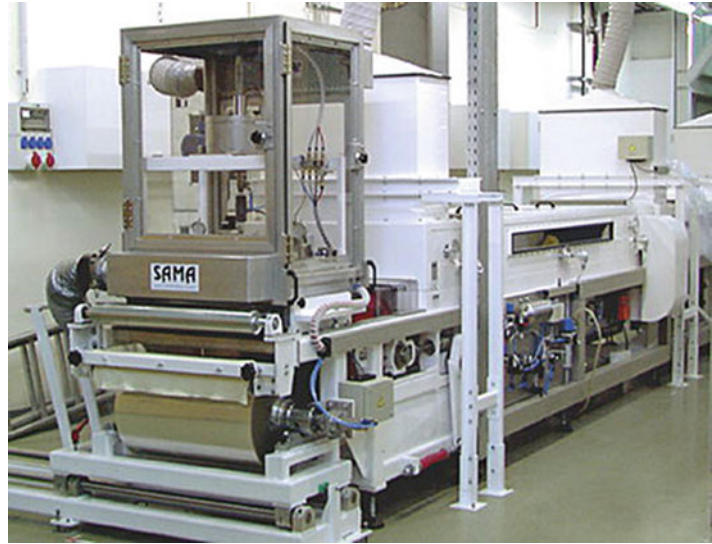
The first step of the process is the preparation/mixing of a slurry consisting of nickel oxide with yttria-stabilized zirconia and graphite powder, as well as several organic additives like solvent, dispersing agents, binder, and softener. The slurry is subsequently cast by means of a tape casting facility. During the process, the slurry flows from

a storage container onto a plastic or metallic foil, which is continuously moved at a controlled velocity beneath the container. The height of the slurry layer is controlled by a doctor blade, which determines the final layer thickness and which creates a smooth and even slurry coating on the carrier foil. After casting the slurry, the formed ceramic foil passes a drying chamber, in which the foil is dried at given temperatures. Thus, a flexible ceramic foil is manufactured (“green tape”), which can be cut, sawn, or punched. Once it is sintered at temperatures  $>1000\ ^\circ\text{C}$ , it is rigid and can be coated. The advantages of the procedure in relation to other methods, e.g., pressing, are the continuous operation with a high manufacturing throughput, an economical production, the high reproducibility, the possibility to recycle green tape leftovers, and the compatibility with standard industrial manufacturing processes [64].

**Electrolyte** In this specific fabrication process, the electrolyte is deposited by slip casting on the anode substrate.

**Solid Oxide Fuel Cells:  
Sustainability Aspects,**

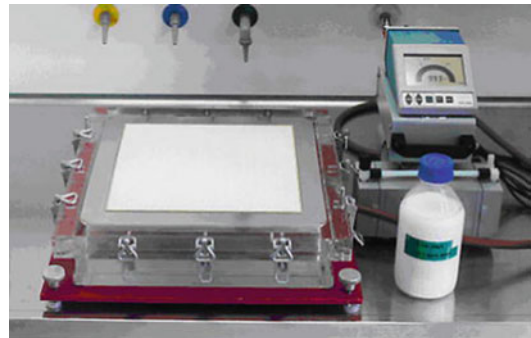
**Fig. 16** Tape casting equipment at Forschungszentrum Jülich



In general, the slip casting process is used to manufacture three-dimensional ceramic components. With the vacuum slip casting process, the process flow is accelerated using vacuum suction. In principle, slip casting processes are based on filling a porous casting mold with a solid-containing suspension (slip). The solvents of the slip will be drawn into the pores of the casting mold, taking along the solid. The solid is deposited at the outline of the casting mold and adds up in a layer that can be separated from the casting mold after drying.

For the production of thin anode functional layers and electrolyte layers when producing planar solid oxide fuel cells, a modified slip casting process is used. Here, the suspension is applied on a planar, porous anode substrate in a special apparatus as shown in Fig. 17. The solvent is drawn through the pores by a vacuum. When the substrate is aligned horizontally, the solids of the suspension deposit evenly on the surface. This process of manufacturing thin layers has the following advantages:

- Easy and straightforward handling.
- Series production, if automated.
- Excellent quality of the produced layers.
- Reproducibility of the layer thickness, uniform thickness, and structure throughout the layer.



**Solid Oxide Fuel Cells: Sustainability Aspects,**  
**Fig. 17** Vacuum slip casting equipment for production of planar SOFCs

- 2  $\mu\text{m}$  to 50  $\mu\text{m}$  layers can be realized.
- Low amount of waste (the solvent can be reused).
- Long-term stable suspensions can be produced with little effort.

The disadvantage of this process is the handling of large quantities of solvents and the limitation in the thickness of the layer. There is also a big influence of the structure of the substrate (surface topography, pore size, pore distribution, density distribution, and absorbency) on the quality of the layer in terms of voids and impermeability [66].

## Cathode

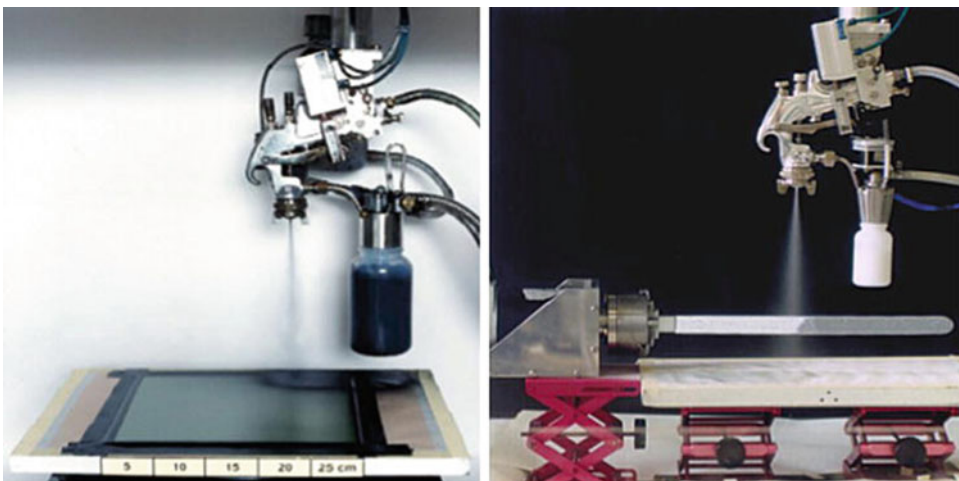
*Wet Powder Spraying* Bilayer cathodes consisting of cathode and cathode current collector layer can, for instance, be manufactured by wet powder spraying (WPS). The cathode contact layer is also applied on the metallic interconnects by spraying. Limitations of the technology are the overspray (the amount of suspension which is sprayed past the object to be coated) and the formation of a suspension mist which needs to be extracted by suction. The overspray can be recycled, though.

By WPS, a suspension composed of solvent, powder, and additives is sprayed by a nozzle (cf. Fig. 18). The thickness of the coating is adjusted by the amount of spray runs with intermediate drying steps. Various geometries, e.g., planar-type or tubular-type SOFC, can be coated by a PC-controlled x-y-axis system and a rotational system in case of the tubes. The thickness obtained so far varies between 5 and 100  $\mu\text{m}$ . The major parameters affecting the spray result are the spray pressure, the spray distance, the nozzle type (with varying apertures), the viscosity and the solid fraction of the suspension, and the grain size distribution and grain morphology of the powder. The intermediate drying steps to obtain thicker layers are necessary to suppress cracking during drying.

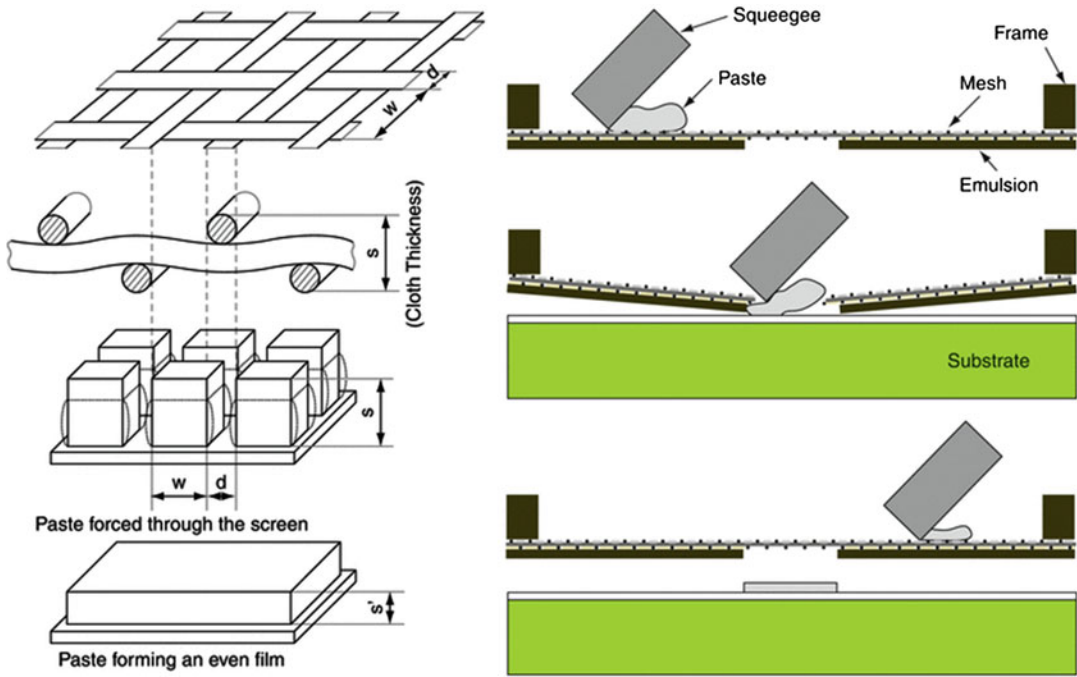
The major advantages of WPS compared to screen printing or plasma spraying are the low-cost fabrication, the possibility for automation, the flexibility concerning size and shape of the samples to be coated, and the facile integration into an industrial process chain.

*Screen Printing* With the screen printing process, a standard industrial manufacturing process can also be applied to manufacture the cathode.

In this process, the cathode material paste is squeezed through the mesh openings of a screen and onto the underlying object. The high-viscosity paste contains particles, binder, and solvent. After drying, i.e. evaporation of the solvent, the layer adheres to the object (cf. Fig. 19). Reproducibility, continuity, and the low materials consumption are the main advantages of this state-of-the-art process. Increasing the cycle time reduces the costs. A variety of patterns can be printed (used, for instance, in electronics industry for integrated circuits) on various surfaces, depending on the size of the printer. Evenness of the substrate and size and resolution of the screen, given by the mesh openings, are the main limitation factors. Another limitation is the layer thickness. Only certain thicknesses are producible as the thickness of the resulting layer is given by the screen [67].



**Solid Oxide Fuel Cells: Sustainability Aspects, Fig. 18** Wet powder spraying process for planar (*left*) and tubular (*right*) geometries



**Solid Oxide Fuel Cells: Sustainability Aspects, Fig. 19** Concept of screen printing (*left*); schematic screen printer (*right*)

Screen printing is expected to replace wet powder spraying in cathode production in the long run. The same procedure can also be applied for electrolyte production. With electrolyte layers, special care has to be taken to produce an even layer with little impact of the screen on layer smoothness and thickness. The development target is multilayer printing, i.e., all layers will be printed on top of an anode substrate to form the SOFC cell, followed by co-sintering. This would result in a reduction of sintering steps and therefore in considerable effort and cost reduction.

#### Material and Energy Demand for Processing/Manufacturing

Table 5 gives an overview of the materials used for SOFC fabrication. The third column refers to the raw material and the upstream processes, preparing the final product/material from the raw material.

Figure 20 illustrates that stainless steel is the main material of a stack. The interconnects, which separate the cells, are metallic, and their weight dominates the complete unit.

The second most used material is nickel oxide which is processed from nickel ore and used for the anode substrate and anode together with yttrium-stabilized zirconia in the form of a cermet and as a nickel mesh for the anode contact layer. Yttrium-stabilized zirconia is produced from rare earths and mineral sands.

The manufacturing process is relatively energy intensive as several electricity-operated high-temperature processes are necessary, for instance, the sintering of the anode substrate, the sheet metal working, the melting of the sealing material, or the heating while assembling, as shown in Table 6. Major processes contributing to environmental impacts are the anode substrate sintering, the production of the metallic interconnectors, and of course the assembling of the components to a stack.

#### Lightweight SOFC Cassette-Type Stack Design

Since automotive applications require a rather robust SOFC design with rapid starting capability, good thermal cycling properties, and high

**Solid Oxide Fuel Cells: Sustainability Aspects, Table 5** Materials for the stationary design SOFC. The processing includes mining and metallurgical and chemical processes for all these materials

Material	Abbreviation	Occurrence
Nickel oxide	NiO	nickel ore
Yttrium-stabilized zirconia	8YSZ	Y: rare earth metal Zr: in minerals
Lanthanum manganite doped with strontium oxide (LSM)	$(\text{La}_{0.8}\text{Sr}_{0.2})_{0.98}\text{MnO}_{3-\delta}$	La: rare earth metal Sr: as mineral Mn: ore component
Lanthanum nitrate hexahydrate	$\text{La}(\text{NO}_3)_3 \cdot 6\text{H}_2\text{O}$	La: rare earth metal
Strontium nitrate	$\text{Sr}(\text{NO}_3)_2$	Sr: alkaline earth metal
Lanthanum cobalt oxide	$\text{LaCoO}_3$	La: rare earth metal Co: cobalt ore
Manganese nitrate	$\text{Mn}(\text{NO}_3)_2 \cdot 4\text{H}_2\text{O}$	Mn: ore component
Barium oxide	BaO	Ba: alkaline earth metal
Calcium oxide	CaO	Ca: component of minerals
Aluminum oxide	$\text{Al}_2\text{O}_3$	Al: component of minerals (i.e., bauxite)
Silicium oxide	$\text{SiO}_2$	Si: quartz, silicate minerals
Nickel	Nickel mesh	Nickel ore

tolerance of the anode to oxidizing atmospheres, the replacement of the nickel cermet anode substrate by a material less sensitive to oxygen and with improved thermomechanical stability appears advisable.

In an alternative approach to standard SOFC manufacturing techniques using sintering of ceramics, various groups such as Ceres Power are developing cells with a porous metal sheet as the supporting layer for the thin active layers of the cell. The Deutsches Zentrum für Luft- und Raumfahrt (DLR) has developed a planar thin-film concept which is based on vacuum plasma spray technology for the manufacture of the

cell layers. This concept, whose principle is schematically shown in Fig. 21, enables an electrolyte thickness of 20–30  $\mu\text{m}$  which allows for operating temperatures of 800 °C or below with still sufficiently high performance. Similar to the “stationary” concept described previously, the lower operating temperature allows for inexpensive materials in the stack as well as for the peripheral high-temperature components [31]. The metal-supported cell (MSC) concept is coupled with thin metal frames and interconnects in a so-called cassette design [69] especially interesting for automobile applications. Therefore, the stack concept referred to in this section is termed “lightweight plasma-sprayed design.” Other designs of cassette-type SOFC stacks have also used ASC cells [70].

The mechanical strength of the thin-film cell and the electrical and thermal conductivity are provided by an open porous metallic substrate which also serves as a fuel gas distributor. The functional layers of the cell – anode, electrolyte, and cathode – are consecutively deposited onto this substrate by a multistep vacuum plasma spray process. The contact from the cathode to the ferritic steel interconnect (bipolar plate) is provided by a flexible and ductile perovskite coating. An important precondition for this design concept is the availability of a long-term stable and corrosion-resistant substrate material with an adequate thermal expansion behavior related to the ceramic cell components [31, 68].

#### SOFC Components and Stack Manufacturing Processes

*Interconnect, cell frame, and metallic substrate* are made of the ferritic steels CroFer22APU [55] and IT-11 (Plansee) [71].

For the soldering of substrate and interconnect, a nickel-based solder foil is required.

The *anode* of the lightweight SOFC is made from nickel oxide (NiO) and yttria-stabilized zirconia. For the *electrolyte*, yttria-stabilized zirconia is also used, while the cathode is made from lanthanum strontium manganite (LSM) (cf. previous section). The same material is used for the *contact layer*. Lanthanum strontium chromite is applied as a ceramic *protective coating* for





**Solid Oxide Fuel Cells: Sustainability Aspects, Fig. 20** Single repeating units and 15 kW class stack of the stationary SOFC design

chromium retention. The noble gas argon is used as an auxiliary medium in the vacuum plasma spraying process [72].

A summary of the material categories used in this lightweight concept is given in Table 7.

Three technical processes are characteristic for the plasma spray SOFC manufacturing.

The central technology is the multistep vacuum plasma spray process (Fig. 22) by which the SOFC cell is deposited onto the substrate-interconnect unit. For an optimum cermet anode layer, doped zirconia (with yttria) and NiO powders are internally injected into a nozzle. At a pressure of 200 mbar and a power level of 30 kW resulting in a relatively low velocity of the particles at impact in the range of 250–350 m/s, a porous cermet anode layer is formed as a result of the weak flattening and densification. At the cell's operating conditions, the NiO in the anode is later completely reduced by hydrogen to pure Ni. This leads to a further increase in porosity to about 20–25 vol% which ensures sufficiently high gas diffusion. The thickness of the anode layer depends on the surface properties of the substrate used; generally, it is in the range of 30–40  $\mu\text{m}$ . For the production of high-performance SOFCs, it is necessary to spray thin gastight electrolyte layers with high deposition efficiency. This is only achievable with completely molten particles which are

accelerated to high velocity in the plasma jet and therefore flattened to dense lamellae on impact. Lamellar microstructured and dense electrolyte layers with high interparticle bonding can be achieved with a thickness of only 20–40  $\mu\text{m}$  [31].

The plasma-sprayed cathodes are obtained in a similar way as the anodes. The variation of the spray parameters has shown that the perovskite phase tends to decompose, especially when  $\text{H}_2$  is added to the plasma gas. With an Ar/He or a pure Ar plasma, best results were achieved with a standard F4V nozzle at a power level of 20 kW, 100 mbar, and internal injection of the powder with  $15^\circ$  in opposite direction to the plasma gas flow. With identical parameters, LSF and LSCF powders in addition to LSM have also been processed to cathode coatings. The lack of a “pore-forming process” as it is used with the reduction process of the anodes leads to a significantly lower overall porosity of plasma-sprayed cathodes in the range of only 10 vol%. This results in a relatively high cathodic polarization resistance, and hence, strong efforts are made to improve the cathode's pore structure. A promising approach is given by the possibility of in situ synthesis and deposition of cathode coatings by applying RF plasma technology.

A vacuum soldering process is the second technical process of relevance. It is used to solder the porous metallic substrate to the interconnect, whereby a nickel-based solder foil is applied [74].



**Solid Oxide Fuel Cells: Sustainability Aspects, Table 6** Electricity intensive steps in stationary SOFC design production

<i>Anode substrate</i>	
Preparation of powder and suspension	
Anode substrate	Coat-Mix
Sintering	1250 °C
<i>Anode substrate and functional layer</i>	
Mixing powder and suspension	
Applying anode functional layer	Slip casting process
<i>Electrolyte</i>	
Prepare powder and suspension	
Applying the electrolyte	Slip casting process
Firing	1400 °C
<i>Cathode functional layer</i>	
Cathode functional layer – paste	
Applying cathode functional layer	Screen printing
<i>Cathode</i>	
Cathode-paste, preparation	
Applying the cathode	Screen printing
Co-firing	1100 °C
<i>Interconnector, cell frames</i>	
Metal plate processing	Sheet metal working
<i>Facing the interconnector</i>	
Ceramic-powder suspension preparation	
Interconnect coating	Wet powder spraying
<i>Glass sealing</i>	
Glass preparation	Melting
Glass sealant paste preparation	Milling-mixing
<i>Stack assembling</i>	
Joining and sealing the stack	~ 800 °C

The third characteristic process is wet powder spraying, by which the contact layer (between cathode and interconnect) is applied to the cathode or interconnect.

#### Feedstock Material for the Cell Components

The “lightweight plasma-sprayed” SOFC concept in principle uses the same materials set as the “stationary” concept. The plasma spray process consumes a certain amount of the noble gas argon, which has its own process chain and the specific

feature that it is produced by air separation technologies [75, 76].

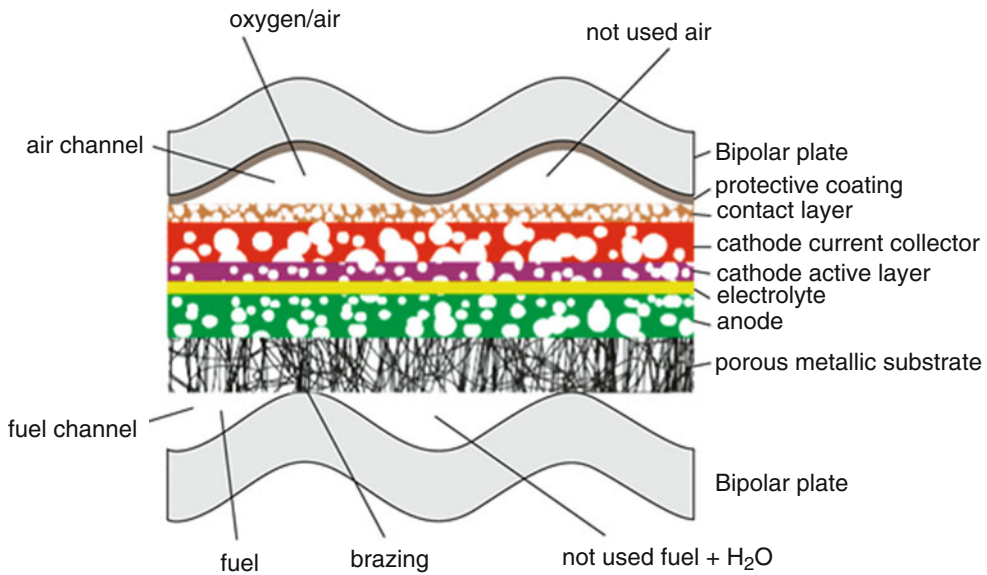
#### Integrated Planar SOFC Concept

The “integrated planar” (IP) SOFC stack concept specifically applied by Rolls-Royce Fuel Cell Systems (today LG Fuel Cell Systems Inc.) uses an array of series-connected cells deposited by screen printing onto a flat support tube, a schematic cross section of which is shown Fig. 23. The support tube, an inert, porous ceramic, is fabricated from a magnesia-magnesium aluminate (MMA) spinel, whereby the desired coefficient of thermal expansion is adjusted by the ratio of the base materials [78].

On the left, Fig. 24 shows an IP-SOFC assembly and on the right the ceramic substrate with the channels shown in front. These channels enable the fuel supply through the support structure and the removal of the reaction products ( $H_2O$ ,  $CO_2$ ). The support tube is made by extrusion. The properties of the MMA ceramic are a function of the precursor powder and the extrusion process used to produce the support tubes. The extrusion process involves combining the MMA with a binder system to produce a dough-like mix.

This is then extruded through an appropriately shaped form to produce a 1.5 m length of support module. Following a drying process, the module supports are cut to approximate length before firing at high temperature to burn out the binders and partially sinter the extrudate. The module supports are then finished by accurately machining to length [79].

Each of the three functional layers of the cell, *anode*, *electrolyte*, and *cathode*, is deposited onto the substrate using screen printing. In practice, each of the functional components requires multiple layers to provide the necessary functionality and manufacturability. Unlike other SOFC designs and similar to the metal-supported cell, the IP-SOFC uses neither the electrolyte nor electrodes to provide structural support. This allows very thin cells with consequently very small material quantities (cf. previous section). The cell functional layers again are made of conventional SOFC materials: yttria-stabilized zirconia



**Solid Oxide Fuel Cells: Sustainability Aspects, Fig. 21** Principle of the planar metal substrate-supported lightweight SOFC concept [68]

electrolyte, nickel cermet anode, and rare earth manganese oxide cathode. The choice of conventional materials allows the use of standard materials suppliers. This ensures that bulk quantities of high-quality materials can be obtained which is essential in producing the quantity of product for scale-up future production. It also allows the efforts in research activities to focus on fine-tuning the material performance and not developing fundamentally new materials. New materials can be introduced as future enhancements after a first product is introduced to the market [78].

For the *anode*, a nickel oxide-YSZ cermet is applied, though the limitations of the current state of that type with respect to redox stability, coking, and sulfur tolerance are known. More recently, the integration of oxide anodes into the concept has been analyzed and tested [79].

Like other concepts, the IP-SOFC design uses yttria-stabilized zirconia as *electrolyte* material. By screen printing, the electrolyte is fabricated with a layer thickness of about 10  $\mu\text{m}$ , which leads to a minimal ionic resistance so that the electrolyte resistance has only a small contribution to the total losses in the cell [78].

For the *cathode*, a mixture of strontium-doped lanthanum manganite (LSM) proved most

suitable, and as the slurry spray process was not scalable to larger modules and production volumes, the screen printing process was chosen for the cathode fabrication [78].

The stack assembly includes ceramic manifold components not further specified, metallic interconnect compounds, and glass ceramics for sealing and joining. The main components are silicon dioxide, calcium oxide, aluminum oxide, and barium oxide.

## Environmental Impacts

### LCA Studies of SOFC

Life cycle assessment of SOFC technology is still uncommon due to the relatively early stage in technical development. However, several studies have been performed since the end of the 1990s. Since there is a lack of “standard” commercial equipment that could serve as a basis and reference point for analysis, LCA studies mostly refer to hypothetical concepts and/or extrapolate from laboratory and early market prototypes to commercial units. While the first studies had only little access to operation data at all (for the fuel cell system itself but also for production processes),

**Solid Oxide Fuel Cells: Sustainability Aspects, Table 7** Materials for metallic substrate, plasma-sprayed lightweight SOFC [31, 68, 72]. The processing includes mining and metallurgical and chemical processes for all these materials

Material	Abbreviation	Occurrence
Nickel oxide	NiO	Nickel ore
Yttrium-stabilized zirconia	8YSZ	Y: rare earth metal Zr: in minerals
LSM	$(La_{0.8}Sr_{0.2})_{0.98}MnO_{3-\delta}$	La: rare earth metal Sr: as mineral
	$La_{0.8}Sr_{0.2}MnO_3$	Mn: ore component
LSCr	$La_{0.7}Sr_{0.15}Ca_{0.15}CrO_3$	La: rare earth metal
		Sr: as mineral
		Ca: in minerals
		$CrO_3$ : in minerals
Barium Oxide	BaO	Ba: alkaline earth metal
Calcium Oxide	CaO	Ca: component of minerals
Alumina (aluminum oxide)	$Al_2O_3$	Al: component of minerals (i.e., bauxite)
Silicium oxide	$SiO_2$	Si: quartz, silicate minerals
Nickel	Nickel mesh	Nickel ore

the main effort was set in the assessment of inventory data using assumptions, simplifications, and correlations [80, 81]. The main outcomes of these studies were the identification of weak points and the setting of benchmarks for further development. With more information about fuel cells available today and a simultaneous advancement in LCA methodology, the studies became more reliable and detailed, regarding system description [82] as well as the assessment of environmental impacts connected with inputs and outputs [83]. Especially the extensive data of these two studies found their way to commercial databases for LCA [84] and thereby became available to LCA practitioners. In 2005, the Federal Ministry for the Environment, Nature Conservation and Nuclear Safety (BMU) commissioned a study investigating ecological aspects of fuel cells

besides economical factors [85]. The most recent LCA analyses were performed in the European integrated projects Real-SOFC [86, 87] and Large SOFC [27]. In the NEEDS project, fuel cells are one technology among others to build up future sustainable energy systems [88]. The European H2FC-LCA project was the latest to systematically develop analysis spreadsheets for LCA assessment of various fuel cell types, among others SOFC [89].

### LCA Results

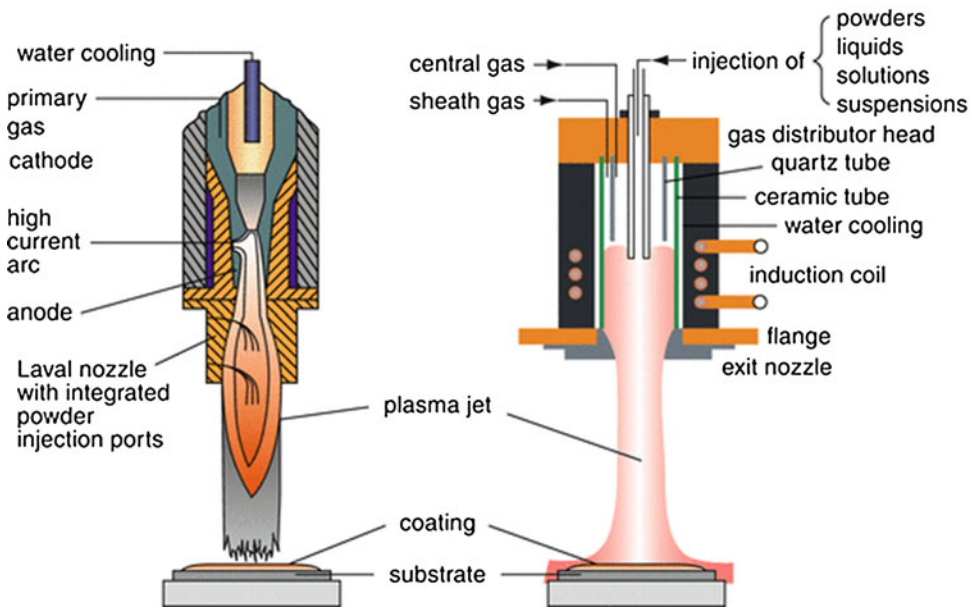
With increasing environmental operating standards for modern energy conversion systems, the upstream and downstream processes, e.g., fuel supply or system component production as well as waste treatment or recycling, are increasingly gaining in relevance. More important than the relative contribution of the production is the absolute impact of production. Very often, technologies showing good characteristics in the use phase lead to high absolute environmental impacts in the production phase due to the use of more “sophisticated” materials and components as well as newly developed or adjusted production processes. Therefore, the entire life cycle has to be included in the investigation.

### Goal and Scope

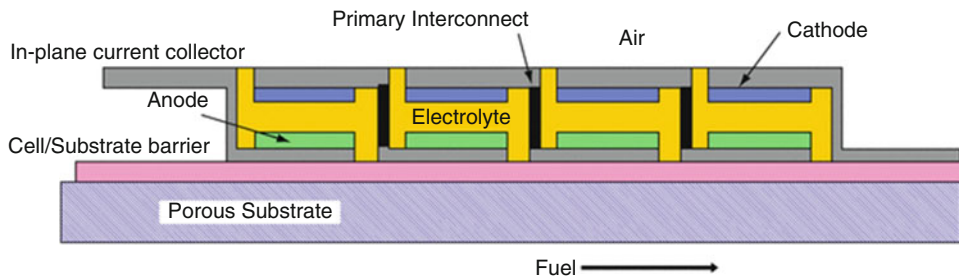
In the different LCA studies, the investigated fuel cell systems vary in their system boundaries. While some studies focus exclusively on the stack itself, others also include the balance of plant (BoP) into the investigations. Major impacts on the results can also be identified due to the variation of fuels used and the end-of-life concept considered in the analysis.

The main goals of the studies are twofold:

- Determination of weak points along the life cycle of fuel cells through identification of materials or processes with potentially high environmental impacts. The results can be used to give some recommendations to avoid or reduce impacts.
- Comparison of ecological characteristics of fuel cell systems and future competing systems



**Solid Oxide Fuel Cells: Sustainability Aspects, Fig. 22** Principles of direct current plasma (*left*) and radio-frequency plasma (*right*) torches [73]



**Solid Oxide Fuel Cells: Sustainability Aspects, Fig. 23** Integrated planar solid oxide fuel cell concept [77]

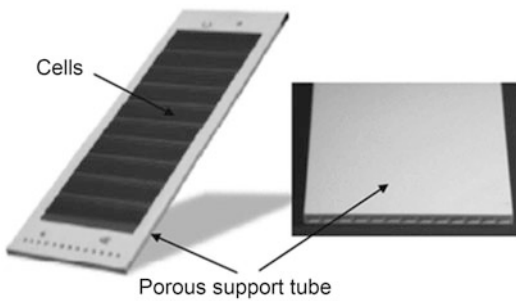
to help decision-makers in terms of optimal applications for fuel cells.

Depending on the focus of the study, the functional unit varies for the different studies. In all studies, the manufacturing of the fuel cell itself is included. Input and output data are related to a 1 kW<sub>el</sub> fuel cell stack, distinguished in tubular or planar cell concepts. The Real-SOFC study focused exclusively on the stacks, accompanying the research activities performed in that project. The other studies include the balance of plant (BoP) and auxiliary components as well. All other studies expand the investigated life cycle

by integrating the use phases as well, thus defining 1 kWh of electricity produced as the basis for comparison.

The impact assessment varies between the projects. While older studies consider mostly material and energy inputs as well as selected emissions to the atmosphere, the newer studies describe the environmental effects using aggregated impact categories.

Parameters with high impact on the results are technical data such as cell performance, electrical efficiency, technical lifetime of the stack, the end-of-life concept considered, and the fuel used. Methodologically speaking, the evaluation and



**Solid Oxide Fuel Cells: Sustainability Aspects, Fig. 24** Active tube and extruded porous support tube [77, 78]

allocation of the coproduct “heat” play an important role. These parameters are not handled equally in the different studies and thus make comparison between the studies difficult.

#### Inventory

**Stack Manufacturing** The environmental impacts of the fuel cell stack can be classified on the one hand into the life cycle stage “material provision and manufacturing of the stack” and on the other hand into the “operation phase of the fuel cell.” The sensitive parameters for the stack system manufacturing are the material input, the manufacturing processes, and the cell performance. The materials used in the planar, sintered fuel cell concept are described in detail in section “Stationary SOFC Stack Design.” It is typical for this type of stacks for stationary applications that the stacks include a high amount of chrome alloy for the interconnect. More recent designs already tackle this issue for reasons of materials, weight, and cost reduction. The relatively high amount of NiO is specific for cells with a thick anode substrate (up to 1.5 mm in Fig. 12, for instance). Again, more recent developments reduce this thickness to 300 to 600  $\mu\text{m}$ . The amount of  $\text{ZrO}_2(\text{Y}_2\text{O})$  is caused by the comparatively low yield of the first sintering phase ( $\sim 80\%$ ), where a number of plates crack or bend and have to be rejected [82]. In contrast, the materials used in tubular cell design are dominated by ceramics. However, the manufacturing process is far more complex. The major materials contribution is

from  $\text{LaMnO}_3$ .  $\text{ZrCl}_4$  and  $\text{YCl}_3$  amounts are increased due to a low material utilization of electrochemical vapor deposition (EVD) ( $\sim 20\%$ ). This process consumes about 15% of the energy necessary for the production of the cell. Together with atmospheric plasma spraying, it sums up to almost 90% of the total energy required for manufacturing. This equals the energy necessary to supply the materials used. The sum of this energy requirement for the tubular concept is lower than that for the sintered ceramic planar design (stationary design), almost by a factor 7. For the sintered ceramic planar concept, energy inputs for materials production are almost 100 times higher than the energy used during manufacturing, mostly related to the supply of the chromium alloy. However, detailed information about the production of some key materials is not available. To compensate the data gaps, assumptions had to be made. The materials affected are  $\text{LaMnO}_3$ , doped  $\text{LaCrO}_3$ ,  $\text{ZrCl}_4$ ,  $\text{YCl}_3$ , and YSZ. In a sensitivity study [82], it was shown that a doubling of the energy values of these materials only results in a 1.6% increase in total energy requirement. For tubular concepts, this source finds the opposite trend. With the dominant material being  $\text{LaMnO}_3$ , a doubling of materials energy expenditure would cause an increase of the total figure of energy effort by about 96%. For the sintered ceramic planar concept, a possible recycling of the interconnect Cr alloy material would reduce the energy requirement significantly [83]. The energy demand for the manufacturing stage is dominated by thermal processes such as sintering and drying. According to furnace manufacturers, the energy demand for a sintering furnace can be decreased by 65% for series production in an industrial furnace and optimized packing of samples in the furnace [83]. The Real-SOFC project showed that the manufacturing processes of slip casting (Fig. 17) and screen printing (Fig. 19) require more than five times more energy than the vacuum plasma-sprayed layers (Fig. 22) of the plasma spray metal support concept. The energy-intensive manufacturing processes for the tubular concept are expected to decrease for mass production [82].

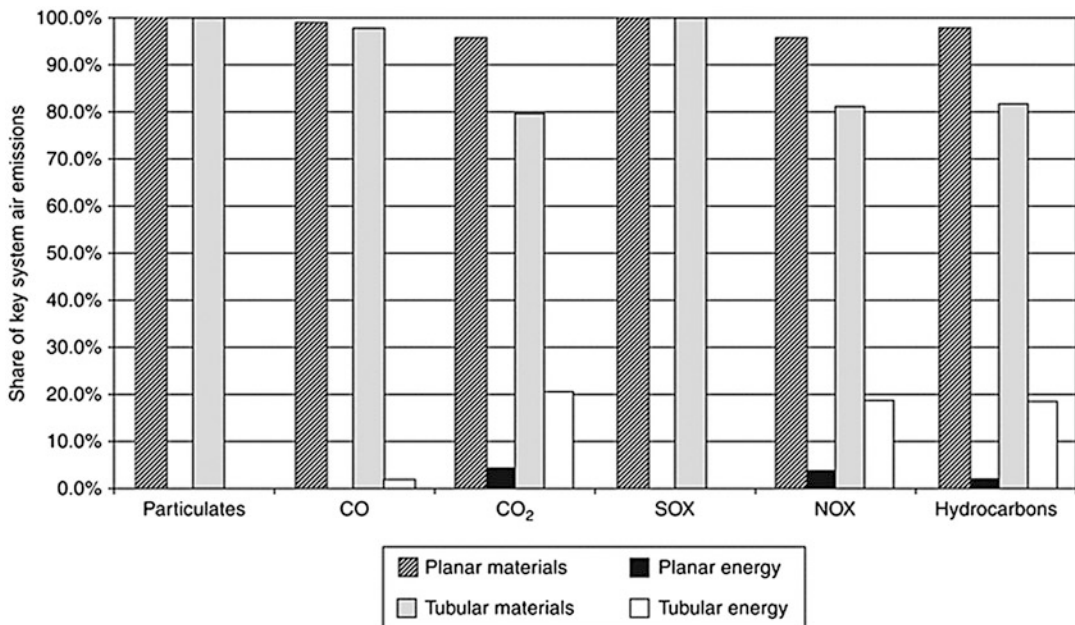


**Balance of Plant Manufacturing** The balance of plant (BoP) of a fuel cell system consists of all system components except the fuel cell stack itself. The BoP therefore includes the complete set of heat exchangers, reformer, afterburner, pumps, blowers, control, etc. that is necessary to build the operational fuel cell system. In contrast to the stack, the BoP for both planar and tubular designs consists mostly of conventional materials. This is predominately steel (~99% for the stationary planar concept). Additionally, alumina (~7%) is used in the tubular concept to a greater extent. As the components are well established, the energy requirements for the manufacturing processes are lower compared to the stack manufacturing. In the NEEDS project, which is more oriented toward future developments and in which technology descriptions for 2025 and 2050 are evaluated, no improvements for heat exchanger, inverter, or gas turbine are expected due to the high maturity of these components. The other BoP components are expected to reduce material intensity by 20% until 2025 and further 30% until 2050, which results in a 42% material reduction (mainly steel). For the fuel cell stack

itself, an improvement of 10% for each time step is estimated.

**Sensitivity Analysis of Power Density** Another sensitive parameter for the results is the cell performance, regulating the amount of cells necessary to provide a given level of power. In a sensitivity analysis, Karakoussis [82] showed the effects of a change in power density of the cell from 0.2 to 0.5 W/cm<sup>2</sup>. As more cells with lower power density are necessary for a 1 kW stack, the material and energy demand for manufacturing increases in a linear relationship. A shift from 0.2 to 0.5 W/cm<sup>2</sup> decreases the values for materials consumption by 40%.

**Key Emissions** The key emissions to air for BoP-related emissions are higher than those for manufacturing the stack. This reflects the higher specific mass of the materials used for the BoP and the associated energy requirements. Figure 25 shows the share of some key emissions differentiated for materials production and process energy [82].



**Solid Oxide Fuel Cells: Sustainability Aspects, Fig. 25** Share of key atmospheric emissions from materials production and process energy [82]



All emissions are much higher from activities related to materials production than from the processes involved in manufacturing fuel cell and BoP. The share of some process-related emissions is more significant for the tubular type, reflecting primarily the much higher process energy requirements for manufacturing. The Real-SOFC project additionally showed high argon emissions for the plasma deposition process [86].

**Comparison of the Manufacturing and the Operation Phase** Finally, the manufacturing phase must be compared with the operation phase of the fuel cell. Because fuel cell systems do not involve a combustion process like that of reciprocating engines, most of the atmospheric emissions during operation are much lower. Due to the low operating temperatures, the NO<sub>x</sub> emissions are very low. The higher reaction temperatures lead to low CO and hydrocarbon emissions. The SO<sub>2</sub> emissions are derived from the sulfur content of the fuel. Because sulfur is toxic to the catalysts, it is removed before entering the fuel cell. The SO<sub>2</sub> emissions therefore do not occur during operation but when the catalyst is regenerated.

Table 8 shows emission values during operation with natural gas from some studies.

Including also the fuel supply into the investigation, CO<sub>2</sub> and other GHG are mainly emitted during operation, with about 80% of the total. The rest is mainly related to the fuel supply, whereas the manufacturing is negligible. For all other emissions, the fuel supply is responsible for the biggest share (between 50% and 90%), with the construction phase mainly causing the rest. In the case of SO<sub>2</sub> emissions, the construction phase is significant because no SO<sub>2</sub> is emitted during operation and natural gas has a low sulfur content.

Additionally, some materials employed in the fuel cells (e.g., nickel and other metals) are produced from sulfidic ores [88].

#### Impact Assessment

In the third phase of an LCA, the life cycle impact assessment (LCIA), the inventory data are allocated to possible environmental impacts. Thereby, different impact categories can be considered. Table 9 summarizes the different impact categories considered in the various studies, the allocated inventory data, and the chosen characterization factor.

**Stack Manufacturing** The differences in the stationary planar and integrated tubular concepts are also visible in the impact assessment, as shown in Fig. 26. The high amount of chromium in the stationary planar concept is decisive for the impacts in all emission-related categories. Also for energy-related emissions, the chromium production shows the highest figures. It has to be kept in mind that no recycling of the interconnect is considered in any of the studies reviewed, but it is technically possible and would result in a considerable reduction in emissions. For the cassette-type designs mentioned earlier, the amount of steel used could be reduced by a factor of up to ten. The impacts of the yttrium-stabilized zirconium are significant in all categories. Although the mass fraction of yttrium is only 8%, it has a high environmental impact and in some categories shows higher impacts than the production of ZrO<sub>2</sub>. For the integrated tubular concept, this environmental sensitivity becomes visible in the impact of YCl. Although its specific amount is quite small, it is noticeable in the environmental impacts. However, LaMnO<sub>3</sub> dominates the environmental impacts, being the material with the

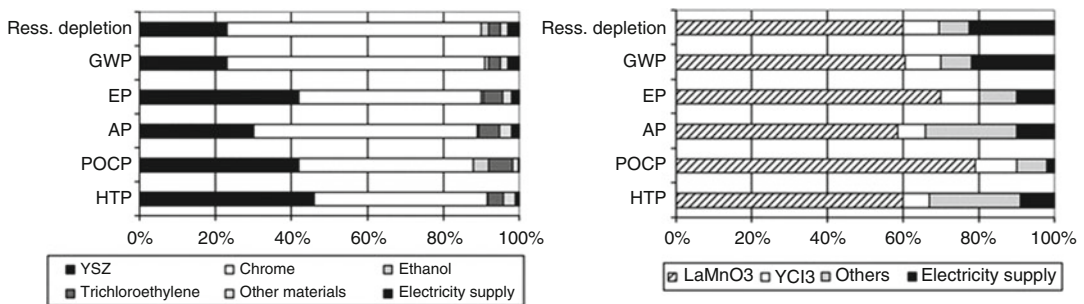
**Solid Oxide Fuel Cells: Sustainability Aspects, Table 8** Atmospheric emissions for SOFC systems operated on natural gas

CO [g/kWh]	CO <sub>2</sub> [g/kWh]	So <sub>x</sub>	No <sub>x</sub> [g/kWh]	Hydrocarbons [g/kWh]	Sources
0.001	218	0.005	0.021	0.202	Karakoussis [82]
0.004	218	0.005	0.021	0.15	Bauen and Hart [90]
0.006	213	0	0.003	0.03	Pehnt [83]
0.006	202	0.002	0.007	0.016	Ecoinvent [84]

**Solid Oxide Fuel Cells: Sustainability Aspects, Table 9** Impact categories of LCIA (Adopted from [91])

Impact category	Allocated inventory data	Characterization factor	Studies
Resource depletion	Material and energy resources	Cumulated energy demand (CEA) kg antimony-eq.	[DLR], [Large SOFC], [Pehnt], [Real-SOFC]
Global warming potential (GWP)	CO <sub>2</sub> , CH <sub>4</sub> , N <sub>2</sub> O, C <sub>2</sub> F <sub>6</sub> , CF <sub>4</sub>	kg CO <sub>2</sub> -eq.	[DLR], [LargeSOFC], [Pehnt], [Real-SOFC]
Acidification potential (AP)	SO <sub>2</sub> , NO <sub>x</sub> , NH <sub>3</sub> , HCl, HF, H <sub>2</sub> S	kg SO <sub>2</sub> -eq.	[DLR], [LargeSOFC], [Pehnt], [Real-SOFC]
Eutrophication potential (EP)	NO <sub>x</sub> , NH <sub>3</sub>	kg PO <sub>4</sub> <sup>3-</sup> -eq.	[DLR], [LargeSOFC], [Pehnt], [Real-SOFC]
Human toxicity potential (HTP)	Particles, SO <sub>2</sub> , NO <sub>x</sub> , NMHC, CO	Years of Lost Life (YOLL) Unit risk Factor kg 1.4 DCB-eq.	[DLR], [Pehnt], [Real-SOFC]
Photochemical ozone creation potential (POCP)	NO <sub>x</sub> , NMHC, CH <sub>4</sub> , ethanol, butane, hexane,	kg ethylene-eq.	[DLR], [LargeSOFC], [Pehnt]
Ecotoxicity potential (FAETP, FSETP)	NH <sub>3</sub> , chromium, HCl, Ni, NO <sub>2</sub> , SO <sub>2</sub>	kg 1.4 DCB-eq.	[Real-SOFC]
Ozone depletion potential (ODP)	CFC, trichloroethane	kg CFC-11-eq.	[LargeSOFC]

[DLR] = [85], [LargeSOFC] = [27], [Pehnt] = [83], [Real-SOFC] = [86]



**Solid Oxide Fuel Cells: Sustainability Aspects, Fig. 26** Material- and energy-related impacts for the planar (*left*) and the tubular system (*right*) [85]

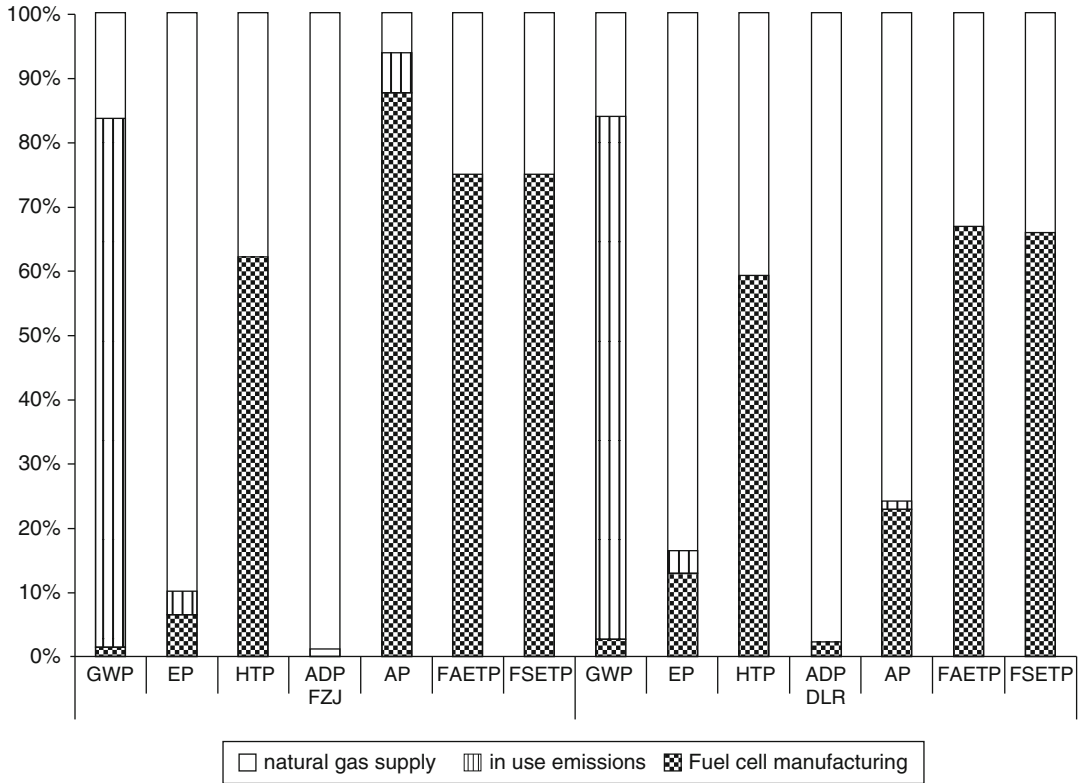
Material- and energy-related impacts for the planar (*left*) and the tubular system (*right*) [85]

highest weight fraction in the support tube. Additionally, the use of electricity in the production phase has a considerable impact on the environment.

During manufacturing of the cells, solvents are used. Although some of them are specified in the inventory of some studies, the environmental relevance is not analyzed in any of the studies due to the lack of detailed information. It is often not clear whether these solvents have a toxic potential or contribute to the creation of photochemical ozone. Therefore, further analysis on the solvent management (for instance, venting of solvent vapor to the atmosphere or condensation and

recycling) is necessary. Due to the impact on the working environment, companies today are increasingly moving toward aqueous-based production processes.

**Environmental Impacts of the Life Cycle Stages** The particular life cycle stages have different effects on the various environmental impacts. Figure 27 compares the qualitative distribution of impacts for the two fuel cell systems investigated in the Real-SOFC project [86], differentiating in the three life cycle stages manufacturing (only fuel cell without BoP), operation, and fuel supply (of natural gas).



**Solid Oxide Fuel Cells: Sustainability Aspects, Fig. 27** Qualitative distribution of the impacts for the stationary sintered cell and lightweight plasma-sprayed planar concepts [86]

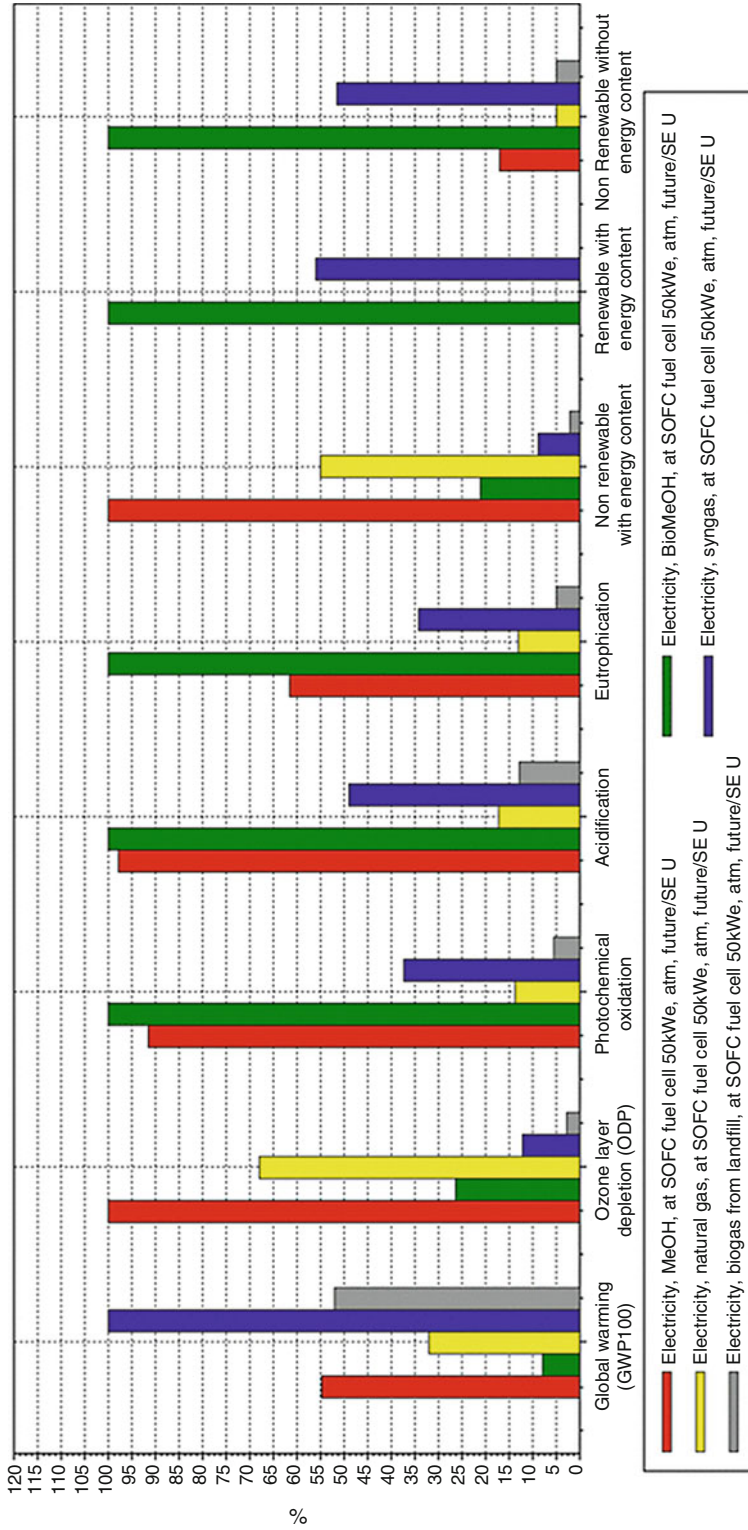
Both fuel cell designs have almost the same impact distribution for all chosen impact categories. Especially the global warming potential is dominated by the operation phase. It is directly connected to the assumed efficiency of the system and the use of natural gas fuel. With comparable efficiencies assumed in all studies, the results are similar. Further contributions are related to methane emissions in fuel extraction and supply.

As expected, the use of resources is nearly exclusively related to the fuel supply chain (about 98%). The eutrophication potential, the potential to form photochemical ozone (only considered in [27, 83, 85]), and the acidification potential are strongly affected by the supply of fuel. However, the results of the stationary sintered cell concept show a high impact of the fuel cell manufacturing also for AP. This is caused by the amount of steel used in this concept. Again, no recycling is considered here.

The effect of fuel cell manufacturing of the cells on human toxicity is not consistent in the different studies. While [86] shows a high share for both concepts analyzed, [83, 85] estimate a higher share of the fuel supply chain.

**Variation of Fuel Supply** As many impact categories are dominated by emissions from the fuel supply chain, the analysis in [27] focuses on the variation of fuels. The study compares methanol (conventional and produced from biomass), natural gas, syngas, and biogas from landfill sites. Figure 28 summarizes the impacts of the overall system for the different fuels used during operation.

For the different categories, no clear winner can be defined. The SOFC fueled with landfill biogas shows the lowest values for all impact categories except global warming potential. Methanol from biomass has the lowest global



**Solid Oxide Fuel Cells: Sustainability Aspects, Fig. 28** Environmental impacts of a 50 kW fuel cell system using different fuels (per kWh) [27]

warming potential but in nearly all other categories the worst performance. In the Real-SOFC project [88], another fuel option considered was hydrogen produced by water electrolysis using electricity from wind turbines. All figures, except the results related to human toxicity, show a significant reduction in impacts. The ten times higher HTP value is exclusively linked to the high amount of steel consumed in the manufacturing of wind turbines.

**Allocation Between Electricity and Heat** As the SOFC systems produce electricity and heat simultaneously, it is necessary to allocate the emissions to the two products. The different studies proceed differently. While some studies allocate all emissions exclusively to the production of electricity, some studies value the heat as well. Two ways are possible to allocate the emissions. One is to give the system a credit for producing heat as a by-product, and the other is to allocate in a way that reflects the physical relationship. References [83, 85] credit the heat production with reference to a modern natural gas burner. This means the impacts of producing the same amount of heat with a natural gas burner are subtracted from the impact of the fuel cell CHP system because it substitutes this energy conversion process (cf. sections “SOFC as High-Efficiency Energy Converters” and “CO<sub>2</sub> Emission Reductions from SOFC Implementation”). This leads to a reduction in the overall impacts of the system proportionally to the amount of heat produced (and utilized). In the NEEDS project, it was chosen to share the emissions between the two products. An often used allocation basis for combined heat and power systems is the exergy. Exergy describes the amount of useful energy that is contained within a product. As exergy of heat is very low, this implies that fuel cell systems with high amounts of heat generated turn out worse in the comparison of electricity compared to fuel cell systems with higher electrical efficiency [88]. In the Real-SOFC project [86], both methods are used. The impacts obtained using the credit method differ much more than those using exergy as allocation base. However, both methods do not

lead to a change in ranking of the different systems investigated.

**End-of-Life Treatment** No study considers end-of-life treatment in its analysis due to the lack of information available at this point of development. However, nearly all studies point out that a reuse or recycling of components would decrease the impacts considerably. In the Real-SOFC project, possible end-of-life options are described qualitatively considering high thermal and chemical processes to show possible solutions to decrease the amount of primary material [86].

## Future Directions

Efficiency and emission balances, as well as materials inventories and end-of-life considerations, are necessary tools in evaluating the environmental performance of fuel cell technology. Due to the complex system of materials and the integration into energy supply systems, for instance, as combined heat and power (CHP) units, the results are not intuitively predictable.

All in all, SOFCs show a considerable potential for increasing energy conversion efficiencies, especially in electricity generation and in CO<sub>2</sub> emission reduction. They do not cause major concerns due to environmental impacts emanating from manufacturing or recycling. SOFCs have the advantage that they do not rely on noble metal catalysts, and the ceramic materials used cause little environmental harm. One of the more serious problems is the working environment hazard of nickel powders that has to be addressed when designing SOFC cell manufacturing plants.

As SOFC technology progresses toward a reduction in the amounts of material, especially for interconnects (cf. section “Materials Inventory of SOFC Concepts”), the analyses presented in the previous sections have to be updated and modified. The same is true for the analysis of the types of materials implemented and their environmental impact from ore mining over materials processing to recycling. New materials and new recipes for pastes and raw materials will be gradually introduced and processes for application of



layers modified or totally changed. Physical vapor deposition, atomic layer deposition, and sol-gel techniques may be used in the manufacturing of high-performance layers [92], as well as roll coating and inkjet printing as cheap and fast methods of applying pastes. These processes have not been evaluated to date.

Further analysis is necessary for all manufacturing processes as they are implemented in industry. The principal methods used in laboratories may deviate considerably from large-scale industrial procedures for a variety of reasons. On the one hand, there is of course the necessity to reduce costs, often at the expense of quality, which may also be coupled to inferior qualities of raw materials with a different environmental footprint (both positive or negative, depending on the circumstances). On the other hand, some processes cannot be implemented under conditions of large-scale manufacturing, whether for reasons of a low throughput of the process, unfulfillable requirements to process parameter control or the workspace, or simply size restrictions. Therefore, the exact layout of an industrial production will have to be analyzed and assessed for every manufacturer separately, unless specific standardized processes establish themselves in SOFC industry.

As the analysis in section “CO<sub>2</sub> Emission Reductions from SOFC Implementation” indicates, the potential of SOFC for contributing toward CO<sub>2</sub> emission reduction obviously depends on the fuels but also on the footprint of the electricity grid an SOFC unit is connected to. This is a rather complex problem that has been recognized by the European Commission and the Fuel Cells and Hydrogen Joint Undertaking (FCH JU) in the formulation of the FCH JU Multi-Annual Implementation Plan [93]. A European project – FC-EuroGrid – will be performing a comprehensive analysis of this problem in the years 2010–2012 [94]. This will lead up to a better understanding of the dependencies of SOFC CO<sub>2</sub> reduction potential on electricity grid carbon footprints and integration of CHP units into heating and electricity supply systems. Eventually, the formulation of minimum efficiency requirements for electrical efficiency as well as for total energy efficiency and CO<sub>2</sub> release – for

a particular fuel – will result from this project. These figures can form the basis for funding decisions in the European programs or, for instance, become elements in certifying fuel cell CHP units under the specific European regulations [10].

## Bibliography

### Primary Literature

1. European Parliament: Directive 2005/32/EC of the European Parliament and of the Council, Official Journal of the European Union, 22 July 2005. <http://eurlex.europa.eu/LexUriServ/LexUriServ.do?uri=OJ:L:2005:191:0029:0058:EN:PDF>. Accessed Mar 2010
2. ISO 14040/14044 (2006) Environmental management – life cycle assessment – principles and framework, – requirements and guidelines. Deutsches Institut für Normung e. V
3. Grausa W, Worrella E (2009) Trends in efficiency and capacity of fossil power generation in the EU. *Energy Policy* 37:2147–2160
4. Arbeitsgemeinschaft Energiebilanzen e.V (2010) Ausgewählte Effizienzindikatoren zur Energiebilanz Deutschland. Daten für die Jahre von 1990 bis 2008 (Selected efficiency indicators for the German energy balances. Data for the years 1990 to 2008). Berlin
5. Brown MH, Sedano RP (2004) Electricity transmission – a primer. National Council on Electric Policy, Washington, DC. ISBN 1-58024-352-5
6. Viebahn P, Patyk A, Fritsche UR, Beer M, Corradini R, Ciroth A, Blesl M, Mayer-Spohn O, Macharey U, Schnettler A, Smolka Th, Fischer M, Schuller O, Große Böckmann Th, Wagner H-J, Mayer H (2008) Erstellung der Grundlagen für einen harmonisierten und fortschreibbaren Datensatz des deutschen Strommixes (Development of base data for a harmonised and updateable data set of the German electricity mix). Stuttgart/Heidelberg/Darmstadt
7. Bundesanstalt für Geowissenschaften und Rohstoffe/Bundesministerium für Wirtschaft und Arbeit (German Ministry of the Economy) (2002) Reserven, Ressourcen und Verfügbarkeit von Energierohstoffen 2002 (Reserves, resources and availability of energy raw materials 2002). E. Schweizerbart'sche Verlagsbuchhandlung, Stuttgart. ISSN 0342- 9288
8. ASUE (2002) .Mikro-KWK – Motoren, Turbinen und Brennstoffzellen (Micro CHP – engines, turbines and fuel cells). Kaiserslautern
9. Slowe J (2008) Market prospects for the CHP equipment industry. *Journal of Cogeneration and On-Site Power Production*. [http://www.delta-ee.com/downloads/ARTICLES\\_COSPP\\_%2008\\_3\\_p29\\_33\\_Slowe.pdf](http://www.delta-ee.com/downloads/ARTICLES_COSPP_%2008_3_p29_33_Slowe.pdf). Accessed May 2011
10. Cogeneration Directive 2004/8/EC. European Commission, Brussels, 2004



11. Herdin GR (2000) Increasing gas engine efficiency. In: Proceedings of the World Energy Engineering Congress, Atlanta
12. Obernberger I, Thek G (2004) Techno-economic evaluation of selected decentralised CHP applications based on biomass combustion in IEA partner countries. IEA Task 32 report, Graz 2004
13. VDI 2067 and VDEW-Lastprofile Materialien M-28/99
14. Föger K (2010) Commercialisation of CFCL's residential power station - BlueGen. In: Proceedings of the 9th European SOFC forum, Lucerne. Paper 0203
15. Bimbaum KU (2010) Brennstoffzellen / Brennstoffzellen Hybridkraftwerke. In *Energietechnologien 2050 – Schwerpunkte für Forschung und Entwicklung, Technologiebericht*, Fraunhofer Verlag, ISBN: 978-3-8396-0102-0
16. Steinberger-Wilckens R, Buchkremer H-P, Malzbender J, Blum L, de Haart LGJ, Pap M (2010) Recent developments in SOFC research at Forschungszentrum Jülich. In: Proceedings of the 9th European SOFC forum, Lucerne, 30 June–2 July 2010. Paper A0105
17. Blum L, Peters Ro, David P, Au SF, Deja R, Tiedemann W (2004) Integrated stack module development for a 20 kW system. In: Proceedings of the 6th European SOFC forum, Lucerne, 30 June–2 July 2004
18. Esdaile-Bouquet T (2011) CHP support mechanisms in the EU, CODE final dissemination workshop, Brussels, 25 March. <http://www.code-project.eu/wp-content/uploads/2011/03/Thomas-Bouquet.pdf>. Accessed May 2010
19. Pillai MR, Bierschenk DM, Barnett SA (2008) Electrochemical partial oxidation of methane in solid oxide fuel cells: effect of anode reforming activity. *Catal Lett* 121:19–23
20. European Commission (2011) A roadmap for moving to a competitive low carbon economy in 2050. COM (2011) 112 final, Brussels, 8 Mar 2011
21. Steinberger-Wilckens R (2005) Hydrogen as a means of transporting and controlling wind power. In: Ackermann T (ed) *Wind energy in power systems*. Wiley, Chichester, pp 505–519. ISBN 0-470-85508-8
22. Brisse A, Schefold J, Stoots C, O'Brien J (2010) Electrolysis using fuel cell technology. In: Steinberger-Wilckens R, Lehnert W (eds) *Innovations in fuel cell technologies*, vol 2, RSC energy and environment series. Royal Society of Chemistry, London, pp 267–286. ISBN 978-1-84973-033-4
23. Jönsson O, Polman E, Jensen JK, Eklund R, Schyl H, Ivarsson S (2003) Sustainable gas enters the European gas distribution system. In: Proceedings world gas conference, Tokyo
24. Oasmaa A Report on biofuels for SOFC applications, part 1: fuel options (D6.1). Report to the large SOFC project. VTT Technical Research Centre of Finland. [http://www.vtt.fi/files/projects/largesofc/large\\_soft\\_biofuels\\_wp6\\_public.pdf](http://www.vtt.fi/files/projects/largesofc/large_soft_biofuels_wp6_public.pdf). Accessed May 2011
25. Global Emission Model for Integrated Systems (GEMIS). <http://www.oeko.de/service/gemis/en/index.htm>. Accessed May 2011
26. Machat M, Werner K (2007) Entwicklung der spezifischen Kohlendioxid-Emissionen des deutschen Strommix (Development of the specific CO<sub>2</sub> emissions of the German electricity mix). Umweltbundesamt, Dessau, ISSN 1862-4359
27. Del Borghi A, et al. (2009) Final report on environmental impact of the operation of high temperature FC. LargeSOFC-Project, Towards a large SOFC power plant, Integrated EU project under the 6th framework programme
28. BMU (2003) Bundeseinheitliche Liste der CO<sub>2</sub>-Emissionsfaktoren. Bundesministerium für Umwelt, Berlin, 1 Nov 2003
29. Steinberger-Wilckens R, Bucheli O, de Haart LGJ, Hagen A, Kiviahio J, Larsen J, Pyke S, Rietveld B, Sfeir J, Tietz F, Zahid M (2009) Real-SOFC – a joint European effort to improve SOFC durability. ECS transactions: solid oxide fuel cells 11 (SOFC XI). In: Proceedings of the SOFC XI meeting, Vienna; ECS Transactions, vol 25, issue 2, "SOFC XI", The Electrochemical Society, Pennington, pp 43–56
30. Blum L, H-P Buchkremer GSM, de Haart LGJ, Quadackers J, Reisinger U, Steinberger-Wilckens R, Steinbrech RW, Tietz F (2006) Overview of the development of solid oxide fuel cells at Forschungszentrum Juelich. *Int J Appl Ceram Technol* 3(6):470–476
31. Schiller G, Henne R, Lang M, Müller M (2004) Development of solid oxide fuel cells by applying DC and RF plasma deposition technologies. *J Fuel Cell Sci Technol* 4(1–2):56–61
32. Cunningham R (2011) Fuel cell gas turbine hybrids – a key part of a clean future, The Rolls-Royce development programme for pressurised hybrid fuel cell systems. <http://www.fuelcellmarkets.com/content/images/articles/H2net%20RAL%20Sep01.pdf>. Accessed May 2011
33. German Federal Government's National Electromobility Development Plan, Berlin, Aug 2009. <http://www.bmwi.de/English/Redaktion/Pdf/national-electromobility-development-plan,property=pdf,bereich=bmwi,sprache=en,rwb=true.pdf>. Accessed May 2011
34. U.S. Geological Survey web-site. <http://minerals.usgs.gov/minerals/pubs/commodity/zirconium/zirconcomcs07.pdf>. Accessed Sept 2011
35. Hedrick JB (2003) U.S. geological survey, mineral commodity, summaries, January 2003. [http://minerals.usgs.gov/minerals/pubs/commodity/rare\\_earths/740303.pdf](http://minerals.usgs.gov/minerals/pubs/commodity/rare_earths/740303.pdf). Accessed Sept 2011
36. U.S. Geological Survey: Fact Sheet 087-02 – Rare earth elements-critical resources for high technology. <http://pubs.usgs.gov/fs/2002/fs087-02/>. Accessed Sept 2011
37. U.S. Geological Survey: rare earths. [http://minerals.usgs.gov/minerals/pubs/commodity/rare\\_earths/mcs-2010-raree.pdf](http://minerals.usgs.gov/minerals/pubs/commodity/rare_earths/mcs-2010-raree.pdf). Accessed Sept 2011
38. Kingsnorth DJ (2009) The rare earth market: can supply meet demand in 2014? Industrial minerals company of Australia, PDAC 2009, Toronto
39. U.S. Geological Survey. [http://minerals.usgs.gov/minerals/pubs/commodity/rare\\_earths/mcs-2009-yttri.pdf](http://minerals.usgs.gov/minerals/pubs/commodity/rare_earths/mcs-2009-yttri.pdf) /. Accessed Sept 2011

40. Mineral Information Institute. <http://www.mii.org/periodic/Y.htm>. Accessed Sept 2011
41. Seilnacht T, Binder H (1999) Lexikon der chemischen Elemente. Stuttgart/Leipzig
42. <http://www.webelements.com/lanthanum/>. Accessed Sept 2011
43. Mineral Information Institute: Lanthanum. <http://www.mii.org/periodic/La.htm>. Accessed Sept 2011
44. MacMillan JP (2004) Strontium. In: Ullmann's encyclopedia of industrial chemistry. Wiley, New York
45. International Manganese Institute. <http://www.manganese.org/>. Accessed Sept 2011
46. Duke JM (1980) Nickel in rocks and ores. In: Nriagu JO (ed) Nickel in the environment. Wiley, New York/Chichester/Brisbane/Toronto, pp 27–50
47. Mining, smelting and refining of nickel. <http://www.nickelinstitute.org/en/NickelUseInSociety/AboutNickel/HowNickelIsProduced.aspx>. Accessed Sept 2011
48. Sanborn D, et al. (1995–1996) Amethyst Galleries, Inc. (updated several times by Covey S.). <http://www.galleries.com/minerals/sulfides/pentland/pentland.htm>. Accessed Sept 2011
49. Hertel RF, Maass T, Muller VR (1991) Nickel. World Health Organization, Geneva. <http://www.inchem.org/pages/ehc.html>. Accessed Sept 2011
50. Nickel. <http://www.seilnacht.com/Lexikon/28Nickel.htm>. Accessed Sept 2011
51. Kerfoot DGE (2004) Nickel. In: Ullmann's encyclopedia of industrial chemistry. Wiley-VCH Verlag GmbH & Co. KGaA. [https://doi.org/10.1002/14356007.a17\\_157](https://doi.org/10.1002/14356007.a17_157)
52. Buchkremer HP, Diekmann U, de Haart LGJ, Kabs H, Stimming U, Stöver D (1997) In: Stimming U, Singhal SC, Tagawa H, Lehnert W (eds). Proceedings of the 5th international symposium. Solid Oxide Fuel Cells (SOFC-V), The Electrochemical Society, Pennington, p 160
53. de Haart LGJ, Vinke IC, Janke A, Ringel H, Tietz F (2001) New developments in stack technology for anode substrate based SOFC. In: Yokokawa H, Singhal SC (eds) Solid oxide fuel cells VII. The Electrochemical Society, PV 2001-16. Proceedings series, Pennington, p 111
54. Piron-Abellan J, Shement V, Tietz F, Singheiser L, Quadackers WJ, Gil A (2001) Ferritic steel interconnect for reduced temperature SOFC. In: Yokokawa H (ed) Proceedings of the 7th international symposium on solid oxide fuel cells (SOFC-VII), Tsukuba, 3–8 Juni 2001 (Proceedings of the electrochemical society; 2001–16, Pennington, 2001) pp 811–819. ISBN 1-56677-322-9
55. Thyssen Krupp VDM, CroFer22APU Material data sheet No. 8005
56. Haanappel VAC, Mertens J, Rutenbeck D, Tropartz C, Herzhof W, Sebold D, Tietz F (2005) Optimization of processing and microstructural parameters of LSM cathodes to improve the electrochemical performance of anode-supported SOFCs. *J Power Sources* 141:216
57. Mai A, Haanappel VAC, Uhlenbruck S, Tietz F, Stöver D (2005) Ferrite-based perovskites as cathode materials for anode-supported solid oxide fuel cells: part I. Variation of composition. *Solid State Ionics* 176:1341–1350
58. Konyshva E, Penkalla H, Wessel E, Mertens J, Seeling U, Singheiser L, Hilpert K (2006) Chromium poisoning of perovskite cathodes by the ODS alloy Cr<sub>5</sub>Fe<sub>1</sub>Y<sub>2</sub>O<sub>3</sub> and the high chromium ferritic steel CroFer22APU. *J Electrochem Soc* 153:A765
59. Shaigana N, Qua W, Iveyb DG, Chen W (2010) A review of recent progress in coatings, surface modifications and alloy developments for solid oxide fuel cell ferritic stainless steel interconnects. *J Power Sources* 195(6):1529–1542
60. Ishihara T, Sammes NM, Yamamoto O (2003) Electrolytes. In: Singhal SC, Kendall K (eds) High temperature solid oxide fuel cells. Elsevier, Oxford/New York/Tokyo. ISBN 1 856 173 879
61. Stöver D, Buchkremer HP, Huijsmans JPP (2003) MEA/cell preparation methods: Europe/USA. In: Vielstich W, Lamm A, Gasteiger HA (eds) Handbook of fuel cells, vol 4, Fuel cell technology and applications, part 2 Wiley, Chichester, pp 1013–1031
62. Haanappel VAC, Shemet V, Vinke IC, Gross SM, Koppitz Th MN, Zahid M, Quadackers WJ (2005) Evaluation of the suitability of various glass sealant-alloy combinations under SOFC stack conditions. *J Mater Sci* 40:1583–1592
63. Gross SM, Koppitz T, Rimmel J, Reisgen U (2005) Glass-ceramic materials of the system BaO-CaO-SiO<sub>2</sub> as sealants for SOFC applications. *Ceramic engineering and science proceedings CODEN CESPDK*, 26(4): 239–245. ISSN 0196-6219
64. Stöver D, Mai HPA, Menzler NH, Zahid M (2006) Processing and properties of advanced solid oxide fuel cells. In: Chandra T, Tsuzaki K, Militzer M, Ravindran C (eds) Proceedings of the THERMEC 2006, Materials Science Forum (vols 539–543), pp 1367–1372
65. Hellerbrand H (1995) Processing of ceramics, part I. In: Cahn RW, Haasen I, Kramer EJ (eds) Materials science and technology, vol 17A. Wiley, Weinheim, p 190
66. Gaudon M, Menzler NH, Djurado E, Buchkremer HP (2005) YSZ electrolyte of anode-supported SOFCs prepared from sub micron YSZ powders. *J Mater Sci* 40:3735–3743
67. Holmes PJ, Loasby RG (1976) Handbook of thick film technology. Electrochemical Publications, Scotland, p 14
68. Franco T, Ruckdäschel R (2006) Diffusion and protecting barrier layers in a substrate supported SOFC concept. In: Proceedings of the 7th European solid oxide fuel cell forum, European fuel cell forum, Oberrohrdorf. Paper No. P0802-051
69. Gubner A, Nguyen-Xuan T, Bram M, Rimmel J, de Haart (2006) Lightweight cassette type SOFC stacks for automotive applications. In: Proceedings of the 7th European SOFC forum, Lucerne, Paper B0402
70. N. Margaritis, L. Blum, P. Batfalsky, S. Ceschini, Q. Fang, D. Federmann, J. Kroemer, N. H. Menzler, R. Peters, R. Steinberger-Wilckens (2015) Status of light weight cassette design of SOFC. In: proceedings of the SOFC XIV symposium, 27-31 July, Glasgow;

- also in *ECS Trans* 68: 209–220. <https://doi.org/10.1149/06801.0209ecst>
71. Montero X, Tietz F, Stöver D, Cassir M, Villarreal I (2009) Evaluation of commercial alloys as cathode current collector for metal-supported tubular solid oxide fuel cells. *Corros Sci* 51(1):110–118
  72. Henne R, Arnold J, Kavka T, Maslani A (2004) Influence of injection mode on properties of DC plasma jets for thermal plasma spraying. *Czech J Phys* 54(3): C766–C771, Springer, Netherlands
  73. Henne R (2003) Was können Brennstoffzellen zur Lösung unserer Energieversorgungsprobleme beitragen? Presentation, VDI Arbeitskreis Technische Gebäudeausrüstung Stuttgart, 20 Oct 2003. [wiv.vdi-bezirksverein.de/HenneVDI.pdf](http://wiv.vdi-bezirksverein.de/HenneVDI.pdf). Accessed May 2011
  74. Schiller G (2006) Metallgestützte SOFC-Zellen. Fortbildungsseminar Werkstofffragen der Hochtemperatur-Brennstoffzelle, Deutsche Gesellschaft für Materialkunde (Hrsg), Jülich, 26–28 .Apr 2006. [http://elib.dlr.de/45395/1/%C3%BClich\\_DGM\\_2006\\_G\\_Schiller.pdf](http://elib.dlr.de/45395/1/%C3%BClich_DGM_2006_G_Schiller.pdf). Accessed May 2011
  75. Lenntech BV (2011). <http://www.lenntech.com/periodic/elements/ar.htm>. Accessed Feb 2011
  76. Praxair, gases, production of argon. [www.praxair.com](http://www.praxair.com). Accessed Feb 2011
  77. Goettler R (2009) Overview of the Rolls-Royce SOFC technology and SECA program. [http://www.netl.doe.gov/publications/proceedings/09/seca/presentations/Goettler\\_Presentation.pdf](http://www.netl.doe.gov/publications/proceedings/09/seca/presentations/Goettler_Presentation.pdf). Accessed May 2011
  78. Hart NT (2004) Scale up of the IP-SOFC to multi kilowatt levels. Report F/01/00197/REP, URN 04/556, DTI. [www.berr.gov.uk/files/file15317.pdf](http://www.berr.gov.uk/files/file15317.pdf). Accessed May 2011
  79. Cassidy M, Boulfrad S, Irvine J, Chung C, Jorger M, Munnings C, Pyke S (2008) Integration of oxide anodes into the Rolls-Royce IP-SOFC concept. *J Fuel Cell Sci Technol* 9(6):891–898
  80. Hart D, Hörmandinger G (1997) Initial assessment of the environmental characteristics of fuel cells and competing technologies. ETSU F/02/00111/REP/1, ETSU, Harwell
  81. Zapp P (1998) Ganzheitliche Material- und Energieflussanalyse von SOFC-Brennstoffzellen. Dissertation Universität-GH Essen, Jülich, Jül-3497
  82. Karakoussis V, Brandon NP, Leach M, van der Vorst P (2001) The environmental impact of manufacturing planar and tubular solid oxide fuel cells. *J Power Sources* 101:10–26
  83. Pehnt M (2003) Assessing future energy and transport systems: the case of fuel cells, part 2: environmental performance. *Int J Life Cycle Ass* 8(6):365–378 <http://ecoinvent.ch>. Accessed Aug 2011
  85. Krewitt W, Pehnt M, Fishedick M, Temming H (2005) Brennstoffzellen in der Kraft-Wärme-Kopplung - Ökobilanzen, Szenarien, Marktpotentiale. Beiträge zur Umweltgestaltung Band A 156, Erich Schmidt Verlag, Berlin
  86. European Institute for Energy Research (EIFER) (2008) Final report on evaluation on the sustainability of the stacks produced in the project. Real-SOFC Project, Realising reliable, durable energy efficient and cost effective SOFC systems, Integrated EU project under the 6th framework programme
  87. Rolls-Royce Fuel Cell Systems Limited (2008) Life cycle inventory analysis of the IP-SOFC stack concept. Real-SOFC Project, Realising reliable, durable energy efficient and cost effective SOFC systems, Integrated EU project under the 6th framework programme
  88. Gerboni R, Pehnt M, Viebahn P, Lavagno E (2008) Final report on technical data, costs and life cycle inventories of fuel cells. NEEDS-Project, New energy externalities developments for sustainability, Integrated EU project under the 6th framework programme
  89. S. Bargigli, F. Barbir, G. Fiorentino, M. Founti, D. Giannopoulos, K.H. Kettl, P. Masoni, A. Moreno, R. Mubbala, M. Narodoslawsky, R. Steinberger-Wilckens, S. Ulgiati, A. Vukman, A. Zamagni, A. Zucaro (2011) An LCA evaluation of MCFCs, SOFCs and PEMFCs, Towards Product Category Rules and Environmental Product Declaration. In: Proceedings of the European Fuel Cells Conference, Rome 14–16 Dec 2011. Scopus EID: 2-s2.0-84923593467
  90. Bauen A, Hart D (2000) Assessment of the environmental benefits of transport and stationary fuel cells. *J Power Sources* 86:482–494
  91. Guinée J, Gorrée M, Heijungs R, Huppes G, Kleijn R, de Koning A, van Oers L, Wegener Sleswijk A, Suh S, de Haes HAU, de Bruijn H, van Duin R, Huijbregts MAJ (2002) Handbook on life cycle assessment: operational guide to the ISO standards. Kluwer, Dordrecht
  92. Han F, Leonide A, van Gestel T, Buchkremer HP (2010) Excellent electrochemical performance with thin YSZ electrolyte for IT-SOFCs. In: Proceedings of the 9th European SOFC forum, European Fuel Cell Forum, Oberrohrdorf/Lucerne
  93. Fuel Cell and Hydrogen Joint Undertaking (FCH JU) (2008) Multi-annual implementation plan (MAIP). Brussels
  94. Project documentation and deliverables of EuroFC-Grid, project funded by the FCH JU, 2010–2012

## Books and Reviews

- Seilnacht T, Binder H (1999) Lexikon der chemischen Elemente, Stuttgart/Leipzig, publishing house Hirzel Stuttgart

---

**Part II**

**Hydrogen Production Science and  
Technology**



## Hydrogen Production Science and Technology

Timothy E. Lipman  
Transportation Sustainability Research Center,  
University of California Berkeley, Berkeley, CA,  
USA

### Article Outline

Definition of the Subject  
Introduction  
Review of Hydrogen Production Methods  
Hydrogen Production Costs  
Hydrogen at Scale  
Conclusion  
Bibliography

### Definition of the Subject

This chapter examines the topic of hydrogen production from a range of different feedstocks and through various production processes. These processes include electrolysis, gasification, pyrolysis, fermentation, photosynthetic algae, as well as through emerging photo- and thermo-electrochemical, high temperature fuel cell, and nuclear cycle-assisted systems. Hydrogen is a widely used industrial molecule and energy carrier that can readily be converted into electricity through fuel cells, now being used in new markets such as vehicle fuel and stationary power production. Hydrogen is expected to be more widely used in the global energy economy moving forward, based on emerging markets and rapid technological progress in production and distribution methods.

### Introduction

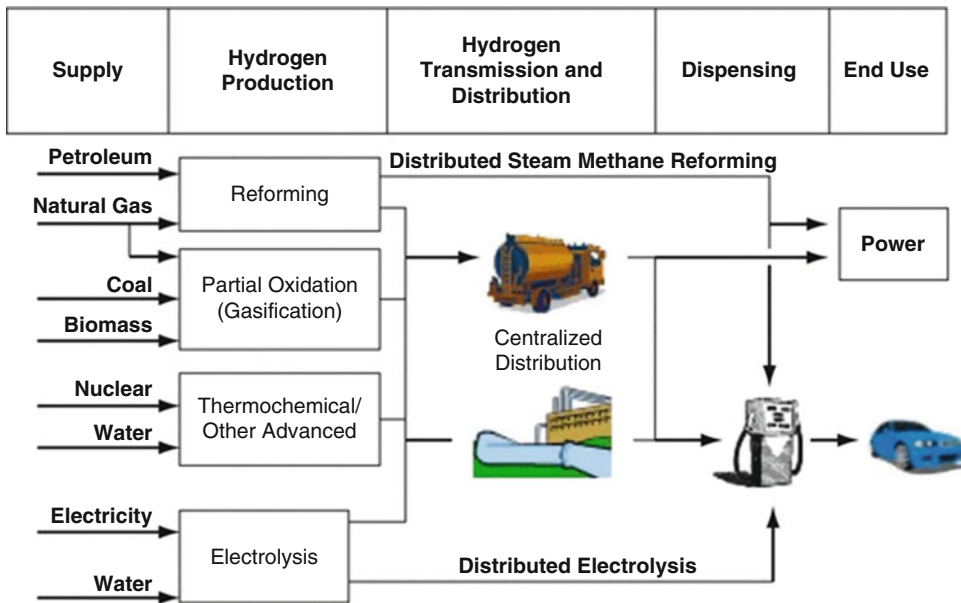
Hydrogen is an abundant element that is currently produced in molecular form for a wide range of

industrial uses. In recent years, it is also starting to be used for stationary power production in fuel cell systems and to power fuel cell electric vehicles including buses, forklifts, and passenger cars. One highly compelling attribute of hydrogen is that it can be produced in many different ways and using a variety of feedstocks; however, it does have to be *produced* through one of a variety of processes rather than simply “discovered” and delivered to market as is, for example, natural gas.

Approximately 10–11 million metric tonnes of hydrogen are produced in the USA each year [1]. For reference, this is enough to power 20–30 million cars (using 700–1,000 gallon energy equivalents per car per year) or about 5–8 million homes. Globally, the production figure was estimated at 22 million metric tonnes in 2013, with growth at 3.5% annually reaching about 27 million metric tonnes in 2018 [2]. Major current uses of the commercially produced hydrogen are for oil refining, where hydrogen is used for hydro-treating of crude oil as part of the refining process to improve the hydrogen to carbon ratio of the fuel, food production (e.g., hydrogenation), treating metals, and producing ammonia for fertilizer and other industrial uses.

A range of potential hydrogen production methods and pathways is presented in Fig. 1. These include reformation, gasification, electrolysis, and other advanced processes. In addition to these well-established pathways, there are various emerging production pathways also possible. These are mostly at the laboratory scale and present and include such concepts as direct “photo-electrochemical” water splitting; a wide array of biological processes involving biogas conversion, algae, and microbial electrolysis cells; and other novel methods such as high-temperature thermo-chemical systems.

This entry reviews a variety of established and emerging hydrogen production methods and their current status. Key remaining issues and research and development (R&D) challenges are highlighted for many of the pathways.



**Hydrogen Production Science and Technology, Fig. 1** Example hydrogen production pathways. (Source: [1])

## Review of Hydrogen Production Methods

Hydrogen in molecular form can be produced from many different sources and in many different ways. Hydrogen is most typically produced today for industrial uses through the steam reformation of natural gas (known as “steam methane reforming”) and from other hydrocarbons in oil refinery locations but also is produced through electrolysis of water and as a by-product of some industrial processes such as chlor-alkali production. While hydrogen production methods often have several aspects and can be grouped in various ways, they can be organized as follows for purposes of this review:

- Reformation of fossil hydrocarbons and bio-derived liquids
- Gasification of coal and other hydrocarbons
- Electrolysis of water
- Biomass gasification and pyrolysis
- Biological production
- Nuclear-related pathways
- Photo-electrochemical methods
- High-temperature thermochemical methods
- Fuel cell-based co-production

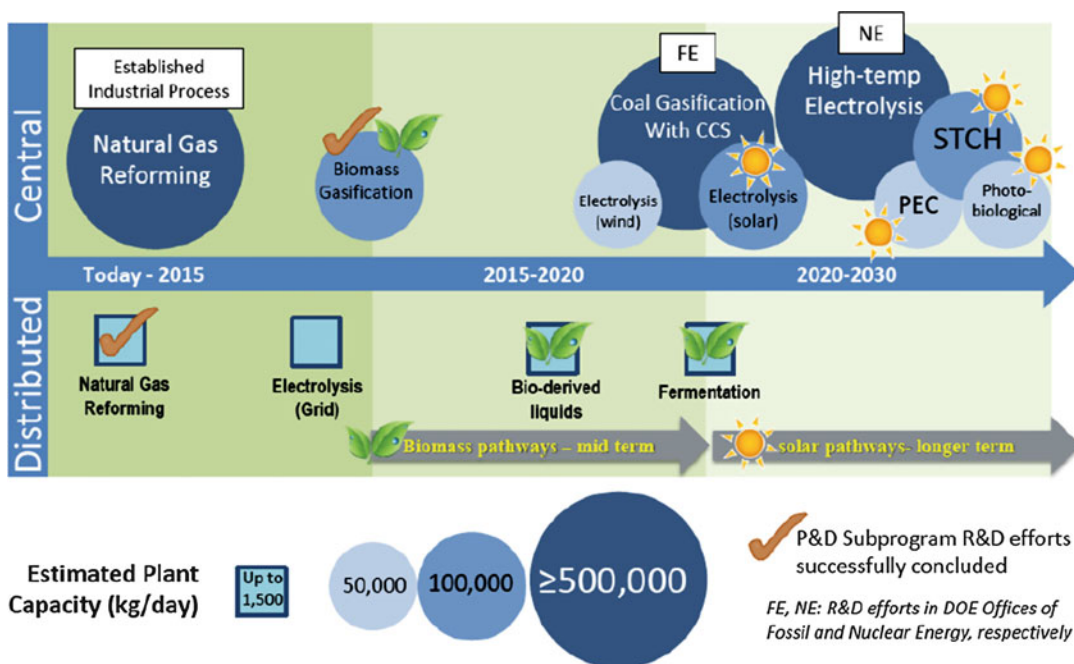
Figure 2 presents a potential timeline for these production methods to become commercial, along with their anticipated scale per production facility.

A review of the primary of these production pathways is presented below, along with identification of key remaining challenges for those that are not yet commercially viable. A section that compares production cost estimates of hydrogen by several of the methods is then presented followed by the overall conclusions of this entry.

### Reformation of Fossil Hydrocarbons and Bio-derived Liquids

The most widely used hydrocarbon reformation process is steam methane reforming (SMR). SMR is the process by which natural gas, other hydrocarbon, or other methane-rich stream such as bio-gas or landfill gas is reacted with steam in the presence of a catalyst to produce hydrogen and carbon dioxide. In the SMR process, carbon monoxide is first produced with hydrogen (this blend is known as “syngas”), and then a series of water-gas shift reactions converts the carbon monoxide to carbon dioxide and additional hydrogen through the injection of additional steam. The water-gas shift occurs first in a high-temperature step at about 350 °C and then in a lower-temperature

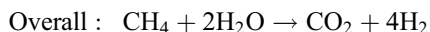
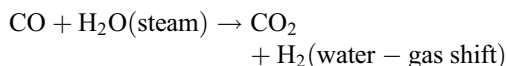
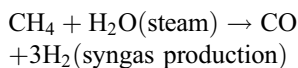




**Hydrogen Production Science and Technology, Fig. 2** Estimated readiness and scale of hydrogen production pathways. (Source: [3])

step at about 190–210 °C. Four hydrogen molecules are produced for every one carbon dioxide molecule, making SMR a relatively low-carbon process when, for example, the use of SMR-based hydrogen is used in a fuel cell vehicle compared with the use of gasoline in a combustion engine vehicle on a “full fuel cycle” basis [4, 5].

The overall SMR reactions are as follows:



SMR produces a hydrogen-rich gas that is typically on the order of 70–75% hydrogen on a dry basis, along with smaller amounts of methane (2–6%), carbon monoxide (7–10%), and carbon dioxide (6–14%) [6]. The efficiency of the SMR process using natural gas as a feedstock is typically about 74% on an LHV basis [7].

Bio-liquids such as ethanol, sugars, and bio-oils can also produce hydrogen through reformation processes as well as via gasification and pyrolysis. Anderson and Carole [8] provide a useful review of the key advantages and disadvantages of various feedstocks as well as potential feedstock prices, hydrogen yield rates, and commercial production timeframes. They examine ethanol, glucose, glycerol, sorbitol, ethylene and propylene glycol, cellulose/hemicellulose, methanol, and bio-oils as potential hydrogen feedstocks that are viable for use in reformation processes. They find that ethanol, glucose, glycerol, and bio-oils are potentially viable in the 2012–2017 timeframe, while sorbitol, ethylene and propylene glycol, cellulose/hemicellulose, and methanol are possible in the 2017+ longer-term timeframe.

For the medium-term feedstocks, they find that the highest yield rates are possible for ethanol (0.26 kg hydrogen/kg ethanol) and crude glycerol (0.24 kg hydrogen/kg crude glycerol), with lower rates possible for pure glycerol (0.15 kg hydrogen/kg pure glycerol), glucose (0.13 kg hydrogen/kg glucose), and bio-oils (0.13 kg hydrogen/kg

bio-oil). The longer-term options all have similar yield rates, ranging from 0.22 kg hydrogen/kg of feedstock (for methanol and propylene glycol) to 0.13 kg hydrogen/kg for sorbitol and cellulose/hemicellulose, while ethylene glycol has a more intermediate estimated hydrogen yield of 0.15 kg per kg of feedstock [8]. Based on the feedstock prices and yield rates presented, it appears from this analysis that glucose, crude glycerol, and cellulose/hemicellulose could be particularly attractive from a rough feedstock cost and yield rate perspective (not yet considering any differences in capital equipment and process energy required).

Key technical challenges for achieving hydrogen cost goals from bio-derived liquids (previously set by the US DOE at under \$3.00 per kg in 2017) include advances in catalyst systems, purification technologies, and system integration. A key issue is catalyst deactivation due to coking, when products from side reactions become deposited on the catalyst. An additional important area of research is low-temperature (<500 °C) reforming, including aqueous-phase reforming that can be applied to glucose, ethylene glycol, sorbitol, glycerol, and methanol. Advantages include reduced energy intensity, better characteristics for the water-gas shift reactions, minimization of decomposition reactions (that can lead to the coking issue described above), and compatibility with membrane separation/purification techniques [8].

### Gasification and Pyrolysis of Coal and Other Hydrocarbons

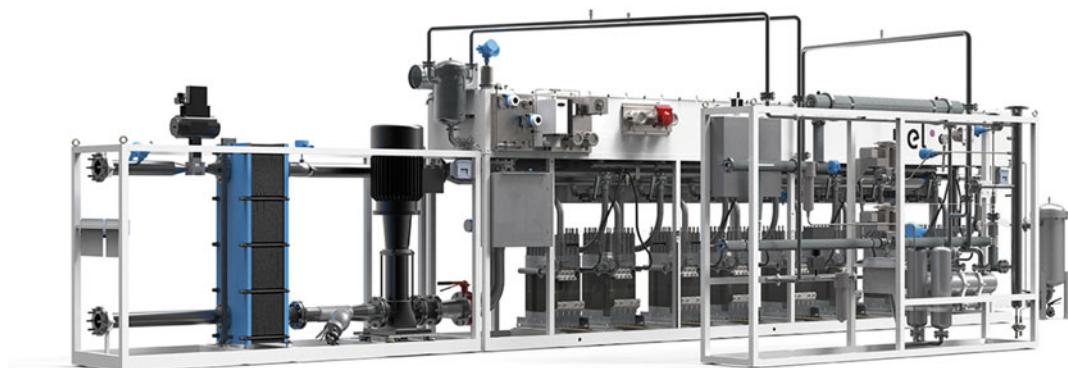
In the partial oxidation (POX) process, also known more generally as “gasification,” hydrogen can be produced from a range of hydrocarbon fuels, including coal, heavy residual oils, and other low-value refinery products. The hydrocarbon fuel is reacted with oxygen in a less than stoichiometric ratio, yielding a mixture of carbon monoxide and hydrogen at 1,200° to 1,350 °C. Hydrogen can also be produced through pyrolysis-based hydrocarbon gasification processes in the absence of oxygen.

The chemistry of hydrogen production from gasification of coal and other heavy hydrocarbons

is complex, involving molecular cracking, POX, steam gasification, water-gas shift, and methanation reactions. The first stages involve progressive devolatilization of the feedstock with increasing temperature, yielding a mix of oils, phenols, tars, and light hydrocarbon gases. This is followed by water-gas shift reactions, where additional hydrogen along with carbon dioxide are produced from carbon monoxide and water, and methanation reactions where methane (which can be later reformed into additional hydrogen) instead of hydrogen is formed with any remaining carbon monoxide. Depending on temperature and pressure conditions, the “syngas” produced from hydrocarbon gasification can have varying amounts of carbon dioxide, methane, and water, along with trace other components [9]. Several metals and metal oxides have been found to catalyze the gasification reactions and can alter the kinetic constants. Iron oxides such as Fe<sub>2</sub>O<sub>3</sub> and Fe<sub>3</sub>O<sub>4</sub> affect the rates of steam gasification of coal and other hydrocarbons, and some gasification reactions are also catalyzed by nickel- and calcium-based substances [9].

One study [10] examined the potential life cycle impacts of hydrogen produced through gasification and pyrolysis of coal, along with two other pathways – the thermochemical sulfur-iodine cycle and the thermochemical “Westinghouse” cycle that both make use of solar thermal energy (or other source of waste heat such as from nuclear power) and sulfuric acid to produce hydrogen. These other chemical cycles are discussed in more detail in the thermochemical and nuclear power-assisted hydrogen production sections later in this review. The study uses SimaPro™ life cycle analysis software for the analysis, which includes major indices for human health impacts, ecosystem impacts (including air, water, and soil impacts), and resource use.

The study referenced above finds that, of these four methods of hydrogen production, from a life cycle (system construction and operation) perspective, gasification of coal has the lowest human health impacts and almost as low ecosystem quality impacts as the Westinghouse cycle, while the Westinghouse cycle has the lowest



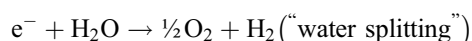
**Hydrogen Production Science and Technology, Fig. 3** Commercial hydrogen production system for proton-exchange membrane electrolysis. (Source: [12])

resource impacts. The sulfur-iodine cycle has somewhat higher ecosystem impacts, comparable human health impacts to the Westinghouse cycle, and comparable resource impacts to coal gasification (i.e., somewhat higher than for the Westinghouse cycle). Pyrolysis of coal, meanwhile, has by far the highest impacts across all three categories, primarily because the amount of hydrogen produced through coal pyrolysis is about 3.5 times lower than for gasification per unit of coal used as feedstock [10].

An interesting aspect of gasification is that it could lend itself to carbon dioxide capture, owing to the large scale of many gasification systems and the production of carbon dioxide through the water-gas shift reactions. Particular attention has focused on calcium oxide (CaO) as an inexpensive carbon dioxide acceptor, yielding calcium carbonate that could then be sequestered [11]. This could prevent the product carbon dioxide from entering the atmosphere, if appropriate geological or oceanic reservoirs are available in the area for long-term storage.

### Electrolysis of Water

Electrolysis is the process through which water molecules are split into hydrogen and oxygen molecules using electricity and an electrolyzer device. Electrolyzers are effectively fuel cell devices that operate in reverse. The overall electrolysis reaction is:



The two most common types of electrolyzers are alkaline (using a potassium hydroxide electrolyte) and PEM (using a solid polymer membrane electrolyte). A picture of a commercial hydrogen electrolysis system is provided in Fig. 3. The electrolysis reaction produces pure oxygen as a by-product along with pure hydrogen. The oxygen can then be used for productive purposes such as enriching the oxygen content of greenhouses for food production. Hydrogen electrolyzers based on both alkaline and PEM technology have now been well established at the megawatt scale. The PEM system pictured in Figure 3 is capable of producing up to about 16,000 SCF of hydrogen per hour, or around 900 kg/day, with a high level of hydrogen purity [12].

Hydrogen can be produced via electrolysis of water from any electrical source, including utility grid power, solar photovoltaic (PV), wind power, hydropower, or nuclear power. The ► [“Electrochemical Hydrogen Production”](#) entry of this encyclopedia reviews the basic science and materials issues with electrochemical hydrogen production in detail.

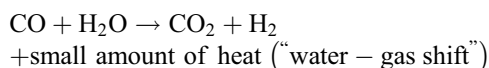
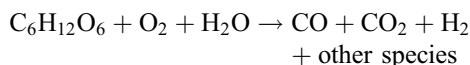
Electrolysis is currently done at a wide range of scales, from a few kW to up to 2,000 kW per electrolyzer device. Additional research involves high-temperature electrolysis, where heat that is co-produced from another process, such as

nuclear power as discussed below, is used to generate steam that can then be electrolyzed into hydrogen and oxygen with less electrical energy input than with lower-temperature electrolysis.

### Biomass Gasification and Pyrolysis

Biomass conversion technologies can be divided into thermochemical and biochemical processes. Thermochemical processes tend to be less expensive because they can be operated at higher temperatures and therefore obtain higher reaction rates. They involve either gasification or pyrolysis (heating biomass in the absence of oxygen) to produce a hydrogen-rich stream of gas known as “syngas” (a blend of hydrogen and carbon monoxide). They can utilize a broad range of biomass types. In contrast, enzyme-based fermentative-type processes (discussed below) are at present mainly limited to wet, sugar-based feedstocks but could include cellulosic feedstocks in the future with continued improvements in process techniques and systems.

Biomass feedstocks can be gasified in a similar manner as fossil hydrocarbons as discussed above and can also be converted through pyrolysis. Gasification involves POX and/or steam reforming to produce a combination of gas and char products, where the char can then be reduced to ultimately produce a mix of hydrogen, carbon monoxide, carbon dioxide, and methane. Water-gas shift can then be used to produce additional hydrogen from carbon monoxide and water, and the methane can also be further reformed into additional hydrogen using SMR. Example chemical reactions include these, using glucose as an example hydrocarbon [13]:



A key issue with biomass gasification is the formation of tar that occurs during the process, which is an unwanted product because it cannot be readily reformed into hydrogen. In order to

minimize tar formation, careful design of the gasifier, incorporation of additives or catalysts, and careful control of operation variables can be effective strategies [13].

Biomass can also produce oxygenated oils through pyrolysis (without oxygen input), which can then be cracked and steam reformed to produce hydrogen and carbon dioxide syngas. An advantage of this method is that bio-oils are easier to transport than either biomass or hydrogen, and hydrogen can thus be produced in a two-step process at different locations with optimization of feedstock supply and hydrogen distribution [13].

A recent area of research has included the production of hydrogen from relatively high water content municipal and food waste streams. A recent investigation has established a process for first converting food wastes into a solid fuel called hydro-char. This process of hydrothermal carbonization followed by steam gasification has been reported to produce 28.8 mmol of hydrogen per gram of dry waste. The study determined that the steam gasification produces more hydrogen than an alternative process of supercritical water gasification. Using the identified steam gasification process, the maximum hydrogen yield was achieved at 450 °C in the presence of a potassium carbonate ( $\text{K}_2\text{CO}_3$ ) catalyst [14].

Depending on application, there are potential additional cleanup steps (with associated costs) that may need to be added for hydrogen produced from biomass and municipal wastes for the provision of high-purity hydrogen (e.g., for low-temperature fuel cell applications for transportation and stationary markets). These may be similar to those required for hydrogen production from other fossil hydrocarbons but with considerable variability in both cases depending on the nature of the application requirements and fuel feedstock (i.e., biogas, natural gas, or refinery coke), the amount of sulfur present, and other factors related to details of the production process.

### Additional Biological Production Methods

There are a wide range of additional biological production methods, beyond gasification or

pyrolysis and reformation of biomass and reformation of biogases. These include:

- Photolytic hydrogen production from water
- Photosynthetic bacterial hydrogen production including dark fermentative methods
- Hydrogen production from algae
- Microbial electrolysis cells
- Other concepts such as combined biological systems

The primary of these additional biological production methods (the first four from the above list) are briefly discussed below.

#### Photolytic Hydrogen Production from Water

The photolytic hydrogen process produces hydrogen from water directly, without the use of a more conventional electrolyzer device. This is accomplished through the use of a photo-electrochemical (PEC) cell that employs a semiconductor material and involves movement of electrons through the material. This is similar to the operation of solar photovoltaic systems, but where instead of the current being collected, it is immediately used at the site of the PEC to split water molecules in either an aqueous or flat-plate type of system.

In the photo-electrochemical water-splitting process, discussed in detail in the ► [“Photocatalytic Hydrogen Production”](#) entry in this encyclopedia [15], a photo-anode is subjected to solar radiation, generating an electronic charge and an electron-hole pair (as in photovoltaics). Second, however, oxidation of water occurs at the holes of the anode, yielding molecular oxygen. Then hydrogen ions and electrons are transported from the photo-anode by way of an electrolyte (for the hydrogen ions) and an electrical connection (for the electrons), forming molecular hydrogen as the hydrogen ions are reduced with the electrons at the cathode. PEC cells can thus use sunlight as the only energy input to produce hydrogen [16].

Since only some of the solar spectrum involves photons with sufficient energy to generate these voltage levels, multilayer photovoltaic junction materials can be used to allow multiple low-

energy photons to be grouped together to exceed the electrolysis threshold. For example, early research investigated GaInP<sub>2</sub>/GaAs “p/n, p/n tandem cells” at the National Renewable Energy Agency, that incorporated a top GaInP<sub>2</sub> junction with a band gap of 1.83 eV, to absorb the visible part of the light spectrum, with a bottom GaAs junction with a band gap of 1.42 eV to absorb the near-infrared portion that gets transmitted through the top junction. This type of system was shown to have a hydrogen production efficiency of 12.4%, based on the estimated hydrogen yield and the incident light intensity of 1,190 mW/cm<sup>2</sup>, consistent with theoretical calculations showing a 24% maximum efficiency. However, efficiencies of more like 10–16% are expected for practical two-layer devices of these types [16].

The selection of semiconductor materials for the photo-anode is critical for PEC cells, as discussed extensively in the ► [“Hydrogen via Direct Solar Production”](#) contribution to this encyclopedia [17]. Key issues identified in the entry are for the semiconductor to have the proper bandgap (the level of energy in electron volts needed, between about 1.6 and 2.0 eV for the primary cell) and the ability to avoid immediate recombination of the charge carriers.

Challenges to PEC cell-based hydrogen production include materials issues including corrosion problems and uncertain performance over time. The lifetimes of current cells being tested in laboratories are on the order of hundreds of hours where tens of thousands of hours of operation are needed for practical systems [18, 19]. Furthermore, there are challenges with the physical assembly of the supramolecular complexes needed for PEC cells, in order to make sure that the various sequential reactions needed are not restricted at any step by poor collection and distribution to the water substrate of the reducing equivalents. It is also important to note that understanding the factors that control multi-electron photochemistry is still at an early stage, meaning that there are both knowledge deficiencies and opportunities for future system improvements.

Practical PEC systems of several different designs can be contemplated, and four of these have undergone recent economic analysis for the



US Department of Energy for an example 10 tonnes per day hydrogen production plant. Of the four types studied – single-bed aqueous suspension, dual bed aqueous suspension, fixed flat panel, and tracking concentrator – the first type was estimated to have the lowest costs of hydrogen produced (\$1.63/kg) compared with \$3.19/kg for the dual bed suspension system, \$4.05/kg for the tracking concentrator system, and \$10.36/kg for the fixed flat panel system [20]. These estimates are consistent with findings from a recent study where the lowest-cost PEC options are estimated to be able to produce hydrogen in the range of \$1.34–2.27/kg at the production site [21].

#### Photosynthetic Bacterial Hydrogen Production

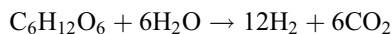
A number of fermentative processes for producing hydrogen using bacteria strains are being investigated. These can generally be categorized into “photobiological” methods where solar energy is captured to help drive the fermentation process or those that use organic materials that were previously produced from photosynthetic process contain hydrogen that is associated with the fixation of carbon. Key issues with the direct photobiological methods are the relatively low conversion efficiencies of solar systems and the fact that oxygen is produced along with hydrogen, creating safety risks as well as difficulties in regulating the oxygen level in the fermentative environment (an important factor to the efficacy of these systems) [22].

Another option that involves conversion of existing organic materials to hydrogen is known as anaerobic or “dark” fermentation. This process uses some type of hydrogenase as an enzyme (the two main types being NiFe and FeFe hydrogenases), uses pyruvate as a key intermediate in the fermentation pathway, and works best with carbohydrate-rich feedstocks. Fermentation of proteins does not yield much hydrogen because protein amino acids are mostly fermented in pairs through “Strickland” reactions where one amino acid is an electron receptor for oxidation of the second amino acid, without hydrogen production [22]. Fermentation of carbohydrate-rich materials such as glucose can yield a series of products following the pyruvate intermediary, including

formate that yields hydrogen and acetyl-CoA that yields acetate and acetaldehyde that can be further processed into ethanol with the addition of NADH. This is known as “enteric-type mixed-acid fermentation.”

As with other biological hydrogen production methods that tend to be relatively slow in terms of yields, low yield rates for practical systems are a constraint for photosynthetic/bacterial methods as well. Based on known metabolic pathways, thermodynamic and metabolic limitations restrict hydrogen production to a maximum of 4 moles of hydrogen per mole of glucose [22]. This is because acetate is necessarily produced as well as hydrogen and carbon dioxide, effectively “locking up” half of the available hydrogen. Strategies to increase yields include optimizing parameters for the fermentation bioprocesses, attempting to limit competing reactions in order to channel more reductant for hydrogen production, decreasing hydrogen partial pressures in the reactor vessels (but then leading to more dilute streams of product gas), using thermophilic strains of bacteria that increase output at higher temperatures (but then requiring additional reactor vessel heating), and identifying and employing more active hydrogenases as enzymes [22].

Hallenbeck [22] reviews these strategies in some detail and concludes that it will be difficult to exceed the “Thauer limit” of 4 moles of hydrogen produced per mole of glucose, even though it is theoretically possible to produce 12 moles of hydrogen per mole of glucose by the reaction:



The existing conversion efficiency of only 33% (maximum) of this theoretical limit is too low for practical systems unless additional steps can be employed to convert more of the organic feedstock into useful products. These have been proposed in the forms of a second stage fermentation for methane production, a second stage photo-fermentation for additional hydrogen production, and (more radically) metabolic engineering to develop novel hydrogen producing pathways. Active research continues to address



the current limitations, with the goal of developing more efficient and complete conversion levels in practical systems.

### Hydrogen Production from Algae

The ability of various strains of algae to produce hydrogen has been studied for some time, with particular attention on unicellular green algae and potential combination of hydrogen production from green algae with additional hydrogen production from bacteria in a co-production concept. Melis and Melneki [23] have proposed this type of system, where photosynthesis is employed in the first step to produce algae biomass and hydrogen gas using the [Fe]-hydrogenase enzyme. In the second stage, the green algal process is coupled with production of an anoxygenic bacteria (such as *Rhodospirillum rubrum*) to produce adenosine triphosphate (ATP), which is required for the evolution of hydrogen using the nitrogenase enzyme. Finally, during a third stage, fermentative bacteria such as *Clostridium pasteurianum* catabolize the algae/bacteria biomass and further enhance the hydrogen yield [23].

In a recent review of microalgae for hydrogen production system progress, Kethorn et al. [24] highlight developments in bioreactor design to improve hydrogen yields for a given amount of light input. They examine recent research studies, along with some older studies, and report that the latest results indicate that hydrogen production rates of up to about 1.3 ml/l/h are now demonstrated based on the widely investigated *C. Reinhardtii* strain of bacteria, up from around 0.6 ml/l/h in some earlier studies. This strain has shown a high level of sustained hydrogen production with better oxygen tolerance than other strains. They discuss the trade-offs associated with different bioreactor designs as well as the use of mutant *C. Reinhardtii* and other types of bacteria [24].

Key areas of continuing research with algal-based hydrogen production systems include limiting oxygen evolution during the algal growth phase, exploring the role of sulfate availability to the chloroplasts to regulate the rate of photosynthesis, examining various means for further increasing hydrogen yields to enable more

practical hydrogen production systems, and improving bioreactor design schemes for maximized production [23, 24].

### Microbial Electrolysis Cells

In a related concept to photosynthetic biological production, microbial electrolysis cells (MECs) can be used to produce hydrogen by providing some of the voltage potential needed for electrolysis, thus reducing energy requirements. Experiments have determined that the bacteria can produce an anode working potential of around 0.3 V and that only an additional 0.11 V are needed to produce hydrogen in theory – but that in practice more like an additional 0.25 V are needed due to overpotential at the cathode [25]. This means that it appears that approximately halving the energy needed for electrolysis is possible with MECs but with still unexplored overall system efficiency. The complete system includes maintaining MEC operating conditions, delivering feedstocks to the production facility, replacing other expendable materials, and performing any gas separation and cleanup needed.

The MEC-based production concept requires two key steps. First, one group of bacteria turns unused sugar and unwanted vinegar from improper fermentation into electricity. Only a small amount of electricity is produced, however, and not enough to reach the 1.2 V necessary to split water in a typical electrolysis reaction. Therefore, some additional electricity from the power grid is also used. Second, another group of bacteria uses the electricity to split water molecules into oxygen and hydrogen in what is known as “microbial electrolysis” [25].

One of the biggest problems that practical systems have to overcome is the bacteria variability of the runoff water, making production rates difficult to predict because the bacteria have to build to a certain level of concentration to be effective. Another issue is that much of the hydrogen can be consumed by “methanogenic” microbes before leaving the solution, leading to much greater production of methane than hydrogen. While this methane could then be “reformed” into hydrogen by SMR, direct production would be far preferable from an overall energy-use standpoint.

Research is underway in the laboratory to improve this hydrogen-to-methane production ratio [25].

### Nuclear-Related Pathways

Many nuclear energy-based hydrogen production schemes are possible. These include nuclear thermal conversion of water using various chemical processes such as the sodium-iodine cycle, electrolysis of water using nuclear power, and high-temperature electrolysis that additionally would use nuclear system waste heat to lower the electricity required for electrolysis. The basic concept is that heat from nuclear plants can be used to assist the production of hydrogen in various ways, with over 100 identified cycles that could benefit from association with nuclear power [26].

A recent US national laboratory study examined hydrogen production costs from nuclear cycles based on the sulfur-iodine (S-I) thermochemical water-splitting cycle, a hybrid sulfur (HyS) thermochemical water-splitting cycle (a modified Westinghouse type cycle), and a high-temperature steam electrolysis (HTSE) cycle. The study focused on various sensitivities associated with cost estimates for these systems and generally found somewhat higher expected

costs than have been reported previously (see Table 1 for details).

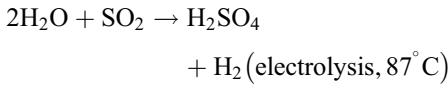
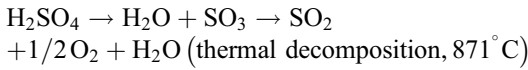
The S-I cycle has been studied since the 1970s and involves a three-step chemical reaction process. The first produces HI and sulfuric acid ( $\text{H}_2\text{SO}_4$ ) from  $\text{I}_2$ ,  $\text{SO}_2$ , and water at about 120 °C; the second produces  $\text{SO}_2$ , water, and  $\text{O}_2$  from the  $\text{H}_2\text{SO}_4$  at about 830 °C (assisted with heat from nuclear power); and the third produces  $\text{I}_2$  and  $\text{H}_2$  from the initial HI at about 450 °C [27]. The sulfur and iodine compounds are recovered and reused. Based on a reactive distillation design, hydrogen production costs of about \$7.27/kg are believed possible with this design with a system producing 380 tonnes per day of hydrogen, assuming some future system cost reductions [28].

The HyS design differs from S-I in that it uses thermal input energy for oxygen generation and a separate low-temperature electrolysis step for hydrogen generation but also involves sulfuric acid decomposition. The HyS cycle was first explored by Westinghouse in the 1980s and is sometimes called the “Westinghouse hybrid cycle.” The key steps in the Westinghouse HyS cycle are [29]:

**Hydrogen Production Science and Technology, Table 1** Estimated hydrogen production costs

Technology and fuel	Production capacity (1,000 kg/day)	Hydrogen production cost (\$/kg)				Source
		Capital	Feedstock	O&M	Total	
Central SMR of natural gas	380	\$0.16	\$1.15	\$0.14	\$1.47	[1]
Distributed SMR of natural gas	1.5	\$0.40	\$1.72	\$0.51	\$2.63	[1]
Central coal gasification with CCS	308	\$0.83	\$0.56	\$0.43	\$1.82	[1]
Central coal gasification w/out CCS	284	\$0.57	\$0.56	\$0.09	\$1.21	[1]
Biomass gasification	155	\$0.37	\$0.52	\$0.55	\$1.44	[1]
Distributed electrolysis	1.5	\$0.96	\$5.06	\$0.73	\$6.75	[1]
Central wind electrolysis	124.5	\$1.46	\$1.69	\$0.65	\$3.82	[1]
Distributed wind electrolysis	0.5	\$3.00	\$3.51	\$0.74	\$7.26	[1]
Central nuclear thermochemical	1,200	\$0.76	\$0.20	\$0.43	\$1.39	[1]
Nuclear S-I	343.5	\$2.61	\$0.35	\$5.31	\$7.27	[28]
Nuclear HyS	343.5	\$1.48	\$0.22	\$2.25	\$4.95	[28]
Nuclear HTSE	343.5	\$1.05	\$0.03	\$3.15	\$4.23	[28]
Single-bed aqueous PEC	1	–	–	–	\$1.63	[20]
Dual bed aqueous PEC	1	–	–	–	\$3.19	[20]
Fixed panel PEC	1	–	–	–	\$4.05	[20]
Tracking concentrator PEC	1	–	–	–	\$10.36	[20]

Notes: *CCS* carbon capture and sequestration, *HTSE* high-temperature steam electrolysis, *HyS* hybrid sulfur cycle, *O&M* operations and maintenance, *PEC* photo-electrochemical cell, *S-I* sulfur-iodine, *SMR* steam methane reforming



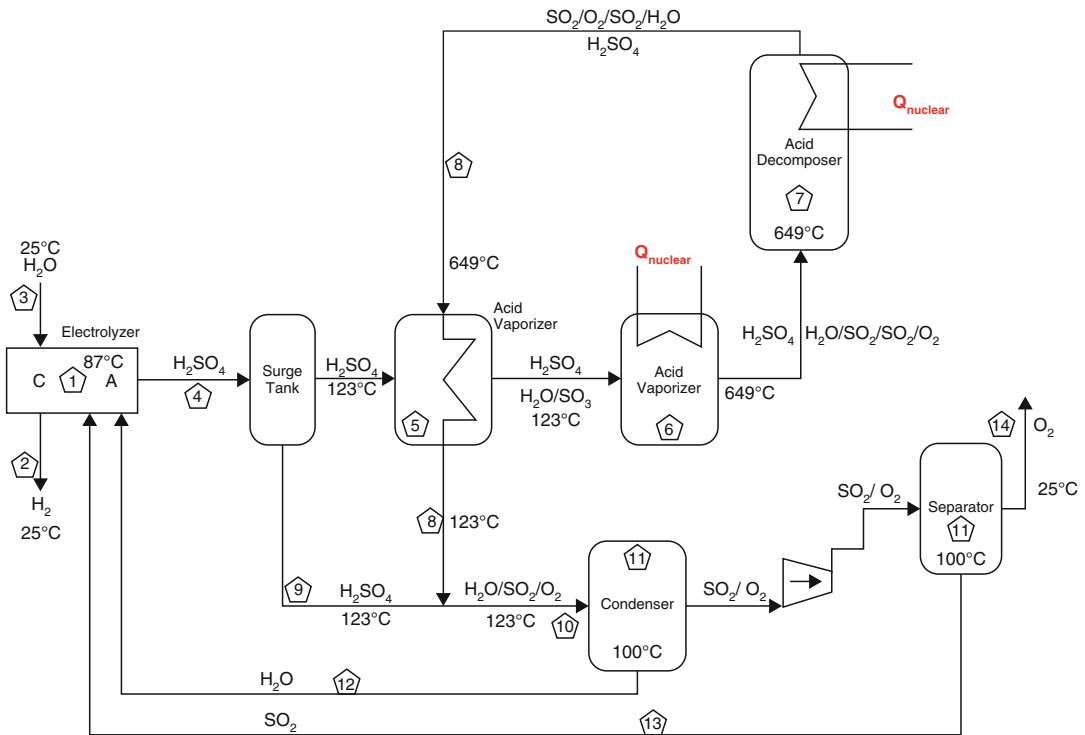
Hydrogen production costs of about \$4.95/kg are believed possible with this type of hybrid system design with a system producing 345 tonnes per day of hydrogen [28]. A schematic of the HyS cycle is presented in Fig. 4.

The third design explored in the recent study, HTSE, involves electrolysis of water at about 800 °C, assisted with heat from nuclear power systems. Key elements of the system include sweep gas coupling heat exchangers, process coupling heat exchangers, solid oxide electrolyzer systems, and feed and product purification systems. Hydrogen production costs of about \$4.23/kg are believed possible with HTSE with a system producing 345 tonnes per day of hydrogen [28].

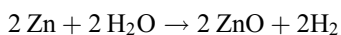
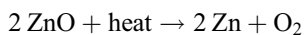
**Thermochemical Production Methods**

In this set of pathways, high-temperature (500–2,000 °C) heat is used to drive chemical reactions to produce hydrogen, including via direct thermolysis of water. This can be done in conjunction with solar thermal power, nuclear power, or other heat sources.

Of the over 200 pathways that have been identified, several are being pursued by the US DOE for further research [30]. Thermochemical production typically involves the use of metal oxides in a two-step process where a metal oxide is first decomposed into the metal and oxygen in an endothermic step and then the metal is then combined with water to re-form the metal oxide and hydrogen in a second exothermic step [31]. In one example known as the zinc oxide cycle, zinc oxide powder passes through a reactor heated by a solar concentrator operating at about 2,300 K. At this temperature, the zinc oxide dissociates to zinc and oxygen gases. The zinc cools, separates, and reacts with water to form hydrogen gas and solid zinc oxide:



Hydrogen Production Science and Technology, Fig. 4 Westinghouse hybrid sulfur cycle schematic. (Source: [27])



The net result is hydrogen and oxygen, produced from water, where the hydrogen can be separated and purified for subsequent use. The zinc oxide can be recycled and reused to create more hydrogen through subsequent phases of the process. Key limitations at present include the rapid reoxidation of the zinc vapor and challenges with keeping the receiver windows clean when the system is coupled with solar thermal systems for delivery of the heat required [31].

An additional type of thermochemical system has been proposed that would also involve a photon component, essentially coupling thermochemical and photo-electrochemical hydrogen production pathways. One concept would use a carbon dioxide/carbon monoxide cycle, where carbon dioxide molecules would absorb near-ultraviolet photons and high temperatures and dissociate into carbon monoxide, helping to enable the production of hydrogen. Research has demonstrated that this can be done at temperatures of around 2,000–2,500 K, which would be compatible with solar thermal concentrator systems [31].

Other concepts involve modifications to the Westinghouse cycle discussed above, including a proposed sulfur-ammonia cycle that makes use of solar power in two ways – to drive both a solar photo-catalytic reactor and a sulfuric acid decomposition reactor. The process would use ammonia, sulfuric acid, and aqueous ammonium sulfate –  $(\text{NH}_4)_2\text{SO}_4$  – at various stages, with the principal advantages using solar photons to directly produce the chemical energy of hydrogen along with using solar heat in the thermochemical step, thus eliminating the need for electrical energy input [31].

### Fuel Cell Co-production

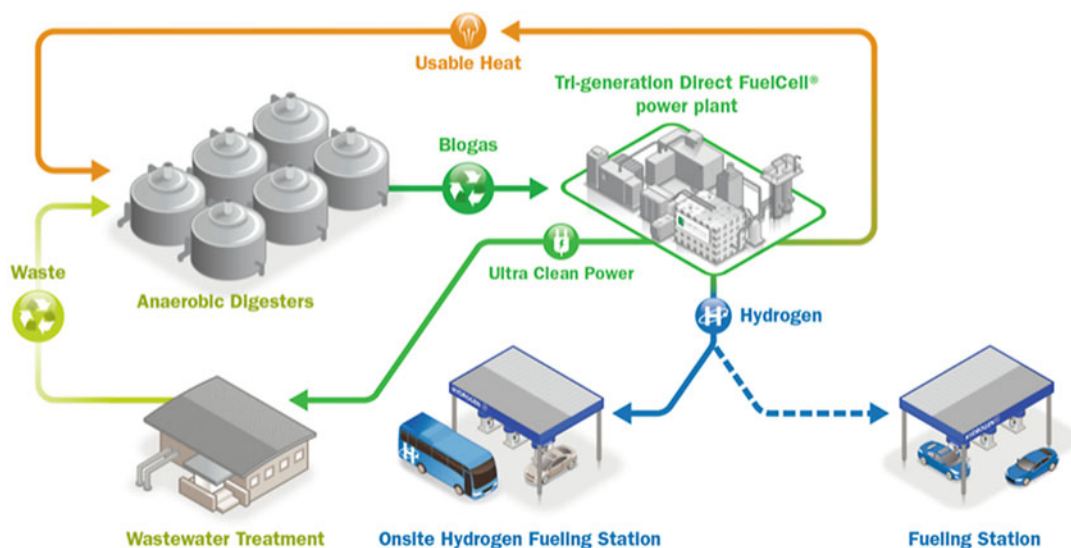
High-temperature fuel cells based on molten carbonate (MCFC) or solid oxide (SOFC) technology operate at sufficiently high temperatures to run directly on methane. This is sometimes called

“internal reforming.” Thus, MCFC and SOFC systems do not need a pure or relatively pure hydrogen stream as do proton-exchange membrane (PEM) and phosphoric acid (PAFC) systems but can run directly on natural gas or biogas or landfill gas. Furthermore, such systems can be designed to produce additional purified hydrogen as a by-product (e.g., for use as a vehicle fuel), by feeding additional fuel and then purifying the hydrogen-rich “anode tail gas” from the fuel cell into purified hydrogen. This concept is discussed in some detail in the case studies section below. A detailed review of this concept for hydrogen production can be found in the ► “Hydrogen Production from High-Temperature Fuel Cells” entry in this encyclopedia [32].

FuelCell Energy (FCE) of Danbury, Connecticut, has teamed up with Air Products and Chemicals, Inc. (APCI) to demonstrate renewable hydrogen production based on the FCE molten carbonate fuel cell technology and a novel hydrogen gas cleanup system. The system was tested at a landfill site at the Orange County Sanitation District in southern California starting in 2012, with performance expectations based on prior hydrogen tri-generation analysis work at the University of California-Irvine [33]. A figure of the system installation is presented in Fig. 5.

The basic concept behind the tri-generation system is that hydrogen and electricity are co-produced, where the electricity is produced using methane (natural gas or biogas) as a feedstock in the high-temperature fuel cell, but additional hydrogen is produced within the fuel cell stack leading to a hydrogen-rich stream of gas leaving the fuel cell unit. This hydrogen-rich “anode tail gas” can then be purified for other uses, such as fuel cell vehicles or other types of fuel cells (e.g., PEM and PAFC) that require pure hydrogen. The following schematic presents the concept and how there are also opportunities for waste heat recovery to help boost overall efficiency.

Analysis of this type of system suggests that 125 kg/day of hydrogen can be produced along with an electrical output of 250 kW, based on over 8,500 h of system testing and a pressure-swapping adsorption (PSA) process for hydrogen



**Hydrogen Production Science and Technology, Fig. 5** Fountain Valley, California tri-generation pilot project. (Source: [34])

separation. The purity of the product hydrogen was measured at 99.99%, while also meeting a target of 0.2 ppm of carbon monoxide. The project team believes that a novel electrochemical hydrogen separation unit, that they are also testing, could offer up to a 50% reduction in operating cost compared to the more conventional PSA hydrogen purification unit, while offering an overall electrical power plus hydrogen production efficiency increase to 68% from 66% (with no waste heat recovery) on a lower-heating value basis [35].

## Hydrogen Production Costs

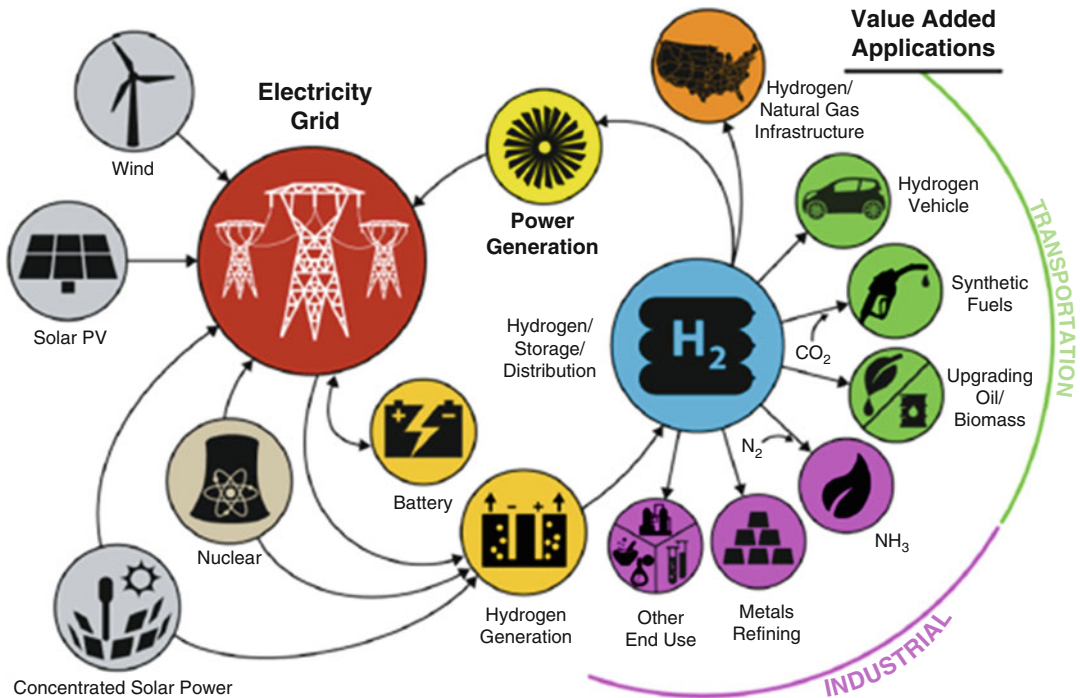
Table 1 presents a set of hydrogen production-only costs (i.e., not including delivery if centralized production) by some of the production methods discussed in this entry that are either used at present or that are possible in the future. These estimates are all as reported by the US Energy Information Administration or based on analysis for the National Academy of Science or the US Department of Energy. These and other estimates were used to report the production cost ranges by production method that were discussed

in the preceding sections of this entry. Note that some of the cleanest methods of producing hydrogen are currently the most expensive (e.g., based on electrolysis from wind or other clean electricity sources), but biomass gasification offers a renewable hydrogen pathway with costs that can potentially be competitive with fossil sources.

These results are consistent with reported progress in a broad review that shows a similar range in production cost estimates. The review shows similarly that the lowest-cost PEC options are estimated to be able to produce hydrogen in the range of \$1.34–2.27/kg, at the lower end of the spectrum of all hydrogen production methods and becoming comparable to conventional SMR and other methods. In comparison with other renewable hydrogen production options, the review study suggests that the biological methods discussed above are promising, but efforts are still needed to improve their production rates. Meanwhile, low conversion efficiencies in combination with high capital costs are the key restrictions for water-splitting technologies to compete with more conventional methods [36].

In comparison with these basic hydrogen production cost projections, in the current hydrogen





**Hydrogen Production Science and Technology, Fig. 6** Concept for hydrogen at scale. (Source: [38])

market, deliveries of industrial-grade high-purity (99.95%+) hydrogen at medium to large volumes of hundreds to a few thousands of kilograms are typically priced at around \$4–5 per 100 standard cubic feet (SCF) (or \$17–21/kg), plus freight, rental, and hazmat charges. For smaller volumes of between 4 and 15 kg, or about 1,600–6,100 SCF, gas costs are estimated to vary widely from \$5 to \$20 per 100 SCF (\$21–83/kg) depending on service model, delivery frequency, and distance from the gas supplier fill plant [37]. Hydrogen delivery to the site of use can add considerable costs depending on delivery distance, providing an advantage for onsite production where possible.

## Hydrogen at Scale

With hydrogen as an energy carrier now proliferating in stationary and transportation power markets, and produced in quantities of tens of millions of metric tonnes per year globally, future planning

is now considered a further scale-up of hydrogen production to meet a range of value-added applications for industry and transportation. Shown in Fig. 6 is a concept for a scaled-up and more deeply embedded role for hydrogen in the global economy. Initial analysis of this concept has shown a significant ability to divert fuels production away from the use of fossil fuels, providing the potential for major energy system and emissions benefits. The “H<sub>2</sub>@Scale” concept by the US Department of Energy shown in the figure considers the potential to increase the role of hydrogen in the US energy economy from approximately 1.2 quadrillion BTUs (or “Quads”) at present to up to 9.2 quads by 2040 by expanding its role in industrial, transportation, and power generation markets [38]. Note that along with the hydrogen generation pathways shown in the figure, additional pathways for hydrogen generation are possible based on biological production, municipal and forest wastes, wastewater treatment, and advanced solar-based applications as discussed above.



## Conclusion

In conclusion, hydrogen is a promising energy carrier and fuel for stationary and transportation uses, but the potential expanded use of hydrogen involves many technical and infrastructure-related challenges. Approximately 10–11 million metric tonnes of hydrogen are used each year in the USA and about 40 million tonnes globally but mostly in internal industrial settings. Dispensing hydrogen to wider consumer and fleet-use markets, such as for private and fleet vehicles and for stationary power uses, involves considerable challenges due to hydrogen's low-energy density (by volume) and other unusual characteristics (i.e., small molecule size, relative ease of ignition in mixes with air, and need for high gas purity when used in certain applications such as in PEM fuel cells).

There are many available and emerging hydrogen production pathways based on a myriad of thermochemical, photochemical, and electrochemical mechanisms and reactions. Perhaps the most compelling aspect of hydrogen as a potential fuel is the incredible diversity in the means and methods by which it can be produced – literally by everything from basic algae to high-temperature fuel cells using ceramic materials and customized catalysts. Hydrogen can be produced from a wide range of feedstocks – from fossil sources such as natural gas or coal to a variety of renewable sources including those based on solar power and wind, geothermal, and biomass energy.

The varied options for hydrogen production include pathways using fossil hydrocarbons or biogas using gasification or pyrolysis processes, steam methane reforming, electrolysis of water, nuclear power-assisted cycles including the sulfur-iodine cycle, fermentative, algae-based, and other biological pathways. Also included are more recently developed electrochemical and thermochemical processes including the use of PEC cells, microbial electrolysis cells, and tailored molecules that can facilitate the splitting of water molecules into hydrogen and oxygen with lower energy requirements than conventional electrolysis.

Of these, several pathways have been studied with regard to potential production costs at

commercial-scale operations. While cost estimates are somewhat preliminary for some of the more novel production methods, particularly attractive hydrogen production costs appear possible for centralized SMR of natural gas, gasification of coal and biomass, nuclear thermochemical systems, and single-bed aqueous photo-electrochemical methods. Also potentially attractive are smaller-scale decentralized production systems based on SMR or electrolysis, as these can avoid the expense and difficulty of transporting bulky hydrogen gas or cryogenic liquid by generating the hydrogen close to the point of end use.

## Bibliography

1. US Energy Information Administration (EIA) (2008) The impact of increased use of hydrogen on petroleum consumption and carbon dioxide emissions. Report #: SR-OIAF-CNEAF/2008-04. [www.eia.doe.gov/oiaf/servicert/hydro/appendixc.html](http://www.eia.doe.gov/oiaf/servicert/hydro/appendixc.html), August
2. Freedonia Group, Inc. (2014) World Hydrogen - Demand and Sales Forecasts, Market Share, Market Size, Market Leaders. Study #3165, February, <https://www.freedoniagroup.com/World-Hydrogen.html>, Accessed May 2018.
3. US Department of Energy (2018) Hydrogen production. <https://www.energy.gov/eere/fuelcells/hydrogen-production>. Accessed Mar 2018
4. Lipman TE, Delucchi MA (2010) Expected greenhouse gas emission reductions by battery, fuel cell, and plug-in hybrid electric vehicles. In: Pistoia G (ed) Battery, hybrid, and fuel cell vehicles. Elsevier Press. ISBN 978-0-444-53565-8
5. Wang M, Wu Y, Elgowainy A (2007) GREET1.7 fuel-cycle model for transportation fuels and vehicle technologies. Argonne National Laboratory
6. Hirschenhofer JH, Stauffer BD, Engleman RR, Klett MG (2000) Fuel cell handbook, 4th edn. US Department of Energy, Federal Energy Technology Center, B/T Books, Orinda
7. US Department of Energy (2011) The Department of Energy Hydrogen and Fuel Cells Program Plan: An integrated strategic plan for the research, development, and demonstration of hydrogen and fuel cell technologies, September, [https://www.hydrogen.energy.gov/pdfs/program\\_plan2011.pdf](https://www.hydrogen.energy.gov/pdfs/program_plan2011.pdf), Accessed May 2018.
8. Anderson A, Carole T (2006) Bio-derived liquids to hydrogen distributed reforming working group background paper. US Department of Energy, HFCIT Program, September
9. Navarro RM, Pena MA, Fierro JLG (2007) Hydrogen production reactions from carbon feedstocks: fossil fuels and biomass. *Chem Rev* 107:3952–3991

10. Smitkova M, Janicek R, Riccardi J (2011) Life cycle analysis of processes for hydrogen production. *Int J Hydrog Energy* 36:7844–7851
11. US Department of Energy (2011) Hydrogen production: biomass gasification. Web document. [http://www1.eere.energy.gov/hydrogenandfuelcells/production/biomass\\_gasification.html?m=1&](http://www1.eere.energy.gov/hydrogenandfuelcells/production/biomass_gasification.html?m=1&)
12. Proton Onsite (2018) Hydrogen fueling. <http://www.protononsite.com/products-proton-site/m-series>. Accessed Mar 2018
13. Czernik S, French R, Penev M (2010) Distributed bio-oil refining. DOE Hydrogen Program FY 2010 annual progress report, pp 38–41
14. Duman G, Akarsu K, Yilmazer A, Gundogdu TK, Azbar N, Yanik J (2018) Sustainable hydrogen production options from food wastes. *Int J Hydrog Energy*. <https://doi.org/10.1016/j.ijhydene.2017.12.146>
15. Zhu J (2011) Photocatalytic hydrogen production (this volume)
16. Khaselev O, Turner JA (1998) A monolithic photovoltaic-photoelectrochemical device for hydrogen production via water splitting. *Science* 280:425–427
17. Arachchige SM, Brewer KJ (2011) Hydrogen via direct solar production (this volume)
18. Joshi AS, Dincer I, Reddy BV (2010) Exergetic assessment of solar hydrogen production methods. *Int J Hydrog Energy* 35:4901–4908
19. Brewer KJ, White T, Quinn K, Wang J, Arachchige S, Knoll J (2011) Photoinitiated electron collection in mixed-metal supramolecular complexes: development of photocatalysts for hydrogen production. DOE Hydrogen and Fuel Cells Program 2011 annual merit review meeting
20. James BD, Baum GN, Perez J, Baum KN (2009) Technoeconomic analysis of photoelectrochemical (PEC) hydrogen production. Prepared by Directed Technologies Inc. for the US Department of Energy under DOE Contract Number: GS-10F-009J, December
21. Yumin H, Wang D (2018) Toward practical solar hydrogen production. *Chem* 4:399–408
22. Hallenbeck PC (2009) Fermentative hydrogen production: principles, progress, and prognosis. *Int J Hydrog Energy* 34:7379–7389
23. Melis A, Melnecki MR (2006) Integrated biological hydrogen production. *Int J Hydrog Energy* 31:1563–1573
24. Kethorn W, Rastogi RP, Incharoensakdi A, Lindblad P, Madamwar D, Pandey A, Larroche C (2017) Microalgal hydrogen production – a review. *Bioresour Technol* 243:1194–1206
25. Logan BE, Regan JM (2006) Microbial fuel cells – challenges and applications. *Environ Sci Technol* 40:5172–5180
26. Brown LC, Besenbruch GE, Funk JE, Marshall AC, Pickard PS, Showalter SK (2002) High efficiency generation of hydrogen fuels using nuclear energy. Presentation at US Department of Energy Hydrogen Fuel Cells and Hydrogen Review, Nuclear Energy Research Initiative (NERI)
27. Mathias PM, Brown LC (2003) Thermodynamics of the sulfur-iodine cycle for thermochemical hydrogen production. Presented at the 68th annual meeting of the Society of Chemical Engineers, Japan, 23 Mar
28. Allen D (2009) FY09 projected hydrogen cost estimates for nuclear hydrogen initiative baseline processes, SAND2009-6630P. Sandia National Laboratory
29. Jeong YH, Kazimi MS, Hohnholt KJ, Yildiz B (2005) Optimization of the hybrid sulfur cycle for hydrogen generation. MIT–NES–TR–004, May
30. US Department of Energy (2011) High-temperature water splitting. [http://www1.eere.energy.gov/hydrogenandfuelcells/production/water\\_splitting.html](http://www1.eere.energy.gov/hydrogenandfuelcells/production/water_splitting.html)
31. T-Raissi A, Muradov N, Huang C, Adebisi O (2007) Hydrogen from solar via light-assisted high-temperature water splitting cycles. *Trans ASME* 129:184–189
32. Brouwer J, Margalef P (2011) Hydrogen production from high temperature fuel cells (this volume)
33. Margalef P, Brown T, Brouwer J, Samuelsen S (2011) Conceptual design and configuration performance analyses of poly-generating high temperature fuel cells. *Int J Hydrog Energy* 36(16):10044–10056
34. FuelCell Energy (2018) Transportation Applications, <https://www.fuelcellenergy.com/supply/hydrogen>, Accessed May 2018.
35. Patel P, Lipp L, Jahnke F, Heydorn E, Abdallah T, Holcomb F (2010) Co-production of renewable hydrogen and electricity: technology development and demonstration. *ECS Trans* 26(1):493–504
36. Nikolaidis P, Poullikkas A (2017) A comparative overview of hydrogen production processes. *Renew Sust Energ Rev* 67:597–611
37. Cohen M, Snow GC (2008) Hydrogen delivery and storage options for backup power and off-grid primary power fuel cell systems. Published in IEEE Intelec 2008 proceedings
38. Pivovar B et al (2016) H2 at Scale: deeply decarbonizing our energy system. Available in 2016 US Department of Energy AMR proceedings at [https://www.hydrogen.energy.gov/pdfs/review16/2016\\_amr\\_h2\\_at\\_scale.pdf](https://www.hydrogen.energy.gov/pdfs/review16/2016_amr_h2_at_scale.pdf)



## Hydrogen Production Through Electrolysis

Abudukeremu Kadier<sup>1</sup>, Mohd Sahaid Kalil<sup>1</sup>, Washington Logroño<sup>2,3</sup>, Azah Mohamed<sup>4</sup> and Hassimi Abu Hasan<sup>1</sup>

<sup>1</sup>Department of Chemical and Process Engineering, Faculty of Engineering and Built Environment, National University of Malaysia (UKM), Bangi, Selangor, Malaysia

<sup>2</sup>Department of Biotechnology, University of Szeged, Szeged, Hungary

<sup>3</sup>Centro de Investigación de Energías Alternativas y Ambiente, Escuela Superior Politécnica de Chimborazo, Chimborazo, Ecuador

<sup>4</sup>Department of Electrical, Electronic and System Engineering, Faculty of Engineering and Built Environment, National University of Malaysia (UKM), Bangi, Selangor, Malaysia

### Article Outline

Glossary

Definition of the Subject

Introduction

Advantages of MECs over Other Hydrogen Production Technologies

Microbial Electrolysis Cell (MEC): Fundamentals Crucial Operating Factors Affecting H<sub>2</sub>

Production in MECs

Various Applications of MECs Beyond Hydrogen Production

Conclusions and Future Application of MECs

Bibliography

### Glossary

**Applied voltage E<sub>ap</sub> (V)** is also called supplemental voltage, in order to obtain measurable current and hydrogen at the cathode of MEC from the combination of these protons and electrons, 0.2 V or more is needed

**Biocathode** A biocathode can be defined as an electrode from cheap material (e.g., carbon) with a microbial population present at the electrode or in the electrolyte that catalyzes the cathodic reaction. To act as a biocathode in an MEC, microorganisms need to be able to take up electrons from the electrode material and use these electrons to produce hydrogen

**British thermal unit (Btu or BTU)** A BTU was originally defined as the amount of heat required to raise the temperature of 1 avoirdupois pound of liquid water by 1 degree Fahrenheit at a constant pressure of one atmosphere

**COD removal (%)**  $\Delta COD = COD_f - COD_{in} / COD_{in} \times 100\%$  Where COD<sub>in</sub> was the initial COD concentration of the electrolyte; COD<sub>f</sub> was the final COD concentration of the effluent after each batch cycle

**Coulombic efficiency (CE)** the number of electrons or H<sub>2</sub> recovered in the circuit over the number of electrons or H<sub>2</sub> theoretically available from the substrate

**Electrochemically active bacteria (EAB)** EAB are a group of microorganisms which are able to consume organic matter and transfer the electrons derived from metabolic processes to the electrode

**Extracellular electron transfer (EET)** EET is a microbial metabolism that enables efficient electron transfer between microbial cells and extracellular solid material

**Hydrogen recovery** is a significant index for MEC performance, which was defined as the ratio of the hydrogen recovered and the maximum theoretical hydrogen produced based on substrate utilization

**Hydrogen yield** is the theoretical number of moles H<sub>2</sub> produced based on substrate usage ( $\Delta COD$ )

**HPR** is volumetric hydrogen production rate, unite of HPR is m<sup>3</sup> H<sub>2</sub>/m<sup>3</sup> reactor/d

**Microbial electrolysis cell (MEC)** MEC is a promising and cutting-age technology for the disposal of wastewater treatment and eco-friendly hydrogen and other bioenergy/biofuel

production including  $\text{CH}_4$ , acetate,  $\text{H}_2\text{O}_2$ , ethanol, and formic acid

**Volatile fatty acids (VFAs)** The three main volatile fatty acids produced in ruminants are acetic acid, butyric acid and propanoic acid

## Definition of the Subject

Microbial electrolysis cell (MEC) is a promising sustainable technology for wastewater treatment, bioenergy and value-added chemicals production. MECs have both operational and functional superiorities over the other technologies presently used for producing hydrogen ( $\text{H}_2$ ) from renewable biomass. Nevertheless, this technology is still in its infancy period and poses various performance limitations and obstacles in real-world applications. Thus, the present chapter mainly focuses on the comprehensive discussion of development of a practical MEC technology and structured as follows: First, a general introduction to MECs, their working principles, thermodynamics and electrochemistry of MECs are provided. Afterwards, key performance parameters and their impacts on the MEC performance are comprehensively discussed. Finally, their various applications beyond hydrogen production and outlooks for future research directions of MECs are highlighted. All in all, the main aim of the current chapter is to assist researchers and engineers to gain fundamental understandings of MEC, and to highlight several future research directions.

## Introduction

Currently, the world is facing the challenges of energy confrontation and clean water shortage. In 2012, the global energy consumption was 549 quadrillion British thermal units (BTUs) that is predicted to increase to 629 quadrillion BTUs in 2020 and to 815 quadrillion BTUs in 2040 (48% increase from 2012 to 2040) [19]. Presently, the fossil fuels (FFs) are the most exploited energy sources (up to 90%) in the world that are not only depleting the natural resources but also damaging

the environment and changing our climate [19]. FF combustion produces greenhouse gasses, for instance, carbon dioxide ( $\text{CO}_2$ ), which contribute to climate change. As part of sustainable energy production, transportation, and use framework, there is a high demand for energy recovery technologies to supplement the renewable energy for powering the Earth.

Hydrogen is an environment-friendly, high-energy fuel, with an energy content of 121 MJ/kg.  $\text{H}_2$  is used as fuel in turbines, internal combustion engines, fuel cells, as well as ovens and heaters [68].  $\text{H}_2$  has the lowest flash point of most common fuels, which allows for simpler starting and ignition equipment. Devices that use  $\text{H}_2$  can perform well even at low temperature [68].  $\text{H}_2$  is also a reagent for Haber process to produce ammonia, the single most important compound produced at industrial scale, 144 million metric tons/year worldwide, which is the major intermediate for fertilizers [12]. Among other industrial applications,  $\text{H}_2$  is needed to convert heavy oil to engine fuels and as a reducing gas in industrial processes.

A number of approaches are available for  $\text{H}_2$  production, namely, coal gasification, natural gas steam reforming, thermochemical conversion (pyrolysis), and water electrolysis (WE) [1, 40, 51], but most of these processes are not feasible for large-scale application by reason of high electricity cost and excessive  $\text{CO}_2$  emissions. Currently, 4% of global total  $\text{H}_2$  production is accounted by water electrolysis, which relies on the burning of FFs to produce the electrical power needed for the water splitting process [75]. The development of sophisticated technologies for producing  $\text{H}_2$  from biomass and other renewable energy resources that reduce environmental issues is now given high priority. In recent times,  $\text{H}_2$  productions from biological processes such as direct/indirect biophotolysis, photo/dark fermentation, and microbial electrolysis cell (MEC) using renewable resources are gaining considerable attention because of reduced catalytic cost and process energy requirements [48]. Nonetheless, the efficiency of these approaches changes with the types of substrate, working mechanisms, end products, and energy inputs [28].

## Advantages of MECs over Other Hydrogen Production Technologies

MEC is an innovative technology for  $H_2$  production that utilizes domestic and industrial wastewater as a substrate through the catalytic action of bacteria in the presence of electric current and absence of oxygen ( $O_2$ ). The MEC was firstly nominated as “electrochemically assisted hydrogen generation” [57], then “biocatalyzed electrolysis” [82], “electrohydrogenesis” [10], and was finally accepted by researchers as “microbial electrolysis cells (MECs)” [60]. MECs have numerous advantages over other biological  $H_2$  production processes. First, the substrates can be from renewable and waste materials rather than FFs: various organic matters such as cellulose, glucose, glycerol, acetic acid, sewage sludge, and different wastewater can be converted to  $H_2$  in MECs [10, 43, 57, 60, 76]. Furthermore, the  $H_2$  production efficiencies are greatly higher in MECs (80–95%) [2, 6, 34, 100] in comparison with the fermentation process (33%) [26, 29] and WE (65%) [101]. Moreover, MECs need relatively low electrical or applied voltage (0.2–0.8 V) [45, 51], which is much smaller

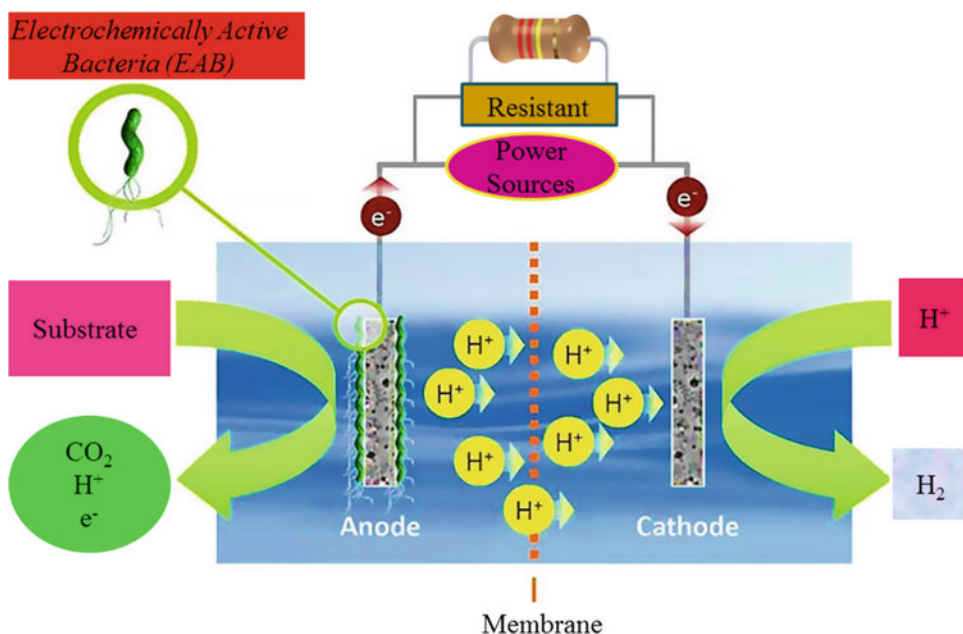
than that needed for traditional WE (typically 1.8–2.0 V) [44, 92]. The phototrophic conversion of organic substrate to  $H_2$  by microalgae and photosynthetic bacteria because of low solar efficiencies and large surface area requirements could not produce higher energy than MEC, which is 90% at the rate of  $0.5 \text{ kW h/m}^3 H_2$  [13, 20, 60].

## Microbial Electrolysis Cell (MEC): Fundamentals

The main focus of this section is to introduce the fundamental concepts of MEC technology, for instance, operating principles, thermodynamics and electrochemical evaluation of MECs, and various extracellular electron transfer (EET) mechanisms in MECs.

### The Major Hydrogen Production Route in MECs

Basically, a typical MEC is composed of three major components: anaerobic anode chamber, cathode chamber, and separator or membrane. Figure 1 illustrates the essential physical

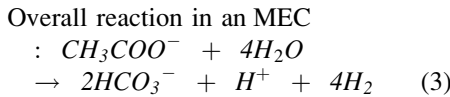
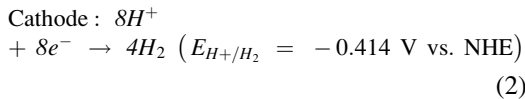
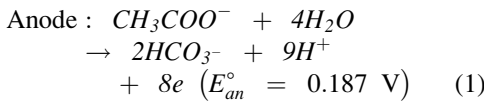


**Hydrogen Production Through Electrolysis, Fig. 1** Schematic illustration of a typical two-chamber MEC reactor and its operation



components of an MEC that consists of an anode, a cathode, an exchange membrane, electrochemically active bacteria (EAB), and an external power supply.

In an MEC, EAB colonize on the anode surface and break down the organic matter or wastes into  $\text{CO}_2$ , electrons ( $e^-$ ), and protons ( $\text{H}^+$ ) as a part of its metabolism. The EAB transfer the produced electrons to the anode, while the protons are diffused directly into the electrolyte solution of MEC to participate in reduction reactions at the cathode. In the meanwhile, the electrons then transfer continuously through an electrical circuit to the cathode with the help of external power supply and combine with the free protons in the solution produce  $\text{H}_2$ . When acetate is used as a substrate, the process can be described in the following electrochemical reactions:



It is worth to mention that the final reduction of protons to  $\text{H}_2$  is a thermodynamically non-spontaneous reaction. Therefore it demands an external energy input, supplemental or applied voltage [46, 62, 82].

### Thermodynamics and Electrochemical Evaluation of an MEC

At pH of 7, the theoretical reduction potential of each half cell reactions in the MEC is written and calculated according to Nernst equation. For the cathode half reaction, the theoretical reduction potentials are written and calculated based on Eq. (4):

$$\begin{aligned} E_{cat} & = E_{cat}^\circ - \frac{RT}{2F} \ln \frac{P_{\text{H}_2}}{[\text{H}^+]^8} = 0 \\ & - \frac{(8.314 \times 298.15)}{(2 \times 96485)} \ln \frac{1}{[10^{-7}]^8} \\ & = -0.414 \text{ V} \end{aligned} \quad (4)$$

where  $E_{cat}^\circ$  is the standard electrode potential for  $\text{H}_2$  (0 V),  $R$  is the universal gas constant (8.314 J/K/mol),  $T$  (K) is the absolute temperature, and  $F$  is Faraday's constant (96,485 C/mol  $e^-$ ). For the anode half reaction, the theoretical reduction potential is written and calculated as stated in Eq. (5):

$$\begin{aligned} E_{an} & = E_{an}^\circ - \frac{RT}{8F} \ln \frac{[\text{CH}_3\text{COO}^-]}{[\text{HCO}_3^-]^2[\text{H}^+]^9} \\ & = 0.187 - \frac{(8.314 \times 298.15)}{(8 \times 96485)} \ln \frac{0.0169}{[0.005]^2 [10^{-7}]^9} \\ & = -0.3000 \text{ V} \end{aligned} \quad (5)$$

where  $E_{an}^\circ$  is the standard electrode potential for acetate oxidation (0.187 V), for a solution with  $\text{HCO}_3^- = 0.005 \text{ M}$ ,  $\text{CH}_3\text{COO}^- = 0.0169 \text{ M}$ ,  $\text{pH} = 7$  [60]. Thus, the cell voltage ( $E_{cell}$ ) necessary for a MEC to produce  $\text{H}_2$  at the cathode under these conditions is

$$\begin{aligned} E_{cell} & = E_{cat} - E_{an} = (-0.414 \text{ V}) \\ & - (-0.300 \text{ V}) = -0.114 \text{ V} \end{aligned} \quad (6)$$

Equation (6) demonstrates that the  $E_{cell}$  is negative, and this shows that  $\text{H}_2$  cannot be produced from acetate spontaneously. In order to make the reaction favorable and produce  $\text{H}_2$ , an additional input voltage ( $>0.114 \text{ V}$ ) must be supplied. In practice, the applied voltage ( $E_{ap}$ ) is generally higher than the theoretical ( $E_{cell}$ ) by cause of ohmic loss, activation loss, and mass transport loss in the MECs. Previous MEC studies demonstrated that  $E_{ap} = 0.2 \text{ V}$  or more is needed to obtain measurable current and  $\text{H}_2$  production in MEC [51, 62]. Nevertheless, this voltage (0.2 V) is much lower than the voltages needed for WE (typically 1.8–2.0 V) [111].



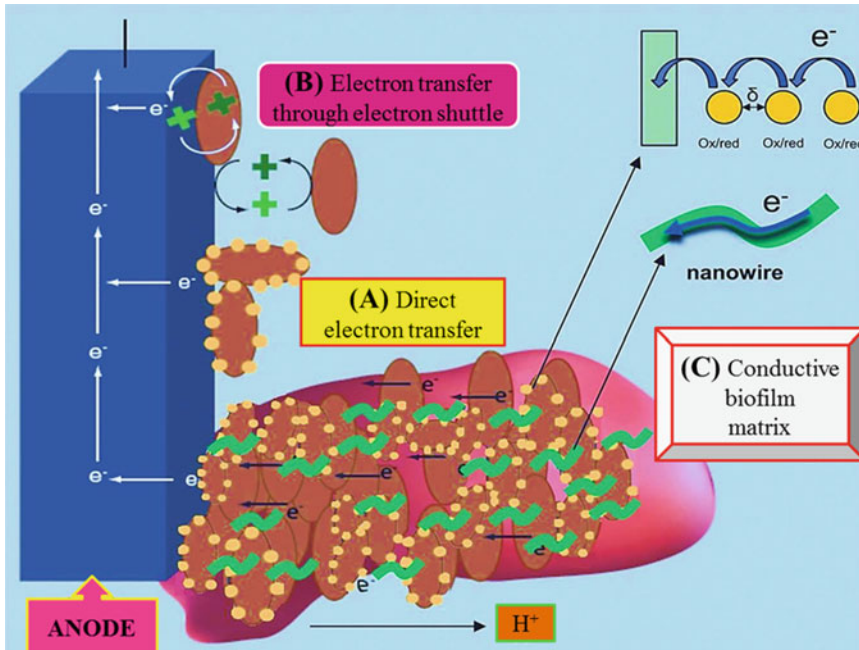
**Main Extracellular Electron Transfer Pathways in MECs**

EAB play a key role in H<sub>2</sub> production in MECs. The performance of MECs is greatly influenced by the ability of EAB on the anode to facilitate the transfer of electrons from substrate to anode (electronic generation). Extracellular electron transfer (EET) refers to the transfer of electrons obtained from a substrate to the anode electrode. A better understanding about the microbial EET may promote the development of new strategies for engineering MECs. The experiments conducted by Torres et al. [94] demonstrated that most forms of respiration involve a soluble compound (e.g., oxygen, nitrate, and sulfate) as an electron acceptor; nevertheless, some microorganisms are able to respire solid electron acceptors, for instance, metal oxides, carbon, and metal electrodes, in order to obtain energy. Although the mechanism of EET has not yet been fully elucidated, however several possible pathways have been proposed. Currently, the most persuasive general descriptions

on the EET mechanisms are illustrated in Fig. 2. The first mechanism is the direct electron transfer between electron carriers in the bacteria and the solid electron acceptor [94]. The second mechanism occurs in the presence of a soluble electron shuttle, which is a compound (e.g., melanin, phenazines, flavins, and quinones) that carries electrons between EAB and the electrode by diffusive transport [72, 97]. The third mechanism proposes a solid component (cellular pili as nanowires) that is part of the extracellular biofilm matrix and is conductive for electron transfer from EAB to the solid surface [25, 79].

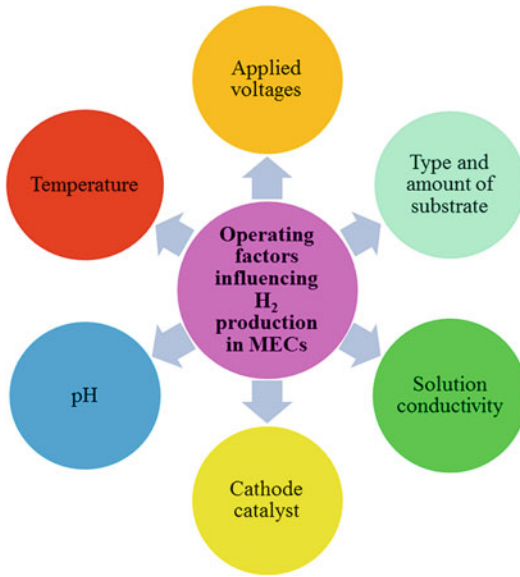
**Crucial Operating Factors Affecting H<sub>2</sub> Production in MECs**

In the MEC, the major operating parameters including pH, temperature, substrate, applied voltage, conductivity, and cathode materials affect the H<sub>2</sub> yield and production (Fig. 3).



**Hydrogen Production Through Electrolysis, Fig. 2** Schematic diagram describing the EET mechanisms in an MEC anode: (a) direct electron transfer – cell in direct contact with electron acceptor via surface c-type

cytochromes, (b) electron transfer through electron shuttle, (c) electron transfer through conductive biofilm and conductive pili (Adapted from [47, 53])



**Hydrogen Production Through Electrolysis,**  
**Fig. 3** Schematic representation of key operating factors affecting performance of MECs

### pH

The pH of electrolyte solutions plays a crucial role in MECs, as it governs both the kinetic and thermodynamics of the anode and cathode reactions. A research effort shows that  $E_{\text{cell}}$  is inversely proportional to the pH, for instance, for each unit rise in the pH, the anodic potential decreases by  $-0.059$  V [58]. The potential associated with the hydrolysis of acetate ( $\text{CH}_3\text{COO}^-$ ) producing electrons,  $\text{H}^+$ , and  $\text{HCO}_3^-$  is approximately  $-0.28$  V at the pH of 7 [59]. In case of MECs using ion-exchange membranes, variation in the pH is a common phenomenon that results in MEC under performance. Liu et al. [58] reported that pH of 9 is optimum for  $\text{H}_2$  production and chemical oxygen demand (COD) removal. While, the gas production rate decreases at the pH value higher or lower than the optimum pH value. Since the anodic potential drops with an increase in the pH, thus the overall potential difference raises as the pH of the anolyte increases.

To ensure the growth of EAB in MECs, controlling the pH is an essential factor. An alkaline pH is always favorable for bacteria although the case for fungi is opposite that needs an acidic pH for its microbial growth activity. The EAB

population also needs a high pH for transferring their electrons to anode [49]. Nimje et al. [74] employed cyclic voltammetry to investigate the effects of the pH on the performance of MEC. Their experimental results showed a raise in the electrochemical activity with increase in pH value of the anolyte solutions from 7 to 9. Similarly, Rozendal et al. [84] reported a loss of output cell potential by 0.38 V, when the pH is raised by approximately 6 units.

### Temperature

Temperature (K or  $^{\circ}\text{C}$ ) is another vital parameter that affects the current density ( $I_p$ ) and energy efficiency of MECs, since the major part of MECs is anaerobic (anodic chamber where the actual substrate degradation occurs), wherein the activity of microbes is temperature dependent (mesophilic phase;  $35\text{--}40$   $^{\circ}\text{C}$ ) [50]. What's more, the performance of MEC is hugely affected by fluctuations in temperature; however, the extent of variation of EAB is lower than methanogenesis [35]. Additionally, Lorenzo et al. [61] evaluated the performance of MEC at three different temperatures of  $20$   $^{\circ}\text{C}$ ,  $25$   $^{\circ}\text{C}$ , and  $30$   $^{\circ}\text{C}$  and reported that COD removal and coulombic efficiencies (CE) were highest with  $30$   $^{\circ}\text{C}$ . Interestingly, MEC can operate even at lower temperature ( $\leq 20$   $^{\circ}\text{C}$ ) in comparison to the methanogenic reactors [77]. Overall, it may be said the effects of temperature on EAB reflect in: (a) the microbial growth of EAB, (b) the transfer rate of mass, (c) the activity of the substrate, and (d) the potential of the electrodes. The appropriate temperature directly and significantly impacts  $\text{H}_2$  yield in MECs.

### Type and Amount of Substrate

Substrate or fuel source is considered as one of the most crucial factors affecting  $\text{H}_2$  production in MECs. Different types of substrate lead to different organic degradation rates and protons release and, hence, consequence in various  $\text{H}_2$  yields [10, 43]. Acetate ( $\text{CH}_3\text{COONa}$ ) is the most extensively used substrate in MECs, by the reason of it is a common end product of dark fermentation. The best MEC performance was achieved using acetate as the fuel source. Jeremiassé et al. (2010b) achieved the highest hydrogen

production rate (HPR) of  $50 \text{ m}^3 \text{ H}_2/\text{m}^3 \text{ d}$  in a two-chamber MEC with the  $E_{\text{ap}}$  of 1 V. Hydrogen recoveries ( $R_{\text{H}_2}$ ) were also high applying the acetate as fuel sources and approached close to the theoretical limitation of 4 mol  $\text{H}_2$ /mol acetate [4]. Cheng and Logan [10] studied different fermentable (glucose, cellulose) and non-fermentable substrates (e.g., VFA: acetic, butyric, lactic, propionic, and valeric). They achieved lower results for fermentable substrates in terms of  $R_{\text{H}_2}$ : 71% and 68% for glucose and cellulose, respectively, while 91% for acetic and lactic acids. Overall energy efficiencies were 64%–63% with glucose and cellulose, compared to 82% for acetic and lactic acids. Cellulose had the lowest HPR with  $0.11 \text{ m}^3 \text{ H}_2/\text{m}^3 \text{ d}$  compared with over  $1.0 \text{ m}^3 \text{ H}_2/\text{m}^3 \text{ d}$  for acetic acid, lactic acid, and glucose. Khan et al. [50] reported the differences in output power densities, CEs, and the microbial community profiles in two identical BESs that were fed with two different substrates, for instance, azo dye-reactive orange 16 and acid navy blue r (a naphthalenedisulfonate dye). The substrate concentration was very high at the time of fresh batch addition that favors the growth of non-EAB population, including methanogens [3].

### Applied Voltage ( $E_{\text{ap}}$ )

Research efforts demonstrate that applying the lower voltage results in lower  $\text{H}_2$  yield. Particularly, when the  $E_{\text{ap}}$  is kept below 0.3 V, the HPR is low. If the applied voltage is raised to 0.8–1.0 V, the HPR reached a peak [60]. The commonly used  $E_{\text{ap}}$  value appears to be 0.5 V [55, 98]. Furthermore, fermentation coupled with hydrogenolysis into the two-stage  $\text{H}_2$  production system achieved 9.95 mol  $\text{H}_2$ /mol glucose [55]. Using an ethanol– $\text{H}_2$  coproducing fermentation with  $E_{\text{ap}}$  of 0.5–0.8 V, the overall  $R_{\text{H}_2}$  could achieve 96%, while using the effluent as the feed of MEC and maintaining the  $E_{\text{ap}}$  of 0.6 V achieved 83% of the overall  $R_{\text{H}_2}$  [63].

As to the research efforts of a voltage regulator for enhancing anode potential, Nam et al. [70] found that when the anode potential in a single-MEC was kept on  $-0.2 \text{ V}$ , both the overall  $\text{H}_2$  production were higher than those for the same conditions under  $E_{\text{ap}} = 0.6 \text{ V}$  [70]. With the

applied voltage, temperature, and pH of 0.2–0.8 V, 25 °C, and 7, respectively, both of the fermentative  $\text{H}_2$  production and the MEC could obtain superior hydrogen yield. On the other hand, lower anode potential without current limitation could reduce the energy loss of anode [56].

### Solution Conductivity

Electrolyte conductivity also affects the HPR in MECs; however this affect is not very considerable. Electrolyte solution of higher conductivity supports better ion transfer that may enhance the overall performance of MEC. Solution conductivity is inversely related to the internal resistance of the MEC system. Call and Logan [4] demonstrated an increase in HPR when the conductivity was raised from 7.5 to 20 mS/cm. Furthermore, Logan et al. [59] showed that ohmic losses can be decreased by applying solutions of higher conductivity. Moreover, these losses can be decreased by reducing the electrode distances and checking the connections properly and employing a membrane of low resistivity [59]. A small variation in electrode distances results in a substantial reduction in internal resistance (IR) of the system with solution of low conductivities. While in solution of higher conductivities, the effect of electrode distances on IR is not remarkable [84]. Hutchinson et al. [38] reported that raising the electrode distances from 0.4 to 1.4 cm and decreasing solution conductivity from 7.8 mS/cm to 1.8 mS/cm would raise the IR of MEC system.

### Cathode Catalyst

A catalyst is employed to accelerate the reaction and to decrease the kinetics hurdle occurring in the reduction of proton to  $\text{H}_2$  gas [8]. The use of catalyst loading on the cathode surface enhances the HPR (Table 1). Platinum (Pt) is the most widely used catalyst for cathode in MECs by the reason of its excellent catalytic properties, inert nature, and low overpotential [8]. Liu et al. [58] investigated the effect of Pt loadings on output power densities and concluded that  $0.2 \text{ g}/\text{cm}^2$  of Pt catalyst would be adequate for maximum power density in MECs. If the loading is very low, the power density and energy efficiency of MECs will be consequently low. The major

**Hydrogen Production Through Electrolysis, Table 1** Summary of cathodic electrode materials and catalysts used in MECs. It includes key performance

parameters of MEC tests, hydrogen production rate (HPR), cathodic hydrogen recovery (RCAT), over all energy efficiency or recovery ( $\eta_{E+S}$ )

Type of cathodic catalyst used in MECs		Hydrogen production rate (HPR) ( $\text{m}^3\text{H}_2/\text{m}^2\text{d}$ )	Cathodic hydrogen recovery ( $R_{\text{CAT}}$ ) (%)	Overall energy efficiency or recovery (%)	Reference
Cathode	Catalyst				
Stainless steel (SS)-based cathode catalyst					
Stainless steel A268	–	$1.50 \pm 0.04$	$61 \pm 3$	$46 \pm 3$	[86]
Stainless steel 304	–	$0.59 \pm 0.01$	$53 \pm 1$	$38 \pm 1$	
Stainless steel 316	–	$0.35 \pm 0.08$	$27 \pm 6$	$19 \pm 4$	
Stainless steel 420	–	$0.58 \pm 0.07$	$43 \pm 2$	$30 \pm 1$	
Stainless steel brush		$1.7 \pm 0.1$	84	$78 \pm 5$	[5, 9, 92]
SS 304 (mesh size #60)		$2.1 \pm 0.3$	$98 \pm 4$	$74 \pm 4$	[110]
3D macroporous stainless steel fiber felt (SSFF)		$3.66 \pm 0.43$	$76.37 \pm 15.04$	$79.61 \pm 13.07$	[89]
Stainless steel wool (SSW)		0.52	$0.7 \pm 0.01$	$0.55 \pm 0.02$	[81]
Stainless steel mesh	Pt coated	1.4	$0.98 \pm 0.02$	$0.75 \pm 0.02$	
Stainless steel mesh	$\text{MoS}_2$	0.67		$0.57 \pm 0.01$	
Stainless steel mesh		$1.13 \pm 0.02$ $1.08 \pm 0.02$	$76 \pm 1$ $76 \pm 1$		[66]
Stainless steel A286	NiOx	0.76	52		[86]
CNT-based electrode alternatives to Pt					
Carbon cloth	Pt/multiwalled carbon nanotube	1.42	65		[99]
	Multiwalled carbon nanotube	1.20	62		
	Polyaniline/multiwalled CNTs	1.04	57		[106]
CNT nanocomposites	75% wt PANI/MWCNTs	1.04	56.7		[107]
	$\text{MoS}_2$	$0.0078 \pm 0.0014$	$46.2 \pm 4.3$		[109]
	$\text{MoS}_2/\text{CNT-30}$	$0.0077 \pm 0.0002$	$43.2 \pm 0.6$		
	$\text{MoS}_2/\text{CNT-60}$	$0.0081 \pm 0.0008$	$46.0 \pm 4.0$		
	$\text{MoS}_2/\text{CNT-90}$	$0.0101 \pm 0.0007$	$49.0 \pm 5.5$		
	Pt	$0.0103 \pm 0.0013$	$48.0 \pm 6.1$		

(continued)

**Hydrogen Production Through Electrolysis, Table 1** (continued)

Type of cathodic catalyst used in MECs		Hydrogen production rate (HPR) (m <sup>3</sup> H <sub>2</sub> /m <sup>3</sup> d)	Cathodic hydrogen recovery (R <sub>CAT</sub> ) (%)	Overall energy efficiency or recovery (%)	Reference
Cathode	Catalyst				
<b>Ni and Ni-based cathode catalysts</b>					
Carbon-fiber weaved cloth	NiMo	2.0	86		[35]
Carbon-fiber weaved	NiW	1.5	75		
Gas diffusion cathodes	Nickel (Ni) particles	5.4 L/LR/day			[33]
Ni 210		0.38 ± 0.04	27 ± 4	20 ± 3	[86]
Ni 400		0.41 ± 0.10	31 ± 5	23 ± 5	
Ni 625		0.79 ± 0.27	43 ± 9	31 ± 8	
Ni HX		0.55 ± 0.11	40 ± 8	29 ± 5	
Ni 625	NiOx	0.76	52		
NiFe LDH	Nickel foam	2.01 ± 0.01 2.11 ± 0.00	97 ± 1 99 ± 0		[66]
Pt/nickel foam		2.12 ± 0.09 2.01 ± 0.00	84 ± 3 84 ± 0		
Nickel foam		1.13 ± 0.01 1.07 ± 0.01	73 ± 0 69 ± 0		
Ni foam		50			[42]
Ni foam		1.1		0.65 ± 0.01	[81]
Ni mesh	Electroformed	4.18 ± 1	119 ± 5	62.9 ± 5	[44]
Ni mesh		0.28 ± 0.01	75.7 ± 0.2	46.7 ± 0.5	[21]
Ti mesh		0.23 ± 0.01	73.3 ± 0.9	44.4 ± 0.9	
<b>Other metal and composite cathode materials</b>					
Ti mesh		0.23 ± 0.01	73.3 ± 0.9	44.4 ± 0.9	[21]
Carbon paper	Pd nanoparticles	2.6 ± 0.5 L/(m <sup>2</sup> d)	46.4 ± 8.5	26.0 ± 4.8 (COD)	[36]
CC		0.0087 ± 0.0007	67.7 ± 10.6		[105]
Carbon cloth	NeFe/Fe <sub>3</sub> C@C	0.0181 ± 0.0011	79.8 ± 8.4		
	N-Fe/Fe <sub>3</sub> C@C (after 20 days)	0.0144 ± 0.0002	79.5 ± 0.8		
Spiral wound electrode		132 A/m <sup>3</sup>		76 ± 5 (COD)	[32]
Nano-Mg(OH) <sub>2</sub> /Gr		0.63 ± 0.11	83 ± 9	71 ± 6	[17]
Carbon cloth	MoS <sub>2</sub>	10.7 A/m <sup>2</sup>			[93]
<b>Biocathode or biocatalyst</b>					
Biocatalyst		0.63	49		[84]
Biocatalyst		0.04	21		[41]
Biocatalyst	Thermophilic biocathode	0.376	70		[24]
Biocatalyst		0.266 ± 0.001 mol Co/mol COD 0.113 ± 0.000 mol CH <sub>4</sub> /mol COD 0.103 ± 0.003 mol acetate/mol COD		3.7 ± 0.05% (Co) 17.5 ± 1.4% (CH <sub>4</sub> ) 0.5 ± 0.001% (acetate)	[37]

(continued)

**Hydrogen Production Through Electrolysis, Table 1** (continued)

Type of cathodic catalyst used in MECs		Hydrogen production rate (HPR) ( $\text{m}^3\text{H}_2/\text{m}^3/\text{d}$ )	Cathodic hydrogen recovery ( $R_{\text{CAT}}$ ) (%)	Overall energy efficiency or recovery (%)	Reference
Cathode	Catalyst				
Modified biocathodes	PANI/MWCNT	0.67	42	86.8% COD	[8]
Biocathode		7.33 $\pm$ 0.37 mg/L/h and 0.301 $\pm$ 0.005 $\text{m}^3/\text{m}^3/\text{d}$ (acetate) & 6.56 $\pm$ 0.38 mg/L/h and 0.127 $\pm$ 0.024 $\text{m}^3/\text{m}^3/\text{d}$ (NaHCO <sub>3</sub> )			[9]

disadvantages of applying Pt are the high cost and poisoning by impurities that led the researchers to look for alternatives. Selembo et al. [86] employed nickel oxide catalyst that enhanced the HPR and energy efficiency of MEC; however, its catalytic activity drops with time. Furthermore, Hu et al. [35] developed an inexpensive NiMo alloy catalyst that showed higher HPRs; nevertheless, they were toxic and caused environmental issues. This has led to the development of biocathodes; compared with chemical catalysts, the use of microbes as cathode catalysts has the advantage of being low priced and self-generating without causing secondary pollution.

Rozendal et al. [83] for the first time studied the use of biocathodes in MECs. The results indicated that the use of biocathode resulted in eightfold enhancement in HPR ( $0.63 \text{ H}_2 \text{ m}^3/\text{m}^3 \text{ d}$ ) in comparison to control electrode [83]. Furthermore, Huang et al. [37] employed biocathode MECs to recover some metals, and in their study, the cobalt was effectively recovered with simultaneous  $\text{CH}_4$  and acetate production. At  $E_{\text{ap}} = 0.2 \text{ V}$ , up to 88.1% of Co(II) was reduced concomitantly obtaining yields of  $0.266 \pm 0.001 \text{ mol Co/mol COD}$ ,  $0.113 \pm 0.000 \text{ mol CH}_4/\text{mol COD}$ , and  $0.103 \pm 0.003 \text{ mol acetate/mol COD}$  [37].

### Various Applications of MECs Beyond Hydrogen Production

MEC produces  $\text{H}_2$  from a variety of wastewater such as industrial, domestic, and synthetic. This

makes the MEC technology a veritable and complementary source of bioenergy and biofuels.

#### Treatment of Domestic Wastewater (DWW)

Ditzig et al. [18] first time reported hydrogen production using DWW as substrate in the MEC process and evaluated system performance in terms of  $R_{\text{H}_2}$ , BOD, COD, and DOC removal. Furthermore, to determine the possibilities of treating DWW in larger-scale MECs, a 120 L of MEC was constructed on site in Northern England, using raw DWW to produce  $\text{H}_2$  for a period of over 3 months [30]. Additionally, A 100 L of MEC was built and tested for 12-month period fed with raw DWW with temperatures ranging from  $1 \text{ }^\circ\text{C}$  to  $22 \text{ }^\circ\text{C}$ . The MEC produced an average of 0.6 L/day of  $\text{H}_2$ , with the  $R_{\text{H}_2}$  of 41.2% [31]. Moreover, Ivanov et al. [39] developed a simple quantitative method for comparing the performance of different wastewaters in MECs operated under fed-batch operation mode. The MEC reactors were inoculated using DWW and industrial wastewater (IWW).

#### MECs for Treatment of Industrial Wastewater and Other Types of Wastewater

In other studies, Tenca et al. [91] examined two different types of wastewater in MECs, a methanol-rich IWW and a food processing wastewater (FPWW). The FPWW contained high concentrations of complex carbohydrates ( $1940 \pm 17 \text{ mg/L}$ ) and acetate, while the IWW (from a specialty chemical manufacturing facility) had a high concentration of methanol



( $1537.4 \pm 48.6$  mg/L) and a lower concentration of biodegradable organic matters. Substantially, more biogas was recovered in MECs through cathodic process with the Pt/CC. Furthermore, Cusick et al. [15] investigated  $H_2$  production performance and costs of MECs fed with DWW and winery wastewater; the respective HPRs were  $0.28 \pm 0.04$   $m^3 H_2/m^3 d$  and  $0.17 \pm 0.09$   $m^3 H_2/m^3 d$ . The resulting  $H_2$  production costs were \$4.51/kg  $H_2$  and \$3.01/kg  $H_2$  for winery wastewater and DWW, respectively [15]. According to these results, the first pilot-scale continuous-flow MEC (1000 L) having 144 electrode pairs in 24 modules was constructed and evaluated for current generation and COD removal with winery wastewater [16]. In their experiment, enrichment of EAB biofilm required  $\sim 60$  days, the volumetric current density reached a peak of  $7.4$   $A/m^3$  by the end of the test (after 100 days), while the HPR reached a peak of  $0.19 \pm 0.04$  L/L/day [16]. Moreover, Kiely et al. [52] attempted to treat potato processing and dairy manure wastewater in MECs. Potato processing wastewater was collected from the primary clarifier of the wastewater treatment system and diluted with ultrapure water in order to lower the organic loading rate. At  $E_{ap} = 0.9$  V, the MECs fed with potato processing wastewater produced  $4.5$  mA ( $0.64$   $mA/cm^2$ ) of electrical current and HPR of  $0.74$   $m^3 H_2/m^3 d$ . The biogas produced by potato processing wastewater MEC was on average 73%  $H_2$ ; 13%  $CH_4$ ; and 14%  $CO_2$ . The  $R_{H_2}$  was 80%, with COD removal of 79%.

These results showed that the MECs fed with dairy manure wastewater did not generate measurable quantities of biogas. The current production was extremely low ( $<1$  mA). It was concluded that potato processing wastewater was a favorable substrate for MECs. It was reported that a single-chamber MEC with a graphite-fiber brush anode produced the HPR of  $0.9$ – $1.0$   $m^3 H_2/m^3 d$  using a full-strength or diluted swine wastewater. COD removals ranged from 8% to 29% in 20 h tests and from 69% to 75% in longer tests of 184 h using full-strength wastewater [98]. The results revealed that the MEC is an efficient method for hydrogen recovery from swine wastewater treatment, although the process needs to be

further studied for decreasing  $CH_4$  production, enhancing the efficiency of converting the organic matter into current, and raising  $R_{H_2}$  at the cathode. Similarly, refinery wastewaters were employed as fuels in MECs for the first time by Ren et al. [80]. The treatability of six different refinery wastewater samples collected from different points were examined in the MECs. The experimental results were similar to those obtained using DWW.

Wang et al. [102] examined the Pt/CC catalyzed and microbial catalyzed at cathodes for their hydrogen production performance at a low temperature of  $9^\circ C$  using molasses wastewater as the fuel. In their work, the overall  $R_{H_2}$  of 72.2% ( $E_{ap} = 0.6$  V) was obtained when the Pt/CC was used. In contrast, when a cheaper catalyst (biocathode;  $E_{ap} = 0.6$  V) was applied,  $H_2$  can still be generated but at a lower overall  $R_{H_2}$  of 45.4%. Pre-fermentation of poorly biodegradable landfill leachate (BOD<sub>5</sub>/COD ratio of 0.32) was evaluated for enhanced current density ( $I_V$ ),  $R_{H_2}$ , CE, and removal of organics (BOD and COD) in MECs. Semi-continuously fermented leachate to the anode of an MEC remarkably enhanced its performance: 83% BOD removal, 68%  $R_{H_2}$ , 17.3% CE, and  $23 A/m^3 I_V$  (or  $16$   $mA/m^2$ ), compared to 5.6% BOD removal, 56%  $R_{H_2}$ , 2.1% CE, and  $2.5$   $A/m^3 I_V$  (or  $1.7$   $mA/m^2$ ) for the raw leachate [67].

What's more, the use of synthetic wastewater containing carbon sources of glycerol, milk, and starch was tested in a single-chamber MEC.  $H_2$  production was only sustained with milk as a single substrate and with the simultaneous degradation of the three substrates. The latter had the best results in terms of volumetric current density ( $I_V$ ),  $150$   $A/m^3$ ; HPR,  $0.94$   $m^3 H_2/m^3 d$ ; and  $R_{cathode}$ , 91% with  $E_{ap} = 0.8$  V [69].

Additionally, waste-activated sludge, which contains a large amount of carbohydrates undegradable by EAB, was tested as a substrate in MECs [64, 65, 90]. From the raw waste-activated sludge, an extremely low  $H_2$  was generated ( $0.056 \pm 0.008$   $m^3 H_2/m^3 d$ ) in a two-chambered MEC, though with alkaline-pretreated waste-activated sludge, a larger quantity of  $H_2$  was generated ( $0.91 \pm 0.10$   $m^3 H_2/m^3 d$ ) [64]. An anaerobic-baffled reactor (ARB) was

utilized to degrade complex organic compounds into volatile short-chain fatty acids and ethanol, with the ARB effluent then being supplied to MECs for H<sub>2</sub> production [65]. An integrated dark fermentation-MEC process was evaluated for H<sub>2</sub> production from sugar beet juice [104], the overall H<sub>2</sub> production was 25% of initial COD (equivalent to 6 mol H<sub>2</sub>/mol hexose added), and the energy recovery from sugar beet juice was 57% using the combined biohydrogen.

More recently, spent yeast (SY) is a great challenge for the brewing industry, which was treated using an MEC to recover energy [87]. Concentrations of SY from bench alcoholic fermentation and ethanol were tested, ranging from 750 to 1500 mg COD/L and from 0 to 2400 mg COD/L, respectively. COD removal efficiency (COD<sub>E</sub>), R<sub>H2</sub>, CE, hydrogen production, and current density ( $I_V$ ) were evaluated. The best treatment condition was 750 mg COD/L SY + 1200 mg COD/L ethanol giving higher COD<sub>E</sub>, R<sub>H2</sub>, and CE (90 ± 1%, 90 ± 2%, and 81 ± 1%, respectively), as compared with 1500 mg COD/L SY (76 ± 2%, 63 ± 7%, and 48 ± 4%, respectively). Future work should focus on electron sinks, acclimation, and optimizing SY breakdown.

### Application of MECs in the Removal of Ammonium or Nitrogen from Urine

Kuntke et al. [54] showed the use of a MEC for ammonium removal, COD removal, and H<sub>2</sub> production from diluted urine. During operation with a batch cathode,  $I_V$ , HPR, ammonium removal rate, and COD removal were obtained as of 23.07 ± 1.15 A/m<sup>2</sup>, 48.6 ± 7.47 m<sup>3</sup> H<sub>2</sub>/m<sup>3</sup> d, 173.4 ± 18.1 g N/m<sup>2</sup> d, and 171.0 ± 16.9 g COD/m<sup>2</sup> d, respectively. The stable operation period was prolonged via addition of new cathode media (HRT 6 h), but this resulted in a lower  $I_V$  (14.64 ± 1.65 A/m<sup>2</sup>), HPR (32.0 ± 0.89 m<sup>3</sup> H<sub>2</sub>/m<sup>3</sup> d), ammonium removal rate (162.18 ± 10.37 g N/m<sup>2</sup> d), and COD removal (130.56 ± 4.45 g COD/m<sup>2</sup> d). The role of current generation in MECs on nitrogen fate and the potential of cation exchange membrane (CEM) for nitrogen transmission were addressed through an experimental work carried out by Haddadi et al. [27].

### MECs for Valuable Product Synthesis

The obvious and more common application of the MEC systems is the production of eco-friendly hydrogen and other biofuels. Apart from H<sub>2</sub>, cathode reactions of MECs can also be used to generate a variety of value-added compounds [45]. Table 1 shows some reported value-added bioproducts from MECs, including CH<sub>4</sub>, acetate, H<sub>2</sub>O<sub>2</sub>, ethanol, and formic acid.

#### Methane

Methane (CH<sub>4</sub>) is the most well-known fuel and is being widely consumed worldwide. CH<sub>4</sub> is commonly detected in MECs during H<sub>2</sub> production as a result of the methanogen growth. This will decrease the commercial value of H<sub>2</sub> and raise the energy and economical cost for its purification [76]. A novel perspective on this issue is to employ MECs to produce CH<sub>4</sub> as an alternative energy source. Direct production of CH<sub>4</sub> in MECs has several advantages over the conventional anaerobic digestion (AD) CH<sub>4</sub> processes. Firstly, organic matter oxidation and CH<sub>4</sub> production are two separated processes in MECs which allow high CH<sub>4</sub> content in produced biogas. Secondly, the process occurs at ambient temperature, i.e., heating is not required, thereby saving input energy. Thirdly, methanogens can accept electrons directly from cathode, which may make the process more tolerant to toxic compounds, for instance, ammonia [14]. Fourthly, MECs can use waste streams with low organic matter content, where AD cannot function [96].

Cheng et al. [11] for the first time reported the production of CH<sub>4</sub> from CO<sub>2</sub> in a two-chamber MECs, with CH<sub>4</sub> production rate reached 0.06 mmol/L/h under E<sub>ap</sub> = 1.2 V. Likewise, Villano et al. [95] measured a CH<sub>4</sub> production ratio of 0.055 ± 0.002 mmol/d-mg VSS from CO<sub>2</sub> in a two-chamber MECs with a biocathode incubated with a hydrogenophilic methanogenic culture at potentials more negative than 0.65 V (vs. SHE) (corresponding to 0.85 V vs. Ag/AgCl). It was noted from the work of Chae et al. [7] that the CH<sub>4</sub> production from MECs is varied with inoculum, substrate, and reactor designs. Furthermore, Clauwaert et al. [14] demonstrated that H<sub>2</sub> produced from the MECs can be further converted

to CH<sub>4</sub> in an external AD, where the process was not inhibited even at ammonium concentration of 5 g N/L. Moreover, a two-chamber MEC containing a carbon biocathode was developed and tested to understand the mechanisms for CH<sub>4</sub> bioelectrosynthesis [113]. Significant quantity of CH<sub>4</sub> was obtained at a poised potential of 0.9 V (vs. Ag/AgCl), reaching  $2.30 \pm 0.34$  mL after 5 h of operation with a faradaic efficiency of  $24.2 \pm 4.7\%$ .

These results demonstrated that electrode material is the crucial factor that governs electron exchange and CH<sub>4</sub> formation efficiencies in MECs. To promote CH<sub>4</sub> production, biocathode via modifying plain carbon stick with a layer of graphite felt (GF) was developed and examined in a two-chamber MEC [114]. CH<sub>4</sub> production with hybrid GF-biocathode reached 80.9 mL/L with the potential of  $-1.4$  V after 24 h of incubation.

#### Acetate

An experiment carried out by Nevin et al. [71] demonstrated that the possibility of reduction of CO<sub>2</sub> to acetate by acetogenic microorganism *Sporomusa ovata* with electrons transferred directly from a graphite cathode (GC) (Table 2). It was found from the work of Nevin et al. [71]

that *S. ovata* biofilms on the GC surfaces consumed electrons from electrode and converted CO<sub>2</sub> to acetate and small quantities of 2-oxobutyrate. Up to 85% of supplied electrons were captured into these products. It is for the first time that the concept of microbial electrosynthesis (MESs) has been proposed, which provides a highly attractive and innovative route that might convert solar energy to valuable organic products more effectively than conventional approaches. As a novel technology, the related mechanisms, foundation theory, and process understanding are still being developed. In this topic, a review article describes and addresses the principles, challenges, and opportunities of MESs and gives important point of view on MESs at the nexus of microbiology and electrochemistry [78].

#### Ethanol

Recently, the feasibility of ethanol (C<sub>2</sub>H<sub>5</sub>OH) production by using electrode instead of H<sub>2</sub> as electron donor in a biocathode MEC was demonstrated (Table 2) [88]. In a two-chamber MEC, acetate was reduced to C<sub>2</sub>H<sub>5</sub>OH via the assistance of electron mediator such as methyl viologen (MV). When the cathode potential was set at 0.55 V, a maximum  $I_V$  of 1.33 A/m<sup>2</sup> was

**Hydrogen Production Through Electrolysis, Table 2** Summary of the value-added biochemicals from MECs

Value-added chemicals	Input voltage (V)	MEC reactor	Cathode	Electron acceptor <sup>a</sup>	Production Rate (mmol/L/h) <sup>b</sup>	References
Acetate (C <sub>2</sub> H <sub>3</sub> O <sub>2</sub> <sup>-</sup> )	0.4	Two-chamber	Graphite sticks	CO <sub>2</sub>	- <sup>c</sup>	[71]
Methane (CH <sub>4</sub> )	0.7–1.0	Single-/two-chamber	Biocathode	CO <sub>2</sub>	0.06	[11]
Hydrogen peroxide (H <sub>2</sub> O <sub>2</sub> )	0.5	Two-chamber	Carbon cloth gas diffusion electrode	O <sub>2</sub>	1.17	[85]
Ethanol (C <sub>2</sub> H <sub>6</sub> O)	$-0.55^d$	Two-chamber	Biocathode	Acetate	0.00003	[88]
Formic acid (CH <sub>2</sub> O <sub>2</sub> )	1.13 <sup>e</sup>	Two-chamber	Pb	CO <sub>2</sub>	0.09	[112]

<sup>a</sup>Electron acceptor in the cathode chamber

<sup>b</sup>Calculated based on total reactor volume with the available data

<sup>c</sup>Not stated

<sup>d</sup>Cathode potential

<sup>e</sup>The power source is MFC stack

achieved after MV addition, leading to 1.82 mM  $C_2H_5OH$  production. The  $C_2H_5OH$  production was hugely dependent on the MV concentrations, and the production stopped after 5 days when MV was depleted [88]. MEC platform provides a new approach to overcome the limitation of conventional biological  $C_2H_5OH$  production. However, there are several challenges that need to be addressed. The mechanism of acetate reduction in the cathode is still unknown. Since  $H_2$  (0.0035 normalized  $m^3 H_2/m^2 d$ ) was observed in the cathode, it could also be involved in acetate reduction. Furthermore, the requirement of irreversibly electron acceptors will add the operation cost, which is a critical challenge for the practical application. Selection of electroactive bacteria which can accept electrons directly from cathode rather than via mediator for  $C_2H_5OH$  production could be interesting in future work. Moreover, the  $C_2H_5OH$  production rate and the final concentration produced in the reported system are still low. What's more, further reduction of electrode overpotential, system internal resistance, and energy losses could boost the  $C_2H_5OH$  production and make the  $C_2H_5OH$  production in MECs commercially applicable.

#### Hydrogen Peroxide

Hydrogen peroxide ( $H_2O_2$ ) is a vital industrial chemical, which can also be produced by MECs. The feasibility of  $H_2O_2$  production was recently demonstrated, based on the microbial oxidation of organic substrate in the anode coupled to  $O_2$  reduction in the cathode of MECs [85]. With  $E_{ap}$  of 0.5 V, this system was capable of producing  $H_2O_2$  at a rate of 1.17 mmol/L/h in the aerated cathode, consequent in an overall efficiency of 83% based on acetate oxidation [85]. Compared with conventional electrochemical method, the  $H_2O_2$  production in MECs needs less energy, which was 0.93 kWh/kg  $H_2O_2$  in the reported study. Theoretically,  $H_2O_2$  can be produced in MFCs with simultaneous electricity production, which was showed by several studies [22, 108]. However, the production rate of  $H_2O_2$  in MFCs was much lower than that of MECs.  $H_2O_2$  production has greatly expanded the application

possibilities of MECs. The most attractive application is the combination of Fenton reaction with MECs, as the MECs can serve as the relatively low-priced  $H_2O_2$  source for the Fenton reaction [23, 115].

To become a mature technology, more efforts should be put on the enhancement of  $H_2O_2$  concentration. The reported maximum  $H_2O_2$  concentration that can be achieved in MECs is only 0.13 wt% [85], which is still an order of magnitude lower than the expected level for real-world implications. A life cycle analysis (LCA) suggested that production of  $H_2O_2$  in MECs is more feasible than conventional routes [22]. However, the technology is still limited by several challenges, among which include  $H_2O_2$  supply and the presence of residual  $H_2O_2$  after the Fenton reaction which are two critical issues [73, 103]. An innovative bioelectro-Fenton system capable of alternate switching between MEC and MFC operation mode was developed to meet the abovementioned challenges [111].

#### Formic Acid

Formic acid ( $HCOOH$ ) is an essential chemical used in pharmaceutical syntheses as well as in paper and pulp production and was achieved based on substrate oxidation in the anode and  $CO_2$  reduction at the cathode [112] (Table 2). The electricity needed for this process was supplied by a five series connected MFCs units, which produced an open circuit voltage (OPC) of 2.73 V. Consequently,  $HCOOH$  was produced at a rate of 0.09 mM/L/h, and a CE of 64.8% was obtained [112]. This innovative approach will contribute to recover and recycle the  $CO_2$  produced during wastewater/waste treatment without energy input, thereby promoting the GHG reduction. Nevertheless, the production rate and the final obtained concentration of  $HCOOH$  are still low at the present stage. The mass transfer and the cathode electrodes are two most crucial factors to enhance the conversion rate. Strategies, for instance, gas diffusion through hollow fiber membrane, could be adapted in future work to raise the dissolution of  $CO_2$ , thereby improving the mass transfer.

## Conclusions and Future Application of MECs

MECs have become a promising technology and nature friendly in the fields of hydrogen production and wastewater treatment. The last decade of research efforts has made significant strides toward practical application of MECs. In this chapter, we have provided an up-to-date review of current application and future perspectives of MEC technology from a practical application point of view. The following conclusions have been drawn:

- (a) A better understanding of basic fundamentals and theories of MECs such as operating principles; the EET mechanisms are vital for upscaling of this technology.
- (b) Selection of different types of efficient EAB and further investigation about the mechanism of EET.
- (c) Amplifying oxidation of hydrogen at the cathode of MECs. With the appropriate process parameters, it is essential to control the conditions of MEC for enhancing the growth of EAB.
- (d) Selection of appropriate substrate. The types of substrate directly influence the  $H_2$  yield. Among different substrates, wastewater is a sustainable rich medium which can be treated by MECs. When MECs are fed with DWW, they can accomplish above 75% COD removal with an associated energy consumption below that traditionally associated to conventional processes. However,  $R_{H_2}$  is usually low, while IWW usually presents higher organic concentration which normally results in higher HPR. However, they often demand some kind of amendment before being fed to the MEC.
- (e)  $CH_4$ -producing MECs could be regarded as a suitable alternative to  $H_2$ -producing MECs to accelerate the commercial development of MEC technology.
- (f) Future prospects of MEC technology are promising: during the last years, several pilot-scale reactors have been developed, and first commercial experiences are in course.

- (g) Other application possibilities of MECs such as chemical synthesis, pollutant removal or control, and heavy metal recovery/removal have not yet moved out from lab. A step-change improvement in performance is needed for many applications, which includes much higher power densities and energy efficiencies.

The application scopes of MECs could be further expanded, e.g., for nutrient recovery. MECs can be an alternative and promising technology to store electrical energy generated from renewable energy sources such as wind and solar into biofuels as well as contribute to  $CO_2$  mitigation. Furthermore, the integration of MECs with existing separation, convention, and treatment processes, e.g., AD, is helpful for overcoming drawback and bringing benefits to each other, thereby boosting the waste conversion and  $H_2$  production. Moreover, the development of the integrated MECs with hydrolysis acidification, as to the nonbiodegradable pollutants, the pretreatment of the hydrolysis acidification process is the main technology. The bottleneck of this technology is to strengthen the effect of fermentation. Therefore, hydrolysis acidification coupled with MEC process is the trend of the field.

**Acknowledgments** This work was supported by the National University of Malaysia (UKM), Project No: DIP-2012-30 and the Malaysian Ministry of Higher Education (MOHE). Special thanks to the Head of Project (D-I-P-2012-30), Prof. Dr. Azah Bt Mohamed, and members.

## Bibliography

### Primary Literature

1. Acar C, Dincer I (2014) Comparative assessment of hydrogen production methods from renewable and non-renewable sources. *Int J Hydrog Energy* 39:1–12
2. Almatouq A, Babatunde AO (2017) Concurrent hydrogen production and phosphorus recovery in dual chamber microbial electrolysis cell. *Bioresour Technol* 237:193–203
3. Borole AP, Hamilton CY, Vishnivetskaya T, Leak D, Andras C (2009) Improving power production in acetate-fed microbial fuel cells via enrichment of

- exoelectrogenic organisms in flow-through systems. *Biochem Eng J* 48:71–80
- Call DF, Logan BE (2008) Hydrogen production in a single chamber microbial electrolysis cell (MEC) lacking a membrane. *Environ Sci Technol* 42:3401–3406
  - Call DF, Merrill MD, Logan BE (2009) High surface area stainless steel brushes as cathodes in microbial electrolysis cells. *Environ Sci Technol* 43:2179–2183
  - Catal T, Lesnik KL, Liu H (2015) Suppression of methanogenesis for hydrogen production in single chamber microbial electrolysis cells using various antibiotics. *Bioresour Technol* 187:77–83
  - Chae KJ, Choi MJ, Kim KY, Ajayi FF, Chang IS, Kim IS (2010) Selective inhibition of methanogens for the improvement of biohydrogen production in microbial electrolysis cells. *Int J Hydrog Energy* 35(24):13379–13386
  - Chen Y, Xu Y, Chen L, Li P, Zhu S, Shen S (2015) Microbial electrolysis cells with polyaniline/multi-walled carbon nanotube-modified biocathodes. *Energy* 88:377–384
  - Chen Y, Shen J, Huang L, Pan Y, Quan X (2016) Enhanced Cd(II) removal with simultaneous hydrogen production in biocathode microbial electrolysis cells in the presence of acetate or NaHCO<sub>3</sub>. *Int J Hydrog Energy* 41(31):13368–13379
  - Cheng S, Logan BE (2007) Sustainable and efficient biohydrogen production via electrohydrogenesis. *Proc Natl Acad Sci U S A* 104:18871–18873
  - Cheng S, Xing D, Call DF, Logan BE (2009) Direct biological conversion of electrical current into methane by electromethanogenesis. *Environ Sci Technol* 43(10):3953–3958
  - Cherkasov N, Ibhaddon A, Fitzpatrick PA (2015) review of the existing and alternative methods for greener nitrogen fixation. *Chem Eng Process* 90:24–33
  - Choi C, Hu N (2016) The modeling of gold recovery from tetrachloroaurate wastewater using a microbial fuel cell. *Bioresour Technol* 133:589–598
  - Clauwaert P, Toledo R, van der Ha D, Crab R, Verstraete W, Hu H, Udert KM, Rabaey K (2008) Combining biocatalyzed electrolysis with anaerobic digestion. *Water Sci Technol* 57(4):575–579
  - Cusick RD, Kiely PD, Logan BE (2010) A monetary comparison of energy recovered from microbial fuel cells and microbial electrolysis cells fed winery or domestic waste waters. *Int J Hydrog Energy* 35:8855–8861
  - Cusick RD, Bryan B, Parker DS, Merrill MD, Mehanna M, Kiely PD, Liu G, Logan BE (2011) Performance of a pilot-scale continuous flow microbial electrolysis cell fed winery wastewater. *Appl Microbiol Biotechnol* 89:2053–2063
  - Dai H, Yang H, Liu X, Jian X, Liang Z (2016) Electrochemical evaluation of nano-Mg(OH)<sub>2</sub>/graphene as a catalyst for hydrogen evolution in microbial electrolysis cell. *Fuel* 174:251–256
  - Ditzig J, Liu H, Logan BE (2007) Production of hydrogen from domestic waste water using a bioelectrochemically assisted microbial reactor (BEAMR). *Int J Hydrog Energy* 32(13):2296–2304
  - EIA: International Energy Outlook (2016) Chapter 1 World energy and economic outlook. <https://www.eia.gov/outlooks/ieo/world.cfm>
  - Fang HHP, Liu H, Zhang T (2005) Phototrophic hydrogen production from acetate and butyrate in wastewater. *Int J Hydrog Energy* 30:785–793
  - Farhangi S, Ebrahimi S, Niasar MS (2014) Commercial materials as cathode for hydrogen production in microbial electrolysis cell. *Biotechnol Lett* 36(10):1987–1992
  - Foley JM, Rozendal RA, Hertle CK, Lant PA, Rabaey K (2010) Life cycle assessment of high-rate anaerobic treatment, microbial fuel cells, and microbial electrolysis cells. *Environ Sci Technol* 44(9):3629–3637
  - Fu L, You SJ, Zhang GQ, Yang FL, Fang XH (2010) Degradation of azo dyes using in-situ Fenton reaction incorporated into H<sub>2</sub>O<sub>2</sub>-producing microbial fuel cell. *Chem Eng J* 160(1):164–169
  - Fu Q, Kobayashi H, Kuramochi Y, Xu J, Wakayama T, Maeda H, Sato K (2013) Bioelectrochemical analyses of a thermophilic biocathode catalyzing sustainable hydrogen production. *Int J Hydrog Energy* 38(35):15638–15645
  - Gorby YA, Yamina S, Mclean JS, Rosso KM, Moyses D, Dohnalkova A, Beveridge TJ, Chang IS, Kim BH, Kim KS, Culley DE, Reed SB, Romine MF, Saffarini DA, Hill EA, Shi L, Elias DA, Kennedy DW, Pinchuk G, Watanabe K, Ishii S, Logan B, Nealson KH, Fredrickson JK (2006) Electrically conductive bacterial nanowires produced by *Shewanella oneidensis* strain MR-1 and other microorganisms. *Proc Natl Acad Sci U S A* 103:11358–11363
  - Gralnick JA, Newman DK (2007) Extracellular respiration. *Mol. Microbiology* 65:1–11
  - Haddadi S, Nabi-Bidhendi G, Mehrdadi N (2014) Nitrogen removal from wastewater through microbial electrolysis cells and cation exchange membrane. *J Environ Health Sci Eng* 12:48
  - Hallenbeck PC, Ghosh D, Skonieczny MT, Yargeau V (2009) Microbiological and engineering aspects of biohydrogen production. *Indian J Microbiol* 49:48–59
  - Heidrich ES, Curtis TP, Dolfing J (2011) Determination of the internal chemical energy of wastewater. *Environ Sci Technol* 45:827–832
  - Heidrich ES, Dolfing J, Scott K, Edwards SR, Jones C, Curtis TP (2012) Production of hydrogen from domestic wastewater in a pilot-scale microbial electrolysis cell. *Appl Microbiol Biotechnol* 97(15):6979–6989
  - Heidrich ES, Edwards SR, Dolfing J, Cotterill SE, Curtis TP (2014) Performance of a pilot scale



- microbial electrolysis cell fed on domestic wastewater at ambient temperatures for a 12 month period. *Bioresour Technol* 173:87–95
32. Hou Y, Zhang R, Luo H, Liu G, Kim Y, Yu S, Zeng J (2015) Microbial electrolysis cell with spiral wound electrode for wastewater treatment and methane production. *Process Biochem* 50(7):1103–1109
  33. Hrapovic S, Manuel MF, Luong J, Guiot S, Tartakovskiy B (2010) Electrodeposition of nickel particles on a gas diffusion cathode for hydrogen production in a microbial electrolysis cell. *Int J Hydrog Energy* 35:7313–7320
  34. Hu H, Fan Y, Liu H (2008) Hydrogen production using single-chamber membrane-free microbial electrolysis cells. *Water Res* 42:4172–4178
  35. Hu H, Fan Y, Liu H (2009) Hydrogen production in single-chamber tubular microbial electrolysis cells using non-precious-metal catalysts. *Int J Hydrog Energy* 34:8535–8542
  36. Huang Y-X, Liu X-W, Sun X-F, Sheng G-P, Zhang Y-Y, Yan G-M, Wang S-G, A-W X, Yu H-QA (2011) new cathodic electrode deposit with palladium nanoparticles for cost-effective hydrogen production in a microbial electrolysis cell. *Int J Hydrog Energy* 36:2773–2776
  37. Huang L, Jiang L, Wang Q, Quan X, Yang J, Chen L (2014) Cobalt recovery with simultaneous methane and acetate production in biocathode microbial electrolysis cells. *Chem Eng J* 253:281–290
  38. Hutchinson AJ, Tokash JC, Logan BE (2011) Analysis of carbon fibre brush loading in anodes on startup and performance of microbial fuel cells. *J Power Sources* 196:9213–9219
  39. Ivanov I, Ren L, Siegert M, Logan BEA (2013) quantitative method to evaluate microbial electrolysis cell effectiveness for energy recovery and wastewater treatment. *Int J Hydrog Energy* 38(30):13135–13142
  40. Jain IP (2009) Hydrogen the fuel for 21st century. *Int J Hydrog Energy* 34(17):7368–7378
  41. Jeremiasse AW, Hamelers HVM, Buisman CJN (2010a) Microbial electrolysis cell with a microbial biocathode. *Bioelectrochemistry* 78:39–43
  42. Jeremiasse AW, Hamelers HVM, Saakes M, Buisman CJN (2010b) Ni foam cathode enables high volumetric H<sub>2</sub> production in a microbial electrolysis cell. *Int J Hydrog Energy* 35:12716–12723
  43. Kadier A, Simayi Y, Kalil MS, Abdeshahian P, Hamid AAA (2014) review of the substrates used in microbial electrolysis cells (MECs) for producing sustainable and clean hydrogen gas. *Renew Energy* 71:466–472
  44. Kadier A, Simayi Y, Chandrasekhar K, Ismail M, Kalil MS (2015) Hydrogen gas production with an electroformed Ni mesh cathode catalysts in a single-chamber microbial electrolysis cell (MEC). *Int J Hydrogen Energy* 40(41):14095–14103
  45. Kadier A, Kalil MS, Abdeshahian P, Chandrasekhar K, Mohamed A, Azman NF, Logroño W, Simayi Y, Hamid AA (2016) Recent advances and emerging challenges in microbial electrolysis cells (MECs) for microbial production of hydrogen and value-added chemicals. *Renew Sust Energ Rev* 61:501–525
  46. Kadier A, Simayi Y, Abdeshahian P, Azman NF, Chandrasekhar K, Kalil MS (2016) A comprehensive review of microbial electrolysis cells (MEC) reactor designs and configurations for sustainable hydrogen gas production. *Alexandria Eng J* 55:427–443
  47. Kadier A, Kalil MS, Mohamed A, Hasan AA, Abdeshahian P, Fooladi T, Hamid AA (2017) Microbial electrolysis cells (MEC) as innovative technology for sustainable hydrogen production: Fundamentals and perspective applications. In: Sankir M, Sankir ND (eds) *Hydrogen Production Technologies*. Wiley-Scrivener Publishing LLC, Hoboken, pp 407–458
  48. Kapdan L, Kargi F (2006) Biohydrogen production from waste materials. *Enzyme Microb Technol* 38:569–582
  49. Khan MZ, Sim YL, Lin YJ, Lai KM (2012) Testing biological effects of hand-washing grey water for reuse in irrigation on an urban farm: a case study. *Environ Technol* 34:545–551
  50. Khan MZ, Singh S, Sreekrishnan TR, Ahammad SZ (2014) Feasibility study on anaerobic biodegradation of azo dye reactive orange 16. *RSC Adv* 4:46851–46859
  51. Khan MZ, Nizami AS, Rehan M, Ouda OKM, Sultana S, Ismail IM, Shahzad K (2017) Microbial electrolysis cells for hydrogen production and urban wastewater treatment: A case study of Saudi Arabia. *Appl Energy* 185(P1):410–420
  52. Kiely PD, Cusick R, Call DF, Selembo PA, Regan JM, Logan BE (2011) Anode microbial communities produced by changing from microbial fuel cell to microbial electrolysis cell operation using two different wastewaters. *Bioresour Technol* 102:388–394
  53. Kumar A, Katuri K, Lens P, Leech D (2012) Does bioelectrochemical cell configuration and anode potential affect biofilm response? *Biochem Soc Trans* 40(6):1308–1314
  54. Kuntke P, Sleutel THJA, Saakes M, Buisman CJN (2014) Hydrogen production and ammonium recovery from urine by a Microbial Electrolysis Cell. *Int J Hydrog Energy* 39(10):4771–4778
  55. Lalaurette E, Thammannagowda S, Mohagheghi A, Maness PC, Logan BE (2009) Hydrogen production from cellulose in a two-stage process combining fermentation and electrohydrogenesis. *Int J Hydrog Energy* 34:6201–6210
  56. Lee HS, Rittmann BE (2009) Characterization of energy losses in an upflow single-chamber microbial electrolysis cell. *Int J Hydrog Energy* 35:920–927
  57. Liu H, Grot S, Logan BE (2005) Electrochemically assisted microbial production of hydrogen from acetate. *Environ Sci Technol* 39(11):4317–4320

58. Liu YP, Wang YH, Wang BS, Chen QY (2014) Effect of anolyte pH and cathode Pt loading on electricity and hydrogen co-production performance of the bioelectrochemical system. *Int J Hydrog Energy* 39:14191–14195
59. Logan BE, Aelterman P, Hamelers B, Rozendal R, Schroder U, Keller J, Freguia S, Aelterman P, Verstraete W, Rabaey K (2006) Microbial fuel cells: methodology and technology. *Environ Sci Technol* 40:5181–5192
60. Logan B, Call D, Cheng S, Hamelers HM, Tomh Sleutels JA, Jeremiasse AW, Rozendal RA (2008) Microbial electrolysis cells for high yield hydrogen gas production from organic matter. *Environ Sci Technol* 42:8630–8640
61. Lorenzo DM, Scott K, Curtis TP, Katuri KP, Head IM (2009) Continuous feed microbial fuel cell using an air cathode and a disc anode stack for wastewater treatment. *Energy Fuel* 23:5707–5716
62. Lu L, Ren ZJ (2016) Microbial electrolysis cells for waste biorefinery: A state of the art review. *Bioresour Technol* 215:254–264
63. Lu L, Ren NQ, Xing DF, Logan BE (2009) Hydrogen production with effluent from an ethanol-H<sub>2</sub>-coproducing fermentation reactor using a single-chamber microbial electrolysis cell. *Biosens Bioelectron* 24:3055–3060
64. Lu L, Xing D, Liu B, Ren N (2012a) Enhanced hydrogen production from waste activated sludge by cascade utilization of organic matter in microbial electrolysis cells. *Water Res* 46(4):1015–1026
65. Lu L, Xing D, Ren N (2012b) Pyrosequencing reveals highly diverse microbial communities in microbial electrolysis cells involved in enhanced H<sub>2</sub> production from waste activated sludge. *Water Res* 46(7):2425–2434
66. Lu L, Hou D, Fang Y, Huang Y, Ren ZJ (2016) Nickel based catalysts for highly efficient H<sub>2</sub> evolution from wastewater in microbial electrolysis cells. *Electrochim Acta* 206:381–387
67. Mahmoud M, Parameswaran P, Torres CI, Rittmann BE (2014) Fermentation pre-treatment of landfill leachate for enhanced electron recovery in a microbial electrolysis cell. *Bioresour Technol* 151:151–158
68. Mazloomi K, Gomes C (2012) Hydrogen as an energy carrier: prospects and challenges. *Renew Sust Energy Rev* 16:3024–3033
69. Montpart N, Rago L, Baeza JA, Guisasola A (2015) Hydrogen production in single chamber microbial electrolysis cells with different complex substrates. *Water Res* 68:601–615
70. Nam JY, Tokash JC, Logan BE (2011) Comparison of microbial electrolysis cells operated with added voltage or by setting the anode potential. *Int J Hydrog Energy* 36:10550–10556
71. Nevin KP, Woodard TL, Franks AE, Summers ZM, Lovley DR (2010) Microbial electrosynthesis: feeding microbes electricity to convert carbon dioxide and water to multicarbon extracellular organic compounds. *MBio* 1(2):e00103–e00110
72. Newman DK, Kolter R (2000) A role for excreted quinones in extracellular electron transfer. *Nature* 405(6782):94–97
73. Nidheesh PV, Gandhimathi R, Ramesh ST (2013) Degradation of dyes from aqueous solution by Fenton processes: a review. *Environ Sci Pollut Res* 20:2099–2132
74. Nimje VR, Chen CY, Chen CC, Chen HR, Tseng MJ, Jean JS et al (2011) Glycerol degradation in single-chamber microbial fuel cells. *Bioresour Technol* 102(3):2629–2634
75. Pagliaro MV, Bellini M, Bevilacqua M, Filippi J, Folliero MG, Marchionni A, Miller HA, Oberhauser W, Caporali S, Innocentiae M, Vizza F (2017) Carbon supported Rh nanoparticles for the production of hydrogen and chemicals by the electro-reforming of biomass-derived alcohols. *RSC Adv* 7:13971–13978
76. Pant D, Singh A, Bogaert GV, Olsen SI, Nigam PS, Diels L, Vanbroekhoven K (2012) Bioelectrochemical systems (BES) for sustainable energy production and product recovery from organic wastes and industrial wastewaters. *RSC Adv* 2:1248–1263
77. Pham TH, Rabaey K, Aelterman P, Clauwaert P, De Schampelaere L, Boon N et al (2006) Microbial fuel cells in relation to conventional anaerobic digestion technology. *Eng Life Sci* 6:285–292
78. Rabaey K, Rozendal RA (2010) Microbial electro-synthesis revisiting the electrical route for microbial production. *Nat Rev Microbiol* 8(10):706–716
79. Reguera G, McCarthy KD, Mehta T, Nicoll JS, Tuominen MT, Lovley DR (2005) Extracellular electron transfer via microbial nanowires. *Nature* 435:1098–1101
80. Ren L, Siegert M, Ivanov I, Pisciotta JM, Logan BE (2013) Treatability studies on different refinery wastewater samples using high throughput microbial electrolysis cells (MECs). *Bioresour Technol* 136:322–328
81. Ribot-Llobet E, Nam J-Y, Tokash JC, Guisasola A, Logan BE (2013) Assessment of four different cathode materials at different initial pHs using unbuffered catholytes in microbial electrolysis cells. *Int J Hydrog Energy* 38:2951–2956
82. Rozendal RA, Hamelers HVM, Euverink GJW, Metz SJ, Buisman CJN (2006) Principle and perspectives of hydrogen production through biocatalyzed electrolysis. *Int J Hydrog Energy* 31(12):1632–1640
83. Rozendal RA, Jeremiasse AW, Hamelers HVM, Buisman CJN (2007) Hydrogen production with a microbial biocathode. *Environ Sci Technol* 42:629–634
84. Rozendal RA, Jeremiasse AW, Hamelers HVM, Buisman CJN (2008) Hydrogen production with a microbial biocathode. *Environ Sci Technol* 42:629–634

85. Rozendal RA, Leone E, Keller J, Rabaey K (2009) Efficient hydrogen peroxide generation from organic matter in a bioelectrochemical system. *Electrochem Commun* 11(9):1752–1755
86. Selembo PA, Merrill MD, Logan BE (2009) The use of stainless steel and nickel alloys as low-cost cathodes in microbial electrolysis cells. *J Power Sources* 190:271–278
87. Sosa-Hernández O, Popat SC, Parameswaran P, Alemán-Nava GS, Torres CI, Buitrón G, Parra-Saldívar R (2016) Application of microbial electrolysis cells to treat spent yeast from an alcoholic fermentation. *Bioresour Technol* 200:342–349
88. Steinbusch KJJ, Hamelers HVM, Schaap JD, Kampman C, Buisman CJN (2010) Bioelectrochemical ethanol production through mediated acetate reduction by mixed cultures. *Environ Sci Technol* 44(1):513–517
89. Su M, Wei L, Qiu Z, Wang G, Shen J (2016) Hydrogen production in single chamber microbial electrolysis cells with stainless steel fiber felt cathodes. *J Power Sources* 301:29–34
90. Sun R, Xing D, Jia J, Liu Q, Zhou A, Bai S, Ren N (2014) Optimization of high-solid waste activated sludge concentration for hydrogen production in microbial electrolysis cells and microbial community diversity analysis. *Int J Hydrog Energy* 39(35):19912–19920
91. Tenca A, Cusick RD, Schievano A, Oberti R, Logan BE (2013) Evaluation of low cost cathode materials for treatment of industrial and food processing wastewater using microbial electrolysis cells. *Int J Hydrog Energy* 38(4):1859–1865
92. Tice RC, Kim Y (2014) Methanogenesis control by electrolytic oxygen production in microbial electrolysis cells. *Int J Hydrog Energy* 39:3079–3086
93. Tokash JC, Logan BE (2011) Electrochemical evaluation of molybdenum disulfide as a catalyst for hydrogen evolution in microbial electrolysis cells. *Int J Hydrog Energy* 36:9439–9445
94. Torres CI, Marcus AK, Lee HS, Parameswaran P, Krajmalnik-Brown R, Rittmann BE (2010) A kinetic perspective on extracellular electron transfer by anode-respiring bacteria. *FEMS Microbiol Rev* 34(1):3–17
95. Villano M, Aulenta F, Ciucci C, Ferri T, Giuliano A, Majone M (2010) Bioelectrochemical reduction of CO<sub>2</sub> to CH<sub>4</sub> via direct and indirect extracellular electron transfer by a hydrogenophilic methanogenic culture. *Bioresour Technol* 10:3085–3090
96. Villano M, Monaco G, Aulenta F, Majone M (2011) Electrochemically assisted methane production in a biofilm reactor. *J Power Sources* 196(22):9467–9472
97. Von Canstein H, Ogawa J, Shimizu S, Lloyd JR (2008) Secretion of flavins by *Shewanella* species and their role in extracellular electron transfer. *Appl Environ Microbiol* 74:615–623
98. Wagner RC, Regan JM, SE O, Zuo Y, Logan BE (2009) Hydrogen and methane production from swine wastewater using microbial electrolysis cells. *Water Res* 43:1480–1488
99. Wang L, Chen Y, Huang Q, Feng Y, Zhu S, Shen S (2012) Hydrogen production with carbon nanotubes based cathode catalysts in microbial electrolysis cells. *J Chem Technol Biotechnol* 87(8):1150–1156
100. Wang J, Xu S, Xiao B, Xu M, Yang L, Liu S et al (2013) Influence of catalyst and temperature on gasification performance of pig compost for hydrogen-rich gas production. *Int J Hydrog Energy* 38:14200–14207
101. Wang M, Wang Z, Gong X, Guo Z (2014) The intensification technologies to water electrolysis for hydrogen production – a review. *Renew Sust Energy Rev* 29:573–588
102. Wang Y, Guo WQ, Xing DF, Chang JS, Ren MQ (2015) Hydrogen production using biocathode single-chamber microbial electrolysis cells fed by molasses wastewater at low temperature. *Int J Hydrog Energy* 39(33):19369–19375
103. Wu TT, Englehardt JD (2012) A new method for removal of hydrogen peroxide interference in the analysis of chemical oxygen demand. *Environ Sci Technol* 46:2291–2298
104. Wu T, Zhu G, Jha AK, Zou R, Liu L, Huang X, Liu C (2013) Hydrogen production with effluent from an anaerobic baffled reactor (ABR) using a single-chamber microbial electrolysis cell (MEC). *Int J Hydrog Energy* 38(25):11117–11123
105. Xiao L, Wen Z, Ci S, Chen J, He Z (2012) Carbon/iron-based nanorod catalysts for hydrogen production in microbial electrolysis cells. *Nano Energy* 1:751–756
106. Yang Q, Jiang Y, Xu Y, Qiu Y, Chen Y, Zhu S, Shen S (2014) Hydrogen production with polyaniline/multi-walled carbon nanotube cathode catalysts in microbial electrolysis cells. *J Chem Technol Biotechnol* 70(7):1263–1269
107. Yang Q, Jiang Y, Xu Y, Qiu Y, Chen Y, Zhu S, Shen S (2015) Hydrogen production with polyaniline/multi-walled carbon nanotube cathode catalysts in microbial electrolysis cells. *J Chem Technol Biotechnol* 90(7):1263–1269
108. You SJ, Wang JY, Ren NQ, Wang XH, Zhang JN (2010) Sustainable conversion of glucose into hydrogen peroxide in a solid polymer electrolyte microbial fuel cell. *ChemSusChem* 3(3):334–338
109. Yuan H, Li J, Yuan C, He Z (2014) Facile synthesis of MoS<sub>2</sub>@CNT as an effective catalyst for hydrogen production in microbial electrolysis cells. *ChemElectroChem* 1(11):1828–1833
110. Zhang Y, Merrill MD, Logan BE (2010) The use and optimization of stainless steel mesh cathodes in microbial electrolysis cells. *Int J Hydrog Energy* 35:12020–12028
111. Zhang Y, Wang Y, Angelidaki I (2015) Alternate switching between microbial fuel cell and microbial electrolysis cell operation as a new method to control

- H<sub>2</sub>O<sub>2</sub> level in Bioelectro-Fenton system. *J Power Sources* 291:108–116
112. Zhao HZ, Zhang Y, Chang YY, Li ZS (2012) Conversion of a substrate carbon source to formic acid for carbon dioxide emission reduction utilizing series-stacked microbial fuel cells. *J Power Sources* 217:59–64
113. Zhen G, Kobayashi T, Lu X, Xu K (2015) Understanding methane bioelectrosynthesis from carbon dioxide in a two-chamber microbial electrolysis cells (MECs) containing a carbon biocathode. *Bioresour Technol* 186:141–148
114. Zhen G, Lu X, Kobayashi T, Kumara G, Xu K (2016) Promoted electromethanosynthesis in a two-chamber microbial electrolysis cells (MECs) containing a hybrid biocathode covered with graphite felt (GF). *Chem Eng J* 284:1146–1155
115. Zhuang L, Zhou S, Yuan Y, Liu M, Wang Y (2010) A novel bioelectro-Fenton system for coupling anodic COD removal with cathodic dye degradation. *Chem Eng J* 163(1–2):160–163



## Electrochemical Hydrogen Production

Marc T. M. Koper  
Leiden Institute of Chemistry, Leiden University,  
Leiden, The Netherlands

### Article Outline

Definition of the Subject  
Introduction  
General Theory  
More Detailed Theories and Simulations  
Hydrogen Evolution at Metal Electrodes  
Hydrogen Evolution at (Electrodes Modified  
with) Molecular Catalysts in Aqueous and  
Nonaqueous Solvents  
Concluding Remarks  
Bibliography

### Definition of the Subject

The electrochemical production of hydrogen by photo-electrolysis or electrolysis is one of the most promising ways for making high-purity hydrogen. Water electrolysis is as old as the field of electrochemistry itself, and this entry focuses on some of the fundamental principles that have been established through the years.

### Introduction

Hydrogen ( $H_2$ ) is considered by many as the fuel of the future. In view of the current interest and importance in securing the sustainability of our society's energy needs, many research efforts are invested in making hydrogen, storing hydrogen, and converting hydrogen back to work. One of the most promising ways to make *clean* "solar hydrogen" is by electrochemistry or electrolysis, either in combination with a photovoltaic cell or in an integrated photo-electrochemical device.

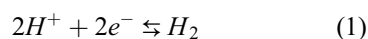
A crucial component of such a device is the catalyst converting water (or protons) into hydrogen. Such a catalyst must be efficient, stable, robust, cheap (or "cost-effective") and be made from abundant sources.

This entry will consider some fundamental considerations associated with the catalysis of the electro-chemical hydrogen production. The entry will focus on the energetic and thermodynamic requirements for such a catalyst [1–3] as opposed to the more usual approach (especially in the field of hydrogen evolution by molecular catalysts) in which emphasis is often on structural aspects of the catalyst. Of course, in an all-encompassing approach or theory, the two must be related, but in the author's view the approach emphasizing the energetic relationships provides a very useful general and basic framework for later, more detailed, approaches. The entry will also discuss these more detailed electrochemical models as well as the role of the solvent in the hydrogen evolution reaction (HER).

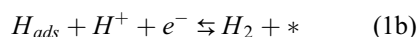
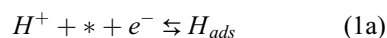
### General Theory

#### Thermodynamic Theory

The hydrogen evolution reaction (HER), or the reverse hydrogen oxidation reaction (HOR), is a classic example of a two-electron transfer reaction



The reaction has a standard equilibrium potential  $E_{H_2/H^+}^0$  of 0 V. The mechanism for the hydrogen oxidation/evolution reaction on metals will be considered first [4]. Later, this will be extended to a more general mechanism that encompasses the framework suggested for molecular catalysts. The classical electrochemical mechanism consists of three steps:



© Springer Science+Business Media, LLC 2012  
T. E. Lipman, A. Z. Weber (eds.), *Fuel Cells and Hydrogen Production*,  
[https://doi.org/10.1007/978-1-4939-7789-5\\_862](https://doi.org/10.1007/978-1-4939-7789-5_862)

Originally published in  
R. A. Meyers (ed.), *Encyclopedia of Sustainability Science and Technology*, © Springer Science+Business Media, LLC 2012  
[https://doi.org/10.1007/978-1-4419-0851-3\\_862](https://doi.org/10.1007/978-1-4419-0851-3_862)



known as the Volmer, Heyrovsky, and Tafel steps, respectively. The symbol \* stands for a free adsorption site on the metal electrode surface, but it may also be considered as a coordination site for hydrogen in a molecular catalyst. The  $H_{ads}$  intermediate is a hydrogen species chemisorbed to such a site on the surface or in the molecular catalyst. Note that in reactions 1a and 1b, the proton and electron transfer are assumed to take place simultaneously. The concerted character of the proton–electron transfer for the Volmer reaction on Pt(111) is supported by recent detailed ab initio density functional theory (DFT) calculations [5, 6].

The above multistep mechanism needs to satisfy thermodynamic constraints in the sense that the combined equilibrium constants need to conform to the Nernst equation of the overall reaction [7]. Let us assume that the reaction follows a Volmer–Heyrovsky mechanism, in which case:

$$\frac{E_{H^+/H_{ads}}^0 + E_{H_{ads},H^+/H_2}^0}{2} = E_{H^+/H_2}^0 = 0 \quad (2)$$

The equilibrium potential of a redox reaction involving an adsorbed or chemisorbed state can be calculated if one defines the concomitant standard state. Consider the Volmer reaction 1a, for which the equilibrium condition is

$$\Delta G(H_{ads}) = \Delta G(H^+ + e^-) \quad (3)$$

Following Nørskov et al. [8], the term on the right-hand side is 0 at  $E = 0$  (vs NHE) by definition, and  $-e_0E$  at any other potential  $E$ , assuming that when the potential is changed only the energy of the electrons changes, and nothing else. The latter assumption may be tested by DFT calculations, showing that the binding energy of  $H_{ads}$  does not depend strongly on potential, or on an applied electric field [9–12]. This implies that the static dipole moment of the  $H_{ads}$  bond to the surface is close to 0, and that the electrosorption valency corresponding to reaction 1a is close to 1 [12]. Therefore, the standard equilibrium potential for the Volmer reaction follows as:

$$E_{H^+/H_{ads}}^0 = -\frac{\Delta G^0(H_{ads})}{e_0} \quad (4)$$

where  $\Delta G^0(H_{ads})$  is the free adsorption energy of  $H_{ads}$  at some suitably defined standard state “0” (for instance, one-fourth coverage on a (111) surface), with respect to the energy of  $H_2$ , which is equal to 0 also by virtue of the above definition. If  $\Delta G^0(H_{ads}) < 0$ , i.e.,  $H_{ads}$  formation onto the catalyst surface yields a thermodynamically more favorable situation than  $H_2$  evolution,  $E_{H^+/H_{ads}}^0 > 0$ . A well-known example of this is hydrogen underpotential deposition (UPD) on platinum and other transition-metal electrodes. Note, however, that in terms of the overall reaction, such a situation implies

$$E_{H^+/H_{ads}}^0 = -E_{H_{ads},H^+/H_2}^0 < 0 \quad (5)$$

so that the Heyrovsky reaction would have a standard equilibrium potential (defined for the same standard state) below 0 V. Neglecting kinetic factors, this analysis would suggest that if in the HER,  $H_{ads}$  formation would be a thermodynamically favorable reaction at  $E = 0$ , molecular hydrogen formation as in the Heyrovsky reaction must be thermodynamically unfavorable. Following Nørskov et al. [8], one could argue that in such a case, the minimal “thermodynamic overvoltage” for the overall reaction,  $\eta_T$ , would be equal to the standard equilibrium potential of the thermodynamically least favorable reaction, i.e.,  $\eta_T = E_{H^+,H_{ads}/H_2}^0 - E_{H^+/H_2}^0$ . This “thermodynamically least favorable reaction step” is termed the *potential-determining step* (not to be confused with the rate-determining step, though often they may correspond to the same reaction step). Since the lowest possible “thermodynamic overvoltage” is 0, it follows that, on the basis of these thermodynamic considerations, we are looking for a catalyst with:

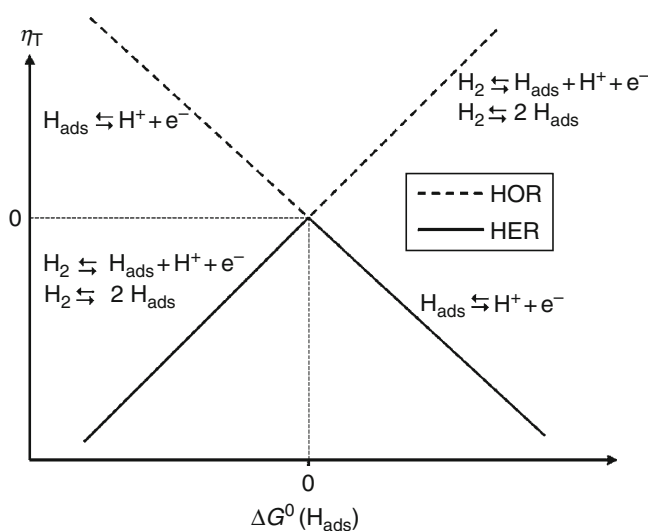
$$\begin{aligned} \eta_T &= E_{H^+/H_{ads}}^0 = E_{H_{ads},H^+/H_2}^0 = \frac{\Delta G^0(H_{ads})}{e_0} \\ &= 0 \end{aligned} \quad (6)$$



Any catalyst with  $\Delta G^0(\text{H}_{\text{ads}}) \neq 0$  will have a  $\eta_{\text{T}} > 0$  as either the Volmer reaction has a standard equilibrium potential more negative than 0 ( $\Delta G^0(\text{H}_{\text{ads}}) > 0$ ) or the Heyrovsky reaction has a standard equilibrium potential more negative than 0 ( $\Delta G^0(\text{H}_{\text{ads}}) < 0$ ). Fig. 1 plots  $\eta_{\text{T}}$  for the HER as a function of  $\Delta G^0(\text{H}_{\text{ads}})$ , and illustrates how the optimal catalyst is a compromise between strong and weak binding of  $\text{H}_{\text{ads}}$ , as expressed by the classical Sabatier principle [13]. Figure 1 is similar but not identical to a volcano relationship, in which the catalytic activity for a reaction is plotted as a function of some property of the catalyst, in this case the catalyst's ability to bind an intermediate. Typically such a plot leads to peak-shaped relationship of the catalytic activity versus the catalyst property, whence the name “volcano relationship.” Such a catalyst property is also known as a “descriptor,” as it gives a general but essential description of the catalyst properties. Although the “thermodynamic overpotential” of multistep electron transfer reactions is not a kinetic measure, the concept of the volcano relationship and associated Sabatier principle straightforwardly

follow from thermodynamics combined with some very mild kinetic assumptions (one of the assumptions that one may make is that of a relation between activation energy and thermodynamic driving force, i.e., the Brønsted–Evans–Polanyi postulate [14]). Therefore, I consider Fig. 1 as a thermodynamic version of the kinetic volcano plot (i.e.,  $\log i_0$  vs  $\Delta G^0(\text{H}_{\text{ads}})$ , with  $i_0$  the standard exchange current density), as originally suggested for the HER by Parsons [15] and Gerischer [16], and recently revived on the basis of DFT-calculated values for  $\Delta G^0(\text{H}_{\text{ads}})$  by Nørskov et al. [17]. Note that the same analysis can be applied to the HOR, leading to the dashed-line volcano plot in Fig. 1, illustrating that for a reduction reaction we obtain a “^”-shaped plot, and for an oxidation reaction we obtain a “v”-shaped plot.

The same analysis may be applied to a Volmer–Tafel mechanism for the HER/HOR. The only difference now is that reaction 1c does not have a standard equilibrium potential, because it is not an electrochemical reaction. However, combined with reaction 1a, it must still satisfy the overall thermodynamic constraints of reaction 1. Defining the standard equilibrium constant of reaction 1c as:



**Electrochemical Hydrogen Production, Fig. 1** “Thermodynamic” volcano plot for the hydrogen evolution reaction (HER) and the hydrogen oxidation reaction (HOR); thermodynamic overpotential (standard equilibrium potential of the potential-determining step) versus the free

binding energy of hydrogen on the electrode surface [15, 17]. The dashed line gives the same plot for the HOR. The potential-determining steps corresponding to the various legs of the curves are indicated

$$K_{\text{H}_{\text{ads}}/\text{H}_2} = \exp\left[\frac{-\Delta G^0(\text{H}_{\text{ads}})}{RT}\right], \quad (7)$$

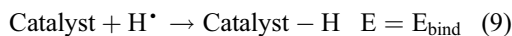
the Tafel–Volmer mechanism has to obey the following relation:

$$E_{\text{H}^+/\text{H}_{\text{ads}}}^0 - \frac{\Delta G^0(\text{H}_{\text{ads}})}{e_0} = 0 \quad (8)$$

In case  $E_{\text{H}^+/\text{H}_{\text{ads}}}^0 < 0$ , the thermodynamic overvoltage is  $\eta_{\text{T}} = E_{\text{H}^+/\text{H}_{\text{ads}}}^0$ , as in the Heyrovsky–Volmer mechanism. In case  $E_{\text{H}^+/\text{H}_{\text{ads}}}^0 > 0$ , the Tafel reaction becomes endothermic (Eq. 8), and therefore thermo-dynamically unfavorable. The most straightforward definition of a “thermodynamic overvoltage” would then follow from Eq. 8, leading to  $\eta_{\text{T}} = -E_{\text{H}^+/\text{H}_{\text{ads}}}^0$ . As a result, we see that the Heyrovsky–Volmer and the Tafel–Volmer mechanisms lead to “thermodynamic volcano curves” that are identical, and that more mechanistic assumptions are needed in order to distinguish between these two mechanisms. One important consequence of a volcano-type relationship such as that illustrated in Fig. 1 is that the potential-determining step is different on each side of the maximum. “Potential determining” means that this step determines the (over)potential at which a certain current density may be reached. For  $\Delta G^0(\text{H}_{\text{ads}}) > 0$ , the Volmer reaction is potential determining; for  $\Delta G^0(\text{H}_{\text{ads}}) < 0$ , either the Heyrovsky or Tafel reaction is potential determining. It is important to point out the difference between potential-determining and rate-determining step. Potential-determining steps are not always rate determining at the relevant potentials, as potential-determining steps suffer from an unfavorable thermodynamics, but not necessarily from an unfavorable kinetics at the potential at which the current finally starts flowing. Nevertheless, this simple analysis lucidly illustrates the thermodynamic constraints applicable to multistep multi-electron transfer reactions, and how catalysis may influence the “thermodynamic overvoltage” by optimizing the binding energy of the key intermediate, in this case  $\text{H}_{\text{ads}}$ . The best catalyst, according to this analysis, is the one that binds hydrogen in such a way that there is no thermodynamic sink or barrier in going from

reactant through intermediate to product. This is the essential point made already by Parsons more than 50 years ago [15]. Experimental volcano plots of the exchange current density of the HER have been suggested many years ago by Trasatti, [18] and such plots may be criticized for various (experimental) reasons [19, 20]. In this section, we will summarize some of the main objections. The section “Hydrogen Evolution at Metal Electrodes” will review the experimental evidence for the existence of a volcano relationship for the HER. At this point, it is stressed again that the approach discussed here does not include explicitly any kinetic aspects of the reaction.

The idea recently suggested by Nørskov et al. [17] is that  $\Delta G^0(\text{H}^*)$  may be calculated for many potential catalysts from first principles by using DFT in combination with some mild assumptions on entropic contributions. In a DFT calculation, one typically calculates the binding energy of the hydrogen atom (or radical):



The free binding energy using  $\text{H}_2$  as a reference can then be estimated from

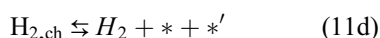
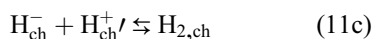
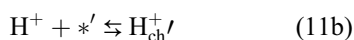
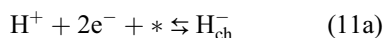
$$\Delta G^0(\text{H}_{\text{ads}}) = E_{\text{bind}} - T^* \Delta S + \Delta \text{ZPE} + E(\text{H}^*) \quad (10)$$

The term  $T^* \Delta S$  takes into account the entropy contribution due to the vibration of hydrogen in its adsorbed state, and  $\Delta \text{ZPE}$  is the corresponding zero-point energy of the adsorbate. Their combined ( $-T^* \Delta S + \Delta \text{ZPE}$ ) value has been estimated for H adsorbed on metals as ca. 0.24 eV by Rossmeisl et al. [11].  $E(\text{H}^*)$  is half the bond energy of the hydrogen molecule, which is 2.24 eV (including the molecule’s ZPE).

Trends in  $\Delta G^0(\text{H}_{\text{ads}})$  or  $E_{\text{bind}}$  among different metals often conform to the so-called d-band model proposed by Hammer and Nørskov [14, 21]. This model claims a close correspondence between the strength of a surface bond (of H, but also of other adsorbates such as O, OH, and CO) and the location of the center of the d band of the metal surface. The energy of the d band may be

“engineered” by changing the properties of the metal surface, for instance by (surface) alloying and overlayer formation [22]. The d-band center also influences the activation energy for dissociative adsorption, primarily through the Brønsted–Evans–Polanyi relationship [14], which assumes a linear relation between reaction energy and activation energy. The role of the d band in bond breaking electron transfer reactions was recently modeled by Santos and Schmickler [23], and will be discussed briefly in the next section.

The above mechanism, based on reactions 1a, 1b, and 1c, is rather specific to the HER on metal electrodes. If such a mechanism takes place on a molecular catalyst, the catalyst typically has two nearby (metal) centers to coordinate the hydrogen and adsorbed hydrogen is often referred to as “hydride.” The mechanism may be termed “homolytic” in this case, akin to the Volmer–Tafel mechanism. On many molecular catalysts or enzymes, however, the general mechanism tends to be different, and may be considered a variant of the Tafel–Heyrovsky mechanism, with the difference that the proton is not dissolved in the liquid phase, but also bound to a nearby “docking” site [1]. In such mechanisms, it is typically assumed that the release of the hydrogen molecule from the active site is an activated process (though the activation barrier may be small). Such a heterolytic mechanism may be written as follows:



where the two different coordination sites have been labeled as  $*$  and  $*'$ . The two-electron transfer character of reaction 11 should be considered as formal; the charge distinction between  $\text{H}^-$  and  $\text{H}^+$  may be exaggerated. Note that we have now the binding energies of  $\text{H}_{\text{ch}}^-$  and  $\text{H}_{\text{ch}}^+$  as the main descriptors for the thermodynamics of hydrogen

evolution, so strictly speaking we have two descriptors now. It is not difficult to understand from Eqs. 11 that the properties of this mechanism will depend on the basicity/acidity of the coordinating sites  $*$  and  $*'$ . As a result, the overall activity for hydrogen evolution will normally be strongly pH dependent. By contrast, hydrogen evolution on metals, which only involves neutral hydrogen as intermediate (at least formally), is typically not strongly pH dependent [1, 4].

## More Detailed Theories and Simulations

The phenomenological theory of the previous section has an old history in the electrochemistry literature, and can be given a much more detailed treatment than given here, for which reference is made to the original literature [15–18, 20]. More detailed molecular-level simulations of the hydrogen evolution (and hydrogen oxidation) reaction have been carried out in recent years, and it is of interest to discuss the main results from those investigations.

Santos and Schmickler consider that modeling hydrogen oxidation or hydrogen evolution fully from first principles is currently still too ambitious a task, and more general insight can be obtained from taking a simpler approach [23–26]. They have formulated a simple Hamiltonian which includes two hydrogens and the metal, and the electronic interaction between them [27]. The interaction with the solvent is treated in a spirit similar to the Marcus model. The ground-state energy of the model Hamiltonian may be calculated (with some approximations) and the interaction parameters entering the expression for the ground-state energy (strength of electronic interaction between hydrogen atoms; strength of electronic interaction of the hydrogen with the metal states; metal surface electronic band structure; strength of interaction of the hydrogen with the solvent) may be obtained from more detailed calculations, such as DFT. Although the effect of the simplifications of such an approach are somewhat difficult to estimate, the great advantage of this method is that it allows for a more detailed description of the HER/HOR without having to

resort to extremely complicated calculations, which may have their own drawbacks. Moreover, the coupling between bond breaking and electron transfer can be followed in an instructive way. The activation energy in the theory of Santos and Schmickler is determined by the interaction of the bonding orbital of the hydrogen molecule with the d band of the metal catalyst as it passes the Fermi level of the metal. At this critical stage, the occupation probability of the bonding orbital is about one, so that one electron has already been transferred to the metal (in terms of the HOR). However, the activation energy for bond making or bond breaking does not only depend on the center of the d band as also predicted by the theory of Hammer and Nørskov. There is an additional important role of the electronic coupling between the hydrogen and the metal surface. The strength of the electronic coupling determines the broadening and splitting of the orbitals involved in the charge transfer reactions, and normally a stronger electronic coupling leads to a lowering of the activation energy. Electronic coupling strengths typically increase toward the lower left-hand corner of the relevant part of the periodic table containing the coinage and transition metals, because of the diffuseness of the metal orbitals involved in the interaction increases in that direction. Based on their detailed calculations, Santos and Schmickler have criticized the use of volcano relationships in understanding trends in the metal-dependent reactivity of the HER/HOR. First of all, for most of the metals for which calculations can be performed, the data points lie on the ascending branch of the volcano curve. Metals that bind hydrogen very strongly also tend to bind oxygen very strongly, and therefore points on the descending branch of the volcano (increasing hydrogen binding strength) pertain to metals covered by an oxide film under aqueous electrochemical conditions. Hence, the experimental evidence for a volcano relationship is weak, if any, according to Santos and Schmickler. While this argument may be correct for the “older” volcano curves encompassing a wide variety of metals, it may not apply to some recent volcano curves (to be discussed in the section “[Hydrogen](#)

[Evolution at Metal Electrodes](#)”). Secondly, the activation energy for hydrogen evolution and hydrogen oxidation depends not only on the strength of the interaction between hydrogen and the metal surface, but also on effects not (directly) incorporated into the simple model discussed in the previous section, such as the strength of the electronic coupling. The weak electronic coupling between nickel and hydrogen may explain the rather low activity of nickel, whereas the strong electronic coupling between rhenium and hydrogen may explain the high HER activity of rhenium [28]. Santos and Schmickler have argued that these two metals indeed appear to deviate from the volcano plot, precisely for the reason mentioned. A final point raised by Santos and Schmickler that is not explicitly included in the analysis of the previous section is that the binding energy of hydrogen is coverage dependent and that different metals may show their optimum activity at different coverages. As a result, Santos and Schmickler refer to the volcano curve, as applied to the HER/HOR as a “venerable” but effectively “defunct” and “oversimplistic” concept.

One of the simplifications made in the Santos–Schmickler approach to the HER/HOR is the way in which the role of the solvent is included. The atomic level modeling of the solvent in the initial stages of proton reduction, without resorting to fully ab initio methods, was considered by Wilhelm et al. [29, 30]. They took the so-called empirical valence bond model (EVBM) to describe proton exchange in water to include proton transfer to a Pt(111) electrode surface. The model was parameterized on the basis of density functional theory calculations. The advantage of this approach over fully ab initio simulations (see below) is that much longer simulation times can be probed and therefore a more meaningful statistics can be obtained. This setup allowed the authors to study the dynamics of proton transfer to Pt(111) as a function of the charge density on the electrode surface. Figure 2 shows the charge dependence of two rate constants obtained from their detailed simulations: the inverse time needed for the proton to reach the

“final” adsorption state, still being a proton, and the inverse time needed for “adsorption-to-discharge.” Figure 2 indicates that at strongly negative surface charge, the proton transfer reaction is dominated by the time the proton needs to approach the surface, and proton discharge is very fast. At less negative surface charge density, the rate for establishing an orientational fluctuation suitable for proton transfer to the surface is rate determining.

Otani et al. [5] have carried out a full ab initio molecular dynamics simulation of the proton transfer reaction on a Pt(111) surface. This was the first ab initio dynamical simulation of an electrode reaction, but it should also be emphasized that this was a single-trajectory simulation, without statistical sampling, and that proton transfer was obtained only if excessively high electric fields were applied. Nevertheless, expect more of this kind of work in the future, and combined with rare-event sampling techniques, this is a potentially very powerful method. More recently, Santana et al. have used a similar approach to study the HOR on Pt(110) [31].

An alternative approach to studying the dynamic aspects of proton reduction and/or hydrogen evolution is to compute the potential

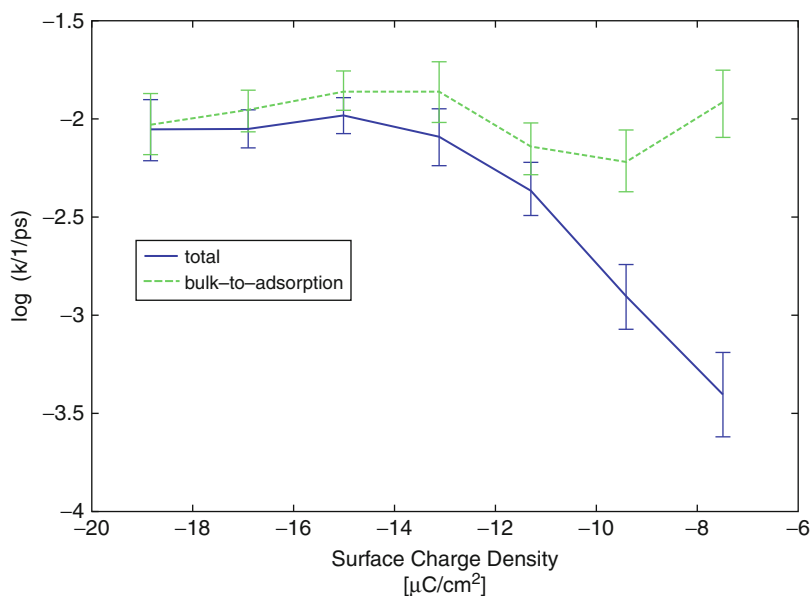
energy surface for such reactions from detailed DFT calculations. A potential energy surface is generated at zero temperature, and therefore it does not include any finite temperature effects. Such an ab initio treatment of the hydrogen evolution reaction has been carried out recently by Skulason et al. [6, 32]. They included the effect of the electrode potential by considering various concentrations of protons (simulating different surface charge densities) within simulation cells of varying size, and extrapolating the obtained energies to infinite cell size to simulate a potentiostatic experiment. For the Volmer reaction on Pt(111), a barrier of ca. 0.5 eV was calculated. The Heyrovsky reaction was concluded to be the reaction with the highest barrier at 0 V, ca. 1.4 eV for the HER, whereas the Tafel reaction has a potential-independent barrier of ca. 0.8 eV at 0 V. As a result, the Tafel reaction is predicted to be the rate-determining step.

## Hydrogen Evolution at Metal Electrodes

### HER at Platinum Electrodes

As platinum is one of the best and most studied catalysts for the HER/HOR, as well as the one

**Electrochemical Hydrogen Production, Fig. 2** Top: Logarithmic representation of the rate for proton discharge (blue, full line) and the proton bulk-to-adsorption rate (green, dashed) on Pt(111). (Reproduced with permission from Ref. [30])



used in fuel cells and in many (acid) electrolyzers, it is useful to summarize here some of the pertinent experimental results. Platinum is generally agreed to be a very active catalyst for HER/HOR, and considered to be located near the apex of the volcano. Standard exchange current densities for the HOR are not easy to obtain because in general it is difficult to correct accurately for mass transport limitations and double-layer charging. Values from  $10^{-3}$  to  $1 \text{ A cm}^{-2}$  have been reported for platinum [4, 33, 34] which would roughly correspond to a turnover rate of  $0.1\text{--}100 \text{ s}^{-1}$  per Pt active site, at the standard equilibrium potential. The Pt “active site” is not well known, and there has been quite some controversy as to whether the HER/HOR is structure sensitive on platinum or not. In contrast to early studies, [35] the groups of Markovic [33] and Conway [34] have found that the Pt(110) surface is the most active in catalyzing the HER/HOR, typically being an order of magnitude more active than the other low-index surfaces.

In electrochemical experiments, rate-determining steps are usually inferred from so-called Tafel slopes, which essentially express the overall potential dependence of the reaction rate (i.e., the current) in a certain potential range. If the Volmer reaction is rate determining and its rate obeys the Butler–Volmer model, then the potential dependence is equivalent to a Tafel slope of  $\ln 10 \times RT/(\alpha FE) \approx 120 \text{ mV/dec}$  if  $\alpha \approx 0.5$ . If, on the other hand, the Heyrovsky reaction is rate determining, and the preceding Volmer reaction in “quasi-equilibrium,” the potential dependence of the reaction is equivalent to a Tafel slope of  $\ln 10 \times RT/[(1 + \alpha) FE] \approx 40 \text{ mV/dec}$  if  $\alpha \approx 0.5$ . Finally, if the Tafel reaction is rate determining, the Tafel slope will be  $\ln 10 \times RT/[2FE] \approx 30 \text{ mV/dec}$ . In these predictions of the Tafel slope, saturation effects on the surface are not included.

Markovic et al. [33] have measured Tafel slopes for both the HER and the HOR on Pt single-crystal electrodes in acidic media. Tafel slopes also appear to depend on the crystal plane; the most active Pt(110) surface exhibits the  $30 \text{ mV/dec}$  Tafel slope well known from polycrystalline Pt [34, 36]. This Tafel slope

corresponds to a Tafel–Volmer mechanism, i.e., a combination of reactions 1a and 1c.

The HER/HOR reaction kinetics is first order in the proton concentration over a wide pH range (0–14), implying that overpotentials are similar on the RHE (reversible hydrogen electrode) scale, in full agreement with the idea that proton and electron transfer are coupled over the entire pH range. However, there is a nontrivial pH effect in the sense that in alkaline media, the rate of the reaction tends to be about an order of magnitude lower than acidic media, at the same overpotential [37]. Conway et al. [37] have explained this effect by a more difficult abstraction of H from  $\text{H}_2\text{O}$  than from  $\text{H}_3\text{O}^+$ . Pt(110) is still the most active surface, also in alkaline media, but the Tafel slope seems to be different, closer to  $60 \text{ mV/dec}$ , although no clear straight line was obtained.

An important discussion in the surface electrochemistry literature concerns the nature of surface-adsorbed hydrogen that acts as a precursor for hydrogen evolution in the HER, or for proton formation in the HOR [4, 38]. It is well known that at potentials above the reversible hydrogen potential, from ca. 0.05 to 0.3 V versus RHE (i.e., where no hydrogen evolution takes place), adsorbed hydrogen is formed on platinum. This form of adsorbed hydrogen is referred to as “underpotential deposited” (upd) hydrogen [38]. The surface coverage of this  $\text{H}_{\text{upd}}$  follows a Frumkin isotherm on Pt(111) and Pt(100) [38–40] with weak repulsive interactions between the adsorbed hydrogens. The coverages of  $\text{H}_{\text{upd}}$  in acidic and alkaline media on Pt(111) are almost identical at the same overpotential, but again the kinetics of its formation is much slower in alkaline media [41]. The adsorbed hydrogen that participates in the HER at potentials around 0 V, is usually termed “overpotential deposited” (opd) hydrogen. The exact relation between  $\text{H}_{\text{upd}}$  and  $\text{H}_{\text{opd}}$  has led to ample discussion and speculation; for an illustrative account, see the paper by Conway and Jerkiewicz [42]. Most probably,  $\text{H}_{\text{upd}}$  and  $\text{H}_{\text{opd}}$  should primarily be distinguished on the basis of the different overall hydrogen coverages applicable to both states, with a typical  $\text{H}_{\text{upd}}$  coverage being lower than 0.5–1.0, and a typical  $\text{H}_{\text{opd}}$  coverage being close to or higher than 1 (i.e.,



including the  $H_{\text{upd}}$  coverage, implying more than 1 H per surface Pt atom), suggesting that  $H_{\text{upd}}$  and  $H_{\text{opd}}$  reside at different sites on the surface. The different coverages lead to different lateral interactions, different energetics, and site preferences, and therefore different activities toward  $H_2$  evolution.

There have been a number of attempts to probe the adsorbed hydrogen on platinum using vibrational spectroscopy. A recent surface-enhanced infrared (IR) study on a platinum film electrode by Kunimatsu et al. [43] confirmed earlier results by absorption–reflection IR [44] that for potentials lower than ca.  $0.1 V_{\text{RHE}}$ , atop-bonded Pt-H is formed. The signal of this band correlated with the hydrogen evolution current, and therefore this species was identified as the intermediate in the HER. Kunimatsu et al. suggest that  $H_{\text{upd}}$  adsorbs below  $0.3 V_{\text{RHE}}$  in hollow sites, though this state has not been resolved spectroscopically, and that, in addition to  $H_{\text{upd}}$ ,  $H_{\text{opd}}$  adsorbs below  $0.1 V_{\text{RHE}}$  at atop sites, and serves as the reaction intermediate.

### Experimental Evidence for Volcano Behavior on Strained Monolayer and Bimetallic Systems

The evidence for a volcano-type relationship has been collected by Trasatti [18], and more recently by Nørskov and Stimming and coworkers [17]. One problem with such a correlation is that it is partially based on including metals that under experimental conditions are most likely covered by an oxide [20]. Recent studies by Kibler et al. [45, 46] have employed the idea of using palladium monolayers on different substrates [from Pd on Re(0001) to Pd on Au(111)] to tune the reactivity toward hydrogen adsorption and hydrogen evolution. Since the potential of the  $H_{\text{upd}}$  peak observed in voltammetry is directly related to the adsorption energy of hydrogen (or more accurately, of  $H_{\text{upd}}$ ), the authors could relate the peak potential to the theoretically predicted d-band shift with respect to Pd (111). The good correlation found suggested that this monolayer approach is a viable and controlled way to tune reactivity. In a subsequent study, the same systems were studied for their HER activity. Figure 3 shows the plot of the

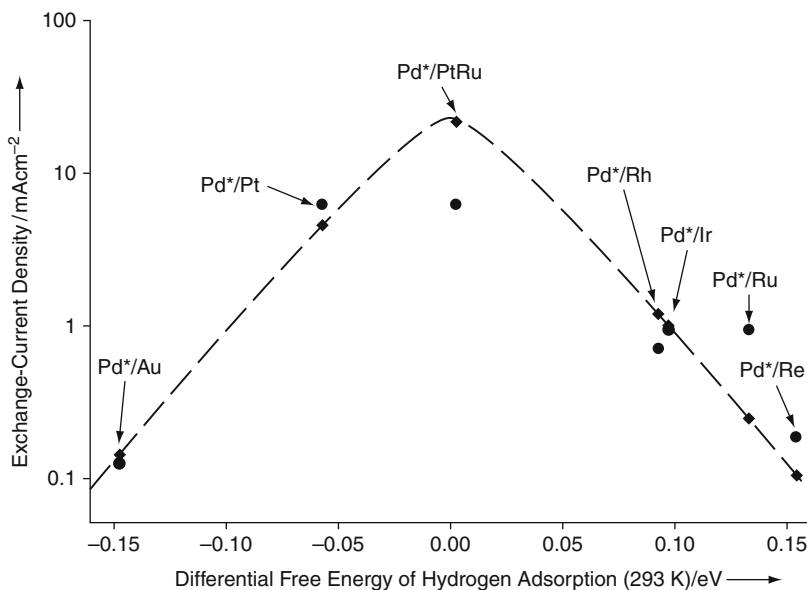
standard exchange current density versus the free energy of adsorption of hydrogen, clearly in agreement with the predictions of the Sabatier principle and the volcano plot. Note that from these results, an optimum standard exchange current density of ca.  $0.01\text{--}0.1 \text{ A cm}^{-2}$  is predicted.

Clearly, a catalyst consisting of Pd, Ru, and Pt is hardly an economical alternative for Pt, which is already quite a good catalyst for the HER/HOR. Therefore, Greeley et al. [47] have carried out an extensive computational study of bimetallic surfaces, screening for specific combinations with a  $\Delta G^0(\text{H}^*)$  close to 0, with a negative formation energy to ensure stability of the material, and preferably consisting of cheaper elements. The counterintuitive combination of Pt and Bi emerged as one of the possibly attractive materials, with a  $\Delta G^0(\text{H}^*)$  closer to zero than Pt. An appropriately prepared Pt-Bi surface alloy was subsequently found to indeed have a higher activity for the HER than Pt, showing the promise and usefulness of this computational screening strategy.

### Hydrogen Evolution at (Electrodes Modified with) Molecular Catalysts in Aqueous and Nonaqueous Solvents

There have been ample efforts to develop molecular catalysts for hydrogen evolution, the majority of them inspired to mimic the activity of natural hydrogenases, resulting in an extensive literature on this subject that will not be summarized here. For some recent reviews, the reader may consult various recent sources [48–51]. These biomimetic complexes are usually organometallic compounds containing Fe, Ni, Co, and/or Ru. It is also known that certain nonmetal containing organic molecules (such as bipyridine) may enhance the HER on metal electrodes otherwise not particularly active for the HER, such as mercury or gold (see, e.g., Ref. [52] and references therein).

Hydrogenases themselves have also been investigated as hydrogen evolution catalysts, and when adsorbed on graphitic electrodes, have been shown to exhibit very good catalytic properties, comparable to platinum. This latter subject has been discussed and reviewed extensively by



**Electrochemical Hydrogen Production, Fig. 3** Hydrogen evolution exchange current density as a function of the theoretical differential free energy of hydrogen adsorption,  $\Delta G^0(\text{H}^*)$ . The dashed line shows the functional form of the theoretical exchange current density, and the black diamonds correspond to the predictions for

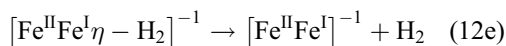
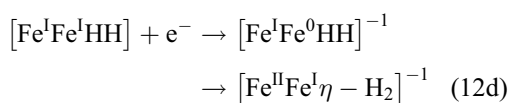
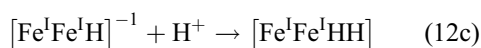
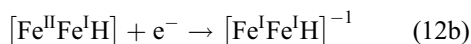
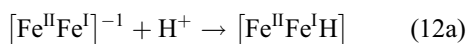
specific overlayers. The black circles represent experimental measurements (the measured exchange current density determines the ordinate for these points, and the abscissa is specified by the theoretical  $\Delta G^0(\text{H}^*)$  value). Pd\*/X denotes a pure overlayer of Pd on a substrate of metal X. (Reproduced with permission from Ref. [46])

Armstrong and coworkers [53]. To elucidate the catalytic function of these enzymes, it is useful to discuss some existing DFT calculations on computational hydrogenase models within the framework of the theory discussed in the section “General Theory.”

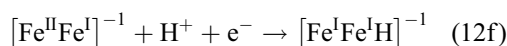
All hydrogenases catalyze both HER and HOR. The [FeFe] hydrogenases are most active for hydrogen formation, while [NiFe] hydrogenases are poised for hydrogen oxidation. Mechanistic information has been obtained from enzyme kinetics, spectroscopy, X-ray structural data, and DFT calculations. A general feature is that hydrogen binding or dissociation, proton exchange, and electron transfer are separate steps. A second distinct difference with the metal surface-catalyzed reaction is the heterolytic splitting or formation of hydrogen (reactions 11). A proton is abstracted by a nearby base, and hydride is stabilized by the metal ions rather than  $\text{H}^*$ , although electron and spin densities are substantially delocalized. This is somewhat similar to the Heyrovsky reaction

proposed for the mechanism on metals (reaction 1b). As mentioned, on a platinum electrode the homolytic bond splitting or making (Tafel reaction 1c) seems to be the preferred pathway.

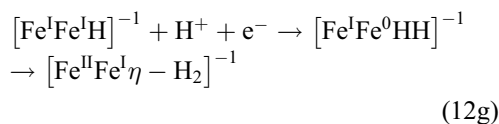
The mechanism of the HER/HOR by [FeFe] hydrogenases, as suggested by DFT calculations and experimental data, can be summarized as follows: [54]



The electrons are rapidly transferred from the reductant (or the electrode) to the active site via the chain of [FeS] clusters. From an electrochemical perspective, these [FeS] clusters thus are intramolecular mediators. Although Fe–H–Fe bridging intermediates have been proposed, the most likely mechanism involves one-Fe bound H-species and side-on bound H<sub>2</sub>. The secondary amine in the bridging ligand and Fe<sup>I</sup> appear to be equally potent as catalytic base. The iron most distant from the nearby [FeS] cluster, called the Fe<sub>d</sub> site that shuttles between the formal 1+ and neutral state in reactions 12a, 12b, 12c, 12d, and 12e, appears as the actual binding site for H and H<sub>2</sub>. By taking together the proton and electron transfer steps in reactions 12a, 12b, 12c, and 12d, we can compare the DFT calculations performed by Sbraccia et al. [54] to the model presented in the section “General Theory.” For reactions 12a and 12b together



the DFT-calculated reaction energy is  $-15.98$  eV. Compared to the H<sub>2</sub> molecule, with a calculated total energy of 31.70 eV, the reaction energy is therefore  $-0.13$  eV. For reactions 12c and 12d together:

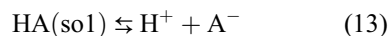


the DFT-calculated reaction energy is  $-15.43$  eV, implying a reaction energy of  $+0.42$  eV. For the final H<sub>2</sub> release, reaction 12e, the reaction energy is  $-0.29$  eV (with a calculated activation energy of 0.07 eV). Note that the three calculated reaction energies now add up to 0, implying that we are considering the reaction at thermoneutral conditions. Although this is an analysis based on total energies, as calculated by DFT, and not on free energies, these numbers still suggest that: (1) for hydrogenases, the key to an efficient catalyst is also to have an active site that binds H just as strong as H<sub>2</sub> (see also Ref. [55]), and (2) that the addition of the second hydrogen, reaction 12g, is

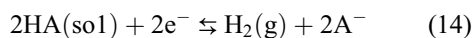
thermodynamically uphill and hence the potential determining step, if we neglect zero-point energy contributions and entropy.

The organometallic nature of hydrogenase structural mimics makes them more soluble in nonaqueous solvents than in water. This has led to the development of activity tests in acetone, propylene carbonate, or acetonitrile for evaluation of model compounds. This is obviously not without consequences for the definition of pH and of the equilibrium potential of the redox couples. The equilibrium potential of the reference couple,  $E_{\text{H}_2/\text{H}^+}^0$ , is indeed strongly dependent on the nature of the protic species (solvated protons or weak acid). The overpotential for hydrogen evolution, which is the relevant experimental quantity when comparing different catalysts in different solutions, must therefore be referred to the reversible potential of the H<sup>+</sup>/H<sub>2</sub> redox couple in the solvent under consideration. Working in a nonaqueous solvent has two important consequences for the determination of the reversible potential. First of all, the solvation energy of the proton is solvent dependent, and leads to a concomitant shift of the standard equilibrium potential. Second, many proton donors dissociate only incompletely in organic solvents, and therefore the dissociation constant should be taken into account in the definition of the standard equilibrium potential. Felton et al. [56] have described how to correct for both effects properly, and have given a useful comparison of various catalysts in a typical nonaqueous solvent, i.e., acetonitrile.

Considering the acid dissociation constant,  $K_{a,\text{HA}}^{\text{sol}}$ , in solvent “sol,” of the reaction:



the standard equilibrium potential of the overall half reaction



in the solvent “sol” is given by

$$E_{\text{H}_2/\text{HA}}^{0,\text{sol}} = E_{\text{H}_2/\text{H}^+}^{0,\text{sol}} - \left( \frac{2.303 RT}{F} \right) \text{p}K_{a,\text{HA}}^{\text{sol}} \quad (15)$$

**Electrochemical Hydrogen Production, Table 1** Dependence of the equilibrium potential of the hydrogen electrode

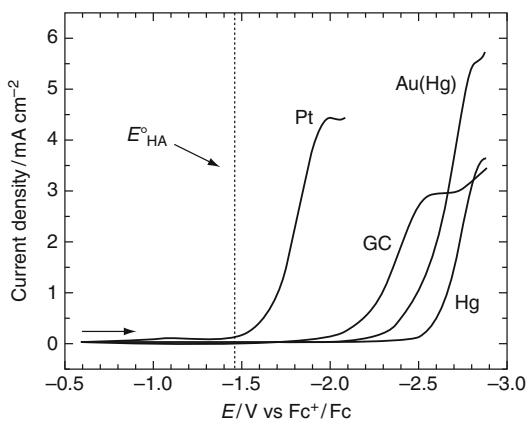
Sol	$E_{\text{H}_2/\text{H}^+}^{0,\text{sol}}$ versus SHE/V (From Eq. 16, Ref. [57])	$E_{\text{H}_2/\text{H}^+}^{0,\text{sol}}$ versus $E_{\text{DMFc}^{+/0}}$ /V (From Refs. [58, 60])	$E_{\text{H}_2/\text{H}^+}^{0,\text{sol}}$ versus SHE/V (Combining [58, 60])
Water	0	-0.099	0
Acetonitrile	0.414	0.435	0.534
DMSO	-0.207	-0.202	-0.103
DMF	-	-0.162	-0.063
Methanol	0.083	-	-

In nonaqueous solvents, values for  $E_{\text{H}_2/\text{H}^+}^{0,\text{sol}}$  or  $E_{\text{H}_2/\text{HA}}^{0,\text{sol}}$  are often referred to the ferrocenium/ferrocene couple in the same solvent. The value of  $E_{\text{H}_2/\text{H}^+}^{0,\text{aq}}$  would be a fundamentally more interesting reference, and if one is not interested in determining absolute electrode potentials, a simple way to look at the solvent dependence of  $E_{\text{H}_2/\text{H}^+}^{0,\text{sol}}$ , as referred to  $E_{\text{H}_2/\text{H}^+}^{0,\text{aq}}$ , is by considering the difference in the absolute solvation energies of the proton in “sol” and water:

$$E_{\text{H}_2/\text{H}^+}^{0,\text{sol}} = E_{\text{H}_2/\text{H}^+}^{0,\text{aq}} + \frac{[\mu^{\text{sol}}(\text{H}^+) - \mu^{\text{aq}}(\text{H}^+)]}{F} \quad (16)$$

Values for the absolute solvation free energy (i.e., the Gibbs free energy of solvation not taking into account the surface potential of the solvent) of the proton in various solvents have been reconsidered recently by Fawcett [57] and the thus calculated values of  $E_{\text{H}_2/\text{H}^+}^{0,\text{sol}}$  (vs  $E_{\text{H}_2/\text{H}^+}^{0,\text{aq}}$ ) are given in Table 1. The experimental estimates of  $E_{\text{H}_2/\text{H}^+}^{0,\text{sol}}$  have also been the subject of much work and debate. Fourmond et al. [58] have recently discussed their proper determination in a limited number of representative solvents, based on original data of Daniele et al. [59]. These values are, however, quoted versus an internal solvent standard, i.e., the ferrocenium/ferrocene  $\text{Fc}^{+/0}$  couple. The equilibrium potential of this couple is usually considered solvent independent, although water appears to be an exception [60].

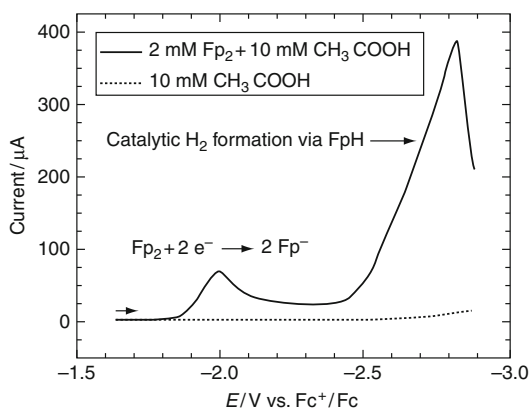
Using the tabulations provided in Ref. [60], the third and fourth columns in Table 1 have been generated, by first referring to decamethylferrocenium (DMFc)/decamethylferrocene couple (third column), which appears to be more



**Electrochemical Hydrogen Production, Fig. 4** Linear sweep voltammograms of hydrogen evolution for 10 mM acetic acid in acetonitrile with 0.10 M tetrabutylammonium hexafluorophosphate at 1.0 V/s. Reversible potential for reduction of acetic acid shown for comparison. (Reproduced with permission from Ref. [56])

solvent independent, and then rescaling such that in water the reference is at 0 V (fourth column). Although there is clearly a lack of data in this table to make any far-reaching conclusions, the differences between the theoretical and experimental values in acetonitrile and dimethylsulfoxide (DMSO) are typically within  $\pm 0.15$  V. More data are obviously needed to further elucidate this correspondence.

To illustrate the influence of a nonaqueous solvent on the HER activity, a comparison of different catalysts in acetonitrile is given in Figs. 4 and 5 [56]. It is seen that Pt is still the best catalyst of the four catalysts illustrated in Fig. 4, and also significantly better than the hydrogenase mimic in Fig. 5, but the overpotential



**Electrochemical Hydrogen Production, Fig. 5** Linear sweep voltammograms for 2 mM Fp<sub>2</sub>, an organometallic Fe compound, plus 10 mM acetic acid in acetonitrile with 0.10 M tetrabutylammonium hexafluorophosphate (*solid curve*) and 10 mM acetic acid alone (*dashed curve*). Hanging mercury drop electrode (area 0.0096 cm<sup>2</sup>). Scan rate: 1.0 V/s. (Reproduced with permission from Ref. [56])

is rather high compared to the situation in an aqueous solvent. As a practical compromise to comparing overpotentials, it has been suggested to compare halfwave potentials. A detailed discussion on the proper comparison of these half-wave potentials has been given recently by Fourmond et al. [58].

## Concluding Remarks

This entry has attempted to address some fundamental issues with studying the electrochemical production of hydrogen under various conditions and with various catalysts. The aim was to provide a common theoretical framework first, and then to show how to build on this framework and to understand the similarities and differences between the different catalytic approaches that have been used to tackle this important problem. It is hoped that this approach may be useful in ultimately developing a cheap, robust, and active catalyst for the electrochemical production of hydrogen. A main future direction for the development of new catalysts for electrochemical hydrogen production could be the combination of heterogeneous and molecular catalysis.

**Acknowledgements** I am grateful to the Catalysis Research Center of Hokkaido University, Sapporo, Japan, for the visiting professorship during which this entry was written, and to Prof. Masatoshi Osawa for his kind hospitality. I am grateful to Dr. Vincent Fourmond for a useful discussion on the correct generation of Table 1.

## Bibliography

### Primary Literature

1. Koper MTM, Heering HA (2010) In: Wieckowski A, Nørskov JK (eds) Fuel cell science: theory, fundamentals, and bio-catalysis. Wiley, New York, p 71
2. Koper MTM, Bouwman E (2010) *Angew Chem Int Ed* 49:3723
3. Koper MTM (2011) Thermodynamic theory of multi-electron transfer reactions: Implications for electrocatalysis. *J Electroanal Chem.* <https://doi.org/10.1016/j.jelechem.2010.10.004>
4. Markovic NM, Ross PN Jr (2002) *Surf Sci Rep* 45:117
5. Otani M, Hamada I, Sugino O, Morikawa Y, Okamoto Y, Ikeshoji T (2008) *J Phys Soc Jpn* 77:024802
6. Skúlason E, Karlberg GS, Rossmeisl J, Bligaard T, Greeley J, Jonsson H, Nørskov JK (2007) *Phys Chem Chem Phys* 9:3241
7. Bard AJ, Faulkner LR (2001) *Electrochemical methods: fundamentals and applications*. Wiley, New York
8. Nørskov JK, Rossmeisl J, Logadottir A, Lundqvist L, Kitchin JR, Bligaard T, Jónsson H (2004) *J Phys Chem B* 108:17886
9. Koper MTM, van Santen RA (1999) *J Electroanal Chem* 472:126
10. Hamada I, Morikawa Y (2008) *J Phys Chem C* 112:10889
11. Rossmeisl J, Nørskov JK, Taylor CD, Janik MJ, Neurock M (2006) *J Phys Chem B* 110:21833
12. Koper MTM (2008) *Faraday Disc* 140:11
13. Sabatier P (1911) *Ber Deutsch Gem Ges* 44:1984
14. Nørskov JK, Bligaard T, Hvolbaek B, Abild-Petersen F, Chorkendorff I, Christensen CH (2008) *Chem Soc Rev* 37:2163
15. Parsons R (1958) *Trans Faraday Soc* 34:1053
16. Gerischer H (1958) *Bull Soc Chim Belg* 67:506
17. Nørskov JK, Bligaard T, Logadottir A, Kitchin JR, Chen JG, Pandalov S, Stimming U (2005) *J Electrochem Soc* 152:J23
18. Trasatti S (1977) *J Electroanal Chem* 39:163
19. Petrii OA, Tsirlina GA (1994) *Electrochim Acta* 39:1739
20. Schmickler W, Trasatti S (2006) *J Electrochem Soc* 153:L31
21. Hammer B, Nørskov JK (1995) *Nature* 376:238
22. Hammer B, Nørskov JK (2000) *Adv Catal* 45:71
23. Santos E, Schmickler W (2007) *Angew Chem Int Ed* 46:8262
24. Santos E, Schmickler W (2007) *Chem Phys* 332:39

25. Santos E, Schmickler W (2008) *Electrochim Acta* 53:6149
26. Santos E, Lundin A, Pötting K, Quaino P, Schmickler W (2009) *Phys Rev B* 79:235436
27. Santos E, Koper MTM, Schmickler W (2008) *Chem Phys* 344:195
28. Schmickler W, Quaino P, Santos E (2010) In: Abstract for the 61st ISE meeting, Nice
29. Wilhelm F, Schmickler W, Nazmutdinov RR, Spohr E (2008) *J Phys Chem C* 112:10814
30. Wilhelm F, Schmickler W, Spohr E, *Phys J* (2010) *Condens Matter* 22:175001
31. Santana JA, Mateo JJ, Ishikawa Y (2010) *J Phys Chem C* 114:4995
32. Skulason E, Tripkovic V, Bjorketun M, Gudmundsdottir S, Karlberg G, Rossmeisl J, Bligaard T, Jonsson H, Nørskov JK (2010) *J Phys Chem C* 114:18182
33. Markovic NM, Grgur BN, Ross PN (1997) *J Phys Chem B* 101:5405
34. Barber J, Morin S, Conway BE (1998) *J Electroanal Chem* 446:125
35. Gomez R, Fernandez-Vega A, Feliu JM, Aldaz A (1993) *J Phys Chem* 97:4769
36. Guerrini E, Trasatti S (2009) *Electrocatalysis in water electrolysis*. In: Barbaro P, Bianchini C (eds) *Catalysis for sustainable energy production*. Wiley, Weinheim, p 235
37. Barber JH, Conway BE (1999) *J Electroanal Chem* 461:80
38. Jerkiewicz G (1998) *Prog Surf Sci* 57:137
39. Koper MTM, Lakkien JJ (2000) *J Electroanal Chem* 485:161
40. Garcia-Araez N, Lakkien JJ, Koper MTM, Feliu JM (2006) *J Electroanal Chem* 588:1
41. Schouten KJP, van der Niet MJTC, Koper MTM (2010) *Phys Chem Chem Phys* 12:15217
42. Conway BE, Jerkiewicz G (2000) *Electrochim Acta* 45:4075
43. Kunimatsu K, Senzaki T, Samjeské G, Tsushima M, Osawa M (2007) *Electrochim Acta* 52:5715
44. Nichols RJ, Bewick A (1988) *J Electroanal Chem* 243:445
45. Kibler LA, El-Aziz AM, Hoyer R, Kolb DM (2005) *Angew Chem Int Ed* 44:2080
46. Greeley J, Nørskov JK, Kibler LA, El-Aziz AM, Kolb DM (2006) *ChemPhysChem* 7:1032
47. Greeley J, Jaramillo T, Bonde J, Chorkendorff I, Nørskov JK (2006) *Nat Mater* 5:909
48. Artero V, Fontecave M (2005) *Coord Chem Rev* 249:1518
49. Radkowski Dubois M, Dubois DL (2009) *Acc Chem Res* 42:1974
50. Dempsey JL, Brunschwig BS, Winkler JR, Gray HB (2009) *Acc Chem Res* 42:1995
51. Artero V, Fontecave M (2010) *Energy Environ Sci* 3:727
52. Uchida T, Mogami H, Yamakata A, Sasaki Y, Osawa M (2008) *J Am Chem Soc* 130:10863
53. Armstrong FA, Belsey NA, Cracknell JA, Goldet G, Parkin A, Reisner E, Vincent KA, Wait AF (2009) *Chem Soc Rev* 38:36
54. Sbraccia C, Zipoli F, Car R, Cohen MH, Dismukes GC, Selloni A (2008) *J Phys Chem B* 112:13381
55. Hinneman B, Moses PG, Bonde J, Jørgensen KP, Nielsen JH, Horch S, Chorkendorff I, Nørskov JK (2005) *J Am Chem Soc* 127:5308
56. Felton GAN, Glass RS, Lichtenberger DL, Evans DH (2006) *Inorg Chem* 45:9181
57. Fawcett WR (2008) *Langmuir* 24:9868
58. Fourmond V, Jacques P-A, Fontecave M, Artero V (2010) *Inorg Chem* 49:10338
59. Daniele S, Ugo P, Mazzochin G-A, Bontempelli G (1985) *Anal Chim Acta* 173:141
60. Noviantri I, Brown KN, Fleming DS, Gulyas PT, Lay PA, Masters AF, Phillips L (1999) *J Phys Chem B* 103:6713





## Hydrogen Production from Biological Sources

Ao Xia<sup>1,2</sup>, Xun Zhu<sup>1,2</sup> and Qiang Liao<sup>1,2</sup>

<sup>1</sup>Key Laboratory of Low-grade Energy Utilization Technologies and Systems (Ministry of Education), Chongqing University, Chongqing, China

<sup>2</sup>Institute of Engineering Thermophysics, Chongqing University, Chongqing, China

### Article Outline

Definition of the Subject

Glossary

Introduction

Substrates for Dark Fermentation

Pre-treatment of Raw Materials

Process Control and Optimization

Bioreactors for Hydrogen Production

Use of Hydrogen as a Transport Fuel

Further Use of Volatile Fatty Acids as a Biorefinery

Potential of Biomass Wastes: A Case Study in China

Concluding Remarks and Future Perspectives

Bibliography

### Definition of the Subject

The wide utilization of fossil fuels has led to massive emission of greenhouse gases. It is urgent to develop clean energy sources. Hydrogen is considered a potential alternative to fossil fuels, due to the cleanliness of its use and high energy density by mass. However, to date, a clean hydrogen production technique has not been defined and commercialized. Conventional hydrogen production techniques usually consume large amounts of fossil fuels and are highly energy-

intensive. In contrast, clean hydrogen may be derived from environmentally friendly biological routes using biomass and organic waste under ambient temperatures and pressures. Among various biological candidates, dark fermentation exhibits advantages in high hydrogen production rate, high hydrogen content and use of a wide range of substrates, has a stable process and requires small amounts of investment. Hydrogen derived from dark fermentation by hydrogen-producing bacteria may play an important role in the future. However, there still are many challenges to realize fully such a process on a large scale. It is important to understand the hydrogen production and consumption mechanisms, and the inhibition, as well as the enhancement strategy of dark fermentation. Additionally, further utilization of the fermentation residue is important to improve the energy balance and economic feasibility of dark fermentative hydrogen production.

### Glossary

**Anaerobic digestion** An anaerobic biological process, which contains hydrolysis, acidogenesis, acetogenesis, and methanogenesis, degrading organic components while producing metabolites primarily consisting of methane and carbon dioxide, through a complex community of bacteria and archaea

**Biomass** Organic compounds which are sourced from living or recently living organisms

**Fermentation** A metabolic process that converts organic compounds to acids, alcohols, and gases, by bacteria and yeast

**Hythane** A gaseous mixture containing 10–25% of hydrogen and 75–90% of methane by volume

**Mass transfer** The net mass movement from one location to another

**Volatile fatty acids** Short-chain fatty acids with fewer than six carbon atoms

## Introduction

### Hydrogen Energy

In 2015, the world primary energy consumption increased to 13,147 Mtoe (or 552.2 EJ), exhibiting shows a 20.2% increase compared with 2005 [1]. Meanwhile, the fossil fuels, including coal, oil, and natural gas, still played the major role, contributing 86.0% of the total primary energy consumption. The excessive utilization of fossil fuels has led to fast release of carbon dioxide and other greenhouse gases (GHGs), which can increase the global average temperature of surface air, acidify oceans, and disrupt weather patterns [2]. The increase of GHGs in the atmosphere and the related temperature increases can cause a number of further environmental problems, including acceleration in the shrinkage of the Antarctic and Greenland ice sheets, a rise in sea level, and the loss of biodiversity [2, 3]. As a result, the use of clean energy sources in place of fossil fuels is an environmentally friendly and sustainable strategy for the future.

Hydrogen is a promising alternative to fossil fuels due to its clean combustion product (water) and high energy density by mass (120 kJ/kg) [4]. Nowadays, hydrogen is mainly produced from steam reforming of natural gas and via water electrolysis. However, such techniques are expensive and energy consuming; they either directly consume fossil fuels or consume electricity which is mainly derived from fossil fuels [5, 6]. Therefore, the current source of hydrogen is not as clean as it might be. A clean and efficient production process for hydrogen is urgently required to help make hydrogen a more viable fuel source.

### Biological Hydrogen Production via Various Routes

Hydrogen production via a biological route using biomass as a substrate usually operates under ambient temperature and pressure, with relatively low parasitic energy demand [6, 7]. As compared with the conventional hydrogen production processes, the biological process is considered more energy efficient and environmentally friendly, especially when the organic wastes are used as substrates [7–9].

Biological hydrogen production may be achieved by various microorganisms under distinct environmental parameters (see Table 1); it can be mainly classified into (1) direct photolysis by green microalgae, (2) indirect photolysis by cyanobacteria, (3) photo fermentation by photosynthetic bacteria (PSB), and (4) dark fermentation by hydrogen-producing bacteria (HPB) [6, 7].

The green microalgae may employ the direct photolysis pathway to split water into hydrogen and oxygen [10]. Nevertheless, the hydrogen production rate (HPR) and hydrogen content are very low. The produced oxygen can inhibit the activity of hydrogenase, which is the key enzyme responsible for hydrogen production. Furthermore, the presence of hydrogen and oxygen may make the gas mixture explosive [11].

An indirect photolysis process by cyanobacteria (also known as blue-green microalgae) may overcome the issue of photosynthetic oxygen, by separating the location and the time of photosynthesis and hydrogen generation. In the first stage, photosynthesis occurs to convert carbon dioxide and water to organic materials while producing oxygen. Subsequently, the generated cyanobacteria cells are transferred to a dark anaerobic environment, which causes the intracellular carbohydrates to degrade to hydrogen, carbon dioxide, and soluble metabolites [12, 13]. Finally, the mixture is transferred to a photo bioreactor for fermentation conducted by cyanobacteria, which further degrades the soluble metabolites to hydrogen and carbon dioxide [13]. The oxygen inhibition can be avoided through separating the photosynthesis and fermentation; however, the hydrogen production efficiency is still low. This can be attributed to the fact that the cyanobacteria act in both roles of hydrogen producers and organic sources. Moreover, the three-stage process requires a complex system, which results in high capital requirements and operational costs.

Photo fermentation is conducted by PSB, which can degrade low-molecular weight organic compounds, such as volatile fatty acids (VFAs), alcohols, and sugars to hydrogen, and produce hydrogen and carbon dioxide, under an anaerobic and nitrogen-deficient environment in the presence of light [6, 14, 15]. The key

**Hydrogen Production from Biological Sources, Table 1** Hydrogen derived from biological processes (Adapted from [6–8])

Element	Dark fermentation	Photo fermentation	Direct photolysis	Indirect photolysis
Microorganism	Fermentative bacteria	Photoheterotrophic bacteria	Green microalgae	Cyanobacteria
Substrates	Organic sources	Sugars, volatile fatty acids, and alcohols	H <sub>2</sub> O	H <sub>2</sub> O
By-product	Volatile fatty acids, alcohols, and CO <sub>2</sub>	CO <sub>2</sub>	O <sub>2</sub>	O <sub>2</sub>
Specific H <sub>2</sub> yield (mol/mol hexose)	4	12	/	12 <sup>a</sup>
Volumetric energy productivity	High	Medium	Low	Low
Light requirement	No	Yes	Yes	Yes <sup>b</sup>
Operation cost	Medium	High	Very high	Very high
Technology level	Demonstration	Pilot	Lab-scale	Lab-scale
Advantage	High H <sub>2</sub> production rate Light independent Wide range substrates Various products No O <sub>2</sub> limitation Possible to treat organic wastes	High specific H <sub>2</sub> yield High hydrogen content No O <sub>2</sub> limitation Possible to treat organic wastes	H <sub>2</sub> from water No requirement for organic substrate input Clean products	H <sub>2</sub> from water No requirement for organic substrate input
Drawback	Further treatment of fermentation effluent required	Light dependent Slow H <sub>2</sub> production	Oxygen hazardous Light dependent Low efficiency Low H <sub>2</sub> concentration High cost	Low H <sub>2</sub> concentration Partial light dependent Complex process Low H <sub>2</sub> concentration Difficult H <sub>2</sub> separation process

<sup>a</sup>Per mol hexose derived from photosynthesis

<sup>b</sup>Photosynthesis and photo fermentation stages

enzymes in this process are nitrogenase and hydrogenase, both of which are very sensitive to oxygen [16, 17]. Fortunately, PSB cannot split water to produce oxygen. High organic content wastewater may be used as a source for photo fermentation. However, this process is very sensitive to ammonium, which may rapidly inhibit photo hydrogen production with concentrations as low as 20 μM [16].

The abovementioned processes are dependent on the light sources. As a result, the availability of light is a crucial factor for light-driven

hydrogen production processes. Due to the mutual shading effects between cells, the light penetration photo bioreactor is quite heterogeneous. The light intensity is reduced significantly with increasing the cell biomass concentration and light path length [18, 19]. An efficient photo bioreactor requires a high surface-to-volume ratio; this would significantly increase the cost of bioreactor construction and maintenance. Artificial light is not realizable for hydrogen production processes on a large scale, as it consumes electricity and is expensive. Sunlight is a cheap

and widely available source; however, it is discontinuous, divided by day and night. Consequently, photo-driven hydrogen production is not stable, and is limited by the availability of sunlight. Furthermore, the increased temperature by excessive solar irradiation can cause damage to the hydrogen system and should therefore be controlled and prevented. In addition, due to the low areal sunlight intensity, as well as the low photosynthetic efficiency, the light-driven hydrogen production techniques usually suffer from the low HPR per unit volume, which results in a difficulty for commercializing such techniques.

In contrast, hydrogen derived from dark fermentation by HPB does not require light input; this facilitates continuous hydrogen production with high performance. Not limited by the light sources, the fermenter can easily achieve a large volume with a relatively simple structure and low cost. The HPB can utilize a wide range of organic substrates, which enables the treatment of biomass and organic wastes. Furthermore, the hydrogen-producing ability of HPB is usually higher than PSB and microalgae, which is advantageous in achieving a high HPR and sufficient hydrogen content. Consequently, dark fermentation is considered as a promising future hydrogen-producing technique and has received extensive research attention in recent years [20–24].

In this entry, biological hydrogen production through dark fermentation is detailed discussed, with the main focus on the areas of pre-treatment, metabolic pathways, bioreactors, and fermentation process control. The further use of hydrogen and VFAs are also reviewed. The potential and challenges for dark fermentative hydrogen production are highlighted.

## Substrates for Dark Fermentation

### Principle of Dark Fermentation

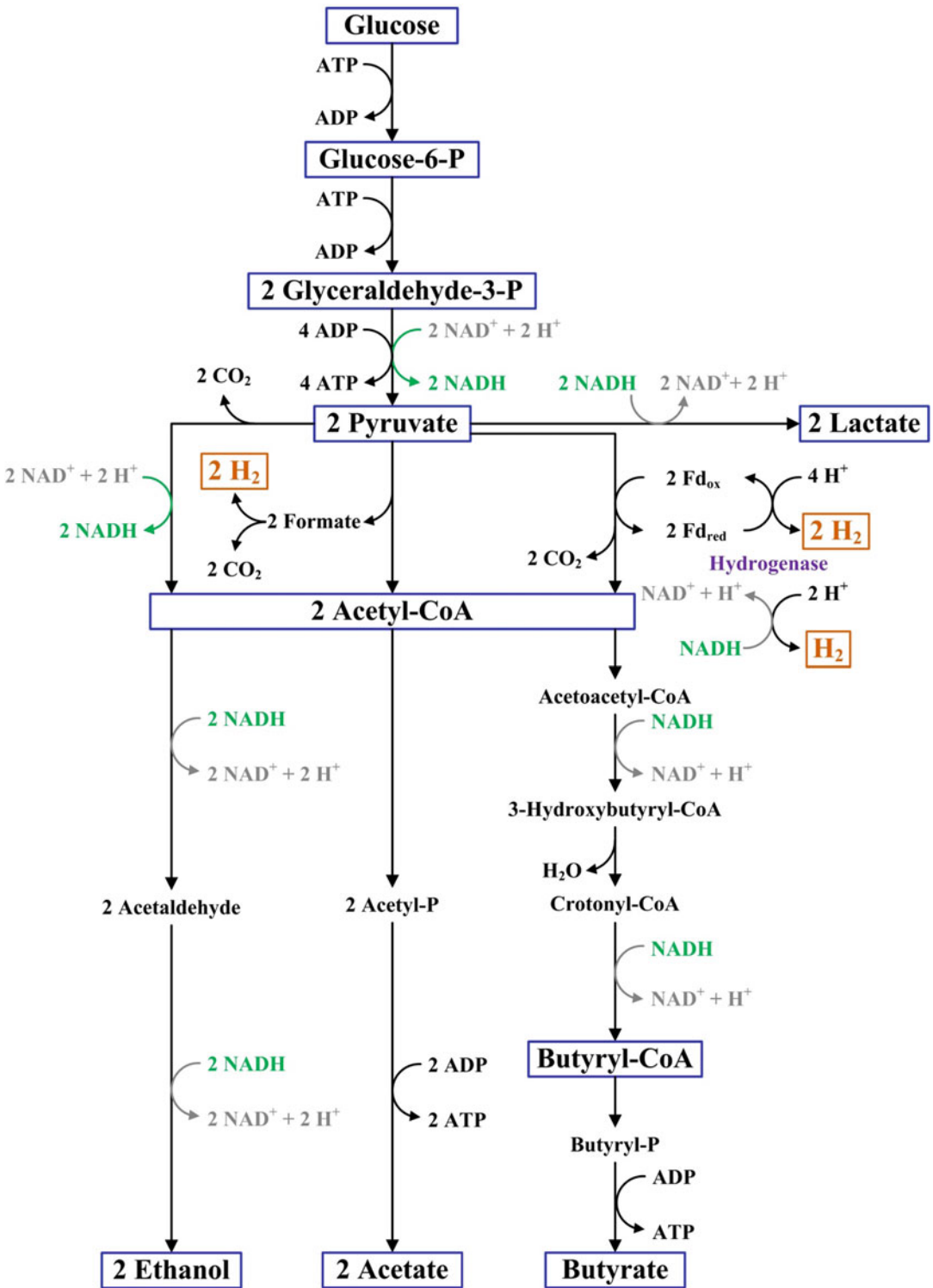
During dark fermentation, the high-molecular-weight organic components, such as carbohydrates, are hydrolysed to smaller compounds, such as reducing sugars, and subsequently degraded anaerobically to hydrogen, carbon

dioxide, and soluble metabolites, such as VFAs and alcohols, by hydrogen-producing bacteria (HPB) [6, 25]. Generally, hydrogen is formed through the combination of electrons and protons with the catalysis by hydrogenase [26]. HPB strains may belong to the families *Clostridiaceae*, *Enterobacteriaceae*, *Thermoanaerobacteriaceae*, *Sporolactobacillaceae*, *Bacillaceae*, etc. [27, 28]. Dark fermentation can be considered as the hydrolysis and acidogenesis steps of anaerobic digestion.

### Mechanism of Metabolic Pathways of Hydrogen Production and Consumption

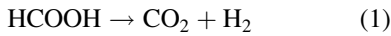
Low-molecular-weight organic components or monomers such as monosaccharides and amino acids, which may be derived from hydrolysis of polymers such as carbohydrates and proteins, are able to diffuse across the cell membrane and transported into HPB cells. Mechanism of hydrogen fermentation is associated with anaerobic degradation of monomers [29]. Glucose is the most common monomer in biomass, such as lignocellulosic biomass, manures, food wastes, and algal biomass, and may be derived from a variety of carbohydrates such as starch, cellulose, glycogen, laminarin, sucrose, and trehalose [8]. The metabolic pathways of glucose during dark fermentation are shown in Fig. 1.

Glucose is anaerobically metabolized to pyruvate, producing reduced nicotinamide adenine dinucleotide (NADH). Pyruvate is further metabolized to acetyl coenzyme A (acetyl-CoA), accompanying by generation of (a) hydrogen and carbon dioxide, (b) NADH and carbon dioxide, or (c) formic acid (which can be further split into hydrogen and carbon dioxide, as shown in Eq. 1) [21]. Alternatively, pyruvate can also be directly converted to end products, such as lactic acid, coupled with NADH consumption. Subsequently, the generated acetyl-CoA is converted to the end products such as acetic acid, butyric acid, and ethanol, without or with NADH consumption. Hydrogen can be produced with the hydrogenase as a catalyst through the combination of protons and electron donors (Eq. 2), which can be sourced from reduced ferredoxin or NADH. The consumption of electron donors can also be considered the

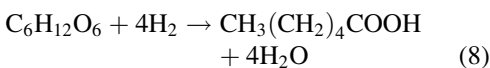
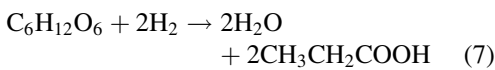
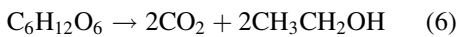
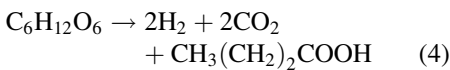
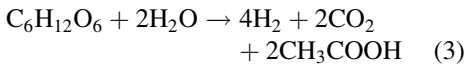


**Hydrogen Production from Biological Sources, Fig. 1** Metabolic pathways of fermentative hydrogen production using glucose as a substrate (Adapted from [8])

same as the consumption of hydrogen production potential [23, 30].

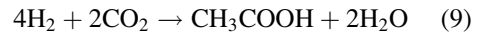


Hydrogen can be generated or consumed upon the metabolic pathways. The acetic acid pathway provides the highest specific hydrogen yield (SHY; 4 mol H<sub>2</sub>/mol glucose or 497.8 mL H<sub>2</sub>/g glucose; Eq. 3), which is followed by butyric acid pathway (2 mol H<sub>2</sub>/mol glucose or 248.9 mL H<sub>2</sub>/g glucose, Eq. 4). Lactic acid (Eq. 5) and ethanol (Eq. 6) pathways do not produce hydrogen. In contrast, hydrogen-consuming routes also exist in glucose fermentation, such as propionic acid (−2 mol H<sub>2</sub>/mol glucose or −248.9 mL H<sub>2</sub>/g glucose, Eq. 7) and caproic acid (−4 mol H<sub>2</sub>/mol glucose or −497.8 mL H<sub>2</sub>/g glucose, Eq. 8) pathways [9, 27].

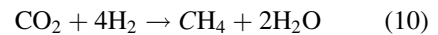


Homoacetogenesis is considered as a major hydrogen consumption pathway which can convert hydrogen and carbon dioxide to acetic acid and water (see Eq. 9), particularly for multi-species cultures. Homoacetogenic bacteria are strict anaerobic bacteria, which exhibit fast growth rates; they may be related to the families *Eubacteriaceae*, *Clostridiaceae*, and *Veillonellaceae*. Some of such bacteria are spore-forming

microbes [9, 30]. Homoacetogenic hydrogen consumption is not dependent on the substrate, origin and pre-treatment of inoculum, fermentation parameters and type of reactor, and is usually accompanied with hydrogen production; overall 11–43% of produced hydrogen may be consumed. Unfortunately, no method to fully block homoacetogenic pathways has yet been reported [30].



Methanogenesis is another possible hydrogen consumption route during dark fermentation. The presence of hydrogenotrophic methanogenic archaea can convert the fermentative gaseous products to methane and water (see Eq. 10). However, methanogenesis is usually not activated in dark fermentation. This is attributed to the fact that the short hydraulic retention time (HRT; usually below 2 days) can cause the wash out of slow growth methanogenic archaea. Furthermore, the low pH, which is caused by production of VFAs, can significantly inhibit the growth and metabolism of methanogenic archaea [31].



In dark fermentation, hydrogen production and consumption pathways are usually thermodynamically favorable with negative Gibbs free energy changes [30, 32]. However, accumulated hydrogen can increase the partial pressure of hydrogen and improve the thermodynamic favorability of hydrogen consumption pathways, while reducing the thermodynamic favorability of hydrogen production pathways [27, 33]. As a result, the hydrogen consumption reactions may be the dominant pathway in dark fermentation. Moreover, the increased carbon dioxide level in the later stage of dark fermentation can also boost homoacetogenesis, resulting in significant hydrogen consumption [30].

### Hydrogen Production Potential of Monomers

Table 2 presents a summary of theoretical values for SHYs from various monomers. Carbohydrate monomers are well understood and considered as the major contribution to fermentative hydrogen



**Hydrogen Production from Biological Sources, Table 2** Hydrogen fermentation reactions using monomers (Adapted from [8, 23, 27])

Monomer	Fermentation reaction <sup>a</sup>	Specific hydrogen yield		Hydrogen content (%) <sup>b</sup>
		(mol/mol)	(mL/g)	
Glucose Galactose Fructose	$C_6H_{12}O_6 + 2H_2O \rightarrow 4H_2 + 2CO_2 + 2CH_3COOH$	4	497.8	66.7
Xylose	$C_5H_{10}O_5 + \frac{5}{3}H_2O \rightarrow \frac{10}{3}H_2 + \frac{5}{3}CO_2 + \frac{5}{3}CH_3COOH$	10/3	497.8	66.7
Mannitol	$C_6H_{14}O_6 + 2H_2O \rightarrow 5H_2 + 2CO_2 + 2CH_3COOH$	5	615.4	71.4
Glycerol	$C_3H_8O_3 + H_2O \rightarrow 3H_2 + CO_2 + CH_3COOH$	3	730.4	75.0

<sup>a</sup>Optimal pathway for hydrogen production

<sup>b</sup>Biogas is mainly composed of H<sub>2</sub> and CO<sub>2</sub>

production [34]. The theoretical SHYs of glucose, galactose, and fructose are 4 mol H<sub>2</sub>/mol monomer (497.8 mL H<sub>2</sub>/g monomer), while that of xylose is 10/3 mol H<sub>2</sub>/mol monomer (497.8 mL H<sub>2</sub>/g monomer) [9, 27]. Mannitol exhibits a higher SHY of 5 mol H<sub>2</sub>/mol monomer (615.4 mL H<sub>2</sub>/g monomer); this is because it has more reducing power, which generates extra NADH during dark fermentation as compared with glucose [23]. Glycerol derived from lipids is another important hydrogen-producing substrate. The theoretical SHYs of glycerol achieves 3 mol H<sub>2</sub>/mol monomer (730.4 mL H<sub>2</sub>/g monomer), which is comparable with carbohydrate monomers. There are numerous existing literatures reported on fermentative hydrogen production from carbohydrate monomers and glycerol [20, 23, 25, 29]. The experimental values are usually in the range of 15–95% of the theoretical values, mainly depending on the sources of inoculum and operation parameters [8].

In contrast, long-chain fatty acids (LCFAs) derived from lipids are difficult to be degraded during dark fermentation; this is attributed to the fact that fermentation of LCFAs to shorter chain equivalents is usually thermodynamically unfavorable, unless coupled with the methanogenesis reaction [35]. Unfortunately, methanogenesis is usually inhibited in most cases of hydrogen fermentation process [30, 36, 37]. Moreover, LCFAs tend to form insoluble hydrophobic aggregates, which adversely affect hydrogen fermentation [38].

Also, protein monomers (i.e., amino acids) have minor contribution to the direct hydrogen production, although they can provide nitrogen sources for

HPB growth during dark fermentation. The experimental SHYs of proteins monomers are very low in common fermentation environments with acidic or a neutral conditions [29, 39, 40]. Such low SHY values are probably due to the slow hydrogen production rates as compared with the fast hydrogen consumption rates during fermentation. However, amino acids do produce a certain amount of hydrogen in extremely alkali environment (pH 10–12) with the aid of chloroform to block the hydrogen consumption pathways [41].

## Pre-treatment of Raw Materials

The rates of hydrolysis and acidogenesis steps during dark fermentation need to be matched to facilitate a balanced and efficient dark fermentation process. However, the hydrolysis step usually acts as the rate-limiting step due to its low rate. This is attributed to the fact that the biomass substrate may contain recalcitrant structures, which are not advantageous for the release and subsequent degradation of organic macromolecules by hydrolytic bacteria [31, 42]. A proper pre-treatment step is desired to disrupt the biomass structure to increase the accessibility of the bacterial enzymes and to degrade the macromolecules to micromolecules to boost the hydrolysis process [9].

## Pre-treatment for Lignocellulosic Substrate

Lignocellulosic biomass, which may be derived from agricultural residues, herbaceous, hard/soft-wood, cellulose wastes, and industry coproducts, contains abundant amounts of the carbohydrate

polymers cellulose (12–61% of TS) and hemicellulose (14–37% of TS), the aromatic polymer lignin (8–31% of TS), as well as small amounts of pectins, soluble sugars, and proteins [43]. Such carbohydrate polymers are built with hexose (e.g., glucose and mannose) and pentose (e.g., xylose), and they are tightly bound to lignin, which provides the structural rigidity and resistance against microbial and enzymatic attacks as well as oxidative stress [36, 44].

Various physical, thermal, chemical, and biological pre-treatment approaches have been employed to alter the lignin structure, to dissolve the lignin and hemicellulose, to increase the accessible surface area, to reduce the crystallization of cellulose (see Table 3), thereby enhancing the hydrogen production performance during dark fermentation [36, 42, 43, 45].

Thermal pre-treatment with or without acid, is well understood (see Table 4). Lopez-Hidalgo et al. [46] investigated the impacts of mechanical and thermal pre-treatments on hydrogen fermentation of wheat straw. The biomass was hammer milled to 425  $\mu\text{m}$  and then heated at 121  $^{\circ}\text{C}$  with steams for 1 h with 0.75% v/v  $\text{H}_2\text{SO}_4$ . The maximum SHY of 140.1 mL/g sugar and HPR of 18 mL/L/h were achieved when the liquid fraction of hydrolysate was used as a substrate. However, the presence of furfural derived from pre-treatment may adversely affect hydrogen fermentation [46]. Gonzales et al. [47] investigated hydrogen fermentation of empty palm fruit bunch, rice husk, and pine tree wood as substrates pre-treated by mechanical mill and autoclave heated at 121  $^{\circ}\text{C}$  for 60 min with 5% v/v  $\text{H}_2\text{SO}_4$ . As a result, the total reducing sugar recovery achieved 56.6–60.7%. Meanwhile, the maximum HPRs of 1510–1860 mL/L/day were achieved, and the maximum SHYs of 0.96–1.25 mol/mol sugar (or 119.5–155.6 mL/g sugar) were obtained. However, in the pre-treatment process, fermentable monosaccharides were partially degraded to VFAs and furans, with hydroxymethylfurfural (HMF) and furfural concentrations of 0.9–1.2 g/L and 3.4–3.6 g/L, respectively [47].

Furanic compounds, such as furfural (derived from pentose) and HMF (derived from hexose),

are considered as common by-products generated via thermal processes, particularly in an acidic environment [36]. Such compounds are known to have a critical impact on microbes through inducing DNA damage and inhibiting enzymes as well as cell growth [48, 49]. Although the inhibitory threshold level varies and is depending on the inoculum and fermentation environments, high concentration of furanic compounds (e.g., above 1 g/L) can significantly inhibit hydrogen fermentation [50–52]. To reduce the inhibitory effects and improve hydrogen production performance, extra detoxification process (e.g., active charcoal adsorption, solvent extraction, alkaline treatment, and evaporation) may be applied [36, 48].

Datar et al. [53] reported hydrogen fermentation of corn stover soaked in 1.2% v/v  $\text{H}_2\text{SO}_4$  for approximately 2 h and subsequently steam exploded at 190  $^{\circ}\text{C}$  for 2 min. Activated charcoal was employed to reduce the concentrations of by-products (i.e., furfural and HMF). Consequently, the lag-phase time of hydrogen fermentation was reduced, with maximal SHY of 3.0 mol/mol sugar (or 373.3 mL/g sugar) and HPR of 176.4 mL/L/h. Most of the glucose and xylose were consumed, with the utilization efficiencies of 91% and 94%, respectively [53]. However, the detoxification process may constitute a major cost of fermentative biofuel production process and may cause a loss of fermentable sugar [24, 36]. A highly selective detoxification process for the removal of by-products derived from thermal pre-treatment with low cost needs to be further explored.

Thermal alkaline pre-treatment also effects lignin disruption and changes to the biomass surface, while it has a minor effect on the formation of furfural and HMF (see Table 3). Lin et al. [54] employed microwave-heated alkali pre-treatment to enhance the enzymatic digestibility of water hyacinth. The biomass was oven-dried, powdered to 0.02 mm, soaked in 0.2% w/v NaOH for 24 h, and then microwave-heated at 190  $^{\circ}\text{C}$  for 10 min. Scanning electron microscopy (SEM) results indicated that the lignocellulose matrix had deconstructed, and the biomass surface had swelled. X-ray diffraction (XRD) results

**Hydrogen Production from Biological Sources, Table 3** Pre-treatment of raw materials (Adapted from [42])

Element	Mechanical	Irradiation	Steam explosion	Hydro thermal	Catalyzed steam explosion	Acid (thermal)	Alkaline (thermal)	Oxidative (thermal)	Ionic liquid	Biological
Alteration of lignin structure	NE	NE	●	○	●○	●	●	●	NE	●
Solubilization of lignin	NE	NE	○	○	●○	○	●○	●○	NE	●
De-crystallization of cellulose	●	○	NE	ND	ND	ND	ND	ND	●	ND
Solubilization of hemicellulose	NE	○	●	●	●	●	○	NE	○	●
Increase of accessible surface area	●	●	●	●	●	●	●	●	●	●
Formation of furfural/hydroxymethylfurfural	NE	○	●	○	●	●	○	○	NE	NE

●: Major effect

○: Minor effect

ND not determined, NE no effect

**Hydrogen Production from Biological Sources, Table 4** Pre-treatment to enhance hydrogen fermentation

Substrate	Pre-treatment	Result	Reference
Wheat straw	Hammer mill to 425 $\mu\text{m}$ and then steam heating at 121 $^{\circ}\text{C}$ for 1 h with 0.75% v/v $\text{H}_2\text{SO}_4$	Straw hydrolysate mainly contained 21 g/L of reducing sugars, 1.0 g/L of formic acid, 3.59 g/L of acetic acid and 0.12 g/L of furfural Specific hydrogen yield increased to 140.1 mL/g sugar Maximum hydrogen production rate increased to 18 mL/L/h Presence of furfural may adversely affect hydrogen production	[46]
Empty palm fruit bunch, rice husk, and pine tree wood	Mill to 1–2 mm and autoclave at 121 $^{\circ}\text{C}$ for 60 min with 5% v/v $\text{H}_2\text{SO}_4$	Total sugar recovery achieved 56.6–60.7% Fermentable monosaccharides were partially degraded to volatile fatty acids and furans HMF and furfural concentrations were 0.9–1.2 g/L and 3.4–3.6 g/L, respectively Maximum hydrogen production rates achieved 1510–1860 mL/L/d Specific hydrogen yields achieved 0.96–1.25 mol/mol sugar (or 119.5–155.6 mL/g sugar)	[47]
Corn stover	Soaked in 1.2% v/v $\text{H}_2\text{SO}_4$ for approximately 2 h and then steam explosion at 190 $^{\circ}\text{C}$ for 2 min	Hydrolysate was mainly derived from hemicellulose and contained xylose, glucose, arabinose, galactose, and mannose The hydrogen lag-phase time can be reduced by the by-product (i.e., furfural and HMF) removal using activated charcoal Specific hydrogen yield increased to 3.0 mol/mol sugar (or 373.3 mL/g sugar) Maximum hydrogen production rate increased to 176.4 mL/L/h Approximately 91% of glucose and 94% of xylose consumed during fermentation	[53]
Miscanthus stems	Chop to a length of 0.5–5 cm, extrusion-NaOH pre-treatment at 70 $^{\circ}\text{C}$ for 4 h, and then enzymatic hydrolysis for 72 h	Sixty-nine percent of cellulose and 38% of hemicellulose were converted to glucose, xylose, and arabinose Thirty-three percent of the initial biomass was converted into monosaccharides <i>Thermotoga elfii</i> was able to grow on hydrolysate, producing higher hydrogen yield compared with glucose medium	[55]
Water hyacinth	Oven-dried, powdered to 0.02 mm, soaked in 0.2% w/v NaOH for 24 h, microwave heated at 190 $^{\circ}\text{C}$ for 10 min, and enzymatic hydrolysis for 24 h	SEM results indicated that lignocellulose matrix was deconstructed, and the biomass surface was swelled XRD results suggested the decrease of crystallinity index from 16.0 to 13.0 due to cellulose amorphization	[54]

(continued)

**Hydrogen Production from Biological Sources, Table 4** (continued)

Substrate	Pre-treatment	Result	Reference
		FTIR results confirmed the destruction of lignin structure and the disruption of the crystalline cellulose to reduce crystallinity Optimal reducing sugar yield of 0.296 g/g VS was achieved Specific hydrogen yield increased to 63.9 mL/g VS	
Cassava residues	Thermal heated at 110 °C for 2 h with 85% NMMO solution and the enzymatically hydrolysed by cellulase for 72 h	SEM results revealed the formation of deep grooves and numerous pores in the surface XRD results showed the decrease of crystallinity index from 40 to 34 FTIR results indicated the partially transformation of crystal cellulose I to amorphous cellulose II The subsequent reducing sugar yield of 51.7 g/g VS, corresponding to 85% of the theoretical value Specific hydrogen yield of enzymatically hydrolysed biomass increased from 92.3 to 126 mL/g VS Maximum hydrogen production rate increased from 174.4 mL/L/h to 227.2 mL/L/h Soluble metabolites increased from 41.8 mM to 50.8 mM	[57]
Sugarcane top	Autoclave at 121 °C for 15 min and fungal pre-treatment at 28 °C for 21 d	Lignin was reduced by 60.4% SEM results indicated biomass was degraded with formation of cavities inside, and microfibrils were separated and fully exposed FTIR results suggested dissolution of lignin and hemicellulose Hemicellulose and cellulose losses were 24.3% and 5.0%, respectively Acetate and butyrate and concentrations were increased by 119.7% and 150.3%, respectively Specific hydrogen yield increased by 40.4% (77.2 mL/g VS) Maximum hydrogen production rate increased by 34.3% (11.0 mL/g VS/h) Lag-phase time reduced by 5.6%	[56]
Microalgae <i>Chlamydomonas reinhardtii</i>	Cell wall disruption and then simultaneous saccharification by $\alpha$ -amylase and fermentation at 75 °C	Almost no hydrogen was produced using intact microalgal cells without pre-treatment as substrates Specific hydrogen yield increased to 2.5 mol/mol glucose equivalent with hydrogen content of 64% Maximum hydrogen production rate increased to 227.3 mL/L/h	[67]
Microalgae <i>Nannochloropsis oceanica</i>	Microwave irradiation at 140 °C with 1% H <sub>2</sub> SO <sub>4</sub> for 15 min	Significant increase of reducing sugars and amino acids yields to 0.29 g/g VS and 0.05 g/g VS Specific hydrogen yield increased	[32]

(continued)

**Hydrogen Production from Biological Sources, Table 4** (continued)

Substrate	Pre-treatment	Result	Reference
		from near zero to 39.0 mL/g VS Maximum hydrogen production rate increased from near zero to 50.3 mL/L/h	
Macroalgae <i>Laminaria japonica</i>	Washed with water, oven-dried, powdered to 0.5 mm, heated at 170 °C for 20 min	Negligible lignin content in macroalgal biomass effected a high SHY of 69.1 mL/g COD <sub>added</sub> without harsh pre-treatment, compared with terrestrial lignocellulosic biomass Increasing temperature from 150 °C to 180 °C improved biomass solubilization, and reduce the cellulose and hemicellulose contents, thereby enhancing the hydrolysis performance Furfural concentration increased from 1.1 to 3.2 g/L with increasing temperature from 150 °C to 180 °C, which may adversely affect hydrogen fermentation Specific hydrogen yield increased by 63.9% (110.8 mL/g COD <sub>added</sub> ); Maximum hydrogen production rate increased by 221.1% (0.61 L/L/h); Total organic acids increased by 91.7% (12.9 g/L) Lag-phase time reduced by 14.4% (10.7 h) Carbohydrate removal efficiency increased by 50.9% (80%)	[68]
Canteen food waste	Selected manually to remove undesirable materials, mixed in blender, and then enzymatically hydrolysed by <i>Aspergillus awamori</i> and <i>Aspergillus oryzae</i> at 55 °C	Maximum glucose yield of 0.39 g/g substrate was obtained in hydrolysate, corresponding to the starch conversion efficiency of 87% Most of the glucose was consumed during fermentation Specific hydrogen yield achieved 219.9 mL/g VS <sub>added</sub> Pre-treatment can effectively boost the hydrolysis rate, enhance substrate utilization, and improve hydrogen production	[69]
Food wastes from a fruit wholesaler, catering kitchen, and brewery	Chopped, pressed, washed, blended, and then hydrothermal pre-treated at 200 °C and 50 bar for 15 min	Hydrolysate was detoxicated by activated carbon to remove HMF Specific hydrogen yield of 3.0 mol/mol hexose was achieved during electro-fermentation Up to 99% of food waste was destructed via hydrothermal pre-treatment and subsequent fermentation	[70]

TS total solids, VS volatile solids, HMF hydroxymethylfurfural, SEM scanning electron microscopy, XRD X-ray diffraction, FTIR Fourier transform infrared spectroscopy, NMMO N-methylmorpholine-N-oxide



suggested the decrease of crystallinity index because of cellulose amorphization. Fourier transform infrared spectroscopy (FTIR) results confirmed the destruction of lignin structure and the disruption of the crystalline cellulose to reduce crystallinity. Consequently, the pre-treated biomass was effectively hydrolysed by enzymes, generating a reducing sugar yield of 0.296 g/g VS and an SHY of 63.9 mL H<sub>2</sub>/g VS [54]. Vrije et al. [55] suggested a one-step extrusion-NaOH (12% w/v) pre-treatment at 70 °C for 4 h for *Miscanthus* stems. The pre-treated biomass was enzymatically hydrolysed, resulting in the conversion 69% of cellulose and 38% of hemicellulose to glucose, xylose, and arabinose. Normal growth of *Thermotoga elfii* on biomass hydrolysate under a thermophilic environment was reported, producing more hydrogen when compared with glucose medium [55].

Fungal pre-treatment is one of representative biological pre-treatments for lignocellulosic biomass; it can selectively degrade lignin and hemicellulose while consuming little cellulose [42]. Kumari and Das [56] carried out fungal pre-treatment of sugarcane top inoculated with white rot fungus *Pleurotus pulmonarius* for 21 d. SEM results indicated the biomass was degraded, with cavities having formed inside, and microfibrils were separated and fully exposed. FTIR results suggested dissolution of lignin and hemicellulose. The contents of lignin, hemicellulose, and cellulose were reduced by 60.4%, 24.3%, and 5.0%, respectively. As a result, the maximum SHY and HPR were enhanced by 40.4% and 34.3%, respectively, with a slight reduction in lag-phase time. Meanwhile, 119.7% increase of acetate and 150.3% increase of butyrate concentrations were observed [56]. It should be noted that the long pre-treatment period and the loss of fermentable component (particularly of hemicellulose). Further work needs to be devoted to boosting hydrolysis while preserving the fermentable organic materials.

Recently, ionic liquids have been employed to pre-treat the lignocellulosic biomass; this approach has shown advantages in cellulose

de-crystallization and the increase of accessible surface area (Table 4), with little inhibitor production [42]. Cheng et al. [57] assessed the impacts of *N*-methylmorpholine-*N*-oxide (NMMO) pre-treatment on subsequent enzymatic hydrolysis and fermentation. SEM results revealed the formation of deep grooves (ca. 4 μm width) and numerous pores in the surface. XRD results showed a decrease of the crystallinity index from 40 to 34. FTIR results confirmed the partial transformation of crystal cellulose I to amorphous cellulose II, with the lateral order index decreased from 0.86 to 0.7. The NMMO pre-treatment facilitated the subsequent enzymatic hydrolysis, with a reducing sugar yield of 51.7 g/g VS, corresponding to 85% of the theoretical value; this equals to a 16.7% increase as compared with direct use of raw biomass for enzymatic hydrolysis. Consequently, the SHY increased from 92.3 to 126 mL/g VS, the maximum HPR increased from 174.4 to 227.2 mL/L/h, and the soluble metabolites increased from 41.8 to 50.8 mM [57]. The ionic liquid pre-treatment is considered as a green route to efficiently pre-treat lignocellulosic biomass; however, this process may be expensive. An economic assessment should be carried out to evaluate such a process. Furthermore, the efficient recovery of ionic liquids should be further investigated and optimized.

### Pre-treatment for Algal Substrate

Aquatic algae, which may be classified as microalgae (such as *Chlorella* and *Chlamydomonas*) or macroalgae (such as *Laminaria* and *Ulva*) based on their size and morphology, are considered as promising substrates for biofuel production [8, 58, 59]. Algal biomass contains little or no lignin, which is advantageous for fermentative hydrogen production [59, 60]. The composition of algal biomass is various and is mainly dependent on the species and environmental conditions [59, 61, 62]. Microalgal biomass contains abundant carbohydrates (10–67% of TS), proteins (8–61% of TS), and lipids (6–40% of TS), whereas macroalgal biomass contains abundant carbohydrates (28–84% of TS), proteins (7–39% of TS), and

small amounts of lipids (1–7% of TS) [36, 60]. It should be noted that the typical organic components in micro- and macroalgae are quite different. For instance, starch, glycogen, glucosylglycerol, and trehalose are the typical carbohydrates in microalgae, while agar, carrageenan, laminarin, fucoidan, cellulose, and mannitol are the typical carbohydrates in macroalgae [12, 60, 63].

The algal cell wall structure can significantly reduce bacterial accessibility and resist bacterial attack [64–66]. Nguyen et al. [67] found hydrogen production by *Thermotoga neapolitana* was near zero when intact microalgal cells of *Chlamydomonas reinhardtii* were used as substrate. Sonication and methanol exposure can effectively disrupt the cell wall structure, and the subsequent simultaneous saccharification and fermentation process generated a high SHY of 2.5 mol/mol glucose equivalent with high content of 64%. Meanwhile, the maximum HPR achieved 227.3 mL/L/h [67]. Xia et al. [32] investigated hydrogen fermentation using microalgae *Nannochloropsis oceanica* as a substrate. When *N. oceanica* biomass was pre-treated by microwave irradiation at 140 °C with 1% H<sub>2</sub>SO<sub>4</sub> for 15 min, the SHY significantly increased to 39.0 mL/g VS, and the maximum HPR increased to 50.3 mL/L/h [32]. Jung et al. [68] used macroalgae *Laminaria japonica* as a substrate for hydrogen fermentation. The washed, oven-dried, and powdered *L. japonica* showed a relative high SHY of 69.1 mL/g COD<sub>added</sub> without harsh pre-treatment, as compared with terrestrial lignocellulosic biomass. This can be attributed to the negligible lignin content in macroalgal biomass. When the powdered biomass was further pre-treated by thermal heating at 170 °C for 20 min, the SHY increased by 63.9%, the HPR increased by 221.1%, the total organic acids concentration increased by 91.7%, and the carbohydrate removal efficiency increased by 50.9%. Meanwhile, the hydrogen-producing lag-phase time was reduced by 14.4%. An increase of the pre-treatment temperature improved the hydrolysis performance but also increase the furfural concentration, which can inhibit the subsequent fermentation process [68].

### Pre-treatment for Food Wastes

Food waste contains complex polysaccharides and proteins, which usually require an extra hydrolysis step for their utilization as fermentation substrates [69, 70]. Han et al. [69] pre-treated food waste with solid-state fermentation by *Aspergillus awamori* and *Aspergillus oryzae* at 55 °C. The maximum glucose yield of 0.39 g/g substrate was achieved, which corresponded to the starch conversion efficiency of 87%. Such biological pre-treatment can effectively boost the hydrolysis rate, enhance substrate utilization, and improve hydrogen production [69]. However, the biological pre-treatment may take a few hours to a few days to fully hydrolyse the substrate. The slow reaction rate may reduce the feasibility for large-scale application. Furthermore, food waste may contain competitor organisms and pathogens, which are not advantageous for dark fermentation and can cause environmental issues. In contrast, high temperatures and pressures during hydrothermal pre-treatment can sterilize the feedstock while reducing the pre-treatment time significantly. Redwood et al. [70] employed hydrothermal pre-treatment to hydrolyse food waste at 200 °C and 50 bars for 15 min and used activated carbon to remove the formed HMF. The maximal SHY of 3.0 mol/mol hexose was obtained in subsequent fermentation, and 99% of food waste was destructed [70]. Yin et al. [71] investigated the impacts of temperature on the hydrothermal pre-treatment and subsequent fermentation of food waste. The optimal temperature for organic dissolution was 180 °C, effecting a 42.5% increase in soluble COD. However, the optimal temperature for fermentation was 160 °C, with a total VFA yield of 0.91 g/g VS removal [71].

### Process Control and Optimization

#### Inoculum

The inoculum for dark fermentation can be classified into single-species and multi-species cultures (see Table 5) [26, 72, 73]. High performance single-species cultures may be isolated from the natural environment [20]. Alternatively, they may be derived from physiochemical

**Hydrogen Production from Biological Sources, Table 5** Inoculum for hydrogen fermentation (Adapted from [8, 29, 72])

Element	Single-species culture	Multi-species culture
Source	Isolated from environment or modified by physiochemical mutation and genetic methodologies	Pre-treatment of mixed bacteria derived from anaerobic digestion
Specific hydrogen yield	Up to approximately 4 mol/mol hexose	Usually, below 2.5 mol/mol hexose
Advantage	High specific H <sub>2</sub> yield especially under a thermophilic environment Highly efficient in conversion of simple substrates to H <sub>2</sub> and other distinctive products	Resilience to biological contamination and inhibitors Highly adaptable to various substrates High substrate degradation efficiency
Drawback	Sensitive to inhibitors Require a sterilization environment Difficulty in degradation of complex substrates	Low specific H <sub>2</sub> yield due to hydrogen-consuming pathways such as homoacetogenesis Various by-products

mutation and genetic modification [74, 75]. Multi-species cultures are usually isolated and enriched from anaerobic digestion inoculum through various pre-treatment approaches, such as the applications of heat, aeration, irradiation, acid, and alkaline conditions, to inhibit most of the hydrogen consumers [29, 76, 77].

Single-species cultures can achieve high SHYs, particularly under a thermophilic environment, and are highly efficient in conversion of simple substrates (such as sugars and glycerol) to hydrogen and other distinctive products [8, 72]. Nevertheless, multi-species cultures are considered more promising for future large-scale applications, because they are able to utilize a wider range of organic materials, thus increasing the potential of energy production using complex biomass as substrates [29, 72]. Furthermore, multi-species cultures contain more diverse microorganisms, which provide resilience to contamination during the treatment of biomass wastes without sterilization, improving the stability for long-term hydrogen fermentation [78]. Nevertheless, the microbial community can be changed during treating various substrates. Xia et al. [79] reported that the microbial community of AFB was simple and was contained one dominant species (*Clostridium butyricum*), when glucose was used as a substrate. However, the microbial community developed a complex structure with three major species (*Clostridium cochlearium*, *Clostridium acetireducens*, and *Sporanaerobacter*

*acetigenes*), when microalgae *Chlorella pyrenoidosa* was used as a substrate for a long-term fermentation [79]. The variation of microbial communities may change the fermentative pathways and products, thereby affecting the hydrogen fermentation performance. The microbial community should be monitored and controlled for long periods of time to ensure stable fermentation.

### Temperature

Temperature has a significant impact on AFB activity and hydrogen fermentation [28]. Hydrogen fermentation performance may increase with increasing temperature within a proper range. However, a significant drop in hydrogen production occurs at excessively high temperatures. Fermentation can be successfully conducted in mesophilic (ca. 37 °C), thermophilic (ca. 55 °C), or hyperthermophilic (>65 °C) environments [6, 8, 22]. Mesophilic environments have been applied widely in dark fermentation due to the low amounts of energy consumption required to maintain the fermenter temperature. Increase in the temperature to thermophilic and hyperthermophilic levels has significant advantages, such as inhibition of hydrogen consumers, enhancement of thermodynamic favorability of hydrogen production pathways, increase of SHYs, and improvement of hydrogen tolerance and metabolic activity of HPB [25, 26]. Nevertheless, the HPR per volume may be reduced in such a heated

environment, as the cell densities of HPB are lower compared with those in a mesophilic environment [78]. The thermophilic conditions may be more competitive if waste heat sources are available.

### pH

The pH is another critical parameter for hydrogen fermentation, and may affect the metabolic pathways and hydrogenase activity [28]. Increase of pH level in a certain range can improve the hydrogen fermentation performance, whereas further increases may inhibit hydrogen production [23, 28]. The optimal pH values have been reported in the range of 5.5–6.5 [26, 80, 81].

Hydrogen fermentation is accompanied with the production of VFAs, which may cause a significant drop of pH in the fermentation system. The low pH (e.g., <5) is not advantageous for hydrogen production, due to the shift of metabolic pathways (e.g., ethanol production) that consume more NADH, decrease of hydrogenase activity, and charge variation of cell membrane [26, 80].

A stable and optimal pH level is very beneficial for hydrogen fermentation. The addition of alkaline chemicals, such as NaOH and KOH, is usually employed in lab scale fermenters [29, 82]. Nevertheless, such pH adjustment is costly and introduces a high level of ions, which may adversely affect HPB growth and metabolism [9]. The use of slightly alkaline wastewater, such as the effluent from anaerobic digestion, may be a cost-effective strategy to maintain the pH of dark fermentation [83]. Alternatively, the addition of protein-rich substrates may be useful for maintaining pH. Anaerobic degradation of protein compounds can generate ammonia, which further dissolves in water and neutralizes excess protons to form ammonium (Eq. 11) [79].



### Hydraulic Retention Time (HRT) and Organic Loading Rate (OLR)

In large-scale applications of hydrogen fermentation, a continuous mode should be employed

rather than a batch mode. In this case, the HRT and OLR are the critical parameters for hydrogen fermentation [9]. HRT indicates the average time the fermentation liquor remains in the fermenter unit (Eq. 12). HRT should be sufficiently high to improve the substrate degradation and to avoid HPB washout of the reactor. However, excess HRT is also not advantageous for hydrogen production. Long HRTs can lead to accumulation of homoacetogenic bacteria, resulting in rapid hydrogen consumption. To ensure a high performance of dark fermentation, the HRT is usually maintained at 0.5 h–2 d [30, 73, 83].

$$\text{HRT (d)} = \frac{\text{Fermenter capacity (L)}}{\text{Daily fresh substrate added (L/d)}} \quad (12)$$

OLR reflects the daily treating capacity of organic materials of the fermenter per unit volume (Eq. 13). OLR directly corresponds to the organic concentrations of the influent and the HRT in traditional homogeneous reactors (such as continuous stirred tank reactor, CSTR). A high OLR may lead to the accumulation of VFAs that can significantly reduce the pH and inhibit hydrogen production [8, 28]. Furthermore, insufficient substrate degradation occurs with a high OLR. However, the low OLR would reduce the biomass degradation capacity of the fermenter per volume and result in requiring larger fermenters, thereby increasing the capital and operating costs for dark fermentation. Therefore, a proper OLR should be selected, based on the substrate origin, pretreatment, inoculum, fermentation temperature, etc., to ensure a cost-effective hydrogen fermentation process.

$$\text{OLR(g/L/d)} = \frac{\text{Daily organic drysolids added (g/d)}}{\text{Fermenter capacity (L)}} \quad (13)$$

### Macro- and Micronutrients

The supply of nutrients is a critical issue for the long-term operation of hydrogen fermenter. Sufficient levels of macro- and micronutrient would

ensure a stable hydrogen fermentation [84]. Macronutrients, for instance, nitrogen, phosphorus, potassium, sodium, magnesium, iron, and calcium, are essential for the fermentation process. Moreover, the micronutrients, for instance, copper, zinc, and molybdenum, can also play important roles during hydrogen fermentation [84, 85]. Such nutrients are associated with cell metabolism and growth, organic component synthesis of HPB, and enzyme activation and function [28, 84, 86]. Nutrient deficiency may occur when the fermentation process only involves mono-substrate, particularly for the carbohydrate-rich substrates such as straw and grass [9, 87]. Maintenance of the nutrients at certain levels is very beneficial for the fermentation process [84]. The nutrients may be supplied by the addition of refined chemicals [9]. Nevertheless, this approach can be expensive and may be not practical for a large-scale fermenter. Alternatively, the co-fermentation with various substrates, for instance, animal excreta and food waste, is a cost-effective strategy for the nutrient supply [88].

### Inhibition

The experimental values of SHYs of substrates are usually much lower than their theoretical values; this can be attributed to the pathways that consume or do not produce hydrogen, as well as the inhibition of hydrogen production. The inhibitors may originate from substrates, the degradation of substrates, and formation of metabolic products.

### Hydrogen and Carbon Dioxide

The accumulated hydrogen improves the hydrogen concentration in the fermentation liquid phase, while reducing the thermodynamic favorability of hydrogen production pathways [84]. Meanwhile, the increased carbon dioxide level facilitates hydrogen consumption reactions, such as homoacetogenesis [30].

Removal of hydrogen and carbon dioxide has the potential to increase the hydrogen production [89]. Sparging with external gas (e.g., nitrogen and argon) has been demonstrated as an effective approach [90–92]. Nevertheless, the gas-sparging

method requires large quantities of external gases and results in the dilution of the hydrogen mixture, which can significantly increase the costs for the subsequent hydrogen upgrading and utilization processes. Alternatively, hydrogen fermentation can be enhanced by applying a vacuum environment to reduce the hydrogen and carbon dioxide concentrations, by employing chemicals (such as KOH and NaOH) to absorb carbon dioxide from the headspace and by removing the dissolved gases [30]. Recently, Massanet-Nicolau et al. [89] proposed an effective approach integrating electrochemical hydrogen removal (EHR) and carbon dioxide removal (CDR) for biohydrogen systems. The use of CDR can improve the SHY from 0.07 to 0.72 mol/mol hexose. The combination of CDR and EHR can further enhance the SHY to 1.79 mol/mol hexose [89].

### Volatile Fatty Acids (VFAs)

The hydrogen fermentation generates high levels of VFAs, usually dominated by acetic acid and butyric acid [32, 80]. Furthermore, thermal pretreatment of biomass may also form VFAs such as formic and acetic acids [36]. The formation of VFAs can significantly reduce hydrogen production because of the end product inhibition and may cause the cell lysis of HPB [93–95].

Increase of the dilution rate of the fermenter can reduce the VFA inhibition; however, the reduced HRT may have negative impacts on hydrogen fermentation, such as the washout of HPB. VFAs in hydrogen fermentation liquor can be effectively removed through bipolar membrane electrodialysis, thereby enhancing hydrogen production [70, 93, 96]. Nevertheless, this approach can be expensive. A cheaper route to remove VFAs, using conventional electrodialysis (CED), has been reported by Jones et al. [95]. High removal efficiencies of VFAs (up to 99%) can be achieved by treating model solution and fermentation liquor with CED for 60 min [95].

### Ammonia

In dark fermentation, ammonia can be generated via the degradation of nitrogen-based organic compounds, such as proteins and urea, or via the



reduction of nitrates by nitrate-reducing bacteria. Also, some substrates, such as manures, may contain high levels of ammonia. An appropriate ammonia level is beneficial for protein synthesis and growth of HPB cells [34, 97]. However, a high ammonia concentration may result in inhibition.

Total ammonia nitrogen (TAN) includes free (unionized) ammonia nitrogen (FAN) and ionized ammonia nitrogen (ammonium). FAN is considered more inhibitory to HPB, because it easily penetrates the cell membrane; this can cause proton imbalances as well as a potassium deficiency [98]. FAN concentration is increased with increasing TAN concentration, pH, and temperature (Eq. 14) [99].

$$\text{FAN} = \frac{\text{TAN}}{1 + \frac{10^{-\text{pH}}}{10^{-\left(0.09018 + \frac{2729.92}{T(K)}\right)}}} \quad (14)$$

When the fermenter operates with a mesophilic environment (37 °C), FAN only constitutes 0.01% of TAN at pH 5, significantly increases to 1% at pH 7, and further increases to 56% at pH 9. However, dark fermentation operates at low pH due to VFA accumulation, under which conditions the inhibitory effect from FAN is usually not significant. For instance, FAN only represents a minor fraction of TAN (0.04–0.4%) at the optimal fermentation pH of 5.5–6.5.

The optimal TAN concentrations for hydrogen fermentation have been reported in the range of 7–71 mM, which equals to 98–994 mg/L; this is mainly dependent on the inoculum source, pH, and temperature [97, 100]. However, slight ammonia inhibition and hydrogen reduction have been observed when the TAN level increased to 1000–3000 mg/L [23]. Further increase of TAN level to 7000–10,000 mg/L may lead to serious ammonia inhibition with poor substrate degradation and hydrogen production [23, 97, 100].

The protein-rich substrates, such as manures and microalgae, usually have high nitrogen contents and low carbon to nitrogen (C/N) ratios; this may result in ammonia accumulation in the fermenter. Co-fermentation of carbon-rich substrates

to improve the C/N ratio would be a cost-effective strategy to reduce the ammonia concentration. The optimal C/N ratio for dark fermentation is usually in the range of 15–40 [101, 102]. Xia et al. [101] found co-fermentation of microalgae *C. pyrenoidosa* and cassava starch at a C/N ratio of 25 can significantly enhance hydrogen fermentation, achieving an SHY of 276.2 mL/g VS, which was 3.7 and 1.8 times higher compared with the mono-fermentation of *C. pyrenoidosa* and cassava starch. Alternatively, many approaches, such as acclimation or immobilization of inoculum, adjustment of pH, temperature control, dilution of fermentation liquor, and ammonia removal by adsorption (zeolite treatment), can effectively reduce the ammonia inhibition [84, 100, 103, 104].

### Nutrients

Proper levels of nutrients (both macro- and micro-nutrients) can boost hydrogen fermentation, whereas excessive nutrients may exhibit inhibitory effects. For instance, the hydrogen fermentation is not efficient with low SHY and HPR in a sodium-free environment [23]. A proper sodium concentration can increase the activity of NADH-ferredoxin oxidoreductase, leading to enhancing the reduction of ferredoxin, which can further provide more potential electron donors during hydrogen fermentation. Moreover, increased sodium concentration is advantageous for another reason: substrates can be actively transported into HPB cells, driven by a sodium gradient created by a high extracellular sodium concentration [105]. Nevertheless, excessive sodium concentrations can seriously inhibit HPB, as a massive expenditure of cellular energy is required to pump out the excess sodium. In addition, a high ion concentration can result in HPB cell lysis [106, 107]. A number of existing literatures reported the toxicity of excessive nutrients on hydrogen fermentation [28, 86, 108]. For instance, Li and Fang [86] found that the relative toxicity of six metals is as follows: copper > nickel and zinc > chromium > cadmium > lead. The threshold concentration of each nutrient varies and is dependent on factors such as the source of inoculum and fermentation operation parameters. The



strategy to overcome inhibition includes dilution to reduce the nutrient concentration below the inhibitory concentration thresholds and the use of long-term acclimatized inoculum. Alternatively, detoxification and extra removal processes may be employed to reduce the excessive nutrient levels [84].

### Furanic and Phenolic Compounds

Pretreatment, especially of lignocellulosic biomass, can form furanic and phenolic compounds, which may be inhibitory for dark fermentation [36]. Furanic compounds, such as furfural and HMF, are derived from the dehydration of pentose and hexose [36, 84]. Furanic compounds can damage the DNA, suppress cell growth, reduce enzyme activity in glycolysis, alter metabolic pathways, and oxidize NADH, which further reduces the hydrogen potential [48, 109, 110].

Phenolic compounds, such as vanillin and syringaldehyde, can be formed during the degradation of lignin polymers [84, 111]. Furanic compounds have negative impacts on cell membranes either by causing damage or by increasing their permeability [84, 112]. Consequently, the leakage of intracellular components as well as the inactivation of essential enzymatic systems may occur, reducing the cell growth and activity and changing the metabolic pathways of HPB cells [36, 45, 113, 114].

The inhibitory thresholds for furanic and phenolic compounds affecting hydrogen fermentation have been reported to be near zero; this means such compounds, at very low levels, can adversely affect hydrogen production [84]. Several studies have employed activated carbon to remove the inhibitory compounds [24, 115, 116]. Cheng et al. [24] found that the removal efficiencies of vanillin, HMF, and furfural by using activated carbon achieved 84.8%, 45.4%, and 39.5%, respectively. However, the slight loss of glucose (13.8%) was also observed, which may reduce the hydrogen potential. These authors also confirmed the combination of activated carbon detoxification and HPB acclimation can improve the SHY and HPR by 29.7% and 84.7%, respectively, using hydrolysed water hyacinth as a substrate [24]. Alternatively, biological or chemical

techniques can be applied in detoxification process. In addition, the full understanding of the formation mechanism of furanic and phenolic compounds as well as the optimization of the pre-treatment process are important topics of the future research.

### Bioreactors for Hydrogen Production

For large-scale hydrogen production, the fermenter should be operated continuously. In addition to HRT, the solids retention time (SRT) and microbial retention time (MRT) are also critical parameters, which indicate the average time of the solids and microbes, respectively, remaining in the fermentation system [13].

$$\text{SRT (d)} = \frac{\text{Total solids in fermenter (g)}}{\text{Daily solids removed (g/d)}} \quad (15)$$

$$\text{MRT (d)} = \frac{\text{Total microbes in fermenter (g)}}{\text{Daily microbes removed (g/d)}} \quad (16)$$

Conventional CSTR has been widely employed in dark fermentation [117]. HPB cells and substrates are suspended homogeneously in the liquid phase. HPB and substrates have the same MRT and SRT, respectively, which are also equal to the HRT. With a short HRT, insufficient SRTs can lead to a poor degradation of substrates, and low MRTs can result in the washout of microbes, which may further cause the failure of the fermentation process [28, 117, 118].

To separate the MRT and SRT from the HRT, advanced bioreactors, such as sludge retention and attachment-type reactors, have been developed (see Table 6). The upflow anaerobic sludge blanket (UASB) reactor is a breakthrough technology that facilitates the sludge retention by forming a granular sludge blanket rich in microbes suspended in the reactor [13]. The organic components flow with fermentation liquor upward through the blanket and are

**Hydrogen Production from Biological Sources, Table 6** Bioreactors for hydrogen fermentation

Element	Traditional reactor	Sludge retention type reactor	Attachment type reactor
Example	Continuous stirred tank reactor	Upflow anaerobic sludge blanket Expanded granular sludge bed Anaerobic fluidized bed reactor	Anaerobic filter Anaerobic membrane bioreactor
Growth mode	Suspension	Granular	Attachment
Retention time <sup>a</sup>	$HRT = SRT = MRT$	$SRT \text{ and } MRT > HRT$	$MRT > HRT \text{ and } SRT$
Advantage	Wide range substrate Homogeneous process Highly efficient mass transfer between substrate and bacteria Simple structure Low investment and operation cost	High OLR and short HRT Lowland footprint High activity and performance granular	High OLR and short HRT Resistant to environment changes No stir requirement Fast restart process
Drawback	Low OLR and high HRT required Large reactor volume Wash out of inoculum	Low substrate TS content required High operation and control requirement	Low efficiency in high TS content substrate Replacement of packed materials Easily blocked

*HRT* hydraulic retention time, *SRT* solids retention time, *MRT* microbial retention time, *OLR* organic loading rate, *TS* total solids  
<sup>a</sup>[13]

degraded by the microbes. The settling action from gravity, combined with the upward flow, ensures suspension of the solid materials. As a result, the *MRT* and *SRT* are much longer than the *HRT*. This facilitates the high volume and mass of substrate input, while improving the solid and microbe retention, to ensure a high performance fermentation process [13, 117].

In the fermentation of organic wastewater with low solids content, the attachment-type reactor via cell immobilization technology (e.g., adsorption, entrapment, encapsulation) offers an effective solution [119]. Interestingly, such a reactor is more tolerant to metal toxicity and hydraulic shock loadings [120]. An anaerobic filter (AF) is a typical attachment-type reactor, which contains filter medium immobilizing active HPB. The wastewater flows through the filter, while the organic components are efficiently degraded by the microbes. The AF technique can effectively retain the high performance HPB while achieving a short *HRT* and stable hydrogen fermentation performance [13].

UASB and AF are more stable than traditional CSTR under a short *HRT* [118, 121]. Kongjan and Angelidaki [121] reported reducing *HRT* to 2.5 d led to HPB washout in the CSTR, while fluctuations and reduction of hydrogen production were observed in UASB and AF at an *HRT* of 0.5 d. Design of novel bioreactor with sufficient *MRT* and *SRT* while short *HRT* would be very beneficial for hydrogen fermentation. Furthermore, the mass transfer in the bioreactor is very critical in the hydrogen fermentation process [14, 15, 122]. Low-molecular-weight substrates (such as glucose) are dissolved in the liquor phase and then transported into the HPB cells for hydrogen production. Meanwhile, the gaseous products (such as hydrogen and carbon dioxide) and soluble metabolites (such as acetic acid) are inversely released to the environment. The poor mass transfer of substrates can lead to insufficient substrate supply for HPB, which would reduce the HPR. Additionally, the poor mass transfer of the products can lead to the accumulation of metabolites, which can further cause the intracellular

**Hydrogen Production from Biological Sources, Table 7** Current techniques for biogas upgrading with carbon dioxide removal (Adapted from [124–126])

Element	Gas scrubbing	Adsorption	Membrane separation	Cryogenic separation
Principle	Removed by using scrubbing fluids such as water and amines	Adsorbed by using carbon molecular sieves and activated carbon	Separated via different permeation rates	Separated via different boiling and sublimation points
Distribution of upgrading techniques <sup>a</sup>	60.7%	16.8%	20.6%	0.2%
Advantage	No pre-treatment Low investment High gas quality	Dry process No water demand High gas quality	Flexible scale Fast start-up Low mechanical abrasion	No chemical use High gas purity Low extra energy input for methane liquefaction
Drawback	Water demand Waste water treatment	High investment H <sub>2</sub> S pre-treatment required Parallel sheets required	High investment, operation energy demand and cost Pre-treatment required Low methane recovery	High investment, operation energy demand, and cost Complex process

<sup>a</sup>Data are collected from [127]

acidification and change the thermodynamic favorability of hydrogen production reaction, thereby inhibiting the hydrogen fermentation.

### Use of Hydrogen as a Transport Fuel

The gas mixture derived from dark fermentation mostly contains hydrogen and carbon dioxide, as well as small amounts of ammonia, hydrogen sulfide, water, nitrogen, oxygen, etc. To meet the standards of compressed gaseous biofuels or grid injection, the product gas mixture should be cleaned by having harmful trace components removed. To improve the heating value, the gas should also be upgraded by the removal of the carbon dioxide to improve the heating value. Alkaline solutions (e.g., NaOH) are usually used to purify and upgrade the gas mixture at the lab-scale [23]. Unfortunately, such a topic has not been investigated at a large scale, because the hydrogen fermentation has yet to be commercialized and only exists in a few demonstration and pilot projects [123]. However, the cleaning and upgrading processes for biohydrogen can be related to biomethane in biogas industry. The

technologies for biogas purification and upgrading have been comprehensively reviewed by Weiland [31], Ryckebosch et al., [124] and Petersson and Wellinger [125]. In addition, the common biogas upgrading techniques are listed in Table 7 [124–127].

Hydrogen is considered the fuel with the highest energy density by mass (excepting nuclear sources) with that results in clean products, and has a great potential for use in the transport sector [5]. Table 8 presents a comparison of physical and chemical characteristics of typical transport fuels. The lower heating value (LHV) of hydrogen by mass (120 MJ/kg) is 2.7 and 2.4 times higher than isooctane (44.3 MJ/kg) and methane (50 MJ/kg), respectively [128]. Hydrogen offers a wide range of flammable limits ( $0.1 < \varphi < 7.1$ ), with the flammable mixtures ranging from as lean as  $\lambda = 10$  to as rich as  $\lambda = 0.14$ ; this is advantageous to produce a wide range of engine power outputs by the varying the mixture equivalence ratio [4]. The burning speed of hydrogen (265–325 cm/s) is approximately seven times higher than isooctane and methane, thereby leading to a shorter combustion time and less heat loss from the hydrogen flame, compared to isooctane

**Hydrogen Production from Biological Sources, Table 8** Use of hydrogen as a transport fuel (Adapted from [4, 128])

Element	Isooctane	Methane	Hydrogen
Formula	C <sub>8</sub> H <sub>18</sub>	CH <sub>4</sub>	H <sub>2</sub>
Molecular weight (g/mol)	114.236	16.043	2.016
Carbon to hydrogen molar ratio	0.44	0.25	0
Density at NTP (kg/m <sup>3</sup> )	692	0.65	0.08
Mass lower heating value (MJ/kg)	44.3	50	120
Mass higher heating value (MJ/kg)	47.8	55.5	142
Mass diffusivity in air (cm <sup>2</sup> /s)	ca. 0.07	0.16	0.61
Minimum ignition energy (mJ)	0.28	0.28	0.02
Flammability limits in air (vol%)	1.1–6	5–15	4–75
Flammability limits ( $\lambda$ )	1.51–0.26	2–0.6	10–0.14
Flammability limits ( $\varphi$ )	0.66–3.85	0.5–1.67	0.1–7.1
Burning speed in NTP air (cm/s)	37–43	37–45	265–325
Flame temperature in air (K)	2470	2148	2318
Stoichiometric air-to-fuel ratio (kg/kg)	15.0	17.2	34.2
Stoichiometric air-to-fuel ratio (kmol/kmol)	59.666	9.547	2.387
Quenching distance in NTP air (cm)	0.35	0.203	0.064

NTP normal temperature (293.15 K) and pressure (1 atm)

and methane flames. As a result, only approximately 17–25% of the thermal energy generated in hydrogen combustion is lost to the environment via radiative heat transfer, compared to 30–42% for isooctane and 22–33% for methane [128].

The gaseous fuels, such as hydrogen and methane, have low energy densities by volume (hydrogen: 10.0 MJ/m<sup>3</sup>, methane: 32.6 MJ/m<sup>3</sup> at normal temperature and pressure) compared with diesel (37 MJ/L) and gasoline (19.6 MJ/L) [128]. To make such gases amenable for use in transportation, they should be compressed to achieve high volumetric energy density.

The typical pressure of compressed methane is in the range of 20–22 MPa; the compression process may consume 3.3% of the chemical energy stored in methane. To achieve a similar energy density by volume, hydrogen needs to be compressed to approximately 70 MPa, which can consume 15% of the total energy in hydrogen [129]. Apart from the energy consumption, safety is an important issue for high pressure hydrogen [5]. Furthermore, the introduction and subsequent diffusion of hydrogen to metals can cause the metals to become brittle and fracture (viz. hydrogen embrittlement); the everyday use of hydrogen requires massive projects to

construct the hydrogen distribution and storage infrastructure [5, 130]. This may be achieved by significant modification of existing natural gas systems.

### Further Use of Volatile Fatty Acids as a Biorefinery

According to the Eq. 3, the optimal case for hydrogen fermentation only converts one-third of the energy in glucose to hydrogen, whereas two-thirds of the energy remains in the liquid phase in the form of VFAs. The theoretical value may vary, depending on the substrate type (e.g., sugars, amino acids, and glycerol) [8]. However, the energy in produced hydrogen only represents a small fraction of the substrate, compared with that further available from the soluble metabolites. Xia et al. [23] used mannitol as a substrate for hydrogen fermentation. The optimal run generated an SHY of 224.2 mL/g mannitol, corresponding to an energy conversion efficiency (ECE) of 17.2%. Meanwhile, the overall ECE of 96.1% was achieved, dominated by butyric acid (38.3%) and ethanol (34.2%) [23]. Another study used glucose and glutamic

acid as substrates, and an ECE of 83.3% was achieved by considering hydrogen and soluble metabolites. However, produced hydrogen only constituted a small fraction of the energy from the substrates (15.6%) [29].

To increase the feasibility of dark fermentation, a further integration with the utilization of soluble metabolites would be of importance, as shown in Fig. 2. The produced alcohols, mainly ethanol, can be purified and then used as a vehicle fuel. Meanwhile, the VFAs may be used as substrates for hydrogen production through photo fermentation, methane production via anaerobic digestion, electricity generation through microbial fuel cell technology, and biodiesel production by yeasts and microalgae [8, 131]. Moreover, a higher economic benefit can be achieved by VFA purification and use of VFAs as substrates for the production of value-added chemicals, such as aldehydes and polyhydroxyalkanoates [131–133].

### Potential of Biomass Wastes: A Case Study in China

In 2014, the energy consumption of the transport sector in China consumed 271 Mtoe, corresponding to 11.4 EJ; this is equal to 13.6% of total final energy consumption in China or 11.2% of global transport energy consumption [1, 134]. The transport sector of China in 2014 was mainly dominated by oil products (90.8%), followed by natural gas (5.5%). The biofuel fraction is relatively small but it is growing [134].

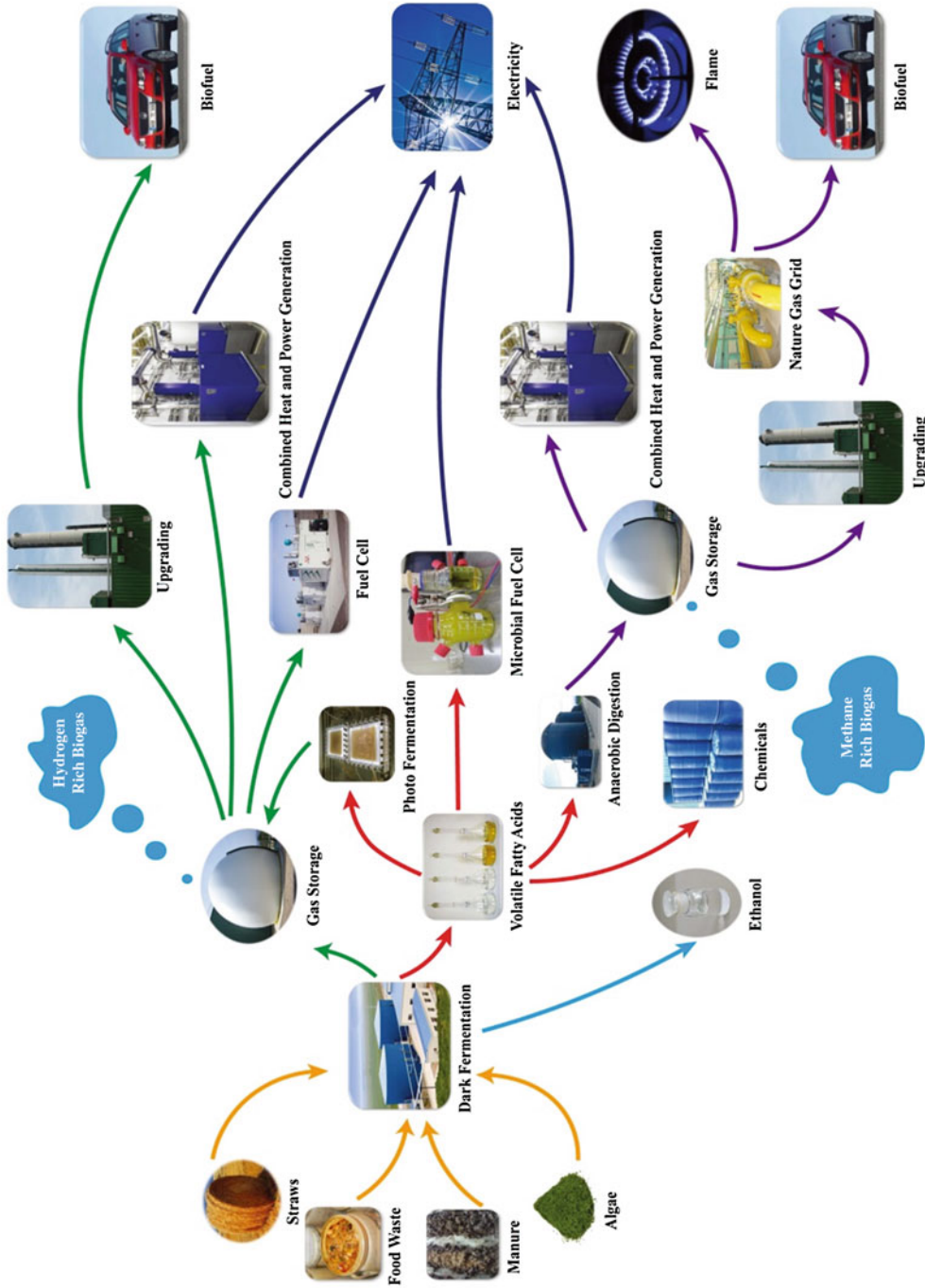
The hydrogen sourced from the treatment of biomass wastes may play a significant role in the transport sector in the future. Various organic wastes are abundant in China, predominantly manure (3800 Mt/a), food waste (83 Mt/a), straw (830 Mt/a), and domestic wastewater (73,532 Mt/a) [135–137]. By applying the simplified calculation indicated in Table 9, manure, food waste, straw, and domestic wastewater can generate 119.1 Gm<sup>3</sup>, 2.5 Gm<sup>3</sup>, 95.4 Gm<sup>3</sup>, and 3.3 Gm<sup>3</sup> of hydrogen, respectively. Meanwhile, the fermentation process can co-generate 225.8 Mt of alcohols

(simplified to ethanol) and 295.2 Mt of VFAs (simplified to acetic acid). The hydrogen and ethanol can fulfill 20.9% and 57.2% of the final consumption of the transport sector in China. The VFAs can be further fermented to hydrogen and methane, which may double the energy production of gaseous biofuel, as estimated from the energy value of VFAs. Alternatively, the VFAs can be used in other applications as shown in Fig. 2.

### Concluding Remarks and Future Perspectives

Fermentative hydrogen derived from biomass waste has significant advantages in waste treatment and renewable energy production. It may play an important role in the future as a clean energy supply, particularly in the transport sector. Until now, however, such a process has not yet become commercially available. There are only a small number of pilot-scale fermenters; more research should be devoted to improving the viability of large-scale dark fermentation through increasing the fermentation efficiency while reducing the cost of the hydrogen production process.

- The pre-treatment of biomass waste can improve subsequent fermentation performance via increasing the SHY, HPR, and substrate degradation efficiency, as well as reducing HRT. However, the optimal pre-treatment strategy has yet to be defined. Different substrates and fermentation systems require various pre-treatment parameters. A viable pre-treatment should simultaneously minimize the parasitic energy use and economic investment. Thermal and chemical pre-treatments can effectively hydrolyse the biomass; however, the cost and the environmental impacts should be carefully assessed. Moreover, such processes can generate by-products, such as furanic and phenolic components, which may inhibit the subsequent fermentation. The mechanism of inhibitor formation and control during pre-treatment should be further



Hydrogen Production from Biological Sources, Fig. 2 Dark fermentation as a platform for energy and chemical production



**Hydrogen Production from Biological Sources, Table 9** Energy and products derived from hydrogen fermentation: a case study in China

Biomass wastes	Productivity (fresh weight, Mt/a)	Volatile solids content	Productivity (volatile solids, Mt/a)	Hydrogen fermentation <sup>a,b</sup>		
				Hydrogen (Gm <sup>3</sup> /a)	Volatile fatty acids (Mt/a)	Alcohols (Mt/a)
Manure	3,800 <sup>c</sup>	21% <sup>d</sup>	798	119.1	159.6	122.1
Food wastes	83 <sup>e</sup>	20% <sup>f</sup>	16.6	2.5	3.3	2.5
Straws	830 <sup>e</sup>	77% <sup>g</sup>	639.1	95.4	127.6	97.8
Domestic wastewater	73,532 <sup>h</sup>	/	22.2 <sup>h,i</sup>	3.3	4.4	3.4

<sup>a</sup>Fermentation substrate was simplified to glucose with 60% of degradation efficiency

<sup>b</sup>Glucose was used as a model substrate during fermentation, which is then converted via mixed metabolic pathway including 50% volatile fatty acids (acetic acid) and 50% alcohol (ethanol) production

<sup>c</sup>[135]

<sup>d</sup>[138]

<sup>e</sup>[136]

<sup>f</sup>[139]

<sup>g</sup>[140]

<sup>h</sup>[137]

<sup>i</sup>Mt COD/a

explored. Alternatively, biological pre-treatment may reduce the energy demand while minimizing inhibitor production. However, the reaction rate of biological pre-treatment requires further improvement, and the loss of the substrates should be minimized.

- Multi-species cultures, such as heat pre-treated anaerobic digestion sludge, are widely employed as inoculum in dark fermentation. Such cultures are able to utilize a wide range of substrates and are resistant to bacterial contamination, compared with the single-species cultures. Nevertheless, the full understanding of microbes in multi-species cultures and their functions, interactions, and metabolic pathways, would be very beneficial to improve the performance and stability of hydrogen fermentation. More work should be devoted to enhancing the hydrogen production pathways and to reducing the hydrogen consumption pathways. High performance hydrogen-producing strains may be isolated from the natural environment, or produced through genetic modification or physiochemical mutation. The addition of such novel strains to multi-species cultures may be advantageous for hydrogen production. Meanwhile, in long-

term continuous fermentation, the microbial community should be monitored and controlled.

- Enhancement of mass transfer in the fermenter is beneficial for hydrogen production. The fermenter design and the control of mixing and flow can significantly affect the mass transfer in the fermenter. More work should be carried out to develop a quantitative model relating the mass transfer to the production of hydrogen and other metabolites, and to intensify the fermentation process.
- The energy remaining in VFAs contained in dark fermentation effluent should be recovered. Many approaches may be integrated to improve the energy conversion, with examples including anaerobic digestion, photo fermentation, bioelectrochemical processes, microbial biodiesel, etc. Anaerobic digestion may be an attractive candidate to combine with dark fermentation. The two-stage process integrating dark fermentation and anaerobic digestion can produce hythane, which is considered as a cleaner and more efficient fuel as compared with methane. Compared with single-stage biogas systems, the addition of a dark fermentation stage to biogas systems can achieve a

higher energy yield, a more stable process, make it more resistant to inhibitory compounds, and attain a shorter overall HRT while increasing the OLR. This can be realized in a biogas system by adding a hydrogen fermenter. Alternatively, VFAs from dark fermentation may also be extracted or used as substrates to produce chemicals. Detailed technical-economic analyses for various integrating systems should be carried out to further elucidate the relative technical and economic feasibility of these options.

**Acknowledgments** This work was supported by the National Science Foundation for Young Scientists of China (No. 51606021), the International Cooperation and Exchange of the National Natural Science Foundation of China (No. 51561145013), and the National Key Research and Development Program of China (No. 2016YFB0601002).

## Bibliography

- BP (2016) BP statistical review of world energy 2016. BP. <http://www.bp.com/>. Accessed 17 Jan 2017
- Obama B (2017) The irreversible momentum of clean energy. Science. doi:10.1126/science.aam6284
- Nigam PS, Singh A (2011) Production of liquid biofuels from renewable resources. Prog Energy Combust Sci 37:52–68
- Verhelst S, Wallner T (2009) Hydrogen-fueled internal combustion engines. Prog Energy Combust Sci 35:490–527
- Murphy JD, Thamsiriroj T (2011) What will fuel transport systems of the future? Mater Today 14:518–524
- Hay JXW, Wu TY, Juan JC, Jahim JM (2013) Biohydrogen production through photo fermentation or dark fermentation using waste as a substrate: overview, economics, and future prospects of hydrogen usage. Biofuels Bioprod Biorefin 7:334–352
- Das D, Veziroglu TN (2001) Hydrogen production by biological processes: a survey of literature. Int J Hydrog Energy 26:13–28
- Xia A, Cheng J, Song W, Su H, Ding L, Lin R, Lu H, Liu J, Zhou J, Cen K (2015) Fermentative hydrogen production using algal biomass as feedstock. Renew Sust Energy Rev 51:209–230
- Xia A, Cheng J, Murphy JD (2016) Innovation in biological production and upgrading of methane and hydrogen for use as gaseous transport biofuel. Biotechnol Adv 34:451–472
- Ghirardi ML, Zhang JP, Lee JW, Flynn T, Seibert M, Greenbaum E, Melis A (2000) Microalgae: a green source of renewable H<sub>2</sub>. Trends Biotechnol 18:506–511
- Holladay JD, Hu J, King DL, Wang Y (2009) An overview of hydrogen production technologies. Catal Today 139:244–260
- Carrieri D, Momot D, Brasg IA, Ananyev G, Lenz O, Bryant DA, Dismukes GC (2010) Boosting auto-fermentation rates and product yields with sodium stress cycling: application to production of renewable fuels by cyanobacteria. Appl Environ Microbiol 76:6455–6462
- Yuan Z, Wu C, Ma L (2016) Principles and technologies of bioenergy utilization. Chemical Industry Press, Beijing
- Zhu X, Guo C-L, Wang Y-Z, Liao Q, Chen R, Lee D-J (2012) A feasibility study on unsaturated flow bioreactor using optical fiber illumination for photo-hydrogen production. Int J Hydrog Energy 37:15666–15671
- Liao Q, Liu D-M, Ye D-D, Zhu X, Lee D-J (2011) Mathematical modeling of two-phase flow and transport in an immobilized-cell photobioreactor. Int J Hydrog Energy 36:13939–13948
- Koku H, Eroglu I, Gunduz U, Yucel M, Turker L (2002) Aspects of the metabolism of hydrogen production by *Rhodobacter sphaeroides*. Int J Hydrog Energy 27:1315–1329
- Oh YK, Raj SM, Jung GY, Park S (2011) Current status of the metabolic engineering of microorganisms for biohydrogen production. Bioresour Technol 102:8357–8367
- Sun YH, Liao Q, Huang Y, Xia A, Fu Q, Zhu X, Zheng YP (2016) Integrating planar waveguides doped with light scattering nanoparticles into a flat-plate photobioreactor to improve light distribution and microalgae growth. Bioresour Technol 220:215–224
- Imaizumi Y, Nagao N, Yusoff FM, Taguchi S, Toda T (2014) Estimation of optimum specific light intensity per cell on a high-cell-density continuous culture of *Chlorella zofingiensis* not limited by nutrients or CO<sub>2</sub>. Bioresour Technol 162:53–59
- Khamtib S, Reungsang A (2012) Biohydrogen production from xylose by *Thermoanaerobacterium thermosaccharolyticum* KCU19 isolated from hot spring sediment. Int J Hydrog Energy 37:12219–12228
- Song WL, Cheng J, Zhao JF, Carrieri D, Zhang CX, Zhou JH, Cen KF (2011) Improvement of hydrogen production by over-expression of a hydrogen-promoting protein gene in *Enterobacter cloacae*. Int J Hydrog Energy 36:6609–6615
- Zhao C, Karakashev D, Lu W, Wang H, Angelidaki I (2010) Xylose fermentation to biofuels (hydrogen and ethanol) by extreme thermophilic (70 °C) mixed culture. Int J Hydrog Energy 35:3415–3422

23. Xia A, Jacob A, Herrmann C, Tabassum MR, Murphy JD (2015) Production of hydrogen, ethanol and volatile fatty acids from the seaweed carbohydrate mannitol. *Bioresour Technol* 193:488–497
24. Cheng J, Lin R, Song W, Xia A, Zhou J, Cen K (2015) Enhancement of fermentative hydrogen production from hydrolyzed water hyacinth with activated carbon detoxification and bacteria domestication. *Int J Hydrog Energy* 40:2545–2551
25. Maru BT, Bielen AAM, Constanti M, Medina F, Kengen SWM (2013) Glycerol fermentation to hydrogen by *Thermotoga maritima*: proposed pathway and bioenergetic considerations. *Int J Hydrog Energy* 38:5563–5572
26. Argun H, Kargi F (2011) Bio-hydrogen production by different operational modes of dark and photo-fermentation: an overview. *Int J Hydrog Energy* 36:7443–7459
27. Angenent LT, Karim K, Al-Dahhan MH, Domiguez-Espinosa R (2004) Production of bioenergy and biochemicals from industrial and agricultural wastewater. *Trends Biotechnol* 22:477–485
28. Wang J, Wan W (2009) Factors influencing fermentative hydrogen production: a review. *Int J Hydrog Energy* 34:799–811
29. Xia A, Cheng J, Ding LK, Lin RC, Song WL, Su HB, Zhou JH, Cen KF (2015) Substrate consumption and hydrogen production via co-fermentation of monomers derived from carbohydrates and proteins in biomass wastes. *Appl Energy* 139:9–16
30. Saady NMC (2013) Homoacetogenesis during hydrogen production by mixed cultures dark fermentation: unresolved challenge. *Int J Hydrog Energy* 38:13172–13191
31. Weiland P (2010) Biogas production: current state and perspectives. *Appl Microbiol Biotechnol* 85:849–860
32. Xia A, Cheng J, Lin R, Lu H, Zhou J, Cen K (2013) Comparison in dark hydrogen fermentation followed by photo hydrogen fermentation and methanogenesis between protein and carbohydrate compositions in *Nannochloropsis oceanica* biomass. *Bioresour Technol* 138:204–213
33. Xia A, Jacob A, Herrmann C, Murphy JD (2016) Fermentative bio-hydrogen production from galactose. *Energy* 96:346–354
34. Sambusiti C, Bellucci M, Zabaniotou A, Beneduce L, Monlau F (2015) Algae as promising feedstocks for fermentative biohydrogen production according to a biorefinery approach: a comprehensive review. *Renew Sust Energy Rev* 44:20–36
35. Oh ST, Martin AD (2010) Long chain fatty acids degradation in anaerobic digester: thermodynamic equilibrium consideration. *Process Biochem* 45:335–345
36. Monlau F, Sambusiti C, Barakat A, Quemeneur M, Trably E, Steyer JP, Carrere H (2014) Do furanic and phenolic compounds of lignocellulosic and algae biomass hydrolyzate inhibit anaerobic mixed cultures? A comprehensive review. *Biotechnol Adv* 32:934–951
37. Liu Z, Zhang C, Lu Y, Wu X, Wang L, Wang L, Han B, Xing X-H (2013) States and challenges for high-value biohythane production from waste biomass by dark fermentation technology. *Bioresour Technol* 135:292–303
38. Chen JL, Ortiz R, Steele TWJ, Stuckey DC (2014) Toxicants inhibiting anaerobic digestion: a review. *Biotechnol Adv* 32:1523–1534
39. Xia A, Cheng J, Lin RC, Liu JZ, Zhou JH, Cen KF (2013) Sequential generation of hydrogen and methane from glutamic acid through combined photo-fermentation and methanogenesis. *Bioresour Technol* 131:146–151
40. Cheng J, Ding LK, Xia A, Lin RC, Li YY, Zhou JH, Cen KF (2015) Hydrogen production using amino acids obtained by protein degradation in waste biomass by combined dark- and photo-fermentation. *Bioresour Technol* 179:13–19
41. Xiao ND, Chen YG, Chen AH, Feng LY (2014) Enhanced bio-hydrogen production from protein wastewater by altering protein structure and amino acids acidification type. *Sci Rep* 4:3992
42. Zheng Y, Zhao J, Xu F, Li Y (2014) Pretreatment of lignocellulosic biomass for enhanced biogas production. *Prog Energy Combust Sci* 42:35–53
43. Ruiz HA, Rodriguez-Jasso RM, Fernandes BD, Vicente AA, Teixeira JA (2013) Hydrothermal processing, as an alternative for upgrading agriculture residues and marine biomass according to the biorefinery concept: a review. *Renew Sust Energy Rev* 21:35–51
44. Karimi K, Taherzadeh MJ (2016) A critical review of analytical methods in pretreatment of lignocelluloses: composition, imaging, and crystallinity. *Bioresour Technol* 200:1008–1018
45. Chen R, Wang Y-Z, Liao Q, Zhu X, Xu T-F (2013) Hydrolysates of lignocellulosic materials for biohydrogen production. *BMB Rep* 46:244–251
46. Lopez-Hidalgo AM, Sanchez A, De Leon-Rodriguez A (2017) Simultaneous production of bioethanol and biohydrogen by *Escherichia coli* WDHL using wheat straw hydrolysate as substrate. *Fuel* 188:19–27
47. Gonzales RR, Sivagurunathan P, Parthiban A, Kim SH (2016) Optimization of substrate concentration of dilute acid hydrolyzate of lignocellulosic biomass in batch hydrogen production. *Int Biodeterior Biodegrad* 113:22–27
48. Almeida JRM, Bertilsson M, Gorwa-Grauslund MF, Gorsich S, Liden G (2009) Metabolic effects of furaldehydes and impacts on biotechnological processes. *Appl Microbiol Biotechnol* 82:625–638
49. Palmqvist E, Hahn-Hagerdal B (2000) Fermentation of lignocellulosic hydrolysates. II: inhibitors and mechanisms of inhibition. *Bioresour Technol* 74:25–33
50. Quemeneur M, Hamelin J, Barakat A, Steyer JP, Carrere H, Trably E (2012) Inhibition of fermentative

- hydrogen production by lignocellulose-derived compounds in mixed cultures. *Int J Hydrog Energy* 37:3150–3159
51. Veeravalli SS, Chaganti SR, Lalman JA, Heath DD (2013) Effect of furans and linoleic acid on hydrogen production. *Int J Hydrog Energy* 38:12283–12293
  52. Monlau F, Aemig Q, Trably E, Hamelin J, Steyer JP, Carrere H (2013) Specific inhibition of biohydrogen-producing *Clostridium* sp after dilute-acid pretreatment of sunflower stalks. *Int J Hydrog Energy* 38:12273–12282
  53. Datar R, Huang J, Maness PC, Mohagheghi A, Czemik S, Chornet E (2007) Hydrogen production from the fermentation of corn stover biomass pretreated with a steam-explosion process. *Int J Hydrog Energy* 32:932–939
  54. Lin RC, Cheng J, Song WL, Ding LK, Xie BF, Zhou JH, Cen KF (2015) Characterisation of water hyacinth with microwave-heated alkali pretreatment for enhanced enzymatic digestibility and hydrogen/methane fermentation. *Bioresour Technol* 182:1–7
  55. de Vrije T, de Haas GG, Tan GB, Keijsers ERP, Claassen PAM (2002) Pretreatment of *Miscanthus* for hydrogen production by *Thermotoga elfii*. *Int J Hydrog Energy* 27:1381–1390
  56. Kumari S, Das D (2016) Biologically pretreated sugarcane top as a potential raw material for the enhancement of gaseous energy recovery by two stage biohythane process. *Bioresour Technol* 218:1090–1097
  57. Cheng J, Zhang J, Lin R, Liu J, Zhang L, Cen K (2017) Ionic-liquid pretreatment of cassava residues for the cogeneration of fermentative hydrogen and methane. *Bioresour Technol* 228:348–354
  58. Jones CS, Mayfieldt SP (2012) Algae biofuels: versatility for the future of bioenergy. *Curr Opin Biotechnol* 23:346–351
  59. Dismukes GC, Carrieri D, Bennette N, Ananyev GM, Posewitz MC (2008) Aquatic phototrophs: efficient alternatives to land-based crops for biofuels. *Curr Opin Biotechnol* 19:235–240
  60. Wei N, Quarterman J, Jin Y-S (2013) Marine macroalgae: an untapped resource for producing fuels and chemicals. *Trends Biotechnol* 31:70–77
  61. Chen C-Y, Zhao X-Q, Yen H-W, Ho S-H, Cheng C-L, Lee D-J, Bai F-W, Chang J-S (2013) Microalgae-based carbohydrates for biofuel production. *Biochem Eng J* 78:1–10
  62. Tabassum MR, Xia A, Murphy JD (2016) The effect of seasonal variation on biomethane production from seaweed and on application as a gaseous transport biofuel. *Bioresour Technol* 209:213–219
  63. Xia A, Jacob A, Tabassum MR, Herrmann C, Murphy JD (2016) Production of hydrogen, ethanol and volatile fatty acids through co-fermentation of macro- and micro-algae. *Bioresour Technol* 205:118–125
  64. Chen PH, Oswald WJ (1998) Thermochemical treatment for algal fermentation. *Environ Int* 24:889–897
  65. Mussgnug JH, Klassen V, Schlueter A, Kruse O (2010) Microalgae as substrates for fermentative biogas production in a combined biorefinery concept. *J Biotechnol* 150:51–56
  66. Ward AJ, Lewis DM, Green B (2014) Anaerobic digestion of algae biomass: a review. *Algal Res* 5:204–214
  67. Nguyen TAD, Kim KR, Nguyen MT, Kim MS, Kim D, Sim SJ (2010) Enhancement of fermentative hydrogen production from green algal biomass of *Thermotoga neapolitana* by various pretreatment methods. *Int J Hydrog Energy* 35:13035–13040
  68. Jung KW, Kim DH, Shin HS (2011) Fermentative hydrogen production from *Laminaria japonica* and optimization of thermal pretreatment conditions. *Bioresour Technol* 102:2745–2750
  69. Han W, Ye M, Zhu AJ, Zhao HT, Li YF (2015) Batch dark fermentation from enzymatic hydrolyzed food waste for hydrogen production. *Bioresour Technol* 191:24–29
  70. Redwood MD, Orozco RL, Majewski AJ, Macaskie LE (2012) An integrated biohydrogen refinery: synergy of photofermentation, extractive fermentation and hydrothermal hydrolysis of food wastes. *Bioresour Technol* 119:384–392
  71. Yin J, Wang K, Yang Y, Shen D, Wang M, Mo H (2014) Improving production of volatile fatty acids from food waste fermentation by hydrothermal pretreatment. *Bioresour Technol* 171:323–329
  72. Jobard M, Pessiot J, Nouaille R, Sime-Ngando T (2014) Microbial diversity supporting dark fermentation of waste. *Trends Biotechnol* 32:549–550
  73. Fang HHP, Liu H (2002) Effect of pH on hydrogen production from glucose by a mixed culture. *Bioresour Technol* 82:87–93
  74. Cheng J, Liu M, Song W, Ding L, Liu J, Zhang L, Cen K (2017) Enhanced hydrogen production of *Enterobacter aerogenes* mutated by nuclear irradiation. *Bioresour Technol* 227:50–55
  75. Song W, Cheng J, Zhao J, Zhang C, Zhou J, Cen K (2016) Enhancing hydrogen production of *Enterobacter aerogenes* by heterologous expression of hydrogenase genes originated from *Synechocystis* sp. *Bioresour Technol* 216:976–980
  76. Van Ginkel S, Sung SW, Lay JJ (2001) Biohydrogen production as a function of pH and substrate concentration. *Environ Sci Technol* 35:4726–4730
  77. Zhu H, Beland M (2006) Evaluation of alternative methods of preparing hydrogen producing seeds from digested wastewater sludge. *Int J Hydrog Energy* 31:1980–1988
  78. Pawar SS, van Niel EWJ (2013) Thermophilic biohydrogen production: how far are we? *Appl Microbiol Biotechnol* 97:7999–8009
  79. Xia A, Cheng J, Ding L, Lin R, Song W, Zhou J, Cen K (2014) Effects of changes in microbial community on the fermentative production of hydrogen and soluble metabolites from *Chlorella pyrenoidosa* biomass in semi-continuous operation. *Energy* 68:982–988

80. Cheng J, Su H, Zhou J, Song W, Cen K (2011) Hydrogen production by mixed bacteria through dark and photo fermentation. *Int J Hydrog Energy* 36:450–457
81. Xie B, Cheng J, Zhou J, Song W, Cen K (2008) Cogeneration of hydrogen and methane from glucose to improve energy conversion efficiency. *Int J Hydrog Energy* 33:5006–5011
82. Jung K-W, Kim D-H, Shin H-S (2012) Continuous fermentative hydrogen and methane production from *Laminaria japonica* using a two-stage fermentation system with recycling of methane fermented affluent. *Int J Hydrog Energy* 37:15648–15657
83. Chu CF, Li YY, Xu KQ, Ebie Y, Inamori Y, Kong HN (2008) A pH- and temperature-phased two-stage process for hydrogen and methane production from food waste. *Int J Hydrog Energy* 33:4739–4746
84. Bundhoo MAZ, Mohee R (2016) Inhibition of dark fermentative bio-hydrogen production: a review. *Int J Hydrog Energy* 41:6713–6733
85. Cheng J, Xia A, Song W, Su H, Thou J, Cen K (2012) Comparison between heterofermentation and auto-fermentation in hydrogen production from *Arthrospira (Spirulina) platensis* wet biomass. *Int J Hydrog Energy* 37:6536–6544
86. Li CL, Fang HHP (2007) Inhibition of heavy metals on fermentative hydrogen production by granular sludge. *Chemosphere* 67:668–673
87. Wall DM, Allen E, Straccialini B, O'Kiely P, Murphy JD (2014) The effect of trace element addition to mono-digestion of grass silage at high organic loading rates. *Bioresour Technol* 172:349–355
88. Demirel B, Scherer P (2011) Trace element requirements of agricultural biogas digesters during biological conversion of renewable biomass to methane. *Biomass Bioenergy* 35:992–998
89. Massanet-Nicolau J, Jones RJ, Guwy A, Dinsdale R, Premier G, Mulder MJJ (2016) Maximising biohydrogen yields via continuous electrochemical hydrogen removal and carbon dioxide scrubbing. *Bioresour Technol* 218:512–517
90. Kim DH, Han SK, Kim SH, Shin HS (2006) Effect of gas sparging on continuous fermentative hydrogen production. *Int J Hydrog Energy* 31:2158–2169
91. Massanet-Nicolau J, Guwy A, Dinsdale R, Premier G, Esteves S (2010) Production of hydrogen from sewage biosolids in a continuously fed bioreactor: effect of hydraulic retention time and sparging. *Int J Hydrog Energy* 35:469–478
92. Mizuno O, Dinsdale R, Hawkes FR, Hawkes DL, Noike T (2000) Enhancement of hydrogen production from glucose by nitrogen gas sparging. *Bioresour Technol* 73:59–65
93. Tang J, Jia SR, Qu SS, Xiao YA, Yuan Y, Ren NQ (2014) An integrated biological hydrogen production process based on ethanol-type fermentation and bipolar membrane electro dialysis. *Int J Hydrog Energy* 39:13375–13380
94. Choudhari SK, Cerrone F, Woods T, Joyce K, O'Flaherty V, O'Connor K, Babu R (2015) Pervaporation separation of butyric acid from aqueous and anaerobic digestion (AD) solutions using PEBA based composite membranes. *J Ind Eng Chem* 23:163–170
95. Jones RJ, Massanet-Nicolau J, Guwy A, Premier GC, Dinsdale RM, Reilly M (2015) Removal and recovery of inhibitory volatile fatty acids from mixed acid fermentations by conventional electro dialysis. *Bioresour Technol* 189:279–284
96. Redwood MD, Orozco RL, Majewski AJ, Macaskie LE (2012) Electro-extractive fermentation for efficient biohydrogen production. *Bioresour Technol* 107:166–174
97. Wang B, Wan W, Wang J (2009) Effect of ammonia concentration on fermentative hydrogen production by mixed cultures. *Bioresour Technol* 100:1211–1213
98. Chen Y, Cheng JJ, Creamer KS (2008) Inhibition of anaerobic digestion process: a review. *Bioresour Technol* 99:4044–4064
99. Rajagopal R, Masse DI, Singh G (2013) A critical review on inhibition of anaerobic digestion process by excess ammonia. *Bioresour Technol* 143:632–641
100. Salerno MB, Park W, Zuo Y, Logan BE (2006) Inhibition of biohydrogen production by ammonia. *Water Res* 40:1167–1172
101. Xia A, Cheng J, Ding LK, Lin RC, Song WL, Zhou JH, Cen KF (2014) Enhancement of energy production efficiency from mixed biomass of *Chlorella pyrenoidosa* and cassava starch through combined hydrogen fermentation and methanogenesis. *Appl Energy* 120:23–30
102. Lay CH, Sen B, Chen CC, Wu JH, Lee SC, Lin CY (2013) Co-fermentation of water hyacinth and beverage wastewater in powder and pellet form for hydrogen production. *Bioresour Technol* 135:610–615
103. Ho L, Ho G (2012) Mitigating ammonia inhibition of thermophilic anaerobic treatment of digested piggery wastewater: use of pH reduction, zeolite, biomass and humic acid. *Water Res* 46:4339–4350
104. Hansen KH, Angelidaki I, Ahring BK (1998) Anaerobic digestion of swine manure: inhibition by ammonia. *Water Res* 32:5–12
105. Lee MJ, Kim TH, Min B, Hwang SJ (2012) Sodium (Na<sup>+</sup>) concentration effects on metabolic pathway and estimation of ATP use in dark fermentation hydrogen production through stoichiometric analysis. *J Environ Manag* 108:22–26
106. van Niel EWJ, Claassen PAM, Stams AJM (2003) Substrate and product inhibition of hydrogen production by the extreme thermophile, *Caldicellulosiruptor saccharolyticus*. *Biotechnol Bioeng* 81:255–262
107. Zheng XJ, Zheng YM, Yu HQ (2005) Influence of NaCl on hydrogen production from glucose by anaerobic cultures. *Environ Technol* 26:1073–1080

108. Lin CY, Shei SH (2008) Heavy metal effects on fermentative hydrogen production using natural mixed microflora. *Int J Hydrog Energy* 33:587–593
109. Lin R, Cheng J, Ding L, Song W, Zhou J, Cen K (2015) Inhibitory effects of furan derivatives and phenolic compounds on dark hydrogen fermentation. *Bioresour Technol* 196:250–255
110. Ask M, Bettiga M, Mapelli V, Olsson L (2013) The influence of HMF and furfural on redox-balance and energy-state of xylose-utilizing *Saccharomyces cerevisiae*. *Biotechnol Biofuels* 6
111. Barakat A, Monlau F, Steyer J-P, Carrere H (2012) Effect of lignin-derived and furan compounds found in lignocellulosic hydrolysates on biomethane production. *Bioresour Technol* 104:90–99
112. Kumar G, Bakonyi P, Periyasamy S, Kim SH, Nemestothy N, Belafi-Bako K (2015) Lignocellulose biohydrogen: practical challenges and recent progress. *Renew Sust Energ Rev* 44:728–737
113. Siqueira MR, Reginatto V (2015) Inhibition of fermentative H<sub>2</sub> production by hydrolysis byproducts of lignocellulosic substrates. *Renew Energy* 80:109–116
114. Kelly C, Jones O, Barnhart C, Lajoie C (2008) Effect of furfural, vanillin and syringaldehyde on *Candida guilliermondii* growth and xylitol biosynthesis. *Appl Biochem Biotechnol* 148:97–108
115. Chang ACC, Tu Y-H, Huang M-H, Lay C-H, Lin C-Y (2011) Hydrogen production by the anaerobic fermentation from acid hydrolyzed rice straw hydrolysate. *Int J Hydrog Energy* 36:14280–14288
116. Orozco RL, Redwood MD, Leeke GA, Bahari A, Santos RCD, Macaskie LE (2012) Hydrothermal hydrolysis of starch with CO<sub>2</sub> and detoxification of the hydrolysates with activated carbon for biohydrogen fermentation. *Int J Hydrog Energy* 37:6545–6553
117. Ren N, Guo W, Liu B, Cao G, Ding J (2011) Biological hydrogen production by dark fermentation: challenges and prospects towards scaled-up production. *Curr Opin Biotechnol* 22:365–370
118. Gavala HN, Skiadas IV, Ahring BK (2006) Biological hydrogen production in suspended and attached growth anaerobic reactor systems. *Int J Hydrog Energy* 31:1164–1175
119. Kumar G, Mudhoo A, Sivagurunathan P, Nagarajan D, Ghimire A, Lay C-H, Lin C-Y, Lee D-J, Chang J-S (2016) Recent insights into the cell immobilization technology applied for dark fermentative hydrogen production. *Bioresour Technol* 219:725–737
120. Karadag D, Koroglu OE, Ozkaya B, Cakmakci M (2015) A review on anaerobic biofilm reactors for the treatment of dairy industry wastewater. *Process Biochem* 50:262–271
121. Kongjan P, Angelidaki I (2010) Extreme thermophilic biohydrogen production from wheat straw hydrolysate using mixed culture fermentation: effect of reactor configuration. *Bioresour Technol* 101:7789–7796
122. Beckers L, Masset J, Hamilton C, Delvigne F, Toye D, Crine M, Thonart P, Hiligsmann S (2015) Investigation of the links between mass transfer conditions, dissolved hydrogen concentration and biohydrogen production by the pure strain *Clostridium butyricum* CWBI1009. *Biochem Eng J* 98:18–28
123. De Gioannis G, Muntoni A, Poletini A, Pomi R (2013) A review of dark fermentative hydrogen production from biodegradable municipal waste fractions. *Waste Manag* 33:1345–1361
124. Ryckebosch E, Drouillon M, Veruaeren H (2011) Techniques for transformation of biogas to biomethane. *Biomass Bioenergy* 35:1633–1645
125. Petersson A, Wellinger A (2009) Biogas upgrading technologies – developments and innovations. IEA Bioenergy. <http://task37.ieabioenergy.com/technical-brochures.html>. Accessed January 18 2017
126. Chaemchuen S, Kabir NA, Zhou K, Verpoort F (2013) Metal-organic frameworks for upgrading biogas via CO<sub>2</sub> adsorption to biogas green energy. *Chem Soc Rev* 42:9304–9332
127. IEA Bioenergy (2015) Task 37 country reports summary. IEA Bioenergy. <http://www.iea-biogas.net/country-reports.html>. Accessed 18 Jan 2017
128. Bauer CG, Forest TW (2001) Effect of hydrogen addition on the performance of methane-fueled vehicles. Part I: effect on SI engine performance. *Int J Hydrog Energy* 26:55–70
129. Jensen JO, Vestbo AP, Li Q, Bjerrum NJ (2007) The energy efficiency of onboard hydrogen storage. *J Alloys Compd* 446:723–728
130. Thamsiriroj T, Smyth H, Murphy JD (2011) A roadmap for the introduction of gaseous transport fuel: a case study for renewable natural gas in Ireland. *Renew Sust Energ Rev* 15:4642–4651
131. Motte J-C, Sambusiti C, Dumas C, Barakat A (2015) Combination of dry dark fermentation and mechanical pretreatment for lignocellulosic deconstruction: an innovative strategy for biofuels and volatile fatty acids recovery. *Appl Energy* 147:67–73
132. Chang HN, Kim N-J, Kang J, Jeong CM (2010) Biomass-derived volatile fatty acid platform for fuels and chemicals. *Biotechnol Bioprocess Eng* 15:1–10
133. Guwy AJ, Dinsdale RM, Kim JR, Massanet-Nicolau J, Premier G (2011) Fermentative biohydrogen production systems integration. *Bioresour Technol* 102:8534–8542
134. IEA (2016) IEA Sankey diagram. IEA. <http://www.iea.org/Sankey/>. Accessed 20 Jan 2017
135. National Development and Reform Commission (2014) Annual report of comprehensive utilization of resources. National Development and Reform Commission. <http://www.sdpc.gov.cn/>. Accessed 18 Jan 2017



136. Kiran EU, Trzcinski AP, Wun Jern N, Liu Y (2014) Bioconversion of food waste to energy: a review. *Fuel* 134:389–399
137. National Bureau of Statistics of China (2016) China statistical yearbook. National Bureau of Statistics of China. <http://www.stats.gov.cn/>. Accessed 18 Jan 2017
138. Miao HF, Wang SQ, Zhao MX, Huang ZX, Ren HY, Yan Q, Ruan WQ (2014) Codigestion of Taihu blue algae with swine manure for biogas production. *Energy Convers Manag* 77:643–649
139. Zhang W, Wu S, Guo J, Zhou J, Dong R (2015) Performance and kinetic evaluation of semi-continuously fed anaerobic digesters treating food waste: role of trace elements. *Bioresour Technol* 178:297–305
140. Chen XH, Zhang YL, Gu Y, Liu ZG, Shen Z, Chu HQ, Zhou XF (2014) Enhancing methane production from rice straw by extrusion pretreatment. *Appl Energy* 122:34–41



## Biohydrogen Production

Suphi Ş. Öncel and Ayşe Köse  
Department of Bioengineering, Ege University,  
Izmir, Turkey

### Article Outline

Glossary  
Definition of the Subject  
Introduction  
Metabolic Machinery Microalgal Biohydrogen  
Production  
Conventional Methods for Genetic Optimization  
Genetic Modifications in Terms of Biohydrogen  
Production  
Systems Biology Approach for Understanding  
Biohydrogen Production  
Targeted Genome Engineering (TGE)  
Bioethics  
Opinions on Biohydrogen Research  
Conclusion  
Future Directions  
Bibliography

### Glossary

**Microalgae** As a general terminology, this word covers all the prokaryotic and eukaryotic algae without considering the taxonomic specifications. However, from a taxonomic point of view, it specifically comprises the eukaryotic photosynthetic microorganisms such as green algae and diatoms.

**Green algae** The unicellular or colony-forming single-celled eukaryotic photosynthetic organisms abundant in aquatic environments.

**Cyanobacteria** The unicellular or filamentous single-celled prokaryotic photosynthetic organisms abundant in aquatic environments, also known as blue-green algae.

**Photobiological hydrogen production** The capability of microalgae to catalyze the conversion reaction of  $H^+$  to  $H_2$  in gas form via hydrogenase enzymes under illuminated conditions.

**D1 protein** A major photosynthetic protein responsible for the constant repair of the photosystem II (PSII) damage from the oxygen generation.

**Homologous expression** The expression of a gene in the same species using recombination and transformation techniques.

**Heterologous expression** The expression of a gene in the bacteria of another organism, plant, animal, fungi, or algae.

**Targeted genome engineering** The site-specific endonuclease activated genome-editing tools, which can generate custom-made genome alterations.

### Definition of the Subject

Today, humans come to a junction where they can choose a way for the future considering energy sources and the environment and, in fact, their existence. In a route to a better future, using every option and tool will be the key and any alternative should not be underestimated. In this regard, renewables and with a special emphasis on microorganisms like microalgae are worth discussing as a promising source of energy. Considering that various microorganisms produce biofuels such as biodiesel, bioethanol, and biomethane, one of the highest priorities will be focused on the production of hydrogen. Hydrogen is known to be an energy carrier rather than an energy source; however, due to its favorable specifications, hydrogen will always be an important player in the arena of energy. Putting aside the conventional fossil industry-based processes, renewable processes especially using microalgae for biohydrogen production through photosynthetic and fermentative pathways are becoming important topics for science but similar to the

other biological processes, low efficiency and productivity is a great challenge for a reliable commercialization route. At this point, using genetics to modify the microalgae to achieve a meaningful level on a commercial scale is an important tool that cannot be ignored. Within this scope, the aim of this entry is to highlight the possibility of biohydrogen production from microalgae with regard to genetic modification within the framework of tools, options, and risks.

## Introduction

Today, energy sustainability is one of the main threats to the future of planet Earth, because it is in a dynamic interrelation between other critical factors as the environment. In its present form, the energy web of our society spins between the blocks of fossil fuels, which are irreversibly destructing the environment. The average person hearing some pessimistic news everyday about the energy crisis, wars, or pollution can develop a defensive behavior, but this will not be sufficient for an immediate change in energy policy unless this behavior becomes a strong awareness that will force policy makers as well as society to take the lead in making changes to protect the environment.

At the junction of possibly the last turn before a dead end, which only leads to a great wall of extinction, humanity should determine how to slow down and then stop the negative effects of energy consumption on the environment. In this regard, hydrogen can be a valuable alternative to provide a solution to the problem of sustainable energy. Hydrogen is the most abundant element in the universe with the lightest atomic weight. It is a highly combustible, nontoxic gas that should be a part of the future of energy.

Currently, apart from the minimal share of water electrolysis, global hydrogen production is dominated by the conventional fossil fuel processes such as steam reforming and gasification [1]. On the other hand, bio-based processes, e.g., obtaining hydrogen from biomass as a substitute for fossil sources through conventional chemical conversion or biochemical conversion reactions, are also important routes to mention especially

when considering a clean, renewable, affordable, and sustainable energy future [2]. The use of microorganisms for direct or indirect hydrogen, or popularly termed as *biohydrogen*, production is becoming an important alternative process [3]. Basically biohydrogen production is accomplished by microorganisms such as microalgae and bacteria through biological conversion processes like biophotolysis or photofermentation in which the metabolic pathways take the control [4–6].

Specifically considering the great advantage of using solar energy as the main driving force in metabolic reactions, photobiological hydrogen production is prominent among the other biohydrogen production processes [7]. Therefore, microalgae having the ability to convert solar energy to biohydrogen in an efficient way should be taken into account [8]. Briefly compared to photosynthetic bacteria, microalgae having a simpler nutrient need such as sunlight (artificial illumination sources are also possible) and minerals other than air, easy cultivation methods and a potential CO<sub>2</sub> utilizer make microalgae a good candidate for hydrogen production [9, 10].

From an engineering point of view, microalgae in general terminology comprise all the prokaryotic cyanobacteria and eukaryotic green algae without considering the taxonomic specifications [3, 11]. On the other hand, the routes for biohydrogen production from microalgae will be different from that of cyanobacteria depending on the taxonomy [12]. Basically, the difference between prokaryotic and eukaryotic biohydrogen mechanism lies in the enzymes of the process [13, 14]. In cyanobacteria, nitrogenase is the main enzyme for indirect biohydrogen production, in which the bidirectional hydrogenase enzyme is the key in both direct and indirect biophotolysis in green algae [4, 15, 16].

Starting with the first attempts of Gaffron and Rubin in the 1940s [17], microalgal hydrogen metabolism has attracted the researchers. However, meaningful productivity can only be reached by the two-stage protocol based on the sulfur starvation during anaerobic cultivation, with the model microalgae *Chlamydomonas reinhardtii* of the Melis Lab. This approach more rapidly increased the attention on microalgae when the authors published their findings in 2000 [18].

Following this development, the number of papers focusing on microalgal biohydrogen increased. Although there are disadvantages to the use of microalgae in the biohydrogen production process, an increase in the interest in the scientific arena was also supported by the high fossil fuel prices and the need to search for alternative fuel sources.

The main bottlenecks in microalgal biohydrogen production can be classified into two aspects: the physical constraints that comprise the production and downstream systems and the biological constraints comprising solar energy utilization capacity and cellular productivities.

Starting with the first bottleneck, microalgal production conventionally runs on the open pond systems which are simple cultivation units having a direct interaction with the environment [18, 19]. Thus, their use is limited with regard to biohydrogen production, in which the culture conditions should be well controlled and require anaerobic conditions [20]. In this regard, the photobioreactors, in other words, the fully controlled cultivation systems leading to isolating the microalgae from the outdoor environment, are an important focus of interest [21]. With their advantages over open systems, photobioreactors and their various designs play a key role in current biohydrogen research [22, 23]. Progress toward an economic design and an energy efficient management will lead to a conventional microalgal biohydrogen process. Another key issue is the downstream processes that comprise one of the main economic loads on the microalgal industry in terms of the scale-up, separation efficiency, and stages for the product. Even if biohydrogen can be separated directly from the culture medium, the microalgal cells will depend on the downstream processes, especially in respect of a biorefinery approach [24–26].

The second bottleneck focuses more on the cell. Basically, all the cells in their natural routine have a limit to their biohydrogen productivity. From an engineering point of view, all the effort is given to the overproduction of the desired product. To motivate or, in a more realistic term, to force the cells to produce the required amount, protocols such as applying stress through different

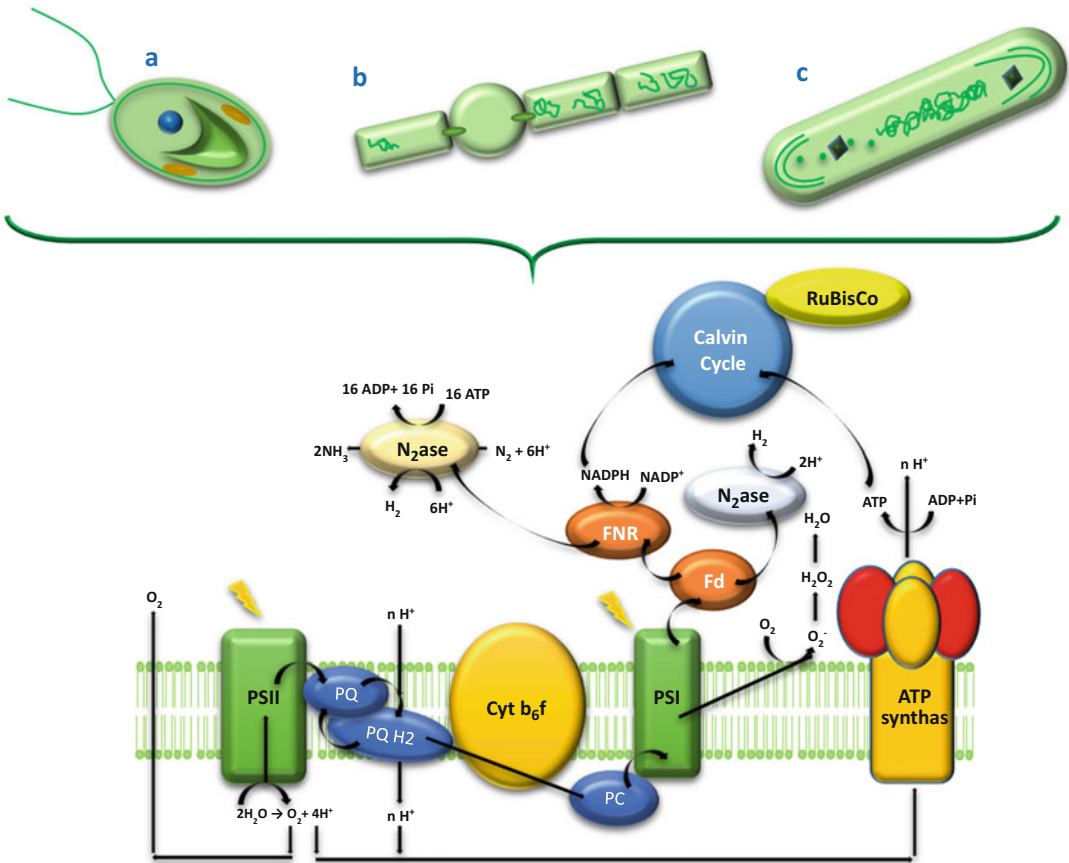
factors and providing optimum culture conditions can be followed [15]. However, it is not always possible to reach the desired productivity, especially considering the limits of an economic process. In this situation, the micro approaches of targeting the cells informatics or the genetics are the strongest trigger [27–29]. With the progress in genetics which considers each cell as a production factory, physical dominators such as the design of the production system are reaching engineering heights from which a leap can be accomplished with support from the molecular level.

### **Metabolic Machinery Microalgal Biohydrogen Production**

When Hans Gaffron focused on biohydrogen mechanism in green algae in the 1930s, the importance of hydrogen was considered from a biological perspective rather than an energy issue. However, with the increasing demand for energy, this topic has become one of the keys to providing sustainable and renewable energy solutions.

After Gaffron's work on hydrogen metabolism [30], studies on microalgae considering both green algae and cyanobacteria attracted scientific attention more than before. Microalgae are a diverse group of microorganisms that can produce hydrogen through their metabolic machinery using different routes, which makes them a valuable source in biohydrogen production (Fig. 1). Their main ability of converting solar energy to carbon sources and O<sub>2</sub> by utilizing water and CO<sub>2</sub> through photosynthesis makes these microorganisms an excellent tool to harvest the Earth's biggest fuel source, the Sun [31, 32].

Starting with cyanobacteria, nitrogen fixation is the dominant route in terms of hydrogen generation. On the other hand, in green algae, the basic biohydrogen route depends on the electrons from photosynthesis as the reducers of hydrogen (H<sup>+</sup>) [33]. In order to determine the overall machinery, a more concentrated analysis is required because the cellular metabolism is like a web with almost every pathway affecting another pathway or is affected by another pathway.



**Biohydrogen Production, Fig. 1** Basic light reactions with special emphasis on hydrogen production during photosynthesis taking place in the chloroplast thylakoid membranes of green algae (a) or photosynthetic membranes of

the cyanobacteria (both nitrogen fixing (b) or not (c) in other words with or without heterocyst) (Modified from Ref. [42])

### Cyanobacterial Biohydrogen Production

Biohydrogen production in cyanobacteria is dominantly catalyzed by bidirectional and uptake [NiFe] hydrogenases. In addition, nitrogen-fixing heterocystous cyanobacteria may have molybdenum, vanadium, or iron atoms in the prosthetic group of nitrogenases [34, 35]. Biohydrogen production in cyanobacteria can follow three alternative routes. First is the photolysis of water using photosystems (PS). Collaboration of PS II and PS I via light-based electron transfer from water to ferredoxin produces nicotinamide adenine dinucleotide phosphate (NADPH), which is the key mechanism for biohydrogen production [13].

Second, the fermentative pathway in which light-dependent photosynthetic storage carbon

sources are catabolized in light-independent reactions; in other words, NADPH from degraded polysaccharides or lipids is the main supplier of electrons which are transferred to the plastoquinone pool (PQ-pool) for the hydrogen production mechanism as a light-independent route [36].

Third is the photofermentative pathway which is a hybrid of the other two pathways [34]. Cyanobacteria with the nitrogen fixation ability use this mechanism in nitrogen fixing units referred to as *heterocysts*. Heterocysts are used as the sites of the spatial separation of oxygenic photosynthesis and hypoxic nitrogen fixation reactions for an indirect biophotolysis. A vegetative cell-originated NADP<sup>+</sup> triggered from the electrons and H<sup>+</sup> transported to the

PQ-pool is reduced through PSI alone inside the heterocysts where the anoxygenic environment is dominant. During the process inside this cell, anaerobic conditions take up hydrogenase *Hup* [34] and the bidirectional hydrogenase is inactivated, leading the vegetative cell originated saccharides to become the source of electrons for nitrogenase reactions [37–40].

### Green Algae Biohydrogen Production

In green algae, there are two light-dependent pathways and possibly one light-independent fermentative pathway for hydrogen evolution mediated by either [Fe] or [FeFe] hydrogenases, both of which are unidirectional [41]. Similar to cyanobacteria, hydrogen is the key secondary metabolite that is used during the balance of redox energetics in green algae to balance the cell's interior redox potential. Green algae have different routes for hydrogen production, catalyzed by unidirectional [Fe] or [FeFe] hydrogenases, in which the reduced ferredoxin is the basic electron supplier of the process [42].

The first route is the direct biophotolysis of water into hydrogen and oxygen where the water splitting PSII and ferredoxin-reducing PSI act together using water as a sink for electrons [43]. The second route is the PSII-independent route of the indirect biophotolysis where the electrons from the glycolysis or citric acid cycle are transferred to the electron transport chain and utilized only by a PSI active hydrogen evolution pathway. This pathway is basically utilized for endogenous carbohydrate storage or other resources such as lipids. A third route other than these light-dependent routes is the dark fermentation of the decarboxylated pyruvate from glycolysis by pyruvate ferredoxin oxidoreductase. In this pathway, cells under dark anaerobic conditions utilize their endogenous starch reservoirs to survive and produce formate, acetate, ethanol, and hydrogen [18, 29, 44–46].

#### *Chlamydomonas reinhardtii* a Key Model for Photobiohydrogen Production

*Chlamydomonas* nominalized from the Greek *chlamys* (a cloak) and *monas* (solitary) is a genus of the Chlorophyte algae under which

various members can be differentiated under microscope depending on their size, shape, chloroplast, pyrenoids, flagella, contractile vacuoles, eye spot organelle, and other cellular features. *Chlamydomonas* has nine basic morphological groups having two interior flagella, a basal chloroplast surrounding one or more pyrenoids, and a significant cell wall [47].

Among the other members, *C. reinhardtii* is the dominant specie especially due to its ability to utilize acetate as a carbon source other than photo-synthetically. It is a unicellular haploid green alga which has been used as a model microorganism for various topics, e.g., photosynthesis, respiration, light acclimation, nitrogen assimilation, flagellar motility, and basal body function [48, 49]. With the increasing attention on biohydrogen, *C. reinhardtii* has also become a model tool for biohydrogen studies [50]. Specifically, the key features of *C. reinhardtii* in becoming the model tool for laboratory studies can be summarized as follows [3, 47–52]:

- Ability to grow rapidly in defined liquid or agar media at neutral pH, without the need for supplementary vitamins or other cofactors.
- Ability to utilize acetate makes this species an isolation- and maintenance-friendly microalga.
- Ability to cultivate photoautotrophically, mixotrophically, or heterotrophically with great survival rate.
- Acetate assimilation helps the survival of non-photosynthetic mutants.
- It is a powerful tool to study light sensitivity and acclimation due to heterotrophic cultivation.
- It has both mitotic and meiotic life cycles; therefore, gametic differentiation, zygote production, induction of meiosis, isolation of diploid strains, and haploid cytoductant studies make this species a valuable platform for the studies of genetic analysis in nuclear, chloroplast, and mitochondrial genomes.
- *Chlamydomonas* is a model platform for strain selection and engineering, especially for valuable products with a fully sequenced genome.
- Effective spectroscopic and transformation methods led this species to be a platform for



investigating genetic, biophysical, and biochemical manipulations.

- Being sensitive to sulfur deprivation makes an ideal model for the efficient two-stage hydrogen production method.

The key issue in biohydrogen production from microalgae is the oxygen sensitivity of the hydrogenase enzymes [53]. In order to circumvent this sensitivity, the basic approach is to understand the oxygen-evolving process in the photosynthesis, i.e., the PSII reaction center which is responsible for the oxygen evolution. Locking the PSII mechanism is essential to downregulate the oxygen production. There are some possible methods such as the dark and light cycle applications or the use of PSII inhibitor chemicals, e.g., DCMU, SAL, and C1-CCP. Unfortunately, these methods have low productivities of biohydrogen, and in particular, using inhibitors is irreversible due to the damage to the cell [3, 44, 54].

The clue to achieving a higher biohydrogen production was found in the oxygen downregulating effect of the deprivation of a nutrient, such as sulfur [55]. Under sulfur-starved conditions, anaerobiosis can be established, giving the opportunity for the hydrogenase enzyme to work [45]. The downregulation of oxygen in photosynthesis leads to the relation of the PSII reaction center and its D1 protein [56]. This 32 kD protein turns over rapidly with photo damage and should be repaired in order to continue its activity. During sulfur starvation, which is the key component of cysteine and methionine in the D1 protein, the repair mechanism of the D1 protein will be blocked resulting in the oxygen downregulation and a decline in the water oxidation rate [44, 45, 54]. This phenomenon is the construct of the basics of the two-stage protocol introduced in 2000 [54].

The two-stage protocol is the temporal separation of the aerobic photosynthetic activity in which the active PSII mechanism produces oxygen that inhibits the hydrogenase enzyme, the key enzyme for hydrogen production from the hydrogen producing stage, in which sulfur starvation is applied under anaerobic conditions in order to lock the PSII mechanism to maintain a sustainable hydrogen production under illuminated

conditions [54]. The relation between photosynthesis and mitochondrial respiration, utilization of cellular storage molecules, and hydrogenase activity are of significance in the two-stage protocol [17, 44]. Today, most studies have focused on the two-stage sulfur deprivation protocol, but some microalgae such as *Platymonas subcordiformis*, *Platymonas helgolandica*, and *Chlamydomonas moewusii* are not as sensitive to sulfur deprivation as *C. reinhardtii*; however, the utilization of inhibitors and nitrogen starvation is still an option to enhance hydrogen production [3].

Considering *C. reinhardtii*, the two-stage protocol has several steps in the light-mediated biohydrogen process. The photosynthetic production of the cells provides the opportunity to increase their population, i.e., biomass. The cells increase in number and density and also accumulate higher amounts of chlorophyll. Later, the grown culture is continued until all the sulfur has been consumed. This stage also needs the anaerobic environment; thus, the cells need to be transferred to a sealed culture vessel.

After the transfer, the sulfur deficiency will react with the photosynthesis and respiration mechanism of the cells in a way that the photosynthetic activity declines due to the photo damage of PSII which cannot be repaired without sulfur. The mitochondrial respiration activity stays constant, leading the cells to consume all the oxygen and face in about the first 24 h. This response can be monitored by the fluorescence measurement which shows the inactivation of PSII with a loss of nearly 90% of its original value [57]. After this stage, the cells start to produce biohydrogen under light by utilizing their storage materials as starch and proteins. This catabolic mechanism supports the oxidative phosphorylation in the mitochondria and a possible NADPH-related electron transport in chloroplasts to both produce enough ATP and allow the cells to survive in an anaerobic environment and produce sustainable biohydrogen. During the process RuBisCo declines rapidly while the PSII and PSI proteins rather gradually lead to a change in the light harvesting system composition [58]. Also the amount of starch in the cells will increase in the first stage until the use of the remainder of the oxygen in

the environment before crossing the respiration level; in other words, they try to store as many substrates as possible with the limited amount of oxygen [59]. This reaction can also be observed in the morphology of the cells. Normal ellipsoid cells become bigger and spherical in the first 24 h followed by a biomass reduction with the start of the biohydrogen production. After the maximum time, about 72 h, the biohydrogen production starts to decrease overlapping the reduction in biomass, supporting the idea of using storage materials as the key for sustainable biohydrogen production [44].

The electron transport related with the hydrogenase activity resulting in hydrogen sustains limited photosynthesis and supports the respiratory electron transport for ATP production. This helps the cells to survive under stress conditions, but prolonged sulfur stress will lead to cell death and a sharp decline in the biohydrogen productivity [17, 44–46, 60]. However, a batch was tested after 35 days, and the cells still produced a small amount of hydrogen, which can be a good indicator of the survival response of *Chlamydomonas* [61].

## Conventional Methods for Genetic Optimization

Microalgae are photosynthetic organisms that offer promise for industrial biotechnology applications. To date, the metabolites from microalgae have been used in several diverse industries for the production of pharmaceuticals, food, feed, cosmetics, and biofuels [62]. To produce a certain metabolite or a product, the strain selection and/or media and growth condition optimization have been tools that are used to enhance the yield efficiency of a desired product, but they are limited to the physical environment [63–65]. Limitations and scientific barriers exist which are derived from the microalgae's own metabolism. In order to manipulate the nature of the species, a deep focus and understanding of metabolic regulation is required. Thus, genetic engineering techniques have become a part of the scientific field investigating cellular regulation, strain development, biofuel production, and other actions to draw attention to microalgal metabolisms [26, 66, 67].

The basic targets of a genetic modification using microalgae as a host are either the over-expression of a desired metabolite for commercial importance, e.g., astaxanthin, fatty acids, and omega-3 acids [29, 68, 69], or the heterologous expression of a metabolite in microalgae [70]. Both of these approaches are designed to integrate an algae-dependent commercial application that benefits from algal metabolism in a positive way. However, there is not only one way to manipulate algae; several approaches and methods can be applied; therefore, the pros and cons of the system should be well considered. The risks of genetic engineering techniques should also be assessed; thus, from a simple lab protocol to legal authorization, all the steps should be precisely evaluated to design a fully controlled system that pays particular attention to industrial strain development [71]. The key term in genetic manipulation in microalgae should be the long-lasting effect and standardization of the product with validated stable transformation techniques, as well as the strain improvement which will increase the reliability of the product or technology that has been developed.

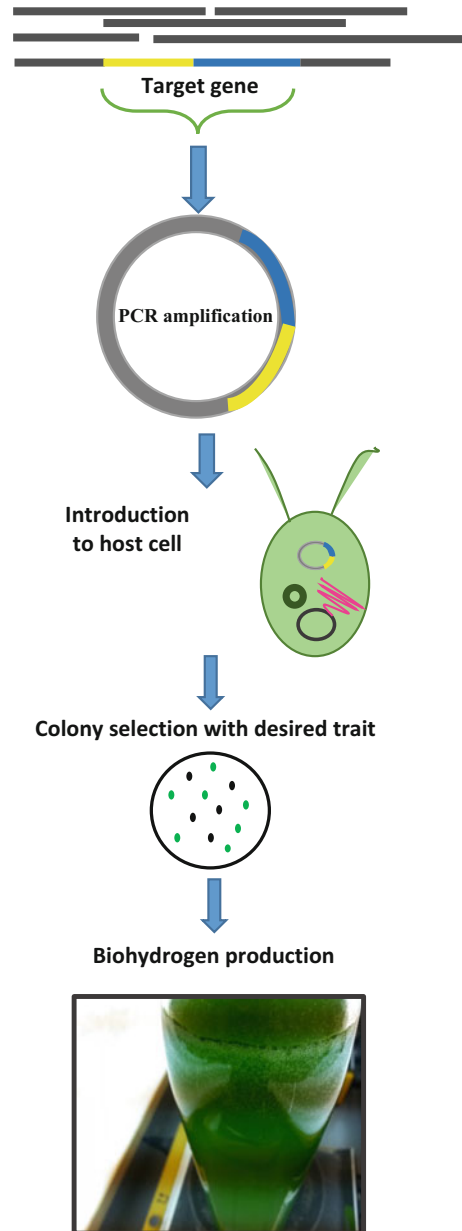
Genetic engineering strategies have fundamental benefits and can be a game changer in biotechnology field [72]. Today, microalgal chloroplasts are conventionally used as machinery for heterologous expression of eukaryotic proteins, hormones, vaccine antigens, antibodies, and other recombinant therapeutics with the advantage of having post-translational modification pathways [73, 74]. Genetically engineered microalgae cells become an individual bioreactor for the production of a desired product [75]. Other than therapeutic purposes, microalgal genomes are also sustainable vectors for biofuel development [29, 76–79].

Regardless the industry it may serve, genetic and metabolic engineering techniques aim to achieve a cost-effective and competitive production strategy in the emerging topics [29, 80]. The other fundamental aim is to exploit the cellular mechanism for the benefit of life sciences [81]. The existing methods can be applied to microalgal genetics; however, the choice of the right procedure is dependent on the aim of the

work. There are some species whose genomes are fully sequenced but they are few in number considering the thousands of other wild-type strains found in nature [82]. Known microalgal sequences highlight the gene functions, annotations, and possibility to respond with a high ratio to homologous recombination and comparative genetics [83]. As in the development path of the genetic engineering techniques, there are a large number of tools for applications, such as genome mining [84], trait analyzing, and industrial strain development [85]. From simple chemical mutagenesis to programmable genome engineering, microalgal genomes can be used as sustainable, reliable, and green hosts.

In order to select the right technique, the regulation of algal genome should be evaluated. Microalgae including cyanobacteria display diversities in terms of metabolism and cellular compartmentation [11]. Green algae, being a eukaryotic host, have three large genomes of nucleus, chloroplasts, and mitochondria. However, as prokaryotic hosts, cyanobacteria lack the chloroplasts and have a plasmid-like genome. The special compartmentation of the chlorophyll containing a thylakoid-like part plays a major role in photosynthesis and other regulatory mechanisms [86].

There are two ways to increase the genetic ability or stability of microalgae, via mutations or the introduction to a transgene (Fig. 2) using transformation techniques, such as electroporation, agrobacterium, chemical poration, DNA-coated gold or tungsten particles, glass bead operations, and bombardment [87–91]. The mutagenesis techniques are the combination of chemical exposure or exposure to high levels of UV light in the long or short term. The survival colonies are cultivated and tested for activity, expression, or suppression levels of the desired product [92]. However, in site-directed or site-specific mutations, the known sequence is mutated in the host organism via polymerase chain reaction (PCR)-based methods, which is a more controlled way to deal with genomes [93]. The PCR products can be a way to screen the gene expression and the level of mutagenesis. Mutagenesis can also be utilized to decipher the activity of a gene or a



**Biohydrogen Production, Fig. 2** Transgene expression in microalgae: Gene of interest is transformed into the genome of microalgae. Mostly the preferred gene insertion is done via chloroplast transformation due to the stable characteristics. However, nuclear transformations are also possible for microalgal genomes (Photograph: courtesy of authors)

gene product, which will also be a useful tool to annotate the function and the role of the target gene in the overall metabolism. The introduction of a transgene to the intracellular environment of

the microalgae cells first requires the design of the transgene and selection of the transformation method [89]. In order to deliver the gene into the cell, the cell membrane should be permeabilized for a while. In some cases, as in cyanobacteria, lack of a thick or rigid cell wall is an advantage. However, in green algae or diatoms, harsh techniques may be required, such as bombardment and electroporation [94]. When the transgene passes the membrane barrier, it is inserted into the nucleus or chloroplast DNA [95]. The latter is for the cultivation and selection of the transgenic colonies.

The main problem of the application of the genetic transformation techniques is the low percentage of stable transformation. Since microalgae have various abilities or structures related to photosynthesis, flagellar movement, photosystems, sulfur uptake lipid pathway, and D1 protein, being a host for post-translational modifications, phototaxis, lipid metabolism, photosynthesis, photorespiration, lipid accumulation, trophic conversion, RuBisCo enzyme activity, starch determination, hydrogenase enzyme activation, and biohydrogen production, it is difficult to develop a model that includes adequate frequency of stable transformations [87, 96, 97]. Somehow microalgae silence the transgene expression and it can only be stable only for a couple of months. In terms of being an industrial application, this is a major limitation to the process. Genome-wide analysis shows that microalgae may have an endogenous protection system as in bacteria to protect itself from viral, plasmid, or other invasions, and due to that mechanism, transgene expression may be precluded.

The genetic manipulation can be implemented by either the nuclear or chloroplast genomes of the eukaryotic microalgae [70, 87]. However, it is stated that the stability of heterologous expression in the chloroplast genome is higher than that of the nuclear transformation. Thus, chloroplast engineering is mostly used to produce recombinant proteins or other molecules. The chloroplast, on the other hand, has a circular structure of almost 200 kb genome. The plasmid structure and code-dependent genomic information flow is the great success of independent transgene expression

studies. Successful chloroplast transformation systems are well defined for *C. reinhardtii* cells, and the database of EST is a good tool to design a new transgene. In other words, nuclear transformation can be used for metabolic control, such as sulfur transfer, hexose transport system, trophic conversion, photosynthetic activity, enzyme control, and pathway editing. The success of nuclear transformation is dependent on few factors because the random transgene expression in the nucleus is harder to track with regard to the changes in the nuclear genome. Another issue is the gene silencing mechanism of the act [98]; thus, a codon optimization approach is a good basis [99]. It is reported that the *C. reinhardtii* nucleus has a G-C rich codon and also its DNA is rich in terms of introns. Since the activity of the noncoding regions is still not clear, achieving stable transformation codon optimization offers promise [99].

Work on microalgae selectable markers, homologues or heterologous expressions, RNA-mediated transformations, amino acid deletion or insertions, recombination and gene-silencing approaches has been undertaken and to date they have displayed stable transformation and change in the desired characteristics [100]. Selectable markers are used as recombination markers and indicate the success of the applied technique. Until now, antibiotic resistance (*ble*, *rnmL*), photosynthetic apparatus, and herbicide resistance traits have been used as controls for marker selection [87, 101]. The homologous expression of the nucleus and chloroplast remains low in frequency, and attempts to overcome this problem by programmable techniques need to be further discussed [96, 102, 103].

What is known about the homologous expression is that it has been successful for the overexpression of the microalgal metabolites, such as omega-3 fatty acids, astaxanthin, and other color pigments [104]. RNA-mediated techniques have been introduced due to the low survival rates of the other transformation techniques. Gene silencing via RNA is a new issue and seems promising for microalgae [81]. There are sequences, such as transcription factors, noncoding sections of the DNA, and noncoding RNA [105]. Thus,

RNA-mediated silencing of the genes is considered to be a functional tool for understanding gene regulation and the mechanistic, as well as the response and stress physiology of the environmental changes. RNA-mediated silencing is undertaken via 20–30 amino acid sequences of micro RNAs and a small interfering RNA [106]. These RNAs are mostly found in genome-sequenced microalgae species, and the underlying control mechanism should be further explored [107].

Apart from eukaryotic microalgae genomes, cyanobacteria species are also a target for recombination techniques [86]. These techniques aim to explore the photosynthetic apparatus, lipid synthesis, cell development, nitrogen fixation metabolism, secondary metabolite production, and circadian rhythms in the cells. The photosynthesis mechanism is mostly enacted through the cyanobacteria intracellular regulation and effects of the extracellular environment. The genome of the cyanobacteria is similar to the chloroplast genome of the eukaryotic microalgae [108]; however, cyanobacteria have a special component in their metabolism, called natural transformation [86]. Thus, apart from the artificial transformation, it has the ability to be transformed naturally by extracellular nuclease enzymes. The number of strains capable of this mechanism is limited and how this natural transformation mechanism works remains unknown; however, it may be similar to the process in the bacterial immune system. Novel methods proposed for eukaryotic microalgae are also applicable for cyanobacteria; however, due to the taxonomic differences there may be some problems. The most used tool is rapid mutagenesis through the induction of chemicals by UV light as in classical systems. Transformations provide a better and clear understanding of the mechanism of the action. The prokaryotic nature of the cyanobacterial cells makes the survival and transformation of the DNA to the cell more successful than in eukaryotic microalgae.

Since the cellular metabolism is dependent on photon energy harvesting, chloroplasts are considered as a sustainable genome mine for stable transformations [87]. Chloroplasts are the main targets for stable expressions of diverse metabolites from fatty acids to human growth hormones

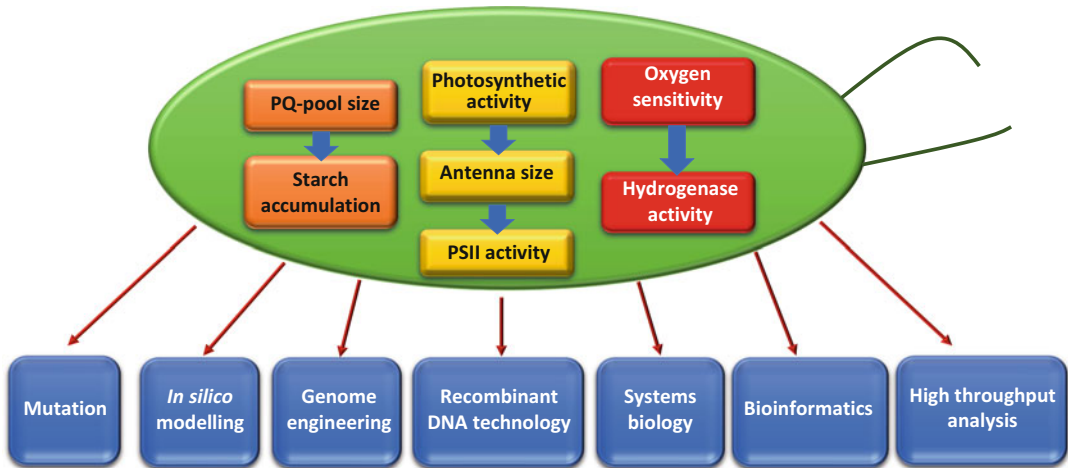
because chloroplasts house the vital pathways in the algal metabolism and correspond to the regulation of intracellular information flow [66, 109]. The heterologous expression of a certain gene is one of the easiest and most conventional ways to engineer microalgal genomes. Each microalgae host can be considered as a unique bioreactor to activate the certain gene of interest. There are various approaches to genetically modify an algae genome; however, sustainable and stable platforms for genetic modification are required to increase efficiency.

This section has briefly presented an overview of the conventional techniques possible for eukaryotic and prokaryotic microalgal transformation. This will be further discussed in relation to biohydrogen production and how yield-efficient microalgal biohydrogen production can be achieved.

### **Genetic Modifications in Terms of Biohydrogen Production**

Metabolic pathway manipulation and genetic engineering aim to reach sustainable levels of hydrogen production. In scientific thinking, genetic engineering can be the toolset that may help to identify the unknown aspects of the biohydrogen metabolism and regulatory machinery [67]. Biohydrogen production in microalgae is highly correlated with the regulation of the photon energy transformation, photosynthetic activity, RuBisCo enzyme activity, turnover rate of the D1 protein for oxygen O<sub>2</sub> evolution, and finally the catalytic activity of the hydrogenase enzymes. The metabolic engineering of microalgae for biohydrogen production can be definitive in preventing bottlenecks, the limitation and reorganization of the electron flow through the H<sup>+</sup> via manipulating photosynthesis, nutrient uptake, and enzyme activity (Fig. 3). Even if the term microalgae taxonomically includes eukaryotic species, it should be noted that cyanobacteria, a prokaryotic host, are also used as models for genetic responses for biohydrogen research. As a brief overview of developments, Table 1 represents some key studies related to hydrogen production via microalgae. However, as a eukaryotic





**Biohydrogen Production, Fig. 3** The representation of fundamental energetic pathways in microalgal biohydrogen production and existing genetic engineering technologies applicable to increase the biohydrogen production yield

host, *C. reinhardtii* has been used as a model for  $H_2$  production; thus, the next section mostly presents eukaryotic microalgae with a special focus on *C. reinhardtii*-related systematics.

### Engineering on Photosynthesis

Light capturing efficiency is fundamental for biohydrogen production [110]. The active hydrogenase enzyme is ready to reduce  $H^+$  to  $H_2$  in gas form under anaerobiosis. However, individual photosynthetic efficiency defines the output amount of the  $H_2$  generated. As in the mass balance dynamics, cells should also be in an energetically balanced state. In this balanced state, the role of the photobiological conversion efficiency determines the partial utilization of the electrons via conveyance through the electron transport chain. In natural environment, 60–80% of the light energy is lost in the form of heat with a small portion remaining for cell survival, growth, and maintenance, and in some cases to generate  $H_2$  [111]. This loss is massive and it depends on the antenna size [112], the amount of chlorophyll, and the capacity of the cells to harvest electrons, which is measured as photosynthetic activity or chlorophyll fluorescence [113]. To increase the light to  $H_2$  conversion which is around 1–2%, a sustainable way is to engineer the photosynthetic regulation [114].

The photosynthesis in microalgae is controlled via light-harvesting complexes (LHCI for PSI and LHCII for PSII) [115]. The responsible genes are nine genes of LHCA1-9 for LHCI and LHCBM1-11 for LHCII in the *C. reinhardtii* cells [116, 117]. The activation of these genes and isoforms controls the regulation of protein complexes in the thylakoid membrane and also in pigments like the chlorophylls and carotenoids [118]. LHC genes are encoded in the nuclear genomes; thus, nuclear genetic manipulations are required to reorganize this function and understand the role in microalgal photosynthesis physiology and relation with biohydrogen production. A few alterations can be made to increase the photosynthetic activity using the LHC. In wild-type strains, the response to the increasing light intensity is the down-regulation of the LHC, which results in cells being triggered to the death path because the intensity is much higher than the maximum tolerance levels. A study published by Melis and coworkers concluded that mutant strains of *C. reinhardtii* with decreased antenna size have increased the capacity to capture light [119], and this raises the key question of “*What is the function of the manipulation of antenna size?*”

Smaller antenna size in microalgae provides a homogenous light distribution into the culture [120]. It is known that photo-oxidation leads to



**Biohydrogen Production, Table 1** The key genetic engineering studies on microalgal biohydrogen production (Modified from Ref. [82])

Aim	Specie/strain	Method	Results	References
Decrease the PSII repair activity of D1 protein	<i>Chlamydomonas reinhardtii</i>	Antisense transformation	Decrease in the <i>SulP</i> synthesis Impaired sulfate uptake Decrease the O <sub>2</sub> evolution rate Hydrogen production under anaerobic sulfur-containing conditions	[58]
Understanding electron transfer and its role in microalgal biohydrogen production metabolism	<i>Chlamydomonas reinhardtii</i>	PSII-deficient strain (FuD7) and RuBisCo deficient strain (CC-2803)	FuD7 activated <i>HydA1</i> genes but no further H <sub>2</sub> production occurred Strain CC-2803 showed decreased photosynthetic efficiency but hydrogen is produced after a fast anaerobiosis	[33, 45]
Identifying the role of hydrogenase coding genes in hydrogen production	<i>Chlamydomonas reinhardtii</i>	Artificial mRNA silencing	Downregulation of <i>HydA1</i> (fourfold lower activity), <i>HydA2</i> and hydrogenase-like protein ( <i>Hyd3</i> ) <i>HydA2</i> and <i>Hyd3</i> mutations have no significant effect on hydrogen production	[106]
Role of light-harvesting complexes	<i>Chlamydomonas reinhardtii</i>	RNAi knockdown mutation	<i>Stm6Glc4L01</i> mutant exhibited a light green phenotype Reduced expression of LHCBM1 (20.6% 60.27%), LHCBM2 (81.2% 60.037%), and LHCBM3 (41.4% 60.05%) compared to 100% control levels 100 mEm-2s2-1 (180%) and biomass (165%) conversion efficiencies H <sub>2</sub> production at increased solar flux densities (450 instead of, 100 mEm22 s21) and	[117]
Cyclic electron flow optimization	<i>Chlamydomonas reinhardtii</i>	State transition mutations ( <i>stm6</i> )	Increased starch deposits Reduced cyclic electron flow around PSI Increased hydrogen photoproduction (540 mL <sup>-1</sup> , 4–5-fold than wild-type strain)	[123]
Understanding the role of starch degradation and hydrogen generation	<i>Chlamydomonas reinhardtii</i>	DNA insertional mutations via electroporation	15,000 mutants are obtained 18 mutants are selected ( <i>sta1-8</i> ; <i>sda1-10</i> ) Reduced PSII-independent hydrogen production Identification of starch-dependent hydrogen production	[135]

(continued)

**Biohydrogen Production, Table 1** (continued)

Aim	Specie/strain	Method	Results	References
To overcome oxygen sensitivity		Rational mutagenesis in silico mutagenesis and volumetric oxygen accessibility Gene shuffling, DNA extraction	Mutant strain L283 W 29% increase in hydrogen Redox properties of H cluster is sequenced. Fe-S bonding sequence is highlighted Conserved genetic structure is observed	[138]
Understanding the role of isoamylase gene	<i>Chlamydomonas reinhardtii</i>	DNA insertional mutations	sta7-10 mutant containing <3% of the glucose Rapid changes in <i>HydA1</i> and <i>HydA2</i> transcript levels Decreased amounts of hydrogen generation of isoamylase deficient mutants	[149]
To reduce RuBisCo levels, activity, and stability	<i>Chlamydomonas reinhardtii</i> strain <i>rbcS</i> <sup>-</sup> T60 <sup>-</sup> 3 mt <sup>-</sup>	Transformation with a wild-type <i>rbcS1</i> gene	Significant decrease in O <sub>2</sub> evolution RuBisCo mutant Y67A accounted for 10–15-fold higher hydrogen production than wild type	[157]
D1 protein activity and PSII repair	<i>Chlamydomonas reinhardtii</i>	Amino acid substitution at D1 protein	Higher amount of D1 protein content Higher carbohydrate storage capacity Sustained PSII activity PAR (photosynthetically active radiation) reached 3.22%	[162]
Decreased oxygen sensitivity	<i>Chlamydomonas reinhardtii</i>	Single or double amino acid deletion mutations at D1 protein	Higher sensitivity to photoinhibition Reduced amount of chl/dry weight and per/cell Higher respiration-to-photosynthesis ratio Higher carbohydrate accumulation at aerobiosis Higher synthesis of xanthophyll-cycle pigments 12–18-fold higher hydrogen biogas production	[163]
D1 protein activity	<i>Chlamydomonas reinhardtii</i>	Single or double amino acid deletion mutations at D1 protein	Increase in the light intensity Shortened lag phase of hydrogen production Maximum biohydrogen production with a double-deletion mutant strain of D239-40 (490 ± 10 mL <sup>-1</sup> ) and D240-41 (388 ± 10 mL <sup>-1</sup> )	[164]

(continued)

**Biohydrogen Production, Table 1** (continued)

Aim	Specie/strain	Method	Results	References
Transcriptome analysis of sulfur-deprived hydrogen generation	<i>Chlamydomonas reinhardtii</i>	Time serial mRNA RT-PCR microarray analysis	Repression of photosynthesis-related transcripts Abundance of LHCBM9 gene transcript Transcriptome-based relation of hydrogen production with photosynthesis, carbon utilization, starch degradation, and electron transfer has been modeled	[186]
Increasing the photobiological hydrogen production	<i>Chlamydomonas reinhardtii</i> cc849	Random insertional mutants, by the ble gene encoding the enzyme with	T1 mutant with 7.8-fold of H <sub>2</sub> yield and about increased 23% of respiration rate Declined photosynthetic rate and Fv/Fm, the efficiency of PSII Reduced photosynthesis/respiration capacity ratio	[211]
Truncated light-harvesting chlorophyll antenna size	<i>Chlamydomonas reinhardtii</i>	DNA insertional mutagenesis	tla1 mutant with a functional chlorophyll antenna size Lower amount of light-harvesting proteins Lower steady-state levels of Lhcb mRNA Higher light intensity for the saturation of photosynthesis Greater solar conversion efficiencies Higher photosynthetic productivity	[215]
Increasing the photosynthetic efficiency with regulating LHC size	<i>Chlamydomonas reinhardtii</i>	DNA insertion Mutagenesis	Smaller size in the LHC-I and LHC-II complexes Increase in the Chl a/Chl b ratio (from 2.6 to 6) Decrease in the total chlorophyll/cell Ability to work under highlight conditions (outdoor experiments)	[216]
Increasing the photochemical utilization of light	<i>Chlamydomonas reinhardtii</i>	RNAi approach to downregulate LHC gene family	<i>Stm3LR3</i> had significantly reduced levels of LHCI and LHCII mRNAs and proteins Reduced levels of fluorescence, sensitivity to photoinhibition Higher photosynthetic quantum yield Increased efficiency of cell cultivation	[217]
Expression of [FeFe] hydrogenases at chloroplasts	<i>Chlamydomonas reinhardtii</i> FUD50	Codon optimized <i>HydA1</i> gene transformation	Chloroplast encoded [FeFe] hydrogenases Hydrogenase expression both aerobic and anaerobic conditions	[218]

the transcriptional downregulation of the photosynthetic apparatus and changes the direction to a carotene pathway. However, the aim is to maintain the photosynthesis active even at high levels of light exposure. The importance of this issue for biohydrogen production is that large-scale cultivation of microalgae can be successfully implemented in open pond systems where natural light can be used. Due to low efficiency of hydrogen, light-dependent inhibition of the culture brings another challenge [121, 122].

Studies investigating truncated antenna size via genetic engineering techniques are vital to increase photosynthetic efficiency [112, 113, 119]. After developing an understanding of translational control of LHC, the findings of another study showed that the cytosolic RNA-binding protein NAB1 has a major role in the regulation of antenna size [120]. This results in the translational silencing of the LHCBM genes. NAB1 in the *stm6* mutant strain named as *Stm6Glc4* which has reduced antenna size (10–17%) and has increased chlorophyll fluorescence activity (50%). This mutant strain can be used for sustained hydrogen production [120] because the host-mutated strain is *stm6*, which has larger starch reserves and a decreased cyclic electron flow around PSI, which is a limitation for electron sinks directed toward hydrogen generation [123]. One step forward is to observe the effect of these strains in terms of biohydrogen production. An RNAi knockdown study in *stm6* mutant strains provided good results to postulate the relationship between photosynthesis and H<sub>2</sub> generation [117]. Knockdown strains called *Stm6Glc4L01* represent a decreased total chlorophyll ratio, which makes cells light green. The LHCBM1, LHCBM2, and LHCBM3 genes are knockdown and the solar to hydrogen and biomass conversion levels are increased, and even at higher light intensities, the hydrogen photo production does not cease [117].

Insertional mutagenesis directed by truncated antenna size also displays the relation between the photosynthetic regulations and amounts of chlorophyll [57, 112]. The results of all the studies

describe the importance of the regulation of photosynthesis and how to manipulate the physiological responses of the cells using genetic engineering techniques. Additionally, the *tlal* gene, which has a major role in the regulation of antenna size, is also described [119]. Light plays a major role in the regulation of electron flow through the hydrogenase enzymes, which is undoubtedly essential for phototrophic or photoheterotrophic hydrogen generation studies; however, strains capable of producing hydrogen under heterotrophic conditions are not dependent on light requiring cell signaling [124]. Under heterotrophic conditions, the fermentative pathway is activated rather than photosynthesis; however, organic carbon assimilation has a major impact on fermentative hydrogen generation. Most microalgae cannot survive in dark conditions and some species cannot metabolize glucose. Thus, inducing the *HUP* genes to transport hexose sugars also shows great variation in the dark fermentative photobiological hydrogen production [125].

If the photosynthesis-driven pathway is the key not only for biohydrogen production but also for the toleration of light stress and variable light intensities, the antenna size is a major issue that should be discussed. The role of antenna regulation is vital for biohydrogen production due to the photosynthetic active radiation efficiencies. Mutagenesis, either random or site-directed, needs to be in correlation with the light to biohydrogen conversion term, which should be increased to reach meaningful levels.

### Engineering on Hydrogenase Enzymes

Microalgal hydrogenase enzymes are key enzymes in the hydrogen production mechanism and are similar in structure to bacterial hydrogenases [126]. Early research on hydrogenases undertaken with bacterial (*Clostridium*, *Desulfovibrio* species) enzymes and from amino acid sequences in the crystal structure has been defined well [127]. The hydrogenase enzyme has approximately a molecular weight of 48 kDa with 350 amino acid residues [41]. The gene activation

mechanism of hydrogenases is more complex because the metabolic pathways do not directly produce the active enzyme; they require a series of gene expression and assembly of the proteins, which can also be called a “*maturation process*” [128, 129]. These enzymes are localized at the chloroplasts but the assembly of the protein particles occurs at the ribosomes [128]. The whole process and the function of the maturation accessory system have not yet been fully understood but it is thought to be an evolutionary regulation against the existence of the oxygen in the environment or within the cell to feed the electron transport chain with the final electron acceptor, which is  $H^+$  in the anaerobic phase.

The hydrogenase enzyme is composed of an active site, called an *H-cluster*, where the redox reactions take place and  $H_2$  is generated in gas form [130]. The enzyme is covered with an apoenzyme part containing microchannels where  $H^+$ ,  $O_2$ , and  $e^-$  are transferred through the active site. The synthesis of the mature hydrogenase enzyme is regulated by the activation of the *HydA1* and *HydA2* genes [123]. The main challenge in hydrogenase enzymes is their sensitivity to even trace amounts of oxygen inside the cell or in the culture medium [44]. Crystallography studies reveal that many microchannels may exist to guide the oxygen to reach the active site of the mature enzyme [42].

Gene expression studies show that the activation of the maturation genes *HydEF*, *HydG*, and *HydA1* is suppressed in aerobic conditions [131, 132]. When anaerobiosis occurs, the genes are activated and the signalization to build a mature enzyme starts. This evidence also reveals the reversible nature of *HydA* and the hydrogenase activation [133]. There are few ideas concerning how to increase the efficiency of the hydrogenase enzymes. One of these is decreasing the sensitivity of  $O_2$ , which is a metabolic suppressor of gene activation [134]. The main target, in other words the challenge, is to engineer hydrogenase tolerant to  $O_2$ . This can be implemented to modify the active site (H-cluster domain) or engineer the microchannels, which is a complex process. Another point regarding microalgal hydrogenases, which are known to have the highest

catalytic activity among the hydrogenase enzymes ( $10^4$ ), is to increase the catalytic conversion efficiency of the  $H^+ \rightarrow H_2$  conversion. An additional indirect option can be the continuous feed of the electrons and redirection pathway of electrons to the active site of the enzyme via decreasing the cyclic electron flow around PSI [135].

Returning to the gene activation metabolism, RNA silencing is an effective technique to observe the knockdown response on the phenotype [98]. Apart from *HydA1* and *HydA2*, there is a third gene called *Hyd3* [132]. The artificial RNA-mediated gene silencing showed that when *HydA1* gene is knocked down, a decrease in the hydrogen generation efficiency is observed. However, silencing other responsible components does not affect the efficiency of the hydrogen generation [106]. These results offer strong evidence to recognize what regulates the hydrogen generation in terms of hydrogenase activation. The insertional mutagenesis of the *HydA1* and *HydA2* genes were examined to understand the activity and generate a heterologous expression platform [131]. The role of *HydA2* was determined as accepting reductants from the fermentative pathway. Even if the expression level was increased when anoxia conditions were introduced, the *HydA2* knockdown mutants showed no elevated hydrogen production. Thus, as the machine for hydrogen generation, *HydA1* is responsible both for the photofermentative and dark fermentative  $H_2$  generation in microalgae [133, 136]. Based on this idea and the accumulation or loss of electrons around the cyclic electron flow through the PSI, it can be concluded that biohydrogen production is firstly dependent on the activation of the hydrogenase enzyme; however, the yield efficiency is related to the supplied electrons [136]. Thus, another approach to increase the genetic engineering related to  $H_2$  generation efficiency is silencing the electron competing pathways. Due to the competition in the electron share, even though the  $O_2$  sensitivity of the active site of the enzyme is decreased, problems still remain in suppressing the yield efficiency due to the electron loss [137].

The crystal structure of the hydrogenase enzymes shows that there is a channel theory in

which  $O_2$  is in competition with other ions [130]. If the  $O_2$  sensitivity can be decreased to a level in which the hydrogenase enzymes can function under aerobic conditions, the hydrogen production process will be more effective [127]. For this purpose the random or site-directed mutagenesis can be used as an efficient tool [124, 131, 138]. Mutant strains can exhibit increased  $O_2$  tolerance, which is a clue that with further research, the  $O_2$  sensitivity can be overcome. However, to understand the relation with active site theory and competition between the ions and molecules, the 3D enzyme structure should be well defined. Since microalgal hydrogenases are smaller than the other hydrogenases, active site confirmation and responsible gene activation has not been well defined yet.

Considering prokaryotic cyanobacteria, attempts to overcome the oxygen tolerance in [NiFe] hydrogenase with amino acid substitution and this approach may be useful for the [FeFe] hydrogenases [139]. Membrane-bound hydrogenase enzymes are found to tolerate  $O_2$ , in contrast to the eukaryotic microalgal hydrogenases [129]. The main question here is “*What drives bacterial enzymes to tolerate  $O_2$  when eukaryotic microalgal hydrogenases cannot cope with oxygen?*” The bacterial membrane-bound hydrogenase enzymes have Ni-Fe bimetallic active site conformation when algal hydrogenase enzymes have an Fe-S orientation [140]. Thus, there is a new clue that metal residues in the active site of the enzyme can be the trigger to the toleration of oxygen levels.

### Engineering on Starch Metabolism

Starch has an essential role in the regulation of cellular energy metabolism in microalgae to support maintenance and survival, as well as reproduction and growth [141]. The journey of electrons obtained from water pyrolysis ends with the formation of starch deposits in green microalgae and  $CO_2$  exhaust as proposed in the Calvin–Benson–Bassham cycle. In microalgal biohydrogen production, starch is used as the primary energy deposits for cells to survive in anoxic conditions and decomposes to feed the PQ-pool in anoxia [142]. With this metabolic

adaptation, microalgae cells use chloro-respiratory pathways to survive, and  $H_2$  gas is produced simultaneously. Keeping this background information in mind, starch anabolism and catabolism play a major role in understanding electron shuttles, energy generation, the role of the PQ-pool, metabolic regulation in genome basis, and cell maintenance [143–145]. Thus, the main question is “*How do microalgae cells know when to accumulate excess amounts of starch which can later to be degraded when anaerobiosis is introduced?*” The response to this question is based on the genetic codes of the microalgae; firstly, it is necessary to identify the genes related to the inner cellular mechanism for starch and lipid production and regulation. The overproduction of starch accumulating genes results from the cell signaling death and increases the starch deposits to provide more energy in anaerobic conditions. Starch metabolism through light is associated with not only pathway-based research but also how the enzymes in the process can be characterized to discover the catabolic regression.

### The Codependent Pathway of Starch and Lipids (TAGs)

Lipid biosynthesis and genetic regulation in microalgae cannot be separated from the other metabolic pathways including the starch metabolism. In some cases, lipid and starch metabolisms can confer each other, and this results in the downregulation of one of these pathways [146]. Even though pathway-based sequencing and metabolomics studies are generalized, microalgae serve as diversifying organisms in the evolutionary terms. Some species are rich in starch accumulation, such as *C. reinhardtii* and *Chlorella vulgaris* [147–149]; however, other species including *Chlorella pyrenoidosa*, *Nannochloropsis salina*, and diatom species, e.g., *Phaeodactylum tricorutum*, deposit higher amounts of fatty acids [104, 150, 151]. Thus, the very first step for starch manipulation should be to choose the appropriate strain for biohydrogen production.

The mass starch production in microalgae cells is triggered via stress conditions, such as nitrogen depletion and sulfur starvation. In nitrogen-depleted cultures, the starch metabolism and



lipid pathways compete with each other; thus, the strain selection of a specified production is of importance [152]. However, with the genetic regulation, the overexpression of the desired product can be obtained.

The responsible genes for starch production in *C. reinhardtii* revealed that gene expression in this manner highly conserved and shows similarities with plant ancestors. This evolutionary mechanism can be identified with UV mutagenesis, site-directed mutagenesis, X-ray studies, and insertional genetic modification techniques [59, 152, 153]. High throughput screening of the mutants can provide the required information to understand the metabolism of cellular starch. Nitrogen starvation or limitation is the preferred method because under nitrogen stress, the cells are triggered to overaccumulate starch. In this condition, insoluble starch deposits can be observed even under a light microscope [154]. An interesting mutant study is related with the flagella movement of *C. reinhardtii* cells in water and the relation with starch accumulation [155]. Considering starch as an energy carrier for algal metabolism, the starch is degraded to produce biohydrogen, provide movement, cell growth and reproduction, and under anaerobic conditions, the priority is to survive. These are all ATP-dependent processes. Considering that flagella require high amounts of ATP to move through the water, during this movement, the cells decompose starch to provide the required energy. The mutants showed that the cells lacking the ability to move contain higher amounts of starch. This excess starch can be used to trigger hydrogen production. Thus, nonmotile *C. reinhardtii* cells could accumulate higher amounts of hydrogen [155]. As mentioned above, the relation between the lipid and starch pathways can be identified with mutant or knockdown strains which are not capable of producing starch but are able to produce almost eightfold lipid accumulation. If silencing a starch pathway is helpful in increasing lipid accumulation, “*What will be the effect of silencing the lipid pathway for starch accumulation and indirectly, what will be the effect on H<sub>2</sub> photoproduction?*”

DNA insertional mutation studies revealing the mutant strains with diverse hydrogen production capacity have presented one major conclusion: in sustaining the anaerobic electron flow, starch is the main cellular component [149]. Mutants lack the ability to synthesize the isoamylase gene responsible for starch anabolism; thus, they cannot accumulate starch as with the wild-type strains. These mutants showed attenuated levels of hydrogen production, which leads to an idea that the starch controlling pathways can be a trigger for photobiological hydrogen production. For example, a *C. reinhardtii* mutant named *sta6* cannot synthesize starch due to the deformation in the ADP-glucose pyrophosphorylase enzyme [144]; thus, this mutant is used as an elevated lipid-producing strain. Studies show that *sta6* mutants have decreased hydrogen production capacities [135, 141]. High light accumulation can also trigger the starch synthesis. Due to antenna-size limitations, the responses to the changing light conditions may also change when the *tlal* gene is mutated. These *tlal* mutants also show varying starch levels as a response to photosynthetic activity, and H<sub>2</sub> generation is increased due to the excellent portioning of the starch-derived electrons [119].

Rather than knockdown of starch production, the overaccumulation of the starch in microalgae results as elevated levels of hydrogen generation. The decomposition rates of the starch are related with the electron flow, and these electrons are shuttled to the hydrogenase enzyme [116]. Random insertional mutagenesis showed that the inhibition of the PSI cyclic electron flow recovers the electron sharing, and the blockage in the stage transition1 results in the increased hydrogen production [123, 156]. Another outcome of the *stm6* mutant strain is the increased amount of starch granules. With random mutagenesis studies, the isolated *stm6* strain has larger deposits of starch due to the rearrangement in the mitochondrial respiration. Thus, downregulation of the cyclic electron flow results in not only elevation of the levels of electron use but also the reorganization of starch deposits. Under dark conditions, there is an opportunity to accumulate larger starch reserves and cells can access more sources of

carbon. This is also useful for the dark fermentative biohydrogen generation. A lower dissolved oxygen concentration has a significant effect on the regulation of the PSII and D1 protein repair cycle. Due to the lower oxygen levels, anoxia can be obtained earlier, and the hydrogen efficiency increases.

In the experiments to obtain genetically altered strains capable of elevated hydrogen production, strain selection is crucial. Respiration rates, starch accumulation, photosynthetic activity, and RuBisCo enzyme activity are the vital parameters to determine the phenotypic differentiation in newly formed strains [157]. An ideal starting point for the mutant strains in terms of starch accumulation is the existence of the isoamylase gene and its activity. A DNA insertional mutant study for selecting the desired strain covers 15,000 species, which is a huge number of selections, and in the end, the strain should provide elevated hydrogen generation; thus, it is a good example showing the potential of mutation.

The approaches to activate the starch response in genomic basis are mainly to increase the yield efficiency of biohydrogen production from microalgae. The synergistic effect of PSII activity starch catabolism and the activation of the hydrogenase enzymes are the main building blocks to firstly visualize the microalgal biohydrogen production and later to sustain it in a more energy efficient way. Most of the starch-related studies as mentioned above are focused on the mutant strains that have no starch production to discover the role and impact of starch on biohydrogen generation, and all these studies concluded that starch is one of the essentials for biohydrogen.

### **Engineering on D1 Protein and Sulfur Metabolism**

The PSII mechanism activity is dependent on the turnover rate of the D1 protein, responsible for the repair of oxygen damage [158]. Hydrogen production in photosynthetic machinery resembles a cascade system in which the reaction steps cannot be separated. The turnover rate and PSII repair with the combination of light harvesting capacity is a rate-limiting step for the gene expression and the maturation of hydrogenase enzymes [121]. D1

protein and photosynthetic activity are highly connected with each other; thus, mutations and gene alterations in the D1 protein may affect photosynthetic activity and hydrogen production yield [159]. The repair cycle of the D1 protein is a continuous process in illuminated conditions. D1 protein encoding gene *psbA* is constantly degraded and expressed to keep the PSII repair cycle active [160]. The gene expression level and number of the transcripts are highly regulated by the environmental conditions, especially light intensity which is a major factor. Other relations of the D1 protein with systemic regulation are metal binding and herbicide pigment production, which are the current trending subjects of stable transformation in chloroplast genome engineering [158].

The D1 protein is encoded in the chloroplast genome [159]. The *psbA* gene is found in microalgae as two sets consisting of approximately 91 nucleotides and having a bacterial end-loop-like structure at the 3' UTR. These inverted sequences are considered to be termination signals. Algal *psbA* genes have a self-splice mechanism [160, 161].

The chemicals, such as DCMU were once used to sustain hydrogen production, and this chemical exposure helped to achieve a visible amount of biohydrogen production. Studies have shown that the addition of DCMU and similar chemicals stops the elongation of the D1 protein; however, the activity of PQ-pool is alive. This kind of study has inspired the genetic regulation and interfering the gene regulations and activity of both PSII and the D1 protein machinery to sustain hydrogen production via inhibiting the oxygen generation and achieve yield efficient biohydrogen generation.

*What happens in the D1 repair cycle when a blockage is observed? A new fully functioning D1 protein cannot be replaced by the damaged one. This results in a decrease in the PSII activity and can be translated as a decrease in the rate of oxygen evolution. When oxygen evolution is hampered, the anoxic conditions can be achieved and easily maintained; thus, the rapid activation of maturation proteins of the hydrogenase enzyme and assembly can be prolonged but are highly*

sensitive to even trace amounts of oxygen. As a final result, hydrogen production is also prolonged.

For the D1 protein mutations, chloroplast transformation and/or mutations are required. The evidence shows that the *psbA* gene is composed of highly conserved sequences, and its genetic structure is composed of four introns [158]. The introns in the gene structure of *psbA* indicate that intronless mutants have a 1.1 kb of length whereas introns occupy a space of approximately 5.6 kb. The results also showed that the photosynthetic activity and growth of the IL-*Chlamydomonas* mutant strain is comparable with the wild type. This study is a key to understanding the intron and exon relation and the translation of these genetic parts into a mature D1 protein [158]. Although most of the species do not have introns in their *psbA* region, the existence of introns of a large size must have a meaning for the *C. reinhardtii* chloroplast genomes.

Most of the studies concerning the D1 protein are related to the amino acid alterations to change the activity of both the D1 protein rebuilt efficiency and the oxygen evolution rate [162]. The deleted amino acid or substituted mutants were reported to produce a higher amount of H<sub>2</sub>, but some mutant strains were not capable of hydrogen evolution. The common responses of these mutant strains are low chlorophyll/dry weight or cell number ratio but increased photosynthetic activity and high respiration rates together with increased starch accumulation [163]. Increased respiration rates are an advantage for hydrogen production, because the oxygen consumption is increased, and this shortens the time required for anaerobiosis and elevates the time-dependent efficiency of hydrogen production. Increased starch deposits also prolong the cell survival metabolism; in other words, cells contain larger amounts of starch for catabolism and survival compared to the wild-type strains [82, 122, 164].

The mutations are achieved with the D1 protein either through amino acid deletions or amino acid substitutions of the different regions and the active sites of the proteins. The double amino acid deletion mutants of D239-40 and D240-41 are in

the region of Q<sub>B</sub> binding and the D1 degradation site whereas L159I/N230Y amino acid substitution is at a location that is responsible for the oxygen-evolving complex [60]. Leucine in 159 site is replaced with isoleucine, and asparagine at 230 site is replaced with tyrosine amino acids. Torzillo et al. claimed that this strain has a hydrogen revolution capacity five times greater than the common strain CC124 [60, 162]. The protein measurement analysis also showed that the amount of the D1 protein in the L159I/N230Y mutants were higher than CC124. The overall H<sub>2</sub> production was also measured as two times more than CC124.

The D1 protein turnover mechanism and sulfur metabolism in biohydrogen production are highly dependent on each other [165]. The concentration of sulfate in the culture medium affects the turnover rate of the D1 protein [92]. Microalgae process sulfur in the form of sulfates (medium components composed of sulfated salts). It is an ATP-dependent process, and the sulfate is consumed for the synthesis of amino acids containing sulfur as cysteine and methionine [166]. The transfer of sulfates is undertaken with the sulfate transport systems which are encoded by nuclear genes. There are two systems in the algae that are responsible for sulfate uptake; one is localized at the outer membrane and the other is placed in the chloroplasts [58]. The sulfate permease holocomplex is placed in the chloroplast and the transported sulfates are utilized for photosynthesis. Sulfates are converted into S<sup>-2</sup>, and in machinery, S<sup>-2</sup> is consumed for cysteine and methionine synthesis. These amino acids can be consumed either for use in another protein body or for the synthesis and assembly of the D1 protein. Thus, the sulfurless medium is utilized for the production of hydrogen at the anaerobic stage. The sulfurless medium blocks the continuous synthesis of the D1 protein; a decrease in the oxygen evolution rate occurs; and hydrogen is produced. There is another way to modify the sulfate and its relation with algal biohydrogen production. Melis and coworkers identified the genes responsible for sulfate transport [58]. Engineering in this gene body may alter the metabolism of algae, resulting in sustained and prolonged hydrogen production.

It has been found that *SulP* gene in green algae contains four introns and five exons. Research has concluded that this gene shows no similarities with prokaryotic systems. Melis and coworkers also used an antisense transformation to understand the function of *sulP* and its relation with biological hydrogen generation [166]. The antisense transformant mutants exhibited a lower protein synthesis, and the photosystem machinery was also affected by the mutations. The authors reported lower D1 protein synthesis together with the RuBisCo activity and also oxygen evolution. However, the mitochondrial respiration activity was not affected; thus, one of the approaches for maintaining hydrogen production in microalgae could be the engineering of the sulfate metabolism, which is critical for the responsible accessory proteins.

*C. reinhardtii* contains four responsible genes: *SulP*, *SulP2*, *Sabc*, and *Sbp* [58]. The *SulP* and *SulP2* genes are mostly interested with transport in the chloroplasts. However, it is interesting that these genes are encoded by the nuclear genome not via the chloroplast genomes. The antisense transformation technique can diminish the sulfate uptake rate of the chloroplast and downregulates the sulfate conversion into amino acids for the PSII repair mechanism. Even if sulfate exists in the medium, the chloroplasts lack the capability to transfer sulfate to the cytosol, and the PSII repair remains insufficient for a regular oxygenic photosynthesis.

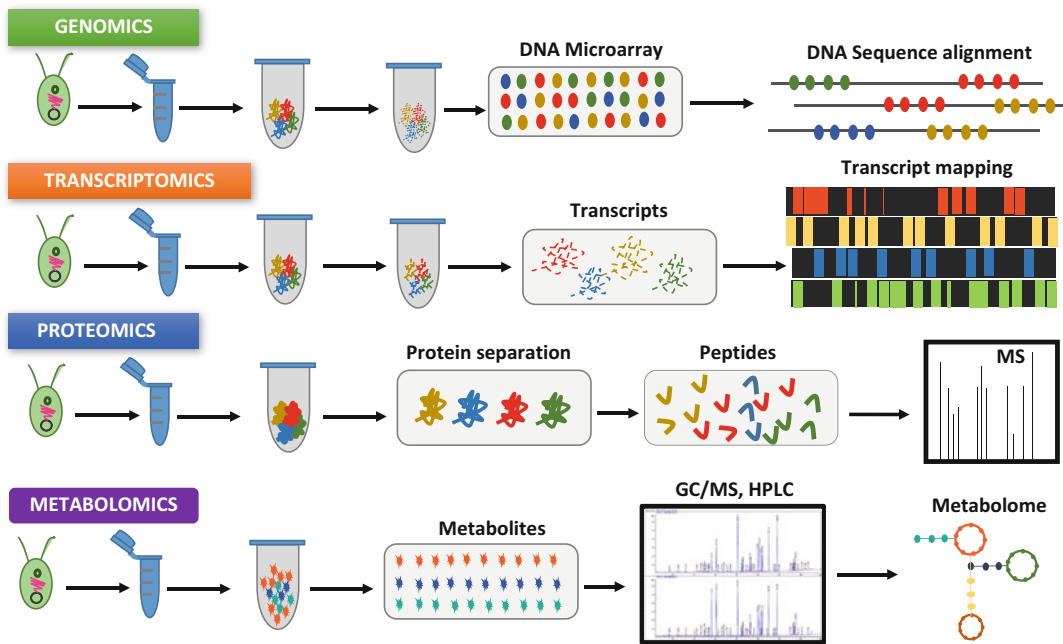
### Systems Biology Approach for Understanding Biohydrogen Production

Biohydrogen production in the microalgal metabolism cannot be separated from other ongoing metabolic processes within the cell. A holistic understanding of the mechanism may be beneficial in designing the future hydrogen-dependent energy systems considering microalgae as a sustainable asset in combination with metabolic engineering [31]. Systems biology is a new bioinformatics tool to understand the inner machinery and metabolism of the cell [167]. Computational tools are novel strategies to design in

silico model applications for biotechnological aspects however; systems biology limits its utility via the requirements of the techniques. High-tech analytical infrastructure tools are necessary, such as high throughput gene sequencing, microarray analysis, GC, MS, HPLC, FPLC, and NMR, as well as MS-equipped analytical devices.

Covering the network balances in the microalgae considering photosynthesis, electron transport, starch decomposition, and hydrogen production metabolism is the key to evaluate the strain improvement for industrial applications. These pathways are interpenetrating and the change in one trait can be observed as a change in the whole cellular machinery. What should be known are the gene expression levels, the turnover rate of the accessory proteins, such as the D1 and D2 heterodimers, and the catalytic activity of the enzymes responsible for the reactions and hydrogen gas production.

Most of the systems biology studies on biohydrogen production consider sulfur deprivation as a fundamental method to deliver novel solutions because the current available data of hydrogen production can only be provided via sulfur-deprived conditions. This highlights a critical point that if it was possible to combat biohydrogen production under sulfur-containing aerobic conditions, then the response of the cells and regulation of the pathway would be different from what it is known today. This can be achieved in a computational environment where recent data continuously feed the in silico models. However, it should not be overlooked that studies on the manipulation of regular environmental physiological conditions limited the responses of hydrogen generation which was not possible with the conventional methods. Furthermore, genetic engineering, recombination, and mutations have shown that there is more to be undertaken than altering nucleotides, amino acid sequencing, and engineering the genome for certain cases; comparative analyses are required. These techniques provide data to be mined for a more sustainable understanding. A system-level approach provides for the realization of a hypothesis for algal biohydrogen production. The fundamental metabolism is replete with challenges which should be



**Biohydrogen Production, Fig. 4** General description and flow diagram of the systems biology omics tools

carefully revised within the perspective of metabolic engineering (Fig. 4).

Considering microalgal cells as a closed system, the interactive dynamic changes inside the cells communications via gene activation, protein synthesis, metabolite secretion, and changes in the biochemical composition can be understood as engineers use thermodynamics to express the inner and outer energetic mechanisms.

*Chlamydomonas* cells are mostly preferred for systems biology studies concerning the synchronization characteristics of the culture since they allow more accurate data to be mined. As a photosynthesis model, genome model, and hydrogen producer, biohydrogen-related systems biology studies utilize the *C. reinhardtii* cells for research purposes [67].

From the genome perspective to the final metabolites, microalgal metabolism is open for studies regarding omics. First, it can be used to differentiate the metabolic regulations of cyanobacteria and microalgae. Furthermore, the comparative studies will feed into the understanding how the inner signaling machinery displays variations even though the final product is the

same; not only on the basis of the current technology but also evolutionary studies can also be represented to discover what lies beneath the algal cell walls.

To achieve a holistic understanding, matching the pieces of a puzzle from gene to metabolite, omics offer a great amount of accessible data to complete the puzzle in order to see the big picture. Neither gene activation nor RNA synthesis, protein production, or final metabolite generation is sufficient to fully cover the essentials in the cellular machinery; rather, a comparative and complimentary study is required. Thus, the aim and scope of genomics, proteomics, transcriptomics, and metabolomics should be well defined.

**Genomics** was the very first attempt to fully annotate the regulatory metabolism of the organism at the DNA sequence base [168]. It aims to disclose the whole genome map and integration. In terms of eukaryotic microalgae, the genomics are composed of the chloroplast, nucleus, and mitochondrial genome which increase the number of deliverables because of the three full large-scale genome sizes [94, 169, 170]. Genomics analysis can reveal the native wild nature of an

organism or it can be used to display the new regulatory machinery and gene-coding metabolism after genome engineering [171]. The current tools for screen are next-generation sequencing, microarray techniques, and functional genomics [85, 172, 173]. Genomics are considered to elevate understanding to a new level with the advances in genome-wide analysis. Along with revealing potential tools, genomics can be used to explore the gene function while investigating the role of the gene cluster in the whole cell physiology and the relation with the phenotype-genotype relations.

As within the scope of biohydrogen production, the dynamics steps are the trigger of anaerobiosis, activation of hydrogenase enzymes, enzyme assembly, H<sub>2</sub> gas production, and termination of the H<sub>2</sub> gas generation processes, and each step has a gene activation reservoir in terms of data collection for genomics [14, 133]. This idea can be adapted to certain environmental stress conditions (sulfur, nitrogen, phosphorous deficiencies/starvation) or on/off switches to trigger hydrogenase enzyme activity [55, 116, 174]. In sulfur depletion for hydrogen production, it is reported that more than 100 genes are up- or downregulated [175]. Tracking the particular genes for the responsible traits can be defined via genomics tools. Recently, algal genomics are preferred for the photosynthesis efficiency and characterization of stable nuclear and chloroplast transformation [176–178]. The results can also be applied to biohydrogen generation [173].

In conclusion, the insight offered by genomics through the microalgal biohydrogen studies shows that the uptake rate of the acetate through the medium environment under dark conditions has a significant effect on the H<sub>2</sub> formation [173]. It is found that acetate is converted into starch and deposited as an energy source for the production of H<sub>2</sub> [179]. Models provide information that the *HydA* enzymes supply electrons from ferredoxin and finding the role of the PQ pool, and the amount of the cyclic electron flow through the hydrogenase reaction center is critical for the H<sub>2</sub> yield [173]. From the model, it is derived that the cyclic electron flow inhibition may increase the

H<sub>2</sub> generation, and the *stm6* mutant strains also display similar results [123].

**Transcriptomics** is the analysis of whole transcriptome data obtained in a specific environmental condition [180]. The RNA expression and the fragments of transcriptomics are aligned with the utilization of a microarray technology to decipher the expression of certain genes at a transcript base via the obtained cDNA libraries [177, 181]. The transcriptome analysis provides information about the expressed genes and the expression levels. This analysis can be undertaken either by a direct analysis of transcripts or by the combination of mutated or engineered cells transcriptome [67, 176, 181]. However, the transcriptome analysis does not represent the final situation of the gene regulations and the expression of gene products; it can only be helpful in understanding the transient state of the expressed genes and translation of the gene products into proteins. The advantage of the transcriptome is derived from the ease in using the tools rather than sequencing a whole algae genome [154]. Most of the eukaryotic microalgae species have a genome size larger than 100 mb [154]. Thus, rather than making a genomic analysis for a special feature like biohydrogen production, transcriptome analysis may be more efficient and user friendly. The time spent, effort, and application of the methodology for whole genome sequencing may be extensive; however, the RNA-based next-generation technologies will be more informative in terms of microalgal omics. The transcriptome data can then be translated into a language to allow an understanding the functional genomic regulation.

Lipid accumulation [182], responses to nitrogen levels [183] and stress conditions, and relations with the lipid accumulation have been the very first topics of the microalgal transcriptomics with *Dunaliella*, *Chlorella* sp., and *C. reinhardtii* being used as models [181, 182, 184]. In terms of biohydrogen, microalgal hydrogen production machinery requires a large amount of enzymatic regulation (*HydEGF*, *HydA1*, *HydA2*, *SulP*, *psbA*, *tlc*, *stm*) and protein assembly mechanisms (i.e., maturation of hydrogenase enzyme, assembly of D1 protein, and reorganization of chloroplast



membrane attached protein distribution). The transcriptomic regulation of algal biohydrogen production is an emerging topic. In particular, responses to the sulfurless conditions offer insights into the next-generation genome and in silico mathematical modeling. RNA-seq analysis [185], sulfur-deprived modeling, and comparative analysis of mutant strains have reported to provide efficient data for hydrogen production machinery.

Transcriptome studies have revealed that in sulfur-depleted conditions representing an anaerobic environment, time-dependent dynamics may result in changes inside the cell [186]. There is a transition from an oxygen existing environment to oxygen abundance, and the opposite is that when oxygen exists in the chamber, then hydrogen cannot be generated. It is reduced to a state in which the hydrogen generation peaks while the oxygen value is replenished. Thus, the dissolved oxygen and hydrogen amounts are constantly changing and a time-dependent analysis will be more effective to obtain accurate results. The transcripts show that genes which are responsible for sulfur metabolism, photosynthesis, carbon metabolism, amino acid synthesis, and redox cycle are activated [186]; however, some unknown genes are also expressed. The transcriptome data revealed that *HydA1* activation is not only dependent on anaerobiosis, but sulfur starvation was the initiator of the activation process combined with a light supply. Only anaerobiosis sustained the activity for a long time. This reveals the S-dependent activation and downregulation of the PSII and D1 turnover rates [160].

**Proteomics** is a new tool used to understand the protein synthesis and protein data of specific conditions [170]. The very raw understanding of the proteomic data started with the electrophoretic protein analysis on gel surfaces, such as SDS-PAGE and Western Blot analysis. The idea of using protein data is to understand the translation of DNA into a specific product. The key for proteomics studies is the utilization of mass spectroscopy (MS) [187], which also allows for quantitative proteomics to be searched [188]. The large-scale analysis of proteins also highlights the amino acid sequences. In terms of biohydrogen, *Hyd1A*, *SulP1*, *tlal*, and other

hydrogen-related gene activation of photosynthesis and electron transport chain suggest that protein-engineering tools can be used for further alignments. Proteomics for microalgal biohydrogen studies are not as highly focused as transcriptomics and metabolomics, but the results for general metabolism including photosynthesis, PSII action mechanism, and quantitative approaches using comparative tools can be used to understand the proteome data [146, 189–191]. Before the high throughput proteomics, simple techniques, such as SDS-PAGE, were used to observe the expression levels of particular proteins when H<sub>2</sub> photoproduction is induced. SDS-PAGE data represents the activated photosynthesis proteins with the highest amount of protein being observed at the 24th hour of the culture [192]. At that time, H<sub>2</sub> production starts, and the culture becomes anaerobic. The D1 protein portioning also changes. Most of the proteins obtained from the proteome data showed that the Calvin cycle, photosynthesis, and protein synthesis were responsible for the folding and degradation, sulfur nitrate and acetate assimilation, and ATP synthesis [172, 192, 193]. These results are vital in the comparison of genomic, transcriptomic, and proteomic data in correlation with the metabolomics [192].

**Metabolomics** is also a recent development in omic tools, which highlights certain metabolite levels and their expression quantities together with the up- and/or downregulation of certain pathways [194]. In a particular condition or as a response to a stress (in biohydrogen production light dark cycles, sulfur starvation, light intensity, and addition of organic sources), cells start to activate the genes related to the stress physiology (activation of hydrogenase enzymes), and a shift occurs in the related metabolic frame (catalysis of H<sup>+</sup> ions to H<sub>2</sub> in gas form). This shift is precious in terms of hydrogen production where microalgae cells engage in their survival strategy and multi-coordinated response activation takes place within the cells [195]. Metabolomics can be constructed to understand either a single pathway or multiple pathway interactions. As in the case of microalgal hydrogen production, the energetic pathways are highly correlated with starch accumulation using

the Calvin–Benson cycle [135]. Another cellular activity is related to the upstream  $O_2$  evolution path, which is a rate-limiting step.

The transcriptome studies for biohydrogen production are undertaken within a sulfur-deprived culture, which is the only known cultivation strategy to obtain a visible amount of hydrogen [181]. With metabolomics studies, the consumed starch, acetate, and other minor elements can be detected using GC, GC-MS, GC-TOF-MS, and NMR techniques [194]. Metabolomics studies also require a high throughput analysis. The metabolomics of the biohydrogen production should be separated and analyzed as a four-step approach due to the two-stage cultivation protocol, which is the most efficient protocol found to date due to the oxygen sensitivity of the biohydrogen production in microalgae [196, 197]. The stages are:

- (i) The aerobic stage in which the mass production of biomass occurs and the cells grow logarithmically under sulfur-rich acetate-containing conditions. The cells accumulate higher amounts of chlorophyll and also the TGA cycle is activated to produce specific amounts of fatty acids. Starch is produced with the Calvin–Benson cycle. In this stage, the culture cells cannot activate hydrogenase enzymes; thus, metabolic pathways for enzyme assembly cannot be observed.
- (ii) In the second stage, cells are transferred to a culture condition in which oxygen is absent and sulfur is deprived. In this stage, a gene expression machinery is observed to adapt  $H^+$  as a final electron acceptor. Oxygen is consumed by the respiratory pathways, and in 24–36 h, anaerobiosis can be observed. The culture starts to decompose starch as a primary metabolite for cell survival. As in the metabolomics approach, sulfur deprivation and starch pathways are important in uncovering the metabolic relations.
- (iii) In this stage, there is rapid  $H_2$  generation in which hydrogenase enzyme activity is at the maximum level, triggering a sustaining  $H_2$  gas generation. Starch and some amino acids are catabolized to provide electron for the  $H^+$  ions.

- (iv) In the termination stage,  $O_2$  evolving from the deficient PSII system starts to accumulate within the cell, and hydrogenase enzyme activity decreases.

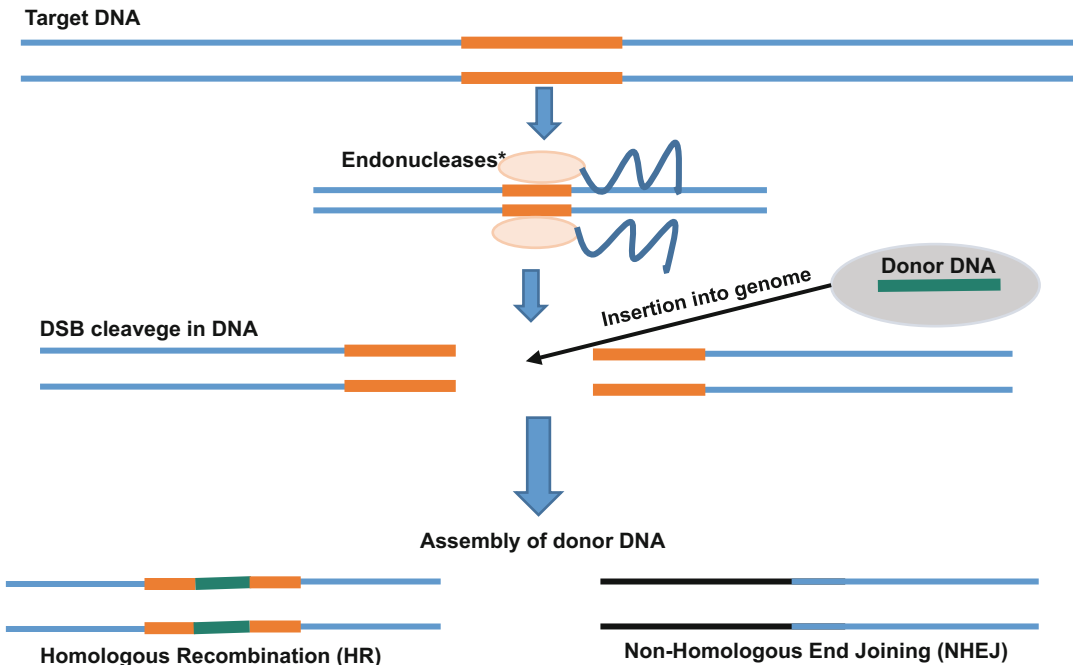
These four steps comprise a whole different area of metabolomics studies, and comparative and quantitative analyses are required in order to understand the regulation of metabolic pathway.

Metabolomics data represents the dynamic pathway analysis of wild-type *C. reinhardtii* under sulfur-deprived conditions; however, it can also be applied to the mutant strains of the D1 protein, chloroplast antenna size, starch metabolism, and SulP deficient strains. Studies reveal that there is a change in an observable range of  $H_2$  photoproduction, and there are also changes in the size or amounts of the proteins, hydrogenase enzymes, and/or starch.

The omics data allows for the metabolic engineering of the target product algal biohydrogen production. The raw data of the wild-type strain, data acquisition for further gene manipulation of transgenic microalgae cell physiology and regulation, and comparative omics tools are the fundamental approaches for strain improvement. All studies regarding  $H_2$  photoproduction physiology have concluded that in hydrogenase activity,  $O_2$  evolution is highly dependent on sulfur deprivation, PQ-size, cyclic electron flow through the PSI together with the rate and yield of the water photolysis to feed required electron.

### Targeted Genome Engineering (TGE)

The introduction of TGE tools does not have a long history with the first tool, *zinc finger nucleases* (ZFNs), being introduced in the early 2000s, followed by the *transcription activator-like effector nucleases* (TALENs). The latest tool, *clustered regularly interspaced short palindromic repeats* (CRISPR), has been introduced as a specific TGE with a high expectation of its performance. Both tools (ZFNs and TALENs) have shown great success and a high number of stable mutations in comparison with the conventional tools. The high throughput analysis also discusses the



**Biohydrogen Production, Fig. 5** The general schematic representation of targeted genome engineering tools. Endonucleases break DNA and donor DNA is

attached into the genome via guidance of the guide-proteins/peptides. “\*” represents for TALEN (*FokI*), ZNF (*FokI*), CRISPR (*Cas9*) tools

activity and utility of the methods. The ease of the tools is that they enable the cells own endogenous DNA repair mechanism while introducing DSBs into the genome (Fig. 5). Even though the technology is relatively new, commercial genome editing kits exist for the researchers. This rapid increase in the use of nuclease technology raises the question, “*Can microalgae genomes be re-written for sustainable hydrogen producing machinery development?*” Thus, the following text presents the general technical information concerning the TGE tools and explains how they can be used in microalgal biohydrogen production [198, 199] (Table 2).

In 1985, ZF motifs were discovered in *Xenopus oocytes* [102]. The ZF motifs and the special DNA cleavage nucleases *FokI* are combined to provide an artificial ZF-dependent genome-editing tool [94]. The ZF domains are 30 amino acid sequences with a zinc atom. These domains are ligated with a 3 bp in the genome. Between the ZFs, there are 5–7 bp of spaces. The ZF domains can be combined to

9–18 bp of the DNA. With the use of programmable DNA restriction enzymes, the genome is cleaved with *FokI* from the location where the ZF domains are paired with its own complementary sequence. When the domains are attached and nucleases cleave the DNA, the breaks in the DNA are rejoined with the insertion of the gene of interest [102, 200, 201].

TALENs also use *FokI* endonucleases to create multiple breaks in the genome. They are composed of a *FokI* domain and a TALE protein domain to recognize the cleavage site [201]. The TALE domain is composed of 30–35 amino acids which recognize single base pairs, attached to the genome [202]. With *FokI*, mediated DSBs are created in the custom-made gene of interest which is ligated with the genome’s own repair system.

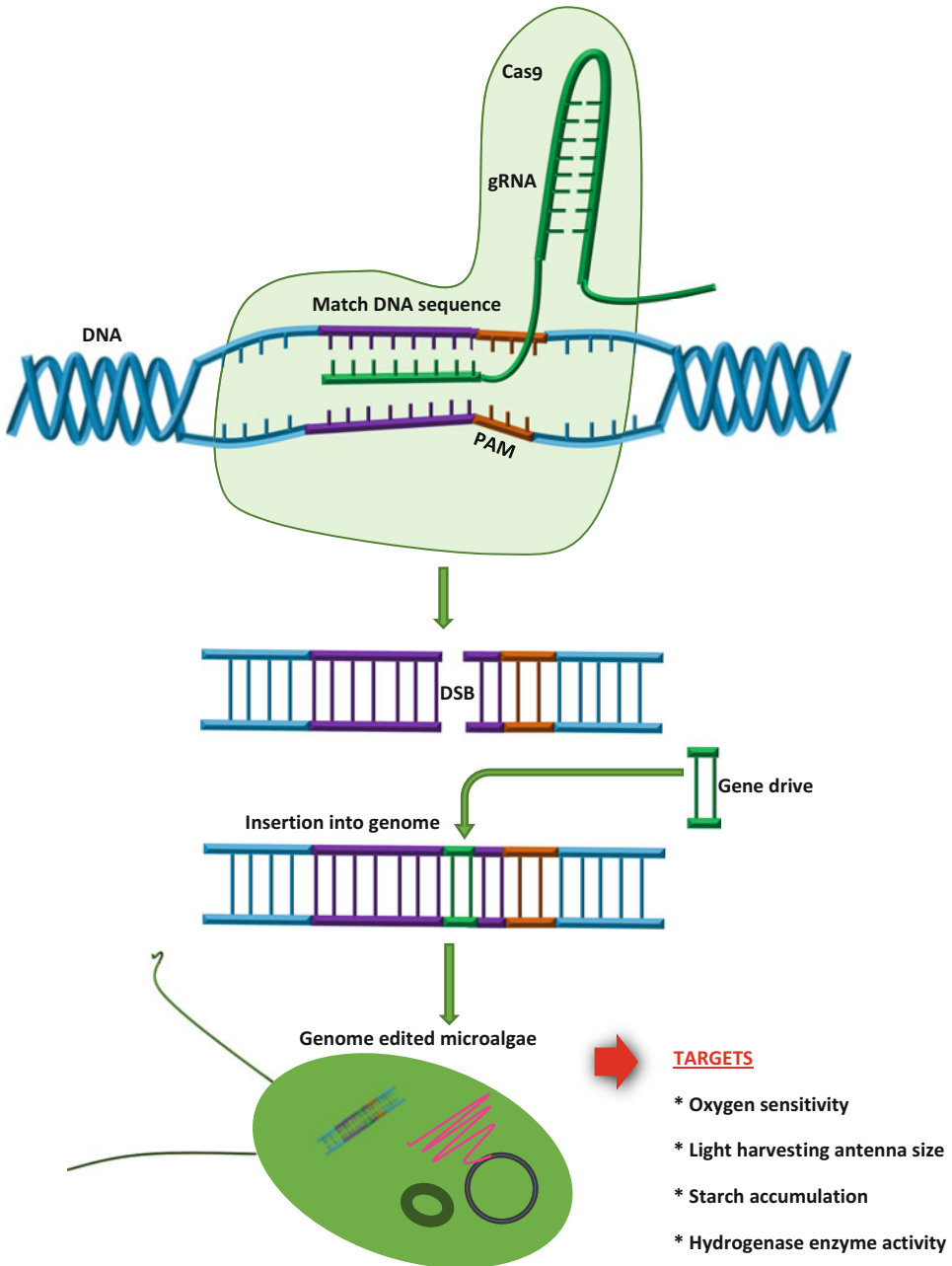
As the latest technology in engineering the genomes of organisms, CRISPR has become one of the most studied tools [203]. The tool is based on bacteria having an adaptive immune system called noncoding repeats (*CRISPRs*), protecting

**Biohydrogen Production, Table 2** The objectives of the targeted genome engineering tools

	TALENs	ZFNs	CRISPR/Cas9
<b>Target</b>	All living organisms		
<b>Aim</b>	Induction of double strand breaks (DSBs) in the genome to insert gene of interest		
<b>Mechanism of action</b>	Nonspecific DNA cleavage regions by nucleases and domains to bind DNA	<i>FokI</i> restriction nuclease-mediated DNA insertion via site specific peptides	CRISPR regions, PAM activator code, gRNA-mediated DNA insertion into the genome via Cas9 endonucleases
<b>Introduction to biotechnology</b>	2010s	2000s	2013
<b>Organisms of success</b>	Bacteria, yeast, mammalian cell, stem cells, plants, microalgae (limited knowledge), transgenic animals	Bacteria, yeast, mammalian cell, stem cells, plants, microalgae (limited knowledge), transgenic animals,	Bacteria, yeast, mammalian cell, embryos, macroalgae cell culture, stem cells, plants, microalgae (recently developing), transgenic animals
<b>Cost</b>	Average	Average	Low
<b>Abilities</b>	Gene knockouts, gene silencing, gene editing, gene correction, gene addition, gene repair		
<b>Recognition type in genome</b>	Protein-DNA	Peptide-DNA	RNA-DNA
<b>Simplicity</b>	++	+	+++
<b>Methylation sensitivity</b>	Sensitive	Sensitive	No
<b>Target</b>	Thymine at 5' end of target sequence	Three base pairs to bind ZFs	Base pairing at PAM sequences
<b>Advantages</b>	Due to small size, effective delivery into the cell Successful clinical results Cost effective	Higher specificity than ZFNs	Independent DNA binding domain RNA guided no need to protein Higher specificity than other tools Cost and time effective Ability to express multiple alterations
<b>Disadvantages</b>	Engineered protein may display adverse immune reactions Requires extensive identical sequences	DNA methylation Time consuming Possibility of bacterial source derived immunoresponse Size-dependent failure into the delivery of cells	Possibility of bacterial source derived immunoresponse Size-dependent failure into the delivery of cells
<b>Microalgae genome</b>	Chloroplast Nucleus	Chloroplast Nucleus	Chloroplast Nucleus
<b>Microalgae genome enhancement</b>	Increase in the photosynthetic activity, manipulations in the PQ pool size, O <sub>2</sub> tolerant hydrogenase, reorientation of electron flow, increasing catalytic activity of hydrogenase, silencing hydrogen competitive pathways		

bacteria from the invasion and infections from viruses [204]. This cluster provides a secure environment for bacteria and archaea genomes from the integration of foreign gene pieces of viral or plasmid genetic materials, creating a natural environment with an on/off switch to differentiate between foreign-DNA and self-DNA. They are

composed of nucleic acid segments divided by a region called spacer [205]. CRISPR regions are in association with **CRISPR-associated proteins** (*Cas*). CRISPR/Cas systems scan the DNA to identify and locate foreign-DNA. Once the foreign-DNA is found, the immune response is activated [105].



**Biohydrogen Production, Fig. 6** CRISPR/Cas9-mediated microalgal genome editing flow diagram and main targets for photobiological hydrogen production (*CRISPR/Cas9*; clustered regularly interspaced short

palindromic repeats–CRISPR-associated proteins 9, *PAM*; protospacer adjacent motif, *DSB*; double stranded break, *gRNA*; guide RNA) (Modified from Ref. [201])

Among the Cas proteins, Cas9 is used in the CRISPR-mediated genome engineering. The Cas9 protein, as an initiator for the activation of gene editing steps, is an RNA-guided DNA

endonuclease enzyme (Fig. 6). There are several steps in the use of CRISPR/Cas9 as a genome-editing tool artificially (in lab conditions). In the process, the Cas9 + guide RNA (gRNA)

complex will find the target region in the genome [206].

Microalgal genome editing with endonucleases is also a recent topic; however, in the literature, the number of studies is limited with most concluding that the algal chloroplast may require additional codon optimization for the effects of the mutations at phenotype level to be observed [206]. To date, *Synechocystis*, *Phaeodactylum tricornutum*, and *C. reinhardtii* species have been examined using ZFNs, TALENs, or CRISPR/Cas9 [96, 198, 207–209]. Genome-engineering techniques generally utilize high throughput screening, genome-wide analysis, or a specific investigation of the phenotype. One study used TALEN for the site-specific HR in *Phaeodactylum tricornutum* in order to silence the urease gene [210]. The TALEN-mediated expression of insertional mutations to the knockdown urease gene was successful but adding a plasmid to the TALEN motif showed better results.

TGE tools have showed great success in gene insertion or knockout mutations in other eukaryotic organisms [211]. Microalgae and plants somehow share common and conserved metabolic routes and photosynthetic ability, representing chloroplast genomes; however, the experiments showed that without a codon optimization, the CRISPR technique has failed at very first trials [206, 212]. Regarding the model green microalgae *C. reinhardtii*, the main problem is that *C. reinhardtii* genome repairs DSBs via the NHEJ repair system; however, CRISPR is dependent on the HR [50]. In order to increase the success rate of CRISPR for algae, the first mutation transformation rate should be tuned. One of the recent studies used *Phaeodactylum tricornutum* for CRISPR editing [209]. This study also reports that codon optimization is necessary for successful use of the CRISPR tool. Knockdown and knockin mutations have been successful in engineering microalgae with CRISPR. The latest study showed that DNA free Cas9 and gRNA expression plasmid provided successful results for zeaxanthin production from *C. reinhardtii* [213]. The knockdown mechanism of the action blocked the zeaxanthin transformation, and the cells continued to accumulate

zeaxanthin in the cytosol. In addition, the knockdown mutations showed diversified photosynthetic activity, which may be a clue for biohydrogen production.

Currently, there is no study in the literature that deals with biohydrogen production using TGE tools. It is quite possible that these tools may be efficient for the sulfur assimilation mechanism and most of all TGE tools may provide a way to design and rewrite the microalgae genomes expressing hydrogenase with no sensitivity to O<sub>2</sub>. This would be a breakthrough in the microalgal biohydrogen generation and may be a game changer for the commercial scale processes. However, it is necessary to overcome the current limitations, the most important of which is the response of microalgae to genome editing. If microalgae find a way to silence the insertion gene drives, this will create a further barrier. The elimination of these mechanistic barriers will provide data for the metabolic fluxes for the biohydrogen production regulation and offer a practical tool to use microalgae as biohydrogen-generating machineries.

## Bioethics

In terms of biofuel production from genetically modified microalgae species, the extent of bioethics considerations will be argued on the basis of environmental protection, biosafety and biosecurity issues, preservation of nature of the host organism, and interrelation of GM-species with nature. Algal biofuels have been considered as a sustainable alternative compared to land crops and petroleum-based fuel sources; yet, a long list of limitations and uncertain production concepts still exists. Although the food versus fuel debate has been a long-term ethical consideration in relation to finding an alternative source other than using field crops [214], the level of acceptability of algal biofuels produced from GM-algae is greater than that of GM-species for direct human or animal consumption.

Below are some key points to highlight concerns related to these emerging technologies:



- The gap that remains between biology and biotechnological applications
- Lack of knowledge about the environmental risks of the technology
- Lack of infrastructure and production technology
- Unknown stability characteristics of the genome-edited algae strain
- Poorly categorized biosafety and biosecurity protocols
- Political instability and dynamism in the bioeconomy
- Lack of consensus on the risk management issues of genome engineering technologies and algal biofuel production
- Global investments and the market trend of both biofuel and genome engineering strategies (e.g., genome engineering technologies are currently emerging for gene therapy and pharmaceutical applications)
- Monopoly of the techniques and the fuel industry

When these key points are considered together to fully understand the past, present, and future of the related issues, the ethical considerations can be well defined for this sustainable concept.

## Opinions on Biohydrogen Research

This section focuses on some lead scientists in the area of microalgae and energy and the realization of applications that will be catalyzed by genetic tools. At this point, with the acknowledgment for their contribution and kindness in providing their ideas, the quotes will serve as a collection of opinions for biofuel applications, especially biohydrogen studies.

Microalgae can provide a great diversity of biofuels. These include biodiesel from algal crude oil; biohydrogen; bioethanol from algal starch; and biogas from algal biomass. In addition, available technology can be used to convert algal oils to conventional diesel, gasoline and jet fuel. Algal biomass can be gasified into syngas to produce fuels such as ethanol. All this depends, first of all, on an ability to sustainably and cost-

effectively produce algal biomass. This is not an easy task. Large-scale production of affordable algal biomass for fuels is actually highly unlikely without genetic and metabolic engineering of microalgae. Priority targets for genetic enhancements should include a substantial increase in the sunlight capture-conversion efficiency of algae; a capacity for enhanced capture of inorganic carbon from a dilute growth medium; triggered mechanisms to auto-flocculate the biomass for easy recovery; and triggered mechanisms for autolysis of the cell to facilitate extraction of the intracellular material. These, of course, are just some of the options. Without genetic and metabolic engineering, there is no hope for algal fuels. (Prof. Yusuf Chisti, School of Engineering, Massey University, New Zealand)

Photosynthetic microbes are versatile organisms that do produce (or can be engineered to produce) a variety of chemicals of interest to a renewable energy future. Algae, in particular (including cyanobacteria) are being utilized by various industries to commercially produce pharmaceuticals and nutraceuticals. In order to optimize them for production of biofuels at large scale and low cost, however, additional genetic modifications are required. Similarly, the importance of developing renewable sources of H<sub>2</sub> is of fundamental importance for a successful H<sub>2</sub> economy. Photosynthetic microbes represent an efficient and clean source of renewable H<sub>2</sub>, either when H<sub>2</sub> production is linked to photosynthetic water oxidation, or when fermentative H<sub>2</sub> production of cellulosic substrate is linked to microbial fuel cells (the latter extract additional H<sub>2</sub> from the products of fermentation). While fermentation coupled to microbial fuel cells seems to be already reaching high conversion efficiency at bench scale with existing microbes, much more research is needed to take advantage of the high rates (but currently low duration) of H<sub>2</sub> production by photosynthetic microbes. Most of the limiting factors have been identified by numerous research groups and extensive genetic engineering work is being performed to address them. It is my view that only through genetic engineering will we be able to achieve the required light conversion efficiency to bring the system to commercial application. (Prof. Maria L. Ghirardi, National Renewable Energy Laboratory (NREL), USA)

The production of H<sub>2</sub> by biophotolysis of the water is the ultimate purpose regarding “clean” technology, as far as only of H<sub>2</sub> and O<sub>2</sub> are produced and the only one of the solar energy is used. The contributions of numerous disciplines, as the bio-inspired chemistry to produce innovative catalysts, proteins engineering applied to hydrogenases to

reduce their sensibility to O<sub>2</sub>, as well as synthetic biology for the metabolic (re) programming, can have a major impact in this domain, where the coupling between the physiology of microorganisms and the production process is absolutely necessary to hope to reach the expected yields. (Prof. Jack Legrand, University of Nantes, France)

Currently, biohydrogen with *Chlamydomonas reinhardtii* is a sequential two stage process, in which growth and H<sub>2</sub> evolution is separated spatially. However, the efficiency of the process in most cases is below 1% under solar light. The two-step process also carries a penalty in terms of maximum attainable photon conversion, since three photons (instead of two as for direct photolysis) are required to transfer an electron from water to hydrogenase (i.e., one photon to extract one electron from H<sub>2</sub>O; one photon to transport the electron through PSI to form NADPH and starch, and one photon to transport the electron from starch to hydrogenase through PSI). Moreover, adding exogenous acetate is required to promote starch accumulation by cells and establish the anaerobic conditions necessary for hydrogen production. However, one important advantage of the two-step process is that since O<sub>2</sub> is almost totally absorbed by respiration, the purity of the H<sub>2</sub> produced is very high approaching 98% if CO<sub>2</sub> is removed by simply scrubbing system. This fact could have important economic implications if we consider that purification of H<sub>2</sub> represents 50–80% of capital costs. In my opinion, genetically manipulation of strains should be addressed at generating strains with high carbohydrate accumulation capacity during growth and coupled by high respiration rate, which should allow reaching anaerobiosis as soon as possible, in order to protect PSII from inactivation by O<sub>2</sub> and prevent state 1 to state 2 transition. Indeed, high productive strains maintain high effective quantum yield of PSII during the hydrogen production with high contribution by PSII (above 80%) of the total hydrogen output. (Dr. Giuseppe Torzillo, Institute of Ecosystem Study (ISE), National Research Council (CNR), Italy)

These quotes reveal that microalgae are promising feedstock for biofuel production, not only for biohydrogen but other derivatives of biofuels can be produced using algae. However, the critical point is the techno-economic feasibility of algae for large-scale cultivation. Apart from scientific developments, commercial applications are also crucial to compete with existing sources. As stated by researchers, genetic manipulations hold the key to the gate to enter a commercial phase.

## Conclusion

Using genetics as a tool to reach the ultimate goal of realizing microalgal biohydrogen production is vital for the future of sustainable energy. It will also be an important example of the rewarding symbiosis between genetics and energy with regard to the useful interaction of a living being and technology, i.e., a perfect combination of biology and industry. The success of this example can also serve as a great game-changing shift by overcoming the questions related to ethics, efficiency, and economy as well as issues that are of concern to society.

As a final word to this discussion of the essentials of microalgal biohydrogen production and revisiting the mechanism from the perspective of genetic engineering techniques, the existing data provides researchers with the known fundamentals of the techniques, regulations, and outcomes of a selection of the current studies. However, if microalgal biohydrogen production is considered to be a future biofuel, it should undoubtedly be accepted that every step from production to storage is essential for success and has their own advantages and limitations. Genetic engineering techniques to engineer super hydrogen producing microalgae are just a small portion of the whole process but its role is vital to design the pre- and post-production steps. Thus, in order to achieve a level of commercial production, an effective way of genetically enhancing the metabolism must be found.

## Future Directions

As it has been discussed in this chapter; microalgae can be named as a promising source for alternative biohydrogen generation. Apart from fundamental issues such as biohydrogen production systems, scale up operations, storage and utilization; there are major requirements still holds the challenge for developing sustainable production strategies. Even if there are still limited numbers of algae species for biohydrogen production; in the future it is expected to discover more

microalgae species capable of biohydrogen generation through direct screening, metagenomic analysis and in silico tools. Within this regard genetic engineering is a huge opportunity; especially targeted genome engineering has a great potential to increase the volumetric biohydrogen productivity. On the other hand, increasing tolerance to oxygen which is the major drawback for lab and industrial scale is the key topic for sustainability and reliability. When these bottlenecks will be passed; novel tools for biohydrogen production will be developed in the context of both science and industry.

## Bibliography

- Voldsund M, Jordal K, Anantharaman R (2016) Hydrogen production with CO<sub>2</sub> capture. *Int J Hydrog Energy* 41(9):4969–4992
- Hosseini SE, Wahid MA (2016) Hydrogen production from renewable and sustainable energy resources: promising green energy carrier for clean development. *Renew Sust Energ Rev* 57:850–866
- Oncel SS (2013) Microalgae for a macroenergy world. *Renew Sust Energ Rev* 26:241–264
- Ghirardi ML, Dubini A, Yu J, Maness P-C (2009) Photobiological hydrogen-producing systems. *Chem Soc Rev* 38(1):52–61
- Tekucheva DN, Tsygankov AA (2012) Coupled biological hydrogen-producing systems: a review. *Prikl Biokhim Mikrobiol* 48(4):357–375
- Boboescu IZ, Gherman VD, Lakatos G, Pap B, Biró T, Maróti G (2016) Surpassing the current limitations of biohydrogen production systems: the case for a novel hybrid approach. *Bioresour Technol* 204:192–201
- Zhang D, Vassiliadis VS (2015) *Chlamydomonas reinhardtii* metabolic pathway analysis for biohydrogen production under non-steady-state operation. *Ind Eng Chem Res* 54(43):10593–10605
- Rashid N, Rehman MSU, Memon S, Ur Rahman Z, Lee K, Han JI (2013) Current status, barriers and developments in biohydrogen production by microalgae. *Renew Sust Energ Rev* 22:571–579
- Dasgupta CN, Jose Gilbert J, Lindblad P, Heidorn T, Borgvang SA, Skjanes K, Das D (2010) Recent trends on the development of photobiological processes and photobioreactors for the improvement of hydrogen production. *Int J Hydrog Energy* 35(19):10218–10238
- Lopes Pinto FA, Troshina O, Lindblad P (2002) A brief look at three decades of research on cyanobacterial hydrogen evolution. *Int J Hydrog Energy* 27(11–12):1209–1215
- Pulz O (2001) Photobioreactors: production systems for phototrophic microorganisms. *Appl Microbiol Biotechnol* 57(3):287–293
- Mathews J, Wang G (2009) Metabolic pathway engineering for enhanced biohydrogen production. *Int J Hydrog Energy* 34(17):7404–7416
- Carrieri D, Wawrousek K, Eckert C, Yu J, Maness PC (2011) The role of the bidirectional hydrogenase in cyanobacteria. *Bioresour Technol* 102(18):8368–8377
- Peters JW, Schut GJ, Boyd ES, Mulder DW, Shepard EM, Broderick JB, King PW, Adams MWW (2015) [FeFe]- and [NiFe]-hydrogenase diversity, mechanism, and maturation. *Biochim Biophys Acta* 1853(6):1350–1369
- Huesemann MH, Hausmann TS, Carter BM, Gerschler JJ, Benemann JR (2010) Hydrogen generation through indirect biophotolysis in batch cultures of the nonheterocystous nitrogen-fixing cyanobacterium *Plectonema boryanum*. *Appl Biochem Biotechnol* 162(1):208–220
- Allahverdiyeva Y, Aro EM, Kosourov SN (2014) Recent developments on cyanobacteria and green algae for biohydrogen photoproduction and its importance in CO<sub>2</sub> reduction. In *Bioenergy research: advances and applications*. Eds: Gupta VK, Tuohy MG, Kubicek CP, Saddler J, Xu F. Amsterdam Elsevier
- Gaffron H, Rubin J (1942) Fermentative and photochemical production of hydrogen in algae. *J Gen Physiol* 26:219–240
- Melis A, Happe T (2001) Hydrogen production. Green algae as a source of energy. *Plant Physiol* 127:740–748
- Oncel S, Kose A, Vardar F, Torzillo G (2015) From Ancient Tribes to Modern Societies, Microalgae Evolution from a Simple Food to an Alternative Fuel Source. In: *Handbook of Marine Microalgae* Ed: Kim SK, Biotechnology Advances Academic Press 127–144
- Scoma A, Giannelli L, Faraloni C, Torzillo G (2012) Outdoor H<sub>2</sub> production in a 50-L tubular photobioreactor by means of a sulfur-deprived culture of the microalga *Chlamydomonas reinhardtii*. *J Biotechnol* 157(4):620–627
- Wang B, Lan CQ, Horsman M (2012) Closed photobioreactors for production of microalgal biomasses. *Biotechnol Adv* 30:904–912
- Giannelli L, Torzillo G (2012) Hydrogen production with the microalga *Chlamydomonas reinhardtii* grown in a compact tubular photobioreactor immersed in a scattering light nanoparticle suspension. *Int J Hydrog Energy* 37(22):16951–16961
- Oncel S, Kose A (2014) Comparison of tubular and panel type photobioreactors for biohydrogen production utilizing *Chlamydomonas reinhardtii* considering mixing time and light intensity *Bioresour Technol* 151: 265–270
- Vanthoor-Koopmans M, Wijffels RH, Barbosa MJ, Eppink MHM (2013) Biorefinery of microalgae for food and fuel. *Bioresour Technol* 135:142–149

25. Yen H, Hu I, Chen C, Ho S, Lee D, Chang J (2013) Biore source technology microalgae-based biorefinery – from biofuels to natural products. *Bioresour Technol* 135:166–174
26. Jones CS, Mayfield SP (2012) Algae biofuels: versatility for the future of bioenergy. *Curr Opin Biotechnol* 23(3):346–351
27. Rochaix JD (1995) *Chlamydomonas reinhardtii* as the photosynthetic yeast. *Annu Rev Genet* 29:209–230
28. Angermayr SA, Gorchs Rovira A, Hellingwerf KJ (2015) Metabolic engineering of cyanobacteria for the synthesis of commodity products. *Trends Biotechnol* 33(6):352–361
29. Lee SK, Chou H, Ham TS, Lee TS, Keasling JD (2008) Metabolic engineering of microorganisms for biofuels production: from bugs to synthetic biology to fuels. *Curr Opin Biotechnol* 19(6):556–563
30. Reaction O, Algae IN, Gaffron BYH (1942) OXY-HYDROGEN REACTION IN ALGAE (From the Department of Chemistry, The University of Chicago, Chicago). *J Gen Physiol*
31. Oh YK, Raj SM, Jung GY, Park S (2011) Current status of the metabolic engineering of microorganisms for biohydrogen production. *Bioresour Technol* 102(18):8357–8367
32. Akkerman I, Janssen M, Rocha J, Wijffels RH (2002) Photobiological hydrogen production: photochemical efficiency and bioreactor design. *Int J Hydrog Energy* 27(11–12):1195–1208
33. Hemschemeier A, Melis A, Happe T (2009) Analytical approaches to photobiological hydrogen production in unicellular green algae. *Photosynth Res* 102(2):523–540
34. Tamagnini P, Axelsson R, Lindberg P, Oxelfelt F, Wünschiers R, Lindblad P (2002) Hydrogenases and hydrogen metabolism of cyanobacteria. *Microbiol Mol Biol Rev* 66(1):1–20, table of contents
35. Tamagnini P, Leitão E, Oliveira P, Ferreira D, Pinto F, Harris DJ, Heidorn T, Lindblad P (2007) Cyanobacterial hydrogenases: diversity, regulation and applications. *FEMS Microbiol Rev* 31(6):692–720
36. Ghirardi M (2000) Microalgae: a green source of renewable H<sub>2</sub>. *Trends Biotechnol* 18(12):506–511
37. Rupprecht J, Hankamer B, Mussgnug JH, Ananyev G, Dismukes C, Kruse O (2006) Perspectives and advances of biological H<sub>2</sub> production in microorganisms. *Appl Microbiol Biotechnol* 72(3):442–449
38. Kufryk G (2013) Advances in utilizing cyanobacteria for hydrogen production. *Adv Microbiol* 3(6):60–68
39. Hallenbeck PC, Abo-Hashesh M, Ghosh D (2012) Strategies for improving biological hydrogen production. *Bioresour Technol* 110:1–9
40. Madamwar D, Garg N, Shah V (2000) Cyanobacterial hydrogen production. *World J Microbiol Biotechnol* 16(8–9):757–767
41. Meyer J (2007) [FeFe] hydrogenases and their evolution: a genomic perspective. *Cell Mol Life Sci* 64(9):1063–1084
42. Srirangan K, Pyne ME, Perry Chou C (2011) Biochemical and genetic engineering strategies to enhance hydrogen production in photosynthetic algae and cyanobacteria. *Bioresour Technol* 102(18):8589–8604
43. Benemann JR (2000) Hydrogen production by microalgae. *J Appl Phycol* 12:291–300
44. Melis A (2002) Green alga hydrogen production: progress, challenges and prospects. *Int J Hydrog Energy* 27(11–12):1217–1228
45. Torzillo G, Scoma A, Faraloni C, Giannelli L (2014) Advances in the biotechnology of hydrogen production with the microalga *Chlamydomonas reinhardtii*. *Crit Rev Biotechnol* 8551:1–12
46. Torzillo G, Seibert M (2013) Hydrogen production by *Chlamydomonas reinhardtii*. in *Handbook of Microalgal Culture: Applied Phycology and Biotechnology*, 2nd Edition. Eds: Richmond A, Hu Q, Wiley Blackwell 417–432
47. Harris EH (2001) *Chlamydomonas* as a model organism. *Annu Rev Plant Physiol Plant Mol Biol* 52(1):363–406
48. Rochaix JD (2002) *Chlamydomonas*, a model system for studying the assembly and dynamics of photosynthetic complexes. *FEBS Lett* 529(1):34–38
49. Hanikenne M (2003) *Chlamydomonas reinhardtii* as a eukaryotic photosynthetic model for studies of heavy metal homeostasis and tolerance. *New Phytol* 159(2):331–340
50. Scranton MA, Ostrand JT, Fields FJ, Mayfield SP (2015) *Chlamydomonas* as a model for biofuels and bio-products production. *Plant J* 82:523–531
51. Nickelsen J, Kück U (2000) The unicellular green alga *Chlamydomonas reinhardtii* as an experimental system to study chloroplast RNA metabolism. *Naturwissenschaften* 87(3):97–107
52. Rupprecht J (2009) From systems biology to fuel-*Chlamydomonas reinhardtii* as a model for a systems biology approach to improve biohydrogen production. *J Biotechnol* 142(1):10–20
53. Márquez-Reyes LA, del Pilar Sánchez-Saavedra M, Valdez-Vazquez I (2015) Improvement of hydrogen production by reduction of the photosynthetic oxygen in microalgae cultures of *Chlamydomonas gloeopara* and *Scenedesmus obliquus*. *Int J Hydrog Energy* 40(23):7291–7300
54. Melis A, Zhang L, Forestier M, Ghirardi ML, Seibert M (2000) Sustained photobiological hydrogen gas production upon reversible inactivation of oxygen evolution in the green alga *Chlamydomonas reinhardtii*. *Plant Physiol* 122(1):127–136
55. Antal TK, Krendelevea TE, Rubin AB (2011) Acclimation of green algae to sulfur deficiency: underlying mechanisms and application for hydrogen production. *Appl Microbiol Biotechnol* 89(1):3–15
56. Wykoff DD, Davies JP, Melis A, Grossman AR (1998) The regulation of photosynthetic electron transport during nutrient deprivation in *Chlamydomonas reinhardtii*. *Plant Physiol* 117(1327):129–139

57. Godaux D, Emonds-Alt B, Berne N, Ghysels B, Alric J, Remacle C, Cardol P (2013) A novel screening method for hydrogenase-deficient mutants in *Chlamydomonas reinhardtii* based on in vivo chlorophyll fluorescence and photosystem II quantum yield. *Int J Hydrog Energy* 38(4):1826–1836
58. Melis A, Chen HC (2005) Chloroplast sulfate transport in green algae – genes, proteins and effects. *Photosynth Res* 86(3):299–307
59. Chochois V, Comstans L, Dauvillée D, Beyly A, Solivèrs M, Ball S, Peltier G, Cournac L (2010) Relationships between PSII-independent hydrogen bioproduction and starch metabolism as evidenced from isolation of starch catabolism mutants in the green alga *Chlamydomonas reinhardtii*. *Int J Hydrog Energy* 35(19):10731–10740
60. Torzillo G, Scoma A, Faraloni C, Ena A, Johannngmeier U (2009) Increased hydrogen photoproduction by means of a sulfur-deprived *Chlamydomonas reinhardtii* D1 protein mutant. *Int J Hydrog Energy* 34(10):4529–4536
61. Oncel S, Vardar-Sukan F (2009) Photobioproduction of hydrogen by *Chlamydomonas reinhardtii* using a semi-continuous process regime. *Int J Hydrog Energy* 34(18):7592–7602
62. Olaizola M (2003) Commercial development of microalgal biotechnology: From the test tube to the marketplace. *Biomol Eng* 20(4–6):459–466
63. Yu N, Dieu LTJ, Harvey S, Lee D-Y (2015) Optimization of process configuration and strain selection for microalgae-based biodiesel production. *Bioresour Technol* 193:25–34
64. Simonato D, Basso S, Giacometti GM, Morosinotto T (2013) Optimization of light use efficiency for biofuel production in algae. *Biophys Chem* 182:71–78
65. Skjånes K, Rebours C, Lindblad P (2012) Potential for green microalgae to produce hydrogen, pharmaceuticals and other high value products in a combined process. *Crit Rev Biotechnol* 33:1–44
66. Gimpel JA, Specht EA, Georgianna DR, Mayfield SP (2013) Advances in microalgae engineering and synthetic biology applications for biofuel production. *Curr Opin Chem Biol* 17(3):489–495
67. Guarnieri MT, Pienkos PT (2015) Algal omics: unlocking bioproduct diversity in algae cell factories. *Photosynth Res* 123(3):255–263
68. León R, Couso I, Fernández E (2007) Metabolic engineering of ketocarotenoids biosynthesis in the unicellular microalga *Chlamydomonas reinhardtii*. *J Biotechnol* 130(2):143–152
69. De Bhowmick G, Koduru L, Sen R (2015) Metabolic pathway engineering towards enhancing microalgal lipid biosynthesis for biofuel application – a review. *Renew Sust Energ Rev* 50:1239–1253
70. Gong Y, Hu H, Gao Y, Xu X, Gao H (2011) Microalgae as platforms for production of recombinant proteins and valuable compounds: Progress and prospects. *J Ind Microbiol Biotechnol* 38(12):1879–1890
71. de Vos MG, Poelwijk FJ, Tans SJ (2013) Optimality in evolution: new insights from synthetic biology. *Curr Opin Biotechnol* 24(4):797–802
72. Harun R, Singh M, Forde GM, Danquah MK (2010) Bioprocess engineering of microalgae to produce a variety of consumer products. *Renew Sust Energ Rev* 14(3):1037–1047
73. Bogorad L (2000) Engineering chloroplasts: an alternative site for foreign genes, proteins, reactions and products. *Trends Biotechnol* 18(6):257–263
74. Mayfield SP, Manuell AL, Chen S, Wu J, Tran M, Siefker D, Muto M, Marin-Navarro J (2007) *Chlamydomonas reinhardtii* chloroplasts as protein factories. *Curr Opin Biotechnol* 18(2):126–133
75. Walker TL, Purton S, Becker DK, Collet C (2005) Microalgae as bioreactors. *Plant Cell Rep* 24(11):629–641
76. Malcata FX (2011) Microalgae and biofuels: a promising partnership? *Trends Biotechnol* 29(11):542–549
77. Zhang F, Rodriguez S, Keasling JD (2011) Metabolic engineering of microbial pathways for advanced biofuels production. *Curr Opin Biotechnol* 22(6):775–783
78. Jones JA, Toparlak ÖD, Koffas MA (2015) Metabolic pathway balancing and its role in the production of biofuels and chemicals. *Curr Opin Biotechnol* 33:52–59
79. Stephenson PG, Moore CM, Terry MJ, Zubkov MV, Bibby TS (2011) Improving photosynthesis for algal biofuels: toward a green revolution. *Trends Biotechnol* 29(12):615–623
80. Mukhopadhyay A, Redding AM, Rutherford BJ, Keasling JD (2008) Importance of systems biology in engineering microbes for biofuel production. *Curr Opin Biotechnol* 19(3):228–234
81. Cerutti H, Ma X, Msanne J, Repas T (2011) RNA-mediated silencing in algae: biological roles and tools for analysis of gene function. *Eukaryot Cell* 10(9):1164–1172
82. Oncel S, Kose A, Faraloni C (2015) Genetic Optimization of Microalgae for Biohydrogen Production. In: *Handbook of Marine Microalgae* Ed: Kim, SK Biotechnology Advances Academic Press 384–404
83. Chien LF, Kuo TT, Liu BH, Di Lin H, Feng TY, Huang CC (2012) Solar-to-bioH<sub>2</sub> production enhanced by homologous overexpression of hydrogenase in green alga *Chlorella* sp. DT. *Int J Hydrog Energy* 37(23):17738–17748
84. Mertens R, Liese A (2004) Biotechnological applications of hydrogenases. *Curr Opin Biotechnol* 15(4):343–348
85. Warner JR, Patnaik R, Gill RT (2009) Genomics enabled approaches in strain engineering. *Curr Opin Microbiol* 12(3):223–230
86. Rosgaard L, de Porcellinis AJ, Jacobsen JH, Frigaard NU, Sakuragi Y (2012) Bioengineering of carbon fixation, biofuels, and biochemicals in cyanobacteria and plants. *J Biotechnol* 162(1):134–147

87. Wannathong T, Waterhouse JC, Young REB, Economou CK, Purton S (2016) New tools for chloroplast genetic engineering allow the synthesis of human growth hormone in the green alga *Chlamydomonas reinhardtii*. *Appl Microbiol Biotechnol*:1–11
88. Keasling JD (1999) Gene-expression tools for the metabolic engineering of bacteria. *Trends Biotechnol* 17(11):452–460
89. Doron L, Segal N, Shapira M (2016) Transgene expression in microalgae—from tools to applications. *Front Plant Sci* 7:505
90. Beer LL, Boyd ES, Peters JW, Posewitz MC (2009) Engineering algae for biohydrogen and biofuel production. *Curr Opin Biotechnol* 20(3): 264–271
91. Galva A, Gonza D, Ferna E (2004) Transgenic microalgae as green cell-factories. *Trends Biotechnol* 22(1):45–52
92. Takahashi Y, Utsumi K, Yamamoto Y, Hatano A, Satoh K (1996) Genetic engineering of the processing site of D1 precursor protein of photosystem II reaction center in *Chlamydomonas reinhardtii*. *Plant Cell Physiol* 37(2):161–168
93. Cano M, Volbeda A, Guedeney G, Aubert-Jousset E, Richaud P, Peltier G, Cournac L (2014) Improved oxygen tolerance of the *Synechocystis* sp. PCC 6803 bidirectional hydrogenase by site-directed mutagenesis of putative residues of the gas diffusion channel. *Int J Hydrog Energy* 39(30):16872–16884
94. Jinkerson RE, Jonikas MC (2015) Molecular techniques to interrogate and edit the *Chlamydomonas* nuclear genome. *Plant J* 82(3):393–412
95. Eichler-Stahlberg A, Weisheit W, Ruecker O, Heitzer M (2009) Strategies to facilitate transgene expression in *Chlamydomonas reinhardtii*. *Planta* 229(4):873–883
96. Daboussi F, Leduc S, Maréchal A, Dubois G, Guyot V, Perez-Michaut C, Amato A, Falciatore A, Juillierat A, Beurdeley M, Voytas DF, Cavarec L, Duchateau P (2014) Genome engineering empowers the diatom *Phaeodactylum tricoratum* for biotechnology. *Nat Commun* 5:3831
97. Doron L, Segan N, Shapira M (2016) Transgene expression in microalgae—from tools to applications. *Frontiers in plant science* 7:505
98. Kim E-J, Ma X, Cerutti H (2015) Gene silencing in microalgae: mechanisms and biological roles. *Bioresour Technol* 184:23–32
99. Wu S, Xu L, Huang R, Wang Q (2011) Improved biohydrogen production with an expression of codon-optimized hemH and lba genes in the chloroplast of *Chlamydomonas reinhardtii*. *Bioresour Technol* 102(3):2610–2616
100. Bashir KMI, Kim M-S, Stahl U, Cho M-G (2016) Microalgae engineering toolbox: selectable and screenable markers. *Biotechnol Bioprocess Eng* 21(2):224–235
101. Guo S-L, Zhao X-Q, Tang Y, Wan C, Alam MA, Ho S-H, Bai F-W, Chang J-S (2013) Establishment of an efficient genetic transformation system in *Scenedesmus obliquus*. *J Biotechnol* 163(1):61–68
102. Kim H, Kim JS (2014) A guide to genome engineering with programmable nucleases. *Nat Rev Genet* 15(5):321–334
103. Shin S-E, Lim J-M, Koh HG, Kim EK, Kang NK, Jeon S, Kwon S, Shin W-S, Lee B, Hwangbo K, Kim J, Ye SH, Yun J-Y, Seo H, Oh H-M, Kim K-J, Kim J-S, Jeong W-J, Chang YK, Jeong B (2016) CRISPR/Cas9-induced knockout and knock-in mutations in *Chlamydomonas reinhardtii*. *Sci Rep* 6:27810
104. Radakovits R, Eduafo PM, Posewitz MC (2011) Genetic engineering of fatty acid chain length in *Phaeodactylum tricoratum*. *Metab Eng* 13(1):89–95
105. Held NL, Childs LM, Davison M, Weitz JS, Whitaker RJ, Bhaya D (2013) CRISPR-Cas systems to probe ecological diversity and host-viral interactions. In *CRISPR-Cas Systems: RNA-Mediated Adaptive Immunity in Bacteria and Archaea* (pp. 221–250). Springer Berlin Heidelberg
106. Godman JE, Molnár A, Baulcombe DC, Balk J (2010) RNA silencing of hydrogenase(-like) genes and investigation of their physiological roles in the green alga *Chlamydomonas reinhardtii*. *Biochem J* 431(3):345–351
107. Di Lin H, Liu BH, Kuo TT, Tsai HC, Feng TY, Huang CC, Chien LF (2013) Knockdown of PsbO leads to induction of HydA and production of photobiological H<sub>2</sub> in the green alga *Chlorella* sp. DT. *Bioresour Technol* 143:154–162
108. Cai F, Axen SD, Kerfeld CA (2013) Evidence for the widespread distribution of CRISPR-Cas system in the Phylum Cyanobacteria. *RNA Biol* 10(5):687–693
109. Specht E, Miyake-Stoner S, Mayfield S (2010) Microalgae come of age as a platform for recombinant protein production. *Biotechnol Lett* 32(10):1373–1383
110. Ringsmuth AK, Landsberg MJ, Hankamer B (2016) Can photosynthesis enable a global transition from fossil fuels to solar fuels, to mitigate climate change and fuel-supply limitations? *Renew Sust Energ Rev* 62:134–163
111. Sekar N, Ramasamy RP (2015) Recent advances in photosynthetic energy conversion. *J Photochem Photobiol C: Photochem Rev* 22:19–33
112. Shin W-S, Lee B, Jeong B, Chang YK, Kwon J-H (2016) Truncated light-harvesting chlorophyll antenna size in *Chlorella vulgaris* improves biomass productivity. *J Appl Phycol*
113. Kirst H, Melis A (2014) The chloroplast signal recognition particle (CpSRP) pathway as a tool to minimize chlorophyll antenna size and maximize photosynthetic productivity. *Biotechnol Adv* 32(1):66–72



114. McKinlay JB, Harwood CS (2010) Photobiological production of hydrogen gas as a biofuel. *Curr Opin Biotechnol* 21(3):244–251
115. Thompson GA (1996) Lipids and membrane function in green algae. *Biochim Biophys Acta Lipids Lipid Metab* 1302(1):17–45
116. Zhang L, Happe T, Melis A (2002) Biochemical and morphological characterization of sulfur-deprived and H<sub>2</sub>-producing *Chlamydomonas reinhardtii* (green alga). *Planta* 214(4):552–561
117. Oey M, Ross IL, Stephens E, Steinbeck J, Wolf J, Radzun KA, Kügler J, Ringsmuth AK, Kruse O, Hankamer B (2013) RNAi knock-down of LHCBM1, 2 and 3 Increases photosynthetic H<sub>2</sub> production efficiency of the green alga *Chlamydomonas reinhardtii*. *PLoS One* 8(4)
118. Biggins J, Svejkovsky J (1980) Linear dichroism of microalgae, developing thylakoids and isolated pigment-protein complexes in stretched poly (vinyl alcohol) films at 77 K. *Biochim Biophys Acta Bioenerg* 592(3):565–576
119. Melis A (2009) Solar energy conversion efficiencies in photosynthesis: minimizing the chlorophyll antennae to maximize efficiency. *Plant Sci* 177(4): 272–280
120. Beckmann J, Lehr F, Finazzi G, Hankamer B, Posten C, Wobbe L, Kruse O (2009) Improvement of light to biomass conversion by de-regulation of light-harvesting protein translation in *Chlamydomonas reinhardtii*. *J Biotechnol* 142(1):70–77
121. Raven JA (2011) The cost of photoinhibition. *Physiol Plant* 142(1):87–104
122. Lardans A, Gillham NW, Boynton JE (1997) Site-directed mutations at residue 251 of the photosystem II D1 protein of *Chlamydomonas* that result in a nonphotosynthetic phenotype and impair D1 synthesis and accumulation. *J Biol Chem* 272(1):210–216
123. Kruse O, Rupprecht J, Bader KP, Thomas-Hall S, Schenk PM, Finazzi G, Hankamer B (2005) Improved photobiological H<sub>2</sub> production in engineered green algal cells. *J Biol Chem* 280(40):34170–34177
124. Meuser JE, Boyd ES, Ananyev G, Karns D, Radakovits R, Murthy UMN, Ghirardi ML, Dismukes GC, Peters JW, Posewitz MC (2011) Evolutionary significance of an algal gene encoding an [FeFe]-hydrogenase with F-domain homology and hydrogenase activity in *Chlorella variabilis* NC64A. *Planta* 234(4):829–843
125. Doebbe A, Rupprecht J, Beckmann J, Mussnug JH, Hallmann A, Hankamer B, Kruse O (2007) Functional integration of the HUP1 hexose symporter gene into the genome of *C. reinhardtii*: impacts on biological H<sub>2</sub> production. *J Biotechnol* 131(1):27–33
126. Kim D-H, Kim M-S (2011) Hydrogenases for biological hydrogen production. *Bioresour Technol* 102(18):8423–8431
127. Leroux F, Liebgott PP, Cournac L, Richaud P, Kpebe A, Burlat B, Guigliarelli B, Bertrand P, Léger C, Rousset M, Dementin S (2010) Is engineering O<sub>2</sub>-tolerant hydrogenases just a matter of reproducing the active sites of the naturally occurring O<sub>2</sub>-resistant enzymes? *Int J Hydrog Energy* 35(19):10770–10777
128. Shepard EM, Mus F, Betz JN, Byer AS, Duffus BR, Peters JW, Broderick JB (2014) [FeFe]-Hydrogenase maturation. *Biochemistry* 53(25):4090–4104
129. Kim S, Lu D, Park S, Wang G (2012) Production of hydrogenases as biocatalysts. *Int J Hydrog Energy* 37(20):15833–15840
130. Swanson KD, Ratzloff MW, Mulder DW, Artz JH, Ghose S, Hoffman A, White S, Zadovnyy OA, Broderick JB, Bothner B, King PW, Peters JW (2015) [FeFe]-hydrogenase oxygen inactivation is initiated at the H cluster 2Fe subcluster. *J Am Chem Soc* 137(5):1809–1816
131. Posewitz MC, King PW, Smolinski SL, Smith RD, Ginley AR, Ghirardi ML, Seibert M (2005) Identification of genes required for hydrogenase activity in *Chlamydomonas reinhardtii*. *Biochem Soc Trans* 33(Pt 1):102–104
132. Cao X, Wu X, Ji C, Yao C, Chen Z, Li G, Xue S (2014) Comparative transcriptional study on the hydrogen evolution of marine microalga *Tetraselmis subcordiformis*. *Int J Hydrog Energy* 39(32): 18235–18246
133. Mulder DW, Shepard EM, Meuser JE, Joshi N, King PW, Posewitz MC, Broderick JB, Peters JW (2011) Insights into [FeFe]-hydrogenase structure, mechanism, and maturation. *Structure* 19(8): 1038–1052
134. Friedrich B, Fritsch J, Lenz O (2011) Oxygen-tolerant hydrogenases in hydrogen-based technologies. *Curr Opin Biotechnol* 22(3):358–364
135. Chochois V, Dauvillée D, Beyly A, Tolleter D, Cuié S, Timpano H, Ball S, Cournac L, Peltier G (2009) Hydrogen production in *Chlamydomonas*: photosystem II-dependent and -independent pathways differ in their requirement for starch metabolism. *Plant Physiol* 151(2):631–640
136. Meuser JE, D'Adamo S, Jinkerson RE, Mus F, Yang W, Ghirardi ML, Seibert M, Grossman AR, Posewitz MC (2012) Genetic disruption of both *Chlamydomonas reinhardtii* [FeFe]-hydrogenases: insight into the role of HYDA2 in H<sub>2</sub> production. *Biochem Biophys Res Commun* 417(2):704–709
137. Godaux D, Bailleul B, Berne N, Cardol P (2015) Induction of photosynthetic carbon fixation in anoxia relies on hydrogenase activity and proton-gradient regulation-like1-mediated cyclic electron flow in *Chlamydomonas reinhardtii*. *Plant Physiol* 168(2): 648–658
138. Ghirardi ML (2015) Implementation of photobiological H<sub>2</sub> production: the O<sub>2</sub> sensitivity of hydrogenases. *Photosynth Res* 125(3):383–393

139. Horch M, Lauterbach L, Lenz O, Hildebrandt P, Zebger I (2012) NAD(H)-coupled hydrogen cycling – structure-function relationships of bidirectional [NiFe] hydrogenases. *FEBS Lett* 586(5):545–556
140. Lambertz C, Chernev P, Klingan K, Leidel N, Sigfridsson KGV, Happe T, Haumann M (2014) Electronic and molecular structures of the active-site H-cluster in [FeFe]-hydrogenase determined by site-selective X-ray spectroscopy and quantum chemical calculations. *Chem Sci* 5(3):1187
141. Blaby IK, Glaesener AG, Mettler T, Fitz-Gibbon ST, Gallaher SD, Liu B, Boyle NR, Kropat J, Stitt M, Johnson S, Benning C, Pellegrini M, Casero D, Merchant SS (2013) Systems-level analysis of nitrogen starvation-induced modifications of carbon metabolism in a *Chlamydomonas reinhardtii* starchless mutant. *Plant Cell* 25(11):4305–4323
142. Antal TK, Krendeleva TE, Laurinavichene TV, Makarova VV, Ghirardi ML, Rubin AB, Tsygankov AA, Seibert M (2003) The dependence of algal H<sub>2</sub> production on photosystem II and O<sub>2</sub> consumption activities in sulfur-deprived *Chlamydomonas reinhardtii* cells. *Biochim Biophys Acta Bioenerg* 1607(2–3):153–160
143. Zabawinski C, Van den Koornhuysen N, Hulst CD, Schlichting R, Giersch C, Delrue B, Lacroix J, Preiss J, Ball S (2001) Starchless mutants of *Chlamydomonas reinhardtii* lack the small subunit of a heterotetrameric ADP-glucose pyrophosphorylase. *J Bacteriol* 183(3):1069–1077
144. Krishnan A, Kumaraswamy GK, Vinyard DJ, Gu H, Ananyev G, Posewitz MC, Dismukes GC (2015) Metabolic and photosynthetic consequences of blocking starch biosynthesis in the green alga *Chlamydomonas reinhardtii* sta6 mutant. *Plant J* 81(6):947–960
145. Scoma A, Bertin L, Pintucci C, Raddi S, Fava F (2012) Inhibition of photosystem 2 in starch-enriched *Chlamydomonas reinhardtii* cells prevents the efficient induction of H<sub>2</sub> production in sulfur-depleted cultures. *Int J Hydrog Energy* 37(14):10604–10610
146. Li Y, Xu H, Han F, Mu J, Chen D, Feng B, Zeng H (2015) Regulation of lipid metabolism in the green microalga *Chlorella protothecoides* by heterotrophy-photoinduction cultivation regime. *Bioresour Technol* 192:781–791
147. Van Den Koornhuysen N, Delrue B, Decq A, Iglesias A, Carton A, Preiss J, Ball S, Libessart N, Zabawinski C (1996) Carbohydrates, lipids, and other natural products: control of starch composition and structure through substrate supply in the monocellular alga *Chlamydomonas reinhardtii*. *Plant Cell* 8(13):2711–2727
148. Biller P, Ross AB (2011) Potential yields and properties of oil from the hydrothermal liquefaction of microalgae with different biochemical content. *Bioresour Technol* 102(1):215–225
149. Posewitz MC, Smolinski SL, Kanakagiri S, Melis A, Seibert M, Ghirardi ML (2004) Hydrogen photo-production is attenuated by disruption of an isomylase gene in *Chlamydomonas reinhardtii*. *Plant Cell* 16(8):2151–2163
150. Beacham TA, Macia VM, Rooks P, White DA, Ali ST (2015) Altered lipid accumulation in *Nannochloropsis salina* CCAP849/3 following EMS and UV induced mutagenesis. *Biotechnol Rep* 7:87–94
151. Li L, Zhang L, Liu J (2015) The enhancement of hydrogen photoproduction in marine *Chlorella pyrenoidosa* under nitrogen deprivation. *Int J Hydrog Energy* 40(43):14784–14789
152. Philipps G, Happe T, Hemschemeier A (2012) Nitrogen deprivation results in photosynthetic hydrogen production in *Chlamydomonas reinhardtii*. *Planta* 235(4):729–745
153. Busi MV, Barchiesi J, Martín M, Gomez-Casati DF (2014) Starch metabolism in green algae. *Starch/Staerke* 66(1–2):28–40
154. Shin H, Hong S-J, Kim H, Yoo C, Lee H, Choi H-K, Lee C-G, Cho B-K (2015) Elucidation of the growth delimitation of *Dunaliella tertiolecta* under nitrogen stress by integrating transcriptome and peptidome analysis. *Bioresour Technol* 194:57–66
155. Hamilton BS, Nakamura K, Roncari DA (1992) Accumulation of starch in *Chlamydomonas reinhardtii* flagellar mutants. *Biochem Cell Biol* 70(3–4):255–258
156. Volgusheva A, Styring S, Mamedov F (2013) Increased photosystem II stability promotes H<sub>2</sub> production in sulfur-deprived *Chlamydomonas reinhardtii*. *Proc Natl Acad Sci* 110(18):7223–7228
157. Pinto TS, Malcata FX, Arrabaça JD, Silva JM, Spreitzer RJ, Esquivel MG (2013) Rubisco mutants of *Chlamydomonas reinhardtii* enhance photosynthetic hydrogen production. *Appl Microbiol Biotechnol* 97(12):5635–5643
158. Johanningmeier U, Heiss S (1993) Construction of a *Chlamydomonas reinhardtii* mutant with an intronless psbA gene. *Plant Mol Biol* 22(1):91–99
159. Giardi MT, Rea G, Lambrevia MD, Antonacci A, Pastorelli S, Bertalan I, Johanningmeier U, Mattoo AK (2013) Mutations of photosystem II D1 protein that empower efficient phenotypes of *Chlamydomonas reinhardtii* under extreme environment in space. *PLoS One* 8(5):18–20
160. Mulo P, Sakurai I, Aro E-M (2012) Strategies for psbA gene expression in cyanobacteria, green algae and higher plants: from transcription to PSII repair. *Biochim Biophys Acta Bioenerg* 1817(1):247–257
161. Preiss S, Schrader S, Johanningmeier U (2001) Rapid, ATP-dependent degradation of a truncated D1 protein in the chloroplast. *Eur J Biochem* 268(16):4562–4569
162. Scoma A, Krawietz D, Faraloni C, Giannelli L, Happe T, Torzillo G (2012) Sustained H<sub>2</sub> production

- in a *Chlamydomonas reinhardtii* D1 protein mutant. *J Biotechnol* 157(4):613–619
163. Faraloni C, Torzillo G (2010) Phenotypic characterization and hydrogen production in *Chlamydomonas reinhardtii* Qb-binding D1-protein mutants under sulfur starvation: changes in chl fluorescence and pigment composition. *J Phycol* 46(4):788–799
  164. Oncel SS, Kose A, Faraloni C, Imamoglu E, Elibol M, Torzillo G, Sukan FV (2014) Biohydrogen production using mutant strains of *Chlamydomonas reinhardtii*: the effects of light intensity and illumination patterns. *Biochem Eng J* 92:47–52
  165. Ghysels B, Franck F (2010) Hydrogen photo-evolution upon S deprivation stepwise: an illustration of microalgal photosynthetic and metabolic flexibility and a step stone for future biotechnological methods of renewable H<sub>2</sub> production. *Photosynth Res* 106(1–2):145–154
  166. Chen HC, Newton AJ, Melis A (2005) Role of SulP, a nuclear-encoded chloroplast sulfate permease, in sulfate transport and H<sub>2</sub> evolution in *Chlamydomonas reinhardtii*. *Photosynth Res* 84(1–3):289–296
  167. Reijnders MJMF, van Heck RGA, Lam CMC, Scaife MA, dos Santos VAPM, Smith AG, Schaap PJ (2014) Green genes: bioinformatics and systems-biology innovations drive algal biotechnology. *Trends Biotechnol* 32(12):617–626
  168. Ball SG (2005) Eukaryotic microalgae genomics. The essence of being a plant. *Plant Physiol* 137:397–398
  169. Henriquez V, Gimpel J, Escobar C, Gutierrez C, Cadoret JP, Marshall S (2009) Identification of microalgal chloroplast sequences: genetic tools to develop microalgal heterologous expression systems for aquaculture applications. *New Biotechnol* 25:S40
  170. Stauber EJ, Hippler M (2004) *Chlamydomonas reinhardtii* proteomics. *Plant Physiol Biochem PPB/Société Fr Physiol végétale* 42(12):989–1001
  171. Liu D, Hu R, Palla KJ, Tuskan GA, Yang X (2016) Advances and perspectives on the use of CRISPR/Cas9 systems in plant genomics research. *Curr Opin Plant Biol* 30:70–77
  172. Weckwerth W (2011) Green systems biology – from single genomes, proteomes and metabolomes to ecosystems research and biotechnology. *J Proteome* 75(1):284–305
  173. Lopez D, Casero D, Cokus SJ, Merchant SS, Pellegrini M (2011) Algal functional annotation tool: a web-based analysis suite to functionally interpret large gene lists using integrated annotation and expression data. *BMC Bioinformatics* 12(1):282
  174. Zhang L, He M, Liu J, Li L (2015) Role of the mitochondrial alternative oxidase pathway in hydrogen photoproduction in *Chlorella protothecoides*. *Planta* 241(4):1005–1014
  175. Zhang Z, Pendse ND, Phillips KN, Cotner JB, Khodursky A (2008) Gene expression patterns of sulfur starvation in *Synechocystis* sp. PCC 6803. *BMC Genomics* 9:344
  176. Jammers A, Blust R, De Coen W (2009) Omics in algae: paving the way for a systems biological understanding of algal stress phenomena? *Aquat Toxicol* 92(3):114–121
  177. Walker TL, Collet C, Purton S (2005) Algal transgenics in the genomic era. *J Phycol* 41(6):1077–1093
  178. Qin S, Lin H, Jiang P (2012) Advances in genetic engineering of marine algae. *Biotechnol Adv* 30(6):1602–1613
  179. Meuser JE, Ananyev G, Wittig LE, Kosourov S, Ghirardi ML, Seibert M, Dismukes GC, Posewitz MC (2009) Phenotypic diversity of hydrogen production in chlorophycean algae reflects distinct anaerobic metabolisms. *J Biotechnol* 142(1):21–30
  180. Kondo A, Ishii J, Hara KY, Hasunuma T, Matsuda F (2013) Development of microbial cell factories for bio-refinery through synthetic bioengineering. *J Biotechnol* 163(2):204–216
  181. Lv H, Qu G, Qi X, Lu L, Tian C, Ma Y (2013) Transcriptome analysis of *Chlamydomonas reinhardtii* during the process of lipid accumulation. *Genomics* 101(4):229–237
  182. Chen W, Zhou P, Zhang M, Zhu Y, Wang X, Luo X, Bao Z, Yu L (2016) Transcriptome analysis reveals that up-regulation of the fatty acid synthase gene promotes the accumulation of docosahexaenoic acid in *Schizochytrium* sp. S056 when glycerol is used. *Algal Res* 15:83–92
  183. Schmollinger S, Mühlhaus T, Boyle NR, Blaby IK, Casero D, Mettler T, Moseley JL, Kropat J, Sommer F, Strenkert D, Hemme D, Pellegrini M, Grossman AR, Stitt M, Schroda M, Merchant SS (2014) Nitrogen-sparing mechanisms in *Chlamydomonas* affect the transcriptome, the proteome, and photosynthetic metabolism. *Plant Cell* 26(4):1410–1435
  184. Bochenek M, Etherington GJ, Koprivova A, Mugford ST, Bell TG, Malin G, Kopriva S (2013) Transcriptome analysis of the sulfate deficiency response in the marine microalga *Emiliania huxleyi*. *New Phytol*
  185. Yang S, Guarnieri MT, Smolinski S, Ghirardi M, Pienkos PT (2013) De novo transcriptomic analysis of hydrogen production in the green alga *Chlamydomonas moewusii* through RNA-Seq. *Biotechnol Biofuels* 6(1):118
  186. Nguyen AV, Thomas-Hall SR, Malnoë A, Timmins M, Mussgnug JH, Rupprecht J, Kruse O, Hankamer B, Schenk PM (2008) Transcriptome for photobiological hydrogen production induced by sulfur deprivation in the green alga *Chlamydomonas reinhardtii*. *Eukaryot Cell* 7(11):1965–1979
  187. Burja AM, Banaigs B, Abou-Mansour E, Grant Burgess J, Wright PC (2001) Marine cyanobacteria – a prolific source of natural products. *Tetrahedron* 57(46):9347–9377
  188. Bath TS, Singh P, Ramakrishnan VR, Sousa MML, Chan LJG, Tran HM, Luning EG, Pan EHY, Vuu KM, Keasling JD, Adams PD, Petzold CJ

- (2014) A targeted proteomics toolkit for high-throughput absolute quantification of *Escherichia coli* proteins. *Metab Eng* 26:48–56
189. Choi Y-E, Hwang H, Kim H-S, Ahn J-W, Jeong W-J, Yang J-W (2013) Comparative proteomics using lipid over-producing or less-producing mutants unravels lipid metabolisms in *Chlamydomonas reinhardtii*. *Bioresour Technol* 145:108–115
190. Rolland N, Atteia A, Decottignies P, Garin J, Hippler M, Kreimer G, Lemaire SD, Mittag M, Wagner V (2009) *Chlamydomonas* proteomics. *Curr Opin Microbiol* 12(3):285–291
191. Pereira M, Bartolomé CM, Sánchez-Fortún S (2014) Photosynthetic activity and protein overexpression found in Cr(III)-tolerant cells of the green algae *Dictyosphaerium chlorelloides*. *Chemosphere* 108:274–280
192. Chen M, Zhao L, Sun Y, Cui S, Yang B, Wang J, Huang F (2010) Proteomic analysis of hydrogen photoproduction in sulfur-deprived *Chlamydomonas* cells proteomic analysis of hydrogen photoproduction in sulfur-deprived *Chlamydomonas* cells. *J Proteome Res* 9:3854–3866
193. Garnier M, Carrier G, Rogniaux H, Nicolau E, Bougaran G, Saint-Jean B, Cadoret JP (2014) Comparative proteomics reveals proteins impacted by nitrogen deprivation in wild-type and high lipid-accumulating mutant strains of *Tisochrysis lutea*. *J Proteome* 105:107–120
194. Zeng SZ, Herrenknecht C, Mondeguer F, Hess P (2013) Metabolomic approach for the analysis of micro-algae : direct analysis versus passive sampling. 4th International Symposium On Marine & Freshwater Toxin Analysis and AOAC Task Force Meeting, 5–9 May 2013, Baiona, Spain
195. Zeng J, Zhang M, Sun X (2013) Molecular hydrogen is involved in phytohormone signaling and stress responses in plants. *PLoS One* 8(8): 1–10
196. Matthew T, Zhou W, Rupprecht J, Lim L, Thomas-Hall SR, Doebbe A, Kruse O, Hankamer B, Marx UC, Smith SM, Schenk PM (2009) The metabolome of *Chlamydomonas reinhardtii* following induction of anaerobic H<sub>2</sub> production by sulfur depletion. *J Biol Chem* 284(35):23415–23425
197. Yang D, Zhang Y, Barupal DK, Fan X, Gustafson R, Guo R, Fiehn O (2014) Metabolomics of photobiological hydrogen production induced by CCCP in *Chlamydomonas reinhardtii*. *Int J Hydrog Energy* 39(1):150–158
198. Jiang W, Brueggeman AJ, Horken KM, Plucinak TM, Weeks DP, (2014) Successful transient expression of Cas9 and single guide RNA genes in *Chlamydomonas reinhardtii* Eukaryotic cell 13:11 p. 1465–1469
199. Wei Y, Niu J, Huan L, Huang A, He L, Wang G (2015) Cell penetrating peptide can transport dsRNA into microalgae with thin cell walls. *Algal Res* 8:135–139
200. Abelson JN, Simon MI, Pyle AM, Colowick SP, Kaplan NO (2014) The use of CRISPR/cas9, ZFNs, TALENs in generating site specific genome alterations, vol 4
201. Gaj T (2014) ZFN, TALEN and CRISPR/Cas based methods for genome engineering. 2013 31(7): 397–405
202. Schaeffer SM, Nakata PA (2015) CRISPR/Cas9-mediated genome editing and gene replacement in plants: transitioning from lab to field. *Plant Sci* 240:130–142
203. Mohanraju P, Makarova KS, Zetsche B, Zhang F, Koonin EV and van der Oost J (2017) Diverse evolutionary roots and mechanistic variations of the CRISPR-Cas systems *Science* 353 (6299) aad 5147
204. Estrela R, Cate JHD (2016) Energybiotechnology in the CRISPR-Cas9 era. *Curr Opin Biotechnol* 38:79–84
205. Horvath P, Barrangou R (2010) CRISPR/Cas, the immune system of bacteria and archaea. *Science* 327(5962):167–170
206. Jiang W, Brueggeman AJ, Horken KM, Plucinak TM, Weeks DP (2014) Successful transient expression of Cas9 and single guide RNA genes in *Chlamydomonas reinhardtii*. *Eukaryot Cell* 13(11):1465–1469
207. Sizova I, Greiner A, Awasthi M, Kateriya S, Hegemann P (2013) Nuclear gene targeting in *Chlamydomonas* using engineered zinc-finger nucleases. *Plant J* 73(5):873–882
208. Gao H, Wright DA, Li T, Wang Y, Horken K, Weeks DP, Yang B, Spalding MH (2014) TALE activation of endogenous genes in *Chlamydomonas reinhardtii*. *Algal Res* 5:52–60
209. Nymark M, Sharma AK, Sparstad T, Bones AM, Winge P (2016) A CRISPR/Cas9 system adapted for gene editing in marine algae. *Sci Rep* 6:24951
210. Weyman PD, Beeri K, Lefebvre SC, Rivera J, McCarthy JK, Heuberger AL, Peers G, Allen AE, Dupont CL (2015) Inactivation of *Phaeodactylum tricornutum* urease gene using transcription activator-like effector nuclease-based targeted mutagenesis. *Plant Biotechnol J* 13(4):460–470
211. Wu S, Xu L, Wang R, Liu X, Wang Q (2011) A high yield mutant of *Chlamydomonas reinhardtii* for photoproduction of hydrogen. *Int J Hydrog Energy* 36(21):14134–14140
212. Wendt KE, Ungerer J, Cobb RE, Zhao H, Pakrasi HB, Abed R, Dobretsov S, Sudesh K, Lem N, Glick B, Sakai M, Ogawa T, Matsuoka M, Fukuda H, McNeely K, Xu Y, Bennette N, Bryant D, Dismukes G, Liu X, Sheng J, Curtiss R, Deng M-D, Coleman J, Lindberg P, Park S, Melis A, Du W, Liang F, Duan Y, Tan X, Lu X, Yao L, Qi F, Tan X, Lu X, Yu J, Liberton M, Cliften P, Head R, Jacobs J, Smith R, Golden S, Brusslan J, Haselkorn R, Griese M, Lange C, Soppa J, Matsuoka M, Takahama K, Ogawa T, Cong L, Ran F, Cox D, Lin S, Barretto R, Habib N, Xu T,

- Li Y, Shi Z, Hemme C, Li Y, Zhu Y, Jiang W, Bikard D, Cox D, Zhang F, Marraffini L, Horvath P, Barrangou R, Wiedenheft B, Sternberg S, Doudna J, Bhaya D, Davison M, Barrangou R, Deltcheva E, Chylinski K, Sharma C, Gonzales K, Chao Y, Pirzada Z, Sander J, Joung J, Kuzminov A, Cai F, Axen S, Kerfeld C, Scholz I, Lange S, Hein S, Hess W, Backofen R, Heidelberg J, Nelson W, Schoenfeld T, Bhaya D, Yao L, Cengic I, Anfelt J, Hudson E, Cobb R, Wang Y, Zhao H, Mulikidjanian A, Koonin E, Makarova K, Mekhedov S, Sorokin A, Wolf Y, Adir N, Collier J, Grossman A, Marraccini P, Bulteau S, Cassier-Chauvat C, Mermet-Bouvier P, Chauvat F, Zinchenko V, Piven I, Melnik V, Shestakov S, Muth G, Nubaumer B, Wohlleben W, Pühler A, Wolk C, Vonshak A, Kehoe P, Elhai J (2016) CRISPR/Cas9 mediated targeted mutagenesis of the fast growing cyanobacterium *Synechococcus elongatus* UTEX 2973. *Microb Cell Fact* 15(1):115
213. Baek K, Kim DH, Jeong J, Sim SJ, Melis A, Kim J-S, Jin E, Bae S (2016) DNA-free two-gene knockout in *Chlamydomonas reinhardtii* via CRISPR-Cas9 ribonucleoproteins. *Sci Rep* 6:30620
214. Biofuels A, McGraw L (2009) The ethics of adoption and development of case study 1 of the adoption and development of energy technologies. *State of the Art Review*
215. Polle JEW, Kanakagiri S-D, Melis A (2003) tla1, a DNA insertional transformant of the green alga *Chlamydomonas reinhardtii* with a truncated light-harvesting chlorophyll antenna size. *Planta* 217(1): 49–59
216. Tetali SD, Mitra M, Melis A (2007) Development of the light-harvesting chlorophyll antenna in the green alga *Chlamydomonas reinhardtii* is regulated by the novel Tla1 gene. *Planta* 225(4): 813–829
217. Mussgnug JH, Thomas-Hall S, Rupprecht J, Foo A, Klassen V, McDowall A, Schenk PM, Kruse O, Hankamer B (2007) Engineering photosynthetic light capture: Impacts on improved solar energy to biomass conversion. *Plant Biotechnol J* 5(6): 802–814
218. Reifschneider-Wegner K, Kanygin A, Redding KE (2014) Expression of the [FeFe] hydrogenase in the chloroplast of *Chlamydomonas reinhardtii*. *Int J Hydrog. Energy* 39(8):3657–3665



## Biohydrogen Production from Agricultural Residues

Emmanuel Koukios<sup>1</sup> and

Ioannis (John) A. Panagiotopoulos<sup>2</sup>

<sup>1</sup>Department of Synthesis and Development of Industrial Processes, School of Chemical Engineering, National Technical University of Athens, Athens, Greece

<sup>2</sup>Elin Biofuels SA, Athens, Greece

celluloses being xylans, arabinans, mannans and galactans.

**Hydrogen productivity** mmol hydrogen per L culture medium and h of fermentation

**Hydrogen yield** Molar amount of hydrogen divided by the molar amount of consumed hexose equivalent (mol hydrogen/mol hexose)

**Inhibitors** Compounds which have toxic effects on the fermenting microorganisms, thus decreasing hydrogen yield and productivity

**Pretreatment** Process used for the release of fermentable sugars from biomass - typically followed by enzymatic hydrolysis

### Article Outline

Glossary

Definition of the Subject

Introduction

Biohydrogen Production via Dark Fermentation

Process Parameters

Agricultural Residues

Pretreatment of Agricultural Residues for Biohydrogen Production

Fermentation Inhibitors

Future Directions

Bibliography

### Definition of the Subject

Biological methods of hydrogen production include the use of algae and cyanobacteria, photosynthetic bacteria, and fermentative bacteria. Fermentative bacteria have attracted high interest because of their high yield with respect to hydrogen production. The application of thermophilic bacteria in hydrogen production is advantageous compared to, for example, industrial yeasts employed for bioethanol production, since the fermentative action of these bacteria can lead to employment of hexose and pentose sugars as well as oligomeric carbohydrates for hydrogen production.

Today hydrogen is mainly produced from natural gas, but its production is more sustainable when using renewable resources, such as biomass, as the raw materials of the process. In particular, the use of lignocellulosic biomass for biological hydrogen production has increasingly attracted attention. Lignocellulosic biomass mainly includes agricultural, forestry and agro-industrial residues, and energy crops. Agricultural residues are advantageous against other lignocellulosic raw materials because they combine the features of abundance, low cost, and the need for a relatively simple pretreatment.

### Glossary

**Cellulose** Homopolysaccharide composed of D-glucose units linked to each other via  $\beta$ -(1,4) glycosidic bonds

**Dark fermentation** Biological hydrogen production process when the organic compounds constitute the sole carbon and energy source providing metabolic energy

**Fermentability** Tendency of a pretreated raw material to improve or inhibit fermentation.

**Hemicelluloses** Heteropolysaccharides composed of different sugar units, the major hemi-



## Introduction

Hydrogen ( $H_2$ ) is a gaseous biofuel with zero  $CO_2$  emission when burnt, and it is the prime energy carrier to be used in fuel cells for electricity generation. Conventional hydrogen production technologies are regarded as high energy demanding. On the other side, biological hydrogen production is a viable alternative to chemical methods for hydrogen production. Biological conversion has key advantages compared to the other technologies because it is relatively efficient and it has relatively low energy demands. In particular, dark fermentation, commonly termed as “dark hydrogen fermentation,” is the process when the organic compounds, which break down toward hydrogen production, constitute the sole carbon and energy source providing metabolic energy. Hereafter the terms “biological hydrogen production” and “biohydrogen production” refer to “dark hydrogen fermentation” unless noted otherwise.

Biomass as a sink of solar energy is an attractive energy source and includes agricultural and forestry residues, municipal solid wastes, industrial wastes, and terrestrial and aquatic crops grown solely for energy purposes. Biomass is expected to have a major role in providing contribution to the global energy demand in the near future. In particular, lignocellulosic biomass can be utilized for biological hydrogen production, as it is a sustainable source of fermentable substrates due to its abundance and low cost. Lignocellulosic biomass mainly includes agricultural, forestry, and agro-industrial residues and energy crops.

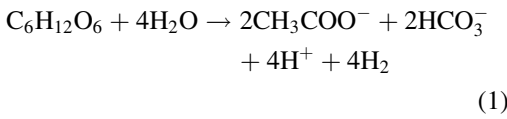
The focus of this chapter is on biohydrogen production from agricultural residues. Firstly, the basic principles of biohydrogen production and the current technology of the process are outlined (section “[Biohydrogen Production via Dark Fermentation](#)”). Then, the influence of the key process parameters on biohydrogen production is summarized (section “[Process Parameters](#)”). Subsequently, the types of agricultural residues that can be used for hydrogen production are discussed (section “[Agricultural Residues](#)”). Pretreatment of the agricultural residues is typically required prior to fermentative hydrogen production because most hydrogen-producing

microorganisms cannot directly utilize cellulose or hemicellulose as a carbon source to grow and produce hydrogen. An overview of the basic pretreatment processes that can be used for biohydrogen production is provided in section “[Pretreatment of Agricultural Residues for Biohydrogen Production](#).” Depending on biomass composition and the pretreatment type, the production of fermentation inhibitors can occur. These substances, which are discussed in section “[Fermentation Inhibitors](#),” tend to inhibit the growth of the microorganisms and lead to decreased hydrogen productivities and yields. Finally, the challenges of biohydrogen production from agricultural residues and the perspectives for further development are discussed in section “[Future Directions](#).”

## Biohydrogen Production via Dark Fermentation

The production of hydrogen is a natural phenomenon under anoxic or anaerobic conditions. A wide variety of bacteria use the reduction of protons to hydrogen to dispose of reducing equivalents which result from primary metabolism. This means that when bacteria grow on organic substrates, these substrates are degraded by oxidation to provide building blocks and metabolic energy for growth. This oxidation leads to the production of electrons which need to be disposed of to maintain electrical neutrality. In aerobic environments, oxygen is reduced and water is produced. In anaerobic environments, other compounds act as electron acceptors and are reduced to molecular hydrogen.

Various organic compounds, such as carbohydrates, sugars, proteins, and lipids, can be used as substrates for the production of biohydrogen via dark fermentation. For the estimation of the theoretical yields of fermentative hydrogen, the reaction of glucose biotransformation toward acetate is generally accepted as reference. According to Eq. (1) the maximum theoretical yield of biohydrogen from hexose fermentation is 4 mol  $H_2$  per mol of consumed hexose [1, 2].



Concurrent production of energy (206 kJ per mol of glucose) takes place and is sufficient to support microbial growth. The remainder of the hydrogen production from hexose is the by-product acetate and, under nonideal circumstances, more reduced products like ethanol or lactate. The complete oxidation of glucose to  $\text{H}_2$  and  $\text{CO}_2$  yields a stoichiometry of 12 mol  $\text{H}_2$  per mol of glucose, but in this case no metabolic energy is obtained. In general, fermentation of glucose (and xylose) results in hydrogen formation, but in addition, depending on the microorganism, also acetate, butyrate, lactate, ethanol, and some other organic compounds, such as formate, butanediol, and succinate, can be produced. These coproducts are typically produced in fermentations with mixed cultures. Their distribution mainly depends on the culture conditions.

Fermentative hydrogen can be produced either through mixed acidogenic microbial cultures, derived from natural environments such as soil or wastewater sludge, or through defined, pure cultures of hydrogen-producing microorganisms. Such microorganisms can be mesophilic (25–40 °C), thermophilic (40–65 °C), extreme thermophilic (65–80 °C), or hyperthermophilic (>80 °C), and they have quite diverse requirements not only in temperature but also in substrate preference, pH, and other parameters. The main advantage of the use of mixed cultures is that no medium sterilization is required for the control and operation of the process, so the overall cost is reduced. The main advantages of the pure cultures are the easier manipulation of the metabolism with modification of the growth conditions and the higher hydrogen yields as a result of the reduced production of undesired coproducts.

A wide variety of microorganisms is able to form hydrogen in dark fermentations. This includes strict anaerobes (*Clostridia*, rumen bacteria, thermophiles, methanogens), facultative anaerobes (*Enterobacter*, *Escherichia coli*, *Citrobacter*), aerobes (*Alcaligenes*, *Bacillus*),

and co- and mixed cultures. *Clostridium butyricum* [3, 4], *Clostridium beijerinckii* [5, 6], *Clostridium tyrobutyricum* [7, 8], *Clostridium thermocellum* [9], and *Clostridium paraputrificum* [10] are examples of strict anaerobic microorganisms that produce hydrogen gas during the exponential growth phase. *Enterobacter aerogenes* [11, 12] and *Enterobacter cloacae* [13] can also be used for hydrogen production. The highest hydrogen yields have been obtained by hydrogen-producing extreme thermophilic anaerobic bacteria, with the strict anaerobic *Clostridia* producing hydrogen with higher yields than facultative anaerobes. The highest hydrogen production rates have been obtained by *Clostridia*, *Enterobacter* and co- and mixed cultures. For the aforementioned reasons, among the hydrogen-producing bacteria, *Clostridia*, *Enterobacter* and co- and mixed cultures are the most widely studied.

Thermophiles and in particular extreme thermophiles and hyperthermophiles are preferred for the production of hydrogen from agricultural residues because the increase of temperature in principle improves the reaction kinetics. Another advantage of fermentations at elevated temperatures is that the process is less sensitive to contaminations by undesirable intruders, so a specific environment enabling maximum production of hydrogen is created. Key thermophiles include *Caldicellulosiruptor saccharolyticus* [14–17], *Thermoanaerobacterium thermosaccharolyticum* [18, 19], *Thermotoga neapolitana* [20–22] and *Thermotoga maritima* [23].

Carbohydrates are the main substrates for fermentative bacteria that produce hydrogen. Cellulose and hemicellulose are the most abundant polysaccharides available in nature, and therefore, glucose and xylose are the predominant monomeric sugars used for hydrogen production. Moreover, starch and sucrose are available in large amounts as they are used as storage material in various plants and can be, therefore, used for hydrogen production.

The main parameters used to characterize hydrogen production efficiency are hydrogen yield and hydrogen productivity. Hydrogen yield is expressed as mol hydrogen per mol C6 sugar.

Hydrogen productivity is typically used in its volumetric version and expressed as mmol hydrogen per L culture medium and h of fermentation. Typically, the maximum volumetric hydrogen productivity is calculated from the time interval with the highest percentage of hydrogen in the off-gas. It should be noted that hydrogen yield has also been expressed in the literature as mol hydrogen per mol C5 sugar. However, for a fair comparison of the results, the hydrogen yields should be reported as H<sub>2</sub> on hexose (mol/mol).

### Process Parameters

The main process parameters that influence the growth of the hydrogen-producing microorganisms and the hydrogen yield and productivity are the organic loading, pH, temperature, hydraulic retention time (HRT) of the reactor, and gas stripping. These parameters, which also influence the economic profile of the process, are discussed below. The growth of hydrogen-producing microorganisms can be inhibited with increased substrate loadings; therefore dilution of the raw hydrolysate is typically required in order to decrease the substrate loading and thus prevent inhibition of the process.

Temperature is one of the most important parameters affecting dark fermentative hydrogen production. Most studies have been based on mesophilic temperatures. However, increased H<sub>2</sub> yields and rates are observed with change in operational conditions from mesophilic to thermophilic temperatures. It has been suggested that the optimal temperature for fermentative hydrogen production seems to be either close to 37 °C or close to 55 °C. However, the investigation of the effect of temperature on fermentative hydrogen production with real biomass substrates is recommended, given that so far mainly pure glucose has been used. It should be noted that cultivation at high temperatures can be a viable strategy to inhibit hydrogen consumers and maximize hydrogen yield. However, the required energy for the operation of the reactor needs to be considerably less than the energy recovered as

hydrogen in order to make the process economically sustainable.

One of the most studied parameters that influence dark fermentative hydrogen production is pH. The concentration of H<sup>+</sup> in the extracellular environment is used not only to control the directions of the metabolic pathways toward oxidized products but also to suppress the activity of methanogenic bacteria. Although there are large variations among different studies, it seems that the optimal pH for hydrogen production from carbohydrates is in the range of 5.2–7.0. This range is mainly related to different raw materials, microbial populations and operational conditions.

Mixed reactors for fermentative hydrogen production can operate in either batch or continuous mode. Batch-mode fermentative hydrogen production is typically performed at laboratory scale for research purposes. Batch-mode reactors offer ease of operation and flexibility. However, continuous bioprocesses are recommended for industrial-scale fermentative hydrogen production. In particular, a typical reactor for these purposes is the continuously stirred tank reactor (CSTR). The CSTR offers simple construction and simple control of pH and temperature. The most important operating parameter in a CSTR is the hydraulic retention time (HRT) of the reactor. Typically a HRT of 12–36 h provides complete conversion of carbohydrates and high hydrogen yields, avoiding the production of methane during dark hydrogen fermentation. A HRT of less than 6 h is known to selectively wash out the methanogens in continuous reactors. At a high HRT product inhibition occurs due to accumulation of volatile fatty acids (VFAs).

The partial pressure of hydrogen (pH<sub>2</sub>) is an important parameter because high partial pressures of hydrogen inhibit hydrogen production. It is known that thermophilic bacteria shift their end product formation upon changes in partial pressure of hydrogen. In the cases of *Caldicellulosiruptor saccharolyticus* [24] and *Caldicellulosiruptor owensis* [25], increased pH<sub>2</sub> leads to increased lactate formation. One way to avoid high partial pressures is gas stripping, which typically takes place with an inert gas such as N<sub>2</sub>. CO<sub>2</sub> can also be used because it is relatively easy

to separate from hydrogen. Regardless of the type of gas, the main disadvantage of the gas stripping techniques is that the stripping gas dilutes the hydrogen content in the reactor and thus creates a further decrease in the separation efficiency. Membrane absorption techniques can be used for hydrogen removal from a gas mixture. However, the use of membrane absorption techniques can result in the development of a biofilm which may favor the emergence of methanogenic bacteria.

## Agricultural Residues

The conversion of lignocellulosic biomass to fermentable sugars and finally hydrogen must be performed at low cost and with high technical efficiency, if it is to compete with other fuel conversion processes. Lignocellulosic biomass represents a cheap and abundant source for hydrogen production. However, the collection, transport, and pretreatment of lignocellulosic biomass pose significant challenges to its use in hydrogen production. Concerning the technical suitability of a lignocellulosic raw material for hydrogen production, the carbohydrate content (Table 1), the pretreatment type, and the hydrogen fermentability of the raw material are the critical factors.

Among other raw materials such as forestry residues and industrial wastes, agricultural residues have advantageous use because they typically require simpler pretreatment. Representative examples of pretreated agricultural residues tested for biohydrogen production are wheat straw [26, 27], barley straw [16, 28], corn stover [29, 30], corn cob [31], and rice straw [21, 32] (Table 1). In Europe, wheat straw has the greatest potential of all agricultural residues because of its wide availability and low cost. Barley straw is also

used in this region. Brazil's biofuel production consumes large quantities of sugar cane, while in the USA, corn is used. Energy crops, such as *Miscanthus* [33], energy crop residues, such as sweet sorghum bagasse [34] and sugarcane bagasse [3], and agro-industrial residues, such as potato steam peels [15], sugar beet molasses [35], and cottonseed cake [36], can also be used for biohydrogen production. However, these raw materials are out of the main scope of the current chapter, which focuses on agricultural residues.

## Pretreatment of Agricultural Residues for Biohydrogen Production

Biohydrogen production from agricultural residues faces a number of challenges. Biomass pretreatment is the most important obstacle to be overcome. The relative difficulty to access the polymers in agricultural residues, i.e., cellulose and hemicellulose, and produce fermentable sugars requires harsher pretreatment than for sugar-based and starch-based materials. In the case of sugary biomass, such as sugar beet and sweet sorghum, most of the sugars are readily fermentable, so the pretreatment is relatively simple. Pretreatment of starchy biomass, such as wheat grains and potato steam peels, is also relatively simple. The starch is typically liquefied prior to saccharification to enhance starch conversion to glucose. Alpha-amylases are typically used in starch liquefaction, and glucoamylases are typically used in the saccharification step.

Cellulose, like starch, is a polymer of glucose but, unlike starch, has a crystalline structure making it water insoluble and resistant to depolymerization. Hemicellulose of agricultural origin is a

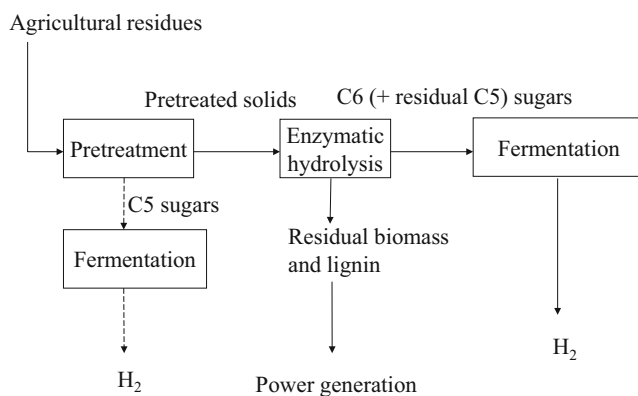
**Biohydrogen Production from Agricultural Residues, Table 1** Chemical composition of typical agricultural residues

Component	Wheat straw	Barley straw	Rice straw	Corn stalk	Corn cob	Corn stover
Cellulose	32–42	34–40	32–44	34–40	32–40	36–40
Hemicellulose	21–26	20–25	19–25	25–30	34–37	22–26
Lignin	14–21	14–20	13–22	12–18	12–16	18–20
Ash	6	7	7	4	1	6

Note: Composition is expressed as (%) percentage of dry matter

### Biohydrogen Production from Agricultural Residues, Fig. 1

A schematic outline of a pretreatment process for biohydrogen production from agricultural residues. The dashed arrows on C5 sugars represent the potential of C5 sugars to be used for hydrogen fermentation



branched polymer of glucose and/or xylose, substituted with arabinose, galactose, mannose, or glucuronic acid, depending on the species. Both cellulose and hemicellulose require pretreatment to be converted to fermentable sugars. The pretreatment step is the first step of the biomass-to-hydrogen process, followed by hydrolysis and one or more fermentation steps (Fig. 1). The step of hydrolysis can be performed with concentrated acids, but today enzymatic hydrolysis is typically performed using cellulases and hemicellulases. Enzymatic hydrolysis, using cellulases, is regarded to be the most attractive way to convert cellulose to glucose. The milder conditions are advantageous since less expensive construction materials are required, as the pH is close to neutral and the temperature and pressure are close to ambient conditions. However, due to the recalcitrant nature of the agricultural residues, enzymatic hydrolysis is very slow, and it is difficult to reach high sugar yields if biomass is not pretreated prior to enzymatic hydrolysis.

The methods for pretreatment can be classified according to various criteria, such as the pH or the principal mechanism during pretreatment. Typically, the pretreatments can be classified into four main groups: mechanical pretreatment (including milling and grinding), thermal pretreatment (including steam explosion and liquid hot water), chemical pretreatment (including acids, alkalis, ionic liquids, oxidizing compounds, etc.), and/or their combinations [37]. The main characteristics of some selected pretreatment methods (Table 2)

are discussed below. Focus is given on the pretreatments that are particularly suited for agricultural residues.

Mechanical pretreatments increase the available specific surface area and reduce the degree of polymerization and cellulose crystallinity. The objective of chipping is to reduce heat and mass transfer limitations. Grinding and milling reduce the particle size and cellulose crystallinity more effectively than chipping probably as a result of the shear forces produced during milling. The type and duration of milling as well as the type of biomass determine the increase in specific surface area, the final degree of polymerization, and the net reduction in cellulose crystallinity. The energy requirements of mechanical pretreatment mainly depend on the characteristics of lignocellulosic biomass. For example, agricultural residues require less energy input than woody materials. However, it is known that mechanical pretreatment generally has high energy costs.

Steam pretreatment is a relatively low-cost pretreatment method that is rapid and requires limited chemical and energy input. In steam pretreatment, chips of biomass are conveyed into large vessels and high-pressure steam is applied (at 200–240 °C) for several minutes. At a set time, some steam is rapidly vented from the reactor to reduce the pressure, and the contents are discharged into a large vessel to flash cool the biomass. Although the method is sometimes referred to as “steam explosion” describing the disruption of the biomass with the rapid decrease of pressure, it is known that explosion is not

**Biohydrogen Production from Agricultural Residues, Table 2** Lignocellulosic biomass pretreatment technologies

Technology	Advantages	Disadvantages	Notes
Steam pretreatment	Relatively low cost	Often catalyst needed	Suitable for a wide variety of feedstocks including agricultural residues
	High glucose yields	Lignin for burning	
Dilute-acid pretreatment	Good removal of hemicelluloses	Release of inhibitors	Particularly suited for agricultural residues
		Typically requires additional size reduction steps	
Organosolv pretreatment	Clean separation of lignin and carbohydrates	High capital and operating costs	
		Solvent may inhibit cell growth	
		Difficult to recover the hemicellulose-derived sugars	
Alkaline pretreatment	Low capital costs	Need to recycle chemicals	
	Low inhibitor release		
Ammonia fiber explosion (AFEX)	Low inhibitor release	High cost due to solvent	Particularly suited for agricultural residues
		Ammonia needs to be recycled	
Ionic liquids	Effective separation of lignin and carbohydrates	Expensive	
		Low ionic liquids tolerance of enzymes and microbes	
Mechanical milling	No inhibitors or residues	High energy costs	

required to achieve good pretreatment and that the main mechanism is rather similar to dilute-acid hydrolysis [38].

Unlike other pretreatment technologies, such as dilute acid that typically require additional size reduction steps, steam pretreatment is used to process a variety of substrates such as chopped straw and conventional pulp chips [39, 40]. The use of catalysts, such as sulfur dioxide and sulfuric acid, and lower pretreatment severities can solubilize and recover more of the hemicelluloses and enhance cellulose hydrolysis, consequently increasing overall sugar recovery [41]. The ability of sulfur dioxide to permeate more uniformly throughout most biomass substrates as compared to sulfuric acid has indicated that it is a more effective catalyst. Steam pretreatment has also

been shown to be particularly effective in processing agricultural residues, such as corn stover and wheat straw, as well as hardwoods, such as poplar, with near-complete hydrolysis of the water-insoluble cellulosic component achieved and more than 60% of the hemicelluloses recovered, at typical cellulase loadings in excess of 15 FPU/g glucan [42]. When enzyme loadings are decreased, one of the few ways to obtain as good hydrolysis yields as were obtained previously at the higher enzyme loadings is to pretreat the biomass substrates more severely. This is usually achieved at the expense of lignin condensation [43]. As well as inhibiting enzymatic hydrolysis, increases in lignin condensation also decrease the potential utility of lignin as a coproduct [44]. Thus, this lignin fraction is typically



utilized as a combustion/energy source to power the overall process.

Concerning steam pretreatment applied on agricultural residues for biohydrogen production, the process has been used with corn stover [29], corn straw [45] and corn stalks [46], giving good results. Given that with steam pretreatment the hemicelluloses is solubilized thus making the cellulose better accessible for enzymatic hydrolysis, high C5 and C6 sugar yields are achieved with the method. This is in favor of applying steam pretreatment for biohydrogen production because hydrogen-producing microorganisms are able to consume both C5 and C6 sugars. In particular, hydrogen-producing microorganisms, such as the extreme thermophilic anaerobic bacterium *Caldicellulosiruptor saccharolyticus*, consume simultaneously glucose and xylose [33, 34], when these sugars are present in ratios that can be expected in hydrolysates from lignocellulosic biomass. On the other hand, other microorganisms, such as *Thermotoga neapolitana*, seem to prefer glucose over xylose [33]. Notable is that *C. saccharolyticus* has a preference for xylose if both sugars are present at equal concentration [47].

Acid pretreatment of lignocellulosic biomass has been studied over the years. Concentrated acids have been traditionally used to treat lignocellulosic materials but are toxic and corrosive, and their use disturbs the economic feasibility of biohydrogen production. Dilute-acid pretreatment, which has received extensive research, can significantly improve the hydrolysis of polysaccharides, mainly hemicelluloses. The acid is mixed with the biomass at an acid concentration of 0.1–2%, and the mixture is held at temperatures of 150–200 °C for periods ranging from seconds to minutes. The hemicelluloses are consequently hydrolyzed. Hydrochloric acid, nitric acid, phosphoric acid, and sulfuric acid have been tested for use in the pretreatment of lignocellulosic biomass and specifically agricultural residues, such as barley straw [16]. Dilute sulfuric acid is commonly used as the acid of choice.

In addition to hydrolyzing the hemicelluloses, dilute-acid pretreatment releases substances that negatively affect the quality of the hydrolysates

by decreasing their fermentability [48]. These substances, known as inhibitors, include weak acids (mainly acetic acid), furans [mainly 5-hydroxymethylfurfural (HMF), a hexose degradation product and furfural, a pentose degradation product], and phenolic compounds from lignin [49]. Fermentation inhibitors are discussed in detail in section “[Fermentation Inhibitors.](#)”

Various types of agricultural residues can be dilute-acid pretreated toward the production of biohydrogen. Corn stover has been pretreated with dilute sulfuric acid for biohydrogen production with *Thermoanaerobacterium thermo-saccharolyticum* W16 [30]. The same acid is known to effectively pretreat rice straw for biohydrogen production with *Thermotoga neapolitana* [21], and wheat and barley straw with *Caldicellulosiruptor saccharolyticus* [50].

Alkaline pretreatments use sodium, calcium, and ammonium hydroxide as reactants. The extensive use of sodium hydroxide over calcium hydroxide is mostly due to the higher solubility of sodium hydroxide and the higher biomass digestibility achieved. Generally, one of the main effects of the alkali is the disruption of the intermolecular bonding between xylan and other biomass components, such as lignin or other hemicellulosic components, resulting in increased porosity of the lignocellulosic material. In addition, applying alkali in a water solution generally leads to swelling of cell wall material, thereby increasing the internal surface of the lignocellulosic matrix. These effects lead to an increase in enzymatic degradability, as the lignocellulosic matrix is more accessible for enzymes. Another effect, less well understood, is the disruption of the lignin structure during alkaline pretreatment. Depending on the alkali used and the biomass type, alkaline pretreatment may lead to lignin depolymerization and partial dissolution of the lignin components.

Concerning alkaline pretreatment applied on lignocellulosic biomass for biohydrogen production, the process has been used with *Miscanthus* [51] and sweet sorghum bagasse [34], resulting in reasonable delignification, low inhibitor release, and efficient hydrogen production. However, agricultural residues are typically pretreated with either steam or dilute acid rather than alkaline

pretreatment. The main reason for this is that in alkaline pretreatment, the chemicals need to be recycled as the used chemical loadings are relatively high.

Ammonia fiber explosion (AFEX) is an alkaline pretreatment method that uses liquid ammonia at elevated pressures to pretreat biomass [52]. The material is treated for 10–60 min at around 100 °C or less. In a closed vessel under pressure, the material and ammonia mix is heated for about 30 min to the desired temperature. After holding the target temperature for about 5 min, the vent valve is opened rapidly to explosively relieve the pressure. The rapid release causes evaporation of the ammonia and a drop in the temperature. The chemical effect of ammonia under pressure causes the cellulosic biomass to swell, thus increasing the accessible surface area while decrystallizing cellulose. The AFEX pretreatment is particularly suited for low-lignin content materials, such as agricultural residues [53], while the effect on woody biomass is less powerful. The main drawback with AFEX is the ammonia itself that needs to be recycled and handled with caution to make the process environmentally feasible. Moreover, from an economic point of view, the ammonia consumption needs to be minimized.

Organosolv pretreatment is known for its ability to produce a substrate amenable to hydrolysis, while maximizing lignin yields. The organosolv process involves treating lignocellulosic biomass with a mixture of water, an organic solvent, and a catalyst at approximately 200 °C and 400 psi. This results in the delignification of the material through the cleavage of lignin-carbohydrate bonds, lignin-lignin bonds, and the solubilization of the lignin in the organic solvent [54]. The advantages of this process include a clean separation of the lignin and carbohydrate components for potential use in coproduct applications and the ability to pretreat recalcitrant substrates such as softwoods. Obviously, organosolv pretreatment is not a typical method for agricultural residues. This is reasonable because of the relatively low lignin content of most of these materials and of the cellulase-inhibitory effect of the increased free phenolic groups in the substrate [55] due to the delignification.

The method of ionic liquids is a new concept in the fractionation of lignocellulosic biomass, such as energy crops, agricultural residues, and also woody biomass [56]. Ionic liquids consist of ions (cations and anions) and have low melting points (<100 °C), high polarities, high thermal stabilities, and negligible vapor pressure. The mode of action for ionic liquids is a disruption of the bonds between cellulose, hemicellulose, and lignin, which results in dissolution of the macromolecules without extensive formation of inhibitory compounds. The cellulose fraction can be recovered by the addition of water, ethanol, or acetone. The solvent can be recovered and reused by various methods such as pervaporation, reverse osmosis, salting out, and ionic exchange. One of the challenges of ionic liquids, apart from their very high cost, is the stability and activity of cellulases in the presence of small amounts of ionic liquids coprecipitated with the recovered cellulose [57].

## Fermentation Inhibitors

The fermentability of hydrolysates produced through pretreatment of agricultural residues is a key challenge in the development of biohydrogen production. Fermentability is the tendency of a pretreated raw material to improve or inhibit fermentation. Typically, some pretreatment processes release substances that negatively affect the quality of the hydrolysates by decreasing their fermentability [48]. These substances, known as inhibitors, tend to inhibit growth of hydrogen-producing bacteria and lead to decreased hydrogen productivities and yields. They include weak acids (mainly acetic acid), furans (mainly 5-hydroxymethylfurfural (HMF), an hexose degradation product and furfural, a pentose degradation product), and phenolic compounds from lignin [49]. The reduction or elimination of fermentation inhibitors is a key factor in the development of pretreatment of agricultural residues.

Acetic acid is generated from the hydrolysis of the acetyl groups in the hemicelluloses. Its generation mainly depends on the temperature and

residence time of dilute-acid pretreatment until the acetyl groups are fully hydrolyzed. At low pH in the fermentation medium, the acetic acid is in the undissociated form and may diffuse into the cells. Once in the cell, the acid dissociates causing a lowering of cell pH that inhibits cell activity. The toxicity varies according to the fermentation conditions. Since the formation of acetic acid is inherent to hemicellulose hydrolysis, its release in the hydrolysate cannot be prevented. However, a higher fermentation pH can reduce this effect, or the acid can be neutralized before fermentation. The release of acetic acid during dilute-acid pretreatment does not seem to be a barrier in hydrogen fermentations given that the acetic acid concentrations typically observed with dilute-acid pretreatment should be tolerable by hydrogen-producing microorganisms. For instance, acetic acid concentrations lower than 3 g/L are fully tolerable by *C. saccharolyticus* [58]. *T. neapolitana* is even more tolerant, being able to grow at acetic acid concentrations as high as 18 g/L [15].

HMF and furfural are formed by dehydration of hexoses and pentoses, respectively. Their level of release in the lignocellulosic hydrolysate varies according to the type of raw material and the pretreatment process. Dilute-acid pretreatment of agricultural residues typically results in the release of both HMF and furfural. These compounds interfere with glycolytic and fermentative enzymes and affect cell growth and respiration. Generally, HMF is considered less toxic than furfural. One possible reason for this is the higher reactivity of HMF. The production of furfural strongly increases with temperature and reaction time. It is known that HMF and furfural concentrations of 1–2 g/L result in 50% inhibition of hydrogen production [33].

Further degradation of HMF can occur, resulting in the formation of levulinic acid and formic acid. Moreover, formic acid is formed when furfural breaks down. Formic acid is more inhibitory than levulinic acid which, in turn, is more inhibitory than acetic acid. Increased toxicity of formic acid is associated with a smaller molecule size, which facilitates its diffusion

through the plasma membrane. The higher toxicity of levulinic acid in comparison with acetic acid seems to be related to the higher hydrophobicity of levulinic acid, which helps its penetration into the cell membrane. It should be noted that the effect of levulinic acid and formic acid on biohydrogen production has not yet been elucidated.

A wide range of phenolic compounds are produced due to lignin breakdown and also carbohydrate degradation during certain types of pretreatment [59]. The amount and type of phenolic compounds depend on the raw material, since lignin in different raw materials has different degrees of methoxylation, internal bonding, and association with hemicelluloses and cellulose in the plant cell wall. Typical phenolic compounds are vanillin, syringaldehyde and catechol. They cause partition and loss of integrity of cell membranes of the fermenting microorganisms, reducing cell growth and sugar assimilation. Phenolic compounds have a considerable inhibitory effect on fermentation and are generally more toxic than furfural and HMF, even at low concentrations. However, it should be noted that the inhibition phenomena in dark hydrogen fermentations have not been fully elucidated yet.

Inhibitors may also originate from the raw material itself. Another group of potential fermentation inhibitors, which is relatively less studied, are the extractives. Extractives are soluble compounds mainly derived from lignocellulosic biomass and include acidic, tannic and terpene acids. Generally, extractives are generally considered to be less toxic compared to the aforementioned lignin degradation products or acetic acid.

Inhibitors can be removed from hydrolysates by detoxification using chemical, physical or biological methods [60]. Inhibitory compounds can be removed before hydrogen fermentation with, e.g., charcoal, cation exchange resin, activated carbon, overliming, or yeasts. Optimization of detoxification conditions is important and can result in an increase in H<sub>2</sub> yield. A different approach to avoid fermentation inhibition is to adapt the pretreatment process, for example, by employing a two-stage pretreatment, where

hemicellulose-derived sugars are released under mild conditions, followed by more severe cellulose pretreatment. Strategies to overcome inhibition that do not involve removal of inhibitors involve changing fermentation conditions in order to reduce the inhibiting effects of certain compounds. However, changing fermentation conditions may also lead to less-than-ideal conditions for the microorganism, longer residence times, and therefore higher process costs. Therefore, employment of these strategies to overcome inhibition should be balanced against possible disadvantages. Finally, the development of more robust hydrogen-producing microorganisms can be an efficient strategy to overcome inhibition.

## Future Directions

Fermentative processes for hydrogen production are advantageous against thermal processes such as gasification and supercritical water gasification. This mainly happens because fermentative processes convert more efficiently biomass with high moisture content to hydrogen. Moreover, fermentative processes do not require large installations for economy of scale, so they can be small scale and cost-effective.

Dark fermentative hydrogen production from biomass is an attractive method for renewable hydrogen production. Depending on the type of biomass, pretreatment is needed to make the available carbohydrates accessible for fermentation toward hydrogen production. Sugar-rich raw materials are highly suitable for dark fermentative hydrogen production. However, sustainable hydrogen production needs to be based on the use of lignocellulosic biomass, which needs complicated pretreatment procedures to become amenable to hydrogen fermentation. Among other lignocellulosic raw materials, such as forestry residues, agricultural residues are advantageous because they are less recalcitrant and, thus, require simpler pretreatment. So far the pretreatment methods that have been developed target primarily toward high sugar yield. The future research on specific pretreatment for biohydrogen production

will focus on achieving high hydrogen fermentability of the produced sugars. Moreover, the ideal pretreatment should limit the release of inhibitory compounds in the hydrolysate because some hydrogen-producing microorganisms are not very tolerant to these compounds. Apart from the pretreatment, the greatest challenge for fermentative hydrogen production from agricultural residues is that the hydrogen yield is relatively low, due to thermodynamic barriers.

## Bibliography

### Primary Literature

1. Thauer RK, Jungermann K, Decker K (1977) Energy conservation in chemotrophic anaerobic bacteria. *Bacteriol Rev* 41(3):100–180
2. Solomon BO, Zeng AR, Biebl H, Schlieker H, Posten C, Deckwer WD (1995) Comparison of the energetic efficiencies of hydrogen and oxychemicals formation in *Klebsiella Pneumoniae* and *Clostridium butyricum* during anaerobic growth on glycerol. *J Biotechnol* 39:107–117
3. Pattra S, Sangyoka S, Boonmee M, Reungsang A (2008) Bio-hydrogen production from the fermentation of sugarcane bagasse hydrolysate by *Clostridium butyricum*. *Int J Hydrog Energy* 33(19):5256–5265
4. Chong ML, Raha AR, Shirai Y, Hassan MA (2009) Biohydrogen production by *Clostridium butyricum* EB6 from palm oil mill effluent. *Int J Hydrog Energy* 34(2):764–771
5. Lin P-Y, Whang L-M, Y-R W, Ren W-J, Hsiao C-J, Li S-L, Chang J-S (2007) Biological hydrogen production of the genus *Clostridium*: metabolic study and mathematical model simulation. *Int J Hydrog Energy* 32(12):1728–1735
6. Skonieczny MT, Yargeau V (2009) Biohydrogen production from wastewater by *Clostridium beijerinckii*: Effect of pH and substrate concentration. *Int J Hydrog Energy* 34(8):3288–3294
7. Jo HJ, Lee DS, Park D, Park JM (2008) Biological hydrogen production by immobilized cells of *Clostridium tyrobutyricum* JM1 isolated from food waste treatment process. *Bioresour Technol* 99(14):6666–6672
8. Mitchell RJ, Kim J-S, Jeon B-S, Sang B-I (2009) Continuous hydrogen and butyric acid fermentation by immobilized *Clostridium tyrobutyricum* ATCC 25755: Effects of the glucose concentration and hydraulic retention time. *Bioresour Technol* 100(21):5352–5355
9. Levin DB, Islam R, Cicek N, Sparling R (2006) Hydrogen production by *Clostridium thermocellum* 27405 from cellulosic biomass substrates. *Int J Hydrog Energy* 31(11):1496–1503

10. Evvyernie D, Yamazaki S, Morimoto K, Karita S, Kimura T, Sakka K, Ohmiya K (2000) Identification and characterization of *Clostridium paraputrificum* M-21, a chitinolytic, mesophilic and hydrogen producing bacterium. *J Biosci Bioeng* 89(6):596–601
11. Tanisho S, Ishiwata W (1994) Continuous hydrogen production from molasses by the bacterium *Enterobacter aerogenes*. *Int J Hydrog Energy* 19(10):807–812
12. Fabiano B, Perego P (2002) Thermodynamic study and optimization of hydrogen production by *Enterobacter aerogenes*. *Int J Hydrog Energy* 27(2):149–156
13. Kumar N, Das D (2000) Enhancement of hydrogen production by *Enterobacter cloacae* IIT-BT 08. *Process Biochem* 35(6):589–593
14. VanFossen AL, Verhaart MRA, Kengen SMW, Kelly RM (2009) Carbohydrate utilization patterns for the extremely thermophilic bacterium *Caldicellulosiruptor saccharolyticus* reveal broad growth substrate preferences. *Appl Environ Microbiol* 75(24):7718–7724
15. Mars AE, Veuskens T, Budde MAW, van Doeveren PFM, Lips SJ, Bakker RR, de Vrije T, Claassen PAM (2010) Biohydrogen production from untreated and hydrolyzed potato steam peels by the extreme thermophiles *Caldicellulosiruptor saccharolyticus* and *Thermotoga neapolitana*. *Int J Hydrog Energy* 35(15):7730–7737
16. Panagiotopoulos IA, Bakker RR, de Vrije T, Claassen PAM, Koukios EG (2012) Dilute-acid pretreatment of barley straw for biological hydrogen production using *Caldicellulosiruptor saccharolyticus*. *Int J Hydrog Energy* 37(16):11727–11734
17. Willquist K, van Niel EWJ (2012) Growth and hydrogen production characteristics of *Caldicellulosiruptor saccharolyticus* on chemically defined minimal media. *Int J Hydrog Energy* 37(6):4925–4929
18. O-Thong S, Prasertsan P, Karakashev D, Angelidaki I (2008) Thermophilic fermentative hydrogen production by the newly isolated *Thermoanaerobacterium thermosaccharolyticum* PSU-2. *Int J Hydrog Energy* 33(4):1204–1214
19. Cao G-L, Ren N-Q, Wang A-J, Guo W-Q, Yao J, Feng Y-J, Zhao Q-L (2010) Statistical optimization of culture condition for enhanced hydrogen production by *Thermoanaerobacterium thermosaccharolyticum* W16. *Bioresour Technol* 101(6):2053–2058
20. de Vrije T, Budde MAW, Lips SJ, Bakker RR, Mars AE, Claassen PAM (2010) Hydrogen production from carrot pulp by the extreme thermophiles *Caldicellulosiruptor saccharolyticus* and *Thermotoga neapolitana*. *Int J Hydrog Energy* 35(15):13206–13213
21. Nguyen T-AD, Kim K-R, Kim MS, Sim SJ (2010) Thermophilic hydrogen fermentation from Korean rice straw by *Thermotoga neapolitana*. *Int J Hydrog Energy* 35(24):13392–13398
22. Eriksen NT, Riis ML, Holm NK, Iversen N (2011) H<sub>2</sub> synthesis from pentoses and biomass in *Thermotoga* spp. *Biotechnol Lett* 33(2):293–300
23. Nogales J, Gudmundsson S, Thiele I (2012) An *in silico* re-design of the metabolism in *Thermotoga maritima* for increased biohydrogen production. *Int J Hydrog Energy* 37(17):12205–12218
24. van Niel EWJ, Claassen PAM, Stams AJM (2003) Substrate and product inhibition of hydrogen production by the extreme thermophile, *Caldicellulosiruptor saccharolyticus*. *Biotechnol Bioeng* 81(3):255–262
25. Zeidan AA, van Niel EWJ (2010) A quantitative analysis of hydrogen production efficiency of the extreme thermophile *Caldicellulosiruptor owensensis* OL<sup>T</sup>. *Int J Hydrog Energy* 35(3):1128–1137
26. Kongjan P, O-Thong S, Kotay M, Min B, Angelidaki I (2010) Biohydrogen production from wheat straw hydrolysate by dark fermentation using extreme thermophilic mixed culture. *Biotechnol Bioeng* 105(5):899–908
27. Panagiotopoulos IA, Bakker RR, de Vrije T, Claassen PAM, Koukios EG (2013) Integration of first and second generation biofuels: Fermentative hydrogen production from wheat grain and straw. *Bioresour Technol* 128:345–350
28. Özgür E, Peksel B (2013) Biohydrogen production from barley straw hydrolysate through sequential dark and photofermentation. *J Clean Prod* 52:14–20
29. Datar R, Huang J, Maness P-C, Mohagheghi A, Czernik S, Chornet E (2007) Hydrogen production from the fermentation of corn stover biomass pretreated with a steam-explosion process. *Int J Hydrog Energy* 32(8):932–939
30. Cao G, Ren N, Wang A, Lee D-J, Guo W, Liu B, Feng Y, Zhao Q (2009) Acid hydrolysis of corn stover for biohydrogen production using *Thermoanaerobacterium thermosaccharolyticum* W16. *Int J Hydrog Energy* 34(17):7182–7188
31. Pan C, Zhang S, Fan Y, Hou H (2010) Bioconversion of corncob to hydrogen using anaerobic mixed microflora. *Int J Hydrog Energy* 35(7):2663–2669
32. Lo Y-C, W-C L, Chen C-Y, Chang J-S (2010) Dark fermentative hydrogen production from enzymatic hydrolysate of xylan and pretreated rice straw by *Clostridium butyricum* CGS5. *Bioresour Technol* 101(15):5885–5891
33. de Vrije T, Bakker RR, Budde MAW, Lai MH, Mars AE, Claassen PAM (2009) Efficient hydrogen production from the lignocellulosic energy crop *Miscanthus* by the extreme thermophilic bacteria *Caldicellulosiruptor saccharolyticus* and *Thermotoga neapolitana*. *Biotechnol Biofuels* 2:12
34. Panagiotopoulos IA, Bakker RR, de Vrije T, Koukios EG, Claassen PAM (2010) Pretreatment of sweet sorghum bagasse for hydrogen production by *Caldicellulosiruptor saccharolyticus*. *Int J Hydrog Energy* 35(15):7738–7747

35. Özgür E, Mars AE, Peksel B, Louwerse A, Yücel M, Gündüz U, Claassen PAM, Eroğlu I (2010) Biohydrogen production from beet molasses by sequential dark and photofermentation. *Int J Hydrog Energy* 35(2):511–517
36. Panagiotopoulos IA, Pasiadis S, Bakker RR, de Vrije T, Papayannakos N, Claassen PAM, Koukios EG (2013) Biodiesel and biohydrogen production from cotton-seed cake in a biorefinery concept. *Bioresour Technol* 136:78–86
37. Mosier N, Wyman C, Dale B, Elander R, Lee YY, Holtzapple M, Ladisch M (2005) Features of promising technologies for pretreatment of lignocellulosic biomass. *Bioresour Technol* 96:673–686
38. Brownell HH, EKC Y, Saddler JN (1986) Steam-explosion pretreatment of wood: Effect of chip size, acid, moisture content and pressure drop. *Biotechnol Bioeng* 28(6):792–801
39. Grous WR, Converse AO, Grethlein HE (1986) Effect of steam explosion pretreatment on pore size and enzymatic hydrolysis of poplar. *Enzym Microb Technol* 8:274–280
40. Ballesteros I, Negro MJ, Oliva JM, Cabañas A, Manzanares P, Ballesteros M (2006) Ethanol production from steam-explosion pretreated wheat straw. *Appl Biochem Biotechnol* 129–132:496–508
41. Mackie KL, Brownell HH, West KL, Saddler JN (1985) Effect of sulphur dioxide and sulphuric acid on steam explosion of aspenwood. *J Wood Chem Technol* 5:405–425
42. Bura R, Chandra R, Saddler J (2009) Influence of xylan on the enzymatic hydrolysis of steam-pretreated corn stover and hybrid poplar. *Biotechnol Prog* 25:315–322
43. Li J, Henriksson G, Gellerstedt G (2007) Lignin depolymerization/repolymerization and its critical role for delignification of aspen wood by steam explosion. *Bioresour Technol* 98:3061–3068
44. Shevchenko SM, Beatson RP, Saddler JN (1999) The nature of lignin from steam explosion/enzymatic hydrolysis of softwood. Structural features and possible uses. *Appl Biochem Biotechnol* 77–79:867–876
45. Li D, Chen H (2007) Biological hydrogen production from steam exploded straw by simultaneous saccharification and fermentation. *Int J Hydrog Energy* 32(12):1742–1748
46. Lu Y, Lai Q, Zhang C, Zhao H, Ma K, Zhao X, Chen H, Liu D, Xing X-H (2009) Characteristics of hydrogen and methane production from cornstalks by an augmented two- or three-stage anaerobic fermentation process. *Bioresour Technol* 100(12):2889–2895
47. Zeidan AA, van Niel EWJ (2009) Developing a thermophilic hydrogen producing co-culture for efficient utilization of mixed sugars. *Int J Hydrog Energy* 34(10):4524–4528
48. Larsson S, Palmqvist E, Hahn-Hägerdal B, Tengborg C, Stenberg K, Zacchi G, Nilvebrant N-O (1999) The generation of fermentation inhibitors during dilute acid hydrolysis of softwood. *Enzym Microb Technol* 24:151–159
49. Palmqvist E, Hahn-Hägerdal B (2000) Fermentation of lignocellulosic hydrolysates. II inhibitors and mechanisms of inhibition. *Bioresour Technol* 74:25–33
50. Panagiotopoulos IA, Bakker RR, de Vrije T, van Niel EWJ, Koukios EG, Claassen PAM (2011) Exploring critical factors for fermentative hydrogen production from various types of lignocellulosic biomass. *J Jpn I Energy* 90:363–368
51. de Vrije T, de Haas GG, Tan GB, Keijsers ERP, Claassen PAM (2002) Pretreatment of *Miscanthus* for hydrogen production by *Thermotoga elfii*. *Int J Hydrog Energy* 27:1381–1390
52. Dale BE, Moreira MJ (1982) A freeze-explosion technique for increasing cellulose hydrolysis. *Biotechnol Bioeng Symp* 12:31–43
53. Teymouri F, Laureano-Peres L, Alizadeh H, Dale BE (2005) Optimization of the ammonia fiber explosion (AFEX) treatment parameters for enzymatic hydrolysis of corn stover. *Bioresour Technol* 96(18):2014–2018
54. McDonough TJ (1993) The chemistry of organosolv delignification. *TAPPI J* 76:186–193
55. Sannigrahi P, Ragauskas AJ, Miller SJ (2010) Lignin structural modifications resulting from ethanol organosolv treatment of loblolly pine. *Energy Fuel* 24:683–689
56. Wasserscheid P, Keim W (2000) Ionic liquids – new “solutions” for transition metal catalyst. *Angew Chem Int Ed* 39:3773–3789
57. Datta S, Holmes B, Park JI, Chen Z, Dibble DC, Hadi M, Blanch HW, Simmons BA, Saprà R (2010) Ionic liquid tolerant hyperthermophilic cellulases for biomass pretreatment and hydrolysis. *Green Chem* 12(2):338–345
58. Panagiotopoulos IA, Bakker RR, Budde MAW, de Vrije T, Claassen PAM, Koukios EG (2009) Fermentative hydrogen production from pretreated biomass: a comparative study. *Bioresour Technol* 100: 6331–6338
59. Popoff T, Theander O (1976) Formation of aromatic compounds from carbohydrates – part III. Reaction of D-glucose and D-fructose in slightly acidic, aqueous solution. *A Chem Scand B* 30:397–402
60. Jönsson LJ, Alriksson B, Nilvebrant NO (2013) Bioconversion of lignocellulose: inhibitors and detoxification. *Biotechnol Biofuels* 6:16

## Books and Reviews

- Claassen PAM, van Lier JB, Contreras AML, van Niel EWJ, Sijtsma L, Stams AJM, de Vries SS, Weusthuis RA (1999) Utilisation of biomass for the supply of energy carriers. *Appl Microbiol Biotechnol* 52(6):741–755
- Galbe M, Zacchi G (2012) Pretreatment: the key to efficient utilization of lignocellulosic materials. *Biomass Bioenergy* 46:70–78



- Kengen SWM, Goorissen HP, Verhaart M, van Niel EWJ, Claassen PAM, Stams AJM (2009) Biological hydrogen production by anaerobic microorganisms. In: Soetaert W, Vandamme EJ (eds) *Biofuels*. John Wiley and Sons, Chichester, pp 197–221
- Levin D, Pitt L, Love M (2004) Biohydrogen production: prospect and limitations to practical application. *Int J Hydrog Energy* 29(2):173–185
- Ragauskas AJ, Beckham GT, Bidy MJ, Chandra R, Chen F, Davis MF, Davison BH, Dixon RA, Gilna P, Keller M, Langan P, Naskar AK, Saddler JN, Tschaplinski TJ, Tuskan GA, Wyman CE (2014) Lignin valorization: improving lignin processing in the biorefinery. *Science* 344(6185):1246843
- Stephanopoulos G (2007) Challenges in engineering microbes for biofuels production. *Science* 315(5813):801–804
- Stolten D (ed) (2010) *Hydrogen and fuel cells – fundamentals, technologies and applications*. Wiley–VCH, Weinheim



# Genetic Optimization for Increasing Hydrogen Production in Microalgae

Cecilia Faraloni and Giuseppe Torzillo  
Istituto per lo Studio degli Ecosistemi, Sede di  
Firenze, Firenze, Italy

## Article Outline

Glossary  
Definition of the Subject  
Introduction  
Potential of Microalgal Engineering: Application Fields and Advantages  
Enzymes Which Catalyze the Biological Hydrogen Production: Hydrogenase and Nitrogenase  
Description of the Mechanisms of Biohydrogen Production Used by Microalgae  
Different Pathways for Hydrogen Production in Microalgae Which May Be Influenced by Genetic Engineering Approach  
Approaches to Promote H<sub>2</sub> Production: Two-Stage Hydrogen Production (Sulfur Deprivation Technique)  
Mutant Strains of Microalgae for Increasing H<sub>2</sub> Production  
Monitoring the PSII Performance During H<sub>2</sub> Production in Mutant Strains by Means of Chlorophyll Fluorescence Changes During Sulfur Starvation  
Future directions  
Bibliography

## Glossary

Hydrogen; microalgae; *Chlamydomonas reinhardtii*; D1 protein; PSII; Fluorescence yield; Hydrogenase; Anaerobiosis

## Definition of the Subject

In recent years, the increasing depletion of fossil resources has increased the necessity to search for alternative sources of energy. What seems imperative is that all efforts have to be addressed to improve the utilization of renewable source of energy. It is well known that under particular conditions, microalgae are capable to produce hydrogen as almost pure biogas. In this respect, the goal would be to use the sole solar light energy and water, a clean and green sustainable source of energy. However, this process has some limitation. The main bottleneck is represented by the reduced photosynthetic efficiency of photosynthetic cells to convert solar light energy into chemical energy (or hydrogen). Many studies have been carried out all over the years in order to solve this problem, but at the moment, only a small improvement has been reached.

Concerning the hydrogen production process, the main problem is the high sensitivity to oxygen of the hydrogenase enzyme, as both its synthesis and functioning are inhibited under aerobic conditions. Many studies have been performed trying to solve the problem by means of genetic engineering. In particular, some microalgae are quite simple microorganisms, and their genome can be easily manipulated. Many studies have considered the microalga *Chlamydomonas reinhardtii*, which is known to produce appreciable amount of H<sub>2</sub> under anaerobic conditions, imposed by sulfur starvation. In particular, mutant strains of this microalga have shown different phenotypic characteristics, with respect to the wild type, which were favorable to induce anaerobiosis and to sustain the productive process for a long time. These characteristics were translated into a hydrogen production higher than in the wild type.

## Introduction

The biohydrogen production is currently considered a promising source of green alternative energy.

Molecular H<sub>2</sub> can be produced by different biological processes based on the utilization of light as energy source. The photosynthetic organisms use light energy for extraction of electrons from water, generating oxygen and energy in the form of ATP and compounds with low redox potential which can be used as substrate for hydrogen production. As sunlight is considered one of the most abundant sources of energy in the world, the photosynthetic conversion of light energy into fuels has acquired increasing relevance due to its renewable nature.

However, the photosynthetic H<sub>2</sub> production exhibits some crucial aspects which have to be considered in order to optimize this “green” source of energy.

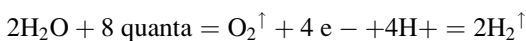
The main problems associated with this form of green energy production are mainly due to: (i) hydrogen-evolving enzyme sensitivity to oxygen; (ii) limitation of light energy conversion efficiency by microalgae, which makes the process not economically viable; and (iii) large-scale cultivation which represents a stressing condition for microorganisms.

When the microalga *Scenedesmus* was found to produce transiently hydrogen under light conditions, after a period of dark incubation [1], it was observed that the process was stopped under illumination by photosynthetic oxygen evolution.

Indeed, one of the most relevant aspects associated with the H<sub>2</sub> production via photosynthetic microorganisms is related to the high sensitivity to oxygen of hydrogenase, enzyme catalyzing the reaction for H<sub>2</sub> production. In particular, the sensitivity to oxygen has been observed for both the expression and functionality of hydrogenase enzyme. This is a very limiting factor considering that the hydrogen production with microalgae is strongly correlated to photosynthesis, which produces oxygen.

Moreover, the photosynthetic efficiency to transfer light energy into chemical energy is low.

Theoretical limit to photobiological H<sub>2</sub> production can be transformed into H<sub>2</sub> energy photosynthetically according to the following equation:



About 10% of the photosynthetically active radiation is reflected by the cultures. Moreover,

under high light, a part of the light energy is not used for photosynthesis, and it is dissipated by heat and utilized to synthesize protective pigments such as xanthophylls that dissipate excess light as heat [2, 3]. Another important aspect is the fact that photons above 700 nm and below 400 nm are not used by microalgae (as in higher plants); consequently, about 55% of incident solar light is unavailable to drive photosynthesis. All these physiological limitations reduce the available light for photosynthesis to about 41%.

The theoretical light conversion efficiency for H<sub>2</sub> production is 13.4% of solar light. It is worth noting that this conversion efficiency is significantly high, compared to the theoretical limit for biomass or biodiesel production [4], which depends on the number of steps necessary to produce a certain compound (i.e., the more the steps required in the biomass case, the lower the efficiency of the process). Finally, assuming that about 20% of the energy can be lost for cell maintenance in cells subjected to diurnal cycle [5], consequently the light conversion efficiency of light into H<sub>2</sub> and biomass is reduced accordingly to 10.7% and 7.6%, respectively. With a light conversion efficiency of about 10%, it would be possible to produce about 600,000 m<sup>3</sup> ha<sup>-1</sup> y<sup>-1</sup> of H<sub>2</sub> in sunny areas.

However, despite this promise, and some decades of research, serious technical barriers need to be overcome before this goal may be reached.

In this respect, genetic engineering represents a very useful tool, in order to better understand the physiological and biochemical mechanisms associated with the photosynthetic biological hydrogen production [6]. Genetic engineering applied to microalgal species able to produce H<sub>2</sub> has been successful in the optimization of H<sub>2</sub> production, in terms of both efficiency and total volume production. In the present chapter, some of the most relevant physiological aspects associated with H<sub>2</sub> production in microalgae are analyzed, focusing on the main pathways involved in H<sub>2</sub> evolution, which may be considered for the improvement of the process by means of genetic optimization.

## Potential of Microalgal Engineering: Application Fields and Advantages

The attractiveness aroused by microalgae derives from their wide range of possible biotechnological applications. Microalgae represent a group of microorganisms among the most ancient and with the greatest phylogenetic diversity of the planet [7–9], counting at least 70,000 species.

They are distributed in a wide spectrum of habitat, adapting their metabolism to complex and extreme environmental conditions (high salinity, extreme temperature, nutrient deficiency, UV radiation). For this reason and for their high capability to adapt to different environmental conditions, they are considered a promising reservoir of genetic diversity.

Microalgae are capable of producing, under stress conditions, significant amounts of substances with high added value (antioxidant carotenoids, phenolic compounds, polyunsaturated fatty acids), and for this reason the study of the physiology of the growth of these microorganisms results in a particular interest. Nowadays microalgae are the main natural sustainable source of these compounds [10, 11].

Therefore several studies have been carried out with the aim of optimizing the production of these metabolites for the commercialization of these by-products [12] having as a result the improvement of know-how of microalgal biotechnology.

Moreover, utilization of microalgae for the production of compounds of commercial interest offers several advantages, compared to higher plants, such as the possibility to utilize extreme environments for cultivation, without subtracting area for agriculture and farming, and reduced costs in culture media. In addition, these photosynthetic microorganisms are quite easy to manipulate from a genetic point of view, due to their simple cellular structure.

Considering the high exploitability of these photosynthetic microorganisms, engineering in microalgae has aroused a large interest, and they have allowed gaining more insight to photosynthetic processes from the physiological, metabolic, and biochemical point of view.

However, most enzymes are encoded in the nucleus but perform their catalytic function in the chloroplast; therefore microalgal engineering has to consider transformation at nuclear, chloroplast, or mitochondrial level, and this can represent a limiting factor to the development of tools for microalgal engineering.

Concerning the capability of certain microalgae to produce hydrogen, owing to the hydrogenase sensitivity to oxygen, most efforts have been carried out in order to bypass this problem, by using experimental procedures aimed to minimize the oxygen concentration in the cultures, screening different microalgal strains, and using genetic engineering, interfering at physiological, metabolic, and biochemical levels, using microalgae as platform for biofuel production in engineered strains.

The microalga *Chlamydomonas* represents a model organism for genetic manipulation, and its chloroplast, mitochondrial, and nuclear genomes have been sequenced. Its chloroplast and nuclear genome can be easily transformed, due to its cellular structure simplicity, and it can be used to obtain mutant strains to study different physiological processes, such as induction of antioxidant carotenoids synthesis, electron transport between PSII and PSI during the photosynthetic processes, and light energy utilization under stress conditions [13]. Indeed *Chlamydomonas reinhardtii* is one of the most studied microorganisms among microalgae, for the hydrogen production process, also by means of mutant strains, as it will be shown further.

## Enzymes Which Catalyze the Biological Hydrogen Production: Hydrogenase and Nitrogenase

The main problem associated with H<sub>2</sub> photobiological production is the high sensitivity to oxygen of the enzymes involved in the reaction.

The reversible reaction which leads to biological hydrogen production is catalyzed by hydrogenase [14] and nitrogenase enzymes [15].

Both enzymes catalyze the reaction  $2\text{H}^+ + 2\text{e}^- \rightarrow \text{H}_2$  with the reduction of H<sup>+</sup> ions to H<sub>2</sub> gas.

Depending on the active site metal content, the hydrogenases are classified as [FeFe] hydrogenases, [NiFe] hydrogenases, and [Fe] hydrogenases [7] (Table 1).

Some authors reported that nonetheless, [FeFe] and [NiFe] hydrogenases are not related; they both have dimetallic compartment, CO and CN ligands attached to iron and cysteine residues [16].

[FeFe] hydrogenases are the best-performing enzyme from the catalytic activity point of view [14, 17, 18]. This enzyme has a unique active site called H cluster characterized by [FeFe] center, with CO and CN<sup>-</sup> and dithiolate ligands, bound with 4Fe-4S cluster via sulfur bridges [14, 19].

Microalgal hydrogenases are known to be the smallest enzymes among H<sub>2</sub> producer microorganisms; even bacteria and different microalgal species share the same cluster, enzymatic activity, and active site and oxygen diffusing channel [14].

These hydrogenases are encoded in the nucleus by *hydA* (*hydA1*, *hydA2*) genes [20–22] with *hydA1* more active than *hydA2* [23]. Maturation of the active enzyme is controlled by a set of genes *hydE*, *hydF*, and *hydG* [24]. The maturation process of the enzyme requires the synthesis of some proteins, and it is also sensitive to oxygen [14, 25–27].

Due to the simple structure of the *C. reinhardtii* hydrogenase, the enzyme has been widely studied in this microalga, and it constitutes the model for studies on the active site maturation [28–30].

Other enzymes which catalyze the reaction of H<sub>2</sub> production are found in cyanobacteria, which can use [NiFe] hydrogenase (bidirectional or uptake) or nitrogenase enzyme, located in the heterocysts, vegetative cells which forms under nitrogen starvation and without oxygen inside [30].

The physiological function of nitrogenase in cyanobacteria consists in fixing nitrogen into ammonium ions [31, 32]. The synthesis of this

enzyme can only occur under starvation of nitrogen source, like ammonium, urea, and nitrate. These nitrogenases are known as MoFe nitrogenases [6, 33]. Hydrogen production by means of nitrogenase enzyme requires too much energy, and it results also in less convenience for its turnover, lower than the [NiFe] and [FeFe] hydrogenases [6, 14, 24].

## Description of the Mechanisms of Biohydrogen Production Used by Microalgae

Among microalgae and cyanobacteria, *Spirulina*, *Synechococcus*, *Anabaena*, *Chlorella*, and *Chlamydomonas* are the most studied genera for biohydrogen production [34]. For cyanobacteria and microalgae, *Synechococcus* [35] and *Chlorella*, *Chlamydomonas reinhardtii*, respectively, are the best hydrogen producers according to today's knowledge.

For all photosynthetic microorganisms able to produce hydrogen, both microalgae and cyanobacteria, the light harvested by the light-harvesting complex II (LHCII), associated with photosystem II (PSII), the first step leads to the split of water into protons and electrons. This process is called biophotolysis, classified as direct or indirect, according to the electron donor (Table 2).

This first step is shared by photosynthetic evolution of oxygen or hydrogen. In this phase, when photosynthesis occurs, absorbed light energy is transferred to the reaction center of PSII and PSI, with a charge separation which is associated with the evolution of molecular O<sub>2</sub>, at PSII level, and reduction of CO<sub>2</sub>, at PSI level, where electrons are driven to ferredoxin PETF (Fdx1) and by ferredoxin-NADP<sup>+</sup> reductase (FNR) to generate NADPH.

### Genetic Optimization for Increasing Hydrogen Production in Microalgae, Table 1

Enzymes catalyzing

the biological H<sub>2</sub> production in microalgae and cyanobacteria

Enzymes		Active site metal content	Microorganism
Hydrogenase	Fe-Fe hydrogenase	Fe-Fe	Microalgae
	Ni-Fe hydrogenase	Ni-Fe	Cyanobacteria
	Fe hydrogenase	Fe	Archaea
Nitrogenase		Fe-MoFe protein	Cyanobacteria

**Genetic Optimization for Increasing Hydrogen Production in Microalgae, Table 2** Summary of the different pathways for H<sub>2</sub> production in microalgae and cyanobacteria

Pathway		Main electron source	Light driven	By-product
Biophotolysis	Direct	Water (PSII dependent)	Yes	O <sub>2</sub>
	Indirect	Starches and proteins (PSII independent, endogenous catabolism)	Yes	CO <sub>2</sub>
Dark fermentation	Glycolysis	Organic substrate	No	Acetic acid CO <sub>2</sub>

Under certain conditions, that is, when oxygen is absent, Fdx1 can also be the electron donor of the enzyme catalyzing H<sub>2</sub> evolution, which is placed in the chloroplast.

However, this process represents alternative mechanisms for the dissipation of reductive potential accumulated inside the cells, when the performance of photosynthetic apparatus is not able to maintain the optimum redox level inside the cells.

The indirect biophotolysis and dark fermentation have in common the electron source, that is, glycolysis, but while the former is light dependent, the latter occurs under dark conditions.

These different pathways contribute in a different manner to the H<sub>2</sub> production, and this aspect will be discussed in more details in the following paragraph.

### Different Pathways for Hydrogen Production in Microalgae Which May Be Influenced by Genetic Engineering Approach

Among microalgae *Chlamydomonas reinhardtii* is one of the most studied microalgae for H<sub>2</sub> production, for its capability of prolonged H<sub>2</sub> production, with a light conversion efficiency of about 0.1%, under sulfur starvation [36]; it can be considered a model organism for H<sub>2</sub> production under laboratory and outdoor conditions [37, 38].

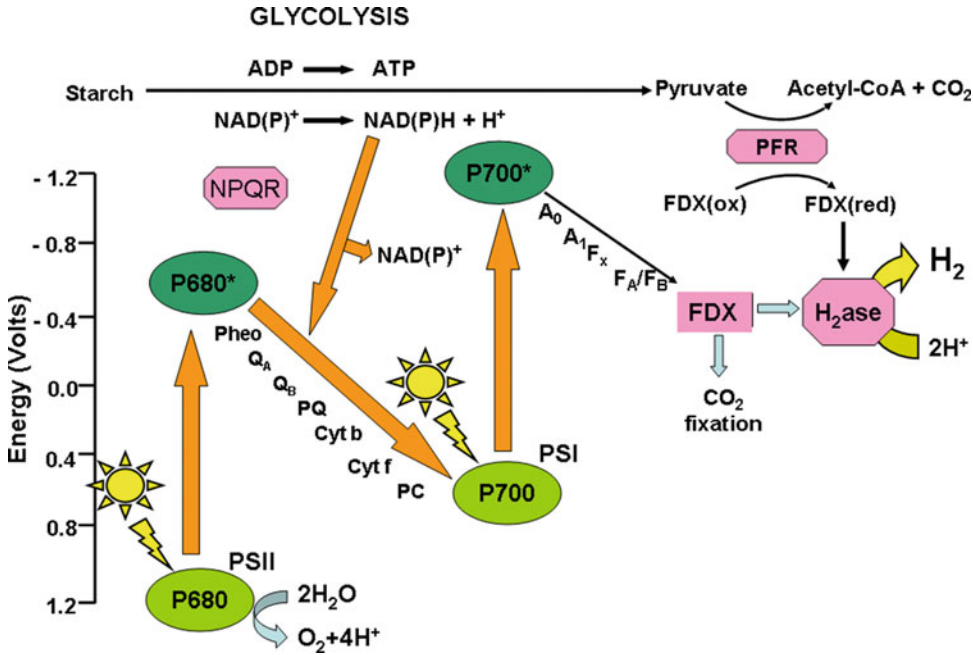
In addition, since its genome is well known, as it has been fully sequenced, many studies have been carried out in order to increase the biohydrogen production capacity by means of genetic optimization of this microalga.

In living *Chlamydomonas* cells, electrons may be driven to the hydrogenase through three different pathways, which are reported in Fig. 1:

1. PSII-dependent pathway, which directly links water-splitting activity to H<sub>2</sub> evolution through PSI, in a process usually referred to as “biophotolysis”
2. PSII-independent pathway, where electrons derived from glycolysis enter the linear electron transport chain at the level of PQ pool, giving rise to a photo-fermentative H<sub>2</sub> release
3. Dark fermentative pathway, where pyruvate derived from glycolysis may be oxidatively decarboxylated by a pyruvate ferredoxin oxidoreductase (PFR), thus likely resulting in a reduced Fdx1 which, in absence of light, may act as an electron donor for hydrogenase

The pathway providing the highest amount of electrons to the hydrogenase is considered to be the PSII-dependent one. On the other hand, sulfur [36] or nitrogen [39] starvation imposed to the culture has been found to significantly enrich cells in internal reserves (e.g., starch), thereby supporting glycolytic pathways and leading to enhanced photo and dark fermentation contribution. Concerning dark fermentative pathway, although in *C. reinhardtii* pyruvate ferredoxin oxidoreductase has been described at genetic [40, 41] and protein levels [42, 43], its link to Fdx1 is not absolutely proven [44]. In any case, this pathway is generally believed to be poorly electrogenic and less efficient than those occurring in the light [44].





**Genetic Optimization for Increasing Hydrogen Production in Microalgae, Fig. 1** Metabolic pathways in microalgae for hydrogen production. These pathways have

been well studied in *Chlamydomonas reinhardtii* cells (Adapted from Torzillo et al. 2014, see Book and Reviews section)

In more details, the direct H<sub>2</sub> production consists of a PSII-dependent pathway, which needs only water and light to provide electrons and protons to the hydrogen production pathway [45]. This reaction is completely independent from the presence of organic compounds, and it is believed as one of the most promising processes for sustainable hydrogen production.

When light reaches PSII, the splitting of water occurs, generating electrons, protons, and oxygen.

Electrons are moved from PSII to PSI through the plastoquinone (PQ) pool and then from PSI are transferred to ferredoxin, which is the final electron donor to hydrogenases.

The limiting factor of this process is the oxygen generation during the water splitting, as the presence of O<sub>2</sub> has to be avoided for the high O<sub>2</sub> sensitivity of hydrogenase enzyme. Some strategies have to be developed in order to remove the oxygen from the cultures during this process. In this contest genetic optimization of strains may be focused on the alteration of metabolism, in order to change the balance between oxygen evolution

and uptake or to make cultures easily encounter anaerobiosis under nutrient starvation or under different light regimes.

It is well known that nutrient starvation decreases cell growth and photosynthetic activity. In particular, the sulfur starvation impairs D1 protein, which is the protein associated with PSII with a higher turnover rate, which is light dependent, containing sulfur amino acids as building blocks. For this reason it is the main target of stress caused by sulfur starvation, as protein degradation under light conditions is not balanced by protein synthesis, as sulfur is absent and all enzymatic photosynthetic apparatus are strongly suppressed [46]. Hence, under sulfur starvation, the photosynthetic activity decreases, leading to the decline of O<sub>2</sub> evolution rate.

Light drives electrons and protons to the PQ pool, which are driven to hydrogenases; hence in the presence of light, there is an increment of transferred H<sup>+</sup> and e<sup>-</sup>, with respect to dark reaction, leading to an appreciable increase in hydrogen production.

Light acts as a reaction accelerator which supports that the photosynthetic electron transport chain is essential for microalgal hydrogen production.

The indirect pathway process offers the advantage of the possibility to use different carbon sources to drive protons and electrons to hydrogenase [47]. Electrons are provided by glycolysis and enter to the linear electron chain at the level of the PQ pool; afterward, they are transferred through the PSI to the (FeFe)-ase.

To carry out the indirect biophotolysis, starch or glycogen is required to be accumulated in the cell.

The interesting aspect of the indirect H<sub>2</sub> production is that these sources are used via anaerobic fermentation and CO<sub>2</sub> results as a by-product rather than O<sub>2</sub>, contrary to what observed with the direct biophotolysis.

The indirect biophotolysis mechanism is studied mostly on cyanobacteria [48]. It is promising in terms of avoiding oxygen and with the perspective to use organic substrates from industrial wastewaters, but it is still a challenging pathway for microalgae.

### **Approaches to Promote H<sub>2</sub> Production: Two-Stage Hydrogen Production (Sulfur Deprivation Technique)**

This approach divides the biological hydrogen production in two stages: the first one is aerobic, and it is needed for the microalgal biomass production which will be used for the hydrogen production stage; in the second one, the biomass is used to produce hydrogen under anaerobic conditions [36].

This approach took place after the findings that in sulfur-deprived cultures, the photosynthetic activity decreased [49]. This was caused by the reduced protein synthesis, and particularly of the D1 protein, which is tightly associated with PSII. Sulfur starvation represented the tool to reach anaerobiosis in microalgal cultures to make hydrogenase able to work and produce hydrogen.

The two-stage H<sub>2</sub> production finds its best application with the microalga *Chlamydomonas*

*reinhardtii*, which has been largely investigated concerning all the physiological aspects of H<sub>2</sub> production also by means of genetic manipulation.

In *Chlamydomonas reinhardtii* the sulfur starvation induces the decrease in photosynthetic activity, which can be low up to 75% of the initial value, within 24 h. When the oxygen evolution rate equalizes the oxygen respiration rate, the cultures reach anaerobic conditions. After a period of anaerobic phase, which is variable according to the strains and light conditions, the hydrogen production may take place. According to these different phases, the hydrogen production phase can be divided into four stages: (I) aerobic phase, the initial phase during which oxygen is always present in the cultures and cells can use already endogenous sulfur reserves; (II) lag phase, when the balance between oxygen evolution and respiration is attained and anaerobiosis can be reached. During this phase, the induction of hydrogenase enzyme can start, and no-hydrogen production can be yet observed; (III) hydrogen production phase, when the hydrogen production occurs; and (IV) no-hydrogen production phase, when the permanence under sulfur starvation has so largely affected protein synthesis, that the cellular metabolism is strongly impaired.

According to the phenotypic characteristics of each strain, these stages can vary, influencing the yield of the hydrogen produced. Indeed, it could be observed that in each stage, some important physiological changes occur, with implication on metabolism. Hence, changing the length of these stages, interfering by genetic manipulation, it has been possible to increase hydrogen production yield.

During the aerobic phase, in *C. reinhardtii* the starch accumulation can be observed, as a response to excess reducing power under sulfur starvation in the light [4, 36]. This phase is very important, as starch catabolism plays a central role in H<sub>2</sub> production, providing electrons to the hydrogenase. Hence, the more starch is accumulated, the more starches can be degraded, under anaerobic conditions, sustaining the H<sub>2</sub> production phase [36]. In addition starch degradation sustains O<sub>2</sub> respiration, so that the largest amount of carbohydrates can facilitate the fast occurrence

of anaerobic conditions. If anaerobiosis occurs soon, when the PSII protein degradation is not so large, the PSII contribution to sustain the electron flow to hydrogenase (direct H<sub>2</sub> production) will be larger than in exhausted cells.

Starch catabolism has been shown to sustain both mitochondrial and chlororespiratory pathways, maintaining anaerobic conditions for the PSII-dependent direct pathway [46] and providing electrons to hydrogenase, through a PSI-dependent process (indirect pathway), respectively [41, 46, 50]. The increase in the pH has been detected, during the aerobic phase, from an initial value of 7.2–8.5. This change has been related to the utilization of acetate, present in the medium, during the aerobic phase, which contributes to the carbohydrate accumulation into the cells [51].

It has been shown that starch breakdown contribution consists in feeding electrons to the PQ pool [52]. During this phase, the PQ pool reduction level increases, causing changes in the internal redox potential, and for this reason the measurement of the redox potential is a good tool to evaluate the physiological response of cells to stress conditions and, more importantly, in the case of H<sub>2</sub> production. In this case, it gives information on the capacity of the cells to accumulate electrons at PQ pool level, to be driven to hydrogenase in the following stage. This is a balance between the starch degradation and the PSII capacity to perform photosynthesis, that is, to dissipate electrons from PQ pool. After the occurrence of a reducing environment, the redox potential that has an initial positive value during the aerobic phase becomes negative up to –550 mV.

This phenomenon may reflect the fact that the induction of H<sub>2</sub> production constituted a response to the excess reducing power accumulated during the aerobic phase and served as a valve to relax the high reduction level inside the cells, by decreasing the degree of reduction of the plastoquinone.

In the following H<sub>2</sub> production phase, during which H<sub>2</sub> is released, both the PSII-dependent (due to the residual PSII activity) and PSII-independent pathways represent important sources of electrons.

During the H<sub>2</sub> production phase, the pH declines down to a value of 7.9.

It has been demonstrated that the PSII contribution to the process is dominant with respect to starch mobilization [53], providing up to 80% of the reducing power supplied [54–56]. The length of the H<sub>2</sub> production phase depends on both the starch catabolism and the PSII contribution and can vary from 2 days to more than 1 week [51]. Most important in this respect is the value of the oxygen respiration rate, as under light exposure and sulfur starvation the O<sub>2</sub> evolution is strongly impaired, but the O<sub>2</sub> uptake is less sensitive to this stress conditions.

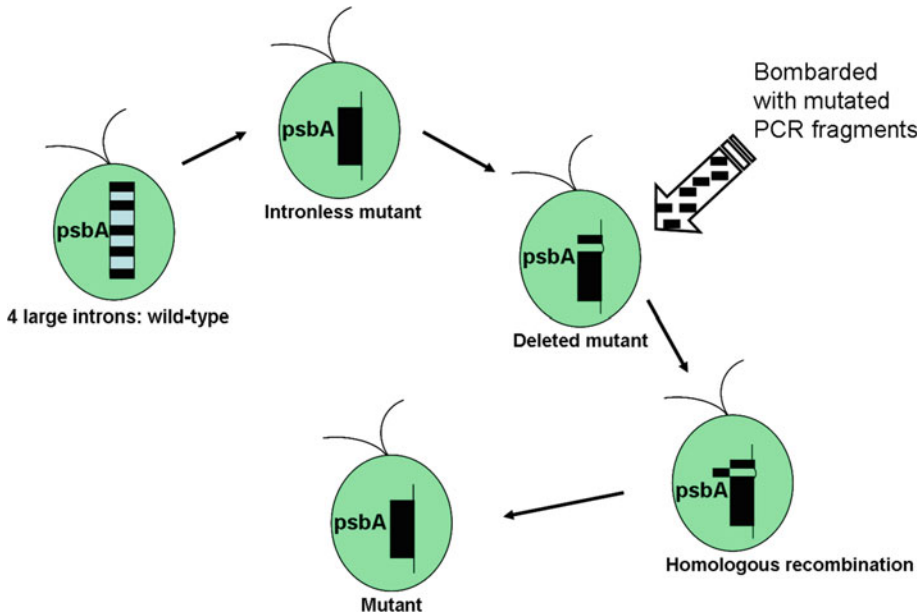
The contribution of the direct or indirect H<sub>2</sub> production can change according to the strain, and what is interesting is that mutant strains with mutation at level of both starch metabolism and PSII activity all exhibited increased H<sub>2</sub> production.

### Mutant Strains of Microalgae for Increasing H<sub>2</sub> Production

The important implication of the D1 protein, encoded by *psbA* gene, in the PSII activity and its high turnover rate have attracted much attention for investigation on a possible role of mutation at D1 protein level in the increment of H<sub>2</sub> production under sulfur starvation. For this reason the screening of *C. reinhardtii* mutant strains has been carried out. An increased H<sub>2</sub> production has been reported in D1 protein mutants [51, 57, 58].

One of the most important sites of the D1 reaction center to drive photosynthetic electron transport through PSII is the Q<sub>B</sub> binding site, which is involved in the signaling of the occurrence of damage. It is placed within a stromal hydrophilic loop between transmembrane helices IV and V (the D–E loop), and it contains an amino acid sequence that is conserved among cyanobacteria, algae, and higher plants [59, 60]. Moreover, the importance of this amino acidic region is due to its implication in the rapid turnover of the D1 protein [61].

Some studies have been carried out on D1 protein mutant strains, obtained from wild-type (11/32b) genetic manipulation, as previously described and reported in Fig. 2 [62].



**Genetic Optimization for Increasing Hydrogen Production in Microalgae, Fig. 2** Scheme of the *psbA* mutagenesis protocol in *Chlamydomonas reinhardtii* for obtaining D1 protein mutant strains

Mutation in different regions of D1 protein has been considered, involving several functions of the D1, which induced diverse phenotypic characteristic and photosynthetic parameters of the strains.

However, the mutated D1 protein conferred the capability to a higher  $H_2$  production than in the wild-type strain (Table 3). Only few exceptions were observed, which did not produce any hydrogen.

Two mutants with amino acid deletion, D240 and D239–40, and one mutant with amino acid substitution, L159I/N230Y, resulted very interesting. The deleted amino acids are located in the D1 protein region involved in the binding of  $Q_B$  and D1 degradation, while the substitution involves a region implicated in the electron donor capacity to the oxygen-evolving complex (OEC).

These strains exhibited phenotypic characteristics which are considered important for the improvement of the  $H_2$  production process. First of all they exhibited an amount of chlorophyll per dry weight biomass 36–56% lower than in the wild type, a useful requisite because the cultures can grow under relatively high cell densities. This

means that with these cells, under sulfur starvation, it is possible to work with higher-dense cultures, which can reach anaerobiosis faster (Table 4).

Concerning the photosynthetic parameters, the deleted mutants exhibited lower oxygen evolution rates and higher respiration rates than those for the wild type. By contrast, double amino acid substitution mutant L159I-N230Y led to increase both oxygen evolution and the respiration rate, 87% and 164% higher than in the wild type. A high respiration to photosynthesis ratio is very useful for the production of hydrogen, because it leads to a faster occurrence of anaerobiosis and faster onset of the hydrogen production phase. The best producer mutant strains showed a  $H_2$  production which was 12–19 times greater than in the wild type; these strains exhibited better performance also in terms of the rate of hydrogen production.

Another important contribution to  $H_2$  production of these mutants came from the great capacity to synthesize carbohydrates combined with a considerably higher level of fluorescence yield (0.300) compared to the wild type (below 0.100)

**Genetic Optimization for Increasing Hydrogen Production in Microalgae, Table 3** Hydrogen output rates measured in wild-type (WT) and the most productive D1

protein mutant strains. The CC124 is shown as a reference strain being used in laboratories worldwide for hydrogen production studies

Strain	Lag time	Production time	H <sub>2</sub> total volume	H <sub>2</sub> final production rate		H <sub>2</sub> maximum production rate <sup>a</sup>
	h	h	ml	ml/l/h	ml/g Chl/h	ml/l/h
WT	50 ± 20	55 ± 5	26 ± 5	0.47 ± 0.11	39 ± 9	1.25 ± 0.13
L159I/N230Y	37 ± 6	285 ± 53	504 ± 22	1.77 ± 0.35	166 ± 29	5.77
D239-40	33 ± 2	183 ± 30	475 ± 50	2.60 ± 0.18	217 ± 15	7.10 ± 1.10
D240	28 ± 4	207 ± 40	318 ± 23	1.54 ± 0.31	128 ± 26	3.54 ± 0.26

<sup>a</sup>H<sub>2</sub> maximum production rate measured over a period of at least 10 hours, during which the rate remained constant. The standard deviation (SD) for each parameter is reported in parentheses

**Genetic Optimization for Increasing Hydrogen Production in Microalgae, Table 4** Phenotypic characteristics of *C. reinhardtii* mutant strains L159I/N230Y, D239-40, and D240 compared with their wild-type (WT) and CC124 strain

Strain	Chl	Chl a/b	Chl cell <sup>-1</sup>	Cell diameter	P <sup>a</sup> <sub>max</sub>	Respiration <sup>b</sup>	R/P ratio <sup>c</sup>
	% of dry weight	ratio	x 10 <sup>-6</sup> µg	µm	µmol O <sub>2</sub> mg <sup>-1</sup> Chl h <sup>-1</sup>	µmol O <sub>2</sub> mg <sup>-1</sup> Chl h <sup>-1</sup>	h <sup>-1</sup>
WT	3.63 ± 0.61	2.90 ± 0.01	3.57 ± 0.12	7.32 ± 0.32	260 ± 2.8	72 ± 0.25	27.70 ± 0.21
D240	1.60 ± 0.18	2.89 ± 0.04	1.56 ± 0.05	9.15 ± 0.30	220 ± 25.0	95 ± 5.8	43.18 ± 2.04
L159I/N230Y	1.80 ± 0.20	3.00 ± 0.05	3.32 ± 0.14	9.43 ± 0.27	487 ± 36.0	190 ± 2.5	39.01 ± 2.22
D239-40	2.33 ± 0.32	2.99 ± 0.05	2.08 ± 0.09	7.38 ± 0.09	119 ± 2.0	78 ± 1.75	65.55 ± 0.36

<sup>a</sup>Maximum rate of (oxygen evolution plus dark respiration)

<sup>b</sup>Dark respiration

<sup>c</sup>Respiration to oxygen evolution rate. The standard deviation (SD) for each parameter is reported in parentheses

during the hydrogen production; thus in these strains, both direct and indirect processes strongly contributed to H<sub>2</sub> production.

The maintenance of a high fluorescence yield value may be related to a higher xanthophylls cycle pool and lutein found in these strains which allows greater protection of PSII from photoinactivation [51].

Recently other important results have been obtained by the selection of *C. reinhardtii* mutant sensitive to high temperature [62]. The screened strains were obtained by random mutagenesis, by UV exposure, and then mutant strains were selected by their ability to evolve oxygen and hydrogen at 25 and 37 °C.

These strains reacted to the high temperature decreasing the photosynthetic activity, which resulted useful in order to obtain anaerobiosis.

These studies resulted very interesting because they helped to better understand the different contributions of the indirect and direct pathways to H<sub>2</sub> production.

The strains exhibited a lowered O<sub>2</sub> evolution within 12–24 h of sulfur starvation at 37 °C. Differences could be appreciated among the strains, in terms of PSII fluorescence yield, D1 and CP43 content, and PSI amount, during the starvation. The mutant with the highest H<sub>2</sub> evolution showed maintenance of the PSII fluorescence yield, and the content of D1 and CP43 proteins and PSI amount did not change, during sulfur starvation [62]. Nonetheless the other mutants displayed a H<sub>2</sub> production lower than this strain, and they showed reduced PSII fluorescence yield and reduced D1 and CP43 proteins. Very important, they found that these mutants displayed an

increased or reduced PSII content, with respect to the wild type, but anyway, they were always able to evolve a higher amount of hydrogen, with respect to the wild type (Table 5). The wild type evolved H<sub>2</sub> within 24 h, and no further accumulation could be observed, so a production rate was not reported for this strain. In addition, when DCMU was added to the cultures, the hydrogen production in mutant and wild type was comparable.

These results indicated how PSII contribution during the H<sub>2</sub> production phase is relevant, as the PSI amount was not the limiting factor for H<sub>2</sub> production. Moreover, these findings supported the idea that the faster occurrence of anaerobiosis the higher hydrogen production, due to the preservation of PSII activity under sulfur starvation.

Deep insights on the different contribution of indirect and direct processes to biogas production erases from studies with mutants with altered state transitions. This is a mechanism by which photosynthetic cells protect themselves from excess light, inducing the partial migration (more than 85% in *C. reinhardtii*) of the LHC II, associated with PSII, from PSII (state 1) to PSI (state 2) [63–65].

It is regulated by the redox level of PQ pool, which signals the oxidative stress level inside the cell.

However, PQ pool plays a major role in the transportation of e<sup>-</sup> and H<sup>+</sup> through electron transport chain either for photosynthesis or for biohydrogen production [49]. Because the substrates of hydrogenase enzymes are e<sup>-</sup> and H<sup>+</sup>, the effective supply of these components directly affects the enzyme activity and hydrogen yield. Thus PQ pool has a crucial role for both of the

processes in both cases either direct or indirect biophotolysis.

*C. reinhardtii* mutant locked in state 1 (i.e., *Stm6*) [54] displayed a lower cyclic electron flow (CEF) around PSI, known to drain electrons out of the H<sub>2</sub> production pathways. With this strain an increased hydrogen production was obtained. Also in this strain, interestingly, a higher respiration rate was observed, which contributed to a faster onset of anaerobiosis than in the WT, preserving PSII from irreversible photodamage [56].

A higher residual PSII activity under sulfur starvation was found to contribute to increased H<sub>2</sub> production in this mutant, strongly supplying electrons during the H<sub>2</sub> production phase.

A further optimization of productivity with this strain was reached by using a transformant of the *Stm6* cell line which expressed the active *Chlorella* HUP1 (hexose uptake protein) hexose transporter and facilitating access to glucose. This mutation allowed a higher accumulation of starches, when glucose was added to the growth medium, enhancing H<sub>2</sub> production in sulfur deprivation by 45–50% [66]. The high carbohydrate content contributed to the higher H<sub>2</sub> production due to prolonged production time, rather than a higher production rate.

Other studies on *C. reinhardtii* mutant, denoted as T1, reported the importance of high oxygen respiration rate, combined with lowering of PSII fluorescence yield and O<sub>2</sub> evolution [67]. In this mutant a respiration rate 23% higher than in the wild type promoted the increase of hydrogen production, which resulted in seven to eight-fold increase, compared to the one with the wild type.

The microalga *Chlorella* has been also investigated in order to permit the hydrogenase expression under aerobic conditions [68]. The authors reported the possibility to engineer the coding region of the *hydA* gene, by means of a plastid and promoters able to work under aerobic conditions. The mutant strain obtained was able to produce an amount of H<sub>2</sub> which was seven to ten-fold higher compared to the wild type. The mutation made the mutant able to produce hydrogen under aerobic conditions and in the presence of sulfur, circumventing the problem of O<sub>2</sub> sensibility. In this way the concomitant aerobic

**Genetic Optimization for Increasing Hydrogen Production in Microalgae, Table 5** Hydrogen production in mutant strain sensitive to high temperature (37 °C). Elaborated from [62]

Mutant strain	H <sub>2</sub> production nmol H <sub>2</sub> ml <sup>-1</sup>	H <sub>2</sub> production rate nmol μg <sup>-1</sup> h <sup>-1</sup>
Wild type	30	–
TSP1	850	3.1
TSP2	5330	11.7
TSP3	1340	3.9
TSP4	170	0.5



respiration of glucose, added to the medium, and the maintained high PSII activity lead the indirect and direct processes to simultaneously and strongly contribute to the production of hydrogen.

Another approach has been undertaken by the construction of a *C. reinhardtii* mutant with a truncated antenna [69]. The findings supported the idea that a reduced antenna permitted the cells to capture more light energy, reducing the self-shading and increasing the light energy utilization efficiency. Interestingly, it was found that under sulfur starvation, it was impossible to reach anaerobic conditions, and only under both sulfur and phosphorus starvation, with immobilized cells in thin layer of alginate, the mutant strains produced hydrogen, in a range of 19–350  $\mu\text{mol photons m}^{-2} \text{s}^{-1}$ . In particular, under higher light intensities of 285 and 350  $\mu\text{mol photons m}^{-2} \text{s}^{-1}$ , the  $\text{H}_2$  production resulted four and six times higher than with the parental strain, respectively.

### Monitoring the PSII Performance During $\text{H}_2$ Production in Mutant Strains by Means of Chlorophyll Fluorescence Changes During Sulfur Starvation

Stating the importance of the direct  $\text{H}_2$  production process, monitoring the photosynthetic activity during the sulfur starvation is extremely useful in order to evaluate the PSII damage and its residual activity during the anaerobic phase. For this purpose, the chlorophyll fluorescence measurement is considered a useful tool, and it is commonly used to evaluate the effect of different kinds of stresses on the photosynthetic apparatus [70].

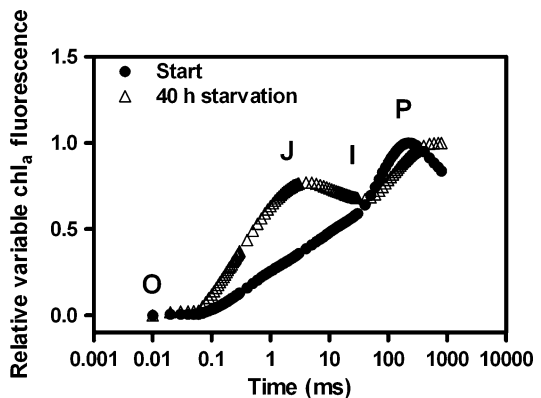
As a consequence of the sulfur starvation, the PSII activity decreases, due to protein degradation and the inability to resynthesize new protein, which is the desired effect of starvation, to induce anaerobiosis and, hence, induction of hydrogenase synthesis and functioning.

Hence the chlorophyll fluorescence can be used to measure the changes in PSII maximum and effective quantum yield during both the aerobic phase and the occurrence of anaerobiosis and hydrogen production.

Figure 3 shows a typical example of kinetics of chlorophyll fluorescence during sulfur starvation. Interestingly, the reduction in chlorophyll fluorescence, measured as effective PSII quantum yield,  $\Delta F/F'_m$ , is concomitant to the oxygen content decrease.

It can be observed that as soon as the  $\Delta F/F'_m$  drop from 0.6 to 0.2, the  $\text{H}_2$  production starts. This behavior has been firstly reported [35] and interpreted as the consequence of a transition from state 1 to state 2 of the photosynthetic apparatus [71]. As soon as anaerobic condition is attained, hydrogenase is expressed and becomes active. The hydrogenase activity partially oxidizes photosynthetic carriers, including the PQ pool, partially establishing the linear electron transfer from PSII, and may induce a partial re-increase in  $\Delta F/F'_m$ .

The non-photochemical reduction of the PQ pool can be estimated by the measurement of chlorophyll induction kinetics. It is generally accepted that the chlorophyll (Chl)*a* fluorescence rise kinetics reflect the progressive reduction of the photosynthetic electron transport chain [72, 73], i.e., the reduction of  $Q_A$  to  $Q_A^-$  and the reduction of the PQ pool. In particular, the increase in the J-step level is taken as an indication of a reduced transfer of electrons further than  $Q_A$  and  $V_J$  parameter and, thus, of an accumulation of reduced  $Q_A^-$  [70] (Fig. 3).



**Genetic Optimization for Increasing Hydrogen Production in Microalgae, Fig. 3** Kinetics of chlorophyll fluorescence in *C. reinhardtii* cells during sulfur starvation for  $\text{H}_2$  production

The effect of sulfur starvation on PSII reaction centers has been studied using Chl $a$  fluorescence [49]. The results indicated the formation of PSII  $Q_B$  nonreducing centers and consequently a limitation of the rapid electron transfer from  $Q_A^-$  to  $Q_B$ . This retardation may have been the cause of further PSII damage, with the reduction of the number of functional PSII reaction centers. The measure of the rate of closure of the PSII reaction centers has been determined by changes in the  $Mo$  parameter, which is a measure of the slope of the transient curve [49, 74, 75]. Hence, the shape of the transient curve, measured during  $H_2$  production, can quickly indicate the level of damage in the photosynthetic apparatus which can be quantified by the measurements of parameters correlated to it. By these measurements, it has been possible to gain more insight to the physiological response of microalgal cells to sulfur starvation and, more important, during the  $H_2$  production. The indications of changes in fluorescence parameters measured in the cultures of different mutant strains provided useful information on the phenotypic characteristics of those mutants able to produce higher hydrogen amount, at a higher rate, than the wild-type strain.

In particular it has been observed in *C. reinhardtii* that the use of mutant strains with a reduced constitutive capability to transfer electrons further than  $Q_A$  has been found to be important for improving  $H_2$  production under sulfur starvation [51]. It has been shown that D1 protein mutant strains which exhibited transient curves with increased  $Mo$  and  $V_J$  parameters with respect to the WT strain were able to a higher  $H_2$  production performance. These parameters were well related to the amplitude of sensitivity the sulfur starvation, and although they indicated that the mutation reduced the photosynthetic activity, for the  $H_2$  production under sulfur starvation, it was not a negative peculiarity. However, these phenotypic characteristics were translated, under sulfur starvation, into an earlier decrease of photosynthetic activity, than in the WT, inducing the anaerobiosis in a very short time, 2 h, whereas the WT reached anaerobic conditions in 34 h [51].

## Future directions

The results obtained with all these different approaches to induce an increase of  $H_2$  production with microalgae demonstrated that genetic engineering may contribute in a very important way, acting at different levels of photosynthetic pathways and metabolism. In particular, the D1 protein mutations could provide different phenotypes to the mutated strains, which, altering the yield of photosynthetic activity and reducing the rate of oxygen evolution, can meliorate the performance in terms of hydrogen production. It has been shown that mutation at the level of  $Q_B$  binding and OEC-interaction site of D1 protein is important in improving  $H_2$  productivity.

Moreover, acting at the level of metabolism in carbohydrates is a crucial step, acting by higher accumulation of starches from a medium and by changing the metabolism.

However, the efficiency of the process in most cases is below 1% under laboratory conditions and only by using mutants in properly designed PBRs or by immobilizing algae or by controlling the partial pressure in the gas phase above the culture. Moreover, the main problem is always represented by the loss of yield when the best-performing mutant strains are transferred outdoor, which is one of the main final objectives to reach, thinking in terms of renewable energy.

The results obtained indicate that further studies have to be carried out, with the aim to cope in one mutant strain the best peculiarity in terms of hydrogen productivity and also considering the robustness of the strain, which have to be able to produce under solar light irradiation. Also the changes of solar light intensity during the day are an important problem to solve, managed with genetic engineering.

Many studies have been focused on the reduction of sensitivity of hydrogenase enzyme, or to reduce the oxygen evolution in the cultures, by mutation impairing the oxygen evolution rate or increasing the oxygen uptake, improving the light capture or the light conversion efficiency, or producing strains resistant to outdoor conditions.

With the prospective of a large-scale system for cultivation and hydrogen production, and in

particular for the utilization of solar energy, as the outdoor cultivation in photobioreactors represents a stressing condition for microorganisms, studies on the physiological aspects of H<sub>2</sub> production process help for the optimization of mutant strains and for their screening.

## Bibliography

### Primary Literature

- Gaffron H, Rubin J (1942) Fermentative and photochemical production of hydrogen in algae. *J Gen Physiol* 26:219–240
- Zhu XG, Long SP, Ort DR (2008) What is the maximum efficiency with which photosynthesis can convert energy into biomass? *Curr Opin Biotechnol* 19:153–159
- Faraloni C, Torzillo G (2013) Xanthophyll cycle induction by anaerobiosis conditions under low light in *Chlamydomonas reinhardtii*. *J Appl Phycol* 25:1457–1471
- Melis A (2009) Solar energy conversion efficiencies in photosynthesis: minimizing the chlorophyll antennae to maximize efficiency. *Plant Sci* 177:272–280
- Pirt SJ, Lee KYK, Richmond A, Pirt Watts M (1980) The photosynthesis efficiency of *Chlorella* biomass grown with reference to solar energy utilisation. *J Chem Technol Biotechnol* 30:25–34
- Srirangan K, Pyne ME, Perry Chou C (2011) Biochemical and genetic engineering strategies to enhance hydrogen production in photosynthetic algae and cyanobacteria. *Bioresour Technol* 102(18):8589–8560
- Bhattacharya D, Yoon HS, Hackett JD (2004) Photosynthetic eukaryotes inite: endosymbiosis connects the dots. *Bioessays* 26:50–60
- Guiry MD (2012) How many species of algae are there? *J Phycol* 48:1057–1063
- Norton TA, Melkonian M, Andersen RA (1996) Algal biodiversity. *Phycologia* 35:308–326
- Borowitzka MA (2013) High value product from microalgae- their development and commercialization. *J Appl Phycol* 25:743–756
- Leu S, Boussiba S (2014) Advances in the production of high value products by microalgae. *Int Biotechnol* 10:169–183
- Davis R, Aden A, Pienkova PT (2011) Technoeconomic analysis of autotrophic microalgae for fuel production. *Appl Energy* 88:3524–3531
- Finazzi G, Furia A, Barbagallo RM, Forti G (1999) State transitions, cyclic and linear transport and photophosphorylation in *Chlamydomonas reinhardtii*. *Biochim Biophys Acta* 1413:117–129
- Meyer J (2007) FeFe hydrogenases and their evolution: a genomic perspective. *Cell Mol Life Sci* 64(9):1063–1084
- Debajyoti D, Debojyoti D, Surabhi C, Sanjoy KB (2005) Hydrogen production by Cyanobacteria. *Microb Cell Factories* 4:36
- Kim DH, Kim MS (2011) Hydrogenases for biological hydrogen production. *Bioresour Technol* 102(18):8423–8431
- Florin L, Tsokoglou A, Happe T (2001) A novel type of iron hydrogenase in the green alga *Scenedesmus obliquus* is linked to the photosynthetic electron transport chain. *J Biol Chem* 276(9):6125–6132
- Vignais PM, Billoud B, Meyer J (2001) Classification and phylogeny of hydrogenases. *FEMS Microbiol Rev* 25(4):455–501
- Nicolet Y, de Lacey AL, Vernède X, Fernandez VM, Hatchikian EC, Fontecilla-Camps JC (2001) Crystallographic and FTIR spectroscopic evidence of changes in Fe coordination upon reduction of the active site of the Fe-only hydrogenase from *Desulfovibrio desulfuricans*. *J Am Chem Soc* 123:1596–1601
- Happe T, Kaminski A (2002) Differential regulation of the Fe-hydrogenase during anaerobic adaptation in the green alga *Chlamydomonas reinhardtii*. *Eur J Biochem* 269:1022–1032
- Forestier M, King P, Zhang L, Posewitz M, Schwarzer S, Happe T, Ghirardi ML, Seibert M (2003) Expression of two [Fe]-hydrogenases in *Chlamydomonas reinhardtii* under anaerobic conditions. *Eur J Biochem* 270:2750–2758
- Ogata H, Lubitz W, Higuchi Y (2009) [NiFe] hydrogenases: structural and spectroscopic studies of the reaction mechanism. *Dalton Trans* 37:7577–7587
- Meuser JE, D'Adamo S, Jinkerson RE, Mus F, Yang W, Ghirardi ML, Seibert M, Grossman AR, Posewitz MC (2012) Genetic disruption of both *Chlamydomonas reinhardtii* [FeFe]-hydrogenases: Insight into the role of HYDA2 in H<sub>2</sub> production. *Biochem Biophys Res Commun* 417(2):704–709
- Boyer ME, Stapleton JA, Kuchenreuther JM, Wang CW, Swartz JR (2008) Cell-free synthesis and maturation of [FeFe] hydrogenases. *Biotechnol Bioeng* 99(1):59–67
- Posewitz MC, King PW, Smolinski SL, Smith RD, Ginley AR, Ghirardi ML (2005) Identification of genes required for hydrogenase activity in *Chlamydomonas reinhardtii*. *Biochem Soc Trans* 33:102–104
- Böck A, King PW, Blokesch M, Posewitz MC (2006) Maturation of hydrogenases. *Adv Microb Physiol* 51:1–72
- Skjånes K, Pinto F, Lindblad P (2010) Evidence for transcription of three genes with characteristics of hydrogenases in the green alga *Chlamydomonas noctigama*. *Int J Hydrog Energy* 35(3):1074–1088
- Posewitz MC, Mulder DW, Peters JW (2008) New frontiers in hydrogenase structure and biosynthesis. *Curr Chem Biol* 2:178–199
- English CM, Eckert C, Brown K, Seibert M, King PW (2009) Recombinant and in vitro expression system for hydrogenases: new frontiers in basic and applied

- studies for biological and synthetic production. *Dalton Trans* 45:9970–9978
30. Bothe H, Schmitz O, Yates MG, Newton WE (2010) Nitrogen fixation and hydrogen metabolism in cyanobacteria. *Microbiol Mol Biol Rev* 74(4):529–551
  31. Carrieri D, Momot D, Brasg IA, Ananyev G, Lenz O, Bryant DA, Dismukes GC (2010) Boosting auto-fermentation rates and product yields with sodium stress cycling. Application to renewable fuel production by cyanobacteria. *Appl Environ Microbiol* 76:6455–6462
  32. Skizim NJ, Ananyev GM, Krishnan A, Dismukes GC (2012) Metabolic Pathways for Photobiological Hydrogen Production by Nitrogenase- and Hydrogenase-containing Unicellular Cyanobacteria Cyanothecae. *J Biol Chem* 287(4):2777–2786
  33. Shestakov SV, Mikheeva LE (2006) Genetic control of hydrogen metabolism in cyanobacteria. *Russ J Genet* 42(11):1272–1284
  34. Oncel S (2013) Microalgae for a macroenergy world. *Renew Sust Energ Rev* 26:241–264
  35. Antal TK, Krendeleva TE, Laurinavichene TV, Makarova VV, Ghirardi ML, Rubin AB, Tsygangov AA, Seibert M (2003) The dependence of algal H<sub>2</sub> production on photosystem II and O<sub>2</sub> consumption in sulfur-deprived *Chlamydomonas reinhardtii* cells. *BBA* 1607:153–160
  36. Melis A, Zhang L, Forestier M, Ghirardi M, Seibert M (2000) Sustained photobiological hydrogen gas production upon reversible inactivation of oxygen evolution in the green alga *Chlamydomonas reinhardtii*. *Plant Physiol* 122:127–135
  37. Scoma A, Giannelli L, Faraloni C, Torzillo G (2012) Outdoor H<sub>2</sub> production in a 50-liter tubular photobioreactor by means of a sulfur-deprived culture of the microalga *Chlamydomonas reinhardtii*. *JBiotechnol* 157:620–627
  38. Oncel S, Kose A, Faraloni C, Imamoglu E, Elibol M, Torzillo G, Vardar Sukun F (2015) Biohydrogen production from model microalgae *Chlamydomonas reinhardtii*: a simulation of environmental conditions for outdoor experiments. *Int J Hydrog Energy* 40(24):7502–7510. Special Issue
  39. Philipps G, Happe T, Hemschemeier A (2012) Nitrogen deprivation results in photosynthetic hydrogen production in *Chlamydomonas reinhardtii*. *Planta* 235:729–745
  40. Hemschemeier A, Jacobs J, Happe T (2008) The pyruvate formate-lyase (Pfl1) of *Chlamydomonas reinhardtii*—a biochemical and physiological characterization of a typically bacterial enzyme in a eukaryotic alga. *Eukaryot Cell* 7:518–526
  41. Mus F, Cournac L, Cardellini V, Caruana A, Peltier G (2005) Inhibitor studies on non-photochemical PQ reduction and H<sub>2</sub> photoproduction in *Chlamydomonas reinhardtii*. *Biochim Biophys Acta* 1708:322–332
  42. Terashima M, Specht M, Naumann B, Hippler M (2010) Characterizing the anaerobic response of *Chlamydomonas reinhardtii* by quantitative proteomics. *Mol Cell Proteomics* 9(7):1514–1532
  43. Terashima M, Specht M, Hippler M (2011) The chloroplast proteome: a survey from the *Chlamydomonas reinhardtii* perspective with a focus on distinctive features. *Curr Genet* 57(3):151–168
  44. Ghirardi ML, Dubini A, Yu J, Maness PC (2009) Photobiological hydrogen-producing systems. *Chem Soc Rev* 38:52–61
  45. Hallenbeck P, Abo-Hashesh M, Ghosh D (2012) Strategies for improving biological hydrogen production. *Bioresour Technol* 110:1–9
  46. Melis A (2007) Photosynthetic H<sub>2</sub> metabolism in *Chlamydomonas reinhardtii* (unicellular green algae). *Planta* 226:1075–1086
  47. Mathews J, Wang G (2009) Metabolic pathway engineering for enhanced biohydrogen production. *Int J Hydrogen Energy* 34:7404–7416
  48. Carrieri D, Wawrousek K, Eckert C, Yu J, Maness PC (2011) The role of the bidirectional hydrogenase in cyanobacteria. *Bioresour Technol* 102(18):8368–8377
  49. Wykoff DD, Davies JP, Melis A, Grossman AR (1998) The Regulation of Photosynthetic Electron Transport during Nutrient Deprivation in *Chlamydomonas reinhardtii*. *Plant Physiol* 117:129–139
  50. Fouchard S, Hemschemeier A, Caruana A, Pruvost J, Legrand J, Happe T, Peltier G, Cournac L (2005) Autotrophic and mixotrophic hydrogen photo-production in sulfur-deprived *Chlamydomonas* cells. *Appl Environ Microbiol* 71(10):6199–6205
  51. Faraloni C, Torzillo G (2010) Phenotypic characterization and hydrogen production in *Chlamydomonas reinhardtii* Q<sub>B</sub>-binding D1-protein mutants under sulfur starvation: changes in chl fluorescence and pigment composition. *J Phycol* 46:788–799
  52. Chochois V, Dauvillée D, Beyly A, Tolleter D, Cuié S, Timpano H, Ball S, Cournac L, Peltier G (2009) Hydrogen Production in *Chlamydomonas*: Photosystem II-dependent and-independent pathways differ in their requirement for starch metabolism. *Plant Physiol* 151:631–640
  53. Ghirardi ML, Zhang L, Lee JW, Flynn T, Seibert M, Greenbaum E, Melis A (2000) Microalgae: a green source of renewable H<sub>2</sub>. *TIBTECH* 18:506–511
  54. Kruse O, Rupprecht J, Bade KP, Thomas-Hall S, Schenk PM, Finazzi G, Hankamer B (2005) Improved photobiological H<sub>2</sub> production in engineered green algal cells. *J Biol Chem* 280:34170–34176
  55. Scoma A, Krawietz D, Faraloni C, Giannelli L, Happe T, Torzillo G (2012) Sustained H<sub>2</sub> production in a *Chlamydomonas reinhardtii* D1 protein mutant. *J Biotechnol* 157:613–619
  56. Volgusheva A, Styring S, Mamedov F (2013) Increased photosystem II stability promotes H<sub>2</sub> production in sulfur-deprived *Chlamydomonas reinhardtii*. *PNAS* 110(18):7223–7228
  57. Melis A, Seibert M, Happe T (2004) Genomics of green algal hydrogen research. *Photosynth Res* 82:277–288

58. Torzillo G, Scoma A, Faraloni C, Ena A, Johanningmeier U (2009) Increased hydrogen photoproduction by means of a sulfur-deprived *Chlamydomonas reinhardtii* D1 protein mutant. *Int J Hydrog Energy* 34:4529–4536
59. Trebst A (1987) The three-dimensional structure of the herbicide binding niche on the reaction center polypeptides of photosystem II. *Z Naturforsch* 42:742
60. Sobolev V, Edelman M (1995) Modeling the Quinone-B binding site of the photosystem-II-reaction center using notions of complementary and contact-surface between atoms. *Proteins Truct Funct Genet* 21:214–225
61. Kettunen R, Tyystjärvi E, Aro EM (1996) Degradation pattern of photosystem II reaction center protein D1 in intact leaves. *Plant Physiol* 111:1183–1190
62. Bayro-Kaiser V, Nelson N (2016) Temperature-sensitive PSII: a novel approach for sustained photosynthetic hydrogen production. *Phptos Res*. <https://doi.org/10.1007/s1120-016-0232-3>
63. Cournac L, Latouche G, Cerovic Z, Redding K, Ravenel J, Peltier G (2002) In vivo interactions between photosynthesis, mitorespiration, and chlororespiration in *Chlamydomonas reinhardtii*. *Plant Physiol* 129:1921–1928
64. Cardol P, Gloire G, Havaux M, Remacle C, Matagne R, Franck F (2003) Photosynthesis and state transitions in mitochondrial mutants of *Chlamydomonas reinhardtii* affected in respiration. *Plant Physiol* 133:2010–2020
65. Endo T, Asada K (1996) Dark induction of the non-photochemical quenching of chlorophyll fluorescence by acetate in *Chlamydomonas reinhardtii*. *Plant Cell Physiol* 37(4):551–555
66. Doebbe A, Rupprecht J, Beckmann J, Mussgnug JH, Hallmann A, Hankmer B, Kruse O (2007) Functional integration of the HUP1 hexose symporter gene into the genome of *C. reinhardtii*: impacts on biological H<sub>2</sub> production. *J Biotechnol* 131:27–33
67. Wu S, Xu L, Wang R, Liu X, Wang QW (2011) A high yield mutant of *Chlamydomonas reinhardtii* for photoproduction of hydrogen. *Int J Hydrog Energy* 36:14134–14140
68. Chien LF, Kuo TT, Liu BH, Lin HD, Feng TY, Huang CC (2012) Solar-to-bioH<sub>2</sub> production enhanced by homologous overexpression of hydrogenase in green alga *Chlorella* sp. DT. *Int J Hydrog Energy* 2012: 17738–17748
69. Kosourov SN, Ghirardi ML, Seibert M (2011) A truncated antenna mutant of *Chlamydomonas reinhardtii* can produce more hydrogen than the parental strain. *Int J Hydrog Energy* 36:2044–2048
70. Strasser R, Srivastava A, Govindjee (1995) Polyphasic chlorophyll a fluorescence transient in plants and cyanobacteria. *Photochem Photo-Dermatology* 61: 32–42
71. Finazzi G, Barbagallo RP, Bergo E, Barbato R, Forti G (2001) Photoinhibition of *Chlamydomonas reinhardtii* in state 1 and state 2. *J Biol Chem* 276:22251–22257
72. Bennoun P (2002) The present model for chlororespiration. *Photosynth Res* 73:273–277
73. Toth SZ, Schansker G, Garab G, Strasser RJ (2007) Photosynthetic electron transport activity in heat treated barley leaves, the role of internal alternative electron donors to photosystem II. *BBA-Bioenergetics* 1767:295–305
74. Antal TK, Volgusheva AA, Kukarskikh GP, Krendeleva TE, Tusov VB, Rubin AB (2006) Examination of chlorophyll fluorescence in sulfur-deprived cells of *Chlamydomonas reinhardtii*. *Biofizika* 51(2):292–298
75. Antal TK, Krendeleva TE, Rubin AB (2007) Study of photosystem 2 heterogeneity in the sulfur-deficient green alga *Chlamydomonas reinhardtii*. *Photosynth Res* 94(1):13–22
76. Oh YK, Raj SM, Jung GY, Park S (2011) Current status of the metabolic engineering of microorganisms for biohydrogen production. *Bioresour Technol* 102:8357–8367
77. Johanningmeier U, Heiss S (1993) Construction of a *Chlamydomonas reinhardtii* mutant with an intronless psbA gene. *Plant Mol Biol* 22(1):91–99

### Books and Reviews

- Edelman M, Mattoo AK, Marder JB (1984) Three hats of the rapidly metabolized 32 kD protein thylakoids. In: Ellis RT (ed) *Chloroplast biogenesis*. Cambridge University Press, Cambridge, pp 283–302
- Ohad I, Kren N, Zer H, Gong H, Mor TS, Gal A, Tal S, Domovich Y (1994) Light-induced degradation of the photosystem II reaction centre D1 protein in vivo, an integrative approach. In: Backer NR, Bowyer JR (eds) *Photoinhibition of photosynthesis, from molecular mechanisms to the field*. Bios Scientific Publishers, Oxford, pp 161–178
- Torzillo G, Seibert M (2013) Hydrogen production by microalgae. In: Richmond A, Hu Q (eds) *Handbook of microalgal culture: applied phycology and biotechnology*, 2nd edn. Wiley, Oxford, pp 417–444
- Torzillo G, Scoma A, Faraloni C, Giannelli L (2014) Advances in the biotechnology of hydrogen production with the microalga *Chlamydomonas reinhardtii*. *Crit Rev Biotechnol* 35(4):485–496
- Vermaas WFI, Ikeuchi M (1991) Photosystem II. In: Bogorad L, Vasil IK (eds) *The photosynthetic apparatus, molecular biology and operation, Cell culture and somatic cell genetics of plants*, vol 7B. Academic Press, San Diego, pp 25–111



## Advances on Inorganic Membrane Reactors for Production of Hydrogen

Adolfo Iulianelli and Angelo Basile  
Institute on Membrane Technology of the Italian  
National Research Council (CNR-ITN),  
University of Calabria, Rende, CS, Italy

### Article Outline

Introduction: Membrane Reactors  
The Role of the Pd-Based Membranes Applied  
to MRs  
Conclusion and Future Trends  
Abbreviations and Symbols  
Bibliography

### Introduction: Membrane Reactors

Over several decades, membrane reactor (MR) technology has been involved in the utilization of new inorganic materials and the development of high-temperature membrane processes as well. The scientific interest about MR technology has attracted particular attention as testified by the extensive literature on the different scientific fields of interest. A general MR subdivision is summarized below, strictly depending on the membrane typology used [1, 2]:

- (a) Dense and porous inorganic membrane reactors
- (b) Electrochemical membrane reactors (fuel cells, electrolytic cells, etc.)
- (c) Zeolite membrane reactors
- (d) Photocatalytic membrane reactors
- (e) Polymeric membrane reactors
- (f) Biomedical membrane reactors or membrane bioreactors

The main characteristic of the MRs used in chemical and biochemical reactions is represented by their ability of intensifying the whole process in the viewpoint of process intensification strategy [2–4]. As a consequence, the membrane choice plays an important role as discussed in the following sections.

Looking at the category of dense and porous inorganic MRs, two different kinds of reforming reactors are allowed: packed-bed membrane reactors (PBMRs) and fluidized-bed membrane reactors (FBMRs). PBMRs are the most studied and can be subdivided into other two distinct configurations such as tubular or plane, with the catalyst loaded inside to constitute a packed bed in direct contact with the membrane [3]. In tubular configuration, the catalyst can be packed either in the membrane core or in the annulus. This configuration is simple due to the easy loading of the catalyst particles even though their dimension plays an important role, being responsible for the performance of the reactor. Smaller-sized particles can be responsible for pressure drop increase, while larger-sized particles can affect negatively the performance in terms of internal mass transfer. In the field of PBMR application for hydrogen production, a critical issue is represented by the mass transfer limitation from the bed to the wall, causing reduced hydrogen permeation and evident temperature profile along the reactor, with consequent detrimental effects on catalyst and membrane performance [4].

Concerning the FBMR technology, as a general description, a common FBMR can be represented by a bundle of membranes immersed in a catalytic bed, exercised at bubbling or turbulent regime [5]. Compared to the PBMRs, the FBMRs show higher catalyst effectiveness and improved mass and heat transfer rates, with consequent more uniform temperature profile along the reactor. Nevertheless, a crucial issue affecting this MR typology is constituted of the minimum fluidization velocity, which is the limit of this kind of reactors. In fact, the catalytic bed is in



suspension only in case the minimum fluidization velocity is overcome. Furthermore, the presence of bubbles makes some mass transfer limitations possible, causing lower MR performance during the specific reaction process [6]. However, up to now, the MRs constitute a concrete option to the conventional reactors (CRs), particularly in the field of hydrogen generation through reforming reactions. Several benefits are realized when an inorganic MR is used instead of a CR, and the most significant of these are summarized below:

1. Potentiality of generating high-grade hydrogen in only one device without needing further hydrogen purification/separation steps
2. Higher conversions than CRs (operated at the same MR conditions) or the same conversion but achieved at milder conditions than the equivalent CR

In the open literature, considerable attention has been paid on the utilization of MRs housing Pd-based membranes because of their high selectivity to hydrogen permeation with respect to all the other gases [7]. Therefore, this chapter focuses on the recent advances on Pd-based MR application with particular reference to hydrogen production from reforming reactions.

### The Role of the Pd-Based Membranes Applied to MRs

In a MR used to carry out such a reaction process for producing high-grade hydrogen (Fig. 1), the so-called shift effect represents the mechanism

useful for overcoming the thermodynamic equilibrium restrictions of an equivalent CR operated at the same MR conditions.

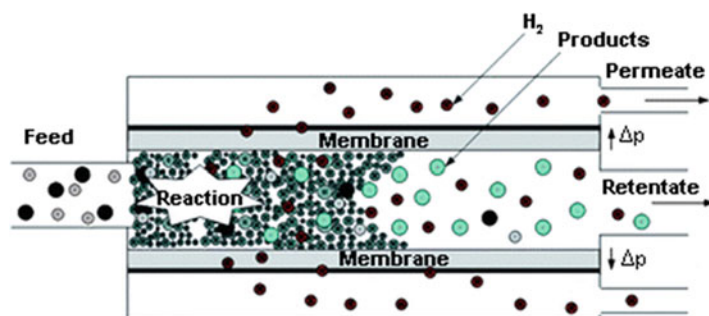
Among the inorganic membranes showing characteristics of high hydrogen permselectivity, niobium, vanadium, and tantalum should be particularly considered due to their higher hydrogen permeability than other metals, with the further behavior of showing hydrogen permeability increase by decreasing the temperature. Unfortunately, these metals are also prone to a severe hydrogen embrittlement phenomenon [8] as a main cause of the transition from a ductile to a brittle behavior. As a consequence, palladium has been greatly considered, although their commercialization is still limited by some issues such as mechanical resistance and high costs [9–12].

The hydrogen molecular transport in a dense layer of palladium occurs through a solution/diffusion mechanism, taking place in six different activated steps:

1. Dissociation of molecular hydrogen at the gas/metal interface
2. Adsorption of the atomic hydrogen on membrane surface
3. Dissolution of atomic hydrogen into the palladium matrix
4. Diffusion of atomic hydrogen through the membrane
5. Recombination of atomic hydrogen to form hydrogen molecules at the gas/metal interface
6. Desorption of hydrogen molecules

Each step may control the hydrogen permeation through the membrane depending on

**Advances on Inorganic Membrane Reactors for Production of Hydrogen, Fig. 1** Scheme of a tubular membrane reactor with the catalytic bed in the membrane core



temperature, pressure, and composition of the gas mixture. The hydrogen permeation flux can be expressed by Eq. (1) as

$$J_{H_2}^{\text{Permeating}} = \frac{B_{H_2}}{\delta} \left( p_{H_2, \text{retentate}}^n - p_{H_2, \text{permeate}}^n \right) \quad (1)$$

where  $J_{H_2}$  is the hydrogen flux permeating through the membrane,  $B_{H_2}$  the hydrogen permeability,  $\delta$  the membrane thickness, and  $p_{H_2, \text{retentate}}$  and  $p_{H_2, \text{permeate}}$  the hydrogen partial pressures in the retentate and permeate sides.  $n$  is a variable in the range 0.5–1 depending on the rate-limiting step of hydrogen diffusion and can be calculated through experiments [13].

When the hydrogen diffusion into the bulk is the rate-limiting step and, meanwhile, no other gas permeation takes place, the hydrogen permeating flux can be calculated by Sieverts-Fick law as expressed by Eq. (2):

$$J_{H_2}^{\text{Permeating}} = \frac{B_{H_2}}{\delta} \left( p_{H_2, \text{retentate}}^{0.5} - p_{H_2, \text{permeate}}^{0.5} \right) \quad (2)$$

where  $B_{H_2}$  is the hydrogen permeability,  $\delta$  the membrane thickness, and  $p_{H_2, \text{retentate}}$  and  $p_{H_2, \text{permeate}}$  the hydrogen partial pressures in the retentate and permeate streams, respectively. Equation (2) indicates the characteristics of full hydrogen permselectivity of the dense palladium layer, meaning that only hydrogen can permeate through the membrane with respect to all the other gases. To consider the temperature effect on the hydrogen permeability of the membrane, the relationship as an Arrhenius law between the hydrogen permeability and the temperature is represented in Eq. (3):

$$B_{H_2} = B_{H_2}^0 \cdot \exp\left(-\frac{E_a}{R.T}\right) \quad (3)$$

where  $B_{H_2}^0$  is the pre-exponential factor,  $E_a$  the apparent activation energy,  $R$  the universal gas constant, and  $T$  the temperature.

Unfortunately, a dense layer of palladium exposed to pure hydrogen permeation below

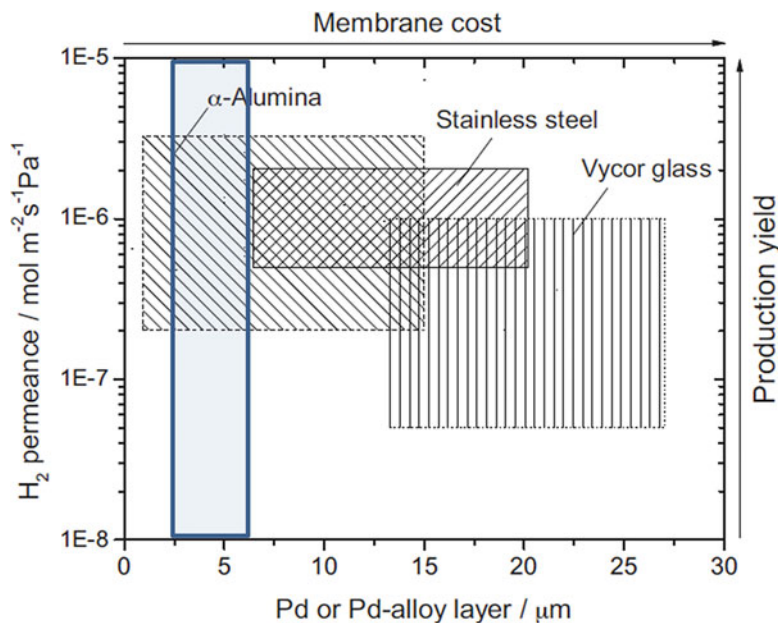
300 °C and 2.0 MPa is prone to the hydrogen embrittlement phenomenon, which may be solved by alloying palladium with other metals, such as silver, nickel, copper, etc. The role of the second metal in the Pd alloy is related to the displaying effect of its electron-donating behavior, being largely similar to that of the hydrogen atom in palladium, making possible competition for the filling of electron holes within the silver and hydrogen [7].

In the last two decades, the role of supported Pd-based membranes has been particularly considered. Indeed, this kind of Pd membranes is constituted by a thin dense layer of palladium or its alloy deposited onto a porous support such as porous Vycor glass (silica gel),  $\text{SiO}_2$ ,  $\text{Al}_2\text{O}_3$ , and  $\text{B}_2\text{O}_3$  or porous stainless steel (PSS). Porous supports having a thermal expansion coefficient close to the palladium allow high mechanical durability and simplify the gas sealing [14]. Nevertheless, PSS support alloys the palladium at relatively high temperatures, leading to lower the hydrogen permeability [15]. This solution allows the reduction of the palladium content and the cost as well, favoring meanwhile a more consistent mechanical resistance [16]. In a recent critical review, You and Ted Oyama [17] pointed out that composite Pd-based membranes prepared by  $\text{Al}_2\text{O}_3$  as a support proved to be more effective than the utilization of other porous supports in terms of membrane cost and hydrogen permeation characteristics (Fig. 2). This can be more emphasized when the dense layer of palladium or palladium alloy is in the range of 2.5–5  $\mu\text{m}$  of thickness, constituting a viable solution to be proposed also at larger scale for achieving a cost-effective and highly hydrogen-permeable and hydrogen-permselective membrane.

Furthermore, among the various Pd deposition techniques, the electroplating and the electroless plating deposition techniques make the deposition of the dense Pd or Pd alloy layer feasible for achieving the most attractive region in a graph of  $\text{H}_2/\text{N}_2$  selectivity vs  $\text{H}_2$  permeability, represented by high value of  $\text{H}_2$  permeance and permselectivity [17]. On the contrary, chemical vapor deposition seems to be not so effective for preparing highly hydrogen-permselective composite

### Advances on Inorganic Membrane Reactors for Production of Hydrogen,

**Fig. 2** H<sub>2</sub> permeance, production yield, and membrane cost vs thickness of the Pd or Pd alloy layer in a composite membrane (Adapted from [17])

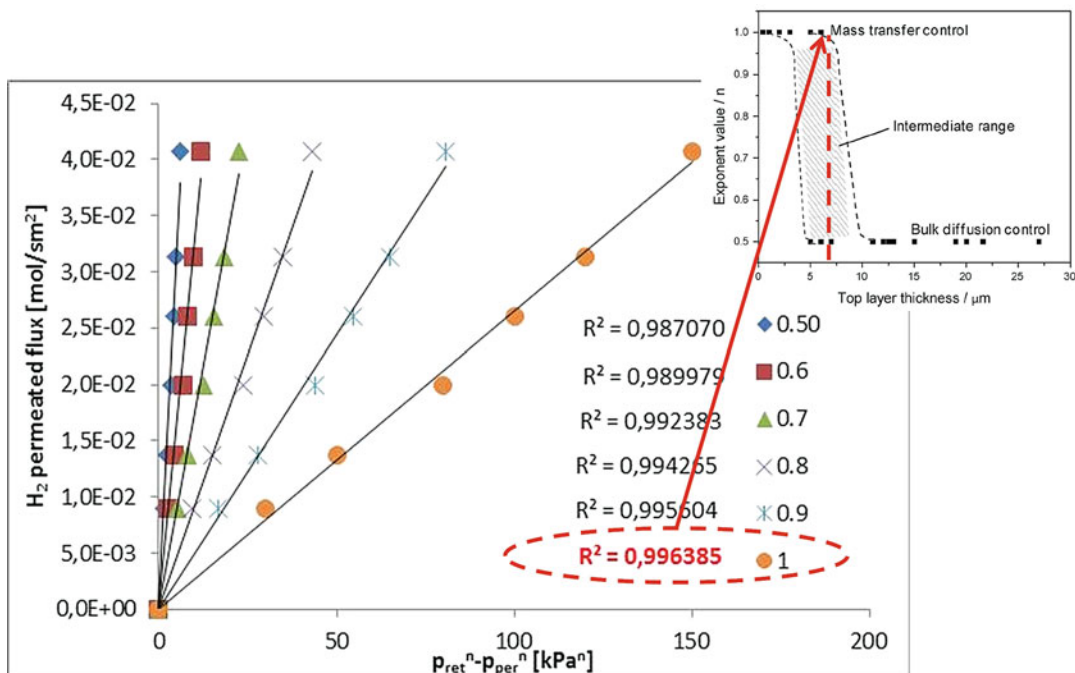


membranes. Another relevant issue related to the supported Pd-based membranes is constituted by the coefficient “*n*” in Eq. (1), which is strictly correlated to the hydrogen permeation characteristics of the composite membrane. As is well known, this coefficient can vary between 0.5 (typical value for expressing the Sieverts-Fick law, regulating fully hydrogen-permselective Pd membranes) and 1.0 (low hydrogen permselectivity). For supported membranes showing a thickness of the dense Pd or Pd alloy layer around 5 μm, the different values of the coefficient “*n*” can exactly describe which kind of mechanism is controlling the hydrogen permeation process through the membrane.

As an example, Fig. 3 shows the graphical calculation of coefficient “*n*” for a Pd-Au/Al<sub>2</sub>O<sub>3</sub> membrane (dense Pd-Au layer of 7 μm) [18], and the value of *n* = 1.0 associated with the highest linear regression factor (*R*<sup>2</sup>) means that the rate-controlling step is the mass transfer instead of the bulk diffusion as for the exponent *n* = 0.5. Apart from the extremities of this range, it is possible to find several exponent “*n*” values describing an intermediate behavior during the hydrogen permeation process. Obviously, “*n*” values closer to 0.5 describe more hydrogen-permselective membranes than values closer to 1.0. As an example,

Table 1 summarizes several experimental data from the open literature regarding composite Pd-based membranes.

As shown, the characteristics of H<sub>2</sub>/N<sub>2</sub> ideal selectivity vary greatly depending on the effectiveness of the dense Pd-based layer deposition (associated with the deposition technique), presence of defects, support typology, and role of the intermediate layer. In some cases, hydrogen permselectivity tends to be complete (highlighted in the table), indicated with the “infinite” term. In this case, the exponent “*n*” is equal to 0.5, and the permeation of hydrogen is regulated by the Sieverts-Fick law (2). Nevertheless, in other cases, the perm-selectivity shows finite values, indicating that the dense layer is not uniform with presence of pin-holes, probably caused by the not effective role of the intermediate layer in the coverage of the pores of the support and for the decrease of its roughness. As a consequence, in the intermediate region (*n* = 0.5–0.8), the other gases can pass through defects with Knudsen mechanism and viscous flow, while hydrogen permeation is through solution/diffusion, Knudsen mechanism, and viscous flow. The contribution of each mechanism on the total hydrogen permeating flux can be taken into account by looking at Eq. (4):



**Advances on Inorganic Membrane Reactors for Production of Hydrogen, Fig. 3** Graphical calculation of coefficient “n” from the linear regression factor (R<sup>2</sup>) for a Pd-Au/Al<sub>2</sub>O<sub>3</sub> membrane with a thin Pd-Au layer of 7 μm

(Adapted from [18]), merged to the rate-controlling step for the hydrogen permeation through the membrane as a function of exponent “n” vs top layer thickness (Adapted from [17])

$$J_{H_2}^{Total} = \frac{1}{\frac{1}{J_{H_2}^{SD}} + \frac{1}{J_{H_2}^K} + \frac{1}{J_{H_2}^{HP}}} \quad (4)$$

where (5) and (6) represent the Knudsen and Hagen-Poiseuille equations, respectively:

$$J_{H_2}^K = \frac{\varepsilon d_p}{\tau L} \left( \frac{8}{9\pi MRT} \right)^{1/2} \Delta p_{H_2} \quad (5)$$

$$J_{H_2}^{HP} = \frac{R^2}{8\eta LP_0} P_{AVE} \Delta p_{H_2} \quad (6)$$

where ε is the membrane porosity, d<sub>p</sub> the pore diameter, τ the tortuosity, L the thickness, M the molecular weight of diffusing gas, Δp<sub>H<sub>2</sub></sub> the trans-membrane hydrogen partial pressure, η the viscosity, P<sub>AVE</sub> the average pressure, P<sub>0</sub> the outlet pressure, and R the radius, while J<sub>H<sub>2</sub></sub><sup>SD</sup> is equal to Eq. (1).

### Membrane Reactors Allocating Pd-Based Membranes

MRs housing Pd-based membranes act on such a reaction process performed inside with the well-known “shift effect,” which allows to overcome the thermodynamic equilibrium restrictions of the reaction carried out in an equivalent CR [4]. This can be observed in the proposed schematic illustration of Fig. 4, in which it is possible to note that the MR conversion doesn’t obey to the limitations of a closed system as the CR. Indeed, a MR represents an open system due to the continuous removal from the reaction side of such a product as hydrogen.

However, for describing the generic behaviors of a MR during a reaction process, depending on the type of the inorganic membrane housed inside, the MR conversion strictly depends on the parameter “H,” defined as permeation rate-to-reaction rate ratio [20]. In case H = 0, the permeation does

**Advances on Inorganic Membrane Reactors for Production of Hydrogen, Table 1** Experimental data from the open literature regarding supported Pd-based membranes (Adapted from [19])

Membrane type	Preparation method	Pd layer ( $\mu\text{m}$ )	T ( $^{\circ}\text{C}$ )	$\Delta p$ (Pa)	$\text{H}_2$ permeance ( $\text{mol}/\text{m}^2 \cdot \text{s} \cdot \text{Pa}$ )	Ideal Selectivity ( $\alpha_{\text{H}_2/\text{N}_2}$ )	Reference
Pd/( $\gamma$ - $\text{Al}_2\text{O}_3/\text{Al}_2\text{O}_3$ )	ELP	5	500	400000	$2.8 \cdot 10^{-6}$	8000	Tanaka et al. [21]
Pd/( $\gamma$ - $\text{Al}_2\text{O}_3/\text{Al}_2\text{O}_3$ )	ELP	2.4	500	100000	$3.9 \cdot 10^{-6}$	32500	Li et al. [22]
Pd/PSS	ELP	10	400	200000	$8.7 \cdot 10^{-7}$	$\sim 11800$	Liguori et al. [23]
Pd/YSZ/PSS	ELP	28	450	40000	$4.5 \cdot 10^{-4 \text{a}}$	$\infty$	Sanz et al. [24]
Pd/( $\gamma$ - $\text{Al}_2\text{O}_3/\text{Al}_2\text{O}_3$ )	ELP	2.6	370	400000	$4.8 \cdot 10^{-7}$	3000	Nair et al. [25]
Pd/ $\text{Al}_2\text{O}_3$	CVD	2	300	30000	$3.3 \cdot 10^{-6}$	5000	Itoh et al. [26]
Pd/ $\text{Fe}_2\text{O}_3$ /PSS	ELP	22	450	100000	$2.7 \cdot 10^{-4 \text{a}}$	$\infty$	Rothenberger et al. [27]
Pd/( $\gamma$ - $\text{Al}_2\text{O}_3/\text{Al}_2\text{O}_3$ )	ELP	6	480	100000	$2.6 \cdot 10^{-6}$	2100	Zhang et al. [28]
Pd/ $\text{Al}_2\text{O}_3$	ELP	0.9	460	199000	$3.1 \cdot 10^{-6}$	1200	Yun et al. [29]
Pd/PSS	ELP	10	400	200000	$5.0 \cdot 10^{-7}$	5000	Mardilovich et al. [30]
Pd/ $\text{Al}_2\text{O}_3$	ELP	0.9	450	105000	$4.0 \cdot 10^{-6}$	9200	Maneering et al. [31]
Pd-Ag-Ru/ $\alpha$ - $\text{Al}_2\text{O}_3$	ELP	6	500	100000	$1.7 \cdot 10^{-4 \text{a}}$	$\infty$	Wang et al. [32]
Pd-Cu/ $\text{SiO}_2/\text{Ni-SS}$	VED	< 2	460	70000	-	> 80000	Nam & Lee. [33]
Pd-Ag/SS	Sputtering	2.6	450	1000000	$3.0 \cdot 10^{-6}$	500 <sup>b</sup>	Peters et al. [34]
Ru/Pd/ $\text{Al}_2\text{O}_3$ /PHA	ELP	6.8	500	100000	-	$\infty$ ( $\text{H}_2/\text{He}$ )	Ryi et al. [35]
Pd/PSS	PP-ELP	20	450	-	-	$\infty$	Sanz et al. [36]
Pd/YSZ/PSS	ELP	25-30	500	-	$3.1 \cdot 10^{-4 \text{a,c}}$	400 <sup>b</sup>	Straczewski et al. [37]
Pd/ $\text{Al}_2\text{O}_3$	ELP	2-4	400	-	-	500	Goldbach et al. [38]
Pd/ $\text{Al}_2\text{O}_3$	ELP	5	400	100000	$4.3 \cdot 10^{-4}$	$\infty$	<b>This work</b>

<sup>a</sup> Sieverts-Fick law considered

<sup>b</sup> Value obtained as separation factor using  $\text{H}_2/\text{N}_2$  mixture

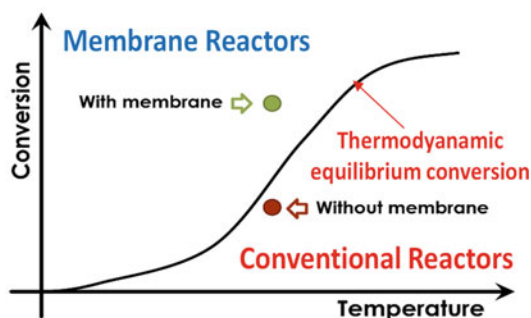
<sup>c</sup> [ $\text{mol}/\text{m}^2 \cdot \text{s} \cdot \text{Pa}^{0.5}$ ]

not take place, and the MR works as a CR. In case of relatively low values of H parameter, this may involve consequently low permeation to reaction rate. Typically, in this region, microporous, dense, and mesoporous membranes show the same behaviors. Otherwise, inorganic membranes showing finite values of ideal selectivity (defined as the ratio between the permeance of a certain gas such as hydrogen and that of a referenced gas such as a blank gas – He, Ar,  $\text{N}_2$ , etc.), when housed inside the MR, make possible to achieve an optimum in terms of H factor. Overcoming the optimum, the reactant loss due to their permeation through the membrane causes a detrimental effect on the conversion. On the contrary, a higher ideal selectivity corresponds to higher conversions. In membranes showing full ideal selectivity (e.g., the Pd-based membranes), the reactant loss does not

take place, because only a product such as hydrogen – in the case of Pd-based membranes – is removed from the reaction side for permeation through the membrane.

As an example of the applications of Pd-based MRs to a reaction process, Table 2 summarizes some of the most recent and significant findings on bioethanol steam reforming process. As presented in those findings, a Pd-based MR coupled with a bio-source reforming process can constitute a renewable and alternative solution for producing hydrogen. As shown, high conversion, hydrogen recovery, and permeate purity are possible using different kinds of supported and unsupported Pd-based MRs. Particular attention should be paid on the results in terms of hydrogen recovery and purity of low Pd-content composite membranes, which allow to reach great experimental





**Advances on Inorganic Membrane Reactors for Production of Hydrogen, Fig. 4** Scheme of an endothermic reaction process (conversion vs T) carried out in both membrane and conventional reactors operated at the same conditions (Courtesy of Prof. Vincenzo Palma)

results with a few microns of deposited Pd. We resumed also some literature data about dense self-supported Pd-based membranes allocated in MRs. Considering the membrane thickness, it is evident that the amount of palladium is quite high, making these membranes not a competitive solution in MRs for the scaling-up of BESR process at industrial level.

Nevertheless, the most critical issue not represented in the table is the difficulty of scaling up this technology at industrial level. In fact, the cost of the membrane, its lifetime, and mechanical resistance as well constitute the main problems affecting the Pd-based MR technology. In particular, about the composite Pd-based membranes, the role of the intermediate layer, the formation of pinholes in the Pd-based dense layer, and the consequent detrimental effects on the hydrogen permselectivity and lifetime represent the most critical obstacles that researchers and scientists have to solve in the near future in order to use the potentiality of this technology in real applications.

Recently, a possible solution to the aforementioned issues can be represented by the MOC (membrane on catalyst), in which the porous substrate itself has the function of a reforming catalyst. Therefore, the integration of catalyst and support makes the cost reduction of the MR module feasible, with further advantages also in terms of MR performance [33].

Figure 5 sketches the scheme of a MR module using a MOC configuration compared to a classic supported membrane. In a steam reforming reaction process, the feed (in Fig. 5 reported as natural gas with steam) goes into the catalytic bed (Fig. 5a), and hydrogen is produced and then removed for permeation through the dense layer of palladium, supported on a porous substrate. On the contrary, Fig. 5b illustrates that in MOC configuration, the feed comes directly in the substrate acting as a catalyst. Figure 6 shows a real Pd-based MOC realized by Tokyo Gas Company Co., Ltd., associated with the scheme of the internal layers [33].

## Conclusion and Future Trends

As foreseen by Dunn [34] regarding hydrogen futures for a sustainable energy system, hydrogen will acquire more and more relevance as a fuel (Fig. 7), up to completely substituting liquid and solid exploitation, while overcoming methane in the near future and playing the role of main fuel in the next century for an increasing economic sustainable growth.

Conventional processes for producing hydrogen from fossil fuels are so far the most used, but they have been strongly revised and redesigned in order to be more sustainable. In this respect, the introduction of MRs has fostered the production of high-purity hydrogen, although the real challenge to make hydrogen really sustainable may be realized when it may be produced from renewable sources. Thus, the potential of Pd-based membranes in hydrogen production systems was illustrated to greatly improve their efficiency and, in the case of biohydrogen production, may represent the critical key factor making the technology sustainable. Future trends will be toward the development of membrane materials and MR configurations able to overcome some membrane application issues, such as cost and performance durability. The application of MR systems on industry may help to promote the “hydrogen economy” on a worldwide scale.

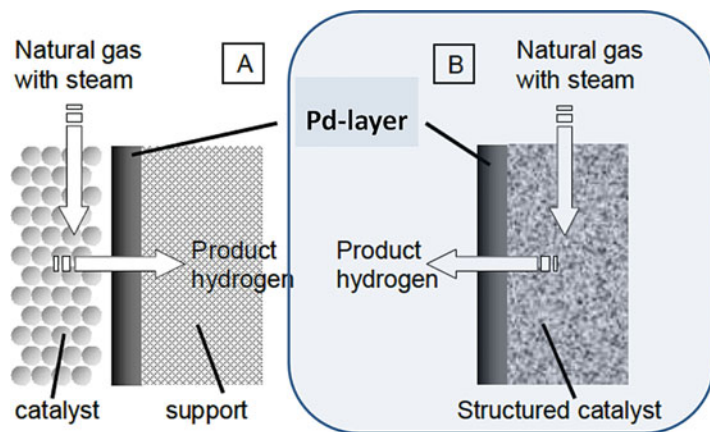


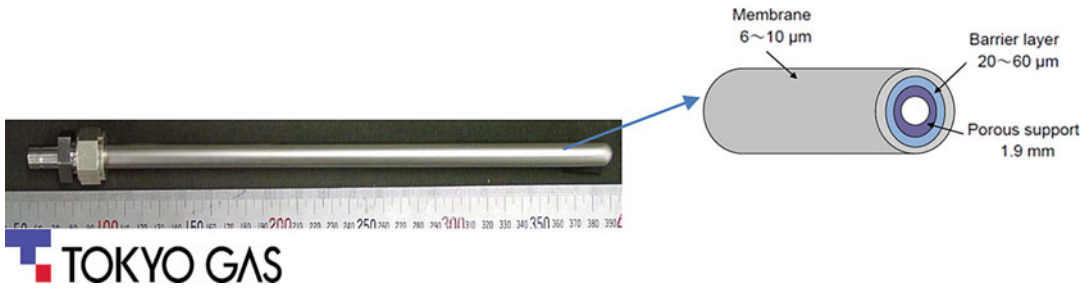
**Advances on Inorganic Membrane Reactors for Production of Hydrogen, Table 2** Recent applications of Pd-based membrane reactors on bioethanol steam reforming for high-grade hydrogen generation

Membrane in the MR	Thickness of the metallic layer [ $\mu\text{m}$ ]	T [ $^{\circ}\text{C}$ ]	p [bar]	Conversion [%]	H <sub>2</sub> recovery [%]	H <sub>2</sub> yield [%]	H <sub>2</sub> purity [%]	Reference
composite Pd/Al <sub>2</sub> O <sub>3</sub>	5	400	2.0	60	70	35	~99.6	[19]
composite Pd-Cu	2	360	1.0	74	–	–	–	[21]
composite Ni-Pd-Ag	<8	450	3.0	~80	–	70	>90	[22]
composite Pd/Al <sub>2</sub> O <sub>3</sub>	4–5	480	10	90	–	80	>99	[23]
composite Pd-Ag/PSS	30	650	4.0	100	70	>50	–	[24]
composite Pd-Ag/PSS	30	600	16	–	80	85	–	[25]
composite Pd-Ag	30	700	6.9	–	–	75	–	[26]
composite Pd/PSS	25	400	8.0	100	55	–	~95	[27]
composite Pd/PSS	25	400	12.0	87	12	17	~95	[28]
composite Pd/Al <sub>2</sub> O <sub>3</sub>	8	400	3.0	98	67	–	~97	[29]
composite Pd/PSS	25	400	8.0	100	55	–	~95	[27]
self-supported Pd-Ag	75	550	–	~100	80	<50	~100	[30]
self-supported Pd-Ag	50	400	3.0	~100	90	53	~100	[31]
self-supported Pd-Ru	50	450	1.0	–	–	~50	~100	[32]

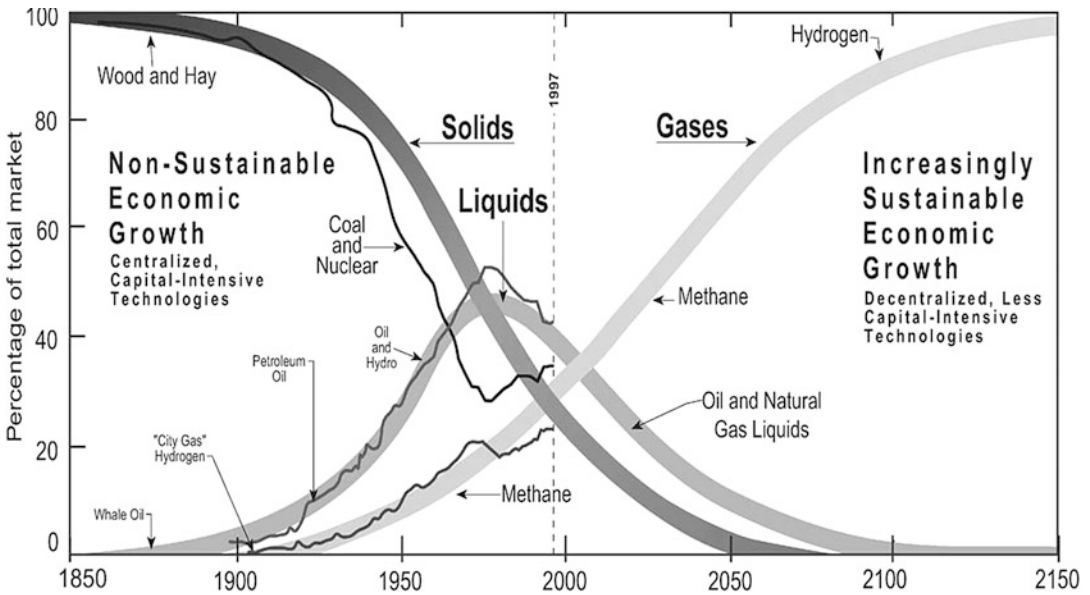
### Advances on Inorganic Membrane Reactors for Production of Hydrogen,

**Fig. 5** Scheme of a steam reforming process MR module housing: (a) classic supported Pd-based MR module, (b) MR module with MOC configuration (Adapted from [33])





**Advances on Inorganic Membrane Reactors for Production of Hydrogen, Fig. 6** Picture of a MOC realized by Tokyo Gas Company Co., Ltd (Adapted from [33])



**Advances on Inorganic Membrane Reactors for Production of Hydrogen, Fig. 7** Hydrogen futures for a sustainable energy system (With permission of reprint from [34])

**Abbreviations and Symbols**

$B_{H_2}$	Hydrogen permeability	$J_{H_2}^K$	Hydrogen permeating flux contribution due to Knudsen flow equations
$B_{H_2}^0$	Pre-exponential factor	$J_{H_2}^{SD}$	Hydrogen permeating flux contribution due to solution/diffusion mechanism
CR	Conventional reactor	$J_{H_2}^{TOT}$	Total hydrogen permeating flux
$d_p$	Pore diameter	L	Length
$E_a$	Apparent activation energy	M	Molecular weight of diffusing gas
FBMR	Fluidized-bed membrane reactor	MR	Membrane reactor
H	Permeation rate-to-reaction rate ratio	n	Dependence factor of the hydrogen flux on the hydrogen partial pressure
$J_{H_2}$	Hydrogen flux permeating through the membrane	p	Pressure
$J_{H_2}^{HP}$	Hydrogen permeating flux contribution due to Hagen-Poiseuille equations	$P_0$	Outlet pressure
		$P_{AVE}$	Average pressure
		PBMR	Packed-bed membrane reactor

$p_{\text{H}_2}$ -permeate	Hydrogen partial pressures in the permeate side
$p_{\text{H}_2}$ -retentate	Hydrogen partial pressures in the retentate side
PSS	Porous stainless steel
R	Radius (in Eq. 6)
R	Universal gas constant
T	Temperature
$\delta$	Membrane thickness
$\eta$	Viscosity
$\Delta p_{\text{H}_2}$	Transmembrane hydrogen partial pressure
$\varepsilon$	Membrane porosity
$\tau$	Tortuosity

## Bibliography

- Westermann T, Melin T (2009) Review – flow-through catalytic membrane reactors – principles and applications. *Chem Eng Process* 48:17–28
- Piomonte V, Di Paola D, De Falco M, Iulianelli A, Basile A (2014) Hydrogen production using inorganic membrane reactors., Ch. 11. In: Basile A, Iulianelli A (eds) *Advances in hydrogen production, storage and distribution*. Woodhead Publishing, pp 283–316. ISBN:978-0-85709-768-2 (print), ISBN:978-0-85709-773-6 (online)
- Iulianelli A, Liguori S, Wilcox J, Basile A (2016) Advances on methane steam reforming to produce hydrogen through membrane reactors technology: a review. *Catal Rev Sci Eng* 58:1–35
- Basile A, Iulianelli A, Tong J (2015) Single-stage hydrogen production and separation from fossil fuels using micro- and macromembrane reactors., Ch. 15. In: Subramani V, Basile A, Nejat Veziroglu T (eds) *Compendium of Hydrogen Energy, Hydrogen Production and Purification*, Woodhead Publishing Series in Energy: Number 83, vol 1, pp 445–468
- Adris AM, Jim Lim C, Grace JR (1994) The fluidized bed membrane reactor system: a pilot scale experimental study. *Chem Eng Sci* 49:5833–5843
- Adris AM, Grace JR (1997) Characteristics of fluidized-bed membrane reactors: scale-up and practical issues. *Ind Eng Chem Res* 36:4549–4556
- Basile A, Iulianelli A, Longo T, Liguori S, De Falco M Pd-based Selective Membrane State-of-the-Art., Ch. 2. In: Marrelli L, De Falco M, Iaquaniello G (eds) *Membrane reactors for hydrogen production processes*. Springer, London/Dordrecht/Heidelberg/New York, pp 21–55
- Lu GQ, Diniz de Costa JC, Duke M, Giessler S, Socolow R, Williams RH, Kreutz T (2007) Inorganic membranes for hydrogen production and purification: a critical review and perspective. *J Colloid Interface Sci* 314:589–603
- Adhikari S, Fernand S (2006) Hydrogen membrane separation techniques. *Ind Eng Chem Res* 45:875–881
- Tereschenko GF, Ermilova MM, Mordovin VP, Orekhova NV, Gryaznov VM, Iulianelli A, Gallucci F, Basile A (2007) New Ti-Ni dense membranes with low palladium content. *Int J Hydrogen En* 32:4016–4022
- Iulianelli A, Basile A (2011) Hydrogen production from ethanol via inorganic membrane reactors technology: a review. *Catal Sci Techn* 1:366–379
- Briceño K, Iulianelli A, Montané D, Garcia-Valls R, Basile A (2012) Carbon molecular sieve membranes supported on non-modified ceramic tubes for hydrogen separation in membrane reactors. *Int J Hydrogen En* 37:13536–13544
- Iulianelli A, Liguori S, Huang Y, Basile A (2015) Model biogas steam reforming in a thin Pd-supported membrane reactor to generate clean hydrogen for fuel cells. *J Power Sources* 273:25–32
- Mallada R, Menéndez M (2008) *Inorganic membranes: synthesis, characterization and applications, technology & engineering*. Elsevier, Amsterdam/Oxford, p 460
- Uemiyama S (1999) State-of-art-the-art of supported metal membranes for gas separation. *Sep Pur Methods* 28:51–85
- Liguori S, Iulianelli A, Dalena F, Pinacci P, Drago F, Broglia M, Huang Y, Basile A (2014) Performance and long-term stability of Pd/PSS and Pd/Al<sub>2</sub>O<sub>3</sub> for hydrogen separation. *Membranes* 4:143–162
- Yun S, Ted Oyama S (2011) Correlations in palladium membranes for hydrogen separation: a review. *J Membr Sci* 375:28–45
- Iulianelli A, Alavi M, Bagnato G, Liguori S, Wilcox J, Rahimpour MR, Eslamlouyan R, Anzelmo B, Basile A (2016) Supported Pd-Au membrane reactor for hydrogen production: membrane preparation, characterization and testing. *Molecules* 21:581–594
- Iulianelli A, Palma V, Bagnato G, Ruocco C, Huang Y, Veziroglu NT, Basile A (2017) From bioethanol exploitation to high grade hydrogen generation: steam reforming promoted by a Co-Pt catalyst in a Pd-based membrane reactor, *in press*, *Renewable Energy*. <https://doi.org/10.1016/j.renene.2017.10.050>
- Keizer K, Zaspalis KVT, De Lange RSA, Harold MP (1994) In: Crespo JG, Boddeker KW. (eds) ISBN:0-7923-2929-5 *Membrane processes in separation and purification*. Kluwer Academic Publishers, Dordrecht, pp 415–429
- Yun S, Lim H, Ted Oyama S (2012) Experimental and kinetic studies of the ethanol steam reforming reaction equipped with ultrathin Pd and Pd-Cu membranes for improved conversion and hydrogen yield. *J Membr Sci* 409-410:222–231
- Lin W-H, Liu Y-C, Chang H-F (2010) Autothermal reforming of ethanol in a Pd-Ag/Ni composite membrane reactor. *Int J Hydrogen En* 35:12961–12969

23. Murmura MA, Patrascu M, Annesini MC, Palma V, Ruocco C, Sheintuch M (2015) Directing selectivity of ethanol steam reforming in membrane reactors. *Int J Hydrogen En* 40:5837–5848
24. Hedayati A, Le Corre O, Lacarrière B, Llorca J (2015) Exergetic study of catalytic steam reforming of bio-ethanol over Pd–Rh/CeO<sub>2</sub> with hydrogen purification in a membrane reactor. *Int J Hydrogen En* 40: 3574–3581
25. Liguori S, Pinacci P, Seelam PK, Keiski R, Drago F, Calabrò V, Basile A, Iulianelli A (2012) Performance of a Pd/PSS membrane reactor to produce high purity hydrogen via WGS reaction. *Catal Today* 193:87–94
26. Papadias DD, Lee SHD, Ferrandon M, Ahmed S (2010) An analytical and experimental investigation of high-pressure catalytic steam reforming of ethanol in a hydrogen selective membrane reactor. *Int J Hydrogen En* 35:2004–2017
27. Basile A, Pinacci P, Iulianelli A, Broglia M, Drago F, Liguori S, Longo T, Calabrò V (2011) Ethanol steam reforming reaction in a porous stainless steel supported palladium membrane reactor. *Int J Hydrogen En* 36:2029–2037
28. Seelam PK, Liguori S, Iulianelli A, Pinacci P, Drago F, Calabrò V, Huuhtanen M, Keiski R, Piemonte V, Tosti S, De Falco M, Basile A (2012) Hydrogen production from bio-ethanol steam reforming reaction in a Pd/PSS membrane reactor. *Catal Today* 193:42–48
29. Iulianelli A, Liguori S, Vita A, Italiano C, Fabiano C, Huang Y, Basile A (2016) The oncoming energy vector: hydrogen produced in Pd-composite membrane reactor via bioethanol reforming over Ni/CeO<sub>2</sub> catalyst. *Catal Today* 259:368–375
30. da Silva AM, Mattos LV, Múnera J, Lombardo E, Noronha FB, Cornaglia L (2015) Study of the performance of Rh/La<sub>2</sub>O<sub>3</sub>-SiO<sub>2</sub> and Rh/CeO<sub>2</sub> catalysts for SR of ethanol in a conventional fixed-bed reactor and a membrane reactor. *Int J Hydrogen En* 40: 4154–4166
31. Iulianelli A, Basile A (2010) An experimental study on bio-ethanol steam reforming in a catalytic membrane reactor. Part I: Temperature and sweep-gas flow configuration. *Int J Hydrogen En* 35: 3170–3177
32. Mironova EY, Ermilova MM, Orekhova NV, Muraviev DN, Yaroslavtsev AB (2014) Production of high purity hydrogen by ethanol steam reforming in membrane reactor. *Catal Today* 236:64–69
33. Shirasaki Y, Yasuda I (2013) Membrane reactor for hydrogen production from natural gas at Tokyo Gas Company: a case study. In: Basile A (ed) *Handbook of membrane reactors: reactor types and industrial applications*. WoodHead Publishing Limited, pp 487–506
34. Dunn S (2002) Hydrogen futures: towards a sustainable energy system. *Int J Hydrogen En* 27:235–264



## Hydrogen Production Through Pyrolysis

Ali Bakhtyari, Mohammad Amin Makarem and Mohammad Reza Rahimpour  
Department of Chemical Engineering, Shiraz University, Shiraz, Iran

### Article Outline

Introduction  
Hydrogen: A Clean and Sustainable Energy Carrier  
Hydrogen Market: A Criterion for Decision  
Hydrogen Applications: Wide Usefulness  
Hydrogen Production: Wide Spread of Routes  
Pyrolysis: An Efficient Route  
Hydrogen from Biomass Feedstock: A Renewable and Sustainable Route  
Biomass: Cheap and Abundant Feedstock  
Bio-oil  
Pyrolysis of Biomass  
Liquefaction of Biomass  
Pyrolysis vs. Liquefaction  
Pyrolysis Specifications  
The Kinetics of Gas Generation Reactions in the Pyrolysis of Biomass  
Pyrolysis of Methane: A Suitable Alternative  
Pyrolysis of Hydrogen Sulfide: Energy Delivery and Decontamination  
Conclusion, Further Studies, and Outlook  
Bibliography

### Introduction

Growing worldwide consumption of energy during the last decades is an outcome of growing world's population and also the strong dependence of human's lifestyle to energy carriers. As an example, 20% of global energy consumption

belongs to the transportation section. Although fossil hydrocarbon-based energy carriers opened new vistas within the procedures of energy production, decreasing sources of natural gas and crude oil is making the governments and industries explore alternatives and even invent novel methods for manufacturing fuels. In addition to the depletion of fossil hydrocarbon sources, increasing emission of greenhouse gases (GHG), as well as  $NO_x$  and  $SO_x$ , is a real challenge of consuming fossil fuels. Global warming, change in climate patterns, and defects in biodiversity are the potential drawbacks of such emissions [1–6]. Besides, necessities of primary separation of impurities such as nitrogen, carbon dioxide, hydrogen sulfide, mercaptans, and salt from hydrocarbon sources make their processing tough and costly [7–10]. As a whole, introducing new routes for manufacturing energy carriers and downstream products that are more environmentally friendly than the current status is state of the art.

### Hydrogen: A Clean and Sustainable Energy Carrier

Due to the aforementioned problems of fossil fuels, there is an urgent need to develop new routes and technologies for renewable and sustainable energy manufacturing. Such routes and technologies must be able to meet the current and planned global energy demand. From a practical point of view, the alternative energy sources, its production, and application must be feasible, economically competitive, environmentally friendly, and easily accessible [11, 12].

Hydrogen, which is the lightest element in the periodic table, is so available in large quantities that it is the most abundant one in the universe. Hydrogen is colorless, odorless, tasteless, and nontoxic. In a wide range of pressure and temperature, hydrogen exists in the gaseous state. Hydrogen is present in small quantities in the air (i.e., 100 ppm) [13]. The properties of hydrogen are

tabulated in Table 1. Accordingly, due to high energy density and abundance, hydrogen can be considered as the most promising candidate for energy delivery. In fact, hydrogen has the highest energy density compared with the conventional fuels and is the most available element. The energy yield of hydrogen is about 120 kJ/g. This quantity is more than two times greater than that of hydrocarbon fossil fuels [12, 16]. Table 2 summarizes the energy contents of various substances. The followings are unique characteristics of hydrogen introducing it as an alternative energy carrier [12]:

- *Very low ignition energy* (i.e., 20 kJ)
- *Broad range of flammability*
- *Broad range of detonation if confined*
- *High ignition temperature*
- *Fast flame speed*
- *High diffusivity*

Furthermore, the variety of production methods is another advantage of hydrogen. In a general point of view, hydrogen is produced from the following sources [11]:

- *Fossil fuels such as natural gas, crude oil, and coal*
- *Unprocessed hydrocarbons such as shale oil and oil from tar sands*
- *Fusion nuclear reactions*
- *Water hydrolysis reaction*
- *Bio-based sources such as biomass*

In the following sections, more details of these methods with the focus on the pyrolysis are presented.

## Hydrogen Market: A Criterion for Decision

Currently, the worldwide market for hydrogen is estimated to be greater than 40 billion dollars per year. As reported by Balat [12], an almost 6% per

**Hydrogen Production Through Pyrolysis, Table 1** Properties of hydrogen (Adopted from [12, 14, 15])

Property	Quantity	Unit
<i>Critical point</i>		
Critical temperature	33.24	K
Critical pressure	1.297	Mpa
Critical density	30.77	Kg.m <sup>-3</sup>
Compressibility factor	0.304	–
<i>Gaseous</i>		
Density	1.33	Kg.m <sup>-3</sup>
Compressibility factor	0.906	–
Enthalpy	1447.4	J.mol <sup>-1</sup>
Entropy	78.94	J.mol <sup>-1</sup> . K <sup>-1</sup>
Constant pressure heat capacity	24.6	J.mol <sup>-1</sup> . K <sup>-1</sup>
Constant volume heat capacity	13.2	J.mol <sup>-1</sup> . K <sup>-1</sup>
Viscosity	1.11 × 10 <sup>-3</sup>	mPa.s
Thermal conductivity	16.5 × 10 <sup>-3</sup>	W.m <sup>-1</sup> . K <sup>-1</sup>
<i>Liquid</i>		
Normal boiling point	20	K
Heat of vaporization	891.2	J.mol <sup>-1</sup>
Density	70.96	Kg.m <sup>-3</sup>
Compressibility factor	0.017	–
Enthalpy	548.3	J.mol <sup>-1</sup>
Entropy	34.92	J.mol <sup>-1</sup> . K <sup>-1</sup>
Constant pressure heat capacity	19.7	J.mol <sup>-1</sup> . K <sup>-1</sup>
Constant volume heat capacity	11.6	J.mol <sup>-1</sup> . K <sup>-1</sup>
Viscosity	13.3 × 10 <sup>-3</sup>	mPa.s
Thermal conductivity	100 × 10 <sup>-3</sup>	W.m <sup>-1</sup> . K <sup>-1</sup>
<i>Combustion</i>		
Autoignition temperature	858	K
Low heating value	119.9	kJ.g <sup>-1</sup>
High heating value	141.8	kJ.g <sup>-1</sup>
Diffusion coefficient in air at STP	0.61	cm <sup>2</sup> .s <sup>-1</sup>
Detonability limits in air	18.3–59	Volume %
Limiting oxygen index	5	Volume %
Flammability limits in air	4–75	Volume %
Minimum energy of ignition in air	20	kJ
Flame temperature in air	2318	K



**Hydrogen Production Through Pyrolysis, Table 2** Energy contents of various substances (Adopted from [16–18])

Substance	Energy content <sup>a</sup>
Coke	27.0
Methane	55.5
Bagasse	9.6
Propane	49.6
Ethanol	29.6
Methanol	19.7
Hydrogen	120.0
Dry wood	16.2
Aviation gasoline	46.8
Automotive diesel	45.6
Automotive gasoline	46.4
Liquefied natural gas (LNG)	54.4

<sup>a</sup>MJ.kg<sup>-1</sup>

year increase in the sales of hydrogen was reported during 2003–2008. Such an increase is due to developed hydrogen applications in the refinery industry with the aim of high-quality fuel processing. An increasing trend was also observed during the last years [19, 20]. However, hydrogen supply and demand in the future strongly depend on the following factors [12]:

- *Progress trend of the technologies producing/consuming hydrogen*
- *Expense of hydrogen in the future*
- *Potential long-term regulations on the emissions of GHG*
- *Expense of rival energy carriers*

Up to 2008, a hydrogen production capacity of 500 billion cubic meters per year was approximated. Such a quantity was equal to 2% of global energy demand [21]. By 2040, it is predicted that hydrogen consumption, as an energy carrier in the vehicles, could save about 18.3 million barrels of petroleum per day, which is equal to approximately 150 million tons of hydrogen. Furthermore, if petroleum reforming was applied to produce such quantity of hydrogen, 11 million barrels per day would be saved [22].

The long-term hydrogen economy requires to deal with the challenges of hydrogen production

routes, feedstocks, facilities of storage and handling, and developments in all the sections of the energy economy [23]. More discussions with an economic point of view could be found elsewhere [12].

## Hydrogen Applications: Wide Usefulness

The utilization of hydrogen as a combustible fuel in the stationary and transportation sections such as rockets, internal combustion engines, fuel cell electric vehicles, and high-temperature industrial furnaces is currently receiving more attentions [24, 25]. In a commercial point of view on the transportation section, the development of fuel cell electric vehicles is more practical due to higher efficiency. In the case of reusing the waste heat, energy efficiency of fuel cell electric vehicles is enhanced up to 90% [12, 24, 26]. The most important advantage of hydrogen, as a fuel, is its carbon neutral ignition. In fact, in the hydrogen ignition, carbon oxides are not generated, and water vapor is the only produced oxidized compound. Besides, for the direct ignition of hydrogen in the internal combustion engines, such as gasoline-ignited engines, no further changes in the structure is required [27]. Blends of hydrogen with alcohols could produce potential non-petroleum fuels in the internal combustion engines. Accordingly, Al Baghdadi [28, 29] investigated the performance and pollutant emission of ignition engines working with blends of hydrogen and ethanol as fuel. Other advantages of hydrogen as a direct transportation fuel are as follows [12, 28, 29]:

- *Rapid burning speed*
- *High effective octane number*
- *No toxicity*
- *Wide limits of flammability in air*
- *Wide gas range in cold weather*
- *Clean combustion product*
- *Small quantities of nitrogen oxides*

In addition to its potential in energy delivery, hydrogen is largely consumed in different aspects of refining, petrochemical, and chemical industries such as the following [21, 22, 30, 31]:

- *Refining and hydro-threating*
- *Fischer–Tropsch synthesis to manufacture alternative fuels*
- *Gas-to-liquid (GTL) technology to manufacture liquid fuels*
- *Ammonia, methanol, ethanol, and dimethyl ether manufacturing*
- *Nitrogenized fertilizers manufacturing*
- *Hydrogenation of acetylene to ethane and ethylene*
- *Bio-oil upgrading by hydrodeoxygenation*
- *Hydrogenation of dangerous residues, e.g., dioxins and polychlorinated biphenyls*

Ammonia manufacturing with about 50% contribution in the global hydrogen consumption is the leading process in industrial hydrogen consumption [12, 30].

## Hydrogen Production: Wide Spread of Routes

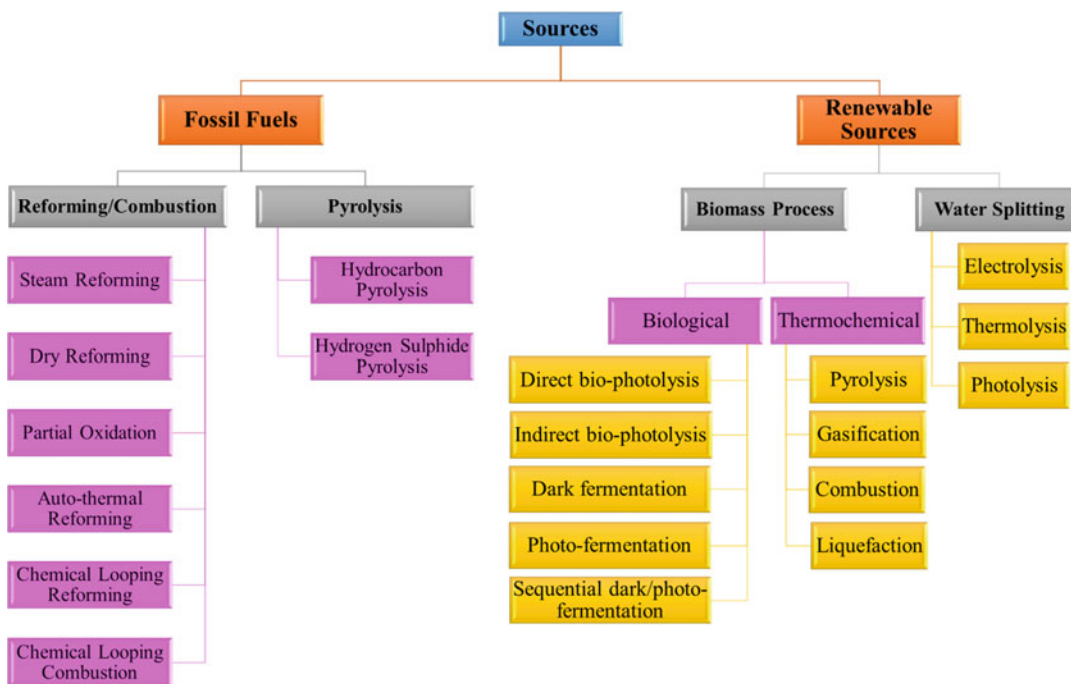
A summary of possible routes for hydrogen production is presented in Fig. 1. Accordingly, fossil fuels and renewable sources are two major feedstocks for hydrogen production. Based on the review of Kothari et al. [11], up to 2008, 96% of produced hydrogen was obtained directly from fossil-fuel sources. In fact, almost all the primary sources of energy could be utilized for hydrogen production. Currently, the major part of hydrogen is produced by serving light hydrocarbons such as natural gas. However, coal and petroleum coke could be practically utilized for hydrogen generation [32]. Accordingly, it was reported that up until the present, methane (i.e., natural gas), heavier hydrocarbons such as naphtha, and solids such as coal had, respectively, 48%, 30%, and 18% shares in the production of hydrogen [11, 33–35].

There is a wide variety of methods to convert the available sources to hydrogen. Thermochemical method [36, 37], electrochemical method [38], photochemical method [38, 39], photocatalytic method [40], and photo-electrochemical method [41, 42] are well-known among which

thermochemical method is currently the most common one. In this method, hydrogen is produced through thermally enhanced chemical reactions, e.g., steam reforming and partial oxidation. In this method, both catalytic and non-catalytic routes are possible, and hydrocarbons and water are the reactants of hydrogen releasing chemical reactions. The main advantages of thermochemical method for hydrogen production are considerably high overall efficiency and low production cost [12].

In the current status, various pioneer thermochemical methods for large-scale hydrogen production from different fossil-fuel sources are conventional steam reforming [43–54], partial oxidation (PO) [55–59], autothermal reforming (ATR) [60–62], dry reforming [63, 64], and pyrolysis of methane [65, 66] and hydrogen sulfide [67]. However, some new technologies such as chemical looping combustion [46, 68–70], chemical looping reforming [71–75], and onboard dehydrogenation [76–80] have been developed recently. Onboard hydrogen production as a valuable by-product of dehydrogenation reactions is currently the state of art. This approach has further benefits such as negligible emissions of carbon oxides and elimination of storage and transportation facilities [31, 81]. Among the abovementioned processes, catalytic steam methane (or natural gas) reforming (SMR) is a widely used route for hydrogen production with 80–85% contribution in the world's total hydrogen production capacity [43–46, 82]. This is due to abundance of natural gas (i.e., methane) sources [83].

Although it is prevalent and energy efficient, SMR needs high-temperature condition, and the most common strategy for providing such condition is burning natural gas. SMR is applied to produce hydrogen in three steps. Methane (or natural gas) is primarily reformed with steam at high temperature and pressure condition to obtain a mixture of hydrogen, carbon monoxide, carbon dioxide, and water. A catalytic water gas shift (WGS) reaction is then carried out to convert carbon monoxide and water to carbon dioxide and hydrogen. The gaseous hydrogen-rich mixture is then purified by a variety of purification processes such as pressure swing adsorption (PSA) [84] or



**Hydrogen Production Through Pyrolysis, Fig. 1** Hydrogen production routes

membranes [85, 86]. More details of SMR method could be found elsewhere [82, 83].

PO is an exothermic reaction of hydrocarbons (e.g., natural gas) in the presence of oxygen. An alternative to both SMR and PO is autothermal reforming (ATR), in which SMR and PO reactions are carried out simultaneously in a single reactor. Accordingly, natural gas, steam, and air are injected into the reactor, and internal combustion of the natural gas (i.e., PO reaction) that is an exothermic reaction drives the endothermic reactions (i.e., SMR reactions). As a consequence of autothermalism inside the reactor, a stand-alone system for hydrogen production from natural is managed [25, 86–88]. In addition to this, high system efficiency, high hydrogen-to-carbon ratio, and relatively low cost are advantages of ATR method [25, 89, 90].

### Pyrolysis: An Efficient Route

The main focus of the present contribution is on the production of hydrogen by pyrolysis of

various feedstocks. Accordingly, more details of the processes employing pyrolysis for hydrogen production are provided in this section. Pyrolysis is a well-known route for hydrogen production, in which hydrogen-containing compounds such as hydrocarbons are the only reactants. In fact, these compounds are decomposed by heating in the absence of oxygen. In this regard, pyrolysis of biomass as a renewable source and pyrolysis of methane and hydrogen sulfide as the feedstocks obtained from fossil fuels are investigated with details.

### Hydrogen from Biomass Feedstock: A Renewable and Sustainable Route

Although the abovementioned processes have their merits, in almost all the cases, hydrogen production leads to the generation of side products such as carbon dioxide. Hence, due to the presence of compounds magnifying the GHG effect, they are considered as non-sustainable routes with non-renewable energy sources [12, 33, 91]. Recently,

Nikolaidis and Poullikkas [66] have presented a detailed discussion on the methods applied to produce hydrogen from fossil-fuel sources. Owing to declining fossil fuels and increasing attention to GHG effects, the contribution of renewable routes is expected to increase in the near future. Furthermore, it is predicted to become the dominant route in the long term [66, 92–95].

As presented in Fig. 1, there are renewable sources for the hydrogen production. In fact, the aforementioned drawbacks prove the necessity of exploring new sources and developing new routes for hydrogen production. Accordingly, hydrogen production from water sources by means of various natural intermediates such as solar energy [96, 97], hydropower energy [98], geothermal energy [99], wind energy [96], and nuclear energy [100] has been extensively studied by different researchers. As shown in Fig. 1, water splitting by means of photolysis, thermolysis, or electrolysis is a candidate for renewable and sustainable hydrogen production.

Although, in the current status, it is not a common route, hydrogen can be obtained from bio-based procedures. Unlimited quantities of hydrogen are anticipated to be produced from biomass sources in the near future [12, 33, 91]. In this regard, the following are different routes for biohydrogen production:

- *Solid biomass such as crops and waste biomass to hydrogen*
- *Fermentation of liquid manure to hydrogen*
- *Biological hydrogen production*

In a general point of view, methods of biohydrogen production from biomass are split into two categories of thermochemical and biological methods. The category of thermochemical routes is made of the following processes:

- *Pyrolysis*
- *Gasification*
- *Combustion*
- *Liquefaction*

while the major biological routes are as follows:

- *Direct bio-photolysis*
- *Indirect bio-photolysis*
- *Dark fermentation*
- *Photo-fermentation*
- *Sequential dark/photo-fermentation*

Based on the economic evaluation of Padró and Putsche [101], hydrogen production from pyrolysis of biomass is a cost-effective route comparing the one from wind electrolysis and photovoltaic electrolysis systems. In fact, the costs of the process are considerably lower in the case of pyrolysis of biomass. More details on the process capability and economic aspects of biological routes and water splitting for renewable hydrogen production are well presented in the recent studies of Nikolaidis and Poullikkas [66] and Shah [102].

Among the bio-based procedures, conversion of solid biomass seems to be more practical than other two routes (i.e., fermentation and biological routes). However, fermentative biohydrogen production from sweet sorghum biomass was declared to be an economic route [103]. Based on the work of Encinar et al. [104], woody biomass and agricultural residues could be economically converted to hydrogen by pyrolysis or gasification in the presence of carbon dioxide. As reported by Ni et al. [17], conversion of biomass obtained from organic wastes is a potential route for economic and environmentally friendly hydrogen production. As an instance, the accessible energy by biohydrogen production is predicted to be as much as 40% of total energy consumed in the transportation section [12, 33, 91].

As mentioned previously, thermochemical and biological routes are the two common ones for conversion of biomass to hydrogen. Thermochemical routes are faster than biological ones, and also they provide higher stoichiometric hydrogen yield with applying gasification method. On the other hand, thermochemical routes, in terms of economic and environmental rules, are introduced as promising candidates for hydrogen production from biomass feedstocks [105, 106]. Biological routes are more environmentally friendly and less energy intensive since they are accomplished under mild conditions.

However, they offer lower rates and hydrogen yields (i.e., mol produced hydrogen/mol consumed biomass) depending on the biomass feedstock type [33, 103, 107]. Hence, the knowledge of biomass types and proper selection is of a great importance. Accordingly, in the following section, a short introduction of biomass and the products derived from biomass is presented. In fact, the knowledge of biomass and the properties of its derivatives could help to proceed with the optimum route for biohydrogen production.

### **Biomass: Cheap and Abundant Feedstock**

The first step in the biohydrogen production is providing cheap and abundant biomass feedstock. Biomass, which is a renewable energy carrier, is obtained from a vast variety of materials such as plants, animal residues, and urban wastes [108]. With this regard, the following are considered as the primary sources of biomass feedstocks [109]:

- *Waste substances, e.g., urban residues, crop residues, agricultural residues, and wood*
- *Products of forests, e.g., trees, shrubs, wood, and residues of logging*
- *Energy and starch crops, e.g., corn, wheat, barley, sugar crops, grasses, and vegetable oils*
- *Water-based substances or creatures such as water weed, water hyacinth, and algae*

Based on the sources, biomass feedstocks are classified into three main categories as the following [109]:

- *Cellulosic biomass*
- *Starch/sugar biomass*
- *Triglyceride biomass*

Although cellulosic biomass is the cheapest and the most abundant type, its conversion to other products is constrained. This is because of its solid state and low energy density. Hence, available technologies for conversion of cellulosic

biomass feedstocks impose extra charges [6, 109]. Considering the influence of biomass type on the composition of the gaseous product and the yield of biohydrogen, properties of different biomass types are of great significance. Cellulosic biomass consists of cellulose, hemicellulose, and lignin, in which cellulose and hemicellulose are the most abundant ones. On the other hand, cellulose and hemicellulose are constituents of approximately 90% of terrestrial biomass (i.e., the biomass generated from earth). More details of their chemical structures are available in the literature [109–111]. The major difficulty in the cellulosic biomass processing is providing efficient technologies to convert the solid-state biomass to a proper fluid. The following are the available technologies to transform the solid cellulosic biomass to fluid [6, 109, 111–115]:

- *Hydrolysis to generate aqueous sugar solutions*
- *Pyrolysis and liquefaction to generate bio-oils and syngas*
- *Gasification to generate syngas*

Edible biomass or starch/sugar biomass is almost gained from vegetables. This type of biomass is potentially transformed into fuels in simpler procedures [6]. Triglyceride biomass (i.e., fats) is gained from vegetable oils, animal fats, and even water-based substances or creatures such as algae. This type of biomass is transformed into glycerol and fatty acids which could be then practically converted to hydrogen by steam reforming, to olefins by catalytic upgrading, and to biodiesel by transesterification [6, 116–118]. However, the major difficulty with the triglyceride biomass is their high processing cost in comparison with cellulosic biomass [6, 116]. More details on the biomass feedstocks and physical and chemical properties are available in a recent contribution by Stedile et al. [119]. A practical route to produce biohydrogen is bio-oil transformation. On the other hand, conversion of cellulosic biomass into bio-oil followed by a second process such as pyrolysis, reforming, and gasification is an indirect route to produce hydrogen from biomass feedstock [6, 120]. In fact, solid biomass is converted into a fluid that is more



practical to be processed, and then the fluid is transformed to valuable products such as hydrogen. However, a portion of hydrogen is produced through the process of biomass pyrolysis into bio-oil. Hence, identification of bio-oil characteristics is of a great interest.

## Bio-oil

Bio-oil is mostly derived from cellulosic biomass feedstock such as wood, agricultural residues, and forest wastes by either pyrolysis [6, 109, 121–125] or liquefaction [126–128]. However, algae transformation into bio-oil is currently the state of art [129, 130]. Bio-oil composition strongly depends on biomass type, the method of biomass conversion to bio-oil, and operating conditions. Accordingly, more than 400 compounds, including aromatics, phenols, aldehydes, alcohols, esters, ketones, and acids could, exist in the bio-oil [6, 128].

## Pyrolysis of Biomass

In the pyrolysis method, biomass feedstock is instantaneously heated in the absence of oxygen and water to reach a high temperature (i.e., 375–525 °C) in a short time. As a result of thermal decomposition, a liquid mixture is generated inside a gaseous mixture, which then liquefies [6, 109, 121–125]. The rate of heating, residence time, and temperature range are the effective factors in the generation of solid, liquid, and gas product during pyrolysis. As stated by Klass [131] and Huber et al. [6, 120], at very high heating rates, temperature ranges of 1000–3000 °C, and residence times less than 1 s, the gaseous product is obtained by flash pyrolysis. However, at a lower temperature range (i.e., 400–900 °C), the generation of liquid product is certain. Furthermore, higher residence times lead to the formation of solid product (i.e., charcoal). Although solid product could be useful in further processes such as metallurgy and chemical industries, its formation during pyrolysis decreases the yields of gaseous product and bio-oil. Therefore, fast or flash pyrolysis (i.e., pyrolysis with short

residence time and high heating rate) is more desirable. An advantage of biomass pyrolysis is low-pressure operation (i.e., 0.1–0.5 MPa) [108]. Up to 80% yield was reported in the previous studies of fast pyrolysis [122, 132]. Bridgwater [121] summarized the characteristics of conventional reactor configurations for fast pyrolysis of biomass feedstock. In this regard, the performances of fixed beds, bubbling fluid beds, circulating fluid beds, transported beds, and rotating cone reactors were evaluated based on their production rate, heating rate, solid production rate, and separation mechanism. More details on the commercial processes of biomass pyrolysis to bio-oil could be found elsewhere [121, 122, 128, 132, 133].

## Liquefaction of Biomass

In liquefaction method, which is a high-pressure and low-temperature (i.e., up to 20 MPa and 250–325 °C) process, reaction rates and mechanisms are controlled to derive liquid bio-oil [6, 126–128]. Thus, a bio-oil type, which is insoluble in water, is generated. Although bio-oil production by pyrolysis method is less expensive, the one obtained by liquefaction method contains less oxygenated compounds. It means that applying liquefaction method leads to bio-oil with higher quality [6]. Catalyst type, pressure range, and reducing gases are the effective means for controlling the rates and mechanisms of desired reactions for high-quality bio-oil. Slurry feed stream made of catalyst particles, biomass, liquid solvent, and reducing gas is injected into the reactor. Different types of liquefaction such as hydrothermal, solvolysis, and hydropyrolysis are well introduced in the literature [126–128, 134, 135]. Differences in their solvents and pressure conditions of these processes make them distinct. Goudriaan et al. [136] developed a commercial liquefaction process for bio-oil production.

## Pyrolysis vs. Liquefaction

Typical properties of bio-oils generated by fast pyrolysis and liquefaction reveal that the one

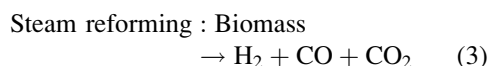
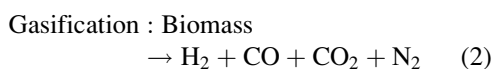
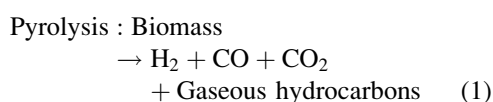


produced by fast pyrolysis contains higher moisture and oxygen contents and lower carbon and hydrogen contents [6, 133, 137–140]. Such characteristics lead to lower heating specifications, lower viscosity, and the pH in the range of acids. Although higher carbon and lower oxygen contents of liquefaction bio-oils lead to higher heating value, its viscosity makes further processes such as ignition in engine fuels and reforming difficult and less efficient. As a whole, the chemical composition of bio-oil has significant effects on the homogeneity, polarity, heating specifications, viscosity, blending, and acidity. Properties of some bio-oil samples are summarized by Gollakota et al. [141]. Liquefaction bio-oils have characteristics more similar to conventional petroleum oil. Thus, it seems to be more beneficial in long term. However, in terms of process economy, the required capital cost for high-pressure equipment in the liquefaction process makes it less attractive for the industries and persuades them to develop fast pyrolysis for bio-oil production [6, 128, 136, 137, 142, 143]. It is worth mentioning that the bio-oil per se is a low value energy carrier. Hence, conversion of bio-oil into value-added energy carriers such as hydrogen is currently the state of art.

As mentioned previously, thermochemical routes, in which biomass feedstock is transformed into hydrogen or even hydrogen-rich gaseous streams, are the most practical ones [144]. In fact, hydrogen production from biomass or the derived syngas from biomass could be an effective step in a climate with zero GHG emission, which is vital in the development of sustainable and renewable energy systems [145]. Although combustion and liquefaction are proposed, thermochemical routes mainly include pyrolysis and gasification. The main reasons of preferring pyrolysis and gasification over the first two are the emission of pollutants in the combustion and necessity of high-pressure facilities in the liquefaction. However, both pyrolysis and gasification produce methane and carbon monoxide in addition to hydrogen, which could be subsequently converted into hydrogen through steam reforming and WGS reactions [146]. Although pyrolysis of biomass was introduced as an option for bio-oil production, it could be singly applied to produce hydrogen. On the

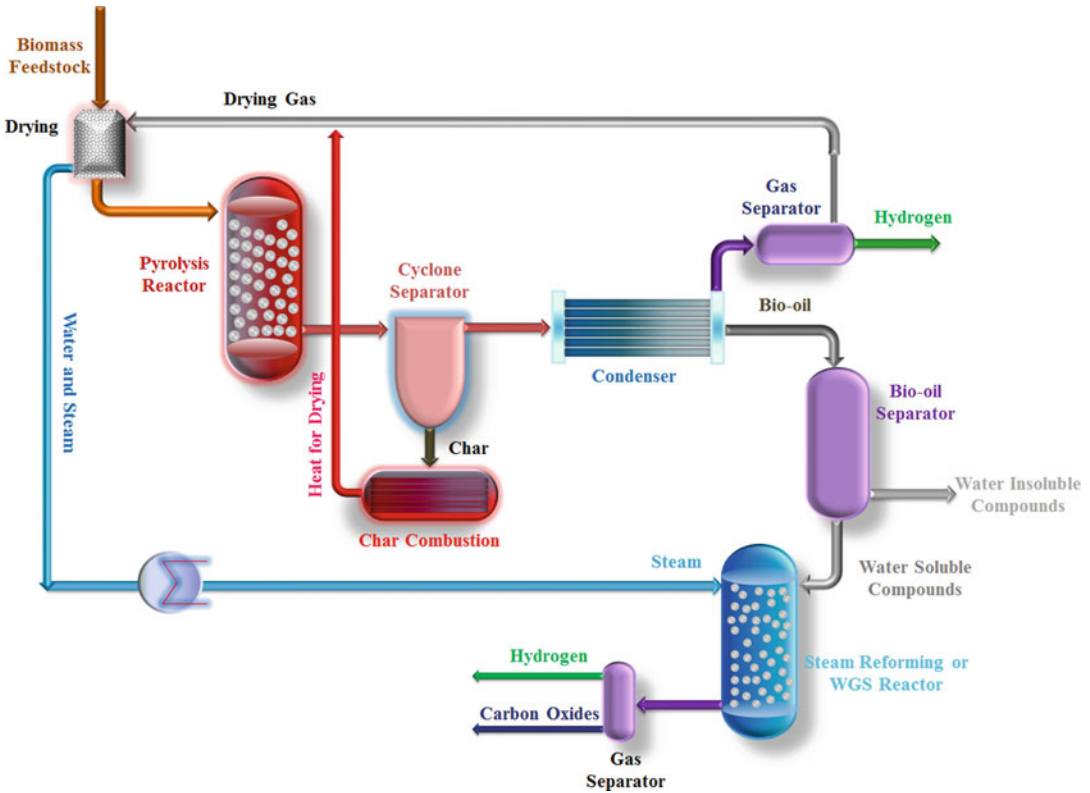
other hand, pyrolysis is a thermochemical route of producing bio-oil (liquid oil) and charcoal (solid) inside a gaseous stream by heating the biomass in the total absence of oxygen. In addition to hydrogen, considerable quantities of methane and light hydrocarbons exist in the gaseous stream, which could be then steam reformed to produce more hydrogen. Besides, presented carbon monoxide in the gaseous steam could be converted into hydrogen and carbon dioxide by further WGS reaction [106, 108, 147]. Afterward, the desired purity of hydrogen is obtained by proper separation units such as pressure swing adsorption (PSA) [84] and membranes [148–150]. The process is well presented in Fig. 2.

As a whole, pyrolysis, gasification, and steam gasification are the most effective routes to produce hydrogen from biomass [106, 108, 151–153]. As an instance, Demirbas and Caglar [154] conducted an experimental study on the hydrogen production by steam reforming of pyrolytic oils obtained from the pyrolysis of lignocellulosic biomass. As declared, this route could be potentially a cost-effective rival for conventional routes of hydrogen production. Although these routes are considered as distinct ones, the associated reactions might occur simultaneously in each case. The following are the major gaseous products obtained from biomass in each route [12]:

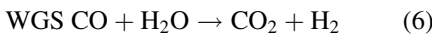
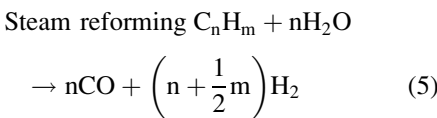
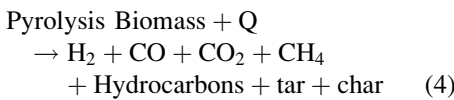


In addition to differences in the hydrogen yield, the side products are different through various biomass treatments.

Generally, the following are the chemical reactions of each step in a biomass pyrolysis process followed by further complementary steam reforming and WGS reactors:



**Hydrogen Production Through Pyrolysis, Fig. 2** Schematic diagram of biomass feedstock pyrolysis (Adopted from [66])



In this route, the yield of hydrogen production strongly depends on the type of biomass feedstock, characteristics of catalyst, temperature range, and residence time (or heating rate) [105]. The syngas obtained from gasification is treated in the same way as the gaseous product obtained from pyrolysis of biomass. In steam gasification of biomass, the yield of hydrogen production is higher than that of fast pyrolysis. With

the overall efficiency (i.e., thermal to hydrogen ratio) which could be managed up to 52%, steam gasification is considered as an efficient and renewable hydrogen production alternative. A steam gasification unit with subsequent steam reforming and PSA units is estimated to require about 2.4 TJ of input primary energy per TJ of produced hydrogen [155]. Besides, in a plant with hydrogen production capacity of 139.7 metric tons per day, with the price of biomass feedstock in the range of 46–80 dollar per tons (dry basis), the hydrogen production cost is estimated to be 1.77–2.05 dollar per kg hydrogen [156]. Depending on the equipment size and biomass feedstock type, the cost of hydrogen production by pyrolysis is estimated to be in the range of 8.86–15.52 dollar per GJ energy (i.e., 1.25–2.20 dollar per kg hydrogen) [146].

In a comprehensive study by Hossain et al. [16], the prospect of hydrogen production from

oil palm biomass was investigated. In this regard, a cost analysis of different hydrogen production routes was carried out. A portion of results is adopted and summarized in Table 3. Clearly, routes that are using biomass have the least feedstock cost. Although process employing natural gas has similar selling price, its process of conversion (i.e., SMR) has higher capital and feedstock costs comparing the process employing biomass. Besides, natural gas sources are not permanently available like biomass. As clear, pyrolysis of biomass with very low feedstock and capital costs as well as the reasonable retail selling price of hydrogen is a promising route. In a recent study, Nikolaidis and Poullikkas [66] compared different routes of hydrogen production, i.e., conventional and new renewable ones, comprehensively and presented relating data for the assessment of technical and economic aspects. Although some advantages are proposed for conventional routes such as SMR, PO, and ATR, pyrolysis of hydrocarbons offers the possibility of reduced step and even emission-free procedure. Furthermore, carbon is the only side product requiring treatment. It was previously mentioned that the produced carbon could be utilized in other processes. Considering the advantages of utilizing biomass such as renewability, low price, and abundance, the pyrolysis process provides an effective route of hydrogen production with the efficiencies in the range of 35–50%. A major drawback of applying biomass pyrolysis is varying hydrogen

content as a result of seasonal availability and impurities existing in the biomass feedstock. The major advantages and disadvantages of other possible routes are collected in the review of Nikolaidis and Poullikkas [66]. It could be concluded that large-scale hydrogen production from biomass feedstock is only feasible by means of thermochemical pathways such as pyrolysis and gasification, while biological biomass treatments offer small-scale facilities for hydrogen production. Pyrolysis of woody biomass with a 3.1–53.4 M\$ capital cost for a 2.7–72.9 tons per day hydrogen production capacity and 1.25–2.20 dollars per kg hydrogen cost proposes a cost-effective route [66].

### Pyrolysis Specifications

As mentioned previously, pyrolysis of biomass is of the promising candidates for large-scale hydrogen production. Hence, investigating the effect of operating parameters on the performance of this process is currently of a great interest. Temperature, residence time, type of catalyst, and type of biomass feedstock are the most determining factors which control the yield of hydrogen production in the pyrolysis of biomass. In a general point of view, higher temperature, longer residence time, and selective catalysts are crucial [157]. However, there are some evidences in the literature proving the negative effect of long residence time on the yield of hydrogen [158].

**Hydrogen Production Through Pyrolysis, Table 3** Cost analysis of different hydrogen production routes (Adopted from [16])

Route	Feedstock	Feedstock cost <sup>a</sup>	Capital cost <sup>b</sup>	Hydrogen retail selling price <sup>c</sup>
Pyrolysis (high estimate)	Biomass	0.92	4.20	2.57
Pyrolysis (low estimate)	Biomass	2.57	73.70	1.47
Gasification (low estimate)	Biomass	2.57	241.40	1.44
Gasification (high estimate)	Biomass	0.92	8.80	2.83
Gasification	Biomass	2.81	167.50	1.99
Steam methane reforming	Methane	10.55	254.10	2.55
Gasification with sequestration	Coal	562.5	1.24	1.25

<sup>a</sup>\$/GJ

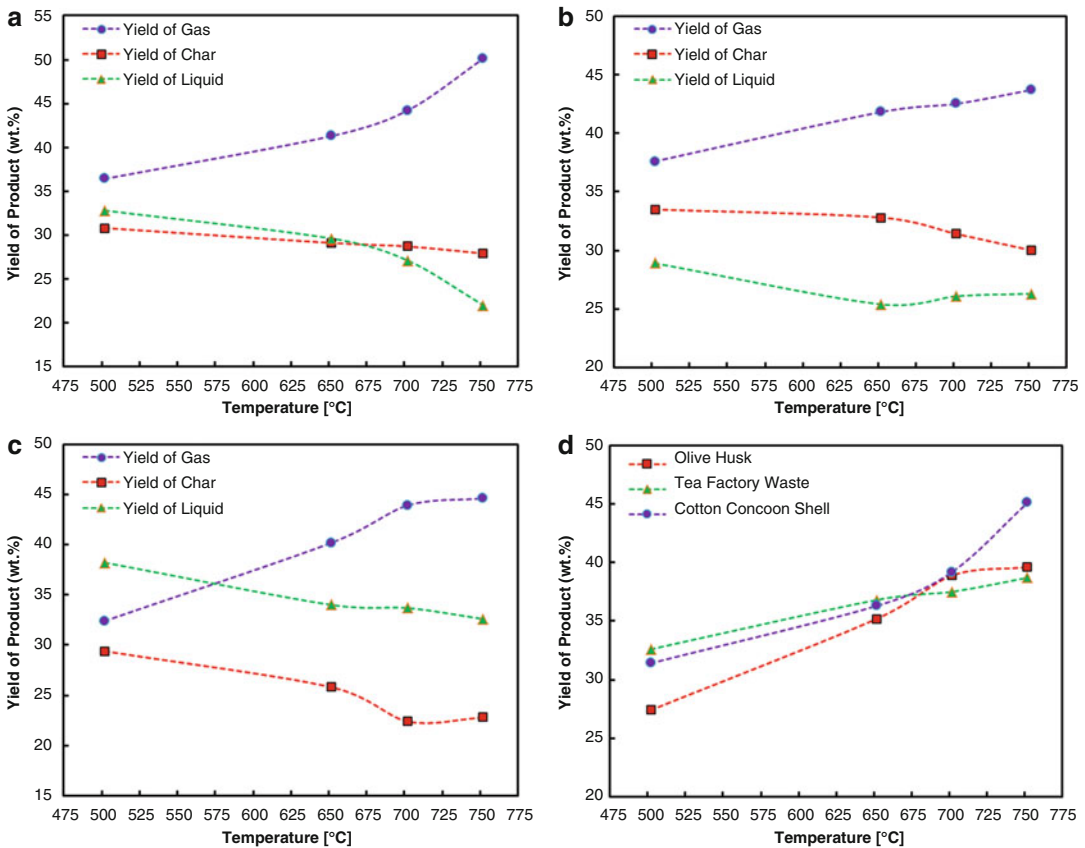
<sup>b</sup>M\$

<sup>c</sup>\$/kg

In order to adjust the determining factors precisely, selection of feedstock source and appropriate reactor type and heat transfer pattern is essential. Accordingly, investigation of different biomass feedstocks is available in the literature. Besides, solid–solid conductive and gas–solid convective patterns are the available heat transfer strategies [159]. Bridgwater et al. [159] summarized the characteristics of various reactors that are operational in the pyrolysis process, i.e., ablative, fluidized bed, circulating fluidized bed, and entrained flow. The fluidized-bed reactor was introduced as the most suitable one for hydrogen production due to higher heating rate, which is essential in the fast pyrolysis of biomass. In addition to this, in order to eliminate the deposition of coke and char on the surface of catalyst particles and then to enhance the operability of biomass

pyrolysis toward hydrogen production, fluidization is applied [160].

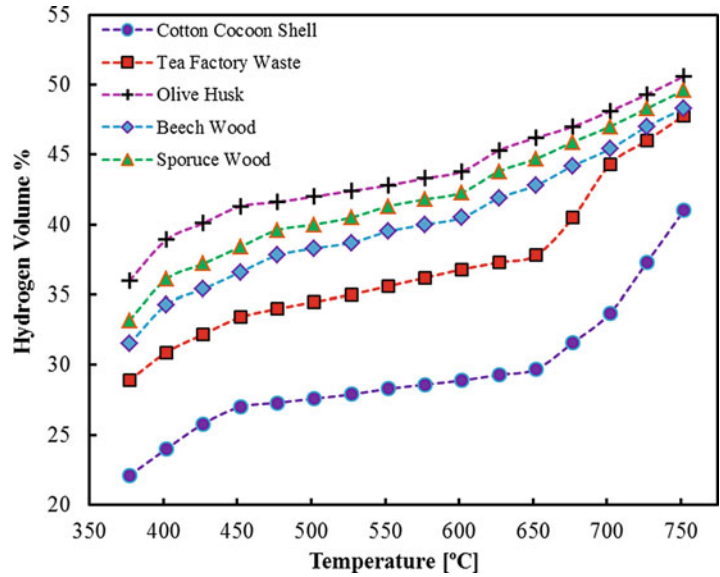
Demirbaş and his colleague [157, 161] investigated the effect of temperature on the performance of pyrolysis process. In this regard, Fig. 3 shows the effect of temperature on the yields of gaseous, liquid, and solid (char) products of three biomass samples processed in fast pyrolysis. It is obvious that the yields of gaseous products are increased by increasing temperature. The yields of liquid and char products show decrease in the studied temperature range. However, the trends are not strictly descending. Besides, the effect of temperature on the yield of hydrogen production in the pyrolysis of various biomass feedstocks is presented in Fig. 4. As shown, increasing temperature in the range of 377–752 °C leads to considerable



**Hydrogen Production Through Pyrolysis, Fig. 3** The effect of temperature on the yields of (a) cotton cocoon shell, (b) tea factory waste, and (c) olive husk biomass and (d) the gaseous product in pyrolysis process

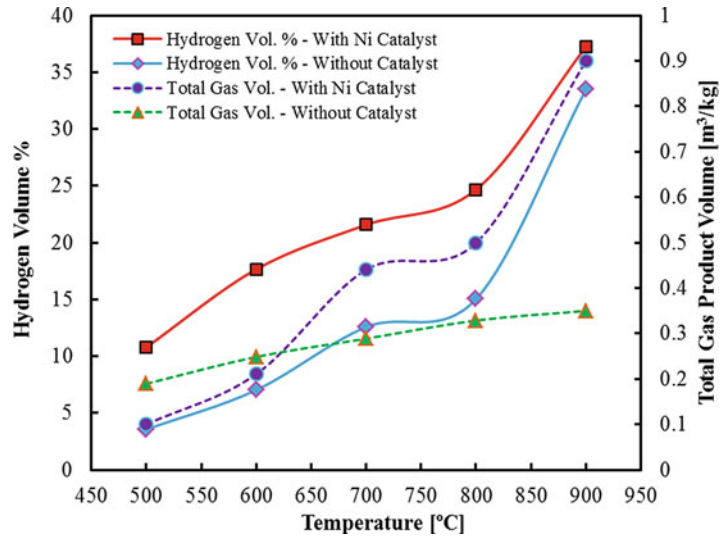
**Hydrogen Production Through Pyrolysis,**

**Fig. 4** The effect of temperature on the yield of hydrogen production in the pyrolysis of various biomass feedstocks



**Hydrogen Production Through Pyrolysis,**

**Fig. 5** The effect of temperature on the yield of gaseous product and hydrogen by pyrolysis of palm oil wastes



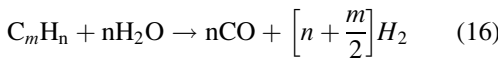
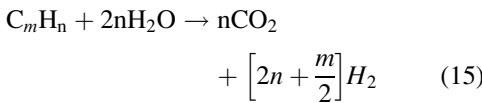
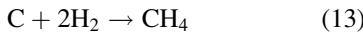
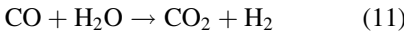
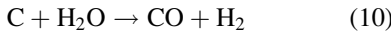
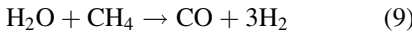
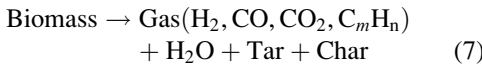
enhancement in the yields of hydrogen. The trends vary by changing the feedstock.

Yang et al. [158] carried out an experimental study on the hydrogen production by pyrolysis of palm oil wastes in a fixed-bed reactor flowing countercurrently. In this regard, the effects of various parameters such as temperature, residence time, and catalyst characteristics on the yield of hydrogen production were investigated.

Figure 5 is to show the effect of temperature on the yield of gaseous product and hydrogen in the

pyrolysis of palm oil wastes in two cases, i.e., without catalyst and with 5 wt % catalyst (Ni) [158]. Increasing the yield of gaseous product and hydrogen with increasing temperature in two cases and enhancing yields by adding the catalyst are evident. The interesting feature is the similar trend of the yield of hydrogen production with temperature in two cases. However, the yields of gaseous product are different in two cases. The thermal cracking of heavier hydrocarbons such as tar and shift reactions at the higher temperatures

could be the reason of such observations [158, 162]. Accordingly, the following reaction network was presented by Yang et al. [158]:



Reactions (7), (8), (9), (10), (11), (14), (15), and (16) are responsible for hydrogen production.

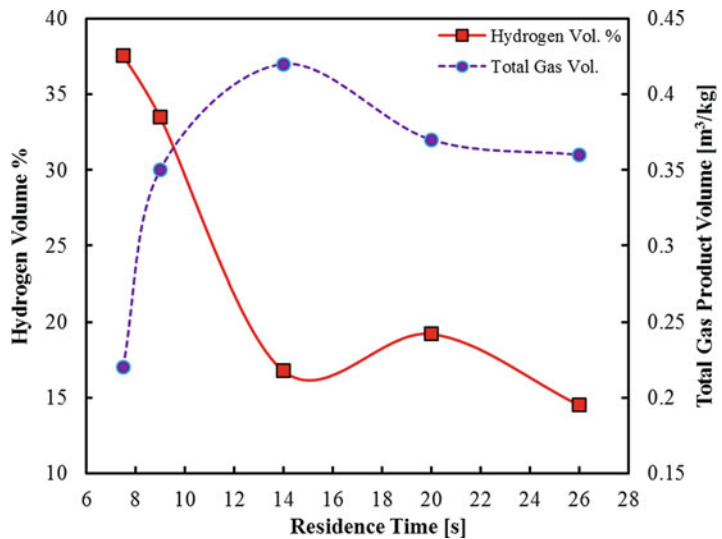
Steam reforming of methane (i.e., reaction (9)) cannot proceed at higher temperatures. However, in the presence of an active catalyst, this reaction could proceed even at higher temperatures. As a result, the higher yield of hydrogen production in the presence of the catalyst is justified.

Another determining factor in the pyrolysis of biomass is residence time. Figure 6 shows the effect of residence time on the yield of gaseous product and hydrogen by pyrolysis of palm oil wastes in the absence of catalyst [158]. The total gas product volume increases first with increasing residence time and reaches the maximum value at about 14 s. Then, it starts to decrease slightly with further increase in the residence time. In a different manner, lengthening the residence time leads to early sudden decrease in the yield of hydrogen, while further increase of the residence time results in higher hydrogen production. However, excessive increase in residence time leads to the reduction of hydrogen production. Although lengthening residence time makes the system proceed toward thermal cracking of heavier hydrocarbons (i.e., reaction (8)) and thus higher gas production rate, it leads to the production of other gaseous components such as carbon oxides and methane.

Utilizing catalysts in the pyrolysis of biomass may lead to production of various components. This is due to the surface characteristics of catalyst and their effects on the product selectivity. In this

**Hydrogen Production Through Pyrolysis,**

**Fig. 6** The effect of residence time on the yield of gaseous product and hydrogen by pyrolysis of palm oil wastes

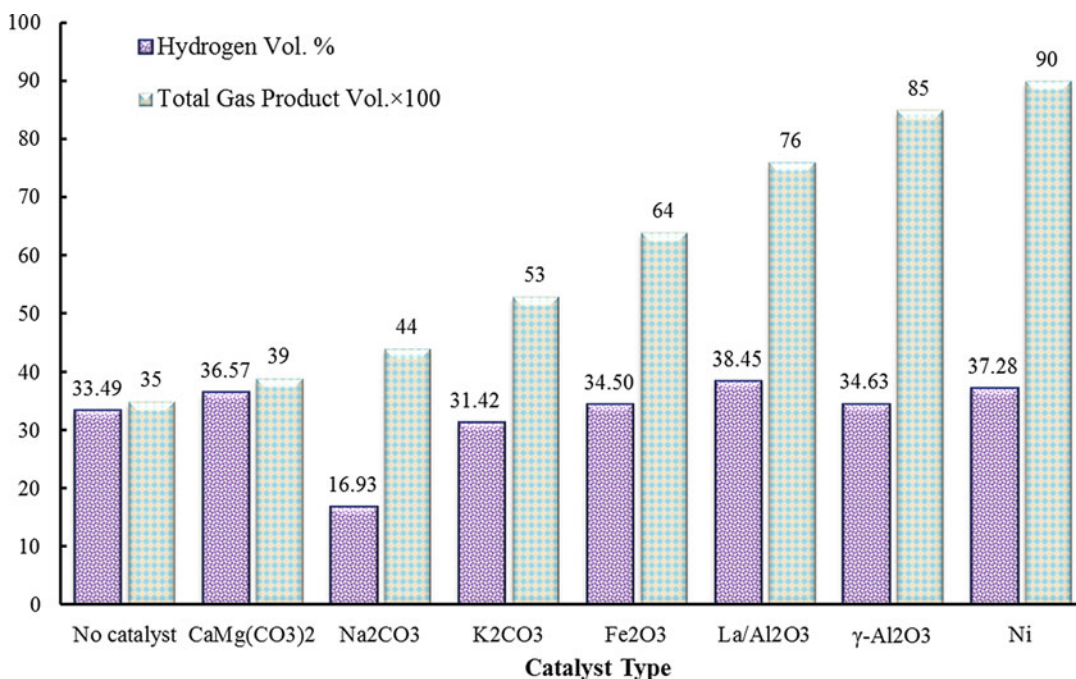




regard, Yang et al. [158] investigated the effect of adding various catalysts in the pyrolysis of palm oil wastes. The results are presented in Fig. 7. Obviously, the presence of a catalyst, regardless of type, leads to higher yields of gaseous product. Besides, Ni catalyst provides stronger catalytic effect than the other ones. In fact, pyrolysis of palm oil wastes in the presence of Ni catalyst is carried out with almost 160% increase in the total yield of gaseous product, whereas the presence of  $\text{CaMg}(\text{CO}_3)_2$  (i.e., dolomite) shows a less catalytic effect on the total yield of gaseous product. The presence of catalyst, in almost all the cases, improves the yield of hydrogen production. However, sodium carbonate (i.e.,  $\text{Na}_2\text{CO}_3$ ) and potassium carbonate (i.e.,  $\text{K}_2\text{CO}_3$ ) show less selectivity toward hydrogen. The highest hydrogen content (i.e., 38.45 vol. %) was obtained by utilizing  $\text{La}/\text{Al}_2\text{O}_3$  catalyst. By considering both the yield of gas and hydrogen selectivity, Ni catalyst provides higher hydrogen production rate. The effect of temperature on the yield of gaseous product and hydrogen content in the presence of Ni catalyst was previously shown in Fig. 5.

Garcia et al. [163] investigated the effect of catalyst (Ni/Al) pretreatment on the pyrolysis of sawdust biomass at the temperature range of 650–700 °C. They found that the temperature of catalyst calcination has a significant effect on the reaction performance. By calcination of the catalyst at 850 °C, the highest yield of hydrogen was obtained. Inside the catalytic effect, the load of the catalyst has a further effect on the yield of hydrogen production. In this regard, Chen et al. [164] found that oxide of chromium ( $\text{Cr}_2\text{O}_3$ ) is the most effective catalyst for the pyrolysis of rice straw and sawdust biomass feedstocks. In addition, they stated that at least 30 wt. % of catalyst load is recommended for practical pyrolysis process in the further studies.

Other researchers have studied the potential of catalyst type in the pyrolysis of biomass toward hydrogen production. In this regard, gasification of tar and dissociation of heavier hydrocarbons by utilizing various catalysts such as  $\text{CaMg}(\text{CO}_3)_2$  and  $\text{CaO}$  [165]; zeolite Y [166]; Ni-based catalysts [167]; carbonates such  $\text{K}_2\text{CO}_3$ ,  $\text{Na}_2\text{CO}_3$ , and  $\text{CaCO}_3$  [164]; and different metal oxides such as  $\text{Cr}_2\text{O}_3$  [164],  $\text{Al}_2\text{O}_3$ ,  $\text{SiO}_2$ ,  $\text{ZrO}_2$ , and  $\text{TiO}_2$  [168]



**Hydrogen Production Through Pyrolysis, Fig. 7** The effect of adding various catalysts in the pyrolysis of palm oil wastes

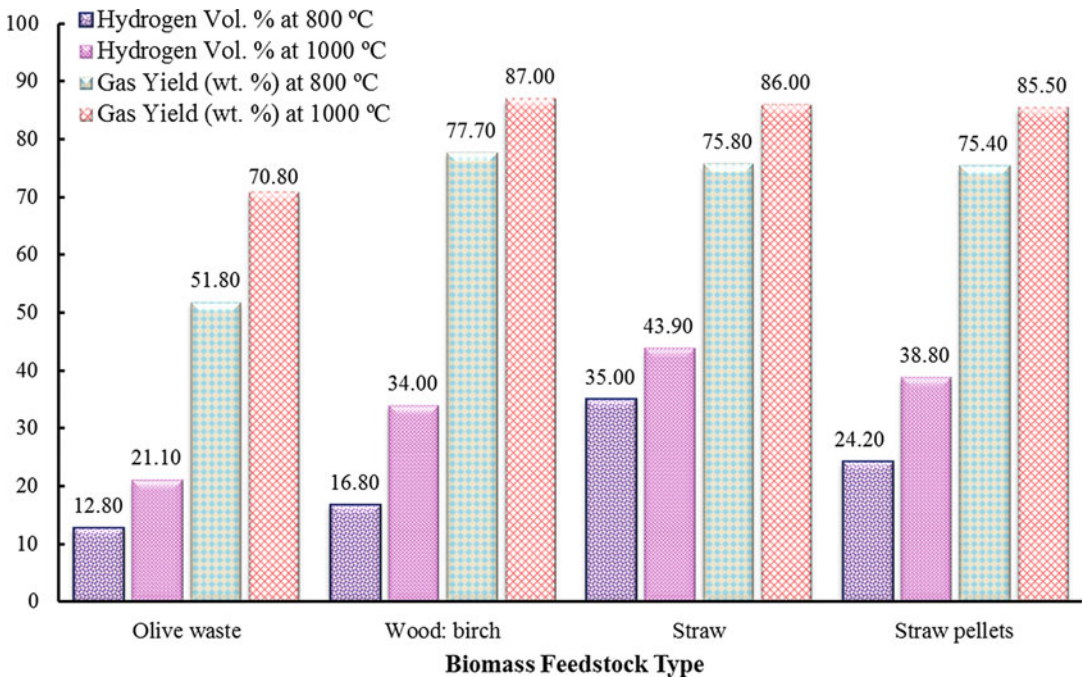
were evaluated. Generally, utilizing Ni-based catalyst significantly improves the hydrogen production rate. Positive effects of utilizing Ni catalyst on the hydrogen production from pyrolysis of palm oil wastes were previously shown in Fig. 5. It is worth mentioning that further hydrogen production could be managed by applying subsequent steam reforming or WGS reactions [168, 169].

In an earlier study, Zanzi et al. [170] conducted an experimental study on the fast pyrolysis of agricultural wastes in the range of 800–1000 °C. The obtained results in terms of gas yield (weight %) and hydrogen content (volume %) are presented in Fig. 8. As prefigure, biomass feedstock type strongly affects the pyrolysis process, the yield of gaseous product, and the hydrogen content. Besides, increasing temperature from 800 °C to 1000 °C results in higher yield of gaseous product and hydrogen content in all the cases. The biomass feedstock prepared from birchwood provides a higher yield of gaseous product, whereas the biomass feedstock of straw offers a higher hydrogen content. Besides, Fig. 4 shows the differences between capabilities of various biomass feedstocks in hydrogen production by

pyrolysis. As stated by Zabaniotou et al. [171], biomass feedstocks containing higher cellulose and hemicellulose lead to gaseous products with higher hydrogen contents. The results of Demirbaş and his colleagues [157, 161] presented in Fig. 4 confirm such a statement. The structural analysis of biomass feedstocks presented in Fig. 4 is presented in the study of Demirbaş and Arin [161]. Up to the present, pyrolysis of a vast variety of biomass feedstocks with the aim of hydrogen production was the object of researchers. In this regard, the potentials of peanut shell [172, 173], plastics, trap grease, synthetic polymers, mixed biomass [169], rapeseed [174], and agricultural wastes [175] were evaluated by different researchers.

### The Kinetics of Gas Generation Reactions in the Pyrolysis of Biomass

Because of the complexity of biomass composition, it is difficult to determine the involved reactions in the biomass processing routes completely. Therefore, some simplified reactions are considered either in series or parallel [176]. As an



**Hydrogen Production Through Pyrolysis, Fig. 8** The effect of biomass feedstocks in the pyrolysis process

instance, Shafizadeh [177] considered a set of parallel reactions for the decomposition of cellulosic biomasses feedstocks (e.g., woody biomass). These reactions were applied to describe the rates of tar, char, and gaseous products. Afterwards, tar decomposing can also lead to char and gaseous products by further reactions. Balci et al. [178] developed a more complex reaction pathway based on the nature of pyrolysis.

In a general point of view, different kinetic models of pyrolysis reactions could be categorized in the following classes [179]:

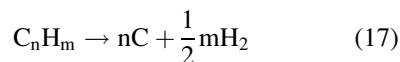
- *Single-step global reaction models*
- *Multiple-step models*
- *Semi-global models*

Although single-step models are in reasonable agreement with the experimental data, they assume that the mass ratios of products (i.e., volatiles and chars) are constant. Such an assumption prevents the accurate prediction of the yields of products at different process conditions [180]. In the semi-global models, it is assumed that pyrolysis products are categorized into chars, tars, and volatiles. Such an approach is beneficial in evaluating and correlating the kinetic data from various biomass feedstocks under similar reaction conditions. However, it is not suitable for comprising thermal decomposition data gained from the dissimilar reaction conditions [181]. Accordingly, researchers have put effort to develop more complex models (i.e., multiple-step models). Such models utilize three [182], seven [183], ten [184], or even twelve [185] consecutive pyrolytic reactions to evaluate the process. More details of the pyrolytic reactions are well provided in the review of White et al. [179]. In this regard, a comprehensive study was conducted to review the established kinetic models and mathematical approximations applicable in the analysis of solid-state reactions.

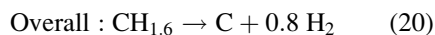
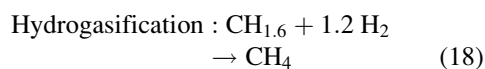
### Pyrolysis of Methane: A Suitable Alternative

As mentioned previously, in the pyrolysis, hydrogen-containing compounds such as

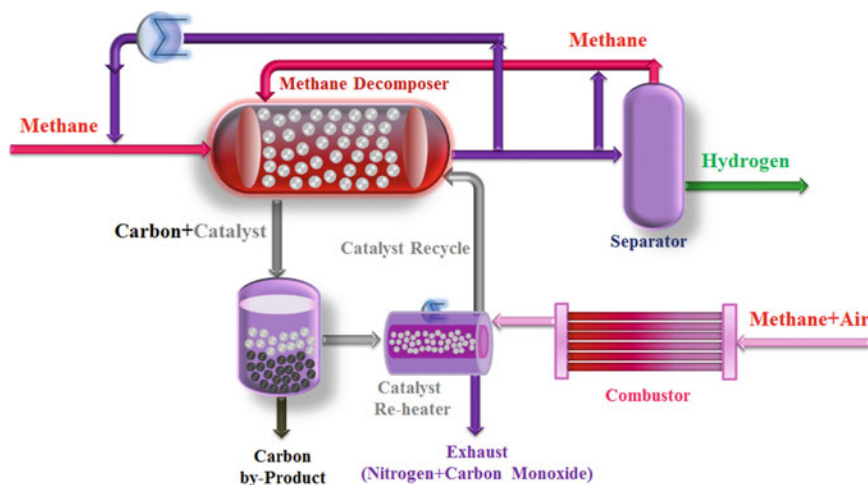
hydrocarbons are decomposed by heating in the absence of oxygen. Accordingly, their thermal decomposition through the following general reaction leads to hydrogen release [65]:



Catalytic thermal decomposition of light hydrocarbons (with the boiling point range of 50–200 °C) leads to the generation of elemental carbon inside hydrogen, while in the case of utilizing heavier hydrocarbons (with the boiling point range higher than 350 °C), a two-step procedure consisted of hydrogasification, and methane cracking is applied to produce hydrogen. In the hydrogasification step, the reaction of hydrocarbons with hydrogen leads to the generation of intermediate methane, followed by methane decomposition to elemental carbon and hydrogen. In this regard, the following reactions are carried out [65, 66]:



In a different manner, hydrogen could be produced by atmospheric direct decarbonization of methane at temperature up to 980 °C. The whole process, which is schematically shown in Fig. 9, is carried out in the absence of oxygen and water. Lower energy consumption (i.e., 37.6 kJ per moles of hydrogen) of pyrolysis comparing conventional steam methane reforming (i.e., 63.3 kJ per moles of hydrogen) is the major primacy of this process. Furthermore, the omission of WGS steps and subsequent carbon dioxide removal and storage sections are other significant advantages. Besides, by carbon management, which is useful in the metallurgy and downstream chemical industries, extra benefits are managed. As a result, large-scale developments of this process could lead to 25–30% lower cost of hydrogen production. Moreover, a suitable market for the carbon byproduct leads to the reduction of production cost. Considering environmental



**Hydrogen Production Through Pyrolysis, Fig. 9** Schematic diagram of methane pyrolysis process (Adopted from [66])

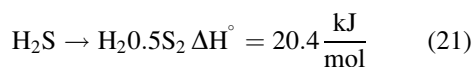
aspects, converting natural gas (i.e., methane) into hydrogen by catalytic decomposition would be more beneficial than the conventional SMR. Such superiority is due to the elimination of carbon dioxide from the manufacturing cycle [65, 66, 186–188].

A possible strategy to increase the conversion of methane in the pyrolysis process is in situ hydrogen separation by utilizing perm-selective membranes. Metallic membranes such as multilayered vanadium and palladium are the promising candidates for in situ hydrogen removal from reaction side due to their suitable hydrogen permeability. However, the latter suffers from low mechanical strength, while the former provides appropriate mechanical properties inside suitable hydrogen diffusivity [148, 149]. Palladium-silver (Pd/Ag) membranes are typical candidates for this purpose [150]. Besides, such a strategy makes it possible to accomplish the process at lower temperatures as well as to reduce the coke formation. However, low-pressure condition in this process could lead to weak hydrogen separation. Problems arising from limited membrane durability and further clean up are other drawbacks of this strategy [76–79, 189].

### Pyrolysis of Hydrogen Sulfide: Energy Delivery and Decontamination

Although there exist conventional routes for the elimination of hydrogen sulfide ( $H_2S$ ) and then

sulfur recovery (e.g., the well-known Claus process [190]), the elemental hydrogen is consumed and converted into other compounds in these routes. Owing to the aforementioned interest for hydrogen production, simultaneous hydrogen sulfide removal, sulfur recovery, and hydrogen production is currently state of the art. In fact, hydrogen production from the hazardous compound is a multipurpose process as a combination of a decontamination strategy with the manufacturing of valuable chemicals and a new energy source is managed [191]. Hence, due to several favorable environmental impacts, it is currently of a great interest. Accordingly, thermolysis (i.e., thermal pyrolysis), photocatalysis, catalytic methods, and multi-step non-catalytic dissociation method are the possible routes for this purpose [192]. Pyrolysis of hydrogen sulfide, which is one of the pioneer techniques, is accomplished according to the following reaction [192]:



Based on the investigation of Kaloidas and Papayannakos [193], lower pressures and higher temperatures are suitable for hydrogen production through pyrolysis of hydrogen sulfide. However, theoretical and experimental investigations reveal that this process suffers from low conversion problem due to the combined effects of



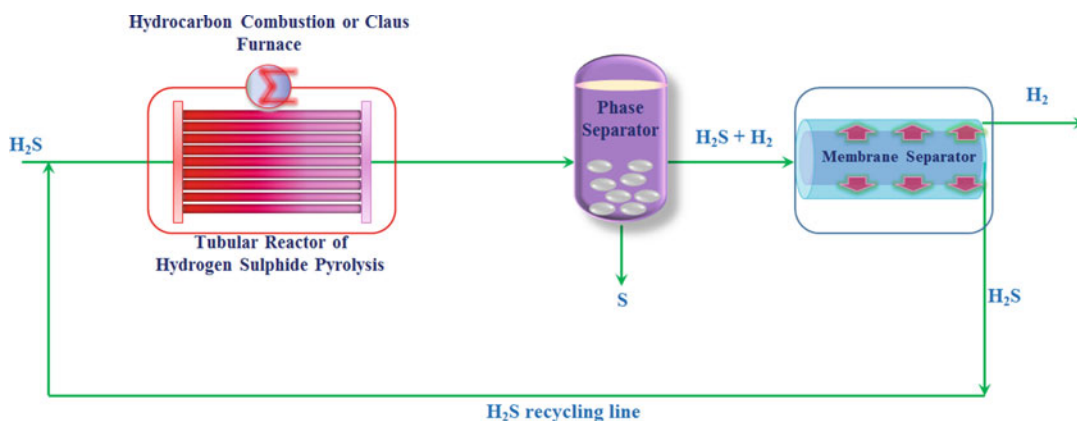
undesirable thermodynamic and kinetic constraints concerning the reversibility of Eq. (21). In fact, at ordinary pressures, the conversion is less than 10% [192]. In situ removal of the products by utilizing selective membranes, condensation of sulfur, or even thermal diffusion is wisely proposed to thermodynamically shift the reaction toward higher hydrogen sulfide conversion [148]. As mentioned previously, palladium-silver membranes are the suitable options [148–150].

Pyrolysis of hydrogen sulfide is generally accomplished in plug flow reactors with different heat sources. In small-scale hydrogen production, i.e., pilot plants or laboratory scales, the reaction side is heated by utilizing furnaces or thermoelectric modules [192, 194]. Cox et al. [195] carried out a feasibility study on the economics of industrial applications of hydrogen sulfide pyrolysis and then compared the feasible process schemes. As a general procedure, two different configurations are proposed for pyrolysis of hydrogen sulfide, first of which is a set of parallel plug flow reactors with external burners. The burners are supplied by natural gas. In the second one, in order to recover the generated heat of an in-operation Claus process and then to enhance the thermal efficiency of the unit, the assembly of plug flow reactors is installed in the burner of the Claus plant. The simplified pyrolysis plug flow reactor is schematically presented in Fig. 10. Although the first configuration is definitely more cost-effective than the second one, none of them could be, in terms of hydrogen price, the rival of the conventional SMR process [195]. Adewale et al. [196] studied hydrogen production from the thermal decomposition of hydrogen sulfide in a commercial sulfur recovery unit and then analyzed the economic benefits obtaining by retrofitting a Claus burner for this purpose. Although an early reduction in the sulfur recovery of the unit was observed, economic analyses showed that the return of capital investment is feasible within less than four years.

Pyrolysis of hydrogen sulfide is possible even in catalytic mode. However, at the temperature ranges higher than 800 °C, the kinetics of reactions allows to achieve chemical equilibria in a short time. Hence, application of catalyst does not make sense in such conditions [197].

Nevertheless, application of catalyst might be beneficial if the options concerning material resistance and shorter residence times are considered. In this regard, Zaman and Chakma [148] provided a comprehensive review on the literature of catalytic decomposition of hydrogen sulfide. Transition metal sulfides, e.g., sulfides of iron, cobalt, nickel, copper, molybdenum, tungsten, vanadium, and zinc were investigated in the literature. More details on the catalytic hydrogen sulfide decomposition could be found in their contribution [148]. More recently, a portion of researches has been devoted to the evaluation of non-conventional catalysts with super performance. The work of Ozaki et al. [198] is a case in point in which they compared the performance of an activated carbon catalyst composed of 3% ferrocene with an as-produced carbon catalyst sample synthesized without added ferrocene. As reported, the ferrocene-containing sample in a fixed-bed reactor offers lower temperature range (i.e., 300–400 °C) for hydrogen sulfide dissociation to hydrogen with reasonable conversion. More recently, Guldal et al. [199] developed a new class of catalysts composed of rare-earth metals and transition-element cations for hydrogen production via pyrolysis of hydrogen sulfide. The samples containing molybdenum were more active in the temperature range less than 850 °C with considerably higher conversion compared with the non-catalytic case.

Developing fluidized-bed catalytic reactors could lead to some merits in the pyrolysis of hydrogen sulfide. Elimination of mass transfer limitations and minimizing catalyst deactivation are of these kinds. In this regard, Cao and Adesina [200] evaluated the transition bimetallic sulfide catalysts in a fluidized-bed reactor for hydrogen production by decomposition of hydrogen sulfide. Accordingly, the combination of ruthenium (Ru) and molybdenum (Mo) provided the best catalysis characteristics for hydrogen production. The obtained results of their study prove the superiority of fluidized-bed over the fixed-bed reactor in the same operating condition. On the other hand, conversion of hydrogen sulfide in the fluidized-bed reactor loaded with Ru/Mo catalyst particles is higher than the case in the fixed-bed one. Besides, fluidization close to the minimum



**Hydrogen Production Through Pyrolysis, Fig. 10** Schematic diagram of hydrogen sulfide pyrolysis process (Adopted from [192])

bubbling point could lead to conversions higher than the equilibrium values. This observation could be possibly due to the membranous effect occurring in the fluidized beds, which would be favorable in shifting the reactions toward higher hydrogen production rate. However, by increasing the flow beyond this condition, a considerable conversion drop was observed owing to the onset of slugging [200].

## Conclusion, Further Studies, and Outlook

Owing to the undeniable necessity of exploring new routes for sustainable energy generation, production of hydrogen by applying pyrolysis process from different sources was investigated in the present contribution. Production of hydrogen by pyrolysis of biomass, natural gas, and hydrogen sulfide feedstocks was introduced as an efficient route. The impacts of various variables such as temperature, residence time, feedstock type, and catalyst characteristics on the production of hydrogen by pyrolysis of biomass feedstocks were investigated.

In spite of the mentioned defects in the developed commercial plants for hydrogen production from fossil hydrocarbon sources and even growing theoretical and experimental studies over production of hydrogen from bio-based sources, lack of codified regulations for large-scale production from such sources is still felt. However, there are

currently some examples of efforts that developed the theoretical achievements into the practical ones, as mentioned in the literature [121]. In spite of this, investigation and application of new efficient technologies for the production of biohydrogen is still a vast and novel field of research and study. New recuperative configurations such as membrane reactors, energy-efficient thermally coupled reactors, the configurations combining these two concepts and the chemical looping concept are the examples of such technologies [74, 77–79, 201–204].

## Bibliography

### Primary Literature

1. Mortensen PM, Grunwaldt J-D, Jensen PA, Knudsen K, Jensen AD (2011) A review of catalytic upgrading of bio-oil to engine fuels. *Appl Catal A Gen* 407:1–19
2. Balat M (2011) Production of bioethanol from lignocellulosic materials via the biochemical pathway: a review. *Energy Convers Manag* 52:858–875
3. Sorrell S, Speirs J, Bentley R, Brandt A, Miller R (2010) Global oil depletion: a review of the evidence. *Energy Policy* 38:5290–5295
4. van Ruijven B, van Vuuren DP (2009) Oil and natural gas prices and greenhouse gas emission mitigation. *Energy Policy* 37:4797–4808
5. Nigam PS, Singh A (2011) Production of liquid biofuels from renewable resources. *Prog Energy Combust Sci* 37:52–68
6. Huber GW, Iborra S, Corma A (2006) Synthesis of transportation fuels from biomass: chemistry, catalysts, and engineering. *Chem Rev* 106:4044–4098



7. Bakhtyari A, Mofarahi M (2014) Pure and binary adsorption equilibria of methane and nitrogen on zeolite 5A. *J Chem Eng Data* 59:626–639
8. Mofarahi M, Bakhtyari A (2015) Experimental investigation and thermodynamic modeling of CH<sub>4</sub>/N<sub>2</sub> adsorption on zeolite 13X. *J Chem Eng Data* 60:683–696
9. Parvasi P, Khaje Hesamedini A, Jahanmiri A, Rahimpour MR (2014) A novel modeling and experimental study of crude oil desalting using microwave. *Sep Sci Technol* 49:1029–1044
10. Kohl AL, Nielsen R (1997) Gas purification. Gulf Professional Publishing. Houston, Texas
11. Kothari R, Buddhi D, Sawhney R (2008) Comparison of environmental and economic aspects of various hydrogen production methods. *Renew Sust Energy Rev* 12:553–563
12. Balat M (2008) Potential importance of hydrogen as a future solution to environmental and transportation problems. *Int J Hydrog Energy* 33:4013–4029
13. Suban M, Tušek J, Uran M (2001) Use of hydrogen in welding engineering in former times and today. *J Mater Process Technol* 119:193–198
14. Saxena R, Seal D, Kumar S, Goyal H (2008) Thermochemical routes for hydrogen rich gas from biomass: a review. *Renew Sustain Energy Rev* 12:1909–1927
15. Mohammed M, Salmiaton A, Azlina WW, Amran MM, Fakhru'l-Razi A, Taufiq-Yap Y (2011) Hydrogen rich gas from oil palm biomass as a potential source of renewable energy in Malaysia. *Renew Sustain Energy Rev* 15:1258–1270
16. Hossain MA, Jewaratnam J, Ganesan P (2016) Prospect of hydrogen production from oil palm biomass by thermochemical process—a review. *Int J Hydrog Energy* 41:16637–16655
17. Ni M, Leung MK, Sumathy K, Leung DY (2006) Potential of renewable hydrogen production for energy supply in Hong Kong. *Int J Hydrog Energy* 31:1401–1412
18. Dutta S (2014) A review on production, storage of hydrogen and its utilization as an energy resource. *J Ind Eng Chem* 20:1148–1156
19. Konieczny A, Mondal K, Wiltowski T, Dydo P (2008) Catalyst development for thermocatalytic decomposition of methane to hydrogen. *Int J Hydrog Energy* 33:264–272
20. Mohan SV, Bhaskar YV, Sarma P (2007) Biohydrogen production from chemical wastewater treatment in biofilm configured reactor operated in periodic discontinuous batch mode by selectively enriched anaerobic mixed consortia. *Water Res* 41:2652–2664
21. Dupont V, Steam reforming of sunflower oil for hydrogen GAS (2007) Production/oxidación catalítica del aceite de girasol en la producción del gas hidrógeno/reformage à la vapeur de l'huile de tournesol dans la production de gaz hydrogène. *Helvia* 30:103–132
22. Armor J (2005) Catalysis and the hydrogen economy. *Catal Lett* 101:131–135
23. McDowall W, Eames M (2007) Towards a sustainable hydrogen economy: a multi-criteria sustainability appraisal of competing hydrogen futures. *Int J Hydrog Energy* 32:4611–4626
24. Cherry RS (2004) A hydrogen utopia? *Int J Hydrog Energy* 29:125–129
25. Hoang D, Chan S (2004) Modeling of a catalytic autothermal methane reformer for fuel cell applications. *Appl Catal A Gen* 268:207–216
26. H. Energy (2003) Fuel cells – a vision of our future. Summary Report, High Level Group for Hydrogen and Fuel Cells
27. Balat M (2005) Current alternative engine fuels. *Energy Sources* 27:569–577
28. Al-Baghdadi M (2003) Hydrogen–ethanol blending as an alternative fuel of spark ignition engines. *Renew Energy* 28:1471–1478
29. Al-Baghdadi MA-RS (2002) A study on the hydrogen–ethyl alcohol dual fuel spark ignition engine. *Energy Convers Manag* 43:199–204
30. Forsberg CW (2007) Future hydrogen markets for large-scale hydrogen production systems. *Int J Hydrog Energy* 32:431–439
31. Khanipour M, Mirvakili A, Bakhtyari A, Farniaei M, Rahimpour MR (2017) Enhancement of synthesis gas and methanol production by flare gas recovery utilizing a membrane based separation process. *Fuel Process Technol* 166:186–201
32. Wiltowski T, Mondal K, Campen A, Dasgupta D, Konieczny A (2008) Reaction swing approach for hydrogen production from carbonaceous fuels. *Int J Hydrog Energy* 33:293–302
33. Balat H, Kurtay E (2010) Hydrogen from biomass – present scenario and future prospects. *Int J Hydrog Energy* 35:7416–7426
34. Acar C, Dincer I (2014) Comparative assessment of hydrogen production methods from renewable and non-renewable sources. *Int J Hydrog Energy* 39:1–12
35. Dincer I, Acar C (2015) Review and evaluation of hydrogen production methods for better sustainability. *Int J Hydrog Energy* 40:11094–11111
36. Funk JE (2001) Thermochemical hydrogen production: past and present. *Int J Hydrog Energy* 26: 185–190
37. Kaneko H, Gokon N, Hasegawa N, Tamaura Y (2005) Solar thermochemical process for hydrogen production using ferrites. *Energy* 30:2171–2178
38. Levchenko A, Dobrovolsky YA, Bukun N, Leonova L, Zyubina T, Neudachina V, Yashina L, Tarasov A, Shatalova T, Shtanov V (2007) Chemical and electrochemical processes in low-temperature superionic hydrogen sulfide sensors. *Russ J Electrochem* 43:552–560
39. Amao Y, Tomonou Y, Okura I (2003) Highly efficient photochemical hydrogen production system using zinc porphyrin and hydrogenase in CTAB micellar system. *Sol Energy Mater Sol Cells* 79:103–111
40. Nada A, Barakat M, Hamed H, Mohamed N, Veziroglu T (2005) Studies on the photocatalytic hydrogen production using suspended modified TiO<sub>2</sub> photocatalysts. *Int J Hydrog Energy* 30:687–691

41. Sedirolu V, Eroglu In, Yücel M, Türker L, Gündüz U (1999) The biocatalytic effect of *i*Halobacterium halobium on photoelectrochemical hydrogen production. *J Biotechnol* 70:115–124
42. Sedirolu V, Yücel M, Gunduz U, Turker L, Eroglu I (1998) The effect of halobacterium halobium on photoelectrochemical hydrogen production. In: *BioHydrogen*. Springer, Boston, pp 295–304
43. Levent M, Gunn DJ, El-Bousiffi MA (2003) Production of hydrogen-rich gases from steam reforming of methane in an automatic catalytic microreactor. *Int J Hydrog Energy* 28:945–959
44. Gunn D, El-Bousiffi M (2004) Production of hydrogen-rich gases from steam reforming of methane in an automatic catalytic microreactor. *Int J Hydrog Energy* 29:1427–1428
45. Farniaei M, Abbasi M, Rahnama H, Rahimpour MR, Shariati A (2014) Syngas production in a novel methane dry reformer by utilizing of tri-reforming process for energy supplying: modeling and simulation. *J Nat Gas Sci Eng* 20:132–146
46. Rahimpour MR, Hesami M, Saidi M, Jahanmiri A, Farniaei M, Abbasi M (2013) Methane steam reforming thermally coupled with fuel combustion: application of chemical looping concept as a novel technology. *Energy Fuel* 27:2351–2362
47. Basile A, Palma V, Ruocco C, Bagnato G, Jokar S, Rahimpour MR, Shariati A, Rossi C, Iulianelli A (2015) Pure hydrogen production via ethanol steam reforming reaction over a novel Pt-Co based catalyst in a dense Pd-Ag membrane reactor (An experimental study). *Int J Mem Sci Technol* 2:5–14
48. Jokar SM, Rahimpour MR, Shariati A, Iulianelli A, Bagnato G, Vita A, Dalena F, Basile A (2016) Pure hydrogen production in membrane reactor with mixed reforming reaction by utilizing waste gas: a case study. *PRO* 4:33
49. Lee JK, Park D (1998) Hydrogen production from fluidized bed steam reforming of hydrocarbons. *Korean J Chem Eng* 15:658–662
50. Ko K-D, Lee JK, Park D, Shin SH (1995) Kinetics of steam reforming over a Ni/alumina catalyst. *Korean J Chem Eng* 12:478–480
51. Seo JG, Youn MH, Park S, Lee J, Lee SH, Lee H, Song IK (2008) Hydrogen production by steam reforming of LNG over Ni/Al<sub>2</sub>O<sub>3</sub>-ZrO<sub>2</sub> catalysts: effect of ZrO<sub>2</sub> and preparation method of Al<sub>2</sub>O<sub>3</sub>-ZrO<sub>2</sub>. *Korean J Chem Eng* 25:95–98
52. Seo JG, Youn MH, Cho KM, Park S, Lee SH, Lee J, Song IK (2008) Effect of Al<sub>2</sub>O<sub>3</sub>-ZrO<sub>2</sub> xerogel support on hydrogen production by steam reforming of LNG over Ni/Al<sub>2</sub>O<sub>3</sub>-ZrO<sub>2</sub> catalyst. *Korean J Chem Eng* 25:41–45
53. Yu C-Y, Lee D-W, Park S-J, Lee K-Y, Lee K-H (2009) Study on a catalytic membrane reactor for hydrogen production from ethanol steam reforming. *Int J Hydrog Energy* 34:2947–2954
54. Barbieri G, Di Maio FP (1997) Simulation of the methane steam re-forming process in a catalytic Pd-membrane reactor. *Ind Eng Chem Res* 36: 2121–2127
55. Wang J, Wan W (2009) Application of desirability function based on neural network for optimizing biohydrogen production process. *Int J Hydrog Energy* 34:1253–1259
56. Kim P, Kim Y, Kim H, Song IK, Yi J (2004) Synthesis and characterization of mesoporous alumina with nickel incorporated for use in the partial oxidation of methane into synthesis gas. *Appl Catal A Gen* 272: 157–166
57. Gao X, Huang CJ, Zhang N, Li J, Weng WZ, Wan H (2008) Partial oxidation of methane to synthesis gas over Co/Ca/Al<sub>2</sub>O<sub>3</sub> catalysts. *Catal Today* 131:211–218
58. Karimipourfard D, Kabiri S, Rahimpour MR (2014) A novel integrated thermally double coupled configuration for methane steam reforming, methane oxidation and dehydrogenation of propane. *J Nat Gas Sci Eng* 21:134–146
59. Onozaki M, Watanabe K, Hashimoto T, Saegusa H, Katayama Y (2006) Hydrogen production by the partial oxidation and steam reforming of tar from hot coke oven gas. *Fuel* 85:143–149
60. Takeguchi T, Furukawa S-N, Inoue M, Eguchi K (2003) Autothermal reforming of methane over Ni catalysts supported over CaO–CeO<sub>2</sub>–ZrO<sub>2</sub> solid solution. *Appl Catal A Gen* 240:223–233
61. Youn MH, Seo JG, Cho KM, Jung JC, Kim H, La KW, Park DR, Park S, Lee SH, Song IK (2008) Effect of support on hydrogen production by auto-thermal reforming of ethanol over supported nickel catalysts. *Korean J Chem Eng* 25:236–238
62. Youn MH, Seo JG, Park S, Jung JC, Park DR, Song IK (2008) Hydrogen production by auto-thermal reforming of ethanol over Ni catalysts supported on ZrO<sub>2</sub>: effect of preparation method of ZrO<sub>2</sub> support. *Int J Hydrog Energy* 33:7457–7463
63. Luna AEC, Iriarte ME (2008) Carbon dioxide reforming of methane over a metal modified Ni-Al<sub>2</sub>O<sub>3</sub> catalyst. *Appl Catal A Gen* 343:10–15
64. Nandini A, Pant KK, Dhingra SC (2006) Kinetic study of the catalytic carbon dioxide reforming of methane to synthesis gas over Ni-K/CeO<sub>2</sub>-Al<sub>2</sub>O<sub>3</sub> catalyst. *Appl Catal A Gen* 308:119–127
65. Muradov N (1993) How to produce hydrogen from fossil fuels without CO<sub>2</sub> emission. *Int J Hydrog Energy* 18:211–215
66. Nikolaidis P, Poullikkas A (2017) A comparative overview of hydrogen production processes. *Renew Sustain Energy Rev* 67:597–611
67. Palma V, Vaiano V, Barba D, Colozzi M, Palo E, Barbato L, Cortese S (2015) H<sub>2</sub> production by thermal decomposition of H<sub>2</sub>S in the presence of oxygen. *Int J Hydrog Energy* 40:106–113
68. Abbasi M, Farniei M, Rahimpour MR, Shariati A (2015) Hydrogen production in an environmental-friendly process by application of chemical looping combustion via Ni-and Fe-based oxygen carriers. *Theor Found Chem Eng* 49:884–900

69. Abbasi M, Farniaei M, Rahimpour MR, Shariati A (2014) Methane dry reformer by application of chemical looping combustion via Mn-based oxygen carrier for heat supplying and carbon dioxide providing. *Chem Eng Process Intensif* 79:69–79
70. Abbasi M, Farniaei M, Rahimpour MR, Shariati A (2013) Enhancement of hydrogen production and carbon dioxide capturing in a novel methane steam reformer coupled with chemical looping combustion and assisted by hydrogen perm-selective membranes. *Energy Fuel* 27:5359–5372
71. Alirezai I, Hafizi A, Rahimpour MR, Raeissi S (2016) Application of zirconium modified Cu-based oxygen carrier in chemical looping reforming. *J CO<sub>2</sub> Util* 14: 112–121
72. Hafizi A, Jafari M, Rahimpour MR, Hassanajili S (2016) Experimental investigation of sorption enhanced chemical looping reforming for high purity hydrogen production using CeO<sub>2</sub>–CaO CO<sub>2</sub> sorbent and 15Fe–5Ca/Al<sub>2</sub>O<sub>3</sub> oxygen carrier. *J Taiwan Inst Chem Eng* 65:185–196
73. Hafizi A, Rahimpour MR, Hassanajili S (2016) High purity hydrogen production via sorption enhanced chemical looping reforming: application of 22Fe<sub>2</sub>O<sub>3</sub>/MgAl<sub>2</sub>O<sub>4</sub> and 22Fe<sub>2</sub>O<sub>3</sub>/Al<sub>2</sub>O<sub>3</sub> as oxygen carriers and cerium promoted CaO as CO<sub>2</sub> sorbent. *Appl Energy* 169:629–641
74. Hafizi A, Rahimpour MR, Hassanajili S (2016) Hydrogen production by chemical looping steam reforming of methane over Mg promoted iron oxygen carrier: optimization using design of experiments. *J Taiwan Inst Chem Eng* 62:140–149
75. Hafizi A, Jafari M, Rahimpour MR, Hassanajili S (2016) Experimental investigation of sorption enhanced chemical looping reforming for high purity hydrogen production using CeO<sub>2</sub>–CaO CO<sub>2</sub> sorbent and 15Fe–5Ca/Al<sub>2</sub>O<sub>3</sub> oxygen carrier. *J Taiwan Inst Chem Eng* 65:185–196
76. Bakhtyari A, Darvishi A, Rahimpour MR (2016) A heat exchanger reactor equipped with membranes to produce dimethyl ether from syngas and methyl formate and hydrogen from methanol. *Int J* 3:65
77. Bakhtyari A, Haghbakhsh R, Rahimpour MR (2016) Investigation of thermally double coupled double membrane heat exchanger reactor to produce dimethyl ether and methyl formate. *J Nat Gas Sci Eng* 32:185–197
78. Bakhtyari A, Mohammadi M, Rahimpour MR (2015) Simultaneous production of dimethyl ether (DME), methyl formate (MF) and hydrogen from methanol in an integrated thermally coupled membrane reactor. *J Nat Gas Sci Eng* 26:595–607
79. Bakhtyari A, Parhoudeh M, Rahimpour MR (2016) Optimal conditions in converting methanol to dimethyl ether, methyl formate, and hydrogen utilizing a double membrane heat exchanger reactor. *J Nat Gas Sci Eng* 28:31–45
80. Bayat M, Rahimpour MR (2011) Simultaneous utilization of two different membranes for intensification of ultrapure hydrogen production from recuperative coupling autothermal multitubular reactor. *Int J Hydrog Energy* 36:7310–7325
81. Brown LF (2001) A comparative study of fuels for on-board hydrogen production for fuel-cell-powered automobiles. *Int J Hydrog Energy* 26:381–397
82. Simpson AP, Lutz AE (2007) Exergy analysis of hydrogen production via steam methane reforming. *Int J Hydrog Energy* 32:4811–4820
83. Jin H, Xu Y, Lin R, Han W (2008) A proposal for a novel multi-functional energy system for the production of hydrogen and power. *Int J Hydrog Energy* 33:9–19
84. Rahimpour MR, Ghaemi M, Jokar S, Dehghani O, Jafari M, Amiri S, Raeissi S (2013) The enhancement of hydrogen recovery in PSA unit of domestic petrochemical plant. *Chem Eng J* 226:444–459
85. Ravanchi MT, Kaghazchi T, Kargari A (2009) Application of membrane separation processes in petrochemical industry: a review. *Desalination* 235: 199–244
86. Chang H-F, Pai W-J, Chen Y-J, Lin W-H (2010) Autothermal reforming of methane for producing high-purity hydrogen in a Pd/Ag membrane reactor. *Int J Hydrog Energy* 35:12986–12992
87. Wilhelm D, Simbeck D, Karp A, Dickenson R (2001) Syngas production for gas-to-liquids applications: technologies, issues and outlook. *Fuel Process Technol* 71:139–148
88. Aasberg-Petersen K, Christensen TS, Nielsen CS, Dybkjær I (2003) Recent developments in autothermal reforming and pre-reforming for synthesis gas production in GTL applications. *Fuel Process Technol* 83:253–261
89. Simeone M, Saleme L, Allouis C (2008) Reactor temperature profile during autothermal methane reforming on Rh/Al<sub>2</sub>O<sub>3</sub> catalyst by IR imaging. *Int J Hydrog Energy* 33:4798–4808
90. Ding O, Chan S (2008) Autothermal reforming of methane gas—modelling and experimental validation. *Int J Hydrog Energy* 33:633–643
91. Balat M, Balat M (2009) Political, economic and environmental impacts of biomass-based hydrogen. *Int J Hydrog Energy* 34:3589–3603
92. Hites RA (2006) Persistent organic pollutants in the Great Lakes: an overview. In: *Persistent organic pollutants in the Great Lakes*. Springer, Berlin/Heidelberg, pp 1–12
93. Lund H (2007) Renewable energy strategies for sustainable development. *Energy* 32:912–919
94. Ćosić B, Krajačić G, Duić N (2012) A 100% renewable energy system in the year 2050: the case of Macedonia. *Energy* 48:80–87
95. Mathiesen BV, Lund H, Karlsson K (2011) 100% Renewable energy systems, climate mitigation and economic growth. *Appl Energy* 88:488–501
96. Granovskii M, Dincer I, Rosen MA (2007) Exergetic life cycle assessment of hydrogen production from renewables. *J Power Sources* 167:461–471

97. Charvin P, Stéphane A, Florent L, Gilles F (2008) Analysis of solar chemical processes for hydrogen production from water splitting thermochemical cycles. *Energy Convers Manag* 49:1547–1556
98. Tarnay DS (1985) Hydrogen production at hydro-power plants. *Int J Hydrog Energy* 10:577–584
99. Sigurvinnsson J, Mansilla C, Arnason B, Bontemps A, Maréchal A, Sigfusson T, Werkoff F (2006) Heat transfer problems for the production of hydrogen from geothermal energy. *Energy Convers Manag* 47:3543–3551
100. Utgikar V, Ward B (2006) Life cycle assessment of ISPRA mark 9 thermochemical cycle for nuclear hydrogen production. *J Chem Technol Biotechnol* 81: 1753–1759
101. C.E.G. Padró, V. Putsche (1999) Survey of the economics of hydrogen technologies. National Renewable Energy Laboratory Golden, CO
102. S. Shah (2015) Hydrogen production processes from biomass. Master Science Thesis, Aalto University
103. Antonopoulou K, Gavala HN, Skiadas IV, Angelopoulos G, Lyberatos G (2008) Biofuels generation from sweet sorghum: fermentative hydrogen production and anaerobic digestion of the remaining biomass. *Bioresour Technol* 99:110–119
104. Encinar J, Beltran F, Ramiro A, Gonzalez J (1998) Pyrolysis/gasification of agricultural residues by carbon dioxide in the presence of different additives: influence of variables. *Fuel Process Technol* 55:219–233
105. Demirbaş A (2001) Yields of hydrogen-rich gaseous products via pyrolysis from selected biomass samples. *Fuel* 80:1885–1891
106. Parthasarathy P, Narayanan KS (2014) Hydrogen production from steam gasification of biomass: influence of process parameters on hydrogen yield – a review. *Renew Energy* 66:570–579
107. Rollin JA, del Campo JM, Myung S, Sun F, You C, Bakovic A, Castro R, Chandrayan SK, Wu C-H, Adams MW (2015) High-yield hydrogen production from biomass by in vitro metabolic engineering: mixed sugars coutilization and kinetic modeling. *Proc Natl Acad Sci* 112:4964–4969
108. Demirbaş A (2001) Biomass resource facilities and biomass conversion processing for fuels and chemicals. *Energy Convers Manag* 42:1357–1378
109. Huber GW, Corma A (2007) Synergies between bio- and oil refineries for the production of fuels from biomass. *Angew Chem Int Ed* 46:7184–7201
110. Lynd LR, Cushman JH, Nichols RJ, Wyman CE (1991) Fuel ethanol from cellulosic biomass. *Science* 251:1318–1323
111. Wyman CE, Decker SR, Himmel ME, Brady JW, Skopec CE, Viikari L (2005) Hydrolysis of cellulose and hemicellulose. *Polysaccharides Struct Divers Funct Versatility* 1:1023–1062
112. Lynd LR, Wyman CE, Gerngross TU (1999) Biocommodity engineering. *Biotechnol Prog* 15:777–793
113. Mosier N, Wyman C, Dale B, Elander R, Lee YY, Holtzapple M, Ladisch M (2005) Features of promising technologies for pretreatment of lignocellulosic biomass. *Bioresour Technol* 96:673–686
114. Wyman CE, Dale BE, Elander RT, Holtzapple M, Ladisch MR, Lee Y (2005) Coordinated development of leading biomass pretreatment technologies. *Bioresour Technol* 96:1959–1966
115. Kamm B, Gruber PR, Kamm M (2006) Biorefineries—industrial processes and products, Wiley Online Library. WILEY-VCH, Weinheim
116. Zakaria ZY, Amin NAS, Linnekoski J (2013) A perspective on catalytic conversion of glycerol to olefins. *Biomass Bioenergy* 55:370–385
117. Corma A, Huber GW, Sauvanaud L, O'Connor P (2008) Biomass to chemicals: catalytic conversion of glycerol/water mixtures into acrolein, reaction network. *J Catal* 257:163–171
118. Murata K, Takahara I, Inaba M (2008) Propane formation by aqueous-phase reforming of glycerol over Pt/H-ZSM5 catalysts. *React Kinet Catal Lett* 93:59–66
119. Stedile T, Ender L, Meier HF, Simionatto EL, Wiggers VR (2015) Comparison between physical properties and chemical composition of bio-oils derived from lignocellulose and triglyceride sources. *Renew Sustain Energy Rev* 50:92–108
120. Huber GW, Dumesic JA (2006) An overview of aqueous-phase catalytic processes for production of hydrogen and alkanes in a biorefinery. *Catal Today* 111:119–132
121. Bridgwater AV (2012) Review of fast pyrolysis of biomass and product upgrading. *Biomass Bioenergy* 38:68–94
122. Mohan D, Pittman CU, Steele PH (2006) Pyrolysis of wood/biomass for bio-oil: a critical review. *Energy Fuel* 20:848–889
123. Isahak WNRW, Hisham MWM, Yarmo MA, Hin T-y Y (2012) A review on bio-oil production from biomass by using pyrolysis method. *Renew Sustain Energy Rev* 16:5910–5923
124. Papari S, Hawboldt K (2015) A review on the pyrolysis of woody biomass to bio-oil: focus on kinetic models. *Renew Sustain Energy Rev* 52:1580–1595
125. Sharma A, Pareek V, Zhang D (2015) Biomass pyrolysis—a review of modelling, process parameters and catalytic studies. *Renew Sustain Energy Rev* 50:1081–1096
126. Behrendt F, Neubauer Y, Oevermann M, Wilmes B, Zobel N (2008) Direct liquefaction of biomass. *Chem Eng Technol* 31:667–677
127. Toor SS, Rosendahl L, Rudolf A (2011) Hydrothermal liquefaction of biomass: a review of subcritical water technologies. *Energy* 36:2328–2342
128. Elliott D, Beckman D, Bridgwater A, Diebold J, Gevert S, Solantausta Y (1991) Developments in direct thermochemical liquefaction of biomass: 1983–1990. *Energy Fuel* 5:399–410

129. Saber M, Nakhshiniev B, Yoshikawa K (2016) A review of production and upgrading of algal bio-oil. *Renew Sustain Energy Rev* 58:918–930
130. Rahimpour MR, Biniiaz P, Makarem MA (2017) 14 – Integration of microalgae into an existing biofuel industry. In: *Bioenergy systems for the future*. Woodhead Publishing, Kidlington, pp 481–519
131. Klass DL (1998) Chapter 1 – energy consumption, reserves, depletion, and environmental issues. In: *Biomass for renewable energy, fuels, and chemicals*. Academic Press, San Diego, pp 1–27
132. Bridgwater A, Peacocke G (2000) Fast pyrolysis processes for biomass. *Renew Sustain Energy Rev* 4:1–73
133. Czernik S, Bridgwater A (2004) Overview of applications of biomass fast pyrolysis oil. *Energy Fuel* 18:590–598
134. Moffatt J, Overend R (1985) Direct liquefaction of wood through solvolysis and catalytic hydrodeoxygenation: an engineering assessment. *Biomass* 7:99–123
135. Vanasse C, Chornet E, Overend R (1988) Liquefaction of lignocellulosics in model solvents: creosote oil and ethylene glycol. *Can J Chem Eng* 66:112–120
136. Goudriaan F, Van de Beld B, Boerefijn F, Bos G, Naber J, Van der Wal S, Zeevalkink J (2008) Thermal efficiency of the HTU<sup>®</sup> process for biomass liquefaction. In: *Progress in thermochemical biomass conversion*, Blackwell Science Ltd. Osney Mead, Oxford, pp 1312–1325
137. Elliott DC, Schiefelbein GF (1989) Liquid hydrocarbon fuels from biomass. *Pap Am Chem Soc* 34:1160
138. Yuan X, Wang J, Zeng G, Huang H, Pei X, Li H, Liu Z, Cong M (2011) Comparative studies of thermochemical liquefaction characteristics of microalgae using different organic solvents. *Energy* 36:6406–6412
139. Miao X, Wu Q, Yang C (2004) Fast pyrolysis of microalgae to produce renewable fuels. *J Anal Appl Pyrolysis* 71:855–863
140. Bakhtyari A, Makarem MA, Rahimpour MR (2017) 4 – light olefins/bio-gasoline production from biomass. In: *Bioenergy systems for the future*. Woodhead Publishing, Kidlington, pp 87–148
141. Gollakota AR, Reddy M, Subramanyam MD, Kishore N (2016) A review on the upgradation techniques of pyrolysis oil. *Renew Sustain Energy Rev* 58:1543–1568
142. Towler GP, Oroskar AR, Smith SE (2004) Development of a sustainable liquid fuels infrastructure based on biomass. *Environ Prog* 23:334–341
143. Elliott D, Baker E, Beckman D, Solantausta Y, Tolonen V, Gevert S, Hörnell C, Östman A, Kjellström B (1990) Technoeconomic assessment of direct biomass liquefaction to transportation fuels. *Biomass* 22:251–269
144. Liu S, Zhu J, Chen M, Xin W, Yang Z, Kong L (2014) Hydrogen production via catalytic pyrolysis of biomass in a two-stage fixed bed reactor system. *Int J Hydrog Energy* 39:13128–13135
145. Fremaux S, Beheshti S-M, Ghassemi H, Shahsavani-Markadeh R (2015) An experimental study on hydrogen-rich gas production via steam gasification of biomass in a research-scale fluidized bed. *Energy Convers Manag* 91:427–432
146. Ni M, Leung DY, Leung MKH, Sumathy K (2006) An overview of hydrogen production from biomass. *Fuel Process Technol* 87:461–472
147. Iribarren D, Susmozas A, Petrakopoulou F, Dufour J (2014) Environmental and exergetic evaluation of hydrogen production via lignocellulosic biomass gasification. *J Clean Prod* 69:165–175
148. Zaman J, Chakma A (1995) Production of hydrogen and sulfur from hydrogen sulfide. *Fuel Process Technol* 41:159–198
149. Edlund DJ, Pledger WA (1993) Thermolysis of hydrogen sulfide in a metal-membrane reactor. *J Membr Sci* 77:255–264
150. Itoh N (1987) A membrane reactor using palladium. *AIChE J* 33:1576–1578
151. McKendry P (2002) Energy production from biomass (part 1): overview of biomass. *Bioresour Technol* 83:37–46
152. Wang D, Czernik S, Montane D, Mann M, Chornet E (1997) Biomass to hydrogen via fast pyrolysis and catalytic steam reforming of the pyrolysis oil or its fractions. *Ind Eng Chem Res* 36:1507–1518
153. Demirbas MF (2006) Hydrogen from various biomass species via pyrolysis and steam gasification processes. *Energy Sources Part A* 28:245–252
154. Demirbaş A, Çağlar A (1998) Catalytic steam reforming of biomass and heavy oil residues to hydrogen, energy, education. *Sci Technol* 11:45–52
155. Koroneos C, Dompros A, Roubas G (2008) Hydrogen production via biomass gasification—a life cycle assessment approach. *Chem Eng Process Process Intensif* 47:1267–1274
156. Damen K, Troost Mv, Faaij A, Turkenburg W (2006) A comparison of electricity and hydrogen production systems with CO<sub>2</sub> capture and storage. Part A: review and selection of promising conversion and capture technologies. *Prog Energy Combust Sci* 32:215–246
157. Demirbaş A (2002) Gaseous products from biomass by pyrolysis and gasification: effects of catalyst on hydrogen yield. *Energy Convers Manag* 43:897–909
158. Yang H, Yan R, Chen H, Lee DH, Liang DT, Zheng C (2006) Pyrolysis of palm oil wastes for enhanced production of hydrogen rich gases. *Fuel Process Technol* 87:935–942
159. Bridgwater A (1999) Principles and practice of biomass fast pyrolysis processes for liquids. *J Anal Appl Pyrolysis* 51:3–22
160. Magrini-Bair KA, Czernik S, French R, Chornet E (2003) Fluidizable catalysts for hydrogen production from biomass pyrolysis/steam reforming, FY

- 2003 Progress Report, National Renewable Energy Laboratory
161. Demirbas A, Arin G (2004) Hydrogen from biomass via pyrolysis: relationships between yield of hydrogen and temperature. *Energy Sources* 26:1061–1069
  162. Xianwen D, Chuangzhi W, Haibin L, Yong C (2000) The fast pyrolysis of biomass in CFB reactor. *Energy Fuel* 14:552–557
  163. Garcia L, Salvador M, Arauzo J, Bilbao R (2001) Catalytic pyrolysis of biomass: influence of the catalyst pretreatment on gas yields. *J Anal Appl Pyrolysis* 58:491–501
  164. Chen G, Andries J, Spliethoff H (2003) Catalytic pyrolysis of biomass for hydrogen rich fuel gas production. *Energy Convers Manag* 44:2289–2296
  165. Simell PA, Hirvensalo EK, Smolander VT, Krause AOI (1999) Steam reforming of gasification gas tar over dolomite with benzene as a model compound. *Ind Eng Chem Res* 38:1250–1257
  166. Williams PT, Brindle AJ (2002) Catalytic pyrolysis of tyres: influence of catalyst temperature. *Fuel* 81:2425–2434
  167. Narváez I, Corella J, Orío A (1997) Fresh tar (from a biomass gasifier) elimination over a commercial steam-reforming catalyst. Kinetics and effect of different variables of operation. *Ind Eng Chem Res* 36:317–327
  168. Sutton D, Kelleher B, Ross JR (2002) Catalytic conditioning of organic volatile products produced by peat pyrolysis. *Biomass Bioenergy* 23:209–216
  169. Czernik S, French R, Evans R, Chornet E (2003) Hydrogen from post-consumer residues. In: US DOE hydrogen and fuel cells merit review meeting. Berkeley
  170. Zanzi R, Sjöström K, Björnbom E (2002) Rapid pyrolysis of agricultural residues at high temperature. *Biomass Bioenergy* 23:357–366
  171. Zabanitoutou A, Ioannidou O, Antonakou E, Lappas A (2008) Experimental study of pyrolysis for potential energy, hydrogen and carbon material production from lignocellulosic biomass. *Int J Hydrog Energy* 33:2433–2444
  172. Evans R, Boyd L, Elam C, Czernik S, French R, Feik C, Philips S, Chaomet E, Parent Y (2003) Hydrogen from biomass-catalytic reforming of pyrolysis vapors. In: US DOE Hydrogen, Fuel Cells & Infrastructure Technologies Program—2003 Annual Merit Review Meeting
  173. Yeboah Y, Bota K, Day D, McGee D, Realff M, Evans R, Chornet E, Czernik S, Feik C, French R (2002) Hydrogen from biomass for urban transportation. In: Proceedings of the US DOE hydrogen program review. San Ramon, California, pp 130–140
  174. Onay O, Mete Koçkar O (2004) Fixed-bed pyrolysis of rapeseed (*Brassica napus* L.) *Biomass Bioenergy* 26:289–299
  175. Abedi J, Yeboah YD, Realff M, McGee D, Howard J, Bota KB (2001) An integrated approach to hydrogen production from agricultural residues for use in urban transportation. In: Proceedings of the 2001 DOE hydrogen program review, NREL/CP-570-30535, National Renewable Energy Laboratory
  176. Encinar JM, Beltrán FJ, González JF, Moreno MJ (1997) Pyrolysis of maize, sunflower, grape and tobacco residues. *J Chem Technol Biotechnol* 70:400–410
  177. Shafizadeh F (1982) Introduction to pyrolysis of biomass. *J Anal Appl Pyrolysis* 3:283–305
  178. Balci S, Dogu T, Yucel H (1993) Pyrolysis kinetics of lignocellulosic materials. *Ind Eng Chem Res* 32:2573–2579
  179. White JE, Catallo WJ, Legendre BL (2011) Biomass pyrolysis kinetics: a comparative critical review with relevant agricultural residue case studies. *J Anal Appl Pyrolysis* 91:1–33
  180. Di Blasi C (1998) Comparison of semi-global mechanisms for primary pyrolysis of lignocellulosic fuels. *J Anal Appl Pyrolysis* 47:43–64
  181. Nunn TR, Howard JB, Longwell JP, Peters WA (1985) Product compositions and kinetics in the rapid pyrolysis of sweet gum hardwood. *Ind Eng Chem Process Des Dev* 24:836–844
  182. Alves S, Figueiredo J (1989) Kinetics of cellulose pyrolysis modelled by three consecutive first-order reactions. *J Anal Appl Pyrolysis* 17:37–46
  183. Diebold JP (1994) A unified, global model for the pyrolysis of cellulose. *Biomass Bioenergy* 7: 75–85
  184. Vargas JM, Perlmutter DD (1986) Interpretation of coal pyrolysis kinetics. *Ind Eng Chem Process Des Dev* 25:49–54
  185. Mangut V, Sabio E, Gañán J, González J, Ramiro A, González C, Román S, Al-Kassir A (2006) Thermogravimetric study of the pyrolysis of biomass residues from tomato processing industry. *Fuel Process Technol* 87:109–115
  186. Muradov N (2001) Hydrogen via methane decomposition: an application for decarbonization of fossil fuels. *Int J Hydrog Energy* 26:1165–1175
  187. Muradov N, Veziroğlu T (2005) From hydrocarbon to hydrogen-carbon to hydrogen economy. *Int J Hydrog Energy* 30:225–237
  188. Muradov N (2001) Catalysis of methane decomposition over elemental carbon. *Catal Commun* 2:89–94
  189. De Falco M, Marrelli L, Iaquaniello G (2011) Membrane reactors for hydrogen production processes. Springer, Surrey
  190. Zhang X, Tang Y, Qu S, Da J, Hao Z (2015) H<sub>2</sub>S-selective catalytic oxidation: catalysts and processes. *ACS Catal* 5:1053–1067
  191. Miltner A, Wukovits W, Pröll T, Friedl A (2010) Renewable hydrogen production: a technical evaluation based on process simulation. *J Clean Prod* 18:S51–S62
  192. Reverberi AP, Klemeš JJ, Varbanov PS, Fabiano B (2016) A review on hydrogen production from hydrogen sulphide by chemical and photochemical methods. *J Clean Prod Part B* 136:72–80



193. Kaloidas V, Papayannakos N (1987) Hydrogen production from the decomposition of hydrogen sulphide. Equilibrium studies on the system  $H_2S/H_2/Si_i$  ( $i=1, \dots, 8$ ) in the gas phase. *Int J Hydrog Energy* 12:403–409
194. Chiarioni A, Reverberi A, Fabiano B, Dovi V (2006) An improved model of an ASR pyrolysis reactor for energy recovery. *Energy* 31:2460–2468
195. Cox BG, Clarke PF, Pruden BB (1998) Economics of thermal dissociation of  $H_2S$  to produce hydrogen. *Int J Hydrog Energy* 23:531–544
196. Adewale R, Salem DJ, Berrouk AS, Dara S (2016) Simulation of hydrogen production from thermal decomposition of hydrogen sulfide in sulfur recovery units. *J Clean Prod* 112:4815–4825
197. Moghiman M, Javadi S, Moghiman A, Hosseini SB (2010) A numerical study on thermal dissociation of  $H_2S$ . *World Acad Sci Eng Technol* 62:824–829
198. Ozaki J-i, Yoshimoto Y, Oya A, Takarada T, Kuzunetsov VV, Ismagilov ZR (2001)  $H_2S$  decomposition activity of TS carbon derived from furan resin. *Carbon* 39:1611–1612
199. Guldal N, Figen H, Baykara S (2015) New catalysts for hydrogen production from  $H_2S$ : preliminary results. *Int J Hydrog Energy* 40:7452–7458
200. Cao D, Adesina A (1999) Fluidised bed reactor studies of  $H_2S$  decomposition over supported bimetallic Ru catalysts. *Catal Today* 49:23–31
201. Rahimpour MR, Dehghani Z (2016) Membrane reactors for methanol synthesis from forest-derived feedstocks. *Membr Technol Biorefining*, pp 383–410
202. Rahimpour MR, Nategh M (2016) Hydrogen production from pyrolysis-derived bio-oil using membrane reactors. *Membr Technol Biorefining*, pp 411–434
203. Rahimpour MR (2015) 10 – Membrane reactors for biodiesel production and processing. In: *Membrane reactors for energy applications and basic chemical production*. Woodhead Publishing, Amsterdam/Boston, pp 289–312
204. Bagnato G, Iulianelli A, Vita A, Italiano C, Laganà M, Fabiano C, Rossi C, Basile A (2015) Pure hydrogen production from steam reforming of bio-sources. *Int J* 2:49



## Hydrogen Production from Algal Pathways

Muhammad Aziz and Ilman Nuran Zaini  
Institute of Innovative Research, Tokyo Institute of Technology, Tokyo, Japan

### Article Outline

Glossary  
Definition of the Subject and Its Importance  
Introduction  
Algae Potential  
Key Technologies  
Highly Energy-Efficient Integrated Systems  
Conclusions  
Bibliography

### Glossary

**Algae** Diverse and large group of photosynthetic and aquatic organisms ranging from unicellular to multicellular. They have no true stems, roots and leaves.

**Autotrophic** An organism that has a capability to produce energy-containing organic compounds from simple substance, generally by using sunlight as an energy source.

**Chemical looping** Novel technology that can provide the means of converting fuel to heat and provide CO<sub>2</sub> separation with high energy efficiency.

**Combined cycle** Combination of two or more thermodynamic cycles that work from the same source of heat and convert it into

mechanical energy. Practically, it is a combination of a gas turbine (Brayton cycle) and a steam turbine (Rankine cycle) for power generation.

**Exergy** The maximum available work that can be used through a process that brings the system into equilibrium with the environment. It represents the quality of energy.

**Gasification** Process that converts fossil or organic-based carbonaceous materials into gaseous fuels (syngas).

**Hydrogen carrier** Material that can store hydrogen in a certain chemical state rather than as free hydrogen molecules. The hydrogen atoms or ions are bonded in the molecule.

**Hydrogenation** A chemical reaction between hydrogen and another unsaturated compounds or elements. The hydrogen atoms are added to a molecule, thus double and triple hydrocarbons are reduced.

**Oxygen carrier** A material used to transport the oxygen so that direct contact between the fuel and air can be avoided.

**Process integration** A holistic method to design the process by considering the interactions among the unit operations and optimize them altogether. It aims to minimize the energy consumption through optimum heat recovery.

**Pyrolysis** A thermochemical decomposition process of an organic substance at elevated temperatures in the absence of oxygen (inert atmosphere).

**Supercritical condition** A condition in which both temperature and pressure of any substance are higher than its thermodynamic critical point. Hence, the material shows no distinct liquid and gas phases.

**Syngas** Abbreviation of synthesis gas. A mixed gaseous fuel that mainly consists of hydrogen, carbon monoxide, and carbon dioxide.

## Definition of the Subject and Its Importance

Algae are autotrophic organisms ranging from unicellular to multicellular and are promising as an energy resource. Algae possess some exceptional characteristics compared with other terrestrial bio-masses, especially regarding growth rate, growth density, starch and lipids content, and CO<sub>2</sub> absorption capability. In addition, algae are non-food-based feedstock resources. Their relatively rich starch and lipids content have urged researchers and industries to utilize algae in more effective ways. Enormous focus has been placed on algae utilization as an energy resource in bio-fuel production, especially bio-diesel and bio-ethanol. Unfortunately, this kind of energy harvesting is considered to be ineffective due to its low conversion efficiency and production rate [1]. Recently, new utilization of algae for hydrogen production and power generation has been studied, which is believed to improve the total energy efficiency as well as provide better energy storage and transportation. This chapter focuses on the description of the state-of-the-art hydrogen production from algae, including some important processes and techniques. In addition, some novel integrated systems for hydrogen production from algae are also presented, incorporating some evaluated parameters for optimum system operation.

## Introduction

Algae are aquatic and photosynthetic plants representing large groups of different organisms that are widely distributed in the sea, freshwater, moist land, etc. Algae have some excellent advantages compared with the terrestrial plants, including fast growing rate, high-efficiency of CO<sub>2</sub> mitigation, and capability to grow under severe conditions [2–4]. Algae can effectively convert sunlight into chemical energy during photosynthesis, up to 9%, leading to high areal productivity [5, 6]. It is estimated that algae are responsible for about 40% of the global carbon fixation [7]. In

addition, algae are emerging as new potential resources for the production of bio-fuels, whereas they are not directly competing with food, different to other bio-fuels. Unfortunately, algae contain a high moisture content, about 70–90 wt% on a wet basis (wb), leading to some difficulties in their utilization.

Because of their high ability to fix CO<sub>2</sub>, algae can serve the possibility to combine their cultivation with the fixation of exhausted CO<sub>2</sub> during conversion toward energy harvesting. This bio-sequestration is considered to be the efficient strategy for abating the greenhouse gases. Hence, energy production from algae is believed to be environmentally benign with minimum CO<sub>2</sub> emission. In addition, co-location of the algae cultivation site to a nearby CO<sub>2</sub> emitting industrial point, such as a power plant, is an appropriate strategy to effectively grow the algae as well as reduce the emission. According to previous research, algae can be productively cultivated under a CO<sub>2</sub> concentration of 15% [8].

Generally, algae can be utilized as industrial and chemical feedstock, nutritious food, and an energy resource in terms of economic, environmental, and sustainable points of view. However, the utilization of algae as an energy resource has been emphasized since the last decade. Algae are mainly utilized for producing the so-called fine chemicals that are utilized further for medicines, food additives, health supplements, and cosmetics. As the concern to reduce the CO<sub>2</sub> emission and other environmental problems increases, algae began to receive intensive attention as one of the renewable energy sources. Algae are rich in lipid content, leading to their potential to be utilized as a primary energy source. This can be converted to different fuels such as bio-hydrogen, bio-diesel, bio-gas, and bio-oil [4]. The calorific value of algae under optimum conditions commonly ranges from 17 to 23 GJ t-dried-algae<sup>-1</sup> [9].

As algae grow in an aqueous environment, their cultivation is generally located remotely, which might be far from their demand sites. Therefore, the produced fuel from algae needs to be stored and transported in the form of secondary

energy forms. Among the secondary energy resources, hydrogen has some advantages of high versatility and efficiency, high variety of production, and utilization technologies, cleanliness, etc. [10]. The utilization of hydrogen is widespread and increasing. It includes combustion in a reciprocating engine or potential combined cycle with steam generation, as well as direct electro-chemical conversion to electricity using fuel cells. Hydrogen can also be blended with other fuels for improved combustion characteristics such as with natural gas to produce hythane. In addition, water is produced during oxidation of hydrogen, resulting in clean and environmentally benign energy utilization.

This section explains the potential and technologies of harvesting algae as a primary energy source and conversion to the secondary energy source, especially hydrogen. A brief description on algae, including their classification, distribution, and potential as an energy source, is provided in the next section. Further, some key technologies related and potentially involved in the conversion of algae to hydrogen are also explained. Thereafter, several integrated systems to effectively convert algae to hydrogen employing different technologies are introduced, including some evaluated operating parameters to find the optimum conversion process.

## Algae Potential

### Algae Classification

Algae are diverse and basically can be sub-classified into microalgae (unicellular) and macroalgae (multicellular), mainly depending on their cell structure.

Microalgae are defined as photosynthetic unicellular or simple-multicellular microorganisms. They are normally found in fresh water and marine habitats [11]. Microalgae such as *Chlamydomonas*, *Scenedesmus*, *Chlorella*, *Dunaliella*, *Spirulina* have a significant amount (more than 50% of their dry weight) of starch and glycogen. Most microalgae belong to the algal

groups like dinoflagellates, *Chlorophyceae*, *Chrysoophyceae*, and diatoms [12]. Microalgae are varied due to the large diversity of its pigments, photosynthetic storage products, cell walls and mucilages, fatty acids and lipids, oils, sterols and hydrocarbons, and bioactive compounds [13].

Unlike microalgae, macroalgae are multicellular and pose plant-like characteristics. Macroalgae, also known as seaweeds, display a complex and dynamic taxonomy [14]. The three common algal phyla are *Phaeophyta* (brown algae), *Rhodophyta* (red algae), and *Chlorophyta* (green algae) [15]. Algae are different from *Cyanophyta*, class *Cyanophyceae* (the blue-green algae) which are eubacteria (true bacteria) [15].

The brown algae are classified into approximately 265 genera, with more than 1500 species. Furthermore, *Phaeophyta* is divided into 13 orders in which common orders include *Laminariales* and *Fucales* that are abundant in nature and have the most complex structure. *Laminariales* are commonly referred to as kelps and are cultivated for many commercial industries, including the frozen food industry, syrups, explosives, ceramics, welding rods, and cleaners. On the other hand, *Fucales* are a large order with a wide range of morphological diversity [15].

In red algae phyla, *Rhodymeniales* are one of the most distinctive and well-defined orders of red algae that currently covers over 42 genera with 300 species and six families, i.e., *Rhodymeniaceae*, *Champiaceae*, *Lomentariaceae*, *Faucheaceae*, *Hymenocladaceae*, and *Fryeellaceae* [16]. In addition, common species of red algae utilized for commercial industries includes the carrageenophytes *Sarcothalia crispata*, *Mazzaella laminarioides*, *Gigartina skottsbergii*, *Chondracanthus chamissoi*, and the agarophytes *Gracilaria chilensis* and *Gelidium linguatum* [17].

### Algae Distribution

Microalgae can be found in terrestrial environments and they can be found in a wide range of habitats, from snowfields to the edges of hot

springs, even from the leaves of the plants to hot and dry desert soils. However, most species of microalgae need at least a film of liquid water to be metabolically active [13]. Microalgae, as a unicellular species, also can utilize planktonic living, i.e., suspended throughout the lighted regions of all water bodies including under ice in polar regions. In addition, they can also be benthic which means attached to the bottom or living within the sediments, limited to shallow areas due to the rapid attenuation of light with depth. Benthic microalgae can grow attached to stones, mud or sand, other algae or plants, or animals [18].

Besides a natural habitat, microalgae also can be grown in an artificial habitat using freshwater, seawater, and wastewater within open ponds or a closed photo-bioreactor. Certain species of microalgae can sustain a wide variety of environmental conditions, i.e., different pH, temperature, light, etc., and they can be growth all year round [11].

As a marine organism, macroalgae can only grow and survive when the physiochemical conditions of seawater are suitable for them. Macroalgae's growth is intimately affected mainly by specific temperature and salinity of the seawater. It also needs adequate water movement, tolerable UV radiation, and sufficient light to optimally grow [19].

Figure 1 shows the global distribution of seaweed species, adapted from the report by Steneck et al. [20]. In Europe, brown seaweed *Laminaria* sp. naturally grows mainly in Western Europe, especially in Norway, France, and Iceland [20, 21]. Those countries have rocky coastal areas which provide enough hard substrate to accommodate extensive kelp plantation [21]. *Laminaria* sp., especially *Laminaria japonica* (kombu), is also found to grow along the coast of east Asia, particularly in the North Pacific from Japan [20, 22]. The seaweed distribution on the coast of Chile and North America is dominated by *Macrocystis* spp., e.g., *Macrocystis pyrifera* (giant bladder kelp) [22], which can grow to 45 m long. In addition, *Macrocystis* spp. is also

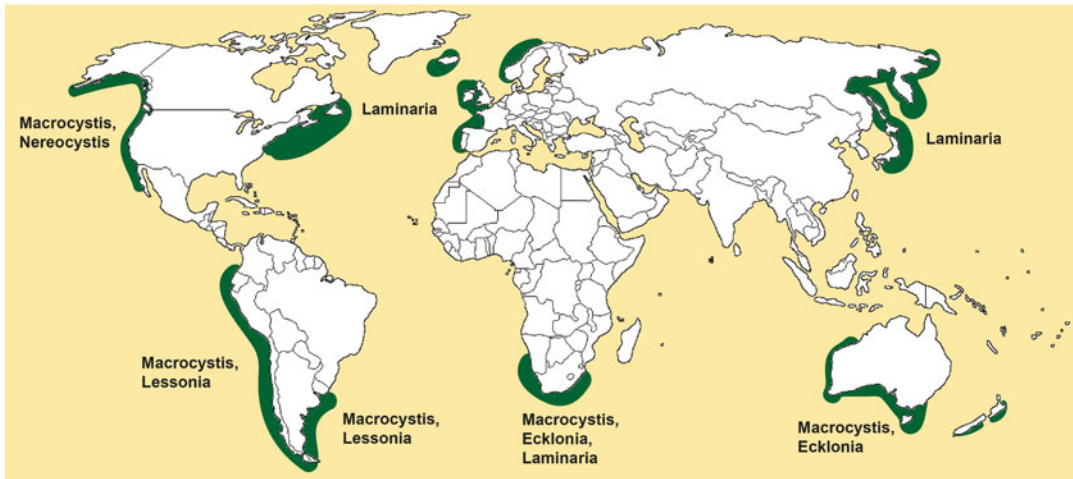
found to grow in the South Pacific Ocean including, South America, South Africa, southern Australia, New Zealand, and some sub-Antarctic islands [20]. Other seaweeds are found to grow on other specific areas such as *Nereocystis leuhtana* which spreads from Central California to Alaska, *Ecklonia maxima* in South Africa [20], *Ecklonia raditata* in Australia [23], and *Alaria fistulosa* in Alaska and the Pacific coast of Asia [20].

### Algae as an Energy Source

In general, algae can produce biomass faster than terrestrial feedstock. Certain species of algae can double in size in approximately 6 h and many species can double in a day [24]. This high growth rate, in addition to excellent capability of CO<sub>2</sub> fixation and growth densities, becomes compelling reasons to invest in algae as energy source. Both starch and lipids are the main components of algae which are used to reserve the carbon and energy for growth and reproduction. However, their ratio differs depending on the algal type and living conditions.

Starch is more likely to be species-dependent rather than dependent on the ecological conditions in which algae were growing. Starch is the most common glucose unit (polyglucans) produced by green algae to store carbon and energy. There are some forms of polyglucans such as amylose, amylopectin (such as in green algae), chrysolaminarin (such as in *Bacillariophyceae*), floridean (such as in *Rhodophyta*), paramylon (such as in *Euglenophyta*), and glycogen (such as in *Cyanophyta*) [25].

On the other hand, lipids are a more concentrated energy store than starch. For comparison, the energy yields of fatty acids (one category of lipid) and carbohydrate in complete oxidation are about 38 and 17 kJ g<sup>-1</sup>, respectively [26]. Lipids basically can be categorized into two different groups: polar and nonpolar (neutral) lipids. The former are the parts of cell membranes, while the latter are the energy storage. Nonpolar lipids are accumulated in the form of triacylglycerols and their composition.



**Hydrogen Production from Algal Pathways, Fig. 1** Seaweed global distribution [20]

Therefore, both glucose and nonpolar lipids are considered as the most important factors to select the algae when they are utilized as an energy resource.

As one of the major biomass resources, algae have potential to be utilized as an energy resource. Recently, the high content of both glucose and lipids has attracted the utilization of algae for bio-fuel production. In addition, energy harvesting from algae in the forms of electricity and hydrogen receive very little attention. Conversion of algae to hydrogen and electricity is also believed very promising.

Figure 2 shows the possible energy utilization pathways of algae [6]. In general, there are four main stages involved during energy harvesting from algae: cultivation, pretreatment, conversion, and posttreatment. Some important technologies related to hydrogen production are discussed later. The conversion of algae to fuel and products is predicated on some important process decision points: (1) conversion of the whole algal biomass, (2) extraction of algal metabolites, and (3) processing of direct algal secretions.

Conversion of algae to hydrogen is considered as one very potential method to harvest the energy from algae. Algae grow in aqueous

environments and are located in remote areas far from the energy demand. Effective storage and transportation are needed to handle the produced fuel from algae. Compared to other secondary energy resources, hydrogen possesses benefits of high versatility, excellent efficiency, high variety of production and utilization technologies, and cleanliness [10].

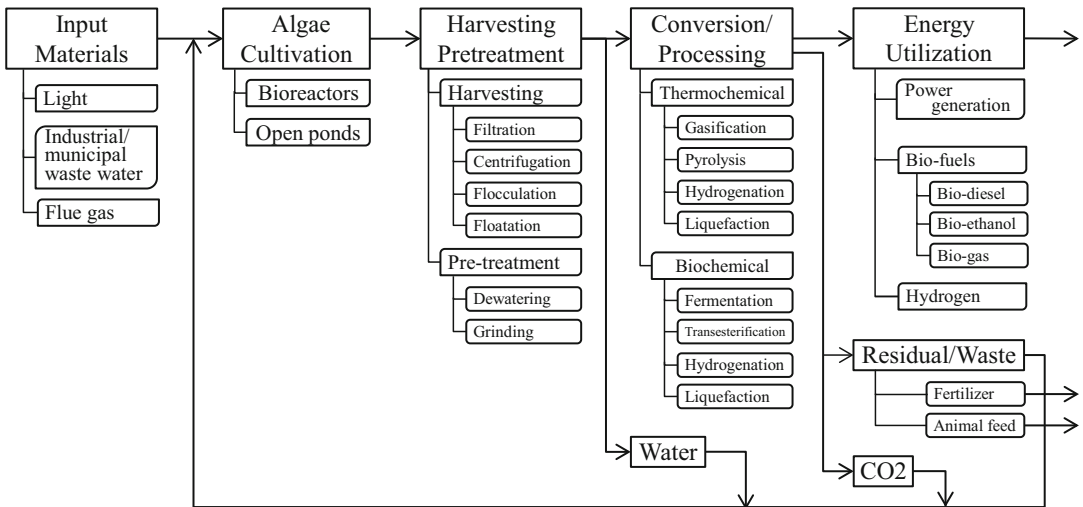
## Key Technologies

Energy production, especially hydrogen, from algae involves and can be performed with various technologies. These technologies are widespread, starting from cultivation, pretreatment, conversion, and posttreatments. In this subsection, some important technologies which are correlated to energy harvesting from algae, especially to hydrogen production, are explained.

### Cultivation

Cultivation of algae deals strongly with the metabolic nature of algae, nutrient supply, light exposure, optimum cultivation environment, handling during harvest, etc. The cultivation methods for microalgae and macroalgae





**Hydrogen Production from Algal Pathways, Fig. 2** Possible algal utilization routes as an energy resource

are quite different. Microalgae cultivation can be performed in an open pond (raceways), closed pond, plastic bag, photo bioreactor system, and a well system [27]. On the other hand, macroalgae cultivation faces more challenging problems, especially related to their characteristics including growth rate, shape, and size.

Table 1 shows the advantages and disadvantages of the cultivation method for both microalgae and macroalgae. In general, compared to an open pond system, a photo bioreactor system offers an excellent axenic culture and a more controllable growth environment for algae, resulting in higher algal productivity [28]. However, a photo bioreactor still faces its original problems related to cost competitiveness due to high capital cost compared to an open pond system [29].

### Drying

High moisture content becomes a significant barrier in algae utilization as the utilization process demands lower moisture content. Although it varies according to the types and living environment, algae have moisture content ranging from 70 to 90 wt% wb. To reduce the moisture content as well as increase the

calorific value, drying becomes very crucial in order to preserve the conversion to be efficient and stable.

Doe et al. [30] reported that to achieve the gasification temperature of 900 °C, moisture content of lower than 10 wt% wb is demanded [30]. Unfortunately, algae drying can reach about 85% of the total energy consumed in algae utilization [31]. Therefore, drying of algae is one of the main bottlenecks in algae culturing. Algae drying is conventionally carried out in a natural convection way of solar drying by hanging or spreading the algae over the net for a relatively long time. Moreover, thermal drying of algae consumes up to 3.6 MJ kg<sup>-1</sup> of fossil-fuel based energy [32]. Hence, an innovative method of drying algae with high energy efficiency is demanded.

Drying is a complex process dealing with moisture evaporation, capillary forces, chemical bonding forces, etc. Hence, drying is strongly influenced by the equilibrium moisture content, i.e., the correlation between the moisture inside the material and the surrounding conditions. The equilibrium moisture content,  $MC_{eq}$ , of *Fucus serratus* can be calculated based on the experiment conducted by Mohamed et al. [33] which is written as the following equation:

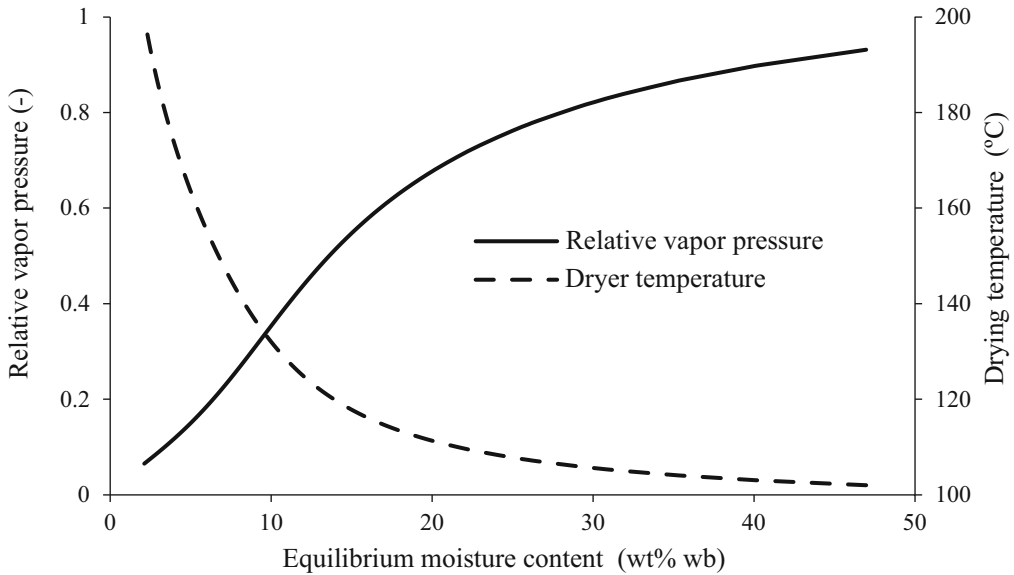
**Hydrogen Production from Algal Pathways, Table 1** Advantages and disadvantages of each cultivation method for algae

Algal type	Cultivation method	Advantages	Disadvantages
Microalgae	Open ponds	Simple engineering system Low capital cost Relatively maintained temperature due to evaporative cooling Lower productivity	Influenced strongly by surrounding environment (temperature, humidity) Low light exposure Risk of contamination and problems in mixing
	Closed ponds	Simple construction Low capital cost (higher than open ponds) Lower risk of contamination	Low light exposure, needs intensive light supply Requires roof and isolation construction Needs starter chemical
	Photo bioreactors	High productivity Less water loss Controllable condition Longer term culture maintenance High surface to volume High volumetric cell density	Higher capital cost Poor scalability Needs temperature maintenance Needs periodic cleaning because of biofilm formation Needs starter chemicals
	Plastic bag	Low capital cost Less water loss Simple construction Low contamination risk	Overheating potential Poor durability
	Well	Less area, high areal productivity Less water loss	Less light supply
Macroalgae	Natural cultivation (ocean)	No need for water supply Low capital cost Natural nutrients supply	Strongly influenced by the natural condition (ocean)
	Artificial ponds	Controllable conditions Better harvest	Need for water supply Need for nutrients supply

$$\begin{aligned}
 & MC_{eq} \\
 &= \frac{1.0078 e^{\left(\frac{-1076}{RT}\right)} e^{\left(\frac{15261}{RT}\right)} \left(\frac{p}{p_{sat}}\right)}{\left[1 - 1.3638 e^{\left(\frac{-1076}{RT}\right)} \left(\frac{p}{p_{sat}}\right)\right] \left[1 - 1.3638 e^{\left(\frac{-1076}{RT}\right)} \left(\frac{p}{p_{sat}}\right) + 0.1124 e^{\left(\frac{-1076}{RT}\right)} e^{\left(\frac{15261}{RT}\right)} \left(\frac{p}{p_{sat}}\right)\right]} \quad (1)
 \end{aligned}$$

where  $p$ ,  $p_{sat}$ ,  $R$ , and  $T$  are the partial pressure (kPa), the saturation pressure (kPa), the gas constant ( $8.314 \text{ J mol}^{-1} \text{ K}^{-1}$ ), and the temperature (K), respectively. Here,  $MC_{eq}$  depends strongly on  $p/p_{sat}$  which is the relative vapor pressure (i.e., the ratio of partial vapor pressure to saturated vapor pressure) of the environment. Figure 3 shows the required drying temperature in correlation to  $MC_{eq}$  in the case of steam drying of algae at atmospheric pressure [6].

Drying of algae to a moisture content higher than 15 wt% wb seems to show a linear relationship among the equilibrium moisture content, drying temperature, and relative vapor pressure because the required energy for drying is almost equal to the latent heat for water evaporation. On the other hand, drying to less than 15 wt% wb presents a significant decrease in relative vapor pressure but a significant increase in the drying temperature due to the removal of bound water.



**Hydrogen Production from Algal Pathways, Fig. 3** Correlation between the relative vapor pressure,  $MC_{eq}$  and drying temperature in the case of steam drying of algae under atmospheric pressure

The removal of this bound water requires much larger energy than that which is needed for water evaporation.

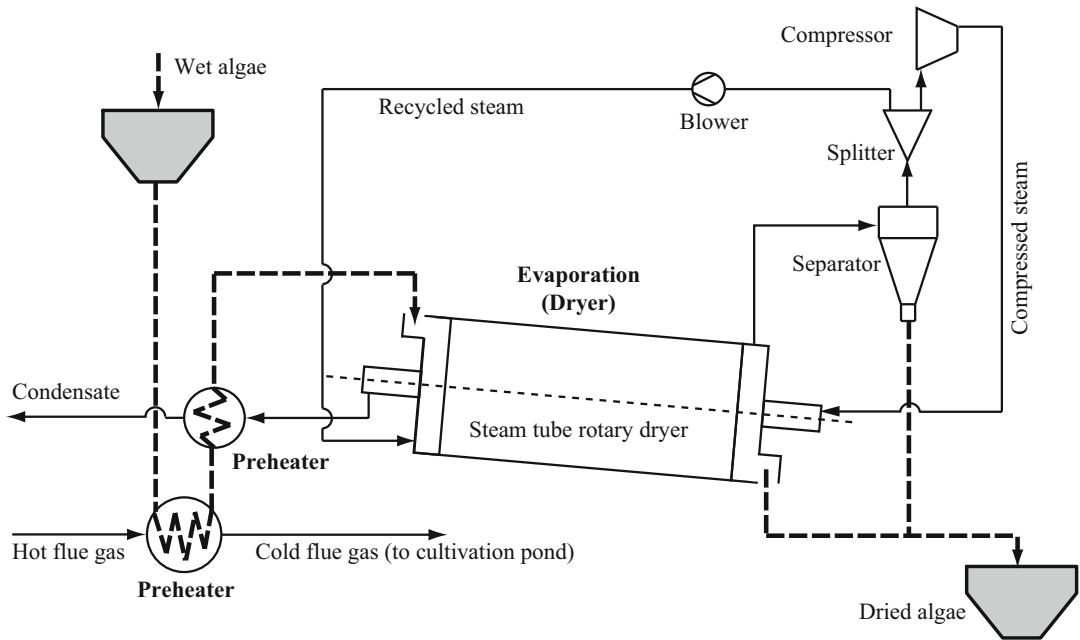
Future research and development efforts with energy-efficient drying have been proposed. These include the heat recovery, heat and mass transfer intensification, and dryer selection. Recently, exergy recovery-based drying has been proposed to further reduce the energy consumption during high moisture content biomass [34, 35].

Aziz et al. [4, 6] have developed an innovative drying system for algae with high energy efficiency. Figure 4 shows their proposed algae drying system adopting a steam tube rotary dryer as the evaporator. The advantages of this kind of dryer include the possibility of a large heat transfer area with high thermal efficiency, high handling ability and suitable for continuous operation, excellent drying control, simple operation, and easy to use, etc. [36].

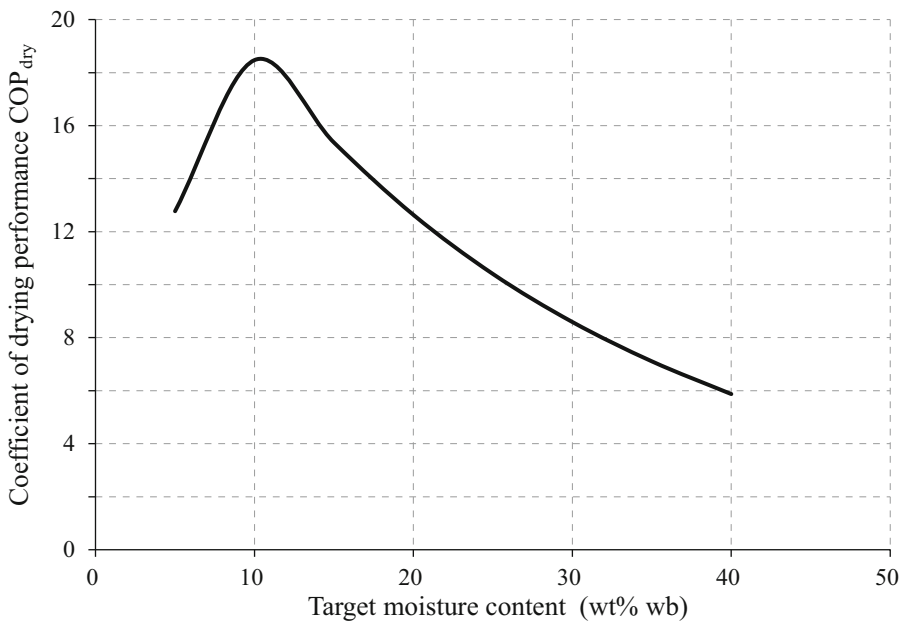
In the steam tube rotary dryer, heat is exchanged conductively in which the heat source is isolated from the material to be dried, which is wet algae. The heating tubes installed inside the steam tube rotary dryer are filled with compressed

steam and arranged in concentric circles inside the dryer to provide the heat required for drying. The heating tubes rotate along with the rotary drum. The heat for drying is provided largely by the condensation heat of the compressed steam in the heating tubes. Wet algae are fed continuously at a uniform rate, tumbled, and agitated by the rotation of the cylinder. A steam tube rotary dryer has a slope rotating cylinder to move the material by gravity, and finally the dried algae are discharged from the outlet. During traveling inside the cylinder, algae are heated by contact with, and radiant heat from, the surfaces of the steam tubes. The mode of heat exchange inside the dryer is set to be counter current to achieve a minimum exergy loss following the heat exchange.

Figure 5 shows the calculated coefficient of drying performance,  $COP_{dry}$ , of the algae drying system based on the exergy recovery technology. In general, the performance of algae drying, based on exergy recovery, is very high,  $COP_{dry}$  is highest at 18.5 when the target moisture content is set to 10 wt% wb. As the target moisture content increases,  $COP_{dry}$  gradually decreases because of a material imbalance, in which the amount of



**Hydrogen Production from Algal Pathways, Fig. 4** Process flow diagram of algae drying, based on exergy recovery



**Hydrogen Production from Algal Pathways, Fig. 5** Relationship between the coefficient of drying performance and target moisture content in algae drying using the exergy recovery technology

compressed steam is insufficient to achieve the optimum heat pairing. On the other hand,  $COP_{dry}$  also decreases sharply as the drying progresses to lower moisture contents due to the large energy requirement for drying and the overall energy input required in the system.

### Thermochemical Conversion

Compared with biochemical conversion, thermochemical conversion can achieve a faster conversion rate and higher carbon conversion efficiency. The thermochemical conversion of algae includes gasification, pyrolysis, liquefaction, and direct combustion. Among them, pyrolysis and gasification are two main thermochemical technologies especially due to their higher conversion efficiency. Furthermore, two gasification technologies are available today for algae: conventional thermal-gasification and supercritical water gasification.

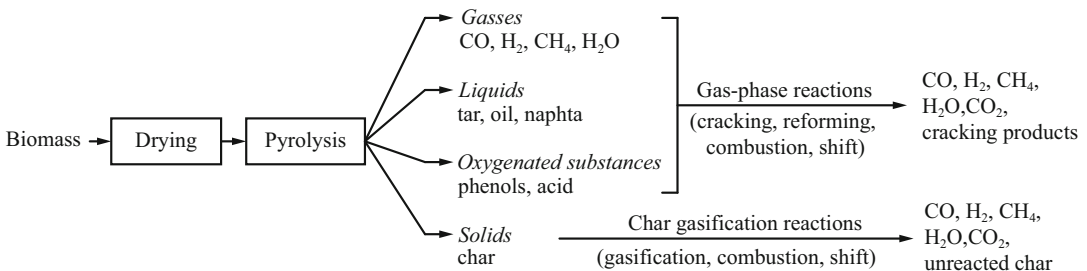
### Thermal Gasification

Gasification is a thermochemical conversion of carbonaceous solid fuel into gas involving the partial oxidation process in the presence of gasifying agents [37]. Common feedstock in gasification includes coal, biomass, and municipal solid waste. Common substances used as gasifying agents include air, steam, oxygen,  $CO_2$ , and a mixture of these. Gas produced from gasification are called “synthetic gas” (syngas) which normally consist of  $H_2$ ,  $CO$ ,  $CO_2$ ,  $CH_4$ , unreacted carbonaceous particles, ashes, tars, and oils. Gasification occurs at high temperature (500–1400 °C) with operating pressure ranging from atmospheric pressure to 3.3 MPa [37]. Compared to other

thermochemical methods, gasification is found to provide better results in terms of increased material decomposition and chemical energy [38]. Compared with pyrolysis, gasification has a higher carbon conversion efficiency and conversion rate [39]. Moreover, gasification has been considered as a feasible option to produce renewable hydrogen through highly efficient and clean large-scale plants [40].

Gasification of biomass is a sequenced process that consists of the following overlapping steps: drying, pyrolysis (devolatilization), reduction (char gasification), and combustion reactions, as illustrated in Fig. 6. Table 2 provides the reactions occurring during gasification of the biomass. During drying, inherent moisture residing between the cell structures of the biomass particles is liberated. Pyrolysis, which precedes gasification, takes place involving the thermal decomposition of larger hydrocarbon molecules of biomass into smaller condensable and noncondensable gas molecules without any major chemical reaction with the gasifying agent.

The products of pyrolysis reactions are gases, liquids, oxygenated substances, and solids. The pyrolysis step is then followed by the gasification step in which a chemical reaction occurs among the hydrocarbons in the biomass, steam,  $CO_2$ ,  $O_2$ ,  $H_2$ , and among the evolved gas. Among those gasification reactions, the gasification of char is produced from pyrolysis, which is the most important reaction. Gasification reactions are mainly endothermic. Hence, a certain amount of exothermic combustion (oxidation) reaction is necessary to provide heat for gasification as well as for drying and pyrolysis.



**Hydrogen Production from Algal Pathways, Fig. 6** Steps of biomass gasification (Adapted from Basu [41]).

There are several reactor designs used for gasification of biomass, including updraft, downdraft, fluidized bed, and entrained flow gasifier, all with their respective advantages and disadvantages. Figure 7 shows the basic principle of each reactor. In Europe, there are approximately 50 commercial gasifier manufacturers that can be classified based on their gasifier product as shown in Fig. 8.

There are some important process parameters that determine the produced syngas yield, particularly the hydrogen yield, from gasification of the biomass as well as gasification of algae. In gasification of algae, the main parameters are algae type, gasifying agent, algae feed particle size, temperature, catalysts, etc.

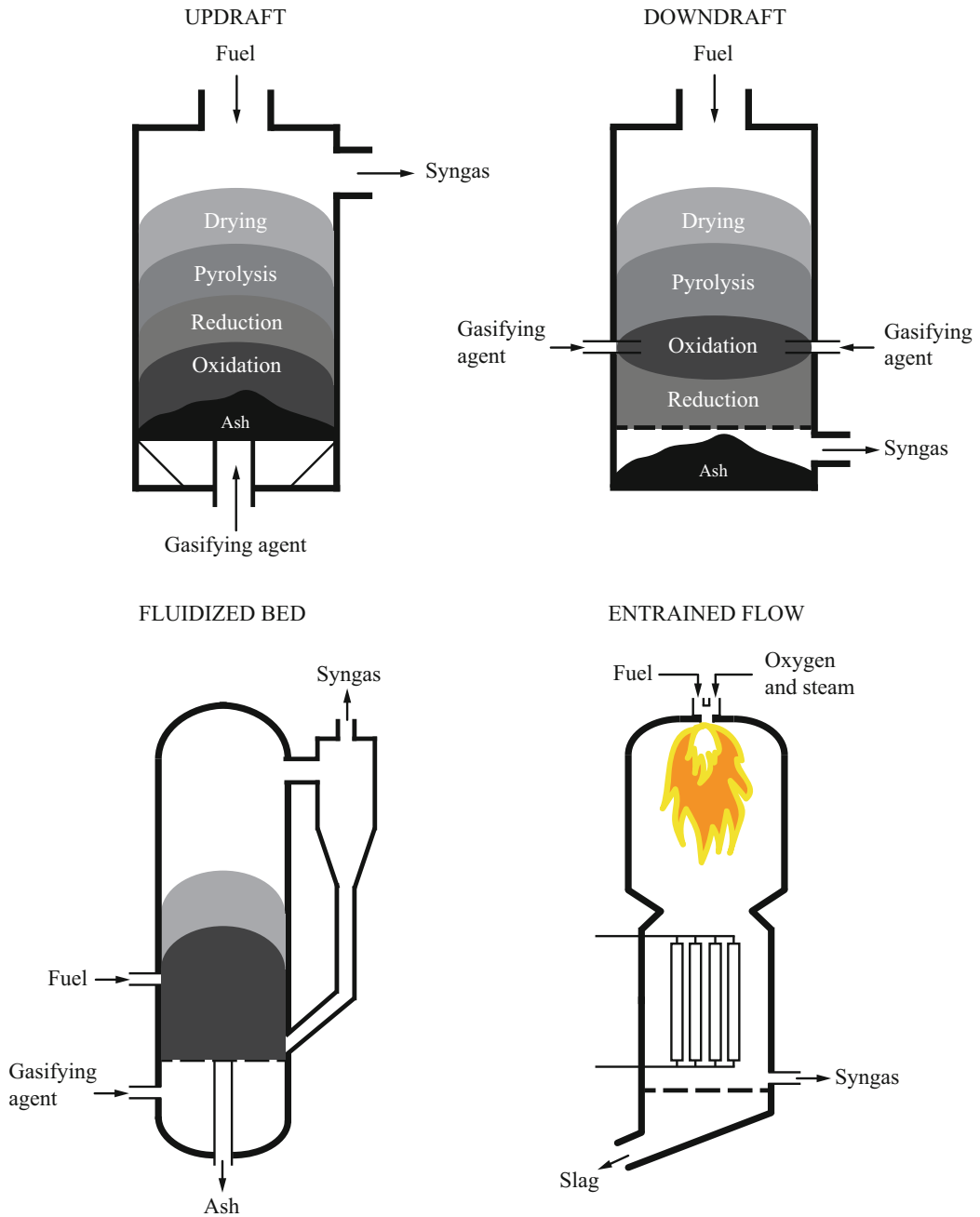
- Algae type

During gasification of algae, the reaction rate and gas yield is predominantly determined by the algae type as each type has a different composition. The gasification process of algae is greatly influenced by the activity of mineral matter content in the algae material. A study was carried out by Duman et al. to investigate the hydrogen production from gasification of two seaweed species (*Fucus serratus* and *Laminaria digitata*) and a microalgae species (*Nannochloropsis oculata*) using steam as a gasifying agent in a laboratory-scale updraft gasifier [43]. The results show that the gasification of seaweeds produced significantly higher hydrogen yield compared to microalgae at the same operating gasification parameters. The different gas yield resulted from the different amounts and composition of inorganics between the seaweeds and microalgae. Furthermore, there was no difference in the gas yield from both seaweed species as they have similar elemental and inorganic compositions. A comparison study was done by Gonzalez et al. to investigate the performance of steam gasification of three different microalgae species by means of thermogravimetric analysis [44]. According to the result, *Scenedesmus almeriensis* produces significantly higher hydrogen as well as CO and CO<sub>2</sub>

**Hydrogen Production from Algal Pathways, Table 2** Reactions occurring during gasification [41, 42]

Reaction	Type	$\Delta H$ (kJ mol <sup>-1</sup> )
<i>Primary devolatilization</i>		
Biomass → CO, CO <sub>2</sub> , CH <sub>4</sub> , C <sub>2</sub> H <sub>4</sub> , H <sub>2</sub> O, carbon, primary tar (CH <sub>x</sub> O <sub>y</sub> )		
<i>Tar cracking and reforming</i>		
Primary tar → CO, CO <sub>2</sub> , CH <sub>4</sub> , C <sub>2</sub> H <sub>4</sub> , H <sub>2</sub> , secondary tar		
<i>Char gasification</i>		
C + CO <sub>2</sub> → 2CO	Boudouard reaction	+159.9
C + H <sub>2</sub> O → CO + H <sub>2</sub>	Water gas reaction/steam reforming	+118.5
C + 2H <sub>2</sub> → CH <sub>4</sub>	Hydrogasification/methane production reaction	-87.5
C + 0.5O <sub>2</sub> → CO	Partial oxidation	-111
<i>Oxidation reaction</i>		
C + O <sub>2</sub> → CO <sub>2</sub>	Oxidation of carbon	-394
CO + 0.5O <sub>2</sub> → CO <sub>2</sub>	Combustion	-283
CH <sub>4</sub> + 2O <sub>2</sub> → CO <sub>2</sub> + 2H <sub>2</sub> O	Combustion	-110
H <sub>2</sub> + 0.5O <sub>2</sub> → H <sub>2</sub> O	Combustion	-242
<i>Shift reaction</i>		
CO + H <sub>2</sub> O → CO <sub>2</sub> + H <sub>2</sub>	Water gas-shift reaction	-40.9
<i>Methanation reactions</i>		
2CO + 2H <sub>2</sub> → CH <sub>4</sub> + CO <sub>2</sub>		-247
CO + 3H <sub>2</sub> → CH <sub>4</sub> + H <sub>2</sub> O		-206
CO <sub>2</sub> + 4H <sub>2</sub> → CH <sub>4</sub> + 2H <sub>2</sub> O		-165
<i>Steam reactions</i>		
CH <sub>4</sub> + H <sub>2</sub> O → CO + 3H <sub>2</sub>	Steam reforming reaction	+206
CH <sub>4</sub> + 0.5O <sub>2</sub> → CO + 2H <sub>2</sub>		-36

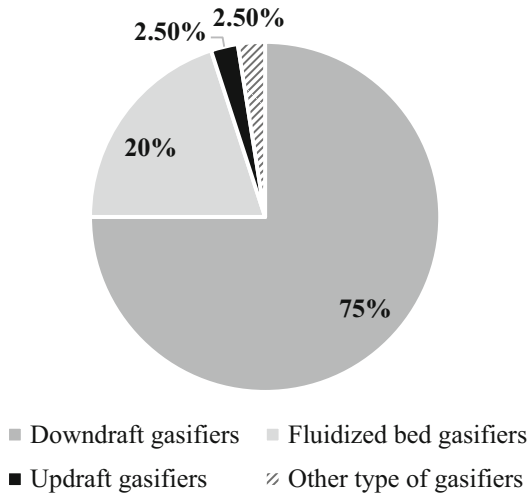




**Hydrogen Production from Algal Pathways, Fig. 7** Type of biomass gasifier/reactor

than *Chlorella vulgaris* and *Nannochloropsis gaditana*, in which the latter produces the lowest gas yield. The reason for the phenomenon is because *Scenedesmus* contains the highest

number of catalytic species, such as K and Mg. The presence of those species promotes the water-gas shift and steam reforming reactions that lead to a higher production of hydrogen.



**Hydrogen Production from Algal Pathways, Fig. 8** Distribution of gasifier manufacturers in Europe based on their gasifier products [37]

- Gasifying agent

Air is the most common medium used as the biomass gasification agent as it is the most economical. However, air produces syngas with lower calorific value due to high  $N_2$  content [37]. Syngas with moderate calorific value can be produced when steam is used as the gasifying agent. A steam medium also costs somewhere between air and oxygen [37]. It can produce more hydrogen yield compared to gasification using other agents. Water vapor has been identified as a catalyst for the char formation mechanism that improves the hydrogen concentration in syngas due to the promotion of the water-gas shift reaction [45]. It is also favorable over oxygen gasification as it does not need another penalty cost in which oxygen gasification needs to meet the high purity oxygen requirement [46]. Furthermore, steam gasification is already well established for producing gaseous fuels in the past decades, making it more readily applicable than other promising gasification methods, such as supercritical water gasification [47]. On the other hand,  $CO_2$  as a gasifying agent generally produces lower hydrogen and CO yields in biomass gasification [45].

- Algae feed particle size

In most biomass gasification cases, it is believed that larger particle size causes greater heat transfer resistance. Hence, higher temperature gradients occur inside the particles that lead to lower inner temperature than the exterior, at a given time. As a result, smaller particle size produces a higher dry gas yield and carbon conversion efficiency. A study was performed by Yan et al. to determine the effect of the fuel particle size on the gas field and carbon conversion efficiency of steam gasification using char, derived from cyanobacterial blooms as fuel at a temperature range of 600–850 °C [48]. The result suggested that at the same gasification temperature, a smaller particle size requires less time for completing the gasification process owing to the increase in the effective thermal conductivity. Thus, a smaller particle size has a higher reaction speed. However, the study also indicated that the effect of particle size on gasification was obvious at lower temperatures, and it becomes less evident with increasing temperature.

#### Reaction temperature

Reaction temperature is the most important parameter in the gasification process. According to Ahmad et al. [49], generally, a higher temperature of gasification contributes to a lower concentration of char and heavy tars, and at the same time it contributes to a higher concentration of hydrogen as well as a higher overall gas yield. The increase in hydrogen concentration is due to the tar thermal cracking reaction that also leads to lower tar production. Furthermore, higher gas yield is caused by higher volatile release at higher temperatures. A study reported that the hydrogen yield from steam gasification of macroalgae and microalgae increased when the temperature of gasification was raised from 700 °C to 850 °C owing to the promotion of the thermal cracking and steam reforming of tar [43]. Another study reported the effect of reaction temperature on the high heating value (HHV) of the produced syngas from gasification of *Scenedesmus almeriensis* in the presence of a catalyst [45]. The result indicated that the HHV increased from 23.58 to 24.67  $MJ Nm^{-3}$  when the reaction temperature

increased from 500 °C to 700 °C. This is also followed by the increase of the H<sub>2</sub>/CO concentration ratio in syngas from 0.17 to 0.81.

- Catalysts

The addition of a catalyst in biomass gasification facilitates effective heat and mass transfer between particles. As a result, it improves the efficiency of the gasification reactions (Boudouard, water-gas, methanation, CO shift, steam reforming) that contribute to the rise in hydrogen and CO yield [42]. A study carried out by Diaz-Rey et al. investigated the effect of three different Ni-based catalysts on the gas yield produced from gasification of *Scenedesmus almeriensis* (Chlorophyceae-class algae) using a mixture of CO<sub>2</sub> and steam as the gasifying agent [45]. The results show that Pt-Ni/Al<sub>2</sub>O<sub>3</sub> is the most effective catalyst that promotes the tar cracking into smaller molecules (H<sub>2</sub>, CO, and CO<sub>2</sub>). Consequently, the catalyst increased the gas yield as well as the hydrogen production. Furthermore, it can reduce the H<sub>2</sub>S contaminant concentration in the syngas composition. In another study, it is reported that the Fe<sub>2</sub>O<sub>3</sub>-CeO<sub>2</sub> catalyst produced higher hydrogen yield compared to the red mud and activated red mud catalyst when they are used for steam gasification of algae [43]. The results demonstrated that Fe<sub>2</sub>O<sub>3</sub>-CeO<sub>2</sub> is an effective catalyst to promote the water gas-shift reaction. Moreover, red mud produced higher hydrogen than activated red mud owing to the higher amount of alkali metal.

Although the production of hydrogen through the thermal gasification route is promising, its utilization is challenging mainly due to the high mineral content in algae. Algae typically have higher amounts of alkali earth and heavy metals than terrestrial biomass, which causes problems for some thermo-chemical conversion methods. The high metal content of algae produces high ash deposition during thermo-chemical conversion which probably would be followed by severe slagging and fouling [50] as also commonly occurs in the case of terrestrial biomass with high metal content [51]. Several studies were performed to attempt the utilization of marine algae by using fluidized bed reactors [52]. Fluidized bed-type

gasifiers offer high: heat and mass transfer, efficiency, and heating values during gasification [47].

In addition, fluidized bed gasification is considered as a flexible technology which can convert solid fuels of varying quality [53]. However, gasification of marine algae in a fluidized bed is expected to be challenging due to the high salt content which can cause fouling and also agglomeration and defluidization of the fluidized bed gasifier that will lead to the shutdown of the reactor [52]. Gasification of *Tetraselmis sp.* using fluidized bed gasifier and a mixture of steam and air as the gasifying agent was attempted by Alghurabie et al. The gasification was carried out at a steam-to-algae mass ratio of 0.5 and temperature of 850 °C. It was found out that the reactor had to be shut down after 10 min of the gasification process due to severe defluidization in the reactor following the rapid bed sintering and agglomeration. Therefore, further intensive studies are needed to utilize algae as a single fuel in fluidized bed gasification.

Algae, however, shows promising results to be used as a secondary fuel in fluidized bed co-gasification with coal [53] and woody biomass [54]. The addition of 10 wt% macroalgae (*Derbesia tenuissima*) or microalgae (*Scenedesmus sp.*) to coal gasification produces more gas yield compared to pure coal gasification. Moreover, the co-gasification of *Derbesia tenuissima* and coal can be performed without any significant problem. In contrast, the co-gasification of *Scenedesmus sp.* and coal had to be stopped after 2.5 h due to severe agglomeration. Therefore, considerable attention should be given in choosing the appropriate algae to be utilized in the fluidized bed co-gasification application. On the other hand, addition of macroalgae and microalgae to gasification of woody biomass increases the H<sub>2</sub>, CO, and CH<sub>4</sub> yields by 6–31%, 3–20%, and 9–20%, respectively [54].

Aziz et al. proposed a generation system to generate power from macroalgae through a novel integration of drying, gasification, and combined cycle [47]. The process design and evaluation of the proposed system was performed using a commercial process simulator. According to the result, the proposed

integrated system demonstrated a relatively high-power generation efficiency of approximately 60%. Hence, it indicated that high-power generation efficiencies are possible when using macroalgae as a fuel source, especially in power generation applications. It is also suggested that algae may be used to supply base-load power, replacing the current use of natural gas, nuclear energy, and coal.

### Supercritical Water Gasification

As a thermochemical conversion technology, supercritical water gasification (SCWG) utilizes the positive characteristics of supercritical water, in which both pressure and temperature are higher than 22.1 MPa and 374 °C, respectively. Under these conditions, the decomposition of biomass feedstock into syngas containing H<sub>2</sub>, CO, CH<sub>4</sub>, and steam is performed. Therefore, like other gasification technologies, the produced syngas can be used as fuel for power generation. In SCWG, water is needed as a solvent which behaves as a reactant and reaction medium. Higher than the critical point, the density of water significantly decreases, leading to a significant decrease of the static relative dielectric constant [55]. As a nonpolar solvent [56], water has excellent transport properties and a strong ability to decompose hydrocarbons and carbohydrates [57]. In addition, hydrogen bonds become significantly weak allowing a complete miscibility among gases; therefore, the reaction occurs in a single homogeneous phase of fluid. Thus, a faster chemical reaction and higher gasification efficiency can be achieved, compared with conventional thermal gasification [58].

The formation of tar and char can be avoided. Hence, almost a complete conversion can be obtained [59]. Because the water is in a single phase, the latent heat to change the phase of water is unnecessary and drying can be eliminated [58, 60]. In addition, the gasification can be performed at relatively lower temperatures compared to conventional thermal gasification. SCWG can produce very clean syngas containing almost no NO<sub>x</sub> and SO<sub>x</sub>, with a low concentration of CO.

Algae conversion through SCWG is very advantageous because algae, especially microalgae, can easily dissolve in water and require a very simple treatment to make them slurry. Slurry with high viscosity is crucial in the success of continuous feeding in SCWG. Unfortunately, although no latent heat of evaporation is required, the total energy required to elevate the water to a temperature of 600 °C at 30 MPa is almost the same as the energy consumed for water evaporation and a temperature increase at 0.1 MPa [55]. In addition, according to some reports [61, 62], the total consumed energy to perform SCWG can be the same as the heating value of the feedstock. Therefore, an efficient heat circulation technology is urgently required to be developed and employed to solve this problem.

Calzavara et al. [63] presented an energy analysis of SCWG for biomass material and explained that energy recovery management is an important point in its process design. Furthermore, Fiori et al. [64] developed an energetically self-sustained SCWG process for biomass employing simple heat recovery. In addition, simple heat recovery was applied in an SCWG reactor driven by concentrated solar energy [65].

To improve the gasification efficiency, some catalysts have been studied. It was reported that the total gas yield and composition differ for different catalysts [57]. Generally, rich hydrogen and low carbon monoxide contents of syngas can be produced [66]. Gasification performed under supercritical conditions is considered still under research and relatively far for its application. In addition, the high salt content of macroalgae results in corrosion and salt precipitation. Although drying can be bypassed in supercritical water gasification, the energy consumption to provide the supercritical condition is very large and almost approaches the heating value of the feedstock [55].

### Other Thermochemical Processes

Biomass pyrolysis is also a popular thermochemical conversion option to produce hydrogen from biomass. The concept of hydrogen production through pyrolysis is similar to gasification;

however, pyrolysis takes place at a lower temperature in the absence of the gasification agent [67]. The main products of pyrolysis are a solid (char), an organic liquid (crude oil), and a low calorific value gas (pyrogas), in different ratios depending on the process conditions, reactor type, and fuel characteristics [68]. The biomass pyrolysis process produces less hydrogen than gasification. Low heating rate, long residence time, and high temperature are favored to enhance the gas yield from the pyrolysis process. [67]. Therefore, recent studies regarding algae pyrolysis are mainly focused on bio-oil production, instead of syngas, through flash and fast pyrolysis that operates at a high heating rate and short vapor residence time. Fast and flash pyrolysis maximizes liquid yield (pyrolysis oil, also called bio-crude oil) when temperatures are in the range of approximately 450–550 °C [68]. According to Chiaramonti et al., in a general scheme coupling microalgae cultivation and pyrolysis process to produce oil as the main product, the noncondensable gas product from pyrolysis could be used to provide heat for the pyrolysis process itself and even for algae drying in the coupling system [68].

Beside pyrolysis, hydrothermal liquefaction (HTL) is also another common route to convert algae into bio-oil. The HTL takes place at a low temperature (300–350 °C) and high pressure (5–20 MPa) and utilizes the high-water activity in subcritical conditions to decompose biomass materials down to shorter and smaller molecular materials with a higher energy density [69].

### Biochemical Conversion to Hydrogen

Algae conversion to hydrogen can also be carried out through a biochemical route by utilizing microorganisms and enzymes to breakdown the algae into liquid or gaseous fuels. In general, biochemical conversion leads to lower conversion efficiency and a slower conversion rate than a thermochemical route, which uses a lower conversion efficiency and requires a larger area [70, 71]. The common biochemical conversion route for hydrogen production includes biophotolysis (direct and indirect), photo-fermentation, and dark fermentation.

Direct photolysis occurs by utilizing the photosynthetic ability of algae and cyanobacteria to split water directly into oxygen and hydrogen. The advantage of direct photolysis is that the principal feed is water, which is readily available and cheap [72]. In indirect biophotolysis, an organic compound and H<sub>2</sub>O act as an electron donor during the process reaction, instead of only H<sub>2</sub>O, as in direct biophotolysis. Furthermore, biophotolysis technology might not be economically feasible for sustainable hydrogen production in the near future, due to several existing technological limitations, such as costly photobioreactor systems, inefficient photosynthesis, and low hydrogen evolution yields of biological systems [73].

The dark fermentation process has recently been gaining attention for biohydrogen production owing to its simplicity and ability to convert various substrates [11]. Dark fermentation can be performed by using either pure or mixed cultures of hydrogen-producing bacteria (HPB). However, the yield of biohydrogen production via dark fermentation is relatively low, because hydrogen is produced as an intermediate product which would be converted later to methane, acetic, and propionic acid by hydrogen-consuming bacteria (HCB) during dark fermentation. Hence, more attention should be given to develop a method that inhibits the activity of HCB and enhances the activity of HPB to improve the yield of biohydrogen production [74]. Furthermore, according to Sambusiti et al., macroalgae and microalgae have chemical and structural barriers that would inhibit their degradation during dark fermentation. This suggestion is confirmed by the low biodegradability of algae (below 36%) during the dark fermentation process [11].

The photo-fermentation process depends on the capability of photosynthetic microorganisms to directly convert solar energy into hydrogen from organic substrates. The photosynthetic system of purple bacteria used in the photo-fermentation process is a relatively simpler photosynthetic system compared to the green algae used in biophotolysis. It consists of only one photosystem which is fixed in the intracellular membrane [72]. There are several drawbacks of

the photo-fermentation process, which includes the high-energy demand owing to the use of the nitrogenase enzyme, the low solar energy efficiencies, and the large area required for anaerobic photo-bioreactors [75].

### Chemical Looping

Chemical looping is considered an advanced technology which can convert and harvest the energy from carbon-based material with free CO<sub>2</sub> emission [76]. Carbon in algae will react with the oxygen carrier producing CO<sub>2</sub>, which is further separated. The separated CO<sub>2</sub> in chemical looping might be sequestered realizing a carbon negative energy harvesting or circulated back to the cultivation for material recirculation. The oxidation in chemical looping is performed without any direct contact between the fuel and oxygen (air). Oxygen is brought and transferred by metal oxide which is acting as the oxygen carrier. Some potential oxygen carriers include: iron oxide (Fe<sub>2</sub>O<sub>3</sub>), nickel oxide (NiO), and manganese oxide (Mn<sub>3</sub>O<sub>4</sub>). Among them, the iron-based oxygen carrier is considered promising due to its low cost, high oxygen carrying capacity, no catalytically dependent reaction, favorable mechanical strength, and high conversion of syngas to combustion products and steam to hydrogen [77]. In addition, it is nontoxic and easy to handle because it is stable under ambient conditions.

Chemical looping can be divided into syngas chemical looping (SCL) and direct chemical looping (DCL). In SCL, the produced syngas from the conversion process, especially gasification, reacts with the oxygen carrier producing a reduced oxygen carrier, CO<sub>2</sub> and H<sub>2</sub>O. Compared to direct chemical looping, it has some benefits, especially regarding better solids handling [78]. On the other hand, in DCL, the solid fuel directly reacts with the oxygen carrier producing almost the same products of SCL with additional remaining materials. DCL has some benefits of fewer unit operations, higher H<sub>2</sub>-to-CO<sub>2</sub> ratio, and a lower oxygen requirement [78].

To produce hydrogen, chemical looping with three circulating reactors are employed: reducer (fuel reactor), oxidizer (steam reactor), and combustor (air reactor). CO<sub>2</sub> and H<sub>2</sub> are basically

produced in the reducer and oxidizer, respectively. Figure 9 shows the basic schematic diagram of chemical looping for hydrogen production with three continuous reactors. Generally, a counter current moving-bed reactor is employed in the case of both the reducer and the oxidizer, while an entrained fluidized bed is adopted for the combustor [79, 80]. Therefore, it is important to note that in both the reducer and the oxidizer, the fluidization velocity must be lower than the minimum fluidization velocity. Because the flow rate of the syngas is fixed, the size of the reactor must be set accordingly.

In the case of SCL, syngas is initially compressed and directly used as a fluidizing gas. Overall, the reduction is primarily endothermic, although it can also be slightly exothermic depending on the composition of the syngas. The reactions assumed to occur during reduction are listed in Table 3 [76]. In the case of DCL, the algae, C<sub>x</sub>H<sub>y</sub>O<sub>z</sub>, will react directly with iron oxide producing Fe, FeO, CO<sub>2</sub>, and H<sub>2</sub>O.

CO<sub>2</sub> and steam are produced during the reduction and then leave the reducer, after which they are further cooled in preparation for separation in the condenser. The reduced iron particles, consisting mainly of Fe and FeO, flow to the oxidizer in which oxidation, with steam as the reactant, takes place to generate highly pure hydrogen after separation in the condenser. The main reactions taking place inside the oxidizer in the presence of excess steam are listed in Table 4 [76].

The partially oxidized oxygen carriers move to the combustor for reclamation. The reaction inside the combustor is shown below:

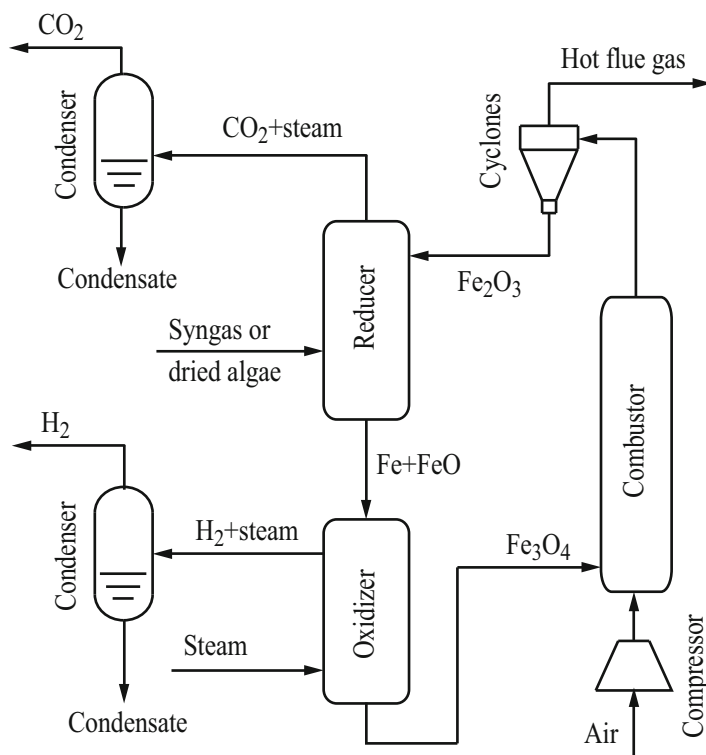


### Hydrogen Storage

Under atmospheric conditions, hydrogen has a high gravimetric energy density of 33 kWh kg-H<sub>2</sub><sup>-1</sup>. However, the volumetric energy density of hydrogen is very low compared to other hydrocarbon fuels, which is only 3 Wh L-gaseous-H<sub>2</sub><sup>-1</sup>. This presents a challenge to store and transport the produced hydrogen. Some effective



**Hydrogen Production from Algal Pathways, Fig. 9** Basic schematic diagram of chemical looping for hydrogen production



**Hydrogen Production from Algal Pathways, Table 3** Reactions during reduction in SCL

Reaction	Heat of reaction
$\text{Fe}_2\text{O}_3 + \text{CO} \rightarrow 2\text{FeO} + \text{CO}_2$	$\Delta H = -2.8 \text{ kJ mol}^{-1}$
$\text{FeO} + \text{CO} \rightarrow \text{Fe} + \text{CO}_2$	$\Delta H = -11 \text{ kJ mol}^{-1}$
$\text{Fe}_2\text{O}_3 + \text{H}_2 \rightarrow 2\text{FeO} + \text{H}_2\text{O}$	$\Delta H = 38.4 \text{ kJ mol}^{-1}$
$\text{FeO} + \text{H}_2 \rightarrow \text{Fe} + \text{H}_2\text{O}$	$\Delta H = 30.2 \text{ kJ mol}^{-1}$
$4\text{Fe}_2\text{O}_3 + 3\text{CH}_4 \rightarrow 8\text{Fe} + 3\text{CO}_2 + 6\text{H}_2\text{O}$	$\Delta H = 897.175 \text{ kJ mol}^{-1}$

**Hydrogen Production from Algal Pathways, Table 4** Reactions during oxidation in chemical looping

Reaction	Heat of reaction
$\text{Fe} + \text{H}_2\text{O} \rightarrow \text{FeO} + \text{H}_2$	$\Delta H = -30.2 \text{ kJ mol}^{-1}$
$3\text{FeO} + \text{H}_2\text{O} \rightarrow \text{Fe}_3\text{O}_4 + \text{H}_2$	$\Delta H = -60.6 \text{ kJ mol}^{-1}$

storage and transportation methods for hydrogen have been developed and applied. These include compression, liquefaction, and chemical and physical storages. Although compressed and liquid hydrogen storages are regarded as the established methods to store and transport

hydrogen, they encounter some problems related to large energy consumption and relatively low safety. Recently, liquid organic hydrogen carrier (LOHC) is believed to be promising to store hydrogen due to its high safety, high storage capacity, excellent reversibility, longer storage time, and lower  $\text{CO}_2$  emissions [81, 82]. In addition, ammonia is also considered as a promising liquid hydrogen carrier, but unfortunately it is toxic and corrosive, has a potent odor and must be transported by a specially designed tanker.

With the LOHC, the hydrogen is covalently bonded through hydrogenation. Furthermore, when the hydrogen is demanded, hydrogen can be released from the LOHC via dehydrogenation. Some available LOHC cycles include cyclohexane-benzene, decaline-naphthalene, and toluene-methylcyclohexane (MCH). The cycle of toluene ( $\text{C}_7\text{H}_8$ )-methylcyclohexane ( $\text{C}_7\text{H}_{14}$ ) is considered very probable to store and transport the hydrogen because it is cheap, stable, and easy to transport. Both toluene and MCH have a wide temperature range as a liquid which is favorable

for long storage under fluctuating environments. Also, a large-scale demonstration test has been conducted successfully by Chiyoda Corporation in Japan proving their applicability [83]. Hydrogenation is considered as a well-established technology including the used catalyst. The reaction, in the case of toluene-MCH, occurs as follows:



## Highly Energy-Efficient Integrated Systems

To produce hydrogen from algae, there are some available studies dealing with the integrated systems with high energy efficiency, employing different options of technologies. These integrated systems are mainly designed based on the principles of enhanced process integration technology (EPI) to minimize the exergy destruction throughout the integrated systems.

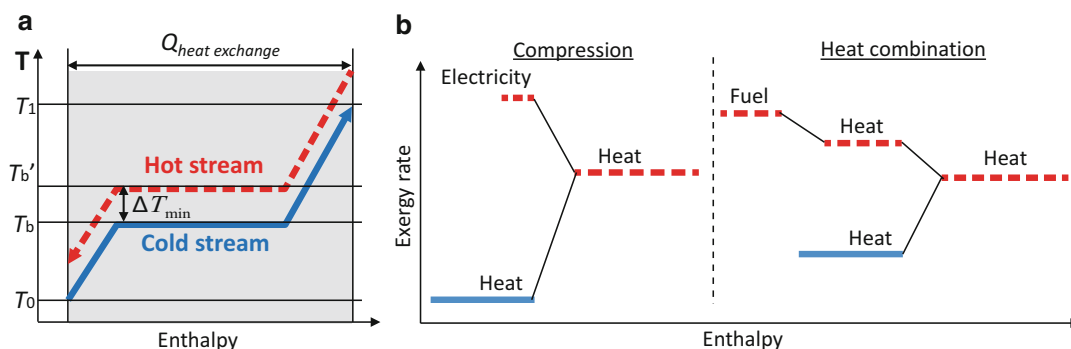
### Enhanced Process Integration

Enhanced process integration (EPI) consists of heat circulation (exergy recovery) and process integration technologies. The former focuses on any single process in which the energy or the heat associated throughout the process is effectively recirculated. The idea of heat circulation is significantly different from the conventional heat recovery which is generally adopted today [84–88]. In heat circulation, the quality of the recovered

energy/heat is maintained to be the same through the optimal self-heat exchange throughout the process. Therefore, a large amount of energy/heat can be recirculated and high energy efficiency can be achieved.

Heat circulation can be realized by combining the exergy-rate elevation with heat pairing. Figure 10 shows the principle of elevation of exergy-rate and its two examples conducted through compression and heat combination. The exergy rate of the process stream, as a cold stream, can be elevated through compression, heat combination, and the heat pump to create the hot stream. Furthermore, to obtain a maximum amount of recovered heat, heat pairing between the hot and cold streams is conducted in consideration of heat type, amount, and exergy rate. Hence, an optimum balance of heat exchange among the streams can be achieved.

Unfortunately, due to various factors, the amount of heat between the hot and cold streams in any single process cannot be matched effectively, resulting in generation of unrecoverable heat. Hence, an imbalance in heat pairing among hot and cold streams occurs, especially in heat pairing of latent heat between the process and the compressed streams. This imbalanced amount of heat exchange results in an unrecoverable energy/heat in any single process. In addition, a minimum temperature approach which is required for heat exchange also causes additional unrecoverable heat. Therefore, the process integration is introduced to utilize the unrecoverable



Hydrogen Production from Algal Pathways, Fig. 10 Principle of enhanced process integration technology [47]

energy/heat in any process to other processes. Hence, the total exergy destruction throughout the integrated system can be minimized.

**Integrated SCWG, Hydrogen Separation, and Hydrogenation**

Aziz [89] has developed an innovative system converting algae to hydrogen by integrating SCWG, hydrogen separation, and hydrogenation. Figure 11 shows the material (solid line) and energy (dotted line) flow diagram of the integrated system.

The system consists of several continuous processes: SCWG, hydrogen separation, hydrogenation, and a combined cycle. The harvested algae are initially treated by creating a slurry before being fed to the SCWG reactor for conversion. The produced syngas then goes through hydrogen separation to produce highly pure and clean hydrogen. The separated hydrogen then flows to the hydrogenator to be covalently bonded to toluene, producing MCH. On the other hand, the remaining gas from the separation is utilized as fuel for combustion in the combined cycle to produce electricity. In addition, a portion of the heat from the combined cycle is utilized to elevate the exergy rate in the SCWG module through heat combination. Furthermore, the flue gas from the combined cycle is recycled back to the cultivation, providing the nutrients for algae (CO<sub>2</sub> bio-sequestration).

The produced hydrogen-rich syngas from SCWG is going to separate without being shifted for enrichment of hydrogen content. The shift reaction, which is the reaction of CO with steam to produce hydrogen, is an endothermic reaction. Therefore, energy must be provided, leading to

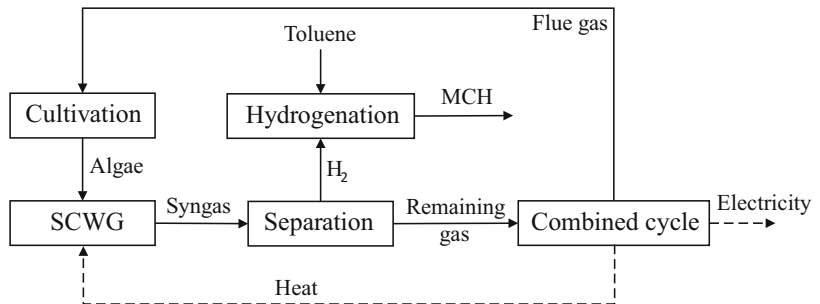
the decrease of overall energy efficiency. Furthermore, co-production of hydrogen and electricity is regarded capable of maximizing the total energy conversion efficiency. In situ power generation using the remaining syngas is expected to be able to cover the electricity required by the internal system, such as pumps, compressors, and other auxiliaries. In addition, the remaining generated electricity can be delivered and sold to the grid for additional revenue.

The schematic process flow diagram of the integrated system is presented in Fig. 12. Algae slurry is pumped to the target pressure for SCWG and then it flows to the gasifier after being preheated using the condensation from the steam turbine and condensed mixture of syngas and steam from the SCWG reactor. On the other hand, water is also pumped and preheated in parallel with the algae slurry. The water is utilized as a fluidizing gas and reactant, and it is fed from the bottom of the gasifier. Algae are converted into syngas in the gasifier and the mixture of syngas and steam is exhausted from the overhead of the gasifier. This mixture is then superheated utilizing the hot flue gas from the gas turbine to raise its exergy rate to facilitate a self-heated exchange. The superheated mixture of syngas and steam is then recirculated back to the gasifier through heating tubes immersed inside the gasifier and then flow to the preheaters. Syngas and steam are separated in the condenser producing relatively pure syngas. In addition, the compression energy generated by syngas is recovered by the expander.

The expanded syngas then flows to the separator for hydrogen separation. The separated highly pure hydrogen (permeate) is preheated before

**Hydrogen Production from Algal Pathways,**

**Fig. 11** Basic material and energy flow diagram of the integrated system consisting of SCWG, hydrogen separation, hydrogenation, and combined cycle





[91]. Hence, in the proposed system, a polymeric membrane is adopted for hydrogen separation.

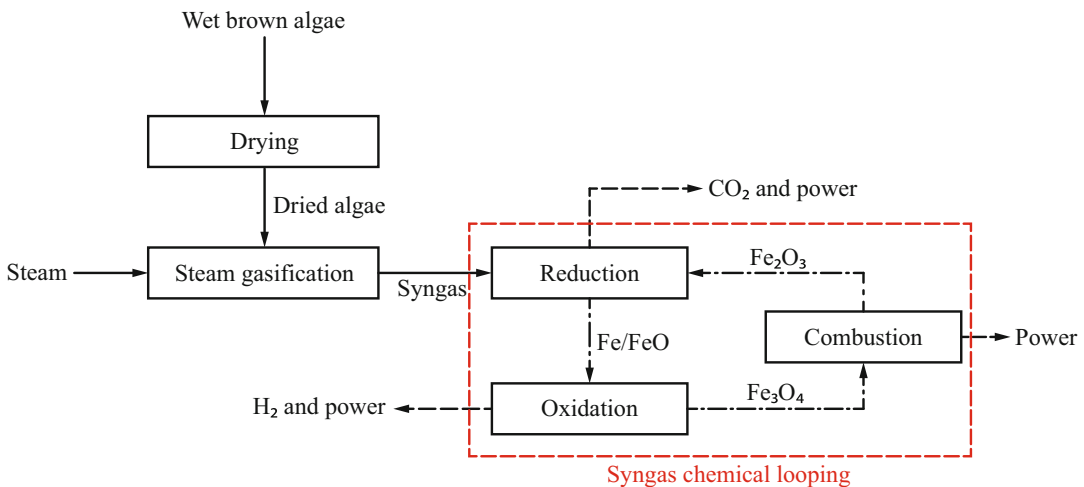
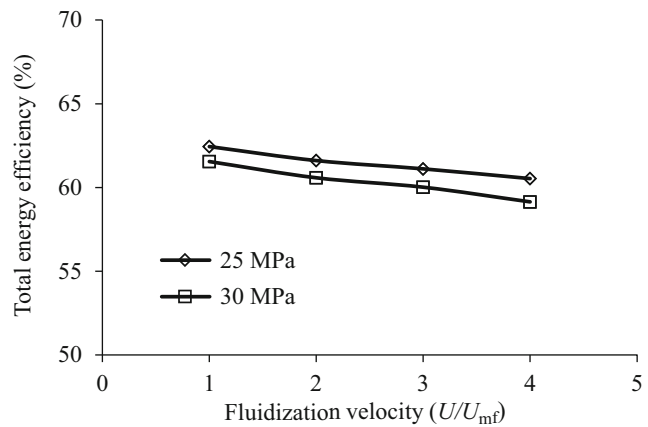
Figure 13 shows the performance of the integrated system in terms of total energy efficiency correlated with fluidization velocity and pressure during SCWG. *Chlorella vulgaris* with moisture content and flowrate of 90 wt% wb and 1000 t-h<sup>-1</sup>, respectively, is used as the sample. The total energy efficiency of the system is very high, higher than 60%. Regarding the hydrogen production, about 3.5 t-H<sub>2</sub> h<sup>-1</sup> can be produced and hydrogenated with toluene-producing MCH. The total energy efficiency decreases following the increase of fluidization velocity. In addition, gasification that is performed under a gasification

pressure of 25 MPa shows a higher total energy efficiency than that of 30 MPa.

**Integrated Drying, Gasification, and Syngas Chemical Looping**

Zaini et al. [92] have proposed a co-generation system converting algae to hydrogen and power by using a chemical looping-based system. Figure 14 presents the schematic diagram of the integrated co-generation system based on the chemical looping process. The co-generation system consists of drying, steam gasification, a chemical looping process, and power generation. Firstly, wet algae are fed to the drying process to improve their characteristics. The dried algae are

**Hydrogen Production from Algal Pathways, Fig. 13** Total energy efficiency of proposed hydrogen production system combining SCWG, hydrogen separation and hydrogenation [89]



**Hydrogen Production from Algal Pathways, Fig. 14** Schematic diagram of integrated co-generation system [92]

then subjected to the gasification process where they are reduced with steam to produce syngas. To evaluate the performance of the system, brown seaweed (*Fucus serratus*) is used as the fuel feedstock. A study carried out by Duman et al. showed that *Fucus serratus* has higher hydrogen yield from a steam gasification process compared to another seaweed species (*Laminaria digitata*) and microalgae (*Nannochloropsis oculata*) [43].

A steam tube rotary dryer is selected as the evaporator. In the steam tube rotary dryer, heating tubes covering the full length of the dryer are arranged in a concentric circle within the dryer, supplying the heat required for drying. Furthermore, Figure 15 shows the process flow diagram of the algae gasification process integrated with the chemical looping system and the power generation system. A dual circulating fluidized bed gasifier, consisting of a gasifier and a combustor operated at near atmospheric pressure, was used for the algae conversion as this technology has a higher carbon conversion efficiency, higher conversion rate, high mass and heat transfers, and high efficiency [79]. Before entering the gasifier, the dried algae were milled to achieve a smaller particle size distribution. Hence, better fluidization and greater mass and heat transfer inside the gasifier can be accomplished. Steam, which acted as the gasification reactant and fluidizing agent, flowed from the bottom of the gasifier. Moreover, sand (olivine) was loaded into the gasifier to enhance the fluidization and heat transfer across the gasifier bed. The fluidized bed gasifier normally operates at a temperature range of 750–850 °C [93]. Gasification then produces H<sub>2</sub>, CO, CO<sub>2</sub>, and CH<sub>4</sub>-rich syngas which is discharged from the gasifier along with the unreacted char and sand to the cyclone for separation. In the cyclone, the unreacted char and sand are then separated from the raw syngas. Raw syngas is circulated to another separation process to remove the slag content. After separation, the unreacted solid goes into the fluidized bed combustor in which it reacts with preheated air flow from the bottom of the bed. The fluidized bed combustor operates at a higher temperature than the gasifier, which ranged between 900 °C and 950 °C [93].

The SCL system consists of three different reactors, namely, a fuel reactor, a steam reactor, and an air reactor. The chain of reaction occurs in those reactors converting syngas produced from the gasification of algae into H<sub>2</sub>, CO<sub>2</sub>, and power. The iron-based oxygen carrier is utilized to accommodate the reduction and oxidation reactions. To provide more heat for the circulating reactors, inert Al<sub>2</sub>O<sub>3</sub> is added into the system as an additional heat carrier. SiC is also added as inert support particles. The mass fraction of the solids circulating in the SCL was assumed as 70% Fe<sub>2</sub>O<sub>3</sub>, 15% SiC, and 15% Al<sub>2</sub>O<sub>3</sub>, as suggested by Fan [76]. The chemical looping process began with reduction reactions between the syngas fuel and oxygen carried by Fe<sub>2</sub>O<sub>3</sub> in the fuel reactor. The fuel reactor is operated at a pressure range of 1.5–3.5 MPa and a temperature of 900 °C. A mixture of steam and CO<sub>2</sub> is produced from the reduction reactions. The reduction reactions in the fuel reactor produced Fe and FeO that were circulated into the steam reactor to undergo oxidation reactions with steam to produce hydrogen. Subsequently, Fe<sub>3</sub>O<sub>4</sub> was then produced from the steam reaction and carried out into the air reactor to be recovered back to Fe<sub>2</sub>O<sub>3</sub> by combustion with air. It should be noted that the air reactor was operated at 0.2 MPa higher pressure than the fuel and steam reactor, as suggested by Aziz et al. [79]. The remaining energy in the downstream of each reactor is recovered by utilizing expanders to convert the energy to electrical power.

The outcome of the simulation shows promising results, as the total efficiency, hydrogen production efficiency, and power generation efficiency are 71.71%, 57.25%, and 14.46%, respectively, when the co-generation system is performed at target moisture during drying of 5%, steam-to-biomass ratio during gasification of 0.7 and operating pressure of SCL system of 3.0 MPa. Increasing the target moisture content during drying has an adverse effect on the system performance as the efficiency decreased due to the lower hydrogen production in the steam reactor, although the net power could be elevated.

Furthermore, increasing the steam-to-biomass ratio also had a similar effect to the high target moisture content. The presence of more steam





during gasification shifted the syngas composition that later reduced the total efficiency of the co-generation system. On the other hand, increasing the operating pressure had a positive effect on the system performance although the total efficiency did not increase significantly. The net power of the system gradually and linearly increased with increased operating pressure of the SCL, followed by a slight increase of the total efficiency.

## Conclusions

Energy production, especially hydrogen, from algae is considered with high potential. Algae are widely distributed across the globe and have different characteristics depending on the types and other environmental conditions. Conversion of algae to hydrogen involves multiple processes. Therefore, selection of the appropriate technologies is considered very important to effectively convert algae to hydrogen.

Furthermore, some state-of-the-art utilization systems for algae employing EPI technology are shown. In EPI technology, the concepts of heat circulation (exergy recovery) and process integration are employed to minimize exergy destruction. Hence, higher energy efficiency can be realized. Technologies with high energy efficiency are urgently required to improve the energy profit ratio (EPR) from the use of microalgae. Technological deployment of the proposed integrated processes is expected to improve the world's energy security and provide energy in a more environmentally friendly manner.

## Bibliography

### Primary Literature

1. Alba LG, Torri C, Samorì C, Jvd S, Fabbri D, Kersten SRA, Brilman DWF (2012) Hydrothermal treatment (HTT) of microalgae: evaluation of the process as conversion method in an algae biorefinery concept. *Energy Fuel* 26:642–657
2. Bayramoglu G, Akbulut A, Ozalp VC, Arica MY (2015) Immobilized lipase on micro-porous biosilica

- for enzymatic transesterification of algal oil. *Chem Eng Res Des* 95:12–21
3. Hwang KJ, Wu SE (2015) Disk structure on the performance of a rotating-disk dynamic filter: a case study on microalgae microfiltration. *Chem Eng Res Des* 94:44–51
4. Aziz M, Oda T, Kashiwagi T (2013) Enhanced high energy efficient steam drying of algae. *Appl Energy* 109:163–170
5. Saeid A, Chojnacka K (2015) Toward production of microalgae in photobioreactors under temperate climate. *Chem Eng Res Des* 93:377–391
6. Aziz M, Oda T, Kashiwagi T (2014) Integration of energy-efficient drying in microalgae utilization based on enhanced process integration. *Energy* 70:307–316
7. Hannon M, Gimpel J, Tran M, Rasala B, Mayfield S (2010) Biofuels from algae: challenges and potential. *Biofuels* 1:763–784
8. Aziz M, Oda T, Kashiwagi T (2014) Advanced energy harvesting from algae—innovative integration of drying, gasification and combined cycle. *Energies* 7:8217–8235
9. McGinn PJ, Dickinson KE, Bhatti S, Frigon JC, Guiot SR, O'Leary SJB (2011) Integration of microalgae cultivation with industrial waste remediation for biofuel and bioenergy production: opportunities and limitations. *Photosynth Res* 109:231–247
10. Chaubey R, Sahu S, James OO, Maity S (2013) A review on development of industrial processes and emerging techniques for production of hydrogen from renewable and sustainable sources. *Renew Sust Energy Rev* 23:443–462
11. Sambusiti C, Bellucci M, Zabaniotou A, Beneduce L, Monlau F (2015) Algae as promising feedstocks for fermentative biohydrogen production according to a biorefinery approach: a comprehensive review. *Renew Sust Energy Rev* 44:20–36
12. John RP, Anisha GS, Nampoothiri KM, Pandey A (2011) Micro and macroalgal biomass: a renewable source for bioethanol. *Bioresour Technol* 102:186–193
13. Johansen MN (2013) *Microalgae: biotechnology, microbiology and energy*. Nova Science, New York
14. Leal MC, Munro MHG, Blunt JW, Puga J, Jesus B, Calado R, Rosa R, Madeira C (2013) Biogeography and biodiscovery hotspots of macroalgal marine natural products. *Nat Prod Rep* 30:1380–1390
15. Davis TA, Volesky B, Mucci A (2003) A review of the biochemistry of heavy metal biosorption by brown algae. *Water Res* 37:4311–4330
16. Schmidt WE, Gurgel CFD, Fredericq S (2016) Taxonomic transfer of the red algal genus *Gloiosaccion* to *Chrysymenia* (Rhodophyta, Rhodophytales), including the description of a new species, *Chrysymenia pseudoventricosa*, for the Gulf of Mexico. *Phytotaxa* 243:54–70
17. Buschmann AH, Correa JA, Westermeier R, Hernández-González MC, Norambuena R (2001)

- Red algal farming in Chile: a review. *Aquaculture* 194:203–220
18. Barsanti L, Gualtieri P (2014) *Algae: anatomy, biochemistry, and biotechnology*. CRC, Boca Raton
  19. Kerrison PD, Stanley MS, Edwards MD, Black KD, Hughes AD (2015) The cultivation of European kelp for bioenergy: site and species selection. *Biomass Bioenergy* 80:229–242
  20. Steneck RS, Graham MH, Bourque BJ, Corbett D, Erlandson JM, Estes JA, Tegner MJ (2002) Kelp forest ecosystems: biodiversity, stability, resilience and future. *Environ Conserv* 29:436–459
  21. Buck BH, Buchholz CM (2004) The offshore-ring: a new system design for the open ocean aquaculture of macroalgae. *J Appl Phycol* 16:355–368
  22. Ross AB, Jones JM, Kubacki ML, Bridgeman T (2008) Classification of macroalgae as fuel and its thermochemical behaviour. *Bioresour Technol* 99:6494–6504
  23. Mohring MB, Wernberg T, Kendrick GA, Rule MJ (2013) Reproductive synchrony in a habitat-forming kelp and its relationship with environmental conditions. *Mar Biol* 160:119–126
  24. Huesemann MH, Hausmann TS, Bartha R, Aksoy M, Weissman JC, Benemann JR (2009) Biomass productivities in wild type and pigment mutant of *Cyclotella* sp. (diatom). *Appl Biochem Biotechnol* 157:507–526
  25. Vitova M, Bisova K, Kawano S, Zachleer V (2016) Accumulation of energy reserves in Algae: from cell cycles to biotechnological applications. *Biotechnol Adv* 33:1204–1218
  26. Berg JM, Tymoczko JL, Stryer L (2002) Triacylglycerols are highly concentrated energy stress. W. H. Freeman, New York
  27. Bharathiraja B, Chakravarthy M, Kumar RR, Yogendran D, Yuvaraj D, Jayamuthunagai J, Kumar RP, Palani S (2015) Aquatic biomass (algae) as a future feed stock for bio-refineries: a review on cultivation, processing and products. *Renew Sust Energy Rev* 47:634–653
  28. Chisti Y (2008) Biodiesel from microalgae beats bioethanol. *Trends Biotechnol* 26:126–131
  29. Borowitzka MA (1999) Commercial production of microalgae: ponds, tanks, tubes and fermenters. *J Biotechnol* 70:313–321
  30. Aziz M, Oda T, Kashiwagi T (2015) Innovative steam drying of empty fruit bunch with high energy efficiency. *Dry Technol* 33:395–405
  31. Lardon L, Helias A, Sialve B, Stayer JP, Bernard O (2009) Life-cycle assessment of biodiesel production from microalgae. *Environ Sci Technol* 43:6475–6481
  32. Sander K, Murthy GS (2010) Life cycle analysis of algae biodiesel. *Int J Life Cycle Assess* 15:704–714
  33. Mohamed LA, Kouhila M, Lahsasni S, Jamali A, Idlimam A, Rhazi M, Aghfir M, Mahrouz M (2005) Equilibrium moisture content and heat of sorption of *Gelidium sesquipedale*. *J Stored Prod Res* 41:199–209
  34. Aziz M, Fushimi C, Kansha Y, Mochidzuki K, Kaneko S, Tsutsumi A et al (2011) Innovative energy-efficient biomass drying based on self-heat recuperation technology. *Chem Eng Technol* 34:1095–1103
  35. Liu Y, Aziz M, Kansha Y, Tsutsumi A (2013) A novel exergy recuperative drying module and its application for energy-saving drying with superheated steam. *Chem Eng Sci* 100:392–401
  36. Devahastin S, Mujumdar AS (2007) Indirect dryers. In: Mujumdar AS (ed) *Handbook of industrial engineering*. CRC Press, Boca Raton, pp 137–149
  37. Ruiz JA, Juárez MC, Morales MP, Muñoz P, Mendivil MA (2013) Biomass gasification for electricity generation: Review of current technology barriers. *Renew Sust Energy Rev* 18:174–183
  38. Ahmed I, Gupta AK (2009) Syngas yield during pyrolysis and steam gasification of paper. *Appl Energy* 86:1813–1821
  39. Antonini T, Gallucci K, Anzoletti V, Stendardo S, Foscolo PU (2015) Oxygen transport by ionic membranes: correlation of permeation data and prediction of char burning in a membrane-assisted biomass gasification process. *Chem Eng Process* 94:39–52
  40. Udomsirichakorn J, Salam PA (2014) Review of hydrogen-enriched gas production from steam gasification of biomass: the prospect of CaO-based chemical looping gasification. *Renew Sust Energy Rev* 30:565–579
  41. Basu P (2010) *Biomass characteristics, biomass gasification and pyrolysis*. Elsevier, Amsterdam
  42. Parthasarathy P, Narayanan KS (2014) Hydrogen production from steam gasification of biomass: influence of process parameters on hydrogen yield – a review. *Renew Energy* 66:570–579
  43. Duman G, Uddin MA, Yanik J (2014) Hydrogen production from algal biomass via steam gasification. *Bioresour Technol* 166:24–30
  44. López-González D, Fernandez-Lopez M, Valverde JL, Sanchez-Silva L (2014) Comparison of the steam gasification performance of three species of microalgae by thermogravimetric-mass spectrometric analysis. *Fuel* 134:1–10
  45. Díaz-Rey MR, Cortés-Reyes M, Herrera C, Larrubia MA, Amadeo N, Laborde M, Alemany LJ (2014) Hydrogen-rich gas production from algae-biomass by low temperature catalytic gasification. *Catal Today* 257:177–184
  46. Ni M, Leung DY, Leung MKH, Sumathy K (2006) An overview of hydrogen production from biomass. *Fuel Process Technol* 87:461–472
  47. Aziz M (2016) Power generation from algae employing enhanced process integration technology. *Chem Eng Res Des* 109:297–306
  48. Yan F, Zhang L, Hu Z, Cheng G, Jiang C, Zhang Y, Xu T, He P, Luo S, Xiao B (2010) Hydrogen-rich gas production by steam gasification of char derived from cyanobacterial blooms (CDCB) in a fixed-bed reactor:

- influence of particle size and residence time on gas yield and syngas composition. *Int J Hydrog Energy* 35:10212–10217
49. Ahmad AA, Zawawi NA, Kasim FH, Inayat A, Khasri A (2016) Assessing the gasification performance of biomass: a review on biomass gasification process conditions, optimization and economic evaluation. *Renew Sust Energ Rev* 53: 1333–1347
  50. Sander K, Murthy GS (2010) Life cycle analysis of algae biodiesel. *Int J Life Cycle Assess* 15:704–714
  51. Zaini IN, Novianti S, Nurdawati A, Irhamna AR, Aziz M, Yoshikawa K (2017) Investigation of the physical characteristics of washed hydrochar pellets made from empty fruit bunch. *Fuel Process Technol* 160:109–120
  52. Alghurabie IK, Hasan BO, Jackson B, Kosminski A, Ashman PJ (2013) Fluidized bed gasification of Kingston coal and marine microalgae in a spouted bed reactor. *Chem Eng Res Des* 91:1614–1624
  53. Zhu Y, Piotrowska P, Van Eyk PJ, Boström D, Kwong CW, Wang D, Cole AJ, De Nys R, Gentili FG, Ashman PJ (2015) Cogasification of Australian brown coal with algae in a fluidized bed reactor. *Energy Fuel* 29:1686–1700
  54. Zhu Y, Piotrowska P, Van Eyk PJ, Boström D, Wu X, Boman C, Broström M, Zhang J, Kwong CW, Wang D, Cole AJ, De Nys R, Gentili FG, Ashman PJ (2016) Fluidized bed co-gasification of algae and wood pellets: gas yields and bed agglomeration analysis. *Energy Fuel* 30:1800–1809
  55. Aziz M (2015) Integrated supercritical water gasification and a combined cycle for microalgal utilization. *Energ Convers Manage* 91:140–148
  56. Haiduc AC, Branderberger M, Suquet S, Vogel F, Bernier-Latmani R, Ludwig C (2009) SunChem: an integrated process for the hydrothermal production of methane from microalgae and CO<sub>2</sub> mitigation. *J Appl Phycol* 21:529–541
  57. Chakinala AG, Brilman D, Swaaij W, Kersten S (2010) Catalytic and non-catalytic supercritical water gasification of microalgae and glycerol. *Ind Eng Chem Res* 49:1113–1122
  58. Kersten SRA, Potic B, Prins W, VanSwaaij WPM (2006) Gasification of model compounds and wood in hot compressed water. *Ind Eng Chem Res* 45: 4169–4177
  59. Vogel F (2010) Catalytic conversion of high-moisture biomass to synthetic natural gas in supercritical water. In: Crabtree R (ed) *Handbook of green chemistry*, vol 3. Wiley, Weinheim, pp 281–324
  60. Kumar S (2012) Sub- and supercritical water-based processes for microalgae to biofuels. In: Gordon R, Seckbach J (eds) *The science of algal fuels*. Springer, Amsterdam, pp 467–493
  61. Matsumura Y, Minowa T, Potic B, Kersten SRA, Prins W, van Swaaij WPM et al (2005) Biomass gasification in near- and super-critical water: status and prospects. *Biomass Bioenergy* 29:269–292
  62. YJ L, Jin H, Guo LJ, Zhang XM, Cao CQ, Guo X (2008) Hydrogen production by biomass gasification in supercritical water with a fluidized bed reactor. *Int J Hydrog Energy* 33:6066–6075
  63. Calzavara Y, Jousot-Dubien C, Boissonnet G, Sarrade S (2005) Evaluation of biomass gasification in supercritical water process for hydrogen production. *Energ Convers Manage* 46:615–631
  64. Fiori L, Valbusa M, Castello D (2012) Supercritical water gasification of biomass for H<sub>2</sub> production: process design. *Bioresour Technol* 121:139–147
  65. Liao B, Guo L, Lu Y, Zhang X (2013) Solar receiver/reactor for hydrogen production with biomass gasification in supercritical water. *Int J Hydrog Energy* 29:13038–13044
  66. Lange S, Pellegrini LA (2014) Study of hydrogen potentiality from supercritical water gasification of different biomasses: thermodynamic analysis and comparison with experimental data. *Chem Eng Trans* 37:175–180
  67. Abuadala A, Dincer I (2012) A review on biomass-based hydrogen production and potential applications. *Int J Energy Res* 36:415–455
  68. Chiaramonti D, Prussi M, Buffi M, Maria A, Pari L (2016) Review and experimental study on pyrolysis and hydrothermal liquefaction of microalgae for bio-fuel production. *Appl Energy* 185:1–10
  69. Brennan L, Owende P (2010) Biofuels from microalgae – a review of technologies for production, processing, and extractions of biofuels and co-products. *Renew Sust Energ Rev* 14:557–577
  70. Aziz M, Prawisudha P, Prabowo B, Budiman BA (2015) Integration of energy-efficient empty fruit bunch drying with gasification/combined cycle systems. *Appl Energy* 139:188–195
  71. Aziz M, Oda T, Mitani T, Kurokawa T, Kawasaki N, Kashiwagi T (2015) Enhanced energy utilization system of algae: Integrated drying, gasification and combined cycle. *Energy Procedia* 75:906–911
  72. Show KY, Lee DJ, Tay JH, Lin CY, Chang JS (2012) Biohydrogen production: current perspectives and the way forward. *Int J Hydrog Energy* 37: 15616–15631
  73. Srirangan K, Pyne ME, Perry Chou C (2011) Biochemical and genetic engineering strategies to enhance hydrogen production in photosynthetic algae and cyanobacteria. *Bioresour Technol* 102:8589–8604
  74. Lee MJ, Song JH, Hwang SJ (2009) Effects of acid pre-treatment on bio-hydrogen production and microbial communities during dark fermentation. *Bioresour Technol* 100:1491–1493
  75. Hallenbeck PC, Benemann JR (2002) Biological hydrogen production: fundamentals and limiting processes. *Int J Hydrog Energy* 27:1185–1193
  76. Fan LS (2010) *Chemical looping systems for fossil energy conversions*. Wiley, Hoboken
  77. Gupta S, Cox S, Abu-Ghannam N (2011) Effect of different drying temperatures on the moisture of

- phytochemical constituents of edible Irish brown seaweed. *LWT-Food Sci Technol* 44:1266–1272
78. Gnanapragasam NV, Reddy BV, Rosen MA (2009) Hydrogen production from coal using coal direct chemical looping and syngas chemical looping combustion systems: assessment of system operation and resource requirements. *Int J Hydrog Energy* 34:2606–2615
  79. Aziz M, Juangsa FB, Kurniawan W, Budiman BA (2016) Clean co-production of H<sub>2</sub> and power from low rank coal. *Energy* 116:489–497
  80. Aziz M, Zaini IN, Oda T, Morihara A, Kashiwagi T Energy conservative brown coal conversion to hydrogen and power based on enhanced process integration: integrated drying, coal direct chemical looping, combined cycle and hydrogenation. *Int J Hydrog Energy* 42:2904–2913
  81. Huggins RA (2010) *Energy storage*. Springer, New York
  82. Teichmann D, Arlt W, Wasserscheid P (2012) Liquid organic hydrogen carriers as an efficient vector for the transport and storage of renewable energy. *Int J Hydrog Energy* 37:18118–18132
  83. Aziz M, Oda T, Kashiwagi T (2015) Clean hydrogen production from low rank coal: novel integration of drying, gasification, chemical looping, and hydrogenation. *Chem Eng Trans* 45:613–618
  84. Kotani Y, Aziz M, Kansha Y, Fushimi C, Tsutsumi A (2013) Magnetocaloric heat circulator based on self-heat recuperation technology. *Chem Eng Sci* 101:5–12
  85. Liu Y, Aziz M, Kansha Y, Bhattacharya S, Tsutsumi A (2014) Application of the self-heat recuperation technology for energy saving in biomass drying system. *Fuel Process Technol* 117:66–74
  86. Prabowo B, Aziz M, Umeki K, Susanto H, Yan M, Yoshikawa K (2015) CO<sub>2</sub>-recycling biomass gasification system for highly efficient and carbon-negative power generation. *Appl Energy* 158:97–106
  87. Kansha Y, Kotani Y, Aziz M, Kishimoto A, Tsutsumi A (2013) Evaluation of a self-heat recuperative thermal process based on thermodynamic irreversibility and exergy. *J Chem Eng Jpn* 46:87–91
  88. Aziz M, Kurniawan T, Oda T, Kashiwagi T Advanced power generation using biomass wastes from palm oil mills. *Appl Thermal Eng* 114:1378–1386
  89. Aziz M (2016) Integrated hydrogen production and power generation from microalgae. *Int J Hydrog Energy* 41:104–112
  90. Liu K, Song C, Subramani V (2010) *Hydrogen and syngas production and purification technologies*. Wiley, Hoboken
  91. Cersosimo M, Brunetti A, Drioli E, Firorino F, Dong G, Woo KT et al (2015) Separation of CO<sub>2</sub> from humidified ternary gas mixtures using thermally rearranged polymeric membranes. *J Membr Sci* 492:257–262
  92. Zaini IN, Nurdiawati A, Aziz M (2017) Cogeneration of power and H<sub>2</sub> by steam gasification and syngas chemical looping of macroalgae. *Appl Energy*, in press. <https://doi.org/10.1016/j.apenergy.2017.06.071>
  93. Shen L, Gao Y, Xiao J (2008) Simulation of hydrogen production from biomass gasification in interconnected fluidized beds. *Biomass Bioenergy* 32:120–127

### Books and Reviews

- Borowitzka M, Moheimani NR (2013) *Algae for biofuels and energy*. Springer, Amsterdam
- Demirbas A, Demirbas MF (2010) *Algae energy: algae as a new source of biodiesel*. Springer, London
- Pandey A, Lee DJ, Chisti Y, Soccol R (2014) *Biofuels from algae*. Elsevier, Amsterdam



# Hydrogen Production from Photoelectrochemical Water Splitting

Paula Dias and Adélio Mendes  
LEPABE – Faculdade de Engenharia,  
Universidade do Porto, Porto, Portugal

## Article Outline

Glossary  
Definition of the Subject and Its Importance  
Introduction  
PEC Water Splitting: Working Principles  
PEC Materials Overview  
PEC Devices Overview  
Efficiency  
Stability/Photocorrosion  
PEC Reactors  
Measurements Protocols  
Future Directions  
Bibliography

## Glossary

**PEC cell** Photoelectrochemical cell for water splitting that converts solar energy directly to hydrogen fuel from photoelectrolysis. It comprises a photoelectrode and a counter electrode immersed in an electrolyte solution.

**PV cell** Photovoltaic solar cell for electricity generation from sunlight.

**Solar tandem cell** Solar cell consisting of two or more absorbers stacked one over the others, which together convert more of the sunlight spectrum and therefore increase the overall cell efficiency.

**PEC-PV tandem** PV-assisted PEC water splitting system, i.e., an integrated PV-PEC device where a PV cell is stacked on a photoelectrode

for providing the necessary bias voltage to photoelectrochemical water splitting.

**Photoelectrode** Photoelectrode is an electrode capable of initiating electrochemical transformations after absorbing light quanta (definition by IUPAC). In the solar water splitting context, photoelectrode is made of a semiconductor film on an electrically conductive material (substrate) for water oxidation or reduction (photoanode or photocathode, respectively); the generated electric current is then used in the counter electrode to promote the counter-redox reaction of water splitting.

## Definition of the Subject and Its Importance

Hydrogen is a valuable chemical commodity, not only in today's industrial marketplace but also in the emerging green economy. Hydrogen is envisioned as one of the most promising fuel options for the storage and distribution of energy derived from renewable sources. In particular, hydrogen generated from solar energy is described as a potential energy storage medium to offset the variability of solar energy for a sustainable society [1]. Photoelectrochemical (PEC) systems combine solar collection and water electrolysis in a single device to produce hydrogen and oxygen gases, which can recombine in fuel cells to convert the stored energy into electricity. Although the first report on electrochemical photolysis of water by Fujishima and Honda [2] is more than 40 years, there is still no commercial PEC device effectively producing solar hydrogen. Practical PEC solar fuel production on a global scale requires the development of devices that are highly efficient, stable, cost-effective, and simple in design. Moreover, the realization of this vision requires laboratory experiments to be engineered into a large-scale



technology. The present entry summarizes the state-of-the-art semiconductor materials, co-catalysts, coatings, and design configurations, as well as new diagnostics and fundamental mechanisms to target a low-cost high-conversion-efficiency and durable PEC water splitting device for hydrogen production.

## Introduction

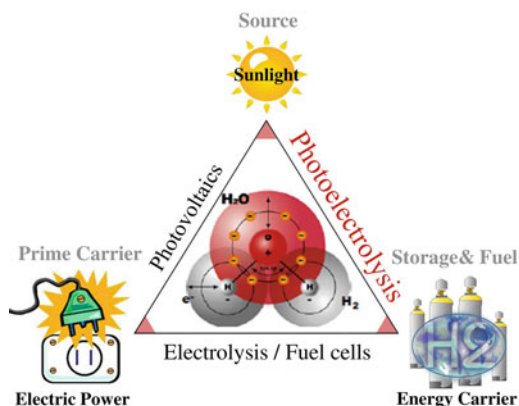
The most important challenge that humanity is currently facing is the development of a long-term and sustainable energy economy. Due to world population increase and industrialization, the total energy consumption is expected to increase from the present 15 TW to 30 TW by 2050 [3, 4]. Presently, fossil fuels provide almost 80% of our energy needs, which will be unable to keep up the global energy demand [5]. Additionally, in the last few years, the consumption of fossil fuels never stopped growing and this behavior is projected for the next decades [6]. As side effects, global warming consequences, natural resources depletion, and global health deterioration are expected to be gradually intensified. Thus, the exploitation of new and promising technologies based on alternative, nonpolluting, and clean energy sources becomes imperative [7].

Solar energy is the largest and most widespread source of renewable energy. The sun irradiance reaching the Earth is plentiful enough to fulfill the humankind energy consumption more than ten thousand times over (120 PW strikes the surface of the Earth, out of which 36 PW is on land) [8]. The solar cell market is one of the fastest growing in the last decade (ca. 40% per year) [9]; however, the photovoltaic (PV) technology only works in a daily basis, and it largely depends on the amount of solar irradiation available. Thus, the intermittency of the solar light flux can cause great fluctuation of the electric grid, which requires the development of efficient approaches to energy storage [7, 10]. Storage approaches such as lithium ion batteries and supercapacitors remain too expensive for grid-scale energy storage, and potentially cheaper alternatives such as

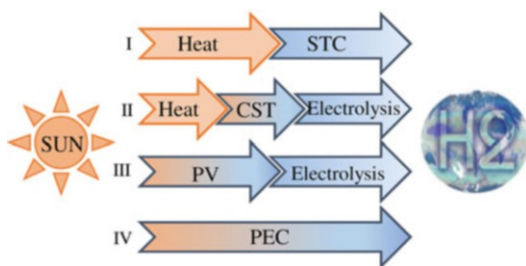
redox flow batteries are still under research and development.

Solar water splitting mimics nature, which achieves solar energy storage for billions of years through photosynthesis, converting solar energy directly into chemical fuels [10]. Hydrogen generated from solar energy is an attractive and flexible energy carrier due to its potential applications across all energy sectors: it is storable and transportable, and it can be efficiently converted into electricity for stationary or mobile applications and used as a feedstock of fuel cells and for the chemical industry [11, 12]. This offers the prospect of a future energy infrastructure based on sunlight, hydrogen, and electricity – Fig. 1 [4].

There are presently several approaches aiming solar-to-hydrogen (STH) conversion as illustrated in Fig. 2 [13]. The two first processes are based on composed devices and consider solar-thermochemical cycles (STC). Process I comprehends two-step STH mechanisms, being the photon-to-thermal energy conversion followed by the thermal-to-chemical conversion. Process II involves the hydrogen generation through three steps, i.e., photon-to-heat, heat-to-electricity, and electricity-to-chemical [14, 15]. Particularly, heat-to-electricity step uses concentrating solar thermal (CST) systems [13]. Process III considers the use of two commercial technologies, namely PV cells, responsible for the photon-to-electric conversion, associated with an electrolyzer to convert electric



**Hydrogen Production from Photoelectrochemical Water Splitting, Fig. 1** A possible future energy triangle based on solar energy (Adapted from Ref. [4])



**Hydrogen Production from Photoelectrochemical Water Splitting, Fig. 2** Solar-to-hydrogen (STH) conversion pathways (Adapted from Ref. [13]). STC is the solar-thermochemical cycles; CST is the concentrating solar thermal systems; PV is the photovoltaic solar cells; and PEC is the photoelectrochemical cell based on a semiconductor/liquid junction (SCLJ)

energy into a chemical fuel [16]. Although such combinations have been demonstrated and tested in several pilot plants [17], PV + electrolyzer approach is too expensive for large solar hydrogen production (cost of hydrogen is around  $\$10 \text{ kg}^{-1}$ ); ca. 30% of the power produced by the PV cell is lost for heat generation rather than to hydrogen production [18]. This motivates research on PEC cells (process IV) based on a semiconductor-liquid junction (SCLJ) that allows the direct photon-to-chemical energy conversion. The major advantage of PEC water splitting is that solar collection, conversion, and storage are combined in a stand-alone system, promoting oxygen and hydrogen evolutions at separate electrodes, which can recombine in fuel cells to convert the stored energy into electricity [19, 20].

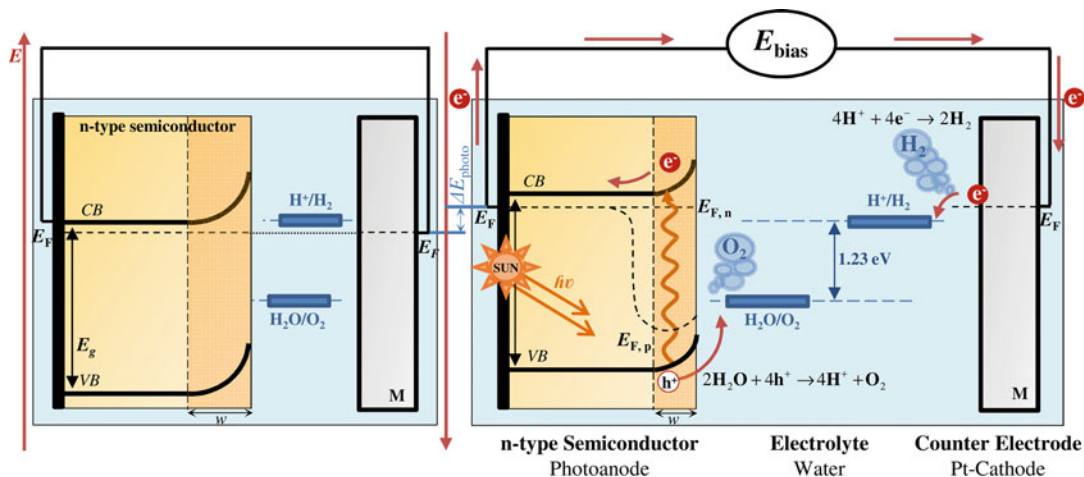
From the different approaches to generate renewable hydrogen, PEC devices are among the most promising, yet probably also the most challenging. PEC water splitting technology remains at an early stage, and research in this area is mostly academic. However, recent techno-economic analyses suggest that a PEC device can only become cost-competitive if it is produced at very low end-cost of ca.  $\$150 \text{ per m}^2$  (device including semiconductor, substrates, housing, and membranes if needed) with improved STH efficiency of 10% and lifetime of 10 years, indicating that solar hydrogen has the potential to be produced at  $\$1$  to  $\$10$  per kg [7, 21]. Further advances require new physical insights into

promising materials with respect to light absorption, charge transport/transfer, stability and photocatalytic activity, and the design and materials used to construct the photoelectrochemical panels.

### PEC Water Splitting: Working Principles

The working principles of a PEC water splitting system based on a single photoelectrode and a metal counter electrode are illustrated in the energy diagram of Fig. 3. This is the simplest possible configuration consisting of two electrodes: a photoactive semiconductor electrode and a metal counter electrode, both immersed in an electrolyte solution that allows the transport of the ionic species. The photoactive material can be either an n-type or p-type semiconductor. A semiconductor having large number of electrons in the conduction band is an n-type semiconductor, whereas in a p-type semiconductor the holes are the majority carriers. Therefore, a photoanode is an n-type semiconductor in PEC water splitting cells, the oxidation of water to oxygen occurs at the semiconductor/electrolyte interface, and the photocathode is a p-type semiconductor evolving hydrogen.

When a semiconductor electrode is immersed in an electrolyte solution in dark, charge equilibration occurs at the interface forming a semiconductor/electrolyte junction (Fig. 3 – left-side). For establishing the thermodynamic equilibrium, the majority charge carriers (electrons in an n-type semiconductor and holes in a p-type semiconductor) are transferred to the second phase upon contact to equalize the Fermi levels. The excess of charges positioned on the semiconductor side is not located at its surface, as it would be in the case of a metallic electrode, but instead it extends into the electrode for a deeper distance, i.e., the space charge layer [22]. For an n-type semiconductor electrode, the Fermi level is normally higher than the redox potential of the electrolyte and then electrons are transferred from the electrode into the solution. Therefore, a positive space charge layer is formed, also called depletion layer since the region is depleted of majority charge carriers.



**Hydrogen Production from Photoelectrochemical Water Splitting, Fig. 3** Energetic diagram of a PEC cell in the dark (left-side) and under illumination (right-side) based on a photoanode and a metal cathode

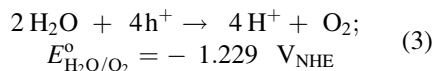
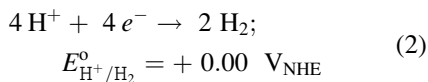
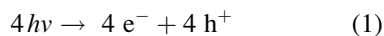
On the other hand, a p-type semiconductor has an initial Fermi level below that of the electrolyte; a negative space charge layer is then formed as holes are transferred into the electrolyte. A charged layer of opposite sign is induced in the electrolyte adjacent to the interface with the solid electrode – Helmholtz layer. This layer consists of charged ions from the adsorbed electrolyte on the solid electrode surface. The Helmholtz layer width (few angstroms) is usually smaller than the space charge layer width [23].

Under illumination, a semiconductor absorbs photons with energies higher than its bandgap energy ( $E_g$ ), injecting electrons from the valence band (VB) to the conduction band (CB) and, consequently, creating electron-hole pairs – Eq. 1. The photovoltage ( $\Delta E_{\text{photo}}$ ) generated by the subsequent separation of the photogenerated charges can directly drive an electrochemical solar-to-fuel production reaction. For an n-type semiconductor photoanode, the case illustrated in Fig. 3 (right-side), photo-generated electrons within the space charge region are driven by the electric field away from the semiconductor/electrolyte interface. Under illumination, the injected electrons raise the Fermi level decreasing the band bending and splitting into a quasi-Fermi level for electrons and for holes close to the interface. The excited electrons flow from the back contact of the

semiconductor, via the external circuit, to the counter electrode, where they reduce water to hydrogen – Eq. 2 or Eq. 4, depending of the electrolyte medium. Either water reacts with the semiconductor surface holes or  $\text{OH}^-$  ions diffuse back to react with holes at the surface of the photoelectrode, oxidizing holes to oxygen – respectively Eqs. 3 or 5.

A different design is also possible with a p-type semiconductor (photocathode) – Fig. 4. In this case, the photocathode, converting incident photons to electron-hole pairs, reduces protons or water to hydrogen – Eqs. 2 or 4, depending on pH medium – at the interface, while oxygen is evolved at the metal anode.

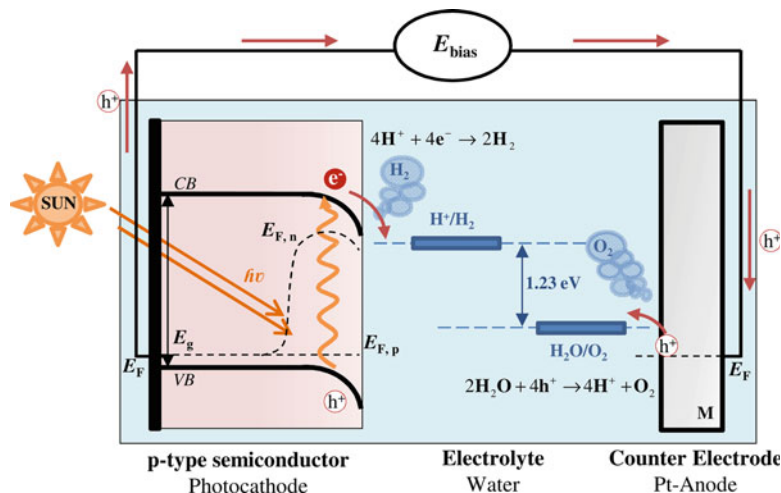
In a PEC cell with an acidic electrolyte the oxygen evolution reaction (OER) and hydrogen evolution reaction (HER) are as follows:



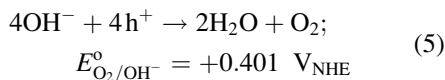
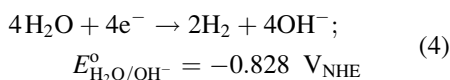
For an alkaline medium, hydroxyl anions are formed from the dissociation reaction of water;

### Hydrogen Production from Photoelectrochemical Water Splitting,

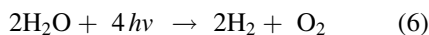
**Fig. 4** PEC cell under illumination based on a photocathode and a metal anode



the reduction and oxidation reactions can be written as [24]:



Therefore, the overall water splitting reaction is the following:



The number of absorbed photons is equal to the number of produced electron-hole pairs, which is twice that of produced  $\text{H}_2$  molecules and four times the produced  $\text{O}_2$  molecules.

The minimum thermodynamic potential needed for driving the water electrolysis is the electric reversible potential of  $\Delta E^\circ = -1.23 \text{ V}$ , based on a Gibbs free energy change of  $\Delta G^\circ = 237 \text{ kJ}\cdot\text{mol}^{-1}$  (based on low heat of combustion, 298 K and 1 bar) [25]. In practice, it takes hundreds of mV overpotential to drive the water splitting reaction, mainly due to overpotentials associated with water oxidation, but also to the counter electrode overpotential, the charge transport in the electrolyte and in the photoelectrode substrate, the distance between the electrodes, and the device geometry [26].

### PEC Materials Overview

The key component of a PEC water splitting cell is the semiconductor photoelectrode, which has to meet several requirements for efficient solar water splitting [27, 28]:

- (i) Strong (visible) light absorption
- (ii) Long-term stability in an aqueous solution
- (iii) Low kinetic overpotentials for the reduction/oxidation reaction
- (iv) Suitable band edge positions to catalyze water reduction and oxidation
- (v) Efficient charge conduction
- (vi) Earth-abundant and cost-effective

The basic parameter that determines the spectral region in which the semiconductor absorbs light is its bandgap energy ( $E_g$ ). Since only 1.23 V are needed for water splitting, a minimum bandgap of 1.23 eV could be sufficient. Based on the standard AM 1.5 G solar spectrum (ca.  $100 \text{ mW}\cdot\text{cm}^{-2}$ ), a semiconductor with such bandgap would give a maximum overall solar-to-hydrogen conversion efficiency of 47.4%, assuming no losses [29]. However, there are significant back processes involved during the solar water splitting, such as the thermodynamic losses (0.3–0.4 eV) and overpotentials required for ensuring sufficiently fast reaction kinetics (0.4–0.6 eV) [4]. As a result, the semiconductor

needs to have a minimum bandgap of ca. 1.9 eV, corresponding to an absorption onset at ca. 650 nm [27]. To achieve the US Department of Energy (DOE) target of 10% STH efficiency, a minimum photocurrent density of ca. 8 mA·cm<sup>-2</sup> is necessary, which means a maximum bandgap of ca. 2.3–2.4 eV. Therefore, the optimum value of the bandgap should be between 1.9 and 2.4 eV. This is consistent with the study by Murphy et al. [30] that indicates an ideal bandgap of ca. 2.03 eV. The semiconductor must have high chemical stability in direct contact with the electrolyte in the dark and under illumination. The stability against corrosion generally increases with semiconductor bandgap, but larger bandgaps limit the visible light absorption. However, very few promising semiconductors are intrinsically stable (with the exception of some oxides), and conformal and stable protection layers may be necessary in a scalable and cost-effective manner.

The carrier diffusion length,  $L_D$ , is also a useful criterion, which can be calculated from the carrier lifetime,  $\tau$ , and mobility,  $\mu$ , as follows:  $L_D = (k_B T \tau \mu / e)^{0.5}$ , where  $k_B$  is the Boltzmann constant,  $T$  is the absolute temperature, and  $e$  is the electron charge. The carriers lifetime and mobility can be measured by, e.g., time-resolved microwave conductivity [31], electrochemical impedance spectroscopy (EIS) [32], intensity modulated photocurrent/voltage spectroscopy (IMPS and IMVS) [33], and transient absorption spectroscopy (TAS) [34]. If  $L_D$  is only a few nanometers or the signal is too small to measure, the semiconductors may be intrinsically poor or susceptible to the formation of recombination centers [35].

The fourth requirement above mentioned is given by the band edge positions in relation to the redox potentials of the desired half-reaction, which implies that the conduction band has to be above water reduction potential,  $E^\circ(\text{H}^+/\text{H}_2)$ , and the valence band has to be below the water oxidation potential,  $E^\circ(\text{H}_2\text{O}/\text{O}_2)$ . This criterion is less strict than the previous ones, since the band edges can be shifted by surface functionalization by dipole layers. Moreover, the charge transport in the semiconductor must be efficient and with minimal recombination losses [27].

Only Earth-abundant materials and scalable thin film technology can meet the target cost of 5 €·kg<sup>-1</sup> H<sub>2</sub> set by the European Commission [36] and the target cost of \$2 to \$4·kg<sup>-1</sup> set by the DOE for future solar hydrogen production [37]. A recent techno-economic analysis showed that a PEC panel needs to cost less than \$150 per m<sup>2</sup> to become commercially competitive [38].

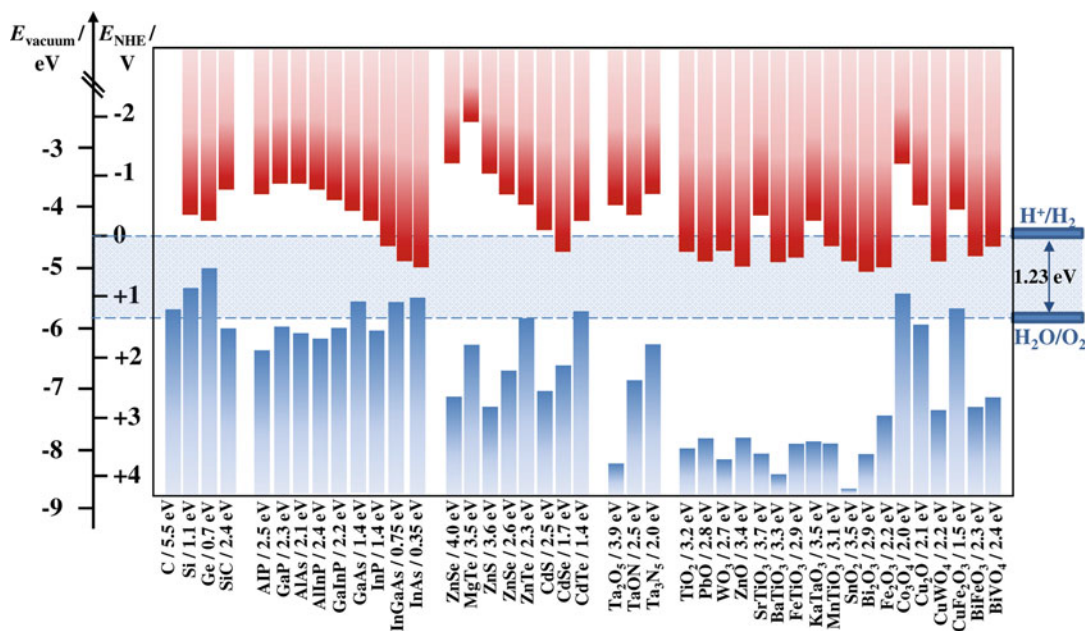
Due to the previously mentioned stringent requirements, no single semiconductor material was identified to promote unbiased water splitting, delivering high solar-to-hydrogen conversion efficiency, and displaying a long-time stability of years. It is likely that the viability of PEC water splitting technology rests on meeting this challenge. During the last decades, various metal oxide (TiO<sub>2</sub>, ZnO,  $\alpha$ -Fe<sub>2</sub>O<sub>3</sub>, WO<sub>3</sub>, BiVO<sub>4</sub>, Cu<sub>2</sub>O, etc.) and nonoxide (silicon, GaAs, GaP, CdS, InP, TaON, Ta<sub>3</sub>N<sub>5</sub>, etc.) semiconductors have been extensively studied [39–41]. Metal oxides are often considered as the class of material suitable for solar water splitting, mainly due to their general stability in aqueous solution and relatively low cost. However, they usually do not have very good semiconducting properties, such as carrier mobility, compared to III-V semiconductors or even Si. The challenge is then to overcome these limitations while taking advantage of the metal oxides properties. Fig. 5 shows the relative band edge positions of several semiconductors.

### Photoanodes for Solar Water Splitting

A photoanode material for solar water splitting is responsible for the oxygen evolution, such that the electric field generated by band bending drives holes toward the surface and electrons to the current collector. Table 1 summarizes the important breakthroughs in the design of photoanode materials.

Since the pioneering work by Fujishima and Honda [2] in 1972, using a titanium dioxide (TiO<sub>2</sub>) photoanode illuminated with UV light, PEC cells with different types of TiO<sub>2</sub> (single crystal, polycrystalline, thin films) have received special attention [43, 44]. TiO<sub>2</sub> material presents an adequate stability but the overall PEC performance is low due to its large bandgap





**Hydrogen Production from Photoelectrochemical Water Splitting, Fig. 5** Energy band edge positions for semiconductors at pH 0 (Adapted from Ref. [42])

( $E_g = 3.2$  eV), which only absorbs in UV range of the solar spectrum; the maximum thermodynamic STH efficiency is then limited to 2.2% [30]. Also, the conduction band edge of this semiconductor is slightly positive to the HER. This limitation can be overcome using titanates, such as  $\text{SrTiO}_3$  ( $E_g = 3.2$  eV) and  $\text{BaTiO}_3$  ( $E_g = 3.2$  eV); the addition of  $\text{Sr}^{2+}$  and  $\text{Ba}^{2+}$  cations moves the potential of the conduction band edge to more negative values [10]. Although these materials can accomplish the direct water splitting, the energy efficiency is very small, e.g., less than 1% STH efficiency was obtained for  $\text{SrTiO}_3$  [45]. Several other attempts have been made doping  $\text{TiO}_2$  with ions such as Fe [46], Cr [47], Ni [48], and C [10, 49] without noticeable energy efficiency increase.

Small bandgap binary metal oxides, such as  $\text{WO}_3$  and  $\alpha\text{-Fe}_2\text{O}_3$ , exhibit conduction band potentials more positively than water reduction and so an external bias potential should be provided to promote complete water splitting. Tungsten trioxide ( $\text{WO}_3$ ) is an interesting semiconductor material due to its high stability against photocorrosion in acidic aqueous

solutions ( $\text{pH} < 4$ ). Moreover, it has an indirect bandgap ( $E_g = 2.6\text{--}2.8$  eV), which absorbs not only the near-UV but also the visible blue portion of the solar electromagnetic spectrum [50]. Unfortunately, the thermodynamic STH efficiency is only around 4.8% [51]. Usually,  $\text{WO}_3$  crystalline and amorphous thin films can be used for water splitting, but a highly crystalline structure is desirable to reduce charge trapping and carrier recombination, therefore, improving its energy performance [52]. A photocurrent density of ca.  $2.7 \text{ mA}\cdot\text{cm}^{-2}$  at 1.0  $V_{\text{RHE}}$  was reported using a nanocrystalline  $\text{WO}_3$  thin film synthesized by an aqueous sol-gel method on a conducting glass electrode; it remained stable over 144 h under 1-sun AM 1.5 G illumination [53]. A methane sulfonic acid solution was used to avoid the deactivation of the photoanode due to the formation and accumulation of peroxy species on its surface. The formation of secondary species becomes kinetically competitive with  $\text{O}_2$  production; though, this aspect can be improved by placing a suitable  $\text{O}_2$  evolution catalyst to enhance the photostability and efficiency toward water splitting reaction, e.g., low-cost co-catalysts such as



**Hydrogen Production from Photoelectrochemical Water Splitting,** incident photon-to-current conversion efficiency – IPCE, STH conversion efficiency –  $\eta_{\text{STH}}$ , and stability); ordered by type of photoelectrode and reverse chronological Table 1 Overview of emerging photoanode materials for PEC water splitting, including experimental conditions and corresponding performance (photocurrent density  $-J_p$ , publication

Photoanode materials	$E_g$ /eV	$E_{\text{fb}}/V_{\text{RHE}}$	Electrolyte	Performance	Stability	Advantages/challenges	Ref./date
<b>TiO<sub>2</sub></b> H <sub>2</sub> -treated rutile TiO <sub>2</sub> ; hydrothermal method	3.0	-0.25 to -0.40	1 M NaOH (pH = 13.6) AM 1.5 G 100 mW·cm <sup>-2</sup>	@ 0.4 V <sub>RHE</sub> : $J = 1.97 \text{ mA}\cdot\text{cm}^{-2}$ $\eta_{\text{STH}} = 1.63\%$ IPCE = 95% at 370 nm; onset potential ca. 0.1 V <sub>RHE</sub>	2 h stable current	Bandgap limits thermodynamic $\eta_{\text{STH}}$ to 2.25%; not viable for maximum $\eta_{\text{STH}} = 10\%$	[90]/2011
<b>WO<sub>3</sub></b> 2-step-16 h hydrothermal reaction	2.6-2.8	0.32	0.1 M H <sub>2</sub> SO <sub>4</sub> (pH = 0) AM 1.5 G 100 mW·cm <sup>-2</sup>	@ 1.23 V <sub>RHE</sub> : $J = 3.7 \text{ mA}\cdot\text{cm}^{-2}$ IPCE = 67% at 350 nm; onset potential ca. 0.6 V <sub>RHE</sub>	30 min 20% current drop	Bandgap limits thermodynamic $\eta_{\text{STH}}$ to 4.8%; not viable for maximum $\eta_{\text{STH}} = 10\%$	[56]/2016
<b>Fe<sub>2</sub>O<sub>3</sub></b> Chemical bath deposition + H <sub>2</sub> -treated; coated with Co-Pi OER co-catalyst	2.0	-	1 M KOH (pH = 13.6) AM 1.5 G 100 mW·cm <sup>-2</sup>	@ 1.23 V <sub>RHE</sub> : $J = 6 \text{ mA}\cdot\text{cm}^{-2}$ IPCE = 50% at 320 nm; onset potential ca. 0.55 V <sub>RHE</sub>	100 h stable current	Potentially viable for maximum $\eta_{\text{STH}} = 10\%$	[71]/2017
<b>BiVO<sub>4</sub></b> SiO <sub>x</sub> /Pt/SnO <sub>2</sub> Mo-doped BiVO <sub>4</sub> nanocone coated with FeOOH/NiOOH OER co-catalyst	2.4	0	0.5 M Na <sub>2</sub> SO <sub>3</sub> AM 1.5 G 100 mW·cm <sup>-2</sup>	@ 1.23 V <sub>RHE</sub> : $J = 5.82 \text{ mA}\cdot\text{cm}^{-2}$ IPCE > 75% at 460 nm; onset potential ca. 0.2 V <sub>RHE</sub>	5 h stable current	Bandgap limits thermodynamic 7.5 mA·cm <sup>-2</sup> ; potentially viable for up to $\eta_{\text{STH}} = 9.2\%$	[91]/2016
<b>WO<sub>3</sub>/Fe<sub>2</sub>O<sub>3</sub> heterojunction</b> WO <sub>3</sub> nanosheets/Fe <sub>2</sub> O <sub>3</sub>	2.7/2.2	-	0.5 M Na <sub>2</sub> SO <sub>4</sub> (pH = 7)	@ 1.23 V <sub>RHE</sub> : $J = 1.66 \text{ mA}\cdot\text{cm}^{-2}$ IPCE ~ 74% at 390 nm; onset potential ca. 0.7 V <sub>RHE</sub>	10 h stable current	Potentially viable for maximum $\eta_{\text{STH}} = 10\%$	[92]/2016
<b>WO<sub>3</sub>/BiVO<sub>4</sub> heterojunction</b> WO <sub>3</sub> -NRs/BiVO <sub>4</sub> coated with Co-Pi OER co-catalyst	2.6/2.4	-	KPi buffer (pH = 7)	@ 1.23 V <sub>RHE</sub> : $J = 6.72 \text{ mA}\cdot\text{cm}^{-2}$ IPCE ~ 90% at 516 nm; onset potential ca. 0 V <sub>RHE</sub>	1 h stable current	ca. 90% of its maximum thermodynamic limit; potentially viable for maximum $\eta_{\text{STH}} = 9.2\%$	[82]/2015
<b>Ta<sub>3</sub>N<sub>5</sub></b> Ni(OH)/Fh/TiO <sub>x</sub> /Ta <sub>3</sub> N <sub>5</sub> Coated with molecular OER catalysts (Co cubane and Ir complex)	2.1	-0.1	1 M NaOH (pH = 13.6) AM 1.5 G 100 mW·cm <sup>-2</sup>	@ 1.23 V <sub>RHE</sub> : $J = 12.1 \text{ mA}\cdot\text{cm}^{-2}$ IPCE ~ 90-100% at 400-500 nm; onset potential ca. 0.6 V <sub>RHE</sub>	Unstable	ca. 94% of its theoretical photocurrent limit; viable for maximum $\eta_{\text{STH}} = 10\%$ ; not transparent – Ta foil substrate	[88]/2016
<b>Ta<sub>3</sub>N<sub>5</sub></b> TaO <sub>x</sub> N <sub>y</sub> ALD film on top of Ta-doped TiO <sub>2</sub> layer, followed by nitridation at 750 °C, coated with Co-Pi OER catalyst	2.1	-0.1	0.5 M K <sub>2</sub> HPO <sub>4</sub> (pH = 13) AM 1.5 G 100 mW·cm <sup>-2</sup>	@ 1.23 V <sub>RHE</sub> : $J = 1.1 \text{ mA}\cdot\text{cm}^{-2}$ ; onset potential ca. 0.8 V <sub>RHE</sub>	Unstable	Viable for maximum $\eta_{\text{STH}} = 10\%$	[93]/2016

cobalt-phosphate (Co-Pi) [54] and FeOOH [55]. However, the best-performing  $\text{WO}_3$  film on FTO-glass showed a photocurrent-density of  $3.7 \text{ mA}\cdot\text{cm}^{-2}$  at  $1.23 \text{ V}_{\text{RHE}}$  without using co-catalysts, corresponding to 93% of its maximum thermodynamic photocurrent [56]. Kwong et al. [55] reported unbiased water splitting using nanoparticulate FeOOH-decorated  $\text{WO}_3$  and 2-junction Si solar cell and a Ni-Mo hydrogen evolution co-catalyst with a STH conversion efficiency of 1.8%.

Hematite ( $\alpha\text{-Fe}_2\text{O}_3$ ) is one of the most abundant and inexpensive oxide semiconductors with suitable energy bandgap ( $E_{\text{g}} = 2.0\text{--}2.2 \text{ eV}$ ) [57]. The thermodynamic maximum STH conversion efficiency is ca. 14–17%, which corresponds to a photocurrent density of  $11\text{--}14 \text{ mA}\cdot\text{cm}^{-2}$  under AM 1.5 G illumination [58]. The first study on hematite ability for water photolysis was published in 1976 by Hardee and Bard [59]. These authors found hematite to be highly stable in neutral and alkaline electrolyte solutions that is of great importance for the commercial viability of the PEC systems [60]. Very recently it was reported a bare hematite thin film (ca. 19 nm) photoelectrode that showed a record-breaking stability over 1000 h of PEC operation under 1-sun AM 1.5 G illumination, with no evidences of film degradation neither of photocurrent density losses [61]. As a drawback, in pure-phase  $\alpha\text{-Fe}_2\text{O}_3$  the photogenerated carriers show low mobility, which implies a short hole diffusion length ( $L_{\text{D}} = 2\text{--}4 \text{ nm}$ ) [62]. These intrinsic disadvantages combined with the sluggish water oxidation reaction are bound to give rise to the recombination of photogenerated electron-hole pairs, thereby leading lower PEC performances [28, 63]. Therefore, the main ongoing studies on hematite concern: (i) improvement of photogenerated current density by morphology optimization (e.g., using different deposition methods [28]) and doping (Si [64], Ti [65], Sn [66], Pt [67], or other atoms); (ii) improvement of generated photopotential minimizing the electron-hole recombination, especially at the photoelectrode surface [68]; and (iii) reduction of the electrochemical activation overpotential using co-catalysts (e.g.,  $\text{IrO}_2$  [69], Co-Pi [67],  $\text{NiFeO}_x$

[70]). Kim et al. [67] used a solution-based colloidal method to prepare a photoelectrode of hematite nanowires (ca. 500 nm thick) doped with Pt and activated with Co-Pi co-catalyst; the prepared photoelectrode showed ca.  $4.32 \text{ mA}\cdot\text{cm}^{-2}$  at a bias potential of  $1.23 \text{ V}_{\text{RHE}}$  and remained stable over 180 min [67]. Recently, a new hematite record breaking of ca.  $6 \text{ mA}\cdot\text{cm}^{-2}$  at  $1.23 \text{ V}_{\text{RHE}}$  was achieved by Jeon et al. [71] with  $\alpha\text{-Fe}_2\text{O}_3$  nanorod arrays modified with Co-Pi catalyst. Nevertheless, the performance of hematite is still considerably lower than the thermodynamic value and current efforts aimed at improving its low-bias performance (reduction of the onset potential for OER and higher photocurrents at lower potentials) [72, 73]. Through the combination of high-temperature annealing and surface modifications with catalysts a cathodic shift on the photocurrent onset potential ( $E_{\text{onset}}$ ) is observed [74]. The low-bias performance of hematite thin films was improved combining an annealing treatment at  $800 \text{ }^\circ\text{C}$  with the use of highly active bimetal oxide co-catalyst layer of  $\text{IrO}_2/\text{RuO}_2$ .  $\text{IrO}_2/\text{RuO}_2$ -coated hematite photoanode exhibited a low turn-on potential of  $0.48 \text{ V}_{\text{RHE}}$  and a final photovoltage of 1.20 V, which is the highest photovoltage reported for hematite-based photoelectrodes; it showed a quite stable performance at  $0.80 \text{ V}_{\text{RHE}}$  for over 72 h [75]. A stand-alone PEC device based on a hematite photoanode catalyzed with  $\text{NiFeO}_x$  in a tandem arrangement with an amorphous Si photocathode (with  $\text{TiO}_2/\text{Pt}$  overlayers) was reported showing an overall efficiency of ca. 0.91% [76], which it is also considerably lower for viable applications.

The limitations of binary oxides have prompted the study of ternary and more complex multinary oxides; there are about 19,000 possible ternary metal oxides and more than 220,000 quaternary oxides with ca. 50 candidate metals in the periodic Table [35]. Therefore, a strategy is needed to identify potential complex oxide candidates, which may well be obtained by rationally engineering the bandgap combining different cations ( $\text{Sn}^{2+}$ ,  $\text{Bi}^{3+}$ ,  $\text{V}^{5+}$ ,  $\text{Ti}^{4+}$ , and  $\text{Nb}^{5+}$ ) in the semiconductor. By far the most successful ternary metal-oxide photoanode was bismuth vanadate ( $\text{BiVO}_4$ ).  $\text{BiVO}_4$  semiconductor has a bandgap

energy of 2.4–2.5 eV and a reasonable band edge alignment with respect to water redox potentials, showing a thermodynamic STH efficiency of ca. 9.2% ( $7.5 \text{ mA cm}^{-2}$ ) [77]. Moreover, it has also been reported that  $\text{BiVO}_4$  shows both n- and p-type semiconducting properties and exhibit high photon-to-current conversion efficiencies under visible light radiation (>40% at 420 nm) [78–80]. Doping  $\text{BiVO}_4$  with  $\text{Mo}^{6+}$  or  $\text{W}^{6+}$  at the  $\text{V}^{5+}$  sites was found to be effective in increasing the electronic conductivity and carrier collection efficiencies; the use of co-catalysts such as Co-Pi and dual-layer Fe and Ni oxy-hydroxides improved slow kinetics and reduced surface recombination, thus enhancing PEC performance. A tungsten-gradient-doped  $\text{BiVO}_4$  photoanode was reported to display a photocurrent of  $3.6 \text{ mA}\cdot\text{cm}^{-2}$  at  $1.23 V_{\text{RHE}}$  [81]. Another approach is to fabricate a type II heterojunction with  $\text{WO}_3$  that improves the carrier separation; a record value of  $6.72 \text{ mA}\cdot\text{cm}^{-2}$  was obtained at  $1.23 V_{\text{RHE}}$ , which is one of the highest photocurrents reported for any metal-oxide photoanode [82]. Various demonstrations of unbiased solar water splitting based on  $\text{BiVO}_4$  have been reported using PEC-PV tandem cells with STH efficiencies of 5.2%, 5.7%, and 8.1% for devices with double junction amorphous silicon [81, 83], dye-sensitized solar cells [84], and GaAs-InGaAsP cells [82], respectively. Despite  $\text{BiVO}_4$  demonstrated already performance levels close to their thermodynamic maximum, for practical PEC devices STH efficiencies of 10% or higher are needed.

Recent studies motivated by bandgap engineering strategy report different ternary oxides, such as copper tungsten oxide ( $\text{CuWO}_4$ ) and ferrite materials ( $\text{ZnFe}_2\text{O}_4$  and  $\text{CaFe}_2\text{O}_4$ ).  $\text{CuWO}_4$  presents a bandgap of 2.0–2.25 eV and a flatband potential similar to  $\text{WO}_3$ ; currents of ca.  $0.2 \text{ mA}\cdot\text{cm}^{-2}$  at  $1.23 V_{\text{RHE}}$  and reasonable stability (tens of hours) were reported for photoelectrodes prepared by sol-gel technique [85].

In addition to tuning the bandgap playing with the cation elements, substituting an oxygen atom by a nitrogen atom decreases the bandgap, e.g., the wide bandgap of tantalum oxide ( $\text{Ta}_2\text{O}_5$ ) can be reduced with high-temperature treatment under

$\text{NH}_3$  to form  $\text{TaO}_x\text{N}_y$ ,  $\text{TaON}$  ( $E_g = 2.5 \text{ eV}$ ) and  $\text{Ta}_3\text{N}_5$  ( $E_g = 2.0 \text{ eV}$ ) have experienced a rapid development as high-performance photoanodes [86], showing narrow bandgaps for visible light absorption ( $\lambda < 600 \text{ nm}$ ) and suitable band edge positions straddling over water redox potentials [12]. A photocurrent density of ca.  $6.7 \text{ mA}\cdot\text{cm}^{-2}$  at  $1.23 V_{\text{RHE}}$  was obtained for the Ba-doped  $\text{Ta}_3\text{N}_5$  nanorod array modified with Co-Pi in an electrolyte solution of 0.5 M  $\text{K}_2\text{HPO}_4$  (pH 13) [87]. This photoanode material showed a maximum STH conversion efficiency of 1.56% at  $0.87 V_{\text{RHE}}$  and remained stable over 100 min. More recently,  $\text{Ta}_3\text{N}_5$  was shown to be able of a photocurrent of  $12.1 \text{ mA}\cdot\text{cm}^{-2}$  (close to its maximum thermodynamic limit of  $12.9 \text{ mA}\cdot\text{cm}^{-2}$ ), but its long-term stability in water is currently an issue [88]. Liu et al. [89] further modified  $\text{Ta}_3\text{N}_5$  with the  $\text{Ni}(\text{OH})_x/\text{MoO}_3$  bilayer and improved its stability up to 24 h in 1 M LiOH aqueous solution (pH 12). Continuous efforts on fundamental knowledge about the factors that most influence the PEC efficiency is still needed, as well as the identification of material preparation routes for economically viable PEC cell development.

### Photocathodes for Solar Water Splitting

Photocathodes used for water splitting need to supply sufficient cathodic current for reduction of protons to  $\text{H}_2$  and must be stable in aqueous environments. Single-crystal phosphides such as GaP ( $E_g = 2.3 \text{ eV}$ ) [94], InP ( $E_g = 1.4 \text{ eV}$ ) [95], and GaInP ( $E_g = 2.2 \text{ eV}$ ) [96] have been studied as nonoxide photocathode semiconductors, but polycrystalline materials are desirable for large-scale applications of PEC systems due to their higher stability [97]. Polycrystalline-Si ( $E_g = 1.1 \text{ eV}$ ) decorated with a variety of catalysts can be used to reduce water [98]. The stability is higher in acids but it also suffers from limited durability due to surface oxidation. The formation of an oxide can be prevented by passivating the surface, e.g., with methyl groups [99]. Recently, an amorphous Si photocathode with  $\text{TiO}_2/\text{Pt}$  protective overlayers was reported exhibiting an impressive photocurrent of ca.  $6.1 \text{ mA}\cdot\text{cm}^{-2}$  and reasonable stability at a large positive bias of  $0.8 V_{\text{RHE}}$ ; this is the

highest photoelectrochemical performance of all reported Si photocathodes [100].

Cuprous oxide ( $\text{Cu}_2\text{O}$ ) has been used as both photoanode and photocathode [10], but it appears as an attractive p-type oxide for solar hydrogen production with a direct bandgap energy of 2.0–2.1 eV suitable for visible light harvesting [101]. Thermodynamic calculations indicate that  $\text{Cu}_2\text{O}$  can produce up to  $14.7 \text{ mA}\cdot\text{cm}^{-2}$ , corresponding to a STH conversion efficiency of 18% based on the AM 1.5 G spectrum [102]. It is abundant, cheap, and environmentally friendly and has favorable energy band positions [103]. However,  $\text{Cu}_2\text{O}$  is easily reduced to Cu when exposed to aqueous electrolytes. This instability can be addressed by depositing protective layers on the electrode surface. Paracchino et al. [102] reported an electrodeposited cuprous oxide electrode protected with nanolayers of Al-doped zinc oxide (AZO) and  $\text{TiO}_2$ , and activated for HER with nanoparticulated Pt co-catalyst, showing photocurrents up to  $7.6 \text{ mA}\cdot\text{cm}^{-2}$  at 0  $V_{\text{RHE}}$ . Furthermore,  $\text{RuO}_x$  top layer was investigated as a co-catalyst [104] and, together with a steam treatment of the multilayer structures, showed optimized electrodes with a stable photocurrent of ca.  $5 \text{ mA}\cdot\text{cm}^{-2}$  during 50 h (photocurrent loss <10%) under 1-sun AM 1.5 G of light chopping (biased at 0  $V_{\text{RHE}}$  in pH 5 electrolyte) [103]. More recently, an unprecedented high current density of  $10 \text{ mA}\cdot\text{cm}^{-2}$  (ca. 70% of its thermodynamic limit) was obtained with  $\text{Cu}_2\text{O}$  nanowire arrays using these ALD protective overlayers [105]. An innovative tandem device made of a transparent  $\text{Cu}_2\text{O}$  photocathode atop a perovskite photovoltaic cell demonstrated unassisted sunlight-driven water splitting up to 2.5% STH efficiency [106].

Copper-based ternary oxides of  $\text{CuFeO}_2$  and  $\text{CuRhO}_2$  have been investigated as photocathode candidates.  $\text{CuFeO}_2$  is more attractive as it is made of widely available elements, it has appropriate absorption properties and relatively high conductivity, and its conduction band, located at ca. 0.4  $V_{\text{RHE}}$ , is suitably positioned to reduce water. An important criterion is its favorable stability under reductive conditions, being one of the few oxides that naturally displays a stable p-type behavior, unlike  $\text{Cu}_2\text{O}$ . Moreover,  $\text{CuFeO}_2$  has a

bandgap energy of ca. 1.5 eV, which enables to reach efficiencies higher than 10% in a tandem device when combined with a photoanode with a bandgap range of 1.8–2.3 eV. Prévot et al. [107], using a simple sol-gel technique to deposit this material and an oxygen intercalation treatment to address the poor majority carrier conductivity, reported photocurrent densities of up to  $1.5 \text{ mA}\cdot\text{cm}^{-2}$  at 0.35  $V_{\text{RHE}}$  for  $\text{O}_2$  reduction and  $0.4 \text{ mA}\cdot\text{cm}^{-2}$  at 0  $V_{\text{RHE}}$  for  $\text{H}^+$  reduction. Importantly, bare  $\text{CuFeO}_2$  is highly stable at potentials at which photocurrent is generated. No degradation is observed after 40 h under operating conditions in basic electrolyte, which turns this photocathode very promising if the charge separation and catalytic activity can be further improved [35].

An overview of the best-performing photocathode materials are summarized in Table 2.

### Challenges for Improving Photoelectrodes Performance

Various strategies have been followed to improve the photoelectrode performance for PEC water splitting, including [108]:

- (i) Doping the bare semiconductor.
- (ii) Morphology control of the photoelectrode.
- (iii) Surface treatment of the semiconductor.
- (iv) Other methods, e.g., band structure engineering using heterojunction structures [109], change the distribution of electromagnetic energy using plasmonic metal nanoparticles on the semiconductors [110].

Doping a semiconductor material is used to simultaneously improve the visible light absorbance (decrease the energy of bandgap) and the mobility of charge carriers. The band structural modification involves the introduction of foreign ions (cations or anions) into the semiconductor material to change its electronic and optical properties. Various dopants including metal ions (e.g., Ti, Sn, Fe) and nonmetal elements (e.g., N, Si, C) have been used to improve the PEC efficiency. A review of the doping effect on a number of promising semiconductors is reported elsewhere [42].

**Hydrogen Production from Photoelectrochemical Water Splitting, Table 2** Overview of emerging photocathode materials for PEC water splitting, including experimental conditions and corresponding performance

(photocurrent density –  $J$ , incident photon-to-current conversion efficiency – IPCE, STH conversion efficiency –  $\eta_{\text{STH}}$ , and stability); ordered by type of photoelectrode and reverse chronological publication

Photocathode materials	$E_g$ / eV	$E_{\text{fb}}$ / $V_{\text{RHE}}$	Electrolyte	Performance	Stability	Advantages/ challenges	Ref./ date
<b>Si</b> a-Si (n-i-p) ZnO layer as TCO-glass TiO <sub>2</sub> overlayer, Pt OER co-catalyst	1.7	–	0.5 M potassium hydrogen phthalate (pH = 4) AM 1.5 G 100 mW·cm <sup>-2</sup>	@ 0 $V_{\text{RHE}}$ : $J = 11.6 \text{ mA}\cdot\text{cm}^{-2}$ IPCE = 80% at 450 nm; onset potential ca. 0.48 $V_{\text{RHE}}$	12 h stable current	Viable for maximum $\eta_{\text{STH}} = 10\%$	[100]/ 2013
<b>Cu<sub>2</sub>O</b> Cu <sub>2</sub> O NWs ZnO:Al/TiO <sub>2</sub> overlayers RuO <sub>2</sub> HER co-catalyst	2.0	0.8	0.5 M Na <sub>2</sub> SO <sub>4</sub> and 0.1 M KH <sub>2</sub> PO <sub>4</sub> at (pH = 5) AM 1.5 G 100 mW·cm <sup>-2</sup>	@ 0 $V_{\text{RHE}}$ : $J = 10 \text{ mA}\cdot\text{cm}^{-2}$ IPCE = 80% at 450 nm; onset potential ca. 0.48 $V_{\text{RHE}}$	10 h stable current; >30% drop after 60 h	Viable for maximum $\eta_{\text{STH}} = 10\%$ ; low stability	[90]/ 2011
<b>CuFeO<sub>2</sub></b> AZO/TiO <sub>2</sub> overlayers Pt HER co-catalyst	1.5	1.0	0.5 M Na <sub>2</sub> SO <sub>4</sub> (pH = 6.1)	@ 0 $V_{\text{RHE}}$ : $J = 0.4 \text{ mA}\cdot\text{cm}^{-2}$ ; current up to 1.5 mA·cm <sup>-2</sup> IPCEs up to 15%; onset potential ca. 0.45 $V_{\text{RHE}}$	10 h stable current	Potentially viable for maximum $\eta_{\text{STH}} = 10\%$ ; poor interface with water reduction catalysis	[107]/ 2015

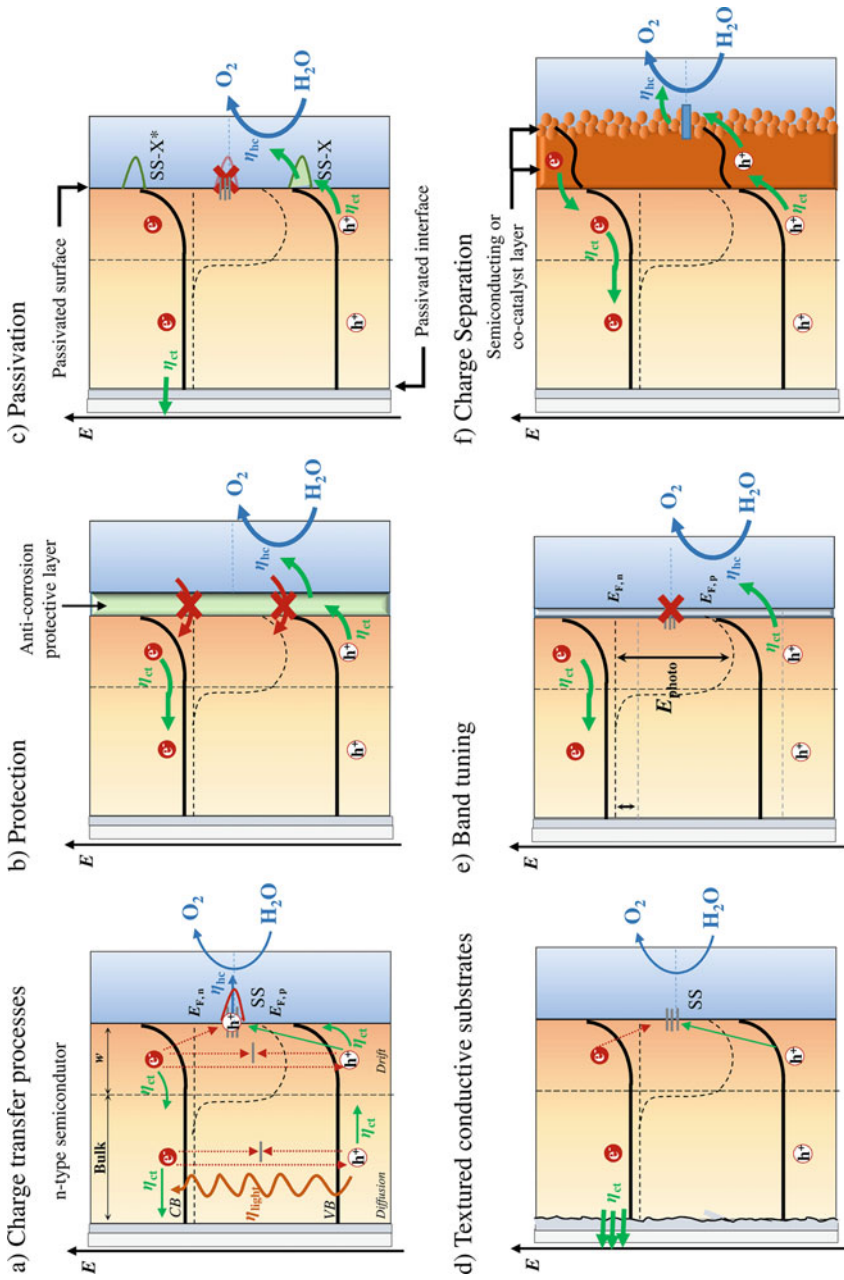
An efficient photoelectrode must have a film thick enough to absorb more light, and the deep photogenerated carriers must be able to reach the surface and then be collected [10]. Therefore, the morphology control of the photoelectrodes by nanostructuring is widely used to overcome the trade-off between enhancing the optical absorption and shortening the diffusion lengths of minority carriers, as well as to improve the catalytic activity by increasing surface area [111]. A good example is the nanostructured hematite photoanode that showed a performance increase by a factor of 10 from the single crystal case. However, the higher surface area generally leads to lower intrinsic photovoltage and increased surface recombination, which are both important loss mechanisms [35]. To minimize surface recombination, it may be efficient to nanostructure only the co-catalyst, especially if the system is limited by surface reaction kinetics.

Surface treatments can be classified as: (i) protection of the surface against

photocorrosion; (ii) forming a surface- and interface-layers for passivation of surface states; (iii) using textured conductive substrates for improved charge collection; (iv) tuning of the band edge positions or band bending for improving the photovoltage; and (v) selective extraction of carriers and improved catalytic activity [112]. These functions are shown schematically in Fig. 6. A recent comprehensive perspective on this topic for further information is described elsewhere [112].

The photoelectrode stability can be enhanced by adding protective overlayers, which should be sufficiently thick to act as a physical barrier between the semiconductor and the electrolyte, but also semitransparent and conductive to avoid the limiting of the light harvesting efficiency or charge transfer [102]. The surface passivation can suppress the deleterious role of the surface trapping states, which act as trapping sites and recombination centers of photoinduced carriers [108]. The third criterion consists of the increase



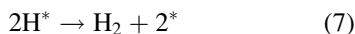


**Hydrogen Production from Photoelectrochemical Water Splitting, Fig. 6** (a) Schematic energy band diagrams and charge transfer processes limiting PEC performance, e.g., using n-type photoanodes. The photocurrent is controlled by the efficiency of light harvesting ( $\eta_{light}$ ), charge transport ( $\eta_{ct}$ ), and holes collection ( $\eta_{hc}$ ), and red arrows indicate the recombination pathways. Main effects of semiconductor surface treatments by: (b) protection against (photo)corrosion with an encapsulating layer; (c) passivation of surface states (SS) by reaction with acid/basic reagents (X) which creates new bonding (SS-X) and antibonding ( $SS-X^*$ ) states out of the bandgap; (d) texturing a conductive substrate; (e) tuning of the band bending and band edges; (f) depositing a semiconducting or co-catalyst layer



of charge carrier collection efficiency modifying the photoelectrode structure with conductive scaffolds (or textured conductive substrates). These conductive substrates include mainly nano-textured transparent conducting oxide (TCO), nanocarbon materials, and a few other unique conductive nanostructures [109]. The degree of band bending and band positions (surface energetics) can be tuned to balance the driving force for the charge transfer processes and the photovoltage [72], e.g., attaching dipolar molecules can afford a relative shift in the semiconductor band edge positions and flatband potential [35].

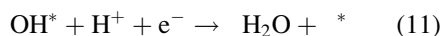
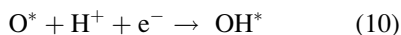
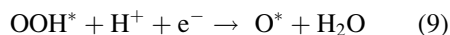
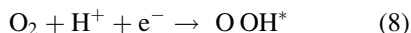
Since the synthesis of chemical products can occur via multistep electron transfer reactions with large overpotential, surface-functionalized catalysis can improve the slow kinetics of surface reactions and minimize the overpotential needed to drive the gases evolution reaction [113]. Improving the reaction kinetics, the onset potential is reduced and then the photovoltage increases. A good catalyst also increases the plateau photocurrent and may contribute for the chemical and photochemical stability [114]. Co-catalysts can be divided into WRC (water reduction catalyst) and WOC (water oxidation catalyst), acting as activation sites for the evolution of H<sub>2</sub> (photocathode) or O<sub>2</sub> (photoanode), respectively. The HER is a two-electron transfer reaction with one catalytic intermediate, H\* (where \* denotes a site on the electrode surface), and may occur by:



(Volmer Tafel mechanism)

The rate of the overall reaction is largely determined by hydrogen adsorption free energy,  $\Delta G_{\text{H}}$ ; thus,  $\Delta G_{\text{H}} \approx 0$  is the condition needed for an active WRC [115]. Platinum sits very near to the top of the hydrogen volcano, with an almost neutral  $\Delta G_{\text{H}}$ , and is well known as the best-performing co-catalyst for the HER [102], also requiring negligible overpotentials to achieve high reaction rates in acidic solutions. However, the scarcity and high cost of Pt limits its widespread use; earth-abundant co-catalysts, such as MoS<sub>2</sub> [116] and Ni-Fe [117], are excellent alternatives for HER. On the other hand, the OER is

limited by sluggish four-electron transfer reaction to produce one molecule of oxygen, justifying the need of improved co-catalysts for increasing its reaction rate. The four-electron pathway can proceed via several different mechanisms, such as the associative mechanism [115]:

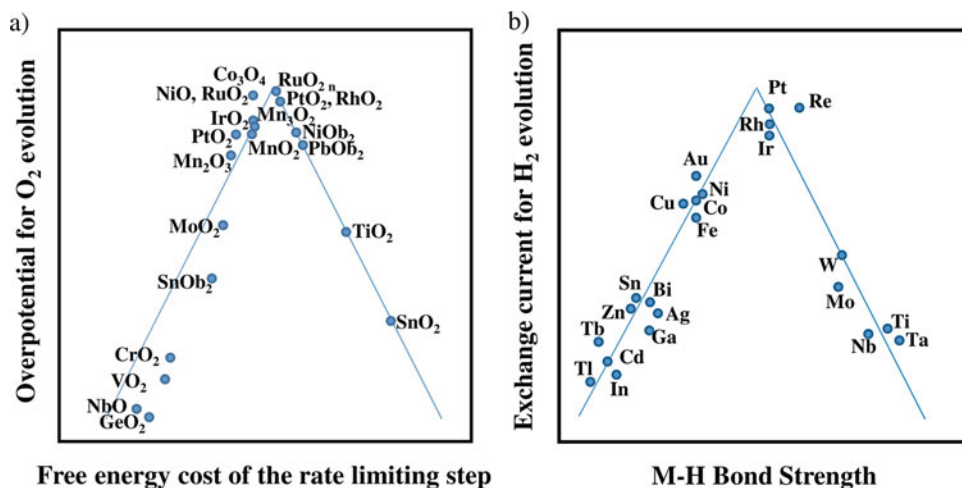


The OER involves multiple intermediates (OOH\*, OH\*, O\*), resulting in a nonzero overpotential of 0.3–0.4 V [115], unlike the case of the HER with one reaction intermediate. Among the WOCs employed so far, IrO<sub>2</sub> [69], RuO<sub>2</sub> [118], cobalt-based (e.g., Co<sub>3</sub>O<sub>4</sub> [119] and Co-Pi [120]), and nickel-based and iron-based (e.g., FeOOH and NiFeO<sub>x</sub> [76]) are most used for OER. The catalytic activity of the oxygen and hydrogen evolution reactions can be shown in volcano plots as shown in Fig. 7a, b, respectively.

A co-catalyst overlay on a semiconductor surface contributes then to improve the catalysis, but it can also contribute for: surface state passivation, tuning the band structure energetics, and improve the stability of the photoabsorber material by serving as a corrosion protection layer [113]. A deeper understanding of the working state of these co-catalysts and the nature of their active sites is needed to control their properties. To address these critical issues a combination of theory, computational studies, and sophisticated characterization technique will be essential for obtaining best-performing materials. Moreover, innovation and developments in new materials are needed as well as innovative PEC cell designs.

## PEC Devices Overview

The PEC research over the past years allowed to develop innovative material systems,



**Hydrogen Production from Photoelectrochemical Water Splitting, Fig. 7** (a) Volcano plot of the overpotential of OER on various oxide surfaces vs. the free energy cost of the rate-limiting step (Adapted from Ref.

[35]); (b) volcano plot of the exchange current density for the HER for several native metals as a function of the metal-hydrogen bond strength (Adapted from Ref. [121])

functionalized interfaces, and devices aiming at stable 10% solar-to-hydrogen efficiency, the target that will make this technology to move to the industrialization level [20]. Furthermore, it is also important to split water without any external bias supply.

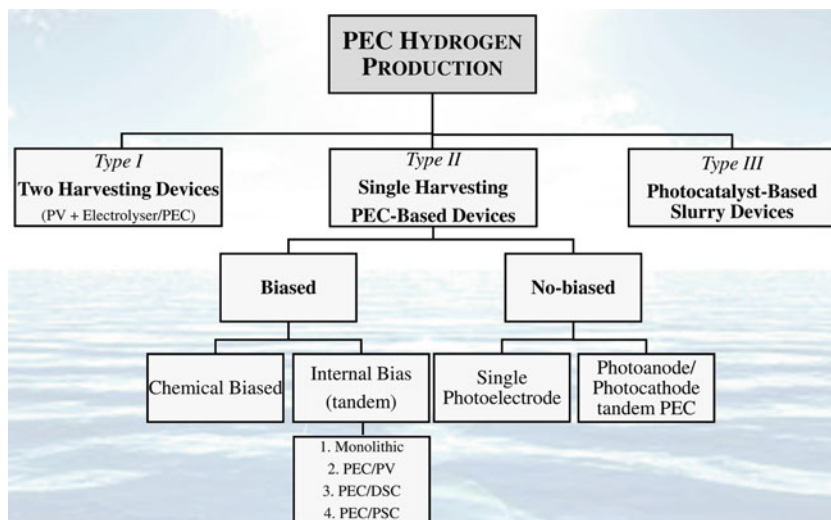
Figure 8 summarizes the configurations of PEC devices for solar hydrogen production: (i) two harvesting devices combining PV cells coupled to an electrolyzer system or to a PEC cell (Type I); (ii) single harvesting PEC-based devices with at least one semiconductor-liquid junction (Type II); and (iii) photocatalyst-based slurry devices (Type III). Type III consists of photoactive semiconductor particles (photocatalysts) free-floating as slurry in a solution bed [122]. This configuration still presents many drawbacks for solar water splitting and so it will not be considered in this entry.

The success of PEC hydrogen production depends on the balance between device performance (STH efficiency and stability), complexity, and cost; the simpler the device, the better. Single-junction photoelectrode systems offer the greatest simplicity but their energy efficiencies are generally low. On the other hand, tandem PEC devices are more complex but also more efficient, emerging as the best approach for solar water splitting

[123]. Table 3 presents the advantages and disadvantages of these PEC configurations.

### Type I: Two Harvesting Devices

Type I combines two physically separated devices to directly drive electrolysis; the only coupling between the PV and electrolysis components is electrical. This configuration prevents the degradation of PV by the water. The most developed approaches are based on a PV cell integrated with an electrolyzer system (PV + electrolyzer). The most significant energy efficiency loss in a PV + electrolysis arrangement arises from the high overpotentials for driving the water oxidations and reduction reactions, summing up to >0.5 V [17]. This represents more than 29% of the voltage needed for the water electrolysis. The PV cells usually generate photovoltages over 2 V, converting sunlight to electricity, whereas the electrolysis unit converts electricity to hydrogen at efficiencies near 65% [122]. The typical photovoltaic cell types are monocrystalline silicon (c-Si) and polycrystalline silicon (p-Si) and thin-film technologies, namely amorphous silicon (a-Si), cadmium telluride (CdTe), copper indium gallium diselenide (CIGS) [124], dye sensitized solar cells (DSC) [125], and perovskite solar cells (PSC) [9]. The viability of this type of approaches



**Hydrogen Production from Photoelectrochemical Water Splitting, Fig. 8** Photoelectrochemical device configurations for solar hydrogen production

**Hydrogen Production from Photoelectrochemical Water Splitting, Table 3** Advantages and disadvantages of the PEC configurations for  $H_2$  production

Device configurations	Advantages	Disadvantages
<i>Type I</i> Two harvesting devices $\eta_{STH, \max} > 20\%$	Nontransparent substrates can be used More efficient utilization of the solar spectrum No stability issues (PV contact with electrolyte solution is avoided)	Twice the collector area for the devices Need to balance the current flow of both devices Auxiliary system losses (e.g., collection of current from PV cell and transmission of electrons through external wiring) Add complexity and cost for large-scale deployment
<i>Type II</i> Single photoelectrode $\eta_{STH, \max} < 5\%$	Only one substrate and one photoanode or photocathode is needed Cheap nontransparent substrate can be used	Poor utilization of the solar spectrum since large bandgap ( $E_g > 1.7$ eV) is needed
<i>Type II</i> Tandem photoelectrodes $\eta_{STH, \max} < 30\%$	Needs only one substrate More efficient utilization of the solar spectrum Use of two smaller bandgap materials Enhanced photovoltages (the photovoltages of each cell are additive)	Need to identify suitable photoanode and photocathode or use a photoelectrode and PV solar cell Need a transparent conducting substrate Need adequate transmittance from front electrode Photocurrent limited by the component generating the smallest current value Optical coupling effects between cells (minimize reflection at front surface) Adds complexity

is limited by the cost of both devices; using commercially available PV and electrolyzer technologies, the hydrogen production cost would be greater than  $\$10 \cdot \text{kg}^{-1}$ , far exceeding the US DOE targets of  $\$2$ – $\$4 \cdot \text{kg}^{-1}$  [122]. Table 4 shows

the STH efficiencies of relevant PV + electrolyzer approaches.

Alternatively, the PV cell can be connected in series with a PEC cell based on a SCLJ, instead of an electrolyzer, resulting in a cheaper but not

necessarily more efficient arrangement [20]. Figure 9 shows a nontandem configuration consisting of a photoanode PEC cell coupled to a PV cell; the majority carriers generated in the PV cell reduce water on the metal cathode and the minority holes generated in the photoanode oxidize water at its surface [20].

Recently, a highly efficient and low-cost cell using a double-junction perovskite PSC cell wired to bifunction earth-abundant NiFe layered double hydroxide catalyst submerged in a NaOH electrolyte solution was reported by Grätzel’s group [126]. The device can provide sufficient potential to drive water photolysis showing a STH efficiency of ca. 12.3% with stable current of 10 mA·cm<sup>-2</sup>. Alternate multiple-bandgap PSCs

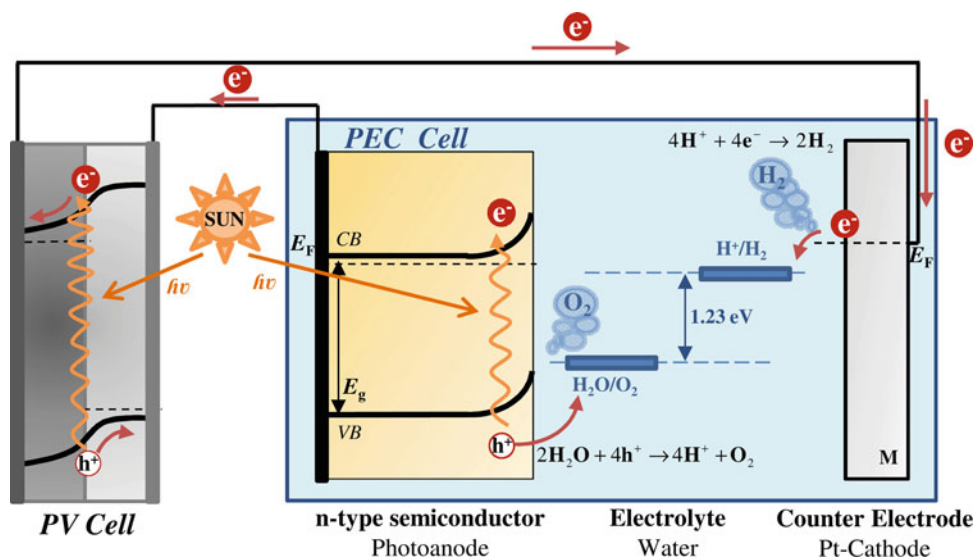
photoelectrodes have been calculated to reach more than 30% solar conversion efficiency, corresponding to  $\eta_{STH}$  of ca. 20% in such devices [127]. In the PV + PEC configuration the available solar exposure area must be substantially larger since both PV and PEC cells have to be directly illuminated [124]. To avoid these drawbacks, a more effective approach would incorporate PV cell and PEC photoelectrode into a single harvesting device, as described in the following section.

**Type II: Single Harvesting PEC-Based Devices**

Single harvesting PEC-based devices have been investigated as a promising alternative for large-scale solar hydrogen production. Type II devices are then divided into biased and nonbiased systems – Fig. 8. Concerning biased systems, the cells operate under illumination in combination with an appropriate bias source to directly promote hydrogen generation; there are chemically biased photo-assisted photoelectrolysis cells and internal biasing devices [16, 20]. Nonbiased devices are based on single photoelectrodes or two photoelectrodes (photoanode and photocathode) in a tandem arrangement.

**Hydrogen Production from Photoelectrochemical Water Splitting, Table 4** Examples of two harvesting devices; photovoltaic efficiency ( $\eta_{PV}$ ) and solar-to-hydrogen efficiency ( $\eta_{STH}$ ), with an electrolyzer efficiency of 65% (extracted from Ref. [124])

PV+ Electrolyzer	$\eta_{PV}/\%$	$\eta_{STH}/\%$
a-Si multijunction	12.1	7.8
III-V multijunction	32	20.8
c-Si modules	13.5	8.8
DSC	8.2	5.3



**Hydrogen Production from Photoelectrochemical Water Splitting, Fig. 9** PV solar cell connected in series with a PEC device (nontandem arrangement)

Biased Devices

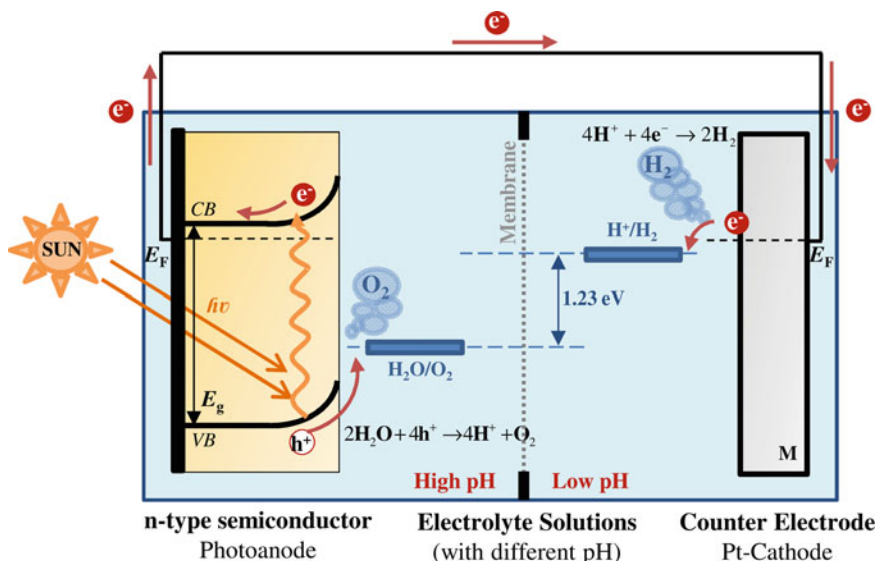
1. Chemically Biased

A chemical bias is achieved using acidic and alkaline environments, placed in two half-cells separated by an ion exchange membrane – Fig. 10. The electrolyte solutions are chosen to reduce the potential required to induce the chemical splitting. The photocurrent flowing between the electrodes lead to the consumption of ion species at the anodic and cathodic cell compartments, resulting in the electrolyte neutralization and the potential bias reduction. Therefore, this configuration is not self-sufficient, relying not only on sunlight but also on additional input of chemicals to maintain the pH gradient [20]. This

approach is then unattractive for practical applications. Table 5 shows two examples of chemically biased PEC cells.

2. Internally Biased

An internal bias with an appropriate match of current and potential will directly increase the STH conversion efficiency, since the PEC system and the PV element with different absorption spectra can address a broader fraction of the solar spectrum [20]. In this configuration, at least one of the substructures must work as a bias source; the total bandgap should be large enough for unassisted water splitting. These systems, also called tandem devices, are normally characterized



Hydrogen Production from Photoelectrochemical Water Splitting, Fig. 10 PEC cell with chemical biasing

Hydrogen Production from Photoelectrochemical Water Splitting, Table 5 Examples of chemically biased PEC cells, device conditions, and correspondent

performance: photocurrent-density ( $J$ ), STH conversion efficiency ( $\eta_{STH}$ ), and stability

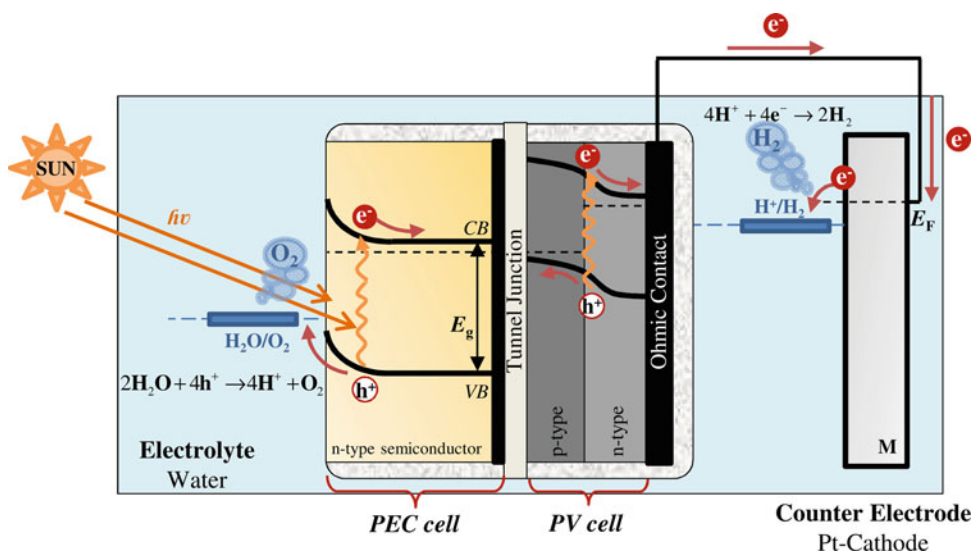
Device configurations	Electrolyte and illumination conditions	Performance	Stability	Ref./date
TiO <sub>2</sub> photoanode Pt cathode	1 M HCl 1 M KOH	Chemical bias = 0.84 V	Not reported	[2]/1972
TiO <sub>2</sub> photoanode Cu-Ti-O photocathode	1 M KOH 0.1 M Na <sub>2</sub> HPO <sub>4</sub> 100 mW·cm <sup>-2</sup>	Chemical bias = 0.40 V $J = 0.25 \text{ mA}\cdot\text{cm}^{-2}$ ; $\eta_{STH} = 0.30\%$	Photocathode corrosion after 4 h	[128]/2008

by layered stacked or hybrid structures involving several different semiconductor films placed on top of each other. Figure 11 shows a top PEC cell stacked to a PV cell in a two-junction (2 J) tandem arrangement; the back contact of the PEC cell and the front contact of the PV cell are connected by a tunnel junction and the back contact of the PV cell is directly connected to the counter electrode. This approach eliminates the electron transmission through wires, reducing ohmic losses, but the process compatibility in fabricating the PEC cell directly onto the PV cell affects device quality and efficiency.

For tandem arrangements connected in series, the overall voltage is given by the sum of the voltages of the individual cells, whereas the total photocurrent is bound by the photocurrent limits of the highest bandgap material. Thus, in order to benefit from this construction, the gain in voltage must be larger than the loss in current. Further optimization is achieved if a large bandgap material (LBG) is layered in front of a small bandgap material (SBG) [129]. Layering the photo-absorbers in this manner allows the short wavelength, greater energy photons, to be absorbed in the LBG and the long ones to be absorbed in the SBG. The top cell has to be semitransparent to enable light transmission to the back

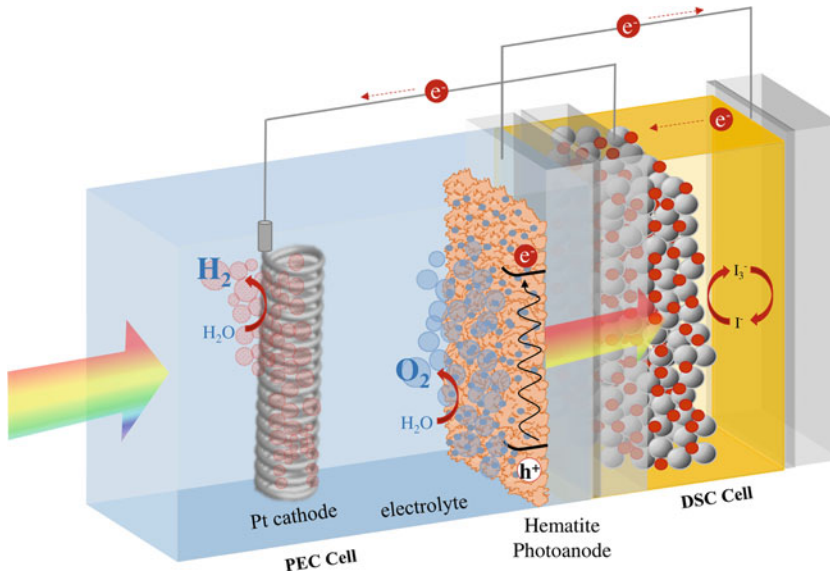
photoelectrode, i.e., a transparent conducting oxide (TCO) substrate must be used. However, if the two junctions are stacked onto the same substrate as a single monolithic structure, no transparent substrate is needed [122]. On the other hand, tandem cells must be carefully optimized based on power and light management of the individual cells, as well as the coupling between them. A detailed viewpoint aiming at these strategies to boost the efficiency of PEC/PV tandem cells by minimizing the coupling loss was recently reported by Rothschild and Dotan [17].

The internally biased tandem structures can then be divided into: (i) stacked monolithic devices (Fig. 11); (ii) PEC/PV tandem systems where the photoelectrode layer is semitransparent, e.g., PEC/DSC (Fig. 12) and PEC/PSC (Fig. 13) devices; and (iii) PEC/PV tandem systems where the PV layer is semitransparent. A further extension of the PV/PEC device is based on the use of a triple-junction (3 J) hybrid system (a PEC top cell and a double-junction PV cell) due to low photovoltages generated by the conventional PV materials (e.g., c-Si, p-Si, CIGS). This configuration develops higher photovoltages, but the photocurrent is limited by the component generating the smallest photocurrent value [122].

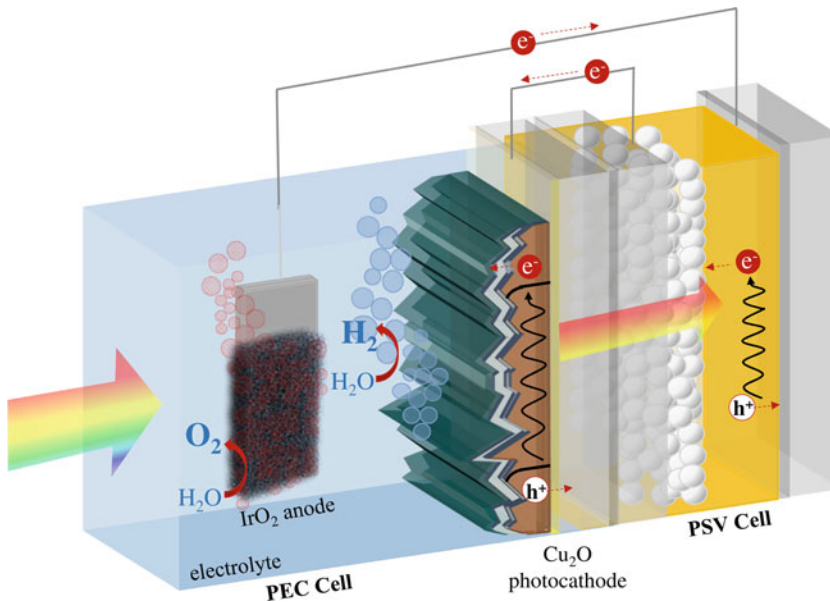


**Hydrogen Production from Photoelectrochemical Water Splitting, Fig. 11** PEC/PV monolithic system using a two-junction hybrid tandem device





**Hydrogen Production from Photoelectrochemical Water Splitting, Fig. 12** PEC/DSC tandem system using a semitransparent hematite photoanode as PEC element and a DSC cell in series for overall water splitting



**Hydrogen Production from Photoelectrochemical Water Splitting, Fig. 13** PEC/PSC tandem system using a semitransparent  $\text{Cu}_2\text{O}$  photocathode as PEC

element and PSC cells in series for overall water splitting (Adapted from Ref. [106])

The best performing PEC/PV tandem system consists of a two-junction monolithic hybrid device: a p-type  $\text{GaInP}_2$  ( $E_g = 1.8$  eV) PEC electrode interconnected by a tunnel junction to a

$\text{GaAs}$  ( $E_g = 1.4$  eV) PV cell grown on a  $\text{GaAs}$  wafer substrate [96]. Sunlight enters through the top  $\text{GaInP}_2$  photocathode and is then filtered down to the  $\text{GaAs}$  PV solar cell. While this system

performs a champion  $\eta_{\text{STH}} = 12.4\%$  under concentrated 11-sun illumination, and in 3 M  $\text{H}_2\text{SO}_4$  electrolyte, the high cost III-V materials and the corrosion of the  $\text{GaInP}_2$  limit its practical use. Therefore, finding semiconductor materials able to form stable junctions has been a major challenge in the field of PEC water splitting; stable metal oxides, e.g.,  $\text{WO}_3$ ,  $\text{Fe}_2\text{O}_3$ , and  $\text{BiVO}_4$ , are a promising option.

Grätzel and coworkers [130] proposed for the first time the use of a semitransparent dye-sensitized solar cell (DSC), instead of the conventional PV solar cell, in a dual-absorber tandem configuration – see Fig. 12. The DSC cell is made of a cheap semiconductor material of  $\text{TiO}_2$ , reducing the final costs [125]. In this system, the semitransparent photoanode PEC cell (e.g., thin films of  $\text{WO}_3$  [131] or  $\text{Fe}_2\text{O}_3$  [132]) absorbs the blue part of the solar spectrum to generate  $\text{O}_2$  from water, whereas the DSC cell captures the green and red lights to generate the external bias needed for  $\text{H}_2$  production at the counter electrode. The successful demonstration of the PEC/DSC tandem device is, therefore, restricted to the use of two DSCs connected in series due to the additional energy required to overcome nonidealities of the photoanodes in the OER [125].

Recently, promising hybrid organic–inorganic lead halide perovskites ( $\text{CH}_3\text{NH}_3\text{PbI}_3$ ) have emerged as exceptional materials for the next-generation photovoltaic technologies [9, 133]. In a few short years of development, perovskite solar cell (PSC) efficiencies have already surpassed the mature DSC solar cells and organic photovoltaics [134, 135]. The lead iodide hybrid perovskites have a low bandgap and large absorption coefficient that facilitate light harvesting into the near-IR region of the solar spectrum. Moreover, PSCs exhibit extremely high photopotential in comparison to nearly all other single-junction PV technologies, fostering the exploration of this material in tandem water splitting architectures. Therefore, the design of low-cost tandem assemblies employing single-junction hybrid perovskite materials establishes a potentially promising new frontier for solar water splitting research. The tunability of the halide perovskite family

(1.1–2.3 eV) may enable the design of a PEC/PSC tandem devices in which a LBG PSC is used to drive SBG photoelectrodes PEC [127]. With the development of sufficient electrode stabilization strategies, tandem systems employing hermetic glass sealed PSC cells [136] with Si photoelectrodes may yield  $\eta_{\text{STH}} > 20\%$  in the near future. Figure 13 shows a PEC/PSC tandem arrangement, where a semitransparent  $\text{Cu}_2\text{O}$  photocathode is used as the PEC element.

Table 6 summarizes relevant experimental reports of internally biased tandem devices for direct solar water splitting, including the performance and device configuration; Fig. 14 depicts the configurations considered.

### Nonbiased Devices

Photoelectrochemical devices with no additional bias represent a prospective pathway to overcome the complexity of biased systems. Nonbiased devices comprise two types of PEC systems: (i) single photoelectrode system, which can be divided into a typical PEC cell (equipped with a large bandgap photoelectrode and a counter electrode); and (ii) a photoanode/photocathode PEC tandem cell.

#### 1. Single Photoelectrode System

The ideal PEC system for solar hydrogen production should aim at the use of a single-junction photoelectrode without any bias, as shown in Figs. 3 and 4 respectively for n-type and p-type semiconductor materials. Up to now, only materials with a very large bandgap, such as  $\text{SrTiO}_3$  [45] and  $\text{KTaO}_4$  [150], have demonstrated direct water splitting; however, they exhibit STH efficiencies below 1% [13]. Therefore, improvements on semiconductor fundamental electronic structure and stability are needed for the viability of this approach.

#### 2. Photoanode/Photocathode PEC Tandem System

The most direct and simple way to construct a dual photosystem for PEC water splitting is using an n-type semiconductor (photoanode)

**Hydrogen Production from Photoelectrochemical Water Splitting, Table 6** Internally biased tandem devices for direct solar water splitting, including experimental conditions and corresponding performance (STH

conversion efficiency –  $\eta_{\text{STH}}$ , and stability); grouped by type of arrangement and ordered by reverse chronological publication

Device configurations	Electrolyte and illumination	$\eta_{\text{STH}}/\%$	Stability, notes	Ref./ date
<b>Monolithic PV (2 J)</b> Top PV: GaInP with AlInP/PO <sub>x</sub> layers Bottom PV: GaInAs coated with RuO <sub>2</sub> OER co-catalyst	1 M HClO <sub>4</sub> 100 mW·cm <sup>-2</sup>	14%	40 h with > 50% drop in current	[137]/2015
<b>Monolithic PV (2 J)</b> Top PV: GaInP <sub>2</sub> Bottom PV: GaAs coated with Pt OER co-catalyst; wired Pt HER co-catalyst	2 M KOH 100 mW·cm <sup>-2</sup>	18.3%	9 h stable current in outdoor test	[138]/2001
<b>Monolithic PV (3 J)</b> PV: 3 × [CuIn <sub>x</sub> Ga <sub>1-x</sub> Se (CIGS)] wired side by side; wired Pt HER and OER co-catalysts	3 M H <sub>2</sub> SO <sub>4</sub> 100 mW·cm <sup>-2</sup>	10%	27 h stable H <sub>2</sub> production	[5]/2013
<b>Monolithic PV (3 J)</b> PV: 3 × (a-Si) Coated with FTO OER co-catalyst; wired Pt or Ni HER co-catalyst	5 M KOH 100 mW·cm <sup>-2</sup>	6.2%	31 days stable current	[139]/2006
<b>Monolithic PEC/PV (2 J)</b> Top PEC – dual photoelectrode: Fe <sub>2</sub> O <sub>3</sub> /TiO <sub>2</sub> -treated and BiVO <sub>4</sub> coated with Ni <sub>2</sub> FeO <sub>x</sub> /Co-Pi and FeOOH/NiOOH OER co-catalysts, respectively Bottom PV: c-Si; wired Pt HER co-catalyst	1.0 M KCl (pH ≈ 9.2) 100 mW·cm <sup>-2</sup>	7.7%	8 h stable current; 2 h measurement of O <sub>2</sub> and H <sub>2</sub>	[140]/2016
<b>Monolithic PEC/PV (2 J)</b> Top PEC: Fe <sub>2</sub> O <sub>3</sub> core-shell NW coated with Au OER co-catalyst Bottom PV: c-Si; wired Pt HER co-catalyst	1 M Na <sub>3</sub> PO <sub>4</sub> 60 mW·cm <sup>-2</sup>	6.0%	40 min measurement of O <sub>2</sub>	[141]/2014
<b>Monolithic PEC/PV (2 J)</b> Top PEC: TiO <sub>2</sub> core-shell NW Coated with IrO <sub>x</sub> OER co-catalyst Bottom PV: c-Si coated Pt HER co-catalyst	1 M H <sub>2</sub> SO <sub>4</sub> 1080 mW·cm <sup>-2</sup> (ca. 11-sun)	0.12%	4.5 h measurement of O <sub>2</sub> and H <sub>2</sub>	[142]/2014
<b>Monolithic PEC/PV (2 J)</b> Top PEC: GaInP <sub>2</sub> Bottom PV: GaAs coated with Pt HER co-catalyst; wired Pt OER co-catalyst	3 M H <sub>2</sub> SO <sub>4</sub> 11-sun	12.4%	20 h with 20% drop in current	[96]/1998
<b>Monolithic PEC/PV (3 J)</b> Top PEC: WO <sub>3</sub> /BiVO <sub>4</sub> coated with Co-Pi OER co-catalyst Bottom PV: GaAs/InGaAsP; wired Pt HER co-catalyst	KPi buffer (pH 7) 100 mW·cm <sup>-2</sup>	8.1%	60 min measurement of O <sub>2</sub> and H <sub>2</sub>	[143]/2016
<b>Monolithic PEC/PV (3 J)</b> Top PEC: BiVO <sub>4</sub> coated with Co-Pi OER co-catalyst Medium PV: a-Si:H Bottom PV: c-Si:H; wired Pt HER co-catalyst	0.1 M KPI (pH 7) 100 mW·cm <sup>-2</sup>	5.2%	1 h with 5% drop in current	[83]/2014
<b>Monolithic PEC/PV (3 J)</b> Top PEC: WO <sub>3</sub> Bottom PV: 2 × (a-Si); wired Pt HER co-catalyst	0.3 M H <sub>3</sub> PO <sub>4</sub> 100 mW·cm <sup>-2</sup>	3%	Not reported	[144]/2010
<b>PEC/DSC tandem (2 J)</b> Top PEC: WO <sub>3</sub> /BiVO <sub>4</sub> coated with FeOOH/NiOOH OER co-catalyst, its back side is a hybrid cDBR consisting of alternating ITO layers on top of TiO <sub>2</sub> /SiO <sub>2</sub> stack Bottom: High- $V_{\text{oc}}$ DSC wired Pt cathode	Phosphate buffer (pH 6.9) 100 mW·cm <sup>-2</sup>	7.1%	10 h stable current 2 h stable H <sub>2</sub> production	[145]/2016

(continued)

**Hydrogen Production from Photoelectrochemical Water Splitting, Table 6** (continued)

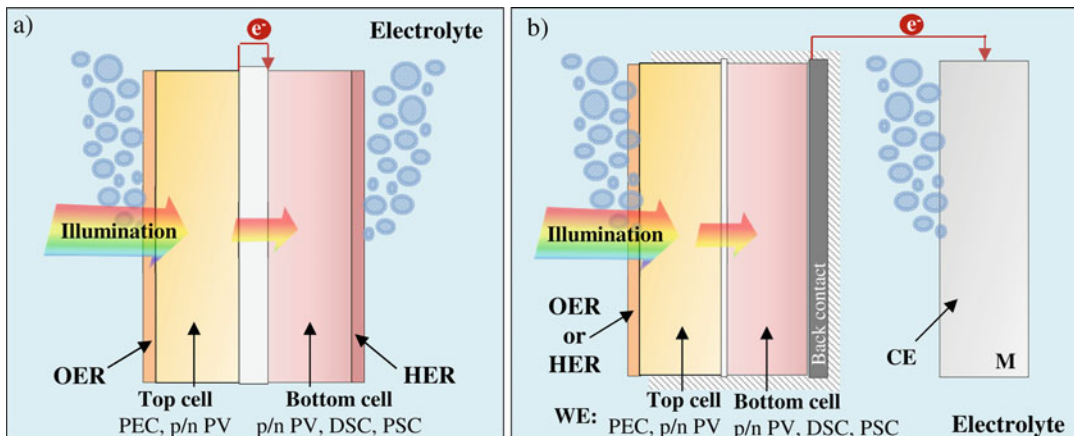
Device configurations	Electrolyte and illumination	$\eta_{\text{STH}}/\%$	Stability, notes	Ref./ date
<b>PEC/DSC tandem (2 J)</b> (1) Top PEC: WO <sub>3</sub> (2) Top PEC: Fe <sub>2</sub> O <sub>3</sub> coated with AlO <sub>3</sub> underlayer and Co OER co-catalyst; wired Pt HER catalyst Bottom: High- $V_{\text{oc}}$ DSC; wired Pt cathode	(1) 1 M HClO <sub>4</sub> (pH 0) (2) 1 M NaOH (pH 13.6) 100 mW·cm <sup>-2</sup>	(1) 3.1% (2) 1.2%	8 h with 30% current drop	[146]/ 2012
<b>PEC/DSC tandem (3 J)</b> Top PEC: Fe <sub>2</sub> O <sub>3</sub> with AlO <sub>3</sub> underlayer coated with Co OER co-catalyst Bottom: 2 × (DSC); wired Pt HER co-catalyst	1 M NaOH (pH 13.6) 100 mW·cm <sup>-2</sup>	1.4% 1.2%	Not reported	[70]/ 2010
<b>PEC/PSC tandem (2 J)</b> Top PEC: Fe <sub>2</sub> O <sub>3</sub> nanorods/SnO <sub>x</sub> -treated coated with Co-Pi OER co-catalyst Bottom PSC: MAPbI <sub>3</sub> ; wired Pt OER catalyst	1 M NaOH (pH 13.6) 100 mW·cm <sup>-2</sup>	3.4%	120 s stable current	[147]/ 2017
<b>PEC/PSC tandem (2 J)</b> Top PEC: BiVO <sub>4</sub> /WO <sub>3</sub> /SnO <sub>2</sub> coated with CoO <sub>x</sub> OER co-catalyst Bottom PSC: MAPbI <sub>3</sub> ; wired IrO <sub>2</sub> OER catalyst	Phosphate buffer (pH 7) 100 mW·cm <sup>-2</sup>	3.5%	120 min stable current; 1 h measurement of H <sub>2</sub>	[148]/ 2017
<b>PEC/PSC tandem (2 J)</b> Top PEC: Mo:BiVO <sub>4</sub> coated with NiOOH/FeOOH OER co-catalyst on SiO <sub>x</sub> /Pt/SnO <sub>2</sub> nanocone arrays Bottom PSC: MAPbI <sub>3</sub> ; wired Pt OER catalyst	0.5 M KH <sub>2</sub> PO <sub>4</sub> buffer (pH 7) 100 mW·cm <sup>-2</sup>	6.2%	10 h with 6% current drop	[91]/ 2016
<b>PEC/PSC tandem (2 J)</b> Top PSC: MAPbI <sub>3</sub> or MAPbBr <sub>3</sub> Bottom PEC: CuIn <sub>x</sub> Ga <sub>1-x</sub> Se <sub>2</sub> (CIGS) coated with Pt HER co-catalyst; wired DSA OER catalyst	0.5 M H <sub>2</sub> SO <sub>4</sub> (pH 0) 100 mW·cm <sup>-2</sup>	6%	180 s stable current	[149]/ 2015
<b>PEC/PSC tandem (2 J)</b> Top PEC: Cu <sub>2</sub> O coated Al:ZnO/TiO <sub>2</sub> overlayers and RuO <sub>x</sub> HER co-catalyst Bottom PSC: (FAPbI <sub>3</sub> ) <sub>1-x</sub> (MAPbBr <sub>3</sub> ) <sub>x</sub> ; wired IrO <sub>2</sub> OER catalyst	0.5 M Na <sub>2</sub> SO <sub>4</sub> 100 mW·cm <sup>-2</sup>	2.5%	2 h with 30% current drop	[106]/ 2015

electrically connected in series with an appropriate p-type semiconductor (photocathode) – Fig. 15.

For the PEC tandem arrangement, the materials should be carefully selected since the following requirements have to be fulfilled: the energy level of the photocathode conduction band ( $E_{\text{CB, PC}}$ ) has to be above the water reduction energy  $-E^\circ(\text{H}^+/\text{H}_2)$  – and the photoanode valence band energy ( $E_{\text{VB, PA}}$ ) has to be below the water oxidation energy  $-E^\circ(\text{H}_2\text{O}/\text{O}_2)$ . Moreover, the photocathode valence band energy level ( $E_{\text{VB, PC}}$ ) should be higher than  $E^\circ(\text{H}_2\text{O}/\text{O}_2)$ , whereas the photoanode conduction band energy level ( $E_{\text{CB, PA}}$ ) should be lower than  $E^\circ(\text{H}^+/\text{H}_2)$ . Briefly,  $E_{\text{CB, PC}} > E^\circ(\text{H}^+/\text{H}_2) > E_{\text{CB, PA}} > E_{\text{VB, PC}} > E^\circ(\text{H}_2\text{O}/\text{O}_2) > E_{\text{VB, PA}}$ . Complete solar-to-hydrogen

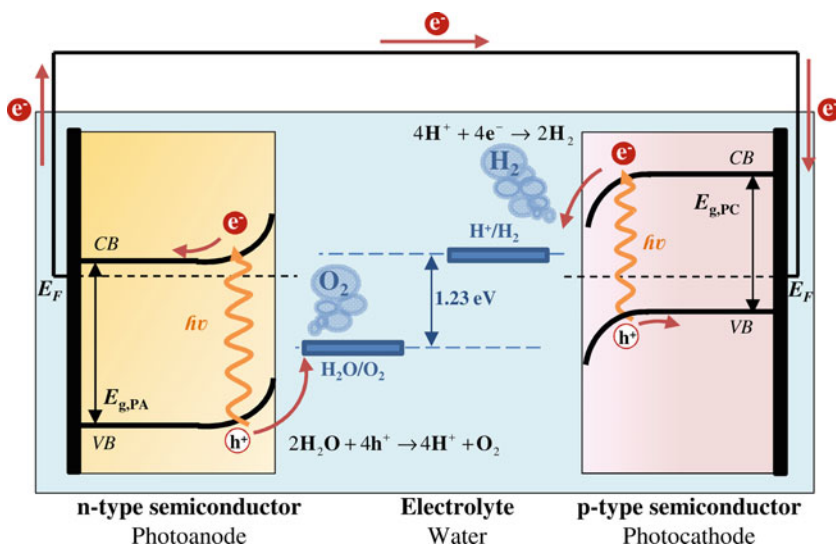
conversion can be achieved if the total photovoltage (given by the potential difference between the quasi-Fermi energy of the holes in the photoanode,  $E_{\text{QF, PA}}$ , and of the electrons in the photocathode,  $E_{\text{QF, PC}}$ ) developed by the PEC tandem cell is greater than the difference between the oxidation and reduction redox levels (1.23 V at room temperature) plus the kinetic overpotentials ( $\eta_{\text{OER}}$  and  $\eta_{\text{HER}}$ ) and any resistive losses that may occur at the system [35].

Only few works have considered this approach due to the lack of suitable photocathode materials for HER; the performance and the stability in aqueous solutions of these p-type materials (e.g., GaInP<sub>2</sub>, Si, SiC, WS<sub>2</sub>, Cu(In,Ga)Se<sub>2</sub>, Cu<sub>2</sub>O, CuYO<sub>2</sub>, CaFeO<sub>4</sub> and p-type Mg doped Fe<sub>2</sub>O<sub>3</sub>) are actually a limiting factor [16]. Relevant



**Hydrogen Production from Photoelectrochemical Water Splitting, Fig. 14** Configurations of internally biased tandem devices for overall water splitting: (a) the semiconductor elements are monolithically integrated (without wire connections); and (b) the light-absorbing elements are electrically wired, where the top element

(PEC or PV) with the larger bandgap has to be semitransparent to transmit the nonabsorbed sunlight spectrum to the bottom element (normally the PV cell). The photoelectrodes can be coated with co-catalysts, e.g., n-type PEC coated with an OER co-catalyst and p-type PEC coated with a HER co-catalyst



**Hydrogen Production from Photoelectrochemical Water Splitting, Fig. 15** Photoanode/photocathode PEC tandem cell, in which a LBG photoanode absorbs

the high-energy portion of the incoming solar irradiation and transmits the remainder to the photocathode

works on photoanode (PA)/photocathode (PC) PEC tandem devices are presented in Table 7. In general, the photocurrent densities in PEC tandem devices using earth-abundant and stable photoelectrodes are about two orders of magnitude smaller than those in commercial

PEC + electrolyzer systems, i.e.,  $1\text{--}2\text{ mA}\cdot\text{cm}^{-2}$  vs.  $10\text{--}20\text{ mA}\cdot\text{cm}^{-2}$  [35]. However, theoretical studies by Bolton [151] suggested that maximum STH efficiencies  $>20\%$  are feasible using semiconductors with bandgaps of ca. 1.7 eV and 1.2 eV for the top and bottom absorber, respectively.

**Hydrogen Production from Photoelectrochemical Water Splitting, Table 7** Photoanode/photocathode PEC tandem devices for direct solar water splitting,including experimental conditions and corresponding performance (STH conversion efficiency –  $\eta_{\text{STH}}$ , and stability); ordered by reverse chronological publication

Device configurations	Electrolyte and illumination	$\eta_{\text{STH}}/\%$	Stability, notes	Ref./ date
<b>PA/PC PEC (2J tandem)</b> Top PEC: Mo-doped BiVO <sub>4</sub> coated with Co-Pi OER co-catalyst Bottom PEC: p-Si decorated with Pt HER co-catalyst	0.1 M KPi (pH 5) 100 mW·cm <sup>-2</sup>	0.57%	3.5 h with 25% drop in current	[152]/ 2016
<b>PA/PC PEC (2J tandem)</b> Top PEC: Mo-doped BiVO <sub>4</sub> coated with NiOOH/FeOOH OER co-catalyst Bottom PEC: CuGa <sub>3</sub> Se <sub>5</sub> /(Ag,Cu)GaSe <sub>2</sub> with CdS overlayer and coated with Pt HER co-catalyst	0.1 M KPi buffer (pH 7) 100 mW·cm <sup>-2</sup>	0.91%	2 h stable current	[153]/ 2015
<b>PA/PC PEC (2J tandem)</b> Top PEC: Fe <sub>2</sub> O <sub>3</sub> coated with NiFe <sub>x</sub> OER co-catalyst Bottom PEC: a-Si with TiO <sub>2</sub> overlayer and coated with Pt HER co-catalyst	Phosphate buffer (pH 11.8) 100 mW·cm <sup>-2</sup>	0.67%	10 h stable current	[76]/ 2015
<b>PA/PC PEC (2J tandem)</b> Top PEC: Fe <sub>2</sub> O <sub>3</sub> coated with IrO <sub>x</sub> OER co-catalyst Bottom PC: a-Si (PV) with TiO <sub>2</sub> /Pt overlayers HER	0.1 M KNO <sub>3</sub> (pH 1.01) 100 mW·cm <sup>-2</sup>	0.44%	5 h with 5% drop in current	[154]/ 2015
<b>PA/PC PEC (2J tandem)</b> Top PEC: BiVO <sub>4</sub> coated with CoPi OER co-catalyst Bottom PEC: Cu <sub>2</sub> O coated with RuO <sub>x</sub> HER co-catalyst	K <sub>3-x</sub> H <sub>x</sub> PO <sub>4</sub> buffer (pH 6) 100 mW·cm <sup>-2</sup>	0.5%	2 min with 20% drop in current	[155]/ 2014
<b>PA/PC PEC (2J tandem)</b> Top PEC: WO <sub>3</sub> coated with NiO <sub>x</sub> OER co-catalyst Bottom PEC: Cu <sub>2</sub> O	0.1 M Na <sub>2</sub> SO <sub>4</sub> (pH 6) 100 mW·cm <sup>-2</sup>	0.04%	Not reported	[156]/ 2012
<b>PA/PC PEC (2J tandem)</b> Top PEC: TiO <sub>2</sub> Bottom PEC: CaFe <sub>2</sub> O <sub>4</sub>	0.1 M NaOH 100 mW·cm <sup>-2</sup>	<0.01%	Not reported	[157]/ 2011
<b>PA/PC PEC (2J tandem)</b> Top PEC: Fe <sub>2</sub> O <sub>3</sub> Bottom PEC: Zn-doped Fe <sub>2</sub> O <sub>3</sub>	0.1 M H <sub>2</sub> SO <sub>4</sub> 100 mW·cm <sup>-2</sup>	0.11%	Not reported	[158]/ 2006
<b>PA/PC PEC (2J tandem)</b> Top PEC: GaAs coated with MnO OER co-catalyst Bottom PEC: InP coated Pt HER co-catalyst	6 M KOH	8.2%	10 h with 10% drop in current	[159]/ 1987
<b>PA/PC PEC (2J tandem)</b> Top PEC: Si-doped Fe <sub>2</sub> O <sub>3</sub> Bottom PEC: SiC	0.01 M NaOH 100 mW·cm <sup>-2</sup>	5 × 10 <sup>-4</sup> %	320 h stable current	[160]/ 1984
<b>PA/PC PEC (2J tandem)</b> Top PEC: Fe <sub>2</sub> O <sub>3</sub> coated with RuO <sub>2</sub> OER co-catalyst Bottom PEC: GaP coated with Pt HER co-catalyst	1 M Na <sub>2</sub> SO <sub>4</sub> fritted compartments sunlight	0.02–0.1%	Not reported	[161]/ 1981
<b>PA/PC PEC (2J tandem)</b> Top PEC: SrTiO <sub>3</sub> Bottom PEC: GaP	1 M NaOH 100 mW·cm <sup>-2</sup>	10.7%	6 h measurement of H <sub>2</sub>	[162]/ 1977
<b>PA/PC PEC (2J tandem)</b> Top PEC: TiO <sub>2</sub> Bottom PEC: GaP	0.2 M H <sub>2</sub> SO <sub>4</sub> 85 mW·cm <sup>-2</sup>	0.3%	Not reported GaP photocorrosion	[163]/ 1976

## Efficiency

The energy conversion efficiency is one of the key performance indicators of the PEC cell. The four

fundamental processes involved in solar water splitting are: light harvesting (ratio of the electron-hole pairs created to the amount of incident photons), separation of the photogenerated electrons and



holes, transport of photoinjected electric charges, and transfer of charge carrier at the electrolyte interface. These photogenerated electrons and holes are then separated by two possible transport mechanisms such as drift and diffusion. Drift is the motion of these charged particles in response to the electric field inside the semiconductor, while diffusion is associated with a gradient in the local concentration of the charged particles. Therefore, the external quantum efficiency of the PEC water splitting reaction, EQE (also called solar-to-hydrogen efficiency,  $\eta_{\text{STH}}$ ), can be defined as [164]:

$$\text{EQE}(\lambda) = \eta_{\text{light}}(\lambda) \times \eta_{\text{ct}}(\lambda) \times \eta_{\text{cat}} \quad (12)$$

where  $\lambda$  is the wavelength,  $\eta_{\text{light}}$  is the light absorption efficiency (ratio of the electron-hole pairs created to the amount of incident photons),  $\eta_{\text{ct}}$  is the charge separation/transport efficiency (ratio between the amount of electrons and holes reaching the interfaces to the photogenerated electron-hole pairs), and  $\eta_{\text{cat}}$  is the quantum efficiency of the catalytic charge transfer to the redox species in the electrolyte.

An alternative definition for the STH efficiency is based on the ratio of the chemical energy produced by the solar energy input, as described in Eq. 13 [8]. The chemical energy produced is the rate of hydrogen production ( $\phi_{\text{H}_2}$ , in  $\text{mmol H}_2 \cdot \text{s}^{-1}$ ) multiplied by the change in Gibbs free energy per mol of  $\text{H}_2$  ( $\Delta G^\circ = 237 \text{ kJ} \cdot \text{mol}^{-1}$ ).

$$\eta_{\text{STH}} = \frac{\phi_{\text{H}_2} \times \Delta G^\circ}{P_{\text{light}} \times A} \quad (13)$$

The solar energy input is the incident illumination power density,  $P_{\text{light}}$ , and  $A$  is the illuminated area. This equation involves the measurement of the  $\text{H}_2$  production rate, which may be difficult when very small devices are used. However, assuming a Faradaic efficiency of 100%, the STH efficiency can be determined simply from:

$$\eta_{\text{STH}} = \frac{E_{\text{redox}} \times J_{\text{photo}}}{P_{\text{light}}} \Bigg|_{\text{AM 1.5 G}} \quad (14)$$

where  $J_{\text{photo}}$  is the photocurrent density responsible for  $\text{H}_2$  generation ( $\text{mA} \cdot \text{cm}^{-2}$ ) obtained from the photocurrent-voltage ( $J$ - $V$ ) characteristics;  $E_{\text{redox}}$  is the potential corresponding to the Gibbs energy and corresponds to the thermodynamic potential needed to drive the water electrolysis,  $\Delta E^\circ = \Delta G^\circ / nF = -1.23 \text{ V}$  ( $n$  is the number of moles of electrons used to produce one mole of  $\text{H}_2$  – in this case  $n = 2$ ). Assuming 1-sun AM 1.5 G incident sunlight ( $P_{\text{light}} = 100 \text{ mW} \cdot \text{cm}^{-2}$ ) under zero bias conditions, which means that no external potential is applied between the working and the counter electrodes, Eq. 14 can be related directly to the photocurrent density of a PEC cell [13]:

$$\eta_{\text{STH}}|_{\text{AM 1.5 G}} (\%) = 1.23 \times J_{\text{photo}} \quad (15)$$

It is then clear that the PEC photocurrent density is the main determining factor for STH efficiency. When an external potential bias is applied to the PEC system, a new efficiency is defined, named as “applied bias photon-to-current efficiency” (APCE) [165]:

$$\begin{aligned} \eta_{\text{APCE}} &= \frac{P_{\text{electrical}}^{\text{out}} - P_{\text{electrical}}^{\text{in}}}{P_{\text{light}}} \\ &= \frac{(E_{\text{redox}} - E_{\text{bias}}) \times J_{\text{photo}}}{P_{\text{light}}} \end{aligned} \quad (16)$$

where  $P_{\text{electrical}}^{\text{out}}$  is the electric power output,  $P_{\text{electrical}}^{\text{in}}$  is the electric power input, and  $E_{\text{bias}}$  is the potential applied to the system to obtain the  $J_{\text{photo}}$ .  $\eta_{\text{APCE}}$  is the IUPAC suggested definition of the solar-conversion efficiency of a cell that has a dark electrode and a semiconductor-based photoelectrode [166]; it measures the fraction of the energy stored in the chemical products that can be assigned to the photovoltage provided by the input solar illumination. This value can be negative, meaning that the electrical energy input is in excess of the free energy stored in the products. To separately assess the properties of individual photoelectrodes, a three-electrode configuration should be employed. This configuration is advantageous because when a reference electrode is present, the potential of the working photoelectrode can be

accurately determined, which provides an estimate of how much electrical energy is put into the electrode. This allows obtaining power conversion efficiency of photoelectrodes based on the half reaction of water splitting. The efficiency of a photoanode ( $\eta_{PA}$ ) should translate its ability to convert photonic energy into chemical energy used for oxidizing water [167]:

$$\eta_{PA} = \frac{(E_{O_2/H_2O}^{\circ} - E_{bias}) \times J_{photo}|_{MPP}}{P_{light}} \quad (17)$$

For a photocathode, the efficiency becomes as follows:

$$\eta_{PC} = \frac{(E_{bias} - E_{H^+/H_2}^{\circ}) \times J_{photo}|_{MPP}}{P_{light}} \quad (18)$$

where the  $J_{photo}$  is the photocurrent-density obtained at the maximum power point (MPP) and the  $E^{\circ}(O_2/H_2O)$  and  $E^{\circ}(H^+/H_2O)$  are the thermodynamic potential of water splitting half reactions [167]. These two equations are meaningful when no additional energy is supplied to the counter electrode for the other half reaction; therefore, they should be used mainly for comparing the performance of various photoelectrodes.

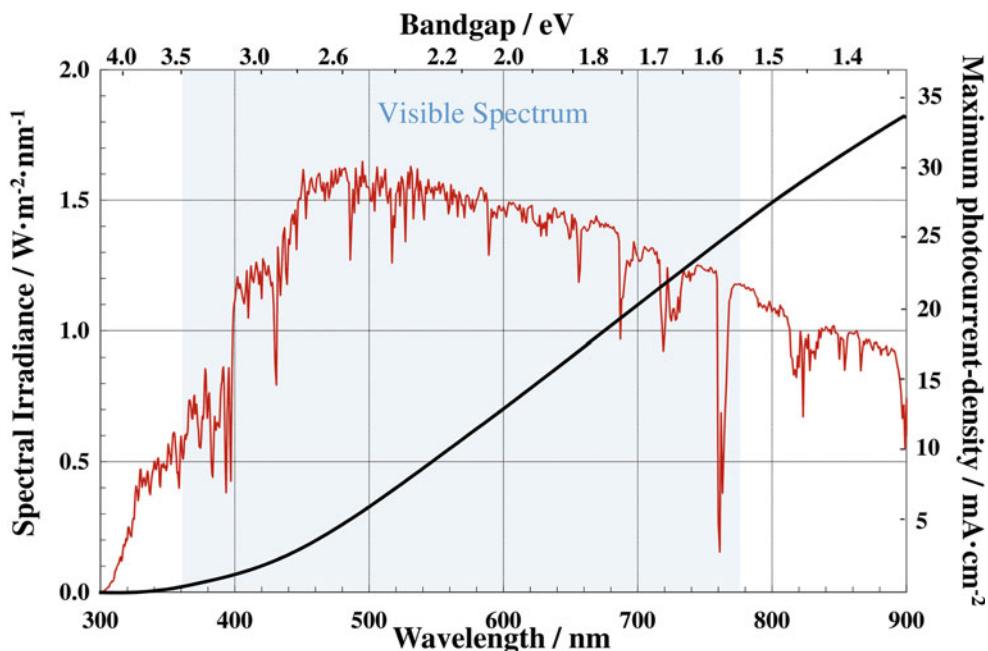
The parameter that determines the light harvesting ability of the photoelectrode is its bandgap  $E_g$ . Radiation of energy lower than  $E_g$  is not absorbed, while energy higher than the bandgap,  $E \geq E_g$ , is partly lost as heat by intraband thermalization processes [13]. Additional losses may occur as: (i) thermodynamic losses related to the water splitting process; and (ii) bulk and interfacial transport losses related to recombination, interfacial kinetics (overpotentials), and band bending in the semiconducting electrodes. Then, it is difficult to achieve high STH conversion efficiencies in a single-junction PEC photoelectrode system. Large bandgap semiconductors with adequate band edge positions would be needed to generate sufficient usable photopotential to drive the redox reactions for water splitting; this limits photon absorption and, therefore, reduces the photocurrent. Thus,

the bandgap tradeoff between photopotential and photocurrent is detrimental for single junctions.

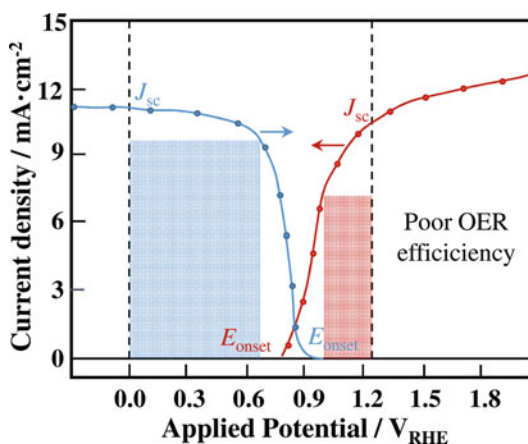
Taking this into account, for semiconductor materials exhibiting bandgaps greater than 3.2 eV, the photocurrent is limited to less than  $1 \text{ mA}\cdot\text{cm}^{-2}$ , which corresponds to a maximum STH efficiency of  $<1.23\%$ , according to Eq. 15. Under ideal conditions, i.e., including thermalization losses but with no overpotential losses, a bandgap of  $E_g = 1.6 \text{ eV}$  should be sufficient and the thermodynamic maximum efficiency of a device involving a single semiconductor photoelectrode is  $30.7\%$  – Eq. 15 [151]. Figure 16 plots the maximum attainable photocurrent densities and STH efficiencies as a function of the bandgap energy for standard AM 1.5 G illumination.

While a multijunction device (tandem arrangement) is more complicated, some recent calculations have shown that this approach has the potential to yield PEC water splitting efficiencies up to  $29\%$  [129]. The tandem strategy allows the use of two smaller bandgap materials, which in turn absorb a much larger fraction of the solar spectrum. Many researchers have investigated the optimal bandgaps for two-junction systems taking energy losses into account; the general conclusion is that the LBG should have a bandgap of  $1.7 \text{ eV}$  while the SBG's bandgap should be  $1.0 \text{ eV}$  [129].

In the case of PEC tandem devices for unassisted water splitting, the maximum thermodynamic photocurrent density and corresponding  $\eta_{STH}$  are predicted from the interception point of the  $J$ - $V$  characteristic curves of the photoanode and photocathode (when each photoelectrode is operating in a single PEC configuration), as shown in Fig. 17. It is, therefore, important to shift the two curves so that the operation point is close to the MPP of each individual  $J$ - $V$  curve. This means that the combined onset potential ( $E_{onset}$ ) values, i.e., the potential at which a photocurrent is first measured, or the sum of the photopotentials ( $E_{photo}$ ), should be greater than  $1.23 \text{ V}$ . For a photoanode  $E_{photo} = 1.23 \text{ V} - E_{onset}$ ; whereas  $E_{photo} = E_{onset}$  for the photocathode [167]. Currently, the practical STH efficiencies are much lower than the thermodynamic values, due to the mismatch of their  $J$ - $V$  curves.



**Hydrogen Production from Photoelectrochemical Water Splitting, Fig. 16** Spectral irradiance at AM 1.5 G and maximum thermodynamic photocurrent densities for a single system (Adapted from Ref. [13])



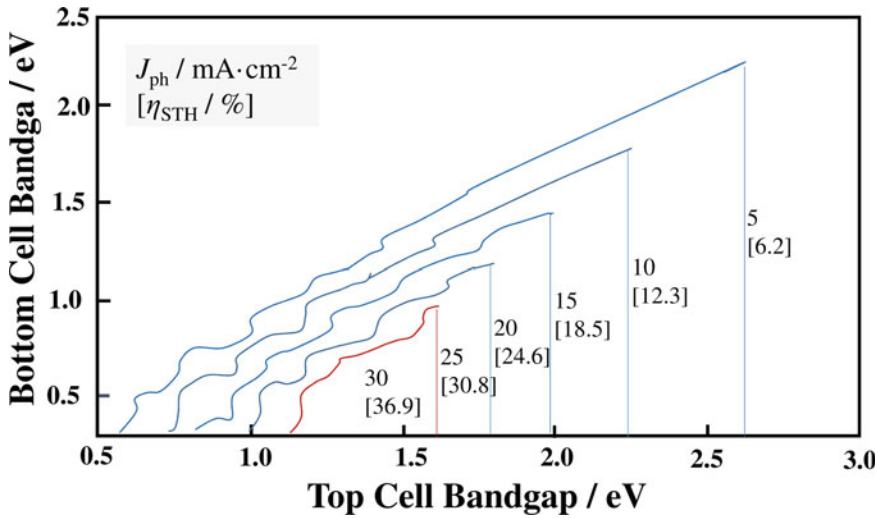
**Hydrogen Production from Photoelectrochemical Water Splitting, Fig. 17** Photocurrent density-voltage curves for a photoanode and photocathode with external bias potential vs. reversible hydrogen electrode (RHE). The blue shadow is the maximum power conversion efficiency of a photoanode, while the red shadow is for the photocathode (Adapted from Ref. [167])

According to Fig. 18, a photoanode/photocathode system composed by a photoanode with a bandgap of  $E_{g, PA} = 2.0$  eV and a photocathode with a bandgap of  $E_{g, PC} = 1.0$  eV has a

thermodynamic STH efficiency of ca. 19%; this corresponds to a modest increase over the approximately 16% predicted with a single semiconductor configuration with  $E_g = 2.0$  eV.

### Stability/Photocorrosion

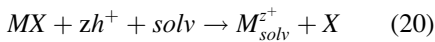
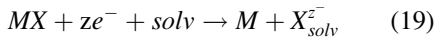
In solar water splitting, the stability/long-term performance of the photoelectrodes is one of the present critical research topics [27]. The electrolytic photoreduction of a semiconductor is often associated with the electrons in the valence band, while the electrolytic photooxidation reaction is related to holes in the conduction band as electronic reactants [168]. The Pourbaix diagram is used to analyze the thermodynamic potential for corrosion of the photoelectrodes, since it maps the possible stable phases in an aqueous electrochemical system. Photochemical corrosion can be described by the Gerischer and Bard model [169, 170]. The photochemical corrosion of a binary semiconductor MX and the solvation (complexing) of the elements (labeled hereafter as “solv”), which leads to the anodic



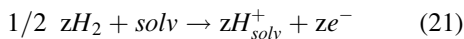
**Hydrogen Production from Photoelectrochemical Water Splitting, Fig. 18** Maximum attainable AM 1.5 G photocurrent densities for dual bandgap devices, as a function of top cell and bottom cell bandgaps,

corresponding to the higher and lower bandgap materials, respectively. Included in brackets are the corresponding STH efficiencies in tandem devices determined by Eq. 10 (Adapted from Ref. [13])

and cathodic decomposition, may be represented by the following reaction, respectively [171]:



where  $z$  is the number of holes or electrons. Using  $H^+/H_2$  standard potentials as reference, the corresponding reaction for hydrogen may be written as [6]:



The addition of Eq. 21 to Eq. 19 or to Eq. 20 yields the corresponding equations for the free energy values,  $_n\Delta G_{sH}$  and  $_p\Delta G_{sH}$ , respectively. The equations for determining the decomposition potentials for the oxidation and reduction of the semiconductor are, respectively:

$$_pE_d = _p\Delta G_{sH}/z \quad (22)$$

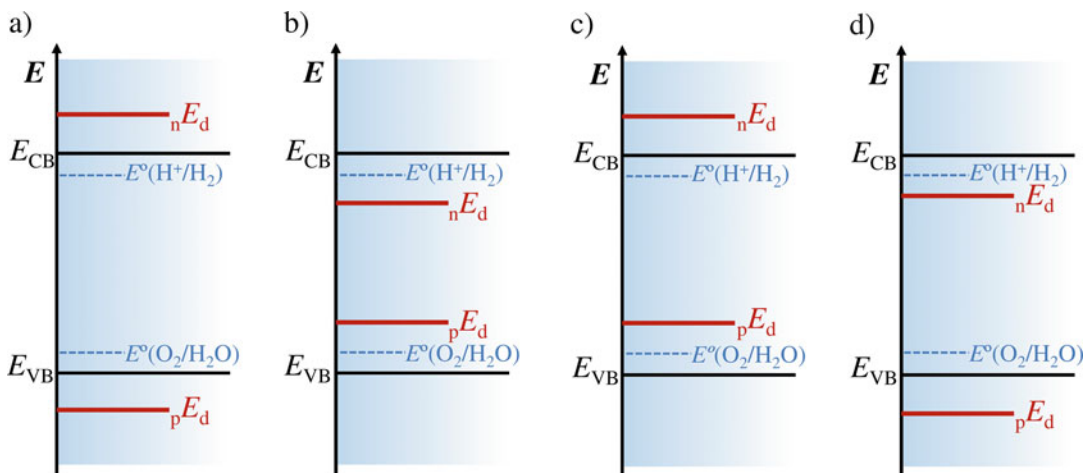
$$_nE_d = -_n\Delta G_{sH}/z \quad (23)$$

The energy positions of the electron-induced potential  $_nE_d$  and the hole-induced corrosion

value  $_pE_d$  can be plotted with respect to the band edges  $E_{CB}$  and  $E_{VB}$  – Fig. 19. In fact, the criterion for thermodynamic stability of the semiconductor is:

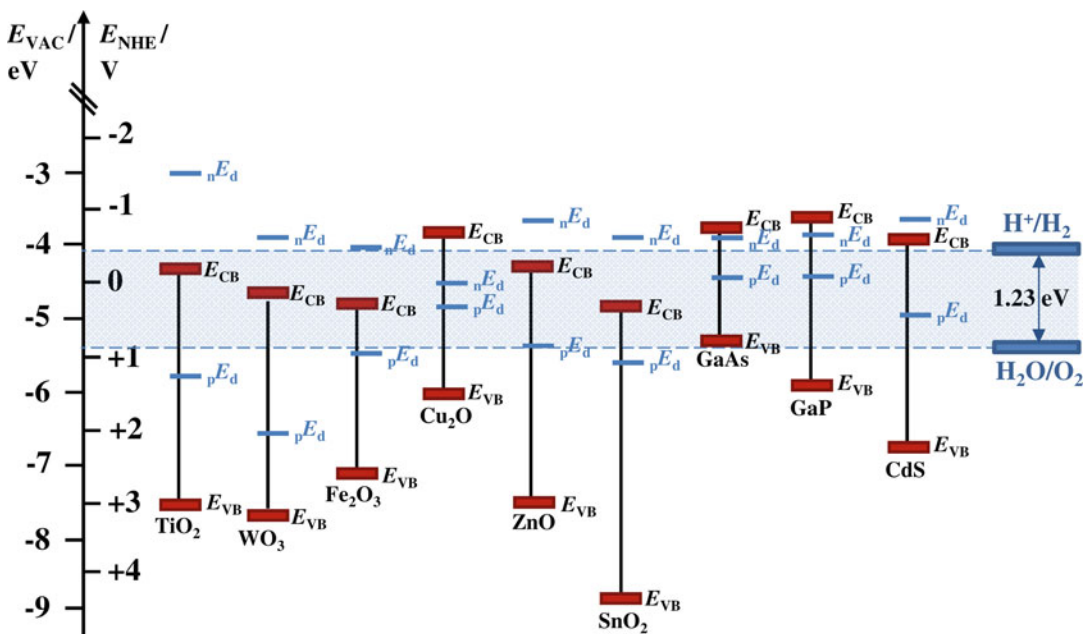
$$_pE_d > E_{redox} > _nE_d \quad (24)$$

Figure 20 shows the decomposition potentials for different oxide and nonoxide semiconductors. Actually, none of the semiconductors presented in Fig. 20 show their Fermi level edges positioned as in Fig. 19a, meaning that they are cathodically and/or anodically unstable. Therefore, the stability of a semiconductor in contact with an electrolyte solution strongly depends on the competition between anodic dissolution and redox reaction, which are controlled by thermodynamic and kinetic parameters, respectively [171]. Thus, even if the semiconductor oxides are not thermodynamically stable, following the calculations of Gerischer [172], they can be kinetically stabilized in the presence of a suitable redox system. For instance, even if the metal oxide semiconductors are thermodynamically stable toward cathodic photocorrosion, most of them are



**Hydrogen Production from Photoelectrochemical Water Splitting, Fig. 19** Relative positions of decomposition Fermi levels of a semiconductor with respect to its

band edges: (a) stable; (b) unstable; (c) cathodically stable but anodically unstable; and (d) anodically stable but cathodically unstable (Adapted from Ref. [6])



**Hydrogen Production from Photoelectrochemical Water Splitting, Fig. 20** Positions of band edges and decomposition Fermi levels for different oxide and nonoxide semiconductors at pH 7 (Adapted from Ref. [171])

unstable toward anodic photocorrosion. Accelerating the kinetics of water oxidation prevents the oxidation of the photoelectrode, e.g., the slow kinetics of water oxidation at hematite photoelectrode often leads to hole accumulation [108]. The instability can also be prevented by

passivating the surface via applying an optically transparent metal and/or metal-oxide coatings by atomic layer deposition (ALD) or physical vapor deposition (PVD) or by adding a suitable co-catalyst to favor the water splitting reaction. However, the corrosion of the electrocatalysts



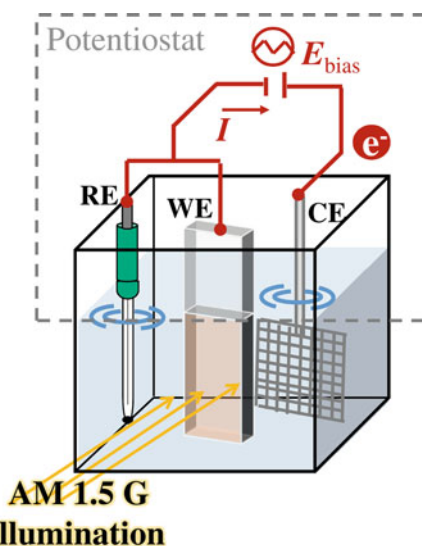
should also be considered. For example,  $\text{RuO}_2$  and  $\text{IrO}_2$  are more stable in acidic media, while anodic dissolution occurs in alkaline conditions,  $\text{Co}_3\text{O}_4$  and Co-Pi are more stable in alkaline than in acidic media.

Extensive overview of existing PEC systems and their performance (photocurrent-density and stability) can be found in the literature [25]. However, hard technological and economic targets have to be met for bringing photoelectrochemical water splitting commercial – 10% STH conversion efficiency stable for more than 10 years. Most reports assess lifetime of semiconductors during less than 24 h; but only few semiconductor-liquid junction (SCLJ) devices demonstrated to display stabilities of more than 1 day [25].

## PEC Reactors

A PEC cell consists of a reservoir containing the electrolyte, where the two electrodes are immersed: the photoactive material (working electrode – WE) and the counter electrode (CE); however, both electrodes can be photoactive [173]. When a three-electrode configuration is used, mainly in a laboratory setup, there is also the reference electrode (RE) – Fig. 21.

The main aspect that distinguishes a PEC cell design from a standard electrochemical cell is the presence of an optically transparent window through which the photoelectrode is illuminated. This window is normally made of soda lime glass, but other materials may be used such as borosilicate glass, quartz, fused silica (amorphous silica) or plastic, namely of acrylic polymers [173]. A normal soda lime glass is quite cheap and stable but cut-off the transmission for wavelengths lower than 350 nm; on the other hand, quartz has a transmittance higher than 90% from 250 nm up to 2500 nm though it is quite more expensive [173]. Instead of quartz, fused silica (amorphous silica) may be considered since it allows a high transmittance, ca. 90%, and shows an excellent stability in both alkaline and acid solutions (except for fluoridric acid), but is slightly cheaper [173]. A good compromise between transmittance



**Hydrogen Production from Photoelectrochemical Water Splitting, Fig. 21** Scheme of a PEC cell for water splitting in a three-electrode configuration: WE – working electrode; CE – counter electrode; and RE – reference electrode

(ca. 280 nm and 2500 nm), stability, and price can be achieved with a borosilicate window. More recently, acrylic-based windows are considered for cheaper devices; this material shows a high transmittance between ca. 350 nm and 900 nm and it is the cheapest material, not fragile but it is easier to get scratched.

## PEC Cell Design

There are some lab PEC devices available commercially; however, most of the PEC reactors reported in the literature were fabricated for testing and optimizing new photoelectrodes [173]. Among these devices, the “Cappuccino” PEC cell designed by LPI at EPFL [173] and “PortoCell” designed by LEPABE at UPORTO [174] are the most known and widely used. The “Cappuccino” cell is made from PEEK (polyether ether ketone) and has a compact design with small distances between electrodes for minimizing the ohmic losses. It has a small chamber in the bottom for allowing a magnetic stirrer to be used, which can help to distribute reactants and disperse products during the electrochemical reaction. Additionally, this cell allows an illumination area of



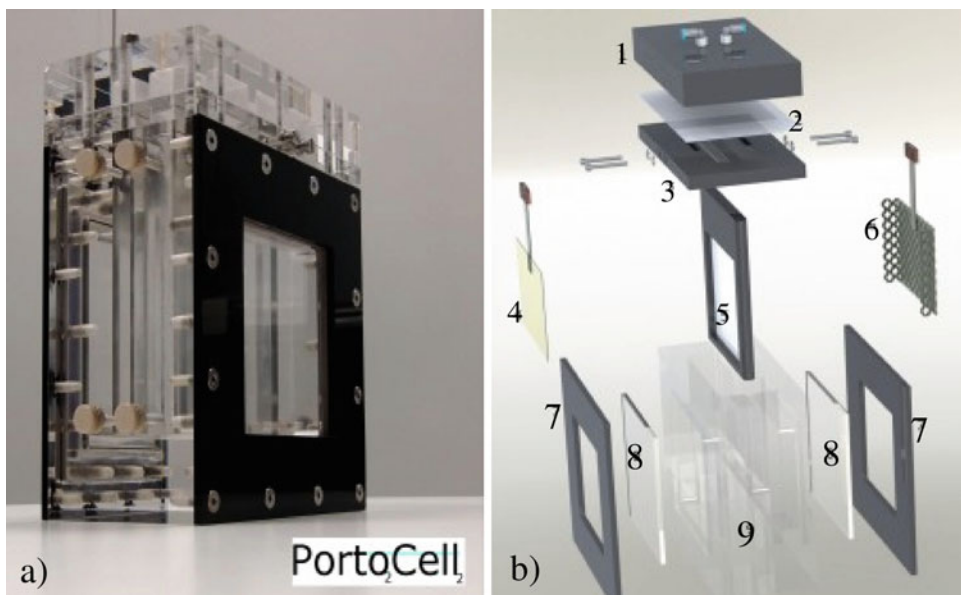
only approximately  $0.5 \text{ cm}^2$ . Therefore, PEC cells like the “Cappuccino” cell cannot respond to the requirements for continuous and larger production of hydrogen, e.g., efficient separation of hydrogen from oxygen, efficient heat dissipation, and versatility for different photoelectrode arrangements [173].

For these reasons, the best performing PEC cell should be “PortoCell” – Fig. 22 [174]. “PortoCell” complies with several requirements for lab applications [175]: (i) maximizes the light penetration through the cell to reach the photoelectrodes; (ii) the illuminated photoelectrode area is completely immersed in the electrolyte; (iii) allows different photoelectrodes configurations; (iv) the cell is resistant to corrosive electrolytes; (v) provides a continuously electrolyte feeding; (vi) allows the use of a membrane to maintain the evolved gases separated; (vii) has facilities to electrically connect the electrodes to the external bias source; and finally (viii) has a robust construction and user-friendly assembly.

“PortoCell” device allows using photoelectrodes up to  $10 \times 10 \text{ cm}^2$  an area crossing

the board between lab-scale and pilot-scale [175]. As observed in Fig. 22, the cell includes two compartments separated by different types of membranes, such as an ion-exchange membrane or a porous membrane, and has fused silica windows on both sides, electrolyte inlets and outlets on both compartments assuring continuous electrolyte feed. These properties enable detailed characterization of PEC configurations with separated collection of evolved gases allowing further analyses, for example, through a connection to a GC.

A new upgrade to the original “PortoCell” design considers [176]: (i) optimized electrolyte flow path for an efficient gas bubbles detachment from the windows and photoelectrode and for efficient heat dissipation – useful when concentrated solar light is used; (ii) counter electrodes placed side by side for allowing light penetration through the cell, crucial for tandem arrangements, though detrimental for ionic transport; and (iii) compact and durable embodiment with a cost-effective construction. Figure 23 shows the “PortoCell” PEC cells mounted and operated



**Hydrogen Production from Photoelectrochemical Water Splitting, Fig. 22** “PortoCell” assembled (a) and disassembled (b): 1 – acrylic cap (gas collection chamber); 2 – porous teflon membrane; 3 – acrylic cap (electrode contacts); 4 – photoelectrodes; 5 – ion exchange

membrane or diaphragm to separate both electrodes; 6 – Pt-counter electrode; 7 – black acrylic for light blocking; 8 – transparent window; 9 – transparent PEC cell body (Adapted from Ref. [175])



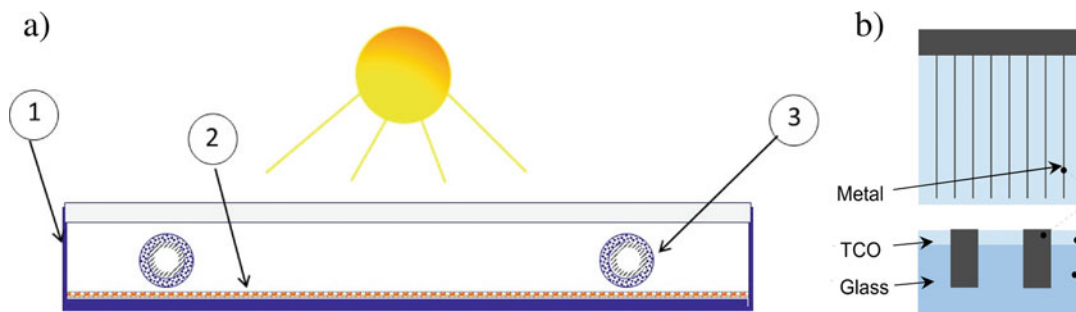
**Hydrogen Production from Photoelectrochemical Water Splitting, Fig. 23** Image of the demonstrative PEC/PV prototype module hosting four new “PortoCell,” which contains photoelectrodes and silicon PV cells with an active surface area of 50 cm<sup>2</sup> each. The prototype has

under homogeneously concentrated solar irradiation – SoCRatus (Solar Concentrator with a Rectangular Flat Focus) [176]. The solar concentrator uses Fresnel lenses capable of concentrating solar radiation at least 10-fold, which offers a significant potential for the reduction of the costs of a PEC hydrogen production plant. Solar concentrator systems focus the direct part of the incident solar radiation on the optical inlet of the PEC panels. As a result, the employment of solar concentrators in combination with PEC panels allows decreasing the active illuminated area and consequently the size of the PEC panel system, while keeping the hydrogen output mostly constant.

A disruptive new PEC design is now being developed, which minimizes the counter electrode overpotential, the charge transport resistance both in the semiconductor and in the electrolyte, and minimizes further the construction costs. The new

been mounted in the focal plane of the DLR test facility SoCRatus in Cologne (Germany), where homogeneously concentrated solar irradiation is provided with a maximum concentration ratio of about 17.5 (Adapted from Ref. [176])

PEC panel comprehends a front glass window and an embedded transparent conductive oxide (ETCO) [177] glass back panel coated with the semiconductor and encapsulating a PV panel – Fig. 24; alternatively, the front window is the back illuminated photoelectrode if applied on a transparent substrate. The counter electrode is a half-MEA (membrane electrode assembly) such as the ones used in proton exchange membrane fuel cells (PEMFC); it is made of platinum metal ultrananoparticles supported in carbon black applied as a coat directly over the ion-exchange membrane shaped as a tube; non-noble metals may be used such as nickel for hydrogen evolution or nickel oxide for the oxygen evolution. Hydrogen or oxygen is produced inside this tube, where water needed for the electrochemical reaction permeates through the membrane originating hydrogen or oxygen, which evolves as gas phase saturated with humidity. The ETCO [177]



**Hydrogen Production from Photoelectrochemical Water Splitting, Fig. 24** (a) Sketch of the innovative photoelectrochemical panel: 1 – PEC panel device; 2 – ETCO glass back panel coated with the photoelectrode (encapsulating a PV panel); and 3 – selective membrane

electrode and nanoparticulated counter electrode; and (b) sketch of a TCO substrate with engraved metal lines (ETCO technology [177]): top view and cross section, respectively top and bottom images

technology comprehends chromium metal lines engraved on a TCO glass, beneath the semiconductor layer, and minimizes the electricity harvesting overpotentials – Fig. 24.

One of the major challenges in large-area PEC panels is the separation of hydrogen and oxygen gas products, as well as hydrogen collection and transport in large solar fields. In state-of-the-art PEC cell designs, anode and cathode compartments are separated by a membrane or diaphragm, and the entire cell must be sealed and fitted with pipes for  $H_2$  gas collection. This translates into a large sealing and piping construction in large-area solar hydrogen production plants. To overcome this problem, Landman et al. [178], from Technion – IIT, designed a new cell concept that addresses these challenges. These authors propose the separation of the oxygen and hydrogen cells using auxiliary electrodes. The electrodes used are  $Ni(OH)_2/NiOOH$ , commonly used in rechargeable alkaline batteries, which can be cycled many times with minimal energy loss. During electrolysis, the  $NiOOH$  auxiliary electrode in the oxygen cell charges, while the  $Ni(OH)_2$  auxiliary electrode in the hydrogen cell discharges; electrolysis can be performed in two separate cells. Using suitable photoanodes, the PEC cell can generate oxygen, which can then be discharged to the atmosphere, alleviating the need for sealing and piping. Since metal wires connect the separated cells to each other, hydrogen is generated at the end-user location; this

concept was successfully demonstrated in small-area cells showing 7.5% solar-to-hydrogen conversion efficiency.

#### The Working Electrode

In PEC water splitting devices, the light absorbing material (photoelectrode) needs to be deposited or grown on a highly conductive substrate. The substrate (current collector) should then form an ohmic back contact with the photoactive material for allowing the charge transfer between working electrode (WE) and counter electrode (CE). When it is necessary for a transparent ohmic contact to have a back-side illumination, or for a tandem device, the most widely used materials are glasses previously coated with a thin layer of a transparent conducting oxide (TCO), such as fluorine doped tin oxide (FTO), indium doped tin oxide (ITO), and aluminum doped zinc oxide (AZO). FTO is currently the conducting substrate of choice due to its commercial availability, high carrier concentration and mobility, acceptable electric conductivities at higher temperatures, and an optical transparency higher than 80% [173]. The development of a transparent semiconductor will allow to transmit the fraction of solar radiation not absorbed by the material and to convert it by other photosystems, improving their overall energy performance. On the other hand, when the transparency is not important, a metal substrate can be a potential alternative. For n-type photoanodes, conducting materials with a work

function that is lower than that of the photoanode itself is required; while for p-type photocathodes, high-work function back-contacts such as gold and platinum should be used [173].

In addition to the transparency requirement, there are severe implications for practical efficiency of a PEC device using front-side and back-side illumination [26]. For the case of front-side illumination and using an n-type photoanode, the absorption occurs near its surface, i.e., the light is absorbed through the thickness of the electrode material and less light reaches the back-contact. Near the surface the density photo-generated charge carriers is greater than at the back-contact; the holes are generated very close to the semiconductor-liquid junction (SCLJ) and thus the hole diffusion length avoids to be very long. On the other hand, the photogenerated electrons need to diffuse through the bulk of the semiconductor to the back-contact, where they are extracted to the counter electrode to reduce water and produce hydrogen; this justifies the need of an electron diffusion length higher or equal than the thickness of the semiconductor film. In the case of a photoanode illuminated from the back-side, the back-contact has higher density of the photo-generated charge carriers, and thus the holes must be able to diffuse through the bulk without recombining with the electrons that only need to diffuse a very short length to reach the back-contact. When a p-type photocathode is used, the diffusion of charge carriers occurs in the opposite direction, i.e., the photogenerated electrons need to reach the SCLJ, whereas the holes diffuse to the back-contact. Therefore, diffusion length of the minority and majority charge carriers is an important parameter to determine the best type of illumination for such a photoelectrode and the

optimum film thickness balancing the maximum light absorption with the charge transport properties. Table 8 presents the electron and hole diffusion length and mobility for the best-performing photoelectrodes.

#### The Electrolyte

The electrolyte in an electrochemical cell consists of a polar solvent with active species to be reduced or oxidized, depending on if it is an alkaline medium or an acidic medium; the electrolyte should not conduct electrons. Photoactive semiconductor materials immersed in a redox electrolyte are greatly affected by the electrolyte solution properties; therefore, the choice of a suitable solution is very important, mainly in what concerns the redox couple selection and the pH compatibility with the photoelectrode [179]. It should contribute to improve charge transfer kinetics, stability, as well as assist in preventing undesirable phenomena, such as surface recombination and trapping. Also, the electrolyte concentration should be sufficiently high to minimize the ohmic potential losses (concentrations of at least 0.5 M are recommended) and should display a high conductivity [173]. The properties of the electrolyte solutions, namely conductivity ( $\kappa$ ), resistance ( $R_E$ ), and potential loss ( $V_{\text{loss}}$ ) at  $5 \text{ mA}\cdot\text{cm}^{-2}$ , are shown in Table 9 for each electrolyte composition.

#### The Counter Electrode

The reaction at the counter electrode (CE) should be as fast as possible and have high catalytic activity. In a single photon-system PEC cell, platinum is usually used as counter electrode for hydrogen evolution; this material presents good stability over a wide range of electrolytes and pH, as well as it shows low overpotentials for

**Hydrogen Production from Photoelectrochemical Water Splitting, Table 8** Diffusion length, carrier mobility, and carrier lifetime properties of the best-performing photoelectrodes (Adapted from Ref. [26])

Photoelectrode material	Carrier mobility/ $\text{cm}^2\cdot\text{V}^{-1}\cdot\text{s}^{-1}$	Carrier lifetime/s	Diffusion length/nm
$\text{Fe}_2\text{O}_3$	0.5	$3 \times 10^{-12}$	2–4
$\text{WO}_3$	10	$(1-9) \times 10^{-9}$	150–500
$\text{Cu}_2\text{O}$	6	$40 \times 10^{-12}$	25
$\text{BiVO}_4$	0.044	$40 \times 10^{-9}$	70
TaON	0.01	$1 \times 10^{-3}$	–31
$\text{Ta}_3\text{N}_5$	0.07	$1 \times 10^{-3}$	–84

**Hydrogen Production from Photoelectrochemical Water Splitting, Table 9** Electrical conductivity ( $\kappa$ ), resistance ( $R_E$ ), and potential losses ( $V_{\text{loss}}$ ) at 5 mA·cm<sup>-2</sup>

for typical electrolyte compositions and pH media;  $R_E$  and  $V_{\text{loss}}$  are calculated using a cell constant ( $K_{\text{cell}}$ ) of 1 cm<sup>-1</sup> (Adapted from Refs. [26] and [173])

Electrolyte pH	Electrolyte composition	$\kappa/\Omega^{-1}\cdot\text{m}^{-1}$	$R_E/\Omega$	$V_{\text{loss}}$ at 5 mA·cm <sup>-2</sup> /mV	$T/^\circ\text{C}$
Neutral	Distilled water	$10^{-3} \approx 10^{-4}$	$10^5\text{--}10^6$	$\infty$	20
Neutral	Purified water	$\approx 5.5 \times 10^{-6}$	$\approx 18 \times 10^6$	$\infty$	25
Neutral	0.1 M NaCl	1.07	93	467	18
	0.5 M NaCl	3.8	26	132	18
	1.0 M NaCl	7.44	13	67	18
Acid	0.5 M H <sub>2</sub> SO <sub>4</sub>	6.2	16	81	20
	1.0 M H <sub>2</sub> SO <sub>4</sub>	36.6	2.7	14	18
	3.5 M H <sub>2</sub> SO <sub>4</sub>	73.9	1.4	7	18
Alkaline	0.1 M KOH	2.26	44	221	18
	0.5 M KOH	10.7	9.3	47	18
	1.0 M KOH	20.1	5.0	25	20

hydrogen evolution (ca. 0.1 V) [173]. In a PEC/PV tandem configuration, the surface area of a CE should be several times larger than the illuminated photoelectrode area as a tactic toward reducing the overpotential required for supporting tandem photocurrent in a tandem device [106]. In PEC devices, a compromise must be maintained between the WE, the CE, and the electrolyte solution in order to ensure low overpotentials, fast charge transport, and efficient light absorption.

#### The Reference Electrode

Two-electrode and three-electrode systems are used to measure the efficiency of a whole PEC cell and the performance of a working electrode as a half cell, respectively. In a two-electrode configuration, the dark- and photocurrents are recorded as a function of potential against a counter electrode. The three-electrode configuration allows measuring the applied potential with respect to a fixed reference electrode, which allows to turn visible the independent response of the working electrode to any change in the applied potential. The most common reference electrodes used in PEC cells are overview in Table 10. In water splitting studies the applied potential is normally reported against RHE (reversible hydrogen electrode). Zero volt on the RHE scale corresponds to the H<sup>+</sup>/H<sub>2</sub> redox potential in the actual solution, independent of the pH; this makes the use of RHE scale more

convenient than NHE (normal hydrogen electrode) scale.

An important selection criterion for a reference electrode is its stability in the electrolyte solution. Silver/silver chloride electrodes are more frequently used as reference electrodes in the PEC systems under three-electrode configuration and thus the potential measured with the Ag/AgCl electrode ( $E_{\text{Ag/AgCl}}$ ) must be converted into RHE scale ( $E_{\text{RHE}}$ ) as follows [173]:

$$E_{\text{RHE}} = E_{\text{Ag/AgCl}} + 0.059 \text{ pH} + E_{\text{Ag/AgCl vs. SHE}}^{\circ} \left( E_{\text{Ag/AgCl vs. SHE}}^{\circ} = 0.1976 \text{ V at } 25^\circ\text{C} \right) \quad (25)$$

where  $E^{\circ}(\text{Ag/AgCl vs. SHE})$  is the potential of the Ag/AgCl reference electrode with respect to the SHE (Standard Hydrogen Electrode). All the reference electrodes are very sensitive and so their maintenance is crucial; they should be stored in the appropriate solution when not in use for avoiding to dry. The potential difference between individual electrodes should be checked every 2 weeks and their deviation should be less than  $\pm 3$  mV; maintenance is needed for larger differences. In this case, the electrode solution should be refreshed and/or the frit should be immersed in a 1 M HCl solution overnight [173]. The lifetime of a reference electrode typically last 2–3 years, depending on its design and manufacturer.



**Hydrogen Production from Photoelectrochemical Water Splitting, Table 10** Overview of reference electrodes frequently used in PEC water splitting research (Adapted from Ref. [173])

Reference electrode	Filling solution	Potential/ <i>E</i> vs. SHE	Remarks
Reversible hydrogen	Actual electrolyte, purged with H <sub>2</sub> gas	0.0–0.059 × pH	RHE
Standard/normal hydrogen	[H <sup>+</sup> ] = 1.18 mol·L <sup>-1</sup> <i>P</i> (H <sub>2</sub> ) = 10 <sup>5</sup> Pa	0	SHE = NHE
Silver/silver chloride (Ag/AgCl)	0.1 M KCl	0.289	
	1.0 M KCl	0.237	
	3.0 M KCl	0.210	
	3.5 M KCl	0.205	
	Saturated KCl	0.198	Workhorse for PEC research
	3 M NaCl	0.209	
	Saturated NaCl	0.197	
Calomel (Hg/Hg <sub>2</sub> Cl <sub>2</sub> )	0.1 M KCl	0.334	
	1.0 M KCl	0.281	NCE
	3.5 M KCl	0.250	
	Saturated KCl	0.242	SCE
	Saturated NaCl	0.236	SSCE

## Measurements Protocols

The energy-conversion efficiency is the key metric for evaluating the performance of photoelectrochemical devices that produce fuels from sunlight, biased or unbiased [180]. The solar-to-hydrogen efficiency is obtained based on the input energy, solar illumination and internal bias, and the energy content of the produced hydrogen. The energy conversion efficiency of the photoelectrodes can be assessed based on its photocurrent, photovoltage, and the Fermi levels; it does not need the construction of a complete PEC cell. A PEC water splitting cell is typically characterized based on UV-vis spectroscopy analysis, steady-state electrochemical methods (*I-V* and CV tests), advanced electrochemical dynamic measurements (EIS, IMPS/IMVS and TAS), incident monochromatic photon-to-current conversion efficiency (IPCE), and Faradaic efficiency.

The UV-vis spectroscopy is used to assess the optical bandgap properties of the bulk semiconductor, e.g., using Tauc plots of  $(\alpha \cdot h \cdot \nu)^n$  vs.  $h \cdot \nu$ , where  $\alpha$  is the semiconductor absorption coefficient at a specific wavelength,  $h \nu$  is the photon energy, and  $n$  depends on the type of transition

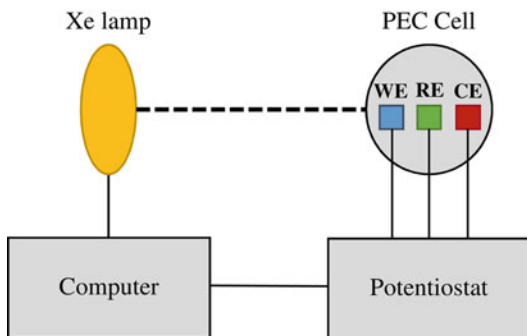
and it may have values between  $n = 1/2$ ,  $n = 2$ ,  $n = 3/2$ , and  $n = 3$  corresponding to the allowed direct, allowed indirect, forbidden direct, and forbidden indirect transitions, respectively [8]. Moreover, the absorption data allows estimating the film thickness, assuming a Lambertian absorption behavior [23]:

$$\ln(1 - abs) = -\alpha \cdot \ell \quad (26)$$

where *abs* is the absorbance,  $\alpha$  is the semiconductor absorbance coefficient at a specific wavelength, and  $\ell$  is the thickness of the film.

Current-voltage (*I-V*) measurement is the most important technique to evaluate the performance of a photoelectrode for PEC water splitting; it consists of applying an external potential bias to the cell and measuring the photocurrent density generated by the photoelectrode,  $J_{\text{photo}}$ , immersed in an electrolyte. These measurements are recorded using a potentiostat, which has at least two leads: one connects to the CE, while the other connects to the WE. Often a standard three-electrode configuration is used, a third lead is provided for the RE and, then, the current is passed between the WE and CE – Fig. 25. In





**Hydrogen Production from Photoelectrochemical Water Splitting, Fig. 25** Experimental arrangement for a potentiostatic measuring system: WE – working electrode; RE – reference electrode; and CE – counter electrode

three-electrode measurements, the potentiostat is used to control the potential difference between the WE and the RE, while the current is measured between the WE and the CE, with negligible current passed between the WE and the RE.

This steady-state technique allows obtaining the current-voltage response in dark and under different light conditions, the photocurrent onset potential,  $E_{\text{onset}}$ , and, therefore, understanding the electron vs. hole transport limitations and transient effects that indicate recombination [173]. The photocurrent density tends to saturate at a certain applied potential bias,  $E_{\text{app}}$ , establishing the upper photocurrent limit that can be used for calculating the applied bias photon-to-current efficiency ( $\eta_{\text{APCE}}$ ) – Eq. 16. Figure 26 shows the ideal behavior of the  $I$ - $V$  curves for an n-type semiconductor in the dark and under illumination conditions (conventionally, 1-sun AM 1.5 G illumination [181]).

When the applied potential to the photoelectrode is equal to the flatband potential ( $E_{\text{fb}}$ ), the applied potential annuls the band bending in the space-charge layer [35]. Thus, the semiconductor energy band becomes flat and there is no longer an electric field for assisting the separation of the photogenerated charge carriers. Determining  $E_{\text{fb}}$  is useful for estimating the positions of the conduction and valence bands with respect to the redox energy levels in the electrolyte, which allows to estimate the maximum photovoltage ( $E_{\text{photo}}$ ) and photocurrent onset potential ( $E_{\text{onset}}$ )

that can be produced. In an ideal scenario, the photocurrent onset potential should be equal to the flatband potential; however, the redox kinetic overpotentials have to be taken into account [35]. Thus,  $E_{\text{fb}}$  is usually measured using other electrochemical techniques, e.g., based on the Mott-Schottky relation [23]; this will be explained in the electrochemical impedance spectroscopy section.

Another metric commonly used to evaluate the effects of input solar illumination is the system-level power converted,  $P_{\text{conv}}$  [182]. In a three-electrode system, the power converted at any current,  $I$ , is given by the product of the current  $I$  and the difference between the potential required to drive the half-reaction in dark,  $E_{\text{dark}}(I)$ , and under illumination,  $E_{\text{light}}(I)$ :

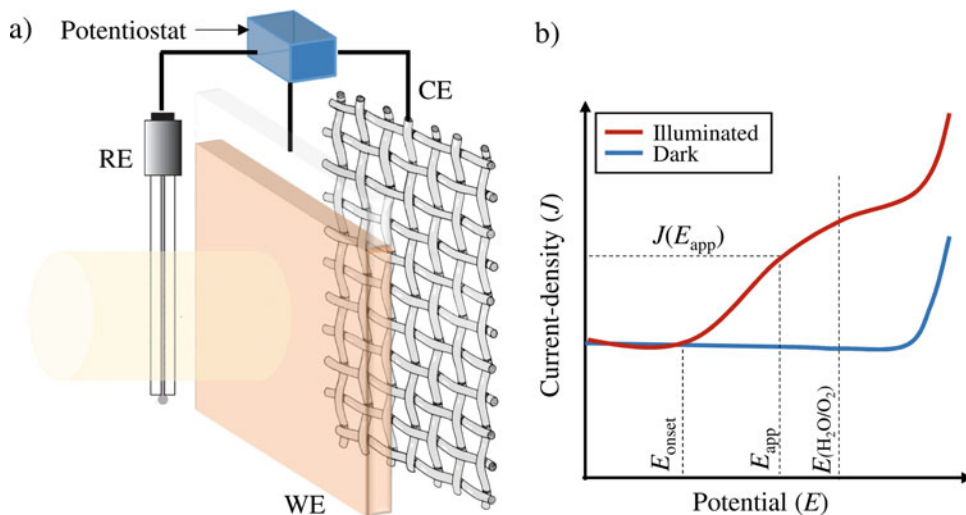
$$\begin{aligned} P_{\text{conv}}(I) &= I \cdot (E_{\text{dark}}(I) - E_{\text{light}}(I)) \\ &= I \cdot E_{\text{conv}}(I) \end{aligned} \quad (27)$$

The ratiometric power converted,  $\Phi_{\text{conv}}$  is still given by the ratio of the  $P_{\text{conv}}$  to the input solar power,  $P_{\text{light}}$ . Figure 27 illustrates the power saved measurements used to characterize the photoelectrode performance.

In cyclic voltammetry (CV) test the potential of a system is swept between two voltage limits while the current response is measured. The CV curves are used for acquiring information about electrochemical reactions, similar to  $I$ - $V$  characteristics, and mainly for analyzing photocorrosion activity in a PEC cell [8].

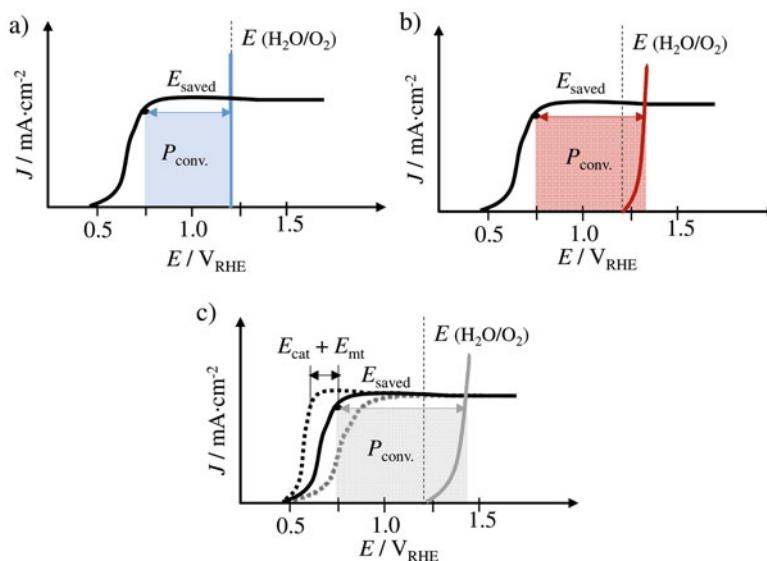
Once it is considered that the photoelectrode is a promising material for solar water splitting, its durability is clearly desired. Stability tests consist in applying a constant potential on a PEC cell system over several hours and measure the resulting time-dependent photocurrent response, under 1-sun AM 1.5 G illumination. The overall stability is controlled by physical and chemical factors; physical stability is related to electrolyte evaporation, which heats up under the solar simulator illumination; the chemical stability is associated to irreversible electrochemical and thermal degradation of the semiconductor and electrolyte [183].

Dynamic techniques should be considered to characterize the pathway losses (ohmic,



**Hydrogen Production from Photoelectrochemical Water Splitting, Fig. 26** (a) Schematic of a three-electrode PEC configuration with incident solar simulated

illumination; (b) ideal  $J$ - $V$  curve for an n-type semiconductor in the dark (blue line) and under illumination conditions (red line) – (Adapted from Ref. [35])



**Hydrogen Production from Photoelectrochemical Water Splitting, Fig. 27** Effect of the dark electrode on the determination of system power-converted,  $P_{\text{conv.}}$ , in three-electrode  $J$ - $V$  measurements using: (a) a photoanode (solid black line) and an ideally dark electrode (solid blue line), where the measured ratiometric power converted is  $\Phi_{\text{conv.}} = 4.2\%$  (for  $P = 100 \text{ mW}\cdot\text{cm}^{-2}$ ); (b) a photoanode and the state-of-the-art dark anode for the water-oxidation reaction (solid red line), in which the dark electrode

exhibits an overpotential of 100 mV at 8 mA –  $\Phi_{\text{conv.}} = 5.0\%$ ; (c) an identically engineered photoanode (black dashed line), e.g., using a co-catalyst, and a dark doped-electrode (solid gray line), showing an overpotential gain of 200 mV due to co-catalyst loading and mass-transport effect –  $\Phi_{\text{conv.}} = 5.8\%$ . The catalyst/mass-transport effects can be observed using a photoelectrode prepared from the photoactive substrate without added co-catalyst layer (dashed blue line) – (Adapted from Ref. [180])

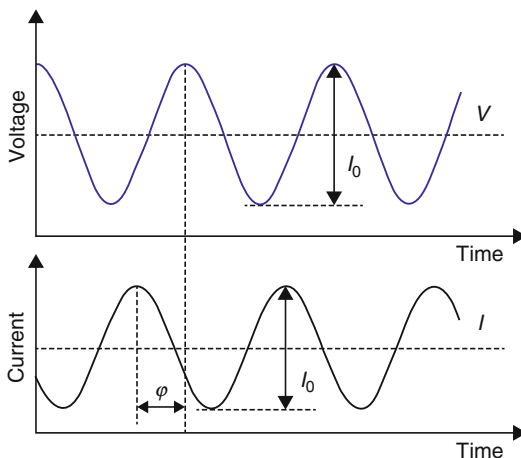
activation, and concentration) that limit the performance of the PEC water splitting cells, namely the properties of the semiconductor electrode: photocurrent, photovoltage, and fill factor [184]. These techniques allow the interpretation of the charge transfer kinetics, mainly characterized by diffusion coefficients and lifetime of the charge carriers [185].

Electrochemical impedance spectroscopy (EIS) is one of the most powerful characterization techniques involving transient studies, which allow a deep diagnostics of the PEC cell: (i) external and shunt resistances; (ii) electron injection and its lifetime; (iii) recombination of the electron-hole pairs; (iv) charge transport resistance in the electrolyte; (v) reduction reaction at the counter electrode (Pt wire); and (vi) diffusivity of the ionic species in the electrolyte [186]. EIS analysis is also of great importance for understanding the specific processes that cause changes in the  $I$ - $V$  curve. For this reason, EIS measurements can be performed in the dark, under bias illumination and in any working condition of the PEC cell, e.g., applying different bias potentials. In the EIS standard procedure, a small sinusoidal voltage perturbation  $V(t)$  is applied to the system (1–20 mV, ensuring that the response is in the pseudo-linear range, and the amplitude and phase shift of the resulting current response  $I(t)$  are monitored at the corresponding frequency – Fig. 28. The response in current has the same period as the voltage perturbation but is phase-shifted by  $\varphi$  [184].

The impedance technique is a measure of the ability of a system to impede the flow of electrical current and is given by the ratio of a time-dependent voltage and a time-dependent current as defined by [184]:

$$\begin{aligned} Z &= \frac{V(t)}{I(t)} = \frac{V_0 \cos(\omega t)}{I_0 \cos(\omega t - \varphi)} \\ &= Z_0 \frac{\cos(\omega t)}{\cos(\omega t - \varphi)} \end{aligned} \quad (28)$$

where  $V_0$  and  $I_0$  are the amplitudes of voltage and current signals, respectively, and  $\omega = 2\pi\nu$  is the angular frequency in radians per second.



**Hydrogen Production from Photoelectrochemical Water Splitting, Fig. 28** Sinusoidal voltage perturbation and resulting sinusoidal current response, phase-shifted by an amount  $\varphi$ .  $V_0$  – amplitude of the voltage signal;  $I_0$  – amplitude of the current signal;  $V$  – work voltage;  $I$  – generated current (Adapted from Ref. [187])

Alternatively, the impedance response can be expressed in terms of a magnitude,  $Z_0$ , and a phase shift,  $\varphi$ , or in terms of real and imaginary components, as follows [188]:

$$\begin{aligned} Z &= Z_0 \frac{\exp(j\omega t)}{\exp(j\omega t - j\varphi)} \\ &= Z_0 (\cos \varphi + j \sin \varphi) \end{aligned} \quad (29)$$

where  $j$  is the imaginary number ( $j = \sqrt{-1}$ ). After knowing the impedance values of real ( $Z' = Z_0 \cos \phi$ ) and imaginary ( $Z'' = Z_0 j \sin \varphi$ ) parts and the phase angle  $\varphi$ , the Nyquist and Bode diagrams can be plotted. The former is the representation of  $-Z''$  vs.  $Z'$ , while the Bode diagram is the representation in a semi-logarithmic plot of the symmetric of the phase angle  $\varphi$  vs. the frequency [187].

Provided that the system is stable, the analysis of the frequency domain response can be performed at the potential range of the  $I$ - $V$  curve, which allows obtaining different features at each point of the frequency variation [189]. Despite being a relatively easy method to apply, the correct interpretation of the EIS spectra requires the use of suitable theoretical tools. Equivalent

electric analogues are used to fit the experimental EIS data for extracting the capacitances and resistances, which are related to charge accumulation, recombination, and charge transfer processes. The resistances are associated to different processes of carrier flux in the bulk of the semiconductor or at the semiconductor/electrolyte interface, whereas the capacitances represent a charge storage mechanism.

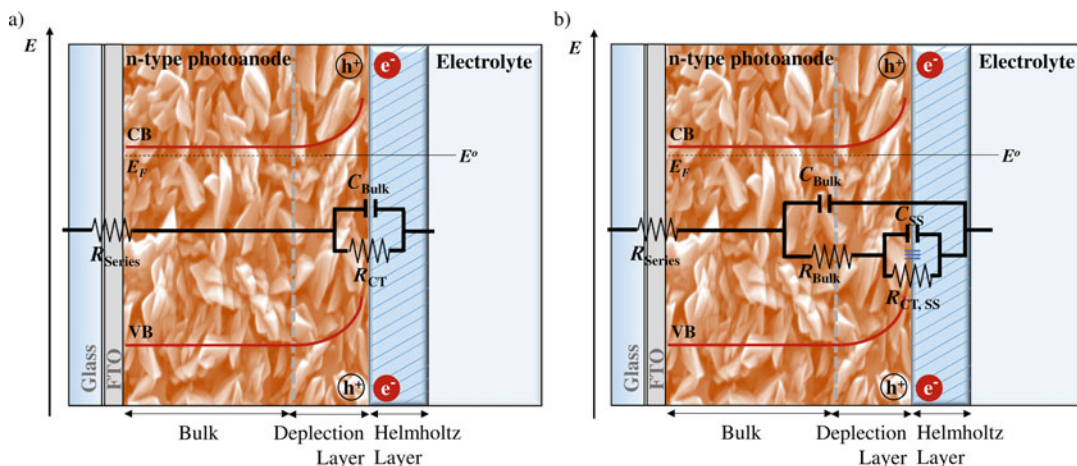
PEC cells have been extensively characterized applying the well-known Mott-Schottky relation, which allows determining the flatband potential ( $E_{fb}$ ) and the donor density of the semiconductor ( $N_D$ ). This relation requires plotting the inverse square route of the space charge capacitance as a function of the applied bias potential. A straight line can be fitted from the linear region of the plot;  $N_D$  value is determined from the slope of this line, while  $E_{fb}$  value is obtained extrapolating the interception of the straight line with the axis of the applied potential [23]. The capacitance is usually determined fitting the experimental data to a Randles electrical analogue circuit, comprising a series resistance and a simple-capacitor (RC) element, as shown in Fig. 29a [6].

A comprehensive equivalent circuit model that highlights the central role of surface states is needed for a deeper interpretation of the kinetics of interfacial reactions at illuminated photoelectrodes, which are expected to influence the PEC performance. Suitable equivalent circuit models for PEC systems have been well described in several publications over the years [23, 32, 33, 68]. Figure 29b shows the equivalent circuit proposed by Klahr et al. [32], consisting of a series resistance ( $R_{Series}$ ), then a bulk capacitance ( $C_{Bulk}$ ) in parallel with a resistance from the charge transport/recombination within the bulk semiconductor ( $R_{Bulk}$ ) and a RC unit consisting of a charge transfer resistance from the surface states ( $R_{CT, SS}$ ) to electrolyte in parallel with its correspondent capacitance ( $C_{SS}$ ). Bisquert and coworkers [189] described the recent advances in the application of EIS technique in PEC water splitting, aiming at establishing suitable circuit models and at characterizing the kinetic steps that contribute to the PEC performance, with particular attention to the role of surface states.

Other examples of frequency-dependent techniques are the intensity modulated photocurrent spectroscopy (IMPS) and the intensity modulated voltage spectroscopy (IMVS), which probe the dynamic relation between irradiation and electrochemical response of the photoelectrode. While in the EIS technique the light intensity is held constant and the electrode potential is modulated, the IMPS/IMVS analyses involve measuring the frequency response of the photocurrent/voltage to sinusoidal modulation of the illumination intensity [6]. IMPS method was introduced in the pioneering work by Peter and coworkers [190] in the 1990s; more recently, IMPS technique has been used combined with EIS technique for obtaining the rate constants for charge transfer and recombination [33, 191]. Contrarily, IMVS technique is relatively underdeveloped for water splitting devices, since it is applied under open circuit conditions, i.e., when the current is zero. Klotz et al. [33] reported the importance of IMVS in alleviating the need to fit EIS data to complex electric circuit models. This study teaches about the processes that limit the low-bias performance in PEC water splitting devices, mainly for the oxygen evolution reaction on n-type photoanodes.

Transient absorption spectroscopy (TAS) has been employed as an useful tool to directly probe charge carriers dynamics, allowing monitoring the mechanisms of photogenerated holes and electrons on the timescale of microseconds to seconds; this technique is particularly relevant for understanding the water oxidation mechanism [34]. TAS is usually performed in a pump-probe configuration based on a pump pulse used for photo-inducing the valence band electrons with a laser source; the dynamics of the transient species formed (valence band holes and conduction band electrons) are then followed by probing their absorption from visible to near infrared wavelengths using a probe pulse or beam [109]. This technique allows determining the role of external electrical bias in the rates of electron-hole recombination, trapping, and interfacial charge transfer to the electrolyte, which is an important factor limiting the efficiency of solar-driven water splitting devices [68].

Quantum efficiency metric, such as the incident monochromatic photon-to-current



**Hydrogen Production from Photoelectrochemical Water Splitting, Fig. 29** (a) Randles electrical circuit analogue used to fit the impedance data under dark

conditions; and (b) electrical circuit analogue proposed by Klahr et al. [32] used to fit the impedance data under illumination

conversion efficiency, IPCE, is also an advantageous parameter to evaluate the PEC performance. IPCE quantifies the effectiveness in converting photons from monochromatic light incident to photocurrent flowing between the working and counter electrodes, allowing to determine which photon contribute to the solar photocurrent. Thus, IPCE is defined as the ratio of the number of electrons generated by light that follows in the external circuit ( $N_{\text{electrons}}$ ) to the number of incident photons as a function of wavelength ( $N_{\text{photons}}$ ) [47]:

$$\text{IPCE}(\lambda) = \frac{N_{\text{electrons}}}{N_{\text{photons}}} \quad (30)$$

Substituting the current definition ( $I = qN_{\text{electrons}}/t$ ) in the previous equation, the IPCE is therefore defined as:

$$\begin{aligned} \text{IPCE}(\lambda) &= \frac{N_{\text{electrons}}}{N_{\text{photons}}} = \frac{qN_{\text{electrons}}/t}{qN_{\text{photons}}/t} \\ &= \frac{I}{qN_{\text{photons}}/t} \end{aligned} \quad (31)$$

where  $q$  is the elementary charge and  $t$  is the time [187]. The number of incident photons with a given wavelength relates to the power of the incident power density ( $P_{\lambda}$ ) by:

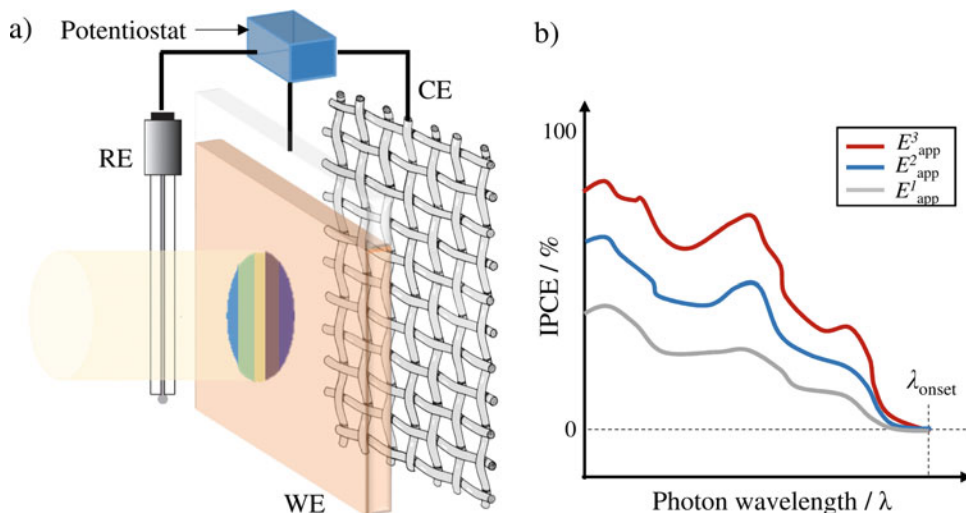
$$P_{\lambda} = \frac{N_{\text{photons}}}{t} h\nu = \frac{N_{\text{photons}}}{t} h \frac{c_0}{\lambda} \quad (32)$$

where  $h$  is the Planck constant,  $\nu$  is the frequency,  $c_0$  is the speed of light, and  $\lambda$  is the wavelength. Manipulating Eq. 32 in order to obtain  $N_{\text{photons}}$  and after introducing it into Eq. 31, the IPCE value can be rewritten as [187]:

$$\begin{aligned} \text{IPCE}(\lambda) &= \frac{I}{q\lambda P_{\lambda}/hc_0} = \frac{Ihc_0}{P_{\lambda}q\lambda} \\ &= \frac{I}{P_{\lambda}} \frac{1240}{\lambda} \times 100\% \end{aligned} \quad (33)$$

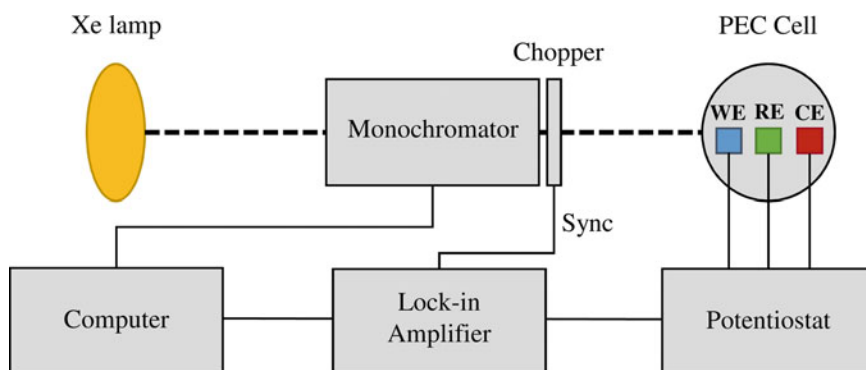
Finally, the IPCE is calculated measuring the current in a cell when particular wavelength ranges with known irradiance  $P_{\lambda}$  focus on the photoelectrode. The IPCE is normally determined at the bias potentials corresponding to the maximum power point. Efficient cells display very high IPCE values over a broad range of visible spectrum. Nevertheless, efficiencies lower than 100% are expected due namely to reflection losses of incident photons and recombination of charge carriers [16]. Figure 30 displays the IPCE plot, showing how the IPCE can vary with the applied potential. The onset wavelength,  $\lambda_{\text{onset}}$ , is closely related to the semiconductor bandgap, and we note that the IPCE at specific wavelength multiplied by the spectral distribution of standard solar





**Hydrogen Production from Photoelectrochemical Water Splitting, Fig. 30** (a) Schematic of a three-electrode PEC configuration with incident monochromatic

illumination; (b) IPCE response measured at a fixed applied potential,  $E_{app}$  (Adapted from Ref. [35])



**Hydrogen Production from Photoelectrochemical Water Splitting, Fig. 31** Experimental arrangement for an IPCE measuring system: WE – working electrode; RE – reference electrode; and CE – counter electrode (Adapted from [192])

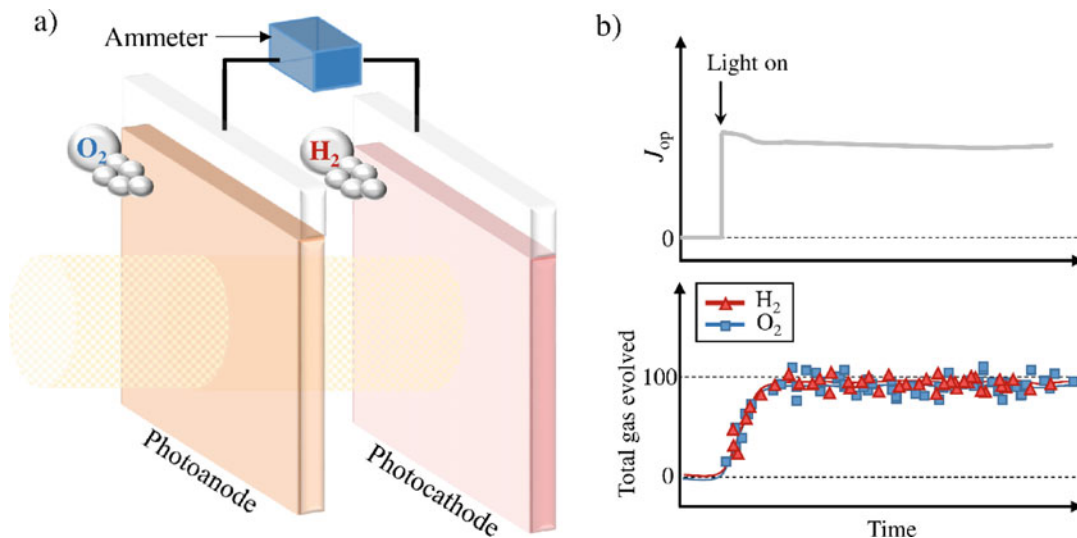
illumination (1-sun AM 1.5 G illumination) can be integrated to give an estimation of the expected  $J_{photo}$  under solar illumination [35].

Figure 31 shows the usual setup of an IPCE apparatus. A high-pressure xenon lamp with an AM 1.5 G filter delivers the standard solar spectrum. The incident wavelength is selected by a grating monochromator, and appropriate filters are used. The incident light intensity is generally low, so that photodecomposition reactions and thermal effects are minimized. The mechanical

chopper interrupts the light periodically in order to allow a lock-in amplifier to be used to distinguish small photocurrents from dark currents [192].

Although initial measurements are often made assuming a Faradaic efficiency for water splitting of 100%, this assumption is not always valid, i.e., when there are parasite reactions [8]. Solar-to-chemical conversion efficiency cannot be made in a three-electrode configuration –Fig. 32. The direct detection of evolved  $H_2$  and  $O_2$  gases,





**Hydrogen Production from Photoelectrochemical Water Splitting, Fig. 32** (a) Schematic of a tandem PEC cell with incident solar simulated illumination, where the light not absorbed by the LBG photoanode is

transmitted to the SBG photocathode; (b) stability response and detection of evolved gases over time (Adapted from Ref. [35])

typically by mass spectroscopy or gas chromatography, is used to obtain the Faradaic efficiency,  $\eta_F$  [8]. The quantitative detection of  $H_2$  and  $O_2$  evolved requires perfect sealing of the PEC cell reactor. Measuring the operating photocurrent density,  $J_{op}$ , with an ammeter as a function of the time gives an indication of the stability of the whole PEC device. The integrated  $J_{op}$  gives the total charge passed, which can be compared with the total amount of gas evolved (accounting for the stoichiometry) for obtaining the Faradaic efficiency and then achieve the overall solar-to-hydrogen conversion efficiency,  $\eta_{STH}$  – Eq. 15.

## Future Directions

In the last few years, research on PEC water splitting technology has been growing quite fast and remarkable developments have been achieved, mainly concerning the development of new semiconductors capable of better stabilities, photocurrents, and photovoltages. Nevertheless, the primary goal of PEC research is to develop a system that balances complexity, cost, and performance in a stand-alone device. Ambitious

technological and economic targets have to be met for making PEC water splitting commercial: a minimum STH efficiency of ca. 10% and 10-year lifetime and a hydrogen threshold cost of \$2–\$4 per kg. Future directions should address four critical topics: (i) development of stable and efficient photoelectrodes, displaying a photocurrent of  $>8 \text{ mA}\cdot\text{cm}^{-2}$ ; (ii) optimization of tandem cell configurations for delivering the highest current density and where the possible electrical power production is used for driving auxiliary systems in a PEC farm; (iii) PEC cell scale-up to panel sizes, minimizing overpotentials and maximizing light use and the construction simplicity; and (iv) techno-economic and life-cycle assessments.

## Bibliography

### Primary Literature

1. Yilmaz F, Balta MT, Selbaş R (2016) A review of solar based hydrogen production methods. *Renew Sust Energ Rev* 56:171–178
2. Fujishima A, Honda K (1972) Electrochemical photolysis of water at a semiconductor electrode. *Nature* 238(5358):37–38

3. EIA (2015) Annual energy outlook 2015. [cited 2015 September]. [www.eia.doe.gov](http://www.eia.doe.gov)
4. van de Krol R, Grätzel M (2012) Introduction. In: van de Krol R, Grätzel M (eds) Photoelectrochemical hydrogen production. Springer, New York, pp 3–11
5. REN21 (2015) Renewables 2015 global status report. [cited 2015 October]. [www.ren21.net](http://www.ren21.net)
6. Lopes T, Andrade L, Mendes A (2013) Photoelectrochemical cells for hydrogen production from solar energy. In: Akbarzadeh NEA (ed) Solar energy sciences and engineering applications. CRC Press, Boca Raton, pp 293–341
7. Pinaud BA et al (2013) Technical and economic feasibility of centralized facilities for solar hydrogen production via photocatalysis and photoelectrochemistry. *Energy Environ Sci* 6(7):1983–2002
8. Chen Z et al (2010) Accelerating materials development for photoelectrochemical hydrogen production: standards for methods, definitions, and reporting protocols. *J Mater Res* 25(01):3–16
9. SPE. Global market outlook for solar power 2015–2019. [cited 2015 May]. [www.solarpowerurope.org](http://www.solarpowerurope.org)
10. Walter MG et al (2010) Solar water splitting cells. *Chem Rev* 110(11):6446–6473
11. Nowotny J et al (2005) Solar-hydrogen: environmentally safe fuel for the future. *Int J Hydrog Energy* 30(5):521–544
12. Hisatomi T, Kubota J, Domen K (2014) Recent advances in semiconductors for photocatalytic and photoelectrochemical water splitting. *Chem Soc Rev* 43(22):7520–7535
13. Miller EL (2010) Solar hydrogen production by photoelectrochemical water splitting: the promise and challenge. In: Vayssieres L (ed) On solar hydrogen & nanotechnology. Wiley, New York, pp 3–32
14. Coelho B, Oliveira AC, Mendes A (2010) Concentrated solar power for renewable electricity and hydrogen production from water – a review. *Energy Environ Sci* 3(10):1398–1405
15. Grimes CA, Varghese OK, Ranjan S (2008) Hydrogen generation by water splitting. In: Light, water, hydrogen. Springer, New York, pp 35–114
16. Grimes CA, Varghese OK, Ranjan S (2008) Photoelectrolysis. In: Light, water, hydrogen. Springer, New York, pp 115–190
17. Rothschild A, Dotan H (2017) Beating the efficiency of photovoltaics-powered electrolysis with tandem cell photoelectrolysis. *ACS Energy Lett* 2:45–51
18. Krol R (2012) Photo-electrochemical production of hydrogen. In: van de Krol R, Schoonman J (eds) Photoelectrochemical hydrogen production. Springer US, New York, pp 121–142
19. Aruchamy A, Aravamudan G, Subba Rao G (1982) Semiconductor based photoelectrochemical cells for solar energy conversion – an overview. *Bull Mater Sci* 4(5):483–526
20. Minggu LJ, Wan Daud WR, Kassim MB (2010) An overview of photocells and photoreactors for photoelectrochemical water splitting. *Int J Hydrog Energy* 35(11):5233–5244
21. Dumortier M, Tembhumne S, Haussener S (2015) Holistic design guidelines for solar hydrogen production by photo-electrochemical routes. *Energy Environ Sci* 8(12):3614–3628
22. Nozik AJ (1978) Photoelectrochemistry: applications to solar energy conversion. *Annu Rev Phys Chem* 29(1):189–222
23. Lopes T et al (2014) Hematite photoelectrodes for water splitting: evaluation of the role of film thickness by impedance spectroscopy. *Phys Chem Chem Phys* 16(31):16515–16523
24. Lopes T et al (2012) E-MRS/MRS bilateral energy conference innovative technological configurations of photoelectrochemical cells. *Energy Procedia* 22:35–40
25. Ager Iii JW et al (2015) Experimental demonstrations of spontaneous, solar-driven photoelectrochemical water splitting. *Energy Environ Sci* 8(10):2811–2824
26. Smith WA (2016) Photoelectrochemical cell design, efficiency, definitions, standards, and protocols. In: Giménez S, Bisquert J (eds) Photoelectrochemical solar fuel production: from basic principles to advanced devices. Springer International Publishing, Cham, pp 163–197
27. Krol R, Liang Y, Schoonman J (2008) Solar hydrogen production with nanostructured metal oxides. *J Mater Chem* 18(20):2311–2320
28. Sivula K, Le Formal F, Grätzel M (2011) Solar water splitting: progress using hematite ( $\alpha$ -Fe<sub>2</sub>O<sub>3</sub>) photoelectrodes. *ChemSusChem* 4(4):432–449
29. Weber MF, Dignam MJ (1984) Efficiency of splitting water with semiconducting photoelectrodes. *J Electrochem Soc* 131(6):1258–1265
30. Murphy AB et al (2006) Efficiency of solar water splitting using semiconductor electrodes. *Int J Hydrog Energy* 31(14):1999–2017
31. Abdi FF et al (2013) The origin of slow carrier transport in BiVO<sub>4</sub> thin film photoanodes: a time-resolved microwave conductivity study. *J Phys Chem Lett* 4(16):2752–2757
32. Klahr B et al (2012) Water oxidation at hematite photoelectrodes: the role of surface states. *J Am Chem Soc* 134(9):4294–4302
33. Klotz D et al (2016) Empirical in operando analysis of the charge carrier dynamics in hematite photoanodes by PEIS, IMPS and IMVS. *Phys Chem Chem Phys* 18(34):23438–23457
34. Barroso M et al (2013) Charge carrier trapping, recombination and transfer in hematite ([small alpha]-Fe<sub>2</sub>O<sub>3</sub>) water splitting photoanodes. *Chem Sci* 4(7):2724–2734
35. Sivula K, van de Krol R (2016) Semiconducting materials for photoelectrochemical energy conversion. *Nat Rev Mater* 1:16010
36. Lancelle-Beltran E et al (2008) *Eur J Inorg Chem*:903

37. James BD et al (2009) Technoeconomic analysis of photoelectrochemical (PEC) hydrogen production, U.D. Report, editor. Directed Technologies, Virginia
38. Zafer C et al (2005) *Sol Energy Mater Sol Cells* 88:11
39. Grimes CA, Varghese OK, Ranjan S (2008) Oxide semiconducting materials as photoanodes. In: *Light, water, hydrogen*. Springer, New York, pp 191–255
40. Grimes CA, Varghese OK, Ranjan S (2008) Non-oxide semiconductor nanostructures. In: *Light, water, hydrogen*. Springer, New York, pp 427–483
41. Osterloh FE (2008) Inorganic materials as catalysts for photochemical splitting of water. *Chem Mater* 20(1):35–54
42. Wang G et al (2014) Chemically modified nanostructures for photoelectrochemical water splitting. *J Photochem Photobiol C: Photochem Rev* 19:35–51
43. Nowotny J et al (2007) Titanium dioxide for solar-hydrogen I. Functional properties. *Int J Hydrog Energy* 32(14):2609–2629
44. Grimes CA, Varghese OK, Ranjan S (2008) Oxide semiconductors: nano-crystalline, tubular and porous systems. In: *Light, water, hydrogen*. Springer, New York, pp 257–369
45. Mavroides JG, Kafalas JA, Kolesar DF (1976) Photoelectrolysis of water in cells with SrTiO<sub>3</sub> anodes. *Appl Phys Lett* 28(5):241–243
46. Wang C et al (2014) Enhancing visible-light photoelectrochemical water splitting through transition-metal doped TiO<sub>2</sub> nanorod arrays. *J Mater Chem A* 2(42):17820–17827
47. Bak T et al (2002) Photo-electrochemical hydrogen generation from water using solar energy. Materials-related aspects. *Int J Hydrog Energy* 27(10):991–1022
48. Liu Q et al (2015) Black Ni-doped TiO<sub>2</sub> photoanodes for high-efficiency photoelectrochemical water-splitting. *Int J Hydrog Energy* 40(5):2107–2114
49. Khan SUM, Al-Shahry M, Ingler WB Jr (2002) Efficient photochemical water splitting by a chemically modified n-TiO<sub>2</sub>. *Science* 297(5590):2243–2245
50. Dias P et al (2016) Photoelectrochemical water splitting using WO<sub>3</sub> photoanodes: the substrate and temperature roles. *Phys Chem Chem Phys* 18(7):5232–5243
51. Liu X, Wang F, Wang Q (2012) Nanostructure-based WO<sub>3</sub> photoanodes for photoelectrochemical water splitting. *Phys Chem Chem Phys* 14(22):7894–7911
52. Zhu T, Chong MN, Chan ES (2014) Nanostructured tungsten trioxide thin films synthesized for photoelectrocatalytic water oxidation: a review. *ChemSusChem* 7(11):2974–2997
53. Solarska R, Jurczakowski R, Augustynski J (2012) A highly stable, efficient visible-light driven water photoelectrolysis system using a nanocrystalline WO<sub>3</sub> photoanode and a methane sulfonic acid electrolyte. *Nanoscale* 4(5):1553–1556
54. Seabold JA, Choi K-S (2011) Effect of a cobalt-based oxygen evolution catalyst on the stability and the selectivity of photo-oxidation reactions of a WO<sub>3</sub> photoanode. *Chem Mater* 23(5):1105–1112
55. Kwong WL, Lee CC, Messinger J (2016) Transparent nanoparticulate FeOOH improves the performance of a WO<sub>3</sub> photoanode in a tandem water-splitting device. *J Phys Chem C* 120(20):10941–10950
56. Wang S et al (2016) Synergistic crystal facet engineering and structural control of WO<sub>3</sub> films exhibiting unprecedented photoelectrochemical performance. *Nano Energy* 24:94–102
57. Satsangi VR, Dass S, Shrivastav R (2010) Nanostructured  $\alpha$ -Fe<sub>2</sub>O<sub>3</sub> in PEC generation of hydrogen. In: *On solar hydrogen & nanotechnology*. Wiley, New York, pp 349–397
58. Warren SC et al (2013) Identifying champion nanostructures for solar water-splitting. *Nat Mater* 12(9):842–849
59. Hardee KL, Bard AJ (1976) Semiconductor electrodes: V. The application of chemically vapor deposited iron oxide films to photosensitized electrolysis. *J Electrochem Soc* 123(7):1024–1026
60. Kim JY et al (2014) A stable and efficient hematite photoanode in a neutral electrolyte for solar water splitting: towards stability engineering. *Adv Energy Mater* 4(13):1614–6840
61. Dias P et al (2016) Extremely stable bare hematite photoanode for solar water splitting. *Nano Energy* 23:70–79
62. Satsangi VR et al (2008) Nanostructured hematite for photoelectrochemical generation of hydrogen. *Int J Hydrog Energy* 33(1):312–318
63. Mayer MT et al (2013) Forming heterojunctions at the nanoscale for improved photoelectrochemical water splitting by semiconductor materials: case studies on hematite. *Acc Chem Res* 46(7):1558–1566
64. Cesar I et al (2008) Influence of feature size, film thickness, and silicon doping on the performance of nanostructured hematite photoanodes for solar water splitting. *J Phys Chem C* 113(2):772–782
65. Hu Y-S et al (2009) Improved photoelectrochemical performance of Ti-doped  $\alpha$ -Fe<sub>2</sub>O<sub>3</sub> thin films by surface modification with fluoride. *Chem Commun* (19):2652–2654
66. Ling Y et al (2011) Sn-doped hematite nanostructures for photoelectrochemical water splitting. *Nano Lett* 11(5):2119–2125
67. Kim JY et al (2013) Single-crystalline, wormlike hematite photoanodes for efficient solar water splitting. *Sci Rep* 3:2681
68. Le Formal F et al (2014) Back electron-hole recombination in hematite photoanodes for water splitting. *J Am Chem Soc* 136(6):2564–2574
69. Tilley SD et al (2010) Light-induced water splitting with hematite: improved nanostructure and iridium oxide catalysis. *Angew Chem Int Ed* 49(36):1521–3773
70. Morales-Guio CG et al (2015) An optically transparent iron nickel oxide catalyst for solar water splitting. *J Am Chem Soc* 137(31):9927–9936

71. Jeon TH et al (2017) Ultra-efficient and durable photoelectrochemical water oxidation using elaborately designed hematite nanorod arrays. *Nano Energy* 39:211–218
72. Lefrou C, Fabry P, Poinet J-C (2012) Thermodynamic features. In: *Electrochemistry*. Springer, Berlin/Heidelberg, pp 119–168
73. Iandolo B et al (2015) The rise of hematite: origin and strategies to reduce the high onset potential for the oxygen evolution reaction. *J Mater Chem A* 3(33):16896–16912
74. Zandi O, Hamann TW (2015) The potential versus current state of water splitting with hematite. *Phys Chem Chem Phys* 17(35):22485–22503
75. Dias P, Andrade L, Mendes A (2017) Hematite-based photoelectrode for solar water splitting with very high photovoltage. *Nano Energy* 38:218–231
76. Jang J-W et al (2015) Enabling unassisted solar water splitting by iron oxide and silicon. *Nat Commun* 6:7447
77. Abdi FF, Firet N, van de Krol R (2013) Efficient BiVO<sub>4</sub> thin film photoanodes modified with cobalt phosphate catalyst and W-doping. *ChemCatChem* 5(2):490–496
78. Sayama K et al (2006) Photoelectrochemical decomposition of water into H<sub>2</sub> and O<sub>2</sub> on porous BiVO<sub>4</sub> thin-film electrodes under visible light and significant effect of Ag ion treatment. *J Phys Chem B* 110(23):11352–11360
79. Walsh A et al (2009) Band edge electronic structure of BiVO<sub>4</sub>: elucidating the role of the bi s and V d Orbitals. *Chem Mater* 21(3):547–551
80. Wang Z et al (2011) BiVO<sub>4</sub> nano-leaves: mild synthesis and improved photocatalytic activity for O<sub>2</sub> production under visible light irradiation. *CrystEngComm* 13(7):2500–2504
81. Abdi FF et al (2013) Efficient solar water splitting by enhanced charge separation in a bismuth vanadate-silicon tandem photoelectrode. *Nat Commun* 4:2195
82. Pihosh Y et al (2015) Photocatalytic generation of hydrogen by core-shell WO<sub>3</sub>/BiVO<sub>4</sub> nanorods with ultimate water splitting efficiency. *Sci Rep* 5:11141
83. Han L et al (2014) Efficient water-splitting device based on a bismuth vanadate photoanode and thin-film silicon solar cells. *ChemSusChem* 7(10):2832–2838
84. Shi X et al (2015) Unassisted photoelectrochemical water splitting beyond 5.7% solar-to-hydrogen conversion efficiency by a wireless monolithic photoanode/dye-sensitized solar cell tandem device. *Nano Energy* 13:182–191
85. Yourey JE, Bartlett BM (2011) Electrochemical deposition and photoelectrochemistry of CuWO<sub>4</sub>, a promising photoanode for water oxidation. *J Mater Chem* 21(21):7651–7660
86. Zhen C et al (2016) Tantalum (oxy)nitride based photoanodes for solar-driven water oxidation. *J Mater Chem A* 4(8):2783–2800
87. Li Y et al (2013) Cobalt phosphate-modified barium-doped tantalum nitride nanorod photoanode with 1.5% solar energy conversion efficiency. *Nat Commun* 4:2566
88. Liu G et al (2016) Enabling an integrated tantalum nitride photoanode to approach the theoretical photocurrent limit for solar water splitting. *Energy Environ Sci* 9(4):1327–1334
89. Liu G et al (2015) Efficient hole extraction from a hole-storage-layer-stabilized tantalum nitride photoanode for solar water splitting. *Chem Eur J* 21(27):9624–9628
90. Wang G et al (2011) Hydrogen-treated TiO<sub>2</sub> Nanowire arrays for photoelectrochemical water splitting. *Nano Lett* 11(7):3026–3033
91. Qiu Y et al (2016) Efficient solar-driven water splitting by nanocone BiVO<sub>4</sub>-perovskite tandem cells. *Sci Adv* 2(6):e1501764
92. Li Y et al (2016) WO<sub>3</sub>@ $\alpha$ -Fe<sub>2</sub>O<sub>3</sub> Heterojunction arrays with improved photoelectrochemical behavior for neutral pH water splitting. *ChemCatChem* 8(17):2765–2770
93. Hajibabaei H, Zandi O, Hamann TW (2016) Tantalum nitride films integrated with transparent conductive oxide substrates via atomic layer deposition for photoelectrochemical water splitting. *Chem Sci* 7(11):6760–6767
94. Memming R, Schwandt G (1968) Electrochemical properties of gallium phosphide in aqueous solutions. *Electrochim Acta* 13(6):1299–1310
95. Heller A (1981) Conversion of sunlight into electrical power and photoassisted electrolysis of water in photoelectrochemical cells. *Acc Chem Res* 14(5):154–162
96. Khaselev O, Turner JA (1998) A monolithic photovoltaic-photoelectrochemical device for hydrogen production via water splitting. *Science* 280(5362):425–427
97. Abe R (2010) Recent progress on photocatalytic and photoelectrochemical water splitting under visible light irradiation. *J Photochem Photobiol C: Photochem Rev* 11(4):179–209
98. Nakato Y et al (1987) Hydrogen photoevolution at p-type silicon electrodes coated with discontinuous metal layers. *J Electroanal Chem* 228(1–2):97–108
99. Hamann TW, Lewis NS (2006) Control of the stability, electron-transfer kinetics, and pH-dependent energetics of Si/H<sub>2</sub>O interfaces through methyl termination of Si(111) surfaces. *J Phys Chem B* 110(45):22291–22294
100. Lin Y et al (2013) Amorphous Si thin film based photocathodes with high photovoltage for efficient hydrogen production. *Nano Lett* 13(11):5615–5618
101. Meyer BK et al (2012) Binary copper oxide semiconductors: from materials towards devices. *Phys Status Solidi B* 249(8):1487–1509
102. Paracchino A et al (2011) Highly active oxide photocathode for photoelectrochemical water reduction. *Nat Mater* 10(6):456–461

103. Azevedo J et al (2014) On the stability enhancement of cuprous oxide water splitting photocathodes by low temperature steam annealing. *Energy Environ Sci* 7(12):4044–4052
104. Tilley SD et al (2013) Ruthenium oxide hydrogen evolution catalysis on composite cuprous oxide water-splitting photocathodes. *Adv Funct Mater* 24(3):1616–3028
105. Luo J et al (2016) Cu<sub>2</sub>O nanowire photocathodes for efficient and durable solar water splitting. *Nano Lett* 16(3):1848–1857
106. Dias P et al (2015) Transparent cuprous oxide photocathode enabling a stacked tandem cell for unbiased water splitting. *Adv Energy Mater* 5(24):1614–6840
107. Prévot MS, Guijarro N, Sivula K (2015) Enhancing the performance of a robust sol–gel-processed p-type Delafossite CuFeO<sub>2</sub> photocathode for solar water reduction. *ChemSusChem* 8(8):1359–1367
108. Li Z et al (2013) Photoelectrochemical cells for solar hydrogen production: current state of promising photoelectrodes, methods to improve their properties, and outlook. *Energy Environ Sci* 6(2):347–370
109. Shen S et al (2016) Hematite heterostructures for photoelectrochemical water splitting: rational materials design and charge carrier dynamics. *Energy Environ Sci* 9(9):2744–2775
110. Gross Koren M, Dotan H, Rothschild A (2016) Nano gold rush: on the origin of the photocurrent enhancement in hematite photoanodes decorated with gold Nanoparticles. *J Phys Chem C* 120(28):15042–15051
111. Osterloh FE (2013) Inorganic nanostructures for photoelectrochemical and photocatalytic water splitting. *Chem Soc Rev* 42(6):2294–2320
112. Guijarro N, Prevot MS, Sivula K (2015) Surface modification of semiconductor photoelectrodes. *Phys Chem Chem Phys* 17(24):15655–15674
113. Montoya JH et al (2017) Materials for solar fuels and chemicals. *Nat Mater* 16(1):70–81
114. Fabbri E et al (2014) Developments and perspectives of oxide-based catalysts for the oxygen evolution reaction. *Cat Sci Technol* 4(11):3800–3821
115. Seh ZW et al (2017) Combining theory and experiment in electrocatalysis: insights into materials design. *Science* 355(6321)
116. Morales-Guio CG et al (2014) Hydrogen evolution from a copper(I) oxide photocathode coated with an amorphous molybdenum sulphide catalyst. *Nat Commun* 5:3059
117. Zhang D et al (2015) One-step preparation of optically transparent Ni-Fe oxide film electrocatalyst for oxygen evolution reaction. *Electrochim Acta* 169:402–408
118. Zeradjanin AR et al (2014) Rational design of the electrode morphology for oxygen evolution – enhancing the performance for catalytic water oxidation. *RSC Adv* 4(19):9579–9587
119. Chang JA et al (2012, 1863) *Nano Lett* 12
120. Gamelin DR (2012) Water splitting: catalyst or spectator? *Nat Chem* 4(12):965–967
121. Faughnan BW, Kiss ZJ (1968) *Phys Rev Lett* 21:1331
122. Chang JA et al (2010) *Nano Lett* 10:2609
123. Prévot MS, Sivula K (2013) Photoelectrochemical tandem cells for solar water splitting. *J Phys Chem C* 117(35):17879–17893
124. Conibeer GJ, Richards BS (2007) A comparison of PV/electrolyser and photoelectrolytic technologies for use in solar to hydrogen energy storage systems. *Int J Hydrog Energy* 32(14):2703–2711
125. Grätzel M (2005) Solar energy conversion by dye-sensitized photovoltaic cells. *Inorg Chem* 44(20):6841–6851
126. Luo J et al (2014) Water photolysis at 12.3% efficiency via perovskite photovoltaics and earth-abundant catalysts. *Science* 345(6204):1593–1596
127. Zhang K et al (2016) Water splitting progress in tandem devices: moving photolysis beyond electrolysis. *Adv Energy Mater* 6(15):1600602
128. Mor GK et al (2008) P-type Cu–Ti–O nanotube arrays and their use in self-biased heterojunction photoelectrochemical diodes for hydrogen generation. *Nano Lett* 8(10):3555–3555
129. Seger B et al (2014) 2-photon tandem device for water splitting: comparing photocathode first versus photoanode first designs. *Energy Environ Sci* 7(8):2397–2413
130. Grätzel M (2001) Photoelectrochemical cells. *Nature* 414(6861):338–344
131. Grätzel M, Augustynski J Tandem cell for water cleavage by visible light 2001. EPFL
132. Duret A, Gratzel M (2005) Visible light-induced water oxidation on Mesoscopic  $\alpha$ -Fe<sub>2</sub>O<sub>3</sub> films made by ultrasonic spray Pyrolysis. *J Phys Chem B* 109(36):17184–17191
133. Park N-G (2013) Organometal perovskite light absorbers toward a 20% efficiency low-cost solid-state Mesoscopic solar cell. *J Phys Chem Lett* 4(15):2423–2429
134. Tan S et al (2004) *J Phys Chem B* 108:18693
135. Cervini R, Cheng Y, Simon G (2004) *J Phys D Appl Phys* 37:13
136. Magalhães MAM et al (2010) Glass sealing of dye-sensitized solar cells. Google Patents
137. May MM et al (2015) Efficient direct solar-to-hydrogen conversion by in situ interface transformation of a tandem structure. *Nat Commun* 6:8286
138. Khaselev O, Bansal A, Turner JA (2001) High-efficiency integrated multijunction photovoltaic/electrolysis systems for hydrogen production. *Int J Hydrog Energy* 26(2):127–132
139. Kelly NA, Gibson TL (2006) Design and characterization of a robust photoelectrochemical device to generate hydrogen using solar water splitting. *Int J Hydrog Energy* 31(12):1658–1673
140. Kim JH et al (2016) Hetero-type dual photoanodes for unbiased solar water splitting with extended light harvesting. *Nat Commun* 7:13380

141. Wang X et al (2013) Silicon/hematite core/shell nanowire array decorated with gold nanoparticles for unbiased solar water oxidation. *Nano Lett* 14(1):18–23
142. Liu C et al (2013) A fully integrated nanosystem of semiconductor nanowires for direct solar water splitting. *Nano Lett* 13(6):2989–2992
143. Sonya K et al (2016) Tandem photo-voltaic–photoelectrochemical GaAs/InGaAsP–WO<sub>3</sub>/BiVO<sub>4</sub> device for solar hydrogen generation. *Jpn J Appl Phys* 55(4S):04ES01
144. Gaillard N et al (2010) Status of research on tungsten oxide-based photoelectrochemical devices at the University of Hawai'i
145. Shi X et al (2016) Unassisted photoelectrochemical water splitting exceeding 7% solar-to-hydrogen conversion efficiency using photon recycling. *Nat Commun* 7
146. Brillet J et al (2012) Highly efficient water splitting by a dual-absorber tandem cell. *Nat Photon* 6(12):824–828
147. Gurudayal et al (2017) Atomically altered hematite for highly efficient Perovskite tandem water-splitting devices. *ChemSusChem* 10(11):2449–2456
148. Gurudayal et al (2016) Highly active MnO catalysts integrated onto Fe<sub>2</sub>O<sub>3</sub> Nanorods for efficient water splitting. *Adv Mater Interfaces* 3(15):1600176
149. Luo J et al (2015) Targeting ideal dual-absorber tandem water splitting using perovskite photovoltaics and CuIn<sub>x</sub>Ga<sub>1-x</sub>Se<sub>2</sub> photocathodes. *Adv Energy Mater* 5(24):1501520
150. Mor GK et al (2009) *Nano Lett* 9:4250
151. Bolton JR, Strickler SJ, Connolly JS (1985) Limiting and realizable efficiencies of solar photolysis of water. *Nature* 316(6028):495–500
152. Xu P et al (2016) Photoelectrochemical cell for unassisted overall solar water splitting using a BiVO<sub>4</sub> photoanode and Si nanoarray photocathode. *RSC Adv* 6(12):9905–9910
153. Kim JH et al (2016) Overall photoelectrochemical water splitting using tandem cell under simulated sunlight. *ChemSusChem* 9(1):61–66
154. Li W et al (2015) Hematite-based solar water splitting in acidic solutions: functionalization by mono- and multilayers of iridium oxygen-evolution catalysts. *Angew Chem Int Ed* 54(39):11428–11432
155. Bornoz P et al (2014) A bismuth Vanadate–cuprous oxide tandem cell for overall solar water splitting. *J Phys Chem C* 118(30):16959–16966
156. Lin C-Y et al (2012) Cu<sub>2</sub>O/NiO<sub>x</sub> nanocomposite as an inexpensive photocathode in photoelectrochemical water splitting. *Chem Sci* 3(12):3482–3487
157. Snaith HJ et al (2011) Lead-sulphide quantum-dot sensitization of tin oxide based hybrid solar cells. *Sol Energy* 85(6):1283–1290
158. Ingler WB, Khan SUM (2006) A self-driven p/n-Fe<sub>2</sub>O<sub>3</sub> tandem photoelectrochemical cell for water splitting, vol 9. ETATS-UNIS: Institute of Electrical and Electronics Engineers, Pennington
159. Kainthla RC, Zelenay B, Bockris JO (1987) Significant efficiency increase in self-driven photoelectrochemical cell for water photoelectrolysis. *J Electrochem Soc* 134(4):841–845
160. Turner JE, Hendewerk M, Somorjai GA (1984) The photodissociation of water by doped iron oxides: the unblased p/n assembly. *Chem Phys Lett* 105(6):581–585
161. Mettee H, Otvos JW, Calvin M (1981) Solar induced water splitting with p/n heterotype photochemical diodes: n-Fe<sub>2</sub>O<sub>3</sub>/p-GaP. *Sol Energy Mater* 4(4):443–453
162. Ohashi K, McCann J, Bockris JOM (1977) Stable photoelectrochemical cells for the splitting of water. *Nature* 266(5603):610–611
163. Nozik AJ (1976) P-n photoelectrolysis cells. *Appl Phys Lett* 29(3):150–153
164. Jacobsson TJ et al (2015) A theoretical analysis of optical absorption limits and performance of tandem devices and series interconnected architectures for solar hydrogen production. *Sol Energy Mater Sol Cells* 138:86–95
165. Dias P et al (2014) Temperature effect on water splitting using a Si-doped hematite photoanode. *J Power Sources* 272:567–580
166. Bard AJ, Faulkner LR (2001) *Electrochemical methods fundamentals and applications*, 2nd edn. Wiley, New York, p XXI, 833
167. Yang X et al (2015) Enabling practical electrocatalyst-assisted photoelectron-chemical water splitting with earth abundant materials. *Nano Res* 8(1):56–81
168. Gadgil PN (1990) Preparation of iron pyrite films for solar cells by metalorganic chemical vapor deposition. Simon Fraser University, Burnaby, p 241
169. Gerischer H (1977) On the stability of semiconductor electrodes against photodecomposition. *J Electroanal Chem* 82(1–2):133–143
170. Bard AJ, Wrighton MS (1977) Thermodynamic potential for the anodic dissolution of n-type semiconductors. *J Electrochem Soc* 124(11):1706–1710
171. Memming R (2001) *Semiconductor electrochemistry*, 1st edn. Wiley-VCH, Weinheim
172. Sinn C, Meissner D, Memming R (1990) Charge transfer processes at WSe<sub>2</sub> electrodes with pH-controlled stability. *J Electrochem Soc* 137(1):168–172
173. van de Krol R (2012) Photoelectrochemical measurements. In: Van de Krol R, Grätzel M (eds) *Photoelectrochemical hydrogen production*. Springer, New York, pp 13–67
174. Snaith HJ et al (2008) *Nanotechnol* 19:424003
175. Lopes T et al (2014) An innovative photoelectrochemical lab device for solar water splitting. *Sol Energy Mater Sol Cells* 128:399–410
176. PECDEMO (2017) *Photoelectrochemical Demonstrator Device – PECDEMO*. [cited 2017 10th January]



177. Magalhães MAM et al. (2014) Substrate and electrode for solar cells and corresponding manufacturing process. Google Patents
178. Landman A et al. (2017) Photoelectrochemical water splitting in separate oxygen and hydrogen cells. *Nat Mater*. Advance online publication
179. Lopes T (2014) Characterization and phenomenological modeling of photoelectrochemical cells for hydrogen production from solar energy, in Chemical Engineering Department. University of Porto – FEUP, Porto
180. Coridan RH et al (2015) Methods for comparing the performance of energy-conversion systems for use in solar fuels and solar electricity generation. *Energy Environ Sci*
181. Ding IK et al (2009) Pore-filling of Spiro-OMeTAD in solid-state dye sensitized solar cells: quantification, mechanism, and consequences for device performance. *Adv. Funct. Mater* 19(19):2431–2436
182. Dotan H et al (2014) On the solar to hydrogen conversion efficiency of photoelectrodes for water splitting. *J Phys Chem Lett* 5(19):3330–3334
183. Hirsch A et al (2001) Long-term stability of dye-sensitized solar cells. *Prog Photovolt Res Appl* 9(6):425–438
184. O’Hayre R et al (2006) Fuel cell fundamentals. Wiley, New York, p XXII, 409
185. Macdonald JR, Johnson WB (2005) Fundamentals of impedance spectroscopy. In: Impedance spectroscopy. Wiley, Hoboken, pp 1–26
186. Barsoukov E, Macdonald JR (eds) (2005) Impedance spectroscopy: theory, experiment, and applications, 2nd edn. Wiley-Interscience, Hoboken, p 595
187. Andrade L, Ribeiro HA, Mendes A (2011) Dye-sensitized solar cells: an overview. In: Encyclopedia of inorganic and bioinorganic chemistry. Wiley, Hoboken
188. Barsoukov E, Macdonald JR (2005) Impedance spectroscopy: theory, experiment and applications. Second ed. Wiley, Hoboken
189. Bisquert J et al (2016) Analysis of photoelectrochemical systems by impedance spectroscopy. In: Giménez S, Bisquert J (eds) Photoelectrochemical solar fuel production: from basic principles to advanced devices. Springer International Publishing, Cham, pp 281–321
190. Peter LM, Vanmaekelbergh D (2008) Time and frequency resolved studies of photoelectrochemical kinetics. In: Alkire RC, Kolb DM (eds) Advances in electrochemical science and engineering. Wiley, Weinheim, pp 77–164
191. Li W et al (2016) Comparison of heterogenized molecular and heterogeneous oxide catalysts for photoelectrochemical water oxidation. *Energy Environ Sci*
192. Archer MD, Nozik AJ (2008) Nanostructured and photoelectrochemical systems for solar photon conversion. Series on photoconversion of solar energy, v. 3. Imperial College Press/World Scientific, London/Singapore/Hackensack

## Books and Reviews

- Ager Iii JW et al (2015) Experimental demonstrations of spontaneous, solar-driven photoelectrochemical water splitting. *Energy Environ Sci* 8(10): 2811–2824
- Archer MD, Nozik AJ (2008) Nanostructured and photoelectrochemical systems for solar photon conversion. Series on photoconversion of solar energy, vol 3. Imperial College Press/World Scientific, London/Singapore/Hackensack
- Bard AJ, Faulkner LR (2001) Electrochemical methods fundamentals and applications, 2nd edn. Wiley, New York, p XXI, 833
- Barsoukov E, Macdonald JR (2005) Impedance spectroscopy: theory, experiment, and applications, 2nd edn. Wiley-Interscience, Hoboken
- Bisquert J (2014) Nanostructured energy devices: equilibrium concepts and kinetics. CRC Press, Boca Raton
- Bisquert J, Giménez S (2016) Photoelectrochemical solar fuel production: from basic principles to advanced devices. Springer International Publishing, Cham
- Coridan RH et al (2015) Methods for comparing the performance of energy-conversion systems for use in solar fuels and solar electricity generation. *Energy Environ Sci* 8:2886–2901
- Dotan H et al (2014) On the solar to hydrogen conversion efficiency of photoelectrodes for water splitting. *J Phys Chem Lett* 5(19):3330–3334
- Grätzel M (2001) Photoelectrochemical cells. *Nature* 414(6861):338–344
- Grimes CA, Varghese OK, Ranjan S (2008) Light, water, hydrogen. Springer, New York
- Guijarro N, Prevot MS, Sivula K (2015) Surface modification of semiconductor photoelectrodes. *Phys Chem Chem Phys* 17(24):15655–15674
- Hamann CH, Hamnett A, Vielstich W (2007) Electrochemistry. Wiley, Weinheim
- Huggins RA (2010) Energy storage. Springer US, New York
- Lopes T, Andrade L, Mendes A (2013) Photoelectrochemical cells for hydrogen production from solar energy. In: Enteria N, Akbarzadeh A (eds) Solar energy sciences and engineering applications. CRC Press, Boca Raton, pp 293–341
- Memming R (2001) Semiconductor electrochemistry, 1st edn. Wiley-VCH, Weinheim
- Montoya JH et al (2017) Materials for solar fuels and chemicals. *Nat Mater* 16(1):70–81
- Nozik AJ (1978) Photoelectrochemistry: applications to solar energy conversion. *Annu Rev Phys Chem* 29(1):189–222
- O’Hayre R et al (2006) Fuel cell fundamentals. Wiley, New York, p XXII
- Peter LM, Vanmaekelbergh D (2008) Time and frequency resolved studies of photoelectrochemical kinetics. In: Alkire RC, Kolb DM (eds) Advances in electrochemical science and engineering. Wiley, Weinheim, pp 77–164

- Pierret RF (2003) *Advanced semiconductor fundamentals. Modular series on solid state devices, vol VI.* Addison-Wesley, Reading
- Pinaud BA et al (2013) Technical and economic feasibility of centralized facilities for solar hydrogen production via photocatalysis and photoelectrochemistry. *Energy Environ Sci* 6(7):1983–2002
- Rothschild A, Dotan H (2017) Beating the efficiency of photovoltaics-powered electrolysis with tandem cell photoelectrolysis. *ACS Energy Lett* 2:45–51
- Seh ZW et al (2017) Combining theory and experiment in electrocatalysis: insights into materials design. *Science* 355(6321):eaad4998
- Shen S et al (2016) Hematite heterostructures for photoelectrochemical water splitting: rational materials design and charge carrier dynamics. *Energy Environ Sci* 9(9):2744–2775
- Sivula K (2013) Metal oxide photoelectrodes for solar fuel production, surface traps, and catalysis. *J Phys Chem Lett* 4(10):1624–1633
- Sivula K, Le Formal F, Grätzel M (2011) Solar water splitting: progress using hematite ( $\alpha$ -Fe<sub>2</sub>O<sub>3</sub>) photoelectrodes. *ChemSusChem* 4(4):432–449
- Sivula K, van de Krol R (2016) Semiconducting materials for photoelectrochemical energy conversion. *Nat Rev Mater*:16010
- Smith WA et al (2015) Interfacial band-edge energetics for solar fuels production. *Energy Environ Sci*
- van de Krol R, Grätzel M (2012) *Photoelectrochemical hydrogen production.* Springer US, New York
- van de Krol R, Liang Y, Schoonman J (2008) Solar hydrogen production with nanostructured metal oxides. *J Mater Chem* 18(20):2311–2320
- Vayssieres L (2010) *On solar hydrogen & nanotechnology.* Wiley, New York
- Walter MG et al (2010) Solar water splitting cells. *Chem Rev* 110(11):6446–6473
- Würfel P (2007) *Physics of solar cells.* Wiley-VCH, Weinheim, pp 37–84
- Yang X et al (2015) Enabling practical electrocatalyst-assisted photoelectron-chemical water splitting with earth abundant materials. *Nano Res* 8(1): 56–81
- Zhang K et al (2016) Water splitting progress in tandem devices: moving photolysis beyond electrolysis. *Adv Energy Mater* 6(15):1600602



## Hydrogen via Direct Solar Production

Shamindri M. Arachchige and Karen J. Brewer  
Department of Chemistry, Virginia Polytechnic Institute and State University, Blacksburg, VA, USA

### Article Outline

Glossary  
Definition of the Subject  
Introduction  
Photochemical Water Splitting  
Components for Supramolecular Solar Hydrogen Photocatalysis  
Solar Hydrogen Photocatalysis  
Iron-Based System  
Rh-Based Supramolecular and Multicomponent Systems  
Co-Based Supramolecular and Multicomponent Systems  
Pt and Pd-Based Homogeneous Systems for Solar Hydrogen Production  
Palladium-Based Supramolecular Solar Hydrogen Photocatalysts  
Conclusions and Future Directions  
Bibliography

### Glossary

- BL** A ligand that is located between two metals in a supramolecule, bridging ligand.
- bpy** A bidentate terminal ligand, 2,2'-bipyridine.
- CAT** The site of a reaction that occurs via catalysis, facilitated by the catalyst without the destruction of this subunit occurring multiple times in a cycle.
- dmgBF<sub>2</sub>** (Difluoroboryl) dimethylglyoximate.
- dmgH** Dimethylglyoximate.
- dpp** A bidentate bridging ligand, 2,3-bis(2-pyridyl) benzoquinoxaline.
- dpgBF<sub>2</sub>** (Difluoroboryl)diphenylglyoximate.
- dpp** A bidentate bridging ligand, 2,3-bis(2-pyridyl) pyrazine.
- dpg** A bidentate bridging ligand, 2,3-bis(2-pyridyl) quinoxaline.
- EA** A subunit that functions to accept an electron in a redox reaction, electron acceptor.
- ED** A subunit that functions to donate an electron in a redox reaction, electron donor.
- et** Excited state electron transfer, oxidation or reduction reaction involving the loss or gain of an electron that occurs in an electronic excited state.
- GS** Electronic ground state of a molecule.
- HOMO** Highest occupied molecular orbital for a molecule.
- I<sub>a</sub>** Intensity of incident light.
- ic** Internal conversion, a non-radiative process that allows conversion between two electronic states of the same spin multiplicity.
- isc** Intersystem crossing, a non-radiative process that allows conversion between two electronic states of different spin multiplicity.
- k<sub>x</sub>** Rate constant of process "x."
- LA** Ground electronic state of a light absorber.
- \*LA** Excited electronic state of a light absorber.
- L-pyr** A monodentate terminal ligand, [(4-pyridine) oxazolo(4,5-f)phenanthroline].
- LUMO** Lowest unoccupied molecular orbital for a molecule.
- Me<sub>2</sub>bpy** A bidentate terminal ligand, 4,4'-dimethyl-2,2'-bipyridine.
- Me<sub>2</sub>phen** A bidentate terminal ligand, 4,7-dimethylphenanthroline.
- MLCT** Metal-to-ligand charge-transfer, an electronic excited state.
- MMCT** Metal-to-metal charge-transfer, an electronic excited state.
- nr** Non-radiative decay or movement between electronic states via processes that do not involve the absorption or emission of light.
- phen** A bidentate terminal ligand, 1,10-phenanthroline.

- ppy** A monodentate terminal ligand, 2-phenylpyridine.
- py** A N containing aromatic ring, pyridyl.
- q** Bimolecular deactivation, a reaction of an electronic excited state of a molecule which results in relaxation to the ground state via interaction with another molecule without transfer of electrons or generation of an excited state.
- Q** Quencher, a molecule that is engaged in a reaction with an electronic excited state of another molecule leading to generation of the ground state of the excited molecule.
- rxn** Photochemical reaction from the electronic excited state of a molecule.
- TL** A ligand that is located at the end of a supra-molecule and bound to only one metal center, terminal ligand.
- tpy** A tridentate terminal ligand, 2,2':6',2''-terpyridine.
- $\lambda_{\max}^{\text{abs}}$  Absorption maximum.
- $\lambda_{\max}^{\text{em}}$  Emission maximum.
- $\Phi$  Quantum yield or a process provides the number of events of interest that occur from an electronic excited state as related to the number of excited molecules.
- $\Phi^{\text{em}}$  Quantum yield of emission providing the number of photons emitted by an electronic excited state of a molecule divided by the number of photons absorbed.

## Definition of the Subject

Developing renewable sources of energy to replace reliance on fossil fuels remains a major challenge. Sunlight is recognized as the largest of all carbon-neutral energy sources with  $4.3 \times 10^{20}$  J reaching the earth's surface in 1 h, larger than the current energy consumption by humans in a year [1, 2]. Plants harness solar energy through photosynthesis, which is used to power the biological world and ultimately stored in carboniferous fossil fuels. The rate of production of fossil fuels is exceeded by current consumption leading to interest in artificial means to harvest solar energy. Growing energy demands due to rising living standards and increased population have stimulated a global initiative to exploring alternative means to harness solar

energy and alternative energy sources. Current methods to harness solar energy for practical purposes do not compete with fossil fuel use. Artificial photosynthesis, use of synthetic systems that mimic photosynthetic energy conversion, provides an attractive avenue for solar fuel production [1–4]. The “hydrogen economy,” transformation from an oil-based economy to a hydrogen-based one, has been proposed as an attractive energy solution for the future [1–6]. Hydrogen provides a high energy content per gram (120 kJ/g), can be used in fuel cells, and has low environmental impact. Hydrogen is found in various feedstocks on earth, combined with oxygen in water and carbon in fossil fuels. Steam-methane reforming currently provides about 95% of the hydrogen used in the United States [7]. Visible light-induced solar hydrogen production from water would be the ultimate clean, renewable energy solution. Molecule-based systems for artificial photosynthesis offers unique insight into electron transfer processes amenable to study by conventional experimental techniques. A molecular-based artificial photosynthetic fuel production system requires an antenna to capture light, generation of a potential, and a catalyst for reduction of the substrate, water. Water reduction to produce hydrogen fuel is complex involving charge separation, multielectron reactions, and chemical bond reorganization. Functioning molecular photocatalysts for water reduction have emerged recently, but practical systems do not yet exist. Engineering systems that can efficiently produce hydrogen from water is a topic of extensive research and developmental efforts with significant progress made in identifying the molecular components necessary for this complicated chemistry.

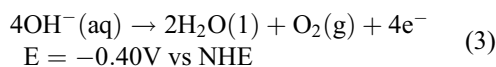
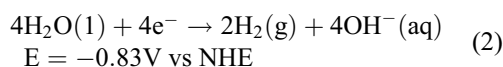
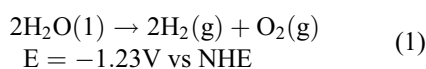
## Introduction

This contribution highlights recent progress in the use of complex molecular systems that reduce water or protons for solar hydrogen production. Supramolecular complexes in this forum are large molecular assemblies composed of multiple components whose individual properties provide a unique function to the supramolecule [8]. The focus will be

on supramolecular complexes that couple a light-absorbing unit (LA) to a reactive metal center that is the catalyst (CAT). Systems are designed so that the orbital energetics of the molecular components allow efficient intramolecular charge-transfer to the CAT upon light activation. Although the properties of the components are typically perturbed in the supramolecular assemblies, the individual components bring to the molecular device a unique function retained by each subunit in the assembly. A sacrificial electron donor (ED) is typically used to reductively quench the oxidized LA. The foundation for supramolecular photochemistry was established by the pioneering work using separate LAs and hydrogen-generating CATs in solar energy conversion schemes [9–11]. Recent progress using homogeneous multicomponent systems in solar hydrogen production will also be presented. The multicomponent systems consist of a LA, electron relay (ER), and a CAT that are not covalently linked. Illustrative examples of different molecular architectures are provided and the photochemistry discussed. Factors impacting system efficiency, including light-absorbing ability at desired wavelengths, the quantum yield of product formation ( $\Phi$ ), and the turnover number (TON) for system components, will be highlighted.

## Photochemical Water Splitting

Solar water splitting uses energy from the sun to split water into hydrogen and oxygen. The splitting of water is an energetically uphill process requiring 1.23 eV. The overall reactions for water splitting are multielectron processes (Eqs. 1, 2, and 3):



The redox potentials are pH dependent with proton reduction at pH = 1 occurring at 0.00 V vs. NHE. Multielectron chemistry is key as multielectron water is energetically much more favorable (1.23 V vs. NHE) [1] than water splitting using single electron pathways (5 V vs. NHE) [11]. Most of the solar spectrum has energies >1.23 eV and can be used for the multielectron splitting of water. Many systems are reported to split water using ultraviolet radiation but the fraction of available solar power in this region is smaller, and focus has been to use more abundant, lower energy light to power water photolysis [3, 4]. Due to the complicated nature of designing complete water splitting systems, researchers typically focus on understanding either water oxidation or water reduction, by replacing the other half with a sacrificial electron acceptor or a sacrificial ED.

## Components for Supramolecular Solar Hydrogen Photocatalysis

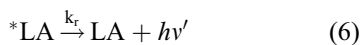
The individual components within the supramolecule provide the overall photocatalytic activity to the supramolecule, thus careful consideration must be given to selecting structural components. The perturbation of each component upon assembly in a supramolecule must be predictable and controllable, with the overall function being maintained.

**Light Absorption** LA is used in this forum to absorb light and transfer that energy or an electron to other parts of the supramolecule. Incorporation of a LA within the molecular architecture that absorbs in the visible region allows for the use of more of the solar spectrum in solar hydrogen production schemes. A LA absorbs a photon of light to form an electronically excited state,  $^*LA$ , which has distinctive properties compared to the ground state system, Eq. 4:

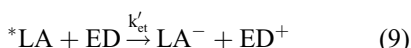
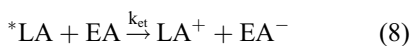
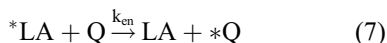


Once excited, relaxation of the  $^*LA$  to the ground state can occur in a non-radiative fashion,

through heat loss or in a radiative fashion by emitting light, Eqs. 5 and 6:



Excited states can be quenched by energy or electron transfer, see Eqs. 7, 8, and 9:



The thermodynamic driving force ( $E_{\text{redox}}$ ) of excited state electron transfer depends on the excited state reduction potential of the LA ( $E(*LA^{n+}/LA^{(n-1)+})$ ) and the ground state oxidation potential of the ED ( $E(ED^{0/+})$ ) for excited state reduction, Eq. 10, or the excited state oxidation potential of the LA ( $E(*LA^{n+}/LA^{(n+1)+})$ ) and the ground state reduction potential of the EA ( $E(EA^{0/-})$ ) for excited state oxidation, Eq. 11. The excited state redox potentials,  $E(*LA^{n+}/LA^{(n-1)+})$  and  $E(*LA^{n+}/LA^{(n+1)+})$ , differ significantly from the ground state potentials as electronic excited states are both better oxidizing and reducing agents relative to their ground states. The excited state redox potentials can be calculated based on the ground state reduction or oxidation potential of the LA and the energy gap between the ground vibronic state of the electronic ground and excited states ( $E^{0-0}$ ), Eqs. 12 and 13:

$$E_{\text{redox}}(\text{red}) = E\left(*LA^{n+}/LA^{(n-1)+}\right) - E\left(ED^{0/+}\right) \quad (10)$$

$$E_{\text{redox}}(\text{oxd}) = E\left(*LA^{n+}/LA^{(n+1)+}\right) - E\left(EA^{0/-}\right) \quad (11)$$

$$E\left(*LA^{n+}/LA^{(n-1)+}\right) = E\left(LA^{n+}/LA^{(n-1)+}\right) + E^{0-0} \quad (12)$$

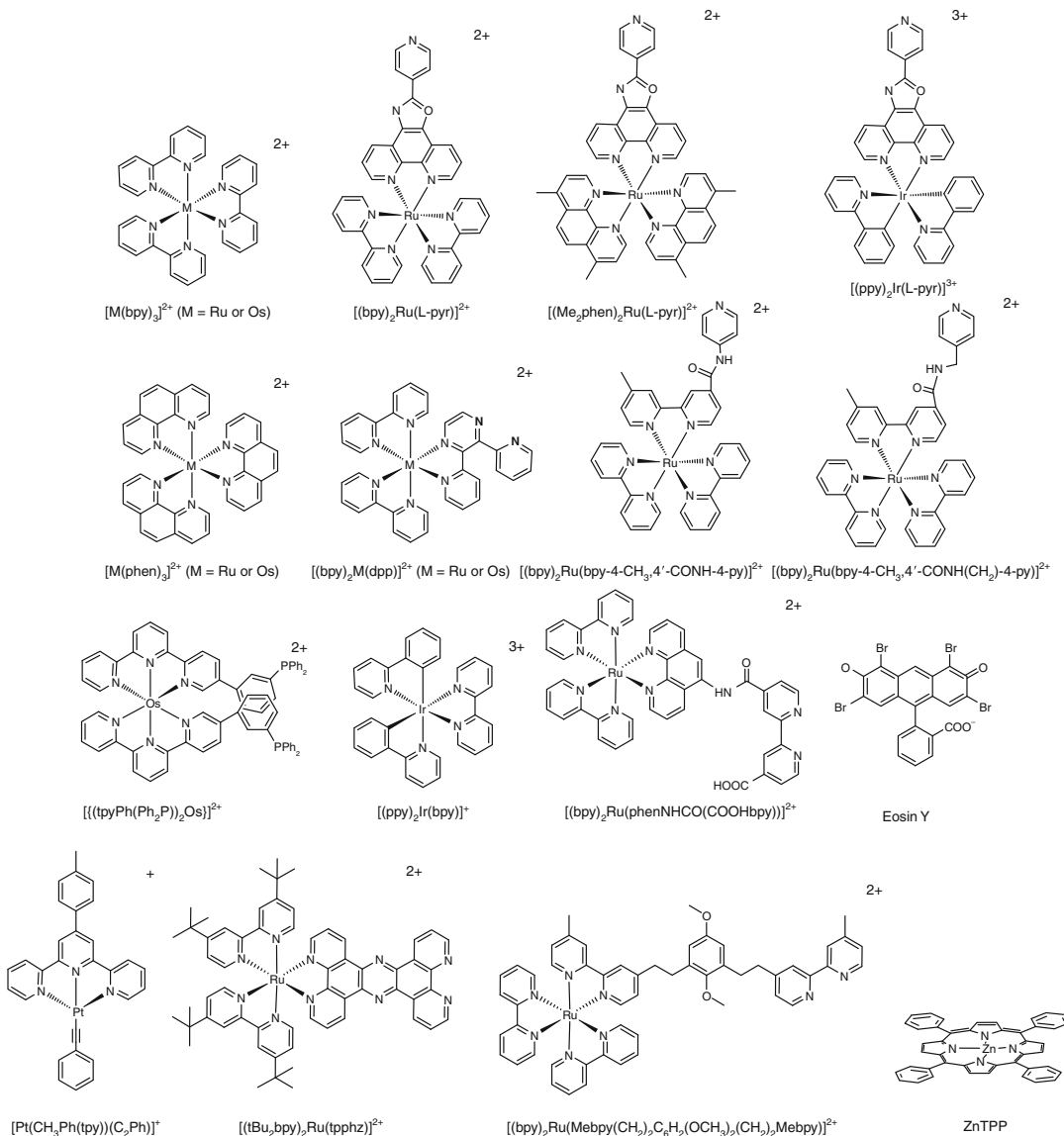
$$E\left(*LA^{n+}/LA^{(n+1)+}\right) = E\left(LA^{n+}/LA^{(n+1)+}\right) - E^{0-0} \quad (13)$$

*Common Light Absorbers* Ruthenium and late transition metal complexes are widely applicable LAs with strong absorptivity and good spectral coverage as well as long-lived emissive metal-to-ligand charge-transfer (MLCT) excited states [9, 10, 12–15]. Some commonly used LAs used in solar energy conversion schemes are shown in Fig. 1. The excited state of  $[Ru(\text{bpy})_3]^{2+}$  is capable of excited state electron- [16–18] and energy-transfer reactions.  $[Ru(\text{bpy})_3]^{2+}$  absorbs light with high extinction coefficients in the ultraviolet and visible regions of the spectrum. The UV-region is dominated by intense absorptions that are intraligand (IL)  $\pi \rightarrow \pi^*$  in nature, while the visible region is dominated by  $Ru(d\pi) \rightarrow \text{bpy}(\pi^*)$  MLCT transitions with  $\lambda_{\text{max}}^{\text{abs}} = 450 \text{ nm}$  [12–14]. Following the absorption of a photon of light to generate the  $^1\text{MLCT}$  excited state, rapid intersystem crossing occurs with unit efficiency to populate a relatively long-lived  $^3\text{MLCT}$  excited state (excited state lifetime,  $\tau = 850 \text{ ns}$  in room temperature (RT) acetonitrile solution, quantum yield,  $\Phi = 0.07$  emitting at  $\lambda_{\text{max}}^{\text{em}} = 620 \text{ nm}$  in RT) [13]. The excited state lifetime,  $\tau$ , is the inverse of the sum of all the rate constants for deactivation of an electronic excited state in the absence of a quencher, Eq. 14:

$$\tau = \frac{1}{k_r + k_{nr}} \quad (14)$$

The quantum yield for emission,  $\Phi^{\text{em}}$ , for an excited state can be calculated by considering the ratio between the rate constants for the process of interest and the sum of all the rate constants for the deactivation of a state, multiplied by the fraction of light that populates this state, Eq. 15:





**Hydrogen via Direct Solar Production, Fig. 1** Representative light absorbers used in solar hydrogen production schemes

$$\Phi^{em} = \Phi_{3MLCT} \frac{k_r}{k_r + k_{nr}} \quad (15)$$

$\Phi_{3MLCT}$  is the quantum efficiency for generation of the  $^3MLCT$  state, which is one for  $[\text{Ru}(\text{bpy})_3]^{2+}$  and most Ru(II) polyazine LAs. The relationship between  $\Phi$  of photochemical processes with concentration of a Q is described using Stern-Volmer kinetics, Eq. 16:

$$\Phi^0 / \Phi = 1 + K_{sv}[\text{Q}] \quad (16)$$

$\Phi^0$  and  $\Phi$  are quantum yields in the absence and presence of Q, respectively, and  $K_{sv}$  is the Stern-Volmer quenching constant. The excited state properties of Ru polyazine-type LAs can be modulated by modification of the ligands bound to the metal center. Complexes use similar properties with higher energy Os(d $\pi$ ) orbitals and

**Hydrogen via Direct Solar Production, Table 1** Spectroscopic and redox properties of Ru<sup>II</sup> and Os<sup>II</sup> polyazine complexes

Complex	$\lambda_{\text{max}}^{\text{abs}}$ (nm)	$\lambda_{\text{max}}^{\text{em}}$ (nm)	$\tau$ (ns)	Ref.
[Ru(bpy) <sub>3</sub> ] <sup>2+</sup> a	449	605	850	[13]
[Ru(phen) <sub>3</sub> ] <sup>2+</sup> a	443	604	400	[13]
[Ru(Ph <sub>2</sub> phen) <sub>3</sub> ] <sup>2+</sup> b	460	613	4,680	[23]
[Os(bpy) <sub>3</sub> ] <sup>2+</sup> a	640	723	20 <sup>b</sup>	[24]
[(bpy) <sub>2</sub> Ru(dpp)] <sup>2+</sup> a	470	675	240	[25, 26]
[(phen) <sub>2</sub> Ru(dpp)] <sup>2+</sup> a	465	652	252	[27]
[(bpy) <sub>2</sub> Os(dpp)] <sup>2+</sup> a	485	798	37	[28, 29]
[Ru(tpy) <sub>2</sub> ] <sup>2+</sup>	476 <sup>c</sup>	629 <sup>a</sup>	0.25 <sup>b</sup>	[30, 31]
[Os(tpy) <sub>2</sub> ] <sup>2+</sup>	477 <sup>c</sup>	718 <sup>c</sup>	269 <sup>a</sup>	[31]

<sup>a</sup>In acetonitrile solution at room temperature

<sup>b</sup>In aqueous solutions

<sup>c</sup>In ethanol–methanol (4/1)

lower energy-excited MLCT states. Table 1 provides spectroscopic properties of Ru and Os LAs. Although the excited state of [Ru(bpy)<sub>3</sub>]<sup>2+</sup> is thermodynamically capable of reducing water to produce hydrogen, this reaction does not occur. Recent studies have also used Ir- or Pt-based LA in photochemical hydrogen production schemes [19–21]. The use of metalloporphyrin types of complexes as LAs have been investigated as they mimic dyes found in nature in photosynthesis [22].

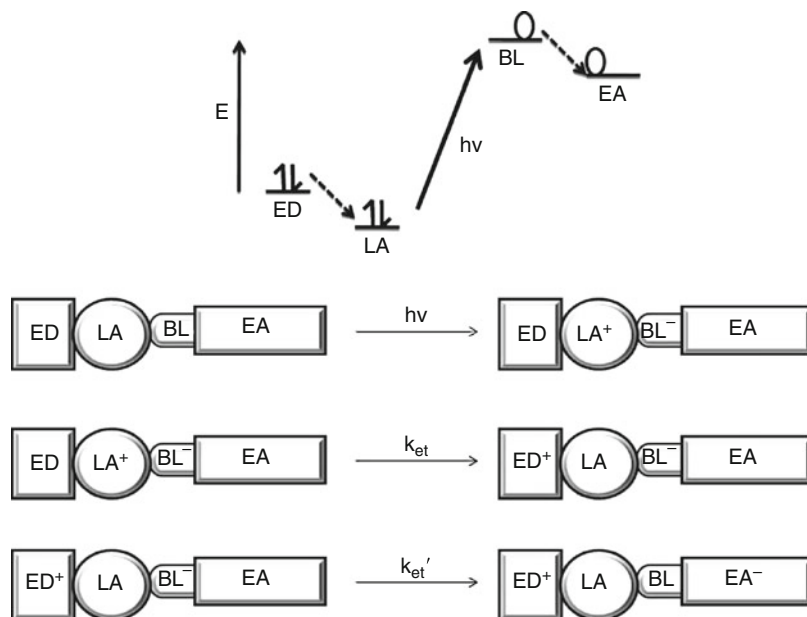
**Electron Relay** Multicomponent systems rely on a suitable relay to transport electrons from an excited LA to the CAT. This electron relay must be able to accept electrons from the <sup>\*</sup>LA. In supramolecular complexes, bridging ligands (BL) are used as electron relays and serve to covalently couple the individual components. A wide range of BLs has been used for this purpose, providing varied degrees of coupling between the LA and CAT and with varied acceptor orbital energetics [12]. Polyazine BLs are commonly used to couple molecular components within supramolecular assemblies. Polyazine BLs separated by short rigid spacers allow for significant electronic communication between components and directional electron or energy transfer [32–35]. [(bpy)<sub>2</sub>Ru(dpp)]<sup>2+</sup> is a well-studied LA derived from [Ru(bpy)<sub>3</sub>]<sup>2+</sup> with one of the bpy replaced by the polyazine BL, dpp (dpp = 2,3-bis(2-pyridyl)pyrazine) [25, 26, 33, 34]. The lowest lying excited state of [Ru(bpy)<sub>2</sub>(dpp)]<sup>2+</sup> is a Ru(dπ) → dpp(π<sup>\*</sup>)

CT state, transferring charge from the ruthenium to the dpp ligand. This <sup>1</sup>MLCT absorption occurs at 470 nm with the <sup>3</sup>MLCT emission at 675 nm ( $\tau = 210$  ns). The two remote nitrogen donor atoms on the dpp ligands provide points of attachment for a second metal center, allowing the construction of polymetallic complexes. The dpp(π<sup>\*</sup>) acceptor orbital is stabilized when it is bridging two metals. In the homobimetallic system [(bpy)<sub>2</sub>Ru]<sub>2</sub>(dpp)<sup>4+</sup>, a red shifted Ru(dπ) → dpp(π<sup>\*</sup>) CT transition at 525 nm is observed with a shortened <sup>3</sup>MLCT lifetime of 80 ns [10, 25].

**Catalysts** Photochemical water reduction to produce hydrogen is an energetically uphill process involving bond dissociation and formation. Catalysts are used to promote this reaction. Most multicomponent systems are heterogeneous with considerable progress being made recently in homogeneous photocatalysis [19–21]. These systems typically use Pt, Pd, Rh, Co, or bioinspired diiron dithiolate (contains an Fe<sub>2</sub> core) catalysts. The non-precious metal-based Co and Fe systems are proposed as being economically viable. Homogeneous catalysis allows catalyst engineering to promote electron transfer from the LA and allows understanding of the mechanism of action through conventional solution-based analysis methods. Care must be taken in the selection of CATs to ensure that they do not compete for light with the LA.

### Hydrogen via Direct Solar Production,

**Fig. 2** Photoinduced charge separation in a ED-LA-BL-EA molecular device (*ED* electron donor, *LA* light absorber, *EA* electron acceptor)



*Turnover Number (TON) and Quantum Yield ( $\Phi$ )* The observed TON and  $\Phi$  of a reaction are key parameters describing catalytic system efficiency and stability. The TON relative to the CAT is defined as the ratio of amount of hydrogen produced ( $n \text{ H}_2$ ) to the initial amount of CAT present ( $n_o \text{ CAT}$ ), Eq. 16:

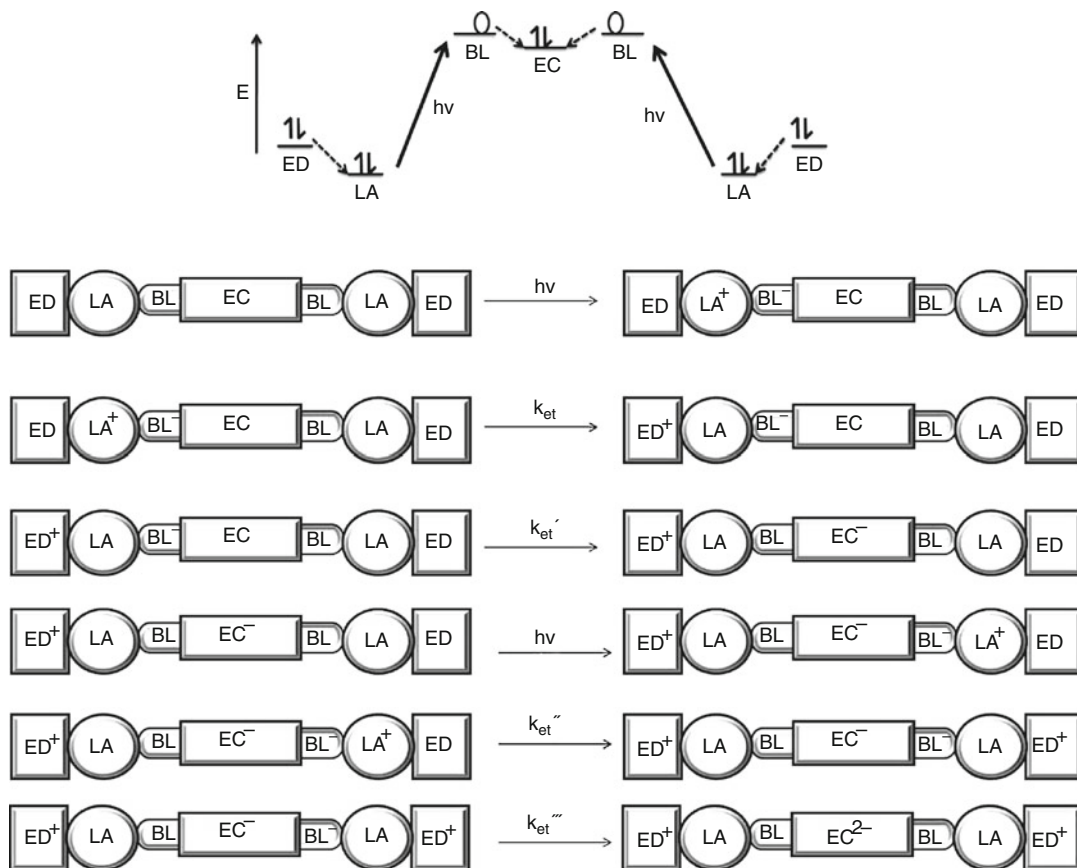
$$\text{TON} = \frac{n \text{ H}_2}{n_o \text{ CAT}} \quad (17)$$

**Photoinitiated Charge Separation** Solar energy conversion schemes that proceed via photoreduction of substrates are initiated with photoinduced charge separation that generates a potential at the molecular level. A simplified supramolecular device for photoinitiated charge separation is represented in Fig. 2. Optical excitation, followed by intramolecular electron transfer affords a charge separated state consisting of a positively charged electron donor,  $\text{ED}^+$ , and negatively charged electron acceptor,  $\text{EA}^-$ . The photogenerated charge separated (CS) state should persist for enough time to drive useful chemistry during the excited state lifetime. In supramolecular systems, the duration of charge separation can be modulated by fine tuning the orbital overlap between the ED and

LA through modification of distance between these two subunits. The efficiency of charge separation is also key to functioning and often factors enhancing lifetime reduce quantum efficiency.

**Photoinitiated Electron Collection** Photo-initiated electron collection (PEC) is a process by which at least two electrons are collected on a central site following optical excitation. For PEC, supramolecular complexes can be designed so that two ED-LA units are connected to a single EA that can accept at least two electrons (an electron collector, EC) to give a ED-LA-BL-EC-BL-LA-ED structural motif. Following multiple optical excitations, this system collects two electrons at the EC creating two  $\text{ED}^+$ , Fig. 3. PEC is of considerable importance in solar fuel production as multielectron reduction of the substrate is required in many fuel producing reactions. In the important monograph by Balzani in 1987, the design considerations for functioning photoinitiated electron collectors were discussed [8]. Since then many supramolecular systems that couple multiple LAs have been constructed, but only a few functioning PEC systems exist.

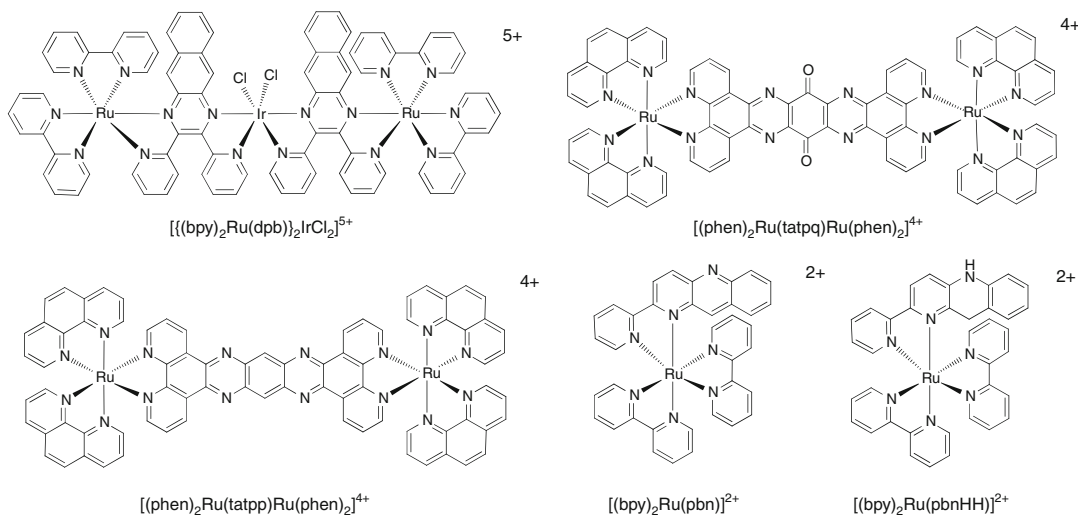
*Photoinitiated Electron Collectors that Collect Electrons on Ligand Orbitals* Photoinitiated



**Hydrogen via Direct Solar Production, Fig. 3** Photoinduced electron collection in a ED-LA-EA-LA-ED molecular device (ED electron donor, LA light absorber, EA electron acceptor)

electron collectors are devices that allow the use of light energy to collect the reducing equivalents needed to produce fuels. Molecular-based PEC systems are engineered so that the subunits are connected in an order with orbital energetics that allow multiple electrons to be collected on a single site following light activation. Current systems that undergo PEC have LA units connected to EC through BLs that function as electron relays. The first functioning photoinitiated electron collector is  $[\{(bpy)_2Ru(dpb)\}_2IrCl_2](PF_6)_5$  ( $dpb = 2,3$ -bis(2-pyridyl)benzoquinoxaline) which collects two electrons on the  $dpb(\pi^*)$  orbitals upon two sequential excitations and electron transfer events, Fig. 4 [36]. Electron transfer from the  $dpb(\pi^*)$  orbitals to the Ir-based orbitals is energetically uphill. Homobimetallic ruthenium systems,  $[(phen)_2Ru(tatpq)Ru(phen)_2]^{4+}$  ( $phen = 1,10$ -Phenanthroline,

$tatpq = 9,11,20, 22$ -tetraazatetrapyrido[3,2-a:2'3'-c:3''-2''-1:2''',3'''-n]pentacene-10,21-quinone) and  $[(phen)_2Ru(tatpp)Ru(phen)_2]^{4+}$  ( $tatpp = 9,11,20, 22$ -tetraazatetrapyrido [3,2-a:2'3'-c:3''-2''-1:2''', 3'''-n]pentacene) are the next PECs studied with multiple electrons also being collected on the BL ( $\pi^*$ ) orbitals, Fig. 4 [37, 38]. Although these initial systems undergo PEC, they are not known to reduce substrates. The monometallic system,  $[Ru(bpy)_2(pbn)]^{2+}$  ( $pbn = 2$ -(2-pyridyl) benzo[b]-1, 5-naphthyridine), couples a Ru-based LA to an  $NAD^+$  ( $NAD^+ =$  nicotinamide adenine dinucleotide) model ligand, Fig. 4. The  $NAD^+$  model ligand acts as a reservoir for two electrons and uses proton coupled electron transfer. Photolysis of a solution containing  $[Ru(bpy)_2(pbn)]^{2+}$  and triethylamine ( $Et_3N$ ) leads to the formation of  $NADH$  like  $[Ru(bpy)_2(pbnHH)]^{2+}$ , a potential



**Hydrogen via Direct Solar Production, Fig. 4** Photoinitiated electron collectors that collect electrons on ligand orbitals

hydride donor for reduction of organic substrates [39, 40].

## Solar Hydrogen Photocatalysis

This entry will focus on the recent developments in molecular-based solar hydrogen photocatalysis using Fe, Co, Rh, Pt, and Pd-based CATs and Ru, Os, Pt, Re, and Ir-based LAs. Illustrative examples will be provided with discussions on system function, TON, and efficiency. The hydrogen TON, quantum yield, and system properties are summarized in Table 2.

### Iron-Based System

Metabolism of protons in certain bacteria and algae are catalyzed by a certain class of metalloenzymes coined hydrogenases. Iron hydrogenases are important in proton reduction producing hydrogen gas. Recent research efforts focus on biomimetic diiron systems containing an  $Fe_2S_2$  core, structurally similar to the iron hydrogenase active sites, for solar hydrogen photocatalysis [19–21, 41]. Interest in these systems has been inspired by the superior catalytic activity of hydrogenases which can reach 6,000–9,000

molecules of hydrogen  $s^{-1}$  [42]. Most  $Fe_2S_2$  systems have been used in electrocatalytic proton reduction, requiring strongly acidic conditions and large overpotentials [43].

**Supramolecular Iron-Based System** The Ru- $Fe_2S_2$  dyads,  $[(bpy)_2Ru(Me bpy CONHPh COO(Fe_2\{\mu-S_2(CH_2)_2CH\}(CO)_6)))]^{2+}$ ,  $[(tpy)Ru(tpyC_2Ph(Fe_2\{\mu-S_2(CH_2)_2N\}(CO)_6)))]^{2+}$ ,  $[(bpy)_2Ru(Me bpy CONHPh(Fe_2\{\mu-S_2(CH_2)_2N\}(CO)_6)))]^{2+}$ , and  $[(bpy)_2Ru(bpyC_2Ph(Ph_2)P(Fe_2\{\mu-S_2(CH_2)_3\}(CO)_5)))]^{2+}$ , in which a model iron hydrogenase active site is attached to a  $[Ru(bpy)_3]^{2+}$  type chromophore, are supramolecular architectures constructed for possible application in solar hydrogen production, Fig. 5 [44–47]. These systems couple the favorable optical properties of the Ru-based chromophore to the catalytic properties of the diiron active site. It was anticipated that the optically populated  $^3MLCT$  excited state would reduce the diiron species by two electrons and catalyze water reduction to produce hydrogen. It was found that electron transfer to the diiron dyads is thermodynamically unfavorable in this structural motif as the reduction potentials of the diiron units are more negative than the excited state oxidation potential of the ruthenium LAs. These Ru- $Fe_2S_2$  dyads are not solar hydrogen photocatalysts, but provide important design considerations for

Hydrogen via Direct Solar Production, Table 2 Summary of hydrogen photocatalysis data

Solvent (electron donor)	$\lambda$ (nm)	LA	LA-CAT	CAT	TON (time, h)	QY	Ref
$\text{CH}_2\text{Cl}_2/\text{CF}_3\text{COOH}$ (2-mercaptopbenzoic)	$\geq 400$		$[\text{ZnTPP}(\text{pyCOO}(\text{CH}_2)_2(\text{Fe}_2\{\mu\text{-S}_2(\text{CH}_2)_2\text{N}\}(\text{CO})_6)]$		0.16 ( $\text{Fe}_2$ ) (2) 16 (LA) (2)		[48]
$\text{CH}_3\text{CN}/\text{H}_2\text{O}$ (ascorbic acid)	$> 400$	$[\text{Ru}(\text{bpy})_3]^{2+}$		$[\text{Ph}(\text{CH}_2)(\text{Fe}_2\{\mu\text{-S}_2(\text{CH}_2)_2\text{N}\}(\text{CO})_5(\text{P}(\text{N-pyr}_3)))]$	4.3 ( $\text{Fe}_2$ ) (3) 86 (LA) (3)		[51]
$\text{CH}_3\text{CN}/\text{H}_2\text{O}$ (ascorbic acid)	$> 400$	$[(\text{bpy})_2\text{Ru}(\text{Me}_2\text{bpy})]^{2+}$		$[\text{Ph}(\text{CH}_2)(\text{Fe}_2\{\mu\text{-S}_2(\text{CH}_2)_2\text{N}\}(\text{CO})_5(\text{P}(\text{N-pyr}_3)))]$	3.9 ( $\text{Fe}_2$ ) (3) 76 (LA) (3)		[51]
$\text{CH}_3\text{CN}/\text{H}_2\text{O}$ (ascorbic acid)	$> 400$	$[\text{Ru}(\text{Me}_2\text{bpy})_3]^{2+}$		$[\text{Ph}(\text{CH}_2)(\text{Fe}_2\{\mu\text{-S}_2(\text{CH}_2)_2\text{N}\}(\text{CO})_5(\text{P}(\text{N-pyr}_3)))]$	1.9 ( $\text{Fe}_2$ ) (3) 38 (LA) (3)		[51]
$\text{CH}_3\text{CN}/\text{H}_2\text{O}$ (ascorbic acid)	$> 400$	$[\text{Ru}(\text{bpy})_3]^{2+}$		$[\text{Ph}(\text{CH}_2)(\text{Fe}_2\{\mu\text{-S}_2(\text{CH}_2)_2\text{N}\}(\text{CO})_6)]$	0.78 ( $\text{Fe}_2$ ) (3)		[51]
$\text{CH}_3\text{CN}/\text{H}_2\text{O}$ (ascorbic acid)	$> 400$	$[\text{Ru}(\text{bpy})_3]^{2+}$		$[\text{Ph}(\text{CH}_2)(\text{Fe}_2\{\mu\text{-S}_2(\text{CH}_2)_2\text{N}\}(\text{CO})_5(\text{P}(\text{N-pyr}_3)_2))]$	1.7 ( $\text{Fe}_2$ ) (3) 34 (LA) (3)		[51]
$\text{DMF}/\text{H}_2\text{O}$ (ascorbic acid)	455–850	$[\text{Ru}(\text{bpy})_3]^{2+}$		$[\text{Fe}_2(\mu\text{-Cl}_2\text{bdt})(\text{CO})_6]$	200 ( $\text{Fe}_2$ ) (2.5)	0.01	[52]
$\text{CH}_3\text{COCH}_3/\text{H}_2\text{O}$ ( $\text{Et}_3\text{N}$ )	$> 400$	$[(\text{ppy})_2\text{Ir}(\text{bpy})]^{+}$		$[\text{Ph}(\text{CH}_2)(\text{Fe}_2\{\mu\text{-S}_2(\text{CH}_2)_2\text{N}\}(\text{CO})_5(\text{P}(\text{N-pyr}_3)))]$	466 ( $\text{Fe}_2$ ) (8) 660 (LA) (8)		[53]
$\text{CH}_3\text{CN}/\text{H}_2\text{O}$ ( <i>N,N</i> -Dimethylamine)	470		$[\{(\text{bpy})_2\text{Ru}(\text{dpp})\}_2\text{RhCl}_2]^{5+}$		28 (CAT) (4) 20 (CAT) (2)		[54]
$\text{CH}_3\text{CN}/\text{H}_2\text{O}$ ( <i>N,N</i> -Dimethylamine)	470		$[\{(\text{bpy})_2\text{Ru}(\text{dpp})\}_2\text{RhBr}_2]^{5+}$		38 (CAT) (4) 26 (CAT) (2) 3 (CAT) (4) <sup>a</sup>		[55–57]
$\text{CH}_3\text{CN}/\text{H}_2\text{O}$ ( <i>N,N</i> -Dimethylamine)	470		$[\{(\text{phen})_2\text{Ru}(\text{dpp})\}_2\text{RhCl}_2]^{5+}$		18 (CAT) (2)		[56]
$\text{CH}_3\text{CN}/\text{H}_2\text{O}$ (triethylamine)	470		$[\{(\text{bpy})_2\text{Ru}(\text{dpp})\}_2\text{RhCl}_2]^{5+}$		4 (CAT) (2)		[56]
$\text{CH}_3\text{CN}/\text{H}_2\text{O}$ (triethylamine)	470		$[\{(\text{bpy})_2\text{Ru}(\text{dpp})\}_2\text{RhBr}_2]^{5+}$		6 (CAT) (2)		[56]



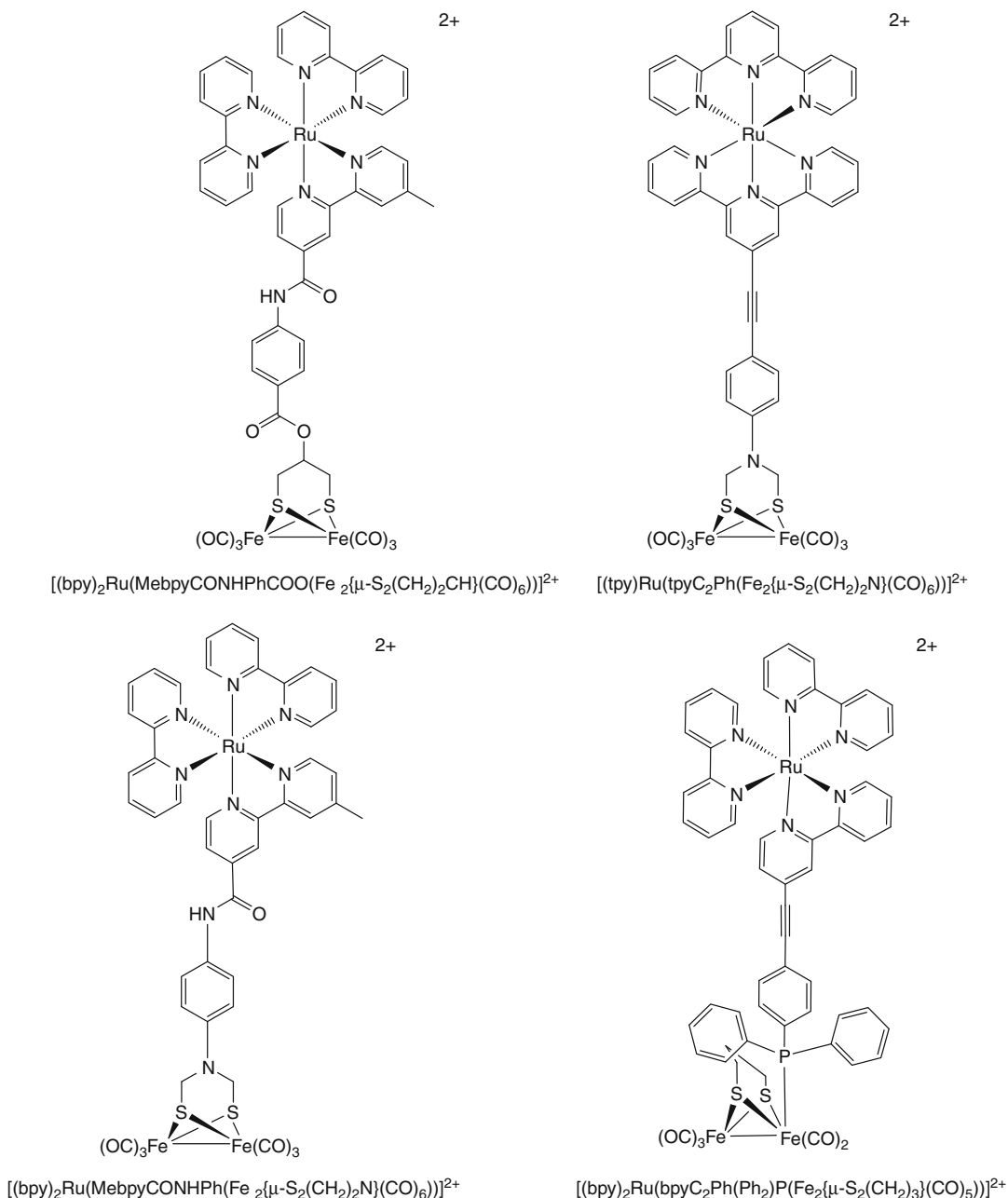
CH <sub>3</sub> CN/H <sub>2</sub> O (triethylamine)	470				[{(phen) <sub>2</sub> Ru(dpp)} <sub>2</sub> RhCl <sub>2</sub> ] <sup>5+</sup>		3 (CAT) (2)	[56]
CH <sub>3</sub> CN/H <sub>2</sub> O (triethanolamine)	470				[{(bpy) <sub>2</sub> Ru(dpp)} <sub>2</sub> RhBr <sub>2</sub> ] <sup>5+</sup>		1 (CAT) (2)	[56]
CF <sub>3</sub> SOOH/H <sub>2</sub> O (sodium ascorbate)	> 380				[{(tpy)Ph(Ph <sub>2</sub> P) <sub>2</sub> Os} RhCl(CO)] <sup>2+</sup>		36 (CAT) (18)	[58]
CF <sub>3</sub> SOOH/H <sub>2</sub> O (sodium ascorbate)	> 380				[{(tpy)Ph(Ph <sub>2</sub> P) <sub>2</sub> Os} RhCl <sub>2</sub> ] <sup>3+</sup>		87 (CAT) (18) 594 (CAT) (240)	0.007 [58]
CF <sub>3</sub> SOOH/H <sub>2</sub> O (sodium ascorbate)	> 380					RhCl <sub>3</sub> ·3H <sub>2</sub> O/dppe	24 (CAT) (18)	[58]
HCl/THF	300–400				[Rh <sub>2</sub> <sup>0,II</sup> (dfpma) <sub>3</sub> X <sub>2</sub> (L)]		27/h (CAT) (3)	0.01 [59]
H <sub>2</sub> O (triethanolamine)	450				[Ru(bpy) <sub>3</sub> ] <sup>2+</sup> [Rh (bpy) <sub>3</sub> ] <sup>3+</sup>	Pt	500 (LA) (240)	0.11 <sup>b</sup> [11, 60]
THF/H <sub>2</sub> O (triethanolamine)	UV-VIS				[Ir (f-mppy) <sub>2</sub> (dtbbpy)] <sup>+</sup>	[Rh(dtbbpy) <sub>3</sub> ] <sup>3+</sup>	5,000 (LA or CAT) (20–24)	0.34 [61]
CH <sub>3</sub> COCH <sub>3</sub> /Et <sub>3</sub> NH <sup>+</sup> (triethylamine) <sup>c</sup>	UV-VIS						56 (Co) (4)	[62]
CH <sub>3</sub> COCH <sub>3</sub> /H <sub>2</sub> O (triethylamine) <sup>c</sup>	UV-VIS						22 (Co) (4)	[62]
CH <sub>3</sub> COCH <sub>3</sub> /Et <sub>3</sub> NH <sup>+</sup> (triethylamine) <sup>c</sup>	> 350						103 (Co) (15)	[62]
CH <sub>3</sub> COCH <sub>3</sub> /Et <sub>3</sub> NH <sup>+</sup> (triethylamine) <sup>c</sup>	UV-VIS						17 (Co) (4)	[62]
CH <sub>3</sub> COCH <sub>3</sub> /Et <sub>3</sub> NH <sup>+</sup> (triethylamine) <sup>c</sup>	UV-VIS						12 (Co) (4)	[62]
CH <sub>3</sub> COCH <sub>3</sub> /Et <sub>3</sub> NH <sup>+</sup> (triethylamine) <sup>c</sup>	> 380						9 (Co) (4)	[63]
CH <sub>3</sub> COCH <sub>3</sub> /Et <sub>3</sub> NH <sup>+</sup> (triethylamine)	> 380						90 (Co) (4) 210 (Co) (15) <sup>e</sup>	[63] [63]
CH <sub>3</sub> COCH <sub>3</sub> /Et <sub>3</sub> NH <sup>+</sup> (triethylamine) <sup>c</sup>	> 380						165 (Co) (15)	0.11 <sup>d</sup> [63]
CH <sub>3</sub> COCH <sub>3</sub> /Et <sub>3</sub> NH <sup>+</sup> (triethylamine) <sup>c</sup>	> 380						273 (Co) (15)	0.16 <sup>f</sup> [63]
CH <sub>3</sub> COCH <sub>3</sub> /Et <sub>3</sub> NH <sup>+</sup> (triethylamine) <sup>d</sup>	> 400						38 (Co) (8)	[64]

(continued)

Hydrogen via Direct Solar Production, Table 2 (continued)

Solvent (electron donor)	$\lambda$ (nm)	LA	LA-CAT	CAT	TON (time, h)	QY	Ref
CH <sub>3</sub> COCH <sub>3</sub> /Et <sub>3</sub> NH <sup>+</sup> (triethylamine) <sup>d</sup>	>400		[(bpy) <sub>2</sub> Ru(bpy-4-CH <sub>3</sub> ,4 <sup>0</sup> -CONH (CH <sub>2</sub> )-4-py)Co(dmgBF <sub>2</sub> ) <sub>2</sub> (OH <sub>2</sub> ) <sup>2+</sup>		47 (Co) (8)		[64]
CH <sub>3</sub> CN/H <sub>2</sub> O (Eu <sup>2+</sup> )	450	[Ru(bpy) <sub>3</sub> ] <sup>2+</sup>		[Co <sup>II</sup> L]	10 (LA)		[65]
CH <sub>3</sub> CN/H <sub>2</sub> O (triethanolamine)	465	[Ir(F-nppy) <sub>2</sub> (bpy)] <sup>+</sup>		[Co(bpy) <sub>3</sub> ] <sup>2+</sup>	1 (Co)		[66]
CH <sub>3</sub> CN/H <sub>2</sub> O (triethanolamine)	>410	[Pt(tpy)(C $\equiv$ CPh) ClO <sub>4</sub> ]		[Co(dmgH) <sub>2</sub> ppyCl]	920 (LA)		[67]
CH <sub>3</sub> CN/H <sub>2</sub> O (triethanolamine)	>450	Eosin Y		[Co(dmgH) <sub>2</sub> ppyCl] <sup>2+</sup>	18 (Co)		[68]
DMF/H <sub>2</sub> O/AcOH (triethanolamine)	>400	[ReBr(CO) <sub>3</sub> bpy]		[Co(dmgH) <sub>2</sub> ]	2,100 (10)	0.04 <sup>h</sup>	[69]
H <sub>2</sub> O/acetate buffer (EDTA)	>350		[(bpy) <sub>2</sub> Ru(phenNHCO(COOHbpy)) PtCl <sub>2</sub> ] <sup>2+</sup>		900 (LA) (14) <sup>g</sup>	0.01	[70]
CH <sub>3</sub> CN/H <sub>2</sub> O (N,N <sup>0</sup> - Dimethylamine)	470		[{(phen) <sub>2</sub> Ru(dpp)} <sub>2</sub> Ru(dpq)PtCl <sub>2</sub> ] <sup>6+</sup>		115 (CAT) (5)		[71]
CH <sub>3</sub> CN/H <sub>2</sub> O (N,N'- Dimethylamine)	530		[{(bpy) <sub>2</sub> Ru(dpp)} <sub>2</sub> Ru(dpq)PtCl <sub>2</sub> ] <sup>6+</sup>		40 (CAT) (3)	0.01	[72]
H <sub>2</sub> O/MES (EDTA)	350-550		[PtCl(tpy)Cl]		3 (LA or CAT) (7)	0.02	[73]
CH <sub>3</sub> CN/triethylamine (triethylamine)	470		[ <sup>t</sup> Bu <sub>2</sub> bpy) <sub>2</sub> Ru(tpphz)PdCl <sub>2</sub> ] <sup>2+</sup>		56 (CAT) (30)		[74]

<sup>a</sup>in water/phosphate buffer using TEOA ED (Ref. [57])<sup>b</sup>Ref. [11]<sup>c</sup>100-fold excess of both Et<sub>3</sub>NH<sup>+</sup> and Et<sub>3</sub>N were used<sup>d</sup>300-fold excess of both Et<sub>3</sub>NH<sup>+</sup> and Et<sub>3</sub>N were used<sup>e</sup>600-fold excess of both Et<sub>3</sub>NH<sup>+</sup> and Et<sub>3</sub>N were used<sup>f</sup> $\lambda$  = 412 nm, irradiation time 2 h<sup>g</sup>dmgH was added to the system<sup>h</sup> $\lambda$  = 520 nm, irradiation time 2 h

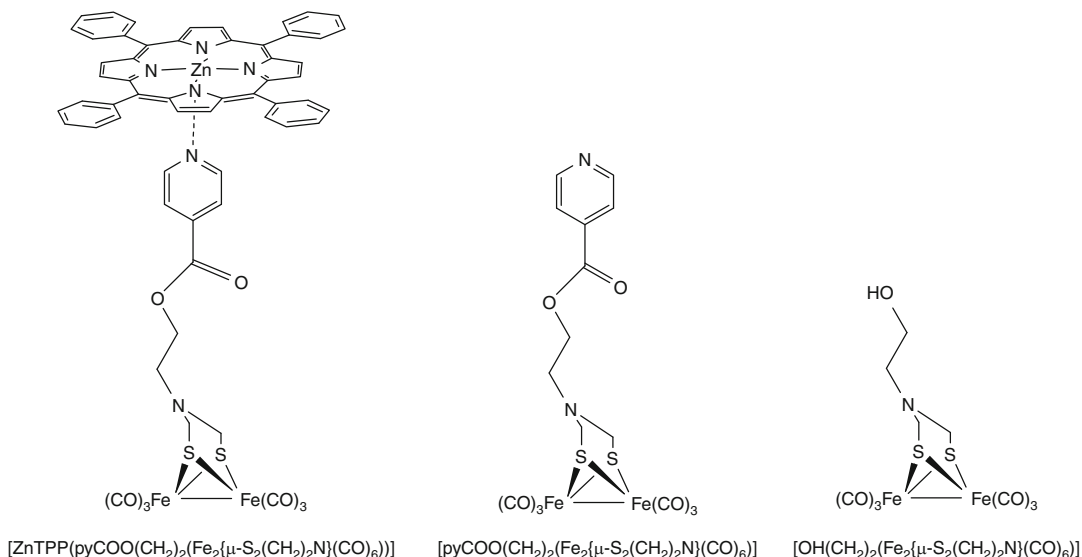


**Hydrogen via Direct Solar Production, Fig. 5** Systems that couple a ruthenium chromophore to an iron-based catalyst

catalyst engineering. Component modification at the diiron center to facilitate electron transfer from the  $^3MLCT$  excited state of the photosensitizer and/or photogeneration of a  $^3MLCT$  excited state with a higher energy acceptor orbital have been

suggested as a means to promote excited state electron transfer from the ruthenium LA to the diiron core [45–47].

A pyridine (py)-functionalized hydrogenase active site model complex bound to a zinc



**Hydrogen via Direct Solar Production, Fig. 6** Representations of ZnFe self-assembling system and the FeFe subunits

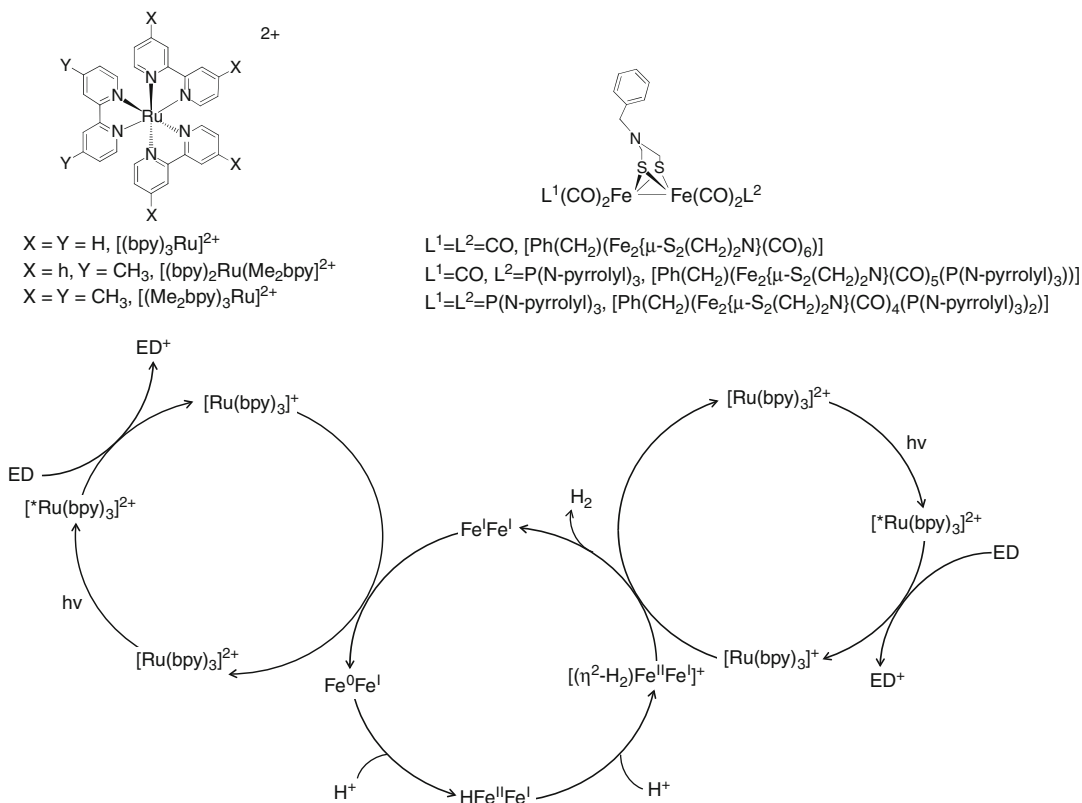
tetraphenyl-porphyrin [ZnTPP] LA, [ZnTPP(pyCOO(CH<sub>2</sub>)<sub>2</sub>(Fe<sub>2</sub>{μ-S<sub>2</sub>(CH<sub>2</sub>)<sub>2</sub>N}(CO)<sub>6</sub>))], has been used in solar hydrogen production, Fig. 6 [48]. The photoinduced intra-molecular electron transfer from the <sup>1</sup>MLCT state of the LA to the diiron unit has been established by fluorescence spectroscopy and laser flash photolysis technique. The weak interaction between the diiron center and the LA allows the two units to separate following intramolecular electron transfer, minimizing charge recombination through back electron transfer. The system can also reassemble to mediate intramolecular electron transfer.

Photolysis of ZnTPP, [pyCOO(CH<sub>2</sub>)<sub>2</sub>(Fe<sub>2</sub>{μ-S<sub>2</sub>(CH<sub>2</sub>)<sub>2</sub>N}(CO)<sub>6</sub>)], and the electron donor 2-mercaptobenzoic acid in presence of CF<sub>3</sub>COOH acid as the proton source in methylene chloride at λ > 400 nm resulted in photochemical hydrogen production with 0.16 TON based on [pyCOO(CH<sub>2</sub>)<sub>2</sub>(Fe<sub>2</sub>{μ-S<sub>2</sub>(CH<sub>2</sub>)<sub>2</sub>N}(CO)<sub>6</sub>)] and 16 TON based on [ZnTPP]. The amount of hydrogen increases almost linearly in the first 40 min and reaches a plateau in 2 h. This decrease in rate of hydrogen production is attributed to CAT decomposition through CO loss.

Hydrogen production does not occur when [pyCOO(CH<sub>2</sub>)<sub>2</sub>(Fe<sub>2</sub>{μ-S<sub>2</sub>(CH<sub>2</sub>)<sub>2</sub>N}(CO)<sub>6</sub>)] is

replaced by [OH(CH<sub>2</sub>)<sub>2</sub>(Fe<sub>2</sub>{μ-S<sub>2</sub>(CH<sub>2</sub>)<sub>2</sub>N}(CO)<sub>6</sub>)]. This suggests that assembly of the system and the intramolecular electron transfer events are crucial for solar hydrogen catalysis as [OH(CH<sub>2</sub>)<sub>2</sub>(Fe<sub>2</sub>{μ-S<sub>2</sub>(CH<sub>2</sub>)<sub>2</sub>N}(CO)<sub>6</sub>)] does not coordinate with ZnTPP and hydrogen production does not occur. It is proposed that the singlet excited state intramolecular electron transfer forms the charge separated state [ZnTPP<sup>+</sup>pyCOO(CH<sub>2</sub>)<sub>2</sub>(Fe<sub>2</sub>{μ-S<sub>2</sub>(CH<sub>2</sub>)<sub>2</sub>N}(CO)<sub>6</sub>)<sup>-</sup>], which undergoes dissociation to form [ZnTPP<sup>+</sup>] and [pyCOO(CH<sub>2</sub>)<sub>2</sub>(Fe<sub>2</sub>{μ-S<sub>2</sub>(CH<sub>2</sub>)<sub>2</sub>N}(CO)<sub>6</sub>)<sup>-</sup>]. [ZnTPP<sup>+</sup>] is reductively quenched by the ED, while [pyCOO(CH<sub>2</sub>)<sub>2</sub>(Fe<sub>2</sub>{μ-S<sub>2</sub>(CH<sub>2</sub>)<sub>2</sub>N}(CO)<sub>6</sub>)<sup>-</sup>] is protonated. The protonated radical anion facilitates the second electron transfer event, which is followed by further protonation and hydrogen release. Further protonation of the protonated radical anion prior to the second electron transfer has been observed in electrochemical hydrogen production catalyzed by Fe<sub>2</sub>S<sub>2</sub> hydrogenases [49]. This is the first photoactive hydrogenase model system that incorporates the self-assembling principle for photochemical hydrogen production. This system is interesting as both CAT and LA are based on bioinspired materials.

In photosynthesis, the light-dependent reactions are carried out by two photosystems,

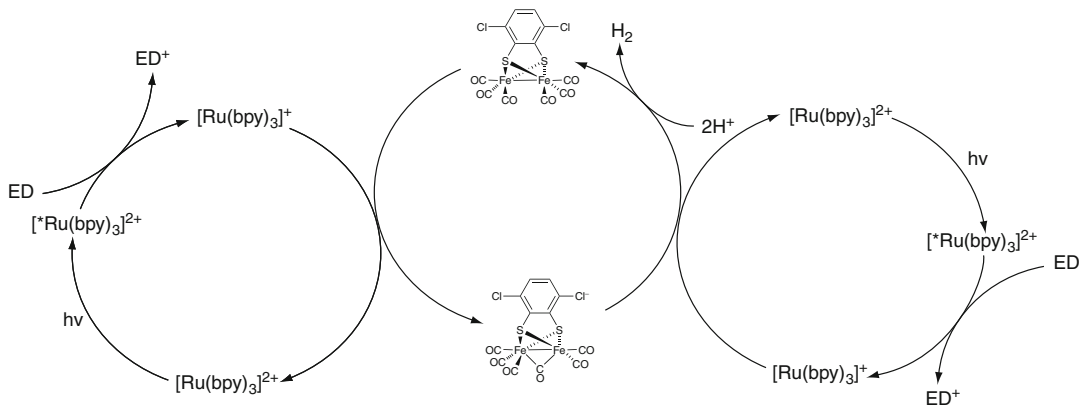


**Hydrogen via Direct Solar Production, Fig. 7** Homogeneous three-component system for solar hydrogen production catalyzed by biomimetic diiron hydrogenase catalyst

photosystem I (PS I) and photosystem II (PS II). PS I catalyzes the optically induced electron transfer from reduced cytochrome *c* to oxidized ferredoxin that are directly used to reduce nutrients or used to produce NADH. Systems that couple PS I to active hydrogen producing CATs are known. A recent review describes this technology employing molecular wires to connect PS I directly to CAT including Pt nanoparticles or the distal  $[4\text{Fe-4S}]$  of a  $\text{Fe}_2$  or NiFe hydrogenase [50].

**Multicomponent Iron-Based Systems** A few multicomponent systems have been reported that use biomimetic iron hydrogenase model complexes as CATs in solar hydrogen production schemes. Multicomponent systems are solution systems with multiple molecules interacting through diffusion to allow individual molecules to perform the acts associated with solar hydrogen production. The photocatalytic system typically

consists of three main components: LAs, CATs, and EDs functioning through intermolecular interactions in solution. A photoactive multicomponent system for solar hydrogen production using biomimetic iron hydrogenase model complexes was first reported in 2008 [51]. This system uses  $[\text{Ru}(\text{bpy})_3]^{2+}$  type LAs,  $\text{Fe}_2\text{S}_2$  CATs, and ascorbic acid as the ED irradiating at  $\lambda > 400$  nm, Fig. 7. The system consisting of  $[\text{Ru}(\text{bpy})_3]^{2+}$  LA,  $[\text{Ph}(\text{CH}_2)(\text{Fe}_2\{\mu\text{-S}_2(\text{CH}_2)_2\text{N}\})(\text{CO})_6]$  CAT containing all CO ligands, and ascorbic acid in  $\text{CH}_3\text{CN}/\text{H}_2\text{O}$  has the lowest activity attributed to decomplexation of the CO from the CAT. One or two of the CO ligands on the  $\text{Fe}_2\text{S}_2$  unit were replaced by a phosphine-based ligand to improve the photostability and catalytic activity of the system. The photosystem consisting of the  $\text{P}(\text{pyr})_3$ -monosubstituted CAT ( $\text{Ph} = \text{phenyl}$ ,  $\text{P}(\text{pyr})_3 = \text{tris}(\text{N-pyrrolyl})\text{phosphine}$ ),  $[\text{Ph}(\text{CH}_2)(\text{Fe}_2\{\mu\text{-S}_2(\text{CH}_2)_2\text{N}\})$



**Hydrogen via Direct Solar Production, Fig. 8** Proposed mechanism for photochemical hydrogen generation using  $[\text{Ru}(\text{bpy})_3]^{2+}$  LA,  $[\text{Fe}_2(\mu\text{-Cl}_2\text{bdt})(\text{CO})_6]$  CAT, and ascorbic acid in DMF/ $\text{H}_2\text{O}$

$(\text{CO})_5(\text{P}(\text{N-pyr})_3)]$ , showed greater photo-stability and catalytic activity albeit low turn-overs, 4.3 TON relative to CAT and 86 TON relative to the LA. The photosystem consisting of  $[\text{Ru}(\text{bpy})_3]^{2+}$  showed the greatest hydrogen production relative to  $[(\text{bpy})_2\text{Ru}(\text{Me}_2\text{bpy})]^{2+}$  or  $[(\text{Me}_2\text{bpy})_3\text{Ru}]^{2+}$  LAs. The decline in the hydrogen production when  $[(\text{bpy})_2\text{Ru}(\text{Me}_2\text{bpy})]^{2+}$  or  $[(\text{Me}_2\text{bpy})_3\text{Ru}]^{2+}$  is used is attributed to inefficient reductive quenching of the excited LA by the ascorbate anion. Methyl substitution renders the excited state reduction potential of the LA more negative making reductive quenching by ascorbate anion less thermodynamically favorable.

It is proposed that the excited  $[\text{Ru}(\text{bpy})_3]^{2+}$  LA is reductively quenched by the electron donor to form  $[\text{Ru}(\text{bpy})_3]^+$ . Intermolecular electron transfer to the diiron unit is thermodynamically feasible and a  $\text{Fe}^0\text{Fe}^{\text{I}}$  species is formed. Based on the redox potentials it is established that further reduction of the CAT is thermodynamically unfavorable. Protonation of the  $\text{Fe}^0\text{Fe}^{\text{I}}$  species to form  $\text{HFe}^{\text{II}}\text{Fe}^{\text{I}}$  followed by further reduction  $\text{HFe}^{\text{I}}\text{Fe}^{\text{I}}$  is likely. One proposal is that hydrogen production occurs through protonation of  $\text{HFe}^{\text{I}}\text{Fe}^{\text{I}}$  with regeneration of the CAT. An alternative mechanism is the second protonation of  $\text{HFe}^{\text{II}}\text{Fe}^{\text{I}}$  to generate  $[(\eta^2\text{-H}_2)\text{Fe}^{\text{II}}\text{Fe}^{\text{I}}]^+$  that is capable of being reduced to generate hydrogen and regenerate the CAT, Fig. 7.

Higher TON for photochemical hydrogen production has been achieved using  $[\text{Fe}_2(\mu\text{-Cl}_2\text{bdt})$

$(\text{CO})_6]$  ( $\text{Cl}_2\text{bdt} = 3,6\text{-dichlorobenzene-1,2-dithiolate}$ ) as the CAT [52].  $[\text{Fe}_2(\mu\text{-Cl}_2\text{bdt})(\text{CO})_6]$  is a known electrocatalyst for hydrogen production, allowing electrochemical reduction of protons at low potentials [75]. This complex is unusual displaying electrochemical reversibility. Electrochemical reversibility in these systems could be particularly relevant for hydrogen photocatalysis as proton reduction occurs by consecutive one electron reduction steps. Photolysis of a system consisting of  $[\text{Ru}(\text{bpy})_3]^{2+}$ ,  $[\text{Fe}_2(\mu\text{-Cl}_2\text{bdt})(\text{CO})_6]$ ,  $[\text{Ru}(\text{bpy})_3]^{2+}/[\text{Fe}_2(\mu\text{-Cl}_2\text{bdt})(\text{CO})_6]$  10:1), and ascorbic acid (pH = 5.5) in DMF/ $\text{H}_2\text{O}$  at  $\lambda = 455\text{--}850$  nm provides over 200 TON relative to the CAT in 2.5 h at which time photocatalysis discontinues attributed to CAT deactivation. The maximum TON frequency is  $2.7 \text{ H}_2 \text{ CAT}^{-1} \text{ min}^{-1}$ . The  $\Phi$  of hydrogen production is 0.01 per absorbed photon. A  $\Phi = 0.014$  with a frequency of  $3.7 \text{ H}_2 \text{ CAT}^{-1} \text{ min}^{-1}$  has also been obtained at pH = 6.4, but with lower TON and system stability. The proposed mechanism of action is represented in Fig. 8. Transient absorption and emission spectral data have established the elementary steps of the catalytic cycle to involve the reductive quenching of the excited LA by ascorbic acid to form  $[\text{Ru}(\text{bpy})_3]^+$  and reoxidation of  $[\text{Ru}(\text{bpy})_3]^+$  by the diiron unit.

Photochemical hydrogen production in a more basic medium has been investigated using the three-component system using  $[(\text{ppy})_2\text{Ir}(\text{bpy})]^+$  LA ( $\text{ppy} = \text{phenylpyridine}$ ),  $[\text{Ph}(\text{CH}_2)$



(Fe<sub>2</sub>{μ-S<sub>2</sub>(CH<sub>2</sub>)<sub>2</sub>N}(CO)<sub>5</sub> (P(N-pyr)<sub>3</sub>)) CAT, and Et<sub>3</sub>N electron donor in CH<sub>3</sub>COCH<sub>3</sub>/H<sub>2</sub>O irradiating at λ > 400 nm [53]. Turnover numbers of 466 relative to the CAT and 660 relative to the LA in 8 h has been achieved in this system. The impact of solvent, ED, LA, and CAT concentrations on solar hydrogen production has been investigated to determine the optimized concentrations to achieve the high TON reported. Unlike in the previous diiron systems, system deactivation occurs through decomposition of the LA, as re-addition of the LA showed total system recovery. The mechanism of catalyst function under basic conditions is unclear but it is proposed to occur through a Fe<sup>0</sup>Fe<sup>I</sup> species which is formed through reductive quenching of the LA by Et<sub>3</sub>N followed by reduction of the Fe<sup>I</sup>Fe<sup>I</sup> form of the CAT.

### Rh-Based Supramolecular and Multicomponent Systems

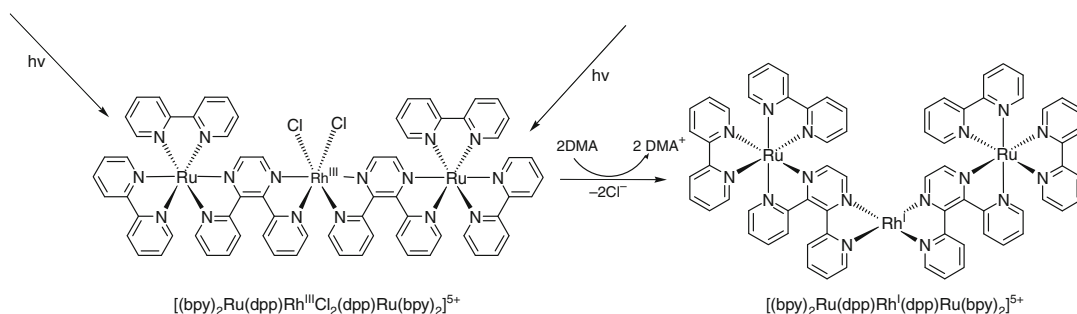
Tris-(2,2'-bipyridine)Rh<sup>III</sup>, [Rh(bpy)<sub>3</sub>]<sup>3+</sup>, is known to undergo excited state electron transfer of [<sup>\*</sup>Ru(bpy)<sub>3</sub>]<sup>2+</sup> [76]. The one electron reduction product, [Rh(bpy)<sub>3</sub>]<sup>2+</sup>, is kinetically unstable and rapidly disproportionate to form [Rh(bpy)<sub>3</sub>]<sup>+</sup> and [Rh(bpy)<sub>3</sub>]<sup>3+</sup>. Rh-based systems are used as the electron relays in solar hydrogen production schemes.

**Systematic Studies Using Rh-Based Supramolecular Photocatalysts for Solar Hydrogen Production** The coupling of Rh centers to Ru light absorbers in supra-molecular frameworks is reported [77–81]. The majority of this work focuses on the study of chelated complexes of Rh<sup>III</sup> coupled to Ru polyazine charge-transfer complexes. In these studies the Rh acts as an intramolecular electron acceptor for the MLCT excited state of the Ru LA. In many of the systems, the Rh centers are bound to only chelating ligands, which can limit the chemistry that can follow intramolecular electron transfer. Brewer et al. reported the supramolecular complex [{(bpy)<sub>2</sub>Ru(dpp)}<sub>2</sub>RhCl<sub>2</sub>]<sup>5+</sup>, the first photoinitiated electron collector that collects multiple electrons on a metal capable of photocatalyzing hydrogen

production from water [54–57, 82, 83]. This supra-molecular system incorporates two [(bpy)<sub>2</sub>Ru(dpp)]<sup>2+</sup> LAs and a single Rh EC allowing for multiple electron reduction. This system is unique from the previously reported systems as the Rh center is bound to monodentate Cl<sup>-</sup> ligands that can be lost following photoreduction. This allows the metal to become coordinatively unsaturated, allowing complexation and/or reaction with substrates. The redox properties of [{(bpy)<sub>2</sub>Ru(dpp)}<sub>2</sub>RhCl<sub>2</sub>]<sup>5+</sup> demonstrate that the Ru LAs are electronically isolated, important to PEC and multi-electron photochemistry.

Brewer et al. subsequently reported other systems incorporating a similar architecture that are photoinitiated electron collectors catalyzing solar hydrogen production. These systems also couple two Ru<sup>II</sup> or Os<sup>II</sup> LAs to a single Rh<sup>III</sup> acceptor. The supramolecular assemblies provide a LA-BL-RhX<sub>2</sub>-BL-LA structural motif (LA = Ru<sup>II</sup> or Os<sup>II</sup> polyazine LA, X = Cl<sup>-</sup> or Br<sup>-</sup>, BL = dpp). Visible light irradiation affords PEC resulting in Rh reduction and loss of the labile ligands, Fig. 9. Studies have established [{(bpy)<sub>2</sub>Ru(dpp)}<sub>2</sub>RhX<sub>2</sub>]<sup>5+</sup> (X = Cl<sup>-</sup> or Br<sup>-</sup>) and [{(phen)<sub>2</sub>Ru(dpp)}<sub>2</sub>RhCl<sub>2</sub>]<sup>5+</sup> as photochemical molecular devices for electron collection at a metal center and are photocatalysts for solar hydrogen production from water with a hydrogen yield of Φ ≈ 0.01 [54, 56, 82]. Modification of the LA to Os and/or the TL to tpy and a Cl destabilizes the LA metal-dp orbitals providing systems that absorb light at lower energy. The complexes [{(bpy)<sub>2</sub>Os(dpp)}<sub>2</sub>RhCl<sub>2</sub>]<sup>5+</sup>, [{(tpy)OsCl(dpp)}<sub>2</sub>RhCl<sub>2</sub>]<sup>3+</sup>, and [{(tpy)RuCl(dpp)}<sub>2</sub>RhCl<sub>2</sub>]<sup>3+</sup> have been studied and their photocatalytic activity evaluated [56]. Studies show that [{(bpy)<sub>2</sub>Os(dpp)}<sub>2</sub>RhCl<sub>2</sub>]<sup>5+</sup> and [{(tpy)RuCl(dpp)}<sub>2</sub>RhCl<sub>2</sub>]<sup>3+</sup> are solar hydrogen photocatalysts but provide lower activity consistent with significantly lower driving forces for excited state reductive quenching by the ED. Factors that impact photocatalytic efficiency have been evaluated by studying the redox and photophysical properties of these systems.

*Rhodium-Based Supramolecular Photocatalysts: Redox Properties* The electrochemical analysis of the supramolecular systems provides

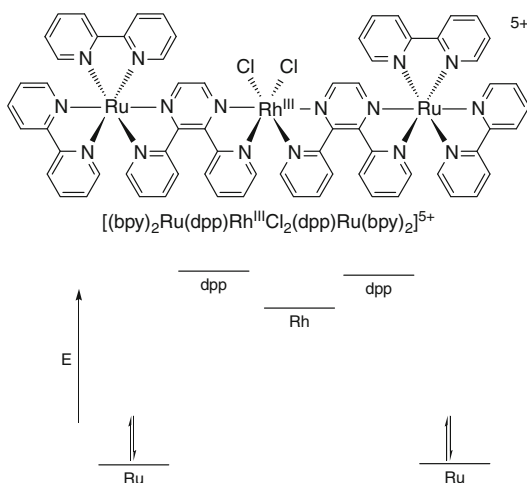


**Hydrogen via Direct Solar Production, Fig. 9** Photoinitiated electron collection on a metal center

meaningful information to understand excited state electron transfer and photocatalyst function. Electrochemical analysis provides a good estimation of the energy of the highest occupied molecular orbital (HOMO) and the lowest unoccupied molecular orbital (LUMO), allowing the study of the orbital energetics. Electrochemically the trimetallic complexes of the general formula  $\{[(TL)_2M(dpp)]_2RhX_2\}^{5+}$  ( $TL = bpy$  or  $phen$ ,  $M = Ru$  or  $Os$ ,  $X = Cl$  or  $Br$ ) and  $\{[(tpy)MCl(dpp)]_2RhCl_2\}^{3+}$  ( $M = Ru$  or  $Os$ ) demonstrate reversible metal-based oxidations and irreversible Rh and reversible ligand-based reductions [56]. All the trimetallics show overlapping  $Ru^{II/III}$  or  $Os^{II/III}$  based oxidations for the two terminal ligands, indicating minimal electronic interaction between the two terminal metal LA subunits. The Ru centers of the RuRu bimetallic systems  $\{[(bpy)_2Ru]_2(dpp)\}^{4+}$  or  $\{[(phen)_2Ru]_2(dpp)\}^{4+}$  are electronically coupled showing two  $Ru^{II/III}$  oxidations at *ca.* +1.47 and +1.66 V vs. SCE [84]. These bimetallic systems do not display photoinitiated electron collection and/or reduction of substrates.  $\{[(bpy)_2Ru(dpp)]_2RhX_2\}^{5+}$  systems ( $X = Cl$  or  $Br$ ) or  $\{[(phen)_2Ru(dpp)]_2RhCl_2\}^{5+}$  show overlapping oxidative couples at *ca.* 1.60 V vs. SCE.  $Rh^{III}$  centers coordinated to polyazine ligands typically display irreversible reductions corresponding to  $Rh^{III/II/I}$  processes [85]. The  $Rh^{III/II/I}$  reductions are followed by the loss of halides as observed for  $[Rh(bpy)_2Cl_2]^+$ . In the trimetallic systems, the  $Rh^{III/II/I}$  reduction is followed by two reversible  $dpp^{0/-}$  reductions. The halides on the  $Rh^{III}$  center impact the redox properties as evidenced by a slightly more

positive  $Rh^{III/II/I}$  reduction,  $-0.36$  V vs. SCE for  $\{[(bpy)_2Ru(dpp)]_2RhBr_2\}^{5+}$  relative to  $\{[(bpy)_2Ru(dpp)]_2RhCl_2\}^{5+}$ ,  $-0.40$  V vs. SCE [54–56]. This positive shift in the  $Rh^{III/II/I}$  couple is consistent  $Br^-$  being a weaker  $\sigma$  donor than  $Cl^-$ . The  $Os^{II/III}$  couple occurs at 1.17 V vs. SCE in  $\{[(bpy)_2Os(dpp)]_2RhCl_2\}^{5+}$ . The more positive oxidation potential is a result of more destabilized  $Os(d\pi)$  orbitals relative to the  $Ru(d\pi)$  orbitals in the Ru-based systems. The  $Ru^{II/III}$  oxidation of  $\{[(tpy)RuCl(dpp)]_2RhCl_2\}^{3+}$  occurs at 1.09 V vs. SCE, more positive than the  $Ru^{II/III}$  oxidations of the analogous  $bpy$ -based systems, and consistent with a more electron rich ruthenium center due to  $Cl^-$  coordination in place of a pyridine ring. The  $Os^{II/III}$  couple in  $\{[(tpy)OsCl(dpp)]_2RhCl_2\}^{3+}$  occurs at 0.81 V vs. SCE, consistent with even more destabilized  $Os(d\pi)$  orbitals. The reductive electrochemistry of  $\{[(tpy)MCl(dpp)]_2RhCl_2\}^{3+}$  shows irreversible  $Rh^{III/II/I}$  reductions at  $-0.51$  and  $-0.55$  V vs. SCE ( $M = Ru$  or  $Os$ ), respectively, followed by two reversible  $dpp^{0/-}$  couples. The electrochemistry of the trimetallic supramolecular complexes predict  $Ru(d\pi)$ - or  $Os(d\pi)$ -HOMOs with energy tuned by the TL or LA metal and  $Rh(d\sigma^*)$ -based LUMOs with energy tuned by the halides bound to Rh. The electrochemistry predicts a lowest lying metal-to-metal charge-transfer state (MMCT) with an oxidized Ru and a reduced Rh, Fig. 10.

*Rhodium-Based Supramolecular Photocatalysts: Spectroscopic Properties* The optical properties of the trimetallic supramolecular complexes are evaluated by electronic absorption spectroscopy [54–56]. The trimetallic

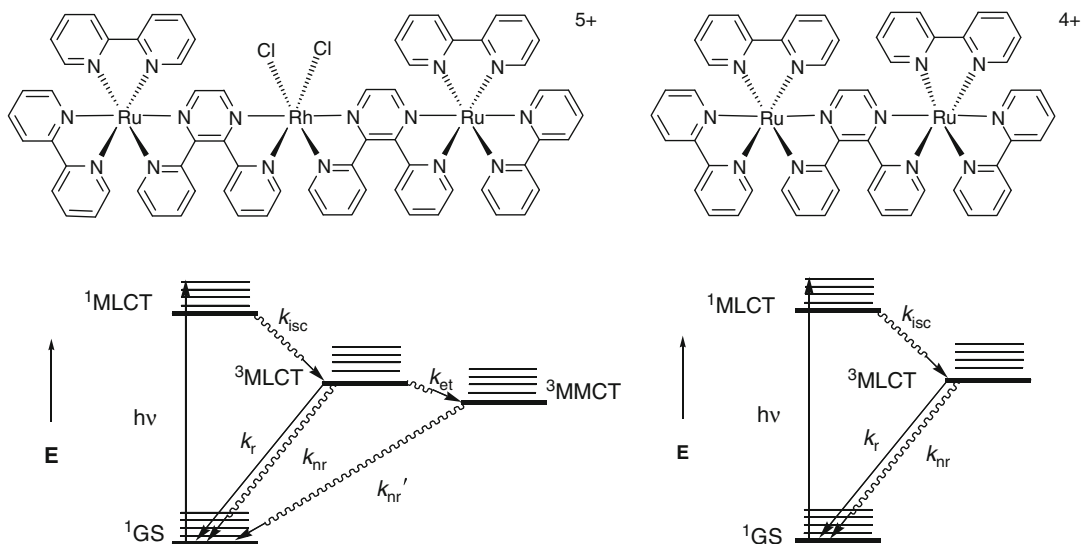


**Hydrogen via Direct Solar Production, Fig. 10** Orbital energy diagram of Rh-centered photoinitiated electron collection of the form LA-BL-RhX<sub>2</sub>-BL-LA (LA = bpy or phen, BL = dpp, X = Cl or Br)

supramolecular assemblies are efficient light absorbers throughout the UV and visible regions of the spectrum with transitions characteristic of each subunit of the LA-BL unit. The electronic absorption spectra of  $[\{(bpy)_2Ru(dpp)\}_2RhX_2]^{5+}$  (X = Cl or Br) and  $[\{(phen)_2Ru(dpp)\}_2RhCl_2]^{5+}$  exhibit intense  $\pi \rightarrow \pi^*$  TL and dpp transitions in the UV, Ru( $d\pi$ )  $\rightarrow$  TL ( $\pi^*$ ) (TL = bpy or phen) CT transitions between 410 and 420 nm, and Ru( $d\pi$ )  $\rightarrow$  dpp( $\pi^*$ ) CT transitions at  $\lambda_{max}^{abs} = 520$  nm ( $\epsilon = 2.6 \times 10^4$  M<sup>-1</sup> cm<sup>-1</sup>) [56]. The lowest energy Ru( $d\pi$ )  $\rightarrow$  dpp( $\pi^*$ ) CT transition for  $[\{(bpy)_2Ru(dpp)\}_2(dpp)]^{4+}$  or  $[\{(phen)_2Ru(dpp)\}_2(dpp)]^{4+}$  occurs at  $\lambda_{max}^{abs} = 526$  nm demonstrating that the Ru (dp)  $\rightarrow$  dpp( $\pi^*$ ) CT are dominating in this region. This is verified by the nearly identical electronic absorption spectra of  $[\{(bpy)_2Ru(dpp)\}_2RhCl_2]^{5+}$  and  $[\{(bpy)_2Ru(dpp)\}_2RhBr_2]^{5+}$  demonstrating that the halide on the Rh does not significantly impact the optical properties. The electronic absorption spectra for the tpy-based systems are similar to the bpy analogs showing changes consistent with the destabilized metal orbitals showing Ru( $d\pi$ )  $\rightarrow$  dpp( $\pi^*$ ) CT transitions at  $\lambda_{max}^{abs} = 540$  nm. For the Os analogs,  $[\{(bpy)_2Os(dpp)\}_2RhCl_2]^{5+}$  and  $[\{(tpy)OsCl(dpp)\}_2RhCl_2]^{3+}$ , the Os( $d\pi$ )  $\rightarrow$  dpp( $\pi^*$ ) CT transitions occur at slightly

lower energies relative to the ruthenium-based systems, consistent with the destabilized Os( $d\pi$ ) orbitals. The Os systems show pronounced intensity of the <sup>3</sup>MLCT absorption in the low energy region due to a high degree of spin-orbit coupling.

*Rhodium-Based Supramolecular Photocatalysts: Photophysics* Emission spectroscopy is used to probe intramolecular electron transfer within a supramolecular assembly possessing emissive MLCT light absorbers. The Ru-based  $[\{(TL)_2Ru(dpp)\}_2RhX_2]^{5+}$  (TL = bpy or phen, X = Cl or Br) systems possess <sup>3</sup>MLCT emissive excited states [54–56]. Model systems are used for comparison of the excited state properties to better understand the nature of energy and/or electron transfer within the supramolecular architecture. The bimetallic complex  $[\{(bpy)_2Ru(dpp)\}_2(dpp)]^{4+}$  that lacks the Rh<sup>III</sup> typically serves as the model for the interpretation of the emissive properties of these supramolecules due to the similar excited state energies and nature of the emissive <sup>3</sup>MLCT excited states. Determination of the rate of electron transfer requires that the energy and nature of the emissive state of the model must closely match that of the supramolecular assembly. In the  $[\{(TL)_2Ru(dpp)\}_2RhX_2]^{5+}$  (TL = bpy, X = Cl or Br) and  $[\{(phen)_2Ru(dpp)\}_2RhCl_2]^{5+}$  systems, the optically excited <sup>1</sup>MLCT state populates a <sup>3</sup>MLCT state that is quenched by intramolecular electron transfer to populate a low-lying <sup>3</sup>MMCT state (see Fig. 11) [54–56]. The complexes  $[\{(bpy)_2Ru(dpp)\}_2RhCl_2]^{5+}$ ,  $[\{(bpy)_2Ru(dpp)\}_2RhBr_2]^{5+}$ , and  $[\{(phen)_2Ru(dpp)\}_2RhCl_2]^{5+}$  display weak emissions from the Ru( $d\pi$ )  $\rightarrow$  dpp( $\pi^*$ ) <sup>3</sup>MLCT state at  $\lambda_{max}^{em} = 760$  nm for  $[\{(bpy)_2Ru(dpp)\}_2RhCl_2]^{5+}$  and  $[\{(bpy)_2Ru(dpp)\}_2RhBr_2]^{5+}$  and  $\lambda_{max}^{em} = 746$  nm for  $[\{(phen)_2Ru(dpp)\}_2RhCl_2]^{5+}$  with  $\Phi^{em} = 7.3 \times 10^{-5}$ ,  $1.5 \times 10^{-4}$ , and  $1.8 \times 10^{-4}$ , respectively, at RT in deoxygenated acetonitrile solutions following excitation at 520 nm. The emission from the <sup>3</sup>MLCT state is quenched by ca. 85–90% relative to  $[\{(bpy)_2Ru(dpp)\}_2(dpp)]^{4+}$  ( $\lambda_{max}^{em} = 744$  nm,  $\Phi^{em} = 1.38 \times 10^{-3}$ ) indicating intramolecular electron transfer to populate a lower lying state. Electrochemical analysis predicts this state to be a <sup>3</sup>MMCT excited state with oxidized Ru LAs and a reduced Rh. The  $\tau$  of the

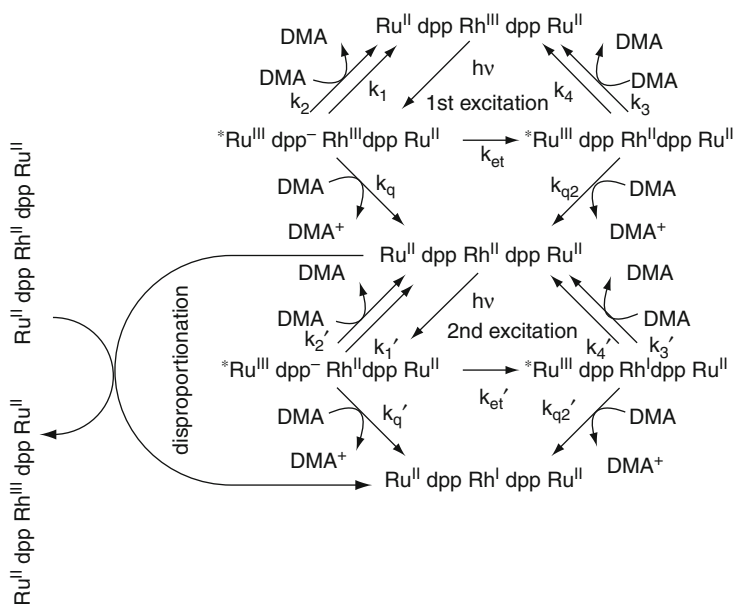


**Hydrogen via Direct Solar Production, Fig. 11** State diagrams for  $[\{(bpy)_2Ru(dpp)\}_2RhX_2]^{5+}$  ( $X = Cl^-$  or  $Br^-$ ) and  $[\{(phen)_2Ru(dpp)\}_2RhCl_2]^{5+}$  (left) and  $[\{(bpy)_2Ru\}_2(dpp)]^{4+}$  (right)

$^3MLCT$  states in deoxygenated acetonitrile solutions at RT for  $[\{(bpy)_2Ru(dpp)\}_2RhCl_2]^{5+}$ ,  $[\{(bpy)_2Ru(dpp)\}_2RhBr_2]^{5+}$ , and  $[\{(phen)_2Ru(dpp)\}_2RhCl_2]^{5+}$  are 32, 26, and 27 ns, respectively, reduced relative to the  $\tau$  of  $[\{(bpy)_2Ru\}_2(dpp)]^{4+}$ ,  $\tau = 140$  ns [56, 84]. The  $k_{et}$  to populate the  $^3MMCT$  states, estimated by assuming  $k_r$  and  $k_{nr}$  of the trimetallic systems are the same as  $[\{(bpy)_2Ru\}_2(dpp)]^{4+}$ , are comparable with  $k_{et} = 1.2 \times 10^8$  s $^{-1}$ ,  $5.2 \times 10^7$  s $^{-1}$ , and  $4.4 \times 10^7$  s $^{-1}$ , respectively, for  $[\{(bpy)_2Ru(dpp)\}_2RhCl_2]^{5+}$ ,  $[\{(bpy)_2Ru(dpp)\}_2RhBr_2]^{5+}$ , and  $[\{(phen)_2Ru(dpp)\}_2RhCl_2]^{5+}$ . Efficient intramolecular electron transfer is seen in this trimetallic motif.

*Rhodium-Based Supramolecular Photocatalysts: Solar Hydrogen Production* Solar hydrogen production from water using a series of supramolecular photoinitiated electron collectors of the general form LA-BL-RhX $_2$ -BL-LA has been evaluated [54–56]. These systems photoreduce by two electrons, following visible light excitation in the presence of DMA. This mechanism proposes that  $[\{(bpy)_2Ru(dpp)\}_2Rh]^{5+}$  species is formed by the excited trimetallic molecule using a sacrificial electron donor and passes through an intermediate Rh $^{II}$  species, Fig. 12.

These complexes are unusually oxidizing in their excited states, allowing for excited state oxidation of a variety of electron donors. Reductive quenching of both the  $^3MLCT$  and  $^3MMCT$  states are feasible. Kinetic investigation by Stern-Volmer emission quenching as well as product formation was performed focusing on the formation of the single electron reduced Rh $^{II}$  species. The rate of reductive quenching to generate the Rh $^{II}$  species from the  $^3MLCT$  excited state would be  $1.9 \times 10^9$  M $^{-1}$  s $^{-1}$  if reduction only occurs via this pathway [82]. A Stern-Volmer emission quenching analysis showed that the  $^3MLCT$  excited state is efficiently quenched by DMA close to diffusion limit,  $k_q = 2 \times 10^{10}$  M $^{-1}$  s $^{-1}$ . The estimated excited state reduction potentials of the  $^3MLCT$  and  $^3MMCT$  states for  $[\{(bpy)_2Ru(dpp)\}_2RhCl_2]^{5+}$  are 1.23 and 0.84 V vs. SCE, respectively. Positive driving forces for reductive quenching of both excited states are predicted, using Eq. 10, the oxidation potential of DMA,  $E_{1/2} = 0.81$  V vs. SCE. Very similar driving forces for reductive quenching of the excited states by DMA are also predicted for  $[\{(bpy)_2Ru(dpp)\}_2RhBr_2]^{5+}$  and  $[\{(phen)_2Ru(dpp)\}_2RhCl_2]^{5+}$  based on their excited state reduction potentials and the oxidation potential of DMA.



### Hydrogen via Direct Solar Production,

**Fig. 12** Proposed mechanism for photoinitiated electron transfer. bpy, Cl, and charges are omitted for clarity.  $\text{Ru}^{\text{II}}\text{dppRh}^{\text{III}}\text{dppRu}^{\text{II}}$  is  $[\{(\text{bpy})_2\text{Ru}(\text{dpp})\}_2\text{RhCl}_2]^{5+}$ , where bpy = 2,2'-bipyridine and dpp = 2,3-bis-2-pyridylpyrazine. DMA is dimethylaniline.  $k_1$  and  $k_4$  are the unimolecular decay pathways from the  $^3\text{MLCT}$  and

$^3\text{MMCT}$  states, respectively, whereas  $k_2$  and  $k_3$  are the bimolecular deactivation rates from the same states.  $k_{\text{et}}$  is the rate of electron transfer to generate the  $^3\text{MMCT}$  state.  $k_q$  and  $k_{q2}$  are the rates of reductive quenching by DMA to generate the  $\text{Rh}^{\text{II}}$  complex from the  $^3\text{MLCT}$  and  $^3\text{MMCT}$  states, respectively

The trimetallic complexes  $[\{(\text{bpy})_2\text{Ru}(\text{dpp})\}_2\text{RhCl}_2]^{5+}$ ,  $[\{(\text{bpy})_2\text{Ru}(\text{dpp})\}_2\text{RhBr}_2]^{5+}$ ,  $[\{(\text{phen})_2\text{Ru}(\text{dpp})\}_2\text{RhCl}_2]^{5+}$ ,  $[\{(\text{bpy})_2\text{Os}(\text{dpp})\}_2\text{RhCl}_2]^{5+}$ ,  $[\{(\text{tpy})\text{RuCl}(\text{dpp})\}_2\text{RhCl}_2]^{3+}$ ,  $[\{(\text{tpy})\text{OsCl}(\text{dpp})\}_2\text{RhCl}_2]^{3+}$ , and the first photoinitiated electron collector  $[\{(\text{bpy})_2\text{Ru}(\text{dpp})\}_2\text{IrCl}_2]^{5+}$  were evaluated with respect to their functioning as hydrogen photocatalysts in the presence of water and DMA,  $\text{Et}_3\text{N}$ , or TEOA [56]. All complexes demonstrate photocatalytic activity with the exceptions of  $[\{(\text{bpy})_2\text{Ru}(\text{dpp})\}_2\text{IrCl}_2]^{5+}$  and  $[\{(\text{tpy})\text{OsCl}(\text{dpp})\}_2\text{RhCl}_2]^{3+}$ . The lack of photocatalysis by  $[\{(\text{bpy})_2\text{Ru}(\text{dpp})\}_2\text{IrCl}_2]^{5+}$  demonstrate that the functioning systems require a Rh center and a  $^3\text{MLCT}$  and/or  $^3\text{MMCT}$  states with sufficient driving forces for excited state reduction by the ED. It is predicted that the coordinatively unsaturated species generated by Rh reduction,  $[\{(\text{TL})_2\text{Ru}(\text{dpp})\}_2\text{Rh}^{\text{I}}]^{5+}$  (TL = bpy or phen), is reactive and susceptible to interaction with substrates such as water.

Photolysis of acetonitrile solutions of  $[\{(\text{bpy})_2\text{Ru}(\text{dpp})\}_2\text{RhX}_2]^{5+}$  ( $\text{X} = \text{Cl}^-$  or  $\text{Br}^-$ ) or  $[\{(\text{phen})_2\text{Ru}(\text{dpp})\}_2\text{RhCl}_2]^{5+}$  in the presence of DMA and water at  $\lambda = 470$  nm leads to water reduction to produce hydrogen with  $\Phi = 0.01$  with 18–26 TON in 2 h (36–54 TON relative to the LA as 2 TON of the LA are needed per catalytic cycle).  $[\{(\text{bpy})_2\text{Ru}(\text{dpp})\}_2\text{RhBr}_2]^{5+}$  shows higher photocatalytic activity relative to the chloride analog implying that the rate of halide loss is kinetically important. The complexes  $[\{(\text{bpy})_2\text{Os}(\text{dpp})\}_2\text{RhCl}_2]^{5+}$  and  $[\{(\text{tpy})\text{RuCl}(\text{dpp})\}_2\text{RhCl}_2]^{3+}$  yield similar amounts of hydrogen when irradiated at 470 nm in the presence of DMA and water, but with much lower efficiency than  $[\{(\text{bpy})_2\text{Ru}(\text{dpp})\}_2\text{RhCl}_2]^{5+}$ . The excited state reduction potentials of the  $^3\text{MLCT}$  and  $^3\text{MMCT}$  were predicted as 0.91 and 0.54 V vs. SCE, respectively, for  $[\{(\text{bpy})_2\text{Os}(\text{dpp})\}_2\text{RhCl}_2]^{5+}$  and 1.01 and 0.61 V, respectively, for  $[\{(\text{tpy})\text{RuCl}(\text{dpp})\}_2\text{RhCl}_2]^{3+}$  making

quenching of the  $^3\text{MMCT}$  excited state by DMA unlikely.

The production of hydrogen despite the negative driving force for reductive quenching of the  $^3\text{MMCT}$  excited state suggests that hydrogen production can occur through quenching of only the  $^3\text{MLCT}$  excited state. The lower driving force for reductive quenching of the  $^3\text{MLCT}$  and the lower  $\tau$  may account for the lower photocatalytic efficiency of these complexes.  $[\{(\text{tpy})\text{OsCl}(\text{dpp})\}_2\text{RhCl}_2]^{3+}$  does not function as a photocatalyst under the conditions investigated. Based on the excited state reduction potentials of the  $^3\text{MLCT}$  and  $^3\text{MMCT}$  states, 0.71 and 0.37 V vs. SCE, respectively, the reductive quenching of both excited states by DMA are thermodynamically unfavorable, explaining the lack of photocatalytic activity of this system. Addition of Hg(l) to the photocatalytic systems does not impair hydrogen production suggesting that hydrogen production catalyzed by Rh colloid formation is not an active pathway and that the supramolecular architecture remains intact during photocatalysis [54, 86, 87]. Interestingly,  $[\{(\text{bpy})_2\text{Ru}(\text{dpp})\}_2\text{IrCl}_2]^{5+}$  is not a solar hydrogen photocatalyst although PEC occurs on the  $\text{dpp}(\pi^*)$  orbitals and a thermodynamically favorable driving force for reductive quenching of the  $^3\text{MLCT}$  state by DMA exists. This implies that other factors in addition to PEC and favorable thermodynamics for reductive quenching are important for solar hydrogen production. The lack of hydrogen production by the Ir-system implies that the Rh center is essential for photocatalysis.

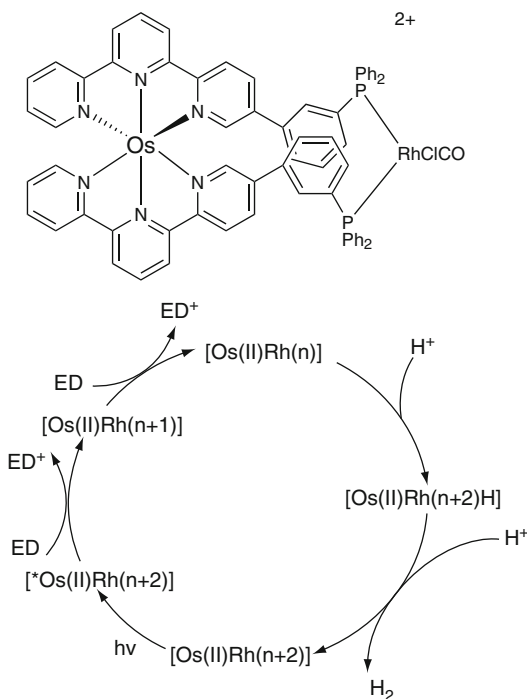
The impact of the ED on the most efficient photocatalysts  $[\{(\text{bpy})_2\text{Ru}(\text{dpp})\}_2\text{RhCl}_2]^{5+}$ ,  $[\{(\text{bpy})_2\text{Ru}(\text{dpp})\}_2\text{RhBr}_2]^{5+}$ , and  $[\{(\text{phen})_2\text{Ru}(\text{dpp})\}_2\text{RhCl}_2]^{5+}$  shows that the efficiency of hydrogen production varies in the order DMA (18–26 TON in 2 h) >  $\text{Et}_3\text{N}$  (3–6 TON in 2 h) > TEOA (1 TON in 2 h) [56]. TEOA has a slightly higher driving force for reductive quenching of the photocatalysts than  $\text{Et}_3\text{N}$ , but results in lower hydrogen yields. An important factor to be considered in water reduction is the solution pH. The effective pH of the photolysis solutions using DMA,  $\text{Et}_3\text{N}$ , or TEOA were

estimated as *ca.* 9.1, 14.7, and 11.8, respectively, on the assumption that the  $\text{pK}_a$  values of their conjugated acids remain unchanged in the photocatalytic solutions relative to aqueous conditions ( $\text{pK}_a = 5.07$  ( $\text{DMAH}^+$ ), 10.75 ( $\text{Et}_3\text{NH}^+$ ), and 7.76 ( $\text{TEOAH}^+$ )). The lower catalyst function when TEOA is the ED may be attributed to the higher effective pH of the solution. The reduction potential of water is pH dependent occurring at lower potentials at lower pH. In addition the protonation of the Rh center may be critical to photocatalysis and this equilibrium would be very sensitive to pH. In addition, the ability of DMA to form donor-LA  $\pi$ -stacking interactions may be advantageous for more efficient reductive quenching of the excited states affording the highest hydrogen yields compared to the aliphatic electron donors. Recent studies have focused on the scale up of photochemical hydrogen production using the lead photocatalyst  $[\{(\text{bpy})_2\text{Ru}(\text{dpp})\}_2\text{RhBr}_2]^{5+}$ . Studies show that increased [DMA], increased headspace, volume, and a DMF solvent provide enhanced catalyst function [88].

Photochemical properties of  $[\{(\text{bpy})_2\text{Ru}(\text{dpp})\}_2\text{RhBr}_2]\text{Br}_5$  in aqueous medium have been investigated [57]. Studies have established this complex to function as a photoinitiated electron collector in water, the first system shown to display this function in aqueous medium.  $[\{(\text{bpy})_2\text{Ru}(\text{dpp})\}_2\text{RhBr}_2]\text{Br}_5$  functions as a photocatalyst for the production of hydrogen in the presence of TEOA with added triflic acid, hydrobromic acid, or phosphoric acid. The photocatalytic efficiency is lower in the aqueous medium, typical of these systems.

The Rh-centered supramolecular complexes are efficient photocatalysts for water reduction to produce hydrogen fuel. The variation of component identity within this molecular architecture allows for optimization of functioning of these systems and the understanding of the mechanism of action. The functioning of these systems is also modulated by system parameters such as solvent, temperature, reagent concentrations, hydrogen partial pressure, etc. This provides a unique forum to explore the multi-dimensional space needed to optimize solar





**Hydrogen via Direct Solar Production, Fig. 13** OsRh dyad systems for solar hydrogen production

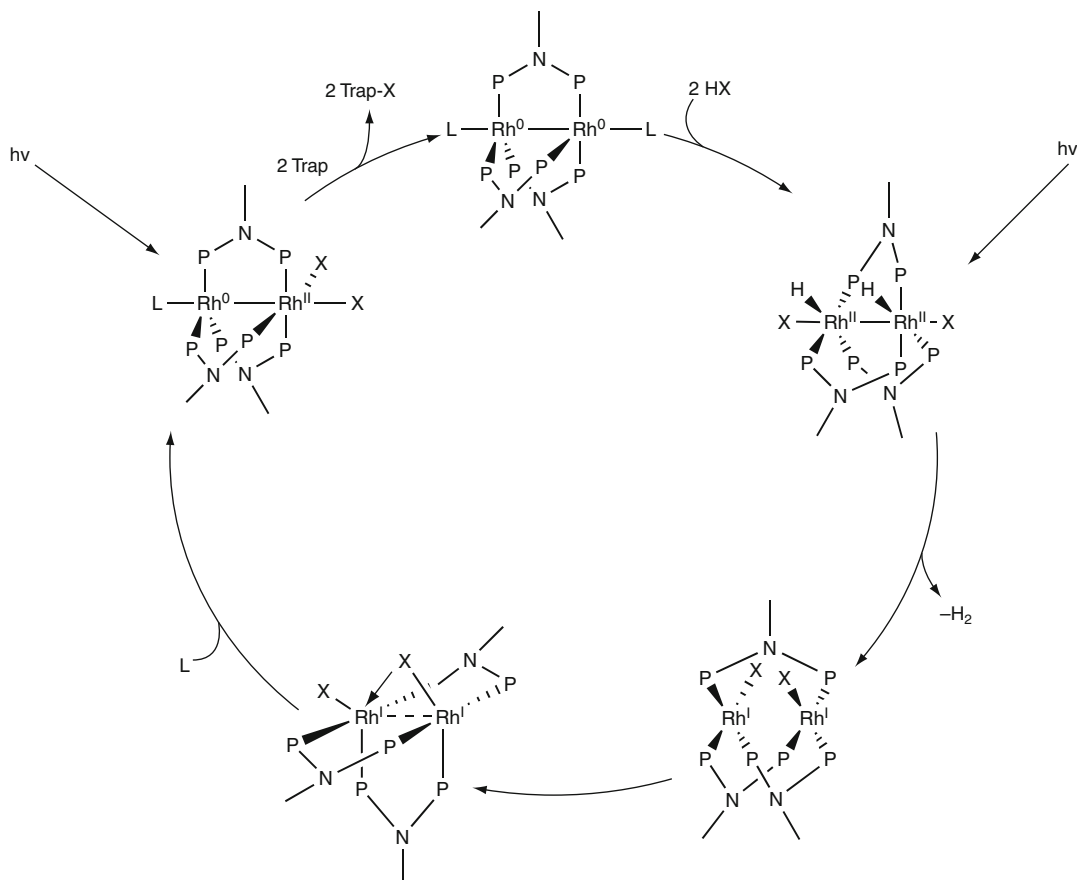
hydrogen production via direct water reduction. Often preliminary studies appear without the long-term study needed to explore the full potential of these new supramolecular catalysts for hydrogen production.

Supramolecular solar hydrogen photocatalysts that couple a  $[\text{Os}(\text{tpy})_2]^{2+}$  LA to a Rh CAT are reported, Fig. 13 [58]. The OsRh dyads have been synthesized and analyzed in situ by treatment with  $[\text{RhCl}(\text{CO})_2]_2$  or  $\text{RhCl}_3$ . The dyads are potent LAs absorbing in the visible at 480 and 655 nm, attributed to  $\text{Os}(d\pi) \rightarrow \text{tpy}(d\pi^*)$   $^1\text{MLCT}$  and  $^3\text{MLCT}$  absorptions, respectively. An  $\text{Os}(d\pi) \rightarrow \text{tpy}(d\pi^*)$   $^3\text{CT}$  emission is observed at 728 nm ( $\Phi^{\text{em}} = 0.52$  in an acetonitrile/water mixture) with reduced intensity relative to the parent LA ( $\Phi^{\text{em}} = 0.73$  in an acetonitrile/water mixture) suggestive of intramolecular electron transfer to the Rh. The emission is decreased when sodium ascorbate is added to the dyad efficient quenching of the excited state by sodium ascorbate.

Irradiation of catalytic amounts of the dyad generated in situ at  $\lambda > 380$  nm in a

trifluoromethanesulfonic acid/sodium ascorbate mixture at pH = 5.2 for 18 h affords hydrogen with 36 TON [58]. Use of  $\text{RhCl}_3$  in place of  $[\text{RhCl}(\text{CO})_2]_2$  yields 87 TON with  $\Phi = 0.007$ . Electron donors including TEOA or L-cysteine are not effective for hydrogen photocatalysis. Lower catalytic function is observed when  $\text{RhCl}_3 \cdot 3\text{H}_2\text{O}/\text{dppe}$  (dppe = 1,2-bis(diphenylphosphino)ethane) with  $[\text{Os}(\text{tpy})_2]^{2+}$  is used as the photosystem (24 TON) with no detectable hydrogen if only  $\text{RhCl}_3 \cdot 3\text{H}_2\text{O}/\text{dppe}$ ,  $\text{RhCl}(\text{CO})(\text{dppe})$ , or only the LA is used. This suggests that the supramolecular architecture is important for photocatalysis and intramolecular electron transfer from Os to Rh is a key step. A schematic for the proposed mechanism is shown in Fig. 13. It is proposed that upon optical excitation, intramolecular electron transfer to Rh by two electrons leads to a reduced Rh which can react with a proton to form a Rh-H, which generates hydrogen.

Photochemical hydrogen production from hydrohalic acid solutions by a Rh-based dinuclear mixed-valence complex capable of multielectron photochemistry has been reported, Fig. 14 [59, 89]. Hydrogen production occurs with  $\Phi = 0.01$  with 27 TON/h during the initial 3 h, in the presence of a halogen trap. The mixed-valence compounds have been constructed to drive multielectron chemistry and are of the form  $\text{M}^{n+} \dots \text{M}^{n+2}$ . Rhodium bimetallics,  $[\text{Rh}_2(\text{dfpma})_3\text{X}_4]$ , when ligated by three dfpma ligands transform to a two-electron mixed-valence state,  $[\text{Rh}_2^{0,\text{II}}(\text{dfpma})_3\text{X}_2(\text{L})]$  (dfpma =  $\text{MeN}(\text{PF}_2)_2$ , X = Cl or Br, L = CO,  $\text{PR}_3$ , or CNR) when irradiated at excitation wavelengths between 300 and 400 nm in the presence of excess L and a halogen-atom trap. The dfpma ligand provides stability to the mixed-valence state by acting as both a  $\pi$ -acceptor and a  $\pi$ -donor. Further irradiation activates a  $\text{Rh}^{\text{II}}\text{-X}$ , which is the rate limiting step, to generate a doubly reduced form,  $[\text{Rh}_2^{0,0}(\text{dfpma})_3\text{L}_2]$ . Photolysis of  $[\text{Rh}_2^{0,0}(\text{dfpma})_3\text{L}_2]$  in the presence of HCl results in an intermediate  $\text{Rh}^{\text{II}}\text{,Rh}^{\text{II}}$  dihydride, dihalide,  $[\text{Rh}_2^{\text{II,II}}(\text{dfpma})_3\text{Cl}_2\text{H}_2]$ , which upon photolysis produces hydrogen with the generation of the  $[\text{Rh}_2^{\text{I,I}}(\text{dfpma})_3\text{Cl}_2]$  which undergoes internal disproportionation affording  $[\text{Rh}_2^{0,\text{II}}(\text{dfpma})_3\text{X}_2(\text{L})]$ .

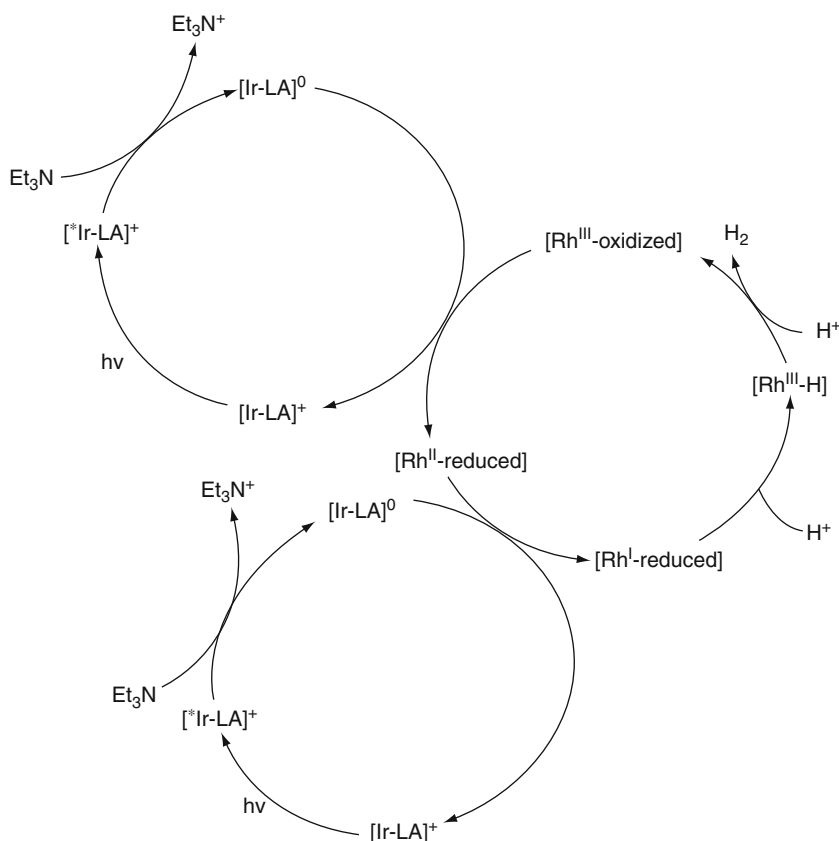


**Hydrogen via Direct Solar Production, Fig. 14** Mechanism for the photocatalytic generation of hydrogen from hydrohalic acids using a dirhodium mixed-valence photocatalyst. (Figure adapted from Ref. [59])

New systems  $[\text{Rh}^{\text{I}}\text{Au}^{\text{I}}(\text{tfepma})_2(\text{CN}^t\text{Bu})_2]^{2+}$  and  $[\text{Pt}^{\text{II}}\text{Au}^{\text{I}}(\text{dppm})_2\text{PhCl}]^+$  (tfepma =  $\text{MeN}(\text{P}(\text{OCH}_2\text{CF}_3)_2)_2$  and dppm =  $\text{CH}_2(\text{PPh}_2)_2$ ) have been constructed with the aim of promoting more efficient M-X bond activation [90, 91]. The  $\text{Pt}^{\text{III}}\text{-Au}^{\text{II}}$  species,  $[\text{Pt}^{\text{III}}\text{Au}^{\text{II}}(\text{dppm})_2\text{PhCl}_3]^+$ , formed by photooxidation displays enhanced efficiency of metal-halide bond activation with respect to the dirhodium complexes.

**Rhodium-Based Multicomponent Photocatalysis** The pioneering work in photochemical hydrogen production using molecular systems used  $[\text{Rh}(\text{bpy})_3]^{3+}$  as an electron relay in solar hydrogen production schemes using  $[\text{Ru}(\text{bpy})_3]^{2+}$  and TEOA [11, 60]. In the presence of a heterogeneous platinum catalyst, photocatalytic hydrogen production from water occurs with  $\Phi = 0.11$  irradiated at  $\lambda = 450$  nm with *ca.*

80 TON relative to  $[\text{Rh}(\text{bpy})_3]^{2+}$  reported under similar conditions [11, 60]. The MLCT excited state of  $[\text{Ru}(\text{bpy})_3]^{2+}$  undergoes intermolecular electron transfer to  $[\text{Rh}(\text{bpy})_3]^{3+}$  to produce the oxidized LA and  $[\text{Rh}(\text{bpy})_3]^{2+}$ . The photo-generated  $\text{Rh}^{\text{II}}$  system is kinetically unstable and can rapidly disproportionate to  $[\text{Rh}^{\text{I}}(\text{bpy})_2]^+$  and  $[\text{Rh}^{\text{III}}(\text{bpy})_3]^{3+}$  deactivating the system. The catalytic species in this system is colloidal Pt, which facilitates hydrogen photocatalysis by accepting electrons from the reduced Rh. In-depth studies of  $[\text{Rh}^{\text{I}}(\text{bpy})_2]^+$  have established that at low concentrations in alkaline solutions  $[\text{Rh}^{\text{I}}(\text{bpy})_2]^+$  predominates, while a dimer,  $[\text{Rh}^{\text{I}}(\text{bpy})_2]_2^{2+}$ , is dominant at higher  $[\text{Rh}^{\text{I}}(\text{bpy})_2]$  [92, 93].  $[\text{Rh}^{\text{III}}(\text{bpy})_2(\text{H})(\text{H}_2\text{O})]^{2+}$  and  $[\text{Rh}^{\text{I}}(\text{bpy})_2]_2(\text{H})^{3+}$  are formed by protonation of  $[\text{Rh}^{\text{I}}(\text{bpy})_2]^+$  or  $[\text{Rh}^{\text{I}}(\text{bpy})_2]_2^{2+}$  at low pH. Thermodynamic and



**Hydrogen via Direct Solar Production, Fig. 15** Mechanism for the photocatalytic generation of hydrogen from water in a Ir-Rh multicomponent system with Et<sub>3</sub>N electron donor

kinetic parameters for the oxidative addition of hydrogen to  $[\text{Rh}^{\text{I}}(\text{bpy})_2]^+$  and photoinduced reductive elimination of hydrogen have been studied,  $K_{\text{H}} = 1.45 \times 10^3 \text{ M}^{-1}$  [94]. Studies show that *cis*- $[\text{Rh}^{\text{III}}(\text{H})_2(\text{bpy})_2]^+$  dissociates to hydrogen and  $[\text{Rh}^{\text{I}}(\text{bpy})_2]^+$  when irradiated ( $\lambda > 300 \text{ nm}$ ).

Cyclometalated Ir<sup>III</sup> complexes have been used as LAs in photochemical schemes for production of hydrogen from water using tris-2,2'-bipyridyl Rh<sup>III</sup> complexes as CATs, Fig. 15 [61]. The study of the system function with varied  $[\text{Ir}(\text{C}\wedge\text{N})_2(\text{N}\wedge\text{N})]^+$  LAs and  $[\text{Rh}(\text{N}\wedge\text{N})]^{3+}$  CATs has allowed the development of an optimized photosystem for solar hydrogen production. An optimal catalyst combination of  $[\text{Ir}(\text{f-mppy})_2(\text{dtbbpy})]^+$  and  $[\text{Rh}(\text{dtbbpy})_3]^{3+}$  has been identified through catalyst screening, studies of the impact of hydrogen production by LA,

CAT, solvent environment, and electron donor (f-mppy = 5-methyl-2-(4-fluoro)phenylpyridine). Irradiation of 80% THF-H<sub>2</sub>O system at 460 nm shows 5,000 TON relative to either the LA or the CAT when one component is limiting in excess of the other. The use of 1:1 of LA and CAT balances the performance of both components resulting in 3,400 TON and a maximum catalytic rate of turnovers of  $520 \text{ h}^{-1}$  with  $\Phi = 0.32$  in *ca.* 20–24 h. The rate constants for reductive quenching of the excited state of the LA by Et<sub>3</sub>N and oxidative quenching by  $[\text{Rh}(\text{dtbbpy})_3]^{3+}$  are similar,  $k_{\text{ox}} = 6.7 \times 10^7 \text{ M}^{-1} \text{ s}^{-1}$  and  $k_{\text{red}} = 6.4 \times 10^7 \text{ M}^{-1} \text{ s}^{-1}$ , but the presence of excess of Et<sub>3</sub>N suggests that a reductive quenching mechanism is dominant. Addition of Hg does not impede system function providing evidence that the system is a true homogeneous system for photocatalytic hydrogen production.

## Co-Based Supramolecular and Multicomponent Systems

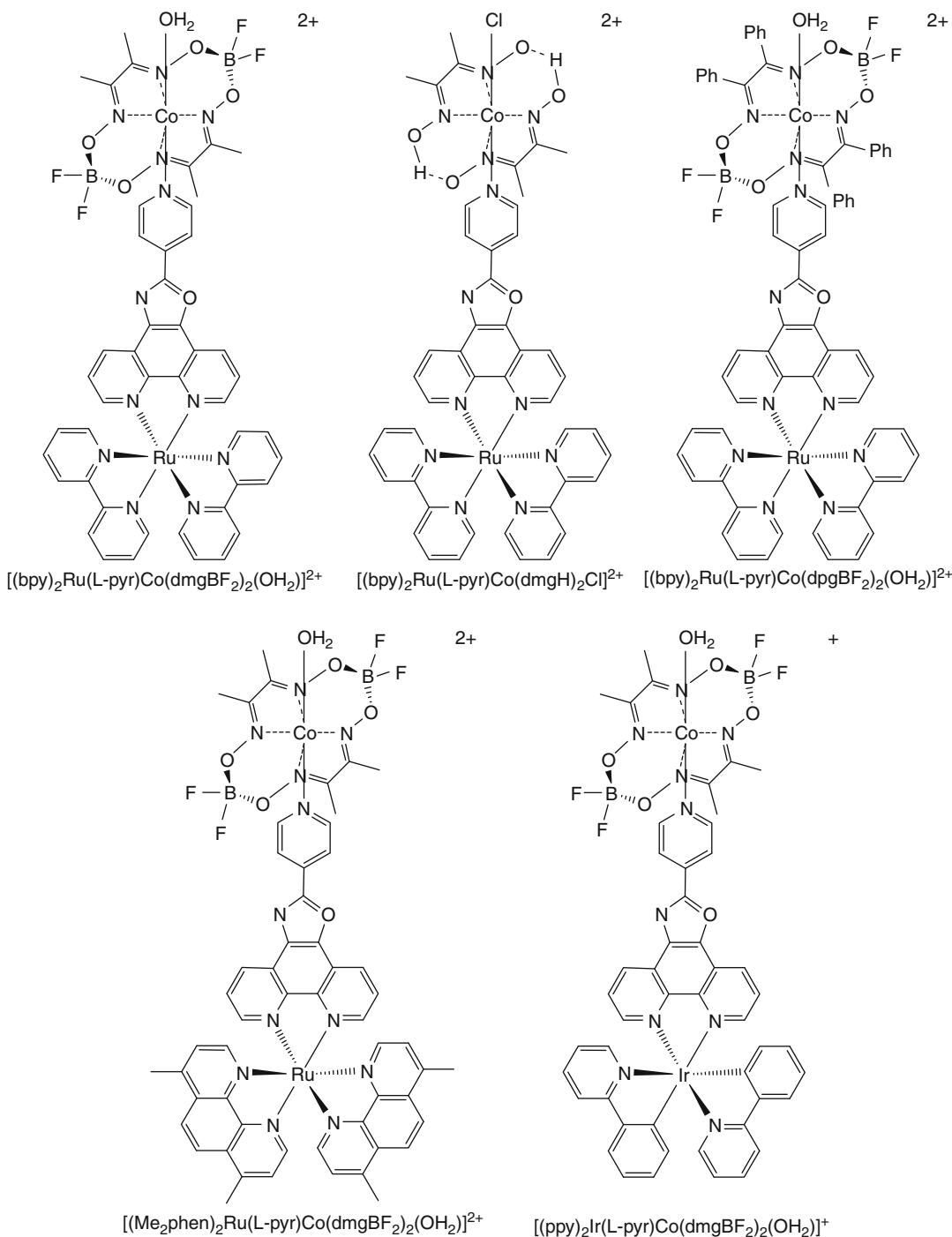
Cobalt complexes with diglyoxime ligands are electrocatalysts for hydrogen production at low overpotentials. The electrochemical and photochemical hydrogen evolution catalyzed by cobaloximes with thermodynamic analysis of hydrogen evolution pathways has been reviewed recently [95]. Supramolecular systems as well as multicomponent systems which incorporate cobaloximes sensitized by Ru or Ir base LAs are known. These systems provide a means to utilize first-row transition metal complexes as CATs.

**Co-Based Supramolecular Systems** Supramolecular systems have been engineered taking advantage of the light-absorbing properties of Ru<sup>II</sup> or Ir<sup>III</sup> chromophores and the catalytic properties of cobaloximes in single molecules [62, 63]. Supramolecular dyads [(bpy)<sub>2</sub>Ru(L-pyr)Co(dmgBF<sub>2</sub>)<sub>2</sub>(OH<sub>2</sub>)]<sup>2+</sup>, [(bpy)<sub>2</sub>Ru(L-pyr)Co(dmgH)<sub>2</sub>Cl]<sup>2+</sup>, [(bpy)<sub>2</sub>Ru(L-pyr)Co(dpgBF<sub>2</sub>)<sub>2</sub>(OH<sub>2</sub>)]<sup>2+</sup> [62], [(Me<sub>2</sub>phen)<sub>2</sub>Ru(L-pyr)Co(dmgBF<sub>2</sub>)<sub>2</sub>(OH<sub>2</sub>)]<sup>2+</sup>, and [(ppy)<sub>2</sub>Ir(L-pyr)Co(dmgBF<sub>2</sub>)<sub>2</sub>(OH<sub>2</sub>)]<sup>+</sup> (L-pyr = [(4-pyridine)oxazolo(4,5-f)phenanthroline], dmgH = dimethylglyoximate, dmgBF<sub>2</sub> = (difluoroboryl)dimethylglyoximate, dpgBF<sub>2</sub> = (difluoroboryl)diphenylglyoximate, Me<sub>2</sub>phen = 4,7-dimethylphenanthroline, ppy = 2-phenylpyridine) [63] are photocatalysts for solar hydrogen production, Fig. 16. The BF<sub>2</sub>-bridged systems are more resistant toward acid hydrolysis and undesired hydrogenation reactions. The Co<sup>II</sup> state is easier to reduce in the BF<sub>2</sub>-bridged systems vs. the H-bridged cobaloximes. The L-pyr BL facilitates intramolecular excited state electron transfer.

Photochemical hydrogen production from Et<sub>3</sub>NH<sup>+</sup> occurs when acetone solutions of [(bpy)<sub>2</sub>Ru(L-pyr)Co(dmgBF<sub>2</sub>)<sub>2</sub>(OH<sub>2</sub>)]<sup>2+</sup>, [(bpy)<sub>2</sub>Ru(L-pyr)Co(dmgH)<sub>2</sub>Cl]<sup>2+</sup>, or [(bpy)<sub>2</sub>Ru(L-pyr)Co(dpgBF<sub>2</sub>)<sub>2</sub>(OH<sub>2</sub>)]<sup>2+</sup> are photolyzed using a CdI-doped Hg light source in the presence of 100-fold excesses of Et<sub>3</sub>N and Et<sub>3</sub>NH<sup>+</sup> [62]. Turnover numbers of 56, 17, and 12 over 4 h are seen for [(bpy)<sub>2</sub>Ru(L-pyr)Co(dmgBF<sub>2</sub>)<sub>2</sub>(OH<sub>2</sub>)]<sup>2+</sup>, [(bpy)<sub>2</sub>Ru(L-pyr)Co

(dmgH)<sub>2</sub>Cl]<sup>2+</sup>, or [(bpy)<sub>2</sub>Ru(L-pyr)Co(dpgBF<sub>2</sub>)<sub>2</sub>(OH<sub>2</sub>)]<sup>2+</sup>, respectively. Increasing Et<sub>3</sub>N and Et<sub>3</sub>NH<sup>+</sup> to 300-fold excess had slight effect with 60 TON observed for [(bpy)<sub>2</sub>Ru(L-pyr)Co(dmgBF<sub>2</sub>)<sub>2</sub>(OH<sub>2</sub>)]<sup>2+</sup> in 4 h. The impact of solvent on photocatalytic efficiency of [(bpy)<sub>2</sub>Ru(L-pyr)Co(dmgBF<sub>2</sub>)<sub>2</sub>(OH<sub>2</sub>)]<sup>2+</sup> showed lower TON in acetonitrile (TON = 10), methanol (TON = 9), DMF (TON = 3), or 1,2-dichloroethane (TON = 0). The lower TON in DMF or 1,2-dichloroethane is attributed to decomplexation of the photocatalyst in these solvents. When the proton source is water (100-fold excess of both water and Et<sub>3</sub>N), 22 TON in 4 h is seen for [(bpy)<sub>2</sub>Ru(L-pyr)Co(dmgBF<sub>2</sub>)<sub>2</sub>(OH<sub>2</sub>)]<sup>2+</sup>. It is likely that the lower activity is due to pH changes that are significant when water is used as the proton source. Visible light-induced excitation (λ > 350 nm) of the [(bpy)<sub>2</sub>Ru(L-pyr)Co(dmgBF<sub>2</sub>)<sub>2</sub>(OH<sub>2</sub>)]<sup>2+</sup> system afforded 103 TON in 15 h. Lower TON is obtained when a UV cutoff filter is used, implying both UV and visible light promote photocatalysis. It is mentioned that the analogous system of [(bpy)<sub>2</sub>Ru(L-pyr)Co(dmgBF<sub>2</sub>)<sub>2</sub>(OH<sub>2</sub>)]<sup>2+</sup> with the BL oxazole O replaced by NH shows a twofold increased photocatalytic activity with 104 TON achieved in 4 h using 100-fold excesses of Et<sub>3</sub>N and Et<sub>3</sub>NH<sup>+</sup>. For comparison, photolysis of the multicomponent system consisting of [Ru(bpy)<sub>3</sub>]Cl<sub>2</sub> and one equivalent of [Co(dmgBF<sub>2</sub>)<sub>2</sub>(OH<sub>2</sub>)<sub>2</sub>] in 100-fold excess of both Et<sub>3</sub>N and Et<sub>3</sub>NH<sup>+</sup> yields only 20 TON using UV-VIS light with only traces of hydrogen observed when a UV cutoff filter is used.

Photochemical hydrogen production occurs when acetone solutions of [(Me<sub>2</sub>phen)<sub>2</sub>Ru(L-pyr)Co(dmgBF<sub>2</sub>)<sub>2</sub>(OH<sub>2</sub>)]<sup>2+</sup> (Me<sub>2</sub>phen = 4,7-dimethylphenanthroline), in which bpy has been substituted by Me<sub>2</sub>phen, or [(ppy)<sub>2</sub>Ir(L-pyr)Co(dmgBF<sub>2</sub>)<sub>2</sub>(OH<sub>2</sub>)]<sup>+</sup>, in which an Ir-based LA is used, are irradiated at λ > 380 nm in the presence of 300 equivalents of Et<sub>3</sub>N and Et<sub>3</sub>NH<sup>+</sup> with 9 and 90 TON in 4 h, respectively [63]. The Ir-based system demonstrates enhanced photocatalytic efficiency to the Ru-based system, with 210 turnovers in 15 h in the presence of 600 equivalents of ED and proton source.



**Hydrogen via Direct Solar Production, Fig. 16** Representations of cobalt-based supramolecular dyads

For comparison the multicomponent system  $[Ir(ppy)_2(phen)]^+$  and  $[Co(dmgBF_2)_2(OH_2)_2]$  under the same irradiation conditions yields similar initial rates, but the dyad shows greater stability

as the hydrogen production rate levels off at 165 TON in 15 h. This implies that intramolecular electron transfer in the dyad may not be the rate limiting step in the hydrogen

production scheme, but the reductive quenching of the excited photosensitizer by  $\text{Et}_3\text{N}$  may be important.

This study also uses a multicomponent system based on a  $[\text{Re}(\text{CO})_3\text{Br}(\text{phen})]$  LA and  $[\text{Co}(\text{dmgBF}_2)_2(\text{OH}_2)_2]$  CAT with 273 TON in 15 h using 600-fold excess of both  $\text{Et}_3\text{N}$  and  $\text{Et}_3\text{NH}^+$  [63]. The use of the Re-based LA provides enhanced system functioning with  $\Phi$  ( $\frac{1}{2} \text{H}_2$ ) = 0.16 relative to  $\Phi$  ( $\frac{1}{2} \text{H}_2$ ) = 0.10 in the Ir-based multicomponent system ( $\lambda = 412 \text{ nm}$ , irradiation for 2 h). This study demonstrates superior system functioning when Ir-or Re-based LAs are employed relative to the Ru-based LAs. The Ru-based dyads demonstrate superior photocatalytic efficiency to the multicomponent  $[\text{Ru}(\text{bpy})_3]^{2+}$ /cobaloxime system. By contrast, the Ir-based dyad shows similar catalytic efficiency to the multicomponent  $[\text{Ir}(\text{ppy})_2(\text{phen})]^+$ /cobaloxime system, but the supramolecular dyad shows greater stability. It is predicted that intramolecular electron transfer affords a  $\text{Co}^{\text{I}}$  species which is protonated to yield a  $\text{Co}^{\text{III}}\text{-H}$  intermediate that can be further protonated to generate hydrogen. Electron transfer to the catalytic Co center can occur either directly from oxidative quenching of the photoexcited LA or from a reduced LA generated from the reductive quenching by an electron donor. A favorable driving force for oxidative quenching of the LA by the attached  $\text{Co}^{\text{II}}$  site is predicted, as the observed electrocatalytic potentials are more positive than the standard excited state reduction potential for  $[\text{Ru}(\text{bpy})_3]^{2+}$  [96]. Thus, the mechanism for photochemical hydrogen production by the supramolecular Ru-based systems is predicted to proceed through intramolecular electron transfer to the cobalt center from a photoexcited Ru LA. Faster reductive quenching of the excited Re-or Ir-based LA by  $\text{Et}_3\text{N}$  is attributed to the enhanced hydrogen production observed when the photosystem uses these LAs.

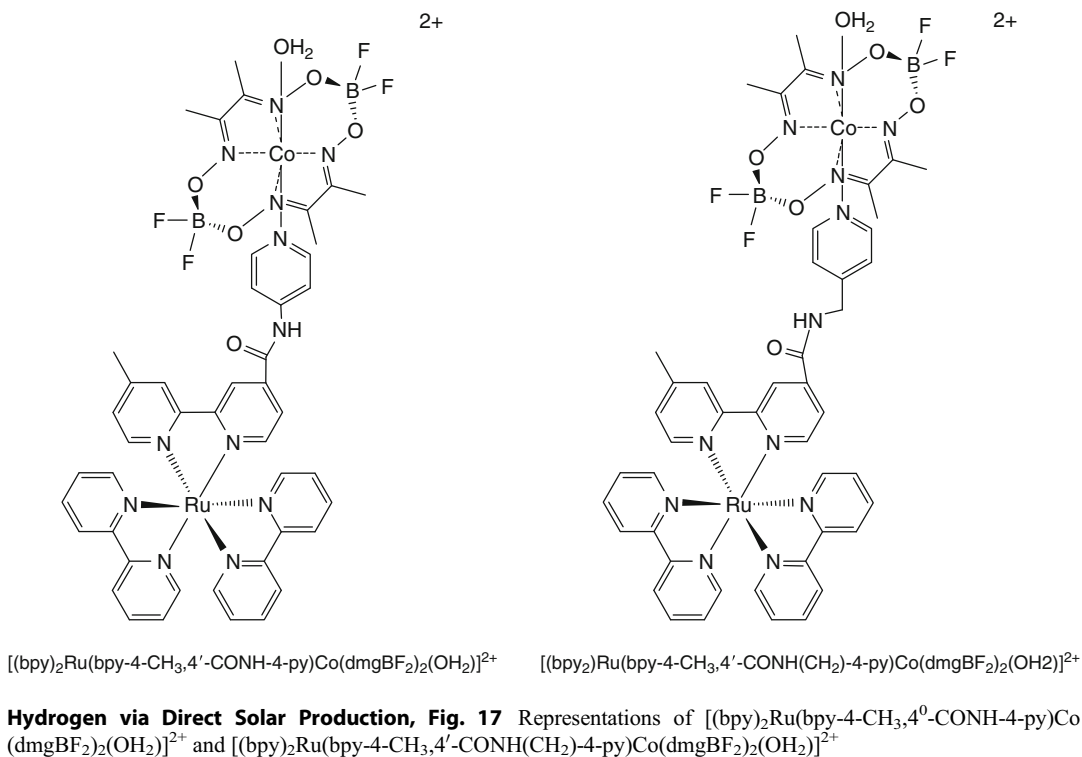
The complex  $[(\text{bpy})_2\text{Ru}(\text{bpy-4-CH}_3,4'\text{-CONH-4-py})\text{Co}(\text{dmgBF}_2)_2(\text{OH}_2)]^{2+}$  in which the Ru LA and the cobaloxime CAT are connected by a conjugated bridge, and  $[(\text{bpy})_2\text{Ru}(\text{bpy-4-CH}_3,4'\text{-CONH}(\text{CH}_2)\text{-4-py})\text{Co}(\text{dmgBF}_2)_2(\text{OH}_2)]^{2+}$ , in which the two components are connected by an unconjugated

bridge, have been used in solar hydrogen production schemes, Fig. 17 [64]. Intramolecular electron transfer is evidenced by the emission quenching of the  $^3\text{MLCT}$  charge-transfer state by 35% and 25% relative to the parent LAs  $[(\text{bpy})_2\text{Ru}(\text{bpy-4-CH}_3,4'\text{-CONH-4-py})]^{2+}$  and  $[(\text{bpy})_2\text{Ru}(\text{bpy-4-CH}_3,4'\text{-CONHCH}_2\text{-4-py})]^{2+}$ , respectively. The lower emission intensity in the dyad containing the conjugated bridge is attributed to more efficient deactivation through radiative and nonradiative decay, due to the shorter distance between the LA and the cobaloxime. Photolysis of  $[(\text{bpy})_2\text{Ru}(\text{bpy-4-CH}_3,4'\text{-CONH-4-py})\text{Co}(\text{dmgBF}_2)_2(\text{OH}_2)]^{2+}$  or  $[(\text{bpy})_2\text{Ru}(\text{bpy-4-CH}_3,4'\text{-CONH}(\text{CH}_2)\text{-4-py})\text{Co}(\text{dmgBF}_2)_2(\text{OH}_2)]^{2+}$  at  $\lambda = 400 \text{ nm}$  in the presence of 300-fold excess of both  $\text{Et}_3\text{N}$  and  $\text{Et}_3\text{NH}^+$  in acetone results in hydrogen production with 38 and 48 TON in over 8 h for  $[(\text{bpy})_2\text{Ru}(\text{bpy-4-CH}_3,4'\text{-CONH-4-py})\text{Co}(\text{dmgBF}_2)_2(\text{OH}_2)]^{2+}$  and  $[(\text{bpy})_2\text{Ru}(\text{bpy-4-CH}_3,4'\text{-CONH}(\text{CH}_2)\text{-4-py})\text{Co}(\text{dmgBF}_2)_2(\text{OH}_2)]^{2+}$ , respectively. Lower TONs are observed when DMF or acetonitrile are the solvent. The complex  $[(\text{bpy})_2\text{Ru}(\text{bpy-4-CH}_3,4'\text{-CONH-4-py})\text{Co}(\text{dmgBF}_2)_2(\text{OH}_2)]^{2+}$  with a conjugated bridge shows similar photocatalytic efficiency to  $[(\text{bpy})_2\text{Ru}(\text{L-pyr})\text{Co}(\text{dmgBF}_2)_2(\text{OH}_2)]^{2+}$ . The unconjugated bridge may impede the possible deactivation routes promoting higher photocatalytic TON. In  $[(\text{bpy})_2\text{Ru}(\text{bpy-4-CH}_3,4'\text{-CONH-4-py})\text{Co}(\text{dmgBF}_2)_2(\text{OH}_2)]^{2+}$  and  $[(\text{bpy})_2\text{Ru}(\text{bpy-4-CH}_3,4'\text{-CONH}(\text{CH}_2)\text{-4-py})\text{Co}(\text{dmgBF}_2)_2(\text{OH}_2)]^{2+}$ , oxidative quenching of the excited Ru LA by the  $\text{Co}^{\text{II}}$  through intramolecular electron transfer has been suggested as the dominant quenching process based on the favorable driving forces and the fact that the excited states of the parent LAs are not quenched efficiently with  $\text{Et}_3\text{N}$ .

#### Other Multicomponent Co-Based Systems

The pioneering work using Co-based CAT for solar hydrogen production was in the late 1970s utilizing  $[\text{Ru}(\text{bpy})_3]^{2+}$  LA and a Co(II) macrocycle system as the CAT. Optical excitation of a system containing  $[\text{Ru}(\text{bpy})_3]^{2+}$ ,  $[\text{Co}^{\text{II}}\text{L}]$  ( $[\text{Co}^{\text{II}}\text{L}] = \text{Co}^{\text{II}}(\text{Me}_6[14]\text{dieneN}_4)(\text{H}_2\text{O})_2^{2+}$ , and  $\text{Eu}^{2+}$  at  $\lambda = 450 \text{ nm}$  afforded hydrogen providing 10 TON with respect to  $[\text{Ru}(\text{bpy})_3]^{2+}$  and 1 TON

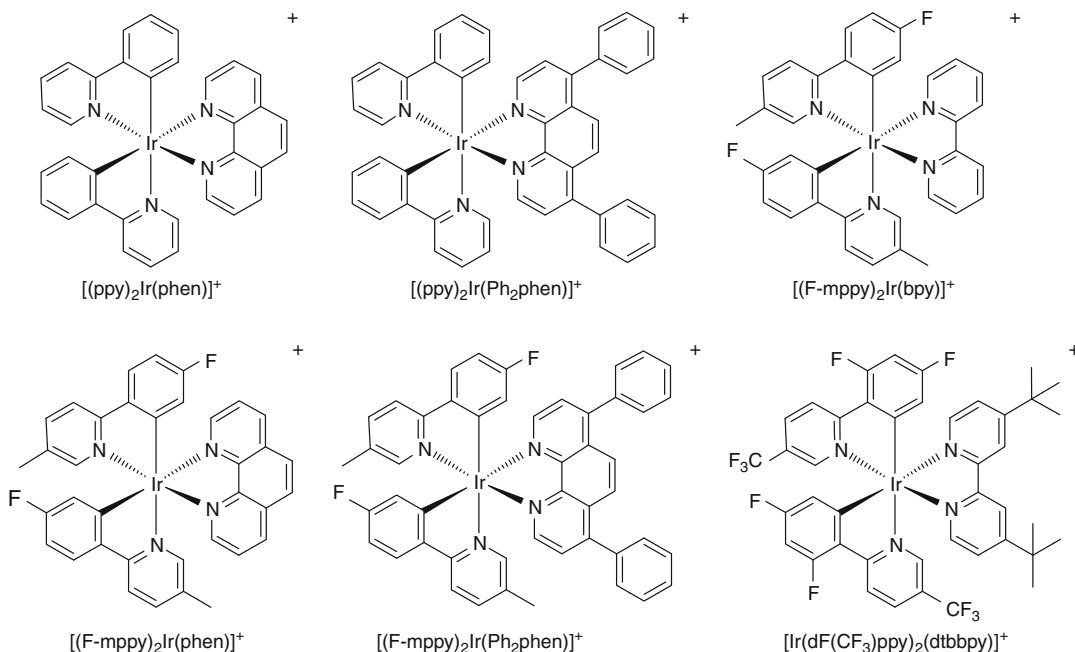




with respect to  $[Co^{II}L]$ , with a  $\Phi = 0.05$  [65]. Optical excitation of the LA leads to intermolecular electron transfer generating a  $Co^I$  species which reduces water to produce hydrogen. Early work using cobaloximes for photochemical hydrogen production entailed a photosystem consisting of  $[Ru(bpy)_3]^{2+}$ ,  $[Co(dmgH)_2(OH_2)_2]$ , and triethanolamine (TEOA) in DMF with 16 TON in 1 h relative to the CAT [97].

A series of heteroleptic Ir complexes of the molecular architecture  $[Ir(C^{\wedge}N)_2(N^{\wedge}N)]^+$  ( $C^{\wedge}N = ppy$  or  $F-mppy$  and  $N^{\wedge}N = bpy$ , phen,  $Ph_2phen$  (4,7-diphenyl-1,10-phenanthroline)) have been investigated as LAs in photochemical hydrogen production from water using  $[Co(bpy)_3]^{2+}$  as the CAT, Fig. 18 [66]. Irradiation of photosystems consisting of an Ir-based LA,  $[Co(bpy)_3]^{2+}$  and TEOA in a  $CH_3CN$ /water mixture at  $\lambda = 465$  nm affords hydrogen with 800–920 TON relative to the LA and 16–18 TON relative to the CAT with the system consisting of  $[Ir(F-mppy)_2(bpy)]^+$  LA providing the highest TON. The fluorinated compounds typically show slightly higher activity. It is

proposed that intramolecular electron transfer from the excited LA to the CAT affords a reduced Co species that promotes proton reduction to make hydrogen. The Ir-based systems are about 20 times more efficient than  $[Ru(bpy)_3]^{2+}$  and 3–6 times more efficient than  $[Ru(Me_2phen)_3]^{2+}$ . The multicomponent Ru-based photosystem consisting of  $[Ru(bpy)_3]^{2+}$  or  $[Ru(Me_2phen)_3]^{2+}$  ( $Me_2phen = 4,7$ -dimethyl-1,10-phenanthroline) provides lower TON (100 TON relative to  $[Ru(bpy)_3]^{2+}$  and 2 TON relative to the CAT or 290 TON relative to  $[Ru(Me_2phen)_3]^{2+}$  and 12 TON relative to the CAT). The excited states of the Ir-based systems are quenched efficiently by both  $[Co(bpy)_3]^{2+}$  and TEOA whereas the excited states of the Ru LAs are only quenched by  $[Co(bpy)_3]^{2+}$ . The rate of quenching of the excited state of the Ir-system by  $[Co(bpy)_3]^{2+}$  is about an order of a magnitude faster than TEOA quenching rate and also faster than for the Ru-based systems. The rates of quenching of the Ir-based excited states by  $[Co(bpy)_3]^{2+}$  range from  $4.8$  to  $6.9 \times 10^8 M^{-1} s^{-1}$ . System modification of the LA has provided  $[Ir(dF$



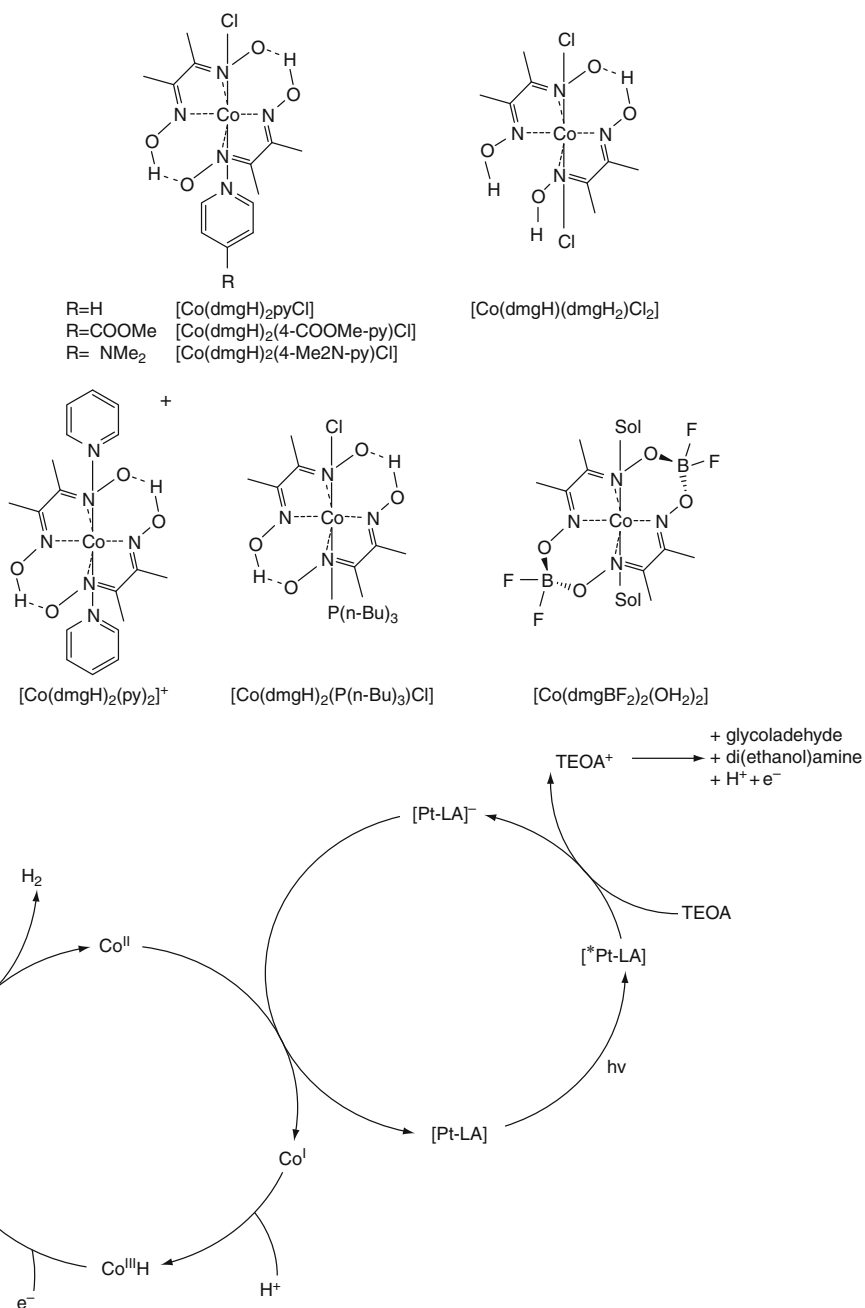
**Hydrogen via Direct Solar Production, Fig. 18** Ir-based LAs used in photosystems incorporating  $[Co(bpy)_3]^{2+}$  CAT for photochemical hydrogen production from water

$(CF_3)ppy)_2(dtbbpy)](PF_6)$  ( $dF(CF_3)ppy = 2-(2,4\text{-difluorophenyl})\text{-}5\text{-trifluoromethylpyridine}$  and  $dtbbpy = 4,4'\text{-di-tert-butyl-}2,2'\text{-dipyridyl}$ ) with enhanced excited state lifetime and significant reducing power that shows dramatically improved system function with a relative  $\Phi$  that is ca. 14 times larger than  $[Ru(Me_2phen)_3]^{2+}$  [98].

A series of cobaloxime complexes,  $[Co(dmgH)_2(py)Cl]$ ,  $[Co(dmgH)_2(4\text{-COOMe-py})Cl]$ ,  $[Co(dmgH)_2(4\text{-Me}_2\text{N-py})Cl]$ ,  $[Co(dmgH)(dmgH)_2Cl_2]$ ,  $[Co(dmgH)_2(py)_2]^+$ ,  $[Co(dmgH)_2(P(n\text{-Bu})_3)Cl]$ , and  $[Co(dmgBF_2)_2(OH_2)_2]$ , ( $dmgH_2 = \text{dimethylglyoxime}$ ) have been investigated as molecular catalysts photochemical hydrogen generation from water in systems containing a Pt terpyridyl acetylide chromophore and TEOA in acetonitrile, Fig. 19 [67, 99]. Characterization of the cobaloximes, hydrogen photocatalysis, and the investigation of the impact of photosystem functioning with respect to LA, CAT, TEOA, solvent, and  $CH_3CN/\text{water}$  ratio are reported. The cobaloximes oxidatively quench the emission of the excited state LA efficiently, close to the diffusion controlled limit, with

the fastest quenching of  $1.7 \times 10^9 \text{ M}^{-1} \text{ s}^{-1}$  by  $[Co(dmgH)_2(4\text{-COOMe-py})Cl]$ .

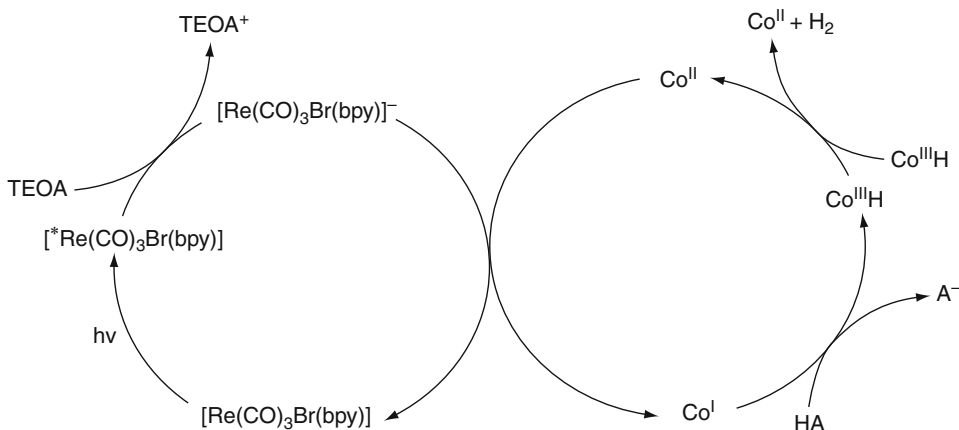
The rate of oxidative quenching by  $[Co(dmgH)_2(py)_2]^+$  is  $4.0 \times 10^7 \text{ M}^{-1} \text{ s}^{-1}$ ; this lower rate is attributed to the lack of a Cl ligand in this complex that can interact with the Pt LA during the quenching process. It was found that a photosystem consisting of  $[Pt(tpy)(C \equiv CPh)]ClO_4$  ( $tpy = 4'\text{-p-tolyterpyridine}$ ),  $[Co(dmgH)_2(py)Cl]$ , TEOA, and water in  $CH_3CN$  gives 2100 TON in 10 h, irradiated at  $\lambda > 410 \text{ nm}$ , when the optimized  $[TEOA]$  and  $CH_3CN/H_2O$  ratio are used. No hydrogen is observed after 5 h of photolysis in systems consisting of  $[Pt(tpy)(C \equiv CPh)]ClO_4$ ,  $[Co(dmgH)_2(P(n\text{-Bu})_3)Cl]$  or  $[Co(dmgBF_2)_2(OH_2)_2]$ , and TEOA. In the system consisting of  $[Co(dmgH)_2(P(n\text{-Bu})_3)Cl]$ , it is likely that the stable hydride formed,  $[CoH(dmgH)_2(P(n\text{-Bu})_3)]$  known to yield hydrogen only upon thermolysis at  $150 \text{ }^\circ\text{C}$ , prevents hydrogen photocatalysis. The complex  $[Co(dmgBF_2)_2(OH_2)_2]$  is thermodynamically incapable of proton reduction as evidenced by the  $Co^{II/I}$  reduction potential of  $-0.29 \text{ V vs. NHE}$



**Hydrogen via Direct Solar Production, Fig. 19** Representative cobaloximes used for solar hydrogen photocatalysis and the proposed photocycle for hydrogen production by reductive quenching of the LA

which is more positive of proton reduction (-0.48 V) at the pH used for photocatalysis (pH = 8.5). Induction periods of 1–2 h are observed for the hydrogen-generating systems. This induction period is impacted by the solvent

conditions, LA, and TEOA concentration. The induction period is consistent with the requirement for the formation of Co<sup>I</sup> for photogeneration of hydrogen to occur. The photochemical cycle can proceed through the oxidative quenching of the



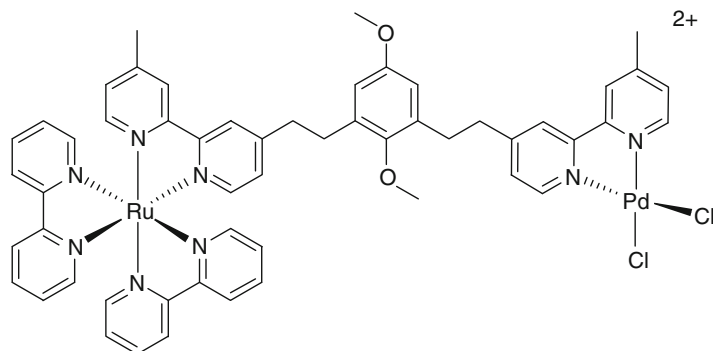
**Hydrogen via Direct Solar Production, Fig. 20** General representation of a homolytic pathway using a Co-based hydrogen producing photosystem

photoexcited LA by  $\text{Co}^{\text{III}}$  to form  $\text{LA}^+$  and  $\text{Co}^{\text{II}}$ , or through reductive quenching by TEOA to form  $\text{LA}^-$  and  $\text{TEOA}^+$ , Fig. 19. Electron transfer from the  $\text{LA}^-$  to  $\text{Co}^{\text{III}}$  occurs regenerating the LA. The catalytic cycle proceeds with further reduction of  $\text{Co}^{\text{II}}$  to  $\text{Co}^{\text{I}}$  followed by protonation to give a  $\text{Co}^{\text{III}}\text{-H}$  intermediate. One pathway is the protonation of  $\text{Co}^{\text{III}}\text{-H}$  to yield hydrogen and  $\text{Co}^{\text{III}}$ . An alternative pathway is utilizing a single Co pathway, which entails reduction of the  $\text{Co}^{\text{III}}\text{-H}$  to  $\text{Co}^{\text{II}}\text{-H}$  which subsequently gets protonated to generate hydrogen and  $\text{Co}^{\text{II}}$ . This single Co mechanism is supported by the observed linear dependence of the Co concentration on photochemical hydrogen production in a system consisting  $[\text{Pt}(\text{ttpy}) (\text{C} \equiv \text{CPh})\text{ClO}_4]$  ( $\text{ttpy} = 4'\text{-p-tolyterpyridine}$ ),  $[\text{Co}(\text{dmgH})_2\text{pyCl}]$ , TEOA, and water in  $\text{CH}_3\text{CN}$  irradiating at  $\lambda > 410 \text{ nm}$ . An alternative kinetically distinguishable proposal is the homolytic reaction mechanism involving two  $\text{Co}^{\text{III}}\text{-H}$  to give hydrogen and  $\text{Co}^{\text{II}}$ . Kinetics of electron transfer reactions of hydrogen evolving cobaloximes have been reported recently [100]. Studies demonstrate that the homolytic pathway ( $\text{Co}^{\text{III}}\text{H} + \text{Co}^{\text{III}}\text{H} \rightarrow 2 \text{Co}^{\text{II}} + \text{H}_2$ ) is favored over a pathway involving protonation of  $\text{Co}^{\text{III}}\text{-H}$  to yield hydrogen and  $\text{Co}^{\text{III}}$ .

A photocatalytic system using the organic dye, Eosin Y as the LA,  $[\text{Co}(\text{dmgH})_2\text{pyCl}]^{2+}$ , and TEOA produces hydrogen with an initial rate of 100 TON/h upon irradiation at  $\lambda > 450 \text{ nm}$

[68]. Addition of free  $\text{dmgH}_2$  provides increased stability to the photosystem providing 900 TON relative to the LA (*ca.* 20 mL of hydrogen) in 14 h. A maximum  $\Phi = 0.04$  is observed when a bandpass filter at 520 nm is employed, but with a lower TON relative to  $\lambda > 450 \text{ nm}$ . The rate of hydrogen evolution shows marked pH dependence with maximum at  $\text{pH} = 7$  and decreases sharply at more acidic or basic pH.

Photochemical hydrogen production occurs in a photosystem consisting of  $[\text{ReBr}(\text{CO})_3\text{bpy}]$ ,  $[\text{Co}(\text{dmgH})_2]$ , acetic acid/water, TEOA in DMF at  $\lambda > 400 \text{ nm}$  [69]. Turnover numbers are approximately twice compared to when  $[\text{Ru}(\text{bpy})_3]^{2+}$  is the LA under the same conditions (150 TON in 9 h for  $[\text{ReBr}(\text{CO})_3\text{bpy}]$  relative to 65 TON when  $[\text{Ru}(\text{bpy})_3]^{2+}$  is the LA). The quantum yield for hydrogen production is 0.26. The rate of hydrogen production shows a square dependence on the total Co concentration. This square dependence implies a homolytic pathway for hydrogen photocatalysis. The rate of hydrogen production exhibited a linear dependence on the photon flux. Forward electron transfer between the LA and the CAT occurs at a rate close to diffusion control, with a rate of  $2.5 \times 10^8 \text{ M}^{-1} \text{ s}^{-1}$ . An excess of dimethylglyoxime is systematically added to the system to ensure the complete formation of the CAT and reduce the portion of free  $[\text{Co}]_{\text{soln}}^{2+}$ , which is also an efficient quencher of the excited state of the LA, Fig. 20.



**Hydrogen via Direct Solar Production, Fig. 21** Representation of  $[(bpy)_2Ru(Mebpy)(CH_2)_2C_6H_2(OCH_3)_2(CH_2)_2Mebpy)PdCl_2]^{2+}$  (bpy = 2,2'-bipyridine)

### Pt and Pd-Based Homogeneous Systems for Solar Hydrogen Production

Pt- and Pd-based systems have been used in solar hydrogen production schemes. Supramolecular systems that couple polyazine LAs with bridged Pt or Pd CATs for proton reduction are known [70, 73, 74, 101, 102]. The use of the supramolecular design allows for increased electron transfer rates and component modification to enhance device function and light-absorbing properties. The bridged systems use rigid or flexible spacers between the LA and the CAT which controls the level of electronic communication between components. The formation of metallic colloids during photoreduction of the supramolecular assembly has been reported in some studies using similar supramolecular assemblies, implying that heterogeneous catalysis is dominant with the colloidal metal being the active catalytic species [103, 104]. Photo-induced decomposition of  $[(bpy)_2Ru(Mebpy)(CH_2)_2C_6H_2(OCH_3)_2(CH_2)_2Mebpy)PdCl_2]^{2+}$ , Fig. 21, was observed by ESI-MS and the formation of Pd colloid observed by TEM and XPS of evaporated reaction mixtures during photochemical hydrogen production [103]. Mercury tests are employed to deactivate photoproduced metal colloids via formation of inactive alloys with colloidal metals eliminating the impact of the colloid on photochemical activity [86, 87].

These tests can provide meaningful information regarding the mechanism of action for solar

hydrogen production, but care must be taken in drawing conclusions as this is a complicated issue. Concentration of the medium to study solids through TEM and XPS can also lead to system decomplexation resulting in formation of metallic solids. Reduced polyazine complexes including those produced electrochemically are known to adsorb to electrodes or metal surfaces such as Hg (I) and this could deactivate a catalytic system. The study of complicated multistep photocatalytic processes is complex, and detailed analyses with carefully selected comparison to determine the catalytically active species are necessary.

A RuPt bimetallic system  $[(bpy)_2Ru(phenNHCO(COOHbpy))PtCl_2]^{2+}$ , which employs an amide linkage on the phenanthroline as a bridge, produces hydrogen from water when illuminated at  $\lambda > 350$  nm in aqueous acetate buffer solutions in the presence of EDTA, with a  $\Phi = 0.01$  and 5 turnovers in 10 h [70]. This complex displays an emission from the  $^3MLCT$  state at  $\lambda_{max} = 610$  nm in an aqueous solution with its intensity quenched by 67% relative to the parent  $[(bpy)_2Ru(phenNHCO(COOHbpy))]^{2+}$  suggestive of intramolecular electron transfer process occurring in the bimetallic system. To ascertain that there is no interference from any photodecomposition products, comparisons are made with analogous multicomponent photosystems. The system consisting of  $[Ru(bpy)_3](NO_3)_2$ , *N,N'*-dimethyl-4,4'-bipyridinium, and  $[PtCl_2(dcbpy)]$  (*dcbpy* = 4,4'-dicarboxy-2,2'-bipyridine) is effective providing a  $\Phi = 0.02$ ,

but completely retarded in the absence of *N,N'*-dimethyl-4,4'-bipyridinium. Hydrogen production does not occur when  $[\text{Ru}(\text{bpy})_2(5\text{-aminophen})]^{2+}$  and  $[\text{PtCl}_2(\text{dcbpy})]$  or the parent LA,  $[(\text{bpy})_2\text{Ru}(\text{phenNHCO}(\text{COOHbpy}))]^{2+}$ , and  $\text{K}_2\text{PtCl}_4$  is the photosystem. The lack of activity by these multicomponent systems suggests the bridge between Ru and Pt is essential for photoreactivity in this system. Hydrogen production shows a linear response to photon flux implying that one-photon excitation of a molecule operates. Rate of hydrogen production shows a linear dependence on supramolecular complex concentration. Lower photocatalytic activity is observed when the COOH on bpy is replaced by a COOEt group demonstrating that a clear relationship exists between the energy of the LUMO and the hydrogen evolving activity which was greatest when the more electron withdrawing COOH is the substituent [105].

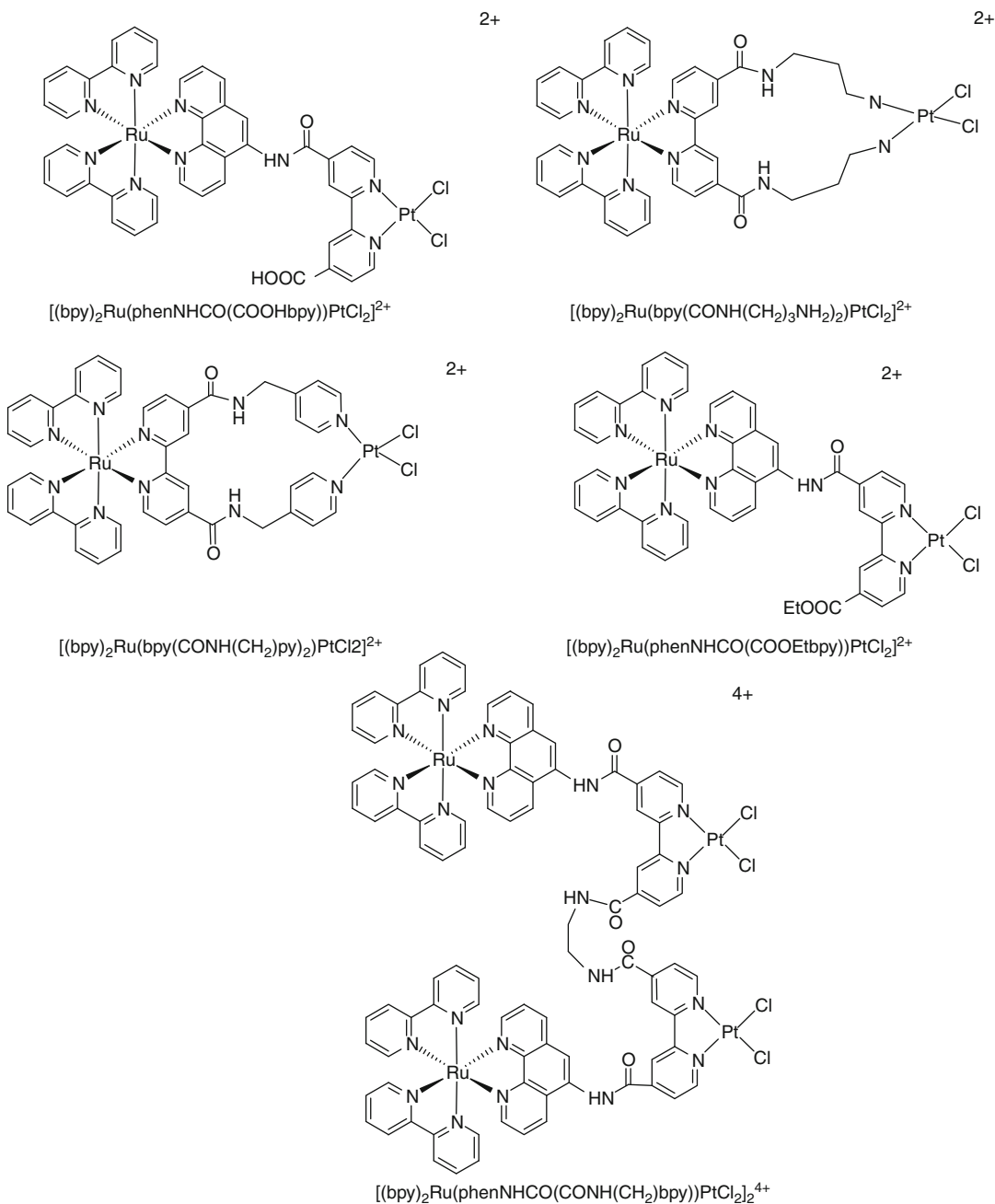
The hydrogen evolution rate by  $[(\text{bpy})_2\text{Ru}(\text{phenNHCO}(\text{COOHbpy}))\text{PtCl}_2]^{2+}$  is shown to obey Michaelis-Menten enzymatic kinetics with regard to the concentration of EDTA, suggesting that an ionpair formation between  $[(\text{bpy})_2\text{Ru}(\text{phenNHCO}(\text{COOHbpy}))\text{PtCl}_2]^{2+}$  and  $\text{EDTA}^{2-}$  is an important step in the photocycle [106]. Bimetallic RuPt systems that incorporate aliphatic linkages to bridge  $[(\text{bpy})_2\text{Ru}(\text{bpy}(\text{CONH}(\text{CH}_2)_3\text{NH}_2)_2)\text{PtCl}_2]^{2+}$  and  $[(\text{bpy})_2\text{Ru}(\text{bpy}(\text{CONH}(\text{CH}_2)_2\text{py})_2)\text{PtCl}_2]^{2+}$ , Fig. 22, do not display photocatalytic activity. This implies that aromaticity of the bridge connecting the LA and the CAT is important for intramolecular electron transfer in  $[(\text{bpy})_2\text{Ru}(\text{phenNHCO}(\text{COOHbpy}))\text{PtCl}_2]^{2+}$ . Recently a tetrametallic system that shows higher catalytic activity to the original bimetallic system has been reported,  $[(\text{bpy})_2\text{Ru}(\text{phenNHCO}(\text{CONH}(\text{CH}_2)\text{bpy}))\text{PtCl}_2]^{2+}$  [106]. This system shows enhanced catalytic activity with a  $\Phi = 0.014$ .

The tetrametallic  $[\{(\text{phen})_2\text{Ru}(\text{dpp})\}_2\text{Ru}(\text{dpq})\text{PtCl}_2]^{6+}$  and  $[\{(\text{bpy})_2\text{Ru}(\text{dpp})\}_2\text{Ru}(\text{dpq})\text{PtCl}_2]^{6+}$  systems have been investigated as photoinitiated electron collectors (dpq = 2,3-bis(2-pyridyl)quinoxaline), which photocatalyze the production of hydrogen from water with  $\Phi = 0.01$  [71,

72]. These systems couple two terminal  $(\text{TL})_2\text{Ru}^{\text{II}}(\text{dpp})$  LA units to a central ruthenium which is connected to a reactive platinum component through a dpq bridge, Fig. 23.  $[\{(\text{phen})_2\text{Ru}(\text{dpp})\}_2\text{Ru}(\text{dpq})\text{PtCl}_2]^{6+}$  displays a Ru( $d\pi$ )  $\rightarrow$  dpp( $\pi^*$ ) CT absorption observed at 541 nm and an emission from the  $^3\text{MLCT}$  state ( $\lambda_{\text{max}}^{\text{em}} = 752$  nm and  $\Phi^{\text{em}} = 3.0 \times 10^{-4}$ ) with reduced intensity relative to  $[\{(\text{phen})_2\text{Ru}(\text{dpp})\}_2\text{Ru}(\text{dpq})]^{6+}$  ( $\lambda_{\text{max}}^{\text{em}} = 752$  nm and  $\Phi^{\text{em}} = 12.3 \times 10^{-4}$ ) in acetonitrile [71]. The  $\tau$  of  $[\{(\text{phen})_2\text{Ru}(\text{dpp})\}_2\text{Ru}(\text{dpq})\text{PtCl}_2]^{6+}$  is 120 ns, also reduced relative to the  $[\{(\text{phen})_2\text{Ru}(\text{dpp})\}_2\text{Ru}(\text{dpq})\text{PtCl}_2]^{6+}$ , 170 ns. The reductions in the  $\Phi^{\text{em}}$  and  $\tau$  are characteristic of intramolecular electron transfer in  $[\{(\text{phen})_2\text{Ru}(\text{dpp})\}_2\text{Ru}(\text{dpq})\text{PtCl}_2]^{6+}$  populating a lowest energy CS state with  $k_{\text{et}} = 2.5 \times 10^6 \text{ s}^{-1}$ . The  $\tau = 1.7 \mu\text{s}$  at 77 K in a solid glass matrix in both tetrametallic and trimetallic systems. The emission of  $[\{(\text{phen})_2\text{Ru}(\text{dpp})\}_2\text{Ru}(\text{dpq})\text{PtCl}_2]^{6+}$  is quenched efficiently by DMA with  $k_{\text{q}}$  of  $4.8 \times 10^9 \text{ M}^{-1} \text{ s}^{-1}$ . The properties of  $[\{(\text{bpy})_2\text{Ru}(\text{dpp})\}_2\text{Ru}(\text{dpq})\text{PtCl}_2]^{6+}$  with bpy substituted TL are similar.  $[\{(\text{bpy})_2\text{Ru}(\text{dpp})\}_2\text{Ru}(\text{dpq})\text{PtCl}_2]^{6+}$  displays Ru( $d\pi$ )  $\rightarrow$  dpp( $\pi^*$ ) CT absorption at 540 nm and an emission from the  $^3\text{MLCT}$  state ( $\lambda_{\text{max}}^{\text{em}} = 745$  nm and  $\Phi^{\text{em}} = 2.5 \times 10^{-4}$ ) with reduced intensity relative to  $[\{(\text{bpy})_2\text{Ru}(\text{dpp})\}_2\text{Ru}(\text{dpq})]^{6+}$  ( $\lambda_{\text{max}}^{\text{em}} = 745$  nm and  $\Phi^{\text{em}} = 6.0 \times 10^{-4}$ ) in acetonitrile [72]. The  $\tau$  of  $[\{(\text{bpy})_2\text{Ru}(\text{dpp})\}_2\text{Ru}(\text{dpq})\text{PtCl}_2]^{6+}$  is 92 ns, also reduced relative to the  $[\{(\text{bpy})_2\text{Ru}(\text{dpp})\}_2\text{Ru}(\text{dpq})]^{6+}$ , 133 ns. The reductions in the  $\Phi^{\text{em}}$  and  $\tau$  are characteristic of intramolecular electron transfer in  $[\{(\text{bpy})_2\text{Ru}(\text{dpp})\}_2\text{Ru}(\text{dpq})\text{PtCl}_2]^{6+}$  populating a lowest energy CS state with  $k_{\text{et}} = 3.4 \times 10^6 \text{ s}^{-1}$ . Intramolecular electron transfer is hindered at 77 K in a solid glass matrix with  $\tau = 1.7 \mu\text{s}$  in both tetrametallic and trimetallic systems. The emission of  $[\{(\text{bpy})_2\text{Ru}(\text{dpp})\}_2\text{Ru}(\text{dpq})\text{PtCl}_2]^{6+}$  is quenched efficiently by DMA with  $k_{\text{q}}$  of  $5.4 \times 10^9 \text{ M}^{-1} \text{ s}^{-1}$ .

A unique feature in these tetrametallic systems is that a greater degree of reduction of the  $\Phi^{\text{em}}$  in the tetrametallic vs. the trimetallic is observed relative to the reduction of the  $\tau$  of the tetrametallic vs. trimetallic. For  $[\text{Ru}(\text{bpy})_3]^{2+}$  and similar systems, the  $F_{3\text{MLCT}} = 1$ . The differences in the degrees of quenching of



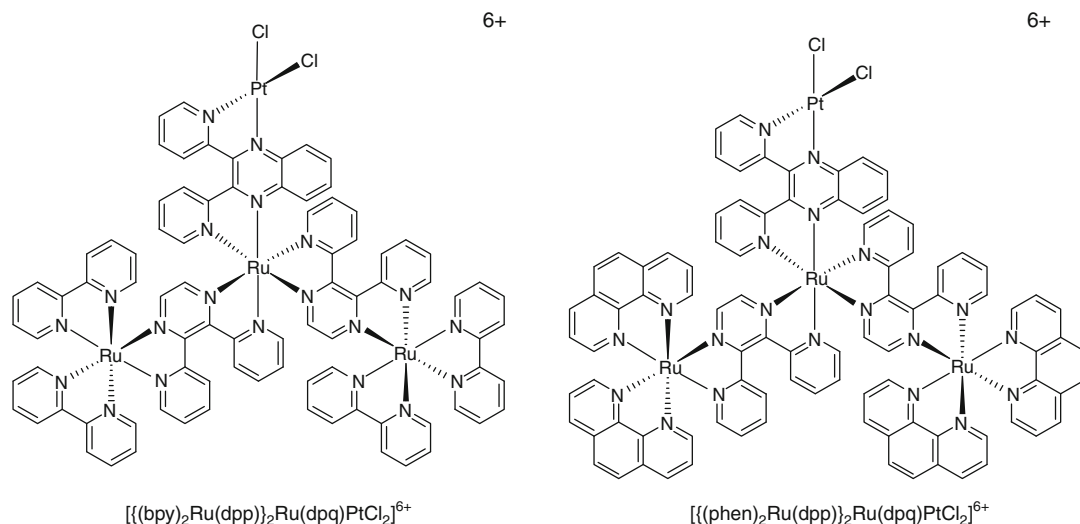


**Hydrogen via Direct Solar Production, Fig. 22** RuPt supramolecular systems for solar energy conversion

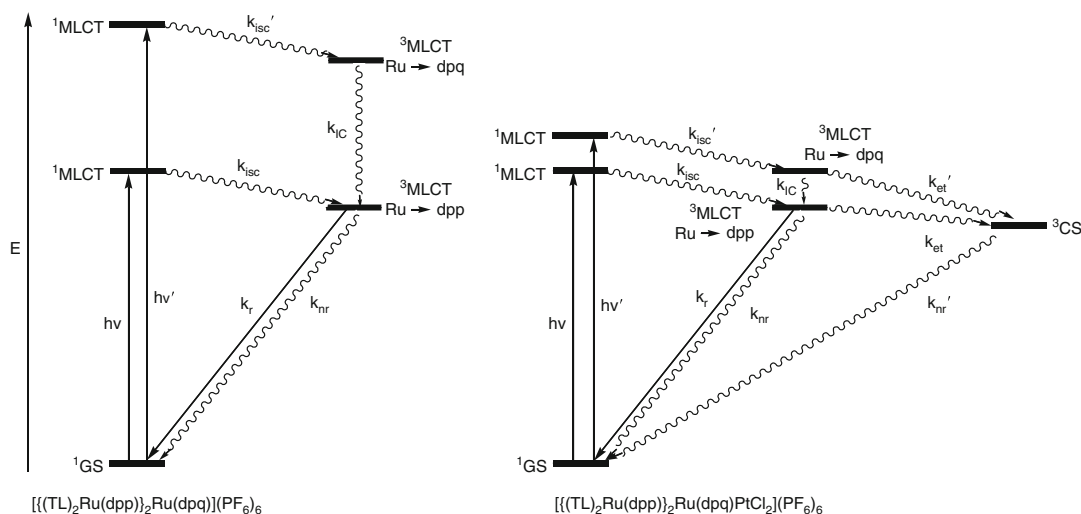
$\Phi^{em}$  and  $\tau$  of the tetrametallic vs. model trimetallic systems imply that  $F_{3MLCT} \neq 1$ , which suggests a reduction in population of the emitting  $^3MLCT$  excited state due to an alternative intramolecular electron transfer

pathway ( $k_{ct}'$ ) in which the higher-lying central  $Ru(d\pi) \rightarrow dpq(\pi^*)$  CT state directly populates the  $^3CS$ , Fig. 24.

Both  $[\{(bpy)_2Ru(dpp)\}_2Ru(dpq)PtCl_2]^{6+}$  and  $[\{(phen)_2Ru(dpp)\}_2Ru(dpq)PtCl_2]^{6+}$  are



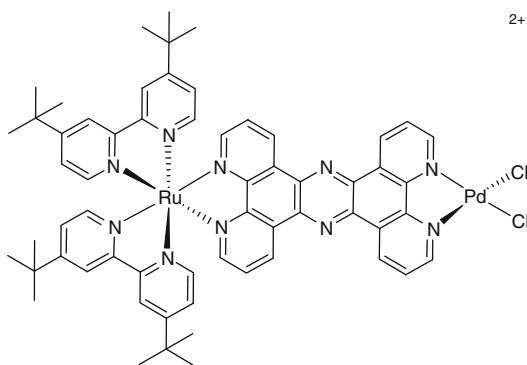
**Hydrogen via Direct Solar Production, Fig. 23** Representations of  $[\{\text{bpy}\}_2\text{Ru}(\text{dpp})]_2\text{Ru}(\text{dpq})\text{PtCl}_2]^{6+}$  and  $[\{\text{phen}\}_2\text{Ru}(\text{dpp})]_2\text{Ru}(\text{dpq})\text{PtCl}_2]^{6+}$



**Hydrogen via Direct Solar Production, Fig. 24** State diagram showing excited state photophysical properties of  $[\{(\text{TL})_2\text{Ru}(\text{dpp})\}_2\text{Ru}(\text{dpq})\text{PtCl}_2]^{6+}$  and  $[\{(\text{TL})_2\text{Ru}(\text{dpp})\}_2\text{Ru}(\text{dpq})\text{PtCl}_2]^{6+}$  (TL = bpy or phen)

photoinitiated electron collectors with electrons being collected on the molecular orbitals of the central Ru and the surrounding BLs. Spectroscopic changes that occur when the systems are photochemically reduced in the presence of DMA or electrochemically reduced by two electrons are almost identical, implying

that the photoproduct and electrochemically reduced product are the same. For  $[\{\text{bpy}\}_2\text{Ru}(\text{dpp})]_2\text{Ru}(\text{dpq})\text{PtCl}_2]^{6+}$ , photochemical hydrogen production occurs in the presence of DMA and water when photoexcited at  $\lambda = 530$  nm with  $\Phi = 0.01$  representing 40 turnovers in 3 h. The amount of hydrogen produced by  $[\{\text{bpy}\}_2\text{Ru}$



**Hydrogen via Direct Solar Production, Fig. 25** Representation of  $[(^t\text{Bu}_2\text{bpy})_2\text{Ru}(\text{tpphz})\text{PdCl}_2]^{2+}$

$(\text{dpp})_2\text{Ru}(\text{dpq})\text{PtCl}_2]^{6+}$  is much higher than that produced by  $[(\text{bpy})_2\text{Ru}(\text{dpp})]_2\text{Ru}(\text{dpq})]^{6+}$  and Pt colloid. For  $[(\text{phen})_2\text{Ru}(\text{dpp})]_2\text{Ru}(\text{dpq})\text{PtCl}_2]^{6+}$ , photochemical hydrogen production occurs in the presence of DMA when photoexcited at  $\lambda = 470$  nm with 115 TON in 5 h. Addition of excess Hg does not impede catalytic activity, which implies that the supramolecular architecture remains intact during the photocycle and colloidal Pt is not operative.

**Bifunctional Pt-Based System** The complex  $[\text{PtCl}(\text{tpy})\text{Cl}]$  is a single molecule that acts in a bifunctional manner promoting both photosensitization and catalysis [73]. Photolysis of  $[\text{PtCl}(\text{tpy})\text{Cl}]$  in aqueous buffer at  $\lambda = 350\text{--}550$  nm in the presence of EDTA affords 3 TON in 7 h with a  $\Phi = 0.02$ . 2-Morpholinoethanesulfonic acid is the buffer used to avoid coordination of buffer reagents to the  $\text{Pt}^{\text{II}}$  by replacing Cl, shown to lower hydrogen yield. Contribution from catalytically active Pt colloids seems not operative as the system functions with added Hg(l). It is suggested that photochemical hydrogen production proceeds through a bimolecular mechanism. Photosensitization is suggested to occur through a <sup>3</sup>MMLCT state (MMLCT = metal-metal-to-ligand charge-transfer) in dimer formation facilitated by  $\text{Pt}\cdots\text{Pt}$  association. The saturation kinetics with regard to the EDTA concentration suggests that the dimer of  $[\text{PtCl}(\text{tpy})]^+$  and the dianionic form of EDTA form an ion-pair adduct to facilitate reductive quenching by EDTA during the photochemical processes.

## Palladium-Based Supramolecular Solar Hydrogen Photocatalysts

The RuPd bimetallic system  $[(^t\text{Bu}_2\text{bpy})_2\text{Ru}(\text{tpphz})\text{PdCl}_2]^{2+}$  (<sup>t</sup>Bu = tertiary butyl, tpphz = tetrapyrrophenazine, Fig. 25) is a solar hydrogen photocatalyst producing hydrogen, with 56 TON in 30 h, in the presence of the electron donor,  $\text{Et}_3\text{N}$ , in acetonitrile when optically excited at  $\lambda = 470$  nm [74]. The proton source is  $\text{Et}_3\text{N}$ . A weak emission at  $\lambda_{\text{max}} = 650$  nm with  $\tau = 27$  ns is observed significantly quenched relative to the parent  $[(^t\text{Bu}_2\text{bpy})_2\text{Ru}(\text{tpphz})]^{2+}$  ( $\lambda_{\text{max}} = 638$  nm,  $\tau = 154$  ns). It is suggested that the  $\text{Ru}^{\text{II}}\text{-phenazine}^- \text{-Pd}^{\text{II}}$  radical photogenerated in the presence of  $\text{Et}_3\text{N}$  is involved in the photochemical hydrogen generation step, initiating chloride loss from palladium. Photoinduced electron transfer processes to reduce the Pd site have been studied by resonance Raman and ultrafast time-resolved spectroscopy showing rapid Pd reduction [107].

## Conclusions and Future Directions

The conversion of solar energy to a transportable fuel is challenging but important in meeting increasing energy demands. The production of hydrogen fuel via solar water splitting is an attractive approach to alternative energy conversion and storage as the amount of energy reaching the Earth's surface from the sun in 1 h is sufficient to power our planet for more than a year. Photocatalysis to reduce water to produce hydrogen is complicated involving multielectron transfer, bond breaking, and bond formation. Despite these challenges and the lack of consistent substantial long-term funding, a number of photosystems for solar hydrogen production have been developed recently. Pioneering work on multi-component systems was critical to success. Water splitting to produce hydrogen is complicated and involves energetically demanding chemical reactions with bond breaking and formation and is a multielectron process. Solar energy conversion is promoted via water reduction by multistep processes with multiple photons used sequentially.

Work has focused on the LA and/or CAT design for solar hydrogen production schemes. Structural diversity is starting to be available. Many systems incorporate Ru-based LAs and reactive metal centers in the photocatalytic schemes. Ir, Pt, Re, and Zn-based systems have emerged recently showing promise as LAs. Biomimetic iron-based systems, Rh, Co, Pt, and Pd-based CATs have been typically used in these schemes. The Rh- and Co-based systems take advantage of ability of Rh or Co to cycle through three oxidation states reducing from  $M^{III}$  to  $M^{II}$  and  $M^I$  for multielectron chemistry. The application of typical Ru (II) trischelate systems with ligands such as bpy or phen provide for absorption in the visible region to *ca.* 450 nm. The light absorption energy can be modulated by ligand substitution and the use of ligands with stabilized  $\pi^*$  orbitals provide for longer wavelength excitation often to *ca.* 550–650 nm.

Using bridging ligands provides a means to covalently attach the LA to the CAT allowing more efficient intramolecular electron transfer pathways from the LA to the catalytic site. In addition, factors that impact intramolecular electron transfer can be studied and modulated within molecular systems. Coupling of a LA to CAT often dramatically perturbs the properties of these components. The ability to modulate the electrochemical and photochemical properties by component modification in supramolecular systems can be exploited in molecular design. The application of large molecular systems to address hydrogen photocatalysis allows system study using conventional molecular characterization methods allowing for the ability to probe the processes involved in the photocatalytic process.

Many factors are considered during photosystem design for hydrogen photocatalysis. The redox potentials of the LA, CAT, and coordinated ligands dictate the driving force of electron transfer reactions. LA properties including absorptivity and excited state lifetimes are contributing factors which determine wavelength response and overall photosystem efficiency. System parameters including, solvent, electron donor, pH, wavelength of excitation, etc., also determine functioning system efficiency and stability. Often solvent

choice can have dramatic impact with systems showing good photoreactivity in organic solvents that are not functional in aqueous media. Catalysts and electron donors selected should not compete for light with the LA. Study and comparison of system parameters that impact hydrogen photocatalysis is crucial as many conditions impact photocatalysis and no set of standard conditions exist. For example, some solvents that show enhanced system function for photocatalytic systems have been shown to deactivate other systems. Comparison of systems is complicated by these widely varied conditions.

The study of electron transfer between components is key to understanding photosystem properties. The electron transfer events occurring in supramolecular systems are studied with comparison using model systems that should have similar spectroscopic and photophysical properties, but is always not the case. Careful selection of model systems is essential to these studies as the assumption that  $k_r$  and  $k_{nr}$  are the same in the model systems and supramolecular systems is inherent to this analysis. Sample purity is also important in these studies as the rate of electron transfer could be underestimated in the presence of other emissive impurities or overestimated in the presence of impurities which quench the emissive excited state. The study of these electron transfer events become more complicated as model systems to probe excited state processes are not readily available.

Design and development of functioning photocatalysts for the reduction of water to produce hydrogen fuel has become an international effort as the world recognizes the significance for the need for environmentally friendly, renewable, economically viable alternatives for fuel production. There has been much success in this field given the complexity of the systems and processes.

The iron-based systems exploit the ability of iron-based hydrogenases to catalyze water reduction to produce hydrogen. Interesting biomimetic assemblies have been produced that couple ruthenium to diiron catalytic centers but these complexes have not shown applicability to solar hydrogen photocatalysis. The unfavorable

thermodynamic driving force for electron transfer from the ruthenium to the CAT impedes the use of the supramolecules diiron systems as photocatalysts for solar hydrogen production. The coupling of alternative ZnTPP LA units to these diiron cores provides for thermodynamically favorable electron transfer and has provided for photocatalytic systems with low TON. The ZnTPP LA unit possesses a higher energy singlet excited state that allows electron transfer to the diiron unit. These supramolecular assemblies reduce acidic solutions of 2-mercaptobenzoic acid to produce hydrogen following optical excitation with low turnovers. The multicomponent systems using diiron catalytic centers and Ru-based LA have shown promise providing higher TON using high CAT loading. In these systems, the stability of the CAT determines system stability with system malfunction occurring often after few hours due to CAT decomposition. Use of Ir-based LAs have shown better promise with higher TON relative to the LA and CAT, but system deactivation occurs due to decomplexation of the CAT.

Rhodium-centered photoinitiated electron collectors are known to catalyze water reduction to hydrogen.  $[\{(bpy)_2Ru(dpp)\}_2RhCl_2]^{5+}$ ,  $[\{(bpy)_2Ru(dpp)\}_2RhBr_2]^{5+}$ , and  $[\{(phen)_2Ru(dpp)\}_2RhCl_2]^{5+}$  are the lead photocatalysts in this area, demonstrating higher hydrogen yields and turnover capacities. The use of a bridging dpp on the Ru LA provides significant coverage of the solar spectrum to the low energy visible. The Ru LA displays an emissive  $^3MLCT$  excited state. The spectroscopic and photophysical properties display population of the emissive  $^3MLCT$  excited state followed by intramolecular electron transfer to populate the  $^3MMCT$  excited state. Optical excitation in the presence of an electron donor leads to at least two intramolecular electron transfer steps affording a coordinatively unsaturated  $Rh^I$  species which can interact with and reduce a substrate such as water. These systems couple two charge-transfer light absorbers to a single electron collector. Studies on the design considerations for a functioning system for optical multielectron reduction of water to produce hydrogen have shown that this general structural

motif is applicable in solar hydrogen production schemes. A related photoinitiated electron collector,  $[\{(bpy)_2Ru(dpb)\}_2IrCl_2]^{5+}$ , does not demonstrate photocatalytic activity implying that the Rh center is necessary and facilitates the chemical steps involved in bond transformations. The coordination environment on the rhodium center impacts the photocatalytic activity as evidenced by the greater hydrogen yields when weaker  $\sigma$ -donors are present on rhodium (Br vs. Cl), further implying that the reactive rhodium center and/or the  $^3MMCT$  excited state may be important.  $[\{(bpy)_2Ru(dpp)\}_2RhBr_2]^{5+}$  provides a system with a lower lying  $Rh(d\sigma^*)$  acceptor orbital with a larger driving force for intramolecular electron transfer to produce the  $^3MMCT$  state and/or promotes halide loss to generate the  $Rh^I$  system. Systematic studies on factors impacting hydrogen production, including the driving force for reductive quenching of the excited states by the electron donor, excited state lifetime of the photocatalyst, effective pH of the solution, and electron donor-catalyst interactions, has been studied. Photocatalytic activity of  $[\{(tpy)RuCl(dpp)\}_2RhCl_2]^{3+}$  and  $[\{(bpy)_2Os(dpp)\}_2RhCl_2]^{5+}$  is observed with lower efficiency, consistent with the lower driving force for reductive quenching of the  $^3MLCT$  excited state by DMA. The result is important, showing hydrogen can be evolved employing the  $^3MLCT$  excited state as electron transfer quenching of the  $^3MMCT$  state is not thermodynamically favorable in these systems. The system pH and the electron donor-catalyst interactions are important factors to be considered as varied photocatalytic activity is observed with variation of electron donors.

Multicomponent systems incorporating cyclometalated Ir complexes have been used as LAs in photochemical schemes for production of hydrogen from water using  $[Rh(NN)_3]^{3+}$  CATs. A preliminary study of a library of LA and CAT has enabled the identification of the most efficient system providing high TON and good system stability. Ir LAs provide varied excited state lifetimes and redox potentials relative to the classical Ru LAs.

The use of cobalt CATs have been investigated in solar hydrogen production schemes. The often substitutionally labile cobalt centers are stabilized

by the use of cobaloximes often with excess ligand in solution. The supramolecular systems incorporating Ir-based LAs show superior activity to the Ru-based system and enhanced stability relative to the analogous multicomponent system. The use of a Re-based LA with cobaloxime CAT has provided good functioning. Use of Pt- or Ir-based LAs with cobaloxime CATs has shown to be the most promising, providing high TON and good system stability.

Recent studies have focused on the coupling of Pd and Pt reactive metal centers to Ru charge-transfer light absorbers for multielectron solar hydrogen photocatalysis. There have been conflicting reports on these systems with follow-up studies showing that in some RuPt and RuPd systems the reduction of the complex may lead to colloidal Pd or Pt. It was proposed that Pt(s) or Pd (s) are the active catalyst for hydrogen generation. Some systems are proposed to function without colloidal metal formation. Careful analysis of these catalytic systems is needed to provide insight into the function of these photocatalysts and the optimization of the future generation of catalysts.

The area of solar hydrogen production through the use of photocatalysts that collect and deliver reducing equivalents is an active area of current research in inorganic photochemistry. The design and development of systems that catalyze this complicated process can play a significant role in the development of efficient photocatalysts for solar hydrogen production. The fundamental understanding of the properties of the LA, bridging ligand, CAT, and system parameters that determine hydrogen production efficiency is critical to the successful development of efficient and stable photocatalysts for the reduction of water to produce hydrogen fuel. The development of structurally diverse systems which couple a LA to a CAT is needed in this field with systematic variation of device components. Basic chemical studies of the perturbation of properties upon assembly of the supramolecules are also needed. Careful analysis of results and comparisons are needed. It is important that long-term studies of these important systems for light to fuel conversion are undertaken to understand the functioning of these systems and

explore the multidimensional parameter space needed to optimize the performance of these systems that are still in their infancy. Detailed mechanistic studies are necessary to uncover factors that limit the functioning of these systems and design of more promising molecular architectures that carry out this complicated photocatalytic reaction. A wide array of system parameters can impact system functioning further complicating this process. The research and development in this very important area requires long-term interest and research funding to assemble the fundamental chemical knowledge needed to establish efficient solar hydrogen production schemes. Sustained and focused research is needed to bring these systems to completion.

**Acknowledgments** Acknowledgment is made to all the students and research scientists who have worked in this area in the Brewer Group. Special acknowledgment to Ms. Jessica D. Knoll for help with the manuscript. Acknowledgment is also made to the Chemical Sciences, Geosciences and Biosciences Division, Office of Basic Energy Sciences, Office of Sciences, US Department of Energy for their generous support of our research and to the financial collaboration of Phoenix Canada Oil Company which holds long-term license rights to commercialize our Rh-based technology.

## Bibliography

1. Bard AJ, Fox MA (1995) Artificial photosynthesis: solar splitting of water to hydrogen and oxygen. *Acc Chem Res* 28:141–145
2. DOE (2005) Report of the basic energy sciences workshop on solar utilization. Department of Energy, Washington, DC
3. Lewis NS (2009) A perspective on forward research and development paths for cost-effective solar energy utilization. *ChemSusChem* 2:383–386
4. Nocera DG (2009) Living healthy on a dying planet. *Chem Soc Rev* 38:13–15
5. Bockris JO'M (1999) Hydrogen economy in the future. *Int J Hydrogen Energy* 24:1–15
6. Lubitz W, Tumas W (2007) Hydrogen: an overview. *Chem Rev* 107:3900–3903
7. <http://www.fsec.ucf.edu/EN/consumer/hydrogen/basics/pro-duction.htm>
8. Balzani V, Moggi L, Scandola F (1987) Towards a supramolecular photochemistry: assembly of molecular components to obtain photochemical molecular devices. In: Balzani V (ed) *Supramolecular photochemistry*. Reidel, Dordrecht, pp 1–28



- Kalyanasundaram K (1982) Photophysics, photochemistry and solar energy conversion with tris (bipyridyl)ruthenium(II) and its analogues. *Coord Chem Rev* 46:159–244
- Juris A, Balzani V, Barigelletti F, Campagna S, Belsler P, Von Zelewsky A (1988) Ru (II) polypyridine complexes: photophysics, photochemistry, electrochemistry, and chemiluminescence. *Coord Chem Rev* 84:85–277
- Kirch M, Lehn J-M, Sauvage J-P (1979) Hydrogen generation by visible light irradiation of aqueous solutions of metal complexes. An approach to the photochemical conversion and storage of solar energy. *Helv Chim Acta* 62:1345–1384
- Balzani V, Juris A, Venturi M, Campagna S, Serroni S (1996) Luminescent and redox-active polynuclear transition metal complexes. *Chem Rev* 96:759–834
- Kawanishi Y, Kitamura N, Tazuke S (1989) Dependence of spectroscopic, electrochemical, and excited-state properties of tris chelate ruthenium (II) complexes on ligand structure. *Inorg Chem* 28:2968–2975
- Durham B, Caspar JV, Nagle JK, Meyer TJ (1982) Photochemistry of  $\text{Ru}(\text{bpy})_3^{2+}$ . *J Am Chem Soc* 104:4803–4810
- Demas JN, Adamson AW (1971) A new photosensitizer. Tris (2,2'-bipyridine)ruthenium(II) chloride. *J Am Chem Soc* 93:1800–1801
- Gafney HD, Adamson AW (1972) Excited state Ru (bipyridyl) $_3^{2+}$  as an electron-transfer reductant. *J Am Chem Soc* 94:8238–8239
- Bock CR, Meyer TJ, Whitten DG (1974) Electron transfer quenching of the luminescent excited state of tris(2,2'-bipyridine)ruthenium(II). Flash photolysis relaxation technique for measuring the rates of very rapid electron transfer reactions. *J Am Chem Soc* 96:4710–4712
- Bock CR, Connor JA, Gutierrez AR, Meyer TJ, Whitten DG, Sullivan BP, Nagle JK (1979) Estimation of excited-state redox potentials by electron-transfer quenching. Application of electron-transfer theory to excited-state redox processes. *J Am Chem Soc* 101:4815–4824
- Tinker LL, McDaniel ND, Bernhard S (2009) Progress towards solar-powered homogeneous water photolysis. *J Mater Chem* 19:3328–3337
- Wang M, Na Y, Gorlov M, Sun L (2009) Light-driven hydrogen production catalysed by transition metal complexes in homogeneous systems. *Dalton Trans* 33:6458–6467
- Inagaki A, Akita M (2010) Visible-light promoted bimetallic catalysis. *Coord Chem Rev* 254:1220–1239
- Balzani V, Credi A, Venturi M (2008) Photochemical conversion of solar energy. *ChemSusChem* 1:26–58
- Lin CT, Böttcher W, Chou M, Creutz C, Sutin N (1976) Mechanism of the quenching of the emission of substituted polypyridineruthenium (II) complexes by iron (III), chromium(III), and europium(III) ions. *J Am Chem Soc* 98:6536–6544
- Kober EM, Sullivan BP, Dressick WJ, Caspar JV, Meyer TJ (1980) Highly luminescent polypyridyl complexes of osmium (II). *J Am Chem Soc* 102:7383–7385
- Braunstein CH, Baker AD, Streckas TC, Gafney HD (1984) Spectroscopic and electrochemical properties of the dimer tetrakis (2,2'-bipyridine)( $\mu$ -2,3-bis (2-pyridyl)pyrazine)diruthenium(II) and its monomeric analogue. *Inorg Chem* 23:857–864
- Fuchs Y, Lofters S, Dieter T, Shi W, Morgan R, Streckas TC, Gafney HD, Baker AD (1987) Spectroscopic and electrochemical properties of dimeric ruthenium(II) diimine complexes and determination of their excited state redox properties. *J Am Chem Soc* 109:2691–2697
- Wallace AW, Murphy WR, Petersen JD (1989) Electrochemical and photophysical properties of mono- and bimetallic ruthenium(II) complexes. *Inorg Chim Acta* 166:47–54
- Richter MM, Brewer KJ (1991) Synthesis and characterization of osmium(II) complexes incorporating polypyridyl bridging ligands. *Inorg Chim Acta* 180:125–131
- Abdel-Shafi AA, Worrall DR, Ershov AY (2004) Photosensitized generation of singlet oxygen from ruthenium(II) and osmium (II) bipyridyl complexes. *Dalton Trans* 7:30–36
- Winkler JR, Netzel TL, Creutz C, Sutin N (1987) Direct observation of metal-to-ligand charge-transfer (MLCT) excited states of pentaammineruthenium (II) complexes. *J Am Chem Soc* 109:2381–2392
- Beley M, Collin J-P, Sauvage J-P, Sugihara H, Heisel F, Miehé A (1991) Photophysical and photochemical properties of ruthenium and osmium complexes with substituted terpyridines. *J Chem Soc Dalton Trans* 23:3157–3159
- Rillema DP, Mack KB (1982) The low-lying excited state in ligand p-acceptor complexes of ruthenium (II): mononuclear and binuclear species. *Inorg Chem* 21:3849–3854
- Berger RM (1990) Excited-state absorption spectroscopy and spectroelectrochemistry of tetrakis (2,2'-bipyridine)( $\mu$ -2,3-bis (2-pyridyl)pyrazine) diruthenium(II) and its Monomeric counterpart: a comparative study. *Inorg Chem* 29:1920–1924
- Balzani V, Campagna S, Denti G, Juris A, Serroni S, Venturi M (1998) Designing dendrimers based on transition-metal complexes: light-harvesting properties and predetermined redox patterns. *Acc Chem Res* 31:26–34
- Campagna S, Pietro CD, Loiseau F, Maubert B, McClenaghan N, Passalacqua R, Puntoriero F, Ricevuto V, Serroni S (2002) Recent advances in luminescent polymeric dendrimers containing the 2,3-Bis(2'-pyridyl)pyrazine bridging ligand. *Coord Chem Rev* 229:67–74
- Molnar SM, Nallas GNA, Bridgewater JS, Brewer KJ (1994) Photoinitiated electron collection in a mixed-metal trimetallic complex of the form  $[\{(\text{bpy})_2\text{Ru}(\text{dpb})\}_2\text{IrCl}_2](\text{PF}_6)_5$  (bpy = 2,2'-bipyridine

- and dpb = 2,3-bis(2-pyridyl)benzoquinoxaline). *J Am Chem Soc* 116:5206–5210
37. Konduri R, Ye H, MacDonnell FM, Serroni S, Campagna S, Rajeshwar K (2002) Ruthenium photocatalysts capable of reversibly storing up to four electrons in a single acceptor ligand: a step closer to artificial photosynthesis. *Angew Chem Int Ed* 41:3185–3187
  38. Konduri R, de Tacconi NR, Rajeshwar K, MacDonnell FM (2004) Multielectron photoreduction of a bridged ruthenium dimer, [(phen)<sub>2</sub>Ru(tatpp)Ru(phen)<sub>2</sub>](PF<sub>6</sub>)<sub>4</sub>: aqueous reactivity and chemical and spectroelectrochemical identification of the photoproducts. *J Am Chem Soc* 126:11621
  39. Polyansky DE, Cabelli D, Muckerman JT, Fukushima T, Tanaka K, Fujita E (2008) Mechanism of hydride donor generation using a Ru(II) complex containing an NAD<sup>+</sup> model ligand: pulse and steady-state radiolysis studies. *Inorg Chem* 47:3958–3968
  40. Fukushima T, Fujita E, Muckerman JT, Polyansky DE, Wada T, Tanaka K (2009) Photochemical stereospecific hydrogenation of a Ru complex with an NAD<sup>+</sup>/NADH Type ligand. *Inorg Chem* 48:11510–11512
  41. Lomoth R, Ott S (2009) Introducing a dark reaction to photochemistry: photocatalytic hydrogen from [FeFe] hydrogenase active site model complexes. *Dalton Trans* 7:9952–9959
  42. Frey M (2002) Hydrogenases: hydrogen-activating enzymes. *Chembiochem* 3:153–160
  43. Capon J-F, Gloaguen F, Pétilion FY, Schollhammer P, Talamin J (2009) Electron and proton transfers at diiron dithiolate sites relevant to the catalysis of proton reduction by the [FeFe]-hydrogenases. *Coord Chem Rev* 253:1476–1494
  44. Wolpher H, Borgström M, Hammarström L, Bergquist J, Sundström V, Styring S, Sun L, Åkermark B (2003) Synthesis and properties of an iron hydrogenase active site model linked to a ruthenium tris-bipyridine photosensitizer. *Inorg Chem Commun* 6:989–991
  45. Ott S, Kritikos M, Åkermark B, Sun L (2003) Synthesis and structure of a biomimetic model of the iron hydrogenase active site covalently linked to a ruthenium photosensitizer. *Angew Chem Int Ed* 42:3285–3288
  46. Ott S, Borgström M, Kritikos M, Lomoth R, Bergquist J, Åkermark B, Hammarström L, Sun L (2004) Model of the iron hydrogenase active site covalently linked to a ruthenium photosensitizer: synthesis and photophysical properties. *Inorg Chem* 43:4683–4692
  47. Ekström J, Abrahamsson M, Olson C, Bergquist J, Kaynak FB, Eriksson L, Sun L, Becker H-C, Åkermark B, Hammarström L, Ott S (2006) Bio-inspired, side-on attachment of a ruthenium photosensitizer to an iron hydrogenase active site model. *Dalton Trans* 38:4599–4606
  48. Li X, Wang M, Zhang S, Pan J, Na Y, Liu J, Åkermark B, Sun L (2008) Noncovalent assembly of a metalloporphyrin and an iron hydrogenase active-site model: photo-induced electron transfer and hydrogen generation. *J Phys Chem B* 112:8198–8202
  49. Chong D, Georgakaki IP, Mejia-Rodriguez R, Sanabria-Chinchilla J, Soriaga MP, Darensbourg MY (2003) Electrocatalysis of hydrogen production by active site analogues of the iron hydrogenase enzyme: structure/function relationships. *Dalton Trans* 21:4158–4163
  50. Lubner CE, Grimme R, Bryant DA, Goldbeck JH (2010) Wiring photosystem I for direct solar hydrogen production. *Biochemistry* 49:404–414
  51. Na Y, Wang M, Pan J, Zhang P, Åkermark B, Sun L (2008) Visible light-driven electron transfer and hydrogen generation catalyzed by bioinspired [2Fe2S] complexes. *Inorg Chem* 47:2805–2810
  52. Streich D, Astuti Y, Orlandi M, Schwartz L, Lomoth R, Hammarström L, Ott S (2010) High-turnover photochemical hydrogen production catalyzed by a model complex of the [FeFe]-hydrogenase active site. *Chem Eur J* 16:60–63
  53. Zhang P, Wang M, Na Y, Li X, Jiang Y, Sun L (2010) Homogeneous photocatalytic production of hydrogen from water by a bioinspired [Fe<sub>2</sub>S<sub>2</sub>] catalyst with high turnover numbers. *Dalton Trans* 39:1204–1206
  54. Elvington M, Brown J, Arachchige SM, Brewer KJ (2007) Photocatalytic hydrogen production from water employing a Ru, Rh, Ru molecular device for photoinitiated electron collection. *J Am Chem Soc* 129:10644–10645
  55. Arachchige SM, Brown J, Brewer KJ (2008) Photochemical hydrogen production from water using the new photocatalyst [(bpy)<sub>2</sub>Ru(dpp)]<sub>2</sub>RhBr<sub>2</sub>(PF<sub>6</sub>)<sub>5</sub>. *J Photochem Photobiol A Chem* 197:13–17
  56. Arachchige SM, Brown JR, Chang E, Jain A, Zigler DF, Rangan K, Brewer KJ (2009) Design considerations for a system for photocatalytic hydrogen production from water employing mixed-metal photochemical molecular devices for photoinitiated electron collection. *Inorg Chem* 48:1989–2000
  57. Rangan K, Arachchige SM, Brown JR, Brewer KJ (2009) Solar energy conversion using photochemical molecular devices: photocatalytic hydrogen production from water using mixed-metal supramolecular complexes. *Energy Environ Sci* 2:410–419
  58. Miyake Y, Nakajima K, Sasaki K, Saito R, Nakanishi H, Nishibayashi Y (2009) Design and synthesis of diphosphine ligands bearing an osmium(II) bis(terpyridyl) moiety as a lightharvesting unit: application to photocatalytic production of dihydrogen. *Organometallics* 28:5240–5243
  59. Heyday AF, Nocera DG (2001) Hydrogen produced from hydrohalic acid solutions by a two-electron mixed-valence photocatalyst. *Science* 293:1639–1641
  60. Brown GM, Chan SF, Creutz C, Schwarz HA, Sutin N (1979) Mechanism of the formation of dihydrogen

- from the photoinduced reactions of tris(bipyridine) ruthenium(II) with tris (bipyridine)rhodium(III). *J Am Chem Soc* 101:7638–7640
61. Cline ED, Adamson SE, Bernhard S (2008) Homogeneous catalytic system for photoinduced hydrogen production utilizing iridium and rhodium complexes. *Inorg Chem* 47:10378–10388
  62. Fihri A, Artero V, Razavet M, Baffert C, Leibl W, Fontecave M (2008) Cobaloxime-based photocatalytic devices for hydrogen production. *Angew Chem Int Ed* 47:564–567
  63. Fihri A, Artero V, Pereira A, Fontecave M (2008) Efficient H<sub>2</sub>-producing photocatalytic systems based on cyclometalated iridium-and tricarbonylrhenium-diimine photosensitizers and cobaloxime catalysts. *Dalton Trans*:5567–5569
  64. Li C, Wang M, Pan J, Zhang P, Zhang R, Sun L (2009) Photochemical hydrogen production catalyzed by polypyridyl ruthenium-cobaloxime heterobinuclear complexes with different bridges. *J Organomet Chem* 694:2814–2819
  65. Brown GM, Brunschwig BS, Creutz C, Endicott JF, Sutin N (1979) Homogeneous catalysis of the photoreduction of water by visible light. Mediation by a tris(2,2'-bipyridine)ruthenium(II)-cobalt (II) macrocycle system. *J Am Chem Soc* 101:1298–1300
  66. Goldsmith JI, Hudson WR, Lowry MS, Anderson TH, Bernhard S (2005) Discovery and high-throughput screening of heteroleptic iridium complexes for photoinduced hydrogen production. *J Am Chem Soc* 127:7502–7510
  67. Du P, Schneider J, Luo G, Brennessel WW, Eisenberg R (2009) Visible light-driven hydrogen production from aqueous protons catalyzed by molecular cobaloxime catalysts. *Inorg Chem* 48:4952–4962
  68. Lazarides T, McCormick T, Du P, Luo G, Lindley B, Eisenberg R (2009) Making hydrogen from water using a homogeneous system without noble metals. *J Am Chem Soc* 131:9192–9194
  69. Probst B, Kolano C, Hamm P, Alberto R (2009) An efficient homogeneous intermolecular rhenium-based photocatalytic system for the production of H<sub>2</sub>. *Inorg Chem* 48:1836–1843
  70. Ozawa H, Haga M-A, Sakai K (2006) A photohydrogen-evolving molecular device driving visible-light-induced EDTA-reduction of water into molecular hydrogen. *J Am Chem Soc* 128:4926–4927
  71. Knoll JD, Arachchige SM, Brewer KJ (2011) A structurally diverse Ru(II), Pt(II) tetrametallic motif for photoinitiated electron collection and photocatalytic hydrogen production. *ChemSusChem* 4:252–261
  72. Miao R, Zigler DF, Brewer KJ Manuscript to be submitted to *Inorg Chem*
  73. Okazaki R, Masaoka S, Sakai K (2009) Photohydrogen-evolving activity of chloro(terpyridine) platinum(II): a single-component molecular photocatalyst. *Dalton Trans*:6127–6133
  74. Rau S, Schäfer B, Gleich D, Anders E, Rudolph M, Friedrich M, Görls H, Henry W, Vos JG (2006) A supramolecular photocatalyst for the production of hydrogen and the selective hydrogenation of toluene. *Angew Chem Int Ed* 45:6215–6218
  75. Schwartz L, Singh PS, Eriksson L, Lomoth R, Ott S (2008) Tuning the electronic properties of Fe<sub>2</sub>( $\mu$ -areneedithiolate) (CO)<sub>6-n</sub>(PMe<sub>3</sub>)<sub>n</sub> (n = 0, 2) complexes related to the [Fe–Fe]-hydrogenase active site. *C R Chim* 11:875–889
  76. Sutin N, Creutz C, Fujita E (1997) Photo-induced generation of dihydrogen and reduction of carbon dioxide using transition metal complexes. *Comments Inorg Chem* 19:67–92
  77. Balzani V, Credi A, Venturi M (1998) Photochemistry and photophysics of coordination compounds: an extended view. *Coord Chem Rev* 171:3–16
  78. Venturi M, Credi A, Balzani V (1999) Electrochemistry of coordination compounds: an extended view. *Coord Chem Rev* 185:233–256
  79. Scandola F, Argazzi R, Bignozzi CA, Indelli MT (1994) Photoinduced energy and electron transfer in inorganic covalently linked systems. *J Photochem Photobiol A Chem* 82:191–202
  80. Serroni S, Juris A, Campagna S, Venturi M, Denti G, Balzani V (1994) Tetranuclear bimetallic complexes of ruthenium, osmium, rhodium and iridium. Synthesis, absorption spectra, luminescence and electrochemical properties. *J Am Chem Soc* 116:9086–9091
  81. Indelli MT, Scandola F, Collin J-P, Sauvage J-P, Sour A (1996) Photoinduced electron and energy transfer in rigidly bridged Ru(II)-Rh(III) binuclear complexes. *Inorg Chem* 35:303–312
  82. Elvington M, Brewer K (2006) Photoinitiated electron collection at a metal in a rhodium-centered mixed-metal supramolecular complex. *Inorg Chem* 45:5242–5244
  83. White TA, Rangan K, Brewer KJ (2010) Synthesis, characterization, and study of the photophysics and photocatalytic properties of the photoinitiated electron collector [(phen)<sub>2</sub>Ru(dpp)]<sub>2</sub>RhBr<sub>2</sub>](PF<sub>6</sub>)<sub>5</sub>. *J Photochem Photobiol A Chem* 209:203–209
  84. Kalyanasundaram K, Nazeeruddin MK (1990) Photophysics and photoredox reactions of ligand-bridged binuclear polypyridyl complexes of ruthenium (II) and of their monomeric analogs. *Inorg Chem* 29:1888–1897
  85. Kew G, DeArmond K, Hanck K (1974) Electrochemistry of rhodium-dipyridyl complexes. *J Phys Chem* 78:727–734
  86. Anton DR, Crabtree RH (1983) Dibenzo[a, e] cyclooctatetraene in a proposed test for heterogeneity in catalysts formed from soluble platinum-group metal complexes. *Organometallics* 2:855–859
  87. Baba R, Nakabayashi S, Fujishima A, Honda K (1985) Investigation of the mechanism of

- hydrogen evolution during photocatalytic water decomposition on metal-loaded semi-conductor powders. *J Phys Chem* 89:1902–1905
88. Arachchige SM, Shaw R, White TA, Shenoy V, Tsui H-M, Brewer KJ (2011) Modification of system parameters for high turnover in a photocatalytic system for water reduction to produce hydrogen using a Ru, Rh, Ru photoinitiated electron collector. *ChemSusChem* 4:514–518
  89. Esswein AJ, Veige AS, Nocera DG (2005) A photocycle for hydrogen production from two-electron mixed-valence complexes. *J Am Chem Soc* 127:16641–16651
  90. Esswein AJ, Dempsey JL, Nocera DG (2007) A Rh<sup>II</sup> – Au<sup>II</sup> bimetallic core with a direct metal-metal bond. *Inorg Chem* 46:2362–2364
  91. Cook TR, Esswein AJ, Nocera DG (2007) Metal – halide bond photoactivation from a Pt<sup>III</sup>Au<sup>II</sup> complex. *J Am Chem Soc* 129:10094–10095
  92. Chou M, Creutz C, Mahajan D, Sutin N, Zipp AP (1982) Nature of bis(2,2′-bipyridine)rhodium(I) in aqueous solutions. *Inorg Chem* 21:3989–3997
  93. Schwarz HA, Creutz C (1983) Reactions of tris- and bis(2,2′-bipyridine)rhodium(II) complexes in aqueous solution. *Inorg Chem* 22:707–713
  94. Fujita E, Brunschwig BS, Creutz C, Muckerman JT, Sutin N, Szalda D, van Eldik R (2006) Transition state characterization for the reversible binding of dihydrogen to Bis(2,2′-bipyridine) rhodium(I) from temperature- and pressure-dependent experimental and theoretical studies. *Inorg Chem* 45:1595–1603
  95. Dempsey JL, Brunschwig BS, Winkler JR, Gray HB (2009) Hydrogen evolution catalyzed by cobaloximes. *Acc Chem Res* 42:1995–2004
  96. Kölle U (1992) Transition metal-catalyzed proton reduction. *New J Chem* 16:157–169
  97. Hawecker J, Lehn JM, Ziessel R (1983) Efficient homogeneous photochemical hydrogen generation and water reduction mediated by cobaloxime or macrocyclic cobalt complexes. *Nouv J Chim* 7:271–277
  98. Lowry MS, Goldsmith JJ, Slinker JD, Rohl R, Pascal RA, Malliaras GG, Bernhard S (2005) Single-layer electroluminescent devices and photoinduced hydrogen production from an ionic iridium(III) complex. *Chem Mater* 17:5712–5719
  99. Du P, Knowles K, Eisenberg R (2008) A homogeneous system for the photogeneration of hydrogen from water based on a platinum (II) terpyridyl acetylide chromophore and a molecular cobalt catalyst. *J Am Chem Soc* 130:12576–12577
  100. Dempsey JL, Winkler JR, Gray HB (2010) Kinetics of electron transfer reactions of H<sub>2</sub>-evolving cobalt diglyoxime catalysts. *J Am Chem Soc* 132:1060–1065
  101. Sakai K, Ozawa H (2007) Homogeneous catalysis of platinum (II) complexes in photochemical hydrogen production from water. *Coord Chem Rev* 251:2753–2766
  102. Ozawa H, Yokoyama Y, Haga M-A, Sakai K (2007) Syntheses, characterization, and photo-hydrogen-evolving properties of tris(2,2′-bipyridine)ruthenium(II) derivatives tethered to a cis-Pt(II)Cl<sub>2</sub> unit: insights into the structure–activity relationship. *Dalton Trans*:1197–1206
  103. Lei P, Hedlund M, Lomoth R, Rensmo H, Johansson O, Hammarström L (2008) The role of colloid formation in the photoinduced H<sub>2</sub> production with a Ru<sup>II</sup>-Pd<sup>II</sup> supramolecular complex: a study by GC, XPS, and TEM. *J Am Chem Soc* 130:26–27
  104. Du P, Schneider J, Li F, Zhao W, Patel U, Castellano FN, Eisenberg R (2008) Bi- and terpyridyl platinum (II) chloro complexes: molecular catalysts for the photogeneration of hydrogen from water or simply precursors for colloidal platinum? *J Am Chem Soc* 130:5056–5058
  105. Masaoka S, Mukawa Y, Sakai K (2010) Frontier orbital engineering of photo-hydrogen-evolving molecular devices: a clear relationship between the H<sub>2</sub>-evolving activity and the energy level of the LUMO. *Dalton Trans* 39:5868–5876
  106. Ozawa H, Kobayashi M, Balan B, Masaoka S, Sakai K (2010) Photo-hydrogen-evolving molecular catalysts consisting of polypyridyl ruthenium (II) photosensitizers and platinum(II) catalysts: insights into the reaction mechanism. *Chem Asian J* 5:1860–1869
  107. Tschierlei S, Presselt M, Kuhnt C, Yartsev A, Pascher T, Sundström V, Karnahl M, Schwalbe M, Schäfer B, Rau S, Schmitt M, Dietzek B, Popp J (2009) Photophysics of an intramolecular hydrogen-evolving Ru-Pd photocatalyst. *Chem Eur J* 15:7678–7688



## Photo-Catalytic Hydrogen Production

Jiefang Zhu

Department of Materials Chemistry, Ångström Laboratory, Uppsala University, Uppsala, Sweden

### Article Outline

Glossary

Definition of the Subject

Introduction

Principle of Photocatalytic H<sub>2</sub> Production

Evaluation of Photocatalytic H<sub>2</sub> Production

Experimental Setup for Photocatalytic H<sub>2</sub> Production

Photocatalysts for H<sub>2</sub> Production

Development and Modification of H<sub>2</sub> Production Photocatalysts

Future Directions

Bibliography

### Glossary

**Band gap** In solid-state physics, a band gap, also called an energy gap, is an energy range in a solid where no electron states can exist. In graphs of the electronic band structure of solids, the band gap generally refers to the energy difference (in electron volts) between the top of the valence band and the bottom of the conduction band in insulators and semiconductors. This is equivalent to the energy required to free an outer shell electron from its orbit about the nucleus to become a mobile charge carrier, able to move freely within the solid material.

**Conduction band** In the solid-state physics field of semiconductors and insulators, the conduction band is the range of electron energies, higher than that of the valence band, sufficient to free an electron from binding with its individual atom and allow it to move freely within

the atomic lattice of the material. Electrons within the conduction band are mobile charge carriers in solids, responsible for conduction of electric currents in metals and other good electrical conductors.

**Dopant** A dopant, also called a doping agent, is a trace impurity element that is inserted into a substance (in very low concentrations) in order to alter the electrical properties or the optical properties of the substance. In the case of crystalline substances, the atoms of the dopant very commonly take the place of elements that were in the crystal lattice of the material.

**Doping** In semiconductor production, doping is the process of intentionally introducing impurities into an extremely pure (also referred to as intrinsic) semiconductor to change its electrical properties.

**Dye sensitization** The process in which the dye absorbs light to yield an excited state, which in turn transfers an electron (or energy) onto the semiconductor.

**Hydrogen production** The industrial method for generating hydrogen.

**Hydrogen** The chemical element with atomic number 1. It is represented by the symbol H. At standard temperature and pressure, hydrogen is a colorless, odorless, nonmetallic, tasteless, highly combustible diatomic gas with the molecular formula H<sub>2</sub>.

**Photocatalysis** In chemistry, photocatalysis is the acceleration of a photoreaction in the presence of a catalyst (called photocatalyst). In catalyzed photolysis, light is absorbed by an adsorbed substrate (called photocatalyst). In photogenerated catalysis, the photocatalytic activity depends on the ability of the catalyst (called photocatalyst) to create electron–hole pairs, leading to secondary reactions.

**Photocatalyst** A substance that is able to promote, by absorption of light quanta, chemical transformations of the reaction participants, repeatedly participating in intermediate chemical interactions and regenerating its chemical composition after each cycle of such interactions.

**Photocatalytic** water splitting The production of hydrogen ( $H_2$ ) and oxygen ( $O_2$ ) from water by directly utilizing the energy from light. Photocatalytic water splitting has the advantage of the simplicity of using powder or film photocatalysts in solution and (sun) light to produce  $H_2$  and  $O_2$  from water.

**Semiconductor** A material that has an electrical conductivity due to flowing electrons (as opposed to ionic conductivity) which is intermediate in magnitude between that of a conductor and an insulator. This means roughly in the range  $10^{-8}$ – $10^3$  S/cm. In semiconductors, current is often schematized as being carried either by the flow of electrons or by the flow of positively charged “holes” in the electron structure of the material. Actually, however, in both cases only electron movements are involved.

**Valence band** In solids, the valence band is the highest range of electron energies where electrons are normally present at absolute zero temperature. The valence electrons are bound to individual atoms, as opposed to conduction electrons, which can move freely within the atomic lattice of the material. On a graph of the electronic band structure of a material, the valence band is located below the conduction band, separated from it in insulators and semiconductors by a band gap. In metals, the conduction band has no energy gap separating it from the valence band.

## Definition of the Subject

Increasing environmental concerns from using non-sustainable fossil fuels and a growing energy demand are forcing human beings to pursue clean and sustainable sources of energy. Hydrogen exists as a light, diatomic gas with high energy content by weight, but small energy content by volume. Hydrogen can react cleanly with oxygen in a highly exothermic reaction, with pure water as the only product. The energy stored in the chemical bond of hydrogen can be released by simply burning it in a combustion engine, or more efficiently by oxidizing it in a fuel cell. Based on the above properties, hydrogen is often considered an

attractive alternative to the current, fossil fuel-based energy carrier. However, the currently most widely used methods to produce hydrogen are based on the conversion of fossil fuel resources and thus deviate completely from the environmentally friendly intention of using hydrogen.

Photocatalysis is a technique to convert light (ideally sunlight) energy to chemical energy or electrical power. Photocatalytic  $H_2$  production is a technique utilizing the energy from (sun)light to produce  $H_2$  from water (or other hydrogen resources). Photocatalytic  $H_2$  production from water has been accepted as one of the most promising ways to realize a hydrogen economy for three reasons: (1) this technology is based on photon (or solar) energy, which is a clean, perpetual source of energy, and mainly water, which is a renewable resource; (2) it is an environmentally safe technology without undesirable by-products and pollutants; and (3) the photochemical conversion of solar energy into a storable form of energy, i.e., hydrogen, allows one to deal with the intermittent character and seasonal variation of the solar influx [1].

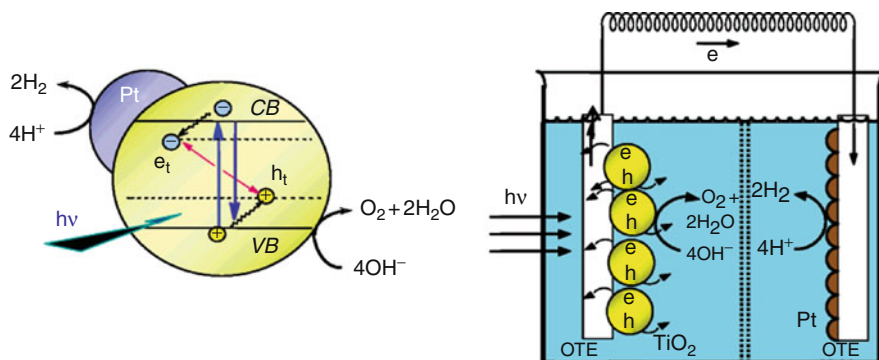
Photocatalytic water splitting has the advantage of simply using powder or film photocatalysts, and in this entry, it excludes the contents on photoelectrochemical (PEC) water splitting, which is described in another entry of this encyclopedia. The redox mechanism of photocatalytic  $H_2$  production is similar to that of PEC  $H_2$  generation. The main difference between the two approaches lies in the location of the redox reactions, as illustrated in Fig. 1. In the photocatalytic process, both oxidation and reduction reactions occur on the surface of a photocatalyst (powder or film), and as a result, a mixture of  $H_2$  and  $O_2$  is evolved together (the left-hand side of Fig. 1). In the photoelectrochemical process, oxidation and reduction take place at spatially separated photoanode and cathode, respectively, resulting in  $H_2$  and  $O_2$  being evolved separately (the right-hand side of Fig. 1). It should be noted that the efficiency of photocatalysts is normally lower than that of photoanodes in  $H_2$  generation, since hydrogen and oxygen have a tendency to react back to



water if they are evolved at the same location. However, compared to photoanodes, photocatalysts do not need a conductive substrate for charge collection, so that a much broader selection of synthetic methods, such as solid-state high temperature synthesis, can be adopted. This allows photocatalysts to be prepared with relative ease and at a competitive cost. In a photocatalytic system, cocatalysts can be easily introduced by firing and mixing. Furthermore, research on photocatalysts may provide a convenient screening approach for the selection of suitable photoanodes.

### Introduction

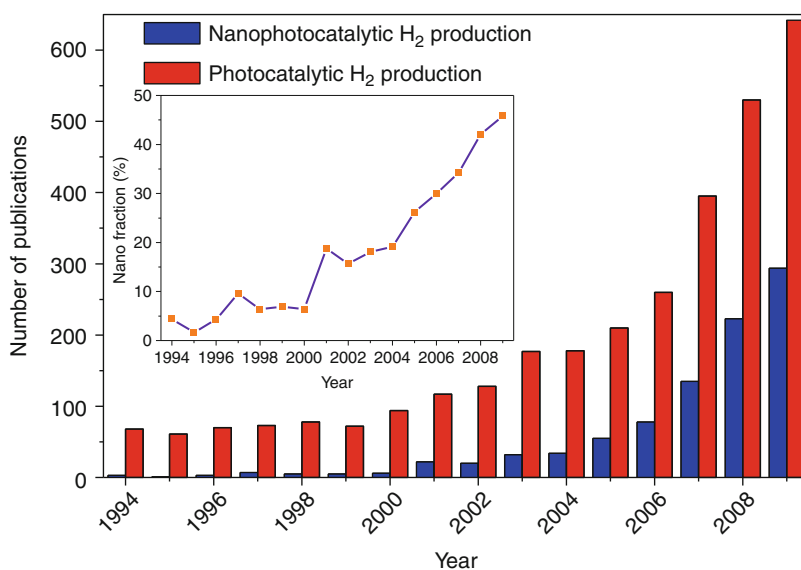
Photocatalytic H<sub>2</sub> production has been developing for 40 years. The increasing number of scientific publications constitutes clear bibliographical evidence for the significance of this hot field, as shown in Fig. 2. Recently, nanoscience and nanotechnology opened a new vista in this field. Since 2004, the number of publications on nanophotocatalytic H<sub>2</sub> production has increased by a factor of about 1.5 times every year. Many papers recently studied the impact of different nanostructures and nanomaterials on the performance



**Photo-Catalytic Hydrogen Production, Fig. 1** Photocatalytic splitting of water following the band gap excitation of the semiconductor nanoparticle (left-hand side) and a

photoelectrolysis cell based on a nanostructured semiconductor film electrode (right-hand side). (Reprinted with permission from [2]. Copyright 2007 American Chemical Society)

**Photo-Catalytic Hydrogen Production, Fig. 2** The number of publications on (nano) photocatalytic H<sub>2</sub> production sorted by year. The inset shows the fraction of publications on photocatalytic H<sub>2</sub> production that deal with nano-aspects. (Data were collected from the “Web of Science,” and entries until October 14, 2010, have been considered)



of photocatalysts, since it was found that the total energy conversion efficiency is largely determined by nanoscale properties of photocatalysts. Although progress has been made in many fields concerning photocatalytic H<sub>2</sub> production during these years, such as photocatalytic reactor design, product separation and detection, and light harvesting, the key factor determining its practical application is the materials, i.e., photocatalysts.

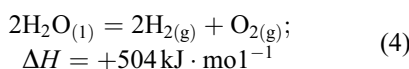
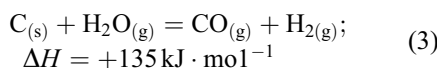
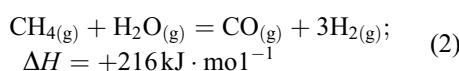
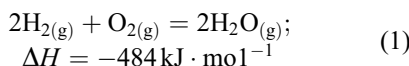
In 1972, the initial work of Fujishima and Honda indicated that PEC water splitting could be performed by using a TiO<sub>2</sub> photoanode [3]. The setup in that work is similar to that shown on the right-hand side of Fig. 1. Photo-generated electrons and holes are formed in TiO<sub>2</sub> when it is irradiated by UV light. The photo-generated electrons flow to a Pt counter electrode to reduce water to H<sub>2</sub>, while water is oxidized to O<sub>2</sub> by photogenerated holes on the TiO<sub>2</sub> side. Following this exciting finding, H<sub>2</sub> production by semiconductor photocatalysis and electrolysis has been attracting more and more attention. During the 1970s and the first half of the 1980s, the photocatalysts used for H<sub>2</sub> production from water splitting mainly focused on TiO<sub>2</sub>, SrTiO<sub>3</sub> [4, 5], and ZnO. Compared to TiO<sub>2</sub>, SrTiO<sub>3</sub> can split water without an external bias due to its higher conduction band level. In the middle of the 1980s, Pt/CdS [6–8] and ZnS [9] were identified as highly active photocatalysts for H<sub>2</sub> evolution under visible-light irradiation in the presence of sacrificial reagents. In the second half of the 1980s, new photocatalysts, such as K<sub>4</sub>Nb<sub>6</sub>O<sub>17</sub> [10–13], Na<sub>2</sub>Ti<sub>3</sub>O<sub>7</sub> [14], K<sub>2</sub>Ti<sub>2</sub>O<sub>5</sub> [14], and K<sub>2</sub>Ti<sub>4</sub>O<sub>9</sub> [14], were used for water splitting. Many tantalate [15–19], tungstate [20, 21], and molybdate [20] photocatalysts have shown high activity for H<sub>2</sub> production from an aqueous solution containing a sacrificial reagent since the second half of the 1990s. After coming into the new century, the database of photocatalysts for water splitting has become more plentiful. Many oxide photocatalysts consisting of the metal cations Ga<sup>3+</sup>, In<sup>3+</sup>, Ge<sup>4+</sup>, Sn<sup>4+</sup>, and Sb<sup>5+</sup>, with d<sup>10</sup> configuration (i.e., metal cations having fully filled (with ten electrons) outermost d orbitals), and assisted with RuO<sub>2</sub> as a cocatalyst have recently been reported [22–26]. Non-oxide Ge<sub>3</sub>N<sub>4</sub> with a RuO<sub>2</sub>

cocatalyst was also found to be a photocatalyst for H<sub>2</sub> production [27]. Oxynitrides [28–31] and oxysulfides [32, 33] have been widely developed in research led by K. Domen for H<sub>2</sub> and O<sub>2</sub> evolution under visible-light irradiation in the presence of sacrificial reagents. Cr-Rh oxide/GaN:ZnO is a solid solution of GaN and ZnO, which is also active for overall water splitting [34]. The solid solution of ZnO and ZnGeN<sub>2</sub>, (Zn<sub>1-x</sub>Ge<sub>x</sub>)(N<sub>2</sub>O<sub>x</sub>) was recently discovered as another active d<sup>10</sup> metal oxynitride photocatalyst for pure water splitting under visible light [35]. A Z-scheme photocatalytic water splitting system, which involved two-step photoexcitation under visible-light irradiation, was recently developed by mimicking the natural photosynthesis of green plants [36, 37].

## Principle of Photocatalytic H<sub>2</sub> Production

As mentioned above, H<sub>2</sub> is an energy carrier, and the combustion of it produces only water and traces other pollutants with a large amount of heat releasing (Eq. 1). Moreover, H<sub>2</sub> is also an important raw material in chemical industries, e.g., industrial ammonia synthesis. However, a large fraction of hydrogen production is currently based on fossil fuel resources. The processes involved in the conversion of fossil fuels, such as the reforming of natural gas (Eq. 2), coal gasification (Eq. 3)/liquefaction, and coal electrolysis, require large amounts of energy, either in the form of heat or electricity, and all these processes are accompanied with the release of vast amounts of carbon dioxide. In order to actualize the hydrogen economy, there is a demand for other carbon-neutral feedstocks from which hydrogen can be produced with the energy provided by a sustainable source. Alternative feedstocks under consideration include wood, other biomass, organic waste, and water, where the former options are not necessarily carbon neutral, however. The latter option constitutes an entirely sustainable energy system, where hydrogen is produced from water (Eq. 4) and later on recovered back into water in a combustion engine or a fuel cell. This entry therefore focuses on hydrogen production from water.

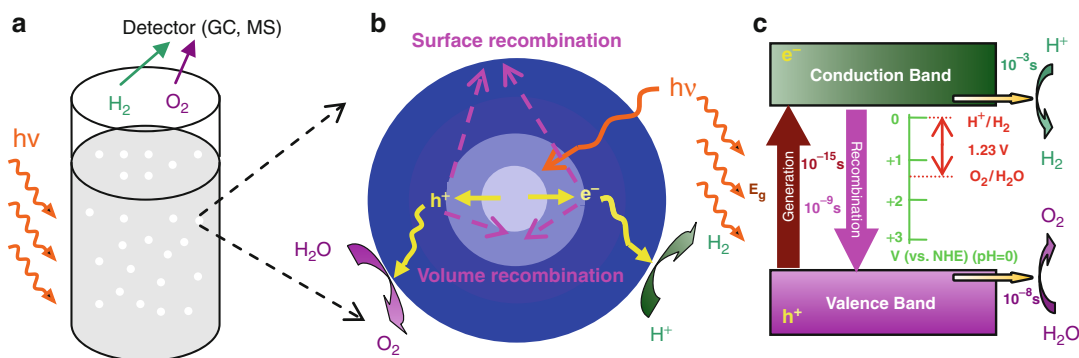
In principle, water can be split into  $H_2$  and  $O_2$  by several different pathways and utilizing various energy sources. The commonly used method is to dissociate water in an electrolysis cell. However, electrolysis is a two-step process, and the potential of achieving a highly efficient, simple, and cost-effective conversion is limited. A better idea is to directly split water in a single device into its component gases, without the production of electricity in advance. Photocatalysis can directly utilize photon energy to decompose water into  $H_2$  and  $O_2$ .



Photocatalytic  $H_2$  production (or water splitting) occurs on the surface of semiconductor materials, as shown in Fig. 3. Figure 3 shows three basic steps in photocatalytic  $H_2$  production. The first step is the absorption of photons. A semiconductor has a valence band (VB) and a

conduction band (CB), which are separated from one another by a band gap ( $E_g$ ), as shown in Fig. 3c. In the ground state, all electrons exist in the VB. Under irradiation by photons with energy equivalent to or larger than  $E_g$ , some of the electrons are excited from the VB to the CB, leaving empty states, so-called holes, in the VB. The second step is the charge separation and migration, as shown in Fig. 3b. The photogenerated electrons and holes from the first step may recombine in the bulk or on the surface of the semiconductor on a time scale which is slower than the time required for their generation (Fig. 3b, c). Some electrons and holes that travel to the surface of the semiconductor without recombination can cause reduction ( $H_2$  formation) and oxidation ( $O_2$  formation) reactions, respectively, in the last step called surface chemical reactions. The important parameters in photocatalysts are the width of the band gap and the levels of the conduction and valence bands. From Fig. 3c, the theoretical minimum band gap (or photon energy) for water splitting is 1.23 eV, corresponding to a wavelength of 1008 nm, according to the formula  $E_g$  (eV) equal to  $1240/\lambda$  (nm).

However, if taking into account thermodynamic losses at various steps in the photocatalytic process, overpotential is necessary to ensure a reasonable reaction rate, and effective photocatalysts exhibit band gaps larger than 2 eV, corresponding to a wavelength below 620 nm. If



**Photo-Catalytic Hydrogen Production, Fig. 3** (a) A suspension of photocatalyst powders in water under irradiation. (b) The processes involved in water splitting by a photocatalyst particle are photon absorption, electron-hole generation (and recombination), charge transport,

and oxidation/reduction reactions on the semiconductor surface. (c) The principle and energy diagram for photocatalytic water splitting on a semiconductor. (Reprinted from [1], Copyright (2009), with permission from Elsevier)

the sunlight is to be used for water splitting, visible-light-responsive photocatalysts should have band gaps between 2 and 3.1 eV, since the intensity of sunlight is small in the UV region, i.e., for wavelengths below 400 nm (3.1 eV). Apart from the band gap requirement, for H<sub>2</sub> production to take place, the CB bottom edge should be more negative than the reduction potential of H<sup>+</sup>/H<sub>2</sub> ( $E_{\text{H}^+/\text{H}_2} = 0\text{V vs NHE at pH 0}$ ), while the VB top edge should be more positive than the oxidation potential of O<sub>2</sub>/H<sub>2</sub>O ( $E_{\text{O}_2/\text{H}_2\text{O}} = 1.23\text{V vs NHE at pH 0}$ ) for O<sub>2</sub> evolution from water to occur, as shown in Fig. 3c. Figure 4 lists the band edge positions for commonly used semiconductors. It can be seen that there are not many semiconductors meeting the requirements of band gap and band levels for ideal photocatalysts for water splitting. Besides thermodynamic requirements, an ideal photocatalyst should also have kinetic advantages, e.g., high photocatalytic activity for H<sub>2</sub> and O<sub>2</sub> production. There are a few non-oxide semiconductors that meet requirements mentioned above. However, they are unstable and/or easily corroded (e.g., CdS). It has proven difficult to find a simple and cost-effective photocatalyst meeting all the requirements [1].

## Evaluation of Photocatalytic H<sub>2</sub> Production

There is no perfect standard for comparing H<sub>2</sub> productivity of different photocatalysts in different photocatalytic systems. Therefore, researchers normally compare their homemade photocatalysts in their setups with some references, e.g., commercial TiO<sub>2</sub> photocatalysts, which are well known for their high activity, like P25 (a product of Evonik Degussa GmbH), Hombikat UV-100 (a product of Sachtleben Chemie GmbH), and ST-01 (a product of Ishihara Sangyo Kaisha, Ltd.). However, there are some terms that are commonly used to describe photocatalytic activity, and these are discussed below.

### Turnover Quantities

The quantitative measurements of photocatalytic activity of a solid photocatalyst are normally

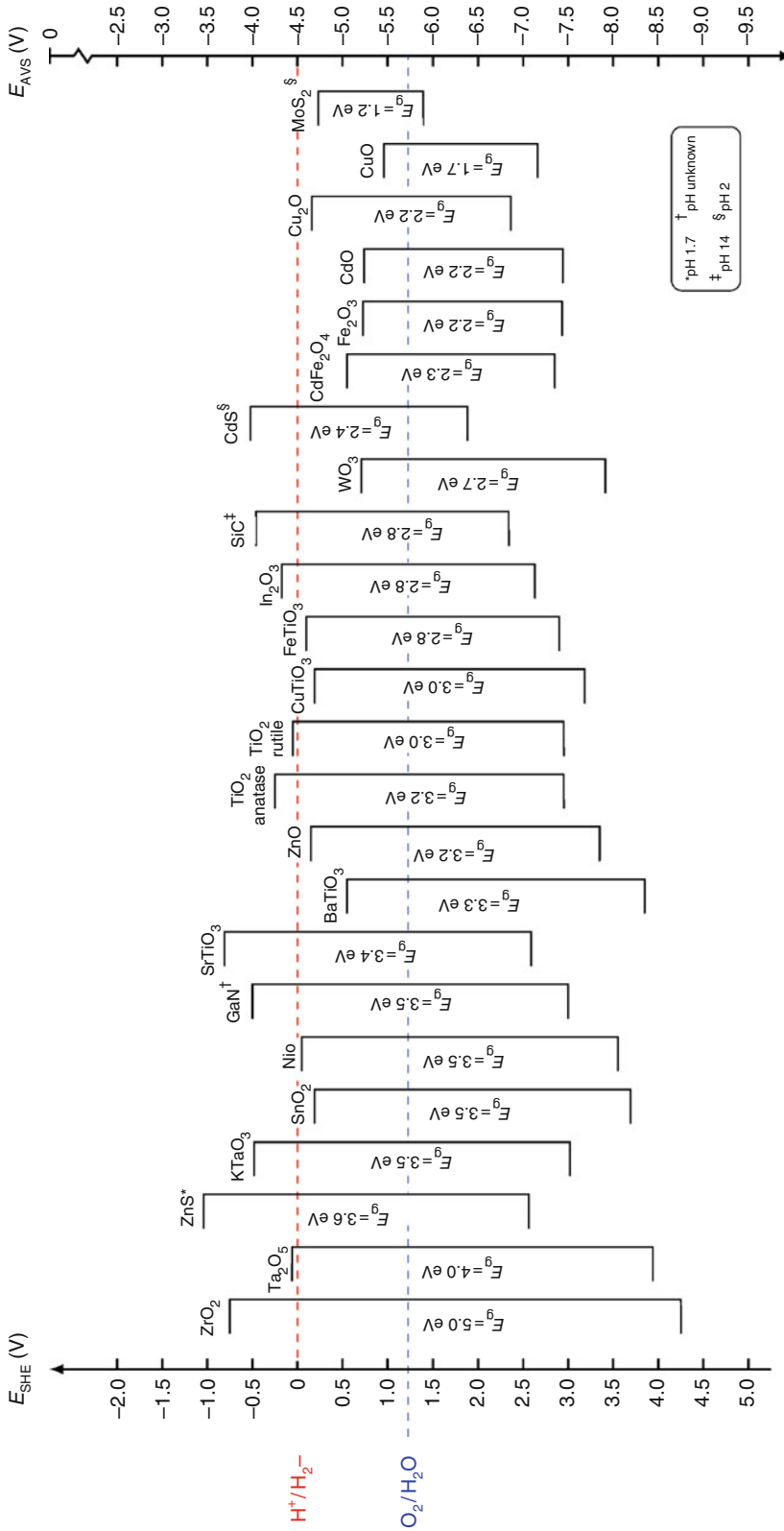
derived from process kinetics to express a rate referenced to the number of photocatalytic sites to infer how many times a catalytic cycle turns over. Traditionally, these parameters are the turnover number (TON), turnover rate (TOR), and turnover frequency (TOF). In H<sub>2</sub> production, turnover rate (TOR) is considered as the number of H<sub>2</sub> molecules produced per active site per unit time (units: molecules site<sup>-1</sup> time<sup>-1</sup>) (Eq. 5); turnover frequency (TOF) as the number of H<sub>2</sub> molecules produced per unit time (units: molecules time<sup>-1</sup>) (Eq. 6); and turnover number (TON) as a quantity that describes how many times a H<sub>2</sub> evolution reaction or process turnovers at active sites integrated over time (units: molecules site<sup>-1</sup>) (Eq. 7).

$$\text{TOR} = \frac{\text{Number of H}_2 \text{ molecules produced}}{\text{Number of activesites} \cdot \text{Reaction time}} \quad (5)$$

$$\text{TOF} = \frac{\text{Number of H}_2 \text{ molecules produced}}{\text{Reaction time}} \quad (6)$$

$$\text{TON} = \frac{\text{Number of H}_2 \text{ molecules produced}}{\text{Number of activesites}} \quad (7)$$

Using these turnover quantities, it can be judged whether a given process is truly photocatalytic, as TON of a real photocatalytic reaction is much higher than 1. In addition, these turnover quantities are also supposed to be useful in assessing new materials as photocatalysts, and reproducible or comparable across various laboratories. Normally, it is difficult to determine the number of active sites for a photocatalyst, and the active sites and non-active sites can switch during photocatalytic process. Therefore, the number of atoms in a photocatalyst or on the surface of a photocatalyst, instead of the number of active sites, is often employed in Eqs. 5, 6, and 7. However, the irradiated surface area is not equal to the total surface area of the photocatalyst, and the active sites can only lie in the irradiated surface area. Thus, the practical determination of turnover quantities remains very complex, and cannot be accurate.



**Photo-Catalytic Hydrogen Production, Fig. 4** Valence and conduction band edge positions of various semiconductors with respect to the standard hydrogen electrode ( $SHE$ ) scale and the vacuum reference energy scale  $E_{AVS}$ . All values were reported being tested at pH 1, unless otherwise noted

### Quantum Yield and Photonic Efficiency

Quantum yield ( $\Phi$ ) is defined as the number of defined events that occur per photon absorbed by the system, or as the amount (mol) of reactant consumed or product ( $H_2$ ) formed per amount of photons (mol or Einstein) absorbed (Eq. 8). The definition of quantum yield makes it difficult to describe photocatalytic efficiency in real heterogeneous media, particularly for complex reactor geometries. In suspension systems, the sum of reflection, scattering, and transmission should be measured precisely, in order to determine the amount of photons absorbed by the photocatalyst.

$$\Phi = \frac{\text{Number of } H_2 \text{ molecules produced}}{\text{Number of photons absorbed by photocatalyst}} \quad (8)$$

A simple alternative method of comparing process efficiencies for equal absorption of photons has been proposed by N. Serpone for heterogeneous photocatalysis: (relative) photonic efficiency [38]. Photonic efficiency ( $\xi$ ) describes the number (or mols) of reactant molecules transformed or product ( $H_2$ ) molecules formed divided by the number or Einsteins of photons at a given wavelength incident on the reactor cell (Eq. 9). Alternatively, the photonic efficiency can also be described by the ratio of the initial rate of the event to the rate of incident photons reaching the reactor as obtained by actinometry (Eq. 10).

$$\xi = \frac{\text{Number of } H_2 \text{ molecules produced}}{\text{Number of incident photons on reactor}} \quad (9)$$

$$\xi = \frac{\text{The rate of } H_2 \text{ production}}{\text{The rate of photons impinging on reactor}} \quad (10)$$

To avoid unnecessary errors and the effects from reactor geometry and light source, together with the properties (e.g., size, surface area) of the photocatalyst material used, another kind of efficiency has been defined so that it could be used to compare experiments within the same laboratory or even with other laboratories, and it

would be reactor independent: the relative photonic efficiency ( $\xi_r$ ). It is related to an acceptable standard process, a standard photocatalyst material, or a standard “secondary actinometer” in photocatalytic processes (Eq. 11). For example, the determination of the total incident photon in the wavelength regions by chemical actinometry ferrioxalate has been performed in the same reactor, in order to avoid the corrections for any influence of light reflection, beam position, and reactor geometry. In the experimental description of a relative photonic efficiency, reactor geometry, light source, and photocatalyst properties should be constant in assessing  $\xi_r$ . To be really useful and comparable,  $\xi_r$  values should not depend on light irradiance and reactor geometry, or even on other parameters such as pH, photocatalyst loading, substrate concentration, and temperature [38], which is not easy in practice.

$$\xi_r = \frac{\text{The rate of } H_2 \text{ production}}{\text{The rate of standard process under identical conditions}} \quad (11)$$

### Experimental Setup for Photocatalytic $H_2$ Production

There are several kinds of setups for photocatalytic  $H_2$  production and/or water splitting. Generally speaking, these setups consist of four parts. The first part is a light source. A high-pressure mercury lamp is often used with quartz apparatuses for broad band gap semiconductors, since UV-light irradiation is needed. A xenon lamp is used for visible-light irradiation, when a cut-off filter is employed to avoid infrared heating. A solar simulator (AM1.5) with its radiance of  $100 \text{ mW cm}^{-2}$  is ideal for solar hydrogen production study. Alternatively, a xenon lamp and several filters can be assembled for a solar simulator. In this case, the emission spectrum should be measured to make sure of its identity to solar spectrum, and the intensity should be calibrated by a thermopile or Si photodiode. The second part is a reaction cell. There are different shapes and sizes of reactors for photocatalytic  $H_2$  production



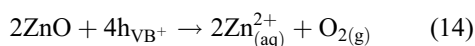
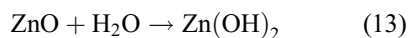
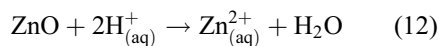
and/or water splitting. They should be transparent enough for light irradiation, and they are connected to the third part, a gas line. Vacuum pump, pressure gauge, and carrier gas are normally connected to the gas line. The last part is gas detection and/or collection part, which draws in the produced gases ( $H_2$  and  $O_2$ ) from gas line. Gas chromatography and mass spectrometry are employed for microanalysis, while volumetric measurement is suitable for a large amount of gas evolution. The whole system (including reactor, gas line, gas detector, and collector) should stay gas tight during operation.

## Photocatalysts for $H_2$ Production

Most photocatalysts are composed of both metal and nonmetal ions. Metal cations show their highest oxidative states with  $d^0$  (red area in Fig. 5) or  $d^{10}$  (green area) electronic configuration, while O, S, and N (blue area) exist as their most negative states. The conduction band bottom consists of the d and sp orbitals of the metal cations, while the valence band top in metal oxides is composed of O 2p orbitals, which is normally located at ca. +3 V (vs SHE) or higher. The valence bands of metal oxysulfides and oxynitrides are formed by S 3p and O 2p, and N 2p and O 2p, respectively. In some compounds, alkali (Li, Na, K, Rb, and Cs), alkaline earth (Mg, Ca, Sr, and Ba), and transition metal (Y, La, and Gd) ions can constitute the crystal structures of these compounds, rather than make any contribution to the energy structures. In this section, the commonly used materials for photocatalytic  $H_2$  production will be introduced.

$TiO_2$  has been one of the most important photocatalysts for  $H_2$  production, due to its availability, low price, nontoxicity, high photoactivity, and stability. The biggest disadvantage of  $TiO_2$  is the low utilization of visible light, as a consequence of its wide band gaps, which are 3.2 eV (corresponding to an absorption edge of 380 nm) and 3.0 eV (400 nm) for anatase and rutile, respectively. At any rate,  $TiO_2$  is a good reference and starting material for research. ZnO has the similar advantages (including availability, low price,

nontoxicity, high photoactivity, and enough potential for both  $H_2$  and  $O_2$  evolution) with  $TiO_2$  and single-crystalline ZnO even has fast electron mobility. However, it is unstable in strong acids (Eq. 12) and alkalis (Eq. 13), and after long-time irradiation, ZnO suffers from photocorrosion, due to the oxidation of  $O^{2-}$  in ZnO by photogenerated holes (Eq. 14).  $WO_3$  has a relatively narrow band gap of 2.7 eV, but enables it to utilize part of the visible light.  $WO_3$  is a successful photocatalyst for  $O_2$  evolution from water, while its conduction band is not negative enough to reduce  $H^+$  to  $H_2$ . In practice,  $WO_3$  is applied to water splitting by coupling to another semiconductor or by doping.  $\alpha-Fe_2O_3$  has several advantages of narrow band gap of 2.2 eV, good photo stability, chemical inertness, and low cost. However, it has the same problem as  $WO_3$  with respect to its positive conduction band level. Furthermore, it suffers from fast  $e^-h^+$  recombination and poor charge transportation.



When  $TiO_2$  is fused with other metal oxides ( $SrO$ ,  $BaO$ ,  $Ln_2O_3$  ( $Ln = \text{lanthanide}$ )), metal titanates with perovskite structure are formed. Perovskites have the general formula  $ABX_3$ , and several hundred oxides own this structure. Among them,  $SrTiO_3$  and  $BaTiO_3$  both with a band gap of 3.3 eV have been widely studied as semiconductors for photocatalytic water splitting. Alkaline metal hexatitanates ( $M_2Ti_6O_{13}$ ;  $M = Na, K, Rb$ ) are normally used in powder form in suspensions, together with a cocatalyst. There are more complex perovskites containing two different cations, and many of these have a layered structure. Two main classes of such oxides, which have been studied in water splitting, are the Dion–Jacobson series ( $AM_n - 1B_nO_{3n+1}$ , e.g.,  $KCa_2Ti_3O_{10}$ ), and the Ruddlesden–Popper series ( $A_2M_n - 1B_nO_{3n+1}$ , e.g.,  $K_2La_2Ti_3O_{10}$ ). Another type of layered perovskites has the generic composition  $A_nB_nO_{3n+2}$  ( $n = 4, 5$ ;  $A = Ca, Sr, La$ ;

H																	Non-metal					He
Li	Be											B	C	N	O	F	Ne					
Na	Mg											Al	Si	P	S	Cl	Ar					
K	Ca	Sc	Ti	V	Cr	Mn	Fe	Co	Ni	Cu	Zn	Ga	Ge	As	Se	Br	Kr					
Rb	Sr	Y	Zr	Nb	Mo	Tc	Ru	Rh	Pd	Ag	Cd	In	Sn	Sb	Te	I	Xe					
Cs	Ba	Ln	Hf	Ta	W	Re	Os	Ir	Pt	Au	Hg	Tl	Pb	Bi	Po	At	Rn					
			d <sup>0</sup> configuration					d <sup>10</sup> configuration														
La	Ce	Pr	Nd	Pm	Sm	Eu	Gd	Tb	Dy	Ho	Er	Tm	Yb	Lu								

**Photo-Catalytic Hydrogen Production, Fig. 5** Elements constructing photocatalysts. (Reprinted from [1], Copyright (2009). With permission from Elsevier)

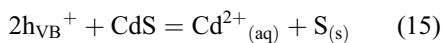
B = Nb, Ti). Among them,  $\text{La}_2\text{Ti}_2\text{O}_7$  (i.e.,  $\text{La}_4\text{Ti}_4\text{O}_{14}$ ) and  $\text{La}_4\text{CaTi}_5\text{O}_{17}$  are representative titanates. The band gaps of  $\text{La}_2\text{Ti}_2\text{O}_7$  and  $\text{La}_4\text{CaTi}_5\text{O}_{17}$  are 3.2 and 3.8 eV, and when loaded with nickel they showed a quantum yield of 12% (<360 nm) and 20% (<320 nm) for water splitting, respectively [39].

Tantalates and niobate oxides with corner-sharing octahedral  $\text{MO}_6$  ( $M = \text{Ta}, \text{Nb}$ ) structures have shown high photocatalytic activity for the cleavage of water, since the photogenerated electron-hole pairs can easily migrate and separate through the corner-shared  $\text{MO}_6$  units. Tantalates,  $\text{MTaO}_3$  ( $M = \text{Li}, \text{Na}, \text{K}$ ) were reported as effective photocatalysts for water splitting under UV irradiation. These oxides own perovskite structure, and their band gaps are 4.7 eV (Li), 4.0 eV (Na), and 3.7 eV (K), respectively [40]. Some layered oxides (e.g.,  $\text{K}_4\text{Nb}_6\text{O}_{17}$ ) have two kinds of interlayers, which exist alternately.  $\text{H}_2$  is evolved from one interlayer, where cocatalysts are selectively introduced. In  $\text{K}_4\text{Nb}_6\text{O}_{17}$  case,  $\text{H}_2$  and  $\text{O}_2$  evolutions are separated by the photocatalytic niobate sheet, which will be described later.

Generally speaking, oxides containing d<sup>0</sup> transition metal cations, like  $\text{Ti}^{4+}$ ,  $\text{Nb}^{5+}$ , or  $\text{Ta}^{5+}$ , have wide band gaps (>3.0 eV). Thus, these materials

can only be excited under UV irradiation. Interestingly, K Ce M O ( $M = \text{Ta}, \text{Nb}$ ) and their solid solutions  $\text{K}_4\text{Ce}_2\text{Ta}_{10-x}\text{Nb}_x\text{O}_{30}$  ( $x = 0-10$ ) were found to have band gaps of ca. 1.8–2.3 eV (corresponding to absorption edges of 540–690 nm), and they performed well under visible-light irradiation. This may be ascribed to the hybrid construction of their valence bands [41].

Many metal sulfide photocatalysts are active under visible-light irradiation. The valence bands of metal sulfides consist of S 3p orbitals, which make the valence band potential more negative and thus narrows the band gap, compared to the valence bands composed of O 2p orbitals in corresponding metal oxides. CdS with wurtzite structure is the most studied metal sulfide photocatalyst. It has a narrow band gap (2.4 eV), which makes it absorb visible-light below a wavelength of 510 nm. Although the valence and conduction bands of CdS are perfectly suitable for  $\text{O}_2$  and  $\text{H}_2$  evolution, CdS is apt to be photo-corroded (Eq. 15), which is common for most metal sulfides. In order to avoid photo-corrosion, scavengers (electron donors, such as cysteines, EDTA, sulfide, or sulfite species) are often used to consume photogenerated holes during the photocatalytic water splitting by CdS.



Enlightened by the N doping effect,  $\text{Ta}_3\text{N}_5$  was prepared by nitriding  $\text{Ta}_2\text{O}_5$  in an  $\text{NH}_3$  atmosphere. Reasonably, the band gap shrinks from  $\sim 4.0$  eV for  $\text{Ta}_2\text{O}_5$  to  $\sim 2.1$  eV for  $\text{Ta}_3\text{N}_5$ . The narrower band gap results from a higher-lying valence band derived from N 2p orbitals in  $\text{Ta}_3\text{N}_5$  other than O 2p orbitals in  $\text{Ta}_2\text{O}_5$ . This material photocatalytically produced  $\text{H}_2$  and  $\text{O}_2$  under visible irradiation ( $< 600$  nm) [42]. Nitrides with  $d^{10}$  electronic configuration, such as  $\text{Ge}_3\text{N}_4$  and GaN, also performed the cleavage of water under UV-light irradiation. In these  $d^{10}$  electronic configuration nitrides, the conduction band formed by broad hybridized sp orbitals makes it easy to transfer the photogenerated electrons to cocatalysts, e.g.,  $\text{RuO}_2$  [27, 43].

Oxynitrides and oxysulfides were recently designed to split water under visible-light irradiation. For oxynitrides and oxysulfides with  $d^0$  electronic configuration metal ions, such as TaON and  $\text{Sm}_2\text{Ti}_2\text{S}_2\text{O}_5$ , the valence band mainly consists of hybridized N 2p (or S 3p) and O 2p orbitals, while the conduction band is still composed of the empty d orbitals of the corresponding metal. In such compounds, photogenerated holes can move smoothly in the broad valence band, which benefits to the oxidation of water. Oxynitride photocatalysts consisting of  $d^0$  configuration metal cations such as  $\text{Ti}^{4+}$ ,  $\text{Nb}^{5+}$ , and  $\text{Ta}^{5+}$  are active for  $\text{H}_2$  or  $\text{O}_2$  evolution in the presence of sacrificial reagents. TaON prepared by partial nitridation of  $\text{Ta}_2\text{O}_5$  showed high activity under visible-light irradiation ( $420 \text{ nm} \leq \lambda \leq 500 \text{ nm}$ ). The band gap of TaON was estimated to be 2.5 eV. Photocatalytic  $\text{H}_2$  production by TaON was performed in an aqueous methanol solution and with a Ru cocatalyst [28, 30]. As mentioned above, compared to photocatalysts containing  $d^0$  metal ions, the photocatalysts composed of  $d^{10}$  metal ions (such as Ge and Ga) have the conduction band bottom made up of hybridized sp orbitals of  $d^{10}$  metal ions. These hybridized sp orbitals increase the mobility of photogenerated electrons in the conduction band and high photocatalytic activity for reduction of water. The solid solutions

$(\text{Ga}_{1-x}\text{Zn}_x)(\text{N}_{1-x}\text{O}_x)$  [34] and  $(\text{Zn}_{1-x}\text{Ge}_x)(\text{N}_2\text{O}_x)$  [35] are two examples of these  $d^{10}$  metal oxynitrides.

P-type III–V semiconductors have several attractive features, such as a high charge carrier mobility, an ideal band gap, and high photoelectrochemical stability, which make them suitable photocatalytic materials for reducing water to  $\text{H}_2$ . P-InP photocathodes are capable of producing  $\text{H}_2$  from HCl or  $\text{HClO}_4$  electrolytes with high efficiency [44]. Photocathodes of p-GaInP<sub>2</sub> (a solid solution of GaP and InP) have also evolved  $\text{H}_2$  efficiently by using a GaAs p-n junction bias [45].

## Development and Modification of $\text{H}_2$ Production Photocatalysts

Whether photocatalytic  $\text{H}_2$  production can have practical application depends largely on the development of photocatalytic materials. That is why material research is the focus of this topic. Both the development of existing photocatalysts and the exploitation of new photocatalysts are necessary. The progress of related fields in materials science, chemistry, and physics also add new vigor to the field of photocatalytic  $\text{H}_2$  production.

### Nanosize Effect

With the development of advanced fabrication and characterization, nanosized photocatalysts have become the main object of material study. When a photocatalyst becomes smaller, it has a larger surface area, which provides more active sites for reactant adsorption and decomposition, and light harvest. In photocatalysts, photogenerated electrons and holes transfer to the surface to have effect. Small particles provide a short distance for the charge carrier transfer, largely avoiding the bulk recombination. When a particle is smaller than some critical size (normally in the nanosize range), the energy levels within the filled (valence band) and empty (conduction band) states become discrete, and simultaneously the band gap increases, compared to its bulk counterpart. This leads to a blue shift in the absorption spectra for nanosized particles. Different materials

have different critical sizes. With the broadening of the band gap, electrons at the bottom edge of the conduction band and holes at the top edge of the valence band acquire more negative and positive potentials, respectively, which means that they have stronger redox powers in such nanoparticles.

### Porous Structures

Porous materials have high surface area and good adsorption ability, and can concentrate reactants around active sites. Selective photocatalysis can be achieved by adjusting the pore size. Recently, advanced fabrication techniques have been developed to prepare porous photocatalysts with high surface area and suitable pore size. It has been reported that hydrothermally synthesized TiO<sub>2</sub> nanoparticles without calcination had a large specific surface area (438 m<sup>2</sup>/g) and small crystallites (2.3 nm) dispersed among amorphous mesoporous domains, and exhibited much better photocatalytic activity for H<sub>2</sub> production compared with samples calcined at various temperatures, and also the commercial photocatalyst P25 [46].

A novel synthesis was carried out by using KCl electrolyte to control the electrostatic repulsive force between TiO<sub>2</sub> nanoparticles toward the formation of a mesoporous structure, which showed the highest photocatalytic activity for H<sub>2</sub> production, compared to nonporous colloidal TiO<sub>2</sub>, and commercial Degussa P25 and Hombikat UV-100 (HBK) samples [47]. Cocatalysts can also be easily deposited and dispersed onto these porous photocatalysts. The photocatalytic reduction of metal cations (M = Ni<sup>2+</sup>, Co<sup>2+</sup>, Cu<sup>2+</sup>, Cd<sup>2+</sup>, Zn<sup>2+</sup>, Fe<sup>2+</sup>, Ag<sup>+</sup>, Pb<sup>2+</sup>) on the surface of mesoporous TiO<sub>2</sub> (specific surface area 130–140 m<sup>2</sup>/g, pore diameter 5–9 nm, and anatase content 70–90%) resulted in the formation of nanostructured metal–semiconductor composites (TiO<sub>2</sub>/M). These metal–TiO<sub>2</sub> nanostructures showed a remarkable photocatalytic activity for hydrogen production from water–alcohol solutions, and the efficiency was 50–60% greater than that of the metal-containing nanocomposites based on Degussa P25. The anatase content and pore size proved to be the main parameters determining the photoreaction rate [48].

Porous materials are often used as supports for catalysts and photocatalysts. Highly dispersed and coordinated metal species on microporous zeolite and mesoporous silica materials have shown very high photocatalytic activity, and were referred to as “single-site photocatalysts.” Photocatalytic H<sub>2</sub> production by CdS has been improved by its porous supports, such as aluminum-substituted mesoporous silica molecular sieve (Al-HMS) [49], microporous and mesoporous silicas [50], porous polyethylene terephthalate fibers (PET) [51], and ETS-4 zeolite [52].

### Low-Dimensional Nanostructure

One-dimensional (1D) nanostructures (nanowires, nanorods, nanotubes, and nanofibers) have shown their outstanding properties in photocatalytic H<sub>2</sub> production. Compared to aspheric nanoparticles with the same volume or weight, 1D nanomaterials have higher surface areas. They can normally provide fast charge transportation, especially for those single-crystalline 1D nanostructures. Anders et al. found that photoelectrodes with nanorods oriented perpendicular to the conductive substrate can shorten the transport distance for electrons to the back contact (electron collector) and avoid recombination losses at grain boundaries between nanoparticles, compared to photoelectrodes with nanoparticle deposits [53]. Disorder, order, and different orientations of the 1D units also affect the photoelectrochemical properties. In the same research [53], the reported photon-to-current efficiency is lower for the Fe<sub>2</sub>O<sub>3</sub> electrode with the nanorods parallel to the substrate, compared to nanorods perpendicular to the substrate. The electrons have a more straightforward pathway to the back contact with nanorods perpendicular to the substrate, which leads to the elimination of recombination losses at nanorod boundaries and higher incident photon-to-electron conversion efficiency (IPCE) values.

As mentioned above in the section Photocatalysts for H<sub>2</sub> Production, the poor charge transportation (mainly due to low mobility of holes) of a-Fe<sub>2</sub>O<sub>3</sub> largely limits its application in photoelectrochemical and photocatalytic H<sub>2</sub> production. One way to solve this problem is to use 1D

a-Fe<sub>2</sub>O<sub>3</sub> with high aspect ratios. It was demonstrated that the transportation distance for photogenerated holes to the a-Fe<sub>2</sub>O<sub>3</sub>/solution interface was largely shortened in a-Fe<sub>2</sub>O<sub>3</sub> nanowires [54]. The limitation from hole transportation can be reasonably overcome, if the a-Fe<sub>2</sub>O<sub>3</sub> nanowire radius is shorter than the hole diffusion length. 1D nanostructured photocatalysts, e.g., TiO<sub>2</sub> nanotubes [55–58], nanocolumns [59], nanowires [60] and nanofibers [61], and CdS nanorods [62] and nanowires [63], have been playing a very important role in photocatalytic H<sub>2</sub> production.

Two-dimensional (2D) structured materials (nanosheets, nanoscrolls, and nanolayers) have attracted special interest in catalysis and photocatalysis. They can have a high surface area, expose a certain facet with high photocatalytic activity, and provide fast charge transfer. Pt/TiO<sub>2</sub> nanosheets with exposed (001) facets showed high photocatalytic activity for H<sub>2</sub> production [64]. High surface energy of (001) facets is effective for dissociative adsorption of reactant molecules, and water molecules can chemically dissociate on the (001) surface. So the authors believed that the exposed (001) facets contributed to the high photocatalytic activity in H<sub>2</sub> production [64], which had been also suggested by Amano [65] and Lu et al. [66].

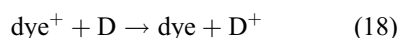
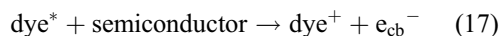
The following example shows the fast charge transfer of nanosheets and nanoscrolls. In a dye-sensitized semiconductor photocatalytic H<sub>2</sub> production system, the semiconductor transfers electrons from the photoexcited dye to the hydrogen evolution catalyst (typically Pt or Rh). Niobate nanoscrolls and nanosheets acted as good electron transfer mediators between a phosphonated [Ru(bpy)<sub>3</sub>]<sup>2+</sup> derivative and Pt, as shown in Fig. 6. An external quantum yield (incident photo-to-current yield) of 20–25% was observed for hydrogen evolution in this system [67].

Layered structures have been widely used in photocatalytic H<sub>2</sub> production. K<sub>4</sub>Nb<sub>6</sub>O<sub>17</sub> has a structure with two types of interlayers. H<sub>2</sub> is produced from one interlayer, in which cocatalysts are introduced by ion exchange or interlayer reaction, while O<sub>2</sub> is evolved in the other interlayer, as shown in Fig. 7. In this way, the sites for H<sub>2</sub> and

O<sub>2</sub> evolution are separated by the photocatalytic niobate sheet [68].

### Dye-Sensitized Semiconductor

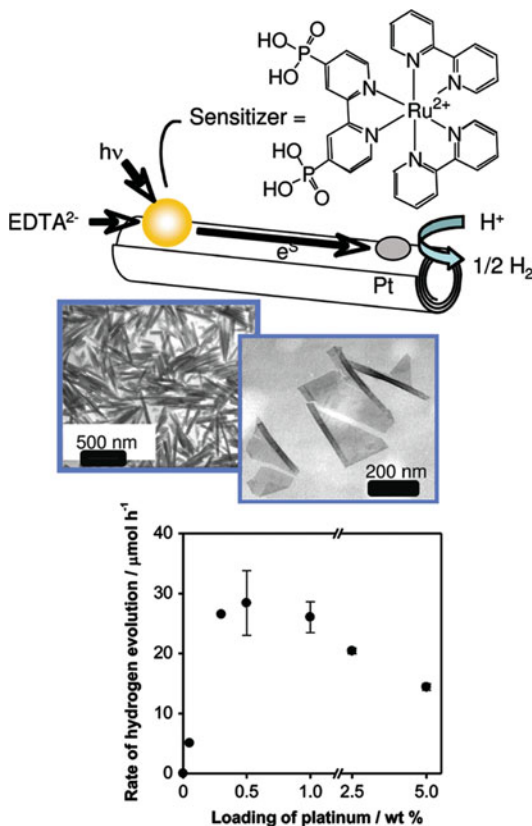
Some wide band semiconductors (such as TiO<sub>2</sub>, SrTiO<sub>3</sub>, and ZnO) show very high photocatalytic activity in H<sub>2</sub> production under UV illumination, but cannot absorb visible light, which limits their application in solar energy conversion. One way to extend their light response to visible range is to use a dye, which can absorb visible light. This system is called a dye-sensitized semiconductor system. In this system, the dye absorbs the visible light, becomes excited, and its excited state injects electrons into the semiconductor conduction band, on which H<sub>2</sub> is produced usually in the presence of a metal cocatalyst. In order to regenerate dyes, electron donors, such as I<sub>3</sub><sup>-</sup>/I<sup>-</sup> pair and EDTA, are added into the solution to supply the dyes with electrons and sustain the reaction cycle. The excitation, electron injection, and dye regeneration can be expressed as in the following Eqs. 16, 17, and 18. The steps involved are illustrated in Fig. 8. Porphyrins, [Ru(bipy)<sub>3</sub>]<sup>2+</sup>, [Fe(CN)<sub>6</sub>]<sup>4-</sup>, carboxylic (c-RuL<sub>3</sub>) compounds, phosphonic (p-RuL<sub>3</sub>) compounds, diamine and dithiolate complexes of Pt<sup>IV</sup>, eosin, Cu phthalocyanine, and dipyrindyl complexes of Ru, and complex of Zn with cytochrome C are commonly used as dye sensitizers. It is not easy to find a stable dye without any degradation by sensitized photocatalyst after long time irradiation. The dye should also have a strong absorption in visible light and a suitable energy level of its excited state (more negative than the conduction band of the sensitized semiconductor).



### Cocatalyst Deposited Semiconductor

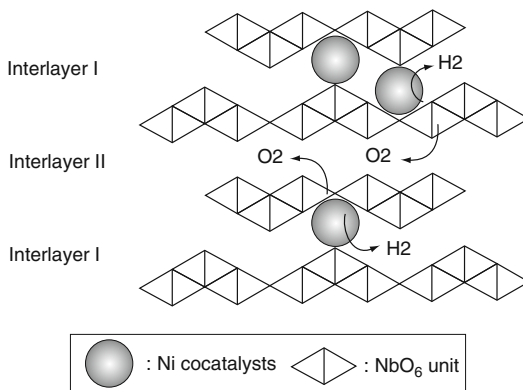
Cocatalysts, typically noble metal nanoparticles, are normally needed in photocatalytic systems for H<sub>2</sub> production. Apart from noble metals, cocatalyst chemistries also include RuO<sub>2</sub>, Ni and





**Photo-Catalytic Hydrogen Production, Fig. 6** (Top) Schematic representation of photoinduced electron transfer from a phosphonated [Ru(bpy)<sub>3</sub>]<sup>2+</sup> sensitizer to Pt catalyst particles, mediated by H<sub>4</sub>Nb<sub>6</sub>O<sub>17</sub> nanoscrolls. (Center) TEM images of individual nanosheets (right) and of nanoscrolls precipitated from a suspension of exfoliated H<sub>4</sub>Nb<sub>6</sub>O<sub>17</sub> (left). (Bottom) The dependence of hydrogen evolution rate on Pt loading. (Reprinted with permission from [67]. Copyright 2009 American Chemical Society)

its oxide, the mixed oxides of Rh and Cr, tungsten carbide, MoS<sub>2</sub>, and so on. The promoting mechanism by cocatalysts is illustrated in Fig. 1. When a semiconductor is excited by light irradiation with enough energy, photogenerated electrons are transited from the valence band to the conduction band of the semiconductor, raising the Fermi level of the semiconductor. The Fermi level difference between the semiconductor and the deposited noble metal drives the photogenerated electrons to the noble metal, and this increases the Fermi level of the noble metal, which drives the electrons from the noble metal to an electron acceptor in the solution (H<sup>+</sup> for H<sub>2</sub> production). From this



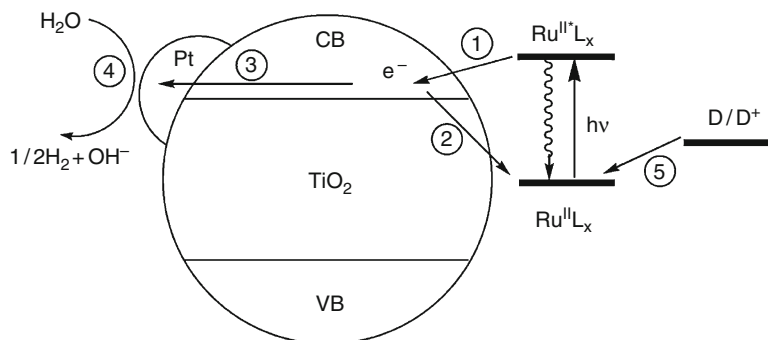
**Photo-Catalytic Hydrogen Production, Fig. 7** Water splitting over K<sub>4</sub>Nb<sub>6</sub>O<sub>17</sub> photocatalyst with layered structure. (From [68]. Reproduced by permission of The Royal Society of Chemistry)

process, the cocatalyst improves photocatalytic H<sub>2</sub> production by acting as (1) an electron sink to separate electrons and holes, reducing their recombination, and (2) an electron transfer to shuttle photogenerated electrons from the semiconductor to an acceptor, reducing the activation energy for the reduction of water. Both the species and size of the noble metal affect the energetics and the electron transfer between the semiconductor and noble metal. From the practical viewpoint, it is economical to exploit and develop cheap noble metal species for deposition modification.

### Doped Semiconductor

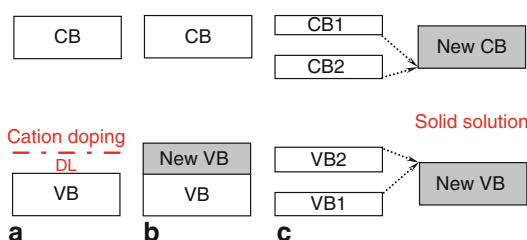
Doping has been widely used to extend the optical response of wide band gap semiconductors to visible range. Transition metal doped TiO<sub>2</sub> was systemically investigated [70]. The photo-reactivity of doped TiO<sub>2</sub> appears to be a complex function of the dopant concentration, the energy level of dopants within the TiO<sub>2</sub> lattice, their d electronic configuration, the distribution of dopants, the electron donor concentration, and the light intensity. It is important to tune the species, content, depth, and distribution of dopants inside the structure of host photocatalysts. Sometimes, cation-doping-induced visible-light absorption cannot become a substantial condition for photocatalytic activity in the visible range, since the absorption of doped semiconductors results from several absorption transitions of different origins.





**Photo-Catalytic Hydrogen Production, Fig. 8** Illustration of visible light-induced  $H_2$  production on a ruthenium complex-sensitized  $TiO_2$  particle in water. The number represents the major electron pathways: 1, electron injection from the excited sensitizer to CB; 2, back electron transfer to the oxidized sensitizer ( $Ru^{II}L_x$ );

3, electron migration and trapping in Pt deposits; 4, interfacial electron transfer to  $H_2O$  (or  $H^+$ ) on Pt; 5, sensitizer regeneration by an electron donor (D). (Reproduced with permission from [69]. Copyright 2007 Society of Photo Optical Instrumentation Engineers)



**Photo-Catalytic Hydrogen Production, Fig. 9** Existing band engineering approaches: (a) cation doping, which creates a discrete impurity energy level (DL) within the forbidden band gap; (b) valence band modification, which forms a new valence band with higher top; and (c) solid solution formation, producing a new couple of valence and conduction bands, whose band gap is between those of the component semiconductors. (Reprinted from [1], Copyright (2009). With permission from Elsevier)

The doping of wide band gap semiconductors with transition metal ions creates discrete new energy levels within the forbidden band. Visible-light absorption and photoactivity are induced by the interband, as shown in Fig. 9a. This induced visible-light photoactivity is normally low, due to the limited amount of dopants that can be incorporated, as indicated by a small shoulder in the visible-light region, instead of a total red shift of the absorption edge. Increasing the dopant concentration in the semiconductor matrix can, to some extent, improve visible-light absorption, but excessive doping can easily disturb the original structure, or form separate impurity phases.

Sometimes, doping can extend the lifetime of photogenerated charge carriers by transient and shallow charge carrier trapping. In most cases, dopants can also act as recombination centers for photogenerated electrons and holes and decrease photocatalytic activity.

Anion doping to improve photocatalytic  $H_2$  production under visible-light irradiation is a quite new field, compared to transition metal cation doping. Although there has been some work on anion doping, the state of anion dopants, and the origin of visible-light absorption and photoactivity are still in the debate. Among all the anion dopants (N, F, C, S, and P), N-doped  $TiO_2$  has been mostly investigated as a representative, since N has the similar atomic radius and chemical state with O, which makes it easy to substitute O in metal oxide lattice. N-doped  $TiO_2$  and its visible-light response were first reported by Asahi et al. in 2001 [71], and this work has been followed by various theoretical and experimental studies. Asahi et al. suggested that the N 2p level (above the O 2p level in  $TiO_2$ ) could mix with the valence band of  $TiO_2$  composed of O 2p orbits, which forms a new valence band and narrows the band gap (Fig. 9b). The conduction band of N-doped  $TiO_2$  remains unchanged and higher than the  $H_2$  reduction potential, while the valence band is shifted up, but still enough for water oxidation. However, this mechanism was challenged by arguing that a low level of doping ( $\leq 2$  at.%) can

only form midgap state above the valence band of  $\text{TiO}_2$ , like cation doping, and cannot shift up the valence band unless a high level of doping ( $\leq 20\%$ ) is carried out. In practice, high-level doping may form oxynitrides (or oxysulfides) or even nitrides (or sulfides). It was also argued that the visible-light response is due to the advent of color centers (e.g.,  $\text{F}$ ,  $\text{F}^+$ ,  $\text{F}^{++}$ , and  $\text{Ti}^{3+}$ ), and the formation of midgap energy level and oxygen vacancies induced by doping [72, 73].

### Solid Solution Semiconductor (Semiconductor Alloy)

Another approach to adjust the band gap and band positions is to form a solid solution semiconductor (or a semiconductor alloy) between wide and narrow band gap semiconductors (Fig. 9c). If two (or more) semiconductors have similar crystal lattice structures, solid solution is likely formed by them. The band gap of solid solution can be tuned, to some extent, by varying the composition of the solid solution. The reported solid solutions include GaN-ZnO, ZnS-CdS, ZnS-AgInS<sub>2</sub>, ZnS-AgInS<sub>2</sub>-CuInS<sub>2</sub>, CdS-CdSe, ZnO-ZnGeN<sub>2</sub>, GaP-InP, and others. Interestingly, despite the large band gaps of pure GaN and ZnO ( $>3$  eV), GaN-ZnO solid solutions have visible absorption with band gaps of 2.4–2.8 eV, and can decompose water under visible light. Density functional theory (DFT) calculations indicated that the conduction band bottom of GaN-ZnO was mainly composed of 4s and 4p orbitals of Ga, while the valence band top consisted of N 2p orbitals, followed by Zn 3d orbitals. The presence of Zn 3d and N 2p electrons in the upper valence band might provide p-d repulsion for extending the valence band, narrowing the band gap [34].

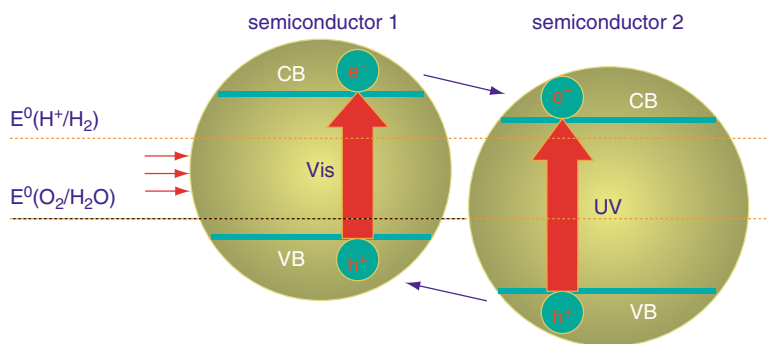
### Semiconductor Composites

Photogenerated charge carrier recombination can be minimized by coupling two semiconductors, if their band positions are crossed, as illustrated in Fig. 10. Photogenerated holes tend to accumulate in the semiconductor with the less positive valence band (semi-conductor 1 in Fig. 10), while photogenerated electrons are collected by

the semiconductor with the less negative conduction band (semiconductor 2 in Fig. 10). This efficient charge separation largely enhances the photocatalytic efficiency. It is very useful to choose a narrow band gap semiconductor as one coupling semiconductor in order to utilize visible light. Semi-conductors, such as CdS, PbS, Bi<sub>2</sub>S<sub>3</sub>, CdSe, InP, and n-Si, that can absorb visible light serve as inorganic sensitizers in semiconductor/semiconductor composites. Photocatalytic H<sub>2</sub> production by semiconductor composites can be successfully achieved if the following conditions are met: (1) the band levels of two semiconductors should be matched well, leading to wide charge carrier separation, (2) the less negative conduction band of the composite should still be more negative than the water reduction potential, and (3) there should be good contact between the two semiconductors, which ensures fast and efficient charge carrier injection between them.

### Multiphotonic System (Z-Scheme) for H<sub>2</sub> Production

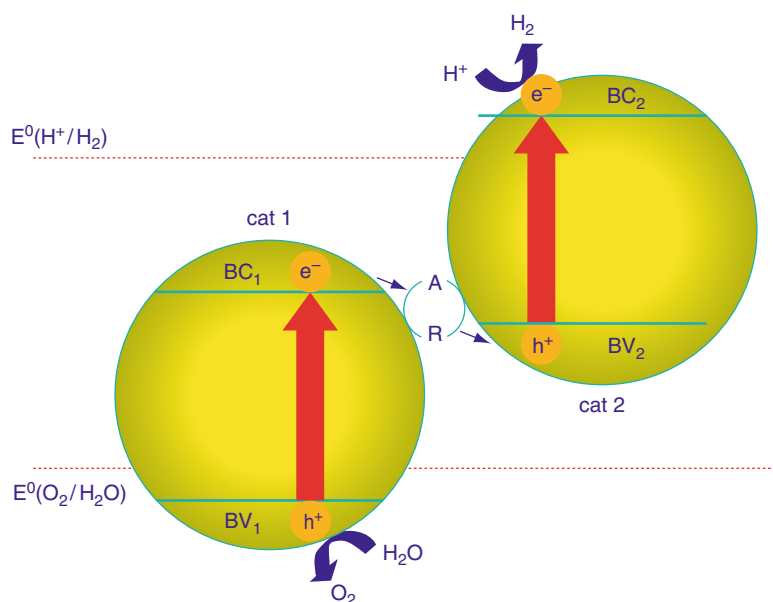
By mimicking the natural photosynthesis by green plants, a Z-scheme photocatalytic water splitting system was developed [36]. This system involved two-photon-excitation under visible light. The Z-scheme system consisted of a H<sub>2</sub>-evolution photocatalyst (Cat 2 in Fig. 11), an O<sub>2</sub>-evolution photocatalyst (Cat 1 in Fig. 11), and a reversible redox mediator (Ox/Red) that acted separately as the electron donor (R in Fig. 11) and acceptor (A in Fig. 11) for the respective half reactions. Protons are reduced to hydrogen molecules by the conduction band electrons of the photocatalyst with the more negative conduction band level, and R scavenges its valence band holes. Water is oxidized to oxygen by the photocatalyst with the more positive valence band level, and A reacts with its conduction band electrons. Photocatalysts, which only work in half reactions in water splitting, combine with each other to run the whole water splitting in this system. These photocatalysts are partly free of the strict energy limitations for the band structure of a single water splitting photocatalyst. They can have narrow



**Photo-Catalytic Hydrogen Production, Fig. 10** Band structure of a composite photocatalyst with an enhanced visible-light response, prepared by a mixture of wide and

narrow band gap photocatalysts. (Reproduced with permission from [74]. Copyright 2009 Wiley-VCH Verlag GmbH & Co. KGaA)

**Photo-Catalytic Hydrogen Production, Fig. 11** Diagram of a dual photocatalyst system employing a redox shuttle (A/R). (Reproduced with permission from [74]. Copyright 2009 Wiley-VCH Verlag GmbH & Co. KGaA)



band gaps with only one band (conduction or valence band) level enough for water reduction or oxidation.  $\text{SrTiO}_3$ ,  $\text{TaON}$ ,  $\text{CaTaO}_2\text{N}$ , and  $\text{BaTaO}_2\text{N}$  can work as  $\text{H}_2$  evolution photocatalysts, while  $\text{WO}_3$ ,  $\text{BiVO}_4$ , and  $\text{Bi}_2\text{MoO}_6$  can act as  $\text{O}_2$  evolution photocatalysts. The  $\text{IO}_3^-/\text{I}^-$ ,  $\text{Fe}^{3+}/\text{Fe}^{2+}$ , and  $\text{Ce}^{4+}/\text{Ce}^{3+}$  redox couples normally act as reversible electron shuttles. The key factors for designing a good Z-scheme system are to find a pair of photocatalysts for separate  $\text{H}_2$  and  $\text{O}_2$  production with high efficiency, and an efficient reversible electron mediator, the redox potential

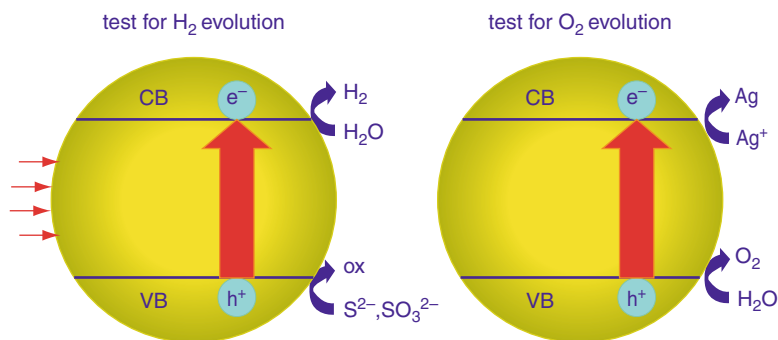
of which can meet the energy requirements of being electron donor and acceptor in the respective half reactions.

### Dissolved Additives for $\text{H}_2$ Production Improvement

Photocatalytic  $\text{H}_2$  or  $\text{O}_2$  production is often carried out in the presence of electron donors including low aliphatic alcohols (methanol, ethanol, isopropanol), sulfides ( $\text{H}_2\text{S}$ ,  $\text{Na}_2\text{S}$ ), sulfites ( $\text{Na}_2\text{SO}_3$ ), hydrazine, aliphatic amines (triethylamine, triethanolamine), carboxylic acids

### Photo-Catalytic Hydrogen Production,

**Fig. 12** Half reactions of water splitting for H<sub>2</sub> and O<sub>2</sub> evolution reactions in the presence of sacrificial reagents. (Reproduced with permission from [74]. Copyright 2009 Wiley-VCH Verlag GmbH & Co. KGaA)



(formic acid, EDTA), carbohydrates and other organic compounds, or electron acceptors including persulfate, Ag<sup>+</sup>, and Fe<sup>3+</sup>. The mechanism of photocatalytic reaction using these sacrificial reagents is illustrated in Fig. 12.

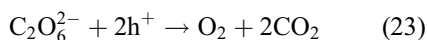
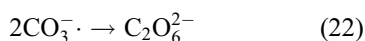
Taking photocatalytic H<sub>2</sub> production for example, after the excitation of the photocatalyst by light with enough energy, the photogenerated electrons in the conduction band reduce absorbed water molecules to H<sub>2</sub>, while a hole in the valence band is filled with an electron from a sacrificial reagent (S<sup>2-</sup>, SO<sub>3</sub><sup>2-</sup> in Fig. 12). The thermodynamic requirement for the occurrence of such a process is the potential of the conduction band more negative than the water reduction potential, and the potential of the valence band more positive than the oxidation potential of the electron donor, rather than water. This requirement sometimes does not need strong oxidation ability of photocatalyst, depending on the reducing reagent used.

Although these half reactions are not overall water splitting reaction, they are very useful to test a given semiconductor's kinetic and thermodynamic performance for H<sub>2</sub> or O<sub>2</sub> evolution. Scavengers, e.g., S<sup>2-</sup>/SO<sub>3</sub><sup>2-</sup>, are commonly used when hydrogen production is performed by metal sulfides. When metal sulfides are used for photocatalytic hydrogen production, photo-corrosion occurs due to the S<sup>2-</sup> in metal sulfides being oxidized by photogenerated holes in the valence band. As a sacrificial reagent, S<sup>2-</sup> can easily react with two holes to form S. Then, the added SO<sub>3</sub><sup>2-</sup> can dissolve S into S<sub>2</sub>O<sub>3</sub><sup>2-</sup>, preventing any detrimental deposition of S on CdS. Therefore, photo-corrosion of CdS is avoided.

Interestingly, a process of simultaneous hydrogen production and H<sub>2</sub>S removal was performed by a composite photocatalyst made of bulk CdS decorated with TiO<sub>2</sub> nanoparticles, i.e., CdS (bulk)/TiO<sub>2</sub>, under visible light. Hydrogen originated from both H<sub>2</sub>S and H<sub>2</sub>O when H<sub>2</sub>S was dissolved in alkaline water [75].

Since electron donors are sacrificially consumed during photocatalytic H<sub>2</sub> production, continuous addition of electron donors is normally necessary for sustaining H<sub>2</sub> production. The effect from different hydrocarbon electron donors was qualitatively investigated. It was found that the decomposition of these hydrocarbons could also contribute to a higher H<sub>2</sub> yield, since H<sub>2</sub> is one of their decomposition products [76]. The integration of clean H<sub>2</sub> fuel production and pollutant decomposition is promising and significant in practical application, since some pollutants (oxalic acid, formic acid, and formaldehyde) can act as electron donors [77].

Addition of carbonate salts was found to enhance H<sub>2</sub> and O<sub>2</sub> production stoichiometrically [78]. Several carbonate species were formed through the following reactions (Eqs. 19, 20, 21, and 22). Photogenerated holes were consumed by reacting with HCO<sub>3</sub> to form carbonate radicals (HCO<sub>3</sub><sup>·</sup>, CO<sub>3</sub><sup>·-</sup>) (Eqs. 20 and 21), which is beneficial for photogenerated charge carrier separation. Peroxycarbonates (C<sub>2</sub>O<sub>6</sub><sup>2-</sup>) could be easily decomposed by holes into O<sub>2</sub> and CO<sub>2</sub> (Eq. 23). The evolution of CO<sub>2</sub> promoted the desorption of O<sub>2</sub> from the photocatalyst surface, and thus minimized the back reaction between H<sub>2</sub> and O<sub>2</sub>. Then desorbed CO<sub>2</sub> could be dissolved and converted into HCO<sub>3</sub><sup>-</sup> again.



Addition of iodide was also found to promote hydrogen production [79]. Iodide anion ( $\text{I}^-$ ) in a suspension can be adsorbed preferentially onto cocatalyst surface, forming an iodine layer. The iodine layer can suppress backward reaction between  $\text{H}_2$  and  $\text{O}_2$ , which enhanced the production of hydrogen and oxygen significantly. However, adding too much carbonate salts or iodide anions could make these species excessively enriched on the photocatalyst surface, decreasing light harvesting.

## Future Directions

Worldwide energy consumption and man-made global warming result from humans excessively using limited fossil fuel on the earth, so it is time for society to pursue sustainable, clean energy systems. It is likely that the topic of this entry (photocatalytic  $\text{H}_2$  production) will contribute greatly to a sustainable, clean energy system, but with uncertain timing for deployment. Although the efficiency of photocatalytic  $\text{H}_2$  production is lower than that of photoelectrochemical (PEC) water splitting, the former technology provides a simple and convenient manipulation platform and valuable information for the development of the latter. There are also other promising technologies for sustainable, clean energy systems, which should also be paid attention to, and can be studied together with photocatalytic and PEC water splitting. Photocatalytic fuel generation from  $\text{CO}_2$  is one of them. It converts  $\text{CO}_2$  and  $\text{H}_2\text{O}$  to chemical fuels (e.g., methanol) by using solar energy, which decreases global emission of  $\text{CO}_2$  and keeps global neutral carbon cycle. It allows, to

some extent, human beings to keep using fossil fuel. This technology has many similarities with photocatalytic  $\text{H}_2$  production, e.g., water oxidation is also evolved in its process. The research outcomes from photocatalytic  $\text{H}_2$  production may well be applicable to the rising technology of photocatalytic  $\text{CO}_2$  fixation.

Although photocatalytic water splitting ( $\text{H}_2$  production) has been studied for almost 40 years, a further understanding of this process has dropped behind the reported phenomena. Although this field has seen some achievements, the total solar-to-hydrogen conversion efficiency is still much lower (about 1%) than the expected (about 10%) for practical application. Fundamental research on scientific details is necessary. For instance, is the charge carrier recombination so fast that too few reductive and oxidative sites can be reached by water? Where are the surface-active sites? What is their nature? Does desorption of products mainly determine the low efficiency? Besides studying the mechanism, the criteria for evaluation of photocatalytic  $\text{H}_2$  production should be established, which makes the comparison of results from different labs much easier. This kind of criteria has already been set up in the solar cell field. Material development can strongly promote the breakthroughs in this technology. Some traditional semiconductors (metal oxides, metal sulfides) should be modified, rather than discarded, since they have their potential advantages in practical application. Of course, the study of their modification is always important.

Simultaneously, there is an increasing opportunity to exploit novel photocatalysts for  $\text{H}_2$  production with the accumulation of theoretical and experimental knowledge. The focus should still be on stable, low-cost photocatalysts that can be manufactured on a large scale. Since using sunlight for  $\text{H}_2$  production is a trend or target, the sensitization of photocatalysts and multiphotonic systems are expected topics in this field. Nanoscience and nanotechnology will continue to play an important role in many aspects, including the preparation and characterization of photocatalysts, the modification of optical and electronic structures of photocatalysts, and the design for light harvesting and management.

Nanoreactors and well-controlled model systems are expected to be very useful for better understanding of the basic physics and chemistry involved in photocatalytic H<sub>2</sub> production. Further down the road, there will be a significant engineering challenge to integrate individual components into a fully functional device, the scalability and sustainability of which should also be achieved.

## Bibliography

### Primary Literature

- Zhu J, Zäch M (2009) Nanostructured materials for photocatalytic hydrogen production. *Curr Opin Colloid Interface Sci* 14:260–269
- Kamat PV (2007) Meeting the clean energy demand: nanostructure architectures for solar energy conversion. *J Phys Chem C* 111:2834–2860
- Fujishima A, Honda K (1972) Electrochemical photolysis of water at a semiconductor electrode. *Nature* 238:37–38
- Domen K, Naito S, Onishi T, Tamaru T, Soma M (1982) Study of the photocatalytic decomposition of water vapor over a nickel (II) oxide-strontium titanate (SrTiO<sub>3</sub>) catalyst. *J Phys Chem* 86:3657–3661
- Domen K, Kudo A, Onishi T, Kosugi N, Kuroda H (1986) Photocatalytic decomposition of water into hydrogen and oxygen over nickel (II) oxide-strontium titanate (SrTiO<sub>3</sub>) powder. I. Structure of the catalysts. *J Phys Chem* 90:292–295
- Matsumura M, Saho Y, Tsubomura H (1983) Photocatalytic hydrogen production from solutions of sulfite using platinumized cadmium sulfide powder. *J Phys Chem* 87:3807–3808
- Kakuta N, Park KH, Finlayson MF, Ueno A, Bard AJ, Campion A, Fox MA, Webber SE, White JM (1985) Photoassisted hydrogen production using visible light and coprecipitated ZnS·CdS without a noble metal. *J Phys Chem* 89:732–734
- Reber JF, Rusek M (1986) Photochemical hydrogen production with platinumized suspensions of cadmium sulfide and cadmium zinc sulfide modified by silver sulfide. *J Phys Chem* 90:824–834
- Reber JF, Meier K (1984) Photochemical production of hydrogen with zinc sulfide suspensions. *J Phys Chem* 88:5903–5913
- Kudo A, Tanaka A, Domen K, Maruya K, Aika K, Onishi T (1988) Photocatalytic decomposition of water over NiO–K<sub>4</sub>Nb<sub>6</sub>O<sub>17</sub> catalyst. *J Catal* 111:67–76
- Kudo A, Sayama K, Tanaka A, Asakura K, Domen K, Maruya K, Onishi T (1989) Nickel-loaded K<sub>4</sub>Nb<sub>6</sub>O<sub>17</sub> photocatalyst in the decomposition of H<sub>2</sub>O into H<sub>2</sub> and O<sub>2</sub>: structure and reaction mechanism. *J Catal* 120:337–352
- Domen K, Kudo A, Tanaka A, Onishi T (1990) Overall photodecomposition of water on a layered niobate catalyst. *Catal Today* 8:77–84
- Yoshimura J, Kudo A, Tanaka A, Domen K, Maruya K, Onishi T (1988) H<sub>2</sub> evolution caused by electron transfer between different semiconductors under visible light irradiation. *Chem Phys Lett* 147:401–404
- Shibata M, Kudo A, Tanaka A, Domen K, Maruya K, Onishi T (1985) Photocatalytic activities of layered titanium compounds and their derivatives for H<sub>2</sub> evolution from aqueous methanol solution. *Chem Lett* 16:1017–1018
- Kato H, Kudo A (1998) New tantalate photocatalysts for water decomposition into H<sub>2</sub> and O<sub>2</sub>. *Chem Phys Lett* 295:487–492
- Mitsui C, Nishiguchi H, Fukamachi K, Ishihara T, Takita Y (1999) Photocatalytic decomposition of pure water over NiO supported on KTa(M)O<sub>3</sub> (M = Ti<sup>4+</sup>, Hf<sup>4+</sup>, Zr<sup>4+</sup>) perovskite oxide. *Chem Lett* 28:1327–1328
- Ishihara T, Nishiguchi H, Fukamachi K, Takita Y (1999) Effects of acceptor doping to KTaO<sub>3</sub> on photocatalytic decomposition of pure H<sub>2</sub>O. *J Phys Chem B* 103:1–3
- Kato H, Kudo A (1999) Photocatalytic decomposition of pure water into H<sub>2</sub> and O<sub>2</sub> over SrTa<sub>2</sub>O<sub>6</sub> prepared by a flux method. *Chem Lett* 28:1207–1208
- Machida M, Yabunaka J, Kijima T (1999) Efficient photocatalytic decomposition of water with the novel layered tantalate RbNdTa<sub>2</sub>O<sub>7</sub>. *Chem Commun* 1999:1939–1940
- Kudo A, Hiji S (1999) H<sub>2</sub> or O<sub>2</sub> evolution from aqueous solutions on layered oxide photocatalysts consisting of Bi<sup>3+</sup> with 6 s<sup>2</sup> configuration and d<sup>0</sup> transition metal ions. *Chem Lett* 28:1103–1104
- Kudo A, Kato H (1997) Photocatalytic activities of Na<sub>2</sub>W<sub>4</sub>O<sub>13</sub> with layered structure. *Chem Lett* 26:421–422
- Sato J, Saito S, Nishiyama H, Inoue Y (2001) New photocatalyst group for water decomposition of RuO<sub>2</sub>-loaded p-block metal (In, Sn, and Sb) oxides with d<sup>10</sup> configuration. *J Phys Chem B* 105:6061–6063
- Ikarashi K, Sato J, Kobayashi H, Saito S, Nishiyama H, Inoue Y (2002) Photocatalysis for water decomposition by RuO<sub>2</sub>-dispersed ZnGa<sub>2</sub>O<sub>4</sub> with d<sup>10</sup> configuration. *J Phys Chem B* 106:9048–9053
- Sato J, Saito S, Nishiyama H, Inoue Y (2003) Photocatalytic activity for water decomposition of indates with octahedrally coordinated d<sup>10</sup> configuration. I. Influences of preparation conditions on activity. *J Phys Chem B* 107:7965–7969
- Sato J, Kobayashi H, Inoue Y (2003) Photocatalytic activity for water decomposition of indates with octahedrally coordinated d<sup>10</sup> configuration. II. Roles of geometric and electronic structures. *J Phys Chem B* 107:7970–7975
- Sato J, Kobayashi H, Ikarashi K, Saito S, Nishiyama H, Inoue Y (2004) Photocatalytic activity



- for water decomposition of RuO<sub>2</sub>-dispersed Zn<sub>2</sub>GeO<sub>4</sub> with d<sup>10</sup> configuration. *J Phys Chem B* 108: 4369–4375
27. Sato J, Saito N, Yamada Y, Maeda K, Takata T, Kondo JN, Hara M, Kobayashi H, Domen K, Inoue Y (2005) RuO<sub>2</sub>-loaded b-Ge<sub>3</sub>N<sub>4</sub> as a non-oxide photocatalyst for overall water splitting. *J Am Chem Soc* 127:4150–4151
  28. Hara M, Takata T, Kondo JN, Domen K (2004) Photocatalytic reduction of water by TaON under visible light irradiation. *Catal Today* 90:313–317
  29. Yamasita D, Takata T, Hara M, Kondo JN, Domen K (2004) Recent progress of visible-light-driven heterogeneous photocatalysts for overall water splitting. *Solid State Ionics* 172:591–595
  30. Kasahara A, Nukumizu K, Takata T, Kondo JN, Hara M, Kobayashi H, Domen K (2003) LaTiO<sub>2</sub>N as a visible-light (≤600 nm)-driven photocatalyst (2). *J Phys Chem B* 107:791–797
  31. Liu M, You W, Lei Z, Zhou G, Yang J, Wu G, Ma G, Luan G, Takata T, Hara M, Domen K, Li C (2004) Water reduction and oxidation on Pt–Ru/Y<sub>2</sub>Ta<sub>2</sub>O<sub>5</sub>N<sub>2</sub> catalyst under visible light irradiation. *Chem Commun* 2004:2192–2193
  32. Ishikawa A, Takata T, Kondo JN, Hara M, Kobayashi H, Domen K (2002) Oxysulfide Sm<sub>2</sub>Ti<sub>2</sub>S<sub>2</sub>O<sub>5</sub> as a stable photocatalyst for water oxidation and reduction under visible light irradiation (λ ≤ 650 nm). *J Am Chem Soc* 124:13547–13553
  33. Ishikawa A, Takata T, Matsumura T, Kondo JN, Hara M, Kobayashi H, Domen K (2004) Oxysulfides Ln<sub>2</sub>Ti<sub>2</sub>S<sub>2</sub>O<sub>5</sub> as stable photocatalysts for water oxidation and reduction under visible-light irradiation. *J Phys Chem B* 108:2637–2642
  34. Maeda K, Teramura K, Lu DL, Takata T, Saito N, Inoue Y, Domen K (2006) Photocatalyst releasing hydrogen from water-enhancing catalytic performance holds promise for hydrogen production by water splitting in sunlight. *Nature* 440:295
  35. Lee Y, Terashima H, Shimodaira Y, Teramura K, Hara M, Kobayashi H, Domen K, Yashima M (2007) Zinc Germanium Oxynitride as a photocatalyst for overall water splitting under visible light. *J Phys Chem C* 111:1042–1048
  36. Sayama K, Mukasa K, Abe R, Abe Y, Arakawa H (2002) A new photocatalytic water splitting system under visible light irradiation mimicking a Z-scheme mechanism in photosynthesis. *J Photochem Photobiol A Chem* 148:71–77
  37. Tada H, Mitsui T, Kiyonaga T, Akita T, Tanaka K (2006) All-solid-state Z-scheme in CdS–Au–TiO<sub>2</sub> three-component nanojunction system. *Nat Mater* 5:782–786
  38. Parmon V, Emeline AV, Serpone N (2002) Glossary of terms in photocatalysis and radiocatalysis. *Int J Photoenergy* 4:91–131
  39. Kim HG, Hwang DW, Kim J, Kim YG, Lee JS (1999) Highly donor-doped (110) layered perovskite materials as novel photocatalysts for overall water splitting. *Chem Commun* 1999:1077–1078
  40. Kato H, Kudo A (2001) Water splitting into H<sub>2</sub> and O<sub>2</sub> on alkali tantalate photocatalysts ATaO<sub>3</sub> (A = Li, Na, and K). *J Phys Chem B* 105:4285–4292
  41. Shangquan WF (2007) Hydrogen evolution from water splitting on nanocomposite photocatalysts. *Sci Technol Adv Mater* 8:76–81
  42. Hitoki G, Ishikawa A, Takata T, Kondo JN, Hara M, Domen K (2002) Ta<sub>3</sub>N<sub>5</sub> as a novel visible light-driven photocatalyst (λ < 600 nm). *Chem Lett* 31:736–737
  43. Kida T, Minami Y, Guan G, Nagano M, Akiyama M, Yoshida A (2006) Photocatalytic activity of gallium nitride for producing hydrogen from water under light irradiation. *J Mater Sci* 41:3527–3534
  44. Heller A (1984) Hydrogen-evolving solar cells. *Science* 223:1141–1148
  45. Khaselev O, Turner JA (1998) A monolithic photovoltaic-photoelectrochemical device for hydrogen production via water splitting. *Science* 280:425–427
  46. Yi H, Peng T, Ke D, Ke D, Zan L, Yan C (2008) Photocatalytic H<sub>2</sub> production from methanol aqueous solution over titania nanoparticles with mesostructures. *Int J Hydrogen Energy* 33:672–678
  47. Lakshminarasimhan N, Bae E, Choi W (2007) Enhanced photocatalytic production of H<sub>2</sub> on mesoporous TiO<sub>2</sub> prepared by template-free method: role of interparticle charge transfer. *J Phys Chem C* 111:15244–15250
  48. Korzhak AV, Ermokhina NI, Stroyuk AL, Bukhtiyarov VK, Raevskaya AE, Litvin VI, Kuchmiy SY, Ilyin VG, Manorik PA (2008) Photocatalytic hydrogen evolution over mesoporous TiO<sub>2</sub>/metal nanocomposites. *J Photochem Photobiol A Chem* 198:126–134
  49. Zhang YJ, Zhang L (2008) Synthesis of composite material CdS/Al-HMS and hydrogen production by photocatalytic pollutant degradation under visible light irradiation. *J Inorg Mater* 23:66–70
  50. Ryu SY, Balcerski W, Lee TK, Hoffmann MR (2007) Photocatalytic production of hydrogen from water with visible light using hybrid catalysts of CdS attached to microporous and mesoporous silicas. *J Phys Chem C* 111:18195–18203
  51. Lunawat PS, Senapati S, Kumar R, Gupta NM (2007) Visible light-induced splitting of water using CdS nanocrystallites immobilized over water-repellant polymeric surface. *Int J Hydrog Energy* 32:2784–2790
  52. Guan GQ, Kida T, Kusakabe K, Kimura K, Fang XM, Ma TL, Abe E, Yoshida A (2004) Photocatalytic H<sub>2</sub> evolution under visible light irradiation on CdS/ETS-4 composite. *Chem Phys Lett* 385:319–322
  53. Beermann N, Vayssières L, Lindquist S-E, Hagfeldt A (2000) Photoelectrochemical studies of oriented nanorod thin films of hematite. *J Electrochem Soc* 147:2456–2461
  54. van de Krol R, Liang Y, Schoonman J (2008) Solar hydrogen production with nanostructured metal oxides. *J Mater Chem* 18:2311–2320
  55. Lin CH, Lee CH, Chao JH, Kuo CY, Cheng YC, Huang WN, Chang HW, Huang YM, Shih MK

- (2004) Photocatalytic generation of H<sub>2</sub> gas from neat ethanol over Pt/TiO<sub>2</sub> nanotube catalysts. *Catal Lett* 98:61–66
56. Nam W, Han GY (2007) Preparation and characterization of anodized Pt-TiO<sub>2</sub> nanotube arrays for water splitting. *J Chem Eng Jpn* 40:266–269
57. Khan MA, Akhtar MS, Woo SI, Yang OB (2008) Enhanced photoresponse under visible light in Pt ionized TiO<sub>2</sub> nanotube for the photocatalytic splitting of water. *Catal Commun* 10:1–5
58. Kuo HL, Kuo CY, Liu CH, Chao JH, Lin CH (2007) A highly active bi-crystalline photocatalyst consisting of TiO<sub>2</sub> (B) nanotube and anatase particle for producing H<sub>2</sub> gas from neat ethanol. *Catal Lett* 113:7–12
59. Thimsen E, Rastgar N, Biswas P (2008) Nanostructured TiO<sub>2</sub> films with controlled morphology synthesized in a single step process: performance of dye-sensitized solar cells and photo watersplitting. *J Phys Chem C* 112:4134–4140
60. Jitputti J, Suzuki Y, Yoshikawa S (2008) Synthesis of TiO<sub>2</sub> nanowires and their photocatalytic activity for hydrogen evolution. *Catal Commun* 9:1265–1271
61. Lin CH, Chao JH, Liu CH, Chang JC, Wang FC (2008) Effect of calcination temperature on the structure of a Pt/TiO<sub>2</sub> (B) nanofiber and its photocatalytic activity in generating H<sub>2</sub>. *Langmuir* 24:9907–9915
62. Janet CM, Viswanath RP (2006) Large scale synthesis of CdS nanorods and its utilization in photo-catalytic H<sub>2</sub> production. *Nanotechnology* 17:5271–5277
63. Jang JS, Joshi UA, Lee JS (2007) Solvothermal synthesis of CdS nanowires for photocatalytic hydrogen and electricity production. *J Phys Chem C* 111:13280–13287
64. Yu JG, Qi LF, Jaroniec M (2010) Hydrogen production by photocatalytic water splitting over Pt/TiO<sub>2</sub> nanosheets with exposed (001) facets. *J Phys Chem C* 114:13118–13125
65. Amano F, Prieto-Mahaney OO, Terada Y, Yasumoto T, Shibayama T, Ohtani B (2009) Decahedral single-crystalline particles of anatase titanium(IV) oxide with high photocatalytic activity. *Chem Mater* 21:2601–2603
66. Liu G, Yang HG, Wang XW, Cheng L, Lu H, Wang L, Lu GQ, Cheng HM (2009) Enhanced photoactivity of oxygen-deficient anatase TiO<sub>2</sub> sheets with dominant 001 facets. *J Phys Chem C* 113:21784–21788
67. Youngblood WJ, Lee SHA, Maeda K, Mallouk TE (2009) Visible light water splitting using dye-sensitized oxide semiconductors. *Acc Chem Res* 42:1966–1973
68. Kudo A, Miseki Y (2009) Heterogeneous photocatalyst materials for water splitting. *Chem Soc Rev* 38:253–278
69. Choi W (2007) Photocatalytic hydrogen production using surface modified titania nanoparticles. In: Guo J (ed) *Solar hydrogen and nanotechnology II*. Proceedings SPIE 6650:66500L
70. Choi W, Termin A, Hoffmann MR (1994) The role of metal-ion dopants in quantum-sized TiO<sub>2</sub>: correlation between photoreactivity and charge-carrier recombination dynamics. *J Phys Chem* 98:13669–13679
71. Asahi R, Morikawa T, Ohwaki T, Aoki K, Taga Y (2001) Visiblelight photocatalysis in nitrogen-doped titanium oxides. *Science* 293:269–271
72. Serpone N (2006) Is the band gap of pristine TiO<sub>2</sub> narrowed by anion-and cation-doping of titanium dioxide in second-generation photocatalysts? *J Phys Chem B* 110:24287–24293
73. Fujishima A, Zhang X, Tryk DA (2008) TiO<sub>2</sub> photocatalysis and related surface phenomena. *Surf Sci Rep* 63:515–582
74. Yerga RMN, Galván MCÁ, del Valle F, de la Mano JAV, Fierro JLG (2009) Water splitting on semiconductor catalysts under visible-light irradiation. *ChemSusChem* 2:471–485
75. Jang JS, Kim HG, Borse PH, Lee JS (2007) Simultaneous hydrogen production and decomposition of H<sub>2</sub>S dissolved in alkaline water over CdS-TiO<sub>2</sub> composite photocatalysts under visible light irradiation. *Int J Hydrogen Energy* 32:4786–4791
76. Nada AA, Barakat MH, Hamed HA, Mohamed NR, Veziroglu TN (2005) Studies on the photocatalytic hydrogen production using suspended modified TiO<sub>2</sub> photocatalysts. *Int J Hydrogen Energy* 30:687–691
77. Li YX, Lu GX, Li SB (2003) Photocatalytic production of hydrogen in single component and mixture systems of electron donors and monitoring adsorption of donors by in situ infrared spectroscopy. *Chemosphere* 52:843–850
78. Sayama K, Arakawa H (1992) Significant effect of carbonate addition on stoichiometric photodecomposition of liquid water into hydrogen and oxygen from platinum-titanium (IV) oxide suspension. *J Chem Soc Chem Commun* 2:150–152
79. Abe R, Sayama K, Arakawa H (2003) Significant effect of iodide addition on water splitting into H<sub>2</sub> and O<sub>2</sub> over Pt-loaded TiO<sub>2</sub> photocatalyst: suppression of backward reaction. *Chem Phys Lett* 371:360–364

## Books and Reviews

- Ashokkumar M (1998) An overview on semiconductor particle systems for photoproduction of hydrogen. *Int J Hydrogen Energy* 23:427–438
- Best JP, Dunstan DE (2009) Nanotechnology for photolytic hydrogen production: colloidal anodic oxidation. *Int J Hydrogen Energy* 34:7562–7578
- Fujishima A, Zhang X, Tryk DA (2007) Heterogeneous photocatalysis: from water photolysis to applications in environmental cleanup. *Int J Hydrogen Energy* 32:2664–2672
- Getoff N (1990) Photoelectrochemical and photocatalytic methods of hydrogen production: a short review. *Int J Hydrogen Energy* 15:407–417
- Kaneko M, Okura I (2002) *Photocatalysis: science and technology*. Kodansha/Springer, Tokyo/Berlin
- Kitano M, Hara M (2009) Heterogeneous photocatalytic cleavage of water. *J Mater Chem* 20:627–641

- Kudo A (2007) Photocatalysis and solar hydrogen production. *Pure Appl Chem* 79:1917–1927
- Kudo A (2007) Recent progress in the development of visible lightdriven powdered photocatalysts for water splitting. *Int J Hydrogen Energy* 32:2673–2678
- Kudo A, Kato H, Tsuji I (2007) Strategies for the development of visible-light-driven photocatalysts for water splitting. *Chem Lett* 33:1534–1539
- Maeda K, Domen K (2007) New non-oxide photocatalysts designed for overall water splitting under visible light. *J Phys Chem C* 111:7851–7861
- Moon SC, Matsumura Y, Kitano M, Matsuoka M, Anpo M (2003) Hydrogen production using semiconducting oxide photocatalysts. *Res Chem Intermed* 29:233–256
- Navarro RM, Sánchez-Sánchez MC, Alvarez-Galvan MC, del Valle F, Fierro JLG (2009) Hydrogen production from renewable sources: biomass and photocatalytic opportunities. *Energy Environ Sci* 2:35–54
- Osterloh FE (2008) Inorganic materials as catalysts for photochemical splitting of water. *Chem Mater* 20:35–54
- Paleocrassas S (1974) Photocatalytic hydrogen production: a solar energy conversion alternative? *Sol Energy* 16:45–51
- Rajeshwar K, McConnell R, Licht S (2008) *Solar hydrogen generation*. Springer, New York
- Stroyuk AL, Kryukov AI, Kuchmii SY, Pokhodenko VD (2009) Semiconductor photocatalytic systems for the production of hydrogen by the action of visible light. *Theor Exp Chem* 45:209–233
- Zhang H, Chen G, Bahnemann DW (2009) Photoelectrocatalytic materials for environmental applications. *J Mater Chem* 19:5089–5121
- Zäch M, Hä gglund C, Chakarov D, Kasemo B (2006) Nanoscience and nanotechnology for advanced energy systems. *Curr Opin Solid State Mater* 10:132–143



# Hydrogen Production from High-Temperature Fuel Cells

Jacob Brouwer and Pere Margalef  
National Fuel Cell Research Center, University of California, Irvine, CA, USA

## Article Outline

- Glossary
- Definition of the Subject
- Introduction
- Background
- Key Principles of Poly-Generation of H<sub>2</sub> with HTFC
- Cycle Configurations for Poly-Generating HTFC
- Comparative Efficiency Analyses
- Hydrogen Transport Impacts on Comparative Analyses
- Discussion of Scientific Basis for Observed Performance
- World's First Poly-Generating HTFC System
- Future Directions
- Bibliography

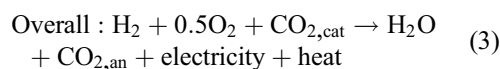
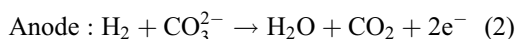
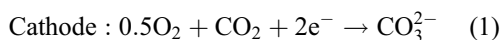
## Glossary

**Distributed energy resources (DER)** Small-scale power generation, energy conversion, storage, and/or control technologies (typically in the range of 3–10,000 kW) that are installed and operated close to the energy demand (e.g., a home or business). These resources can provide an alternative to or an enhancement of the existing electric power and thermal energy systems. Among the main advantages of the DER are the energy saving associated with the transport of energy from the centralized plants to the points of use and the potential to poly-generate power, heating, cooling, and/or fuels close to the point of use.

**Distributed generation (DG)** According to the California Energy Commission [1], distributed

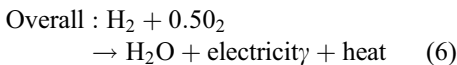
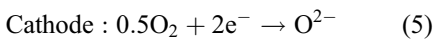
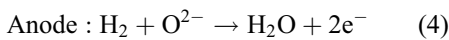
generation (DG) comprises small-scale power generation technologies (typically in the range of 3–10,000 kW) located close to where electricity is used (e.g., a home or business) to provide an alternative to or an enhancement of the existing electric power system. Among the main advantages of the distributed generation are the energy saving associated with the transport of energy from the centralized plants to the points of use and the potential for cogeneration of heat and power.

**High-temperature fuel cells (HTFC)** HTFC are electrochemical conversion devices that produce electricity directly from the chemical potential difference between a fuel and oxidant. There are two common types of high-temperature fuel cells: (1) molten carbonate fuel cells (MCFC) and (2) solid oxide fuel cells (SOFC). The *molten carbonate fuel cell* uses a carbonate electrolyte, which is generally a mixture of lithium and potassium carbonates (salts). At the high operating temperature (typically 550–650 °C) the alkali carbonates become a highly conductive molten salt, with CO<sub>3</sub><sup>2-</sup> ions providing ionic conduction. Anode materials are typically Ni–Cr/Ni–Al alloys and cathode materials are comprised of lithiated NiO [2]. The fuel cell operation is the result of a complex conjunction of physical, chemical, and electrochemical processes that together oxidize fuel and reduce oxidant in separate compartments to produce electricity, heat, and redox reaction products. The anode and cathode half reactions and overall electrochemical reaction are [3].



Note that carbon dioxide must be supplied to the cathode as well as oxygen. The CO<sub>2</sub> is converted

to carbonate ions which provide the means of ion transfer between the cathode and the anode. Therefore, there is a net transfer of CO<sub>2</sub> from cathode to anode. There are different ways of CO<sub>2</sub> recycling. The most common method feeds the anode exhaust gas to an anodic gas oxidizer (AGO), which converts any unused hydrogen or carbon monoxide into water and CO<sub>2</sub>. A portion of the exhaust gas from the anodic gas oxidizer is then mixed with fresh air and fed into the cathode inlet. This process also serves to preheat the reactant air, burn the unused fuel, and bring the waste heat into one stream for use in a bottoming cycle [4]. The *solid oxide fuel cell* uses an oxide ion-conducting ceramic material as the electrolyte. Since only two phases (solid and gas) are required and CO<sub>2</sub> recirculation is not required, these systems are conceptually simpler than other fuel cells [5]. As in the molten carbonate case, no precious metal catalysts are needed due to the high operating temperatures (700–1000 °C). SOFC have typically used materials sets based upon a yttria-stabilized zirconia (YSZ) electrolyte comprised of 8–10% Y<sub>2</sub>O<sub>3</sub> in ZrO<sub>2</sub> [2]. Above 700 °C, YSZ becomes a conductor of oxygen ions (O<sup>2-</sup>). The negatively charged ion (O<sup>2-</sup>) is transferred from the cathode to the anode [6]. The half-reactions produce water in the anode as follows:



The remaining SOFC fuel from the anode reactions is typically oxidized by the remaining oxygen from the cathode in a combustor to produce heat. This heat is used in the fuel cell plant to preheat the inlet streams and/or overcome the endothermicity of steam reforming reactions elsewhere in the system.

**Hydrogen separation** When hydrogen is produced by thermochemical processes such as steam methane reformation (SMR), the output

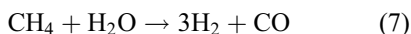
gas is a hydrogen-rich gas (i.e., reformat) that contains water vapor, carbon monoxide, carbon dioxide, and other trace gases. Therefore, hydrogen must be separated from the reformat gas and purified to reach the specific requirements for hydrogen use. Hydrogen separation in refineries has been traditionally done by established technologies such as pressure swing adsorption (PSA), selective permeation processes using polymer membranes, or cryogenic separation processes. Each process is based upon different separation principles. Economic aspects and other project considerations such as process flexibility, reliability, and scalability have to be taken into account to decide the hydrogen separation method [7]. Besides the traditional methods, alternative techniques for hydrogen separation are being developed. These include the Electrochemical Hydrogen Separation method (EHS) and Hydrogen Separation Membrane Reactor (HSMR) [8].

**Parasitic loads** In power generation devices, parasitic loads are those loads associated with the normal operation of the system that are required to sustain the normal operation of the system in a safe and reliable manner. Typical parasitic loads are associated with the preparation of the reactants, handling of products, exchanging of heat and flows, and thermal management. The power required for these parasitic loads must be produced by the same generator and subtracted from the generator power to produce the net system power output. Ideally, parasitic loads should be minimized in order to achieve higher system efficiencies.

**Poly-generation** Poly-generating systems include energy conversion systems that convert fuel chemical energy into multiple useful forms of energy or power. For instance, a specific poly-generation system instance that produces only two products is a combined heat and power (CHP) system that generates electrical and thermal power from fuel in a single, integrated system. Poly-generating systems are typically comprised of a number of individual components, including for example a heat engine, generator, heat recovery equipment,

and electrical interconnection hardware that are configured into an integrated whole system. The primary energy conversion device (i.e., the prime mover) is typically used to identify the type of poly-generating system. Prime movers include reciprocating engines, gas or steam turbines, and fuel cells that can produce electrical and thermal power from a variety of fuels, including natural gas, coal, and biofuels. Thermal energy from the system can be used in direct process applications or indirectly to produce steam, hot water, hot air for drying, or chilled water for process cooling [9]. High-temperature fuel cells, in particular, can be designed and operated to poly-generate electricity, heat, and useful chemicals (such as hydrogen) in a variety of configurations [10].

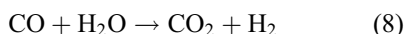
**Steam methane reformation (SMR)** Steam methane reforming is a mature industrial technology that is typically used for hydrogen production. The basic reforming reaction for methane is



SMR is an endothermic reaction so that heat must be provided to drive the reaction forward to produce hydrogen. The overall process for hydrogen production typically also includes the water–gas-shift reaction defined below.

**Synergy Synergy** describes the complementary interaction of processes to create an outcome that is in some way of more value than the sum of the individual values that would otherwise have been produced by the individual processes operating independently.

**Water–gas shift (WGS)** The reaction of carbon monoxide with water to produce hydrogen and carbon dioxide as follows:



The WGS reaction is reversible and exothermic.

**Well-to-tank (WTT) efficiency** Well-to-tank efficiency is defined as the total energy of a ready-to-be-used fuel (i.e., in the tank of the vehicle), divided by the total energy required for the extraction, preparation, transport, and

dispensing of the same fuel. This efficiency calculation is widely used in the automotive sector to compare the energy intensity of different fuels. On the other hand, well-to-wheel (WTW) efficiency accounts for the inefficiencies of the vehicle propulsion system. WTT are higher than WTW efficiencies.

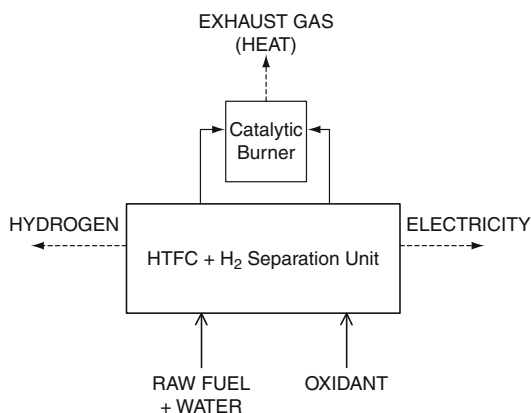
## Definition of the Subject

Hydrogen is a likely energy carrier of the future due to the absence of carbon, low emissions when converted in various end-use technologies, and ability to be cleanly and efficiently produced from various domestic primary energy sources. In 2003 the Federal government launched the Hydrogen Fuel Initiative with a total budget of \$1.2 billion over 5 years in order to accelerate research and development of fuel cell technologies [11]. Importantly, major automobile manufacturers are operating fuel cell vehicles that run on pure hydrogen gas, and several fuel cell buses are in operation in major cities around the world. Companies such as Shell, Air Products and Chemicals, Chevron, and Air Liquide are developing hydrogen production, distribution, and dispensing technologies for hydrogen vehicles along with strategies to deploy them. Moreover, the state of California intends to reduce the carbon content of transportation fuels through the Low Carbon Fuel Standard. Additional legislation in the areas of energy and climate, such as that contained in California laws entitled AB32, AB1493, SB76, and SB1368, highlight California's commitment to ensuring low greenhouse gas emissions for both electricity and transportation fuels [11]. Many other places around the world, including Germany and fellow European Union countries, Japan, China, and Korea, are advancing hydrogen fueling and vehicle technology. Therefore, developing a highly efficient, low-emission, and economically viable hydrogen production and delivery methodology is of great importance from environmental, social, economic, and political perspectives.

The production of hydrogen from high-temperature fuel cells is accomplished by a synergistic integration of fuel processing,



electrochemical conversion in a fuel cell, and hydrogen separation that leads to an ability to locally produce and deliver hydrogen with ultra-low criteria pollutant and greenhouse gas emissions. The resulting system comprised of a high-temperature fuel cell that produces electricity, heat, and hydrogen fuel uses a hydrogen separation unit (HSU) that separates and purifies the hydrogen from the anode off-gas, and is typically referred to as a poly-generating or tri-generating fuel cell. Figure 1 shows a basic schematic of a poly-generating HTFC.



**Hydrogen Production from High-Temperature Fuel Cells, Fig. 1** Basic schematic of a poly-generating HTFC

## Introduction

Since it is not naturally occurring, hydrogen must be produced from water via electrolysis, photolysis, or thermal splitting, or from hydrocarbon fuels (e.g., natural gas, coal, biogas, biomass) via reformation or gasification. Currently, hydrogen is typically produced at large centralized steam methane reformation (SMR) plants from natural gas. SMR is a convenient and cost-effective method that has been implemented to produce a substantial commercial supply for petroleum refining, metals processing, and other industrial uses. Not only hydrogen production (e.g., SMR plants and a host of other cost-effective and environmentally sensitive production technologies) but also energy-efficient and environmentally sensitive technologies for transport, distribution, and dispensing of hydrogen will be needed in the future [12].

Distributed generation of hydrogen, while typically less efficient than centralized generation, is foreseen by many as a viable strategy to produce hydrogen due to the savings associated with transport and distribution of the hydrogen, which can be energy and emissions intensive. Significant efforts to develop small-scale hydrogen production plants have led to commercialization of relatively affordable systems. Ogden [13] reviewed the development and commercialization status of various types of small-scale reformers.

Conventional steam methane reformers consisting of long catalyst-filled tubes that operate at high pressures (15–25 atm) and high temperatures (850 °C) have been successfully scaled

down to units that produce as little as 10–100 kg/h. However, at such small sizes, relative capital costs are too high to compete with large-scale hydrogen production. In addition, the footprint of these systems may be too large to be placed at conventional fueling stations. For this reason, more compact and inexpensive designs have been, and are being, developed by many manufacturers. The average hydrogen production efficiency reported for good systems ranges between 60% and 77% (on a LHV basis) [13]. The main technical challenges of distributed reformers include relatively larger system heat losses at small scale and inability to produce hydrogen on demand that may require large hydrogen storage capabilities, especially during the early stages of hydrogen vehicle deployment.

## Background

As indicated above, most hydrogen is produced today from fossil fuels in large SMR plants and is used at or near the production site [12]. As fuel cells and hydrogen vehicles become more widely used, an entire infrastructure for the distribution and dispensing of hydrogen will be needed with the additional goal of producing and delivering hydrogen to consumers in an environmentally sensitive manner [14].

An integrated energy future that meets transportation fuel and stationary power and thermal

energy demands could be made from the same primary energy sources. For example, the primary feedstock currently used for the production of hydrogen (i.e., natural gas) is also a significant primary energy source for electricity production. As both energy sectors (transportation and electricity generation) come to rely on the same primary energy sources, there are significant opportunities to integrate them, which can introduce profound changes in how our energy is converted and distributed. The integration of these two energy sectors at the level of a production plant via poly-generation of hydrogen, heat, and electricity could lead to lower prices for both transportation and stationary applications and ultimately enhance overall efficiency and flexible use of diverse resources [10].

Electricity and hydrogen poly-generation can be accomplished at large or at small scale. For the large-scale approach, hydrocarbon feedstocks such as coal, natural gas, or biomass can be converted via thermochemical processes to a syngas. Syngas is comprised of hydrogen, water, carbon monoxide, and carbon dioxide and can be used to generate electricity in a fuel cell, steam cycle, gas turbine, or combination of these technologies (i.e., combined cycle). Since the syngas produced has a high concentration of hydrogen, part of the gas stream can be diverted and the hydrogen can be separated from the rest of the gas to produce high-purity hydrogen for fuel cell vehicle use.

For the small-scale approach, poly-generating fuel cells represent a viable technology to produce hydrogen, electricity, and heat on demand in a distributed fashion. Excess heat released during the electrochemical fuel cell reactions can be used to produce hydrogen through steam reformation of hydrocarbon fuels. The highly synergistic nature of the poly-generating concept at high temperatures leads to higher production efficiencies compared to conventional hydrogen and electricity generation [15]. If successfully developed, poly-generating HTFC that produce electricity, heat, and hydrogen from a variety of hydrocarbon fuels will provide high efficiency and low emissions distributed hydrogen production and delivery. In addition, such a concept could aid fuel cell

market viability, stakeholder confidence, and energy security and sustainability together with emissions reduction [16].

### **Key Principles of Poly-Generation of H<sub>2</sub> with HTFC**

The key principles that apply to high-temperature fuel cell systems that poly-generate electricity, heat, and hydrogen are as follows:

1. Fuel flexibility of high-temperature fuel cells
2. High-temperature fuel cell–fuel processing relationship
3. Low entropy associated with exchanging heat at similar temperature
4. Fuel utilization concept requires excess fuel processing
5. Lower fuel utilizations lead to higher electrochemical efficiencies
6. Endothermicity of hydrocarbon reformation provides needed cell cooling
7. Production of excess hydrogen produces higher fuel cell efficiency
8. Chemical synergy associated with reactant/product interactions
9. All synergies lead to lower fuel cell system parasitic losses
10. Electrochemical and catalytic processes are inherently low emissions
11. Processes are efficient even at small size enabling distributed production
12. Hydrogen transport involves emissions and energy penalties

A brief description of each of these key principles is presented in this section.

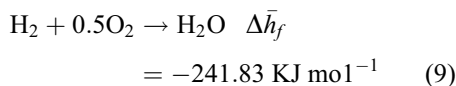
#### **Fuel Flexibility of High-Temperature Fuel Cells**

High-temperature fuel cells, such as the molten carbonate fuel cell (MCFC) and solid oxide fuel cell (SOFC), can be operated on a variety of hydrocarbon fuels including natural gas, digester gas, landfill gas, coal and biomass synthesis gases. MCFC and SOFC technologies comprise specific characteristics that make them especially amenable to operation on such hydrocarbon fuels. These characteristics include the use of an oxidizing ion

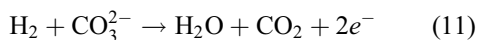
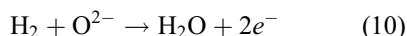
in the electrochemical reactions ( $\text{CO}_3^{2-}$  for MCFC and  $\text{O}^{2-}$  for SOFC) and high-temperature operation (550–650 °C for MCFC and 700–1000 °C for SOFC) which promotes sufficiently rapid chemical and electrochemical reactions.

### High-Temperature Fuel Cell: Fuel Processing Relationship

Solid oxide fuel cells (SOFC) and molten carbonate fuel cells (MCFC) generate electricity and heat through exothermic electrochemical reactions. Oxidation of hydrogen takes place in the anode compartment, which overall thermodynamics are described by the global reaction:

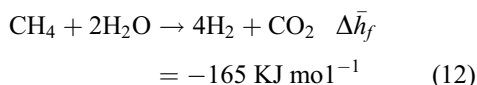


The electrochemical oxidation reactions that convert hydrogen to water in the SOFC and MCFC anode compartments are, respectively:



These reactions are complemented by corresponding oxidant reduction reactions in the cathode compartment, ion transport, and electron flow to perpetuate the electrochemical reactions. Since electricity is produced by these electrochemical reactions at less than 100% efficiency, the remaining portion of the enthalpy of reaction produces heat as reactants are converted to products.

HTFC system designs typically incorporate fuel processing with electrochemical conversion. The global fuel processing reaction includes steam methane reforming and water–gas-shift reactions and is described by:



The heat generated by the electrochemical reactions of Eq. 9 tends to be greater than the

heat required by the endothermic fuel processing reactions of Eq. 12 for the amount of electricity produced [6]. Surplus heat is typically used to preheat the fuel and oxidant streams before they enter the fuel cell and to produce the steam required for system operations. Therefore, more hydrocarbon fuel than that required for the electric power generation could be processed in a HTFC, creating a hydrogen-rich stream that could be subsequently purified and delivered to the point of use without the need of an additional reformer.

### Low Entropy Associated with Exchanging Heat at Similar Temperature

To proceed at a sufficiently fast rate and to completion (i.e., consume all the hydrocarbon fuel to produce hydrogen-rich syngas), the fuel processing reactions (e.g., steam reformation reaction of Eq. 12) must occur at a reasonably high temperature. Irreversible heat transfer processes between the exothermic fuel cell reactions (i.e., heat source) and the endothermic reforming reactions (i.e., heat sink) increase the entropy generation of the system. This irreversible heat transfer must be provided to a typical reformer reactor in a fuel cell system, using either fuel combustion or fuel cell exhaust heat at temperatures above those at which the reformation reactions proceed. However, the operating temperatures of HTFC (550–650 °C for MCFC and 700–1000 °C for SOFC) are similar to the temperatures at which hydrogen production rate and reaction completion are acceptable for steam methane reformation processes (i.e., ~700 °C). Therefore, heat can be transferred from the exothermic to the endothermic process with minimal (or zero) temperature difference leading to low entropy generation for heat exchange, resulting in overall high efficiency.

### Fuel Utilization Concept Requires Excess Fuel Processing

Fuel and oxidant utilization factors refer to the fractions of the total fuel and oxidant flowing through the anode and cathode compartments that are consumed to generate electricity. If fuel and/or oxidant species concentrations become too low, the chemical potential difference becomes unable to sustain a voltage difference. The Nernst

potential ( $V_{\text{Nernst}}$ ) describes the relationship between voltage and reactant and product concentrations that applies to a fuel cell

$$V_{\text{Nernst}} = E_0 + \frac{RT}{2F} \ln \frac{x_{\text{H}_2} x_{\text{O}_2}^2}{x_{\text{H}_2\text{O}}} \quad (13)$$

where  $E_0$  is the ideal reversible potential,  $F$  is Faraday's constant [96,487 kC/kmol],  $R$  is the gas constant,  $T$  is the operating temperature, and  $x_k$  is the concentration of the species  $k$  [6].

Since fuel cell electrodes are good electronic conductors (they act as equipotential surfaces), low reactant concentrations anywhere in the anode or cathode compartments leads to voltage that cannot be sustained. Therefore, fuel utilization ( $U_f$ ) and oxygen utilization ( $U_{\text{O}_2}$ ) must be always lower than 100%. In other words, the amount of fuel and oxidant fed into the fuel cell must always and continuously be greater than the amount consumed within the stack to produce electricity even when hydrogen is not produced.

### Lower Fuel Utilizations Lead to Higher Electrochemical Efficiencies

In operational fuel cell systems, cell voltage increases as fuel utilization decreases, which results in higher electrochemical efficiencies. The electrochemical efficiency is defined as the actual cell voltage ( $V_{\text{cell}}$ ) divided by the thermodynamically possible cell voltage ( $V_{\text{max}}$ ), or

$$\eta_{\text{cell}} = \frac{V_{\text{cell}}}{V_{\text{max}}} \quad (14)$$

where  $V_{\text{max}}$  is defined as the maximum theoretical voltage that would be achieved if all the energy from the hydrogen fuel were transformed into electrical energy [15], or

$$V_{\text{max}} = \frac{-\Delta \bar{g}_f}{n_i F} \quad (15)$$

where  $\Delta \bar{g}_f$  is the Gibbs free energy,  $n_i$  is the number of electrons transferred during the electrochemical oxidation of fuel species  $i$  ( $n_i = 2$

for  $\text{H}_2$  and  $\text{CO}$ ,  $n_i = 8$  for  $\text{CH}_4$ ), and  $F$  is Faraday's constant.

From the Nernst voltage equation Eq. 13, it can be observed that higher species concentrations lead to higher cell voltages. At lower fuel utilizations, reactant species concentrations are higher along the electrode channels. Thus, it can be stated that lower fuel utilization results in higher cell voltages that raise the electrochemical efficiency of the fuel cell as described by Eq. 14.

An alternative concept that provided insight into the effects of the fuel utilization on the electrochemical efficiency relates to the mixing of products with reactants to dilute the electrochemically active species concentrations. Water product mixes with the anode gas as it is formed by the electrochemical reactions in an MCFC or SOFC. The concentration of water product in the anode increases as the fuel utilization factor increases. Mixing processes are irreversible so they produce entropy. As a result, a completely reversible fuel cell operation would be only approached as  $U_f \rightarrow 0$ . In other words, irreversibilities increase as the utilization factor increases [17].

Consequently, one desires to operate a fuel cell at the lowest possible utilization factor to maximize the cell voltage and reduce mixing irreversibilities. However, unless one recycles or otherwise uses the anode off-gas then one alternatively desires high utilization to achieve high overall stack electrical efficiency. Typically, fuel utilization is selected in the 70–90% range to balance these considerations.

One of the key principles of poly-generating fuel cells is related to the capability of operating the fuel cell at lower fuel utilizations without compromising the overall system electrical efficiency. As already stated, hydrogen that is not electrochemically oxidized will be separated and considered as a valuable system output. Therefore, inasmuch as additional hydrogen is separated and used, there is the opportunity to take advantage of the higher electrochemical efficiency that is a natural by-product of the lower fuel utilizations required for hydrogen production.

### Endothermicity of Hydrocarbon Reforming Provides Needed Cell Cooling

The fact that fuel cells must be cooled to maintain steady state operating temperature allows for synergistic coupling of endothermic steam reforming with exothermic fuel cell electrochemical reactions to yield unprecedented efficiency. Adding more endothermic reforming reactions for the same amount of electrochemical reactions results in a reduced requirement for air cooling of the cell. The synergistic performance benefits related to these lower cooling requirements are caused by: (1) the additional endothermic reformation at lower fuel utilization that provides additional cooling to the fuel cell stack; and (2) less electrochemical heat generated per mol of input fuel due to the higher voltages achieved at lower fuel utilizations. Both phenomena reduce the auxiliary power associated with forcing air through the cathode compartment, which is the primary means of otherwise removing heat from the fuel cell.

### Chemical Synergy Associated with Reactant/Product Interactions

High-temperature fuel cells operate at high enough temperatures to convert methane into fuels that are more amenable to electrochemical oxidation such as hydrogen and carbon monoxide within the anode compartment. This concept is known as internal reformation (IR) and represents one of the key features of high-temperature fuel cells that can yield exceptionally high electrical efficiencies when compared with low-temperature fuel cells that process fuel in a separate reactor (i.e., external reformation). The main synergy associated with IR is related to the direct consumption of the hydrogen product of the reforming reaction by the electrochemical fuel cell reactions that produce water, a reformation reactant, which all occurs at the same time and physical location [16]. The immediate consumption of products and provision of reactants by the fuel cell reactions drives the reformation reaction forward and assures reaction completeness. Continual production of hydrogen and consumption of water by reformation also directly facilitates electrochemical reaction progress. This chemical synergy is introduced in addition to the heat

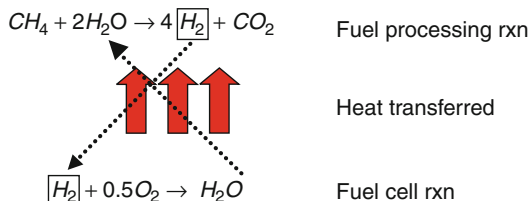
exchange synergy between exothermic fuel cell reactions and endothermic fuel processing reactions with minimum losses since both reactions occur at the same time and place. Figure 2 shows the main reactions, chemical exchange synergy, and heat transfer processes occurring during internal reformation in high-temperature fuel cells.

### All Synergies Together Work in the Same Direction to Increase Fuel Cell System Efficiency

At low fuel utilizations, the ratio between endothermic heat from the fuel processing reactions and exothermic heat from the electrochemical reactions increases, leading to a reduction of the auxiliary power required to circulate cooling air through the cathode. In addition, thermodynamic analyses demonstrate that cooling required per mol of fuel input drops at lower fuel utilizations due to the higher operational voltages at low fuel utilizations [15]. The design and operating changes that produce these synergies require changes in the same direction. Therefore, all of the described synergies of poly-generating high-temperature fuel cells can work together to result in higher fuel cell efficiencies compared to conventional fuel cell system designs that do not poly-generate. There remain design challenges, such as managing the fuel cell temperature gradient in poly-generating systems, but, the overall design and operating changes required for poly-generation work together to improve efficiency.

### Integration with Hydrogen Separation Produces Higher System Efficiency

Fuel cells are by nature required to produce somewhat more hydrogen than is electrochemically



**Hydrogen Production from High-Temperature Fuel Cells, Fig. 2** Internal reformation chemical and thermal synergy mechanisms



converted in the anode compartment. However, operating at lower fuel utilization leads to higher electrochemical efficiency and the chemical synergies of internal reforming, and the endothermicity of fuel processing reactions leads to lower parasitic losses due to reduced air blower power. These features by themselves would not be beneficial to overall system efficiency until and unless they are integrated into a system design that produces a significant amount of product hydrogen leading to remarkably higher overall efficiency. This is accomplished by using the above principles in combination with hydrogen separation technology that is integrated with the system design requirements in a manner that exchanges more heat for useful electrochemical and hydrogen production purposes.

### **Electrochemical and Catalytic Processes Are Inherently Low Emissions**

The inherent electrochemical and catalytic nature of high-temperature fuel cells and poly-generating fuel cells yields ultralow criteria pollution emissions.

–Thermal  $\text{NO}_x$  requires high-temperature combustion in air whereas in HTFC, all of the fuel is processed and converted either electrochemically or by catalytic processes at low temperature.

– $\text{SO}_x$  cannot be produced since sulfur is removed from the fuel before entering the system.

–Particulate matter (PM) is not produced due to high water content, catalyst presence, and low-temperature conditions extant in the anode compartment, followed by catalytic and/or low-temperature oxidation of the anode off-gas.

–CO is amenable to the electrochemical oxidation to release electrons in the anode compartment and the remainder is consumed by catalytic and/or low-temperature oxidation of the anode off-gas.

–Hydrocarbons are usually converted into methane in a pre-converter reactor before entering the fuel cell stack and the remainder is consumed by catalytic and/or low-temperature oxidation of the anode off-gas.

–Air toxics, such as higher hydrocarbons, aldehydes, and alcohols, are not present or are

removed from the incoming fuel and typically no air toxic compounds are produced by any of the processes involved in a fuel cell system. If any air toxics would be produced then they would likely be destroyed at the high-temperature catalytic conditions of the anode compartment or anode off-gas oxidizer.

### **Processes Are Efficient Even at Small Size Enabling Distributed Production**

Heat engine energy conversion is driven by a temperature difference while fuel cell energy conversion is driven by a chemical potential difference. The efficiency of any heat engine is limited by the efficiency that could be achieved by the reversible cycle operating upon a temperature difference, known as the Carnot efficiency [18]. On the other hand, fuel cells are limited by the Nernst equation and chemical potential difference that can be established in the cell, since they convert the chemical potential difference directly into electrical energy [6]. Heat engines for electricity production also have additional losses associated with the conversion of mechanical energy (e.g., piston movement, spinning turbine) to electricity through cranks, gears, and a generator.

Heat engines have reduced efficiency at reduced size because surface-to-volume ratios increase leading to higher percentage heat losses and inability to sustain the high cycle temperature for smaller engines. This leads to an inherent inability to establish a high temperature difference leading to a lower efficiency limit (i.e., lower Carnot efficiency). In addition, small-scale heat engines have proportionally larger friction, non-isentropic compressions and expansion, and other losses in comparison to larger heat engines. As a result, we currently tend to produce most of our power in very large central power plants based upon the heat engine – smaller plants are inherently less efficient.

On the other hand, fuel cell power production and efficiency depends upon the establishment of a chemical potential difference which can be established in equal difference regardless of the size of the cell.



### Hydrogen Transport Involves Emissions and Energy Penalties

Today, most hydrogen is produced from natural gas in large steam methane reformation (SMR) plants in a centralized fashion. To produce hydrogen at large scale in centralized reformation plants is more efficient than producing hydrogen at small-scale reformation plants.

The main steps of a well-to-tank hydrogen supply chain may be defined as production, treatment, distribution, storage, and dispensing. Each step can be accomplished with a variety of different technologies which may be more or less energy intensive and environmentally friendly [19]. For long distances, transportation of liquefied hydrogen by diesel truck is the most common strategy. However, liquefaction of hydrogen is the most energy intensive process and it makes sense only for very long delivery distances. Shorter distance hydrogen transport may be resolved by the transportation of compressed hydrogen which takes less energy than liquefaction, but delivers less hydrogen per unit truck volume. Hydrogen can also be transported via high-pressure pipeline, which is one of the least energy intensive methods. But, in comparison to other gaseous or liquid fuels, hydrogen pipeline delivery is more energy intensive [20]. In all of these cases, the relatively low volumetric energy density of hydrogen leads to relatively large energy and emissions penalties associated with hydrogen transport and delivery. These penalties can result in mediocre well-to-tank efficiencies compared to other fuels. These penalties can be averted by the production of hydrogen in a distributed fashion with a technology that scales down with high efficiency, such as poly-generating HTFC [15]. Nonetheless, energy and emissions penalties associated with hydrogen transport must be accounted for in all analyses.

### Cycle Configurations for Poly-Generating HTFC

Brouwer and Leal [21] investigated the production of hydrogen with high-temperature fuel cells by analyzing and comparing eight different cycle

configurations using solid oxide fuel cells (SOFC) and molten carbonate fuel cells (MCFC). Six of the eight configurations use fuel cell heat to drive hydrogen production in an external reformer placed in different positions in the cycle. The other two configurations use the internal reformation capabilities of high-temperature fuel cells to produce hydrogen.

Based upon the cycle configurations developed by Brouwer and Leal [21], Margalef et al. [10] investigated in detail how placing the external reformer in different positions affects the fuel cell performance and the hydrogen production efficiency. In addition, Margalef et al. investigated the performance of the poly-generating plant at different fuel utilizations together with the integration of commercially available hydrogen separation and purification technologies (i.e., pressure swing adsorption) with the fuel cell balance of plant (BOP).

### High-Temperature Fuel Cell Subsystem

High-temperature fuel cells (HTFC) generate electricity and heat through exothermic electrochemical reactions. Generated heat by the fuel cell reactions is typically utilized internally or externally by the endothermic fuel processing reactions, which in turn provide cooling to the system [22]. Surplus heat is used to preheat the fuel and oxidant streams before they enter the fuel cell and to produce the steam required for system operations. In addition, the remaining thermal energy contained in the exhaust gases can be used downstream of the fuel cell for poly-generation applications that require or value heat [22].

One possible configuration is to use the fuel cell heat to produce hydrogen via steam methane reforming in an external reformer (i.e., external reformation). Another possibility relies on the internal reforming capabilities of HTFCs and on the fact that the amount of high-quality heat produced by the exothermic reactions within the stack is typically greater than the heat required for fuel processing [6]. Therefore, more hydrocarbon fuel than that required for the electricity generation can be processed in an HTFC, creating a hydrogen-rich stream that could be subsequently purified and delivered at the point of production

without the need of an external reformer [16] (i.e., internal reformation). This mode of operation implies lower stack fuel utilization factors and has been associated with synergies such as lower cell polarization losses and lower parasitic losses correlated with lower cooling air [15].

**Separation/Purification Subsystem (Hydrogen Separation Unit (HSU))**

Hydrogen separation and purification in refineries has been traditionally accomplished by using established technologies such as pressure swing adsorption (PSA), selective permeation processes using polymer membranes, or cryogenic separation process. Each process is based on a different separation principle, so each method differs significantly from each other. Economic aspects and other project considerations such as process flexibility, reliability, and scalability have to be taken into account to decide the hydrogen separation method [23].

Other hydrogen separation technologies include electrochemical hydrogen separation (EHS), which is foreseen as a promising technology to separate hydrogen fuel from a fuel cell anode exhaust stream. However, EHS technology is not currently mature and has not been used in poly-generating applications to date. In any case, the hydrogen-rich stream is treated and prepared in the hydrogen separation unit (HSU) according to the selected separation/purification technology. For this work, PSA technology has been selected due to its commercial readiness and recent use in poly-generating systems [24].

The HSU configuration depends upon the specific requirements of the hydrogen separation technology and the anode off-gas conditions. PSA technology requires relatively low inlet temperatures and high inlet pressures. Additionally, hydrogen separation with PSA becomes more efficient at high hydrogen partial pressures [23]. Therefore, to extract the hydrogen from the anode off-gas of a HTFC using a PSA, the HSU is required to:

- Decrease the hydrogen-rich stream temperature
- Increase the hydrogen-rich stream pressure
- Increase the hydrogen partial pressure of the hydrogen-rich stream

Table 1 shows representative PSA feed gas requirements and the current configuration design points.

A simplified HSU block consisting of a series of heat exchangers and compressors designed to meet the PSA temperature and pressure requirements is shown in Fig. 3.

As shown in Fig. 3, an electric chiller has been placed upstream of the PSA reactor to meet the temperature requirements when ambient air temperature (used as a cold media in the upstream heat exchangers) is too high. The electric chiller represents a small fraction of the total parasitic loads. Interestingly, required PSA inlet temperature is low enough to condense out sufficient water vapor from the gas stream. As shown in Fig. 3, condensed water may be removed upstream of the PSA reactor resulting in higher hydrogen partial pressures and facilitating the PSA separation process.

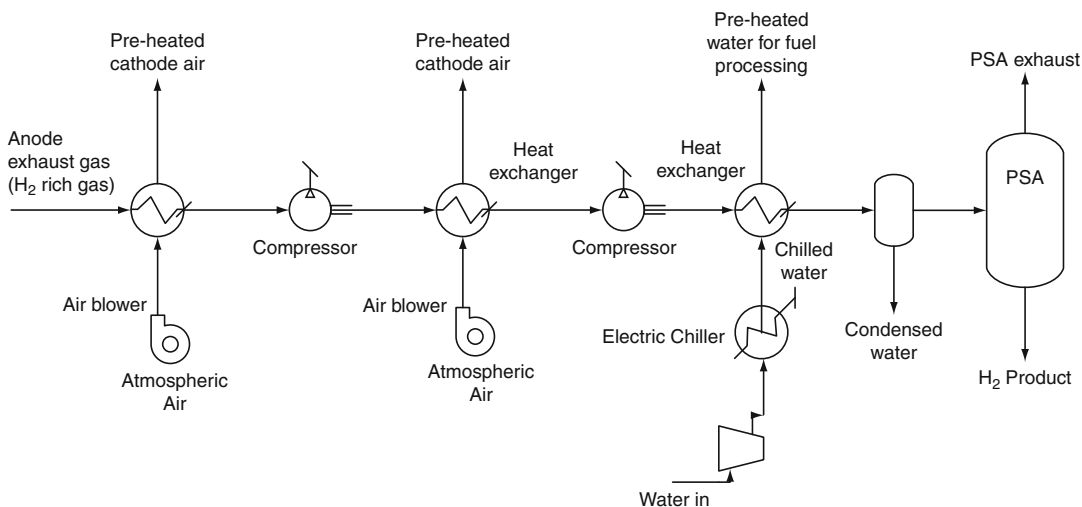
In the internal reformation cases, the air and water that is heated in the HSU represents an opportunity to thermally integrate the HSU with fuel cell balance of plant. This thermal integration strategy is crucial in order to ensure overall thermal balance within the plant, which may be jeopardized at certain operating conditions if hydrogen is separated from the anode off-gas [15].

**Integrated Poly-Generating HTFC Cycles According to Fuel Processing**

Steam methane reformation (SMR) and water–gas shift (WGS) are the main fuel processing reactions that convert raw fuel (i.e., natural gas) into fuels more amenable to electrochemical oxidation (i.e., hydrogen and carbon monoxide) occurring on the nickel-based anode of HTFC.

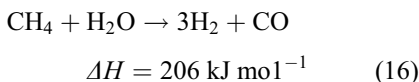
**Hydrogen Production from High-Temperature Fuel Cells, Table 1** State-of-the-art PSA feed gas requirements

Parameter	State-of-the-art value range	Notes
Absolute pressure (kPa)	303–2026	Based on the state of the art [25]
Temperature (°C)	4–50	Based on the state of the art [25]



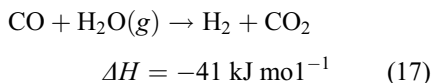
**Hydrogen Production from High-Temperature Fuel Cells, Fig. 3** Hydrogen separation unit configuration

Steam methane reforming is an endothermic reaction that consists of the reaction of methane and steam over a supported nickel catalyst to produce a mixture of hydrogen, carbon monoxide, carbon dioxide, and methane. The basic reforming reaction for methane is



Heat has to be provided to drive the reaction forward to the hydrogen production direction. As shown in Fig. 4, hydrogen concentration under equilibrium conditions is highest between 900 and 1100 K [16].

The water–gas–shift (WGS) reaction (starting from steam) is slightly exothermic and occurs at the same time as steam reforming [6]. During the shift reaction, additional hydrogen is produced. The basic water–gas–shift reaction for carbon monoxide is



In poly-generating HTFC, if external reformer is used to produce hydrogen, special attention has to be given to the temperature at which heat from

the fuel cell stack is transferred to the external reformer. Therefore, it is important to analyze different cycle configurations consisting on different positions of the external reformer within the system.

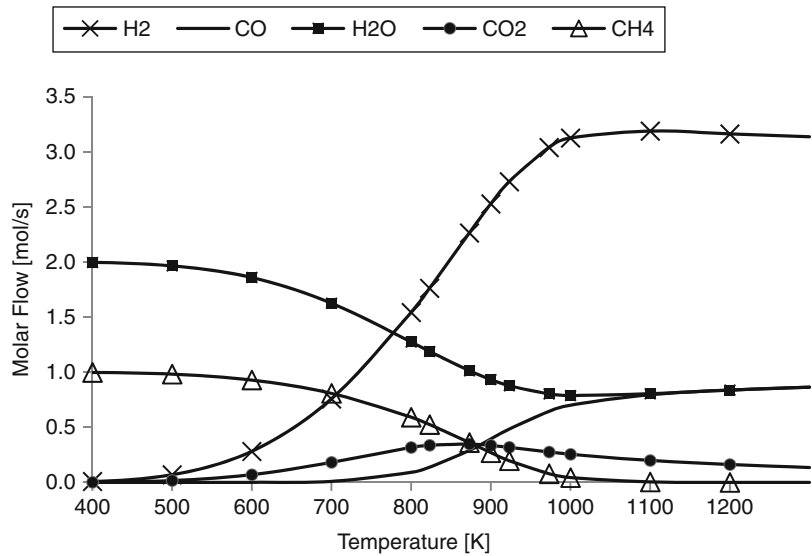
In the internal reformation cases where additional hydrogen production occurs at the same physical location than fuel cell reactions (i.e., direct internal reformation) or in a location that is thermally connected with the anode (i.e., indirect internal reformation), the temperature at which heat is transferred to the fuel processing reactions corresponds to the operating stack temperature which is equal to the temperature at which hydrogen production is maximized. This feature constitutes one of the key principles that lead to unprecedented high efficiencies achieved by poly-generating HTFC [9].

**External Reformation Configurations** High-temperature fuel cells (HTFC) can be integrated with an external reformer in multiple ways. Based on preliminary designs by Brouwer and Leal [16], Margalef et al. [10] analyzed in detail the external reforming configurations of poly-generating HTFC shown in Fig. 5.

In all cases, steam reformation is driven by the fuel cell exhaust heat in an external reformer, which takes as much heat as possible without compromising the fuel cell operating temperatures. Inlet

### Hydrogen Production from High-Temperature Fuel Cells,

**Fig. 4** Equilibrium composition as a function of temperature (steam-to-carbon ratio  $S/C = 2$ ) [16]



temperatures of the fuel, steam, and air streams are kept constant at 1173 K in order to sustain the electrochemical reactions within the stack. Therefore, depending upon the external reformer location, more or less heat is available to produce hydrogen with the external reformer. Note that in all the configurations, a hydrogen separation unit (HSU) block, based on PSA technology, is placed downstream of the reformer to separate and purify the hydrogen stream from the reformat gas.

**Internal Reformation Configurations** Internal reforming promotes hydrogen production within the fuel cell stack and provides cooling to the fuel cell stack due to its endothermic nature. Generally, fuel cell systems do not electrochemically consume all the fuel that is supplied (a fundamental limitation for all fuel cells) and they produce enough heat to reform much more fuel than the amount they consume. Remaining fuel exiting the anode presents a unique opportunity for low-cost hydrogen [16].

Margalef et al. [15] analyzed in detailed one internal reformation SOFC configuration at 80% and 60% fuel utilization ( $U_F$ ). Figure 6 shows the schematic of this configuration. As shown, the HSU block is placed at the anode gas exit upstream the catalytic oxidizer.

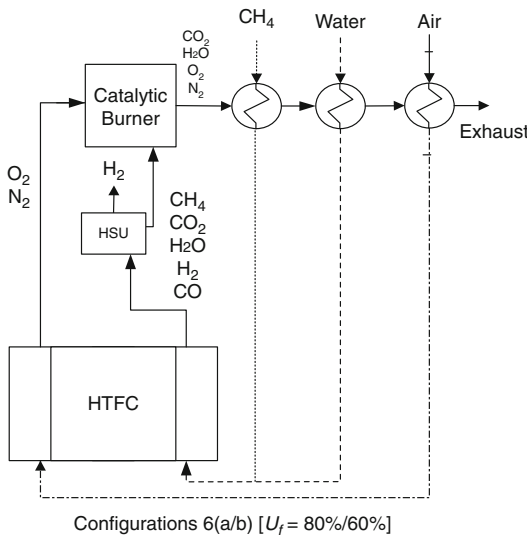
**Representative Performance Characteristics** Modeling capabilities developed at the National Fuel Cell Research Center (NFCRC) of

the University of California, Irvine have been used to evaluate the fuel cell performance and the hydrogen production capabilities of the presented poly-generating HTFC configurations. The complete model consists of an SOFC stack; heat exchangers to preheat the fuel, water, and air; an external SMR reactor placed in different locations for each of the different configurations; an adiabatic catalytic combustor that captures the thermal energy of the unused fuel downstream of the stack; and an HSU block based on PSA technology.

Each configuration has been analyzed following the same approach. For the external reformation cases (Conf. 1–5), stack input temperatures of the fuel, air, and steam have been fixed at 1173 K whereas the amount of reformed methane varies depending upon how much heat is available after preheating all the input streams. Pinch analyses for each heat exchanger have been performed in order to avoid temperature crossovers within the heat exchangers. Similarly, for the internal reformation cases (Conf. 6a/6b), the amount of hydrogen extracted in the HSU block depends upon how much thermal energy has to be extracted from the anode off-gas in order to preheat the input streams to the specified temperatures [10].

**Bulk Stack and External Reformer Temperatures** For the external reformation cases, the heat available to produce hydrogen without





**Hydrogen Production from High-Temperature Fuel Cells, Fig. 6** Poly-generating HTFC based upon internal reformation

compromising the thermal balance of the fuel cell determines how much methane will be taken by the external reformer. However, the hydrogen yield will be a function of the temperature at which the reformation takes place. As shown in Fig. 4, hydrogen yield peaks between 900 and 1000 K and it flattens out after this point. Therefore, the external reformer should operate in this temperature range in order to maximize the hydrogen production.

Figure 7 shows both fuel cell stack and external reforming temperatures for all the configurations.

As expected, stack temperatures are the same for all cases since inlet stream temperatures have been fixed to a certain value. Importantly, in configurations 6a and 6b, stack and reformation temperatures are equal due to the fact that hydrogen is produced by internal reforming.

Configuration 1 presents the lowest reformation temperature. This makes sense since the external reformer is placed downstream of all the heat exchangers where exhaust gas temperatures are lowest. Configuration 3b achieves the highest reformation temperature among the configurations. This configuration is the only external reforming configuration where the

fuel utilization factor has been lowered to 60%. Therefore, more hydrogen will be oxidized in the catalytic combustor raising the exhaust gas temperature considerably. The rest of the configurations present similar reformation temperature values, all of them in range where hydrogen yield is high.

**Hydrogen Production Rate** Figure 8 shows the amount of hydrogen produced with each configuration. As observed, there is a significant difference between the hydrogen produced with the external reforming configurations and the amount of hydrogen produced with the internal reformation configurations.

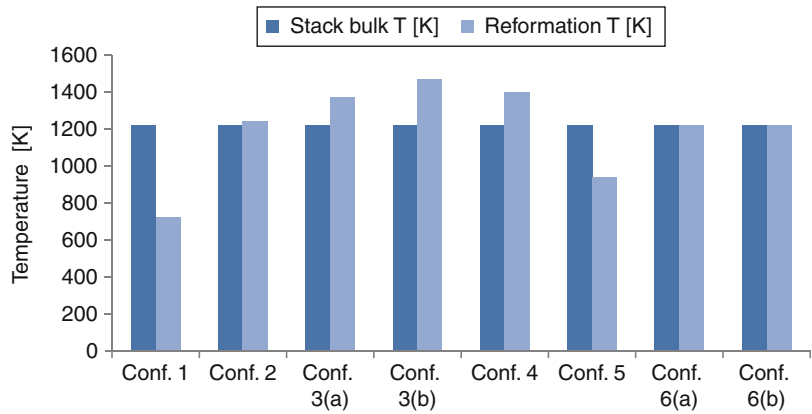
The amount of hydrogen produced with configuration 1 is low. As shown in Fig. 7, the temperature at which reformation occurs in configuration 1 is 724 K, at which temperature hydrogen yield under equilibrium conditions is very small.

Figure 7 shows that in configurations 2, 3a, 3b, and 4, external reforming occurs at temperatures at which hydrogen yield is high. However, the amount of hydrogen produced is not comparable to the internal reformation cases or configuration 5. As mentioned previously, hydrogen production is a function of the temperature at which the reformation occurs but is also a function of the amount of transferred heat from the exhaust gas stream to the external reformer. Although in configurations 2, 3, and 4, steam reforming occurs at relatively elevated temperatures, the heat that can be transferred from the fuel cell exhaust to the reformer without compromising the fuel cell thermal balance is not enough to reform large amounts of methane. As a result, the amount of hydrogen that can be produced with these configurations is not large.

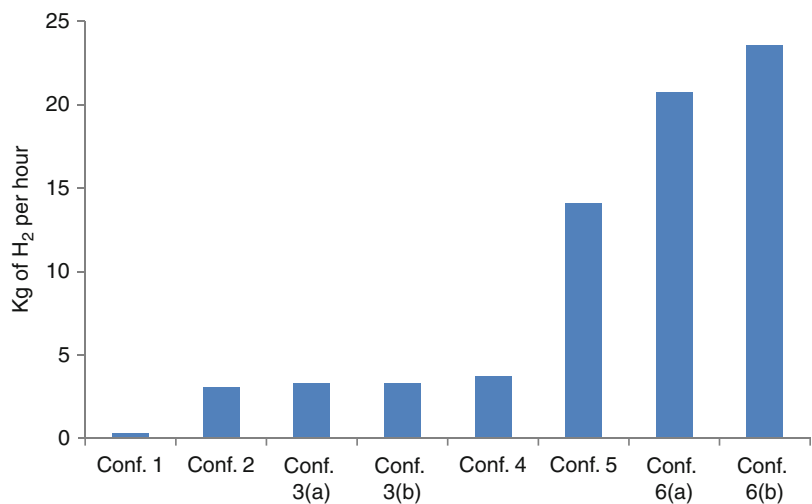
Configuration 5 presents higher hydrogen production than the other external reforming configurations. In this case, since the external reformer is placed after the catalytic combustor, the temperature at which the reformation occurs is high enough to achieve significant hydrogen yields. Importantly, since there is no preheater downstream of the reformer, more heat can be extracted from the fuel cell exhaust stream without affecting any fuel cell stream input temperatures.



**Hydrogen Production from High-Temperature Fuel Cells, Fig. 7** Stack and reformer temperatures



**Hydrogen Production from High-Temperature Fuel Cells, Fig. 8** Hydrogen production after PSA



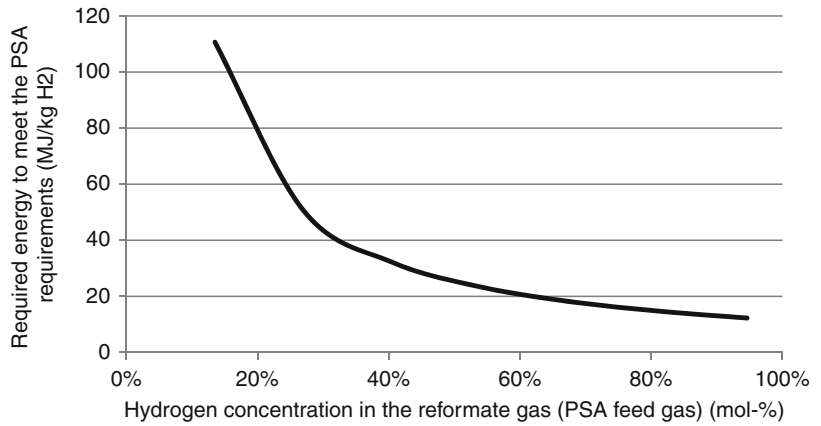
Finally, configurations 6a and 6b achieve the highest hydrogen production. This is due to the fact that the reformation takes place within the SOFC stack, which operates within the range of temperatures at which hydrogen yield is high. Additionally, the reformation reactions and the fuel cell reactions occur in the same physical space. Therefore, heat from the source (i.e., exothermic fuel cell reactions) to the sink (i.e., endothermic reformation reactions) is directly transferred without the need of a heat exchanger. Thus, more heat can be captured resulting in higher hydrogen yields. The total hydrogen production for each configuration is shown in Fig. 8.

**Parasitic Loads Associated with the Hydrogen Separation Unit** Energy required to separate the hydrogen from the reformat stream varies in each configuration. The HSU is required to

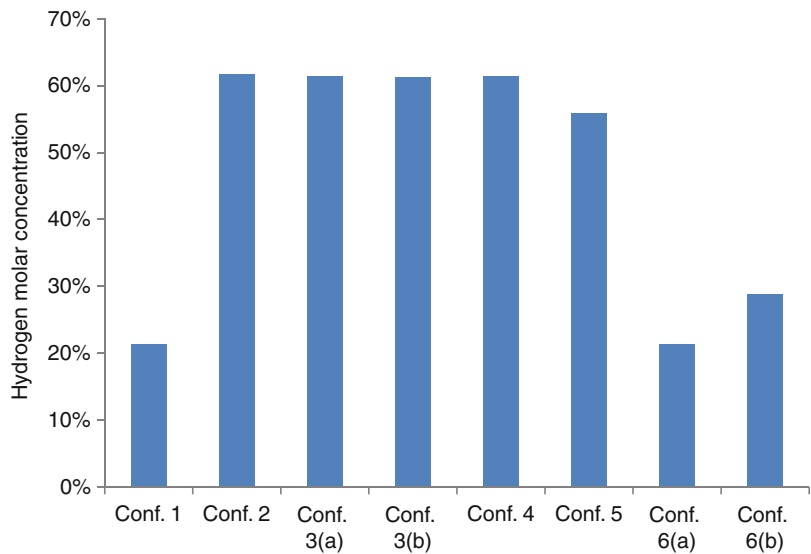
increase the pressure and drop the temperature of the reformat gas in order to meet the PSA requirements. This process requires energy and as a result, decreases the overall efficiency of the poly-generating plant. Margalef et al. [10] estimated the amount of energy required to separate 1 kg of hydrogen with the HSU design presented in Fig. 3. The HSU model consists of a series of heat exchangers and compressors that decrease the temperature and increase the pressure of the reformat gas to the design point levels, accordingly, for each configuration. Figure 9 shows the energy per kilogram of hydrogen required for the preparation of the reformat gas to meet the PSA requirements, as a function of the molar concentration of hydrogen.

As seen, the energy required to separate 1 kg of hydrogen from the reformat stream does not

**Hydrogen Production from High-Temperature Fuel Cells, Fig. 9** Specific energy required for the PSA process



**Hydrogen Production from High-Temperature Fuel Cells, Fig. 10** Hydrogen concentration in the PSA feed gas



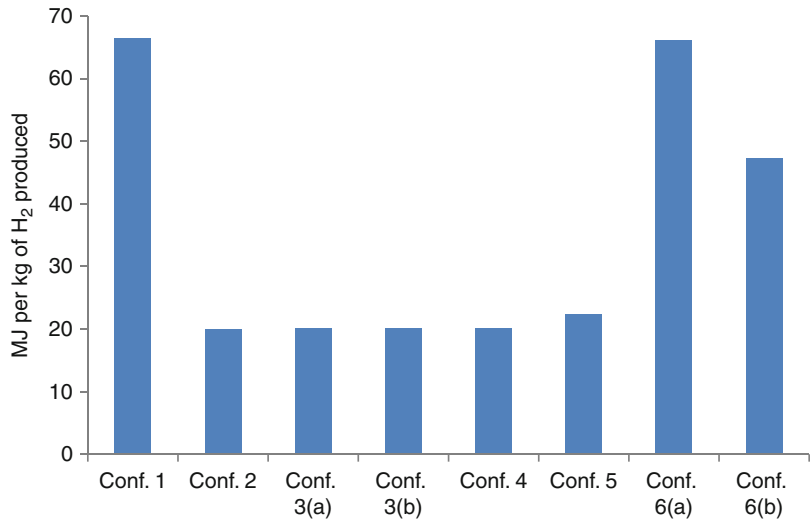
decrease linearly with the hydrogen molar concentration and depends upon the hydrogen concentration in the anode off-gas. This is due to the fact that for lower hydrogen concentrations, relatively more gas has to be cooled and compressed to produce the same amount of hydrogen. Therefore, the amount of energy required to separate 1 kg of hydrogen with PSA technology is lower when the hydrogen concentration of the feed gas is high [10]. Figure 10 shows the molar hydrogen concentrations of the PSA feed gas for each configuration.

For all of the external reformation configurations except for configuration 1, hydrogen concentrations remain around 60%. Although the

heat available to produce hydrogen in configuration 1 is comparable to the rest of the configurations, the temperature at which the reformation occurs is not high enough to achieve significant methane conversion. Similarly, configurations 6a and 6b present low hydrogen concentrations compared to the rest of the configurations. This makes sense since the produced hydrogen is mixed with the anode off-gas products which include all the carbon dioxide and steam products from the stack reactions, including internal reforming and electrochemical reactions. As a result, the hydrogen concentration of the reformat gas for the internal reformation cases is relative low when compared with the external reformation configurations.

**Hydrogen Production from High-Temperature Fuel Cells,**

**Fig. 11** Parasitic load required to separate 1 kg of H<sub>2</sub> at the HSU



**Hydrogen Production from High-Temperature Fuel Cells, Table 2** Efficiency equations for (1) state-of-the-art method, (2) ideal poly-generation method, and (3) supplemental input method [9]

	Electrical efficiency	Thermal efficiency	Hydrogen efficiency	Total mixed efficiency
1	$\frac{P_{net}}{E_{tot}} \frac{Q_{net}}{\eta_{boiler}} \frac{H_2}{\eta_{SMR}}$	$\frac{Q_{net}}{E_{tot}} \frac{P_{net}}{\eta_{CC}} \frac{H_2}{\eta_{SMR}}$	$\frac{H_2}{E_{tot}} \frac{P_{net}}{\eta_{CC}} \frac{Q_{net}}{\eta_{boiler}}$	$\frac{P_{net} + Q_{net} + H_2}{E_{tot}}$
2	$\frac{P_{net}}{E_{tot} + Q_{net} + H_2}$	$\frac{Q_{net}}{E_{tot} + P_{net} - H_2}$	$\frac{P_{PSA}}{E_{tot} - P_{net} - Q_{net}}$	$\frac{P_{net} + Q_{net} + H_2}{E_{tot}}$
3	External reforming $\frac{P_{net}}{E_{tot}} \frac{Q_c}{\eta_{boiler}} \left( F_{H_2} + \frac{P_{PSA}}{\eta_{CC}} \right)$	$\frac{Q_{net}}{\eta_{boiler}} = \eta_{boiler}$	$\frac{H_2}{F_{H_2} + \frac{P_{PSA}}{\eta_{CC}}}$	$\frac{P_{net} + Q_{net} + H_2}{E_{tot}}$
	Internal Reforming. $\frac{P_{net}}{E_{tot}} \frac{Q_c}{\eta_{boiler}} \left( (U_f - U_{f,H_2ES}) E_{tot} + \frac{P_{PSA}}{\eta_{CC}} \right)$		$\frac{(U_f - U_{f,H_2ES}) E_{tot} + \frac{P_{PSA}}{\eta_{CC}}}{H_2}$	

Figure 11 shows the energy required to separate 1 kg of hydrogen with each configuration. As shown, higher hydrogen concentration streams require less energy to separate the hydrogen from the reformat gas.

**Comparative Efficiency Analyses**

Because a poly-generating HTFC simultaneously produces electricity, hydrogen, and useful thermal energy, efficiencies can be measured and expressed in a number of different ways. Margalef et al. developed three different methods to appropriately calculate the overall and coproduct production efficiencies [9]. Table 2 shows the developed equations for each method. The

methods have been labeled as: (1) *State-of-the-art Method*; (2) *Ideal Poly-generation Method*, and (3) *Supplemental Input Method*.

These methods are based upon different and reasonable assumptions for the allocation of input energy to each of the coproducts. It should be clear that there is not a unique or superior method for calculating poly-generation efficiencies so that each of the methodologies proposed can be used in comparative analyses if based upon accurate assumptions. For the current specific analyses, the *Supplemental Input Method* is used to estimate the overall electrical and hydrogen production efficiencies for each configuration. Thermal efficiency has not been calculated since it depends upon the thermal requirements of each specific application and there may be cases when thermal

**Hydrogen Production from High-Temperature Fuel Cells, Table 3** Efficiency results obtained with the Supplemental Input Method (LHV)

Configuration	1	2	3a	3b	4	5	6a	6b
Electrical efficiency	53.4%	53.3%	53.3%	46.9%	53.3%	52.8%	50.0%	58.4%
Hydrogen efficiency	18.0%	73.5%	73.2%	68.2%	73.2%	62.1%	90.7%	83.5%
Overall efficiency	52.3%	54.7%	54.8%	48.5%	55.0%	55.7%	70.0%	69.5%

energy is not required. Results are presented in Table 3.

The efficiency results shown in Table 3 correspond to the Supplemental Input Method [9] and do not include the heat products shown in the equations presented in Table 2. With this method, electrical efficiency is the net power output  $P_{\text{net}}$  divided by the energy flow allocated exclusively for the electricity production, which corresponds to the total energy flow in  $E_{\text{tot}}$  minus the energy flow that has been specifically used to produce hydrogen product. The energy flow used to produce hydrogen product includes feedstock energy (i.e., additional fuel) as well as the necessary fuel to generate the electricity required for the hydrogen separation as if it was produced with a state-of-the-art combined cycle plant. The lowest electrical efficiency value corresponds to configuration 3b. In this case, hydrogen is produced externally and the fuel cell is operating at 60% utilization factor. As expected, the electrical efficiency is low since more fuel is used without obtaining any additional energy flow output (i.e., hydrogen fuel). On the other hand, the highest electrical efficiency value corresponds to configuration 6b, in which hydrogen is produced internally and the fuel cell is operated at 60% utilization factor. Due to the synergies associated with higher voltages at lower fuel utilizations, electrical efficiency is significantly higher than the rest of the configurations. Nevertheless, one must recall the discussion associated with the key principles above that this analysis confirms that these synergies are only captured if hydrogen is separated from the anode off-gas. Otherwise, more fuel is being used to obtain the same mix of energy outputs. The rest of configurations present similar electrical efficiencies.

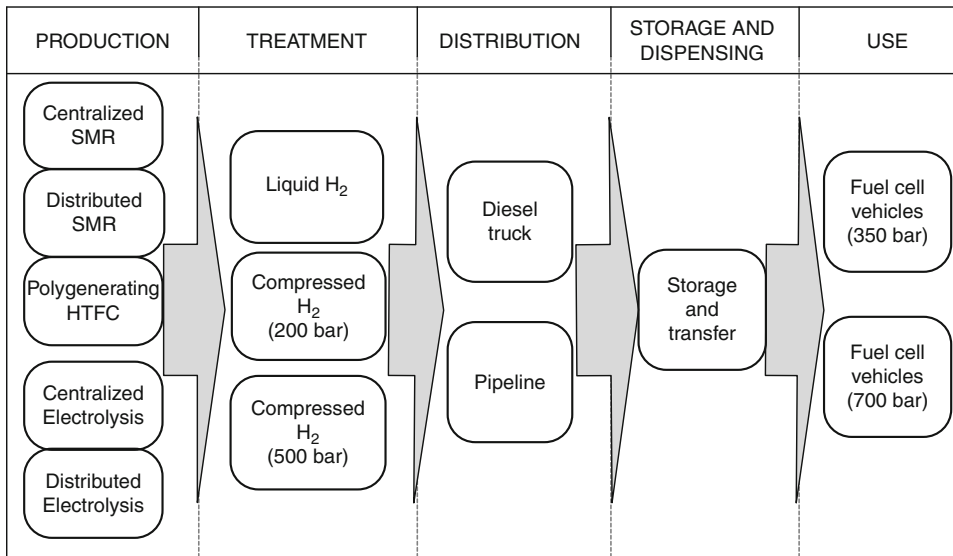
With the Supplemental Input Method, hydrogen efficiency is calculated in a similar way as

specified in Table 2. The chemical power output of the hydrogen produced,  $H$ , is divided by the energy flow input specifically allocated to produce hydrogen. Once again, it corresponds to the feedstock energy (i.e., additional fuel) as well as the necessary fuel to generate the electricity required for the hydrogen separation as if it was produced with a state-of-the-art combined cycle plant. As seen in Table 3, the highest values correspond to the internal reformation cases. Interestingly, although the parasitic load per kilogram of hydrogen produced is higher in configuration 6a than in configuration 6b (see Fig. 11), hydrogen production efficiency is greater in the former case due to the fact that when hydrogen is produced at 80% utilization factor, the additional fuel feedstock allocated to produce hydrogen is equal to zero.

Finally, overall efficiency values are similar in all the external reformation cases, even for configuration 1 where the hydrogen output is almost negligible. This indicates that the hydrogen production does not affect the overall performance when the amount of hydrogen is relatively small (i.e., external reformation cases). As expected, both internal reformation cases achieve the highest overall fuel-to-product efficiency values.

### Hydrogen Transport Impacts on Comparative Analyses

Today, most hydrogen is produced from natural gas in large steam-methane reformation (SMR) plants in a centralized fashion. To produce hydrogen at large scale in a centralized plant is more efficient than producing hydrogen at small scale [20]. Stephens-Romero et al. [19] define production, treatment, distribution, storage, and dispensing as the main steps of a well-to-tank hydrogen



**Hydrogen Production from High-Temperature Fuel Cells, Fig. 12** Steps in well-to-tank efficiency analysis of H<sub>2</sub>

supply chain. Each step can be accomplished with a variety of different technologies. Figure 12 shows the main steps of a generic hydrogen supply chain from well to tank with the most widely used technologies.

One of the main benefits of producing hydrogen in a distributed manner versus centralized manner is the elimination of the fuel transport and delivery steps (fuel distribution) which can be energy intensive. Furthermore, if hydrogen is produced on demand as in poly-generating HTFC, hydrogen storage may be considerably reduced compared with the distributed reformer case.

### Comparative Analysis of Ten Different Hydrogen Supply Chains

To evaluate the benefits of producing hydrogen in a distributed fashion versus centralized production, different hydrogen supply chains with different technologies for each step are analyzed from an energy perspective, resulting in ten different cases. Details of each supply chain are provided in Table 4. As shown, two different final uses corresponding to the two available fuel cell vehicle tank pressures (i.e., 350 bar and 700 bar) [26] are evaluated. In addition, when hydrogen is produced in a centralized SMR plant, the three

available treatment methodologies are investigated. As a result, ten different supply chains have been evaluated.

After evaluating the energy required for each step from *production* to *dispensing* of hydrogen, well-to-tank (WTT) efficiencies of the ten different hydrogen supply-chain scenarios were calculated. Figure 13 shows the main results obtained from the analyses.

As shown, the lowest WTT efficiency values are observed for the distributed steam-methane reformation (SMR) cases whereas the highest values correspond to poly-generating HTFC. As expected, due to the significant energy penalties associated with liquefaction processes, WTT efficiencies of centralized SMR with liquid hydrogen transportation are almost as low as the distributed SMR cases. Importantly, the production step includes the energy content of the fuel feedstock. The WTT efficiency values have been obtained by dividing the energy content of 1 kg of hydrogen (on a LHV basis) by the total energy required from WTT corresponding to each case.

From these energy-based comparative analyses, it is concluded that, of all the analyzed cases, poly-generating HTFC provide the most efficient way to produce and deliver hydrogen.

**Hydrogen Production from High-Temperature Fuel Cells, Table 4** Definition of the ten unique hydrogen supply chain cases

CCase	Production	Treatment	Distribution	Storage	Dispensing
1	Centralized SMR	Liquid H <sub>2</sub>	Diesel truck (100 km)	Liquid H <sub>2</sub>	Use = 350 bar (Transfer = 7 bar to 400 bar)
2	Centralized SMR	Liquid H <sub>2</sub>	Diesel truck (100 km)	Liquid H <sub>2</sub>	Use = 700 bar (Transfer = 7 bar to 800 bar)
3	Centralized SMR	Compressed H <sub>2</sub> (200 bar)	Diesel truck (100 km)	Compressed H <sub>2</sub> (200 bar)	Use = 350 bar (Transfer = 200 bar to 400 bar)
4	Centralized SMR	Compressed H <sub>2</sub> (200 bar)	Diesel truck (100 km)	Compressed H <sub>2</sub> (200 bar)	Use = 700 bar (Transfer = 200 bar to 800 bar)
5	Centralized SMR	Compressed H <sub>2</sub> (500 bar)	Diesel truck (100 km)	Compressed H <sub>2</sub> (500 bar)	Use = 350 bar (Transfer = 500 bar to 400 bar)
6	Centralized SMR	Compressed H <sub>2</sub> (500 bar)	Diesel truck (100 km)	Compressed H <sub>2</sub> (500 bar)	Use = 700 bar (Transfer = 500 bar to 800 bar)
7	Distributed SMR	Compressed H <sub>2</sub> (500 bar)	n/a (0 km)	Compressed H <sub>2</sub> (500 bar)	Use = 350 bar (Transfer = 500 bar to 500 bar)
8	Distributed SMR	Compressed H <sub>2</sub> (500 bar)	n/a (0 km)	Compressed H <sub>2</sub> (500 bar)	Use = 700 bar (Transfer = 500 bar to 800 bar)
9	Poly-generating HTFC	Compressed H <sub>2</sub> (500 bar)	n/a (0 km)	Compressed H <sub>2</sub> (500 bar)	Use = 350 bar (Transfer = 500 bar to 500 bar)
10	Poly-generating HTFC	Compressed H <sub>2</sub> (500 bar)	(0 km)	Compressed H <sub>2</sub> (500 bar)	Use = 700 bar (Transfer = 500 bar to 800 bar)

### Discussion of Scientific Basis for Observed Performance

High-temperature fuel cells (HTFC) operate at high enough temperature and produce enough heat and water from the electrochemical reactions to provide heat to the internal fuel processing reactions (i.e., internal reformation). Importantly, the overall heat generated by the fuel cell reactions is typically greater than the heat consumed by the endothermic fuel processing reactions occurring within the fuel cell stack [6]. Surplus heat is partially used to preheat the fuel and oxidant streams before they enter the fuel cell and to produce the steam required for system operations. Therefore, more hydrocarbon fuel than that required for the electricity generation could be processed in an HTFC, creating a hydrogen-rich stream that could be subsequently purified and delivered to the point of use without the need of an external reformer. This represents the main concept that defines and allows the production of hydrogen in addition to electricity and heat with an HTFC. Such systems have been

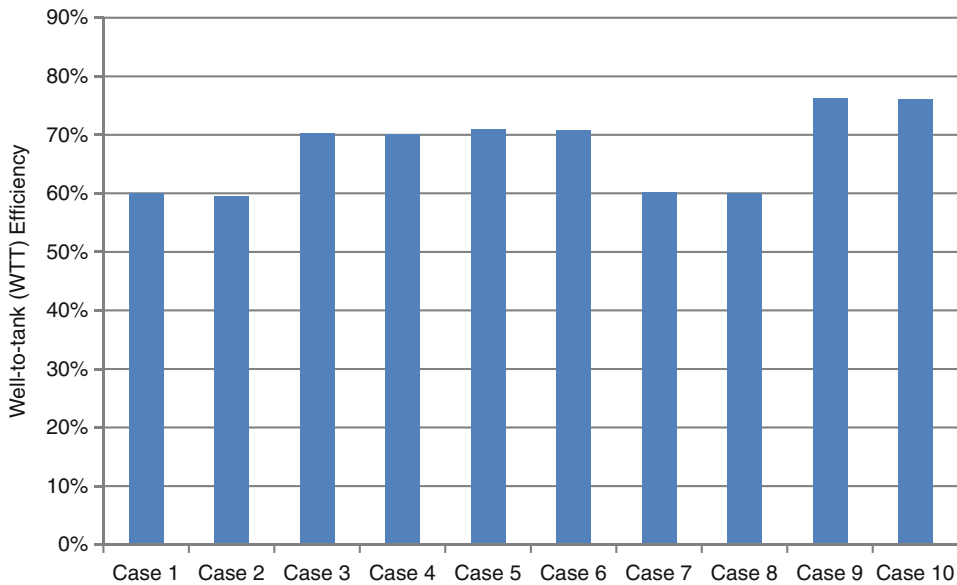
identified as poly-generating HTFC or tri-generation systems (Fig. 14).

Poly-generation systems can produce and deliver hydrogen fuel with lower marginal costs, fuel use, and emissions than conventional hydrogen production and delivery methods [27]. Since hydrogen is produced in a distributed generation fashion there is no energy or emissions penalty associated with the transport and delivery of the hydrogen to its point of use. Recent studies performed at the National Fuel Cell Research Center (NFCRC) of the University of California Irvine demonstrate that less energy is needed to transport and deliver hydrogen to vehicles compared with distributed and centralized steam methane reforming (SMR) resulting in higher well-to-tank (WTT) efficiencies [15].

### Definition and Quantification of the Synergies Associated with Poly-Generating HTFC

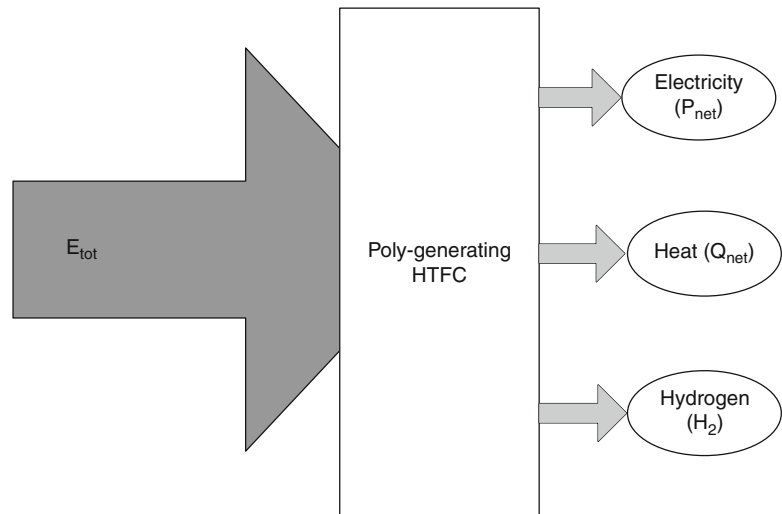
Among the main benefits associated with the production of hydrogen with HTFC, there are





**Hydrogen Production from High-Temperature Fuel Cells, Fig. 13** Well-to-tank efficiencies of the evaluated supply-chains

**Hydrogen Production from High-Temperature Fuel Cells, Fig. 14** Inputs and outputs of a poly-generating HTFC



synergistic effects intimately related with operating the fuel cell at low fuel utilization factors:

1. Synergistic impact of lower fuel utilization leads to higher cell voltages which result in:

(a) Higher electrochemical efficiencies

(b) Less electrochemical heat generated per mol of input fuel

2. Synergistic impact of lower fuel utilization increases the heat sink associated with the endothermic SMR reaction (i.e., internal fuel processing), reducing excess air requirements for cooling.

Synergies 1(b) and 2 reduce the excess air requirements for the stack cooling. Consequently,

lower cooling requirements will lower the parasitic loads from the cathodic air blowers, increasing the net power of the system and the overall system efficiency. In this section, more details about each of the identified synergies are provided.

**Synergistic Impact of Lower Fuel Utilization Leads to Higher Electrochemical Efficiencies** Ideal reversible voltage ( $E_0$ ) drops as soon as current is being produced due to the changes in product and reactant concentrations. Importantly, reactants and products concentrations along the electrode channels vary at different utilization factors. Therefore, operating the fuel cell at different fuel utilizations may affect the cell voltage. The voltage reduction caused by the change of species concentrations is known as *Nernstian losses* ( $\eta_{\text{Nernst}}$ ), which added to the reversible voltage  $E_0$ , results on the Nernst Voltage ( $V_{\text{Nernst}}$ ).

$$V_{\text{Nernst}} = E_0 + \eta_{\text{Nernst}} = E_0 + \frac{RT}{2F} \ln \left( x_{\text{H}_2} x_{\text{O}_2}^{\frac{1}{2}} \right) \quad (18)$$

$x_{\text{H}_2\text{O}}$

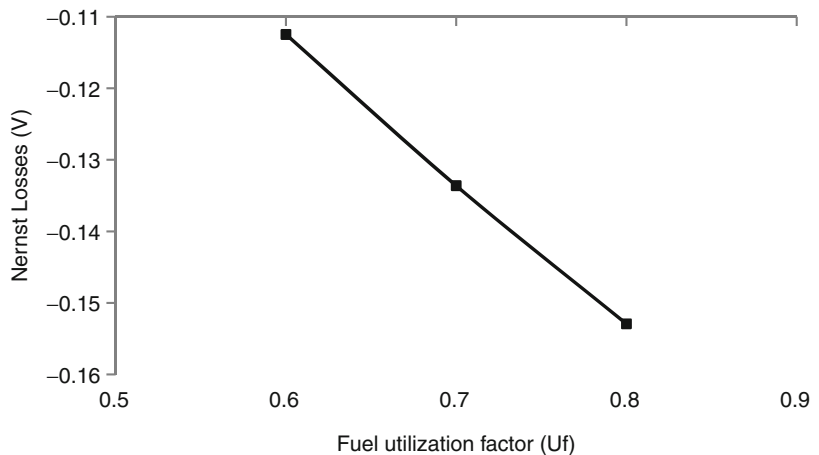
Figure 15 shows the Nernstian losses ( $\eta_{\text{Nernst}}$ ) as a function of the utilization factor obtained with the poly-generating SOFC modeling efforts by Li and Margalef [15, 28].

As shown in Fig. 15, voltage drop related with the Nernstian losses decreases at lower fuel utilizations. This effect represents in fact one of the synergies associated with poly-generating fuel cells, which typically operate at lower fuel utilizations than stand-alone fuel cells (i.e., electricity and heat production only).

To quantify this synergy, the system can be analyzed at two different fuel utilizations. The first value corresponds to the typical utilization factor of a stand-alone SOFC (e.g.,  $U_f = 0.9$ ) whereas the second value corresponds to the typical utilization factor of a poly-generating SOFC (e.g.,  $U_f = 0.6$ ). The difference in Nernst losses ( $V_{\text{Nernst}}$ ) between both operating points represents the voltage gain of operating the fuel cell at lower fuel utilizations and quantifies this synergistic effect. Approximately, a gain of 0.06 V in the Nernst voltage has been observed by operating the fuel cell at typical utilization factor used in poly-generating fuel cells ( $U_f = 0.6$  compared to  $U_f = 0.9$ ).

Additionally, the utilization factor affects the fuel cell performance through reaction kinetics since they also depend upon the reactant and product concentrations at the reaction sites [22]. The voltage drop associated with the reaction kinetics at different fuel utilizations is known as *reaction loss* ( $\eta_{\text{rxn rate}}$ ). However, previous analyses performed by Margalef et al. [15] show that reaction losses represent a small fraction of the total voltage drop related with the concentration changes associated with different fuel utilizations. Therefore, the overall effects of

**Hydrogen Production from High-Temperature Fuel Cells, Fig. 15** Nernst losses ( $\eta_{\text{Nernst}}$ ) versus the fuel utilization factor



operating the fuel cell at lower fuel utilizations on the cell voltage can be defined as

$$\begin{aligned} \Delta V_{\text{cell,conc}} &= \Delta V_{\text{cell,Nernstian}} \\ &+ \Delta V_{\text{cell,rxn rate}} \sim \Delta V_{\text{cell,Nernstian}} \end{aligned} \quad (19)$$

If all the energy from the hydrogen fuel were transformed into electrical energy, the cell voltage would correspond to the maximum voltage  $V_{\text{max}}$ . The maximum voltage would be given by

$$\begin{aligned} V_{\text{max}} &= \frac{-\Delta \bar{g}_f}{n_i F} \\ &= 0.97 \text{ V if using the LHV} \end{aligned} \quad (20)$$

where  $-\Delta \bar{g}_f$  is the Gibbs free energy at 900 °C,  $n_i$  is the number of electrons transferred during the electrochemical oxidization of fuel species  $i$  ( $n_i = 2$  for  $\text{H}_2$  and  $\text{CO}$ ,  $n_i = 8$  for  $\text{CH}_4$ ), and  $F$  is the Faraday's constant. This voltage would be obtained from a 100% efficient system [6]. Therefore, the actual efficiency of the cell (or electrochemical efficiency) is the actual voltage divided by the maximum voltage, or

$$\eta_{\text{cell}} = \frac{V_{\text{cell}}}{V_{\text{max}}} = \frac{V_{\text{cell}}}{0.97} \text{ if using the LHV} \quad (21)$$

Therefore, the electrochemical efficiency gain associated with lower utilization factors can be written as

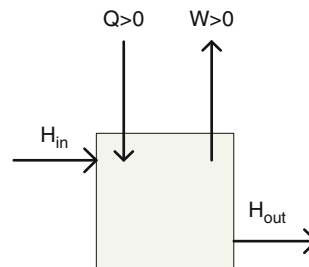
$$\begin{aligned} \Delta \eta_{\text{cell}} &= \frac{\Delta V_{\text{cell,conc}}}{V_{\text{max}}} = \frac{0.06}{0.97} \times 100 \\ &= 6.2\% \text{ if using the LHV} \end{aligned} \quad (22)$$

This result demonstrates and quantifies the first synergy associated with generating hydrogen with HTFC. As seen, by lowering the utilization factor at typical values of poly-generating SOFC, the electrochemical efficiency increases by 6.2%.

A more philosophical approach to explain the cell voltage drop as the fuel utilization factor increases is related to the mixing of products with reactants to dilute electrochemically active

species concentrations. Water product mixes with the anode gas as it is formed throughout the electrochemical reactions. Note that mixing of products with reactants can occur in either the anode (e.g., MCFC, SOFC) or cathode (e.g., PEMFC, PAFC) compartments. The concentration of water product in the anode increases as the fuel utilization factor increases. Mixing processes are irreversible so they produce entropy. As a result, a completely reversible SOFC operation would be only approached as  $U_f \rightarrow 0$ . In other words, irreversibilities increase as the utilization factor increases. Consequently, one wants to operate a fuel cell at the lowest possible utilization factor in order to reduce the mixing irreversibilities. However, there is a compromise between the cell efficiency and the fuel utilization efficiency that counterbalances this consideration with a desire for high utilization to achieve high overall system electrical efficiency.

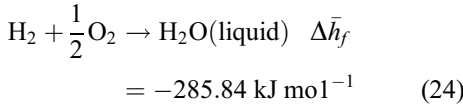
**Synergistic Impact of Lower Fuel Utilization Increases the Heat Sink Associated with the Endothermic SMR Reaction, Reducing Excess Air Requirements for Cooling** A high-temperature fuel cell (HTFC) is an electrochemical device that converts chemical energy of a fuel and oxidant directly to electricity. Fuel cell electrochemical reactions are exothermic, thus electrochemical heat is produced. In addition, during the operation of an HTFC, ohmic resistance across the electrodes and bipolar plates generates heat. The specific electrochemical heat released  $q_{FC}$  can be calculated applying the first law of thermodynamics, according to Eq. 23. Sign convention for this analysis is specified in Fig. 16:



**Hydrogen Production from High-Temperature Fuel Cells, Fig. 16** Sign convention

$$\Delta \bar{h}_f = qFC - wFC \quad (23)$$

where  $\Delta \bar{h}_f$  is the enthalpy of combustion of hydrogen corresponding to the reaction



and  $w_{FC}$  is the electric work produced by the fuel cell, given by the Eq. 23

$$w_{FC} = n_e F V_{\text{cell}} \quad (25)$$

where  $V_{\text{cell}}$  is the operational cell voltage,  $n_e$  is the number of electrons transferred during the electrochemical reactions (i.e.,  $n_e = 2$  for hydrogen), and  $F$  is the Faraday's constant. Combining Eqs. 23 and 25, the specific heat generated during a real fuel cell operation can be calculated as follows:

$$\begin{aligned} qFC &= \Delta \bar{h}_f + w_{FC} \\ &= \Delta \bar{h}_f + n_e F V_{\text{cell}} \left[ \frac{\text{kJ}}{\text{mol H}_2} \right] \end{aligned} \quad (26)$$

In a real fuel cell, although part of the heat is exchanged and used in several ways, including fuel processing and air preheating, excess air is usually required to prevent overheating [29]. Assuming that the fuel processing consists of steam reformation (SMR) and water-gas shift (WGS), the total specific heat absorbed by the fuel processing reactions  $qFC$  including the steam production is

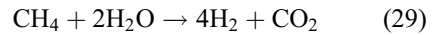
$$\begin{aligned} qFP &= \Delta \bar{h}_{SMR} + \Delta \bar{h}_{WGS} + 2 \times \Delta \bar{h}_{vap} \\ &= 206.1 - 41.2 + 2 \times 44.1 \\ &= 253.1 \left[ \frac{\text{kJ}}{\text{mol CH}_4} \right] \end{aligned} \quad (27)$$

where  $\Delta \bar{h}_{SMR}$  is the enthalpy of steam reforming reaction,  $\Delta \bar{h}_{WGS}$  is the enthalpy of water-gas-shift reaction, and  $\Delta \bar{h}_{vap}$  is the enthalpy of vaporization of water. Therefore, remaining heat that has to be transferred to the excess air for cooling purposes  $q_{\text{cool}}$  is the difference between the heat liberated

during the fuel cell reactions  $qFC$  and the heat absorbed by the fuel processing reactions  $qFP$ :

$$q_{\text{cool}} = m \cdot qFC + qFP \left[ \frac{\text{kJ}}{\text{mol CH}_4} \right] \quad (28)$$

where  $m$  is the number of moles of hydrogen produced during the fuel processing reactions. For this specific case, the overall fuel processing reaction includes SMR and WGS, and is given by Eq. 29.



Therefore,  $m$  is equal to 4. Combining Eqs. 27–29, the specific cooling required can be written as

$$\begin{aligned} q_{\text{cool}} &= 4(\Delta \bar{h}_f + n_e F V_{\text{cell}}) \\ &\quad + qFP \left[ \frac{\text{kJ}}{\text{mol of CH}_4} \right] \end{aligned} \quad (30)$$

As expected, more electrochemical heat is liberated per mole of hydrogen  $qFC$  at higher fuel utilizations. Consequently, by operating the fuel cell at lower utilization factors reduces the fuel cell cooling requirements per mole of input fuel, due to the higher cell voltages that result in less electrochemical heat generated. Lower cooling requirements mean lower parasitic loads from the air blowers, increasing the net power of the system and the overall system efficiency.

## World's First Poly-Generating HTFC System

The world's first installation to poly-generate electricity and hydrogen with high-temperature fuel cells (i.e., a molten carbonate fuel cell) has been installed at the Orange County Sanitation District (OCSD) in Fountain Valley, California [24]. The system that has been installed at OCSD is the world's first hydrogen coproduction system installed at a customer site. In addition, it has begun to produce electricity, heat, and hydrogen from renewable digester gas fuel. The prime

contractor in the effort is Air Products and Chemicals, Inc., who is working with FuelCell Energy and the National Fuel Cell Research Center and OCS D on the project. The main funding agencies are the US Department of Energy, California Air Resources Board, and the South Coast Air Quality Management District.

This important installation of a prototype poly-generating HTFC operating on digester gas at OCS D will provide important data and experience that will benefit the advancement of the poly-generation concept. The installation itself and measured performance characteristics may also identify important areas for research, development, improvement, and application of the concept.

## Future Directions

Recommendations for future research work on poly-generating HTFC development include the development of a detailed dimensional and dynamic SOFC model that is required to solve the complicated internal temperature and species concentration profiles that are not resolved by nondimensional models. Thermodynamic and nondimensional SOFC insights are nonetheless useful for system design and comparative analyses. In addition, the overall system performance obtained by these models generally sets the ideal system performance target. However, since the outlet flow temperatures do not necessarily represent the maximum temperatures in the SOFC, and peak temperatures often occur internal to the stack, a dimensional SOFC model and/or internal temperature measurements could be used to determine if the SOFC working voltage is achievable and practical.

All the analyses performed in previous literature have been performed at a fixed current density value. Therefore, the same analyses described in this chapter should be performed at lower current densities. At such operating conditions, it is likely that the operational cell voltage will rise, increasing the electrochemical efficiency. However, less electrochemical heat will be generated, which is likely to reduce the hydrogen production potential. Therefore, it is possible to adjust the

system performance for each specific market depending upon which product is more valuable by varying the operational current density in addition to the fuel utilization.

It has been found that pressure swing adsorption (PSA) might not be the best technology for extraction and purification of the hydrogen from the anode off-gas due to the PSA feed gas requirements. A complex HSU configuration is required in order to meet pressure, temperature, and hydrogen concentration requirements. Therefore, different purification strategies such as electrochemical hydrogen separation and selective permeation membranes might be more suitable for the poly-generation application.

An economic analysis of poly-generating high-temperature fuel cells should be performed in detail. From an efficiency perspective and considering only the configurations presented herein, poly-generating HTFC are the best solution. However, the economics of such novel systems should be analyzed and compared with conventional production methods. Additionally, due to the poly-generating nature of these systems, different strategies to fit each of the specific market requirements should be designed. These strategies might be resolved by dynamic modeling efforts to investigate the ability of system configurations to dynamically dispatch each of the respective products depending upon demand profiles for each product.

## Bibliography

1. Online resource available at: <http://www.energy.ca.gov/distgen/>
2. EG & G Technical Services, Inc. (2004) Fuel cell handbook, 7th edn. U. S. Department of Energy Office of Fossil Energy, Morgantown
3. Brouwer J, Jabbari F, Leal EM, Orr T (2006) Analysis of a molten carbonate fuel cell: numerical modeling and experimental validation. *J Power Sour* 158(1):213–224
4. Sundmacher K et al (2007) Molten carbonate fuel cells modeling, analysis, simulation, and control. Wiley, Weinheim
5. Aguiar P, Chadwick D, Kershenbaum L (2002) Modelling of an indirect internal reforming solid oxide fuel cell. *Chem Eng Sci* 57:1665–1677
6. Larminie J, Dicks A (2003) Fuel cell systems explained. Wiley, West Sussex

7. Dufour J et al (2009) Life cycle assessment of processes for hydrogen production. Environmental feasibility and reduction of greenhouse gases emissions. *Intl J Hydrog Energy* 34:1370–1376
8. Holladay JD, Hu J, King DL, Wang Y (2009) An overview of hydrogen production technologies. *Catal Today* 139(2009):244–260
9. Margalef P, Brown T, Brouwer J, Samuelsen GS (2010) Efficiency of polygenerating high temperature fuel cells. *J Power Sour POWER\_POWER-D-10-02363*
10. Margalef P, Brown T, Brouwer J, Samuelsen GS (2010) Conceptual design and configuration performance analyses of polygenerating high temperature fuel cells. *Intl J Hydrog Energy*. Accepted 11 May 2011
11. California Fuel Cell Partnership Action Plan (2009) Hydrogen fuel cell vehicle and station deployment plan: a strategy for meeting the challenge ahead. California Fuel Cell Partnership Action Plan, West Sacramento
12. Spath P, Mann M (2001) Life cycle assessment of hydrogen production via natural gas steam reforming. NREL/TP-570-27637. NREL National Renewable Energy Laboratories, Golden
13. Ogden JM (2002) Review of small stationary reformers for hydrogen production. Technical Report to the International Energy Agency
14. Sverdrup GM et al (2006) Status of hydrogen production pathways – comparison of energy efficiencies, fossil fuel use, greenhouse gas emissions, and costs. In: WHEC 16, 13–16 June 2006, Lyon
15. Margalef P (2010) On the polygeneration of electricity, heat and hydrogen with high temperature fuel cells. PhD dissertation, University of California, Irvine
16. Brouwer J, Leal E (2006) A thermodynamic analysis of electricity and hydrogen polygeneration using a solid oxide fuel cell. *J Fuel Cell Sci Technol* 3:137–143
17. Singhal SC, Kendall K (2003) High temperature solid oxide fuel cells: fundamentals, design and applications. Elsevier, Oxford
18. Cengel YA, Boles MA (2006) Thermodynamics: an engineering approach, 6th edn. McGraw Hill, Boston
19. Stephens-Romero S (2010) Systematic planning to optimize investments in hydrogen infrastructure deployment. *Intl J Hydrog Energy* 35:4652–4667
20. Bossel U (2003) Energy and the hydrogen economy
21. Brouwer J, Leal E (2005) Production of hydrogen using high-temperature fuel cell: energy and exergy analysis. In: 18th international congress of mechanical engineering, ABCM, Ouro Preto
22. O’Hayre R, Cha S, Colella W, Prinz FB (2006) Fuel cell fundamentals. Wiley, New York
23. Miller QM, Stocker J (1989) Selection of a hydrogen separation process. In: NPRA annual meeting held 19–21 Mar 1989, San Francisco
24. Heydorn EC, Patel P (2010) Development of a renewable hydrogen station. ICEPAG, Costa Mesa
25. QuestAir H-3200 Commercial Brochure. <http://www.xebecinc.com/hydrogen-purification-h3200.php>
26. Air Products & Chemicals Inc. Recovery process using pressure swing adsorption technology. <http://texasiof.ces.utexas.edu/texasshowcase/pdfs/presentations/c6/pcook.pdf>
27. Vollmar HE et al (2000) Innovative concepts for the coproduction of electricity and syngas with solid oxide fuel cells. *J Power Sour* 86:90–97
28. Li M (2010) Detailed fuel cell modeling for coal-based integrated gasification fuel cell system design and analysis. Mechanical and aerospace doctoral studies dissertation. University of California, Irvine
29. Van Herle J et al (2003) Energy balance model of a SOFC cogenerator operated with biogas. *J Power Sour* 118:375–383
30. Samuelsen GS (2005) Energy station concept. In: California hydrogen blueprint plan, vol 2. California Environmental Protection Agency, Sacramento [http://www.hydrogenhighway.ca.gov/plan/reports/volume2\\_050505.pdf](http://www.hydrogenhighway.ca.gov/plan/reports/volume2_050505.pdf)





## Nuclear-Assisted Hydrogen Production

Rami S. El-Emam<sup>1,2</sup> and Ibrahim Dincer<sup>2</sup>

<sup>1</sup>Faculty of Engineering, Mansoura University, Mansoura, Egypt

<sup>2</sup>Faculty of Engineering and Applied Science, University of Ontario Institute of Technology, Oshawa, ON, Canada

### Article Outline

Glossary

Definition of the Subject

Introduction

Routes of Nuclear Energy for Hydrogen Production

Generation IV Nuclear Reactors for Hydrogen Production

Safety Aspects of Nuclear Hydrogen Production Plants

Concluding Remarks

Bibliography

### Glossary

**CANDU** CANadian Deuterium Uranium reactor that uses heavy water as moderator and coolant.

**Gibbs free energy** A chemical thermodynamic function that describe the energy available to do useful work.

**Hybrid thermochemical cycles** Series of electrochemical and thermochemical series of reactions for water splitting hydrogen production.

**Hydrolysis** The chemical reaction between water and another substance to form new substances including the ionization of water molecule and splitting of the hydrolyzed compound.

**Thermochemical cycles** The process of water splitting for hydrogen production using heat

source in chemical reactions where the chemical compounds used are continuously recycled.

**Thermolysis** The process of thermal decomposition through a chemical reaction where a chemical substance breaks up into two or more substances using heat.

**Water electrolysis** The decomposition of water for hydrogen production using electric current.

**Water radiolysis** The process of water molecule dissociation into hydrogen and hydroxide ions through the exposure to high energy ionizing radiation.

### Definition of the Subject

Right after the 2015 United Nations Climate Change Conference in Paris, two solutions, namely, renewable energy and carbon free fuels, have come out. In this regard, several nations have started re-planning their future with hydrogen to help combat global warming and solve energy issues. One of the most recent historical events is that the chief executive officers of thirteen leading energy, transport and industrial global companies established the hydrogen council during the recent Davos Economic Forum in 2017. All these attempts show how shifting to hydrogen economy will take place. However, the technology currently utilized for the generation of hydrogen, steam reforming of natural gas, is not environmentally benign in a satisfactory manner and leads to some environmental impact due the life cycle emissions of some greenhouse gases, such as CO<sub>2</sub>. Several innovative clean technologies of hydrogen production, especially for large-scale production, would be possible and feasible when incorporating the nuclear energy of the advanced nuclear fission-based technologies, and ultimately the nuclear fusion energy. This chapter sheds light on the potential of the current routes and the future of hydrogen production using nuclear energy and the associated safety aspects of such projects. It also highlights the role of nuclear hydrogen

production for securing a sustainable and clean energy future.

## Introduction

The interest and need of large-scale production of hydrogen is growing, and it is seen to be playing an important role in the current millennium. Hydrogen is vital basic element in a wide range of chemical processes. It is a clean energy carrier that can be stored in various forms including forming ammonia (which is the essential element in fertilization industry as well as pharmaceuticals and large-scale cooling applications). It is also considered as the future fuel for fuel cell vehicles. Hydrogen is also crucial for the methanol economy.

Currently, hydrogen is mostly produced through fossil based driven technologies. However, there is a growing awareness of the impact of greenhouse gases emissions of such technologies. The historic Paris Agreement of COP21 to combat climate change initiated a flourishing potential for politicians, stakeholders, and the public of all nations of the world to work towards sustainable low-carbon energy future. Carbon-free large-scale hydrogen production is considered one of the innovative technologies which is expected to serve as the platform of the Paris Agreement. Renewable and nuclear energy alternatives are the main players in this market. Concentrated solar thermal technologies and high temperature reactors are the most appropriate options with high potential to drive the high temperature hydrogen production technologies (e.g., High Temperature Steam Electrolysis (HTSE), thermochemical and hybrid-thermochemical hydrogen production cycles). Wind and nuclear generated electricity are also the competent for driving conventional large-scale electrolysis plants at economic and environmentally benign operation. However, generally speaking, even with employing energy storage techniques, solar- and wind-based energy systems for hydrogen production will always face the challenge of availability and fluctuating nature of the energy source.

The cost is another factor that plays a huge role in the choice of the nuclear technology for

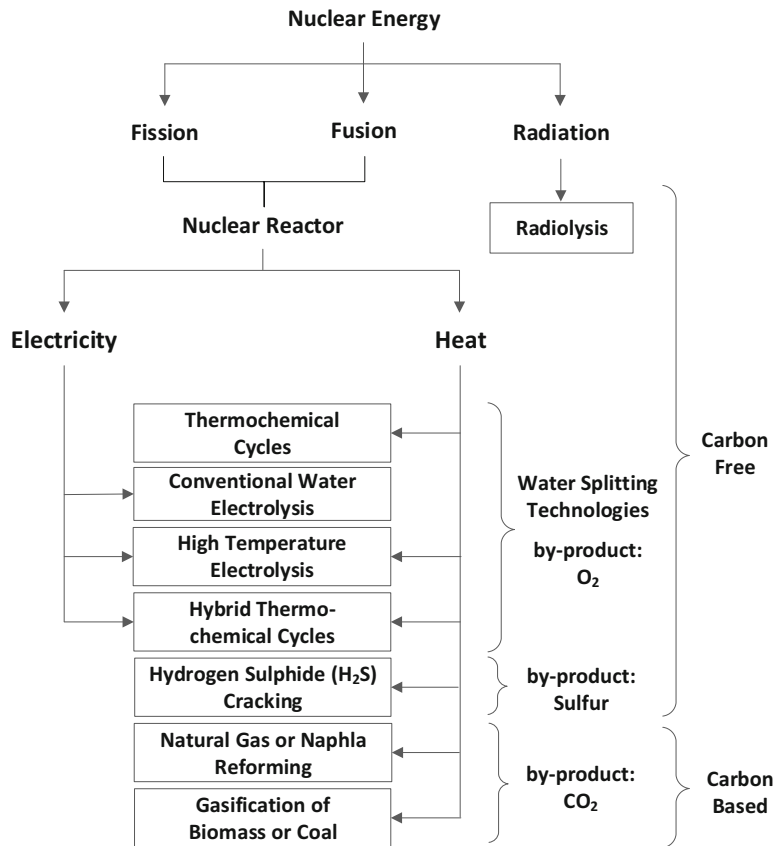
hydrogen production as well as emerging the nuclear hydrogen into the global market. Although steam methane reforming technology, which is the most dominant method for hydrogen production to meet the current hydrogen demands, is of relatively low cost compared with the other cleaner alternatives for hydrogen production, yet using the off-peak operating periods of power nuclear reactors for hydrogen production through electrolysis technologies, or using the nuclear energy for the cogeneration of electric power along with hydrogen production through water splitting technologies may be more cost effective, as well as being more attractive compared with hydrogen-only nuclear reactors, especially considering small size reactors and the use of light water reactors.

It is important to note that the most dominant and cost-effective approach for hydrogen generation is based on the steam methane reforming. Yet the cost associated with its environmental impact brings the attention to other innovative technologies which are very promising when coupled with nuclear reactors. The direct use of nuclear-produced electricity for conventional electrolysis of water is a direct mature approach. However, thermochemical and hybrid thermochemical water splitting cycles using the nuclear heat and electricity are of promising potential for large-scale clean hydrogen production, considering the energy usage and operating efficiency, as will be discussed in the following sections.

## Routes of Nuclear Energy for Hydrogen Production

Energy of nuclear radiation can be envisaged to generate hydrogen through direct water radiolysis (chemo-nuclear) process, or using the generated high temperature heat of fission/fusion reactors and/or the electric power of nuclear power plants in thermal, electric, or hybrid hydrogen production plant. Figure 1 shows the different routes of using the nuclear energy for hydrogen generation through several carbon-free and carbon-based hydrogen production technologies.

**Nuclear-Assisted Hydrogen Production,**  
**Fig. 1** Technology routes of hydrogen generation using nuclear energy



In radiolytic water splitting process, high-energy radiation and the kinetic energy associated with the fission products are used for exciting the water molecule resulting in its direct split into hydrogen and oxygen. Carty et al. [1], in 1981, reported 15% efficiency with splitting six water molecules using 100 eV alpha radiation in steam irradiation process. The containment of radioactive materials as per safety regulations and designs of current commercial reactors seize the progress of such process for large-scale hydrogen production.

Nuclear reactor technologies enable the conversion of the nuclear radiation energy to useful high temperature heat by thermalizing the nuclear particles in collision-slowng process. The thermal energy is carried by heat transfer fluid to the power plant for electricity generation. Based on the temperature level of the generated heat, nuclear generated thermal energy and/or the produced electric power can be employed for

hydrogen production in several hydrogen generation technologies.

Thermodynamically, heat can be used for water splitting by supplying the required enthalpy difference,  $\Delta H$ , and the Gibbs free energy,  $\Delta G$  (the latter cannot be transferred in form of heat, for hydrogen production processes it is mostly in the form of electric work) for splitting water molecules. For instance, in the electrolysis water splitting technology, only electric power is provided; however, part of it is internally converted to heat equal to  $-T\Delta S$  by the Joule effects within the electrolyte. The ratio of required change of enthalpy to the change in Gibbs energy is linked to the temperature of the process. The reaction enthalpy increases with higher temperature values, yet the Gibbs energy decreases. This brings the operation of conventional electrolysis to be considered at relatively low temperatures (around the standard temperature), where the ratio of  $\Delta G$  to  $\Delta H$  is very high compared with

high temperature operation for this specific process.

Using conventional electrolysis for hydrogen production coupled with nuclear power plant is not bringing too much complication to the system integration as the hydrogen plant is only resembling an electric load which shall be connected to the electric grid. Although low-temperature electrolysis is currently the ready technology for nuclear hydrogen production, yet the thermodynamic potential of using the energy of nuclear reactors for high-temperature hydrogen production processes is higher. In high-temperature thermal energy processes for hydrogen production, the required energy is directly supplied in form of heat. Heat-based processes have the thermodynamic advantage of not being constrained by the Carnot efficiency ruling heat engines converting heat to electric power. This also applies to the hybrid processes where electric work is supplied to conduct certain steps of the process along with thermal energy, which still release the thermodynamic efficiency from Carnot limitations compared with purely electric driven processes.

### Generation IV Nuclear Reactors for Hydrogen Production

The new generation of nuclear power plants has higher potential for positive contribution in the domestic energy sources for achieving energy security and stability, along with the safe, reliable, and economic operation. In 2002, The Generation IV (GEN IV) International Forum (GIF) selected six fission systems from nearly 100 different concepts, and developed a technology roadmap for the development of these technologies [2]. The updates on the development, time line, and status of these technologies can be found in the reports released by GIF [3]. Table 1 shows the six types of innovative nuclear technologies considered by the nations incorporated in GIF and the possible routes for integration with the different hydrogen generation technologies. In the following, some of the nuclear hydrogen technologies based on the concepts of GEN IV reactors are highlighted.

### SCWR for Hydrogen Production

There are several projects on the SCWR, based on thermal and fast spectrum bases, developed in six countries. The CANDU-SCWR thermal pressure tubes reactor presents a viable potential for hydrogen production application by integration with Copper–Chlorine (CuCl) hybrid thermochemical plant [4]. This also applies to all other SCWRs based on the operating temperature of the reactor core and the temperature requirements for this cycle. The CANDU-SCWR is fueled with uranium dioxide, cooled by supercritical water, and moderated using heavy water. Thorium is the secondary option to fuel this reactor. The referential plant of the CANDU-SCWR is of 2,540 MWth, the pressure tube reactor allows for modification of the power, reducing the fuel channel in the core. It allows the insertion of reheaters in the steam cycle (for example, see [5]).

The CANDU-SCWR core outlet temperature of 625 °C may be used for supplying heat to the HI decomposition step of the S-I thermochemical cycle which required heat at the temperature of 450 °C. This step takes about 10% of the cycle heat demand, and the rest of the heat demand is required at about 850 °C which cannot be provided by this reactor. This also applies to the HyS process which required high-temperature heat. Several studies have been conducted on upgrading the heat of the CANDU-SCWR to provide heat at elevated temperature. Chemical and electric heat pumps have been studied, yet not been considered as a solid option to be used for the cogeneration application of this reactor. Due to this, the national research and development on nuclear hydrogen production in Canada has been more focused on the development of the CuCl process as the most promising alternative for integration with the CANDU-SCWR. This is also the case for the other countries developing SCWRs including the USA, Japan, China, France, and Republic of Korea.

The CuCl cycle was developed by the Atomic Energy of Canada Limited (AECL) and the Argonne National Laboratory (ANL) as a low-temperature thermochemical cycle. Several CuCl cycle configurations were tested and investigated to identify the most optimized cycle design

**Nuclear-Assisted Hydrogen Production, Table 1** Hydrogen technologies adaptability with the advanced nuclear reactor technologies

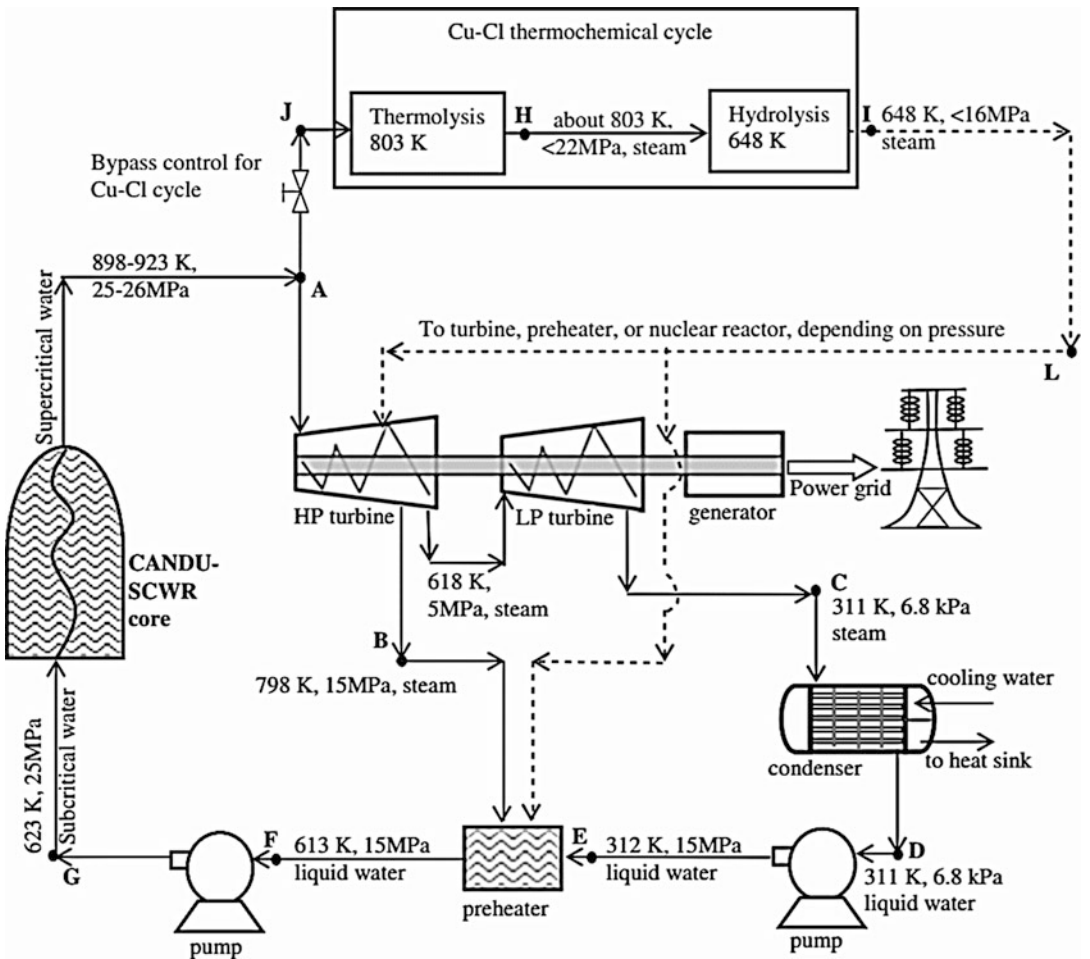
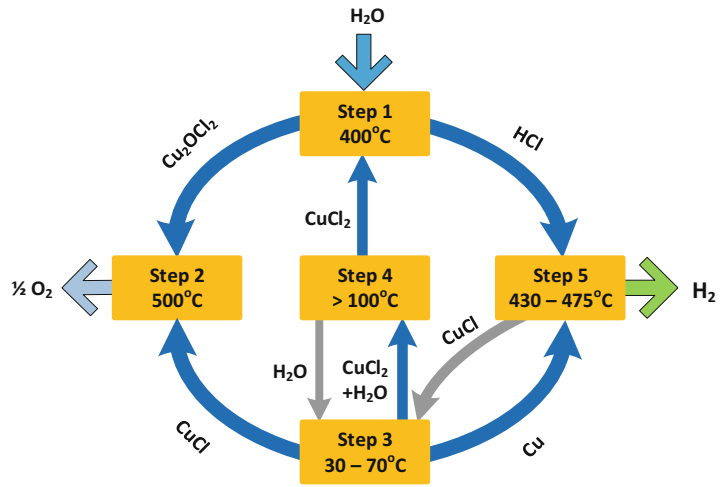
		GEN IV – advanced nuclear technologies					
		SCWR	VHTR	SFR	GFR	MSR	LFR
Specifications	Core outlet temperature (°C)	500–625	750–950	450–550	750–850	650–850	450–800
	Efficiency (electric based) (%)	44–48	40–50	38–42	45–48	45–55	42–45
	<b>Thermodynamic power cycle</b>						
	Brayton cycle	–	He	S-CO <sub>2</sub>	He	He	S-CO <sub>2</sub>
	Rankine cycle	Steam	Steam	Steam	–	–	Steam
Hydrogen production technologies	<b>Electrolysis</b>						
	PEM electrolysis (<100 °C)	✓	✓	✓	✓	✓	✓
	Alkaline electrolysis (~200 °C)	✓	✓	✓	✓	✓	✓
	High temp electrolysis (>800 °C)	–	✓	–	✓	✓	✓
	<b>Thermochemical/hybrid cycles</b>						
	Sulfur iodine (>800 °C)	–	✓	–	✓	–	–
	Hybrid sulfur (>800 °C)	–	✓	–	✓	–	–
	Copper chlorine (>600 °C)	✓	✓	–	✓	✓	–
	<b>Carbon-based thermochemical</b>						
	Steam methane reforming (>700 °C)	–	✓	–	✓	✓	–
Coal/biomass gasification (>650 °C)	✓	✓	–	✓	✓	–	

*GFR* gas cooled fast reactor, *LFR* lead cooled fast reactor, *MSR* molten salt reactor, *SCWR* super critical water reactor, *SFR* sodium cooled fast reactor, *VHTR* very high temperature reactor

considering the energy (thermal and electric) requirements and the associated cost among other factors. The cycle proved being of positive potential for generation of hydrogen using the nuclear power [6–10]. In general, CuCl cycle consists of set of closed loop reactions of intermediate copper and chloride compounds with the overall net water splitting reaction. The cycle internal loop recycles all the chemicals on a continuous basis without any greenhouse gas emissions. A schematic of the five-step CuCl cycle is shown in Fig. 2. The figure shows the paths of the different compounds in the closed loop steps with the temperature requirements for each step of the process.

In general, indirect integration incorporating intermediate heat exchangers is needed for linking the SCWR and CuCl plant, due to safety considerations. In addition, the heat extraction points and water flow arrangements of the power cycle are governed by the level of operating temperature values of the main operations of the CuCl plant. One of the conceptual system integration schemes of the CANDU-SCWR with the CuCl hydrogen generation plant, proposed by Wang et al. [11], is shown in Fig. 3. The power cycle in this system is proposed to be steam Rankine cycle with single reheat, preheater, and two turbines. Part of the supercritical water at the core exit condition, state A, is bypassed to provide heat to the

**Nuclear-Assisted Hydrogen Production, Fig. 2** Schematic of the five-steps Copper–Chlorine hybrid thermochemical cycle



**Nuclear-Assisted Hydrogen Production, Fig. 3** Schematic of integrated SCWR power cycle and CuCl hydrogen generation plant, modified from Wang et al. [11]

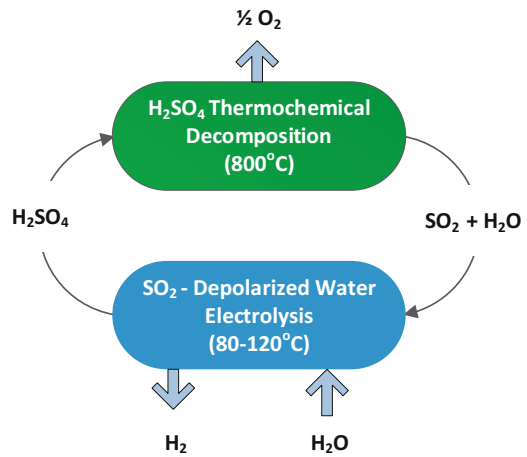


thermolysis and hydrolysis processes of the CuCl plant at around 520–530 °C and 365–375 °C, respectively. Based on the condition of the return flow of the power cycle working fluid after the heat transfer process to the hydrogen generation plant (state I), it may be returned to the main cycle as the path shown in the figure. Different system integration schemes have been proposed in the literature considering double-reheat power cycle and providing heat to the different CuCl processes through different extraction points from the power cycle based on the temperature level.

### VHTR for Hydrogen Production

VHTRs are generally helium cooled thermal reactor designs, moderated by solid graphite, with a core outlet temperature of 750–950 °C (up to 1,000 °C). This very high operating temperature results in a high electric efficiency and a great potential for cogeneration applications, especially hydrogen production. It is actually seen as the most suitable among the other six GEN IV concepts for highly efficient hydrogen production. There are several projects on the VHTR concept designed as Small Modular Reactors (SMRs) with pebble bed or prismatic block core. Several conceptual designs have been considered for the integration of hydrogen production technologies with the VHTR projects processed and considered by GIF. The Sulfur Iodine (S-I), the Hybrid Sulfur (HyS), and the HTSE are the three hydrogen production technologies taken into consideration for VHTR hydrogen production projects. The Next Generation Nuclear Plant (NGNP) of the US VHTR program suggests the use of HTSE due to its relatively simpler design [12]. Different studies have been performed to investigate the performance of such system integration, and an overall operating efficiency of 30–34% were reported [13]. Steam methane reforming was also considered for system integration with the NGNP.

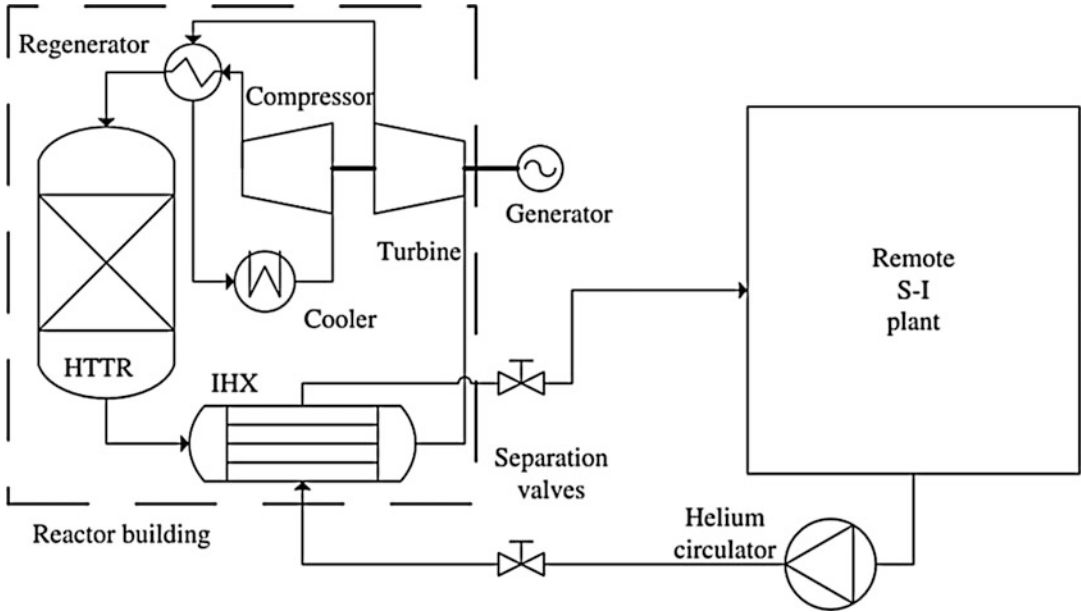
The S-I thermochemical cycle (simplified schematic of the cycle processes is shown in Fig. 4) is considered for hydrogen production using the heat of the Gas Turbine Temperature Reactor for hydrogen production (GTHTR300C) of the Japan Atomic Energy Research Institute, Japan Atomic Energy Agency, and the US-DOE



**Nuclear-Assisted Hydrogen Production, Fig. 4** Schematic of the Sulfur Iodine S-I thermochemical cycle

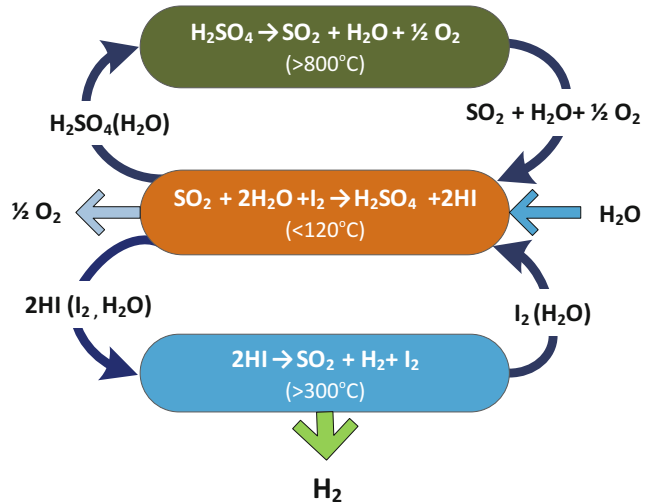
NERI (Nuclear Energy Research Initiative) General Atomics modular helium reactor concept. The GTHTR300C considers the coupling of the S-I plant through intermediate heat exchangers with a helium Circulator. The reactor has a secondary helium cooling loop for the S-I integration. Helium in the main loop circulates from 950 to 590 °C at its highest and lowest temperature values, respectively. Helium leaves the intermediate heat exchanger with temperature difference of 100 °C from the inlet temperature (core exit temperature). The secondary helium cycle operated with helium circulating from around 900 °C, exiting the intermediate heat exchanger, supplying heat to the  $\text{H}_2\text{SO}_4$  vaporizer, and the HI decomposer, and leaves at around 470 °C. Different versions of the system cogeneration are considered. Figure 5 shows the schematic of the cogeneration plant for power and hydrogen, producing 45–60 ton of hydrogen daily, along with 175–202 MW at 45–48% of overall efficiency.

Another integrated conceptual system for nuclear hydrogen production is the Pebble Bed Modular Reactor (PBM) of the South African VHTR program for cogeneration of power and hydrogen. However, the program was terminated in 2010. One of the main reasons of terminating the program is the immaturity of the helium gas turbine power plant among other issues. In this program, the Hybrid Sulfur (HyS) water splitting



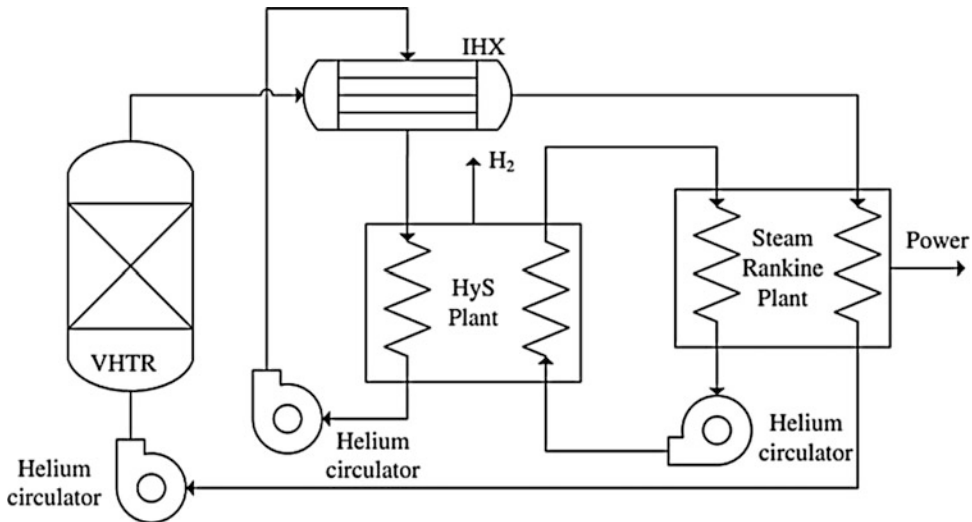
**Nuclear-Assisted Hydrogen Production, Fig. 5** Schematic of the integrated GTHTR300C with S-I plant for hydrogen production, adopted from Naterer et al. [4]

**Nuclear-Assisted Hydrogen Production, Fig. 6** Schematic of the Hybrid Sulfur HyS hybrid thermochemical cycle



thermochemical cycle was considered for the hydrogen generation plant. Figure 6 shows a schematic of the HyS process. The configuration of the integrated system can be seen in Fig. 7. The integrated system was designed as four linked PBMR/HyS modules to a steam power cycle. Each reactor unit generates 500 MWth, which is used to raise the helium temperature to 950 °C in the

primary loop. One hundred and ninety five MW of the thermal power is to be transferred to each unit of the HyS plant through the helium secondary loop. In addition, 55 MW of the generated electric power is fed to each of the HyS units in the hydrogen generation plant. With regards to the overall system operation, it was designed to generate about 600 MW of electric power which is



**Nuclear-Assisted Hydrogen Production, Fig. 7** Schematic of the integrated PBMR and HyS plant for cogeneration application, adopted from Naterer et al. [4]

partially used for hydrogen cogeneration, producing around 20 Mt per day along with 380 MW of electric power delivered to the grid.

### Safety Aspects of Nuclear Hydrogen Production Plants

The information provided in this section would give the reader a good understanding of the practical and general safety concerns and considerations associated with nuclear hydrogen production. The topic may have much more to be discussed, but it was seen to be beyond the scope of this chapter.

On the nuclear plant side, even though nuclear energy is carbon-free, yet other concerns exist regarding the safety of reactor operation and nuclear waste transporting and storing. The severe and long-term damage to the surrounding environment after the Fukushima Daiichi accidents in 2011 has led the world to be more concerned with the development of improved safety regulations of existing nuclear power plants and the modern designs under development (which adapt much safer systems). Several regulations and considerations were also implemented, mainly in the new designs, to secure the plant from terrorist attacks

or collision of civil airplanes. Other design aspects of the safety systems were already in place in most of operating reactors in response to military flights attacks, yet there are differences in size, weight, and amount of fuel involved in civil airplanes compared with military ones.

With respect to hydrogen generation plants; the fundamental philosophy of safety for a chemical plant for hydrogen production is completely different than that of a nuclear power plant. The latter is mainly built on confinement of all the radioactive materials into the facility. However, in a chemical facility, confining chemical materials increase the hazard and explosion potential, putting workers and the public in risk. This for sure applies on water splitting hydrogen plants where there is a possibility of inadvertent mix of the resulting hydrogen and oxygen causing the hazard of internal explosions.

In a hydrogen production plant, the two main safety concerns are the uncontrolled release of hydrogen, and the release of interim toxic gases and compounds of the hydrogen production process. Although leakage detectors and shut-off valves would be part of safety regulations of chemical plants, yet, proper measures shall be considered to face any failure through the operation and ensure the capability of maintaining the

safety of the control room of the nuclear power plant.

The main hazard associated with the hydrogen leakage in hydrogen production plant is being ignited. The jet flames of ignited hydrogen can be extended to several meters and could cause severe damage of the structure and components of the hydrogen plant due to overheating. Safety design shall consider safe distance between the nuclear power plant and the co-located hydrogen plant to avoid any damage to the nuclear facility. If the released hydrogen did not ignite, it may generate a hydrogen air cloud that may move and spread over a long distance or penetrate to the nuclear facility through the ventilation system. This cloud is associated with the hazard of delayed non-overpressure flash fire with strong heat wave. Such incident shall not alert the overpressure emergency response and falsely would not interrupt the safe operation signal in the control room. Another hazard of unignited released hydrogen is the explosion of the hydrogen air cloud causing damaging overpressure waves.

Thermochemical and hybrid thermochemical hydrogen production technologies involve the hazard of the release of toxic gases into the plant. For instance, there is possibilities of uncontrolled release (or leak) of toxic gases such as  $\text{H}_2\text{SO}_4$ ,  $\text{SO}_2$ ,  $\text{SO}_3$ ,  $\text{HI}$ ,  $\text{I}_2$  in S-I hydrogen production plant;  $\text{H}_2\text{SO}_4$ ,  $\text{SO}_2$  and  $\text{SO}_3$  in HyS hydrogen production plant; and the chlorine gas in CuCl hydrogen production plant. Safety considerations to mitigate the consequences of the penetration of such toxic gases to the nuclear power plant control room have to be taken into account in the safety designs of nuclear hydrogen plants. Applying safe separation distance between the co-located nuclear power plant and hydrogen production plant is a simple approach to secure the nuclear facility from the effects of any accidental release of such gases in the hydrogen generation facility. Proper actions have to be applied to isolate the control room including ventilation system shutdown based on the concentration of these gases with applying recirculated filtered air in the control room until the hazard of the released gases is over.

## Concluding Remarks

Nuclear energy, as relatively clean energy source, has the potential to contribute to the growing hydrogen economy. Nuclear power plants coupled to electrolysis, thermochemical, or hybrid water splitting plants is considered as a promising route for large-scale carbon-free hydrogen production routes. In the short term, coupling nuclear and hydrogen generation plants would serve in reducing the carbon emissions accompanied with the currently fossil-powered steam methane reforming hydrogen plants. In the long term, nuclear hydrogen is believed to be serving as a direct fuel for hybrid hydrogen fuel cell vehicles which are expected to replace currently operating ones as one of the strategies adopted by several nations for decarbonization of the transportation sector.

## Bibliography

1. Carty RH, Mazumder MM, Schreiber JD, Pangborn JB (1981) Thermo-chemical hydrogen production. Final report IGT Project 30517, Institute of Gas Technology, Chicago
2. Technology Roadmap Update for Generation IV Nuclear Energy Systems, Issued by the OECD Nuclear Energy Agency for the Generation IV International Forum, 2014
3. Generation IV International Forum (2017). <https://www.gen-4.org/>
4. Naterer GF, Dincer I, Zamfirescu C (2012) Hydrogen production from nuclear energy. Springer, New York
5. Chow CK, Khatabil HF (2008) Conceptual fuel channel designs for CANDU-SCWR. *Nucl Eng Technol* 40(2):139–147
6. Lewis MA, Serban M, Basco JK (2003) Hydrogen production at  $<550^\circ\text{C}$  using a low temperature thermochemical cycle. In: Proceedings of the nuclear production of hydrogen: second information exchange meeting, Argonne
7. Lewis MA, Masin JG, Vilim RB, Serban M (2005) Development of the low temperature Cu–Cl cycle. In: Proceedings 2005 international congress on advances in nuclear power plants, American Nuclear Society, Seoul
8. Naterer GF, Gabriel K, Wang ZL, Daggupati VN, Gravelins R (2008) Thermochemical hydrogen production with a copper–chlorine cycle. I: oxygen release from copper oxychloride decomposition||. *Int J Hydrog Energy* 33:5439–5450

9. Naterer GF, Daggupati VN, Marin G, Gabriel KS, Wang ZL (2008) Thermochemical hydrogen production with a copper–chlorine cycle. II: flashing and drying of aqueous cupric chloride. *Int J Hydrog Energy* 33:5451–5459
10. Naterer GF, Suppiah S, Lewis M, Gabriel K, Dincer I, Rosen MA, Fowler M, Rizvi G, Easton EB, Ikeda BM, Kaye MH, Lu L, Piro I, Spekkens P, Tremaine P, Mostaghimi J, Avsec J, Jiang J (2009) Recent Canadian advances in nuclear-based hydrogen production and the thermochemical Cu–Cl cycle. *Int J Hydrog Energy* 34:2901–2917
11. Wang ZL, Naterer GF, Gabriel KS (2010) Thermal integration of SWCR nuclear and thermochemical hydrogen plants. In: Second Canada–China joint workshop on supercritical water cooled reactor, Toronto
12. Varrin RD, Reifsneider K, Scott DS, Irving P, Rolfson G (2011) NGNP hydrogen technology down selection, Idaho National Laboratory, Idaho Falls
13. Elder R, Allen R (2009) Nuclear hydrogen production: coupling a very high/high temperature reactor to a hydrogen production plant. *Prog Nucl Energy* 51:500–525

# Index

- A**
- Acceleration method, 665
  - Acetate, 804, 811
  - Acetic acid, 913, 914
  - AC impedance method, 542
  - Activation loss, 203, 208
  - Activation overpotential, 531
  - Adenosine triphosphate (ATP), 791
  - Advent TPS<sup>®</sup>, 114
  - Agricultural residues
    - chemical composition, 909
    - pretreatment process, biohydrogen production (see Biohydrogen production)
  - Air Pollution Emission Experiments and Policy Analysis Model (APEEP), 37
  - Alcohol-based fuels, 618
  - Algae, 975, 976
    - biochemical conversion to hydrogen, 990–991
    - biomass gasification, 984
    - classification, 977
    - cultivation, 979, 981
    - distribution, 977, 979
    - drying, 980–983
    - as energy source, 978, 980
    - uses, 976
  - Algal biomass, 894
  - Alkaline (anion) exchange membrane (AEM), 441
    - application in fuel cells, 448–449
    - patent literature, 449–450
    - preparation, 444–445
    - properties, 464–466
  - Alkaline fuel cells (AFCs), 15, 91, 93, 96, 706
  - Alkaline membrane fuel cells (AMFCs), 326, 441
    - fuel cell reactions, 440, 442
    - H<sub>2</sub> as fuel, 446–448
  - Alkaline pretreatments, 912–913
  - Allis-Chalmers, 140
  - Alloy stability, 220
  - Alternative energy, 478
  - Alumina tubes, 670
  - Ammonia fiber explosion (AFEX), 913
  - Anaerobic digester gas (ADG), 515
  - Anaerobic digestion, 833
  - Anaerobic filter (AF), 852
  - Anaerobiosis, 924, 931
  - Ang and Sammells' mechanism, 536
  - Anionomer, 440
  - Anode, 89, 91, 93, 95, 295, 531, 569, 591
    - catalyst layer, 519–520
    - tail-gas oxidizer, 121
  - Anodic faradaic impedance, 545
  - Apatite-type oxide electrolytes
    - La<sub>10</sub>Si<sub>6</sub>O<sub>27</sub>, 600
    - La<sub>9.33+x</sub>Ge<sub>6</sub>O<sub>26+3x/2</sub> (x = 0?2.67), 602
    - structure, 600
  - AP2 damage factors, 37
  - Applied voltage E<sub>ap</sub> (V), 799
  - Aquivion<sup>®</sup>, 244
  - Area specific resistance (ASR), 573
  - Automotive PEMFCs, 135
    - acceleration/deceleration, 147–149
    - alkaline anion exchange membranes, 166
    - Ballard Power Systems, 141
    - bipolar plate targets, 158
    - cold temperatures, 151–153
    - contamination/impurities, 153
    - cost breakdown, 154
    - durability targets, 154
    - electrocatalyst targets, 155
    - general motors, 140–141
    - idling/low load, 145–147
    - membrane targets, 155–158
    - metal pathways for future fuel cell electrocatalysts, 163, 164
    - modes of operation, 145
    - overall status and targets, 153–154
    - Pt-based electrocatalysts, 159
    - research and development, 139–140
    - start-up/shutdown, 149–151
    - UTC power/fuel cells, 141
  - Automotive transportation, 503
  - Auto-thermal reforming (ATR), 951, 957
  - Autotrophics, 975
  - Auxiliary power units (APU), 701, 711
    - on diesel, 726, 727
    - heavy duty truck, 712
    - military applications, 712



**B**

- Ba<sub>2</sub>In<sub>2</sub>O<sub>5</sub>-based oxides electrolytes, 600  
 Ba<sub>0.6</sub>La<sub>0.4</sub>CoO<sub>3</sub> cathode, 610  
 Balance of plant (BOP), 27, 410, 515, 528, 733, 771  
   air subsystem, 58  
   component costing analysis, 33–34  
   controls and meters subsystem, 59  
   coolant subsystem, 58  
   direct manufacturing cost, 59–60  
   fuel processing subsystem, 58  
   power subsystem, 59  
   protection systems, 59  
   subsystem costs, 59  
   support structures, 59  
   thermal management subsystem, 58  
 Band gap, 1099  
 Ba<sub>0.5</sub>Sr<sub>0.5</sub>Co<sub>0.8</sub>Fe<sub>0.2</sub>O<sub>3-δ</sub> (BSCF) cathode, 608  
 Bifunctional Pt-based system, 1091  
 Binary friction model (BFM), 251  
 Biocathode, 799  
 Biochemical conversion, 990  
 Biogas fuels, 619  
 Biogas upgrading techniques, 853  
 Biohydrogen production, 906, 952–953  
   acid pretreatment, 912  
   alkaline pretreatments, 912  
   cellulose, 909  
   fermentation inhibitors, 913–915  
   hemicellulose, 909  
   hydrolysis, 910  
   ionic liquids, 913  
   lignocellulosic biomass pretreatment technologies, 911  
   mechanical pretreatments, 910  
   organosolv pretreatment, 913  
   process parameters, 908–909  
   starchy biomass, 909  
   steam pretreatment, 910–912  
 Biological hydrogen production  
   dark fermentation (*see* Dark fermentation)  
   direct photolysis by green microalgae, 834  
   indirect photolysis process, 834  
   photo fermentation, 834–835  
 Biomass, 833  
   cheap and abundant, 953–954  
   gas generation reactions, 962–963  
   hydrogen production, 951–953  
   liquefaction, 954  
 Biomass gasification, 788, 984, 985  
   algae feed particle size, 987  
   algae type, 985  
   catalysts, 988  
   gasifying agent, 987  
   reaction temperature, 987  
 Biomass gasifier, 986  
 Biomass pyrolysis, 788, 954, 989–990  
   effect, 962  
   schematic diagram, 956  
   temperature effect, 959  
 Biomass wastes, China, 855, 857  
 Bio-oil, 954–955  
 Biophotolysis, 869, 894, 922, 923, 925  
 Bioreactors for hydrogen fermentation, 851–853  
 Biorefinery, volatile fatty acids as, 854–855  
 Bipolar plates, 175, 195, 211–212, 226–227, 239  
   manufacturing, 52–55  
   targets, 158  
 Block copolymers  
   biphenol-based disulfonated arylene ether sulfone  
     units, 398  
   block length, 398, 399  
   BPSH, 398, 400  
   BPSH-BPS, 401  
   effect of, 398  
   higher proton conductivity, 397, 398  
   high molecular weight, 398  
   linkage groups, 398  
   Nafion membranes, 401  
   proton exchange membranes, 398  
   strategy, 397  
   unsulfonated equivalents, 398  
 BOP, *see* Balance of plant (BOP)  
 Boron poisoning, 617, 618  
 Bottom up cost modelling, 31  
 Bridging ligands (BL), 1055  
 British thermal unit (Btu/BTU), 799  
 Bruggemann model, 252  
 Bubble pressure, 515  
 Bulk-like regime, 433  
 Burying effect, 300
- C**  
 Calcia-stabilized zirconia (CSZ), 577  
 CANadian Deuterium Uranium reactor (CANDU), 1151  
 Carbon black (CB), 348, 358  
 Carbon corrosion, 125, 215, 221–222  
   kinetic models, 244  
 Carbon deposition, 689  
 Carbon deposition ratio  
   biogas fuels, 620  
   city gas, 617  
   hydrocarbon fuels, 613  
   hydrocarbon fuels, 615  
 Carbonization, 355, 515  
 Carbon-support corrosion, 179–182  
 Carbon to ionomer (C:I) ratio, 419  
 Carman-Kozeny constant, 251  
 Carnot efficiency, 1131  
 Catalyst(s), 323, 1060–1061  
   roadmap, 334–335  
 Catalyst coated membrane (CCM), 50–53, 55, 298  
 Catalyst contaminants  
   at anode, 220–221  
   at cathode, 220–221  
   internal sources, 221  
 Catalyst layer (CL), 235, 242, 418  
   contributions to O<sub>2</sub> transport resistance, 418  
   interface models, 242

- ionomer covered catalyst particle (ICCP) model, 243
- ionomers in, 424
- macro-homogeneous models, 242
- multiscale models, 242
- phases, 242
- uptake and swelling data, 424
- Catalytic activity, 365–372
- Catalytic stability, 372–377
- Cathode, 295, 531, 569, 591
  - catalyst layer, 519
  - catalysts, 805, 808
  - Pt loading, 325
- Cathodic faradaic impedance, 545
- Cell components, raw materials, 747
- Cell-/stack-/system-level testing, 107
- Cellulose, 905
- Cellulosic biomass, 953
- Cell voltage, 87–88
- CeO<sub>2</sub>-based oxide electrolytes, 597
- CeO<sub>2</sub>-Rh anodes, 612
- Ceramic Fuel Cell Ltd. (CFCL), 718
- Chalcogenides, 345–350
- Chemical looping, 975, 991, 992, 998
- Chemical oxygen demand (COD), 804
  - removal, 799
- Chemical synergy associated with reactant/product interactions, HTFCs, 1130
- Chlamydomonas reinhardtii*, 866, 869–871, 886, 922, 924, 929, 931
  - chlorophyll fluorescence in, 930
  - mutant strains, 926
  - phenotypic characteristics of, 928
  - starch accumulation, 925
  - sulfur starvation, 925
- Chlorella vulgaris*, 996
- Chlorine poisoning, 617, 618
- Chlorophyte algae, 869
- Chloroplast genome, 873, 874
- C-H-O ratio, hydrocarbon fuels, 614, 615, 618
- CHP, *see* Combined heat and power (CHP)
- Chromium, 755, 757, 759
  - poisoning, 665, 674, 686–688
- City gas fuels, 614
- Clean Power Plan (CPP), 40
- ClearEdge Power, 503
- Cloud tower, 515
- Clustered Regularly Interspaced Short Palindromic Repeats (CRISPR), 889, 890
- Coal gas fuels, 620
- Coat-Mix Process<sup>®</sup>, 759
- Cobaloxime complexes, 1084, 1085
- Co-based supramolecular systems, 1080–1082
- Cocatalyst deposited semiconductor, 1111–1112
- Coefficient of drying performance (COP<sub>dry</sub>), 982
- Coefficient of thermal expansion (CTE), *see* Thermal expansion coefficient (TEC)
- CO<sub>2</sub> emission, 738
  - per unit of useful energy, 740
  - total reduction, 742
- Cold temperatures, 151
- Combined cycle, 975
- Combined cycle power plant (CCPP), 13
- Combined heat and power (CHP), 27, 84, 477, 515, 516, 570, 713–714, 733, 825–826
  - devices, 499
  - generation, 735
  - high-electrical-efficiency, 737
  - PEM (*see* Polymer electrolyte membrane (PEM) fuel cell systems)
  - SOFC (*see* Solid oxide fuel cell (SOFC))
  - total energy efficiency of, 742
- Commercialization, SOFC
  - alcohol-based fuels, 618–619
  - alternative materials and fuels, 621–622
  - anode materials, 610–612
  - applications, 592
  - biogas fuels, 619–620
  - cathode types, 605–607
  - C-H-O ratio, fuels, 614, 615, 618
  - city gas fuels, 614–618
  - coal gas fuels, 620–621
  - Cr poisoning phenomena, cathode, 608–609
  - Cu-based cermet anodes, 612
  - fuel flexibility, 612–614
  - impurity poisoning (*see* Impurity poisoning)
  - ionic conductivity (*see* Ionic conductivity)
  - I-V characteristics, 603, 619–621
  - LaCrO<sub>3</sub>-based oxide anodes, 611–612
  - limitations, 592
  - Ni/YSZ cermet anodes, 611
  - oxygen ionic conductors (*see* Oxygen ionic conductors)
  - perovskite-related oxide cathode, 607–610
  - protonic conductors, 602–605
  - S/C ratio, fuels (*see* Steam-to-carbon (S/C) ratio)
- Compression creep and creep recovery method, 491
- Concentrating solar thermal (CST) systems, 1004
- Conduction band, 1099
- Continuously-stirred tank reactor (CSTR), 908
- Continuum surface force (CSF) model, 248
- Conventional imbibing method, 477, 482, 483
- Conventional reactors (CRs), 936, 939, 941
- Conversion electron yield x-ray absorption method (CEY-XAS), 349
- Copper-ceria, 642
  - catalysis, 643–645
  - conductivity, 642–643
  - poisoning and stability, 645–646
- Copper chlorine (CuCl) hybrid thermochemical cycle, 1154–1157
- Cost breakdown, 154
- Cost issues, SOFCs
  - constant current operation, 693
  - constant voltage operation, 693
  - high cost element, identification of, 692
  - low-cost materials, 692
  - raw materials, roles of, 692

- Coulombic efficiency (CE), 799  
 Counter electrode (CE), 1037  
 CPP, *see* Clean Power Plan (CPP)  
 Criteria air pollutants, 27  
 Cr poisoning phenomena, cathode, 608  
 Current density, 86–88  
   cell level, 684  
   stacks level, 685  
 Current interruption, 542  
 Cu-UPD-mediated electrodeposition method, 309  
 Cyanobacteria, 865, 867–869, 872, 886  
 Cyanobacterial biohydrogen production, 868–869  
 Cyclometalated Ir<sup>III</sup> complexes, 1079
- D**
- Dark fermentation, 905–908  
   algal substrate, pre-treatment for, 845–846  
   ammonia, 849–850  
   for energy and chemical production, 856  
   food wastes, pre-treatment for, 846  
   furanic and phenolic compounds, 851  
   hydraulic retention time, 848  
   hydrogen and carbon dioxide removal, 849  
   inhibition, 849  
   inoculum for, 846–847  
   lignocellulosic substrate, pre-treatment for, 839–845  
   macro-and micronutrients, 848–849  
   metabolic pathways, mechanism of, 836–838  
   nutrients, 850–851  
   organic loading rate, 848  
   pH, 848  
   principle of, 836  
   process, 990  
   temperature, 847–848  
   volatile fatty acids, 849
- Degradation, 195  
 Density functional theory (DFT), 108, 298, 442, 576  
   calculations, 822, 823  
 Department of energy (DoE), 202, 203, 208  
 Design for manufacturing and assembly (DFMA), 31  
 Design verification test, 119  
 Deuterium exchange experiments, 442  
 DG, *see* Distributed generation (DG)  
 Diels-Alder polymerization, 396  
 Diffusion models, 245  
 Dilute-acid pretreatment, 912  
 Direct acid casting (DAC) technique, 481  
 Direct hydrocarbon solid oxide fuel cells  
   anodes for hydrocarbon fuels, 635–637  
   cell potential and power density, 635  
   copper-ceria, 642–646  
   double perovskites, 652–655  
   electronic conductivity for, 641  
   fluorite, 658  
   lanthanum chromates, 646–652  
   oxidation of hydrocarbons in, 637–640  
   poisoning and stability, 641–642  
   pyrochlore structured oxides, 657, 658  
   strontium titanates, 655–657  
   structures and defect chemistry, 640–642  
   tungsten bronzes, 659  
 Direct hydrogen-fuel-cell-powered vehicles, 159  
 Direct manufacturing cost model, 30–32  
 Direct methanol fuel cells (DMFCs), 296, 345, 448, 706  
 Dissociation constants, carbonate melts, 534  
 Dissolved additives, for hydrogen production, 1115–1117  
 Distributed energy resources (DER), 1123  
 Distributed generation (DG), 701, 712–713, 725–726, 733, 735, 1123  
   CHP, 713–714  
   mobile applications, 714, 715  
   off-grid and secondary, 714  
   prime power, 713  
 3D microtomography, 583–584  
 DOE 2020 target costs, 78  
 Dopant, 1099  
 Doped semiconductors, photo-catalytic hydrogen production, 1112–1114  
 Doping, 1099  
 Double perovskites, 652–653  
   catalysis, 653–654  
   conductivity, 653  
   stability, 654–655  
 Dow membranes, 390  
 D1 protein, 865, 883, 924, 926, 931  
 Dry agglomerate model, 535  
 Dual proton-oxygen ion-conducting cells, 573, 574  
 Durability/reliability, SOFC systems, 135, 195  
   air flow, 679  
   anomalous gaseous leakage, 683  
   carbon deposition, 689  
   cell performance, degradation in, 683  
   chromium poisoning, 686–688  
   combusted gases, back diffusion of, 683  
   contamination, 681–682  
   current density, effects of, 684–685  
   current flow, redistribution of, 683  
   distribution of current, 681  
   edge effect, 681  
   electrical path, 679  
   electrical shorting, 683  
   electrochemical conversion, 679  
   emergency stops, 682, 683  
   exothermic and endothermic effects, 683–684  
   field tests, 679–680  
   fuel and fuel treatment, 679  
   gas distribution, 681  
   generalized model for degradation, gaseous impurities, 690–691  
   impurities, 689–690  
   long-term operation, 680, 681  
   nickel sintering, 688–689  
   oxygen potential, 685–686  
   stack weight, effect of, 681  
   sulfur poisoning, 689  
   thermal cycles/redox cycles, 681  
 Durability targets, 154

- Dusty gas model (DGM), 250  
Dye sensitization, 1099  
Dye-sensitized semiconductors, 1111  
Dye-sensitized solar cells, 20  
Dynamic mechanical analyses (DMA), 407
- E**  
EEA, *see* Electrolyte-electrode assembly (EEA)  
Effectiveness factor, 531  
Electrical conductivity, 633, 672  
Electrical efficiency, 735  
Electrical generators, 13  
Electrically driven vehicles, 20  
Electroactive catalyst layers (ECLs), 84  
Electrocatalysis (EC), 92  
    facet-and shape-controlled Pt-Alloy nanocrystal, 312–317  
    Pt-Alloy, 301–306  
    Pt and Pt-alloy nanowire and nanotube, 309–312  
    Pt monolayer, 306–309  
Electrocatalyst, 135, 295  
    targets, 155  
Electrocatalytic reaction, 633  
Electrochemical area (ECA), 515  
Electrochemical double layer capacitors (EDLC), 16  
Electrochemical hydrogen production, *see* Hydrogen evolution/oxidation reaction (HER/HOR)  
Electrochemical hydrogen separation (EHS), 1133  
Electrochemical impedance spectroscopy (EIS), 1042  
Electrochemically active bacteria (EAB), 799, 802, 804  
Electrochemically active surface area values (ECSA), 208–209, 218, 323  
Electrochemical reaction, PEMFC, 262  
    Butler-Volmer and Tafel kinetics, 262  
    double trap model, 264  
    dual-path kinetic model, 263  
    Heyrovsky-Volmer mechanism, 263  
Electrochemical surface area, 312  
Electrochemical systems  
    alkaline fuel cell, 15  
    direct methanol fuel cell, 15  
    energy conversion and storage, 13  
    high-temperature proton exchange membrane fuel cell, 14–15  
    molten carbonate fuel cell, 16  
    phosphoric acid fuel cell, 15–16  
    photovoltaic system, 19–20  
    polymer electrolyte membrane fuel cell, 14  
    redox flow batteries, 16–17  
    solid oxide fuel cell, 16  
    supercapacitors, 16  
    thermodynamic efficiency, 14  
Electrochemical vapor deposition (EVD), 665, 668, 669, 688  
Electrode(s), 102, 326–328, 468  
    materials, 577–578  
Electrode electrolyte assembly (EEA), 27  
Electrolysis of water, 787  
Electrolyte, 84, 89, 90, 531, 569, 591, 760  
    membranes, 439, 458  
    role, 89–91  
Electrolyte-electrode assembly (EEA), 64, 67–69  
Electrolyte take-up (ETU), 515  
Electromobility, 20–22  
Electronic conductivity, 641, 648  
    cathode types, 605–606  
Electron relay, 1060  
Electroosmotic drag, 199  
Element-sensitive electron energy loss spectroscopy (EELS), 309  
Ellingham diagrams, 677  
Emissions, 771  
Empirical valence bond model (EVBM), 824  
End-of-life treatment, 776  
Endothermicity, of hydrocarbon reformation, 1130  
Energy, 949, 950, 952, 964, 966  
    conversion processes, 12  
    output/input, 515  
Energy dispersive X-ray (EDX), 410  
Enhanced process integration (EPI), 993–994, 999  
Enzymatic hydrolysis, 910  
Equilibrium moisture content (MCEq), 980, 982  
Equivalent annual cost (EAC), 725  
Equivalent weight, 439  
Ethanol (C<sub>2</sub>H<sub>5</sub>OH), 811  
Eukaryotic host, 872  
Eukaryotic microalgae, 874, 886, 887  
European Directive on CHP, 735  
Eutectic alkali metal carbonates, 534  
Exchange current density, 531  
Exergy, 975  
Extended X-ray absorption fine structure (EXAFS), 302, 582, 583  
Extracellular electron transfer (EET), 799, 803
- F**  
Factory acceptance test, 119  
Fe/Cr system, 17  
[FeFe] hydrogenases, 828  
Fe-N-C catalyst, 343, 376  
Fermentability, 905  
Fermentation, 833  
Ferritic alloys, 673  
Field readiness demonstration test, 119  
Field tests, 679–680  
First-generation cells, 665, 668, 673, 678, 688, 692  
Fixed-grid models, 247  
Fluidized-bed membrane reactors (FBMRs), 935  
Fluorenyl groups, 407, 408  
Fluorescence yield, 927, 929  
Fluorinated cyclic compounds, 393  
Fluorinated ethylene propylene (FEP), 515  
Fluorite, 658  
Fluorite-type oxides electrolytes  
    CeO<sub>2</sub>-based oxide, 597–598  
    pyrochlore-type oxide, 598

- Fluorite-type oxides electrolytes (*cont.*)  
 types, 593  
 ZrO<sub>2</sub>-based oxide, 593–597
- Formic acid (HCOOH), 812, 914
- Fossil fuels, 478
- Free (unionized) ammonia nitrogen (FAN), 850
- Freezing, 218
- Fucus serratus*, 980, 985, 997
- Fuel cell(s), 1, 11, 27, 102–103, 531, 733  
 vs. alternate technologies, 12  
 applications, 89  
 classification, 296  
 electricity generation, 84  
 energy conversion, 84, 85  
 flexibility, 591  
 future works, 79  
 H<sub>2</sub>/air, 403, 404  
 high-temperature, 2  
 life time and reliability, 196  
 performance, 135  
 power and energy capabilities, 17  
 reactants, 103  
 supply chain, 774  
 technology, 84  
 temperature in, 296
- Fuel cell cathode, transport reaction, 327
- Fuel cell electric vehicles (FCEV), 324
- FuelCell Energy (FCE), 533, 794
- Fuel cell system (FCS), 27, 28
- Fuel cell vehicles, on Pt consumption, 325
- Fullerene groups, 408, 409
- G**
- Gas batteries, 13
- Gas diffusion electrode (GDE), 84, 85, 94
- Gas diffusion layer (GDL), 84, 94, 95, 199, 203, 210, 212, 222, 235, 240, 515, 517–519
- Gas diffusion media (GDM), 199, 201, 203, 208, 211, 212
- Gas engine CHP unit, 736
- Gasification, 975  
 biomass, 788  
 of coal, 786  
 reactions, 984, 985, 996, 998
- Gasifying agent, 987
- Gas-phase mass-transfer coefficient, 540
- Gas solubility, 535
- Gas transport, PEMFC  
 binary friction model, 251  
 dusty gas model, 250  
 Maxwell-Stefan models, 251  
 tortuosity model, 252
- Gd<sub>2</sub>O<sub>3</sub>-doped CeO<sub>2</sub> electrolyte, 597
- Gd<sub>2</sub>Ti<sub>2</sub>O<sub>7</sub> (GZT) electrolytes, 598
- General motors, fuel cell vehicles and FCV model, 141
- Generation IV nuclear reactors, hydrogen production, 1154–1159
- Genetic modifications, biohydrogen production  
 D1 protein and sulfur metabolism, 883–885  
 enzymes, 879–881  
 photosynthesis, 875–879  
 starch metabolism, 881
- Genetic optimization conventional methods, 871–874
- Gibbs free energy, 4, 86, 1151
- Global energy challenge  
 global challenges, 703–704  
 pollution and emissions, restrictions on, 703  
 renewable-based power production increase, 703, 704  
 structural investments, 702–703  
 world electricity consumption, 702  
 world primary energy demand, 702
- Glucose, pathways during dark fermentation, 836, 837
- Graphite-based bipolar plates, 166
- Graphite plates, 239
- Graphitic nitrogen atoms, 353
- Graphitization, 515
- Grazing-incidence small-angle X-ray Scattering (GISAXS), 426, 428
- Green algae, 865, 867, 869, 872  
 biohydrogen production, 869
- Greenhouse gases (GHGs), 834  
 analysis, 34  
 MEF, 37
- Green-house gases, regulated emissions, and energy use in transportation (GREET) software, 21
- Grid electricity, annual displacement of, 743
- H**
- H<sub>2</sub>/air-powered PEM fuel cells, 296
- Heat engines, 12–13
- Heat pipe effect, 267
- Heat transport, PEMFC, 266  
 interface models, 266  
 non-isothermal model, 266  
 Soret and Dufour effects, 267
- Hemicelluloses, 905
- Heterocysts, 868
- Heterologous expression, 865
- Heterostructure, 569
- Hexafluoroisopropylidene-containing polybenzimidazole, 489
- H<sub>2</sub>-fed PEFC, 93–95
- High conductive electrolyte, 693–694
- High electrical conductivity, 672
- High power density (HPD), 717
- High-temperature fuel cells (HTFC), 2, 16, 1123–1124  
*See also* Poly-generating high-temperature fuel cells
- High temperature polymer electrolyte fuel cells, 95–96
- High-temperature polymer electrolyte membrane fuel cells (HT-PEMFC), 515, 516
- High-temperature polymer electrolyte membranes, 114–115
- High-temperature proton exchange membrane (HTPEM) fuel cell, 14  
 polarization curve, 15
- High-temperature steam electrolysis (HTSE), 793
- Hofmann elimination reaction, 442, 443
- Homoacetogenesis, 838

- Homologous expression, 865  
Honda, 144  
H<sub>2</sub>S poisoning, 614, 617  
Humidified fuel, 633  
Hybrid electric vehicles, 20  
Hybrid sulfur (HyS) hybrid thermochemical cycle, 1157, 1158  
Hybrid sulfur (HyS) process, 508  
Hybrid sulfur (Hy-S) thermochemical water splitting cycle, 792–793  
Hybrid thermochemical cycles, 1151  
*HydA1*, 880  
*HydA2*, 880  
Hydraulic models, 245  
Hydraulic retention time (HRT), 848, 908  
Hydrocarbon ionomer membranes  
  block copolymers, 397–401  
  composite membranes, 409–410  
  high-IEC ionomers, rigid rod backbone, 393–397  
  pendant acidic groups, polymers with, 404–407  
  sulfonic acid clusters, polymers with, 399–405  
  superacid groups, 407–409  
Hydrocarbon PEMs, 463  
Hydro-char, 788  
Hydrogen, 515, 1003, 1099  
  applications, 949  
  from biomass, 951  
  characteristics, 948  
  cost analysis, production, 957  
  diffusion, 937  
  market, 948  
  partial pressures, 937, 939  
  permeation flux, 937  
  production, 948, 950  
  production routes, 951  
  properties, 947, 948  
  sustainable energy system, 943  
  temperature effect, 937  
Hydrogen-air fuel cells, 125  
Hydrogenase enzymes, 870, 875, 880, 881, 889  
  crystal structure, 880  
  molecular weight, 879  
Hydrogenases, 920, 926, 929, 931  
Hydrogenation, 1, 975, 994–996  
Hydrogen carrier, 975  
Hydrogen contaminants impacts, 217  
Hydrogen energy, 236, 834  
Hydrogen evolution/oxidation reaction (HER/HOR), 297  
  ab initio dynamical simulation, 825  
  d-band model, 822–823  
  DFT calculations, 822, 823  
  at electrodes modified with molecular catalysts, 827–831  
  empirical valence bond model, 824  
  metal-dependent reactivity, 824  
  molecular-level simulations, 823  
  at platinum electrodes, 825–827  
  potential-determining step, 820, 822  
  Santos–Schmickler approach, 823–825  
  standard equilibrium potential, 819  
  Tafel–Volmer mechanism, 822, 823  
  thermodynamic overvoltage, 820  
  thermodynamic volcano plot, 821  
  Volmer–Heyrovsky mechanism, 820, 821  
Hydrogen fermentation reactions, using monomers, 838, 839  
Hydrogen oxidation reaction (HOR), 87, 92, 96, 104, 173–175, 297, 326, 439  
Hydrogen PEMFC vehicle, 323  
Hydrogen peroxide (H<sub>2</sub>O<sub>2</sub>), 812  
Hydrogen photocatalysis data, 1064–1066  
Hydrogen-producing bacteria (HPB), 836  
Hydrogen production, 801, 1099  
  algae, 791  
  aspects, 784  
  from bio-algae systems, 1  
  biomass gasification and pyrolysis, 788  
  costs, 795–796  
  development and modification, 1109–1117  
  dissolved additives for, 1115–1117  
  electrolysis of water, 787–788  
  fuel cell co-production, 794–795  
  gasification and pyrolysis of coal and hydrocarbons, 786–787  
  hydrogen at scale, 796  
  methods, 1  
  microalgae (*see* Microalgae, hydrogen production)  
  microbial electrolysis cells, 791–792  
  nuclear-related pathways, 792–793  
  photocatalysts for, 1107–1109  
  photolytic, 789–790  
  photosynthetic bacterial, 790–791  
  reformation of fossil hydrocarbons and bio-derived liquids, 784–786  
  Rh-based supramolecular photocatalysts, 1071–1078  
  route, 801–802  
  thermochemical production methods, 793–794  
  and utilization, 2  
Hydrogen production, nuclear energy, 1153  
  conventional electrolysis, 1154  
  cost, 1152  
  hydrogen production plants, safety aspects of, 1159–1160  
  radiolytic water splitting process, 1153  
  SCWR for, 1154–1156  
  VHTR for, 1157–1159  
Hydrogen production rate (HPR), 799, 805, 806  
Hydrogen production systems, Pd-based membranes, *see* Pd-based membrane reactors  
Hydrogen productivity, 905  
Hydrogen pump, 505  
Hydrogen recovery, 799  
Hydrogen separation, 994, 1124  
  integration with, 1130–1131  
Hydrogen separation unit (HSU)  
  configuration, 1134  
  parasitic loads associated with, 1138–1140  
  separation and purification, 1133



- Hydrogen storage, 991–993  
 Hydrogen sulphide (H<sub>2</sub>S), 964  
 Hydrogen yield, 799, 905  
 Hydrolysis, 1151  
 Hydrophilic/hydrophobic phase separation, 387  
 Hydrothermal liquefaction (HTL), 990  
 5-Hydroxymethylfurfural (HMF), 914  
 Hythane, 833
- I**
- Impregnation technique, 358  
 Impurity poisoning, 591  
   boron poisoning, 617, 618  
   chlorine poisoning, 617, 618  
   H<sub>2</sub>S poisoning, 614–617  
   phosphorus poisoning, 617, 618  
   siloxane poisoning, 617, 618  
 Inert gas step addition (ISA)  
   anodic overpotential, 555–557  
   cathodic overpotential, 553–555  
   measurements, 547  
   overpotential analysis, 547–552  
   overpotential relations, 557–558  
 Inhibitors, 905  
 Injection molded carbon plates, 54–55  
 Inoculum, for dark fermentation, 846–847  
 Inorganic membrane reactors, *see* Membrane reactors (MRs)  
 Integrated co-generation system, 996  
 Integrated planar SOFC stack concept, 766  
 Interface resistivity, 684  
 Intermediate temperature gaseous species, 694  
 Internal combustion engine (ICE), vehicle catalytic converter, 324  
 Internal reformation (IR), 1130  
   configurations, 1135  
 Internal resistance, 531  
 Ion and water transport, 177–178  
 Ion exchange capacity (IEC), 187, 387, 389–391, 423, 425, 431  
   high-IEC ionomers, 393–397  
 Ionic channels, 387  
 Ionic conductivity, 444  
   Ba<sub>2</sub>In<sub>2</sub>O<sub>5</sub>-based oxide electrolyte, 600  
   cathode types, 606–607  
   Gd<sub>2</sub>O<sub>3</sub>-doped CeO<sub>2</sub> electrolyte, 597  
   LaGaO<sub>3</sub>-based oxides electrolyte, 599  
   La<sub>10</sub>Si<sub>6</sub>O<sub>27</sub> electrolyte, 601–602  
   proton-conductive perovskite type oxides electrolyte, 604–605  
   ScSZ electrolyte, 596  
   Sm<sub>2</sub>O<sub>3</sub>-doped CeO<sub>2</sub> electrolyte, 597  
   yttria-stabilized ZrO<sub>2</sub> electrolyte, 594  
   ZrO<sub>2</sub> doped conductors, 594–596  
 Ionic resistance, 515  
 Ionic species contamination, 226  
 Ionomer, 323, 387, 417, 439, 459  
   ion and water transport, 177–178  
   membranes, 417  
   sulfonate groups, 333  
   thin film, 330–334  
 Ionomer covered catalyst particle (ICCP) model, 243  
 Ionomer-Pt interface, 330  
 Ionomer thin films, PEM, 417, 420  
   characterization and diagnostic techniques, 421  
   ionomers comparison, 420  
   morphology, 426  
   structure/property relationship, 430  
   substrate/film interactions, 431  
   swelling and sorption behavior, 423  
   thickness regime, 433  
 Iron phthalocyanine, 351  
 I-V characteristics, SOFC  
   alcohol-based fuel, 619  
   coal gas fuel, 620  
   protonic conductors, 603
- J**
- Japan's Ene-Farm program, 118
- K**
- Kilo watts, 515  
 Kinetic losses, 235  
 Knudsen diffusion coefficient, 252
- L**
- LaCrO<sub>3</sub>-based oxide anodes, 611  
 LaGaO<sub>3</sub>-based oxides electrolytes, 599  
 Laminaria digitata, 985  
 316L and 310 austenitic stainless steel, 536  
 LaNi<sub>0.6</sub>Fe<sub>0.4</sub>O<sub>3</sub> (LNF) cathodes, 608  
 Lanthanum, 749  
 Lanthanum chromates, 646–647  
   catalysis, 649–651  
   conductivity, 647–649  
   stability, 652  
 Lanthanum nickel-iron oxide cathodes, 687  
 Lanthanum strontium cobaltite ferrites (LSCF), 667, 670, 676, 679, 685  
 Lanthanum strontium manganites (LSM), 668, 670, 674, 676–679, 684–688  
 La<sub>10</sub>Si<sub>6</sub>O<sub>27</sub> electrolytes, 600  
 La<sub>0.6</sub>Sr<sub>0.4</sub>Co<sub>0.2</sub>Fe<sub>0.8</sub>O<sub>3</sub> (LSCF) cathodes, 608  
 La<sub>9.33+x</sub>Ge<sub>6</sub>O<sub>26+3x/2</sub> (x = 0–2.67) electrolytes, 602  
 LCA, *see* Life cycle assessment (LCA)  
 LCC model, *see* Lifecycle cost (LCC) model  
 LCI, *see* Life cycle inventory (LCI)  
 LCIA model, *see* Life cycle impact assessment (LCIA)  
 LCOE, *see* Levelized cost of electricity (LCOE)  
 Levelized cost of electricity (LCOE), 41  
 Level set (LS) method, 248  
 Leverett J-function, 256  
 Levulinic acid, 914  
 Li-air systems, 21  
 Life cycle assessment (LCA), 733  
   goal and scope, 768  
   phases, 745

- Life-cycle cost (LCC) model, 27, 34, 35  
Life cycle impact assessment (LCIA), 27–28, 772  
  AP2 damage factors, 37–40  
  commercial buildings, emission, 37  
  CPP, 40  
  emission factors, 37–39  
  environmental and health externalities, 34–37  
  fuel cells emission factors, 39–40  
  LCOE, 41–43  
  MBA, 36, 37, 40  
  MEF, 36–37  
Life cycle inventory (LCI), 733  
Lifetime, 195  
Light absorption, 1055, 1057–1060  
Lignocellulosic biomass, 906, 909–912, 915  
Lipid biosynthesis, 881  
Liquefaction  
  of biomass, 954  
  vs. pyrolysis, 954  
Liquid organic hydrogen carrier (LOHC),  
  992–993  
Liquid phase mass transfer rate, 540  
Liquid water, in membrane electrode assembly  
  capillary-based models, 257  
  pore-scale models, 255  
  saturation-based models, 256  
  two-phase flow transport, 255  
Ln<sub>0.8</sub>Sr<sub>0.2</sub>Co<sub>1-y</sub>Fe<sub>y</sub>O<sub>3-δ</sub> cathode  
  cathodic polarization, 609  
  electrical conductivity, 608  
Loan repayment factor (LRF), 725  
Local transport loss, 323, 329  
Local transport resistance, 329–330  
Los Alamos National Laboratory (LANL), 296  
Low equivalent weight (EW) membranes  
  ionomer chemical modification, 465  
  mechanical stabilization, 465  
Lower heating efficiency (LHV), 204–205  
Lowest unoccupied molecular orbital  
  (LUMO), 1055  
Low-Pt fuel cell  
  durability of, 335–336  
  performance, 328–329  
Low-temperature PEM fuel cells, 104
- M**  
Macroalgae, 977, 978, 988–989  
Macrocycle, 343  
Macro-scale mathematical models, 237  
Manganese, 752, 753  
Marginal benefit of abatement (MBA), 36, 37, 40  
Marginal emission factor (MEF), 36, 37  
Marketing issues, SOFCs  
  applications, 709  
  APU, 711–712, 726  
  Bloom Energy, 717–718  
  Ceramic Fuel Cell Ltd., 718  
  Ceres Power, 719  
  cost and availability, 723  
  distributed generation, 712–714, 725–726  
  experience/learning curves, 723–725  
  FuelCell Energy, 717  
  high-volume field testing and production, 720  
  interrelated challenges in, 720  
  large central power plants, 727  
  large-scale test and demonstration, 720  
  manufacturing cost calculations, 722–723  
  micro-CHP, 709–711, 726–727  
  Mitsubishi Heavy Industries, 718  
  primary market drivers and estimated  
    market sizes, 715  
  REAL-SOFC, 720  
  reliability, 721, 722  
  Rolls Royce Fuel Cell Systems, 718  
  Siemens Westinghouse, 716, 717  
  Topsoe Fuel Cell, 719, 721  
  US SECA program, 720, 721  
  validation and proof, 720  
  Wärtsilä, 719–720  
Mars-van Krevelen-type (MvK) mechanism,  
  649, 650  
Mass transfer, 531, 833  
Mass transport losses, 235  
Mass-transport phenomenon, 107  
Materials degradation, PEMFC  
  alloy stability, 220  
  bipolar plates, 226  
  carbon corrosion, 221  
  catalyst contaminants, 220  
  chemical stability, 223  
  freezing conditions, 226  
  gas diffusion layer, 222  
  ionic species contamination, 226  
  mechanical degradation, 225  
  micro porous layer, 222  
  Pt coarsening, 218  
  seals degradation, 227  
Mathematical modeling, 235  
Matrix, 531  
Maximum entropy method (MEM), 581, 582  
MBA, *see* Marginal benefit of abatement (MBA)  
m-Dichlorobenzene, 396  
Mechanical pretreatment, 910  
MEF, *see* Marginal emission factor (MEF)  
Melt/solid polymerization, 480  
Membrane electrode assembly (MEA), 27, 103, 173, 195,  
  197, 323, 326, 458, 477, 491–496  
  and voltage-loss terms, 174–176  
Membrane electrolytes  
  hydrocarbon ionomer membranes (*see* Hydrocarbon  
    ionomer membranes)  
  PFSA (*see* Perfluorosulfonic acid (PFSA))  
Membrane on catalyst (MOC), 941  
Membrane reactors (MRs), 935  
  benefits, 936  
  characteristic of, 935  
  FBMRs, 935  
  PBMRs, 935  
  Pd-based membranes

- Membrane targets, 155  
MeN<sub>4</sub>, 355, 358–365  
Me–N–C catalysts, 355, 358–365  
Metal-air batteries, 21  
Metal support cells, 665, 676  
Metal-to-ligand charge-transfer (MLCT), 1055, 1058  
Metal-to-metal charge-transfer (MMCT), 1055  
Methane (CH<sub>4</sub>), 515, 533, 810, 950, 963  
Methanogenesis, 838  
Methanol-fed fuel cell, 95  
Microalgae, hydrogen production, 865, 977–978, 988  
  and cyanobacteria, 922, 923  
  genetic engineering approach, 923–925  
  mechanisms, 922–923  
  mutant strains, 926–931  
  PSII, 930–931  
  two-stage hydrogen production, sulfur deprivation technique, 925–926  
Microalgal biohydrogen production  
  bioethics, 893–894  
  biohydrogen research, 894–895  
  chlamydomonas reinhardtii for, 869  
  cyanobacterial biohydrogen production, 868–869  
  genetic modifications (*see* Genetic modifications, biohydrogen production)  
  green algae biohydrogen production, 869  
  systems biology approach (*see* Systems biology approach, biohydrogen production)  
  targeted genome engineering (TGE), 889–893  
Microalgal chloroplasts, 871  
Microbial electrolysis cell (MEC), 791, 799  
  advantages, 801  
  ammonium/nitrogen from urine, 810  
  applications, 808  
  cathode catalyst, 805  
  domestic wastewater (DWW) treatment, 808  
  electrolyte conductivity, 805  
  fundamentals, 801–803  
  hydrogen production route, 801  
  industrial wastewater, 808  
  main extracellular electron transfer pathways, 803  
  operating factors, H<sub>2</sub> production, 803–808  
  pH, 804  
  substrate/fuel source, 804, 805  
  temperature, 804  
  thermodynamics and electrochemical evaluation, 802  
  valuable products synthesis, 810  
  voltage, 805  
Micro-combined heat and power (micro-CHP), 701, 709, 710, 726–727  
  domestic application, products for, 710  
  in Europe, 710, 711  
  in Japan and South Korea, 711  
  in North America, 711  
Microelectricalmechanical (MEM) systems, 505  
Micro-planar SOFCs, 572–574  
Micro porous layer (MPL), 174, 201, 222, 240  
Micro-scale models, 272  
Microtubular SOFCs, 570–572  
Minor species, 694–695  
Mirai, 128  
Mitsubishi Heavy Industries (MHI), 718  
Mixed ionic-electronic conducting (MIEC), 591, 637, 638  
Molecular-based PEC systems, 1062  
Molten carbonate fuel cells (MCFCs), 16, 29, 91, 93, 96, 667, 706  
  anode, 536–537  
  cathode, 537–538  
  characteristics, 531  
  coal and organic wastes, 533  
  current-voltage behaviors, 532, 533  
  developments, 533  
  electrolyte loss, 535–536  
  electrolytes, 533–535  
  performance analysis (*see* Performance analysis, MCFCs)  
  reactant gas addition method, 557  
Moving-mesh models, 247  
MTU, 533  
Multiblock copolyimides, 404, 405  
Multiblock poly(arylene ether sulfone ketone)s, 401, 402  
Multicomponent Co-based systems, 1082–1086  
Multicomponent iron-based systems, 1069–1071  
Multiphotonic system, for hydrogen production, 1114–1115  
Mutagenesis, 872
- N**  
Nafion<sup>®</sup>, 110, 244  
Nafion thin films  
  contact angle, 429  
  GISAXS patterns, 427, 428  
  properties, thicker nafion membrane, 422, 423  
  swelling data, 425  
Nanosized photocatalysts, 1109–1110  
Nanostructured thin film (NSTF), 209, 330  
  catalyst, 310  
  electrodes, 111  
Natural gas, 515  
Net present value (NPV), 725  
Neutron scattering studies, 581–582  
Next Generation Nuclear Plant (NGNP), 1157  
Nickel, 754, 755  
  sintering, 688–689  
Nicotinamide Adenine Dinucleotide Phosphate (NADPH), 868, 895  
[NiFe] hydrogenases, 828  
Niobium oxide, 349  
Nissan, 144  
Nitrides, 345–350  
Nitrogenases, 921–922  
Nitrogen-doped carbon, 353  
Non-Fickian O<sub>2</sub> transport resistance, 331  
Non-fluorinated ionomers, *see* Hydrocarbon PEMs  
Non-noble metal catalysts (NNMC), 343  
  activity, 365–372

- carbon-based materials with carbon and/or nitrogen sites, 352–357
  - carbonized materials, molecular centers in, 352
  - commercial applicability, 378
  - Me–N–C catalysts with MeN<sub>4</sub>, 355, 358–365
  - with molecular centers, 350–351
  - non-pyrolyzed macrocycles, 351–352
  - stability, 372–377
  - Non-polar lipids, 978
  - Normal hydrogen electrode (NHE), 295
  - Numerical modeling, 235
- O**
- Ohmic loss, 203, 208, 531
  - Ohmic transport losses, 235
  - O<sub>2</sub> local component, 329
  - Open circuit potential (OCP), 633, 634, 638, 639, 644, 650
  - Open-circuit voltage (OCV), 86, 391, 531, 538
  - Open-source fuel cell software, 235
  - Operating conditions, PEMFC
    - air contaminants impacts, 216–217
    - anode and cathode feed interruption, 215
    - cell voltage variations and excursions, 214–215
    - freezing, 218
    - hydrogen contaminants impacts, 217
    - real-life conditions, fuel cell impacts, 213–214
    - temperature overshoots, 215–216
  - Operating window, 195
  - Operation phase, 772
  - Organic loading rate (OLR), 848
  - Organometallic nature, of hydrogenase structural mimics, 829
  - Organosolv pretreatment, 913
  - Os<sup>II</sup> polyazine complexes, spectroscopic and redox properties of, 1060
  - Oswald ripening, 244
  - Overpotential, 531, 633
  - Oxygen, 515
    - carrier, 975
    - permeation, 684
    - reduction catalyst, 353
    - stoichiometry, 633
  - Oxygen ionic conductors, 591
    - apatite-type oxides electrolytes, 600–602
      - La<sub>10</sub>Si<sub>6</sub>O<sub>27</sub> electrolytes, 600–602
      - pyrochlore-type oxides electrolytes, 598
      - ZrO<sub>2</sub>-based oxide electrolytes, 593
  - Oxygen potential
    - changes in, 685
    - electrode/electrolyte interface, 686
    - fuel/air starvation, 686
    - short circuit with/without outer resistance, 686
  - Oxygen reduction reaction (ORR), 87, 91, 95, 96, 104, 173–175, 203, 295–297, 323, 326, 343, 391, 439
    - electrocatalysis at platinum surfaces, 297–301
  - Oxynitrides, 348
- P**
- Packed-bed membrane reactors (PBMRs), 935
  - Palm oil pyrolysis
    - catalysts effect, 961
    - residence time effect, 960
    - temperature effect, 959
  - Parasitic loads, 1124
  - Paris Agreement, 1152
  - Partially fluorinated ionomers, *see* Hydrocarbon PEMs
  - Pd-based membrane reactors
    - bioethanol steam reforming process, 940, 942
    - endothermic reaction process, 941
    - MOC, 941
    - role of, 936–939
    - steam reforming process, 941, 942
  - Pebble Bed Modular Reactor (PBMR), 1157
  - PEC, *see* Photoinitiated electron collection (PEC)
  - PEC-PV tandem, 1003
  - PEMFCs, *see* Proton exchange membrane fuel cell (PEMFC)
  - Pendant acidic groups, 404–407
  - Perfluorinated sulfonic acid-containing polymer (PFSA), 439
    - conductivity vs. relative humidity, 461
    - EW ionomer conductivity, 462
    - morphology, 461
    - structure, 460
    - water solubility, 463
  - Perfluorinated sulfonic acid (PFSA) membranes, 105
  - Perfluorosulfonic acid (PFSA), 173, 184, 187, 387, 411, 418, 420, 423, 428, 434, 435
    - FTIR study, 426
    - general chemical structure of, 388, 389
    - hydration behavior, 424, 425
    - membrane, 331
    - new synthetic routes, 393
    - short side chain, 390–391
    - stabilized, 391–393
    - swelling, 423
    - terpolymers, 391
    - thickness properties impacts, 422
    - trends in, 389, 390
  - Performance analysis, MCFCs
    - AC impedance method, 542–547
    - current interruption, 542–544
    - ISA (*see* Inert gas step addition (ISA))
    - reaction characteristics, 540–541
    - steady-state polarization, 541–542
  - Performance decay, 515
  - Perovskite-related oxide
    - anode materials, 611
      - Ba<sub>2</sub>In<sub>2</sub>O<sub>5</sub>-based oxide electrolytes, 600
    - cathode materials, 607, 608
      - LaGaO<sub>3</sub>-based oxide electrolytes, 599
      - proton based conductors electrolytes, 603
    - structure, 598
  - Peroxide path mechanism, 537
  - Phaeophyta* (brown algae), 977
  - Phenolic resin, 354

- Phenoxy side chains, 395
- Phosphoric acid, 515
- Phosphoric acid fuel cells (PAFCs), 15, 92, 96, 515, 667, 706
- ambient pressure, 518
  - anode catalyst layer, 519–520
  - applications, 524–525
  - balance of plant, 528
  - bipolar plates, 520
  - catalyst decay, 522
  - cathode catalyst layer, 519
  - cathode exhaust, 517
  - coolers, 521
  - edge seals, 520–521
  - electrolyte management, 522–524
  - electrolyte matrix, 519
  - gas diffusion layers, 517–519
  - natural gas, 517
  - non-repeat components, 521–522
  - payback period, 516
  - sub stack, 517
  - UTC Power, 517, 521, 522
- Phosphoric acid/polybenzimidazole fuel cell system, 496
- automotive transportation, 503
  - CHP devices, 499
  - in depth analysis of, 497–499
  - hybrid sulfur process, 508–509
  - hydrogen pump, 505
  - MEA manufacturing, 499
  - microelectricalmechanical systems, 505
- Phosphorus poisoning, 617, 618
- Photobiological hydrogen production, 865, 866
- Photobioreactors, 867
- Photocatalysis, 1099, 1100
- for hydrogen production, 1107–1109
- Photo-catalytic hydrogen production
- cocatalyst deposited semiconductor, 1111–1112
  - development and modification, 1109–1117
  - dissolved additives for, 1115–1117
  - doped semiconductors, 1112–1114
  - dye-sensitized semiconductor, 1111
  - evaluation of, 1104–1106
  - experimental setup, 1106–1107
  - low-dimensional nanostructure, 1110–1111
  - multiphotonic system, 1114–1115
  - nanosized photocatalysts, 1109–1110
  - number of scientific publications, 1101
  - photocatalysts for, 1107–1109
  - photonic efficiency, 1106
  - porous structures, 1110
  - principle of, 1102–1104
  - quantum yield, 1106
  - semiconductor composites, 1114
  - solid solution semiconductor, 1114
  - turnover quantities, 1104
- Photocatalytic water splitting, 1100
- Photochemical hydrogen production, 1070–1071, 1077
- Photochemical water splitting, 1057
- Photo-electrochemical cell (PEC), 789, 795, 797, 1003
- Photoelectrochemical (PEC) systems, 1003
- advantages and disadvantages, PEC configurations, 1018
  - devices overview, 1016–1027
  - efficiency, 1027–1030
  - materials overview, 1007–1016
  - measurements protocols, 1038–1046
  - reactors, 1033–1038
  - stability/photocorrosion, 1030–1033
  - water splitting, working principles, 1005–1007
- Photoelectrode, 1003
- Photo-fermentation process, 990–991
- Photoinitiated charge separation, 1061
- Photoinitiated electron collection (PEC), 1061–1063
- Photolytic hydrogen production, 789
- Photonic efficiency, 1106
- Photosynthesis, 1068–1069
- Photosynthetic bacteria, 866
- hydrogen production, 790
- Photosystem II (PSII), 922, 926, 928
- chlorophyll fluorescence, sulfur starvation, 930
  - PSII-dependent pathway, 923, 924
  - PSII-independent pathway, 923
  - and starch degradation, 926
- Photovoltaic solar cell, 1003
- Picard method, 274
- Planar device, 569
- Platinum-based catalysts degradation, 178–179
- Platinum electrodes, for HER/HOR, 825
- nontrivial pH effect, 826
  - overpotential deposited hydrogen, 826
  - reaction kinetics, 826
  - surface-adsorbed hydrogen, 826
  - surface-enhanced infrared study, 827
  - Tafel slopes, 826
  - volcano behavior on monolayer and bimetallic systems, 827
- Platinum group metals (PGM), 323
- Plug Power, 101
- Poka-yoke, 128
- Polarization, 531
- resistance, 633
- Poly(2,2'-(1,4-phenylene)5,5'-bibenzimidazole), 484–486
- Poly(2,2'-(dihydroxy-1,4-phenylene)5,5'-bibenzimidazole), 490
- Poly(2,2'-*m*-phenylene-5,5'-bibenzimidazole), 482–483
- Poly(2,5-polybenzimidazole), 483
- Poly(*m*-phenylene phosphonic acid), 396, 397
- Poly(vinylidene di fluoride) (PVDF), 409
- Poly(vinylphosphonic acid) (PVPA), 407
- Polyacrylonitrile, 362, 515
- Polyazine bridging ligands, 1060
- Poly(phenylene)-based polyelectrolytes, 395
- Polybenzimidazole (PBI), 184, 477, 480, 519
- with inorganic composites, 487
  - poly(2,2'-(1,4-phenylene)5,5'-bibenzimidazole), 484

- poly(2,2'-m-phenylene-5,5'-bibenzimidazole), 482
- poly(2,5-polybenzimidazole), 483–484
- pyridine, 485
- sulfonated, 486
- synthesis of, 480–482
- Polyetherketones (PEK), 519
- Polyfullerene, 409
- Poly-generating high-temperature fuel cells
  - chemical synergy associated with reactant/product interactions, 1130
  - comparative efficiency analyses, 1140–1141
  - cycle configurations, 1132–1140
  - electrochemical and catalytic processes, 1131
  - electrochemical efficiency, 1129
  - endothermicity of hydrocarbon reformation, 1130
  - external reformation configurations, 1134–1135
  - fuel and oxidant utilization factors, 1128–1129
  - fuel flexibility, 1127–1128
  - fuel processing relationship, 1128
  - future research work recommendations, 1148
  - heat engine energy conversion, 1131
  - hydrogen production rate, 1137–1138
  - hydrogen transport, 1132, 1141–1142
  - integration with hydrogen separation, 1130–1131
  - internal reformation configurations, 1135
  - low entropy generation for heat exchange, 1128
  - representative performance characteristics, 1135
  - schematics of, 1126
  - stack and external reformer temperatures, 1135–1137
  - synergistic effects, 1143–1147
  - world's first installation, 1147–1148
- Poly-generating systems, 1124–1125
- Polygeneration, 738
- Polyimide ionomer membranes, 404, 405
- Polymer-electrolyte fuel cells (PEFCs), 2, 85, 92, 93, 96, 418, 431, 434, 667
- Polymer electrolyte membrane (PEM) fuel cell systems, 14, 15, 477, 478
  - advancements, 107–116
  - advantages, 478
  - alkaline polymer electrolyte membranes, 115–116
  - bipolar plates, 52, 54, 55
  - BOP (*see* Balance of plant (BOP))
  - CCM, 50, 55
  - CCP, 64
  - chalcogenides, 345–350
  - components lifetimes, 44
  - computational fluid dynamics, 107
  - CO poisoning, 126–127
  - cost and reliability of, 127–129
  - critical parameters/specifications, 106–107
  - design, 116–122
  - efficiency, 479
  - electrocatalysts, 108–109
  - emissions, 41
  - externality benefits, 60, 61
  - freezing, 123–124
  - functional specifications, 44–47
  - future research, 130
  - high-temperature polymer electrolyte membranes, 114–115
  - industry, 100–102
  - injection molded carbon plates, 54
  - LCC model, 60, 63
  - LCIA model, 60, 63
  - LCOE, 62, 64
  - line availability, 49
  - low-and intermediate-temperature proton-conducting polymer electrolyte membranes, 111–114
  - manufacturing costs, 49, 50 (*see also* Phosphoric acid/polybenzimidazole fuel cell system)
  - mass-transport phenomenon, 107
  - nanostructured electrodes, 110–111
  - nitrides, 345–350
  - porous electrodes, 109–110
  - private costs, 62, 65
  - process yield, 50, 51
  - purification device for hydrogen gas, 496
  - schematic diagram, 50
  - setup time, 49, 51
  - social costs, 62, 65
  - stack cost sensitivity analysis, 56–57
  - stack manufacturing cost vs. annual production volume, 55–56
  - stack size, 47
  - start/stop, 124–125
  - and sustainability, 129–130
  - system design, 44–45
  - system requirements and architecture, 116–120
  - TCO savings, 62, 64
  - technical readiness, 122–127
  - transition metal carbides, 345
- Polymer electrolyte membranes, 244
- Poly(arylene ether)s, 400, 402, 408
- Poly(arylene ether sulfone)s, 400, 402, 407
- Polysulfone-based AEMs, 447
- Polysulfophenylated poly(phenylene), 396
- Polytetrafluoroethylene, 515
- Pore diffusion resistance, 531
- Pore-filling method (PFM), 363, 370, 374
- Porous stainless steel (PSS), 937
- POSCO Energy Co., 533
- PowerCore™, 705–707
- Power density, 196, 771
- Pressure swing adsorption (PSA), 794, 950, 955, 956
- Primary energy input, 736
- Prime power, 713
- Process integration, 975
- Product development process map, 119–120
- Prokaryotic cyanobacteria, 866, 881
- Prokaryotic hosts, 872
- Protogenic group, 188–189
- Proton conductivity, 184–185, 477
  - of segmented block copolymers, 484
- Proton diffusion coefficient, 397, 398
- Proton-exchange membrane (PEM), 173, 235, 387, 417, 418, 434
  - for transportation applications, 388



- Proton exchange membrane fuel cell (PEMFC), 195, 235, 295, 296, 389, 706
- bipolar plates, 211, 239
  - carbon-support corrosion, 179–182
  - catalyst layers, 242
  - challenges in development, 173–174, 190
  - charge transport, 258
  - CO<sub>2</sub> emissions, 137–138
  - conductivity stabilizing inorganic additives, 467–468
  - costs, 196, 201
  - design, 235
  - electrochemical reactions, 262
  - electrodes, 468–471
  - electrolyte, 197
  - electrolyte membranes, 458–459
  - future aspects, 472
  - gas diffusion layers, 240
  - gas diffusion media, 208
  - gas transport, 250
  - greenhouse gas emissions reduction, 138
  - heat transport, 266
  - historical background, 167
  - Honda, 144–148
  - HOR and ORR reactions, 174, 175
  - hydrocarbon PEMs, 463–465
  - ion and water transport, 177–178
  - ionomer chemical modification, 465–466
  - liquid water, 255
  - low equivalent weight membranes, 465
  - materials degradation (*see* Materials degradation, PEMFC)
  - MEA and voltage–loss terms, 174–176
  - membrane, 205
  - membrane development, 182–183
  - membrane electrode assembly (MEA), 458
  - microporous layer, 240
  - microscale simulation, 268
  - model implementation, 273
  - morphology, 185–188
  - operating conditions (*see* Operating conditions, PEMFC)
  - operating window and performance, 199
  - operation, 235
  - perfluorinated sulfonic acid containing polymers (PFSA), 459–463
  - performance breakdown, 201
  - polymer electrolyte membranes, 244
  - protogenic group, choice of, 188–189
  - proton conductivity, 184–185
  - Pt-based catalysts degradation, 178–179
  - reactant gas permeability, 185, 186
  - safety of hydrogen, 138
  - seals and edge protection, 212
  - stack components, 197, 198
  - temperature targets, 183–184
  - Toyota, 142–144
  - two-phase flow in fuel cell channel, 247
  - vehicles, 236
  - voltage losses, 175–176
  - water transport, 253
  - well-wheels green house emissions, 137
- Protonic conductors, 591–592
- characteristics, 603
  - perovskite-type oxides, 603–605
  - types, 602–603
- Proton transport, 244
- Pseudocapacitors, 16
- Pseudomorphic monolayers, 306
- PSII, *see* Photosystem II (PSII)
- Pt coarsening, 218–220
- PtCoMn alloy, 208
- Pt mass activity, 295
- Pt monolayer catalysts, advantages of, 306
- Pt nanoparticles, on KetjenBlack carbon particles, 328
- Pt roughness factor, 323
- Pt-specific activity, 295
- PV-assisted PEC water splitting system, 1003
- PV cell, *see* Photovoltaic solar cell
- 3,5-pyridine-para copolymer, 493
- Pyridine polybenzimidazoles, 485–486
- Pyridinic nitrogen atoms, 353
- Pyrochelates, 343
- Pyrochlore structured oxides, 657, 658
- Pyrochlore-type oxides electrolytes, 598
- Pyrolysis, 951, 975
- biomass, 788, 954
  - of coal, 787
  - hydrogen sulphide, 964–966
  - kinetic models, 963
  - vs. liquefaction, 954–957
  - methane, 963–964
  - palm oil, 960
  - sawdust biomass, 961
- Q**
- Quality function deployment (QFD) process, 116
- Quantum yield, 1106
- catalysts, 1061
- Quartz-crystal microbalance (QCM), 424, 425
- R**
- Radiation-grafting of vinylbenzyl chloride, 445
- Ragone plot, 17
- Raman spectroscopy, 584
- Rankine cycle, 1155
- Reactant gas addition (RA) method, 557–566
- Reactant gas permeability, 185, 186
- Reaction kinetics, 531
- Redox flow batteries (RFBs), 17, 18
- Redox stability, 665
- Redox supercapacitors, 16
- Reference electrode, 1038
- Relative humidity (RH), 174
- effects, 300
- Renewable sources, gases from, 740
- Reversible hydrogen electrode (RHE), 104, 295

- Rhodium-based multicomponent photocatalysis, 1078–1079
- Rhodium-based supramolecular photocatalysts, 1071–1078
- Rhodophyta (red algae), 977
- Robustness, 195
- Rotating disk electrode (RDE) tests, 326
- Rotating ring disk electrode (RRDE), 303, 343
- RuBisCo enzyme activity, 873, 874, 883
- Ru<sup>II</sup> polyazine complexes, spectroscopic and redox properties of, 1060
- RuPd bimetallic system, 1091
- RuPt bimetallic system, 1087
- Ruthenium, 345
- S**
- Santos–Schmickler approach, 823–825
- Scanning transmission electron microscopy (STEM), 309
- Scenedesmus almeriensis*, 985, 987, 988
- Sc<sub>2</sub>O<sub>3</sub>-stabilized ZrO<sub>2</sub> (ScSZ) electrolyte, 596
- Screen printing process, 762
- Sc stabilized zirconia (ScSZ), 582, 583
- Sealless tubular cells, 668
- cell configuration, 669
  - cell performance degradation, 670
  - improvement of, 671
  - metal support cells, 672
  - nickel, 669
  - planar design, 671
  - stack configuration, 669
  - stack design, 671
  - status of, 671
- Seals degradation, 227–228
- Seal technology, 675
- Secondary ion mass spectrometry (SIMS), 681, 682, 686
- Second-generation cells, 665, 670, 671, 673, 676, 678, 688, 692
- Semiconductor, 1100
- composites, 1114
- Serenergy, 501
- Short side chain PFSA
- higher-IEC membranes, 391
  - humidity dependence of proton conductivity, 390
  - monomers, structure and molecular weight of, 390
  - plotted proton conductivity, 390, 391
- Shutdown-startup cycling tests, 498
- Sieverts-Fick law, 937, 938
- Silicon carbide, 515
- Siloxane poisoning, 617, 618
- SimaPro<sup>TM</sup> lifecycle analysis software, 786
- Single-site photocatalysts, 1110
- SION1 alkaline ionomer, 446
- Site density, 343
- Small-angle X-ray scattering (SAXS), 187, 407
- Sm<sub>2</sub>O<sub>3</sub>-doped CeO<sub>2</sub> electrolyte, 597
- SOFC, *see* Solid oxide fuel cell (SOFC)
- Solar energy, 1004
- Solar hydrogen photocatalysis, 1063–1066
- Solar tandem cell, 1003
- Solar-thermochemical cycles (STC), 1004
- Solar-to-hydrogen (STH) conversion, 1004
- pathways, 1005
- Solar water splitting, 1004, 1057
- photoanodes for, 1008–1012
  - photocathodes for, 1012–1014
- Solid oxide electrolysis (SOEC), 701, 708, 714
- Solid oxide fuel cell (SOFC), 5, 16, 93, 97, 569, 633, 667, 701, 706, 728, 729, 733
- accelerated materials discovery, 578–579
  - active components of, 573
  - active parts, 734
  - advantages, 734
  - area specific resistance, 573
  - balance of plant, 70
  - commercialization (*see* Commercialization, SOFC)
  - components, 764
  - components lifetimes, 47
  - conventional power generation technologies, 708
  - cost issues (*see* Cost issues, SOFCs)
  - CPP, 72
  - definition, 733
  - design production, 766
  - developments, 667
  - devices and configurations, 570
  - direct manufacturing costs, 69–71
  - distinguishing feature of, 634
  - dual proton-oxygen ion-conducting cells, 573, 574
  - durability/reliability (*see* Durability/reliability, SOFC systems)
  - EEA, 64–67
  - electrochemical process, 704, 705
  - electrode materials, 577–578
  - electrolyte/electrode assembly, 704, 705
  - electrolyte materials, 575–577
  - fuel cell stack, 705, 706
  - fuel flexibility, 707
  - functional specification, 49
  - functional specifications, 47–49
  - High-Efficiency Energy Converters, 734–738
  - higher electrical efficiency, 707
  - highly flexible material, 704, 705
  - LCA studies of, 767
  - LCC, 71, 74
  - LCIA, 71, 74
  - LCOE, 71, 75
  - line availability, 67
  - line performance, 67
  - lower emission and noise levels, 708
  - lower maintenance cost, 707–708
  - manufacturing parameters, 66
  - markets, 29 (*see also* Marketing issues, SOFCs)
  - metal support cells, 676
  - microtubular, 570–572
  - mixed reactant fuel cells, 571–573
  - negative terminal of, 569

- Solid oxide fuel cell (SOFC) (*cont.*)  
 neutron scattering studies, 581–582  
 operating principle, 634  
 operation temperature, 676–679  
 oxide interconnect vs. metal interconnect, 672–674  
 vs. PEM  
 balance of plant cost, 70  
 direct manufacturing cost, 73  
 positive terminal of, 569  
 PowerCore™, 705–707  
 process yield, 67  
 Raman spectroscopy, 584  
 redox issues, 675  
 sealless tubular performance, 668–673  
 seals, 675  
 in situ diagnostics, development of, 579–580  
 in situ materials characterization, 580  
 societal cash flow, 72  
 stack configuration, 66  
 stack material costs, 67–69  
 stack modules, 705, 706  
 synchrotron X-ray studies (*see* Synchrotron X-ray studies)  
 synergies with coupled technologies, 708  
 system cost, 70, 72  
 system design, 47, 48  
 TCO savings, 75  
 types of, 747  
 YSZ, 635
- Solid solution semiconductor, 1114
- Solid State Energy Converter Alliance (SECA), 693
- Sorption behavior, 423
- Specific hydrogen yield (SHY), theoretical values, 838, 839
- Spin-casting, 419
- Stack, 27, 569, 733  
 behavior, 693  
 manufacturing, 770, 772
- Starch/sugar biomass, 953
- Steady-state polarization (SSP), 541
- Steam methane reforming (SMR), 784, 785, 788, 795, 950–951, 957, 965, 1125  
 method, 1126, 1133, 1134, 1141
- Steam pretreatment, 910
- Steam reforming of natural gas, 6
- Steam-to-carbon (S/C) ratio  
 city gas, 614  
 hydrocarbon fuels, 613, 614
- Stress, volume changes, 666
- Strontium, 751, 752
- Strontium titanates, 576  
 catalysis, 657, 658  
 conductivity, 655–657
- Structural diffusion mechanism, 105
- Sulfonated perfluorovinyl monomers, 393
- Sulfonated polybenzimidazoles, 486–487
- Sulfonated poly(p-phenylene) copolymer, 394–396
- Sulfonated Polyether ether ketone (S-PEEK), 207
- Sulfonated poly(phenylene sulfone)s (sPSO<sub>2</sub>), 396, 397
- Sulfonate group interaction, 333
- Sulfopropylated polysilsesquioxane (SiOPS), 410
- Sulfur iodine (S-I) thermochemical cycle, 1157
- Sulfur-iodine (S-I) thermochemical water splitting cycle, 792
- Sulfur poisoning, 666, 689
- SunHydro, 504
- Supercapacitors, 16
- Supercritical condition, 975
- Supercritical water gasification (SCWG), 989, 994–996
- Superoxide path mechanism, 537
- Supplemental Input Method, 1140, 1141
- Supramolecular iron-based system, 1063, 1067–1069
- Supramolecular solar hydrogen photocatalysis  
 Co-based supramolecular systems, 1080–1082  
 components for, 1057–1063  
 iron-based system, 1063, 1067–1069  
 multicomponent Co-based systems, 1082–1086  
 palladium-based homogeneous systems, 1091  
 photophysics, 1073–1074  
 Pt- and Pd-based homogeneous systems, 1087–1091  
 redox properties, 1071–1072  
 Rh-based, 1071–1079  
 solar hydrogen production, 1074–1078  
 spectroscopic properties, 1072–1073
- Suski's mechanism, 536
- Swelling, 423
- Synchrotron X-ray studies  
 3D microtomography, 583–584  
 synchrotron diffraction, 582–583  
 XANES and EXAFS, 583
- Synergy, 1125
- Syngas, 784, 786, 788, 975
- Syngas chemical looping (SCL), 991, 992, 996
- Systems biology approach, biohydrogen production  
 genomics, 886–888  
 metabolomic analysis, 888–889  
 proteomic analysis, 888  
 transcriptome analysis, 887–888
- System shutdown ratio, 44
- ## T
- Tafel–Volmer mechanism, 822, 823
- Targeted genome engineering, 865
- Targeted genome engineering (TGE), 889
- Temperature targets, 183–184
- Terpolymers, 391
- Thermal expansion, cathode types, 607
- Thermal expansion coefficient (TEC), 633, 672
- Thermochemical cycles, 1151
- Thermochemical method, 950, 952, 955
- Thermochemical production methods, 793
- Thermolysis, 1151
- Thermoneutral potential, 4
- Thermo-osmosis, 254
- Thin-film heterostructures, 575–577

- Thin-film regime, 433  
Third-generation cells, 666, 670  
Three-phase boundary, 439, 531  
Topsoe Fuel Cell (TOFC), 709, 710, 715, 716, 718, 719, 721, 722, 728  
Tortuosity model, 252  
Total ammonia nitrogen (TAN), 850  
Total cost of ownership (TCO) modeling framework, 28  
  direct manufacturing cost model, 30, 32  
  LCC model, 30, 34, 35  
  LCIA model (*see* Life cycle impact assessment (LCIA))  
  manufacturing cost shared parameters, 32–33  
Toyota, 142  
Toyota Mirai FCEV, 335  
Transcription Activator-Like Effector Nucleases (TALENs), 889, 890, 893  
Transcriptome analysis, 887  
Transition metal carbides, 345  
Transition metal chalcogenides, 343, 345–350  
Transport fuel, hydrogen use as, 853–854  
Transport losses, 203, 210  
Triglyceride biomass, 953  
Trimetallic complexes, 1075  
Triple-phase boundary (TPB), 92, 93, 103, 583–585  
Tris-(2,2'-bipyridine)Rh<sup>III</sup>, 1071  
Tris(2,4,6-trimethoxyphenyl) polysulfone-methylene quaternary phosphonium hydroxide (TPQPOH), 448  
Tungsten carbide, 345  
Turnover frequency (TOF), 343  
Turnover number (TON), catalysts, 1061  
Two-phase cathode models, 255  
Two-phase flow model, PEMFC  
  continuum surface force model, 248  
  fixed-grid models, 247  
  level set method, 248  
  moving-mesh models, 247  
  Navier-Stokes and continuity equations, 247
- U**  
Ullmann coupling reaction, 396  
Ultra-thin films regime, 433, 528  
Underpotential deposition (UPD), 306  
Unmanned aerial vehicles (UAV), 711, 712  
Upflow anaerobic sludge blanket (UASB) reactor, 851–852  
Use-phase modeling, *see* Lifecycle cost (LCC) model  
UTC power/fuel cells, 141
- V**  
Valence band, 1100  
Vehicle diffusion, 105  
Volatile fatty acids (VFAs), 799, 833, 854–855  
Volcano behavior, 307  
Volmer–Heyrovsky mechanism, 820, 821  
Voltage efficiency, 86, 88  
Volume-average model, 243  
Volume of fluid (VOF) method, 247
- W**  
Wastes, as feedstock, 739  
Water electrolysis, 1151  
Water–gas shift (WGS) reaction, 1125, 1134  
Water management, 105  
Water radiolysis, 1151  
Water transport, polymer electrolyte, 253  
Well-to-tank (WTT) efficiency, 1125  
  analysis, of H<sub>2</sub>, 1142  
Westinghouse cycle, 786  
Wet powder spraying (WPS), 762  
Working electrode (WE), 1036, 1037
- X**  
X-ray absorption near edge spectroscopy (XANES), 302, 309, 582, 583  
X-ray absorption spectroscopy (XAS), 302  
X-ray adsorption near edge structure, 649
- Y**  
Yttria-stabilized zirconia (YSZ), 572, 575, 576, 635, 638, 639, 642, 643, 647, 658, 668, 669, 672, 673, 676, 677  
  electrolyte, 594–596  
Yttrium (Y), 748
- Z**  
Zinc Finger Nucleases (ZFNs), 889  
Zirconium (Zr), 747  
  oxynitrides, 348  
  phosphate, 488  
ZrO<sub>2</sub>-based oxide electrolytes  
  ionic conductivity, 594  
  limitations in higher temperature, 597  
  ScSZ, 596  
  thin-film electrolytes, 596–597  
  yttria-stabilized ZrO<sub>2</sub>, 594